Proceedings of the 12th International Conference on Structures in Fire

Edited by

Liming Jiang, Paulo Vila Real,
Xinyan Huang, Mhd Anwar Orabi, Jin Qiu, Tianwei Chu,
Zhuojun Nan, Cheng Chen, Zhiruoyu Wang,
Asif Usmani

Organised by

The Hong Kong Polytechnic University
香港理工大學

Department of Building Environment and Energy Engineering
建築環境及能源工程學系

Sponsored by

Faculty of Construction and Environment
建設及環境學院

Croucher Foundation
裘槎基金會

HKIE
The Hong Kong Institution of Engineers
香港工程師學會

Proceedings of the 12th International Conference on Structures in Fire

Hosted by

The Hong Kong Polytechnic University

Proceedings of the 12th International Conference on Structures in Fire
(SiF 2022)

Hosted by The Hong Kong Polytechnic University

30 November to 2 December 2022

Editors: Liming Jiang, Paulo Vila Real, Xinyan Huang, Mhd Anwar Orabi, Jin Qiu, Tianwei Chu, Zhuojun Nan, Cheng Chen, Zhiruoyu Wang, Asif Usmani

Published by The Hong Kong Polytechnic University © 2022

ISBN: 978-962-367-869-8

Organised by:

THE HONG KONG POLYTECHNIC UNIVERSITY
香港理工大學

Department of
Building Environment and Energy Engineering
建築環境及能源工程學系

Sponsored by:

FACULTY OF CONSTRUCTION AND ENVIRONMENT
建設及環境學院

Croucher Foundation
裘槎基金會

HK工E THE HONG KONG INSTITUTION OF ENGINEERS
香港工程師學會

File service sponsored by:

figshare

TABLE OF CONTENTS

PREFACE

As the name suggests, SiF or "Structures in Fire" is a sub-discipline of critical importance for the sustainability and resilience of civil engineering infrastructure and urban environments. It is a complex interdisciplinary subject and one that does not usually find space in undergraduate civil engineering curricula other than a few exceptions. The main reason for this is that the traditional approaches to ensuring the safety of structures in fire have been based on simplifying assumptions, both about the fire hazard and about the structural behaviour under elevated temperatures. Much of the research that is conducted and presented by scholars in this event is related to improving upon the traditional "prescriptive" approach for structural fire resistance design and increasingly towards considering more and more realistic estimates of the hazard and the corresponding material and structural responses in order to quantify the overall structural "performance" more reliably. This field has made enormous strides during the past 20 plus years, and much of the credit for this must go the opportunity for scholarly interactions provided by SiF and the innovations inspired by these regular interactions.

It is therefore our great pleasure to be hosting this 12th International Conference on Structures in Fire at Hong Kong Polytechnic University. It is particularly heartwarming since we have all yearned for a return to some level of normalcy after many of our cherished opportunities for scholarly exchange have had to be curtailed on account of the global pandemic. The previous conference at University of Queensland had to be largely online. On this occasion we are expecting more than a quarter of the presentations to be presented in person and also expect a good number of delegates to physically attend the presentations, albeit the majority of the presentations would still be online.

It has been over twenty years since the "SiF Movement" was established with the first conference in Copenhagen having an attendance in low double figures. It is a testament to the vision of the originators (Primarily Professor Jean-Marc Franssen) that this event has become the most prestigious and most eagerly awaited by both researchers and leading practitioners in the field of structural engineering for fire resistance and fire safety. For most of the recent conferences the number of papers submitted far exceed (by almost double) the number of papers that can be accommodated in the three-day programme, even with two parallel sessions. This conference has been no exception and a similar situation exists. We received 224 abstracts before the deadline and accepted 156 abstracts after the review process by at least three reviewers from the scientific committee. Eventually, 115 papers are successfully submitted as full papers for presentation in SiF2022 from 30 Nov 2022 to 2 Dec 2022.

Taking this opportunity, we would like to thank the continuous support from the SiF steering committee chaired by Prof Jean-Marc Franssen. We also would like to thank all the supporting stuff in the Department of Building Environment and Energy Engineering of PolyU and the volunteer team of SiF2022!

On behalf of the local organizing committee:

Prof Asif Usmani
The Hong Kong Polytechnic University
Dr Liming Jiang
The Hong Kong Polytechnic University

On behalf of the scientific committee:

Prof Paulo Vila Real
University of Aveiro

COMMITTEES

Organising Committee

Prof Asif Usmani (The Hong Kong Polytechnic University)
Dr Liming Jiang (The Hong Kong Polytechnic University)
Prof Ben Young (The Hong Kong Polytechnic University)
Prof Kwok-Fai Chung (The Hong Kong Polytechnic University)
Dr Xinyan Huang (The Hong Kong Polytechnic University)
Dr Mustesin Khan (The Hong Kong Polytechnic University)
Dr Xiqiang Wu (The Hong Kong Polytechnic University)
Dr Anwar Orabi (The Hong Kong Polytechnic University)
Dr Aatif Khan (The Hong Kong Polytechnic University)
Prof Francis Au (Hong Kong University)
Dr Young Wong (Arup Hong Kong)
Prof Guoqiang Li (Tongji University)
Prof Suwen Chen (Tongji University)
Prof Guobiao Lou (Tongji University)
Prof Jihong Ye (China University of Mining and Technology)
Prof Jian Jiang (China University of Mining and Technology)
Prof Yong Du (Nanjing Technology University)
Prof Weiyong Wang (Chongqing University)
Prof Peijun Wang (Shandong University)
Prof Chao Zhang (Wuhan University)
Dr Yaqiang Jiang (Sichuan Fire Research Institute)
Dr Qingfeng Xu (Shanghai Research Institute of Building Sciences)
Dr Linzhu Chen (Shanghai Research Institute of Building Sciences)

Steering Committee

Prof Jean Marc Franssen (Chair) (The University of Liege)
Prof Paulo Vila Real (The University of Aveiro)
Prof Venkatesh Kodur (Michigan State University)
Prof Kang Hai Tan (Nanyang Technological University)

Chair of Scientific Committee

Prof Paulo Vila Real

Members of Scientific Committee

Alar Just
Aldina Santiago
Ali Nadjai
Andrea Frangi
Andy Buchanan
Anil Agarwal
Ann Jeffers
Anthony Abu
Antonio Bilotta
Asif Usmani
Bin Zhao
Birgit Östman
Bo Wu
C.S. Manohar
Carlos Couto
Charles Clifton
Christian Dagenais
Christophe Renaud
Colleen Wade
Cristian Maluk
Daniel Brandon
David Barber
David Lange
Dhionis Dhima
Eleni Asimakopoulou
Emidio Nigro
Eric Tonicello
Erica Fischer
Faris Ali
Felix Wiesner
Florian Block
François Hanus
František Wald
Fuminobu Ozaki
Guo-Qiang Li
Haiyan Zhang
Holly Warren
Ignacio Paya Zaforteza
Ian Burgess
Iolanda del Prete
Jean-Marc Franssen
Jian Jiang
Jiayu Hu
Joachim Schmid
João Paulo Rodrigues
Jochen Zehfuß
John Gales
Kang Hai Tan
Katherine Cashell
Kazunori Harada
Leroy Gardner
Li Ye
Liming Jiang
Linus Lim
Lou Guobiao
Luke Bisby
Mohannad Zeyad Naser
Mahen Mahendran
Manuel Romero
Mark Green
Markus Knobloch
Martin Mensinger
Massimo Fragiacomo
Michael Engelhardt
Michael Klippel
Michal Jandera
Mitsuo Ozawa
Muhammad Masood Rafi
Mustesin Khan
Nicola Tondini
Norman Werther
Nuno Lopes
Olivier Vassart
Panwei Du
Paulo Piloto
Pedro Palma
Peijun Wang
Peter Schaumann
Piergiacomo Cancelliere
Pietro Gambarova
Raul Zaharia
Richard Emberley
Roberto Felicetti
Ruben Van Coile
Serdar Selamet
Shan-Shan Huang
Shengxin Fan
Susan Lamont
Suwen Chen
Takeo Hirashima
Thomas Gernay
Timo Jokinen
Tom Molkens
Tomaž Hozjan
Vasant Matsagar
Venkatesh Kodur
Weiyong Wang
Yong Du
Yong Wang
Yuzhuo Wang
Zhi Zhang
Zhong Tao
Dong Zhang
Chao Zhang

Proceedings of the 12th International Conference on Structures in Fire

Applications of Structural Fire Engineering

STEEL SECTION EQUIVALENT UNIFORM TEMPERATURE DISTRIBUTION IN PERFORMANCE-BASED FIRE DESIGN – EC3 CALCULATION METHOD GENERALIZED FOR NON-UNIFORM FIRE EXPOSURE

Timo Jokinen[1], Risto Ranua[2], Mikko Salminen[3]

ABSTRACT

This paper presents modifications for Eurocode 3 (EC3) unprotected steel section equivalent uniform temperature distribution formulas, that generalizes them for non-uniform fire exposure to better serve the demands in performance-based fire design. The validation for these formulas is also presented by using 2D FEM (Finite Element Method) temperature analysis (with SAFIR software). The modified formulas are designed to fit well with FDS (Fire Dynamics Simulator) fire simulations, and they should not be limited to specific type of fire (i.e. they should work with localized fire, fully developed fire, travelling fire, etc.). The modified formulas are presented as a supplementary tool for determining the section temperatures that are compared against member critical temperatures, and they should be used in tandem (not as a substitute) with more advanced structural analysis as required in EC3 for performance-based structural fire design.

Keywords: steel structures; section temperature; performance-based fire design; SAFIR; FDS; Eurocode

1 EQUIVALENT UNIFORM TEMPERATURE DISTRIBUTION FORMULAS

1.1 Calculation formulas presented in EC3

If the conditions outside the steel section have uniform temperature distribution, the development of the equivalent uniform temperature distribution in the unprotected steel section θ_a can be calculated using the formulas in Eurocodes EN 1993-1-2 section 4.2.5.1 and EN 1991-1-2 section 3.1 [1, 2]:

$$\theta_a(t+\Delta t) = \theta_a(t) + k_{sh}\frac{A_m/V}{c_a\rho_a}\dot{h}_{net}\Delta t \tag{1}$$

$$\dot{h}_{net} = \dot{h}_{net,c} + \dot{h}_{net,r} = \alpha_c(\theta_g - \theta_a) + \Phi\varepsilon_m\varepsilon_f\sigma[(\theta_r + 273°C)^4 - (\theta_a + 273°C)^4] \tag{2}$$

$$k_{sh} = \begin{cases} 0.9\cdot\left(A_m/V\right)_b/\left(A_m/V\right), & \text{for I-sections} \\ 1.0, & \text{for other sections} \end{cases} \tag{3}$$

where

θ_a is the equivalent uniform temperature distribution in the unprotected steel section (shortened also to just "section temperature" in this paper) [°C],

t is the time [s],

[1] Senior Fire Safety Specialist, M.Sc, Markku Kauriala Ltd, Fire engineering and fire safety design consultants, Finland e-mail: timo.jokinen@kauriala.fi

[2] Senior Fire Safety Consultant, M.Sc, Markku Kauriala Ltd, Fire engineering and fire safety design consultants, Finland e-mail: risto.ranua@kauriala.fi

[3] Senior Fire Safety Specialist, D.Sc, Markku Kauriala Ltd, Fire engineering and fire safety design consultants, Finland e-mail: mikko.salminen@kauriala.fi

https://doi.org/10.6084/m9.figshare.22153451

Δt	is the time interval ($\Delta t \leq 5$ s) [s],
(A_m/V)	is the section factor for unprotected steel members [1/m],
A_m	is the surface area of the member per unit length [m²/m],
V	is the volume of the member per unit length [m³/m],
c_a	is the specific heat of steel (temperature dependant; EN 1993-1-2 section 3.4.1.2 for carbon steel),
ρ_a	is the unit mass of steel (ρ_a = 7850 kg/m³) [kg/m³],
$\dot{h}_{net}$	is the net heat flux to unit surface area [W/m²],
$\dot{h}_{net,c}$	is the net heat flux to unit surface area due to convection [W/m²],
$\dot{h}_{net,r}$	is the net heat flux to unit surface area due to radiation [W/m²],
α_c	is the coefficient of heat transfer by convection (in standard fire α_c = 25 kW/m²; in natural fires / performance-based fire design α_c = 35 kW/m² [2]) [kW/m²],
θ_g	is the gas temperature near the member [°C],
θ_r	is the effective radiation temperature of the fire environment (in case of fully fire engulfed members $\theta_r = \theta_g$) [°C],
Φ	is the configuration factor (can be ignored by using Φ = 1.0),
ε_m	is the surface emissivity of the member (ε_m = 0.7 for carbon steel),
ε_f	is the emissivity of the fire (in general ε_f=1.0),
σ	is the Stephan Boltzmann constant $5.6704 \cdot 10^{-8}$ W/m²K⁴,
k_{sh}	is the correction factor for the shadow effect (can be ignored by using k_{sh} = 1.0) and
$(A_m/V)_b$	is the box value of the section factor; i.e. the surface area of the member per unit length is calculated from the smallest rectangular box that can surround the member [1/m].

There seems to be no changes planned to these formulas in the upcoming Eurocode revisions based on preliminary drafts seen by the authors.

1.2 Calculation formulas modified for performance-based fire design

In performance-based design the temperature distribution around the steel section is typically not uniform, and the net heat fluxes differ from each other around the section. In fire simulations (for example using Fire Dynamics Simulator, FDS [3], Figure 1a), it's common to utilize Adiabatic Surface Temperatures (AST) [4] when transferring the temperature data to the structural analysis. Adiabatic Surface Temperature method takes into account the convective and radiative heat transfer between the gas and the solid structure, and converts them to a single equivalent AST value.

In fire simulations it is common to measure the AST values from four different section directions. In this case the steel section can be divided into four different sides with four separate heat fluxes, separate section factors and separate shadow effect correction factors (Figure 1b).

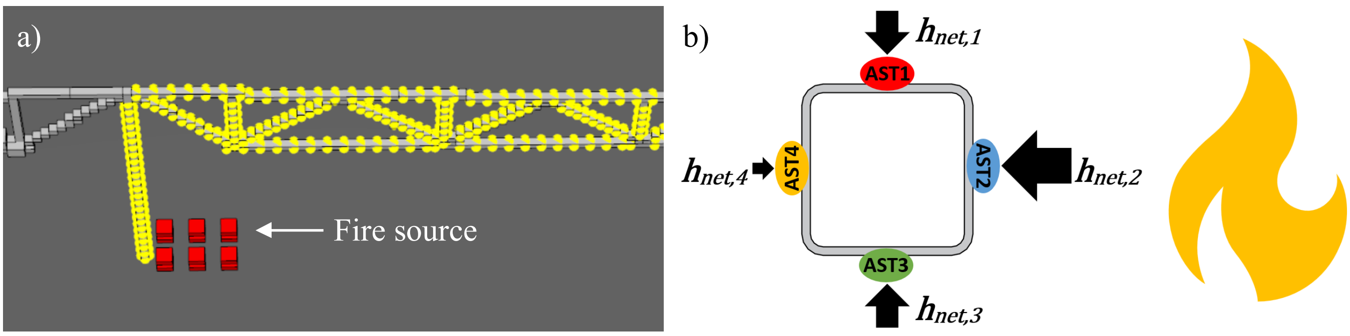

Figure 1. The principle for determining the temperatures that heat the structural steel sections using virtual Adiabatic Surface Temperatures (AST) measurement devices in fire simulations a) detail from FDS model b) the placement of AST measurement devices around the steel section and their corresponding net heat fluxes.

Thus, the steel section temperature development (when longitudinal heat transfer along the member is neglected) can now be calculated by modifying the previous Eurocode formulas the following way:

$$\theta_a(t+\Delta t)=\theta_a(t)+\frac{\Delta t}{c_a\rho_a}\sum_{k=1}^{4}\left[k_{sh,k}\left({}^{A_{m,k}}/_{V}\right)\dot{h}_{net,k}\right] \quad (4)$$

$$\dot{h}_{net,k}=\alpha_c\left(\theta_{AST,k}-\theta_a\right)+\varepsilon_m\varepsilon_f\sigma\left[\left(\theta_{AST,k}+273°C\right)^4-\left(\theta_a+273°C\right)^4\right] \quad (5)$$

$$k_{sh,k}=\begin{cases}\chi_{sh,web}\cdot\left({}^{A_{m,b,k}}/_{V}\right)_b\Big/\left({}^{A_{m,k}}/_{V}\right), & \text{for I-section web sides}\\ 1.0, & \text{for I-section flange sides and for other sections}\end{cases} \quad (6)$$

where

$(A_{m,k}/V)$ is the section factor for unprotected steel member on each of the four different sides of the section [1/m], the sum of each should result in the original section factor; i.e. $\sum_{k=1}^{4}({}^{A_{m,k}}/_{V})={}^{A_m}/_{V}$,

$A_{m,k}$ is the surface area of the each section side per unit length, [m²/m]; $\sum_{k=1}^{4}A_{m,k}=A_m$,

$\dot{h}_{net,k}$ is the net heat flux on each side of the section [W/m²],

$\theta_{AST,k}$ is the AST-temperature on each side of the section [°C],

$k_{sh,k}$ is the correction factor for the shadow effect determined separately for each side of the section,

$(A_{m,b,k}/V)_b$ is the section factor of the I-section web side surface simplified to a box [1/m] and

$\chi_{sh,web}$ is an additional web cavity correction factor (by default $\chi_{sh,web}=0.9$).

When $k_{sh}=1.0$ and the temperature exposure is uniform, these formulas (4) - (5) should result in exactly the same section temperature development than with the regular EC3 formulas (1) - (3). Formulas could be designed so, that they would also work identically when $k_{sh}<1.0$ in uniform fire, but this would require that the I-section flat outer flange surfaces would have a $k_{sh,k}$ value that is < 1.0, and intuitively this would not make sense. For this reason the formula (6) works slightly differently than the original formula (3): in the modified formula, $k_{sh,k}=1.0$ in all flat or convex surface regardless of the rest of the section shape (i.e. $k_{sh,k}=1.0$ in tube surfaces, I-section outer flange surfaces, etc), and actual value for $k_{sh,k}$ is only calculated for concave surfaces (i.e. I-section web surfaces and inner flange surfaces, etc). This also means, that a new correction factor $\chi_{sh,web}$ is required, because the default value of 0.9 given in formula (3) may not be ideal anymore. In this paper, the effect of $\chi_{sh,web}$ is studied in the section 2.5; all the other calculations are done by using the default value $\chi_{sh,web}=0.9$.

Figure 2 shows an example how to calculate $(A_{m,k}/V)$ and $k_{sh,k}$ values for an I-section.

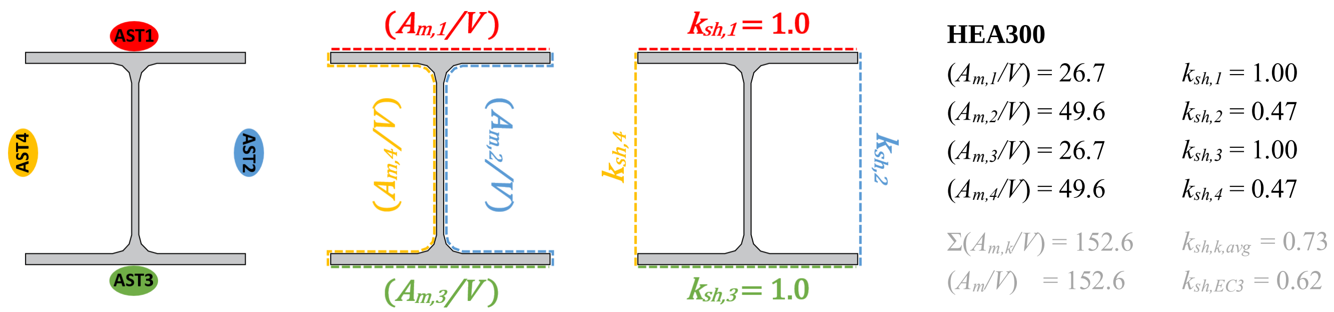

Figure 2. Example from $(A_{m,k}/V)$ and $k_{sh,k}$ calculation with the modified formulas using HEA300 profile. Comparison of the modified method to the regular EC3 method is shown in grey. (In this example $\chi_{sh,web}=0.9$).

An example why these modified formulas (4) - (6) are needed at all is shown in Figure 3. One could think that by calculating an average curve from the four different temperature exposures (and heat fluxes) and by using the regular EC3 formulas (1) - (3), it would lead to the correct steel section temperature development, but this is not the case. Figure 3 shows an example where this averaging method would underestimate the section temperature by as much as 61 °C, which could be quite dangerous in performance-based structural fire design.

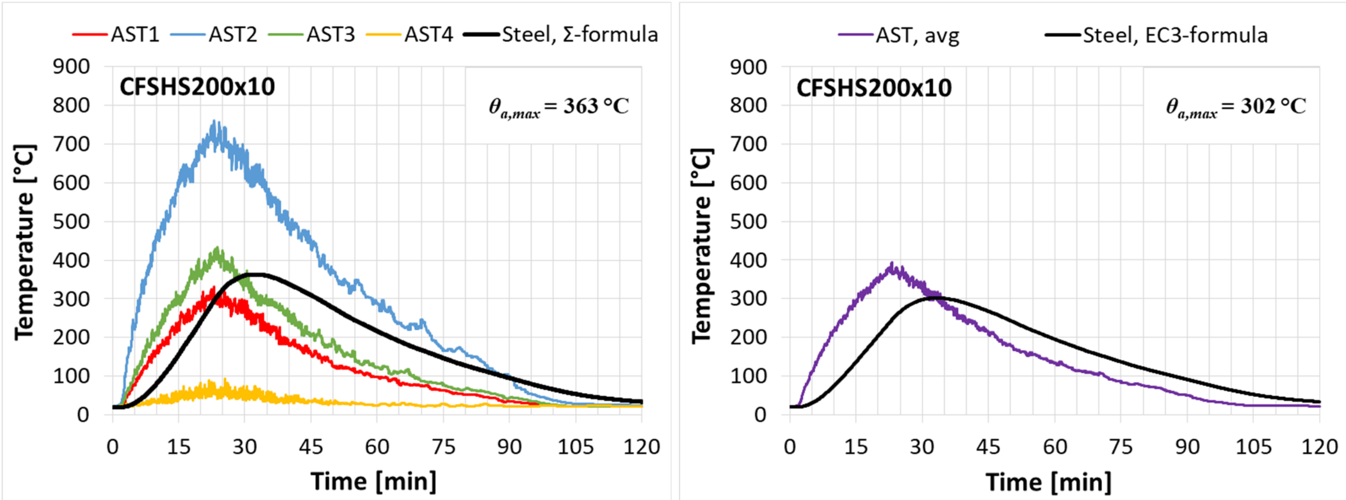

Figure 3. An example of why averaging the different temperature exposures and then using the regular EC3 formulas should be avoided in performance-based fire design (i.e. it can lead to underestimation of the section temperature).

Some steel structures are not exposed to fire from all four sides. If one or more sides of the steel section is right next to an obstruction (e.g. wall columns, corner columns, floor beams etc.), the obstructed side of the section should be assumed to have an adiabatic surface if better heat flux measurement between the section and obstruction is not available (i.e. for the obstructed sides the $\dot{h}_{net,k} = 0$). This should be a conservative assumption for wide range of obstruction materials, since usually during the heating phase, the heat flux direction is from the steel section towards the obstruction [5]. Conversely, assuming a constant 20 °C temperature to the obstructed section sides may lead to an underestimation of the steel section temperatures. In this paper, the sections are exposed to fires from all four sides in all the studied cases. A case study shown in a separate paper [6] presents also members with fire exposures only on 2 or 3 sides of the section.

2 VALIDATION OF THE MODIFIED FORMULAS USING FEM

2.1 Validation methods and models

This paper also aims to present validation studies for the presented modified formulas (4) - (6) (hence referred here also as the Σ-formulas) by comparing the section temperature development from the Σ-formulas to the development of section temperature average calculated with 2D FEM analysis using SAFIR software [7]. SAFIR is extensively validated [7, 8, 9, 10] and widely used software for analysing structures in elevated temperatures.

Several different variables are studied in the validation analyses: different fire exposures (from highly non-uniform to completely uniform), section sizes (light profiles to heavy profiles and column profiles to beam profiles), section types (convex sections to concave sections), and the shadow effect of the section (from no shadow effect / omitted shadow effect to fully utilized shadow effect).

The studied fire exposures are shown in Figure 4 and they are:

- ISO-Fire: standard temperature-time curve (also known as standard fire or ISO 834 fire), uniform fire exposure, no cooling phase (EN 1991-1-2, section 3.2.1 [2])
- Fire 1 (F1): highly non-uniform fire exposure, medium fire intensity
- Fire 2 (F2): non-uniform fire exposure (relatively similar on three sides, but significantly cooler on one side), high fire intensity
- Fire 3 (F3): slightly non-uniform fire exposure, low fire intensity

The standard fire somewhat depicts a fully developed compartment fire (although without an ignition and a cooling phase), the rest of the fires are localized fires taken from FDS fire simulation projects.

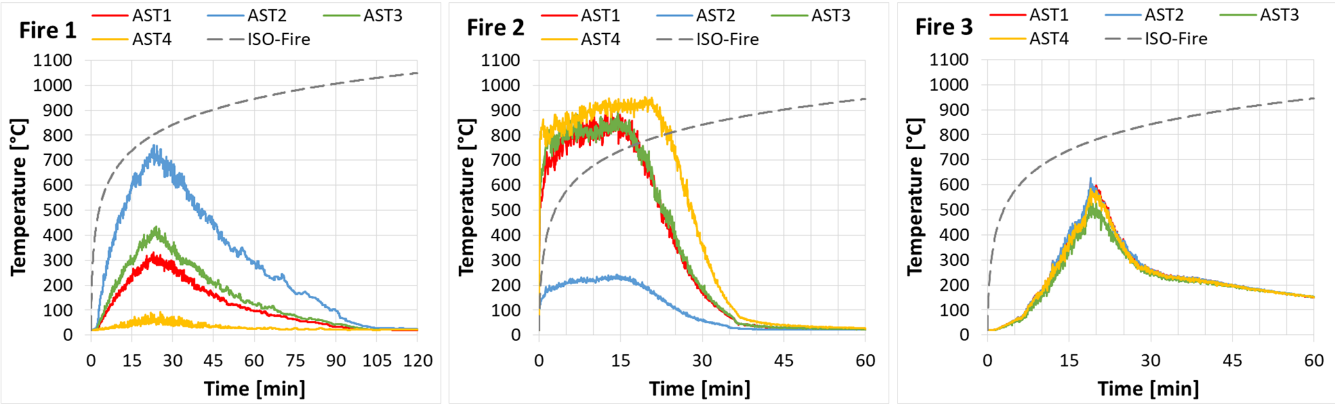

Figure 4. Fires 1-3 (or F1-F3) that are used in the validation calculations. ISO-fire shown as a comparison.

Four different steel sections are studied, and some of the cases are also studied in two different section orientations; regular orientation and 90° rotated orientation in relation to the non-uniform fire exposure:

- SHS200x10, a tubular square section
- HEA300, an I-section commonly used in columns
- IPE300, an I-section commonly used in beams
- HEM300, a very bulky I-section

The SAFIR validation models that do not include the shadow effect (i.e convex sections, and the concave sections when shadow effect is omitted) are relatively simple; 2D section is modelled with four temperature frontier constraints acting on the section boundaries (Figure 5a). In tubular sections the heat exchange in the internal cavity is also considered by utilizing a Void constraint. The models that do include the shadow effect of a concave section are modelled by utilizing the method described in [7]: by using fictitious radiative elements that close the cavity in the web of the section (Figure 5b). The temperatures of the fictitious radiative elements directly follow the temperature curve prescribed to that section side, and these elements have an emissivity value of one (i.e. similarly than $\varepsilon_f = 1.0$ in formula (5)). Direct heat conduction between fictitious radiative elements and steel section is prevented.

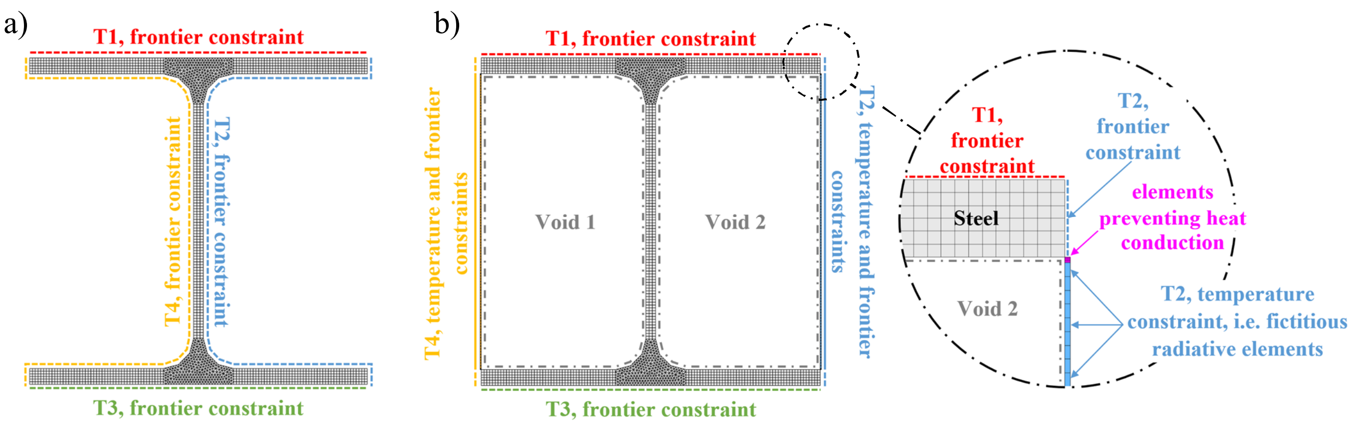

Figure 5. Example of the SAFIR 2D temperature analysis models used in the validation calculations.
a) a model disregarding the shadow effect ($k_{sh} = 1.0$), b) a model utilizing the shadow effect ($k_{sh} < 1.0$).

In the SAFIR models, the parameters of the steel and the fire (c_a, ρ_a, ε_m, α_c,) are set to the same values than described in chapter 1.1. The models consist of 1216 – 6656 elements depending on the section type, and a calculation time step of 1.0 s is used. From the resulting SAFIR temperature data, an average steel section temperature curve is calculated (as a weighted arithmetic mean where the element temperature is weighted by the element area, fictitious radiative elements are omitted). Figure 6 shows examples from the resulting temperature gradients and SAFIR section temperature curves compared against the formulas (4) - (6).

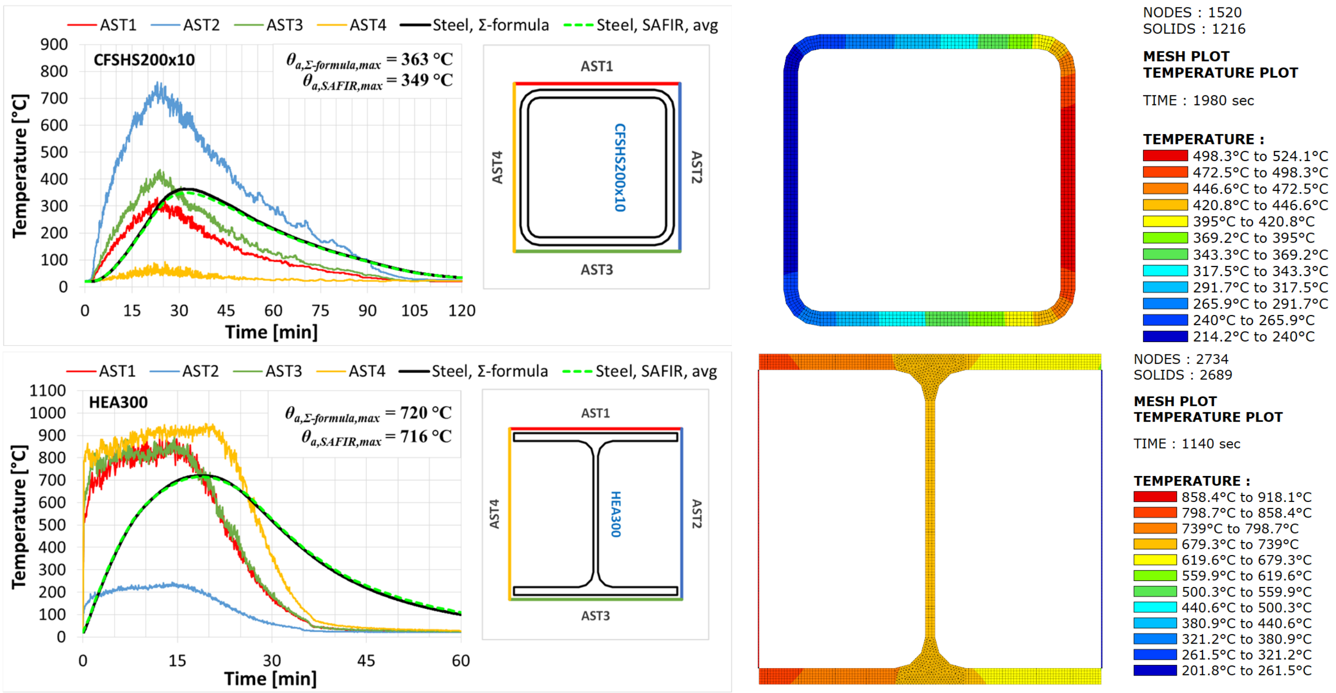

Figure 6. Example figures comparing the section temperature development with Σ-formulas vs. SAFIR model averages (left), and the corresponding temperature gradient at the hottest timepoint in the SAFIR model (right). Example calculations for a section without shadow effect (top) and for a section with shadow effect (bottom).

2.2 Validation results in standard fire

In the validation analyses with uniform fire (ISO-fire, cases 1 - 7), three different section temperature deviations are studied in order to judge the performance of the methods: difference between Σ-formula temperatures and SAFIR temperatures ($\Delta\theta a,0(t)$, (7)), difference between EC3 temperatures and SAFIR temperatures ($\Delta\theta a,1(t)$, (8)), and difference between Σ-formula temperatures and EC3 temperatures ($\Delta\theta a,2(t)$, (9)). In each of these, the section temperature curves are compared against each other at 60 s intervals, and maximum, minimum, mean, and standard deviation values are recorded from the temperature deviations in question. The results are shown in Table 1.

$$\Delta\theta_{a,0}(t) = \theta_{a,\Sigma-formula}(t) - \theta_{a,SAFIR,avg}(t),\ \ t = 0\,\text{s}, 60\,\text{s}, 120\,\text{s} \ldots 7200\,\text{s} \tag{7}$$

$$\Delta\theta_{a,1}(t) = \theta_{a,EC3-formula}(t) - \theta_{a,SAFIR,avg}(t),\ \ t = 0\,\text{s}, 60\,\text{s}, 120\,\text{s} \ldots 7200\,\text{s} \tag{8}$$

$$\Delta\theta_{a,2}(t) = \theta_{a,\Sigma-formula}(t) - \theta_{a,EC3-formula}(t),\ \ t = 0\,\text{s}, 60\,\text{s}, 120\,\text{s} \ldots 7200\,\text{s} \tag{9}$$

Table 1. Validation results in standard fire; temperature deviations in the different calculation methods.

#	Fire	Section	k_{sh}	$\Delta\theta_{a,0}(t)$ [°C]				$\Delta\theta_{a,1}(t)$ [°C]				$\Delta\theta_{a,2}(t)$ [°C]			
				max	min	mean	st.dev	max	min	mean	st.dev	max	min	mean	st.dev
1	ISO	CFSHS200x10	NO	2.3	-1.0	0.4	0.7	2.3	-1.0	0.4	0.7	0.0	0.0	0.0	0.0
2	ISO	HEA300	NO	9.9	-0.6	2.0	3.0	9.9	-0.6	2.0	3.0	0.0	0.0	0.0	0.0
3	ISO	HEA300	YES	0.0	-9.2	-1.6	2.7	0.0	-23.2	-4.6	6.8	14.1	0.0	2.9	4.2
4	ISO	IPE300	NO	7.9	-0.7	1.2	2.1	7.9	-0.7	1.2	2.1	0.0	0.0	0.0	0.0
5	ISO	IPE300	YES	3.1	-3.8	-0.3	1.0	0.4	-10.5	-1.6	2.7	8.6	0.0	1.3	2.2
6	ISO	HEM300	NO	18.4	-0.3	4.9	5.1	18.4	-0.3	4.9	5.1	0.0	0.0	0.0	0.0
7	ISO	HEM300	YES	0.4	-13.8	-3.5	4.9	0.0	-28.7	-9.4	9.9	15.0	0.0	5.9	5.4
				max	min	mean	st.err	max	min	mean	st.err	max	min	mean	st.err
				18.4	-13.8	0.4	2.7	18.4	-28.7	-1.0	4.7	15.0	0.0	1.5	2.3

The results show, that when k_{sh} = 1.0, the modified method and the regular EC3 method result in exactly the same temperature development in uniform fire exposure (Table 1, see $\Delta\theta_{a,2}(t)$). The results also show, that the modified method seems to result in very slightly better temperature estimation than the regular EC3 method in standard fire (Table 1, compare $\Delta\theta_{a,0}(t)$ vs. $\Delta\theta_{a,1}(t)$; slightly less underestimation and deviation in $\Delta\theta_{a,0}(t)$). However, in standard fire the differences seem to be very minor between the two calculation methods and SAFIR validation results as can also be seen from the curves in Figure 7.

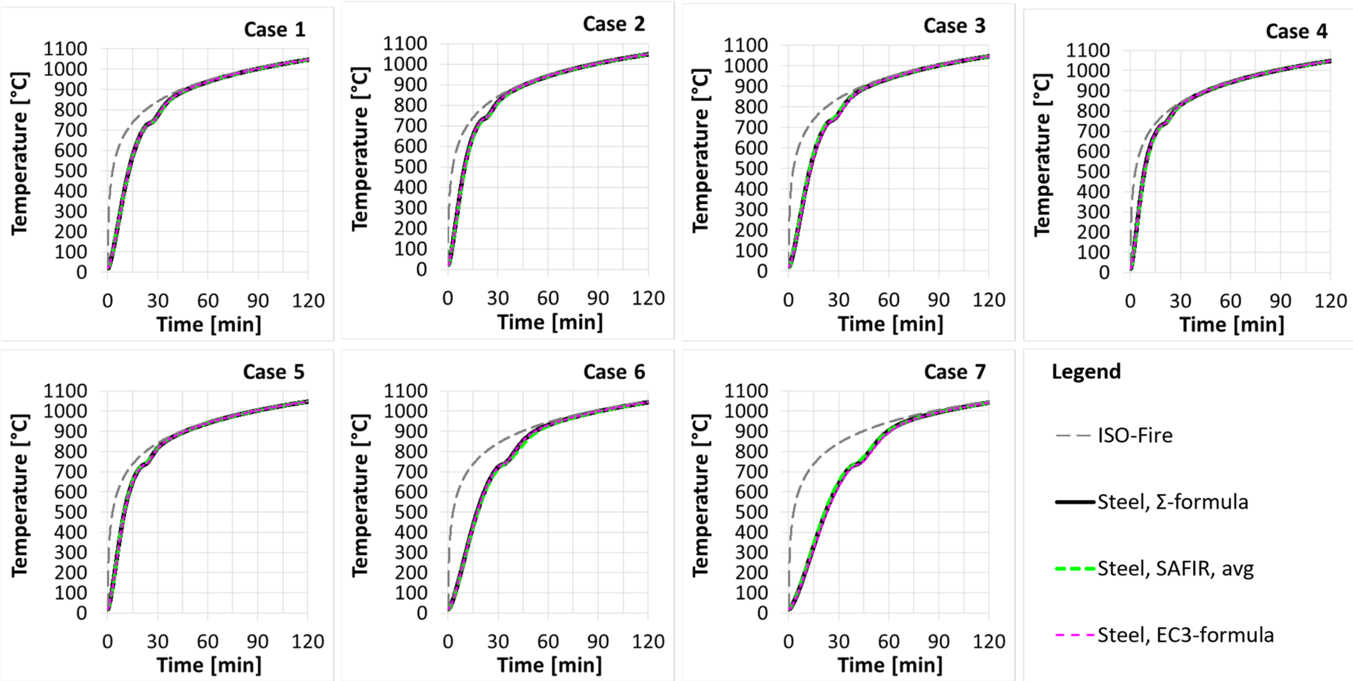

Figure 7. Validation results in standard fire; steel section temperature curves with different calculation methods.

2.3 Validation results in non-uniform fire without shadow effect correction factor

In the validation analyses with non-uniform fire, section temperature deviations are analysed similarly than in previous chapter: differences between Σ-formula temperatures and SAFIR temperatures are compared at 60 s intervals (formula (10)), and maximum, minimum, mean, and standard deviation values are recorded. But in addition to these, special attention is needed for the maximum equivalent uniform section temperature in fires with cooling phase, since it is often the most important result attained from these types of calculations. The differences in these maximum temperatures are analysed using formulas (11) - (14).

$$\Delta\theta_a(t) = \theta_{a,\Sigma-formula}(t) - \theta_{a,SAFIR,avg}(t), \quad t = 0\ \mathrm{s}, 60\ \mathrm{s}, 120\ \mathrm{s} \ldots 7200\ \mathrm{s} \tag{10}$$

$$\theta_{a,\Sigma-formula,max} = \max\left(\theta_{a,\Sigma-formula}(t)\right), \quad t = 0 \ldots 7200\ \mathrm{s} \tag{11}$$

$$\theta_{a,SAFIR,max} = \max\left(\theta_{a,SAFIR,avg}(t)\right), \quad t = 0 \ldots 7200\ \mathrm{s} \tag{12}$$

$$\Delta\theta_{a,max} = \theta_{a,\Sigma-formula,max} - \theta_{a,SAFIR,max} \tag{13}$$

$$\Delta\theta_{a,max,\%} = \frac{\theta_{a,\Sigma-formula,max} - \theta_{a,SAFIR,max}}{\theta_{a,SAFIR,max}} \tag{14}$$

The results for cases without shadow effect correction factors (convex sections, and the concave sections when shadow effect is omitted; cases 8 - 19) are shown in Table 2 and Figure 8.

Table 2. Validation results in non-uniform fire **without** shadow effect correction factors; the deviations between the two maximum equivalent uniform section temperatures, and the deviations between the two curves.

#	Fire	Section	k_{sh}	$\theta_{a,\Sigma\text{-}formula,max}$ [°C]	$\theta_{a,SAFIR,max}$ [°C]	$\Delta\theta_{a,max}$ [°C]	$\Delta\theta_{a,max,\%}$ [-]	$\Delta\theta_a(t)$ [°C] max	min	mean	st.dev
8	F1	CFSHS200x10	NO	363.1	348.8	**14.3**	**4.1 %**	14.4	-0.1	4.2	4.6
9	F2	CFSHS200x10	NO	720.4	700.9	**19.5**	**2.8 %**	29.6	-4.8	5.1	10.7
10	F3	CFSHS200x10	NO	352.2	351.4	**0.8**	**0.2 %**	0.9	-0.7	0.1	0.4
11	F1	HEA300	NO	417.0	398.3	**18.7**	**4.7 %**	19.0	-0.7	4.2	6.1
12	F2	HEA300	NO	728.2	719.6	**8.6**	**1.2 %**	25.0	-7.4	3.1	10.9
13	F3	HEA300	NO	411.4	403.0	**8.4**	**2.1 %**	7.9	-1.6	1.0	2.8
14	F1	IPE300	NO	450.0	437.5	**12.5**	**2.9 %**	12.4	-0.4	2.5	3.8
15	F2	IPE300	NO	729.6	728.3	**1.3**	**0.2 %**	14.3	-5.7	0.8	6.4
16	F3	IPE300	NO	459.0	450.2	**8.8**	**1.9 %**	6.9	-1.7	0.5	2.4
17	F1	HEM300	NO	329.1	318.0	**11.1**	**3.5 %**	11.1	-1.0	3.3	4.0
18	F2	HEM300	NO	634.1	609.9	**24.2**	**4.0 %**	24.0	-4.2	6.5	9.4
19	F3	HEM300	NO	273.7	269.2	**4.5**	**1.7 %**	4.5	-0.1	1.8	1.5
						mean	mean	max	min	mean	st.err
						11.1	**2.4 %**	29.6	-7.4	2.7	2.0

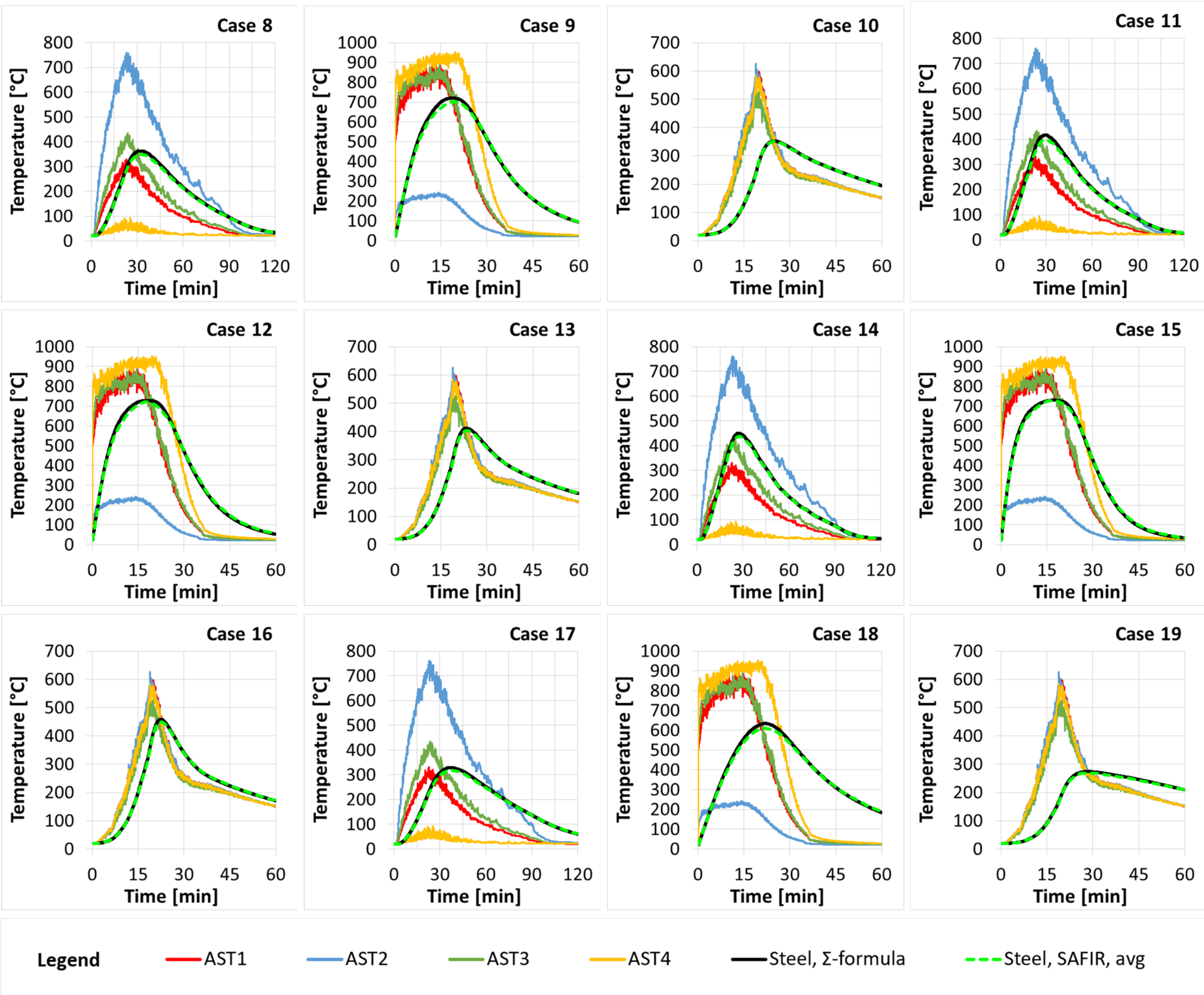

Figure 8. Validation results in non-uniform fire **without** shadow effect correction factors; steel section temperature curves with Σ-formulas vs. SAFIR average section temperature curves.

The results show, that in non-uniform fire exposure without shadow effect correction factors the Σ-formulas slightly overestimate the maximum section temperature compared to the SAFIR results: on average 11 °C or 2.4 % higher maximum section temperatures and there are no cases where Σ-formulas would result in underestimation. This can be regarded as a positive result since overestimation of the temperatures is more tolerable than underestimation in terms of the safety of the structural design.

When the section temperature curves are compared to each other point by point, somewhat larger deviations can be observed. Some of these differences in the section temperature development can probably be attributed to the different behaviour of the models when the section temperature is near the very large spike in specific heat of steel at 735 °C (see EN 1993-1-2 section 3.4.1.2 [1]). I.e. in SAFIR model parts of the section may reach 735 °C and thus the heating is temporarily slowed in these parts of the section, meanwhile the average section temperature may never reach 735 °C and thus Σ-formulas are never slowed down by the specific heat spike (for example, see Case 9 in Figure 8). This is an inherent difference between 2D FEM analysis and hand calculation approach, and it might be difficult to try to correct in the calculation formulas. However, the differences in the temperature development still relatively minor, and overall the curve shape is much less important for the use of these formulas compared to the maximum section temperature values.

2.4 Validation results in non-uniform fire with shadow effect correction factor

The results for cases with shadow effect correction factors (cases 20 - 37) are shown in Table 3 and Figure 9. The deviations are analysed similarly, than in previous chapter.

Table 3. Validation results in non-uniform fire **with** shadow effect correction factors; the deviations between the two maximum equivalent uniform section temperatures, and the deviations between the two curves. ($\chi_{sh,web} = 0.9$).

#	Fire	Section	k_{sh}	$\theta_{a,\Sigma\text{-}formula,max}$ [°C]	$\theta_{a,SAFIR,max}$ [°C]	$\Delta\theta_{a,max}$ [°C]	$\Delta\theta_{a,max,\%}$ [-]	$\Delta\theta_a(t)$ [°C] max	min	mean	st.dev
20	F1	HEA300	YES	353.8	360.5	**-6.7**	**-1.9 %**	1.9	-7.1	-4.1	2.4
21	F1	HEA300, 90°	YES	364.3	342.4	**21.9**	**6.4 %**	21.7	-3.9	4.8	8.5
22	F2	HEA300	YES	719.9	715.7	**4.2**	**0.6 %**	7.0	-11.0	-5.1	5.8
23	F2	HEA300, 90°	YES	713.2	696.8	**16.4**	**2.4 %**	23.4	-10.2	0.7	11.4
24	F3	HEA300	YES	344.8	342.9	**1.9**	**0.5 %**	3.7	-2.0	0.4	1.6
25	F3	HEA300, 90°	YES	346.1	343.6	**2.5**	**0.7 %**	3.8	-2.0	0.5	1.7
26	F1	IPE300	YES	417.3	423.3	**-6.0**	**-1.4 %**	6.4	-8.7	-4.5	4.0
27	F1	IPE300, 90°	YES	372.5	356.2	**16.3**	**4.6 %**	17.3	-6.8	0.8	8.0
28	F2	IPE300	YES	729.6	734.3	**-4.7**	**-0.6 %**	0.8	-19.9	-10.3	7.1
29	F2	IPE300, 90°	YES	753.7	761.8	**-8.1**	**-1.1 %**	40.2	-17.4	-1.3	15.8
30	F3	IPE300	YES	414.5	406.8	**7.7**	**1.9 %**	11.1	-3.8	1.0	5.0
31	F3	IPE300, 90°	YES	408.1	400.6	**7.5**	**1.9 %**	10.6	-4.0	0.8	4.9
32	F1	HEM300	YES	260.7	266.8	**-6.1**	**-2.3 %**	0.7	-6.2	-4.4	2.2
33	F1	HEM300, 90°	YES	261.5	250.8	**10.7**	**4.3 %**	10.7	-2.7	4.0	4.4
34	F2	HEM300	YES	565.5	568.8	**-3.3**	**-0.6 %**	0.0	-7.5	-4.8	1.7
35	F2	HEM300, 90°	YES	565.0	558.9	**6.1**	**1.1 %**	8.5	-9.4	-0.2	5.3
36	F3	HEM300	YES	221.5	220.6	**0.9**	**0.4 %**	1.5	0.0	0.6	0.4
37	F3	HEM300, 90°	YES	221.5	220.3	**1.2**	**0.6 %**	1.6	0.0	0.8	0.5
					Average	mean	mean	max	min	mean	st.err
						3.5	**1.0 %**	40.2	-19.9	-1.1	3.7

The results show, that in non-uniform fire with shadow effect correction factors the Σ-formulas still slightly overestimate the maximum section temperature compared to the SAFIR results (on average 3.5 °C or 1.0 %), but in these cases underestimations were also observes (in 6 cases out of 18, or 33 %). However, these underestimations remained relatively small (at worst -8.1 °C or 1.1 %), so the result can still be deemed to be acceptable.

Similar differences in the steel section temperature development (i.e. the differences Σ-formula and SAFIR average curve shapes) were observed, than described in the previous chapter.

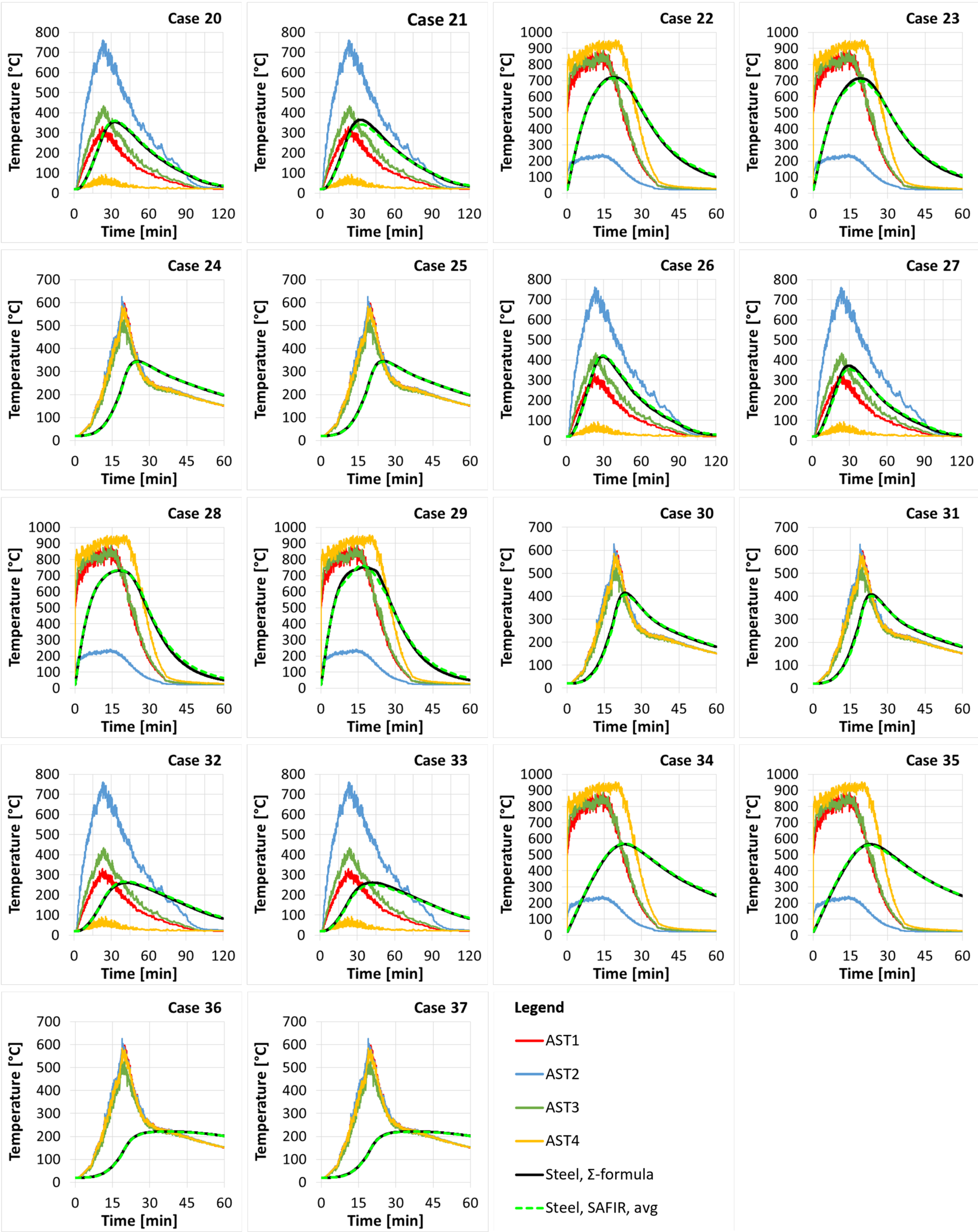

Figure 9. Validation results in non-uniform fire **with** shadow effect correction factors; steel section temperature curves with Σ-formulas vs. SAFIR average section temperature curves. ($\chi_{sh,web} = 0.9$).

2.5 The effect of the additional web cavity correction factor in shadow effect formula

The cases with shadow effect correction factors (cases 20 - 37) were recalculated using different values for the additional web cavity correction factor $\chi_{sh,web}$ (value of 0.90 was used in the previous chapter), and the results are presented in Table 4. The results show that with $\chi_{sh,web} = 0.80$ the maximum section temperatures would be on average underestimated by 3.6 °C or 0.8 %, and thus it is clearly not very good choice. $\chi_{sh,web} = 0.85$ would result the best estimation on average, but yet 61 % studied cases resulted in underestimated maximum section temperature values. $\chi_{sh,web} = 0.90$ seems like quite good compromise; slightly higher temperature on average but significantly less underestimated cases. Increasing $\chi_{sh,web}$ value to 0.95 would perhaps already overestimate section temperatures too much, while not decreasing the number of underestimated cases significantly.

Table 4. The effect of the additional web cavity correction factor in shadow effect formula; the deviations between the two maximum equivalent uniform section temperatures in the 18 studied cases recalculated with different $\chi_{sh,web}$ values, and percentage of the cases that resulted in underestimated maximum section temperature.

$\chi_{sh,web}$	$\Delta\theta_{a,max}$ [°C]				$\Delta\theta_{a,max,\%}$ [°C]				$n_{underestimated}$
	max	min	mean	st.dev	max	min	mean	st.dev	
0.95	22.0	-4.6	**6.8**	8.2	6.4 %	-0.7 %	**1.8 %**	2.1 %	28 %
0.90	21.9	-8.1	**3.5**	8.8	6.4 %	-2.3 %	**1.0 %**	2.3 %	33 %
0.85	21.7	-12.8	**0.0**	9.8	6.3 %	-4.1 %	**0.1 %**	2.6 %	61 %
0.80	21.4	-17.1	**-3.6**	11.1	6.3 %	-6.0 %	**-0.8 %**	3.0 %	72 %

3 DISCUSSION

The results show that there seems to be a good fit between the proposed Σ-formulas vs. SAFIR validations, although in highly non-uniform fires Σ-formulas tends to produce slightly higher section temperatures on average, but this is conservative result in terms of practical design.

The proposed method is presented as an additional tool for the performance-based fire design (i.e. checking section temperatures against member critical temperatures), but the final design should also be checked accounting also the indirect effects of the design fires (indirect thermal actions and displacements from thermal expansions, thermal gradients within cross-sections, non-linear material models, etc. like required for example in EN 1991-1-2 section 4.1 [2]). Trying to consider these indirect effects just by using section temperatures and critical temperatures may prove difficult, so it is recommended that the final structural fire design is analysed using advanced calculation models (see EN 1993-1-2 section 4.3 [1]), for example by utilizing combined thermal and mechanical analysis in SAFIR software.

However, the proposed Σ-formulas are still very useful in performance-based fire design, for example:

- during preliminary design,
- as a tool for identifying most critical structures and design fire scenarios, and then focusing the advanced structural analyses just to them,
- as a demonstrative tool for presenting the results for non-experts (e.g. during authority approval phase); difference between section temperature and critical temperature can be much easier to understand than advanced structural analysis models.

4 CONCLUSIONS

This paper presented modifications for EC3 unprotected steel section equivalent uniform temperature distribution formulas, that generalizes them for non-uniform fire exposure to better serve the demands in performance-based fire design (named here the Σ-formulas). The modified formulas were designed to fit well with FDS fire simulations, and they should not be limited to specific type of fire (i.e. they should work with localized fire, fully developed fire, travelling fire, etc.). If one or more sides of the steel section is right next to an obstruction (e.g. wall columns, corner columns, floor beams etc.), the obstructed side of the section should be assumed to have an adiabatic surface.

The validation for these formulas was done by using 2D FEM temperature analysis (with SAFIR software), and several different variables were studied in the validation analyses: different fire exposures (from highly non-uniform to completely uniform), section sizes (light profiles to heavy profiles and column profiles to beam profiles), section types (convex sections to concave sections), and the shadow effect of the section (from no shadow effect / omitted shadow effect to fully utilized shadow effect).

The validation results showed that there seems to be a good fit between the procedures (Σ-formulas vs. SAFIR models), although in very non-uniform fires Σ-formulas tends to produce slightly higher section temperatures (which is conservative result in terms of practical design). In non-uniform fire exposure and without shadow effect, Σ-formulas resulted on average 11 °C or 2.4 % higher maximum section temperatures, and with shadow effect on average 3.5 °C or 1.0 % higher maximum section temperatures. It was also shown that the Σ-formulas produce identical results with the original Eurocode formulas, when the fire exposure is completely uniform (e.g. standard fire) and when there is no shadow effect. With shadow effect the results are very close to each other in uniform fire.

In the modified method, the way of calculating the shadow effect of the section was slightly altered from EC3 method, which required introducing additional correction factor $\chi_{sh,web}$. Based on the analysis presented in the paper a value of $\chi_{sh,web} = 0.90$ is recommended.

The proposed method is presented as a useful tool for the preliminary performance-based fire design (section temperatures vs. critical temperatures), but the final design should also be checked using more advanced methods to better account for the indirect effects of the design fires (indirect actions and displacements from thermal expansions, thermal gradients within cross-sections, non-linear material models, etc.).

REFERENCES

1. EN 1993-1-2. 2005. Eurocode 3: Design of steel structures. Part 1-2: General rules. Structural fire design
2. EN 1991-1-2. 2002. Eurocode 1: Actions on structures. Part 1-2: General actions. Actions on structures exposed to fire
3. Fire Dynamics Simulator (FDS), https://pages.nist.gov/fds-smv/
4. Wickström, U., McGrattan, K. 2007. Adiabatic surface temperature for calculating heat transfer to fire exposed structures. Proceedings of the Eleventh Interflam Conference.
5. Heinisuo, M., Jokinen, T. 2014. Tubular composite columns in a non-symmetrical fire. Magazine of Civil Engineering. 49. 107-120. 10.5862/MCE.49.11.
6. Jokinen, T., Ranua, R., Salminen, M. 2022. Recent developments in holistic performance-based fire design of steel structures - Case study: a padel-center. 12th International Conference on Structures in Fire (SiF'22)
7. Gernay, T., Franssen, J.M. 2017. "Modeling structures in fire with SAFIR®: Theoretical background and capabilities". Journal of Structural Fire Engineering, Vol. 8, issue 3, pp. 300-323.
8. Pintea, D., Franssen, J.M. 1997. Evaluation of the thermal part of the code SAFIR by comparison with the code TASEF. Proc. 8th Int. Conf. on Steel Structures, Vol. 2, M. Ivan ed., MIRTON, Timisoara, pp. 636-643
9. Franssen, J.M. 2003. Heat transfer by radiation in internal cavities with a complex shape. Proc. of the SEI-SFPE conf. Designing structures for fire, Baltimore, DEStech Publ. Inc., pp. 33-42
10. Zaharia, T., Gernay, T. 2012. Validation of the Advanced Calculation Model SAFIR Through DIN EN 1991-1-2 Procedure. 10th Int. Conf. ASCCS, Singapore

SiF 2022– The 12th International Conference on Structures in Fire
The Hong Kong Polytechnic University, Nov 30 - Dec 2, 2022

FRAMEWORK TO INCORPORATE SPRINKLER SYSTEM IN STRUCTURAL FIRE ENGINEERING

Mikko Salminen[1], Mikko Malaska[2], Timo Jokinen[3], Risto Ranua[4]

ABSTRACT

Sprinkler system can be very reliable and effective way to reduce fire risks in buildings if maintained properly. Even though there are options to account sprinkler system in Structural Fire Engineering (SFE), there is a lack of consistent guideline (at least in Finland). This can lead to totally different structural fire design in similar buildings, depending on the interpretation and assumptions made. This paper presents a framework to take the effect of the sprinkler system consistently into account in SFE. The framework is based on Finland's fire regulations and on experience of multiple projects. A case-example, where this framework has been applied is presented in the paper.

Keywords: Sprinkler System; Structural Fire Engineering; Sprinkler Reliability; Case Study

1 INTRODUCTION

Automatic sprinkler systems are an effective way to reduce the fire risks in buildings. Recent study from Finland (main results presented e.g. in [1]) shows that sprinkler system can be very reliable if maintained properly. Moreover, it has been shown that when the sprinkler system operates fully as designed, the temperatures affecting the load-bearing structures are often relatively low and the structural resistance is typically not compromised as shown e.g. in [2 - 4]. In holistic Structural Fire Engineering (SFE) it does not make sense to ignore an active system which is reliable and efficient. On the other hand, it should be ensured that if the sprinkler system does not operate as designed, the consequences are still tolerable.

The fundamental background in prescriptive structural fire safety, such as in prescriptive regulations of Finnish fire regulations [5], seems to be that the higher the potential consequences of structural failure in fire, the more the structural fire design should be based on passive systems (i.e. fire resistance ratings of structural elements). If the potential consequences are smaller, the benefits from sprinkler system can often be utilized in larger extent as illustrated in Figure 1.

EN 1991-1-2 [6] Annex E allows the reduction in the design fire load in sprinklered buildings. In Finland, the use of EN 1991-1-2 Annex E is prohibited per Finnish national annex, but the Finnish fire regulations [5] allow to take the cooling effect from sprinkler system into account in SFE. However, the guidance is vague: *"slower rise in temperature and the cooling of load-bearing building elements may be taken into consideration"* [5]. This guidance can lead to totally different structural fire design in similar buildings,

[1] Senior Fire Safety Specialist, Markku Kauriala Ltd Fire Engineering and Fire Safety Design Consultants, Tampere, Finland
e-mail: mikko.salminen@kauriala.fi
[2] Professor, Tampere University, Tampere, Finland
e-mail: mikko.malaska@tuni.fi, ORCID: https://orcid.org/0000-0002-8215-9765
[3] Senior Fire Safety Specialist, Markku Kauriala Ltd Fire Engineering and Fire Safety Design Consultants, Tampere, Finland
e-mail: timo.jokinen@kauriala.fi
[4] Senior Fire Safety Consultant, Markku Kauriala Ltd Fire Engineering and Fire Safety Design Consultants, Tampere, Finland
e-mail: risto.ranua@kauriala.fi

https://doi.org/10.6084/m9.figshare.22153469

depending on the interpretation and assumptions made. Therefore, a guideline or framework is needed (at least in Finland) to take the effect of the sprinkler system into account in SFE process in consistent way.

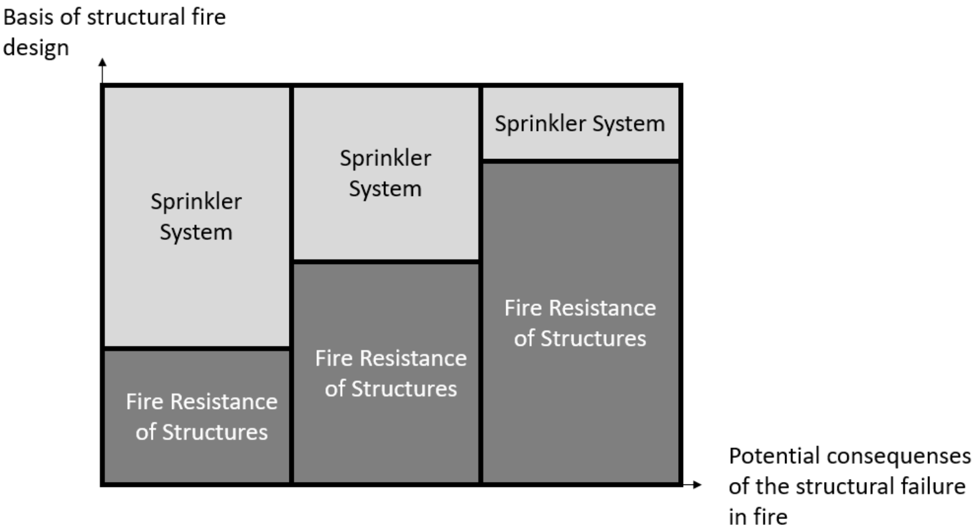

Figure 1. The fundamental background of structural fire safety e.g. in [5].

Generally, there are different options to implement sprinkler system in SFE, e.g. EN 1991-1-2 Annex E approach. An event tree analysis has also been used in many projects to determine the design fire load so that the risk of structural collapse in fire is tolerable. The event tree analysis requires data on sprinkler reliability, which is relatively well available in Finland [1]. Figure 2 presents a simple example of event tree analysis, which shows clearly how sprinkler reliability is related to design fire load (or the probability that the fire load is less than the critical fire load for the structures). This kind of event tree analysis also requires the target probability for the unwanted event (structural collapse in fire).

Sprinkler operation can also be taken into account in fire simulations, such as Computational Fluid Dynamics (CFD) and there are multiple options to make conservative assumptions in the CFD-analysis. Even though there are options to account sprinkler system in SFE, it is often unclear which approach to use, and what and how conservative assumptions should be made so that the design solution represents the desired/required level of safety.

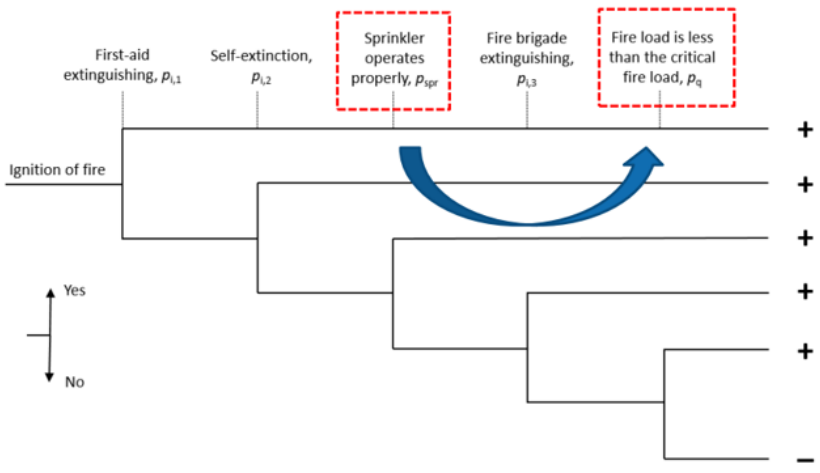

Figure 2. Simple event tree to take sprinkler system into account in fire design (in design fire load).

2 RELIABILITY OF AUTOMATIC SPRINKLER SYSTEMS

Modern automatic sprinkler systems have demonstrated very high operational reliability and design regulations have opened up new opportunities to incorporate sprinklers in building design. For robust and fire safe design solutions, it is of great importance that the sprinkler reliability levels applied are well justified. Sprinklers can be utilized in structural solutions when they operate as designed. Sprinkler system reliability is a probabilistic measure of assurance that a system will operate in the field as intended when required. The reliability of sprinkler systems can be quantified for example by system-based approach, which estimates the reliability of the entire sprinkler system directly from past performance in actual fire incidents.

A large number of system-based research have been reported. In Table 1 four recent system-based studies providing data on sprinkler system operational reliability and performance reliability (efficiency) are presented [7 - 11]. Operational reliability is a measure that, the system operates when required. Performance reliability is a measure that, given the sprinkler has correctly operated according to its design specifications, the development of the fire will be affected as intended. Statistics state that sprinkler systems were effective in controlling the fire in 96-99 % of the fires in which they operated [7,10]. This high value of reliability assumes that the systems are correctly designed and installed, and that the lack of maintenance and other human errors are designed out, for example, by using detection and alarm provisions. By combining the two reliability components, the overall reliability of sprinkler systems can be calculated. The research data indicates that the overall reliability levels of general fire sprinkler systems vary significantly depending on the source of information. This is due to differences in data and interpretations about successful operation of the system. For the risk-based fire engineering and design approach, data with such a large dispersion are not likely applicable. As there is no access to those fire statistics, a uniform analysis of different sources is not possible and direct application of the data in the risk-based fire design approach is difficult.

Table 1. Studies providing system-based data on operational and performance reliabilities of automatic sprinkler systems.

Source	Operational [%]	Performance [%]	Overall [%]
Ahrens 2021 (USA, residential) [7,8]	95 *	97	92
Ahrens 2021 (USA, commercial, offices) [7,8]	90 *	96	86
Nieminen 2018 (Finland) [9]			98
Optimal Economics 2017 (UK, residential) [10]	97	99	96
Optimal Economics 2017 (UK, all) [10]	94	99	93
Frank et al. 2012 (New Zeeland) [11]			86
* Failures also include cases where the system was not available			

In order to produce more accurate data with more specific information about the definitions used for successful sprinkler operation, a system-based study was carried using the statistics system of Finnish rescue services [9,12]. The statistics cover actual fire incidents in Finland over the 1996-2016 period. A total of 2821 cases were analysed. Cases where the fire was extinguished and restrained were counted as successful and the cases where operation or effect was deficient, or sprinkler system didn’t operate at all were counted as failed. Cases where the sprinkler system was covering only an individual device, where the temperature rise was not high enough to activate sprinkler head, where the fire was outside of the protected area, or where the fire may had been extinguished by someone or self-extinguished before sprinkler head would have activated were excluded from the study. The number of excluded cases was 2045. There were 761 successful cases and in total 15 cases which were estimated as unsuccessful, so the reliability of sprinkler systems was 98,1 %. This represents the system overall reliability as operational and performance reliabilities were taken into account.

3 CURRENT REGULATIONS AND GUIDANCE IN FINLAND

The basis of Finnish fire regulations is explained below so that it is easier for the reader to understand the starting point of the developed framework.

In prescriptive design of Finnish fire regulations [5] there are some benefits available when using sprinkler system, such as larger fire compartments, mitigations in surface classes and lower fire resistance requirements of load-bearing structures. Moreover, some types of buildings are not allowed without sprinkler system (e.g. more than two-storey timber buildings). The benefits in surface classes and in fire resistance requirements are often relatively small, e.g. B-s1, d0 → C-s2, d1 or R120 → R90.

Finnish fire regulations have allowed performance-based fire engineering generally since 1997, and it is relatively often applied in larger projects. However, there is not much guidance related to acceptable methods and design criteria. The last revision of fire regulations [5] includes more guidance and requirements related to SFE, such as:

- The required fire resistance of essential load-bearing structures in a fire (varying between 30 minutes without cooling phase to the full fire duration depending on the building type)
- Design fire load density (in most cases 80 % fractile should be used, and in some cases the minimum value is limited to 600 MJ/m^2 or 900 MJ/m^2. In buildings with more than two storeys and more than 28 m in height, 80 % fractile value should be multiplied by factor 2).
- Guidance specifying when localized fire can be used and when flashover should be assumed to be occurred (average smoke layer temperature 500 °C or more, or the radiation intensity from smoke layer to floor is at least 20 kW/m^2)
- Guidance on how to account sprinkler system in design: "*In design of the load-bearing structures that is based on a design fire scenario, a slower rise in temperature and the cooling of load-bearing building elements may be taken into consideration provided that the building is provided with an automatic fire-extinguishing system that is suitable for its purpose*."

From authors' perspective, the abovementioned guidance can be useful and add clarity in SFE-projects, however there are also some items that are not logical:

- Arbitrary (or so it seems) fire load factor 2 in buildings that are higher than 28 m and have more than two storeys. This can create huge difference in the fire risks e.g. between 27 and 29 m high buildings, which does not make sense in performance-based engineering.
- The guidance related to sprinkler system is vague which can lead to in similar buildings totally different design solutions depending on the assumptions made. Consistent level of crudeness should also apply to guidance (now the fire load is specified in detail but the guidance related to sprinkler is vague).

In summary, it is often unclear what and how conservative assumptions related sprinkler system should be made so that the design solution represents the desired/required level of safety.

4 DIFFERENT APPROACHES TO ACCOUNT SPRINKLER SYSTEM IN SFE

As mentioned, there are multiple different options to account sprinkler system in structural fire design. Feasible approach depends on the level of analysis (e.g. CFD-analysis / zone model / parametric fire curve, etc) and the desired level of conservatism (which is related also to other factors, e.g. the fractile of design fire load).

Tables 2 and 3 present different approaches to take sprinkler system into account in design, such as reducing the fire area (e.g. to localized fire / protection area of sprinkler system), taking advantage of the cooling effect and reducing heat release rate (HRR) of the design fire curve. The most conservative approach is naturally not to take the sprinkler system into account in any way.

Table 2 presents the assumptions that are recommended in the proposed framework and Table 3 presents also alternative options which can be useful in some cases.

In the proposed framework, the cooling effect and reduction in the fire area can be taken into account as shown in Table 2. It is recommended that HRR of the design fire is not reduced locally in SFE (e.g. by “cutting” the HRR curve after the sprinkler activation). However, it should be noted that the reduction in fire area also reduces HRR as the fire doesn’t spread as much as it would spread without sprinkler system. Reduction in fire area can be taken into account in different types of methods such as parametric fires, zone models, CFD. Cooling effect can be taken into account only in advanced methods as in CFD.

Table 2. Recommended conservative assumptions for modelling sprinkler system in SFE.

Level of conservatism	Reduction in fire area	Cooling effect, but at least 1 critical spr-head not operating	Cooling effect as full	Reduction in HRR
Conservative (C)	Yes	-	Yes	No
Very Conservative (VC)	Yes	Yes	-	No
Extremely Conservative (EC)	Yes	No	No	No
Not taken into account (-)	No	No	No	No

Table 3. Alternative assumptions for modelling sprinkler systems in SFE.

Level of conservatism	Reduction in fire area	Cooling effect, but at least 1 critical spr-head not operating	Cooling effect as full	Reduction in HRR
Realistic (R)	Yes	-	Yes	Yes
Alternative Conservative (AC)	Yes	No	No	Yes

The alternative assumptions presented in Table 3 are not recommended for actual structural fire design in this framework. Realistic (R) assumptions per Table 3 may be useful e.g. when remodeling an actual fire where sprinkler system operated or to understand better the realistic performance in design case. Alternative Conservative (AC) assumptions are often used e.g. in egress analysis, and it used to be more popular in SFE before the cooling effect could be taken into account in the fire simulation software.

It is noted that there are also other methods to take sprinkler system into account in SFE, such as in EN 1991-1-2 Annex E, where the design fire load can be reduced if there is sprinkler system in the considered building. However, it is assumed that this method and reduction of fire load is based on risk analysis (similar as presented in Figure 2): the probability that sprinkler system doesn’t operate, and high fire load occurs in the critical location, is very low, and lower fire load fractile can be justified. Therefore, this method is not considered as an actual modelling of sprinkler system.

5 PROPOSED FRAMEWORK

5.1 General

The proposed framework is based on the guidance given by the Finnish fire regulations [5] (described in Chapter 3) and experience from multiple SFE-projects. The goal of this framework is to systematize SFE procedure in the case where sprinkler system is applied so that:

1. Sprinkler system is taken into account in the design and
2. The risks related to the case where sprinkler system does not operate as designed, are tolerable

The steps to use the proposed framework are as follows:

1. Determine the risk category of the building (Table 4: Low, Low+, Moderate, Moderate+, High, High+)
2. Determine the Basis of Design (BOD) for SFE-analysis where sprinkler system is taken into account (Table 5: BOD 1a or 1b)
    - The BOD in this context contains the fractile of the fire load, the level of conservatism applied for sprinkler system and the acceptance criteria.
    - BOD 1a assumes that the sprinkler system is modelled in the analysis, e.g. by using CFD-tools.
    - BOD 1b assumes that the sprinkler system is not modelled in the analysis (e.g. parametric fire curve), and the effect of sprinkler system is taken into account in the design fire load (in similar way as in EN 1991-1-2 [6]).
3. Determine the BOD for SFE-analysis where sprinkler system is not taken into account in any way (Table 6: BOD 2)
    - BOD 2 is used as an additional check to ensure that also in extremely severe scenario there is enough time to evacuate from the building. It is assumed that in most cases it is relatively simple to verify that the design meets the acceptance criteria of BOD 2.
4. Conduct the analysis using BOD 1a or 1b and BOD 2

5.2 Classification of buildings

The proposed framework is based on similar classification of buildings as Finnish fire regulations regarding to SFE. The Risk categories' names from *Low* to *High+* have been proposed for the purpose of this framework. Note, that institution refers here to hospitals, nursing homes, etc.

Table 4. Classification of buildings in different risk categories.

<table>
<tr><th>Risk Category</th><th colspan="2">Exemplar building(s)</th></tr>
<tr><td>Low</td><td colspan="2">One storey, general, height no greater than 9 m</td></tr>
<tr><td>Low+</td><td colspan="2">Two-storey, general, height no greater than 9 m</td></tr>
<tr><td>Moderate</td><td>One-storey:
- accommodation premise with more than 50 places
- institution with more than 25 places
- assembly and business premise with more than 250 people</td><td>One-storey, general, height exceeding 9 m</td></tr>
<tr><td>Moderate+</td><td colspan="2">Two-storey, general, height exceeding 9 m</td></tr>
<tr><td>High</td><td>Two-storey:
- accommodation premise with more than 50 places
- institution with more than 25 places
- assembly and business premise with more than 250 people</td><td>More than two storeys, height no greater than 28 m</td></tr>
<tr><td>High+</td><td colspan="2">More than two storeys, height exceeding 28 m</td></tr>
</table>

5.3 Basis of design

The basis of design (BOD) of the proposed framework are described in the following (Table 5 and 6). The BOD depends on the consequences of the failure. The assumptions become more conservative as the consequences increase. It should be noted that BOD is given only at high level. The designer needs to define the actual fire scenarios, design fires and their locations in detail. It is recommended that the whole process is conducted in close co-operation with the relevant stakeholders (building user, design team, building and fire authorities) to achieve an agreement on the feasible fire scenarios and design fires for the project.

Table 5 presents BOD 1a and 1b as described below:

- The first value indicates the applied fractile for the design fire load (50 %, 80 % or 95 %)
- The second value indicates the assumptions related to the operation of sprinkler system (C, VC, EC, -, see also Table 2).
- Acceptance criteria 1 (same for BOD 1a and 1b) indicates the period that the load-bearing structure must resist the fire.

Either one of BOD 1a and 1b can be applied in the analysis. It is assumed that BODs 1a and 1b are approximately as severe scenarios. In BOD 1a, it is assumed that sprinkler operates at some level, and relatively high fire load fractile should be applied. In BOD 1b the fire load fractile is smaller, but the assumptions related to sprinkler system are more conservative (does not operate or only controls the area of the fire). It should be noted that the design fire load fractile 80 % in BOD 1a is based on Finnish regulations, and the reduction in design fire load fractile in BOD 1b is based on the following reasoning:

- EN 1991-1-2 Table E.2 allows to reduce the design fire load by factor 0,61 if building has sprinkler system. Per EN 1991-1-2 Table E.4, the average value of fire load in different occupancies is approximately 0,82 x the 80 % fractile. Therefore, it can be concluded that EN 1991-1-2 allows to use lower values for design fire load than the average value of fire load (0,61 < 0,82).
- In this framework at least 50 % fractile of fire load is recommended for all cases to increase the robustness of the design solution. Therefore, it can be concluded that BOD 1b is on the safe side compared to EN 1991-1-2.

Using the values of Table 5, the probability that the chosen fire load is exceeded is 2 – 2,5 times higher in BOD 1b than in 1a (50 % / 20 % = 2,5 in Low – High, 10 % / 5 % = 2 in High+).

Table 5. Basis of Design (BOD) 1a and 1b (fractile of the fire load, the level of conservatism applied for sprinkler system and the acceptance criteria by risk category of the building).

	Risk Category of the Building					
	Low	Low+	Moderate	Moderate+	High	High+
BOD 1a	80 % C	80 % * VC	80 % VC	80 % * VC	80 % * VC	95 % ** VC
BOD 1b	50 % EC	50 % -	50 % -	50 % -	50 % -	90 % -
Acceptance Criteria 1 – Required fire resistance time	30 min	30 min	60 min	60 min	Full Fire	Full Fire

* At least 600 MJ/m^2

** At least 900 MJ/m^2

Table 6 presents BOD 2 similarly. As mentioned earlier, BOD 2 can be considered as an additional check to ensure that even in extremely severe case there is still enough time to evacuate the building. Therefore, sprinkler system is not considered, and relatively high fractile for fire load is applied. The RSET-value needs to be obtained from egress simulations.

Table 6. Basis of design (BOD) 2 (fractile of the fire load, the level of conservatism applied for sprinkler system and the acceptance criteria by risk category).

Risk Category	Low	Low+	Moderate	Moderate+	High	High+
BOD 2	80 % -	80 % * -	80 % -	80 % * -	80 % * -	95 % ** -
Acceptance Criteria 2 – Required fire resistance time	RSET	RSET	RSET	RSET	RSET	RSET

* At least 600 MJ/m^2

** At least 900 MJ/m^2

6 CASE STUDY – STEEL TRUSSES OF A MUSIC HALL

6.1 Introduction and SFE-analysis

The considered music hall will be located in Vaasa, Finland. It is a part of a larger building complex Wasa Station, which includes shopping centre, hotel and apartments (at left in Figure 3). The whole building will be equipped with sprinkler system.

The roof structure of the music hall will be built of steel trusses (at right in Figure 3). The prescriptive requirement for these trusses per [5] is R60.

SFE analysis were done to optimize the fire protection of the trusses which locate relatively high from the floor in the music hall. Fire simulations were conducted using FDS-software (Fire Dynamics Simulator [13]) and SFE-analysis were done using SAFIR -software [14]. The design fires included the fires of the stand, stage and different lofts as shown in Figure 4. Figure 4 also shows the FDS-model including the steel trusses and the devices measuring the Adiabatic Surface Temperatures (AST) (in yellow) [15]. AST:s are used to transfer the temperatures from fire simulations to structural analysis. AST method takes into account the convective and radiative heat transfer between the gas and the solid structure and converts them to a single equivalent AST value.

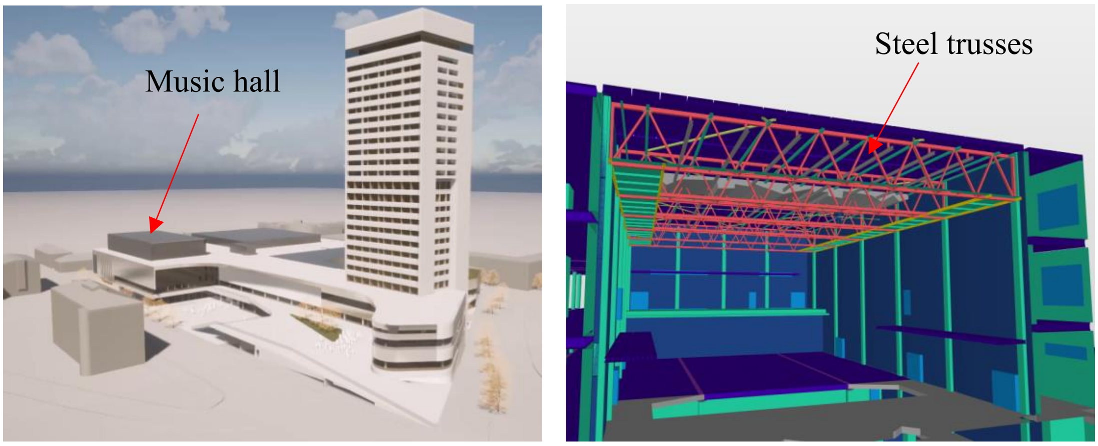

Figure 3. Considered building (at left) and the steel trusses of the music hall (at right).

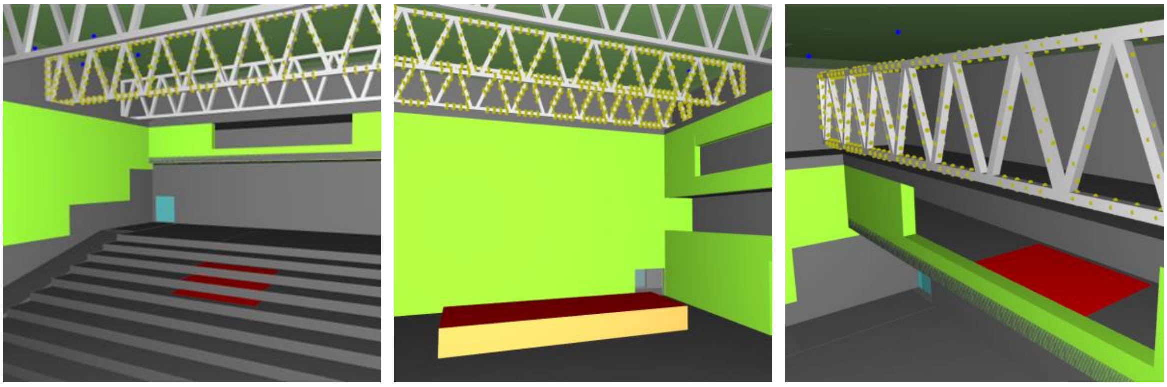

Figure 4. Design fires in the FDS-model: stand fire (at left), stage fire (in the middle) and loft fire (at right).

6.2 Applying the sprinkler system in design

The music hall is approximately 15 m high and has 3 stories and the total number of people is 1350. Therefore, the risk category of the building per Table 4 is "High". It should be noted that the risk category of the higher part of the building is "High+". However, in this case the tower is in different fire compartment with the music hall and therefore left out of this consideration. Per Table 5 and 6, the following design Basis of Design (BOD) should be applied in the design (BOD 1a or 1b and BOD 2):

- BOD 1a (sprinkler system taken into account):
    - Fire load fractile: 80 % (at least 600 MJ/m^2)
    - Assumptions related to sprinkler system: Very Conservative per Table 2
    - Acceptance criteria: resistance for full fire duration
- BOD 1b (sprinkler system not taken into account):
    - Fire load fractile: 50 %
    - Sprinkler system is not taken into account
    - Acceptance criteria: resistance for full fire duration
- BOD 2
    - Fire load fractile: 80 % (at least 600 MJ/m^2)
    - Sprinkler system is not taken into account
    - Acceptance criteria: resistance for RSET -time

In this case, the fire simulations were conducted using FDS where sprinkler system can be modelled. Therefore, BOD 1a was selected to be applied in the analysis. Per Table 2, the reduction in fire area and cooling effect can be taken into account. However, at least one sprinkler head should be non-operative. Moreover, the heat release curve of the design fire should not be reduced. In the final FDS-analysis, all the sprinkler heads above the design fire were conservatively assumed to be non-operative (see also Figure 5).

The egress simulations showed that the required safe egress time (RSET) for the music hall was at maximum approximately 11:30 min. Typically unprotected steel structures with similar dimensions as in this case, achieve approximately at least 13 – 15 minutes fire resistance in extremely severe conditions (standard fire). Therefore, it was concluded that the acceptance criteria of BOD 2 were met in this case.

Figure 5. Example of taking sprinkler system into account in the analysis: stand fire at left, stage fire at right.

6.3 Results

Figure 6 shows a visualization of the stand fire (at left) and stage fire simulations (at right). It can be seen that the sprinkler heads directly above the design fire are not operating. Figure 7 shows the heat release rates in the simulations (input vs. output).

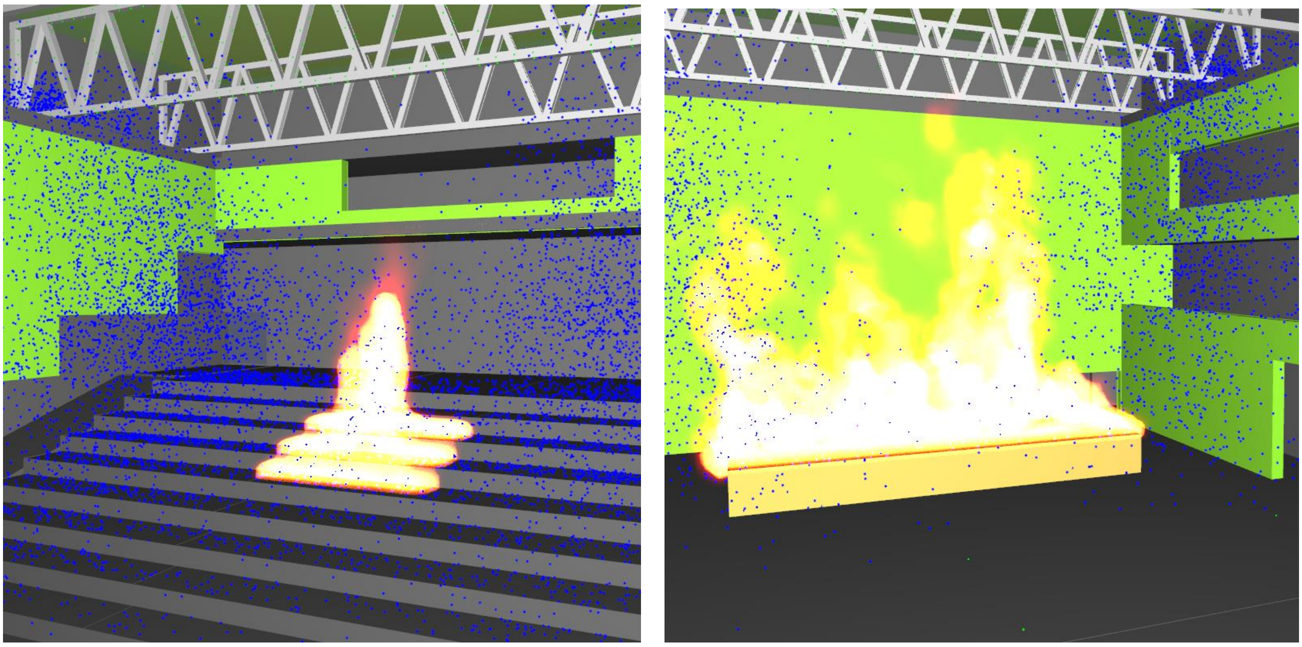

Figure 6. Visulization of the fire simulations where sprinkler system is taken into account conservatively (stand fire at left, stage fire at right).

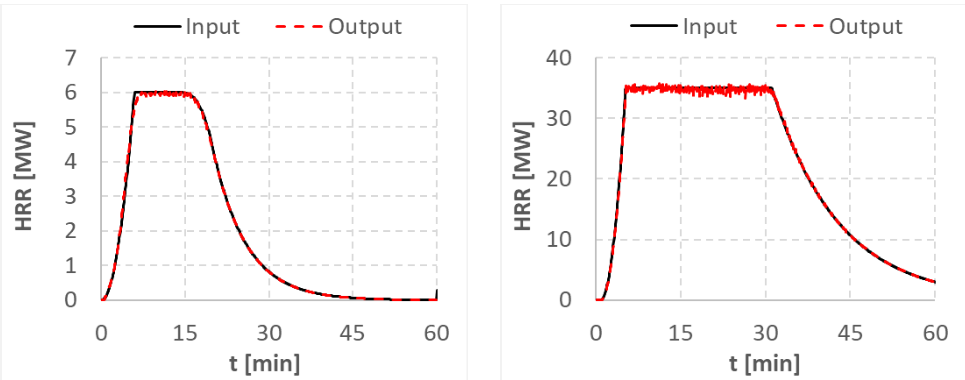

Figure 7. Heat release rates in the simulation (stand fire at left, stage fire at right).

Based on the conducted analysis, it was concluded that the stage fire is the most critical fire scenario for the steel trusses. Figure 8 presents the temperature development of the hottest steel profile in the stage fire. The temperatures were compared to the corresponding critical temperatures per EN 1993-1-2 [16]. It should be noted that this comparison of temperatures is done for preliminary design and the final design is done using advanced structural calculations with SAFIR-software. Figure 9 presents the SAFIR-model of the most critical steel truss. The deformations of the steel truss (scaled by factor 10, presented on blue color) are plotted at 30 minutes, which is approximately the time when the steel profiles reach their maximum temperature.

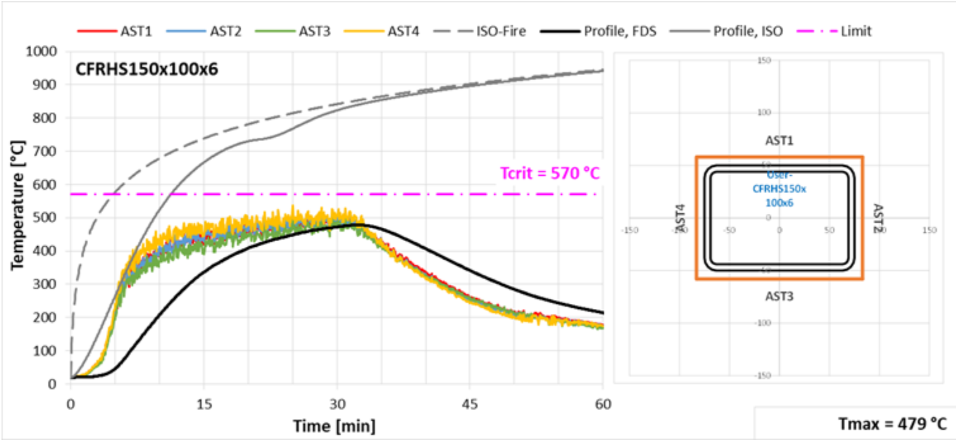

Figure 8. Temperature development of the hottest steel profile in the most critical fire scenario (stage fire).

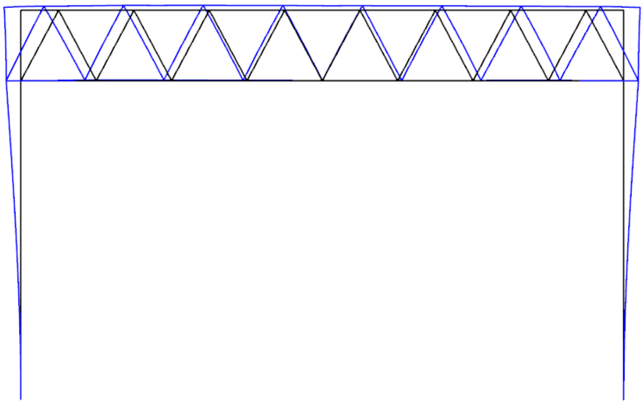

Figure 9. SAFIR-model of the most critical steel truss and columns. Displacements at 30 minutes of stage fire on blue colour (scaled by factor 10).

Based on the conducted SFE-analysis it is concluded that unprotected steel trusses were able to resist the full fire durations, including the cooling phase. Therefore, no passive protection was required for the truss profiles. The columns need to be fire protected to the prescriptive class R60.

7 CONCLUSIONS

The following general conclusions related to utilizing sprinkler system in SFE are drawn in this paper:

- Sprinkler system can be very reliable and effective way to reduce fire risks in buildings if maintained properly.
- There are multiple options to account sprinkler system in SFE.
- However, there is a lack of consistent guideline or framework (at least in Finland) which may lead to totally different structural fire design in similar buildings, depending on the interpretation and assumptions made.

This paper proposes a framework to include sprinkler system in SFE. The framework is based on the guidance given by the Finnish regulations and experience from multiple SFE-projects. The goal of this framework is to systematize SFE procedure in the case where sprinkler system is applied so that sprinkler system can be taken into account in the design and the risks related to the case where sprinkler system does not operate as designed, are tolerable. Based on the experience gained from projects (e.g. the case presented here), the framework seems to be feasible for typical SFE-applications.

REFERENCES

1. Salminen, M., Nieminen, M. & Malaska, M.. Sprinklerilaitteiston luotettavuuden vaikutus teräsrakenteiden palomitoitukseen. Rakenteiden Mekaniikka, Vol. 52, Nro 1, 2019, pp. 23-37 (In Finnish).
2. Outinen, J. & Kansa, J., Fire protection of steel structures using sprinkler systems. Proceedings – Nordic Steel Construction Conference 2009: Malmö, Sweden, September 2-4, 2009.
3. Outinen, J. & Vaari, J., Fire Protection of Tall Steel Columns using Water Sprinklers. Application of Structural Fire Engineering, 19-20 April 2013, Prague, Czech Republic, 2013.
4. Zelinka, S., Hasburgh, L.E., Bourne, K.J., Tucholski, D.R., Ouellette, J.P., Compartment Fire Testing of a Two-Story Mass Timber Building. General Technical Report FPL-GTR-247. USDA – United States Department of Agriculture, Forest Service, Forest Products Laboratory, May 2018.
5. Ympäristöministeriö. Ympäristöministeriön asetus rakennusten paloturvallisuudesta annetun ympäristöministeriön asetuksen muuttamisesta 927/2020 (Finnish Fire Regulations, In Finnish), 2020.
6. EN 1991-1-2. Eurocode 1: Actions on structures. Part 1-2: General actions. Actions in structures exposed to fire. CEN. Brussels, 2003.
7. Ahrens, M., US Experience with Sprinklers, National Fire Protection Association NFPA, Quincy, MA, USA, 2021.
8. Ahrens, M., US Experience with Sprinklers, Supporting Tables, National Fire Protection Association NFPA, Quincy, MA, USA, 2021.
9. Nieminen, M., Rakennusten automaattisten sprinklerilaitteistojen luotettavuus. M.Sc. Thesis. Tampere University (In Finnish), 2018. Available: https://trepo.tuni.fi/handle/123456789/25673
10. Optimal Economics, Efficiency and effectiveness of sprinkler systems in the United Kingdom: An analysis from fire service Data, 2017.
11. Frank, K., Spearpoint, M. & Challands, N., Uncertainty in estimating the fire control effectiveness of sprinklers from New Zealand fire incident reports. Fire Technology. 50, 2012, s. 611-632. DOI: 10.1007/s10694-012-0297-2
12. Salminen, S., Nieminen, M. & Malaska, M., Determination of sprinkler system reliability and its effect on structural fire design of steel structure. 9th International Conference on Steel and Aluminium Structures (ICSAS19), 3-5 July 2019, Bradford, UK, 2019.
13. McGrattan, K., McDermott, R., Hostikka, S., Floyd, J, & Vanella, M., Fire Dynamics Simulator (Version 6). User' Guide. NIST Special Publication 1019, 2022.
14. Gernay, T., Franssen, J.M., "Modeling structures in fire with SAFIR®: Theoretical background and capabilities". Journal of Structural Fire Engineering, Vol. 8, issue 3, 2017, pp. 300-323.
15. Wickström, U., McGrattan, K., Adiabatic surface temperature for calculating heat transfer to fire exposed structures. Proceedings of the Eleventh Interflam Conference, 2007.
16. EN 1993-1-2, Eurocode 3: Design of steel structures. Part 1-2: General rules. Structural fire design, Brussels, European committee for standardization, 2005. 83 p.

SiF 2022– The 12th International Conference on Structures in Fire
The Hong Kong Polytechnic University, Nov 30 - Dec 2, 2022

STEEL FAILURE OF ANCHORS MADE OF C-STEEL UNDER FIRE CONDITIONS – A PROPOSAL FOR A NEW DESIGN CRITERION ACCORDING TO EN 1993-1-2

Samir Haddadi[1], Omar Al-Mansouri[2]

ABSTRACT

The use of post-installed and cast-in anchors is a world-wide practice. They are needed for structural and non-structural connections. They can offer high load-bearing capacity and ease of use for various types of systems. Their design covers a variety of failure modes at ambient temperature (e.g., concrete cone breakout, pull-out, steel...). Under fire conditions, the load-bearing capacity of these systems decreases for all failure modes and can lead to the failure of the connection that can no longer withstand the applied loads.

Currently, the resistance to steel failure under fire conditions can be either evaluated according to EAD 330232 or calculated according to EN 1992-4, Annex D. The EN 1992-4 method offers a suitable alternative without testing to get default values of resistance to steel failure under fire conditions. However, it can be very penalizing for commercial threaded rods with high steel grades as it does not take the steel grade into consideration. When this method was developed, it was validated against a limited number of fire tests. In addition, it offers fire ratings (i.e., resistance for a given fire exposure time) that are limited to 30, 60, 90 and 120 min.

This paper presents two alternative fire design methods for steel failure mode of commercial threaded rods made of carbon steel (c-steel). Reduction factors applicable to the ultimate tension steel strength of c-steel are used according to EN 1993-1-2 Tables 3.1 and D.1. These methods determine the reduction factor based on the temperature of the steel rod with fire exposure time. The temperature was calculated numerically using FE simulation of transient thermal analysis, using the commercial software ANSYS. The anchors were modelled in uncracked concrete and ISO 834-1 fire conditions were applied to the fire exposed surfaces.

The study is based on three test campaigns with over 270 fire tests resulting in steel failure, carried out in three different laboratories (CSTB, TU Kaiserslautern and IWB Stuttgart) according to EOTA TR 020. The database includes 6 anchor sizes (M6, M8, M10, M12, M16 and M20) and steel grades (5.6, 5.8, 8.8 and 12.9) according to ISO 898-1. The observed steel failure mode on the specimens was either failure of the shaft or the nut (melting of threads). The influences of anchor diameter and steel grade are presented. The precision of each method (current one according to EN 1992-4, Annex D, EN 1993-1-2 Tables 3.1 and D.1) against the database is evaluated and discussed. Consequently, recommendations for adoption of rational-based methods such as the ones presented in this paper are given for design purposes in the conclusions of this work.

Keywords: steel-failure, nut failure, rod failure, commercial threaded rods, fire conditions, post-installed, cast-in place anchors

[1] Intern, Centre Scientifique et Technique du bâtiment (CSTB), Champs-sur-Marne, France
e-mail: samirhaddadi21@gmail.com
[2] Dr., Studies and Assessment Engineer, R&D Project Manager, Centre Scientifique et Technique du Bâtiment (CSTB), Champs-sur-Marne, France
e-mail: omar.almansouri@cstb.fr, ORCID: https://orcid.org/0000-0002-4458-9182
https://doi.org/10.6084/m9.figshare.22153496

1 INTRODUCTION

Anchorage systems are becoming increasingly important in civil engineering and construction works all over the world. Anchors ensure the transfer of loads from various building elements to the base material (e.g., concrete). The load transfer between anchorage and concrete can be ensured by mechanical connections (threading, locking, expansion) or by adhesion (organic or inorganic bonding). Anchors loaded in tension can show different failure modes: steel, concrete cone, pull-out, combined pull-out and concrete (for bonded anchors), concrete splitting, and concrete blow-out (for cast-in headed studs) [1]. Although millions of fasteners are installed worldwide, knowledge of this technology is in continuous development. Several research studies have been conducted for decades to evaluate and improve the strength of anchors. The behaviour of fasteners can be influenced by several parameters: environmental and accidental conditions such as temperature, atmosphere, fatigue, earthquakes or fire can cause anchors to undergo effects that degrade the resistance in different modes of failure, which can cause human and material losses.

Fire exposure of anchor systems is an essential justification for certain construction projects. Assessment and test conditions of mechanical anchors exposed to fire may be performed in accordance with EAD 330232-01-0601 [2], and the design in accordance with the EN 1992-4, Annex D [1]. Recommendations for assessment, testing and design of bonded anchors under fire conditions are being developed in EOTA (European Organisation for Technical Assessment).

The focus of this research is on the steel failure of anchors under fire. Assessment is usually done by testing in accordance with the testing conditions of EOTA TR 020 [3]. In EN1992-4, tables D.1 and D.2 give a design method for unprotected steel part of anchors exposed to fire conditions. For steel failure under fire conditions, research studies were conducted by Reichert (2020) [4], based on experimental data of anchors under fire with steel failure. A comparison was made between the values obtained by the evaluation according to (EOTA TR 020, 2009) and a method based on the reduction factors given by the EN 1993-1-2 [5] applied on the temperature of the anchor taken experimentally and numerically. The fire resistance according to the TR 020 were the most conservative values. The outcome of this proposal was a review of the steel stress values given by EN 1992-4, tables D.1 and D.2. However, the proposal is empirical (based on highly scattered fire tests), and no correlation was made between the steel grade and the appropriate reduction under fire conditions.

In this work, a method for design of the steel failure of anchors under fire is presented. The model considers the influence of the anchor diameter, also the steel grade. The model is rational, e.g., based on the calculation of the temperature field along the anchor. The thermal distribution along the anchor is determined at each time during the fire exposure by a finite element model of the anchorage configuration (anchor installed in concrete). The temperature as a function of time is then used to calculate the resistance of the steel by associating it with the reduction factors applicable for c-steel in EN 1993-1-2 [5]. Thermal properties of the materials (c-steel and concrete) are a function of temperature were taken from the Eurocodes 2 and 3.

2 DESCRIPTION OF TEST CAMPAIGNS

2.1 Description of fire tests

The testing campaigns presented in this paper were conducted in three different laboratories, *Centre Scientifique et Technique du Bâtiment* (CSTB), France, *Technische Universität Kaiserslautern* (TUK), Germany and *Institut für Werkstoffe im Bauwesen* (IWB Stuttgart), Germany. The tests were conducted according to the specifications of EOTA TR 020 [3]. The tested anchor types were headed studs, post-installed mechanical anchors (torque-controlled expansion anchors and wedge anchors) and post-installed bonded anchors with 6 anchor sizes (M6, M8, M10, M12, M16 and M20) and steel grades (5.6, 5.8, 8.8 and 12.9). The test conditions were the same for all the campaigns, a constant tension load was applied to the anchor and ISO 834-1 [6] fire conditions were applied to the exposed surfaces as it shown in

Figure 1. The tests were conducted until anchor failure under constant load. For each test, the applied load and time of failure were reported.

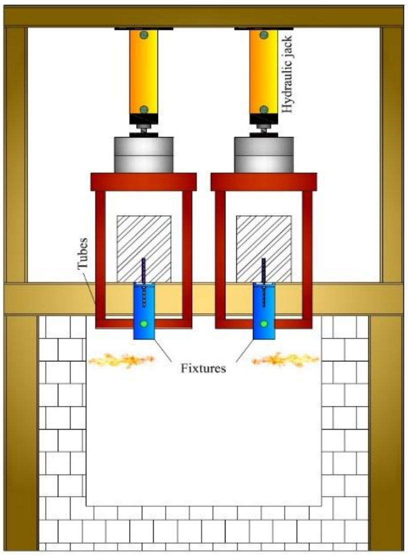

Figure 1. Gas furnace and loading system (CSTB) [7]

2.2 Summary of tested anchors

CSTB's test campaign contained mechanical anchors (2 types of torque-controlled expansion anchors and wedge anchors), bonded anchors (with epoxy and acrylate-based adhesives) and headed studs. TUK's test campaign also contained mechanical and bonded anchors with different diameters. IWB's test campaign contained cast-in-place anchors (headed studs) and bonded anchors. The total of tested anchors is 271, all performed in uncracked concrete. All the tests resulted in steel failure, the failure was observed in the rod (shaft failure) or the nut (melting of threads).

3 NUMERICAL MODEL

3.1 Description of the model

This section describes the numerical model used for the determination of temperature distribution of an anchors in uncracked concrete under ISO 834-1 fire conditions [6].Temperature profiles are then used to determine the steel failure resistance of anchors under fire.

The numerical model is based on the geometry shown in Figure 2. The geometry is a model of a metallic rod anchored in a concrete cylinder. A 2D axisymmetric simplification has been considered for this study. The external part of the anchor and the bottom part of the concrete cylinder are directly exposed to fire, the upper part is exposed to ambient air and the lateral surfaces are supposed under adiabatic conditions.

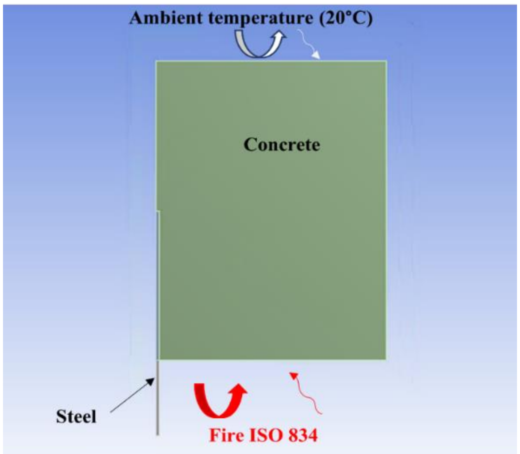

Figure 2. Boundary conditions applied in the heat transfer model for anchors exposed to fire conditions

The study consists of a numerical resolution of the heat conduction equation, and this is done via a finite element simulation of transient heat transfer analysis. Heat transfer is done by convection and radiation between fire gas temperature (as a function of time) and the exposed surfaces and also between ambient temperature (constant with time) and unexposed surfaces. The governing Partial Differential Equation (PDE) of the model is the heat conduction equation (without energy source) expressed in Equation 1:

$$\rho c \frac{\partial T}{\partial t} = k \nabla^2 T \qquad \text{Equation 1}$$

For the 2D axisymmetric case, the expression is presented in Equation 2:

$$\rho c \frac{\partial T}{\partial t} = \frac{\partial}{r \partial r}\left(kr \frac{\partial T}{\partial r}\right) + k \frac{\partial^2 T}{\partial z^2} \qquad \text{Equation 2}$$

The boundary conditions of the studied problem are second-type conditions (Neumann conditions), and are outlined in the following paragraph. The heat flux exchanged by convection and radiation on the exposed surfaces is expressed by Equation 3, the part exposed to ambient air (unexposed surfaces) is expressed in Equation 4. The heat exchange coefficients for convection and radiation are taken according to EN 1991-1-2 [8].

$$-k \frac{\partial T}{\partial n} = h_{fire}\left(T_s - T_{fire}\right) + \varepsilon.\sigma\left(T_s^4 - T_{fire}^4\right) \qquad \text{Equation 3}$$

$$-k \frac{\partial T}{\partial n} = h_{air}(T_s - T_{air}) + \varepsilon.\sigma(T_s^4 - T_{air}^4) \qquad \text{Equation 4}$$

And for the lateral part (adiabatic), no heat transfer (Equation 5):

$$-k \frac{\partial T}{\partial n} = 0 \qquad \text{Equation 5}$$

Where:

ρ	is the density (kg/m^3).
c	is specific heat (J/kg·K).
k	is the thermal conductivity (W/m·K).
h_{fire}	is the convective heat transfer coefficient for the fire exposed surface (25 W/m²·K).
h_{air}	is the convective heat transfer coefficient for the surface exposed to ambient air (4 W/m²·K).
ε	is surface emissivity (0.7).
σ	is the Stephan-Boltzmann constant (5.667×10-8 W/m²·K4).
T_s	is the solid surface temperature (K).
T_{feu}	is the fire temperature (K).
T_{air}	is ambient temperature (K).

The geometric values correspond to those of a tension test of anchors on concrete cylinders. The two materials used in this study (c-steel and concrete) are in perfect interaction with each other, i.e., perfect contact at both interfaces is modelled in ANSYS. The thermal and physical properties (thermal conductivity, specific heat, and density) of concrete and c-steel are time dependent (see Figure 3) and are taken from the Eurocode 3 part 1-2 [5]. The density of the steel is considered constant with respect to temperature, and its value is $\rho = 7850$ kg/m^3.

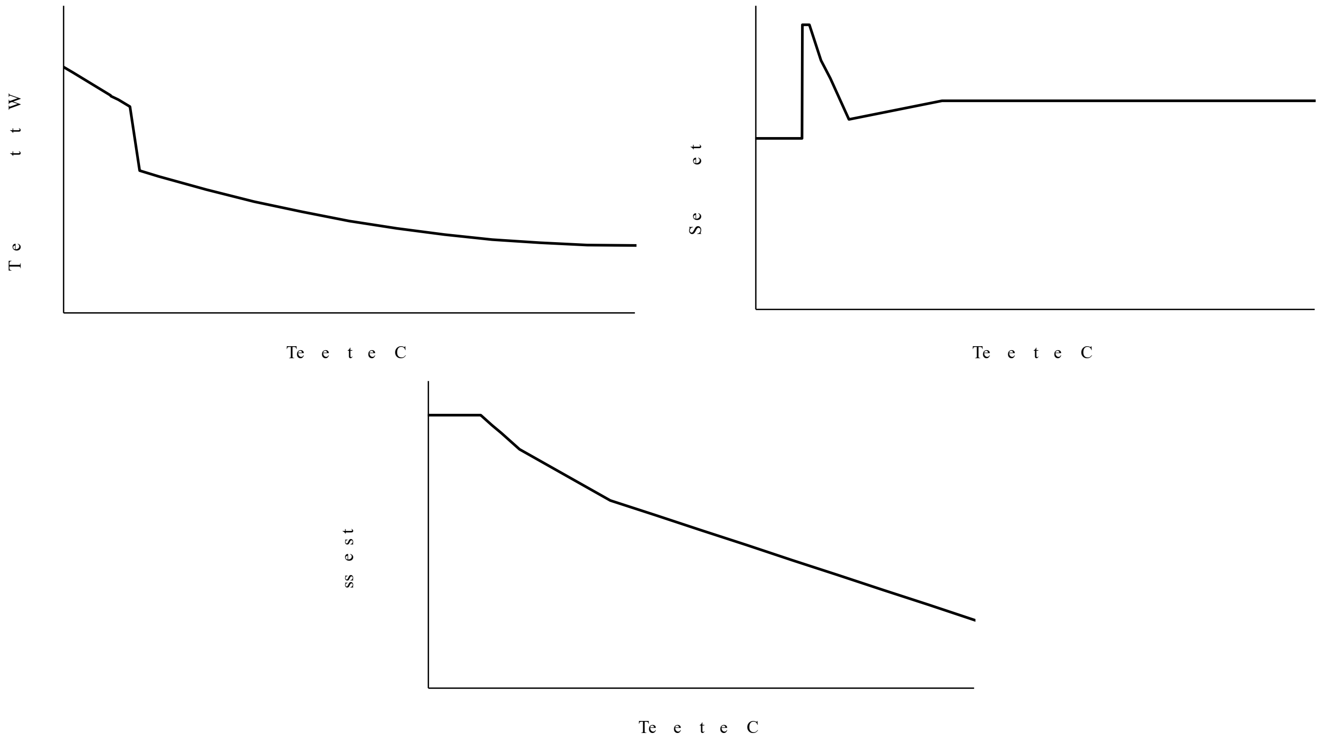

(a) Concrete

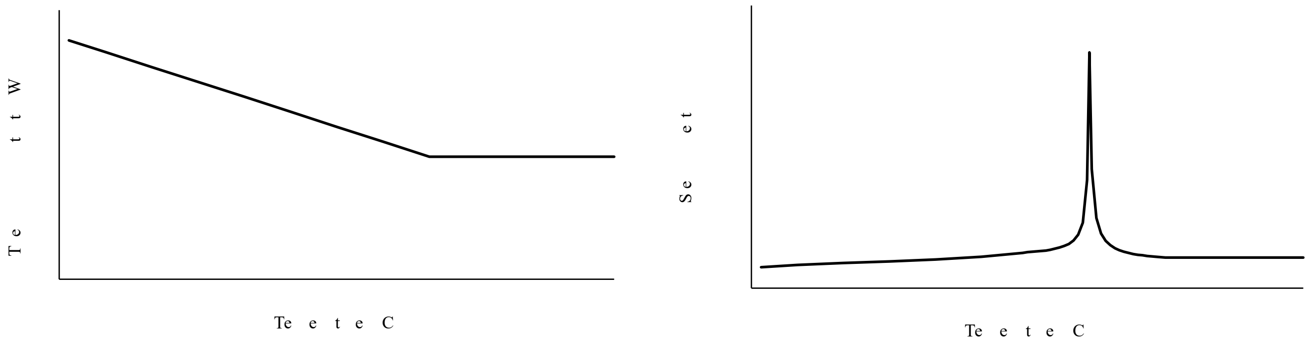

(b) Steel

Figure 3. Thermal properties of concrete and steel

3.2 The influence of anchor diameter on the temperature

The diameter of the anchor is an influential parameter to be taken into account. A study of the influence of the diameter on the maximum temperature along the rod was conducted on anchor nominal diameters from M6 to M39 (according to the scope of EN 1992-4). Figure 4 shows the maximum temperature along the rod of the anchor as a function of time. Big diameters tend to diffuse heat faster than small diameters, which results in lower maximum temperatures for big sizes, but more homogeneous temperature along the embedment depth of the anchor (inside the concrete).

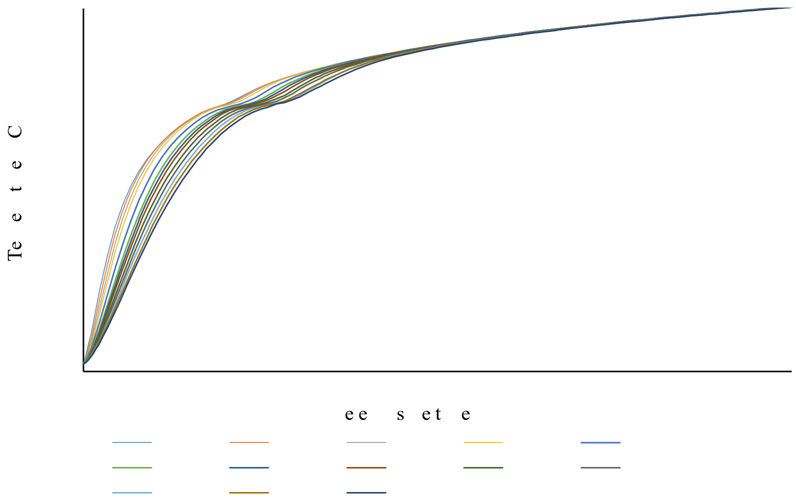

Figure 4. Maximum temperature as a function of time

4 CALCULATION OF THE FIRE RESISTANCE

The characteristic resistance for steel failure of anchors loaded in tension, can be calculated for steel rods having a constant strength along the element, as shown in Equation 6 according to the EAD 330499 [9]:

$$N_{Rk,s} = A_s \cdot f_{uk} \qquad \text{Equation 6}$$

Where:

A_s: = nominal cross section area of the rod.

f_{uk} = characteristic ultimate steel tension strength at 20°C.

In the following, two methods are proposed, the principle being to apply the reduction factor as a function of temperature on the evaluated resistance at ambient temperature.

Method 1

This method applies the ultimate limit reduction factor to the ultimate strength of the steel rod, as shown in Equation 7.

$$N_{Rk,s,fi(t)} = k_{u,\theta} \cdot f_{uk} \cdot A_s \qquad \text{Equation 7}$$

Where:

$k_{u,\theta}$ = reduction factor for the ultimate tension strength under fire conditions. EN 1993-1-2, Table 3.1 provides the factor $k_{y,\theta}$ which is the reduction factor for the yield strength at high temperature. As the main interested of this work is related more to the ultimate strength f_{uk}. Annex A of EN 1993-1-2 allows the determination of the ultimate strength as follow:

For $T < 300°C$

$$f_{u,\theta} = f_{u,20°C}$$

For $T \geq 400°C$

$$f_{u,\theta} = f_{y,\theta}$$

For $300°C \leq T < 400°C$

Linear interpolation between $300°C$ and $400°C$

Method 2

This method applies a reduction factor $k_{b,\theta}$ is applied to the ultimate resistance of the bolts made of steel, as expressed in Equation 8:

$$N_{Rk,s,fi(t)} = k_{b,\theta} \cdot f_{uk} \cdot A_s \qquad \text{Equation 8}$$

$k_{b,\theta}$ = reduction factor determined for the appropriate bolt temperature.

The difference between the two methods is that method 1 takes in consideration the ratio between the tension and yield strength of the steel unlike method 2 that only takes into account the ultimate strength of the steel. According to EN 1993-1-2, Annex A, method 1 express the ultimate tension strength at high temperature in terms of the yield strength for different temperature ranges (20°C-300°C, 300°C-400°C and 400°C-1200°C). Therefore, a steel grade of 5.8 will not have the same ultimate tension strength at high temperature as a steel of 5.6 grade despite the fact that the two grades have the same ultimate tension strength at ambient temperature (500 N//mm²). This is due to the ratio f_{yk}/f_{uk} which is equal to 0.8 for the steel grade 5.8 and 0.6 for the grade 5.6. It should be noted that the characteristic failure strength of steel at ambient temperature is only based on the ultimate tension strength at 20°C without taking this ratio into account. The hypothesis changes at high temperature according to the Annex A of EN 1993-1-2. The other difference between method 1 and method 2 is maximum temperature covered by the reduction factors, which is 1200°C for method 1 and 1000°C for method 2. The influence of this difference will be discussed later.

5 REDUCTION FACTOR FOR STEEL TENSION STRENGTH

5.1 Reduction factor vs. temperature

Steel structures progressively lose their resistance when exposed to fire conditions. In EN1993-1-2 [5], the table 3.1 gives the factor $k_{y,\theta}$ that is related to the yield strength f_y as a function of temperature. Table D.1 in EN 1993-1-2 gives the factor $k_{b,\theta}$ as a function of temperature, which is specific to the reduction of the ultimate tension strength of bolts. The two factors are presented in Figure 5.

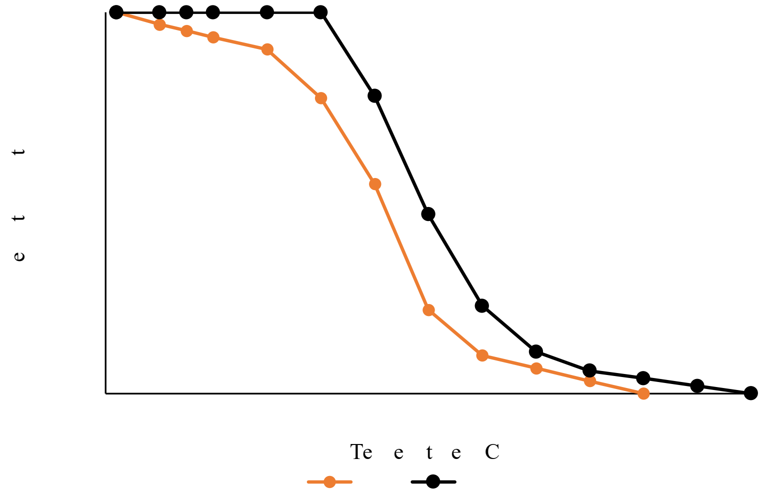

Figure 5. The reduction factors for c-steel

The focus of this study is on the ultimate tension strength f_{uk} of steel, and as the factor $k_{y,\theta}$ given in Table 3.1 of EN 1993-1-2 concerns the yield strength. The idea is to deduce a factor $k_{u,\theta}$ that applies to the ultimate f_{uk} strength from $k_{y,\theta}$, and this for common ratios of rods in the market $f_{yk}/f_{uk} = 0.6; 0.8$ or 0.9 see .

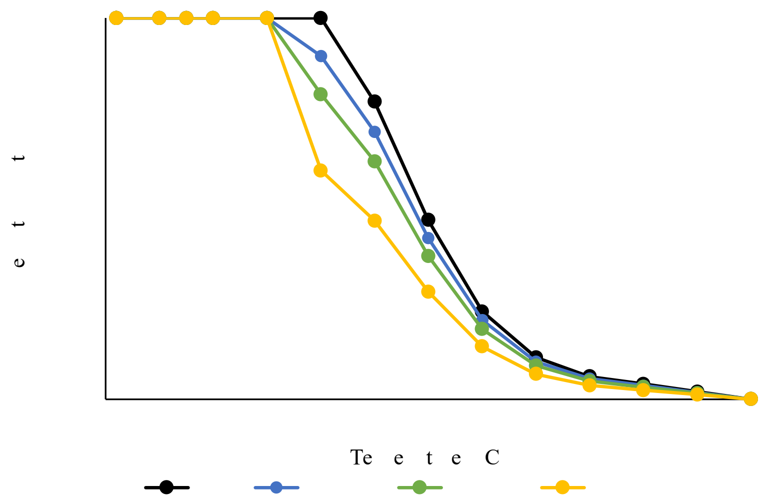

Figure 6.

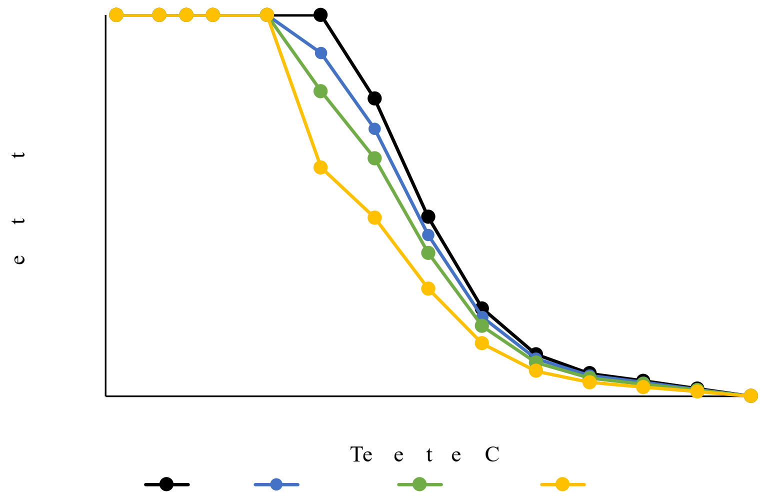

Figure 6. Reduction factor of steel ultimate tension strength as a function of temperature

6 DESIGN MODEL FOR STEEL FAILURE

This method is developed for the design of steel-failure mode of anchors under fire. The principle of the method is based on the reduction of the steel strength at high temperatures, given in the EN 1993-1-2. The steel failure resistance under fire is obtained in two steps; the maximum temperature at the anchor at any time is obtained by thermal calculations using a finite element method. Then, the reduction factor vs. fire exposure time relationship is obtained through the temperature vs. fire exposure time relationship. Finally, the reduction factor is applied to the ultimate tension steel strength at ambient temperature to obtain the steel fire resistance vs. fire exposure time relationship. An illustration of the method is presented in Figure 7.

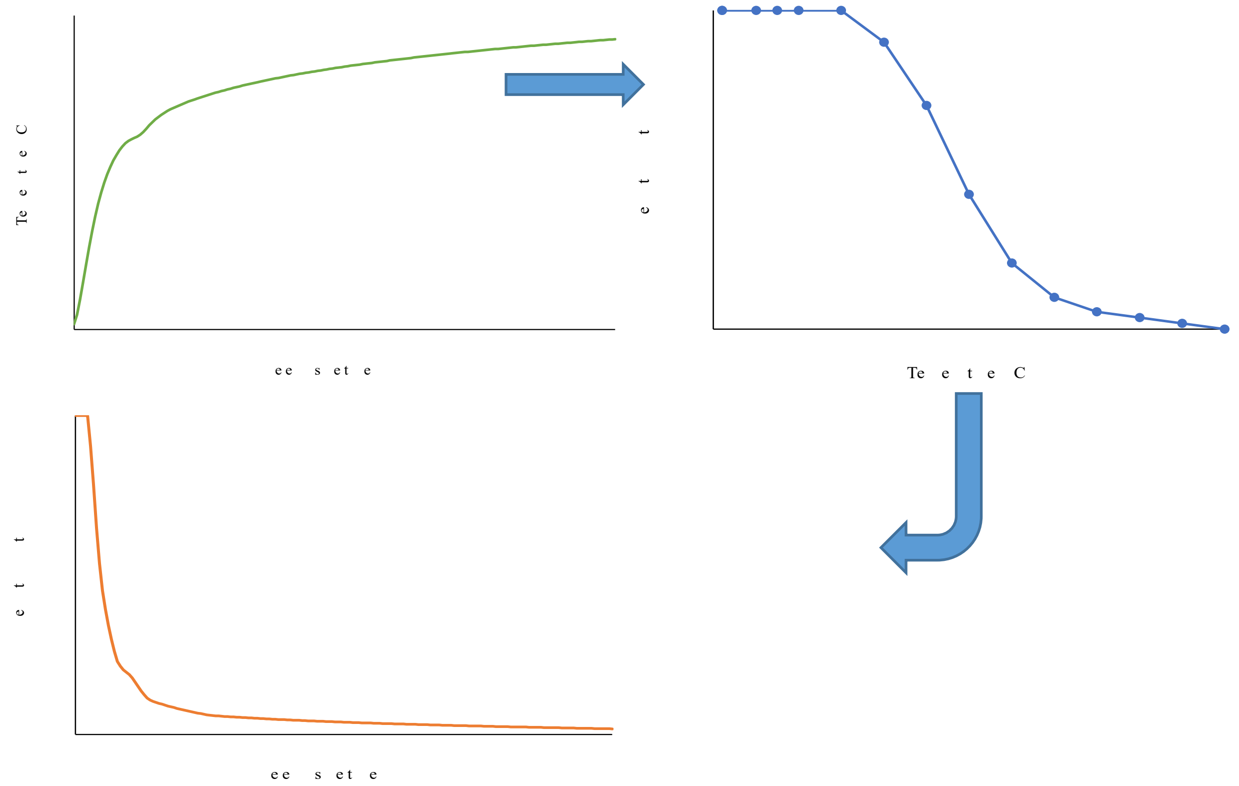

Figure 7. Schematic representation of the model

7 EXPERIMENTAL VALIDATION

Considering the 2 methods presented previously, the following presents the details of the tests results. The following figures (Figure 8, Figure 9 and Figure 10) show a comparison between the proposed methods against the fire tests results from the three campaigns. As an example, the diameter M12 is shown for the steel grades 5.8 and 8.8 (having a ductility ratio $f_{yk}/f_{uk} = 0.8$) for each test campaign.

For the 3 tests campaigns, the figures show conservative results. all the fire test points are above the $k_{b,\theta}$ curve (model based on $k_{b,\theta}$) and almost all the points are also above the $k_{u,\theta}$ curve (model based on $k_{u,\theta}$).

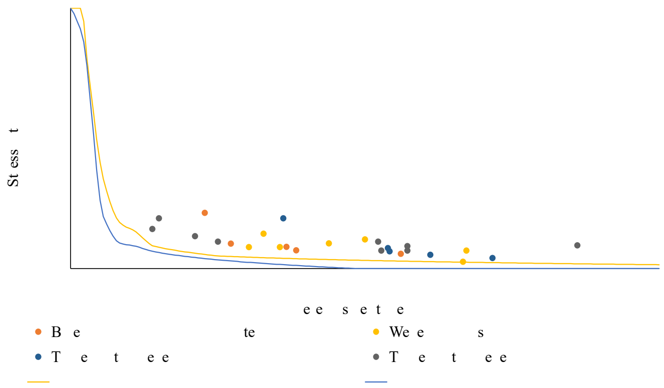

Figure 8. Reduction factor of steel resistance for M12 (CSTB)

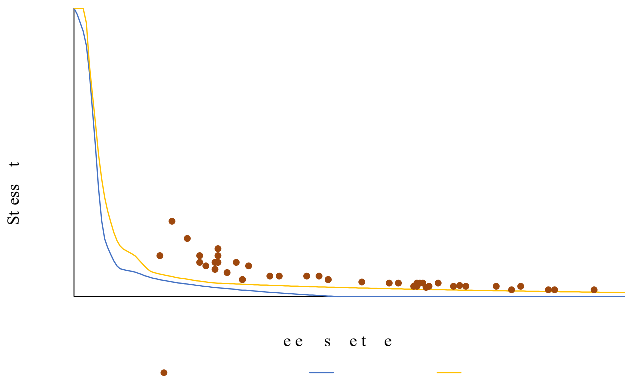

Figure 9. Reduction factor of steel resistance for M12 (TUK)

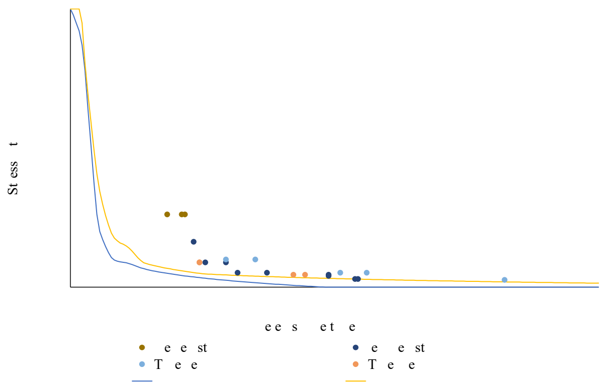

Figure 10. Reduction factor of steel resistance for M12 (IWB)

The $k_{b,\theta}$ curve, based on the factor in table D.1 of EN 1993-1-2 gives more conservative results than the $k_{u,\theta}$ curve, but this method can be considered too conservative. In fact, the model considers that the steel has no more resistance after about 80 minutes of fire exposure (equivalent to 1000°C of maximum temperature along the rod) and can result in penalizing calculations where the fire test data shows that the resistance of the anchors can last for longer fire exposure times. Therefore, method 1 (based on $k_{u,\theta}$ from table 3.1 of EN 1993-1-2) is recommended and will be considered for the rest of the paper, as it covers temperatures up to 1200°C and can yield calculated resistances > 0 kN for longer fire exposure times (until 180 min).

The previous figures were an example of reduction calculated via the model against the reduction measured from tests on one diameter (M12). To study the degree of conservatism of the model, the following figures (Figure 11, Figure 12 and Figure 13) show the ratio between the measured reduction factor (from the fire test results) and calculated reduction factor (from the model based on method 1) for all three test campaigns.

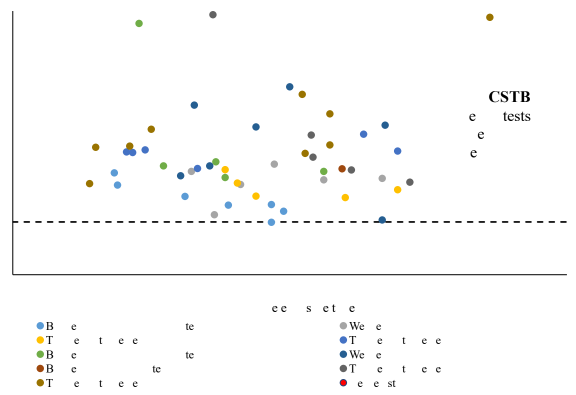

Figure 11. Measured factor/calculated factor (CSTB)

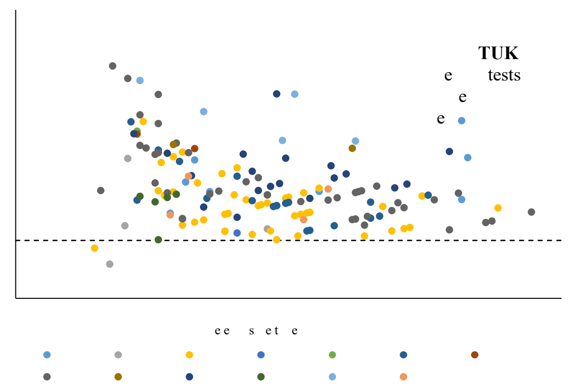

Figure 12. Measured factor/calculated factor (TUK)

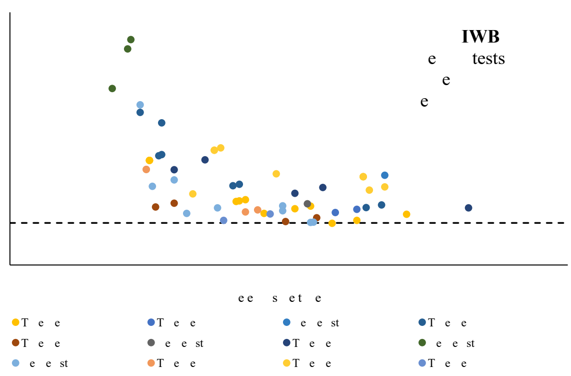

Figure 13. Measured factor/calculated factor (IWB)

The design model based on method 1 yields conservative results compared to the fire tests results. For the CSTB campaign, it shows that for the 52 tests, the calculated reduction factor using the model is smaller than the measured factor, i.e., 100% of the database. For the TUK campaign, only 2 points are unconservative for the 158 tests in the database (a degree of conservatism of 98.7% shown in Figure 12). For the IWB campaign, the model also yielded conservative results with a degree of 98.4% on 61 tests (Figure 13).

8 CONCLUSION

This paper presents a method for the design of steel failure of anchors under tensile load under fire condition. The method uses numerical resolution of the heat transfer equation to obtain the temperature along the anchor as a function of time. The temperature is then used as an input for the reduction factor calculation model. The numerical model of transient thermal calculation is a 2D axisymmetric modelling of a metallic anchor embedded in a concrete cylinder under IS0 834-1 [6] fire conditions. First, a parametric study was conducted on all the anchor diameters covered by EN 1992-4 (from M6 to M39). The variation of the maximum temperature along the rod is observed. The temperature changes with the diameter as a function of fire exposure time. Bigger diameters tend to diffuse heat more, and the maximum temperature along the anchor is higher for smaller diameters.

In this study, the model was validated experimentally, using fire test results from three different laboratories (CSTB, TUK and IWB). More than 270 fire tests resulting in steel failure are adopted in the study. Anchor types integrated in the study are: post-installed mechanical anchors, cast-in headed studs and post-installed bonded anchors of different diameters (M6 to M20) and of different steel grades (5.6, 5.8, 8.8, 10.9).

Two methods were presented in this paper, based on table D.1 (factor $k_{b,\theta}$) and table 3.1 (factor $k_{y,\theta}$) from EN 1993-1-2 [5] gives the factor $k_{b,\theta}$ for bolts and screws in table D.1. The calculation based on this reduction factor yielded conservative results against the experimental results, but this method was deemed too conservative and can over-penalizing. In fact, the reduction from EN 1993-1-2 table D.1 considers the steel having no resistance when exposed to temperatures above 1000°C (equivalent to approximately 80 minutes of fire exposure time), unlike what is observed in the tests results where the anchors can resist to fire exposure times longer than 80 minutes.

EN 1993-1-2 [5] gives the factor $k_{y,\theta}$(allowing to deduce $k_{u,\theta}$) in table 3.1. The calculation based on this reduction factor also yielded conservative results. However, this method is less penalizing and can produce steel fire resistance values for fire exposure times up to 3 hours. The reduction factor also considers the f_{yk}/f_{uk} ratio of each steel grade ad recommended by EN 1993-1-2, Annex A.

REFERENCES

[1] *EN 1992-4. Eurocode 2 – Design of concrete structures – Part 4 : Design of fastenings for use in concrete,* Sept 2018.

[2] EOTA, *EAD 330232-01-0601. Mechanical fasteners for use in concrete,* Dec 2019.

[3] *EOTA TR 020. Evaluation of Anchorages in Concrete concerning Resistance to Fire. European Organization for Technical Approvals Technical report no. 20; May 2005.*

[4] M. Reichert, «Zur Bestimmung des Feuerwiderstands von,» Technische Universität Kaiserslautern , 2020.

[5] *EN 1993-1-2. Eurocode 3: Design of steel structures – Part 1-2: General rules – Structural fire design,* November 2005.

[6] *ISO 834-1 International Standard Fire-resistance tests – Elements of building construction – Part 1: General requirements,* First edition, 1999.

[7] O. Al-Mansouri, R. Mège, N. Pinoteau, T. Guillet et S. Rémond, «Influence of testing conditions on thermal distribution and resulting load-bearing capacity of bonded anchors under fire».

[8] *Eurocode 1: Actions on structures - Part 1-1: General actions - Densities, self-weight, imposed loads for buildings,* 1991.

[9] EOTA, *EAD 330499-01-0601. Bonded fasteners for use in concrete,* Dec 2018.

SiF 2022– The 12th International Conference on Structures in Fire
The Hong Kong Polytechnic University, Nov 30 - Dec 2, 2022

COMPARATIVE ANALYSIS OF THE FIRE PERFORMANCE OF A STEEL ARCH BRIDGE

Patrick Covi[1], Nicola Tondini[2], Enrico Giuriati[3]

ABSTRACT

Bridges are strategic infrastructures and must be designed to withstand operating and exceptional load conditions. However, the current structural standards of bridges do not explicitly consider fire actions. In fact, unlike most structures and infrastructures (buildings and tunnels), there is no specific regulatory obligation that requires the designer to verify a bridge according to fire resistance criteria. However, the fire risk is not negligible, as highlighted by the scientific literature. This aspect can lead to a high vulnerability to the fire of bridges and in the event of a fire, a significant impact on the functionality of the infrastructural network can therefore be expected. The present work fits into this context by analyzing the fire vulnerability of an arched steel overpass with an orthotropic slab deck. Different plausible fire scenarios, such as heavy good trucks, were considered below the bridge and were modelled according to nominal curves and natural fire curves, such as computational fluid dynamics (CFD). A series of thermomechanical analyses were then developed to identify the failure modes and times of collapse, as well as the deformation behaviour that can cause the loss of functionality.

Keywords: Arch bridge, fire, CFD, orthotropic deck.

1 INTRODUCTION

The safety of road networks is a fundamental prerequisite for the economy, the environment, and society. The most vulnerable elements in a road network are bridges. Several researchers have studied bridge failures and monitoring systems [1-6]. The causes of collapses include flood, earthquake, fire, collision, wind, overload, settlement, and environmental degradation of the bridge elements.

Fire is an action that can severely damage bridge structures, which are not generally designed with fire resistance criteria. In addition, to assess the possibility of structural collapse, which can occur despite the beneficial effect of the ventilation that cools the hot gas that spreads during the fire, it is often essential to check the extent of the deformations in the structure. In fact, too high deformations not only may cause the loss of functionality of the bridge, with severe repercussions for vehicular traffic, but can also cause damage to systems and underground services, both urban and extra-urban, often incorporated into the structure, with even more extensive consequences.

[1] Postdoctoral Researcher, Department of Civil, Environmental and Mechanical Engineering, University of Trento (Italy)
e-mail: patrick.covi@unitn.it, ORCID: https://orcid.org/0000-0002-0570-4061
[2] Associate Professor, Department of Civil, Environmental and Mechanical Engineering, University of Trento (Italy)
e-mail: nicola.tondini@unitn.it, ORCID: https://orcid.org/0000-0003-2602-6121
[3] MSc student, Department of Civil, Environmental and Mechanical Engineering, University of Trento (Italy)
e-mail: giuriati.enrico@gmail.com
https://doi.org/10.6084/m9.figshare.22153505

In recent years, several researchers have studied the structural behaviour of bridges subject to fire scenarios using numerical models [7-16], experimental tests [17-18], fire behaviour bridge girders [8,20], and more generally on the fire risk applied to bridges [22-26].

Among these, the research by Moya et al. (2014) [9] concerned the study of the fire that occurred at the I-65 flyover in Birmingham, Alabama, USA in 2002 through numerical analysis. Some computational fluid dynamics models (CFD) were used to reproduce the real fire scenario during the accident.

The research conducted by Dotreppe et al. (2006) [15] concerned the Vivegnis bridge near Liège, a Tied-arch bridge made of steel and a composite steel-concrete deck. The bridge collapsed following a fire caused by a gas pipe explosion. Several numerical simulations were performed with the SAFIR software to simulate the behaviour of the bridge subject to a localized fire. Choi (2008) [16] conducted numerical analyses of the behaviour of the I-80/880 junction bridge in Oakland (USA) during the fire that destroyed part of the composite steel-concrete deck. Some experimental campaigns were also carried out on bridges subject to the action of fire, including the experimental tests conducted by Moya et al. (2017) [18] concerned a bridge with steel beams and reinforced concrete slab. A six meter span bridge subjected to four realistic fire scenarios.

Zhang et al. [20] presented an overview on fire behaviour of bridge girders. Bridge girders subject to fire could exhibit a large deflection or, in some cases, torsion and lateral-torsion problems [20]. Possidente et al. [21] developed a 3D-beam finite element code to model open cross-section steel elements subjected to torsional and lateral-torsion effects under fire condition.

Garlock et al. (2012) [24] presented a detailed overview of bridges that have been subject to fires in the past, post-fire repair strategies in bridges and an overview of the fire risk in bridges. Kodur et al. (2021) [29] examined the risk of fires in transport infrastructure such as bridges and tunnels. In particular, some strategies were analysed to mitigate the fire risks in these types of structures. Finally, the research by Khan et al. (2021) [26] developed a framework for assessing the fire risk of bridges based on data from six case studies.

In 2002, average annual losses of $1.28 billion from fire-damaged bridges were estimated in the United States alone. In particular, the fires that are triggered on the infrastructural network are mainly caused by the collision of vehicles with combustible materials and gas explosion from a leaking pipeline attached to the bridge structure [29-30]. Therefore, their intensity can be exceptionally high, also due to the fact that collisions produce the rapid ignitions of highly flammable materials. Bridges and overpasses with girders and with cables / stays made of steel and steel-concrete composite are therefore particularly vulnerable, since: i) being in most cases not designed with fire resistance criteria, the load-bearing capacity decreases rapidly due to the rapid heating of the steel structural elements and ii) are often made with statically determined schemes with low robustness in case of fire. Furthermore, the closure of a bridge can have significant repercussions on the infrastructural network and economic consequences.

2 CASE STUDY

(a) (b)

Figure 1. General view of the bridge (3D render): (a) Highway overpass; (b) Overpass on a suburban area.

The bridge geometry, material models and other assumptions are provided in this section. The bridge analyzed in this paper is an unprotected single-span steel arch overpass, as shown in Figure 1. The bridge is 65 m long and 14.7 m wide and it consists of an orthotropic slab deck with two traffic lanes. The transverse beams are placed every 3 m. Figure 2 shows its cross section and some tridimensional render details. The bridge has one arch along the span that is centred in the middle of the bridge deck. The steel bridge deck is fully fixed at the junction of the arch and provides lateral stability to the arch. Two different steel grades were used. In detail, high-strength steel grade (fy ≥ 750 N/mm^2) was adopted for the hangers, while steel grade S355 (EN 10025-2, 2019) was adopted for all other elements, i.e. steel deck and arch.

(a)

(b)

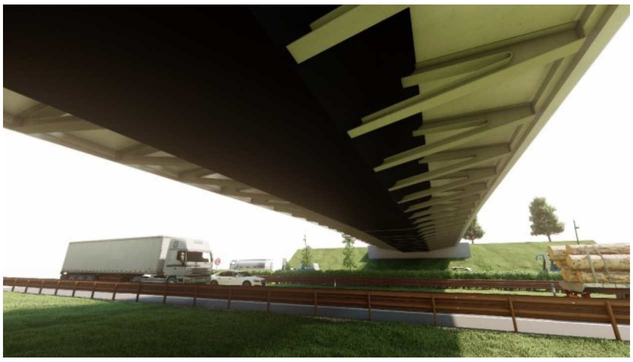

(c)

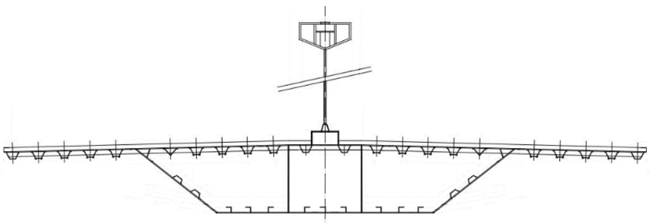

(d)

Figure 2. (a-c) 3D render details; (d) Section of the bridge.

3 FEM

Typically, the restraints at the end of the bridge are considered as free or fixed end conditions (Figure 3a-b). Bridges and the infrastructures anchored to them (i.e. pipes, electrical cables, monitoring systems) are designed to allow thermal expansion within certain displacement limits using thermal joints [31-33]. Maximum and minimum air temperature values are used to estimate the axial displacements of the bridge due to thermal expansion and expansion joints are designed to accommodate them. However, when a fire occurs, the thermal expansions can be higher than the maximum displacement of the designed expansion joint. In this scenario, the presence of the thermal joints induces restraint conditions that are in between the two limit cases (Figure 3c).

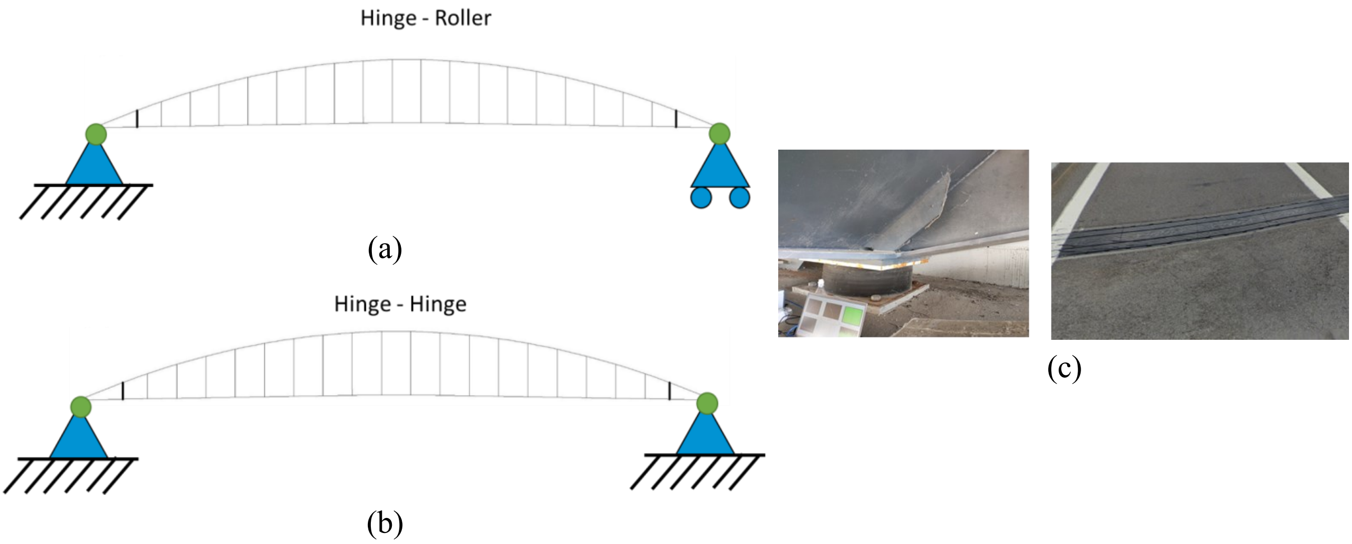

Figure 3. (a) bridge free end condition; (b) bridge fixed end condition; (c) dissipator and thermal joint.

In this respect, SAFIR [34] does not include a gap element to model expansion joints. Since it is a proprietary software, it was not possible to implement a GAP element directly in the source code. Therefore, a different approach was used in order to implement the GAP with only the elements already inside the SAFIR software. Figure 4 illustrates the configuration of the mechanical system that was used to simulate the GAP.

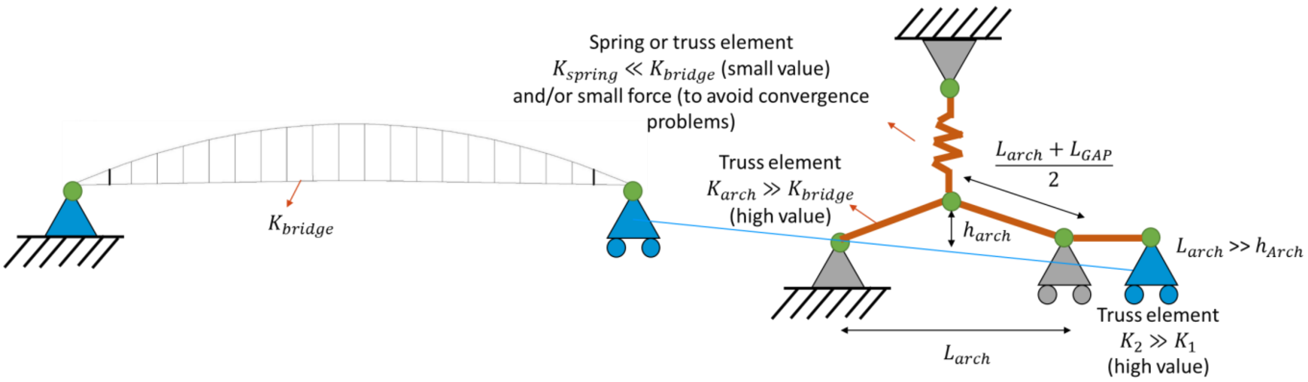

Figure 4. mechanical configuration to simulate the bridge's gap.

The mechanical system works in a similarly to a Von Mises Planar Truss/Arch [35] and a Pantograph. The system was made of two straight hinges truss elements for the arch and a third horizontal truss element that connects the arch with the rest of the structure. To avoid convergence problems due to the lability condition or snap-through and to have a small force in order to re-open the GAP, a spring was applied at the crown of the arch.

The system can extend along the horizontal axis for the desired displacement of the bridge thermal joint (L_{GAP}). Based on the geometrical parameter of the mechanism, such as the desired gap length (L_{GAP}) and the initial span of the arch (L_{arch}), it is possible to obtain the initial height of the arch (h_{arch}) using Equation 1.

$$h_{arch} = \sqrt{\frac{L_{GAP}}{2} * \left(L_{arch} + \frac{L_{GAP}}{2}\right)} \tag{1}$$

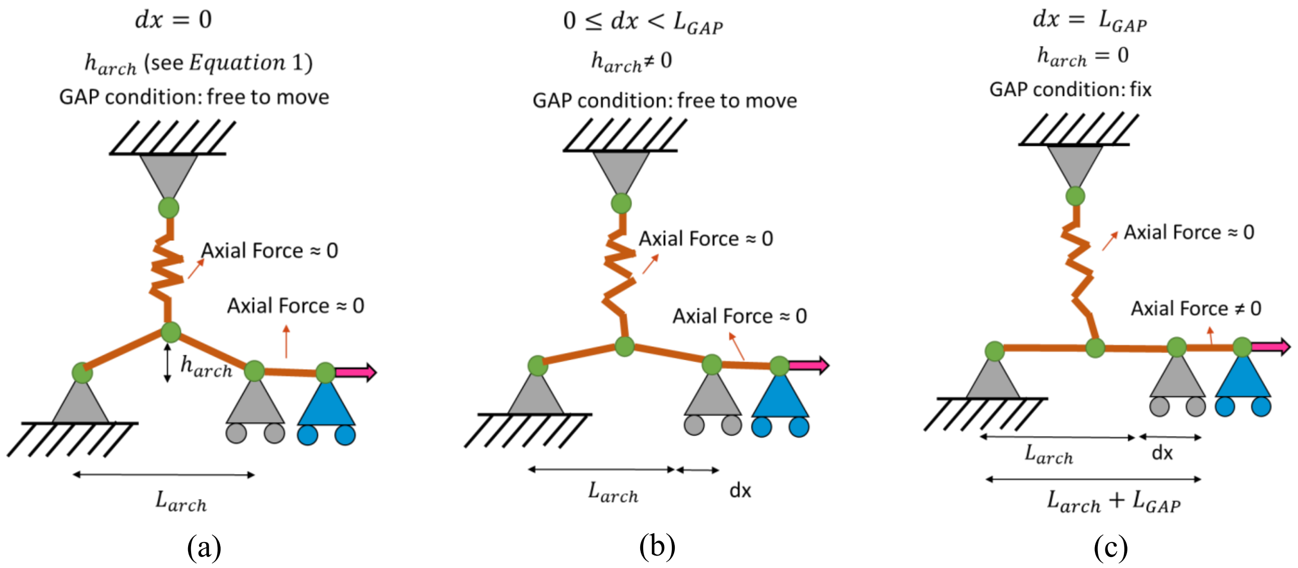

Figure 5. Operation of the mechanical system (GAP): (a) at rest; (b) partially opened; (c) fully closed.

Figure 5 illustrates the mechanism during different steps. In detail, Figure 5a shows the GAP mechanism at rest. When the bridge or the structures starts to expand, the arch starts closing, giving a minimal resistance to the horizontal movement of the structure that could be considered negligible (see Figure 5b). Finally, when the maximum length of the GAP setting is reached, the GAP is fully closed and prevents the bridge or the structure from moving forward in the horizontal direction, as shown in Figure 5c.

The spring force should not be too big or small value to avoid convergency problems caused by out-of-range values in the matrix operations. For the same reason, the stiffness of the truss elements must not be a very high value. A round cross-section with area equal to A = 1.0 m^2, Young's modulus E = 6000 GPa was chosen for the truss elements.

In order to demonstrate the effectiveness of the GAP methodology and to illustrate the implementation of a real scenario using SAFIR, the proposed mechanical system was added to a simply supported beam. Results of the SAFIR analysis were then verified against the GAP element developed in the software OpenSees [36]. Figure 6a shows the numerical model of the simply supported beam with the GAP mechanism in both horizontal directions, while Figure 6b illustrates the horizontal input force imposed at the end of the beam. Figure 6c compares the horizontal displacement responses measured at the end of the beam; instead, Figure 6 compares the force of the GAP element. As can be appreciated in Figure 6c-d, the structure's response obtained using SAFIR well matches the reference OpenSees solution.

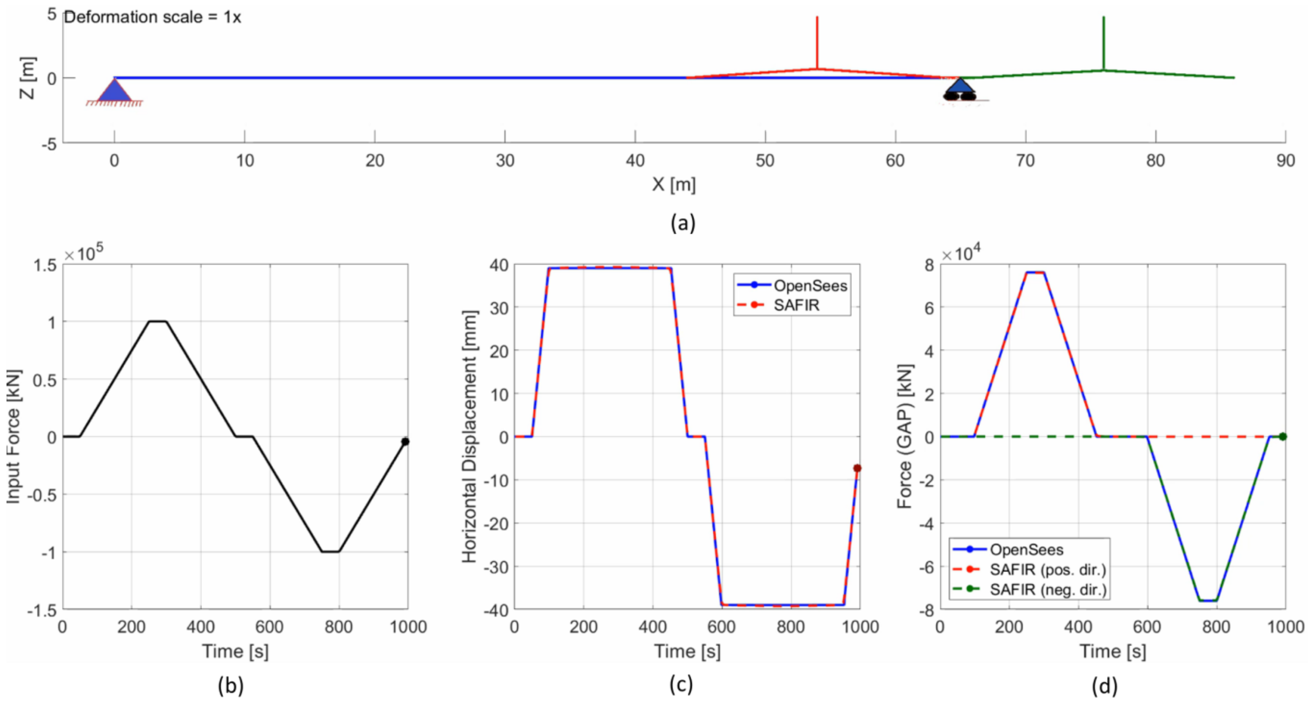

Figure 6. Comparison between SAFIR and OpenSees: (a) FEM model with the GAP mechanism in both horizontal directions. (b) Horizontal input force; (c) horizontal displacement; (d) Axial forces of the GAP mechanism.

A 3D thermomechanical model of the bridge was created in the thermomechanical software SAFIR using nonlinear Euler-Bernoulli beam elements, as shown in Figure 7.

In this work, modelling the gap that simulates the thermal expansion joints of the bridge was considered. In detail, a gap of 0.2 m was modelled to allow for the thermal expansion of the bridge up to the end of the thermal joint. A series of thermomechanical analyses were performed to investigate the structural fire behaviour, including the deformation behaviour that can cause the loss of functionality of the bridge.

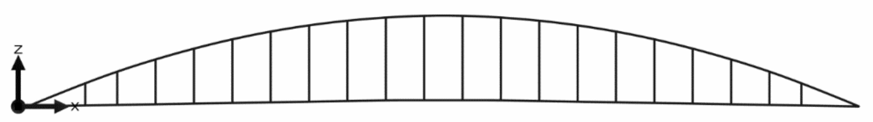

Figure 7. Numerical model

4 FIRE ANALYSIS

Both a prescriptive and a performance-based approach were applied by employing different fire curves and by selecting different plausible fire scenarios. Indeed, the most common way to define the gas temperature is to use prescriptive code-based fire curves. Therefore, preliminary analyses were performed using nominal curves such as the hydrocarbon and the ISO 834 curve, the former being more appropriate, as illustrated in Figure **9**. Another type of curve used to analyse the fire behaviour of bridges is the fire curve proposed by Stoddard [37] (see Fig. 4). This curve was conceived to estimate the air temperature following a collision between tanker trains, which happened on 11 December 2002.

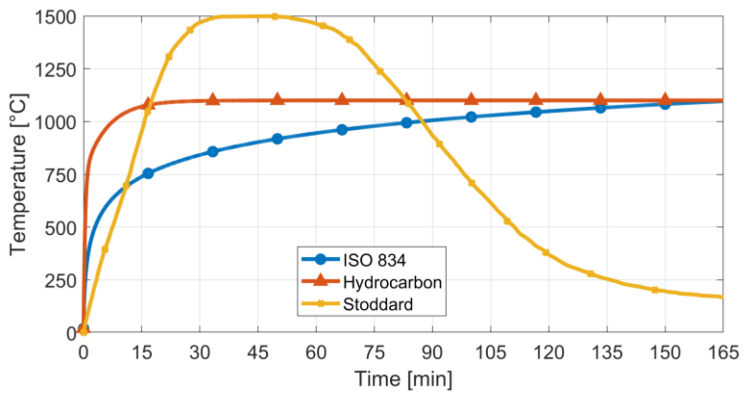

Figure 8. prescriptive code-based fires curves and Stoddard curve

Because of the length of the bridge, a vehicle fire will naturally induce a non-uniform thermal action on the structure. Indeed, the nominal fire curves were applied not only to the whole length of the bridge but to different portions, i.e. total length, half-length and one quarter, as illustrated in Figure 9.

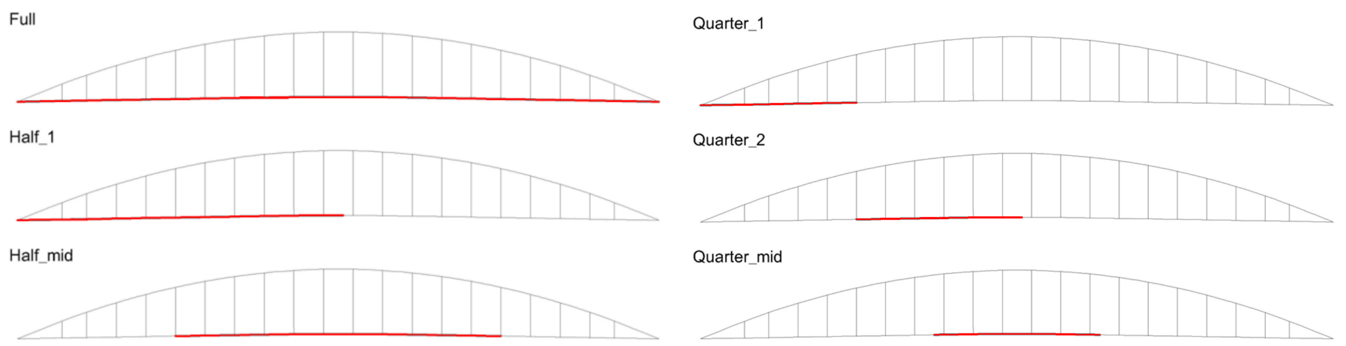

Figure 9. Portion of the bridge under fire action

The simulation results using the nominal fire curves are summarized in Table 1. It is possible to observe that applying the fire curve to the entire bridge length leads to structural failure. The Stoddard fire curve was the more severe and entailed the collapse under all heating configurations. No structural failure was observed when the bridge was half heated for the ISO 834 and the hydrocarbon fire curve. In terms of residual deformation, all maximum vertical displacement values exceed L/150. By assuming a limit value of L/250 as for the serviceability limit state for steel structures, the full functionality of the bridge cannot be assured.

Table 1. Results of the prescriptive code-based fires curves and Stoddard curve.

ID	Nominal curve	Fire location	(min)	Residual deflection (m)	Residual deflection over bridge's length
#1	ISO834	Full	64	Not applicable	Collapse
#2	ISO834	Half_1	102	-0.49	L/135
#3	ISO834	Half_Mid	120	-0.45	L/145
#4	ISO834	Quarter_1	120	-0.48	L/135

#5	ISO834	Quarter_2	120	-0.46	L/140
#6	ISO834	Quarter_Mid	120	-0.46	L/140
#7	Hydrocarbon	Full	28	Not applicable	Collapse
#8	Hydrocarbon	Half_1	55	-0.47	L/140
#9	Hydrocarbon	Half_Mid	78	-0.51	L/130
#10	Hydrocarbon	Quarter_1	120	-0.48	L/135
#11	Hydrocarbon	Quarter_2	120	-0.46	L/140
#12	Hydrocarbon	Quarter_Mid	120	-0.46	L/140
#13	Stoddard	Full	28	Not applicable	Collapse
#14	Stoddard	Half_1	38	Not applicable	Collapse
#15	Stoddard	Half_Mid	32	Not applicable	Collapse
#16	Stoddard	Quarter_1	42	Not applicable	Collapse
#17	Stoddard	Quarter_2	42	Not applicable	Collapse
#18	Stoddard	Quarter_Mid	41	Not applicable	Collapse

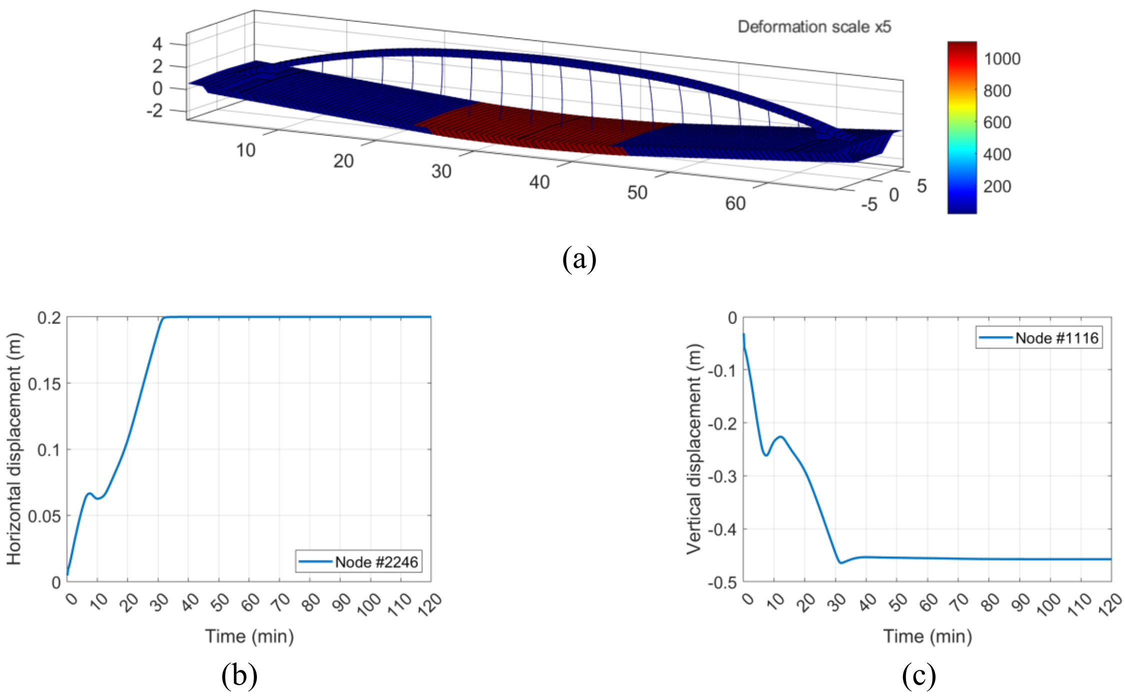

Figure 10. Analysis #12: Results at the end of the simulation: (a) Deformed shape and steel temperature; (b) Horizontal displacement; (c) Vertical displacement at mid-span.

Figure 10b-c illustrates the horizontal and vertical displacement responses measured respectively at the end node and mid-span node of the bridge. It is worth pointing out that a 0.2 m expansion joint effect was included and after 38 minutes the axial expansion of the bridge reaches the gap, as shown in Figure 10b. It is possible to notice an inversion of the horizontal and vertical displacements between 7 minutes and 13 minutes from the beginning of the fire. This is caused by the vertical variation of the stiffness center caused by the differential increase in the temperatures in the section.

Moreover, different plausible natural fire scenarios were also considered, such as heavy good trucks, below the bridge and they were modelled according to computational fluid dynamics (CFD) models using FDS (Fire Dynamics Simulator) software [38]. A 3D model of the bridge has been created. The model domain was 65.0 m wide, 20.0 m deep and 15.0 m high to allow the fire sufficient volume for air entrainment and extension of flames. All boundaries were left open to ambient and the initial temperature was 20°C. The model included the ground slope. The geometry of the modelled bridge is shown in Figure 11.

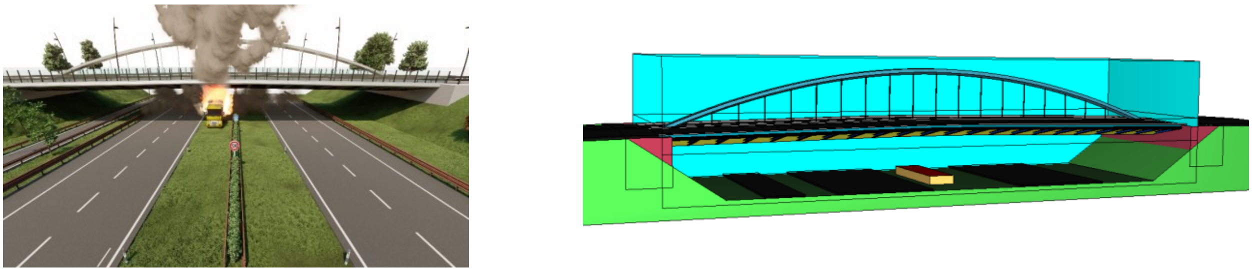

(a) (b)

Figure 11. FDS fire scenario (Truck location A) a) 3d render b) FDS general view.

In order to model a real fire in a CFD analysis, it is possible to apply an HRR (Heat Release Rate) thermal release curve, as also described in the Italian Ministerial Fire Prevention Decree of 3 August 2015 (DM 3AGO (2015)) (Fire Prevention Code). The HRR curve is the variation of the thermal release power in a combustion reaction, which depends on the fuel, the ventilation conditions and the geometric characteristics of the material.

One HRR curve was used for the simulations:

- Truck: the heavy goods vehicle loaded with wood and plastic pallets (Figure 12) [39].

The fires were placed in four different locations underneath the bridge:

- Location A: the fire was centered at mid-span, both longitudinally and transversely (Figure 13).
- Location B: The fire location was offset longitudinally from the center of the bridge near the end of the bridge.

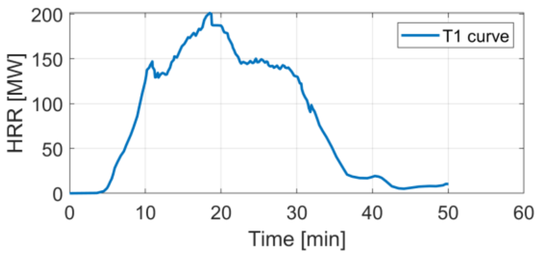

Figure 12. HRR of the heavy goods vehicle loaded with wood and plastic pallets [39].

Figure 13 illustrates the development of fire and smoke after 23 minutes from the beginning of one fire scenario as an example of the fire development stages.

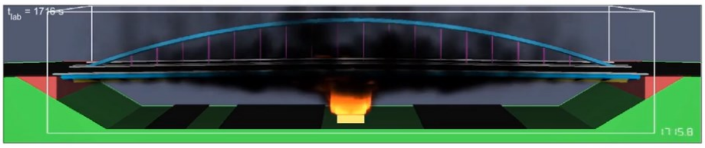

Figure 13. FDS results general view of the bridge after 25 min (Truck location A).

To measure the temperature evolution of the gas, a total of 2022 adiabatic surface temperature gas-phase devices were placed across the bridge deck, arch and hangers. The output values from these devices were used for performing thermal-structural analysis of the sections in SAFIR.

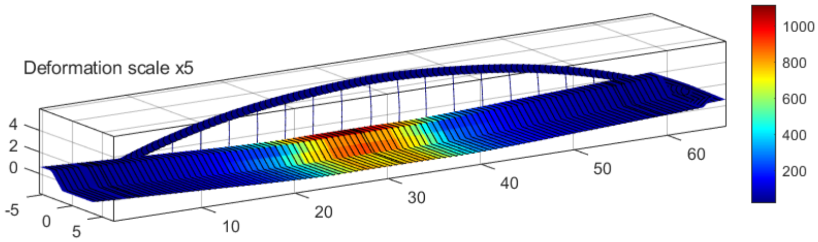

Figure 14. Deformed shape and steel temperature of the deck after 25 min.

The simulation results using the FDS scenarios are summarized in Table 2. As an example, Figure 14 shows the deformed configuration and steel temperature of the deck 23 minutes after the beginning of the fire scenario modelled in FDS that involved the heavy goods vehicle loaded with wood and plastic pallets. Figure 15 illustrates the horizontal and the deflection time history of the bridge under the FDS fire load. No structural failure was observed with residual vertical displacement between 20 cm (L/310) and 30 cm (L/240) depending on the fire scenario. In this case, given the fact that a smaller part of the bridge is affected by the fire, it is not trivial to state that a residual displacement less than L/250 can lead to full functionality because the deformation can be highly localised with steep gradients of vertical displacement near the maximum value. This should be investigated more in depth.

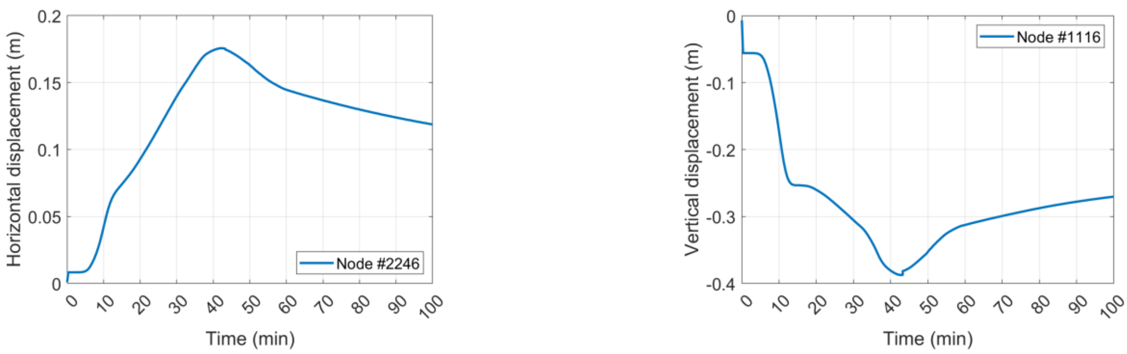

(a) (b)

Figure 15. Displacements time history of the bridge: (a) Horizontal; (b) Deflection.

Table 2. Results of the FDS scenarios.

ID	Nominal curve	Fire location	(min)	Residual deflection (m)	Residual deflection over bridge's length
#1	Truck	Location A	100	-0.27	L/240
#2	Truck	Location B	100	-0.21	L/310

5 CONCLUSIONS

The paper presented numerical fire analysis and thermal-structural analysis to investigate a steel arch bridge under fire using CFD and SAFIR software.

The results showed that nominal curves are generally conservative and predict much shorter failure times. CFD analyses provided more realistic representations of the bridge fire scenario and in the analysed cases the collapse was not even attained. However, in all cases in which failure was not reached, the final deformation state was to such an extent that the bridge was not fully functional after fire for nominal fire curves by assuming a vertical limit of L/250. For the CFD analyses, smaller residual deformations were observed, but more localised. The modelling of the expansion joint (GAP) in the numerical model allowed to obtain a more realistic constraint condition compared to the boundary conditions frequently used in other studies, such as hinge-hinge or hinge-roller constraints.

ACKNOWLEDGMENT

The support received from the Italian Ministry of Education, University and Research (MIUR) in the framework of the 'Departments of Excellence' (grant L 232/2016) is gratefully acknowledged

REFERENCES

1. Lee, G. C., Mohan, S., Huang, C., & Fard, B. N. (2013). A study of US bridge failures (1980-2012). Buffalo, NY: MCEER.
2. Scheer, J. (2011). Failed bridges: case studies, causes and consequences. John Wiley & Sons.
3. Diaz, E.E.M., Moreno, F.N., and Mohammadi, J. (2009). Investigation of Common Causes of Bridge Collapse in Colombia. Practice Periodical on Structural Design and Construction. 14(4): p. 194-200
4. Deng L, Wang W, Yu Y (2016) State-of-the-art review on the causes and mechanisms of bridge collapse. J Perform Constr Facil. https://doi.org/10.1061/(ASCE)CF.1943-5509.0000731
5. Ceravolo R., Tondini N.*, Abbiati G. and Kumar A. (2012) Dynamic characterization of complex bridge structures with passive control systems. Structural Control and Health Monitoring, 19(4): 511–534. doi: 10.1002/stc.450.
6. Tonelli, D., Rossi, F., Brighenti, F. et al. Prestressed concrete bridge tested to failure: the Alveo Vecchio viaduct case study. J Civil Struct Health Monit (2022). https://doi.org/10.1007/s13349-022-00633-w
7. Payá-Zaforteza, I. and Garlock, M.E.M., 2012. A numerical investigation on the fire response of a steel girder bridge. Journal of Constructional Steel Research, 75, pp.93-103.
8. Aziz, E. and Kodur, V., 2013. An approach for evaluating the residual strength of fire exposed bridge girders. Journal of Constructional Steel Research, 88, pp.34-42.
9. Alos-Moya, J., Paya-Zaforteza, I., Garlock, M. E. M., Loma-Ossorio, E., Schiffner, D., & Hospitaler, A. (2014). Analysis of a bridge failure due to fire using computational fluid dynamics and finite element models. Engineering Structures, 68, 96-110.
10. Liu, Z., Silva, J.C.G., Huang, Q., Hasemi, Y., Huang, Y. and Guo, Z., 2021. Coupled CFD–FEM Simulation Methodology for Fire-Exposed Bridges. Journal of Bridge Engineering, 26(10), p.04021074.
11. Song, C., Zhang, G., Kodur, V., Zhang, Y. and He, S., 2021. Fire response of horizontally curved continuous composite bridge girders. Journal of Constructional Steel Research, 182, p.106671.
12. Timilsina, S., Yazdani, N. and Beneberu, E., 2021. Post-fire analysis and numerical modeling of a fire-damaged concrete bridge. Engineering Structures, 244, p.112764.
13. Alos-Moya, J., Paya-Zaforteza, I., Hospitaler, A. and Loma-Ossorio, E., 2019. Valencia bridge fire tests: Validation of simplified and advanced numerical approaches to model bridge fire scenarios. Advances in Engineering Software, 128, pp.55-68.
14. Zhang, G., Song, C., Li, X., He, S. and Huang, Q., 2021. Fire performance of continuous steel-concrete composite bridge girders. KSCE Journal of Civil Engineering, 25(3), pp.973-984.
15. Dotreppe JC, Majkut S, Franssen JM. 2006. Failure of a tied-arch bridge submitted to a severe localized fire, structures and extreme events. IABSE Symposium; p. 272–273.
16. Choi J. (2008) Concurrent fire dynamics models and thermomechanical analysis of steel and concrete structures. Ph.D. dissertation. Atlanta (USA): Georgia Institute of Technology.
17. Kaundinya, I., Bergerhausen, U. and Schmidt, J., 2017. Effects of extreme fire scenarios on bridges. Bridge Structures, 13(4), pp.159-167.

18. Alos-Moya, J., Paya-Zaforteza, I., Hospitaler, A. and Rinaudo, P., 2017. Valencia bridge fire tests: Experimental study of a composite bridge under fire. Journal of Constructional Steel Research, 138, pp.538-554.
19. Thiébaud, R., Lebet, J. P., Beyer, A., & Boissonnade, N. (2016). Lateral torsional buckling of steel bridge girders. In Proceedings of the Annual Stability Conference Structural Stability Research Council, Orlando, USA (pp. 12-15).
20. Zhang, G., Zhao, X., Lu, Z., Song, C., Li, X., & Tang, C. (2022). Review and discussion on fire behavior of bridge girders. Journal of Traffic and Transportation Engineering.
21. Possidente L., Tondini N.*, Battini J.-M. (2020) 3D beam element for the analysis of torsional problems of steel structures in fire, Journal of Structural Engineering, 146:(7), 10.1061/(ASCE)ST.1943- 541X.0002665.
22. Naser, M.Z. and Kodur, V.K.R., 2015. A probabilistic assessment for classification of bridges against fire hazard. Fire Safety Journal, 76, pp.65-73.
23. Aziz, E.M., Kodur, V.K., Glassman, J.D. and Garlock, M.E.M., 2015. Behavior of steel bridge girders under fire conditions. Journal of Constructional Steel Research, 106, pp.11-22.
24. Garlock, Maria, et al. "Fire hazard in bridges: Review, assessment and repair strategies." Engineering structures 35 (2012): 89-98.
25. Kodur, Venkatesh, and M. Z. Naser. "Fire hazard in transportation infrastructure: Review, assessment, and mitigation strategies." Frontiers of Structural and Civil Engineering (2021): 1-15.
26. Khan, M.A., Khan, A.A., Anwar, G.A. and Usmani, A., 2021, October. Framework for fire risk assessment of bridges. In Structures (Vol. 33, pp. 523-532). Elsevier.
27. Possidente L., Tondini N.*, Battini J.-M. (2020) 3D beam element for the analysis of torsional problems of steel structures in fire, Journal of Structural Engineering, 146:(7), 10.1061/(ASCE)ST.1943- 541X.0002665.
28. Aziz, E.M., Kodur, V.K., Glassman, J.D. and Garlock, M.E.M., 2015. Behavior of steel bridge girders under fire conditions. Journal of Constructional Steel Research, 106, pp.11-22.
29. Kodur, Venkatesh, and M. Z. Naser (2021) "Fire hazard in transportation infrastructure: Review, assessment, and mitigation strategies." Frontiers of Structural and Civil Engineering.
30. Hu, Jiayu, Ricky Carvel, and Asif Usmani. (2021) "Bridge fires in the 21st century: A literature review." Fire Safety Journal.
31. Roeder, C. W. (2003). Proposed design method for thermal bridge movements. Journal of Bridge Engineering, 8(1), 12-19.
32. Parke, G., & Hewson, N. (Eds.). (2022). ICE manual of bridge engineering. ICE Publishing.
33. Caspani, V.F.; Tonelli, D.; Poli, F.; Zonta, D. Designing a Structural Health Monitoring System Accounting for Temperature Compensation. Infrastructures 2022, 7, 5. https://doi.org/10.3390/infrastructures7010005
34. Franssen, J-M, Gernay, T. (2017): Modeling structures in fire with SAFIR©: Theoretical background and capabilities. Journal of Structural Fire Engineering, 8 (3), 300-323.
35. R. von Mises, "Über die Stabilitätsprobleme der Elastizitätstheorie," ZAMM, vol. 3, pp. 406–422, 1923
36. McKenna, F. (2011). "Opensees: a framework for earthquake engineering simulation,"Computing in Science & Engineering, vol. 13, no. 4,pp. 58–66.
37. Stoddard R. (2004), "Inspection and repair of a fire damaged prestressed girder bridge," in Proceedings of International Bridge Conference, Pittsburgh, PA, USA.
38. McGrattan, K. , McDermott, R. , Weinschenk, C. and Forney, G. (2013), Fire Dynamics Simulator, Technical Reference Guide, Sixth Edition, Special Publication (NIST SP), National Institute of Standards and Technology, Gaithersburg, MD, [online], https://doi.org/10.6028/NIST.sp.1018
39. Hurley, M. J., Gottuk, D. T., Hall Jr, J. R., Harada, K., Kuligowski, E. D., Puchovsky, M., and Wieczorek, C. J. (Eds.). (2015). SFPE handbook of fire protection engineering. Springer.

SiF 2022– The 12th International Conference on Structures in Fire
The Hong Kong Polytechnic University, Nov 30 - Dec 2, 2022

A DESIGN FRAMEWORK FOR FIRE PROTECTED STEEL CONNECTIONS WITH ANCILLARY MEMBERS IN AUSTRALIA

Wong, Andy Hoa Wei[1], Walden, Matthew[2], Spyridakis, Stavros[3], Ingolfsson, Sigurjon[4] and Song, Yuanyuan[5]

ABSTRACT

In steel structural steel construction, it is common to have non-protected ancillary members interface with fire protected members. Current guidance and accepted practice do not consider the actual fire exposure risk present in the building or size of the member. A practical design framework was established to consider applied fire scenarios and the resultant structural behaviour of a building in a combined setting.

The application of coat-back was also discussed. The 500mm coat-back is only applicable up to a 2-hour rating based on a hydrocarbon or ISO 834 fire curve. Higher fire resistance ratings may require increased coat-back. A 1-D heat transfer calculation can be used in application for coat-back lengths. The 3,000mm^2 per metre length rule, for ancillary members not to be protected, appears to be still valid, although its threshold is not strictly 3,000mm^2. These findings should be further investigated ideally with a full parametric study, including testing.

Keywords: Steel connections; ancillary members; design framework; applications of structural fire engineering

1. INTRODUCTION

Within the context of protecting steel elements from fire exposure, primary members are typically coated with intumescent paint, vermiculite, encapsulated or alike. In steel construction, it is quite common to have non-protected secondary or ancillary members interface with fire protected members, as shown in Figure 1 below. In a majority of structural design, the capacity of these connections is just as important, if not more critical than the overall member or section.

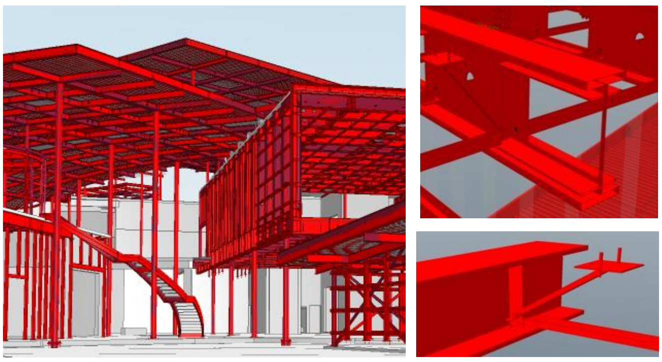

Figure 1: Typical ancillary connections into protected members, (Left) Overall steel structure; (Right) primary beam with secondary/ancillary members connections

Despite how important these connections are, prescriptive design requirements and criteria, in Australia and many jurisdictions around the globe, lack guidance and design approaches. There are magic numbers suggested by industry bodies [1] [2], however, they are generally guidance without the consideration of the use of the space, size of the members or geometry. To date, there is no prescriptive design methodology to address non-protected secondary or ancillary members interface with protected members, and its impact to the local member or section; the methodologies and such are largely left to the designer to prescribe.

A design framework has been iteratively developed on a composite steel and concrete structure building; to set a methodology on how these connections should be addressed for fire exposure, taking into

[1] Engineer, Arup, e-mail: Andy-HW.Wong@arup.com
[2] Senior Engineer, Arup, e-mail: Matthew.Walden@arup.com
[3] Senior Engineer, Arup, e-mail: Stavros.Spyridakis@arup.com
[4] Senior Engineer, Arup, e-mail: Sigurjon.Ingolfsson@arup.com
[5] Associate, Arup, e-mail: Yuan-yuan.song@arup.com
https://doi.org/10.6084/m9.figshare.22153520

consideration the actual use of the building, its members and geometry and the variation of tested or untested products. This framework could form the foundation as an exemplar methodology for industry.

2. STATE OF THE ART

2.1. Industry Design Approach

In design, steel connection designs are bespoken for that building and its classification of use. Manufacturers of protective coatings have test reports and data but often are confidential, not widely available for public and tested as single structural elements and not within the context of wider structural behaviour in fire. Furthermore, test conditions vary, some are based on the ISO 834 standard fire, ASTEM E119, hydrocarbon curves or fixed heat load. The test details are unclear, e.g., how many elements has been tested and why/how we could apply this test result to a wide range of connections which are under different heating and loading conditions.

Theoretically, the best approach would be to test every connection in a laboratory environment. However, this is practically unattainable when considering design variations and constructability constraints, cost and project delivery timeframes. The prescriptive guidance in the Building Code of Australia [3], is very open broad with no set design framework.

"The method of attaching or installing a finish, lining, ancillary element or service installation to the building element must not reduce the fire-resistance of that element to below that required."

Therefore, it inherently drives for a performance-based solution, which is difficult without understanding the actual performance of the structural connection in fire.

Industry guidance is that heat transfer from unprotected structural steel into protected structural steel should be considered. The industry best and accepted practice is to apply a coat-back on all secondary or ancillary elements for a distance of 450-500mm [2] [4] [5], where the contact area exceeds 3,000mm^2 per metre of length of the protected primary member [1].

This is to limit the effects of heat transfer from the unprotected member impacting on the protected primary member. For a complex connection, this approach could lead to significant over engineered designs. The guidance and accepted practice do not consider the actual fire exposure risk present in the building or size of the member.

2.2. Heat Transfer Theory

From a theoretical perspective, the root problem relates to heat transfer, limiting the transfer of heat from the secondary or ancillary elements to the primary members. Linear 1-D heat transfer is described by Fourier's Law of Conduction [6]:

$$q" = -k\frac{dT}{dx} \qquad (1)$$

Where, (q") is the heat energy, (k) is the thermal conductivity, with respect to the Temperature (T) gradient at a depth (x) in a solid. When evaluating temperature gradients within a solid, a dimensionless ratio of thermal resistance is expressed as the Biot number [7]:

$$Bi = \frac{hL}{k} \qquad (2)$$

Where the heat transfer coefficient (h) and the characteristic length of the considered geometry (L) is taken over the thermal conductivity.

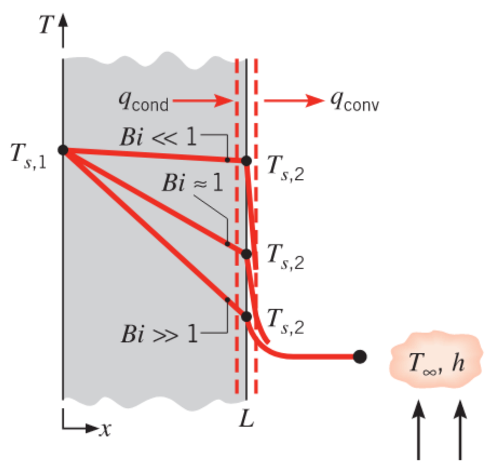

Figure 2: A representation of the temperature gradient through a 1-D element for different Biot numbers [7]

For Bi <<1, they are typically characterised as "thermally thin", where the thermal resistance to conduction is low and as such heat transfer is faster and expected to be more uniform through the solid – i.e. assuming a constant temperature throughout.

For Bi >>1, they are typically characterised as "thermally thick", where the solid has more thermal resistance, as such the heat transfer through the solid is slower and a temperature gradient through the material is expected – i.e. indicating a transient heat conduction through the volume of the material over a given time period.

2.3. Heat Transfer in Steel

Expanding the effects of heat transfer in 2-D and 3-D for steel, the rate of temperature rise of a protected or unprotected steel member is dependent on the *section factor*, which is a ratio of the heated perimeter to the area or mass of the cross-section [8] [9]. This is represented as:

$$Section\ Factor = \frac{H_P}{A} \quad or\ Section\ Factor = \frac{A_P}{V} \tag{3}$$

Where, the numerator is the heated perimeter (H_P) or perimeter area (A_P) per unit length, with denominator as the cross-sectional area of the member (A) or member volume (V) per unit length. The higher the Section Factor, the higher the heated perimeter relative to its cross-sectional area is [10].

In Eurocode 3 [9], the Section Factor is used as lumped capacity analytical model to determine the temperature of steel elements for both unprotected and protected. This is typically used on I-Beams or members alike where the thickness of its elements, web and flanges are thin. Steel has a relatively high thermal conductivity (k), and when observing the direct impact of heat into thin elements with a small characteristic length (L) and a uniform heated perimeter; the results of equation (2) will result in a Biot number <<1. This approach would be consistent in simple exposure of steel elements.

When a steel element is partially exposed, such as exposure on a portion of the bottom flange as shown in Figure 3, especially for large I-beam sections, in a simplistic sense, it is expected that there will be a larger characteristic length (L) when evaluating the Biot Number.

Applying equation (2), the I-beam in Condition 3.2 would have a higher Biot number than Condition 3.1, as such a temperature gradient would be expected to be more apparent in Condition 3.2 considering it has a small, heated surface area thus a larger characteristic length. Eurocode 3 [9], relies on a lumped capacity analytical model to evaluate steel temperature, which assumes uniform heating of the entire cross-sectional area of the beam, taking an average rather than the expected temperature gradient from the member section.

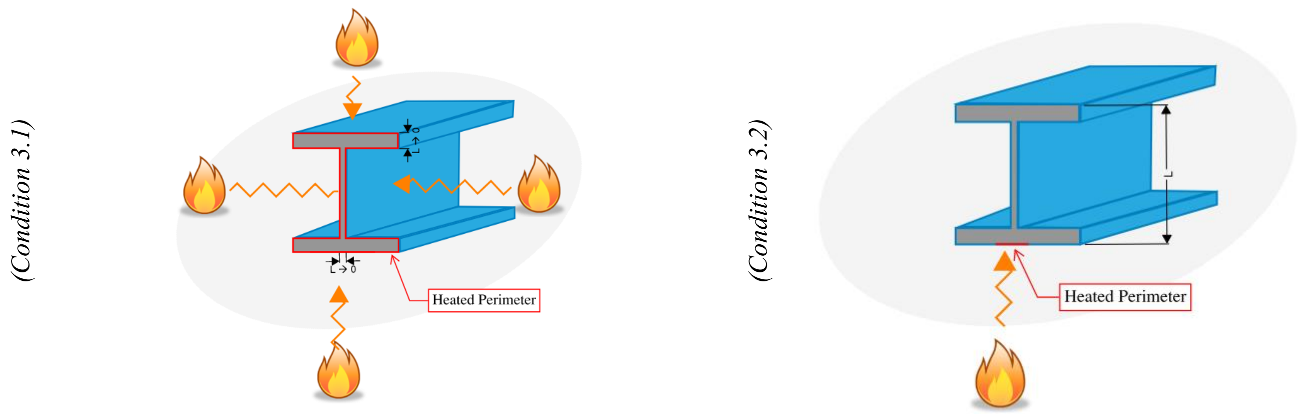

Figure 3: Simplistic relation to the characteristic length of the Biot number related to the heated perimeter. (Left) Uniform heated perimeter, (Right) Non-uniform heated perimeter with heating from one direction.

Burgan and Selby [11], and Amdahl, et al. [12] demonstrate that for both fire protected and unprotected ancillary members, causing non-uniform heating, there is a wide temperature deference in the member section (i.e. temperatures in the flanges, webs or distance from connections).

A temperature gradient can be more apparent when considering a 1-D heat transfer of steel element longitudinally, such as a distance of 500mm (only assuming heating in one-direction with perfect bounding insulation). Yasseri demonstrates a notable temperature gradient with a 1-D heat transfer analytical model [10].

Like most material, steel's thermal and mechanical properties change with increased temperatures. Figure 4 is an extract from Eurocode 3 which shows the reduction factors for the stress-strain relationships such as its effective yield strength. The critical temperature is often prescribed to be around 550°C-600°C, based on the assumption that with safety factors most elements are loaded at 50% of their ambient temperature capacity and that failure occurs when the material had a 50% reduction in strength [13].

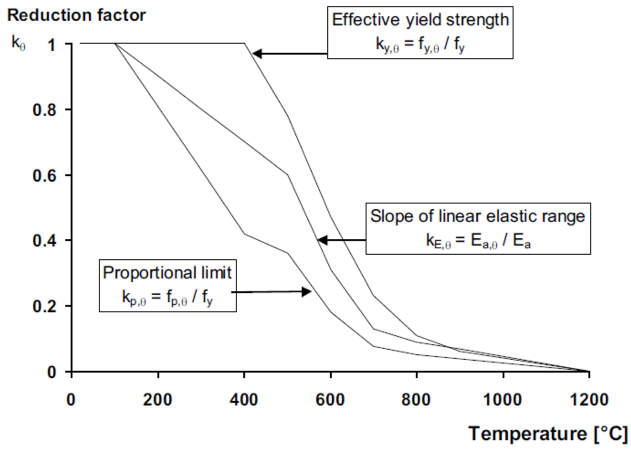

Figure 4: Reduction factors for the stress-strain relationship of carbon steel at elevated temperatures [9]

2.4. Fire Exposure

In Australia, the fire resistance of elements is described as the Fire Resistance Level (FRL) and is graded for its "*structural adequacy/ integrity/ insulation ratings*", in that order [3]. For instance, an FRL of 120/-/- represents that a member has a 120 minutes IS0 834 furnace time equivalence, for structural adequacy with nil ratings for integrity and insulation – i.e., a column member carrying predetermined structural load other than its self-weight for 120 minutes under the subject fire curve. This rating is set out by the Australian Standard AS 1530.4, and similar representations of fire ratings are present in other jurisdictions in the world based on either the ISO 834 or ASTM E119 furnace curves.

The intent is to standardise the fire protection to the structural elements as per the risks associated with its usage and height of the building. It is irrelevant to a real fire or structure behaviour. In some instances, a hydrocarbon, RABT-ZTV or other temperature-time curves may be used more in infrastructure settings, but, in Australia, the FRLs are still defined by the ISO 834 curve.

Through historical compartment research by Kawagoe, Law, Harmathy, Thomas, Heselden and others [14], we know that the temperatures in some regimes can be governed by openings in a compartment, rather than the present fuel loads.

There are different design curves which can accommodate different heating regimes, one of which is the parametric fire curves as described in Eurocode 1, EN 1991-1-2 in Annex A [15], which can be used instead of the ISO 834 furnace curve. The parametric fire takes in consideration the expected fuel loads of the space and the opening conditions and is a considered a widely used methodology. Figure 5 shows a comparison between steel temperatures applying the Eurocode 3 unprotected and protected steel equations [9] with fire inputs of either ISO 834 or a parametric curve from Eurocode 1 [15].

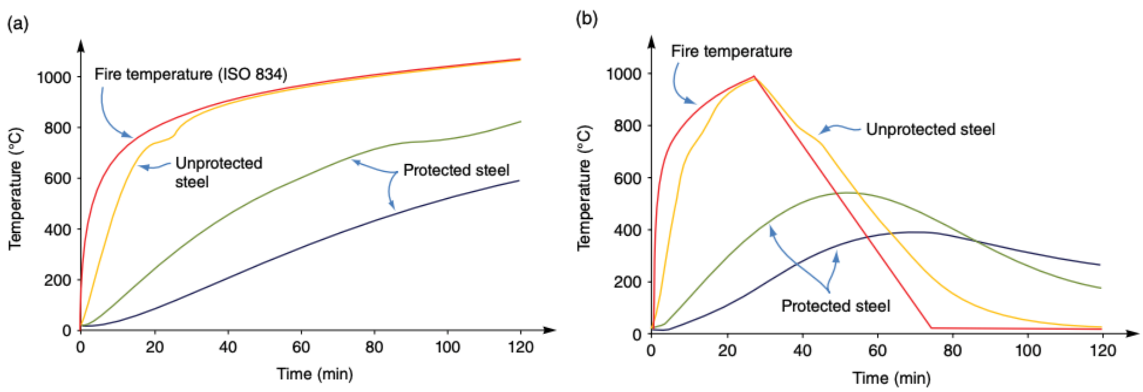

Figure 5: A comparison of steel member temperatures when exposed to a standard fire (ISO 834) and a parametric fire [8].

2.5. Coat-back

The adopted industry coat-back design approach on all secondary or ancillary elements is for a distance of 450-500mm, where the contact area exceeds 3,000mm^2 per metre of length. This is based on the source reference, from the Fire and Blast Information Group / Steel Construction Institute (FABIG/SCI) technical note [1], Burgan and Selby [11], also from SCI, conducted various finite element models (FEM) to observe the effects of the coat-back.

Burgan and Selby analysis was validated with a hydrocarbon curve up to 2 hours, with an insulation product Thermolag 440 as the coat-back up to 450mm. Although the authors did note that the analysis was still valid with another unspecified insulation product (Poldolski et al. disagrees for intumescent products [16]), the resultant empirical equation [11] was given as the following:

$$T_a = T_p + \frac{N\sqrt{t}}{[1 + A_r\,(\frac{L_p}{300})^2]L"_p} \tag{4}$$

The paper does mention modelling akin to a parametric study, however, the full result is not published. As such, it is hard to observe the correlation between the section factors of the primary and secondary members with coat-back. There was no mention on the 3,000mm^2 exception on coat-back as described in the FABIG/SCI technical note [1]. Even applying equation (4), using 3,000mm^2 as the ancillary member's area and applying the limits of the equation's validation ($A_r = 0.02$, L_p=5mm, t=2 hours and assume square perimeter), there is an expected temperature rise of ~38°C. Whether this is the temperature rise to be considered non-significant is unknown.

Various other published papers have assessed coat back, tested to either 1-hour or 2-hour exposure with both ISO 834 and hydrocarbon curves; majority have concluded that the coat-back has been applicable in their specific applications. Generally, the longer the coat-back the better the protection [17].

Burgan and Selby and Yasseri et al. [11] [10], do acknowledge the ratios of, the cross-sectional areas and the section factors of the primary and the ancillary members to have an effect; section factors are generally higher on ancillary members. Poldolski et al. and Dobrovolny et al. [16] [18], further confirm with correlations showing increased thickness of protection and lower section factors, provided better insulation and thus a bigger gradient along a coat-back length.The general consensus is that 450-500mm is applicable for a fire resistance level up to 2-hours equivalence, whether it is ISO 834 or hydrocarbon curves.

Due to the vastness of the inputs and different arrangements, it is very difficult to directly collate with each other as many are not like-for-like (i.e., different fire curves or materials). Further investigation is required in academia and industry, with a full parametric case study, that has a standardised approach with validation and testing to observe if there is an overarching correlation that, perhaps dimensionless, such that it can be applicable to all cases.

3. THE PROBLEM

In the applied design process of structural fire design on buildings, there is a fine balance on what inputs are adopted such that you deliver the best outcome for your project. There are many factors to consider, technical, buildability, time, unknown product information and client expectations.

As a designer you try to balance all these factors, how do you protect the connection to achieve a safe outcome? The current approach and literature have no consideration of the actual fire or structural behaviour in a combined setting. For example, there are instances where localised temperatures could be considered more important than the lumped temperature of a steel member. This may be more critical in beams where the flanges of an I-beam typically carry the compression and tension of the bending moment, while the web of the I-beam takes up the lateral and shear loads of the structure.

What type of fire is present? As this will influence the applied heat loading onto a connection and the global structure. A short and hot fire will impact the structure very differently to a long and cool fire.

For this project, a thermal fire analysis was conducted on an intricate composite steel and concrete structure in Australia. Some sample connections from this building are shown in Figure 6, showcasing a wide range of steel connections, some of which are partially protected where ancillary members connect into primary protected members.

Taking account of the current State of the Art, including knowledge gaps and project constraints, a design framework has been developed to help solve the complexity of the problem.

Figure 6: Sample sections, in a finite element model, with ancillary member connections attached.

4. FINDINGS AND DISCUSSIONS

4.1. Intricate Connections

For intricate connections where no coat-back is applied and hotspot attachments cannot be limited, this was assessed on a case-by-case basis with a finite element heat transfer analysis. This can be useful in a complex scenario with multiple attachments, as shown in Section 4.2. LS-DYNA was used, a general-purpose nonlinear finite element analysis package which is capable of simulating thermal analysis of concrete and steel structures.

This methodology is based on the specified design limiting temperature (550°C), which was selected for this project. A baseline reference model (R) is taken with a layer of fire protection (plasterboard used in this instance), such that lumped steel temperature of the baseline reference model is less than 550°C. This will be compared to the proposed actual connection arrangement model (A) with the same thickness and thermal properties of the baseline reference model, with the thermal bridge (ancillary attachments).

Temperatures for the proposed model (A) were examined at the flange and web of the section to evaluate the reduction of the yield strength of steel, as per AS 1530.4-2014. Sections of the two models are shown in Table 1.

Table 1: Intricate Connection Methodology Outline

Baseline Reference Model (R)		**Proposed Actual Model (A)**	
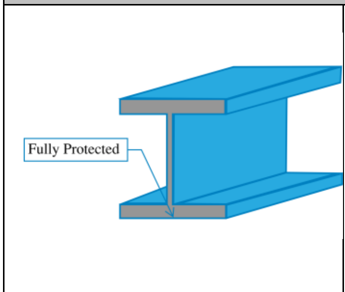	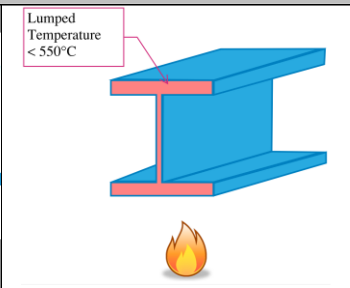	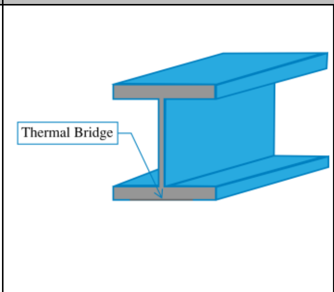	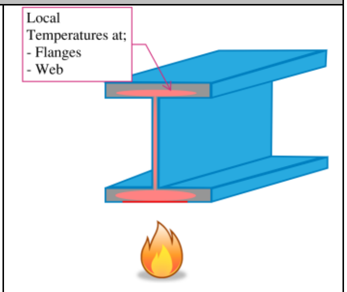
R1: Reference Geometry State	R2: Reference Heating State	A1: Proposed Geometry State	A2: Proposed Heating State

The approach and steps would be the following:

1. Categorise the critical elements of the connections that are required to be modelled.
2. Use Eurocode 3, Section 4.2.5.2 of EN 1993-1-2:2005 [9] calculation method, to determine thickness of plasterboard needed to achieve steel temperature less than 550°C.
3. Apply the properties to the baseline reference model (R) with all elements protected.

4. Verify the baseline reference model (R) to see if the lumped temperature is less than 550°C using the standard ISO 834 fire curve, per AS 1530.4-2014.
5. Test the proposed model (A) with:
    a. The ISO 834 fire curve, or;
    b. Parametric fire curve.
6. Record temperatures after the specified time for FRL for ISO 834 fire curve or maximum temperature for the parametric fire.
7. Check the yield strength of the flange/web where applicable and check the Ultimate Limit State design under fire load to confirm the connection does not fail (Local and Global).
8. Repeat with adjustments if connection fails.

Measured temperature locations are in line with the thermocouple locations specified in AS 1530.4-2014.

Calculation of Limiting Temperature is taken as the maximum difference between

$$(R) - (A) + \text{Design Temperature} \qquad (5)$$

taken at the individual measurement points in Table 2 and their average. Equation (5) is based on:

$$T_{web} \geq T_{limit} \geq T_{flange} \qquad (6)$$

Table 2: Temperature measurement locations per AS 1530.4-2014 [19]

Beams	Columns
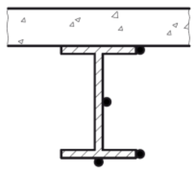	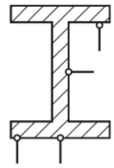

Ordinarily, the web temperature governs the limiting temperature of the overall section, due to its thinner section. When the flange temperate exceeds the web temperature, equation (5) no longer applies. With the flange taking the flexural loads, it becomes more critical. Highest shear forces, taken by the web, may not occur at the same position of a member where the highest bending moment is taken by the flange. In such cases, the flange temperature (A) governs and becomes Limiting Temperature.

4.2. Finite Element Modelling Results

The fire protection of members in the building were a combination of vermiculite or intumescent paint coatings. As the thermal properties of these coatings differ between supplier and paint formulation and the expansion behaviours cannot be accurately quantified, a surrogate material was used. The material properties are not as critical, the assessment is a comparative approach with respect to the reference model (R), thus is not reliant on precise material properties as both (A) and (R) share the same properties.

A parametric fire curve was deemed more appropriate for the space, based on the assumed fuel loads and compartment geometry, including ventilation. The parametric fire curve provided a better representation of a likely exposure fire event rather than based on furnace temperatures under ISO 834, which is common practice in industry. A sample connection from the project is presented here. It is a 3-sided exposed steel beam with multiple attachments with its topside connected to the concrete slab.

Table 3: Example FEM modelled connection

3D BIM Model	LS-DYNA Model	Information:	
	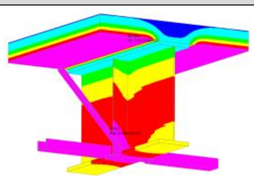	Beam Type:	700 WB 150
		Protection Design Limiting Temperature:	550° C at 120 FRL
		Resultant Temperature with ancillary connections:	560° C

The results from the LS-DYNA model (summarised in Table 4) show that the critical temperature averaged across the bottom flange of the beam reaches 560ºC, which is the critical section of the beam. It was confirmed in the structural model that this temperature increase at this location would not result in the connection to fail. The higher temperature produced a higher steel yield stress, this modified value was inputted into the structure model to check the beam's capacity under a fire limit state load case.

Table 4: Section Result Summary

Section	Model (R)	Model (A)	Units
700 WB 150	R	A	
Fire	ISO Fire	Parametric	
Section	465	427	[°C]
Web	586	451	[°C]
Flange Bottom	496	560	[°C]
Flange Top	284	231	[°C]
Resultant limiting Temperature:		560	[°C]

Considering the fire curve representative of the space (fuel loads and ventilation) and having the concrete slab acting in as a heat sink, the increases in temperatures due to the unprotected element connected to the beam did not result in structural failure under fire limit state design. Specifically, model (A) resulted in lower maximum average temperatures than the temperature taken at 120 minutes in model (R). Figure 7 and Figure 8 show the output temperatures from the measurement points.

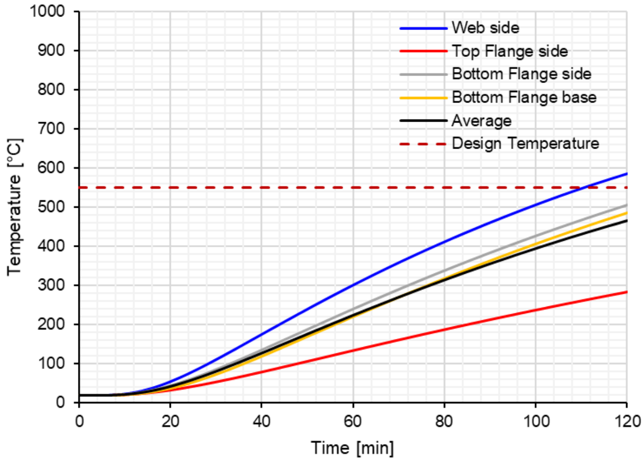

Figure 7: Model (R) Temperature vs. Time

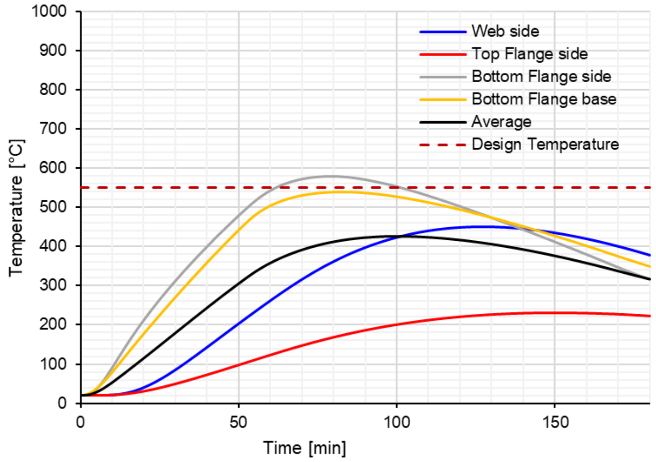

Figure 8: Model (A) Temperature vs. Time

4.3. Minor Connection Discussion

For minor connections, limiting the exposure of unprotected surface was based on the generally accepted rule of protection adopted by industry. It was highlighted in Section 2.5 that 3,000mm^2 per metre length rule, where no coat-back was required, was taken as the industry best guidance. However, the origins of this could not be found and more is needed to confirm the exact threshold. The impact of unprotected ancillary members for the 3,000mm^2 per metre length rule is discussed in this Section.

Applying the same connection as the one shown in Section 4.2, Figure 10 compares the presence of an ancillary stub at the bottom of the connection. The stub is a 100mm x 100mm connected at the bottom of the flange and has a coat-back of 90mm from the surface of the flange (as shown in Figure 9). The baseline model (no stub) has unprotected existing ancillary connections of 6,950mm^2.

Figure 10 shows the temperate and its difference, along the bottom flange longitudinally of the primary member from the stub attachment at the section's base. An FRL 120 heating curve is applied in both cases for this comparison.

The temperature difference are relatively minor in Figure 10, <10°C at 200mm. Table 5 shows the resultant yield stress reduction factor from Eurocode 3 [9] and utilisation of the section increase based on a design temperate of 550°C, with a corresponding yield reduction factor of 0.625.

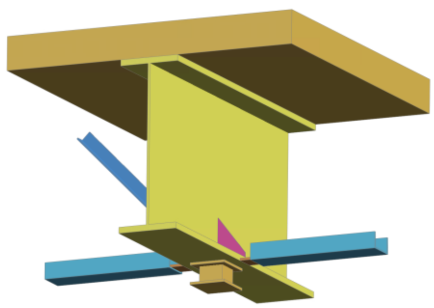

Figure 9: Connection with stub located attached to the bottom flange

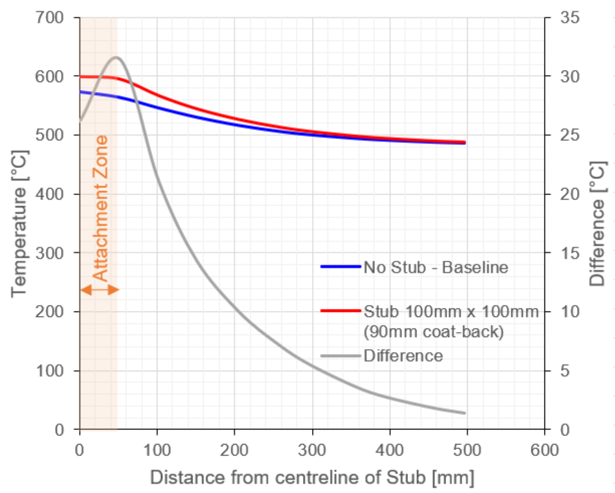

Figure 10: Resultant temperatures along the primary member from the ancillary attachment interface

For both cases, particularly when you move away from the attachment zone, the utilisation factor increase (%) is in a similar magnitude for 5th percentile structural design for failure [3] [8].

From a structural standpoint, slight increases in the utilisation factor is generally acceptable, as it would assume that the section is full loaded, which is rare. In design structures are not fully optimised, it discounts conservatism taken in section sizing, load redistribution, accounting extra for buildability. Furthermore, the ultimate limit state for fire may not be the overall worst-case scenario compared to wind, earthquake and serviceability. As such slight increases under fire limit state may be perceived as lower risk, compared to other scenario.

Table 5: Resultant structural yield reduction and utilisation factor increase relative to 550°C design temperature

x =	0	50	100
Yield Reduction Factor (No Stub)	0.55	0.58	0.64
Stub	0.47	0.49	0.57
Utilisation Factor Increase (No Stub)	12.6%	7.1%	-2.2%
Stub	32.0%	28.6%	8.9%

A connection with a contact area of 3,000mm^2, may well below the 5% range, thus fall within the 5th percentile envelope for design structural failure.

As calculated in Section 2.5, if the 38°C temperature rise was the ‘threshold’, the resultant ~32°C increase is below that ‘threshold’.

Although applying equation (4), for a 90mm coat-back in this configuration from Burgan and Selby [11], we would have an expected temperature rise of ~2°C in the hotspot zone instead. As such, the equation could not be used uniformly in all situations.

Figure 11 shows the fractional temperature decrease from the hotspots in the same connection but also compares it to another FEM connection, where the ancillary connection is less than 3,000mm^2 to its primary member. The bracket value is the area ratio of the ancillary member with its connected primary member.

- Purple line – same 10,000mm^2 stub.
- Red line – same connection but with an unprotected fly brace (5,150mm^2) connected to the stiffener *(taken as the ‘primary member’)*.

- Blue line – a 2,400mm^2 RHS section attached to an I-beam (different section - Figure 6 (b)).

For both ancillary connections of 10,000mm^2 and 2,400mm^2, where the area ratio is the same magnitude, the temperature away from the attachment appears to decrease at a similar rate. Further research is needed to help conclude if such correlation exists, and it could provide a better definition on when coat-back is not needed.

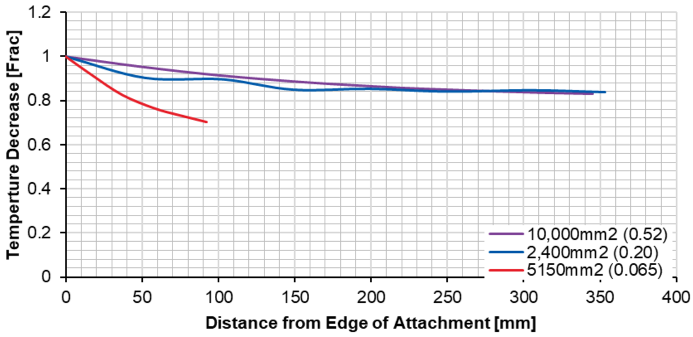

Figure 11: Resultant fractional temperature decreases along the primary member from the ancillary attachment interface for three attachment types

The unprotected fly brace (5,150mm^2) has an area ratio a magnitude lower, as the fly brace was relatively small in cross-sectional area compared to the wider cross-sectional area of the stiffener. With a higher mass, the stiffener sinks in a majority of heat away from the fly brace. This makes sense when looking at Equation (1) but in a 2-D sense; as the temperature gradient would be greater but also more difference in mass on a pure energy per area basis. It is suggested that further research is needed to pinpoint the exact threshold.

4.4. Coat-back Discussion

Applying a 500mm coat-back for FRLs up to 120 is generally supported as noted in in Section 2.5. This section evaluates a 1-D heat transfer analysis to provide a simpler method of calculating the required coat-back in future applications.

Applying methodologies found in Bergman et al. [7], notes from Maluk [20] and properties from Eurocode 1 and 3 [15] [9], an iterative 1-D heat transfer analysis was developed using an ISO 834 fire curve up to FRL 120. A similar assessment was previously done by Yasseri et al. for the hydrocarbon curve up to 2-hours [10]. The analysis was conducted with 500mm (Figure 12) and 1,000mm (Figure 13) length of steel, exposed to heat at (x) =0 and no heat loses at the end.

Figure 12 and Figure 13 show the progression of temperatures through the steel for a depth of (x), with each progressive line representing 12-minute intervals. By 120-minute exposure of the ISO 834 fire curve, at 500mm in both cases, temperatures are less than 300°C, with lower temperatures in Figure 13, around the mid 200°C s. According to Equation (2) and its theory, a larger gradient is present with a higher Biot number and as such the temperature at 500mm would be lower in Figure 13 than in Figure 12. At 300°C, the effective yield strength of steel would not have been reduced [9].

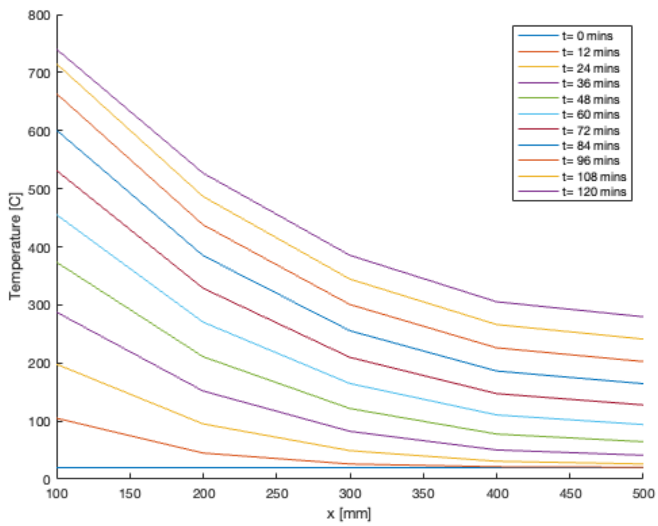

Figure 12: 1-D heat transfer for steel with a length 500mm

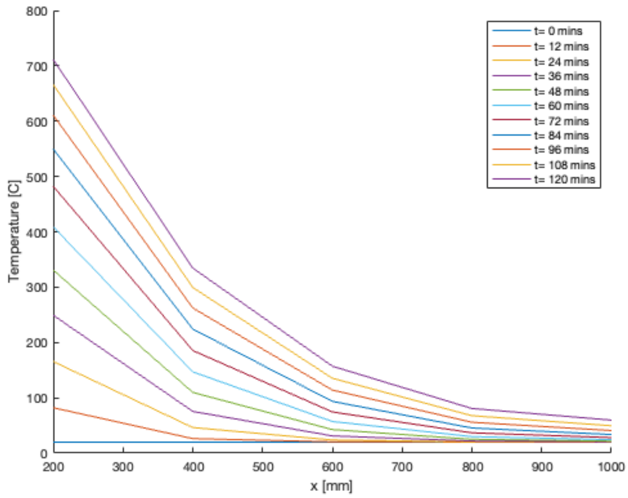

Figure 13: 1-D heat transfer for steel with a length 1,000mm

Both figures are a simplified representation of heat flow through a coat-back ancillary member into the primary protected member. Figure 12 shows heating from the unprotected portion of the ancillary member through the insulated 500mm coat-back to the expected temperature, assuming no heat losses in the end. Figure 13 applies additional 'distance' to simulate heat loss through to the primary member as shown in Figure 15 (note that 1,000mm is taken arbitrarily for comparison).

A 1-D model assumes no thickness or volume in the ancillary member. If this was considered, temperatures would be more distributed and thus result in lower temperatures along the 500mm length (assuming perfect insulation). Figure 14 shows the effect on this on a large beam (refer to Figure 6(d)) that was heated in one direction by an ISO 834 fire curve, whereby the temperature is much lower due to the thickness and volume, as it is able to dissipate due to its three-dimensional mass.

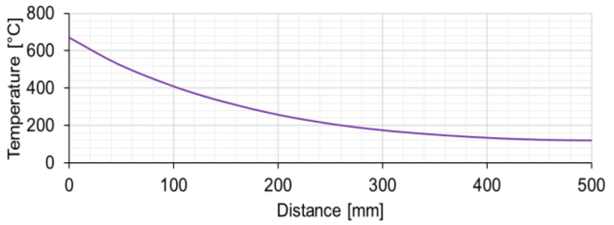

Figure 14: LS-DYNA model example of one-directional heating along a splice plate connection of 1200WB 392 section at 120 minutes of exposure of ISO 834 fire curve

Conversely, as shown in Figure 16, there would be heating perpendicular to the ancillary member. As described by Yasseri et al [10], the heating could be assumed uniform through its length. Burgan and Selby mentioned that ancillary members are typically under protected, as the coat-back is based on the Section Factor of the primary member, and the Section Factor of the ancillary member is typically higher than the primary member [11]. Therefore, the ancillary member may heat up faster than the primary member.

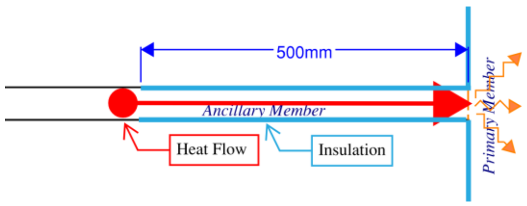

Figure 15: Ancillary member attachment 1-D heat flow

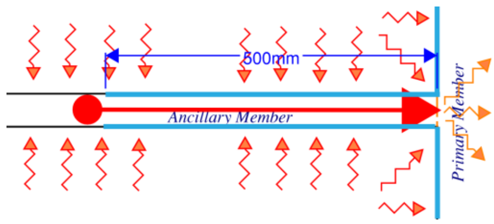

Figure 16: Ancillary member attachment with external exposure

As the heating is assumed to be uniform through the length of the ancillary member, a constant value could be applied for each time step of the 1-D model based on a correction by measuring the difference in temperature of the same protection thickness using Eurocode 3, Section 4.2.5.2 of EN 1993-1-2:2005 [9].

However, considering the effects of heat loss by distance and volume, as shown in Figure 13 and Figure 15, this may counterbalance heat gains, and further investigation could be done to confirm. For simplicity and practical application purposes, the method of 1-D heat flow analysis – up to the coat-back length of 500mm with no heat loss at the end, as shown in Figure 12 – may be sufficient enough up to a 2-hour exposure (hydrocarbon or ISO-834), which is supported by other literature, as noted in Section 2.5.

5. THE DESIGN FRAMEWORK

The design framework takes in, best industry practice, current available research, design considerations and the variability of protective coatings offered by manufacturers. It accounts of unknown information or untested system and provides a practical approach to address the issue.

The approach considers the use of the building and actual design loads to help inform the protected arrangement. It takes a comparative approach from an unprotected baseline with protected arrangement. A parametric fire curve may be used, as it provides a design fire based on the actual usage of the space and the expected fire exposure, which is then assessed against the actual structural response of the primary steel connection's capacity. The framework is as follows:

The steel elements are protected with either intumescent paint or vermiculite spray, to meet the design limiting temperature of 550°C (example) to achieve the required FRL requirements, taking precedence from the State of the Art, as defined by the structural engineering team in their design.

Where unprotected secondary elements are connected to a fire-rated primary structural member, a thermal bridge is created, which may cause temperatures within the primary structural element to exceed the design limiting temperature of 550°C.

The following protection scheme is proposed for the unprotected steel elements supported by the fire rated steel members. Due to the amount of present connection, the members are triaged into relevant connection types, Type A, B and C.

- **Type A Connection** – When non-fire rated steel elements connect to a fire rated element, which lead to a total unprotected area less than 3,000mm^2 per metre length of the fire rated element, no additional protection is provided.
- **Type B Connection** – When non-fire rated steel elements connect to a fire rated element, which lead to a total unprotected area over 3,000 mm^2 per meter length of the fire rated element, the non-fire rated element is to be protected at least 500 mm at the connection.
- **Type C Connection** – When non-fire rated steel elements connect to a fire rated element, which lead to a total unprotected area over 3,000mm^2 per meter length of the fire rated element, and the non-fire rated element cannot be protected at least 500mm at the connection, the required fire protection scheme is proposed on case-by-case basis.

This is shown as a flowchart in Figure 17.

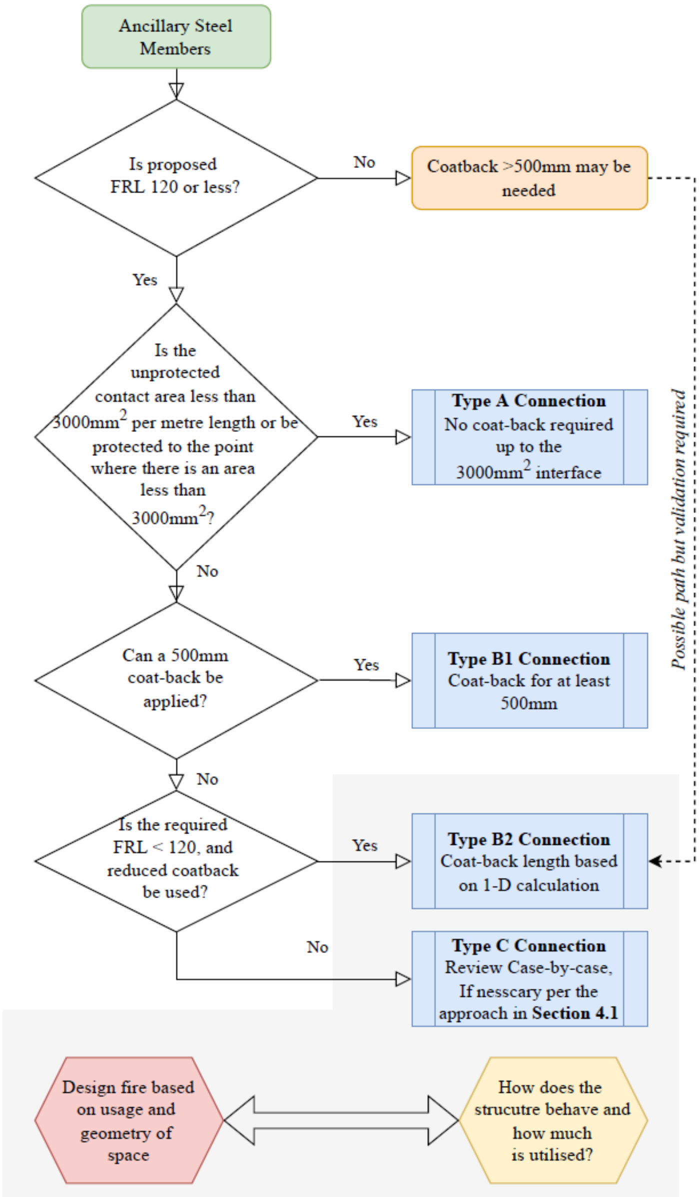

Figure 17: Flowchart of design framework

6. CONCLUSION

A practical design framework was established to consider applied fire scenarios and the resultant structural behaviour of a building in a combined setting.

The application of coat-back was also discussed with some potential correlations noted as follows.

- The 3,000mm^2 per metre length rule for ancillary members not to be fire protected, appears to be still valid, although its threshold may not just be at 3,000 mm^2, this needs to be explored and verified.
- The 500mm coat-back is only applicable up to a 2-hour rating (hydrocarbon and ISO 834), based on literature and the above study, higher ratings may require increased coat-back. Coat-back length could be supported by an iterative 1-D heat transfer calculation.

The above findings should be further investigated, ideally with a full parametric study, including laboratory testing.

ACKNOWLEDGEMENT

We would like to acknowledge the support and contribution provided by Arup's seed funding. Acknowledgment of Jon Dufty who was involved with the finite element modelling geometry on the project and both to Michaela Brown and Lisa Kaluzni as the main structural engineers on the project, who were involved through the design process.

7. REFERENCES

[1] Fire and Blast Information Group (FABIG), "Design Guidance for Hydrocarbon Fires," Steel Construction Institute, Ascot, United Kingdom, 2014.

[2] Associated for Specialist Fire Protection (ASFP), Code of practice for junctions between different fire protection systems when applied to load bearing structural steel elements., Kingsley, United Kingdom: Associated for Specialist Fire Protection (ASFP), 2010.

[3] Australian Building Codes Board, "National Construction Code, Building Code of Australia 2019 Amendment 1," Australian Building Codes Board, Canberra, Australia, 2020.

[4] Underwriter's Laboratrories (UL), "UL's Best Practice Guide for Passive Fire Protection for Structural Steelwork," Underwriter's Laboratrories (UL), Northbrook, United States of America, 2018.

[5] DNV, "Offshore Stanfards DNV-OS-D301: 2019 Amdt 2021 Fire Protection," DNV, Baerum, Norway, 2019.

[6] O. A. Ezekoye, "Conduction of Heat in Solids," in *SFPE Handbook of Fire Protection Engineering Fifth Edition*, New York, United States of America, Society of Fire Protection Engineers (SFPE), 2016, pp. 53-101.

[7] T. L. Bergman, A. S. Lavine, F. P. Incropera and D. P. Dewitt, Fundamentals of Heat Transfer Seventh Edition, Jefferson City, United States of America: John Wiley & Sons, 2011.

[8] A. H. Buchanan and A. K. Abu, Strucutral Design for Fire Safety Second Edition, Chichester, United Kingdom: Wiley, 2017.

[9] European Committee for Standardization, "EN 1993-1-2 Eurocode 3: Design of steel structures - Part 1-2: General rules - Structural fire design," European Committee for Standardization, Brussels, Belgium, 2005.

[10] S. F. Yasseri, "Coat-back length in Passive Fire Protection of Offshore Installations," in *21st International Conference on Offshore Mechanics and Arctic Engineering*, Oslo, Norway, 2002.

[11] B. A. C. A. Burgan, "Rules for the Determination of Coat-back Requirements," Steel Construction Institute, Ascot, United Kingdom, 1997.

[12] J. Amdahl, T. Holmas and B. Skallerud, "Ultimate Strength of Strucutral Members with Attachments during Accidental Fires," in *International Conference Resposne of Structures to Extreme Loading*, Toronto, Canada, 2003.

[13] A. Lucherini, "Fundamentals of thin intumescent coatings for the design of fire-safe structures," The University of Queensland School of Civil Engineering, Brisbane, Australia, 2020.

[14] D. Drysdale, An Introduction to Fire Dynamics Third Edition, West Sussex, United Kingdom: John Wiley & Sons, 2011.

[15] European Standards Committee, "BS EN 1991-1-2, Eurocode 1: Actions on structures - Part 1-2: General actions - Actions on structures exposed to fire," European Standards Committee, Brussels, Belgium, 2002.

[16] D. Podolski, Y.-C. Wang and J. Yuan, "Numerical investigation of intuimescent 'coatback' on unportected secondary beams," in *Applications of Fire Engineering*, Manchester, United Kingdom, 2017.

[17] M. Friebe, B.-S. Jnag and Y. Jim, "A parametric study on the use of passive fire protection in FPSE topside module," *International Journal of Naval Architecture Ocean Engineering,* no. 6, pp. 826-839, 2014.

[18] P. Dobrovolny, J. Sejna and F. Wald, "Temperture Distrubutiom in the Coatback of a Partially Fire-Protected Member," in *Applications of Strucutral Fire Engineering*, Ljubljana, Solvenia, 2021.

[19] Australian Standards, "AS1530.4:2014 Methods for fire tests on building materials, components and structures, Part 4: Fire-resistance tests for elements of construction," Australian Standards, Sydney, Australia, 2014.

[20] C. Maluk, *Notes on Heat Conduction - Course Notes,* Brisbane, Australia: The University of Queensland, 2018.

SiF 2022– The 12th International Conference on Structures in Fire
The Hong Kong Polytechnic University, Nov 30 - Dec 2, 2022

RECENT DEVELOPMENTS IN HOLISTIC PERFORMANCE-BASED FIRE DESIGN OF STEEL STRUCTURES - CASE STUDY: A PADEL-CENTER

Timo Jokinen[1], Risto Ranua[2], Mikko Salminen[3]

ABSTRACT

This paper presents an overview of the performance-based fire safety analysis of steel structures of padel-center built in Nokia, Finland. The analyses are conducted using advanced calculation models (FDS and SAFIR) in support with less sophisticated models (critical temperatures of steel member). The aim of the paper is showcase recent developments in design processes and methods that are in practical use today in performance-based fire design (PBD), and to demonstrate that relatively extensive performance-based studies can be (commercially) viable also in relatively small and mundane steel buildings. As a result of the performance-based design, most of the steel structures in the case building could be constructed without fire protection, but some critical structures were identified and protected to class R30.

Keywords: steel structures; performance-based fire design; case study; SAFIR; FDS

1 THE BUILDING IN THE CASE STUDY

The building studied with performance-based fire design is relatively tall (approx. 10 m) but quite small 1-story padel-center (approx. 1500 m²) built to Nokia, Finland. The load bearing structure is steel skeleton frame (columns, trusses and braces, see Figure 1b), and the building will not be equipped with a sprinkler system. The building consist of padel fields, a lounge area, and a locker room area which is a separate fire compartment and which has HVAC machinery above it (Figure 1a).

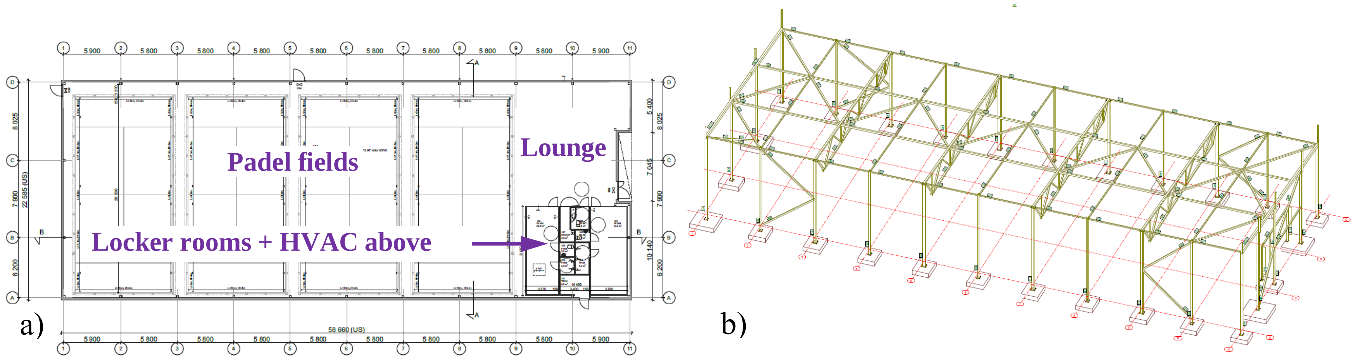

Figure 1. The case building: a) the architectural plan of the ground floor b) the steel skeleton.

[1] Senior Fire Safety Specialist, M.Sc, Markku Kauriala Ltd, Fire engineering and fire safety design consultants, Finland
e-mail: timo.jokinen@kauriala.fi
[2] Senior Fire Safety Consultant, M.Sc, Markku Kauriala Ltd, Fire engineering and fire safety design consultants, Finland
e-mail: risto.ranua@kauriala.fi
[3] Senior Fire Safety Specialist, D.Sc, Markku Kauriala Ltd, Fire engineering and fire safety design consultants, Finland
e-mail: mikko.salminen@kauriala.fi
https://doi.org/10.6084/m9.figshare.22153547

2 REGULATORY BASIS

The PBD is done according to Finnish fire safety decrees [1, 2] utilizing Eurocodes (especially EN 1991-1-2 and EN 1993-1-2 [3, 4]) and their Finnish national annexes (as closely as they can be in PBD). According to prescriptive design, the fire resistance requirement for the steel structures in the case building is R30 and the aim of the PBD is to reduce the required fire protection where possible. PBD is explicitly allowed in Finnish fire safety decrees, but some additional design criteria are presented for the PBD of load-bearing structures (Table 1).

Table 1. Design criteria when the design of essential load-bearing structures is based on a design fire scenario. Shortened from the full table presented in Decrees 848/2017 & 927/2020 [1, 2], (unofficial English translation).

Building	**Restrictions**	**Resistance of essential load-bearing structures in a fire**	**Design fire load density [MJ/m²]**
One-storey, general	Height exceeding 9 m	60 minutes without cooling phase	$Q_{fi,k}$
$Q_{fi,k}$ is the statistically or computationally determined characteristic value of the total fire load density (80 % fractile).			
The study is carried out for a completely developed fire. If it can be demonstrated that no flashover will occur, the design can be made for a local fire. Flashover is regarded as having taken place if the average temperature of the hot smoke layer reaches 500 degrees Celsius, or if the radiation from the smoke layer to the floor exceeds 20 kW/m².			

3 FIRE SCENARIOS AND DESIGN FIRES

Due to nature of the building, the potential fire load is quite small (padel is a racket sport similar to tennis or squash), thus the design fire scenarios consist of localized fire load concentrations. The building is equipped with locker rooms, but they are separated from the main hall with EI30 fire compartment borders and fire in there will not affect the hall part (see Figure 3). The use of localized fires will require that flashover will not occur, which is verified during the fire simulations.

The studied fire scenarios and design fires are:

- **Fire I:** Lounge area furniture fire: Design fire of four 3-person sofas on lounge area. (Figure 2 a), First sofa ignites 5 min before the other three. Two different locations are studied.
- **Fire II:** Sporting equipment fire: Design fire of 10 sporting bags filled with flammable clothing (Figure 2 b).
- **Fire III**: Fire during maintenance: scissor lift fire with miscellaneous temporary fire load. Design fire approximated to a forklift fire and three wooden pallets (Figure 2 c & d).
- **Fire IV**: Fire on HVAC balcony near the trusses: fire load in HVAC machine is very small; design fire approximated to three wooden pallets left during maintenance on the balcony (Figure 2 d).

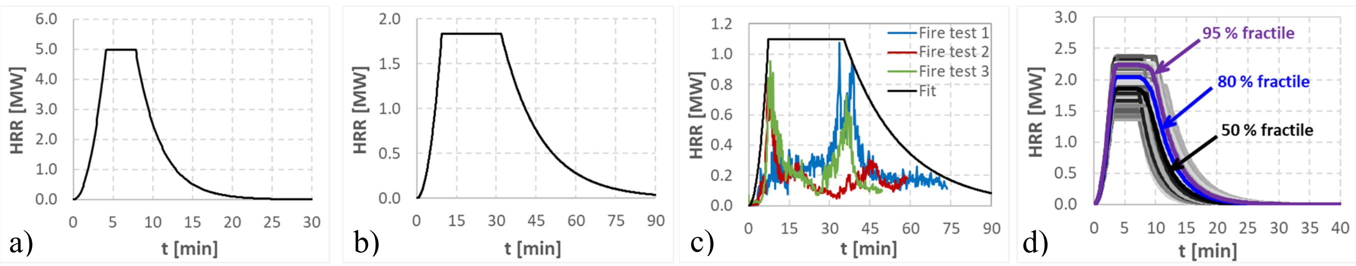

Figure 2. Heat release rate (HRR) curves for the design fires: a) one 3-person sofa [5], 99.9 % fractile, b) 10 sporting bags filled with flammable clothing [5], 99.9 % fractile, c) scissor lift fire based on forklift fires from [6] d) three wooden pallets (Monte Carlo simulations based on formulas in [7]).

The locations of the fire scenarios and design fires are shown in Figure 3. All of the shown fire scenarios and design fires were simulated in the case project, but due to length constraints of this paper, only Fires Ia, Ib and II are documented here in more detail (which were the most critical fire scenarios). The design fires of I and II are based on 99,9 % fractiles [5], which is much greater than required in Table 1.

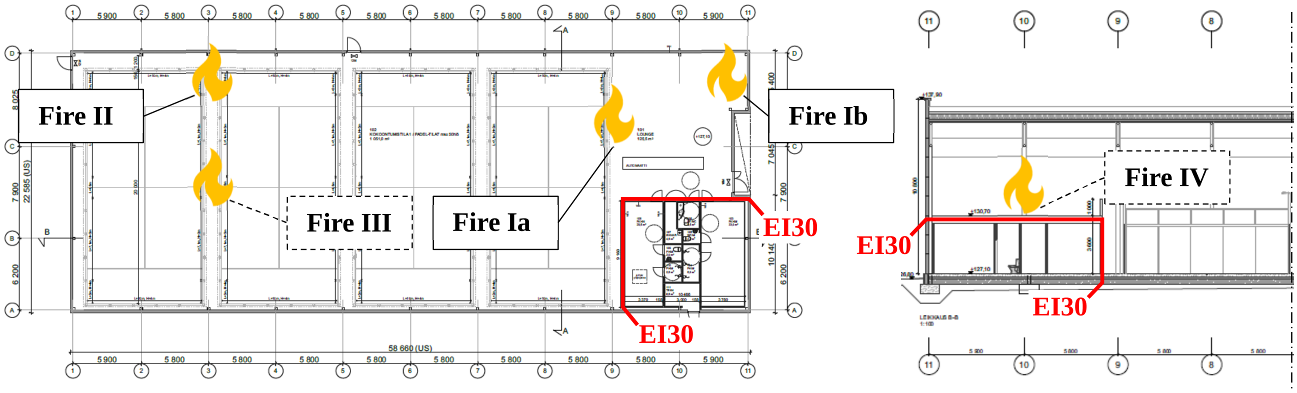

Figure 3. Locations of the fire scenarios and design fires. EI30 compartment borders around the locker rooms.

4 ACCEPTANCE AND PERFORMANCE CRITERIA

Following acceptance and performance criteria are used:

- Design fires should cover all feasible fire scenarios in the building (848/2017, 3§ [1]).
    - If localized fires are used, the radiation heat flux towards the floor should remain below 20 kW/m² to ensure flashover doesn't occur (see Table 1).
- Analysed steel structures should withstand the whole design fire including cooling phase without collapse (technically the requirement is 60 min without cooling phase, see Table 1, but since chosen design fires are mostly shorter than 60 min, it doesn't matter). This can be determined by:
    - **Simple calculation models**: Simple analysis according to Eurocode EN 1993-1-2 section 4.2 [3] using steel section temperatures and critical temperatures; section temperatures must remain below the critical temperatures of members during the whole fire.
    - **Advanced calculation models:** advanced analysis according to Eurocode EN 1993-1-2 section 4.3 [3] using FEM software (e.g. SAFIR); the structure must maintain its resistance without collapse the whole design fire in the advanced analysis model.
    - Since EN 1991-1-2 section 4.1 [4] requires, that in PBD indirect effects of the design fires (i.e. indirect thermal actions and displacements from thermal expansions, thermal gradients within cross-sections, non-linear material models, etc) must be considered, the final design is checked using the advanced calculation models. Simple calculation models are used to find the most critical members and design fires where the advanced models should focus.

5 CALCULATION METHODS

5.1 Fire simulations

Fire simulations are performed using the Fire Dynamics Simulator (FDS, v. 6.7.9). FDS is computational fluid dynamics (CFD) software, and it is based on numerically solving a form of Navier-Stokes equations optimized for fire-driven fluid flows. FDS is designed and validated to work well in typical building fire conditions [8, 9]. In this study, FDS models are built using Pyrosim pre-processor. The used FDS models are shown in Figure 4; measurement points are shown in yellow and design fire surfaces are red. Smoke exhaust systems are assumed to be closed during the whole simulations, but the building is assumed to have enough doors open to ensure that the fire will not become oxygen limited.

The resolution of the simulation mesh is the most important parameter affecting the FDS simulation quality. The sufficiency of the mesh resolution can be assessed with $D^*/\delta x$ ratio [8, 9], where δx is the nominal size of a mesh cell [m] and D^* characteristic fire diameter [m] (see calculation formula in [8]). The commonly accepted lower limit for $D^*/\delta x$ ranges between 4 – 16 (e.g. [10]). There is no upper limit; larger values capture more details. In the simulations $\delta x_{Fire\ I} = 0.2$ m and $\delta x_{Fire\ II} = 0.1$ m near the fire source and near the measurement points (multiple of 2× or 4× further away from these critical areas). Therefore, in these simulations the ratio $D^*/\delta x$ is between 12 - 15 and thus the mesh resolution can be deemed to be sufficient.

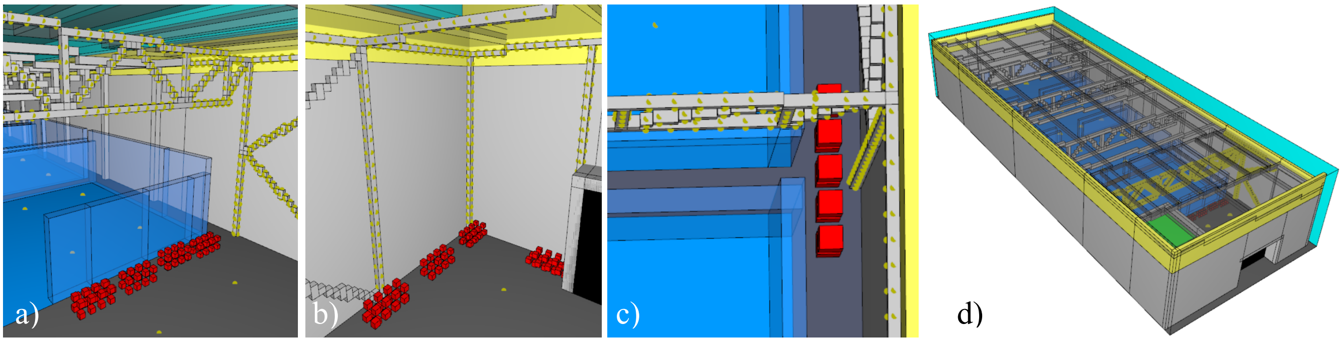

Figure 4. a) a picture from the FDS model in Fire Ia, b) a picture from the FDS model in Fire Ib, c) a picture from the FDS model in Fire II, d) the whole calculation domain in the FDS simulations.

5.2 Structural fire resistance using simple calculation models

Temperatures are transferred from the fire simulations to the structural analysis by using Adiabatic Surface Temperature (AST) measurements [11]. Adiabatic Surface Temperature method takes into account the convective and radiative heat transfer between the gas and the solid structure and converts them to a single equivalent AST value.

If the steel section is exposed to a uniform fire, the development of the unprotected steel section temperature θ_a can be calculated using the formulas presented in Eurocodes EN 1993-1-2 section 4.2.5.1 and EN 1991-1-2 section 3.1. However, in PBD the temperature exposure is often not uniform. In these simulations the AST values have been measured from four different section directions at 20 - 40 cm intervals (Figure 4, Figure 5a). To account the non-uniform fire exposure, the aforementioned Eurocode formulas can be modified by dividing the steel section into four different sides with four separate heat fluxes, separate section factors and separate shadow effect correction factors (Figure 5b).

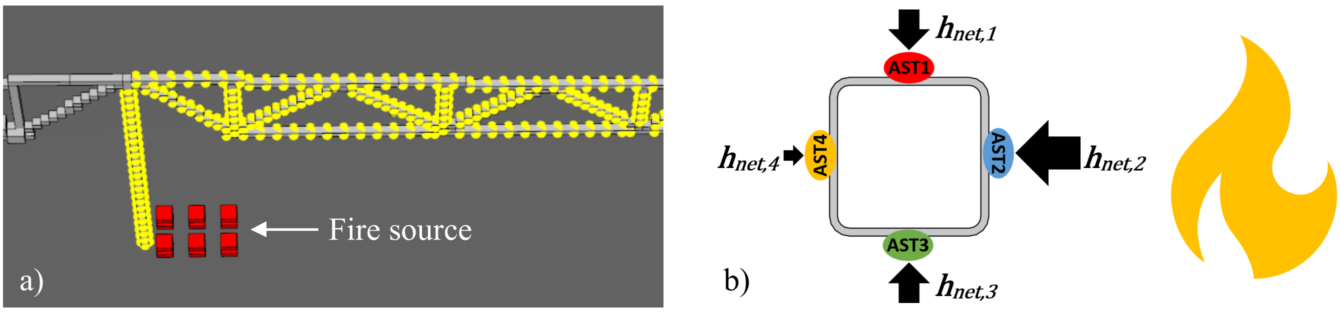

Figure 5. The principle for determining the temperatures that heat the structural steel sections using virtual Adiabatic Surface Temperatures (AST) measurement devices in fire simulations a) example from an FDS model (not from the case building) b) the placement of AST measurement devices around the steel section and their corresponding net heat fluxes.

The steel section temperature development can now be calculated with these modified formulas (when longitudinal heat transfer along the member is neglected):

$$\theta_a(t+\Delta t) = \theta_a(t) + \frac{\Delta t}{c_a \rho_a} \sum_{k=1}^{4} \left[k_{sh,k} \left({}^{A_{m,k}}/_{V} \right) \dot{h}_{net,k} \right] \quad (1)$$

$$\dot{h}_{net,k} = \alpha_c(\theta_{AST,k} - \theta_a) + \varepsilon_m \varepsilon_f \sigma[(\theta_{AST,k} + 273°C)^4 - (\theta_a + 273°C)^4] \quad (2)$$

$$k_{sh,k} = \begin{cases} \chi_{sh,web} \cdot \left({}^{A_{m,b,k}}/_{V} \right)_b \Big/ \left({}^{A_{m,k}}/_{V} \right), & \text{for I-section web sides} \\ 1.0, & \text{for I-section flange sides and for other sections} \end{cases} \quad (3)$$

These modified formulas, their use and their validation are explained in detail in a separate paper [12], and thus is not in the scope of this paper. If one or more sides of the steel section is right next to an obstruction (e.g. wall columns, corner columns), the obstructed side of the section is assumed to have an adiabatic surface. This should be a conservative assumption for wide range of obstruction materials, since usually during the heating phase, the heat flux direction is from the steel section towards the obstruction [13].

The steel section temperature development is compared against the critical temperatures of the members. The critical temperatures are calculated using the usual Eurocode rules [3, 4] and load combinations for the fire limit state design using the Finnish national annex. The indirect effects of the fires (i.e. indirect thermal actions and displacements from thermal expansions, thermal gradients within cross-sections, non-linear material models, etc) have **not** been accounted in the calculation of the critical temperatures, because this can be difficult to execute properly, and because they **will be** accounted in the structural analysis with advanced methods (Section 5.3). The critical temperatures of the studied members are shown in Table 2.

5.3 Structural fire resistance using advanced calculation models

The most critical fire scenarios are analysed using advanced calculation models using finite element method (FEM) and utilizing SAFIR software. SAFIR is extensively validated [14] and has been relatively widely applied in practical PBD projects (e.g. [15]). With SAFIR analyses, the requirements presented in EN 1991-1-2 section 4.1 and EN 1993-1-2 section 4.3 [3] can be fulfilled:

- Thermal response should be based on the acknowledged principles and assumptions of the theory of heat transfer.
- The mechanical response should be based on the acknowledged principles and assumptions of the theory of structural mechanics, taking into account the changes of mechanical properties with temperature (non-linear temperature dependent mechanical properties, EN 1993-1-2 section 3.2).
- The effects of non-uniform thermal exposure should be considered.
- The effects of thermally induced strains and stresses both due to temperature rise and due to temperature differentials, should be considered (i.e. constrained thermal expansion of the members themselves, thermal expansion of adjacent members, thermal gradients within cross-sections).

For most accuracy, it would be ideal to measure the temperature developments in all the members of the building and study all of the structure as a whole in FEM analysis, but in many projects this is not feasible and some simplifications must be made. Especially in localized fires, only partial FEM model of the structures can be utilized (often a single frame). However, during this simplification process special attention towards the support conditions and how to model the stiffness of the building must be made. In this paper, single frame is analysed, and the stiffness of the building is converted to a single equivalent spring in the plane of the truss (see, Figure 6a .The effect of the stiffness in the perpendicular plane is often not as significant and can be assumed to be rigid at intersection points of the frame and rest of the structure). The equivalent spring of the stiffening system k_{eq} has been calculated using formula:

$$k_{eq} = k_{eq,0} k_{E,\theta} \tag{4}$$

where

$k_{eq,0}$ is the equivalent spring of the stiffening system of the building at 20 °C. This can be calculated, for example, by using regular structural FEM model (by assigning a lateral point load to the studied location and measuring the deflection) or by using a “component method” with simpler hand calculation estimates (i.e. the overall stiffness consists of serial and parallel springs from different stiffening components, e.g. stiffening trusses on the walls and lateral stiffening trusses on the roof).

$k_{E,\theta}$ is the reduction factor for the slope of the linear elastic range of steel (EN 1993-1-2 section 3.2.1 [3]). In SAFIR, this cannot be a time dependant value in springs, so a single average temperature of the stiffening system must be estimated, for example, by using the temperatures in faraway measurement points from the fire simulations.

In these analyses $k_{eq,FireI}$ = 4600 kN/m and $k_{eq,FireII}$ = 5000 kN/m. The ends of the truss braces and the connections between the column and truss are assumed to be hinged.

The applied loads are determined using the most critical load combinations in accidental limit state design according to the Eurocodes and Finnish national annexes (which in this case was the maximum snow loads, see Figure 6b). The result of the SAFIR analysis is binary; either the structure withstands the design fire, or it does not. So, in order to assess if the structure was near the collapse, separate sensitivity studies are made, where the applied loads are multiplied by a factor of 1.25 and the SAFIR analysis is run again.

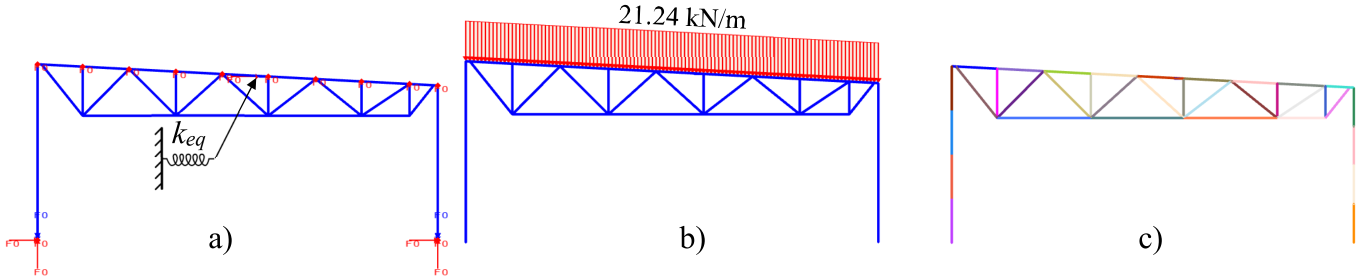

Figure 6. SAFIR model of the analysed frame a) support conditions and the building stiffening system simplified to a single spring at the location of the horizontal stiffening truss b) imposed loads during fire c) different steel sections and different temperature developments corresponding to the measurements from FDS simulations.

The temperatures are transferred to the SAFIR model using AST measurement curves from the FDS simulations (see chapter 5.2) and applied to the four sides of each section (Figure 7a). Heat transfer in the internal cavities is also considered. Each short member (e.g. truss braces) has temperature curves applied from the hottest location measured along that member; longer members are divided into shorter parts (e.g. columns, truss chords) and then processed similarly (see Figure 6c).

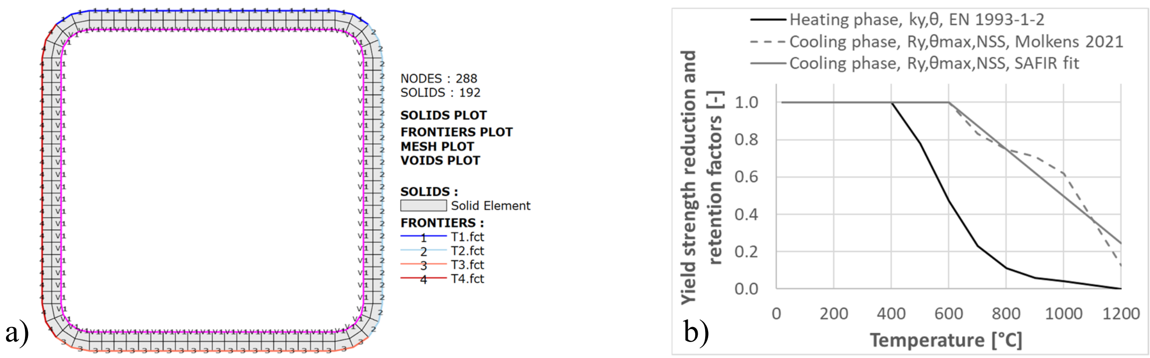

Figure 7. a) Example of the used SAFIR model for sections (Truss top chord, CFRHS180x180x10) b) The model used for the retention factor for yield strength of normal strength steel during cooling phase [16] and the SAFIR fit of it.

The default material models presented in EN 1993-1-2 section 3.2 [3] do not differentiate the steel mechanical properties between the heating phase and the cooling phase of the fire. However in reality, the steel may not retain its original mechanical properties after it has been heated up and cooled down. For this reason, the yield strength model has been supplemented with yield strength retention model after the heating and cooling cycle (see Figure 7b), which is based on the research by Molkens et al. presented in [16]. The retention factors presented by Molkens et al. are based on statistical evaluation of the mechanical data from hundreds of test results and different models are presented for different steel types and grades (in this case study, all the members are S355 grade, so only the retention factors for normal strength steel, NSS, are utilized). However, as of writing SAFIR only supports bi-linear relationship for the cooling phase retention factors, and thus the Molkens et. al model has been simplified to a fit line (Figure 6b, solid grey line).

In the heating phase the yield strength of the steel $f_{y,\theta}$ is calculated using the regular formula $f_{y,\theta} = k_{y,\theta} f_y$, where $k_{y,\theta}$ is the EC3 yield strength reduction factor (Figure 6b, solid black line) [3] and f_y the original yield strength at 20 °C (here 355 MPa). In the cooling phase, the additional formula $f_{y,R} = R_{y,\theta max} f_y$ is used, where $f_{y,R}$ is the maximum yield strength value the steel can recover to and $R_{y,\theta max}$ is the yield strength retention factor (Figure 6b, solid grey line), which is calculated based on the maximum reached steel temperature. Nevertheless, in PBD, the failure during cooling phase should be quite infrequent occurrence, since the retention factor for normal strength steel starts to decrease only after 600 °C, and the structural failure would require that the maximum stresses are much higher during the cooling phase than during the maximum temperature (both of which should be quite rare for pure steel structures).

The SAFIR calculations are done in 3D space and by using dynamic analysis. Each section model consists of 192 solid elements and the frame models consist of 494 beam elements.

5.4 Determining the required fire protection rating for the selected members

If the studied steel sections do not pass the acceptance criteria unprotected, the required fire protection rating is determined. This can be more difficult in PBD than when using standard fire (ISO-fire), since many (or most) fire protection system manufactures do not provide an easy way to utilize their products in PBD (intumescent paints can be especially difficult). In this study, the required fire protection rating is determined by using the following procedure:

0. The following steps are proceeded, if the unprotected steel section exceeds the member critical temperature (or if there is a safety margin of < 50°C), or if the structure fails the analysis using the advanced models.
1. The steel section temperature development is calculated in ISO-fire as fire protected utilizing the calculation formulas for protected members shown in EN 1993-1-2 section 4.2.5.2. However, the calculation method is modified in a somewhat similar way as shown in [12] in order to make the formulas better support non-uniform fire exposures.
2. The thickness of the fire protection material is optimized in a way that the steel section temperature in ISO-fire is exactly the same as the member critical temperature at the chosen fire protection rating time point (i.e. at 30 min in R30, at 60 in R60, at 90 min in R90, etc.).
3. The steel section temperatures are calculated again in the design fire using the exactly same fire protection than in previous step, and if the section temperature now remains below the critical temperature, the fire protection rating is sufficient for the studied design fire in PBD.

In the shown procedure, the accuracy of the actual temperature development of the protected steel section is not paramount, since the method is used comparatively between the design fires and ISO-fire. Also, the procedure is agnostic towards the actual selected fire protection system; the aim of the procedure is not to directly determine the required fire protection thickness with the selected system, but only to determine the required fire protection rating (R-class). Afterwards, the results can be utilized for many different fire protection systems (e.g. intumescent paints, fire protection boards, fire protection wools), and the actual required fire protection thicknesses can be determined utilizing the regular tabulated values from the system manufacturers (using the determined fire protection rating in combination with the section factor of the steel profile and the critical temperature of the member).

Although, if the structure is close to fulfilling the acceptance criteria unprotected, it can be more beneficial to change to a larger section size rather than to prescribe additional fire protection (if it's not too late in the design process for structural changes in the frame).

6 RESULTS

6.1 Fire simulations

Pyrosim visualisation of flames at peak heat release rate during the fire simulation is presented in Figure 8.

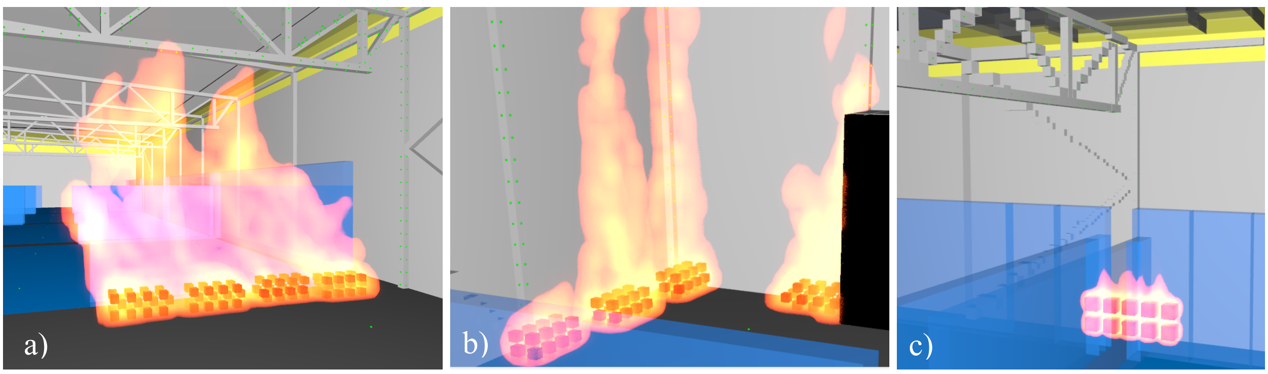

Figure 8. Pyrosim visualisation of flames at peak HRR in a) Fire Ia, b) Fire Ib, c) Fire II.

The figures below (Figure 9 a & b) show a comparison between the input HRR curves and the output HRR curves measured from the simulations, and they seem to match each other well (i.e. the fire is not oxygen limited). The figures below (Figure 9 c & d) also shows heat fluxes measured from the floor level of the models, and they remain significantly below the flashover criterium; i.e. the acceptance criteria for the use of localised fires is fulfilled.

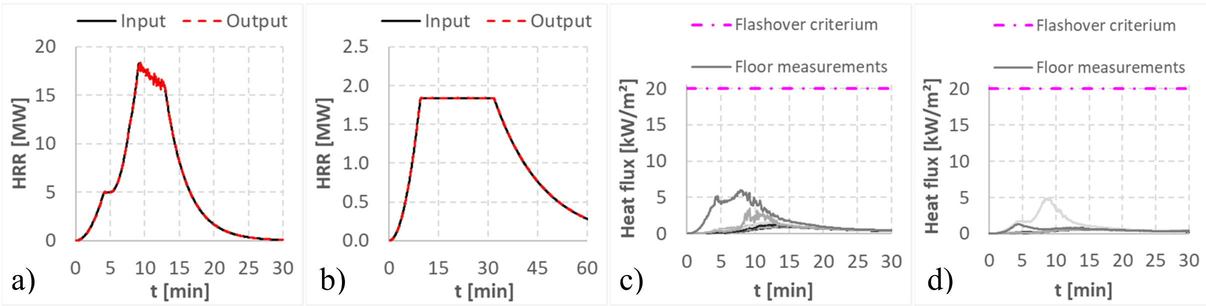

Figure 9. a) HRR check in Fire Ia, b) HRR check in Fire II, c) flashover check from the heat flux measurements on the floor in Fire Ia, d) flashover check from the heat flux measurements on the floor in Fire Ib.

6.2 Structural fire resistance using simple models

The Figure 10 shows the temperature development of the unprotected steel sections of some selected structural members at their hottest locations in Fires Ia, Ib and II (solid black curves, Steel section), which are compared against their critical temperatures (dash dot magenta lines, Limit); i.e. the section temperature must stay below this line at all timepoints to pass the acceptance criterium. The adiabatic surface temperature curves and their relation to the section sides are also shown (solid red, blue, green and orange curves, AST#). Standard fire is shown as a reference temperature (dashed gray curves, ISO-Fire).

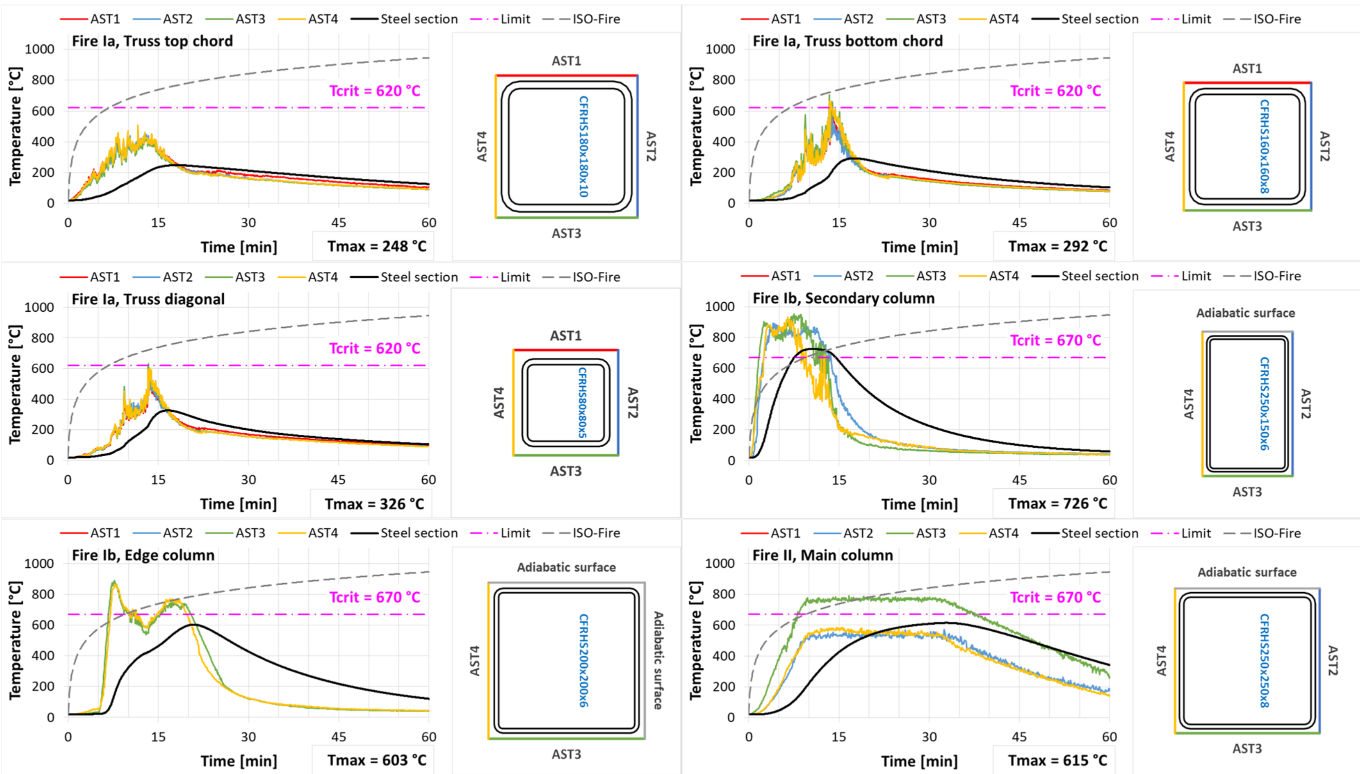

Figure 10. Temperature development of the unprotected steel sections of some selected members at their hottest locations in Fires Ia, Ib and II vs. their critical temperatures.

Table 2 shows the maximum section temperatures $\theta_{a,max}$ of all studied members (unprotected) in Fires Ia, Ib and II compared to their critical temperatures $\theta_{a,crit}$, and a margin between the two; i.e. results of the structural fire resistance using simple models. It can be seen, that the acceptance criteria are fulfilled in Fires Ia and II, but not in Fire Ib for every member; i.e. some fire protection is needed (see chapter 6.4)

Table 2. Maximum section temperatures $\theta_{a,max}$ of all studied members (unprotected) in Fires Ia, Ib and II vs. their critical temperatures $\theta_{a,crit}$, and a margin between the two.

Fire	Member	Section	Material	$\theta_{a,crit}$ [°C]	$\theta_{a,max}$ [°C]	$\theta_{a,crit}$ - $\theta_{a,max}$ [°C]
Ia	Main column	CFRHS250x250x8	S355	670	215	**455**
Ia	Truss top chord	CFRHS180x180x10	S355	620	248	**372**
Ia	Truss bottom chord	CFRHS160x160x8	S355	620	292	**328**
Ia	Truss diagonal	CFRHS80x80x5	S355	620	326	**294**
Ia	Truss vertical	CFRHS80x80x5	S355	620	306	**314**
Ib	Secondary column	CFRHS250x150x6	S355	670	726	**-56**
Ib	Edge column	CFRHS200x200x6	S355	670	603	**67**
Ib	End column	CFRHS200x200x8	S355	670	503	**167**
Ib	Roof brace	CFRHS100x100x4	S355	750	682	**68**
Ib	Wall brace	CFRHS140x140x5	S355	780	737	**43**
Ib	Roof brace	CFRHS100x100x5	S355	750	433	**317**
Ib	Edge beam	CFRHS300x200x8	S355	710	527	**183**
II	Main column	CFRHS250x250x8	S355	670	615	**55**
II	Secondary column	CFRHS250x150x6	S355	670	601	**69**
II	Truss top chord	CFRHS180x180x10	S355	620	163	**457**
II	Truss bottom chord	CFRHS160x160x8	S355	620	76	**544**
II	Truss diagonal	CFRHS80x80x5	S355	620	173	**447**
II	Truss vertical	CFRHS80x80x5	S355	620	123	**497**
II	Roof brace	CFRHS100x100x4	S355	750	181	**569**
II	Wall brace	CFRHS140x140x5	S355	780	630	**150**

6.3 Structural fire resistance using advanced models

Since Fire Ib did not pass the acceptance criteria unprotected using the simple models, the advanced models are focused to Fires Ia and II. The results are shown in Figure 11 and Figure 12. The figures on the left show the midpoint deflections of the truss (Figure 11a, solid black line) and the column (Figure 12a, solid black line) during the design fires. It can be seen, that there are no sudden spikes in the deflection curves, the FEM analysis converges all the way to the end, and towards the end the deflections start to recover (i.e. if the structure were to fail, it would be very evident from these figures). Thus, it can be concluded, that the structure maintains its resistance without collapse the whole design fire also when using advanced calculation models; acceptance criterion is fulfilled. The results of the sensitivity studies are also shown (Figure 11a & Figure 12a, dashed grey lines), where the loads were multiplied by 1.25. It can be seen, that the structures maintain their resistance without collapse even with this increased loading. Therefore, the structural capacity is not very near its limit. The figures on the right (Figure 11b & Figure 12b) show the overall deformations of the structure at the 15 min time point (deformations are scaled here by 10x).

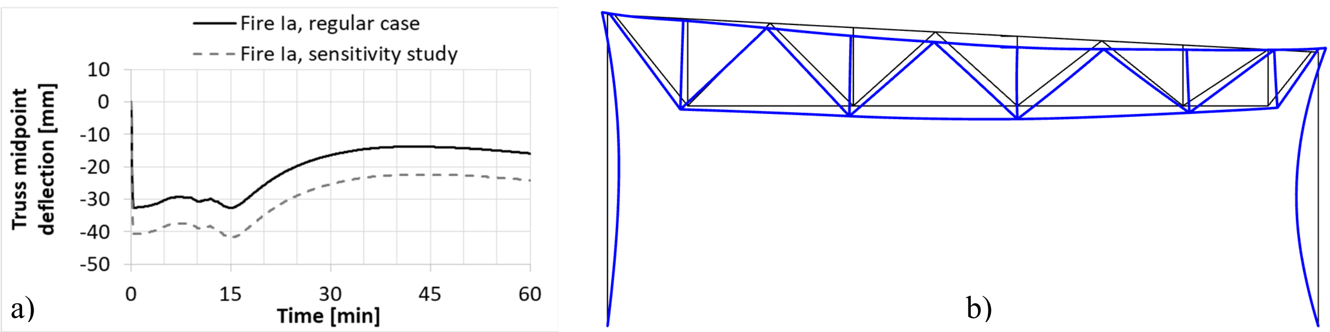

Figure 11. Fire Ia: a) Truss midpoint deflection during SAFIR analysis (the regular case and the sensitivity study with loads multiplied by 1.25) b) The overall deformations of the structure at the 15 min time point (deformations are scaled by 10x).

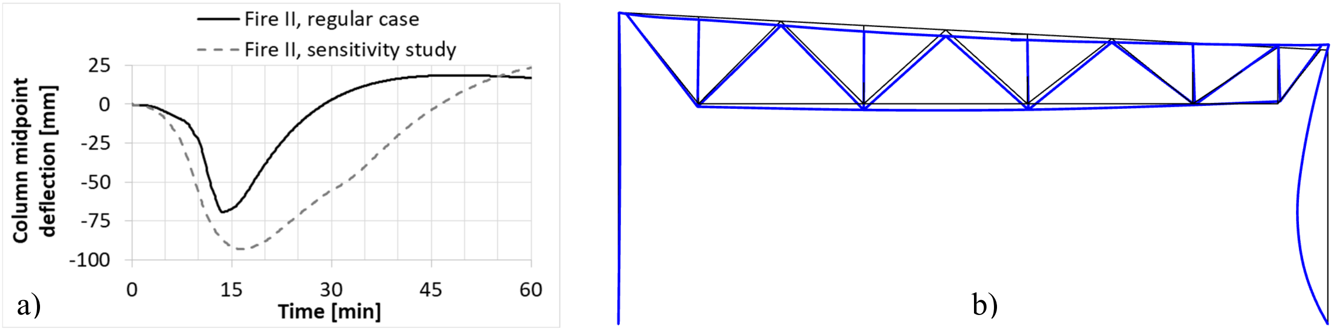

Figure 12. Fire II: a) Column midpoint deflection during SAFIR analysis (the regular case and the sensitivity study with loads multiplied by 1.25) b) The overall deformations of the structure at the 15 min time point (deformations are scaled by 10x).

6.4 Determining the required fire protection rating for the selected members

Since the structures in Fire Ib did not pass the acceptance criteria without fire protection, the required fire protection rating is determined for the affected members by using the procedure described in chapter 5.4. The results for CHRHS250x150x6 secondary columns are shown in Figure 13. It can be seen that, fire protection rating of R30 is enough to provide over 200 °C margin between the section temperature and the critical temperature (Figure 13a). It can also be seen that no fire protection is required above 3 meters from the floor, since the effect of the design fire has sufficiently diminished (Figure 13b).

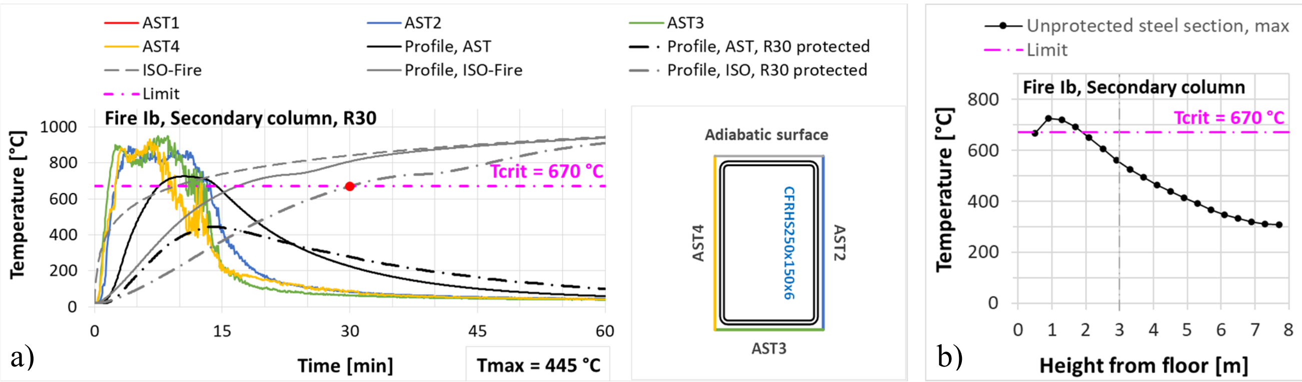

Figure 13. Determining the required fire protection for CHRHS250x150x6 secondary columns a) determining the required fire protection rating (R30) b) determining the required fire protection extent (no protection needed above 3 m from the floor).

The final result of the performance-based design is shown in Figure 14: i.e. the columns near the corner of the lounge area require R30 fire protection from +0.00 m to +3.00 m, the structures inside the EI30 compartment (which were excluded from the PBD) require R30 fire protection and all other steel structures can be left unprotected.

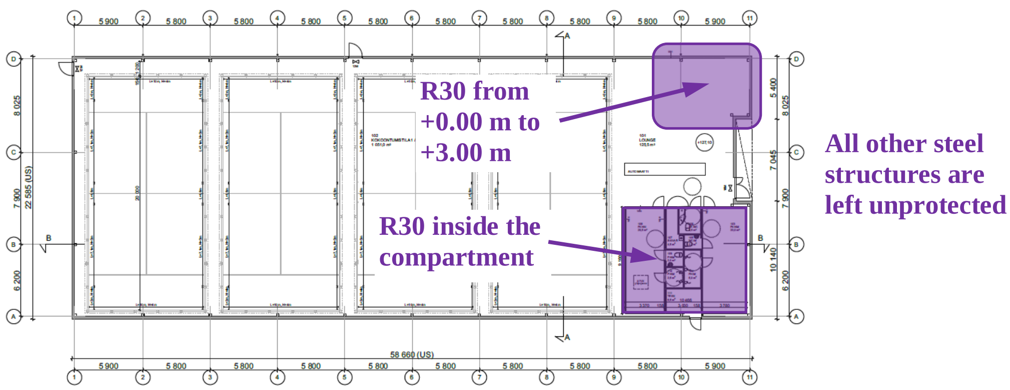

Figure 14. The final result of the performance-based design.

7 CONCLUSIONS

As a result of the performance-based design, most of the steel structures in the case building could be constructed without fire protection, but some critical structures were identified and protected to class R30. The methods presented in the paper form a relatively robust framework for PBD of similar steel structures and are directly applicable to other similar buildings especially in Finland (and have already been widely applied by the authors). Furthermore, many of the design steps described in this paper can be, and has been, automated to significantly speed up the design process (e.g. placement of the AST measurement points to FDS, structural fire resistance analysis using the simple models and partially the assembly of the SAFIR models), which makes relatively extensive performance-based studies (commercially) viable also in relatively small and mundane steel buildings.

ACKNOWLEDGMENT

Construction company Meijou Oy is acknowledged for letting us publish this project, structural design office Tolppa Oy is acknowledged for providing the steel frame and the critical temperatures, and both are gratefully acknowledged for seamless co-operation.

REFERENCES

1. Finnish Ministry of Environment. 2017. Decree of the Ministry of the Environment on the Fire safety of Buildings, 848/2017
2. Finnish Ministry of Environment. 2020. Decree of the Ministry of the Environment on the Amendment to the Decree of the Fire safety of Buildings, 927/2020
3. EN 1993-1-2. 2005. Eurocode 3: Design of steel structures. Part 1-2: General rules. Structural fire design
4. EN 1991-1-2. 2002. Eurocode 1: Actions on structures. Part 1-2: General actions. Actions on structures exposed to fire
5. Hietaniemi, J. 2007. Palon voimakkuuden kuvaaminen toiminnallisessa paloteknisessä suunnittelussa. VTT, JH WORKING PAPERS 1, Espoo, Finland.
6 Audouin, L., Coutin, M. 2017. Experimental Characterization of a Forklift Fire. SMiRT 24, 15th International Post-Conference Seminar on Fire Safety in Nuclear Power Plants and Installations.
7. Babrauskas, V. 2008. Heat Release Rates. In: The SFPE Handbook of Fire Protection Engineering. 4. Painos. Quincy: National Fire Protection Association. Pp. 3-1 - 3 59.
8. McGrattan, K., McDermott, R., Hostikka, S., Floyd, J, & Vanella, M. 2022. Fire Dynamics Simulator (Version 6). User' Guide. NIST Special Publication 1019.
9. McGrattan, K., McDermott, R., Hostikka, S., Floyd, J, & Vanella, M. 2022. Fire Dynamics Simulator (Version 6). Technical Reference Guide. Volume 3: Validation. NIST Special Publication 1018-3.
10. U.S. Nuclear Regulatory Commission. 2007. NUREG-1824. Verification & Validation of Selected Fire Models for Nuclear Power Plant Applications. Volume 7: Fire Dynamics Simulator.
11. Wickström, U., McGrattan, K. 2007. Adiabatic surface temperature for calculating heat transfer to fire exposed structures. Proceedings of the Eleventh Interflam Conference.
12. Jokinen, T., Ranua, R., Salminen, M. 2022. Steel section equivalent uniform temperature distribution in performance-based fire design – EC3 calculation method generalized for non-uniform fire exposure. 12th International Conference on Structures in Fire (SiF'22)
13. Heinisuo, M., Jokinen, T. 2014. Tubular composite columns in a non-symmetrical fire. Magazine of Civil Engineering. 49. 107-120. 10.5862/MCE.49.11.
14. Gernay, T., Franssen, J.M. 2017. "Modeling structures in fire with SAFIR®: Theoretical background and capabilities". Journal of Structural Fire Engineering, Vol. 8, issue 3, pp. 300-323.
15. Salminen, M., Hietaniemi, J. 2016. Performance-Based Fire Design of Steel Structures of Helsinki Olympic Stadium. Applications of Structural Fire Engineering. 15-16 October 2015, Dubrovnik, Croatia.
16. Molkens, T., Cashell, K., Rossi, B. 2021. Post-fire mechanical properties of carbon steel and safety factors for the reinstatement of steel structures. Engineering Structures. 234. 111975.

GALVANIZATION EFFECT ON STEEL FRAMES EXPOSED TO FIRE

Margherita Autiero[1], Donatella de Silva [2], Antonio Bilotta [3], Emidio Nigro [4]

ABSTRACT

One of the materials mostly penalized in case of fire is the steel, because of its elevated thermal conductivity and the small dimensions of the structural member sections. Therefore, if the bare steel structures do not reach the required level of fire resistance it is necessary to use fire protections. Recent studies have shown that hot-dip galvanization which is already efficient to protect steel members from corrosion, can also provide a beneficial effect on the temperature of steel members exposed to fire thanks to a reduction in surface emissivity. This paper shows the main results of high-temperature small-scale tests on galvanized and not-galvanized steel plates, investigating and quantifying the effect of galvanization on the temperatures of steel elements, in a common and economical electrical furnace. Moreover, in the second part of this work, the effect of galvanization was assessed by varying the fire curve and the element section factors A_m/V, underlining when it could be significant for improving structural fire resistance. An application of the galvanization benefit was also presented referring to advanced thermo-mechanical analyses of a single-story steel building, finding that, thanks to the galvanisation, this structure satisfies the required performance level, according to the fire safety engineering approach.

Keywords: galvanization; fire resistance; experimental tests; steel frames

1 INTRODUCTION

Galvanization is a surface coating process to protect steel members from corrosion, in which the steel is coated with zinc to prevent it from rusting. The most common galvanization method is hot-dip galvanizing, where the protective zinc coating is obtained by dipping the steel element into a bath of molten zinc usually at about 450°C. The zinc coating is formed by a metallurgic reaction during which several zinc-iron alloy layers are formed. Therefore, the coating is chemically bound to steel beneath, and it is not only laid on top of it. The formation of the zinc coating depends on several factors. On one hand, it depends on the galvanizing conditions such as melting temperature, dipping time and chemical composition of zinc bath. On the other hand, it is influenced by surface conditions and chemical composition of the steel (e.g. silicon and phosphorous content). Silicon concentration in quantities between 0.04% and 0.14% (Sandelin steel) or above 0.22% (hyper-Sandelin steels) can accelerate the iron-zinc reaction to form a thicker zinc coating with a different alloy layer structure [1]. Four steel categories (C_x), according to EN ISO 14713-2 [2] are defined based on the silicon concentration: C_A - Low silicon content steel (Si ≤ 0.04%), C_B: Non-Sandelin intermediate composition steels (14% < Si ≤ 0.22%), C_C: Sandelin steel (0.04% < Si ≤ 0.14%) and C_D: hyper-Sandelin steels (Si > 0.22 %).

[1] Margherita Autiero, Department of Structures for Engineering and Architecture, University of Naples Federico II (Italy), e-mail: margherita.autiero2@unina.it ,
[2] Donatella de Silva, Department of Structures for Engineering and Architecture, University of Naples Federico II (Italy) e-mail: donatella.desilva@unina.it , https://orcid.org/0000-0002-4058-902X
[3] Antonio Bilotta, Department of Structures for Engineering and Architecture, University of Naples Federico II (Italy) e-mail: antonio.bilotta@unina.it , https://orcid.org/0000-0002-2414-5488
[4] Emidio Nigro, Department of Structures for Engineering and Architecture, University of Naples Federico II (Italy) e-mail: eminigro@unina.it , https://orcid.org/0000-0002-3848-7454

https://doi.org/10.6084/m9.figshare.22153568

The surface coating can modify the emissivity that is the ratio between the energy radiated from a surface of a material and the energy radiated from a black body, under same conditions, at same temperature and wavelength. The radiative component of the net heat flux depends on the emissivity of flame ε_f, and on the member surface ε_m one [3]. The emissivity ranges between zero and one and lower is the emissivity of a surface, slower is the heating.

The radiation of metal surfaces depends on atomic and molecular level. Sala [4] states that the radiation behavior depends on the chemical composition in a layer with a thickness of few microns. The radiation behavior of galvanized surfaces should hence be provided exclusively by the alloy layer (40 µm to 250 µm) or from the upper pure zinc layer alone, which is only a few micrometers thick .

Therefore, the emissivity of hot-dip galvanized steel elements is influenced by the alloy layer composition, by the oxidation of zinc, and by the melting of the outer zinc layer at a temperature of 419°C. As a result, the emissivity of the galvanized surface is variable with temperature [5].

The current Eurocode for structural steel EN1993-1-2 [3] provides a constant surface-independent emissivity value ε_m = 0.70, whereas recent studies [5 - 8] showed that galvanization can also reduce the surface emissivity with a beneficial effect on the temperature of steel members exposed to fire. Jirku and Wald (2013) [6] performed a fire test in a real scale building and two fire tests in furnace on steel members with IPE200 and hollow tube cross-sections, obtaining a constant value of emissivity for galvanized steel equal to 0.32. While Bihina et al.[7] carried out three standard fire tests on hot-rolled steel structural members, finding an equivalent emissivity for hot-dip galvanized specimens, that increases with temperature. Mensinger and Gaigl (2019) [5] assessed emissivity curves as a function of temperature for hot-dip galvanized steel elements by small-scale and full-scale tests. The temperature-dependent emissivity was determined for various hot-dip galvanized surfaces and steel categories C_A, C_B, and C_D were tested, combined with all possible surface conditions. The results showed an emissivity dependent not only on temperature, but also by the weathering, with the negative influence of outdoor storage. Moreover, the results highlighted that the zinc-iron alloy layers have a big influence on the emissivity value. In particular, only for steel of C_A and C_B, the emissivity value is lower than 0.7, for steel temperatures up to 530 °C. Due to chemical reactions, a new layer structure is formed with a higher roughness and a consequent increasing of surface emissivity. Therefore, while EN1993-1-2 [3] suggests a simplified surface independent constant emissivity for carbon steel ε_m = 0,70, the experimental results showed a temperature-dependent emissivity for hot-dip galvanized steel, with values lower than 0.7 for steel temperatures up to 500 °C. Since the studies conducted in literature showed a positive effect of galvanization on the steel temperature due to the variation of the emissivity, Mensinger and Gaigl [5] suggested an emissivity (ε_m) equal to 0,35 for steel temperature ($\theta_{a,t}$) lower than 500 °C and equal to 0,70 for $\theta_{a,t}$ greater than 500 °C.

Starting from these considerations, the first part of the paper shows the main results of high-temperature small-scale tests on square galvanized and not-galvanized steel plates, investigating and quantifying the effect of galvanization on the temperatures of steel elements, in order to calculate the emissivity of galvanized steel in a common and economical electrical furnace. Moreover, in the second part of this work, the effect of galvanization was assessed by varying the fire curve and the element section factors A_m/V, underlining when it could be significant for improving structural fire resistance. Finally, in the last part, an application of the galvanization benefit is presented referring to advanced thermo-mechanical analyses of a single-story steel building.

2 EXPERIMENTAL AND ANALYTICAL INVESTIGATION AT ELEVATED TEMPERATURE

2.1 Experimental programme

The experimental tests were performed in an electrical furnace by exposing to heat only the upper surface of specimens, while the remaining parts were protected with an insulating material in order to reduce heat exchange. Therefore, the steel samples consisted of 44 plates, placed inside a box composed by a sequence of five calcium silicate boards 12.7 mm thick, in order to approximately obtain laterally adiabatic conditions (see Figure 1a). The box was placed on a rockwool layer and finally on refractory bricks. Inside the box, a variable layer of rockwool was placed, to ensure that the sample and the box upper surfaces were aligned to each other (see Figure 1b). The square samples had dimensions of 50x50mm, with a variable thickness, in order to obtain different section factors A_m/V (ratio between the surface area exposed to fire and the volume of the element) ranging between 20 and 200m^{-1}. For each section factor, one non-galvanized (NG) and three galvanized (G) specimens were tested to have a direct comparison between their temperatures.

The test samples were galvanized using a galvanizing bath according to UNI EN 1461:09. As a result, the galvanized specimens have a mean galvanizing thickness of about 120μm. The ID of the specimen is X-Y-Z: where X is the section factor of the specimen, Y indicates if the sample is galvanized (G) or not galvanized (NG) and Z indicates the number of the tested specimen. The thickness of the specimens and their section factors are listed in Table 1.

Table 1 Test matrix

Not galvanized (NG)	Galvanized (G)			A_m/V [m^{-1}]	s [mm]
20_NG_1	20_G_1	20_G_2	20_G_3	20	50
30_NG_1	30_G_1	30_G_2	30_G_3	30	35
40_NG_1	40_G_1	40_G_2	40_G_3	40	25
50_NG_1	50_G_1	50_G_2	50_G_3	50	20
60_NG_1	60_G_1	60_G_2	60_G_3	60	17
70_NG_1	70_G_1	70_G_2	70_G_3	70	14
80_NG_1	80_G_1	80_G_2	80_G_3	80	12.5
90_NG_1	90_G_1	90_G_2	90_G_3	90	11
100_NG_1	100_G_1	100_G_2	100_G_3	100	10
125_NG_1	125_G_1	125_G_2	125_G_3	125	8
200_NG_1	200_G_1	200_G_2	200_G_3	200	5

To measure the temperature in the steel samples three Chromel/Alumel K thermocouples were inserted from the furnace inspection hole while the fourth one was assembled in the furnace (see Figure 1b). In particular, the thermocouple (TR_1) was used to measure the steel temperature in the directly exposed face, while the (TR_2) measured the temperature in the non-exposed face. To insert these two thermocouples each steel sample was previously drilled with a hole diameter of 2.5mm and a depth of 4mm. The (TR_3) was used to monitor the furnace temperature, as also the furnace thermocouple (TR_4).

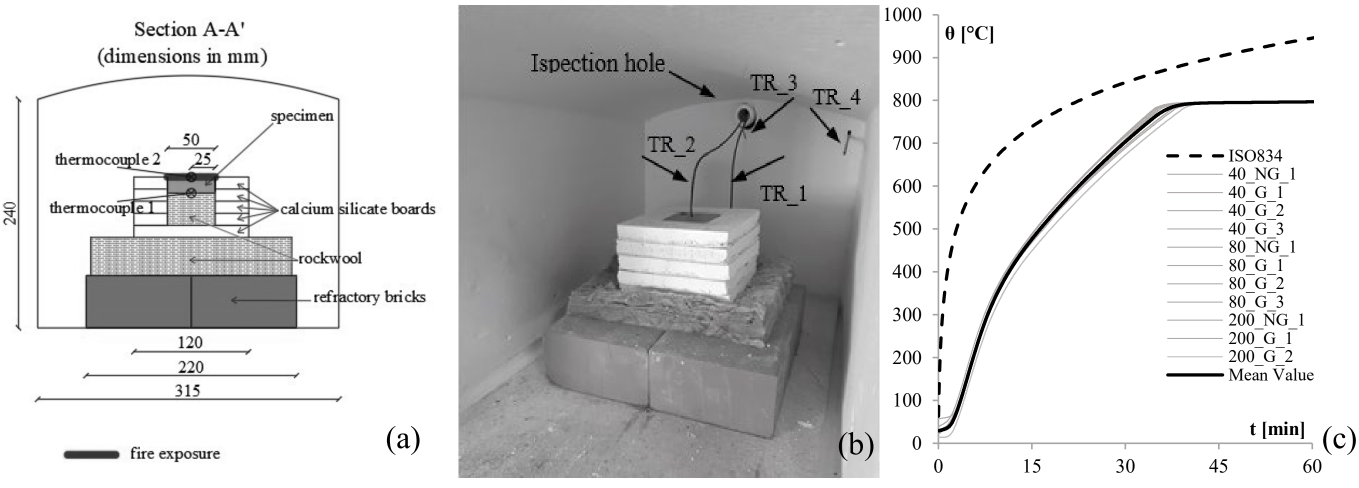

Figure 1 Test set up: (a) cross section, (b) setup in the furnace with position of the thermocouples, (c) thermal input curves: temperatures recorded by TR_3.

An acquisition system allows to record all the temperatures detected by each thermocouple. The tests were carried out by using an input fire curve slower than the standard fire curve ISO834 with a development from 20°C to 800°C, because of this particular type of furnace. Figure 1c shows the values of these temperatures recorded by TR_3, for some selected tests, demonstrating a very good agreement between all the input curves, and thus allowing to make direct comparisons between the experimental results.

2.2 Results and discussion

The results obtained for three representative section factors (A_m/V = 40, 80, 200 m^{-1}) are discussed below. Figure 2 shows the temperature recorded by TR_1 for each galvanized sample and their mean value (black curve) for the three selected section factors. Furthermore, the graphs of Figure 2 also contain the input fire curve obtained as the mean of each test with same A_m/V (Mean_input_A_m/V). For the section factors 40 and 80 m^{-1}, all the test results were available and so the results obtained for the three galvanized and one ungalvanized specimens are shown. While, for the section factor equal to 200 m^{-1} only the results obtained for two galvanized and one ungalvanized specimens are available, because one thermocouple didn't work during the test.

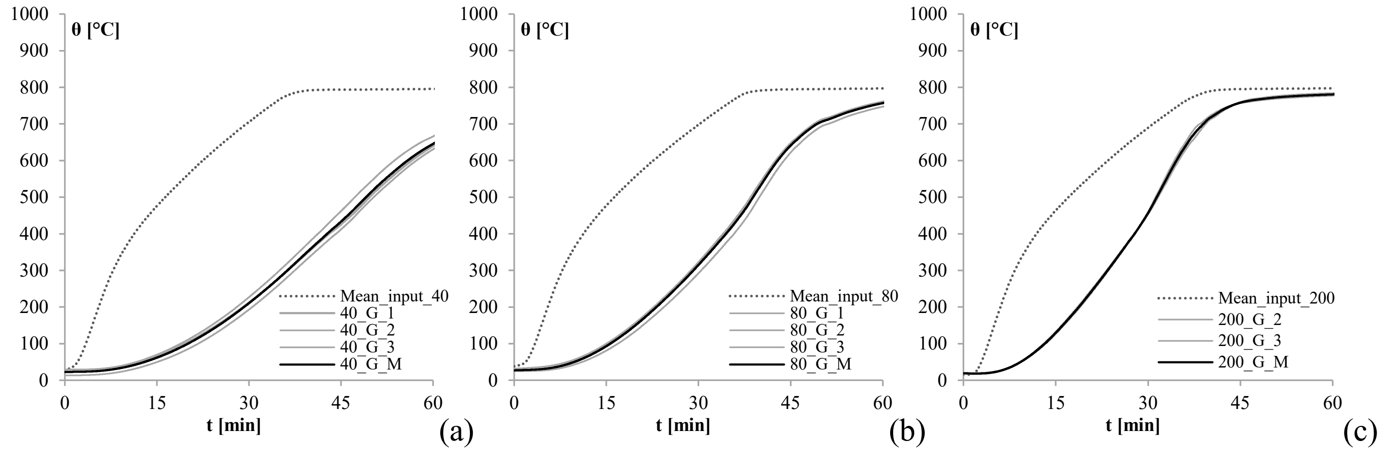

Figure 2 Comparison between temperatures of three galvanized specimens with same Am/V and their mean value (G_M); A_m/V= 40 m^{-1} (a), A_m/V= 80 m^{-1} (b), and A_m/V= 200 m^{-1} (c)

In all the cases the steel temperatures recorded in the specimens during each test are very similar to each other, demonstrating not only the stability of the results, but also the reliability of the test setup. Since the stability of the results, the mean temperature value (Am/V_G_M) for each section factor is considered in the following comparisons. Figure 3a shows the experimental results obtained for the non-galvanized (40_NG) and galvanized (40_G_M) specimens with dashed and continuous curves respectively. These results show the effect of galvanizing in terms of lower temperatures of the hot-dip galvanized specimens. For example, at 30 minutes of exposure time the temperature of blank specimen θ_{40_NG} reached 250 °C while the same galvanized specimens have a temperature θ_{40_G} of 211 °C. This difference of about 40°C changes during the heating with a maximum value ($\Delta\theta_{max}$) of 111 °C at 47 minutes, when the temperatures are 572 °C for the blank specimen and 462 °C for the galvanized ones.

In the Figure 3b the results obtained for non-galvanized (80_NG) and galvanized (80_G_M) specimens are represented. First of all, faster heating than the previous case is observed due to a lower thickness of the samples and a greater section factor (A_m/V= 80 m^{-1}), obtaining higher temperatures, both for galvanized and non-galvanized samples. Nevertheless, the effect of galvanizing on the steel heating is still appreciable, indeed the galvanized samples have lower temperatures than the corresponding non-galvanized. For example, at 30 minutes in the not galvanized specimen θ_{80_NG} is 400 °C while in the same galvanized specimens θ_{80_G} is 315 °C. This difference of 86°C changes during the heating with a maximum value of 169 °C at 37 minutes, when the temperatures are θ_{80_NG} = 625 °C and θ_{80_G} = 456 °C respectively.

Passing from a section factor of 80 m^{-1} to 200 m^{-1} the specimens show faster heating (see Figure 3a,c), and the maximum beneficial effect of galvanizing on the steel temperatures appears already at 28 minutes; at this time $\Delta\theta_{max}$ is equal to 162 °C with θ_{200_NG} of 614 °C and θ_{200_G} of 457 °C. With the increase of exposure time, the beneficial effect of galvanizing is reduced due to the rapid heating of the steel element characterised by a high value of A_m/V.

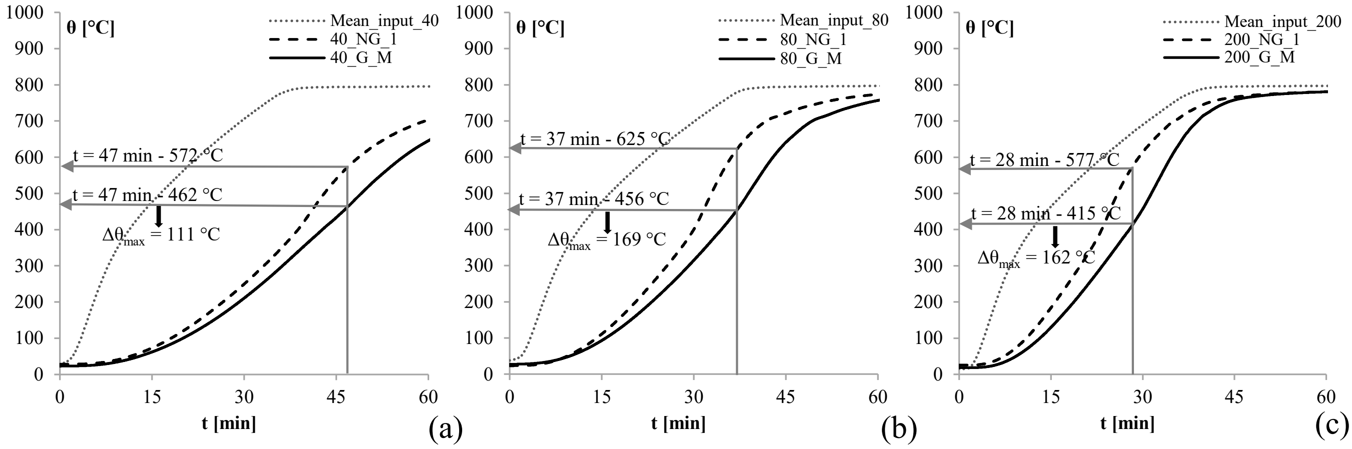

Figure 3 Comparison between the recorded temperatures of the non-galvanized samples (NG_1) and the mean value of the galvanized ones (G_M) with the same Am/V: (a) Am/V= 40 m-1, (b) Am/V= 80 m-1, and (c) Am/V= 200 m-1

Figure 4 plots a direct comparison between the experimental results of galvanized and non-galvanized specimens obtained for the three A_m/V = 40, 80, 200 m^{-1}. Due to the different values of A_m/V, the steel temperature curves are clearly different, but for the same A_m/V, the maximum temperature difference between galvanized and blank samples is reached when the temperatures in galvanized specimens are about 450 °C at different heating times.

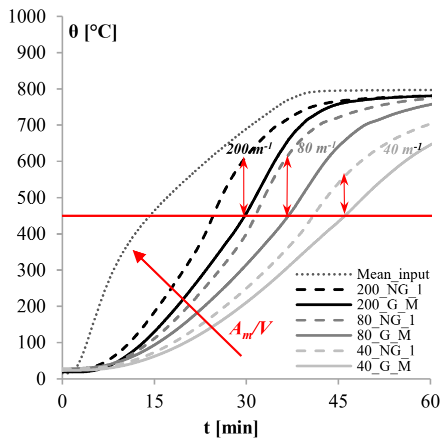

Figure 4 Comparison between experimental results of different galvanized (G) and non-galvanized (NG) specimens

2.3 Analytical modelling of galvanized steel members

Starting from the experimental results, a simulation of the tests on galvanized samples was carried out by implementing the analytical method for the steel temperature development, suggested also by Eurocode EN1993-1-2 [3], the effect of galvanizing was modelled according to the two-stages emissivity relationship suggested in [5] (ε_m = 0,35 for $\theta_{a,\,t} \leq 500$ °C; ε_m = 0,70 for $\theta_{a,\,t} > 500$ °C), later called NEW_EN_G. As thermal action the thermal input curves obtained from each test was considered, a convection coefficient, α_c, lower than the one related to the standard fire curve was used to consider the convective thermal flux specific for these tests. This α_c value was calculated for non-galvanized specimens with three different section factors based on the mean of the temperatures recorded by the lower TC_1 and the upper TC_2 thermocouples and by considering the sample as a grey emitter and the furnace walls area bigger than the sample surface; in this way, a mean value α_c equal to 6.4 W/m^2K was calculated.

Moreover, some calibrations were conducted to obtain the surface emissivity variation with the steel temperatures. Starting from all the data analyzed in the first part of the paper, the following analytical function was calibrated by comparing the experimental results obtained for the galvanized specimens with the analytical ones by varying the four parameters: ε_{max}, ε_{min}, β and γ:

$$\varepsilon = 0.5 \cdot (\varepsilon_{max} - \varepsilon_{min}) \cdot tanh\left[\left(\frac{1}{\beta}\right) \cdot (\theta_{a,t} - \gamma)\right] + 0.5 \cdot (\varepsilon_{max} + \varepsilon_{min}) \quad (1)$$

In particular, two different calibrations were carried out: CAL_1, which refers to each A_m/V, and CAL_2, which refers to all the A_m/V. The Figure 5 shows the development of the two curves obtained from equation (1) for CAL_1 and CAL_2 and a comparison with the two-stages emissivity relationship (NEW_EN_G). Even though these two curves are based on results of small-scale tests performed in a common and cheap electrical furnace, they confirmed that the development of galvanized steel emissivity depends on the steel temperature.

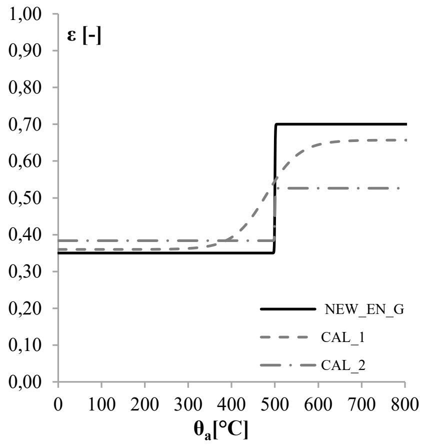

	$\varepsilon_{m,min}$ [-]	$\varepsilon_{m,max}$ [-]	β [-]	γ [-]
NEW_EN_G	0.35	0.7	-	-
CAL_1	0.36	0.66	77	480
CAL_2	0.38	0.53	1	500

Figure 5 Comparison between emissivity curves obtained for the two different calibrations, (CAL_1, CAL_2) and the NEW_EN_G.

Figure 6 compares the experimental temperatures and the analytical ones calculated using the emissivity values of CAL_1, CAL_2 and NEW_EN_G: a very good agreement with the experimental curves can be observed for A_m/V= 80 m^{-1}, while a small difference is found in the case of A_m/V= 40 m^{-1} and A_m/V= 200 m^{-1}.

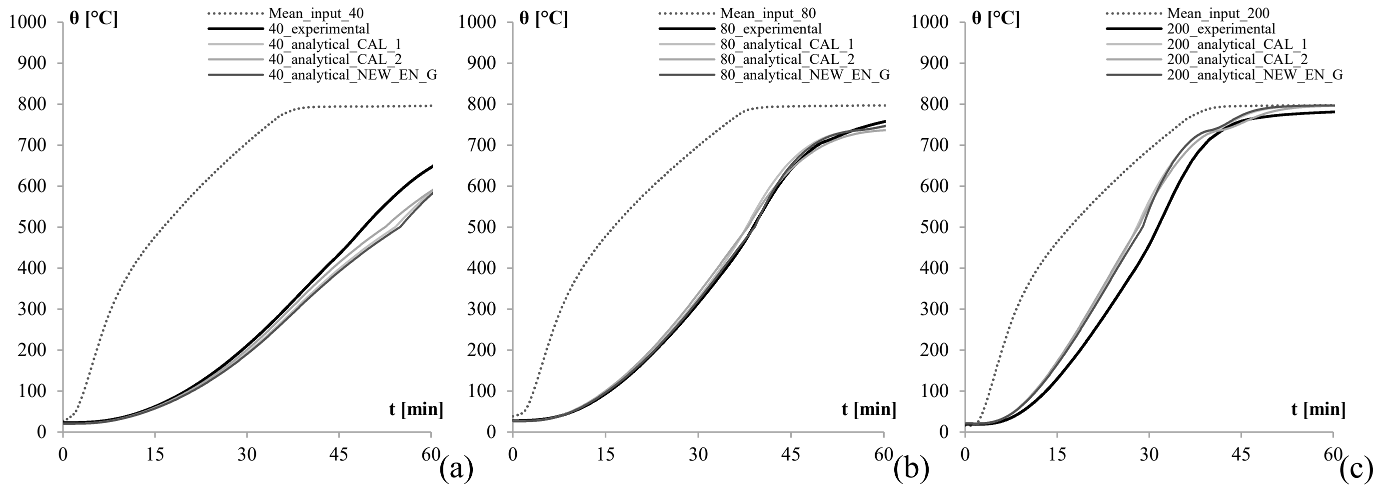

Figure 6 Comparison between experimental and analytical results.

Furthermore, the analytical curves are very similar to each other using emissivity values according to CAL_1, CAL_2 and NEW_EN_G. Therefore, considering that CAL_1, CAL_2 were calibrated using an input curve slower than the standard ISO834 fire curve, the comparison results of Figure 6 show that the several applied emissivity formulations may be used also for fire curves different from the standard one, as they are able to provide emissivity values for properly modelling the behaviour of galvanized steel elements with good accuracy.

3 ASSESSMENT OF THE GALVANIZATION EFFECT UNDER NATURAL FIRE CURVES

On the base of experimental results, the second part of the paper presents an analytical assessment of the galvanizing effect by varying both the fire curves and the section factors. For assessment and verification in fire situation, the Italian code [9], in accordance with European ones, defines five performance levels (PL), depending on the importance of the building; for example, in the case of industrial ones, PLI and PLII can be chosen. In particular, in PLI the absence of external consequences due to structural collapse has to be demonstrated, whereas according to the PLII the structure has also to maintain its fire resistance capacity for a period of time sufficient for the evacuation of occupants to a safe area outside of the building. In order to comply with the performance level, different design solutions can be chosen, based on prescriptive or performance-based approaches. The main difference between the prescriptive (PA) and the performance based (PBA) approaches is that the first one is based on standard fire resistance tests or empirical calculation methods, using nominal fire curves. In particular, the code provides three types of conventional fire curves (standard ISO834, hydrocarbon, and external nominal curve), selected according to the nature of the combustible materials in the compartment. On the other hand, in the PBA, the thermal input assessment is conducted through the selection of design fire scenarios, which represent qualitative description of the fire development, based on key aspects that characterize the real fire (e.g., compartment dimension, ventilation, fire loads...). The natural fire curves can be obtained through simplified or advanced models. One of the most simplified methods, described in Annex A of EN1991-1-2 [10], is called “Parametric temperature-time curves”, which provides a simple tool for modelling the post-flashover fire, assuming a uniform temperature distribution in the compartment. This method is adopted below.

3.1 Parametric temperature-time fire curves

Parametric temperature-time curves are analytical functions that provide the evolution of the gas temperature in a compartment as a function of time, based on physical parameters that influence the development of a fire compartment such as the dimensions of the compartment, the design fire load density related to the floor area (q_{fd}), the ventilation conditions through opening factor (O) and the thermal properties of the closing elements (e.g., walls). In particular, in this paper, the opening factor O was considered equal to 0.02, 0.04 and 0.09 $m^{1/2}$, while q_{fd} equal to 500 MJ/m^2. In the following, the different parametric fire curves will be indicated with the corresponding O as (P_O) – see Figure 7a. From this figure it can be observed that, in the case of a fire controlled by ventilation, the fire duration increases with the decrease of the opening factor O while the temperature peak increases with the increase of O, fixing all the other parameters. Moreover, Figure 7a shows that for a time interval between 0 and 26 minutes the $P_{0.09}$ parametric fire curve have higher temperatures than the ISO834 ones, underlining the importance of assessing the structure fire resistance with the PBA.

3.2 Effect of galvanization on the steel member fire resistance

In order to quantify the beneficial effect of galvanization, the behaviour of the galvanized steel member compared to the non-galvanized one are investigated at different specific temperatures. In particular, according to the reduction factors $k_{y,\theta}$ and $k_{E,\theta}$ [3] the structural steel can withstand approximately 400°C before it begins to soften. At about 600°C, the steel will lose about half of its strength. While its stiffness starts to reduce at about 100°C, till losing the the 60% at 500°C (see Figure 7). Therefore, deflections, local buckling, and twisting of the steel member can occur, and if the bare steel structures do not reach the required level of fire resistance it is necessary to use fire protections. However, if this required level of fire resistance is not very high, considering the beneficial effect of the galvanization can be crucial for satisfying the fire resistance requirement.

The behaviour of the galvanized steel member compared to the non-galvanized one are investigated at the temperatures equal to 500,550,600, and 650°C. For each of these steel temperatures the corresponding time in the galvanized element (t^G_θ) and in the non-galvanized one (t^{NG}_θ) are considered (see Figure 7b).

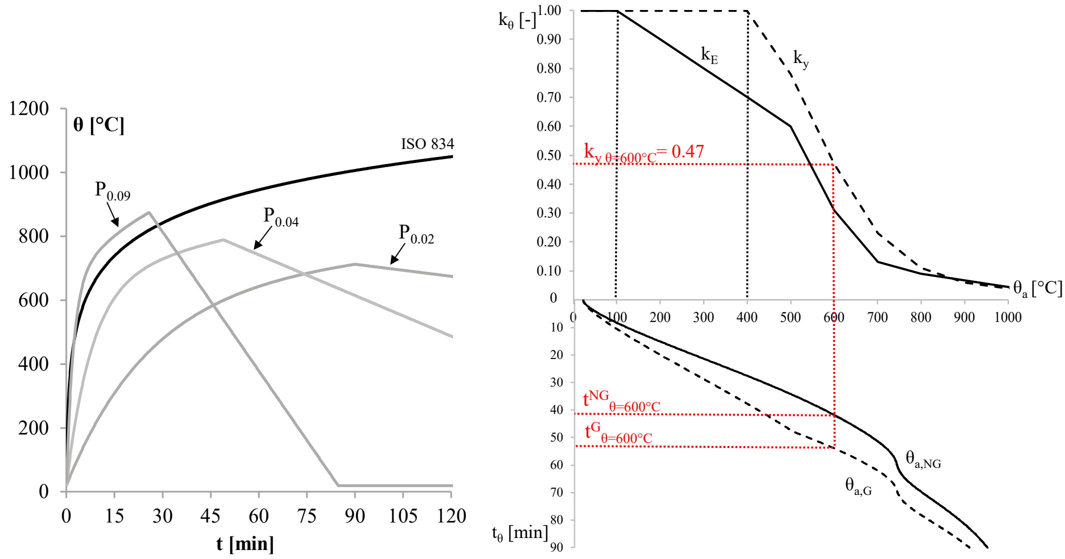

Figure 7 (a) Comparison between standard ISO834 fire curve and parametric ones, (b) Identification of the time to which the selected temperatures (e.g., 600°C) are reached in galvanized ($t^G{}_\theta$) and blank steel ($t^{NG}{}_\theta$)

These time values are represented in Figure 8 respect to four A_m/V in the case of the previous selected fire curves ($P_{0.02}$, $P_{0.04}$, $P_{0.04}$ and ISO 834 standard fire curve).

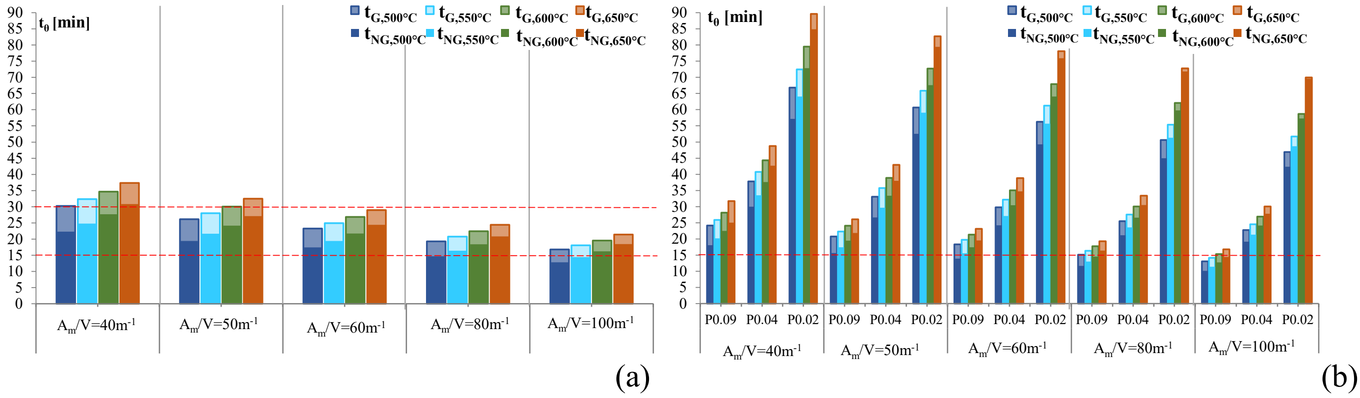

Figure 8 t_θ representation varying A_m/V and the fire curve for galvanized and non-galvanized elements (a) standard ISO834 fire curve, (b) parametric fire curves

The effect of the A_m/V on the element heating can be observed, indeed higher is A_m/V lower is the time for reaching a certain θ_a. It can be also seen that for each A_m/V, $t^G{}_\theta$ is always higher than $t^{NG}{}_\theta$; this means that a fixed temperature θ_a, in the case of G steel element, is reached later than the NG one; this effect reduces with the increasing of A_m/V. Moreover, it is possible to identify, for each A_m/V, a similar trend. In particular, considering A_m/V= 40m^{-1}, for a slower fire curve, t_θ increases and the galvanization effect can be much appreciated. Furthermore, by fixing the fire curve, the maximum effect can be observed between 400 and 500°C confirming the experimental results where the effect of the galvanization was maximum at about 450°C. It is worth noting that even though at 100ºC the beneficial effect is less, it can be significant to delay the steel local and member buckling effect. The galvanizing is often used to protect industrial steel buildings from corrosion; for these structures, the Italian technical fire prevention regulation requires to satisfy the performance level PLII. According to the prescriptive based approach, using the standard ISO834 fire curve, the structure has to maintain its load bearing capacity for a minimum period of time related to the building fire load; herein 15 and 30 minutes are considered. According to the performance-based approach the structure should maintain the load-bearing capacity under natural fire for a period of time sufficient for the safe evacuation of the occupants (*RSET- required safe escape time*). In particular, the structural collapse time has to be greater than 2·RSET with a minimum of 15 minutes. So, on the base of all the previous considerations, the effect of the galvanization can be relevant in these time intervals. In the case of standard ISO834 fire curve (Figure 8a), used for assessing the fire resistance of a single structural member (PA), the effect of the galvanization can be appreciable both for low A_m/V (e.g. 40,50m^{-1}) at t_θ =30min and for greater A_m/V (e.g. 60,80 and 100 m^{-1}) at t_θ=15min. While in the case of natural fire curves (Figure 8b), referring to t_θ =15min, the effect of galvanization can be beneficial for all considered A_m/V. Therefore, even if PBA requires advanced thermo-mechanical analysis considering the indirect actions, it allows to introduce the beneficial galvanization effect on the behaviour of the whole structure. Indeed, the slow heating of the structural members can influence positively the fire effects on the structural behaviour during the fire exposure, reducing the indirect actions and the requirements in terms of capacity of the structure to redistribute stresses and internal forces according to the different stiffness of the structural members.

4 ADVANCED FIRE ANALYSES OF GALVANIZED STEEL FRAMES

In order to analyse the galvanization effect on the behaviour of an whole structure, an application of the galvanization benefit was also presented referring to advanced thermo-mechanical analyses of a single-story steel building.

4.1 Description of the analysed structural typology

The steel structure analysed in this paper is the one provided in the European Report [11]; after a benchmark analysis to validate the model, several thermo-mechanical analyses were carried out by using SAFIR software [12]. The building structures are composed of double steel frames with beams and columns made with H-shaped profiles, as shown in Figure 9 and listed in Table 2. The same frame has been analysed for the galvanized and non-galvanized elements, in 3D space by allowing the out-of-plane displacements. The frame is hinged with additional fixations provided by 11 purlins in the third direction.

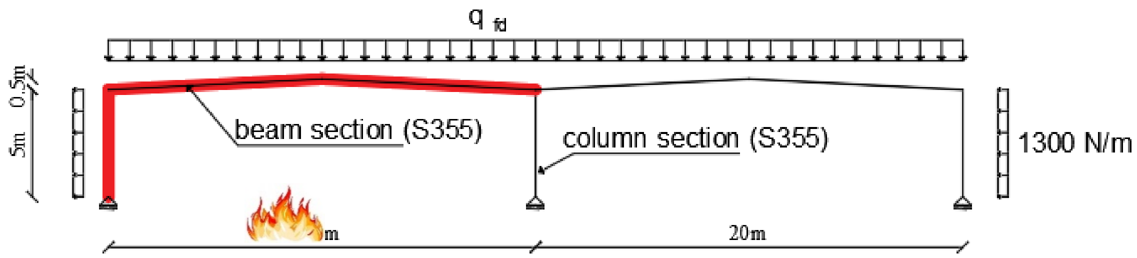

Figure 9 steel frame analysed

Dynamic analyses were carried out, by considering that the fire is localized in only one bay; materials' thermal and mechanical properties are assumed according to the EN1993-1-2 and the strain hardening is not considered. All the profiles are class 1 sections during the fire. For the steel temperature calculation, no shadow effect is considered; the effect of galvanizing was modelled according to the two-stages emissivity relationship (ε_m = 0,35 for $\theta_{a,t} \leq$ 500 °C; ε_m = 0,70 for $\theta_{a,t} >$ 500 °C), while for the non-galvanized structure the value suggested by EN1993-1-2 [3] for carbon steel ε_m = 0,70 was used.

Table 2 cross sections and loads used

Fire curve	q_{fd} [N/m]	Beam section	Column section
ISO834 for R15	6540	IPE500	IPE450
ISO834 for R30	7470	HE400B	HE450B
Natural fire curves	4700	IPE500	IPE450

The thermo-mechanical analyses were carried out by considering the fire curves shown in Figure 7a, which means the standard fire curve ISO834 and the three parametric natural fire curves $P_{0.02}$, $P_{0.04}$, $P_{0.09}$. Based on the results obtained from preliminary analyses, for each fire curve, different A_m/V and in particular utilization factors were used (see Table 2) in order to optimize the galvanization effect for each case.

4.2 Assessment with standard fire curve ISO834

In order to underline the difference between the galvanized and non-galvanized structures the first results are provided in terms of collapse time in both cases. In the case of the standard fire curve two different case were studied, in order to obtain the fire Resistance R15 and fire Resistance R30.

Therefore, in the first case the collapse time for the non-galvanized structure t_{col_NG} is equal to 14 min, while for the galvanized one, t_{col_G} is 17 min. The critical structural element in fire is the beam, for both non galvanized and galvanized case. The beam section factor IPE550, exposed on four sides, is $A_m/V = 151m^{-1}$ and the utilization factor μ_0=0.15. Figure 10a shows that at 15 min of fire exposure the temperature for the galvanized element is lower than the temperature of the non-galvanized one. The beam collapse is also assessed in terms of Axial Force-Bending Moment Resistance Domain, in which the collapse is caused by combined bending and compression from axial forces (see Figure 10b). The resistance domains are reduced to consider the lateral-torsional instability, using the χ_{LT} coefficient, calculated according to EN1993-1-2.

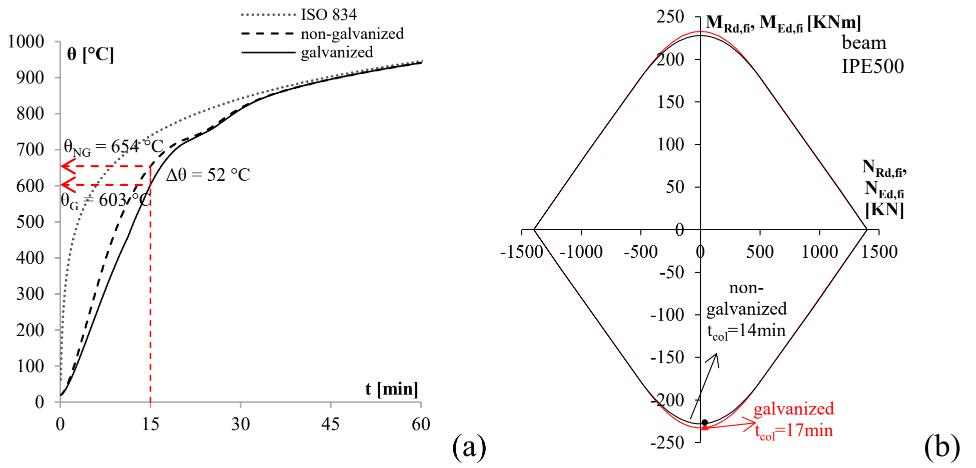

Figure 10 Comparison between temperatures (a) and Axial Force-Bending Moment Resistance Domains (b)

To guarantee 30 min of fire resistance, the cross sections of the structural members and the loads are changed, (see Table 2), the collapse time for the non-galvanized structure t_{col_NG} is equal to 29 min, while for the galvanized one, t_{col_G} is 31 min.

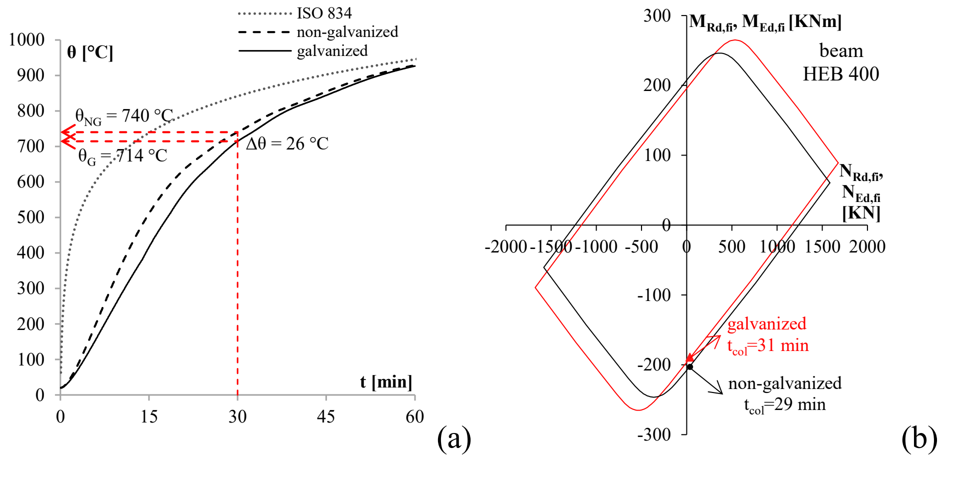

Figure 11 Comparison between temperatures (a) and Axial Force-Bending Moment Resistance Domains (b)

Also in this case, the critical structural element in fire is the beam, for both non galvanized and galvanized case. The beam section factor HE400B, exposed on four sides, is $A_m/V = 82m^{-1}$ and the utilization factor μ_0=0.1. Figure 11a shows that at 30 min of fire exposure the temperature for the galvanized element is lower than the temperature of the non-galvanized one. The beam collapse is also assessed in terms of Axial Force-Bending Moment Resistance Domain (Figure 11b), in which the collapse is caused by combined bending and compression from axial forces. In this case the domain is not symmetric because the beam is exposed on three sides.

4.3 Assessment with natural fire curves

Also, in this case the results are provided in terms of collapse times, for the non-galvanized structure (t_{col_NG}) and the galvanized one (t_{col_G}). Table 3 shows the effect of galvanizing on the steel heating: for natural fire curves slower than standard ISO834, the time for reaching a certain temperature increases and the galvanizing effect can be much appreciated.

Table 3 collapse time for the natural fire curves

	$P_{0.09}$		$P_{0.04}$		$P_{0.02}$	
	t_{col_NG}	t_{col_G}	t_{col_NG}	t_{col_G}	t_{col_NG}	t_{col_G}
[min]	14	16	29	31	70	74

In all the cases, the critical element is the beam IPE550 with a section factor A_m/V = 151m^{-1}. Figure 12 shows the galvanizing beneficial effect in terms of temperature, indeed the temperature for the galvanized element is lower than the temperature of the non-galvanized one. Figure 12a shows the temperatures obtained for the parametric fire curve O=0.09 m^{-1}, where thanks to the galvanization and without any fire protection the structure could satisfy the 15min requirement (see Table 3), even though at these collapse times the temperature difference is only equal to 12°C. As also said before the value of 15 min is considered according to the Italian fire regulation.

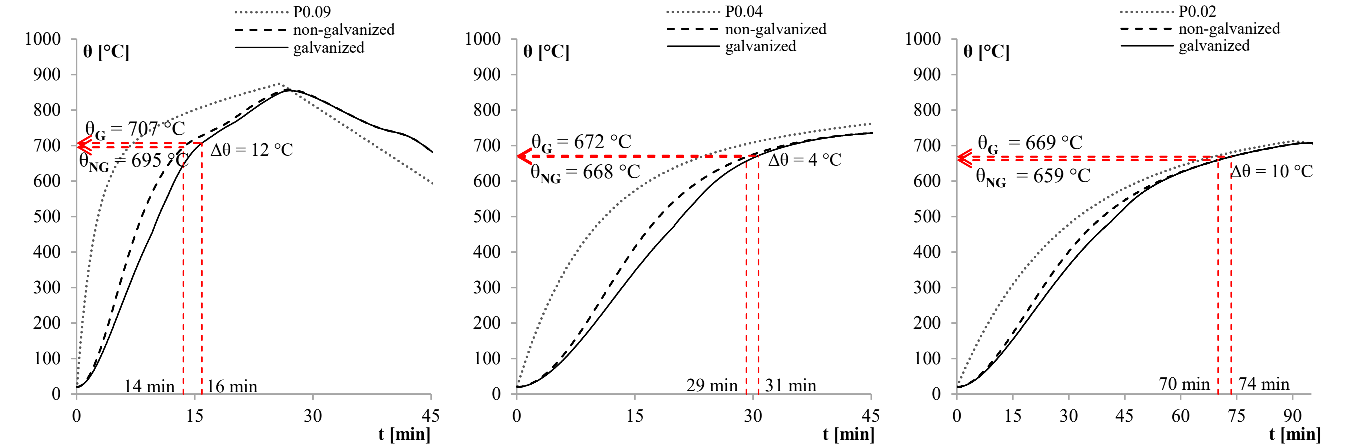

Figure 12 Comparison between temperatures of the non-galvanized beam and galvanized one for the parametric fire curves (a) $P_{0.09}$, (b) $P_{0.04}$, (c) $P_{0.02}$.

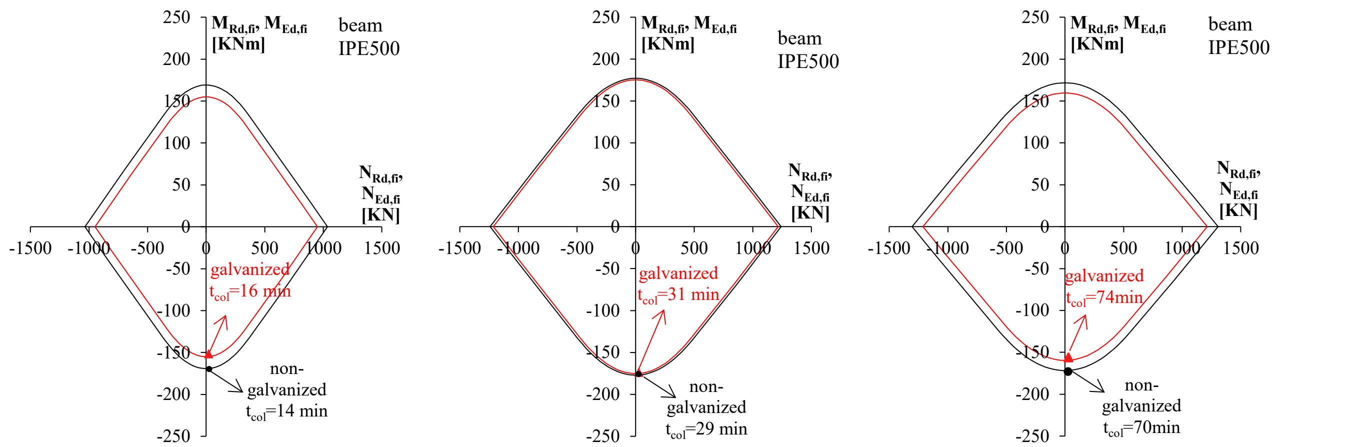

Figure 13 Axial Force-Bending Moment Resistance Domain for the parametric fire curves (a): P0.09, (b): P0.04, (c): P0.02.

Figure 12b shows that, in case of parametric fire curve O=0.04 m^{-1}, the temperature at collapse time of both galvanized and non-galvanized steel beams are very close to each other, however, the different heating can be particularly appreciated between 10 and 25 min. In the case of parametric fire curve O=0.02 m^{-1}, Figure 12c shows that, in this case, the temperature at collapse time of both galvanized and non-galvanized steel beams has a difference of about 10°C. The beam collapse is assessed in terms of Axial Force-Bending

Moment Resistance Domain, see Figure 13, in which the collapse is caused by combined bending and compression from axial forces. Figure 13b, shows that, in the case of parametric fire curve O=0.04 m^{-1}, since the temperature at collapse time of both galvanized and non-galvanized steel beams are very close to each other also the Axial Force-Bending Moment Resistance Domain are very similar.

5 CONCLUSIONS

This paper presents an experimental program aimed at the investigation of the behaviour of galvanized steel members and the characterization of its surface emissivity starting from the temperatures measured during small-scale tests in an electrical furnace. The results confirm the beneficial effect of galvanization on slowing down the heating, while the emissivity formulations obtained may be used also for fire curves different from the standard one. Therefore, an analytical assessment of the galvanizing effect by varying both the fire curves and the section factors, was carried out. Showing that for the standard ISO834 fire curve, the effect is more appreciable for low section factors and for times of fire exposure from 15 to 30 minutes. On the contrary in the case of natural fire curves, a larger number of section factors can benefit from this effect, for a larger time of fire exposure. In order to assess the effect of the galvanization on the structural fire behaviour, advanced thermo-mechanical analyses of steel single story frames were carried out. These analyses have shown how this effect is useful to satisfy the fire resistance requirement when the whole structure is modelled and so the slower heating of the members can play a relevant role also on the structural behaviour, reducing the indirect actions and influencing the redistribution of the stresses and internal actions according to the different stiffness of the structural members. In particular, this effect was found useful for steel industrial building, for which, the technical fire prevention regulations require to satisfy a performance level not particularly high. Indeed, in these cases, the galvanization allows guaranteeing the required performance level, saving the application of fire protection.

REFERENCES

1. Pernice L. (2021). Zincatura a caldo. Mirapromotion Srl. (In Italian)
2. ISO 14713-2:2009, Zinc coatings — Guidelines and recommendations for the protection against corrosion of iron and steel in structures — Part 2: Hot dip galvanizing
3. EN 1993-1-2, Eurocode 3: Design of steel structures - Part 1-2: General rules -Structural fire design, 2005.
4. Sala A. (1986) . Radiant properties of materials: Tables of radiant values for black bodies and real materials, Elsevier Science Ltd.
5. Gaigl C., (2019). Fire resistance of hot-dip galvanized steel structures, PhD Thesis, Technical University of Munich.
6. Jirku J., Wald F., (2013). Influence of zinc coating to a temperature of steel members in fire, in ASFE'13 - Application of Structural Fire Engineering, 19-20 April 2013, Prague, Czech Republic.
7. Bihina G., Zhao B. (2021). Hot dip galvanizing of steel structural members: an alternative to passive fire insulation? Ce/papers 4, Proceedings of Eurosteel 2021: 1–3 September 2021, Sheffield, England.
8. Autiero M., Bilotta A., de Silva D., Nigro E., Pernice L. (2021). Temperature of galvanized steel specimens heated in electrical furnace, in ASFE 2021 - Applications of Structural Fire Engineering, 10-11 June 2021, Lubiana, Slovenia. Paper Id. 62, 6 pp.
9. D.M. 3 agosto 2015 "Approvazione di norme tecniche di prevenzione incendi, ai sensi dell'articolo 15 del decreto legislativo 8 marzo 2006, n. 139", GU n. 192 del 20/8/2015 – S.O. n. 51.
10. EN 1991-1-2, Eurocode 1: Actions on structures - Part 1-2: General actions - Actions on structures exposed to fire, 2002.
11. Fire safety of industrial halls - A valorisation project - EUROPEAN COMMISSION Directorate-General for Research Research Fund for Coal and Steel Unit - Contract No RFS2-CT-2007-00032 1 July 2007 to 31 December 2008
12. Franssen, J.M., Gernay, T. (2017), Modeling structures in fire with SAFIR®: Theoretical background and capabilities, Journal of Structural Fire Engineering, 8(3):300-323. https://doi.org/10.1108/JSFE-07-2016-0010

CHALLENGES AND OPPORTUNITIES ASSOCIATED WITH STRUCTURAL FIRE ENGINEERING DESIGN OF AN OPEN-PLAN EXOSKELETON BUILDING

Sigurjon Ingolfsson[1], Berna Zaragoza Solis[2], Andy Wong[2] , Eoin O'Loughlin[3]

ABSTRACT

Large and unusual buildings pose a challenge for codified prescriptive fire engineering approaches. Performance-based structural fire engineering is often a more appropriate approach. This paper presents a selection of key challenges and potential opportunities for the application of SFE learned by the authors through the assessment of structures in fire for real commercial building projects.

Current design practices responding to these challenges are discussed and it is noted that adding a degree of conservatism to designs in order to deal with the uncertainty involved is the typical approach taken by designers. However, there is limited research that underpins some of those assumptions and improved datasets and methods would lend themselves to improved fire protection designs.

Keywords: Exoskeleton; External Structural Steel; Case Study; Applications of Structural Fire Engineering

1 INTRODUCTION

Performance-based structural fire engineering (SFE) offers an alternative to simple codified prescriptive approaches to fire resistance design. Through SFE, designers can refine which structural elements should achieve fire resistance, and what fire resistance ratings are required. Of note for steel structures, SFE can help reduce environmental impact, in the form of the carbon associated with the supply, application, and maintenance of passive fire protection [1].

When considering the structural fire resistance design of a building, designers must ask themselves the following questions:

1. **The design goals** – What constitutes success? What constitutes failure? How safe or resilient is a code-compliant design? How can a structure designed outside the bounds of prescriptive codes be reliably shown to be sufficiently 'safe' in fire?
2. **The fire scenarios** – What fire exposure(s) are appropriate and relevant, given the available fuel, structure location, etc.?
3. **The structural response** – How will the structure (protected or unprotected) behave at elevated temperatures due to fire?

These questions have implicit answers in prescriptive codes, but they are founded in simplified approaches which serve as proxies for actual design. Using this approach, designers can end up designing 'unknowingly', particularly where a structure is less 'common' or representative of prescriptive testing standards.

[1] Arup Australia,
Corresponding author e-mail: ,
[2] Arup Australia

[3] Arup UKMEA

https://doi.org/10.6084/m9.figshare.22153574

A commercial project journey includes engagement with various stakeholders such as statutory approvers, building insurers, the developer, and the ultimate building operator. Opportunities may get lost or discarded as carrying overly high project risk at the early stages unless there is a very clear and robust framework, analysis methodologies, and ways of communicating the outcomes of a performance based SFE route.

This paper presents a selection of key challenges and potential opportunities for the application of SFE learned by the authors through the assessment of structures in fire for real commercial building projects. A particular case study is offered into an ambitious arts and culture building with large open plan compartments which illustrates the opportunities and challenges that building projects can pose to fire designers as well as some of the intricate design of SFE.

2 CASE STUDY BUILDING DESCRIPTION

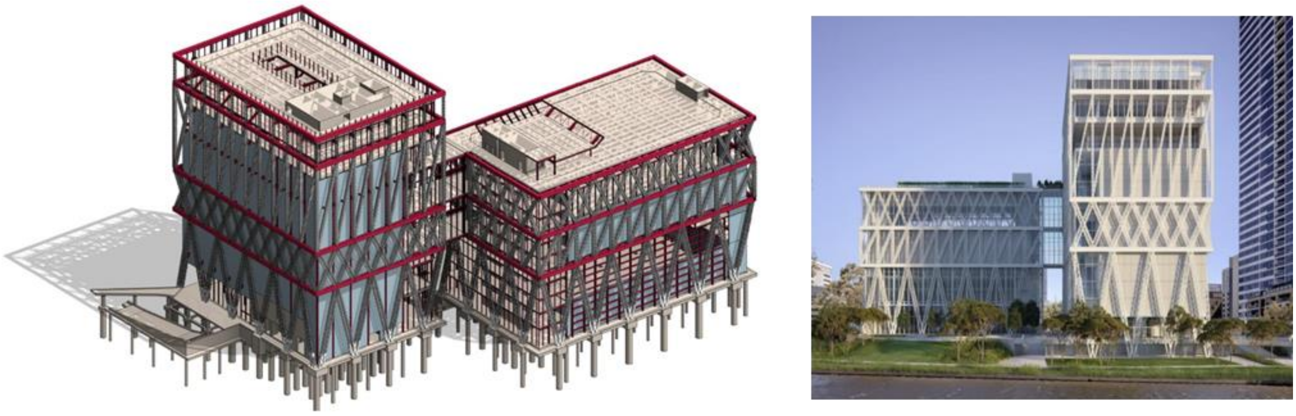

Figure 1: Case Study Building

The case study building is approx. 70 m tall (Figure 1), and the overall structure consists of a large latticework steel exoskeleton which supports the slabs of individual storeys and is paired to the stair cores. The building itself has very few internal columns to maintain a clear space for flexible exhibits. Resulting from this requirement there are also large steel trusses internal to each tower that typically connect to the exoskeleton or a larger truss to transfer the forces from the individual slabs to the exoskeleton.

An indicative elevation of the described building is shown below.

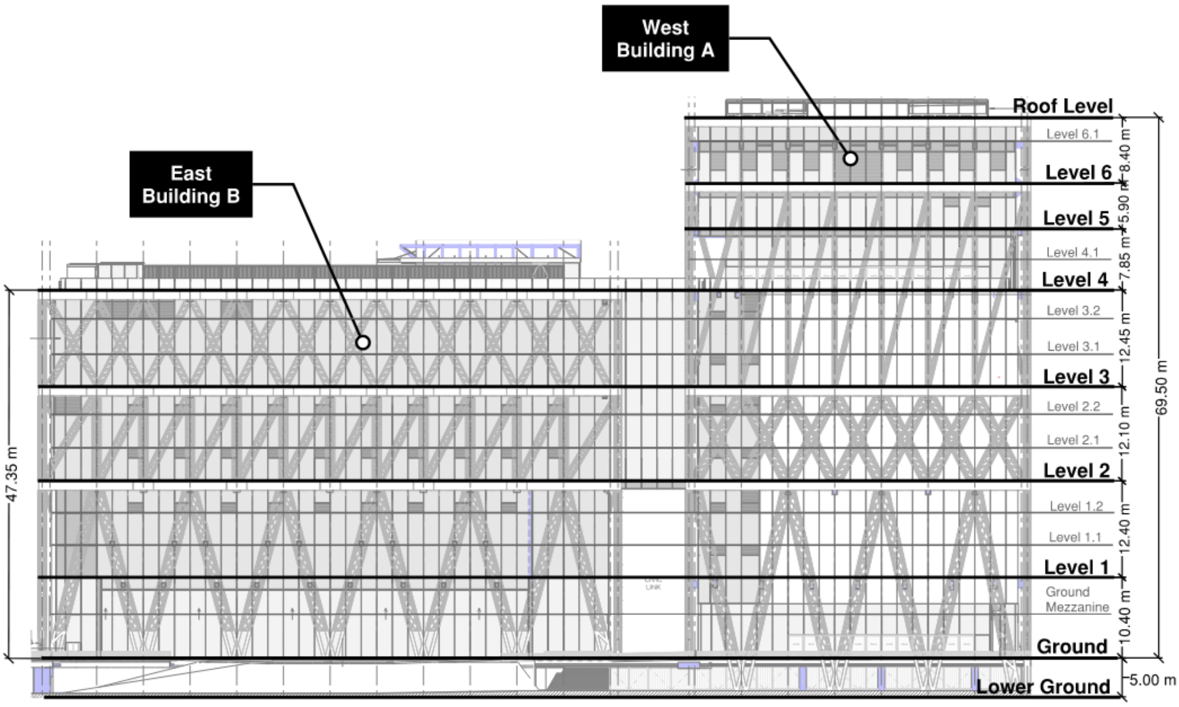

Figure 2: Case Study Building elevation

3 CHALLENGES AND OPPORTUNITIES

3.1 Exoskeleton Analysis

For the analysis of the external steel structure (Exoskeleton), two main fire scenarios are considered to have an impact on these elements:

- An external flame generated by a fire within a compartment (e.g., plant room, loading dock, etc) in any of the two buildings.
- A second major scenario is an external fire such as vehicle fire originated near the Exoskeleton. Note that at Ground level, goods vehicle traffic is expected for loading of exhibition spaces and thus a vehicle fire is a relevant design scenario.

3.1.1 External Fire Exposure Generated by a Fire Within a Compartment Internal to the Building

To evaluate the effects of an external flame impacting the Exoskeleton, the maximum temperature of the external flames of the most onerous compartments can be estimated first by applying a methodology pioneered by Law & O'Brien [2]. This methodology, which was published by the Steel Construction Institute, has demonstrated good correlation with small compartments but is less verified for larger compartments such as the ones evaluated as part of the subject building. Conservative results for large compartments are expected [2]. More accurate and validated methodologies for external flames emanating from larger compartments than those originally investigated by Law would present an opportunity to optimise designs further.

Once the maximum temperature of the external flames has been estimated, the duration of these elevated temperatures needs to be evaluated. One method leans on the parametric curve method described in EN1991-1-2 [3] originally derived by Wickstrom [4][5]. However, again this methodology was defined for smaller compartments (less than 500 m^2, which have been shown to be generally inappropriate for modern compartment sizes [6]) and thus using it for large compartments needs to be done with care as the fundamental assumptions are as follows:

(i) Uniform gas temperature in the fire compartment

(ii) Total fuel burnout inside the compartment

(iii) Ventilation-controlled fire

(iv) Natural ventilation

All those assumptions are challenged by large open plan and high compartments (which sit outside testing that has been undertaken as part of the derivation of temperature/time curves (Figure 3)) which may contain mechanical smoke exhaust. However, it is considered that the use of the methods above leads to conservative designs and thus they are commonly applied in practice.

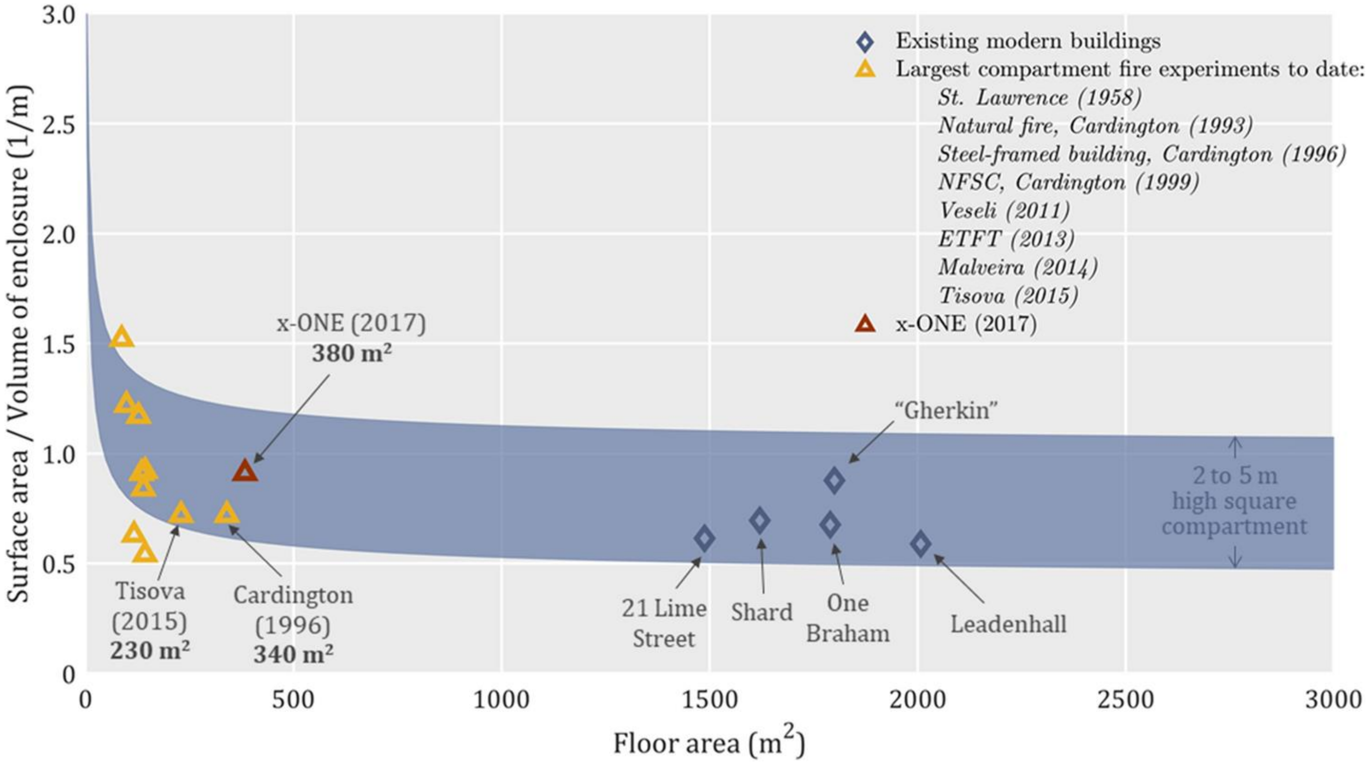

Figure 3: Comparison of the surface area to volume ratio of compartments within which experiments have been carried out to date, and recently constructed tall buildings in London, UK. From [7]

Another method would be to use computational fluid dynamics (CFD) simulators or other pre-flashover methodologies. However, to the authors' knowledge, the ability to reliably predict fire dynamics in compartments that may have varied fire loads for structural design purposes is not practicable [8].

Once the temperatures and duration of those temperatures have been established, heat transfer to the structure needs to be addressed. This presents another opportunity which is discussed in a later section of this paper.

3.1.2 External Fire Exposure Generated by an external fire

The most critical external fire scenario is considered to be a truck fire as it represents the largest fuel load that is anticipated by the base of the building. The building has access to heavy goods vehicles, hence, the traffic of these types of heavy vehicles around some external areas of the buildings can be expected. As a result, the possibility of one of them catching fire near the external exoskeleton is considered possible.

In this context, experimental data for truck fires was investigated. It is noted that, most of the experimental data of large-scale test available for heavy vehicles has been analysed in tunnels, where the internal conditions can lead to different fire conditions in comparison to the expected truck fire in an open area which would be expected to be less intensive. Therefore, three different truck fires scenarios were considered within the analysis with the intention to cover as wide a scenario as feasible. Two of these scenarios were considered to be a fast-short fires corresponding to the data obtained from large-scale fire tests 00 of heavy good trucks within a tunnel and a third is a fire utilising reported maximum heat release rates for HGVs from NFPA 502 [9].

The behaviour of this type of fire can be varied from fire in open spaces as the expected truck fire impacting the exoskeleton. One of these large-scale tests was conducted at the TST tunnel facility in Spain, March 2012 [10]. The test(s) simulated heavy goods vehicles consisting of 228 pallets with 48 plastic pallets (20% by volume) and 180 wooden pallets (80% by volume) were used in all fire tests. The truck had approximate dimensions of 10 m(L) × 4.5 m (H) × 2.5 m (W).

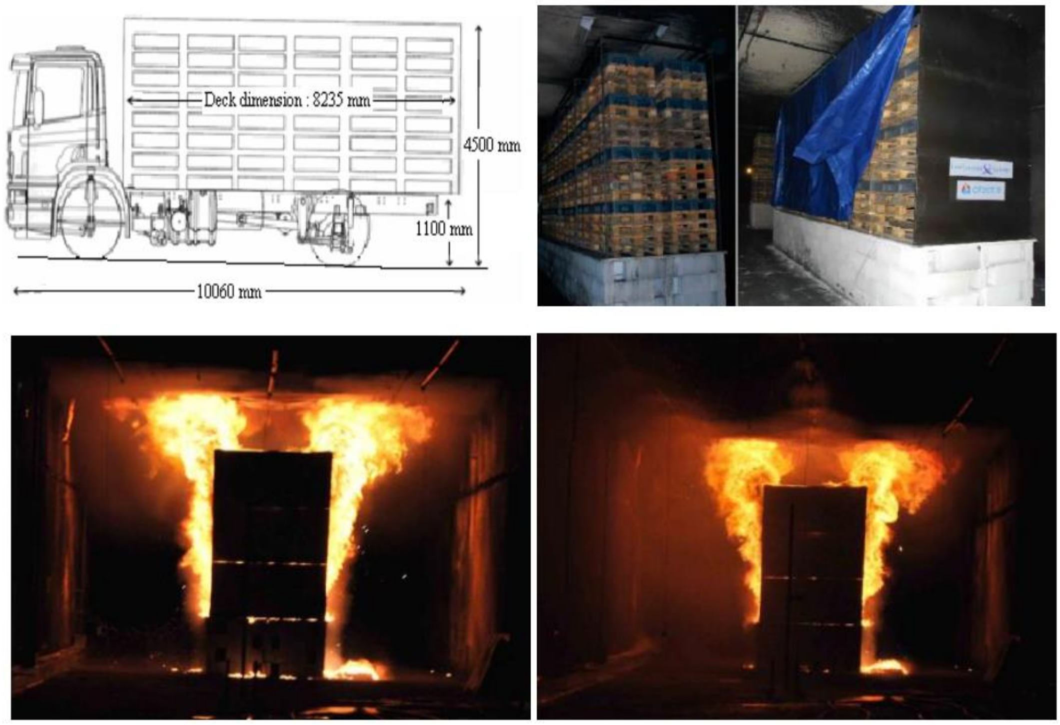

Figure 4: Large-scale fire truck test conducted at the TST tunnel facility in Spain, March 2012 [10].

The fire had a duration of approximately 40 mins. The Heat Release Rate (HRR) recorded during the test is illustrated in the figure below.

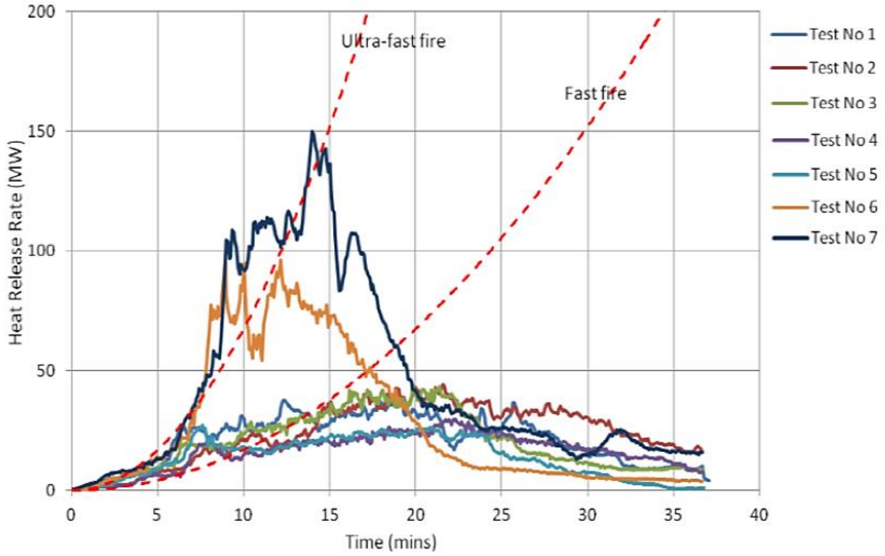

Note: Test 1 to 5 - deluge system operate at 4 minutes
Test 6- deluge system operate at 8 minutes
Test 7- free burning

Figure 5: HHR for Heavy Good Vehicle (HGV) fire with and without fire suppression, Spain 2012 [10].

The second design truck fire was obtained from the SFPE Handbook [11]. This guideline described the results obtained for another large-scale of an HGV with approximate dimensions of 12.5 m(L) × 2.5 m (H) × 2.4 m (W). During this test, a maximum peak HHR of about 130 MW was recorded during the approximately 60 minutes of fire duration. With the HRR vs time graph shown below, it has been estimated that about 109 GJ were released during this fire.

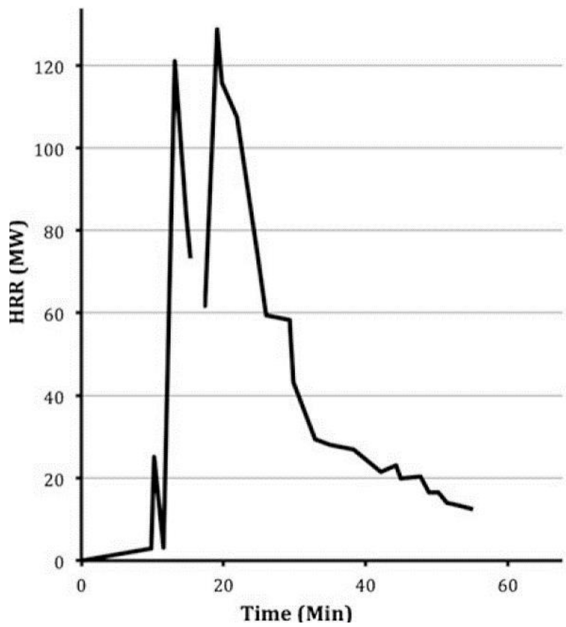

Figure 6: Large-scale fire HGV data from SFPE Handbook [11].

These scenarios are wildly different and thus additional a potential alternative methodology where the design truck fire can be adopted considering the total amount of energy released during the two large-scale truck fires (~100 GJ) presented above. While the behaviour of fire of a heavy good truck in a tunnel is not expected to be the same as in an open area, the total amount of energy that can be released is expected to be the same.

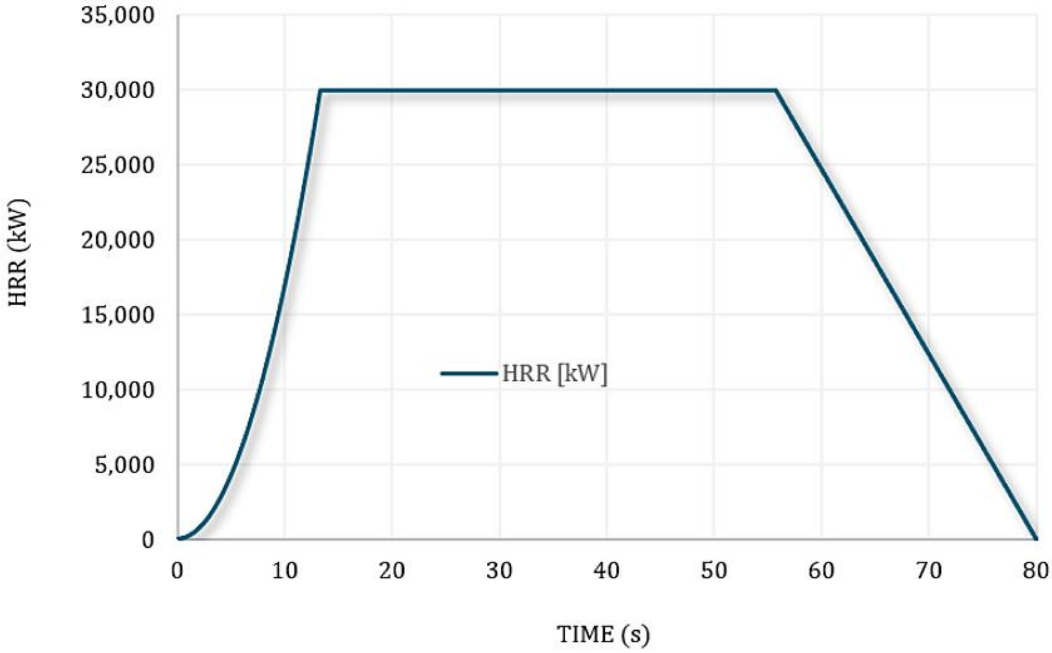

Figure 7: Modified truck fire scenario.

This design fire scenario is a fabrication as it is not based on direct testing information but, in the absence of good datasets for external fires and the wide variability of data which does exist, is considered to represent one in a suite of scenarios which the structure needs to be tested against.

3.1.3 Thermal expansion forces

Evaluating induced thermal expansionary forces experienced by the exoskeleton configuration is essential as regardless of fire protection methods the structural frame is subject to failure mechanisms due to thermal effects but is not a part of standard structural design or the standardised way that fire resistance is measured [12][13].

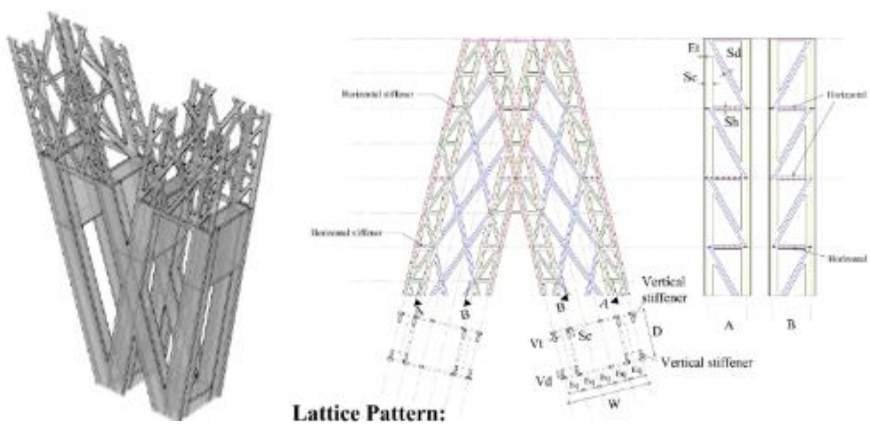

Figure 8: Illustration of Lattice pattern

Of particular note for the subject building is the potential for a travelling fire as this is actually the more onerous design scenario as (with colder restraining members) the heated lattice patterned member is more susceptible to failure than in the scenario where all members are uniformly heated.

3.2 Internal Structural Element Analysis

3.2.1 Fuel Load Analysis

The internal compartments of the building are largely comprised of ~1500 m^2 exhibition spaces (Figure 9) with floor to ceiling heights of 11 m. This creates challenges as experimental set-ups (and thus the methodologies derived from them) have not been conducted for such large height or area compartments as noted before.

Notably, the feature exhibition space poses a unique fire hazard, as a 23 m high space intended to contain Very Large Objects (VLOs). This space is likely to contain combinations of large hanging objects such as planes and objects such as train cars and steam engines. Truck access is also provided to this space.

This combination results in a diverse potential fire load and the potential for hanging objects to obstruct sprinkler coverage to objects below and for greatly delayed sprinkler activation due to the increased ceiling height. An indicative example of this type of arrangement is shown below.

Figure 9: Very Large Objects in Exhibition spaces.

This space provides immense challenges for designers to tackle. In order to determine appropriate design fire scenarios, the following must be resolved amongst others:

1. What is the fuel load present?
2. How much of this fuel load is available to any potential fire?
3. How will the fire spread and grow?
4. Is the fuel load distributed uniformly?
5. What is the available ventilation to the space? Will there be additional ventilation created by the fire itself?

The datasets available are both limited or aging. As an example of this a commonly used, within Australia, survey of fuel loads was published in the International Fire Engineering Guidelines [14] in 2005 but this fundamentally relies upon a fuel load study conducted between 1967 to 1969 in Switzerland. Given the different nature of compartments in modern buildings, it is suggested by the authors that this may no longer be a fully viable dataset to be used.

The techniques for fuel load surveys also appear not to be standardised and usually include only the full calorific value of contents but not necessarily the available fuel for combustion which introduces another source of uncertainty to the calculations.

The subject of fuel loads therefore comprises both a challenge and an opportunity to refine designs from potential conservatisms.

3.2.2 Unprotected small connections on to protected steelwork

Within the exhibition spaces, a number of secondary members connect to primary truss members at the roof of the exhibition spaces. When analysed under the structural fire load case, it is found that the secondary members are not required for overall stability of the structure. Thus, presenting an opportunity for optimised fire protective design. However, the interface between these unprotected members and protected steel members must be considered carefully.

Industry guidance is that heat transfer from unprotected structural steel into protected structural steel should be considered. The industry best and accepted practice is to apply a coat-back on all secondary or ancillary elements for a distance of 450-500mm [15] [16] [17], where the contact area exceeds 3,000 mm^2 per metre of length of the protected primary member [18].
This is to limit the effects of heat transfer from the unprotected member impacting on the protected primary member. For a complex connection, this approach could lead to significant over engineered designs.
The guidance and accepted practice do not consider the actual fire exposure risk present in the building or size of the member.

To illustrate this analysis of internal elements within the exhibition spaces (mainly trusses and beams at ceiling level) within the compartments of the subject buildings, considers two main fire scenarios. The first is the potential of a fire located at floor level that can potentially impact the subject elements located at ceiling and mezzanine.

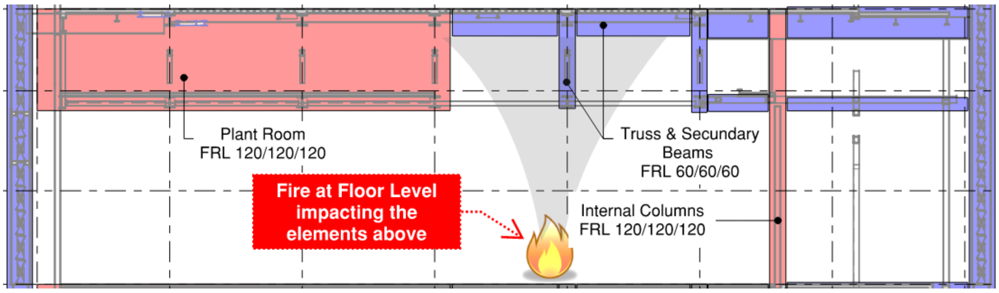

Figure 10: Fire scenario at Floor Level (FL) impacting the trusses and beams located at ceiling level.

A second major scenario impacting the elements with proposed reduced FRLs is a fire coming from equipment such as speakers or TV screen media located at mezzanine level that can directly impact the subject elements.

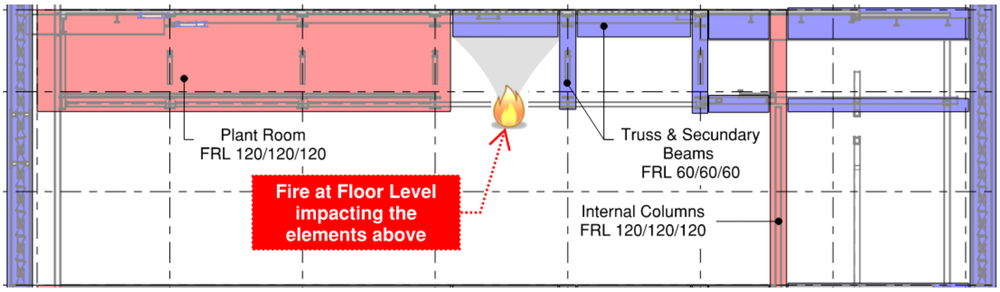

Figure 11: Fire scenario at Mezzanine Level impacting the trusses and beams located at ceiling level.

3.2.3 Areas with inherent limited ventilation

This section discusses a potential practical methodology to evaluate the potential for flashover conditions in large spaces with limited ventilation as is the case for the subject building as the exhibition spaces must be acoustically separated from adjacent areas and some do not have windows direct to outside resulting in a scenario where the only ventilation is provided through the main door openings.

The results from this analysis identify the compartments which are likely to reach post-flashover conditions. Hence, this analysis provides an indication of the compartments that are most likely to be subjected to more onerous conditions during a fire.

In order to estimate the probability of the occurrence of a flashover within the compartments, the required Heat Release Rate (HRR) to reach flashover can be estimated using the Thomas' flashover criterion (Walton and Thomas, 2008) described in the Structural Design for Fire Safety guideline [19].

$$Q_{FO} = 0.0078\ A_t + 0.378\ A_v\ (\sqrt{H_v})$$

Q_{FO} *Heat release rate necessary for flashover (MW)*

At *Total area of the compartment enclosing surface boundaries excluding area of vent openings (m^2)*

Av *Area of ventilation opening (m^2)*

hv *Height of ventilation opening (m)*

Noting that, as before, the correlation was derived for smaller compartments and thus could be subject to error when applied to large compartments. For designers, this leads to the use of additional conservative safety margins

4 CONCLUSION

When designing commercial buildings for structural fire resistance, a number of challenges are encountered by designers, these include:

- The use of correlations which may be outside the limitations of their original derivations. Particularly for large open compartments
- Lack of specific datasets for fuel loads within bespoke areas of a building
- Fixing connections from unprotected steel elements on to protected steel elements
- The ability to consider compartments with limited ventilation.
- The impact of localised fires (or travelling fires) on the structure through thermal expansion

The current design practices which respond to these are largely by adding a degree of conservatism to designs in order to deal with the uncertainty involved which are then agreed upon by project stakeholders (e.g., fire engineering designer, authority having jurisdiction, local fire service, fire engineering peer reviewer). However, there is limited to no explicit research that underpins some of those assumptions and improved datasets & methods would lend themselves to improved fire protection designs.

5 REFERENCES

[1] Bisby L(2021), *Structural Fire Safety when responding to the climate emergency*. The Journal of the Institution of Structural Engineers, Vol 99

[2] Margaret Law, Engineering Journal, "Fire Safety of External Building Elements – The Design Approach", American Institute of Steel Construction (AISC), USA, 1978.

[3] British Standards, "Eurocode 1: Actions on structures. Part 1-2: General actions – Actions on structures exposed to fire", BS EN 1991-1-2:2002.

[4] Wickström U. 1981. Temperature calculation of insulated steel columns exposed to natural fire. Fire Safety Journal, 4(4), 219-225.

[5] Wickström U. 1985. Application of the standard fire curve for expressing natural fires for design purposes. Fire Safety: Science and Engineering, ASTM International.

[6] Jonsdottir AM, Rein G (2009) "Out of range". Fire Risk Management, pp 14-17

[7] Rackauskaite E, Bonner M, Rein G, Et. Al (2022). *Fire Experiment Inside a Very Large and Open-Plan compartment: x-ONE.* Fire Technology, pp 905-939.

[8] Rein, G, Torero J.L, Jahn, W, *et al, Round-Robin Study of a priori Modelling Predictions of the Dalmarnock Fire Test One*

[9] NFPA, *NFPA 502 : Standard for Road Tunnels, Bridges and Other Limited Access Highways*, 2023

[10] M. K. Cheong, W. O. Cheng and others, "Heat Release Rates of Heavy Goods Vehicle Fires in Tunnels", BHR International Symposium on Aerodynamics, Ventilation and Fire Tunnels, Barcelona, Spain, 2013.

[11] Morgan J. Hurley, " SFPE Handbook of Fire Protection Engineering, Fifth Edition, 2016.

[12] Bisby L, Gales J, Maluk C (2013), *A contemporary review of large-scale non-standard structural fire testing*. Fire Science Reviews.

[13] Gales J, Maluk C, Bisby L(2012), *Structural Fire Testing – Where are we, how did we get here, and where are we going?*. 15th International Conference on Experimental Mechanics (ICEM)

[14]"International Fire Engineering Guidelines, Edition 2005", Australian Building Codes Board, Canberra, Australia, 2005.

[15] Associated for Specialist Fire Protection (ASFP), Code of practice for junctions between different fire protection systems when applied to load bearing structural steel elements., Kingsley, United Kingdom: Associated for Specialist Fire Protection (ASFP), 2010.

[16] Underwriter's Laboratories (UL), "UL's Best Practice Guide for Passive Fire Protection for Structural Steelwork," Underwriter's Laboratories (UL), Northbrook, United States of America, 2018.

[17] DNV, "Offshore Standards DNV-OS-D301: 2019 Amdt 2021 Fire Protection," DNV, Baerum, Norway, 2019.

[18] Fire and Blast Information Group (FABIG), "Design Guidance for Hydrocarbon Fires," Steel Construction Institute, Ascot, United Kingdom, 2014.

[19] Andrew H. & Anthony K., "Structural Design for Fire Safety", Second Edition, 2017.

[20] P. H. Thomas, "Design Guide: Structural Fire Safety - Workshop Cib W14."

HOTSPOTS JEOPARDISING THE FIRE PROTECTION PERFORMANCE

An established issue becoming a new challenge in construction

Iolanda Del Prete[1], Lukas Rutkauskas [2], Florian M. Block[3]

ABSTRACT

The functionality of intumescent paint is based on its ability to char and expand if exposed to heat. Objects located within the expansion zone of the paint or connecting not fire protected steelwork can lead to a local temperature increase in the protected steelwork causing so-called hotspots, which could compromise the stability of the primary structure in fire. Whilst the UK Association of Specialist Fire Protection (ASFP) and intumescent paint manufacturers have been providing guidelines to deal with this issue since the early 2000's, it appears to be a new challenge for the construction industry. Only the much-heightened awareness of fire safety measures on site, after the Grenfell tragedy, makes the construction industry address this issue.

This paper provides an insight into this complex problem and proposes a methodology to solve this challenge in a performance-based way. As a first step a Qualitative Risk Assessment (QRA) is proposed and then in some cases followed by advanced Finite Element Method (FEM) analyses.

The presented case studies in this paper demonstrate on the example of large stadia and mixed-use developments, how the proposed methodology was applied.

Keywords: hotspots, fire protected primary steelwork, unprotected secondary steelwork, qualitative risk assessment, finite element modelling

1 INTRODUCTION

The charring and expansion of intumescent paint when exposed to heat leads to the formation of an insulating layer that is typically 30-50 times the dry film thickness of the paint (DFT). If the charring and expansion of the intumescent is restricted by objects that are located within the expansion zone of the paint, then the required thickness of the char layer cannot be generated. Therefore, the steelwork will be heated more in these areas and hotspots in the steelwork are formed. The same applies in areas where unprotected primary or secondary steelwork is connected to fire protected steelwork. Examples of secondary steelwork likely to lead to hotspots, if not accurately dealt with, are lift bracket connections within steel frame lift shafts, secondary steelwork supporting riser floors, cladding support brackets, balustrade supports, MEP services supports or similar.

According to the prescriptive guidance, depending on several factors, it might be required to fire protect the secondary steelwork elements. The main factors are the size of the attachment, the required fire resistance, the number of attachments per surface area/length of primary steelwork member and the rules of the fire protection manufactures. Negligence in the observation of the rules set out by fire protection

[1] Dr. Iolanda Del Prete, Buro Happold Engineering
e-mail: iolanda.delprete@burohappold.com
[2] Mr. Lukas Rutkauskas, Holmes Aus & NZ
e-mail: lukas.rutkauskas@holmesgroup.com
[3] Dr. Florian Block, Buro Happold Engineering
e-mail: florian.block@burohappold.com
https://doi.org/10.6084/m9.figshare.22153634

manufacturers or other available guidance may adversely impact the warranty of the fire protection performance provided by the fire protection manufacturers and more importantly could lead to a structural collapse of the primary steelwork. Paint manufacturers are usually prepared to underwrite the performance of the protected structural element provided that the size of the area, over which no intumescent is present/functional, is lower or equal to the size of a pound coin (circa 450 mm^2) in an A4 page. However, different acceptance criteria may be provided by different paint manufactures.

According to the ASFP Technical Guidance Document 8 (TGD8) [1], a so-called "coatback", i.e. an extension of the intumescent paint by 500mm on the unprotected elements, would be required to prevent the conduction of excessive heat through the unprotected element into the protected element. Therefore, any secondary steelwork interfacing with primary steelwork will need to either:

- Be locally painted in accordance with the ASFP or fire protection manufacturer's guideline or
- Justify through structural fire engineering (SFE) calculations that the unprotected hotspot is negligible

The two-step methodology proposed in this paper, which is aimed to solve this challenge in a performance-based way, is summarised in the following: as a first step a Qualitative Risk Assessment (QRA) is proposed, which is followed by advanced Finite Element Method (FEM) analyses in some cases.

2 METHODOLOGY

The methodology presented herein is aimed to solve in a performance-based way the challenge posed on the construction industry by the prescriptive requirements set out to prevent structural failures in presence of hotspots on the steelwork in case of fire.

Given the size and complexity of some developments, which Buro Happold have been recently designing, such as stadia and large mixed-use building, compliance with the prescriptive requirements, which are usually defined for ordinary structures, have proven to be unpracticable. On the other hand, the application of a performance-based design completely relying on advanced FEM would be challenging too due to the required computational effort. Therefore, a certain level of engineering judgement by educated and experienced structural fire engineers is often required to solve the hotspot issue in an efficient way.

The authors of this paper developed a two stages approach, whereby a QRA is carried out in the first step, followed by FEM, where required.

2.1 Qualitative Risk Assessment

The QRA is a relatively simple tool, which requires the application of engineering judgement to estimate the hazardous conditions and the consequence of failure, which determine the risk of a structure failing due to hotspots. Based on this approach, many low-risk hotspots can be addressed. In order to assess the risk of a hotspot to life safety, the following tasks are implemented:

- Severity of hazard assessment, which accounts for the likelihood of a fire with a certain size to occur and affect the structure with a certain number/location of unprotected attachments. The categories considered to be relevant for the definition of the severity of hazard are usually the exposure condition (H1), shielding conditions (H2), severity of hotspot (H3).
- Definition of the consequence of failure of the member potentially affected by hotspots. This is usually done in a qualitative way and based on engineering judgement. However, reference is also made to the recommendations of Approved Document B [7] and BS EN1991-1-7 [2] (including commentary provided in SCI P391 [3]), for Class 3 buildings to prevent the disproportionate collapse in case of accident.

Five classes (low - L, medium low - ML, medium - M, medium high – MH, and high - H) are assigned to Severity and Consequence.

The resulting hotspot risk is categorized in three groups being: Negligible risk (no fire protection is required); Tolerable/medium risk (passive fire protection may be required, but further review/calculations are proposed); Unacceptable/high risk (passive fire protection is required).

2.2 Advanced Finite Element Method Analysis

Advanced FEM calculations are used in cases, where the connection details potentially subject to hotspot are too complex, or the consequence of failure are too high for the QRA. In general, the FEM analysis involves a heat transfer assessment considering the locally reduced performance of the intumescent paint followed by structural modelling at elevated temperatures. The thermo-structural analysis, carried out with SAFIR [3], accounts also for the expansion of the intumescent paint when the steel temperature achieves 180-200°C in average, according to the information provided by the intumescent paint manufacturers appointed for the projects used as case studies. This is done by means of a stepped heat transfer analysis, where the steel is considered unprotected in the first step of the analysis, followed by another step where activation of the paint is considered. The authors are aware that temperatures higher than 200°C have been observed during experimental tests [4], where certain intumescent paints were used. However, the step analysis, described herein, is just aimed to explain the methodology and it can be reapplied by setting different parameters, such as activation temperatures higher than 180-200°C, more appropriate for the specific products.

3 CASE STUDIES

3.1 54,000 Seater Football Stadium

The methodology is presented on the example of a new 54,000 seater stadium being designed and built in the UK. The North, South and Corner stands superstructure consist of frames of steel columns and beams, supporting precast lattice slab floors. The roof structure is made of steel cantilever structure over the East and West Stands, and long span trusses over the North and South Stands. The East and West Stands are made of concrete. The support to the facades is included in the 'roof structure'. Figure 1 shows the exploded view of the stadium structure.

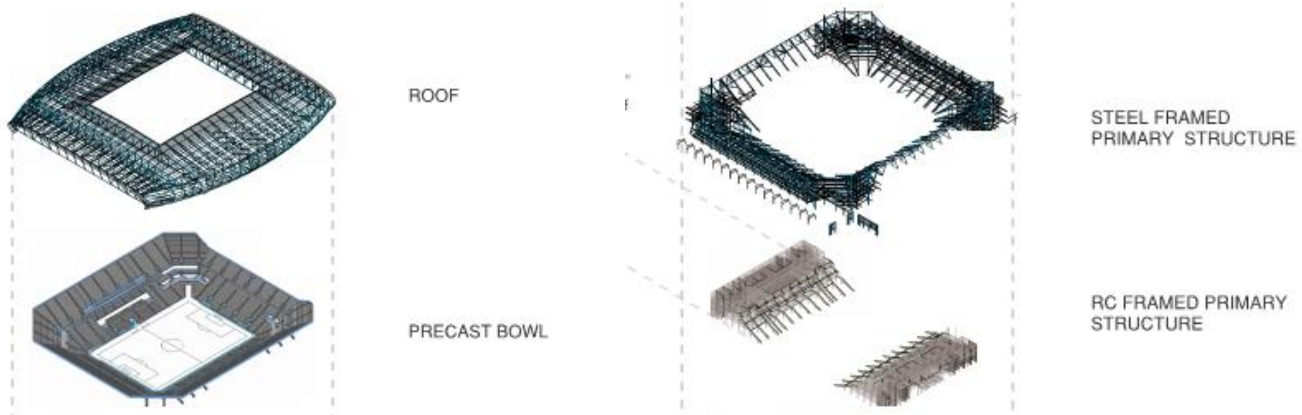

Figure 1. Exploded view of stadium superstructure

The presented case is the assessment of the hotspots due to façade secondary steelwork connections on primary steelwork, which has been carried out in two steps summarised in Section 2.1 and 2.2.

During the Step 1 (QRA), the following tasks were implemented:

- Severity of hazard definition: examples of exposure conditions, shielding and severity of hotspot with corresponding rates are shown in Table 1. Once assigned a certain rating to the different items affecting the severity of hazard, the total severity rating is calculated as product of the individual rates (H=H1·H2·H3). Based on the total severity of hazard rating, the severity of hazard classes can be defined as in the following: Low (H≤5); Medium-Low (5<H≤12); Medium (12<H≤27); Medium-High (27<H≤64); High (H>64).

- Definition of the consequence of failure, which is the most important part of the QRA process, because it largely affects its response. Examples of consequence of failure with corresponding ratings are shown in Table 2.
- Definition of Risk by cross referencing the outcomes of the severity of hazard and consequence of failure assessments using Table 3.

It should be noted that Table 1 and Table 2 provide only examples considered relevant for the specific application by the authors. The appropriate parameters should be tailored on a case-by-case basis.

Table 1. Severity of Hazard Definition

	L	ML	M	MH	H
EXPOSURE CONDITION	1	2	3	4	5
Fire breaking out of a compartment with flames **unlikely to engulf** members In large **fire-sterile** circulation space, lobbies, stairs, toilette	1				
Secondary steelwork affected by fire spreading out of fire resisting construction **lower** than the required fire resistance of the member		2			
In **non-fire sterile** circulation space (e.g. hospitality lounge with customer bar) Fire breaking out of a compartment with flames **likely to engulf** members External fire with flames likely **to engulf** members Steelwork at the edge of **non-compartment floor** in large circulation space (or similar low fire hazard spaces) which could be affected by a **fire spreading from the level below (medium hazard space)** through the façade			3		
Steelwork at the edge of **non-compartment floor** in large circulation space (or similar low fire hazard spaces) which could be affected by a **fire spreading from the level below (medium-high hazard space)** through the façade				4	
Inside a fire compartment Inside a riser					5
SHIELDING	1	2	3	4	5
Hotspot is **shielded by fire resisting material** (fire resistance **higher** than resistance of the structure)	1				
Hotspot is **shielded by fire resisting material** (fire resistance **lower** than resistance of the structure)		2			
Hotspot is **shielded by non-combustible** material (e.g. material **with insulating properties**)			3		
Hotspot is shielded by **non-combustible material** (e.g. material **with non-insulating properties**, steel sheets, etc.)				4	
Not shielded or **shielded by combustible** material					5
SEVERITY OF HOTSPOT	1	2	3	4	5
Individual attachment in low stress area (e.g close to the beam's support) **engulfed** by fire Multiple attachments **NOT simultaneously affected** by fire (e.g. localised fire with low flame height and small diameter likely to radiate from a certain distance no more than a couple of close attachments on beams)	1				
Individual attachments in highly stressed areas (e.g. beam's midspan) **engulfed** by fire		2			
Couple of close attachments **engulfed** by fire in highly stressed area (e.g. localised fire with high flame height and small diameter likely to engulf no more than a couple of close attachments on beams)			3		
Multiple or continuous attachments simultaneously **exposed** to a fire (e.g. localised fire radiating all the attachments along a column from a certain distance)				4	
Multiple or continuous attachments simultaneously **engulfed** by fire (e.g. fully developed fire in a compartment)					5

Table 2. Consequence of failure definition

CONSEQUENCE OF FAILURE	
Beams putting less than $50m^2$ slab area at risk Columns putting less than $50m^2$ total slab area at risk (one or multiple floors)	LOW
Beams putting less than $50m^2$ slab area at risk (compartment floor)	MEDIUM-LOW
Beams putting more than $50m^2$ and less than $100m^2$ slab area at risk Columns putting more than $50m^2$ and less than $100m^2$ total slab area at risk (one or multiple floors)	MEDIUM
Beams putting more than $50m^2$ and less than $100m^2$ slab area at risk (compartment floor) Beams putting more than $100m^2$ slab area at risk but not *Key Elements* Columns supporting any area of compartment floor	MEDIUM-HIGH
Key Elements	HIGH

NOTE: if a beam provides lateral restraint to a column at MJ location, then the consequence of this beam failing should be increased at least to the next class to consider the consequence of the column losing the lateral restraint.

Table 3. Evaluation of Risk

	Severity of hazard/ Consequence	Consequence of failure				
		Low	**Medium-Low**	**Medium**	**Medium-High**	**High**
Severity of Hazard	**Low**	Negligible	Negligible	Negligible	Negligible	To be reviewed
	Medium-low	Negligible	Negligible	Negligible	To be reviewed	To be reviewed
	Medium	Negligible	To be reviewed	To be reviewed	To be reviewed	To be reviewed
	Medium-high	Negligible	To be reviewed	To be reviewed	To be reviewed	Attachment to be protected
	High	Negligible	To be reviewed	To be reviewed	Attachment to be protected	Attachment to be protected

In general, the details classified as "To Be Reviewed" were further reviewed to assess the feasibility of reducing the severity of the hazard and/or the consequence of failure, such to reduce the overall risk. Mitigation measures were explored to allow, in a safely manner, the secondary steelwork to remain unprotected. The details, which fell in "To Be Protected" were further reviewed to interpret the requirements set out by the fire protection manufacturer in terms of protection to be applied on the secondary steelwork and advise on how to comply with the rules provided by the manufacturer.

Alternatively, the details "To Be Reviewed" or "To Be Protected" could be analysed by means of FEM.

In the following, the application of the QRA of façade brackets (billets – see Figure 2), which are connected to an edge beam on the Level 02 (L02) (red rectangle in Figure 3) is shown.

As shown in Figure 4, the unprotected secondary steelwork connected to the edge beam supporting the slab on L02 falls in the service corridor and the fire hazard on this floor from the accommodation rooms is negligible because the rooms are enclosed in fire resisting constructions remote from the secondary steelwork. Therefore, the rate assigned to **H1 is equal to 1.**

According to the fire strategy drawings (Figure 4), the façade is not shielded by fire rated constructions, however in case of fire in the service corridor, it is very unlikely for the flames to directly impinge the unprotected secondary steelwork. In a space like the service corridor, it is expected that a fire not larger than a small bin fire would occur. As discussed with approving authorities, a small bin fire would be characterised by a maximum HRR of 0.2MW, diameter of fire D=0.6m and height of the flame h=1.33m.

Since the height of the flame is significantly shorter than the height of the unprotected secondary steelwork above the floor, the absence of shielding is irrelevant, and the severity of hazard rating should be low. However, to add redundancy to the QRA, **H2 has been considered equal to 3**.

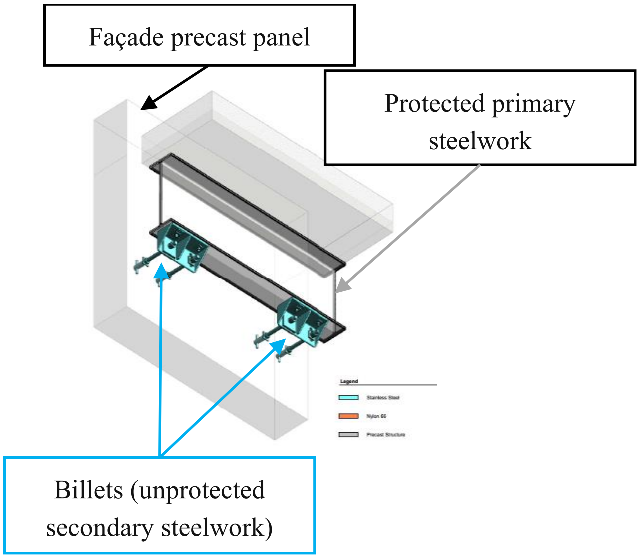

Figure 2. Connection detail

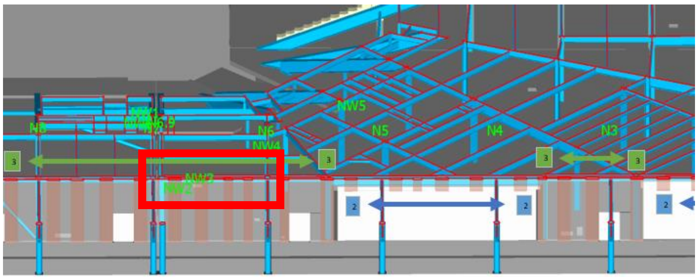

Figure 3. Identification of the location of the beam potentially affected by hotspots

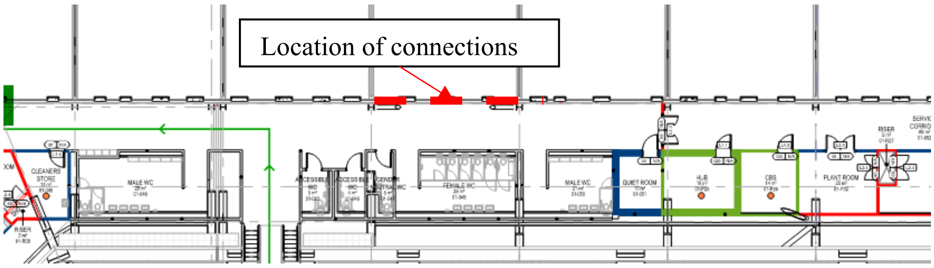

Figure 4 Use of the space where the fire hazard could be (continuous coloured lines represent the rating of fire resisting constructions)

In order to assess the severity of hotspot, it has been considered that multiple attachments are provided along the length of the beam (4 panels - 8 billets). However, as discussed above, a localised fire typical of the use of this space (e.g. small bin fire 0.2MW, D=0.6m, h=1.33m) is unlikely to affect more than a couple of billets. This is because the precast piers are at a distance of at least 2 m centre to centre and each pier requires two support billets at the minimum distance of 350 mm, according to the information provided by the façade contractor. Therefore, the diameter of the fire would cover a maximum of two billets, which would not be directly engulfed in the fire, because their height above the floor is higher than the flame height. Therefore, the rating assigned to **H3 is equal to 1.** According to Table 3, the total Severity of Hazard rating is **H1 x H2 x H3 equal to 3**, which falls in the **Low** severity class.

For the definition of the consequence of failure, it has been assumed that the beam (red dotted in Figure 5) would fail in case of fire due to hotspots. According to the structural drawings, this is a primary beam exposing about 106m^2 slab area to risk (only 6m^2 exceed of the 100m^2 given in ADA and therefore not considered a Key Element). The slab at this level is not a compartment floor and the robustness assessment did not identify this element as critical. Therefore, according to Table 3, a medium consequence of failure could be assigned to this case. However, since the beam provides lateral restrain to a column on the MJ, the consequence is increased to **medium-high**.

According to Table 4, the risk of hotspots on the assessed beam is **Negligible** and therefore the secondary steelwork connecting to the assessed beam **does not require fire protection**.

3.2 Large Mixed-Use Development

A QRA, similar to the one described in Section 3.1 above, was carried out on selected connections to the primary steelwork of a very large mixed-use development in London. The outcome of the QRA suggested that some connection details would need further review and therefore a detailed structural fire engineering (SFE) assessment was carried out by implementing FEM analyses. The case described herein is a cruciform mullion connection to H columns in the basement level of the lifts of the development (Figure 5), where the secondary steelwork could not be protected on site fulfilling the requirement of the ASFP guidance (see Section 1). As shown in Figure 5, the steelwork surface highlighted with blue lines was unpractical to be protected due to the narrow space and interface with the glazing of the lift.

A 2D heat transfer model of the structural element was built in GID [8] and analysed with SAFIR [5, 6]. The heat transfer model comprises of the following components and materials (see Figure 5): primary element (steel column), secondary connection (steel), intumescent paint.

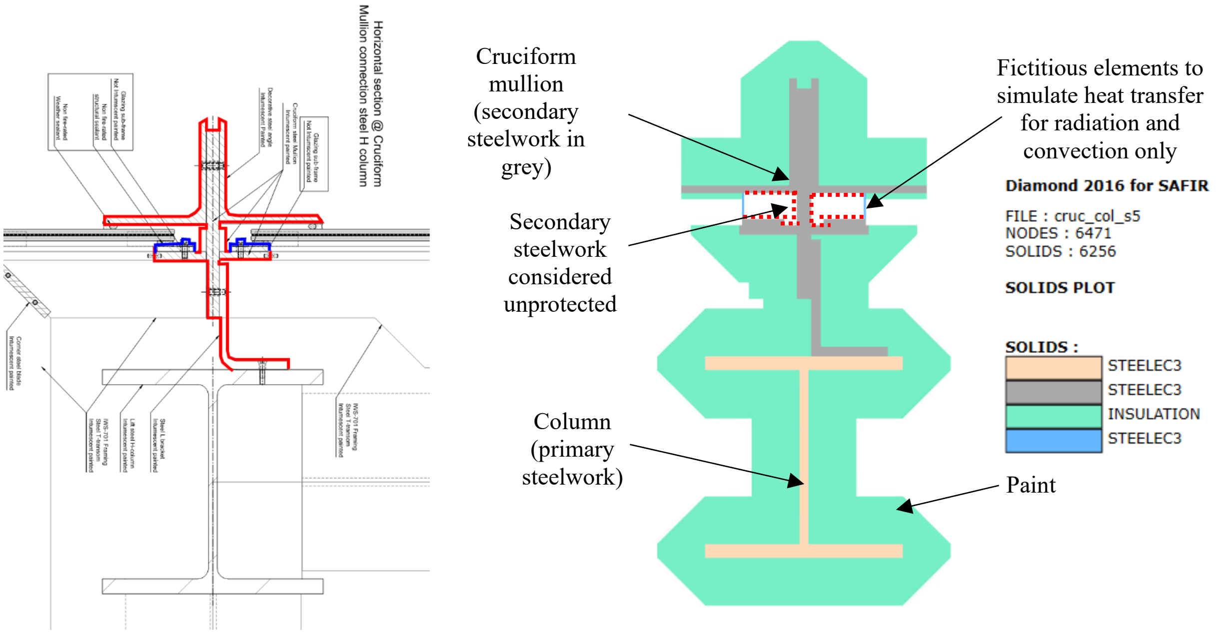

Figure 5. Connection detail and 2D heat transfer model

A generic insulation material with a constant thickness and nominal thermal properties was defined to represent the intumescent paint applied to the primary steelwork. The intumescent paint was designed to activate at 200°C. In order to consider the initial behaviour of the intumescent paint, when the intumescent paint is not active yet, the heat transfer analyses were divided into a number of steps, described below.

Where the secondary elements are provided with a coatback, the properties of the paint at the secondary structure are as per primary element. For the calibration of the intumescent paint's thermal properties to be used in the heat transfer analyses, the calculation of the element temperature was preliminarily carried out in accordance with Equation 4.27 in BS EN1993-1-2 [9] for protected steel. A nominal value was assumed for the thickness, density, and specific heat capacity of the insulation with the thermal conductivity of the insulation adjusted using the goal seek method in Microsoft Excel such that the protected element reaches its critical temperature at the designed time into the Standard Fire. The critical temperature of 539ºC was defined based on recommendations given in [10] for hot rolled H sections columns in compression in shopping/congregational areas.

A multiple-step process was used to ensure the model accounts for the activation of intumescent paint when the steel temperature reaches 200°C. Based on the temperature distribution in the section, the activation of the intumescent paint has been designed in five steps (including three actual and two numerical fictitious steps as explained in the following). This is due to the activation temperature in some thin parts of the sections being achieved significantly faster than in other thicker parts. With the multiple steps, the design of the paint activation is closer to the reality. The description of the different steps is shown in following:

1. The first step is run with no protection layer. The standard fire 'FISO' was applied to the section. When the average temperature in certain parts of the section reaches 200°C the step is completed.

2. The second step resumes from the end of the first step and adds the protective layer. The protective layer is activated only on the parts of the element achieving the activation temperature. This is a fictitious step implemented with the only aim to introduce a new set of elements into the analyses. These new elements represent the intumescent paint, which is considered to be at the same temperature as the standard fire temperature (ISO834) at the time the previous step ended. This step runs for 5-10 seconds. The constraint of the temperature is to prevent the artificial cooling of steel that would occur if the layer of protection was introduced as being at ambient temperature. The application of an ISO fire temperature to the insulation layers is a conservative assumption. The ISO fire curve is applied on the steelwork where the paint has not been activated yet from the time of activation of the intumescent paint on the remaining part of the section.
3. The third step continues from the end of the second step. The temperature constraint on the insulation is removed so the temperature begins to spread evenly through the section and insulation. The ISO fire curve is again applied from the time, when the intumescent paint activates. This step runs until the intumescent paint activation temperature is achieved on other parts of the section (Figure 6).

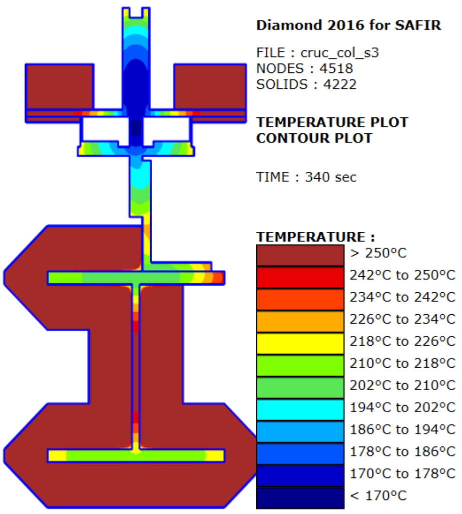

Figure 6. Temperature at the End of Step 3 (note: legend only for Figure 6)

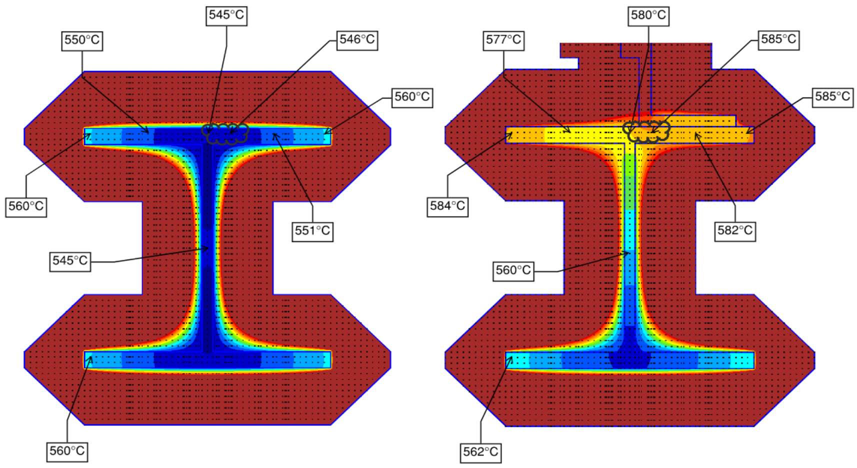

Figure 7. Temperature Field after 120 min of standard fire exposure

4. Additional steps, similar to the previous ones, are implemented until the intumescent paint activation is simulated on the whole section.

The analysis showed that the top flange temperature in the model with secondary steel attachment is on average 25-30°C higher than in a model without the attachment (Figure 7), therefore the decrease of the yielding strength ranges between 5% and 15% and the decrease in the elasticity of steel ranges between 7% and 19%. The maximum temperature difference between the models is 39°C (546°C in undisturbed model to 585°C in model with secondary steelwork).

This a local increase in the top flange where the corner of the secondary steel angle is connected to the flange, the area is marked in Figure 7. The difference in the yield strength reduction between the models is 21% (k_y=0.65 for T=546°C and k_y=0.515 for T=585°C) and 25% for the reduction of the elasticity of steel (k_E=0.467 for T=546°C and k_E =0.35 for T=585°C). However, this is only a local reduction on the area bubbled in Figure 7. The reduction is significantly lower for the other areas. In addition to the above it is also worth noting that some conservative assumptions have been implemented in the model, such as: omission of the expansion of the intumescent paint at the tips of the elements with a thickness below 10mm; neglection of the temperature dissipation into the steel column in the 3rd direction (along the axis of the column); activation of the intumescent paint based on averaged temperature in the model (the intumescent paint on some parts of the section, such as tips of the flange of the column, would activate earlier, resulting with lower temperature in these areas).

Based on the analysis carried out and summarised above, it is concluded that the presence of the cruciform mullion connected to the flange of the H column with the proposed fire protection regime (not compliant with ASFP) would be unlikely to cause an unacceptable increase of temperature in the affected columns. These elements would have similar levels of safety to sections fire protected in accordance with the rules provided by the ASFP guidance.

3.3 82,000 Seater Rugby Stadium

A QRA, similar to the one described in Section 3.1, was carried out on the cladding brackets connected to the primary steelwork supporting the façade of an existing 82,000 seater rugby stadium in the UK, which was being redeveloped in the 2018. The outcome of the QRA suggested that some connection details would need further review and therefore a detailed SFE assessment was carried with the following methodology.

- Parametric analysis of 3D heat transfer models of a typical cladding bracket connected to the edge beam with varied extent of the fire protection along the bracket.
- Analysis of a 2D heat transfer model of the undisturbed section (no cladding bracket to the beam).
- Preliminary structural analysis of the perimeter beam (steel beam composite with concrete) with non-uniform temperature along the beam, according to the heat transfer analyses results.
- Advanced structural analysis of the perimeter steel beam with detailed shell models to account for local and global effects of both vertical and horizontal loads.

The case presented herein is the analysis of the most typical beam in the stand of the stadium under assessment, which is a UB356x127x33 with 3 cladding brackets connected to it.

Design Fires

Since the aim of the analysis is not to assess whether the element survive in a natural fire, but rather to assess whether the hotspots lead to worse performance of the structural element in comparison to the fully protected case, the analyses were carried out in case of exposure to the standard fire curve for the time of fire resistance required to the building (R90) according to the prescriptive regulation.

Acceptance Criteria

The set of acceptance criteria, which limit the deflection and rate of deflection of the beam, are taken from BS EN 13501-1-2016 for fire testing of structural elements.

Heat Transfer Modelling

Three 3D heat transfer models of a typical cladding bracket connected to the edge beam were built in GID [8] and analysed in SAFIR [5, 6]. These comprised (see Figure 8): the edge beam (steel), the end plate (steel), the PFC (steel) and intumescent paint. The difference between the three models is the extent of the fire protection along the PFC bracket (steel beam protected only; steel beam and cladding bracket fully protected as standard compliant option; steel beam and steel end-plate protected – Figure 8b).

To reduce the computational effort due to the size of the 3D models, a generic insulation material with constant thickness with nominal thermal properties has been defined to represent the intumescent paint applied to the primary steelwork (no step analysis implemented in this case). By considering a generic insulation material with constant thickness, the initial steel temperature is slightly underestimated, since the intumescent paint does not activate before the steel temperature achieves about 200°C. However, this is considered reasonable, since this generic insulation material is defined such to provide the equivalent insulation properties that allow the protected beam to achieve its design temperature (553 °C according to the Yellow Book) at the required time in the Standard Fire.

In order to reduce the modelling and computational time, the undisturbed section was modelled in 2D.

Heat Transfer Results

The bottom flange was chosen as the critical area to be monitored because a significant reduction of the strength of the bottom flange could lead to the failure of the beam in bending. Therefore, the temperature after 90 minutes of fire exposure in the centre of the bottom flange of the steel beam was normalised against the maximum temperature in the bottom flange and plotted versus the distance from the centre of symmetry of the model, in the three modelled cases. The analyses showed that when the fully unprotected cladding bracket is exposed to a standard fire, this leads to a hotspot in the web of the beam where the bracket is connected. This causes, due to heat transfer via conduction, a high temperature in the bottom flange (about 780°C). The temperature in the bottom flange reduces as the distance from the cladding brackets increases, and the temperature in the undisturbed area (600 mm away from the centre of the connection) of the beam reduces by about 30%.

In the case where the steel beam and the steel plate are protected, the maximum temperature in the bottom flange, due to the hotspot, is about 86% of the maximum temperature observed in the previous case (cladding bracket fully unprotected). The temperature in the undisturbed area of the beam reduces by about 20%. The lower reduction of strength in this case maximises the chances for the beam to survive.

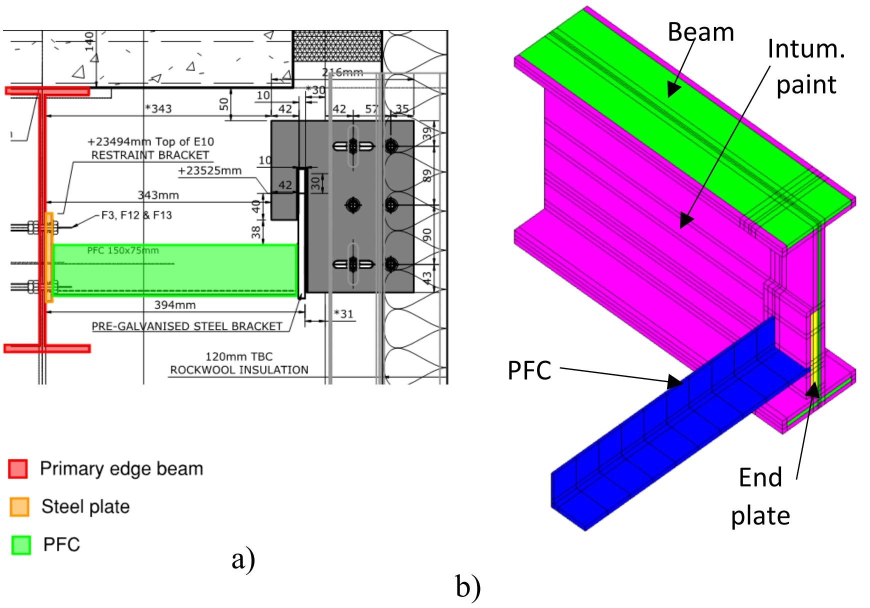

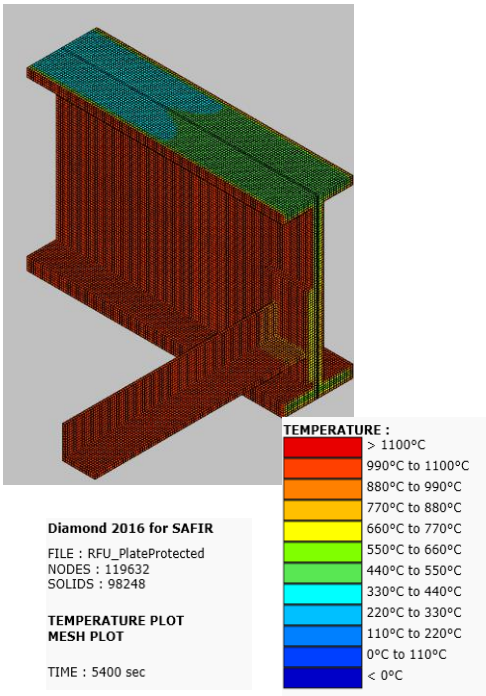

Figure 8. (a) Detail and (b) 3D Model of bracket-to-beam connection (steel beam and steel end-plate protected)

Figure 9. Temperature field after 90 minutes (steel beam and steel end-plate protected)

<u>Structural Analysis</u>

The analysis of a simple 2D structural model of the perimeter beam with simply supported end conditions and non-uniform temperature along the beam, extracted from the heat transfer models, was carried out for its two benefits: making preliminary considerations and evaluating the benefits in fire of a steel beam composite with the concrete slab; reduce significantly the computation time required for the analysis of composite beams with complex shell or brick models.

In order to account for the non-uniform temperature distribution along the beam, two different cross-sections were assigned along the beam. Based on the outcomes of the 3D heat transfer analysis (Figure 9), the following assumptions were considered reasonable: the temperature in the section affected by hotspots was applied to the beam finite elements for a length of 200 mm on both sides of the centre of the cladding bracket location; the temperature in the undisturbed section was applied elsewhere.

The unfactored vertical loads were provided by the structural engineers, combined in Fire Limit State (FLS) and applied to the model. The beam was modelled as a steel beam acting compositely with a concrete slab.

As shown in Figure 10, the structural analysis showed that the beam is able to sustain its load carrying capacity for more than 90 minutes in case of standard fire exposure, however, the effects of horizontal loads on the beams could not be taken into account with this simple model. Therefore, more advanced analyses were carried out. The case of a fully unprotected cladding bracket was not further analysed with more advanced analyses, because the simple 2D structural model showed that the beam would not survive for 90 minutes under vertical loads only (Figure 11).

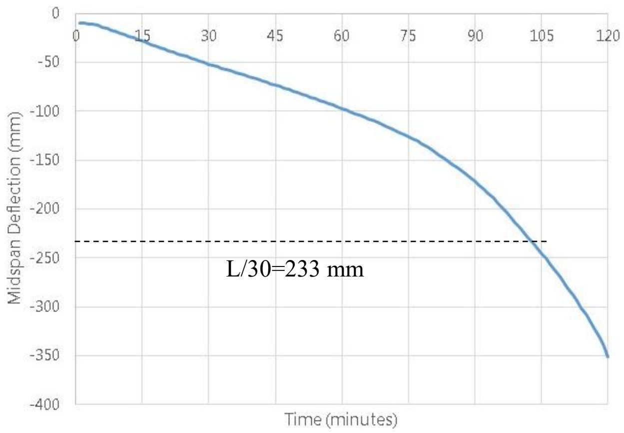

Figure 10. Mid-span displacement vs. time – steel beam and end-plate protected - no H loads

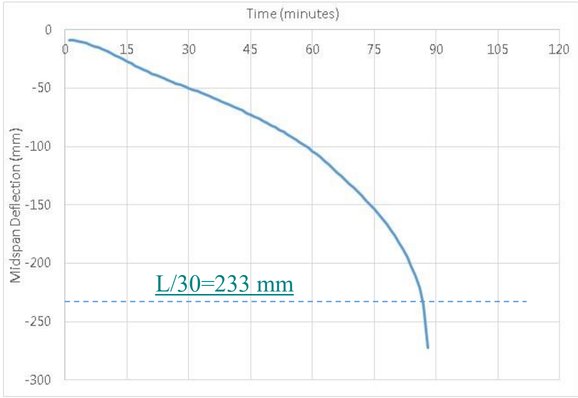

Figure 11. Mid-span displacement vs. time – steel beam protected only – no V loads, no H loads

Figure 12 shows the shell model of the beam, where 32 different sections were assigned to the thickness of the shell areas. The different sections were assigned to the bottom flange (**bf**), the web (**web**) and the top flange (**tf**), in the undisturbed area (**no-b**: no-bracket) and where the cladding brackets are connected to the beam (**b**: bracket). Note, the sections assigned to the shell areas had the same geometry along the length of the beam. Only the temperature-time histories assigned to the sections along the beam vary according to the results of the thermal analyses. The thermal fields obtained by the analysed thermal models of the beams were transferred to the corresponding sections assigned to thickness of the shell elements.

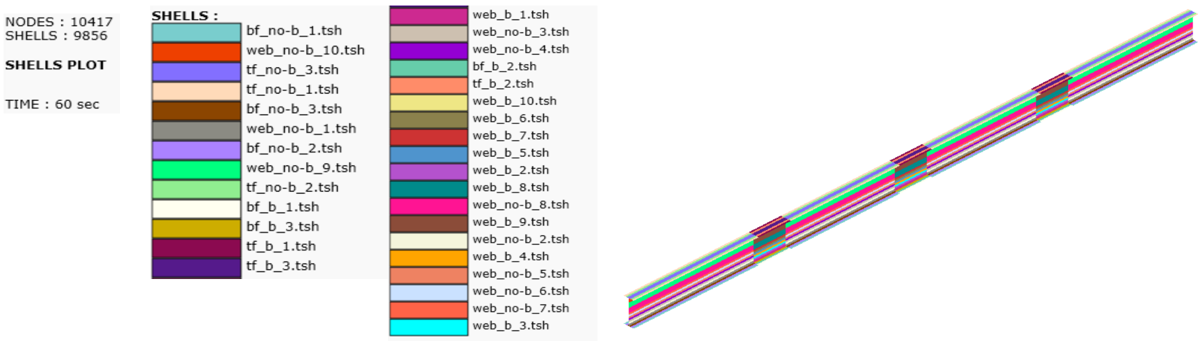

Figure 12. Shell model geometry of the beam

The beam was considered simply supported with the top flange having lateral and torsional restraint from the presence of the slab. Pressure, due to the dead load from the slab spanning across the beams, point loads, due to the vertical loads from façade, and horizontal loads, due to the barrier and wind loads, were provided by the structural engineer and façade contractor. The torsional moment due to the offset between the façade vertical load and centre of torsion of the beam was also considered. The loads were combined in FLS.

The thermo-structural analysis showed that the beam fails after about 79 minutes of standard fire exposure with a deformed shape as shown in Figure 13 (5x scale). Figure 13 and Figure 14, which plots the mid-span deflection versus time of fire exposure, suggest that a “run-away” failure type occurs accompanied by significant compressive deformations in the top flange of the beam in the mid-span. However, this behaviour is not realistic because of the connection with the slab, which was not modelled in 3D due to the required high computational effort. Therefore, in order to understand whether the analysis results of the 2D model (Figure 10), which account for the composite action but disregard the horizontal loads, can be considered valid, we needed to understand whether the failure of the beam, modelled in 3D, was due to either the out-of-plane behaviour associated with high values of horizontal forces or the lack of composite action. Therefore, the analysis of the 3D model was also carried without horizontal loads. Since the failure time and behaviour of the beam in the 3D model did not significantly change, it was deduced that the effect of the horizontal forces was negligible. Therefore, the 2D thermo-structural analysis carried out by neglecting the horizontal forces but including the composite action of the steel beam with concrete slab, is a valid model to assess the capacity of the edge beam in case of fire.

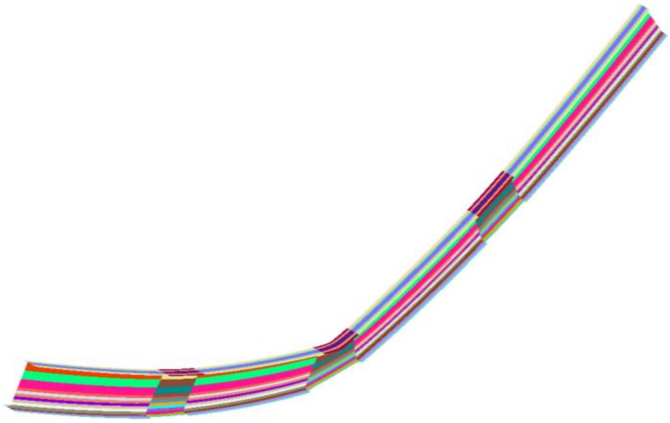

Figure 13. Deformed shape (5x scale) at failure

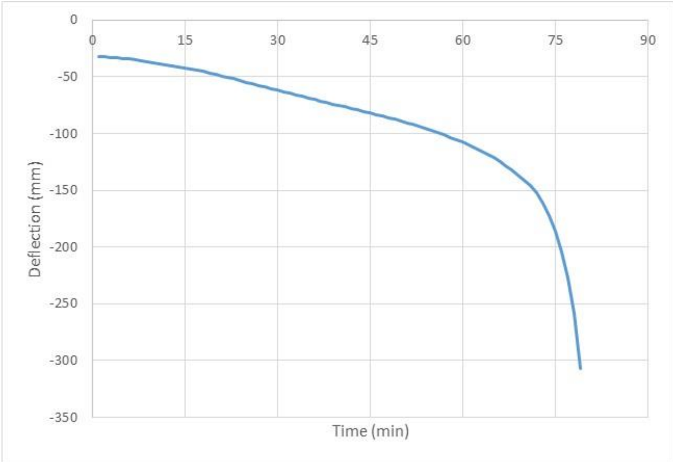

Figure 14. Deflection versus time of fire exposure

As previously shown in Figure 10, the composite beam is able to maintain its stability in case of fire for more than 90 minutes. Therefore, the acceptance criterion is met.

4 CONCLUSIONS

This paper proposed a performance-based methodology, based either on QRA or use of FEM analyses, to solve a construction challenge posed by prescriptive guidance to prevent hotspots in the protected primary steelwork. The presented case studies demonstrated on the example of large stadia (54,000 seater stadium being designed and built the UK and an existing 82,000 seater rugby stadium in the UK) and a mixed-use development in London that the proposed methodology was successfully applied to rationalise the extent of fire protection on secondary steelwork connected to fire protected primary steelwork. The SFE assessments described herein, ranging from the simplest engineering judgement driven QRA to more advanced assessments including complicated 3D modelling, allowed the delivery of multiple optimised structures by ensuring a robust structural behaviour and considering the life safety aspects as stipulated in the Building Regulations. In several cases, such SFE assessment allowed for fully unprotected secondary steelwork.

REFERENCES

1. ASFP Technical Guidance Document 8 Code of practice for junctions between different fire protection systems when applied to load bearing structural steel elements, www.asfp.org.uk , 2010
2. BS EN1991-1-7 Action on structures – Part 1-7: General actions – Accidental actions, July 2014
3. SCI P391 Structural robustness of steel framed buildings, Institute of Steel Construction Inc pp. 143-158
4. Lucherini, A., Maluk, C., Novel test methods for studying the fire performance of thin intumescent coatings. IFireSS 2017 – 2nd International Fire Safety Symposium Naples, Italy, June 7-9, 2017
5. Franssen, J.M., Gernay, T., Modelling structures in fire with SAFIR®: Theoretical background and capabilities, Journal of Structural Fire Engineering, 8(3):300-323 (2017)
6. Franssen, J.M., SAFIR: A thermal-structural program for modelling structures under fire, Engineering Journal, 143–158 (2005)
7. Approved Document B - Volume 2 – Buildings other than dwellinghouses, 2019
8. Melendo, A., Coll, A., Pasenau, M., Escolano, E., Monros, A., *www.gidhome.com.* Accessed 2016
9. Eurocode 3: Design of steel structures - Part 1-2: General rules - Structural fire design, April 2005
10. ASFP: Fire protection for structural steel in buildings 5th Edition (Yellow Book), July 2014

Proceedings of the 12th International Conference on Structures in Fire

Composite Structures in Fire

FIRE PERFORMANCE OF TAPERED CONCRETE-FILLED STEEL TUBULAR COLUMN PROTECTED BY INTUMESCENT FIRE COATING

Jian Wang[1] and Qian-Yi Song[2]

ABSTRACT

Tapered concrete-filled steel tubular (CFST) columns have been used in various structures due to their aesthetic appearance and excellent structural behaviour. However, the research on their fire performance is still insufficient at this stage. In this paper, fire tests of three tapered CFST columns under eccentric load are carried out, and all specimens are protected by intumescent fire coating (IFC). The test results show that the IFC and tapered CSFT specimen can reliably work together under fire. Under remarkable heat insulation effects of the IFC, the fire rating of the tapered CFST specimen can exceed 180min, even if the load ratio is up to 0.56. A verified finite element analysis (FEA) model to predict the fire performance of CFST tapered column was established, taking into account the passive confinement effect of steel tube on the in-filled concrete. Combined with typical cases, the influence of tapered angle and slenderness ratio on the fire performance of tapered CFST column was discussed.

Keywords: Tapered concrete-filled steel tubular column; fire performance; intumescent fire coating; experimental investigation; finite element analysis.

1 INTRODUCTION

Numerous experimental and theoretical study for the fire performance of concrete-filled steel tubular (CFST) columns have been carried out since CFST columns were applied to various structures, and extensive research achievements have been summarized to establish simplified design methods [1-4]. The current research towards fire performance of CFST columns mainly focused on circular, square and rectangular cross-sectional columns. Meanwhile, with the increasing requirements of modern infrastructure for economy and aesthetics, tapered CFST has also been widely used in engineering practice [1,2]. Figure 1 shows a tapered CFST large column and its diagram used in an airport terminal engineering in China. However, the research on the fire performance of tapered CFST columns is still limited. As the basis for the study of fire performance, the mechanical behaviour of tapered CFST columns has been studied extensively [5-8]. It can be understood that in addition to the material strength and sectional dimension, the slenderness ratio (λ) and tapered angle (θ) have significant effects on the structural behaviour of tapered CFST members.

In general, the fire rating of unprotected CFST columns can reach 30~60min or even higher, depending on the geometric sizes and load level [9,10]. Thus, although CFST columns offer enhanced fire resistance, additional fire protection is still necessary for the cases where high load level is applied or high fire rating is required. Despite the issue of aging effects [11], intumescent fire coating (IFC) exhibits numerous benefits including lightweight, thin thickness, convenient construction, ease of maintenance, efficient thermal insulation and aesthetic appearance, and have been widely used in steel and steel-concrete

[1] Ph.D. Candidate, Tsinghua University,
e-mail: j-wang18@mails.tsinghua.edu.cn, ORCID: https://orcid.org/0000-0002-4652-4163
[2] Ph.D., China Southwest Architectural Design and Research Institute Corp. Ltd,
e-mail: soujy.qy@gmail.com, ORCID:https://orcid.org/0000-0002-3126-6261
https://doi.org/10.6084/m9.figshare.22153673

composite structures for fire safety purpose [12]. There have been relevant research reports on the IFC protected CFST columns [9,12-14] and the experimental studies shows that with the insulation effects of the IFC, the fire rating of the circular CFST column with a diameter of 600mm can still exceed 180min even with a load ratio of 0.6. In this paper, fire performance of tapered CFST under eccentric load was studied by combining experimental investigation and numerical analysis. The influence of tapered angle and slenderness ratio on the fire rating of tapered CFST columns was also discussed.

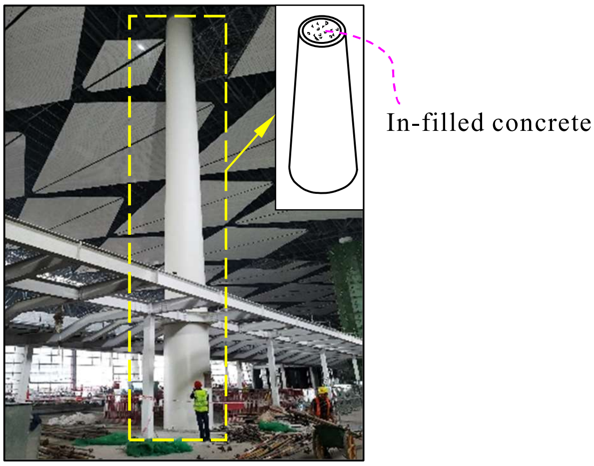

Figure 1. Tapered CFST column protected by intumescent fire coating

2 EXPERIMENTAL PROGRAM

2.1 Test specimens and parameters

Three tapered CFST specimens and one straight CFST specimen were designed and details of the specimens are listed in Table 1. Three major types of IFC materials on the market were selected, of which type A and C are solvent-based while type B is water-based. For the tapered CFST specimens, the outer diameter of the steel tube was (400~600) mm and the wall thickness was 10mm; for the straight CFST specimen, the outer diameter of the steel tube was 400 mm and the wall thickness was 8mm. The measured DFT of the intumescent coating ranged from 2.53mm to 5.02mm. The load applied on the tapered specimens ranged from 1437kN to 3013kN, and the corresponding load ratio of the specimens under fire was from 0.27 to 0.59. The load ratio can be calculated by equation (1).

$$R = \frac{N_F}{N_u} \qquad (1)$$

where N_F is the value of the load applied on the specimen under fire,

N_u is the ultimate strength of the specimen, which can be obtained from finite element analysis as suggested by Lam et al [7].

Table.1 Details of IFC protected CFST specimens

Lable.	$D \times t_s$/mm	H/mm	H_{eq}/mm	d_p/mm	λ	θ/°	Loading Conditions				t_R/min
							N/kN	e/mm	N_u/kN	R	
TA	(400~600) ×10	3720	2630	2.74	24.8	1.54	1437.3	100	5420.6	0.27	>180
TB	(400~600) ×10	3720	2630	5.02	24.8	1.54	3013.3	100	5420.6	0.56	>200
TC	(400~600) ×10	3720	2630	2.78	24.8	1.54	1450.5	100	5420.6	0.27	>180
SC	400 ×8	3720	3720	2.53	37.2	0	2238.6	100	3812.7	0.59	166

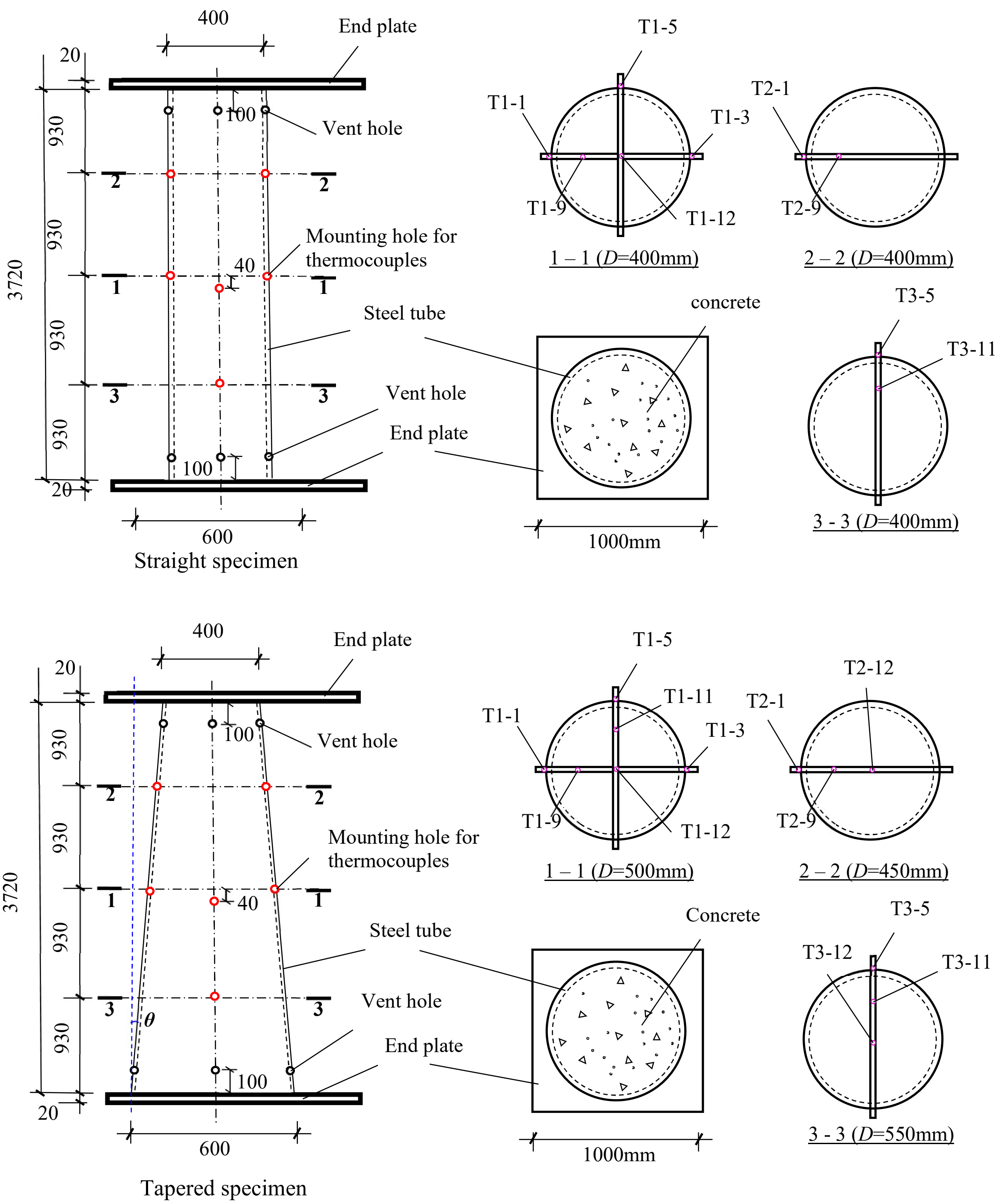

Figure 2. Details of the CFST specimens and location of thermocouples (Unit: mm).

The detailed information of the test specimens is shown in Figure 2. Vent holes are pre-drilled during the processing of steel tubes, and they are located at 100mm distance from the top and bottom ends of the tube. Mounting holes for the installation of thermocouples are also drilled at three cross-sections. The measured yield strength of steel was 389.9Mpa and the compressive strength of concrete was 44.4Mpa.

The finishing paint was also applied after the nominal DFT of IFC was reached and the curing was satisfied. The primer, intermediate paint and finishing paint compatible with the applied IFC materials were used for all the specimens.

2.2 Data measurement

The furnace temperature was measured by furnace thermocouples. Type-K thermocouples were mounted at the locations marked in Figure 2 to measure the temperature of specimens during fire exposure. The temperature of the outer surface of tube and the concrete at distances of 100mm and 200mm from the outer surface of tube was measured. There were thermocouples set in the same cross-section and at the same distance from the steel surface to verify the accuracy of temperature measurement and the uniformity of temperature rise.

The displacement sensor set on the bottom plate was used to measure the axial displacement of the specimen during fire exposure. The bottom plate was equipped with a load sensor, which can monitor the axial load value during the test. In the tests, the failure of column was deemed to occur when one of the following two criteria has been exceeded [15]: 1) Limiting axial contraction, $0.01H$ mm, and 2) Limiting rate of axial contraction, $0.003H$ mm/min. H is the initial height of the specimen, and should be taken as H_{eq} for the tapered CFST columns [8], as shown in equation (2). Besides, although some specimens did not fail after fire exposure of 180min, the tests were also terminated for safety purpose.

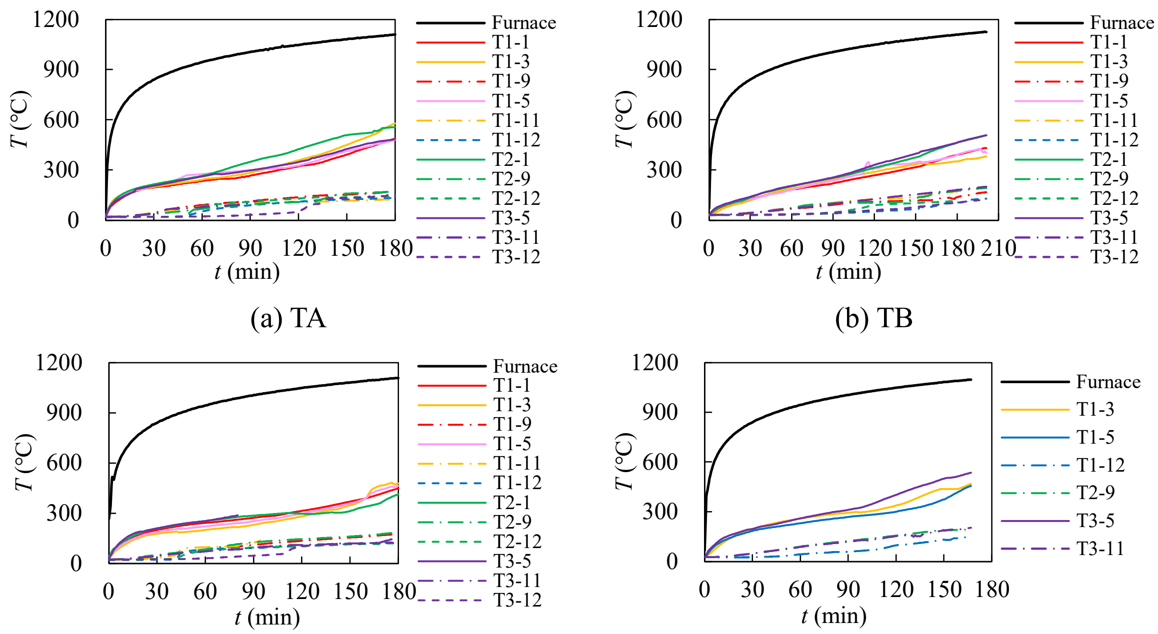

(a) TA (b) TB

(c) TC (d) SC

Figure 3. The measured temperature of the furnace and CFST specimens.

$$H_{\text{eq}} = \frac{H}{\sqrt{2\gamma + 1}} \qquad (2.1)$$

$$\gamma = \frac{D_{\text{b}} - D_{\text{t}}}{D_{\text{t}}} \qquad (2.2)$$

where H_{eq} is the equivalent height of the tapered CFST column,

γ is the tapered ratio of tapered CFST specimen,

D_b and D_t is the diameter of the top and bottom cross-sections, respectively.

2.3 Test setup and fire condition

ISO-834 standard heating curve [15] was employed and the measured furnace temperature and ISO-834 standard temperature is shown in Figure 3. The measured furnace temperature of all the tests basically coincided with the standard temperature. All the specimens were exposed to fire from four sides, and the total length of the specimen was 3760mm (including end plates) while only 3420mm in the middle was under fire. The top and bottom ends of all the specimens were protected by thermal insulation blankets during heating. Both ends of the specimen were hinged, and the eccentric load was applied from the bottom by hydraulic jack fixed under the furnace. Keep the axial load applied on the specimen stable, and then ignite to heat up. The heating stage lasted for 166min~201min.

3 EXPERIMENTAL RESULTS AND ANALYSIS

3.1 Fire rating (t_R)

At the end of the test, all the tapered specimens except the straight specimen SC, do not reach their fire rating although the heating time lasted for 180min even 200min, as shown in Table 1 and Figure 4. The IFC protected CFST columns have excellent fire performance with a fire rating exceed 150min within the DFT applied in the tests, even if the load ratio of the specimens is up to 0.59. For tapered CFST columns with a load ratio up to 0.56, under the reliable protect of the IFC, its fire rating even exceeds 200min.

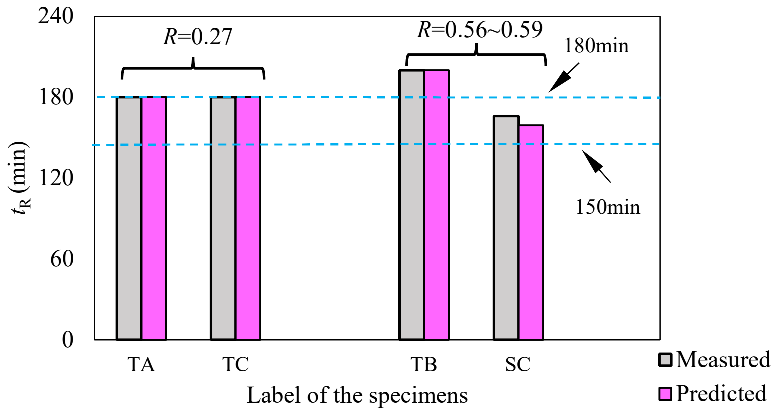

Figure 4. The fire rating of the IFC protected CFST specimens.

3.2 Failure mode

After the test, all the tapered specimens have no obvious overall deformation, and only the expanded coatings of specimen TC has fallen off locally, as shown in Figure 5(a)~(c). This indicates that al the tapered CFST specimens remain intact after 180 min of fire exposure. However, the straight CFST specimen SC failed by global buckling, obvious lateral deflection can be observed. Stripping the expanded coatings and then the convex buckling of the steel tube can be observed on the cross-section in middle height. Meanwhile, the expanded coatings on the south side fell off in a large area, indicating that the integrity of the coating has been damaged, as shown in Figure 5(d).

3.3 Temperature versus time relationship

The measured temperature rise curves are shown in Figure 3, in which the positions of the temperature measuring points were located according to Figure 2. The solid line in Figure 3 represents the temperature rise curves measured on the steel outer surface, while the dot dash line and dashed line represents the curves measured in the concrete at distances of 100mm and 200mm from the outer surface of tube, respectively.

3.4 Displacement versus time relationship

Figure 6 shows the axial displacement (δ) versus time (t) relationship of the specimens during fire exposure, with expansion deformation as positive and compression deformation as negative. By the end of the tests, all the tapered specimens were still in the expansion state while the straight specimen SC has reached its fire rating due to the excessive axial displacement.

(a) TA

(b) TB

(c)TC

(d) SC

Figure 5. The IFC protected tapered CFST specimens before and after heating.

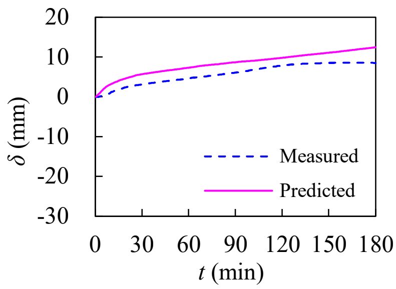

(a) TA

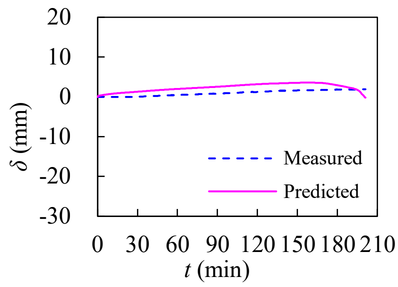

(b) TB

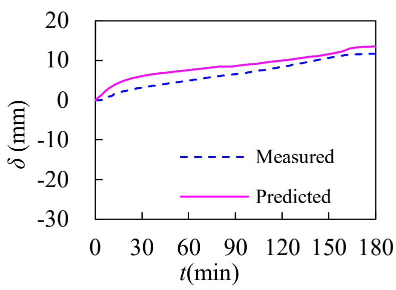

(c) TC

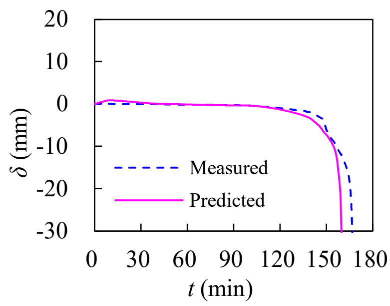

(d) SC

Figure 6. Axial displacement Temperature changes at different heights of tapered CFST specimens

4 FINITE ELEMENT ANALYSIS

4.1 Model establishment

The sequentially coupled thermal-stress analysis approach was employed to calculate the fire performance of CFST columns [16,17]. There are two main steps in this approach: heat transfer analysis and mechanical analysis. The thermal-mechanical coupled finite element analysis (FEA) model [2] of CFST was established on the *ABAQUS* [18] platform in this section. As the research on the thermal properties of IFC is not yet mature, heat transfer analyses were carried out by using the measured temperature of the steel outer surface as the temperature boundary condition [14]. The thermal properties of steel and concrete proposed by EN 1994-1-2 [19] were adopted. However, it has not been reported about the interface thermal conductance of IFC protected CFST sections. In this paper, h_j=200 W/(m^2·K) was temporarily adopted by referring to Espinos et al. [20].

At the ambient and heating stage, the stress-strain relationship of steel proposed by EN 1994-1-2 [19] was adopted and the reduction factor for yield strength $k_{y,T}$ was determined according to GB 51249 [10] considering that the steel tube was manufactured according to Chinese specifications. The stress-strain relationship of core concrete under uniaxial compression in the heating stage was determined according to Song et al. [14]. Because the sectional diameter of the tapered columns changes along the axis, the stress-strain relationship of the confined concrete at each section is not completely consistent. Han et al. [6] pointed out through experimental investigation that the failure of the tapered CFST column mainly concentrated on the minimum section, so the stress-strain relationship of the core concrete was temporarily determined by the parameters of the top section for simplification purpose.

A surface-based interaction, with a contact pressure model in the normal direction and a Coulomb friction modelling in the tangential direction, was used between steel tube and concrete core [14,17]. The friction factor μ was defined as 0.6 during the analyses. 3D hexahedral eight-node solid elements with reduced integration (C3D8R) were used for the core concrete and the end plates, while four-node shell elements with reduced integration (S4R) were used for the steel tube. The established FEA model was shown in Figure 7.

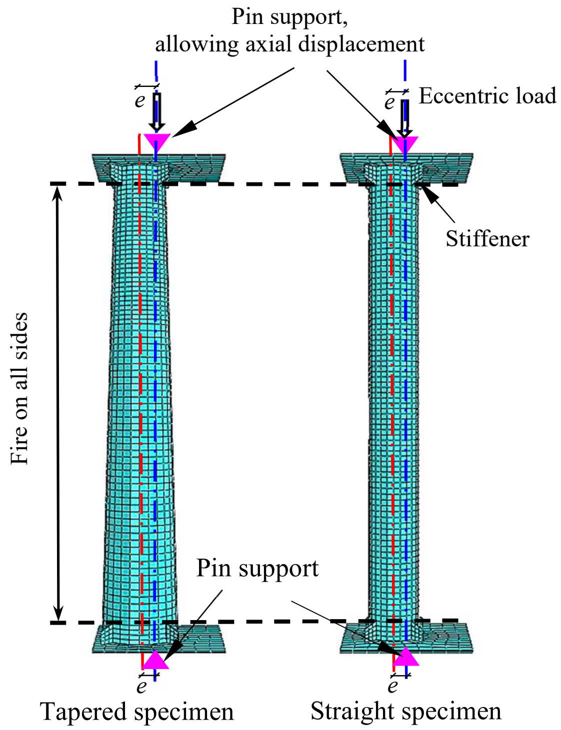

Figure 7. Thermal-mechanical coupled FEA model of CFST columns

4.2 Model verification

The established FEA model was verified from four aspects: temperature rise curve, failure mode, axial displacement versus time relationship and fire rating. The measured temperature of steel tube was introduced into the heat transfer analysis model, and the calculated temperature rise curve of concrete is shown in the Figure 8, which is in good agreement with the measured curve. The curve label was explained in Section 3.3. Figure 9 shows the predicted failure mode of the straight specimen SC and the tapered specimen TB. It can be seen that the predicted failure modes are generally in good agreement with the test results shown in Figure 5. Although the tapered specimen TB has not been damaged at the end of the heating, it has entered the compression stage and will reach its fire rating soon. The calculated failure position is close to the top section, which is similar to the experimental results at normal temperature [5-8]. See Figure 6 and Figure 4 for the comparison between the calculated and measured values of axial displacement and fire rating, which indicates that the calculation results have sufficient accuracy.

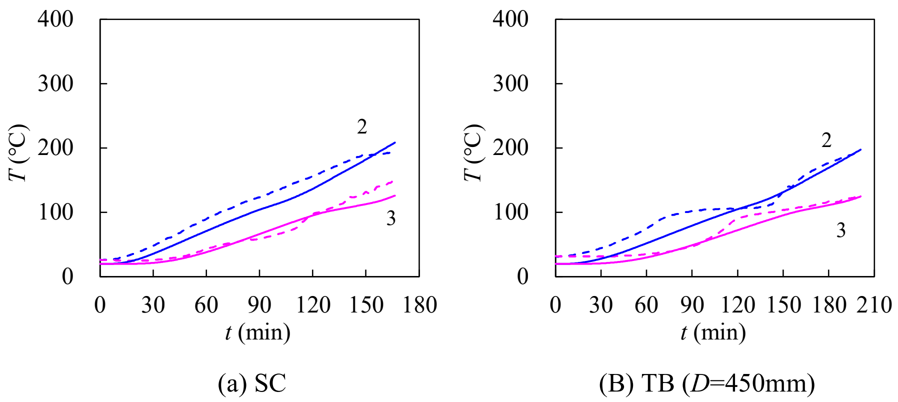

Figure 8. The typical predicted temperature rise curves of CFST specimens

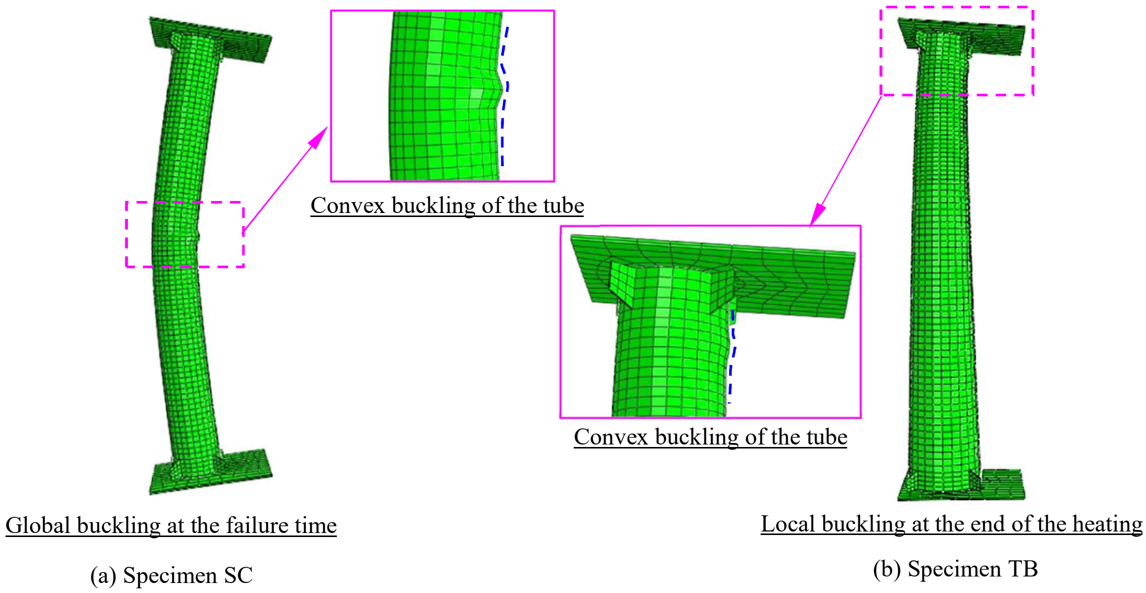

Figure 9. The predicted failure modes of CFST specimens

4.3 Parametric study

For the fire performance of straight CFST columns, Han [2] has carried out a series of parametric studies and determined the main influencing factors, such as the sectional dimension, slenderness ratio, and the fire protection thickness. Different from the straight columns, tapered columns have a unique geometric parameter, namely, tapered angle; In addition, the influence of slenderness ratio will be different due to the changing sectional dimension of the tapered column along the axis. The influence of these two important parameters on the fire rating of the tapered CSFT columns were calculated and discussed in this section. For tapered columns with circular cross-section, the tapered angle (θ) and the slenderness ratio (λ) can be determined as equation (3) and (4), respectively [8].

$$\theta = \text{acrtan}\frac{D_b - D_t}{2H} \qquad (3)$$

$$\lambda = \frac{4H}{D_b} \qquad (4)$$

Typical calculation cases are shown in Table 2. During calculation, the measured temperature rise curve of measuring point T3-5 of the specimen TB is uniformly selected as the boundary condition for heat transfer analysis. The temperature of the steel tube is 465°C when the heating time lasted for 180 min, which is very representative for the CFST columns protected by IFC. Although the temperature of steel tubes at different sections may be different for tapered specimens in actual, it was not taken into account in detail in this section. In all cases, the wall thickness of steel tube is taken as 10mm; The yield strength of steel tube and compressive strength of concrete is f_y=345N/mm^2 and f_{cu}=50N/mm^2, respectively.

Table.2 Details of the calculation cases for parametric study

Label	D_t/mm	D_b/mm	H/mm	H_{eq}/mm	λ	θ/°	Loading Conditions				t_R/min
							N/kN	e/mm	N_u/kN	R	
T-1	600	600	3720	3720	24.8	0	6312	100	10521	0.60	154
T-2	400	600	3720	2630	24.8	1.54	3156	100	5260	0.60	185
T-3	200	600	3720	1664	24.8	3.08	844	100	1407	0.60	198
T-4	519	600	1500	1310	10.0	1.54	5405	100	9008	0.60	138
T-5	197	600	7500	3321	50.0	1.54	770	100	1283	0.60	175

It is worth noting that the failure modes of straight columns and tapered columns at ambient temperature are significantly different: global buckling occurs in straight columns, while tapered columns fail because the cross-section near the top reached the ultimate strength, as shown in Figure 10. It can be seen that even if the ultimate load is reached, the tapered column can still hold the load without degradation and allow continuous deformation, which is a typical elastoplastic strength failure. This is because the stress of other locations beyond the failure section is still at a low level, thus the load can be sustained continuously. However, the load ratio of the tapered columns is still defined as equation (1).

(1) Tapered angle (θ)

Figure 11(a) shows the influence of tapered angle (θ) on the fire rating of tapered CFST columns. With the same load ratio and steel temperature, the t_R increases when θ increases from 0° to 3.08°. In fact, it is related to the actual load effects of the tapered column. As illustrated in Section 2.2, the fire rating is determined according to ultimate deformation or ultimate deformation rate. However, for tapered CFST columns, the failure of top cross-section which reaches its ultimate strength will not directly lead to global buckling of the whole column. With the increase of tapered angle, the ultimate bearing capacity of the column decrease remarkably, as shown in Table 2. Although the defined load ratio is both 0.6, the applied load of T-3 is only 13.4% of that of T-1. For tapered CFST columns, using equation (1) to define the load ratio will overestimate the actual effects of applied load on the fire performance.

(2) Slenderness ratio (λ)

Figure 11(b) shows the influence of slenderness ratio on the fire rating of tapered CFST columns. With the same load ratio and steel temperature, the t_R increases when λ increases from 10 to 24.8, while decreases when λ increases from 24.8 to 50. This phenomenon is similar to that of straight CFST columns [2].

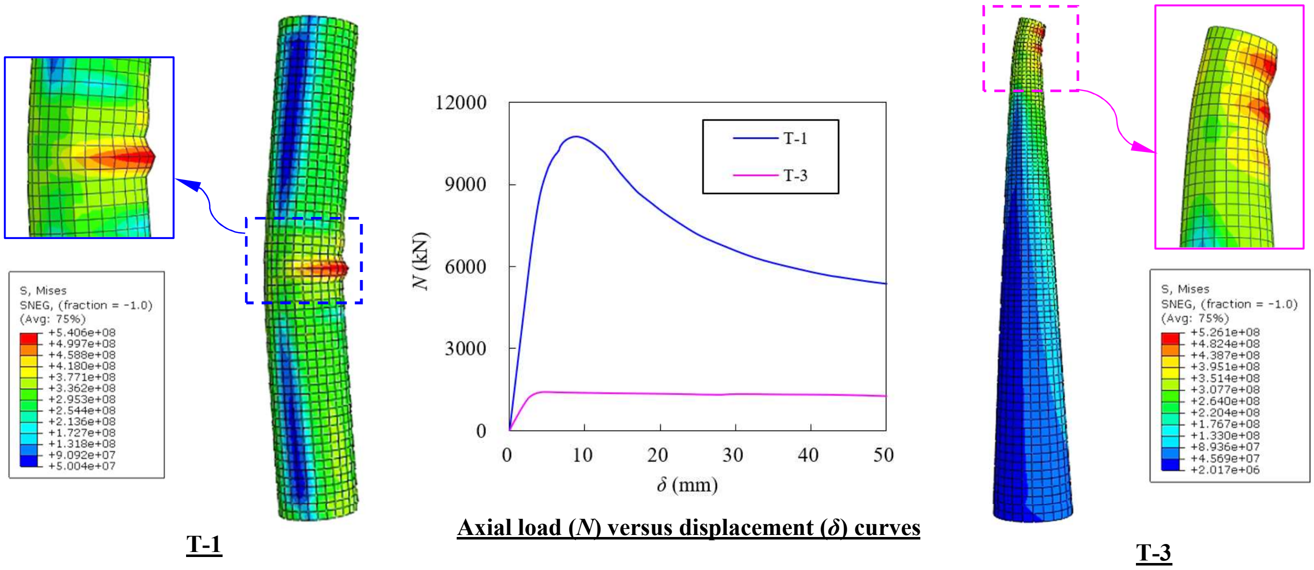

Figure 10. Failure modes and N-δ relations of straight and tapered CFST columns at ambient temperature

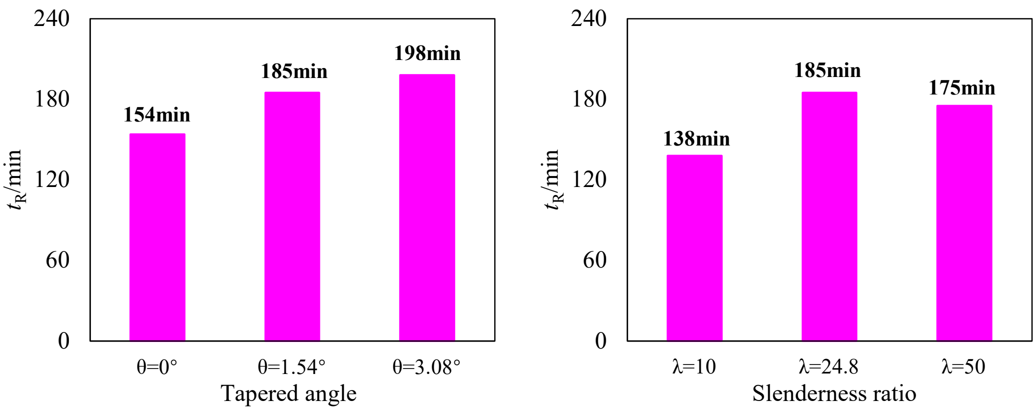

(a) t_R-θ relationship (b) t_R-λ relationship

Figure 11. Influence of tapered angle (θ) slenderness ratio (λ) on fire rating (t_R)

5 CONCLUSIONS

The following conclusions can be drawn within the limitations of this paper:

(1) With the reliable thermal insulation of IFC, the fire rating of straight CFST column with a load ratio of 0.59 can exceed 150min; While for IFC protected tapered CFST column with a load ratio up to 0.56, the fire rating can exceed 180min.

(2) The IFC protected straight CFST column under fire failed by global buckling, and the convex buckling of the steel tube can be observed on the cross-section in middle height; The predicted failure mode for IFC protected tapered CFST is convex buckling of the steel tube and the failure position is close to the top cross-section, which is similar to the experimental results at normal temperature.

(3) The tapered angle and slenderness ratio can both influence the fire performance of tapered CFST column. Because the failure mode of tapered CFST column under fire is cross-sectional strength failure near the top rather than global buckling, using the method of defining the load ratio of straight columns to determine the load ratio of tapered columns will overestimate the actual effects of applied load on the fire performance of tapered columns.

REFERENCES

1. Han L., Li W. & Bjorhovde R., Developments and advanced applications of concrete-filled steel tubular (CFST) structures: Members. Journal of Constructional Steel Research, 100, 211-228 (2014).
2. Han L., Concrete-Filled Steel Tubular Structures – Theory and Practice (3rd edition). Beijing (China): Science Press, 2016 [in Chinese].
3. Lie T., Fire resistance of circular steel columns filled with bar-reinforced concrete, Journal of Structural Engineering, ASCE,1994, 120(5): 1489-1509.
4. Sakumoto Y., Okada T., Yoshida M., & Tasaka S., Fire resistance of concrete-filled fire-resistant steel-tube columns. Journal of Materials in Civil Engineering, 6(2), 169-184 (1994)
5. Han L., Li W., Wang W. & Tao Z., Advanced Composite and Mixed Structures: Testing, Theory and Design Method (2nd edition). Beijing (China): Science Press, 2017 [in Chinese].
6. Han L., Ren Q. & Li W., Tests on inclined, tapered and STS concrete-filled steel tubular (CFST) stub columns. Journal of Constructional Steel Research, 66,1186-1195 (2010).
7. Lam D., Dai X., Han L., Ren Q. & Li W., Behaviour of inclined, tapered and STS square CFST stub columns subjected to axial load. Thin-Walled Structures, 54,94-105 (2012).
8. Ren Q., Han L., Hou C. & Hua Y., Experimental behaviour of tapered CFST columns under combined compression and bending. Journal of Constructional Steel Research, 128,39-52 (2017).
9. Song Q., Han L., Feng Y. & Zhou K., Temperature rise distribution of circular concrete-filled steel tubular cross-sections with intumescent coating, Journal of Constructional Steel Research, 168, 105869 (2020).
10. Ministry of Housing and Urban-Rural Development of the People's Republic of China, Administration of Quality Supervision, Inspection and Quarantine of the People's Republic of China. Code for fire safety of steel structures in buildings. Beijing: China Architecture & Building Press, 2019. (GB 51249-2019, In Chinese)
11. Wang L., Wang Y. & Li G., Experimental study of hydrothermal aging effects on insulative properties of intumescent coating for steel elements. Fire Safety Journal, 55, 161-181 (2013).
12. Jafarian M., Wang Y. & Yuan J., Temperature attained in intumescent coating-protected concrete filled circular steel tubular sections under the standard fire condition. Journal of Structural Engineering, 148(1), 04021224 (2022).
13. Rush D., Bisby L., Gillie M., Jowsey A. & Lane B., Design of intumescent fire protection for concrete filled structural hollow sections. Fire Safety Journal, 67, 13-23 (2014).
14. Song Q., Han L., Zhou K. & Feng Y., Fire resistance of circular concrete-filled steel tubular (CFST) column protected by intumescent coating. Journal of Constructional Steel Research, 147, 154-170 (2018).
15. International Organization for Standardization, Fire-resistance tests-element of building construction-Part 1, IS0 834-1. Switzerland, Geneva, 1999.
16. Espinos A., Romero M.L. & Hospitaler A., Advanced model for predicting the fire response of concrete filled tubular columns, Journal of Constructional Steel Research 66, 1030-1046 (2010).
17. Song T., Han L. & Yu H., Concrete filled steel tube stub columns under combined temperature and loading. Journal of Constructional Steel Research, 66,369-384 (2010).
18. ABAQUS, ABAQUS 2017 Documentation, DassaultSystèmes, Providence, RI, USA, 2017.
19. CEN, BS EN 1994-1-2:2005 EN 1994-1-2, Design of composite steel and concrete structures. Part 1-2: General rules - Structural fire design, 2008.
20. Espinos A., Romero ML. & Hospitaler A., Advanced model for predicting the fire response of concrete filled tubular columns. Journal of Constructional Steel Research, 66,1030-1046 (2010).

IMPROVED TENSILE MEMBRANE ACTION MODEL OF COMPOSITE SLABS AT ELEVATED TEMPERATURES

Hong-hui Qi[1], Yong Du[2], Jian Jiang[3], Guo-qiang Li[4]

ABSTRACT

Different from reinforced concrete slabs, composite slabs appear more complicated tensile membrane action (TMA) in fire conditions. An improved TMA model is proposed to accurately determine the fire resistance of composite slabs exposed to ISO834 fire. It is assumed that the fracture of steel reinforcement in the long span is the governing failure mode of composite slabs at elevated temperatures. The slab is divided into four concrete rigid plates and one elliptic reinforcement net at centre considering TMA, and the contribution of rotation of concrete rigid plates on the deflection in short-span is taken into account. It is found that the improved model has a great prediction of the mid-span deflection and fire resistance. Meanwhile, coupling thermo-mechanical finite element analyses are carried out to simulate the TMA response of composite slabs at elevated temperatures. The results show that the failure mode is the fracture of the reinforcement in long span, the same as the assumption of the improved model.

Keywords: composite slabs; tensile membrane action; ISO834 fire; fire resistance; finite element analysis

1 INTRODUCTION

Large displacement is acceptable when the slabs suffer from high temperatures in fire environment. Tensile membrane action (TMA) would occur in slabs with vertical edge-restraint at large displacements, leading to higher fire resistance of the slab at large displacements than that at small deflections.

Significant work has been conducted by Bailey et al. [1] to analyse TMA in both reinforced concrete slabs and composite slabs in fire. However, previous fire testes have showed that TMA between composite slabs and reinforced concrete slabs is different, as shown in Figure 1. Li et al. [2] proposed a novel TMA model in composite slabs under fire, following the crack path. This model agrees with composite slabs well except the failure mode assumption that composite slab should collapse due to the fracture of the reinforcement in the short span, which seems to be inconsistent with the actual situation, as shown in Figure 2.

A large number of numerical models have been established to analyse the coupled thermo-structural behaviour of composite slabs. Jiang et al. [3] analysed the response of composite slabs under fire conditions fully considering the effect of ribs. The coupled thermo-structural model used composite shell elements for the composite slab with temperature distribution captured from the heat transfer model. A “dummy material” was employed to fill the space between the ribs. This numerical analysis had a better agreement with the test results than others due to the effect of ribs on both heat transfer and structural properties of composite

[1] PhD, Tongji University,
e-mail: honghuiqi_mail@163.com
[2] Professor, Nanjing Tech University,
e-mail: yongdu_mail@njtech.edu.cn
[3] Professor, China University of Mining and Technology,
e-mail: jian.jiang@cumt.edu.cn
[4] Professor, Tongji University,
e-mail: gqli@tongji.edu.cn
https://doi.org/10.6084/m9.figshare.22153679

slabs. Most of previous numerical studies focused on the parametric analysis, but limited investigations concentrated on the failure stage of TMA progress in composite slabs at elevated temperature.

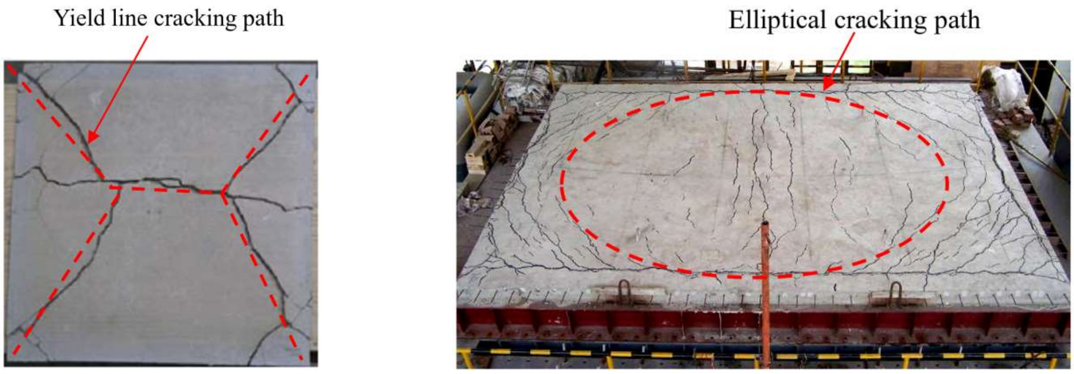

(a) reinforced concrete slab (b) composite slab with profiled steel decking

Figure 1. Different deformation patterns

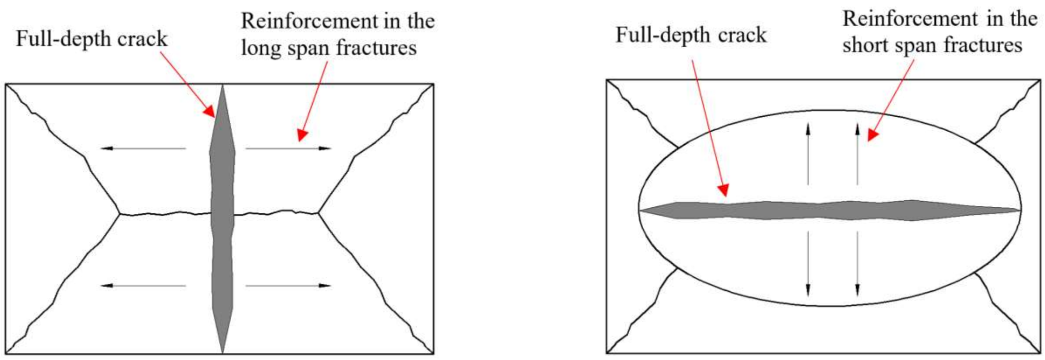

(a) reinforced concrete slabs in tests (b) composite slabs in Li's model

Figure 2. Different failure mode

With the aim to present an improved TMA model of composite slabs at high temperatures, the present paper assumed that the composite slab failed due to the fracture of the reinforcement in long span in this TMA model. The force and moment equilibrium equations of composite slabs were set up to determine the fire resistance of the composite slabs at elevated temperatures. A coupling thermo-structural finite element model was established to simulate the behaviours of the composite slab under fire. The results of the improved TMA model, finite element model and fire tests were compared and discussed.

2 IMPROVED TMA MODEL

2.1 Assumptions of the improved model

According to the experiments [4], the cracks along the perimeter of the composite slab would occur firstly at high temperatures. It is significant that the cracks along the long edges occurred before those along the short edges. Before the occurrence of cracks, the strain of the reinforcement in two directions increased at the same rate. When the cracks along the long edges occurred, the rotation of the rigid concrete plates reduced the increase of the strain of the reinforcement in the short span, but induced larger deflection in the mid-span of composite slabs. This caused higher strain of the reinforcement in the long span than that in the short span, and led to fracture of the reinforcement in the long span.

Considering the contribution of the rotation of the concrete plates to the deflection in fire tests, there are two critical assumptions in the improved TMA model. The first assumption is that the rotation of the concrete rigid plates along the long span can contribute to the deformation of reinforcement in the short span. The second assumption is that the composite slab collapses when the reinforcement in the long span reaches its ultimate tensile strength.

The slab can be divided into four concrete rigid plates and one central reinforcement net considering of TMA, as shown in Figure 2. The geometric parameter α in Figure 2 is determined by the traditional yield line theory The shape of reinforcement net is supposed to be elliptic paraboloid under a load of q. The half lengths of the ellipse are defined as KL and KB, and $0<K<0.5$. The elliptic paraboloid is given by:

$$\frac{x^2}{\frac{1}{w_i}\cdot(KL)^2}+\frac{y^2}{\frac{1}{w_i}\cdot(KB)^2}=w_i-z \qquad (1)$$

where L is the long edge length of the slab,

B is the short edge length of the slab,

w_{i} is the deflection of the reinforcement net in i direction.

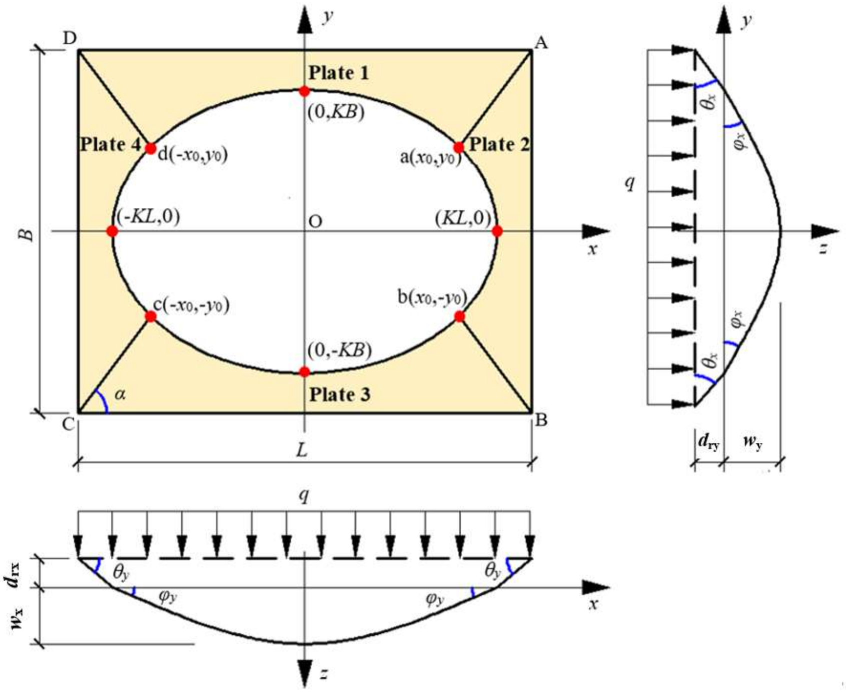

Figure 2. Geometric and deformation parameters of the composite slab with TMA at high temperature

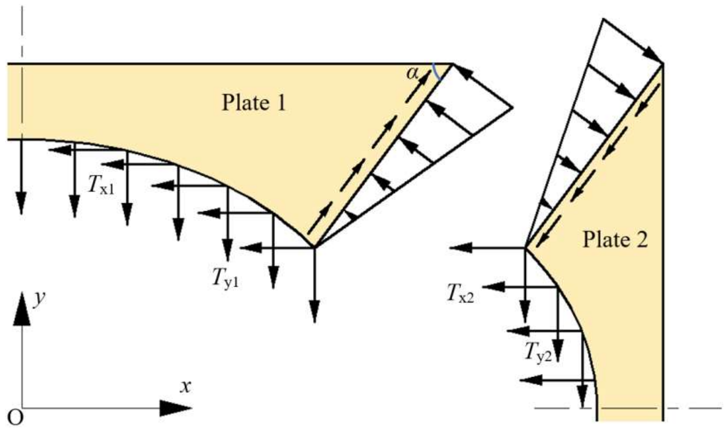

Figure 3. Force distribution on a quarter of the composite slab with TMA at high temperature

The points a, b, c and d in Figure 2 are four intersecting points of the yield line and the ellipse. The deflection of the reinforcement net in x direction is different from that in y direction, but the mid-span deflection of the slab is the same due to the rotation of the rigid plate.

Due to symmetrical geometrical shape and load, the force distribution can be simplified on a quarter of a composite slab, as shown in Figure 3. The parameters C and S denote the compression force and shear force on the interface between adjacent plates, respectively; T_{xi}, T_{yi} are the tensile force due to the reinforcement net on plate i in x and y direction, respectively.

2.2 Deflection of composite slabs at elevated temperature

The total deflection of a composite slab is divided into the deflection of the reinforcement net and concrete rigid plate. The deflection of the reinforcement net is determined by the thermal elongation given as:

$$w_{\mathrm{x}} = KL\sqrt{\frac{3}{8}\left[\varepsilon_{\mathrm{uk}} + \alpha_{\mathrm{s}} \cdot \Delta T\right]} \tag{2}$$

$$w_{\mathrm{y}} = KB\sqrt{\frac{3}{8}\left[\varepsilon_{\mathrm{uk}} + \alpha_{\mathrm{s}} \cdot \Delta T\right]} \tag{3}$$

where $\varepsilon_{\mathrm{uk}}$ is the ultimate elongation of reinforcement at elevated temperature,

α_{s} is the average coefficient of thermal expansion for the reinforcement,

ΔT is the increased temperature of reinforcement at elevated temperature.

The deflection of the concrete rigid plate is determined by the rotation. However, there is lack study on the rotation of the slab in the long span. Zhang et al. [5] noted that the rigid plates in the short span and the tangent of the elliptic paraboloid are continuous on the boundaries. It indicates that θ_{x} is equal to the gradient of the elliptic paraboloid at point (0, KB). However, θ_{y} cannot be derived by θ_{x} directly, due to the contribution of the rotation of the concrete rigid plates along the long span on the deformation of reinforcement in the short span. Therefore, a virtual parameter θ_{x}' is proposed to correspond to θ_{y} and equal to the tangent inclination of the elliptic paraboloid at the same time, given as:

$$\theta_{\mathrm{x}}' = \arctan\left(\left.\frac{\partial z}{\partial y}\right|_{y=KB}\right) = \arctan\left(\frac{2w_{\mathrm{x}}}{KB}\right) \tag{4}$$

Based on the deformation compatibility condition of rigid plates 1 and 2 at the point of (x_0, y_0), the rotation of plates in the long span can be determined by:

$$\theta_{\mathrm{y}} = \arctan\left(\frac{\frac{B}{2} - y_0}{\frac{L}{2} - x_0} \cdot \tan\theta_{\mathrm{x}}'\right) \tag{5}$$

According to the assumption, the ultimate deflection of a composite slab is determined by the reinforcement in long span. It indicates that the final deflection is the sum of w_{x} and d_{rx} as below:

$$w_{\mathrm{total}} = KL\sqrt{\frac{3}{8}\left(\varepsilon_{\mathrm{uk}} + \alpha_{\mathrm{s}} \cdot \Delta T\right)} + \tan\theta_{\mathrm{y}} \cdot \left(\frac{L}{2} - KL\right) \tag{6}$$

2.3 Force and moment equilibrium equations

According to the force equilibrium of rigid plate 1 in y axis and rigid plate 2 in x axis, the compression force C and shear force S on the interface between adjacent plates, as shown in Figure 3 can be obtained as:

$$\begin{cases} S = \sin\alpha \cdot \int_0^{x_0} T_y(x)\,dx - \cos\alpha \cdot \int_0^{y_0} T_x(y)\,dy \\ C = \cos\alpha \cdot \int_0^{x_0} T_y(x)\,dx + \sin\alpha \cdot \int_0^{y_0} T_x(y)\,dy \end{cases} \quad (7)$$

where $T_y(x)$ is the component forces of the reinforcement net in y axis per unit length,
$T_x(y)$ is the component forces of reinforcement net in x axis per unit length.

Figure 4 shows that the forces leading to bending moments of the rigid plate 1 include the applied uniform load (q), the compressive and shear forces between the plates (C and S), the vertical and horizontal component forces in the reinforcement (T_{z1} and T_{y1}) and the bending resistance of the slab along the yield line (M_{ux}). the bending moment equilibrium equation of the plate 1 about line DA can be obtained as:

$$M_{q_1} + M_{T_{z1}} + M_{T_{y1}} - M_{C1} - M_{S1} - M_{ux} = 0 \quad (8)$$

where M_{q1} is the bending moment about line DA due to the external load in the plate 1,
M_{Tz1} is the bending moment about line DA due to the component force in the reinforcement in z direction in the plate 1,
M_{Ty1} is the bending moment about line DA due to the component force in the reinforcement in y direction in the plate 1,
M_{C1} is the bending moment about line DA due to the compressive force in the plate 1,
M_{S1} is the bending moment about line DA due to the shear force in the plate 1,
M_{ux} is the bending resistance of the plate 1 along the yield lines in x direction.

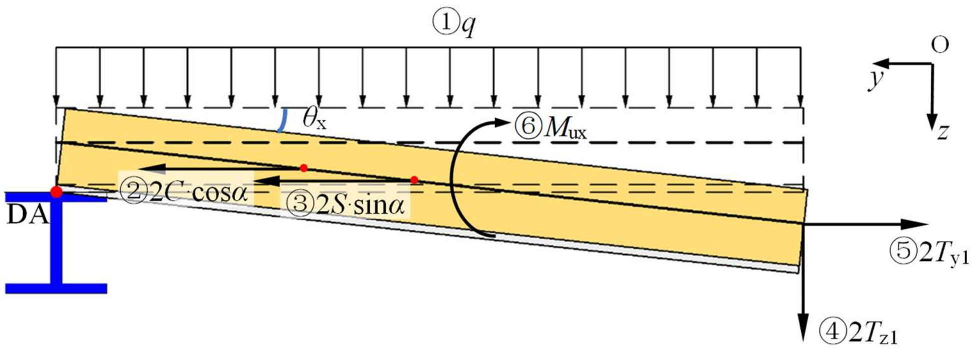

(a) elevation view

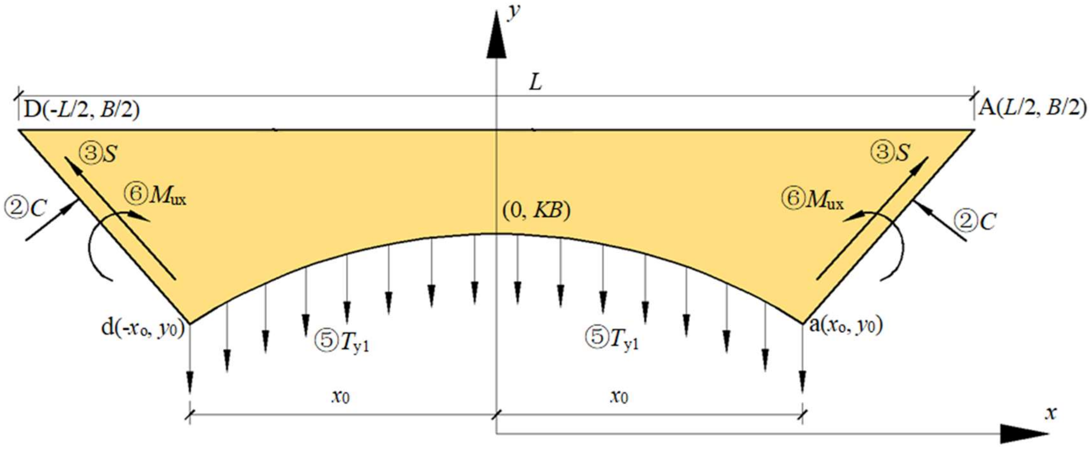

(b) plan view

Figure 4. Bending moment equilibrium of rigid plate 1

The bending moment equilibrium equation of the plate 2 about line AB can be determined in this way as below:

$$M_{q_2} + M_{T_{z2}} + M_{T_{x2}} - M_{C2} + M_{S2} - M_{uy} = 0 \qquad (9)$$

where M_{q2} is the bending moment about line DA due to the external load in the plate 2,

M_{Tz2} is the bending moment about line DA due to the component force in the reinforcement in z direction in the plate 2,

M_{Ty2} is the bending moment about line DA due to the component force in the reinforcement in y direction in the plate 2,

M_{C2} is the bending moment about line DA due to the compressive force in the plate 2,

M_{S2} is the bending moment about line DA due to the shear force in the plate 2,

M_{uy} is the bending resistance of the plate 2 along the yield lines in y direction.

The bending moment equilibrium of the plates 3 and 4 is the same as that of the plates 1 and 2.

2.4 Load capacity of composite slabs at elevated temperature

The central reinforcement net resistance is dependent on the tensile force of reinforcement in z direction. When the resistance is smaller than the load, the reinforcement would fail. In the ultimate state, the resistance is equal to the load given as:

$$q = \frac{4\left[\int_0^{KL} T_z(x)\cdot dx + \int_0^{KB} T_z(y)\cdot dy\right]}{\pi\cdot(KL)\cdot(KB)} \qquad (10)$$

where $T_z(x)$ is the component forces of the reinforcement net in z direction per unit length,

$T_z(y)$ is the component forces of reinforcement net in z direction per unit length.

The load capacity considering the coordination between the reinforcement and the plate 1 is obtained by solving the bending moment equilibrium of plate 1 and the central reinforcement net resistance. The load capacity considering the coordination between the reinforcement and the plate 2 is obtained by solving bending moment equilibrium of plate 2 and the central reinforcement net resistance. The load capacity of the composite slab at elevated temperatures is the minor value of the calculated load capacity above.

2.5 Comparison between the improved model and fire tests

Although there has been a number of tests on composite slabs under fire, there were no fire tests on composite slabs conducted till failure. Therefore, the results of calculation models to determine the ultimate fire resistance of the composite slab should be greater than that of tests. Table 1 and Table 2 summarise the maximum mid-span deflection and load capacity from the fire tests, improved model, Li's model and Bailey's model, respectively.

Table 2 Summary of the maximum mid-span deflection

ID	Source	Maximum mid-span deflection (mm)			
		Test value	Improved model	Li's model	Bailey's model
S1	Purdue tests [6] FA-2	265	273	233	172
S2	Purdue tests [6] FA-3	250	270	230	170
S3	BRANZ [7] Hi-bond slab	253	263	194	149
S4	COSSFIRE [8] Composite floor	550	539	394	403

Table 3 Summary of the load capacity

ID	Source	Load capacity (kN/m^2)			
		Test value	Improved model	Li's model	Bailey's model
S1	Purdue tests [6] FA-2	4.8	4.4	4.1	3.5
S2	Purdue tests [6] FA-3	4.8	5.2	4.7	3.8
S3	BRANZ [7] Hi-bond slab	3	16.4	14.7	3
S4	COSSFIRE [8] Composite floor	3.75	10.7	9.7	4.4

Table 2 shows that the maximum mid-span deflection obtained by the improved mode was 1.03, 1.08, 1.04 and 0.98 of that of tests, respectively, while the results from other models are smaller than that of tests. It indicates that the mid-span deflection predicted by the improved model has a better agreement with the test than other models.

Table 3 shows the load capacity predicted by the models is greater than that of tests, especially for S3 and S4. It may be due to the fact that they were loaded at a small level compared to the load capacity. The load capacity predicted by Bailey's model is the most conservative than the other two models, with 0.73, 0.79, 1.00 and 1.17 of the test values, respectively.

3 FINITE ELEMENT ANALYSIS

3.1 Establishment of the model

A heat transfer model was established firstly by LS-DYNA. Due to the periodicity of the composite slab and uniform temperature at the bottom of the slab, one half-strip of the composite slab was modelled. The solid element and shell element were used to simulate the concrete slab and profiled steel decking, respectively. The reinforcement was not modelled in the heat transfer model because the effect of the reinforcement on the temperature distribution was negligible. The concrete slab and steel decking shared the same mesh and nodes on the contact surface. Adiabatic boundary conditions were assigned at the symmetric boundaries. The heat was transferred by convection and radiation at the top and bottom surface. For the bottom of the composite slab, the ISO 834 standard fire curve was employed to simulate the gas temperature as thermal boundary. The thermal properties of the steel and concrete as specified in EC4 [9] were used in this model. The convective transfer coefficient of the top concrete surface was 8 $W/(m^2 \cdot K)$ and the emissivity was 0.78. The convective heat transfer coefficient was taken as 25 $W/(m^2 \cdot K)$ for the lower flange, and 15 $W/(m^2 \cdot K)$ for the web and upper flange of the steel decking.

A coupling thermo-structural model was established where the temperatures were obtained from the heat transfer analysis and then input in the structural model. In the structural model, the composite slab was simulated by layered composite shell element, and a "dummy material" with negligible strength and stiffness was filled in the blank zone to make sure the same thickness and layers between thin strips and thick strips [3]. The composite slab was simply supported at the four edges. The temperature-dependent stress-strain relationship of concrete and steel in this model was taken from EC2 [10]. A specific parameter FRACR in the material model (MAT_CONCRETE_EC2) was used to simulate the mechanical properties combining the concrete and dummy material in the rib.

3.2 Validation of the model

Figure 5 shows certain numbered points where the temperature was captured in tests. The temperature time history at certain numbered points simulated by finite element analysis is compared with the test results.

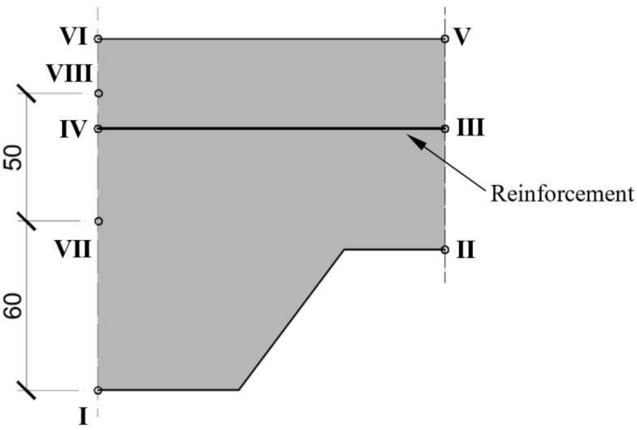

Figure 5. Location of temperature markers

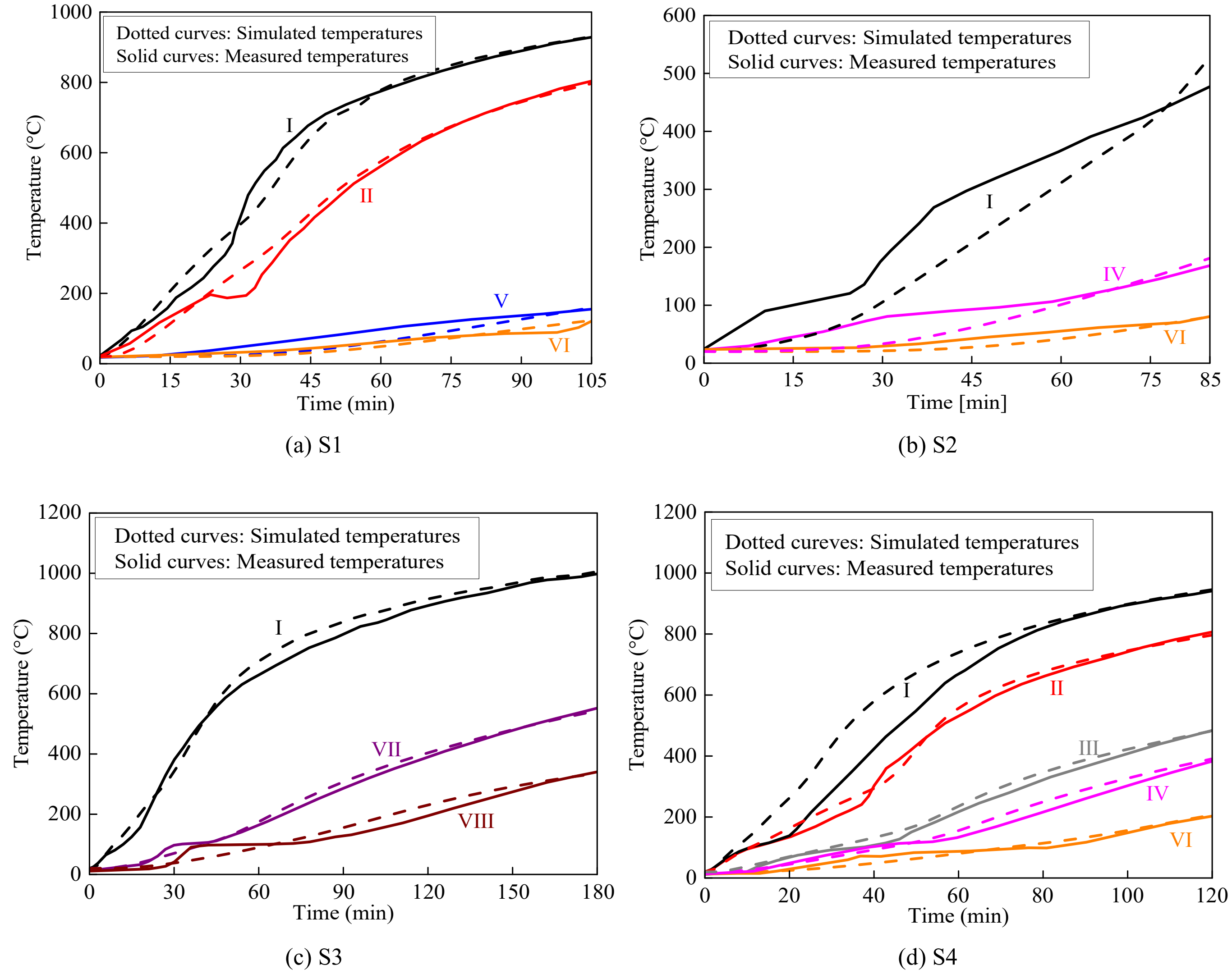

Figure 6. Comparison of the temperature distribution between simulation and test

Figure 6 shows a comparison of the measured and simulated temperature distribution in the four test slabs. It can be found that the simulated temperature has a good agreement with measured results. The difference by 6.7% between the simulated and test results at Point I in Figure 6(b) is mainly due to the effect of the emissivity of the galvanized steel decking when the zinc layer melted. The difference by 46.5% between the simulated and test results in Figure 6(d) at about 100℃ is likely due to the evaporation and irregular migration of the water vapor in the concrete, which could absorb heat.

The mid-span deflection of the four test slabs simulated by finite element analysis is compared with the test results, as shown in Figure 7. Totally, the simulated mid-span deflection agrees well with the measured results. When the test terminated, the relative errors between the simulated and measured deflection for the four test slabs are 3.54%, 9.31%,0.80% and -2.90%, respectively. The difference of S2 is mainly due to the inaccurate simulated of the temperature distribution obtained by heat transfer model.

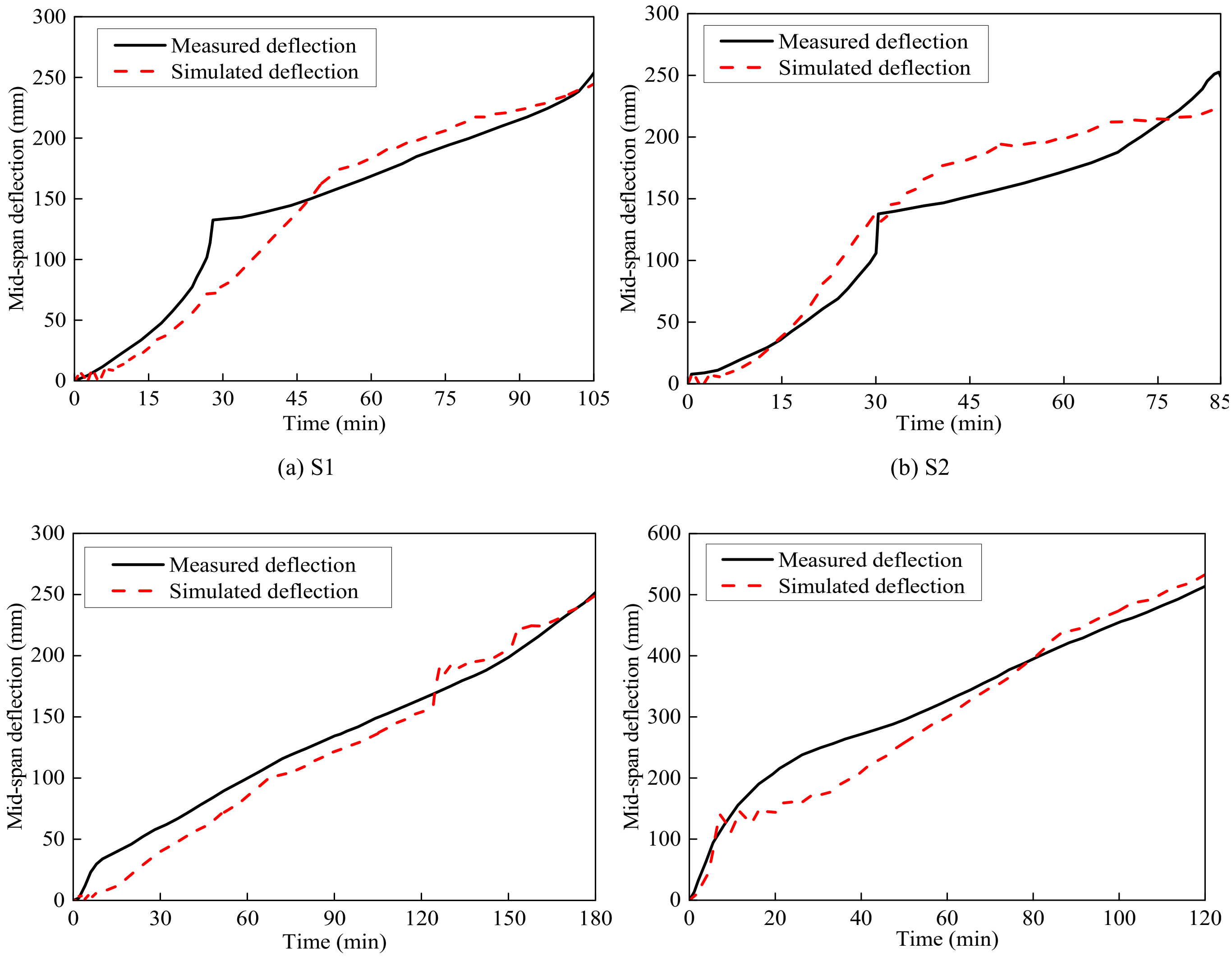

(a) S1 (b) S2

(c) S3 (d) S4

Figure 7. Comparison of the mid-span deflection between simulation and test

3.3 Discussion of the assumptions in the improved model

The improved model is based on a serious of assumptions which has not been proved by tests. By comparing the numerical model and test results, some critical assumptions in the improved model are discussed.

In previous studies, the effect of the profiled steel decking was negligible due to the degraded mechanical behaviours of steel at high temperature. The improved model disagreed this view and proposed that profiled steel decking may be affect the configuration of the development of TMA in composite slabs, which was vividly different from that in reinforced concrete slabs. Figure 8 shows the comparison of the numerical model with or without the profiled steel decking. It can be found that the mid-span deflection in the model without profiled steel decking was 39.7% greater than the other model and test result, due to higher temperature distribution. Hence, it is reasonable to assume that the profiled steel decking could affect the fire resistance of composite slabs.

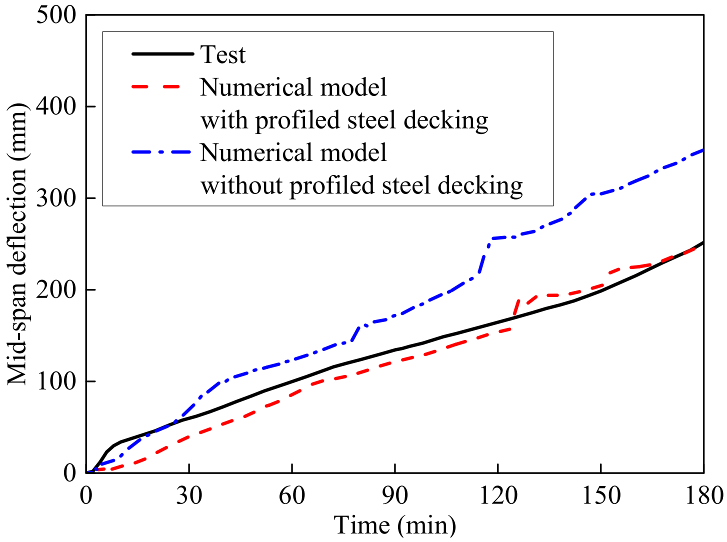

Figure 8. Comparison of the numerical model with or without profiled steel decking

Figure 9 shows the comparison of the numerical model with or without the rotation of the concrete rigid plates. It can be found that the numerical model with the rotation had a better agreement with the test result, whist the model without the rotation differed from the test result by 19.1% at 180 min. It indicated that the rotation of the concrete rigid plates occurred in the test, and affected the deflection of the slab. Therefore, it is necessary to consider the rotation of concrete rigid plates, and the contribution of the rotation of the concrete plates to the deflection of the slab.

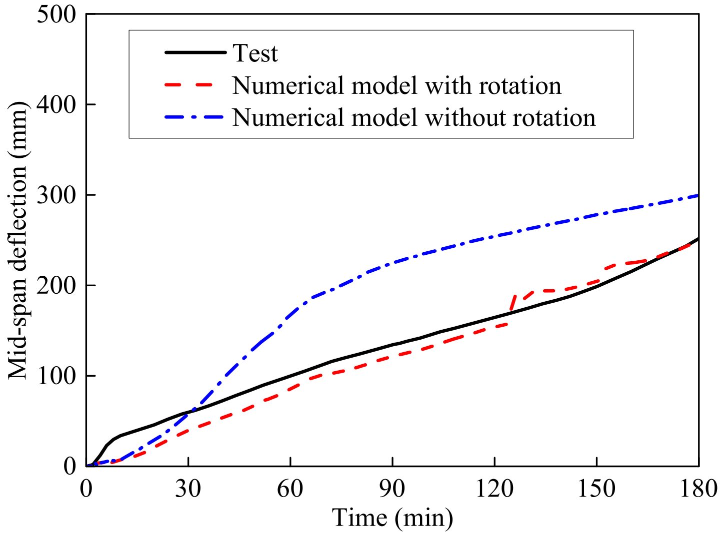

Figure 9. Comparison of the numerical model with or without the rotation of the concrete rigid plates

The other critical assumption is the failure mode of the composite slab in fire conditions. To explore the failure mode, a new composite slab called S5 was simulated and compared. The size of S5 was 5.23 m×3.72 m. The yield strength of reinforcement was 400 MPa and the compressive strength of concrete was 30 MPa. The applied load on S5 was 50 kN/m^2. The ISO 834 standard fire curve was used to simulate the elevated temperature.

Figure 10 shows the simulated stress of the reinforcement in two directions in S5 by finite element model. At the beginning, the stress of the reinforcement in long span increased rapidly, and reached the yield strength at about 28min. The stress redistribution occurred at about 40min, indicating that the stress of reinforcement decreased in long span and increased in short span, due to the degradation of the mechanical properties of the reinforcement at high temperatures. This stress redistribution kept stable for approximately 10 mins. Then, the stress of the reinforcement in two directions decreased, and finally the stress of the reinforcement in long span first reached zero at about 60min, which represented the failure of the composite slab. Therefore, the result of the finite element analysis is consistent with the assumption in the improved model that the composite slab collapses when the reinforcement in the long span fractures.

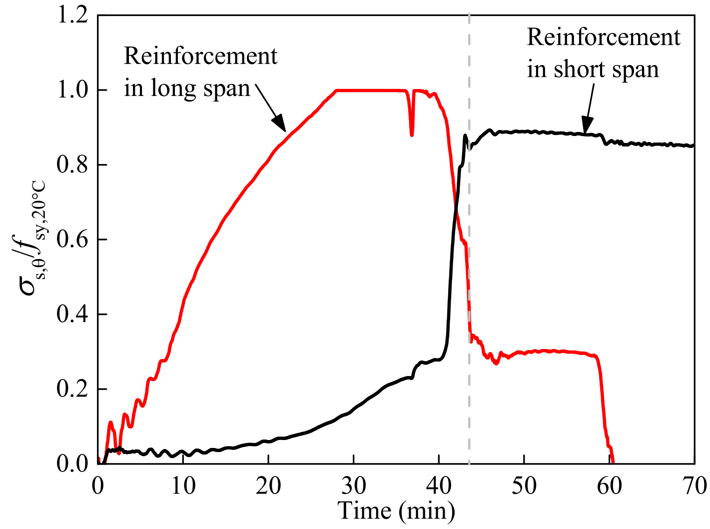

Figure 10. Stress of the reinforcement simulated by finite element model

4 CONCLUSIONS

This paper proposed an improved method to calculate tensile membrane action of composite slabs with profiled steel decking exposed to fire. Numerical models were also established to simulate the response of composite slabs considering TMA at high temperatures. The conclusions have been drawn as follows:

1. The improved model was proposed for predicting the fire resistance of rectangular composite slabs. The contribution of rotation of concrete rigid plates on the deflection in short-span should be taken into account. The fracture of the reinforcement in long span was assumed as the failure mode of composite slabs at high temperatures in the improved TMA model.
2. The mid-span deflection and fire resistance predicted by the improved TMA model had a better agreement with the test results than other models. The mid-span deflection predicted by the improved model was up to 8% greater than the test results.
3. Numerical analysis was used to simulate the previous fire tests of composite slabs. Corresponding to the improved TMA model, the assumptions in the improved model were discussed based on the numerical analysis. It was also found in numerical model that the fracture of the reinforcement in long span is prior to that of short span.

REFERENCES

1. Bailey, C. G., Toh, W. S., Chan, B. M., Simplified and Advanced Analysis of Membrane Action of Concrete Slabs, Aci Structural Journal, vol. 105, no. 1, 2008, pp. 30-40.
2. Li, G. Q., Guo, S. X., Zhou, H. S., Modeling of membrane action in floor slabs subjected to fire, Engineering Structures, vol. 29, no. 6, 2007, pp. 880-887.
3. Jiang, J., Main, J. A., Weigand, J. M., Sadek, F., Reduced-order modeling of composite floor slabs in fire. II: Thermal-structural analysis, Journal of Structural Engineering, vol. 146, no. 6, 2020, 04020081.
4. Li, G. Q., Zhang, N. S., Jiang, J., Experimental investigation on thermal and mechanical behaviour of composite floors exposed to standard fire, Fire Safety Journal, vol. 89, 2017, pp. 63-76.
5. Zhang, N. S., Li, G. Q., A New Method to Analyze the Membrane Action of Composite Floor Slabs in Fire Condition, Fire Technology, vol. 46, no. 1, 2010, pp. 3-18.
6. Wellman, E. I., Varma, A. H., Fike, R., Kodur, V., Experimental evaluation of thin composite floor assemblies under fire loading, Journal of Structural Engineering, vol. 137, no. 9, 2011, pp. 1002-1016.

7. Lim, L., Buchanan, A., Moss, P., Franssen, J. M., Numerical modelling of two-way reinforced concrete slabs in fire, Engineering Structures, vol. 26, no. 8, 2004, pp. 1081-1091.
8. Zhao, B., Roosefid, M., Breunese, A., Connections of steel and composite structures under natural fire conditions (COSSFIRE), Europe: Research Fund for Coal and Steel; 2011.
9. Eurocode 4: Design of composite steel and concrete structures, Part 1-2: General rules General rules Structural fire design. Brussels, European Committee for Standardization; 2005.
10. Eurocode 2: Design of concrete structures, Part 1-1: General rules and rules for buildings, Brussels, European Committee for Standardization; 2004.

FIRE BEHAVIOR OF CONCRETE-FILLED HOLLOW SECTION COLUMNS WITH HIGH STRENGTH BAR-BUNDLE AS CORE

Shaghayegh Ameri[1], Rudolf Röß[2], Jochen Zehfuß[3], Martin Mensinger[4]

ABSTRACT

Concrete-filled hollow section (CFHS) columns with solid steel core are being used more in the construction industry, benefiting their high load-bearing capacity, slender design, prefabrication capability, and exceptional structural fire performance. The current research proposes an innovative approach to improve the structural performance of these columns in both ambient and fire conditions by replacing solid steel core with high-strength bar-bundles. The bar-bundles with different configurations operate equivalent to a solid element, but with a smaller element size, reducing the imperfection caused by thickness-dependent internal residual stress in the steel. The configuration of the bar-bundles and the ribs on the rebar's surface improves the composite behaviour and increases the interaction between the steel and in-filler mortar, especially at elevated temperature. Furthermore, the point contacts between the bars reduce conductive thermal transfer between them. Finally, utilizing high-strength steel increases the load-bearing capacity of these composite columns and results in designing more slender columns and reducing material consumption.

This paper presents the fire behaviour of the proposed columns in large-scale fire tests and an advanced nonlinear finite-element model which has been calibrated and can robustly estimate the fire behaviour of the proposed composite columns.

Keywords: Composite columns; high-strength steel; bar-bundle; fire tests; finite element modelling;

1 INTRODUCTION

Concrete-filled hollow sections (CFHS) became a conventional type of composite columns by achieving high fire resistance without extra fire protection materials. Concrete with low thermal conductivity work as fire protection, and the hollow section keeps concrete confinement during fire exposure. Utilizing additional steel core is a method proposed by different researchers for increasing load bearing capacity of these composite columns and designing more slender structural elements which are more favourable for architectural purposes. The CFHS columns have been extensively investigated experimentally and numerically in both ambient conditions and fire. The joint European research on the fire performance of CFHS [1] and the large-scale tests conducted by the National Research Council of Canada [2] are the wide studies on this topic.

Effects of different parameters have been investigated on CFHS columns: 1) geometrical parameters: using elliptical geometry [3], circular and square shape [4, 5]; 2) boundary conditions: application of fire load with non-uniform exposure on the sections [6]; effect of support condition [7] or large eccentricity [8]; and

[1] Msc., Technische Universität Braunschweig, Institute of Building materials, Concrete construction and Fire safety (iBMB), Germany
e-mail: s.ameri@ibmb.tu-bs.de, ORCID: https://www.tu-braunschweig.de/ibmb
[2]Msc., Technical University of Munich, Chair of metal construction, Germany
e-mail: r.roess@outlook.com, ORCID: www.cee.ed.tum.de/metallbau/
[3] Prof. Dr.-Ing., Technische Universität Braunschweig, Institute of Building materials, Concrete construction and Fire safety (iBMB), Germany
e-mail: j.zehfuss@ibmb.tu-bs.de, ORCID: https://www.tu-braunschweig.de/ibmb
[4] Prof. Dr.-Ing., Technical University of Munich, Chair of metal construction, Germany
e-mail: mensinger@tum.de, ORCID: www.cee.ed.tum.de/metallbau/
https://doi.org/10.6084/m9.figshare.22153685

finally 3) Post-fire mechanical performance of these sections under constant axial loads [9] or with considering cyclic thermal and mechanical loads [10]. Furthermore, researchers are proposed different methods for improving the thermo-mechanical performance of these composite columns. Utilizing double skin sections is one of the famous methods studied from different points of view. Geometry is again the first parameter for both circular and square hollow sections [11] and then the type of concrete used for filling, which can be normal self-consolidating concrete [12] or Ultra-high performance concrete [13].

The single fire test conducted by Klingsch in 1984 [14] was one of the first studies on CFHS columns with a steel core. The most recent studies from Kleibömer [15] and Neuenschwander [16] were on CFHS columns with a solid steel core in the middle. Their focus was on the behaviour of these columns in the event of a fire, and the strength of contact between core and concrete was studied at different temperatures.

Besides experimental investigations, numerical methods were developed for predicting the thermal or thermo-mechanical behaviour of different types of CFHS columns. One-dimensional models were mainly used for global structural models, in which the performance of the whole structure made by CFHS elements under fire was a matter of control [17, 18]. The three-dimensional models developed by the finite element method focused on one specific element or the connection between the beam and column. Most of the researchers used sequential method for investigating the thermo-mechanical behaviour of the composite sections with different software, such as: DYNA3D as a strong software for predicting the behaviour of concrete under extreme loading [19], Programing in Visual Fortran [20], Ansys [21], Abaqus [22] and computer code BoFIRE [23] which researchers used for simulating thermal or thermo-mechanical behaviour of CFHSs.

The recent study reports a series of large-scale experimental tests of a novel composite column at elevated temperatures to investigate their thermo-mechanical performance and develop a calibrated and validated numerical model, which implies the observed composite behaviour in the fire.

2 COLUMNS FABRICATION

The columns for this fire tests were manufactured under the supervision of industrial partners, started with setting the bars in their location utilizing some stencils (Figure 1, a), and then the bars were bundled together with straps (Figure 1, b) and fixed by several tack welds throughout their length (Figure 1, c). Both ends of the bar bundles flattened to provide full contact between the bar bundle and the head plate, and thus the force introduction via the head plate into the entire rod bundle could be ensured. For centralizing the bar bundle inside the cladding tube, spacers made of fibre-reinforced concrete were fixed around the bar-bundles (Figure 1, b), besides two alignment plates welded at both ends of the cladding tube (Figure 1, d) to keep bar-bundles in the centre.

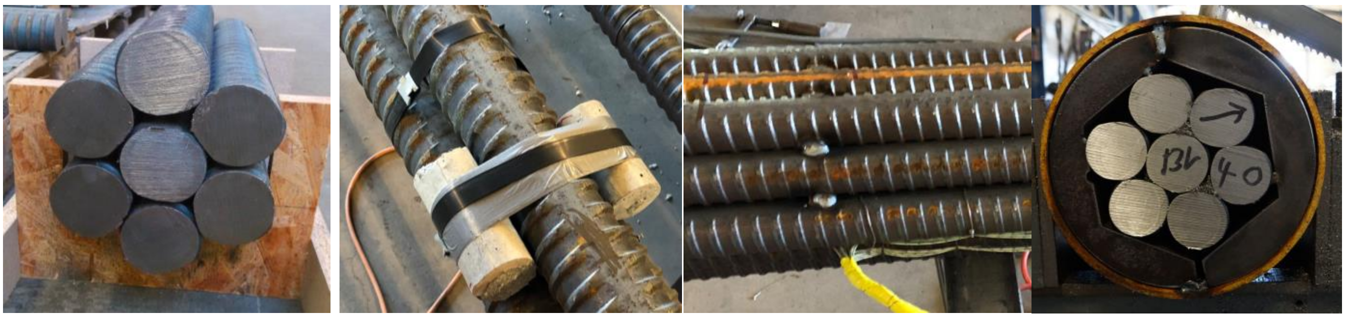

a b c d

Figure 1. fabrication process of bar-bundle columns

The temperature measuring points were planned in 5 levels according to the number of bars in several points between the rebars in the section. Thermocouples were fixed to rebars by the spot-welding to avoid any loose connection during the grouting. After all adjustments, the tube was fixed to the end plates by circumferential fillet welds. Then the columns were placed vertically, and the mortar was pumped by high pressure into the columns from the inlet located at the bottom of the cladding tube. The swelling mortar without aggregate was used to assure that all spaces between the bars were filled completely. Columns were stored for 100 days to reach their highest strength. Four vapour outlets, two on top and two on bottom considered on the tube to avoid explosive failure of the tube caused by the high vapour pressure building up by the heated mortar (evaporated moisture content of mortar during fire test).

3 FULL-SCALE FIRE TESTS

3.1 Test details and set-up

Fire tests were conducted on three columns with different configurations of bars (3, 7, and 19 bars) in the core with a similar length of 4,09 m. The geometrical and structural details of the columns are defined in Table 1. All columns were manufactured by a cladding tube made of cold-formed structural hollow sections of steel grade S355 and high-strength rebars with grade S670. The columns were filled with mortar with strength equivalent to C80/95. All fire tests were conducted with nominally pinned-fixed support conditions. The pinned end was realized by rocker bearing set-up using a half cylinder installed on the hydraulic jack. The mechanical load was applied by a hydraulic press with a capacity of 6 MN from the bottom of the furnace with 10 mm eccentricity, and columns were fixed by a reaction beam from the top. To minimize heat loss and avoid any thermal damage to the equipment, columns were insulated with 20 cm mineral wool from the top and bottom. The amount of axial force and the vertical deformation were continuously recorded by sensors inside the hydraulic press, and the Horizontal deformation was measured by a LVDT (Linear Variable Differential Transformer) sensor installed from the side to the middle of the columns' height.

Table 1. Geometrical and structural details of the columns

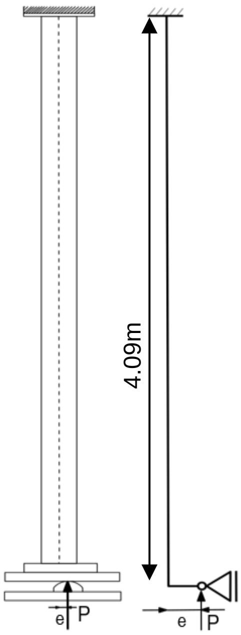

Configuration	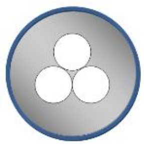	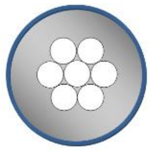	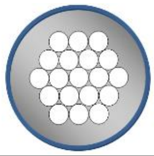
Col. No.	C1	C2	C3
Tube Diameter [mm]	219.1	273.0	244.5
Tube thickness [mm]	5	6	6.3
Tube-steel grade	S355	S355	S355
Bar diameter [mm]	75	57.5	35
Bar number	3	7	19
Rebar-steel grade	S670	S670	S670
min mortar cover	23.7	44.2	28.4
Support condition	Fixed-pinned	Fixed-pinned	Fixed-pinned
P_0	640	2000	1600
R90 [kN] (ecc. 10mm)	1420	2946	2095

The tests started with applying an axial pre-load (P_0) with an eccentricity of 10 mm and held constant for 30 minutes prior to the fire exposure, and after starting the fire, kept constant for 90 minutes. After 90 minutes, the load increased with a speed of 8 kN/s till the nonlinear geometrical failure (buckling) occurred, and once the columns buckled, the load was defined as the load-bearing capacity of the columns under 90 minutes of standard fire.

The fire exposure followed the standard ISO-834 curve using 6 oil burners located at the bottom of the furnace, and the fire temperature was measured by 6 plate thermocouples installed near the column on both sides and at 3 different levels. The temperature-time history of a different part of the sections in 5 levels was recorded by K-type thermocouples installed on the rebars before the construction of the column.

3.2 Thermal results

As mentioned above, the temperature distribution in the section of the columns was recorded by thermocouples installed on rebars and in 5 levels. The results shown in Figure 2 are the measured temperature of the rebars named by the number of the bar and their level (A to E from top to bottom). The temperature measured by thermocouples in levels A and E are showing the lowest temperature because the thermocouples were located near the top and bottom of the columns near insulation parts.

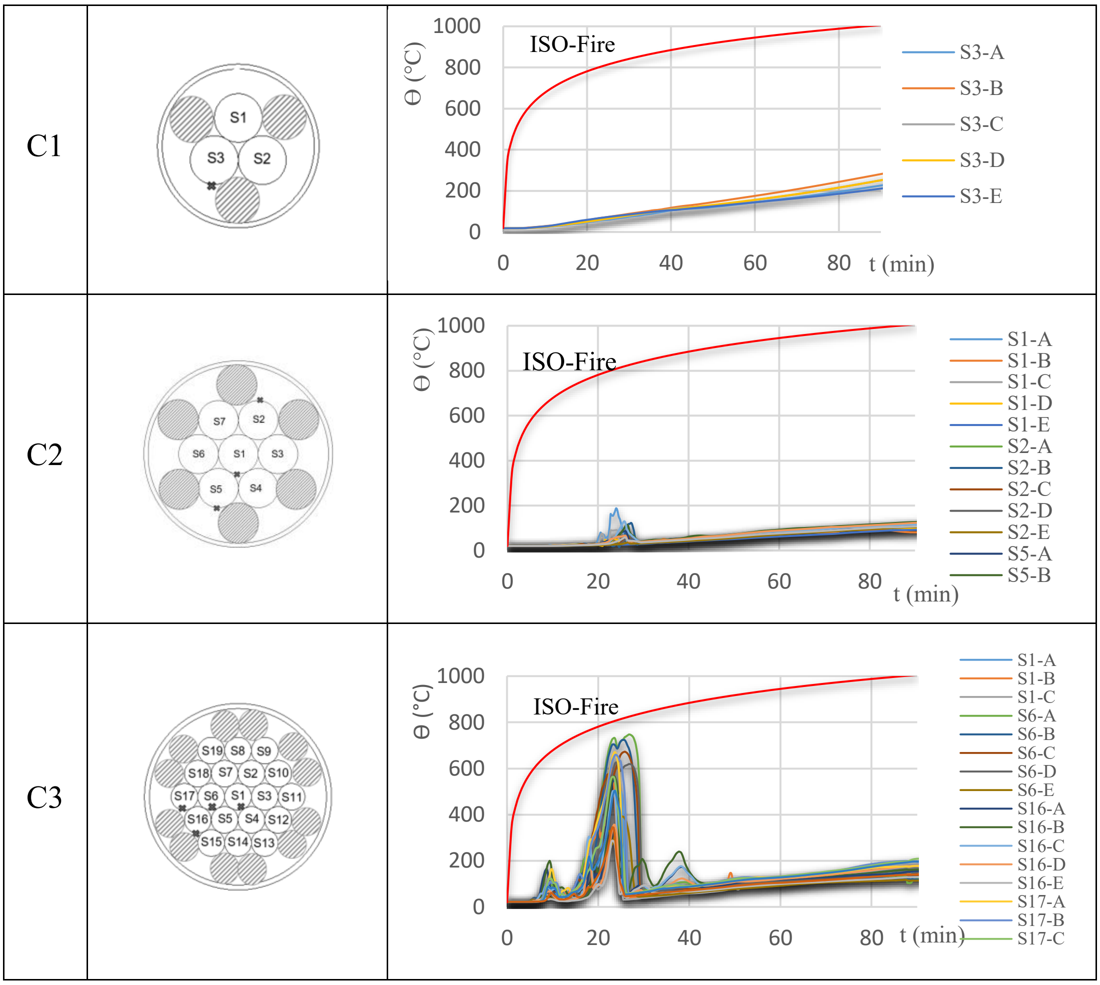

Figure 2. The recorded temperature of the bar-bundles in columns C1, C2, and C3

The maximum temperature of the rebars in columns C1, C2, and C3 reached to respectively 250°C, 110°C, and 200°C after 90 minutes of exposure to standard fire (Figure 2). The difference in the results is reasonable according to the thickness of the mortar cover in the columns, which are respectively 23.5 mm, 44.2 mm, and 28.4 mm, and the lower the core temperature, the thicker the mortar cover. However, the range of the core temperature is much lower than the temperatures were reported for the CFHS columns with solid steel core [16] with identical section sizes, which reached to approximately 600 °C under 90 minutes standard fire. There are two major effective parameters on the low temperature recorded in the proposed columns: 1) the thermal resistance of mortar is higher than normal concrete conventionally used as filler of concrete-filled hollow section columns, 2) The thickness of air layer build-up by increasing the temperature in the section of the column. It is known that by starting the fire and increasing the temperature of the steel tube, the tube starts to expand radially, which builds up an air layer between the tube and mortar, performing as an extra insulating layer. By increasing the temperature of mortar and its radial expansion, the thickness of the air layer reduces over time. Since the connection between the mortar and bar-bundle is strong, the mortar cannot expand freely, which means the reduction of the air layer's thickness will be slow over time, besides the low thermal conductivity of mortar which reduces the temperature transfer into the section. In contrast, the connection between concrete and solid steel core in CFHS columns with the solid core is so weak, and by increasing the temperature, both tube and concrete expand freely, which reduces the air layer thickness faster and affects core temperature raise.

The considerable point in the temperature results of the bars is in the peaks measured in the time between app. 20 and 40 minutes after applying fire load in C2 and C3, whilst no sudden increase was measured in column C1. The peaks are linked to the number of bars, their size, and their configuration. The mortar between the bars has a moisture content that evaporates over time and needs to find a way between the bars to release. In C1, there is only one space between the bars with big size, which lets the vapour distribute in a larger space to find a way for releasing. When the size of the bar is small, and the number of them is high, it means there are small spaces between them, and with the assumption that the spaces are filled completely by mortar, the evaporated moisture of this mortar would trap between the bars until finding a way to release and cause partially high pressure inside the column that is more significant in C3 with more numbers of peaks. High moisture and vapour pressure cause errors in recorded temperature by thermocouples. However, after all, vapour was released, the peaks were eliminated from the recorded temperature and increased semi-linearly till the end of fire tests.

3.3 Thermo-mechanical results

The thermo-mechanical result of all columns follows a similar principle, as presented in Figure 3. The diagram shows the vertical deformation of the columns during the fire tests. By starting the ISO fire, the tube heats up very fast and expands longitudinally. In the first minutes of the test (app. 20 min) tube takes the whole load. Before the tube reaches its critical temperature expands linearly, and after that, the material goes to the plastic phase, and in a short time tube fails, and all load is re-distributed to the core elements. The amplitude and range of the peak depend on the amount of the load and thickness of the tube. For similar columns size, The lower the load and the thicker the tube, the higher the amplitude and range of the peak.

During the failure of the tube, the core temperature raise slowly, and the mortar and bars elongate longitudinally and radially for 90 minutes; then, the load increased till buckling failure occurs.

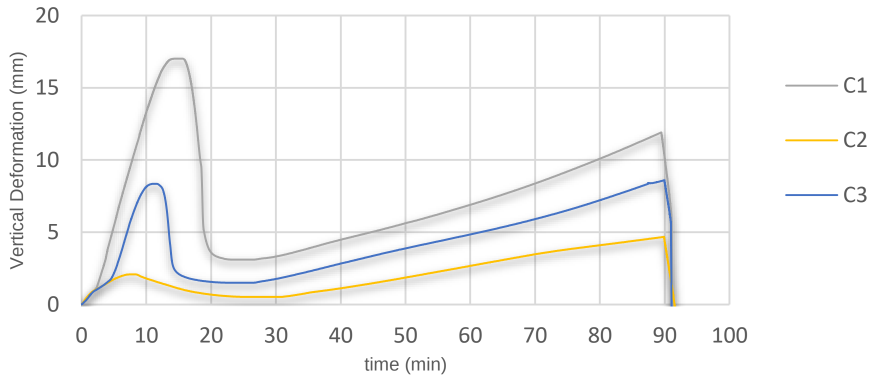

Figure 3. Vertical deformation of the columns C1, C2 & C3 throughout the 90 minutes standard fire tests

4 NUMERICAL SIMULATION

Numerical models were developed by ABAQUS standard software. Two-dimensional models were developed for heat transfer analysis and parametric study for the definition of effective parameters on the thermal behaviour of the columns, besides calibrated three-dimensional thermo-mechanical models for the simulation of fire tests. For developing a validated numerical model, besides considering the boundary conditions mentioned in fire test details, temperature-dependent mechanical properties of high-strength rebars and thermal properties of mortar were defined by experimental tests. Then the models were calibrated by the result of fire tests.

4.1 Material properties

The cladding tubes were made of steel grade S355, which is a standard material with known thermo-mechanical properties; therefore, the test was only conducted on Rebars with steel grade S670 and the mortar.

4.1.1 *Temperature-dependent material properties of steel S670*

The steady-state tensile tests were conducted on non-standard specimens. The specimens were rebars with 18, 28, and 35 mm sizes and 1.1 m lengths. The middle of the rebars for measurement by extensometer was milled to a round rod with respectively 14, 20, and 20 mm diameter with an original gauge length of L_0=100 mm. the temperature of the specimen in the top, middle, and bottom of the L_0 part were measured throughout the tests by K-type thermocouples. Before the tensile tests at elevated temperature, the material properties at room temperature were measured on standard specimen cut from the rebars of the same size and same production batch, and the tests were repeated twice for each bar size; the rounded average values for the material properties are:

Young's modulus = 210000 N/mm^2

Effective yield strength f_y = 850 N/mm^2

The steady-state tests are used to determine the modulus of elasticity, yield, and ultimate tensile strength at high temperatures. Specimens were subjected to a constant temperature (400°C, 500°C, 600°C, 700°C), and The specimen was loaded by path control method at a specified strain rate to failure. The temperature reached the desired limit by 3K/min speed, and a speed of 0.005 mm/s is considered for increasing the deformation after reaching the constant temperature in the L_0 part. Results of steady-state tests on the high-strength rebars show a bigger reduction in yield and ultimate tensile strength in comparison with the proposed temperature-dependent diagrams by Eurocode [24] for normal steel (Figure 4).

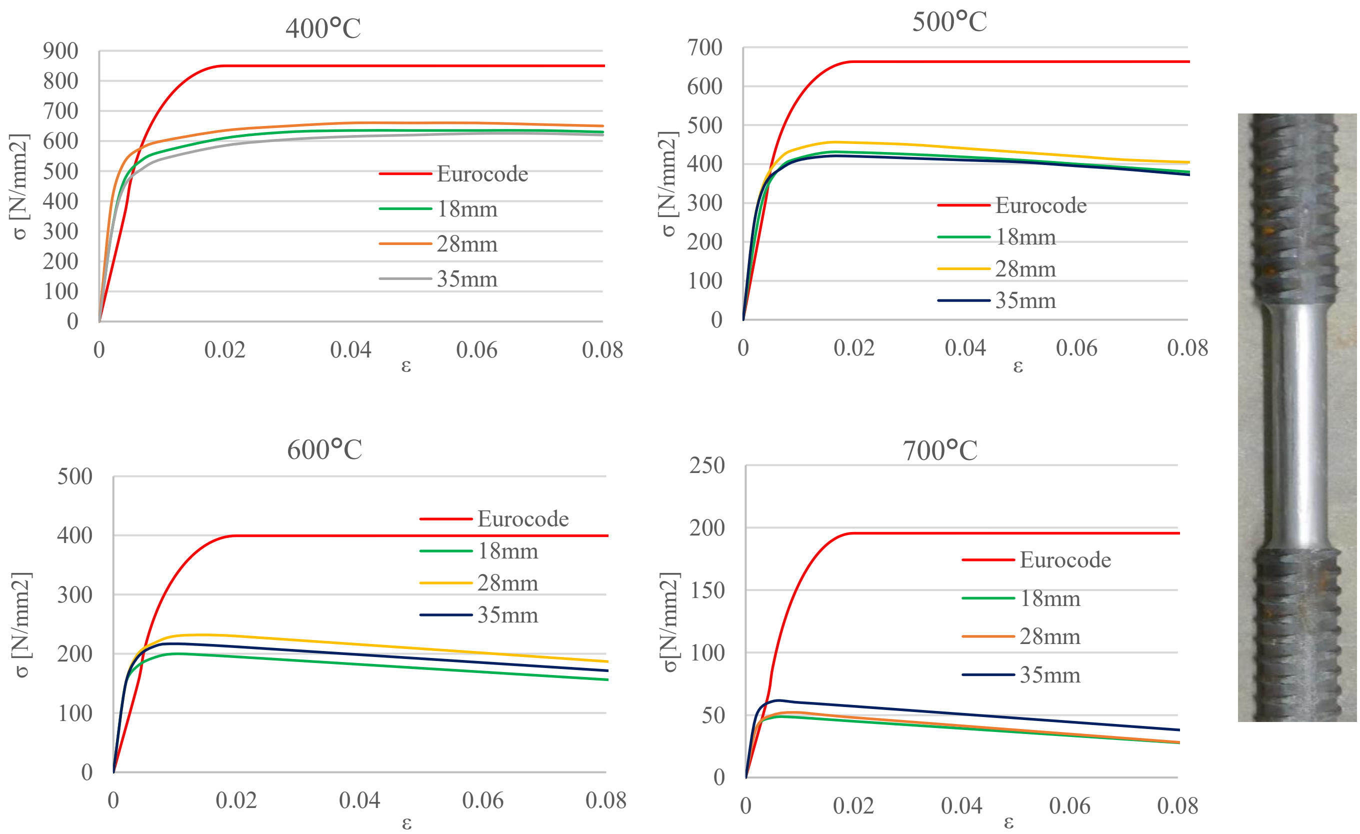

Figure 4. Comparison of steady-state test on bars with 18, 28, and 35mm size under 400, 500, 600, and 700°C with Eurocode3

The average reduction factors for the effective yield strength ($k_{y,\theta} = f_{y,\theta} / f_y$) and for the proportional limit ($k_{p,\theta} = f_{p,\theta} / f_y$) as well as for the slope in the elastic range ($k_{E,\theta} = E_{a,\theta} / E_a$) are calculated and compared with the factors suggested by the Eurocode for normal steels in Table 2.

Table 2. comparison of measured reduction factors for steel grade S670 with Eurocode

θ	$k_{y,\theta} = f_{y,\theta} / f_y$		$k_{p,\theta} = f_{p,\theta} / f_y$		$k_{E,\theta} = E_{a,\theta} / E_a$	
	Eurocode	Test	Eurocode	Test	Eurocode	Test
400°C	1	0.81	0.42	0.51	0.7	0.75
500°C	0.78	0.56	0.36	0.40	0.6	0.6
600°C	0.47	0.29	0.18	0.19	0.31	0.36
700°C	0.23	0.11	0.075	0.05	0.13	0.15

4.1.2 Thermal properties of mortar

The thermal material properties of the pressed mortar significantly influence the heating of the bar-bundle cross-section. Therefore, the determination of thermal conductivity, bulk density, and specific heat capacity as a function of the material temperature is required.

For the production of the columns, a grout cement of the grade CEM I 42.5 R - Rheoment from the company Thomas Zement GmbH & Co. KG was chosen. This cement is characterized by its high flowability at low water-cement ratios. Since the voids to be filled between the individual bars are very small, no aggregate was added. The water-cement ratio was chosen to be 0.3. The specimens for each test were prepared and stored for at least 100 days under normal climatic conditions (23 °C, 50 % relative humidity) until they were tested. The summary of the result of experimental tests and final diagrams considered in the numerical simulation are shown in Figure 5. The detail of the conducted tests is not the focus of the current paper; therefore, only the final results are presented.

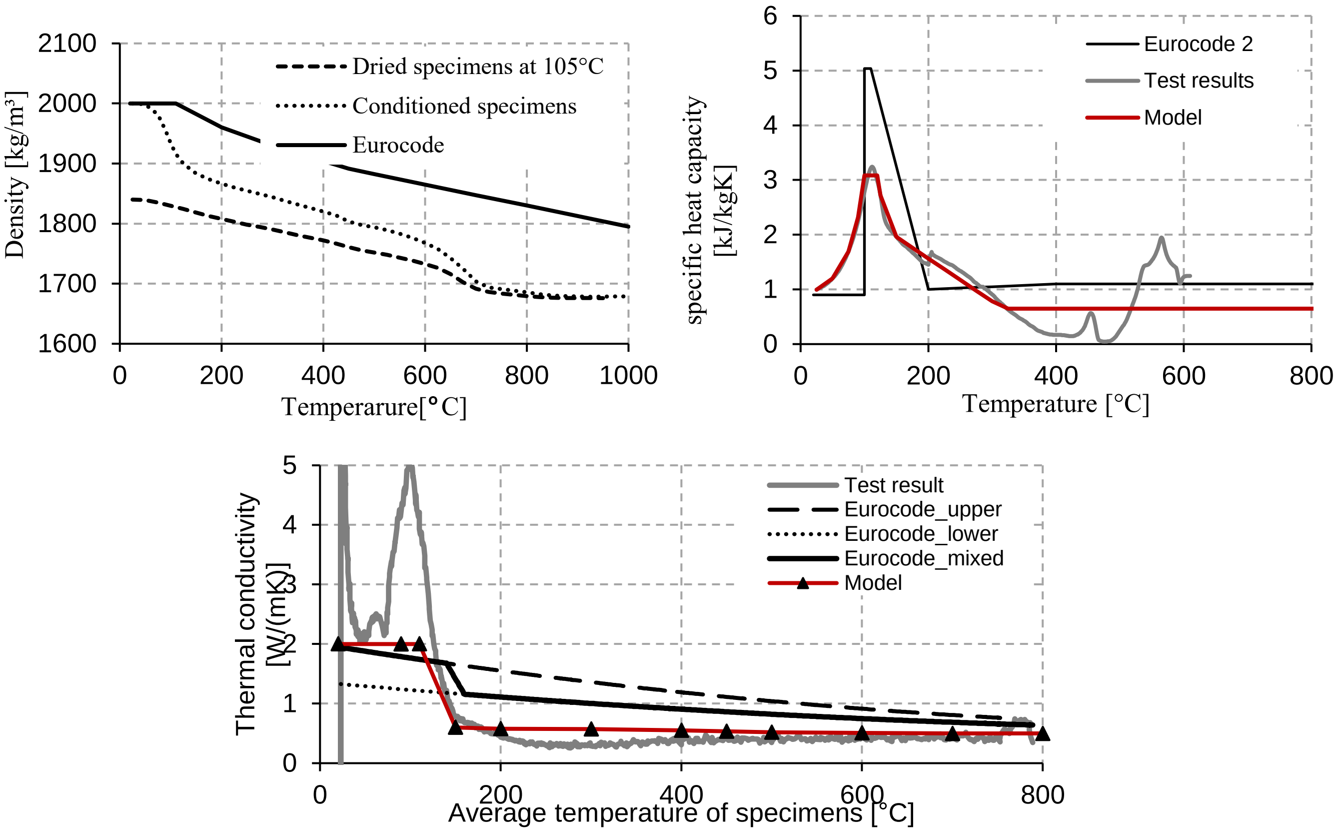

Figure 5. Thermal properties of the mortar: density (top-left), Specific heat (top-right), and thermal conductivity (bottom)

4.2 Heat transfer analysis

Thermal analysis was done first on the two-dimensional model to control different parameters and calibrate the model by fire test results. The effect of air layer build-up between tube and mortar by increasing temperature can be defined by gap conductance in ABAQUS software. However, the correct definition of the parameters has a direct effect on results. For this purpose, some initial simulations were performed, which show the thickness of the air layer varies between 1.5 to 2 mm after 90 minutes of ISO-fire exposure, considering reasonable column size according to standard tube sizes. It is known that the gap conductance depends on many parameters besides the thickness of the air layer, like its temperature by time and its partial pressure or moisture content, etc. For a conventional concrete-filled hollow section, Espinos [8] considered 200 W/(m^{2}K), and for a Concrete filled hollow section with a solid steel core, Neuenschwander [22] proposed 100 W/(m^{2}K). In this study, constant gap conductance of 50 W/(m^{2}K) is considered, which shows good agreement with test results (Figure 6).

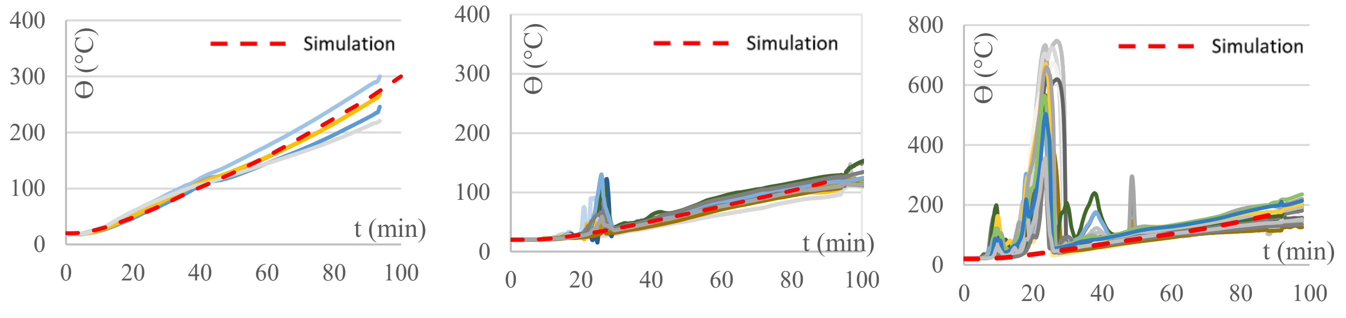

Figure 6. Comparison of bar temperature in fire tests and numerical simulation (Red dashed lines)

The sensitive analyses were performed on section diameter, tube thickness, mortar cover thickness, and the number of bars. The results show that the tube thickness has the lowest effect on temperature distribution in the section. The effect of sections' diameter as the next parameter was evaluated under constant cladding tube thickness of 5mm and concrete cover of 20mm, and then the temperature of bars with column size 100, 200, and 300 mm and for 1, 3, 7, and 19 bar were calculated. Results show by increasing the column size, the temperature of the bars decreases. Increasing column size means increasing material volume, which needs more energy to increase its temperature. Therefore, under standard fire load, the temperature of the section with a smaller size increases faster, although the concrete cover is equal in all of them.

The next parameter was the effect of concrete cover thickness in sections with constant size. Obviously, by increasing the concrete cover, the temperature of the bars decreases.

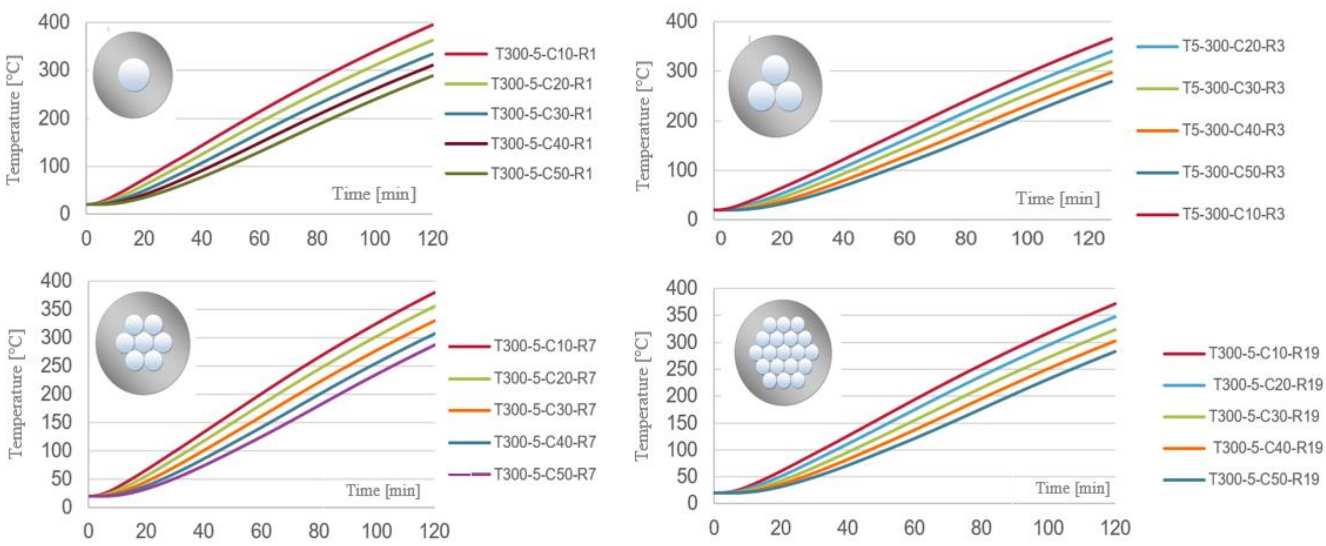

Figure 7. Effect of concrete cover changes (10, 20, 30, 40, 50mm) on bar temperature - with constant column size (300mm) and different bar configuration

This effect is shown in Figure 7 for a constant column size of 300mm and tube thickness of 5mm, and different configurations of bars. The changes in maximum temperature of bars with changing concrete cover from 10 to 50 mm are approximately 100 degrees. These results indicate the realization of one of the goals of this project. Using a bar-bundle as a core instead of a solid core by decreasing the volume of steel reduces the temperature of the core, which leads to lower stiffness reduction of material and reaching higher fire resistance columns.

4.3 Thermo-mechanical analysis:

A three-dimensional advanced nonlinear model was developed here to simulate the thermo-mechanical performance of the columns tested in this project. For avoiding time-consuming and highly nonlinear coupled temperature-displacement analysis with complex convergence problems, the sequential method is considered for the simulation method. Firstly, buckling analysis was carried out, and the nodal deformation of the first mode was transferred by a very small factor to the final model as imperfection. Secondly, a pure heat transfer analysis was done on the column, and the nodal temperature history was transferred to the final model. And eventually, the mechanical analysis was done on a model considering initial imperfection and nodal temperature-time changes. All geometrical properties and boundary conditions were defined according to the fire tests.

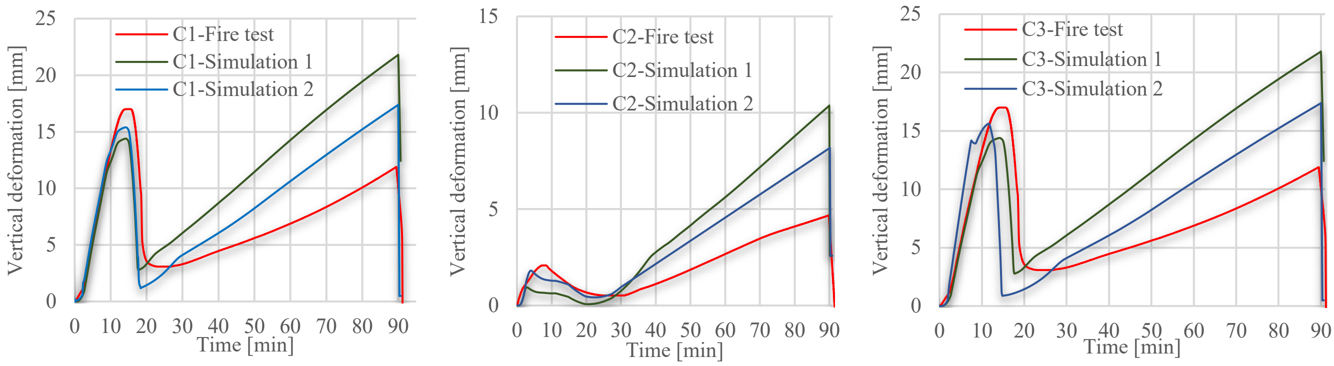

Figure 8. Compare the vertical deformation of columns in fire tests with two series of simulation results

Two series of simulations were performed with two accuracy levels (Figure 8). The initial series of models was carried out with considering material properties according to Eurocode 3, 2 [24, 25] (steel: elasto-plastic and mortar: elastic), nominal support condition, and big mesh size with a maximum 30 mm dimension. The second series with more accurate definitions for all boundary conditions. Material properties defined based on experimental tests and temperature-dependent concrete damage plasticity were considered for mortar mechanical performance. The support condition is simulated by spring with pre-calculated deformation and rotation stiffness. And finally, the mesh size was reduced to a maximum of 20 mm size which resulted in more comparable results with fire tests. The maximum difference between the measured and calculated load-bearing capacity of the columns under 90 minutes of ISO fire was 1.5%.

Parametric analyses were also performed on the thermo-mechanical performance of the columns. For this purpose, the fire resistance of the columns was calculated under 60, 90, and 120 minutes of standard fire and with similar sections and different column lengths (Table 3).

Table 3. Simulation results of columns load bearing capacity with different length, fire resistance duration and similar boundary condition as fire tests

Load bearing capacity[kN]									
L[m]	C1 (3 Bars)			C2 (7 Bars)			C3 (19 Bars)		
	R60	R90	R120	R60	R90	R120	R60	R90	R120
2	5090	4300	3260	9200	8350	7110	8040	6400	4300
4.09	1810	1440	1005	3270	2980	2020	2880	2120	1440
6	1630	1390	870	2850	2660	1960	2640	2100	1120
8	1020	830	635	1920	1595	1345	1565	1250	870
10	630	530	410	1160	1010	880	1000	815	570

In comparison with the load-bearing capacity of columns with a 2 m length under ISO fire, by increasing the length to 4.09 m, the load-bearing capacity reduces an average of 67%. For a length of 6 m, this reduction reaches 71%, and for columns with 8 m and 10 m length, the load-bearing reduces respectively, 80% and 88%.

With a similar simulation method performed in parametric analysis, the buckling coefficient was calculated, which is the ratio of buckling resistance calculated from simulation to the cross-sectional plastic resistance. The results, which are shown in Figure 9, have been superimposed on buckling curve "c" proposed by Eurocode.

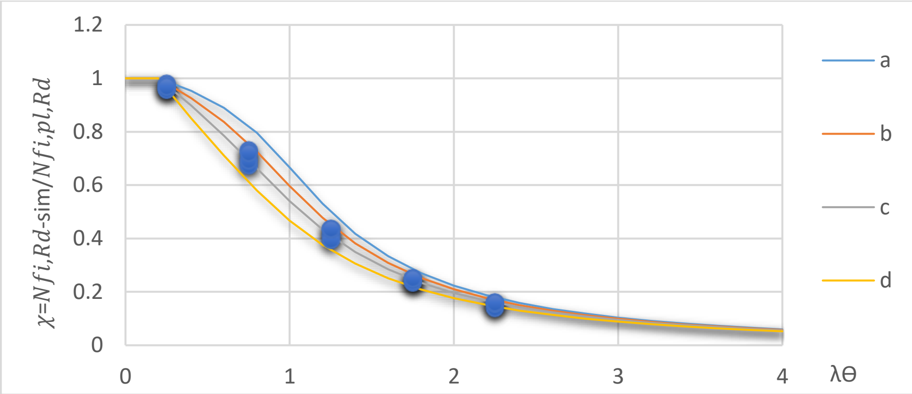

Figure 9. Evaluation of the buckling coefficient with the relative slenderness at elevated temperature with Eurocode

For having a closer look at the results and comparing the results of fire simulation with the load-bearing capacity calculated in ambient conditions for each configuration type of bars, the diagrams in Figure 10 are created.

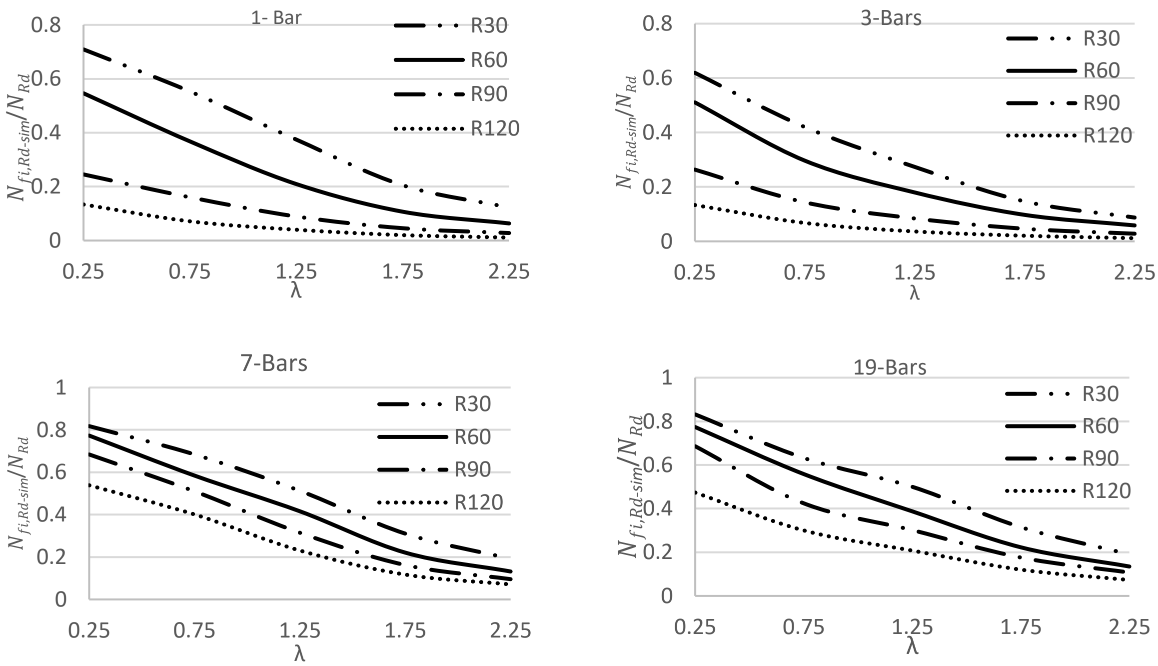

Figure 10. Comparison of load-bearing capacity in fire and ambient temperature

The results show that the load-bearing capacity in columns with 1 and 3 bars reduces much more than the columns with 7 and 19 bars in the event of a fire. Especially, the columns with 1 and 3 bars have a significant reduction of load bearing after 60 minutes of fire, which is mainly related to the configuration and size of the bars, which have a positive effect in sections with 7 and 19 bars on the distribution of the load.

5 CONCLUSION

In summary, the paper proposes a novel approach for developing the thermo-mechanical performance of CFHS columns with solid steel cores by replacing the solid core with high-strength bar bundles with pressed grout as filler. The results of experimental tests and numerical simulation shows that the new approach fulfils the initial purposes of the project:

Injection of swelling mortar without aggregate with high pressure into the tube filled the space between the bars bundles completely and made strong contact with the bar bundles. The strong contact doesn't let mortar expand freely, which results in a thicker air layer between the tube and mortar and delays the temperature transfer to the core for a longer time.

The high thermal resistance of the utilized mortar has a significant effect on the reduction of core temperature-time development and also temperature distribution in the mortar, which slows down the radial expansion of the mortar.

Using bar-bundles with different configurations and the ribs on their surface strengthens the contact between mortar and bar-bundle, which lets mortar have more contribution to load bearing capacity of the columns. And, of course, the point contact between them reduces the thermal conduction in the steel core.

Utilizing high-strength steel for bar-bundle increase remarkably the load-bearing capacity of the columns.

The tube could keep the confinement of the mortar throughout the fire tests and avoid any explosion failure or local buckling because of internal vapour pressure.

The developed numerical models can reasonably estimate the fire performance of the proposed columns, which can be a reliable replacement for costly large-scale fire tests.

ACKNOWLEDGEMENT

The authors gratefully acknowledge the financial support of the German Federation of Industrial Research Associations (AIF), the scientific supervision of the Steel Application Research Association (FOSTA), and the technical support of industrial partners in the manufacture and provision of the test specimens.

REFERENCES

1. Grandjean, G., Grimault, J. P., & Petit, L. (1981). Determination de la duree au feu des profils creux remplis de beton. Office des publications officielles des Communautés européennes.
2. Kodur, V. K. R., and Lie, T. T. (1995). "Experimental studies on the fire resistance of circular hollow steel columns filled with steel-fiber-reinforced concrete." NRC (National Research Council Canada), Institute for Research in Construction, Internal Report No. 691, Ottawa, Canada.
3. Espinos, Ana, Leroy Gardner, Manuel L. Romero, and Antonio Hospitaler. "Fire behaviour of concrete filled elliptical steel columns." Thin-walled structures 49, no. 2 (2011): 239-255.
4. Espinos, A., Manuel L. Romero, E. Serra, and A. Hospitaler. "Circular and square slender concrete-filled tubular columns under large eccentricities and fire." Journal of Constructional Steel Research 110 (2015): 90-100.
5. Bailey, Colin. "Effective lengths of concrete-filled steel square hollow sections in fire." Proceedings of the Institution of Civil Engineers-Structures and Buildings 140, no. 2 (2000): 169-178.
6. Yang, Hua, Faqi Liu, Sumei Zhang, and Xuetao Lv. "Experimental investigation of concrete-filled square hollow section columns subjected to non-uniform exposure." Engineering structures 48 (2013): 292-312.
7. Rodrigues, João Paulo C., and Luís Laim. "Fire response of restrained composite columns made with concrete filled hollow sections under different end-support conditions." Engineering Structures 141 (2017): 83-96.
8. Espinos, A., Romero, M. L., Serra, E., & Hospitaler, A. (2015). Circular and square slender concrete-filled tubular columns under large eccentricities and fire. Journal of Constructional Steel Research, 110, 90-100
9. Rush, David I., Luke A. Bisby, Allan Jowsey, and Barbara Lane. "Residual capacity of fire-exposed concrete-filled steel hollow section columns." Engineering Structures 100 (2015): 550-563.

10. Yang, Hua, Lin-Hai Han, and Yong-Chang Wang. "Effects of heating and loading histories on post-fire cooling behaviour of concrete-filled steel tubular columns." Journal of Constructional Steel Research 64, no. 5 (2008): 556-570.
11. Lopes, Rúben FR, and João Paulo C. Rodrigues. "Behaviour of restrained concrete filled square double-skin and double-tube hollow columns in case of fire." Engineering Structures 216 (2020): 110736.
12. Lu, Hui, Lin-Hai Han, and Xiao-Ling Zhao. "Fire performance of self-consolidating concrete filled double skin steel tubular columns: Experiments." Fire safety journal 45, no. 2 (2010): 106-115.
13. Romero, Manuel L., Ana Espinós, J. M. Portolés, Antonio Hospitaler, and C. Ibañez. "Slender double-tube ultra-high strength concrete-filled tubular columns under ambient temperature and fire." Engineering Structures 99 (2015): 536-545.
14. Klingsch, W. (1984). "Analyse des Tragverhaltens von Geilinger Baustützen bei Normaltemperatur und bei Brandbeanspruchung sowie der zughörigen Bemessungsverfahren." Bergische Universität Wuppertal, Gutachten Nr. 84-11, Wuppertal, Germany.
15. Schaumann, P., and Kleibömer, I. (2015). "Thermal and structural response of concrete-filled tubular columns with massive steel core in case of fire." Bautechnik, 92, 330-334.
16. Neuenschwander, Martin, Markus Knobloch, and Mario Fontana. "Fire behavior of concrete filled circular hollow section columns with massive steel core." In Proceedings of the international colloquium stability and ductility of steel structures SDSS. 2010.
17. Bailey, C. (2000). Effective lengths of concrete-filled steel square hollow sections in fire. Proceedings of the Institution of Civil Engineers-Structures and Buildings, 140(2), 169-178.
18. Wang, Y. C., & Kodur, V. K. R. (1999). An approach for calculating the failure loads of unprotected concrete filled steel columns exposed to fire. Structural Engineering and Mechanics, 7(2), 127-146.
19. Zha, X. X. "FE analysis of fire resistance of concrete filled CHS columns." Journal of Constructional Steel Research 59, no. 6 (2003): 769-779.
20. Yang, H., Han, L. H., & Wang, Y. C. (2008). Effects of heating and loading histories on post-fire cooling behaviour of concrete-filled steel tubular columns. Journal of Constructional Steel Research, 64(5), 556-570.
21. Ding, J., and Y. C. Wang. "Realistic modelling of thermal and structural behavior of unprotected concrete filled tubular columns in fire." Journal of Constructional Steel Research 64, no. 10 (2008): 1086-1102.
22. Neuenschwander, Martin, Markus Knobloch, and Mario Fontana. "Modeling thermo-mechanical behavior of concrete-filled steel tube columns with solid steel core subjected to fire." Engineering Structures 136 (2017): 180-193.
23. Schaumann, Peter, Venkatesh Kodur, and Oliver Bahr. "Fire behavior of hollow structural section steel columns filled with high strength concrete." Journal of Constructional Steel Research 65, no. 8-9 (2009): 1794-1802.
24. EN 1993-1-2:2010-12, Eurocode 3: Design of steel structures - Part 1-2: General rules - Structural fire design
25. DIN EN 1992-1-2:2010-12, Eurocode 2: Design of concrete structures - Part 1-2: General rules - Structural fire design

STUDY ON FIRE RESISTANCE OF PREFABRICATED DEMOUNTABLE COMPOSITE BEAMS USING BOLTED SHEAR CONNECTORS

Mengjie Wang[1], Guobiao Lou[2], Zhaohan Wen[3], Binhui Jiang[4,*], Yongchang Wang[5], Yaqiang Jiang[6]

ABSTRACT

Using bolts as shear connectors of the steel-concrete composite beams enables prefabricated assembly and makes it possible to demountable and reuse the prefabricated components. However, studies on the fire resistance of prefabricated demountable composite beams (PDCBs) connected by bolts are limited. In this paper, four full-scale fire resistance tests were conducted to investigate the fire resistance of PDCBs connected by shear bolts with profiled sheet ribs parallel to the steel beam. Test phenomena, heating curves, deformation curves, and critical temperatures of specimens were obtained through fire-resistant tests. Test results show that the shear failure of bolted connectors occurred in the partially connected PDCBs instead of in the fully connected ones. Under the same load ratio, the fire resistance limit of PDCBs with fire protection was 4.4 times that of PDCBs without fire protection. The temperatures of the upper flanges of the steel beams in the PDCBs were overestimated by the existing codes. Moreover, numerical heat transfer analysis was carried out to investigate the effect of steel beam upper flange dimensions and concrete slab thickness on the temperature distribution of the steel beam upper flange. Finally, formulas were proposed for calculating the temperature distribution of the steel beam upper flange, which agrees well with the FEM simulated values.

Keywords: Prefabricated; demountable; composite beam; bolted connection; fire resistance; heat transfer

1 INTRODUCTION

Steel-concrete composite beams are usually composed of steel beams, reinforced concrete slabs, and shear connectors, which generally exhibit excellent structural performance in terms of strength and stiffness [1]. Structural Fire safety is an important research topic [2-4]. With the widespread application of steel-concrete composite beams in building and bridge structures, increasing attention has been attracted to the fire resistance and fire design methods of composite beams [5]. Currently, extensive research studies on the fire resistance of conventional composite beams have been conducted, including experiments, and numerical and theoretical analyses [6-10].

Shear connectors between the concrete slab and the steel beam are usually used to transfer the longitudinal shear forces at the concrete-steel interface [11]. In conventional composite beams, the shear connectors are mostly welded on the upper flange of steel beams (such as stud, channel steel, etc.) and embedded in the

[1] PhD Candidate, School of Civil Engineering, Tongji University, Shanghai 200092, China
e-mail: mengjieang@tongji.edu.cn
[2] Associate professor, School of Civil Engineering, Tongji University, Shanghai 200092, China
e-mail: gblou@tongji.edu.cn
[3] Postgraduate, School of Civil Engineering, Tongji University, Shanghai 200092, China
e-mail: wzhtj@qq.com
[4] Associate professor, School of Civil Engineering, Central South University, Changsha 410075, China
e-mail: binhuijiang@csu.edu.cn, ORCID: https://orcid.org/0000-0003-3774-9587
[5] Professor, School of Mechanical, Aerospace and Civil Engineering, University of Manchester , UK
e-mail: yong.wang@manchester.ac.uk
[6] Research Assistant, Sichuan Fire Science and Technology Research Institute of MEM, Sihchuan 610036, China
e-mail: jiang.yaqiang@scfri.cn
https://doi.org/10.6084/m9.figshare.22154159

cast in situ concrete slab, which requires extensive wet work and makes the deconstruction and reuse of the structural components almost impossible [11]. A prefabricated demountable composite beam (PDCB) was developed wherein the steel beam is attached to the prefabricated concrete slab using demountable bolts as shear connectors [12]. The use of demountable bolted connectors in steel-concrete composite beams allows prefabricated assembly, disassembly, and recyclability. In previous studies, extensive push-out tests on bolted shear connectors and bending test studies on composite beams have been carried out at room temperature [11, 13-17]. However, research studies on the fire resistance of steel-concrete composite beams connected by bolts, especially full-scale experimental studies, are limited.

In this paper, four full-scale PDCBs with different shear connection ratios and fire protection situations were tested under fire based on the ISO-834 standard heating curve. The failure phenomenon was observed, and temperature-time curves, mid-span vertical displacement-time curves, critical temperatures, and mid-span vertical maximum displacements of the specimens were obtained. Moreover, numerical heat transfer analysis was carried out to investigate the temperature distribution of the steel beam upper flange in the PDCB, and formulas were proposed to calculate the temperature of the steel beam upper flange considering the heat absorption effect of the concrete slab.

2 EXPERIMENTAL PROGRAM

2.1 Test specimens

A total of four full-scale PDCBs specimens (CB1, CB2, CB3 and CB4) with various shear connection ratios and fire protection situations were constructed and loaded to failure. Details of the specimens are presented in Table 1Table 1. Specimens CB1 and CB2 were designed with 46% shear connection (partially connected), and constructed with a total of 18 bolted connectors. Specimens CB3 and CB4 were designed to be fully connected with a total of 34 bolted connectors. In particular, steel beams in specimens CB2 and CB4 are covered with lightweight non-intumescent fire protection, while CB1 and CB3 are not.

The length and height of the test PDCBs were 5600 mm and 480 mm, respectively, and the width of the concrete slab was 1500 mm. The geometry of the cross-section is illustrated in Figure 1. The concrete slab is made of C40 commercial concrete. To facilitate the installation and removal of the test specimens, two symmetrical concrete slabs with a thickness of 130 mm were used, and a 40 mm wide post-casting joint was reserved in the middle of the span. The steel beams have a section of HN350 × 175 × 7 × 11 (mm) and the steel grade of them is Q345B. Profiled sheet ribs are parallel to the steel beam. The steel and concrete were connected through the use of M19 shear bolted connectors. Lightweight non-intumescent fire protection coatings used in specimens CB2 and CB4 were 10 mm thick and had a density of 400 kg/m^3, a heat capacity of 1 kJ/(kg·℃), and a thermal conductivity of 0.11 W/(m·℃).

Table 1 Specimens detail.

Specimen	Fire protection coating	Bolt number	Shear connection ratios	Test load (kN·m)
CB1	No	18	Partially connected	240
CB2	10 mm	18	Partially connected	240
CB3	No	34	Full connected	270
CB4	10 mm	34	Full connected	270

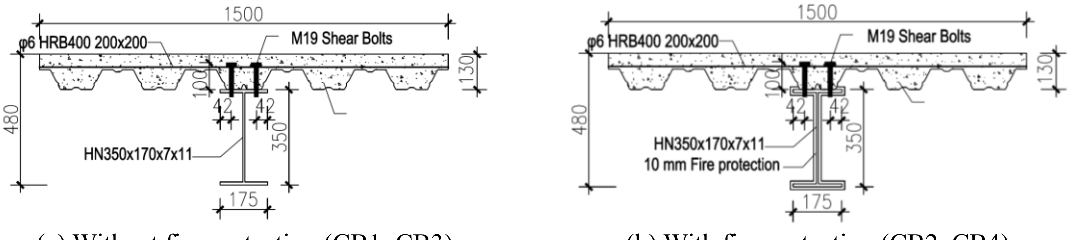

(a) Without fire protection (CB1, CB3) (b) With fire protection (CB2, CB4)

Figure 1 Sketch of specimens (unit in mm).

2.2 Test device and test procedure

The fire tests were conducted in the Fire Laboratory of Tongji University. A concentrated load was applied in the mid-span by a jack and then distributed to the composite beam specimen by a 1400 mm long distribution beam, as illustrated in Figure 2. Firstly, the specimens were loaded to 10 kN and kept at the constant load for 5 min to observe if the test equipment operates properly. Then the specimens were loaded to the test load value and kept constant for 15 min. The load ratio was 0.65 for all the specimens. Then, the specimens were heated according to the ISO-834 standard heating curve using a gas furnace with internal dimensions of 4500 mm×3000 mm×2200 mm. The load was kept constant during the heating stage. Finally, when the limit state was reached, the heating was stopped and the specimen was unloaded. According to the ref. [18], the specimen can be considered to reach the limit state when the mid-span deflection of the steel-concrete composite beam reaches $L/30$ (L denotes the simply supported span of the composite beam).

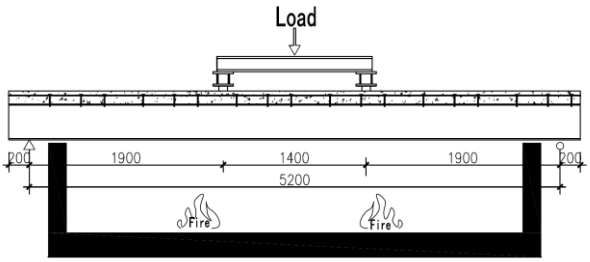

Figure 2 Sketch of experiment (unit in mm).

2.3 Instrumentation

The deformation and temperature of the test beams were monitored using displacement transducers and thermocouples, respectively. The arrangement of the thermocouples and displacement transducers can be seen in Figure 3. Three displacement transducers were attached at the mid-span (D1) and two load positions (D2 and D3) of the test beam to record the vertical displacements. In order to obtain an accurate temperature distribution for different parts of each specimen, the thermocouples were arranged on the mid-span (M) and quarter-span (N) sections of the specimens, as shown in Figure 3(a). At each section, thermocouples were installed on the steel beam, shear bolt and concrete slab to measure temperature development during the fire test. As illustrated in Figure 3(b), thermocouples S1, S2 and S3 measured the temperature at the bottom flange, middle web and top flange of the steel beam, B1, B2 and B3 measured the temperatures of shear bolt at the bottom, middle and top, C1 and C2 measured the temperatures of concrete slab at the bottom and top.

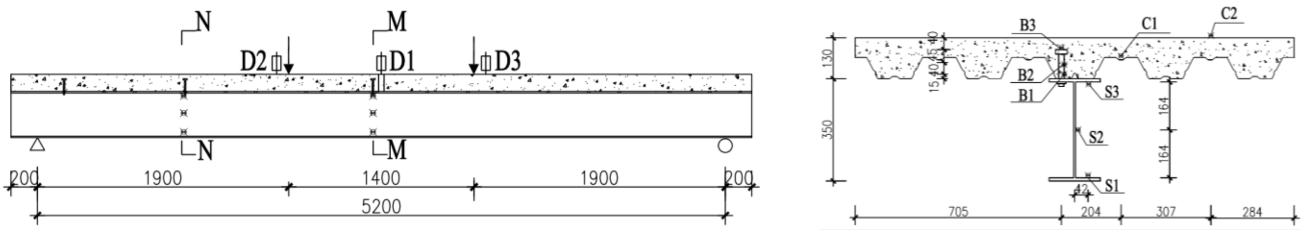

(a) Displacement transducer (b) Thermocouples

Figure 3 The arrangement of displacement transducers and thermocouples (unit in mm).

3 TEST RESULTS AND DISCUSSION

3.1 Overall observations

Post-test photos of the test beams are shown in Figure 4. As shown in these photos, one or two longitudinal shear cracks were observed in all four specimens. During the test, cracks first appeared on the concrete slab near the loading points and supports, and then gradually developed and widened as the temperature continues to rise, eventually penetrating the full length of the composite beam. It is noted that the longitudinal shear crack widths were about 2 to 3 mm for partially connected PDCBs (CB1 and CB2), while those for fully connected PDCBs (CB3 and CB4) were about 5 mm. In addition, the shear connection ratios have an effect on the failure of PDCBs. Firstly, the damage of concrete slabs in fully connected PDCBs was more severe than that in partially connected ones. Secondly, the shear failure of bolted connectors occurred in the partially connected PDCBs (CB1 and CB2), while no shear failure of bolted connectors occurred in the fully connected PDCBs (CB3 and CB4). As presented in Figure 5, three bolts at the end of specimen CB1 were sheared off with a flat section, and one bolt near the left loading point of specimen CB2 was sheared off.

(a) CB1

(b) CB2

(c) CB3

(d) CB4

Figure 4 Specimen photos after the fire test

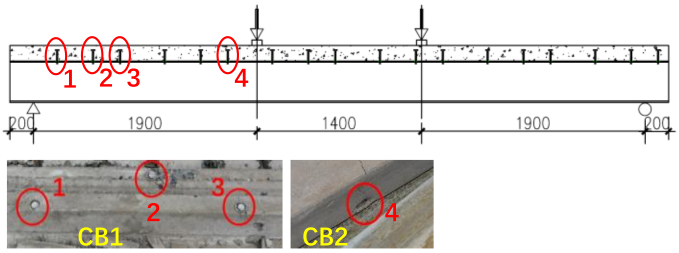

Figure 5 Fracture failure of bolted connectors

3.2 Thermal response

3.2.1 Furnace temperature

The comparison of temperature-time curves in the furnace with the ISO-834 standard heating curve is shown in Figure 6. As shown in Figure 6(a), for specimen CB1, the development of furnace temperature was generally consistent with the ISO-834 standard heating curve, while the furnace temperature for specimen CB3 was obviously higher than the ISO-834 standard heating curve due to equipment problems. As shown in Figure 6(b), the developments of furnace temperature were generally similar to the ISO-834 standard heating curve for specimens CB2 and CB4. It is also noted that in the initial heating stage (0-20 min), the furnace temperature-time curves exhibited a certain difference from the ISO-834 standard heating curve.

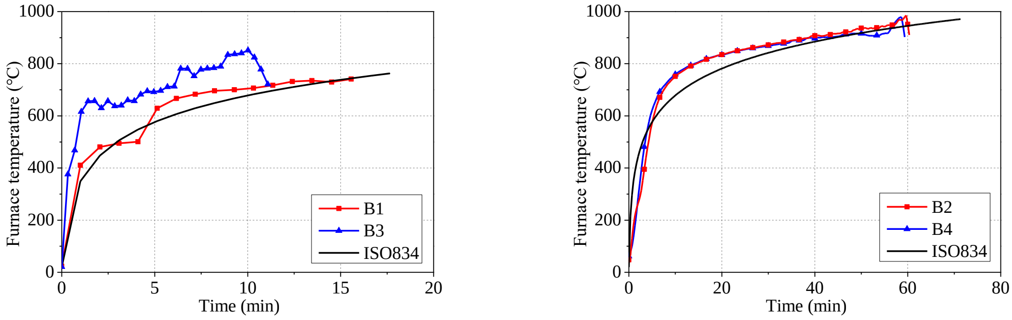

(a) CB1 and CB3

(b) CB2 and CB4

Figure 6 Furnace temperature

3.2.2 Comparison of temperatures at different sections

Specimen CB2 is taken as an example to illustrate the temperature distribution of cross-sections M and N in the PDCBs. Figure 7(a), (b) and (c) compare the temperature developments of steel beams, bolts and concrete slabs, respectively. It can be seen that the temperature developments of the steel beam, bolts and concrete slabs on different sections were generally similar, which represents the temperature distribution of PDCBs along the length direction was generally uniform. Therefore, the temperature distribution of the steel beam, bolts and concrete slabs in the PDCBs can be analysed using the mid-span section (section M) as a representative.

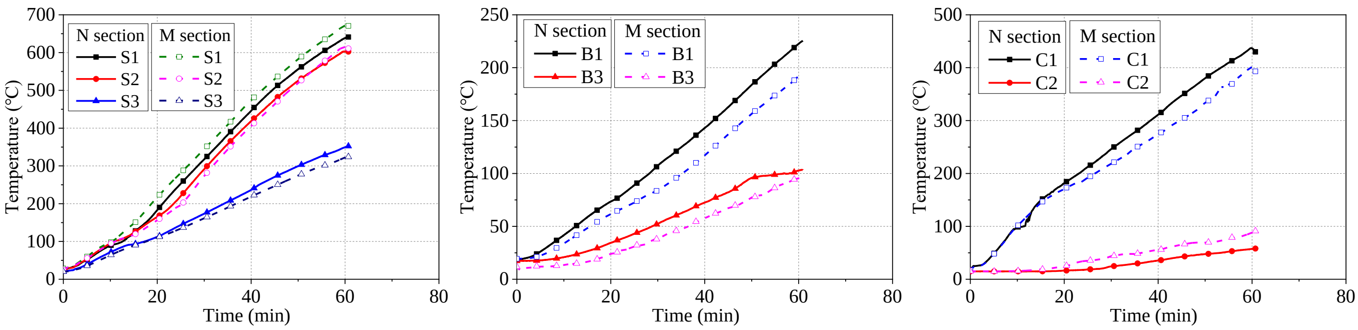

(a) Steel beam

(b) Bolts

(c) Concrete slab

Figure 7 The comparison of the temperature profiles at different cross-sections.

3.2.3 Development of temperature in the composite beam

3.2.1 Steel beams

The temperature-time curves in the mid-span section of the steel beam during the fire test are shown in Figure 8. It can be seen that the temperatures of the lower flange and the web of the steel beam were close to each other, while they were much higher than that of the upper flange of the steel beams. This is because the upper flange of the steel beam is attached to the concrete slab, resulting in a large amount of heat being absorbed by the concrete slab during the heating process.

Moreover, the measured temperatures are compared with the recommended values by GB51249 [19] and Eurocode 4 [20]. The steel beam is divided into an upper flange (noted as GB-up) and a remaining inverted T-shape (noted as GB-T) in the GB51249, whereas in the EC4 code the beam is considered as a single unit (noted as EC4). As presented in Figure 8(a) and (c), the temperatures of the lower flange and web of unprotected steel beams can be well predicted by the GB51249, whereas the temperatures predicted for EC4 are relatively lower. However, the temperatures of the lower flange and web of protected steel beams were overestimated by the GB51249 and EC4, as shown in Figure 8(b) and (d). In general, for all specimens, the calculated temperatures for the upper flange of the steel beam in both EC4 and GB51249 were significantly conservative as they do not take into account the heat absorption of the concrete slab.

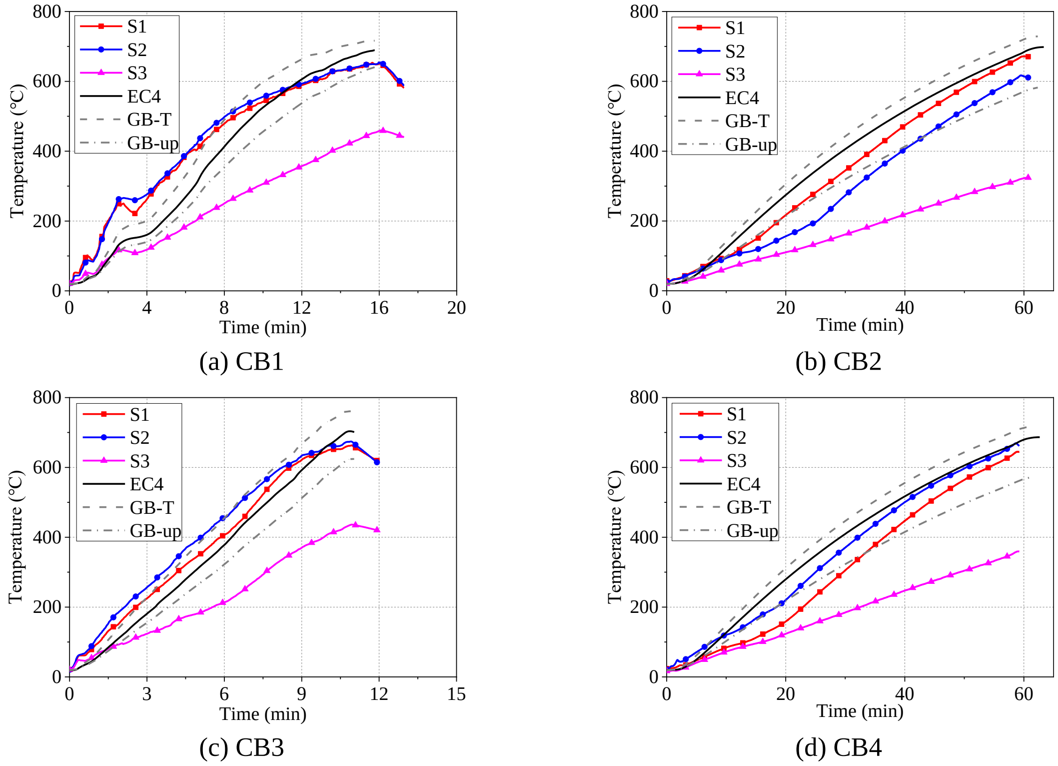

Figure 8 Temperature developments of the steel beam.

3.2.2 Bolts

The temperature-time curves of the mid-span section of the bolts during the fire test are shown in Figure 9. The temperatures of the shear bolt continuously decreased from the bottom to the top along with the height direction, namely: B1 > B2 > B3.

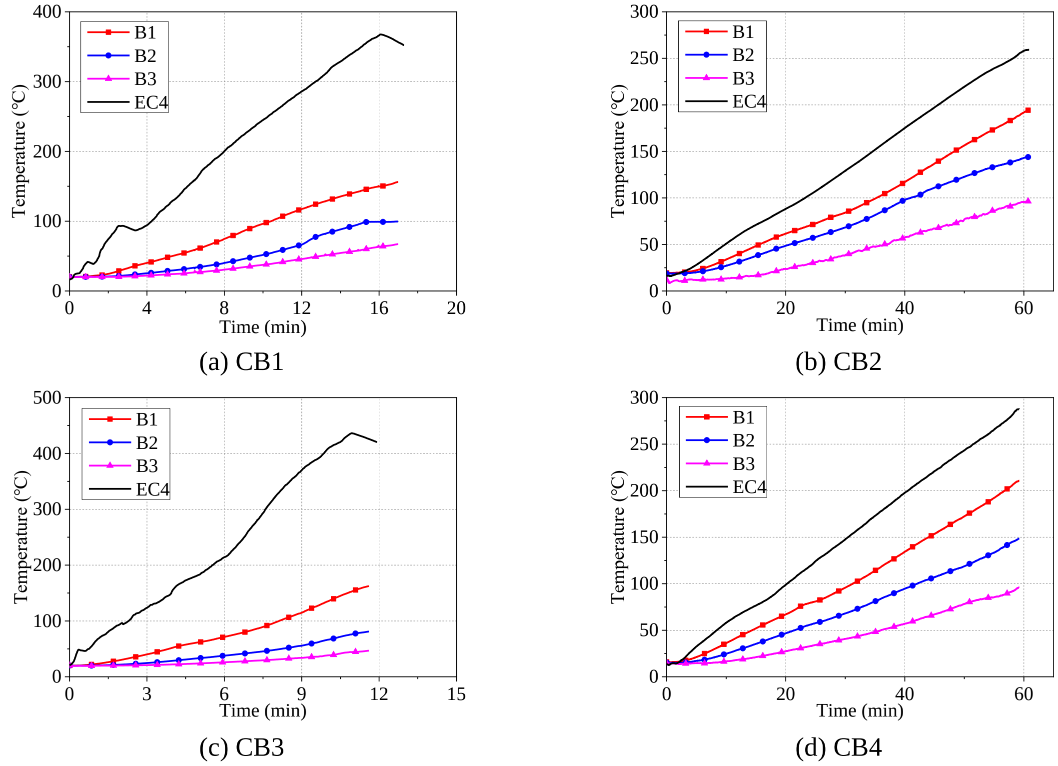

Figure 9 Temperature developments of bolts.

Moreover, the measured temperatures of the bolts are compared to the recommended values of the EC4, which assumes that the bolt temperature is 80% of the upper flange temperature of the steel beam. As can be seen from Figure 9, the calculated values of EC4 were significantly higher than the measured bolt temperatures, especially when the PDCB is without fire protection. This may be due to the fact that the bolts are completely encased in concrete, resulting in a large amount of heat being absorbed by the surrounding concrete.

On the other hand, for PDCBs with fire protection, the temperatures of the bolts and upper flange of the steel beam both increase uniformly. It is therefore possible to estimate the temperature of the bolts at different heights by multiplying the temperature of the steel beam upper flange by a reduction factor. According to the test results of specimens CB2 and CB4, the reduction factors for the bottom, middle and top of the bolts were 0.75, 0.56 and 0.37, respectively.

3.2.3 Concrete slabs

The temperature-time curves of the concrete slab during the fire test are shown in Figure 10. It can be seen that the temperature of the concrete slab on the lower surface (C1) was higher than that at the upper surface (C2).

Moreover, the measured temperatures are compared to the recommended values of the EC4, which assumes that the concrete slab temperature is 40% of the upper flange temperature of the steel beam (denoted as EC4). As presented in Figure 10(a) and (c), the calculated values of EC4 were much higher than the temperatures of the concrete slab for specimens CB1 and CB3. This is due to the fact that the fire resistance limit of the PDCBs without protection is within 16 min, during which the temperature of the steel beam rises rapidly while the temperature of the concrete rises slowly. As presented in Figure 10(b) and (d), the calculated values of EC4 were generally close to the values of C2, while they were significantly smaller than the values of C1. In general, 40% of the upper flange temperature of the steel beam cannot well represent the temperature of concrete slab in the PDCBs.

In addition, appendix D to EC4 gives the temperature distribution of the concrete slab along the thickness direction, from which the temperature at the bottom and top of the concrete slab can be calculated (denoted as EC4-bot and EC4-top). As shown in Figure 10(c) and (d), the values of EC4-bot and EC4-top were close to the measured temperatures of concrete slab.

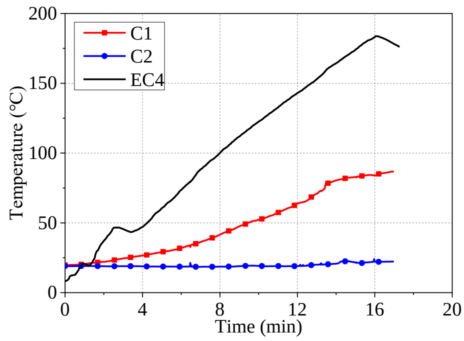

(a) CB1

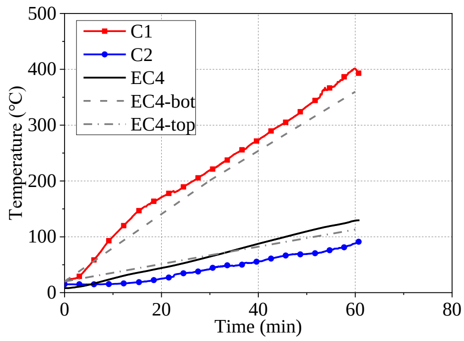

(b) CB2

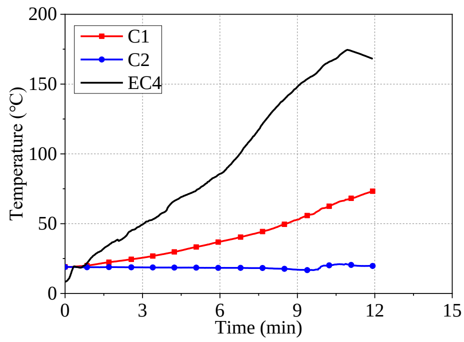

(c) CB3

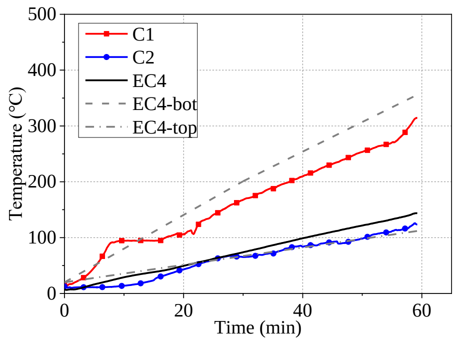

(d) CB4

Figure 10 Temperature developments of concrete slabs.

3.3 Displacements and critical temperature

The mid-span vertical displacement-time curves for specimens are shown in Figure 11. The specimens can be considered to reach the limit state when the mid-span displacement of PDCBs reaches $L/30$. The fire resistance limits of specimens CB1, CB2, CB3 and CB4 were 16 min, 60 min, 11 min and 59 min, respectively, with the maximum displacements being 194 mm, 211 mm, 193 mm and 234 mm, respectively. It can be seen that under the same load ratio, the fire resistance limits of PDCBs with fire protection (CB2, CB4) were about 4.4 times those of PDCBs without fire protection (CB1, CB3). The mid-span displacements of PDCBs with fire protection were approximately 15% greater than those of PDCBs without fire protection. The shear connection ratio has little effect on the fire resistance limit and mid-span displacement of the PDCBs. It is noted that the fire resistance limit of specimen CB3 was lower than that of specimen CB1 may be due to the furnace temperature of specimen CB3 being obviously higher than that of specimen CB1.

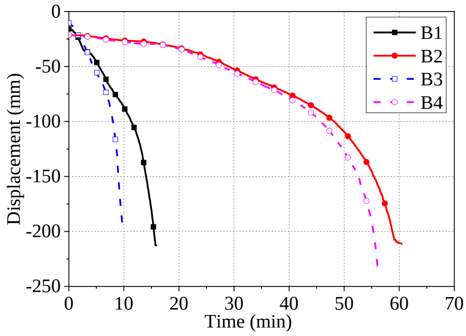

Figure 11 Displacement development

When the test specimens reached the fire resistance limit, the temperatures of the steel beam, bolt and concrete slab in the mid-span of the specimens are presented in Table 2. It can be seen that a certain temperature gradient existed when the composite beam specimen reached the fire resistance limit. The temperatures of the steel beam were considerably higher than the temperatures of the shear bolt and concrete slab. In this paper, the temperature of the lower flange of the steel beam when the fire resistance limit was reached was considered as the critical temperature of the composite beam. Hence, the critical temperatures of specimens CB1, CB2, CB3 and CB4 were 650℃, 671℃, 663℃and 644℃, respectively.

Table 2 Temperature at fire resistance limit

Specimen	Temperature (℃)							
	S1	S2	S3	B1	B2	B3	C1	C2
CB1	650	654	459	150	100	63	85	22
CB2	671	617	323	192	143	96	401	88
CB3	663	674	436	154	76	45	68	21
CB4	644	670	360	210	148	96	318	127

4 NUMERICAL SIMULATION ON TEMPERATURE RISING

4.1 General description

It is essential to accurately calculate the temperature distribution of PDCB in a fire. However, the temperature distribution of steel beam upper flange was overestimated by the existing codes, as they do not take into account the heat absorption of the concrete slab. In this section, numerical heat transfer analysis is carried out to investigate the temperature distribution of the steel beam upper flange in composite beams using the finite element software ABAQUS. A two-dimensional composite beam heat transfer model was developed as shown in Figure 12. The dimensions of the model were consistent with that of the test specimen. Each model consisted of four-node quadrilateral elements DC2D4. Thermal conductivity, specific heat, and mass density of steel beam and bolt were defined using the models in EC4, and those of concrete were defined according to GB51249. The thermal parameters of the fire protection coating are set according to the actual situation. The steel beam, bolts and concrete slab were assumed to be connected completely continuously by the “tie” constraint to transfer heat. The convective heat transfer coefficient is taken as 25 W/ (m^2 ℃) for surfaces exposed to fire and 9 W/ (m^2 ℃) for surfaces not exposed to fire. The thermal radiation coefficient is taken as 0.5, however, for the lower corrugated part of the plate ribs, the radiation angle is considered to be reduced and the combined thermal radiation coefficient is taken to be 0.15. The recorded fire heating curves from the tests were used as the input temperature of the thermal load. The initial temperature of the model was set at 20 ℃ by using the predefined temperature field in the FE model.

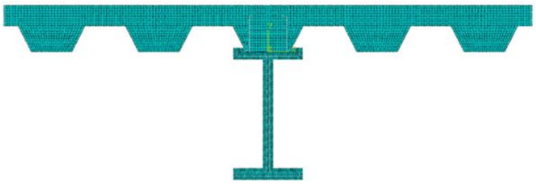

Figure 12 Finite element model

4.2 Verification of the numerical model

The results of heat transfer analyses were compared with fire tests results and the accuracy of the finite element model was verified. Taking specimen CB4 as an example, the temperature curves of steel beam, bolts and concrete slab between the test results and the model results are compared in Figure 13. It can be seen that the finite element model developed in this paper can well predict the temperature rise curves of steel beams, bolts and concrete slabs.

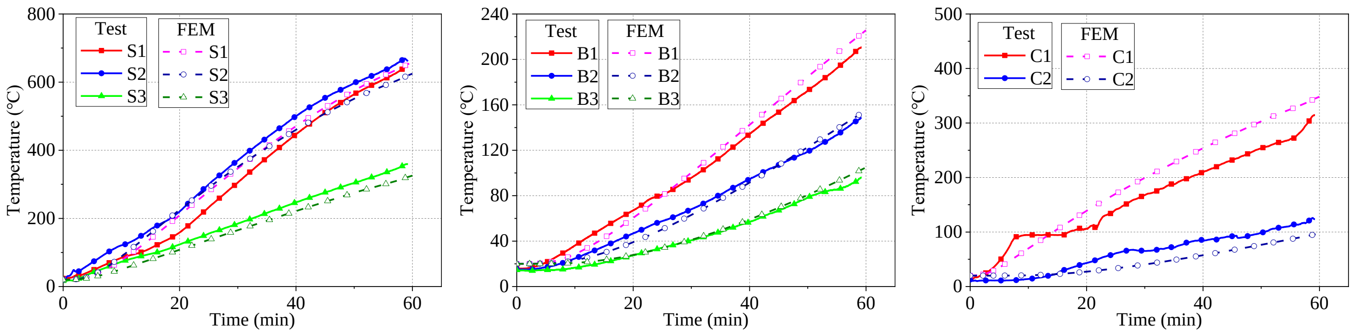

(a) Steel beam (b) Bolts (c) Concrete slab

Figure 13 comparing curves of experiment and simulation models.

4.3 Parametric study

The effect of steel beam upper flange dimensions and concrete slab thickness on the temperature curves of the upper flange was investigated by parametric analysis. The concrete slab was replaced with a flat plate without ribs to facilitate parametric analysis. The ISO 834 curve was used as the input temperature. The heating time is set to be 20 min for cases without fire protection and 120 min for cases with fire protection.

4.3.1 Effects of steel beam upper flange dimensions

Figure 14 shows a comparison of the temperature curves of upper flange of the steel beam between the FEM simulated values and GB51249 calculated values. The upper flange dimensions of a steel beam are expressed as flange width (b) * flange thickness (t_f).

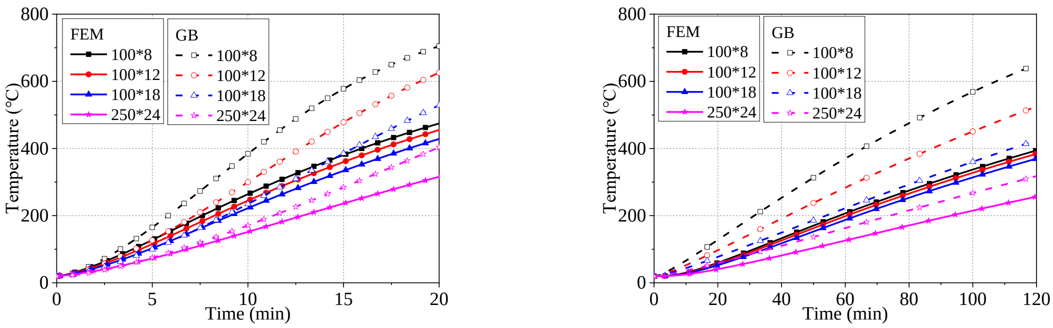

(a) Without fire protection (b) With fire protection

Figure 14 The effect of the width-to-thickness ratio of the upper flange of a steel beam on its temperature.

It can be seen that the temperatures calculated by GB51249 were generally higher than the finite element results, and the deviation is sensitive to the change in the dimensions of the upper flange of the steel beam. In general, with the increase in width-to-thickness ratio of the steel beam upper flange, the deviation between the calculated values of the specification and the FEM simulated values enlarges.

4.3.2 Effects of thickness of concrete slab

Figure 15 shows the temperature curves of the upper flange of the steel beam for different concrete thicknesses. It can be seen that the temperature of the steel beam upper flange decrease with the increase of the concrete slab thickness when the concrete slab thickness is within 75 mm. When the concrete slab is thicker than 75 mm, the temperature of the steel beam upper flange no longer decrease with the increase of the concrete slab thickness.

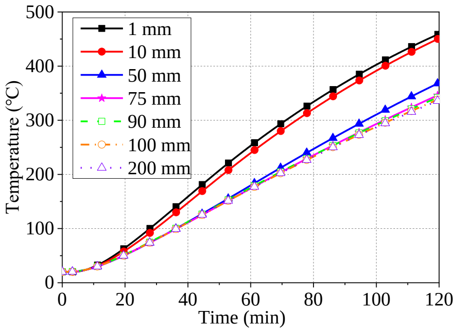

Figure 15 Effect of concrete slab thickness on the temperature of the steel beam upper flange.

5 EQUATION FOR CALCULATING THE TEMPERATURE OF STEEL BEAM

The temperatures of the steel beam upper flange calculated in the GB51249 were significantly higher than the test values, due to the neglect of the heat absorption effect of the concrete slab. An incremental method is specified in GB51249 to calculate the temperature curve of steel members. The temperature of the steel member at the target time T_s is obtained by calculating the temperature increment ΔT_s within each time increment Δt, and accumulating all ΔT_s to the initial temperature T_0, as shown in (1).

$$T_s(t)=\sum_{0}^{t}\Delta T_s+T_0 \tag{1}$$

It is noted that the temperature of the steel beam upper flange increases linearly with the increase of fire time, both as calculated by finite elements and as predicted by the GB51249. It is therefore possible to estimate the temperature of the steel beam upper flange by multiplying the predicted temperature values of GB51249 by a discount factor. In this paper, all ΔT_s are multiplied by a discount factor β to obtain the discounted temperature increment ΔT_s^*, as presented in (2). The discounted temperature increments ΔT_s^* were used to calculate the temperature of the steel beam upper flange by the incremental method, as shown in Equation (3).

$$\Delta T_s^*=\Delta T_s\times\beta \tag{2}$$

$$T_s^*(t)=\sum_{0}^{t}\Delta T_s^*+T_0 \tag{3}$$

The results of the parametric analysis show that the most important factor influencing the discount factor β is the width-to-thickness ratio b/t_f of the steel beam upper flange after the concrete slab is thicker than 75 mm. Formulas were proposed to calculate the discount factor β based on the results of parametric analysis. The formula for calculating the discount factor β for the PDCB without fire protection is shown in (4), and that for the PDCB with fire protection is shown in (5). The discount factors calculated by the equations were compared with those obtained from the finite element parametric analysis, as shown in Figure 16. It can be seen that the formula proposed in this paper can well calculate the discount factor.

It is noted that (4) and (5) proposed in this paper have some scope of application. The thickness of the concrete has an effect on the discount factor within a certain range. (4) and (5) presented in this paper apply where the thickness of the concrete slab is greater than 90 mm and greater than four times the thickness of the upper flange of the steel beam. In addition, lightweight non-intumescent fire protection coatings were used in this paper. The equations presented in this paper may not be applicable for composite beams using other fire protection measures such as non-lightweight fire protection coatings or fire panels.

$$\beta=\begin{cases}0.78, & \dfrac{b}{t_{\mathrm{f}}}<5\\ -0.0072\dfrac{b}{t_{\mathrm{f}}}+0.816, & 5\le\dfrac{b}{t_{\mathrm{f}}}\le 30\\ 0.6, & \dfrac{b}{t_{\mathrm{f}}}>30\end{cases}\tag{4}$$

$$\beta=\begin{cases}0.91, & \dfrac{b}{t_{\mathrm{f}}}<5\\ -0.029\dfrac{b}{t_{\mathrm{f}}}+1.05, & 5\le\dfrac{b}{t_{\mathrm{f}}}\le 16\\ 0.57, & \dfrac{b}{t_{\mathrm{f}}}>16\end{cases}\tag{5}$$

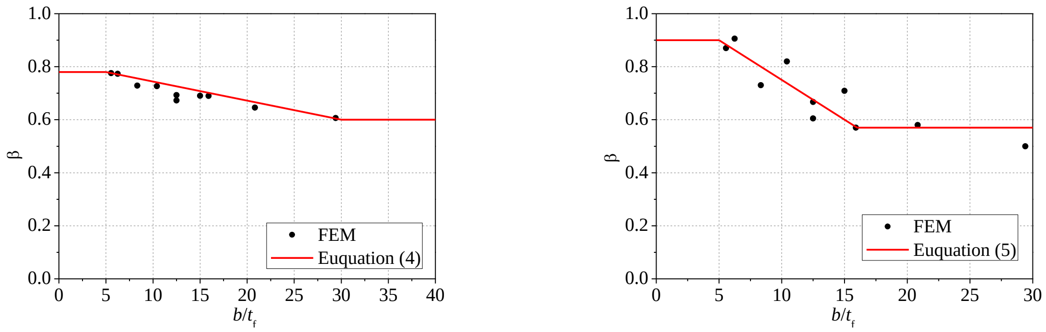

(a) Without fire protection (b) With fire protection

Figure 16 Comparison of the discount factor calculated by the Equations with that of the finite element parametric analysis

6 CONCLUSIONS

In this paper, four full-scale fire tests were conducted to investigate the effect of the fire protection and shear connection ratios on the fire resistance of prefabricated demountable composite beams (PDCBs) connected by shear bolts. The failure phenomena, temperature distribution, vertical displacement, and critical temperature of specimens were obtained. Then, numerical heat transfer analysis is carried out to investigate the temperature distribution of the steel beam upper flange in a PDCB. Formulas were proposed to calculate the temperature of the steel beam upper flange considering the heat absorption effect of the concrete slab. The following is a summary of the findings:

a. When exposed to fire, one or two longitudinal shear cracks occur in the concrete slab of the PDCBs. The shear failure of bolted connectors occurred in the partially connected PDCBs but not in the fully connected ones. Additionally, concrete slab damage in fully connected PDCBs is more severe than that in partially connected ones.
b. Under the same load ratio, the fire resistance limits of PDCBs with fire protection were around 4.4 times those of PDCBs without fire protection. However, the shear connection ratios have little effect on the fire resistance limit of PDCBs.
c. The temperature distribution of PDCB along the length direction was generally uniform. However, there is a temperature gradient in the cross section of the composite beam. The temperature of the steel beam is considerably higher than the temperature of the bolt and concrete slab.
d. The temperatures of the upper flanges of the steel beams in the PDCBs were overestimated by the EC4 and GB51249, the reason may be that they do not take into account the heat absorption of the concrete slab.
e. With the increase in the width-to-thickness ratio of the steel beam upper flange, the deviation between the specification calculated values and the FEM simulated values enlarges. When the thickness of the

concrete slab is within 75 mm, the heat absorption properties of the concrete slab on the upper flange of the steel beam increase with the thickness of the concrete slab.

f. Formulas were proposed for calculating the temperature of the upper flange of steel beams in PDCBs. The proposed formulas can well predict the temperature of the upper flange of the steel beam in the PDCBs.

REFERENCES

[1] N. Loqman, N.A. Safiee, N.A. Bakar, N.A.M. Nasir. Structural Behavior of Steel-Concrete Composite Beam using Bolted Shear Connectors: A Review. MATEC Web of Conferences. 203 (2018), 6010

[2] T.T. Nguyen, K.H. Tan, I.W. Burgess. Behaviour of composite slab-beam systems at elevated temperatures: Experimental and numerical investigation. ENG STRUCT. 82 (2015), 199-213.

[3] Y. Li, M. Wang, G. Li, B. Jiang. Mechanical properties of hot-rolled structural steels at elevated Temperatures： A review. FIRE SAFETY J. 119 (2021), 103237.

[4] M. Wang, Y. Li, G. Li, W. Wang, B. Jiang. Comparative experimental studies of high-temperature mechanical properties of HSSs Q460D and Q690D. J CONSTR STEEL RES. 189 (2022).

[5] B. Jiang, G. Li, A. Usmani. Progressive collapse mechanisms investigation of planar steel moment frames under localized fire. J CONSTR STEEL RES. 115 (2015), 160-168.

[6] J. Martinez, A.E. Jeffers. Analysis of restrained composite beams exposed to fire. ENG STRUCT. 234 (2021), 111740.

[7] E.M. Aziz, V.K. Kodur, J.D. Glassman, M.E. Moreyra Garlock. Behavior of steel bridge girders under fire conditions. J CONSTR STEEL RES. 106 (2015), 11-22.

[8] M. Wu, S. Fan, H. Zhou, Y. Han, D. Liang. Experimental and numerical research on fire resistance of stainless steel-concrete composite beam. J CONSTR STEEL RES. 194 (2022), 107342.

[9] E.C. Fischer, A.H. Varma. Fire behavior of composite beams with simple connections: Benchmarking of numerical models. J CONSTR STEEL RES. 111 (2015), 112-125.

[10] D. Shi, X. Hu, H. Du, Z. Xie, Y. Meng. Study on shear performance of notched connections for glulam-concrete composite beams under fire. FIRE SAFETY J. 126 (2021), 103482.

[11] N. Loqman, N.A. Safiee, N.A. Bakar, N.A.M. Nasir. Structural Behavior of Steel-Concrete Composite Beam using Bolted Shear Connectors: A Review. MATEC Web of Conferences. 203 (2018), 6010.

[12] H.Y. Ban, J.W. Fan, L. Yang, Research advances and application prospects of deconstructable steel structures. The 27th China Academic Conference on Structural Engineering, (2018), pp. 8. (in Chinese)

[13] M. Tran, V.N. Van Do, T. Nguyen. Behaviour of steel-concrete composite beams using bolts as shear connectors. IOP conference series. Earth and environmental science. 143 (2018), 12027.

[14] H. Du, X. Hu, Y. Meng, G. Han, K. Guo. Study on composite beams with prefabricated steel bar truss concrete slabs and demountable shear connectors. ENG STRUCT. 210 (2020), 110419.

[15] J.W. Luo, H.Y. Ban, Y.Q. Yuan, Research advances of deconstructable composite beams and joints in full life cycle. The 17th Structural Stability and Fatigue Branch of China Steel Structure Association, (2021), 230-234. (in Chinese)

[16] H. Du, B. Zhang, X.M. Hu, L.Y. Kou, Y. Xia, Experimental study on shear behavior of bolt connectors in steel- concrete composite beams. Journal of Building Structures. 38 (2017), 308-314. (in Chinese)

[17] H.Y. Ban, J.W. Luo, Y.Q. Yuan, L. Yang, Research on mechanical behavior of shear connectors in deconstructable steel-concrete composite beams. Progress in Steel Building Structures, 24 (2022), 35-46.

[18] G.Q. Li, H.Y. Zhou, Experimental study on the fire-resistance of steel-concrete composite beams. China Civil Engineering Journal, 40 (2007), 19-26. (in Chinese)

[19] Chinese standard, Code for Fire Safety of Steel Structures in Buildings, GB51249-2017, China Architecture & Building Press, Beijing (2017). (in Chinese)

[20] Eurocode 4 Design of Composite Steel and Concrete Structures—Part 1-2: Structural Fire Design, EN 1994-1-2, CEN, Brussels (1994)

EXPERIMENTAL INVESTIGATION ON STEEL-REINFORCED CFST COLUMNS AFTER FIRE EXPOSURE

David Medall[1], Carmen Ibáñez[2], Vicente Albero[3], Andrés Lapuebla[4], Ana Espinós[5], Manuel L. Romero[6]

ABSTRACT

Steel-reinforced concrete-filled steel tubular (SR-CFST) columns may be an alternative to improve the fire resistance of concrete-filled steel tubular (CFST) columns, which is limited by the direct exposure of the outer steel tube to the heat source. In SR-CFST sections an open steel profile is embedded within the concrete infill of the CFST section. In a fire situation, this form of construction enhances the performance of the section since the inner steel profile is thermally protected by the surrounding concrete, thus delaying its degradation at high temperatures. In this experimental program, six SR-CFST specimens are tested. First, the specimens are uniformly exposed to high temperatures inside an electric furnace; then the post-fire resistance of the columns subject to increasing axial load is tested in a vertical frame. The SR-CFST specimens are grouped into two series comprising circular and square geometries respectively and, for the sake of comparison, the selected circular and square steel tubes utilised the same cross-sectional area of steel. The experimental results show the high ductility of the SR-CFST stub columns after heating, with the circular specimens reaching higher peak loads than the square columns. For each series, the peak load at post-fire increases as the size of the embedded steel profile does. RSI values are similar for both circular and square SR-CFST columns. Data indicate that, for circular columns confinement is still active in the post-fire situation, but the influence of the size of the embedded steel profile is not notable in the RSI.

Keywords: Steel-reinforced concrete-filled steel tubular columns; Post-fire behaviour; Residual strength

1 INTRODUCTION

Steel-reinforced concrete-filled steel tubular (SR-CFST) columns may be an alternative to improve the fire resistance of concrete-filled steel tubular (CFST) columns, which is limited by the direct exposure of the outer steel tube to the heat source. In SR-CFST sections an open steel profile is embedded within the concrete infill of the CFST section. In a fire situation, this form of construction enhances the performance of the section since the inner steel profile is thermally protected by the surrounding concrete, thus delaying its degradation at high temperatures.

[1] PhD student, Concrete Science and Technology Institute (ICITECH), Universitat Politècnica de València, Spain
e-mail: damemar@posgrado.upv.es, ORCID: https://orcid.org/0000-0001-9212-5326
[2] Associate Profesor, Concrete Science and Technology Institute (ICITECH), Universitat Politècnica de València, Spain
e-mail: caribus@upv.es, ORCID: https://orcid.org/0000-0002-9354-5637
[3] Associate Profesor, Department of Mechanical Engineering and Construction, Universitat Jaume I, Spain
e-mail: valbero@uji.es, ORCID: https://orcid.org/0000-0001-7193-9232
[4] Associate Profesor, Concrete Science and Technology Institute (ICITECH), Universitat Politècnica de València, Spain
e-mail: anlafer0@mes.upv.es, ORCID: https://orcid.org/0000-0001-9667-236X
[5] Lecturer, Concrete Science and Technology Institute (ICITECH), Universitat Politècnica de València, Spain
e-mail: aespinos@mes.upv.es, ORCID: https://orcid.org/0000-0001-7335-4676
[6] Full Profesor, Concrete Science and Technology Institute (ICITECH), Universitat Politècnica de València, Spain
e-mail: mlromero@mes.upv.es, ORCID: https://orcid.org/0000-0001-5247-4767

https://doi.org/10.6084/m9.figshare.22154264

Given their novelty, investigations into the behaviour of SR-CFST columns are still limited, particularly with regard to their fire and post-fire performance, but the many advantages of their application are making their study appealing for the research community. It is worth highlighting the tests performed at the University of Liège [1], those carried out in Shanghai [2, 3] and the tests conducted at Southeast University [4]. In the first experimental program, the fire resistance of ten slender composite columns was tested using self-compacting concrete. Four of the ten sections were SR-CFST (with an embedded HEB120 steel profile), combining circular and square shapes for the outer steel tube. The fire resistance times ranged from 39 up to 79 min for a load level of 0.4 thanks to the application of intumescent paint in some specimens. The maximum studied external dimension was 219.1 mm and for greater outer dimensions a complementary numerical study was carried by means of the software SAFIR.

In the works by Meng et al. [2, 3], fire resistance tests on eight SR-CFST columns were presented. The specimens combined square and circular geometries and, in this case, the effect of non-uniform heating was also considered. The columns were 1800 mm long although only the central 1200 mm were heated. The SR-CFST had an embedded HW150x150. The results of the experiments showed that the inner steel profile considerably enhanced the fire behaviour of the specimen, exceeding 240 min for the 1-side and 2-sides exposed columns. Lately, Mao et al. [4] also investigated the fire behaviour of SR-CFST columns but with cruciform section profiled steel. The specimens were tested under the ISO-834 standard fire and parameters including the shape of the outer steel tube (circular or square) or the load ratio were considered. Once more, it was found that the fire resistance of SR-CFST columns had substantial improvement compared with CFST columns.

Recently, the residual strength of SR-CFST stub columns after exposure to ISO-834 standard fire curve was assessed by Meng et al. [5], through a series of tests on non-uniformly heated columns. Three 600 mm long square specimens composed of an outer square steel tube of dimensions 300×300×6 mm and an inner steel profile HW150×150 were tested. The parameter studied was the number of sides exposed to the heating source, so the columns were 2, 3 and 4-sides exposed inside a small electric furnace, where a hysteretic pre-heat process was initially applied in order to approach the standard fire curve. Once cooled down, the columns were tested to failure to obtain their residual strength. As expected, the residual strength of the columns decreased with the fire exposure time. In general, a high ductility level was observed for the stub SR-CFST columns since they maintained their load bearing capacity reasonably constant after reaching the peak point instead of showing a sharp drop. Expressions for the residual strength after different types of fire exposure were presented based on parametric studies.

In view of the literature analysis, it can be seen that the number of available fire and post-fire test results on SR-CFST columns is scarce. Therefore, in this paper, the results of an experimental program on the behaviour of SR-CFST columns after fire exposure is presented.

2 EXPERIMENTAL PROGRAM

2.1 Column specimens

In this experimental program, six SR-CFST specimens are tested. The SR-CFST specimens are grouped into two series comprising circular and square geometries respectively (see Figure 1a and 1b). For the sake of comparison, the selected circular and square steel tubes utilised the same cross-sectional area of steel (with a maximum difference of a 2.51%).

a) b)

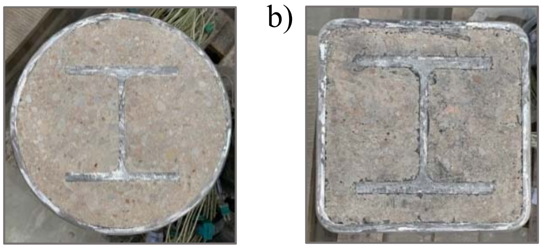

Figure 1. SR-CFST configurations analysed: a) circular; b) square

In Table 1, cross-sectional properties of all test specimens and other data corresponding to each series are summarized. For convenience, the test specimens were named as follows: SR-CFST-S-Ti (i.e. SR-CFST-C-T1), where S stands for the cross-sectional shape of the outer steel tube (C for circular and S for square); and Ti represents the type of embedded section, where T1 stands for HEB100, T2 for HEB120 and T3 for HEB140.

As summarised in Table 1, for the circular columns, ϕ273x10 steel tubes are employed as the external profile whereas the square steel tubes are #220x10. For the embedded steel profiles, three different sections are considered in both series: HEB100, HEB120 and HEB140.

Table 1. Specimens details

	Specimen	D or B (mm)	t_o (mm)	f_{yo} (MPa)	f_{uo} (MPa)	Inner section	f_{yi} (MPa)	f_{ui} (MPa)	f_c (MPa)	N_0 (kN)	N_{post} (kN)	RSI
	SR-CFST-C-T1	273	10	451	504	HEB100	315	445	24.3	8774	4799	0.547
	SR-CFST-C-T2	273	10	451	504	HEB120	308	437	24.3	9016	>5000	0.554*
	SR-CFST-C-T3	273	10	451	504	HEB140	315	441	24.3	9331	>5000	0.536*
	SR-CFST-S-T1	220	10	560	680	HEB100	315	445	24.3	7547	4153	0.550
	SR-CFST-S-T2	220	10	560	680	HEB120	308	437	24.3	7856	4615	0.587
	SR-CFST-S-T3	220	10	560	680	HEB140	315	441	24.3	8245	4896	0.594

Note: D and B are the outer diameter or dimension for circular and square sections respectively; t_o is the outer steel tube thickness; f_{yo} and f_{yi} are the yield strength of steel for the outer steel tube and inner embedded section respectively; f_{uo} and f_{ui} are the ultimate strength of steel for the outer steel tube and inner embedded section respectively; f_c is the concrete cylinder compressive strength; N_0 and N_{post} are the room temperature and post-fire ultimate load respectively; and RSI is the residual strength index.

2.2 Material properties

- Steel

In this experimental program, all steel tubes were cold-formed carbon steel and had a nominal yield strength of S355. Regarding the embedded steel profiles, all of them were hot rolled with a nominal yield strength of S275. In order to provide enough material for the coupon tests, extra material than strictly needed was supplied. For all the hollow steel tubes and embedded steel profiles, the actual values of the yield strength (f_{yo} and f_{yi}, respectively) and the ultimate strength (f_{uo} and f_{ui}, respectively) were determined through the corresponding coupon tests (three tests per tube) and are shown in Table 1. According to the European standards, the modulus of elasticity of steel was set to 210 GPa.

- Concrete

In order to obtain the actual compressive strength of concrete (f_c), the pertinent standard tests were carried out on the 100 mm cube. From the values of the strength of the cubic samples, the equivalent cylinder compressive strength was obtained according to Eurocode 2 [6], and is shown in Table 1. The sets of concrete samples were prepared in a planetary mixer and cured in standard conditions during 28 days. The day when the experiment of a certain specimen was going to be performed, the corresponding samples were tested.

3 TEST SETUP AND PROCEDURE

The first step of the experiments consisted on heating the SR-CFST specimens, which were uniformly exposed to high temperatures inside the furnace. After cooling at room temperature, the post-fire resistance of the columns subject to increasing axial load was tested in a vertical frame.

3.1 Thermal test setup

For the thermal tests, a small electric furnace of 10000 W power was used. The furnace has an inner diameter of ϕ400 mm, consisting of two semicylinders joined by a hinge. On the inner refractory wall of each semicylinder, the electric elements are distributed evenly in parallel layers through the whole cylinder length for both sides, as can be seen in Figure 2.

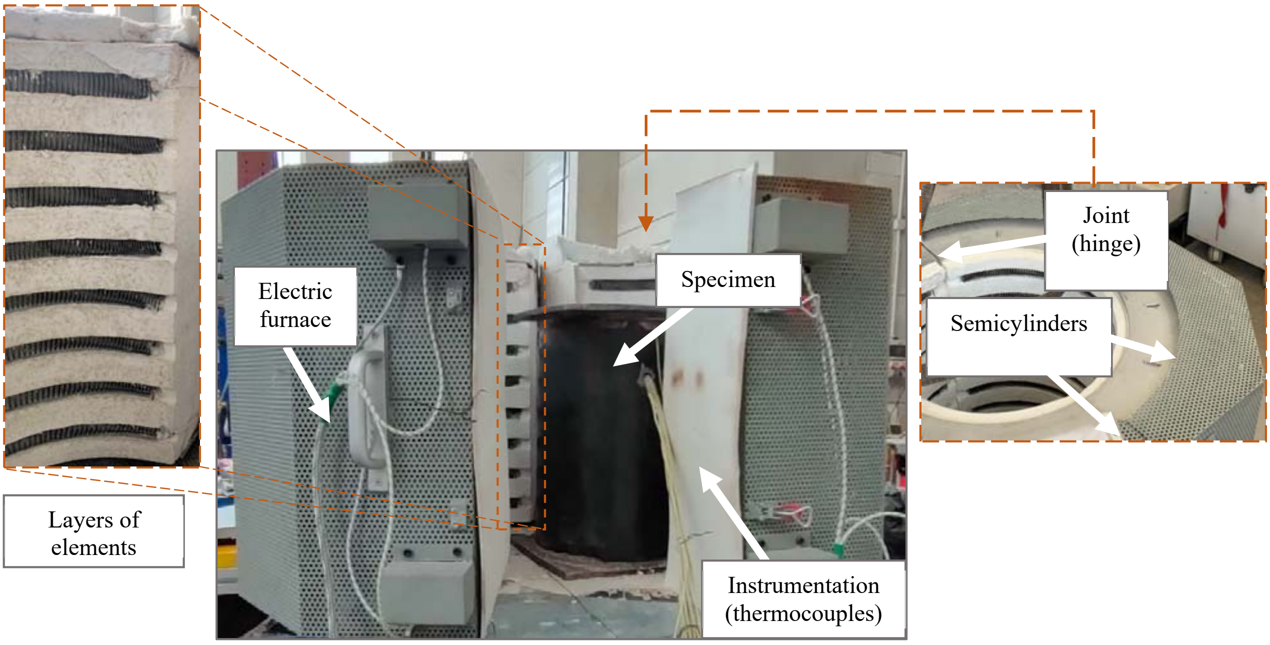

Figure 2. Thermal test setup

To register the temperature evolution during the thermal test, a set of 12 thermocouples were positioned at the mid-length of the section following the layout presented in Figure 3. Thermocouples number 1 and 6 were welded to the outer steel tube surface and thermocouples number 7, 8, 9 and 10 were welded at different points of the embedded steel profile. The rest of the thermocouples were embedded in the concrete core. Thermocouples number 2, 3 and 4 were place equidistantly, with a separation of 1/6 of the section width, and number 5 was positioned at 1/4 of the section width.

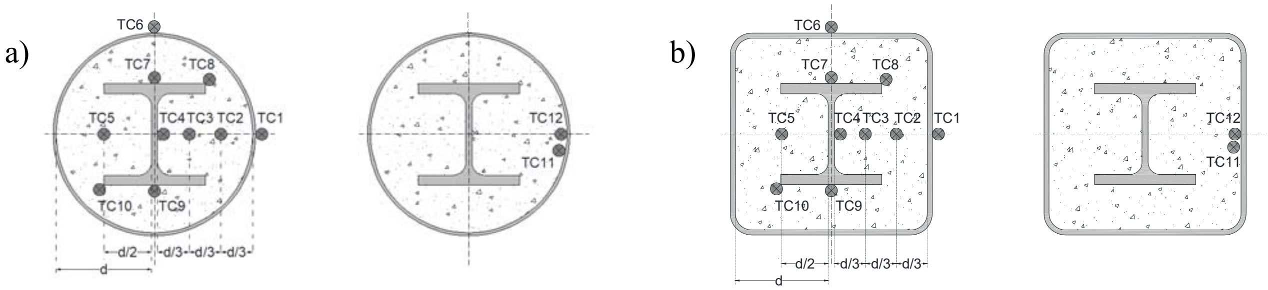

Figure 3. Thermocouples layout: a) circular sections; b) square sections.

3.2 Post-fire test setup

The second part of the experiments consisted of testing the post-fire resistance of the columns subject to increasing axial load. For that purpose, a vertical testing frame with a hydraulic jack with capacity of 5000 kN was employed as shown in Figure 4 together with the setup of one of the experiments. All the columns had a length of 400 mm with pinned-fixed (P-F) boundary conditions during the experiment. The tests were monitored by means of four LVDTs placed at the four sides of the column to register the top end axial displacemtent and with two sets of strain gauges attached to the four sides of the column in the longitudinal and transversal directions.

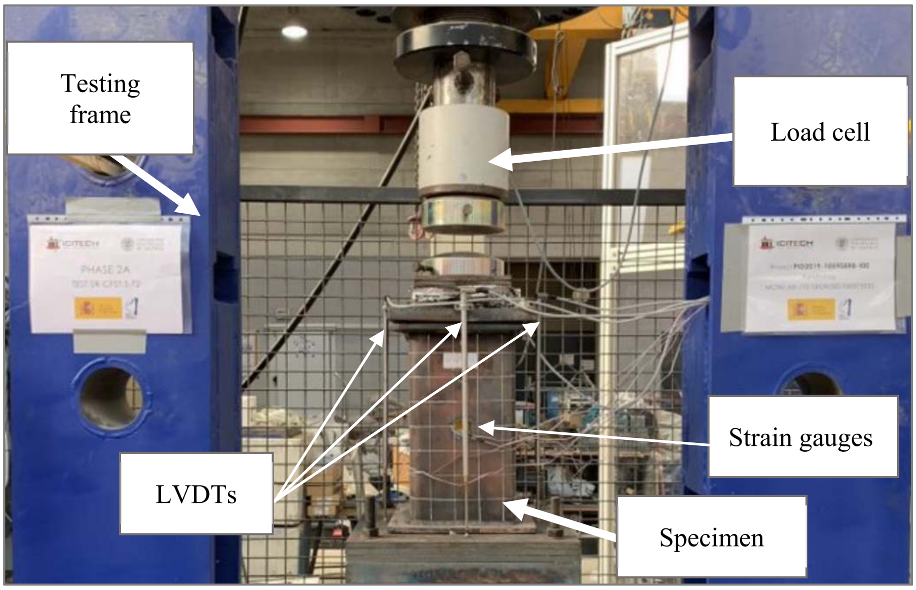

Figure 4. Post-fire test setup

3.3 Test procedure

All the columns were prepared and tested at the Concrete Science and Technology Institute (ICITECH), at Universitat Politècnica de València (Spain). At both ends of each specimen, steel plates with dimensions 300x300x10 mm were placed. First, a steel plate was welded to the bottom of the embedded steel profile. Next, the thermocouples were positioned together with the hollow steel tube in order to correctly place the wires. A hole was drilled at the top end of the columns for this purpose and to allow vapour ventilation during heating. Later, the bottom of the hollow steel tube was welded to the steel plate. Once the column was filled with concrete and it was settled with the help of a needle vibrator, the specimen was covered with a plastic film. Finally, the second plate was welded to the top end of the column right after smoothing the top surface in order to assure planarity and the contact of the steel plate with all the components.

The circular and square SR-CFST columns were first heated unloaded in the described electric furnace, since this condition is considered to be more conservative in the evaluation of the residual strength of concrete after heating [7-9]. To prevent heat loss, both top and bottom surfaces were protected with fibre blankets. The furnace temperature target was set to 1000 ºC to guarantee that the embedded steel profile, in all the cases, had a significant reduction in its mechanical properties. Due to the electric furnace power specifications, this led to heating times higher than 240 min for all the specimens. Once the target temperature was attained, the electric furnace was switched off and it was opened so that the specimen cooled at ambient temperature. During the heating and part of the cooling process the temperatures of the furnace and specimens were registered (Figure 5).

Once the specimen had cooled down (Figure 6a), the experiment continued with the compression test to obtain the residual strength of the SR-CFST column after heating. As part of the pertinent displacement control test, at the start of each experiment and right after the correct positioning of the specimen, data from the four LVDTs were monitored to assure that the columns were, in fact, axially loaded and that the compression was uniformly applied. The load cell allowed to measure the applied load during the test, being the loading rate 0.1mm/min. During the loading process, the applied axial load was monitored and recorded together with the evolution of the axial displacement of the columns, showing its shortening due to the applied load (Figures 6b, 7 and 8).

4 TEST RESULTS AND DISCUSSION

4.1 Cross-sectional temperatures

The registered temperatures during the heating process are shown in Figure 5. For the sake of clarity only the data of four of the thermocouples are displayed together with the evolution of the furnace temperature.

a) Circular sections b) Square sections

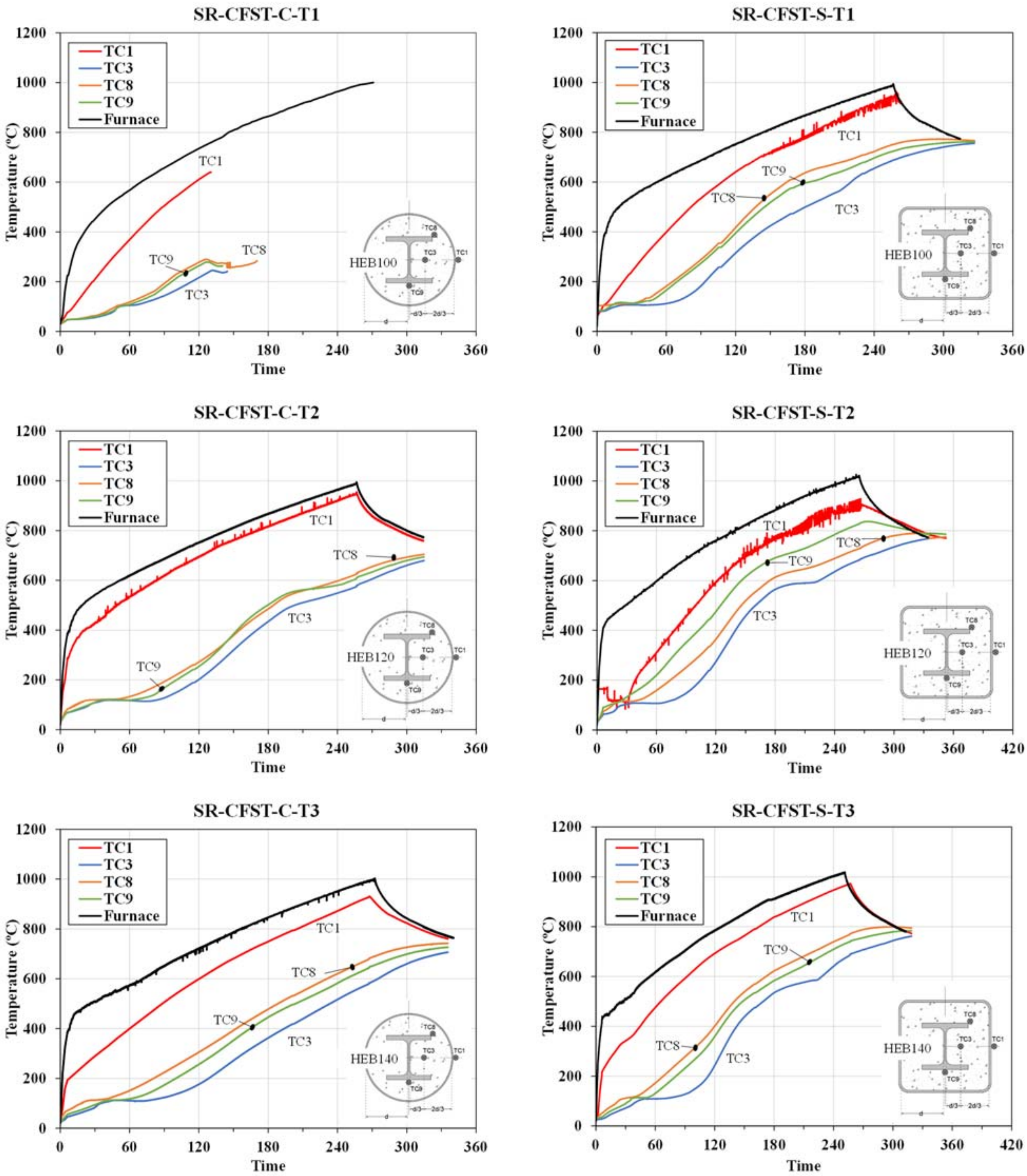

Figure 5. Cross-sectional temperatures

Note that for specimen SR-CFST-C-T1, temperatures are missing from 120 min on for TC1, from 150 min on for TC3 and TC9; and from approximately 180 min on for TC9, because the corresponding thermocouples and the data acquisition system failed during the test.

As observed in Figure 5, temperatures are generally higher for the square SR-CFST columns than for the corresponding circular columns, which may be explained with the effect of the section factor, since for the same cross-sectional area, the square sections present a higher exposed perimeter. For both series, the delay of temperature rise in the concrete core can be observed. The thermal protection provided by the outer steel tube together with the low thermal diffusivity of concrete are responsible for this effect.

For each series, it can be seen that in the specimens SR-CFST-C-T3 and SR-CFST-S-T3, the embedded steel profile, HEB140, reaches higher temperatures than the other two types of sections. For the same external dimensions, the greater the embedded steel profile, the less the concrete cover that protects the profile. In Figure 6a the state of all the columns after the thermal test is shown.

Figure 6. Columns after the thermal and the post-fire mechanical test

4.2 Failure mode

Figure 6b displays the state of all the columns after the post-fire mechanical tests, where the columns are highly damaged and cracked due to the high level of compression achieved during the mechanical test. As shown in Figure 6b, the columns at failure developed the characteristic elephant foot due to local buckling of the outer steel tube, especially the square specimens. As pointed out by Meng et al. [5], this phenomenon is caused by the different thermal expansion of the different materials and the uneven temperature field, which enables the steel tube to support the increasing axial load and yield. In the case of the tested columns, the outward bulges appeared near the columns' top end, which may be due to the fact that it is on this end where the hole for water evaporation was drilled. Also, the ball joint of the load cell is located at this side, facilitating the folding of the steel tube closer to the top end.

In Figure 7, the graphs show the axial load versus axial displacement histories for both series of columns. The initial response was mostly linear elastic up to approximately 65-70% of the peak load (N_{post}), which is concordance to the response observed by other authors [5]. The columns then enter the plastic range and the stiffness of the columns decreased gradually. Finally, the specimens achieved the peak load which kept constant for a significant period instead of presenting a sharp drop, showing the high ductility of the columns. For all the tests, Table 1 shows the peak load registered during the experiments.

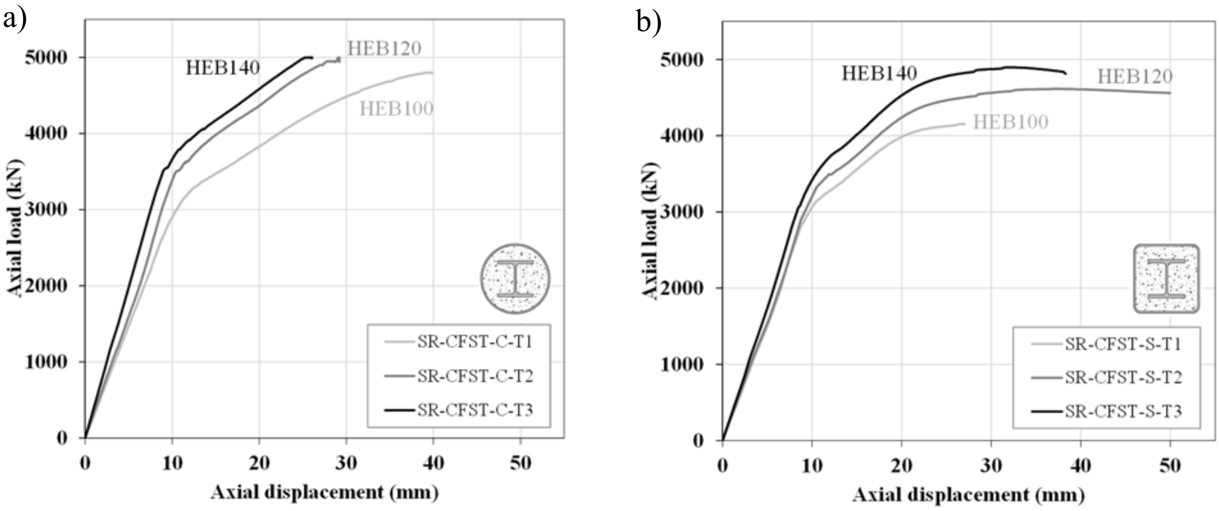

Figure 7. Axial load-displacement curves: a) circular sections; b) square sections.

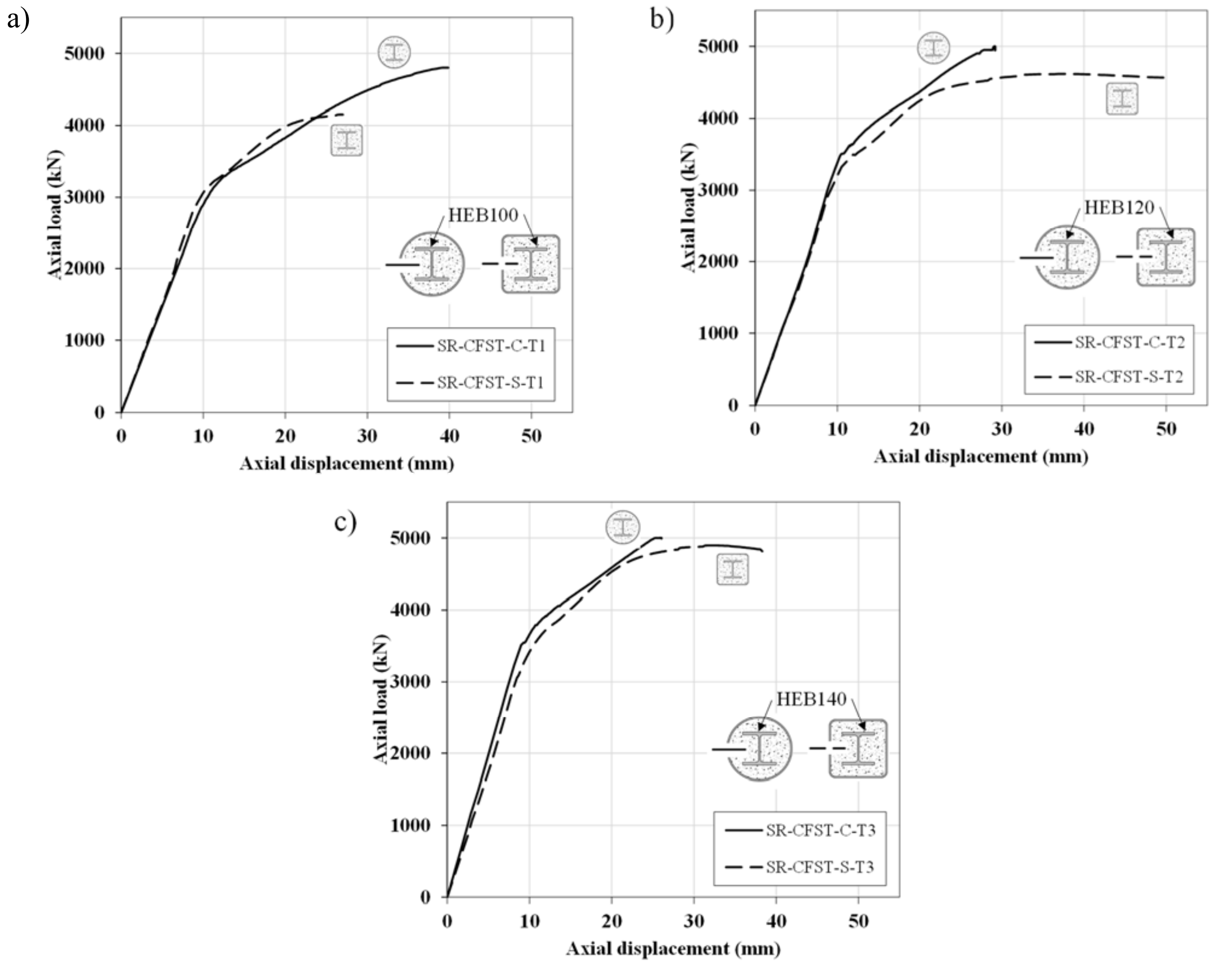

Figure 8. Axial load-displacement curves for different embedded profiles: a) HEB100; b) HEB120, c) HEB140.

Note that in Figure 7a, for columns SR-CFST-C-T2 and SR-CFST-C-T3, the tests were manually paused due to the technical limitations of the vertical frame (5000 kN) and this fact did not allow to register the maximum load experimentally (see also column N_{post} in Table 1).

In general, circular SR-CFST columns had higher peak loads than their square counterparts. For each series, the peak load at post-fire increased as the size of the embedded steel profile did, being the maximum values for the specimens with and embedded HEB140 (Figure 8).

4.3 Residual strength index (RSI)

To quantify the loss of load bearing capacity experienced by the columns after being exposed to high temperatures, the residual strength index (RSI) is calculated. The approach proposed by Han et al. [10] has been adopted, where RSI is defined as:

$$RSI = \frac{N_{\text{post}}}{N_0} \tag{1}$$

where N_0 and N_{post} are the room temperature and post-fire ultimate load respectively.

For the calculation of N_0 the next equations are used. In the case of square SR-CFST sections, confinement at room temperature is neglected. Therefore, N_0 is calculated as follows:

$$N_0 = A_a f_{uo} + A_c f_c + A_s f_{ui} \tag{2}$$

where A_a and f_{uo} are the cross-sectional area and the ultimate strength of the steel tube; A_c and f_c are the cross-sectional concrete area and the compressive cylinder strength of concrete; and A_s and f_{ui} are the cross-sectional area and the ultimate strength of the embedded steel profile.

However, in the case of circular sections, the expression of clause 6.7.3.2 of Eurocode 4 Part 1-1 [11] for the plastic resistance to compression of CFST sections is adapted in order to consider the effect of confinement in the ultimate load at room temperature for SR-CFST columns. This is given by:

$$N_0 = \eta_a A_a f_{uo} + A_c f_c \left(1 + \eta_c \frac{t}{D} \frac{f_{uo}}{f_c}\right) + A_s f_{ui} \tag{3}$$

where t is the wall thickness of the steel tube; D refers to the external diameter of the column; and η_a and η_c are the factors related to the confinement of concrete. For axially loaded members, with e/D<0.1 and relative slenderness $\bar{\lambda}$<0.5, these factors are given by:

$$\eta_a = 0.25\left(3 + 2\bar{\lambda}\right) \tag{4}$$

$$\eta_c = 4.9 - 18.5\bar{\lambda} + 17\bar{\lambda}^2 \tag{5}$$

Note that Eurocode 4 Part 1-1 [11] uses the design value for the yield strength of steel and for the concrete compressive strength, which in this investigation have been replaced for the actual values of the ultimate strength of steel and the actual concrete cylinder compressive strength derived from the material tests and reported in Table 1.

For all the columns, the values of the RSI are calculated and summarised in Table 1. For the circular SR-CFST columns, account for the confinement has been made. Note that for columns SR-CFST-C-T2 and SR-CFST-C-T3, the values of the RSI in Table 1 appear marked with * since they have been calculated assuming a N_{post} of 5000 kN, but the real values for those RSI would be slightly higher.

Figure 9 illustrates the RSI values for both series. Generally, the RSI has the same order of magnitude for both circular and square columns, all of them around 0.55-0.60. The fact that the loss of capacity is similar for both shapes, implies that confinement, which has been considered for the calculation of N_0 in circular columns, is still active in the post-fire situation. For the square SR-CFST columns, the difference between the RSI values of all the columns is not very important (7.4% and 1.2% with respect to the lowest value of

0.55 corresponding to SR-CFST-S-T1). This can be due to the fact that the higher degradation of the larger inner steel profiles (less concrete cover to protect them from fire) compensates somehow with the greater cross-sectional area of the profile, thus leading to values of RSI quite similar for all of the specimens.

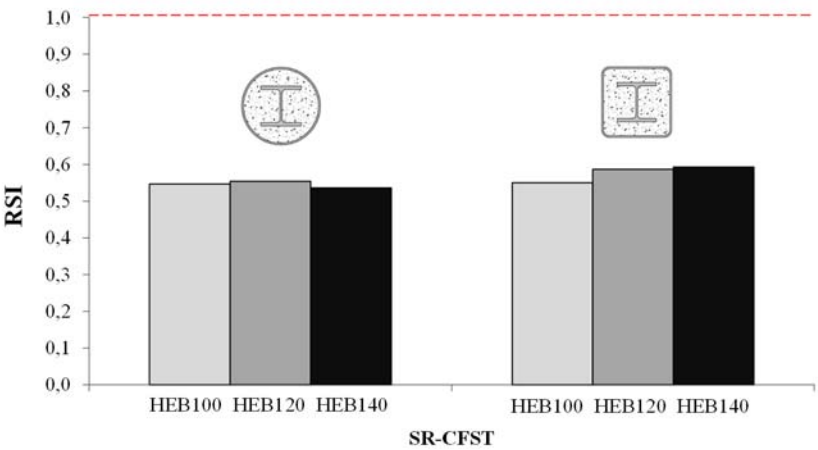

Figure 9. Residual strength index (RSI)

5 CONCLUSIONS

Through the experimental investigation described in this paper, the mechanical response of stub SR-CFST columns after heating has been studied. The evolution of the cross-sectional temperatures with time and the axial load versus axial displacement histories were analysed. Six SR-CFST specimens were tested. First, the columns were uniformly heated inside an electric furnace; then, the post-fire resistance of the columns subject to increasing axial load was tested in a vertical frame. According to their external shape, the columns were grouped into two series comprising circular and square geometries respectively and, for the sake of comparison, the selected circular and square steel tubes utilised the same cross-sectional area of steel (with a maximum difference of a 2.51%). From this study, some conclusions can be drawn:

- Temperatures are generally higher for the square SR-CFST columns than for the corresponding circular columns, which may be due to the effect of the higher section factor of square columns.
- For the same external dimensions, the larger the embedded steel profile, the higher the temperatures reached. This is because the bigger the embedded steel profile, the less the concrete cover that protects the profile from heating.
- The experimental results show the high ductility of the SR-CFST stub column after heating, with the circular specimens reaching higher peak loads than the square columns. For each series, the peak load at post-fire increases as the size of the embedded steel profile does.
- RSI values are similar for both circular and square SR-CFST columns, but the influence of the size of the embedded steel profile is not notable. For circular columns confinement is still active in the post-fire situation.

ACKNOWLEDGMENTS

The authors would like to express their sincere gratitude for the help provided through the Grant PID2019-105908RB-I00 and for the first author's pre-doctoral contract through the Grant PRE2020-093106 funded by MCIN/AEI/ 10.13039/501100011033 and by "ESF Investing in your future". The authors would like to thank Dr Enrique Serra (https://orcid.org/0000-0002-8823-6450) for his help and assessment to prepare and conduct the experiments and Dr David Pons (https://orcid.org/0000-0002-9034-9550) for his help in conducting the material tests.

REFERENCES

1. Dotreppe, J.C., Chu, T.B. & Franssen, J.M., Steel hollow columns filled with self-compacting concrete under fire conditions. Proceedings of the 3rd Congress of the International Federation for Structural Concrete (FIB) and PCI Conference (2010).
2. Meng, F-Q., Zhu, M-C., Clifton, G.C., Ukanwa, K.U. & Lim, J.B.P., Performance of square steel-reinforced concrete-filled steel tubular columns subject to non-uniform fire. J Constr Steel Res, vol. 166, 105909, (2020). https://doi.org/10.1016/j.jcsr.2019.105909
3. Meng, F-Q., Zhu, M-C., Clifton, G.C., Ukanwa, K.U. & Lim, J.B.P., Fire performance of edge and interior circular steel-reinforced concrete-filled steel tubular stub columns. Steel Compos Struct, vol. 41, 115–22, (2021). https://doi.org/10.12989/scs.2021.41.1.115
4. Mao, W-J., Wang, W-D., Zhou, K. & Du, E-F., Experimental study on steel-reinforced concrete-filled steel tubular columns under the fire. J Constr Steel Res, vol. 185 (2021). https://doi.org/10.1016/j.jcsr.2021.106867
5. Meng, F-Q., Zhu, M-C., Mou, B. & He, B., Residual strength of steel-reinforced concrete-filled square steel tubular (SRCFST) stub columns after exposure to ISO-834 standard fire. Int J Steel Struct, vol. 19, 850–66, (2019). https://doi.org/10.1007/s13296-018-0174-z
6. CEN EN 1992-1-1, Eurocode 2: Design of concrete structures. Part 1.1: General rules and rules for buildings. Brussels, Belgium: Comité Européen de Normalisation (2004).
7. Hertz, K.D., Concrete strength for fire safety design. Mag Concr Res, vol. 57(8), 445-53, (2005). https://doi.org/10.1680/macr.2005.57.8.445
8. Huo, J.S., Huang, G.W. & Xiao, Y., Effects of sustained axial load and cooling phase on post-fire behaviour of concrete-filled steel tubular stub columns. J Constr Steel Res, vol. 65, 1664-76, (2009). https://doi.org/10.1016/j.jcsr.2009.04.022
9. Liu, F., Gardner, L. & Yang, H., Post-fire behaviour of reinforced concrete stub columns confined by circular steel tubes. J Constr Steel Res, vol. 102, 32-103, (2014). http://dx.doi.org/10.1016/j.jcsr.2014.06.015
10. Han, L., Huo, J. & Wang, Y., Compressive and flexural behaviour of concrete filled steel tubes after exposure to standard fire. J Constr Steel Res, vol. 61(7), 882-901, (2005). http://dx.doi.org/10.1016/j.jcsr.2004.12.005
11. CEN EN 1994-1-1. Eurocode 4: Design of composite steel and concrete structures. Part 1.1: General rules and rules for buildings. Brussels, Belgium: Comité Européen de Normalisation (2004).

FIRE TESTS ON STEEL-TIMBER COMPOSITE BEAMS

Antoine BÉREYZIAT[1], Dhionis DHIMA[2], Sébastien DURIF[3], Maxime AUDEBERT[4], Abdelhamid BOUCHAÏR[5], Amir SI LARBI[6].

ABSTRACT

The fire resistance and the thermomechanical behaviour of Steel-Timber Composite (STC) beams are studied through 4 fire tests. 35 non-loaded reduced specimens and 2 mechanically loaded real-scale beams are tested considering standard fire conditions (ISO 834 temperature-time curve). They consist in various steel profiles associated with timber elements in such a way that steel is fully or partially protected from fire. Timber is used as a fire protective material since it has a low conductivity and a low charring rate. Fire tests on non-loaded reduced specimen allow to investigate a wide variety of configurations, and to identify key parameters. It is found that full timber protection is very efficient as steel remains below 250°C during 35 or 70 minutes when timber protection is respectively 30 or 50mm thick. Moreover, timber moisture is found to have a beneficial impact on steel temperature, while hollow sections favour timber combustion and steel heating during the cooling phase. Full-scale mechanically loaded fire tests highlight the importance of assembly joints, because deflexion can open it, which accelerate the heating of steel. Finally, an 81 min fire resistance is measured for a STC beam with 45mm timber protection. These finding contribute to better understand the behaviour of steel-timber structural elements in fire situation. It appears that judicious mixing of timber and steel can lead to improved performances in both normal and fire situations. The presented results can be used to improve the design of STC beams.

Keywords: Steel; timber; composite; fire tests; STC beams.

1 INTRODUCTION

The use of timber as a fire protective material for steel may seems counter-intuitive considering the combustible nature of wood. Nevertheless, it is also an insulating material whose charring rate is low and well known (about 0.65mm/min for softwood according the EN 1995-1-2). Therefore, it is possible to use timber to protect a steel structure from fire during a certain period of time, which depends on the thickness of the timber elements used. It is partly for this reason that the use of steel-timber beams (flitch beams) was proposed as early as the 19th century [1].

[1] Ph. D., ENISE, ADEME
e-mail: antoine.bereyziat@enise.fr, ORCID: https://orcid.org/0000-0002-1223-9735
[2] Senior Researcher, CSTB
e-mail: dhionis.dhima@cstb.fr, ORCID: https://orcid.org/0000-0002-3372-5759
[3] Associate professor., UCA
e-mail: sebastien.durif@uca.fr, ORCID: https://orcid.org/0000-0002-1202-4179
[4] Associate professor, ENISE
e-mail: maxime.audebert@enise.fr, ORCID: https://orcid.org/0000-0003-2974-468X
[5] Full professor, UCA
e-mail: abdelhamid.bouchair@uca.fr, ORCID: https://orcid.org/0000-0003-2179-421X
[6] Full professor, ENISE
e-mail: amir.si-larbi@enise.fr, ORCID: https://orcid.org/0000-0002-4532-7512
https://doi.org/10.6084/m9.figshare.22154372

This idea is tested in Netherlands in 1974 by Twilt and Witteveen [2]. They seek to design a solution that is efficient, lightweight, and resistant. They also want to minimize the amount of fuel available, because they are concerned that the combustion of timber could cause the steel to heat up critically. They choose a solution consisting in encasing the steel profiles they wish to protect using the thinnest timber boards possible. They test two 3.40m columns, which are mechanically loaded and exposed to a standard fire corresponding to the ISO 834 curve. They show that a 28mm thick wood protection, despite being combustible, has a strong influence on the fire resistance of steel profiles, increasing it to durations between 50 and 60 minutes. They note that steel profiles heat up heterogeneously due to local perforations of the timber protection caused by combustion.

This protection principle reappears in the 2000s in Japan, but the studied configurations include much more massive timber elements, and timber pieces embedded between the flanges of fire protected steel profiles [3 – 6]. Sakamoto et al. [6] give their conclusions on the fire tests conducted in these studies. They indicate that configurations with a 60mm timber thickness have a guaranteed fire resistance of one hour. They highlight the fact that the tested beams and columns show a "self-extinguishing" behaviour [6,7], without "re-ignition, progress of char, or a rise of temperature" during the cooling phase [6]. Indeed, at the end of the fire exposure, the temperature of steel does not rise again, and remains around 100°C for several hours [4,5]. This suggests that the wood combustion is stopped or too low to induce an increase in the temperature of steel. In addition, the tested elements are found to be able to withstand the applied load during and after fire exposure.

These studies have made it possible to construct several buildings in Japan, where timber is used as a fire protective material for steel structures between two and seven stories high [7,8].

More recently, the fire resistance of steel-timber composite elements has been studied further and has been developed to involve other materials. For example, Jang et al. [9] performed fire tests on 3.5m steel columns glued with 60mm thick glulam covers. The temperature of steel remains under 100°C for configurations with timber between the flange of the steel profile, and a one-hour fire resistance is confirmed. A hollow configuration with gypsum in it is found to be less effective as the temperature of steel reach 170°C after a one-hour fire exposure. Jang et al. point out that timber and gypsum do not only act as insulating elements since the moisture they contain actively affects the temperature of the protected steel profile. Finally, Riola Parada et al. [10] test cold-formed steel profiles embedded between two glulam beams (GL24) and associated with a reinforced concrete compression flange. The timber elements covering steel profiles are at least 50mm thick, and the two test specimens are subjected to a standard fire (ISO 834) for 90 minutes without mechanical loading. This fire exposure time is longer than those considered in the studies carried out so far, while the thickness of the protective timber is comparable or even lower. Riola Parada et al. measure temperatures around 500°C in steel after 83 minutes of exposure to a standard fire. Authors consider that this temperature is significant because "at this temperature, the steel has already lost 50% of its load capacity" [10].

Therefore, literature shows that the association of timber and steel can be beneficial in fire situation as timber can be used as fire protection for steel, but it can also be interesting at room temperature. Indeed, studies suggest that STC (Steel-Timber Composite) elements allow mutual mechanical reinforcement of both steel and timber components [11 – 14]. Thus, STC beams have a great potential, both in normal and fire situations.

This study aims to use tests results to better understand the behaviour of STC beams in fire situation. It is proposed to investigate it through two bending tests conducted in standard fire conditions. The thermomechanical study is supplemented by two fire tests on non-loaded reduced specimens (0.8m long).

2 TEST FACILITIES

Fire tests are conducted in the CSTB[7] laboratories. The used test furnace (Figure 1) has a 3.0 x 4.0 m footprint and reproduces a standard fire following the ISO 834 heating curve by means of eight gas burners. The temperature in the furnace chamber is measured using plate thermometers. The test protocols conform to the European standard EN 1363-1 [15]. Both mechanically loaded (bending) and non-loaded fire tests are performed. Bending tests on STC beams at room temperature are conducted at the Pascal Institute[8] to complement the study.

Figure 1. Test furnace (thermal test on reduced specimens).

3 THERMAL TESTS ON REDUCED SPECIMENS

3.1 Test specimens

33 non-loaded specimens are tested in two separate fire tests. They are 80cm long and are made from steel plates or from IPE 120, IPE 300, or HEA 140 profiles, which are pre-drilled at their extremities and then connected by screwing with timber elements, arranged in such a way that steel is partially or completely protected from fire (Figure 2). A total of 18 distinct configurations are tested:

- Configurations D, F, G, H, J, L, N, O, and Q are tested during test n°1 and are all duplicated (18 specimens), fire protective timber has a 30mm thickness (Figure 2), and the fire exposure period is 34 minutes.
- Configurations A, B, C, E, K; I, M, P and R are tested in test n°2 and are all duplicated except for A, B and C (15 specimens), fire protective timber has a 50mm thickness (Figure 2), and the fire exposure period is 68 minutes.

In order to limit assembly clearances, timber and steel parts are clamped together during the assembly process. Configurations are classed into families based on the nature of the steel components they comprise (Table 1).

Table 1. Configuration types

Configurations	Steel component	Specimens
A B C	IPE 300	3 (A, B, C)
D E F	Steel plate 120 x 4mm	6 (D1, D2, E1, E2, F1, F2)
H I J	IPE 120	6 (H1, H2, I1, I2, J1, J2)
L M N O P Q R	HEA 140	14 (L1, L2, M1, M2, N1, N2, O1, O2, P1, P2, Q1, Q2, R1, R2)
G K	Timber only	4 (G1, G2, K1, K2)

[7] https://www.cstb.fr/en/test-facilities/fire-testing/

[8] http://www.institutpascal.uca.fr/index.php/en/presentation-m3g / https://msgc-cust.fr/equipements/

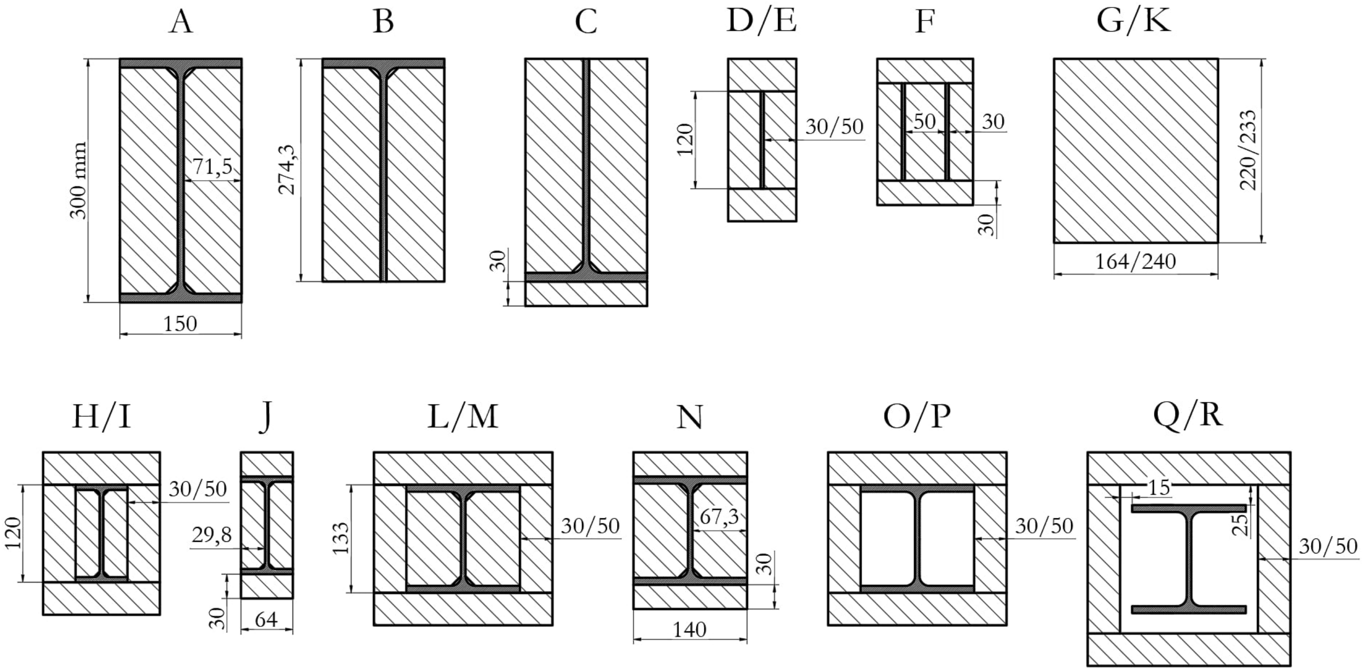

Figure 2. Sections of reduced specimens (80cm long).

Timber used to make the test specimens is sourced from two different suppliers. The moisture content on dry basis of the used timber is determined in accordance with the EN 13183-1 [16], by oven drying some samples (Table 2). The obtained ranges of values are corroborated by 113 measurements carried out with a spike moisture meter. The density of timber is also measured on this occasion (Table 2).

Table 2. Timber properties (tests on reduced specimens).

Timber	Specimens	Basic wood density [kg/m^3] (avg. / SD)	Dry wood density [kg/m^3] (avg. / SD)	Moisture content on dry basis [%] (avg. / SD)	Number of measurement samples
Test n°1 softwood lumber	D2, F2, H2, J2, L2, N2, O2, Q2	459 *(calculated)*	407 / 50.4	12.8 / 0.7	3
Test n°1 GL28h (Spruce)	D1, F1, G1, G2, H1, J1, L1, N1, O1, Q1	455 *(calculated)*	409 / 53.3	11.3 / 0.4	2
Test n°2 softwood lumber	E2, I2,	448 / 40.4	423 / 39.5	11.3 / 0.6	8
Test n°2 GL28h (Spruce)	A, B, C, E1, K1, K2, I1, M1, M2, P1, P2, R1, R2	455 / 43.2	430 / 42.5	10.7 / 0.3	7

3.2 Test setup

Test specimens are suspended from the cover slabs of the test furnace by means of threaded rods welded to the steel components. They are arranged so that specimens A, B and C are exposed on three sides (the upper side being protected by a slab), and all others on four sides (Figure 3). Extremities of specimens are protected by a mineral insulation which also covers the heads of the fastening screws.

At the end of the exposure to the ISO fire, specimens are not extinguished, because we wish to observe how the timber continues to burn or not during the cooling phase. We also want to check whether the burning of the timber constituting the specimens causes an increase in the temperature of the steel components to such an extent that their structural integrity is threatened during the cooling phase. Therefore, the analysis is divided between the observation of the fire exposure phase and the cooling phase.

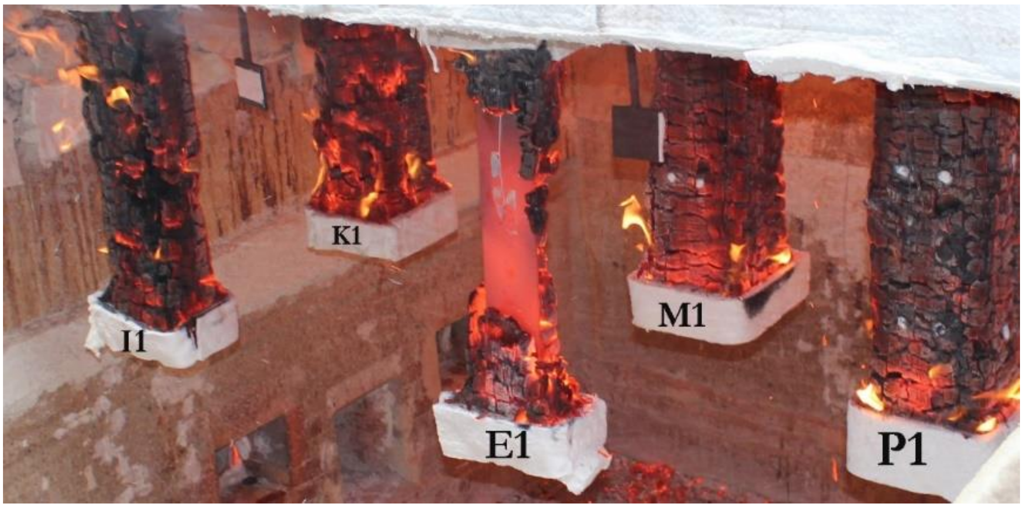

Figure 3. Test n°2 – specimens exposed on four sides.

Some of the test specimens are removed from the furnace after the fire exposure while the others are left to cool inside. In this way, two very different cooling conditions are tested which allow the observations to be nuanced. Indeed, test specimens removed from the furnace are exposed to a relatively cool but largely ventilated environment, whereas those left in the furnace, which is closed, are subjected to a warmer environment and a weaker ventilation. The specimens which stay in the furnace are subjected to residual thermal solicitations generated by the refractory walls of the furnace, and to moderate ventilation generated artificially to cool the furnace down over several hours. The drawback of this approach is that it does not allow direct assessment of the charring rate of the timber composing the specimens, since this would require extinguishing them as soon as the furnace is shut down, and then measuring the residual timber sections.

The temperature of steel is measured at flanges (f) and the web (w) of each profile constituting the test specimens. For this purpose, type K thermocouples with a copper disc head are used (Figure 4). Wires are insulated with a 400°C resistant glass silk and are routed through the interior of the test specimens thanks to notches made in timber. The head of thermocouples is held in place by aluminium adhesive tape and then by the timber elements themselves, which are notched so that the copper disc heads are maintained against the steel. When steel surfaces are not covered with timber, thermocouples head are welded against the steel profile (Figure 4). The measured values do not show any singular evolution of the temperature above 400°C, so the measured temperature curves are considered in their entirety. Only one measurement requires the thermocouple wires to be passed through the fire, a shielded thermocouple capable of withstanding these conditions is then used.

Figure 4. Test n°2 - specimen P2 - thermocouples n°3 and n°17, respectively used for temperature measurement on the web and on the flange of the steel profile.

3.3 Results and discussion

Due to the large number of tested specimens, only major findings are exposed on this paper, but comprehensive results can be found in [17].

3.3.1 Fire protection of steel using timber during fire exposure

Firstly, the temperature curves obtained experimentally show that the thermal protection provided by timber is very effective. Fully protected configurations allow steel to be held below 250°C for over 34 minutes when using 30mm thick timber protection boards (Figure 5 – L1 and O1). This duration increases to over 68 min for 50mm boards (Figure 6 – M1 and R1). Steel remains intact during this time. For comparison, an unprotected steel section of this type can reach a temperature of 600°C after 13 min only, which can be considered as a critical temperature under certain conditions (degree of utilisation = 45% according to the EN 1993-1-2). Figure 5 and Figure 6 show that hollow configurations (O1 and R1) have an efficiency that is comparable to that of timber filled configurations (L1 and M1). It is clear that the proposed method for protecting steel with timber can largely achieve an R30 fire resistance rating using 30mm thick cladding, and R60 when 50mm thick boards are used.

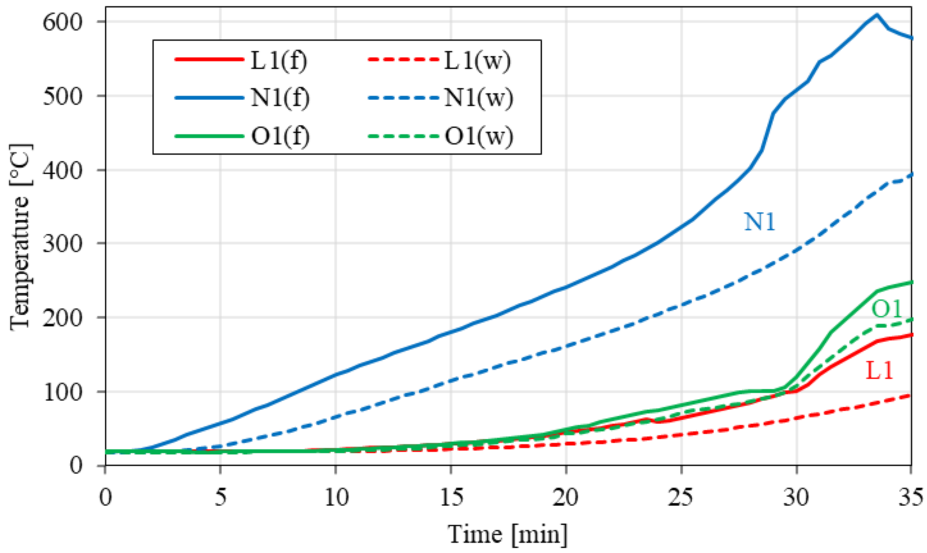

Figure 5. Test n°1 - temperature evolution of the flange (f) and the web (w) of HE140 steel profiles partially (N1) or fully (L1 and O1) protected by 30mm thick timber pieces.

Secondly, Figure 5 shows that configurations that are partially exposed to fire (N1) perform less well than those that are fully protected (L1 and O1). However, they do have some effectiveness, as the temperatures measured in steel remain below 500°C for approximately 30 minutes. If the steel profile was not protected at all, it would reach this temperature after 10 minutes only. It can be seen that the thermal field in the steel profile is very heterogeneous, with differences up to 200°C being observed between the flange and the web (Figure 5 – N1).

Thirdly, there is a "temperature dwell" [18] at 100°C for several minutes on some curves of Figure 5 and Figure 6, which reflects the beneficial action of the moisture contained in timber. A non-negligible proportion of it accumulates against steel [19 – 21] as a result of the mass transfers that occur within timber during its combustion [18]. The high enthalpy of vaporization of water causes the steel temperature to stay around 100°C until it is completely evacuated. This results in a slowing down of the heating of steel which is not negligible. The hollow configurations (O1 and R1), show a particularly marked temperature dwell, for about 10 minutes (Figure 6), which reflects the action of the vapour trapped in the timber casing. The sealing of the latter is therefore an important factor. However, there is no such temperature dwell for configurations partially exposed to fire (N1). In this case heat is transferred to the centre of the profile by thermal conduction in steel, which heats up the surrounding timber. The heat flow is locally directed from the steel to the external parts, and the thermo-migration phenomenon causes the water to move away from the steel profile. Thus, it cannot benefit from the accumulation of water and the subsequent reduction of the heating rate.

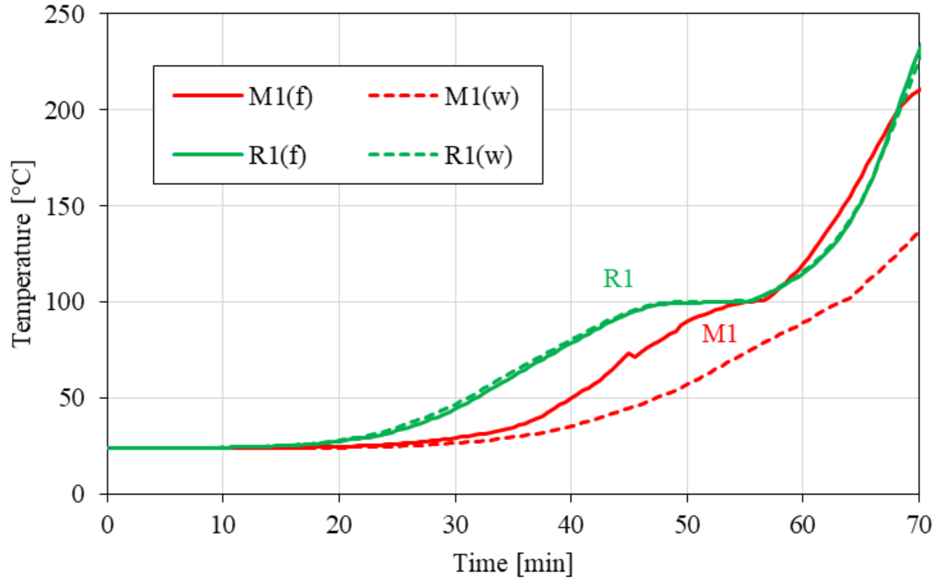

Figure 6. Test n°2 - temperature evolution of the flange (f) and the web (w) of HE140 steel profiles fully protected by 50mm thick timber pieces (M1 and R1).

3.3.2 Thermal behaviour during the cooling phase

During the cooling phase, the continuation or resumption of timber combustion is frequently observed (Figure 7 – c), sometimes several hours after the end of the fire exposure. Some specimens have their timber completely consumed, while others keep a residual section of intact timber (Figure 7 – a & b).

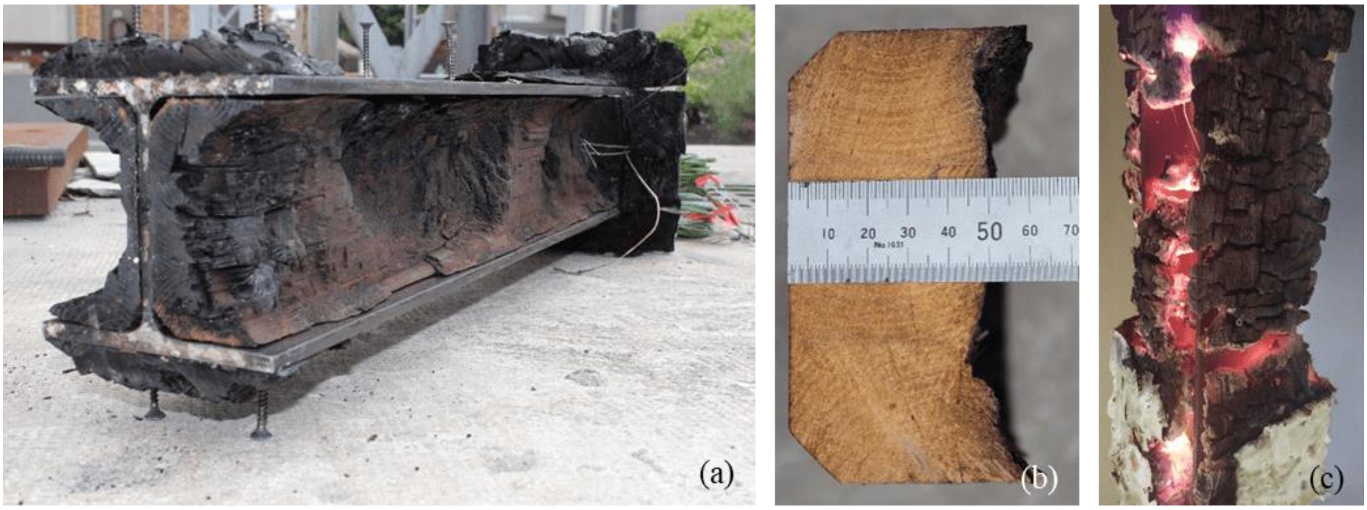

Figure 7. (a): M2 specimen after the cooling phase and the removal of char. (b): M2 specimen – residual section of timber at mid-length, initial thickness = 67mm. (c): O2 specimen – burning of residual timber and heating of steel during the cooling phase.

It is difficult to guess whether steel components will collapse during the cooling phase due to the heating generated by timber combustion. Nevertheless, Figure 7 (c) shows that hollow sections facilitate the combustion of timber by allowing the circulation of oxygen within them. This intense burning, which most often occurs shortly after the fire exposure has ended, heats up steel to temperatures that can compromise its mechanical strength (Figure 8 – P1, P2, R1, R2). Therefore, seeking to reduce the amount of fuel (timber) contained in STC beams can be counterproductive. It seems more appropriate to fill sections with timber, because its combustion does not necessarily lead to significant heating of steel in this case (Figure 8 – M2).

In addition, if significant heating occurs, it manifests itself several hours (3-4 h) after the end of the fire exposure (Figure 8 – M1). Results obtained by Uesugi et al. [3], who test two beams and the same kind of configuration (hollow and timber-filled), tend to confirm this observation.

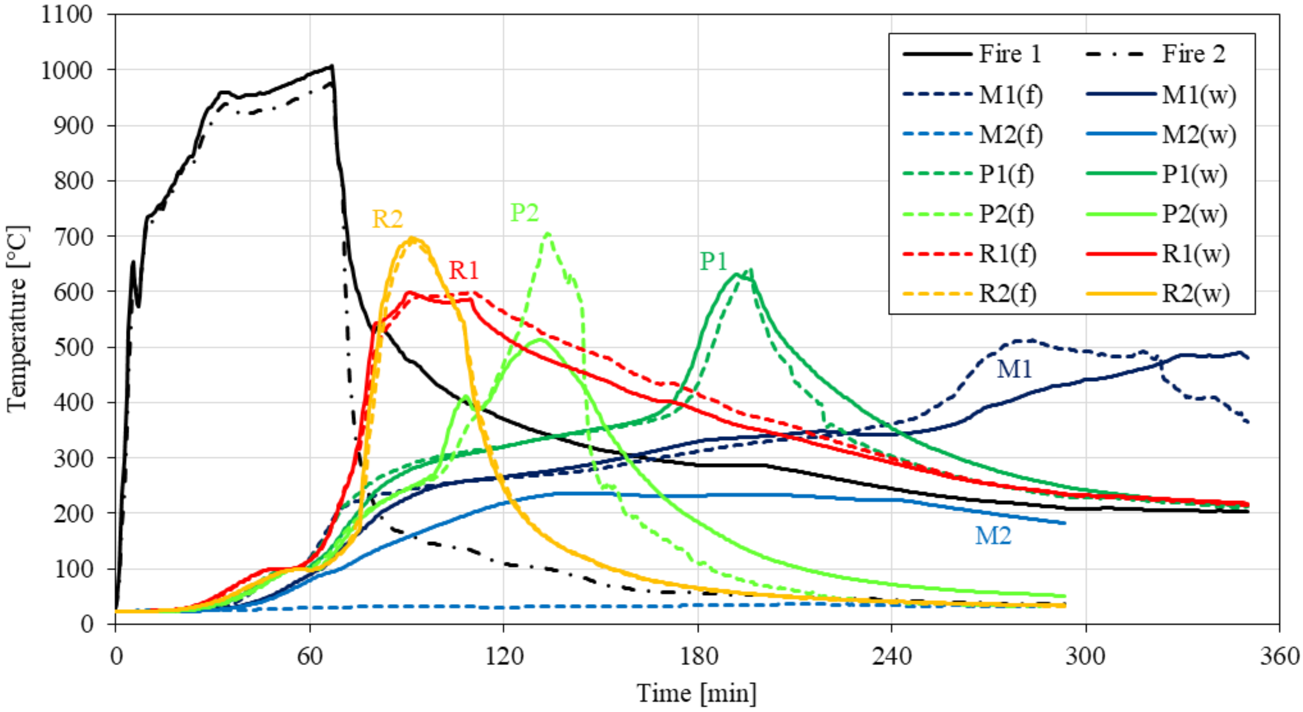

Figure 8. Temperature evolution of the flange (f) and the web (w) of HE140 steel profiles fully protected by 50mm thick timber pieces. M1, P1, and R1 stay in the furnace during the cooling phase (Fire 1), but M2, P2, and R2 are removed from it (Fire 2).

4 REAL-SCALE THERMOMECHANICAL TESTS

4.1 Tested configurations and setup

Two fire tests are performed on real-scale Steel-Timber Composite (STC) beams (Figure 9), with a span of 4.4 m. The beams are put through a constant four-point bending load while being exposed to the ISO 834 fire on three faces until collapse (Figure 10). The STC beams are made of IPE 270 steel profiles (S275) associated with lateral pieces of glulam (GL24h) embedded between the flanges. STC1 is partially exposed to fire, while STC2 is fully protected thanks to a U-shaped timber part fixed on the bottom of the beam, and timber planks fixed along the upper flange. In both cases, the upper face is protected by an insulating slab made of foamed concrete, which is used to close the furnace. Beams components are held together by screws without structural capacity, and loads are shared between steel and timber by simple contact interactions. In order to ensure good contact, thin steel plates are fitted into the gap between the upper flange and the lateral timber pieces at loading points. The two loading points are spaced 1.0m apart, and the applied bending moment is given in Table 3 for each test. These loads represent about 43% of the failure loads at room temperature measured thanks to 7 bending tests carried out at the Pascal Institute. Mechanical loads considered for an unprotected IPE 270 are given in Table 3 for comparison.

Type K thermocouples are used to record temperatures on steel and in timber in three cross-sections, and the mid-span vertical displacement is measured. Temperatures are also measured on one-meter-long non-loaded beams for comparison. The average basic density of timber is 451 kg.m^{-3} for lateral pieces, and 418 kg.m^{-3} for the U-shaped bottom part of STC2. The oven drying of 27 wood samples allows to determine an average moisture content on dry basis equal to 13.2%. This value is confirmed by 70 non-destructive measurements performed with a pinless (EMF) moisture-meter.

Table 3. Mechanical load.

Beam considered	Bending moment at failure (avg. at room temperature) [kN.m]	Bending moment considered in fire situation [kN.m]	Load ratio considered in fire situation [%]
STC1	210.9 (test)	91.0 (test)	43
STC2	258.2 (test)	110.7 (test)	43
IPE 270*	92.3 (test)	65.5 (calculation)	43

**Without fire protection.*

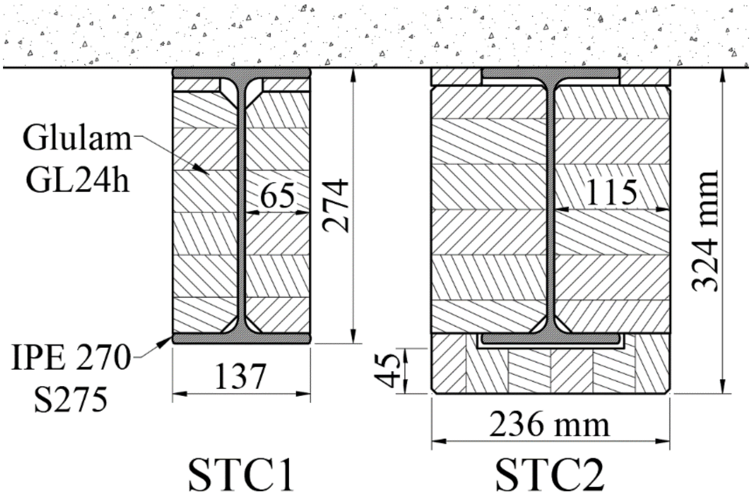

Figure 9. Sections of the real-scale configurations tested.

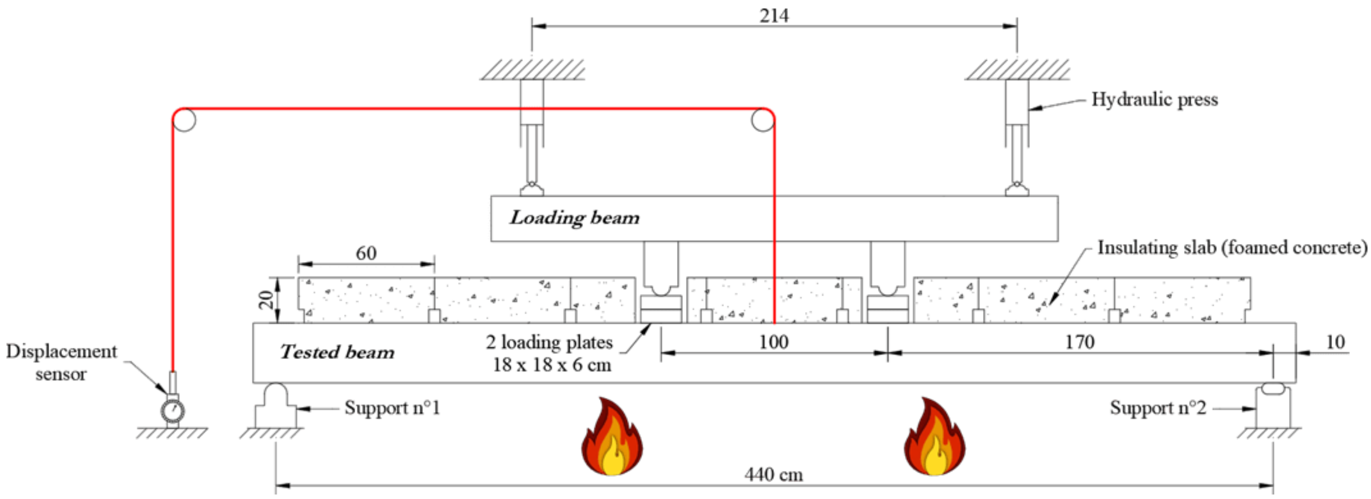

Figure 10. Setup for real scale fire tests.

4.2 Results

4.2.1 Fire resistance

Figure 11 shows the evolution of the deflection affecting STC1 and STC2 during their exposure to the ISO fire. By comparing them, it can be seen that STC1 deforms much earlier due to the thermal expansion of its lower flange, which is exposed to fire. In contrast, STC2 barely deflects during the first hour of exposure to fire, and then bends with an increasing rate due to the combined effect of the thermal expansion and the deterioration of the mechanical properties of the bottom flange, both caused by the degradation of the U-shaped bottom timber protection.

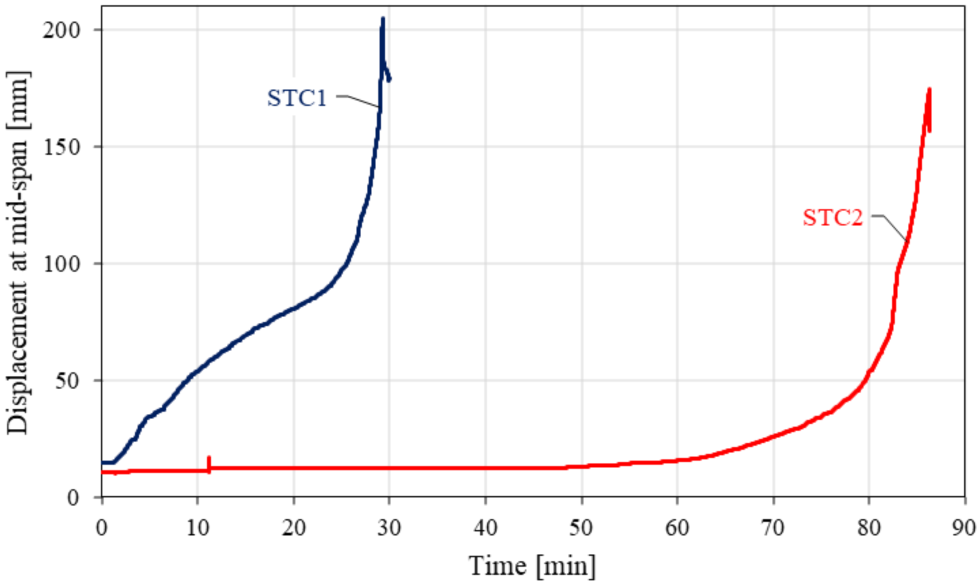

Figure 11. Vertical displacement measured at mid-span during full-scale fire-tests.

EN 1363-1 [15] gives two criteria helping identify the failure of fire tested beams in bending. These criteria relate to the mid-span vertical displacement: one sets a maximum deflection value, while the other sets a displacement speed limit. The tested beam is considered ruined if both criteria are met, or if the deflection reaches 1.5 times the limit displacement. In the case of beams STC1 and STC2, the displacement limit is 177mm, and the displacement speed limit is 7.88mm/min. Both criteria are met when testing STC1, but the deformation of STC2 does not allow to measure a mid-span displacement equivalent to the limit displacement. The STC2 beam is finally removed from the furnace for safety reasons (stability of the insulating slabs), and the speed criterion is the only one used for this test.

These criteria are used to determine the fire resistance times given in Table 4. These durations are compared to the one calculated for an IPE 270 profile without fire protection and subjected to the same loading ratio: 43%. The temperature rise of this unprotected steel profile is calculated in accordance with the EN 1993-1-2 and then compared to the critical temperature associated with a 43% loading rate, i.e., 609 °C (according the EN 1993-1-2). This calculation establishes that an unprotected IPE 270 has a 13 min fire resistance time when placed under the same conditions as those considered in the performed tests. Table 4 show that STC1 and STC2 configurations can respectively withstand 40 and 70% more load, and resist fire 2.2 and 6.3 times longer. Therefore, the fire protection and the mechanical reinforcement provided by timber are significant. Finally, it is shown that while the STC1 configuration does not achieve R30 (by one minute), the STC2 configuration largely achieves R60. Therefore, protecting the bottom flange with a 45mm thickness of timber increases the fire resistance considerably.

Table 4. Fire resistances.

Configuration	Time at failure [min]	Bending moment considered in fire situation (reminder) [kN.m]
STC1	81 (measured)	91.0
STC2	29 (measured)	110.7
IPE 270*	13 (calculated)	65.5

**Without fire protection*

4.2.2 Temperature of steel

Figure 12 shows temperatures measured on the bottom flange of the STC2 configuration. The temperature increases much more severely for the loaded beam than for the non-loaded beam. These two beams are strictly similar, so the mechanical load is the only one responsible for the observed differences. It can be said that the mechanical load impacts the thermal behaviour of the STC2 configuration. A much larger 100°C temperature dwell is also observed for non-loaded beams than for mechanically loaded beams. In the case of non-loaded beams, the vapour released from timber remains trapped inside the section and contributes to slow the heating of steel. In the case of loaded beams, the deflection causes the joints between the different pieces of timber to open. This allows water vapour to escape and hot gases to come into contact with steel. These phenomena accelerate the degradation of the timber protection and the heating of steel. This observation shows that the tightness of the assembly joints is an important factor in the fire resistance of steel-timber composite beams.

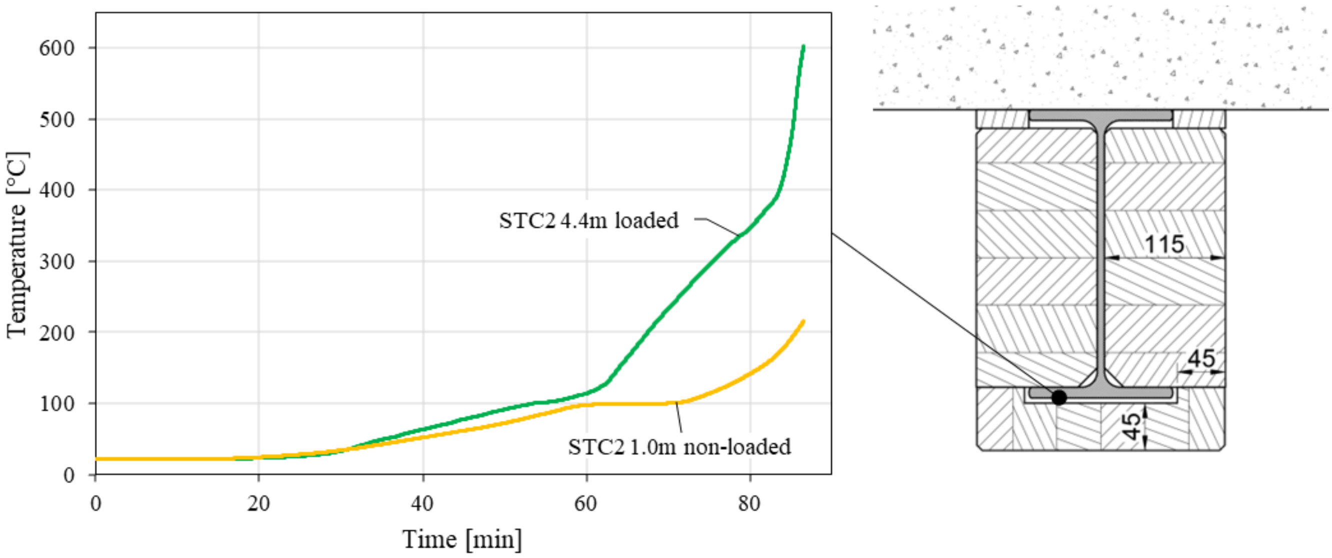

Figure 12. Effect of the mechanical load on the temperature measured on the bottom flange of STC2.

5 CONCLUSIONS

Four fire tests performed at the CSTB allow to refine knowledges on the behaviour of Steel-Timber Composite (STC) structural elements in fire situation:

- Full timber protection is efficient to protect steel against fire. Non-loaded tests suggest that 30 min fire resistance is easily reached using 30mm thick timber protection, and more than one hour with 50mm protection. 81 min fire resistance is reached during a mechanically loaded test on a STC beam with a 45mm thick timber protection (load ratio 43%).
- Configurations with steel partially exposed to fire are far less efficient, but a 30 min fire resistance can be reached depending on the amount of exposed steel and the load ratio considered in fire situation.
- Mass transfer occurring in timber exposed to fire have a significant and beneficial impact on the temperature of steel by leading to the accumulation of water against it.
- Hollow sections allow oxygen flow in beams. It leads to a significant heating of the steel during the cooling phase because of the combustion of timber. Timber filled sections tend to reduce this risk.
- The sealing of assembly joints is an important factor. Deflection tends to open joints, which allow the water initially contained in timber to escape, the hot gas to reach steel, and the protection to burn faster. Increasing the sinuosity of the joints could allow to improve the performance of tested beams.

These fire tests provide thermal measurement in both steel and timber for 35 non-loaded specimens and 2 mechanically loaded STC beams. Fire resistance of these two beams is also measured. These results can be used as a database for a MEF thermomechanical model. Further work consists in using such a model to investigate various parameters, e. g., the span of the STC beam or the load ratio in fire situation.

ACKNOWLEDGMENT

Authors thank the Scientific and Technical Centre for Building (CSTB) and the Environmental and Energy Management Agency (ADEME) for funding this work. Authors thank the following companies for providing timber and steel: Gagne construction métal, Coladello, Arbonis, and Racineo.

REFERENCES

1. Flitch-plate, riveted and trussed girders. Am. Archit. Build. News, vol. 13, pp. 255–258, 1883. Available: https://archive.org/details/americanarchitec13newyuoft/page/n457/mode/2up.
2. L. Twilt and J. Witteveen, The fire resistance of wood-clad steel columns. Fire Prev. Sci. Technol., vol. 11, pp. 14–20, 1974.
3. Uesugi, T. Harada, and Y. Namiki, Fire resistance of sugi covering materials for structural steel. J. Wood Sci., vol. 48, no. 4, pp. 343–345, 2002. doi: 10.1007/BF00831358.
4. M. Shiraiwa, S. Yusa, H. Masuda, T. Kawai, Y. Namiki, and H. Saito, Fire resistance on hybrid wooden structure, Part 8: Experimental fire resistance study on self-charring-stop wooden column structure. Annual meeting of Architectural Institute of Japan, 2004, pp. 137–138.
5. H. Masuda, S. Yusa, T. Kawai, and Y. Namiki, Fire resistance of hybrid wooden structure, Part 9: Loaded fire resistance test on heavy-timber beam structure. Annual meeting of Architectural Institute of Japan, 2004, pp. 139–140.
6. I. Sakamoto, N. Kawai, H. Okada, and S. Yusa, Final Report of a Research and Development Project on Timber-based Hybrid Building Structures, 2004.
7. JR East Design Corporation, Kunimi Town Office Building. Steel construction Today & Tomorrow, no. 49, pp. 15–18, 2016.
8. Timbersize, 木質ハイブリッド集成材：ノンブラケット型, 2017. http://www.timberize.com/index.html?target=417 (accessed Jul. 03, 2022).
9. S. Jang, Y. Kim, Y. Jang, and I. Shin, Fire resistance of steel column glued with structural glulam covers. World Conf. Timber Eng., 2010.
10. F. Riola-Parada, K. Tavoussi, A. Fadai, W. Winter, and L. Stockert, Fire performance of prefabricated timber-steel-concrete ribbed decks. World Conf. Timber Eng., 2018.
11. M. Fujita and M. Iwata, Bending test of the composite steel-timber beam. Appl. Mech. Mater., vol. 351–352, pp. 415–421, 2013. doi: https://doi.org/10.4028/www.scientific.net/AMM.351-352.415.
12. W. Winter, K. Tavoussi, F. Riola Parada, and A. Bradley, Timber-Steel Hybrid Beams for Multi-Storey Buildings: Final Report. World Conf. Timber Eng., 2016.
13. S. Duan, W. Zhou, X. Liu, J. Yuan, and Z. Wang, Experimental Study on the Bending Behavior of Steel-Wood Composite Beams. Adv. Civ. Eng., vol. 2021, p. 1315849, 2021. doi: 10.1155/2021/1315849.
14. B. Jurkiewiez, S. Durif, A. Bouchair, and C. Grazide, Experimental and analytical study of hybrid steel-timber beams in bending. Structures, vol. 39, pp. 1231–1248, 2022. doi: 10.1016/j.istruc.2022.03.055.
15. European Committee for Standardization, EN 1363-1 - Fire resistance tests - Part 1: general requirements. 2020.
16. European Committee for Standardization, NF EN 13183-1 - Moisture content of a piece of sawn timber - Part 1: determination by oven dry method. 2002.
17. A. Béreyziat, Étude du comportement thermomécanique de poutres mixtes acier-bois en situation d’incendie. Université de Lyon, 2022.
18. R. H. White and E. L. Schaffer, Transient Moisture Gradient in Fire-Exposed Wood Slab. Wood Fiber Sci., vol. 13, no. 1, pp. 17–38, 1981.
19. M. Audebert, D. Dhima, M. Taazount, and A. Bouchaïr, Experimental and numerical analysis of timber connections in tension perpendicular to grain in fire. Fire Saf. J., vol. 63, pp. 125–137, 2014. doi: 10.1016/j.firesaf.2013.11.011.
20. M. Sedighi Gilani, E. Hugi, S. Carl, P. Palma, and P. Vontobel, Heat Induced Desorption of Moisture in Timber Joints with Fastener During Charring. Fire Technol., vol. 51, no. 6, pp. 1433–1445, 2015. doi: 10.1007/s10694-014-0416-3.
21. A. Samaké, M. Taazount, P. Audebert, and P. Palmili, Thermo-hydric transfer within timber connections under fire exposure: Experimental and numerical investigations. Appl. Therm. Eng., vol. 63, no. 1, pp. 254–265, 2014. doi: 10.1016/j.applthermaleng.2013.10.049.

TEMPERATURE DEVELOPMENT IN THE CROSS SECTION OF COMPOSITE BEAMS WITH GALVANIZED STEEL COMPARED TO UNCOATED STEEL

Mirabela Firan[1], Kurt Tutzer[2], Prof. Martin Mensinger[3], Justus Frenz[4], Prof. Jochen Zehfuß[5]

ABSTRACT

Recent research results [1-3] show a significantly slower heating behavior of hot-dip galvanized steel compared to uncoated steel profiles in the event of a fire. As a result, steel structures in combination with moderate oversizing can achieve the required fire resistance class of R30 without the need for additional passive fire protection measures. In the case of composite beams, the fire resistance R30 can be obtained with significantly increased material efficiency and economy by using higher-strength steels. Additionally, by forming single symmetrical hybrid welded beams, such as a halved rolled section with an optimized (A_m/V ratio) lower flange and in combination with hot-dip galvanization, a fire resistance of R30 can be ensured in an economical way.

The positive effect of hot-dip galvanized composite beams in comparison with uncoated composite beams is investigated during real-scale fire experiments with a series of girders ranging in height, profile thickness, strength category and concrete slab detailing. The focus of the investigation is on the development of the temperature profile over the height of the steel profile and in the concrete slab as well as the stud shear connectors.

Keywords: Composite beams; hot dip galvanizing; section temperature profile; ISO 834, trapezoidal sheet

1 INTRODUCTION

The emissivity of hot-dip galvanized steel components depending on the galvanizing category according to EN ISO 14713-2:2020 [8] differs from the value for the emissivity ε of steel components of ε= 0.7 given in EN 1993-1-2:2010 [6] and EN 1994-1-2:2010 [7]. In particular, significantly lower emissivities occur at component temperatures below 500°C, leading to slower heating of the components, so that fire resistance R30 can be achieved for compact cross-sections without additional fire protection measures.

In the event of a fire, heat is transferred to a steel member by convection and by thermal radiation in the form of electromagnetic waves. In the initial phase of a full fire, the heating of a steel component is dominated by convection, while in the further course of the fire the heating by radiation becomes dominant.

The proportion of energy transferred by radiation is linearly dependent on the emissivity of the component surface. The emissivity ε is the measure that indicates how strongly a material can absorb or emit thermal radiation.

[1] Doctoral Candidate, Technical University of Munich, Chair of Metal Structures
e-mail: m.firan@tum.de, ORCID: https://orcid.org/0000-0002-5879-4515
[2] Doctoral Candidate, Technical University of Munich, Chair of Metal Structures
e-mail: k.tutzer@tum.de
[3] Professor, Technical University of Munich, Chair of Metal Structures
e-mail: mensinger@tum.de, ORCID: https://orcid.org/0000-0001-5210-5400
[4] Doctoral Candidate, Technical University of Brunswick, Institute of Building Materials, Division of fire Safety
e-mail: j.frenz@ibmb.tu-bs.de
[5] Professor, Technical University of Brunswick, Institute of Building Materials, Division of fire Safety
e-mail: j.zehfuss@ibmb.tu-bs.de
https://doi.org/10.6084/m9.figshare.22154474

The temperature increase $\Delta\theta a$, in an unprotected steel cross section during a fire for the time interval Δt can be calculated according to EN 1993-1-2 [6] with the following equation.

$$\Delta\theta_{a,t} = k_{sh} \frac{\frac{A_m}{V}}{c_a \rho_a} \dot{h}_{net} \Delta t \quad [K] \qquad (1)$$

k_{sh} is the correction factor for the shadow effect

A_m/V is the section factor for unprotected steel members [1/m]

$\dot{h}_{net}$ is the design value of the net heat flux per unit area [W/m²]

The heating behaviour of the cross section is strongly influenced by geometrical parameters, for example by the section and it is significantly influenced by the net heat flux $\dot{h}_{net}$. Spatial heat energy transfer occurs through convection and radiation. By combination, they provide the net heat flux in structural fire design:

$$\dot{h}_{net} = \dot{h}_{net,c} + \dot{h}_{net,r} \quad [\mathrm{W/m^2}] \qquad (2)$$

$\dot{h}_{net,c}$ is the net convective heat flux component

$$\dot{h}_{net,c} = \alpha_c(\theta_g - \theta_a) \quad [\mathrm{W/m^2}] \qquad (3)$$

$\dot{h}_{net,r}$ is the net radiative heat flux component

$$\dot{h}_{net,r} = \phi \cdot \varepsilon_m \cdot \varepsilon_f \cdot \sigma \cdot \left[(\theta_g + 273)^4 - (\theta_a + 273)^4\right] \quad [\mathrm{W/m^2}] \qquad (4)$$

ε_m is the surface emissivity of the member

The emissivity of steel is considered when heating is caused by radiation. The lower the emissivity, the slower the heating of the component progresses. Hot-dip galvanizing can have an influence on the emissivity. The greater the temperature difference between the component surface and the furnace temperature, the greater the influence of emissivity. A positive effect occurs especially at the beginning of the fire and with small profile factors (Figure 1).

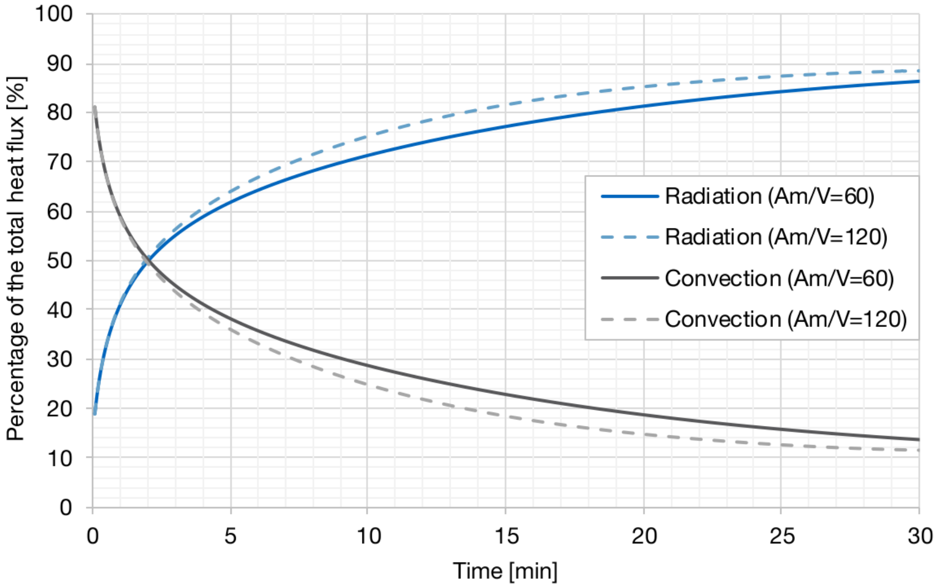

Figure 1: Ratio of radiation and convection of the total net heat flux [5]

Hot-dip galvanizing of steel components is carried out in accordance with EN ISO 1461 [11]. In this process, steel components are immersed in a liquid zinc bath. As a result of a reciprocal diffusion of the liquid zinc bath with the iron of the steel profile, a coating of several, differently composed iron-zinc alloy layers is formed [1]. The formation of the alloy layers depends on several factors. One of the most important parameters is the chemical composition of the steel in terms of silicium and phosphorus content. Depending on this, EN ISO 14713-2 distinguishes four different categories: low-silicium area (category A), Sebisty area (category B), Sandelin area (category C) and high-silicium area (category D).

As part of the research project IGF 18887 N [12], small-scale fire tests and large-scale fire tests were carried out at the Technical University of Munich to investigate the influence of hot-dip galvanizing on the emissivity of steel components in the case of fire. For the tests, specimens in steel categories A to D and with different storage conditions after galvanisation (new galvanized, stored inside and stored outside for about one year) were compared. The research results show a more favourable heating behavior of all hot-dip galvanized steel components of category A and B according to EN ISO 14713-2 compared to the specified global emissivity of $\varepsilon = 0.70$, according to EN 1993-1-2 as shown in figure 2.

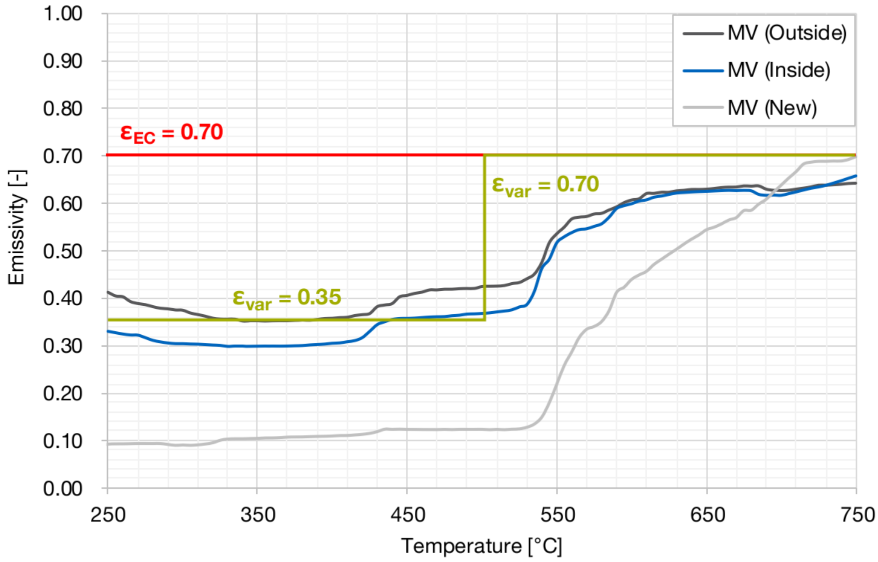

Figure 2: Comparison of the two-stage emissivity approach for category A and the normative emissivity [5]

As a result of the investigations from [12], a temperature-dependent two-stage emissivity was specified: ε=0.35 for a component temperature up to 500°C and ε=0.7 for a component temperature above 500°C. This temperature dependence of the emissivity was adopted in the course of the revision of EN 1994-1-2.

Table 1: Values of the surface emissivity ε_m

Type of steel	$\varepsilon_m (\theta_m \leq 500°C)$	$\varepsilon_m (\theta_m > 500°C)$
carbon steel	0,7	
HDG steel[a]	0,35	0,7

[a] Hot-dip galvanised steel according to EN ISO 1461 with a steel composition corresponding to category A or B according to EN ISO 14713-2, Table 1.

This paper focusses on the temperature development of the steel profile for composite beams in the case of fire. For this purpose, tests on composite girders were compared with galvanized and non-galvanized steel girders. Another difference between the tests is the execution of the concrete slab as a solid slab, Holorib sheet and trapezoidal profile.

2 EXPERIMENTAL INVESTIGATIONS

2.1 Test specimens

The present experimental investigations consist of composite beams subjected to large-scale fire tests executed in three different research projects (Project A: IGF 19105 [4], Project B: IGF 21536 N and Project C: IGF 21403 N). All projects were (Project A) and still are (Project B and C) carried out at the Technical University of Munich and Technical University of Braunschweig. To allow direct comparison of the test results, similar dimensions and bearing conditions were chosen in all three projects. The beams were manufactured with both solid concrete chord and different trapezoidal sheets, spanning perpendicular to the profile axis. Due to the high degree of propagation and available test data, the profile sheets Holorib51 from Montana, Cofraplus60 from ArcelorMittal and Comflor80 from Tata Steel were used for the production of the composite beams with steel deck. In order to evaluate the favourable influence of hot-dip galvanizing on the fire behaviour, the steel sections of the composite beams with Holorib51 were immersed in a zinc bath before casting the concrete cord. Table 1 gives an overview of all composite beams subjected to fire tests that are part of this paper. It should be mentioned that additional beam tests have been carried out which indeed are not included in this publication but can be found in past [4] and future publications.

Table 2 Overview over referenced beams below

Project Beam-Nr.	Beam Profile	Steel grade	Trapezoidal sheet	Zink Coating	Comment
A – 1	HEB 300	S355	None	No	
B – 1	HEB 300	S460	HR51/150	Yes	
B – 2	Welded section “HEA300”	S690	HR51/150	Yes	*Flange: 16 x 260 Web: 10 x 268 mm
B – 3	Single Sym. H=280 mm	S460+S690	HR51/150	Yes	*1/2 IPE500 (S460) + bottom flange 30 x 340 mm (S690)
C – 1	HEB 300	S355	CP60	No	
C – 2	HEB 300	S355	CF80	No	

All beams were produced with a length of 9.0 m and a concrete deck width of 1.0 m. The concrete class was chosen with C35/45 for the beams with trapezoidal deck and C40/50 for the beam with the solid slab. The thickness of the concrete cord was ranging from 0.15 to 0.2 m. Beam and concrete deck were connected by stud shear connectors welded through the pre-punched trapezoidal sheets directly onto the flange of the steel profile. The steel grade varied from S355 to S690 and steel section covered both hot-rolled standard profiles and welded optimized sections. Figure 3 exemplarily shows the geometry of one of the beams with the section axes at which temperature measurements are made. Due to the table placed under the beam (see Fig. 5) leading to some shading of the beams from the burners in the furnace at midspan, for the analysis only temperatures from beam sections directly subjected to the fire were considered (the side areas marked in Figure 3).

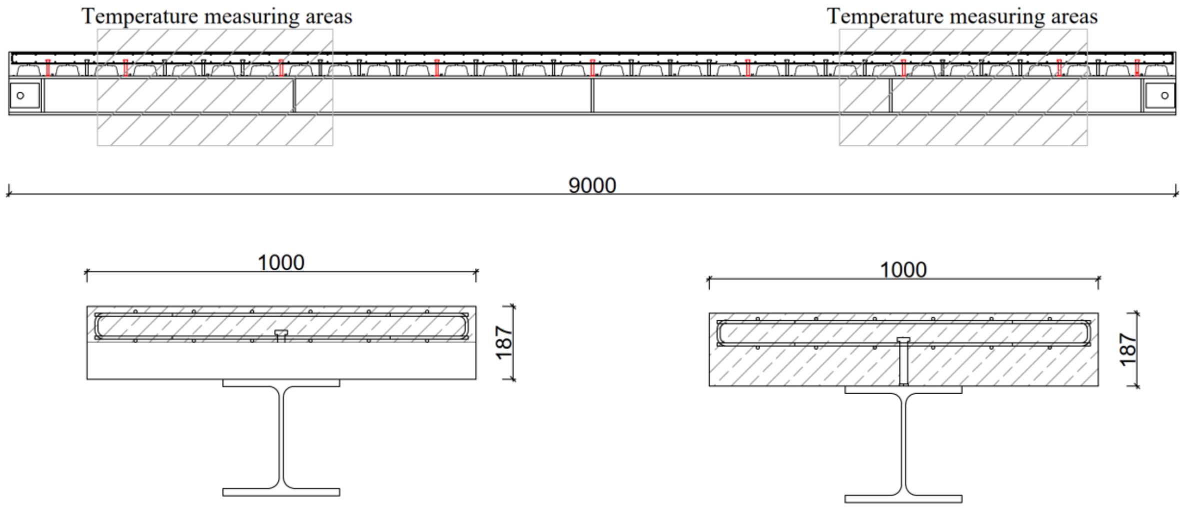

Figure 3: Exemplary beam geometry (beam C-2) with region of the temperature measurements discussed below

2.2 Instrumentations

The tests were carried out in a fire test furnace according to EN 1363-1 [13]. During the fire test, the temperature measurement in the furnace was conducted by surface plate thermocouples, which were arranged uniformly in the furnace directly underneath the steel sections. Type K thermocouples recorded the temperatures throughout the composite beam sections. Temperature measurements were taken at the steel surface for the unprotected steel sections. For all hot-dip galvanized parts, thermocouples were placed in small boreholes (3 mm diameter) at a depth of half of the thickness of the respective section element. In the concrete, temperatures were measured with thermocouple-ladders, so that temperature development over the deck height can be understood. Thermocouple ladders were placed in both the high and low rib locations for concrete decks with trapezoidal sheets. The measurement was carried out on several sections over the beam length. The arrangement of the thermocouples on the steel profile was staggered over the length of the beam in order to compensate possible temperature differences due to shadowing effects. Some stud shear connectors were modified with a borehole so that the temperature could be recorded near the connection point to the beam inside of the connector (connector height: 125 mm, borehole depth from the top: 100 mm). Beam deformation, end rotation and slip between concrete deck and steel section was recorded but will not be discussed in this paper. Nevertheless, the focus of this work is on the temperature development of the steel profile, recorded by the arrangement of the thermocouples according to Figure 4.

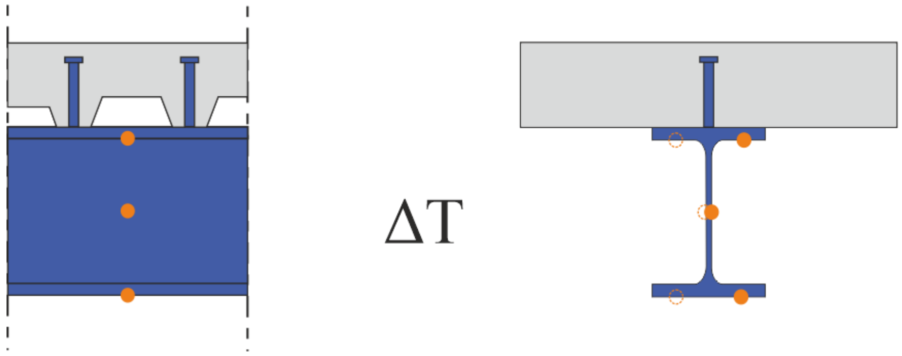

Figure 4: thermocouples arrangement on steel beam

2.3 Experimental Setup

All fire tests were carried out in the slab testing furnace at iBMB, part of TU Braunschweig. The furnace chamber has dimensions of 8.0 m x 4.0 m and thus provides a large area for fire exposure to the beams. At the beam ends, the beam crosses the furnace wall and is supported by hinges on both ends. Gas concrete elements were placed on the upper side of the concrete girders to close the top side of the furnace. The beams were mechanically loaded with three presses aligned in the longitudinal center line and placed at midspan and both quarter-span points. All beams were loaded before the start of the fire with some beams of project A being exposed to cyclic loading while all other beams had only a static loading phase. After 20 minutes of mechanical loading, the ISO 834 fire was introduced for all beams. For projects B & C the target duration was 30 min of ISO fire, whereas shorter durations were chosen in project A. One table was placed at midspan to restrict the maximum deflection and prevent the beam from collapsing into the furnace in case of total failure. In order to avoid excessive deformation, leading to uncontrolled heat leakage and subsequently damage to the furnace and the load application device, sand-lime bricks were placed centrally under the beams, limiting the maximum deformation of the beams. Figure 5 and Figure 6 illustrate the test setup.

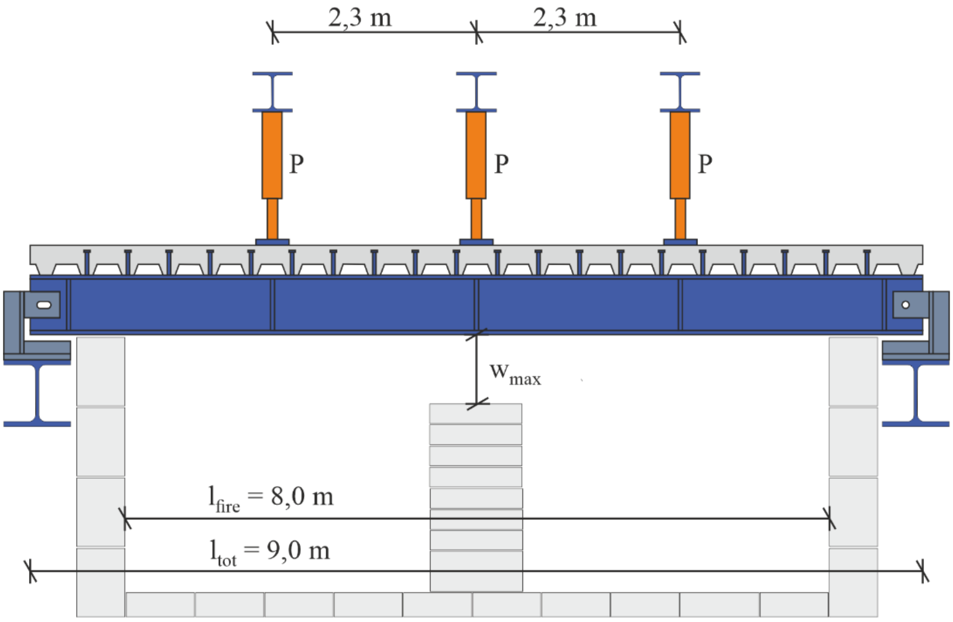

Figure 5: Schematic representation of the test setup and furnace at iBMB in Braunschweig

Figure 6: Large-scale fire test setup: furnace and composite beams

3 RESULTS

3.1 Observations

Figure 7 gives an overview of the beams before and after the start of the heating process. When the load was applied, all girders showed an initial vertical deformation and slip, depending on their flexural stiffness, which resulted from the beam geometry and the realized degree of shear connections in the composite cross-section. As the fire started, the vertical deformations of all beams increased significantly. After approximately 9-14 minutes of fire exposure, moist areas appeared on the surface of the concrete (Figure 8, left). This phenomenon results from inner mass transport of water vapor, which condenses on the surface of the concrete slab[8, 10]. In addition, spalling of the concrete chord occurred during the tests, which was characterized by loud popping noises. Although after the fire test, damage caused by spalled concrete was mainly seen on the side of the concrete chord (Figure 8, right). Spalling was also observed in on the upper side of the concrete belt, which was not directly exposed to the fire. In [10], these are attributed to thermomechanical and thermohydraulic processes in the concrete. At the beam ends, the occurrence of slip from mechanical loading was observed at the beginning of the test, which developed in the reverse direction soon after the start of heating process, caused mainly by the thermal expansion of the steel profile. Shortly before reaching the maximum deflection, a strongly nonlinear increase in vertical deformations was observed for all beams.

Figure 7: Composite beams before and during fire test

Figure 8: Pots of moisture condensed on the surface of the concrete slab (left), spalling of the concrete recorded after the experiments (right)

Temperature development

This paper focusses on the temperature development of the steel profile. For the short duration of the fire tests of less than 32 minutes for all fire tests with ISO curve, temperatures in the concrete deck taken at 30 mm above the inner surface of the profile sheets did not exceed 150 °C. It was observed that the temperature of the concrete was higher for the thermocouples rib of the profile sheet than for the thermocouples above the crown of the profiled sheet. Similar, relatively low temperatures were observed for the sheer studs. At 25 mm above the top flange of the steel sections, temperatures did not exceed 300 °C for all configurations. The furnace for the fire tests conducted at iBMB, TU Braunschweig, Germany were fitted with oil burners to produce the standard fire according to ISO 834. As seen in Figure 9, an acceptable temperature development was achieved in all tests so that beam temperature measurement data from all tests will be compared in the following. The test/ ISO 834 standard fire curve ran for 22 minutes for beam A-1 (project A) as well as 24 and 31 minutes for beams B-1 & B-2, B-3 (project B) and 31 minutes for beams C-1 & C-2 (project C) respectively.

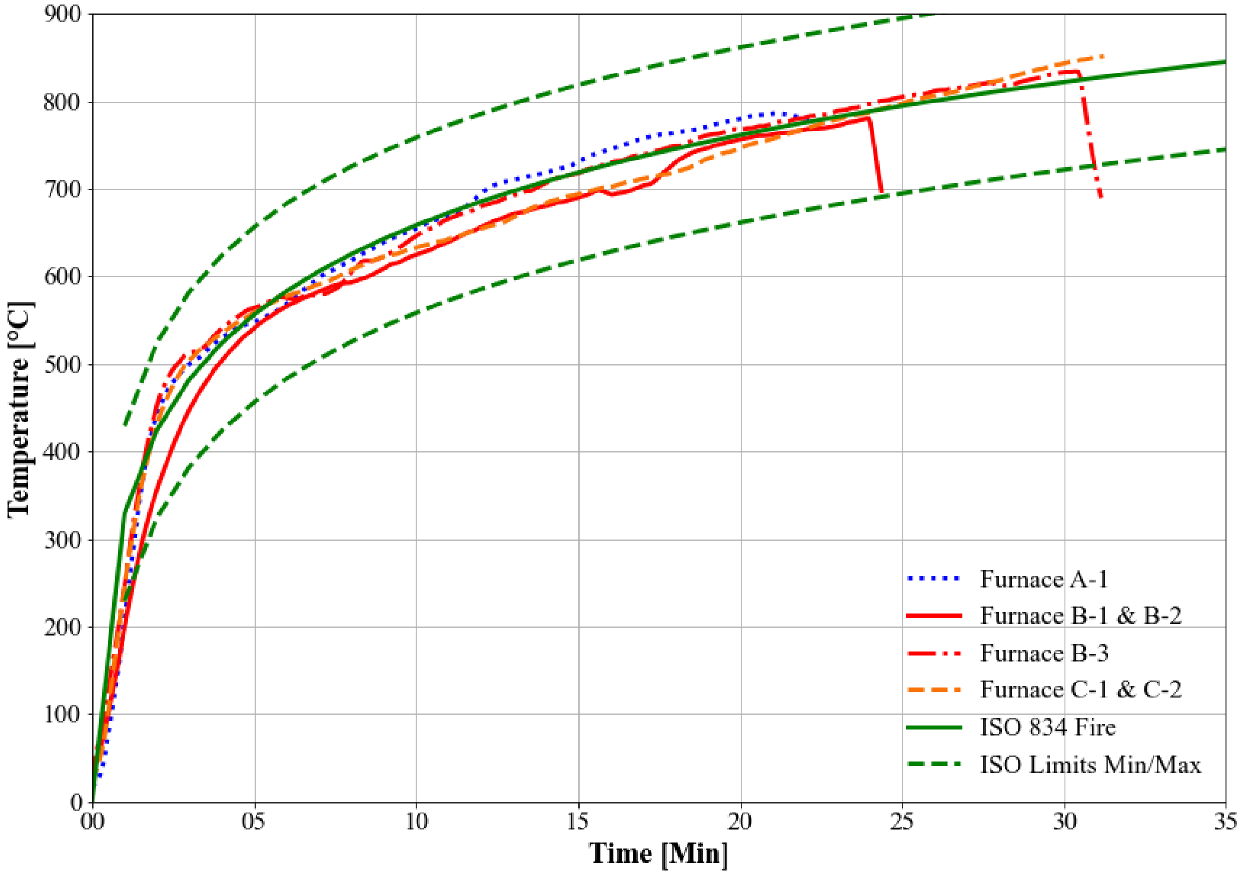

Figure 9: Average measured furnace temperature during the fire tests

In all projects, HEB300 profiles were used so that measurements could be compared. In project A, uncoated beams were topped with a directly-adjacent concrete chord. High trapezoidal sheets were added in project C, so that the top flange was not in direct contact with the concrete chord and due to the size of the ribs, the top side of the top flange was somewhat (C-1, sheet: Cofraplus60) or more (C-2, sheet: Comfloor80) exposed to the open fire. Project B used trapezoidal sheets with rather small ribs (HR51/150), so that the top flange was not in contact with the concrete chord but still almost completely covered. Also, all beams in project B were hot-dip galvanized.

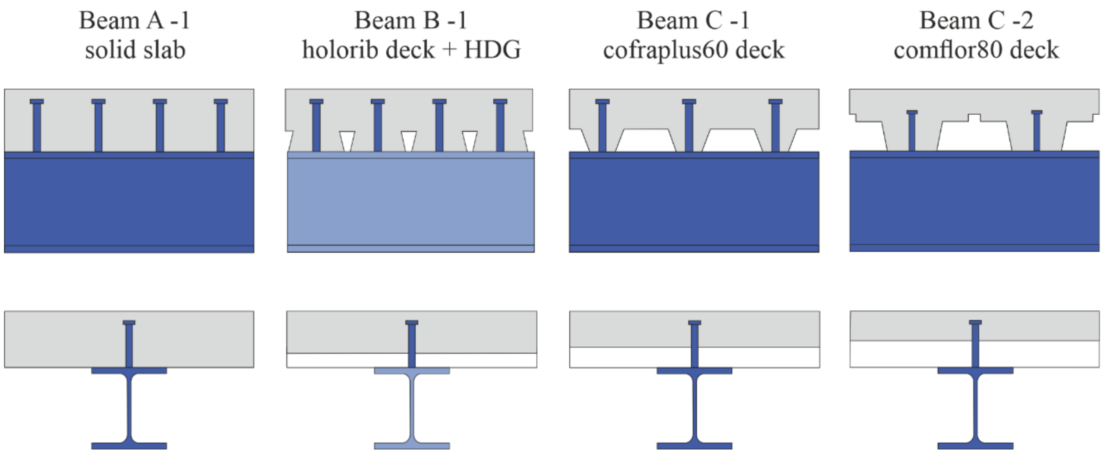

Figure 10: Overview of beam configurations with HEB-300 from projects A, B and C

The mean values of the temperature profile development in Figure 11 show some clear characteristics. The steel section profile from beam B-1 shows the smallest temperatures throughout the fire test so that heating retardation due to the zinc coating may be assumed. The measurements of the temperature development seem to be approximated well by the simplified method from EN 1994-1-2 where the emissivity of steel is set to 0.35 for steel temperatures up to 500 °C and to 0.7 for steel temperatures above 500 °C in the three-sided exposure situation. Beams from project A show a slightly increased speed of heating but seem to benefit from the cooling effect of the directly adjacent concrete deck. The temperature increase is slightly below the estimated values for three-sided exposure with constant emissivity 0.7 given by the simplified method in EN 1994-1-2. The beams in project C however show the fastest increase in temperature, that exceeds the EN 1994-1-2 temperature estimation for a 3-sided fire exposure. This temperature increase can be attributed to the openings between the ribs of the profiled sheet which provide a reduced protection for the steel flange.

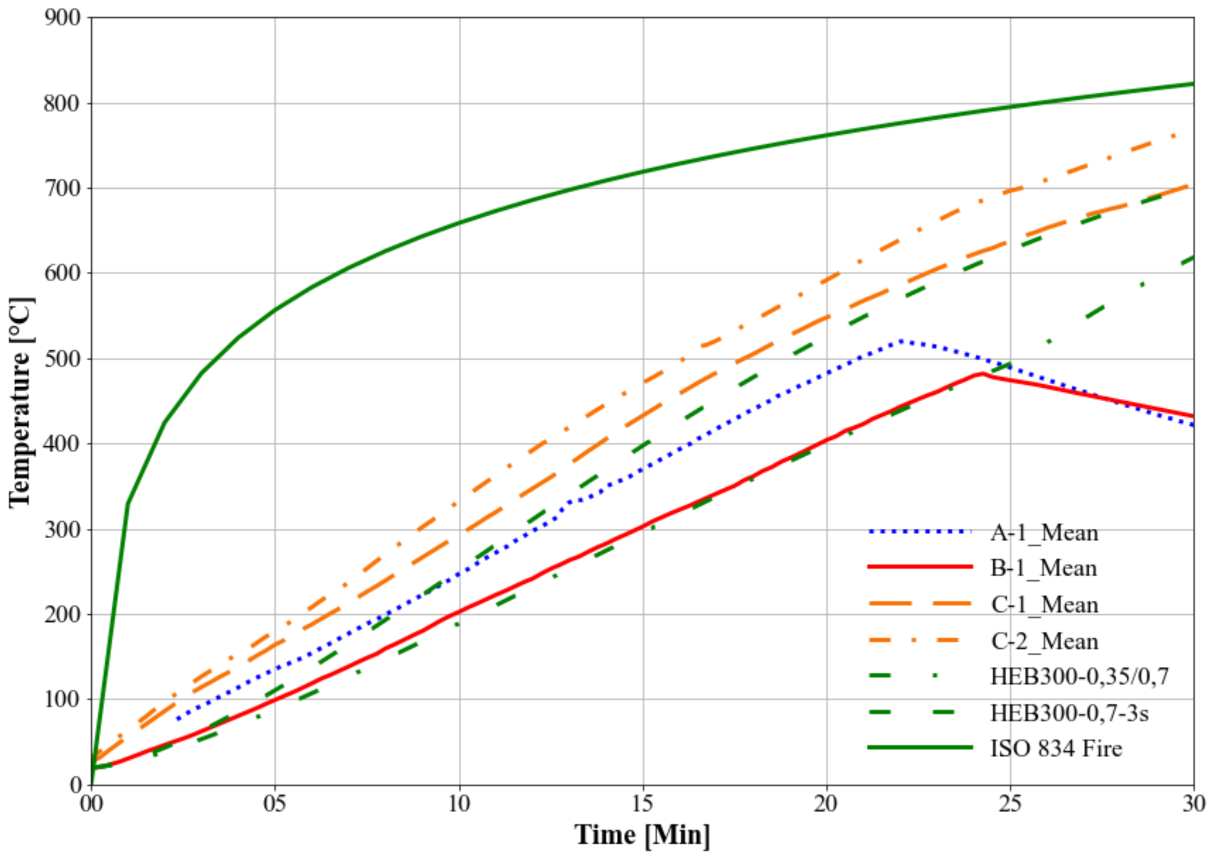

Figure 11: HEB-300 – temperature mean values for measurements equally distributed from top flange, bottom flange and web according to Figure 4

The comparison of the temperatures of flanges and webs in Figure 12 show some clear differences in the characteristic heating behavior. The more exposed top flange of beams C-1 and C-2 records significantly higher temperatures than all other beams with fully covered top sides. This reduced cooling effect can still be seen in the web temperatures that are still higher than the unprotected beams in project A. Bottom flange temperatures are also slightly higher in project C, but the difference is rather small.

The positive effect of reduced emissivity of the hot-dip galvanized steel section is specifically evident in the web temperatures, where the largest surface with a relatively small section thickness leads to the largest gap in temperatures compared to the unprotected section.

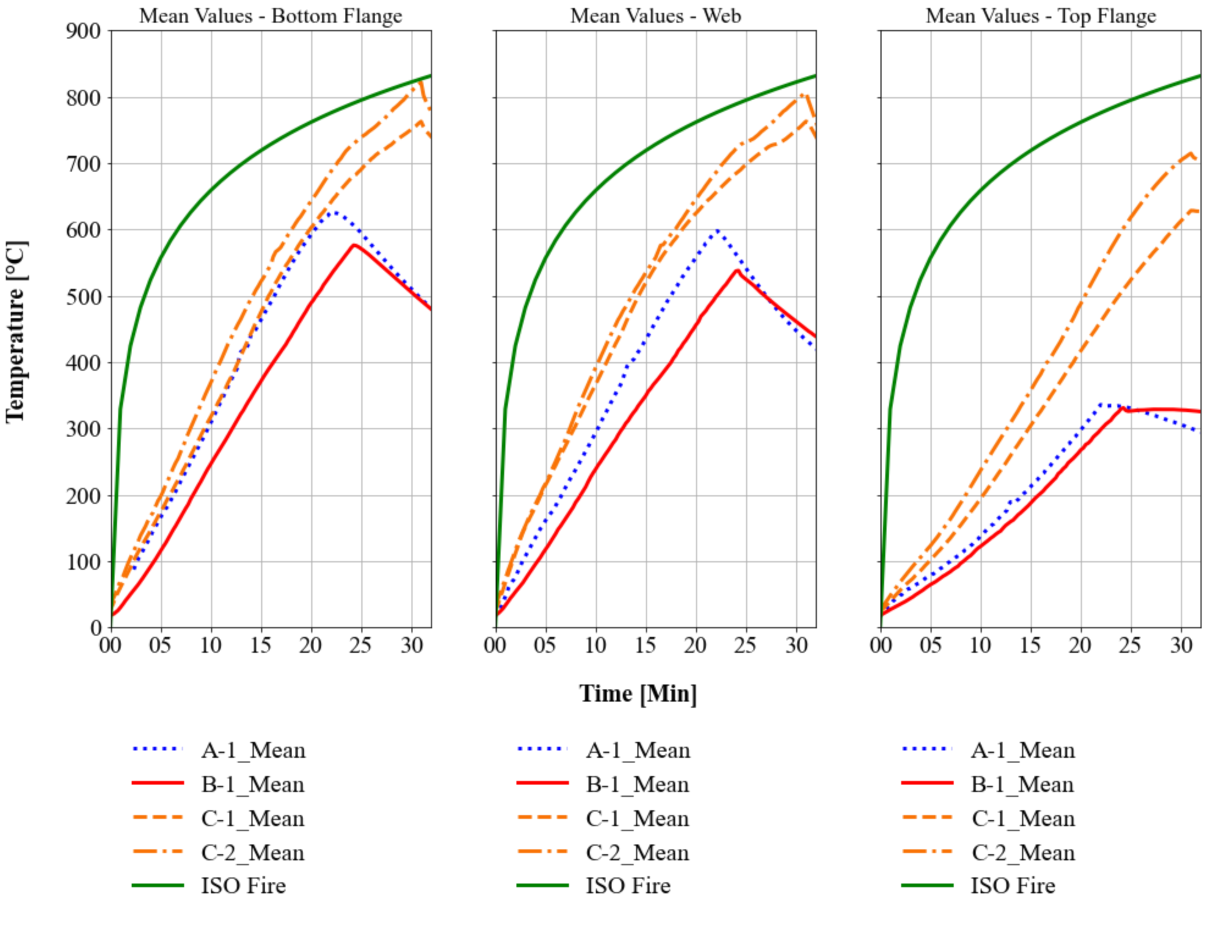

Figure 12: HEB-300 – Comparison of temperatures in flanges and web

The approach of a reduced emissivity of 0.35 in case of hot-dip galvanizing for steel temperatures up to 500°C appears to be valid for other cross sections as well. Section B-2 is welded from two flanges 16 x 260 mm and a web 10 x 268 mm. Since the section dimensions are smaller than in the hot-rolled section HEB300 (B-1), the temperature rises faster in this section. Section B-3 is produced from a halved IPE500 for top flange and web with an optimized bottom flange 340 x 30 mm.

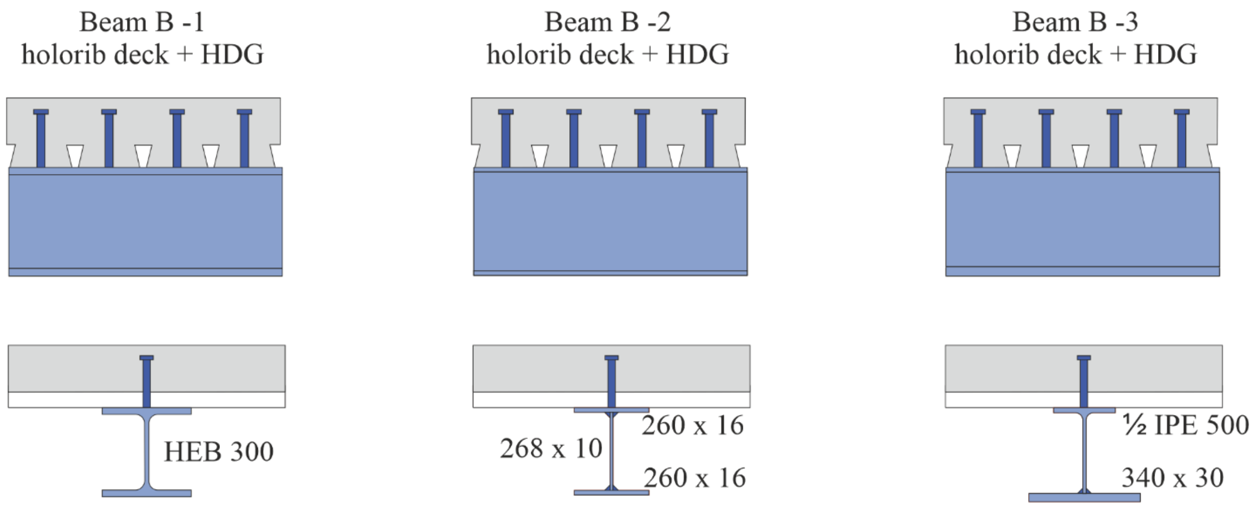

Figure 13: Overview of beam configurations from project B

The IPE500 dimensions are comparable to the thicknesses of the other beams, only the bottom flange is larger. Due to the thickness of the bottom flange, heating occurs slower so that in this profile the web temperature ends up being the largest after 30 minutes.

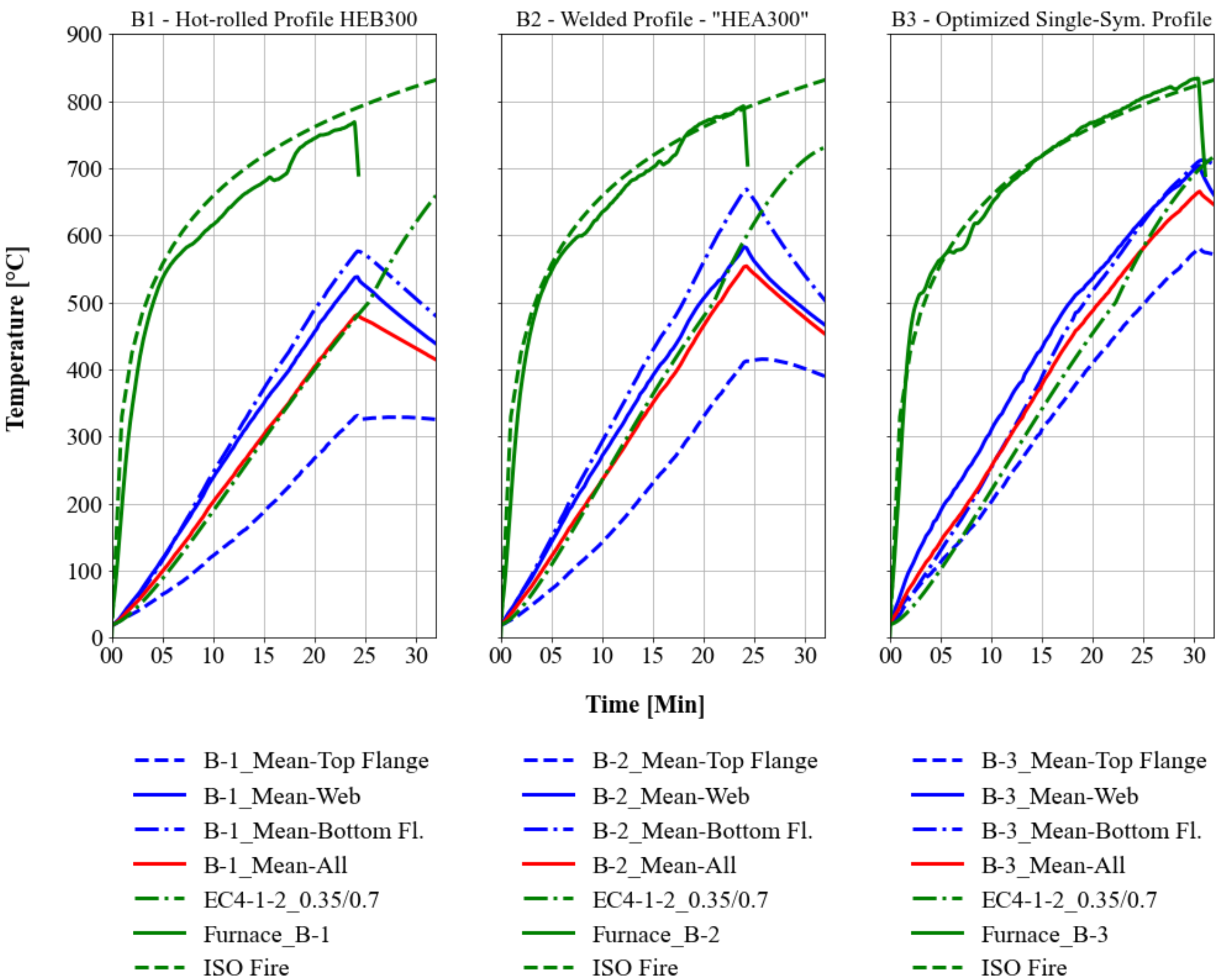

Figure 14: HEB-300 – Temperature development of galvanized steel profiles from project B

4 CONCLUSIONS

This paper presented four full-scale fire tests carried out on simply supported composite steel-concrete beams with solid slabs and steel sheeting perpendicular to the steel profile. Temperature development was measured and reported in the paper. The measured temperatures of the galvanized steel profiles show that the proposed approach from [5] is applicable, with a temperature-dependent emissivity, being reduced to $\varepsilon_m = 0.35$ until a component temperature of 500°C is reached and subsequently increased to $\varepsilon_m = 0.7$. Due to the positive effect of hot-dip galvanising and the application of composite construction, a significant proportion of the fire protection measures for R30 requirements can be saved. It was also shown that the heating rate increases sharply with increasing height of the profiled sheets with open shape. For higher profiled sheets, such as Comflor80, without additional fire protection measures the assumption of pure 3-sided fire exposure can be questioned and requires further investigation.

ACKNOWLEDGMENT

The research project IGF 21536 N from the GAV - Gemeinschaftsausschuss Verzinken e.V., Düsseldorf, FOSTA - e. V., Düsseldorf and DASt Deutscher Ausschuss für Stahlbau e.V., Düsseldorf and the research project IFG 21403 from DASt, are supported by the Federal Ministry of Economic Affairs and Climate Action the German Federation of Industrial Research Associations (AiF) as part of the programme for promoting industrial cooperative research (IGF) on the basis of a decision by the German Bundestag. The project are carried out at TU-Munich, TU-Braunschweig and at the RWTH Aachen.

REFERENCES

1. M. Mensinger and C. Gaigl, “Feuerwiderstand verzinkter Stahlkonstruktionen”, Stahlbau 88, 1, 3–10, 2019.
2. J. Jirku and F. Wald, “Influence of Zinc Coating to a Temperature of Steel Members in Fire”, Journal of Structural Fire Engineering 6, 2, 141–146, 2015.
3. G. Bihina, B. Zhao, “Hot-dip galvanizing of steel structural members: an alterna-tive to passive fire insulation?”, Proceedings 9. European Conference on Steel and Composite Structures (Eurosteel 2021), 1.-3. September 2021, Sheffield, Großbritannien. https://doi.org/10.1002/cepa.1427.
4. M. Mensinger, S. Pfenning, J. Zehfuß and S. Brunkhorst. 2018. Schlussbericht zu IGF-Vorhaben Nr. 19105 N. Mindestverdübelung von Verbundträgern bei Brand.
5. Gaigl, C.: Fire resistance of hot-dip galvanized steel structures. München, Technische Universität München, Dissertation, 2019.
6. DIN EN 1993-1-2:2010-12, Eurocode 3 (2010) Design of steel structures - Part 1-2: General rules - Structural fire design; German version.
7. DIN EN 1994-1-2:2010-12, Eurocode 4 (2010) Design of composite steel and concrete structures - Part 1-2: General rules - Structural fire design; German version.
8. DIN EN ISO 14713-2 (2020), Zinc coatings - Guidelines and recommendations for the protection against corrosion of iron and steel in structures - Part 2: Hot dip galvanizing; German version.
9. Jiang, S.-C.; Ranzi, G.; Chen, L.-Z. et al.: Behaviour and design of composite beams with composite slabs at elevated temperatures. In: Advances in Structural Engineering 20, 20, 1451-1465.
10. Paliga, K.: Entstehung und Vermeidung von Betonabplatzungen bei extremer Brandeinwirkung. Zugl.: Braunschweig, Techn. Univ., Diss., 2003. Materialprüfanstalt für das Bauwesen, Institut für Baustoffe, Massivbau und Brandschutz der Technischen Universität Braunschweig Heft 172.
11. DIN EN ISO 1461 (2009) Hot dip galvanized coatings on fabricated iron and steel articles - Specifications and test methods (ISO 1461:2009); German version.
12. Martin Mensinger, Christian Gaigl. 2018. Schlussbericht zu IGF-Vorhaben Nr. 18887 N. Feuerwiderstand von feuerverzinkten, tragenden Stahlkonstruktionen im Brandfall.
13. DIN EN 1363-1:2020-05 Fire resistance tests - Part 1: General requirements; German version

COMPARISONS OF THE FIRE PERFORMANCE BETWEEN SQUARE CONCRETE-FILLED STEEL TUBULAR COLUMNS AND SQUARE TUBED-REINFORCED-CONCRETE COLUMNS

Dongdong Yang[1], Faqi Liu[2], Shan-Shan Huang[3], Hua Yang[4]

ABSTRACT

Tubed-reinforced-concrete (TRC) column is an innovated type of composite column that resembles concrete-filled steel tubular (CFST) columns in appearance. Different from CFST columns, the steel tube of a TRC column is terminated at the beam to column connections and the steel tube mainly provides confinement to concrete. In fire conditions, TRC columns may behave very differently as compared to CFST columns. Till now, very few studies have been conducted on the fire behaviour of TRC columns. This paper intends to compare the fire performance of these two kinds of composite columns, which would be helpful to understand the behaviour of TRC columns in fire. Two configurations of CFST columns were investigated, one with rebars and one without. A finite element model was developed using ABAQUS and validated against test results. The effects of load ratios, sectional dimensions, slenderness ratios and load eccentricity ratios on the axial and lateral deformations, load redistributions, fire resistance and failure modes of TRC and CFST columns were analysed. During heating, the axial load is redistributed from the steel tube to the inner section in CFST columns while this load redistribution mainly occurs between concrete and reinforcing bars for TRC columns. The fire resistances of these three kinds of composite are mainly affected by load ratio, sectional dimension and slenderness ratio. The bar-reinforced CFST columns perform best in fire under concentric loading and their fire resistance are around 20% better than those of the TRC columns. As for eccentric loading conditions, the fire performance of TRC columns is the best.

Keywords: Square tubed-reinforced-concrete columns; concrete-filled steel tubular columns; fire performance; comparison; finite element modelling

1 INTRODUCTION

Concrete-filled steel tubular (CFST) columns have become more and more popular in engineering constructions worldwide over the past few decades, due to their high load-bearing capacity, good ductility, excellent seismic performance and ease of construction [1]. As an innovated composite column type, tubed-reinforced-concrete (TRC) columns resemble CFST columns in appearance and possess all the above advantages of CFST columns. However, the steel tube of the TRC column is terminated at the beam-column connections and does not sustain axial load directly though inevitable longitudinal stresses exist due to the

[1] Dr, Department of Civil Engineering, College of Architectural Science and Engineering, Yangzhou University, Yangzhou, 225127, China., e-mail: ddyang@yzu.edu.cn
[2] Dr, Key Lab of Structures Dynamic Behavior and Control, (Harbin Institute of Technology) & Key Lab of Smart Prevention and Mitigation of Civil Engineering Dis-asters (Harbin Institute of Technology), Harbin, 150090, China.
e-mail: fqliu@hit.edu.cn
[3] Dr, Department of Civil and Structural Engineering, The University of Sheffield, Sheffield, S1 3JD, UK.
e-mail: s.huang@sheffield.ac.uk
[4] Professor, Key Lab of Structures Dynamic Behavior and Control, (Harbin Institute of Technology) & Key Lab of Smart Prevention and Mitigation of Civil Engineering Dis-asters (Harbin Institute of Technology), Harbin, 150090, China.
e-mail: yanghua@hit.edu.cn
https://doi.org/10.6084/m9.figshare.22154498

friction and bond at the steel-concrete interface. Since the steel tube of a TRC column is approximately uniaxially loaded in tension in the transverse direction, the tube's local buckling can be generally minimised or significantly delayed and the confinement effect provided by the tube to the concrete core is more effective, as compared to the CFST columns. Generally, relatively thin steel tubes are used in TRC columns and the typical steel to concrete area ratio is 2% - 4%, whereas this ratio is usually between 4% to 20% in CFST columns.

In Europe, bar-reinforced concrete is generally used in CFST columns to improve fire resistance. In China, the concrete infill is mainly plain concrete, and external fire protection is used to provide the required fire rating. Extensive experimental and numerical studies have been carried out on the fire performance of CFST columns, e.g. by Han [1], Lie and Kodur [2], Wang [3], Hong and Varma [4], Romero et al. [5], Tao et al. [6] and Yang et al. [7]. These studies cover CFST columns filled with plain concrete and bar-reinforced concrete. However, studies conducted on the fire behaviour of TRC columns are still limited [8-10]. In fire conditions, the axial load applied on a TRC column is mainly borne by the concrete and reinforcing bars, unlike in the case of a CFST column. Thus, the high-temperature deformation behaviour and failure mode of TRC columns may differ from those of the conventional CFST columns. However, the difference between the fire performance of these two similar composite columns has not been clearly clarified yet.

To provide a better understanding of the working mechanism of TRC columns, the fire performance of TRC columns was analysed in this paper through systemic finite element analysis (FEA) modelling and compared with that of CFST columns. Two configurations of CFST columns were investigated, one with rebars and one without, as shown in Figure 1. To enable comparisons, the total steel consumptions (sum of steel tube and reinforcements) of the analysed columns were identical. Columns under concentric and eccentric loads were investigated. The axial deformation, lateral deformation, internal bending moment, load redistribution, fire resistance and failure mode of these columns were analysed and compared. Based on the FEA modelling, parametric studies were conducted to assess the influence of key parameters, e.g. load ratio, sectional dimension, slenderness ratio, and load eccentricity ratio on the fire resistance of those columns. Finally, an intuitive comparison result of the fire resistance of these three kinds of composite columns was given, to serve as a recommendation for the engineering design.

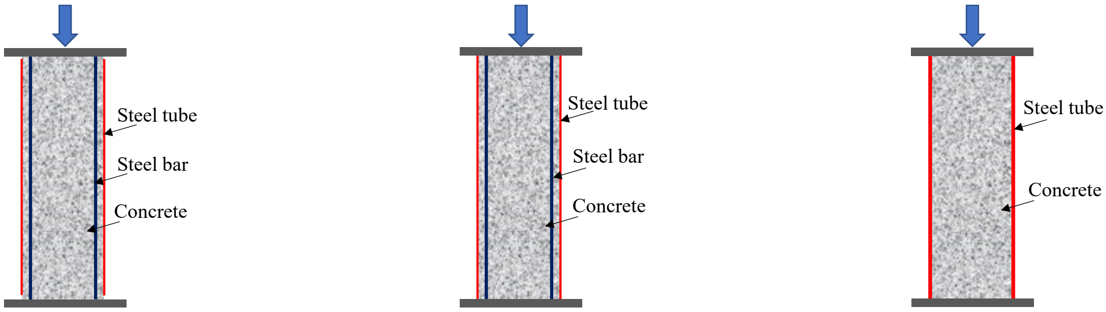

a) TRC b) CFST-bar c) CFST-no bar

Figure 1. Typical illustrations of TRC and two kinds of CFST columns

2 FEA MODELLING AND VALIDATION

2.1 Description of the FEA modelling

A 3-D nonlinear sequentially-coupled thermal-stress FEA model was built to analyse the fire performance of CFST and TRC columns. This model considers the geometrical nonlinearity, material nonlinearity and complex interface behaviour. A pure heat transfer analysis was first conducted and then the temperature outputs were input into the stress analysis model. The meshing details of these two models were the same. There were 15 to 20 elements throughout the column cross section. Due to the geometric and load symmetries, a quarter of each column was built in model.

The details of the heat transfer models of the TRC and CFST columns were identical. ISO 834 standard fire [11] was adopted and the column was exposed to fire at four sides along its whole length. The thermal property models provided by Lie [12] were adopted for concrete and steel. The values for the convective coefficient and emissivity coefficient were 25 W/(m^2·K) and 0.5, respectively. The thermal resistance of 100 W/(m^2·K) was set at the steel-concrete interface. The influence of water evaporation was approximately simulated by modifying the specific heat value of concrete at 100 ºC. The nodes of the rebars were tied to those of the concrete to achieve an identical temperature.

For the stress analysis of TRC columns, the axial load was applied only to the inner reinforced concrete section. For the steel-concrete interface, the interaction in the normal direction was defined using hard contact and a coefficient of 0.3 was used as the coefficient of tangential friction. To model the potential separation between the steel tube and concrete core in axial direction, two steel plates were added to the CFST column model and the steel plates were connected to the steel tube by shell-to-solid coupling. Only normal hard contact was set for the interface between the steel plate and concrete. The high-temperature constitutive model proposed by Lie [12] was adopted for the compressive behaviour of concrete, and the one recommended by Hong and Varma [4] was used for tension. The rebars were embedded in the concrete. The stress-strain relationships in EC4 [13] were used for the steel tube and reinforcements. The thermal expansion coefficient of concrete was assumed to be constant, 6×10^{-6}/ºC [4, 8, 14]. The temperature-dependent thermal expansion coefficients recommended in EC3 [15] were used for the steel tube and reinforcements. The initial geometric imperfection was assumed to be L/1000 multiplied by the amplitude of the first buckling mode given by an eigenvalue buckling analysis, where L is the column length.

2.2 Model validation

The FEA model has been proved effective in predicting the fire behaviour of circular TRC columns [8] and square TRC columns [9]. The model was further validated against fire tests on CFST columns filled with reinforced concrete conducted by Chabot and Lie [16] (SQ-12 and SQ-18) and Espinos et al. [17] (S1 and S5), as well as fire tests on CFST columns filled with plain concrete carried out by Han et al. [18] (SP-2 and SP-3) and Lie and Chabot [19] (SQ-02 and SQ-20). The comparison in the axial-deformation-time relationships between the testing and modelling results are illustrated in Figure 2. Part of the validation results (STCRC-2 and STCRC-3 given in reference [8] and TRC-0.5-0 and TRC-0.5-25 given in reference [9]) for TRC columns are also included in Figure 2. A good agreement was observed, indicating that the FEA model is capable of simulating the high-temperature performance of steel-concrete composite columns.

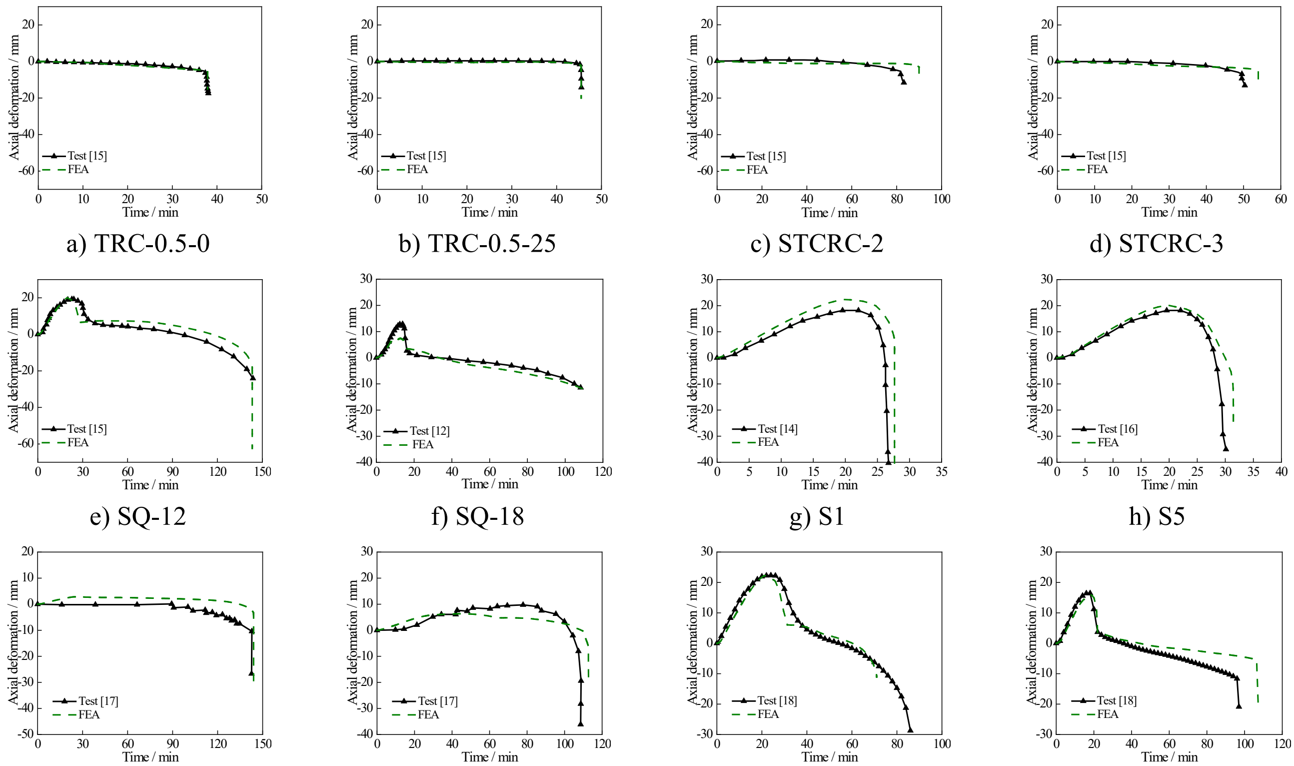

a) TRC-0.5-0 b) TRC-0.5-25 c) STCRC-2 d) STCRC-3

e) SQ-12 f) SQ-18 g) S1 h) S5

i) SP-2 j) SP-3 k) SQ-02 l) SQ-20

Figure 2. Validations of the FEA model against the test results of TRC and CFST columns

3 RESULTS AND DISCUSSIONS

3.1 Deformation behaviour

The fire performance of a TRC column and two CFST columns (one with rebars and one without) were analysed and compared in this section. All columns were of 600 mm square cross section, subject to identical load ratio (0.5). The CFST column with rebars was named as CFST-bar and its steel ratio and reinforcement ratio were the same as those of the TRC column. The other CFST column without rebars was called CFST-no bar. The total steel use of this column equals to the sum of the steel tube and reinforcing bars of the other two bar-reinforced columns. The steel ratio of the TRC column is 3% and its reinforcement ratio is 4%. The concrete cube compressive strength is 50 MPa and the yield strengths of the steel tube and reinforcing bar are 345 MPa and 335 MPa, respectively. The development over time of the axial deformation, lateral deformation, mid-height bending moment of these columns at high-temperature were simulated by the FEA models. The modelling results for columns of 30 and 50 slenderness ratios are displayed in Figures 3 and 4, respectively.

The TRC column experiences no axial elongation and its axial deformation curve can be divided into two parts. The TRC column fails after the occurrence of deformation runaway. The CFST-bar column exhibits very slight axial expansion, no more than 0.3 mm. For column CFST-no bar, the elongation due to steel thermal expansion is obvious, and the max. expansion reaches 1.8 mm. The axial-deformation-time relationships of the CFST columns with and without rebars generally consist of four stages [14]. The axial expansion of column CFST-bar is tiny and this may be attributed to its low steel ratio. The lateral deformation curves of these three composite columns are similar and, at a certain time, column CFST-no bar experiences the largest lateral deformation. The mid-height bending moment-time curves of these three columns resemble the curves for the lateral deformation. It is found that reinforcing bars are necessary in TRC columns to resist bending moments.

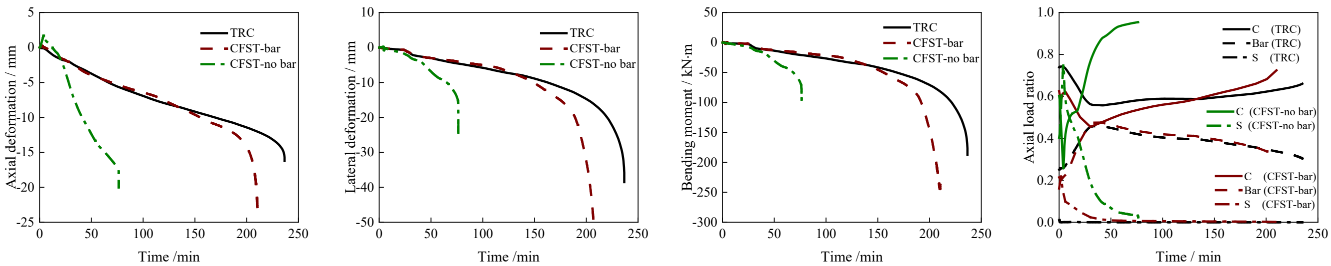

a) Axial deformation b) Lateral deformation c) Mid-height bending moment d) Load redistribution

Figure 3. Comparisons of the fire behaviours between the three kinds of composite columns (D=600 mm, n=0.5, λ=30)

3.2 Load redistribution

Load redistributions occur within the cross-section during heating, due to the differential degradations and thermal expansions of the different materials of a composite column. The load redistributions over heating could reflect the working mechanisms of such columns in fire. The axial loads (in terms of load ratio) distributed to concrete, steel tube and rebars of those columns at the mid-height sections were extracted from the FEA results and are illustrated in Figure 3 d). For CFST columns, the load distribution is in accordance with the axial deformation behaviour. The steel tube is heated the most and so it expands more than the inner reinforced concrete section. Firstly, the axial load is gradually transferred from the inner section to the steel tube until the column reaches its largest axial elongation. Afterwards, the load taken by the steel tube keeps decreasing until failure, due to the strength reduction of the steel tube. It is found that the load in the steel tube at its peak expansion deformation increases with an increase in the tube thickness. For column CFST-no bar, the load ratio of the steel tube increases from 0.4 to 0.75 at 4 min. As expected, the loaded redistribution in the concrete core is opposite to that in the steel tube. For column CFST-bar, its tube thickness is only 4.5 mm and the axial load ratio of the steel tube increases very little, from 0.16 to 0.22. For the two columns with rebars, the axial load is redistributed from the concrete to reinforcing bars until the rebars yield. Although the steel tube of the TRC column is designed not to directly sustain axial load, a very small amount of axial load was found taken by the steel tube. This is due to inevitable interface bond and friction. Comparing Figures 3 and 4, the effect of column slenderness (30, 50) on the load redistribution is insignificant.

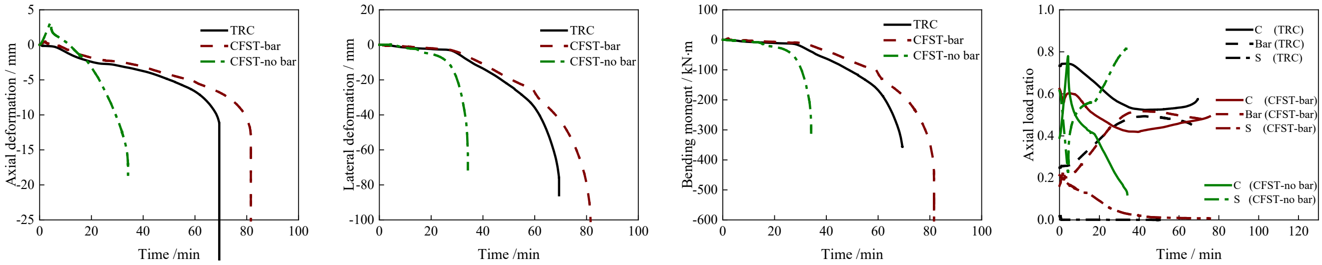

a) Axial deformation b) Lateral deformation c) Mid-height bending moment d) Load redistribution

Figure 4. Comparisons of the fire behaviours between the three kinds of composite columns (D=600 mm, n=0.5, λ=50)

3.3 Failure modes

Figure 5 shows the failure modes of the columns with the above mentioned three cross section configurations of 30 slenderness subject to 0.5 load ratio. All columns fail mainly by global buckling; the local buckling of steel tubes were also overserved. The steel tube local buckling of the TRC column is very little and only occurs at the concave side of the column. This is because the steel tube does not directly sustain axial load, as confirmed by Figure 3 d) and Figure 4 d). For the other two columns, CFST-bar and CFST-no bar, considerate steel tube local buckling occurs on all sides of the columns. The local buckling of column CFST-bar is more severe than that of CFST-no bar. This may be attributed to the fact that the steel tube of the former is much thinner than that of the latter.

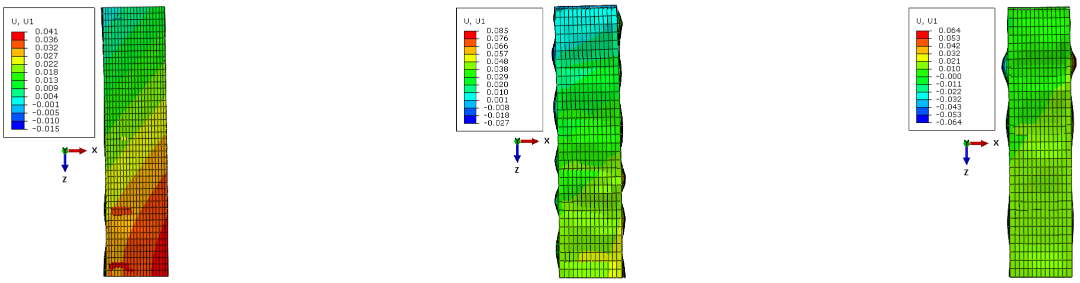

a) TRC b) CFST-bar c) CFST-no bar

Figure 5. Failure modes of these composite columns

3.4 Fire resistance

Figure 6 shows the simulated fire resistances of columns with the above mentioned three cross-section configurations, of various slendernesses (30 - 50) subject to various load ratios (0.5 - 0.8). The failure criteria given in ISO 834 [11] were adopted to define failure.

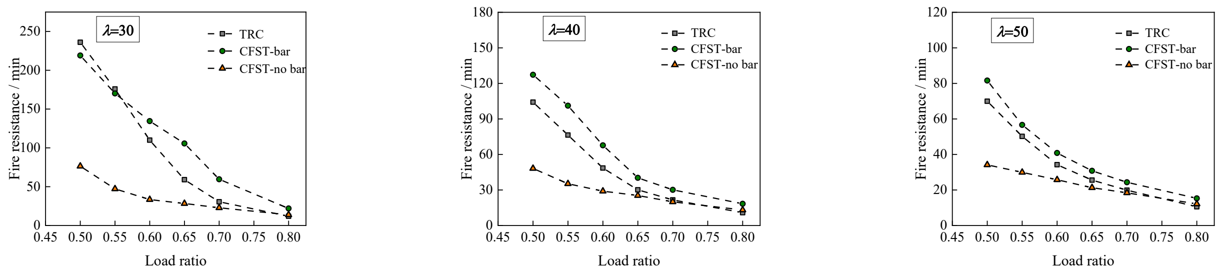

a) λ=30 b) λ=40 c) λ=50

Figure 6. Fire resistance of the three kinds of composite columns under the same axial load ratio (D=600mm)

The fire resistance of the composite columns decreases apparently with the increase of load ratio. When the load ratio maintains constant, column CFST-bar generally has the highest fire resistance while the fire resistance for CFST-no bar is the least. The difference in fire resistance between these three columns may be due to the different ambient-temperature load contributions of their steel tubes. For the CFST column, the steel tube contributes to the capacity directly by sustaining the axial load and indirectly by providing confinement to the inner concrete. However, the steel tube of the TRC column mainly provide confinement to the inner concrete.

When the load ratio maintains constant, the applied loads for these three composite columns are different and that may be another reason for the differences in Figure 6. The ambient-temperature load-bearing capacities of these three kinds of columns of the same steel amount ratio are predicted via FEA modelling and presented in Figure 7. The ambient-temperature capacities of the columns are very close. The average ratio between the load-bearing capacity of the CFST-bar column and that of the TRC column is 0.967 and this ratio is 1.017 for the case of the column CFST-no bar. This could be attributed to the fact that all columns are of the same steel amount ratio. However, in fire, the cooler reinforcing bars contribute more to the capacity than the hotter steel tube does, which can be found in Figure 8.

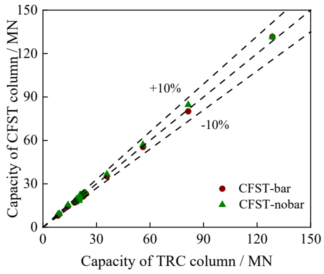

Figure 7. Ambient-temperature load-bearing capacity of these three kinds of columns

a) Temperature b) Strength reduction

Figure 8. Temperatures and strength reductions for the steel tube and rebars

Figure 9 plots the fire resistances of these columns against a normalised load ratio, the ratio between the applied load to the ambient temperature load-bearing capacity of the TRC column. This enables the comparison of the fire resistances of these columns in the context that the applied axial loads are identical. It is found that the difference in fire resistance between the TRC and CFST-bar columns becomes not obvious. This means that these two kinds of composite columns with bar-reinforced concrete infill could achieve almost identical fire performance under the same material usage.

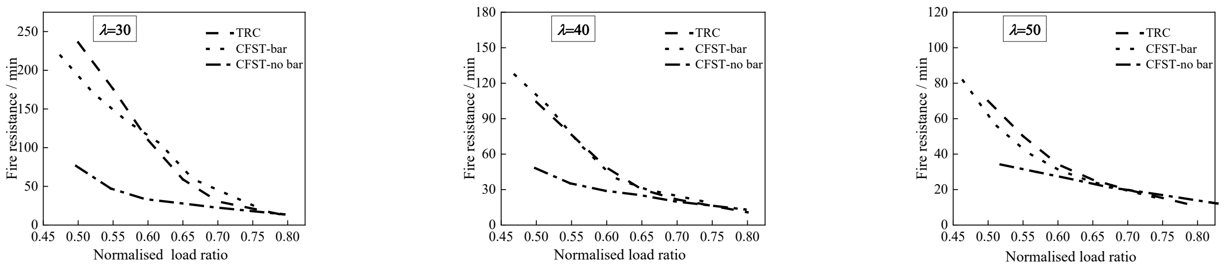

a) λ=30 b) λ=40 c) λ=50

Figure 9. Fire resistance of the three kinds of composite columns under the same axial load (D=600 mm)

4 PARAMETRIC STUDIES

4.1 Columns under concentric loading

Parametric studies were conducted using the developed FEA models. Columns under concentric loading were first analysed. The investigated parameters are load ratio n, sectional dimension D, slenderness ratio λ, concrete cube compressive strength f_{cu}, steel tube yield strength f_y, rebar yield strength f_b, steel ratio α_s and reinforcement ratio α_b. The values of these parameters are listed in Table 1.

Table 1. Values of the investigated parameters for columns under concentric loading

Parameters	Values	Default
Load ratio n	0.4, 0.5, 0.6, 0.7,0.8	0.5
Dimension D (mm)	400, 600, 800, 1000, 1200, 1500	600
Slenderness ratio λ	30, 40, 50	30
Concrete strength f_{cu} (N/mm^2)	30, 40, 50, 60	50
Steel tube strength f_y (N/mm^2)	235, 345, 390, 420	345
Rebar strength f_b (N/mm^2)	335, 400, 500	335
Steel ratio α_s (%)	2.5, 3.0, 3.5, 4.0	3.0
Reinforcement ratio α_b (%)	2.0, 3.0, 4.0, 5.0, 6.0	4.0

The fire resistances of TRC, CFST-bar and CFST-no bar columns of various sectional dimensions and various slenderness ratios are shown in Figures 10 and 11. Generally, the column fire resistance decreases with the increases in load ratio and slenderness ratio, whereas larger sectional dimension leads to higher fire resistance. These results are in accordance with the conclusions in references [1-10]. It is found that sectional dimension and slenderness ratio have significant influences when the load ratio is relatively low, as most of the columns under high load ratios fail very early.

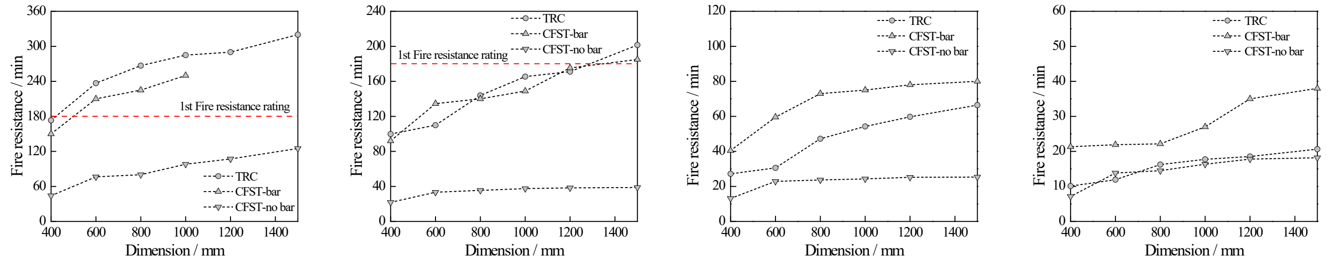

a) n=0.5 b) n=0.6 c) n=0.7 d) n=0.8

Figure 10. Influence of sectional dimension on the fire resistance of columns under concentric loading

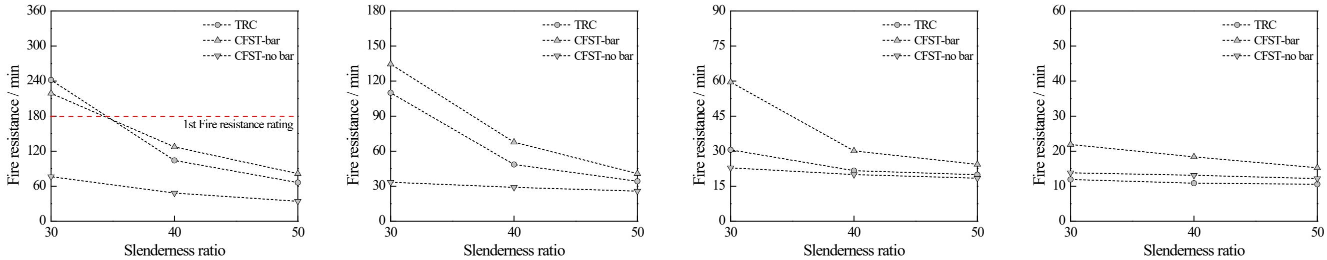

a) n=0.5 b) n=0.6 c) n=0.7 d) n=0.8

Figure 11. Influence of slenderness ratio on the fire resistance of columns under concentric loading

The influence of the concrete compressive strength, steel tube yield strength and reinforcement yield strength on the fire resistance of these composite columns are shown in Figures 12-14. The fire resistances of these three types of composite columns are positively correlated with the concrete strength. This is because the overall temperature of concrete core is relatively low due to its low thermal conductivity and large latent heat, leading to a slight decrease of material property. Therefore, the higher the concrete strength, the lower the load-bearing capacity reduction of the column during heating, and the longer the fire resistance. For TRC and CFST-no bar columns subject to the same load ratio, it is found that columns with steel tubes of higher strength grade have lower fire resistance, as the column capacity is more reliant on the steel tube which is lost very fast in fire.

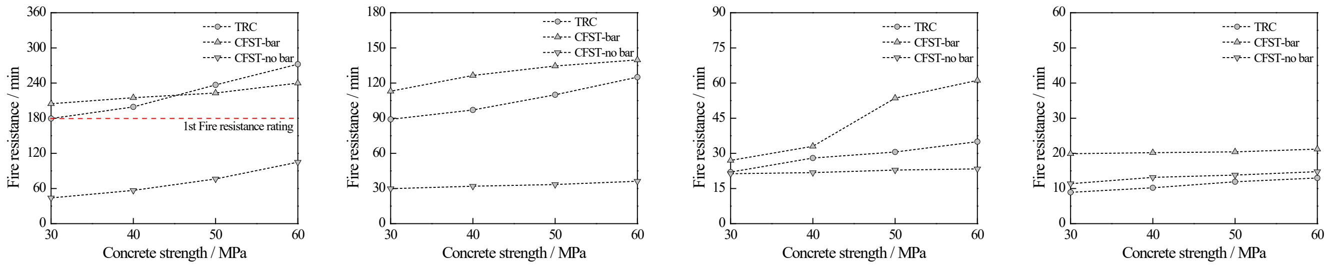

a) n=0.5 b) n=0.6 c) n=0.7 d) n=0.8

Figure 12. Influence of concrete strength on the fire resistance of columns under concentric loading

For TRC columns, higher rebar strength leads to higher fire resistance. This is because that the rebars are not heated much and the increase of rebar strength means a higher contribution of the rebars to the column's capacity in fire. The influence of steel tube yield strength on the fire resistance of column CFST-bar is complicated. For most cases, the fire resistance of the column decreases with the increase of steel tube yield strength and this is in accordance with the trends of the TRC and CFST-no bar columns. However, when the tube yield strength increases from 235 MPa to 345 MPa, the fire resistance of the column increases. This converse trend may be explained by the fact that the difference in the bearing capacities of these two columns with different tube yield strengths is only 0.3%. The applied axial loads of these two columns are almost the same. The steel tube of the column with lower tube yield strength is more prone to local buckling, which governs the column's fire resistance. Increasing the rebar yield strength reduces the fire resistance of column CFST-bar. The reason may be that the axial load on the column increases with the increase of rebar strength, but the thickness and yield strength of the steel tube remain unchanged; the risk of steel tube local buckling therefore increases.

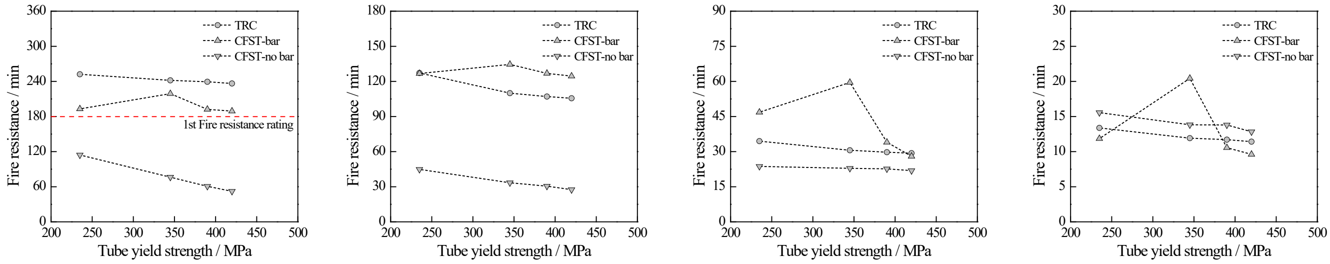

a) n=0.5 b) n=0.6 c) n=0.7 d) n=0.8

Figure 13. Influence of steel tube strength on the fire resistance of columns under concentric loading

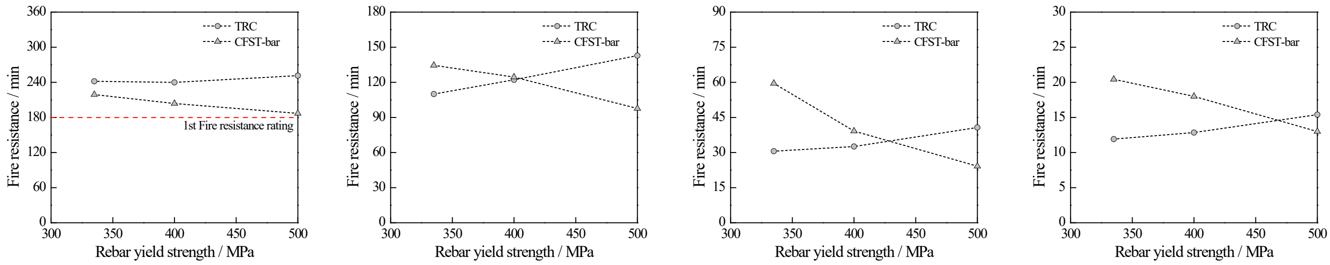

a) n=0.5 b) n=0.6 c) n=0.7 d) n=0.8

Figure 14. Influence of reinforcement strength on the fire resistance of columns under concentric loading

Figures 15 and 16 show the influences of steel to concrete area ratio and reinforcement ratio on the fire resistance of the columns. It should be noted that the steel ratio of column CFST-no bar increases when the reinforcement ratios of the other two columns increase (to keep the total steel use the same between the three cases). Generally, the increase of steel ratio leads to a decrease in fire resistance for all these three kinds of composite columns. When the reinforcement ratio of the CFST column with plain concrete infill exceeds 3%, the increase in reinforcement ratio brings down the fire resistance, possibly caused by the negative influence of steel tube local buckling.

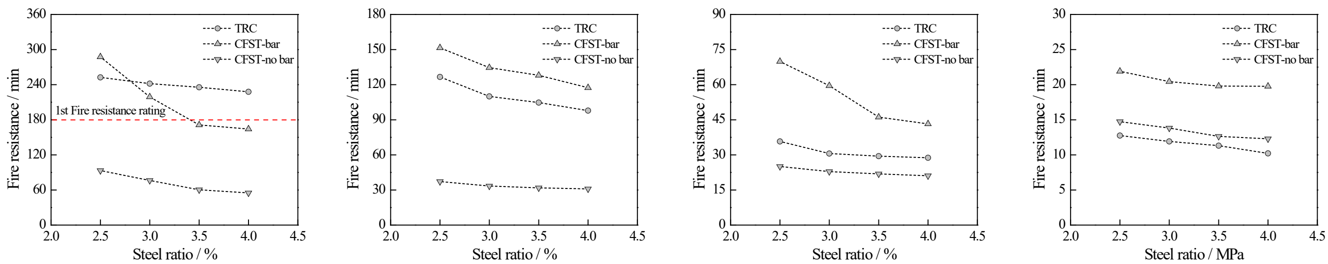

a) n=0.5 b) n=0.6 c) n=0.7 d) n=0.8

Figure 15. Influence of steel ratio on the fire resistance of columns under concentric loading

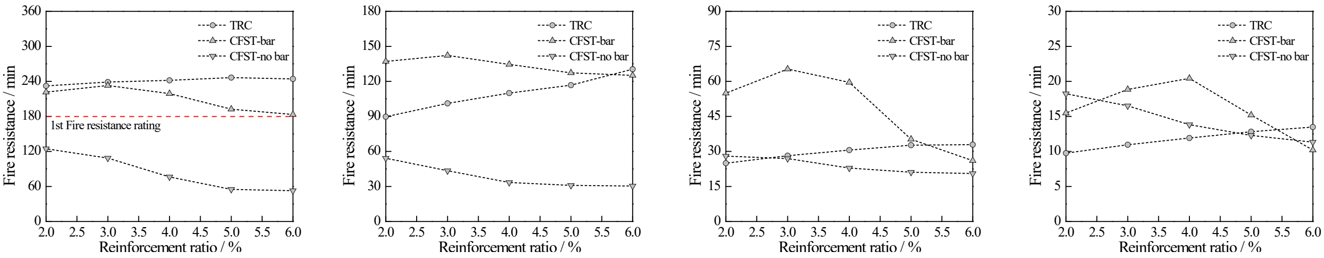

a) n=0.5 b) n=0.6 c) n=0.7 d) n=0.8

Figure 16. Influence of reinforcement ratio on the fire resistance of columns under concentric loading

4.2 Columns under eccentric loading

The influences of load eccentricity on the column fire performance are rather complicated, which can be divided in two folds: a) load eccentricity increases the second-order effect and causes premature failure; b) load eccentricity also leads to a reduction in the compressive force applied on to the column subject to a certain load ratio, which is actually beneficial. Depending on which of these two counteracting effects is dominant, the influence of the load eccentricity varies. To compare the fire performance of TRC and CFST columns under eccentric loading, parametric studies are carried out in this section. The investigated parameters are load ratio n (0.5 - 0.7), slenderness ratio λ (30 - 50) and load eccentricity ratio $2e/D$ (0 - 1.0). Other parameters are set as the default values given in Table 1. It needs to be noted that the load eccentricity ratio studied in this section is relatively low, since TRC columns rely on the steel tube to provide confinement to the concrete, which is largely effective under compression rather than bending [20]. The effect of load eccentricity ratio on the load-bearing capacity at ambient temperature of composite columns is first assessed, as it affects the definition of load ratio.

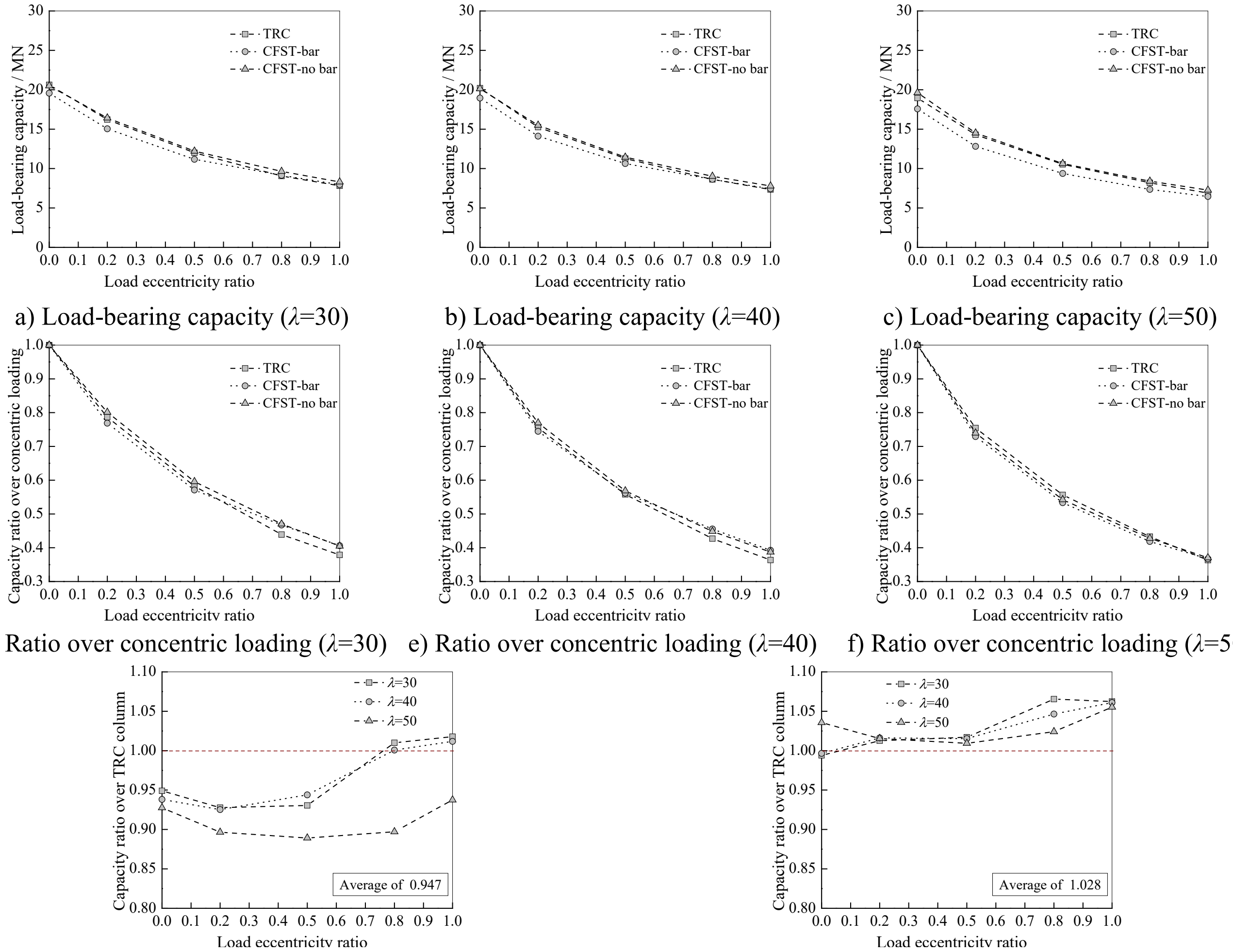

a) Load-bearing capacity (λ=30) b) Load-bearing capacity (λ=40) c) Load-bearing capacity (λ=50)

d) Ratio over concentric loading (λ=30) e) Ratio over concentric loading (λ=40) f) Ratio over concentric loading (λ=50)

g) Capacity ratio over TRC column (CFST-bar) h) Capacity ratio over TRC column (CFST-no bar)

Figure 17. Influences of load eccentricity ratio on the ambient-temperature load bearing capacity of TRC and CFST columns

The calculated results for columns with various slenderness ratios and load eccentricity ratios are shown in Figure 17. For all the three types of columns, the load-bearing capacity decreases continually as the load eccentricity increases. When $2e/D$ is higher than 0.5, the negative effect of load eccentricity on the load-bearing capacity of a TRC column is more significant than the case of a CFST column. This indicates TRC columns are suitable to be used in conditions of relatively low load eccentricity, in terms of ambient-temperature loading bearing. As shown in Figure 17 h), the bearing capacity of a CFST-no bar column is always higher than that of its TRC counterpart, which is consistent with the conclusions drawn in Figure 7. In most cases (relatively high slenderness ratio and relatively low load eccentricity ratio), the load-bearing capacity of a CFST-bar column is inferior to that of a TRC column. For the example columns investigated in Figure 17, the average ratio between the load-bearing capacity of the CFST-bar column and that of the TRC column is 0.947 and this ratio is 1.028 for the case of the column CFST-no bar.

The influences of load eccentricity ratio on the FEA calculated fire resistances of TRC, CFST-bar and CFST-no bar columns are shown in Figure 18. It is interesting to find that the development of fire resistance over load eccentricity ratios vary depending on the type and slenderness ratio of the column. For TRC columns and CFST-no bar columns with a relatively low slenderness ratio (i.e. 30), the fire resistance decreases as load eccentricity ratio increases from 0 to 0.2. After the load eccentricity ratio exceeds 0.2, its negative influence on the fire resistance is insignificant. For the TRC and CFST-no bar columns of a relatively high slenderness ratio (i.e. 50), the effect of load eccentricity on fire resistance is generally negligible and this is consistent with experimental observations [9]. However, the case for the CFST-bar columns is different. The fire resistance of eccentrically-loaded CFST-bar column generally decreases continually with the load eccentricity increases, regardless of the slenderness ratio. The main reason may be the steel tube in the column is very thin and is subject to axial load directly. Increasing load eccentricity increases the negative effect of local buckling on the fire performance of the column.

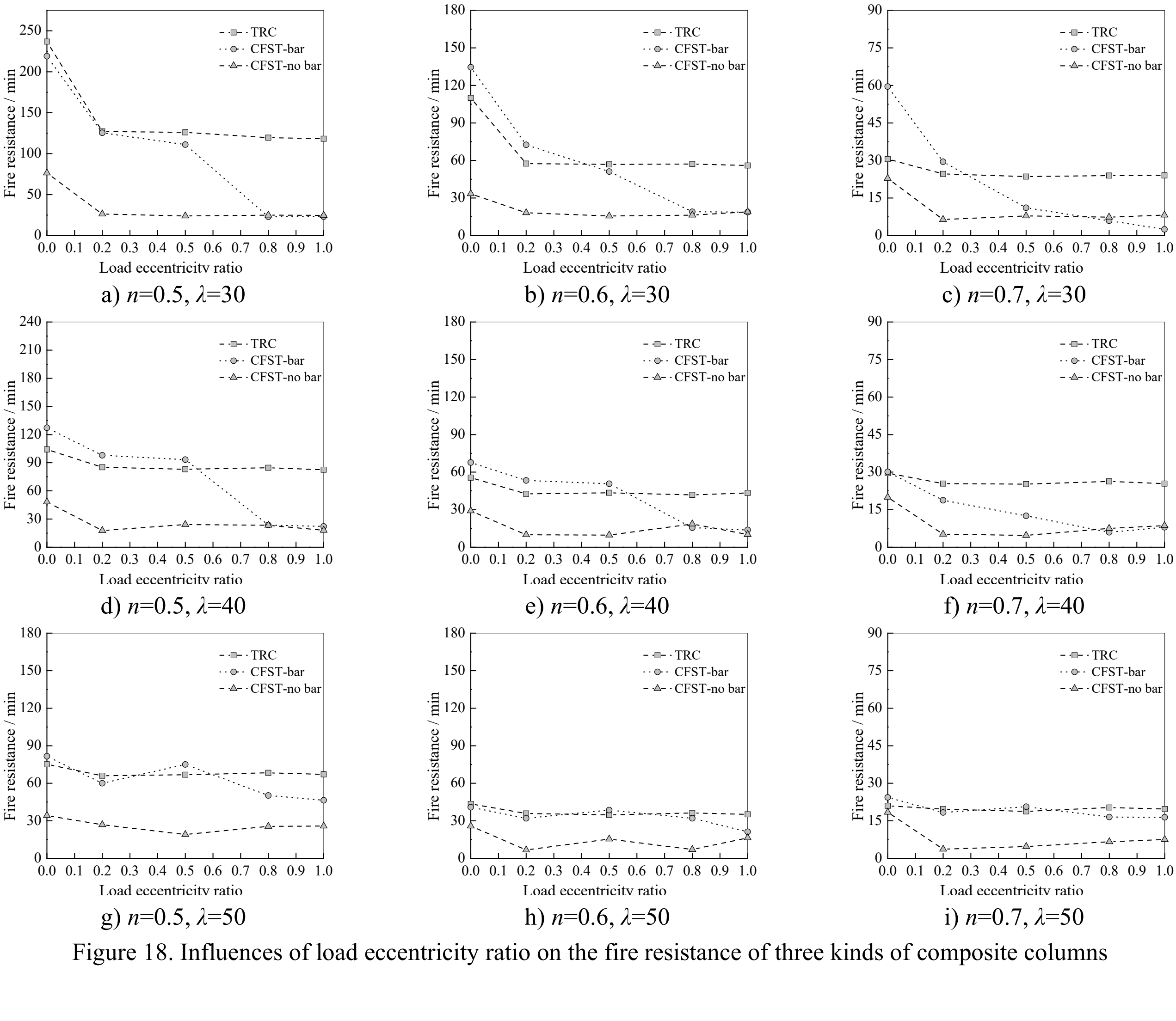

Figure 18. Influences of load eccentricity ratio on the fire resistance of three kinds of composite columns

It is concluded from Figure 18 that load eccentricity affects the fire resistance of the composite columns of a relatively low slenderness more than the other slenderer columns. When the load eccentricity is comparatively small, i.e. $2e/D$ is lower than 0.5, the fire resistance of the CFST-bar column is the highest, followed by that of the TRC column. However, the TRC column performs best in the condition of a relatively large load eccentricity ratio. Considering the applied load onto a TRC column is generally larger than that onto a CFST-bar column under the same load ratio, it is therefore speculated that TRC columns could achieve excellent fire performance under both concentric and eccentric loading conditions.

4.3 Result summary

Figure 19 summaries all fire resistances calculated in the above parametric studies. The fire resistance of the TRC columns is set as reference and the comparison result is based on the same load ratio of each column. For concentrically-loaded columns, in average, the fire resistance of the CFST-bar columns is 20% higher that of the TRC columns, while the fire resistance of the CFST-no bar columns is 40% lower than that of the TRC columns. This indicates that the TRC columns perform slightly worse in fire than the CFST columns filled with bar reinforced concrete. If the applied load is set to be the same, the fire resistance of the columns TRC and CFST-bar may be comparable. It should be pointed out that the fire resistance of a TRC column is lower than that of the CFST-bar column only when the fire resistance is lower than 150min, whereas the former column behaves better in fire than the latter for the relatively long fire resistance cases. As shown in Figure 19 b), the fire resistance of TRC columns is the highest when the load is applied eccentrically. In particular, the fire resistance of a CFST-bar column is around 84% of that of the TRC column, the TRC-no bar column only achieves 33% of the TRC column's fire resistance.

a) Concentric loading b) Eccentric loading

Figure 19. Comparisons of fire resistance between TRC and CFST columns

It is concluded from Figure19 that the majority of steel should be arranged into the section as longitudinal reinforcement rather than as external steel tube, to achieve better fire resistance, for either concentric or concentric loading cases. It should be pointed out that the main aim of this research is to compare the fire performance of TRC columns with that of traditional CFST columns. To keep the total steel usage the same between the different column types to facilitate comparisons, the steel to concrete area ratio of CFST-bar columns adopted in this research is lower than the typical value (4%-20%) used in engineering practice.

5 CONCLUSIONS

The fire performances of TRC and CFST columns were compared via 3D sequentially-coupled FEA modelling. The following key conclusions could be drawn based on the analysis results:

1) During heating, the axial load is redistributed from the steel tube to the inner section in CFST columns. For the TRC columns, the load redistribution mainly occurs between concrete and reinforcing bars. Local buckling of steel tube has a very significant detrimental effect on the fire performance of CFST columns.

2) Load ratio, slenderness ratio and sectional dimension have significant influences on the fire resistance of CFST and TRC columns. The negative effect of load eccentricity on the fire resistance of CFST-bar columns is the largest among the three column types. Generally, load eccentricity affects the fire resistance of the composite columns of a relatively low slenderness more than the other slenderer columns.

3) In general, the more the steel tube contributes to the ambient-temperature loading-bearing capacity of a composite column, the worse the column performs (in terms of fire resistance period) in fire. It is recommended to arrange the majority of steel as longitudinal reinforcement rather than as steel tube.

4) The bar-reinforced CFSTs have the highest fire resistance under concentric loading, which is slightly higher than that of the TRC columns. Under eccentric loading, the fire performance of TRC columns is the best. The fire resistance of the CFST without rebars is far worse than those of the other two columns.

ACKNOWLEDGMENT

The research work in this paper is financially supported by the National Natural Science Foundation of China (51978209) and the Natural Science Foundation of the Jiangsu Province of China (BK20220592), to which the authors are grateful.

REFERENCES

1. L.H. Han, Theory and practice of concrete-filled steel tubular structure (third edition), Beijing: Science Press, 2016. [in Chinese]
2. L. L. Lie, and V. K. R. Kodur, "Fire resistance of steel columns filled with bar-reinforced concrete," J. Struct. Eng., vol. 122, p.p. 30-36, 1996.
3. Y.C. Wang, Steel and composite structures-behaviour and design for fire safety, London: Spon Press, 2002.
4. S. Hong, and A. H. Varma, "Analytical modeling of the standard fire behavior of loaded CFT columns," J. Constr. Steel Res., vol. 65, p.p. 54-69, 2009.
5. M. L. Romero, V. Moliner, A. Espinos, C. Ibañez, and A. Hospitaler, "Fire behavior of axially loaded slender high strength concrete-filled tubular columns," J. Constr. Steel Res., vol. 67, pp. 1953-1965, 2011.
6. Z. Tao, M. Ghannam, T. Y. Song, and L. H. Han, "Experimental and numerical investigation of concrete-filled stainless steel columns exposed to fire," J. Constr. Steel Res., vol. 118, pp. 120-134, 2016.
7. H. Yang, L. H. Han, and Y. C. Wang, "Effects of heating and loading histories on post-fire cooling behaviour of concrete-filled steel tubular columns," J. Constr. Steel Res., vol. 64, pp. 556-570, 2008.
8. F. Q. Liu, Y. Y. Wang, L. Gardner, and A. H. Varma, "Experimental and numerical studies of reinforced concrete columns confined by circular steel tubes exposed to fire," J. Struct. Eng., vol. 145, 04019130, 2019.
9. D. D. Yang, F. Q. Liu, S. Huang, and H. Yang, "ISO 834 standard fire test and mechanism analysis of square tubed-reinforced-concrete columns," J. Constr. Steel Res., vol. 175, 106316, 2020.
10. D. D. Yang, F. Q. Liu, S. Huang, and H. Yang, "Structural fire safety design of square and rectangular tubed-reinforced-concrete columns," Structures, vol. 29, pp. 1286-1321, 2021.
11. ISO, Fire resistance test–Elements of building construction, Part 1: General requirements. Geneva, 1999.
12. T. T. Lie, "Fire resistance of circular steel columns filled with bar-reinforced concrete," J. Struct. Eng., vol. 120, pp. 1489-1509, 1994.
13. CEN, Design of composite steel and concrete structures - Part 1-2: General rules - Structural fire design. Brussels. EN 1993-1-2, Eurocode 3 - Design of Steel Structures - Part 1-2: General Rules - Structural Fire Design, CEN, Brussels, 2005.
14. A. Espinos, M. L. Romero and A. Hospitaler, "Advanced model for predicting the fire response of concrete filled tubular columns," J. Constr. Steel Res., vol. 66, pp. 1030-1046, 2010.
15. CEN, Design of steel structures - Part 1-2: General rules - Structural fire design. Brussels, 2005.
16. M. Chabot and T. T. Lie, "Experimental studies on the fire resistance of hollow steel columns filled with bar-reinforced concrete". Ottawa: NRC-CNRC, Inst. Res. Constr., Internal Rep. No. 628, 1992.
17. A. Espinos, M. L. Romero, E. Serra and A. Hospitaler, "Circular and square slender concrete-filled tubular columns under large eccentricities and fire," J Constr Steel Res., vol. 110, pp. 90-100, 2015.
18. L. H. Han, Y. F. Yang and L. Xu, "An experimental study and calculation on the fire resistance of concrete-filled SHS and RHS columns," J Constr Steel Res., vol. 59, pp. 427-452, 2003.
19. T.T. Lie and M. Chabot, "Experimental studies on the fire resistance of hollow steel columns filled with plain concrete". Ottawa: NRC-CNRC, Inst. Res. Constr., Internal Rep. No. 611, 1992.
20. H. Yang, F.Q. Liu and L. Gardner, "Post-fire behaviour of slender reinforced concrete columns confined by circular steel tubes," Thin-Walled Struct., vol. 87, pp. 12-29, 2015.

SiF 2022– The 12th International Conference on Structures in Fire
The Hong Kong Polytechnic University, Nov 30 - Dec 2, 2022

EFFECT OF STRUCTURAL DAMAGE ON THE THERMAL RESPONSE OF CFST COLUMNS

Smita Singh[1], Prithvi Sangani[2], Anil Agarwal[3]

ABSTRACT

Concrete-filled steel tubular (CFST) members are efficient structural members which are currently increasingly used in the construction industry. Under multi-hazard loading conditions, columns are often subjected to structural damage followed by thermal loading due to fire. This article studies the effect of mechanical damage on the thermal response of CFT columns through a detailed experimental program. Circular and square stub CFST columns were subjected to structural damage by applying axial compression and eccentric compression loading. The columns were loaded to three different levels of damage: (a) no mechanical loading, (b) loading to a maximum deformation of 10 mm at the ends, and (c) loading to a maximum deformation of 19 mm at the ends, respectively. The concentric compression (CC) and eccentric compression (EC) loading were done in a displacement-controlled manner. The corresponding deformation field in the steel tube was recorded digitally using the digital image correlation (DIC) technique. Subsequently, the specimen was unloaded and heated by placing them in a furnace. The temperature in the furnace cavity followed the ISO-834 standard fire curve for 1-hour followed by 2-hour cooling. The insulation effect of the gap created between the steel tube and concrete core, as well as increased resistance to the heat flow due to the development of cracks in concrete, is critical for predicting the temperatures inside the concrete core.

Keywords: Steel-concrete composite columns; Steel-concrete interface behavior; fire tests; Structural fire behavior

1 INTRODUCTION

The CFST columns have gained wide recognition in the past decade in the construction industry and are being widely used. In CFST columns, concrete is filled inside the steel tube, and the structural profile of CFST columns varies in geometry.

When the CFST specimens are subjected to thermal loading steel tube heats up first, and then, because of conduction, the concrete slab heats up. When the outer surface of the specimen is heated to high temperatures, the steel tube goes through large thermal stresses and separates from the concrete core. This separation can further accelerate due to the vapour pressure. When the steel tube separates from the concrete core, it creates a layer of air which works as an insulator and hence slows the rate of temperature rise at the surface of the concrete core. Few researchers have discussed the effect of the gap between steel and concrete in a composite system which has been discussed in the following paragraphs.

[1] Research Scholar, Department of Civil Engineering, Indian Institute of Technology, Hyderabad.
e-mail: ce17resch11007@iith.ac.in, ORCID: https://orcid.org/0000-0003-2997-7651
[2] Research Scholar, Department of Civil Engineering, Indian Institute of Technology, Hyderabad.
e-mail: ce20resch13001@iith.ac.in, ORCID: https://orcid.org/0000-0003-4815-5426
[3] Associate Professor, Department of Civil Engineering, Indian Institute of Technology, Hyderabad.
e-mail: anil@ce.iith.ac.in, ORCID: https://orcid.org/0000-0002-3902-4304

https://doi.org/10.6084/m9.figshare.22154507

Multiple tests with composite beams have been undertaken by Guo and Bailey [1] in natural fire circumstances, including heating and cooling cycles of fire. During the heating process, they reported that the deck was separated from the concrete slab.

Shivam et al. [2] have shown that it is essential to take the insulating effect of the space between the steel deck and concrete slab into account when predicting the temperatures in the slab. This can have a substantial impact on the slab's estimated fire resistance rating.

Espinos et al. [3] have studied the behaviour of elliptical CFST columns under fire loading numerically. They have assumed a constant value of conductance of 200 W/m2-K between the steel tube and concrete core. And they found that the mechanical behaviour of CFST is affected by the interface created between the steel tube and concrete core.

The objective of this research is to understand the effect of applied mechanical damage on the CFST columns on the fire response of CFST columns and ultimately correlate its effect on fire resistance. The DIC data will be used to correlate the lateral deformations of the buckled steel tube with the temperatures inside the concrete core.

2 EXPERIMENTAL PROCEDURE

Using a comprehensive experimental protocol, this study investigates the impact of mechanical damage on the thermal response of CFT columns. Axial compression and eccentric compression loads were used to cause structural damage to circular stub CFST specimens, and their details are shown in table 1. Specimens are labelled based on the type of loading and level of axial deformation applied to them. Specimen labelled as CC-10 represents the circular specimen subjected to concentric compression of 10mm axial deformation.

During the casting, thermocouples were placed inside the concrete core. Thermocouples labelled C1 to C5 were placed inside the concrete core, while the thermocouples labelled as S1 and S2 were spot welded to the steel tube. The location of thermocouples is shown in figure 5(b).

Table 1. Details of the CFST specimens

Specimen	L (mm)	D×t (mm)	f_c(MPa)	f_y(MPa)	E_s (GPa)	Axial Deformation (mm)	Type of Loading
CC-10	350	165.1×4.8	25	446	200	10	Concentric
CC-19	350	165.1×4.8	25	446	200	19	Concentric
EC-10	350	165.1×4.8	25	446	200	10	Eccentric
EC-19	350	165.1×4.8	25	446	200	19	Eccentric
Undamaged	350	165.1×4.8	25	446	200	0	---

The columns were loaded to three different levels of damage: (a) no mechanical loading, (b) loading to a maximum deformation of 10 mm at the ends, and (c) loading to a maximum deformation of 19 mm at the ends, respectively. The concentric compression (CC) and eccentric compression (EC) loading were done in a displacement-controlled manner. Hence, the following four loading cases are considered in the study CC 10, CC 19, EC 10, and EC 19. The corresponding deformation field in the steel tube was recorded digitally using the digital image correlation (DIC) technique. Figure 1 presents the experimental setup, 3-D DIC setup, an image of a damaged specimen, and the stitched all-around image developed from the DIC data. Subsequently, the specimen was unloaded and heated by placing them in a furnace. Figure 2 presents the images of damaged specimens before heating. Figure 3 presents the scanned image using the 3-D DIC for specimen CC-19.

After mechanical damage, specimens were placed inside the furnace and subjected to fire loading. The temperature in the furnace cavity followed the ISO-834 standard fire curve [4] for 1-hour as shown in figure 3. The K-type thermocouples placed inside the specimens recorded the temperature-time histories at different locations in each column. The temperature inside the specimens is shown in figure 4.

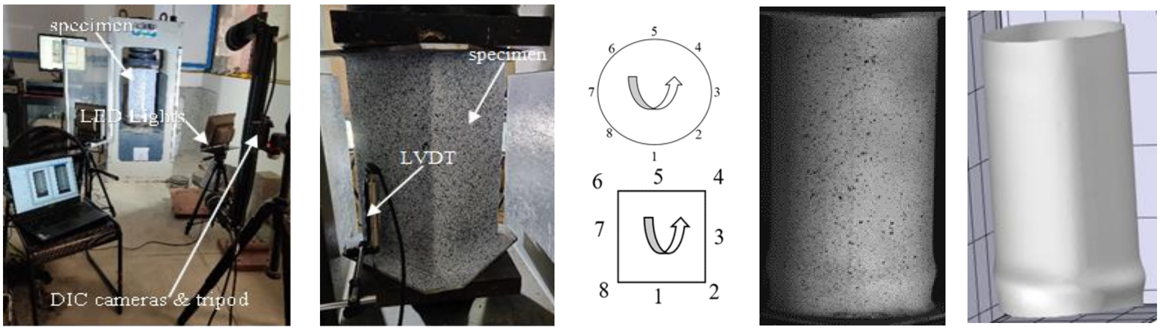

(a) DIC Setup (b) LVDT setup (c) markers (d) after damage (e) Scanned image

Figure 1. Experimental Setup & Circumferential markers for scanning

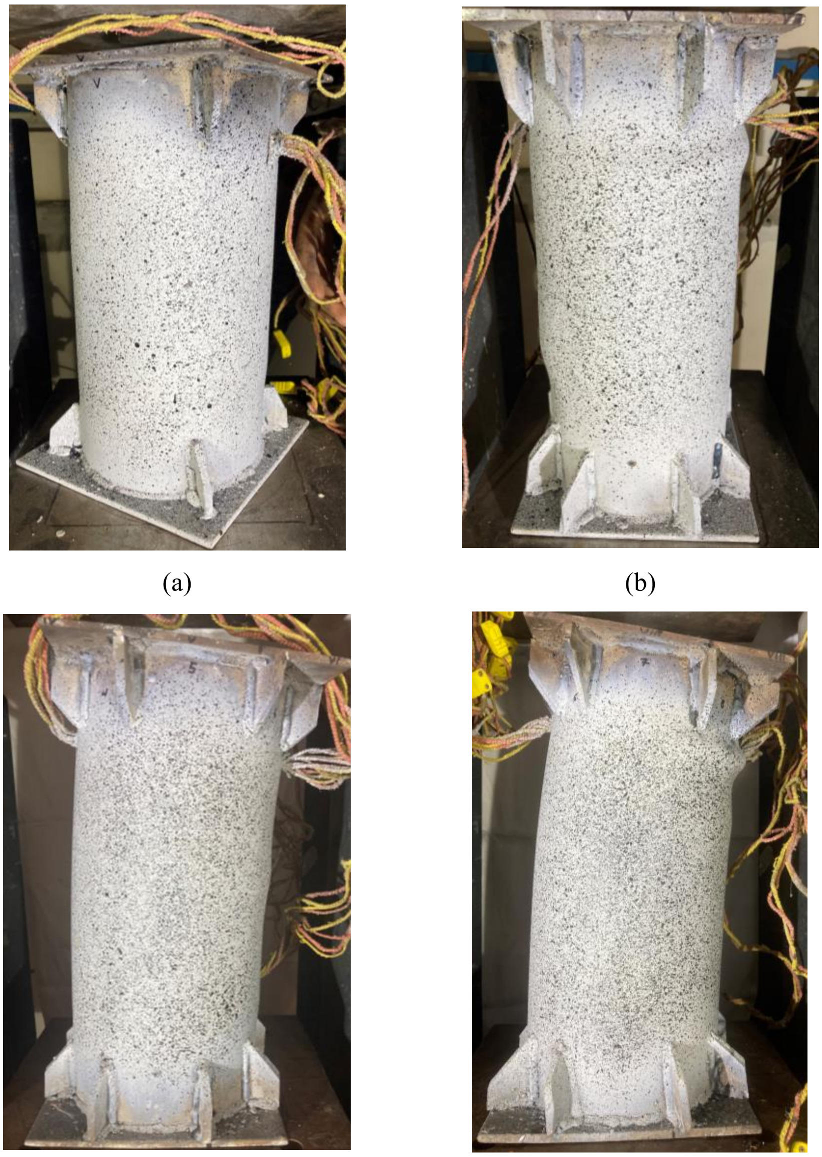

(a) (b)

(c) (d)

Figure 2. Images of specimens after mechanical damage (a)CC-10 (b) CC-19 (c) EC-10 (d) EC-19mm

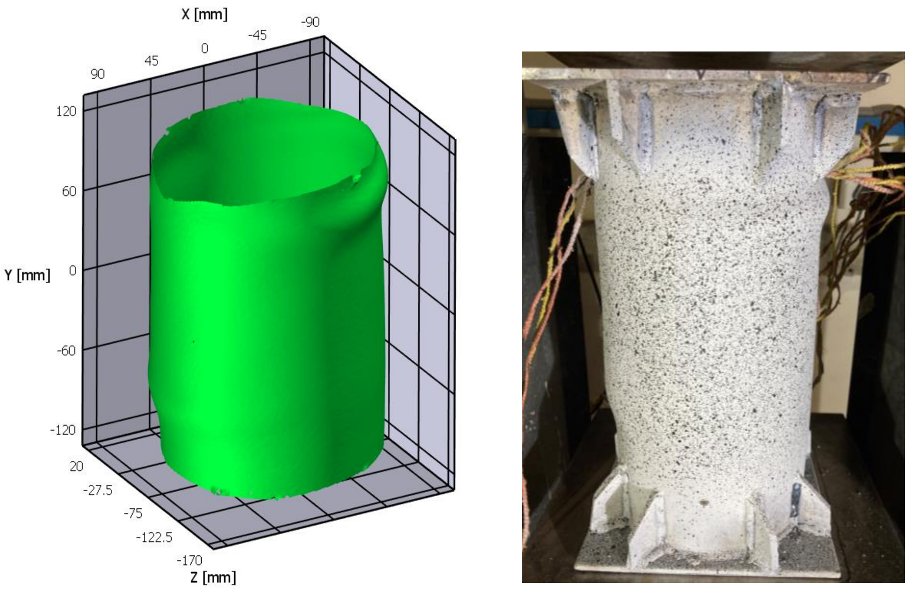

(a) 3-D scan image (b) Image after mechanical damage

Figure 3. Comparison of the specimen after mechanical damage with scanned image after scanning using 3-D DIC

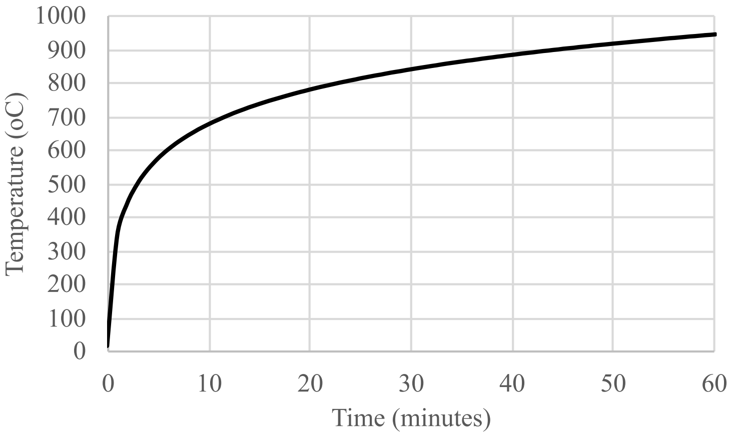

Figure 4. The ISO 834 temperature-time curve

The results presented in this article are a part of ongoing research. The initial experimental results show that even for undamaged columns, differential thermal expansion between the steel tube and the concrete core creates a separation between the two, which acts as a thermal barrier during the heating of the column. Compare the temperature plots of Undamaged-S5 and Undamaged-C5 in Fig. 5(b). The temperatures in the outer portion of the concrete are further reduced due to the local buckling of the steel tube in pure axial compression (CC_19-C5). Due to eccentric compression, the side subjected to a greater amount of compression (C4) experiences a slower temperature rise in comparison to the opposite side (C2) as shown in Fig. 5(c). However, as shown in Fig. 5(d), the temperatures at the centre of the cross-section are affected relatively less by the damage and almost unaffected by the eccentricity in the loading.

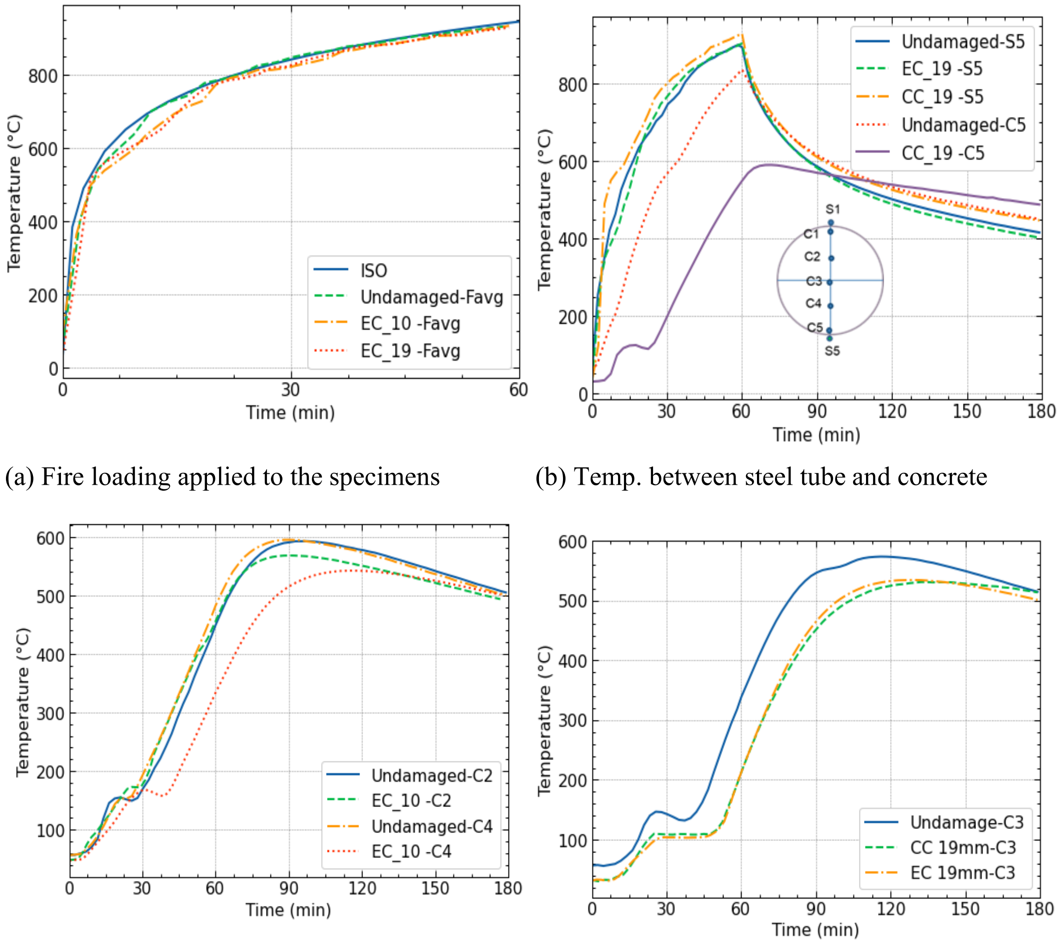

(a) Fire loading applied to the specimens

(b) Temp. between steel tube and concrete

(c) Temp. inside concrete core

(d) Temperatures at the centre location

Figure 5. Temperature profile inside concrete core and steel tube

3 CONCLUSIONS

In this paper, an experimental study was conducted on the CFST specimens the study the effect of mechanical damage on thermal response. The experimental results demonstrated that the temperature at the centre of the specimen is less affected by the damage and the effect is almost negligible in the eccentric compression case.

Due to eccentric compression, the side undergoing a larger degree of compression experiences a slower increase in temperature compared to the opposite side.

Further experiments are being conducted to better understand and quantify the effect of structural damage on thermal response. We are also trying to develop a numerical model from the scanned model after the mechanical damage was introduced and then do the fire analysis on the FE model generated by importing the scanned model.

ACKNOWLEDGMENT

The authors are thankful to the Ministry of Education, Government of India, for the sponsorship which helped in carrying out this research work. The authors would also like to acknowledge the support provided by Pyrodynamics, Bengaluru, for setting up 3D-DIC.

REFERENCES

1. Guo, S., & Bailey, C. G. (2011). Experimental behaviour of composite slabs during the heating and cooling fire stages. *Engineering structures*, *33*(2), 563-571.
2. Sharma, S., Vaddamani, V. T., & Agarwal, A. (2019). Insulation effect of the concrete slab-steel deck interface in fire conditions and its influence on the structural fire behaviour of composite floor systems. *Fire Safety Journal*, *105*, 79-91.
3. A. Espinos, L. Gardner, M.L. Romero, A. Hospitaler, Fire behaviour of concrete filled elliptical steel columns, Thin-Walled Struct. 49 (2) (2011) 239–255.
4. ISO 834-1. Fire resistance tests – elements of building construction –part 1: general requirements. International Standard ISO 834, Geneva;1999

RECONSTRUCT THE LOAD REDISTRIBUTION PATHS IN MULTI-FLOOR FIRE SCENARIOS USING 3D STRUCTURAL MODELS

Jin Qiu[1], Xuesong Cai[2], Liming Jiang[3], Asif Usmani[4]

ABSTRACT

Considering the slabs in the global response of steel framed buildings in fires is important. The deflected floor slabs could redistribute the load to columns leading to column failure and even progressive collapses. Tensile membrane action developed in the composite floor systems helps enhance the structural resistance against collapse. This two-fold role played by floor systems makes it important to reconstruct the collapse modes by analysing the load redistribution mechanisms after considering the slab effect. This paper numerically investigates the load redistribution mechanisms in steel-concrete composite structures subjected to multi-floor spreading fires after considering the slab effect. A 3D mid-rise steel framing office building based on the Cardington building prototype is designed and modelled, where the composite slabs are simulated using a high-efficient slab model with integrated section to simplify the modelling efforts and to enhance the computation efficiency. Four hazard scenarios distinguished by the state of the column (i.e., fully protected, partially protected or failed) in the middle of fire region on different floors are designed. The study shows that the 3D structural building can survive the multi-floor spreading fires under these four scenarios even when the columns are assumed to fail at two floors. Nearly all loads are transferred to the four columns that have connection with the failed column via beams. The 'pull up' effect of floor system plays crucial important in bridging over the failure of columns.

Keywords: Multi-storey buildings; load redistribution; failure mechanism; multiple floor fires; OpenSees

1. INTRODUCTION

Investigations on system-level behaviour of structures in fires have been performed in the past several decades. The full-scale Cardington fire tests [1] in a 8-storey composite steel-framed building presented the mechanisms such as restraint effect on steel frame members and the tensile membrane action of composite slabs in fire, which underlines the shortcomings of fire tests conducted on isolated structural members under prescriptive fire load such as the standard fire curve. The full-scale test findings revealed the importance of considering structural member interaction and load redistribution in a structural system subjected to fire action. With the evolved understanding of the fire resistance of modern steel framed buildings, many research efforts have been devoted to the performance-based fire safety design aiming to reduce the fire protection costs and to maintain the fire safety performance [2–4]. On the other hand, those catastrophic building collapses in fire, such as the WTC buildings in 2001, the Windsor Tower in 2005, the Plasco

[1] Ms., Department of Building Environment and Energy Engineering, The Hong Kong Polytechnic University
e-mail: jinjin.qiu@connect.polyu.hk, ORCID: https://orcid.org/0000-0002-0603-854X
[2] Dr., YanTai Research Institute, Harbin Engineering University
e-mail: caixuesongbest@hrbeu.edu.cn, ORCID: https://orcid.org/0000-0003-3353-2479
[3] Dr., Department of Building Environment and Energy Engineering, The Hong Kong Polytechnic University
e-mail: liming.jiang@polyu.edu.hk, ORCID: https://orcid.org/0000-0001-8112-2330
[4] Prof., Department of Building Environment and Energy Engineering, The Hong Kong Polytechnic University
e-mail: asif.usmani@polyu.edu.hk, ORCID: https://orcid.org/0000-0003-2454-5737
https://doi.org/10.6084/m9.figshare.22154507

Building in 2017, have warned the community of the risk of fire induced structural failure. Especially, the collapse of WTC 7 building was the solely due to the spread fire.

A progressive collapse is defined as the disproportionate spread of failure which eventually leads to the overall collapse of the building. To explore the progressive collapse mechanisms initiated from local failure, many research works have been performed. Two failure modes were identified by Ali et al. [6] through thermo-mechanical analysis on a single-story two-span bare steel frames, exhibiting differently inward or outward deformed shapes due to the heated columns. Jiang et al. [7] suggested four collapse mechanisms of steel frames under different load ratios, beam sizes and fire scenarios, which were found triggered by the buckling of the heated columns. The bracing system is widely adopted in the steel framed structures to enhance the horizontal resistance against wind force and earthquake force. Some studies [8–10] focusing on the effect of braces on the collapse behaviour of structures in fire revealed that the vertical bracing system could decrease the effect of deflected beams on heated columns, and enhance the resistance to progressive collapse when the heated columns failed. The benefit of hat trusses on preventing the collapse of long-span truss frame was found by Flint et al. [11], as the hat truss system could provide a new load path to redistribute the load from the failed column to other structural members effectively. More recently, Agarwal and Varma [12] proposed that the increment of reinforcement in the concrete slabs could facilitate the load redistribution after columns buckled, and thereby helped maintain the stability of the whole structure using 3D analyses. Jiang and Li [13] found that the load redistribution path dominated the collapse modes and more loads from the bucked heated columns were transferred along the short edge to the adjacent columns. Currently, limited literature has explored the load redistribution path in multi-floor composite structural buildings considering a multi-floor spreading fire scenario, which may be more critical fire scenario causing structural collapses. Usmani et al. [5] proposed two collapse mechanisms induced by multi-floor fires, namely, the weak floor failure mechanism and the strong floor collapse mechanism to describe the failure of the external columns due to large deflection of floor systems. The columns as the main vertical load bearing components play critical roles in determining the potential risks of progressive collapse. Meanwhile, the column failure could be induced by largely deflected composite floor systems as restraint effect. To study the load redistribution after column loss, the alternate load path method by assuming one or several columns being removed, is often adopted [3,14]. Although the column removal method ignores the contraction of the heated column in the cooling phase [15], the load redistribution mechanisms using column removal method in the heating period remains valid.

This paper is intended to reconstruct the load redistribution path in steel-concrete composite structures using 3D models, which investigates the global structural responses to multiple-floor fires with the consideration of slabs. An eight-storey steel framed structure is modelled based on the Cardington building. To reduce the modelling efforts of composite slabs with profiled steel decking and improve the computation efficiency, a high-efficient composite slab numerical model with integrated composite section developed in OpenSees for fire ([16], under review) is employed in the building model. The capability of the composite slab model is validated against the Cardington corner fire test and sensitivity analysis on the mesh size of composite slab model is also performed. Four initial column failure scenarios are considered and then a 3-storey vertically spread fire is applied. The global structural performance, column response as well as the load redistribution path between columns are then analysed to demonstrate the 3D structure building subjected to multi-storey spreading fires, which found local failure of columns simultaneously occurring in an upper and lower floor would cause large deflection of floor slabs and even failure of a floor system.

2. COMPOSITE SLAB MODELLING IN STRUCTURAL BUILDINGS

2.1 High-efficient composite slab model with integrated composite slab section

Composite slabs are commonly adopted in modern steel-framed buildings. However, the non-uniform section profile in the direction perpendicular to ribs makes the modelling process difficult on the premise of limited loss of accuracy. The application of solid elements can capture the characteristics of geometric properties and the thermal profiles, but it is not suitable for large-scale numerical models due to the extremely high computational cost. A shell-element model is of higher computation efficiency, whereas it cannot model the section with varying thicknesses. To facilitate the composite slab modelling in full-scale composite structural buildings, a high-efficient composite slab model with integrated composite section (see Figure 1) is implemented by the authors in the open-source program of OpenSees for fire ([16]). Using a unified section with internal representation of ribs and flat segments, it becomes much easier in defining nodes, elements and thermal action.

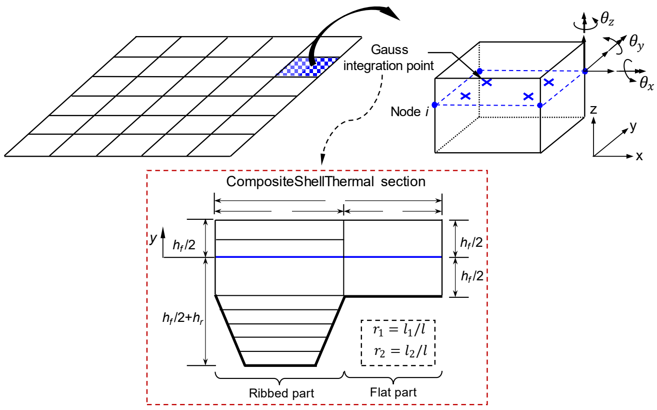

Figure 1. Illustration of composite slab model with integrated section

2.2 Performance validation of the composite slab model with integrated section

The Cardington fire tests in UK have provided well-documented dataset for numerical validation of composite structures in fire. The corner fire test was conducted in a enclosed compartment of a plan size 10 m × 7.5 m (see Figure 2(a)), which is modelled to validate the performance of composite slab model with integrated section. The structural sections for steel members and the geometric details of composite slabs are shown in Figure 2(a) and Figure 2(b) respectively. The composite slabs in Cardington building were made of lightweight concrete onto the 0.9 mm thick steel decking (PMF CF70), of a nominal thickness of 130 mm. Shear studs were used to tie the composite slabs to steel beams. A uniformly distributed load of 5.48 kN/m^2 in total was applied to the composite floor systems[17], and wood cribs of a floor desnity 45 kg/m^2 were distributed throughout the compartment to simulate the fire loading.

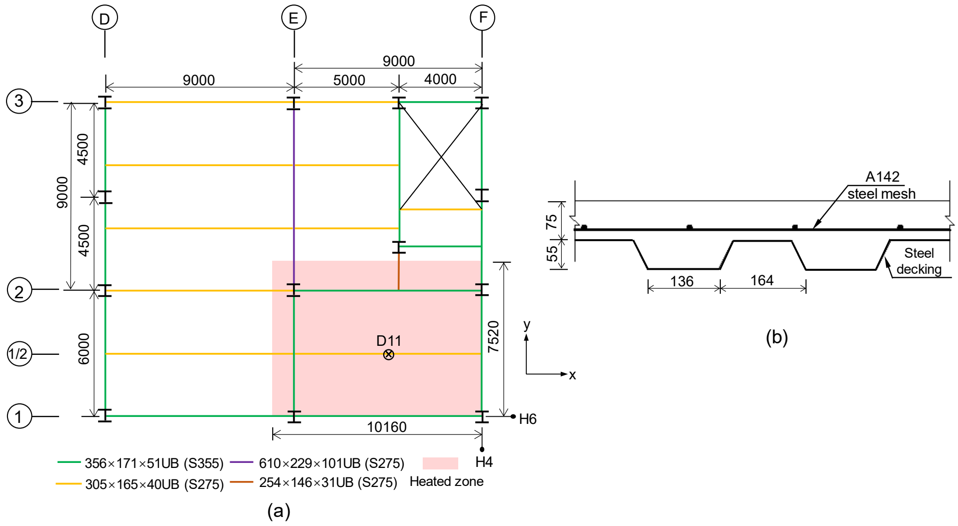

Figure 2. Schematic of the numerical model for Cardington corner test (unit: mm): (a) plan view of numerical model; (b) detailed geometrics of composite slabs adopted in the model.

Thermo-mechanical Concrete Damaged Plasticity (CDP) model is employed for concrete while steel mesh is discretised using a rebar mesh approach. For the steel beams and columns, a fibre-based section of Steel01Thermal material is adopted. The yield strength of steel, f_y, the compressive strength of concrete, f_c, and the corresponding elastic modulus, E, at ambient temperature are summarized in Table 1. The temperature-dependent thermal elongations and material models of concrete and steel recommended in

Eurocode 3 Part 1-2 [18] are deployed. As suggested by this standard, the thermal creep strain in the steel at elevated temperatures is considered implicitly in the given stress-strain relationships.

Table 1. Materials properties for the Cardington corner fire test. (Unit: MPa)

Properties	Materials				
	S275	S355	Steel mesh	Steel decking	Concrete
f_y/f_c (MPa)	308	390	460	350	35
E (GPa)	210	210	210	210	21

The connection between beams and columns were assumed rigid. No shear connectivity loss between composite slabs and the steel-framed supporting system was reported in the test. Thus, the composite slabs were linked to the beams by 'beam' type rigid link which means perfect composite action between steel beam and composite slabs at both ambient and elevated temperatures. Two types of mesh size (300 mm × 300 mm in integrated model 1 and 500 mm × 500 mm in integrated model 2) are adopted to study the effect of mesh fitness on the predicted results of steel framing composite structures.

Time histories of displacement of two nodes are extracted from the numerical model and are plotted in Figure 3. These nearly overlapping deflection-time curves predicted by integrated model 1 and integrated model 2 reveal that the composite slab model with integrated section behaves robustly and is able to obtain accurate predictions in a system-level structure with rather rough mesh. Figure 3(a) and Figure 3(b) show the central deflections of beam 1/2 between the gridlines E&F and the horizontal displacements of column 1F at half column height of the first floor along global X and Y directions, respectively. The test results recorded during the test are also included for comparison. In Figure 3(a), reasonable agreement between predictions by OpenSees and test results can be achieved. From the horizontal displacement-time curves of corner column 1F we can see that the column expanded outwards in global X and Y directions throughout the whole heating period, which is due to the thermally induced 'push-out' effect of the floor system exposure to fire. The outward displacements of column indicate that the deflection of floor is not large enough to pull the corner column inward.

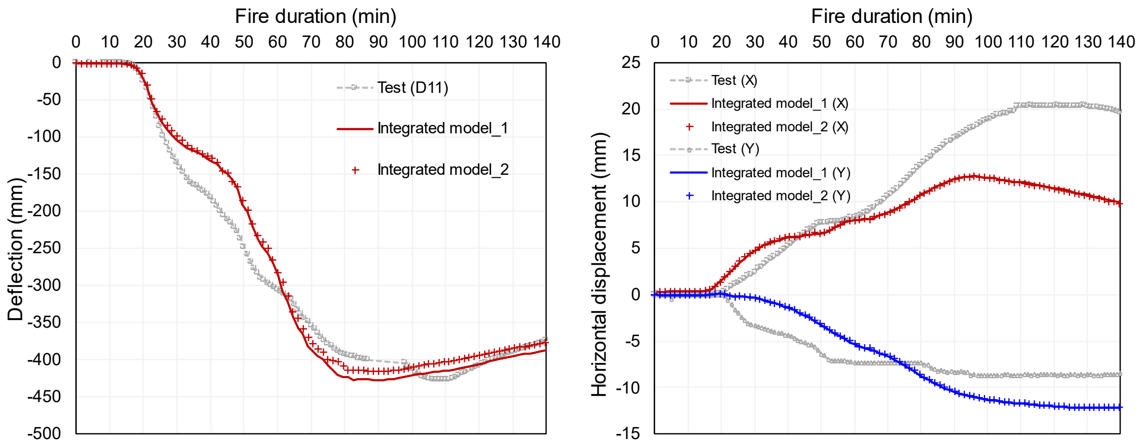

(a) Central deflections of beam 1/2between gridlines E and F

(b) Horizontal displacements of column1 F

Figure 3. Comparison results of different structural components within the heated corner compartment.

3. 3D STRUCTURAL MODELS OF MULTI-STOREY BUILDINGS IN FIRE

3.1 Prototype Steel-framed Composite building

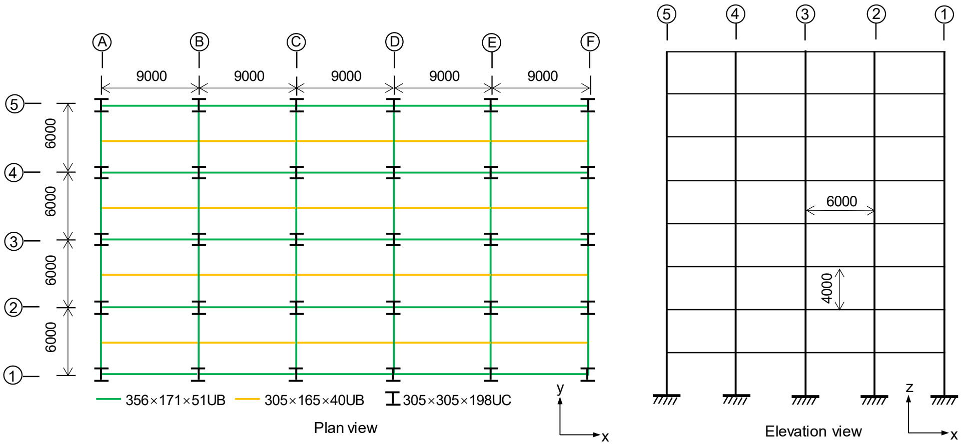

Figure 4. Illustration of the multi-floor composite structural building (unit: mm).

The study considers a typical mid-rise (eight-story) steel frame with composite floors based on the Cardington building [1]. Figure 4 illustrates the plan and elevation layouts of the structural building. The structure is laid out in five 9 m bays in the longitudinal direction and four 6 m bays in the transverse direction, resulting in a total floor area of 45 m × 24 m on plane. Each storey is 4 m high, thus the total height of the modelled building is 32 m. As denoted in Figure 4, the secondary beams, primary beams and columns are taken as 305×165×40 UB, 356×171×51 UB and 305×305×198 UC, respectively. The composite slabs adopted in this building have the same geometric details as that used in the Cardington building. Columns are arranged with strong axes parallel to the gables (see Figure 4) to supplement the resistance against horizontal forces in the short span direction. This building is intented to represent a typical steel moment-resisting frame strucutre which is a commonly form in seismic regions. Hence, all beam-to-column connections are totally rigid. The materials properties at ambient temperature adopted in this multi-floor building directly refer to the correspoding values listed in Table 1.

The mesh size of the column is 400 mm along the length direction. A consistent mesh with element size of 600 mm along global x direction and 600 mm along global y direction is used for both composite slabs and beams. As discussed in **Section 2**, the application of the high-efficient composite slab model enables the mesh size perpendicular to ribs no longer limited to the geometric details of the composite slabs, and the mesh can be rather rough to futher improve the computation efficiency of large-scaled structural model. This model contains 35230 nodes and 33720 elements in total.

3.2 Design fires and hazard scenarios

3.2.1 3-floor spreading fire

A three-floor vertically spreading fire scenario is designed and the fire location on the structural plane and structural elevation is illustrated in Figure 5. In a plan view, the fire occurs in a 18m×12m compartment at the corner, where the internal column 2E of interest is located at the centre of the compartment in fire. Vertically, the fire initially starts from the first floor and then progressively spreads to the second floor and the third floor after 10 min and 20 min respectively, which indicates the delay of fire ignition between different floors is 10 min. Note that some assumptions and simplifications are made for the 3-floor fire scenario. On one hand, the fire at each floor is assumed to be a fully flashed over compartment fire and follows the same gas temperature-rising curve recorded in the Cardington corner test. Hence, the horizontally travelling behaviour of fire on one floor is not considered. A 10 min time delay is adopted based on the realistic fire accidents, where 6-30 min were observed for floor-to-floor fire spreading [23].

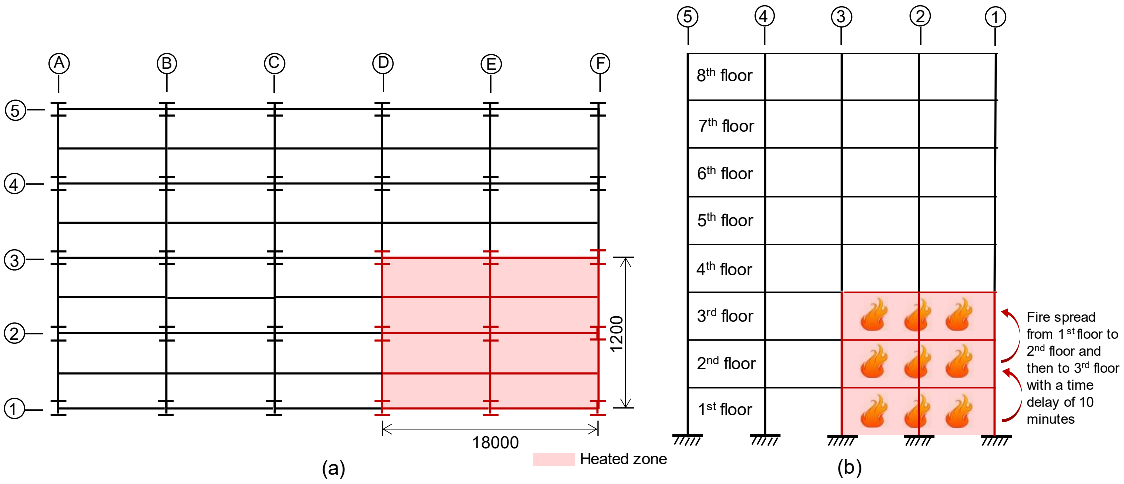

Figure 5. Vertically spreading fire scenario: (a) fire location on plan; (b) fire spreading.

3.2.2 Extreme scenarios

To construct the load redistribution path of 3D structures under multi-floor vertically spreading fires, the following scenarios shown in Figure 6 are designed and analysed. (1) Scenario 1. All columns and external perimeter beams in this model are assumed to be protected using 25 mm ceramic fibre blanket, while all interior primary and secondary beams are left unprotected. This is exactly the fire protection manner adopted in the Cardington corner test. In real buildings, secondary beams are usually left unprotected and exposure to fires directly while all the primary beams are protected. Hence, scenario 1 is a less conservative case than common buildings with intact fire protection. (2) Scenario 2, the insulation on the top 800 mm of internal column 2E on the first floor is removed considering the suspended ceiling might be installed at this location. The Cardington plane frame test studied the column response to fires with this kind of partial insultation. Up to 180 mm squashing was observed under the combined action of material degradation and restrained upward thermal expansion. (3) Scenario 3. column 2E on the first floor is cut off, where the interior column 2E on some floors is assumed to be failed and followed by a spreading fire. (4) Scenario 4. Column 2E on both the first floor and on the third floor are all cut off. As shown in scenario 4, the floor systems at the first floor level and at the second floor level are connected through the column on the second floor while these two-storey floor systems are independent of the structural frame in the interior of fire region due to the failure of columns on the upper and lower storeys.

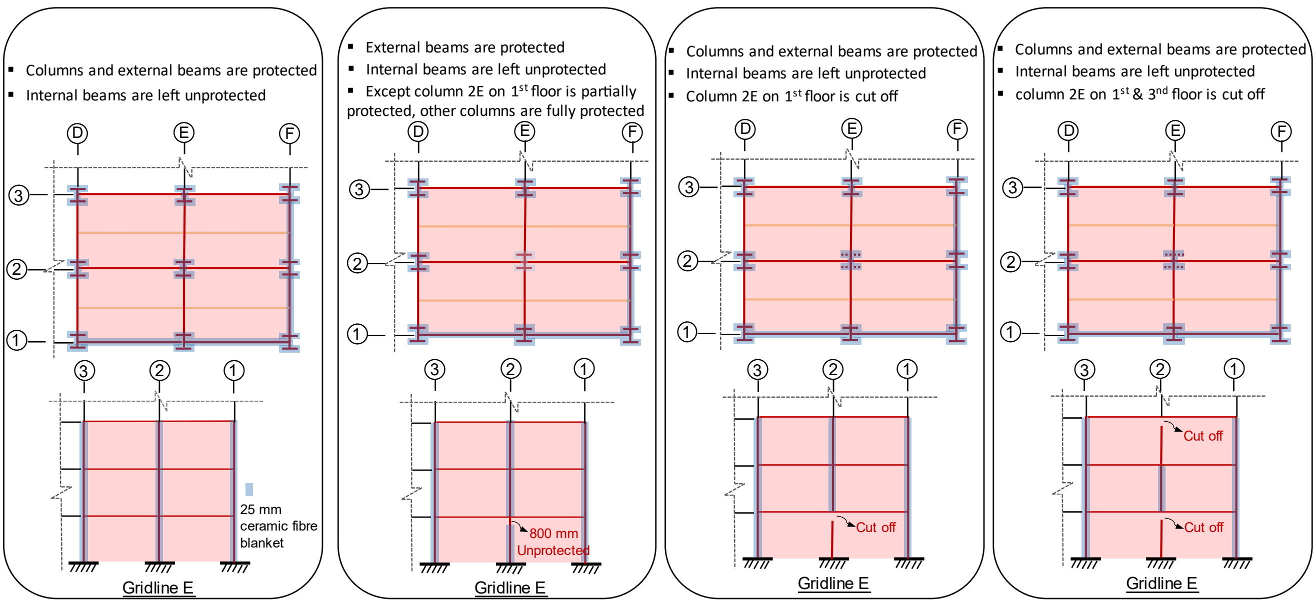

Figure 6. Designed hazard scenarios.

As described previously, the fire on different floors follows the same temperature curve measured in the Cardington corner test and the protection manner is also identical to that adopted in this test. Thus, temperatures of various members recorded in the Cardington corner test can be taken as the thermal loads in these designed scenarios and be applied to the corresponding structural members directly. For the upper segment of column 2E on the first floor exposed to fire directly, heat transfer analysis is performed in OpenSees for fire by taking the gas temperature of the Cardington corner test as thermal boundaries. The fire lasts for 90 min when the fire on the third floor enters cooling phase, and so only the heating stages at all the fire floors are considered.

4. ANALYSES ON MULTI-STOREY COMPOSITE STRUCTURAL BUILDINGS UNDER MULTIPLE FLOOR FIRES

4.1 General thermo-mechanical performance

Figure 7 shows the deformed structures at the end of analysis. Only the deformed shapes in scenario 1 and scenario 4 are presented. In scenario 1, scenario 2 and scenario 3, the overall deformed shapes of the structure are quite similar. In these three scenarios, up to 700 mm deflections can be observed in the middle of each compartment in fire due to the later support of the four corner columns. While for scenario 4, the maximum deflection in the floor systems at both the first storey level and at the second storey level occurs around column 2E after losing support from the upper and the lower steel frame, and the peak deflection is up to 1100 mm. The extensively deflected floor system in scenario 4 results in the inward horizontal displacements of edge column 1E along the global Y direction at the first floor level as presented in Figure 8, where positive values mean inward displacement along Y direction and negative values mean outward displacement along Y direction. For scenario 1, the horizontal displacements of edge column 1E at those fire floor levels are all pushed out due to the thermal expansion of floor systems. The inward displacement of column 1E in scenario 4 is less than that of column 1E at the above non-floor levels which is induced by the downward pull action of floors in fire. Overall, neither signs of global collapse nor progressive collapse is observed, which indicates that the structure is stable enough to survive the 3-floor spreading fires even the interior column 2E is cut off on two floors.

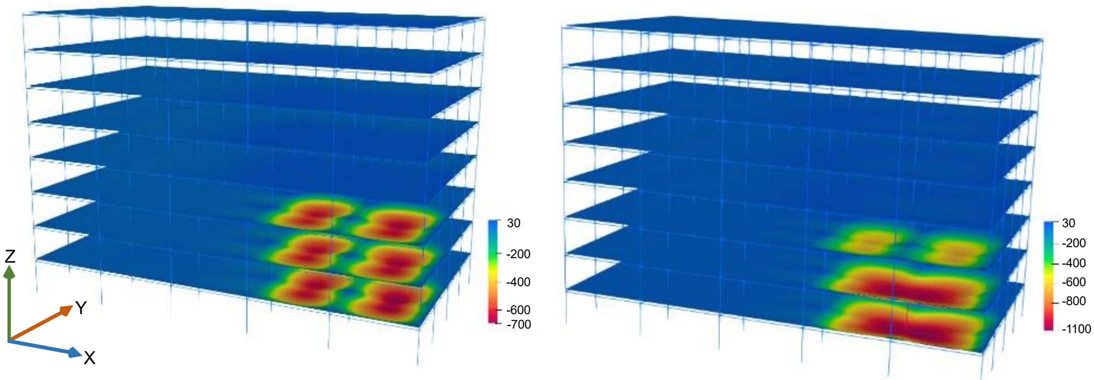

(a) Scenario 1 (b) Scenario 4

Figure 7. Deformed configurations of structures.

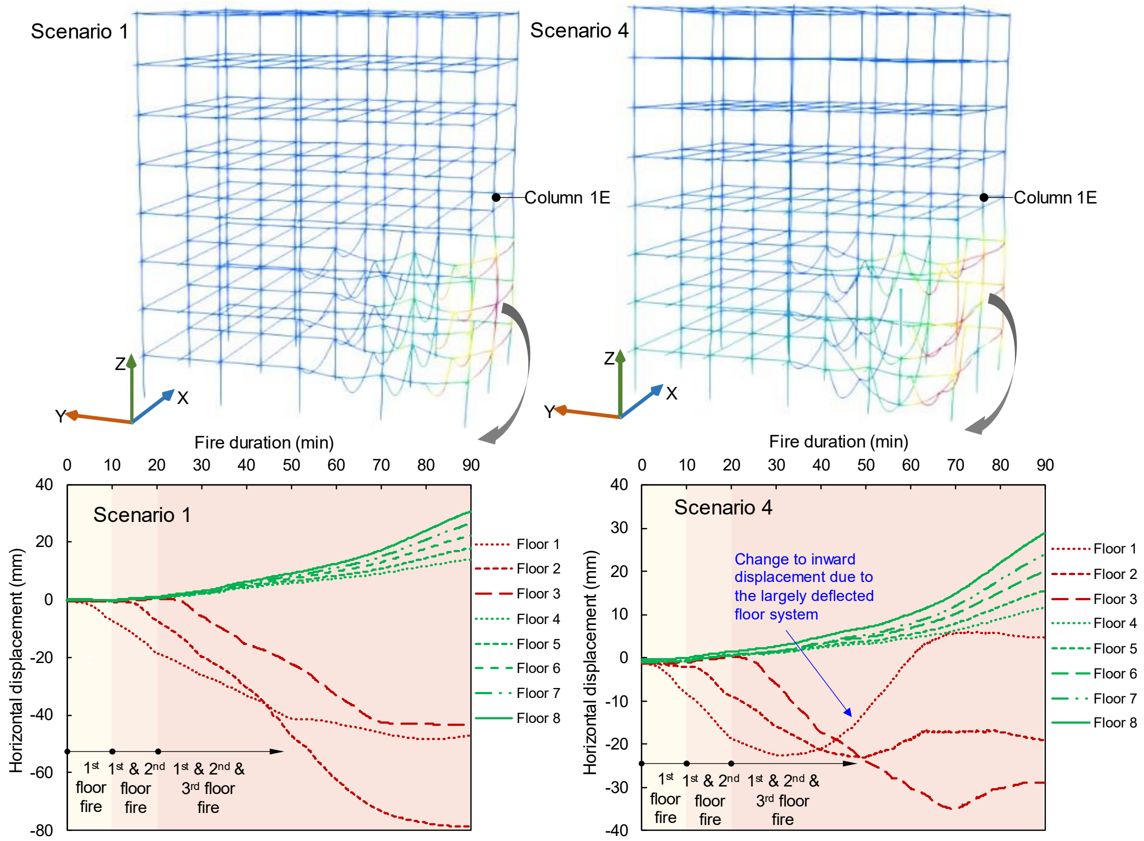

Figure 8. Deformed shape of steel frame along global Y direction (5X) and the horizontal displacements of edge column 2E along Y direction.

4.2 Column response

4.2.1 Load redistribution pattern

At the end of fire, the axial force redistribution patterns of columns on the first floor for scenario 2, scenario 3 and scenario 4 are plotted in Figure 9(a), Figure 9(b) and Figure 9(c) respectively. The percentage of redistributed loads is calculated as the ratio of the axial force difference between the columns in these scenarios and the corresponding columns in scenario 1 to the total redistributed axial force of column 2E. In addition to the load redistribution ratio, the ratios of redistributed load to the axial force originally borne by the column in the scenario 1 are also calculated and denoted in Italics in brackets for those columns that bear most of the load transferred from the failed column. The positive value indicates the increased axial force in the column and the negative value means that the load borne by the column is reduced.

After the interior column 2E on the first floor fails, nearly all the redistributed load from this column is distributed to the four columns that have connection to this interior column through beams. Moreover, larger load is distributed along the short span than the long span. It is worth noting that the redistributed load to perimeter beam 1E results in a load increment of 58.99%, 75% and 80.1% in scenario 2, scenario 3 and scenario 4 respectively. Such largely increased load in the perimeter column induced by the failure of the column 2E is possible to cause the progressive collapse especially when the perimeter column is exposed to fire directly. Due to the upward expansion of the heated columns within the fire compartment, the columns adjacent to the fire compartment tend to move up together, leading to the slight decrease of compression in these columns. The load redistribution path from the failed column to the adjacent structural members in these scenarios will be discussed in the following paragraphs to reveal the effect of floor system in transferring the loads.

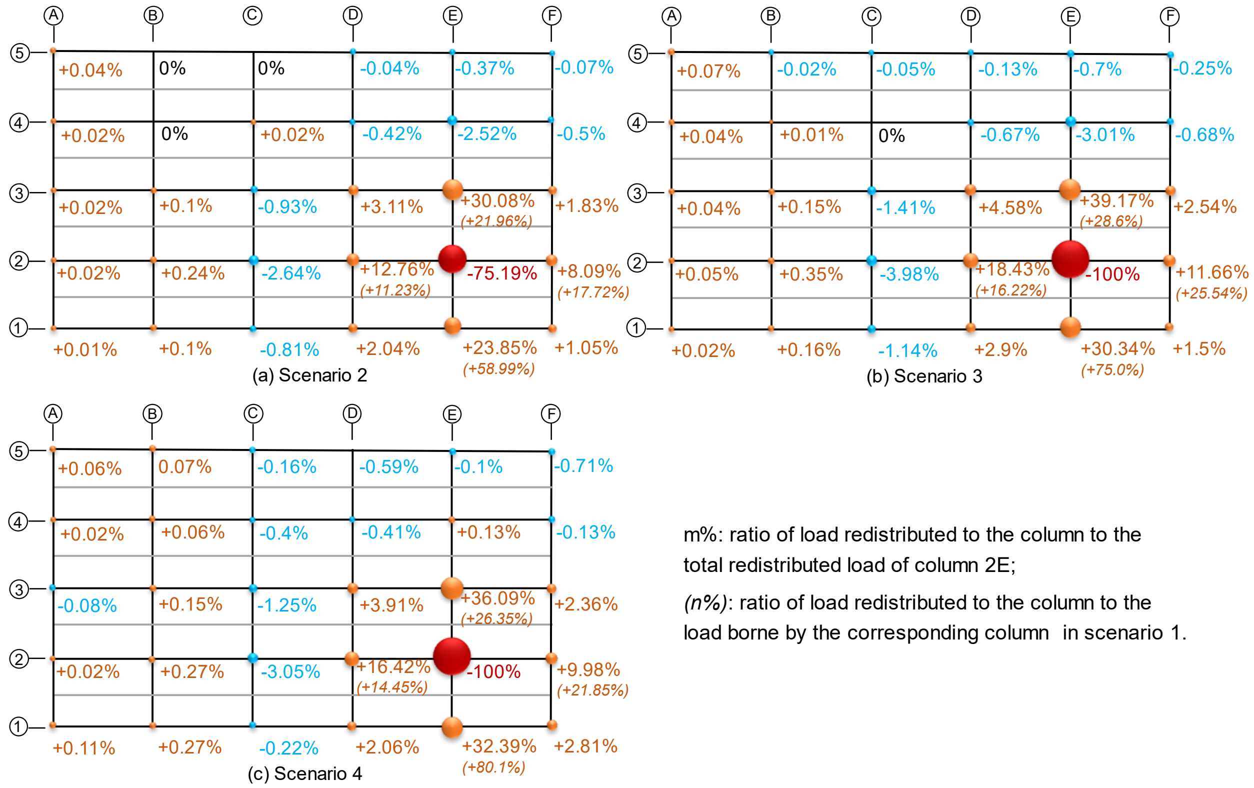

Figure 9. Axial load redistribution pattern in columns at the end of the analysis.

4.2.2 Internal state of column

The vertical displacements and internal axial force of interested column 2E at different floor levels in different scenarios are plotted in Figure 10 and Figure 11, respectively. The negative values in Figure 11 represent compression and the positive values mean tension. Figure 10(a) shows that when the internal column is protected thoroughly, the column 2E at each fire floor level and above the fire floors always moves upwards slowly due to its own thermal expansion and already shoots past the original position at the end of analysis. Due to the restrained effect of floor system, the constrained thermal expansion of column results in the increase of internal axial force in the column. Along with the heating, the steel properties of the column 2E begin to degrade, and hence, the load borne by the column will be transferred to the surrounding stiffer structural members through floor systems. As a result, the axial force in the column 2E on these fire floors decreases slowly.

From Figure 10(b) it can be seen that when the steel column is partially protected, the top of column on the first floor expands upwards till heating for approximately 41 min and then drops dramatically. This sudden reverse in terms of vertical displacements indicates the failure of the column at the unprotected region under the combined effects of thermally-induced material degradation and restrained upward thermal expansion. Because the failure of column occurs on the first floor, the column at the upper floor levels all presents the sudden drop. At approximately 60 min mark, the downward displacement of the internal column 2E nearly approaches 30 mm and then the column starts to move upward. Combining with the axial force evolution in the column 2E shown in Figure 11(b), it can be found that at the moment when the column fails, the axial force in column 2E at all floor levels decreases significantly and the axial force in the column on the non-fire floors changes from compression to tension. This kind of ‘pull’ action from the upper non-fire floors helps stabilize the global structure and efficiently alleviate the further downward displacement induced by the column failure.

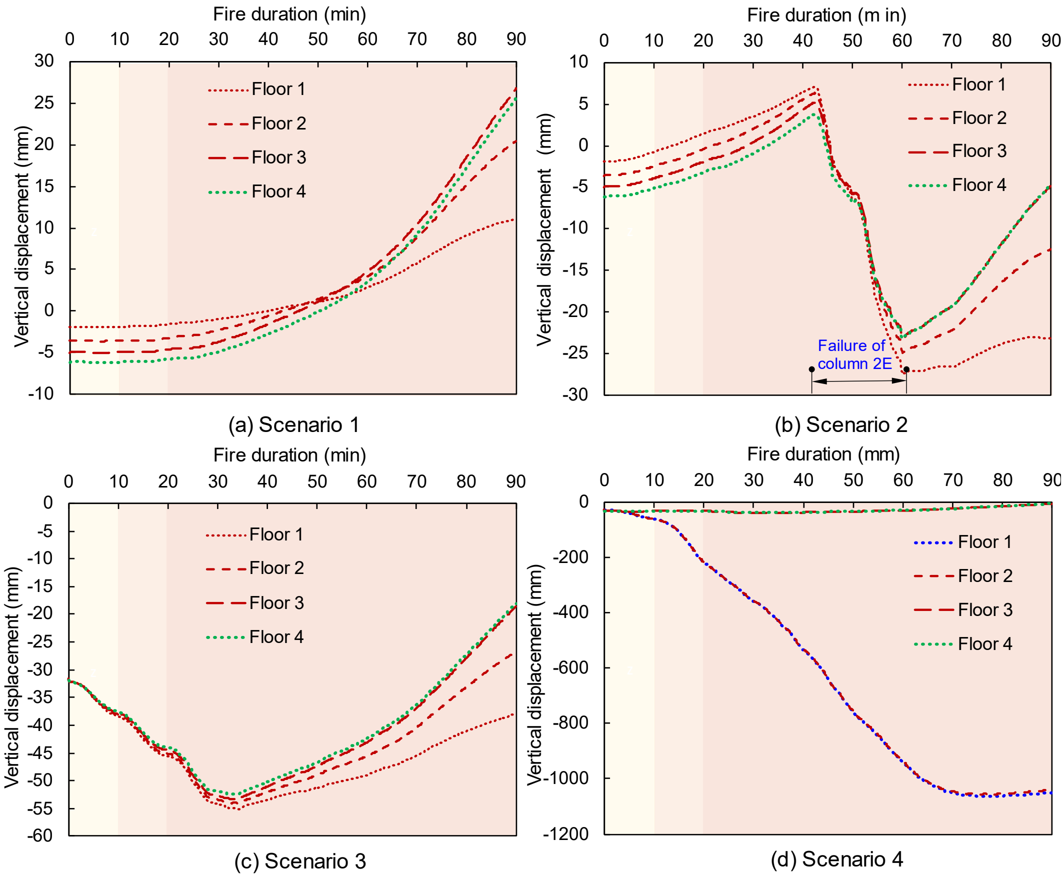

Figure 10. Vertical displacements of interior column 2E at different floor levels.

Due to the failed column on the first floor in scenario 3, the downward displacement of column 2E at different floor levels is significantly larger than that in the scenario 1 and scenario 2, which is up to 55 mm after 30 min. During the first 30 min, it seems that the thermal expansion of columns and the deflection of floor systems in fire further intensifies the downward displacement of the column 2E. This is because the weaker stiffness of the lower part of the structural system induced by the failed column makes it more prone to deform downwards. Within the same fire duration, that is in the first 30 min, the axial force in the column 2E shifts from compression into tension and increases significantly to pull the whole downward floor system in the fire area. After about 30 min, though the floor system with the region demarcated by columns at four corners continues to deflect as discussed previously, the column 2E begins to move upwards coupled with the steadily and slowly decreasing axial force. This indicates that the further deflection of floor systems does not pull the upper floor downwards any more. With the stories increase, the axial force in column 2E gradually increases on these fire floors and on the one non-fire floor above, and then decreases in turn. This may be because after the fire occurs, the column on the fourth floor has to bear the total downward pull forces from the lower three floor systems in fire, while for those non-fire floors above, the robust floor system could help share and then transfer the tension in column 2E to other members.

Column 2E on both the first floor and on the third floor is cut off in scenario 4, resulting in an unsupported state for the column on the second floor. As shown in Figure 10(d), the axial displacements of this column at the first floor level and at the second floor level are nearly overlapping and are significantly larger than that of the column at the above floor levels throughout the fire. The maximum downward displacement exceeds 1000 mm at the advanced stages of fire. From Figure 11(d) where the internal axial force development of the column 2E are illustrated it can be seen that when the fire starts on the first floor, the axial force of column 2E on the second floor changes from compression into tension and increases rapidly. It peaks at about 12 min when the fire on the second floor has started and the floor system starts to move downwards together. For the column on those non-fire floors, the axial compression force maintains until the fire ignites on the third floor. The downward floor system at the third floor level is pulled by the column above, resulting in a rise of tensile force on those above floors.

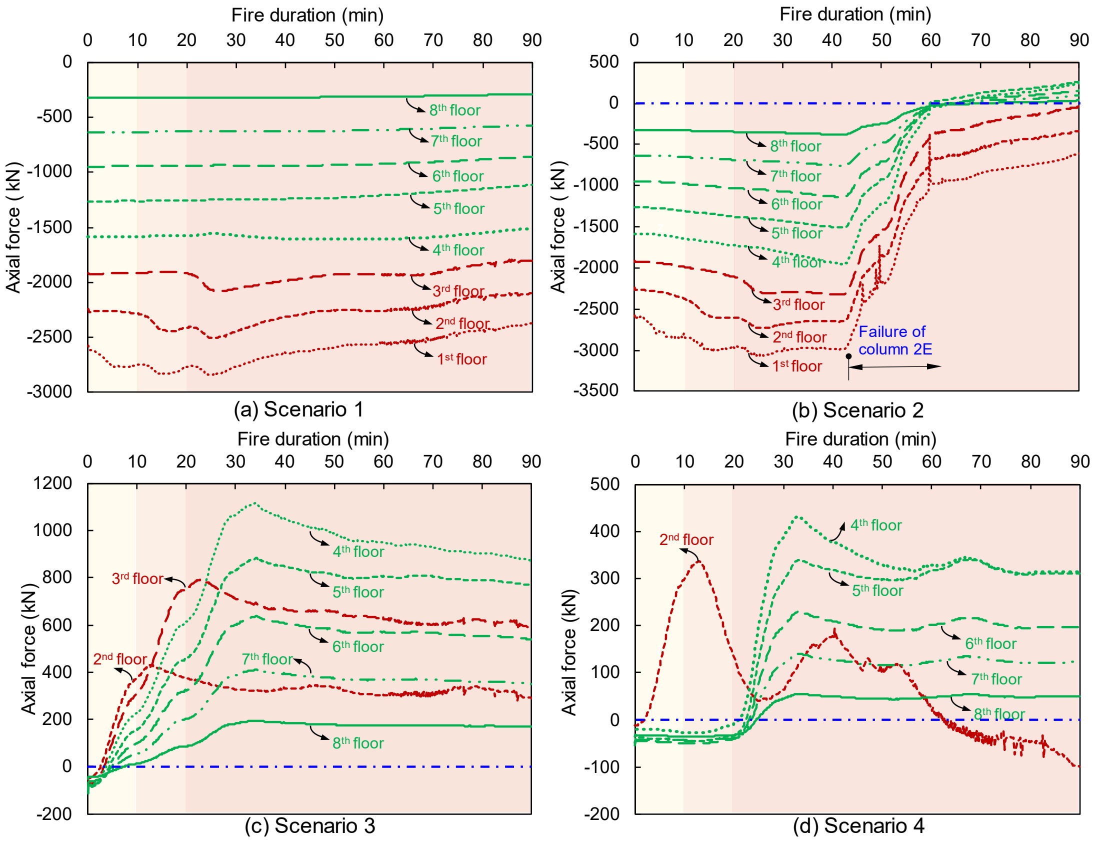

Figure 11. Evolution of internal axial force in the interior column 2E on different floors.

5. CONCLUSIONS

This paper aims to investigate the load redistribution mechanism of multiple steel framing composite structures under multi-floor vertically spreading fires. A high-efficient composite slab model with integrated section is employed. The Cardington corner test is adopted to validate the capability of the modelling approach in capturing the fire response of composite floor system. Four hazard scenarios distinguished by column failure patterns are numerically analysed. The following conclusions can be drawn:

- The composite slab model with integrated composite section is applicable to the large-scale structural model. The application of this composite slab model breaks through the limitation on meshing along the direction perpendicular to ribs due to the different section and can well capture the performance of a system level structure in fire;
- The composite slab model can highly simplify the modelling effort of composite slabs because this model is not sensitive to the mesh size. Quite rough mesh can be adopted in modelling multi-floor composite structural buildings;
- The typical multi-storey office building can survive the 3-floor vertically spreading fires even when the interior column on the first floor and on the third floor fails. The robustness of the structural building benefits from the pull action from the upper floor systems and the load redistribution mechanism of the floor system on the same floor;
- After the interior columns fail, nearly all the load borne by this column is transferred to the four columns that have connection with the failed column through beams;
- When the downward displacement of floor system is large enough, it is possible to pull the edge beam inwards. However, the inward displacement is significantly smaller than that of the above non-fire floors induced by the downward pull action of floors in fire.

This investigation on the 3D multiple storey building subjected to 3-floor vertically spreading fires presents the load redistribution mechanism by discussing the column state. To better reveal the role played by the floor system such that the load redistribution path can be well understood, more work focusing on the floor system in fire need to be performed in the future. Besides, in addition to the moment resisting structural system, the common gravity system is worth studying.

ACKNOWLEDGMENT

This research work was supported by the Start-up Fund of the Hong Kong Polytechnic University (P0031564) and the Open Fund from the State Key Laboratory of Disaster Reduction in Civil Engineering (SLDRCE20-02). The financial supports are greatly appreciated.

REFERENCES

[1] Steel B. The behaviour of multi-storey steel framed building in fire. 1999.

[2] Wang Y, Burgess I, Wald F, Gillie M. Performance-based fire engineering of structures. CRC press; 2012.

[3] Gernay T, Khorasani NE. Recommendations for performance-based fire design of composite steel buildings using computational analysis. J Constr Steel Res 2020;166:105906. https://doi.org/10.1016/j.jcsr.2019.105906.

[4] Vassart O, Zhao B. FRACOF engineering background. Report developed for the leonardo Da vinci programme: fire resistance assessment of partially protected composite floors (FRACOF). European commission. Bordeaux, France: 2011. https://doi.org/10.1090/cbms/068/01.

[5] Usmani AS, Chung YC, Torero JL. How did the WTC towers collapse: A new theory. Fire Saf J 2003;38:501–33. https://doi.org/10.1016/S0379-7112(03)00069-9.

[6] Ali HM, Senseny PE, Alpert RL. Lateral displacement and collapse of single-story steel frames in uncontrolled fires. Eng Struct 2004;26:593–607. https://doi.org/10.1016/j.engstruct.2003.12.007.

[7] Jiang J, Li GQ, Usmani A. Progressive collapse mechanisms of steel frames exposed to fire. Adv Struct Eng 2014;17:381–98. https://doi.org/10.1260/1369-4332.17.3.381.

[8] Jiang J, Li GQ, Usmani A. Effect of Bracing Systems on Fire-Induced Progressive Collapse of Steel Structures Using OpenSees. Fire Technol 2015;51:1249–73. https://doi.org/10.1007/s10694-014-0451-0.

[9] Sun R, Huang Z, Burgess IW. The collapse behaviour of braced steel frames exposed to fire. J Constr Steel Res 2012;72:130–42. https://doi.org/10.1016/j.jcsr.2011.11.008.

[10] Talebi E, Md Tahir M, Zahmatkesh F, Kueh ABH. Comparative study on the behaviour of buckling restrained braced frames at fire. J Constr Steel Res 2014;102:1–12. https://doi.org/10.1016/j.jcsr.2014.06.003.

[11] Flint G, Usmani A, Lamont S, Lane B, Torero J. Structural Response of Tall Buildings to Multiple Floor Fires. J Struct Eng 2007;133:1719–32. https://doi.org/10.1061/(asce)0733-9445(2007)133:12(1719).

[12] Agarwal A, Varma AH. Fire Induced Progressive Collapse of Steel Building Structures: The Role of Interior Gravity Columns. Eng Struct 2014;58:129–40. https://doi.org/10.1016/j.engstruct.2013.09.020.

[13] Jiang J, Li GQ. Progressive collapse analysis of 3D steel frames with concrete slabs exposed to localized fire. Eng Struct 2017;149:21–34. https://doi.org/10.1016/j.engstruct.2016.07.041.

[14] Tavakoli HR, Kiakojouri F. Threat-Independent Column Removal and Fire-Induced Progressive Collapse: Numerical Study and Comparison. Civ Eng Infrastructures J 2015;48:121–31.

[15] Gernay T, Gamba A. Progressive collapse triggered by fire induced column loss: Detrimental effect of thermal forces. Eng Struct 2018;172:483–96. https://doi.org/10.1016/j.engstruct.2018.06.060.

[16] Qiu J, Jiang L. An integrated section model to enable simulating composite slabs in fire simply as modelling a flat slab. Comput Struct n.d.

[17] Huang Z, Burgess IW, Plank RJ. Non-linear structural modelling of a fire test subject to high restraint. Fire Saf J 2001;36:795–814. https://doi.org/10.1016/S0379-7112(01)00040-6.

[18] British Standards Institution. BS EN 1993-1-2: 2005: Eurocode 3: design of steel structures - Part 1-2: general rules-structural fire design 2005.

[19] Hidalgo JP, Goode T, Gupta V, Cowlard A, Abecassis-Empis C, Maclean J, et al. The Malveira fire test: Full-scale demonstration of fire modes in open-plan compartments. Fire Saf J 2019;108:102827. https://doi.org/10.1016/j.firesaf.2019.102827.

[20] Dai X, Welch S, Vassart O, Cábová K, Jiang L, Maclean J, et al. An extended travelling fire method framework for performance-based structural design. Fire Mater 2020;44:437–57. https://doi.org/10.1002/fam.2810.

[21] Stern-Gottfried J, Rein G. Travelling fires for structural design-Part II: Design methodology. Fire Saf J 2012;54:96–112. https://doi.org/10.1016/j.firesaf.2012.06.011.

[22] Stern-Gottfried J, Rein G. Travelling fires for structural design-Part I: Literature review. Fire Saf J 2012;54:74–85. https://doi.org/10.1016/j.firesaf.2012.06.003.

[23] Ronagh M and. Plastic Hinge Length of RC Columns Subjected to Both Far-Fault and Near-Fault Ground Motions Having Forward Directivity. Struct Des Tall Spec Build 2011;24:421–39. https://doi.org/10.1002/tal.

EFFECT OF POST HIGH TEMPERATURE EXPOSURE ON THE BEHAVIOR OF COMPOSITE COLUMN WITH FERROCHROME SLAG AS A FINE AGGREGATE

Kazi M A Sohel[1], Khalifa Al-Jabri[2], Zaher H A Al-Abdulqader[3], B. M Waris[4]

ABSTRACT

Ferrochrome slag (FCS), an industrial solid waste, has promising properties that promote its use as an alternative aggregate in concrete production. This can be a partial solution to reduce the pressure on natural aggregates. This study experimentally studied the effect of FCS fine aggregate on the physical and mechanical behavior of concrete-filled steel tube (CFST) stub columns exposed to different temperatures. The influence of FCS fine aggregate substitution level and heating temperature range (200°C, 400°C, 600°C, and 800°C) on load-displacement behavior, ultimate load, and failure mode was investigated. The CFST stub columns were filled with three different concrete mixes using conventional fine aggregate, 50% and 100% FCS as a fine aggregate replacement. The results showed that increasing the FCS fine aggregate content in the concrete increased the ultimate strength and stiffness of CFST stub columns at both ambient and after being exposed to elevated temperatures. The fine natural aggregate can be fully replaced by the FCS fine aggregate without compromising any mechanical properties of concrete, as well as CFST columns at room and elevated temperatures. The Eurocode 4 (EC4) and ACI codes show a conservative prediction of ultimate strengths for the CFST stub columns at ambient as well as at elevated temperatures compared to the experimental results for all three concrete mixes. However, EC4 gives a closer estimation of the ultimate load for all concrete mixes than the ACI recommendation.

Keywords: Concrete; composite column; Ferrochrome slag; elevated temperature; industrial waste

1 INTRODUCTION

Due to faster construction development and the evolution of economies in many cities, meeting the global demand for concrete is now becoming more challenging as the earth's resources are limited. Despite this, natural aggregates are still used for more than three-quarters of new mixed concrete. Therefore, environmental, economic and technical problems have led to increased attention being paid to the usage of waste materials and by-products in concrete. Furthermore, their utilization may enhance the properties of mortar and concrete such as a microstructure, mechanical and durability properties, which are not achieved easily using only ordinary Portland cement and natural aggregates [1] (Qasrawi et al., 2009). There are many types of waste materials and by-products, namely: steel slag; recycled waste plastic; scrap tyres; waste glass; coal fly ash; wood ash; rice husk ash; etc., which have been researched significantly in several parts of the world. Ferrochrome slag is one of the potential waste materials which can be used as coarse and fine aggregates to produce concrete [2] (Fares et al., 2021). Ferrochrome slag is obtained as a by-

[1] Associate Professor, Civil and Acrhitectural Engineering Department, Sultan Qaboos University, Oman
e-mail: kmasohel@squ.edu.om, ORCID: https://orcid.org/0000-0003-1144-614X
[2] Professor, Civil and Acrhitectural Engineering Department, Sultan Qaboos University, Oman
e-mail: aljabri@squ.edu.om, ORCID: https://orcid.org/0000-0001-9913-5631
[3] Post graduate student, Civil and Acrhitectural Engineering Department, Sultan Qaboos University, Oman
e-mail: za.abdulqader@gmail.com
[4] Assistant Professor, Civil and Acrhitectural Engineering Department, Sultan Qaboos University, Oman
e-mail: waris@squ.edu.om, ORCID: https://orcid.org/0000-0002-8975-7362
https://doi.org/10.6084/m9.figshare.22154735

product from the production of ferrochrome (FeCr) which is an important component in stainless steel. In the sultanate of Oman, most of ferrochrome slag, which is produced by the Mining companies in large quantities, is disposed of without benefit reuse in any application [3] (Al-Jabri et al., 2018). Therefore, any beneficial use (e.g. as construction material) of this waste material will reduce the environmental hazard.

The ferrochrome industries face the disposal problem due to the existence of residuals chromium content (Cr (VI) and Cr (III)) in the solid waste and it can be released to the environment. However, the leaching of harmful Cr (VI) and Cr (III) can be prevented if the ferrochrome slag is used in the confined steel tube to produce composite columns. A recent study shows that high-strength concrete can be produced by using partial replacement of coarse and fine aggregate with ferrochrome slag [4] (Rajasekhar & Reddy, 2015). For these reasons, ferrochrome slag can be safely used in CFST columns without the concern of environmental effects and concrete instability.

Concrete-filled steel tube (CFST) is one of the typical concrete-steel composite structures that is increasingly used in high-rise buildings, bridge piers, offshore structures, military installations and many other structures due to their excellent structural performances including earthquake resistance [5, 6] (Song et al., 2010, Shams and Saadeghvaziri, 1997). Since the first use of CFST column for road bridge in the late 1870's in England, this type of column was gained increasing popularity from 1980's [7,8] (Nishiyama et al. 2002, Schneider, 1998). The strength of filled concrete can be improved by the confinement effect provided by the steel tube, whereas the local buckling of the steel tube can be delayed or even prevented by the concrete core. Also, the steel tube can be utilized as a permanent formwork for concrete casting and thus, the construction duration and cost will be reduced.

The performance of CFST column under different loading conditions including fire resistance and residual strength after exposure has been carried out in many studies [9-11] (Li et al., 2017, Bahrami and Nematzadeh, 2021, Ekmekyapar and Alhatmey, 2019). During the fire exposure, the CFST columns exhibited fire resistance better than those of the conventional steel and reinforced concrete columns because concrete can absorb the heat from the steel tube which is exposed directly to fire while the steel tube can prevent the concrete from spalling [12] (Han et al., 2014). Meanwhile, after the fire, the residual strength of structural member needs to be assessed to check its capability for continual use. Moreover, the utilization of ferrochrome slag as fine aggregates in concrete mixture, can make enhancement to the thermal and mechanical characteristics of the concrete by reducing temperature gradients and raising temperature stability [3, 4, 13] (Al-Jabri et al., 2018; Islam et al., 2021, Rajasekhar & Reddy, 2015). It was found that concrete with FCS fine experienced less internal damage dame and less strength reduction than conventional concrete when exposed to elevated temperatures [13] (Islam et al., 2021). Therefore, it is postulated that ferrochrome slag aggregate concrete-filled steel tube will exhibit better performance over conventional CFST at elevated temperatures.

Many studies were conducted to investigate the behaviour of steel tubular columns filled with concrete containing different waste or by-product materials such as recycled aggregate, steel slag, waste glass, tire rubber, dune sand and agricultural solid waste [14-19]. Some them were investigated for high temperature effect on the structural performances. However, till now, there is no research conducted to investigate the behavior of CFST columns made with ferrochrome slag as a fine aggregate at and after exposure to elevated temperature which is the main goal of this project. Also, the presence of ferrochrome slag in the concrete improves the strength of concrete, it is necessary to know the behavior of structural elements containing ferrochrome slag concrete and the influence of elevated temperature on it. Therefore, this paper presents a study on the behavior and mechanical properties of CFST stub columns with three different concrete mixes using conventional fine aggregate, 50% and 100% ferrochrome slag (FCS) as a fine aggregate replacement at ambient and elevated temperatures (200°C, 400°C, 600°C and 800°C).

2 EXPERIMENTAL INVESTIGATION

2.1 Materials

The materials used for the experiment were cement, coarse aggregate, fine aggregate and ferrochrome slag. The physical properties and chemical composition of the cement in accordance with ASTM C150/150M-12 are Type I. The ferrochrome slag (FCS) was collected form Al Tamman Indsil LCC, Oman. The fine FCS aggregate is shown in Figure 1.

A crushed dolomite stone with a maximum size of 20 mm was used as coarse aggregate to produce concrete. The gradation of the coarse aggregate was within the range limit specified by ASTM C33 [20]. Crushed rock sand was used as fine aggregate for concrete mixes. Crushed siliceous limestone used as fine aggregate has a specific gravity of 2.63 and water absorption of 0.98 %. The gradation of natural fine aggregate along with FCS fine aggregate is shown in Figure 2 as per ASTM C33/C33M [20]. From the figure, the gradation of FCS is finer than the conventional fine aggregate.

The circular steel tubes were cut to the specific length of 300 mm for CFST column. For the stub columns tested by Yu et al. [15] and Li et al. [9], the nominal L/D ratios were in the range of 2 to 5 to avoid the overall buckling and end conditions. The yield strength, ultimate strength and modulus of elasticity of the steel were 291 MPa, 418 MPa and 190 GPa, respectively.

Figure 1. Fine ferrochrome slag aggregate

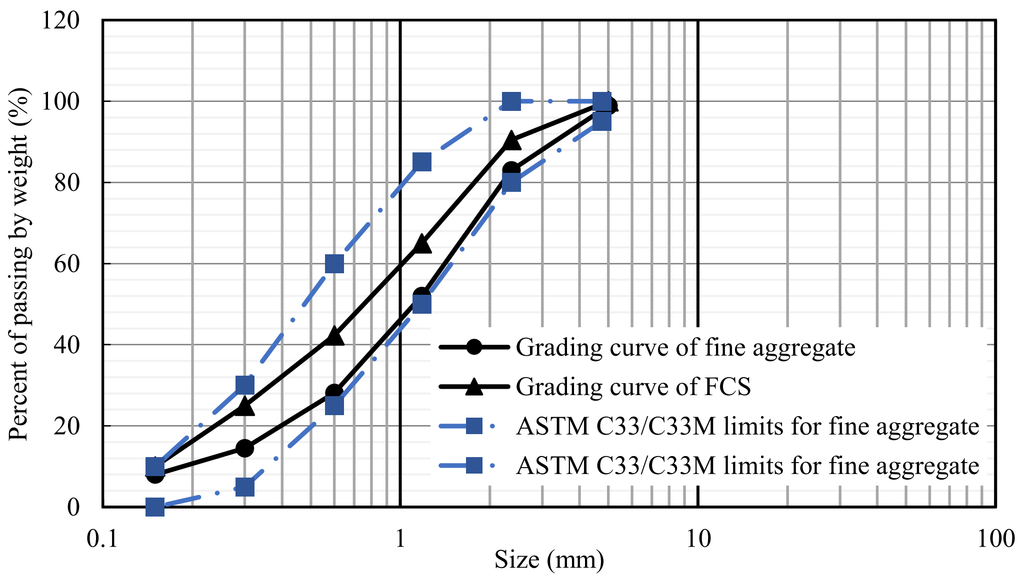

Figure 2. Gradation of the fine natural aggregate and FCS

2.2 Mix design

In this study, three types of concrete with the same mix proportion ratio (1:1.5:2.6) were used to fill the steel tubes (H=300mm, D=109.2mm) and cylinders (H=200mm, D=100mm). The target compressive strength of concrete is 40 MPa. The mix proportions of 1 m^3 of concretes are presented in Table 1.

Table 1 Mix proportions of three types of concrete (kg/m^3)

Components	Mix 1 (0% FCS)	Mix 2 (50% FCS)	Mix 3 (100% FCS)
Cement	447.73	447.73	447.73
Coarse Aggregate 10mm-(30%)	354.67	354.67	354.67
Coarse Aggregate 20mm-(70%)	827.56	827.56	827.56
Fine Aggregate	656.76	328.38	0
Ferrochrome slag	0	328.38	656.76
Water	197	197	197
Water-Cement ratio (w/c)	0.44	0.44	0.44
Measured density	2499	2524	2553

2.3 Preparation of CFST stub columns and cylinders

Two stub columns from each batch were used to evaluate the immediate characteristics strength of CFST stub column at every elevated temperature (25°C, 200°C, 400°C, 600°C and 800°C) and one stub column for residual strength for each temperature. The number and dimension of CFST stub columns are listed in Table 2. The steel tubes were filled with concrete in three layers with tamping and vibration. At the end of pouring concrete, the thermocouples were inserted inside four numbers of tubes till the middle height (150 mm) for each type of concrete mix. These thermocouples were used to observe the core temperature of the stub columns during heating in the oven.

Table 2 Number of CFST stub columns.

Type of Mix	Temperature	Cross-section D × t × H (mm)	No. of CFST stub columns	Total No.
0% FCS (control)	25°C	114 × 2.4 × 300	2	14
	200°C		3	
	400°C		3	
	600°C		3	
	800°C		3	
50% FCS	25°C		2	14
	200°C		3	
	400°C		3	
	600°C		3	
	800°C		3	
100% FCS	25°C		2	14
	200°C		3	
	400°C		3	
	600°C		3	
	800°C		3	

2.4 Test procedure

After 28 days of moist curing, the stub columns and concrete cylinders were kept outside in the room temperature until the test day (10 to 12 days). The stub columns were placed in the electric furnace for heating as shown in Figure 3. Considering the objective of this research, the heating rate was set between 4°C/min and 6°C/min, and the furnace temperature were calibrated with maximum difference between the required temperature of the sample and the furnace was 10-20°C. When the core temperature of the stub columns reached to the targeted temperature, the oven was switched off and the samples remained in the oven for slow cooling to the room temperature. The core temperature was monitored by a data logger via thermocouple which was installed during the casting of columns. After cooling the samples were taken out from the oven and tested for residual compressive strength. At the same time two unheated stub column form the same batch was tested for compressive strength. Strain gauges were mounted in the steel surface of the CFST columns to determine longitudinal and hoop strain during the test. Three concrete cylinder from the same mix were also tested to determine the compressive strength of the concrete.

Figure 3 Electric furnace (left) and CFST column inside the furnace (right)

3 RESULTS AND DISCUSSION

3.1 Performance of CFST stub columns at ambient temperature

The failure modes of the six CFST stub columns for the three types of mixes at ambient temperature are shown in Figure 4. The figure shows that all stub columns are subject to a local outward buckling failure for the three mixes at a different location of the specimens. In general, the use of FCS fine aggregates had no obvious influence on the failure mode.

The effect of ferrochrome slag replacement on the measured axial load versus the deformation curves is shown in Figure 5(a). In the figure, each curve is the average of two curves of two specimens for each mix. From Figure 5(a), the influence of FCS fine aggregates on the shape of load-deformation curves at ambient temperature is not obvious. In general, the load-deformation curves of the columns with three different mixes typically had an ascending branch, a descending branch and a stable branch. It can be seen in Figure 5(a) that the increase in the FCS percentage in the concrete mix increases the ultimate load. For instance, the values of ultimate load for one specimen with 50% FCS mix (N_{ua}=802.24 kN) and 100% FCS mix (N_{ua}=857.76 kN) were increased by 2.84% and 9.95%, respectively, compared with the 0% FCS mix (N_{ua}=780.08 kN). This strength behavior is aligned with strength enhancement concrete with addition of FCS fine aggregate. Compressive strengths of control, 50% FCS, and 100% FCS concrete mixtures were 48.0, 52.5, and 54.4 MPa, respectively. Modulus of elasticity of the mixes were 37, 43 and 46 GPa, respectively.

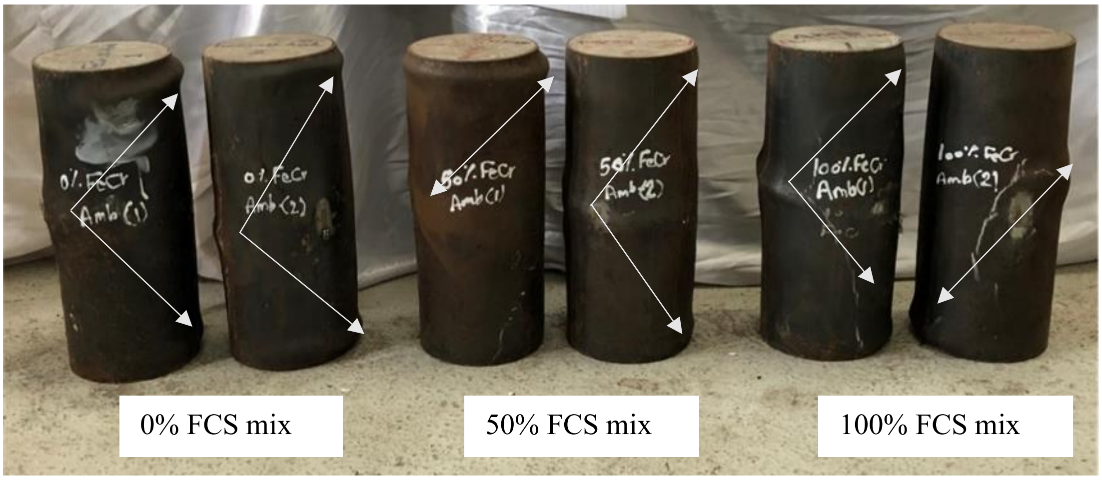

Figure 4 Failure modes of CFST stub columns at ambient temperature

The load versus longitudinal (compressive) and hoop (tensile) strains curves of the CFST stub columns at ambient temperature for the three mixes namely; 0%_FCS mix, 50%_FCS mix and 100%_FCS mix are presented in Figure 5(b), where the negative strain values indicate compression. The curves for one specimen from each group are shown in the figure. The strain values were directly obtained from the reading of the strain gauges installed at the mid-height of specimens. In general, the load-strain curves have an ascending branch till the initial local buckling then a descending branch.

From Figure 5(b), it can be seen that load strain behaviour of CFST column with 100%_FCS is almost linear up to the Peak load, which signify the uniform stiffness of 100%_FCS concrete. On the other hand, the stiffness of column with normal concrete was decreased with non-linear behaviour after 650 kN. This differences is due to stiff behaviour of FCS fine aggregate compared to natural crushed stone fine aggregate. For this reason, at peak load, the failure of 100%_FCS concrete in CFST column was brittle as can be realized from the sharp decrease in load (see Figure 5).

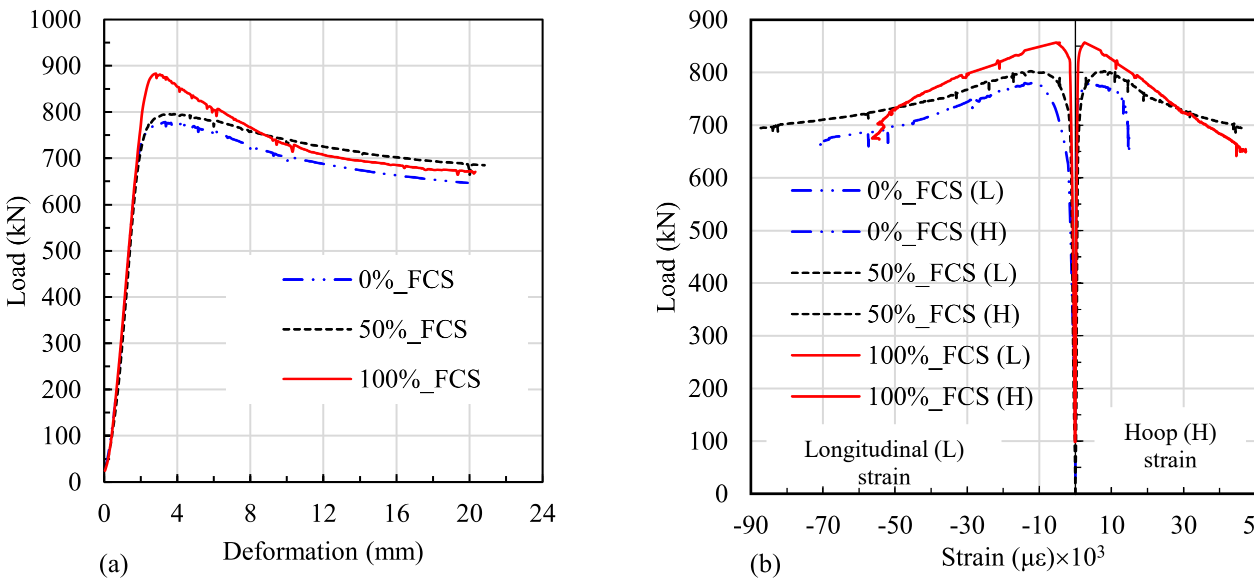

Fig. 5 (a) Load-deformation (b) load-strain curves for composite columns with different mixes at ambient temperature

3.2 Performance of CFST stub columns after exposed to elevated temperature

The failure modes of the 12 CFST stub columns for the three types of mixes after exposed to elevated temperatures (200°C, 400°C, 600°C and 800°C) are presented in Figure 6. All stub columns that exposed to elevated temperatures 200°C and 400°C are subjected to a local and minor global outward buckling failure for the three mixes. The local buckling occurred at the top and bottom height of the specimens and outward global buckling occurred at the mid-height of the specimens. On the other hand, the stub columns that exposed to elevated temperatures 600°C and 800°C are subjected to a local outward buckling failure for the three mixes that located at the top height of specimens and a different location as well.

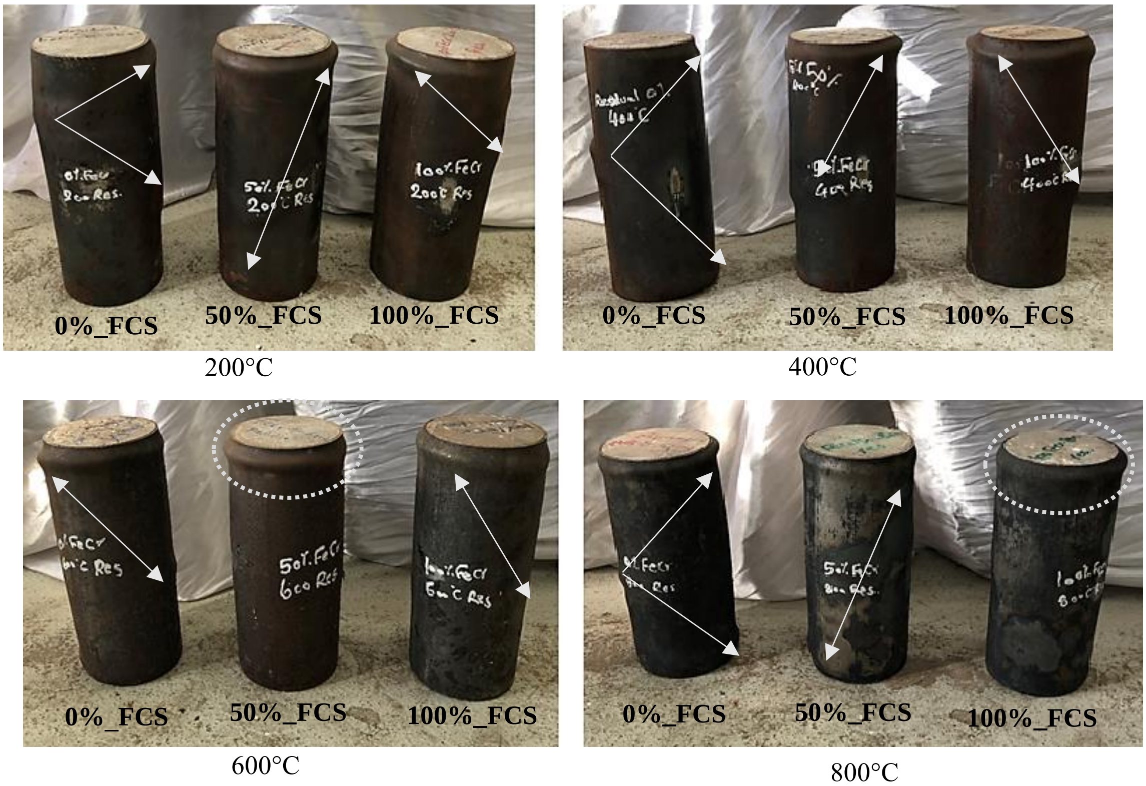

Figure 6 Failure modes of CFST stub columns after being exposed to elevated temperature under compression

After the compression test, the steel tubes for 0%_FCS and 100%_FCS mixes that exposed to elevated temperature 400°C and 800°C were removed to observe the failure mode of the core concrete, as illustrated in Figure 7. From the figure, it can be observed that the core concrete of all specimens was crushed at the region where the outward local or global buckling occurred in the specimens that exposed to elevated temperature. Meanwhile, the concrete was totally cracked for the specimens that was exposed to 800°C.

During the compression test load-displacement curves were obtained using installed displacement transducer attached to cross heard of actuator and load cell via data logger. The measured residual axial load versus the deformation curves of CFST stub columns for the three types of mixes after exposed to elevated temperatures 200°C and 800°C are shown in Figure 8. For each type of concrete mix, two CFST stub columns were tested for residual strength. The curves in Figure 8(a) represented one specimen for each mix.

In general, the residual load-deformation curves for the three mixes typically had an ascending branch, a descending branch and a stable branch after they were exposed to elevated temperatures of 200°C and 400°C, while the residual curves for the three mixes had an ascending, a slightly descending and a stable branch after they were exposed to elevated temperatures 600°C and 800°C. The CFST stub columns showed more ductile behavior with the increase of exposure temperature as shown in Figure 8(a). CFST columns with FCS fine aggregate showed stiffer behavior than the CFST column with conventional concrete, as can be realized from the residual load-displacement curves in Figure 8(a). The residual ultimate load of 100% FCS concrete mix was higher compared with the other mixes after it was exposed to elevated temperatures (200°C, 400°C, 600°C and 800°C).

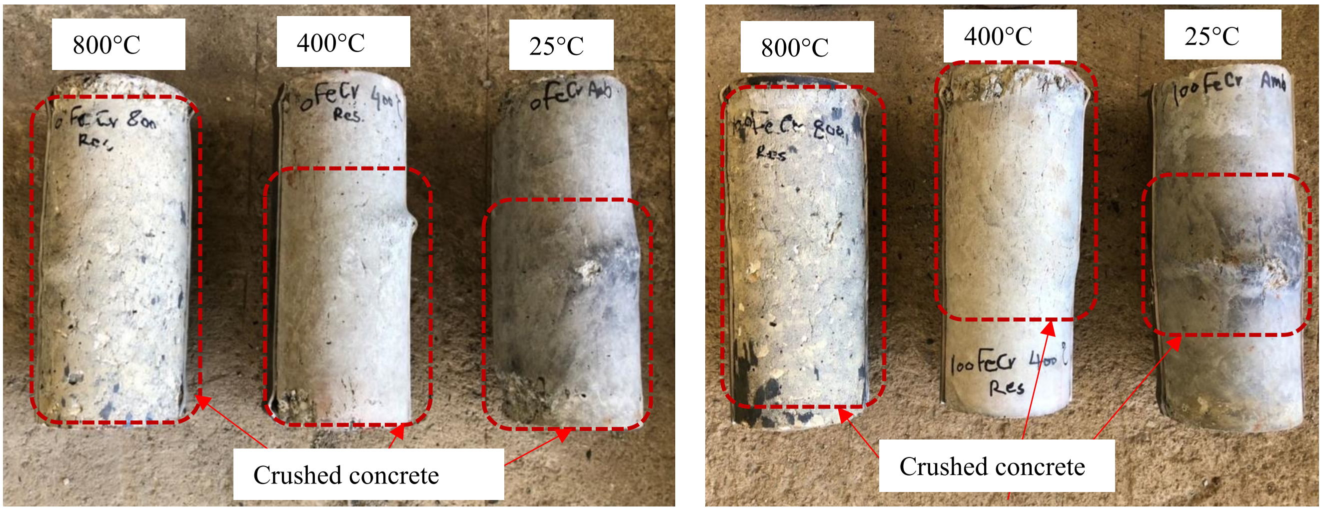

(a) 0% FCS mix (b) 100% FCS mix

Figure 7 Failure modes of the core concrete after being exposed to elevated temperature 400°C and 800°C.

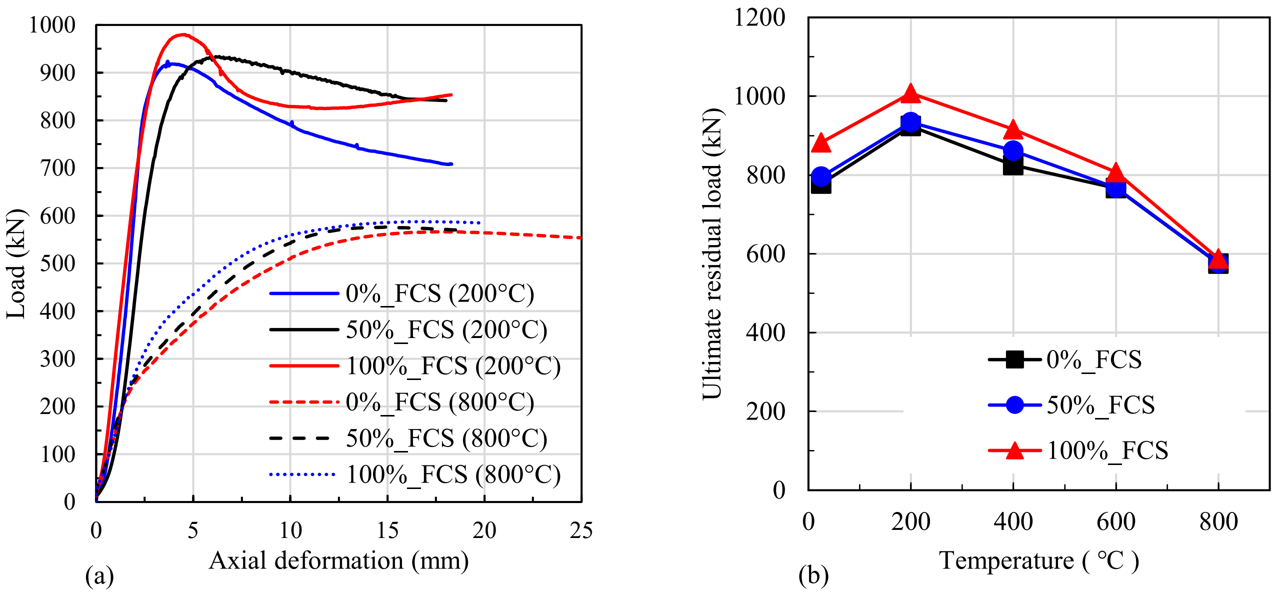

(a) (b)

Figure 8 (a) Load-deformation curves for the different mixes after being exposed to elevated temperatures (b) Variation of residual ultimate strength of CFST stub columns with temperature

In this study, the residual peak load of all stub columns were taken as the residual ultimate loads. The loading point in residual load-displacement curve where the non-linearity starts was taken as yield load the column. The ultimate load and yield load for the all CFST columns exposed to different elevated temperatures are presented in Table 3. The variation of residual strength of the CFST columns with the exposure temperature is plotted in Figure 8(b). From the table and figure, it can be seen that the value of residual ultimate load for the three mixes increased with the increase in the temperature up to 400°C, then it was decreasing gradually after it was exposed to the elevated temperatures 600°C and 800°C compared with the average ultimate load at the ambient temperature. For instance, the values of residual ultimate load at 200°C for control mix (N_{ur}=923.72 kN), 50% FCS mix (N_{ur}=869.44 kN) and 100% FCS mix (N_{ur}=1007.44 kN) were increased by 19%, 9% and 14%, respectively, compared with the ultimate load at ambient temperature for each mix. This is due to slight increase of concrete compressive strength at 200°C, as found in the previous study on the effect of high temperature on the compressive strength of concrete with FCS fine aggregates [13].

Table 3 Residual ultimate and axial yield load of CFST stub columns after exposed to elevated temperatures

Type of Mix	Temperature (°C)	Specimen label	Residual ultimate Load (N_{ur}) (kN)	Axial Yield Load (kN)
0% FCS Mix	25°C	0% FCS -amb.	778.16	670.00
	200°C	0% FCS -200-Res.	923.72	890.00
	400°C	0% FCS -400-Res.	824.80	450.00
	600°C	0% FCS -600-Res.	766.36	460.00
	800°C	0% FCS -800-Res.	566.40	250.00
50% FCS mix	25°C	50% FCS -amb.	795.66	731.00
	200°C	50% FCS -200-Res.	869.44	750.00
	400°C	50% FCS -400-Res.	861.16	530.00
	600°C	50% FCS -600-Res.	767.08	625.00
	800°C	50% FCS -800-Res.	576.08	305.00
100% FCS mix	25°C	100% FCS -amb.	882.70	845.00
	200°C	100% FCS -200-Res.	1007.44	890.00
	400°C	100% FCS -400-Res.	915.56	780.00
	600°C	100% FCS -600-Res.	807.12	600.00
	800°C	100% FCS -800-Res.	587.52	295.00

The load versus longitudinal (compressive) and hoop (tensile) micro strains curves of the CFST stub columns after they were exposed to elevated temperatures are presented in Figure 9, where the negative strain values indicate compression. In the figure, the strain values were obtained from the strain gauges installed at the mid-height of the specimens. Some curves in Figure 9(a) are discontinued or sharply descend after reaching the ultimate strength; this could be due to strain gauge damage or debonding caused by local buckling of steel at the strain gauge location.

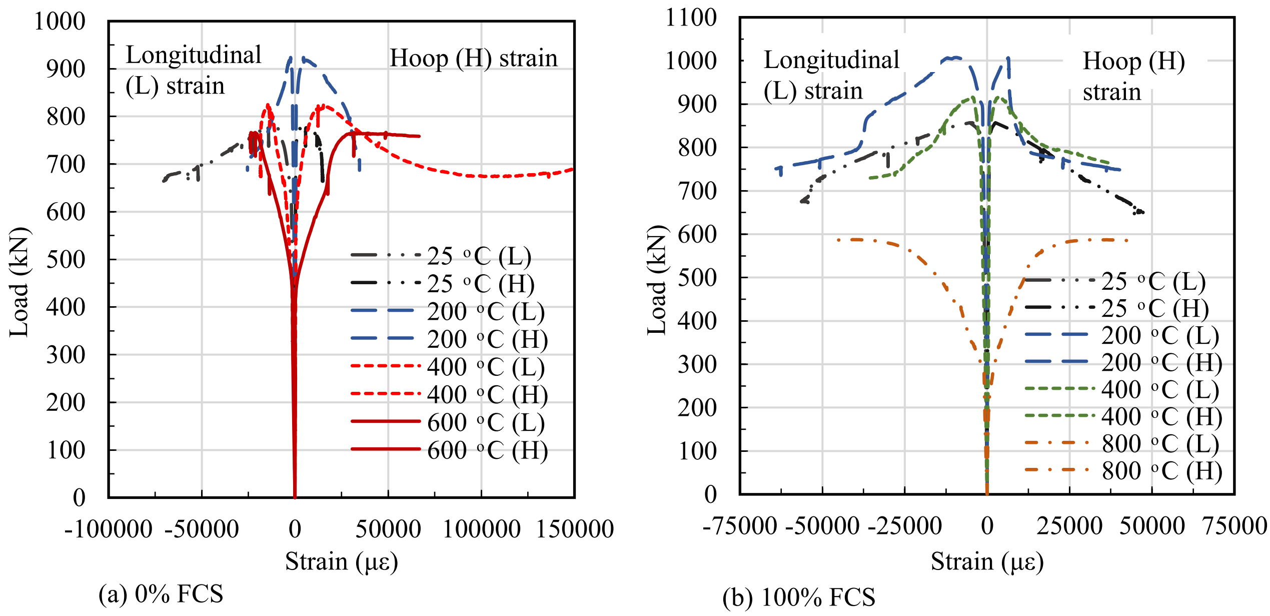

Figure 9 Residual load-strain curves for of CFST stub columns for each mix after being exposed to different elevated temperatures

From Figure 9, the load-strain curves have an ascending branch till they reached the residual ultimate load then a descending branch for the exposure temperatures of 200°C and 400°C, regardless of the type of concrete. Whereas, the residual load-strain curves of the specimens for the exposure temperatures of 600°C and 800°C had a slightly descending branch after they reached the residual ultimate load. This may be due to the fact that the concrete at these high temperatures (600°C and 800°C) lost its strength significantly.

3.3 Comparison of test results to ACI 318-19 and Eurocode 4

The test results of the CFST stub columns at ambient temperature are compared with the result of Eurocode 4 (EC4-1994) [21] and American Concrete Institute (ACI 318-19-2019) [22]. Eurocode provides an Equation (1) to find the axial compressive load for circular CFST stub columns as follow:

$$N_{pl.Rd} = A_a \eta_a \frac{f_y}{\gamma_a} + A_c \frac{f_{ck}}{\gamma_c}\left[1 + \eta_c \frac{t}{d}\frac{f_y}{f_{ck}}\right] \qquad (1)$$

where γ_a and γ_c are the partial material safety factors for steel and concrete, respectively, which can be taken as 1.0 and 1.3, respectively. For stub columns with pure axial loading the values of $\eta_a = \eta_{a0}$ and $\eta_c = \eta_{c0}$ are given by the following formulas:

$\eta_{a0} = 0.25(3 + 2\bar{\lambda})$ and $\eta_{c0} = 4.9 - 18.5\bar{\lambda} + 17\bar{\lambda}^2$

for very short column and eccentricity $e = 0$, $\bar{\lambda} \cong 0$

$\eta_{a0} = 0.75$ *and* $\eta_{c0} = 4.9$

f_y and f_{ck} are the yield strength of the steel section and the characteristic compressive strength of the concrete, respectively.

Whereas, ACI 318-19 provides a formula to find the axial compressive force of the CFST as given in Equation (2),

$$N_{ACI} = 0.85 A_c f'_{ck} + A_{st} f_y \qquad (2)$$

where A_{st} and A_c are the cross-sectional areas of the steel and concrete sections, respectively.

The results obtained from the experimental test, EC4 and ACI 318-19 for the CFST stub columns at ambient temperature and after exposed to 800°C are summarized in Table 4.

Table 4 Comparison of test results with EC 4 and ACI 318-11 for CFST stub columns at different temperatures

Type of Mix	Specimen label	N_{exp} (kN)	f_{ck} (Mpa)	N_{EC4} (kN)	N_{ACI} (kN)	N_{exp}/ N_{EC4}	N_{exp}/ N_{ACI}
Without heating	0%_FCS -amb.	778.16	48.0	746.26	627.54	1.04	1.24
	50%_FCS -amb.	802.24	52.51	778.73	663.44	1.03	1.21
	100%_FCS-amb	857.76	54.42	792.48	678.65	1.08	1.26
After heating to 800°C	0%_FCS-800°C	566.40	5.30	438.75	287.57	1.29	1.97
	50%_FCS-800°C	576.08	6.90	450.20	300.22	1.28	1.92
	100%_FCS-800°C	587.52	8.04	458.50	309.41	1.28	1.90

As can be seen in table, a conservative prediction from the ACI 318-19 code was obtained for the three concrete mixtures. These results are supported by other researches [14,23] for conventional concrete. On average, the experimental results are 24 % and 5% more than the calculated values by ACI 318 [22] and EC4 [21], respectively. The reason behind this difference between the ACI 318 and EC4 is due to the confinement effect which is considered in EC4. In case of heated specimens, the concrete strength was reduced based on the previous research on concrete with FCS fine aggregate [22]. Using the reduced concrete strength, the residual strength of the CFST columns were calculated as shown in Table 4. As can be seen, both EC4 and ACI318 underestimated the peak load of the heated CFST columns. The maximum deviation in predicting the peak load of the post-heated CFST columns by EC4 and ACI318 was 29% and 97%, respectively. Overall, EC4 provides a closer prediction for both unheated and post-heated CFST columns than ACI318.

4 CONCLUSIONS

This research presented a study on the behavior of concrete filled steel tubular (CFST) stub columns that were filled with conventional concrete and concrete with ferrochrome slag (FCS) as a fine aggregate replacement with different percentages (50% and 100%) at ambient temperature and elevated temperatures from 200°C to 800°C. In relation to the objectives of this study, the major conclusions are summarized as follows:

1. The mechanical properties CFST stub columns with FCS concrete were higher than those of the CFST stub columns with conventional concrete. This is due to the enhancement of compressive strength and the modulus of elasticity concrete with FCS fine aggregate.
2. After heating at elevated temperatures, the residual ultimate strength of the CFST stub columns for the three mixes increased slightly by the increasing of temperature up to 400°C. Reduction in strength compared to the room temperature strength was observed at exposure temperature above 400°C. In general, the existence of FCS in the concrete mix enhanced the ultimate strength of CFST stub columns compared to CFST column with conventional concrete at all elevated temperatures.
3. The ACI code provides a conservative prediction of ultimate strength for the unheated and post heated CFST stub columns compared to the experimental results for all three concrete mixes. On the other hand, for both unheated and post-heated CFST columns, EC4 provides a closer prediction than ACI code.
4. As the CFST columns with 100% FCS showed superior performance in terms of ultimate load bearing capacity and stiffness compared to the column with conventional concrete, ferrochrome slag is recommended to be used in the concrete mix for CFST columns.

ACKNOWLEDGMENT

The financial support from Ministry of Higher Education, Research and Innovation (MOHERI), Oman is acknowledged. The financial grant number is RC/RG-ENG/CAED/18/01.

REFERENCES

1. Qasrawi, H., Shalabi, F., & Asi, I., Use of low CaO unprocessed steel slag in concrete as fine aggregate. Construction and Building Materials 23(2), 1118-1125, (2009). https://doi.org/10.1016/j.conbuildmat.2008.06.003.
2. Fares, A. I., Sohel, K. M. A., Al-Jabri, K., & Al-Mamun, A., Characteristics of ferrochrome slag aggregate and its uses as a green material in concrete–A review. Construction and Building Materials 294, 123552, (2021). https://doi.org/10.1016/j.conbuildmat.2021.123552.
3. Al-Jabri, K., Shoukry, H., Khalil, I. S., Nasir, S., & Hassan, H. F., Reuse of waste ferrochrome slag in the production of mortar with improved thermal and mechanical performance. Journal of Materials in Civil Engineering, 30(8), 04018152, (2018). https://doi.org/10.1061/(ASCE)MT.1943-5533.0002345.
4. Rajashekar, K., & Reddy, C. S., An experimental study on use of ferrochrome slag aggregate in concrete making. ICI Journal, 15(4), 25-9, (2015).
5. Song, T. Y., Han, L. H., & Yu, H. X., Concrete filled steel tube stub columns under combined temperature and loading. Journal of Constructional Steel Research, 66(3), 369-384, (2010), https://doi.org/10.1016/j.jcsr.2009.10.010.
6. Shams, M., & Saadeghvaziri, M. A., State of the art of concrete-filled steel tubular columns. Structural Journal 94(5), 558-571 (1997).
7. Nishiyama, I., Morino, S., Sakino, K., Nakahara, H., Fujimoto, T., Mukai, A., et al., Summary of research on concrete-filled structural steel tube column system carried out under the US–Japan cooperative research program on composite and hybrid structures BRI Research Paper No.147, Building Research Institute, Japan (2002).
8. Schneider, S. P., Axially loaded concrete-filled steel tubes. Journal of structural Engineering 124(10), 1125-1138 (1998). https://doi.org/10.1061/(ASCE)0733-9445(1998)124:10(1125).

9. Li, W., Luo, Z., Tao, Z., Duan, W. H., & Shah, S. P., Mechanical behavior of recycled aggregate concrete-filled steel tube stub columns after exposure to elevated temperatures. Construction and Building Materials 146, 571-581, (2017). https://doi.org/10.1016/j.conbuildmat.2017.04.118.
10. Bahrami, A., & Nematzadeh, M., Bond behavior of lightweight concrete-filled steel tubes containing rock wool waste after exposure to high temperatures. Construction and Building Materials 300, 124039, (2021). https://doi.org/10.1016/j.conbuildmat.2021.124039.
11. Ekmekyapar, T., & Alhatmey, I. A., Post-fire resistance of internally ring stiffened high performance concrete filled steel tube columns. Engineering Structures 183, 375-388, (2019). https://doi.org/10.1016/j.engstruct.2019.01.024.
12. Han, L. H., Li, W., & Bjorhovde, R., Developments and advanced applications of concrete-filled steel tubular (CFST) structures: Members. Journal of constructional steel research, 100, 211-228, (2014). https://doi.org/10.1016/j.jcsr.2014.04.016.
13. Islam, M. Z., Sohel, K. M. A., Al-Jabri, K., & Al-Harthy, A., Properties of concrete with ferrochrome slag as a fine aggregate at elevated temperatures. Case Studies in Construction Materials 15, e00599, (2021). https://doi.org/10.1016/j.cscm.2021.e00599.
14. Hamidian, M. R., Shafigh, P., Jumaat, M. Z., Alengaram, U. J., & Sulong, N. R., A new sustainable composite column using an agricultural solid waste as aggregate. Journal of cleaner production 129, 282-291 (2016). https://doi.org/10.1016/j.jclepro.2016.04.072.
15. Yu, X., Tao, Z., & Song, T. Y., Effect of different types of aggregates on the performance of concrete-filled steel tubular stub columns. Materials and Structures 49(9), 3591-3605 (2016). https://doi.org/10.1617/s11527-015-0742-z.
16. Nematzadeh, M., Karimi, A., & Gholampour, A., Pre-and post-heating behavior of concrete-filled steel tube stub columns containing steel fiber and tire rubber. Structures 27, 2346-2364, (2020). https://doi.org/10.1016/j.istruc.2020.07.034.
17. Ren, Q. X., Zhou, K., Hou, C., Tao, Z., & Han, L. H., (2018). Dune sand concrete-filled steel tubular (CFST) stub columns under axial compression: Experiments. Thin-Walled Structures 124, 291–302, (2018). https://doi.org/10.1016/j.tws.2017.12.006.
18. Xu, Q., Zhang, Y., Liu, H., Zhou, M., Wang, Q., & Lin, H., Effect of spontaneous-combustion coal gangue aggregate on axial performance of square concrete-filled steel tube stub columns. Structures 44, 216-235 (2022). https://doi.org/10.1016/j.istruc.2022.07.044.
19. Yang, Y. F., & Hou, R., Experimental behaviour of RACFST stub columns after exposed to high temperatures. Thin-walled structures 59, 1-10, (2012). https://doi.org/10.1016/j.tws.2012.04.017.
20. ASTM C33/C33M-18, Standard specification for concrete aggregates. Technical Report, ASTM International, West Conshohocken, PA., (2018).
21. BS EN 1994-1-1: 2004, Design of Composite Steel and Concrete Structures, Part1.1, General Rules and Rules for Building British Standards Institution, London (2004).
22. ACI 318-19, Building Code Requirements for Structural Concrete: An ACI Standard: Commentary on Building Code Requirements for Structural Concrete (ACI 318R-19). American Concrete Institute. (2019). https://doi.org/10.14359/51716937.
23. Abed, F., AlHamaydeh, M., & Abdalla, S., Experimental and numerical investigations of the compressive behavior of concrete filled steel tubes (CFSTs). Journal of Constructional Steel Research 80, 429-439, (2013). https://doi.org/10.1016/j.jcsr.2012.10.005.

Proceedings of the 12th International Conference on Structures in Fire

Concrete Structures in Fire

A NOMOGRAM FOR PREDICTING FIRE-INDUCED SPALLING

Arash Teymori Gharah Tapeh[1], Mohammad Khaled al-Bashiti[2], Alireza Ghasemi[3], Haley Hostetter[4], Deanna Craig[5], M.Z. Naser[6]

ABSTRACT

Concrete, encountering harsh conditions such as fire, is prone to damage. One of the most critical ones is spalling, and this tragic event continues to be a challenging area of research. A thorough examination of the available literature reveals the difficulty of anticipating spalling. As a result, this work proposes a nomogram as a tool to predict spalling of concrete mixtures. The suggested solutions enable interested academics and engineers to visually assess a concrete mixture's susceptibility to spalling without costly laboratory tests. The outcome of this study is a simple tool for practitioners and structural designers to predict spalling in their designed sections disregarding the complex nature of this long-standing problem.

Keywords: Logistic Regression; Spalling, Fire; Concrete; Nomogram.

1 INTRODUCTION

Due to its high tendency not to interact with external conditions, concrete has become one of the two primary materials used in construction. However, in the harsh conditions of fire, concrete will undertake some degree of damage. Such damage is fundamentally correlated to the main components of concrete (including but not limited to aggregates, sand, (water/sand) ratio, (silica-fume/ binder) ratio, fly-ash, etc.) and is controlled by their portion. Spalling is one of the most complicated damages to consider [1, 2].

The spalling phenomenon is a condition in which we have a disintegrated chunk of concrete from one of its member sides. Reduction in size and exposure of crucial elements (such as bars and other reinforcement) to harsh conditions, as well as high-temperature propagation of concrete due to spalling can result in many unexpected failures in structures [3–5].

Remarkable works and projects have assessed both the traditional and high-strength concrete performance at high temperatures [4, 5]. They have shown that modern concrete (UHPC) is more inclined to spall in comparison to moderate-strength concrete due to the dense microstructure that UHPC concrete has. A deep dive into the open literature [6–9] show that we still suffer from the lack of a reliable and verified procedure

[1] Ph.D. Student, School of Civil & Environmental Engineering and Earth Sciences (SCEEES), Clemson University, USA,
e-mail: ateymor@clemson.edu, ORCID: https://orcid.org/0000-0001-9174-079X
[2] Ph.D. Student, School of Civil and Environmental Engineering & Earth Sciences (SCEEES), Clemson University, Clemson, SC 29634, USA.
e-mail: malbash@clemson.edu, ORCID: https://orcid.org/ 0000-0002-3889-2564
[3] Ph.D. Student, School of Civil and Environmental Engineering & Earth Sciences (SCEEES), Clemson University, Clemson, SC 29634, USA.
e-mail: ghasemi.alireza2121@gmail.com, ORCID: https://orcid.org/0000-0003-4745-8169
[4] Ph.D. Student, School of Civil and Environmental Engineering & Earth Sciences (SCEEES), Clemson University, Clemson, SC 29634, USA.e-mail: hhostet@g.clemson.edu, ORCID: https://orcid.org/0000-0002-4269-9820
[5] MSc. Student, School of Civil and Environmental Engineering & Earth Sciences (SCEEES), Clemson University, Clemson, SC 29634, USA.
e-mail: dcraig3@g.clemson.edu,
[6] Assistant Professor, School of Civil and Environmental Engineering & Earth Sciences (SCEEES), Clemson University, Clemson, SC 29634, USA.
AI Research Institute for Science and Engineering (AIRISE), Clemson University, Clemson, SC 29634, USA
e-mail: mznaser@clemson.edu, ORCID: https://orcid.org/0000-0003-1350-3654
https://doi.org/10.6084/m9.figshare.22154825

by which we can predict the spalling phenomenon. Furthermore, in contrast with many other phenomena in civil engineering, there are limited guidelines and provisions for predicting spalling.

To tackle the difficulties associated with spalling, taking advantage of current computational methods, including artificial intelligence (AI), machine learning, and big data, seems attractive enough to be applied in this project. The fundamental assumption herein is that capturing the correlation through a data-driven analysis could be possible rather than traditional methods[10].

Even though rigorous jobs have been carried out so far to apply AI in engineering, most of these works can be categorized as a black-box procedure (where we have final prediction and output without any insight into the whole process). As a result, we propose to use the logistic regression (LR) algorithm to predict spalling. LR models can demonstrate the correlation between input values and output features in different ways, some of which are graphs or nomograms.

In the current project, we map a path to discover a heuristic nomogram through LR to estimate the appropriate degree of predicting spalling phenomena. In this pursuit, 293 observations from the different tests were gathered and analyzed. Our findings show that predicting spalling through LR has high accuracy and can predict spalling through the model component.

2 DATA COLLECTION AND METHODOLOGY

For the current project, using data from[11], we collected 293 different data samples containing 11 different input variables (ratio of water to binder, ratio of silica-fume to binder, ratio of fly-ash to binder, ratio of GGBS to binder, ratio of fine aggregate to binder, ratio of coarse aggregate to binder, moisture content of concrete mixture, rate of heating per minute, maximum exposure temperature, the maximum size of aggregate, and the characteristic length) and one target variable (this output value categorized as Spalling/No-Spalling) to find a spalling occurrence in concrete sections as a function of different mixtures. Considering Table (1), one can see that the dataset has a balanced and healthy distribution range for identified variables.

Table 1: Concrete mixtures database with statistical features.

Parameters	Mean	Median	Standard Deviation	Range	Minimum	Maximum	Skewness
Water/binder (W/b)	0.371	0.33	0.124	0.42	0.19	0.61	0.4232712
Coarse aggregate/binder (ca/b)	1.733	1.77	0.900	3.95	0	3.95	0.1084053
Fine aggregate/binder ratio(fa/b)	1.658	1.51	0.653	2.93	0.45	3.38	0.7925641
Heating rate (°C/min)	28.55	5	42.028	239.75	0.25	240	1.7831517
Moisture content of concrete(M)	0.03132	0.04	0.020	0.07	0	0.07	-0.386714
Characteristic distance of the concrete (D)	61.91	50	37.606	180	20	200	2.0872133
Maximum exposure temperature (T-max °C)	568.2	600	246.201	1100	100	1200	0.2212357
Silica fume/binder(sf/b)	0.03297	0	0.062	0.207	0	0.207	1.6677876
Maximum size of aggregate (Sa)	12.76	13	6.608	31.88	0.12	32	0.1848011
GGBS/binder (G/b)	0.04328	0	0.100	0.458	0	0.458	2.3875603
Fly ash/binder (F/b)	0.02272	0	0.071	0.546	0	0.546	3.4990225

2.1 Nomogram Development

The logistic regression is one the most used algorithm for classifying two different outputs, developed by David Cox[12], is used for developing the nomogram in this study. The LR algorithm uses the *Sigmoid function*. The suggested nomogram was created in the R programming language (version 4.1.2).

The following algebraic form is used to fit the spalling occurrence once the LR algorithm has been properly validated (Eq. 1). This illustration indicates that the occurrence of spalling is determined using the collected database's specified characteristics. A logistic, *Sigmoid* equation is then used to determine the likelihood that spalling will occur (Eq. 2). Equation 2 returns two distinct values, one for no spalling equal to zero and the other for spalling equal to one, respectively. To build the nomogram and determine the likelihood of spalling, the sigmoid function from the R Toolbox and the *rms* (regression modeling strategy) R package [13]are specially utilized.

$$Spalling \sim W/b + Ca/b + Fa/b + H + M + D + T + Sf/b + Sa + G/b + F/b \quad \text{Eq. 1}$$

$$Propensity \text{ of } Spalling = \frac{1}{1 + exp^{-(\beta 0 + \beta 1 X1 + \beta 2 X2 + \cdots)}} \quad \text{Eq. 2}$$

Where β_0, β_1, etc., are coefficients[3] derived during the training process, and X_1, X_2, etc., are the features identified in our database (and those listed in Eq. 1).

3 FINDINGS AND DISCUSSION

3.1 Validation metrics

For the current project, the collected data set has passed the split procedure in which it has separated into train and test sets that start from 70% in the train set and corresponding 30% in the test set. For the validation assessment, test sets were used. Also, the confusion matrices, which encompass three main elements, are considered for data analysis, usually used for binary and multi-classification problems. The three metrics elements are 1- True Positive Rate (TPR) or Sensitivity or Recall (TP), 2- True Negative Rate (TNR) or Specificity, and 3- Accuracy (ACC). The metrics above define as 1- actual positive cases correctly identified, 2- actual negative cases correctly identified, and the assessment ratio of correct predictions to the total number of samples, respectively. All the metrics formulas are described hereunder[14].

$$\text{True Positive Rate (TPR) =Sensitivity} = \frac{\text{TP}}{\text{TP+FN}} \quad (1)$$

$$\text{True Negative Rate (TNR) =Specificity}= \frac{\text{TN}}{\text{TN+FP}} \quad (2)$$

$$\text{Accuracy (ACC)} = \frac{\text{TP+TN}}{\text{TP+TN+FP+FN}} \quad (3)$$

3.2 Logistic regression result

R programming language (R version 4.1.2 (2021-11-01)) was used, and all the compiled, as well as the compiled dataset were then input into the R for analysis. Additionally, for data training, the logistic regression modeling algorithm adopted a data set formerly divided into train and test. Then, 10-fold cross-validation is used for the train set to avoid any biases stemming from data ordering. Lastly, confusion matrices were calculated to visualize the model performance in different sub-dataset from the original dataset.

[3] *Spalling=-9.6005W/b+0.3444Ca/b+1.2066Fa/b+0.0089H+40.3826M+0.0224D+0.0070T+14.2181Sf/b-0.1055Sa+4.2498G/b+0.3490F/b-6.1001*

At the beginning of the training procedure, the model accuracy was relatively poor (nearly 70%). Therefore, using the ML validation technique can enhance the model's accuracy and prevent overfitting. Also, 10-fold cross-validation was used to increase the data accuracy for the 70/30 ratio and boost the accuracy from 70% to 89%. For the same purpose of increasing data accuracy, the same procedure has been carried out three times to have a better result for 80/20 and 90/10 ratios. Lastly, for the 90/10 split ratio, 96.6% accuracy of the corresponding test set has been achieved, and its nomogram developed. As mentioned earlier, confusion matrices encompassed predicted and actual classes and explored the logistic regression model performance. Entries in diagonal and off-diagonal of these matrices indicate the model's true and false prediction of spalling phenomena. Confusion matrices on the test set based on maximum accuracy for three different split ratios are presented in Tables 2-4.

Table 2: confusion matrix for Spalling (Considering highest accuracy for 70/30 split ratio)

True classes	Predicted classes ('Positive' Class: not spalling)		True sum
	not spalling	spalling	
not spalling	31	7	38
spalling	2	49	51
Sum	33	56	89
Error (%)	0.06	0.12	0.1

Table 3: confusion matrix for Spalling (Considering highest accuracy for 80/20 split ratio)

True classes	Predicted classes ('Positive' Class: not spalling)		True sum
	not spalling	spalling	
not spalling	21	2	23
spalling	1	35	36
Sum	22	37	59
Error (%)	0.04	0.05	0.05

Table 4: confusion matrix for Spalling (Considering highest accuracy for 90/10 split ratio)

True classes	Predicted classes ('Positive' Class: not spalling)		True sum
	not spalling	spalling	
not spalling	10	0	10
spalling	1	19	20
Sum	11	19	30
Error (%)	0.09	0	0.03

The pooled results of different test-train ratio approaches are summarized in Table 5, including sensitivity (precision of model in predicting not spalling classes), and Specificity (precision of model in predicting spalling cases), and accuracy.

Table 5: Sensitivity, Specificity, and Accuracy for the three main test-train split (70%-80%-90% Train and 30%-20%-10%Test)

Performance measure results of LRM models for different split ratio			
Split ratio	Sensitivity	Specificity	Accuracy
70/30%(Train-Test)	0.9394	0.8750	0.8989
80/20%(Train-Test)	0.9545	0.9459	0.9492
90/10%(Train-Test)	0.9091	1.0000	0.9667

3.3 Variable Importance

The importance of variable for the 11-input variables was computed in this analysis. The result is summarized in Figure 1 to visualize the feature's importance. As can be seen, the four most significant variables are the maximum exposure temperature, water/binder ratio, heating rate, and moisture content of concrete correspondingly. On the contrary, the fly ash/binder ratio has the least significance in spalling occurrence, which means that it has the least interaction in any reaction regarding the increasing void pressure in concrete. Furthermore, to eliminate the multiplicity of independent variables, the top five significant variables chose and assigned to the logistic model to find the model with the least variable. The result shows that less than 5% differentiation exists between all and most significant variables, which can be ignored for simplicity in future studies.

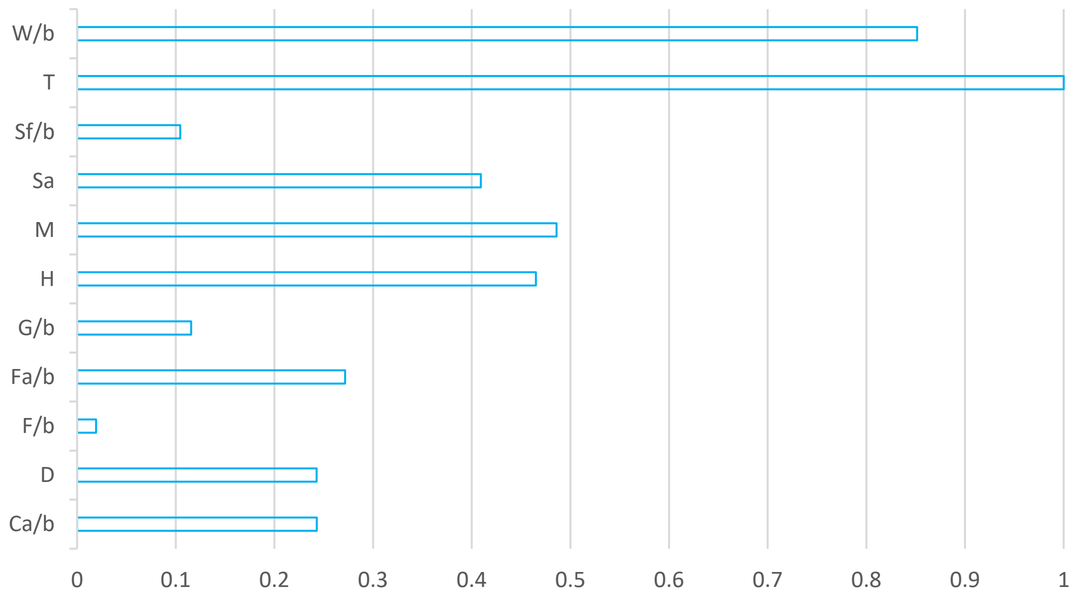

Figure 1: Feature Importance

3.4 Nomogram

Like the previous part, we begin by assessing the logistic regression model, which had an area under the curve metric of 92% and 100% in training and testing, respectively. Additionally, the model's sensitivity, Specificity, and accuracy scores were 0.910, 1.000, and 0.961, respectively; as the data shows, the model has excellent performance.

3.4.1 Development of Nomogram

In Fig. 2, the created nomogram is shown. Based on receiving a total amount of points, this nomogram determines a certain concrete mixture's propensity to spall based on its characteristics (ranging from 0-100). This total number of points is also used to calculate the likelihood of spalling, which is the arithmetical sum of the points allotted to independent features. As one can see, each feature must be scaled separately; hence the scale of the points associated with each feature must also be done correctly. This nomogram shows the possibility of spalling with varying degrees of confidence for concrete mixes with a total summation of numbers starting from 133 for the zero probability (no spalling) and 251 for the one probability(spalling). Table 6, which includes a list of all the variables and their associated scaled points, is also a companion to the nomogram. As a result, rather than using the nomogram to discover points, a user can refer to Table 6 to determine whether the required concrete mixture will be spalled or not. Please refer to the Appendix for a complete solved example.

Table 6: Companion to the developed nomogram

Water-binder ratio	Points	Coarse aggregate/binder ratio	Points	Fine aggregate/binder ratio	Points	Heating rate	Points	Moisture content	Points	Characteristic distance of the concrete	Points
0.15	**62**	0	**0**	0	**0**	0	**1**	0	**0**	20	**0**
0.2	**56**	0.5	**2**	0.5	**8**	20	**2**	0.005	**3**	40	**6**
0.25	**50**	1	**4**	1	**16**	40	**5**	0.01	**5**	60	**12**
0.3	**43**	1.5	**7**	1.5	**23**	60	**7**	0.015	**8**	80	**17**
0.35	**37**	2	**9**	2	**31**	80	**9**	0.02	**10**	100	**23**
0.4	**31**	2.5	**11**	2.5	**39**	100	**11**	0.025	**13**	120	**29**
0.45	**25**	3	**13**	3	**47**	120	**14**	0.03	**16**	140	**35**
0.5	**19**	3.5	**16**	3.5	**54**	140	**16**	0.035	**18**	160	**41**
0.55	**12**	4	**18**			160	**18**	0.04	**21**	180	**46**
0.6	**6**					180	**21**	0.045	**23**	200	**52**
0.65	**0**					200	**23**	0.05	**26**		
						220	**25**	0.055	**29**		
						240	**28**	0.06	**31**		
								0.065	**34**		
								0.07	**36**		

Table 6 (continued)

Maximum exposure temperature	points	Silica fume/binder ratio	Points	Maximum aggregate size	Points	GGBS/binder ratio	Points	Fly ash/binder ratio	Points	Total Points*	Probability of spalling occurrence
100	**0**	0	**0**	0	**48**	0	**0**	0	**0**	**133**	**0.01**
200	**9**	0.02	**4**	5	**41**	0.05	**3**	0.05	**0**	**178**	**0.25**
300	**18**	0.04	**7**	10	**34**	0.1	**5**	0.1	**0**	**192**	**0.5**
400	**27**	0.06	**11**	15	**27**	0.15	**8**	0.15	**1**	**206**	**0.75**
500	**36**	0.08	**15**	20	**20**	0.2	**11**	0.2	**1**	**251**	**0.99**
600	**45**	0.1	**18**	25	**14**	0.25	**14**	0.25	**1**		
700	**55**	0.12	**22**	30	**7**	0.3	**16**	0.3	**1**		
800	**64**	0.14	**26**	35	**0**	0.35	**19**	0.35	**2**		
900	**73**	0.16	**29**			0.4	**22**	0.4	**2**		
1000	**82**	0.18	**33**			0.45	**25**	0.45	**2**		

1100	**91**	0.2	**37**			0.5	**27**	0.5	**2**		
1200	**100**	0.22	**40**					0.55	**2**		

*The values of 192 is expected to spall**.**

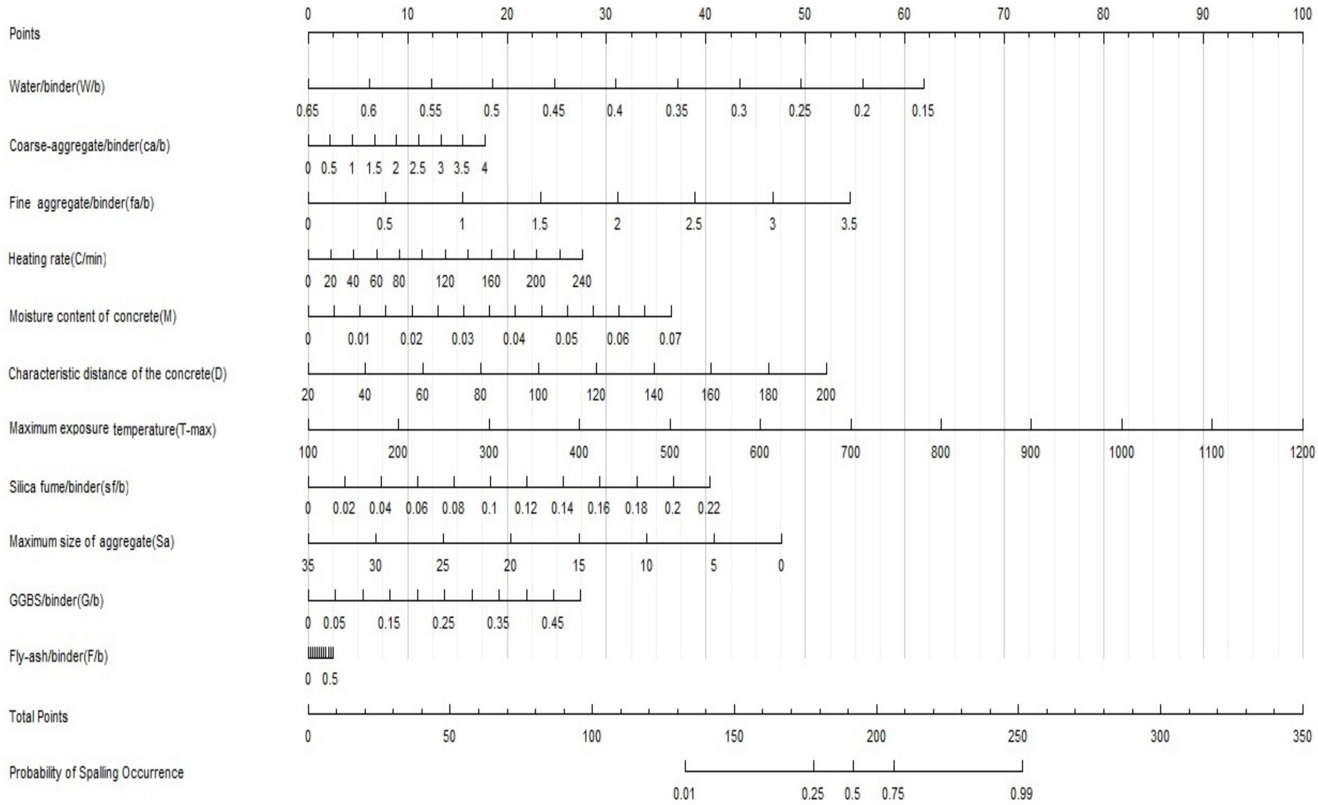

Figure 2: The developed nomogram for predicting spalling in concrete mixtures

4 CONCLUSION

Fire-induced spalling is a challenging issue. This study proposes the LR technique for developing a nomogram. A set of fire tests gathered from 293 observations was assembled and examined to build the suggested techniques. The analysis's conclusion demonstrates the simplicity and possibility of creating one-shot AI-based solutions for challenging structural fire engineering issues.

REFERENCES

1. Buchanan, A.H., Abu, A.K.: Fire Safety in Buildings. In: Structural Design for Fire Safety (2016)
2. Kodur, V., Naser, M.: Structural Fire Engineering. McGraw Hill Professional (2020)
3. al-Bashiti, M.K., Naser, M.Z.: Verifying domain knowledge and theories on Fire-induced spalling of concrete through eXplainable artificial intelligence. Constr. Build. Mater. 348, 128648 (2022). https://doi.org/10.1016/j.conbuildmat.2022.128648
4. Khoury, G.A.: Effect of fire on concrete and concrete structures, Prog. Struct. Eng. 2, 429–447 (2000). https://doi.org/10.1002/pse.51
5. Liu, J.-C.C., Tan, K.H., Yao, Y.: A new perspective on nature of fire-induced spalling in concrete, Constr. Build. Mater. 184, 581–590 (2018). https://doi.org/10.1016/j.conbuildmat.2018.06.204
6. Hertz, K.D.D.: Limits of spalling of fire-exposed concrete, Fire Saf. J. 38, 103–116 (2003).

https://doi.org/10.1016/S0379-7112(02)00051-6
7. Kalifa, P., Menneteau, F., Quenard, D.: Spalling and pore pressure in HPC at high temperatures, Cem. Concr. Res (2000)
8. Jansson, R.: Fire spalling of concrete - A historical overview, in: MATEC Web Conf. 2013,. https://doi.org/10.1051/matecconf/20130601001
9. Hertz, K.D., Sørensen, L.S.: Test method for spalling of fire exposed concrete, Fire Saf. J (2005)
10. Naser, M.Z.: Mechanistically Informed Machine Learning and Artificial Intelligence in Fire Engineering and Sciences. Fire Technol. 1–44 (2021). https://doi.org/10.1007/s10694-020-01069-8
11. Tapeh, A.T.G., Naser, M.Z.: Discovering Graphical Heuristics on Fire-Induced Spalling of Concrete Through Explainable Artificial Intelligence. Fire Technol. 58, 2871–2898 (2022). https://doi.org/10.1007/s10694-022-01290-7
12. Cox, D.R.: The Regression Analysis of Binary Sequences, J. R. Stat. Soc. Ser. B (1959)
13. Regression, T., Strategies, M.: Package ‘ rms .’ (2022)
14. Naser, M., Alavi, A. Insights into Performance Fitness and Error Metrics for Machine Learning. Under Rev. (2020)

APPENDIX A

This section provides an illustration and step-by-step instructions for utilizing the Logistic-Nomogram to assess a typical concrete mixture's propensity to fire-induced spalling. In this investigation, the concrete piece has spalled and possesses the following characteristic:

Note: The problem's probability close to 0 will be considered as a not spalled model, and a probability close to 1 as a spalled model.

- W/b (water to binder) ratio =0.2
- Ca/b (Coarse aggregate to binder ratio) =1.28
- Fa/b (Fine aggregate to binder ratio) =1.11
- Heating rate Hr (°c/m) = 5
- Moisture content=0.05
- Characteristic length of specimen D(mm)=51
- Maximum exposure temperature T-max(°c) =100
- Silica fume/binder ratio=0.1
- Maximum aggregate size Sa(mm)=13
- GGBS/binder ratio=0
- Fly ash/binder ratio=0

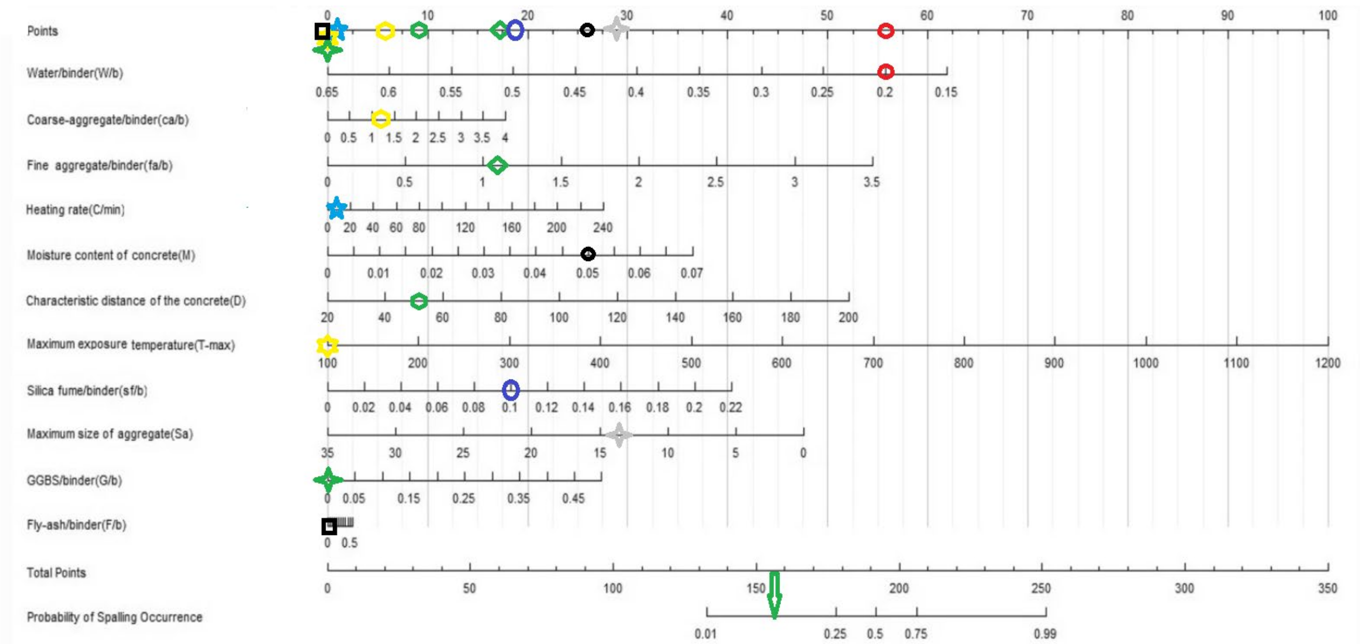

The total score for all 11 independent variables is 159.5, which, when shown on the probability axes, has a rate of about 14%. (Spalling did not happen for the concrete mixture).

(Please help with the dot formatting for the Above figure to show the one-shot Nomogram application)

Using the complementary table, the same conclusion could have been reached.

Total points = 56+5.5+15+1.5+26+9+0+18+28+0+0 = 159.5 points < 192 and is about 14% then No-Spalling is expected.

ON THE PREMISE OF A NEW THEORY FOR FIRE-INDUCED SPALLING OF CONCRETE THROUGH EXPLAINABLE ARTIFICIAL INTELLIGENCE

Mohammad Khaled al-Bashiti[1], Alireza Ghasemi[2], Arash Teymori Gharah Tapeh[3], Haley Hostetter[4], Deanna Craig[5], M.Z. Naser[6]

ABSTRACT

This paper presents preliminary results to describe the fire-induced spalling of concrete using explainable artificial intelligence (XAI). One thousand fire tests were collected from the literature consisting of twenty-two different mechanical, environmental, material, and geometrical parameters, creating the largest spalling database (up to date). This database was used to build, analyze, and verify an XAI model to identify the critical parameters influencing concrete spalling. This preliminary analysis is articulated around the top 5 factors influencing spalling and consists of two exogenous factors (maximum exposure temperature and heating rate) and three endogenous factors (compressive strength of concrete, degree of moisture content, and the amount of polypropylene fibre). The presented analysis showcases the linkage between these factors and quantifies them so that engineers can design a concrete mix that mitigates spalling.

Keywords: Concrete; Fire-induced spalling; Explainable AI; Fire test.

1 INTRODUCTION

Concrete is one of the most widely used materials in the construction industry. During its service lifetime, concrete structures experience various extreme events that can cause damage to the structure. One such event is fire. Fire can adversely affect the integrity of concrete structures and may result in spalling-related damage, which is the breakage or separation of concrete chunks from the bulk of a structural member.

[1] Ph.D. Student, School of Civil and Environmental Engineering & Earth Sciences (SCEEES), Clemson University, Clemson, SC 29634, USA.
e-mail: malbash@clemson.edu, ORCID: https://orcid.org/ 0000-0002-3889-2564
[2] Ph.D. Student, School of Civil and Environmental Engineering & Earth Sciences (SCEEES), Clemson University, Clemson, SC 29634, USA.
e-mail: ghasemi.alireza2121@gmail.com, ORCID: https://orcid.org/0000-0003-4745-8169
[3] Ph.D. Student, School of Civil and Environmental Engineering & Earth Sciences (SCEEES), Clemson University, Clemson, SC 29634, USA.
e-mail: ateymor@clemson.edu, ORCID: https://orcid.org/0000-0001-9174-079X
[4] Ph.D. Student, School of Civil and Environmental Engineering & Earth Sciences (SCEEES), Clemson University, Clemson, SC 29634, USA.
e-mail: hhostet@g.clemson.edu, ORCID: https://orcid.org/0000-0002-4269-9820
[5] MSc. Student, School of Civil and Environmental Engineering & Earth Sciences (SCEEES), Clemson University, Clemson, SC 29634, USA.
e-mail: dcraig3@g.clemson.edu,
[6] Assistant Professor, School of Civil and Environmental Engineering & Earth Sciences (SCEEES), Clemson University, Clemson, SC 29634, USA.
AI Research Institute for Science and Engineering (AIRISE), Clemson University, Clemson, SC 29634, USA
e-mail: mznaser@clemson.edu, ORCID: https://orcid.org/0000-0003-1350-3654
https://doi.org/10.6084/m9.figshare.22154831

Spalling can suddenly occur when the outside surface of the concrete members experiences a relatively high heating temperature (beyond 300ºC) [1].
The ramification of spalling varies, from forming a concrete matrix micro-crack to anticipating significant decreases in the compressive strength of concrete associated with temperature gradients. Such catastrophic events can harm the structure, and the structural members will suffer from a gradual reduction of the concrete capacity [2]. Such an event could trigger a structure to collapse. The degradation of compressive strength has been attributed to a combination of the decomposition of the hydrated pastes, deterioration of the aggregates, and the thermal incompatibilities between paste and aggregate, leading to stress concentrations and microcracking [2–6].

To further elaborate on the above, the moisture content of concrete is another critical factor that could influence concrete spalling, especially when present at above 2–3% of moisture content by weight of concrete [1, 7–9]. Polypropylene fibres have become an efficient solution for reducing the spalling risk of concrete due to fire exposure. Concrete with certain amounts of polypropylene fibre (PPF) and subjected to extreme heating conditions were observed to be free from thermal spalling [1, 10–12] with some exceptions[1]. Alternatively, the heating rate and maximum exposure temperature are considered exogenous critical factors and directly influence concrete spalling[4, 5, 13–16]. The contribution to spalling doesn't end here; many more parameters influence spalling, and the non-linearity nor the monotonic relation of spalling is escalating the complexity of understanding the concrete spalling phenomena.

To date, no consensus has been reached on fire-induced concrete spalling mechanisms [2]. Given the high nonlinearity of the spalling phenomenon, explainable artificial intelligence (XAI) could be perceived as an opportunity to explore the notion of a new theory [17–19]. This research work creates a model that accurately predicts and explains the fire-induced spalling of concrete – which is then can be thought of as the foundation for a possible theory on spalling [15].

2 DATABASE

The database contains more than 1000 test samples collected from the open literature. Twenty-two independent variables are known to be most acceptable for influencing fire-induced spalling in concrete. One dependent variable describes the occurrence of spalling by two labels: no spalling or spalling. The 22 independent variables are: 1) Water/binder ratio, 2) Aggregate type, 3) Aggregate/binder ratio, 4) Sand/binder ratio, 5) Heating rate, 6) Moisture content, 7) Maximum exposure temperature, 8) Silica fume/binder ratio, 9) Max aggregate size, 10) GGBS/binder ratio, 11) Fly ash/binder ratio, 12) Polypropylene fibre quantity, 13) Polypropylene fibre diameter, 14) Polypropylene fibre length, 15) Steel fibre quantity, 16) Steel fibre diameter, 17) Steel fibre length, 18) Shape, 19) Length, 20) Width, 21) Height, 22) Compressive strength. Table 1 shows the results of statistical analysis on this collected database.

Table 1. Summary of statistical insights for the parameters of the database

Parameter	Min	Max	Median	Mean	Standard deviation	Skew
Water/binder ratio (%)	0.13	0.63	0.30	0.31	0.13	0.78
Aggregate/binder ratio (%)	0.00	5.10	1.66	1.42	1.16	0.34
Sand/binder ratio (%)	0.48	3.41	1.20	1.37	0.51	1.40
Heating rate (C/min)	0.10	200.00	10.00	26.02	35.70	1.93
Moisture content (%)	0.000	0.089	0.035	0.035	0.019	-0.311
Maximum exposure temperature	75	1200	600	578	228	0
Silica fume/binder ratio (%)	0.00	0.23	0.00	0.06	0.08	0.82
Max aggregate size (mm)	0.50	32.00	13.00	10.60	7.84	-0.03
GGBS/binder ratio (%)	0.00	0.48	0.00	0.04	0.12	2.92
FA/binder ratio (%)	0.00	0.40	0.00	0.02	0.07	3.60

Compressive strength (MPa)	20	214	84	91	40	1
PP fibre quantity (Kg/m^3)	0.00	16.00	0.00	1.09	2.60	3.91
PP fibre diameter (μm)	0.00	150.00	0.00	10.84	21.19	3.49
S fibre length (mm)	0.00	60.00	0.00	5.02	10.74	3.04
S fibre quantity (Kg/m^3)	0.00	180.00	0.00	18.92	37.68	2.32
S fibre diameter(mm)	0.00	90.00	0.00	1.10	9.51	9.26
PP fibre length (mm)	0.00	30.00	0.00	3.18	5.64	2.00
Length (mm)	28.0	3600.0	100.0	198.2	401.5	6.3
Height (mm)	0.0	3360.0	150.0	203.8	348.0	7.3
Width (mm)	0.0	1200.0	50.0	91.2	162.1	3.5

3 METHODOLOGY

This section describes the methodology used to explore the spalling phenomena and establishes a holistic understanding of the main factors of fire-induced spalling by building, training, and validating an XAI model. This model is then augmented by the explainability methods to identify the key parameters influencing fire-induced spalling to find patterns in our spalling database and quantify them. Figure 1 illustrates a flowchart to detail the process boundaries of this analysis. A multi-step process starts with collecting the database and ends with identifying and quantifying fire-induced spalling influencing parameters.

In the first step, the database is collected and pre-processed to be used as input for the model, which is created to predict spalling. The next stage starts by splitting the data into two sets; the larger set will be used for training purposes, while the testing set will be used to evaluate the model's predictions of spalling. In the subsequent stage, the model will be assessed based on different evaluation metrics to establish its validity. Poor evaluation will lead to repeating the process to the training stage, at which we will need to evaluate the data processing. However, a good evaluation will take the model to its final stage, at which the explainability tools and methods are applied, and the top five parameters are identified and quantified.

3.1 XAI model

In this work, an XAI model was built using Extreme Gradient Boosting (XGBoost) as a decision-tree-based algorithm that uses a gradient boosting framework [20, 21]. It is known as one of the fastest implementations compared to the gradient boosting family, focusing on enhancing the model performance and processing rapid numerical and mathematical computations. XGBoost was used herein to establish a limestone of this preliminary analysis based on building a binary classification predictive model.

The first step in creating a prediction model starts by fitting the algorithm to the training set. In our model, the probability of spalling in the trained dataset is initially predicted to be 50%, regardless of the spalling dataset's default parameters. After which, the residuals (i.e., observations subtracted from the predictions) are calculated. At this point, the model's output has been accurately predicted and validated. However, at this stage, it is considered a 'black-box' model.

AI models are uninterpretable by themselves, which is why they are called 'black-box' models; they are directly created from big 'data,' and users are unable to understand or explain the approaches that the models are proposing as a solution. Still, advanced techniques and explainability methods have been introduced to the computer science domain. These techniques (i.e., XAI) allow us to explain our models and understand the model's outcomes both visually and graphically. With the help of explainability tools and frameworks, engineers can interpret and deliver a transparent model. To investigate our model's behaviour, we are adopting the feature importance plot, summary plot, and partial dependence plot, which will be discussed accordingly.

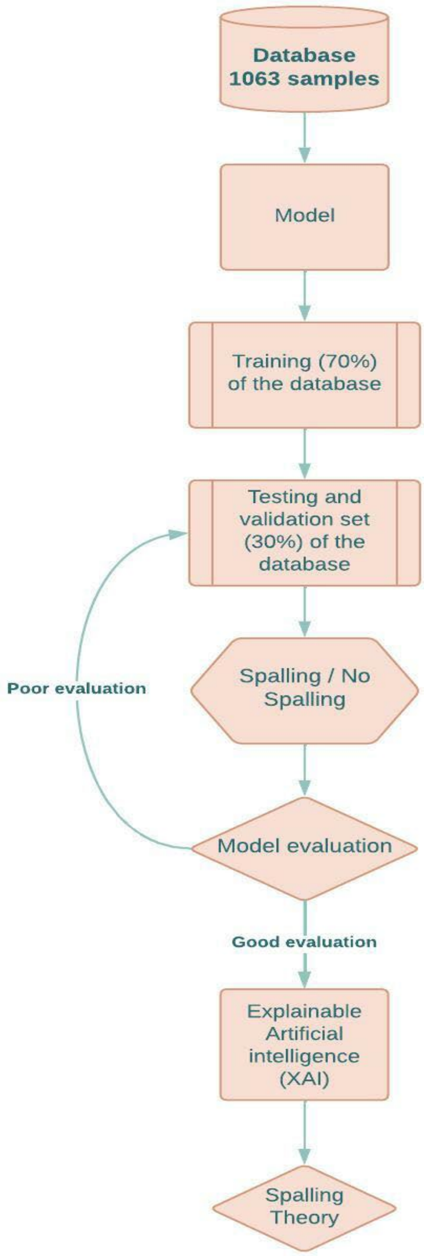

Figure 1. Flowchart for the model process

First, the feature importance plot is the plot where the parameters are ordered in descending order based on how high the impact is on the prediction [22]. Despite its advantages, the major cons related to this figure is that it does not provide information regarding the direction of impact. To overcome this con, the summary plot was put forward with the leverage to combine feature importance and their direct and indirect impact on the model's output [22]. Such an advanced plot explains how the model reached its prediction. However, the summary plot was unable to quantify them. This is where the partial dependence plot (PDP) comes in handy. Finally, the partial dependence plot works by producing a relationship between the parameter's value and its corresponding prediction. At each value of the parameter, the model is evaluated for all observations of the other model inputs, and the output is then averaged. Thus, the relationship they depict is only valid if the parameter of interest does not have a strong correlation with the other parameters.

3.2 XAI model technical details

The developed algorithm was trained and validated over the 1000 specimens mentioned in the previous section. The dataset was split into two sets; the large set contains 70% of the database and is used to train and cross-validate the model, while the smaller set consists of 30% of the database and is used to test and evaluate the trained model. Then, a k-fold cross-validation approach is used to further refine the training process and to prevent the model's overfitting.

In addition, confusion matrices are also used. Confusion matrices measure the quality of the model's predicted values compared to the original values to produce a 2D matrix (Fig. 2) and visualize the model's performance. The most accurate model with the highest accuracy should have a high number of samples in the diagonal line from the top left to the lower right. Similarly, the diagonal line from the lower left to the higher right should have the lowest number of samples.

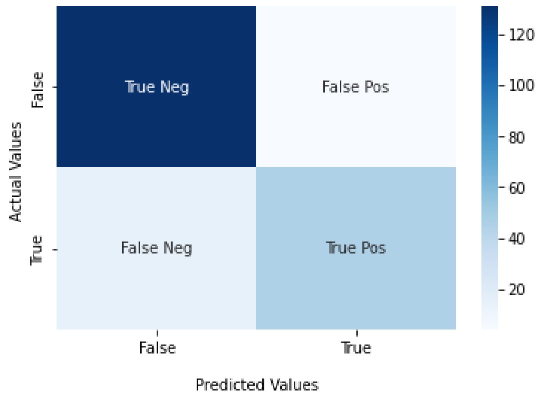

Figure 2. Confusion matrix

Similar to the model that was developed and recently published by the authors with an accuracy of 92% [15], this model consisted of almost identical tuning parameters and was tweaked with the following settings: 1. Objective: binary: logistic, which specifies the learning task and the corresponding learning objective. 2. Seed = 52, used for generating reproducible results and parameter tuning. 3. Learning rate = 0.3, which makes the model more robust by shrinking the weights on each step. 4. Max depth = 4, the maximum depth of a tree, which is used to control over-fitting, as higher depth will allow the model to learn definite relations to a particular sample.

The following settings were used for the data fitting stage: 1. Verbose = True, when the verbose parameter is set to 'True', then the evaluation metric on the validation set is printed at each boosting stage. 2. Early stopping rounds=50 is a technique used to stop training when the loss on the validation dataset starts to increase. 3. Eval metric='AUCpr'. The evaluation metric is to be used for validation data. Which is the Area under the curve in our model. Lastly, the following settings were used in the k-folds validation stage: The number of splits = 10 represents the equal portions of the split datasets. Random state = 7; it shuffles the data before splitting it to avoid the model's overfitting.

4 RESULTS AND DISCUSSION

After examining 22 different parameters, we are focusing our discussion on the top 5 influential parameters that govern concrete spalling thru XAI. Further analysis is ongoing to analyze the resulting parameters.

4.1 Model validation

The model's performance is the key to proving the model's power to predict spalling, and the proposed model prediction accuracy was 92%. Figure 3 demonstrates the confusion matrix for both testing and training datasets. As one can see, both training and testing sets performed well in the confusion matrix evaluation method. The diagonal line, which showcases the true labels in the training set, presents 518 (no spalling) and 215 (spalling), while the model mispredicted only ten samples. Similarly, on the testing dataset, the diagonal line which shows the true labels shows 208 (no spalling) and 86 (spalling), both of which are predicted correctly, in contrast to only 25 samples that have been miss-predicted.

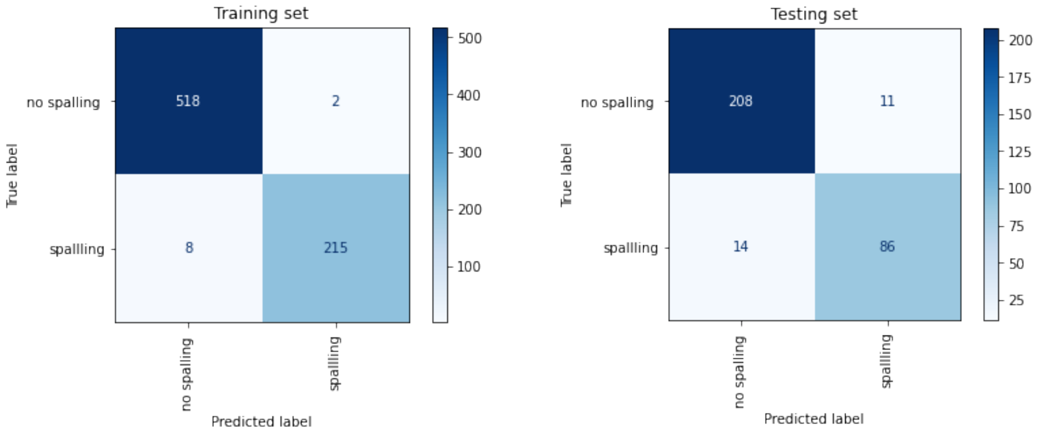

Figure 3. Model's confusion matrix for training and testing sets

4.2 Feature importance plot

Figure 4 shows that the compressive strength of concrete is the most important factor among the five factors included in this study, followed by maximum exposure temperature, moisture content, heating rate, and PP fibres, respectively. The downside of the feature importance plot is that it can only show the order of the influencing parameters. We were able to identify the feature importance, and at this point, we are obliged to define the direction of the feature and how each feature influences spalling to resist or trigger spalling, which introduces the SHAP summary plot.

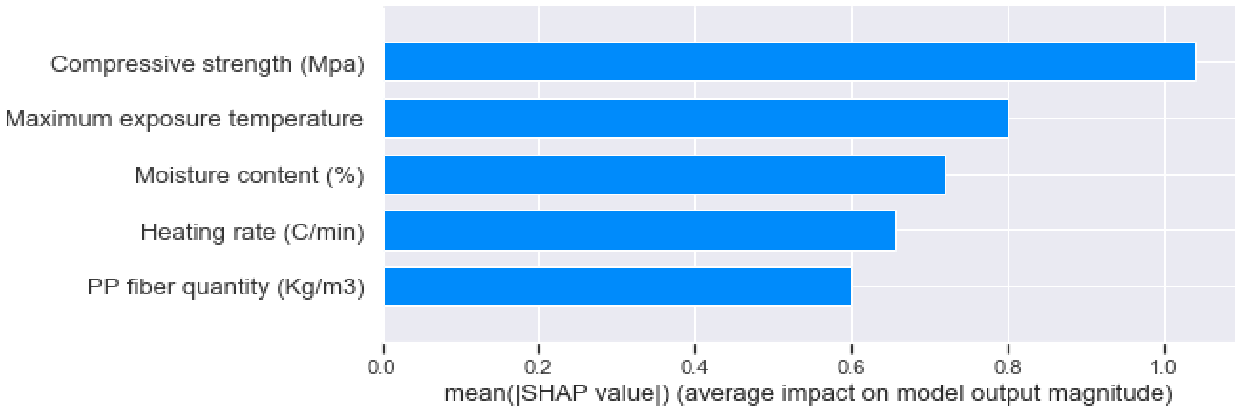

Figure 4. Feature importance plot of SHAP values

4.3 Summary plot

Figure 5 shows the five factors used in this study that influence spalling. Focusing on the compressive strength and its position at the top of the figure indicates how significant the impact is on the model's prediction. In addition, red dots (high compressive strength values) are on the positive SHAP values, which shows that the higher the compressive strength, the higher the chances of spalling. Additionally, maximum exposure temperature, moisture content, and heating rate factors show the exact same direction of impact on the model as the red dots are on the positive side of the SHAP values, but its impact power is correspondingly lower than the compressive strength.

Alternatively, polypropylene fibre quantity in a concrete mix shows an entirely different impact on spalling. The red dots, which indicate a higher amount of PP fibre in the mixture, lay on the negative side of the summary plot indicating that higher quantities of pp fibre negatively impact the spalling occurrence, which will mitigate spalling. Now, quantifying the features is a must, and we must continue our analysis to be able to quantify the feature and create a concrete mix that can mitigate spalling.

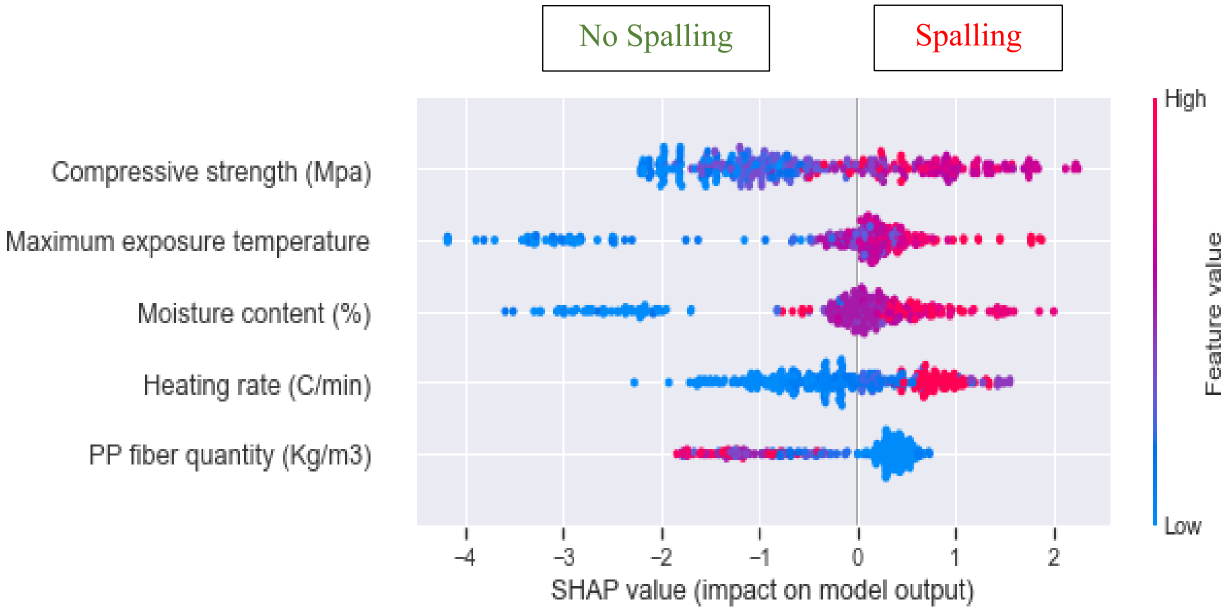

Figure 5. Summary plot of SHAP values

4.4 Partial dependence plot

Figure 6 represents the PDPs for the top five influencers to spalling. One can see some trends which are of interest to the reader. Looking at the compressive strength, PDP confirms the outcome of the SHAP summary plot that the tendency of spalling increases as the compressive strength increases because higher compressive strength increases the density matrix of concrete and decreases the permeability, which makes concrete that is more sensitive to spalling [1, 2, 23]. It should be noted that there are three critical values where the trend increases sharply. Those values lay at (47, 86, and 110 MPa). These values lay where the concrete class roughly changes from normal-strength concrete to high-strength concrete to ultra-high-performance concrete.

A closer look at the maximum exposure temperature plot shows a direct correlation between temperature and concrete spalling. Also, the trend increases sharply between the temperature of 320-380ºC, and this temperature lays at the aggregate dehydration temperature and stabilizes before and after this range. Kang and Hertz [2, 16] mentioned the explanation for such a unique trend. Further, the rise in heating rate (upward of 5 °C/min and from 10-15°C/min) positively correlates with spalling; when the values increase, the likelihood of spalling occurrence also increases. The plot for PP quantity shows a different trend which shows that adding 0.75-0.9kg/m^3 will significantly mitigate spalling in the concrete mix.

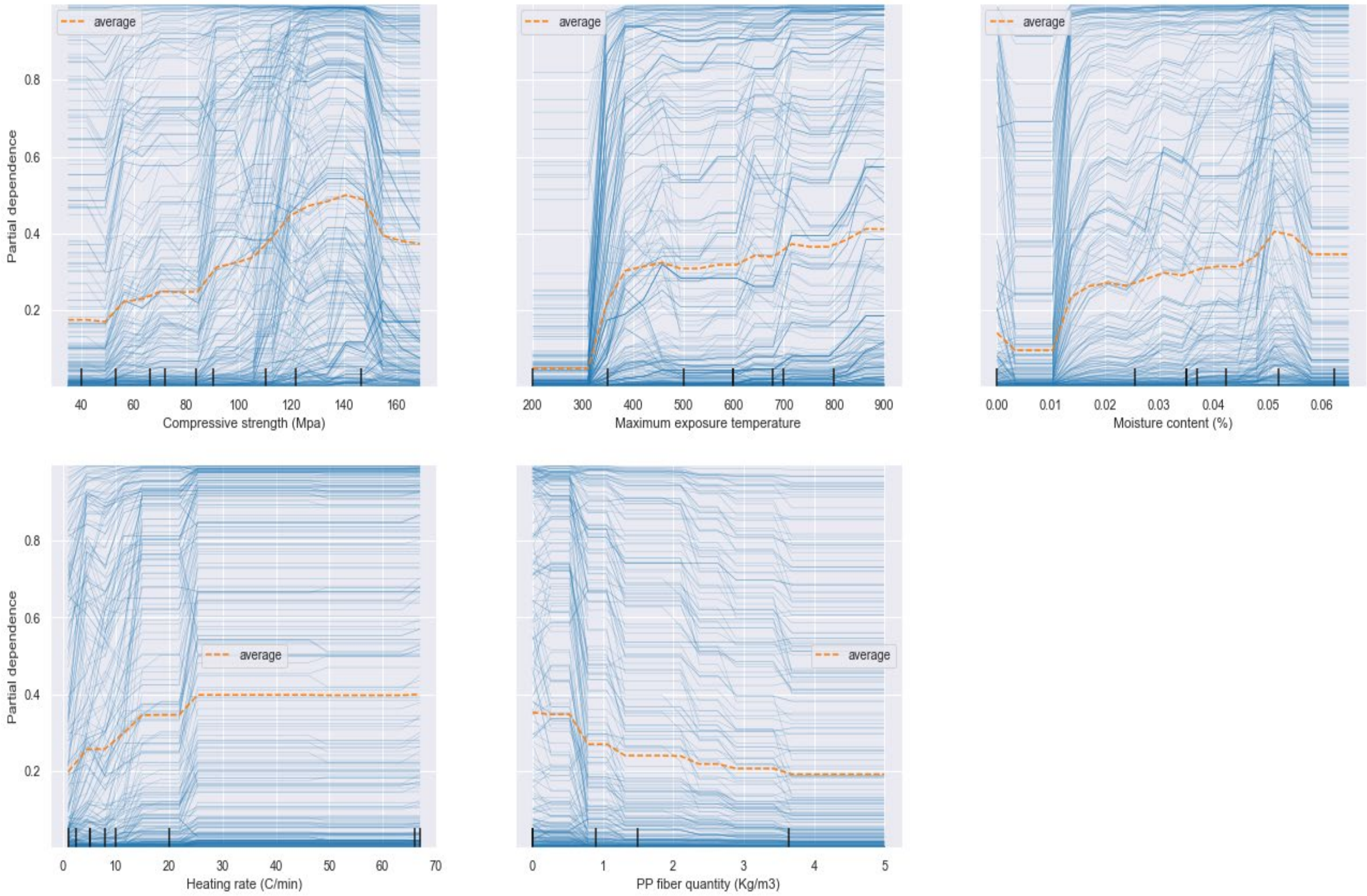

Figure 6. Partial dependence plot for the top five influencers of spalling.

5 CONCLUSIONS

This work presented a preliminary analysis en route to obtaining a spalling-free concrete mixture by analyzing 1000 fire tests (the largest in the literature review) using XAI. We were able to create a model that can predict concrete spalling with high accuracy (i.e., 93%). The following conclusions can be drawn.

- Compressive strength, maximum exposure temperature, moisture content, heating rate, and pp fibre quantity are considered the top 5 influencers of fire-induced spalling of concrete.
- The analysis of this paper confirms that compressive strength has a direct correlation to spalling and can be critical above 85 MPa.
- Maximum exposure temperature is ranked second most critical factor with a critical limit of 300ºC, the chances of spalling increase beyond this limit
- Reducing the moisture content below 1% by the weight of concrete is an effective way to improve the spalling resistance.
- Spalling was detected under high and low heating rates; however, limiting the heating rates below 5oC/min can minimize the spalling risk.
- Adding PP fibres to the concrete mix can reduce the spalling tendency (especially in mixtures of > 0.9 kg/m3).

REFERENCES

1. Khoury, G.A.: Effect of fire on concrete and concrete structures. Progress in Structural Engineering and Materials. 2, 429–447 (2000). https://doi.org/10.1002/pse.51
2. Liu, J.C., Tan, K.H., Yao, Y.: A new perspective on nature of fire-induced spalling in concrete. Constr Build Mater. 184, (2018). https://doi.org/10.1016/j.conbuildmat.2018.06.204

3. Hwang, E., Kim, G., Choe, G., Yoon, M., Son, M., Suh, D., Eu, H., Nam, J.: Explosive Spalling Behavior of Single-Sided Heated Concrete According to Compressive Strength and Heating Rate. Materials. 14, (2021). https://doi.org/10.3390/MA14206023
4. Kodur, V.K.R.: Spalling in High Strength Concrete Exposed to Fire: Concerns, Causes, Critical Parameters and Cures. Structures Congress 2000: Advanced Technology in Structural Engineering. 103, 1–9 (2004). https://doi.org/10.1061/40492(2000)180
5. Kodur, V.K.R., Phan, L.: Critical factors governing the fire performance of high strength concrete systems. Fire Saf J. 42, 482–488 (2007). https://doi.org/10.1016/J.FIRESAF.2006.10.006
6. Liu, J.C., Tan, K.H.: Fire resistance of strain hardening cementitious composite with hybrid PVA and steel fibers. Constr Build Mater. 135, (2017). https://doi.org/10.1016/j.conbuildmat.2016.12.204
7. Lura, P., Terrasi, G. pietro: Reduction of fire spalling in high-performance concrete by means of superabsorbent polymers and polypropylene fibers: Small scale fire tests of carbon fiber reinforced plastic-prestressed self-compacting concrete. Cem Concr Compos. 49, (2014). https://doi.org/10.1016/j.cemconcomp.2014.02.001
8. ACI CODE-318-14: Building Code Requirements for Structural Concrete and Commentary, https://www.concrete.org/store/productdetail.aspx?ItemID=318U14&Language=English&Units=US_Units
9. publication, T.H.-A. special technical, 1965, undefined: Effect of moisture on the fire endurance of building elements. scholar.archive.org.
10. Phan, L.T.: Pore pressure and explosive spalling in concrete. Materials and Structures/Materiaux et Constructions. 41, (2008). https://doi.org/10.1617/s11527-008-9353-2
11. Han, C.G., Hwang, Y.S., Yang, S.H., Gowripalan, N.: Performance of spalling resistance of high performance concrete with polypropylene fiber contents and lateral confinement. Cem Concr Res. 35, (2005). https://doi.org/10.1016/j.cemconres.2004.11.013
12. Naser, M.Z., Kodur, V.K.: Explainable machine learning using real, synthetic and augmented fire tests to predict fire resistance and spalling of RC columns. Eng Struct. 253, 113824 (2022). https://doi.org/10.1016/J.ENGSTRUCT.2021.113824
13. Shaikh, F.U.A., Taweel, M.: Compressive strength and failure behaviour of fibre reinforced concrete at elevated temperatures. 3, 283–293 (2015). https://doi.org/10.12989/acc.2015.3.4.283
14. Zhukov, V. V. (1994). Reasons of explosive spalling... - Google Scholar, https://scholar.google.com/scholar?hl=en&as_sdt=0%2C41&q=Zhukov%2C+V.+V.+%281994%29.+Reasons+of+explosive+spalling+of+concrete+by+fire%2C+Scientific+Research+Institute+for+Concrete+and+Reinforced+Concrete%2C+Moscow.&btnG=
15. al-Bashiti, M.K., Naser, M.Z.: Verifying domain knowledge and theories on Fire-induced spalling of concrete through eXplainable artificial intelligence. Constr Build Mater. 348, 128648 (2022). https://doi.org/10.1016/J.CONBUILDMAT.2022.128648
16. Hertz, K.D.: Limits of spalling of fire-exposed concrete. Fire Saf J. 38, 103–116 (2003). https://doi.org/10.1016/S0379-7112(02)00051-6
17. Dawood, T., Zhu, Z., Zayed, T.: Machine vision-based model for spalling detection and quantification in subway networks. Autom Constr. 81, 149–160 (2017). https://doi.org/10.1016/J.AUTCON.2017.06.008
18. Naser, M.Z., Kodur, V.K.: Explainable machine learning using real, synthetic and augmented fire tests to predict fire resistance and spalling of RC columns. Eng Struct. 253, 113824 (2022). https://doi.org/10.1016/J.ENGSTRUCT.2021.113824
19. Teymori, A., Tapeh, G., Naser, · M Z, Naser, M.Z.: Artificial Intelligence, Machine Learning, and Deep Learning in Structural Engineering: A Scientometrics Review of Trends and Best Practices. Archives of Computational Methods in Engineering 2022. 1, 1–45 (2022). https://doi.org/10.1007/S11831-022-09793-W

20. Chen, T., international, C.G.-P. of the 22nd acm sigkdd, 2016, undefined: Xgboost: A scalable tree boosting system. dl.acm.org. 13-17-August-2016, 785–794 (2016). https://doi.org/10.1145/2939672.2939785
21. Chen, T., Guestrin, C.: XGBoost: A Scalable Tree Boosting System. Proceedings of the 22nd ACM SIGKDD International Conference on Knowledge Discovery and Data Mining. https://doi.org/10.1145/2939672
22. A Unified Approach to Interpreting Model Predictions, https://papers.nips.cc/paper/2017/hash/8a20a8621978632d76c43dfd28b67767-Abstract.html
23. Yermak, N., Pliya, P., Beaucour, A.L., Simon, A., Noumowé, A.: Influence of steel and/or polypropylene fibres on the behaviour of concrete at high temperature: Spalling, transfer and mechanical properties. Constr Build Mater. 132, 240–250 (2017). https://doi.org/10.1016/J.CONBUILDMAT.2016.11.120

EFFECTS OF CARBONATION ON FIRE SPALLING BEHAVIOUR OF CONCRETE: A PRELIMINARY EXPERIMENTAL STUDY

Chao Jiang[1], Hao-Chuan Zhang[2], Yu-Qing Ge[3], Xiang-Lin Gu[4]

ABSTRACT

This paper presented a preliminary experimental study on the effects of carbonation on fire spalling behaviour of concrete. An apparatus was developed to heat concrete under sustained loads and measure multi-field responses simultaneously. By creating concrete slab specimens with a surface half carbonated and half non-carbonated, the effects of carbonation on fire spalling behaviour of concrete were tested by the developed apparatus. Results showed that carbonation may raise the fire spalling risk of concrete but its effects are usually intertwined with other factors, e.g., load and/or moisture. More well-designed experiments that carefully distinguish effects of different factors, including carbonation, load, moisture, etc., should be conducted. Moreover, pore pressures may not necessarily be the necessary condition for spalling of concrete. Experiments that heat fully dried concrete specimens under loads should be conducted to further verify this. In addition, strain measurements should be improved to eliminate the effects of high temperatures to finally realize accurate monitoring and recording of synchronized multi-field responses of concrete to elevated temperatures. The tentative study in this paper contributed to refined investigation on effects of carbonation on fire spalling behaviour of concrete.

Keywords: Concrete; Carbonation; Fire spalling; Elevated temperature

1 INTRODUCTION

Spalling may occur when structural concrete is subjected to high temperature caused by fire accidents. This phenomenon is a great threat to structural safety because it reduces cross-sectional size of members and exposes reinforcing steel bars to elevated temperatures [1,2]. Load stress, thermal stress and pore pressure are the main causes of fire spalling of concrete [3-5]. On the other hand, under common atmospheric environments, concrete structures usually undergo carbonation of concrete. Carbonation changes the chemical composition of hardened cement paste, decreases the porosity and reduces the transport coefficient of concrete [6,7]. As a result, the elastic modulus of surface carbonated concrete increases [8,9] and hence the compressive stress increases there. Moreover, due to decreased transport coefficient of surface carbonated concrete, the pore pressure in concrete with carbonated surface layers may increase as compared with that in non-carbonated concrete under elevated temperatures. Correspondingly, carbonation in surface layer concrete increases the fire spalling risk of concrete. Therefore, effects of carbonation on fire spalling behaviour of concrete deserve more attention. To do so, the authors developed an apparatus that enabled to heat concrete specimens under sustained loads. Based on the developed apparatus, a preliminary experimental study on the effects of carbonation on fire spalling behaviour of concrete under sustained loads was conducted and presented.

[1] Associate Professor for Research, Key Laboratory of Performance Evolution and Control for Engineering Structures (Ministry of Education), Tongji University,
e-mail: cjiang@tongji.edu.cn, ORCID: https://orcid.org/0000-0002-2414-3968
[2] PhD Candidate, Department of Structural Engineering, College of Civil Engineering, Tongji University,
e-mail: 2011132@tongji.edu.cn
[3] PhD Candidate, Department of Structural Engineering, College of Civil Engineering, Tongji University,
e-mail: 1910272@tongji.edu.cn
[4] Professor, Department of Structural Engineering, College of Civil Engineering, Tongji University,
e-mail: gxl@tongji.edu.cn, corresponding author
https://doi.org/10.6084/m9.figshare.22154897

2 EXPERIMENTS

2.1 Materials and specimens

Two concrete slab specimens were cast and designed to undergo heating under different load levels, as shown in Table 1. Meanwhile, three prism concrete specimens were cast to test the strength of concrete. The mix design of concrete was shown in Table 2. Ordinary Portland cement was used. ISO standard sand and granite gravels were used as fine and coarse aggregates, respectively. Coarse aggregates were within sizes ranging from 5 to 16 mm. Moreover, water-reducing agent by 2.2% weight of cement was added to increase the workability of the cement paste during casting. All specimens were cured in a room with a relative humidity higher than 95% and a temperature of 20 °C for 28 days. The tested concrete strength was 55 MPa. For S2, both steel tubes and thermocouples were embedded into different depths to monitor pore pressures and temperatures in inner concrete during heating and cooling, as illustrated by Figure 1. More details about the steel tubes that enable to measure pore pressures in concrete under elevated temperatures could be found in Ref. [5].

Table 1. Arrangement of specimens

Specimen No.	Dimension (mm)	Load level	Tested data	Carbonation time	Heating rate
S1	290×190×80	0.4 (0.32)	load	7 months(2021.5-12)	10 °C/min
S2	280×180×80	0.2 (0.13)	load/displacement /temperature/pore pressure	7 months(2021.5-12)	10 °C/min

Note: in the Load level column, the numbers in brackets denote the actual load levels.

Table 2. Mix design

Water (kg/m³)	Cement (kg/m³)	Sand (kg/m³)	Coarse aggregate (kg/m³)		Water-reducing agent (%, by weight of cement)
			(5-10 mm)	(10-16 mm)	
155	441	541	758	505	2.2

2.2 Carbonation

After the specimens were cured for 28 days, 5 surfaces of the slab specimens were fully sealed and the half of the remaining one surface was sealed by aluminium foils, as illustrated by Figure 1. Then the partially sealed slab specimens were put into a chamber for carbonation for 7 months at a temperature of 30 °C, a relative humidity of 60% and a CO_2 concentration of 20%, as shown in Table 3, following the specifications of the Chinese code [10]. As such, each slab specimen was partially carbonated leaving a surface with a half carbonated and a half non-carbonated.

(a) Specimen 1-before sealing

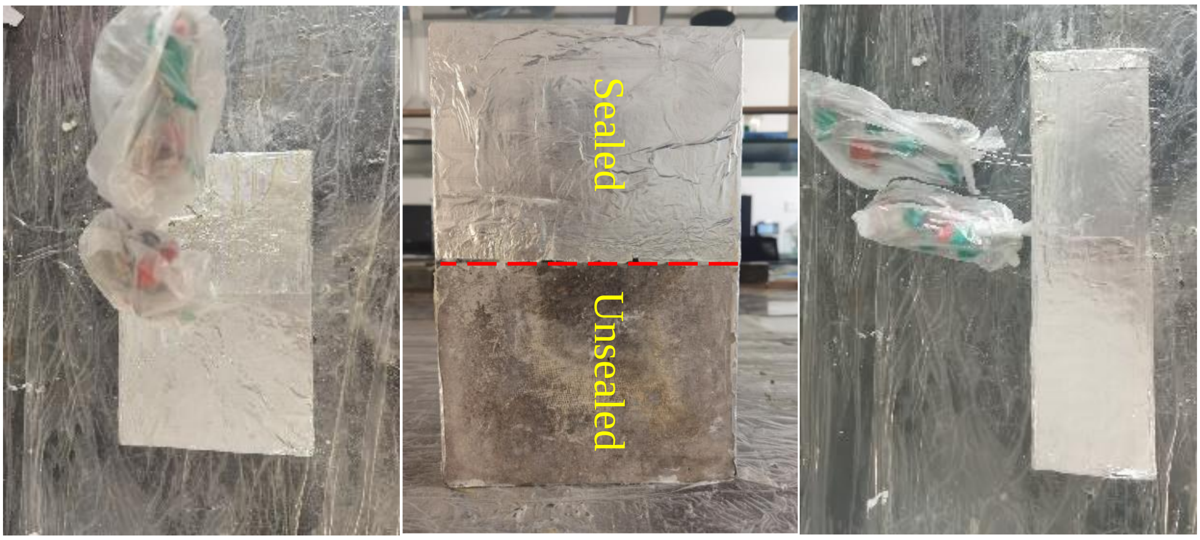

(b) Specimen 1-after sealing

(c) Specimen 2-before sealing

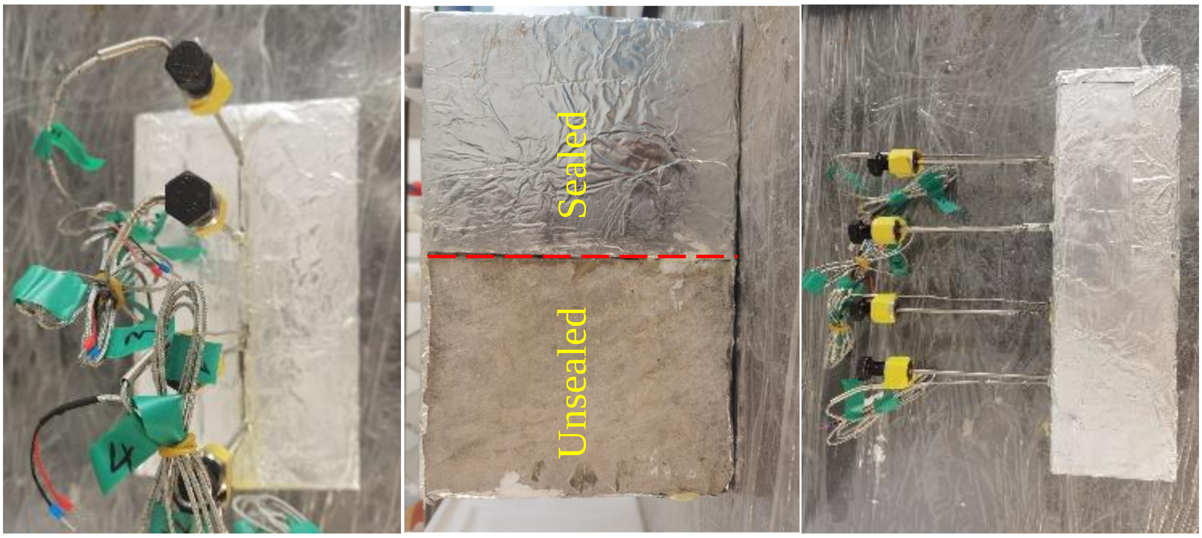

(d) Specimen 2-after sealing

Figure 1. Pre-treatment of concrete specimens

Table 3. Parameters for carbonation tests

Temperature (℃)	Relative humidity (%)	Concentration of CO_2 (%)
30	60	20

2.3 Insulation

After carbonation, the sealing aluminium foils over the exposed surface and its opposite surface were removed and the sealing aluminium foils over the other four surfaces were retained. Then, high temperature-resistant cotton was adhered to retained aluminium foils so that the slab specimens were peripherally sealed and insulated, making the heat and moisture transfer generally in one dimension in the specimen from the exposed surface to its opposite surface.

2.4 Apparatus

To sustain loads on concrete specimens at heating, an apparatus was developed by the authors, as illustrated by Figure 2. The apparatus mainly consists of three systems: 1) loading system; 2) heating system and 3) data acquisition system. The loading system is composed of a self-equilibrated steel frame and a hydraulic pump. Load is exerted by the hydraulic pump to steel beams, which is further transferred to the specimen, as illustrated by Figure 2. Moreover, two force transducers are set in the frame so that the load can be monitored in real time. The heating system is a furnace that enables to increase temperature by multi-linear stages. The data acquisition system monitors and records temperatures, pore pressures, loads, displacements, etc., simultaneously. The procedure of using this apparatus is as follows: 1) insert the specimen into the center of the frame; 2) fasten nuts 1A and 1E; 3) initiate the data acquisition system; 4) start the hydraulic pump and preload to a small level to check the centrality among the specimen and the steel frame; 5) exert load to the expected levels; 6) fasten nuts 1B and close the hydraulic pump; 7) start the furnace to heat the specimen as expected.

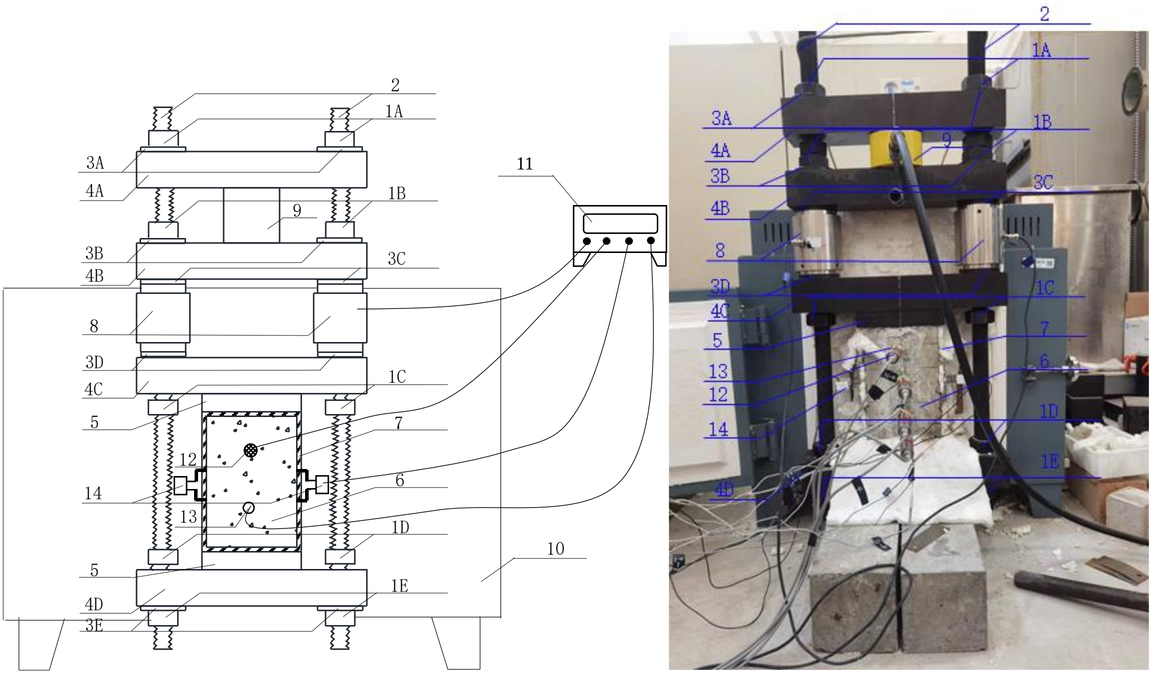

Figure 2. Test apparatus

(1A~E: nuts; 2: screws; 3 A~E: circular plates; 4 A~D: beams; 5: plates; 6: specimen; 7: sealing & insulating; 8: force transducers; 9: pump; 10: furnace; 11: data logger; 12: steel tubes; 13: thermocouples; 14: extensometers)

2.5 Loading

After the specimen was set into the frame, open up the hydraulic pump to exert the designed load and then fasten nuts 1B. After that, close the hydraulic pump for safety during subsequent heating. There was a drop of load after closing the hydraulic pump. The actual load levels were also monitored by the force transducers, as shown in Table 1.

2.6 Heating

The specimens were designed to be heated at a rate of 10 °C/min to 800 °C and undergo a natural cooling to the room temperature. However, if the specimens spalled before 800 °C, the heating was stopped and the specimens were cooled to room temperature naturally.

3 RESULTS AND DISSCUSION

3.1 Observed phenomena

Both specimens failed suddenly during heating, but the failure times and modes were different, as shown in Figure 3. For S1, crushing of concrete occurred at the end of the carbonation part at 44 min after heating when furnace temperature reached 446 °C. A major crack that parallel to the exposed surface was found in the carbonated part, which was however not found in the non-carbonated part. This indicated that carbonation might make concrete more prone to spalling. For S2, the whole exposed surface of the specimen spalled, including the carbonated and non-carbonated parts, at around 60 min after heating when furnace temperature reached 634 °C. Overall, the maximum spalling depth reached 27.45 mm and the average spalling depth was about 13.65 mm. In the carbonation part, the average spalling depth was about 11.11 mm, which was smaller than that in the non-carbonated part, i.e., 16.20 mm. Steel tubes at the embedded depth of 10 mm, in both the carbonated and non-carbonated parts, were right at the spalling surface as shown in Figure 3b. As the load level in S2 was much higher than that in S1, the effects of carbonation on fire spalling of concrete might have been outweighed by the effects of load level, making both the carbonated and non-carbonated parts spall in S2.

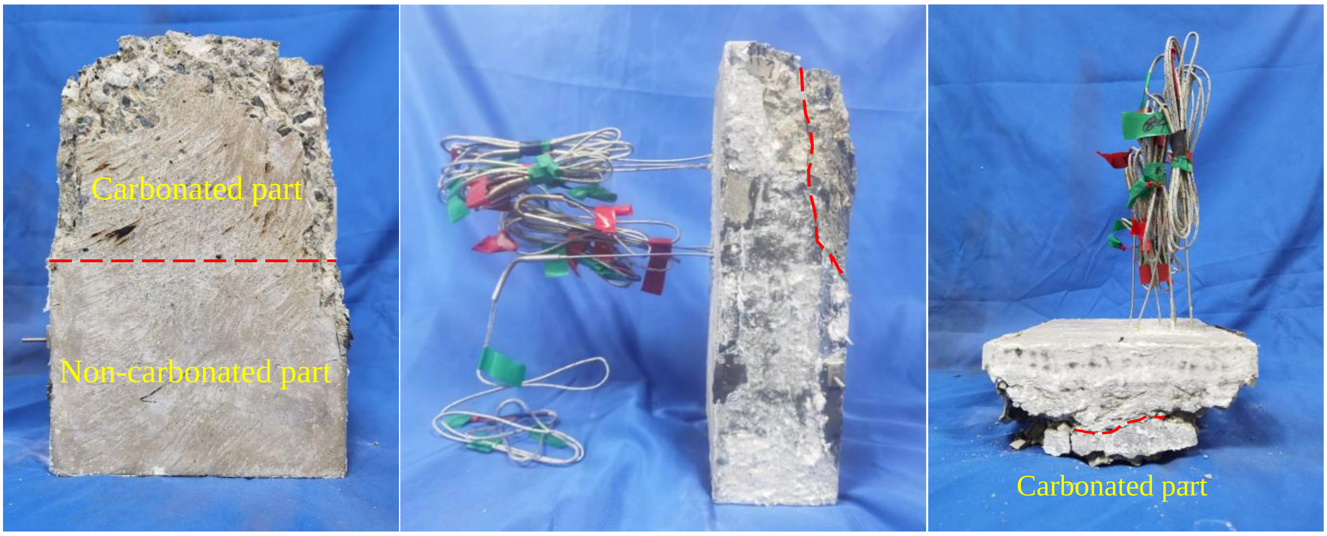

(a)Specimen 1

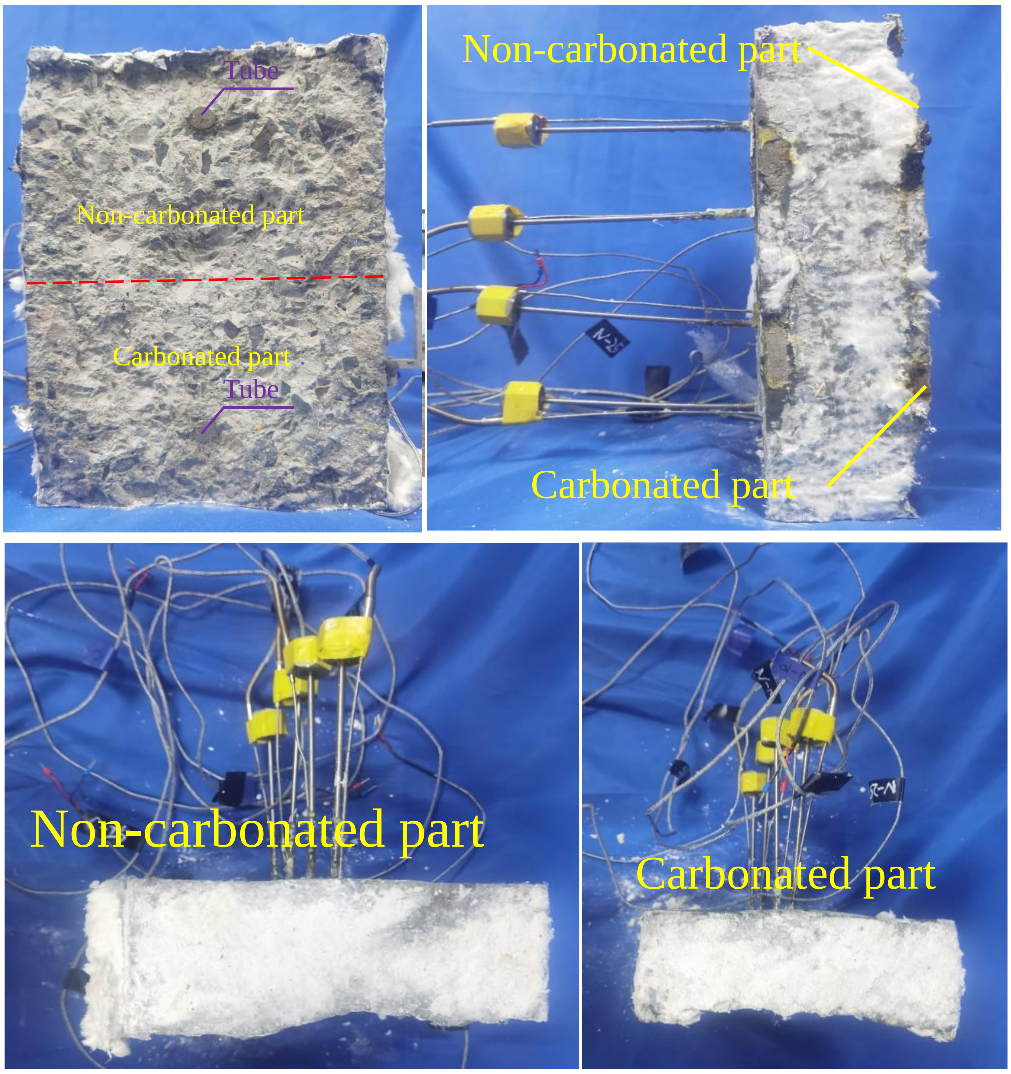

(b)Specimen 2(spalling depth: 27.45 mm in maximum and 13.65 mm on average)

Figure 3. Observed phenomena

3.2 Temperatures

The temperature developments at different depths into S2 during heating and cooling were shown in Figure 4. As shown in Figure 4, there were delays of temperatures at the exposed surface as compared with the furnace temperature. At the depth of 10 mm, the development of temperature in the carbonated part was slightly later than that in the non-carbonated part and the maximum temperature in the non-carbonated part was much higher than that in the carbonated part. Theoretically, the peak temperatures should occur at the same time point, but the peak temperature at the depth of 10 mm in the non-carbonated part occurred later than that in the carbonated part. This might be caused by spalling of concrete. Spalling of concrete was deeper in the non-carbonated part than in the carbonated part so that the thermocouple in the non-carbonated part might be directly exposed to the furnace. Then the “exposed” thermocouple was subjected to a rather high temperature in the furnace at spalling and a faster temperature increase occurred, as shown in Figure 4. At the depth of 25 mm, the temperature increase in the carbonated part was almost the same as that in the non-carbonated part. The delay of peak temperature in the non-carbonated part as compared with that in the carbonated part might be due to spalling of concrete, too.

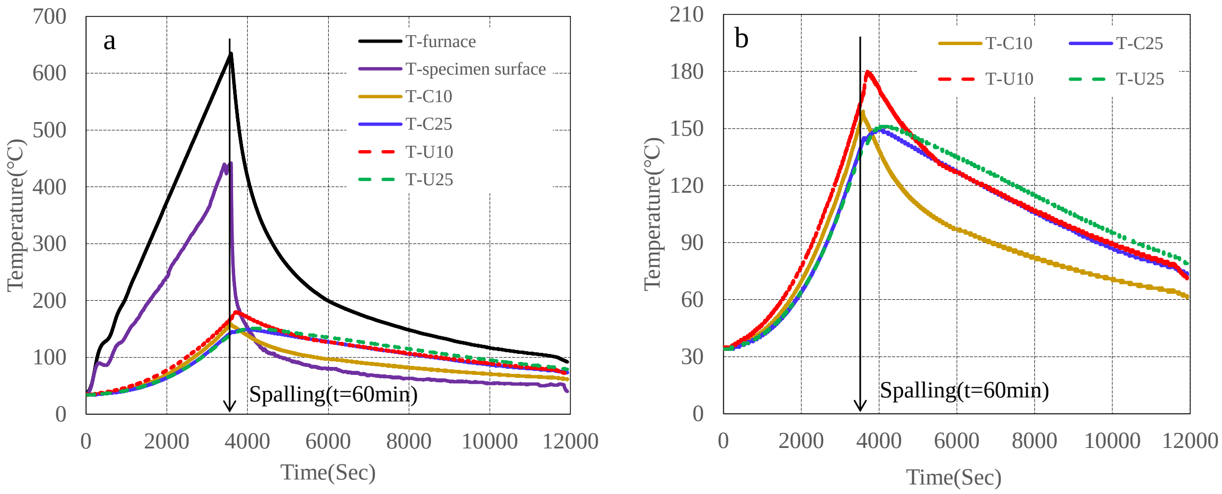

Figure 4. Temperatures

3.3 Pore pressures

The developments of pore pressures at different depths into S2 during heating and cooling were shown in Figure 5. In general, the pore pressures were small, not higher than 0.03 MPa. At spalling, the pressures at the depth of 10 mm were around 0.021 and 0.029 MPa in the carbonated and non-carbonated parts, respectively. As both the steel tubes at the depth of 10 mm in the carbonated and non-carbonated parts were right at the spalling surface, the rather small pressures might indicate that pore pressures were not necessarily the necessary condition for spalling of concrete. In other words, thermo-mechanical stresses alone might cause spalling of concrete, which was also consistent with the points in the literature [11-13].

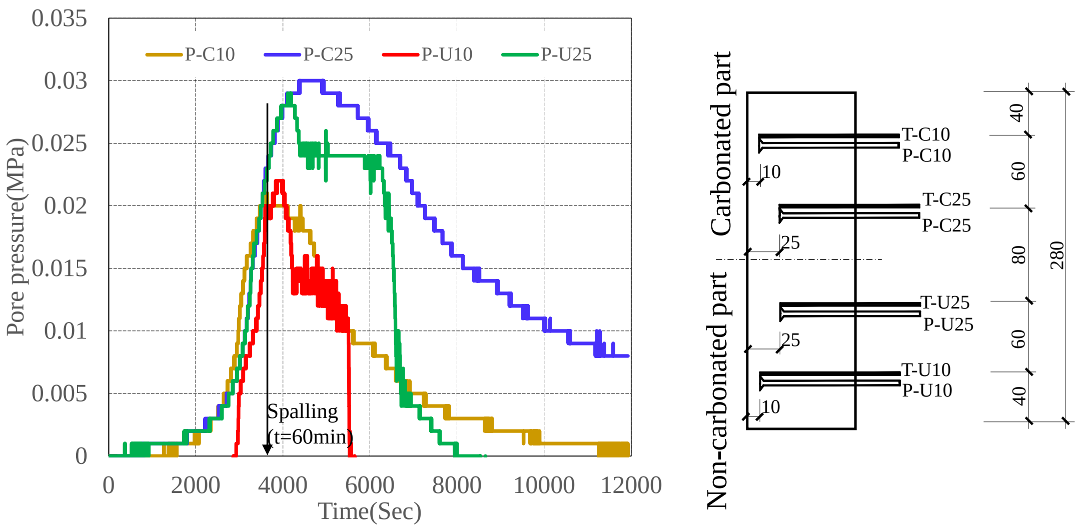

Figure 5. Pore pressures

3.4 Loads and strains

The load and/or strain developments in S1 and S2 during heating and cooling were illustrated in Figure 6. As shown in Figure 6a, during the heating process of S1, the load slowly increased and reached a peak to 301.61 kN at around 39 min, 5 min before spalling, but overall the increase was limited and the load was almost maintained as constant during heating. As shown in Figure 6b, for S2, the load increased much higher with temperature increase and reached the peak 107.26 kN right at the time of spalling. In both specimens, the load dropped suddenly at spalling. The strains at depths of 9 and 74 mm from the exposed surface were also measured. While during the initial heating process, the strains increased with the temperature increase, the strain measurement systems were easily damaged or broken by the high temperatures so that the full-range strains were not correctly monitored and recorded.

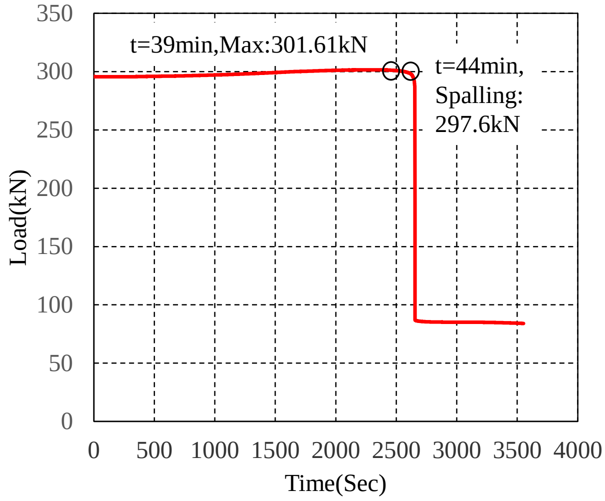

(a)Specimen 1

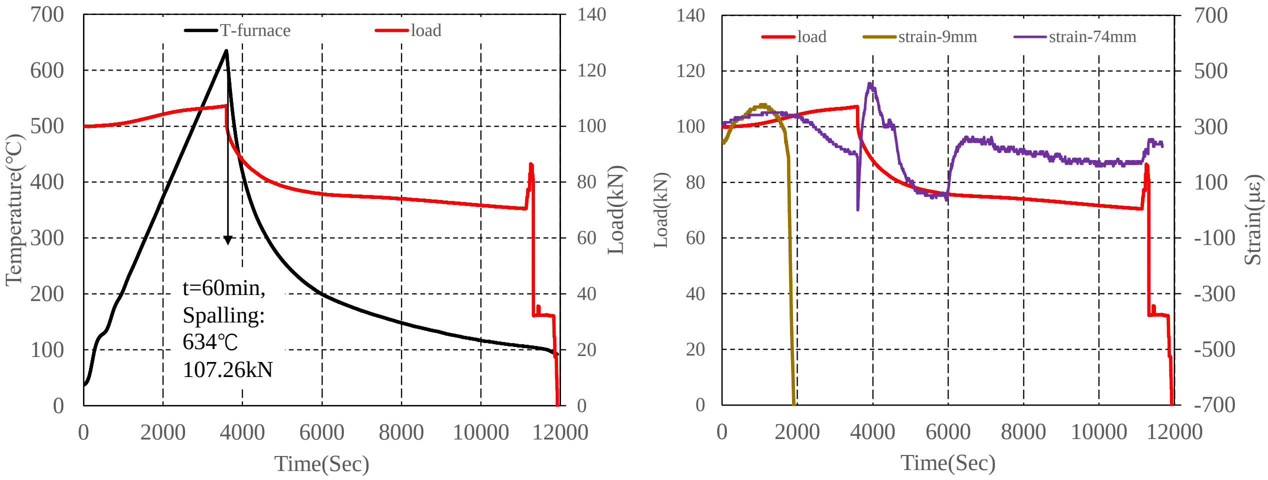

(b)Specimen 2

Figure 6. Loads and strains

4 CONCLUSIONS

This paper presented a preliminary experimental study on the effects of carbonation on fire spalling behaviour of concrete. An apparatus was developed to realize heating and loading concrete specimens and monitoring and recording loads, strains, temperatures and pore pressures, simultaneously. By creating concrete slab specimens with a surface half carbonated and half non-carbonated, the effects of carbonation on fire spalling behaviour of concrete were tested by the developed apparatus. Results showed that:

(1) Carbonation may raise the fire spalling risk of concrete but its effects are usually intertwined with other factors, e.g., load and/or moisture. More well-designed experiments that carefully distinguish effects of different factors, including carbonation, load, moisture, etc., should be conducted.

(2) Pore pressures may not necessarily be the necessary condition for spalling of concrete. Experiments that heat fully dried concrete specimens under loads should be conducted to further verify this.

(3) Strain measurements should be improved to eliminate the effects of high temperatures to finally realize accurate monitoring and recording of synchronized multi-field responses of concrete to elevated temperatures.

The experiments presented in this paper were tentative studies on the effects of carbonation on fire spalling behaviour of concrete. A systematic experimental and numerical study on this topic is on-going in the authors' research group and will be reported in the near future.

ACKNOWLEDGEMENTS

This research work was financially supported by the National Natural Science Foundation of China with Grant No. 51908417 and Shanghai Pujiang Program with Grant No. 20PJ1413400.

REFERENCES

1. Khoury, G.A. and Y. Anderberg Y., Concrete spalling review, Fire Safety Design, 2000.
2. Li, Y., Yang, E.H., Zhou, A. and Liu, T., Pore pressure build-up and explosive spalling in concrete at elevated temperature: A review, Construction and Building Materials, Vol. 284, 2021, 122818. https://doi.org/ 10.1016/j.conbuildmat.2021.122818.
3. Zhang, H. L., Davie, C. T., A numerical investigation of the influence of pore pressures and thermally induced stresses for spalling of concrete exposed to elevated temperatures. Fire Safety Journal., Vol.59, 2013, pp. 102-110. https:// doi.org/10.1016/j.firesaf.2013.03.019.
4. Jiang, C., Fang, J., Chen, J.Y. and Gu, X.L., Modeling the instantaneous phase composition of cement pastes under elevated temperatures. Cement and Concrete Research, Vol. 130, 2020, 105987. https://doi.org/10.1016/j.cemconres.2020.105987.
5. Jiang, C., Ge, Y.Q., Zhang, H.C. and Gu, X.L., Effects of thermal expansion of enclosed medium and direction of pressure bearing plane of metal tubes on pore pressure measurements in cement-based materials under elevated temperatures, Fire Safety Journal, Vol. 130, 2022, 103599. https://doi.org/10.1016/j.firesaf.2022.103599.
6. Song, H.W. and Kwon S.J., Permeability characteristics of carbonated concrete considering capillary pore structure, Cement and Concrete Research, Vol. 37, Iss. 6, 2007, pp. 909-915. https://doi.org/10.1016/j.cemconres.2007.03.011
7. Papadakis, V.G. , Vayenas C.G. and Fardis, M.N., Fundamental Modeling and Experimental Investigation of Concrete Carbonation, ACI Materials Journal, Vol.88, No.4, 1991, pp.363–373.
8. Xiao, J., Li, J., Zhu, B. and Fan, Z., Experimental study on strength and ductility of carbonated concrete elements, Construction and Building Materials, Vol.16, No.3, 2002, pp.187–192. https://doi.org/10.1016/S0950-0618(01)00034-4.
9. Jerga, J., Physico-mechanical properties of carbonated concrete, Construction and Building Materials, vol.18, no.9, 2004, pp.645–652. https://doi.org/10.1016/j.conbuildmat.2004.04.029.
10. China National Standard, Standard for test methods of long-term performance and durability of ordinary concrete, GB/T 50082-2009, Beijing: China Architectural Industry Press, 2009.
11. Ulm, F., Coussy, O., Bazant, Z.P., The "Chunnel" fire. I: Chemoplastic softening in rapidly heated concrete. ASCE Journal of Engineering Mechanics, Vol. 125, No.125, 1999, pp. 272-282.
12. Ulm, F., Acker, P., Levy, M., The "Chunnel" fire. II: Analysis of concrete damage. ASCE Journal of Engineering Mechanics, Vol. 125, No.3, 1999, pp. 283-289.
13. Ju Y., Tian, K., Liu, H., Reinhardt, H.W., Wang, L., Experimental investigation of the effect of silica fume on the thermal spalling of reactive powder concrete. Construction and Building Materials. Vol. 155, 2017, pp. 571-583.

FACTORS GOVERNING THE FLEXURAL RESPONSE OF ULTRA-HIGH PERFORMANCE CONCRETE BEAMS UNDER FIRE CONDITIONS

Srishti Banerji[1], Venkatesh Kodur[2]

ABSTRACT

This paper presents results from a set of numerical studies on critical factors influencing the response of fire-exposed ultra-high performance concrete (UHPC) beams. The numerical model is based on a macroscopic finite element formulation and accounts for fire-induced spalling, temperature-dependent properties of UHPC and steel reinforcement, and realistic failure criteria. Specifically, spalling is evaluated using an advanced analysis approach by taking into consideration the combined stresses generated due to pore pressure, thermal gradients, and structural loading. The validated model is applied to conduct a set of parametric studies to quantify the effect of critical parameters on the fire response of UHPC beams. Results from numerical studies indicate that the fire resistance of UHPC beams is highly influenced by fire scenario, sectional dimensions, and dosage of steel and polypropylene fibres, whereas tensile reinforcement ratio has a minor impact on the fire performance of the UHPC beams.

Keywords: Ultra-high performance concrete beams; fire-induced spalling; numerical model; fire resistance

1 INTRODUCTION

Ultra-high performance concrete (UHPC) is an innovative cementitious material, made with high fineness admixtures, specially graded fine aggregates, steel fibres, and a low water-to-binder ratio. Owing to its pre-tailored mix proportions, UHPC has a dense microstructure and possesses high compressive strength (above 150 MPa) and tensile strength (5 MPa or higher), enhanced ductility, and improved durability characteristics. Since the compressive strength of UHPC is significantly higher than that of conventional normal strength concrete (NSC), cross-sections of UHPC members are much smaller than that of NSC members for carrying the same level of loads. The leaner cross-sections of UHPC members have lower self-weight as compared to NSC members and thus, can contribute to reducing the overall dead load [1], making UHPC increasingly favourable for applications in high-rise buildings. For use in building applications, structural members must satisfy required fire ratings to comply with fire safety requirements in building code. Recent studies have shown that despite superior performance under ambient conditions, UHPC exhibits poor performance under fire conditions as compared to conventional concrete. This is mainly due to the faster degradation of strength and modulus properties of UHPC with temperature, as well as its high susceptibility to fire-induced spalling. Furthermore, the smaller cross-sections of UHPC members lead to a reduction in thermal mass, which can accelerate heat propagation in UHPC structural members and lower their fire performance [2].

At present, the required fire ratings of reinforced concrete (RC) members specified in building codes are assessed through prescriptive rules wherein, required fire resistance is achieved by meeting the minimum

[1] Assistant Professor, Dept. of Civil and Environmental Engineering, Utah State University, Logan, UT, USA.
e-mail: srishti.banerji@usu.edu, ORCID: https://orcid.org/0000-0002-2330-3683
[2] University Distinguished Professor, Dept. of Civil and Environmental Engineering, Michigan State University, East Lansing, MI, USA.
e-mail: kodur@egr.msu.edu, ORCID: https://orcid.org/0000-0003-2058-2725

https://doi.org/10.6084/m9.figshare.22154900

dimensions of the section and concrete cover thickness to reinforcement [3]. The prescriptive provisions are derived from fire tests predominantly conducted on NSC members subjected to 50% load level and standard fire exposure, without taking into account critical parameters such as realistic fire scenarios, loading level, spalling effects, etc. Due to differences in microstructure, sectional dimensions, and vulnerability to spalling, the fire behaviour of UHPC members can differ significantly from conventional NSC members under varying realistic conditions. Moreover, fire-induced spalling is dependent on various test parameters including heating rate, load level, etc., as well as specific concrete properties such as permeability, tensile strength, presence of polypropylene fibres, etc. [4]. To this date, there are no studies in the literature quantifying the effect of these parameters on the fire response of RC beams made of UHPC. To overcome some of these knowledge gaps, a set of parametric studies were carried out to characterize the fire performance of UHPC beams.

2 NUMERICAL MODEL

A numerical model has been recently developed by Kodur and Banerji [5] to predict the fire response of UHPC beams using FORTRAN. The fire resistance analysis is carried out by applying a macroscopic finite-element based approach, wherein temperature-dependent sectional moment-curvature (M-κ) relations are utilized to trace the response of UHPC beam in the entire range from loading till collapse under fire. In the analysis, the beam is divided into a number of segments along its length and the mid-section of each segment is assumed to represent the overall behaviour of that segment. For each segment, the mid-section is further discretized into a two-dimensional mesh of bilinear iso-parametric four-noded rectangular elements. Fire is applied on the bottom and two sides of the beam, by inputting time-temperature relations as per standard fire curve or any given design fire scenario. In the analysis, the fire exposure time is incremented in time steps of 30 seconds. At each time step, the model sequentially performs thermal analysis, spalling analysis, and structural analysis.

Thermal analysis is carried out to evaluate the temperature distribution within the mid-section of each segment. Within the solid cross-section, conduction is the dominant heat transfer mechanism. The heat transfer from the surrounding environment (exposed to fire or unexposed) to the boundary elements is through convection and radiation. At each time step, a heat balance is established in each element of the discretized section to compute the temperature rise through a finite element based heat transfer analysis using the high temperature thermal properties of constituent materials (UHPC and steel reinforcement). Temperature-dependent thermal properties of UHPC are defined in the model using relations given by Kodur et al [6]. For steel rebars, thermal expansion coefficient values from Eurocode 2 [7] were incorporated in the model, whereas thermal conductivity and specific for rebars were not specifically considered as it does not significantly influence the temperature distribution in the beam cross-section.

Following thermal analysis, spalling is evaluated through a sub-model that utilizes hydro-thermo-mechanical stresses generated in heated concrete [8]. The thermal stress in the concrete elements is evaluated by calculating the free thermal expansion using the elemental temperatures and temperature-dependent thermal expansion coefficient of concrete. The mechanical stress generated in each concrete element from the applied loading on the beam is computed by using the high-temperature stress-strain relations of concrete corresponding to the mechanical strain determined from the strength analysis. The stress due to pore pressure is evaluated by calculating the elemental pore pressure through a finite element-based mass transfer analysis, accounting for the vaporization and movement of moisture in heated concrete. The model also accounts for the influence of polypropylene fibers, increasing temperature, pore pressure, and structural loading on the variation of permeability for evaluating pore pressure. Further details on the spalling sub-model are provided elsewhere [8]. When spalling occurs in an element, that element is removed from the cross-section and the reduced cross-section with updated boundary conditions is considered for subsequent steps of analysis.

Thereafter, the structural analysis starts by evaluating concrete strain and stress in all the elements for a given (assumed) curvature, till force equilibrium and strain compatibility are satisfied, within a predefined numerical (convergence) tolerance. The moment corresponding to the assumed curvature represents one point on the M-κ curve and a series of such points form one M-κ curve. The M-κ curves take into account temperature-dependent degradation in mechanical properties of UHPC and reinforcement. For UHPC, the relations proposed for mechanical properties at various temperatures by Banerji and Kodur [9] were utilized. The temperature-dependent stress-strain relations for rebars are adapted from high-temperature tension tests reported in the literature [10] and comprise a linear elastic range, yield plateau, a strain hardening range, and a softening range.

The maximum value of the moment in the M-κ relations determines the moment capacity of the beam. The deflection of the beam is calculated using the moment-area method. To determine failure, each beam segment is checked against predefined strength and deflection limit states at each time increment. Based on the strength limit state, failure is considered if the moment capacity in any beam segment is lower than the moment due to the applied load. According to the deflection limit state, failure is deemed to occur when in any beam segment, the deflection is greater than $L^2/400d$ or the rate of deflection is greater than $L^2/9000d$ (mm/min) where, L is the span length of the beam (mm) and, d is the effective depth of the beam (mm).

The numerical model was validated by comparing the predicted response parameters against data measured in fire tests conducted on UHPC beams, designated as U-B1, U-B2, and U-B10 tested at Michigan State University [11]. Beams U-B1 and U-B2 consisted of steel fibers, whereas beam U-B10 consisted of both steel and polypropylene fibers. The elevation and cross-sectional details of the UHPC beams are shown in Figure 1. The beams were tested under simply supported end conditions and were subjected to two-point flexural loading, wherein each point load was located at 1.4 m from the end support. The middle 2.4 m portion of the beam was exposed to "Design Fire" (DF) to simulate a typical office fire as shown in Figure 2. UHPC beams U-B1, U-B2, and U-B10 were subjected to load ratios of 40% (38 kN), 60% (59 kN), and 45% (43 kN), respectively, of their ultimate flexural capacity at room temperature (97 kN). The validation process included a comparison of thermal response, extent of spalling, deflections, and fire resistance predictions from the analysis with that measured during fire tests [11]. As part of thermal response validation, a comparison of temperatures at rebar and concrete locations matched well with measured temperatures in tests. The predicted values for the extent of spalling were within the range of the measured values. As part of structural response validation, mid-span deflections predicted by the numerical model were in close agreement with deflections measured in fire tests. The measured fire resistances of beams U-B1, U-B2, and U-B10 were 75, 78, and 114 min and the predicted fire resistances are 82, 73, and 112 min respectively. The predicted fire resistances of the UHPC beams are within 10% of the measured fire resistance from the tests. Detailed comparisons of the predicted and measured response parameters are presented in other published works by the authors [8]. The comparisons indicate that the numerical model can predict the behavior of fire-exposed UHPC beams with reasonable accuracy. The numerical model is applied to simulate the fire response of UHPC beams under different scenarios.

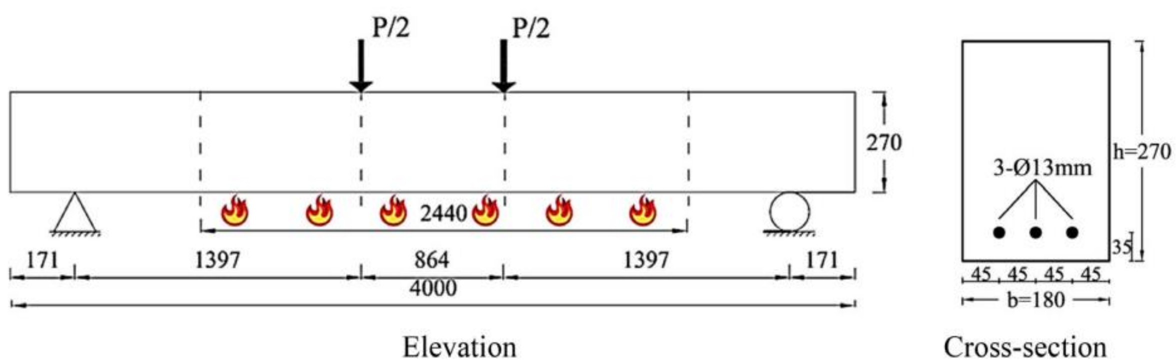

Figure 1. Elevation and cross-section of the analysed UHPC beams for validation (All units are in mm).

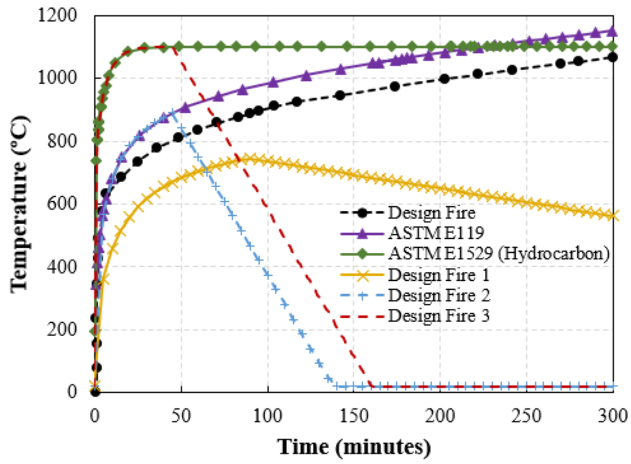

Figure 2. Time-temperature curves for different fire scenarios.

3 PARAMETRIC STUDIES

A simply-supported UHPC beam designated as UHPC-B0 (shown in Figure 1) is taken as the reference beam for the parametric studies. For the baseline case, beam UHPC-B0 is subjected to two-point loads applying 50% of its room temperature moment capacity, and the middle 2.4 m length of the beam is subjected to ASTM E119 standard fire exposure. The varied parameters include fire scenario, sectional dimensions, tensile reinforcement ratio, dosage of steel and polypropylene fibres as tabulated in Table 1. In each set of analyses, one parameter is varied within a practical range, whereas all the other parameters are maintained constant. To investigate the influence of fire scenarios, two standard fire exposures (ASTM E119 and ASTM E1529), and three design fire exposures were considered (see Figure 2). To quantify the effect of varying beam size on the fire response of UHPC beams, cross-sectional dimensions were varied. The considered sectional dimensions are 150 x 230mm^2, 180 x 270mm^2, 240 x 360mm^2, 270 x 410mm^2, and 360 x 540mm^2. The influence of tensile reinforcement ratio (in the range of 0.9% to 1.65%) on the fire resistance of UHPC beams is quantified by varying the number and size of tensile rebars. To evaluate the effect of steel and polypropylene (PP) fibres on the fire behaviour of UHPC beams, steel fibre dosage is varied in the range of 0.75 to 3% by volume and PP fibre content is varied in the range of 0 to 0.3% by volume.

Table 1. Summary of varied parameters and results from parametric studies

Varied Parameter	Beam designation	Parameter value	Fire exposure	Loading ratio	Predicted fire resistance (min)	Predicted extent of spalling (%)
Fire scenario	UHPC-B0	ASTM E119	ASTM E119	0.5	63	6.6%
	UHPC-B1	ASTM E1529 (Hydrocarbon)	ASTM E1529	0.5	50	6.2%
	UHPC-B2	DF 1	DF 1	0.5	107	5.3%
	UHPC-B3	DF 2	DF 2	0.5	No Failure	6.6%
	UHPC-B4	DF 3	DF 3	0.5	50	6.2%
Sectional dimensions	UHPC-B5	150mm x 230mm, Moment capacity-41 kNm	ASTM E119	0.5	53	7.5%
	UHPC-B0	180mm x 270mm, Moment capacity- 70 kNm	ASTM E119	0.5	63	6.6%
	UHPC-B6	240mm x 360mm, Moment capacity- 129 kNm	ASTM E119	0.5	74	5.1%
	UHPC-B7	270mm x 410mm, Moment capacity- 165 kNm	ASTM E119	0.5	80	4.2%
	UHPC-B8	360mm x 540mm, Moment capacity- 379 kNm	ASTM E119	0.5	96	3.3%

Table 1. (cont'd)

Varied Parameter	Beam designation	Parameter value	Fire exposure	Loading ratio	Predicted fire resistance (min)	Predicted extent of spalling (%)
Tensile reinforcement ratio	UHPC-B0	3-D13, ρt=0.9%, Moment capacity-70 kNm	ASTM E119	0.5	63	6.6%
	UHPC-B9	3-D16, ρt=1.24%, Moment capacity-91 kNm	ASTM E119	0.5	64	6.6%
	UHPC-B10	4-D13, ρt=1.09%, Moment capacity-84 kNm	ASTM E119	0.5	62	6.6%
	UHPC-B11	4-D16, ρt=1.65%, Moment capacity-112 kNm	ASTM E119	0.5	63	6.6%
Steel vol. fraction	UHPC-B12	0.75% vol., f'c=157 MPa, f't=5 MPa	ASTM E119	0.5	60	7.8%
	UHPC-B0	1.5% vol., f'c=175 MPa, f't=6 MPa	ASTM E119	0.5	63	6.6%
	UHPC-B13	2.25% vol., f'c=178 MPa, f't=7.5 MPa	ASTM E119	0.5	71	5.8%
	UHPC-B14	3% vol., f'c=182 MPa, f't=9.5 MPa	ASTM E119	0.5	74	2.9%
Polypropylene fiber dosage	UHPC-B0	0 % vol. PP fiber, f'c=175 MPa, f't= 6 MPa	ASTM E119	0.5	63	6.6%
	UHPC-B15	0.1 % vol. PP fiber, f'c=162 MPa,f't=5.8 MPa	ASTM E119	0.5	73	5.3%
	UHPC-B16	0.2% vol. PP fiber, f'c=151 MPa,f't=5.5 MPa	ASTM E119	0.5	74	0.8%
	UHPC-B17	0.3% vol. PP fiber, f'c=143 MPa,f't=5.2 MPa	ASTM E119	0.5	76	0%

3.1 Effect of fire scenario

UHPC beams subjected to 50% load ratio were analysed under varying fire exposure scenarios to study the effect of fire scenario on their fire resistance. The investigated fire scenarios are shown in Figure 2, and include two standard fire scenarios, namely, ASTM E119 and ASTM E1529 hydrocarbon fire, and three design fire scenarios; namely, Design Fire 1 (DF1), Design Fire 2 (DF2), and Design Fire 3 (DF3). The beams subjected to ASTM E1529 (hydrocarbon fire) and DF3 have the fastest temperature progression, followed by ASTM E119 and DF2, and lastly followed by DF1. The progression of mid-span deflections in the analysed UHPC beams under varying fire scenarios is plotted in Figure 3. The beams subjected to fire scenarios with high severity, ASTM E1529 and DF3, have the lowest fire resistance (50 min) due to severe temperature-induced degradation of member capacity and early rebar yielding as a result of rapid rise in rebar temperatures. This was followed by the failure of the UHPC beam subjected to comparatively moderate heating of ASTM E119 standard fire without a cooling phase, at 63 min. Fire scenario DF2 has the same time-temperature curve as ASTM E119 in the heating phase for 45 min, followed by cooling. The UHPC beam exposed to DF2 did not fail and partially recovered deflection due to the presence of cooling phase which lowered the sectional temperatures and facilitated partial recovery of strength and stiffness properties. DF1 had low fire severity with a longer heating duration of 90 min followed by cooling phase. Under fire scenario DF1, the analysed beam attains high temperatures because of the prolonged heating phase of 90 min and fails at 107 min before temperatures start to decrease in the cooling phase. However, the beam experienced the lowest spalling (5.3%) under DF1, which contributed to attainment of the highest fire resistance among the beams that failed. All the other analysed beams experienced similar levels of spalling in the range of 6.2-6.6%. Thus, the analysis results infer that fire scenario has a significant influence on the fire response of the UHPC beams, wherein the rate of increase in deflection is dependent on the severity, heating duration, and the rate of rise in fire temperatures.

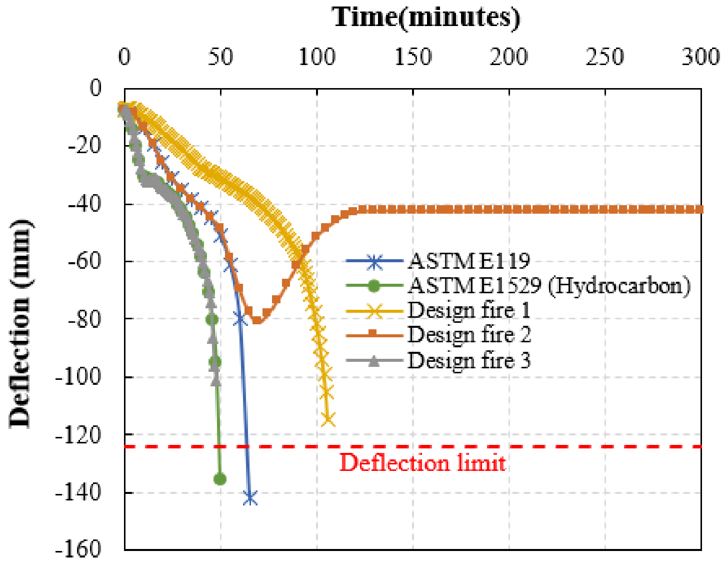

Figure 3. Effect of fire scenario on deflection of UHPC beams.

3.2 Effect of sectional dimensions

The influence of sectional dimensions on the fire resistance of UHPC beams is studied by analysing five UHPC beams of different cross-sectional sizes as summarized in Table 1, subjected to ASTM E119 fire exposure and 50% of their respective load capacity. The clear cover thicknesses to tensile reinforcement and reinforcement ratio were maintained constant at 28 mm and 0.09% respectively, in all the beams in the analysis. Additionally, every beam was designed to have the same width-to-depth ratio of 1.5. The rise in rebar temperatures was at a similar rate across all the beams due to the same cover thickness to tensile reinforcement in the analysed beams. As the sectional size of the beam was increased, heat transmission in the cross-section reduced due to higher thermal mass provided by larger sections and thus, resulting in significantly lower temperatures at interior concrete locations. These lower sectional temperatures in larger UHPC sections resulted in delaying the build-up of pore pressure and lowered the extent of spalling. Also, degradation of strength properties is slower due to lower sectional temperatures in UHPC beams with higher sectional sizes. Figure 4 shows the deflections of the analysed beams and it can be seen that the deflections rise at a faster rate for beams with smaller dimensions. While the fire resistance of the beam of size 150 mm x 230 mm is 53 min, the fire resistance of the beam of size 360 mm x 540 mm is 96 min. Thus, increasing member size increases the fire resistance of the member (see Table 1).

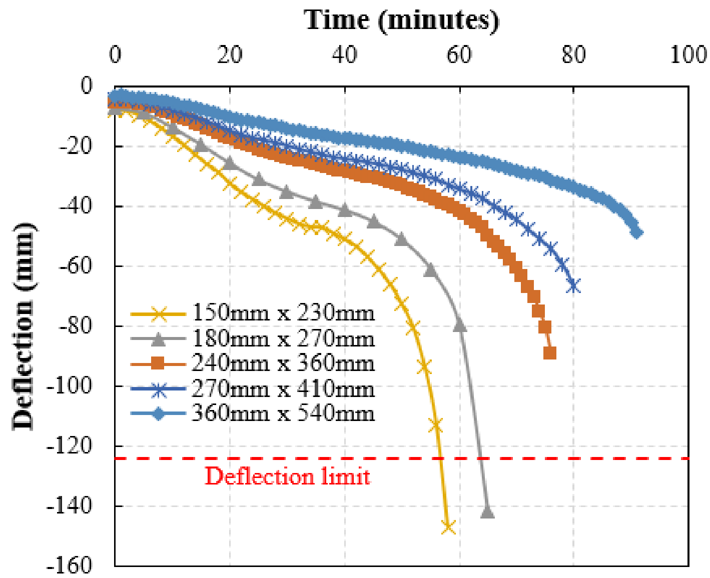

Figure 4. Effect of specimen dimensions on deflection of UHPC beams.

3.3 Effect of tensile reinforcement ratio

To study the effect of tensile reinforcement ratio, which is the ratio of the area of tension steel to the effective area of the beam cross-section, on fire resistance of UHPC beams, four different ratios were considered: 0.9%, 1.09%, 1.24%, and 1.65%. The sectional dimensions and cover thickness were same across the analysed beams, and only the number and diameter of tensile steel reinforcement were varied as shown in Table 1. With the increase in longitudinal reinforcement, the room temperature bending moment capacity of the UHPC beams increased significantly, resulting in a 60% increase in capacity over an increase of 0.85% in reinforcement. For exclusively investigating the effect of tensile reinforcement ratio, the load ratio was maintained constant as 50% of the corresponding load carrying capacity at room temperature for each beam (shown in Table 1). Further, all the analysed UHPC beams were subjected to ASTM E119 fire exposure. The progression of the mid-span deflection of the studied beams is plotted in Figure 5 as a function of fire exposure time. From the analysis results, it was found that the effect of tensile reinforcement ratio on fire resistance of UHPC beams was insignificant with negligible variations in thermal, spalling, and structural response of the beams. This unaltered response for different ratios of tensile reinforcement is because of the equivalent rate of reduction in capacity due to similar temperature rise in rebars provided with the same cover in all the beams. Further, due to the equivalent thermal distribution and load ratio, the level of spalling was uniform across the analysed beams.

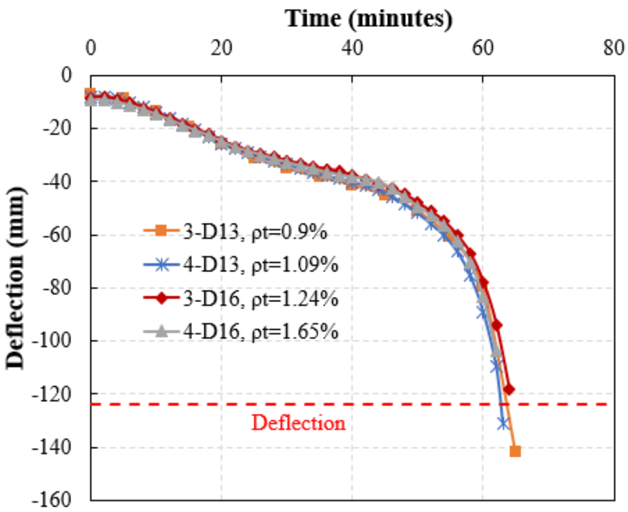

Figure 5. Effect of tensile reinforcement ratio on deflection of UHPC beams.

3.4 Effect of fibre content

To study the influence of the amount of steel fibres on the fire response of UHPC beams, UHPC with varying dosage of steel fibres of 0.75%, 1.5%, 2.25%, and 3% by volume were utilized. Initial strength properties for UHPC with different volume fractions of steel fibres were incorporated as summarized in Table 1. It can be noted the compressive and tensile strength of UHPC increased with increasing steel fibre dosage. Figure 6 shows the comparative variation of mid-span deflection as a function of fire exposure time. In the early stages of fire exposure till 40 min, the response of all the UHPC beams with different dosage of steel fibres is similar due to adequate strength and stiffness in the beams for resisting the applied load level of 50% of their capacity at room temperature. Beyond 45 min into fire exposure, the rate of deflection increase in fire-exposed UHPC beams becomes gradual and slower with increase in steel fibre content. The UHPC beams with higher steel fibre content have higher initial strength than the UHPC beams with lower steel fibre content. Higher initial strength leads to slower degradation of material properties and reduced loss of concrete cross-section (due to the lower fire-induced spalling) in these beams with higher amount of steel fibres. Thus, relatively lower deflections and higher fire resistance is experienced by UHPC beams with higher steel fibre content. According to the results of this analysis, the fire resistance of UHPC beams can be increased to 74 min by incorporating 3% by volume steel fibres as compared to fire resistance of 60 min by including 0.75% steel fibres.

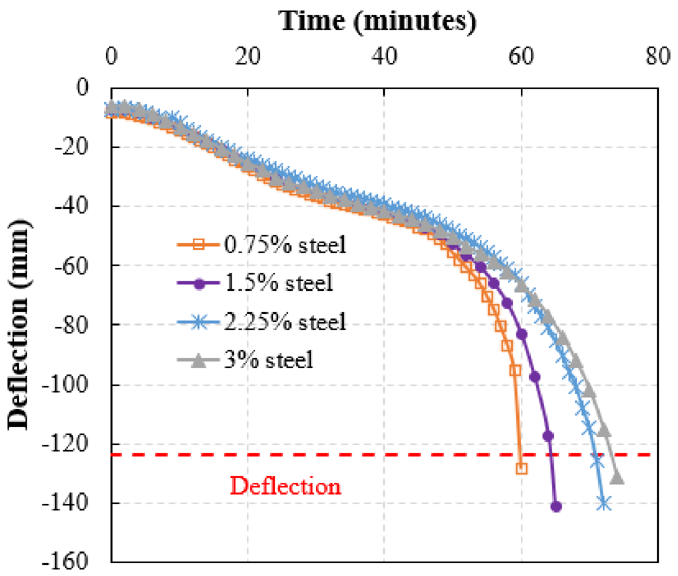

Figure 6. Effect of steel fibres on deflection of UHPC beams.

To evaluate the influence of varying dosage of polypropylene (PP) fibres on the fire response of UHPC beams, four UHPC beams with 0% (no PP fibres), 0.1%, 0.2%, and 0.3% by volume PP fibre content were analysed. All the beams were assumed to contain 1.5% by volume of steel fibres. The relative increase in permeability due to the melting of PP fibres at 160°C is dependent on the fibre dosage amount and is computed according to fibre percolation theory [12,13]. Additionally, increasing PP fibre dosage results in lower strength (as shown in Table 1) due to lower density and introduction of weaker zones in the concrete matrix. The structural response of the four UHPC beams, with varying amount of PP fibres, is compared in Figure 7 by plotting the variation in mid-span deflection as a function of fire exposure time. Overall, it can be seen that the UHPC beam without PP fibres experienced much larger deflections and failed earlier (at 63 min), than the beams with PP fibres throughout the fire exposure. This can be attributed to faster capacity degradation that resulted from the loss of concrete cross section due to severe spalling in the beam without any PP fibres. The rise in deflections was slower in the beams with PP fibres due to slower degradation of strength and stiffness properties owing to spalling mitigation facilitated by melting of PP fibres. The overall deflection progression of the beams with PP fibres was similar. With the inclusion of 0.1%, 0.2%, and 0.3% of PP fibres, the fire resistance was 73 min, 74 min, and 76 min respectively. The improvement in fire resistance with an increase in fibre dosage was relatively lower due to the associated reduction in strength by adding a higher volume of PP fibres.

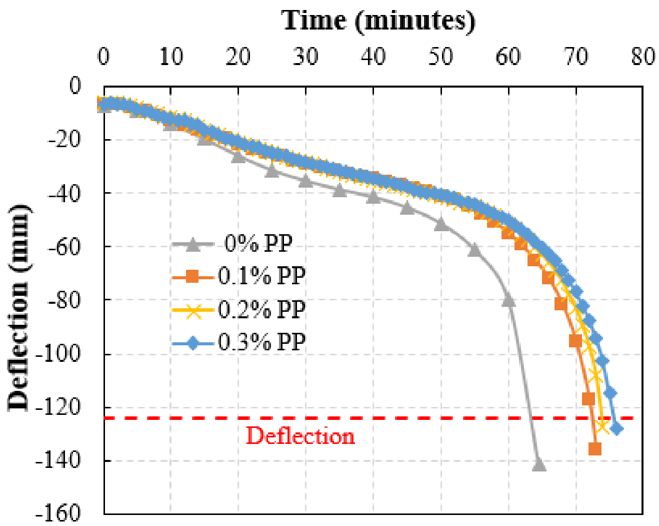

Figure 7. Effect of polypropylene (PP) fibres on deflection of UHPC beams.

4 CONCLUSIONS

Based on the results presented in this paper, the following conclusions can be drawn on the factors governing the fire performance of UHPC beams:

- Fire scenario, cross-sectional dimensions, presence, and dosage of steel and polypropylene fibres have a significant influence on the fire performance of the UHPC beams, whereas tensile reinforcement ratio has a minor impact on the fire performance of the UHPC beams.
- Fire severity has a significant effect on the fire behaviour of UHPC beams, wherein a higher intensity fire results in lower fire resistance. The fire resistance of UHPC beams is also dependent on the duration of heating.
- Cross-sectional dimensions have a significant influence on the response of fire-exposed UHPC beams; with larger beam cross-section (higher thermal mass) leading to higher fire resistance and lower extent of spalling.
- The addition of 3% by volume of steel fibres enhances the fire resistance of UHPC beams and mitigates spalling through slower degradation of tensile strength in UHPC. Incorporating 0.2-0.3% by volume of polypropylene fibres significantly reduces the extent of fire-induced spalling and thereby, enhances the fire resistance of UHPC beams.

REFERENCES

[1] Kromoser B, Preinstorfer P, Kollegger J. Building lightweight structures with carbon-fiber-reinforced polymer-reinforced ultra-high-performance concrete: Research approach, construction materials, and conceptual design of three building components. Struct Concr 2019;20:730–44.

[2] Kodur V, Naser MZ. Structural Fire Engineering. New York: McGraw-Hill Professional; 2020.

[3] ACI 216.1-14. Code Requirements for Determining Fire Resistance of Concrete and Masonry Construction Assemblies. Am. Concr. Inst., Farmington Hills, MI: American Concrete Institute; 2014.

[4] Kodur VKR, Phan L. Critical factors governing the fire performance of high strength concrete systems. Fire Saf J 2007;42:482–8. https://doi.org/10.1016/j.firesaf.2006.10.006.

[5] Banerji S, Kodur V. Numerical model for tracing the response of ultra-high performance concrete beams exposed to fire. Fire Mater 2022.

[6] Kodur V, Banerji S, Solhmirzaei R. Effect of temperature on thermal properties of ultrahigh-performance concrete. J Mater Civ Eng 2020;32:04020210.

[7] Eurocode 2: Design of Concrete Structures, Part 1–2: Structural Fire Design 2004.

[8] Kodur V, Banerji S. Modeling the fire-induced spalling in concrete structures incorporating hydro-thermo-mechanical stresses. Cem Concr Compos 2021;117:103902.

[9] Banerji S, Kodur V. Effect of temperature on mechanical properties of ultra-high performance concrete. Fire Mater 2022;46:287–301.

[10] Felicetti R, Gambarova PG, Meda A. Residual behavior of steel rebars and R/C sections after a fire. Constr Build Mater 2009;23:3546–55.

[11] Banerji S, Kodur V, Solhmirzaei R. Experimental behavior of ultra high performance fiber reinforced concrete beams under fire conditions. Eng Struct 2020;208:110316.

[12] Bentz DP. Fibers, percolation, and spalling of high-performance concrete. Mater J 2000;97:351–9.

[13] Liu X, Ye G, De Schutter G, Yuan Y, Taerwe L. On the mechanism of polypropylene fibres in preventing fire spalling in self-compacting and high-performance cement paste. Cem Concr Res 2008;38:487–99.

NUMERICAL APPROACH FOR EVALUATING SHEAR RESPONSE OF FIRE EXPOSED BRIDGE GIRDERS MADE OF UHPC

Kodur, Venkatesh[1], Gil, Augusto[2]

ABSTRACT

This paper presents the development of a numerical model to trace the shear response of UHPC bridge girders under fire conditions. A standard AASHTO-PCI type II bridge girder cross-section is modelled, and its shear and flexural behavior is compared to a similar conceptual rectangular section. The model takes into consideration temperature-dependent material properties and is validated against experimental data from fire tests. Results indicate that shear capacity becomes a governing limit state in I-shaped UHPC girders due to higher temperatures in the stem and it should be taken into consideration in evaluating fire resistance of UHPC bridge girders.
Keywords: UHPC; bridge girders; fire resistance; shear capacity; numerical modelling

1 INTRODUCTION

Bridge fires usually occur due to collision of vehicles that result in spillage of fuels or chemicals in the vicinity of a bridge [1]. Even though the probability of a fire breakout on a bridge is low, and it does not represent a significant risk to life safety, its occurrence can cause significant economic consequences and long traffic disruptions [2]. Bridge fires are characterized by fast burning and rapid rise in temperatures. There has been a rise in the number of bridge fire incidents over the last decade due to increasing urbanization and transportation of hazardous materials [3]. These fires result in significant economic impact, arising from the large damage (or even collapse) in structural members and the need of repair or reconstruction of bridges. Besides, temporary closure of a fire affected bridge can create big congestions in the surrounding traffic network, as seen in previous bridge fire incidents [4], [5]. Therefore, developing an understanding of the fire behavior of bridge structures is important to implement appropriate mitigation strategies so as to prevent such consequences on critical bridges.

Typically, concrete structures present high inherent fire resistance attributed to the slower heat transmission inside a concrete member and slower degradation of its mechanical properties with temperature rise. There exist provisions in building codes and standards to address fire hazard [6], [7]. However, there is no such provision in current bridge design codes and standards [8]–[10]. The fire provisions used for buildings cannot be extended to bridge structures due to fundamental differences in fire scenarios, material characteristics, and structural configurations adopted in bridge structures. Specifically, modern concrete bridges are designed with concretes of higher strength to achieve high durability and economy. Also, they have slender cross-sections to reduce self-weight and achieve increased span lengths. However, higher concrete strengths present lower fire resistance than conventional concretes due to the faster degradation of its strength with temperature and their high susceptibility to fire-induced spalling [11].

[1] University Distinguished Professor, Department of Civil and Environmental Engineering, Michigan State University,
e-mail: kodur@egr.msu.edu, ORCID: https://orcid.org/0000-0003-2058-2725
[2] Ph.D. Student, Department of Civil and Environmental Engineering, Michigan State University,
e-mail: masierog@msu.edu, ORCID: https://orcid.org/0000-0001-6167-7638
https://doi.org/10.6084/m9.figshare.22177802

Ultra-high-performance concrete (UHPC) is an innovative cementitious composite material that has found interest in bridge applications due to its high strength (over 150 MPa in compression) and durability. To take advantage of its advanced mechanical properties and be economically feasible, bridge girders are designed at ambient conditions with slender cross-sections and less shear reinforcement. However, when exposed to elevated temperatures, such as during a fire incident, these characteristics contribute to a faster propagation of temperatures throughout the member as well as faster degradation of its structural capacity. Previous studies have shown that its compressive and tensile strengths can be reduced by almost 50% after exposure to 500°C and that it is highly sensitive to the rate of temperature increase [12]. At the structural level, it has been reported that the fire resistance of UHPC beams can have less than 50% of the fire resistance of similar beams made with conventional concrete [13].

In current rational fire design methods, the fire resistance of concrete beams and girders is evaluated based on flexural failure limit state only, without any consideration to shear limit state. Although this design philosophy might work for conventional members, it may not be conservative or realistic in certain scenarios where shear capacity degrades at a rapid pace under fire, as in the case of I-shaped girders with slender webs. Specifically, such I-shaped girders made with UHPC can undergo faster degradation in shear capacity, as compared to flexural capacity, under fire conditions. Limited studies have been carried out on the fire behavior of UHPC beams, but almost none of these studies evaluate failure under shear limit state. In order to overcome this knowledge gap, this paper presents the development of a numerical model to trace the flexural and shear response of UHPC bridge girders under fire conditions.

2 SHEAR STRENGTH OF CONCRETE GIRDERS

Shear failure is not a major concern in conventional reinforced and prestressed concrete members under fire conditions. Due to its catastrophic nature, conventional concrete beams are designed with shear reinforcement to ensure that the member would experience flexural failure before shear failure in the case of overloading at ambient conditions [14]. Over the years, alternative methods have been developed for shear design of concrete beams based on different theories. Most commonly, conventional concrete beams are designed for diagonal tension stresses, resulting from shear and longitudinal flexural stresses, based on truss analogy theory [14]. The ACI 318 [15] method is based on this assumption and considers the shear capacity (V_n) of a conventional reinforced concrete beam to be comprised of contribution of concrete (V_c) and shear reinforcement in web (V_s), as shown in Equation 1 and illustrated in Figure 1. The shear strength contribution of the concrete includes the contributions from aggregate interlock (V_i), dowel action of the main reinforcing bars (V_d), and that of the uncracked concrete (V_{cz}). Since these components cannot be estimated individually, the overall contribution of concrete can be calculated using Equation 2, which is an empirical derivation from shear strength tests in concrete beams. The shear strength contribution of the web reinforcement is calculated through Equation 3:

$$V_n = V_c + V_s \tag{1}$$

$$V_c = \left(0.16\,\lambda\,\sqrt{f'_c} + 17\,\frac{\rho_w\,V_u\,d}{M_u}\right) b_w\,d \tag{2}$$

$$V_s = \frac{A_v\,f_{yt}\,d}{s} \tag{3}$$

where λ is a modification factor reflecting the lower tensile strength of lightweight concrete and is assumed to be 1.0 for normal weight concrete, f'_c is the concrete compressive strength, V_u and M_u are the shear force and bending moment at the section being evaluated, b_w and d are the web width and effective depth of the girder, A_v is the area of shear rebars, f_{yt} is the yield strength of the shear rebars, and s is the spacing between shear rebars.

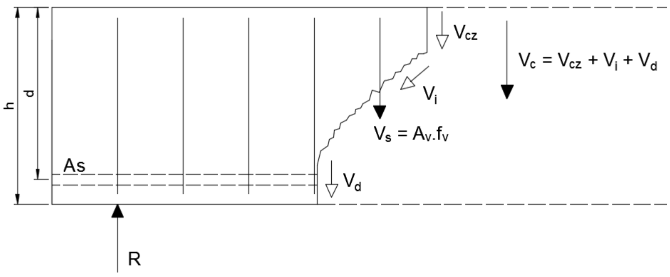

Figure 1. Forces at a diagonal crack in a beam with stirrups

For UHPC, the shear strength contribution of the steel fibers in UHPC (V_f) may be added as a third component to Equation 1. This is the procedure adopted in some design guidelines and recommendations, such as the French National Addition to the Eurocode 2 [16] and the Canadian Highway Bridge Design Code [9]. The French recommendation is used to estimate the contribution of the steel fibers (V_f) to shear strength of UHPC in this study, using Equation 4:

$$V_f = \sigma_{Rd,f}\, b_w\, z\, \cos\theta \tag{4}$$

where $\sigma_{Rd,f}$ is the mean value of the post-cracking strength perpendicular to the shear crack of inclination θ; b_w is the width of the web, and z is the effective shear depth. The value of $\sigma_{Rd,f}$ is obtained from uniaxial tensile stress-strain results derived from a specified inverse analysis of the results of a flexural prism test and includes a partial safety factor and an orientation factor. The inclination angle of the principal compression stress with respect to the longitudinal axis is determined from elastic stress transformation evaluated at the center of gravity of the beam at the expected force demand at the ultimate limit state. The value of θ is taken as equal to or greater than 30°, as per [16]. The French shear design method for beams also requires that the stress in the compression field to be lower than the compressive resistance limit and the flexural reinforcement be able to accommodate the increase in tensile force due to the applied shear force.

The reduced flexural and shear capacity of a reinforced concrete beam exposed to fire can be evaluated at the sectional level by extending room temperature capacity equations with due consideration to temperature induced degradation of material properties. The reduced shear capacity of a beam made with UHPC ($V_{UHPC,T}$) can be considered as the sum (Equation 5) of the degraded shear strength of concrete ($V_{c,T}$), shear reinforcement ($V_{s,T}$), and steel fiber reinforcement ($V_{f,T}$) due to temperature as in Equations 6, 7, and 8, respectively:

$$V_{UHPC,T} = V_{c,T} + V_{s,T} + V_{f,T} \tag{5}$$

$$V_{c,T} = \left(0.16\,\lambda\sqrt{f'_{c,T}} + 17\,\frac{\rho_w\, V_{u,T}\, d}{M_{u,T}}\right) b_w\, d \tag{6}$$

$$V_{s,T} = \frac{A_v\, f_{yt,T}\, d}{s} \tag{7}$$

$$V_{f,T} = \sigma_{Rd,f,T}\, b_w\, z\, \cos\theta \tag{8}$$

where $f'_{c,T}$ is the concrete compressive strength, $f_{yt,T}$ is the yield strength of shear stirrups, and $\sigma_{Rd,f,T}$ is the steel fiber reinforcement. Since specific temperature-dependent values of the post-cracking strength perpendicular to the shear crack ($\sigma_{Rd,f,T}$) have not been measured and reported in the literature, it is proposed in this study the use of the same strength reduction factors used for steel stirrups in Eurocode 2 [17]. Also, it should be noted that temperatures used to account for degradation of properties of steel fibers will be taken to be the same as temperature in the concrete at the same location.

3 INCORPORATION OF SHEAR STRENGTH IN FIRE RESISTANCE ANALYSIS

The aforementioned equations are incorporated to a numerical model developed in ABAQUS to evaluate the fire response of UHPC beams and girders. This finite element model is capable of tracing the thermal (temperatures) and structural (stresses and strains) behavior of beams under combined effects of mechanical and thermal loads. It takes into consideration modeling parameters and material degradation relations (for steel) from Eurocodes [17]–[19]. For UHPC, thermal and mechanical relations derived from experimental tests in previous studies were used [12], [20], considering the compressive and tensile strengths to be 167 MPa and 7 MPa, respectively. More details on the development of this model, including discretization, material models, and analysis details, can be found elsewhere [21].

In order to evaluate failure of UHPC bridge girders, deflection and strength limit states are used. The deflection criterion is based on BS 476 [22] prescriptions and is achieved when mid-span deflection exceeds L/20 (mm) or the rate of deflection exceeds $L^2/9000d$, where “L” is the span length and “d” is the effective depth of the girder in mm. The strength criterion is based on ASTM E119 [23] prescriptions and is said to be achieved when the structural member is unable to resist the applied loading effects (i.e. applied bending moment or shear force). For strength assessment, the temperatures obtained through the finite element model at different points of the beam are used to calculate degradation of flexural and shear capacities considering temperature-induced degradation of steel and concrete properties through an Excel spreadsheet. The level of capacity of the beam (flexural and shear) is calculated based on ACI 318 [15] equations and the derivation previously presented to estimate flexural and shear capacities at elevated temperatures.

The model was validated by comparing model predictions with results from previously undertaken fire tests. Due to lack of fire tests in concrete bridge girders in the literature, results from fire tests in UHPC beams tested by Banerji et al. [11] have been used for validation. The validation was undertaken by comparing measured (in the experimental test) and predicted (by the model) mid-span deflections and sectional temperatures as a function of the fire exposure time. Results from the validation process are not presented here due to space constrains, but they can be found elsewhere [21]. Overall, predicted temperatures and mid-span deflections from the ABAQUS model compared well with data reported in experimental tests.

4 CASE STUDY

The validated numerical model is applied to evaluate the fire behavior (including shear response) of a bridge girder with a standard AASHTO-PCI Type II cross section. In addition, a conceptual rectangular section with same width and depth was modelled in order to investigate the influence of concrete mass on the fire behavior of UHPC bridge girders. Figure 2 presents details of the cross-section and the girder’s structural configuration. Both girders were reinforced with sixteen 12.7 mm-diameter reinforcing bars, distributed in two layers at the bottom part of the girder, spacing 51 mm from each other and from the cross-section contour. Both girders were 6,200 mm-long, with a clear span of 6,000 mm and two concentrated forces of 378 kN applied 1,000 mm from the girder mid-span, while exposed to ASTM E119 standard fire curve. Thermal and mechanical properties of steel and UHCP were assumed to be the same as the ones described in the previous section.

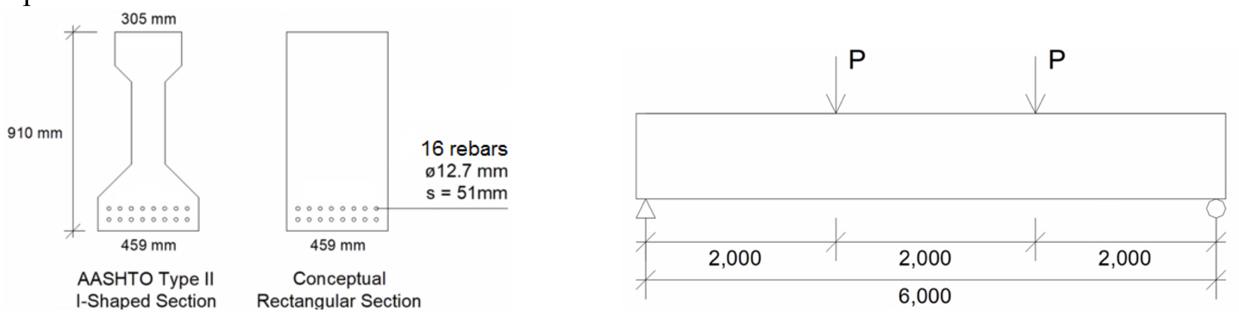

(a) Cross-sections (b) Structural configuration

Figure 2. Details of the modelled UHPC bridge girder

4.1 Thermal response

Figure 3 presents the progression of temperatures with fire exposure time at different points throughout the cross-section of the modeled UHPC bridge girders (both I-shaped and rectangular). Selected points include the location of corner, center and top rebars, as well as at the center of the web and at the top of the girder, as illustrated in Figure 2. It can be seen that the temperature progression in the corner and center rebars is very similar in both girders. However, temperature in other locations progresses more rapidly in the I-shaped girder. For instance, at 60 minutes of fire exposure, the temperature in the center of the web is below 40°C in the web of the rectangular girder, while it is past 350°C in the I-shaped girder. This is attributed to the slender cross-section of the I-shaped girder that allows a faster progression of temperatures throughout the girder cross-section. The thinner web also allows the transmission of heat to the bottom and top flanges, which results in increased temperatures in the top layer of rebars, as well as the top of the girder.

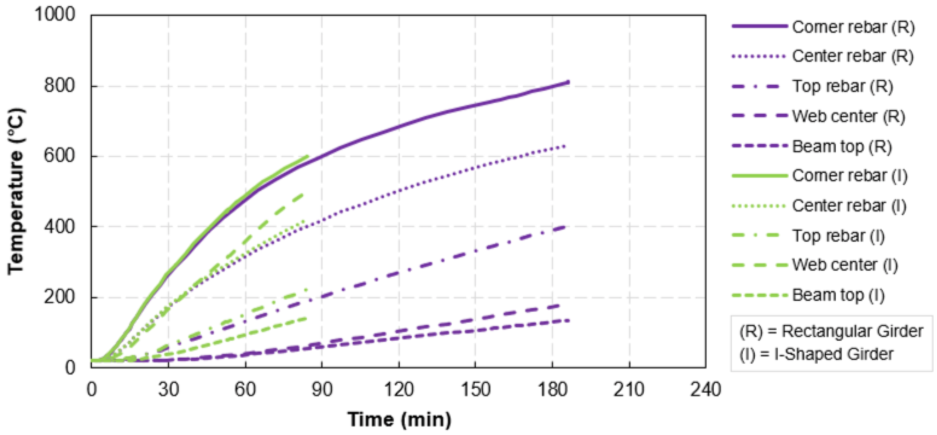

Figure 3. Progression of temperatures with fire exposure time of the modelled UHPC bridge girders

4.2 Structural response

The structural response of these girders is evaluated through degradation of its mid-span deflections as well as its flexural and shear capacity. Figure 4 presents the progression of mid-span deflection with fire exposure time for both girders up to their respective failure time. It can be seen that mid-span deflections were higher and increased much more rapidly in the I-shaped girder compared to the rectangular girder throughout the whole fire exposure. This is mostly attributed to the lower moment of inertia of the I-shaped cross-section compared the rectangular cross-section. Furthermore, the faster degradation of strength and stiffness due to the higher temperatures to which the I-shaped girder experience compared to the rectangular contributes to the rapid increase of mid-span deflections in I-shaped girders during fire exposure, contributing to early failure and lower fire resistance.

Figure 5 presents degradation of the flexural and shear strength of both girders with fire exposure time. From the assessment of moment capacity degradation, it is clear that the I-shaped girder experience faster degradation than the rectangular girder, which is attributed to the higher temperatures experienced that lead to faster degradation of concrete and steel strength. However, only the rectangular girder experience failure under flexural limit state, which occurred after 186 minutes of fire exposure. The I-shaped girder did not reach the flexural limit state because it failed under the shear limit state earlier, at 84 minutes of fire exposure, as can be seen in the Figure 5 (b).

Degradation of shear capacity in the rectangular girder occurred much more slowly compared to the I-shaped girder, attributed to the slower progression of temperatures in the web. To further assess the failure mode of these girders during fire exposure, principal strain contours obtained through the numerical model at the estimated failure time are presented in Figure 6. It can be seen that the mode of failure changed from flexure to shear due to concentration of strains on the bottom of the mid-span (in the rectangular section) to the center of the web (in the I-shaped section), respectively. While both girders presented similar degradation in the strength of steel reinforcement, degradation of the concrete strength in the stem was much higher in the I-shaped section. This is a result of the higher temperatures reached in the concrete due to the lower concrete mass.

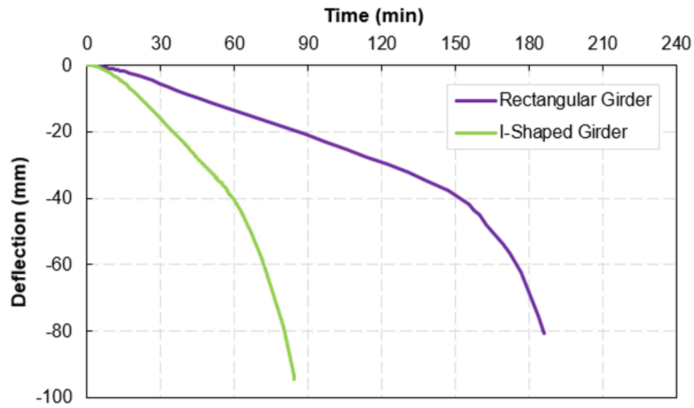

Figure 4. Variation of mid-span deflection with fire exposure time

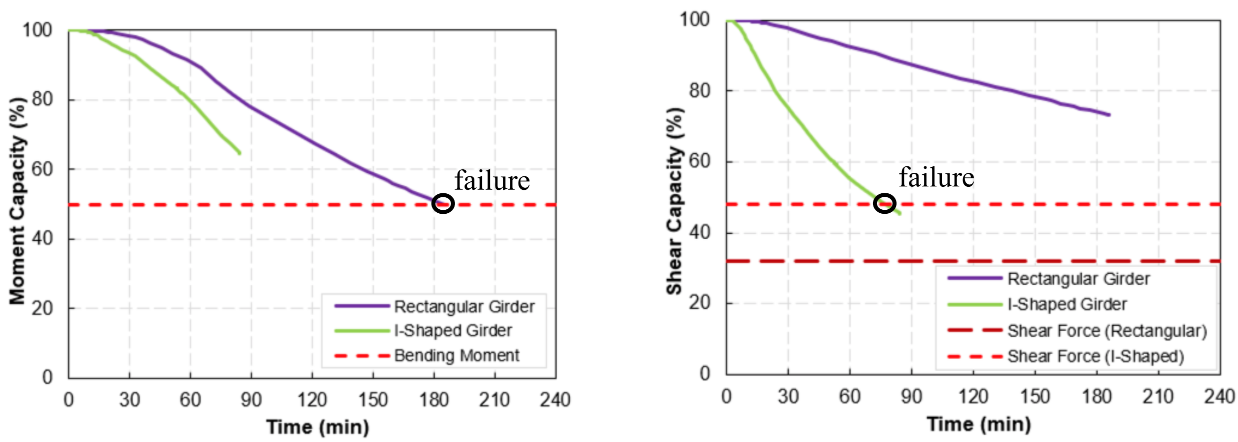

(a) Flexural capacity

(b) Shear capacity

Figure 5. Degradation of flexural and shear capacities as a function of fire exposure time

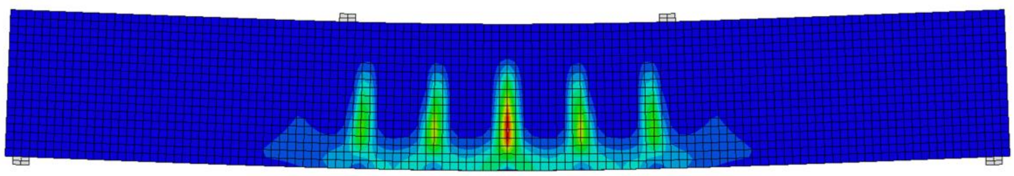

(a) Rectangular section at 186 minutes of fire exposure

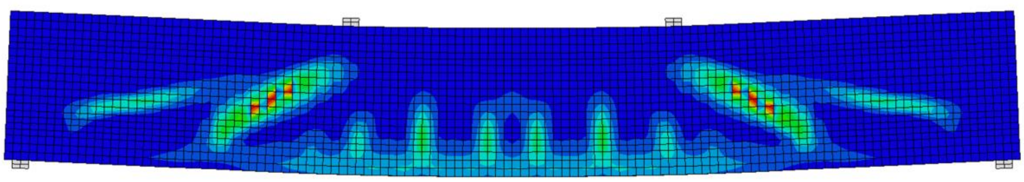

(b) I-shaped section at 84 minutes of fire exposure

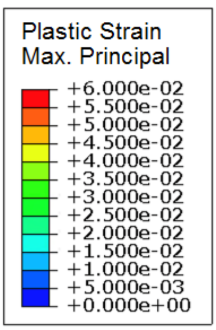

(c) Plastic strain scale

Figure 6. Principal plastic strains through the beam longitudinal cross-section of each girder

4.3 Failure times and failure modes

Table 1 summarizes results obtained from the analysis, including fire resistance failure times. It can be seen that none of the girders failed under deflection limit state and that while the rectangular girder only attained failure under flexural limit state at 186 of fire exposure, the I-shaped girder attained failure only under the shear limit state at 84 minutes of fire exposure. The lower fire resistance of the I-shaped girder is attributed to its reduced web thickness, which allow a faster progression of temperatures throughout the member cross-section, and degradation of concrete strength. As a consequence, shear capacity of the girder is degraded is degraded at a faster pace, leading to early failure and reduced fire resistance.

Table 1. Summary of fire resistance results

Girder cross-section	Fire resistance (minutes)				
	Deflection criteria		Strength criteria		Final
	Deflection*	Rate of deflection*	Flexural*	Shear*	
Rectangular	NF	NF	186	NF	186
I-shaped	NF	NF	NF	84	84

* NF – No failure

5 SUMMARY

This paper presented the development of a numerical approach for analyzing the behavior of UHPC bridge girders under fire exposure. Degradation of flexural and shear capacities are calculated through design equations taking into consideration reduction in steel and concrete mechanical properties with temperature. Results from this study show that temperatures progress more rapidly in I-shaped girder's cross-sections, which makes shear failure a governing limit state in I-shaped UHPC girders. Therefore, shear limit state should be taken into consideration in the fire design of UHPC bridge girders, especially when no shear reinforcement is provided.

REFERENCES

1. Garlock, M., Paya-Zaforteza, I., Kodur, V.K.R. and Gu, L., Fire hazard in bridges: Review, assessment and repair strategies. Engineering Structures 35, 89-98 (2012). https://doi.org/10.1016/j.engstruct.2011.11.002
2. Kodur, V.K.R. and Naser, M.Z., Importance factor for design of bridges against fire hazard. Engineering Structures 54, 207-220 (2013). http://dx.doi.org/10.1016/j.engstruct.2013.03.048
3. Kodur, V.K.R. and Naser, M.Z., Designing steel bridges for fire safety. Journal of Constructional Steel Research 156, 46-53 (2019). https://doi.org/10.1016/j.jcsr.2019.01.020
4. Kodur, V.K.R. and Naser M.Z., Fire hazard in transportation infrastructure: Review, assessment, and mitigation strategies. Frontiers of Structural and Civil Engineering 15, 46-60 (2021). https://doi.org/10.1007/s11709-020-0676-6
5. Peris-Sayol, G., Paya-Zaforteza, I., Balasch-Parisi, S. and Alós-Moya, J., Detailed analysis of the causes of bridge fires and their associated damage levels. Journal of Performance of Constructed Facilities 31 (2017). https://doi.org/10.1061/(ASCE)CF.1943-5509.0000977
6. ACI 216. Code Requirements for Determining Fire Resistance of Concrete and Masonry Construction Assemblies. Farmington Hills, MI, USA: American Concrete Institute; 2014.
7. International Code Council. International Building Code. Washington, DC, USA; 2018.
8. AASHTO (American Association of State Highway and Transportation Officials). LRFD Bridge Design Specifications. Washington, DC, USA; 2009.
9. CSA (Canadian Standards Association). S6:19 Canadian highway bridge design code. Canada; 2019.

10. Taly, N., Highway Bridge Superstructure Engineering: LRFD Approaches to Design and Analysis. Boca Raton, FL: CRC Press; 2015.
11. Banerji, S., Kodur, V. and Solhmirzaei, R., Experimental behavior of ultra high performance fiber reinforced concrete beams under fire conditions. Engineering Structures 208, 110316 (2020). https://doi.org/10.1016/j.engstruct.2020.110316
12. Banerji, S. and Kodur, V., Effect of Temperature on Mechanical Properties of Ultra-High Performance Concrete. Fire and Materials 46, 287-301 (2021). https://doi.org/10.1002/fam.2979
13. Kodur, V. and Banerji, S., Comparative fire behavior of reinforced concrete beams made of different concrete strengths. In: 11th Structures in Fire Conference. University of Queensland Library; 2020.
14. Nilson, A., Darwin, D. and Dolan, C., Design of concrete structures. 14th ed. New York, NY: McGraw Hill; 2010.
15. ACI 318. Building Code Requirements for Structural Concrete and Commentary. Farmington Hills, MI, USA: American Concrete Institute; 2019.
16. AFNOR - French standard institute. NF P 18-710 - National addition to Eurocode 2 - Design of Concrete Structures: Specific Rules for Ultra-High Performance Fibre-Reinforced Concrete (UHPFRC). 2016.
17. Eurocode 2. EN 1992-1-2: Design of concrete structures - Part 1-2: General rules - Structural fire design. Brussels, Belgium; 2004.
18. Eurocode 1. EN 1991-1-2: Actions on structures - Part 1-2: General actions - Actions on structures exposed to fire. Brussels, Belgium; 2002.
19. Eurocode 3. EN 1993-1-2: Design of steel structures - Part 1-2: General rules - Structural fire design. Brussels, Belgium; 2005.
20. Kodur, V., Banerji, S. and Solhmirzaei, R. Effect of Temperature on Thermal Properties of Ultrahigh-Performance Concrete. Journal of Materials in Civil Engineering 32, 04020210 (2020). https://doi.org/10.1061/(ASCE)MT.1943-5533.0003286
21. Gil, A. and Kodur, V., A numerical approach for evaluating shear capacity of concrete beams exposed to fire, Proceedings of the PCI Convention 2022, Precast/Prestressed Concrete Institute: Kansas City, MO, March, 2022.
22. British Standard (BS). BS476-20 - Fire tests on building materials and structures – Part 20: Method from determination of the fire resistance of elements of construction (general principles). London, UK; 1987.
23. ASTM E119. Standard Test Methods for Fire Tests of Building Construction and Materials. West Conshohocken, PA, USA; 2018.

EFFECTS OF CORROSION ON THE BEHAVIOUR OF SHORT REINFORCED CONCRETE COLUMNS EXPOSED TO ELEVATED TEMPERATURES

Lipi Mishra[1], Umesh Kumar Sharma[2]

ABSTRACT

Reinforced concrete (RC) structures are exposed to several deleterious environments which result in their shortened service life. Corrosion of reinforcement is one of the predominant reasons for deterioration of RC structures. In a corroded RC structure, an accidental fire can cause additional damage to the structural integrity. Previous studies have not addressed the combined effect of exposure to high temperature and presence of corrosion on the behaviour of RC columns. This research gap is explored in the current experimental study. Present research was designed to learn the implications of presence of corrosion in RC short columns upon subjection of high temperatures. Twelve RC short square column specimens were cast and the results of mean of three column samples were produced for each category. Six columns were corroded to 10% and 20% degree of corrosion following accelerated corrosion protocol, and the other six columns were left uncorroded. After the accelerated corrosion program was over, the corroded specimens were subjected to high temperature exposure with a target temperature of 800^{0}C, in an electric furnace. Uncorroded specimens were also subjected to the same heating regime. Afterwards the specimens were tested under uniaxial compression test. It was inferred that the presence of corrosion in heated samples had substantial effect on the residual compressive strength, strain ratio, and ductility of the columns.

Keywords: Reinforced concrete column; corrosion; elevated temperature; fire

1 INTRODUCTION

Corrosion of reinforcement is the leading cause of deterioration of RC structures globally. The alkaline medium in concrete generates passive layer on steel surface and protects it from corrosion. But presence of chloride ions in the environment or carbonation process can break the barrier and initiate corrosion. As corrosion products have higher volume than steel, it results in tensile force on surrounding concrete, which leads to cracks in concrete. Corrosion leads to degradation of mechanical properties of the steel bar, loss of cross-section of the steel bar, reduced bond strength between steel and concrete, crack propagation in concrete section [1-5]. Researchers have conducted various studies on the impact of corrosion on the behaviour of RC columns. The compressive strength of RC columns were found to decrease by 3% for corrosion degree of 10% and by 12% for corrosion degree of 25% respectively [6]. Some studies reported that the ductility of RC columns is affected more relative to their compressive strengths due to reinforcement corrosion [7,8]. Degree of corrosion being 7.5% the compressive strength of columns reduced by 6.6% as compared to a reduction of ductility ratio by 7.2 [7]. When only transverse stirrups were targeted for corrosion in RC columns, the peak and ultimate axial compressive strain in columns were more affected relative to their compressive strength [9]. Li et al. [10] tested corroded RC columns under

[1] Ph.D. Candidate, Indian Institute of Technology, Roorkee
e-mail: lmishra@ce.iitr.ac.in, ORCID: https://orcid.org/0000-0001-9680-457X
[2] Professor, Indian Institute of Technology, Roorkee
e-mail: umesh.sharma@ce.iitr.ac.in , ORCID: https://orcid.org/0000-0002-0972-908X
https://doi.org/10.6084/m9.figshare.22177814

sustained loading and found 47.8% decrease in compressive strength for degree of corrosion of 20% under no sustained loading conditions.

Elevated temperature exposure has deleterious effects on RC structures. It is well established that thermal exposure leads to degradation of mechanical properties of concrete [11,12]. Spalling of concrete is observed due to high heat exposure during fire, which results in reinforcing steel being directly exposed, that leads to significantly reduced structural capacity [13]. Researchers have studied the behaviour of RC columns exposed to elevated temperatures. Normal strength concrete columns were found to have better fire resistance compared to high strength concrete columns which are less permeable [14]. Fire performance of RC columns depend on the thermal exposure process such as rate of heating, maximum temperature reached, rate of cooing etc [15]. The detailing of reinforcements, spacing of transverse stirrups, the load-eccentricity also significantly affect the fire resistance of RC columns [15,16].

Although researchers have studied the effect of corrosion and high temperature subjection on the response of RC columns individually, studies on the combined effects of the two is rarely addressed. Current experimental program is designed to address this gap in literature.

2 EXPERIMENTAL STUDY

2.1 Specimen Preparation

Reinforced concrete short columns were cast with square cross-sectional dimensions of 150x150mm. The height of the columns was 650mm. While the test length of the columns was 450mm, 100mm length was provided at both ends of the columns for external confinement purpose during compressive strength test. Four 12mm steel bars with yield strength of 490MPa were used as longitudinal bars in the columns. 8mm steel bars with yield strength of 490MPa were taken as transverse reinforcements. 50mm centre to centre spacing was provided for the transverse stirrups in the test length. Closer spacing of 25mm centre to centre were provided in the two ends of 100mm lengths of external confinement region.

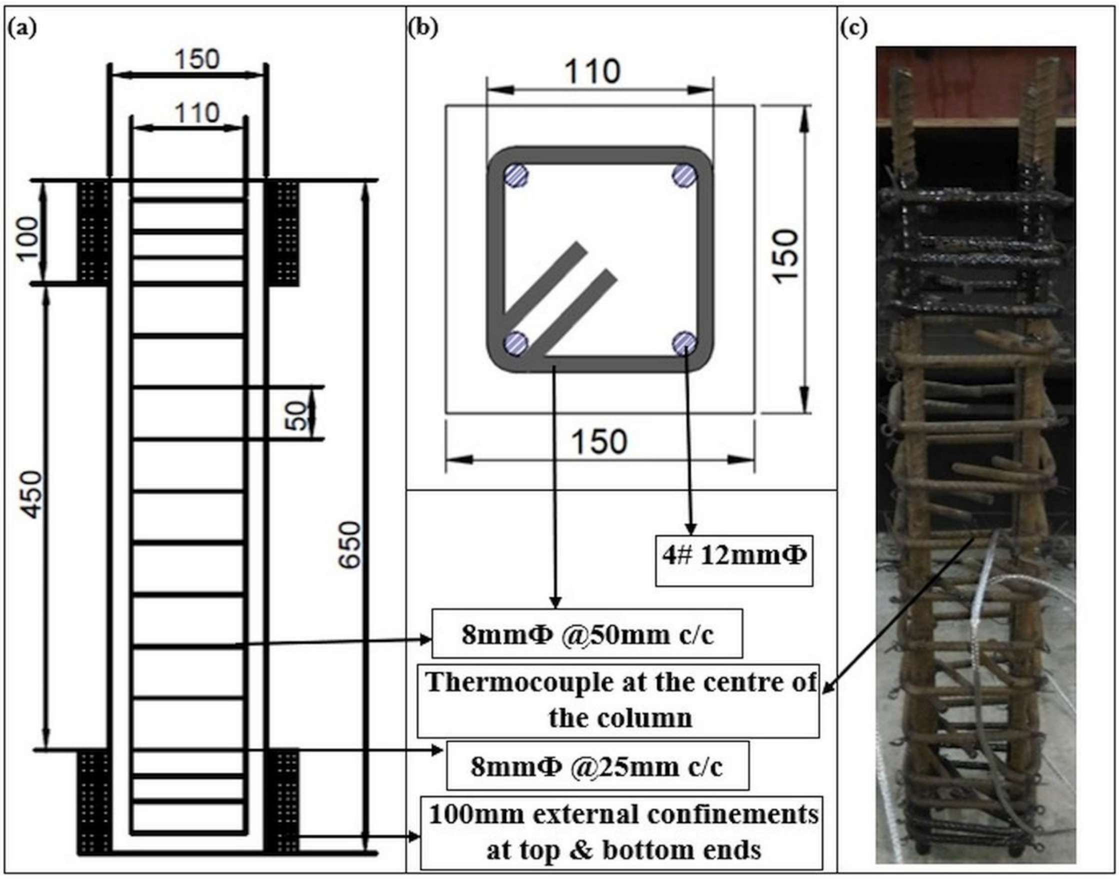

Figure 1. The dimensional details of columns (in mm)

20mm clear cover was provided in all columns. Figure 1 shows the dimension and reinforcement details of the column specimens.Specimens designed for corrosion had all four longitudinal bars projecting out of surface to allow space for electrical connections during accelerated corrosion. In order to measure the time-temperature data inside the specimens, one K-type thermocouple was placed at the centre of each column during casting. All steel bars were weighed before casting specimens, for gravimetric analysis after corrosion.

Concrete mix design was incorporated using ordinary Portland cement 43 grade (OPC 43), zone II fine aggregate and 12.5 mm maximum nominal size coarse aggregate as per IS 10262:2009 [17]. The average compressive strength after 28 days of concrete cubes was 37.5 MPa. The specimen codes were represented as C-X-Y%, where C represents column, X is the target exposure temperature in ^{0}C (8 for 800^{0}C) and Y% denotes the targeted level of corrosion (10% and 20%). Control specimens were represented as C-0-0%. Three column specimens were cast for each batch code. The results furnished are the average of three samples.

2.2 Accelerated corrosion

Accelerated corrosion procedure was followed to induce target level of corrosion in the column specimens. The corrosion degree is defined as the percentage weight loss of the steel bars after corrosion as given in equation (1). Faraday's law was applied to calculate the required duration and amount of current supply as per equation (2). The applied current density was kept constant for the required duration at 200µA/cm^2 throughout the accelerated corrosion process. The accelerated corrosion test arrangement is shown in Figure 2.

$$CD = \frac{W_i - W_f}{W_i} x100 \tag{1}$$

Where *CD* is the degree of corrosion in %, W_i in the initial weight of the steel bar and W_f is the final weight of the steel bar after corrosion.

$$M_{loss} = \frac{M.I.t}{Z.C_F} \tag{2}$$

Where M_{loss} is the mass loss of steel in corrosion. *M* is molar mass of the steel reinforcement. *Z* is the valence equals to 2. *I* is the amount of current supplied in Amperes. *t* is the duration of current supply in seconds. C_F is Faraday's constant, i.e., 96500 C/mol.

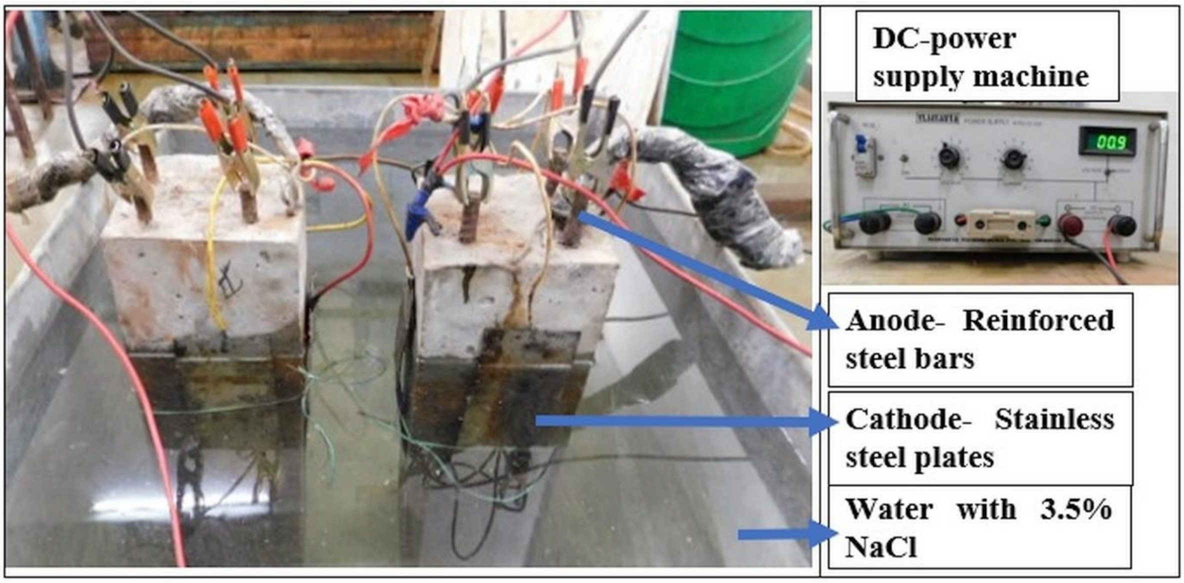

Figure 2. The accelerated corrosion test arrangement

Column specimens were subjected to two target degrees of corrosion, i.e., 10% and 20%. Specimens were partially submerged in a tank with saline water with 3.5% sodium chloride. The four protruded longitudinal bars were used as anodes and stainless-steel plates on four faces of the column in the test length region were used as cathodes. The electrical connections were done as shown in Figure 2. A current and voltage control DC supply machine was used for constant DC current supply to specimens over the required period. Anode was connected to the positive output terminal and cathode was connected to the negative output terminal of the machine. The input current and voltage for each specimen were monitored throughout the investigation. After the target duration of current supply, the specimens were taken out from the saline water and allowed to dry in room temperature. Specimens were cleaned properly, and the crack patterns were observed on each face.

2.3 Exposure to high temperature

After accelerated corrosion process was over, six corroded specimens were taken for thermal test. Three non-corroded specimens were subjected to the same temperature exposure program. A vertical split type of electric furnace of 450mm height was used for the elevated temperature exposure program, accommodating one specimen at a time. The furnace had a capacity of reaching highest temperature of 1000^{0}C. The test length portion of the columns was kept inside the furnace. The thermal test set-up is shown in Figure 3. The heating process consisted of heating rate of 10^{0}C/min, to a target temperature of 800^{0}C, target temperature was maintained for one hour. The furnace was then switched off. Rate of cooling was not programmed. The specimens cooled down to room temperature. Two thermocouples kept track of the temperature history of specimen throughout the heating schedule: one embedded inside the centre of the column and another thermocouple kept inside the furnace on the surface of the specimen at mid height. The thermocouple built-in the furnace produced furnace temperature. The thermocouples were connected to the data-taker system and the temperature profiles throughout the heating and cooling period were saved in the computer.

Figure 3. The furnace test set-up

2.4 Axial Compression Test

After seven days cooling in ambient temperature, the columns were tested in axial compressive test set-up as shown in Figure 4. Steel collars were fastened at the top and bottom ends of the columns of 100mm lengths for external confinement purpose during the axial compression test. Two linear variable differential transducers (LVDT) were fixed along the longitudinal axis at two opposite faces of the specimen for measuring the differential change in vertical displacement during compression. Displacement controlled compression testing machine of 5000kN capacity was used for the column specimens. A constant displacement rate of 0.1mm/minute was maintained during all compression tests. The load cell and the LVDTs were connected to a data-taker system and the data were recorded throughout the compression test.

Figure 4. Axial compression test

3 OBSERVATIONS

3.1 Observations on heat exposure

The time-temperature data plots for all columns are produced in Figure 5. The temperature profiles of all specimens during the whole process of heating and cooling were captured through data-taker system. Three temperature profiles are produced for each column. The furnace temperature, surface temperature at mid-height of the column and temperature at the centre (Tc) of the column. The difference in the value of temperature between surface and the centre of column was calculated in order to measure the thermal gradient inside the column. The values corresponding to the observations are produced in Table 1.

Table 1. Time-temperature data observation for all specimens

Columns	Maximum difference in temperature (^{0}C)		Time at max temperature difference (minutes)		Tcmax (^{0}C)	Time at Tcmax (minutes)
	+ve	-ve	+ve	-ve		
C-8-0%	451.1	-130.9	76	202	609.5	166
C-8-10%	413.9	-105.2	85	204	591.4	158
C-8-20%	381.1	-64.8	90	203	557.0	151

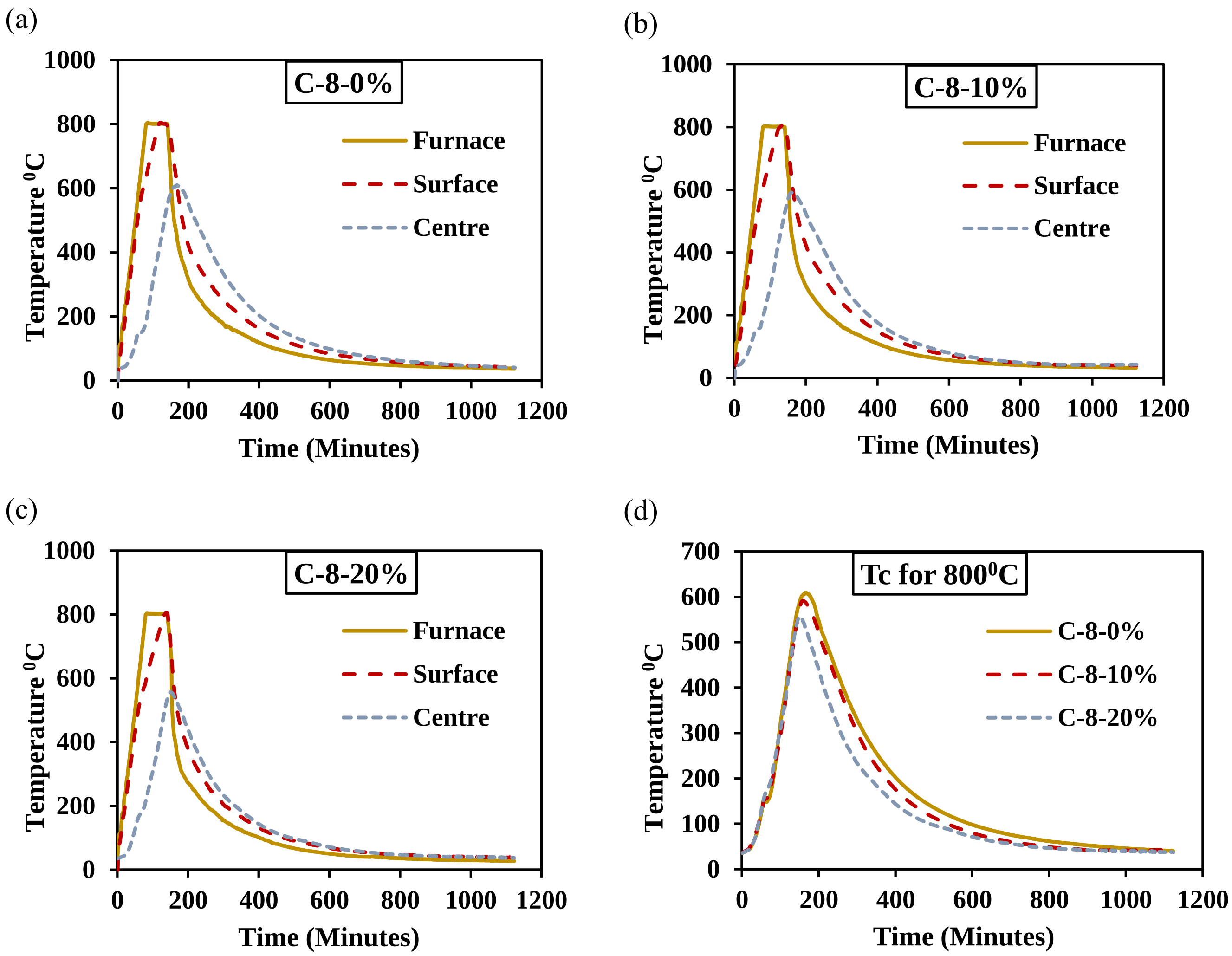

Figure 5. Time-temperature graphs of all specimens

It can be observed from Figure 5 (d) that maximum temperature reached at the centre of the specimens Tcmax decreased with the increase in degree of corrosion. For the similar temperature exposure regime, the specimens with higher corrosion level had lower Tcmax and the duration taken to reach Tcmax was also lower. Tcmax reduced from 609^{0}C for C-8-0% to 591^{0}C for C-8-10%. It further reduced to 557^{0}C for C-8-20%. The phenomenon could be explained as the degree of corrosion increased, the quantity of cracks on the specimens also increased. It might have provided a pathway for thermal energy to diffuse in the specimen, thus declining the value of Tcmax. The difference in the value of temperatures (δT) between the surface and Tc was also observed to reduce with increase in corrosion percentage. During the heating period maximum value of (δTmax) was reached as shown in Table 1. δTmax decreased from 450^{0}C for C-8-0% to 381^{0}C for C-8-20%. It also took more time to reach δTmax in corrosion damaged specimens. Probably the presence of cracks made it difficult to sustain higher values of maximum temperature in corrosion damaged concrete specimens.

3.2 Observations on corrosion damage

After the axial compression test, the cover concrete was removed in order to study the state of the reinforcement. Then the reinforcements were cleaned properly as per ASTM: G1-03 [18] and weighed in order to find out the mass loss percentage. It was observed that corrosion process damaged the transverse reinforcements more than the longitudinal reinforcements. More loss in steel cross section was observed for transverse reinforcements. E.g., in C-8-20% the average corrosion degree was observed to be 18.08%.

Whereas the stirrups underwent an average of 19.97% of corrosion in comparison to only 15.57% corrosion in longitudinal bars. Samples with 20% corrosion had complete loss of steel in some of the transverse reinforcements around the corners as shown in Figure 6. There was pitting corrosion observed along the longitudinal bars as well.

During the axial compression test it was observed that diagonal cracks developed along control columns, and they failed in shear. C-8-0% samples had 0.05mm wide cracks developed mainly horizontally along the stirrups after heat exposure. During compression test initial cracks appeared along the existing lateral cracks, so it appeared the concrete crushed under compression for C-8-0%. For corroded samples C-8-10% and C-8-20%, cracks developed along both longitudinal and transverse directions after corrosion process. During axial compression test it was found that the cracks developed in-line with the existing corrosion cracks. Cover concrete spalled due to degraded bond at concrete and steel interface. The failure mode in corroded specimens was impacted by loss of cross section in transverse steel reinforcements. Due to loss of steel in corrosion process, the confinement provided by stirrups no longer existed. The corroded longitudinal bars gradually buckled and led to column failure.

Figure 6. C-8-20% after demolition

4 ANALYSIS OF RESULTS

4.1 Load-displacement curves

During axial compression test, the value of the compressive load and corresponding axial compression of the specimens were recorded. The load-displacement curves of all column specimens are plotted as shown in Figure 7. Various parameters were calculated from the plots and are presented in Table 2. The yield strength was calculated from the merging point of two lines, a secant line through the load point measuring 65% of peak load and another line tangent to the peak load. The ductility factor of specimens was calculated as the ratio of displacement corresponding the load value equal to 80% of peak load in post-peak curve to the yield displacement. Δu represented the displacement value. Δu_{yield} is the yield point displacement.

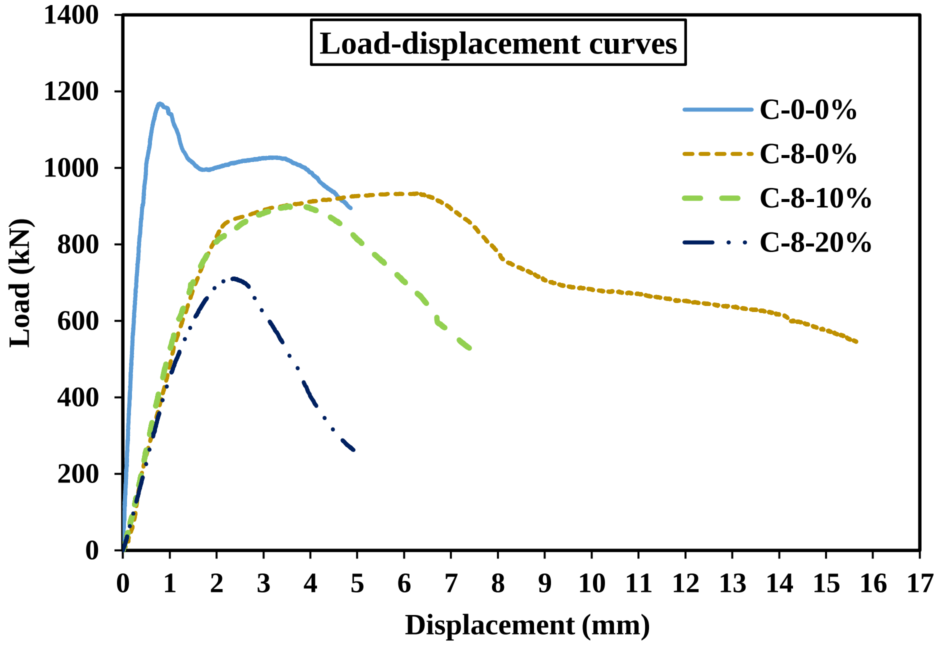

Figure 7. Load-displacement curves of all column specimens

Table 2. Compression test results

Columns	Peak Load (kN)	Peak Load Ratio	Δu at peak load (mm)	Strain ratio at peak load	Yield Strength (kN)	Δu_{yield} (mm)	Δu at 80% of peak load (mm)	Ductility Factor
C-0-0%	1168	1	0.8	1	1003.5	0.5	4.52	9.06
C-8-0%	933.29	0.79	6.28	7.94	826.28	2.03	8.31	4.1
C-8-10%	901.3	0.77	3.7	4.67	765.4	1.76	5.84	3.32
C-8-20%	710.9	0.61	2.31	2.91	621.9	1.61	3.3	2.06

It could be seen from Table 2 that the value of yield strength and ductility factor gradually decreased from control specimen to C-8-20%. C-8-20% had 77.8% reduction is ductility factor relative to the control specimen. The ratio of value of strain at peak load for all specimens to the same for control specimen was presented as strain ratio at peak load for all specimens in Table 2. It was observed that the value of strain at peak load increased with increase with temperature which is observed by previous studies as well. Whereas for the same exposure of heat the specimens with higher level of corrosion had lower value of strain at peak load, indicating brittle failure.

4.2 Peak compressive load

It was observed that peak compressive load gradually reduced as the level of corrosion increased. The values of the peak compressive load and corresponding decline in percentage compared to C-0-0% specimen are plotted in Figure 8. C-8-0% had 79% reduction and C-8-10% had 77% decline in compressive strength whereas for C-8-20% it was 61% compared to C-0-0%.

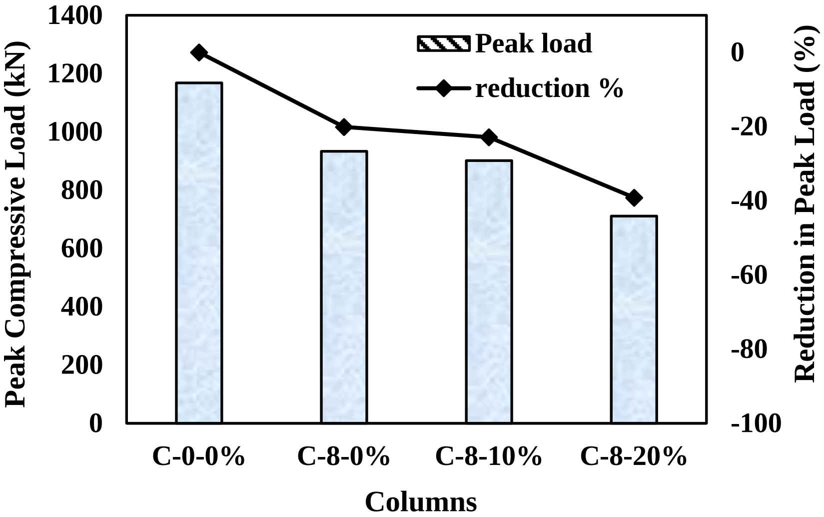

Figure 8. Variation of peak compressive load of all specimens

4.3 Stiffness of columns

The initial stiffness of column specimens was calculated from the load-displacement diagrams. It was calculated as the ratio of load to corresponding displacement pertaining to the point with load value of 65% of peak load. The values of initial stiffness for all specimens are plotted as shown in Figure 9. The percent reduction in stiffness for all specimens was calculated relative to the stiffness value of control specimen, plotted in Figure 9. It can be seen that stiffness value for columns was majorly impacted by subjection of elevated temperature. There was a reduction in stiffness of 80.53% for C-8-20% from the control specimen. There was only 0.8% difference in stiffness values between corroded and non-corroded heated samples. As is seen in the slopes of curves in Figure 7, initial slopes of the load-displacement curves changed drastically with subjection of elevated temperature. With heat exposure remaining same, the degree of corrosion hardly affected the initial slope of the curves. It could be explained that the initial stiffness of columns was affected by the core concrete. Damage due to corrosion affects the cross-section of the steel and bond between steel and concrete, causing cover cracks. As the load level increased, the core dilated and eventually the due to lack of adequate confinement the column failed. During the initial stage of the load application, the strength of the concrete core plays the pivotal role when it comes to initial stiffness values. Elevated temperature subjection of 800^0C results in physicochemical changes in concrete microstructure, reducing its mechanical properties significantly. The core concrete is more affected by elevated temperature of 800^0C as compared to corrosion degrees of 10% and 20%. Thus, resulting initial stiffness was showing significantly reduced values.

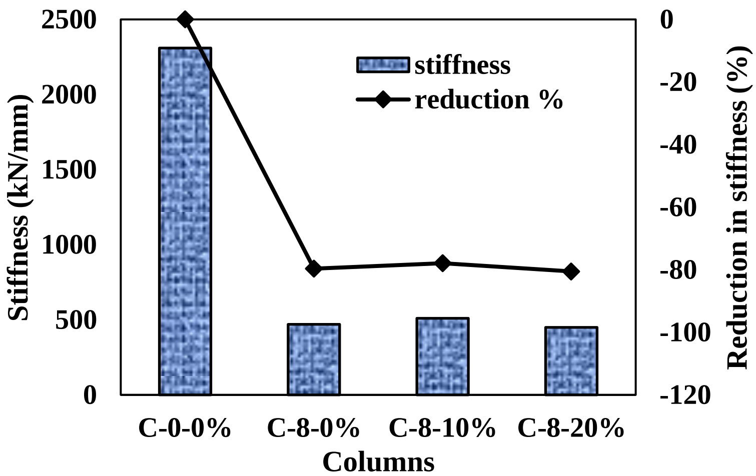

Figure 9. Stiffness values of all specimens

5 CONCLUSIONS

Current experimental study was designed to identify how the behaviour of RC columns changes with the presence of corrosion along with high temperature exposure. Following conclusions could be drawn from the study:

- The presence of corrosion resulted in reduced values of temperature profile inside the specimens. The highest temperature along the centroid of the specimens Tcmax was higher in C-8-0% and gradually decreased with increase in corrosion percentage in C-8-10% and C-8-20%. The value of δTmax and hence maximum temperature gradient also followed the same pattern.
- The difference in the time required to reach Tcmax and the time at beginning of cooling was also lower for C-8-20% compared to C-8-0%. The presence of cracks might have facilitated the heat flow within the specimens.
- During axial compression test, diagonal cracks developed along C-0-0%, and they failed in shear. Concrete crushed under compression for C-8-0%. For C-8-10% and C-8-20% it was found that the cracks developed in-line with the existing corrosion cracks. The failure mode in corroded specimens was impacted by loss of cross section in transverse steel reinforcements. Due to loss of steel in corrosion process, the confinement provided by stirrups no longer existed. The corroded longitudinal bars gradually buckled and led to column failure.
- Peak compressive strength, ductility factor of specimens gradually decreased with increase in degree of corrosion. It was observed that strain at peak load increased with increase with temperature. Whereas for the same exposure of heat, the specimens with higher level of corrosion had lower value of strain at peak load, indicating brittle failure.
- Initial stiffness value for columns was majorly impacted by the subjection of elevated temperature. There was a reduction in initial stiffness of 80.53% for C-8-20% from the control specimen C-0-0%. Whereas there was only 0.8% difference in stiffness values between corroded and non-corroded heated samples.
- Even though the size of the columns was much smaller than the columns in real buildings, the conclusions drawn in this study will be applicable to large scale RC columns as well. As stirrups in columns are located nearest to the surface of the column, they are more affected by corrosion compared to the longitudinal reinforcements. The loss of steel especially at the corners of the stirrups result in inferior confinement to the longitudinal steel and core concrete. In case of fire incidents such columns will be more susceptible to failure compared to non-corroded columns. The compressive strength and ductility will also be diminished, and presence of corrosion will lead to brittle failure. With presence of corrosion, maximum temperature and thermal gradient will also be lesser inside full scale columns compared to non-corroded columns. Further research can be done in future to assess the quantitative analysis for corroded full scale columns subjected to fire.

REFERENCES

1. Bhargava, K., Ghosh, A. K., Mori, Y., and Ramanujam, S. (2007). "Corrosion-induced bond strength degradation in reinforced concrete—Analytical and empirical models." Nucl. Eng. Des., 237(11) 1140–1157. https://doi.org/10.1016/j.nucengdes.2007.01.010
2. Coronelli, D. (2002). Corrosion Cracking and Bond Strength Modelling for Corroded bars in Reinforced Concrete. ACI Materials Journal, 99(3), 267–276.
3. Stanish, K., Hooton, R.D., & Pantazopoulou, S.J., (1999). Corrosion Effects on Bond Strength in Reinforced Concrete. ACI Structural Journal, 96(6).
4. Vidal, T., A. Castel, and R. François. 2004. "Analyzing crack width to predict corrosion in reinforced concrete." Cem. Concr. Res. 34 (1): 165–174. https://doi.org/10.1016/S0008-8846(03)00246-1
5. Zhang, R., Castel, A., & François, R. (2009). The corrosion pattern of reinforcement and its influence on serviceability of reinforced concrete members in chloride environment. Cement and Concrete Research, 39(11), 1077–1086. https://doi.org/10.1016/j.cemconres.2009.07.025

6. Revathy, J., Suguna, K., & Raghunath, P. N. (2009). Effect of Corrosion Damage on the Ductility Performance of Concrete Columns. American Journal of Engineering and Applied Sciences, 2(2), 324–327. https://doi.org/10.3844/ajeassp.2009.324.327
7. Lee, C., Bonacci, J. F., Thomas, M. D. A., Maalej, M., Khajehpour, S., Hearn, N., Pantazopoulou, S., Sheikh, S. (2000). Accelerated corrosion and repair of reinforced concrete columns using carbon fibre reinforced polymer sheets. Canadian Journal of Civil Engineering, 27(5), 941–948. https://doi.org/10.1139/l00-030
8. Bae, S. W., A. Belarbi, and J. J. Myers. 2005. "Performance of corrosion-damaged RC columns repaired by CFRP sheets." ACI Spec. Publ. 230:1447–1464
9. Vu, N. S., Yu, B., & Li, B. (2017). Stress-strain model for confined concrete with corroded transverse reinforcement. Engineering Structures, 151, 472–487. https://doi.org/10.1016/j.engstruct.2017.08.049
10. Li, Q., Huang, L., Ye, H., Fu, C., & Jin, X. (2020). Mechanical Degradation of Reinforced Concrete Columns Corroded Under Sustained Loads. International Journal of Civil Engineering, 18(8), 883–901. https://doi.org/10.1007/s40999-020-00511-w
11. Kodur, V., & McGrath, R. (2003). Fire endurance of high strength concrete columns. Fire Technology, 39(1), 73–87. https://doi.org/10.1023/A:1021731327822
12. Kodur, V. K. R., & Phan, L. (2007). Critical factors governing the fire performance of high strength concrete systems. Fire Safety Journal, 42, 482–488. https://doi.org/10.1016/j.firesaf.2006.10.006
13. Phan, L. T. (2008). Pore pressure and explosive spalling in concrete. Materials and Structures, 41(10), 1623–1632. https://doi.org/10.1617/s11527-008-9353-2
14. Phan, L. T., & Carino, N. J. (2002). Effects of Test Conditions and Mixture Proportions on Behavior of High-Strength Concrete Exposed to High Temperatures. ACI Materials Journal, 99(1). https://doi.org/10.14359/11317
15. Shah, A. H., & Sharma, U. K. (2017). Fire resistance and spalling performance of confined concrete columns. Construction and Building Materials, 156, 161–174. https://doi.org/10.1016/j.conbuildmat.2017.08.167
16. Buch, S. H., & Sharma, U. K. (2019). Empirical model for determining fire resistance of Reinforced Concrete columns. Construction and Building Materials, 225, 838–852. https://doi.org/10.1016/j.conbuildmat.2019.07.183
17. IS 10262: 2009. Indian concrete mix design guidelines; 2009
18. Standard Practice for Preparing, Cleaning, and Evaluating Corrosion Test Specimens. ASTM International, 90(Reapproved 2017), 1–9. https://doi.org/10.1520/G0001-03R11.2

SiF 2022– The 12th International Conference on Structures in Fire
The Hong Kong Polytechnic University, Nov 30 - Dec 2, 2022

TEMPERATURE-DEPENDENT MECHANICAL PROPERTIES OF CONCRETE AND GEOMATERIALS FOR TUNNEL FIRE STUDIES

Marzieh Shahraki[1], Nan Hua[2], Anthony Tessari[3], Negar Elhami-Khorasani[4]

ABSTRACT

Fire hazards can cause severe and irrecoverable damage to reinforced concrete tunnel linings. Historically, major fire events have led to months of downtime and millions of dollars of losses due to repair costs and affected operations. Advanced modeling can be used during the design process or for post-fire assessment to evaluate the level of damage and repairability of tunnel liners subjected to fire. Proper material properties, both at elevated temperatures and post-fire, are needed as inputs to these models. This paper provides a comprehensive review of experimental investigations on the residual compressive strength of concrete after exposure to high temperatures up to 1000 °C. The existing data are analysed to identify attributes that could affect the dispersion in residual strength. The refined datasets are used to develop probabilistic models for the normalized residual compressive strength of concrete. Also, the stiffness of soil or rock that is supporting the tunnel liner impacts the response of the structure. Thus, the paper provides the results of experiments to characterize the elastic modulus of three rock samples, including limestone, mudstone, and gypsum at temperatures ranging from 20 to 80°C. Experimental data in the literature show a larger variation in the stiffness of clay could be expected when compared to rock. The analyses indicate that the vertical crown displacement of a tunnel liner could be underestimated by 26% if the temperature-dependent elastic modulus of clay is not considered in the structural analysis of the tunnel.

Keywords: Residual concrete strength; elastic modulus; rock; clay

1 INTRODUCTION

Extreme fire events in tunnels may have catastrophic consequences, including loss of life, structural damage, and major socio-economic impacts due to service disruptions. Concrete structures typically behave well at high temperatures and do not collapse when subjected to moderate fires. Yet, these structures experience damage and require repair after the fire to resume functionality. Advanced modeling can be used for performance-based engineering of the reinforced concrete tunnel liners during the design process and as part of the damage assessment after a fire event. The goal of using advanced modeling is to evaluate the extent of damage and potential for repair given a fire scenario. Structural damage to the tunnel can be characterized based on the deteriorated depth of concrete, residual strength, and displacement.

Proper temperature-dependent material properties are important inputs to numerical models for evaluating the structural response during and after a fire. The constitutive material models for steel and concrete at high temperatures have been extensively studied in the literature. For example, building on existing datasets in the literature, the authors previously established probabilistic models for the material properties of steel

[1] Geotechnical Engineer, Arup, USA
e-mail: marzieh.shahraki@arup.com, ORCID: https://orcid.org/0000-0001-8142-5374
[2] Tunnel Engineer, Mott MacDonald, USA
e-mail: nan.hua@mottmac.com, ORCID: https://orcid.org/0000-0002-3046-9331
[3] Associate Professor, University at Buffalo, USA
e-mail: atessari@buffalo.edu, ORCID: https://orcid.org/0000-0003-0231-345X
[4] Associate Professor, University at Buffalo, USA
e-mail: negarkho@buffalo.edu, ORCID: https://orcid.org/0000-0003-3228-0097
https://doi.org/10.6084/m9.figshare.22177817

and concrete at high temperatures[1, 2]. However, the assessment of post-fire strength and displacements requires residual properties of the material as well. Thus, this paper focuses on:

(1) Temperature-dependent residual strength of concrete and comparison of findings with Eurocode reduction factors.

(2) Temperature-dependent elastic modulus of clay and rock that sit against the reinforced concrete liner and their effect on the structural response of the tunnel under fire.

2 RESIDUAL COMPRESSIVE STRENGTH OF CONCRETE

2.1 Data collection and analysis

There is a relatively large number of experimental studies on the residual compressive strength of concrete after exposure to high temperatures. A total of 53 articles, published from 1990 to 2020, with about 1240 data points on the residual compressive strength of concrete as a function of maximum temperature reached were reviewed [3-55]. The dataset covered the concrete with compressive strength equal to or less than 55 MPa at room temperature. The specimens included both cubes and cylinders; therefore, conversion factors were applied to cubic samples to adjust the strength measurements before reviewing the data. Also, most of the tests were conducted at 200°C, 400°C, and 600°C.

Siliceous and calcareous aggregates are the two major coarse aggregate types utilized in concrete mixtures. Most experiments in the collected dataset focused on concrete with siliceous aggregate, accounting for 87% of the dataset. Eurocode 2 (EC2) [56] specifies the loss in concrete strength due to temperature based on the type of coarse aggregate and provides reduction factors for concrete compressive strength at high temperatures. Eurocode 4 (EC4) [57] recommends an additional 10% loss of strength with respect to the value at the maximum reached temperature to determine the residual strength after exposure to high temperatures. Figure 1 presents the normalized residual compressive strength of concrete as a function of temperature and based on aggregate type for the collected dataset. The residual compressive strength data (f'_c) were normalized using the average of values recorded at room temperature ($f'_{c,20}$). The plots include the EC2 reduction factors for the compressive strength of concrete at high temperatures as well as the EC4 recommended reduction factors for residual strength. Figure 1 shows that the EC reduction factors are close to the median of the data for concrete with siliceous aggregate but seem to overestimate strength for concrete with calcareous aggregate.

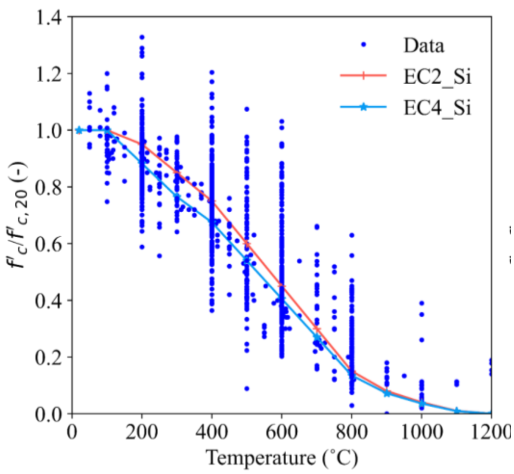

(a)

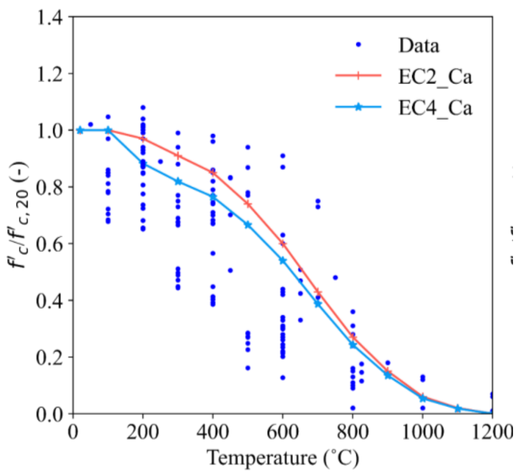

(b)

Figure 1. Collected data on residual strength of concrete as a function of maximum temperature reached, the EC2 reduction factors, and EC4 recommendation for (a) siliceous aggregate and (b) calcareous aggregate

The data in Figure 1 show a relatively large scatter; thus, the influence of other parameters, such as normal versus recycled aggregates, the addition of fibers (steel, polypropylene, and hybrid), supplementary cementing materials (silica fume and fly ash), and w/c ratio, on the residual strength of concrete were studied. It was concluded that differentiation between recycled versus normal aggregates does not have a noticeable effect on the residual compressive strength of concrete. The residual strength of fiber-reinforced concrete with silicious aggregates did not follow a noticeable trend, but calcareous concrete with fibers had lower residual strength. However, data on calcareous concrete with fibers is from a single study [49] and a general conclusion cannot be made. The data did not show a particular trend for concrete mixes with and without silica fume and fly ash. In general, calcareous concrete with a w/c ratio higher than 0.5 maintained strength after exposure to high temperatures better than concrete mixes with a lower w/c ratio, but the same conclusion did not apply to data for concrete with siliceous aggregate.

There is no standard testing protocol to measure the residual strength of concrete and experimental data from the literature are obtained using different protocols. The testing protocol includes the rate of heating, maximum temperature, retaining time, rate of cooling, and type of cooling. Most of the reviewed articles used an electric furnace with slow heating rates due to safety requirements with limited data available using the standard fire curve as the heating protocol. Figure 2 shows the normalized residual compressive strength data based on the retaining time of less than and larger than 2 hours for silicious and calcareous aggregates. The retaining time (t_R) is the duration that a specified furnace temperature is maintained once it has been reached. Longer exposure times are preferred to ensure that the core of the specimen reaches thermal equilibrium with the furnace environment.

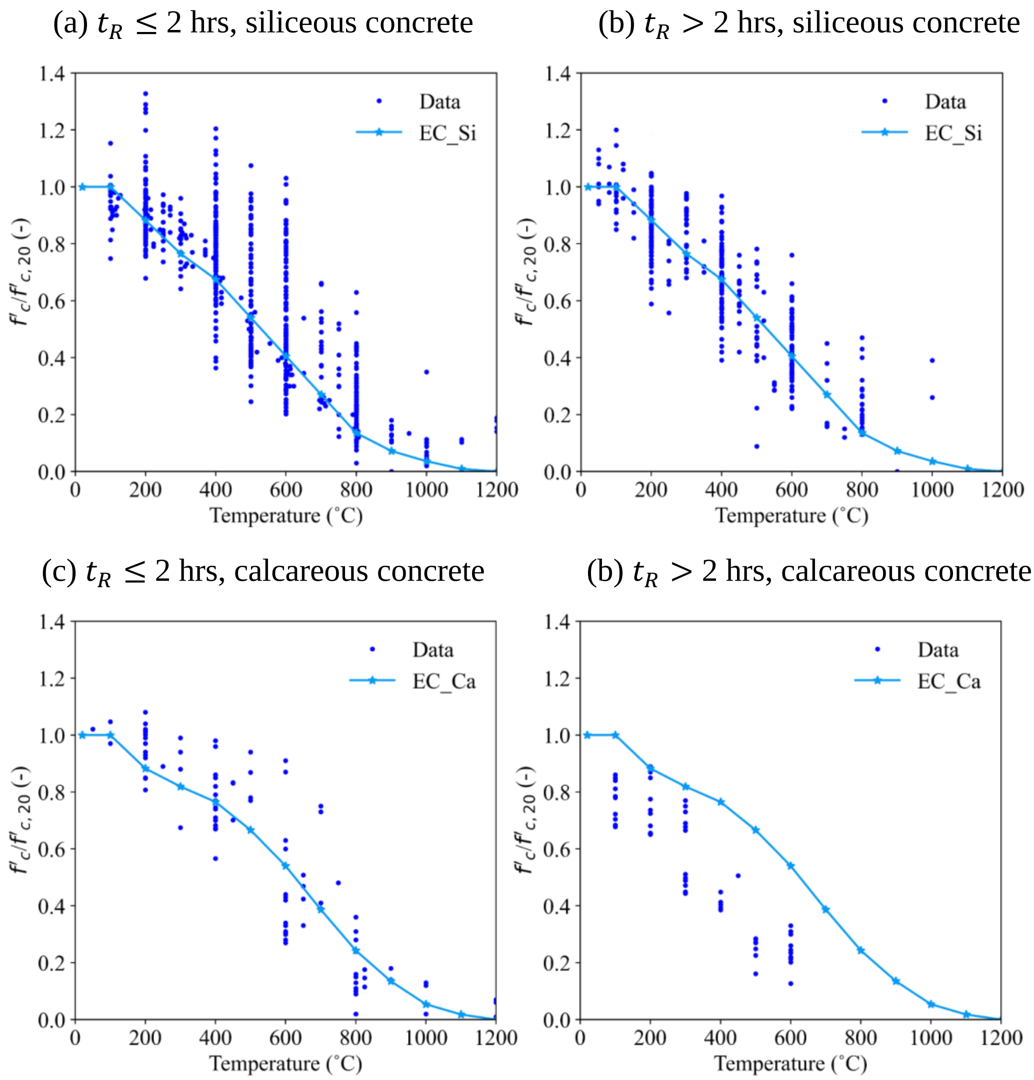

Figure 2. Normalized residual strength of concrete with siliceous and calcareous aggregates and retaining times less than or equal to 2 hours and greater than 2 hours

Figure 2 shows that categorizing the data based on retaining time reduces the scatter for siliceous aggregate, especially in the temperature range of 400 – 700°C. As expected, the residual strength for cases with a retaining time larger than 2 hours tends to be lower than those with retaining times less than 2 hours. The plots confirm the importance of maintaining sufficient heating time for the specimens to reach thermal equilibrium and thus obtain proper measurements. The plots also include the recommended EC4 reduction factors for residual strength, showing that most data for calcareous concrete with a retaining time larger than 2 hours falls below the EC4 recommended factors.

The cooling process may impact the structural behaviour of concrete and the recovered strength after a fire. Among the reviewed articles, only two studies [20, 35] investigated the effect of the cooling rate, indicating that a faster cooling rate would lead to a larger loss of concrete strength and stiffness. All the data for calcareous aggregate concrete were air-cooled. Most of the data for siliceous aggregate concrete were also air-cooled. A handful of experiments reported that the relative strength of water-cooled specimens was lower than those of air-cooled specimens (e.g.,[24, 25, 48]).

2.2 Probabilistic model

A probabilistic model for the residual compressive strength of concrete after exposure to high temperatures is established based on the collected data. The refined dataset included a total of 401 and 159 data points for normal-strength concrete with siliceous and calcareous aggregates, respectively. Data with retaining times larger than 2 hours were kept in the dataset for concrete with siliceous aggregate. Given the small set of available data for concrete with calcareous aggregate, all data with retaining times less than and larger than 2 hours were included when developing the probabilistic model.

The procedure to establish the probabilistic models involved examining the suitability of 13 distinct probability density functions (PDFs). The selected functions to fit data were gamma, normal, lognormal, logistic, log-logistic, inverse Gaussian, Gumbel, generalized t-distributions, beta, Rician, Nakagami, Bimbaum-Saunders, and Weibull. Raw data were grouped at temperature intervals of 50°C to capture variability at distinct temperature intervals. Each temperature group comprised data points within a ±10°C range. Datasets containing less than 5 data points were discarded. Therefore, 11 temperature groups for siliceous aggregate concrete and 7 temperature groups for calcareous aggregate concrete were created. Distributions were fit to the data in each temperature group and the goodness of the fit was compared. Three information criteria were used to compare and quantify the relative goodness of each fit across all temperature groups: (1) Bayesian information criterion or BIC; (2) Akaike information criterion or AIC; (3) Corrected AIC or AICc. The mean of each information criterion (i.e., BIC, AIC, and AICc) was calculated for all the temperature groups. Concrete data with calcareous aggregates had a small number of data points; thus, AICc was a more suitable criterion to identify models with a better fit.

Three additional requirements were imposed to arrive at the probabilistic models: (1) the model should be a "continuous function" covering temperatures from 20°C to 1000°C; (2) the model should have a "closed-form function" to facilitate implementation in analytical and computational frameworks; (3) the model should ensure continuity in reliability appraisals during the transition from ambient to high temperatures. To address the third requirement and capture the scatter in concrete compressive strength at room temperature, a mean value of 1.0 with a coefficient of variation (COV) of 0.12 is imposed at 20°C when developing the probabilistic models. The selected value of the COV is based on the recommendation by Holický and Sýkora (2010) [58] for normal strength concrete compressive strength at 20°C.

Considering all the quantitative and qualitative criteria listed above, Weibull and lognormal distributions were short-listed as viable candidates. Both distributions could represent the data; however, the Weibull function was chosen for both aggregate types to ensure compatibility with established stochastic functions for concrete strength at high temperatures by Qureshi et al. (2020) [2]. The Weibull distribution is a PDF with scale (λ) and shape (k) parameters, as defined below:

$$f(x;\lambda,k) = \begin{cases} \frac{k}{\lambda}\left(\frac{x}{\lambda}\right)^{k-1} e^{-\left(\frac{x}{\lambda}\right)^{k}} & x \geq 0 \\ 0 & x < 0 \end{cases} \qquad (1)$$

The two parameters of the Weibull distribution were determined for each temperature group of the concrete data with siliceous and calcareous aggregates. To provide continuous predictive functions for both parameters, nineteen polynomials were fit to the parameters as a function of temperature. The following are the corresponding equations for the temperature-dependent parameters of the Weibull distribution for siliceous concrete:

$$\lambda(T) = 1.06 \times 10^{-3}T + 1.11 \text{ and } k(T) = \frac{95.27}{5.095 + 23.21 \times 10^{-3}T} \tag{2}$$

Similarly, temperature-dependent parameters of the Weibull distribution for calcareous concrete are determined using the following equations:

$$\lambda(T) = 1.06 \times 10^{-3}T + 1.068 \text{ and } k(T) = \frac{18.92}{1.617 + 8.38 \times 10^{-3}T} \tag{3}$$

Figure 3 shows the data for the residual strength of concrete, the median, 0.05 and 0.95 quantiles of the probabilistic model, and the recommended EC4 reduction factors. The EC4 recommendation is relatively close to the median of the Weibull distribution for siliceous concrete. For calcareous concrete, the median of the Weibull distribution is lower than the EC4 recommendation.

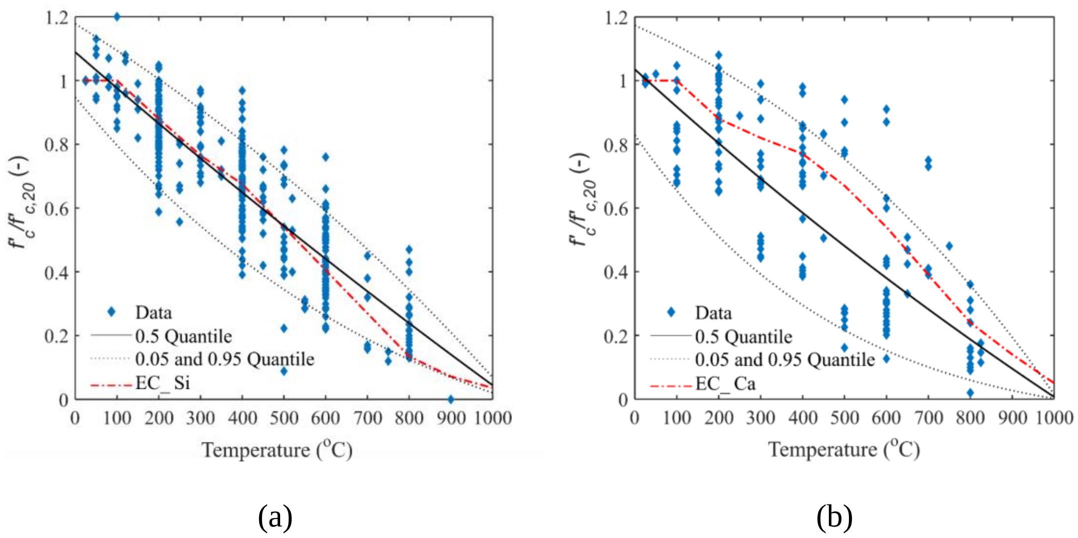

Figure 3. Temperature-dependent residual strength data for normal strength concrete, the Weibull probabilistic model, and the EC4 recommendation for (a) siliceous concrete, and (b) calcareous concrete

3 MODULUS OF ELASTICITY OF ROCK

3.1 Experimental program

This section discusses the elastic modulus of rock at elevated temperatures. The stiffness of geomaterials surrounding the tunnel liner has an impact on the deflections and structural response of the tunnel section. Thermo-mechanical triaxial tests were used to evaluate the elastic modulus of rock core specimens under varying stresses and temperatures in accordance with ASTM D7012 [59]. Core samples of limestone, shale (mudstone), and gypsum with 5 cm diameters were cut to length using 1:2 ratios. The samples were subjected to three confining pressures, which mimic the lateral confinement conditions expected in a shallow soil-tunnel system, and temperatures in the range of 20-80°C. To achieve the desired temperature, a heated circulating bath was connected to the triaxial apparatus. The specimens were heated to the specified temperature in a mechanical loading chamber and kept there for at least 3 hours at 20 and 40°C, and 8 hours at 60 and 80°C. To measure the internal temperature, three thermocouples were placed at three different elevations inside the triaxial apparatus (i.e., top, mid-height, and near the bottom of the specimen) as shown in Figure 4. Except for the test at 20°C, the external temperature control system was set to 10°C above the intended temperature to compensate for the heat loss through the hoses, which supplied heated water to the triaxial chamber. A triaxial compression test was then completed, which involved confining the specimen by pressurizing the cell fluid surrounding the specimen (radial pressure) and gradually increasing the axial force to 10kN.

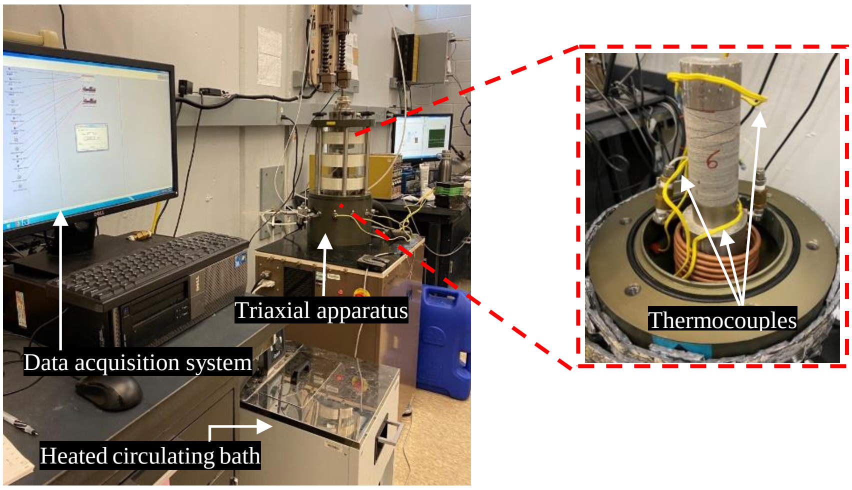

Figure 4. An elevated temperature triaxial test setup, showing the triaxial apparatus, heated circulating bath, and data acquisition system for measuring the stress-strain and temperature

3.2 Experimental results

The elastic modulus of limestone, shale, and gypsum was measured at four different temperatures: 20, 40, 60, and 80°C. For each sample, tests were performed at three confining pressures (CP) of 100, 500, and 1000 kPa, and stress-strain envelopes were obtained. The value of the elastic modulus, E, was calculated using the average slope of the straight-line portion of the stress-strain curve. The average slope was calculated via a linear least-squares fit to the stress-strain data. The findings show a slight decrease in the elastic modulus of limestone and a slight increase in the elastic modulus of shale (mudstone) with the temperature at the lowest confinement; however, the temperature increase had a negligible effect on the results in most trials. The findings from Mao et. al [60] and Zhang et. al [61], who carried out uniaxial compression tests on limestone and mudstone with no confining pressure, are in agreement with the results of experiments with the lowest confining pressure (i.e., 100 kPa). Figure 5 compares the normalized elastic modulus from the literature and the experiments in this study. The values are normalized using the elastic modulus at ambient temperature for a confining pressure of 100 kPa. Overall, additional experiments are needed to generalize conclusions on the effects of temperature and confining pressure on the elastic modulus of rock. More experiments are being conducted at the University at Buffalo.

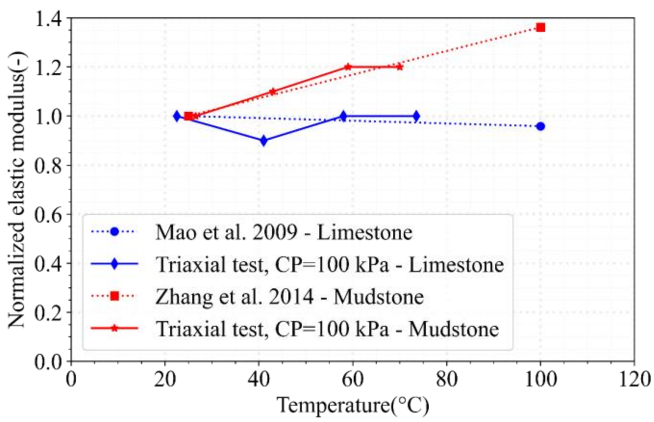

Figure 5. Comparison of the normalized elastic modulus of limestone and mudstone with data from literature [60, 61]

4 MODULUS OF ELASTICITY OF CLAY

4.1 Effect of temperature on material properties

The effect of temperature on saturated clay was studied based on existing data from the literature. Accounting for the change in stiffness of clay due to temperature requires careful consideration. When clay temperature increases, excess pore water pressure is generated due to the differential expansion of the pore water and soil solids. This excess pore pressure reduces the effective stress in the soil. The reduction of the effective stress could decrease the elastic modulus of the clay, while thermal hardening could increase the elastic modulus. Therefore, the elastic modulus of soil is a function of both soil temperature and excess pore pressure. It is the net change in the clay's elastic modulus that would affect tunnel deformation under fire.

Ghaaowd et al. [62] studied the effect of temperature in the range of 0-80 °C on the change in pore water pressure for 13 specimens of 8 different types of clay. For the same specimen, Δu changed at a steady rate with ΔT, where Δu is the change in excess pore pressure in kPa and ΔT is the change in temperature in °C. The upper and lower bounds of Δu (kPa)/ΔT (°C) were obtained as 0.9 kPa/°C and 4.3 kPa/°C, respectively. Cekerevac and Laloui [63] reported secant elastic moduli obtained from tests at 22 °C and 90 °C of Kaolin clay samples (Table 2) using a temperature-controlled triaxial apparatus. In this study, a linear interpolation was adopted to obtain the secant modulus for temperatures between 22 °C to 90 °C.

Table 2: Secant elastic modulus of normally consolidated clay samples [63]

Temperature (°C) \ Confining effective pressure (kPa)	300	600
22	11 MPa	21 MPa
90	15 MPa	24 MPa

The net change in clay's elastic modulus can be calculated as a function of the temperature given the change in excess pore pressure (Δu (kPa)/ΔT) and the effect of thermal hardening (Table 2).

4.2 Effect of temperature on structural response

Considering the larger variation in the elastic modulus of clay with temperature compared to rock, this section studies the influence of including temperature-dependent properties of clay on the structural response of a reinforced concrete tunnel liner. The tunnel section was adapted from the Storebælt Railway Tunnel in Europe [64]. The tunnel section was circular, located about 25 m below the ground surface and 31 m below the sea level. The inner diameter of the adapted section was 7.5 m with a thickness of 0.35 m (slightly different from the actual tunnel). The compressive strength of concrete was taken as 27.5 MPa and the tensile yield strength of the reinforcement was 414 MPa. The average elastic modulus of the surrounding soil was 23 MPa.

The performance of reinforced concrete liner was studied under the RWS fire curve. Sequentially, a coupled thermo-structural analysis conducted via SAFIR was used to simulate the structural response [65]. Figure 6a shows the SAFIR beam-spring model for half of the investigated tunnel section, where the concrete liner was composed of 12 beam elements, and the subgrade reaction was captured by 13 radial spring elements. The horizontal movement and rotation were restrained at the two ends of the liner elements to simulate symmetric boundary conditions. The considered applied loads on the tunnel sections included self-weight, earth pressure, water pressure, live load, and impact load [66]. The temperature-dependent material properties for both concrete and steel were taken from EN 1992-1-2 [67].

The springs were modeled using truss elements in SAFIR, for which the elastic modulus could be updated over time. The stiffness of the springs (K_r) was calculated using Eq. 4 [68], as a function of tunnel radius R, elastic modulus E (calculated based on Section 4.1), and Poisson's ratio ν of the surrounding soil. The springs were only activated when the tunnel expands outward, placing the springs in compression.

$$K_r = \frac{E}{[R(1+\nu)]} \qquad (4)$$

A 2D transient thermal analysis was carried out for the beam cross-section to obtain the time-dependent temperature of each sectional fiber. Figure 6b shows the cross section for the 2D heat transfer analysis, with a 0.35-m thick and 1-m wide reinforced concrete lining section and a soil layer on top. A refined mesh was used on the side that was exposed to fire. The thermal elongation, specific heat, and thermal conductivity of concrete and steel were defined as temperature-dependent per EN 1992-1-2 [67] and EN 1993-1-2 [69]. Thermal conductivity, specific heat, specific mass of the clay material, and water content of the soil were taken as 1 W/mK, 1375 J/kgK, 1600 kg/m^3, and 320 kg/m^3, respectively [70]. The tunnel section was divided into two regions, denoted as "hot" and "cold". The hot region was exposed to the RWS fire curve, and the cold region remained at ambient temperatures throughout the fire.

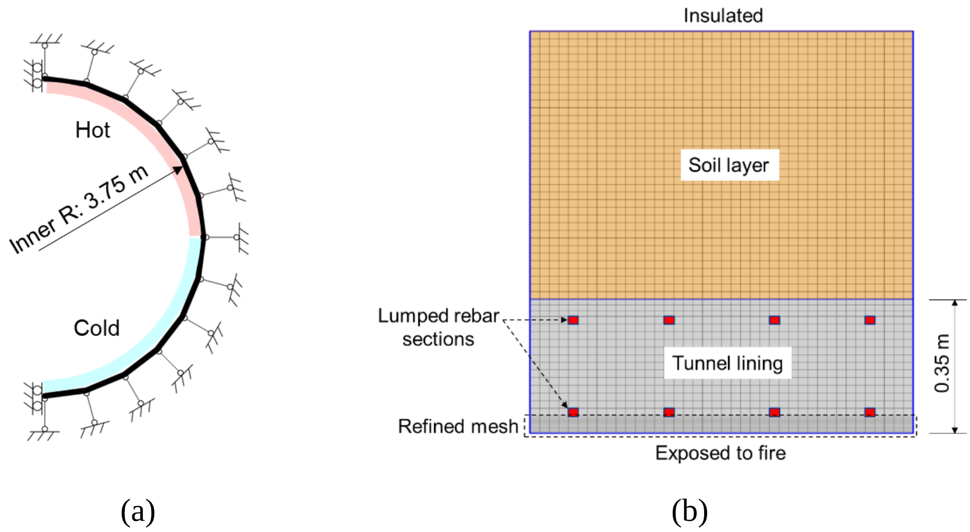

Figure 6. (a) The beam-spring model in SAFIR for the mechanical analysis under fire, (b) cross-section for heat transfer analysis

Figure 7 shows the vertical crown displacement for the tunnel section after 11 hours of exposure to the RWS fire curve. The simulation was stopped at 11 hours as the soil temperature reached 90°C as data on temperature-dependent properties of clay was not available beyond 90°C. The figure compares the vertical crown displacements of the tunnel using (1) the constant elastic modulus at ambient temperature, and (2) the temperature-dependent lower and upper bounds considering the excess pore pressures discussed in Section 4.1. The crown displacement increased from 85 to 115 mm at 11 hours when soil properties with the upper bound of the excess pore pressure were included. The result for the case with a lower bound of the excess pore pressure was less sensitive to soil properties.

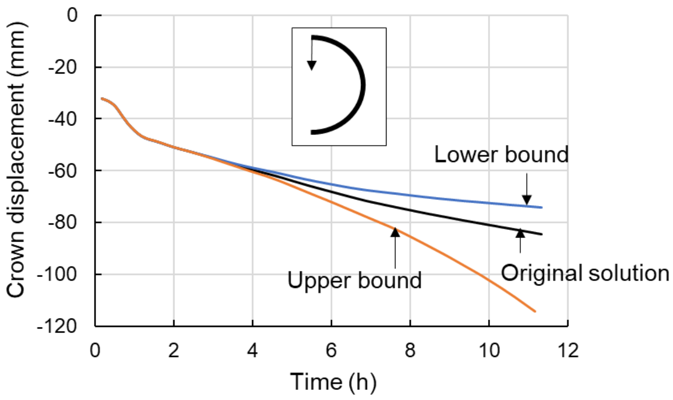

Figure 7. Vertical crown displacement for tunnel section considering soil properties at ambient temperature and temperature-dependent soil properties

5 CONCLUSIONS

Experimental data on the residual compressive strength of normal-strength concrete after exposure to high temperatures were collected and analysed. Most existing research has focused on siliceous concrete with limited data available for calcareous concrete. Analysis of the data showed that the duration of the retaining time at the maximum temperature during the experiments had a significant influence on the results. The specimen should be heated for enough time to ensure the core reaches the target temperature. A minimum retaining time of 2 hours is recommended to achieve uniform temperature in the specimen. Overall, there is a need to research a standard testing protocol defining heating rates, retaining times, and cooling rates. Probabilistic models with Weibull distributions were established to quantify uncertainties in the temperature-dependent residual compressive strength of siliceous and calcareous concrete. The median of the proposed probabilistic model for the siliceous concrete is close to the EC4 recommendation (i.e., EC2 retention factors with an additional 10% reduction in strength). However, the EC4 recommendation tends to overestimate the reduction factors for calcareous concrete when compared with the median of the proposed model.

Experimental data on the elastic modulus of rock samples, including limestone, mudstone, and gypsum were included. Data from the literature were collected to calculate the elastic modulus of clay considering the effect of temperature on excess pore water pressure. It was shown that excluding the change in soil properties could lead to underestimating the displacements of a tunnel lining during a fire. More research is needed to collect high-temperature data on soil properties (such as the elastic modulus and Poisson's ratio) under a wide range of temperatures. Overall, advanced modeling can be used for the performance-based design of tunnels under fire and to guide post-fire damage assessment.

ACKNOWLEDGMENT

This work was supported by the CAIT Region 2 UTC Consortium, and the Institute of Bridge Engineering (IBE) at the University at Buffalo. The authors gratefully acknowledge the Structural Engineering and Earthquake Simulation Laboratory (SEESL) at the University at Buffalo for their generous support. Any opinions, findings, conclusions, or recommendations expressed in this material are those of the authors and do not necessarily reflect the views of the CAIT Region 2 UTC Consortium.

REFERENCES

1. Elhami-Khorasani, N., P. Gardoni, and M. Garlock, *Probabilistic fire analysis: material models and evaluation of steel structural members.* Journal of Structural Engineering, 2015. 141(12): p. 04015050.
2. Qureshi, R., et al., *Probabilistic models for temperature-dependent strength of steel and concrete.* Journal of Structural Engineering, 2020. 146(6): p. 04020102.
3. Sullivan, P. and R. Sharshar, *The performance of concrete at elevated temperatures (as measured by the reduction in compressive strength).* Fire Technology, 1992. 28(3): p. 240-250.

4. Chan, Y., G. Peng, and M. Anson, *Residual strength and pore structure of high-strength concrete and normal strength concrete after exposure to high temperatures.* Cement and concrete composites, 1999. 21(1): p. 23-27.
5. Luo, X., W. Sun, and Y. Chan, *Residual compressive strength and microstructure of high performance concrete after exposure to high temperature.* Materials and Structures, 2000. 33(5): p. 294-298.
6. Zhang, B., et al., *Residual fracture properties of normal-and high-strength concrete subject to elevated temperatures.* Magazine of concrete research, 2000. 52(2): p. 123-136.
7. Barragán, B., G. Giaccio, and R. Zerbino, *Fracture and failure of thermally damaged concrete under tensile loading.* Materials and structures, 2001. 34(5): p. 312-319.
8. Phan, L.T., J.R. Lawson, and F.L. Davis, *Effects of elevated temperature exposure on heating characteristics, spalling, and residual properties of high performance concrete.* Materials and structures, 2001. 34(2): p. 83-91.
9. Poon, C.-S., et al., *Comparison of the strength and durability performance of normal-and high-strength pozzolanic concretes at elevated temperatures.* Cement and concrete research, 2001. 31(9): p. 1291-1300.
10. Tolentino, E., et al., *Effects of high temperature on the residual performance of Portland cement concretes.* Materials research, 2002. 5(3): p. 301-307.
11. Poon, C.-S., et al., *Performance of metakaolin concrete at elevated temperatures.* Cement and Concrete Composites, 2003. 25(1): p. 83-89.
12. Li, M., C. Qian, and W. Sun, *Mechanical properties of high-strength concrete after fire.* Cement and concrete research, 2004. 34(6): p. 1001-1005.
13. Abramowicz, M. and R. Kowalski, *The influence of short time water cooling on the mechanical properties of concrete heated up to high temperature.* Journal of civil engineering and management, 2005. 11(2): p. 85-90.
14. Sakr, K. and E. El-Hakim, *Effect of high temperature or fire on heavy weight concrete properties.* Cement and concrete research, 2005. 35(3): p. 590-596.
15. Anwar Hossain, K.M., *Macro-and microstructural investigations on strength and durability of pumice concrete at high temperature.* Journal of materials in civil engineering, 2006. 18(4): p. 527-536.
16. Chang, Y.-F., et al., *Residual stress–strain relationship for concrete after exposure to high temperatures.* Cement and concrete research, 2006. 36(10): p. 1999-2005.
17. Lau, A. and M. Anson, *Effect of high temperatures on high performance steel fibre reinforced concrete.* Cement and concrete research, 2006. 36(9): p. 1698-1707.
18. Zega, C. and A. Di Maio, *Recycled concrete exposed to high temperatures.* Magazine of Concrete Research, 2006. 58(10): p. 675-682.
19. Arioz, O., *Effects of elevated temperatures on properties of concrete.* Fire safety journal, 2007. 42(8): p. 516-522.
20. Lee, J., Y. Xi, and K. Willam, *Properties of concrete after high-temperature heating and cooling.* ACI Materials Journal, 2008. 105(4): p. 334.
21. Sancak, E., Y.D. Sari, and O. Simsek, *Effects of elevated temperature on compressive strength and weight loss of the light-weight concrete with silica fume and superplasticizer.* Cement and Concrete Composites, 2008. 30(8): p. 715-721.
22. Anagnostopoulos, N., K. Sideris, and A. Georgiadis, *Mechanical characteristics of self-compacting concretes with different filler materials, exposed to elevated temperatures.* Materials and structures, 2009. 42(10): p. 1393-1405.
23. Arioz, O., *Retained properties of concrete exposed to high temperatures: Size effect.* Fire and Materials: An International Journal, 2009. 33(5): p. 211-222.
24. Bingöl, A.F. and R. Gül, *Effect of elevated temperatures and cooling regimes on normal strength concrete.* Fire and Materials: An International Journal, 2009. 33(2): p. 79-88.
25. Chen, B., C. Li, and L. Chen, *Experimental study of mechanical properties of normal-strength concrete exposed to high temperatures at an early age.* Fire Safety Journal, 2009. 44(7): p. 997-1002.
26. Tang, W. and T. Lo, *Mechanical and fracture properties of normal-and high-strength concretes with fly ash after exposure to high temperatures.* Magazine of Concrete Research, 2009. 61(5): p. 323-330.
27. Demirel, B. and O. Keleştemur, *Effect of elevated temperature on the mechanical properties of concrete produced with finely ground pumice and silica fume.* Fire Safety Journal, 2010. 45(6-8): p. 385-391.
28. Ghandehari, M., A. Behnood, and M. Khanzadi, *Residual mechanical properties of high-strength concretes after exposure to elevated temperatures.* Journal of Materials in Civil Engineering, 2010. 22(1): p. 59-64.

29. Tanyildizi, H. and A. Çevik, *Modeling mechanical performance of lightweight concrete containing silica fume exposed to high temperature using genetic programming.* Construction and Building Materials, 2010. 24(12): p. 2612-2618.
30. Yuuml and E. ksel, *The effect of cure conditions and temperature changes on the compressive strength of normal and fly ash-added concretes.* International Journal of Physical Sciences, 2010. 5(17): p. 2598-2604.
31. Rama Seshu, D. and A. Pratusha, *Study on compressive strength behaviour of normal concrete and self-compacting concrete subjected to elevated temperatures.* Magazine of concrete research, 2013. 65(7): p. 415-421.
32. Sarhat, S.R. and E.G. Sherwood, *Residual mechanical response of recycled aggregate concrete after exposure to elevated temperatures.* Journal of Materials in Civil Engineering, 2013. 25(11): p. 1721-1730.
33. Xiao, J., Y. Fan, and M. Tawana, *Residual compressive and flexural strength of a recycled aggregate concrete following elevated temperatures.* Structural Concrete, 2013. 14(2): p. 168-175.
34. Ahmad, S., Y.S. Sallam, and M.A. Al-Hawas, *Effects of key factors on compressive and tensile strengths of concrete exposed to elevated temperatures.* Arabian journal for science and engineering, 2014. 39(6): p. 4507-4513.
35. Chen, G.M., et al., *Compressive behavior of steel fiber reinforced recycled aggregate concrete after exposure to elevated temperatures.* Construction and Building Materials, 2014. 71: p. 1-15.
36. Mathew, G. and M.M. Paul, *Influence of fly ash and GGBFS in laterized concrete exposed to elevated temperatures.* Journal of materials in Civil Engineering, 2014. 26(3): p. 411-419.
37. Al-Jabri, K.S., M.B. Waris, and A.H. Al-Saidy, *Effect of aggregate and water to cement ratio on concrete properties at elevated temperature.* Fire and Materials, 2016. 40(7): p. 913-925.
38. Bideci, Ö.S., *The effect of high temperature on lightweight concretes produced with colemanite coated pumice aggregates.* Construction and Building Materials, 2016. 113: p. 631-640.
39. Martins, D.J., J.R. Correia, and J. de Brito, *The effect of high temperature on the residual mechanical performance of concrete made with recycled ceramic coarse aggregates.* Fire and Materials, 2016. 40(2): p. 289-304.
40. Torić, N., et al., *Mechanical properties of lightweight concrete after fire exposure.* Structural concrete, 2016. 17(6): p. 1071-1081.
41. Yaqub, M. and C. Bailey, *Non-destructive evaluation of residual compressive strength of post-heated reinforced concrete columns.* Construction and building materials, 2016. 120: p. 482-493.
42. Tufail, M., et al., *Effect of elevated temperature on mechanical properties of limestone, quartzite and granite concrete.* International Journal of Concrete Structures and Materials, 2017. 11(1): p. 17-28.
43. Türkmen, İ., et al., *Properties of pumice aggregate concretes at elevated temperatures and comparison with ANN models.* Fire and Materials, 2017. 41(2): p. 142-153.
44. Bui, N.K., T. Satomi, and H. Takahashi, *Effect of mineral admixtures on properties of recycled aggregate concrete at high temperature.* Construction and Building Materials, 2018. 184: p. 361-373.
45. Rafi, M.M., T. Aziz, and S.H. Lodi, *Effects of elevated temperatures on residual properties of low-strength concrete.* Journal of Testing and Evaluation, 2018. 47(5): p. 3448-3469.
46. Varona, F.B., et al., *Influence of high temperature on the mechanical properties of hybrid fibre reinforced normal and high strength concrete.* Construction and Building Materials, 2018. 159: p. 73-82.
47. Xie, J., et al., *Coupling effects of silica fume and steel-fiber on the compressive behaviour of recycled aggregate concrete after exposure to elevated temperature.* Construction and Building Materials, 2018. 184: p. 752-764.
48. Yang, H., H. Zhao, and F. Liu, *Residual cube strength of coarse RCA concrete after exposure to elevated temperatures.* Fire and Materials, 2018. 42(4): p. 424-435.
49. Eidan, J., et al., *Residual mechanical properties of polypropylene fiber-reinforced concrete after heating.* Construction and Building Materials, 2019. 198: p. 195-206.
50. Ren, Q., et al., *Effects of fly ash on the mechanical and impact properties of recycled aggregate concrete after exposure to high temperature.* European Journal of Environmental and Civil Engineering, 2019: p. 1-17.
51. Salahuddin, H., et al., *Effects of elevated temperature on performance of recycled coarse aggregate concrete.* Construction and Building Materials, 2019. 202: p. 415-425.
52. Khan, A.-u.-R., et al., *Behaviour and residual strength prediction of recycled aggregates concrete exposed to elevated temperatures.* Arabian Journal for Science and Engineering, 2020. 45(10): p. 8241-8253.
53. Sachin, V. and N. Suresh, *Residual properties of normal-strength concrete subjected to fire and sustained elevated temperatures: A comparative study.* Journal of Structural Fire Engineering, 2020.

54. Yonggui, W., et al., *Mechanical properties and microstructure of basalt fibre and nano-silica reinforced recycled concrete after exposure to elevated temperatures.* Construction and Building Materials, 2020. 247: p. 118561.
55. Zhao, H., F. Liu, and H. Yang, *Residual compressive response of concrete produced with both coarse and fine recycled concrete aggregates after thermal exposure.* Construction and Building Materials, 2020. 244: p. 118397.
56. CEN-EN1992-1-1, *Eurocode 2: Design of concrete structures - Part 1-1: General rules and rules for buildings*. 2004, European standards.
57. CEN-EN1994-1-2, *Eurocode 4: Design of composite steel and concrete structures - Part 1-2: General rules - Structural fire design.* European standards, 2005.
58. Holický, M. and M. Sýkora. *Stochastic models in analysis of structural reliability*. in *Proceedings of the international symposium on stochastic models in reliability engineering, life sciences and operation management*, *Beer Sheva*, *Israel*. 2010.
59. ASTM, *ASTM D7012, Standard Test Methods for Compressive Strength and Elastic Moduli of Intact Rock Core Specimens under Varying States of Stress and Temperatures*. 2017, ASTM International West Conshohocken.
60. Mao, X.-B., et al., *Properties of failure mode and thermal damage for limestone at high temperature.* Mining Science and Technology (China), 2009. 19(3): p. 290-294.
61. Zhang, L., et al., *The mechanical properties of mudstone at high temperatures: an experimental study.* Rock mechanics and rock engineering, 2014. 47(4): p. 1479-1484.
62. Ghaaowd, I., et al., *Pore water pressure prediction for undrained heating of soils.* Environmental Geotechnics, 2015. 4(2): p. 70-78.
63. Cekerevac, C. and L. Laloui, *Experimental study of thermal effects on the mechanical behaviour of a clay.* International journal for numerical and analytical methods in geomechanics, 2004. 28(3): p. 209-228.
64. Society, B.T., *Tunnel lining design guide*. 2004: Thomas Telford.
65. Franssen, J.-M. and T. Gernay, *Modeling structures in fire with SAFIR®: Theoretical background and capabilities.* Journal of Structural Fire Engineering, 2017.
66. Hua, N., A. Tessari, and N.E. Khorasani, *The effect of geologic conditions on the fire behavior of tunnels considering soil-structure interaction.* Tunnelling and Underground Space Technology, 2022. 122: p. 104380.
67. CEN-EN1992-1-2, *Eurocode 2: Design of concrete structures - Part 1-2: General rules - Structural fire design*. 2004, European standards.
68. Savov, K., R. Lackner, and H.A. Mang, *Stability assessment of shallow tunnels subjected to fire load.* Fire safety journal, 2005. 40(8): p. 745-763.
69. CEN-EN1993-1-2, *Eurocode 3: Design of steel structures - Part 1-2: General rules - Structural fire design*. 2005, European standards.
70. McCartney, J.S., et al., *Emerging thermal issues in geotechnical engineering*, in *Geotechnical fundamentals for addressing new world challenges*. 2019, Springer. p. 275-317.

STUDY ON LOAD-CARRYING CAPACITY AND STRESS DISTRIBUTION OF REINFORCED CONCRETE SLABS AT ELEVATED TEMPERATURES

Takeo Hirashima[1], Akira Seino[2], Eishi Mano[3], Kei Kimura[4]

ABSTRACT

Reinforced concrete slabs are supported in two ways: when the degree of deflections increases during fires, membrane stress occurs within the cross-section of the slab, thereby improving the fire resistance owing to this membrane action. Herein, the deflection behaviour of reinforced concrete slabs under membrane action and the relationship between the reinforcement temperature and the load-carrying capacity were investigated using small-scale square slab tests. Finite element analysis using shell elements was also conducted, which predicted the deflection behaviour and strain distribution obtained from the tests. Furthermore, results obtained using previous calculation methods for load-carrying capacity agreed relatively well with the test results. The stress distribution and the deflection curve are discussed herein based on the finite element analysis results.

Keywords: Reinforced concrete slab; Fire resistance; Membrane action; Stress distribution; FEA

1 INTRODUCTION

Reinforced concrete (RC) slabs and composite slabs are supported in two ways: when the degree of deflections increases during fires, membrane stress occurs within the cross-section of the slab, thereby improving the fire resistance of the slab owing to this membrane action [1–5]. A prediction method for load-carrying capacity considering the membrane action of composite slabs during fires was proposed by Bailey et al. The method was based on the yield-line theory and the enhancement that depends on the amount of deflection [6]. Another study was proposed by Li et al. based on the force and moment equilibrium requirements for deflected slabs [7–8]. However, few studies have compared the calculation results of these methods with the fire resistance test results for floor slabs. Herein, load-bearing elevated-temperature tests of small-scale square RC slabs were conducted until the reinforcement failed. The test results were compared with the calculation results obtained using Bailey's and Li's methods. In addition, a finite element analysis using shell elements was conducted using SAFIR to determine the stress distribution of the reinforcements and the deflection curves of the slabs. This paper reports the associated results.

2 LOAD-BEARING ELEVATED-TEMPERATURE TESTS OF SQUARE RC SLABS

2.1 Test parameters and specimens

The advantage of small-scale tests is that the loading and heating can be continued until the specimen completely fails. Table 1 lists the parameters and specimen names for the ambient and elevated-temperature tests of small-scale square RC slabs. The objective of the loading test at the ambient temperature was to

[1] Professor, Graduate School of Engineering, Chiba University
e-mail: hirashima@faculty.chiba-u.jp, ORCID: https://orcid.org/0000-0003-1462-5370
[2] Researcher, Taisei Advanced Center of Technology, Taisei Corporation
e-mail: sinakr01@pub.taisei.co.jp, ORCID: https://orcid.org/0000-0002-3050-9874
[3] Graduate student, Graduate School of Science and Engineering, Chiba University
e-mail: 21wm3138@student.gs.chiba-u.jp
[4] Senior Researcher, Steel Structures Research Lab., Nippon Steel Corporation
e-mail: kimura.ze8.kei@jp.nipponsteel.com, ORCID: https://orcid.org/0000-0002-7808-3585
https://doi.org/10.6084/m9.figshare.22177820

obtain the stiffness, the maximum load of the slab, and the membrane stress distribution of the reinforcement. The main parameter of the elevated-temperature test was the loading level. A constant load was maintained during heating. Three target loads were determined by the load-carrying capacity of the slab based on the yield-line theory without the enhancement given by Equation (1) and the maximum load obtained from the test result under ambient conditions.

$$P_b = 8 \cdot \frac{L}{2a} \cdot 0.9d \cdot A_s \cdot \sigma_y \quad (1)$$

where P_b is the load-carrying capacity of the slab based on the yield-line theory (19.7 kN);

L is the both support spans (1.5 m);

d is the effective depth of reinforcement (17 mm);

a is the distance from support to the loading line (522 mm);

A_s is the cross-sectional area of reinforcement per unit width (176 mm^2/m);

σ_y is the yield stress of the reinforcement from the inspection certificate (635 N/mm^2)

When the target load was larger than the load P_b, load P_b was applied before heating. The load was gradually increased to reach the target load at 400°C, which was then maintained above 400°C. The target load (45.9 kN) of specimen 2-t30-H was the maximum load obtained from the ambient-temperature test result.

Figure 1 shows the two-way slab and bar arrangement of the specimens. The length and width were 1600 and 1600 mm, respectively. The slab thickness was 30 mm. The reinforcement was a welded wire mesh WFP in accordance with JIS G-3551. The mesh pitch was 75 mm, and the diameter was 4 mm. Mortar was used instead of concrete because the specimens were extremely thin. The compressive strength of the mortar was 32.0 MPa prior to the slab tests. The mechanical properties of the reinforcement and the mortar at elevated temperatures are discussed in the next section. Strain gauges were installed inside the slab for the ambient-temperature test, and thermocouples were installed inside the slab for the elevated-temperature tests, as shown in Figure 1.

2.2 Test setup and measurements

Figures 2 and 3 show the equipment used in the tests. The load was applied as a square-line load with a side length of 456 mm via a loading jig, which was a thick steel plate with four semi-circular bars attached to the bottom, at the centre of the specimen. Four floor perimeters were supported with a supporting frame, and only the downward displacement was restrained at the supports because the boundary conditions at the supports did not significantly affect the deflection behaviour of the slab under membrane action [5]. Vertical displacement was measured at the loading line on the loading jig.

The specimen was heated in an electric furnace (width: 1200 mm; depth: 1200 mm; height: 550 mm) under the supporting frame. To prevent a gap opening due to deflection of the specimen, a ceramic fibre blanket was set up between the specimen and the electric furnace wall. However, this electric furnace could not provide standard fire heating according to ISO 834. Therefore, the voltage of the electric furnace was maximised for heating. The temperature measurement points of the specimen were the points at which the reinforcement bars intersected and the upper and lower surfaces of the mortar slab. A Type K thermocouple covered with ceramic fibre was used for the temperature measurement.

Table 1. Outlines of specimen and test parameters

Slab Specimens	Name	Reinforcement temperature	Target load
Supported spans: 1.5 x 1.5 m Thickness: 30 mm Reinforcement: Welded wire mesh, 75 x 75 mm mesh, diameter 4 mm	2-t30-AT	Ambient temperature	Maximum load
	2-t30-L	Elevated temperature, Transient state	19.7 kN
	2-t30-M		32.8 kN
	2-t30-H		45.9 kN

Figure 4 shows the results of the load control for the load-bearing test at elevated temperatures. In these tests, based on the planned loading schedule, the target load was achieved when the reinforcement temperature reached 400°C, and the load was maintained thereafter. In the 2-t30-H test, the load was supported until the reinforcement temperature exceeded 400°C, despite the maximum load obtained from the ambient-temperature test. This was because the load-carrying capacity of the slab increased as the slab deflected.

2.3 Cracking on upper and lower surfaces of the slabs

Figure 5 (a) and (b) show cracking on the upper and lower surfaces of the specimen, respectively, after the elevated-temperature test. In all specimens, multiple large circular cracks occur outside the loading line on the upper surface, as shown in Figure 5 (a). Between or on the outside of these cracks, a compression ring is formed, where the compressive stresses are developed. On the lower surface, cracks occur along the loading and yield lines based on the yield-line theory, as shown in Figure 5 (b). These cracks that developed on the upper and lower surfaces of the slab are typical cracks when the slab was under membrane action. The test results on temperature and deflection are shown later, together with the analysis of results.

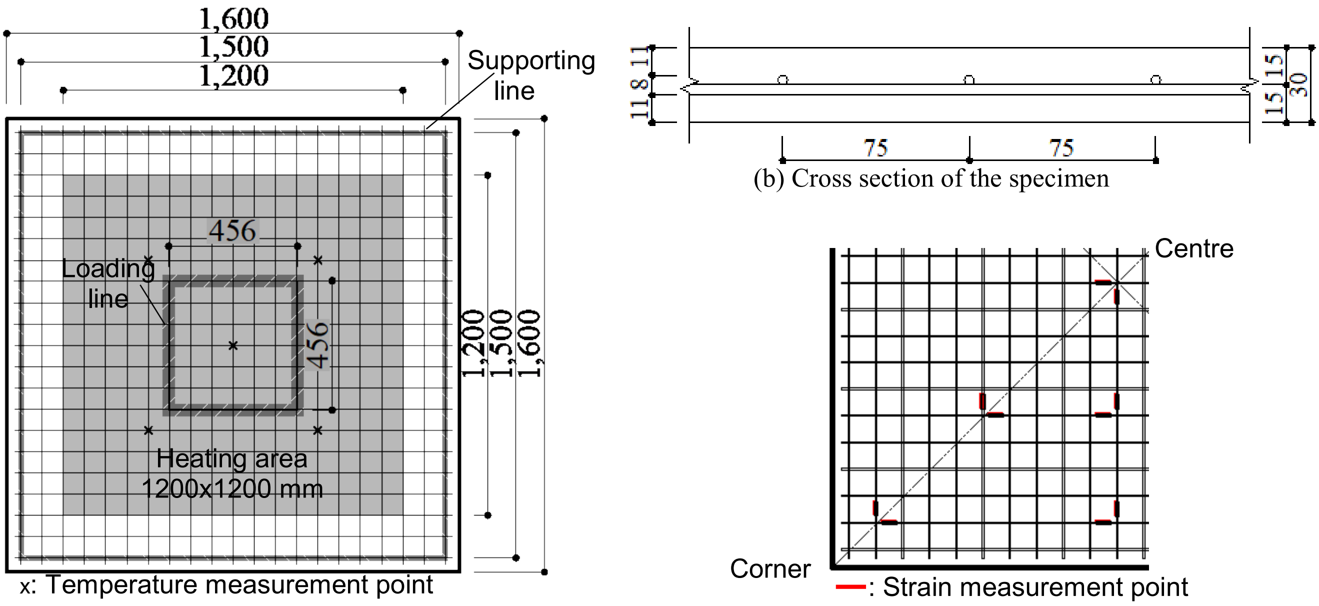

(a) Outline of the specimen
(b) Cross section of the specimen
(c) Arrangement of strain gages for ambient temperature test

Figure 1. Reinforced mortal slab specimen

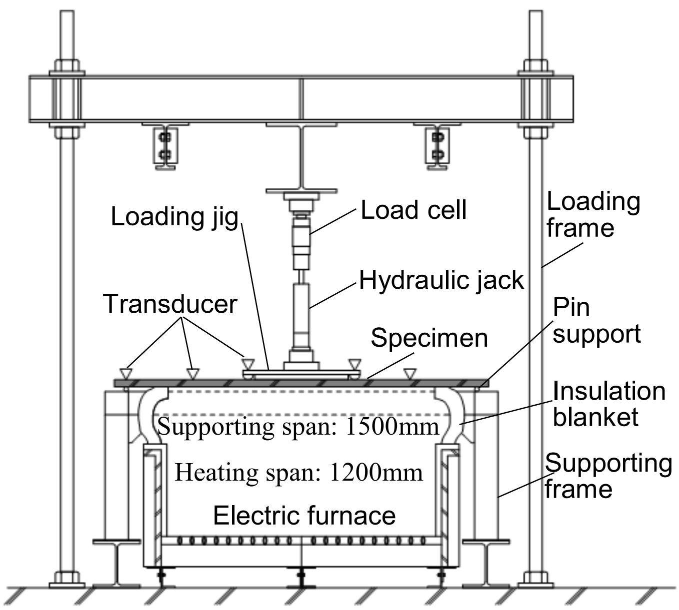

Figure 2. Test set up

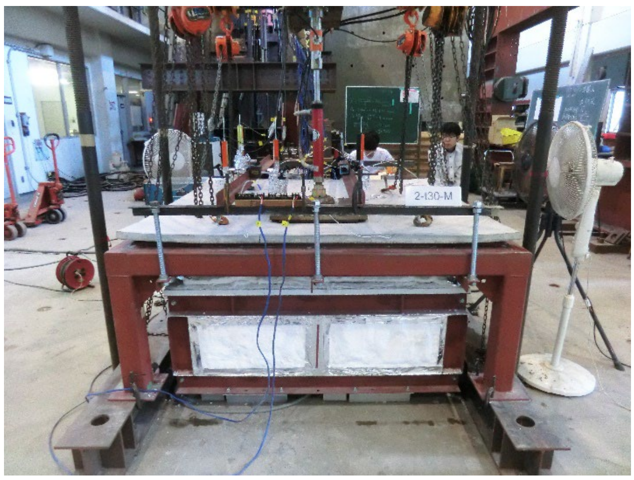
Figure 3. Test equipment

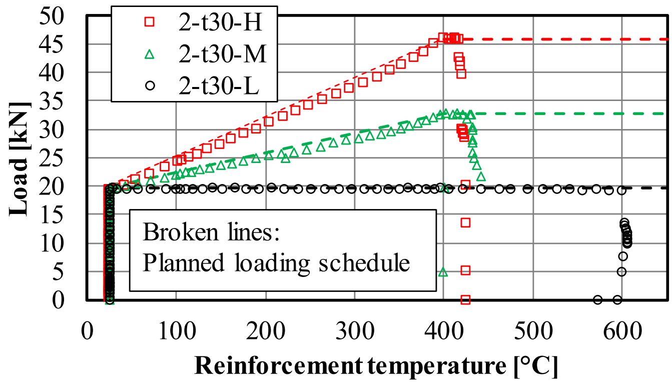

Figure 4. Result of the load control for load-bearing elevated-temperature tests

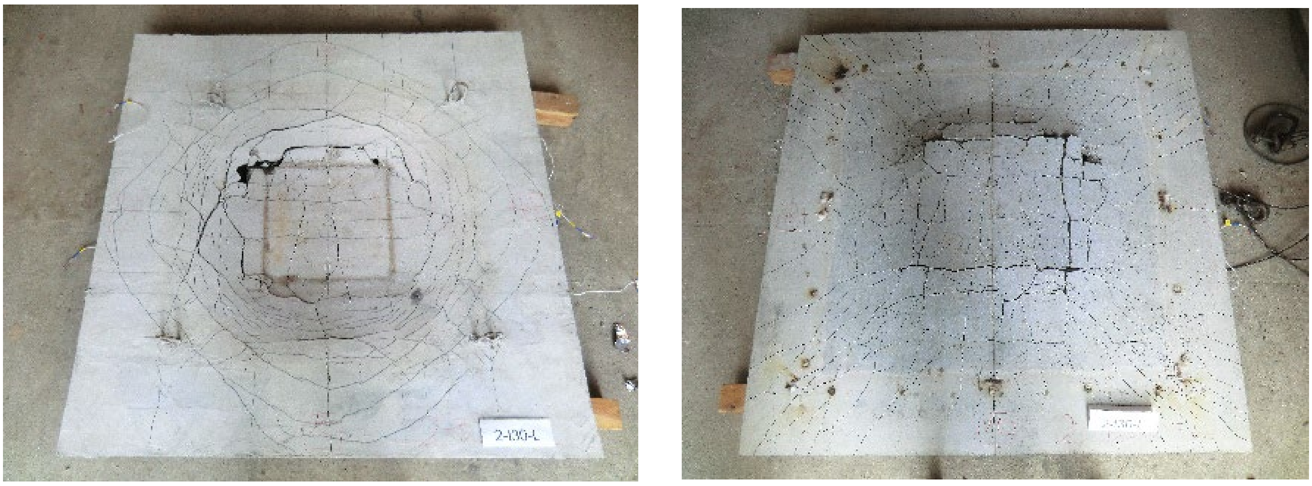
(a) Upper surface (b) Lower surface

Figure 5. Cracking on upper and lower surfaces of the slab after elevated-temperature test (2-t30-L)

3 FINITE ELEMENT ANALISIS

3.1 Objective of the numerical analysis and the analysis software

The objective of the numerical analysis was to confirm the validity of the analysis model and to analyse the membrane stress distribution generated in the slab. The finite element analysis (FEA) software “SAFIR” was used for numerical analysis. First, the temperature distribution in the cross section of the slab was calculated using a thermal analysis program, and the stress and deformation conditions of the slab were estimated using a structural analysis program. For more details regarding SAFIR, refer to reference [9].

3.2 Analysis models

The slab was modelled using the shell elements. Figure 6 shows the analysis model for the slab test, in which (a) shows the mesh and loading points; (b) shows the cross section model, and (c) shows the boundary conditions. The length of the slab specimen used in the analysis was the same as that of the support span. The size of the shell element was set to 74.6 to 76.0 mm according to the mesh pitch, as shown in Figure 6 (a). In the tests, lifting is observed at the corners; therefore, the boundary condition at the 1/4 portion of the corners is free in the analysis, as shown in Figure 6 (c). In the thermal analysis, the thickness direction is divided into six elements. In the structural analysis, the number of integration points in the thickness direction is set to seven, as shown in Figure 6 (b). When the heating range of the slab was the same as in the test and when the entire slab was heated, the deflection behaviours were approximately the same; therefore, the model adopted here was for entire surface heating.

The temperature dependence of the specific heat and the thermal conductivity of the mortar used for the analysis was determined using EN1992-1-2 [10]. The thermal conductivity at the ambient temperature was 1.5 W/mK. The density of the mortar was 2166 kg/m^3, and the water content was 4%. The emissivity was

0.6. The convective heat transfer coefficient was set to 20 W/m^2.K because an electric furnace was used in these tests. These values were either measured or determined through calibration by comparing with the test results.

3.3 Mechanical properties of the materials used for specimens and its analysis

Figure 7 shows the effective yield stress of the reinforcement obtained from the high-temperature coupon tests and analysis model. The effective yield stress is the value of the stress at 1% strain [11]. Reinforcing bars used in welded wire meshes (reinforcement) have a relatively high yield stress and yield ratio at the ambient temperature. The strength obtained in this coupon test was 754 N/mm^2, which was higher than the yield stress in the inspection certificate. This value was used in the ambient-temperature test. As shown in Figure 6, the strength of the reinforcement is similar to that at the ambient temperature before the temperature reached 200°C, but the strength rapidly decreases when the temperature exceeds 300°C; when the temperature reaches 700°C, the strength decreases to 1/10 of that at the ambient temperature. In contrast, the analysis software SAFIR uses Eurocode2 values for the strength reduction factor at high temperatures. Therefore, in the elevated-temperature tests, as shown in Figure 7, the strength at the ambient temperature changes such that the effective yield strength at 500°C is the same as the high-temperature coupon test result. The class N values of cold-worked reinforcing steel were used as the reduction factors. The elastic modulus of the reinforcement at high temperatures is also referred to as Eurocode2.

Figure 8 shows the compressive strength of the mortar obtained using the high-temperature compression tests and its analysis model. The compressive strength at the ambient temperature obtained using this high-temperature test equipment was 26.5 N/mm^2. The strength of the concrete at high temperatures used in the analysis was determined based on this ambient temperature value and the reduction factor of Eurocode2. The difference between the compressive strengths of the concrete obtained from the high-temperature compression tests and the reduction factor from Eurocode2 was relatively low. In the slab tests that were the focus of this study, the load-carrying capacity was determined not through the crushing of the concrete but through the yielding or failure of the reinforcement. Therefore, the analysis model did not consider the decrease in compressive strength at 100°C owing to moisture evaporation. The tensile strength of the concrete was 1/10 of its compressive strength. A model that considers transient strain was used to determine strain at the compressive strength.

3.4 Results for temperatures

Figure 9 (a) and (b) show the temperatures obtained from the load-bearing test of the slab specimen at elevated temperatures and its thermal analysis. The time in these figures includes the time required to apply the force prior to heating. The gas temperature of the electric furnace was determined through thermal analysis. In the analysis, the temperature was increased at the rate of temperature increase at the end of heating in the tests. As shown in both figures, the reinforcement temperature obtained through the analysis agreed approximately with the test results. As discussed below under of structural behaviour, the relationship between the reinforcement temperature and the deflection of the slab was used. Therefore, the error between the test and analysis values of the temperature-time relationship did not affect the deflection behaviours. The temperature of the upper surface of the slab obtained from the 2-t30-L test was higher than the actual value because of the failure of the thermocouple after 120 min. The temperature of the lower surface of the slab was not measured in these tests. Therefore, it was not possible to compare the test and analysis values for the temperature difference between the upper and lower surfaces of the slab; a slight error occurred in the thermal deflection owing to the temperature gradient in the thickness direction.

3.5 Results for the deflection behaviour

Figure 10 shows the load-deflection relationship of the slab at the ambient temperature. The load is a concentrated vertical force applied to the loading jig (see Figure 2) installed at the centre of the specimen. The deflection is the average value measured by the transducers installed on the loading jig, and is the vertical displacement at the loading line (see Figure 1). In the ambient-temperature test, the load stagnated owing to the cracking of concrete on the lower surface at approximately 4 kN, and then increased as the deflection increased. When the load reached 45.9 kN, the reinforcement failed, and the load decreased. The maximum load was approximately 2.3 times of the load-carrying capacity based on the yield-line theory

(P_b, see Equation (1)). The deflection at the maximum load was approximately 1/20 of the support span. The result of the FEA agreed well with the test result, although the deflection under the same load was slightly larger.

Figures 11 (a)-(c) show the deflection behaviour based on the load-bearing elevated-temperature tests. In these tests, the same load of 19.7 kN was applied prior to heating; however, slight differences were observed in the deflection results. In the 2-t30-H and 2-t30-M tests, the load increases until the reinforcement temperature reaches 400°C, as shown in Figure 4. In the 2-t30-H test, in which the target load (45.9 kN) was the maximum load obtained from the ambient-temperature test, the slab failed when the reinforcement temperature reached 416°C. From the results of the high-temperature coupon test of the reinforcement, the effective yield strength of the reinforcement at 400°C is approximately 78% of that at ambient temperature, as shown in Figure 7. The 45.9 kN load was supported in this test because of the enhancement effect caused by the thermal deflection of the slab. The FEA results of the 2-t30-H test agreed well with the test results for deflection increase up to approximately 300°C; however, the analysis stopped at 323°C. Although the load in the 2-t30-M test was considerably lower than that in the 2-t30-H test, the reinforcement temperature of 432°C at the time of failure for the 2-t30-M test was relatively low. In addition, the FEA result for the deflection in the 2-t30-M test agreed with the test result until the failure. In the 2-t30-L test, a constant load corresponding to the load-carrying capacity based on the yield-line theory was supported until the reinforcement temperature reached 599°C. Based on the FEA results, the calculation stopped when the reinforcement temperature was 580°C, and the deflection behaviour agreed with the test result. The FEA was able to accurately predict the deflection behaviour of the slabs at ambient and elevated temperatures.

3.6 Results of the strain distribution on the reinforcement for the ambient-temperature test.

Figures 12 (a)-(f) show the comparison of the values obtained from the strain gauges attached to the reinforcement in the ambient-temperature test and its analysis results. For the strain in the radial direction at the centre of the slab, the FEA value is approximately the intermediate value between the two test values,

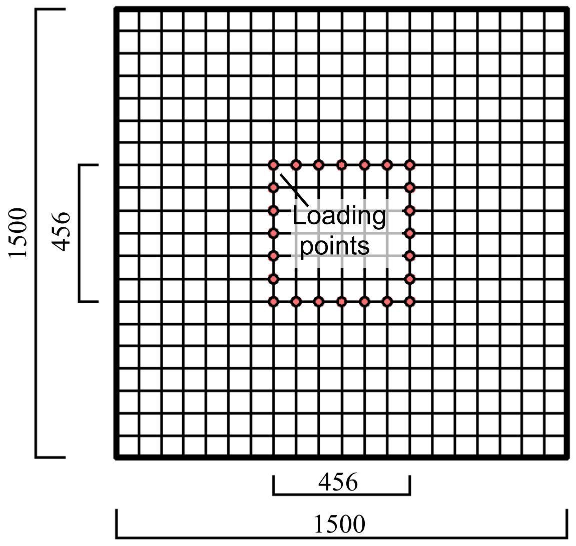

(a) Mesh and loading points

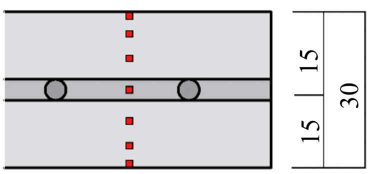

(b) Cross-section model

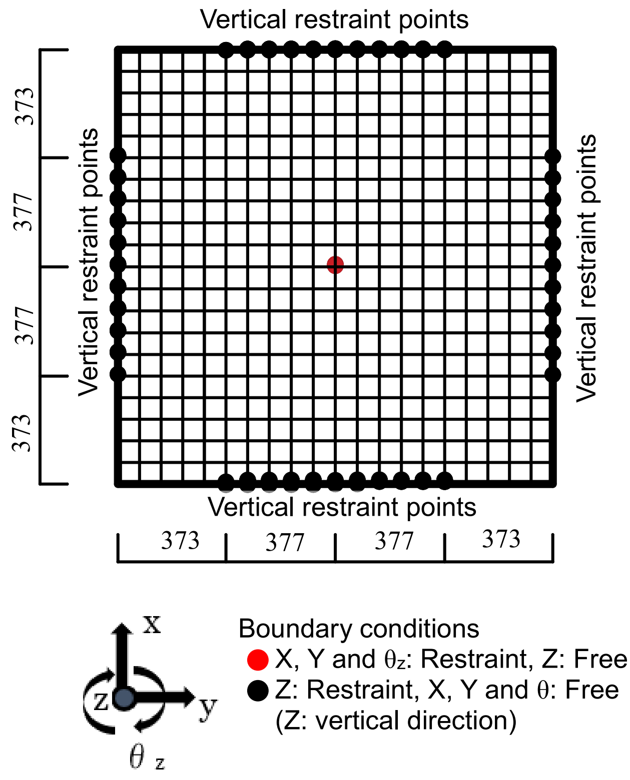

(c) Boundary conditions of displacement

Figure 6. Analysis model of the test specimen

as shown in Figure 12 (a). Regarding the strain of the welded wire mesh, the strain of the lower-side reinforcement was larger than that of the upper-side reinforcement, and the strain exceeded 0.6% at the time of failure. The strain at the middle of the centre and the support (1/4 part) is slightly larger in the test result for the radial direction and slightly larger in the FEA result for the tangential direction, as shown in Figure 12 (b). The tangential strains at the middle of the centre and the corner (diagonal 1/4 part) roughly correspond between the test and FEA values, as shown in Figure 12 (c). Tangential strains near the support are related to compression based on the test and FEA results; however, the compressive strains are relatively low, as shown in Figure 12 (d). For the strain near the corner, the test values were larger at the initial stage, and the test and FEA values were approximately similar at the time of failure. As mentioned above, this FEA was able to predict the strain distribution of the welded wire mesh in the slab.

In this section, it indicates that FEA is able to grasp the deflection behaviour and strain distribution of the two-way RC slabs. The next section discusses the load-carrying capacity models using the FEA results of the deflection curve and membrane stress distribution.

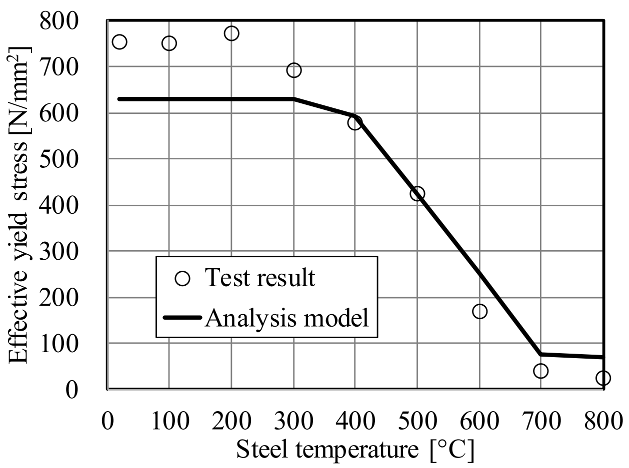

Figure 7. Effective yield stress of the reinforcement

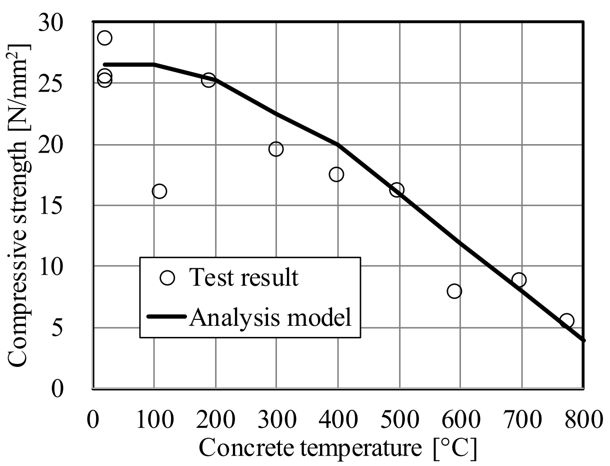

Figure 8. Compressive strength of the concrete

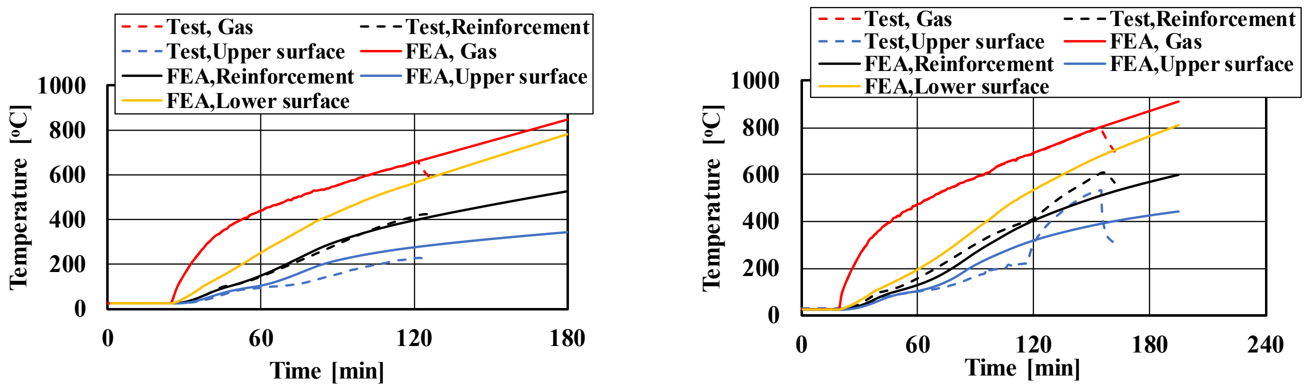

(a) 2-t30-H (b) 2-t30-L

Figure 9. Result of the temperatures

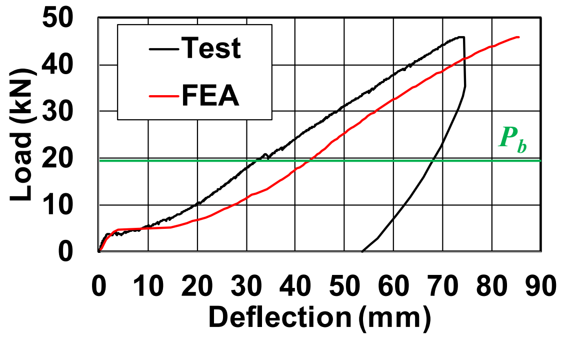

Figure 10. Results of the load-deflection relationship for the ambient temperature tests (2-t30-AT)

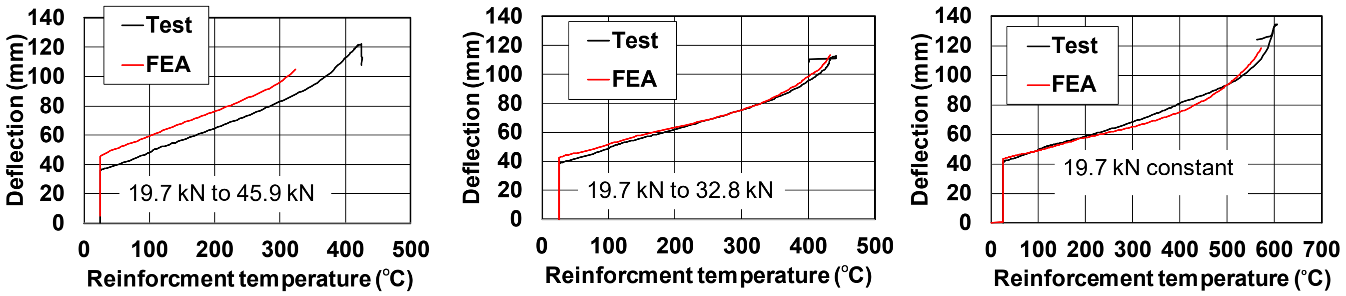

(a) 2-t30-H (b) 2-t30-M (c) 2-t30-L

Figure 11. Results of the deflection behaviour for the load-bearing elevated temperature tests

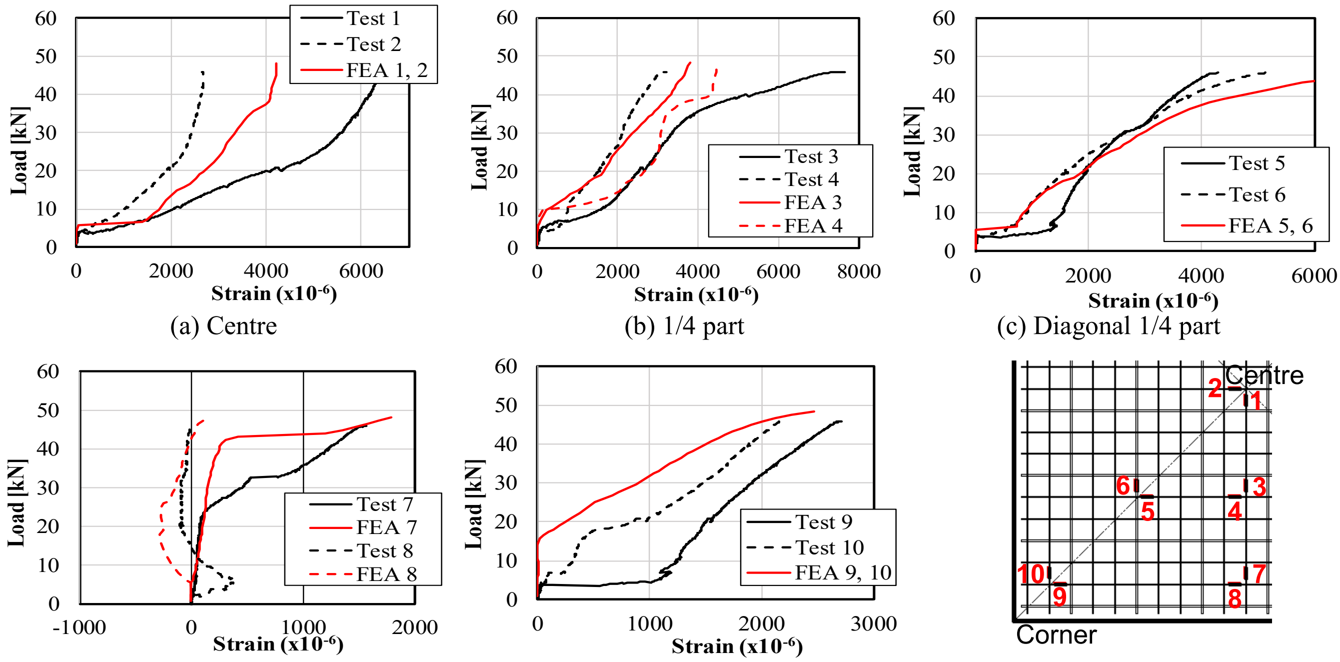

(a) Centre (b) 1/4 part (c) Diagonal 1/4 part

(d) Side (e) Corner (f) Strain measurement points

Figure 12. Results of the strain on reinforcement for the ambient temperature tests

4 DISCUSSION ON LOAD-CARRYING CAPACITY AND STRESS DISTRIBUTION

4.1 Comparison with the load-carrying capacity model by Bailey

In this section, the test results of the slabs described earlier are compared with the results obtained using the evaluation method proposed by Bailey and Moore for load-carrying capacity [6]. Hereafter, the evaluation method refers to the Bailey's method. This method uses a simple energy approach to calculate the load-carrying capacity of a composite flooring system. The energy of the lightly reinforced composite slab was determined based on the modified yield-line approach to account for the enhancement due to in-plane forces.

The load-carrying capacity considering the membrane action of the slab is described in Equation (2). This equation multiplies the value of the enhancement due to the in-plane force by the load-carrying capacity based on the yield-line theory. The enhancement value is given by Equation (3). During the test, a concentrated load was applied to the specimen. The load-carrying capacity from the test results was replaced with that of the uniformly distributed load using Equation (4).

$$q_u = \frac{24}{L^2} \cdot 0.9 d \cdot A_s \cdot \sigma_y(T) \cdot e \qquad (2)$$

$$e = 1 + \frac{2b}{3(3+g_0)} \cdot \frac{v}{d} - \frac{b^2(1-g_0)}{3(3+g_0)} \tag{3}$$

$$q_{test} = \frac{6a}{L^3} \times P_{b,test} \tag{4}$$

where q_u is the load-carrying capacity considering the membrane action of the slab [N/m^2]

L is the both support spans (1.5 m);

d is the effective depth of reinforcement (0.015 m);

a is the distance from support to the loading line (0.522 m);

A_s is the cross-sectional area of reinforcement per unit width (176 mm^2/m);

$\sigma_y(T)$ is the effective yield stress of the reinforcement at the reinforcement temperature T [N/mm^2];

e is the enhancement due to in-plane forces;

b is the membrane force parameter for a square slab (1.5);

g_0 is the parameter fixing depth of compressive stress-blocks when membrane forces are zero (0.6);

v is the deflection at the centre of the slab obtained from the test results [m];

q_{test} is the load-carrying capacity for uniformly distributed load from the test result [N/m^2];

$P_{b,test}$ is the maximum load or applied load for the elevated temperature tests [N/m^2]

Herein, the effective yield stress of the reinforcement is obtained from the high-temperature coupon tests, as shown in Figure 7. As for the deflection, which is the main factor in the enhancement, the deflection of the test results under the limit state condition is provided. Table 2 presents a comparison between the test and calculation results for the load-carrying capacity.

The calculation results obtained using the Bailey's method agreed with the results of the 2-t30-AT test at ambient temperature and the 2-t30-H test at elevated temperature. For the 2-t30-M test, the ratio of the calculated value to the test value was considered to be high because the load-carrying capacity in the test was relatively low. For the 2-t30-L test, the ratio of the calculated value to the test value was low. As shown in Figure 7, the high-temperature strength of the reinforcement used in this specimen decreases significantly from 500 to 600°C. When the reinforcement temperature distribution of 2-t30-L was slightly lower than the temperature at the measurement point, the calculated value was underestimated. In summary, the ratios q_u/q_{test} were within 0.80 to 1.28; therefore, these calculation results using the Bailey's method approximately agreed with the test results.

Table 2. Calculation results using the Bailey's method for the load-carrying capacity of the slab specimens

Specimen	T [°C]	$\sigma_y(T)$ [N/mm^2]	v [mm]	e	q_u [kN/m^2]	q_{test} [kN/m^2]	q_u/q_{test}
2-t30-AT	20	754	74	2.29	43.7	42.6	1.03
2-t30-H	416	551	120	3.14	43.8	42.6	1.03
2-t30-M	432	528	108	2.92	39.0	30.4	1.28
2-t30-L	599	170	133	3.38	14.6	18.3	0.80

4.2 Comparison with the load-carrying capacity model by Li

In this section, the test and analysis results of the slabs described above were compared with the results from the evaluation method proposed by Li et al [7–8] for load-carrying capacity. Hereafter, the evaluation method refers to the Li's method. Li et al. proposed that a slab in the limit state with membrane action is divided into four rigid plates and a reinforcement net, similar to an elliptic paraboloid [7]. The membrane action was considered by solving the equilibria with the deflected slab in the limit state. Li's method can also evaluate the load-carrying capacity based on the strength of a concrete compression ring [8].

Herein, a square slab was used instead of a rectangular slab. Therefore, the elliptical part was replaced with a circular part in the equations described in the Li's method. Figure 13 shows the division and coordinates of the square slab in the limit state. The load-carrying capacity of the slab was calculated using Equations

(5) – (9). These equations can be solved explicitly by setting the value of K. Therefore, the value of K was gradually increased, and K was determined when the values of q_{t1} and q_{t2} were similar based on Equations (5) and (6). The vertical component forces T_{xv} and T_{yv} depend on the effective yield stress of the reinforcement at a high temperature $\sigma_y (T)$, as shown in Table 2. In this calculation, the test value was assigned to the central deflection w_{total} of the slab in the limit state. The value of w_{total} is the same as that of v, as shown in Table 2. Therefore, the value of w in Equation (7) does not depend on the strains ε_{uk} and $\alpha_s \Delta T$ of the reinforcement. The load-carrying capacity based on the strength of the concrete compression ring was obtained using Equation (9). The ratio K_c in its limit state was obtained from Equation (8). In this test, because the compression ring was also involved for the non-heated area, the design strength at the ambient temperature was used for the concrete strength in Equation (8). The table 3 presents a comparison of the test and calculation results for the load-carrying capacity.

$$q_{t1} = \frac{4\int_0^{KL} T_{yv} dx + 4\int_0^{KL} T_{xv} dy}{\pi (KL)^2} = q_t \tag{5}$$

$$q_{t2} = \frac{q_{12}A_{12} + q_{34}A_{34}}{A_{12} + A_{34}} = q_t \tag{6}$$

$$w_{total} = w + d_r = KL\sqrt{\frac{3}{8}(\varepsilon_{uk} + \alpha_s \Delta T)} + \left(\frac{1}{2}L - KL\right)\cdot \theta_x \tag{7}$$

$$\int_0^{K_c L} T_{xh(y)} dy = \left(\frac{1}{2} - K_c\right) L \cdot h_c \cdot f_{cT} \tag{8}$$

$$q_c = \frac{2q_{12,c} + 2q_{34,c} + 4\int_0^{K_c L} T_{yv} dx + 4\int_0^{K_c L} T_{xv} dy}{L^2} \tag{9}$$

where q_t is the load-carrying capacity of the slab due to the effective yield stress of the reinforcement;
q_{t1} is the load-carrying capacity of the circular part contributed from the force of reinforcement;
q_{t2} is the load-carrying capacity of 4 rigid plates equal to q_{t1};
K is the ratio of the circular part diameter to the support span L for the square slab;
T_{xv} and T_{yv} are the vertical component force for the reinforcement in x and y directions, respectively;
q_{12} and q_{34} are the load-carrying capacity of the rigid plates determined by the equilibriums about the axis at the supports;
A_{12} and A_{34} are the area of the rigid plate 1 or 2 and plate 3 or 4, respectively;
d_r is the deflection caused by the rotation of rigid plates;
w is the parabolic deflection of the circular part;
q_c is the load-carrying capacity based on the strength of the concrete compression ring;
K_c is the ratio of the circular part diameter to the support span L determined by Equation (8);
f_{cT} is the ultimate compressive strength of the concrete (21 N/mm^2)

As listed in Table 3, the ratios min (q_t , q_c)/q_{test} q_u/q_{test} are within 1.04 to 1.48; therefore, the calculation results using the Li's method are slightly higher than the test results. In addition, the reinforcements failed in the limit state of the tests; however, the load-carrying capacities were determined based on the strength of the concrete compression ring, except for the 2-t30-L test result. In the following paragraph, the higher load-carrying capacities are discussed using the FEA results.

Figure 14 shows the FEA result for the transition of the distribution of the principal membrane force for the 2-t30-L test. In Figure 14, the red lines represent the tensile forces, and the blue lines represent the compressive forces. As the reinforcement temperature increases, the principal membrane force decreases, whereas the area where the tensile forces are dominant increases. A compression ring is also observed at the outer periphery of the slab. From the results of the principal membrane forces, it is considered that the

FEA results captured the membrane stress distribution in the limit state of the slab at elevated temperatures. In addition, in this test and the FEA, the concentrated load was applied as a square line; therefore, the boundary line between the tension and compression was not circular. Figures 15 (a)-(c) show the tensile stress distribution of the reinforcement in the radical direction in the limit state obtained through FEA. The figure also shows the value of KL, which is the radius of the circular area of a parabolic deflection, obtained using the Li's method. In the calculation of the load-carrying capacity in the limit state using the Li's method, the tensile stress of the reinforcement at the boundary of the circular area was provided by the effective yield stress. However, the yielding areas of the FEA results were smaller than those calculated using the Li's method. This could be one of the reasons for the higher calculated values than the test values. In addition, as shown in Figures 16 (a) and (b), the results from FEA and Li's deflection models are in good agreement. Furthermore, the change in the slopes between the inside and outside of the boundary of the circular area was not significant, indicating that the change in the vertical component force of the reinforcement was insignificant. Therefore, further discussion is required to explain the higher calculated values.

Table 3. Calculation results using the Li's method for the load-carrying capacity of the slab specimens

Specimen	K	d_r [mm]	w [mm]	q_t [kN/m^2]	K_c	q_c [kN/m^2]	q_{test} [kN/m^2]	min (q_t , q_c)/q_{test}
2-t30-AT	0.41	22	52	67.3	0.38	44.3	42.6	1.04
2-t30-H	0.42	32	88	78.6	0.39	46.5	42.6	1.09
2-t30-M	0.42	30	78	70.0	0.39	43.6	30.4	1.43
2-t30-L	0.42	35	97	27.0	0.45	62.7	18.3	1.48

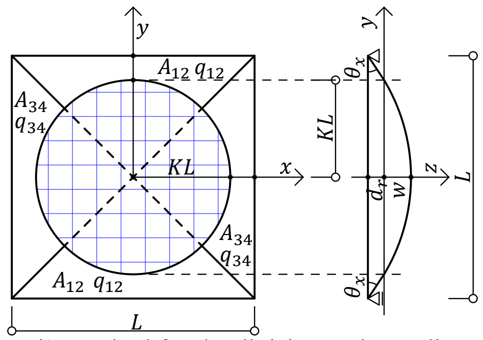

Figure 13. Calculation model by Li's method for the division and coordinates of the square slab at the limit state

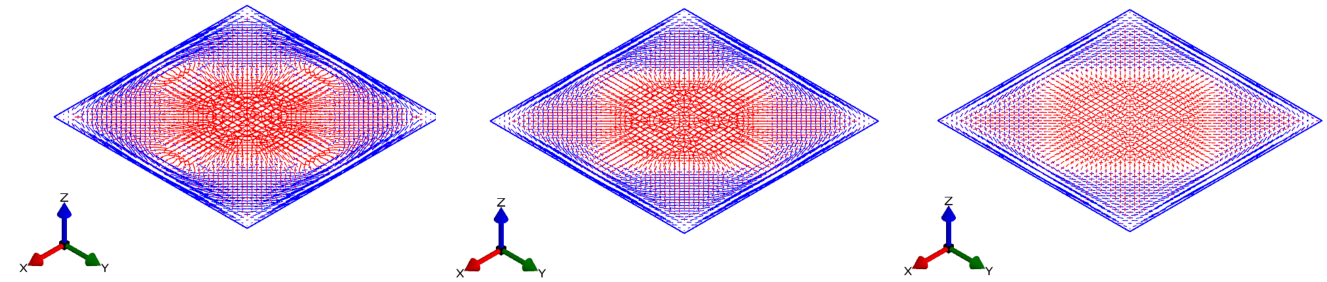

(a) Temp. 26 °C, Def. 42.0 mm (b) Temp. 400 °C, Def. 75.4 mm (c) Temp. 574 °C, Def. 120.0 mm (limit state)

Figure 14. Transition of the distribution of the principal membrane force

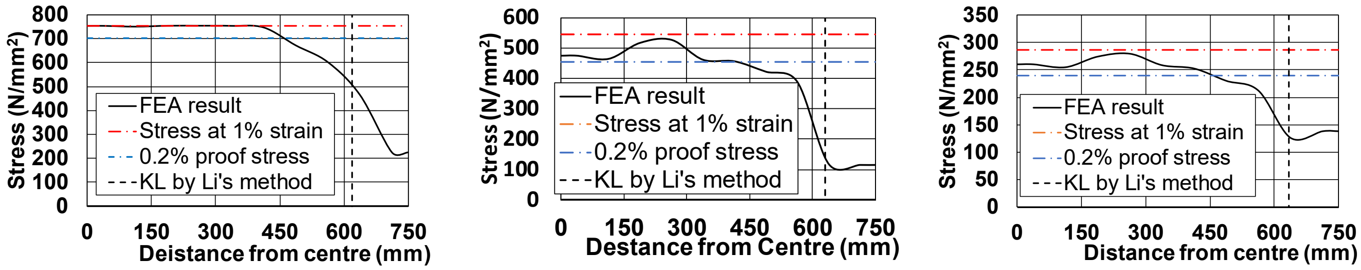

(a) 2-t30-AT (b) 2-t30-M (c) 2-t30-L

Figure 15. Results of the stress distribution of reinforcement for the radical direction in the limit state obtained from FEA

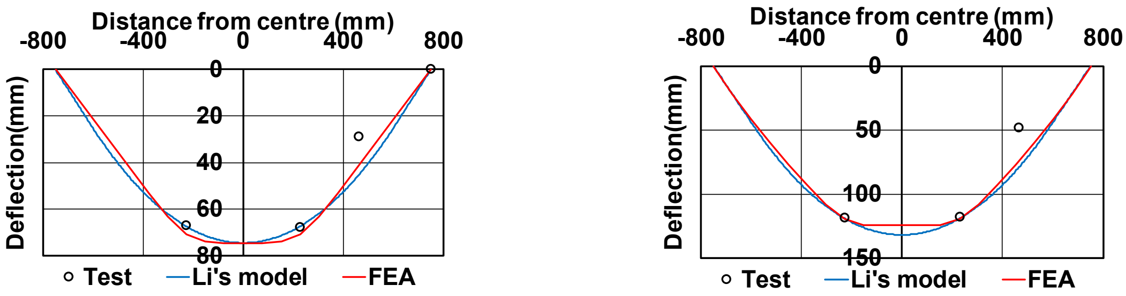

(a) 2-t30-AT (b) 2-t30-L

Figure 16. Comparison of the deflection curves of the slabs obtained from FEA and Li's model

5 CONCLUSIONS

Herein, the deflection behaviour of RC slabs under membrane action and the relationship between the reinforcement temperature and the load-carrying capacity were investigated through small-scale square slab tests. It was found that the FEA using shell elements could predict the deflection behaviour and strain distribution obtained from the tests. Furthermore, it was shown that calculated results using the Bailey's method and the Li's methods for the load-carrying capacity of the slabs approximately agreed with the test results. The stress distribution and the deflection curve were also discussed herein based on the FEA results. The yielding areas of the FEA results were smaller than those calculated using the Li's method, whereas the both results for deflection curves were in good agreement.

Recently, improved calculation methods [12–14] for the load-carrying capacity considering the membrane action of RC slabs have been proposed. It is necessary to compare with the results using these methods in the future.

REFERENCES

1. British Steel plc, Swinden Technology Centre, A European Joint Research Programme, "The behaviour of multi-storey steel framed buildings in fire", 1999
2. L. C. S. Lim, "Membrane action in fire exposed concrete floor systems", Ph D thesis, University of Canterbury, 2003
3. B. Zhao, M. Roosefid, and O. Vassart, "Full scale test of a steel and concrete composite floor exposed to ISO fire", Proceedings of the Fifth International Conference on Structures in Fire, pp. 539-550, 2008
4. N. Zhang, G. Li, G. Lou, S. Jiang, and K. Hao, "Experimental study on full scale composite floor slabs under fire condition", Proceedings of Application of Structural Fire Engineering, Prague, Czech Republic, 2009
5. T. Hirashima, K. Kinoshita, T. Yoshida, J. Suzuki, F. Ozaki, K. Kimura, and Y. Murakami, "Membrane action of floor slabs in fire Part 1: Load-bearing fire tests of a composite flooring system composed of RC slabs and an unprotected steel beam", J. Struct. Constr. Eng., AIJ, Vol. 86, No. 785, pp. 1106-1116, 2021, doi.org/10.3130/aijs.86.1106
6. C. G. Bailey, and D. B. Moore, "The structural behaviour of steel frames with composite floor slabs subject to fire: Part 1: Theory", The Structural Engineer 78, No.11, pp. 19-27, 2000
7. G. Li, S. Guo, and H. Zhou, "Modeling of membrane action in floor slabs subjected to fire", Engineering Structures 29, pp. 880-887, 2007, doi.org/10.1016/j.engstruct.2006.06.025
8. N. Zhang, N. Zhang, and G. Li, "A new method to analyse the membrane action of composite floor slabs in fire condition", Fire Technology, 46, pp. 3-18, 2010, DOI: 10.1007/s10694-009-0086-8
9. T. Gerna, and J. M. Franssen, "Modeling structures in fire with SAFIR®: Theoretical background and capabilities", Journal of Structural Fire Engineering, Vol. 8, issue 3, pp. 300-323, 2017
10. EN 1992-1-2, Eurocode2: Design of concrete structures –Part 1-2 General rules– Structural fire design, 2004
11. Architectural Institute of Japan, Recommendation for fire resistant design of steel structures, 1999
12. I. Burgess, "Yield-line plasticity and tensile membrane action in lightly-reinforced rectangular concrete slabs", Engineering Structures 138, pp. 195-214, 2017, doi.org/10.1016/j.engstruct.2017.01.072
13. Y. Wang, G. Wang, Z. Huang, Y. Huang, Y. Jiang, Y. Zhang, C. Zhang, Y. Bu, W. Song, "An analytical method for determining the tensile membrane action of RC slab panels, Engineering Structures 245, 2021, doi.org/10.1016/j.engstruct.2021.112895
14. H. Qi, Y. Du, J. Jiang, G. Li, "Improved tensile membrane action model of composite slabs at elevated temperatures", Structures 36, pp. 13-31, 2022, doi.org/10.1016/j.istruc.2021.11.042

SiF 2022– The 12th International Conference on Structures in Fire
The Hong Kong Polytechnic University, Nov 30 - Dec 2, 2022

FULL-SCALE TEST AND NUMERICAL ANALYSIS OF COMPOSITE FLOORING SYSTEM EXPOSED TO A LONG-DURATION ISO FIRE

Yusuke Shintani [1], Toshihiko Nishimura [2], Kei Kimura [3]

ABSTRACT

Full-scale fire tests and numerical analyses of the composite flooring system were conducted to understand (a) the effects of supporting condition of the concrete slab on the membrane action and (b) ultimate states of the concrete slab with large displacement where the specimens lost integrity. Two reinforced concrete slabs and three composite slabs were exposed to 3-8 h ISO834 heating under the vertical load bearing condition. The experimental results of RC slabs showed that the displacement of the supporting beams of the slabs affected little the appearance of the membrane action of the concrete slab if the beams could support the slabs. The large relative displacement, which was 1/11 to 1/10 of the short span of the specimen, caused penetration cracks parallel to the shot-side direction of the specimen, which could lead to the loss of integrity. Finite element analysis also showed that the strain at unheated concrete surface in the long-side direction of the specimen caused by the tensile stress in reinforcement was larger than that in the short-side direction, which was consistent with the appearance of the concrete crack in the tests.

Keywords: Full scale fire test; Composite flooring system; Concrete slab; Membrane action

1 INTRODUCTION

Many studies on the membrane action of reinforced concrete slabs in fire have been conducted since the real-scale experiment in Cardington [1]. However, only few experiments considering the deformation of the steel frames that support the slab have been conducted [1,2]. The high load-bearing capacity of slabs owing to membrane action during fires makes observing the ultimate state of slabs in fire tests difficult. Large displacements of concrete slabs cause penetration cracking and loss of integrity. However, this has only been observed in a few studies [3, 4]. Therefore, a real-scale fire test of a composite flooring system composed of a reinforced concrete slab and steel frames exposed to a long-duration ISO834 fire was conducted. To understand the effects on the integrity of the specimen, finite element analysis (FEM) was also conducted, and the distribution of the strain and the stress at the unheated surface of the specimen were studied.

[1] Chief Researcher, Research & Development Institute, Takenaka Corporation,
e-mail: shintani.yuusuke@takenaka.co.jp, ORCID: https://orcid.org/0000-0002-5488-2761
[2] Senior chief Researcher, Research & Development Institute, Takenaka Corporation,
e-mail:nishimura.toshihiko@takenaka.co.jp, ORCID: https://orcid.org/0000-xxxx-xxxx-xxxx
[3] Senior Researcher, Steel Structures Research Lab., Nippon Steel Corporation
e-mail: kimura.ze8.kei@jp.nipponsteel.com, ORCID: https://orcid.org/0000-0002-7808-3585
https://doi.org/10.6084/m9.figshare.22177838

2 EXPERIMENTAL METHODS

2.1 Specimens

Fire tests were conducted on two reinforced rebar truss deck slabs (Tests A1 and A2) and three composite slabs (Tests B1, B2, and B3). The list of specimens and their details are presented in Table 1 and Figures 1 and 2. The specimens were composed of a concrete slab supported by four protected primary beams and an unprotected secondary short-span beam. The dimensions of all specimens were 6200 mm × 3500 mm, which is the area between the centres of the primary beam positions. The primary beams in x-direction were extended and pin-supported at a position 100 mm away from the edge of the extended beams as shown in Figure 1 and 2. The blue lines show the reinforcing bars in the x-direction, and green lines those in the y-direction. The concrete slabs were connected with the primary and secondary beams via the shear studs shown as small circles in Figure 1 and 2.

The depth of the truss deck slab (tests A1 and A2) was 135 mm. Top and bottom reinforcing bars (D13) were installed in the x-direction, shown in Figure 1, at a pitch of 200 mm. They were connected via thin-lattice trussing. The lapping zone of upper reinforcing bars was set in the middle in the long-side direction, in which the vertical deformation of the specimen was the largest. The bottom reinforcing bars were not installed on the secondary beam as shown A-A' section in Figure 1. Only the top reinforcing bars (D10) were installed in y-direction (the short-side direction) at a pitch of 200 mm.

The depth of the composite slab (tests B1, B2, and B3) was 155 mm (thin part of 80 mm). The D10 rebar was installed in a two-way direction at a pitch of 200 mm. The lapping zone was set in the middle of the long-side direction.

To study the effect of the protected steel frames on the vertical deformation, the thickness of the fire protection (AES blanket) of the primary beam were changed in Test A1 (25 mm) and Test A2 (100 mm).

Table 1. List of specimens

	Specimen	Deck	Slab thickness	Concrete	Reinforcement
RC Slab	A1, A2	Truss deck (t = 1.2 mm)	135 mm	Light weight ($\sigma_c = 24.9$ N/mm^2)	SD295 ($\sigma_y = 345$ N/mm^2) X: 2-D13@200* Y: 1-D10@200
Composite Slab	B1, B2	Composite deck (t = 1.2 mm)	80/155 mm	Normal weight ($\sigma_c = 23.8$ N/mm^2)	SD295 ($\sigma_y = 362$ N/mm^2) X: 1-D10@200 Y: 1-D10@200
	B3			Light weight ($\sigma_c = 34.0$ N/mm^2)	

* The bottom reinforcement was not installed on the secondary beam, as shown in the section view in Figure 1.

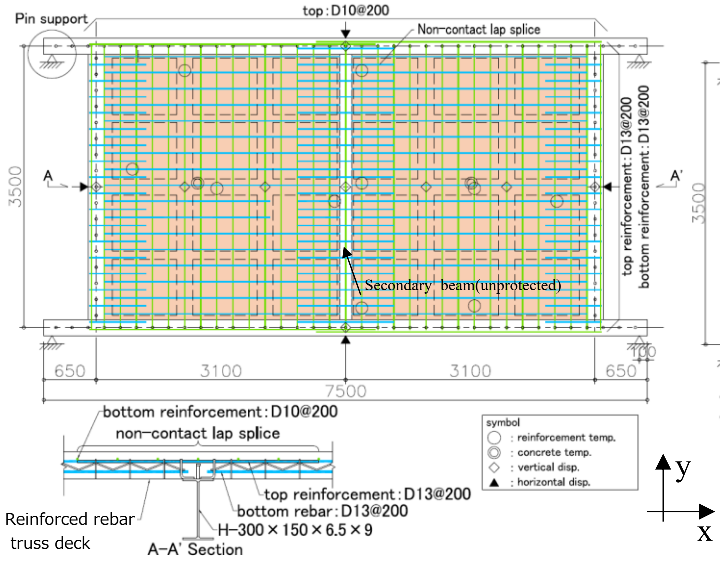

Figure 1. Specimen used in Test A1 and A2

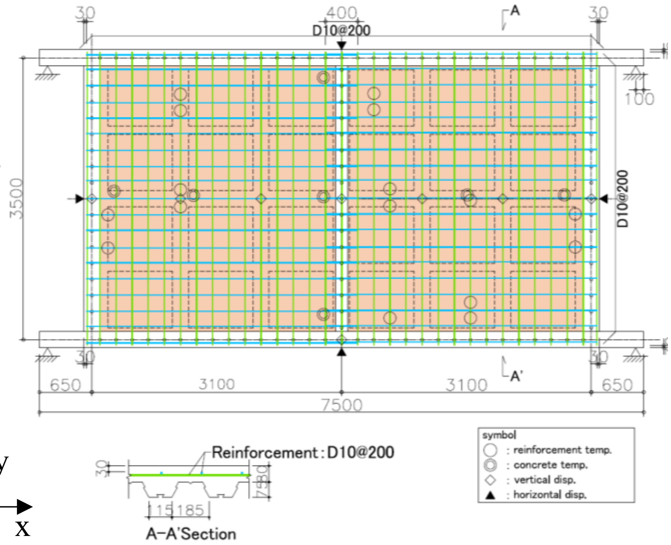

Figure 2. Specimen used in Test B1, B2 and B3

2.2 Experimental setup

The specimens were placed on a fire-test furnace to heat the bottom surface of the specimen, as shown in Figure 3. Twenty-four concrete weights (10.4 kN per 1 unit), shown as the dashed rectangular block in Figure 1 and 2, were used to load the specimens, as shown in Figure 4. The total loads were 13.6 kN/m^2 (Tests A1 and A2) and 14.4 kN/m^2 (Tests B1 and B2) and 13.93 kN/m^2 (Test B3). The specimens were exposed to ISO fire for 3–8 h and subjected to loading until the next day to study the load-bearing capacity in both the heating and cooling phases.

The concrete and steel temperatures and vertical and horizontal displacements were measured at the positions shown in Figures 1 and 2.

Figure 3. Specimen of the heated surface (Test A2)

Figure 4. Experimental setup

3 NUMERICAL ANALYSIS

The nonlinear finite-element software SAFIR [5] was used to conduct the heat transfer analysis and thermal stress analysis in the same manner as in earlier studies [6, 7]. The thermal properties and stress-strain relationships of normal weight concrete were used for those of light weight concrete.The numerical results were compared to the experimental results.

3.1 Heat transfer analysis

Figure 5 shows the heat transfer analysis model of the (a) RC slab, (b) composite slab, (c) unprotected secondary beam, and (d) protected primary beam. They were modelled according to the test specimens. The composite slab was modelled as a flat slab (dashed line in Figure 5(b)). The thickness was the average of the thicknesses of thin and thick parts.

The thermal properties of the concrete and steel followed those prescribed in Eurocode 4 [8]. The moisture content of the concrete was set to 7–10% based on the material test results. The convection heat transfer coefficients at the heated and non-heated surfaces were set to 23 and 4 W/(m^2.K), respectively. The emissivity of the specimen and flame was 0.7 and 1.0, respectively.

3.2 Thermal stress analysis

Figure 6 shows the thermal stress analysis model. The concrete slab including reinforcing bars was modelled using a shell element. Only the top reinforcing bars of the specimen in Test A1 and A2 were modelled. Both the unprotected secondary beam and protected primary beam were modelled using a beam element. The vertical displacement at the edge of extended beams was restricted. A vertical load was uniformly applied to the surface of the concrete slab.

The stress–strain relationships of concrete and steel at high temperatures reflect those published in Eurocode 4[8]. The compression strength of the concrete at ambient temperature was equal to that in the material test data as shown in Table 1. The tensile strength was set to 0 N/mm^2. Meanwhile, the yield points of the reinforcement and primary and secondary steel beams were set equal to that in the material test data (Table 1). The thermal elongation behaviours of concrete and steel at high temperatures were also set based on Eurocode 4.

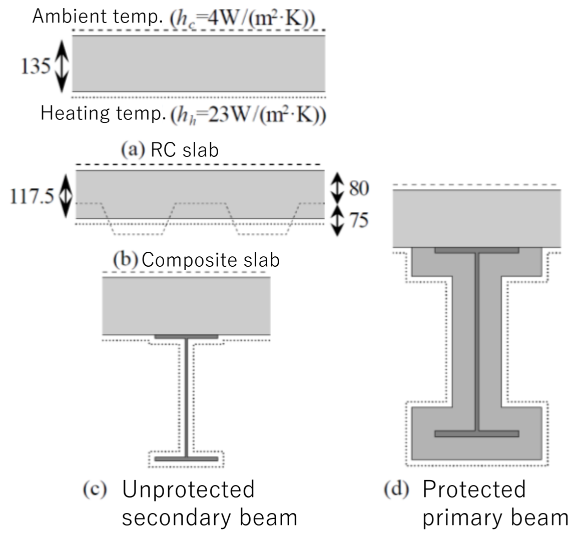

Figure 5 Heat transfer analysis model

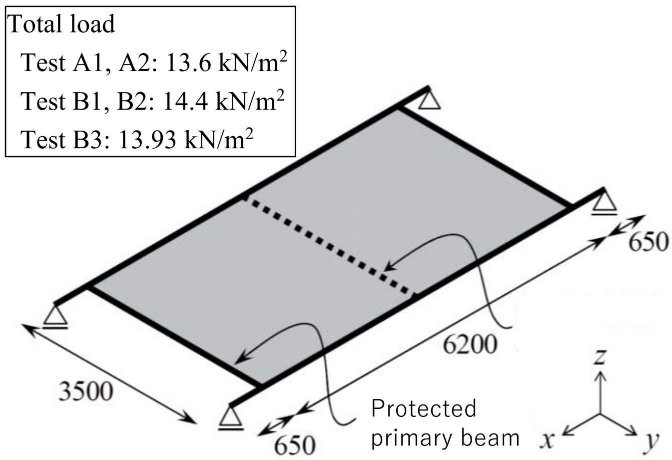

Figure 6 Thermal stress analysis model

4 RESULTS AND DISCUSSION

4.1 Overview

The experimental results are presented in Table 2. Test A1 was stopped at 180 min because the primary beam was in contact with the fire furnace. Other tests were conducted such that the primary beams did not contact the furnace by increasing the depth of fire protection of the primary beams and raising the height of the support of the specimens. Tests A2 and B1 were stopped at 480 min owing to the maximum heating duration of the furnace. The vertical displacements of the primary beams and the concrete slabs and ratio of relative displacement to the short span of the specimen (3,500 mm) when the heating stopped are also shown in Table 2. The relative displacement means the difference of those of the primary beam and the concrete slabs.. The relative displacements were 1/10 to 1/16 of the short span of the specimen, except for that in Test A1.

Figure 6 shows the specimens after the tests. The steel decks on the heating surface in specimen A2 and B1 failed 5-6 h after heating as shown in Figure 7(a). An explosion on the concrete surface was observed. Unprotected secondary beams were twisted. However, failure of unprotected bolted joints of secondary beams was not observed in any of the tests.

Table 2. Experimental results

Test #	A1	A2	B1	B2	B3
Heating duration [min]	180	480	480	330	267
Displacement at stop heating (Primary beam / Slab) [mm]	92/200	97/322	62/391	48/368	44/376
Ratio of relative displacement to short span of specimen	1/32	1/16	1/10.6	1/10.9	1/10.5

(a) Test A2

(b) Test B3

Figure 7. Heated surface of specimen after test

4.2 Temperature of specimen

The temperature history in the concrete slab and upper reinforcement bars in Tests A2 and B3 is shown in Figure 8. The solid lines show the experimental results. The circles indicate the calculation results.

The difference of the concrete temperature at the heated and unheated surfaces were large and caused the large vertical displacement of the specimens as mentioned later. Especially, the concrete temperatures of RC slabs at the unheated surface remained under 200 – 300 °C after 8 h ISO fire as shown in Figure 8(a).

The temperatures of top reinforcing bars in Test A2 were about 400 °C after 6 h, and the calculated temperature was about 480 °C after 8 hours. The temperatures of the reinforcing bars in Test B3 were higher than those in Test A2 because of the thinner concrete slab than the RC slab, which caused the early increase of the vertical displacement in Test B3.

The calculated temperatures of the concrete slabs and reinforcing bars were in good agreement with the experimental results.

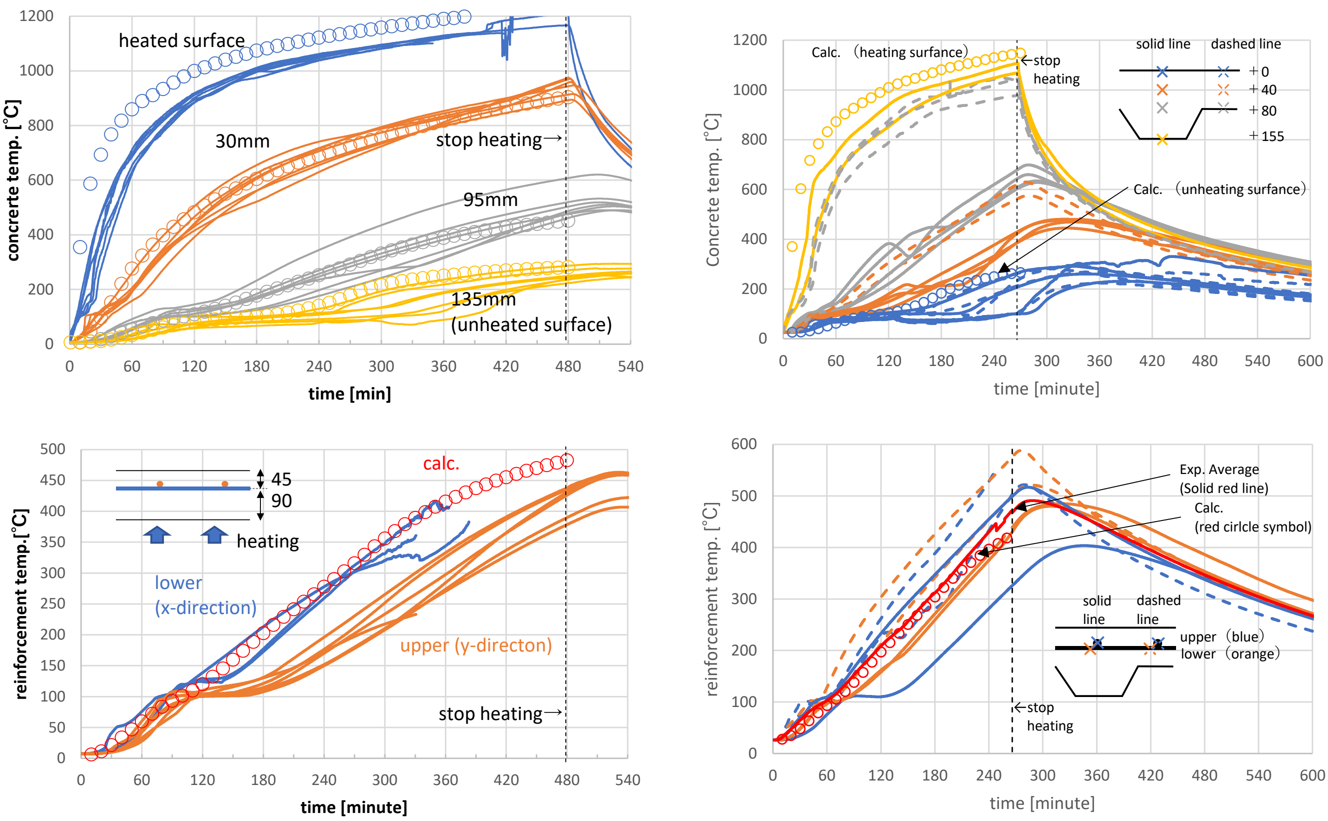

(a) RC slab (Test A2)

(b) Composite slab (Test B3)

Figure 8. Temperature of concrete and reinforcement

4.3 Deformation

The vertical displacements at the central part of the slab and mid-span of the protected primary beam in X-direction and the relative displacements in Tests A2 and B3 are shown in Figure 9. The solid lines and circles show the experimental and calculation results, respectively. The increase in the relative displacement reduced after 30 min because of the membrane action of the slabs in all tests. It is consistent with the results of a previous study [9]. The relative displacements in Test A1 and A2 show the same trend until 180 min, at which the heating was stopped in Test A1, despite the difference of the vertical displacement of the primary beams in Test A1 and A2. This means the displacement of the supporting beams of the slabs affected little the appearance of the membrane action of the concrete slab if the beams could support the slabs.

The histories of the relative displacement were shown in Figure 9. The relative displacement in Test A1 and A2 were smaller than those in Test B1, B2, and B3 because the section area of reinforcing bars in Test A1 and A2 were larger. The vertical displacement in Test B series were almost same until 130 min. In test B1 and B2, the weights to apply load to the specimens were in contact with each other as shown in Figure 12 at 130 and 190 min, respectively. This could affect the specimen as the tension rod as shown in Figure 11 and reduce the bearing load of the specimen and reduce the increase in the vertical displacement. In the test B3, the contact of the weights was not observed because the smaller weights were used to avoid the contact of weights during the test by using smaller weights.

The relative displacements are plotted against the reinforcement temperature in Figure 11. The solid line shows the experimental results, and the circle symbol the calculated results. The relative displacement increased almost linearly with the reinforcing temperature when the temperature was lower than 300-350 °C. When the temperature of reinforcing bars was larger, the increase in the relative displacement tended to accelerate because of the reduction of the strength of the reinforcing bars.

The circular symbol in Figure 9 and 11 shows the calculated results of the displacement. The calculated results of composite slab were in good agreement with the experimental results when the reinforcing temperatures were predicted well. But the relative displacement in RC slab were overestimated. The bottom reinforcing bars in X-direction, which was not considered in analysis model, might bear some load.

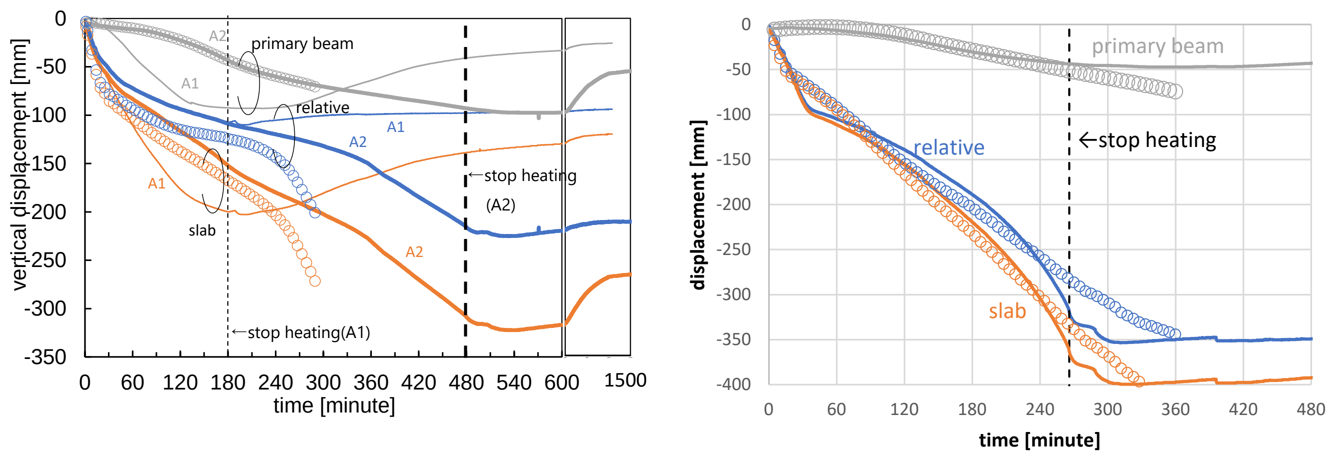

(a) RC slab (Test A2)

(b) Composite slab (Test B3)

Figure 9. Temperature of concrete and reinforcement

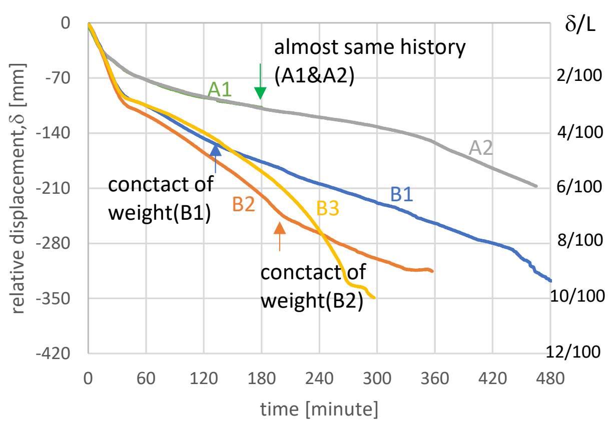

Figure 10. history of relative displacement

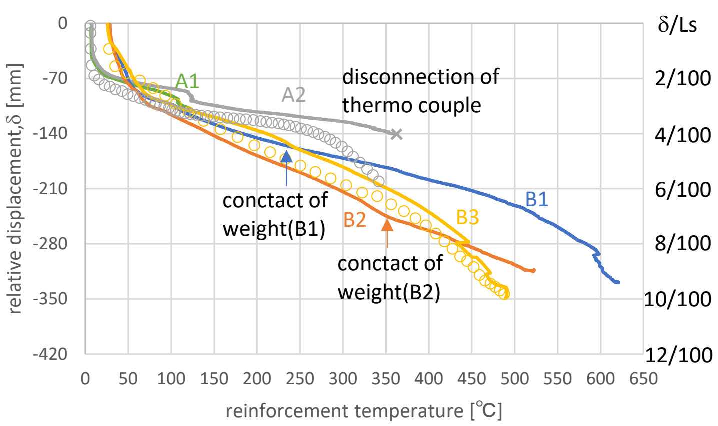

Figure 11. relative displacement plotted against reinforcement temperature

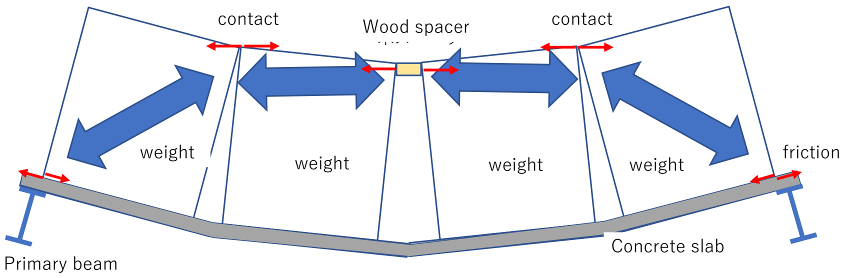

Figure 12. diagram of contact of weight during test (Test B1, B2)

Figure 13 shows the history of the horizontal displacement and rotation angle of the slab in Test B3. The rotation angle was calculated from the difference of the horizontal displacement of the slabs at 38.75 mm high (one-fourth slab thickness) and 116.25 mm high (three-fourth slab thickness). The solid and dashed lines show the experimental and calculation results, respectively.

The specimen was expanded horizontally in x-direction until heating was stopped, as shown blue lines in Figure 13(a). On the contrary, the horizontal displacement became positive due to the increase in the vertical displacement. The calculated results reproduce this tendency well.

The shot-side and long-side of the specimens internally rotated as shown in Figure 13(b). The rotation angle at the long side was overestimated, and that at short-side was underestimated. The rotation restriction by the primary beams were not predicted well.

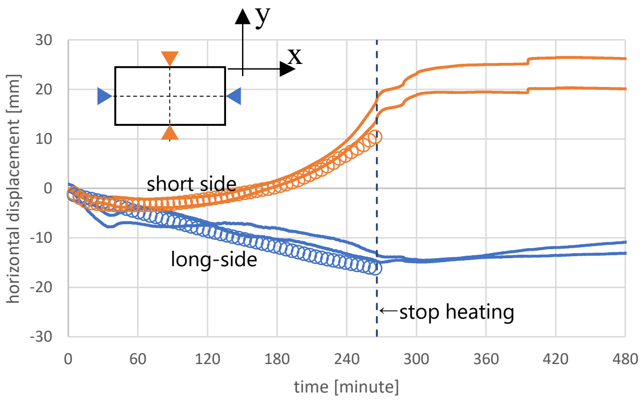

(a) Horizontal displacement

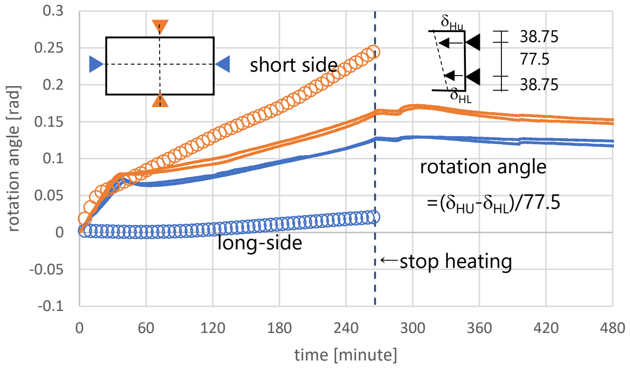

(b) Rotation angle

Figure 13. History of the horizontal displacement and rotation angle of slab (Test B3)

4.4 Crack and strain at concrete surface

Figure 14 shows the cracks on the unheated surface in Tests B1 and B3. Penetration cracking in Y-direction was observed at the centre of the specimen because of the tension stress in the longitudinal direction of the specimen. Penetration cracking in X-direction was also observed in Test B3. Cracking in the circumferential direction was caused by the primary beam restraint.

The calculation results of the strain and stress on the unheated surface in Test B3 at the times when the vertical deformation reached the maximum value (376 mm at 267 min) are shown in Figure 15. The significant tensile strain at the outer periphery caused by the negative bending moment corresponds to the cracks on the concrete surface in the specimen. The tensile strain in the long-side direction at the central part was larger than that in the short-side direction. It corresponds to the direction of the cracks in the unheated surface. The stress in the unheated surface exhibits a compression ring that balances the tension by reinforcement.

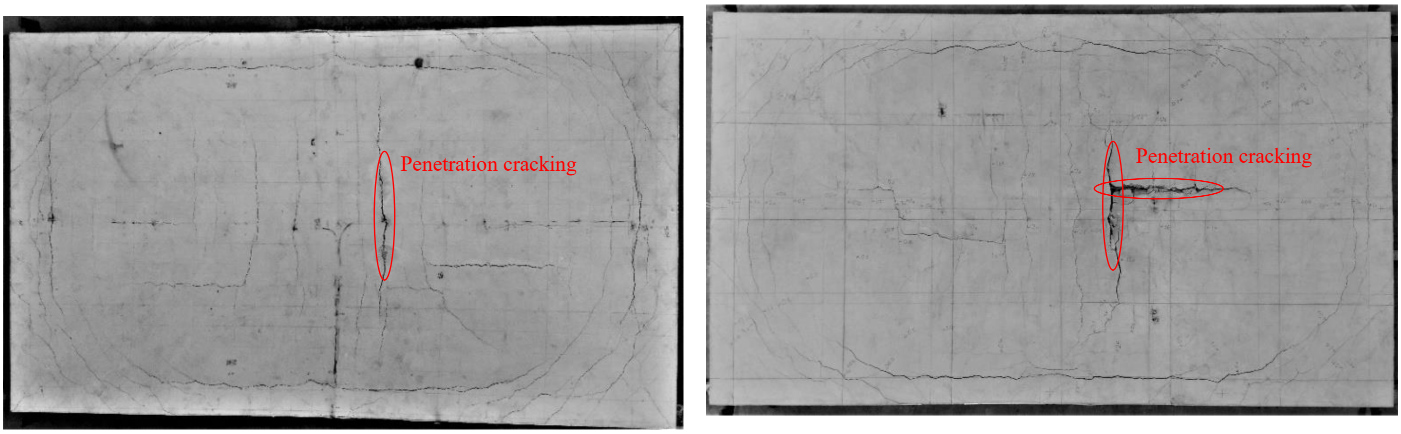

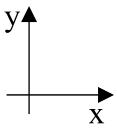

(a) Unheated surface in Test B1 (b) Unheated surface in Test B3

Figure 14. Temperature of the concrete and reinforcement

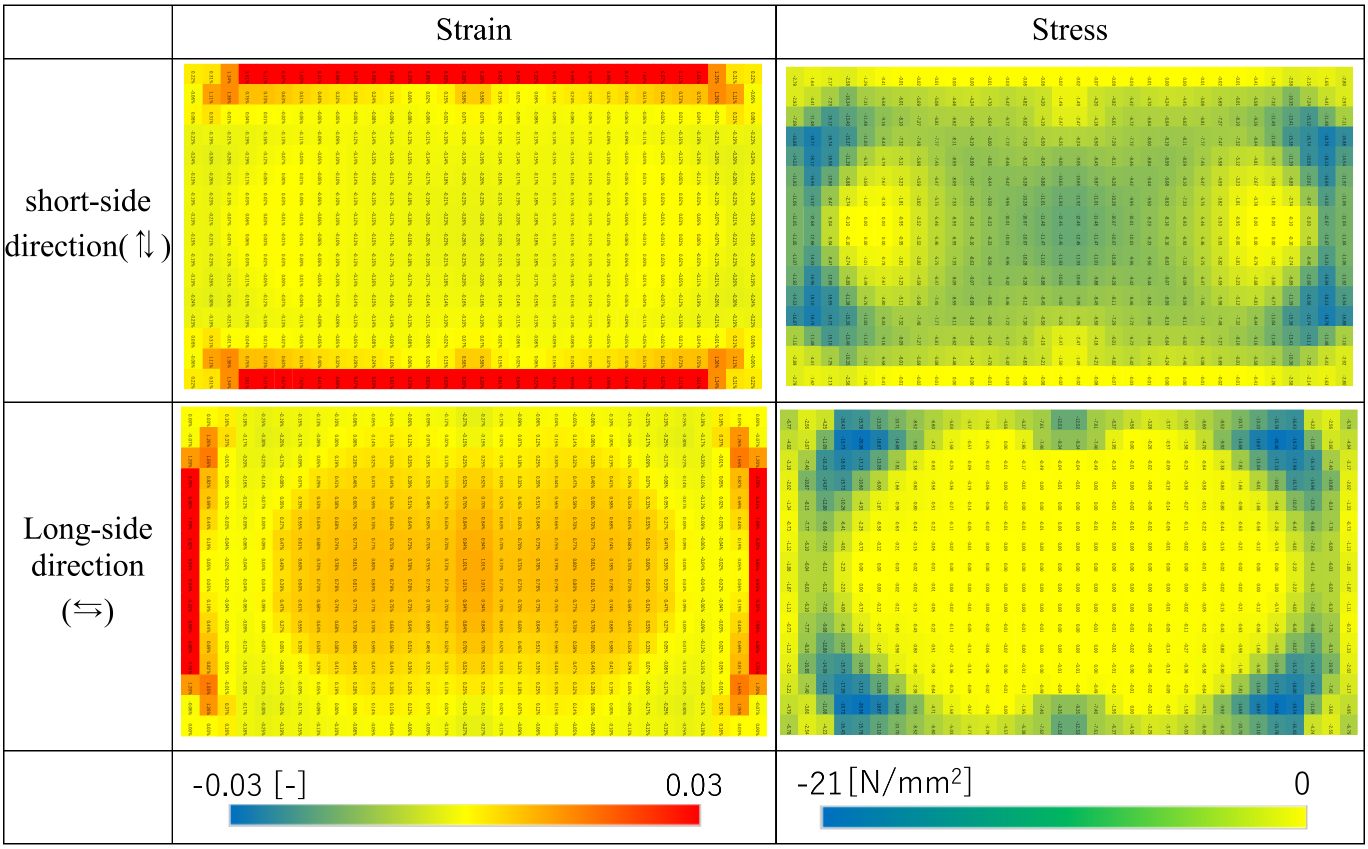

Figure 15. Temperature of concrete and reinforcement

The relationship between the load ratio (the ratio of the applied load (L_T) to the ultimate load at ambient temperature calculated from the yield-line theory (W_p)) and ratio of the relative displacement to the short span is shown in Figure 16. W_p was calculated by Equation (1) [4].

$$W_p = \frac{24\times0.9dA_s\sigma_u}{l^2}\left(\frac{a}{\sqrt{1+3a^2}-1}\right)^2 \tag{1}$$

where, l is short span of specimen [m], d is effective depth [m], a is aspect ratio of specimen, As is section area of reinforcement per unit length [mm^2/m], and σ_u is tensile strength of reinforcement [N/mm^2].

The integrity of the slabs could be lost by the appearance of penetration crack if the ratio of the relative displacement exceeded 1/12– 1/11.

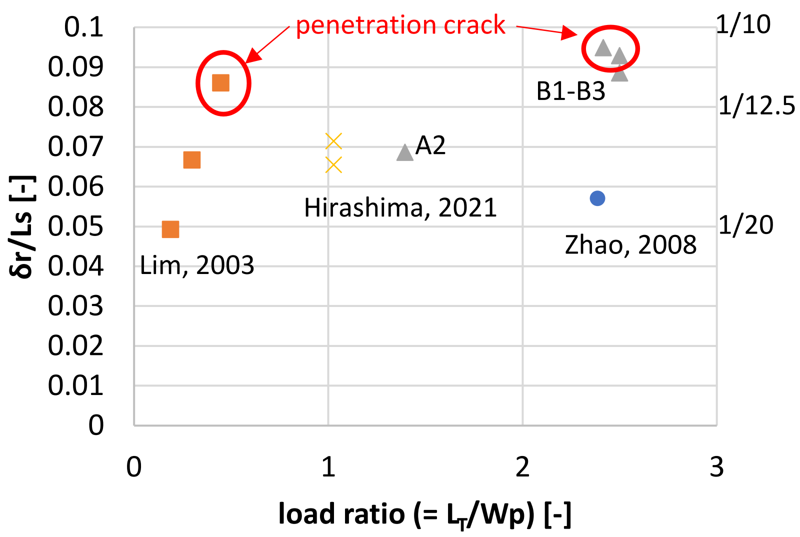

Figure 16. Temperature of concrete and reinforcement

5 CONCLUSIONS

Real-scale fire tests and FEM analysis of five concrete slabs supported by the protected primary beams and unprotected secondary beams were conducted. The fire-protection thickness of the primary beams was varied to study the effect of the vertical displacement of the beam on the membrane action of the reinforced concrete slabs. Three composite slabs were exposed to a long-duration ISO fire to study the ultimate condition of the slabs caused by the significant displacement, which was 1/11–1/10 of the short-side length of the specimen.

All specimens could sustain the vertical load during the heating and cooling phases owing to membrane action. FEM analysis could predict the history of temperature and deformation well.

In the fire tests of the reinforced concrete slab, the relative displacements, which are the differences between the maximum displacement of the concrete slabs and that of the primary beams, show the same tendency. This occurs despite the fact that the maximum displacement of the concrete slabs was unequal in the two tests. Hence, the displacement of the primary beam supporting the concrete slab did not affect the membrane action.

Penetration cracks in the short-side direction at the centre parts of the concrete slab were observed when the relative displacement of the concrete slab reached 1/11–1/10 of the short-span of the specimen. The FEM analysis showed that the tensile strain at the concrete surface in the short-side direction of the specimen was larger than that in the long-side direction. The development of cracks increased the temperature of the reinforcement. This could led to the collapse of the specimen owing to the decrease in the load-bearing capacity.

REFERENCES

1. C. C. Bailey, T. Lennon, D. B. Moore, "The behaviour of full-scale steel framed buildings subjected to compartment fires," The Structural Engineer, 77(8), pp.15-21, 1999
2. B. Zhao, M. Roosefid, O. Vassart, "Full scale test of a steel and concrete composite floor exposed to ISO fire and corresponding numerical investigation," Eurosteel 2008, 2008
3. Linus C. S. Lim, "Membrane action in fire exposed concrete floor systems," Ph D thesis, University of Canterbury, 2003.4
4. T. Yoshida, T. Hirashima, J. Suzuki, F. Ozaki, K. Kimura, Y. Murakmi, "Membrane action of floor slabs in fire (Part 2): Load-bearing fire tests of a flooring system composed of composite slabs and an unprotected steel beam," Journal of Structural and Construction Engineering (Transactions of AIJ), 87(797), pp.646-656, 2022. https://doi.org/10.3130/aijs.87.646
5. J.-M. Franssen, T. Gernay, "Modelling structures in fire with SAFIR: Theoretical background and capabilities", Journal of Structural Fire Engineerting, 8(3), pp.300-323, 2017
6. K. Kimura, T. Hirashima, F. Ozaki, T. Yoshida and J. Suzuki, "Numerical analysis of load-bearing fire test for reinforced concrete slab", 9th International Conference on Composite Construction in Steel and Concrete, 2021
7. K. Kimura, "Membrane actions of reinforced concrete floor slabs exposed to fire", Steel Construction Today & Tomorrow, 60, pp.9-12, 2020
8. EN 1994-1-2, Eurocode 4: Design of composite steel and concrete structures, Part 1.2: General rules – Structural fire design, 2005
9. T. Hirashima, K. Kinoshita, T. Yoshida, J. Suzuki, F. Ozaki, K. Kimura, Y. Murakami, "Membrane action of floor slabs in fire (Part 1): Load-bearing fire tests of a composite flooring system composed of RC slabs and an unprotected steel beam," Journal of Structural and Construction Engineering (Transactions of AIJ), 86(785), pp.1106-1116, 2021. doi:10.3130/aijs.86.1106

THE EFFECT OF KENAF FIBRE AND SUSTAINED TEMPERATURES ON THE RESIDUAL MECHANICAL AND MORPHOLOGICAL CHARACTERISTICS OF BIOFIBROUS HIGH-STRENGTH CONCRETE

Oluwatobi Aluko[1], Jamaludin Yatim[2], Mariyana Ab. Kadir[3], Khairulzan Yahya[4], Kasali Mujedu[5]

ABSTRACT

Fibres play notable roles in concrete bared to extreme temperatures. The high manufacturing cost of convectional fibres and greener initiatives necessitate biofibers in concrete. Mechanical and microstructural characteristics are crucial to fire-damage concrete's serviceability and forensic demands. Thus, this research presents an experimental report on a 28-day cured Kenaf Fibrous High Strength Concrete (KFHSC), heated between 100-800ºC, sustained for 1, 2, and 3 hours, and tested after cooled naturally. The fibres were treated and examined through SEM and TGA to ascertain their interfacial and thermal properties, using an optimum volume (0.75%) and length (25mm) in a grade 60 mix. The KFHSC's residual mechanical properties, weight, ultrasonic pulse velocity, and morphology were determined and compared with Plain High Strength Concrete (PHSC). Both samples degraded with an increase in temperatures and duration. However, kenaf fibre retrained crack extension at a lower temperature phase and reduced pore pressure build-up at a higher temperature phase.

Keywords: Biofibers; kenaf fibre; residual mechanical properties; microstructures; elevated temperature

1 INTRODUCTION

Fibre plays a substantial role in producing tougher and more durable concrete, with minimal deterioration due to cracks, corrosion and fire impact. However, the high manufacturing cost of convectional fibres and the need for greener composites necessitate biofibers in concrete. Plant-based fibre sourced from cotton, hemp, jute, bamboo, flax, ramie, coconut, sisal, bagasse, and kenaf plants has been included in the concrete for over 40 years with significant properties improvement, and more research opportunities [1–3]. Fibres have been reported to improve high-strength concrete fire behaviour by ameliorating vapour pressure built-up and crack extension, most significantly as a hybrid of metallic and polypropylene fibres [4–6]. Research on the behaviour of biofibrous concrete bared to extreme temperatures is still scarce. Nevertheless, previous reports reveal that, apart from sustainability, CO_2 neutrality and relatively high stiffness benefits, biofibers in concrete lessen cracks and pore-pressure build-up in heated high concrete [1–3]. However, the focus has been on high-performance, ultra-high-performance concrete [7,8], with minimal reports on high-strength concrete, which are also prone to explosive spalling. Recent studies have found kenaf fibre beneficial in terms of its strength and durability application in reinforced concrete for marine structures [9]. Kenaf fibre is obtained from the kenaf plant, which originates in Africa. It is planted abundantly and commercially in Malaysia and other Asian countries and is advantageous due to its high yield, tensile strength property, low

[1] Research Student, Dept. of Structure and Materials, Faculty of Civil Engineering, Universiti Teknologi Malaysia.
e-mail: aluko1977@graduate.utm.my, ORCID: https://orcid.org/0000-0002-3221-5730
[2] Assoc Prof, Dept. of Structure and Materials, Faculty of Civil Engineering, Universiti Teknologi Malaysia
e-mail: jamaludin@utm.my, ORCID: https://orcid.org/0000-0002-9568-1317
[3] Assoc Prof, Institute Noise and Vibration, Universiti Teknologi Malaysia
e-mail: mariyanaida@utm.my, ORCID: https://orcid.org/ 0000-0002-3976-1507
[4] Dr, Dept. of Structure and Materials, Faculty of Civil Engineering, Universiti Teknologi Malaysia
e-mail: khairulzan@utm.my, ORCID: https://orcid.org/0000-0002-4089-4438
[5] Dr, Dept. of Structure and Materials, Faculty of Civil Engineering, Universiti Teknologi Malaysia
e-mail: bayomujedu@yahoo.com, ORCID: https://orcid.org/0000-0002-1655-840X
https://doi.org/10.6084/m9.figshare.22177841

density, high aspect ratio, and modulus[5]. Many researchers have explored kenaf fibres from characterisation to structural applications and durability [9–11]. However, its behaviour under elevated temperatures has not been investigated. Also, the increasing quest for biofibrous construction materials must be balanced with concern for their endurance and capability of kenaf fibre in high-strength concrete under thermal load. Notably, mechanical characteristics and microstructural analysis are crucial for fire-damaged concrete's serviceability and forensic requirements. Therefore, this research presents a report of KFHSC of grade 60, exposed to thermal load up to 800ºC, sustained for 1, 2, and 3 hours, and tested after cooling. The KFHSC's residual mechanical properties, weight, Ultrasonic Pulse Velocity (UPV), and morphology were determined and compared with PHSC. These findings would be useful as data for standard development for design and application strategy.

2 EXPERIMENTAL PROGRAM

2.1 Materials and Material Properties

Aggregates, cement, kenaf fibre, potable water, and superplasticiser were used for this research. However, due to their hydrophilicity, kenaf fibres require modification before use in a concrete mixture. Kenaf fibre was collected from the National Tobacco Board at Kelantan, Malaysia. It was treated with an optimum alkaline concentration of 5% NaOH, with the chemical reaction indicated in Equation 1, air-dried, combed, and chopped to 25mm, as shown in Figure1 (a)&(b), before incorporating 0.75% optimum volume into the concrete matrix. Fibre morphology testing was done using Scanning Electron Microscopy (SEM)), JEOL JSM-IT300LV with a working voltage of 20kV. Figure1(c) shows that the alkaline solution had removed the wax and oil protecting the outer face of the fibre cell wall and the hydrogen bonding in the interconnected structure of fibre cellulose, hemicellulose, and lignin, thereby improving the fibre surface roughness and interfacial properties. While the smooth surface of the untreated fibre shows the network of cellulose, wax, and oil covering the surface, as shown in Figure.1d, as reported by [12] on hemp fibre modification. Thermogravimetric Analysis(TGA) of the treated and untreated kenaf fibre was done using the TA instrument, TGA, Q500 model, with a 10ºC/min heating rate to examine the thermal decomposition of the fibre, respectively [12]. The physical and strength characteristics of kenaf fibre used in this study were obtained through tests [13], and the result is shown in Table 1. Fine aggregate use was sharp sand with a maximum grain size of 4.75mm, and crushed granite of 10mm, all adequately graded, according to[14]. Ordinary Portland cement (OPC, 42.5), based on [15] and RHEOBUILD 1100 brand of superplasticiser, in compliance with [16].

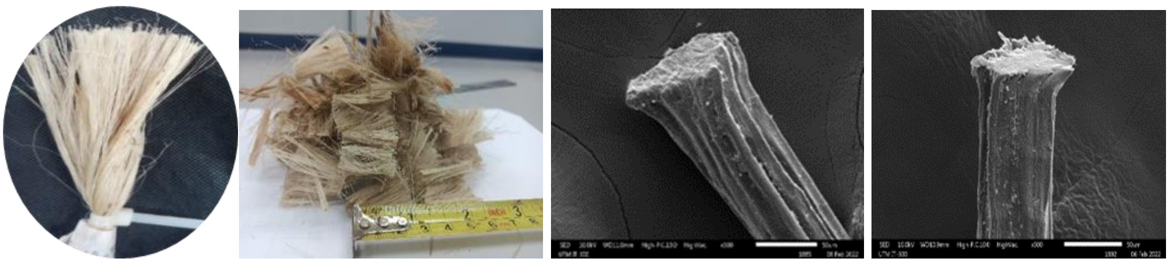

(a) (b) (c) (d)

Figure 1. Kenaf fibre: (a) Treated, (b) Short-discrete form, (c) SEM (treated), (d) Untreated

$$2(OH^{-})fiber + 2NaOH \rightarrow fiber + Na_{2_{aq}}^{+} + 2H_2O + O_2 \quad (1)$$

Table 1. **:** Properties of modified kenaf fibres

Fibre	Length (mm)	Diameter (μm)	Ave. Aspect ratio	Density (Kg/m^3)	Tensile strength (MPa)	Elastic Modulus(GPa)	Elongation at yield(%)
	25	40.1-115.2	500μm	1.05-1.52	136-930	15-54	1.6-1.77

2.2 Concrete Mix Design

Department of the Environment (DOE) method of mix design was used for this study. Two mixes with 312 samples were made for the UPV, compressive strength and split tensile test at ambient and elevated temperatures. The mix proportion is shown in Table 2.

Table 2. Mix proportion for KFRC and control

Mix	Kenaf Fiber(%)	Kenaf Fiber(kg/m^3)	Water (w/c=0.33) (kg/m^3)	Cement (kg/m^3)	Fine agg. (kg/m^3)	Coarse agg. (kg/m^3)	SP(1%)
PHSC	0	0	170	515	692	1037	5.32
KFHSC	0.75	9	170	515	692	1037	5.32

2.3 Samples Preparation

The mixing method used to prepare KFHSC samples was similar to plain concrete, except for fibre. The short discrete kenaf fibres were hydrated for 30mins [17] before the mixing process started. Then the mixer received the aggregates, cement, and water and adequately mixed them before the fibres were dispersedly added and mixed for 3 mins. A superplasticiser dosage was added and mixed for 5 minutes to ensure a uniform mixture. The slump and compaction factor test was done based on [18], and the concrete was placed in the oiled moulds and appropriately compacted on a vibrating table. The concrete samples were de-moulded after 24 hours and water-cured for 28 days. After curing, the samples were allowed to dry, weighed, and tested for their properties at ambient temperature.

2.4 Heating and Cooling of the samples

The standard fire test measures the defiance of structural elements to fire. This study used an unstressed residual testing technique comparable with [19,20], as shown in Figure 3. Each set of KFHSC & PHSC samples was heated for 100, 200, 300, 400, 600, and 800ºC in an electrically controlled furnace (Muffle Cardiolite), with the size 0.8 m^3, shown in Figure 2, with a heating rate of 4.1°C/mins, for 1, 2, 3 hours. They were cooled naturally to ambient temperature, as the cooling rate was monitored with a portable Reed Infrared thermometer, with an average cooling rate of 49°C/mins for 800ºC samples. Then, the weight losses, UPV test, compressive, and splitting tensile strength were examined.

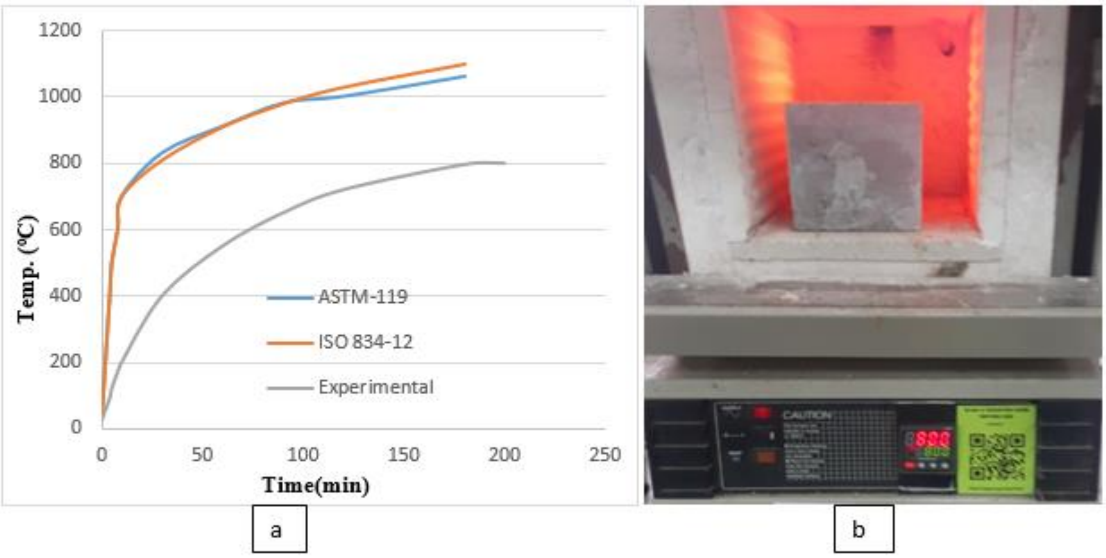

Figure 2. (a)Experimental Heating Curve Vs Standard Curve (b) Furnace

2.5 Tests on Hardened Heated Samples

All test were done at D04, T03, Universiti Teknologi Malaysia, Malaysia. UPV was conducted on the samples to examine the post-fire integrity of KFHSC compared with PHSC. Weight loss in KFHSC cubes samples was determined by obtaining the pre and post-heating weight difference, expressed in percentages as a function of the elevated temperatures for 1H, 2H, and 3H (H: hours). Average UPV test results were estimated as a function of elevated temperature and exposure period. Also, a compressive strength test was done based on [21], and a 2500 kN compression machine with a loading rate of 6kN/s, air-cooled, 100mm cube KFRC samples were applied were tested for each targeted temperature. The average values were recorded as the residual strength. Similarly, the split tensile strength test, based on [22], was carried out on cylindrical samples (100 diameters, 200 mm high) at the loading rate of 1.25kN/s, using the same compressive strength machine, but changed the jaw and packed the samples with a plywood plate at the top and bottom. The average residual and relative residual strength were obtained for compressive and split tensile strength. The relative residual strength at a given temperature represents the residual strength ratio at various target temperatures to the strength at room temperature (26ºC). Samples' microstructure was done using Scanning Electron Microscopy (SEM)), JEOL JSM-IT300LV with a working voltage of 20kV.

3 RESULTS AND DISCUSSIONS

3.1 Residual Mechanical Characteristics of KFHSC

Mechanical properties remain the most crucial properties of concrete bared to extreme temperatures because it influences concrete's performance diversely due to different material compositions and temperature variations [23]. The test results presented in this section include; residual UPV, weight loss, compressive, and split tensile strength, to depict concrete strength reduction as a function of temperature variation and exposure durations.

3.2 Result of Residual Weight Loss and UPV of KFHSC

The deterioration of concrete can easily be estimated through weight loss [24]. Figure 3 shows the impact of exposure temperatures and duration on KFHSC sample weight compared to PHSC. KFHSC samples had a lesser weight than PHSC samples at room temperature, due to low specific gravity, unlike steel fibre. For 1 hour of heating, between 26-300ºC, Both mixes slightly lost weight, which could be linked to the dehydration of the samples. At 300ºC, KFHSC and PHSC lost 2.5% &2.1%, at 800ºC, 9.4%, 8.4% respectively. For 2 hour fire, weight loss for both mixes was noticed between 26-300ºC, but that of KFHSC was remarkable, and at 300ºC, KFHSC and PHSC lost 4.6% and 3.1%, respectively. At 800ºC, KFHSC lost its weight considerably at 9.6% compared to PHSC with 8.8%. Also, for 3H heating, weight loss was more substantial, as shown in Figure 3. At 300ºC, KFHSC lost 4.7%, Compared to PHSC with 3.5%. At 800ºC, KFHSC lost 9.9%, compared to PHSC with 8.9%. Both samples have experienced complete decomposition of kenaf fibre and dehydration of cement paste and aggregates at this temperature. The reason for higher weight loss in KFHSC, apart from the fibre deterioration, is the lower density and high permeable matrix, which dehydrates faster than samples with higher density. Also, due to the fragmentation of concrete materials at high temperatures, the release of bound water from the cement paste and the concrete's porosity [25], This finding agrees with the [12] report that hemp fibre was used.

Kenaf fibre had a tangible impact on the KFHSC UPV results due to the low density compared to PHSC. From Figure 4, UPV results for KFHSC and PHSC were 4.786km/s and 4.856km/s at ambient temperature, respectively, with PHSC having a higher value of 1.5%, depicting good concrete quality [26]. There was a gradual change in both mixes before 400ºC. However, UPV values for KFHSC and PHSC significantly dropped at 400ºC and above. Thus, at 400ºC for 1H, KFHSC and PHSC lost 22% and 19% and 72% and 68% of their pre-heating values at 800ºC, respectively. The exposure temperature and duration effect became significant for 2H exposure, as shown in Figure 4. Therefore, at 400ºC, KFHSC and PHSC lost 28% and 24% of their pre-heating values; at 800ºC, KFHSC and PHSC lost 78% and 71% of their UPV value, respectively. For 3 hours, both samples degraded at 800ºC and lost 82% (0.842km/s) and 76% (1.187km/s) of the original values, respectively. Both mixes experienced coarsening of microstructure due to fire impact. Thus the decline in the UPV result of KFHSC is not attributed to the ashing of kenaf fibres alone but the deformation of C-S-H at 450ºC, making the matrice more porous and permeable, consequently reducing the sample's UPV values. This is similar to the report of [27], which used alfa fibre and [12], which used hemp fibre.

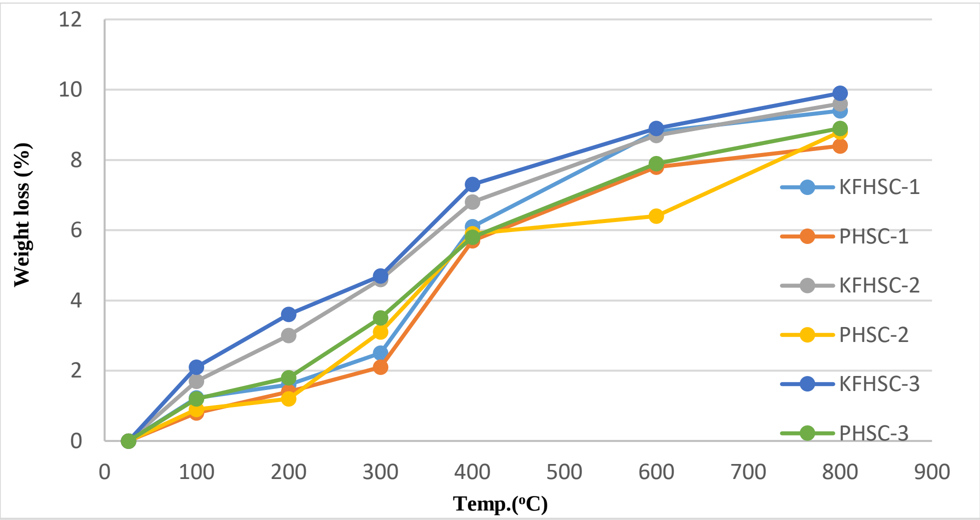

Figure 3: Average Weight Loss Vs Temperature Changes

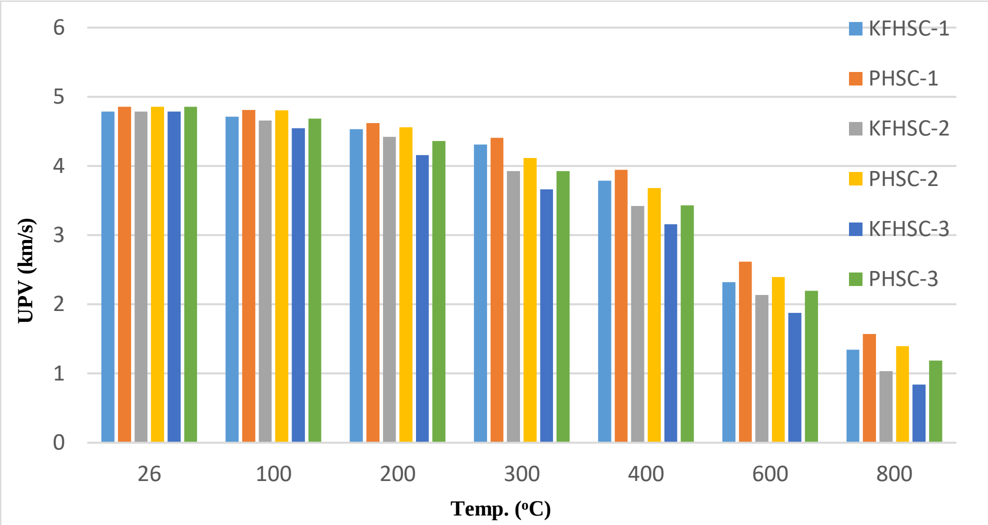

Figure 4: Average UPV Vs. Temperature Changes

3.3 Results of Residual Compressive strength

Kenaf fibre did not improve the compressive strength of the KFHSC mix even at room temperature, which is general to all biofibers. This could be attributed to the 'balling effect' in fresh concrete, low specific gravity, and the inability to distribute the fibre evenly in the mix. Therefore, strength enhancement experienced on the composite was the regular concrete's strength spike initiated at a particular temperature level due to hydration of remaining un-hydrated cement within the composite. The relative compressive strength of the KFHSC and PHSC mixes for exposure durations is shown in Figure 5.

KFHSC met the design strength of 60MPa. From Figure 5, for 1H exposure, KFHSC and PHSC strength improved by 1% and 2% at 100ºC, respectively, agreeing with [28]. The marginal increase in compressive strength could be accredited to the dehydration of samples at a lower temperature range, forming Van Der Waals force, then increasing the strength. Also, the quickening of the release of chemically bound free water, exuding calcium hydro-silicate (C-S-H) and ($Ca(OH)_2$. However, the KFHSC and PHSC strength declined by 200ºC by 14% and 13%, respectively. This could be credited to the loss of water from the samples, resulting in voids formation, thus causing a decline in the compressive strength. This occurrence is referred to as a 'strength recession' [29]. At 300ºC, KFHSC and PHSC climaxed with a 6% strength improvement compared with 200ºC. This could be due to the completion of the hydration phase, with vaporised water moving across the pores and voids of un-hydrated cement. This forms stronger bonds within the KFHSC matrix. However, PHSC and KFHSC recovered 99% and 98% at 400ºC, respectively. Also, KFHSC and PHSC lost 48% and 37% strength at 600ºC and 76% and 68% of their original strength at 800ºC, respectively.

Similarly, for a 2H exposure, shown in Figure 5, both mixes gained 2% strength at 100ºC and lost 12% and 11% at 300ºC, respectively. At 400ºC, the compressive strength shut up slightly, with only 8% and 7% strength loss for KFHSC and PHSC, respectively. At 800ºC, KFHSC and PHSC lost 80% and 71% of their pre-heating strength. Also, for 3H, as shown in Figure 5. Both mixes gained 2% at 100ºC, after which strength rapidly degraded. At 800ºC, KFHSC and PHSC had lost 83% and 76% of their pre-heating strength. The strength upsurge for both mixes during heating could be attributed to the formation of additional hydration products by converting the C–S–H state into a pectolite state [$NaCa_2Si3O_8(OH.)$] KFHSC climaxed its strength, with stability between 200ºC-300ºC. The severe loss was observed between 400ºC-800ºC for both mixes because 600ºC was the beginning of aggregate and C-S-H decomposition. Decomposition of portlandite and second stage breakdown of the C-S-H and generation of β-C_2S [30]. There is not yet a published report on the effect of varying and sustained elevated temperatures on biofibrous concrete for comparison. However, [8,12,27] reported a similar result for Hemp, Jute and Alfa fibres for 1H, 2H, and 3H, respectively. Therefore, it could be concluded that strength loss in KFHSC is less of a fibre effect but more of concrete material deterioration [8].

3.4 Residual Split Tensile Strength

Kenaf fibre(KF) offers a massive advantage to concrete in resisting tensile stresses. KFHSC cylinder samples resisted sudden failure or total breakage, and only small cracks showed on the cylinder sample surface. As shown in Figure 6, KFHSC and PHSC had a 4% strength gain at 100ºC but gradually lost the Split tensile strength as the exposure temperature and duration increased. At 400ºC, KFHSC and PHSC lost 23% and 17% of their original strength; at 800ºC, KFHSC and PHSC lost 72% and 66% of their pre-heating values. For a 2-hour exposure period, both mixes marginally gained 2% strength at 100ºC and gradually lost strength until 800ºC, where both lost 81% and 76% of their original strength. For a 3-hour duration, as shown in Figure 6, both mixes had 100% strength recovery at 100ºC and lost 87% and 81% of their pre-heating strength at 800ºC, respectively. The behaviour of KFHSC from 26ºC-400ºC complies with the previous finding that when the concrete is subjected to indirect tensile stress, the kenaf fibres absorb the tensile force and prevent progressive cracking, through stress distribution and bridging mechanism, unlike non-fibrous samples. This finding agrees with [31] Alfa fibre report. The increase in tensile splitting strength at the lower phase of the temperature is due to the ability of kenaf fibres to bridge across the cracks in the concrete matrix, which provides some post-cracking ductility arresting cracks from further propagation.

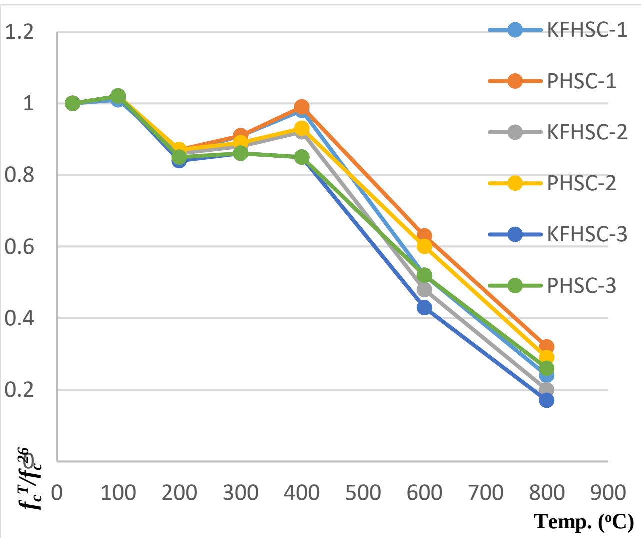

Figure 5:Relative Residual Compressive Strength Vs. Temp.

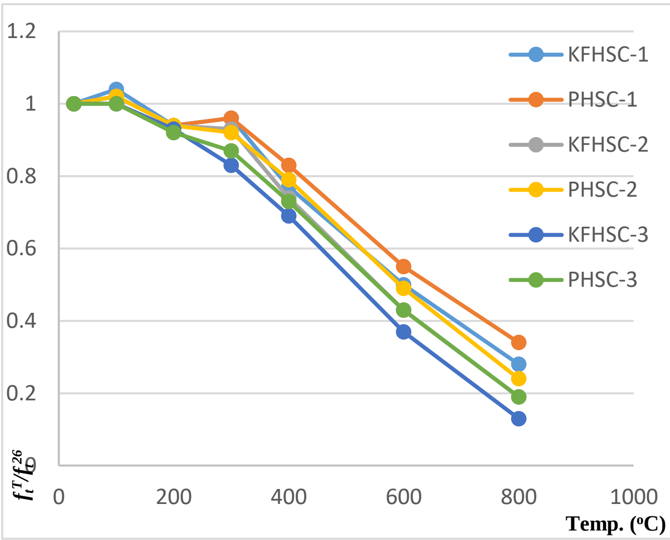

Figure 6: Relative Split Tensile Strength Vs. Temp.

3.5 Microstructure

Due to space, discussion on the microstructures is limited to 1H, 2H and 3H exposure at ambient, 400ºC and 800ºC. Figure 7 (a&b) shows KFHSC and PHSC before heating. Both mixes were reasonably dense, stable and unaltered at ambient temperature, except for some cracks observed around KF in the KFHSC matrix due to fibre pull-out. For PHSC, the C-S-H was well-formed on the matrices. With increasing temperature and exposure duration, the microstructure of the KFHSC matrix experienced some notable transformations

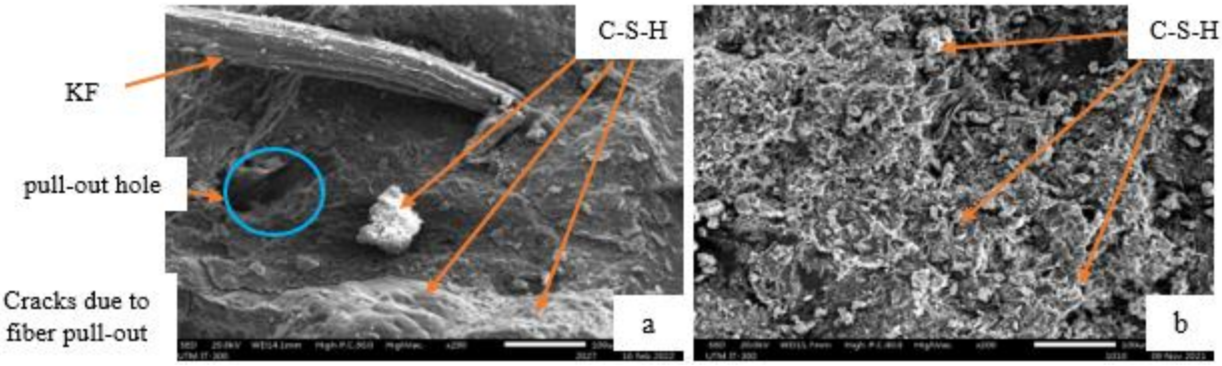

Figure 7: SEM Image(100µm) at Ambient Temperature (a) KFHSC (b) PHSC

3.5.1 1H,2H and 3H Exposure Duration at 400ºC

Figure 8 (a-f) reveals the microstructure of KFHSC for 1, 2&3H exposure at 400ºC and the role of KF within the matrix cracks and spalling reduction compared with PHSC. For 1&2H exposure, as shown in Figures 8 (a&b),(c&d), No cracks were observed on both matrices at this exposure temperature and duration. There were some 'active' KF yet in the KFHSC matrix, spanning across, thus offering a bridging mechanism and cracked mitigation. Although, there was no significant crack observed in the PHSC matrix, except for some microvoids. This agrees with the report of [12] using hemp fibre for 1H exposure. However, some voids were observed under the kenaf fibre, as shown in Figure 8 (a&c). These were not thermally-induced voids but voids caused by the bridging operation of KF during concrete mixing, which also made the matrix less dense [32]. KF probably had thermal endurance due to alkaline treatment, which enhanced thermal performance [12]. C-S-H had become crystallised in both mixes, which caused an upsurge in the compressive strength observed at this temperature.

Also, the transformation of C-S-H gel to crystalline stages enhanced strength more than the preliminary C-S-H gel. Thus, a new crystalline segment with free lime made during cement hydration created a denser microstructure. This was accountable for additional solid volume and bond strength which caused a 13% and 14% upsurge in compressive strength for KFHSC and PHSC at 400ºC, respectively. For 3H, as shown in Figure 8 (e&f),). KF has degraded, though some short ones may restrain crack propagation, as shown in Figure 8(e). However, the autoclaving process in cement paste became ineffective due to the duration, which also affected the strength because the surge in compressive strength was only for 1&2H, excluding the 3H exposure. The long exposure duration was observed with no crystallised C-S-H in both matrices. Also, 3H exposure impacted the matrices, and improvement in compressive strength on both matrices was very marginal. Some microcracks were observed on both KFHSC and PHSC had a long crack line on the cement paste of the matrix, as shown in Figure 8 (e&f).

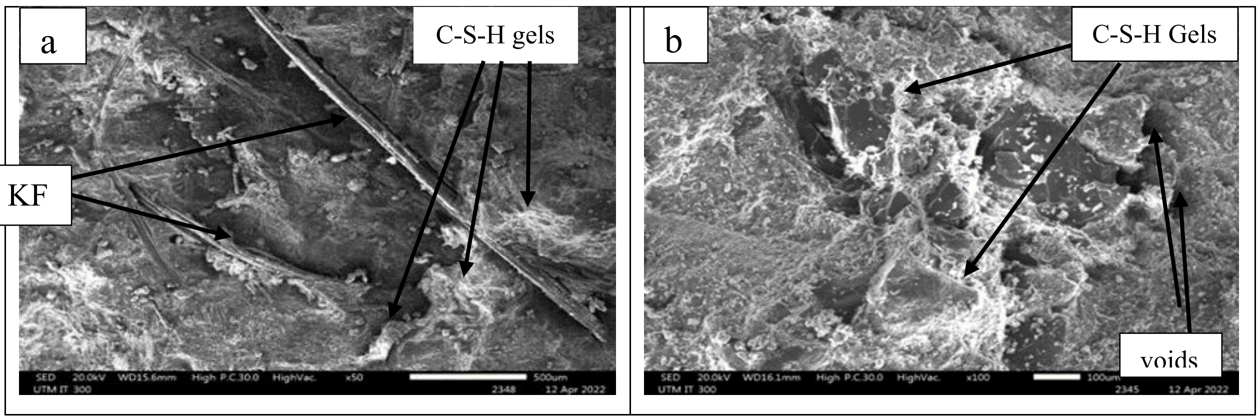

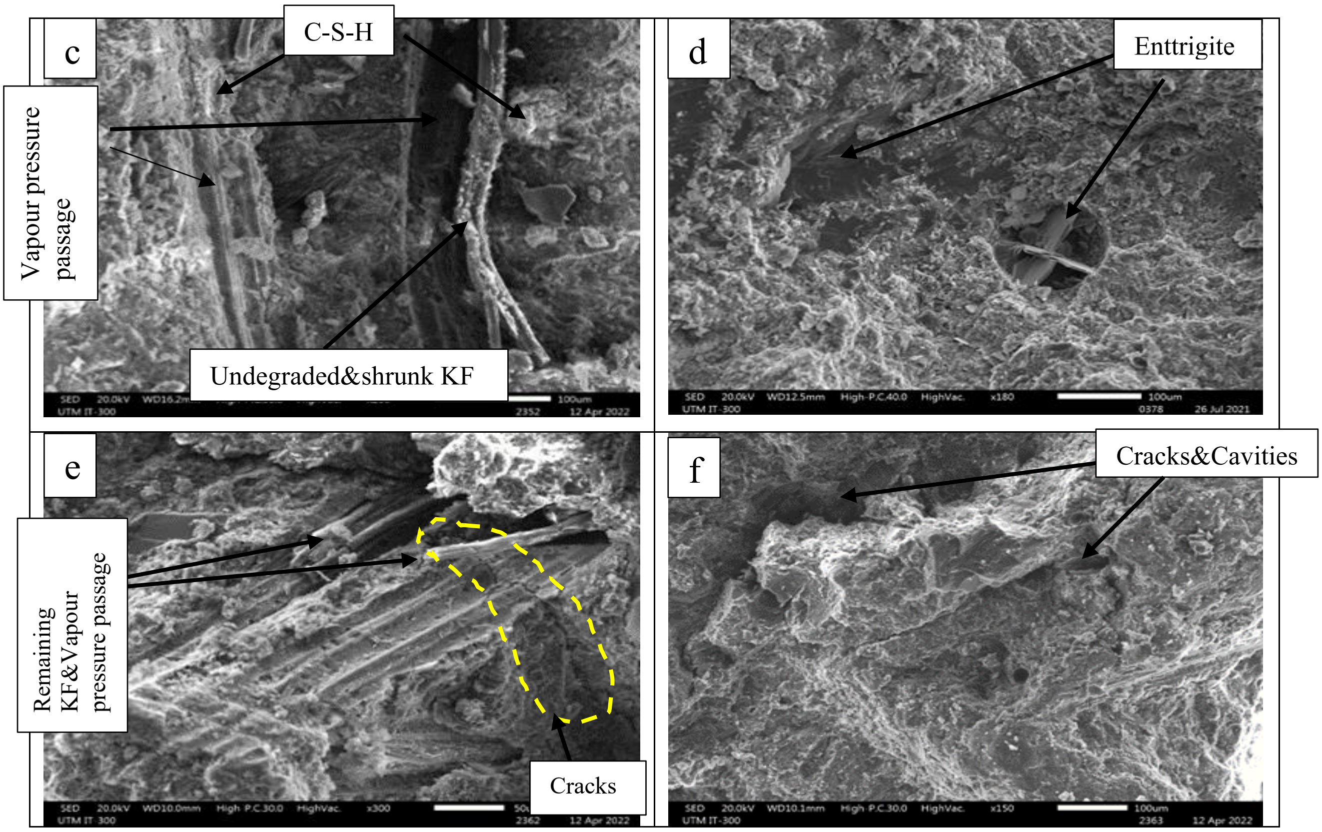

Figure 8: (a)SEM Image@100mμ for 400ºC: (a) KFHSC-1H, (b) PHSC-1H, (c) KFHSC-2H, (d) PHSC-2H, (e) KFHSC-3H, (f) PHSC-3H

3.5.2 1H,2H and 3H Exposure Duration at 800ºC

At 800ºC, for 1H exposure, as shown in Figure 9 (a), incompletely degraded, shrunk KF was observed performing a 'bridging' function. However, the second CSH decomposition stage has changed to form β-C_2S. As a result, the microstructure has become more porous and ladened with microcracks due to the complete dehydration of cement paste and aggregates, causing aggregate expansion and cement paste shrinkage. Although, microcracks were not observed in KFHSC as much in PHSC. Just like how Hager [33] recommended using particle boards to ameliorate thermal spalling in heated concrete. The incompletely degraded kenaf fibre, as shown in Figure 9 (a), acted as an 'expansion joint' Its thermal conductivity is low, consequently mitigating thermal stress in the heated samples. Unlike PHSC, which was faced with constant expansion of aggregate and shrinkage of cement paste, which was the reason for severe cracks seen on the sample, as shown in Figure 9 (b). Also, the contraction of KF at this temperature allowed passage and discharge of vapour pressure and then reduced spalling tendency due to pore pressure development. A similar report about jute fibre was made by [8], although the spalling of PHSC was less significant at this temperature and exposure.

For 2H exposure of KFHSC & PHSC, as shown in Figures 9(c&d), KF had decomposed completely and created voids and cracks within the matrix. The matrices had completely dehydrated, which is one of the reasons for crack propagation, as observed. The PHSC matrix was filled with cracks and cavities. For KFHSC and PHSC, the complete decomposition of C-S-H became practical at this level. There was matrix transformation into an amorphous structure, incurring more cracks and voids, which appeared throughout the concrete samples, as shown in Figures 9 (c&d). C-S-H had deteriorated. The mode of failure of both matrices was satisfactory and retained compressive strength for KFHSC, and PHSC was 20% and 29% of their original strength. These findings agree with [8]. Similarly, for the 3H duration, both samples had begun to experience a 'coarsening effect,' a pore structure development within the matrices [4]. The decomposition of C-S-H is very conspicuous. The fibres have shrunk and frailed, enhancing the microcracks. At this temperature, both matrices had transformed from crystal structure into an amorphous structure, engendering many cracks and widened cavities that appeared vastly on the samples, with tremendous damage to all sample microstructure.

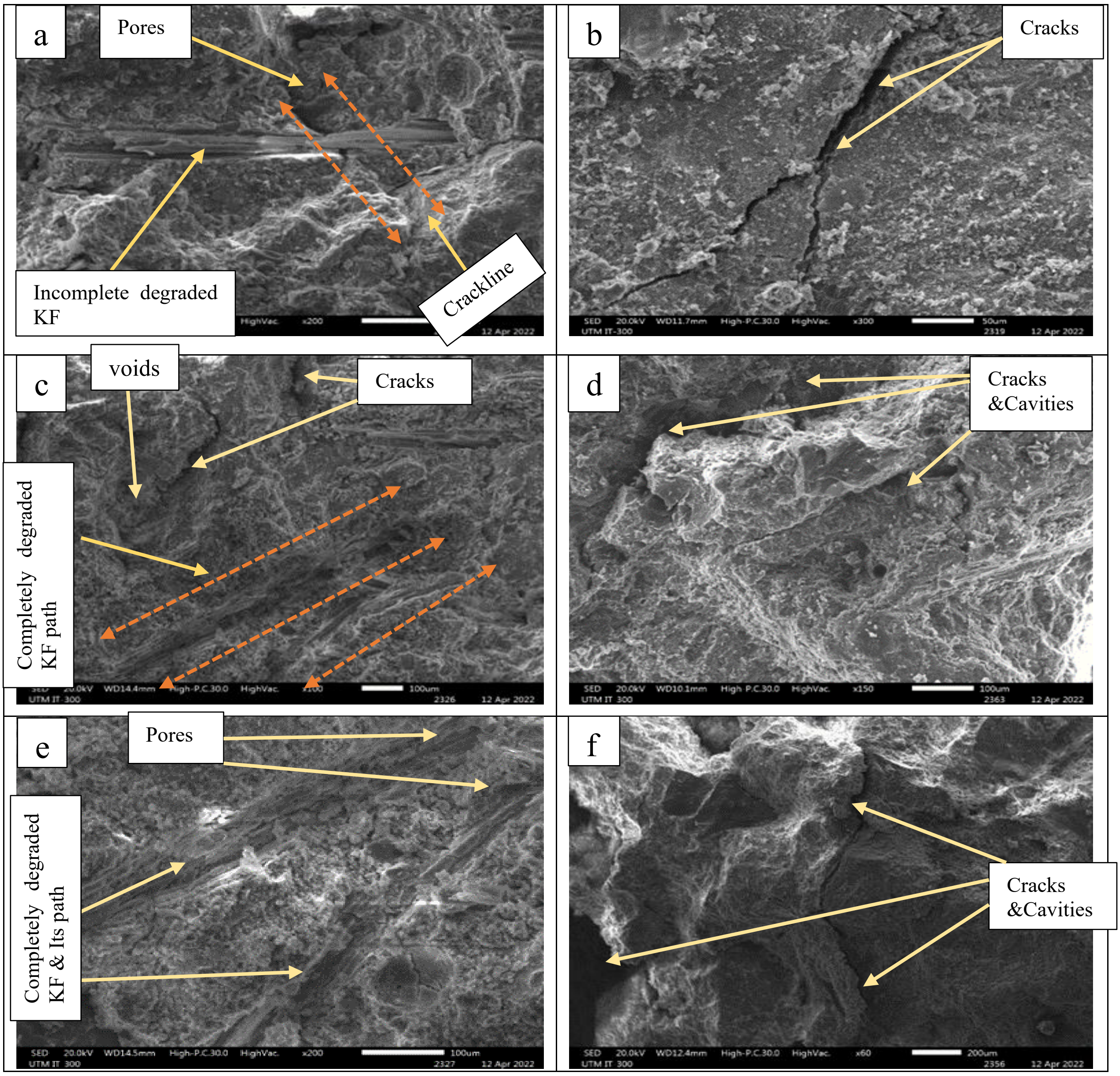

Figure 9:(a)SEM Image@ 800ºC: (a) KFHSC-1H, (b) PHSC-1H, (c) KFHSC-2H, (d) PHSC-2H, (e) KFHSC-3H, (f) PHSC-3H

4 CONCLUSIONS

- Weight loss and UPV value reduction were significant in KFHSC compared to PHSC because of the low density and high permeability of the matrix compared with the PHSC
- KFHSC for 1H climaxed its strength at 300ºC and slightly maintained till 400ºC. Compressive strength loss in KFHSC is less of fibre's consumable effect but more of concrete material deterioration under thermal load.
- KFHSC samples performed comparatively with PHSC samples before 400ºC, with a remarkable ductile failure mode for split tensile strength. Unlike PHSC, which fails suddenly.
- The morphological images were appropriately well-matched with mechanical properties. 1H fire exposure for KFHSC, up to 800ºC, the KF still effectively ameliorated crack propagation and thermal incompatibility of the aggregate and cement paste within the matrix, which was an

advantage over PHSC samples. Also, for 2H heating, this mechanism was sustained till 400ºC before the complete deterioration of the matrix. For a 3H, deterioration of the materials commenced at 400ºC and continued till 800ºC with a massive ‘coarsening effect’ on both matrices. At this temperature, both matrices have transformed from crystal to amorphous structures.

- According to these findings, for an optimum fibre volume fraction of 9kg/m^3, the application of KFHSC should not be exposed to a temperature beyond 600ºC for 1H exposure and 400ºC for 2 and 3H exposure periods.
- The collapse of concrete members becomes imminent if explosive spalling is added to the worsening condition the concrete has suffered under thermal load. Thus, based on this microstructural analysis, KF benefits high-strength concrete exposed to elevated temperatures. Apart from the crack-arresting capability, post-cracking stress distribution, especially at the lower temperature phase, cushions the effect of thermal strain due to thermal incompatibility between aggregates and hardened cement paste.

ACKNOWLEDGMENT

The authors expressed profound gratitude for the support from Research Management Centre through the HiCOE grant, R.J130000.7822.4J222. Also, the Technical Staff at the Structure and Materials laboratory of the School of Civil Engineering, Universiti Teknologi Malaysia. The financial supports received from the Federal Government of Nigeria via TETFund are well-appreciated.

REFERENCES

[1] M. A. Aziz, P. Paramasivam, and S. L. Lee, “Prospects for natural fibre reinforced concretes in construction,” *Int. J. Cem. Compos. Light. Concr.*, vol. 3, no. 2, pp. 123–132, 1981.

[2] A. Elsaid, M. Dawood, R. Seracino, and C. Bobko, “Mechanical properties of kenaf fiber reinforced concrete,” *Constr. Build. Mater.*, vol. 25, no. 4, pp. 1991–2001, 2011.

[3] and K. A. H. Hector Archila, Sebastian Kaminski, David Trujillo, Edwin Zea Escamilla, “Bamboo Reinforced Concrete – a Critical Review.”

[4] G. F. Peng, W. W. Yang, J. Zhao, Y. F. Liu, S. H. Bian, and L. H. Zhao, “Explosive spalling and residual mechanical properties of fiber-toughened high-performance concrete subjected to high temperatures,” *Cem. Concr. Res.*, vol. 36, no. 4, pp. 723–727, 2006.

[5] M. Ozawa and H. Morimoto, “Effects of various fibres on high-temperature spalling in high-performance concrete,” *Constr. Build. Mater.*, vol. 71, pp. 83–92, 2014.

[6] M. A. Moghadam, D. Ph, R. A. Izadifard, and D. Ph, “Effects of steel and glass fibers on mechanical and durability properties of concrete exposed to high temperatures,” *Fire Saf. J.*, vol. 113, no. January, p. 102978, 2020.

[7] M. Ozawa, R. Sato, M.-H. Yoon, K. Rokugo, G.-Y. Kim, and G.-C. Choe, “Thermal properties of jute fiber concrete at high temperature,” *J. Struct. Fire Eng.*, vol. 7, no. 3, pp. 182–192, 2017.

[8] D. Zhang, K. H. Tan, A. Dasari, and Y. Weng, “Effect of natural fibers on thermal spalling resistance of ultra-high performance concrete,” *Cem. Concr. Compos.*, vol. 109, no. January, p. 103512, 2020.

[9] N. N. M. N. &Suriani M. J. Nur Fikriah Hashim, Nuraqilah Mohd Zainal, Nurain Jamil, “Strength and Durability of Kenaf Fiber Reinforced Concrete For Marine Structures,” *Univ. Malaysia Teren. J. Undergrad. Res.*, vol. 1, no. 1, pp. 1–9, 2019.

[10] M. Ramesh, *Hemp, jute, banana, kenaf, ramie, sisal fibers*. Elsevier Ltd, 2018.

[11] O. E. Babatunde, J. M. Yatim, M. Razavi, I. M. Yunus, and N. M. Azzmi, “Experimental Study of Kenaf Bio Fibrous Concrete Composites,” vol. 24, no. 6, pp. 3922–3927, 2018.

[12] I. Netinger Grubeša, B. Marković, A. Gojević, and J. Brdarić, “Effect of hemp fibers on fire resistance of concrete,” *Constr. Build. Mater.*, vol. 184, pp. 473–484, 2018.

[13] BS-EN-14889-2, “Fibres for concrete - Part 2: Polymer fibres. Definitions, specifications and conformity,” *Bsi*, vol. 3, p. 30, 2006.

[14] ASTM C 136-06, “ASTM C 136-06: Standard Test Method for Sieve Analysis of Fine and Coarse Aggregates,” pp. 5–9, 2006.

[15] ASTM-C150, “ASTM C150,” vol. 04, pp. 1–7, 2002.

[16] A. C494-04, “Standard Specification for Chemical Admixtures for Concrete,” *Annu. B. ASTM Stand.*, no. February, pp. 1–9, 2008.

[17] T. F. Lam and J. M. Yatim, “Mechanical properties of kenaf fiber reinforced concrete with different fiber content and fiber length,” *J. Asian Concr. Fed.*, vol. 1, no. 1, p. 11, 2015.

[18] BS EN 12350-2, “Testing fresh concrete, Part 2: Slump-test. BSI,” 2009.

[19] ISO 834-12, “INTERNATIONAL STANDARD:Fire resistance tests — Elements of building construction,” 2012.

[20] ASTM E119-16a, “ASTM E119: Standard Test Methods for Fire Tests of Building Construction and Materials,” *ASTM Int. West Conshohocken, PA*, vol. 552, no. 1, 2016.

[21] B. E. 12390-3:2019, “Testing hardened concrete Compressive strength of test specimens,” *Br. Stand. Inst.*, p. 24, 2019.

[22] BS EN 12390-6, “Testing hardened concrete: Tensile splitting strength of test specimens. BSI,” 2009.

[23] V. Kodur, “Properties of Concrete at Elevated Temperatures,” *ISRN Civ. Eng.*, vol. 2014, pp. 1–15, 2014.

[24] A. S. M. A. Awal and I. A. Shehu, “Performance evaluation of concrete containing high volume palm oil fuel ash exposed to elevated temperature,” *Constr. Build. Mater.*, vol. 76, pp. 214–220, Feb. 2015.

[25] B. Demirel and O. Keleştemur, “Effect of elevated temperature on the mechanical properties of concrete produced with finely ground pumice and silica fume,” *Fire Saf. J.*, vol. 45, no. 6–8, pp. 385–391, 2010.

[26] J. . B. Neville, A.M, *Concrete Technology 2nd edition*, Second edi. Longman Group UK Limited, 2010.

[27] S. Juradin, L. K. Vranješ, D. Jozić, and I. Boko, “Post-fire mechanical properties of concrete reinforced with spanish broom fibers,” *J. Compos. Sci.*, vol. 5, no. 10, pp. 1–17, 2021.

[28] I. Afshoon and Y. Sharifi, “Utilization of micro copper slag in SCC subjected to high temperature,” *J. Build. Eng.*, vol. 29, no. December 2019, p. 101128, 2020.

[29] C. Wang, X. Chen, X. Wei, and R. Wang, “Can nanosilica sol prevent oil well cement from strength retrogression under high temperature?,” *Constr. Build. Mater.*, vol. 144, pp. 574–585, 2017.

[30] O. G. Aluko, J. M. Yatim, M. A. A. Kadir, and K. Yahya, “A review of properties of bio-fibrous concrete exposed to elevated temperatures,” *Constr. Build. Mater.*, vol. 260, p. 119671, 2020.

[31] S. M. Imane Mihoub, Mohammed Rissel Khelifa, “Impact of Elevated Temperature On The Properties of Concretes Reinforced,” *Civ. Environ. Eng. REPORTS*, vol. 30, no. 3, pp. 161–185, 2020.

[32] T. F. Lam, “Effect Of Kenaf Fibre On The Mechanical Properties Of Reinforced Concrete Structures,” Universiti Teknologi Malaysia, 2017.

[33] I. Hager, “Behaviour of cement concrete at high temperature,” *Bull. Polish Acad. Sci. Tech. Sci.*, vol. 61, no. 1, pp. 145–154, 2013.

MULTI-OBJECTIVE OPTIMIZATION OF REINFORCED CONCRETE SLABS EXPOSED TO NATURAL FIRES

Ranjit Kumar Chaudhary[1], Balša Jovanović[2], Thomas Thienpont[3], Thomas Gernay[4] and Ruben Van Coile[5]

ABSTRACT

Risk-based designs are complicated and often computationally challenging, involving numerous design parameters, design objectives and design constraints. In structural fire engineering, single-objective optimization is commonly adopted for risk-based designs, but this approach may converge to a local optimum, leading to uneconomical design solutions. Implementation of multi-objective optimization (MOO) algorithms can address these issues for risk-based designs. This study explores the implementation of MOO for design of reinforced concrete slabs exposed to natural fires. The natural fire exposure is modelled through the Eurocode parametric fire curve, relating the fire load density to the building occupancies (as listed in EN 1991-1-2:2002). To reduce the computational cost, a non-dominated sorting genetic algorithm (NSGA-II) is considered for MOO in this study. Adopting MOO approach, an optimized design is obtained which reduces the reinforcement cost in slab by 40 % and the environmental cost by 25 %, compared to the prescriptive design approach. The results from such risk-based design optimization could be taken into account when defining prescriptive design requirements.

Keywords: Reinforced concrete slab; natural fires; risk-based design; multi-objective optimization; genetic algorithm

1 INTRODUCTION

Fire safety regulations are commonly implemented through prescriptive design guidance. These guidance are based on the historical experience, learnt over time in response to fire disasters. In most cases, adequate safety can be achieved in (common) structures which fall within this experience [1], but adequacy for uncommon structures is unproven. With the increased use of innovative structural materials, preference of exceptional architectural designs and the adoption of advanced engineering solutions, the application of prescriptive guidance is narrowing. Realising the limitations of prescriptive guidance, performance-based design (PBD) is increasingly preferred [2]. One of the commonly accepted tools for PBD is probabilistic risk assessment (PRA) [1]. In performance-based approaches, fire safety objectives are clearly defined.

---

[1] PhD student, Ghent University
e-mail: RanjitKumar.Chaudhary@ugent.be, ORCID: https://orcid.org/ 0000-0002-1104-5859
[2] PhD student, Ghent University,
e-mail: Balsa.Jovanovic@ugent.be, ORCID: https://orcid.org/0000-0001-5200-5848
[3] PhD student, Ghent University
e-mail: Thomas.Thienpont@ugent.be, ORCID: https://orcid.org/ 0000-0003-1466-3377
[4] Assistant professor, Johns Hopkins University
e-mail: tgernay@jhu.edu, ORCID: https://orcid.org/ 0000-0002-3511-9226
[5] Associate professor, Ghent University
e-mail: Ruben.VanCoile@ugent.be, ORCID: https://orcid.org/ 0000-0002-9715-6786
https://doi.org/10.6084/m9.figshare.22177850

Societal objectives such as life-safety form the benchmark for the design and the stakeholders are free to introduce their additional objectives (e.g., reduced structural down-time after damage, higher design life, intact aesthetic appearance, etc.). The PRA based performance criteria for design objectives are aimed at reducing the structural risk to "As Low As Reasonably Practicable" [1,3]. The probabilistic evaluation of these criteria however demands huge computational expense.

Risk-based designs in fire safety engineering are generally single-objective optimization based, especially through cost-benefit analysis by balancing cost of a safety measure against the benefits of risk reduction [4, 5, 6, 7]. In these investigations, when multiple objectives exist, they are combined to form a single objective function. These single-objective based optimizations may converge to a local optimum, potentially leading to uneconomical results [8]. Further, for developing single-objective formulations, all the objectives need to be transformed to a single utility value. For example, when the optimization includes the minimization of CO_2 emissions, the objective is often transformed into an equivalent monetary value. Adoption of a multi-objective optimization (MOO) method has the potential to address these shortcomings of single-objective optimization problems [8], but has yet to be studied in the structural fire engineering context.

The current study shows that risk-based design can be carried out through multi-objective optimization. To demonstrate this, a case study of a fire exposed reinforced concrete (RC) slab is considered. The fire exposure for the slab is modelled by a natural fire, including the decay phase. For the MOO of the RC slab, a computationally efficient genetic algorithm (GA) is adopted [8]. This study therefore demonstrates a novel risk-based design approach for fire exposed structures. Within the approach, additional design objectives, design parameters, and constraints can be introduced, leading to a flexible PBD framework.

2 MULTI-OBJECTIVE OPTIMIZATION METHOD

The solution of a MOO problem involves determining the design variables that result in optimum objective function values. These optimum design variables lie within the feasible region. Eq. (1) represents a general MOO problem:

$$\left\{\begin{array}{lll} Maximize/minimize & f_m\,(x), & m = 1,2,\dots,M \\ subjected\ to & g_j\,(x) \geq 0, & j = 1,2,\dots,J; \\ & h_k\,(x) = 0, & k = 1,2,\dots,K; \\ & x_i^L \leq x_i \leq x_i^U, & i = 1,2,\dots,n \end{array}\right\} \tag{1}$$

where $x = [x_1, x_2 \dots\dots x_n]^T$ is a vector of design variables. The design variables themselves are subjected to the last set of constraints, with L the lower bound and U the upper bound. These bounds constitute the variable design space $\mathcal{D}$. Further, $g_j(x)$ and $h_k(x)$ are a set of J inequality and K equality constraints and $f_m(x)$ is a set of M design objectives. The design objectives form the objective space $\mathcal{Z}$.

Single-objective optimizations result in a single-optimal solution (a point), while the MOO method results in a set of optimal solutions, commonly referred to as Pareto-optimal solutions. The solutions are a set of non-dominated points calculated through the principle of dominance, which states that these sets are the ones that are not dominated by any other solution set. The boundary defined by these Pareto-optimal solutions is called a Pareto-optimal front. The main objective of MOO is finding the set of solutions which are diverse (spread-over the objective space) and close to the Pareto-optimal front.

MOO is a well-recognised approach in engineering for solving a variety of problems [8]. Even in structural engineering, the application of MOO for design optimization is well-recognised. Some of the applications related to seismic design can be found in [9-11], where member cross-sections are optimized by minimizing the structural damage and cost. Other applications relate to the maintenance planning for reinforced concrete bridges [12], minimizing environmental effects of RC frame designs [13], in construction project management [14] etc. MOO algorithms can mainly be classified into two groups: (i) Classical methods and (ii) Evolutionary algorithms. The classical methods have several disadvantages: they are slow and require many computations, resulting in a biased solution. They often converge to a local/sub-optimal solution and are difficult to implement with parallel computing [8]. Most of the evolutionary algorithms overcome these limitations. Therefore, the current study adopts a genetic algorithm (non-dominated sorting algorithm, referred as NSGA-II), which is a type of evolutionary algorithm [8-10].

3 REINFORCED CONCRETE SLAB EXPOSED TO NATURAL FIRES

3.1 Problem description

The considered RC slab is one-way simply supported, 0.2 m thick and reinforced at the bottom face with bars of 10 mm diameter spaced at 100 mm centre to centre. The reinforcement bars have a clear concrete cover of 15 mm (i.e., the reinforcement axis at 20 mm from the bottom face). The concrete slab is a part of a compartment of size 6 m × 4 m × 3 m. The concrete has a characteristic strength of 30 MPa, while the yield strength of reinforcement is 500 MPa. The same slab has been investigated in [16, 17] for probabilistic assessment of fire-exposed structures. The slab is exposed to fire at the bottom face, while the top face is in contact with air at ambient temperature. The fire exposure to the slab is modelled using the Eurocode parametric fire curve [15]. Slabs from two types of building occupancies (office and residential building, considering fire load densities listed in the EN 1991-1-2:2002) are considered for the evaluations [15].

3.2 Bending moment capacity evaluation

The bending moment capacity of the slab (M_R) is evaluated based on Eq (2), which allows determining the bending moment capacity at both the ambient and elevated temperatures. At ambient condition, the temperature of reinforcing bars (T) is considered as 20°C. For fire exposure, a thermal analysis is carried out to evaluate the temperature in the rebars over time. In Eq (2), A_s refers to the area of reinforcement in the slab, $k_{f_y(T)}$ is the yield strength retention factor for reinforcement yield stress, h and b refers to the depth and width of the slab, c is the clear concrete cover to reinforcement and ϕ is the diameter of reinforcement. $f_{y,20°C}$ and $f_{c,20°C}$ stand for yield strength of reinforcing bars and strength of concrete, respectively, at ambient temperature. The design bending moment capacity of the slab at ambient conditions is calculated as 59 kN-m (considering 1.5 and 1.15 as the safety factor for concrete and steel strength).

$$M_R = A_s k_{f_y(T)} f_{y,20°C}\left(h - c - \frac{\phi}{2}\right) - 0.5\frac{\left(A_s k_{f_y(T)} f_{y,20°C}\right)^2}{b f_{c,20°C}} \tag{2}$$

The thermal analysis for RC slab is carried out through a 1-D numerical heat transfer model. In the analysis, the entire cross-section of the slab is modelled as concrete, and the fire exposure at the bottom face is applied through convection and radiation. More details and validation of the numerical heat transfer can be found in [17]. The thermal evaluation for the RC slab is carried out until the temperatures in the section cool down close to ambient, to consider stability until full 'burnout' [18]. Figure 1 shows the maximum temperature of the reinforcing bars evaluated for natural fire exposure of RC slab. Herein, various parametric fires with varying fire load density (q_f) and opening factor (O) are considered. The results are shown for two reinforcement axis distances (20 and 60 mm). In the Figure, the temperatures vary widely for change in both the parameters of parametric fire exposure (q_f and O) and the reinforcement axis distances. With the maximum temperature of reinforcing bars determined, the critical bending moment capacity of RC slab for different fire exposure can be assessed based on Eq (2). Based on the prescriptions in the Eurocode [15], the mean fire load density for an office and residential building corresponds to 420 MJ/m^2 and 780 MJ/m^2, respectively. The maximum temperatures for these fire loads are 380 and 480 °C (for O = 0.04 m$^{1/2}$ and a = 20 mm) and the corresponding moment capacity can be calculated as 59 kN-m (same as design) and 45 kN-m, respectively, considering Eurocode [20] strength reduction factors.

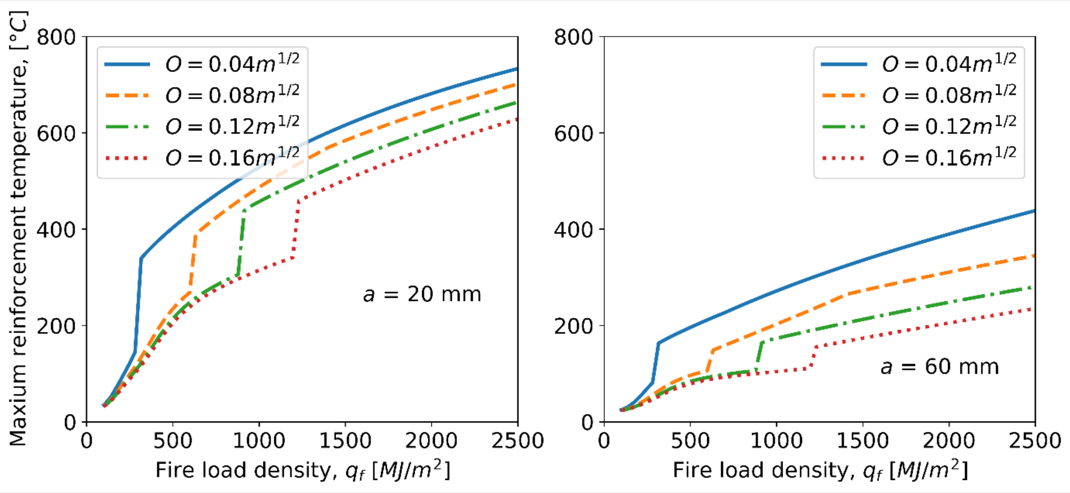

Figure 1. Maximum temperature of reinforcing bars of RC slab for parametric fire exposure, considering reinforcement axis distance, *a* of 20 and 60 mm.

4 DESIGN PARAMETERS AND OBJECTIVES FOR RC SLAB OPTIMIZATION

4.1 Definition of design parameters and objectives

For ambient design conditions, Eurocode [19] recommends a target reliability index of 3.8 for moderate consequences (50 year reference period). The parameters of bending moment capacity in Eq (2) can be adjusted to achieve this design target, e.g., by increasing the area of reinforcement A_s. The design target for fire exposure is however not clear. For fire design, Eurocode [20] tabulates a nominal 20 mm as the required reinforcement axis (*a*) for RC slabs to achieve 60 minutes standard fire rating. This is a prescriptive value and the resulting safety level or economic optimality is unknown. Herein the optimum value of this parameter is decided through a risk-based design approach. As the reinforcement axis distance is varied, the ambient design capacity changes and there is a need to change the reinforcement area to maintain the ambient design capacity constant. These two variables ('a' and A_s) are considered as design parameters in this study. Note also that the influence of other parameters on design moment capacity is relatively smaller. The influence of these parameters on ambient design moment capacity is shown in Figure 2. A_s significantly influences the slab's capacity, while the influence of 'a' increases with an increase in A_s. 'a' will however have a large influence on the slab capacity at elevated temperature, as can be deduced from the rebar temperatures in Figure 1.

Three costs are associated with evaluating the optimum design parameters for the slab: the investment cost (including its obsolescence value), the (lifetime) failure cost, and the environmental cost. The minimization of these costs allows designing the slab at minimum cost and therefore are considered as objective functions for design optimization of RC slab. The investment cost and the environmental cost are proportional to the amount of reinforcement in slab, while the failure cost is governed by the ultimate limit state and the structural failure probability. The impact of failure on the environmental cost is not considered at this point. The upfront justification is that the failure frequency should be so low that the environmental impact is limited. The Eurocode ambient design target [19] for reliability index is considered as constraint for the design optimization.

4.2 Investment cost

Out of the two design parameters, the investment cost is only associated with the increased reinforcement area of the RC slab. The reinforcement area of the slab with reinforcing bars of 10 mm diameter and spacing of 200 mm (centre to centre) is considered as reference case (A_s of 393 mm^2). The maximum A_s considered for the optimization is 3930 mm^2. Note that for this value, the section is not over-reinforced . Figure 3 shows the investment cost as a function of the reinforcement area in the slab. The cost is obtained from RSMeans [21], a database for building and construction costs. The cost of reinforcing bars for the slab is

1.31 USD ($)/lb (i.e., 2.89 $/kg) for US national average. This cost includes the labour, material and overhead costs. For the reference case, the cost of reinforcement for the slab (per m^2) is 2.89 ($/kg) × 7850 (steel density in kg/m^3) × 393/(106) (m^2) = 8.92 $. For the maximum limit of reinforcement area (i.e., 393 mm^2), the cost could increase to 89.2 $/$m^2$. For slab of size (6m × 4 m), the cost is 2141 $, an increase of 1927 $ over the reference case. This cost corresponds to a single slab in the building. Considering all the slabs in the building, the cost would be large. The cost has been evaluated considering the slab size of 6 m × 4 m. In this study, the investment cost includes the obsolescence value (lifetime). An obsolescence rate (ω) of 0.022/year [22] is considered for this. For lifetime evaluation of obsolescence cost, a discounting factor of 0.03/year (for societal stakeholders [23]) is applied. The total investment cost, C_I with obsolescence value can be written as:

$$C_I = C_{I,0}(1 + \frac{\omega}{\gamma}) \tag{3}$$

where, $C_{I,0}$ is the investment cost for reinforcing bars in the slab.

4.3 Environmental cost

Environmentally friendly design solutions are increasingly preferred over cost-effective solutions [24] because of the increased concerns related to greenhouse emissions from the construction industry (amounting to about 12 % of total emissions in Western Europe). This study, therefore, considers reducing the environmental impact of structural design as one of the objectives, with CO_2 emissions as the environmental cost indicator [25]. The cost of added reinforcements for RC slab contributes to the additional CO_2 emission. This is estimated based on [24], where the total life-cycle CO_2 emission per kg of steel is estimated as 3.01 kg. Figure 3 shows the CO_2 emissions calculated for the increased reinforcement area of RC slab. The increased reinforcement area could cause 2000 kg CO_2 emission equivalent and thus there is a need to consider this cost, which in the reference case amounts to 220 kg (10 times lower).

4.4 Life-time failure cost

Failure cost minimization under fire-exposure is another objective considered in the design optimization of the RC slab. The evaluation of the life-time cost (*D*) is risk-based and conditional on the fire exposure scenario, given by:

$$D = \frac{\lambda_{fi} P_{sf} \mu_D}{\gamma} \tag{4}$$

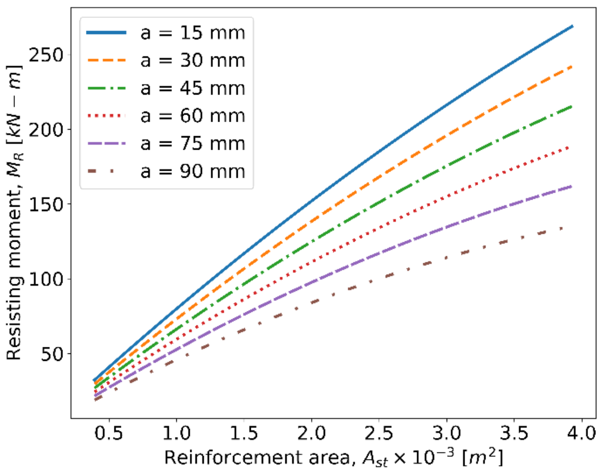

Figure 2 Ambient bending moment capacity of the RC slab as a function of reinforcement area and its axis position.

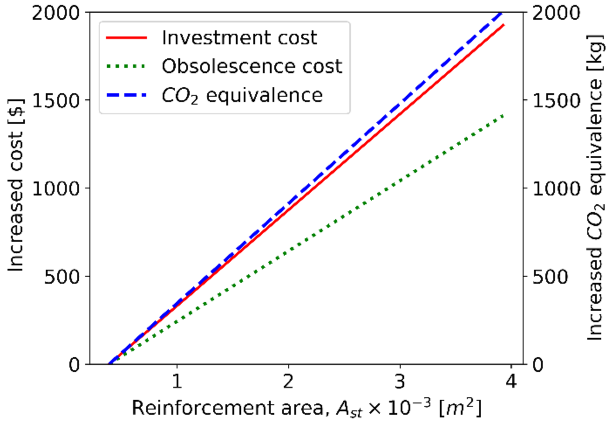

Figure 3. Investment cost, obsolescence cost, and CO_2 emission [kg] equivalent function of the reinforcement area of the slab.

where, λ_{fi} is the yearly probability of a structurally significant fire, P_{sf} is the probability of structural failure given fire, and μ_D is the mean failure cost for the given fire. The same discounting factor (γ) as in the obsolescence life-time cost evaluation is taken here (0.03 for societal stakeholders). Based on [26], the annual fire occurrence frequency for office building is 0.00423, while it is 0.00151 for a residential building (united states). Probability of fire occurrence are reported values, while the failure normally occurs for structurally significant fires. The structurally significant fires are commonly estimated by considering successful early fire suppression because of the presence of active fire protection systems (reduction factor of 0.08 considered [27]) and other factors such as the efficiency of the fire and rescue service system (reduction factor of 0.10 considered [28]). The evaluation of the failure cost for the structure includes direct costs and indirect costs, and is normally evaluated as a factor (ξ) of the initial construction cost (C_0), as in Eq (5). Direct costs involve the costs from structural components, non-structural components, contents of the building, fatalities and injuries of civilians and fire-fighters, and can be statistically determined. Determination of indirect cost is challenging and often subjective.. In this study, the failure cost for the RC slab is evaluated as a factor of the initial structural cost. Based on RSMeans [21], the cost per square foot for an office building is (C_0) 303 $ psf (3261 $/m^2), while that of a multi-family dwelling (1-3) is 215 $ psf (2314 $/m^2). These costs include the cost of both structural and non-structural components. The failure cost is evaluated considering the loss of entire compartment in the event of failure. Here, a failure cost factor of 100 is adopted for the evaluations and also a parametric study is conducted for this. This cost takes into account that the failure of a compartment slab is likely to result in extensive damages to the remainder of the building and inability to use a large part of the structure for a prolonged time. For office buildings a failure cost factor of 7 is commonly considered in earthquake engineering [29]. The cost factor considered here thus assumes that the local structural failure results in a loss of usability in an area with order of magnitude 15 times larger than the 24 m^2 compartment.

$$\mu_D = \xi C_0 \tag{5}$$

The structural failure probability is evaluated considering the exceedance of the bending moment capacity of the slab as a limit state. The limit state equation, Z can be written as:

$$Z = K_R M_{R,fi} - K_E\left(M_G + M_Q\right) \tag{6}$$

where, $M_{R,fi}$ stands for bending moment capacity for fire exposure and M_G and M_Q are the moments from permanent and imposed loads, respectively. $M_{R,fi}$ is evaluated based on Eq (2), while the characteristic moments due to loads are evaluated from the design moment of the considered slab, considering Eurocode safety factors. K_R and K_E are the model uncertainties for the capacity and load evaluations.

The characteristic moments due to loads are:

$$M_G = \frac{M_{Rd}}{max\left\{\left(\gamma_G + \psi_0 \gamma_Q \frac{\chi}{1-\chi}\right); \left(\xi \gamma_G + \gamma_Q \frac{\chi}{1-\chi}\right)\right\}} \tag{7}$$

$$M_Q = \frac{\chi}{(1-\chi)} M_G \tag{8}$$

where, M_{Rd} refers to the design moment capacity of the slab at ambient conditions for the reference design (calculated as 59 kN-m). γ_G (1.35) and γ_Q(1.5) are the partial safety factors for the permanent and imposed load. ξ (0.85) is the reduction factor considering the unfavourable occurrence of permanent load. ψ_0 for office building is commonly 0.7. The same value of ψ_0 is considered for residential building as well. The load factor (χ) is assumed as 0.5 for the load moment evaluations.

The failure probability of the RC slab is evaluated based on Eq (9), where Z is the limit state equation. Table 1 lists the stochastic parameters for evaluating $M_{R,fi}$ and the load moments (M_G and M_G). A Monte-Carlo approach is adopted for the evaluations.

$$P_{sf} \;=\; P[Z < 0] \tag{9}$$

$M_{R,fi}$ involves a thermo-mechanical analysis as discussed in Section 3.2. Note that in Table 2, the probabilistic model for strength retention factor for yield strength of reinforcing bars include the uncertainty in yield strength at 20°C. 10^5 MC (Monte Carlo) realizations are developed for the estimation of $M_{R,fi}$. For computational efficiency, an interpolation function (3-dimensional) is developed to evaluate the temperature of reinforcing bars, with axis distance ('a'), fire load density (q_f) and compartment opening factor (O) as input parameters. The evaluation for load moments is based on 10^{10} MC realizations. Figure **4** shows the failure probability for the slab at different values of design parameters ('a' and A_s). Two fire exposure scenarios are considered (i.e., $q_{f,nom}$ of 420 and 780 MJ/m^2). From the figure, it can be concluded that the addition of reinforcing bars could reduce the failure probability of RC slab from a level of 1.0 to 10^{-9}. Reinforcement axis distance changes the failure probability marginally in slabs with a lower reinforcement area, while significantly with a higher reinforcement area. Comparatively, fire exposure with 780 MJ/m^2 is considerably more critical than 420 MJ/m^2 for the RC slab when comparing failure probability.

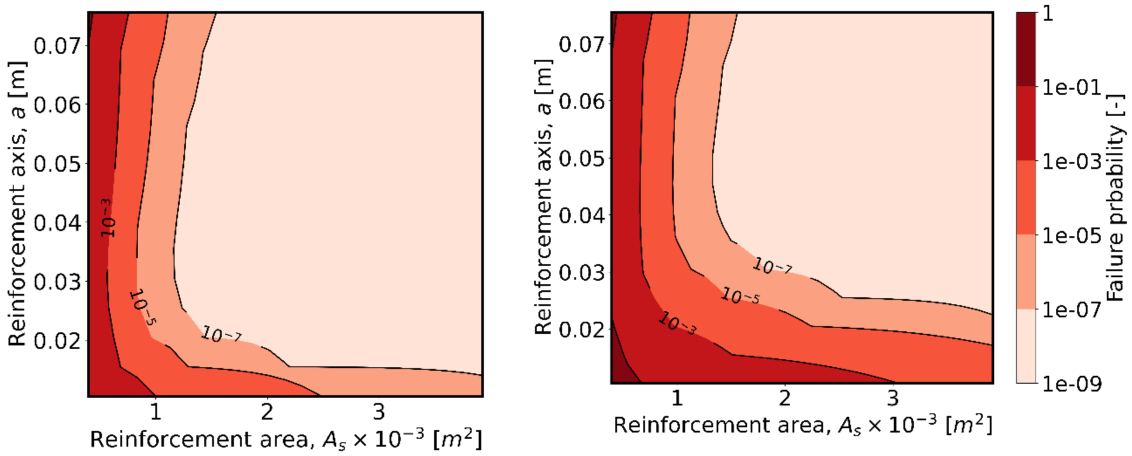

(a) $q_{f,nom}$ = 420 MJ/m^2 (b) $q_{f,nom}$ = 780 MJ/m^2

Figure 4 Failure probability of RC slab for fire exposure with fire load density of (a) 420 and (b) 780 MJ/m^2 at different values of reinforcement area and its axis position (constant compartment opening factor of O = 0.04 m$^{1/2}$).

Table 1 Stochastic parameters for probabilistic evaluation of moment capacity and the moments due to load for RC slab

Variables	Symbol [unit]	Distribution	Mean, μ	SD, σ
Moment capacity, $M_{R,fi}$				
Slab thickness	h [m]	Normal [30]	200	5
Concrete strength	f_c (20°C) [MPa]	Lognormal [30]	42.9	6.4
Reinforcement yield strength retention factor	$k_{fy,T}$ [-]	Temperature dependent lognormal model [31]		
Reinforcement axis	'a' [mm]	Beta(4,4) [30]	a_{nom} + 5 [12 – 80]	5
Reinforcement area	A_s [mm^2/m]	Normal [30]	1.02 $A_{s,nom}$	$0.02\mu_{As}$
Fire load density	q_f [MJ/m^2]	Gumbel [15]	$q_{f,nom}$ [420 and 780]	$0.3\mu_{qf,nom}$
Compartment opening factor	O [m$^{1/2}$]	Deterministic	O [0.04-0.16]	-
Moment due to loads				
Permanent load	M_G [kN-m]	Normal [32]	M_G	0.1 $\mu_{M,G}$
Imposed load	M_Q [kN-m]	Gamma [32]	0.2× M_Q	$0.95\mu_{M,Q}$
Model uncertainties				
capacity estimation	K_R **[-]**	Lognormal [30]	1.1	0.11
Load estimation	K_E **[-]**	Lognormal [32]	1	0.1

4.5 Ambient design verification

In this study, the ambient reliability index is considered as a constraint so that the design of RC slab is optimized for fire exposure only. he considered ambient design target reliability in this study (3.8) is lower than the requirement in EN 1990:2002 since the load models applied are for a 1-year reference period. Figure 5 shows the ambient design target reliability evaluated at different values of the reinforcement area and its axis positions. In the Figure, with an increase in reinforcement area, the ambient capacity of the RC slab increases and thus also the corresponding reliability index. Conversely, an increase in axis distance (from the bottom face) reduces the reliability.

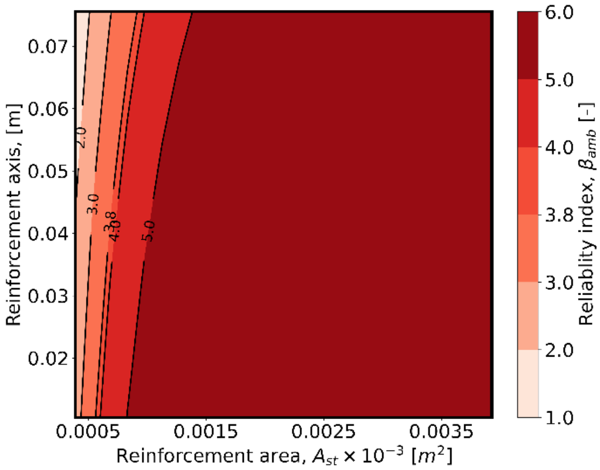

Figure 5 Ambient design target reliability index for RC slab at different values of design parameters.

5 MULTI-OBJECTIVE OPTIMIZATION FOR A RC SLAB EXPOSED TO FIRE

In the RC slab optimization, two design parameters, three design objectives, and one constraint have been identified (in Section 4). The NSGA-II algorithm is adopted for the optimization, where a population size of 100 for 60 generations, with 10 off-springs in each generation are used for the optimization input. Diverse Pareto-front solutions are obtained for these NSGA-II optimization parameters. The Pareto-front solutions can be seen in Figure 6b where the objective space is presented. The design space shows the points corresponding to the Pareto-front solutions of Figure 6a. The results are shown here only for RC slabs of a residential building occupancy, considering q_f of 780 MJ/m^2 and O of 0.04 m$^{1/2}$. A failure cost factor (ξ) equal to 100 times the initial construction cost is considered. The optimum values for A_s and a obtained are 583 mm^2/m and 16 mm, respectively. These are shown by grey lines in the figure. The optimum value is obtained by evaluating the distance of the normalized Pareto-front solutions from an ideal solution where investment, failure and environmental cost have zero values. The Pareto-front point with the minimum distance is the optimum solution. The investment and the failure cost-points are normalized by a maximum value of these two costs for all Pareto-front points, whereas the environmental cost by maximum value of the environmental cost before evaluating the distances. There is a possibility to consider different (need-based) importance factor for the design objectives, for example, environmental costs could be more significant. Additionally, the environmental cost here is CO_2 emission based and could be transformed to an equivalent monetary value. For this situation, the normalization factor would be the maximum of all these three costs and the obtained optimum solution is economically optimum.

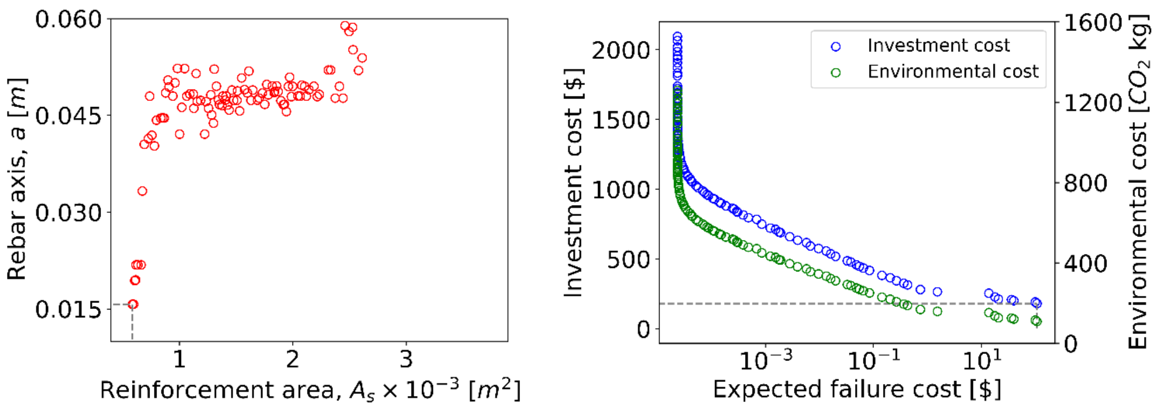

(a) Design space
(Pareto-front points only)

(b) Objective space
(Cost Pareto-fronts)

Figure 6 (a) Design space and (b) objective space for MOO of a RC slab, considering residential occupancy (q_f = 780 MJ/m^2 and O = 0.04 m$^{1/2}$). The failure cost factor is 100 times of the initial structural cost

The determination of failure cost factor (ξ) of a fire-exposed RC slab is problematic, owing to the uncertain costs of the contents inside the building, fatalities and injury to occupants and the associated indirect costs. The failure cost factor is thus considered as a variable in the study. Table 2 presents the optimum value of the design parameters at different failure cost factors. Also, the optimum objective function evaluations are shown in the Table. Results are shown for both the residential and office occupancy of the building. In the Table, the expected annual failure cost evaluated for lower ξ (< 100) is smaller in comparison to the investment cost. This is because ambient design constraint (β_{amb}) governs the optimum parameters for these cases. In Table 2, the optimum reinforcement area for ξ of 3 and 10 is 584 mm^2, while reinforcement axis positions are 16 mm. The optimum 'a' here is based on failure cost minimization and therefore, the total cost value increases for both the increase or decrease in 'a'.

The considered slab in the study has reinforcement area of 785 mm^2 (10 rebars at 100 mm c/c). Based on [20] (see, Table 2) , the axis positions are 20 mm and 40 mm for 1- and 2-hour of ISO fire-rating. When compared to the considered slab, the optimum design (with ξ of 2 and 10) has 25 % less reinforcement cost and the axis position of 16 mm is optimum. Further, considering the depth of slab as fixed, the higher axis positions recommendation in [20] for normal design condition (for 1- and 2-hour of ISO fire-rating) accounts for increase in reinforcement area to 785 mm^2 and 896 mm^2 to maintain constant design bending moment. This shows the reinforcement cost to be 2.4% and 15 % lesser for MOO based optimum design . Also, the CO_2 emissions is 25 % (linear model considered) for the MOO design. The same observation can also be made for the residential building. In Table 2, the failure cost could go as high as 606 \$ for ξ of 10000. The failure cost can be high when a prescriptive approach is adopted, since 20 mm of cover is recommended by [20] for 1-hour of prescriptive fire resistance. Thus, MOO based designs leads to economical design solutions.

These design optimizations are presented here for a single RC slab member. If all of the slabs for a multi-story structure are considered, the overall cost reduction can be significant. In Table 2, we see how the reinforcement area and axis positions vary with the increased ξ and thus "building importance classes" can be defined for these different levels of ξ with target reliabilities, and associated "prescriptive" design provisions.

In this study, a MOO approach is demonstrated for a risk-based design of a RC slab and thus can be generalized for other structural members under fire-exposure. Currently, the presented MOO approach considers only two design parameters and three design objectives, but additional multiple objectives can be introduced in the same framework. Further, minimization of environmental damage is adopted as another dimension of the objective (which is seldom considered in design), leading to a more sustainable design. The MOO framework has environmental damage measured as CO_2 emissions and thus this framework has the possibility to consider diverse objective types and is not limited to a single objective measure (for example, monetary evaluations for failure and investment cost).

Table 2 Optimum design solutions for the RC slab at different failure cost factor values, considering office and residential occupancies.

Failure cost factor (ξ)	**Optimum design parameters**		**Optimum costs**		
	A_s [mm^2]	a [mm]	Investment cost including obsolescence [\$]	Expected annual failure cost [\$]	Environmental cost [kg CO_2]
Office building (q_f = 420 MJ/m^2)					
3	584	16	180	13	108
10	584	16	180	42	108
100	617	22	212	82	127
1000	673	33	264	61	159
10000	673	33	264	606	159
Residential building (q_f = 780 MJ/m^2)					
3	584	16	180	3	108
10	584	16	180	11	108
100	584	16	180	107	108
1000	617	22	212	207	127
10000	673	33	264	153	159
EN1992:1-2 [20] recommendation for 'a'					
ISO Fire rating	R30	R60	R90	R120	R180
a [mm]	10	20	30	40	55

6 CONCLUSIONS

Prescriptive design approach for uncommon structures may be inadequate, either from an economic or reliability standpoint. For these types of structures, a performance-based approach is recommended, with explicit consideration of the risk associated with the design. This study highlights the potential benefits of performing this assessment through a Multi-Objective Optimization (MOO) framework to achieve a safe and economical structural design.

A MOO framework is proposed, which uses a genetic algorithm for the optimization. The framework is applied to evaluate the lifetime optimum design for a RC slab exposed to natural fires, considering multiple objectives, design parameters and design constraints, within a probabilistic framework. The results indicate that the optimum value of design parameter is a function of the fire exposure parameter and the failure cost factor. The study shows that MOO approach leads to economical design solutions. For the considered RC slab, a reduction of about 40 % in reinforcement cost and 25 % in environmental cost can be made in comparison to the prescriptive design of 1- and 2-hour fire resistance rating. In comparison to single-objective optimization , the MOO approach is flexible and allows different metrics for objective functions, for example, investment and failure costs are expressed here in dollars, while environmental costs as CO_2 emissions. In this study, a framework for MOO based design of fire exposed structures is demonstrated where multiple structural performance criteria and objectives can be ascertained. These risk-based design approaches can be considered for defining prescriptive design provisions.

REFERENCES

1. Van Coile, Ruben, Danny Hopkin, David Lange, Grunde Jomaas, and Luke Bisby. The need for hierarchies of acceptance criteria for probabilistic risk assessments in fire engineering. Fire technology 55, no. 4 (2019): 1111-1146.
2. Hurley, Morgan J., and Eric R. Rosenbaum. Performance-based fire safety design. Boca Raton: CRC Press, 2015.
3. BS 7974:2019 Application of fire safety engineering principles to the design of buildings. Code of practice. European Standards,: 2019.
4. De Sanctis, Gianluca, and Mario Fontana., Risk-based optimisation of fire safety egress provisions based on the LQI acceptance criterion. Reliability Engineering & System Safety 152 (2016): 339-350.
5. Fischer, Katharina, Edgar Virguez, Mauricio Sánchez-Silva, and Michael H. Faber., On the assessment of marginal life saving costs for risk acceptance criteria. Structural safety 44 (2013): 37-46.
6. Hopkin, Danny, Michael Spearpoint, Matthew Arnott, and Ruben Van Coile. Cost-benefit analysis of residential sprinklers–Application of a judgement value method. Fire safety journal 106 (2019): 61-71.
7. Hopkin, Danny, Ian Fu, and Ruben Van Coile. Adequate fire safety for structural steel elements based upon life-time cost optimization. Fire Safety Journal 120 (2021): 103095.
8. Deb, Kalyanmoy. Multi-objective optimisation using evolutionary algorithms: an introduction. In Multi-objective evolutionary optimisation for product design and manufacturing, pp. 3-34. Springer, London, 2011.
9. Gudipati, Vamshi Krishna, and Eun Jeong Cha. A resilience-based framework for design optimization of interdependent buildings. (2019).
10. Hu, Sicong, Yixuan Zou, Yufeng Gai, Zheng Huang, and Guquan Song. Risk-Based Multiobjective Optimal Seismic Design for RC Piers Using the Response Surface Method and NSGA-II. Advances in Civil Engineering 2021 (2021), 8852203.
11. Liu, Min, Scott A. Burns, and Y. K. Wen. "Multiobjective optimization for performance-based seismic design of steel moment frame structures." Earthquake Engineering & Structural Dynamics 34, no. 3 (2005): 289-306.
12. Kawamura, K., Frangopol, D. M., Miyamoto, A., & Tanaka, T. (2020). Maintenance planning optimization of a reinforced concrete bridge element using genetic algorithms and dynamic programming. In Reliability and Optimization of Structural Systems (pp. 55-63). CRC Press..
13. Paya-Zaforteza, Ignacio, Victor Yepes, Antonio Hospitaler, and Fernando Gonzalez-Vidosa. CO2-optimization of reinforced concrete frames by simulated annealing. Engineering Structures 31, no. 7 (2009): 1501-1508.
14. Alothaimeen, Ibraheem, and David Arditi. Overview of multi-objective optimization approaches in construction project management. Multicriteria Optimization-Pareto-Optimality and Threshold-Optimality (2019).
15. EN 1991-1-2: Actions on structures. Part 1–2: General actions—Actions on structures exposed to fire. (2002).
16. Chaudhary, Ranjit Kumar, Ruben Van Coile, and Thomas Gernay. Potential of surrogate modelling for probabilistic fire analysis of structures. Fire Technology 57, no. 6 (2021): 3151-3177.

17. Thienpont, Thomas, Ruben Van Coile, Wouter De Corte, and Robby Caspeele. Determining a global resistance factor for simply supported fire exposed RC slabs. In fib symposium 2019: Concrete: Innovations in materials, design and structures, pp. 2191-2197. 2019.
18. Gernay, Thomas. Fire resistance and burnout resistance of reinforced concrete columns. Fire safety journal 104 (2019): 67-78.
19. EN 1990: Eurocode - Basis of structural design. 2002.
20. EN 1992: Eurocode 2: Design of concrete structures - Part 1-2: General rules - Structural fire design. 2004.
21. Gordian. Assemblies Costs Book, RSMeans. 2022.
22. Bokhari S, Geltner D. Characteristics of Depreciation in Commercial and Multifamily Property: An Investment Perspective. Real Estate Econ 2018;46:745–82.
23. Fischer, Katharina, Celeste Barnardo-Viljoen, and Michael H. Faber. Deriving target reliabilities from the LQI. , 5, no. 4.2 (2012): 10. LQI Symposium in Kgs. Lyngby, Denmark.
24. Paya-Zaforteza, I., Yepes, V., Hospitaler, A. and Gonzalez-Vidosa, F., 2009. CO_2-optimization of reinforced concrete frames by simulated annealing. Engineering Structures, 31(7), pp.1501-1508.
25. Oh, Byung Kwan, Se Woon Choi, and Hyo Seon Park. Influence of variations in CO2 emission data upon environmental impact of building construction. Journal of Cleaner Production 140 (2017): 1194-1203.
26. Manes M, Rush D. A Critical Evaluation of BS PD 7974-7 Structural Fire Response Data Based on USA Fire Statistics. Fire Technol 2019;55:1243–93.
27. BSI. PD 7974–7:2019. Application of fire safety engineering princi-ples to the design of buildings: probabilistic risk assessment. BritishStandards Published Document; 2019.
28. Vassart Olivier, Zhao B, Cajot Louis-Guy, Fabienne Robert, Meyer Udo, Frangi Andrea,. 2014. Eurocodes: Background and applications. Structural fire design. Worked examples.
29. Kanda, Jun, and Haresh Shah. Engineering role in failure cost evaluation for buildings. Structural Safety 19, no. 1 (1997): 79-90.
30. Holický, Milan, and Miroslav Sýkora. Stochastic models in analysis of structural reliability. In Proceedings of the international symposium on stochastic models in reliability engineering, life sciences and operation management, Beer Sheva, Israel, pp. 8-11. 2010.
31. Qureshi, Ramla, Shuna Ni, Elhami Khorasani, Negar, Van Coile, Ruben, Hopkin, Danny and Gernay, Thomas. Probabilistic models for temperature-dependent strength of steel and concrete. Journal of Structural Engineering 146, no. 6 (2020): 04020102.
32. Jovanović, Balša, Ruben Van Coile, Danny Hopkin, Negar Elhami Khorasani, David Lange, and Thomas Gernay. "Review of current practice in probabilistic structural fire engineering: Permanent and live load modelling." Fire Technology 57, no. 1 (2021): 1-30.

NEW APPROACH FOR TABULATED AND SIMPLIFIED ASSESSMENT OF FIRE RESISTANCE OF CONCRETE BEAMS: THE YIELD FORCE METHOD

Ruben Van Coile[1], Balša Jovanović [2]

ABSTRACT

Tabulated data is commonly used for a fast evaluation of the fire resistance of reinforced concrete beams. This tabulated data is however limited in the number of configurations listed, and does not allow to take into account the load level (utilization). Especially for the assessment of existing structures, a fast and more flexible approach for evaluating the fire resistance can be beneficial. Taking advantage of the wide availability of modern data storage and retrieval tools, a new calculation method is proposed which relies on precalculated temperature profiles and concrete lever arm data. The method is referred to as the "yield force method" since the core underlying assumption is reinforcement yielding in the fire limit state. The calculation has been elaborated for a single case study, indicating a very precise assessment of the bending moment capacity, as compared with the bending moment capacity obtained through a full nonlinear numerical calculation. For the investigated case, a maximum error of 5% was obtained. As the error is on the non-conservative side, the presented evaluations suggest that multiplying the capacity obtained with the yield force method with a factor of 0.95 is sufficient for reliably obtaining a conservative assessment of the bending moment capacity in fire. Thanks to its computational efficiency, the method also has specific potential for application in probabilistic calculations.

Keywords: Concrete beam; bending capacity; tabulated data; simplified method

1 INTRODUCTION

The tabulated data within EN1992-1-2:2004 is commonly used for the evaluation of the fire resistance of reinforced concrete (RC) beams [1 – 2]. This tabulated data is very practical as it allows for an instantaneous evaluation of the fire resistance while working on-site, as part of a fast engineering check, or even within a meeting with other parties. In some situations, however, issues are encountered while using the tabulated data for beams: (i) the number of configurations listed in the tables is limited; (ii) it is not possible to take into account knowledge on the loading on the beam (notably when the beam is not fully utilized in normal design conditions); (iii) the tabulated data does not give insight in the actual fire resistance of an element. Notably for the fire resistance assessment of concrete beams within existing structures, a fast and easy-to-use tool to evaluate the fire resistance rating based on observations from the site would thus be most valuable.

Addressing the above, a new engineering method has been developed for evaluating the bending moment capacity and fire resistance rating of concrete beams, considering standard fire exposure. The method is denoted as the *yield force method* and takes advantage of the ability for data retrieval and data handling (i.e., simple calculations) which has become widely available in recent years on smartphones, tablets and laptops. The calculation approach is described in Section 2, followed by a validation and background

[1] Associate Professor, Ghent University,
e-mail: ruben.vancoile@ugent.be, ORCID: https://orcid.org/ 0000-0002-9715-6786
[2] PhD researcher, Ghent University
e-mail: balsa.jovanovic@ugent.be, ORCID: https://orcid.org/0000-0001-5200-5848
https://doi.org/10.6084/m9.figshare.22177862

discussion in Section 3 and the calculation of a model error in Section 4. Section 5 demonstrates how the yield force method can be a very convenient tool for the probabilistic assessment of reinforced concrete beams exposed to fire. Section 6 concludes.

2 YIELD FORCE METHOD

2.1 Concept introduction

The *yield force method* allows for the quasi-instantaneous evaluation of the bending moment capacity of reinforced concrete beams exposed to fire. For now, the method has been developed for simply supported beams (i.e., ‘positive’ bending moment) without compression reinforcement, considering the ISO 834 standardized heating regime. By comparing (the design value of) the bending moment capacity with (the design value of) the bending moment induced by the design loads, the fire resistance rating is readily determined. The method can be extended to consider hogging (‘negative’) bending moments and other fire exposures. For many practical situations however, the current status of the approach is expected to be sufficient.

The yield force method relies on precalculated temperature profiles for reinforced concrete cross-sections, combined with precalculated concrete force lever arms (i.e., the vertical position of the resultant concrete compression force). The method then assumes that the capacity is defined by reinforcement yielding. Considering designs governed by yielding in normal design conditions, and the reinforcement yield stress reducing upon heating during the fire exposure, this assumption will be valid in most applications. The error obtained by the method is explored below in Section 4.

2.2 Overview of calculation steps

The calculation steps are shown in Figure 1 and elaborated below.

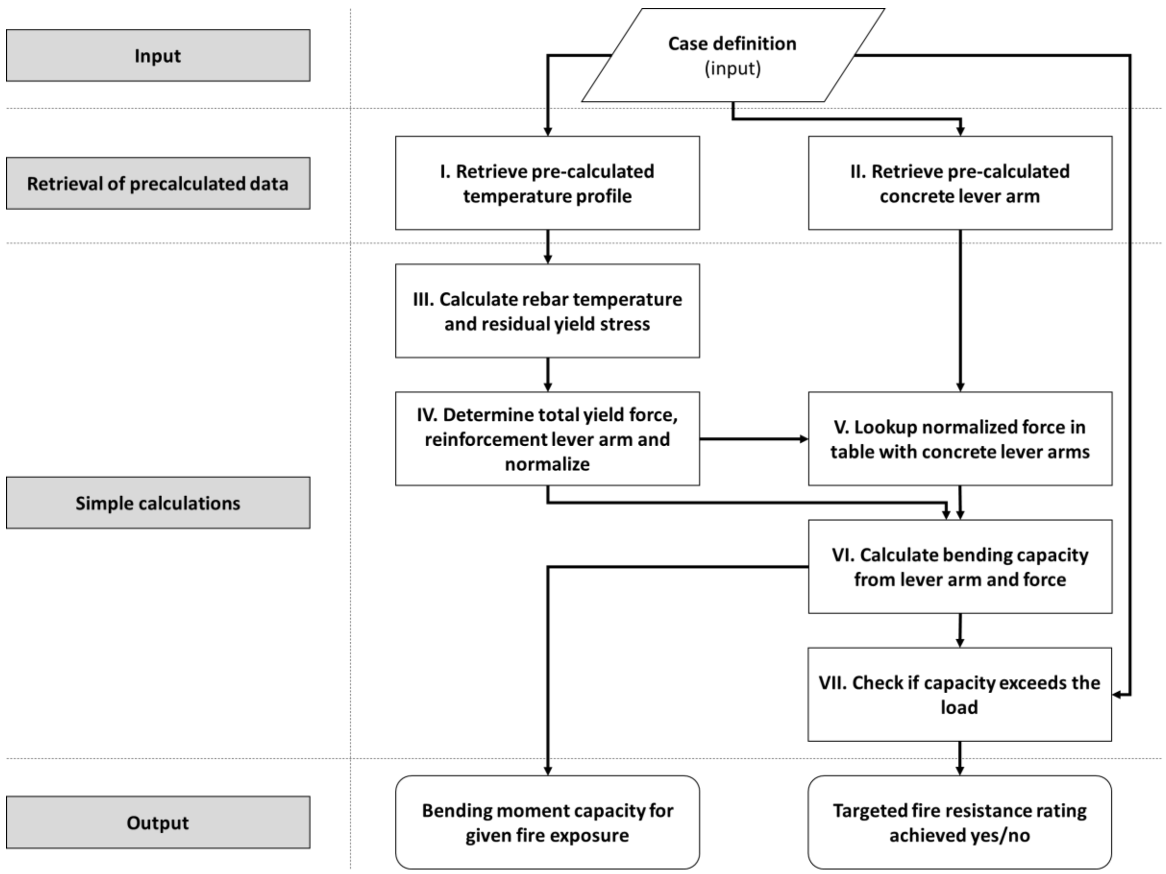

Figure 1. Calculation steps for application of the yield force method. If the goal is to evaluate the bending moment capacity only, then step VII and the resulting evaluation of the fire resistance rating can be omitted.

2.3 Input

The assessor specifies the characteristics of the cross-section, i.e., the width b and the height h of the concrete cross-section, and the position and size of the rebars. Also the fire severity is specified. Within the current implementation for ISO 834 standard heating regimes, this entails the specification of the required fire resistance rating t_E. For a first evaluation, a conservative assessment of the available reinforcement is sufficient (e.g., for an existing structure). Compression reinforcement can be neglected. Further input data relates to the (characteristic) concrete compressive strength and (characteristic) reinforcement yield stress. If a comparison of the resistance effect against the load effect is wanted, then also load parameters need to be defined. Data for the case study shown further in Section 3 is listed in Table 1. The load parameters are presented jointly through the design value of the bending moment, $M_{Ed,fi}$, in principle determined in accordance with EN 1990:2002 (here an example value was used for demonstration purposes).

Table 1– User input

<table>
<tr><th>Parameter</th><th colspan="3">Case study value</th></tr>
<tr><td colspan="4">Cross-sectional characteristics</td></tr>
<tr><td>Height, h</td><td colspan="3">300 mm</td></tr>
<tr><td>Width, b</td><td colspan="3">200 mm</td></tr>
<tr><td>Concrete compressive strength (characteristic), f_{ck}</td><td colspan="3">30 MPa</td></tr>
<tr><td>Reinforcement yield stress (characteristic), f_{yk}</td><td colspan="3">500 MPa</td></tr>
<tr><td rowspan="3">Reinforcement bars</td><td>Diameter [mm]</td><td>Horizontal axis distance to lower left corner [mm]</td><td>Vertical axis distance to lower left corner [mm]</td></tr>
<tr><td>20</td><td>35</td><td>35</td></tr>
<tr><td>20</td><td>165</td><td>35</td></tr>
<tr><td colspan="4">Fire severity</td></tr>
<tr><td>ISO 834 fire duration, t_E</td><td colspan="3">60 min (example value for demonstration purposes)</td></tr>
<tr><td colspan="4">Load situation (optional)</td></tr>
<tr><td>Design value of the bending moment, $M_{Ed,fi}$</td><td colspan="3">40 kNm (example value for demonstration purposes)</td></tr>
</table>

2.4 Retrieval of precalculated data

I. Retrieve pre-calculated temperature profile

The width b and height h are rounded down to the nearest lower precalculated values b^* and h^*, and the temperature field associated with b^*, h^* and t_E is retrieved (Figure 2). For completeness, also additional temperature profiles for selected ISO 834 durations are visualized here as these are used further in the paper.

II. Retrieve pre-calculated concrete lever arm

The precalculated data for the concrete lever arm y_c for the combination of b^*, h^* and t_E is retrieved (see Figure 3 with the definition). This precalculated data contains the vertical position y_c [m] (measured relative to the middle of the beam) of the (resultant) concrete compression force when the maximum bending capacity in the cross-section is achieved. The data is listed for a given fire duration t_E and for given normalized reinforcement force n_s.

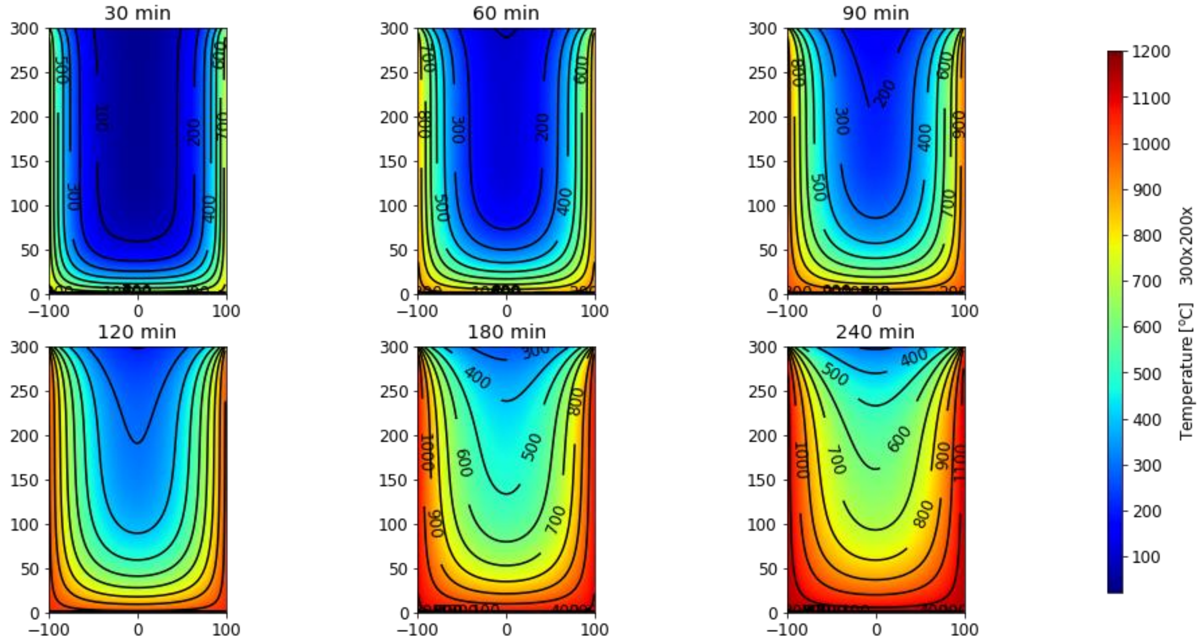

Figure 2. Temperature profiles for example case (300 mm x 200 mm, t_E = 30/60/90/120/180/240 min).

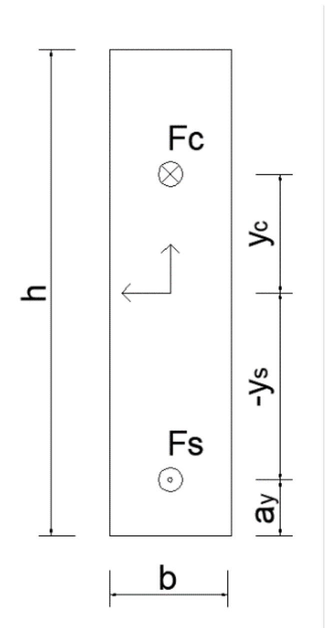

Figure 3. Concrete beam cross-section, with location of resultant concrete force F_c and resultant reinforcement force F_s. Indication of concrete and steel lever arms y_c and y_s. Note that the origin of the element axes is in the center of the beam.

The normalized reinforcement force n_s is defined by (1), with N_s the reinforcement force and N_c the concrete force. Considering the bending limit state, N_c and N_s are equal in magnitude but opposite in sign. The normalization is done with respect to the concrete (characteristic) compressive strength. The normalized concrete force n_s is listed with dimension [m^2] (or [mm^2] for human readability). For the example case of Table 1, such data is listed in Table 2. Within the test implementation, the data is listed for the fire durations considered further in the paper.

$$n_s = \frac{N_s}{f_{ck}} = \frac{|N_c|}{f_{ck}} \tag{1}$$

Table 2 – Concrete force lever arm y_c [mm] upon reaching maximum capacity, in function of the normalized reinforcement force n_s and for different ISO 834 standard fire durations.

n_s [mm^2]	0 min	30 min	60 min	90 min	120 min	180 min	240 min
150	149.7	146.4	145.9	145.8	145.9	146.0	146.0
300	149.4	147.1	146.5	146.4	146.4	146.3	146.3
450	149.0	147.2	146.6	146.5	146.4	146.2	146.1
600	148.7	147.2	146.6	146.4	146.2	146.0	145.8
750	148.4	147.0	146.5	146.2	146.0	145.7	145.5
1500	146.5	145.6	145.1	144.7	144.4	143.9	143.5
2250	144.5	143.3	142.8	142.4	142.0	141.2	140.6
3000	142.5	140.9	140.1	139.5	138.9	137.7	136.8
3750	140.4	138.4	137.5	136.6	135.8	134.1	132.7
4500	138.4	136.0	134.8	133.7	132.6	130.3	128.3
5250	136.4	133.5	132.0	130.7	129.3	126.4	123.4
6000	134.4	131.1	129.3	127.7	126.0	122.3	118.2
6750	132.4	128.6	126.5	124.7	122.6	118.0	112.7
7500	130.4	126.2	123.8	121.6	119.2	113.6	106.7
8250	128.4	123.7	121.0	118.6	115.8	109.0	100.2
9000	126.4	121.2	118.2	115.4	112.2	104.3	93.1
9750	124.3	118.7	115.4	112.4	108.7	99.3	85.8
10500	122.4	116.3	112.6	109.1	105.1	94.4	79.2
11250	120.4	113.7	109.8	106.1	101.5	88.9	73.1
12000	118.3	111.3	106.9	102.8	97.7	83.4	67.7
12750	116.2	108.8	104.1	99.6	94.1	77.9	62.9
13500	114.1	106.3	101.4	96.5	90.3	72.1	NA
14250	112.2	103.7	98.4	93.2	86.4	67.7	NA
15000	110.3	101.3	95.3	89.7	82.1	62.9	NA

2.5 Simple calculations

III. Calculate rebar temperature and residual yield stress

Adopting the temperatures θ_i at the position of the reinforcement axis (obtained from the retrieved temperature profile), the residual yield stress of the reinforcement is determined as $k_{fy}(\theta_i)\cdot f_{yk}$ for each of the identified rebars. Here $k_{fy}(\theta)$ is the temperature-dependent yield stress retention factor as listed in EN 1992-1-2:2004, and f_{yk} is the characteristic reinforcement yield stress in normal design conditions (commonly 500 MPa). For the example case, Table 3 lists the average reinforcement temperatures and k_y values for different fire durations. Note: as the reinforcement layout is symmetrical, the temperature is approximately equal (differences result from rounding errors and interpolation) for both rebars, so there is no loss of information associated with the use of the average temperature.

IV. Determine total reinforcement yield force, lever arm and normalize

The total reinforcement force N_s is the sum of all rebar capacities, i.e. (2), with A_i the area of the ith rebar. The normalized reinforcement force n_s is found by dividing N_s with f_{ck}, i.e. (1). The lever arm is defined from the middle of the beam cross-section (positive towards the top of the section, see Figure 3). To allow for rebars which are not positioned at the same height, a weighted lever arm is determined through (3) with

a_{yi} the vertical axis distance of rebar i to the bottom of the section, as provided by the user (Table 1). Values for the example case are listed in Table 3. As the rebars are in a single layer with $a_{y,i}$ = 35 mm and the section height h = 300 mm, y_s = -115 mm. See Figure 3 for the definition of y_s.

$$N_s = \sum_i A_i k_{y,i} f_{yk} \tag{2}$$

$$y_s = \sum_i \frac{A_i k_{y,i} f_{yk}}{N_s} \left(a_{y,i} - \frac{h}{2} \right) \tag{3}$$

V. Lookup normalized force in table with concrete lever arms

The calculated value of n_s is used to interpolate in the precalculated lever arm, y_c, data from Table 2. For the example case, this corresponds with obtaining an assessment of the concrete lever arm by interpolating the n_s values obtained in Step IV (and listed in Table 3) considering the precalculated lever arm data of Table 2. Results are listed in Table 3.

VI. Calculate bending capacity form lever arm and force

The capacity is calculated as (4). Results are listed in Table 3.

$$M_{Rd,fi,tE} = n_s f_{ck} (y_c - y_s) \tag{4}$$

Table 3 – Intermediate calculation results

	0 min	30 min	60 min	90 min	120 min	180 min	240 min
θ_{rebar} [°C]	20	354	564	697	792	923	1011
k_y [-]	1	1	0.582	0.236	0.119	0.055	0.038
n_s [mm^2]	10000	10000	5818	2364	1193	554	377
y_s [mm]	-115	-115	-115	-115	-115	-115	-115
y_c [mm]	123.7	117.9	130.0	141.9	145.1	146.1	146.2
$M_{Rd,fi,tE}$ [kNm]	71.6	69.9	42.7	18.2	9.3	4.3	3.0
$M_{Rd,fi,tE} \geq M_{Ed,fi}$	Yes	Yes	Yes	No	No	No	No

VII. Check if capacity exceeds the load

The design values for the bending moment capacity in fire can be compared with the design value for the bending moment induced by the design loads. This allows to confirm the fire resistance rating. For the case listed in Table 1, a fire resistance rating of 60 min is confirmed.

3 VALIDATION AND BACKGROUND OF THE YIELD FORCE METHOD

3.1 Validation

The bending moment capacity evaluated through the yield force method is validated against full numerical cross-sectional calculations as described in [3]. This means that the RC beam is discretized using a fine mesh, whereby the temperature and temperature-dependent material properties are determined for each mesh-element, as well as the thermal strain. Considering a plane-section hypothesis and the condition of pure bending (no resultant axial force), the bending moment diagram is then determined. All of the above is done considering the models described in EN1992-1-2:2004. Results are visualized in Figure 4, together with the capacity predicted by the yield force method. For this specific case study, the comparison indicates an excellent approximation of the numerical evaluation.

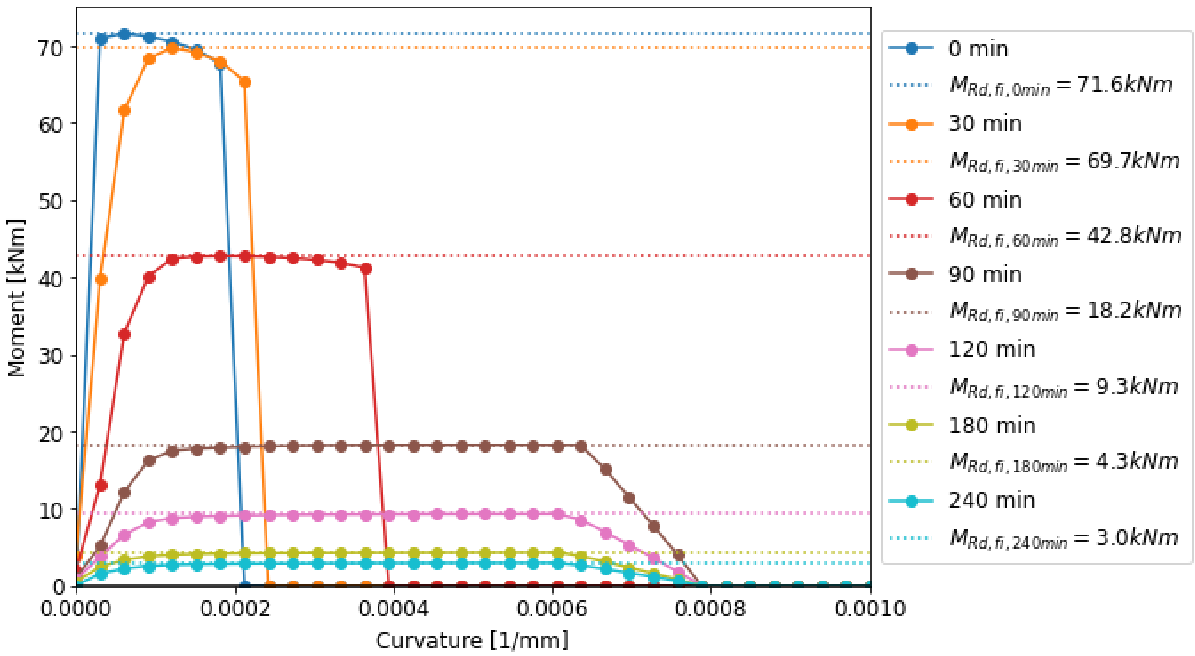

Figure 4. Numerical evaluation of the moment-curvature diagram (full lines) and capacity evaluated through the yield force method (dotted lines), for different ISO 834 durations.

3.2 Background

The precalculated diagrams for the concrete lever arm rely on a large number of nonlinear calculations in accordance with the advanced calculation method of EN 1992-1-2:2004, whereby the moment curvature diagram is evaluated for a given concrete beam cross-section (as demonstrated above in 3.1). The maximum of the moment curvature diagram is adopted as the bending moment capacity.

The results of the nonlinear cross-section calculations have been generalized, acknowledging that when the bending capacity is defined by reinforcement yielding (i.e., has a mechanical strain between 0.02 and 0.15 in accordance with EN 1992-1-2:2004), the reinforcement tensile force is known a priori, and is equal to the resultant concrete compressive force considering axial equilibrium. The only unknown is thus the position of the concrete compressive force. This position is readily obtained through a nonlinear calculation of the bending moment capacity (evaluated as the maximum of the moment curvature diagram), and is independent of the reinforcement position (the bending moment capacity is defined by a maximization of the concrete lever arm for the known tensile/compressive force and is thus not dependent on the precise reinforcement position).

The above clarifies how for a known reinforcement force, under the assumption of reinforcement yielding (i.e., an under-reinforced section), the concrete lever arm which defines the cross-sectional capacity can be pre-calculated. Considering the concrete material model of EN 1992-1-2:2004, the concrete mechanical stress at every location is proportional to the concrete compressive strength in normal design conditions (see Figure 3.1 of EN 1992-1-2:2004). Hence, the cross-sectional strain profile which maximizes the concrete lever arm is the same for all configurations with the same normalized reinforcement force N_s/f_c (in the calculations and demonstration above, the characteristic compressive strength f_{ck} is used as a specific value of f_c). In other words, for a given cross-section, the concrete lever arm for the section capacity is fully determined by the normalized reinforcement force, as defined by (1).

Considering the above, the following limitations apply to the method: (i) the beams are simply supported and the cross-sectional capacity is determined by the sagging bending moment capacity (i.e., the load bearing capacity is defined by the bending limit state); (ii) compression reinforcement is ignored; (iii) no spalling is considered (as in the existing tabulated data); (iv) all tensile rebars are assumed to be yielding in the fire limit state.

4 MODEL ERROR

4.1 Motivation

The fast calculation approach of the yield force method relies on the assumption that all rebars yield in the fire limit state. Due to the nonlinear temperature profile in the cross-section, it is possible that the reinforcement is located in an area with large thermal strains, resulting in limited mechanical strains even for large curvature. As an example, Figure 5 visualizes the ratio of the reinforcement stress and (temperature-dependent) yield stress at the curvature for which the maximum concrete lever arm is obtained. For the investigated cross-section at 30 minutes, this ratio does not go under 95% for the expected positions of the reinforcement. For clarity, ratios below 0.95 all have the same colour (including the top areas in the compression zone). Figure 5 illustrates how the reinforcement is positioned in an area with a resulting stress close to, but not exactly equal to, the yield stress. This explains why the yield force method may result in a small overestimation of the bending moment capacity. If this error can be quantified in a statistical manner, it should be possible to (i) determine a conservative correction factor which ensures that the yield force method does not result in a significant overestimation, and (ii) include the model error in probabilistic calculations for failure probabilities.

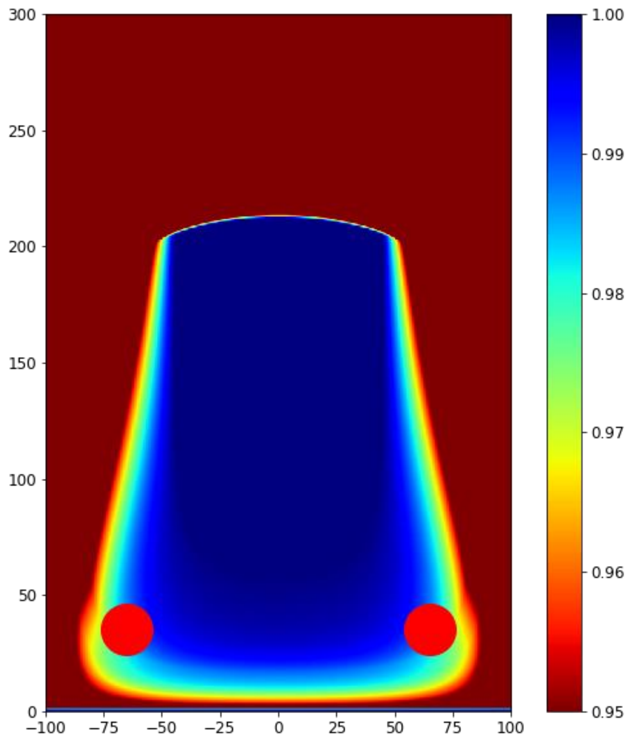

Figure 5. Ratio of the reinforcement stress relative to the yield stress at 30 min of ISO 834 standard fire exposure, for all positions within the cross-section. Ratios below 0.95 (including negative ratios corresponding with compression areas) are visualized in the same colour. The red dots indicate the reinforcement position for the case study.

4.2 Model error

Taking into account the above motivation, a large number of evaluations is done whereby the bending moment capacity is determined through a nonlinear evaluation of the moment-curvature diagram on the one hand, and through application of the yield force method on the other hand. The error is determined as the ratio of the capacity obtained by the yield force method relative to the numerically evaluated capacity. Results are presented in Figure 6, considering 2500 Monte Carlo simulations for the stochastic variables listed in Table 4. These stochastic distributions are compatible with the recommendations of the Joint

Committee on Structural Safety (JCSS) [4], meaning that the results give a view of the error obtained for a specific configuration. To generalize these results, the obtained model errors need to be compared with those obtained for a large number of alternative configurations. Alternative approaches can also be explored.

Based on Figure 6 it is evident that for the considered case study the model error of all fire exposures except the 30 min one is quite small and almost negligible. The errors are however non-conservative and the error at 30 min of fire exposure for this case is larger (up to approximately 5% overestimation of the capacity). The reason for this overestimation by the table method is that the reinforcement is not yielding when the maximum moment for this exposure is achieved, see Figure 5 above. Multiplying the result obtained by the yield force method with a "correction factor" of 0.95 readily ensures a conservative result. Further evaluations are however required to confirm this conclusion for other cross-sections.

Table 4 - Probability distributions considered

Parameter	Explanation	Distribution	Mean	COV
f_c	$20°C$ concrete compressive strength	Lognormal	$\frac{f_{ck}}{1-2COV_{fc}}$	0.15
f_y	$20°C$ reinforcement yield stress	Lognormal	$\frac{f_{ck}}{1-2COV_{fy}}$	0.07
c	Concrete Cover	Beta44	$c_{nom}+5$	$\frac{5\ mm}{c_{nom}}$
A_s	Reinforcement area	Normal	$1.02A_{s,nom}$	0.02

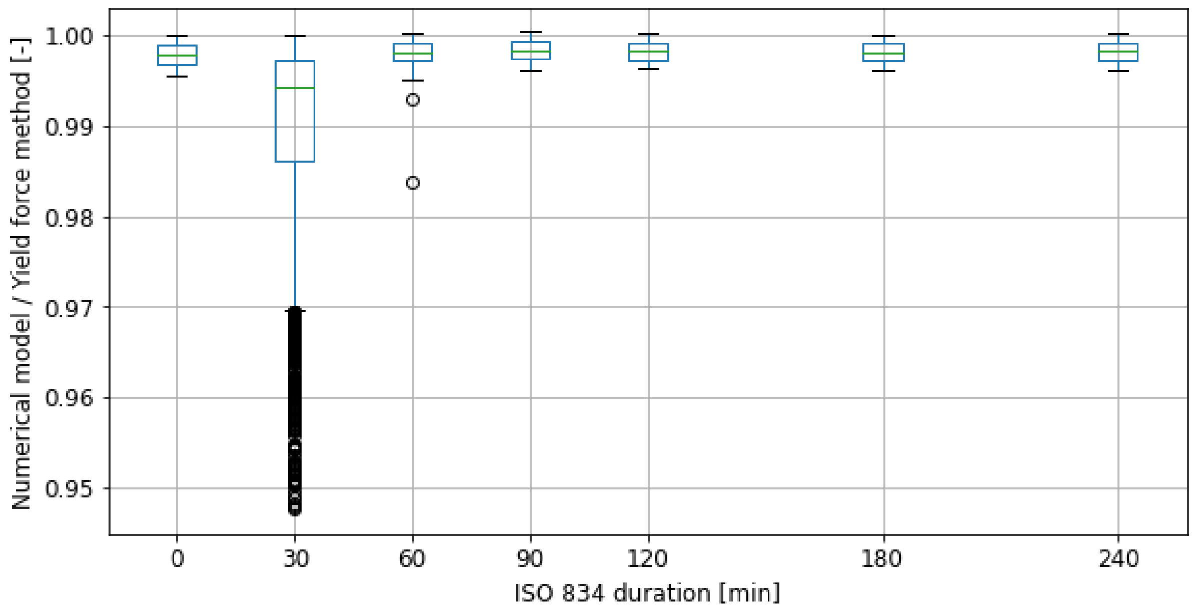

Figure 6. Model error for the case study, defined as the ratio of the numerically evaluated bending moment capacity to the capacity evaluated through the yield force method.

5 APPLICATION: PROBABILISTIC EVALUATION OF RC BEAM CAPACITY IN FIRE

The speed and simplicity of the yield force method is one of its main advantages, together with its ability to maintain a very close approximation of a full nonlinear evaluation. Thus, the yield force method can be used to efficiently conduct probabilistic calculations. Figure 7 and Figure 8 show the PDF, and CDF of the moment capacity based on the 10^6 calculations. It took a regular office PC less than one minute to conduct those calculations using the yield force method. Up to now, limited probabilistic studies of fire exposed RC beams exist [5]. The evaluations presented here demonstrate how the yield force method can help alleviate this.

The results in Figure 7 highlight a very broad distribution for the bending moment capacity at 30 minutes of standard fire exposure. A similar, but less pronounced, effect is observed at 60 min. This demonstrates how the PDF of the capacity in fire is not necessarily best described by a lognormal distribution. Note that this evaluation does not yet include the uncertainty with respect to the retention factors at elevated temperature for the concrete strength and reinforcement yield stress. For state-of-the-art models, see [6]. These effects will increase the variation, but also complicate the application of precalculated diagrams as in the yield force method.

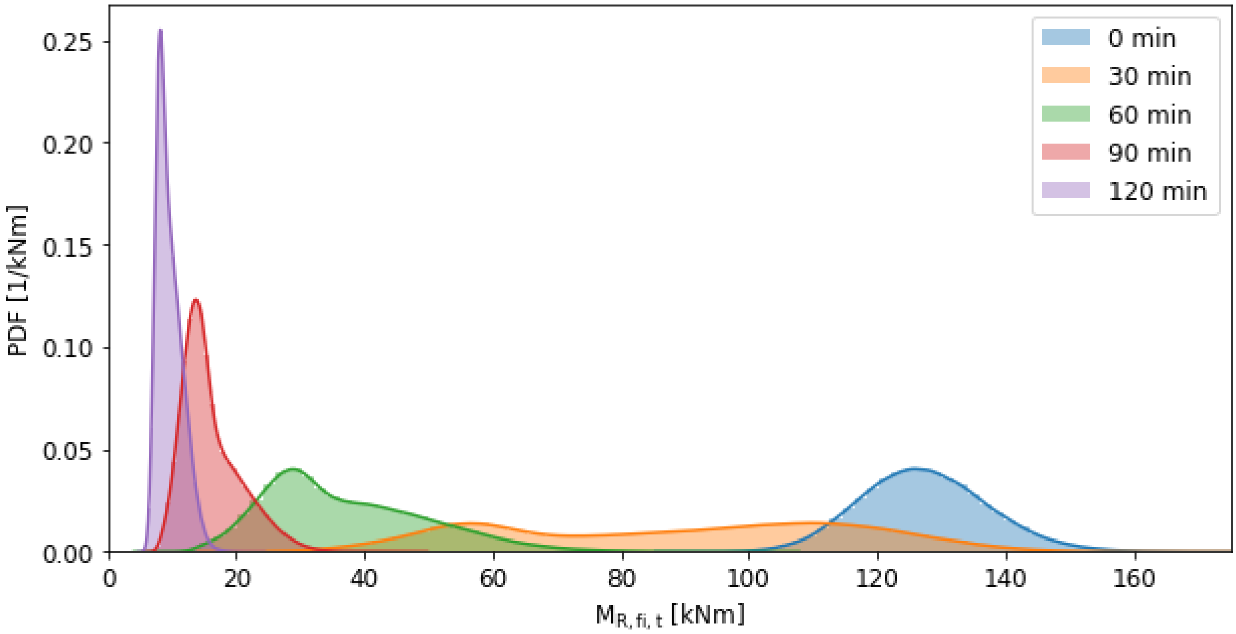

Figure 7. Observed PDF for the bending moment capacity at different ISO 834 standard fire durations, as obtained through 10^6 Monte Carlo evaluations using the yield force method.

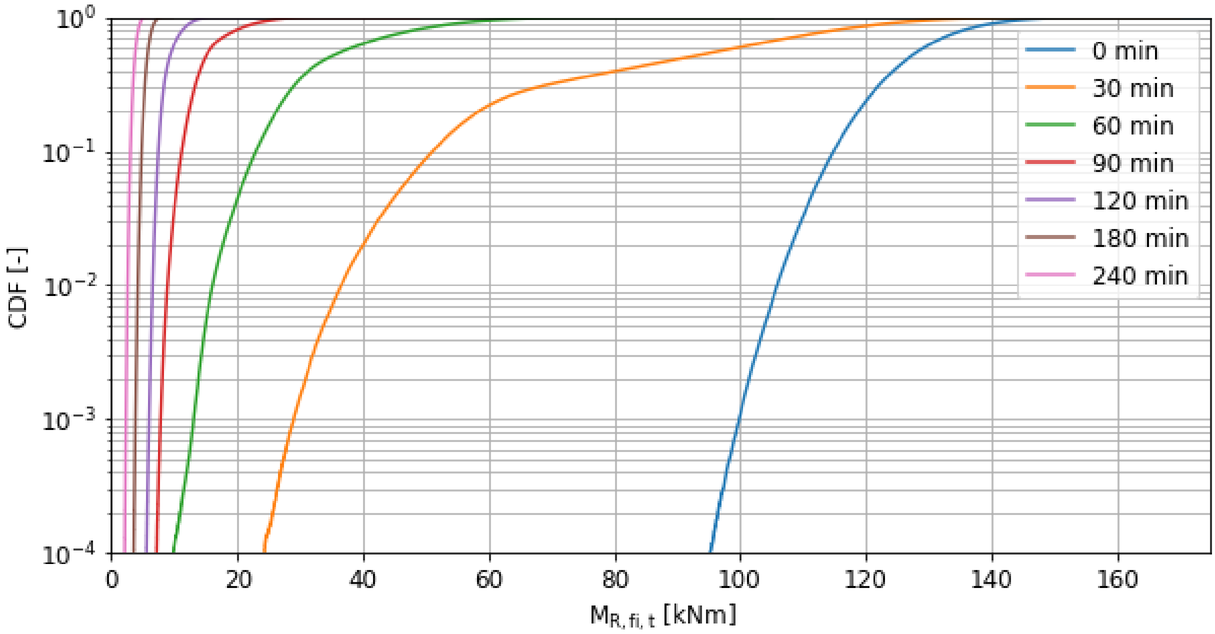

Figure 8. Observed CDF for the bending moment capacity at different ISO 834 standard fire durations, as obtained through 10^6 Monte Carlo evaluations using the yield force method.

6 CONCLUSIONS

A new, fast and easy-to-use method (yield force method) is introduced for the evaluation of the fire resistance (bending moment capacity) of reinforced concrete beams exposed to fire. The yield force method results in a very precise approximation of a full nonlinear evaluation of the bending moment capacity through numerical methods, and can be easily implemented as an automated calculation procedure. The evaluation relies on precalculated temperature profiles and concrete force lever arm data. Thanks to modern data retrieval resources, this is considered not to be an obstacle for the methods' adoption. Thanks to its flexibility and precision, the method in effect makes tabulated fire resistance ratings for reinforced concrete beams obsolete. In the evaluations made so far, the maximum error obtained between the yield force method and a full nonlinear calculation is 5%. As the error is largely due to the reinforcement not fully yielding in the nonlinear calculation, the error is on the non-conservative side. Multiplying the result obtained by the yield force method with a "correction factor" of 0.95 readily ensures a conservative result. Thanks to the computational ease of the yield force method, it is also a very promising approach for probabilistic calculations.

REFERENCES

1. Taerwe, L. (2008). Fire design of concrete structures according to the eurocodes: a review. In ACI spring Convention: Designing concrete structures for fire safety (pp. 75-95). ACI
2. Achenbach, M., Gernay, T., & Morgenthal, G. (2018). Verification of a tabulated method of eurocode for concrete columns using a response surface and advanced methods. In SiF 2018–10th International Conference on Structures in Fire (pp. 101-106). Ulster University, Belfast, UK.
3. Van Coile, R. (2015). Reliability-based decision making for concrete elements exposed to fire. Doctoral dissertation. Ghent University, Belgium.
4. JCSS. (2011). JCSS Probabilistic Model Code. Joint Committee on Structural Safety. Available at: https://www.jcss-lc.org/jcss-probabilistic-model-code/ (Accessed 14/10/2022).
5. Coelho, T., Diniz, S., Rodrigues, F., & Van Coile, R. (2022). State-of-the-art review of the reliability evaluation of concrete beams exposed to fire. Journal of Structural Fire Engineering, (ahead-of-print).
6. Qureshi, R., Ni, S., Elhami Khorasani, N., Van Coile, R., Hopkin, D., & Gernay, T. (2020). Probabilistic models for temperature-dependent strength of steel and concrete. Journal of Structural Engineering, 146(6), 04020102.

SiF 2022– The 12th International Conference on Structures in Fire
The Hong Kong Polytechnic University, Nov 30 - Dec 2, 2022

EXPERIMENTAL STUDY ON HYBRID FIBRE REINFORCED HIGH-PERFORMANCE CONCRETE COLUMNS AT ELEVATED TEMPERATURES

Panwei Du[1], Kang Hai Tan[2]

ABSTRACT

Research in the field of developing innovative concrete materials has been ongoing for the last three decades. The development of high-performance concrete (HPC) is the outcome of these efforts, which has superior performance characteristics such as high strength and good durability. In the design of reinforced concrete (RC) structures, it is a requirement of building codes that all RC structural members be fire resistant. Thus, structural behaviour and fire design of HPC columns are of great importance in the design. However, it was revealed that the majority of the tests focused on the effects of concrete strength, load ratio, fire curve, addition of fibres, heating regime and aggregate type. Insufficient research has been carried out on axial restraint, column dimension and load eccentricity. To address the research gaps, an experimental programme involving ten columns was conducted in this paper to improve understanding of fire performance of HPC columns when subjected to elevated temperatures, focusing on the effects of column dimension, load eccentricity, biaxial bending and axial restraint. Although complex loading conditions such as uniaxial and biaxial bending and axial restraint were applied, there was no evidence of spalling in any of the specimens. The effect of load eccentricity on fire endurance was dependent on the cross-sectional design.

Keywords: High-performance concrete; eccentric loading; explosive spalling; fire resistance; axial restraint

1 INTRODUCTION

Research in the field of improving material properties and developing innovative concrete materials has been ongoing for the past three decades. The development of high-performance concrete (HPC) is the outcome of these efforts, which possesses superior performance characteristics such as high strength and good durability. In this regard, HPC has gained considerable attention within the construction industry in recent years. For structures, it is a requirement of building codes that all reinforced concrete (RC) structural members be fire resistant. However, it is known that HPC is prone to explosive spalling when subjected to fire, especially when the heating rate is high. Therefore, in the design of HPC columns, structural fire behaviour and fire design are very important.

A variety of critical parameters, such as column size, heating profile (standard fire curve or parametric fire curve), load level during fire tests, aggregate type, lateral reinforcement, load eccentricity (uniaxial and biaxial), degree of axial restraint, etc., impact the fire behaviour of HPC columns [1]. There have been several fire tests conducted in the literature to examine how HPC columns behaved at elevated temperatures [2-7]. According to a comprehensive review [8], it was revealed that the majority of the tests focused on the effects of concrete strength, load ratio, fire curve, inclusion of fibre, heating regime and aggregate type. Insufficient research has been carried out on axial restraint, column dimension and load eccentricity. A notable aspect is that almost all columns were evaluated under axial loading only where load eccentricity

[1] Dr, Nanyang Technological University Singapore,
e-mail: pwdu@ntu.edu.sg, ORCID: https://orcid.org/ 0000-0003-3838-2705
[2] Professor, Nanyang Technological University Singapore
e-mail: ckhtan@ntu.edu.sg
https://doi.org/10.6084/m9.figshare.22177877

was not applied, especially for bi-axial loading on HPC columns which has not been documented previously. However, it is essential to consider the effect of load eccentricity as it exists in all columns in practice. Additionally, load eccentricity will aggravate the severity of explosive spalling on the compression side since the stress is higher. Since there is a lack of studies on eccentrically loaded columns, it is necessary to investigate the structural behaviour of such types of columns subjected to elevated temperatures and it can be used as the basis for structural fire design of HPC columns.

Another important factor influencing structural fire behaviour of HPC columns is the degree of restraint, which is also lacking in the literature. An axial restraint occurs when adjacent structural members restrain the thermal expansion of a heated column. According to Kodur and Phan [1], the presence of axial restraint could result in a greater induced force, thereby affecting the degree of spalling and reducing fire resistance. There have been several studies conducted on the fire performance of NSC columns subjected to axial restraint [9, 10]. It was reported that corner spalling occurred in the columns due to combined effect of axial restraint and uniaxial bending. It should be noted that up until now, there has been very limited research on fire performance of HPC columns under axial restraint. Only one experimental study has been conducted by Benmarce and Guenfoud [11] where the behaviour of 12 columns under various load levels, degrees of restraint and heating rates was investigated. According to the report, all specimens showed minor spalling and the columns failed as a result of axial contraction. However, there were several important factors that were not examined in this study, including load eccentricity and fibre inclusion. Since axial restraint has a considerable influence on HPC columns at elevated temperatures and only limited studies have been conducted on this factor, there is a need to conduct tests to understand the fire behaviour of axially restrained HPC columns.

An interesting finding from the literature is that the addition of PP fibres did not prevent the explosive spalling completely for most HPC columns. As stated in EN 1992-1-2 [12], HPC must contain at least 2 kg/m^3 PP fibres to prevent spalling. In spite of this, several researchers have reported that corner spalling still occurred in HPC columns with PP fibres [6, 7]. This suggests that the addition of PP fibre itself may not be sufficient to completely eliminate spalling. Consequently, hybrid fibres should be applied to avoid spalling and improve fire resistance of HPC columns such that structural fire safety of structures can be assured.

The purpose of this research is to fill up the abovementioned research gaps by developing a test programme with 10 full-scale HPC columns subjected to ISO 834 fire curve. Fire tests are being conducted to investigate the structural behaviour of HPC columns subjected to a variety of uniaxial and biaxial load eccentricities, as well as axial restraint. Test results will be discussed in detail.

2 TEST PROGRAMME

2.1 Concrete material properties

Concrete mix design aims to provide a compressive strength of at least 90 MPa and protect the concrete from experiencing explosive spalling when subjected to fire. The mix proportions are presented in Table 1 with a water-to-binder (W/B) ratio of 0.315. Hybrid PP and steel fibres are used to prevent spalling and improve ductility. PP fibres are 12 mm in length and 30 μm in diameter where the dosage is 2 kg/m^3 by weight or 0.2% by volume. Dramix® 3D 6535BG steel fibres are 35 mm in length and 540 μm in diameter with a single hook. Steel fibres are dosed at 78 kg/m^3 by weight or 1% by volume.

Table 1. Concrete mix proportions

Ingredient	Cement	Silica fume	Coarse aggregate	Fine aggregate	Water	Superplasticizer	PP fibre	Steel fibre
kg/m^3	550	85	800	800	200	16	2	78

The compression test was conducted on three cylinders of 100 mm in diameter and 200 mm in height. The compressive strength f_c was 93.2 MPa and the elastic modulus E_c was 40.1 GPa. Three notched beams were tested under bending to examine the flexural strength of concrete. The beams were 150 × 150 × 750 mm in dimension with a span length of 500 mm. The linear elastic flexural strength was 7.28 MPa and the peak flexural strength was 11.7 MPa with the help of 1% steel fibres. Details of flexural strength-*CMOD* curves can be found in Du et al. (2022). Besides mechanical properties, spalling performance at the material level was examined prior to conducting full-scale column tests. Concrete cylinders were heated for 90 min in an electric furnace following ISO 834 fire curve. Spalling did not occur in all the samples which showed that a hybrid of PP and steel fibres proved effective to mitigate spalling.

2.2 Specimen design

This study is primarily concerned with the effects of load eccentricities (uniaxial and biaxial), cross-section dimensions (slenderness ratio) and axial restraint on HPC columns. As shown in Table 2, ten columns with square sections will be tested in two series. All the columns had a length (L) of 2900 mm. To study the effect of cross-section dimensions, two different cross-sections were designed in Series I; one had a width (B) of 270 mm and the other one was 200 mm. There were three levels of uniaxial load eccentricity for each type of cross-section, viz 0, 30 and 50 mm. In Series II, it was intended to explore the behaviour of columns subjected to biaxial load eccentricity and axial restraint. Thus, specimens No. 7 and 8 were designed to have two different levels of biaxial load eccentricity (i.e. $e_y = e_z = 30$ mm for No.7 and $e_y = e_z = 50$ mm for No. 8), and specimens No. 9 and 10 were subjected to an axial restraint ratio (α_R: restraint stiffness over column axial stiffness) of 8.4%. The load ratio of all the specimens, which is defined as the applied load during fire testing (P_{fi}) over load-carrying capacity at ambient (P_c), is targeted at 0.35.

Table 2. Overview of test programme

Series	No.	Specimen ID	B (mm)	L (mm)	l/r -	e_y (mm)	e_z (mm)	α_R -	P_{fi}/P_c
I	1	H-270-00	270	2900	37	0	0	-	0.35
	2	H-270-30	270	2900	37	30	0	-	0.35
	3	H-270-50	270	2900	37	50	0	-	0.35
	4	H-200-00	200	2900	50	0	0	-	0.35
	5	H-200-30	200	2900	50	30	0	-	0.35
	6	H-200-50	200	2900	50	50	0	-	0.35
II	7	H-200-30B	200	2900	50	30	30	-	0.35
	8	H-200-50B	200	2900	50	50	50	-	0.35
	9	H-200-30R	200	2900	50	30	0	8.4%	0.35
	10	H-200-50R	200	2900	50	50	0	8.4%	0.35

Figure 1 demonstrates a typical design of column specimens. For each column, an enlarged concrete block was designed at each end with the dimension of 280 × 400 × 400 mm to create load eccentricity and protect the column end from crushing failure. Steel plates with a thickness of 20 mm were attached to the end block to connect with the knuckle bearing blocks, which were used to support the column on the test rig. The knuckle bearing is free to rotate, thus creating a pin-pin boundary condition.

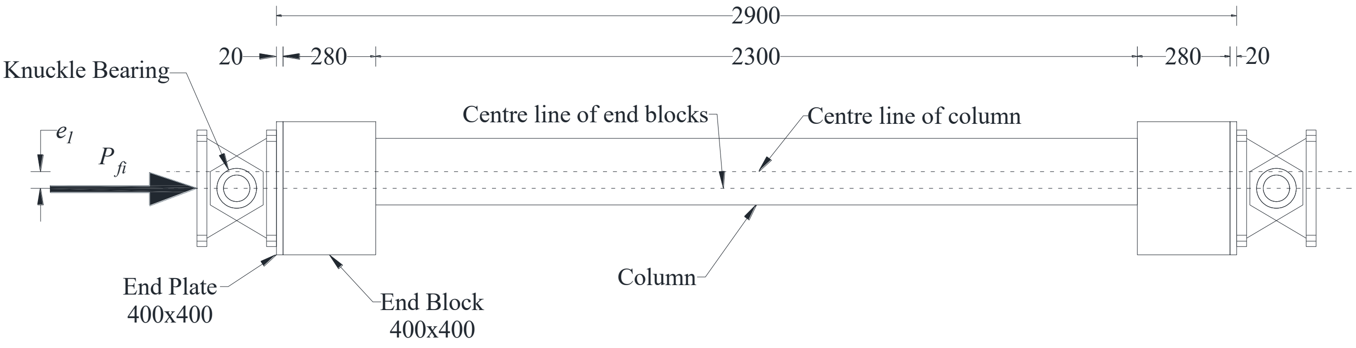

Figure 1. Column design

The cross-sectional layouts of column specimens are shown in Figure 2. There are three types of cross-section design. The first design is for the columns with 270 mm width (Specimen No. 1 – 3), as presented in Figure 2a. For this design, 4H25 was used, which had a yield strength of 567.8 MPa. The second and third designs are for columns (Specimen No. 4 – 10) having 200 mm width reinforced by 4H20 in which the average yield strength was 564.5 MPa, as shown in Figures 2b and 2c, respectively. The difference between Figure 2b and 2c is that equal biaxial load eccentricity was produced to simulate biaxial bending in the third design. All the columns were reinforced by 10 mm plain bars spaced 150 mm apart for stirrups, and the yield strength of stirrups was 281.1 MPa.

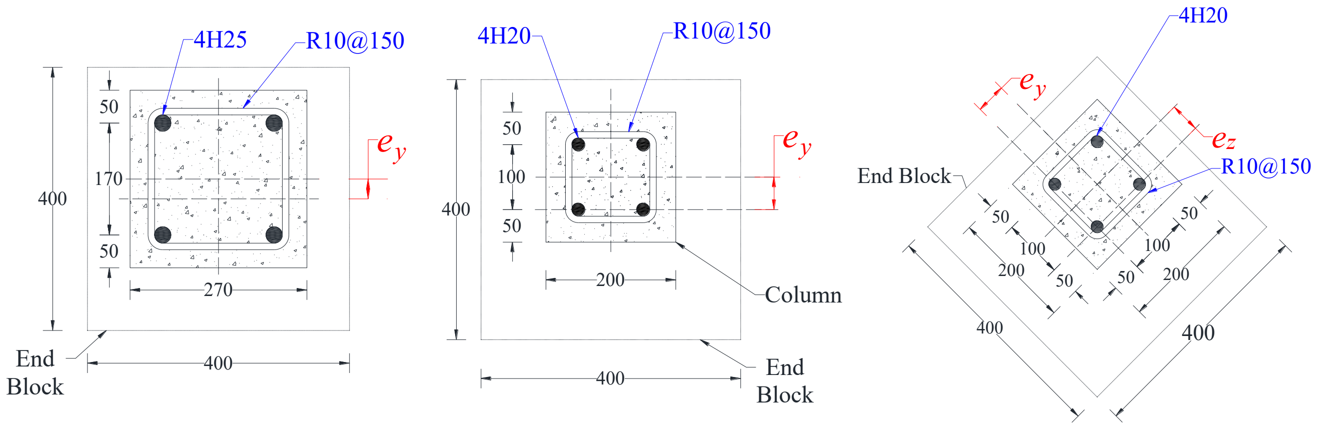

(a) 270 mm (b) 200 mm under uniaxial bending (c) 200 mm under biaxial bending

Figure 2. Cross-section configuration

2.3 Test setup

Test setup is presented in Figure 3. As shown in Figure 3a, the column specimen was placed horizontally in the electric furnace. The loading was applied through a 5000 kN hydraulic actuator. For the restrained column specimens, there was a restraint steel beam positioned between the actuator and the column, and it was supported by two A-frames. The steel beam would restrain the thermal expansion of column specimens under heating. For unrestrained columns, this beam was removed to allow free expansion.

Linear variable differential transformers (LVDTs) were used to evaluate the deformation of specimens. The mid-height deflection was measured by an LVDT that was positioned at the top, as presented in Figure 3b. A total of 8 LVDTs were attached to the ends of specimens (4 at each end) to measure the axial deformation and rotation (Figure 3c).

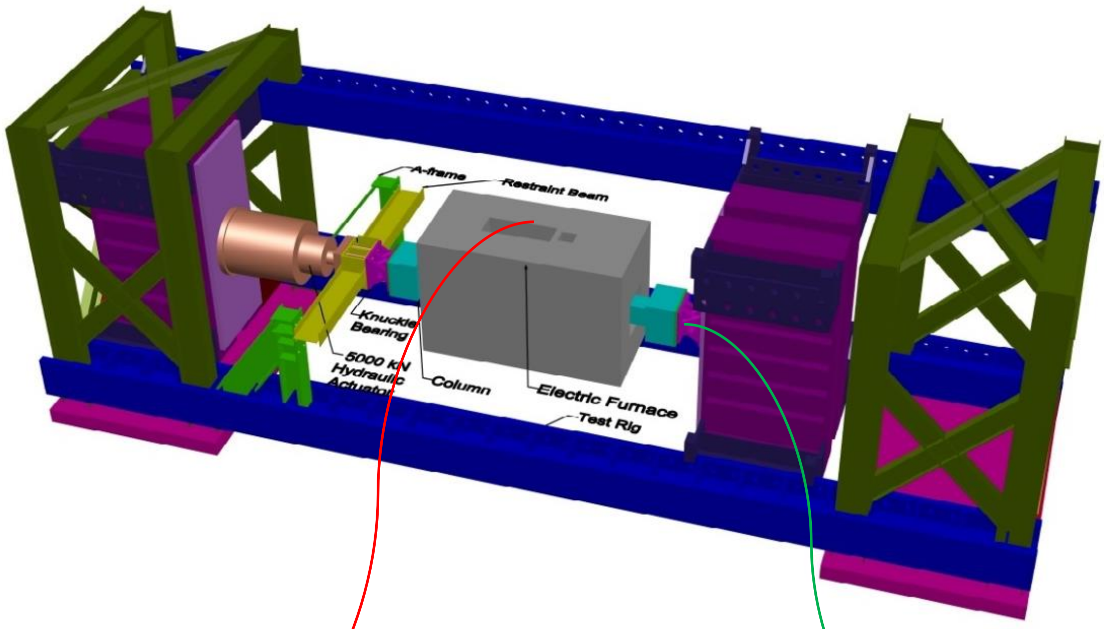

(a) 3D view

(b) LVDT measuring mid-height deflection

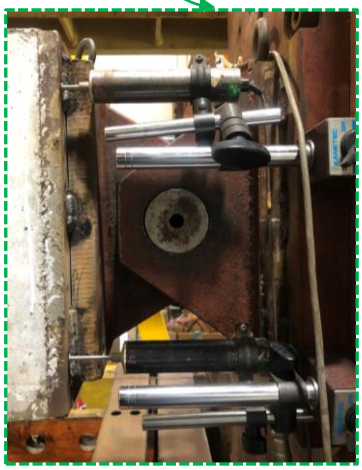

(c) LVDTs measuring axial deformation

Figure 3. Test setup

2.4 Test procedure

This research adopted transient heating conditions for all the column specimens. The specimen was embedded inside the furnace to allow 4-side heating. Insulation wool was used to seal openings to minimise heat loss. After installation of the specimen, a preloading of 15% of the target applied load during fire test (P_{fi}) was applied and released to check the instrumentation and eliminate slack of the setup. Following the release of preloading, P_{fi} was applied and retained for a minimum of 15 min until no further changes to instrumentation readings were observed. The furnace was then switched on to produce ISO 834 fire curve and fire testing officially started. Throughout the heating process, a constant applied load was maintained by adjusting the actuator to allow for free expansion and contraction of the specimen. Readings of LVDTs and thermocouples were recorded at a 5-second interval. When the specimen was unable to support P_{fi} (or the deflection rate was very high), the test ceased and the fire resistance was recorded.

3 RESULTS AND DISCUSSIONS

Test results and key findings from the ten fire tests are presented in this section. More details can be found in [8, 13].

3.1 Failure mode

One of the objectives of this study is to mitigate spalling by using hybrid PP and steel fibres. Figure 4 presents photographs of all the failed specimens after fire testing. It is noteworthy that there was no evidence of spalling in all the column specimens, in spite of different slenderness ratios, load eccentricities and levels of axial restraint. Compared with the tests in the literature where only PP fibre was added and spalling still occurred, this study showed the effectiveness of hybrid PP and steel fibres in mitigating spalling at the structural level. Additionally, structural integrity could be maintained due to the addition of steel fibres.

As for the failure mode, a classical stability failure was observed for specimens subjected to pure concentric loading (H-270-00 and H-200-00) since concrete at the compression zone was severely crushed. When the load eccentricity was getting larger, more tension cracks were observed and the failure mode tended to be combined failure mode (concrete crushing and yield of steel reinforcement).

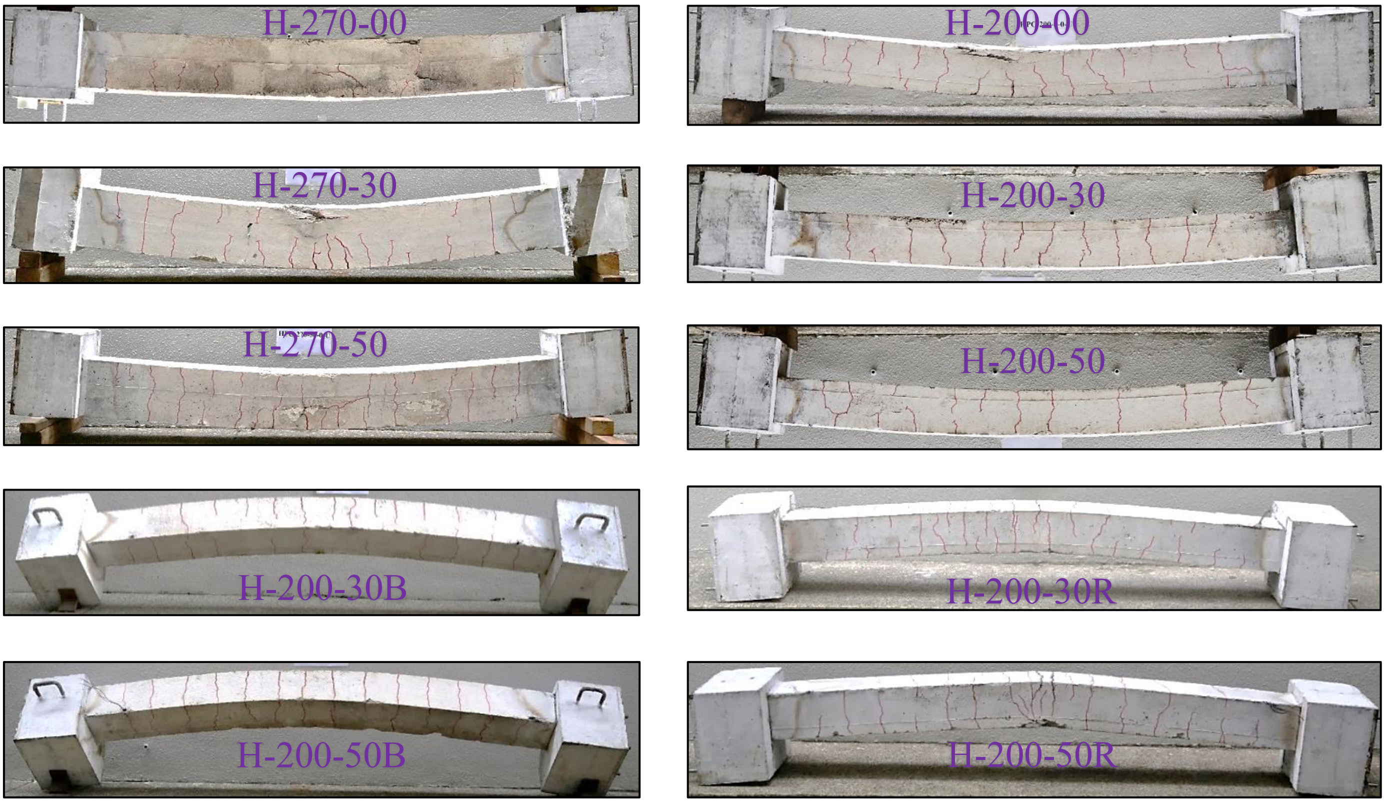

Figure 4. Photograph of failed specimens

3.2 Mid-height column deflection

The mid-height column deflection of the 10 tests is illustrated in Figure 5. It was found that as load eccentricity increased, the deflection increased, resulting in more tension cracks. For columns under pure concentric loading (H-270-00 and H-200-00), the deflection was suddenly increased, also implying a loss of stability.

The specimens generally had a good bending and deformation capacity due to the addition of steel fibres. According to Tan and Nguyen [9] who conducted column tests under uniaxial loading, the deflection at failure was around 45 mm. This study achieved 100 mm for the mid-height column deflection for the same slenderness ratio (H-270-00). Therefore, the mix design presented in Table 1 may potentially be used in beams to improve bending and shear capacity under fire since it is spalling resistant.

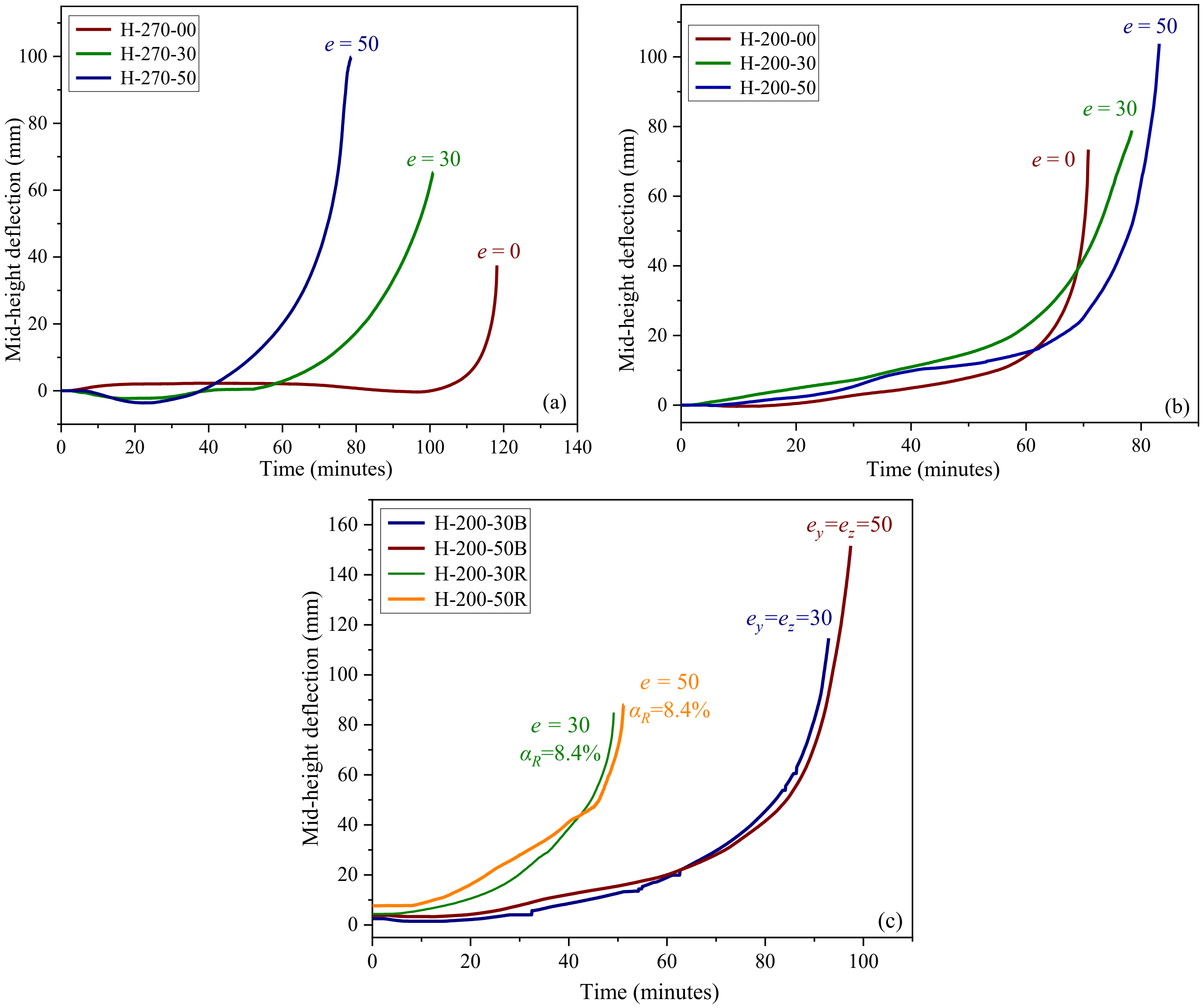

Figure 5. Mid-height column deflection

3.3 Axial deformation

Figure 6 shows the axial deformation of all the specimens. In general, axial deformation of columns exposed to elevated temperatures is characterised by expansion initially due to thermal expansion, followed by contraction due to material degradation. As the load eccentricity increased, an increase in maximum axial deformation (contraction) was observed. However, the restrained columns (H-200-30R and H-220-50R) showed similar axial deformation to the unrestrained columns (H-200-30 and H-220-50), implying that the ultimate deformation was not affected by axial restraint.

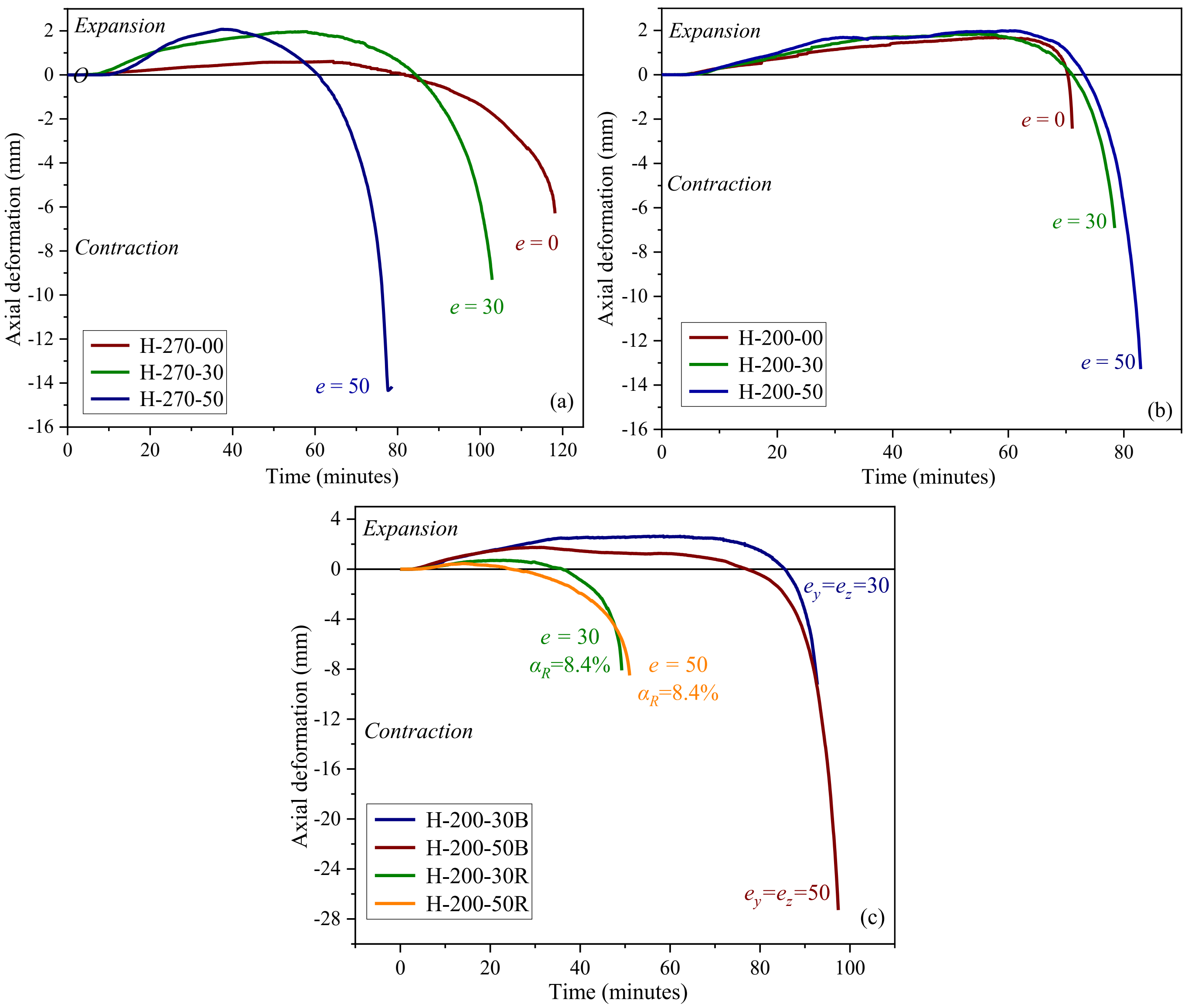

Figure 6. Axial deformation

3.4 Fire endurance

The effects of column dimension, load eccentricity, biaxial bending and axial restraint on fire resistance are presented in Figure 7. H-270-00 achieved the highest fire resistance of 118.2 min while H-200-30R exhibited the lowest fire resistance, with a duration of 49.3 min. It was found that the effect of load eccentricity on fire endurance was dependent on the cross-sectional design. H-270 columns showed decreased fire resistance when the load eccentricity increased, whereas H-200 columns showed an increase (Figure 7a). A detailed explanation of this phenomenon can be found in [8]. Therefore, load eccentricity can have a significant impact on fire resistance when the column dimensions, concrete cover, reinforcement ratios and load levels are taken into account. On the other hand, the axial restraint would speed up the failure of columns and decrease the fire resistance as a result of the additional force generated during the expansion stage of columns (Figure 7c). Consequently, it is essential to consider the effect of load eccentricity and axial restraint in fire design.

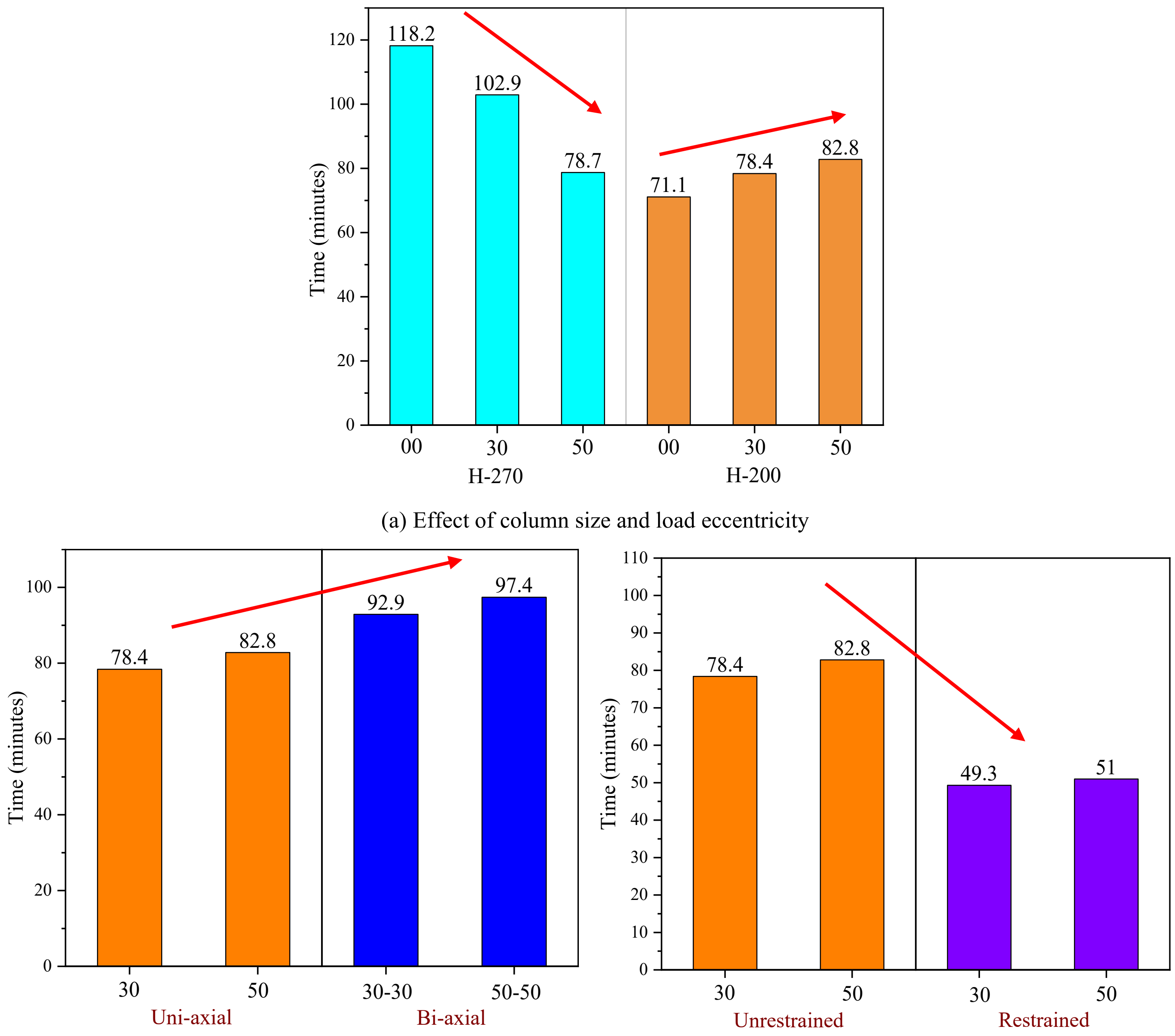

(a) Effect of column size and load eccentricity

(b) Effect of biaxial bending (H-200)

(c) Effect of axial restraint (H-200)

Figure 7. Fire endurance

4 CONCLUSIONS

An experimental programme involving ten columns was conducted in this paper to improve the understanding of fire performance of HPC columns when subjected to elevated temperatures. It focused on the effects of column dimension, load eccentricity, biaxial bending and axial restraint, which were missing in the literature. Data collected in this study may be used to validate numerical and analytical models for HPC columns and improve current codes of practice regarding fire resistance [14]. Based on the test results, key findings are summarised as follows:

- Although complex loading conditions such as uniaxial and biaxial bending and axial restraint were applied, there was no evidence of spalling in any of the specimens. Compared with the tests in the literature where only PP fibre was added and spalling still occurred, this study showed the effectiveness of hybrid PP and steel fibres in mitigating spalling at the structural level. Additionally, structural integrity could be maintained due to the addition of steel fibres.
- It was found that the effect of load eccentricity on fire endurance was dependent on the cross-sectional design. H-270 columns showed decreased fire resistance when the load eccentricity

increased, whereas H-200 columns showed an increase. The effect of load eccentricity should be incorporated into fire design.

- Axial restraint would speed up the failure of columns and decrease the fire resistance because of the additional force generated during the expansion stage of columns

ACKNOWLEDGMENT

This material is based on research/work supported by the Singapore Ministry of National Development and National Research Foundation under L2 NIC Award No. L2NICCFP1-2013-4. Any opinions, findings, and conclusions or recommendations expressed in this material are those of the author(s) and do not necessarily reflect the views of L2 NIC.

REFERENCES

1. Kodur, V. and L. Phan, Critical factors governing the fire performance of high strength concrete systems. Fire safety journal, 2007. **42**(6-7): p. 482-488.
2. Aldea, C.-M., J.-M. Franssen, and J.-C. Dotreppe, Fire test on normal and high-strength reinforced concrete columns. NIST Special Publication 919, 1997: p. 109-124.
3. Ali, F., D. O'Connor, and A. Abu-Tair, Explosive spalling of high-strength concrete columns in fire. Magazine of Concrete Research, 2001. **53**(3): p. 197-204.
4. Kodur, V. and R. McGrath. Performance of high strength concrete columns under severe fire conditions. in CONSEC'01: Third International Conference on Concrete Under Severe Conditions. 2001.
5. Kodur, V., et al., Effect of strength and fiber reinforcement on fire resistance of high-strength concrete columns. Journal of Structural Engineering, 2003. **129**(2): p. 253-259.
6. Raut, N. and V. Kodur, Response of high-strength concrete columns under design fire exposure. Journal of Structural Engineering, 2010. **137**(1): p. 69-79.
7. Khaliq, W. and V. Kodur, Effectiveness of polypropylene and steel fibers in enhancing fire resistance of high-strength concrete columns. Journal of Structural Engineering, 2018. **144**(3): p. 04017224.
8. Du, P., Y. Yang, and K.H. Tan, Fire behaviour and design of hybrid fibre reinforced high-performance concrete columns subjected to uniaxial bending. Engineering Structures, 2022. **251**: p. 113425.
9. Tan, K.-H. and T.-T. Nguyen, Structural responses of reinforced concrete columns subjected to uniaxial bending and restraint at elevated temperatures. Fire Safety Journal, 2013. **60**: p. 1-13.
10. Tan, K.-H. and T.-T. Nguyen, Experimental behaviour of restrained reinforced concrete columns subjected to equal biaxial bending at elevated temperatures. Engineering Structures, 2013. **56**: p. 823-836.
11. Benmarce, A. and M. Guenfoud, Behaviour of axially restrained high strength concrete columns under fire. Construction & Building Materials, 2005. **57**(5).
12. EN 1992-1-2, Eurocode 2: Design of concrete structures-Part 1-2: General rules-Structural fire design, in Bressels: CEN. 2004: Brussels, Belgium.
13. Du, P., Y. Yang, and K.H. Tan, Effects of Biaxial Bending and Axial Restraint on Hybrid Fiber Reinforced High-Performance Concrete Columns at Elevated Temperatures. Journal of Structural Engineering, 2022. **148(**11): p. 04022185.
14. Du, P., Y. Yang, and K.H. Tan, Analytical modelling of high strength concrete columns under ambient and fire conditions. Engineering Structures, 2021. **247**: p. 113216.

FIRE RESISTANCE OF LIGHTWEIGHT ENGINEERED CEMENTITIOUS COMPOSITE: RESIDUAL MECHANICAL PROPERTY AND SPALLING BEHAVIOUR

Bo-Yu Deng[1], Ling-Zhi Li[2]*, Ke-Quan Yu[3], Md Nasir Uddin[4], and Hong-Jun Yu[5]

ABSTRACT

Lightweight engineered cementitious composite cementitious composite (LWECC) is a special type of cement composite material with superior tensile performance, durability, and low self-weight. However, the fire resistance of LWECC is unknown and there is a lack of research in this aspect. This study aimed to study the residual mechanical property and spalling behaviour of LWECC after exposure to elevated temperature. The novel LWECC reinforced by PE fibres was developed by incorporating high-volume fly ash cenosphere (FAC) as lightweight fine aggregate. A total of 15 mixtures were tested to investigate the effects of silica fume (SF), FAC, polyethylene (PE) and polypropylene (PP) fibre on fire resistance experimentally. The introduction of PP fibres could effectively mitigate explosive spalling, while PE fibres failed to provide the benefit on spalling resistance. The SF and FAC had adverse influences on spalling resistance. The post-fire compressive strength began to decrease drastically when the temperature exceeds 800 ℃ . The work provides a promising way to develop high-performance LWECC with high fire resistance, which is helpful for fire resistance design of LWECC structures in the future.

Keywords: Fire resistance; Explosive spalling; Lightweight engineered cementitious composite; Mechanical properties

1 INTRODUCTION

Concrete has become the most widely employed structural material. However, the inherent defect of ordinary concrete material hinders its application in modern building structures, such as brittleness and easily cracking. Over the past 30 years, engineered cementitious composites (ECC) have made breakthrough in improving the ductility and durability of concrete materials [1-3]. As one type of high-performance fibre reinforced concrete (FRC), ECC are extensively concerned by researchers for tensile strain-hardening and multiple-cracking behaviour, which can achieve a high direct tensile strain capacity over 3% and control the crack width around 100 μm [4-6]. The structural performance can be improved significantly by incorporating ECC, in terms of bearing capacity, ductility and corrosion resistance [7-10]. Nevertheless, the spalling resistance and mechanical properties of ECC at elevated temperature is much less understood than conventional concrete[11-14].

[1] Ph.D. candidate, Tongji University,
e-mail: 2010022@tongji.edu.cn
[2] Associate professor, Tongji University,
e-mail: lilingzhi@tongji.edu.cn
[3] Associate professor, Tongji University,
e-mail: 12yukequan@tongji.edu.cn
[4] Master, Tongji University,
e-mail: nasiruddin@tongji.edu.cn
[5] Master, Tongji University,
e-mail: honjunyu@126.com
https://doi.org/10.6084/m9.figshare.22177880

Although ECC exhibits superior performance at ambient temperature, its fire resistance is questionable. The melting of polymer fibre might have two potential influences on the ECC exposed to high temperature [15]. On the one hand, the excellent tensile characteristics of ECC would be reduced and even vanished as the mechanical performance of fibres deteriorate in fire. On the other hand, the fibre melting would alleviate the thermal spalling by increasing the permeability inside ECC. Previous studies have reported that PP, polyvinyl alcohol (PVA), and low-density PE (LDPE) fibres are effective in preventing the explosive spalling of concrete, while high-density PE (HDPE) fibre exhibits poor spalling resistance [16-20]. At elevated temperature, the HDPE fibre would not produce the expansion microcracks or empty channels inside ECC matrix as other types of fibres, due to its low thermal expansion coefficient and high viscosity after melting [21].

The behaviour mechanism in fire is more complicated for LWECC, due to the distinct thermal properties of hollow lightweight aggregates. LWECC is generally developed using the FAC with very low thermal conductivity (0.08 W/m·K) [22]. The thermal insulation of FAC is beneficial in protecting the reinforcement from high temperature [23] and then upgrading the fire resistance rating of structural members. However, this characteristic can be double-edged sword increasing the spalling risk at high temperature gradient. The LWECC has the advantages of reducing the self-weight and enhancing the ductility and durability of structure, due to its high strength-to-density ratio and superior tensile properties. Nevertheless, the research on fire resistance of LWECC is rare. It is necessary for the structural application of LWECC to understand the fundamental behaviour in fire[24].

In this paper, ten different mixtures were tested to study the effect of PE fibres, SF and FAC on the fire resistance of LWECC at high temperature. Five mixtures reinforced with hybrid fibres (i.e., PE and PP fibres) were tested to investigate the improvement in the explosive spalling resistance by PP fibres, where different contents of PP fibres (0.1~0.5% by volume) were considered. In addition, the changes in the physical and mechanical properties of LWECC after exposure to various temperatures were studied, in terms of colour, cracking pattern, mass loss and residual compressive strength.

2 EXPERIMENTAL PROGRAM

2.1 Mixture proportion and preparation

The raw materials of ECC matrix include ordinary Portland cement 52.5R, silica fume (SF, 0.1~1 μm), Class F fly ash (FA), fine silica sand (125~180 μm) and fly ash cenosphere (FAC). FAC is a fly ash hollow sphere that can float on the water, which is derived from the industrial waste residue of coal combustion. The chemical components are SiO_2 (50%~65%), Fe_2O_3 (1%~7%), Al_2O_3 (24%~38%) and CaO (≤ 5%). Due to the hollow micro-structure and thin shell, FAC particles have a low apparent density and exhibit excellent thermal insulation. The physical properties of FAC are listed in Table 1. The mixtures were reinforced with high-strength PE fibres and PP fibres. The geometry and physical properties of fibres are summarized in Table 2.

As shown in Table 3, ten mixtures were prepared to investigate the influence of SF, FAC and PE fibre content on the spalling behaviour of ECC (for the spalling behaviour). The control groups are the ordinary ECC of about 1800 kg/m^3. As for the six LWECCs, the fine silica sand in ECC matrix was replaced by the FAC lightweight aggregate by volume. The densities of LWECCs were reduced to about 1300 kg/m^3, which was 28% lower than the 1800 kg/m^3 of the control mixtures. The LWECC features adequate compressive strengths of 35 MPa, high tensile strength of 7 MPa and strain capacity of 5%. To maintain proper flowability and fibres dispersion of the mix, the hydroxypropyl methylcellulose (HPMC) of 0.5 g/L and the powder-based polycarboxylate superplasticizer (SP) of 4 g/L were used. The water-to-binder ratios (w/b) of the mixtures were 0.30 and 0.32.

To study the influence of PP fibres on the spalling resistance of LWECC (for the spalling prevention)., five mixtures were designed as shown in Table 4, where the volume fraction of PE fibre was fixed at 1%. The dosage in volume of PP fibres varied from 0.1% to 0.5%.

A planetary mixer was used for the preparation of the mixtures. Cement, SF, FA, SP and silica sand or FAC were uniformly blended by mixing for around 1 min. Subsequently, water was added into the mixture during stirring. When a homogenous and consistent fresh paste was obtained (about 3 min mixing), polymer fibres were added, and the stirring lasted for another 2 min mixing. Then, the fresh mixtures were cast into cubic moulds with external vibration to remove entrapped air bubbles. After 24 hours, the specimens were demoulded and cured in hot water at temperature of 60 ± 1 °C for 48 hours and then stored at ambient temperature until 28 days.

Table 1. Physical characteristics of FAC

	Apparent Density (g/cm^3)	Bulk Density (g/cm^3)	Crushing Strength (MPa)	D50 (μm)	D90 (μm)
FAC	0.87	0.72	70	120	250

Table 2. Geometry and physical properties of fibre

	Diameter (μm)	Length (mm)	Strength (MPa)	Strain capacity (%)	Density (g/cm^3)	Melting temperature (°C)
PE	24	18	2900	3	0.97	144
PP	31	12	400	0.3	0.91	160

Table 3. Mixture compositions for spalling behaviour (unit: g/L)

Mix ID	Cement	FA	SF	Sand	FAC	Water	PE fibre (v/v)
C-0	361.0	338.0	85.0	716.6	/	250.9	0%
C-1	361.0	338.0	85.0	716.6	/	250.9	1%
C-2	361.0	338.0	85.0	716.6	/	250.9	2%
C-NSF-0	472.2	338.0	/	716.6	/	250.9	0%
C-NSF-1	472.2	338.0	/	716.6	/	250.9	1%
C-NSF-2	472.2	338.0	/	716.6	/	250.9	2%
L-0	361.0	338.0	85.0	/	238	250.9	0%
L-1	361.0	338.0	85.0	/	238	250.9	1%
L-NSF-0	472.2	338.0	/	/	238	250.9	0%
L-NSF-1	472.2	338.0	/	/	238	250.9	1%

*In the mix ID, "C" denoted "ordinary ECC", "L" denoted "LWECC", "NSF" denoted "no silica fume". For example, "L-NSF-1" denoted "LWECC samples containing 1% PE fibres and no SF".

Table 4. Mixture compositions for spalling prevention (unit: g/L)

Mix ID	Cement	FA	SF	Sand	FAC	Water	PE fibre (v/v)	PP fibre (v/v)
LP-1-1	361.0	338.0	85.0	/	238	250.9	1%	0.1%
LP-1-2	361.0	338.0	85.0	/	238	250.9	1%	0.2%
LP-1-3	361.0	338.0	85.0	/	238	250.9	1%	0.3%
LP-1-4	361.0	338.0	85.0	/	238	250.9	1%	0.4%
LP-1-5	361.0	338.0	85.0	/	238	250.9	1%	0.5%

*In the mix ID, "L" denoted "LWECC", the suffix number denoted "fibre contents". For example, "LP-1-3" denoted "LWECC samples containing 1% PE fibres and 0.3% PP fibres".

2.2 Spalling resistance test

To investigate spalling resistance of ECC and LWECC, the cubic (70.7 mm) specimens were exposed in an electrical furnace at a heating rate of 10 °C/min (started from ambient temperature). The specimens were enclosed in a perforated steel cage to prevent spalling debris from harming the interior heating components while allowing for heat convection, as shown in Figure 1. The temperature was measured in the air inside the furnace. When it reached the prescribed temperature of 150, 200, 300, 400, 600, and 800 °C and then kept the target temperature for 1 hour to achieve a thermal steady-state condition. During the test, the sound in the furnace was checked. After testing, specimens were cooled down naturally for 1 day and the explosive spalling severity was observed visually. For each temperature exposure level, six specimens were tested. All specimens are oven dried at 80 °C for 48 hours before the spalling test, as shown in Figure 2, to eliminate the influence of moisture content on explosive spalling.

Figure 1. Furnace for heating test

Figure 2. Oven dry

2.3 Mechanical test

To study the residual mechanical properties, the cubic specimens with excellent spalling resistance were used for uniaxial compressive tests. The setups for compressive are shown in Figure 3. Five cubic samples of 70.7 mm were subjected to compression test by 30 tones MTS machine with a loading rate of 0.5 mm/min for each group.

Figure 3. Compressive test

3 RESULTS AND DISCUSSION

3.1 Colour change and cracking pattern

Figure 4 shows that the colour change of the LP-1-4 specimen when exposed to a high temperature. The surface colour of LWECC changed from dark grey at 25 °C to light grey at 600 °C due to the loss of water and chemical decomposition. Specimens subjected to 300 °C displayed a light brown colour, possibly due to the evaporation of fibre. When the temperature exceeded 800 °C, the colour turned beige. The post-fire specimens of different material proportion shared a similar colour change and cracking development. For all mixtures, no visible surface cracks occurred until the temperature reached 800 °C. As shown in Figure 5, surface hairline cracks were monitored at 800 °C. The crack width and number increased with the higher temperature. It was found that the LWECC cracked more severely than other normal-weight mixes, which indicated that the FAC may cause the cracking under elevated temperatures. The number and width of post-fire cracks decreased with an increasing content of PP fibres.

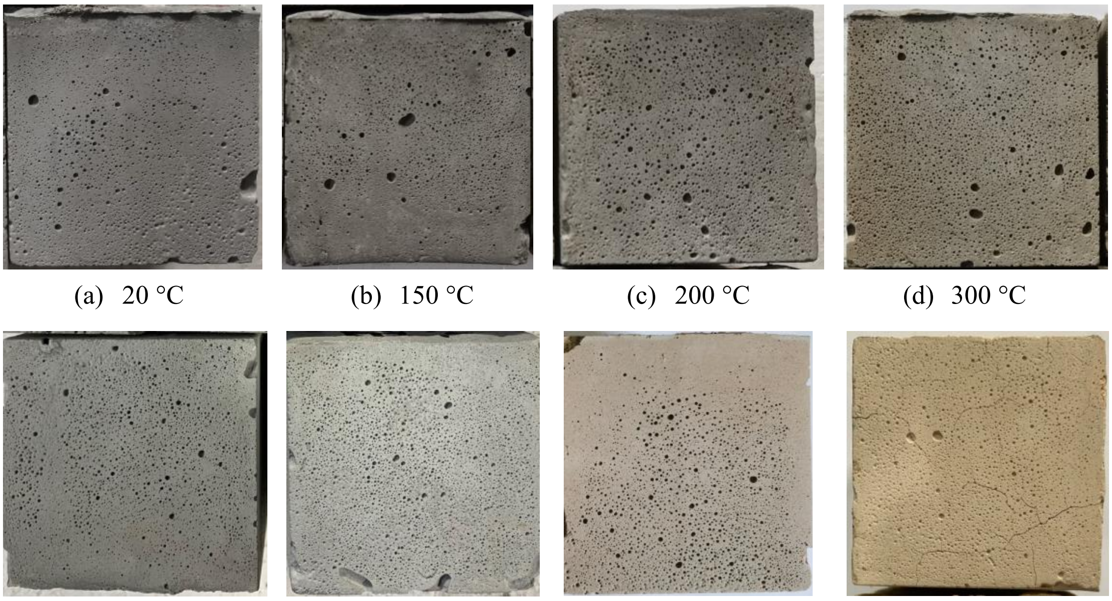

(a) 20 °C (b) 150 °C (c) 200 °C (d) 300 °C

(e) 400 °C (f) 600 °C (g) 800 °C (h) 1000 °C

Figure 4. Surface colour change (LP-1-4)

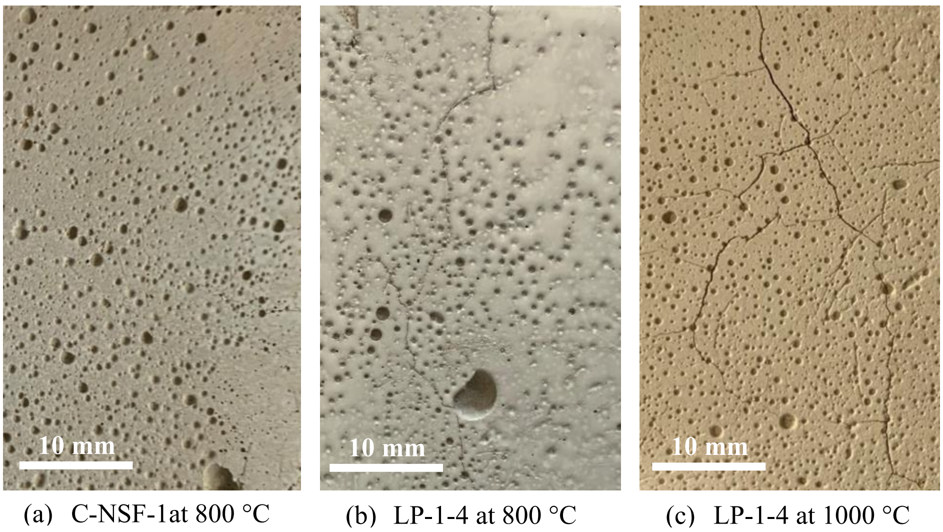

(a) C-NSF-1at 800 °C (b) LP-1-4 at 800 °C (c) LP-1-4 at 1000 °C

Figure 5. Surface cracking

3.2 Mass loss

Figure 6 shows the relationship between the mass loss and the elevated temperature of heat exposed. At the early stage below 300 °C, the mass loss increased rapidly with increasing exposure temperatures, mainly due to the release of free and physically bound water. When temperatures exceeded 400 °C, the mass decrease speed slowed down slightly, and the mass loss of most mixtures was approximately 10%. The polymer fibre has a relatively low melting point (below 200 °C). As it melts in the concrete, a large number of pores will form. Through the connection of these pores, a network of channels will form, allowing water vapor to escape. And the volatilization of the melted or decomposed fibres also has an influence on the mass loss. Therefore, the mixture with the higher fibre content (especially the PP fibre) exhibited slightly higher mass loss. At higher temperatures above 600 °C, the mass change was caused by the dehydration of the paste.

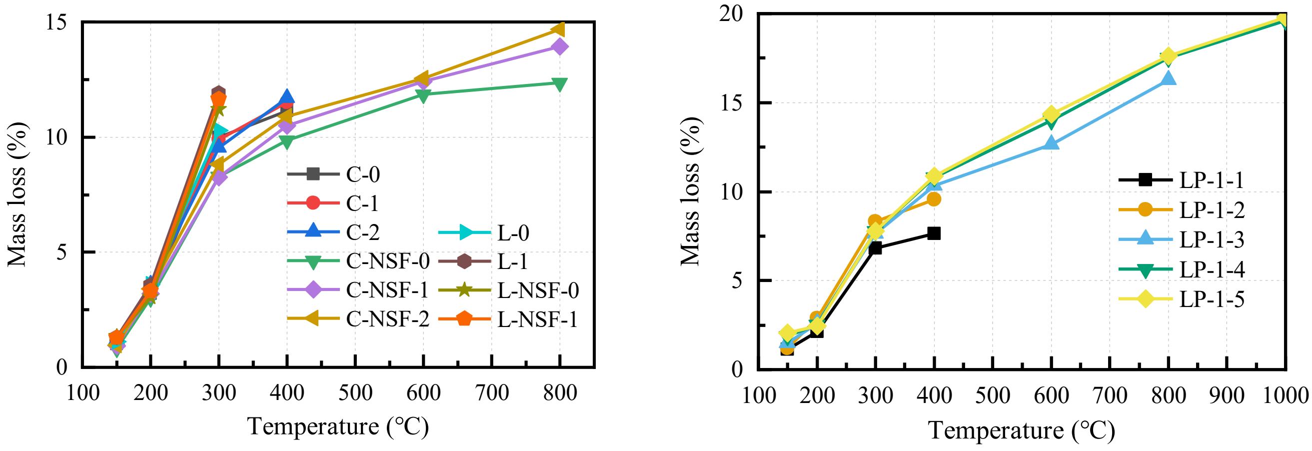

(a) Mixtures without PP fibres

(b) Mixtures with PP fibres

Figure 6. Mass loss of post-fire specimens

3.3 Spalling behaviour and prevention

The spalling test results of control mixture and LWECC are shown in Figure 7. The probability of spalling (the ratio of spalling specimens to total specimens) is defined as spalling risk. The spalling risks of six ECC and four LWECC mixtures are illustrated in Figure 8. Without PP fibre, only the C-NSF group has no spalling risk, whereas the other groups exhibit varying degrees of severe spalling before 400 ℃ . There are no noticeable differences in the spalling risk between the mixtures with different PE fibre content. PE fibres can relieve the spalling very slightly. As for the PP fibre reinforced LWECC (LP group), 0.3% PP fibre is not sufficient to prevent spalling. When the PP fibre content reaches 0.4%, the LWECC could withstand high temperatures of up to 1000 ℃ without spalling. This paper attempts to explain the severe spalling phenomena associated with ECC materials based on generally accepted mechanisms:

(1) According to the theory of vapor pressure, the explosion of concrete is caused by the vapor pressure generated by the internal moisture migration at high temperatures. The low permeability and high compactness of ECC make it difficult for steam pressure generated inside it to escape. The spalling of ECC may happen when the accumulated steam pressure reaches saturation with increasing temperature.

(2) Based on the comparison of the specimens with and without SF (C-0 vs C-NSF-0, L-0 vs L-NSF-0), it can be concluded that the addition of SF will increase the spalling risk effectively. Because the SF of smaller particles can compact the internal structure, and thus reduces the material's permeability.

(3) According to the thermal stress theory, the thermal inertia of concrete causes a large temperature gradient during fire. This results in inconsistent internal and external thermal expansion, which causes the external concrete to be compressed and internal tensed. With the increase of temperature, the thermal stress accumulates continuously, leading the increase of spalling risk.

(4) Considering that FAC is a hollow sphere with high thermal insulation, the inclusion of FAC would decrease the thermal conductivity. The thermal conductivity of ULECCC material is only 0.2 ~ 0.5 W/(m·K), which is much lower than 0.8 ~ 1.7 W/(m·K) of ordinary concrete. A large temperature

gradient within the material is prone to be generated, resulting in high-temperature spalling. Therefore, the LWECC containing FAC suffered higher spalling risk.

(5) PP fibres can mitigate spalling at elevated temperatures by improving the permeability of concrete. However, the mechanism by which PP fibres increase the permeability of concrete is controversial. Some researchers believe that the melting of PP fibres results in the formation of connected empty spindly channels, which increases the permeability of concrete. Some researchers believe that microcracks in caused by the thermal expansion of PP fibres are the source of the enhanced permeability.

(6) The effects of different types of fibres on prevent spalling vary greatly. PP and PVA fibres can significantly prevent high-temperature spalling, while PE fibres have a limited effect. Although the melting point of PE fibre is relatively low (about 144 °C), its higher vaporization temperature (about 500°C) and lower coefficient of expansion make it incapable of creating channels for vapor escape.

(a) C-0 after 600 °C

(b) L-1 after 300 °C

(c) L-1 after 400 °C

(d) LP-1-3 after 600 °C

(e) LP-1-3 after 800 °C

Figure 7. Spalling observation

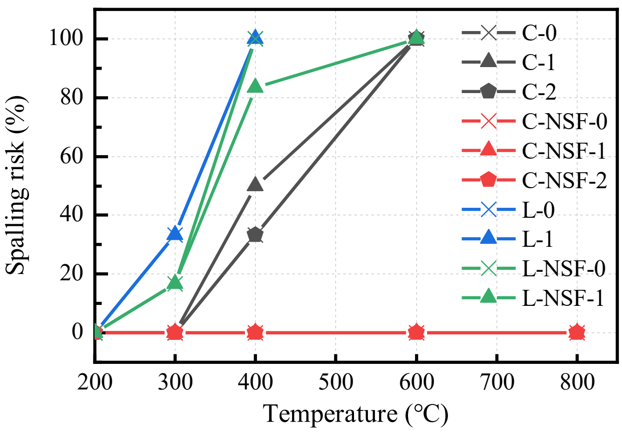

(a) Mixtures without PP fibres

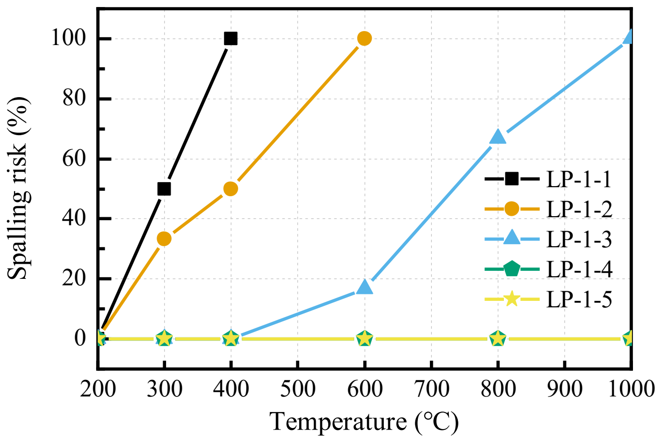

(b) Mixtures with PP fibres

Figure 8. Spalling risk

3.4 Residual compressive strength

The residual compressive strengths of post-fire specimens are presented in Figure 9. The compression strength changes were negligible after exposure to high temperatures below 300 °C, except for the C-NSF group. As the temperature increased to 400 ℃ , the compressive strength was observed to decrease substantially. The residual compressive strength for the LP and C-NSF groups decreased to about 30 MPa at 600 ℃ , and dropped to around 20 MPa at 800 ℃ . It can be found that the incorporation of PP fibres mitigated the degradation in compressive strength. Strength reduction factor for specimens in the LP group ranged from 58%~64%, which was evidently higher than 26%~41% for specimens in the C-NSF group. The content of PE and PP fibres had no significant effect on the compressive strength.

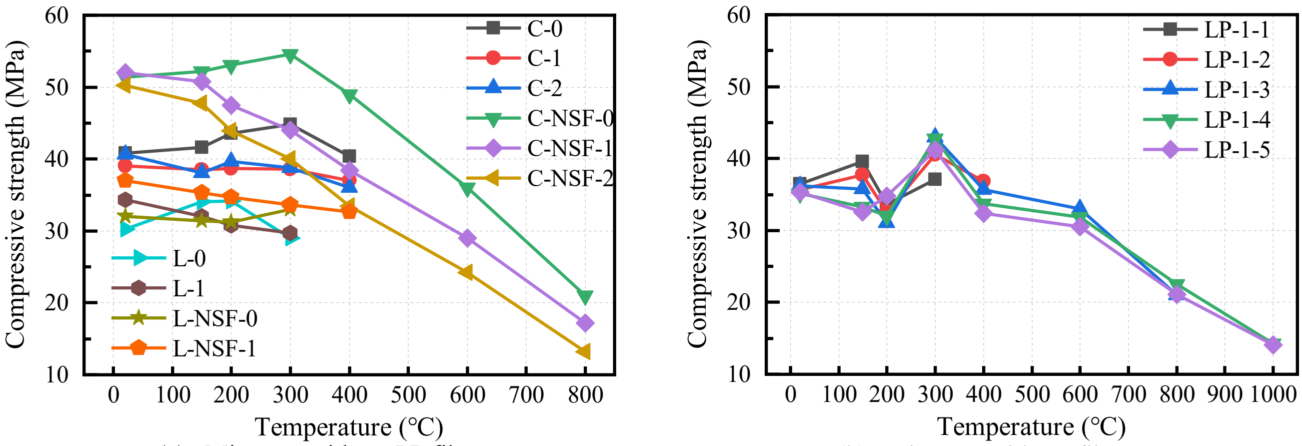

Figure 9. Residual compressive strength

4 CONCLUSIONS

In this paper, the fire resistance of LWECC was investigated from two aspects, i.e., spalling behaviour and residual mechanical property. The following conclusions can be drawn:

(1) The spalling behaviour of cement composites can be easily induced by FAC and SF. Even though the mixtures in the control group contained only 4.85% of SF, it spalled severely after exposure to 400 °C. Since the FAC has a low thermal conductivity, it can increase the thermal inertia of the composite and elevate the spalling risk. LWECC suffered spalling at 300 °C due to the high amount of FAC (about 40% of the volume).

(2) The incorporation of PP fibres improved the spalling resistance. Spalling risks and damage intensity were significantly reduced with an increase in PP fibre content. To prevent high-temperature spalling of LWECC, 0.4 % PP fibres were required. Although PE fibres have a lower melting point (144 ℃) than PP fibres (160 ℃), they failed to provide the expected improvement in spalling resistance.

(3) The high temperature had relatively slight effect on compressive strength of LWECC before 400 °C. Afterward, the strength deteriorated significantly with increased exposure temperature. The introduction of PE and PP fibres had a relatively small impact on the residual compressive strength of specimens. LWECC containing 0.4% PP fibres remained over 50% of original strength at 800 °C.

ACKNOWLEDGMENT

The work described in this paper was financially supported by the National Natural Science Foundation of China (Grants No. 52108243), State Key Lab of Subtropical Building Science, South China University of Technology (No. 2021ZB10) and Fundamental Research Funds for the Central Universities. The authors are grateful for each one of these contributions.

REFERENCES

[1] Li LZ, Cai ZW, Yu KQ, Zhang YX, Ding Y. Performance-based design of all-grade strain hardening cementitious composites with compressive strengths from 40 MPa to 120 MPa. Cement and Concrete Composites. 2019;97:202-17.

[2] Li VC. Engineered cementitious composites (ECC): Bendable concrete for sustainable and resilient infrastructure. Springer. 2019.

[3] Yu KQ, Yu JT, Dai JG, Lu ZD, Shah SP. Development of ultra-high performance engineered cementitious composites using polyethylene (PE) fibers. Construction and Building Materials. 2018;158:217-27.

[4] Yu KQ, Ding Y, Liu JP, Bai YL. Energy dissipation characteristics of all-grade polyethylene fiber-reinforced engineered cementitious composites (PE-ECC). Cement and Concrete Composites. 2020;106:103459.

[5] Yu Kq, Ding Y, Zhang YX. Size effects on tensile properties and compressive strength of engineered cementitious composites. Cement and Concrete Composites. 2020;113:103691.

[6] Wang YC, Liu FC, Yu JT, Dong FY, Ye JH. Effect of polyethylene fiber content on physical and mechanical properties of engineered cementitious composites. Construction and Building Materials. 2020;251.

[7] Qin FJ, Zhang ZG, Yin ZW, Di J, Xu LJ, Xu XQ. Use of high strength, high ductility engineered cementitious composites (ECC) to enhance the flexural performance of reinforced concrete beams. Journal of Building Engineering. 2020;32.

[8] Li LZ, Bai Y, Yu KQ, Yu JT, Lu ZD. Reinforced high-strength engineered cementitious composite (ECC) columns under eccentric compression: Experiment and theoretical model. Engineering Structures. 2019;198:13.

[9] Yuan F, Pan JL, Dong LT, Leung CKY. Mechanical Behaviors of Steel Reinforced ECC or ECC/Concrete Composite Beams under Reversed Cyclic Loading. Journal of Materials in Civil Engineering. 2014;26.

[10] Ismail MK, Hassan AAA. Performance of lightweight SCC beams strengthened with rubberized engineered cementitious composite in shear. Engineering Structures. 2022;252.

[11] Luo JJ, Cai ZW, Yu KQ, Zhu WJ, Lu ZD. Temperature impact on the micro-structures and mechanical properties of high-strength engineered cementitious composites. Construction and Building Materials. 2019;226:686-98.

[12] Yu KQ, Lu ZD, Yu JT. Residual compressive properties of strain-hardening cementitious composite with different curing ages exposed to high temperature. Construction and Building Materials. 2015;98:146-55.

[13] Zhang ZG, Liu JC, Xu XQ, Yuan LQ. Effect of sub-elevated temperature on mechanical properties of ECC with different fly ash contents. Construction and Building Materials. 2020;262:11.

[14] Rawat S, Lee CK, Zhang YX. Performance of fibre-reinforced cementitious composites at elevated temperatures: A review. Construction and Building Materials. 2021;292:39.

[15] Liu JC, Tan KH. Fire resistance of ultra-high performance strain hardening cementitious composite: Residual mechanical properties and spalling resistance. Cement & Concrete Composites. 2018;89:62-75.

[16] Tran NP, Gunasekara C, Law DW, Houshyar S, Setunge S. Microstructural characterisation of cementitious composite incorporating polymeric fibre: A comprehensive review. Construction and Building Materials. 2022;335:18.

[17] Liu JC, Tan KH. Mechanism of PVA fibers in mitigating explosive spalling of engineered cementitious composite at elevated temperature. Cement & Concrete Composites. 2018;93:235-45.

[18] Zhang D, Dasari A, Tan KH. On the mechanism of prevention of explosive spalling in ultra-high performance concrete with polymer fibers. Cement and Concrete Research. 2018;113:169-77.

[19] Zhang D, Tan KH. Effect of various polymer fibers on spalling mitigation of ultra-high performance concrete at high temperature. Cement & Concrete Composites. 2020;114:9.

[20] Li Y, Pimienta P, Pinoteau N, Tan KH. Effect of aggregate size and inclusion of polypropylene and steel fibers on explosive spalling and pore pressure in ultra-high-performance concrete (UHPC) at elevated temperature. Cement & Concrete Composites. 2019;99:62-71.

[21] Zhang D, Liu YC, Tan KH. Spalling resistance and mechanical properties of strain-hardening ultra-high performance concrete at elevated temperature. Construction and Building Materials. 2021;266:9.

[22] Huang ZY, Liew JYR, Li W. Evaluation of compressive behavior of ultra-lightweight cement composite after elevated temperature exposure. Construction and Building Materials. 2017;148:579-89.

[23] Wu YP, Wang JY, Monteiro PJM, Zhang MH. Development of ultra-lightweight cement composites with low thermal conductivity and high specific strength for energy efficient buildings. Construction and Building Materials. 2015;87:100-12.

[24] Huang ZY, Padmaja K, Li S, Liew JYR. Mechanical properties and microstructure of ultra-lightweight cement composites with fly ash cenospheres after exposure to high temperatures. Construction and Building Materials. 2018;164:760-74.

PREDICTION OF COMPRESSIVE STRENGTH OF CONCRETE CONTAINING RECYCLED AGGREGATE AT HIGH TEMPERATURES USING AN ARTIFICIAL NEURAL NETWORK (ANN)

Sanaz Ramzi[1], Mohammad Javad Moradi[2], Hamzeh Hajiloo[3]

ABSTRACT

Recycled aggregates (RA) are widely used around the world as an effective solution to manage construction, renovation, and demolition (CRD) waste and the depletion of natural sources. The behaviour of recycled aggregate concrete exposed to high temperatures is complex, non-linear, and affected by various parameters. In the past decade, artificial neural networks (ANNs) have been frequently used for predicting the properties of different types of concrete. This report aims to predict the compressive strength of recycled aggregate concrete when exposed to high temperatures using an ANN model. A total of 116 data points from previous experimental studies were collected for training, validating, and testing the model. The ANN-based model was developed using nine input parameters: temperature level, recycled aggregate type (siliceous and calcareous), coarse and fine recycled aggregate replacement ratio, cement and water content, and heating rate. The results indicated that the artificial neural networks model is a reliable and efficient method for predicting the compressive strength of recycled aggregate concrete after subjecting to high temperatures. It was found that recycled concrete containing siliceous aggregates and higher water-to-cement ratios has a relatively higher residual compressive strength than calcareous concrete at high temperatures.

Keywords: Recycled aggregate; High temperatures; Compressive strength; Artificial neuronal network

1 INTRODUCTION

Concrete is the most common material used in the construction industry around the world. There is a large amount of concrete waste generated by construction, renovation, and demolition activities [1]. For instance, 17.3 million tonnes of CRD waste in Canada were produced in 2008 [2]. Concrete waste can be crushed into coarse aggregate for new concrete, which has provided an excellent solution to waste management and environmental degradation problems, such as non-renewable natural resources depletion [1, 3]. Over the last decades, the implementation of recycled aggregate has received significant attention [4]. The recycled aggregates extracted from waste concrete have different properties depending on their source and manufacturing process [5]. Concrete containing recycled aggregate has more porosity and less density than concrete made with natural aggregate (NA) due to the residual mortar adhered to the recycled aggregate, which includes 20-30% of recycled aggregate concrete [6, 7]. Therefore, recycled aggregate concrete may have different mechanical behaviours compared to concrete with natural aggregate because of contrasting characteristics between RA and NA under high-temperature exposure conditions [6]. Due to the widespread usage of recycled material in concrete, further information is required to fully understand the behaviour of recycled aggregate concrete in fire conditions [2].

Although in previous years, many studies have investigated the behaviour of concrete produced with natural coarse aggregates at high temperatures, research on the behaviour of concrete containing recycled aggregate

1 Graduate Student, Department of Civil and Environmental Engineering, Carleton University, Canada
e-mail: sanazramziaraghi@cmail.carleton.ca
2 Graduate Student, Department of Civil and Environmental Engineering, Carleton University, Canada
e-mail: mjmoradi@cmail.carleton.ca
3 Assistant Professor, Department of Civil and Environmental Engineering, Carleton University, Canada
e-mail: hamzehhajiloo@cunet.carleton.ca; ORCID: https://orcid.org/0000-0002-5932-2640
https://doi.org/10.6084/m9.figshare.22177895

when exposed to high temperatures is still limited [8]. Moreover, the results of the available studies are contradictory.

Xiao et al. [9] examined the residual compressive strength of recycled aggregate concrete (RAC) prepared with five different recycled coarse aggregates replacement levels of 0%, 30%, 50%, 70%, and 100% after high-temperature exposure (200 ℃ , 400 ℃ , 600 ℃ , and 800 °C). The results revealed that beyond 400 °C, the compressive strength of recycled concrete with at least 50% replacement of RAC was higher than that of natural aggregate concrete. In another experimental study, Zega et al. [10] evaluated the mechanical properties of recycled concrete with three different natural and recycled coarse aggregates (siliceous gravel, quartzite and granite crushed stone) prepared with water to cement (w/c) ratios of 0.4 and 0.7 at a single temperature of 500 °C. It was found that the recycled concrete showed better performance than the corresponding natural aggregate concrete for the three types of aggregate at 500 ℃ . Recycled concrete containing quartzitic coarse aggregate showed the best performance at a w/c ratio of 0.40. This can be attributed to the formation of a high-quality interface zone between the new mortar and the quartzite aggregate. On the other hand, for w/c of 0.70, the best performance was observed in concrete produced with granitic aggregate (natural and recycled) due to the lowest temperature reached within the center of granite aggregate concrete specimens.

Kou et al. [11] examined the compressive strength of recycled aggregate concrete containing ground granulated blast furnace slag and fly ash after exposure to 300 °C, 500 °C, and 800 °C. The replacement ratios of coarse natural aggregates with coarse recycled aggregates were 0%, 50%, and 100%. It was found that recycled aggregate concrete had a higher relative residual compressive strength than natural aggregate concrete (NAC) for all types of binder materials.

Vieira et al. [12] investigated the residual mechanical properties of concrete with 20%, 50%, and 100% recycled coarse aggregates as replacements for natural coarse aggregates after exposure to 400 ℃ , 600 ℃ , and 800 °C. They reported that the mechanical properties of recycled aggregate concrete are similar to the reference concrete made with natural aggregate. In addition, the mechanical properties of concrete with increasing content of recycled coarse aggregate were considerably reduced after subjecting to high temperatures. Galas et al. [13] have also reported similar results for concrete with different recycled aggregate replacement ratios of 0%, 30%, and 100% at a single temperature of 500 °C.

Wang et al. [14] investigated the compressive strength of concrete mixtures made with 100% coarse recycled aggregate, along with different levels of fine recycled aggregate (0%, 50% and 100%) to replace fine natural aggregate after heating to high temperatures between 200 ℃ and 800 °C. The concrete with 50% fine RA was found to have higher compressive strength compared to the concrete specimens without fine RCA. This strength improvement can be explained by the similar thermal expansion properties of mortar adhered with fine recycled aggregate and new mortar. Additionally, greater strength loss was observed in RCA specimens under the water cooling method than in natural cooling.

Pliya et al. [15] evaluated the compressive strength of recycled aggregate concrete after exposure to temperatures of 150 ℃ , 300 ℃ , and 450 ℃ . The specimen was made with 30% coarse and 30 % fine recycled aggregates as the natural aggregate partial substitute. It was observed that the strength of RAC decreased after exposure to high temperatures up to 450 ℃ due to the different physicochemical deformation of the cement matrix. Concrete with 30% coarse and fine recycled concrete aggregate performed adequately at high temperatures, similar to its reference concrete containing natural aggregate.

As seen from the above literature, replacing natural aggregates with recycled aggregates can significantly influence the mechanical properties of concrete. In addition, the performance of RCA concrete under high temperatures is highly complex, non-linear and affected by many parameters. In recent years, many researchers have employed artificial neural networks as reliable tools in modeling the complex behaviour of many problems in civil engineering. Recently, several studies have been conducted to estimate the mechanical properties of RCA concrete at room temperature using an artificial neural network [5, 7, 16-21]. However, studies about recycled aggregate concrete behaviour at high temperatures are scarce in the literature. This study aims to develop an accurate and reliable ANN model to predict the compressive strength of RA concrete after exposure to high temperatures.

2 DEVELOPMENT OF THE ARTIFICIAL NEURAL NETWORK

The artificial neuronal network is inspired by networks of biological neurons [22]. The network learns through training examples that consist of input parameters and corresponding output parameters from past experimental investigations [23]. The basic structure of a feed-forward ANN model is comprised of at least three layers: an input layer, one output layer, and one or more hidden layers; each layer contains many processing units known as neurons [24, 25]. Neurons are linked to each other with modifiable connection weights. The input layer receives data from outside, and for each of the input layer neurons, the input value is multiplied by the connection weights and transmitted to the neurons of the hidden layers. These weighted input values are summed, and a bias value is applied to neurons in the hidden layer. Then, the output value is obtained by applying a non-linear transfer function, such as sigmoid or hyperbolic tangent, to the combined input values. This value is used as input by the neurons in the output layer, where the ANN model produces the result.[26]. Finally, the error is determined by comparing the predicted output of the network and the target values from experimental results. This training process is continued until the error decreases to an acceptable level. The initial connection weights and bias values are selected randomly and then modified to minimize the errors of the network. The backpropagation algorithm based on the gradient search method is extensively used to minimize errors and update the weights and biases. The performance of the trained network can be assessed by mean-square error (MSE) and correlation coefficient (R) according to equations (1) and (2), respectively. The R-value close to 1 and MSE almost 0 demonstrates the reliability of the outcome of the network [27].

$$MSE = \frac{1}{N}\sum_{(i=1)}^{N}(y_i - y_i)^2 \qquad (1)$$

$$R = \frac{\sum\left(y-\bar{y}\right)\left(y-\bar{y}\right)}{\sqrt{\sum\left(y-\bar{y}\right)^2}\sqrt{\sum\left(y-\bar{y}\right)^2}} \qquad (2)$$

Where $\bar{y}$ and $\bar{\hat{y}}$ demonstrate the average values of the target and predicted outputs;y and the $\hat{y}$ are the target and predicted values, respectively.

2.1 Database

A sufficient database is required to train, validate, and test the artificial neural network models. In the present study, a database containing 116 data points from various past experimental studies is gathered to predict the compressive strength of concrete made with recycled concrete aggregate after high temperatures exposure[3, 8-12, 14, 15, 28]. The database was generated based on the following criteria:

1. The temperature of the center of concrete samples was considered the target temperature
2. The specimens with fibres were excluded from the database
3. Only recycled aggregate with no contamination, such as plastic, was selected
4. The specimens used in the database cooled in the air after reaching target temperatures

In this study, the ANN model used nine input variables: the exposure temperature, the type of aggregate of parent concrete used to generate the recycled aggregate (siliceous and calcareous), the amount of recycled coarse and fine aggregate, the amount of natural coarse and fine aggregate, the amount of cement, the water content, and the heating rate. These input variables are the most influential parameters on the compressive strength of RAC exposed to high temperatures. The selected output variable was the ratio of the residual compressive strength of concrete exposed to a given high temperature to the initial compressive strength of concrete at ambient temperature. The input and output (target) variables were normalized into the range of [0,1] to improve learning speed and accuracy [29, 30] using the equation (3) :

$$x_{normalized} = \frac{x - x_{\min}}{x_{\max} - x_{\min}} \qquad (3)$$

Where $x_{normalized}$, x_{min} and x_{max} denotes the normalized, minimum, and maximum values of x from input or output variables, respectively. Table 1 shows the anatomical statistics of the quantitative input parameters used in the model. The histogram of the input parameters used for developing the network is illustrated in Figure 1.

2.2 Modeling the network

The optimal configuration of the neural network must be found in order to save time and preserve the relativity of the prediction process [31]. The optimal structure is determined by varying the number of neurons and layers in the hidden layer using the trial-and-error approach, which is based on reducing the difference between the predicted value of the network and the experimental output [32, 33]. A small number of hidden neurons is selected, then the number of neurons increases progressively, and at the same time, the errors are monitored [30]. In this study, the best configuration of the ANN model to estimate accurately the relative compressive strength of concrete containing RA consists of one hidden layer with 20 neurons, as shown in Figure 2. In the input and output layers, the number of neurons is equal to the number of input and output variables [34]. The ANN model was developed using the neural network toolbox in MATLAB software. The backpropagation Levenberg-Marquardt (LM) algorithm has been used for its fast convergence and high accuracy [30]. The database was randomly segmented into three subsets, 70% for training, 15% for validation, and 15% for testing the performance of the network using the Marquardt algorithm [31]. The training dataset was employed to train the model and find the optimal value for weights and biases. The validating dataset was utilized to evaluate the applicability and generality of the ANN model and to prevent over-fitting. The testing dataset is used to validate the performance of the proposed ANN model [27]. Tansig and Purelin were employed as the hidden and output layer transfer functions, respectively. The equations of these functions are presented as follows (4) and (5):

$$y = Tansig(x) = \frac{2}{(1+e^{(-2x)})} + 1 \qquad (4)$$

$$y = Purelin(x) = x \qquad (5)$$

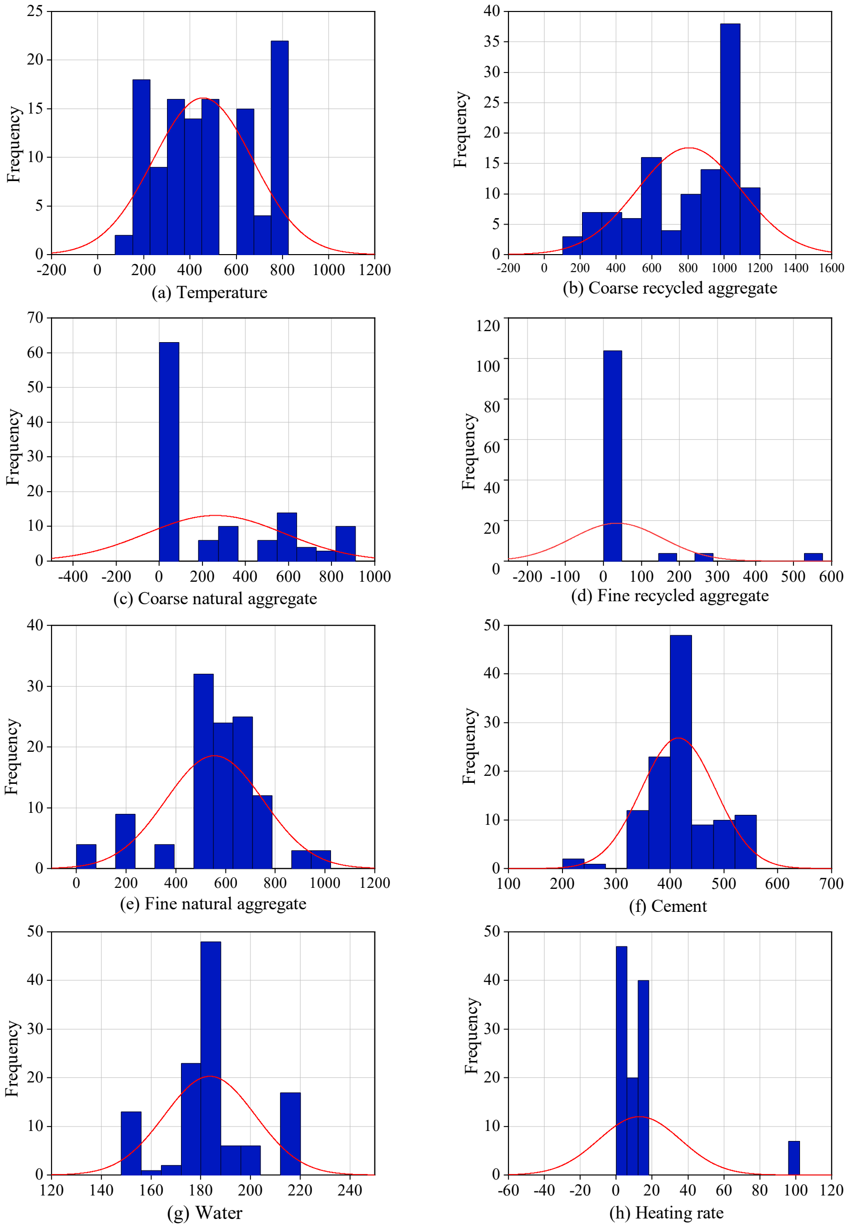

Figure 1. The histograms of input parameters used in the proposed ANN model

Table 1. Anatomical statistics of the input parameters used in the model.

Attribute	Unit	Min	Max	Average
Temperature	℃	100	800	450.59
Coarse recycled aggregate	kg/m^3	181.9	1149	806.3
Coarse natural aggregate	kg/m^3	0	893	499
Fine recycled aggregate	kg/m^3	0	573	27.53
Fine natural aggregate	kg/m^3	0	1020	620.47
Cement	kg/m^3	220	550	414
Water	kg/m^3	150	217	181.87
Heating rate	°C/min	0.5	12	5

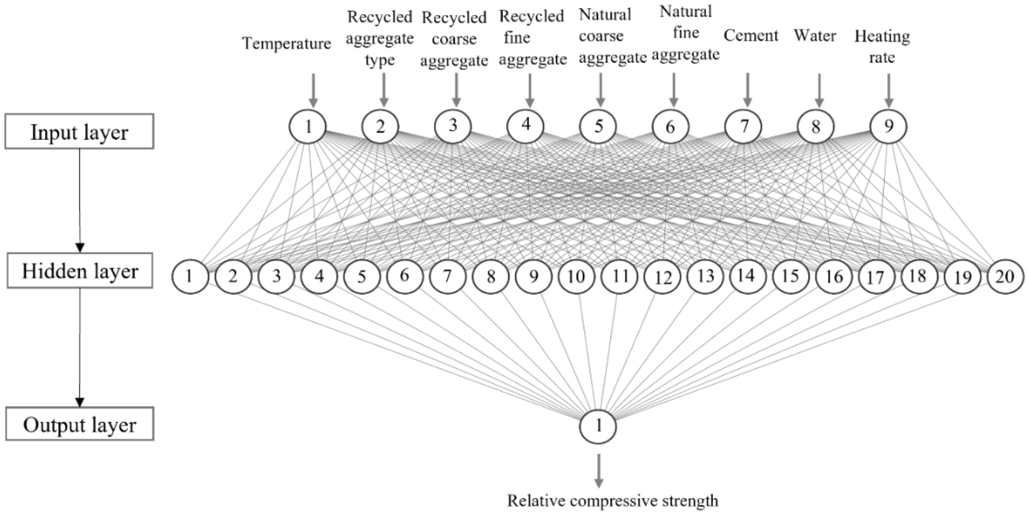

Figure 2. The architecture of the proposed ANN model

2.3 Performance of the developed ANN model

In the present study, the statistical parameters, including Mean Squared Error (MSE) and correlation coefficient (R), were employed to examine the performance of the ANN model. The variation of Mean Squared Error (MSE) as a function of the number of epochs for the training, validation, and testing phases of the proposed ANN model is represented in Figure 3. The MSE value of the network was obtained as 0.011 for the validation dataset. This value shows the suitable precision of this trained ANN model with the wide variation range of data points. The correlation coefficient (R) indicates the correlation between the predicted and desired output (target). The R value obtained was 0.9578 for all data in the network, as shown in Figure 4.

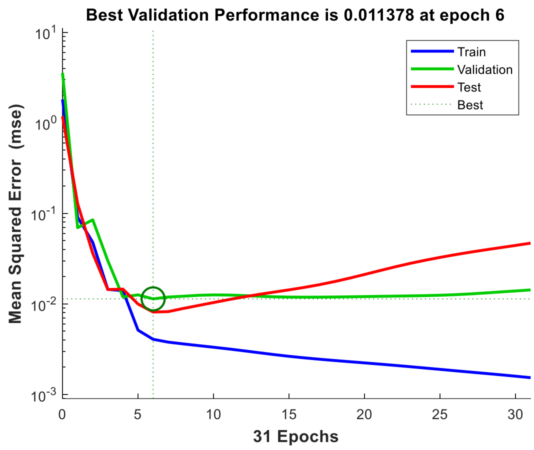

Figure 3. The performance of the proposed ANN model

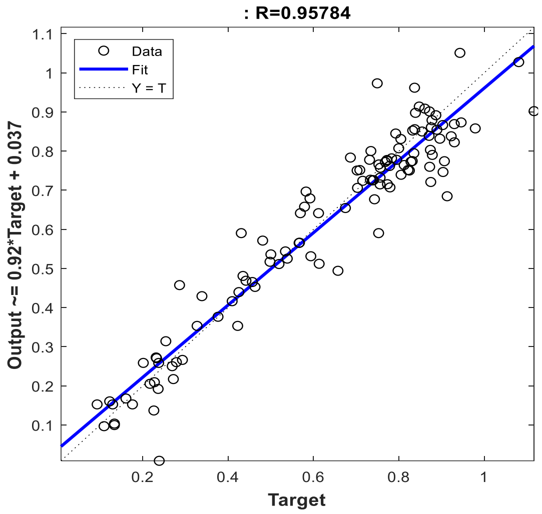

Figure 4. The regression of the proposed ANN model

3 RESULTS AND DISCUSSION

In order to examine the effects of the input parameters on the compressive strength of recycled aggregate concrete exposed to high temperatures, a parametric analysis was conducted using the outcome of the ANN model. The assumed RCA concrete mix designs are represented in Table 2. Moreover, the average value of the available heating rate data in the database (5°C/min) was supplied to the network for parametric study analysis. The variation of compressive strength of siliceous recycled concrete aggregate (Si-RCA) concrete versus different recycled coarse aggregate replacement ratios and at three w/c ratios (0.32, 0.40, and 0.5) after heating up to 800 ℃ has been illustrated in Figure 5. Overall, the compressive strength decreased with increasing the temperature and further decreased in RC with higher w/c ratios. Moreover, in Si-RCA concrete specimens with higher w/c ratios, the variation of the compressive strength is moderately independent of the coarse RCA ratios. However, adding recycled aggregate to concrete has a positive effect on the compressive strength up to 600 ℃ , especially for lower w/c ratios. This may be attributed to the compatibility of the thermal expansion coefficient between the cement paste and recycled aggregates, which results in a reduction of the micro-crack numbers and size in the Interfacial Transition Zone (ITZ). The same results were obtained in the previous experimental tests [8, 10, 11, 35]. For temperatures higher than 600 ℃ , the compressive strength of concrete decreases as the RCA ratios increase due to the more susceptible interface of RCA to cracking. This phenomenon is indicated in the scanning electron microscopy (SEM) analysis of Gales et al. [13] and Da Silva et al. [36].

The compressive strength of concrete with higher w/c ratios sharply decreases beyond 400 °C, as seen in Figure 6 (b) and (c). The superior interface between old and new pastes in lower w/c ratios resulting in a closer thermal expansion between new mortar and recycled aggregate, is the main reason for preventing a significant reduction in the compressive strength for lower w/c ratios. This is in accordance with the outcomes of previous experimental research [10, 35]. Moreover, the results show that adding RCA to concrete positively impacts compressive strength. However, for higher temperatures, i.e., around 800 °C, the trend is reversed owing to the dehydration of CH as well as the transformation of C-S-H morphology. The results of prediction using the ANN model in Figure 6 are in complete accordance with the results of Xie et al. [37] and Khaliq [28], once again verifying the predicted outcomes of the proposed network.

Table 2. The assumed concrete mix designs.

Type of RCA	Coarse aggregate of RCA (kg/m^3)	Coarse aggregate of NA (kg/m^3)	Fine RCA aggregate (kg/m^3)	Fine NA aggregate (kg/m^3)	Cement (kg/m^3)	Water (kg/m^3)
Calcareous [28]	911	0	0	646	550	176
Siliceous [11]	1078	0	0	678	390	195

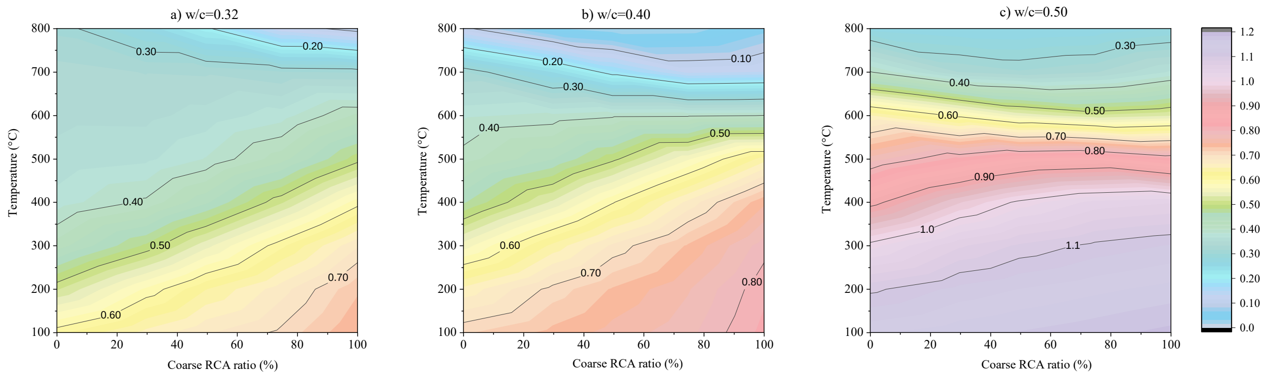

Figure 5. Variation of compressive strength of with natural fine aggregate versus temperatures and Si-RCA replacement ratio at different w/c: a) w/c =0.32, b) w/c=0.40, and w/c=0.5

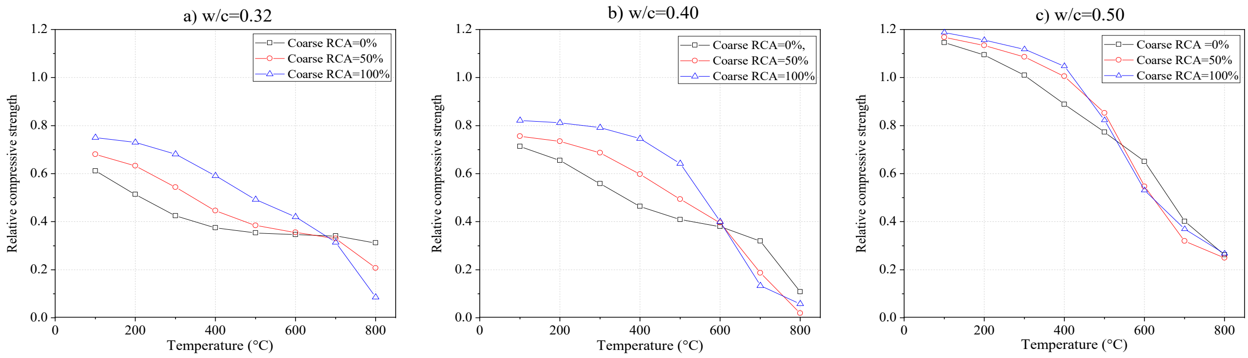

Figure 6. Variation of compressive strength of concrete with replacing natural coarse aggregate with 0%, 50% and 100% of siliceous RCA versus temperatures at different w/c: a) w/c =0.32, b) w/c=0.40, and w/c=0.5 RCA

The interactive effect of temperature and coarse RCA replacement ratio on the relative compressive strength of concrete containing calcareous recycled concrete aggregate (Ca- RCA) at three w/c ratios (0.32, 0.40, and 0.5) is shown in Figure 7. It can be seen that incorporating Ca-RCA as coarse aggregate replacement leads to an improvement in the compressive strength of concrete with a higher w/c ratio. For example, as seen for concrete with 45% and 100% coarse RCA replacement, the strength increased up to 27% and 47%, respectively, compared to concrete without recycled aggregate (see Figure 8). Similar results have been reported by Sarhat et al. [8]. However, the effect of coarse RCA ratios is insignificant in concrete with Ca-RCA at lower w/c ratios, as demonstrated in Figure 8 (a) and (b).

The comparison of all Figures from Figure 5 and Figure 8 demonstrates the effect of aggregate type on the compressive strength of concrete when subjected to elevated temperatures. Since understanding the effect of different aggregates using experimental research is relatively complex and costly, few studies with a limited number of specimens studied the effect of RCA type. Nevertheless, using the ability of the ANN model to predict new results based on the previous experimental tests with reasonable accuracy may pave the way for the recognition of the RCA-type effect. As it was stated before, the accuracy of the ANN outcomes was validated using proven facts and previous experimental results. Therefore, it may be concluded that the prediction shown in Figure 6 and Figure 8 can be compared to understand the effect of RCA type on the compressive strength of recycled concrete. As shown, concrete specimens made with Si aggregates have relatively higher compressive strength in temperatures up to 800 ℃ and in higher w/c ratios than calcareous concrete. This is due to the mineralogical and chemical composition and the petrographic origin of aggregates [38, 39]. According to the results of Razafinjato et al. [40], the presence of silanol groups (Si-O-H) within the crystalline structure is the main reason for thermal instability in Si aggregates. An increase in temperature results in a silanol dihydroxylation and micro-cracks development in the aggregates body. On the other hand, the decarbonation of Ca aggregates occurs at higher temperatures compared with Si aggregate. This may be a reason for the obtained outcomes based on the ANN model, which is also consistent with the experimental results of Razafinjato et al. [41].

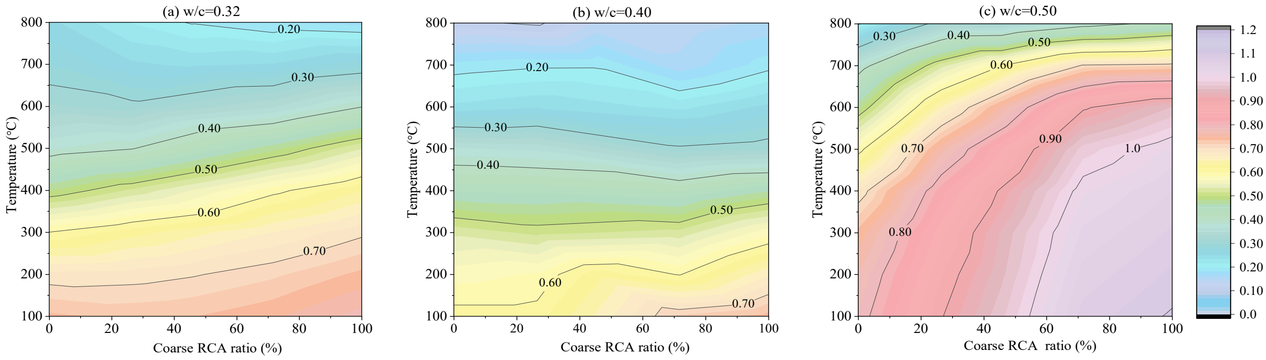

Figure 7. Variation of compressive strength of with natural fine aggregate versus temperatures and Ca-RCA replacement ratio at different w/c: a) w/c =0.32, b) w/c=0.40, and w/c=0.5

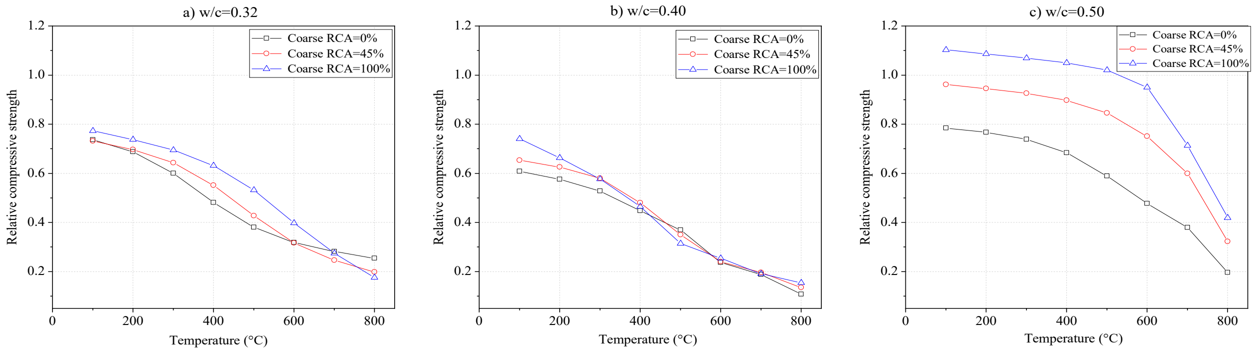

Figure 8. Variation of compressive strength of concrete with replacing natural coarse aggregate with 0%, 45% and 100% of calcareous RCA versus temperatures at different w/c: a) w/c =0.32, b) w/c=0.40, and w/c=0

4 CONCLUSIONS

In this study, an artificial neural network was developed to predict the complex and non-linear compressive strength of recycled aggregate concrete when exposed to high temperatures. The recommended model was developed based on the 116 experimental data points collected from previous studies. The following conclusion can be drawn from this study:

1. The results indicated that the proposed ANN model is able to predict the relative compressive strength of recycled aggregate concrete exposed to high temperatures with an acceptable degree of accuracy. The accuracy of the ANN outcomes was confirmed using the previous experimental results.
2. In concrete with siliceous recycled concrete aggregate, the higher content of RCA with lower w/c improves compressive strength for temperatures under 600℃ . However, the strength decreases beyond this temperature as the RCA content increases. For concrete with higher w/c, the variation of the compressive strength is moderately independent of coarse RCA ratios.
3. The relative compressive strength of concrete with a higher w/c ratio improved with increasing the calcareous coarse RCA replacement levels at all temperatures.
4. Recycled concrete specimens containing silicious aggregates have relatively higher compressive strength in temperatures up to 800 °C and at higher w/c ratios than calcareous recycled concrete.

ACKNOWLEDGMENTS

The authors acknowledge the financial support from the Natural Sciences and Engineering Research Council of Canada (NSERC) for the support.

REFERENCES

1. Rafi, M.M., and Aziz, T., *Experimental testing of fly ash containing recycled aggregate concrete exposed to high temperatures.* Sustainable and Resilient Infrastructure, 2019: p. 1-16.
2. Cree, D., Green, M., and Noumowé, A., *Residual strength of concrete containing recycled materials after exposure to fire: A review.* Construction and Building Materials, 2013. 45: p. 208-223.
3. Yang, H., Zhao, H., and Liu, F., *Compressive stress–strain relationship of concrete containing coarse recycled concrete aggregate at elevated temperatures.* Journal of Materials in Civil Engineering, 2019. 31(9): p. 04019194.
4. Fernandes, B., Carré, H., Mindeguia, J.-C., Perlot, C., and La Borderie, C., *Effect of elevated temperatures on concrete made with recycled concrete aggregates-An overview.* Journal of Building Engineering, 2021. 44: p. 103235.
5. Kandiri, A., Sartipi, F., and Kioumarsi, M., *Predicting compressive strength of concrete containing recycled aggregate using modified ann with different optimization algorithms.* Applied Sciences, 2021. 11(2): p. 485.
6. Yang, H., Zhao, H., and Liu, F., *Residual cube strength of coarse RCA concrete after exposure to elevated temperatures.* Fire and Materials, 2018. 42(4): p. 424-435.
7. Naderpour, H., Rafiean, A.H., and Fakharian, P., *Compressive strength prediction of environmentally friendly concrete using artificial neural networks.* Journal of Building Engineering, 2018. 16: p. 213-219.
8. Sarhat, S.R., and Sherwood, E.G., *Residual mechanical response of recycled aggregate concrete after exposure to elevated temperatures.* Journal of materials in civil engineering, 2013. 25(11): p. 1721-1730.
9. Xiao, J., Fan, Y., and Tawana, M., *Residual compressive and flexural strength of a recycled aggregate concrete following elevated temperatures.* Structural Concrete, 2013. 14(2): p. 168-175.
10. Zega, C.J., and Di Maio, A.A., *Recycled concrete made with different natural coarse aggregates exposed to high temperature.* Construction and Building Materials, 2009. 23(5): p. 2047-2052.
11. Kou, S.C., Poon, C.S., and Etxeberria, M., *Residue strength, water absorption and pore size distributions of recycled aggregate concrete after exposure to elevated temperatures.* Cement and Concrete Composites, 2014. 53: p. 73-82.
12. Vieira, J., Correia, J., and De Brito, J., *Post-fire residual mechanical properties of concrete made with recycled concrete coarse aggregates.* Cement and Concrete Research, 2011. 41(5): p. 533-541.
13. Gales, J., Parker, T., Cree, D., and Green, M., *Fire performance of sustainable recycled concrete aggregates: Mechanical properties at elevated temperatures and current research needs.* Fire Technology, 2016. 52(3): p. 817-845.
14. Wang, Y., Liu, F., Xu, L., and Zhao, H., *Effect of elevated temperatures and cooling methods on strength of concrete made with coarse and fine recycled concrete aggregates.* Construction and Building Materials, 2019. 210: p. 540-547.
15. Pliya, P., Hajiloo, H., Romagnosi, S., Cree, D., Sarhat, S., and Green, M., *The compressive behaviour of natural and recycled aggregate concrete during and after exposure to elevated temperatures.* Journal of Building Engineering, 2021. 38: p. 102214.
16. Hammoudi, A., Moussaceb, K., Belebchouche, C., and Dahmoune, F., *Comparison of artificial neural network (ANN) and response surface methodology (RSM) prediction in compressive strength of recycled concrete aggregates.* Construction and Building Materials, 2019. 209: p. 425-436.
17. Duan, Z.-H., Kou, S.-C., and Poon, C.S., *Prediction of compressive strength of recycled aggregate concrete using artificial neural networks.* Construction and Building Materials, 2013. 40: p. 1200-1206.
18. BKA, M.A.R., Ngamkhanong, C., Wu, Y., and Kaewunruen, S., *Recycled aggregates concrete compressive strength prediction using artificial neural networks (ANNs).* Infrastructures, 2021. 6(2): p. 17.
19. Khademi, F., Jamal, S.M., Deshpande, N., and Londhe, S., *Predicting strength of recycled aggregate concrete using artificial neural network, adaptive neuro-fuzzy inference system and multiple linear regression.* International Journal of Sustainable Built Environment, 2016. 5(2): p. 355-369.
20. Deshpande, N., Londhe, S., and Kulkarni, S., *Modeling compressive strength of recycled aggregate concrete by Artificial Neural Network, Model Tree and Non-linear Regression.* International Journal of Sustainable Built Environment, 2014. 3(2): p. 187-198.
21. Rizvon, S.S., and Jayakumar, K., *Strength prediction models for recycled aggregate concrete using Random Forests, ANN and LASSO.* Journal of Building Pathology and Rehabilitation, 2022. 7(1): p. 1-10.
22. Behnood, A., and Golafshani, E.M., *Predicting the compressive strength of silica fume concrete using hybrid artificial neural network with multi-objective grey wolves.* Journal of Cleaner Production, 2018. 202: p. 54-64.

23. Mukherjee, A., and Biswas, S.N., *Artificial neural networks in prediction of mechanical behavior of concrete at high temperature.* Nuclear engineering and design, 1997. 178(1): p. 1-11.
24. Ashteyat, A.M., and Ismeik, M., *Predicting residual compressive strength of self-compacted concrete under various temperatures and relative humidity conditions by artificial neural networks.* Computers and Concrete, 2018. 21(1): p. 47-54.
25. Atici, U., *Prediction of the strength of mineral admixture concrete using multivariable regression analysis and an artificial neural network.* Expert Systems with applications, 2011. 38(8): p. 9609-9618.
26. Özcan, F., Atiş, C.D., Karahan, O., Uncuoğlu, E., and Tanyildizi, H., *Comparison of artificial neural network and fuzzy logic models for prediction of long-term compressive strength of silica fume concrete.* Advances in Engineering Software, 2009. 40(9): p. 856-863.
27. Golafshani, E.M., Behnood, A., and Arashpour, M., *Predicting the compressive strength of normal and High-Performance Concretes using ANN and ANFIS hybridized with Grey Wolf Optimizer.* Construction and Building Materials, 2020. 232: p. 117266.
28. Khaliq, W., *Mechanical and physical response of recycled aggregates high-strength concrete at elevated temperatures.* Fire safety journal, 2018. 96: p. 203-214.
29. Moradi, M., Daneshvar, K., Ghazi-Nader, D., and Hajiloo, H., *The prediction of fire performance of concrete-filled steel tubes (CFST) using artificial neural network.* Thin-Walled Structures, 2021. 161: p. 107499.
30. Gupta, T., Patel, K., Siddique, S., Sharma, R.K., and Chaudhary, S., *Prediction of mechanical properties of rubberised concrete exposed to elevated temperature using ANN.* Measurement, 2019. 147: p. 106870.
31. Roshani, M.M., Kargar, S.H., Farhangi, V., and Karakouzian, M., *Predicting the effect of fly ash on concrete's mechanical properties by ann.* Sustainability, 2021. 13(3): p. 1469.
32. Altun, F., Kişi, Ö., and Aydin, K., *Predicting the compressive strength of steel fiber added lightweight concrete using neural network.* Computational Materials Science, 2008. 42(2): p. 259-265.
33. Hosseini, M., and Abbas, H., *Neural network approach for prediction of deflection of clamped beams struck by a mass.* Thin-Walled Structures, 2012. 60: p. 222-228.
34. Nasir, M., Gazder, U., Maslehuddin, M., Al-Amoudi, O.S.B., and Syed, I.A., *Prediction of properties of concrete cured under hot weather using multivariate regression and ANN Models.* Arabian Journal for Science and Engineering, 2020. 45(5): p. 4111-4123.
35. Zega, C., and Di Maio, A., *Recycled concrete exposed to high temperatures.* Magazine of Concrete Research, 2006. 58(10): p. 675-682.
36. Da Silva, J.B., Pepe, M., and Toledo Filho, R.D., *High temperatures effect on mechanical and physical performance of normal and high strength recycled aggregate concrete.* Fire Safety Journal, 2020. 117: p. 103222.
37. Xie, J., Zhang, Z., Lu, Z., and Sun, M., *Coupling effects of silica fume and steel-fiber on the compressive behaviour of recycled aggregate concrete after exposure to elevated temperature.* Construction and Building Materials, 2018. 184: p. 752-764.
38. Razafinjato, R.N., *Comportement des bétons à haute température: influence de la nature du granulat*. 2015, Université de Cergy Pontoise.
39. Schmidt, P., Masse, S., Laurent, G., Slodczyk, A., Le Bourhis, E., Perrenoud, C., Livage, J., and Fröhlich, F., *Crystallographic and structural transformations of sedimentary chalcedony in flint upon heat treatment.* Journal of Archaeological Science, 2012. 39(1): p. 135-144.
40. Razafinjato, R.N., Beaucour, A.-L., Hebert, R.L., Ledesert, B., Bodet, R., and Noumowe, A., *High temperature behaviour of a wide petrographic range of siliceous and calcareous aggregates for concretes.* Construction and Building Materials, 2016. 123: p. 261-273.
41. Niry, R., Beaucour, A., Hebert, R., Ledesert, B., Noumowe, A., and Bodet, R., *Comportement à haute température des bétons de granulats naturels siliceux et calcaires, 32 èmes Rencontres de l'AUGC.* Polytech Orléans, 2014: p. 4-6.

BOND BEHAVIOR OF FLEXURAL STEEL REBARS WITH CONCRETE IN FIRE CONDITIONS – THE ROLE OF RATE OF HEATING

Ira Banoth[1], Anil Agarwal[2]

ABSTRACT

When an RC flexural member is subjected to fire, the bond mechanism of concrete and reinforcement becomes more complex due to the material strength degradation and a complex interfacing of the two components. Most of the earlier research employs pull out tests. Only a handful of researchers have employed flexural tests to evaluate the bond performance, but they have studied the performance in post-fire conditions. In this study, the bond behaviour of concrete and deformed steel is evaluated by conducting beam tests at elevated temperature conditions. The specimens were made with 30 MPa strength concrete and 20 mm diameter deformed reinforcement bars. The specimens were prepared by two parallelepipedal concrete blocks with auxiliary reinforcement connected by steel hinges. Rebar for the bond test was placed in concrete at clear cover of 40 mm. The beam specimens followed specifications of Annex C of European Code prEN10080. A length equal to four times the bar diameter is bonded with concrete. The rest of the length was unbonded to ensure that the beam strength is governed by the bond failure shown in Figure 1. The heating and loading set up are presented in Figure. 2. Two different heating protocols, heating rate of 2 ºC/min and ISO 834 standard fire curve were employed. During the tests, the furnace temperature was raised following the one of the two heating protocols until the rebar in the bonded region reached the desired temperature value. Following which, the beam was loaded in four-point bending at the designated points until the bond failed and the rebar slipped at one of the two ends. The mechanical loading was concluded within 120 seconds. The temperature of rebar did not change significantly during this period. Therefore, these tests can be classified as conducted under adiabatic conditions.

The bond stress-slip response and the maximum bond strength are recorded at interface temperatures of 25, 100, 200, 300, 400, and 500 ºC. Typical furnace temperatures and the corresponding rebar interface temperatures time histories are reported in Figure 3 (a). Bond stress-slip behaviour is similar in both the cases irrespective of magnitude at all the temperatures. The reduction of bond strength is more significant in the case of ISO heating than slow heating rate of 2ºC/min. This clearly indicates that tests conducted by slowly heating the entire specimen to a uniform temperature overpredicts the bond strength.

Key words: Concrete; deformed steel; heating rate; beam test; bond

[1] 1Research scholar, Department of Civil Engineering, Indian Institute of Technology Hyderabad (IITH),
e-mail: ira.banoth@gmail.com
[2] Assistant Professor, Department of Civil Engineering, Indian Institute of Technology Hyderabad (IITH),
e-mail: anil@ce.iith.ac.in
https://doi.org/10.6084/m9.figshare.22177901

1 INTRODUCTION

When RC members subjected to fire it is necessary to understand the bond behaviour for the structural integrity of the structures. Bond occurs due to the three kinds of mechanisms; chemical adhesion, mechanical interlocking of the ribs with the surrounding concrete and frictional resistance. The analytical bond stress slip model [1] is developed by conducting pullout tests at ambient conditions as shown in Figure 1. The parameters are considered in these tests are concrete strength, rebar surface, transverse reinforcement etc. But at elevated temperatures there are no such bond stress slip models are developed when the structures are subjected to elevated temperatures.

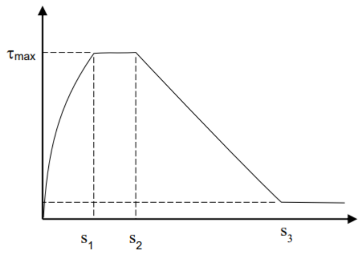

Figure 1. Analytical bond stress slip model

2 LITERATURE REVIEW

Most of the research studies have been carried out pull-out test to study the bond behaviour between steel and concrete due to easiness and handy of the specimens. There are two kinds of tests are conducted: (a) high temperature tests (specimen heated up to the desired temperature at the interfaces and loaded immediately, (b) specimen heated to the desired temperatures and then cooled down to the room temperatures and then loaded.

Most of the studies are conducted in residual conditions, hardly two studies are available at high temperatures [2,3]. Diederichs and schneider are studied the bond behaviour of different kind of rebars in different tests conditions (thermal steady state and non-thermal study state). The conclusions drawn from these studies are the bond stress slip behaviour not only depends on the temperatures but also on the test procedure. The effect of surface of the rebar plays a very significant role on the bond stress slip behaviour. Morley and Royles studied the bond behaviour in stressed and unstressed conditions. At room temperature in the case of stressed conditions the reduction of bond strength is more than the unstressed condition due to the disturbances occurs when the specimen subjected constant stress applied. At high temperatures the reduction of bond strength is more in the case of unstressed conditions than the stressed conditions.

Haddad et. al [4] studied bond behaviour between steel rebars by incorporating of hybrid combinations of fibres. The incorporation of fibers improves the ductility at high temperatures. Eval Lubloy and Viktor Hlavicka [5] studied bond behaviour by considering different combinations of aggregates and fibers. The reduction of bond strength is more significant than the compressive strength. Varona et. al [6] studied the bond behaviour between steel and concrete by considering different combinations of the fibres for the normal strength concrete and high strength concrete. The steel fibres with high aspect ratio improves the peak bond strength at high temperatures. Deshpande et. al [7] studied the bond behaviour for the different conventional concrete and strain hardening cementitious composites (SHCC) with hybrid combination of fibres. At room temperature normalized bond strength is more in the case of conventional concrete than the SHCC. Hybrid fibre reinforced concrete is having more absolute and normalized bond strength at high temperatures.

Lee et. al [8] studied the bond behaviour between steel and concrete by considering different heating rates. Bond strength is decreased with the increasing heating rates due to larger thermal gradients. Bond strength is more in the case of water-cooled specimens than the natural cooling due to the sudden shocks occurs in the water-cooled specimens [9]. Bosnjak et. al [10] studied the bond behaviour between steel and concrete for the modified beam end specimens by following ISO [11] heating rate to replicate the practical scenario.

3 MOTIVATION AND OBJECTIVES

Most of the studied are conducted by following slow heating rates to maintain uniform temperatures at the interface by conducting the pull-out test specimen. These tests are does not reflect the actual behaviour of bond in flexural members. So, in these study beam specimens are considered to replicate the real behaviour of flexural members by considering the Rapid heating rate (ISO) and slow heating rate (2 ºC/min is also considered to develop a data model and the effect of heating rate on the bond behaviour between steel and concrete.

4 EXPERIMENTAL PROGRAM

4.1 Materials

Locally available materials are used. Ordinary Portland Cement of 53 grade, Dhana Laxmi Fe550 grade steel rebars, River sand, coarse aggregates are used. concrete mix design details are presented in Table 1.

Table 1. Concrete mix proportion (kg/m^3)

Cement	Fine aggregate	Coarse aggregate	water	admixture
329	850	1034	164.4	2.63

4.2 Specimen preparation

Two different diameters of rebars (12 mm and 20 mm) are used. The rebar is bonded four times the diameter of rebar with concrete and the remaining length is unbonded by using plastic sleeves. The specifications of the beam specimen are considered according to codes prEN 10080 [12] with the little modification of stirrups. The beam specimen is two parallelepipedal concrete blocks with the auxiliary reinforcement connected on the top by steel hinges and bottom is connected by the rebar as shown in Figure 2. Details and specifications of the beam specimen is given in the Figure 3 and Table 3

Bonding-debonding of rebar **(1,2-bonded length)**

Auxillary reinforcement Steel hinge

Specimen mould

Figure 2. Specimen Preparation

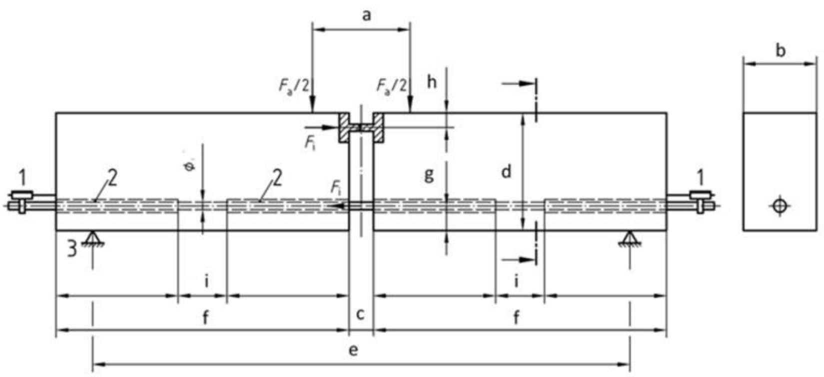

Figure 3. Beam specimen details

Table 3. Specimen details

Dimension	*φ*	*a*	*b*	*c*	*d*	*e*	*f*	*g*	*h*	*i*
Value mm for bar Diameter < 16 mm	12	150	100	50	180	650	375	50	30	48
Value mm for bar Diameter ≥ 16 mm	20	200	150	60	240	1100	600	50	40	80

4.3 Test setup and test procedure

Two steel I-sections with the welded plate are fixed on the loading plateau at a required distance for the two types of beams to ensure the mechanism of simply supported beam. The beam tested for the bond is placed in a chamber arranged by electric ceramic heating panel as shown in Figure 4. The beam is heated from the bottom side to ensure the practical scenario by following different heating rates. Time-temperature profiles are shown in Figure 5. Slips are measured at the two ends of the beams by LVDTs Once the desired temperatures reached at the interface loading will be applied at the deflection rate of 2.5 mm/min. Ultimate bond strength is reached within 2 minutes so the tests can be done at high temperatures.

Ambient Elevated Temperatures

Figure 4. Test setup

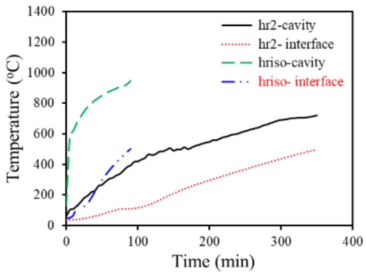

Figure 5. Time-temperature profile

5 TEST RESULTS AND DISCUSSION

5.1 Bond stress slip behavior

Tests results are presented in Table 4. Bond stress slip behavior of all the specimen as shown in Figure 6. Bond stress versus slip behavior is similar for both the diameter of rebar by following slow heating rate and rapid heating rate irrespective of magnitude. The initial part of the curve is very steep, where there is almost no slip due to the chemical bonding and later the bond stress slip curve shows the slip due to mechanical interlocking of the ribs. Once bond stress reached at its ultimate stage the specimen fails due to the bond of the concrete surrounding by the ribs loses. Residual bond stress occurred due to the frictional resistance of the ribs. This behavior of ribs in residual bond stress is more significant up to the temperature of 300 ºC in the case of 12 mm rebar diameter due to the shallower depths of the ribs of 12 mm than the 20 mm diameter of rebar. The bond strength is more in the case of 12 mm diameter of rebar than the 20 mm rebar due to the more area bonded with the concrete in the case of 20 mm rebar so the stress concentration will be less in the bonded area.

Table 4 Test results

Diameter of rebar (mm)	Heating rate (ºC/min)	Interface temp (ºC)	Bond strength (MPa)	Residual bond strength (% of 25 ºC)
12	control	25	27.20	103
12	control	25	25.38	97
12	2	100	20.09	76
12	2	200	24.56	93
12	2	300	19.56	74

12	2	400	16.91	64
12	2	500	14.90	57
12	ISO	100	16.09	61
12	ISO	200	16.76	64
12	ISO	300	13.24	50
12	ISO	400	13.36	51
12	ISO	500	9.39	36
20	control	25	23.83	109.57
20	control	25	22.29	102.45
20	control	25	19.14	87.98
20	2	100	14.35	65.98
20	2	200	14.75	67.80
20	2	300	15.24	70.05
20	2	400	11.07	50.88
20	2	500	7.20	33.11
20	ISO	100	12.68	46.83
20	ISO	200	10.07	46.28
20	ISO	300	8.49	39.52
20	ISO	400	6.76	31.46
20	ISO	500	4.50	24.05

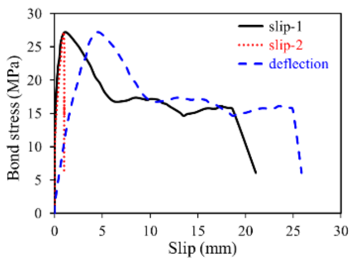

φ12-25-1

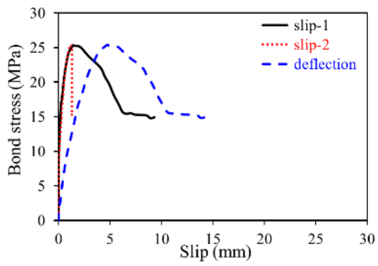

φ12-25-2

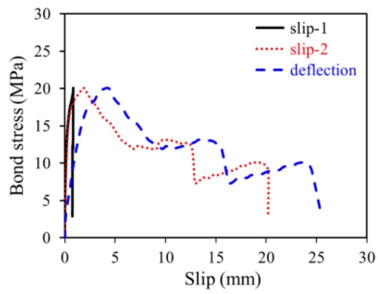

φ12-100-hr2

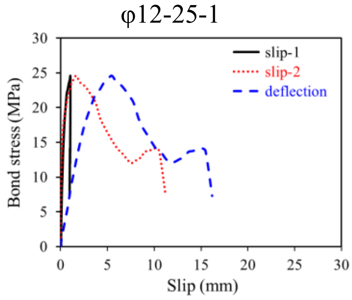

φ12-200-hr2

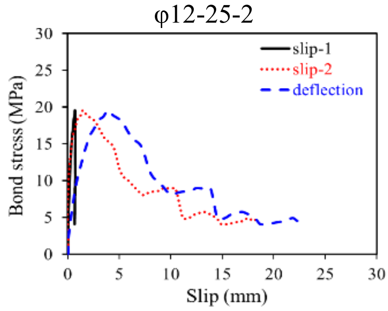

φ12-300-hr2

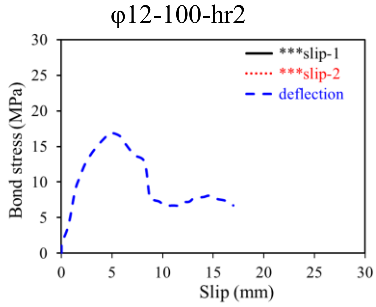

φ12-400-hr2

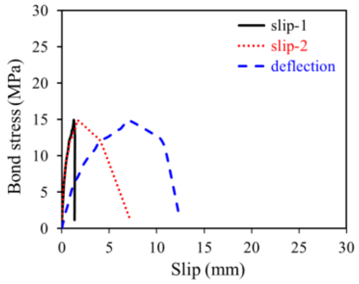

φ12-500-hr2

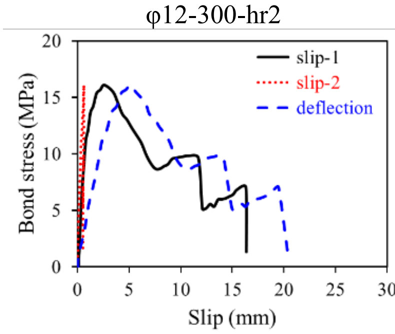

φ12-100-hrISO

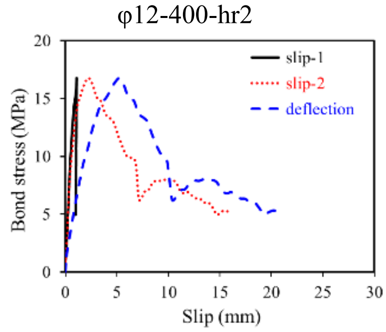

φ12-200-hrISO

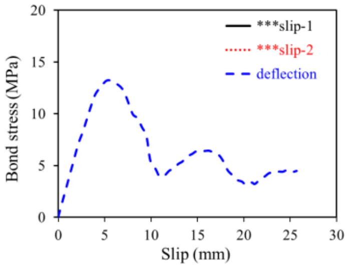

φ12-300-hrISO

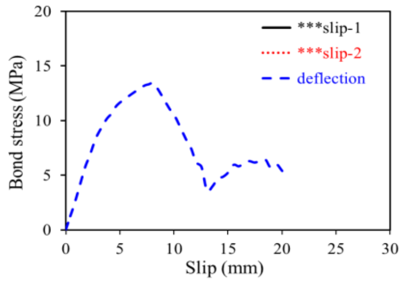

φ12-400-hrISO

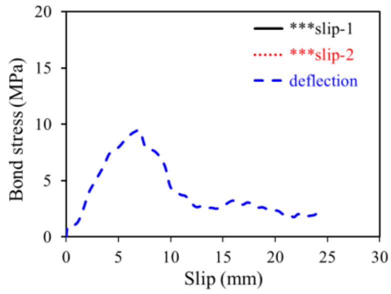

φ12-500-hrISO

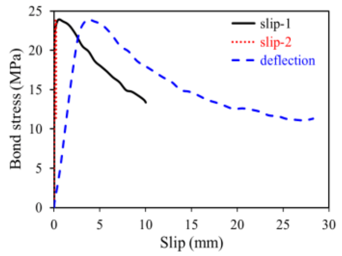

φ20-25-1

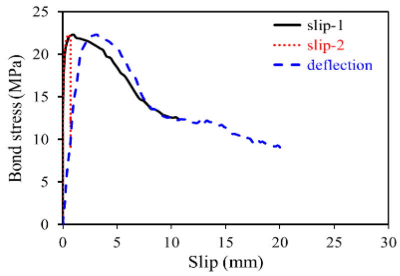

φ20-25-2

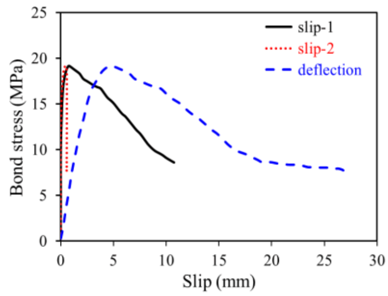

φ20-25-3

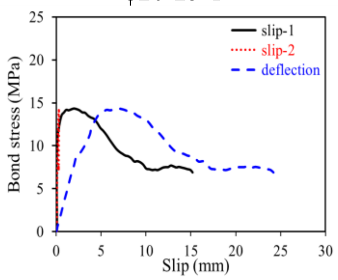

φ20-100-hr2

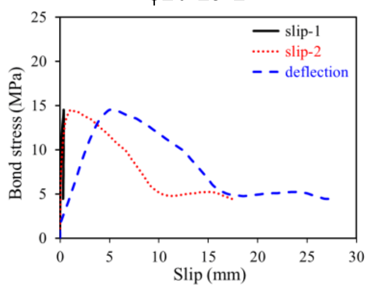

φ20-200-hr2

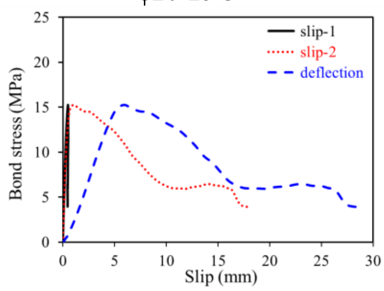

φ20-300-hr2

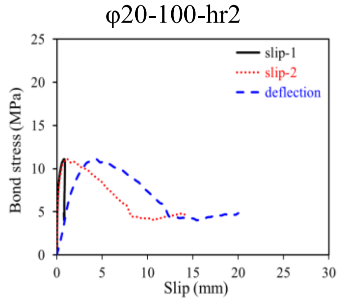

φ20-400-hr2

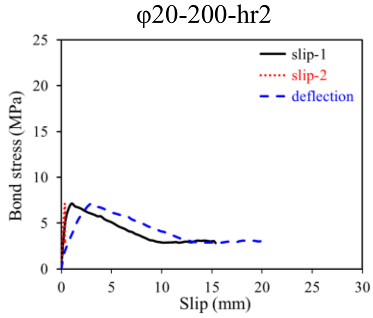

φ20-500-hr2

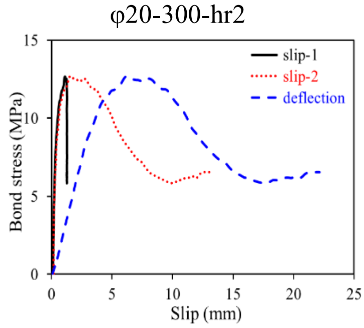

φ20-100-hrISO

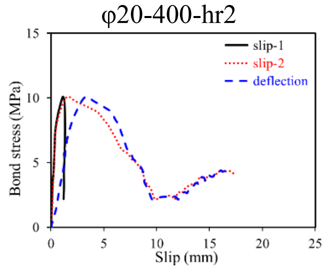

φ20-200-hrISO

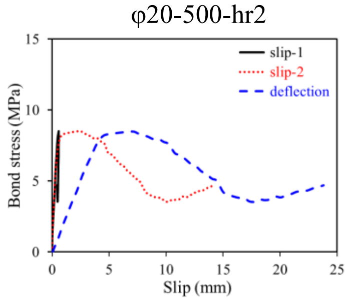

φ20-300-hrISO

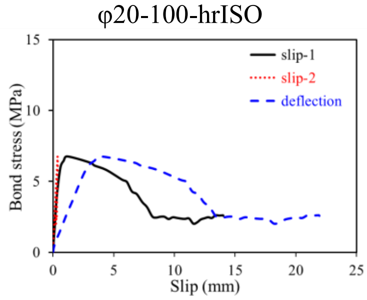

φ20-400-hrISO

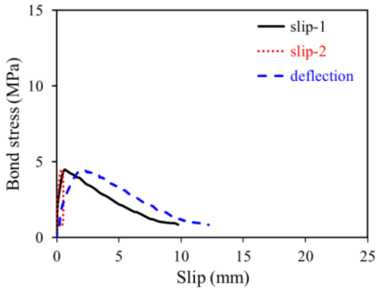

φ20-500-hrISO

Figure 6. Bond stress slip beahviour

5.2 Residual bond strength

Residual bond strength against temperature is shown in Figure 7. The reduction of bond strength is more significant in the case of rapid heating rate than the slow heating rate for both the diameter of rebar due to larger thermal gradients between the surface and interface temperatures. The reduction of bond strength again picked up at the temperature 200 and 300 oC in the case of slow heating rate due to the heat energy is conserved by the moisture evaporation at these temperatures.

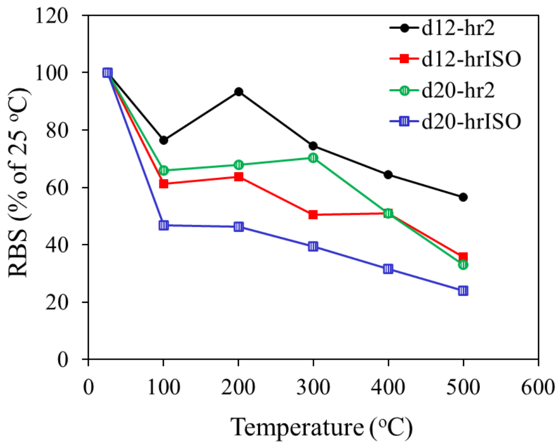

Figure 7. Residual bond strength versus temperature

6 CONCLUSIONS

- Bond stress versus slip behavior is studied by conducting beam tests.
- Bond stress slip behavior is similar in all the cases irrespective of magnitudes. Bond strength is more in the cases of 12 mm diameter of rebar than 20 mm rebar due to less stress concentration in the bonded area in the cases of 12 mm diameter rebar.
- The reduction of bond strength is more in the case of rapid heating rate for both the diameter of the rebars due to larger thermal gradients between the surface and the interface temperatures

REFERENCES

1. FIB, Model code for concrete structures 2010, International Federation for Structural Concrete, Lausanne, Switzerland, 2013.
2. Diederichs, U., Schneider, U., Bond strength at high temperatures. J Mag Concr Res 33(115), 75–84 (1981). https://doi:10.1680/macr.1981.33.115.75.
3. Royles, R., Morley, P.D., Response of the bond in reinforced concrete to high temperatures. J Mag Concr Res 35(124), 157–163 (1983). https://doi: 10.1680/macr.1983.35.124.157.
4. Haddad, R.H., Al-Saleh, R.J., & Al-Akhras N.M., Effect of elevated temperature on bond between steel reinforcement and fibre reinforced concrete. J Fire Saf 43(5), 334–343 (2008). https://doi.org/10.1016/j.firesaf.2007.11.002.
5. Lubloy, É, Hlavička, V., Bond after fire. J Constr Build Mater 132, 210–218 (2017). https://doi:10.1016/j. conbuildmat.2016.11.131.
6. Varona, F.B., Baeza, F.J., Bru, D., Ivorra, S., Evolution of the bond strength between reinforcing steel and fibre reinforced concrete after high temperature exposure. Constr Bulid Mater, 176, 359-370 (2018).
7. Deshpande, A., Kumar, D., Ranade, R., Temperature effects on the bond behavior between deformed steel reinforcing bars and hybrid fiber-reinforced strain-hardening cementitious composite. Constr Build Mater 176, 117337 (2019). https://doi.org/10.1016/j.conbuildmat.2019.
8. Lee, J., Sheesley, E., Jing,Y., Xi. Y., Willam, K., The effect of heating and cooling on the bond strength between concrete and steel reinforcement bars with and without epoxy coating. J Constr Build Mater 177, 230–236 (2018). https://doi:/10.1016/j.conbuildmat.2018.05.128.
9. Bingöl, A.F., Gül, R., Residual bond strength between steel bars and concrete after elevated temperatures. J Fire Saf. 44(6), 854–859 (2009). https:// doi: 10.1016/j.firesaf.2009.04.001.
10. J. Bošnjak, A. Sharma, C. Öttl, Modified beam-end test setup to study the bond behavior of reinforcement in concrete after fire, Mater. Struct. Constr. 51 (2018).
11. ISO: 834-11:2014, Fire Resistance Tests – Elements of Building Construction – Part 11: Specific Requirements for assessment of fire Protection to Structural Steel Elements.
12. ENV 10080:1995, Steel for the reinforcement of concrete- weldable reinforcing steel – General.

RELIABILITY OF CONCRETE SLABS SUBJECTED TO A NATURAL FIRE DESIGNED BY TABULATED VALUES

Marcus Achenbach[1], Guido Morgenthal[2]

ABSTRACT

The design check regarding the fire resistance of concrete slabs can be easily performed using tabulated values. Design codes specify the minimum thickness and minimum axis distance for the desired fire rating. The tables are based on experimental results and are well accepted by engineers and building authorities. However, the actual level of safety of the structural components, that is obtained by this approach, is not known. On the other hand, performance-based methods are more accepted, but require a target reliability as performance criterion. Hence there is a need for calibration of the performance methods using the results of the "traditional" descriptive approach. The calibration is performed for a single span concrete slab, where the axis distance of the reinforcement is chosen in order to meet the design requirements for a fire rating R30 and R90. A "standard" compartment is selected to cover typical fields of application. The opening factor is considered as parameter to obtain the maximum peak temperatures in the compartment. The stochastic basic variables are identified and a Monte-Carlo simulation is set up to calculate the probabilities of failure. The results indicate that the calculated reliability index is within the range, which has been used for the derivation of safety and combination factors in the Eurocodes. It can be observed that members designed for a fire rating R90 have a significant increase of the structural safety compared to a design for a fire rating R30.

Keywords: Concrete; slab; calibration; Monte-Carlo simulation, probabilistic methods

1 INTRODUCTION

The use of tabulated values for the check of the fire resistance are widely accepted by structural engineers and building authorities. The tabulated values given in Eurocode 2 [1] are based on laboratory tests [2] subjected to a standard fire [3]. Tests on structural elements subjected to fire have been performed since the beginning of the 20th century, where the standard temperature-time curve has prevailed as standard heating regime for laboratory tests [4]. It is assumed, that the standard temperature-time curve covers the peak temperatures of fires in office and residential buildings [5]. The experimentally determined "fire resistance" for a standard fire has been adopted in building regulations in various countries [4]. The proof of "adequate" fire safety can be easily carried out using the prescriptive approach. The necessary fire rating is given in building regulations and can be checked using tabulated values for the considered structural members. Although the application is very easy, the determination of the achieved level of safety, expressed in structural reliability or probability of failure, can be challenging.

[1] Dr., LGA KdöR, Nürnberg, Germany
e-mail: marcus.achenbach@lga.de, ORCID: https://orcid.org/0000-0003-1689-1218
[2] Prof. Dr., Bauhaus University Weimar, Germany
e-mail: guido.morgenthal@uni-weimar.de, ORCID: https://orcid.org/0000-0003-1516-8677
https://doi.org/10.6084/m9.figshare.22177913

Previous studies on the structural safety of concrete slabs subjected to different fire scenarios [6–8] are based on a full probabilistic analysis for a chosen set of parameters and stochastic basic variables. This allows to identify the governing stochastic variables and to calculate probabilities of failure for the given set of parameters. But conclusions for the structural reliability of slabs designed using tabulated values are only partly possible.

Assumptions on the structural reliability, namely the reliability index β [9], for members subjected to fire are necessary to determine safety and combination factors. These factors are needed for the semi-probabilistic approach of the Eurocodes [10]. It is assumed, that the reliability index β for concrete members subjected to fire is in a range of 1.0 [11] and 2.5 [2]

In this paper it is examined, which level of safety can be expected for concrete slabs subjected to natural fires, designed for a given fire rating using tabulated values. This allows to conclude from a specified fire rating to a probability of structural failure p_f. The calculated values of p_f are a necessary input to calibrate performance based methods [9, 12], because adequate level of safety using performance-based methods for natural fires can only be shown if the safety level for prescriptive design is known.

The applied methods are presented in Section 2. The results of the Monte-Carlo simulation are presented in Section 3, followed by the conclusions in Section 4. An outlook for further research is given in Section 5.

2 APPLIED METHODS

2.1 Calculated slabs

A simply supported concrete slab subjected to a uniformly distributed load is analysed. The structural system and cross section are displayed in Figure 1, the relevant parameters are given in Table 1. The characteristic dead load g_k and live load q_k, thickness h, span l and area of reinforcement a_s have been chosen according to typical applications in residential buildings. A combination factor $\psi_2 = 0.3$ is assumed for the live load q_k, a concrete strength f_{ck} = 20 MPa and yield strength f_{yk} = 500 MPa for the cold worked reinforcement is considered. The provided area of reinforcement is sufficient to meet the design requirements in the ultimate limit state at room temperature according to Eurocode 2 [13]. The provided thickness of the slab h = 14 cm exceeds the minimum thickness of the slab for a fire rating R90 of 10 cm. The axis distance a of the reinforcement is given by the tabulated values of Eurocode 2 [1] for a fire rating R30 and R90. The minimum axis distance a = 1 cm for a fire rating R30 is less than the necessary minimum concrete cover given at ambient temperatures [13]. But the minimum value of a = 1 cm is examined because it may occur in real buildings due to errors in execution. In addition, this allows to conclude from an axis distance to a level of safety without any "hidden safety" given by detailing rules.

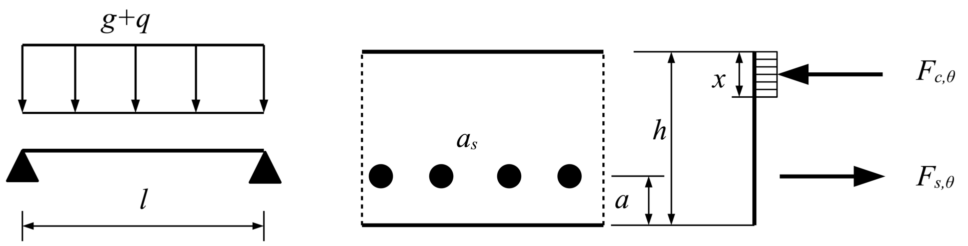

Figure 1. Structural system (left), cross section (middle) and inner forces (right) of the concrete slab

Table 1. Parameters of the simulated concrete slabs

Fire rating	l [cm]	h [cm]	a [cm]	a_s [cm²/m]	f_{ck} [MPa]	f_{yk} [MPa]	g_k [kPa]	q_k [kPa]
R30	330	14	1.0	3.35	20	500	5	3
R90	330	14	3.0	3.35	20	500	5	3

The gas temperatures are calculated for a natural fire acc. to Eurocode 1, Annex A [3]. The fire load densities $q_{f,k}$ = 300, 600 and 900 MJ/m^2, given as 80%-fractile, are considered and the opening factor O is varied in limits of 0.02 to 0.2 m$^{1/2}$ to calculate the peak gas temperatures, shown in Table 2. As reasonable approach for office and residential buildings, the fire growth rate is considered with t_{lim} = 20 min [3] and a ratio of the total area of the enclosure A_t to the floor area A_f of $A_t/A_f = 3$ is chosen. The thermal properties of the enclosure are taken as constant value of b = 1500 J / m^{2}s$^{1/2}$K for concrete or masonry structures [14].

2.2 Parametric temperature-time curves and thermal analysis

The gas temperatures are determined by the parametric temperature-time curves of Eurocode 1 [3]. These curves consist of two parts: an ascending, nonlinear branch in the heating phase and a linear descending part in the cooling phase. The gas temperature θ_g [°C] in the heating phase is given by the empiric equation

$$\theta_g(t) = 20 + 1325\left(1\text{-}0.324e^{-0.2t^*}\text{-}0.204e^{-1.7t^*}\text{-}0.472e^{-19t^*}\right) \tag{1}$$

with the scaled time $t^* = t \cdot \Gamma$, the real time t [h] and the non-dimensional scaling factor Γ. The standard temperature-time curve is approximated by equation (1) for $\Gamma = 1$. The scaling factor is defined by

$$\Gamma = \left(\frac{O}{b}\right)^2 / \left(\frac{0.04}{1160}\right)^2 \tag{2}$$

with the opening factor $O = 0.02 \ldots 0.2$ m$^{1/2}$, describing the ventilation conditions, and the thermal properties of the compartment considered by $b = \sqrt{\rho c \lambda}$ [J / m^2 s$^{1/2}$ K]. The maximum temperature is reached at $t^*_{max} = t_{max} \cdot \Gamma$, with

$$t_{max} = \max\left(0.2 \cdot 10^{-3} \cdot q_{t,d}/O\, ; t_{lim}\right). \tag{3}$$

The fire growth rate is taken into account by the tabulated parameter t_{lim} and the design fire load $q_{f,d}$ is considered by $q_{t,d} = q_{f,d} \cdot A_f/A_t$. After the maximum temperature is reached, the linear ascending branch is given in dependence from $t^{**}_{max} = \left(0.2 \cdot 10^{-3} \cdot q_{t,d}/O\right) \cdot \Gamma$.
The design fire load $q_{f,d}$ is specified in Annex E to EN 1991-1-2 [3] by

$$q_{f,d} = m \cdot q_{f,k} \cdot \delta_{q1} \cdot \delta_{q2} \cdot \delta_n, \tag{4}$$

with the combustion factor m [-], the characteristic fire load density $q_{f,k}$ [MJ/m^2], the factor δ_{q1} to consider the size of the compartment and δ_{q2} for the risk of activating a fire, the product δ_n of the other factors δ_i to take sprinklers or other firefighting measures into account. In this paper, m = 0.8 for mainly cellulosic materials [3] and $\prod \delta = \delta_{q1} \cdot \delta_{q2} \cdot \delta_n = 1.0$ for semi-probabilistic calculations are assumed.
The temperature distribution within the concrete cross section is calculated by an explicit finite difference method [15]. The thermal properties of the concrete are modelled according to Eurocode 2 [1] with the following parameters: concrete density at room temperature $\rho(20°C) = 2400$ kg/m^3, moisture content of concrete weight u = 3 %, thermal conductivity λ_c [W / mK] with its lower limit. It is assumed, that the slabs are heated on the bottom surface, whereas ambient temperatures are on the top surface. The boundary conditions for the heat transfer are modelled with coefficient of heat transfer of $a_c = 35$ W / m^{2}K (natural fires), $a_c = 25$ W / m^{2}K (standard fire), $a_c = 4$ W / m^{2}K (ambient temperature) and a total emissivity of $\varepsilon = 0.7$ [1, 3].

2.3 Mechanical analysis

The acting moment M_E is defined by

$$M_E = (g + q) \cdot \frac{l^2}{8} \tag{5a}$$

for the Monte-Carlo simulation. For the semi-probabilistic analysis, M_E is given by

$$M_E = (g_k + \psi_2 \cdot q_k) \cdot \frac{l^2}{8} \tag{5b}$$

with ψ_2= 0.3. The concrete strength is modelled with the strength f_{ck} at 20 °C, because the slab thickness of 14 cm exceeds the specified minimum thickness of 10 cm for a fire rating R90. The yield strength of the reinforcement $f_{s,\theta} = k_s(\theta_s) \cdot f_{yk}$ is modelled as cold worked steel with the reduction factors k_s given in Eurocode 2 [1]. The bending moment resistance of the cross section can be calculated by the yield strength of the reinforcement $F_{s,\theta} = |F_{c,\theta}| = a_s \cdot f_{s,\theta}$ and the height of the stress block $x = F_{s,\theta}/f_{ck}$ by

$$M_R = F_{s,\theta} \cdot \left(h - a - \frac{x}{2}\right) \tag{6}$$

as illustrated in Figure 1.

2.4 Monte-Carlo simulation

The Monte-Carlo simulation [9] is set up for two different fire scenarios for each fire load density:

- using the minimum allowable opening factor of O = 0.02 $m^{1/2}$, leading to a ventilation controlled fire,
- using the peak gas temperatures with the corresponding opening factor given in Table 2, leading to a fuel controlled fire.

Table 2. Parameters of the parametric fire curve

#	$q_{f,k}$ [MJ/m^2]	O [$m^{1/2}$]	A_t / A_f [-]	b [$J / m^2 s^{1/2} K$]	t_{MC} [min]
1	300	0.02	3	1500	100
2	300	0.04	3	1500	100
3	600	0.02	3	1500	150
4	600	0.09	3	1500	150
5	900	0.02	3	1500	200
6	900	0.14	3	1500	200

A total number of n = 10000 samples is generated for each parameter set of Table 2. The stochastic basic variables with the corresponding distributions are given in Table 3. The model uncertainties of the actions X_e, of the cross section resistance X_r and of the thermal analysis X_t are treated as multiplicative variables. The limit state function is defined by:

$$G = X_r \cdot \left(a_s \cdot k_s(X_t \cdot \theta_s) \cdot f_{yk}\right) \cdot \left(h - a - \frac{x}{2}\right) - X_e \cdot (g + q) \cdot \frac{l^2}{8}. \tag{7}$$

The slab is assumed to fail for $G \leq 0$ and the number total number of failed slabs is given by n_f. The probability of failure can be estimated by

$$p_f \approx \frac{n_f}{n} \tag{8}$$

and the corresponding reliability index is defined by

$$\beta = -\phi^{-1}(p_f), \tag{9}$$

where ϕ^{-1} is the inverse cumulative density function of a normal distribution with mean $\mu = 0$ and standard deviation $\sigma = 1$ [9]. The standard deviation of the estimated probability of failure p_f calculated by the Monte-Carlo simulation [9] is given by

$$\sigma_{p_f} = \sqrt{\frac{p_f - p_f^2}{n}}. \tag{10}$$

The limit state function G is evaluated for every time step of 1 min and the probability of failure is calculated. The considered time domain of the Monte-Carlo Simulation t_{MC} is given in Table 2.

Table 3. Stochastic basic variables (N = normal, LN = log-normal, G = Gumbel)

variable	distribution	parameters of distribution	reference
X_e	LN	$\mu = 1.0$, $v = 0.1$	([6])
g	N	$\mu = G_k$,$v = 0,1$	([16, 17])
q	G	q_k: 98%-quantile , $v = 0.4$	([17])
q_f	G	$q_{f,k}$: 80%-quantile , $v = 0.3$	([16])
X_t	N	$\mu = 1.0$, $v = 0.1$	([18])
X_r	LN	$\mu = 1.1$, $v = 0.2$	([6])
f_c	LN	$\mu = f_{ck} + 0.8$ kN/cm² , $\sigma = 0.5$ kN/cm²	([16, 17])
f_s	N	$\mu = f_{yk} + 2\sigma$, $\sigma = 3$ kN/cm²	([16, 19])
a	N	$\mu = a$, $\sigma = 0.5$ cm	([17, 19])

3 RESULTS

3.1 Thermal analysis

The gas temperatures for a standard fire and for parametric temperature-time curves for fire a load density $q_{f,k} = 600$ MJ/m^2 and opening factors $O = 0.02$, 0.09 and 0.2 m$^{1/2}$ are displayed in Figure 2. Though the standard temperature-time curve is assumed to cover the peak temperatures of fires in office and residential buildings [5], the maximum gas temperature calculated for an opening factor $O = 0.09$ m$^{1/2}$ exceeds the standard temperature-time curve within the first 20 min.

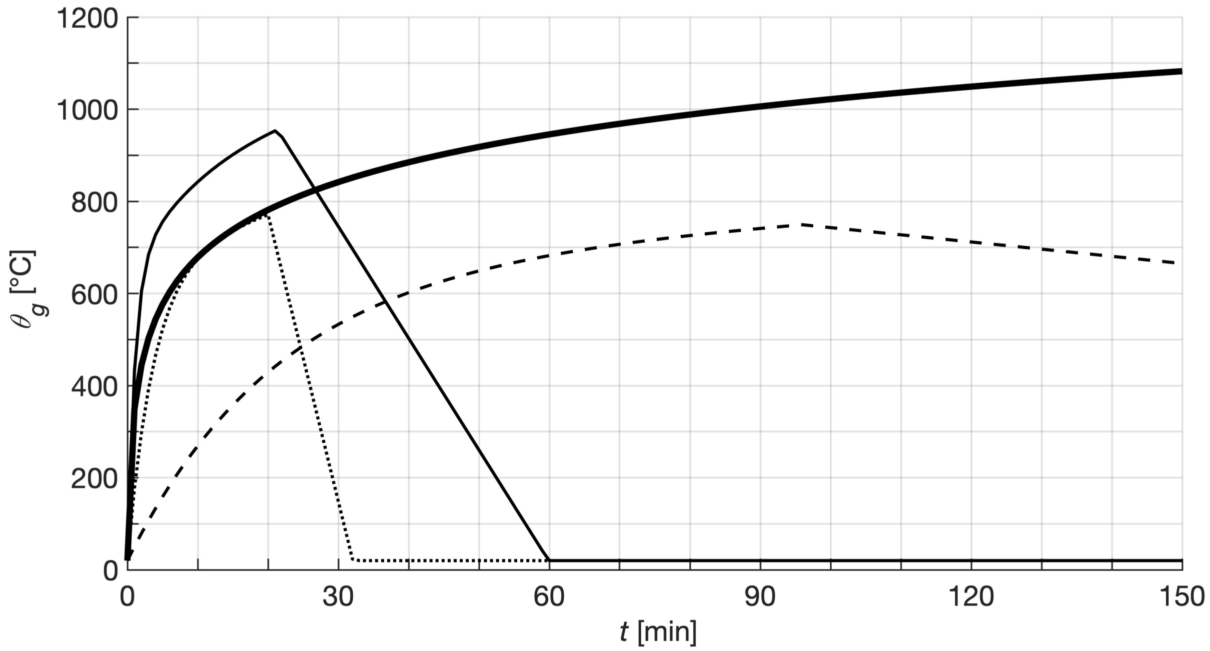

Figure 2. Gas temperatures acc. to EN 1991-1-2 for $q_{f,k}$ = 600 MJ/m^2, m = 0.8, $\prod \delta$ = 1.0, A_t / A_f = 3: standard temperature-time curve (**—**), parametric temperature-time cure with O = 0.09 (—), O = 0.02 (- - -) and O = 0.2 (…) m$^{1/2}$

The influence on the temperature of the rebars is displayed in Figure 3 for an axis distance a = 1 cm. The rebar temperature for a standard fire is 514 °C at t = 30 min. The critical temperature of 500 °C, which is applied for the tabulated values of slabs [1], is exceeded by 2.8 %. The critical temperature is also exceeded for an opening factor O = 0.09 m$^{1/2}$ within the first 30 min (maximum gas temperature) and for O = 0.02 m$^{1/2}$ after 30 min (minimum opening factor). Applying the critical temperature of 500 °C to judge on the fire safety leads to a failure of the considered slabs subjected to natural fires.

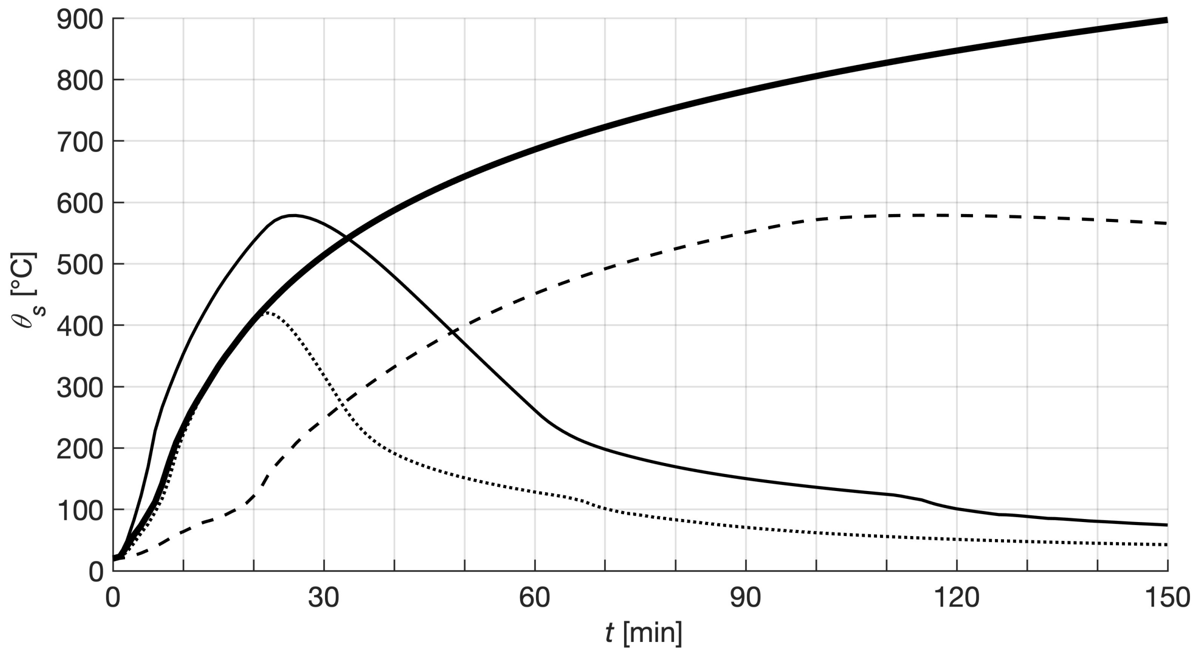

Figure 3. Rebar temperatures for the concrete plate acc. to Table 1, a = 1 cm, gas temperatures acc. to Fig. 2: standard temperature-time curve (**—**), parametric temperature-time curve with O = 0.09 (—), O = 0.02 (- - -) and O = 0.2 (…) m$^{1/2}$

3.2 Semi-probabilistic approach

The calculated rebar temperatures of Figure 3 are considered in the semi-probabilistic evaluation of the moment resistance acc. to equation (5b). Acting moment and moment resistance are plotted in Figure 4. Applying a combination factor of ψ_2= 0.3, introduced by the semi-probabilistic approach of Eurocode 0 [10], reduces the acting moment. The bending moment resistance is bigger than the acting moment and the slab is assumed not to fail.

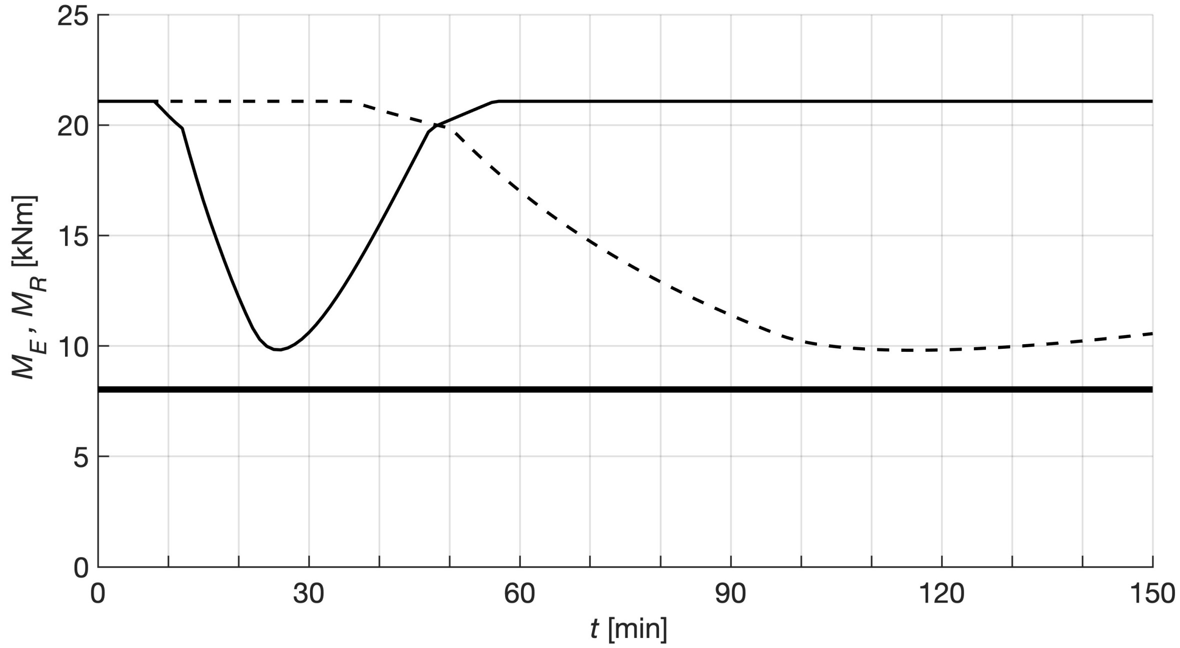

Figure 4. Acting moment and moment resistance for the concrete plate acc. to Table 1, rebar temperatures acc. to Fig. 3: acting moment M_E (━), moment resistance M_R for O = 0.09 (—), O = 0.02 (- - -) $m^{1/2}$

3.3 Monte-Carlo simulation

The limit state function given by equation (7) is evaluated for each time step and the probability of failure is calculated. The maximum probability of failure p_f for the corresponding time t_f is given in Table 4 for an axis distance a = 1 cm.

Table 4. Max. probabilities of failure and corresponding time t_f for a = 1 cm (R30), numbering acc. to Table 2

#	p_f [-]	t_f [min]
1	0.006	84
2	0.015	36
3	0.137	121
4	0.100	27
5	0.350	142
6	0.158	23

The highest probability of failure p_f = 0.350 is calculated for #5 at t_f = 142 min. The mean probability of failure of all six samples is equal to $\bar{p}_f = 0.128$ with a reliability index β =1.14. The standard deviation of $\bar{p}_f$, estimated by the Monte-Carlo simulation, can be calculated by equation (10) as $\sigma_{\bar{p}_f} \approx 0.003$ for

n = 10000 samples. It can be observed that four of six slabs have the highest probability of failure after 30 min. Only #4 and #6 show the highest probability of failure within the first 30 min.

The results of the Monte-Carlo simulation for an axis distance a = 3 cm are given in Table 5. The highest probability of failure is also calculated for #5: p_f = 0.033 at t_f = 200 min. No failure is detected for three samples. Only two slabs show the highest probability of failure within the first 90 min. The mean probability of failure is $\bar{p}_f = 0.006$ (β =2.51) with a standard deviation $\sigma_{\bar{p}_f} =$ 0.001. Hence the mean probability of failure and the reliability index can only be seen as informative value because of the chosen number of n = 10000 samples. It can be expected that the exact probability of failure is smaller than $\bar{p}_f = 0.006$.

Table 5. Max. probabilities of failure and corresponding time t_f for a = 3 cm (R90), numbering acc. to Table 2

#	p_f [-]	t_f [min]
1	0	100
2	0	100
3	0.003	150
4	0	42
5	0.033	200
6	0.001	40

4 CONCLUSIONS

A concrete slab with fixed dimensions and loadings has been analysed in this paper as a sample object to study the influence of the fire rating for a standard fire on the reliability for natural fires. The axis distance has been chosen according to tabulated values [1] and the structural reliability has been determined for different fire scenarios using the parametric temperature-time curves of Eurocode 1 [3]. Due to the limited range of parameters, the conclusions must be interpreted as first indication. General conclusions must be backed by a larger range of examined examples. The conclusions derived from this study are:

- The gas temperatures of the standard temperature-time curve can be exceeded by the parametric temperature-time curve in dependence from the opening factor O.
- The design of a concrete section using tabulated values leads to a rebar temperature close to 500 °C for a standard fire but can be exceeded in case of a natural fire.
- Applying a critical temperature of 500 °C as criteria for structural safety of concrete slabs can identify failure of the slab in case of natural fires, though a mechanical analysis using the semi-probabilistic approach proofs adequate safety.
- The highest probability of failure is observed for a minimum opening factor O = 0.02 $m^{1/2}$ for a ventilation controlled fire. The corresponding time t_f is later than the chosen fire rating of the slab.
- The mean observed reliability index for a concrete slab designed for a fire rating R30 is β =1.14.
- The reliability index for a fire rating R90 can be estimated as $\beta > 2.51$.
- The range of the observed reliability index is within the expected range given in the background literature for the Eurocodes.
- The largest probabilities of failure occur after the nominal time of the fire rating.

5 OUTLOOK

A wider range of parameters and fire models is necessary to generalize these early findings regarding the reliability of concrete members designed using tabulated values. Also, the applied methods for the determination of the reliability index must be suitable to evaluate smaller probabilities of failure. The proposed next steps are:

- Implementation of the FORM algorithm [20] for the determination of the reliability index.
- Consideration of different slab heights.
- Consideration of different ratios q_k/g_k.

REFERENCES

1. EN 1992-1-2 (2004) Eurocode 2: Design of concrete structures – Part 1-2: General rules - Structural fire design
2. Comité Euro-International du Béton (1991) Fire Design of Concrete Structures
3. EN 1991-1-2 (2002) Eurocode 1: Actions on structures – Part 1-2: General actions – Actions on structures exposed to fire
4. Law A, Bisby L (2020) The rise and rise of fire resistance. Fire Saf J 116:1–10. https://doi.org/10.1016/j.firesaf.2020.103188
5. Zehfuß J (2004) Bemessung von Tragsystemen mehrgeschossiger Gebäude in Stahlbauweise für realistische Brandbeanspruchung. PhD Thesis, Technische Universität Braunschweig
6. van Coile R (2015) Reliability-Based Decision Making for Concrete Elements Exposed to Fire. Universiteit Gent
7. Heidari M, Robert F, Lange D, Rein G (2019) Probabilistic Study of the Resistance of a Simply-Supported Reinforced Concrete Slab According to Eurocode Parametric Fire. Fire Technol 55:1377–1404. https://doi.org/10.1007/s10694-018-0704-4
8. Karaki G, Hawileh RA, Kodur VKR (2021) Probabilistic-Based Approach for Evaluating the Thermal Response of Concrete Slabs under Fire Loading. J Struct Eng 147:04021084. https://doi.org/10.1061/(ASCE)ST.1943-541X.0003039
9. Melchers RE (1999) Structural Reliability Analysis and Prediction, 2nd edition. John Wiley & Sons, Chichester
10. Gulvanessian H, Calgaro J-A, Holický M (2002) Designers' Guide to EN 1990, Eurocode: Basis of structural design, 1st edition. Thomas Telfort, London
11. Leonardo da Vinci Pilot Project CZ/02/B/F/PP-134007 (2005) Handbook 5 , Design of buildings for the fire situation
12. Achenbach M (2021) Towards a safety concept for natural fires - the need of code calibration. In: Pečenko R, Huč S, Chifliganec C, Hozjan T (eds) Applications of Structural Fire Engineering – Proceedings of the International Conference in Ljubljana, 10-11 June, 2021. University of Lujubljana, Faculty of Civil and Geodetic Engineering, pp 425–430
13. EN 1992-1-1 (2004) Eurocode 2: Design of concrete structures – Part 1-1: General rules and rules for buildings
14. DIN EN 1991-1-2/NA (2010) Nationaler Anhang – National festgelegte Parameter – Eurocode 1: Einwirkungen auf Tragwerke – Teil 1-2: Allgemeine Einwirkungen – Brandeinwirkungen auf Tragwerke
15. Baehr HD, Stephan K (1998) Wärme- und Stoffübertragung, 3. Auflage. Springer, Berlin
16. Hosser D, Weilert A, Klinzmann C, et al (2008) Sicherheitskonzept zur Brandschutzbemessung. Institut für Baustoffe, Massivbau und Brandschutz, Braunschweig

17. Six M (2001) Sicherheitskonzept für nichtlineare Traglastverfahren im Betonbau. PhD Thesis, Technische Universität Darmstadt
18. Hosser D, Richter E (2006) Überführung von EN 1992-1-2 in EN-Norm und Bestimmung der national festzulegenden Parameter (NDP) im Nationalen Anhang zu EN 1992-1-2. Institut für Baustoffe, Massivbau und Brandschutz, Braunschweig
19. JCSS (2001) Probabilistic Model Code
20. Rackwitz R, Fiessler B (1978) Structural Reliability under Combined Random Load Sequences. Comput Struct 9:489–494

FIRE PERFORMANCE OF CORRODED REINFORCED CONCRETE COLUMNS

Shashank Chandra[1], Umesh Kumar Sharma[2], Mark Green[3], John Gales[4], Pradeep Bhargava[5]

ABSTRACT

The current guidelines for obtaining fire ratings of the reinforced concrete columns are limited to the pristine elements, which do not include the effect of corrosion. An experimental investigation was conducted to examine the effects of corrosion on the fire performance of reinforced concrete (RC) columns. Four full-scale column specimens were cast and tested in this study. Two columns were corroded by the accelerated corrosion regime for the target corrosion of 20%, while the remaining columns were the control specimens and were kept uncorroded. After the desired exposure time for the accelerated corrosion, all the columns were tested in a fire furnace under the standard ISO-834 fire. The experimental results showed that corrosion has a significant influence on the fire performance of the columns. The result shows that the fire rating of the corroded high-strength concrete (HSC) column drops considerably. However, there is a slight improvement in the behaviour of the corroded normal-strength concrete (NSC) column when subjected to fire. The effect of corrosion cracks and spalling on the fire resistance of the corroded RC columns was also noted in this study. This research will enable the design of new reinforced concrete columns for better fire performance despite age-related corrosion deterioration.

Keywords: Reinforced concrete columns; Corrosion deteriorations; Fire ratings.

1 INTRODUCTION

The reinforced concrete structures are crumbling due to ageing and corrosion. Corrosion of the reinforcement is caused by the ingress of chlorides or carbon dioxide from the atmosphere, which causes a reduction in the pH of the concrete surrounding the reinforcement, and favourable conditions got generated for the electrochemical process of corrosion. This electrochemical process of corrosion leads to a decrease in the sectional area of the reinforcement [1], and the bond strength between the reinforcement and concrete also gets compromised [2], [3]. The corrosion products produce the hoop stresses over the surrounding concrete of the reinforcement, which leads to the cracking of the concrete. The strength and integrity properties of RC elements are significantly compromised by the corrosion process. The detrimental effects of corrosion on the various structural properties of the RC elements have been investigated by researchers in the last two decades [4], [5].

Accidental fire is also a potential risk to the infrastructure during its service life. Any structure's fire safety

[1] PhD Candidate, Department of Civil Engineering, IIT Roorkee, India.
e-mail: schandra1@ce.iitr.ac.in , ORCID: https://orcid.org/0000-0003-4584-199X
[2] Professor, Department of Civil Engineering, IIT Roorkee, India.
e-mail: umesh.sharma@iitr.ac.in, ORCID: https://orcid.org/0000-0002-0972-908X
[3] Professor, Department of Civil engineering, Queen's University, Canada.
e-mail: greenm@queensu.ca, ORCID: https://orcid.org/0000-0002-6610-0325
[4] Associate Professor, Department of Civil engineering, Canada
e-mail: jgales061@gmail.com, ORCID: https://orcid.org/0000-0003-2843-2924
[5] Professor, Department of Civil Engineering, IIT Roorkee, India.
e-mail: p.bhargava@ce.iitr.ac.in, ORCID: https://orcid.org/0000-0002-5476-9080
https://doi.org/10.6084/m9.figshare.22177922

objectives are taken care of by incorporating various active and passive fire protection arrangements. The active fire protection arrangements, like sprinklers, fire alarms etc., get activated during the fire incident. The passive fire protection system is the integral fire protection of the structural member. The essential component of passive fire protection is the fire resistance or fire rating, a standard tool to quantify the fire safety ability of the structural elements. Fire resistance is defined as the duration of fire (in terms of minutes or hours) under which a structural element will not lose its strength, stability and integrity. [6]

The column is the main load-bearing element in a structure, and thus, the columns must be able to withstand a design fire. Many studies have been conducted to understand the behaviour of RC columns in the event of fire [7]–[9]. Simple calculation methods to calculate the fire resistance of RC columns have also been developed, as given in Eurocode 2 [10] and Australian code [11]. Yet, the limitation of all these studies and efforts is that these are often developed using pristine RC elements, and the effect of corrosion has not been considered. The corroded structural columns do not behave similarly to their companion non-corroded pristine elements. It should also be believed that corroded RC elements in the event of fire might behave differently from their pristine elements with no effect of ageing and corrosion. This paper investigates the effects of corrosion on the fire performance of RC columns. The corroded RC columns were obtained using a specifically designed accelerated corrosion regime, followed by fire tests.

2 EXPERIMENTAL METHODOLOGY

The experimental program was divided into three stages, stage 1: the casting of RC columns, stage 2: accelerated corrosion of RC columns, and stage 3: fire testing of corroded and non-corroded RC columns in a fire furnace.

In this study, four RC columns (NSC and HSC: each NOS:2), 3150 mm in height, with cross-sectional specifications as shown in Figure 1, were cast (Figure 3). The details of all the columns studied in this investigation are mentioned in Table 1. After 28 days of the curing period, one NSC and one HSC column of these four column specimens were installed for the accelerated corrosion with the current density of 300μA/cm^2 for the central column length of 2150 mm, as shown in Figure 4, following the installation process as shown in Figure 2. This regime's arrangement enabled periodical monitoring of corrosion activities, as discussed in section 3.2 of this paper.

These NSC and HSC columns were kept under this accelerated corrosion process for 70 days and 100 days, respectively, for the targeted mass loss of 20%, but the actual mass loss was found to be 12.29% and 15.38%, respectively, as shown in Table 1 and Figure 8.

After the completion of respective accelerated corrosion time, these two corroded specimens and their companion two non-corroded specimens were tested in the fire furnace with a fire zone of 2175 mm, as shown in Figure 5. The furnace has the capability of applying load along with the desired fire exposure by the four diesel burners installed in it for supplying fuel and air.

During the fire tests of the RC columns, the furnace air temperature was recorded by installing four K-Type shielded thermocouples at different locations of the furnace. A total number of 21, K-type wired thermocouples of 0.85 mm thickness were installed at the various specified places in the reinforcement cage of the RC column before its casting. These internal thermocouples were installed to measure the temperature gradient inside the RC column section during the event of a fire at three different locations, seven at each location (T1 to T7), as shown in Figure 1. Two LVDTs, V1 and V2, were installed at the top of the column to measure the lateral deformations during the fire exposure. LVDTs were also installed at the left face of the column to measure the lateral deformation responses during the fire event. Pinned support was ensured at the top of the column, and bottom support was fixed with a moment-resistant angular assembly. The load was applied through the hydraulic jack and measured through a load cell arrangement. Before the start of the fire event, all the columns were pre-loaded for the load (P) equal to their 33% axial design load capacity. All these instrumentations were connected to a multi-channel data logger to record the respective data during the fire tests.

The corroded specimens (C30220C and C60120C) were then demolished after fire testing. Corroded bars

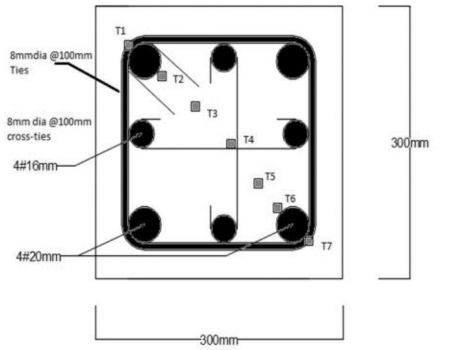

Figure 1. Cross-sectional details of the RC Column

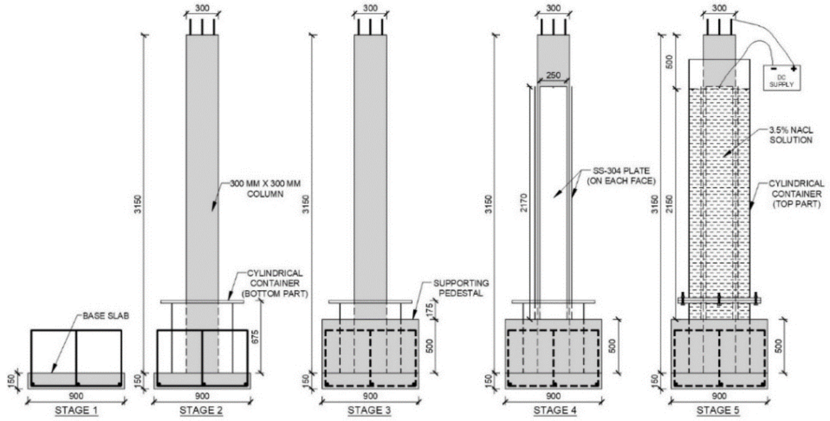

Figure 2. Process of Installation of Corrosion setup

Figure 3. The casting of RC columns

Figure 4. Accelerated Corrosion Setup Regime

Figure 5. Fire furnace

Column designation	Concrete type	Concrete Strength (MPa) (on 28th Day)	Load applied	Measured Fire Resistance	Targeted mass loss	Achieved mass loss	Corrosion Time
C30-3-00C	NSC	36	33%	239 min.	0%	-	-
C30-2-20C	NSC			255 min.	20%	12.29 %	70 Days
C60-5-00C	HSC	67	33%	171 min.	0%	-	-
C60-1-20C	HSC			118 min.	20%	15.38%	100 Days

Table 1. Summary of test parameters and results for Fire Resistance Tests

were extracted, cleaned, and their element-wise residual weights were noted to evaluate actual mass loss due to corrosion, and the results are presented in Figure 8.

3 RESULTS AND DISCUSSION

3.1 Observations from corrosion damage

As mentioned earlier, two out of four column specimens were subjected to accelerated corrosion using an accelerated corrosion setup regime designed for 300µA/cm^2 current density. After achieving the pre-calculated corrosion time, the respective columns were removed from the corrosion setup and examined for corrosion-induced cracks, as shown in Figure 7. Although similar conditions of accelerated corrosion exposure were ensured during the corrosion process, the crack patterns were still different in all the specimens. It may be because concrete is a heterogenous material, and there is a variation in the material's microstructure. The crack widths were found in the range of 0.1 to 8 mm. The longitudinal cracks and diagonal cracks were seen on the faces of the column specimens. It should be noted that the direction of the corrosion cracks primarily indicates the orientation of the reinforcement elements being corroded, which means the longitudinal cracks and diagonal direction cracks shows corrosion of longitudinal reinforcement and transverse reinforcements, respectively.

Gravimetric analysis, as shown in Figure 8, conveys the mass loss experienced by individual elements of the reinforcing cage in the test length of both specimens, which indicates that the transverse reinforcement underwent more severe corrosion than the other elements of the reinforcing cage. It is also evident from Figure 8 that 20 mm longitudinal bars suffered more mass loss than 16 mm bars; it must be because these 20 mm bars were exposed from two faces of the column. The cross ties underwent lesser mass loss, and it must be because the chloride ingress from the surface of the concrete affects less the reinforcing cage elements present near the core of the concrete.

3.2 Half-cell potential measurements

Half-cell potential (HCP) indicates the likelihood of occurrence of the corrosion of the reinforcements embedded inside any concrete element [12]. The arrangement of accelerated corrosion setup used in this experimental investigation permitted the investigation of HCPs periodically. A total of three and four monitoring sessions for C30220C and C60120C, respectively, as shown in Table 2, were conducted to investigate the changes in the potential readings using Ag/AgCl reference electrode-based half-cell equipment. The schematic of half-cell equipment is shown in Figure 6. The surface preparations and HCP tests were conducted by IS 516 (Part 5/Sec 2): 2021[12] and ASTM-c786-15[13]. Before the use of this half-cell equipment, grid lines, as shown in Figure 9, were drawn on the faces of the columns by the use of a rebar locator and a total of 72 points on each face were identified and considered for HCP monitoring for all the periodically conducted monitoring sessions. Based on the various HCP values obtained during the tests, grouping was done in four states, as mentioned in Table 3. As per Table 3, it is evident that state-1 and state-4 are the states where there is a less and high chance of occurrence of corrosion activity, respectively, at the point of the test and the time of measurement. The distribution of percentage frequency occurrence of various states is presented in Figure 10 and Figure 11. It can be inferred that at the same measurement point, the state of corrosion activity occurrence can be different at different monitoring sessions.

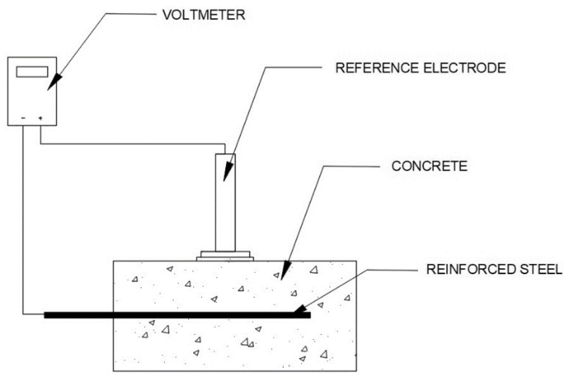

Figure 6. Schematic of Half-cell potential equipment

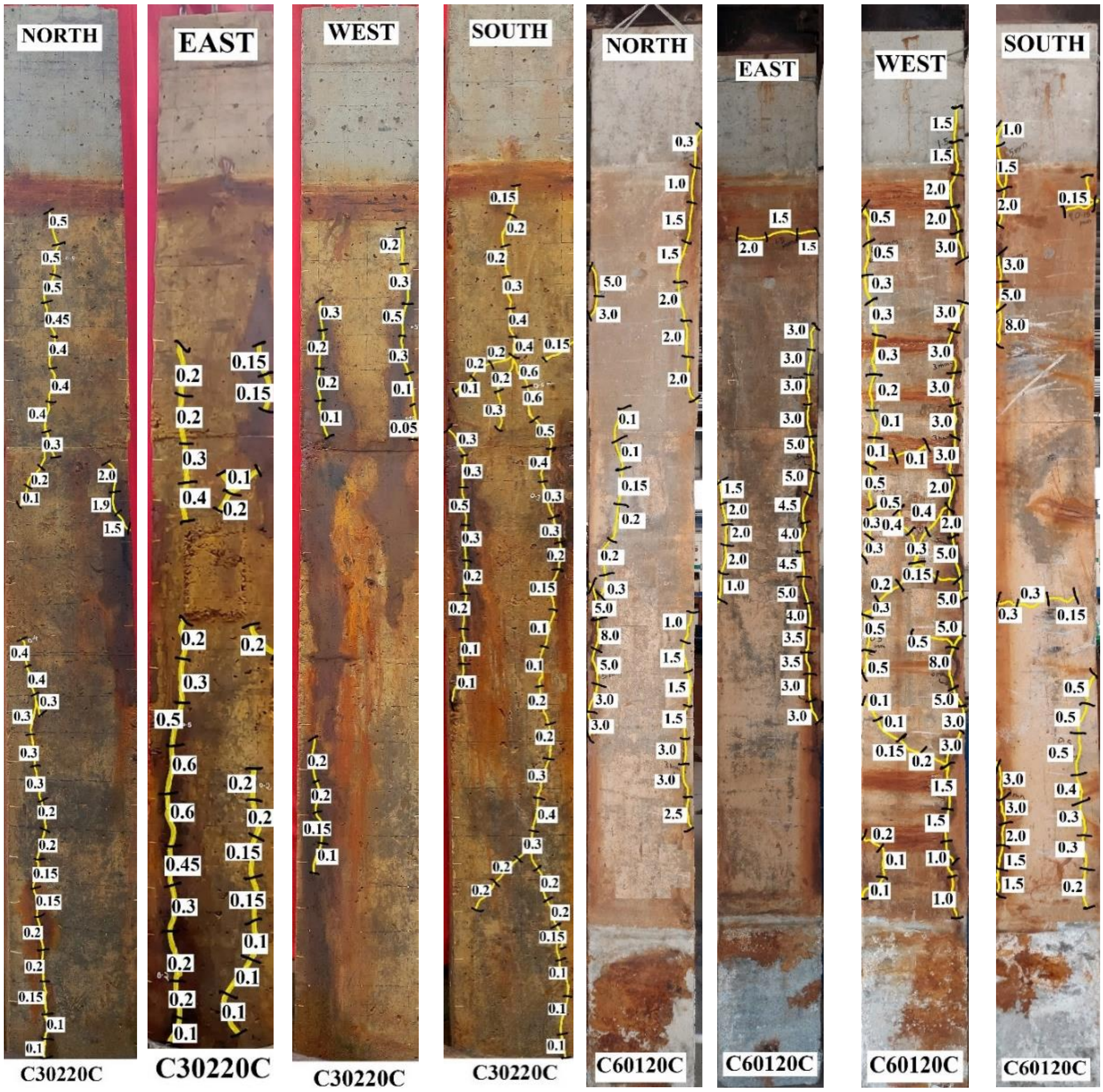

Figure 7. Crack Observation (in mm) for Corroded Specimens

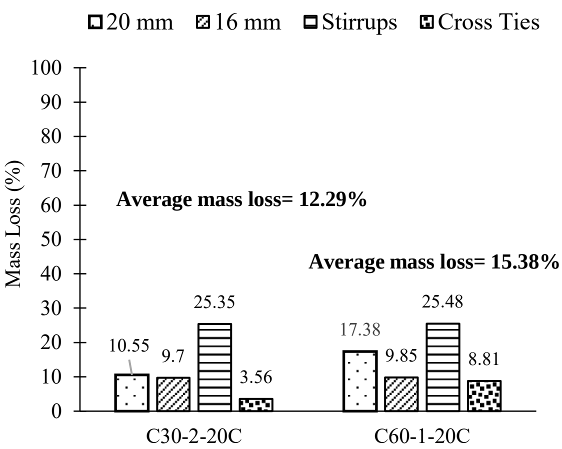

Figure 8. Element-wise Gravimetric analysis.

Column Specification	Monitoring Sessions	Age of accelerated corrosion
C30220C	Monitoring-0	0th day
	Monitoring-1	40th day
	Monitoring-2	70th day
C60120C	Monitoring-0	0th day
	Monitoring-1	40th day
	Monitoring-2	70th day
	Monitoring-3	100th day

Table 2. Monitoring Sessions of HCP measurements.

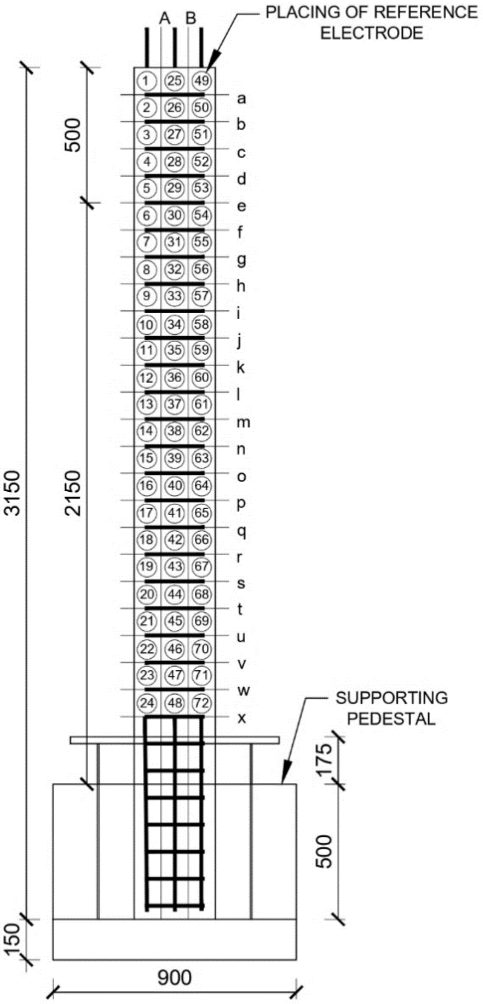

Figure 9. HCP monitoring data points

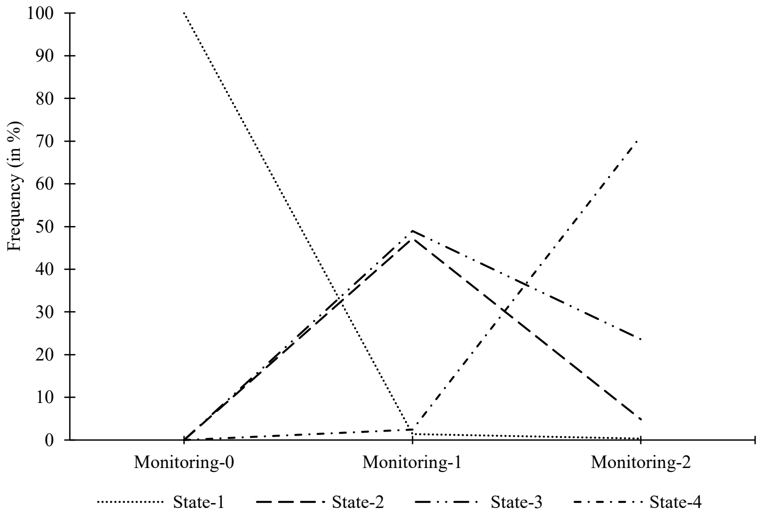

Figure 10. Frequency occurrence distribution of C30220C.

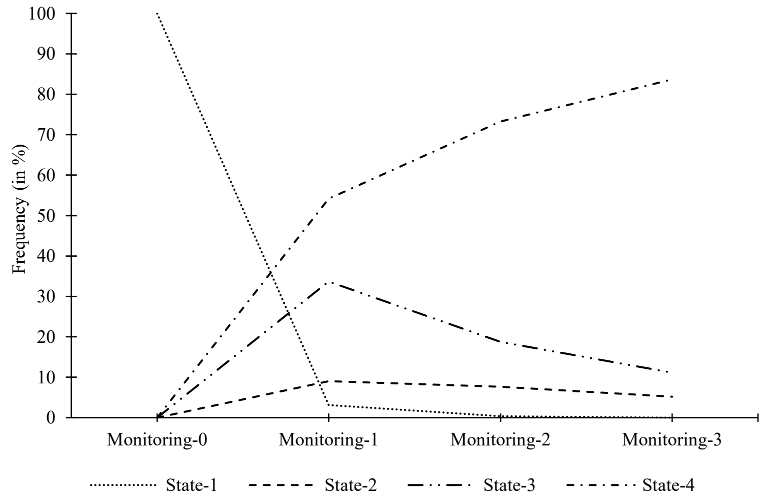

Figure 11. Frequency occurrence distribution of C60120C.

HCP values (Ag/AgCl electrode)	Termed State	Likely Corrosion Condition
> -106 mV	State-1	Low (There is a greater than 90% probability that no reinforcement steel corrosion is occurring at the time of measurement).
-106 mV to -256 mV	State-2	Corrosion activity in that area is uncertain at the time of measurement.
< -256 mV	State-3	High (There is a greater than 90% probability that reinforcement steel corrosion is occurring at the time of measurement).
< -406 mV	State-4	Severe Corrosion.

Table 3. Condition of reinforcing bars based on HCP values[12]

3.3 Temperature profiles during the fire tests

The thermocouples, as shown in Figure 1, recorded the temperature data during the fire testing of column specimens. The Figure 12 and Figure 13 show the average furnace temperature profiles during the time of testing of column specimens in the fire. The temperature profile of the furnace was attempted to follow the ISO-834 standard fire curve during the tests. Although before the tests, it was ensured there is no leakage of fire during the test by filling all the possible gaps with glass wool material, yet it was seen that during the fire testing of corroded specimen, huge explosively spalled portions made some leakage of fire which can be observed in the furnace temperature profile of C60120C column specimen as shown in Figure 13.

Due to the corrosion, most of the internal K- type thermocouples were found to be non-functioning; only the internal thermocouple installed at the core of the concrete was found to be functional and recorded the temperature profiles during the fire testing of column specimens. It may be due the fact the chloride ingress from the surface of the concrete affects lesser the metallic elements present near the core of the concrete. The Figure 14 and Figure 15 show the temperature profiles of internal K-type thermocouples at the core location of the NSC and HSC column specimens respectively, and it can be noticed that the temperature in corroded specimens was found to be on the higher side than that of their companion non-corroded specimens. This must be due to the reason that the corrosion of reinforcing bars in concrete causes tensile stresses on the adjacent concrete, and due to the low tensile strength properties of concrete, the cracks are formed, which provide a convenient passage for the transmission of the heat flux inside the concrete (Q1).

A corroded RC element comprises rust products (Iron oxide and Ferro-ferric oxide) along with the concrete, reinforcing elements and air in the pores. The thermal conductivity of these rust products is much higher than that of the air [14], due to that, in the corroded RC structures, the cracks and the pores are now filled with rust products having much higher thermal conduction properties, and it probably causes the acceleration in the transmission of heat flux inside the concrete element. This may be another reason for noting the core concrete temperature of corroded specimens at the higher side (Q2).

On the other hand, these corrosion cracks might be helpful for the easier evacuation of vapours out of the concrete (V). The illustrations of Q1, Q2 and V are shown in Figure 16.

3.4 Structural Response

3.4.1 Axial deformation

The measured axial deformation through LVDT V1 and V2 of all the columns during the event of fire are mentioned in Figure 17 and Figure 18 as a function of their respective fire exposure time. It was found that all the column specimens in the early fire stage expanded due to the thermal expansion of both concrete and steel. Later, the contraction of the column specimens was seen as the result of a loss of strength in steel reinforcement and concrete. Although the concrete itself behaves better than the reinforcing steel in the event of a fire, as the steel reinforcement starts yielding, the load over the concrete starts progressively increasing; at the same time, concrete strength and stiffness properties are also getting compromised due to the exposure of the high temperatures due to the fire event and ultimately failure occurs when the column is not able to sustain the applied load [8]. It can be seen that the thermal expansion of corroded specimens was found to be less than that of their companion non-corroded specimens; this can be attributed to the higher rebar temperature due to the presence of surface corrosion cracks present over the faces of the column specimens and also due to the faster degradation of strength and stiffness. The axial deformations in the corroded specimens were found to be the function of severe explosive spalling occurring during the fire exposure. Although the applied load was concentric to the axis of the column cross-section, tilting of the specimens was observed, which can be seen in the differences between V1 and V2 values, as shown in Figure 17 and Figure 18. It must be because spalling occurs in a non-uniform manner during the fire event, which weakens one face of the column compared to the other. As soon as the column could no longer sustain the applied load, a sudden drop in the load was observed, and failure occurred. The failure of the C60120C specimen was catastrophic, with the massive sound of breaking corroded reinforcing bars. The failure of all the column specimens studied in this experimental investigation is shown in Figure 25.

3.4.2 Load variation

Load variation during the event of fire as the function of their respective fire exposure time is mentioned in Figure 19 and Figure 20. The applied load over the column specimens increased in the early stage of fire exposure due to the expansion of the column specimen. Later due to the degradation of strength and stiffness properties of both reinforcement and concrete, the contraction occurred, and a reduction in the load was observed. The load over the corroded column specimens was the function of spalling. A sudden decrease in the load was observed at various severe spalling events, and after these reductions, the load again started increasing, as shown in Figure 20.

In the later stage of fire exposure, the load returned to the initially applied load. The reduction in the load was found to be still continuous. At this time, the load was applied through the hydraulic jack, and it was tried to keep the load equal to the initially applied load. After some time, the sudden load reduction was seen, and the column specimen could not sustain the load, and failure occurred. At the time of failure of the C60120C specimen, a sudden and massive load drop was observed, as shown in Figure 20.

3.4.3 Lateral Deformation

Lateral deformation responses of the column specimens during the fire exposure time were measured, and their plots at various time intervals of 0.0T, 0.125T to 1.0T are given in Figure 21 to Figure 24. The T is the total fire exposure time or fire resistance of that particular column specimen.

During the early stage of fire exposure, the column undergoes axial expansion. In the later stage, when the degradation in the strength and stiffness of the concrete and rebars starts, the contraction of the column occurs, as already shown in Figure 17 and Figure 18. The time at which this initiation of degradation was noticed during the fire test was noted and termed Critical Time (CT). The lateral deformation plots of the column specimens at this time of fire exposure are also plotted in Figure 21 to Figure 24. Here, Critical time (CT) can also be defined as the time after which the residual strength of the column plays the role of sustaining the load occurring over it. Here, Critical time is expressed in the multiplication of T, the total fire exposure time. It can also be admitted that the higher the critical time, the lesser the time left with the specimen to sustain the load before the failure. The corroded specimens observed higher critical time compared to their non-corroded specimens. The more significant lateral deformations were observed in the corroded specimen after their respective Critical times, which inferred that the corroded specimens degraded faster in the later stages of fire exposure.

It is evident from Figure 21 and Figure 22 that a slightly lesser lateral deformation of C30220C was recorded compared to its companion non-corroded specimen, C30300C. It must be because corrosion cracks in this corroded specimen helped for easier evacuation of vapors from inside. This minimized the spalling during fire exposure and reduced the lateral deflections. The total fire exposure time of C30120C was increased by 6.7%, with a reduction of 15.2% in final lateral deflection, compared to its non-corroded companion C30300C. In contrast, in C60300C, the total fire exposure time of C60120C dropped by 31.3 %, with a significant increase of 164.46% in final lateral deflection compared to its non-corroded companion-C60500C, as shown in Figure 23 and Figure 24. Such high lateral deflection must be due to the sloughing-off cover concrete after 0.25T, as shown in Figure 24, where T is the total fire exposure time.

3.5 Fire resistance

A comparison of the fire resistance of the four columns studied in this investigation is presented in Table 1. The fire exposure time to reach the failure is termed fire resistance, and the failure is said to occur when the column under the event of fire exposure can no longer sustain the applied load.

Before the fire exposure, each column specimen was loaded with 33% of the axial load carrying capacity (P). In the early stage of fire, expansion of the columns was observed, which increased the load acting over the specimen. In later stages, the column contraction occurred, which reduced the acting load and later, this load reached back to the actual applied load (P), as shown in Figure 19 and Figure 20. Now, the applied load was tried to maintain equal to P, but after some time, the column specimens were found unable to sustain the load (P), and this stage was called a failure of the column.

The fire resistance of C30220C (255 min.) was found to be 6.7% greater than its companion non-corroded specimen C30300C (239 min.), and the fire resistance of C60120C (118 min.) was found to be decreased by 31.4% to its companion non-corroded specimen C60500C (171 min.). It can be stated here that, in the corroded RC structures, the factors Q1, Q2 and V, as mentioned in section 3.3 and Figure 16, play essential roles, as Q1 and Q2 are the factors which will increase the spalling and will rapidly increase the temperature inside the concrete, which further will cause the earlier loss of fire performance. On the other hand, V is the factor which will help enhance the performance of corroded RC elements under fire. If the combined effect of Q1 and Q2 is greater than that of the individual impact of V, it can be concluded that the loss in the performance of corroded RC elements will be observed, as found in C60120C. Also, at the low amount of corrosion, the individual effect of V may be more than the cumulative effect of the Q1 and Q2, then spalling will be minimized (Figure 25), and the fire performance may be enhanced, as found in C30120C.

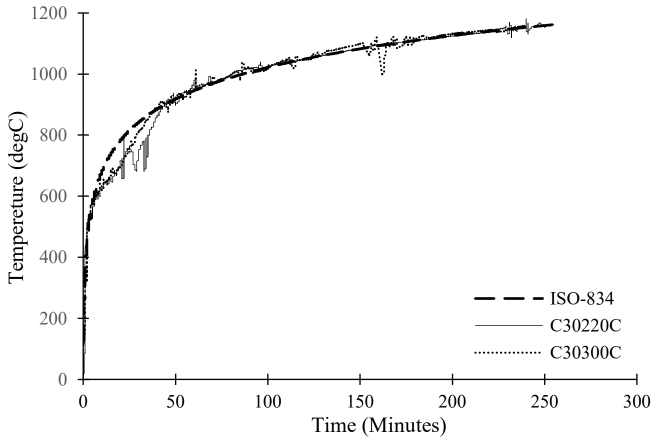

Figure 12. Furnace temperature profiles of NSC columns.

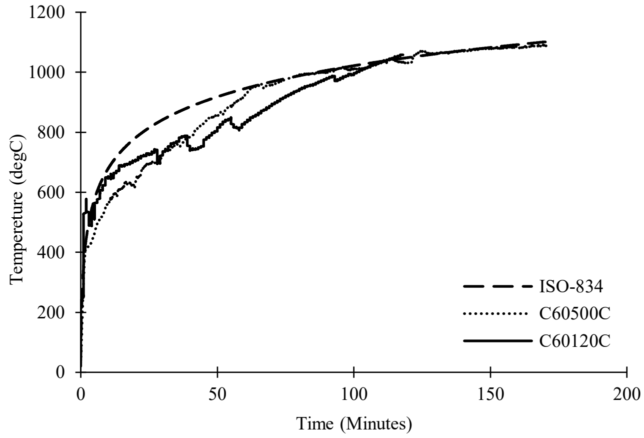

Figure 13. Furnace temperature profiles of HSC columns.

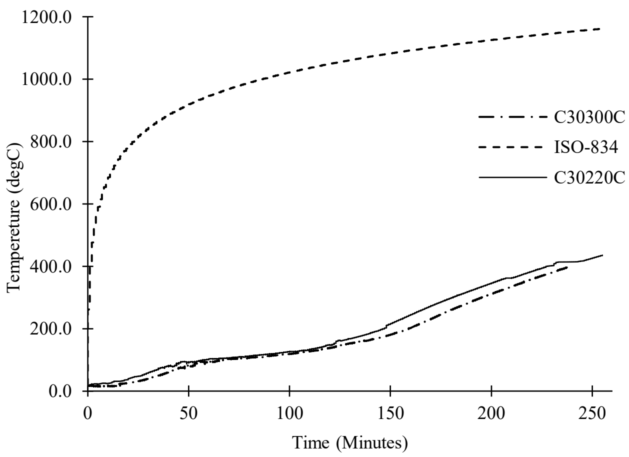

Figure 14. Internal thermocouple at the core concrete location of NSC Columns.

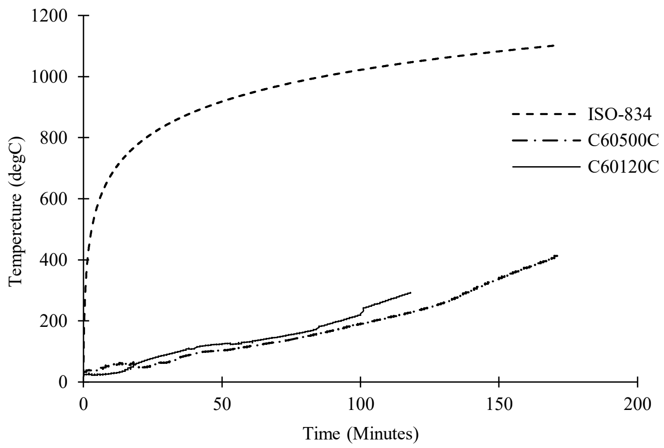

Figure 15. Internal thermocouple at the core concrete location of HSC Columns.

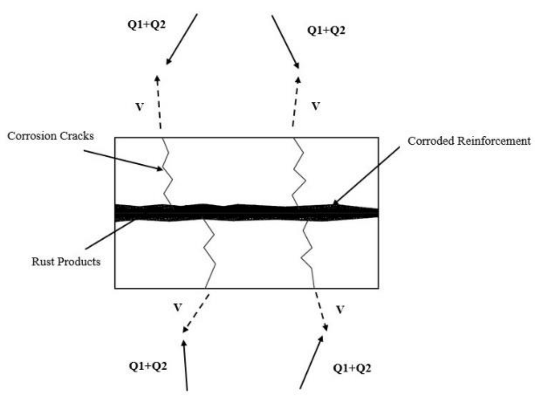

Here,

Q1= Heat flux going inside the concrete due to the convenient passage through cracks.

Q2= Heat flux going inside the concrete due to the higher thermal conductivity of the rust products.

V= Vapors responsible for the spalling evacuating due to the convenient passage through cracks.

Figure 16. Propagation of heat flux through cracks.

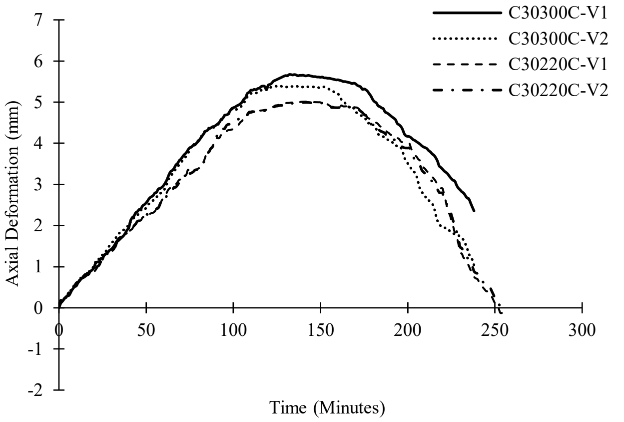

Figure 17. Measured axial deformation as the function of time of NSC columns.

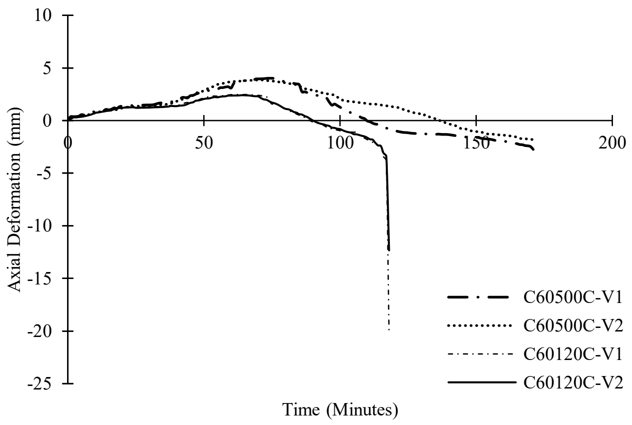

Figure 18. Measured axial deformation as the function of time of HSC columns.

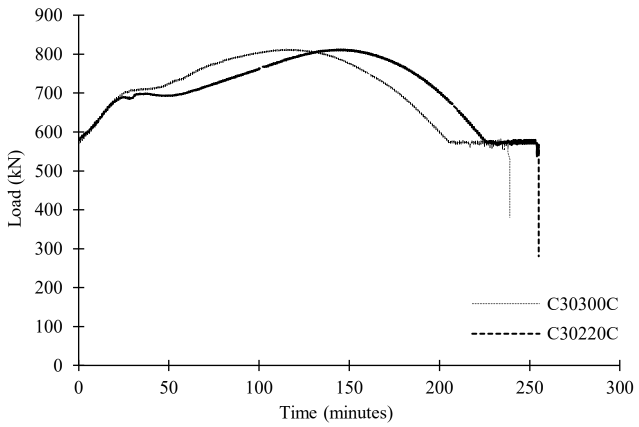

Figure 19. Load variations as the function of time of NSC columns.

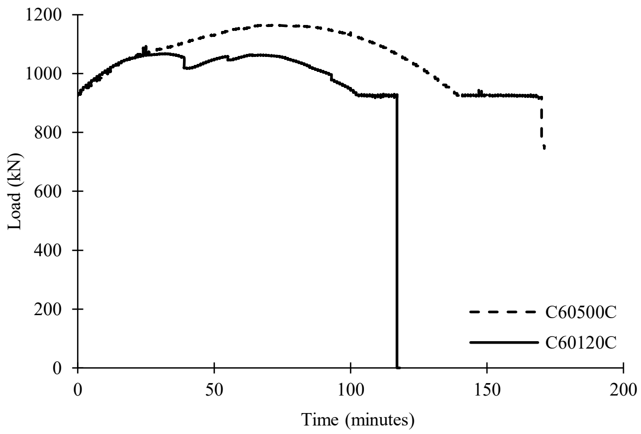

Figure 20. Load variations as the function of time of HSC columns.

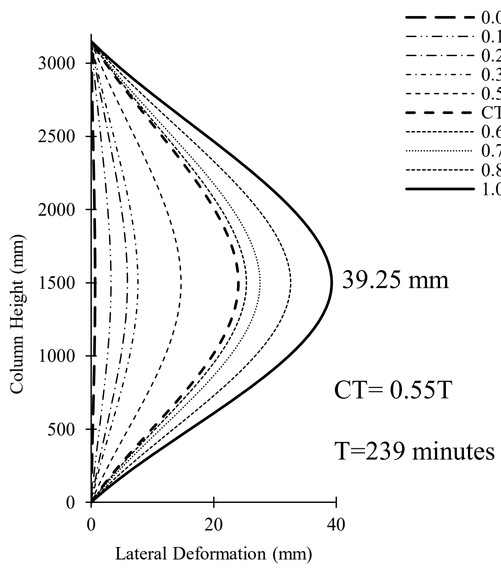

Figure 21. Lateral Deformation of C30300C.

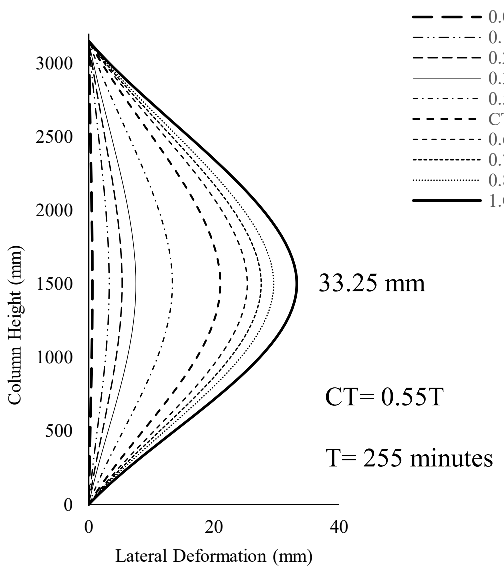

Figure 22. Lateral Deformation of C30220C.

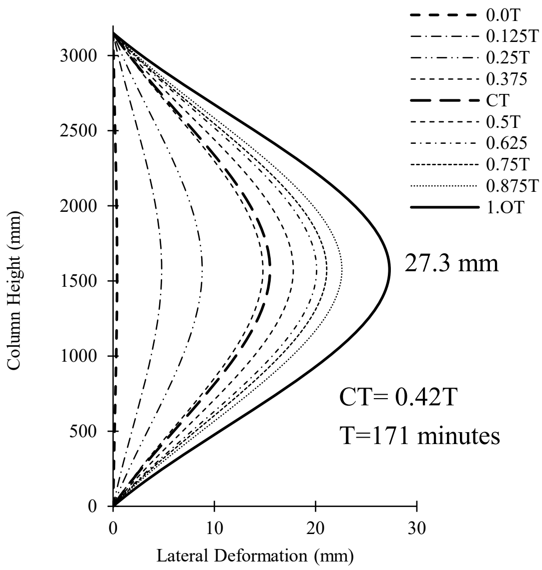

Figure 23. Lateral Deformation of C60500C**.**

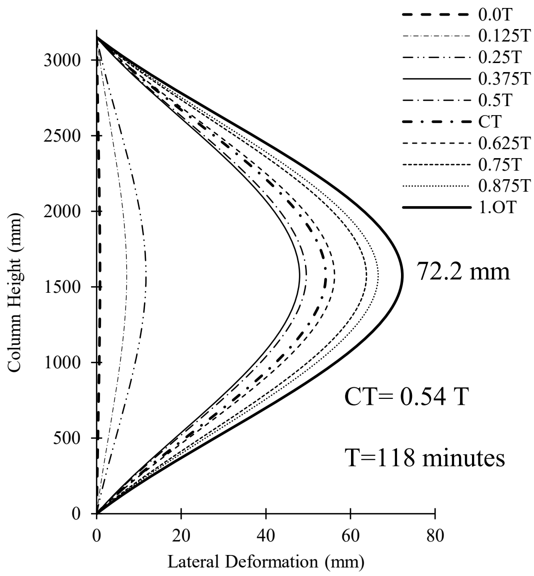

Figure 24. Lateral Deformation of C60120C.

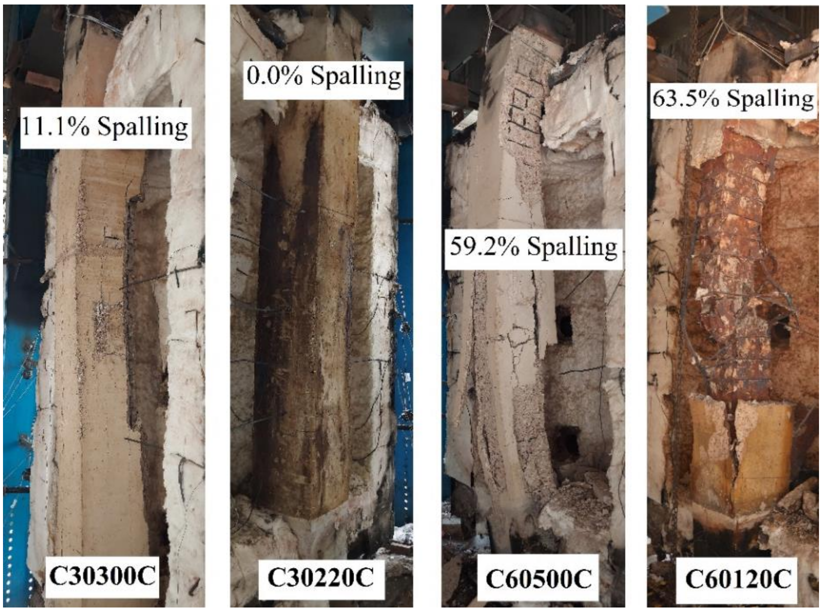

Figure 25. Failure of Column Specimens.

4 CONCLUSIONS

The main objective of this study was to examine the influence of corrosion on the structural fire performance of RC columns. The following conclusions may be drawn from this study:

- Corrosion of reinforcement affects the strength and stiffness properties of RC columns. At 12.29% degree of corrosion though, a slight enhancement in the fire resistance was observed in the NSC column. On the contrary, at 15.38% degree of corrosion, there was a significant loss in fire resistance in HSC columns.
- Due to the surface corrosion cracks and higher thermal conductivity of rust products, the heat flux easily penetrates in the core portion of the concrete section compared to its companion non-corroded specimen, which eventually increases the initial rise of temperatures in the rebars.
- Due to the earlier temperature rise in the corroded specimens' rebars, a comparable less axial expansion of the column was seen in the early stages of fire exposure.

- Corrosion cracks may be vital in easily evacuating the vapours from the RC elements. They can cause a significant reduction in the spalling, which in turn can even enhance fire performance.
- Spalling of concrete must play an important role in the lateral deformation characteristics of the column specimen in the event of fire exposure. As spalling was prevented by corrosion cracks in the NSC column, slightly lesser lateral deformation was observed compared to its companion non-corroded specimen.
- The corroded column specimen exhibits enormous lateral deformation response in the later stages of fire exposure after advancing to its respective Critical Time (CT).
- There are consequences of severe spalling of concrete over the load progression during the fire test.
- HSC corroded specimen undergoes drastic spalling during its fire exposure which eventually causes the earlier loss of strength and stiffness properties of concrete and rebar.

ACKNOWLEDGEMENT

The authors wish to thank the department of science and technology (DST), Government of India, for providing financial support for conducting this experimental investigation.

REFERENCES

[1] W. Zhang, X. Song, X. Gu, and S. Li, ‘Tensile and fatigue behavior of corroded rebars’, *Constr Build Mater*, vol. 34, pp. 409–417, Sep. 2012, doi: 10.1016/j.conbuildmat.2012.02.071.

[2] C. Fang, K. Lundgren, L. Chen, and C. Zhu, ‘Corrosion influence on bond in reinforced concrete’, *Cem Concr Res*, vol. 34, no. 11, pp. 2159–2167, Nov. 2004, doi: 10.1016/j.cemconres.2004.04.006.

[3] S. Coccia, S. Imperatore, and Z. Rinaldi, ‘Influence of corrosion on the bond strength of steel rebars in concrete’, *Materials and Structures/Materiaux et Constructions*, vol. 49, no. 1–2, pp. 537–551, Jan. 2016, doi: 10.1617/s11527-014-0518-x.

[4] A. S. Rajput and U. K. Sharma, ‘Corroded reinforced concrete columns under simulated seismic loading’, *Eng Struct*, vol. 171, pp. 453–463, Sep. 2018, doi: 10.1016/j.engstruct.2018.05.097.

[5] J. Xia, W.-L. Jin, and L.-Y. Li, ‘Performance of Corroded Reinforced Concrete Columns under the Action of Eccentric Loads’, *Journal of Materials in Civil Engineering*, vol. 28, no. 1, Jan. 2016, doi: 10.1061/(asce)mt.1943-5533.0001352.

[6] A. H. Shah and U. K. Sharma, ‘Fire resistance and spalling performance of confined concrete columns’, *Constr Build Mater*, vol. 156, pp. 161–174, Dec. 2017, doi: 10.1016/j.conbuildmat.2017.08.167.

[7] J.-M. Franssen and J.-C. Dotreppe, ‘Fire Tests and Calculation Methods for Circular Concrete Columns’, 2003.

[8] N. K. Raut, V. K. R. Kodur, and F. Asce, ‘Response of High-Strength Concrete Columns under Design Fire Exposure’, doi: 10.1061/ASCEST.1943-541X.0000265.

[9] S. H. Buch and U. K. Sharma, ‘Fire Resistance of Eccentrically Loaded Reinforced Concrete Columns’, *Fire Technol*, vol. 55, no. 5, pp. 1517–1552, Sep. 2019, doi: 10.1007/s10694-019-00823-x.

[10] ‘EN 1992-1-2: Eurocode 2: Design of concrete structures - Part 1-2: General rules - Structural fire design’, 1992.

[11] C. S. Standards Association of Australia. Committee BD-002, *Concrete structures : AS 3600-2009.*

[12] I. Standard, Hardened Concrete-Methods of Test Part 5 Non-Destructive Testing Section 2 Half-Cell Potentials of Uncoated Reinforcing Steel in Concrete’, 2021. [Online]. Available: www.standardsbis.in

[13] ‘Standard Test Method for Standard Test Method for Corrosion Potentials of Uncoated Reinforcing Steel in Corrosion Potentials of Uncoated Reinforcing Steel in Concrete Concrete 1 1’, doi: 10.1520/C0876-15.

[14] M. Takeda, T. Onishi, S. Nakakubo, and S. Fujimoto, ‘Physical properties of iron-oxide scales on Si-containing steels at high temperature’, *Mater Trans*, vol. 50, no. 9, pp. 2242–2246, Sep. 2009, doi: 10.2320/matertrans.M2009097.

THE COMPRESSIVE STRENGTH BEHAVIOUR OF ULTRA-HIGH PERFORMANCE CONCRETE (UHPC) REINFORCED WITH POLY-VINYL ALCOHOL FIBRES AT ELEVATED TEMPERATURES

Branna MacDougall[1], Mark Green[2], Salah Sahart[3], Hamzeh Hajilloo[4]

ABSTRACT

The high compressive and tensile strengths of ultra-high performance concrete (UHPC) result in performance advantages in structural applications, leading to thinner and lighter structures. One drawback to the use of UHPC is its potential for explosive spalling under elevated temperatures. Synthetic fibres, such as polypropylene (PP) and polyvinyl-alcohol (PVA), are commonly added to help mitigate explosive spalling. Most previous research efforts have focused on the residual strength of UHPC following exposure to elevated temperatures, with little focus on the performance of UHPC under simultaneous load and heat effects. This paper presents compressive strength results at steady-state temperatures (25, 300, 400, and 500°C), along with residual compressive strength tests (following exposure to 300, 400 and 500°C). The results show that strength gradually reduced with temperature increase for steady-state and residual conditions. At all temperatures, the residual strength was higher than the steady-state strength, indicating that the cooling phase causes some of the strength to be regained. At 25, 300, 400, and 500°C the steady-state compressive strength was found to be 189.7, 137.9, 134.3, and 113.3 MPa, respectively. At 300, 400, and 500°C, the residual compressive strength was found to be 161.2, 147.1, and 114.8 MPa, respectively.

1 INTRODUCTION

Ultra-High Performance Concrete (UHPC) has a minimum compressive strength of 120 MPa and tensile strength between 8 to 15 MPa [1]. UHPC has increased in use in the past two decades as an alternative to normal strength concrete [2]. The high compressive strength of UHPC is attributed to its unique mix design, which includes only a high quantity of fine aggregates, a high binder content, a low water-to-cement ratio, and high-range water-reducing admixtures. Fibres (steel, glass, or synthetic) are commonly added to increase ductility and tensile strength [3].

The fire performance of UHPC is of concern because the dense microstructure does not allow water vapour formed under elevated temperatures to dissipate; this results in increased tensile stresses, leading to explosive spalling when the tensile strength of UHPC is exceeded. Explosive spalling occurs with little to no warning, resulting in the rapid loss of cross-section. The loss of cross-section exposes deeper layers to fire, increasing the rate of heat propagation [4]. The addition of synthetic fibres, such as polypropylene (PP) fibres, can help mitigate explosive spalling [4 - 6]. Two theories as to how synthetic fibres mitigate explosive spalling are suggested in the literature. The first theory is that when PP fibres melt at approximately 165°C, they create vacant fibre channels, providing spaces for the pore water pressure to dissipate [7]. The second theory is that a difference in coefficients of thermal expansion (CTE) between the

[1] PhD Student, Queen's University,
e-mail: 17bnm2@queensu.ca, ORCID: https://orcid.org/0000-0003-3421-4229
[2] Professor, Queen's University
e-mail: greenm@queensu.ca, ORCID: https://orcid.org/ 0000-0002-6610-0325
[3] Assistant Professor, Purdue University Fort Wayne
e-mail: ssarhat@pfw.edu, ORCID: https://orcid.org/0000-0002-3011-7379
[4] Asssitant Professor, Carleton University, Canada
e-mail: hamzehhajiloo@cunet.carleton.ca, ORCID: https://orcid.org/0000-0002-5932-2640
https://doi.org/10.6084/m9.figshare.22177925

PP Fibres and the UHPC matrix causes the fibres and UHPC to expand at different rates under the same temperature, creating a network of interconnected cracks and thus a pathway for dissipation of pore pressure [5]. Polyvinyl-alcohol (PVA) fibres are another type of synthetic fibre, which have been shown to act similarly to PP fibres in their mechanism to reduce UHPC's propensity for explosive spalling [8].

A literature review has revealed that the majority of research has been focused on the residual fire performance of UHPC, and the mechanisms through which explosive spalling can be mitigated through the use of PP fibres. A comprehensive study on the effects of simultaneous loading and heating UHPC samples is lacking, which must be completed for a realistic fire performance assessment. The present study aims to address this gap in the literature, in assessing the fire performance of UHPC. The results of UHPC with 1% by volume of PVA fibres under steady-state and residual fire exposure are presented.

2 MATERIALS AND METHODS

2.1 UHPC Mixture Procedure and Components

The UHPC mix was a proprietary design provided by ceEntek and the mix design is shown in Table 1. The UHPC mix was prepared using an Imer360 Plus Mortarman mixer, which uses three paddles rotating through the mix. This allows for adequate mixing of low-slump materials, such as UHPC. The mixing procedure requires cement (i.e., UHPC pre-mix in Table 1) to first be added to the mixer. Once mixing began, the superplasticiser, previously diluted with potable water, was added. After two minutes of mixing, PVA fibres, with a diameter of 0.2 mm and a length of 12 mm, were dispersed over the course of four minutes. After 20 minutes of mixing, the slump was measured at 330 mm after 30 seconds of flow, indicating that proper workability had been achieved.

Table 1. Mix design for 1% by volume of PVA fibres

Components	Quantity (kg/m^3)
UHPC pre-mix	2239
PVA fibre	12
Superplasticiser	13.4
Potable water	206.4

2.2 Sample Preparation

In total, 27 cylinders (75 x 150 mm) were cast. The samples were left to cure in their forms for 48 hours, before being demoulded and submerged in water for seven days to accelerate the curing process [2]. Following water submersion, cylinders were left to air-dry for one week. Cylinders were then oven-dried at 105°C to reduce the propensity for UHPC to spall explosively [6]. Pre-drying minimizes the effect of vapour inside the pores of the UHPC microstructure, thereby reducing some of the potential tensile stresses that cause explosive spalling [9]. The cylinders were weighed every 24 hours during the oven-drying process until weight stabilization occurred; typically after five to six days. The cylinders were then left in room-temperature conditions until 28 days had passed or until the testing date.

2.3 Steady-State Conditions

Steady-state temperature tests were completed using the Instron SATEC testing machine fitted with a Eurotherm 2408 heating chamber, shown in Figure 1. Under steady-state conditions, cylinders were brought to a specific temperature, (300, 400 or 500°C). Following the maintenance of thermal equilibrium, cylinders were loaded in compression until failure. Samples were heated at a rate of 2°C/min. The heating rate was selected to be slow enough to reduce the risk of explosive spalling in the UHPC [10]. Once the cylinder reached the desired temperature, a soaking period of two hours commenced allowing for thermal equilibrium to be obtained. The soaking period was determined using Type-K thermocouples. A thermocouple was placed in a select number of samples and showed that an additional two hours were required from when the furnace reached the desired temperature for the cylinder to reach thermal equilibrium. Once thermal equilibrium was reached, a compressive load was applied at a rate of 0.25 MPa/s, as per ASTM C39, until failure occurred.

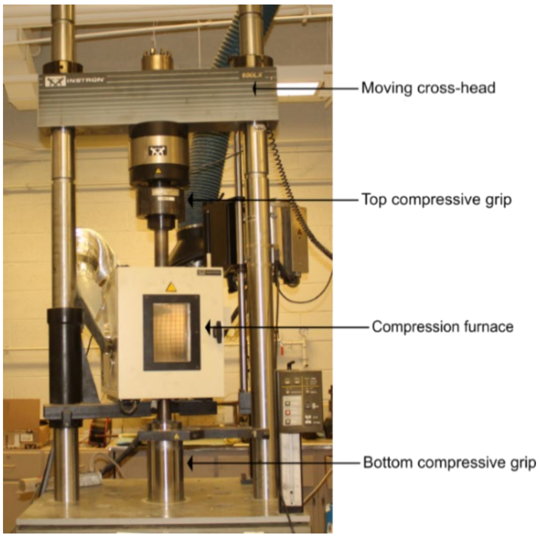

Figure 1. Instron SATEC testing machine

2.4 Residual Conditions

Residual temperature tests were completed using the Instron SATEC testing machine, the Eurotherm 2408 chamber, and the Forney Testing Machine. Cylinders were brought to a specific temperature (300, 400 or 500°C), without any load applied. Following the maintenance of thermal equilibrium, the heating chamber was turned off, and the cylinders were left to cool overnight to return to room temperature. The following day, cylinders were tested in compression, using the Forney Testing machine, until failure occurred. As with steady-state conditions, cylinders were heated at a rate of 2°C /min and were subjected to a soaking period of two hours to maintain thermal equilibrium Cylinders were loaded at a rate of 0.25 MPa/s in compression until failure occurred.

2.5 Scanning Electron Microscopic (SEM) Imaging

Scanning Electron Microscopic (SEM) images were taken of the failed compressive samples from both steady-state and residual testing, allowing for the determination of how increasing temperatures affect UHPC on a microscopic level. The images were taken under the high vacuum mode on an FEI Quanata 650 FEG Environmental SEM at Queen’s University. The microscope collects images using a back-scatter electron (BSE) detector in eight-bit greyscale. In the final images, heavier materials appear brighter, allowing the various materials in a UHPC sample to be differentiated. A fragment of approximately one millimetre in diameter was taken from a failed cylinder at each temperature level and testing condition.

3 RESULTS

3.1 Steady-State Compression Results

The experimental results from the steady-state compression tests are shown in Figure 2. Error bars are included to show the variability in results. Each bar is an average value of three cylinders tested under each steady-state temperature. The highest variability in compressive strengths occurs at 500°C while lower variability is shown in compressive strengths tested at 300 and 400°C. The standard deviation was determined with the minimum required number of samples; therefore no specific conclusions can be made as to why the compressive strength at 500°C had higher variability than those at 300 and 400°C. It is recommended that further tests be completed to obtain a better understanding of the variability of compressive strength at each temperature.

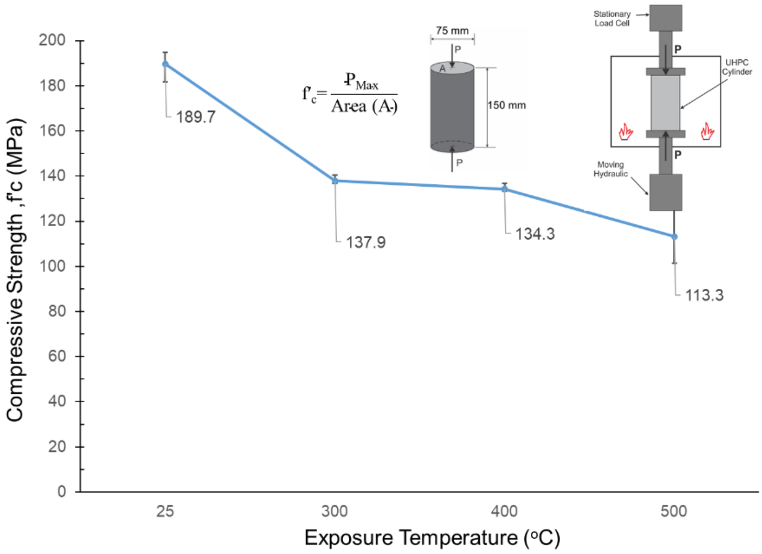

Figure 2. Average compressive strength under various steady-state conditions

Photographs for samples following exposure to 300, 400 and 500°C are shown in Figure 3. At all temperatures, the cylinders failed in a similar manner. Generally, part of the sample split into two larger cone-shaped pieces, while the remainder fragmented into numerous slivers. Visual inspection and measurements revealed that the average size of the fragments varied from approximately 5 to 10 mm. The failure occurred in a sudden manner, with no warning. The left images in Figure 3 show the extent of the fragmentation of the samples when the failure occurred. The right images in Figure 3 show a closer look at the microstructure of the cylinders following failure. At 300°C, the PVA fibres melted, leaving behind vacant black coloured channels. Small white spots were scattered throughout the interior of the failed cylinder, which did not exist prior to heating, indicating that a chemical alteration occurred due to the heat. Figure 3 shows that, at 400°C, the vacant fibre channels were darker in colour, indicating increased damage. Additionally, the bottom of the cylinder shows that the high temperatures may have caused the "burning" of the concrete (or likely the fibres), as brown spots were scattered throughout the base. A strong smell was observed when testing, which increased in intensity as the exposure temperature increased. The smell was attributed to the melting and charring of the PVA fibres. At 500°C the vacant fibre channels lightened in colour, becoming less visible. Following the failure, the concrete cylinders appeared "softer" than those exposed to lower temperature levels, with pieces of the cylinder easily crumbling when touched. This observation indicates that further damage occurred from 400 to 500°C, resulting in a weaker microstructure.

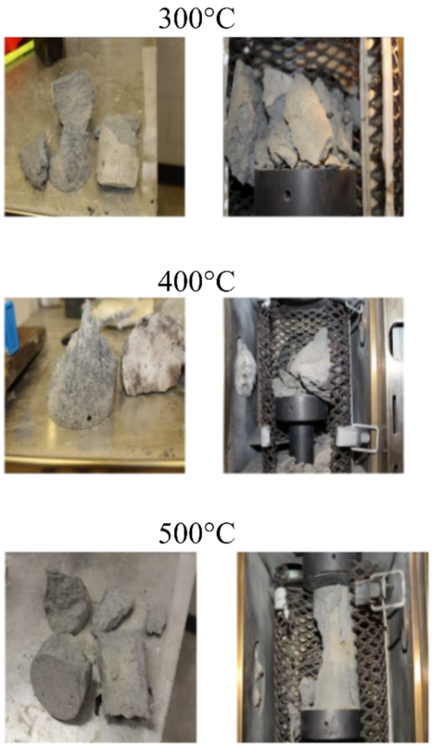

Figure 3. Failed samples under steady-state conditions

3.2 Residual Compression Results

Figure 4 displays the results for compressive strength under residual conditions. In residual tests, cylinders were heated to 300, 400 or 500°C, cooled overnight to room temperature, and tested the following morning in compression using the Forney Testing Machine. Samples exposed to 300°C had the highest average residual compressive strength, while samples exposed to 500°C had the lowest average residual compressive strength. The largest strength decrease occurred within the temperature range of 400 to 500°C. Error bars are used to display the variability in test results. Tests at 400°C had the highest variability, however, only three samples were tested at each temperature level, which is the minimum number to determine standard deviation. Similar to steady-state tests, it is recommended that more tests be completed to get an accurate picture of strength variability at each temperature. It should be noted that the residual compressive strength at each temperature was higher than the corresponding steady-state compressive strength. This indicates a mechanism by which UHPC gains back some of its strength in the cooling phase. This also indicates that residual results may not be a true representation of the compressive strength of UHPC under fire.

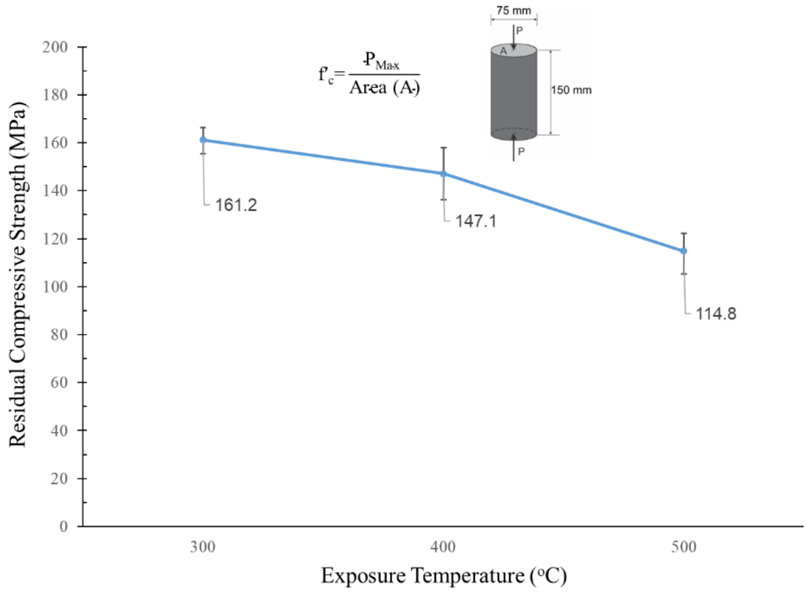

Figure 4. Average compressive strength under various residual conditions

Figure 5 shows photographs of the samples following testing under 300, 400 and 500°C residual conditions. The failure mechanisms for all residual temperature exposures were similar to those found under steady-state conditions. The cylinders generally failed into two main cone pieces, with the remainder of the sample ending up in multiple smaller fragments (typically 5 to 10 mm in size). At 300 and 400°C, the vacant PVA fibre channels were not as dark compared to steady-state conditions. Small white spots were observed throughout the interior of the samples at all temperature exposures. When failure occurred, concrete pieces were spread across a large area compared to the sample size. This can be attributed to the volatile nature of the samples when the failure occurred. The widespread affected area is also a result of melted PVA fibres under high temperatures, meaning that the fibres can no longer provide a “bridging effect”, which would aid in a ductile failure. A large amount of dust can be observed surrounding the cylinder. The failed samples easily crumbled into dust when touched, indicating that low structural integrity remained following failure.

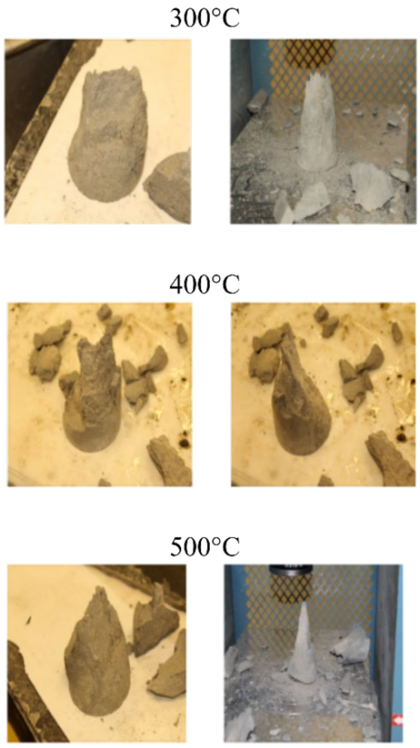

Figure 5. Failed samples under residual conditions

4 DISUCUSSION

4.1 Steady-State Compression

Figure 2 shows that with an increase in temperature, there is a decrease in compressive strength. The highest compressive strength of 189.7 MPa occurs at room temperature, while the lowest compressive strength of 113.3 MPa occurs at 500°C. Other than from room-temperature to 300°C, the largest decrease in compressive strength, 27.3%, occurs from 25 to 300°C. This is attributed to the range having the greatest difference between the lowest and highest temperature vales. Comparatively, from 300°C to 400°C there is a 2.6% reduction in strength, and from 400 to 500°C there is a 15.6% reduction in strength. This indicates that under fire exposure, the temperature range of concern should be 400 to 500°C, where strength decrease is the greatest and occurs at the fastest rate. The strength decrease from 300 to 400°C is comparatively small, meaning that the concern of strength loss in this temperature range is low from a fire safety standpoint. The considerable decrease in compressive strength at 500°C is attributed to the loss of bound water in the cement paste, which occurs between 400 and 500°C, as well as the dehydration of calcium hydroxide in the cement paste, which begins at approximately 500°C [11].

The temperature exposure did not affect the failure mechanism of the cylinders. The failure was consistent, with each cylinder breaking suddenly into two main cone pieces, while the remainder broke off into fragments that flew violently in the surrounding area. Before loading, no explosive spalling was observed in the heating process indicating that PVA fibres may have been effective in mitigating explosive spalling.

4.2 Residual Compression

Figure 4 shows that similar to steady-state conditions, residual compressive strength decreased with increased temperature. The highest residual compressive strength was 161.2 MPa, following exposure to 300°C. The lowest residual compressive strength was 114.8 MPa, following exposure to 500°C. The largest compressive strength decrease, 22%, occurred from 400 to 500°C. The compressive strength decrease from 300 to 400°C was comparatively small, at 9%. This follows a similar trend to steady-state tests, where the largest percent decrease was seen from 400 to 500°C. This further validates that 400 to 500°C is a critical temperature range for fire safety because it is where the greatest strength reduction occurs.

Under residual conditions, failure followed closely to what was observed under steady-state conditions. Cylinders broke into two main cone pieces, while the remainder scattered into small fragments in the surrounding area. The widespread scattering of the cylinder fragments can be attributed to the melting of the PVA fibres when exposed to elevated temperatures. When tested in compression after heating, the fibres had melted and could no longer provide a “bridging effect”, which keeps the cylinder intact under load, and results in a ductile failure mode at room temperature without any exposure to heat.

An important note is that, at all exposure temperatures, residual strength was higher than the steady-state strength at the same temperature. This finding is critical because much of the research thus far has been completed on the residual strength of UHPC as opposed to its performance at high temperatures. However, this testing shows that residual testing is not necessarily an accurate nor conservative representation of the strength of UHPC in fire because strength is regained in the cooling phase. The strength restoration following fire exposure is attributed to the rehydration of cement following dehydration at high temperatures [12].

4.3 SEM Results

SEM results provide a closer look at the failure mechanisms of the UHPC samples under various temperatures and loading conditions. The SEM results for steady-state conditions under 300, 400 and 500°C temperature exposure are shown in Figure 6. The results show a progressive degradation of the UHPC microstructure with increasing temperature. At 300°C, SEM images show that cracks have already formed through the vacant PVA fibre channels. This can be attributed to the difference in coefficients of thermal expansion (CTEs) of the fibres and UHPC microstructure. PVA fibres have a CTE of 10^{-4}/°C, while UHPC has a CTE of 16.9×10^{-6}/°C [11]. A difference in CTEs means that under the same temperature, the fibres and UHPC will expand at different rates, resulting in crack formation. The network of interconnected cracks is believed to prevent an explosive spalling failure during the heating. This theory has been postulated by previous research, which determined that the network of interconnected cracks allowed for excess pore pressure under elevated temperatures to dissipate, thus mitigating the propensity for explosive spalling [5, 13].

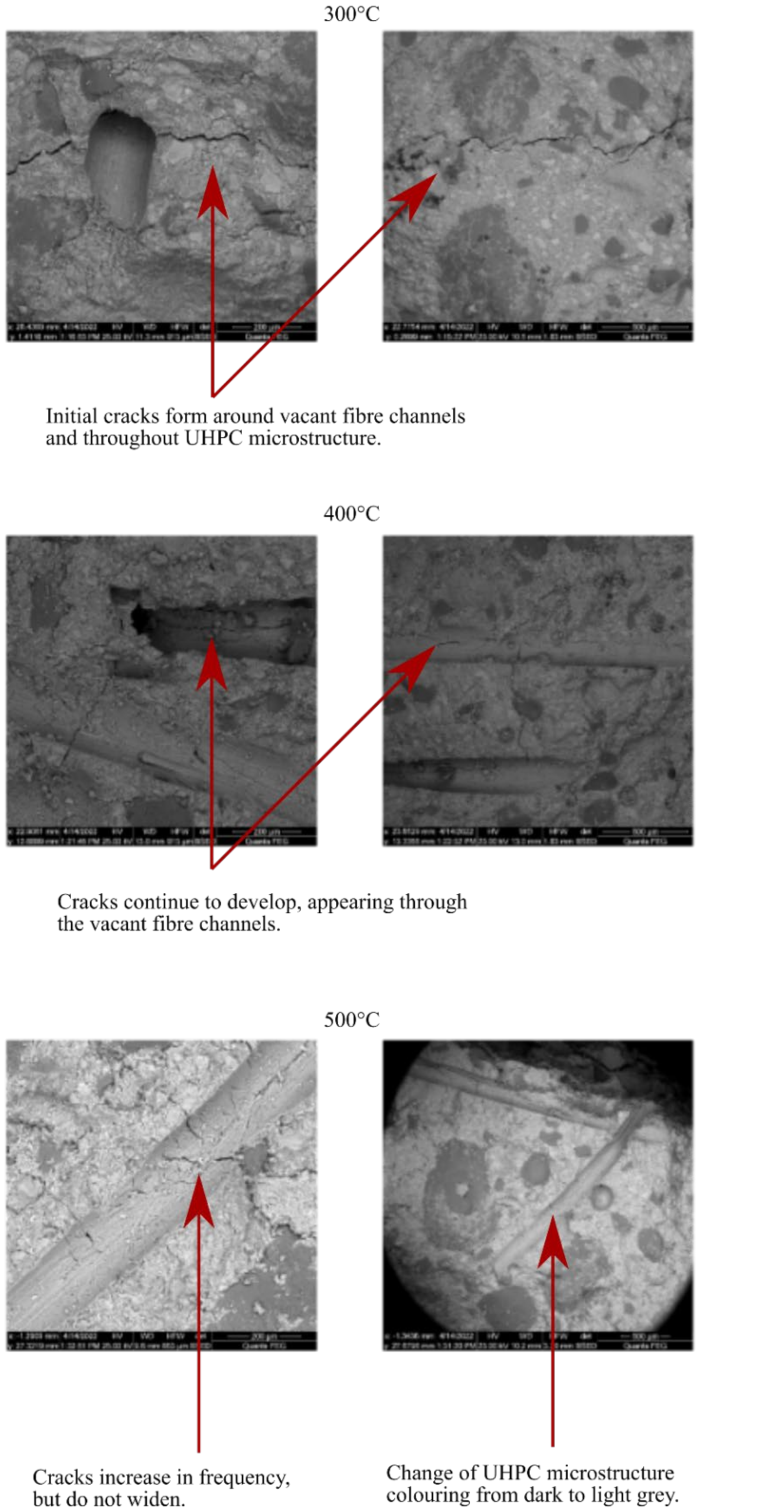

Figure 6: SEM imaging results following exposure to steady-state conditions

The most noticeable change is at 500°C, where the microstructure changes colour from dark to light grey. Cracks surrounding the vacant fibre channels do not appear to widen with temperature increase, however, they do become more frequent, indicating increased damage. The colour change and cracking damage at 500°C provide a visual explanation of the significant compressive strength reduction that occurs at 500°C.

SEM results under residual conditions follow the trend observed under steady-state conditions. At 300°C, a singular deep crack formed through the vacant fibre channel. SEM images at 400°C are similar to those at 300°C, albeit with an increased number of cracks. At 500°C the microstructure changes colour from dark to light grey. Cracks do not deepen or grow in length, however, cracks increase in frequency, indicative of increased damage.

The SEM results for residual conditions under 300, 400 and 500°C temperature exposure, are shown in Figure 7. The results show more visible and deeper cracks than those at steady-state. The increased microstructural damage can be attributed to the additional cooling phase in residual testing. Large temperature differentials under residual conditions induce additional stresses on the UHPC microstructure, causing wider cracks to form. Intuitively, an increased amount of cracking damage should mean a decreased compressive strength. However, as discussed, residual compressive strength is higher than the steady-state compressive strength at all temperatures. It is unclear why this occurs, however, one hypothesis is that the strength increase occurs due to an increase in Van der Waals forces between the gel particles due to water removal and the resulting shrinkage [14].

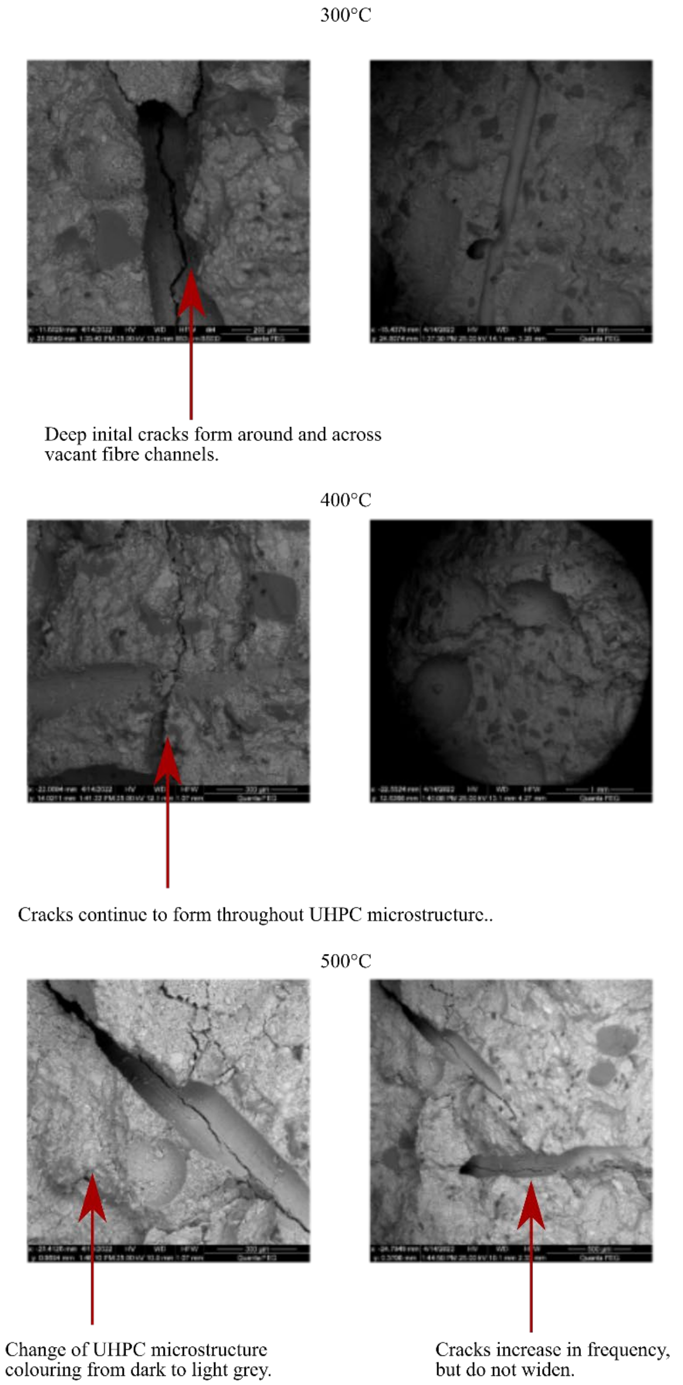

Figure 7: SEM imaging results following exposure to residual conditions

5 CONCLUSIONS

A study was completed on 75 x 150 mm UHPC cylinders reinforced with 1% by volume of PVA fibres to assess fire performance under steady-state and residual conditions. In addition to room-temperature, three temperatures of 300, 400, and 500°C were selected to test the samples under steady-state and residual conditions. After failure, SEM imaging analysis was performed on sample fragments. The following conclusions can be made from the test results:

1) With increasing temperature under steady-state conditions, the compressive strength decreases. With the exception of room-temperature to 300°C, the largest decrease in the compressive strength

was 15.6% when the temperature was increased from 400 to 500°C. Under fire exposure, the temperature range of concern should be 400 to 500°C, where strength decrease is the greatest and occurs at the fastest rate.

2) With increasing temperature under residual conditions, the compressive strength decreases. The largest decrease in compressive strength was 22% when the temperature was increased from 400 to 500°C, further identifying this as the critical temperature range under fire exposure.
3) The residual compressive strength is higher than the steady-state strength at all temperature levels, indicating that strength is regained in the cooling phase.
4) SEM images reveal that cracks occur across and in-between vacant fibre channels under elevated temperatures. No spalling occurred which shows an improved behaviour of UHPC at high temperatures. The interconnected network of cracks is one possible mechanism through which explosive spalling is dissipated. Additionally, the cracks appeared deeper and wider in residual samples, attributed to the additional cooling phase.

ACKNOWLEDGMENTS

The authors would like to thank the Natural Research Council of Canada (NRC), Canadian Precast/Prestressed Concrete Institute (CPCI), the Bert Wasmund Foundation, and the Queen's University Civil Engineering Department for financial support, and ceEntek for materials and advice on mix designs.

REFERENCES

1. Banerji, S. & Kodur, V., Effect of temperature on mechanical properties of ultra-high performance concrete, Fire and Materials, Vol. 46, 2022, pp. 287-301.
2. Rajamane, N.P. & Ambily, P.S. Fly ash as a sand replacement material in concrete – A study, Indian Concrete Journal, Vol. 87, 2013, pp. 1-7.
3. Burke, B., Residual Strength of Ultra-High Performance Concrete After Exposure to Elevated Temperatures, Master's Thesis, 2011, 44.
4. Banerji, S., Kodur, V., & Solhmirzaei, R., Experimental behavior of ultra high performance fiber reinforced concrete beams under fire conditions, Engineering Structures, Vol. 208, 2020.
5. Zhang, D., Dasari A., & Tan K.H., On the mechanism of prevention of explosive spalling in ultra-high performance concrete with polymer fibres, Vol. 113, 2018, pp. 169-177.
6. Kodur, V., Banerji S., & Solhmirzaei, R., Effect of temperature on thermal properties of ultrahigh performance concrete, Journal of Materials in Civil Engineering, 2020, Vol. 32.
7. Heinz, D., Dehn, F., and Urbonas, L. Fire resistance of ultra high performance concrete (UHPC) – Testing of laboratory samples and columns under load, International Symposium on Ultra High Performance Concrete, 2004, pp. 703-716.
8. Ozawa, M. & Morimoto, H. Effects of various fibres on high-temperature spalling in high-performance concrete, Concrete and Building Materials, Vol. 71, 2014, pp. 83-92.
9. Sciarretta, F., Fava, S., Francini, M., Ponticelli, L., Caciolai, M., Briseghella, B., & Nuti, C., Ultra-High performance concrete (UHPC) with polypropylene (Pp) and steel Fibres: Investigation on the high temperature behaviour, Construction and Building Materials, Vol. 304, 2021.
10. Yang, J., Peng, G.-F., Zhao, J., and Shui, G.-S., On the explosive spalling behavior of ultra-high performance concrete with and without coarse aggregate exposed to high temperature, Construction and Building Material, Vol. 226, 2019, pp. 932-944.
11. Hussein, H., Walsh, L., Saragand, S., & Steinberg, E., Effect of Extreme Temperatures on the Coefficient of Thermal Expansion for Ultra-High Performance Concrete, The First International Interactive Symposium on Ultra High Performance Concrete, 2016.
12. Pasztetnik, M. & Wroblewski, R., A Literature Review of Concrete Ability to Sustain Strength after Fire Exposure Based on the Heat Accumulation Factor, Materials, Vol. 14, 2021, pp. 1-35.
13. Zhang, D., Hai Tan, K., Dasari, A., & Weng, Y., Effect of natural fibres on thermal spalling resistance of ultra-high performance concrete, Vol. 109, 2020.

14. Wang, W.C., Compressive strength and thermal conductivity of concrete with nanoclay under various high-temperatures, Vol. 147, 2017, pp. 305-311.

SiF 2022– The 12th International Conference on Structures in Fire
The Hong Kong Polytechnic University, Nov 30 - Dec 2, 2022

SIMPLIFIED APPROACH FOR THE EVALUATION OF THE BEARING CAPACITY OF DEEP R/C TUNNELS EXPOSED TO FIRE

Francesco Lo Monte[1], Patrick Bamonte [2]

ABSTRACT

The structural performance of R/C tunnels when exposed to fire can represent a critical aspect in the design phase, due to some specific issues concerning this kind of infrastructures such as (a) the geometry of the fire compartment (favouring the development of severe fire scenarios) and (b) the inherent structural redundancy (due to the almost axisymmetry and to the presence of the surrounding soil). Both aspects foster the development of sizable indirect actions which can definitely modify the initial state of stress in the lining. It follows the need for a reliable evaluation of the fire performance of tunnels exposed to high temperature, considering the decay of the material properties due to the rise of the temperature, while taking into account the evolution of the internal actions due to the restrained thermal dilation. This task often entails the implementation of complex thermo-mechanical non-linear analyses, which can be properly implemented via advanced finite elements codes capable of multi-physics simulations (as for example Abaqus or Safir). In this regard, in the present study, a simplified approach is described for the non-linear analysis of deep R/C tunnels exposed to fire, based on the main assumption of (I) plane section and (II) axysimmetrically loaded lining. These assumptions allow to reduce the problem into a sectional analysis which can be even implemented in common worksheets. In the paper, the overall method is described, showing sensitivity analyses regarding some parameters involved in the assessment of the structural performance of tunnels exposed to fire.

Keywords: R/C tunnel, fiber-reinforced concrete, segmental lining, simplified approach, non-linear analysis, indirect actions.

1 INTRODUCTION

1.1 Tunnels exposed to fire

The design of tunnels is always critical due to the interaction of different aspects, such as structural and soil layouts, and due to the relevance of such strategic infrastructures which represents essential routes of communication in national and international networks.

Furthermore, it should be highlight as fire in general is a very demanding condition for tunnels, due to some specific issues. First of all, the geometry of the compartment allows the development of severe fire scenarios with very high temperatures lasting for long time (even higher than 1000° [1]). Secondly, the inherent structural redundancy, due to the almost axisymmetry and to the presence of the surrounding soil, and the compression-driven stress state bring in sizable indirect actions which can definitely modify the initial state of stress in the lining [2]. Finally, the severe compression state which usually characterizes the lining already at ambient temperature and, even more during the fire scenario, represents the typical situation fostering spalling phenomenon (this requiring the proper definition of the actual mix design to be used, as for example including polypropylene fibres) [3,4].

Very well-known fire accidents of the past, such as the Channel Tunnel fire in 1996 and the Mont-Blanc Tunnel fire in 1999, strongly increased the common awareness in the community, with a concrete impact

---

[1] Department of Civil and Environmental Enginnering, Politecnico di Milano (Italu)
e-mail: francesco.lo@polimi.it, ORCID: https://orcid.org/0000-0003-4397-6591
[2] Department of Civil and Environmental Enginnering, Politecnico di Milano (Italu)
e-mail: patrick.bamonte @polimi.it, ORCID: https://orcid.org/0000-0002-4967-1089
https://doi.org/10.6084/m9.figshare.22177931

in Standards which in the last decades have become more and more sensitive to this topic.

For the above-mentioned accidents, it is also important to underline the social impacts connected to traffic disruption. For the Channel Tunnel ("Chunnel") fire, the total financial cost (considering the revenue loss and the negative social impact connected to traffic disruption) was about 250 M€ [5] and about four times higher in the case of the Mont-Blanc Tunnel [6].

It follows the need for a reliable evaluation of the fire performance of tunnels exposed to high temperature, considering the decay of the material properties due to the rise of the temperature, while taking into account the evolution of the internal actions due to the restrained thermal dilation. This task generally entails the implementation of analyses which consider the diffusion of heat in the structural elements, the variation of elastic modulus, strength and thermal strain in both concrete and steel rebars (if any), the interaction of the lining with the surrounding soil, and, possibly, the implementation of non-linear mechanical response of the materials. This often requires the need for advanced finite elements code which can perform multi-physics simulations (as for example Abaqus or Safir) [2]

It is worth noting as linear elastic analyses can be also implemented, which however must consider the variation of the elastic modulus of concrete with temperature, in analogy to what usually done at the ULS, but far higher (and too severe) indirect actions are thus obtained, consequently affecting the final design of the tunnel.

1.2 Thermal stresses and indirect actions

The typical temperature and stresses distribution in a concrete slabs exposed to fire on one side is shown in Figure 1. Focusing on thermal stresses, represented by the green line, it is well-known as the dilation of the hottest layer is restrained by the inner cold core of the slab, this introducing compression next to the exposed surface and tension in the inner part, so to guarantee translational equilibrium. Finally, compression rises in the cold side to guarantee rotational equilibrium. Such distribution of stresses brings in zero axial force and bending moment and it is caused by the internal restraint of the section which must maintain its planarity. From the kinematic point of view, such slab is free of undergoing sagging and to dilate axially.

In case of a tunnel lining, however, sagging is not allowed due to the axysimmetry of the problem, which makes every part of the lining assimilable to a clamped-clamped beam. This brings in the bending moment M, as sketched in Figure 1, which reduces or even deletes any sagging introduced by thermal gradient. Such bending moment, leading tension at the cold side and further compression at the hot layer, is the typical flexural action rising during a fire in the case of a tunnel lining.

In addition to sagging, a slab free to move can also dilate due to thermal elongation. On the opposite, in the case of a tunnel lining, sectional elongation would translate to a circumferential elongation of the lining and thus, to an increase of the diameter of the tunnel. This, obviously, finds the opposition of the surrounding soil which reacts increasing the pressure in the lining and consequently increasing the compression N. While bending moment is caused by the flexural stiffness of the lining and by the axysimmetry of the problem, axial force is driven by the stiffness of the soil.

In conclusion, in the case of a tunnel lining, two levels of thermal induced stress can be observed: (1) thermal (self-equilibrated) stresses induced by the internal constrain of plane section and (2) bending moment due to the axisymmetry restraining the thermal sagging and the axial compression induced by the partial restrain of the surround soil to the dilation of the lining.

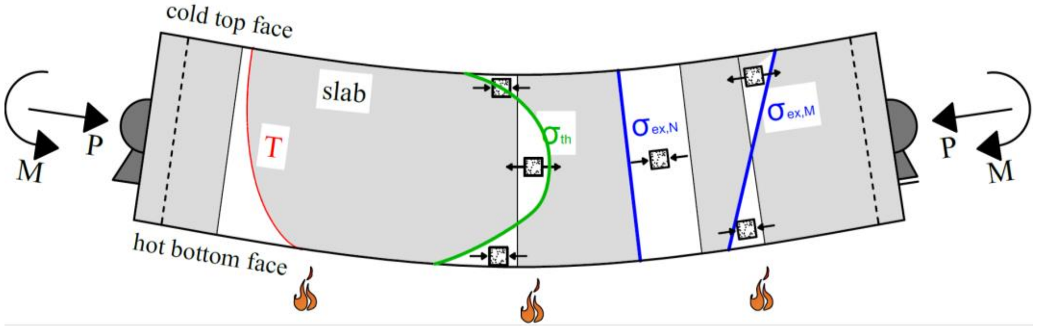

Figure 1. Slab heated at the bottom face: profiles of temperature, thermal stress and load-induced stress.

2 SECTIONAL KINEMATICS OF STRUCTURAL MEMBERS EXPOSED TO FIRE

Studying the section of a slab (or of a tunnel lining) exposed to fire, the assumption of plane section can be maintained (as also currently performed at ULS), thus making the total strain profile describable via a linear equation depending on the strain at the geometrical barycentre ε_0 and on the sectional curvature χ, as $\varepsilon_{tot}(y,t) = \varepsilon_0(t) + \chi \cdot y$, assuming compression positive (and, consequently, shortening positive) and the reference system reported in Figure 2.

The mechanical strain $\varepsilon(y,t)$ can be thus expressed as difference between total strain and thermal strain $\varepsilon_{th}(y,t)$:

$$\varepsilon(y,t) = \varepsilon_{tot}(y,t) - \varepsilon_{th}(y,t) = \varepsilon_0(t) + \chi \cdot y - \varepsilon_{th}(y,t)$$

According to a secant approach, in which any stress can be expressed as the product of mechanical strain and an effective secant modulus $E = \overline{\sigma}/\overline{\varepsilon}$, axial force and bending moment can be calculated via stress integration in the section:

$$N = \int \sigma dA = \int E(\varepsilon_0 + \chi y - \varepsilon_{th})dA = \varepsilon_0 \int EdA + \chi \int EydA - \int E\varepsilon_{th}dA = \varepsilon_0\widetilde{EA} + \chi\widetilde{ES} - \varepsilon_{th,0}\widetilde{EA} = (\varepsilon_0 - \varepsilon_{th,0})\widetilde{EA} + \chi\widetilde{ES}$$

$$M = \int \sigma ydA = \int E(\varepsilon_0 + \chi y - \varepsilon_{th})ydA = \varepsilon_0 \int EydA + \chi \int Ey^2dA - \int E\frac{\varepsilon_{th}}{y}y^2dA = \varepsilon_0\widetilde{ES} + \chi\widetilde{EI} - \chi_{th}\widetilde{EI} = \varepsilon_0\widetilde{ES} + (\chi - \chi_{th})\widetilde{EI}$$

where:

$$\widetilde{EA} = \int EdA \quad \left(= E\int dA = EA \text{ if E does not depend on the temperature}\right)$$

$$\widetilde{ES} = \int EydA \quad \left(= E\int ydA = 0 \text{ if E does not depend on the temperature}\right)$$

$$\widetilde{EI} = \int Ey^2dA \quad \left(= E\int y^2dA = EI \text{ if E does not depend on the temperature}\right)$$

$$\varepsilon_{th,0} = \int E\varepsilon_{th}dA/\widetilde{EA} \quad \left(= E\int \varepsilon_{th}dA/EA = \int \varepsilon_{th}dA/A = \varepsilon_{th,avg} \text{ if E does not depend on the temperature}\right)$$

$$\chi_{th} = \int E\frac{\varepsilon_{th}}{y}y^2dA/\widetilde{EI} \quad \left(= E\int \frac{\varepsilon_{th}}{y}y^2dA/EI = \int \frac{\varepsilon_{th}}{y}y^2dA/I = \chi_{th,avg} \text{ if E does not depend on the temperature}\right)$$

It is interesting to observe as, if the secant modulus E was constant with the temperature, the problem reduces to:

$$N = (\varepsilon_0 - \varepsilon_{th,0})EA$$
$$M = (\chi - \chi_{th})EI$$

where the thermal strain can be expressed in the linearized form $\varepsilon_{th} = \varepsilon_{th,0} + \chi_{th} \cdot y$ with:

$$\int \varepsilon_{th}dA = \int (\varepsilon_{th,0} + \chi_{th}y)dA = \varepsilon_{th,0}\int dA + \chi_{th}\int ydA = \varepsilon_{th,0}A \qquad \Rightarrow \varepsilon_{th,0} = \int \varepsilon_{th}dA/A$$

$$\int \varepsilon_{th}ydA = \int (\varepsilon_{th,0} + \chi_{th}y)ydA = \varepsilon_{th,0}\int ydA + \chi_{th}\int y^2dA = \chi_{th}I \qquad \Rightarrow \chi_{th} = \int \frac{\varepsilon_{th}}{y}y^2dA/I$$

This means that in the (just hypothetic) case of modulus E independent from the temperature, the slab kinematics would not be influenced by the effective distribution of thermal strain, but just by the average thermal elongation $\varepsilon_{th,0}$, and the equivalent thermal curvature χ_{th}.

Furthermore, the following relation can be considered:

$$\frac{\chi_{th}}{\varepsilon_{th,0}} = \frac{\int E\varepsilon_{th}ydA}{\int E\varepsilon_{th}dA}\frac{\widetilde{EA}}{\widetilde{EI}} = e_{th,G}\frac{\widetilde{EA}}{\widetilde{EI}}$$

where it has been defined $e_{th,G} = \int E\varepsilon_{th}ydA/\int E\varepsilon_{th}dA$, namely the distance between the centre of application of $\varepsilon_{th,0}$ and the geometrical barycentre of the section (y = 0).

The equilibrium equation can thus be also written as follows:

$$\begin{cases} N = (\varepsilon_0 - \varepsilon_{th,0})\widetilde{EA} + \chi\widetilde{ES} \\ M = \varepsilon_0\widetilde{ES} + \chi\widetilde{EI} - \varepsilon_{th,0}\widetilde{EA}e_{th,G} \end{cases} \Rightarrow \begin{cases} N = (\varepsilon_0 + \chi e_{k,G} - \varepsilon_{th,0})\widetilde{EA} \\ M = (\varepsilon_0 e_{k,G} - \varepsilon_{th,0}e_{th,G})\widetilde{EA} + \chi\widetilde{EI} \end{cases}$$

In the equation, it has been also introduced the term $e_{k,G} = \widetilde{ES}/\widetilde{EA}$ which represents the distance of the stiffness barycentre with respect to the geometrical barycentre of the section, and it varies during time due to the degradation of the hot layers of the section.

The generalized forces highlighted in the equations are sketched in Figure 2, where it can be noticed the presence of two axial forces, the first one, $-\varepsilon_{th,0}\widetilde{EA}$, applied at centre of application of $\varepsilon_{th,0}$, th_G, and linked to the perfectly-restrained thermal expansion, and the second, $(\varepsilon_0 + \chi e_{k,G})\widetilde{EA}$, applied at barycentre of stiffness, k_G, related to the "de-compression" allowed by the free dilation of the slab.

It is finally of interest, to analyse the case in which the total curvature in constantly zero, as it occurs in a circular ring exposed to fire at the inner face, because of the internal constraint of axysimmetry.

In such case it yields:

$$\begin{cases} N = (\varepsilon_0 - \varepsilon_{th,0})\widetilde{EA} \\ M = \varepsilon_0\widetilde{ES} - \varepsilon_{th,0}\widetilde{EA}e_{th,G} \end{cases} \Rightarrow \begin{cases} \varepsilon_0 = N/\widetilde{EA} + \varepsilon_{th,0} \\ M = (N + \varepsilon_{th,0}\widetilde{EA})e_{k,G} - \varepsilon_{th,0}\widetilde{EA}e_{th,G} \end{cases} \Rightarrow \begin{cases} \varepsilon_0 = N/\widetilde{EA} + \varepsilon_{th,0} \\ M = Ne_{k,G} - \varepsilon_{th,0}\widetilde{EA}(e_{th,G} - e_{k,G}) \end{cases}$$

Let us now consider the two extreme situations, namely slab totally restrained to dilate (hence, $\varepsilon_0 = 0$) and slab free to dilate (hence, N = 0):

$$\varepsilon_0 = 0 \Rightarrow \begin{cases} N = -\varepsilon_{th,0}\widetilde{EA} = -\int E\varepsilon_{th}dA \\ M = -\chi_{th}\widetilde{EI} = -\varepsilon_{th,0}\widetilde{EA}e_{th,G} \end{cases} \qquad N = 0 \Rightarrow \begin{cases} \varepsilon_0 = \varepsilon_{th,0} \\ M = -\varepsilon_{th,0}\widetilde{EA}(e_{th,G} - e_{k,G}) \end{cases}$$

It can be noticed as the first situation ($\varepsilon_0 = 0$) leads to the development of compression during the exposure due to the restrained thermal dilation of the section, while the second situation (N=0) is characterized by nil axial force and higher bending moment (with respect to the case $\varepsilon_0 = 0$), since the "de-compression" force $\varepsilon_0\widetilde{EA}$ applied at a distance e_G with respect to the geometrical barycentre, increases the applied moment (pay attention that, being ε_0 negative since it is an expansion, the red arrow in Figure 2 has the opposite sign).

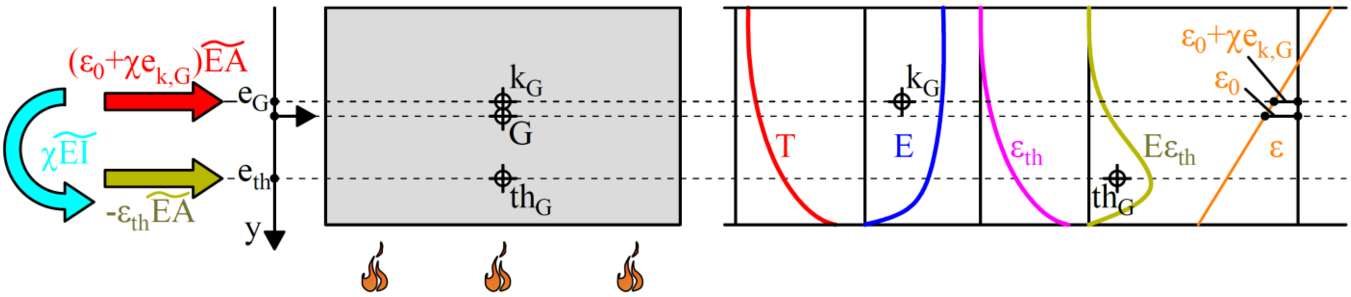

Figure 2. Temperature, T, modulus E, thermal strain ε_{th} and total strain ε profiles in a slab heated at the bottom face and resultant of axial force and bending moment. (G, k_G, th_G, = centre of gross section, stiffness and thermal stress, respectively)

3 SIMPLIFIED SECTIONAL APPROACH FOR TUNNEL LINING EXPOSED TO FIRE

As abovementioned, a simplified approach is herein described for the non-linear analysis of deep tunnels exposed to fire, based on the main assumption of plane section and axysimmetrically loaded lining.

The assumption of axysimmetry is reasonably kept for deep tunnels when the ratio between vertical and horizontal pressure is close to the unit value. However, it is worth noting that the state of bending and compression induced by fire is generally dominating with respect to the initial stress state of the lining, this smoothing down the effects related to the initial lack of axisymmetry.

The assumption of axysimmetry makes it possible to describe the behaviour of the lining via a sectional approach, in which the plane section assumption is kept. Hence, once known the temperature profile along the lining depth at any fire duration, $\varepsilon_{th}(z,t)$ (based on simple thermal analyses or via tabulated data), is thus possible to calculate the mechanical strain profile as above described (namely, $\varepsilon_m(y,t) = \varepsilon_{tot}(y,t) - \varepsilon_{th}(y,t) = \varepsilon_0(t) + \chi \cdot y - \varepsilon_{th}(y,t)$).

The mechanical stress $\sigma(y,t)$ can be then evaluated as a function of ε_0 and χ by assuming a given (non-linear) stress-strain law, as the one provided in EC2 [7], which also takes into account transient thermal strain. The two unknowns ε_0 and χ must be calculated by enforcing the equilibrium in the section in terms of axial force and bending moment.

In this regard, it is worth noting that ε_0 is the relative shortening/elongation of the sectional centroid, namely the relative shortening/elongation of the ring circumference, hence the relative variation of the ring radius. This makes easy the evaluation of the soil pressure around the lining due to the variation of its diameter (triggered by thermal expansion) by multiplying the radial displacement, $\delta_r = \varepsilon_0 \cdot R$ (with R = radius of the tunnel lining), and the elastic constant of the soil k_{soil}:

$p_{th}(t) = \varepsilon_0 \cdot R \cdot k_{soil}$

The elastic constant of the soil k_{soil} can be calibrated on the basis of the convergence law of the soil-tunnel system. As reported in Figure 3, a tangent or a secant approach can be used for the expected range of variation of the displacement $\delta_r = \varepsilon_0 \cdot R$. An iterative procedure can be adopted in this case, by checking the value of δ_r obtained by the simulation and the implemented value of k_{soil}.

The over-pressure $p_{th}(t)$ is a function of the fire duration and must be added to the initial soil pressure, thus varying the initial state of stress in the lining:

$N(t) = N_{20} + p_{th}(t) \cdot b \cdot R$

where N_{20} is the sectional axial force at time 0 and b is the tunnel ring width.

At time 0, axial force and bending moment (N_{20} and M_{20}, respectively) are both known, thus allowing the evaluation of ε_0 and χ via the following system of equations:

$N_{ext} = N_{20} = N_{int} = \int \sigma(y,t)\, dA$

$M_{ext} = M_{20} = M_{int} = \int \sigma(y,t) \cdot y\, dA$

In the presented simplified approach, χ is assumed to remain constant during fire, this being a conservative choice since no structural redistribution of internal forces is allowed during the fire development.

On the other hand, ε_0 is a function of fire duration and can be calculated by imposing the equilibrium in terms of axial force for any following time step:

$N_{ext}(t) = N_{20} + p_{th}(t) \cdot b \cdot R = N_{int} = \int \sigma(z,t)\, dA$

This allows to follow the evolution of ε_0 and N_{ext} (t) due to the thermal dilation of the hot layer of the lining. Finally, the acting bending moment caused by the partially restrained thermal dilation can be calculated via sectional stress-integration.

Since the relationship σ-ε_m already takes into account the actual behaviour of concrete, taking into consideration the decay of stiffness and strength, the non-linear analysis does not require any strength check, since collapse occurs just when the analysis does not converge, namely when at a given fire duration, no value of ε_0 is able to satisfy the equilibrium equation.

The procedure is iterative due to its non-linearity, since at any fire duration, the equation is solved by iteration introducing different values of ε_0, this being easy to be implemented in any calculation sheet of software language.

In the following sensitivity analyses, the initial bending moment is assumed to be nil, this yielding $\chi = 0$.

The iterative procedure at any fire duration can be enforced as follows:

1. an attempt of $\varepsilon_{0,1}$ is arbitrary defined (as for example equal to 0 at time 0, and equal to the final value of the previous time step in the following ones);
2. on the basis of such value of $\varepsilon_{0,1}$, N_{int} is evaluated and the error $\Delta N = N_{int} - N_{ext}(t) = N_{int} - (N_{20} + p_{th}(t) \cdot b \cdot R)$ is calculated;
3. the value of $\varepsilon_{0,2}$ to be implemented in the following iteration is estimated as $\varepsilon_{0,2} = \varepsilon_{0,1} + \Delta\varepsilon_0$, with $\Delta\varepsilon_0 = \Delta N/\widehat{EA}$.

In a few iterations, convergence is obtained.

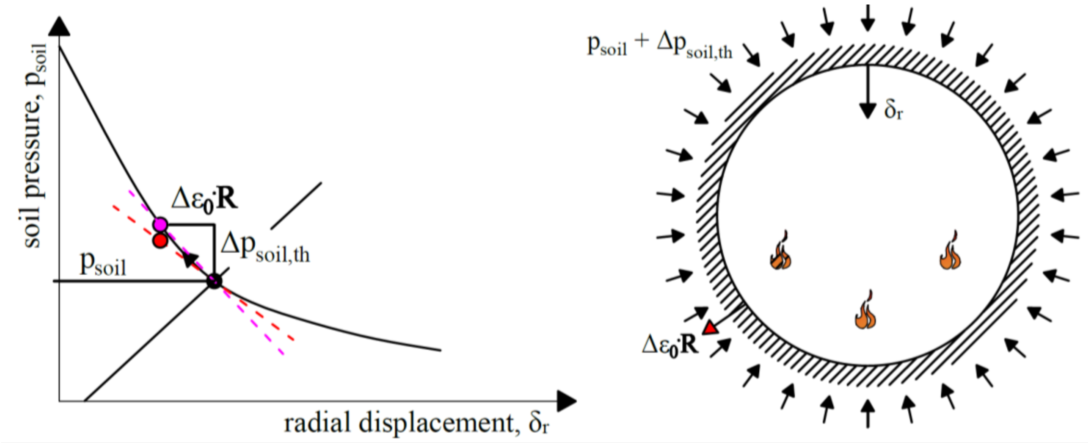

Figure 3. Convergence law of tunnel-soil system.

The described algorithm has been implement in a common programming language together with the algorithm for the evaluation of the temperature in the thickness via the typical finite element approach. As previously described, both thermal and mechanical problems have been reduced to a 1D system.

In Figure 4a, the variation with temperature of f_c^T/f_c^{20}, f_{ct}^T/f_{ct}^{20}, E_c^T/E_c^{20} and $E_c^T/E_c^{20} \cdot \varepsilon_{th}$ is shown, while Figure 4b reports ε_{c1}^T, ε_{cu}^T and ε_{th} with temperature. All parameters are defined according to EC2 [7] in the case of siliceous aggregate. It is worth noting as the thermal strain for perfectly-restrained thermal dilation ($\varepsilon_0 = 0$, leading to $\sigma_{th} = \varepsilon_{th} \cdot E_c^T$) is almost negligible for temperature higher that 1000°C (since the modulus E_c^T approaches the zero value for the high thermally-induced degradation), and also at 20°C (since ε_{th} is zero). For siliceous aggregate, according to the expression defined by EC2 [7], the maximum values of the restrained-dilation stress is reached at 300°C with the value $\sigma_{max} = \varepsilon_{th} \cdot E_c^T \approx E_c^{20}/1000$.

Finally, Figure 5 shows the constitutive laws in compression and in tension for different temperatures.

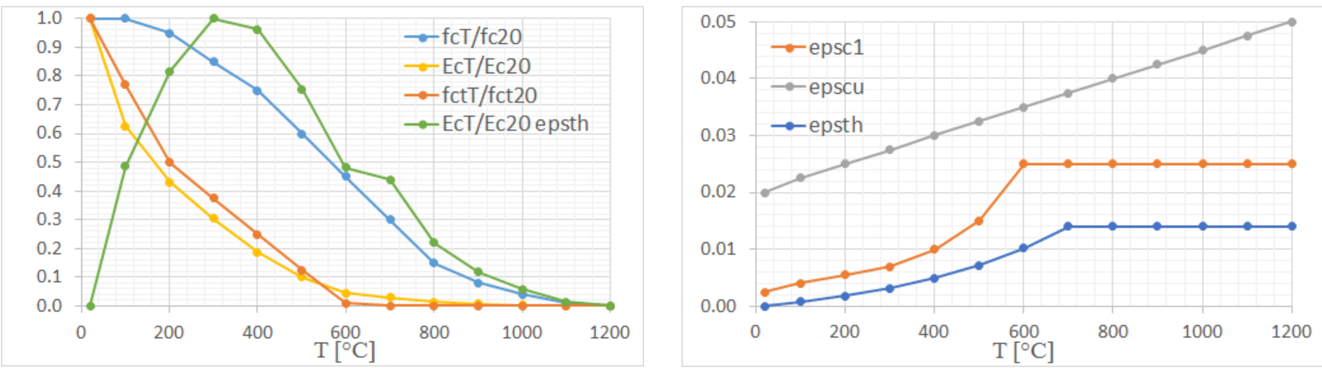

Figure 4. Variation with temperature of f_c^T/f_c^{20}, f_{ct}^T/f_{ct}^{20}, E_c^T/E_c^{20} and $E_c^T/E_c^{20} \cdot \varepsilon_{th}$ and of ε_{c1}^T, ε_{cu}^T and ε_{th} according to EC2.

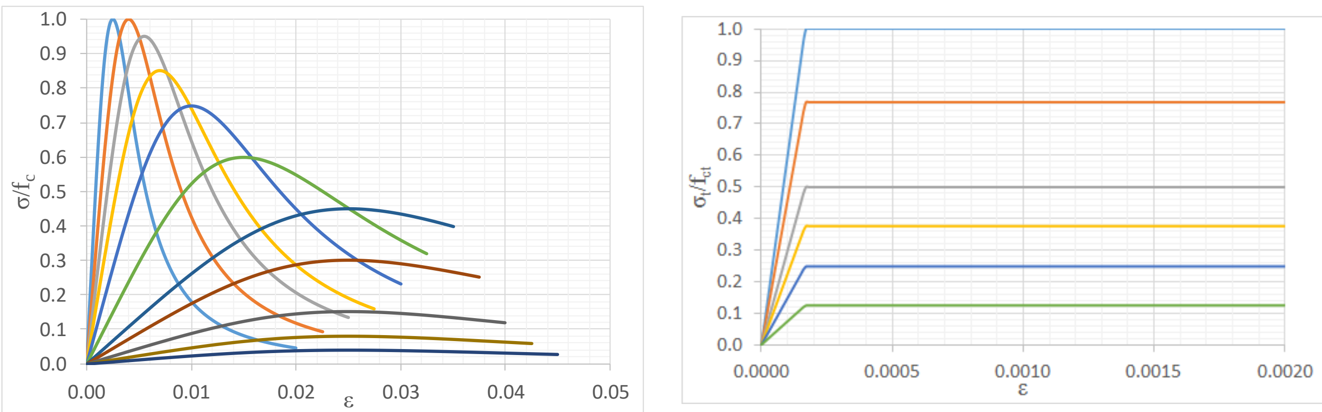

Figure 5. Constitutive laws for plain concrete in compression and for fibre-reinforced concrete in tension.

4 PARAMETRIC ANALYSES

The code has been adopted for several parametric analyses aimed at investigated the main influencing factors in the fire performance of tunnel linings. The main outcomes are described in the following sections.

4.1 Elastic analysis versus non-linear analysis

In Figure 6 it is shown the influence of the type of analyses, namely Elastic Analysis (ELA), in which concrete behaves elastically at any temperature but with a decreasing modulus E according to Figure 4, or Non-Linear Analysis (NLA), in which the constitutive laws described in Figure 5 are implemented. It is worth noting that for sake of simplicity, all the following simulation are carried out in case of Fibre-Reinforced Concrete (thus with a remarkable tensile strength assumed as $f_{ct}^{20} = f_c^{20}/10$) and without rebars.

In Figure 6 the variation with temperature of barycentre strain ε_0, axial force N and bending moment M with time in case of ISO 834 fire curve is shown. On the left, the plots refer to a low initial compression regime (N_{ext}^{20} = 500 kN), while on the right to a medium compression regime (N_{ext}^{20} = 2000 kN). In both cases a ring width of 1 m and a ring external radium of 6 m have been considered. The other parameters are declared within the figures. Thick solid lined refers to NLA, while thin lines refer to ELA.

In the plots showing the bending moment evolution, it has been reported also the evolution of the resistant bending moment of the section according to the temperature profile and the external axial force, by implementing the constitutive laws of Figure 5.

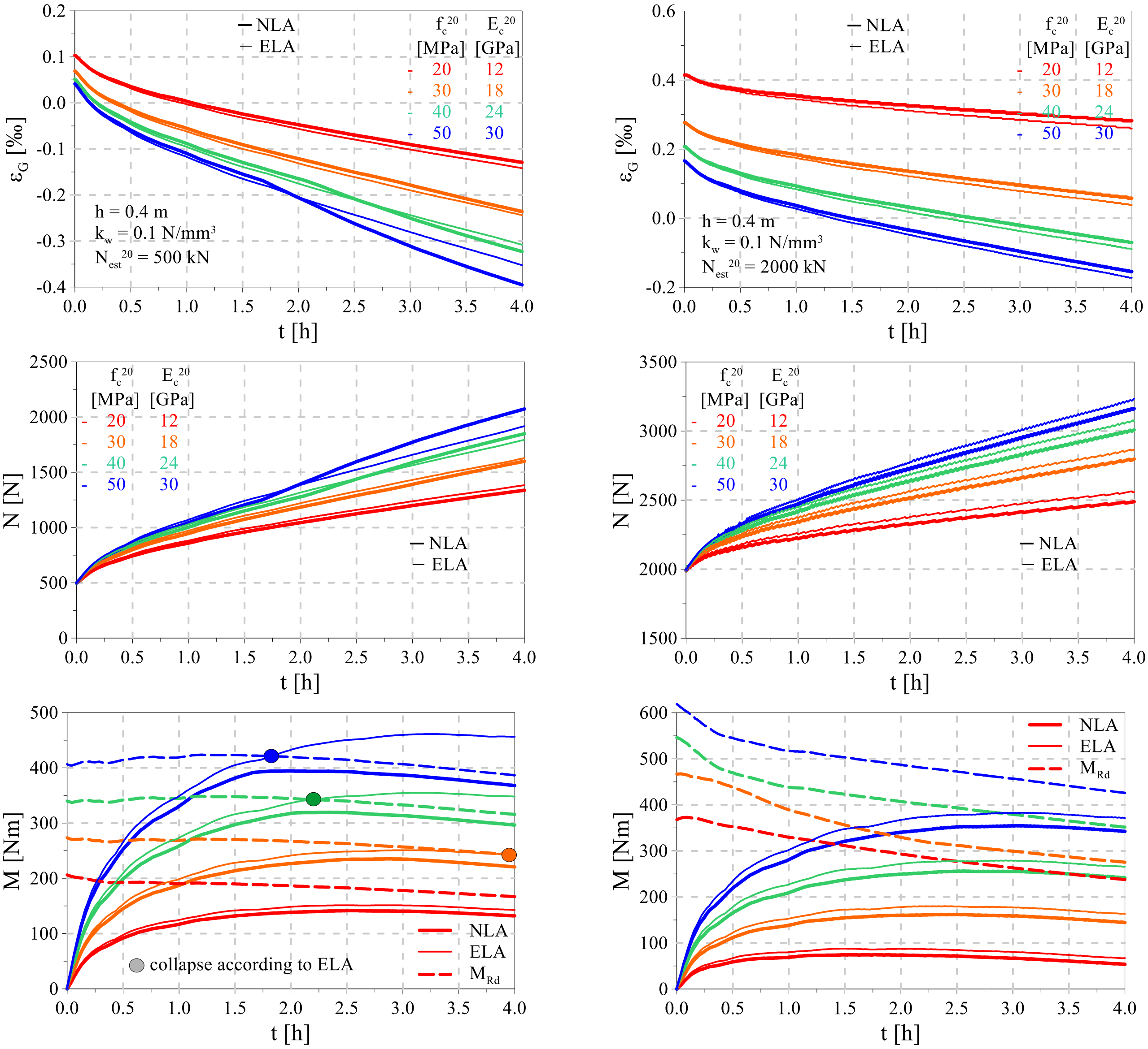

Figure 6. Variation with temperature of barycentre strain ε_0, axial force N and bending moment M with time. On the left, N_{ext}^{20} = 500 kN, while on the right, N_{ext}^{20} = 2000 kN.

It is emblematic the variation of the bending moment according to ELA and NLA for f_c = 50 MPa and N_{ext}^{20} = 500 kN. Comparing its variation for ELA with the variation of M_{Rd}, it yields that failure occurs after about 1.8 h, since M = M_{Rd}. Failure, however, does not occurs for the same case according to NLA, since the "virtual collapse" observed via ELA represents just the configuration in which section plasticization is obtained, namely the attainment of strength in compression or in tension. This is clear in Figure 7, where stress profiles in the thickness are reported for several fire durations.

When plasticization is attained, section stiffness starts reducing (as it can be observed in Figure 8), which in turns translate into a reduction of indirect actions. As it is well known, in fact, while in case of gravitational actions if external forces are higher than bearing ones, failure may occur, in case of indirect actions, if forces attain the bearing ones, cracking (or plasticization) occurs with a subsequent reduction of stiffness and thus a decrease of indirect actions. In this latter case, failure occur only when the bearing capacity of the structure is lower than the initial forces (before the fire), namely the gravitational forces due to the surrounding soil. In the case of a tunnel lining with initial axysimetrical load (thus with an initial nil bending regime) this translates into the condition of an axial force decreasing with the fire duration, which means that the sectional shrinkage due to the compression is higher than the thermal dilation. Such configuration is not stable and thus not engineering allowable.

In the cases in which sectional plasticization does not occurs, ELA and NLA yields very similar results.

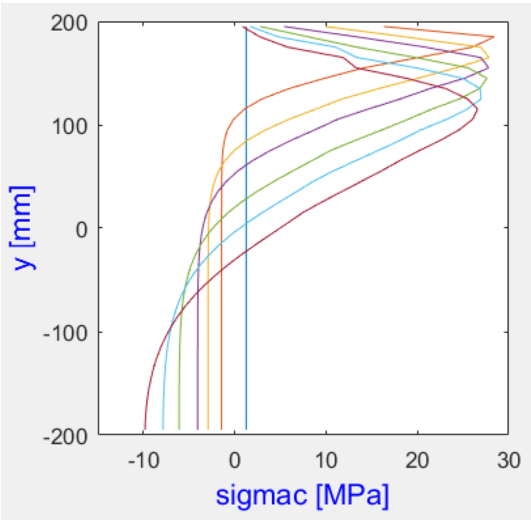

ELA - f_c^{20} = 50 MPa, N=500 kN

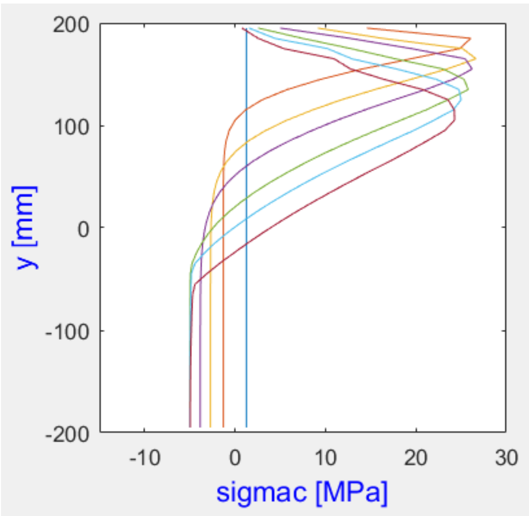

NLA - f_c^{20} = 50 MPa, N=500 kN

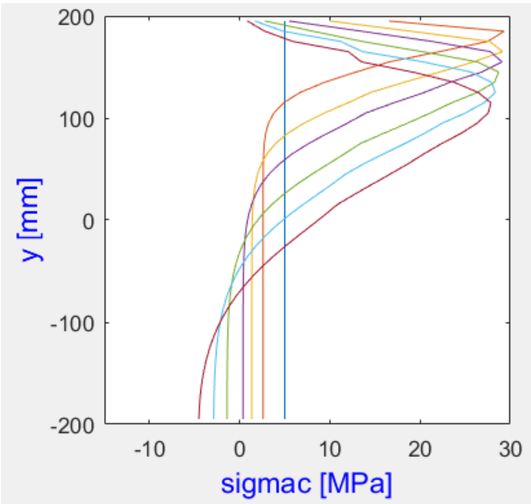

ELA – f_c^{20} = 50 MPa, N=2000 kN

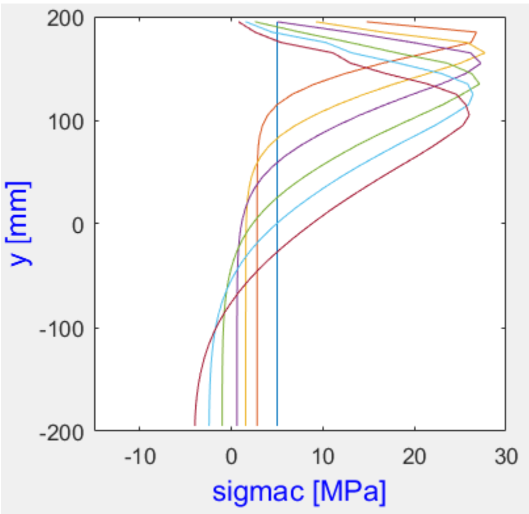

NLA - f_c^{20} = 50 MPa, N=2000 kN

Figure 7. Stress profiles for different fire durations.

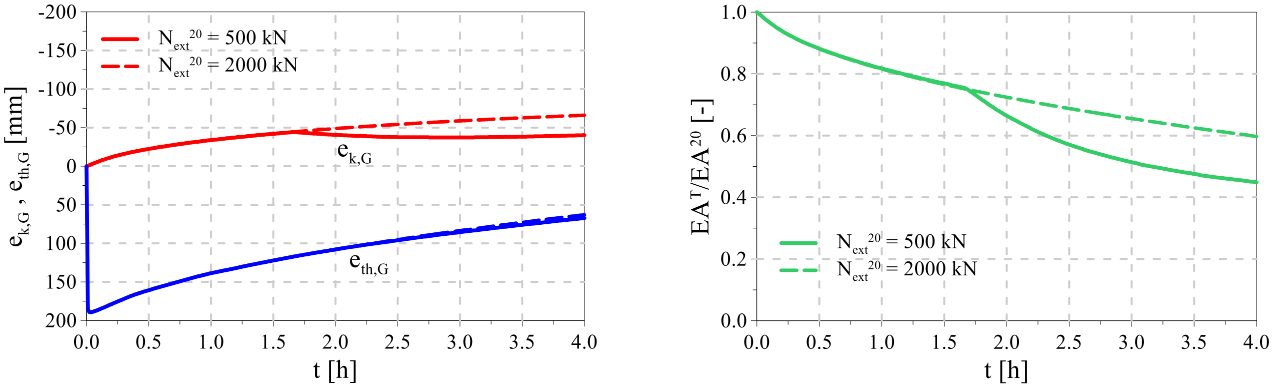

Figure 8. Variation of stiffness and thermal strain eccentricity and variation of sectional axial stiffness with fire duration.

4.2 Effect of soil stiffness and of lining thickness

In Figure 9 it is shown the influence of the soil stiffness (herein represented by k_{soil}) and of the lining thickness, according to Non-Linear Analysis (NLA), on the variation with fire duration of barycentre strain ε_0, axial force N and bending moment M in case of ISO 834 fire curve. In both cases, a low initial compression regime is considered (N_{ext}^{20} = 500 kN), with a width of 1 m and a ring external radius of 6 m. The other parameters are detailed within the figures.

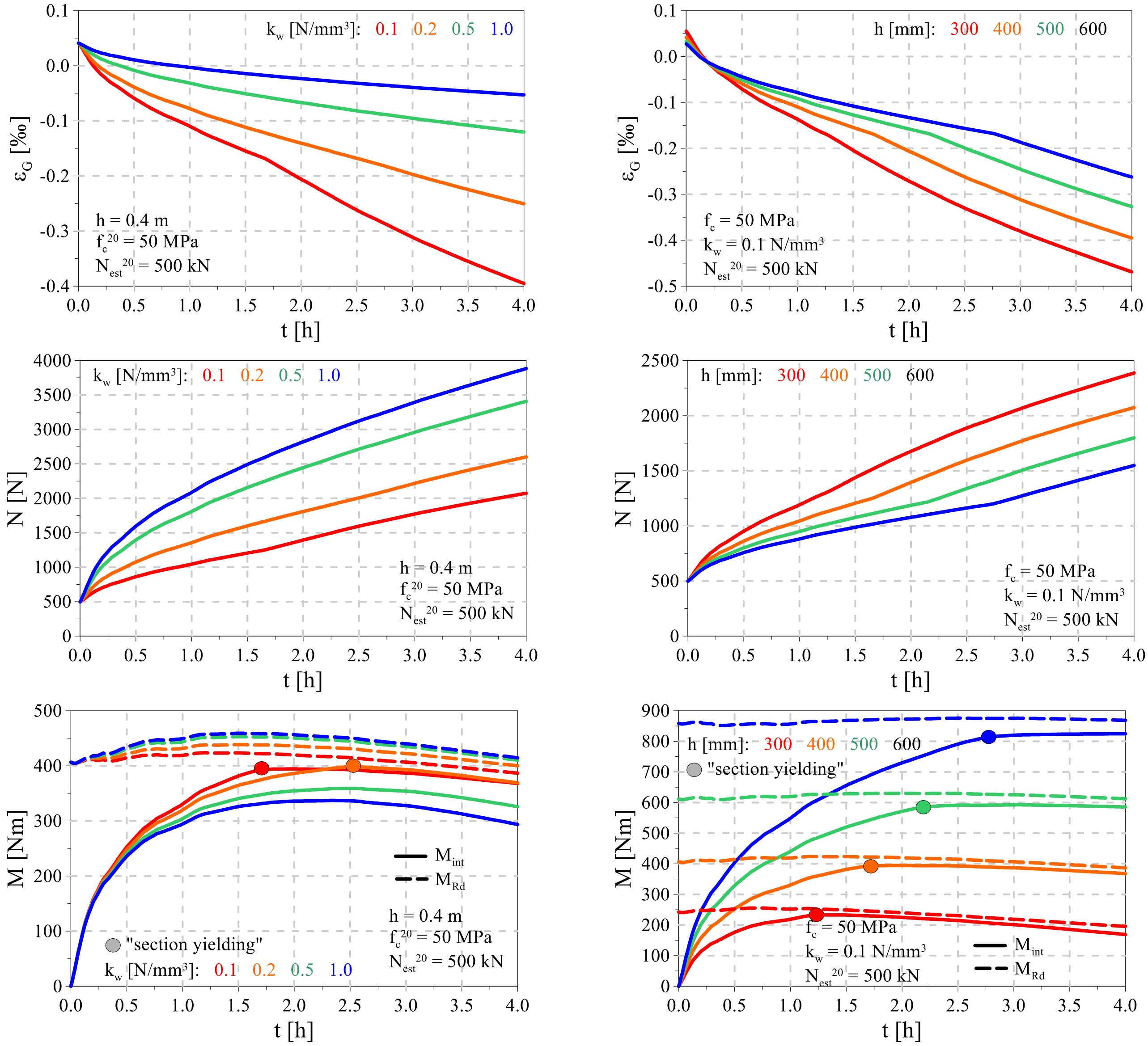

Figure 9. Variation with temperature of barycentre strain ε_0, axial force N and bending moment M with time. On the left, effect of soil stiffness, while on the right, effect of lining thickness.

It is interesting to observe as increasing soil stiffness, the axial force significantly increases, while a minor effect can be observed in the bending moment. The increasing lining thickness, on the other hand, leads to a decrease of the axial compression (since the average temperature and the thermal dilation of the lining decrease), and to an increase of the bending moment, due to the increase of the eccentricity of $\varepsilon_{th} \cdot E$.

5 CONCLUSIONS AND FUTURE STEPS

The possible adoption of a simplified 1D approach has been discussed for the study of the structural performance of tunnel lining exposed to fire. The approach is based on the assumption of axysimmetry (this allowing to reduce the problem to a 1D one) and of plane sections.

The approach is based on the sequential solution of the thermal problem, in order to carried out the temperature distribution within the lining for any fire duration, and of the non-linear mechanical analysis with the implementation of the constitutive laws provided by EC2.

Thanks to its simplicity, the approach allows to investigate the structural behaviour of lining for any fire curve, thickness, soil stiffness, etc… and to easily perform parametric analyses, instrumental in understanding the sensitivity to different factors.

In particular, it has been shown as a linear elastic analysis (taking into account the variation of the elastic modulus with the temperature) can indicate collapse which, however, just correspond to the plasticization of the section (this not necessarily translating to failure).

Increasing concrete stiffness lead to a larger increase of compression and bending moment due to restrained thermal dilation, this even leading to sectional plasticization. Trickier is the role played by lining thickness, since its increase leads to a reduction of the compression (due to the reduction of the average temperature in the lining), but to an increase of the bending moment (due to an increase of the eccentricity of the compression in the hot layer). Finally, stiffer the soil, higher the compression in the lining while a negligible effect is observed in the extent of the bending moment.

Despite the promising adoption of the described approach, several critical aspects need to be further investigated, this being part of the next planned steps of the present study. First of all, the development of the indirect actions must be compared with those obtained by more advanced Finite Element analyses via well-established softwares such as Abaqus or Safir. Secondly, it should be checked the possibility of adopting a 1D approach also in the case of non axysimmetrical problem, this being the most general condition.

REFERENCES

1. FIT, (2005), Technical Report - Part 1: Design Fire Scenarios, European Thematic Network FIT - Fire in Tunnels, Rapporteur A. Haack, supported by the European Community under the 5th Framework Programme 'Competitive and Sustainable Growth' Contract n° G1RT-CT-2001-05017.
2. Lo Monte F., Bamonte P., Beltrami C., (2022), "Study on the Effects of Cooling Phase and Construction Technology on the Fire Performance of R/C Tunnels", Tunnelling and Underground Space Technology, under revision.
3. Cristian Maluk, Jason Tignard, Andrew Ridout, Todd Clarke, Ralf Winterberg, "Experimental study on the fire behaviour of fibre reinforced concrete used in tunnel applications", Fire Safety Journal, Volume 120, 2021, 103173, https://doi.org/10.1016/j.firesaf.2020.103173.
4. Lo Monte, F., Felicetti, R., Meda, A., Bortolussi, A., "Assessment of concrete sensitivity to fire spalling: A multi-scale experimental approach", (2019) Construction and Building Materials, 212, pp. 476-485, DOI: 10.1016/j.conbuildmat.2019.03.332.
5. Smith K. and Atkinson T., (2010), "Factors to consider in using PP fibres in concrete to provide explosive spalling resistance in the event of a fire", Shotcrete: Elements of a System - Bernard (ed), Taylor & Francis Group, London, ISBN 978-0-415-47589-1.
6. Thamm B., (2003), "The new directive onroad tunnel safety", Proceedings of International Symposium on Catastrophic Tunnel Fires (CFT), Boras, Sweden, November 20-21.
7. EN 1992-1-2:2004. (2004). Eurocode 2 - Design of concrete structures - Part 1-2: General rules - Structural fire design. European Committee for Standardization (CEN), Brussels (Belgium).

FEM ANALYSIS OF FIRE SPALLING OF CONCRETE REPAIRED BY PCM USING RING-RESTRAINED HEATING TEST

Mitsuo Ozawa[1], Makiho Sukekawa[2], Yuta Goto[3], Yusuke Sugino[4]

ABSTRACT

Polymer cement mortar (PCM) is a cement mortar mixed with organic polymers; it is widely used to repair the cross-sections of deteriorated parts of reinforced concrete members. PCM is an indispensable material for repairing and reinforcing concrete structures because of its excellent adhesion to concrete, compactness, and workability. However, it has been noted that PCM tends to spall when exposed to high temperatures because it contains organic polymers. Our research group has evaluated the fire spalling properties of PCM using the ring-restrained specimen method, standardised by the Japan Concrete Institute. In this method, the thermal stress and water vapour pressure, which are the main factors in the fire spalling phenomenon, are measured. Furthermore, a heating test using the ring-restrained specimen method has also been conducted for a case in which the concrete was repaired with PCM. The results showed that the fire spalling magnitude of the concrete composite repaired with PCM was larger than that of the concrete specimen without polymers added. As there are a few analytical evaluations of the fire spalling properties of concrete repaired with PCM, we performed a thermal stress analysis using the finite element method on the ring-restrained specimen in this study. In addition, we simulated the experimental value of the fire spalling depth using a tensile strain fracture model and a critical vapour pressure model proposed by the authors.

Keywords: Ring restrained heating test; polymer cement mortar; fire spalling; FEM analysis

1 INTRODUCTION

Polymer cement mortar (PCM) is a cement mortar mixed with organic polymers and is widely used as a cross-section repair material for deteriorated parts of reinforced concrete (RC) members [1]. PCM is an indispensable material for repairing and reinforcing concrete structures because of its excellent adhesion to concrete, compactness, and workability. However, it has been pointed out that PCM tends to spall when exposed to high temperatures because it contains organic polymers [2–6]. Our research group previously evaluated the fire spalling properties of PCM using the ring-restrained specimen method standardised by the Japan Concrete Institute [7–8]. In this method, the thermal stress and water vapour pressure, which are the main factors in the fire spalling phenomenon, are measured [9]. Furthermore, a heating test using the ring-restrained specimen method has been conducted for a case in which concrete was repaired with PCM. The results showed that the fire spalling magnitude of the concrete composite repaired with PCM was larger than that of the concrete specimen without polymers added [10]. In general, spalling occurs in concrete when it is exposed to fire. The thermal stress theory and the water vapour pressure theory have been proposed to explain this phenomenon [11,12]. Several analytical evaluations of fire spalling phenomena in

[1] Professor,Dr.Eng., Gunma University
e-mail: ozawa@gunma-u.ac.jp https://orcid.org/0000-0002-6207-7180
[2] Gaduate Student, Gunma University
e-mail: t201C029@gunma-u.ac.jp
[3] Gaduate Student, Gunma University
e-mail:t221c025@gunma-u.ac.jp
[4] Ph.D, Taiheiyo Materials co ltd.
e-mail: Yusuke-Sugino@taiheiyo-m.co.jp
https://doi.org/10.6084/m9.figshare.22177940

concrete have been reported [13-16]. However, there are only a few studies that have analytically evaluated the fire spalling properties of concrete repaired with PCM. Therefore, we performed a thermal stress analysis using the finite element method (FEM) on ring-restrained specimens and simulated the experimental value of the fire spalling depth using the tensile strain failure model[17]. A model for vapour pressure under saturated conditions was also used for a 2D analysis [16].

2 FIRE TESTING OF CONCRETE REPAIRED BY PCM USING RING-RESTRAINED SPECIMENS

Sukekawa et al. conducted a heating test on a ring specimen in which a concrete member was repaired with PCM [10]. The purpose of their study was to evaluate the fire spalling behaviour of PCM-repaired concrete using a ring test. Figure 1 shows an overview of the ring-restrained specimen. A steel ring with dimensions of 300 × 100 × 8 mm for outer diameter, height, and thickness, respectively, was used. Concrete was placed in the ring to a depth of 50 mm, and the PCM was placed at a height of 50 mm at the bottom to create the specimen. A deformed steel bar with a diameter of 10 mm and length of 250 mm was placed 30 mm from the heating surface. A thermocouple for measuring temperature and a stainless steel pipe for measuring water vapour pressure were installed inside the specimen. After the stainless steel pipe was filled with silicon oil, a pressure sensor was connected to measure the water vapour pressure. In addition, a strain gauge and a thermocouple were placed on the outer surface of the steel ring as counter electrodes. The measurement positions of the internal temperature and the vapour pressure and the positions of the strain gauge and thermocouple on the ring surface were 5, 10, 40, and 60 mm, respectively from the heating surface. Table 1 lists the PCM strength, elastic modulus, and moisture content of the concrete used. The heating test followed the RABT30 heating curve. Figure 2 shows the spalling depth contour after the heating test. The maximum fire spalling depth was approximately 57 mm.

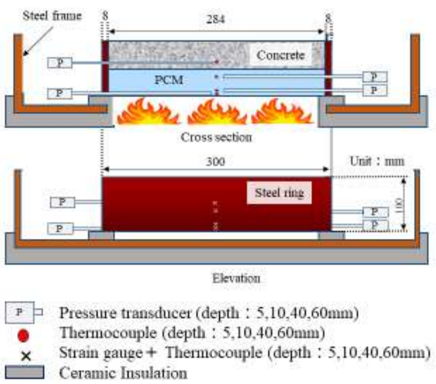

Fig.1 Ring restrained heating test

Table 1 Mechanical properties and water content of NSC,PCM

	Compressive strength (MPa)	Tensile strength (MPa)	Elastic Modulus (GPa)	Water Content (%)
PCM	56.0	3.9	22.4	6.3
NSC	43.1	2.8	30.3	5.7

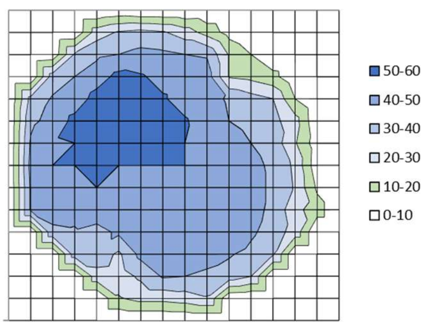

Fig.2 Spalling depth contour (Unit:mm)

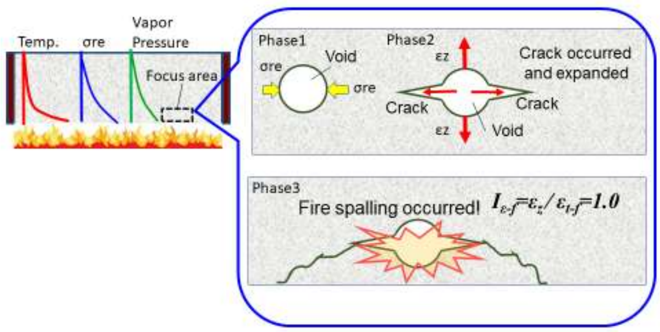

Fig.3 Tensile strain failure model

3 MODEL FOR ESTIMATION OF THERMAL STRESS AND TENSILE STRAIN FAILURE

In this study, a tensile strain failure model [17] was used to evaluate the fire spalling depth. Figure 3 shows the tensile strain failure model. The ring-restrained specimen was assumed to be a cylinder, and a plane stress state was assumed in the cross section at an arbitrary height.

Phase 1: By constraining the thermal expansion of the concrete owing to heating, the restraining stress ($\sigma_{re}(=\sigma_x= \sigma_y)$) acts in a void parallel to the heating surface from the outside toward the core.

Phase 2: The out-of-plane strain (ε_z) is calculated from the strain (ε_x) generated along the x-axis of the void.

Phase 3: It is assumed that fire spalling occurs around the void when the out-of-plane strain (ε_z) exceeds the tensile fracture strain ($\varepsilon_{t\text{-}f}$).

Here, the restraining stress was calculated from the circumferential strain obtained from the ring-heating test. Equations (1)–(5) present the calculation formulas for the tensile strain failure model.

$$\sigma_{re}=\varepsilon_\theta \cdot E_s \cdot t/R \qquad (1)$$

$$\sigma_{re} = \sigma_x = \sigma_y \qquad (2)$$

$$\tau_{xy}=0 \qquad (3)$$

$$\varepsilon_z=\nu_c\ (\sigma_x+\sigma_y)/E_c(T) \qquad (4)$$

$$I_{\varepsilon\text{-}f}=\varepsilon_z/\varepsilon_{t\text{-}f}\ \geqq 1.0 \qquad (5)$$

where σ_{re} is the restraining stress,

ε_θ is the circumferential strain,

E_s is the elastic modulus of the restrained ring,

t is the thickness of the restrained ring,

R is the inner radius of the restrained ring,

σ_x, σ_y, and τ_{xy} are the normal stresses and shear stress in the X-Y plane,

ε_z is the strain in the depth direction from the heating surface,

ν_c is the apparent Poisson's ratio,

$\varepsilon_{t\text{-}f}$ is the tensile failure strain (100, 200, 300 μ in this analysis), and

$I_{\varepsilon\text{-}f}$ is the tensile strain failure index.

4 MODEL FOR VAPOUR PRESSURE UNDER SATURATED CONDITIONS

Figure 4 shows the vapour pressure under saturated condition. Many researchers have reported that the water vapour pressure during the heating of concrete increases along the saturated water vapour pressure (SVP) curve [18]. In this study, the SVP curve was used to model the water vapour pressure, and it was assumed that the fire spalling condition of the water vapour pressure was satisfied when the water vapour pressure exceeded an arbitrary value. The SVP is calculated using the Tetens formula [19]. The critical water vapour pressure model used in this study is shown in equation (6). The vapour pressure limit exponent was set as below. The critical saturated vapour pressure was set to 1.6 MPa based on the temperature range in which PCM spalling occurs, which is 150 to 200 °C [8].

$$P_{svp}(T) = 6.11 \times 10^{\frac{7.5T}{(237.3+T)}} \quad (6)$$

$$I_{p\text{-}f}=P_{svp}(T)/P_{limit} \geqq 1.0 \quad (7)$$

Where

P_{svp} (T) is saturate vapour pressure in water at T °C from Tetens formula.

T : Temperature in concrete during heating

$I_{p\text{-}f}$: Index of critical water vapour pressure model

P_{limit} : Critical saturated vapour pressure is 1.6 MPa in this study

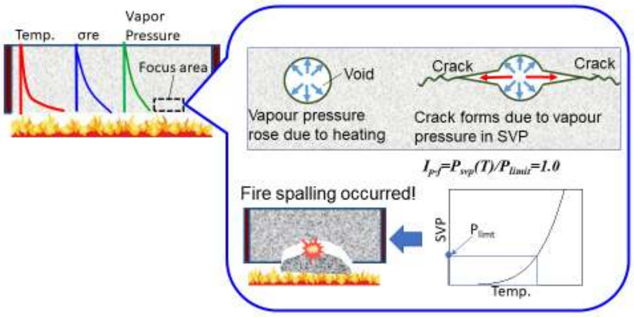

Figure 4 Vapour pressure under saturated condition

Table 2 The analysis cases in 3D and 2D model

Case	Dimension	Limit tensile strain(μ)	Critical vapour pressure(MPa)
1	3D	100	/
2		200	
3		300	
4	2D	100	
5			1.6

5 NUMERICAL ANALYSIS OF FIRE SPALLING OF PCM

5.1 Outline of FEM analysis

Table 2 lists the analysis cases. Thermal stress analysis software for concrete (ASTEA-MACS) was used. The fire spalling analysis of concrete and the PCM-repaired specimens was performed using a ring heating test. For Cases 1 to 3, a tensile strain failure model based on the thermal stress theory was used with a 3D model. The critical tensile strain was 100-300 μ. In Cases 4 and 5, an attempt was made to reproduce fire spalling (peeling-off phenomenon) between PCM and concrete using a 2D axisymmetric model. In Case 4, the tensile strain failure model was used, and the critical tensile strain was set to 100 μ. In Case 5, the tensile strain failure model and the critical water vapour pressure model were used. The ultimate tensile strain was set at 100 μ, and the vapour pressure limit was set at 1.6 MPa.

5.2 3D model analysis

Figure 5 shows the analysis model used in this study. A 1/4 axisymmetric model of the ring-restrained specimen was used for the analysis. The height of the specimen was divided into 20 parts with a width of 5 mm, and the diameter of 142 mm was divided into 8 parts with a width of approximately 17 mm. The thickness of the restrained ring was 8 mm, and it was divided into two parts. The figure 6 shows the heat-transfer boundary conditions of the analysis model. The heat-transfer coefficient of the top surface of the normal-strength concrete (NSC) was set to 12 W/m^2°C. The heat transfer coefficients of the steel ring and the heating surface were set to 400 W/m^2°C and 75 W/m^2°C, respectively. The temperature of the heating surface was given by the RABT30 heating curve. Table 3 lists the density, initial temperature, Poisson's ratio, and mechanical properties of the NSC, PCM, and steel ring.

Figures 7–11 show the physical properties considered in the analysis. The modulus of elasticity, compressive strength, and tensile strength of NSC and steel were set based on the high-temperature residual ratio of the Architectural Institute of Japan [20]. The elastic modulus and residual ratio of the compressive strength and tensile strength of the PCM were set to be the same as those of NSC. The thermal conductivity of the NSC and the specific heat of steel were considered based on a study by Tajima et al. [21]. The thermal conductivity of the PCM was assumed to be the same as that of the NSC. The thermal conductivity of the steel material was set at a constant value of 500 W/m·K. The specific heat of the NSC was adopted from Eurocode2 [22]. The specific heat of the PCM was obtained by adding the latent heat of vapourisation to the cement mortar formula of the Architectural Institute of Japan.

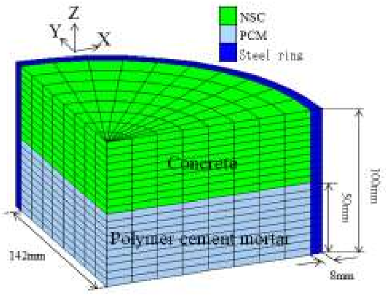

Figure 5 1/4 analysis model in 3D

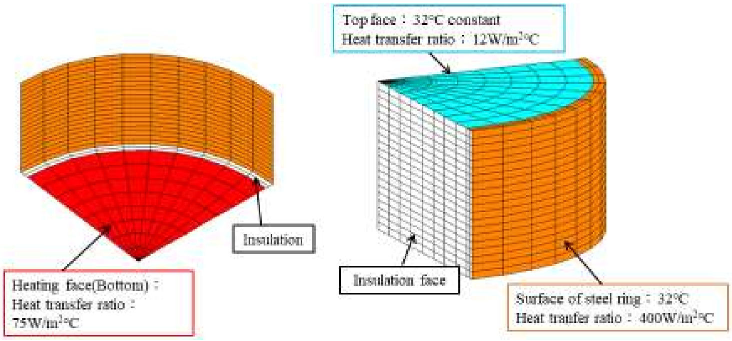

Figure 6 Heat-transfer boundary conditions

Table 3 lists the density, initial temperature, Poisson's ratio, and mechanical properties of the NSC, PCM, and steel ring.

	NSC	PCM	Steel ring
Density (kg/m3)	2400	2100	7850
Initial temperature (°C)	34	34	32
Poison's ratio	0.2	0.2	0.3
Compressive strength (MPa)	43	56	295
Tensile strength (MPa)	2.8	3.9	295
Elastic Modulus (GPa)	30	22	210

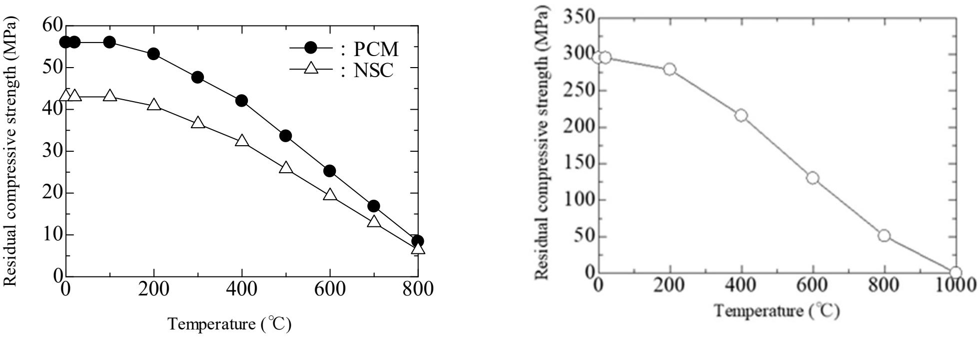

a) PCM ,NSC

b) Steel ring

Figure 7 Residual compressive strength

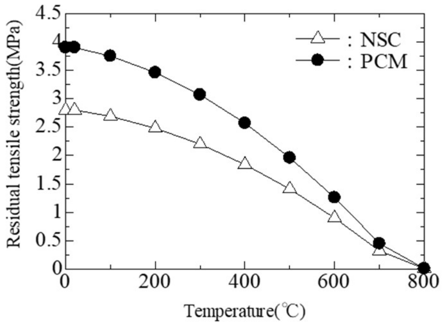

a) PCM ,NSC

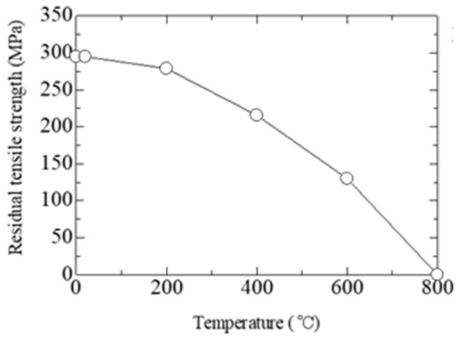

b) Steel ring

Figure 8 Residual tensile strength

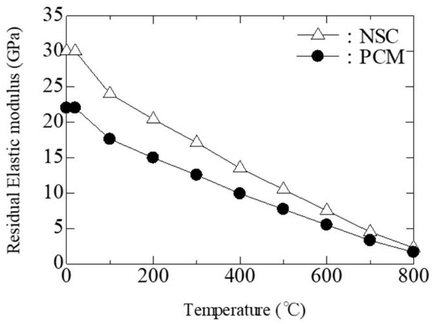

a) PCM ,NSC

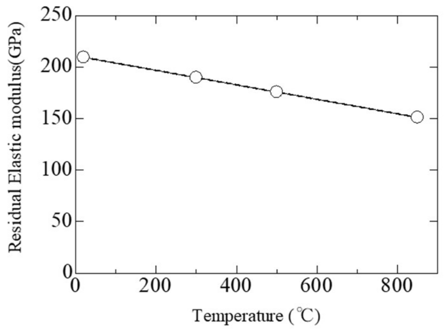

b) Steel ring

Figure 9 Residual elastic modulus

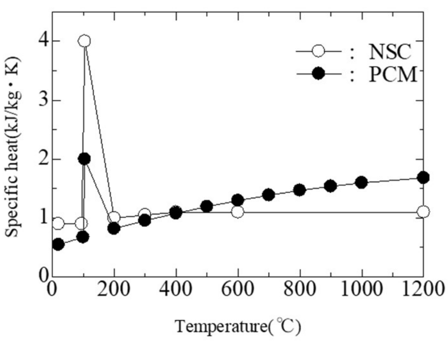

a) PCM ,NSC

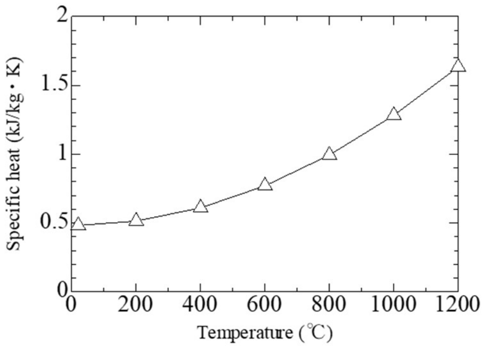

b) Steel ring

Figure 10 Specific heat

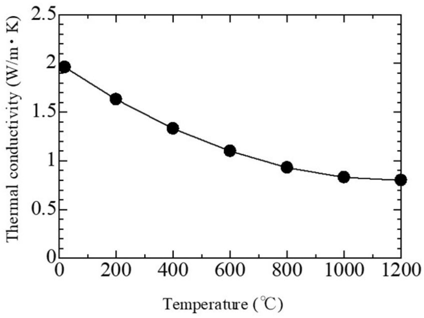

Figure 11 Thermal conductivity(PCM and NSC)

5.3 2D model analysis

Figure 12 shows the 2D analytical model. In the analysis, a 1/2 axisymmetric model of the ring-restrained specimen was used. The height, diameter, and thickness of the specimens were 100, 142, and 8 mm, respectively. Figure 13 shows the heat-transfer boundary conditions of the analysis model. The heat-transfer coefficient of the upper surface of the NSC was set to 12 W/m^2°C, and those of the steel material and heating surface were set to 400 W/m^2°C and 30 W/m^2°C, respectively. The temperature of the heating surface was given by the RABT30 heating curve. The initial conditions were the same as those for the 3D analysis. Regarding the thermal properties of the concrete and PCM, the elastic modulus, compressive strength, tensile strength, and heat-transfer coefficient were the same as those for the 3D analysis. The concrete was assumed to have the same specific heat as in the 3D model. The specific heat of the PCM is shown in Figure 14. The latent heat of vaporisation at 100 °C was assumed to be 4 kJ/kg K. Apparent poison ratio of PCM was 0.15.

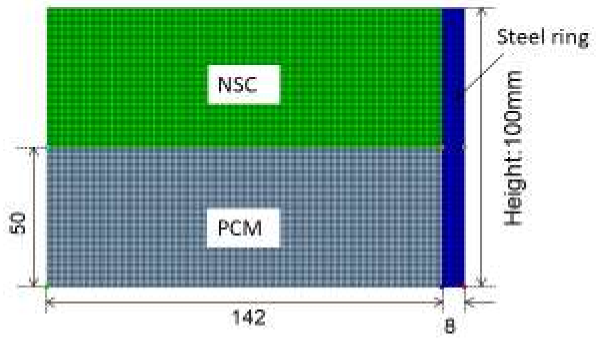

Figure 12 2D analytical model (Unit:mm)

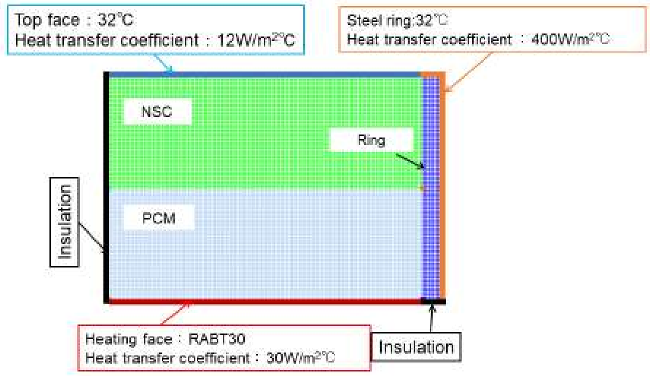

Figure 13 Heat-transfer boundary conditions

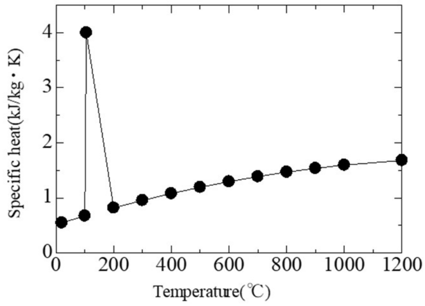

Figure 14 Specific heat of the PCM in 2D model

6 RESULTS AND DISCUSSION

6.1 Fire spalling evaluation of 3D model

Figure 15 shows the contour plot of the maximum temperature inside the specimen. It was confirmed that the maximum temperature reached 807 °C at the lower surface of the specimen, which was the heating surface, and heat was transmitted in the depth direction. Figure 16 shows the measured and analysis values of the internal temperature at the centre of the specimen over time. At positions 5 and 10 mm from the heating surface in the centre of the specimen, the evaluation was performed with good accuracy for approximately 5 min after the start of heating. After 5 min, the measured values showed a rapid temperature increase, indicating a tendency to differ from the analysis values. Regarding this point, in the experiment, fire spalling occurred at a position of 5 mm at approximately 5 min and at a position of 10 mm at approximately 5.5 min. From these results, there was no significant difference between the measured and analysis values until fire spalling occurred in the experiment. Figure 17 shows the temporal change in the tensile strain (εz) in the vertical direction of the specimen. In addition, the red lines in the figure indicate the positions of the tensile fracture strain (εt-f) of 100, 200, and 300 μ set in this experiment. Sugino et al. [23] experimentally demonstrated the relationship between the ratio of polymer to cement (P/C) of polymer cement mortar and the tensile fracture strain (εt-f). It also evaluated high-strength concrete using the strain failure index and stated that the range of tensile failure strain should be 200-400 μ[17]. Based on these results, three cases with tensile failure strains of 100, 200, and 300 μ were selected for this analysis. The evaluation of strain in the Z direction in this analysis was based on the positions 2.5 to 22.5 mm from the heating surface at the centre of the specimen. It was confirmed that the tensile strain (εz) increased with heating from a position closer to the heating surface.

Figure 18 shows a comparison between the experimental and analytical values for the spalling occurrence time. In this analysis, we evaluated the spalling occurrence time as a tensile strain failure index that exceeded 1.0. We plotted the intersection points of the tensile fracture strain (εt-f) and tensile strain (εz). For εt-f = 100 μ, fire spalling occurred 1 min after the start of heating, and the fire spalling analytical start time was much earlier than the measured value. In the case of εt-f of 200 μ and 300 μ, the fire spalling analytical start time was 2 to 3 min; similar to the case of 100 μ, spalling tended to occur earlier than in the actual measurement. In addition, for εt-f = 100 μ, the analytical time when the fire spalling depth exceeded 20 mm was 12 min after the start of heating, which was later than the measured value. The cases of εt-f of 200 μ and 300 μ showed a similar tendency to that of 100 μ. Sugino [23] reported that the tensile failure strain at which PCM spalling occurs is in the range of 50–130 μ, but even if the tensile fracture strain was increased to 300 μ, the analytic fire spalling start time was different from the measured value. The analytical value is slower than the experimental value for the spalling rate. In the heating experiment, the PCM was spalled, and the heat-transfer boundary of the heating surface was reconstructed in the depth direction from the heating surface, resulting in a rapid temperature rise. This caused the thermal stress to spike. As a result, fire spalling continued rapidly. On the other hand, in the analysis, the heating surface did not change, and the increase in temperature and thermal stress due to a constant heat conduction phenomenon was gradual. Additionally, the fire spalling evaluation was performed using tensile strain owing to thermal stress, and it was considered that analytical fire spalling occurred earlier than experimental fire spalling.

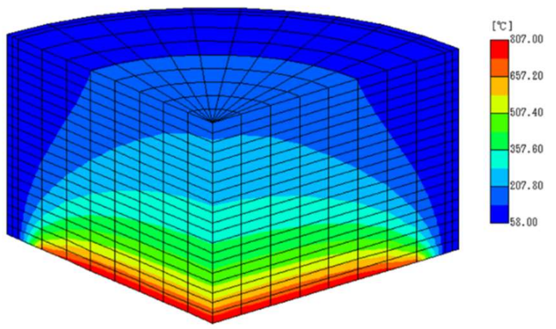

Figure 15 Contour plot of the maximum temperature inside the specimen

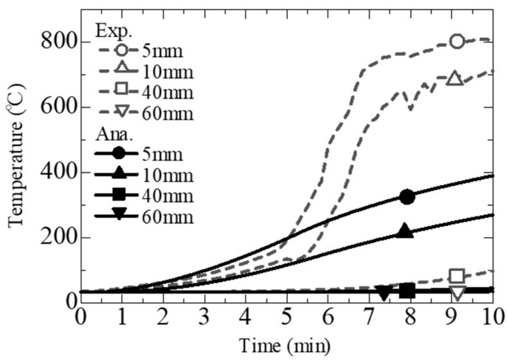

Figure 16 The measured and analysis values of the internal temperature at the centre of the specimen over time

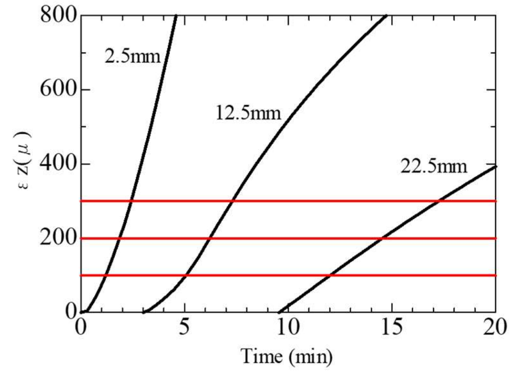

Figure 17 Temporal change in tensile strain (εz) in 3D model

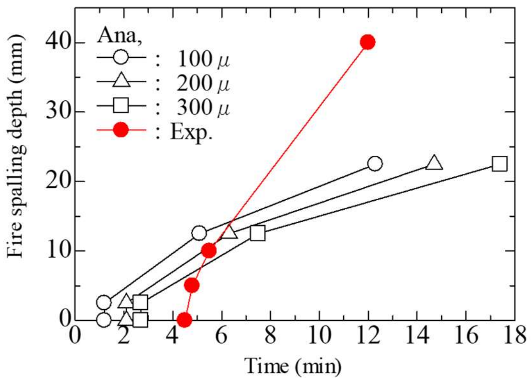

Figure 18 Spalling depth and time in 3D model (Exp. Vs. Ana.)

6.2 Fire spalling evaluation of 2D model

Figure 19 shows the temporal change in the internal temperature of the ring specimen for the analysis in Case 4. In Case 4, a tensile strain fracture model was incorporated, and the limit value of the tensile strain was 100 μ. The temperature data from the calculation at positions 5 mm and 10 mm from the heating surface stopped increasing at approximately 1.5 min. In addition, the temperature at 40 mm from the heating surface stopped increasing at 2.5 min. This indicates that the element spalled because the tensile strain caused by the thermal expansion deformation with heating exceeded 100 μ. Figure 20 shows the temporal change in the internal temperature of the ring specimen in Case 5. In Case 5, the tensile strain limit value of the tensile strain fracture model was set to 100 μ, and the critical vapour pressure was set to 1.6 MPa. The temperature calculated at positions 5 and 10 mm from the heating surface stopped increasing at approximately 5 min.

The temperature at 40 mm from the heating was stopped at 10 min. These results consider the thermal expansion deformation and vapour pressure due to heating. Figure 21 shows a comparison between the measured and analytical values regarding the temporal change in the fire spalling depth. In Case 4, the analysis value is earlier than the actual measurement value. This is probably because only the tensile strain failure model owing to thermal stress was used. On the other hand, in Case 5, the tensile strain exceeds 100 μ and the vapour pressure with the internal temperature is calculated by the saturated water vapour pressure (SVP), and the condition for detachment is satisfied when the limit value exceeds 1.6 MPa. The analytical value in Case 5 is in good agreement with the experimental value.

Figure 22 shows the temporal change in the fire spalling depth contour diagram for Case 5. After 3 min from the start of heating, no peeling of the element was observed. Delamination of the surface layer occurred at approximately 4.5 min, and it was confirmed that the delamination of the element progressed between 6.5 and 10 min.

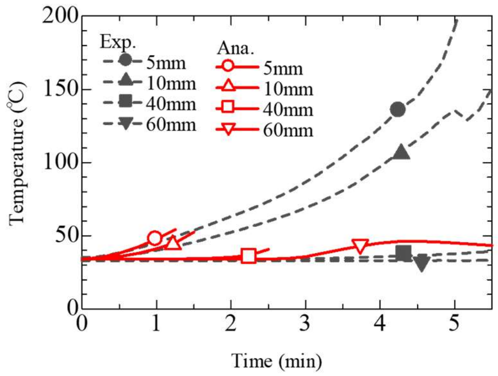

Figure 19 Temporal change of the internal temperature in case 4

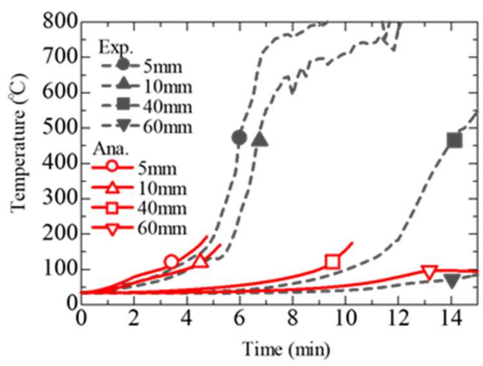

Figure 20 Temporal change of the internal temperature in case 5

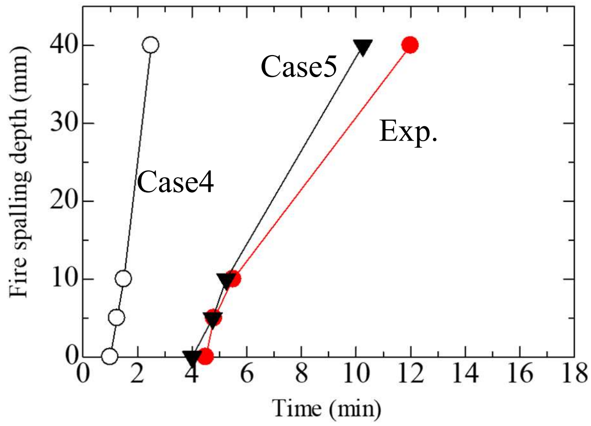

Figure 21 Temporal change of the fire spalling depth
(Case4 ,Case5 and exp.)

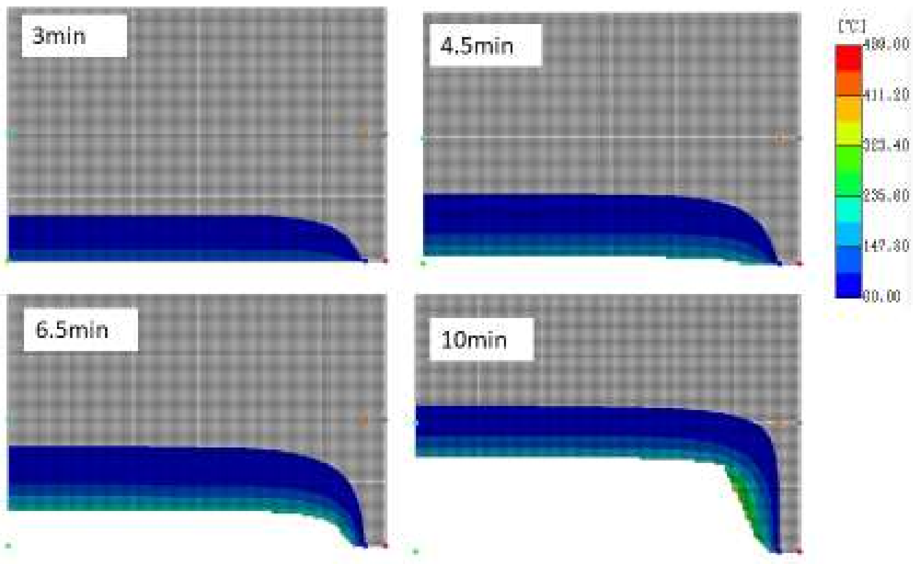

Figure 22 Temporal change of the fire spalling depth contour diagram (Case 5)

7 CONCLUSIONS

In this study, the ability of the tensile strain failure and saturated vapour pressure models to evaluate fire spalling was analysed using the FEM considering a ring-restrained specimen of normal concrete repaired by PCM. The findings of this study are as follows.

(1) By comparing the temperature inside the specimen obtained from the 3D analysis with the actual measurement, it was possible to reproduce the actual measurement up to the time when fire spalling occurred to some extent. However, the time course of the fire spalling depth showed that the fire spalling start time was earlier than the measured value, and the analytical value was different from the measured value even at a position deeper than the heating surface.

(2) In the 2D delamination analysis, it was found that the measured values could be evaluated to some extent by changes in the internal temperature and fire spalling depth over time, using both the tensile strain failure and water vapour pressure models. Additionally, it was considered that by modelling the detachment of concrete pieces due to heating, the measured values could be evaluated well.

ACKNOWLEDGMENT

This study was financially supported by the Japan Society for the Promotion of Science, the Obayashi Foundation, and the Kajima Engineering Foundation. The authors would like to express their gratitude to these organisations for their financial support.

REFERENCES

1. Ohama, Y. and Ota, M., Recent Trends in Research and Development Activities of Polymer-Modified Paste, Mortar and Concrete in Japan, Adv Mater Res, Vol. 687, 2013, pp. 26-34.
2. Chandra, S. and Berntsson, L., Some Effects of Polymer Addition on the Fire resistance of Concrete, Cem Concr Res, Vol. 10, 1980, pp. 367-375.
3. Ohama, Y., Shirai, A., and Imamoto, K., Fire-Protecting Performance of Polymer-Modified Mortars Using Redispersible Polymer Powders, CWB-Special Issue, 2012.pp.4-7
4. Hamasaki, H., Motegi, T., Noguchi, T., Wang, D., and Kim, H., Fire Resistance of Repaired Components by Polymer-Modified Cement Mortar, J Struct Constr Eng, Vol. 75, 2010, pp. 1065-1071 (In Japanese).
5. Kim, H. J. and Park, W. J., Combustion and Mechanical Properties of Polymer-Modified Cement Mortar at High Temperature, Adv Mater Sci Eng 2017, 5853687 (2017). https://doi.org/10.1155/2017/5853687.
6. Lee, S. J., Kim, S. H., and Won, J. P., Strength and Fire Resistance of a High-Strength Nano-Polymer Modified Cementitious Composite, Compos Struct, Vol. 173, 2017, pp. 96-105.
7. Sugino, Y., Ozawa, M., and Tanibe, T., Fire-Related Spalling Evaluation of Ring-Restrained Polymer Cement Mortar and Normal Cement Mortar, Proceedings of the 6th International Workshop on Concrete Spalling due to Fire Exposure, Sheffield, UK, 19-20 September, 2019.
8. Sugino, Y., Ozawa, M., Sukekawa, M., and Tanibe, T., Fire Spalling of Acrylic Polymer Cement Mortar Restrained by Steel Ring, Proceedings of the Sixth International Conference on Construction Materials, ConMat '20, Fukuoka, Japan, 27-29 August, 2020.
9. Japan Concrete Institute, JCI Standards and Guidelines, http://jci-net.or.jp/j/jci/study/standard.html (in Japanese).
10. Sukekawa, M., Sugino, Y., Tanibe, T., and Ozawa, M., Fire-Spalling Evaluation of Concrete Repaired with Polymer Cement Mortar by Ring-Restrained Heating Test, Proceedings of the Structures 20 Congress, Structures20, Seoul, Korea, 25-28 August, 2020.
11. Bazant, Z. P., Analysis of Pore Pressure, Thermal Stress and Fracture in Rapidly Heated Concrete, Proceedings of the International Workshop on Fire Performance of High-strength Concrete, NIST, pp. 155-164, Gaithersburg, MD, USA, 13-14 February, 1997.
12. Anderberg, Y., Spalling Phenomena in HPC and OC, Phan, L. T, Carino, N. J., Duthinh, D., and Garboczi, E. (eds.), NIST, Gaithersburg, MD, USA, pp. 69-73, 1997.
13. Nakamura, H., Yoshida, K., Kunieda, M., Ueda, N., Yamamoto, Y., and Ozawa, M., Simulation about Effect on Explosion Spalling of Thermal Stress and Vapor Pressure, Proceedings of the 2nd International RILEM Workshop on Concrete Spalling due to Fire Exposure, pp. 213-220, Delft, Netherlands, 5-7 October, 2011.
14. Iwama, K., Higuchi, K., and Maekawa, K., Thermo-Mechanistic Multi-Scale Modeling of Structural Concrete at High Temperature, J Adv Concr Technol, Vol. 18, 2020, pp. 272-293.
15. Kodur, V. and Banerji, S., Modeling the Fire-Induced Spalling in Concrete Structures Incorporating Hydro-Thermo-Mechanical Stresses, Cem Concr Compos, Vol. 117, 2021, p. 103902.
16. Ozawa, M., Fujimoto, K., Akutsu, Y., and Akasaka, H., Numerical Simulation for a Fire Spalling Model Based on Thermal Stress and Vapor Pressure of High-Strength Concrete, Proceedings of Applications of Structural Fire Engineering, p. 15, Singapore, 13-14 June, 2019.

17. Ozawa, M., Tanibe, T., Kamata, R., Uchida, Y., Rokugo, K., and Parajuli, S.S., Behavior of Ring-Restrained High-Performance Concrete Under Extreme Heating and Development of Screening Test, Constr Build Mater, Vol. 162, 2018, pp. 215-228.
18. Ozawa, M. and Morimoto, H., Effects of Various Fibres on High-Temperature Spalling in High-Performance Concrete, Constr Build Mater, Vol. 71, 2014, pp. 83-92.
19. Tetens, O. Uber Einige Meteorologische Begriffe, Z. Geophys, Vol. 6., 1930, pp. 297-309.
20. Architectural Institute of Japan, 2017, Guidebook on Fire-Resistive Performance of Structural Materials (in Japanese).
21. Tajima, H., Kishida, M., Kanda, T., and Morita, T., An Analytical Study on the Structural Behavior of TBM Shield Tunnel RC Lining Under High Temperature in Fire, J Jpn Soc Civil Eng E, Vol. 62, 2006, pp. 606-618 (In Japanese).
22. Eurocode 2: Design of Concrete Structures - Part 1-2: General Rules - Structural Fire Design, EN1992-2-1,2-4.12.
23. Sugino, Y., Ozawa, M., Tanibe, T., Tuneto, H., and Sukekawa, M., Study of Spalling Behaviour and Mechanism in Fire of Acrylic Polymer Cement Mortar Using Ring Restrained Specimen, J Jpn Soc Civil Eng E2, Vol. 77, 2021, pp. 150-163 (In Japanese).

PERFORMANCE OF TERNARY BLENDED BASALT-POLYPROPYLENE FIBRE REINFORCED CEMENTITIOUS COMPOSITE AT ELEVATED TEMPERATURES

Aniruddha Tangirala[1], S Rawat[2], Mukund Lahoti[3]

ABSTRACT

This paper aims to provide a sustainable alternative to traditional concrete with improved fire resistance. A total of 76 % cement replacement was achieved with ternary blend of flyash (65 %) and silica fume (11 %). Also, Basalt and polypropylene fibres were incorporated to simultaneously improve the ambient and high temperature performance of the cementitious composite. Cylindrical specimens were exposed to elevated temperature between 200 and 800 °C at an interval of 200 °C. The chosen matrix with fibre combination demonstrated excellent resistance against spalling and provided high strength retention up to 600 °C. Remarkable stability against surface cracking was also observed even at the highest exposure temperature. Scanning electron micrographs are further used to corroborate the trend of residual compressive performance.

Keywords: High volume fly ash; Basalt fibre; Polypropylene fibre; Elevated temperature; Fire

1 INTRODUCTION

Ordinary Portland Cement (OPC) accounts for nearly 80 % of greenhouse gas embodied in concrete [1] and this can be ameliorated by utilization of waste fly ash (FA). OPC production requires 1.5-1.6 tonnes of raw materials and 3000-4300 MJ of fuel and 120-160 kWh of electrical energy [2]. The use of supplementary cementitious materials as OPC replacement in concrete provides a cleaner, environmentally friendly, and economical solution to this problem. Generally, FA as OPC replacement is restricted between 10 and 30 %, as further replacement cause adverse effects in terms of delayed strength development and slow setting [3]. This problem can be mitigated by using ternary blends of silica fume (SF) with high volume fly ash (HVFA), and OPC. SF provides early setting and early strength development and thereby allowing a higher replacement level of waste FA. Global production of FA is around 620-660 million tonnes every year [4] with only a fraction of it being used which necessitates greater rate of consumption in cement based materials. HVFA improves fresh, mechanical, and durability properties of concrete. In addition to improvement in all-round properties of concrete at room temperature, elevated temperature performance improves with increasing FA content owing to proportional decrease in thermal conductivity of concrete.

Fire hazards especially in multi-storied structures and infrastructure located in remote locations such as tunnels are a growing concern. Tunnel is a narrow tubular structure with limited access to safety personnel during rescue operations. In the incidence of a major fire breakout, the temperatures can rise to 1000 °C and can cause degradation of the concrete tunnel lining and of the bond between rebar and concrete. Overall,

[1] Mr., Birla Institute of Technology and Science, Pilani
e-mail: aniruddha.tangirala@gmail.com
[2] Mr., University of New South Whales
e-mail: sanketrawat@gmail.com
[3] Dr., Birla Institute of Technology and Science, Pilani
e-mail: mukund.lahoti@pilani.bits-pilani.ac.in
https://doi.org/10.6084/m9.figshare.22177943

such fire hazards can lead to a significant loss of life and property. Ternary blending causes an improvement in thermal performance because of improvement in hydration and denser microstructure resulting from differences in particle sizes [5]. Furthermore, blending SF and high-volume FA showed improved performance in residual strength capacities of concrete up to 600 °C [6].

Elevated temperatures cause significant degradation to the concrete matrix and often causes spalling which reduces the member cross-section. This may cause the collapse of the structure resulting in greater loss of lives. Fibres with vast differences in melting points is an efficient strategy to restrict the occurrence of spalling [7]. Traditionally, hybrid combination of steel-PP has been found effective in improving the mechanical performance at ambient temperatures and reducing the probability of spalling at elevated temperatures. PP fibres melt at low temperature (~160-170 °C) and help in mitigating the pore pressure [10]. These fibres also have a positive influence on the reduction of plastic and drying shrinkage [8] Steel fibres, on the other hand, resist the propagation of cracks and prevent strength decay, making this hybrid combination very effective at elevated temperatures. However, iron and steel production are responsible for 71 % of the adverse environmental impact originating from the metal production industry. Basalt fibres (BF) are new to civil engineering field and show good compatibility with concrete [9]These fibres have high melting point of 1400-1450 °C, high tensile strength of 2600-4840 MPa, and high Elastic modulus of 80-115 GPa [10]. Additionally, BF are economical with only 5 USD/kg as compared to 15 USD/kg of glass fibre and 30 USD for aramid fibre. Hybridization of BF with low melting point polypropylene (PP) fibres becomes an excellent choice to make the concrete less susceptible to the spalling phenomenon. [11][8]Yao et al. [12] studied the elevated temperature performance of hybrid BF-PP mortar specimens with 0-0.4 % BF and 0.1 % PP. They observed an increase in compressive strength at 200 °C and 400 °C at 12.52 % and 19.35 %, respectively, as opposed to a decrease in strength by 2.33 % and 19.35 %, respectively, in the case of unreinforced mortar mixes. At 600 °C and 800 °C, a residual strength of 27.01% and 45 % respectively was observed for FRCC as compared to 39.1 % and 55 % respectively in case of plain mortar specimen. Koksal et al. [13] used BF up to 0.6 % by volume and observed an increase in the room temperature compressive strength for all inclusion levels.

Sustainability, cost incentives and improvement in mechanical and durability performance of concrete provided by the usage of SF and FA makes their inclusion highly advantageous [14]. Inclusion of BF further improves the sustainability of the mix and its combination with PP creates a spalling resistant mixture. However, there is no available literature studying the use of hybrid BF-PP with ternary blended high-volume fly ash (HVFA-SF) based cementitious composites at elevated temperature. It is important to understand the behaviour of hybrid BF-PP fibre when used with HVFA matrix and the resulting interaction after exposure to different temperature. Therefore, this study analyses the change in the microstructure and chemical composition of the hybrid BF-PP HVFA fibre reinforced cementitious composite (FRCC) mix with varying temperature and its influence on the residual compressive strength and mass loss.

2 MATERIALS AND METHODS

Standard 53 grade cement and class F- FA were used in the present study as the primary binder materials and their chemical composition is given in Table 1. A high-grade SF with 95.11 % SiO_2 content was also used as a secondary SCM. Locally available river sand passing through 300-micron sieve was used as the aggregate. Polycarboxylate ether-based superplasticizer (SP) was selected to achieve the required fluidity in the mix. Hybrid combination of basalt and PP fibres was used, and their properties are specified in Table 2.

Table 1: Oxide composition of primary binders: OPC53 and Flyash

Compounds (%)	Cement	Flyash
SiO_2	18.17	55.99
Al_2O_3	6.98	31.74
CaO	61.42	1.546
MgO	2.35	--
SO_3	0.5	--

Table 2: Properties of BF and PP used in the study

Property	Basalt	Polypropylene
Density (kg/dm3)	2.70	0.91
Melting point (°C)	1350	176
Diameter (µm)	17	12
Length (mm)	12	12
Sizing	Silane	--

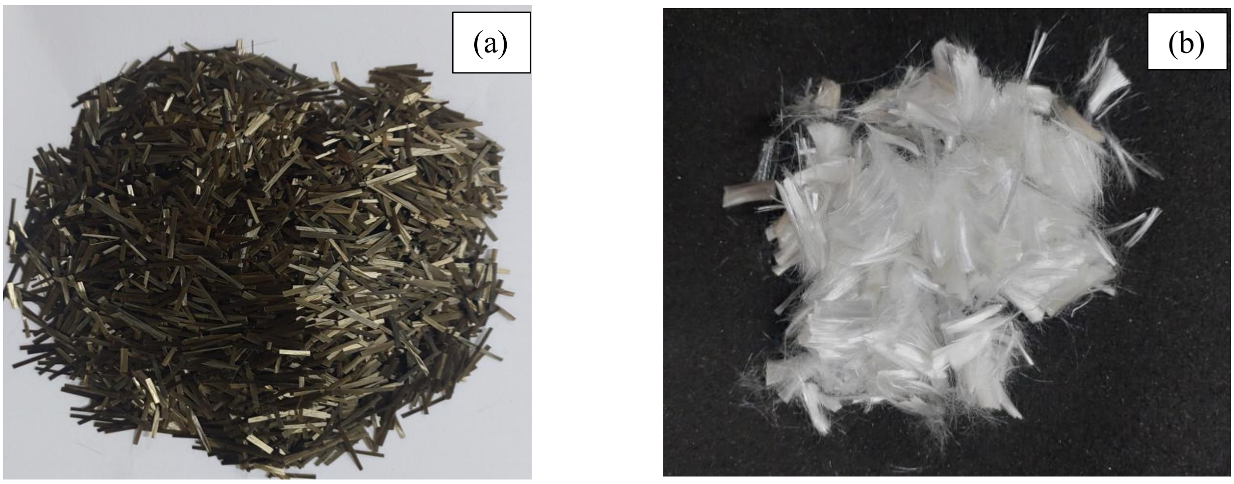

Figure 1. Fibres used HVFA-SF FRCC a) Basalt fibres b) Polypropylene fibres

Initially, all the dry ingredients were added into the pan and dry mixed for a period of 3 minutes. Then the mixture of water and superplasticizer was gradually mixed until a homogenous mixture is obtained. Then half the total volume of fibres was added to the matrix (to avoid stress on the mixer motor) and mixed until homogeneity was achieved and then the other half was added till a final homogeneous mixt was attained. The mix composition is provided in Table 3.

Table 3: Mix design used for the HVFA-SF FRCC

Mix ID	Cement	Flyash	Silica Fume	Sand	Water	SP (kg/m^3)	BF (% vol)	PP (% vol)
65FA	1.00	0.65	0.11	0.44	0.24	6.13	2.00	0.11

Six cylinders of size 75 mm diameter x150 mm height was casted for each set. Three of the six cylinders from each set were used for the ambient temperature testing and the rest were heated in Nabertherm muffle furnace from 200 to 800 °C at an interval of 200 °C with a heating rate of 1 °C/minute. The samples were then allowed to cool down inside the disconnected furnace.

In this study, a prolonged curing time of 56 days (28 days water and 28 days air curing) was adopted to account for slow FA reaction time. Compressive strength tests conforming to ASTM C39 were conducted at ambient and elevated temperatures. Mass loss of the specimen was calculated based on the difference between the masses before and after the subjecting the cylindrical specimens to high temperature. After compressive testing, the broken samples were stored in acetone to inhibit further hydration. The specimens were coated with Chromium to study the microstructure using Apreo-S make Field Emission Scanning Electron Microscope.

3 OBSERVATIONS AND RESULTS

3.1 Surface and colour changes

The specimens subjected to elevated temperature demonstrated very high resistance to surface cracking and remarkably, no major surface cracks were observed even for samples subjected to a temperature of 800 °C. On the other hand, Xu et al. [15] observed severe cracking in their concrete and paste specimens (no fibres) when subjected to temperatures beyond 450 °C (at 1 °C/min heating rate) and suggested that the absence of coarse aggregates increases the prevalence of cracking. In the current study, FRCC didn't have any coarse aggregates and despite that the surface maintained its integrity at elevated temperature. Consequently, the presence of fibres in the matrix has proven to be highly effective in mitigating this behaviour. Cracking at high temperature generally occurs because of build-up of pore pressure and establishment of a thermal gradient. The possible explanation for this excellent behaviour is the release of developed pore pressure by the incorporation of PP combined with slow heating rate that avoids the establishment of a thermal gradient in the FRCC specimens. At temperatures greater than 400 °C, when the PP is completely disintegrated, the high melting point BF may have protected the matrix from further cracking. A change in colour from grey to dull grey was observed with rise in temperature up to 400 °C (Figure 2). Colour further changed from dull grey to patches of dull brick red when the samples were exposed to 600 °C. A comparatively darker shade of brick red was observed when the samples were exposed to 800°C. Overall, the developed FRCC demonstrated excellent surface behaviour at elevated temperature.

Figure 2. Surface and colour change in HVFA-SF FRCC: a) Room b) 200 °C c) 400 °C d) 600 °C e)800 °C

3.2 Mass loss

Mass loss of cylindrical specimens was measured at all temperatures exposures and the variation is depicted in Figure 3. Majority of the mass loss occurred during the initial thermal exposure to 200 °C. The developed HVFA-SF FRCC experienced a 5.93 % of mass loss because of evaporation of free water and PP fibre melting. A steep rise in the mass of loss was observed between 200 and 400 °C as can be seen from Figure 3. At 400 °C, 4.38 % increase was observed because of creation of interconnected channels (PP fibre melting) that allow the adsorbed and capillary water escape. It is usually believed that for temperature greater than 300 °C, decomposition CSH and CH initiate a drop in mass [16]. In this study, an increased pozzolanic reaction at 400 °C, consumed the available portlandite as can be seen from SEM images. Therefore, a portion of the available CSH may have decomposed which accelerated the mass loss. At 600 °C, the composite was found to be stabilized and only a minor increase in mass loss of 0.86 % was observed. Again at 800 °C, an increase of 1.19 % of mass loss was observed. This mass loss is attributed to the loss of chemically bound water as a result of decomposition of hydration products [17]. Despite prolonged exposure to thermal loads, the specimens demonstrated similar mass loss to that of studies available in literature with lower period of exposure [18], indicating the resilience of the material against high temperatures.

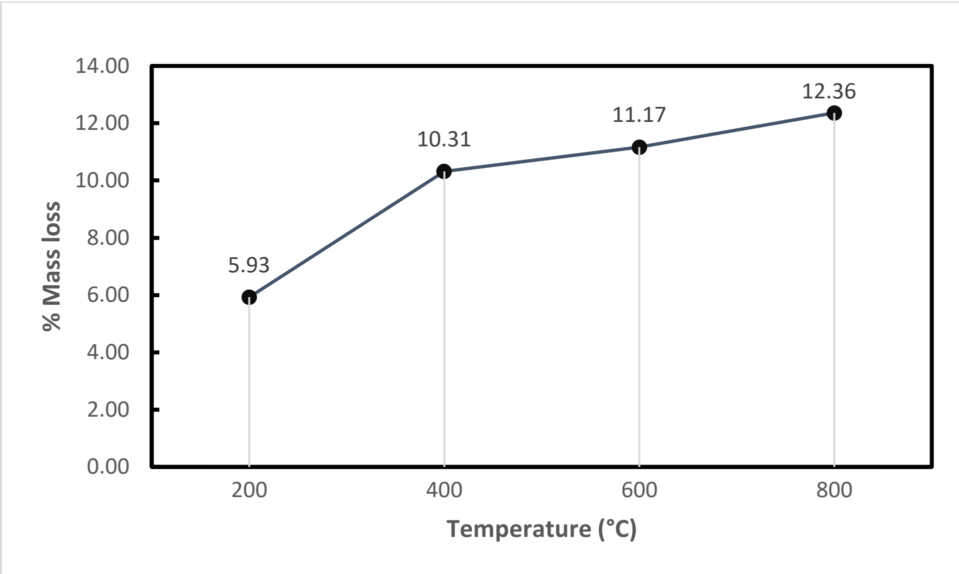

Figure 3. Percentage mass loss of HVFA-SF FRCC at a) 200 °C b) 400 °C c) 600 °C d)800 ℃

3.3 Compressive strength

A room temperature compressive strength of approximately 48 MPa was achieved at the end of 56 days. When exposed to elevated temperatures, the composite initially lost 20.59 % of strength at 200 °C. This loss in strength is attributed to the formation of channels inside the concrete matrix caused by melting of PP fibre. Interestingly, a strength gain of 18.75 % occurred (w.r.t to 200 °C) at 400 °C despite complete disintegration of PP which happens at this temperature. This strength gain was sufficient to make the residual compressive performance at 400 °C to be similar to that of the control specimens. A high residual strength (~79 %) was noted for samples exposed to 600 °C. This minor strength reduction is attributed to the decomposition of Calcium Silicate Hydrate (CSH) and Calcium Hydroxide (CH) [7]. At 800 °C, a drastic loss in residual compressive strength is observed as can be seen from the Figure 4. The dehydration of calcium silicate hydrate (CSH) gel in concrete initiates at about 100 °C and it transforms to di-calcium silicate (C_2S) and tri-calcium silicate (C_3S) at temperatures greater than 600 ℃ [19]. These chemical changes along with the dehydration of calcium hydroxide might be the reason for strength loss of the FRCC specimens after exposure to 800 ℃ . This matrix and hybrid fibre combination demonstrated remarkable stability in terms of strength retention (up to 600 °C) and spalling prevention at elevated temperature.

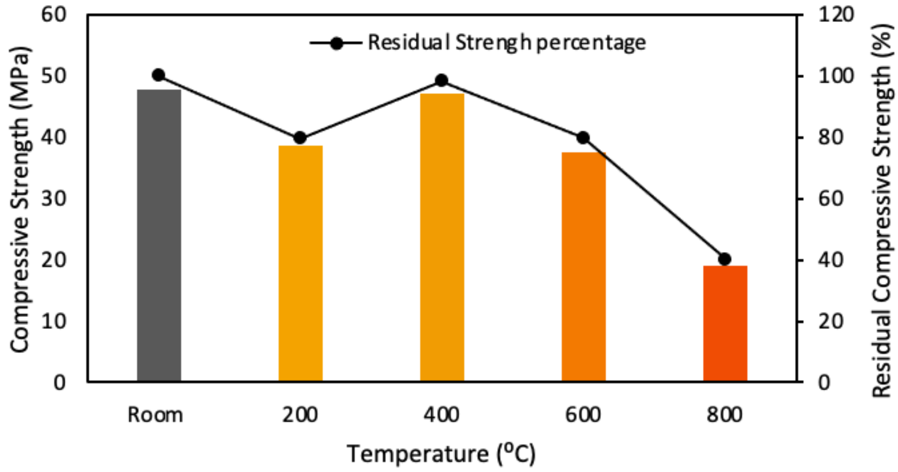

Figure 4. Compressive strength of HVFA-SF FRCC at a) Room temperature b) 200 °C c) 400 °C d) 600 °C e)800 ℃

4 DISCUSSION

4.1 Microstructure observations using SEM

Microstructure of the developed composite was analysed after thermal exposure to validate the findings of the mechanical performance tests. At ambient conditions, a relatively dense microstructure could be observed corroborating the good strength development (~48 MPa) in the FRCC specimens (Figure 5). Correspondingly, the formation of CSH gel could be clearly observed as highlighted in the SEM micrographs. Portlandite crystals can be seen abundantly throughout the microstructure of the HVFA-SF FRCC at ambient temperature. Besides, spherical FA particles could be observed, suggesting the slower pozzolanic reaction of FA particles.

At 200 °C, the porosity of the composite has increased owing to the PP fibre melting and initial dehydration that explains the observed reduction in strength during the compressive testing. Presence of Portlandite and spherical FA particles was found to be less prevalent (comparatively), suggesting an initiation of Pozzolanic reaction at elevated temperature. However, a loss in strength was observed owing to the formation of channels within the matrix (Figure 7) caused by PP fibres melting, loss of bound water and increase in overall porosity of the matrix. These channels allowed the dissipation of the pore pressure developed at elevated temperature that allowed the matrix to be stable against spalling phenomenon.

At 400 °C, densification of microstructure and further hydration can be observed from Figure 6 (b), causing an improvement in compressive strength. Portlandite and spherical FA was found to be absent at 400 °C suggesting their consumption in the pozzolanic reaction. At 600 °C, cracking, and significant increase in porosity can be observed from Fig. 6 (c) causing a drop in the compressive strength of the composite. Also, matrix appeared to be dehydrated in comparison to 400 °C exposure. At 800 °C, more pronounced cracking, high porosity and seems to be completely dehydrated resulting in severe decrease in residual compressive strength. BF have a very high melting point and throughout the study, their morphology was found to be constant at all temperatures suggesting their suitability for fire resistance structures (Figure 8).

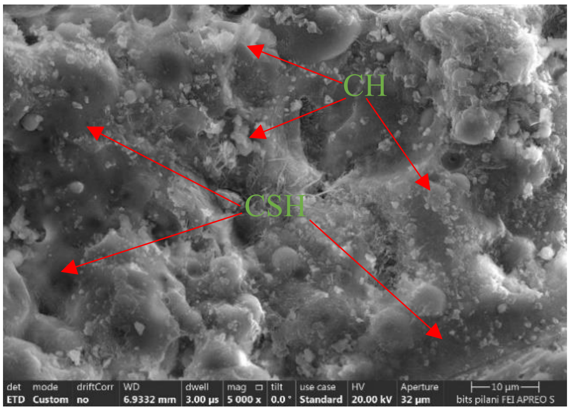

Figure 5. Microstructure at room temperature

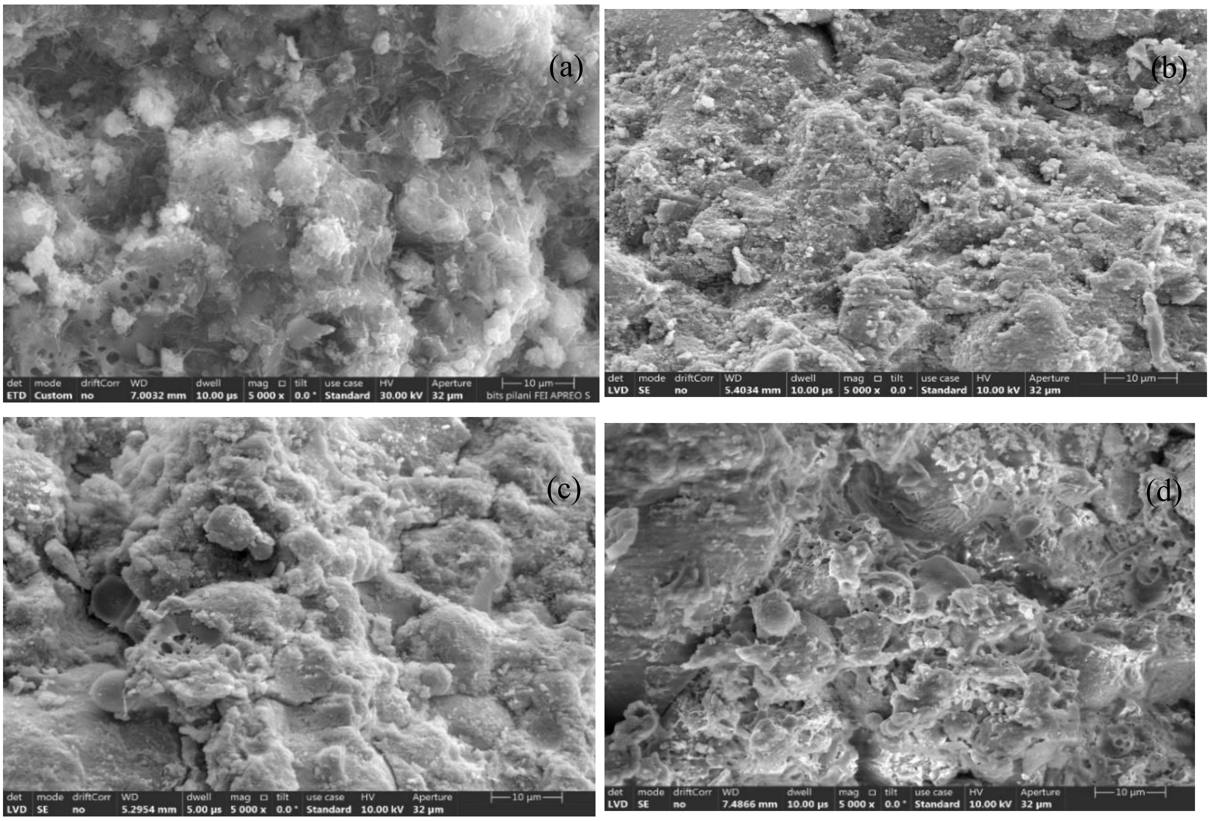

Figure 6. Microstructure in HVFA-SF FRCC at various temperatures: a) 200 °C b) 400 °C c) 600 °C d) 800 °C

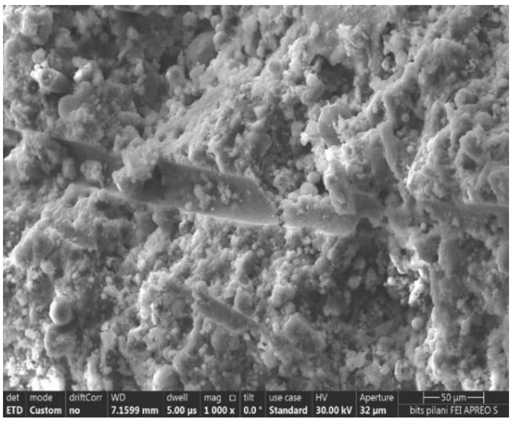
Figure 7. Channels left behind by PP fibre melting at 200 °C in HVFA-SF FRCC

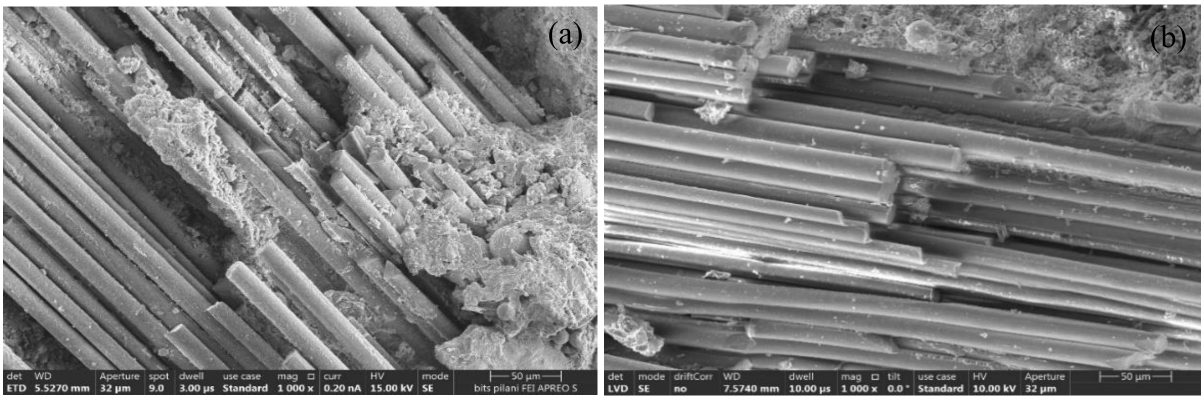

Figure 8. Basalt fibres in HVFA-SF FRCC a) Room temperature b) 800 °C

5 CONCLUSIONS

1. An FRCC mix with 76 % cement replacement and hybrid BF-PP fibres was analysed in this study. This material proved to be excellent at resisting surface cracking. No major surface cracks developed even when the specimens were exposed to 800 °C. BF-PP along with HVFA-SF proved to be an excellent combination for applications where high cracking resistance is pivotal.
2. Mass loss of the developed HVFA-SF based FRCC was significant for 200 and 400 °C. Approximately 83 % of total mass loss was observed at 400 °C. Higher mass loss in the lower temperature exposure conditions is primarily because of low melting point PP fibres which melt and allow the escape of water. Only a minor increase of 0.86 % in mass loss observed at 600 °C. Loss of chemically bound water caused a further 1.19 % of loss in the mass of the specimens at 800 ℃ .

A good strength of approximately 48 MPa was achieved even with 76 % of pozzolanas in this HVFA-SF FRCC. The composite initially lost approximately 21 % of its strength because of formation of channels with PP fibre melting. With the increase in temperature, pozzolanic reaction accelerated and caused a consumption of available Portlandite and FA. This caused a densification of the microstructure at 400°C which improved the residual compressive strength of the FRCC. A good fire resistance with approximately 80 % retention of strength for 600 °C was achieved. With further increase in temperature, a decline in the strength was observed due to the significant increase in porosity, cracking, and decomposition of the microstructure.

REFERENCES

[1] D. J. M. Flower and J. G. Sanjayan, “Green house gas emissions due to concrete manufacture,” *Int. J. Life Cycle Assess.*, vol. 12, no. 5, pp. 282–288, 2007.

[2] A. M. Rashad, “An exploratory study on high-volume fly ash concrete incorporating silica fume subjected to thermal loads,” *J. Clean. Prod.*, vol. 87, no. 1, pp. 735–744, 2015.

[3] S. Donatello, C. Kuenzel, A. Palomo, and A. Fernández-Jiménez, “High temperature resistance of a very high volume fly ash cement paste,” *Cem. Concr. Compos.*, vol. 45, pp. 234–242, 2014.

[4] R. Roychand, S. De Silva, D. Law, and S. Setunge, “Micro and Nano Engineered High Volume Ultrafine Fly Ash Cement Composite with and without Additives,” *Int. J. Concr. Struct. Mater.*, vol. 10, no. 1, pp. 113–124, 2016.

[5] S. Rawat, R. Narula, N. Upasani, and G. Muthukumar, “A relook on dosage of basalt chopped fibres and its influence on characteristics of concrete,” *Lect. Notes Civ. Eng.*, vol. 35, pp. 87–96, 2020.

[6] M. S. Khan and M. Shariq, “Performance of high-volume fly ash concrete after exposure to elevated temperature,” 2019.

[7] L. Liu *et al.*, “Impact of fibre factor and temperature on the mechanical properties of blended fibre-reinforced

cementitious composite," *Case Stud. Constr. Mater.*, vol. 16, no. November 2021, p. e00773, 2022.

[8] A. Behnood and M. Ghandehari, "Comparison of compressive and splitting tensile strength of high-strength concrete with and without polypropylene fibers heated to high temperatures," *Fire Saf. J.*, vol. 44, no. 8, pp. 1015–1022, 2009.

[9] P. Smarzewski, "Flexural Toughness of High-Performance Concrete with Basalt and Polypropylene Short Fibres," *Adv. Civ. Eng.*, vol. 2018, 2018.

[10] A. Adesina, "Performance of cementitious composites reinforced with chopped basalt fibres – An overview," *Constr. Build. Mater.*, vol. 266, p. 120970, 2021.

[11] J. Bošnjak, J. Ožbolt, and R. Hahn, "Permeability measurement on high strength concrete without and with polypropylene fibers at elevated temperatures using a new test setup," *Cem. Concr. Res.*, vol. 53, pp. 104–111, 2013.

[12] Y. Yao, B. Wang, Y. Zhuge, and Z. Huang, "Properties of hybrid basalt-polypropylene fiber reinforced mortar at different temperatures," *Constr. Build. Mater.*, vol. 346, no. July, p. 128433, 2022.

[13] F. Koksal, E. Tugce, O. Gencel, and A. Benli, "The effects of high temperature and cooling regimes on the mechanical and durability properties of basalt fiber reinforced mortars with silica fume," *Cem. Concr. Compos.*, vol. 121, no. August 2020, p. 104107, 2021.

[14] C. Hu and Z. Li, "Cement & Concrete Composites Property investigation of individual phases in cementitious composites containing silica fume and fly ash," *Cem. Concr. Compos.*, vol. 57, pp. 17–26, 2015.

[15] Y. Xu, Y. L. Wong, C. S. Poon, and M. Anson, "Influence of PFA on cracking of concrete and cement paste after exposure to high temperatures," *Cem. Concr. Res.*, vol. 33, no. 12, pp. 2009–2016, 2003.

[16] S. Sanchayan and S. J. Foster, "High temperature behaviour of hybrid steel–PVA fibre reinforced reactive powder concrete," *Mater. Struct. Constr.*, vol. 49, no. 3, pp. 769–782, 2016.

[17] A. Nadeem, S. A. Memon, and T. Y. Lo, "The performance of Fly ash and Metakaolin concrete at elevated temperatures," *Constr. Build. Mater.*, vol. 62, pp. 67–76, 2014.

[18] S. Rawat, C. K. Lee, and Y. X. Zhang, "Performance of fibre-reinforced cementitious composites at elevated temperatures : A review," *Constr. Build. Mater.*, vol. 292, p. 123382, 2021.

[19] M. A. Tantawy, "Effect of High Temperatures on the Microstructure of Cement Paste," *J. Mater. Sci. Chem. Eng.*, vol. 05, no. 11, pp. 33–48, 2017.

Proceedings of the 12th International Conference on Structures in Fire

Experimental Research of Structures in Fire

EXPERIMENTAL ASSESSMENT OF THE BURNOUT RESISTANCE OF TIMBER AND CONCRETE COLUMNS

Thomas Gernay[1], Jochen Zehfuß[2], Jean-Marc Franssen[3], Fabienne Robert[4], Sven Brunkhorst[5], Roberto Felicetti[6], Patrick Bamonte[7], Siyimane Mohaine[8], Robert McNamee[9]

ABSTRACT

Fire-exposed structures may collapse after the available fuel in the compartment has been consumed, while the enclosure is cooling or even after returning to ambient temperatures. But there is no standardized experimental method to study the stability of structural elements until full burnout. The standard fire testing method relies on continuous heating of the element to failure, and in some cases post-fire experiments measure residual load-bearing capacity, but neither of these methods assesses stability of loaded elements throughout the heating and cooling phases of a fire. This paper applies a new experimental method for evaluating the load-bearing capacity function of structural elements until fire burnout. The method adopts the Duration of Heating Phase (DHP) indicator for assessing the burnout resistance of the elements. Full-scale furnace tests on loaded columns are presented, including four on reinforced concrete columns and eight on timber columns, in which identical specimens were subjected to various heating durations followed by controlled cooling. For both the concrete and timber columns, failures occurred during the cooling phase after exposure to ISO 834 heating for a duration shorter than their fire resistance. The timber columns had a measured fire resistance of 55-58 minutes (two specimens) but, when exposed to heating for 15 minutes, failed during cooling after 98-153 minutes (two specimens). These experiments show that delayed thermal-mechanical effects can jeopardize structural stability in real fires and provide a systematic method to assess these effects.

Keywords: Fire tests; concrete columns; glued laminated timber; cooling phase; burnout resistance

---

[1] Assistant Professor, Johns Hopkins University,
e-mail: tgernay@jhu.edu, ORCID: https://orcid.org/0000-0002-3511-9226
[2] Professor, Technische Universität Braunschweig
e-mail: j.zehfuss@ibmb.tu-bs.de
[3] Professor, Liege University
e-mail: jm.franssen@uliege.be
[4] Deputy Director, CERIB Fire Testing Centre
e-mail: f.robert@cerib.com
[5] Researcher, Technische Universität Braunschweig
e-mail: s.brunkhorst@ibmb.tu-bs.de
[6] Associate Professor, Politecnico di Milano
e-mail: roberto.felicetti@polimi.it
[7] Associate Professor, Politecnico di Milano
e-mail: patrick.bamonte@polimi.it
[8] R&D Engineer, CERIB Fire Testing Centre
e-mail: s.mohaine@cerib.com
[9] Research and Business Developer, RISE Research Institutes of Sweden, & Adjunct Senior Lecturer, Lund University
e-mail: robert.mcnamee@ri.se
https://doi.org/10.6084/m9.figshare.22177994

1 INTRODUCTION

Fire-exposed structures may collapse during the cooling phase of the fire, or even thereafter. This poses challenges for building occupants but also for firefighters who must evaluate on the spot whether it is safe to enter a burning building to fight the fire. Incidents of collapse after extinction of a fire have led to casualties [1]. However, currently the concept that is overwhelmingly used to characterize and classify the ability of loadbearing members to withstand fire exposure is the standard fire resistance, which relies on standardized furnace tests that measure the response under heating only. The method of standard fire testing does not include any evaluation of the effects of cooling phases on structural stability.

Researchers have long recognized that structural fire assessments need to go beyond the standard fire resistance rating [2-4]. To better inform about continued stability (or lack thereof) of loadbearing members throughout the different phases of a fire, there needs to be a framework, experimental protocol, and design methods to systematically assess resistance until burnout.

Recently, the concept of burnout resistance evaluated through a standard indicator named 'Duration of Heating Phase' (DHP) was proposed [5]. The DHP quantifies the longest duration of exposure to heating according to the standard ISO 834 fire that will not result in failure of a member when assessing stability throughout the entire fire event. Importantly, the aim of the concept is not to replace a performance-based analysis of the response of a structure under a realistic fire, but rather to adopt a standard method to investigate, measure, and compare the effects of cooling phases on the stability of structural members.

The concept of DHP was applied numerically by Gernay to concrete columns [6] and timber columns [7]. These numerical studies, and subsequent ones [8], showed the relevance and usefulness of the approach as they quantified the maximum thermal exposure that the structural members could withstand to burnout, which is shorter than the members' fire resistance time. But the next necessary step is to apply the concept experimentally and confirm the numerical findings with test data.

In this research, an experimental program was conducted to measure the burnout resistance of full-scale loaded columns in standard furnaces. The experimental program applied for the first time experimentally the concept and method presented numerically in previous research [5-7]. This demonstrates the feasibility and relevance of measuring the ability of columns to maintain stability until full burnout. Experiments were conducted at the University of Liege on four reinforced concrete (RC) columns and at the Technische Universität Braunschweig on eight glued laminated (glulam) timber columns. In both cases, several identical column specimens were tested under identical conditions of loading, in furnaces, but under varying durations of heating according to the ISO 834 time-temperature curve, followed by controlled cooling down phases. Temperatures inside the columns and displacements were measured throughout the tests, for a long duration after the end of the heating to measure possibility of delayed failure. The paper reports the test data from the RC and glulam column fire tests including cases of failure during cooling.

2 BURNOUT RESISTANCE AND DHP

To quantify the resistance to full burnout in furnace testing, this research builds on previous work in which the indicator of Duration of Heating Phase (DHP) [5] was proposed for investigation of delayed failures of structural members during the cooling phase of a fire. The DHP is a systematic measure of the longest heating phase which a structural member will be able to withstand until the end of the fire event, i.e., until the temperatures in the member are back to ambient. The DHP is evaluated by considering a standardized fire exposure with cooling phase and assessing the behaviour of the loaded member continuously throughout the different stages of the fire. The adopted standardized fire exposure, necessary to allow for systematic quantification and comparison between members, has the heating according to the ISO 834 curve followed by linear cooling with the cooling rate from the Eurocode parametric fire model when $\Gamma=1$ (it is close to -10 K/min for short durations of heating, and decreases for longer heating). The definition of the DHP is illustrated in Figure 1 and discussed in detail in previous publications [5-7].

Evaluating the DHP of a structural member requires to successively test the effect of various time-temperature curves on its stability, as illustrated in Figure 1. The DHP is eventually obtained by bounding the behaviour of the member, between a thermal exposure that can be survived to burnout, and one slightly longer that results in collapse during or after the cooling phase. In an experimental setting, this implies constructing several identical specimens and testing them under identical conditions except for the applied duration of the heating phase. This is the concept of the experimental program devised in this research.

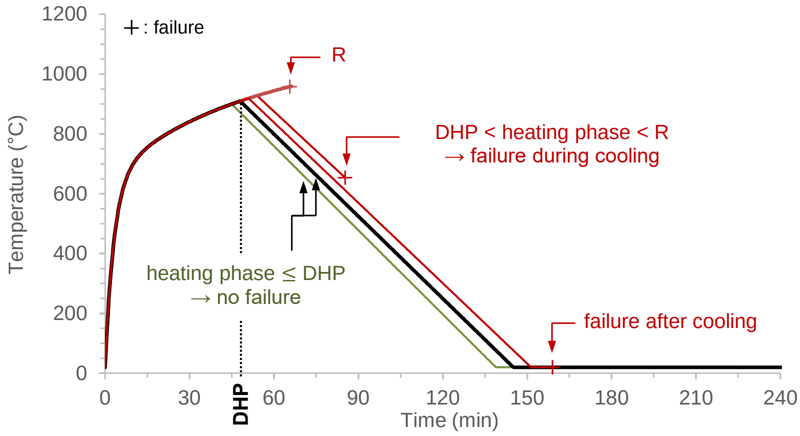

Figure 1. Definition of the DHP indicator to quantify a measure of burnout resistance.

3 DESCRIPTION OF THE EXPERIMENTS

3.1 Experimental method

The experiments are conducted in column furnaces. The columns are tested under heating exposure followed by a cooling phase while the load is maintained, and displacements are measured continuously until stabilization. This stabilization of displacements occurs hours after the end of the heating exposure due to the slow heat transfer across the column section. It is thus important to measure the response for many hours after the end of heating.

For any given test, possible outcomes are that the column: (i) fails during the heating phase, (ii) fails during or after the cooling phase, or (iii) survives the considered exposure. Several tests are conducted on identical specimens to explore the effects of different heating exposures. The heating-cooling exposures are selected with the aim to achieve the different outcomes and bound the behaviour to evaluate the columns' DHP. A priori modelling by the finite element method with SAFIR [9] is used to inform selection of the exposures. Details of the experiments are provided hereafter for the concrete and timber columns, respectively.

3.2 Concrete columns

The experiments on concrete columns were conducted at the Fire Testing Laboratory at the University of Liege, Belgium. The laboratory is accredited ISO 17025. The gas furnace for the column testing is 3.25 m in height. The loading is applied by two hydraulic jacks working in parallel. In each test, the columns were loaded with the same load. The tests varied by the applied time-temperature curve, see Figure 2.

Four identical reinforced concrete columns were cast. Siliceous concrete with a measured cylinder strength at 28 days of 31.3 MPa was used. The columns were designed according to Eurocode for a representative concrete building with five stories. The columns were 3.00 m long with a section of 300 x 300 mm². The longitudinal reinforcement, grade S500 steel, was made of 4 bars of 14 mm in the corners and 4 bars of 10 mm on the medians of the section, with a concrete cover of 20 mm over the 6 mm diameter stirrups. The columns were loaded at 1009 kN during the fire tests, with an eccentricity of 20 mm. This loading represents 56 % of the design load bearing capacity at ambient temperature (1814 kN) calculated according to Eurocode EN1992-1-1 [10]. The degree of utilization at ambient temperature is 90 %. The standard fire resistance rating of the column is 60 minutes according to Eurocode EN1992-1-2 [11] simplified method.

Test 1 was a standard fire resistance test with ISO 834 heating to failure. In Tests 2, 3, and 4, the columns were subjected to respectively 45 minutes, 55 minutes, and 72 minutes of ISO 834 heating followed by cooling, see Figure 2. Additional details on the specimens and experiments are provided in Ref. [12].

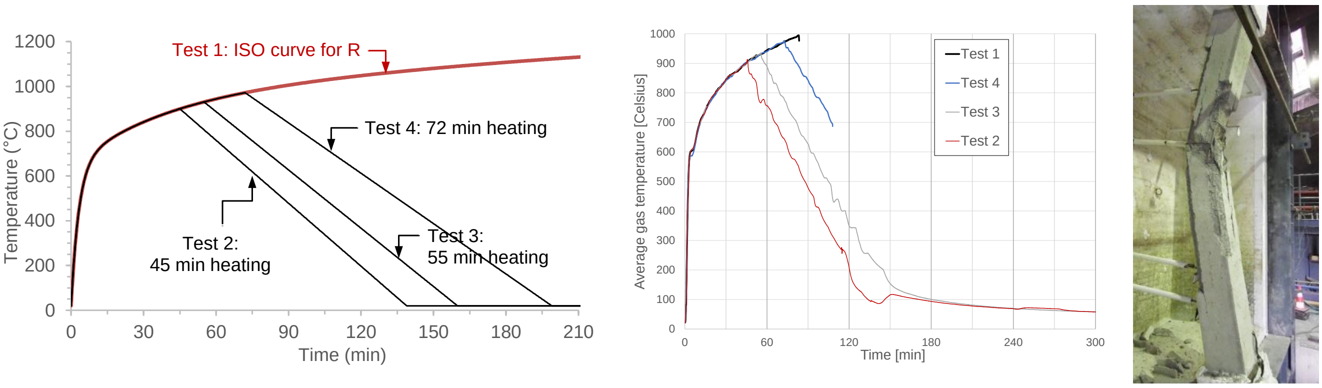

(a) (b) (c)

Figure 2. Concrete column fire tests. (a) Time-temperature curves, planned. (b) Measured furnace temperature. (c) column.

3.3 Timber columns

The experiments on timber columns were conducted at the Institute of Building Materials, Concrete Constructions and Fire Safety (iBMB) of Technische Universität Braunschweig, Germany. The furnace has an inner floor area of 3.60 by 3.60 m² and an inner height of 3.50 m. The furnace uses six oil burners. The mechanical load is applied by a hydraulic press system.

Eight identical timber columns were constructed. The timber columns consisted of glued-laminated spruce made with melamine glue. The single lamellas were 40 mm thick and finger joints were used to produce lamellas of desired length. The strength class was GL 24h. A total of 48 thermocouples were installed at three different heights inside the timber column (16 per section). The measured moisture content for all columns was 9 % ± 0.5 % (in mass percentage) at 5 mm and 13 % ± 0.5 % (in mass percentage) at 30 mm on average. The design of the timber column was also defined to sustain a load representative of a building with five stories with a degree of utilization of 90% at ambient temperature. The cross-section of the timber columns was 280 by 280 mm². The length of the columns was 3.68 m. The columns were loaded at 322 kN during the fire tests, with an eccentricity of 20 mm. The columns were designed to achieve a target fire resistance of R60 according to the Eurocode EN1995-1-2 [13] with consideration of the revised value of the zero-strength layer in prEN1995-1-2 [14]. Details on the specimens and tests are provided in Ref. [15].

Tests 1 and 2 were standard fire resistance tests in which the columns were subjected to ISO 834 heating until failure. Test 1 was hinged-fixed while Test 2 was hinged-hinged; for the remainder of the test program, hinged-hinged conditions were used. In Tests 3 and 4, the columns were subjected to respectively 15 minutes and 10 minutes of ISO 834 heating, followed by a cooling at 10.4 °C/min. Tests 5 to 7 served to verify the repeatability of the previous tests, without inner thermocouples. The time-temperature curves applied in the timber column tests are plotted in Figure 3.

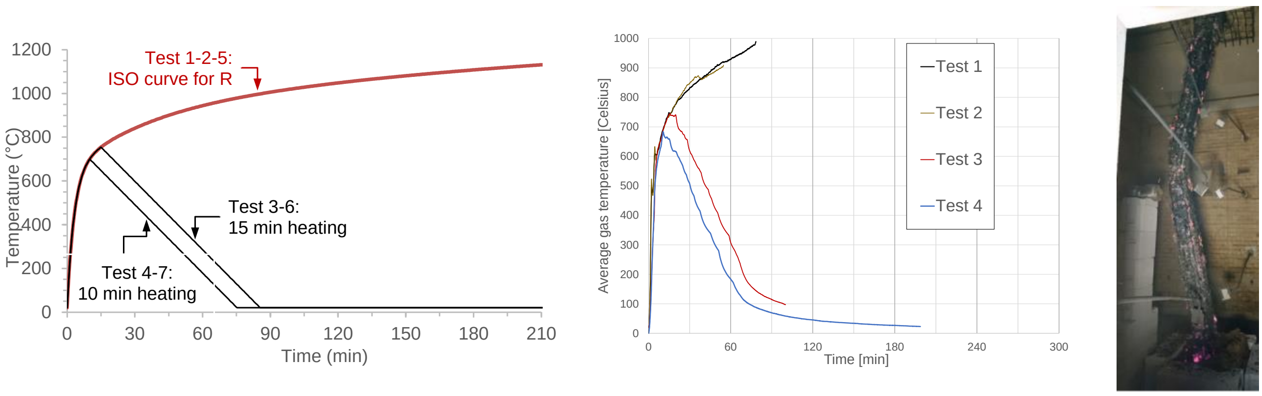

(a) (b) (c)

Figure 3. Timber column fire tests. (a) Time-temperature curves, planned. (b) Measured furnace temperature. (c) column.

4 EXPERIMENTAL RESULTS

4.1 Concrete tests

The tests were conducted at Liege in the summer of 2021. In Test 1, the column failed after 83 minutes of exposure to the ISO 834 time-temperature curve. In Test 2, an identical column was subjected to ISO 834 heating for 45 minutes followed by a linear cooling phase with a rate of -9.4 K/min. No collapse was observed. After 6 hours and 15 minutes, when all temperatures in the section were cooling and were below 150 °C, the load was increased until failure. The post-fire failure load was 1527 kN. In Test 3, the column was heated for 55 minutes followed by cooling at -8.9 K/min (cooling rates are from the Eurocode parametric fire model). No collapse was observed. The column was loaded until failure after 5 hours and 30 minutes. The failure load was 1497 kN. In Test 4, the column was subjected to 72 minutes of ISO 834 heating, followed by cooling at -7.5 K/min. The column failed during cooling after 108 minutes of testing. At time of failure, the temperature in the furnace had dropped from 973 °C to 700 °C.

Figure 4 plots the evolution of the axial displacement at the top of the RC columns. The columns first expand (negative values of axial displacement on the plot) under the effect of thermal expansion. Then, the displacement progressively shifts to a contraction as the column stiffness is reduced by temperatures, transient creep develops [16], and, in Tests 2-3, long cooling leads to partial recovery of the thermal strains.

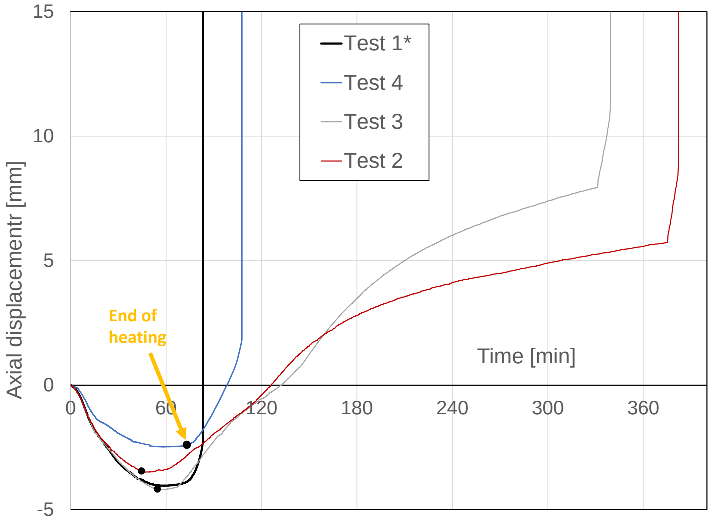

Figure 4. Concrete column tests: evolution of the axial displacement of the columns (negative values are for elongation). Test 1 fails in heating; Test 4 fails in cooling; Tests 2 and 3 are loaded to failure after the end of the heating-cooling sequence.

The experimental program achieved the intended outcome: the tests captured one failure in heating, one failure in cooling, and two cases of survival to burnout. Figure 5 plots the tests outcomes on a timeline. It shows that RC columns may fail during the cooling phase after exposure to ISO 834 heating for a duration shorter than their standard fire resistance. The DHP lies between 55 min and 73 min. The results from the RC column tests are summarised in Table 1.

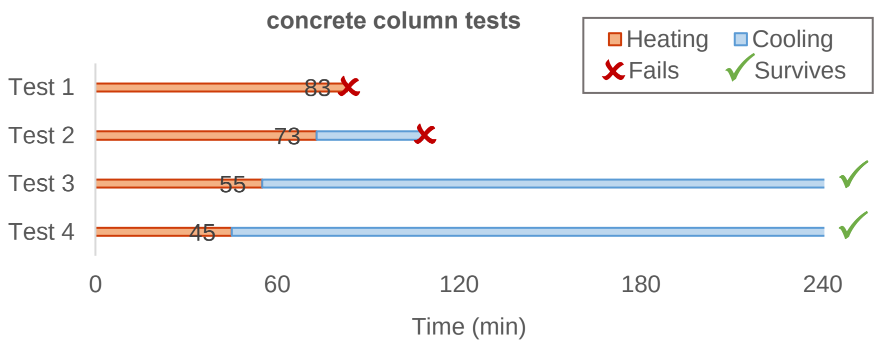

Figure 5. Results from the furnace tests on reinforced concrete columns under heating and cooling.

Table 1. Results of the fire tests on the reinforced concrete columns.

Test	Time of collapse in the heating phase	Start of the cooling phase	Time of collapse in the cooling phase	Failure load after cooling
	Minutes	Minutes	Minutes	kN
1	83	-	-	-
2	-	45	-	1527
3	-	55	-	1497
4	-	73	108	-

Figure 6 shows pictures of the RC columns after the fire tests. The column from Test 1 exhibited corner spalling, but it is unclear whether this spalling developed before the failure or was caused by the failure. The column from Test 3 was loaded to failure after the heating-cooling exposure to determine the residual loadbearing capacity. The column from Test 4 failed during the cooling phase.

Test 1 (failure at 83 min) Test 3 (loading at 330 min) Test 4 (failure at 108 min)

Figure 6. Pictures of the RC columns fire tests.

4.2 Timber tests

The timber tests were conducted at Braunschweig during the spring and summer of 2021. Tests 1, 2, and 5 were standard fire resistance tests under the load of 322 kN. In Test 1, which was hinged-fixed, failure occurred after 78 minutes of fire exposure. In Test 2, which was hinged-hinged, failure occurred after 55 minutes. Test 5 was identical to Test 2 except that no thermocouples were installed in the specimen of Test 5. The column of Test 5 failed at 58 minutes, indicating good repeatability of the fire resistance test. The average charring rate, under the assumption of a charring temperature of 300 °C, was 0.64 mm/min at the axis of the column.

In Tests 3 and 6, the timber column was subjected to the ISO 834 heating for 15 minutes followed by a linear cooling phase at a rate of -10.4 K/min. The tests were nominally identical but the specimen of Test 6 was without inner thermocouples. Both columns collapsed in the late decay phase under the constant load of 322 kN (Figure 7a). During the cooling phase, the temperature continued increasing inside the timber section. A self-extinguishing of flames on the surface of the timber columns in Tests 3 and 6 occurred after approximately 40 minutes, but local smouldering was visible until the failure in Test 3 and until 100 minutes in Test 6. The column in Test 3 collapsed after 98 minutes and that in Test 6 collapsed after 153 minutes.

In Tests 4 and 7, the duration of the ISO 834 heating was 10 minutes. This was followed by a cooling phase at a rate of -10.4 K/min. Visible flaming stopped after 35 minutes. Self-extinguishing of the visible smouldering occurred after 100 minutes. After 150 minutes, all measured temperatures were below 100 °C and decreased very slowly. The vertical displacement progressively increased until about 200 minutes, after which it stabilized. Both columns survived the fire exposure; the columns were then loaded to failure (Figure 7b). The ultimate load capacity was 893.3 kN for Test 4 and 864.9 kN for Test 7. A residual cross-section without discoloration of approximately 230 by 230 mm² was measured after the fire tests.

Test 8 was an ambient temperature test to measure the loadbearing capacity. The ultimate load capacity for Test 8 was 2159 kN. This exceeds by a factor 2.7 the design load-carrying capacity of 800 kN obtained from application of the Eurocode 1995-1-1 [17] equations for a column subjected to combined compression and bending with a strength values of GL 24h, which may be due to the use of the 5% strength fractile in the Eurocode and/or the fact that the producer may have used lamellas with a higher strength classification. From Tests 4 and 7, the residual load capacity of the column after exposure to the fire with a 10 minutes heating phase was 40% of the load-bearing capacity measured at ambient temperature in Test 8.

Figure 8 plots the tests outcomes on a timeline. The timber columns may fail long into the cooling phase after a relatively short exposure to ISO 834 heating. For these specimens which have a measured fire resistance of 55 minutes (Test 2) to 58 minutes (Test 5), the DHP lies between 10 to 15 minutes.

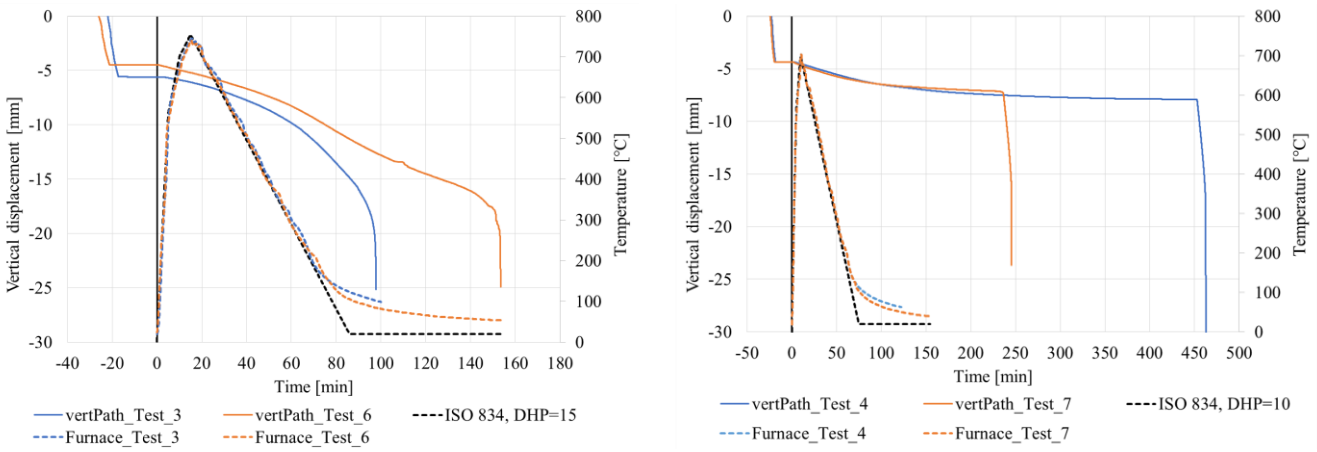

(a) Test 3 and Test 6

(b) Test 4 and Test 7

Figure 7. Timber column tests: evolution of the axial displacement of the columns (negative values are for contraction). Tests 3-6 fail in cooling with the 15 min heating; Tests 4-7 survive with the 10 min heating and are loaded to failure after.

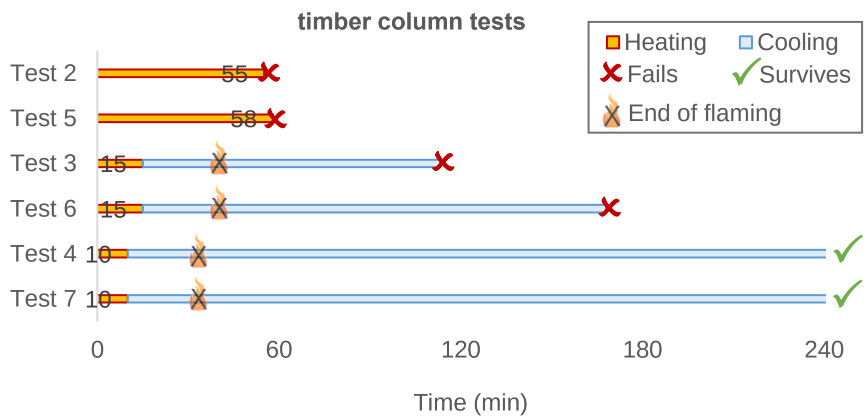

Figure 8. Results from the furnace tests on glulam timber columns under heating and cooling.

The results from the timber column tests are summarised in Table 2. A failure during the late decay phase of the heating-cooling gas temperature-time curve occurred in Tests 3 and 6. On the contrary, the columns of Tests 4 and 7 survived the heating-cooling sequence and were subsequently subjected to increasing load to assess their ultimate load capacity. The results show that there is good repeatability of the experiments and no significant influence of the milling grooves for the thermocouples on the load-carrying behaviour (Test 2 vs Test 5; Test 3 vs Test 6; Test 4 vs Test 7). The test program achieved the intended outcome, with data on failure during heating, failure in the late cooling stage, and survival to full burnout with subsequent loading to failure.

Figure 9 shows pictures of the timber columns from Tests 2, 3, and 4 in the furnace.

Table 2. Results of the fire tests on the glulam timber columns.

Test	Time of collapse in the heating phase	Start of the cooling phase	Time of collapse in the cooling phase	Failure load after cooling
	Minutes	Minutes	Minutes	kN
1	78	-	-	-
2	55	-	-	-
3	-	15	98	-
4	-	10	-	893
5	58	-	-	-
6	-	15	153	
7	-	10	-	865
8	-	-	-	2159 (ambient)

Test 2 (failed during heating)

Test 3 (failed during cooling)

Test 4 (survived the fire)

Figure 9. Pictures of the timber columns fire tests.

Figure 10 shows the residual cross-section of the column from Test 3 at the end of the test. The residual cross-section without discoloration was approximately 220 by 220 mm² for the specimens of Tests 3 and 6. This means that, for the fire with a 15-minute heating duration, approximately 30 mm was consumed on each side over the whole fire exposure. From the standard fire resistance tests (Tests 1, 2, 5), the average charring rate under ISO 834 exposure was 0.64 mm/min. Accordingly, the 15 minutes of exposure to ISO 834 would have resulted in approximately 10 mm of charring depth at the end of the heating phase in Test 3 and Test 6. This shows that, under a fire exposure with a cooling phase, the depth of the section consumed by the thermal exposure (herein, about 30 mm when the column fails at 98 minutes) increases well beyond the charring depth determined at the time of maximum gas temperature (herein, 10 mm at the end of the 15-minute heating).

Figure 10. Residual cross-section for Test 3 of about 220 by 220 mm² (initial section: 280 by 280 mm²).

Figure 11 plots the evolution of the temperature inside the cross-section of the timber column during Test 3. The temperature data that is plotted is an average value of the thermocouple measurements over the three sections at the respective depth. The temperature inside the timber section continues increasing long after the end of the heating phase. It takes 90 minutes for the temperature inside the timber column to decrease below 200 °C.

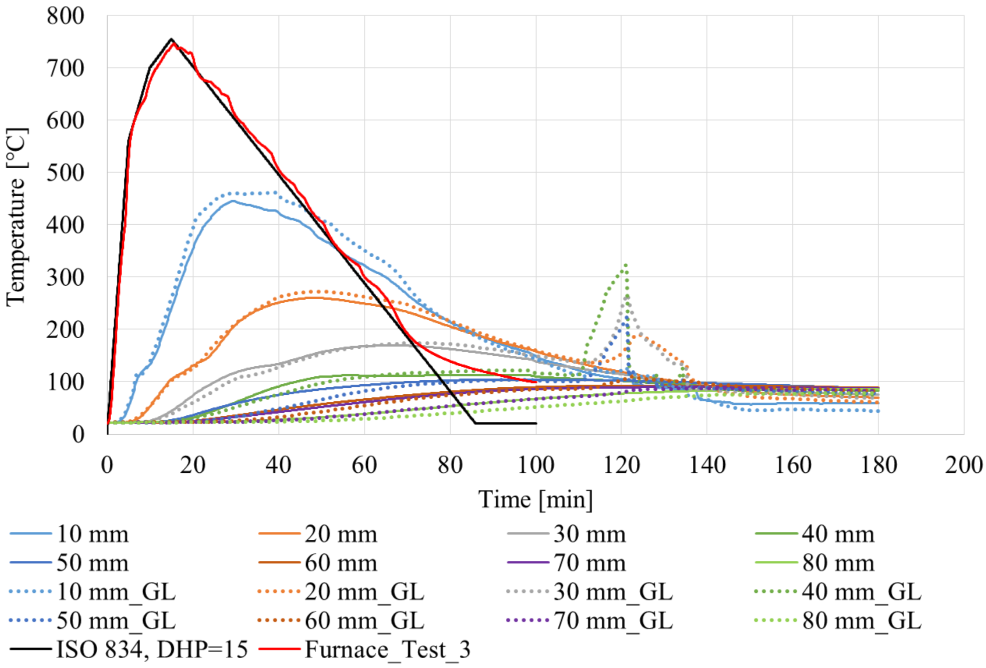

Figure 11. Time-temperature development inside the timber column at different depths under exposure to the 15 minutes heating fire (DHP = 15 min), Test 3.

5 COMPARISON WITH NUMERICAL MODELS

The test program allowed evaluating experimentally the burnout resistance of the RC column and the timber column, based on the DHP indicator [5]. The DHP of the RC column is between 55 and 73 minutes, see Figure 5, because the RC column survived the standardized heating-cooling sequence with a heating phase of 55 minutes but failed under the one with a heating phase of 73 minutes. The DHP of the timber column is between 10 and 15 minutes. Previous FEM studies had been conducted on columns to evaluate their DHP numerically. The new test data can thus be compared with the numerical predictions.

For the RC column, the new test data from this study is compared with the numerical results from the analysis of 74 reinforced concrete columns [6]. The comparison is shown in Figure 12. The experimental fire resistance is 83 minutes (from Test 1), so the "Test data" in Figure 12 shows an interval for R=83min and DHP=[55-73]min. The DHP equation proposed in [6] yields a DHP of 57 min based on the experimental fire resistance of 83 min, which is consistent with the experimentally obtained DHP. The experimental results obtained in this research agree well with the numerical predictions.

For the timber column, the test data from this study is compared with numerical results on 49 glulam timber columns analysed with SAFIR [7] in Figure 13. Two intervals are provided for "Test data" corresponding to the measured values of R equal to 55 and 58 minutes, respectively. The experimental DHP lies between 10 and 15 minutes. Very good agreement is obtained between the experimental data obtained in this study and the numerical predictions of R versus DHP published previously.

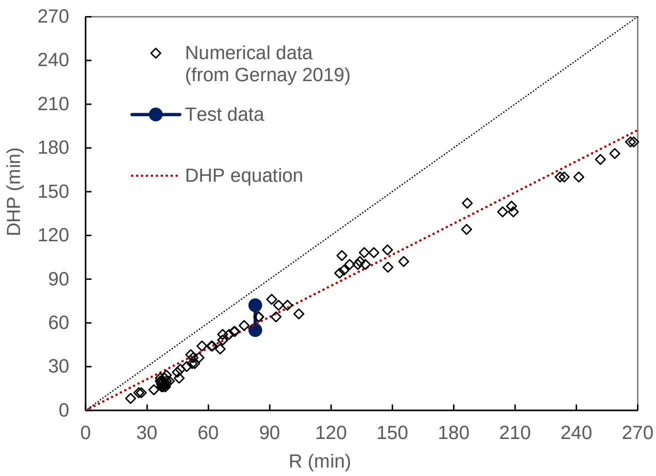

Figure 12. Fire resistance (R) and burnout resistance (DHP) of the concrete column specimen from this study compared with a previously published numerical dataset [6] for 74 reinforced concrete columns.

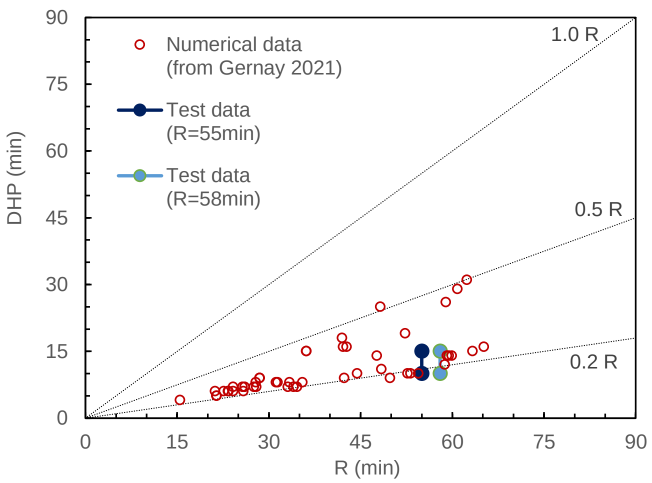

Figure 13. Fire resistance (R) and burnout resistance (DHP) of the timber column specimen from this study compared with a previously published numerical dataset [7] for 49 timber columns.

For both concrete and timber columns, the experiments demonstrate that loadbearing members may fail during the cooling phase when exposed to standardized ISO 834 heating for a duration shorter than their standard fire resistance. The physical phenomena that explain these delayed failures had been explained theoretically and discussed in papers presenting numerical results [6,7,18]. The delayed failures are primarily caused by delayed temperature increase (and charring in case of timber) inside the sections of the columns. As the heat is progressively transferred from the edge to the core of the section, the material strength in the core of the section reaches its minimum reduced value long after the end of the heating phase. The consequences depend on the material since different materials exhibit different laws of strength reduction with temperature. The experimental program presented in this paper confirmed these phenomena, not only qualitatively, but also quantitatively showing that advanced numerical models by the finite element method can be used to accurately assess the behaviour under heating and cooling.

6 CONCLUSIONS

This paper described the application of an experimental method to study the behaviour of columns subjected to fire until burnout. The method assesses the effects of heating-cooling exposure on the structural stability of the columns and determines what severity of fire exposure the columns can survive to full burnout. Application to loaded reinforced concrete columns and glulam timber columns provided new data on their response under controlled heating-cooling exposure. The main findings are:

- While the physical phenomena that explain failure during or even after cooling had been explained theoretically, and the concept of DHP had been introduced and quantified numerically for concrete and timber columns, this testing program brought an experimental confirmation to these theoretical and numerical developments, corroborating models on the prediction of structural failure during cooling.
- Besides qualitatively confirming the phenomena that explain delayed failure, the experimental results agree closely with numerical data previously published based on FE analyses with SAFIR. Numerical predictions of failure during the cooling phase are thus validated by the experiments, both for concrete and timber columns, supporting the validity of advanced analysis for studying burnout resistance.
- The new data include tests on four loaded reinforced concrete columns, 300 by 300 mm^2 and 3.0 m long, under various fire exposure. While the column had a tested fire resistance of 83 minutes, it failed during the cooling phase when the burners were shut off after 72 minutes while the load was maintained. The column survived a shorter fire exposure with 55 minutes heating.
- The new data also include tests on eight loaded glulam columns, 280 by 280 mm^2 and 3.7 m long. Under continuous ISO 834 heating, two column specimens failed at 55 and 58 minutes. Yet when testing identical columns under 15 minutes of ISO 834 followed by a cooling phase, two column specimens collapsed during the ensuing cooling phase after 98 and 153 minutes.
- Flame extinction was not an indicator of whether the timber column would survive to full burnout. The two timber columns subjected to 15 minutes of heating both exhibited self-extinguishing of flames after 40 minutes but failed after 98 and 153 minutes. Fire brigades should thus not take cessation of flaming of timber members as an indication of safety leading them to enter the building.

The findings from the experiments demonstrate that delayed thermal-mechanical effects can jeopardize structural stability in real fires, and they provide a framework to measure these effects in tests. Research is ongoing to further study the effects of different cooling rates, including in natural compartment fire experiments. Moving beyond fire resistance to quantify the response until burnout will support designs for safety of occupants and firefighters throughout the fire and promote repairability and resilience.

ACKNOWLEDGMENT

The support from the project partners is gratefully acknowledged: Johns Hopkins University; CERIB, Fire Testing Centre; Liege University; RISE Research Institutes of Sweden; the Institute of Building Materials, Concrete Construction and Fire Safety of Technische Universität Braunschweig, Division of Fire Safety; and Politecnico di Milano.

REFERENCES

1. Mostafaei H., Sultan M.A., Bénichou N. (2004). Recent Developments on Structural Fire Performance Engineering - a State-of-the-Art Report. https://doi.org/10.4224/20374785
2. Pettersson, O. (1965). Fire research in Scandinavia—A long-term program. Fire Technology 1, 146–150.
3. Harmathy T., Lie T. (1970). Fire test standard in the light of fire research. In Fire Test Performance. ASTM International.
4. Law A., Bisby L. (2020). The rise and rise of fire resistance, Fire Saf J. 116, 103188.
5. Gernay T., Franssen J.-M. (2015). A Performance Indicator for Structures under Natural Fire. Engineering Structures, 100, 94-103.
6. Gernay T. (2019). Fire resistance and burnout resistance of reinforced concrete columns. Fire Safety Journal, 104, 67-78.
7. Gernay T. (2021). Fire resistance and burnout resistance of timber columns. Fire Safety Journal, 122, 103350.
8. Thienpont T., van Coile R., Caspeele R., de Corte W. (2021). Burnout resistance of concrete slabs: Probabilistic assessment and global resistance factor calibration, Fire Safety Journal, 119, 103242.
9. Franssen J.-M., Gernay T. (2017). Modeling structures in fire with SAFIR®: Theoretical background and capabilities. Journal of Structural Fire Engineering, 8(3), 300-323.
10. CEN (European Committee for Standardization), EN 1992-1-1 Eurocode 2: Design of Concrete Structures - Part 1-1: General Rules and Rules for Buildings, Brussels, Belgium, 2004.
11. CEN (European Committee for Standardization), EN 1992-1-2 Eurocode 2: Design of Concrete Structures - Part 1-2: General Rules – Structural Fire Design, Brussels, Belgium, 2005.
12. Gernay T., Franssen J.M., Robert F., McNamee R., Felicetti R., Bamonte P., Brunkhorst S., Mohaine S., Zehfuß J. (2022). Experimental investigation of structural failure during the cooling phase of a fire: Concrete columns. Fire Safety Journal, 134, 103691.
13. CEN (European Committee for Standardization), EN 1995-1-2 Eurocode 5: Design of Timber Structures - Part 1-2: General – Structural Fire Design, Brussels, Belgium, 2004.
14. CEN (European Committee for Standardization), EN 1995-1-2:2020 Eurocode 5: Design of Timber Structures - Part 1-2: General – Structural Fire Design, Brussels, Belgium SC5.T4, Final Draft, May 2021.
15. Gernay T., Zehfuß J., Brunkhorst S., Robert F., Bamonte P., McNamee R., Mohaine S., Franssen J.M. (2023). Experimental investigation of structural failure during the cooling phase of a fire: Timber columns. Fire and Materials, pp 1-16, https://doi.org/10.1002/fam.3110.
16. Gernay T. (2012). Effect of Transient Creep Strain Model on the Behavior of Concrete Columns Subjected to Heating and Cooling. Fire Technology, 48(2), 313-329.
17. EN 1995-1-1:2008-06, Eurocode 5: Design of timber structures - Part 1-1: General - Common rules and rules for buildings, Brussels, Belgium, 2008.
18. Hua N., Khorasani N. E., Tessari A. (2022). Numerical modeling of the fire behavior of reinforced concrete tunnel slabs during heating and cooling. Engineering Structures, 258, 114135.

AN EXPERIMENTAL STUDY OF FIRE PERFORMANCE OF HOLLOWCORE FLOORS

Angela Liu[1], Anthony Abu[2], Vivian Ye[3]

ABSTRACT

An experimental study was undertaken to investigate the impact of mandated link slabs in New Zealand precast hollowcore floor construction on the fire performance of the floors, where the link slabs were required between precast hollowcore floor units and adjacent floor beams due to seismic considerations.

A hollowcore floor system, which included the mandated link slab and the supporting beams, was tested at the systems level. The test was undertaken with the furnace conditions according to the ISO 834 and a superimposed load of 5.3kPa. The test was terminated after the insulation criterion, measured on the unexposed surface, was reached at 116 minutes. Of interest was that premature web failure and loss of lower shell of the hollowcore unit adjacent to the link slab was observed only 29 minutes into the test.

The preliminary findings from the experimental study are summarised as follows:

(1). Hollowcore units could experience considerable thermal gradient across the depth, thus having great web failure potential; (2). Presence of the link slab could significantly exacerbate the sectional distortion of the hollowcore units and horizontal web cracking, leading to increased probabilities of partial collapse of hollowcore units in fires; and (3). Conventional fire rating tests of precast concrete hollowcore floors could overestimate fire resistance ratings.

Keywords: precast; hollowcore floors; fire tests

1 INTRODUCTION

Construction of concrete buildings with hollowcore floors in New Zealand (NZ) became very popular from the 1980s [1]. Typically, hollowcore units are seated on ledges of supporting beams, a topping slab with reinforcing mesh is cast in-situ and the floor system is connected to primary structure through “starter” bars. Due to the concerns about deformation incompatibility between hollowcore floors and surrounding floor frame members in earthquakes, numerous changes were made to NZS3101: Concrete Structures Standard in 2006 [2]. One such change is shown in Figure 1 where the details before 2003 are also shown.

According to NZS3101:2006, the hollowcore unit adjacent to a beam should be placed at a distance equal to or greater than 600 mm or six times the thickness of the topping slab away from the beam. The change as shown in Figure 1(b) was established solely due to seismic considerations. Numerous researchers [3,4] in NZ raised the concern about adequacy of fire resistance of hollowcore floors as detailed according to NZS3101:2006.

[1] Dr. Angela Liu, BRANZ, Building Research Association of New Zealand
e-mail: angela.liu@branz.co.nz
[2] Dr. Anthony Abu, the University of Canterbury, New Zealand
e-mail: anthony.abu@canterbury.ac.nz
[3] Ms. Vivian Ye, the University of Canterbury, New Zealand
e-mail: vivian.ye@pg.canterbury.ac.nz
https://doi.org/10.6084/m9.figshare.22177997

An experimental fire test of a hollowcore floor system was designed and undertaken to address this concern. This paper presents the test results and findings.

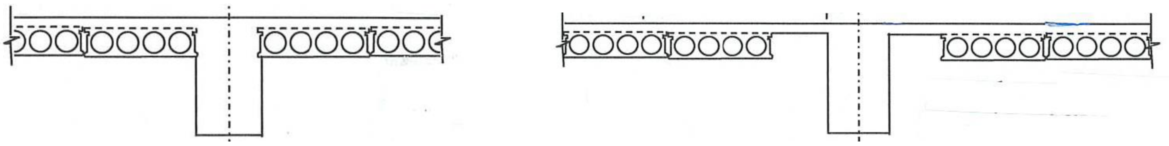

(a) Detail before 2006 (b) Detail in NZS3101:2006

Figure 1. The details for hollowcore units adjacent to beams before and after 2006

2 FIRE PERFORMANCE OF CONCRETE FLOORS

2.1 Fire design of buildings

Fire design of buildings around the world usually takes an elemental approach [5-7]. Fire resistance rating (FRR) demands are determined based on the building's characteristics. All the structural elements necessary for load carrying or separation are required to have fire resistance ratings not less than fire resistance demands.

Fire resistance of a building element is usually rated by a fire resistance test with fire condition according to the ISO 834 [8]. Fire resistance of a building element is defined as the ability of the element to fulfil its designed functions for a period of time in the event of a fire. Three functions are universally used to define fire ratings, and these functions are structural adequacy, integrity and insulation.

2.2 Fire designs of concrete floors

Concrete is generally considered to have good fire performance since it is non-combustible, absorb heat slowly, and does not give off toxic fumes or smoke.

Designs of concrete floors in NZ follow NZS3101:2006 Concrete Structures Standard. According to NZS3101:2006, the criterion for integrity is satisfied if the member meets the criteria for both insulation and structural adequacy for that period. NZS3101:2006 specifies a tabulated method for evaluating the fire resistance ratings of concrete floors. The tabulated method in NZS3101 determines the fire resistance ratings for insulation, based on the equivalent thickness of the floors, and it determines the fire resistance ratings for structural adequacy, based on the concrete cover to tensile reinforcement or strands.

2.3 Research about fire performance of hollowcore floors

Significant research effort has been made to study the fire performance of hollowcore floors across the world in last few decades and most of these studies were undertaken overseas. Some researchers studied the effects of the end restraining actions on fire performance of hollowcore floors [9, 10], and other researchers focused on identifying failure modes of hollowcore floors in fires [11-13]. Most of these studies were designed to investigate the fire resistance of individual hollowcore floor units, rather than fire resistance of hollowcore floor systems in a building environment.

The studies on the effect of the end restraining conditions revealed varied observations. The study by Scheppe et al [9], which was undertaken by conducting fire tests on 200mm thick hollowcore floor units with 80 mm thick topping, concluded that the negative end restraint moment actions at the supports caused premature compression failure on the bottom of the hollowcore units at just 23 minutes into the test. In comparison, the study by Dotreppe and Farnssen [10] concluded that the longitudinal restraining at the supports enhanced not only the flexural behaviour but also the shear capacity of hollowcore units in fires.

With regards to the failure mode identification of hollowcore floors in fires, different failure modes were observed by different researchers. Andersen [11] reported bond failure and shear failure during the fire tests on hollowcore floors with no topping. Van Acker [12] reported that premature shear failure of hollowcore webs occurred 30 minutes into the test and the failure was caused by large tensile thermal stresses due to non-linear thermal gradient across the floor depth. The University of Liege conducted numerical simulations of fire performance of hollowcore floors [10] and the study demonstrated that thermal stresses due to thermal gradient across the slab depth could be large enough to cause shear failure before 30 minutes into the test. This was consistent with Van Acker's observations. Fellinger [13] investigated shear and anchorage behaviour of hollowcore floors in fires. The fire tests by Fellinger were conducted on single hollowcore unit specimens and double web specimens sawn out of hollowcore units. The tests showed different failure modes including anchorage failure, shear failures both in terms of horizontal shear cracking and vertical shear cracking, as well as combined shear and anchorage failures.

Research about fire resistance of hollowcore floors detailed according to NZ practice mainly included the computer simulations using Safir program [18] at the University of Canterbury [3, 14-16] by Chang et al and by Min et al. One of these studies was by Chang et al [15] and it investigated the fire performance of hollowcore floors with the presence of the link slab as recommended by the current concrete standard NZS3101:2006. The study showed that the presence of the link slab could reduce the fire resistance of hollowcore floors. Noted is that Safir modelling can only model the flexural behaviour of the hollowcore floors.

3 THE FIRE TEST OF A HOLLOWCORE FLOOR SYSTEM

3.1 Specimen details

The test specimen of a hollowcore floor system is 3.5m wide and 4.5m long. Figure 2 shows the plan and the edge details.

The test specimen had reinforced concrete beams on all the sides. Two 200 series hollowcore units were seated on the beam ledges along the shorter sides and a link slab of 600 mm wide was introduced as per NZS3101:2006. A 75 mm in-situ concrete topping was cast in-situ on top of the precast hollowcore units. "L" shaped starter bars of 12mm in diameter were used to tie the floor to the edge beams.

3.2 Specimen construction

200 series precast concrete hollowcore units of 4 m long each were transported to BRANZ site from manufacturer's yard. These units were cut from a long unit manufactured at least 5 years ago.

The form work was constructed using timber framing and plywood sheets. After the form work was complete, steel cages of reinforced concrete edge beams were assembled. Figure 3 shows the form work and the cage.

The first pour of concrete was carried out for the edge beams up to the seating level of the hollowcore units. Four weeks after the first pour, the hollowcore floor units were placed on the ledges of the beams along the shorter side, starter bars and ductile reinforcing mesh "SE62" were placed before the second pour.

3.3 Theoretical evaluation of fire resistance of the tested floor system

According to the tabulated method in NZS3101:2006, the FRRs for insulation of concrete floors is dependent on the effective thickness of the slabs. The effective thickness of hollowcore floors is determined as the net cross-sectional area divided by the width of the cross section. For a 200 series hollowcore floor system as used in this test, the effective thickness determined as described above is 102mm for bare hollowcore units and 177 mm for the composite floor with 75mm concrete topping. As such, the FRRs for insulation of the test specimen is 60 minutes for 75mm solid slab (link slab), 105 minutes for bare hollowcore floors, 240 minutes for the composite hollowcore floors.

Based on the tabulated method in NZS3101:2006, the FRRs for structural adequacy depends on the supporting conditions at edges as well as the axis distance to the bottom of reinforcement and tendons. Precast hollowcore floor systems are considered as one-way systems. For the tested floor system, the measured concrete cover to the prestressing strands is 50 mm. As such, the FRRs for structural adequacy is 180 minutes for bare hollowcore units. The topping slab is a two-way continuous flat slab and the concrete cover to the reinforcement is 37.5 mm. This gives the FRRs for structural adequacy of 225 minutes over the link slab.

The FRRs of the hollowcore floor test specimen assessed using the tabulated methods in NZS3101:2006 are summarised in Table 1. In detail, the FRRs for insulation is at least 60 minutes, which is limited by the link slab. The FRRs for structural adequacy is at least 180 minutes, which is limited by the hollowcore floor units. As such, the FRRs for integrity is at least 60 minutes.

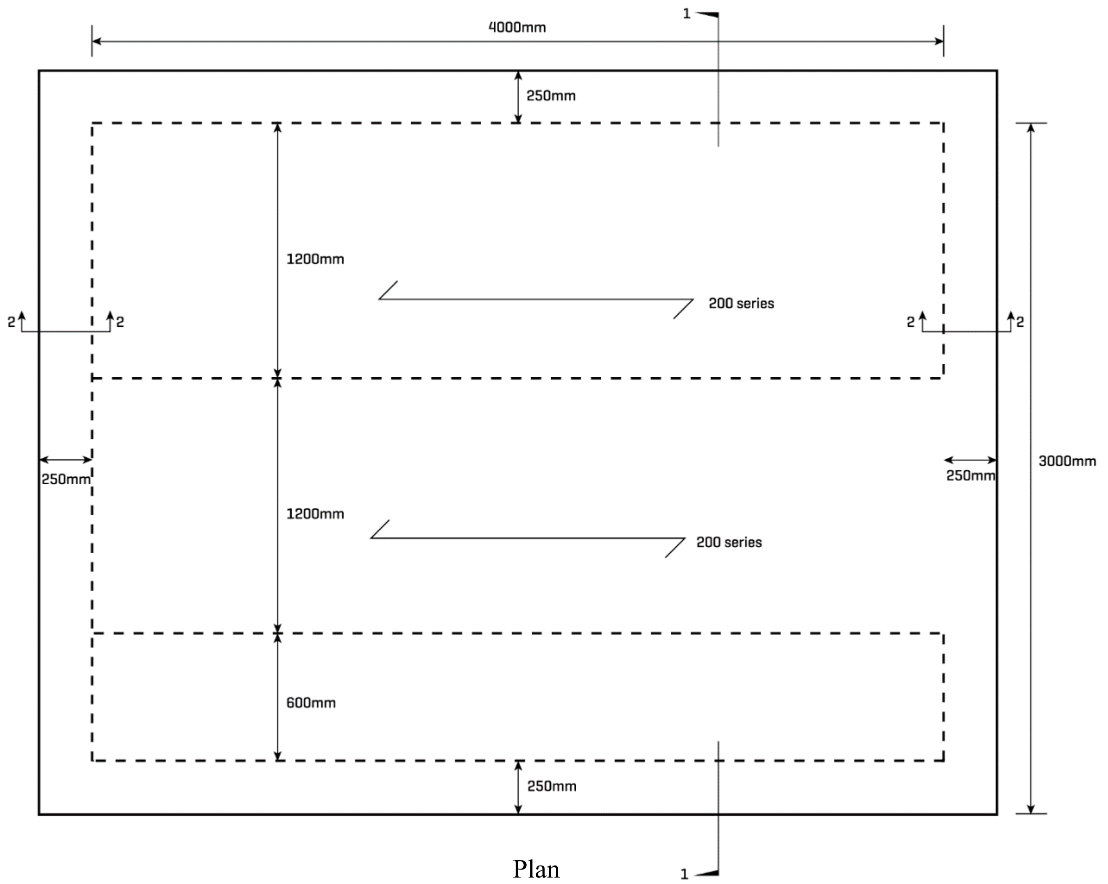

Plan

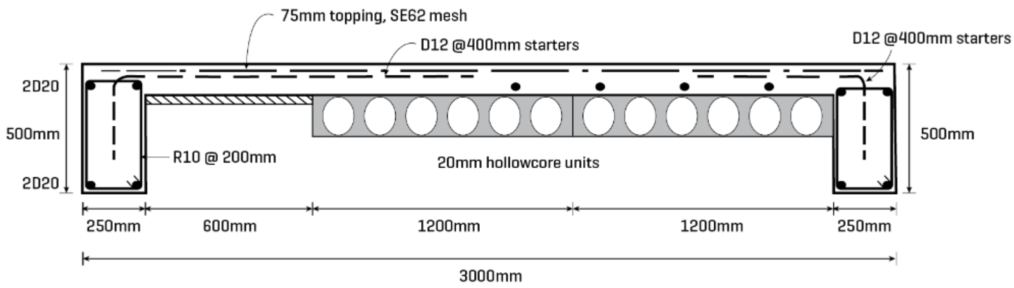

Section 1-1

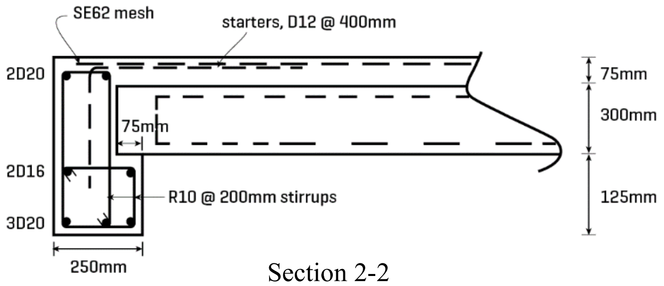

Section 2-2

Figure 2. Plan and section details of the tested hollowcore floor system

Figure 3. Form work and the cage were complete

Table 1. FRRs of 200 series hollowcore floor components (minutes)

	bare hollowcore units	75 mm topping
Insulation	105	60
Structural adequacy	180	225

In real buildings, 200 series hollowcore floor units often span 7 to 8 meters, which are about twice the span of the hollowcore units in this test. This means that the test specimen would be expected to achieve much longer structural adequacy rating than the assessed rating of 180 minutes above.

3.4 Fire test of the hollowcore floor system

The hollowcore floor test specimen was tested, in a horizontal position, on the furnace, which was 3.0 m by 4.0 m, at BRANZ laboratories, Judgeford. The four edge beams of the floor specimen sat on the furnace walls. Figure 4 shows the test setup.

Figure 4. The test setup

Prior to the test, a uniformly distributed load, in addition to the self-weight of the floor, was applied on the floor to simulate live loads. In total, twenty water drums with steel plates were placed, in a uniform grid of four by five, on the slab. Drums were hung off, using steel straps, cross beams in order that the cross beams could support the drums in the event of catastrophic collapse. The combined weight of the water and the steel weights was 316 kg per drum, equivalent to a uniformly distributed load of 5.27 kPa over the floor.

With regards to the test instrumentation arrangements, the instrumentations included potentiometers for vertical displacement measurements and thermocouples for temperature measurements.

Five potentiometers, which were attached to the unexposed floor face to measure the vertical displacements of the floor system at mid-span and quarter points, were shown in Figure 5.

The temperature measurements were taken at different depths and different parts of the floors during the fire test. Figure 6 shows the thermocouples arrangements on the unexposed face of the floor. Figure 7 and Figure 8 respectively show the thermocouples attached at the mesh level and at the interface level between precast hollowcore units and the topping. Thermocouples were also attached along the hollowcore unit joint at three depths within the hollowcore depth as illustrated in Figure 9, where numbers in black, red, and blue are respectively the arrangements of thermal couplers at the depth of 50mm, 100mm and 150 mm from the exposed face.

The potentiometers and thermocouples were connected to the data logger “Agilent 34970A”, which monitored the 5 potentiometers and 50 thermocouples used in the test.

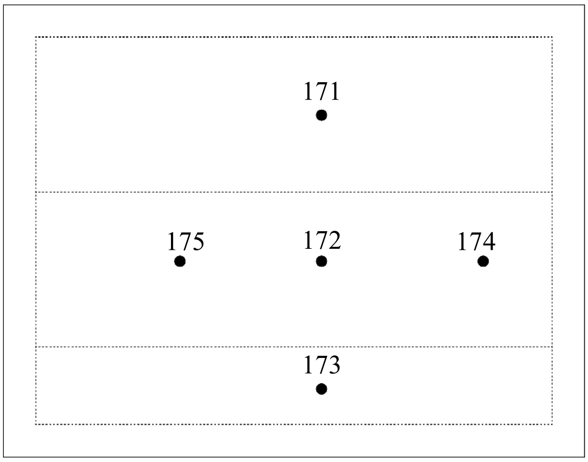

Figure 5. Potentiometer arrangements

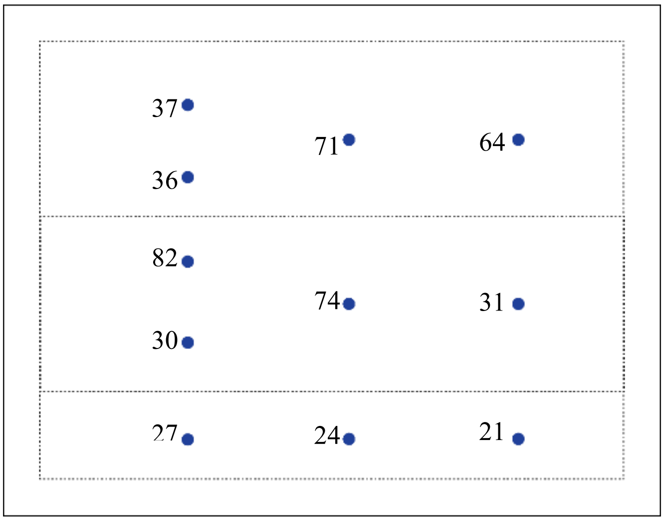

Figure 6. Thermocouples on the unexposed surface

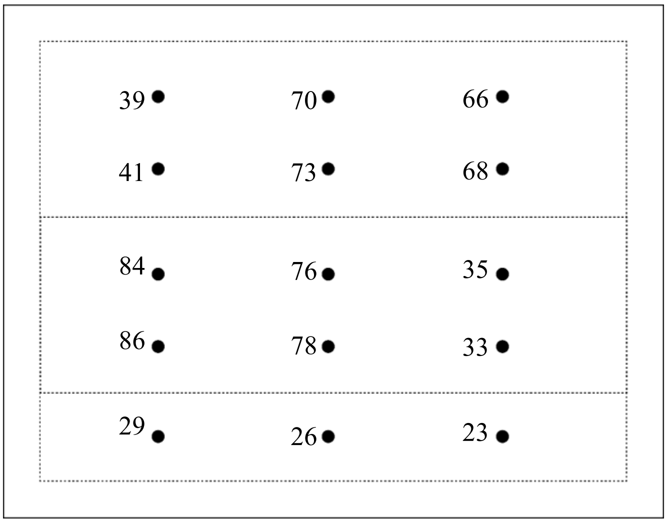

Figure 7. Thermocouples at mesh level

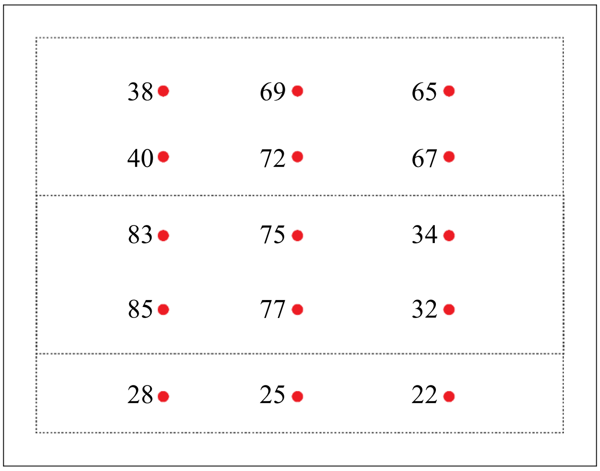

Figure 8. Thermocouples at interface of units and topping

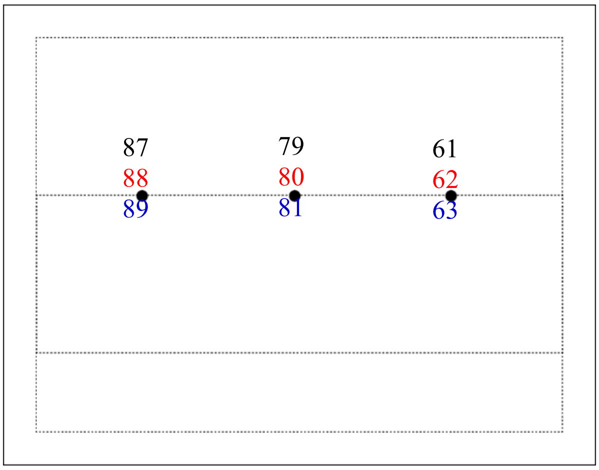

Figure 9. Thermocouples along the joint of hollowcore units

4 TEST OBSERVATIONS AND TEST RESULTS

4.1 Failure mode

The fire test was conducted with the furnace condition according to the ISO 834. The test was terminated soon after the insulation criterion, 140 K average temperature rise on the unexposed surface, was reached at 116 minutes.

The hollowcore floor system deflected insignificantly throughout the entire 120 minutes furnace exposure duration. However, premature shear failure in the web of the hollowcore unit adjacent to the link slab initiated at about 29 minutes into the test, and this was only about 1/6 of the rated structural adequacy rating for this specific hollowcore floor system. As the test continued, the web shear failure progressed in the concerned hollowcore unit. At the completion of the test, the premature web shear failure spread to the entire hollowcore unit adjacent to the link slab, leading to nearly complete loss of lower shell of the hollowcore unit. Figure 10 shows the final appearance of the tested floor system at the completion of the test.

Figure 10. The exposed face of the tested floor system at the completion of the test

4.2 Measured temperatures of furnace gas

Figure 11 compares the average temperature of the furnace gas with the standard ISO 834 fire curve, where the furnace gas temperature represented the average of six furnace thermocouples. Clearly the gas temperature represented ISO 834 curve reasonably well.

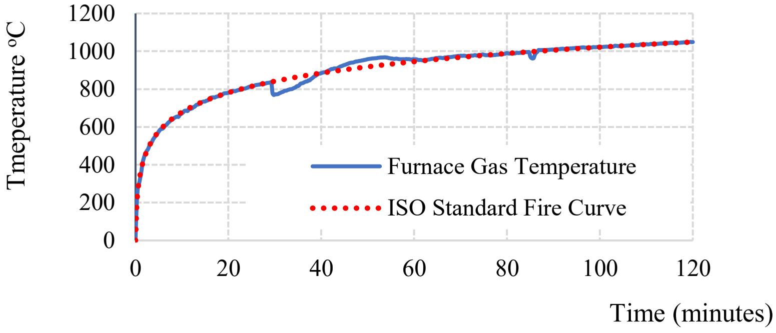

Figure 11. Gas temperature (°C)

4.3 Temperature rises on the unexposed face

Temperatures on the unexposed face were measured using 11 thermocouples. Figure 12 shows the temperature rises obtained from three thermocouples mounted on the unexposed face over the link slab area. Figure 13 shows the temperature rises obtained from eight thermocouples mounted on the unexposed face over the hollowcore floor area. Clearly, the temperature rises on the unexposed face are higher over the link slab than those over the rest floor.

While the average temperature rise over the hollowcore area had been less than 85°C throughout the entire test, the average temperature rises over the link slab did reach 140°C after 116 minutes. The FRRs for insulation is then determined as 116 minutes.

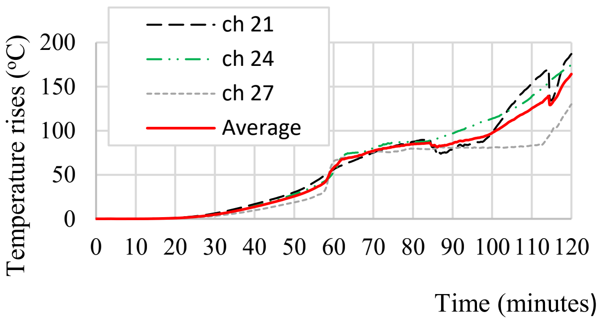

Figure 12. On the unexposed face over the link slab area

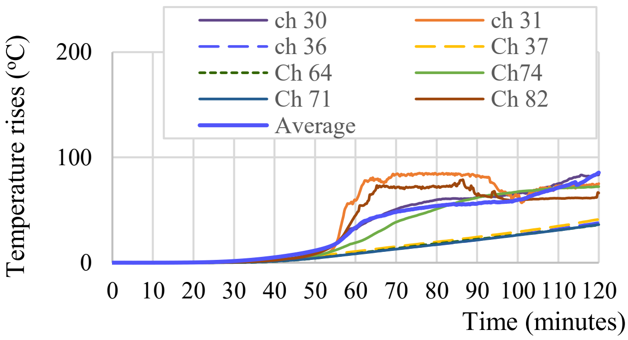

Figure 13. On the unexposed face over hollowcore area

4.4 Temperature variations within the floor slab depth

Apart from the temperature measurements on unexposed floor surface, temperatures were also measured at five pre-determined depths within the slab. One depth was 237.5 mm from the fire-exposed face, which was at mesh level. Another depth was 200 mm from the fire-exposed face, which was at the interface of the precast hollowcore units and the topping over the hollowcore floor area and at the interface of plywood planks and the topping over the link slab area. The remaining three depths were respectively 150 mm , 100 mm , 50 mm from the fire-exposed face, where the thermocouples were placed along the joint of hollowcore units as shown in Figure 9.

Figure 14 and Figure 15 show the average temperature rises respectively at mesh level and at the interface level of hollowcore units and the topping. It is clear that the presence of hollowcore units delayed the temperature rise in topping significantly. Also obvious is that plywood planks of 25 mm provided good protection to the in-situ concrete topping up to 40 minutes, and the protection degraded with time but did not completely disappear throughout the test period of about two hours.

Figure 16 shows the readings from different thermocouples at the interfaces between topping slab and hollowcore units. Clearly, the temperature over the hollowcore unit adjacent to the link slab are much higher because of early damage of this hollowcore unit.

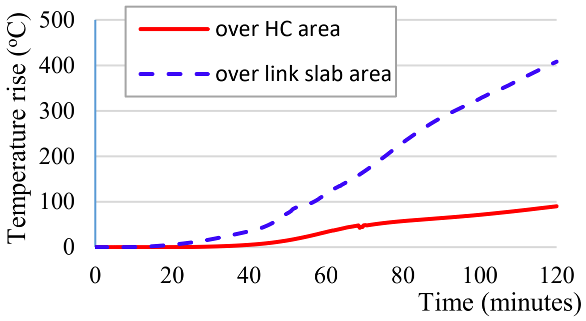

Figure 14. Average temperature rises at mesh level

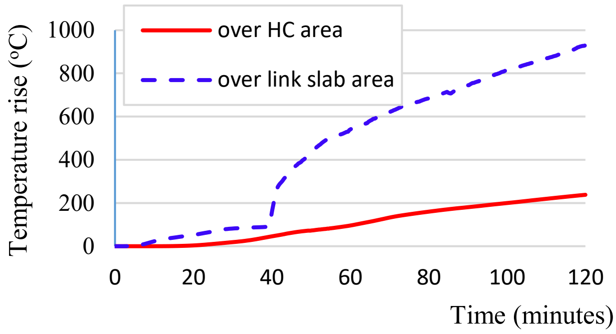

Figure 15. Average temperature rises at interface level

Figure 17 shows the thermal gradients across the floor thickness for different exposure times in hours. In Figure 17, the vertical axis is the depths in mm from the fire-exposed face and the horizontal axis is the measured temperature rises. The temperatures at the depths of 275 mm, 237.5 mm and 200 mm from the fire exposed face were the averaged values from the thermal couplers at midspans of the hollowcore unit adjacent to the link slab. The temperatures at the depths of 150 mm, 100 mm and 50 mm were from the thermal couplers installed along the joint of the two hollowcore units. The temperatures at the depth of zero mm were assumed to be the same as the gas temperatures. It is clear in Figure 17 that the temperature profiles across the section are very non-linear even at 30 minutes into the test and the nonlinearity was more significant as the test progressed.

Noted is that there were no thermocouples installed on the exposed face for this test and the temperature on the exposed face was likely to be lower than gas temperature especially at the beginning of the test. As such, the study also assumed that the temperatures on the exposed face equal to the temperatures reported by Van Acker [12] for the same fire exposure time. Based on this assumption, the thermal gradients across the floor depth for different exposure times are illustrated in Figure 18. Figure 18 again shows that the temperature profiles across the section are very non-linear. Clearly the thermal gradients shown in Figure 18 did not show a rational temperature progression across the depth and this is possibly because the temperatures at different depths measured along the joint of the hollowcore units were different from the temperatures at the same depths but within the hollowcore units.

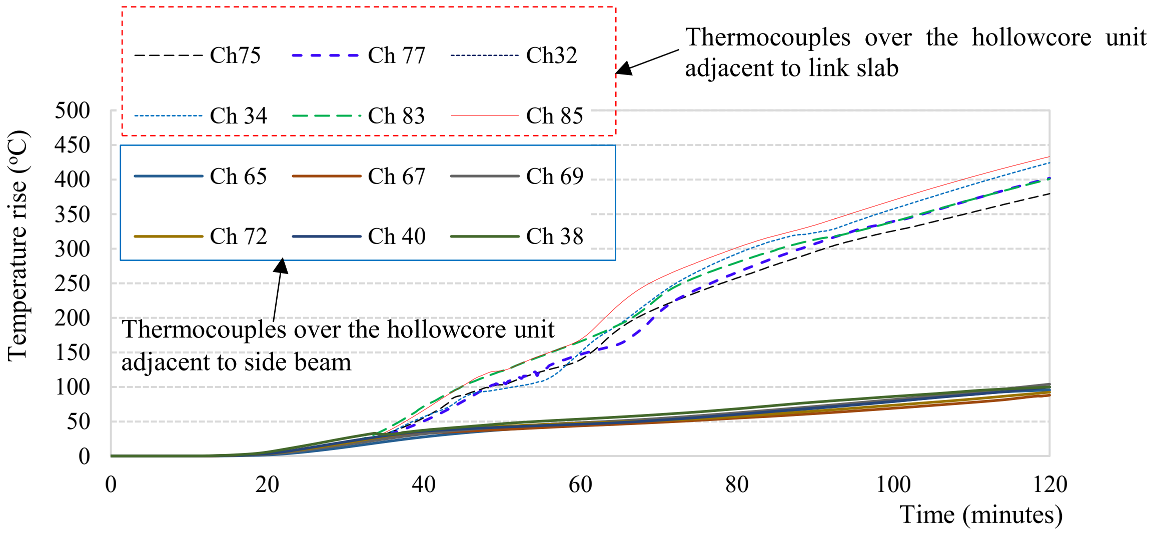

Figure 16. Temperature variations at the interface of hollowcore units and the topping slab

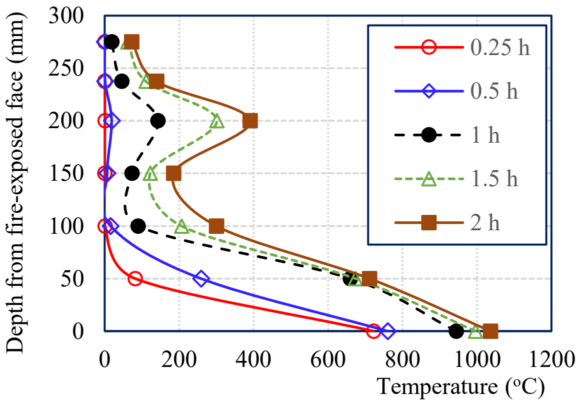

*Temperature on exposed face is gas temperature

Figure 17. Thermal gradients across the depth

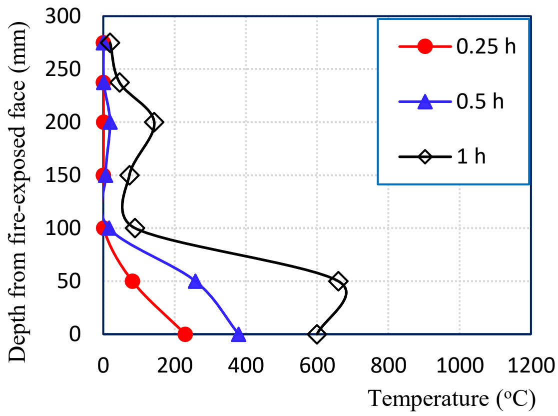

*Temperature on exposed face uses Van Acker's data

Figure 18. Thermal gradients across the depth

4.5 Vertical displacements of the floor

For the studied floor system, the failure criterion in terms of the floor vertical displacement is 146mm, calculated using L2/(400d), and the failure criterion in terms of deflection rate is 6.47mm/minute, calculated using L2/(9000d).

The vertical deflection at mid-span of the unit adjacent to the link slab was significantly greater than that of the unit adjacent to the side beam and this is understandable because of the weakening of the unit adjacent to the link slab. However the maximum measured vertical deflection was 22.0 mm, which is only 15% the deflection failure criterion of 146 mm. Clearly the vertical deflection was not critical.

5 DISCUSSION

The reported experimental study about fire performance of hollowcore floor systems revealed many potential issues of hollowcore floor systems in fires and these issues are discussed as follows.

5.1 Concern about adequacy of conventional fire rating tests of concrete floors

The conventional fire resistance tests of floors were usually performed on individual floor elements, where individual floor elements are supported in the vertical direction only (by bearing or roller supports) with no longitudinal restraining at the supports, as shown in Figure 19. Such an arrangement allows the floor elements exposed to fires to expand freely along two orthogonal horizontal directions and is a typical elemental approach. In contrast, the recent BRANZ test was on a hollowcore floor system that included precast hollowcore units, a topping slab and beams around the floor – a systems approach.

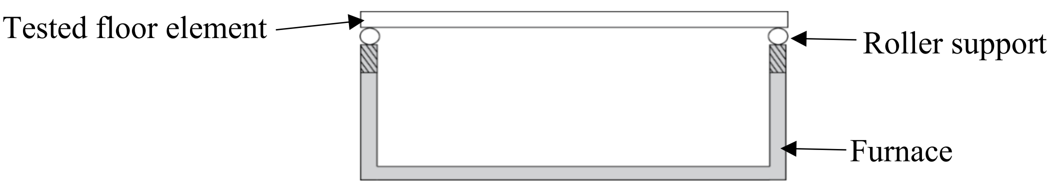

Figure 19. Roller supports only

During the recent BRANZ test, premature shear failure initiated in the web of the hollowcore unit next to the link slab at about 29 minutes, and this was significantly lower than the predicated fire resistance rating for structural adequacy of 180 minutes. Of interest is that the hollowcore unit tightly next to the adjacent beam performed much better and did not have apparent damage throughout the entire test of about 120 minutes.

The test evidence demonstrates that the fire resistance of hollowcore floors, when tested within a system environment, is potentially different from that when tested in an isolated state.

5.2 Possible negative effect of end restraining action

The common belief is that the restraining actions by the surround members, such as floor beams, enhance the fire performance of the hollowcore floors [15, 16]. However the fire test conducted in this study demonstrates that the restraining actions at the supports and/or along the sides could have impacted negatively on the fire performance of the hollowcore floors.

When hollowcore floors are heated, they expand differentially with the hotter part expanding more than the cooler part. When there is no restraining action, the hollowcore units can expand in all directions except upwards. However, when the restraining actions are present at both ends, the expansion is limited to a sideways and/or downwards movement. The sideways expansion of hollowcore units is like a twisting action (as shown in Figure 20) and is more damaging than the downward expansion, which is like normal loading action. The distortion of the hollowcore units potentially causes horizontal web cracking at the uppermost web level, leading to the loss (collapse) of lower shell of the units, similar to the issues discussed by Fenwick [4]. Partial collapse of hollowcore units could progress and lead to significantly compromised fire performance of hollowcore floors, as reported in Netherland by Overbeek [12].

5.3 Negative effect of the link slab on fire performance of hollowcore floors

The introduction of a link slab for hollowcore floor systems as required by the current concrete standards is likely to reduce the fire resistance rating of the hollowcore floors, and reduce the structural adequacy of the hollowcore floors significantly.

When the link slab is introduced to hollowcore floors, the sideway expansion is much greater, significantly exacerbating the horizontal web cracking and subsequent failure of the hollowcore units, as shown in Figure 21. This could cause progressive failure of a hollowcore floor system because the failure of a hollowcore unit adjacent to the link slab provides room for next unit to expand sideways significantly until it fails.

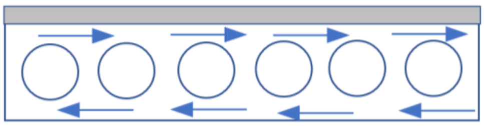

Figure 20. A hollowcore unit subjected to torsion

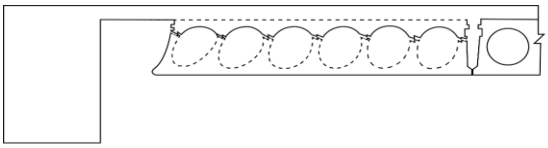

Figure 21. Horizontal web cracking

5.4 Vulnerabilities of hollowcore floors

Hollowcore units are not uniform solid sections and thus vulnerable in fires, in compared with other concrete floor systems. When a hollowcore floor is exposed to fire, the hollowcore units will be subjected to extraordinary nonlinear thermal gradient across the cross section, as illustrated in section 4.4. As a result, thermal stresses induced across the depth of the hollowcore units could be large enough to cause shear failure of the webs, as reported in this test.

6 CONCLUSIONS

A fire test of a precast hollowcore floor system was conducted to investigate fire performance of hollowcore floors with the mandated link slab as required by the current concrete structures standard NZS3101:2006. The preliminary findings as the result of the test are presented as follows:

1. Conventional fire resistance testing method of hollowcore floors, where the individual hollowcore unit can expand horizontally in two orthogonal directions, might incorrectly identify the limiting factors and overestimate the fire resistance of the floors.
2. The commonly used tabulated method in determining the fire resistance of hollowcore floors is based on the flexural performance of hollowcore units. The test presented in this paper demonstrated that premature shear failure due to the thermal gradient over the hollowcore depth could occur much earlier than flexural failure for hollowcore floor systems.

3. Mandated link slab as required by NZS3101:2006 could compromise the fire performance of hollowcore floor systems. This is because presence of the link slab could exacerbate cross sectional distortions of hollowcore units in fires, causing progressive collapse of hollowcore units.
4. The restraining actions by the floor framing could further exacerbate sectional distortion of hollowcore units exposed to fires, exacerbating premature shear failure due to the thermal gradient over the depth of the hollowcore floor units, eventually jeopardising the structural adequacy of hollowcore floors.

ACKNOWLEDGEMENT

The research reported here has been funded by the Building Research Levy. The authors would like to thank BRANZ colleagues, Kevin Frank and George Hare, for the discussions.

REFERENCES:

1. Brunsdon D., Hare J., Elwood K. (2017). Engineering Assessment Processes for Wellington Buildings Following The November 2016 Kaikoura Earthquakes, Bulletin of the New Zealand Society for Earthquake Engineering, 50(2), 338-342
2. SNZ, (2006): Concrete Structures Standard, Standards New Zealand, Wellington, New Zealand
3. Chang, J. J., Buchanan, A. H., Dhakal, R. P., and Moss, P. J. (2008). Hollowcore Concrete Slab Exposed to Fire, Fire and Materials, 32(6), 321-331.
4. Fenwick, R, Bull D & Gardiner D (2010) – Assessment of Hollow-Core Floors for Seismic Performance, Department of Civil and Natural Resources Engineering Research Report 2010-02. University of Canterbury (available https://ir.canterbury.ac.nz/handle/10092/4211)
5. EN (2005). 1993-1-2. Design of Steel Structures, Part 1.2: General Rules-Structural Fire Design. European Committee for Standardization (CEN), Brussels, 2005
6. Ellingwood, B. R. (2007). Structural Design for Fire Conditions: New Developments. Structural Congress, ASCE.
7. NZBC (2019). Clauses C1-C6 Protection from Fire
8. ISO (1975). Fire Resistance Tests – Elements of building construction. ISO 834-1975. International Organization for Standardization
9. Schepper, L., and Anderson, N.E., (2000). Danish Institute of Fire Technology&COWI Technical Report PG10724 -Fire Test of Deck Elements. COWI and Danish Institute of Fire Technology, Denmark
10. Dotreppe, J. and Franssen, J. (2004). Precast Hollow Core Slabs in Fire: Numerical Simulations and Experimental Tests. Proceddings of the Third International Workshop Structures in Fire SiF"04, Ottawa, Canada
11. Andersen N.E., and Lauridsen D.H (1999). Danish Institute of Fire Technology, Technical Report X52650. Part 2. Hollow Core Concrete Slabs. Basismiddel project X52650. 9
12. Van Acker A. (2003), Shear Resistance of Prestressed Hollow Core Floors Exposed to Fire. Structural Concrete. Vol. 4. No 2. pp 65-74.
13. Fellinger, J.H.H (2004), Shear and Anchorage Behaviour of Fire Exposed Hollow Core Slabs, DUP Science, Delft, Netherlands
14. Chang, J. J., (2007). Computer simulation of hollowcore concrete flooring systems exposed to fire, Ph.D Thesis, University of Canterbury, Christchurch, New Zealand
15. Chang, J. J., Buchanan, A. H., DhakA, R. P., and Moss, P. J., (2008). Hollowcore Concrete Slab Exposed to Fire, Fire and Materials, 32(6), 321-331
16. Min, Jeong-Ki. (2011). Numerical Prediction of Structural Fire Performance for Precast Prestressed Concrete Flooring Systems. PhD Thesis, University of Canterbury, Christchurch, New Zealand
17. Overbeek, T. V., Breunese, A., Gijsbers, J., Both, J., Maljaars, J., and Noordijk, L. (2010). New Regulations for Hollow Core Slabs After Premature Partial Collapse. Proceedings of the Sixth International Workshop Structures in Fire SiF'10, Michigan, USA.
18. Franssen, J-M, Kodur, V.K.R & Mason, J. 2002, User's manual for SAFIR2001 Free: A Computer Program for Analysis of Structures at Elevated Temperature Conditions. Liege: University of Liege

THE EFFECT OF HIGH-TEMPERATURE CREEP ON EN6082 T6 ALUMINIUM COLUMNS EXPOSED TO TRANSIENT HEATING

Marko Goreta [1*], Neno Torić [2], Ivica Boko [3]

ABSTRACT

The paper presents an investigation regarding the influence of time-dependent strain on the load-bearing capacity of EN AW 6082 T6 aluminium I section columns with particular emphasis on induced high-temperature creep and its application in a real fire scenario. Current structural design norms lack reliable procedures to determine the exact impact of time-dependent strain on aluminium columns' load-bearing capacity. In the current version of EN 1999-1-2, the effect of creep on columns is implicitly taken into account due to the lack of reliable scientific research in the form of a constant reduction factor of 1.2 that should cover all aspects of the load-bearing capacity reduction due to creep regardless of the heating rate. Since fire protection is in some instances mandatory due to current fire safety laws worldwide, there is a high probability that columns may be exposed to low heating regimes that generally induce substantial high-temperature creep. Therefore, it is necessary to investigate the behaviour of aluminium columns exposed to low heating rates and its influence on the reduction of load-bearing capacity.

Keywords: Creep; time-dependent; columns; fire; aluminium, EN AW 6082 T6

1 INTRODUCTION

1.1 General

Aluminium can be potentially considered as one of the building materials of the future and, next to steel, the second most important metal in construction due to its considerable quantities worldwide and its favourable material properties. It is the third most widespread chemical element on our planet (after oxygen and silicon) found on the surface of the Earth's crust in the form of various silicate and oxide minerals. The desirable properties of aluminium important in construction are achieved in combination with certain alloying elements (manganese, silicon, magnesium, etc) and are manifested in good strength-to-weight ratio, weldability, ductility, corrosion resistance, durability, thermal conductivity, and formability. In addition, aluminium is highly reflective, non-toxic, paramagnetic, absorbs sound and impacts very well, which makes it a good sound insulator. Despite the aforementioned positive properties, aluminium has one major flaw which is its high sensitivity to elevated temperature. Aluminium has a melting point slightly less than three times lower than structural steel, and a significant drop in load-bearing capacity already occurs at temperature interval within 100-200 °C. This significant drawback requires the use of some form of fire protection in everyday structures, even though aluminium is not flammable material.

1.2 Strain at elevated temperature

Load-bearing members exposed to elevated temperatures are subject to several strain components. The total strain can be expressed by equation (1) given by Anderberg [1].

[1] PhD student, University of Split, Faculty of Civil Engineering, Architecture and Geodesy,
e-mail: marko.goreta@gradst.hr, ORCID: https://orcid.org/0000-0001-7645-1623
[2] Associate Professor, University of Split, Faculty of Civil Engineering, Architecture and Geodesy
e-mail: neno.toric@gradst.hr, ORCID: https://orcid.org/0000-0002-7530-7619
[3] Full Professor, University of Split, Faculty of Civil Engineering, Architecture and Geodesy
e-mail: ivica.boko@gradst.hr, ORCID: https://orcid.org/0000-0003-2282-8362
https://doi.org/10.6084/m9.figshare.22178003

$$\varepsilon_{tot} = \varepsilon_{th}(T) + \varepsilon_{\sigma}(\sigma, T) + \varepsilon_{cr}(\sigma, T, t) \quad (1)$$

where $\varepsilon_{th}(T)$ denotes thermal strain, $\varepsilon_{\sigma}(\sigma, T)$ strain due to external load, and $\varepsilon_{cr}(\sigma, T, t)$ time-dependent strain (creep). Thermal strain depends only on the thermal expansion of the element defined by the thermal expansion coefficient of aluminium (α_L=23 · 10^{-6} °C^{-1}) dependent on the temperature T of a heated member. Strain from the external load (mechanical strain) depends on the characteristic of the material, the amount of the load, and the temperature.

When a metal is exposed to a stress that exceeds the yield point, it is permanently (plastically) deformed. If the stress is less than the yield strength, according to the laws of material behaviour defined by the stress-strain curve, the metal is exposed to an elastic strain, which is not valid in the case of metal exposure to elevated temperature. If the temperature exceeds around 25% of the metals' melting temperature, the permanent strain may occur even if the applied stress is lower than the yield value. This temperature and a load-dependent strain refer to creep, and it has a substantial impact on the load-bearing capacity of aluminium columns since it reduces their overall strength and stiffness. Creep is a complex process greatly influenced by the microstructure of the material in terms of crystal structure, particle size, composition, dislocation density, phase constitution, percentage, and size of voids. Mentioned properties can be significantly changed by various thermal and mechanical effects on the aluminium alloy. The exact impact of creep strain on aluminium columns is a scarcely investigated topic. Current regulations for structural fire design of aluminium structures, (EN 1999-1-2 [2]) take creep into account by applying a constant reduction factor of 1.2 for the overall column capacity that should cover all aspects of the load-bearing capacity reduction due to creep regardless of the applied load and the heating rate.

In order to investigate the influence of creep strain on the reduction of the load-bearing capacity of aluminium columns and the global response of entire structure exposed to elevated temperatures, it is mandatory to carry out experimental research with accompanying verification by numerical modelling. To analyse the influence of creep strain on columns, experimental research can be carried out through stationary or transient tests. Generally, stationary tests are used to determine the overall capacity of the column while the transient tests are used as a better approximation of a real fire scenario for constant load and variable temperature.

2 PREVIOUS RESEARCH

Scientific research on aluminium exposed to fire is scarcely a studied topic, although there has been an increase of interest in this field of study in the past few decades. A study with a noticeable impact on the scientific community in terms of determination of the influence of the creep strain on the aluminium columns was conducted by N.K. Langhelle *et al.* [3], [4]. They carried out tests on rectangular tubes of aluminium alloy 6082 T6 in stationary and transient heating conditions. The experimental study has been verified with numerical modelling with a conclusion that the high heating rates (up to 12 °C/min) do not develop significant creep strain that would affect the load-bearing capacity of the columns. This was due low resistance of aluminium at high temperatures and the inability to develop and record notable creep strain.

The most extensive studies in terms of transient heating and its overall influence on aluminium column's capacity were conducted by Maljaars *et al.* [5 – 7]. In the mentioned studies, numerical and experimental analysis for various aluminium columns of different alloys from 5xxx and 6xxx series were tested on various hollow cross sections and heating rates. Maljaars adapted Dorn's theoretical creep model [8] and used it for the analysis of 5xxx alloy series with the main conclusion that the 1.2 reduction factor from EN 1999-1-2 needs to be reconsidered since the creep for lower heating rates accelerates the failure of the column. Kandare *et al.* [9] applied a modified Maljaars creep model on aluminium plates simulated as columns for alloys 5083 and 6082 exposed to transient heating. The presented study was concluded with a good prediction of plate failure due to buckling caused by high temperature creep, with a visible representation of the primary and secondary creep phases, but with an evident deficiency for its application on complex structures and elements such as I-profiles.

Due to a lack of scientific research on I-section aluminium columns exposed to high temperature, Torić *et al.* [10 – 14] carried out a detailed study. Within the study, the coupons together with capacity and stationary tests on aluminium columns made of alloy EN AW 6082 T6 were conducted. An analytical creep model suitable for stationary tests with the capability to predict all creep phases was developed. The main conclusion of the mentioned study was that significant creep develops for temperatures above 150 °C for the presented aluminium alloy on both coupon and column levels. The further objective of this research is to test the effect of creep in various transient heating scenarios.

3 TRANSIENT COLUMN TESTS

3.1 Introduction

An experimental analysis on aluminium columns in transient heating conditions for alloy EN AW 6082 T6 was carried out in Laboratory for Structures at the Faculty of Civil Engineering, Architecture and Geodesy, University of Split. Steel test frame with accompanying equipment which consists of two separate hydraulic systems (for horizontal and transversal force), an induction heating machine, a steel tube that serves as a furnace, separate cooling system, and different measuring equipment, was used to test aluminium columns. Used measuring equipment containing two LVDT-s for vertical and horizontal displacement, a total of 13 thermocouples for temperature readings in five different sections on the column (flanges and the web), acquisition system for data collection and analysis. The test setup is shown in Figure 1.

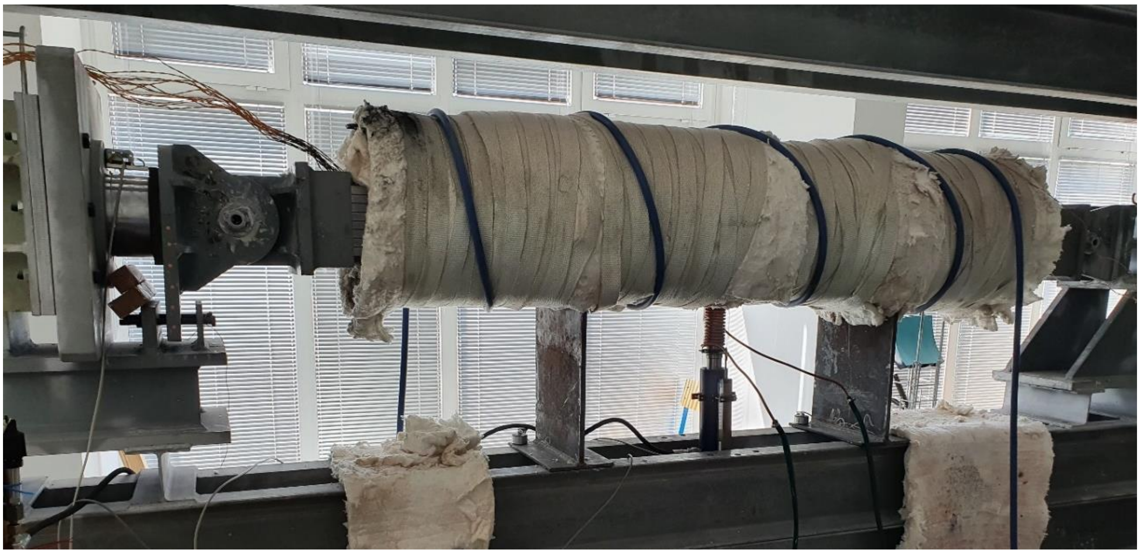

Figure 1. Experimental test setup

3.2 Heating scenario

In the tests, a novel heating arrangement with an induction-generated magnetic field was used. Since aluminium is not ferromagnetic material, the steel tube was used to transfer the heat in the column by uniform radiation. Induction heating compared to classical heating arrangements with heaters or open flame has some significant advantages. Proper coil geometry that generates high-frequency current warms up the object directly and in a targeted manner which reduces the heating time. With different coil designs and power regulation, local heating to the desired temperature can be achieved, easily controlled, and corrected on the control panel of the machine which increases heating accuracy. Automation of the process enables improvement of the productivity and quality of the heating process itself due to the non-contact heating method between the coil and the heating object (without additional interference from the heater in tests). The main advantage of the presented setup is the safety of the entire process since there is no gas and air pollution while the object is heated directly, and no combustible substances are used. In order to define the optimal heating rate for the successful implementation of transient tests, it was necessary to define the effective power of the induction heating machine through the preliminary heat-up tests.

3.3 Preliminary heating tests

A total of six heating tests were performed with a defined machine power of 8, 10, 14, 17, 24, and 30 kW. The reference time interval varied between the tests and was determined based on the rate of formation of near-constant heating rate. The distribution of average heating rates for each test along the specimen is presented in Figure 2 for each power output of the machine.

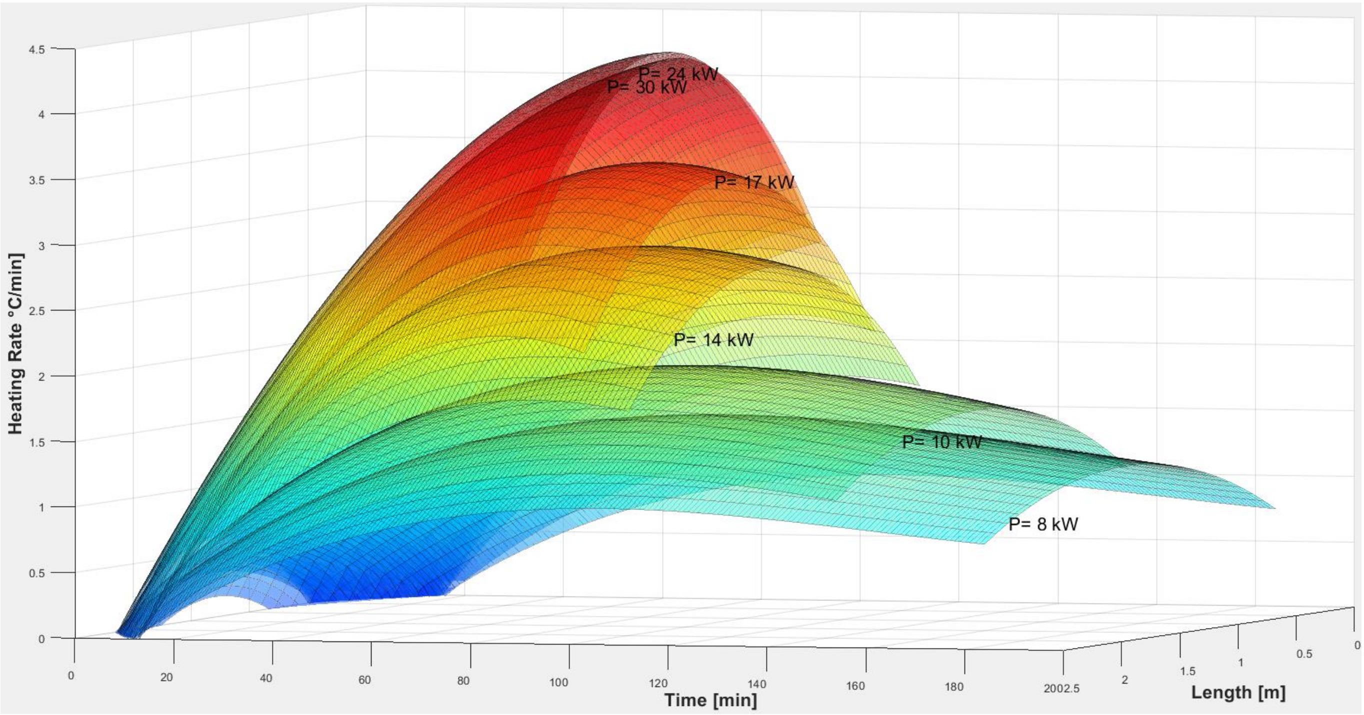

Figure 2. 3D distribution of average heating rates on the aluminium column for each warm-up test

It is evident from Figure 2 that the lower power of the induction machine results in the development of lower heating rates along the column. The adopted heating rate was 17 kW which corresponds to an approximately constant 3 °C/min heating rate 60 minutes into the test.

3.4 Tests on aluminium columns

A total of three aluminium columns made of EN AW 6082 T6 alloy with a length of 2590 mm which corresponds to approximately one clear story height in typical buildings were tested. The cross-section of the column was I-section 220 mm high and 170 mm wide, with a flange thickness of 14 mm and a web of 8 mm which resulted in a slenderness value of 70.

The columns were tested for a transversal force of 15 kN which annulled the geometric imperfections of the columns, self-weight and implied the failure in the vertical direction, and a horizontal load for 250 kN, 300 kN, and 350 kN. Applied loads on the columns were defined based on the capacity and stationary tests [10], preliminary transient tests [15], and to suit obtained coefficients for the previously calibrated creep model [16] through the numerical analysis.

The accuracy of the applied loads was ±5 kN for horizontal forces and ±0.5 kN for transversal forces. The applied average heating rate was approximately 3°C/min in the middle of the columns with a reduction towards the ends of the column. At the thirds of the member, the average heating rate was about 2.5°C/min, and about 1.5 °C/min at the ends. Although the column ends are not directly heated and are outside the steel tube, the shown heating rate was caused by the high thermal conductivity of aluminium.

The applied external load and heating rate affect the vertical displacement rate in the middle of the column where creep strain develops and consequently accelerates the failure of the column due to buckling. The results of vertical displacements presented in Figure 3 show that the influence of creep becomes significant after approximately 60 minutes from the start of the test and reaches its peak just before the failure of the column.

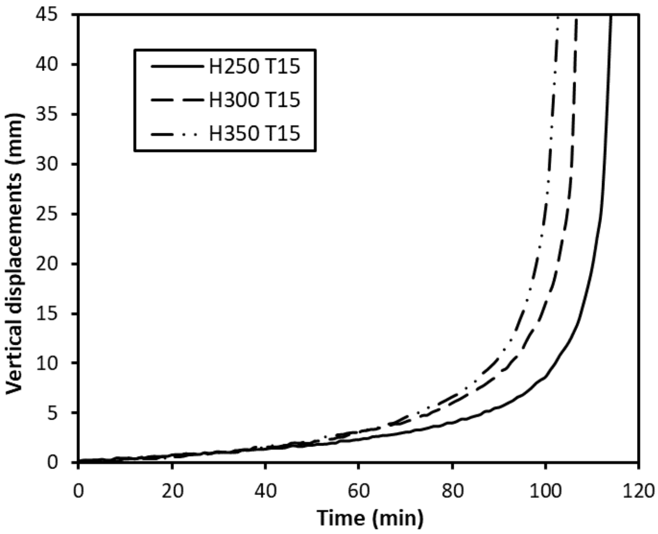

Figure 3. Vertical displacements of tested columns

4 NUMERICAL ANALYSIS

4.1 Geometry

Software ANSYS 16.2 [17] was used for numerical analysis of the column in order to test the performance of the calibrated creep model [16]. The geometry of the numerical model was created in the DesignModeler add-on and consists of a total of seven separate bodies (aluminium column and six steel accessories) with two additional elements used to simulate the horizontal and transversal hydraulic cylinders used to inflict forces on the column. The aluminium column is marked with the number 1 and the steel components with numbers 2-7 in Figure 4. while the numbers 8 and 9 present hydraulic cylinders. The aluminium column is divided into sections to adequately generate a temperature field along the column.

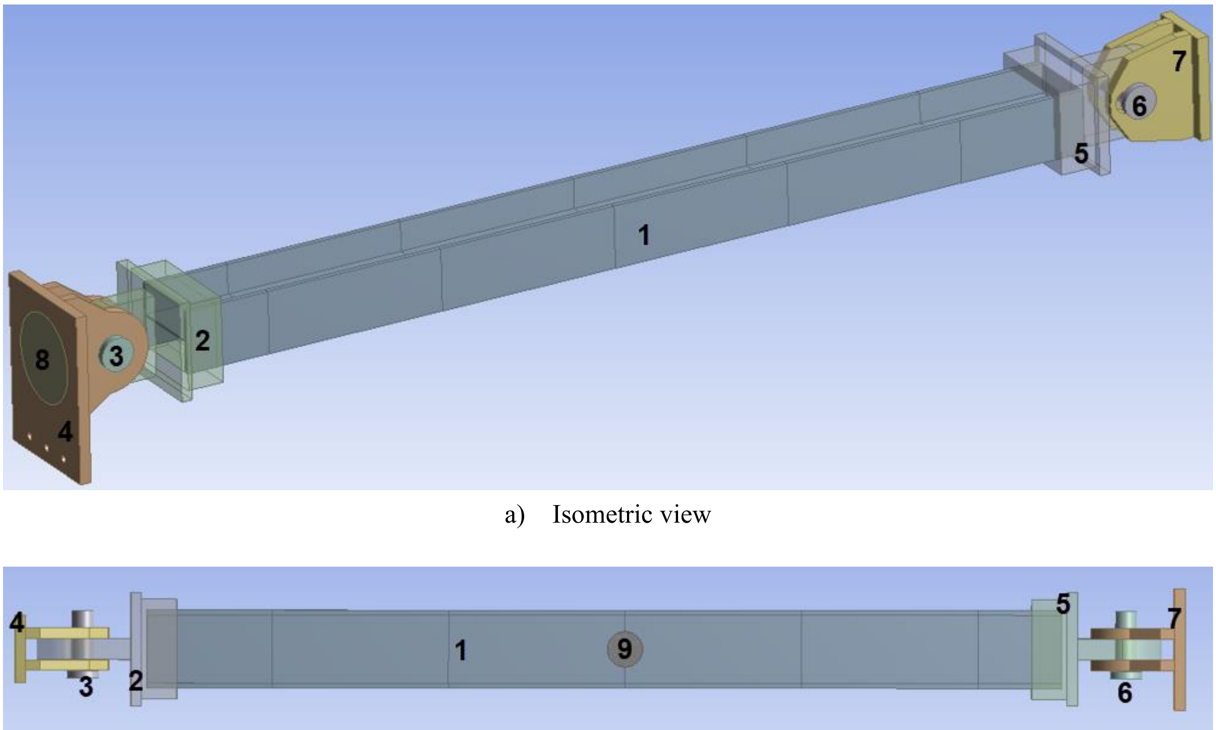

a) Isometric view

b) Bottom view

Figure 4. Numerical model

4.2 Material model

Within the ANSYS material library, there is no aluminium alloy with a material model corresponding to the EN AW 6082 T6 aluminium alloy. In order to successfully carry out numerical analyses, it is necessary to define proper material properties for the aforementioned alloy which was done through the previously conducted stationary tests presented in the paper [13]. The reduction of material properties: proof strength ($f_{0.2,\theta}$), ultimate strength (f_u), elastic modulus (E), and shear modulus (G) is presented in Figure 5.

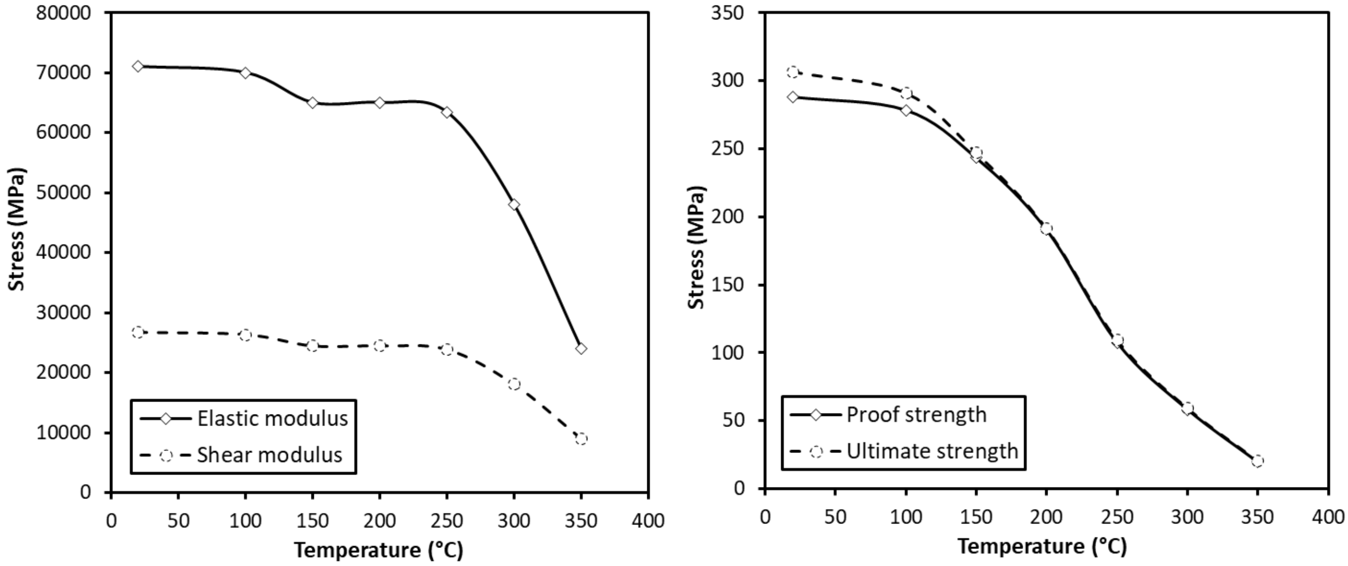

Figure 5. Temperature dependent material properties of alloy EN AW 6082 T6

To perform a nonlinear analysis including material behaviour, the Multilinear Model of Isotropic Hardening was used, which is based on the ratio of the stress and plastic strain at various temperatures. This model is capable of showing yielding graphically, and ultimately the failure of the element by effectively taking into account the influence of creep. The presented material model is shown in Figure 6 for normal temperature and high temperatures significant for the creep development.

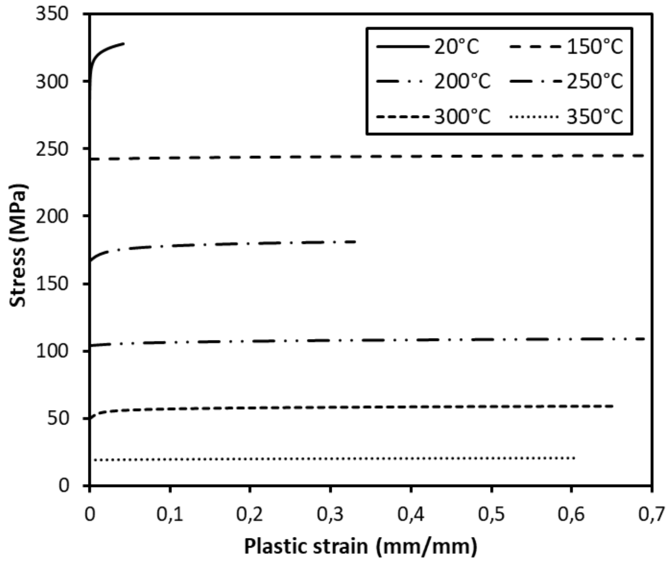

Figure 6. Multilinear Isotropic Hardening material model for alloy EN AW 6082 T6

4.3 Numerical model

For the numerical analysis of steel components and the aluminium column, high-order 3D finite elements were used (SOLID187), suited for modelling complex geometries, irregular meshes and contact elements. The finite element is defined with a total of ten nodes with three degrees of freedom in each node and is used to display plasticity, creep, hardening, large deflections and strains. The average mesh size was around 50 mm with local densities at the contacts of the elements and at the points of application of external load.

In order to simulate experiments conducted on aluminium columns and presented in the previous chapter, it was necessary to divide the column into sections in order to generate the temperature field as accurately as possible to match the temperature records from the tests. Due to the circular cross-section of the furnace, it was assumed, and experimentally confirmed, the near-uniform heating on the column cross-section with the negligible deviation between the flanges and the web. Average temperatures for specific points on the column, on flanges and on the web in the midspan (1/2), at the ends and in between (3/4), are presented in Figure 7 for the presented tests.

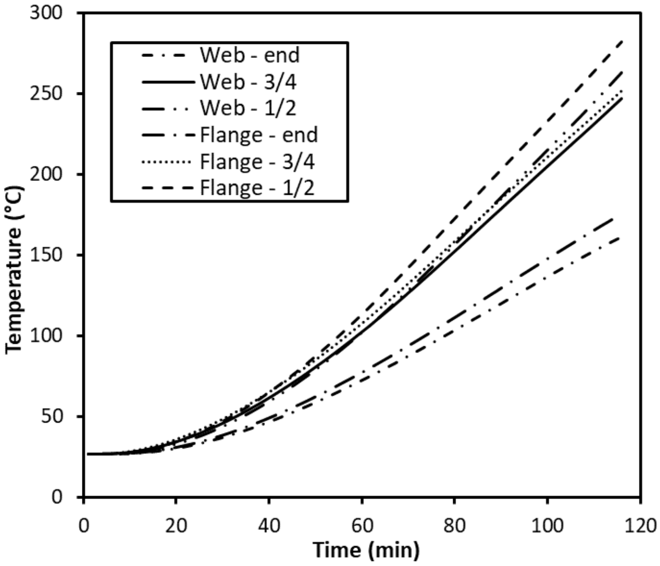

a) H250 T15

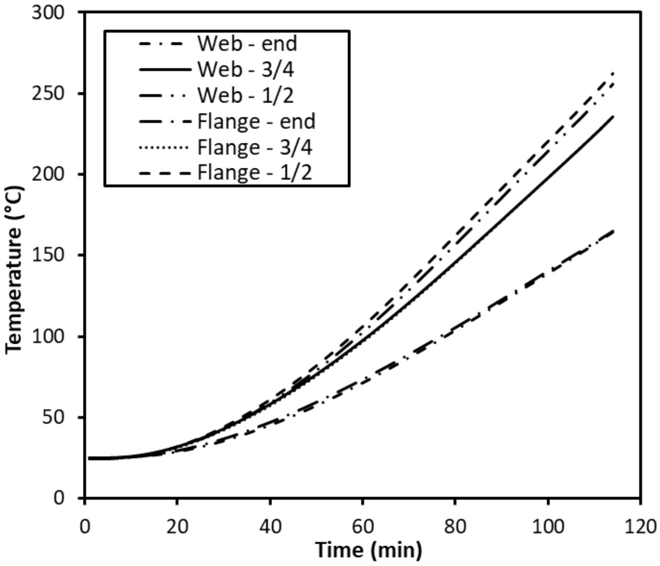

b) H300 T15

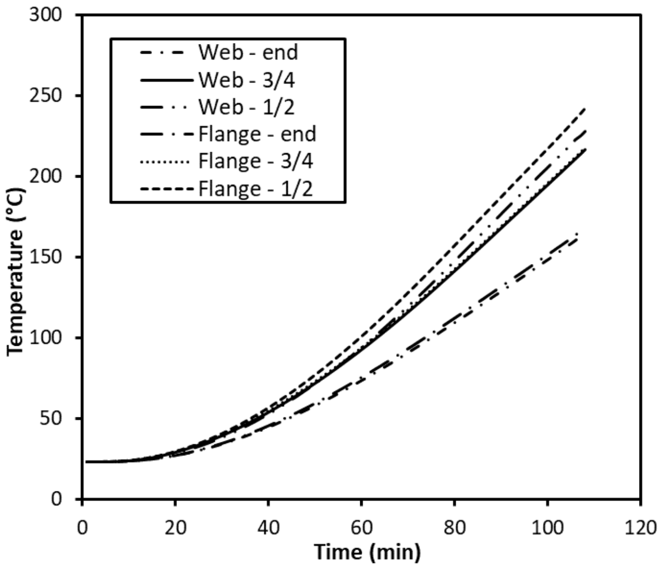

c) H350 T15

Figure 7. Heating curves applied to the numerical model

4.4 Results

Numerical analysis was carried out with and without the influence of creep, and the results of vertical displacements in the middle of the column are presented in Figure 8. Development of creep strain is obtained by using the Modified Time Hardening creep model available in ANSYS, with calibrated coefficients for different temperatures and proof strength rations [16]. Since aluminium alloys are capable of withstanding large plastic strain, it is necessary to define the column failure criteria for the experimental part of the research. Experimentally, yielding manifests through the rapid increase in vertical displacements where the column uses its plastic capacity. Accordingly, the failure criterion for columns in the conducted tests was defined based on the vertical displacement rate at midspan. This condition is met for columns exposed to fire according to the European Committee for Standardization [18] when the member exceeds the value defined by the following equation (2):

$$\frac{L^2}{9000 \cdot d} \frac{mm}{min} \tag{2}$$

where L is the total length of the member (mm), and d is the effective height of the member around the loaded axis (mm). The reference point of failure of the column in accordance with the previous criterion and for the defined geometry is the value when the vertical displacement rate in the experiments exceeds the value of 4.4 mm/min around the loaded, weaker, axis. The point of failure is marked with a black circle in Figure 8. The starting point in Figure 8 presents the time after the initial application of the aforementioned horizontal and transversal loads.

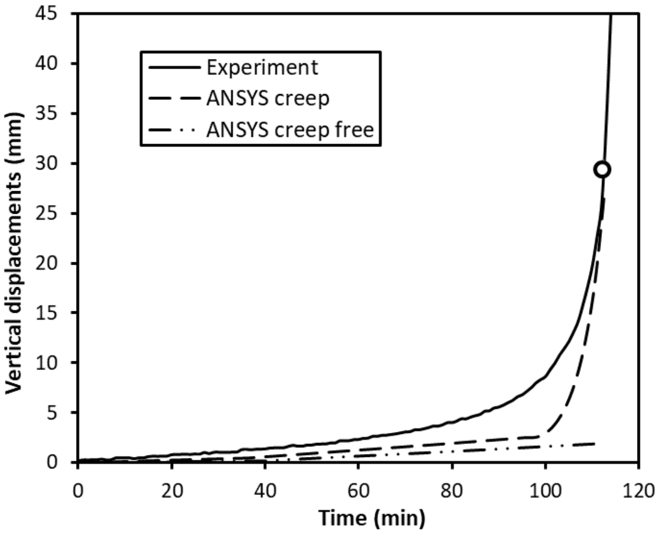

a) H250 T15

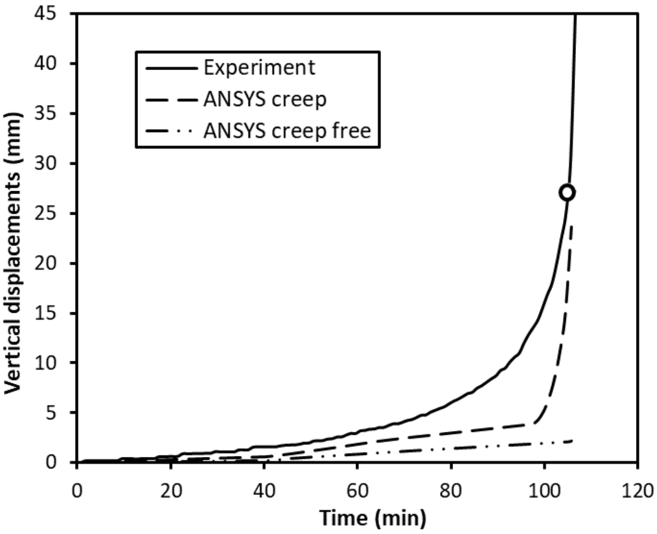

b) H300 T15

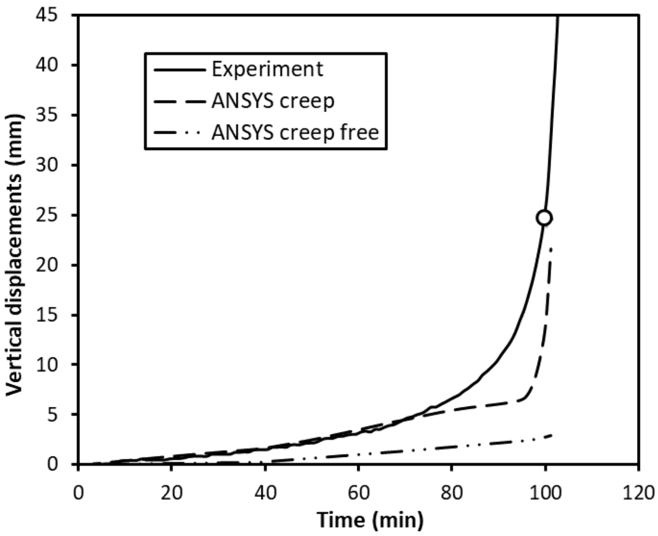

c) H350 T15

Figure 8. Comparison of the experimental and numerical vertical displacements for different horizontal load

5 TIME-DEPENDENT ANALYSIS OF A SIMPLE ALUMINIUM STRUCTURE

A preliminary parametric study based on the load and MTH model coefficients for a 3 °C/min heating rate of the critically loaded column of a simple two-story aluminium frame structure is given. Results of developed creep strain and displacements are presented in Figure 9.

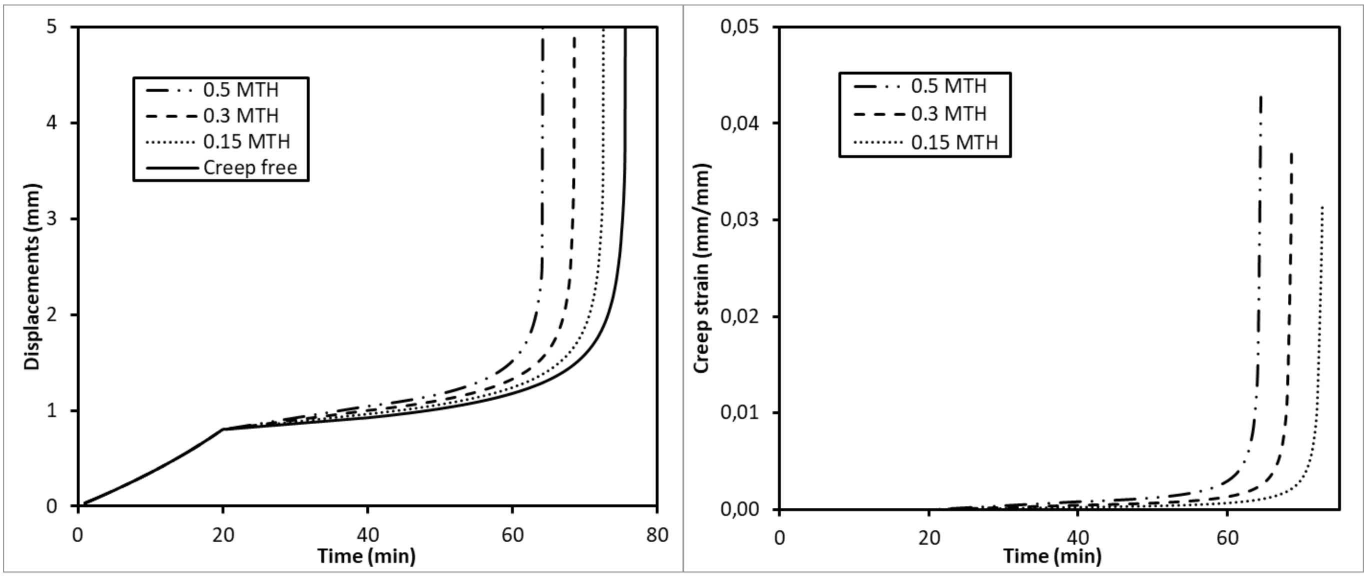

Figure 9. Displacements and creep strain of the critical column

The section geometry of the structure (columns and beams) matches the tested columns with the axial distances of 3 m in one, and 4 m in the other direction. The temperature developed with the heating rate of 3 °C/min was applied on the column uniformly. Line load with a value of 1% of the total applied vertical load around the weaker axis of the central column was used for this preliminary study.

Failure time and the maximal temperature reached upon failure with developed creep strain are presented in Table 1, while the visible yield with presented creep strain at the onset of failure for the critical column is presented in Figure 10 (0.15 MTH creep model, heating rate of 3 °C/min).

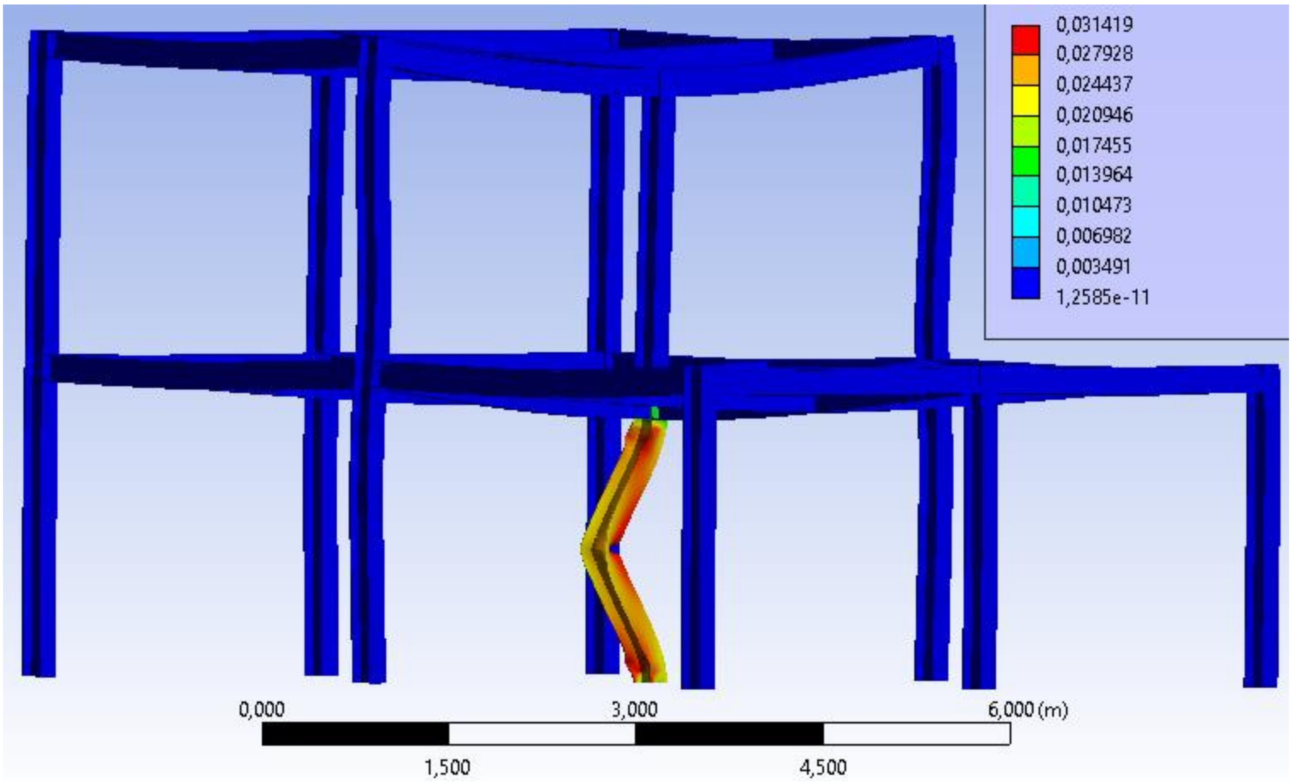

Figure 10. 3D model of simple aluminium structure with developed creep strain for 0.15 MTH model

Table 1. Results of the time-dependent analysis of a simple aluminium structure

MTH	Time of failure (min)	Critical temperature (°C)	Creep strain (mm/min)
0.5	62,42	209	0,0427
0.3	68,58	224	0,0377
0.15	72,71	239	0,0314
0	75,72	250	-

6 DISCUSSION OF THE RESULTS

It can be seen from the comparison between experimental and numerical analysis that the creep strain has a significant influence in terms of the failure time of the column. The critical temperature and failure time of tested columns correlate very well with the numerical simulation values. It can be noted that in the creep-free analysis the column does not fail in the experimental time interval, nor does it develop significant increase in displacements. The displacement ratio between the MTH creep model and creep-free analysis ranges from 183 % in Test 3 (horizontal force 350 kN) and rises with the increase of the horizontal load. In Test 2 with a horizontal force of 300 kN, the difference was 208 % and in Test 1 with a lower force of 250 kN, the displacement ratio difference was 255 %.

It can be seen from Table 1 that creep has a major influence on the failure time and critical temperature of aluminium columns. Failure for the critical 0.5 MTH model occurs around 13 minutes faster and at 41 °C lower temperature in comparison to creep-free analysis for the critically loaded column of the presented simple aluminium structure.

7 CONCLUSIONS

Current results suggest that the creep strain has a significant influence on the overall load-bearing capacity of the aluminium columns made of EN AW 6082 T6 alloy for the heating rate of 3 °C/min. This is evident by observing the failure time and critical temperature for creep-free and explicit creep analysis results. For a more exact representation of the influence of creep more tests need to be carried out in order to strengthen the observations put forward.

ACKNOWLEDGMENT

This work is partially supported through project KK.01.1.1.02.0027, a project co-financed by the Croatian Government and the European Union through the European Regional Development Fund - the Competitiveness and Cohesion Operational Programme.

This work has been partially supported by Croatian Science Foundation under the project Influence of creep strain on the load capacity of steel and aluminium columns exposed to fire (UIP-2014-09-5711). Any opinions, findings, and conclusions or recommendations expressed in this material are those of the authors and do not necessarily reflect the views of Croatian Science Foundation.

REFERENCES

[1] Y. Anderberg, "Modelling steel behaviour," *Fire Saf. J.*, vol. 13, no. 1, pp. 17–26, 1988, doi: 10.1016/0379-7112(88)90029-X.

[2] European Committee for Standardization, "EN 1999-1-2 (2007), Eurocode 9: Design of aluminium structures - Part 1-2: Structural fire design," vol. 1, no. 2005. Brussels, Belgium, 2005.

[3] N. K. Langhelle, E. Eberg, and J. Amdahl, "Comparative study between numerical models and buckling tests of aluminium columns at elevated temperatures," *Proceedings of the International Conference on Offshore Mechanics and Arctic Engineering - OMAE*. 1998.

[4] N. K. Langhelle and J. Amdahl, "Experimental and numerical analysis of aluminium columns subjected to fire," *Proc. Int. Offshore Polar Eng. Conf.*, vol. 4, pp. 406–413, 2001.

[5] J. Maljaars, F. Soetens, and H. H. Snijder, "Local buckling of aluminium structures exposed to fire. Part 1: Tests," *Thin-Walled Struct.*, vol. 47, no. 11, pp. 1404–1417, 2009, doi: 10.1016/j.tws.2009.02.008.

[6] J. Maljaars, F. Soetens, and H. H. Snijder, "Local buckling of aluminium structures exposed to fire. Part 2: Finite element models," *Thin-Walled Struct.*, vol. 47, no. 11, pp. 1418–1428, 2009, doi: 10.1016/j.tws.2008.06.003.

[7] J. Maljaars, "Literature Study on Aluminium Structures Exposed to Fire," *Netherlands Inst. Met. Res.*, p. 128, 2005.

[8] J. E. Dorn, "Some fundamental experiments on high temperature creep," *J. Mech. Phys. Solids*, vol. 3, no. 2, 1955, doi: 10.1016/0022-5096(55)90054-5.

[9] E. Kandare, S. Feih, A. Kootsookos, Z. Mathys, B. Y. Lattimer, and A. P. Mouritz, "Creep-based life prediction modelling of aluminium in fire," *Mater. Sci. Eng. A*, vol. 527, no. 4–5, pp. 1185–1193, 2010, doi: 10.1016/j.msea.2009.10.010.

[10] N. Torić, I. Boko, I. W. Burgess, and V. Divić, "The effect of high-temperature creep on buckling behaviour of aluminium grade EN6082AW T6 columns," *Fire Saf. J.*, vol. 112, no. December 2019, 2020, doi: 10.1016/j.firesaf.2020.102971.

[11] N. Torić *et al.*, "High-temperature properties of aluminum alloy EN6082AW T6," in *The International Conference of Applications of Structural Fire Engineering (ASFE)*, 2017, p. 5.

[12] N. Torić, I. Boko, I. W. Burgess, and M. Goreta, "Experimental analysis of the influence of creep on fire-exposed steel and aluminium columns," in *The 10th International Conference on Structures in Fire*, 2018, p. 6.

[13] N. Torić, J. Brnić, I. Boko, M. Brčić, I. W. Burgess, and I. Uzelac, "Experimental analysis of the behaviour of aluminium alloy EN 6082AW T6 at high temperature," *Metals (Basel).*, vol. 7, no. 4, 2017, doi: 10.3390/met7040126.

[14] N. Torić, I. U. Glavinić, and I. W. Burgess, "Development of a rheological model for creep strain evolution in steel and aluminium at high temperature," *Fire Mater.*, vol. 42, no. 8, pp. 879–888, 2018, doi: 10.1002/fam.2643.

[15] M. Goreta, N. Torić, V. Divić, and I. Boko, "Testing the influence of creep on fire-exposed aluminium columns," in *9th International Congress of Croatian Society of Mechanics*, 2018, no. September, p. 10.

[16] M. Goreta, N. Torić, and I. Boko, "Calibration of an Existing Creep Model for Analysis of Aluminium Members Exposed to Constant Temperature," *Int. J. Eng. Model.*, vol. 34, no. 2, pp. 1–15, 2021, doi: 10.31534/engmod.2021.2.ri.01m.

[17] A. D. Canonsburg, "ANSYS, PA 15317, Release 16.2." 2015.

[18] European Committee for Standardization, "EN 1363-1 (2020), Fire resistance tests - Part 1.: General requirements." Brussels, Belgium, 2020.

FIRE BEHAVIOUR OF STAINLESS STEEL REINFORCEMENT AND STAINLESS STEEL REINFORCED CONCRETE BEAMS

Fazal-ur Rehman[1], Javaria Mehwish[2], Rabee Shamass[3], Katherine A. Cashell[4]

ABSTRACT

This paper is concerned with the behaviour of stainless steel reinforced concrete flexural members during a fire. Recent years have seen a steady increase in the usage of stainless steel reinforcement as an attractive alternative to traditional carbon steel reinforcement. This is mainly owing to its favourable and sustainable attributes, including the excellent corrosion resistance, which can result in a long, maintenance-free life. However, there is a lack of useful performance data and design guidance in the available literature. Therefore, the current paper discusses an experimental and numerical assessment of the behaviour of stainless steel reinforced concrete (SS RC) structural elements during a fire. A material-level test programme was undertaken at Brunel University London to determine the response of stainless steel reinforcement during exposure to different levels of elevated temperature. This data was not previously available. Thereafter, the paper outlines a finite element model which was developed to simulate the response of stainless steel reinforced concrete beams. The model is validated against available data, and then employed to investigate the relative influence of the most salient parameters on the fire behaviour. In particular, the behaviour is compared to that of traditional carbon steel reinforced concrete (CS RC) beams and it is shown that the stainless steel reinforced members behave better in terms of load carrying capacity and sustain fire much longer time than that for the CS RC beam. Additionally, the SS RC beams has higher deflection during the fire exposure in comparison to the CS RC beams.

Keywords: Material testing; finite element modelling; stainless steel; reinforced concrete.

1 INTRODUCTION OF STAINLESS STEEL REINFORCED CONCRETE FLEXURAL MEMBERS DURING A FIRE.

Recent years have seen an increase in the usage of stainless steel reinforcement as an attractive alternative to traditional carbon steel reinforcement. This is mainly owing to its favourable and sustainable attributes, including the excellent corrosion resistance which can result in a long, maintenance-free life. However, there remains a lack of useful performance and design data in the public domain, especially during extreme events such as a fire. Typically, stainless steel reinforcement was used mainly in bridges and structures such as in water treatment plants and other settings susceptible to corrosion, and this has broadened to other structural applications in recent years, such as industrial buildings, car parks and structures in marine environments.

Premature deterioration and failure of concrete buildings and infrastructure due to corrosion of the reinforcement is a severe and well-recognised challenge facing the structural engineering community from

[1] Dr Fazal-ur Rehman, High Tempreture Engineering Scientist, ISIS Neutron and Muon Source, UK
e-mail: fazal-ur.rehman@stfc.ac.uk, ORCID: https://orcid.org/0000-0002-1698-2948
[2] Javaria Mehwish, College of Engineering, Design and Physical Sciences, Brunel University London, UK
e-mail: javaria.mehwish@brunel.ac.uk , ORCID: https://orcid.org/0000-0001-6304-8915
[3] Dr Rabee Shamass, Senior Lecturer in Civil Engineering, LSBU, UK
e-mail: shamassr@lsbu.ac.uk, ORCID: https://orcid.org/0000-0002-7990-8227
[4] Dr Katherine A. Cashell, Assoc. Prof. In Structural Engineering and Design, UCL, UK.
e-mail: k.cashell@ucl.ac.uk, ORCID: https://orcid.org/0000-0003-2804-4542
https://doi.org/10.6084/m9.figshare.22178006

a technical perspective and the wider public from a convenience and economic point of view. In this context, there is an increasing interest in using stainless steel reinforcement in concrete structures to combat the durability problems associated with chloride ingress. There are a number of different approaches to improving durability and, whilst these methods can improve the performance, they may not provide an inherently durable solution to the problem of chloride-induced corrosion and there is still a risk that significant maintenance may be required within the design life of the structure. Meanwhile, stainless steel reinforcement represents an efficient and sustainable solution which, when correctly employed, can prevent the deterioration of infrastructure in the first place, and extend the natural design life of the structure. Moreover, it can enable the use of lower concrete cover values, thus reducing the overall structural weight and material requirements.

The first recognised application of stainless steel as reinforcement was the Progresso Pier, Mexico, in 1941. In this structure, today's equivalent of grade 1.4301 stainless steel was used to reinforce the concrete, and the pier is still in use today (Nickel Institute, 2013) [1]. Between the years 1941-1970, there were very few if any notable applications of stainless steel reinforcing bar in concrete structures. However, in the early 1970s, corrosion of reinforcement became a more pressing issue, and the Building Research Establishment (BRE) conducted a study that spanned over 20 years, concluding with the excellent performance of stainless steel as an alternative to traditional reinforcement (Gedge, 2003) [2]. More recent examples of applications include the Saint George Bridge in Genova, rehabilitation of the Santiago Church, and the New Champlain Bridge in Montreal, Canada.

There are no specific requirements for the manufacturing processes of stainless steel rebars, but BS 6744-10 (2016) [3] provides requirements for the chemical composition and the testing methods. In accordance with this standard, the stainless steel rebar's minimum required mechanical property values are based on the carbon steel B500B specifications as given in Part 7 of BS 4449 (2016) [4]. In terms of structural design, there is a lack of guidance currently available for engineers. Current design codes such as Eurocode 2 do not include specific rules for stainless steel reinforced concrete, and generally suggest using the same criteria as for traditional carbon steel reinforced concrete.

Fig. 1 presents an idealised stress-strain response for (a) carbon steel reinforcement and (b) stainless steel reinforcement, demonstrating the key characteristics for each. In these figures, E is the Youngs modulus, $f_{0.2p}$ is the 0.2% proof strength (used for stainless steel), f_y is the yield strength, f_u is the ultimate strength, ε_u is the elongation at the maximum stress, and ε_f is the total strain at failure. It is noteworthy that ε_u and ε_f are typically significantly larger values for stainless steel compared with carbon steel. It is clear that the behaviour of the two materials is quite different mainly in terms of the much-increased ductility of stainless steel rebars, and therefore employing the same design methods as those devised for carbon steel RC is unlikely to result in an optimal or efficient design outcome for stainless steel reinforced concrete.

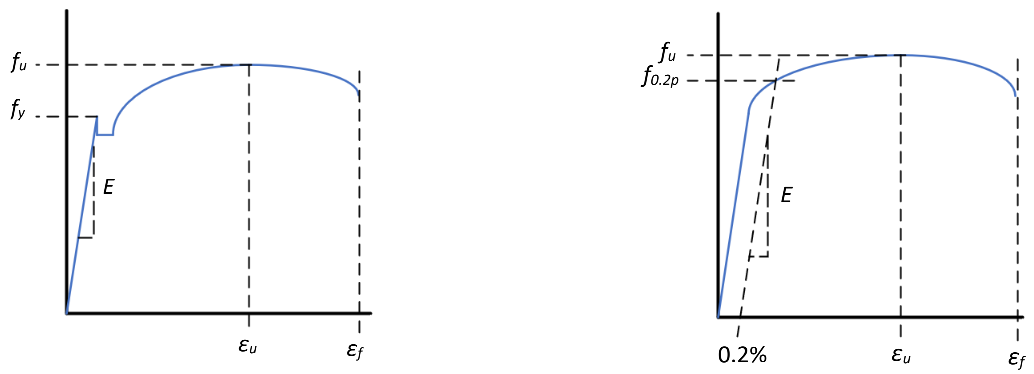

(a) (b)

Figure 1. Idealised stress-strain curve response of (a) carbon steel and (b) stainless steel

In terms of the elevated temperature behaviour, there is a particular dearth of information available on this topic for stainless steel reinforcement. For bare stainless steel structural sections, the retention factors for the yield strength (or 0.2% proof strength) and Young's modulus for both carbon steel [5] and grade 1.4301 stainless steel [6,7]at various levels of elevated temperature are shown in the Fig. 2(a) and (b), respectively. For the strength, although stainless steel initially loses more of its initial strength than carbon steel, this reverses from around 400°C and then stainless steel responds significantly better than carbon steel. Stainless steel behaves even better than carbon steel in terms of stiffness retention. These distinctive properties of stainless steel are very beneficial in the event of fire. On the other hand, stainless steel has a higher coefficient of linear thermal expansion (between 14-17 × 10^{-6} /°C) compared with carbon steel (12× 10^{-6} /°C), which is an important consideration for how it bonds to the surrounding concrete during elevated temperature scenarios. This may be a challenge for reinforced concrete members during a fire, as the composite action between the two constituent materials may be lost, resulting in a loss of bond, greater cracking and greater levels of concrete spalling.

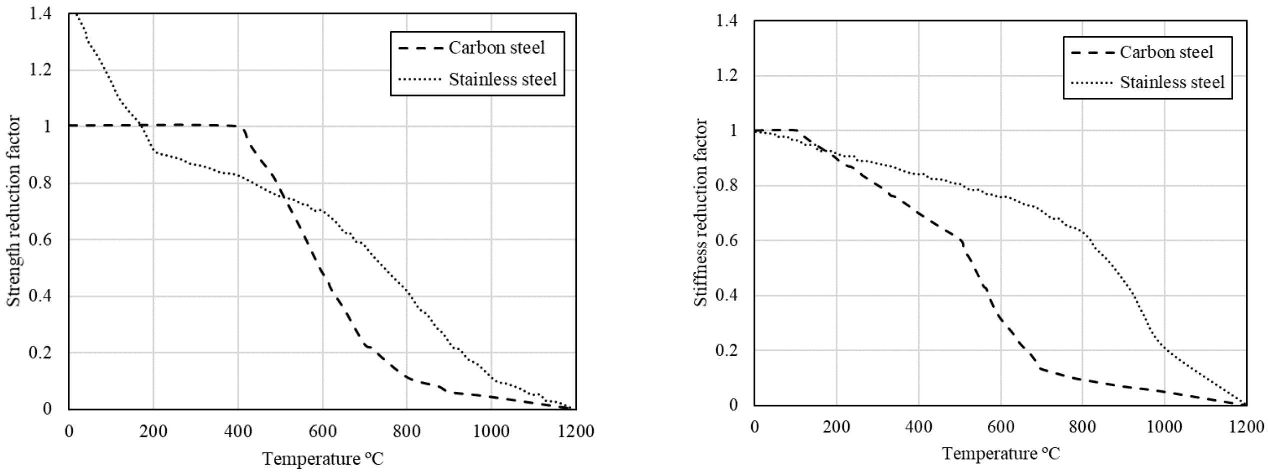

(a) (b)

Figure 2. Retention of mechanical properties for stainless steel and carbon steel including (a) strength and (b) stiffness (adapted from [6]).

In light of the dearth of data on the elevated temperature behaviour of stainless steel reinforcement, this paper proceeds with a description of a series of experiments on these materials, to determine the elevated temperature response of stainless steel reinforcement. This is followed a description of the development and validation of a finite element model to study the behaviour of stainless steel reinforced concrete beams in fire. The data from the experimental programme is incorporated into the model, to reflect the material properties at elevated temperature.

2 EXPERIMENTAL PROGRAMME

2.1 General

In order to determine the real elevated temperature properties, two grades of stainless steel rebar, namely austenitic grade 1.4301 and duplex grade 1.4362, were selected and examined under isothermal test conditions. Both bar types were manufactured through cold-rolling and had a diameter of 12 mm. The testing setup compromised the Instron 5584 150 kN electromagnetic testing frame with an Instron SF-16 2230 furnace, as shown in Fig. 3, and a three-zone Eurotherm 2416 temperature control unit for the elevated temperature testing. For the strain measurement, an extended EX2620-601 extensometer was used.

The isothermal testing was conducted with guidance from BS EN ISO 6892-2 [8]. Each sample had a total length (L_t) of 750 mm, a gauge length (L_0) of 50 mm and parallel length (L_c) between the jaws of 650 mm, and the heating zone was localised to the central 300 mm. The elevated temperature range chosen for the programme was 100°C to 800°C, rising in increments of 100°C. For the heating regime, the samples were heated at a rate of 10°C/min until the target temperature was reached. Following this, all samples were soaked in the target temperature for 1 hour before loading commenced. A 10 kN preload was applied to all samples after the heating regime to remove any slack in the arrangement, and then the samples were subjected to a continuous displacement of 0.5 mm/min until failure occurred.

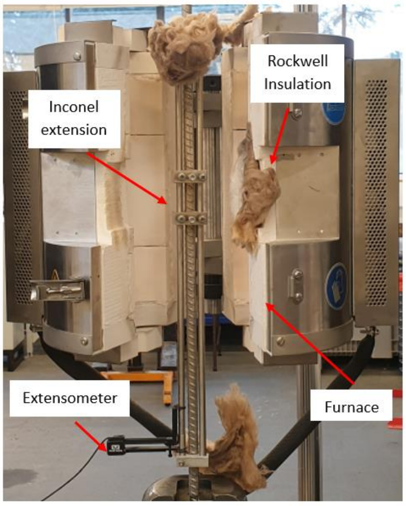

Figure 3. Elevated temperature test arrangement

2.2 Results

Table 1 presents the changes in key properties including the 0.2% proof strength ($f_{0.2p,\theta}$), ultimate strength ($f_{u,\theta}$), elastic modulus (E_θ), and total strain at failure at failure ($\varepsilon_{f,\theta}$) following exposure to various levels of elevated temperature θ between 100 and 800°C for austenitic grade 1.4301 and duplex grade 1.4362. The corresponding stress-strain curves are presented in Figs. 4 and 5, respectively. It is observed that following exposure to temperatures of just 100°C, there was immediately a significant loss in $\varepsilon_{f,\theta}$, total strain at failure, which decreased by 37% and 55% for the austenitic and duplex bars, respectively, compared with the corresponding room temperature values. The failure strains reduced even further with increasing temperature up to around 700℃ , and then the trend was reversed and $\varepsilon_{f,\theta}$ started to increase again. This increase in ductility was due to the rebars reaching the active recrystallization condition of at least 737°C and maintaining the temperature long enough to begin forming new and more ductile austenite grains.

Table 1: Results from the elevated temperature material testing

	Grade 1.4301				Grade 1.4362			
	$f_{0.2p,\theta}$	$f_{u,\theta}$	$\varepsilon_{f,\theta}$	E_θ	$f_{0.2p,\theta}$	$f_{u,\theta}$	$\varepsilon_{f,\theta}$	E_θ
Temp.	(N/mm^2)	(N/mm^2)	(%)	GPa	(N/mm^2)	(N/mm^2)	(%)	GPa
20°C	695.44	885.87	21.22	192.3	836.75	941.46	19.708	200.9
100°C	698.32	797.17	13.34	184.6	674.18	854.52	8.889	192.9
200°C	572.18	732.24	7.43	176.9	607.3	787.01	8.259	184.8
300°C	507.15	712.68	6.67	169.2	615.64	782.49	8.56	176.8
400°C	516.43	691.95	8.13	161.5	606.76	751.46	8.427	168.8
500°C	539.34	649.4	10.21	153.8	523.05	734.35	10	160.7
600°C	418.27	513.73	12.94	146.1	528.25	553.49	9.839	152.7
700°C	310.6	391.49	18.94	136.5	289.05	395.84	10.8	142.6
800°C	155.63	194.09	31.67	121.1	148.19	211.35	18.021	126.6

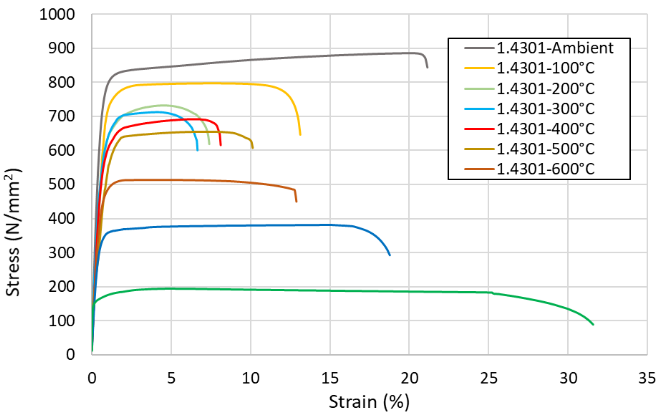

Figure 4. Stress-strain responses for grade 1.4301 at various levels of elevated temperature

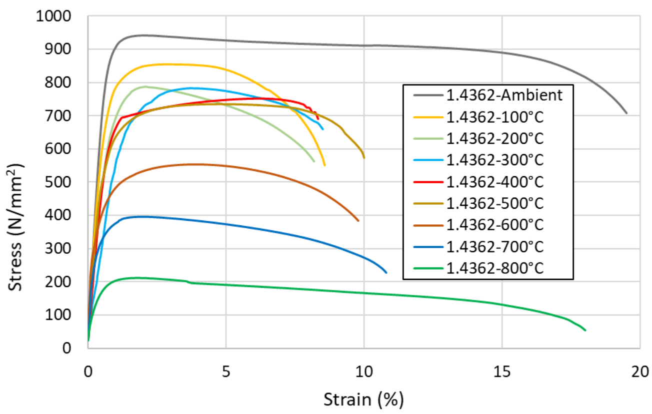

Figure 5. Stress-strain responses for grade 1.4362 at various levels of elevated temperature

For the strength parameters, there were some different behaviours observed between the austenitic and duplex rebars, so each are considered separately hereafter. First, for the austenitic rebars, both $f_{0.2p,\theta}$ and $f_{u,\theta}$ consistently declined as the temperature increased, but in varying proportions, compared with the corresponding room temperature values. At 100°C, there was no significant change to $f_{0.2p,\theta}$, whereas $f_{u,\theta}$ presented a loss of 10% against f_u. After exposure to 200°C, $f_{0.2p,\theta}$ presented a loss of 18% compared with $f_{0.2p}$, whilst $f_{u,\theta}$ lost 17% of its original value. Following exposure to 300°C, 400°C and 500°C, $f_{0.2p,\theta}$ exhibited losses of between 22-27% relative to $f_{0.2p}$ and there were corresponding reductions in $f_{u,\theta}$ of between 20-27% compared with f_u. When exposed to higher temperatures of between 600 and 800°C the losses in strength compared with the ambient temperature values became even more pronounced, with $f_{0.2p,\theta}$ and $f_{u,\theta}$ reducing by 40% and 42%, respectively, following exposure to 600°C, 55% and 56%, respectively, at 700°C and 78% and 79% for samples that were heated to 800℃ .

The duplex rebars also showed significant reductions in strength with increasing temperature, as given in Table 1. In contrast to the austenitic bars, the proof strength $f_{0.2p,\theta}$ reduced by 19% from the ambient temperature value following exposure to 100℃ . Between the temperature exposure range of between 200 and 400°C, there were consistent losses of 26-27% for $f_{0.2p,\theta}$ and 16-20% for $f_{u,\theta}$ compared with $f_{0.2p}$ and f_u. Again, similar to the austenitic rebars, the most significant reduction in strength was following exposure to temperatures of 700°C and above. It is interesting to compare this to the ductility which, as noted before, was quite similar to the virgin values during heating to 800°C. Clearly, the metallurgical phenomena and changes that are occurring in the rebars during this high level of temperature exposure were quite significant.

The test data shown in the Table 1 clearly indicates that there was reduction in the elastic modulus of stainless steel with increasing temperature. The elastic modulus at 100°C for both types of stainless steel slightly reduced by 4% from the ambient temperature value. As the temperature increased, the elastic modulus reduced linearly proportional up to 600°C. At the elevated temperature 800°C, both types of stainless steel exhibited a reduction in elastic modulus by 37% from the ambient temperature.

3 FINITE ELEMENT ANALYSIS

3.1 General

A numerical model was developed in order to simulate and study the behaviour of stainless steel reinforced concrete structural members at elevated temperatures. To date, there is no physical test data for this type of structural behaviour. In terms of the ambient temperature behaviour, a number of researchers have conducted numerical analysis of stainless steel reinforced concrete (SSRC) [e.g., 9-11]. As discussed previously, it is widely accepted that the use of stainless steel in place of carbon steel, for the reinforcement, vastly improves the durability, even in harsh and corrosive environments. In addition, it can improve the flexural performance of RC beams as compared to carbon steel RC beams [11].

As there are no experimental data on the response of stainless steel reinforced concrete beams in fire, and therefore the numerical model developed in this paper is validated in two separate steps. First, the available test data from Mokhtar et al. [12] on stainless steel reinforced concrete beams is employed to examine the stainless steel material model's accuracy at ambient temperature. Then, the elevated temperature modelling of reinforced concrete beams is examined by analysing the tests conducted by Dwaikat and Kodur [13] on traditional carbon steel reinforced concrete beams. Between these two validation steps, the accuracy of the model is assumed, and it is then employed to study the more general response of SSRC beams in fire.

Hereafter, the development of the FE model is described in some detail, with particular attention given to the material modelling. For the elevated temperature analysis, the model is based on the experimental programme conducted by Dwaikat and Kodur [13] which included full-scale fire tests on two similar beams under different fire exposures. One of these specimens, namely Beam B-1 which was tested under standard fire curve ASTM E119 [14], is selected in this study for brevity and its arrangements are described hereafter.

3.2 Structural arrangement

The numerical model was developed based on the details of Beam B-1, which was examined by Dwaikat and Kodur [13], and was made of normal strength concrete with 58MPa compressive strength. As shown in Figure 6, the simply-supported beam was 3960 mm in length, 254 mm in width and had a total depth of 406 mm. The beam had tensile reinforcement of three 19 mm bars and compression reinforcement comprising two 13 mm bars. Shear reinforcement was also included in the cross-section and this was 6 mm bars at a constant spacing of 150 mm. The nominal yield strength of the longitudinal rebar was 420 N/mm^2 and for the stirrups was 280 N/mm^2. The beam was loaded in 4-point loading conditions, as shown in Figure 6 and the two loading points were 1200 mm apart from each other.

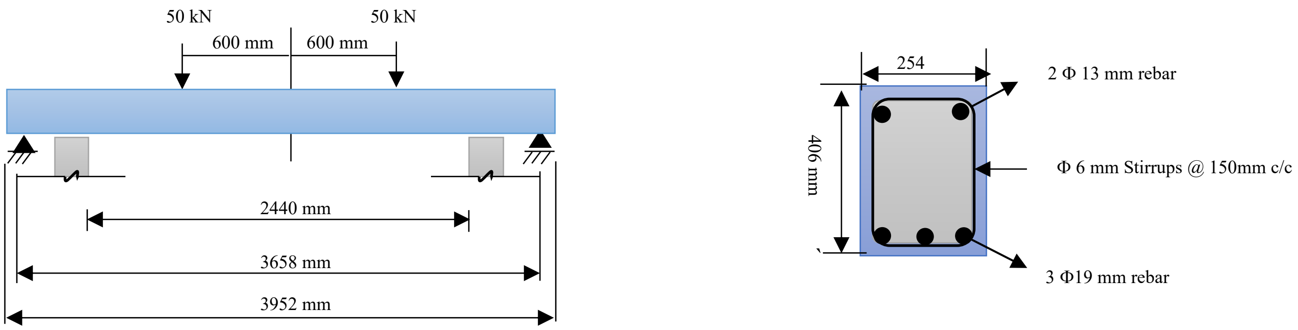

Figure 6. Layout and cross-section of beam examined by Kodur et al. [13].

3.3 Material modelling

3.3.1 Concrete

The concrete material behaviour is defined through the damage plasticity material model (CDP), available in the ABAQUS [15] library. The CDP model includes the effect of elevated temperature and can model the inelastic response of concrete in both tension and compression. The concrete compression behaviour is defined through the stress-strain curve using a constitutive material model taken from Eurocode 2 [6]. The tensile strength of the concrete reduces at elevated temperatures and this reduction is also calculated from Eurocode 2 [6]. The propagation of cracks in the concrete under tension is modelled through the fracture energy G_F . In the absence of experimental data G_F in N/m for ordinary normal weight concrete is estimated from the expression given in Eq. 1, which is taken from the fib Model Code 2010 [16], and in which f_{cm} is the mean compressive strength of the concrete. The compressive strength of concrete varies with temperature, and this is also assumed to occur for the calculation of fracture energy at elevated temperature.

$$G_F = 73.f_{cm}^{.18} \quad [1]$$

Figure 7 shows the compressive stress-strain response of concrete at elevated temperatures, in accordance with Eurocode 2 [6], which is implemented in the validation model.

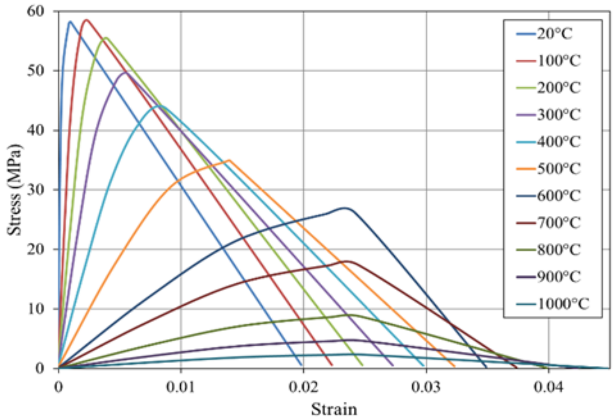

Figure 7. Stress-strain curves of concrete in compression at elevated temperatures [6]

The highly nonlinear behaviour of the concrete can cause significant convergence issues for the solver. The stability of the solution is achieved through use of a viscosity parameter μ (Kmiecik, 2011) [17]. The value of μ is selected as 0.0003 in this analysis determined through an iterative calibration process.

3.3.2 Reinforcement

An isotropic yielding of steel reinforcement can be defined by a uniaxial yield surface against uniaxial plastic strain, which is temperature-dependent. The plastic material data employed in the ABAQUS [15] model is the Cauchy stress and logarithmic strain. The following equations are used for converting the nominal stress–strain values (σ_{nom}-ε_{nom}) into true stress-logarithmic plastic strain (σ_{true}-ε_{ln}^{pl}), as required in ABAQUS:

$$\sigma_{true} = \sigma_{nom} * (1 + \varepsilon_{nom}) \quad [2]$$

$$\varepsilon_{ln}^{pl} = \ln(1 + \varepsilon_{nom}) - \frac{\sigma_{true}}{E} \quad [3]$$

where E is the materials Youngs modulus. For the validation exercise, which was based on the elevated temperature behaviour of carbon steel reinforced concrete, the constitutive material model of the carbon steel reinforcement was taken in accordance with Eurocode 2 [6], as shown in Figure 8.

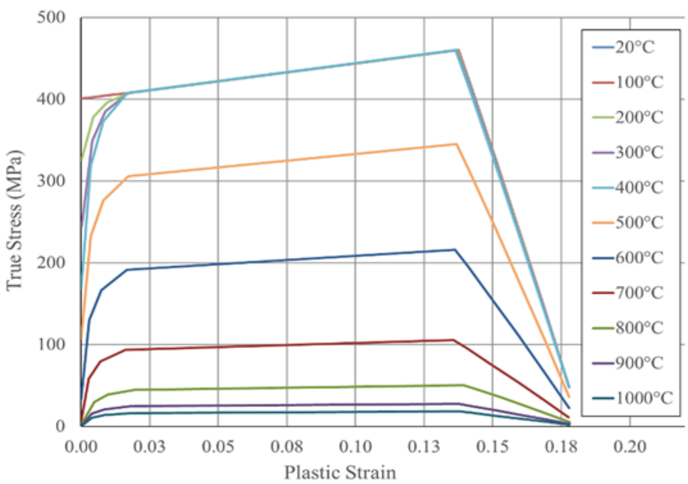

Figure 8. Stress-strain curve for carbon steel at elevated temperatures using Eurocode 2 [6] material model

On the other hand, stainless steel, unlike carbon steel, does not have well-defined yield stress at room temperature. The stress-strain curve for stainless steel is non-linear, with increased strength along with higher strain and a reduction in stiffness. In the absence of definite yield point strength at 0.2% strain which is referred as proof strength $f_{0.2p}$ is considered as design strength for ambient design. In the development of stress-strain curve for stainless steel at elevated temperature, the concept of a modified two-stage Ramberg-Osgood ambient stress-strain relationship for stainless steel is valid [18,19]. For stainless steel reinforcement in the elastic phase, up to stress values equal to the 0.2% proof strength $f_{0.2p,\theta}$, the strain at θ (ε) is related to the stress at θ (σ) by:

$$\varepsilon = \frac{\sigma}{E} + 0.002\left(\frac{\sigma}{f_{0.2p,\theta}}\right)^{n_\theta} \quad \text{for} \quad \sigma \leq f_{0.2p,\theta} \qquad [4]$$

$$\varepsilon = \frac{\sigma - f_{0.2p,\theta}}{E_{0.2,\theta}} + \varepsilon_{u,\theta}\left(\frac{\sigma - f_{0.2p,\theta}}{f_{u,\theta} - f_{0.2p,\theta}}\right)^{m_\theta} + \varepsilon_{0.2,\theta} \quad \text{for} \quad f_{0.2p,\theta} < \sigma \leq f_{u,\theta} \qquad [5]$$

In this expression, $E_{0.2,\theta}$ is the tangent modulus at the elevated temperature $f_{0.2p,\theta}$, $\varepsilon_{0.2,\theta}$ and are the total strains at the elevated temperature 0.2% ($f_{0.2p,\theta}$) proof strengths, respectively, and n_θ ,m_θ are strain hardening exponents at temperature θ. Different values for strain hardening components are proposed for austenitic and duplex stainless steel rebars [7]. In the current study actual stress-strain curve for both austenitic and duplex steel is determined through practical tests, as described earlier in this paper. These are implemented in the ABAQUS model for validation at elevated temperature. Whereas for validation at ambient temperature modified Ramberg-Osgood material model is used. It is applied using Eqs. 6 and 7, which capture the elastic and inelastic stages of the response, respectively:

$$\varepsilon = \frac{\sigma}{E} + 0.002\left(\frac{\sigma}{f_{0.2}}\right)^{n} \quad \text{for} \quad \sigma \leq f_{0.2} \qquad [6]$$

$$\varepsilon = \varepsilon_{0.2} + \frac{\sigma - f_{0.2}}{E_2} + \left(\varepsilon_u - \varepsilon_{0.2} - \frac{f_u - f_{0.2}}{E_2}\right)\left(\frac{\sigma - f_{0.2}}{f_u - f_{0.2}}\right)^{m} \quad \text{for} \quad f_{0.2} < \sigma \leq f_u \qquad [7]$$

3.4 Sequentially coupled thermal stress analysis

There are generally two different approaches in finite element analysis for the solution of structural fire analyses. There are the fully coupled and sequentially coupled thermal-stress analyses. The former of these is hugely computationally demanding and therefore, for RC structures, a sequentially coupled stress analysis is typically employed as it is more computationally efficient; this was employed in the current work. A sequentially coupled thermal-stress analyses is performed in two steps: (i) a heat transfer analysis is first conducted to simulate the spread of elevated temperature through the sections and (ii) a thermal-stress analysis is then performed to apply the loads and displacements. The temperature at each node of the element is calculated in the first step and these are then applied as a predefined field in the second step.

3.4.1 Heat transfer analysis

The input parameters required for the heat transfer analysis are the fire load and the thermal material properties. The fire load was applied in the numerical model using the same approach as in the experiments; that is in accordance with the time-temperature response given in ASTM E119 [14] and presented in Eq. 8:

$$T_f = T_o + 750(1 - \exp(-3.79553\sqrt{t_h}) + 170.41\sqrt{t_h} \qquad [8]$$

where T_0 and T_f are the initial and final temperatures in °C, respectively, and t_h is the time in hours. This fire load was applied in the model in the form of an amplitude at the external boundary of the beam. The temperature transfer through convection was modelled through a surface film condition interaction. Then, the heat transfer from the concrete to the steel was transferred through conduction as the steel was embedded in concrete. In accordance with Eurocode 2 [6], the convective heat transfer coefficient for concrete is taken as 25 W/m^2 °C and 9 W/m^2 °C for fire exposed and unexposed surfaces, respectively. The model was divided into a number of finite elements following a mesh sensitivity study, and an identical mesh was employed for both the thermal and structural stages of the modelling, for compatibility. In the thermal model, the concrete elements were modelled using three-dimensional eight-noded solid linear heat transfer elements known as DC3D8 in the ABAQUS library whilst the reinforcing steel bars were modelled using two-noded heat transfer link elements (DC1D2); both of these element types have a temperature degree of freedom. The thermal properties, including thermal conductivity, specific heat capacity and the coefficient of thermal expansion were taken from the guidance given in Eurocode 2 for the concrete and carbon steel reinforcement [6], and the Design Manual for Stainless Steel [21] for stainless steel.

3.4.2 Thermal stress analysis

The structural thermal-stress analysis was performed in the second step. The concrete was discretized using eight-nodded continuum elements (C3D8) with three degrees of freedom. This element can be used for 3D modelling of solids with or without reinforcement and it is capable of accounting for cracking of concrete in tension, crushing of concrete in compression, creep, and large strains. The steel reinforcement was defined using two-noded link truss elements (T3D2) such that the reinforcing bars could only be deformed by axial stretching. They were pin jointed at their nodes. The interaction between the concrete and the steel was considered as a perfect bond and achieved by embedding the reinforcement in the concrete through embedded region constraints. The tension stiffening behaviour defined in concrete material will allow for the interaction between reinforcement and surrounding concrete.

3.5 Validation of the numerical model

As stated before, there are no experimental data on the response of stainless steel reinforced concrete beams in fire, and therefore the numerical model developed in this paper is validated in two separate steps. First, the available test data from Mokhtar et al. [12] on stainless steel reinforced concrete beams is employed to examine the stainless steel material model's accuracy at ambient temperature. Then, the elevated temperature modelling of carbon steel reinforced concrete beams is examined by analysing the tests conducted by Dwaikat and Kodur [13].

Mokhtar et al. [14] tested four similar beams reinforced with either austenitic (316LN) or duplex (2205) stainless steels. The beams were simply supported, and concrete compressive strength was 37MPa. The details of the tests used for validation are not discussed in depth herein owing to space restrictions, but the results of the validation are given in Figure 9. Overall, the accuracy of the numerical model for reflecting the behaviour of stainless steel reinforced concrete beams at ambient temperature, including, and most importantly, the stainless steel material model is accurate. There were some issues during the testing of beam "Test3M20" which are not reflected in the model, but these issues were resolved during the test programme for the other specimens.

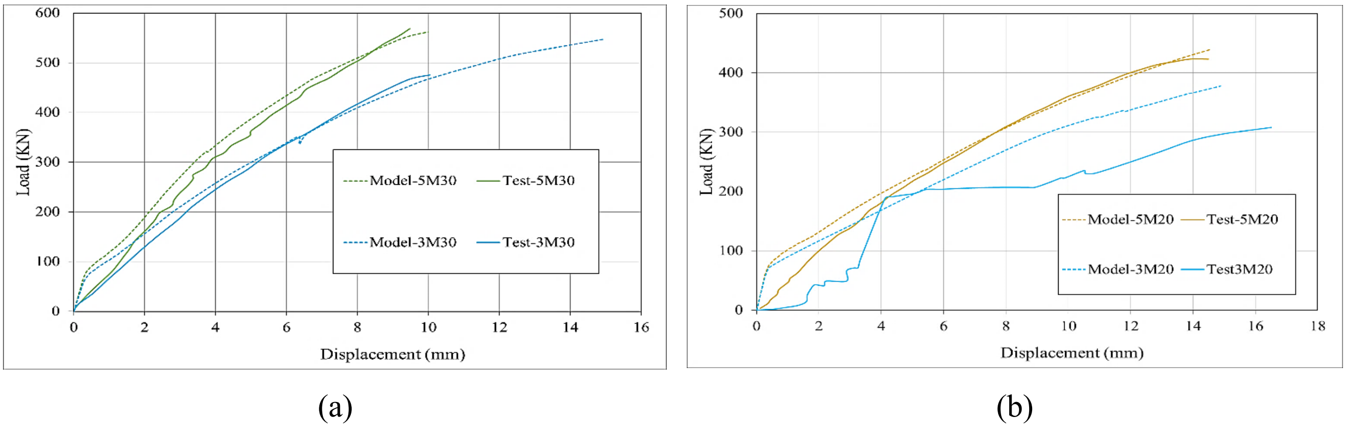

Figure 9. Validation of the numerical model at ambient temperature for beams containing (a) austenitic stainless steel and (b) duplex stainless steel.

As stated before, there are no test data on the elevated temperature behaviour of stainless steel reinforced concrete beams available in the literature. Therefore, the simulation of elevated temperature and its effect on reinforced concrete elements is validated through comparison with test data from traditional carbon steel reinforced concrete beams in fire. The beam test previously described and examined by Dwaikat and Kodur [13] is simulated in the current study, using the numerical model.

During testing, the point loads were firstly applied to the beam and these were held at their target values of 50 kN each, for thirty minutes and until no further deformation occurred. This was then considered to be the starting deflection for the beam when the fire was started, using a furnace, through which the middle two-thirds of the span was directly exposed to the fire. The fire was applied in accordance with the ASTM E119 [14] time-temperature fire curve. During the heating phase, the applied load remained constant for the duration of the fire exposure. The beam failed due to fracture of steel rebar after approximately 180 minutes of fire exposure.

Fig. 10(a) presents a comparison of the temperature development at several key locations of the beam, measured during the tests using thermocouples and also simulated using the numerical model. It is clear that the model is able to replication the temperature development very well, and the results are very similar. As expected, the locations closest to the fire exposure (bottom of the beam) reach the greatest temperatures, with the rebar reaching 600°C by the end of the test. Moreover, Fig. 10(b) presents the beam deflection versus time relationship for the beam during the fire exposure, from both the physical test as well as the numerical simulation. It is clear that the model is able to capture the general behaviour reasonably well, as well as the time at which failure occurs.

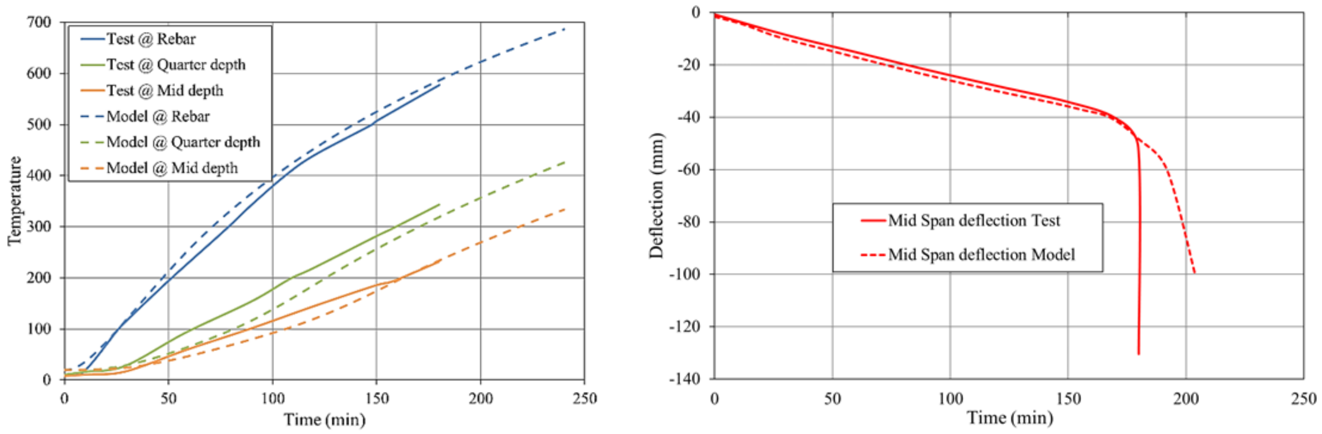

(a) (b)

Figure 10. Comparison of predicted and measured rebar and concrete temperature and displacement.

4 STAINLESS STEEL REINFORCED CONCRETE BEAMS IN FIRE

The validated numerical model is employed for the simulation of SS RC beams under fire. The only difference in the model is the material model for the reinforcement. The interaction between the rebar and the concrete is modelled as perfect bond in both cases, however, the tensile stiffening modelled for concrete allows the effect of interaction in a simple manner [15].

In the current study both austenitic (1.4301) steel and duplex (1.4362) steel rebars were tested at elevated temperature to calculate the reduction of proof strength and ultimate strength under fire. Stress-strain curves measured in practical tests were used in the numerical model to see the fire resistance of SS RC beams under fire. There is a wide difference in the thermal expansion of CS and SS rebars, but it doesn't make any change in the heat distribution among concrete and rebars. This can be viewed in Figs. 11 and 12.

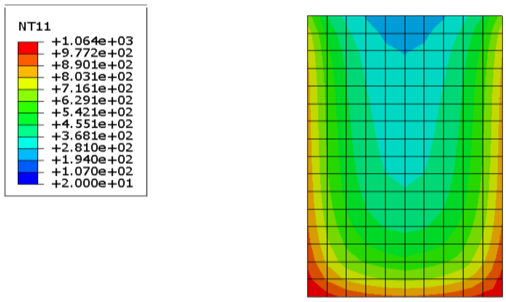

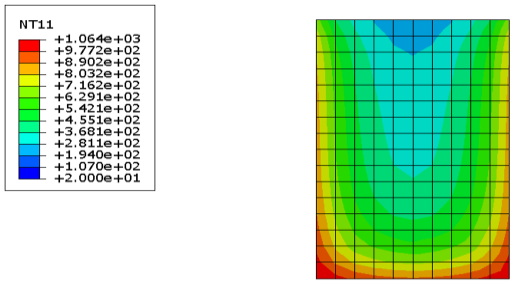

Figure 11. Temp. distribution up to 240 min. for CS RC beam.

Figure 12. Temp. distribution up to 240 min. for austenitic steel RC beam.

Fig. 13 shows the comparison of the CS RC beam with the austenitic RC beam. Both beams have the same cross-sectional geometry, concrete strength and reinforcement ratio. The stainless steel RC beam showed no failure under the given time of the ASTM E119 [14] fire curve. Therefore, the reinforcement ratio of the SS RC beam was reduced as compared to the CS RC beam to analyse the behaviour of the SS RC beam under the full-time-temperature curve of ASTM E119. Fig. 14 shows the behaviour of austenitic and duplex SS RC beams under fire, but with reduced reinforcement ratio, similar cross-section and concrete strength, compared to the behaviour of CS RC beam. The results show that both austenitic and duplex SS RC beams behave similarly such that the deflections values are similar over the period of fire exposure. However, the austenitic RC beam has slightly larger deflection after 170 min. Furthermore, the SS RC beams has higher deflection during the fire exposure in comparison to the CS RC beams since SS has inherently nonlinear properties, high thermal expansion, and survivability at a higher level of deflections. At the same time, carbon steel exhibited lower strains values than those for the stainless steel until yielding. The results show no difference in the heat distribution in all beams; however, SS RC beams sustain loading for a very long time under fire exposure. CS RC beam fails at around 175 min while austenitic and duplex SS RC beams fail at 237 mins and 243 mins respectively. This is mainly due to the SS rebars retain their strength even at the elevated temperature and survive for a much longer period before rupture. In terms of failure mode, SS RC beams failed due to concrete crushing, whereas CS RC beam failed due to the combination of concrete crushing and steel rupture.

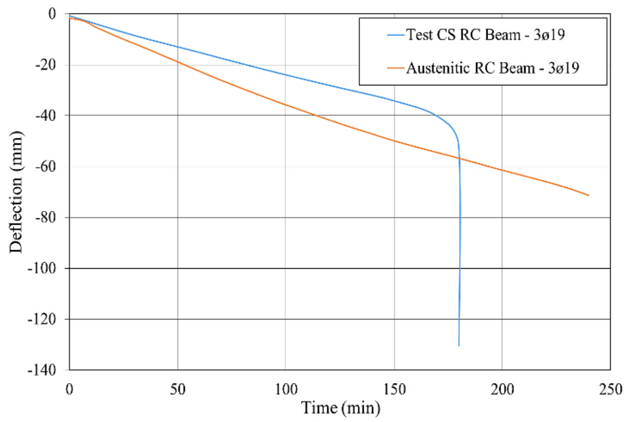

Figure 13. Fire resistance of two similar RC beams reinforced with similar steel ratio of CS and Austenitic steel

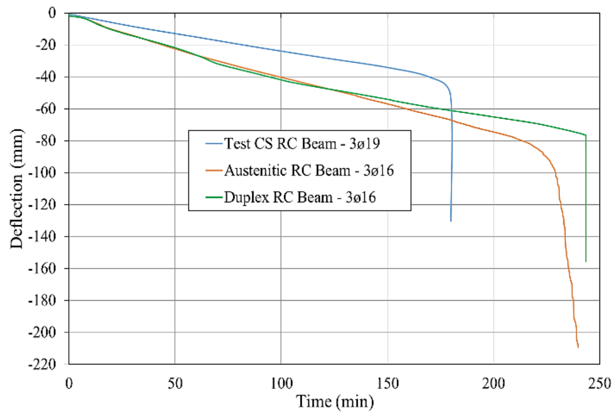

Figure 14. Fire resistance of three similar RC beams reinforced with different steel ratio of CS, Austenitic and Duplex steel.

5 CONCLUSIONS

In this study, the mechanical behaviour of austenitic and duplex stainless steel rebars at elevated temperature was investigated through testing programme. The experimental stress-strain curves were utilised in validated finite element model of RC beam subjected to fire scenario. It was found that all key parameters, including proof strength, ultimate strength, and strain at failure of SS rebars, reduced as the elevated temperature increased, but in varying proportions, compared with the corresponding room temperature values. The elastic modulus also reduced linearly as the temperature increased. The numerical results indicated that the stainless steel RC beams subjected to fire scenario sustain fire much longer time than the that for the CS RC beam. Additionally, the SS RC beams has higher deflection during the fire exposure in comparison to the CS RC beam. Further research studies can be made to investigate the behaviour of SS RC beam at elevated temperatures with different material strength and load ratios.

REFERENCES –

1. Nickel Institute. Stainless rebar: past present and future. Nickel Magazine 2013.
   Available at:
   https://nickelinstitute.org/en/nickel-magazine/nickel-magazine-vol-28-no-1-2013/.
2. Gedge G. The use of stainless steel reinforcement in bridges. The British Stainless Steel Association, 2003.
3. BS 6744:2016 (2016) Stainless Steel Bars—Reinforcement of concrete—requirements and test methods. British Standard Institute
4. BS 4449:2005+A3:2016; Steel for the Reinforcement of Concrete—Weldable Reinforcing Steel—Bar, Coil and Decoiled Product—Specification. British Standard Institute: London, United Kingdom, 2016.
5. EN 1993-1-1, Eurocode 3: Design of steel structures – Part 1.1: General rules and rules for buildings, (2006).
6. EN 1992-1-2., Eurocode 2: Design of concrete structures-Part 1-2: General rules-Structural fire design, European Committee for Standardization (CEN), (2004).
7. EN 1993-1-4, 2006 +A1, Eurocode 3: Design of steel structures – Part 1.4: General rules – Supplementary rules for stainless steels, (2015).
8. BS EN ISO 6892-1:2016 Metallic materials - tensile testing. Method of test at room temperature (ISO 6892-1:2016). British Standard Institute
9. S. Alih, A. Khelil, Behavior of inoxydable steel and their performance as reinforcement bars in concrete beam: Experimental and nonlinear finite element analysis, Constr Build Mater, 37 (2012), pp. 481-492
10. Franco, Noel & Biscaia, Hugo & Chastre, Carlos. (2018). Experimental and numerical analyses of flexurally-strengthened concrete T-beams with stainless steel. Engineering Structures

    Musab Rabi, K.A. Cashell, Rabee Shamass, Ultimate behaviour and serviceability analysis of stainless steel reinforced concrete beams, Engineering Structures, Volume 248,2021,113259, ISSN 0141-0296 https://doi.org/10.1016/j.engstruct.2021.113259.
11. Mokhtar K., Alhadid M. M., Youssef M. A. (2018) 'Early Age Thermal Expansion of Stainless-Steel Reinforced Concrete Sections.' International Conference on Short and Medium Spam Bridges, Quebec City, Quebec, Canada
12. M. B. Dwaikat and V. K. R. Kodur, (2009), Response of restrained concrete beams under design fire exposure, Journal of Structural Engineering, vol. 135, no. 11, pp. 1408–1417, 2009.
13. ASTM E119, “Standard methods of fire test of building construction and materials. American society of testing and materials”, West Conshohocken, PA, 2008.
14. ABAQUS, Finite element software, User Assistance Manual, Simulia, Dassault Systèmes, (2020)
15. fib: Model Code for Concrete Structures 2010, Ernst and Son, 2013
16. Kaklauskas G. A. (1999) 'New Stress-Strain Relationship for Cracked Tensile Concrete in Flexure.' ISSN 1392-1525. STATYBA- Civil Engineering- 1999, V Tomas, Nr. 6

17. L. Gardner, A. Insausti, K.T. Ng, M. Ashraf 'Elevated temperature material properties of stainless steel alloys' J. Constr. Steel Res., 66 (2010), pp. 634-647
18. J. Chen, B. Young 'Stress-strain curves for stainless steel at elevated temperatures' Eng. Struct., 28 (2) (2006), pp. 229-239
19. Ramberg W. (1943) 'Osgood W.R. Description of stress-strain curves by three parameters' Issue 902 of National Advisory Committee for Aeronautics Technical Note
20. Design manual for structural stainless steel 4th edition. SCI publication P413

DETERMINING SFRM THERMAL PROPERTIES THROUGH FIRE TESTS ON I-BEAM SECTIONS

Serdar Selamet[1]

ABSTRACT

Steel structural members exhibit lower fire resistance due to high thermal conductivity, low specific heat, and faster degradation of strength and elastic modulus of steel material with temperature. These structural members are often applied with spray-applied fire-resistive materials (SFRM) to delay temperature rise in the cross-section. This paper investigates the temperature-dependent thermal properties of gypsum-based Cafco 300 and cement-based Cafco Mandolite CP2 fire protection materials through fire furnace tests of protected beam members under constant loading. These properties are crucial for computational heat transfer models, which are utilized to evaluate the fire resistance of protected steel sections. A total of 3 fire furnace tests are conducted under 3-sided standard fire exposure. The average temperature of steel sections from the experiments are compared against the steel section temperature calculated by Eurocode method for steel profiles insulated by fire protection material. Nonlinear regression and random sampling methods are employed to minimize the residual sum of squares between the experimental and numerical temperature results. The results show that the temperature-dependent conductivity of SFRMs ranged from 0.08 W/(m˚C) to 0.25 W/(m˚C) with increasing temperature. The specific heat did not have a significant effect on the section temperature development and therefore kept temperature-independent at 1100 J/(kg˚C). The experimental results are closely captured by using the estimated temperature-dependent SFRM conductivity curves.

Keywords: SFRM; insulation; heat transfer; thermal properties; fire tests

1 INTRODUCTION

Steel structural members exhibit lower fire resistance due to high thermal conductivity, low specific heat, and faster degradation of strength and elastic modulus of steel material with temperature [1]. These structural members are often applied with spray-applied fire-resistive materials (SFRM) to delay temperature rise in the cross-section [2]. SFRMs are typically composed of mineral wool, quartz, perlite and vermiculite along with a binding agent such as cement or gypsum.

Fire resistive materials are currently qualified and certified based on lab-scale fire tests such as those described in the ASTM E119 Standard Test Methods for Fire Tests of Building Construction and Materials [3]. However, these ratings have no quantitative relationship to the actual performance of a SFRM in an actual fire other than the standard fire [4]. To evaluate steel temperatures under fire conditions that differ from the standard fire, thermal analysis can be performed, but such analysis requires knowledge of the thermal material properties of SFRMs [5]. Computational heat transfer models offer the potential to bridge the gap between laboratory testing and field performance. However, these models depend critically on having accurate values for the thermo-physical properties of the SFRM as a function of temperature, to be

[1] Associate Prof, Bogazici University,
e-mail: serdar.selamet@boun.edu.tr, ORCID: https://orcid.org/0000-0001-9444-470X
https://doi.org/10.6084/m9.figshare.22178009

used as inputs along with the system geometry and fire and heat transfer boundary conditions [3]. The thermal performance of gypsum- and cement-based SFRMs were previously studied and there were no consensus on the temperature-dependent specific heat values but the sensitivity analyses shown negligible effect on the steel section temperatures. In addition, the moisture level greatly affected the density measurements at elevated temperatures [6].

This paper investigates the temperature-dependent conductivity of gypsum-based *Cafco 300* and cement-based *Cafco Mandolite CP2* fire protection materials through fire furnace tests of protected beam members under constant loading. The beam members are utilized as part of a 59-story tall steel-concrete building project. The I-beam steel sections in the interior are covered with gypsum-based SFRM and the beams on the exterior connecting steel columns are covered with cement-based SFRM for fire protection. The SFRM thermal properties are estimated by comparing the average temperature of steel sections from the experiments against the temperatures calculated by Eurocode method for steel profiles insulated by fire protection material [7]. Nonlinear regression and random sampling methods are employed to minimize the residual sum of squares between the experimental and numerical temperature results.

2 PROBLEM DESCRIPTION

2.1 Furnace tests

A total of 3 fire furnace tests are conducted under standard fire exposure. In the fire tests, simply supported 4 m long IPE 270, HEM 360 and HEB 360 I-beam sections are exposed to Standard (ISO-834) fire on 3 sides for 120 minutes. All beam sections are loaded with 0.3 utilization ratio (moment capacity) after SFRM application to reflect realistic conditions. IPE 270 and HEM 360 sections are protected with *Cafco 300* and HEB 360 section is protected with *Cafco Mandolite CP2*. The insulation thicknesses are estimated to maintain below the mandated critical temperature of 750°C for 120 minutes standard fire exposure. Accordingly, IPE 270 and HEB 360 sections are protected with 23mm and 10mm Cafco 300, respectively. HEB 360 section is protected with 11mm Cafco Mandolite CP2. The average section temperature is obtained by 9 thermocouples placed on the bottom flange, web and top flange of I-beam sections at 3 different beam lengths as illustrated in Figure 1. The section factors for IPE 270, HEM 360 and HEB 360 are 197 $1/m$, 51 $1/m$ and 86 $1/m$, respectively.

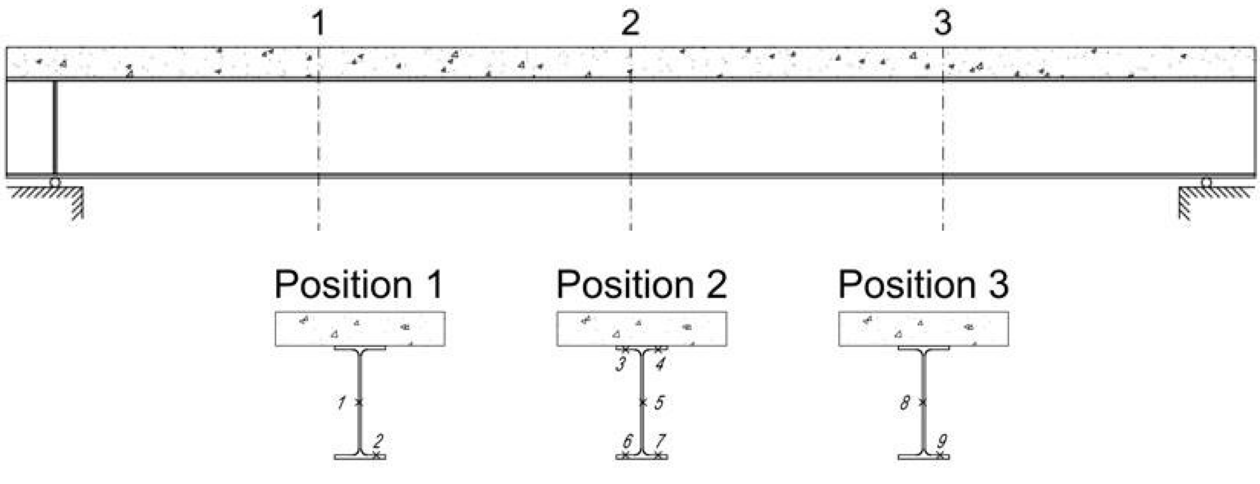

Figure 1. A total of 9 thermo-couple locations within the beam cross section at various lengths for the fire tests.

(a) IPE 270 - 23mm Cafco 300

(b) HEM 360 - 10mm Cafco 300

(c) HEB 360 - 11mm Cafco Mandolite CP2

Figure 2. SFRM applied loaded steel sections after the standard fire exposure.

Before the experiments are conducted, the moisture level of *Cafco 300* and *Cafco Mandolite CP2* are measured between 3-7% during the fire experiments. The post-fire conditions of the insulated beam members are shown in Figure 2. IPE 270 beam member experienced excessive deformations at midspan and therefore the fire test was terminated prematurely at 90 minutes. HEB 360 beam member experienced delamination of the insulation at midspan at around 100 minutes as seen in Figure 2c. Therefore, the thermocouples 5, 6 and 7 of HEB 360 are excluded from the average section temperature readings. Figure 3 plots the average section temperatures of the three profiles. As expected, the temperature development of all sections are fairly similar. This is because the insulation thicknesses are purposefully calculated to keep the section temperature below the mandated critical temperature of 750 °C.

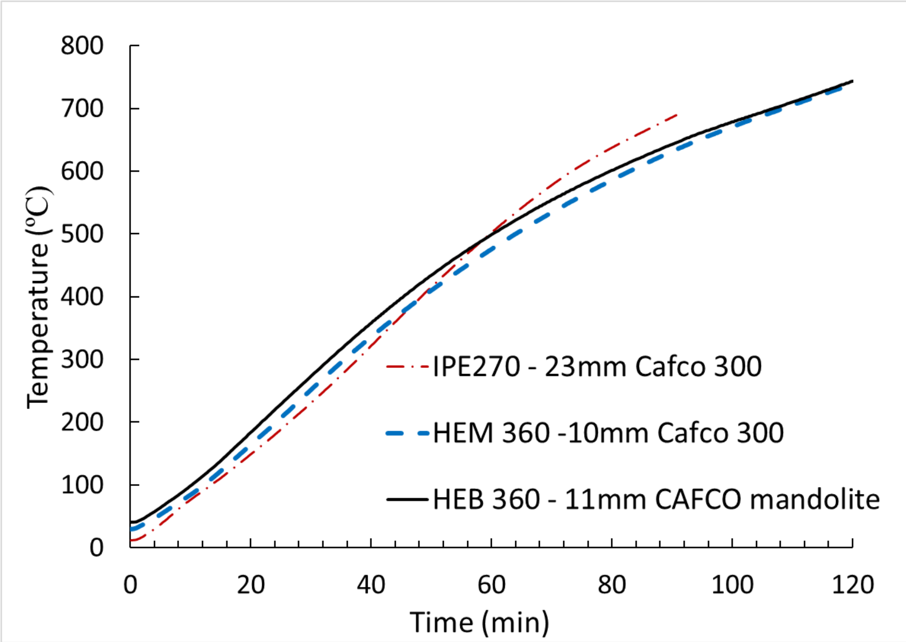

Figure 3. Furnace test results of IPE 270, HEM 360 and HEB 360 steel sections with SFRM under standard fire exposure of 90-120 minutes.

2.2 Heat transfer analyses

Eurocode 3 Part 1-2 provides Eq. 1 for the estimation of uniformly insulated steel cross section temperature. This equation is derived from a condensed one-dimensional (1-D) heat transfer model based on the lumped heat capacity method assuming a uniform temperature within the steel section. Here; T_f is the fire temperature, $\frac{A_p}{V}$ is the section factor and k, ρ, c are density, temperature-dependent conductivity, and temperature-dependent specific heat of the steel material according to Eurocode 3 [7]. For the insulation (SFRM) materials; k_i, ρ_i, c_i, d_i are defined as conductivity, density, specific heat and thickness. The equation to calculate the average section temperatures for IPE 270, HEM 360 and HEB 360 profiles is formulated using Excel spreadsheet. The maximum time increment is taken as 30 seconds.

$$\Delta T = \frac{A_p}{V} \frac{k_i/d_i}{\rho\, c} \frac{T_f - T}{1+\phi/3} \Delta t - \left(e^{\frac{\phi}{10}} - 1\right) \Delta T_f \qquad where \quad \phi = \frac{A_p}{V} \frac{c_i\, \rho_i\, d_i}{c\, \rho} \qquad \text{Eq. 1}$$

The density of *Cafco 300* and *Cafco Mandolite CP2*, which is highly dependent on the moisture level, is taken constant as 315 kg/m^3 and 365 kg/m^3, respectively. As suggested by NIST [4], SFRM specific heat at room temperature is kept constant throughout the fire duration as c_i values of typical SFRM's typically vary only about ± 20% from a mean value. In addition, the variation of SFRM specific heat does not significantly change the average section temperature obtained by Eq. 1 since the SFRM thermal mass is usually minor compared to that of the steel section [8].

The SFRM conductivity, however, greatly affects the steel section temperatures. The manufacture reports of SFRMs provide the room temperature conductivities 0.078 $\frac{W}{m\,°C}$ and 0.095 $\frac{W}{m\,°C}$ of *Cafco 300* and *Cafco Mandolite CP2*, respectively. The temperature range is limited to 800 °C since reliable data on thermal properties of SFRMs at temperatures over 800 °C are not available in the literature due to the limitations of testing techniques.

Several methodologies are streamlined in Excel to estimate SFRMs temperature-dependent conductivity. First, the random sampling method determined to make the first guess of the conductivity range of both

SFRMs from 20 °C to 800 °C at each time increment. The lower limits are taken as the room temperature conductivity values supplied by the manufacturer. The upper limit for both SFRM conductivity is taken as 0.50 $W/_{m\,°C}$ in accordance to data available in the literature. This value is six times of the initial conductivity of *Cafco 300* and *Cafco Mandolite CP2* at room temperature. The upper range closely aligns with NIST investigations on the thermal performance of fire resistive materials [8]. Next, Excel macros are used to randomly select 10000 samples of SFRM conductivity value (with upper and lower limits) at each time increment (i.e. 30 seconds) and compare the section temperature residuals between the three experiments and numerical results. At each increment, the conductivity with the minimum squared-residual is stored and the conductivity for the next time increment is evaluated. Figure 4a-b show the discrete conductivity values of *Cafco* 300 and *Cafco Mandolite CP2*, respectively. It is observed that the graphs are not smooth as expected but the section temperatures obtained from the numerical analysis almost exactly capture the experimental results. In addition, Figure 4a shows that *Cafco 300* conductivity results are slightly different for IPE 270 (thick insulation-small cross-section) and HEM 360 (thin insulation - heavy cross-section). This is attributed to the uncertainties in temperature readings during the furnace tests. It is decided to take the average of the two results in Figure 4a to represent *Cafco 300* temperature-dependent conductivity.

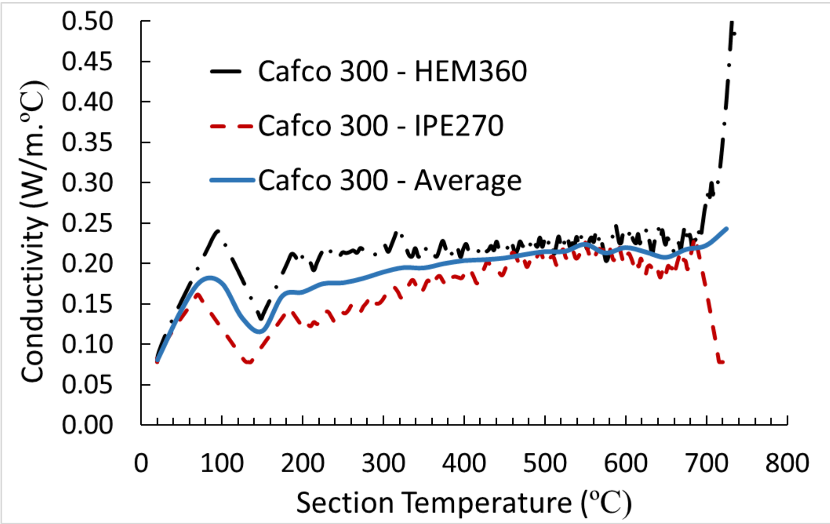

(a)

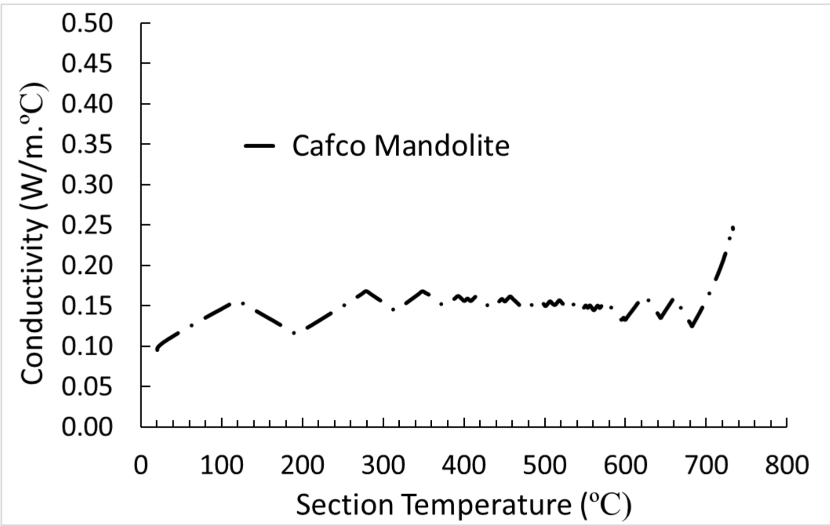

(b)

Figure 4. Discrete conductivity curve for (a) *Cafco 300* and (b) *Cafco Mandolite CP2 obtained from the random sampling method.*

Nonlinear regression method is performed to fit the discrete conductivity values of both *Cafco 300* and *Cafco Mandolite CP2* to a smooth logarithmic function (see Eq. 2). SFRM conductivity asymptotically approaches to a constant value towards 800 °C. The coefficients of the logarithm are shown in Table 1. SFRM conductivity values are plotted in Figure 5. Table 2 lists the thermal properties of SFRMs. It is clear that *Cafco Mandolite CP2* varies much less at elevated temperatures compared to *Cafco 300*.

$$k_i\ (T) = A\ln\ (T) + B \qquad \text{Eq. 2}$$

Table 1. Coefficients for the logarithmic representation of thermal conductivity of SFRMs.

Coefficients	***A***	***B***
Cafco 300	0.0371	-0.0211
Cafco Mandolite CP2	0.015	0.0623

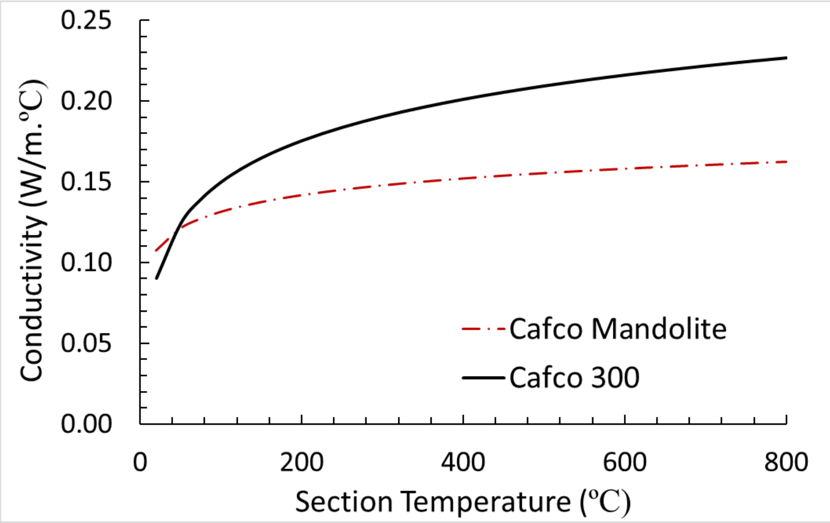

Figure 5. Temperature-dependent conductivity curves for *Cafco 300* and *Cafco Mandolite CP2 obtained from nonlinear regression method.*

Table 2. Thermal Properties of *SFRMs.*

Thermal Properties	**Density** ρ_i kg/m^3	**Specific heat,** c_i J/(kg°C)	**Conductivity,** k_i W/(m°C)								
Temperature (°C)	20-800	20-800	20	100	200	300	400	500	600	700	800
Cafco 300	310	1100	0.078	0.150	0.175	0.191	0.201	0.209	0.216	0.222	0.227
Cafco Mandolite CP2	365	1100	0.095	0.131	0.142	0.148	0.152	0.156	0.158	0.161	0.163

3 RESULTS

Using the temperature-dependent conductivity of SFRMs as shown in Figure 5, the average section temperatures estimated by Eq. 1 closely followed the temperatures from the furnace tests. Figure 6a-c show the section temperature comparison between the numerical and experimental results. The performance of good-fit to the experimental results is measured by the coefficient of determination (i.e. R-squared) method. R-squared method determines the proportion of variance in the dependent variable that can be explained by the independent variable by calculating the residual sum of squares between the experimental and numerical section temperatures as in Eq. 4. Here, y_i is the experimental temperature, $\bar{y}$ is the mean experimental temperature and $\breve{y}_i$ is the numerical (i.e. predicted) value. For all the tests, R^2 is above 95, which indicates a very close fit to the experimental results.

$$R^2 = 1 - \frac{(y_i - \breve{y}_i)^2}{(y_i - \bar{y})^2} \qquad \text{Eq. 4}$$

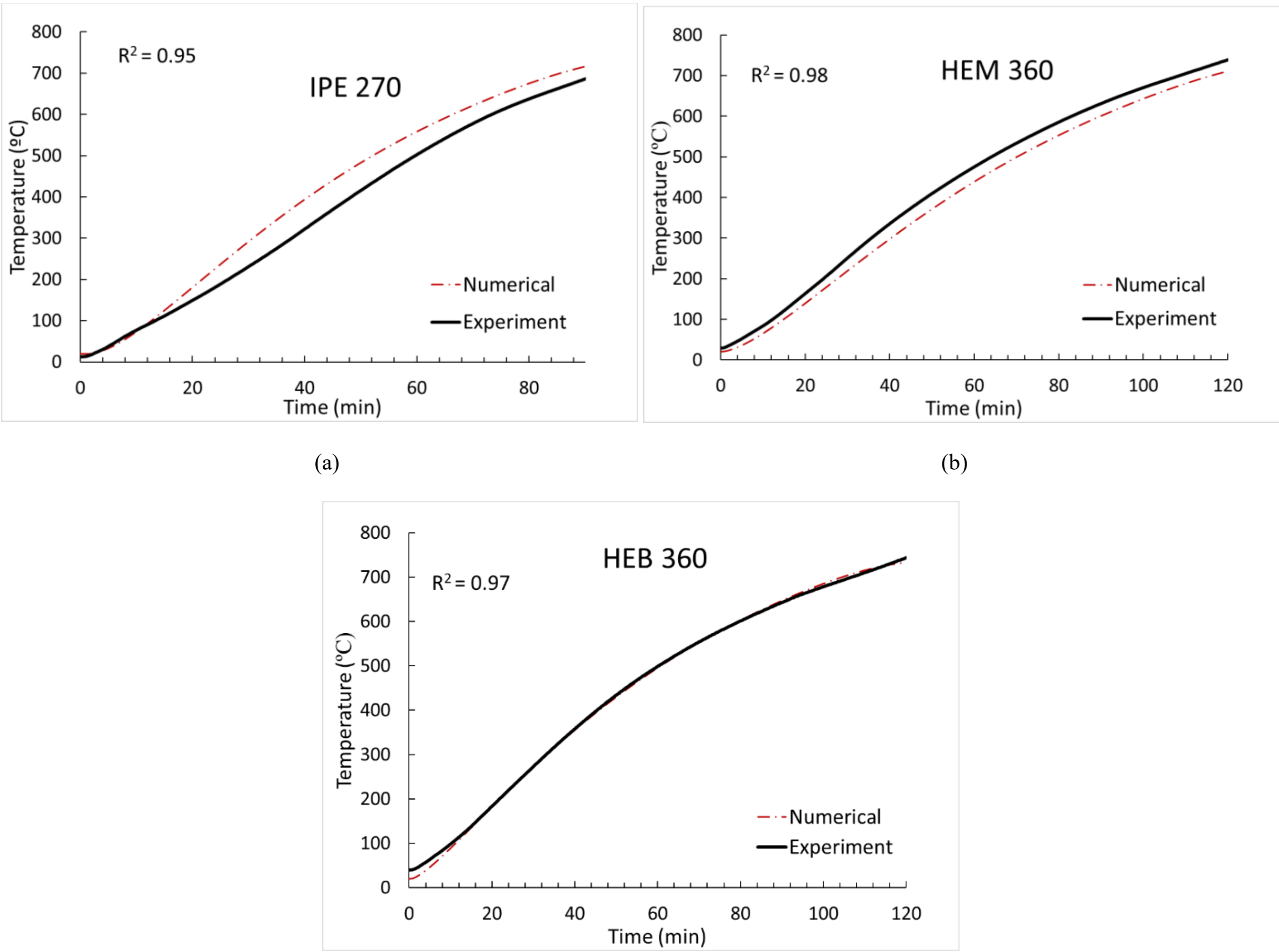

(a) (b) (c)

Figure 6. Average steel section temperature results from the experiments and numerical analyses and the estimated R^2 correlation.

4 CONCLUSIONS

This paper investigates the temperature-dependent conductivity of gypsum-based *Cafco 300* and cement-based *Cafco Mandolite CP2* fire protection materials through fire furnace tests of protected beam members under constant loading. A novel methodology is proposed in reverse calculating SFRM conductivity values from the experimental results. The methodology combines random sampling and nonlinear regression and can be applied to more experimental data of SFRM protected steel sections available in the literature. The study provides a database for the thermal properties of gypsum-based *Cafco 300* and cement-based *Cafco Mandolite CP2* to be utilized in numerical heat transfer simulations. It is found that the variability of the SFRM conductivity greatly changes the steel section temperatures. By utilizing random sampling method, it is determined that temperature-dependent SFRM conductivity can be represented by the logarithmic function. The R-squared method confirms the close match of the numerical results with the section temperatures from the furnace tests with R^2 above 95%.

ACKNOWLEDGMENT

The author would like to acknowledge Efectis Fire Laboratories for the carefully instrumented fire furnace tests and graduate student Ahmet Alperen Orgev for his support in numerical analysis. The author also acknowledge Bogazici University Scientific Research Projects BAP: 7122P, which provided the funding for this study.

REFERENCES

1. Kodur, V.K.R., Dwaikat, M., Fike R., High-temperature properties of steel for fire resistance modeling of structures, Journal of Materials in Civil Engineering 22 (5) (2010) 423–434.
2. Kodur, V.K.R., Shakya, A.M. Effect of temperature on thermal properties of spray applied fire resistive materials, Fire Safety Journal 61 (2013) 314–323.
3. Bentz, D.P. and Prasad, K., 2007. Thermal Performance of Fire Resistive Materials: I. Characterization with Respect to Thermal Performance Models. US Department of Commerce, Technology Administration, National Institute of Standards and Technology.
4. Bentz, D.P., Prasad, K.R. and Yang, J.C., 2006. Towards a methodology for the characterization of fire resistive materials with respect to thermal performance models. Fire and Materials: An International Journal, 30(4), pp.311-321.
5. Zhang, C., Pintar, A., Weigand, J.M., Main, J.A. and Sadek, F., 2021. Impact of variability in thermal properties of SFRM on steel temperatures in fire. Fire Safety Journal, 123, p.103361.
6. Kodur, V.K.R., Bhatt, P.P. and Naser, M.Z., 2019. High temperature properties of fiber reinforced polymers and fire insulation for fire resistance modeling of strengthened concrete structures. Composites Part B: Engineering, 175, p.107104.
7. CEN (European Committee for Standardization), 2005. Design of steel structures. 1–2: General rules—Structural fire design. Eurocode 3, EN1993-1-2, Brussels, Belgium.
8. Carino, N. J., Starnes, M. A., Gross, J. L., Yang, J. C., Kukuck, S. R., Prasad, K. R., Bukowski, R. W.. Federal Building and Fire Safety Investigation of the World Trade Center Disaster, Passive Fire Protection, National Institute of Standards and Technology Report, NIST NCSTAR 1-6A, September 2005.

SiF 2022– The 12th International Conference on Structures in Fire
The Hong Kong Polytechnic University, Nov 30 - Dec 2, 2022

POST-FIRE PROPERTIES OF AN ALUMINIUM BRIDGE AFTER A LOCALISED FIRE

Tom Molkens[1], Maarten Bassier[2], Burak Karabulut[3]

ABSTRACT

Aluminium is acknowledged in machinery, transportation (automotive, aerospace, marine) and building industries as an outstanding material. Nevertheless, in buildings, the material is mostly used in secondary elements and not as primary structural bearing elements. This is mostly thanks to the excellent strength-to-weight ratio, high corrosion resistance, and best possible recycling ratio of all ferrous and non-ferrous metals used in the building industry. Unfortunately, based on pure CO2 emissions, primary aluminium is highly polluting, even up to 8.6 kg CO2/kg equivalent. On the other hand, when 100% recycled aluminium is used, the CO2 emissions decrease to 0.5 kg CO2/kg, a value significantly below the one of concrete and steel. All these arguments highlight the potential that the material itself has promising features for the future. To exploit superior properties of aluminium, structural fire safety concerns must also be addressed in both pre- and post- design phases. Demonstrating the post-fire behaviour of an aluminium bridge under the effect of a car fire has been the driving idea behind this experimental research

Keywords: Aluminium; bridge design; localised fire; residual strength

1 INTRODUCTION

Due to the upcoming material shortages and high energy prices, the use of highly recyclable materials is of paramount importance. This has led to a growing interest in aluminium as a construction material for structures. Regarding circular economy aspects, it is known that the material has a high recycling rate and that the European union is even an exporter of scrap [1] while recycled aluminium decreases the energy demand by 95% [1] and eliminates primary use of raw materials [2]. Both aspects are of extreme importance [3] so as to empower circular economy. The very high intrinsic corrosion resistance is an additional important advantage, as a result of which the structures require little to no maintenance over their life cycle especially in atmospheric conditions when a correct aluminium grade is employed. However, there are important reasons why the material fell into disuse as a construction material after the 1960's, despite its various applications at that time. These reasons can be summarised in one word, namely a lack of knowledge about the structural resilience of structures made of aluminium. Following [4] the resilience of a building includes not only the structural property of robustness, which contributes to the capacity of absorbing an extreme event, but also a recovery capacity that allows the pre-event performance level to be quickly restored or even improved. However, a simple comparison of various construction materials shows that aluminium itself can perform very well as a construction material reducing the mass and CO_2 footprint of structural elements as depicted in Figure 1. Aluminium is fully recyclable, which helps compensate for

[1] Prof. dr. ir, KU Leuven,
e-mail: tom.molkens@kuleuven.be, ORCID: http://orcid.org/0000-0002-3401-9047
[2] Dr. Ing., KU Leuven
e-mail: maarten.bassier@kuleuven.be, ORCID: http://orcid.org/0000-0001-8526-8847
[3] Dr. ir, KU Leuven
e-mail: burak.karabulut@kuleuven.be, ORCID: http://orcid.org/0000-0002-5133-2422
https://doi.org/10.6084/m9.figshare.22178015

its expensive production cost. Due to the relatively low melting point (660 °C) of aluminium, recycling takes only about 5% of the energy needed to produce it from raw materials. The process does not degrade the structural performance and surface quality of aluminium and constitutes one-third of the aluminium production in the European market [2] .

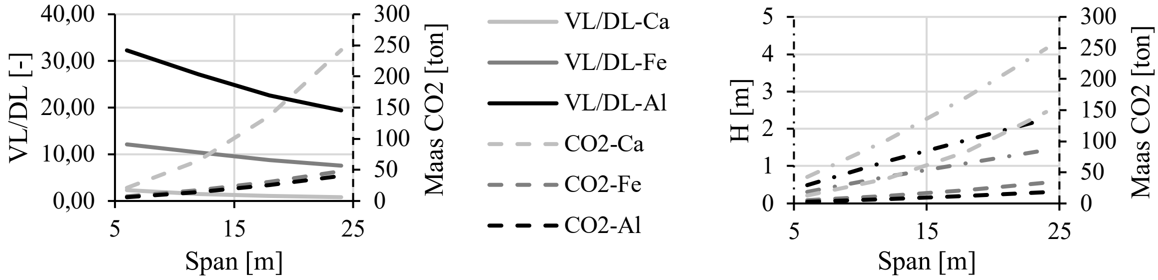

Figure 1. Illustration of the ratio of variable load to own weight, mass CO_2 emission (left), girder height and projected CO_2 emission by 2050 (right) for reinforced concrete (Ca), S355 steel (Fe) and 6061T6 aluminium (Al)

The disappearance of the material in the construction sector almost coincides with the growing interest of the building industry in the fire safety of constructions, around the 60's. Due to the low melting temperature, with a total loss of mechanical properties at 550°C [5] and high thermal conductivity, the material is susceptible to fire. This paper is dedicated to illustrating the potential resistance to a localised fire by a large-scale experiment on a bridge; contrary to compartment fires which are typically very fast growing accompanied with high gas temperatures, and in that way destructive for aluminium structures [6]. However, even the most frequently used building materials today, such as steel and concrete, require necessary protection against the consequences of such temperatures with, for example, intumescent paints or measures against spalling of concrete. In the context of resilience, however, it is not the known behaviour during a fire that is important, but mainly the post-fire behaviour. However, the post-event properties have not been deeply investigated yet, only some non-structural studies can be found [7]. This lack of information means a handicap for the aluminium industry, even though there are existing examples of aluminium in use, in temporary structures as tents [8], podia or even exposed to cyclic loads in civil structures.

2 TEST SET-UP

2.1 Preliminary research

To build upon the above-mentioned expanding trend, and as a part of a research campaign aimed at studying the fatigue and limit-state behaviour of an entire all-aluminium bridge [9], the previous research on the same bridge targeted experimental and numerical studies investigating the structural response of a conceptual aluminium bridge under fatigue and ULS loads. This conceptual bridge was designed and detailed as a proof of concept for a reference continuously supported, plate-girder carbon steel bridge [9] such as the one schematically shown in Figure 1. The span and width of the reference bridge are 45 m and 14.4 m respectively. Those dimensions represent common type of overpass bridges in Europe, based on investigations on 100 examples in Belgium and France (Considering E40 highway in Belgium and E25 highway in France).

The bridge in [9] was first designed based on the EN 1999 standard [10] with the quasi-static and dynamic design loads derived from the EN 1990 [11] and EN 1991-2 [12]. The calculated weight was 283 kg/m compared to 1660 kg/m for a carbon steel equivalent [9]. The design of this conceptual bridge served as the basis for experimental and numerical studies on a down-sized bridge deck [13], which is partially published in [14] by the authors of the current paper. The tested specimen is 5.69 m by 2.2 m in size and 0.57 m high. Its deck is made of eighteen-voided extruded panels, in a transverse-to-traffic orientation, and were riveted (to mimic the bolted connections while saving time) to three longitudinal plate girders for a total span of 5.69m. The tested girders were built-up by riveting extruded hollow panels and L-profile extrusions. This down-sized bridge deck was statically tested in its linear elastic range in order to validate a finite element model (FEM) of the conceptual bridge. The FEM was then used to find a configuration respecting the ultimate (strength and fatigue) and serviceability (displacements) limit states for a light-weight portable (dismountable) bridge such as those for rapid-deployment in disaster-hit regions

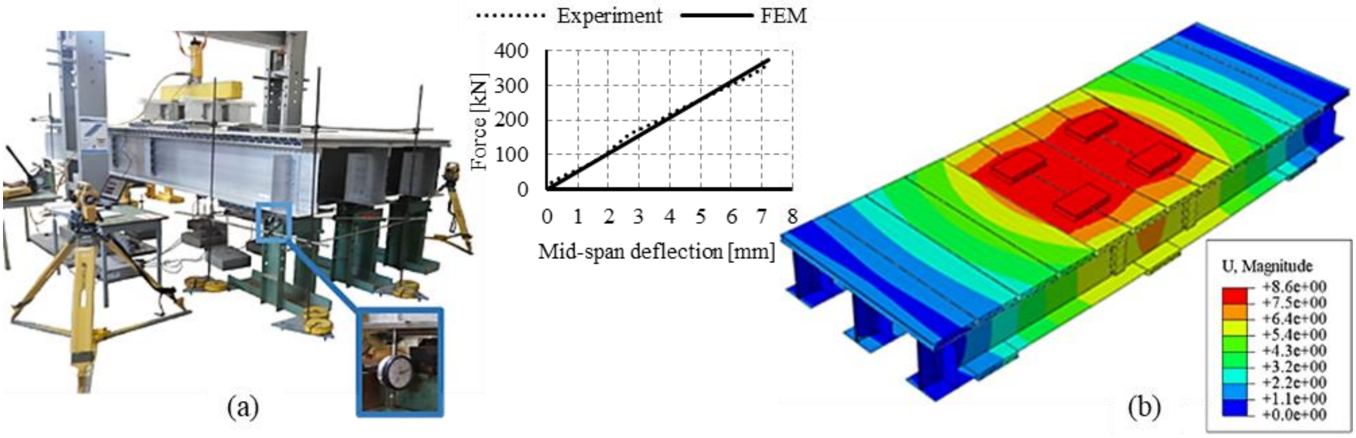

Figure 2. Schematic of the experimental and numerical procedure: (a) component testing; (b) FEM validation

As the meaning of the preliminary research was to show the proof of concept, the loading was only performed in the elastic range without entering in non-linear material and geometrical behaviour (40% of proof strength). In that way, the bridge did not suffer from previous tests.

2.2 Materials

The aluminium grades used are type EN-AW6005-T6 for the web panel and the L-profiles, and EN-AW6005A-T6 used for the bridge deck (with limited increased addition of copper and chromium but mainly extra manganese). The materials undergo typical precipitation hardening temperature treatment (T6 mark) to improve mechanical strength. In [10], the mechanical properties of the EN-AW6005A-T6 alloy can be found in function of the applied production process and material thickness. Under the influence of a temperature (e.g., fire), the mechanical properties decrease starting from relatively low temperatures compared to steel (Fe denotation in Figure 3). However, in contrast to steel, the reduction in Young's modulus is delayed compared to this of the 0.20% proof strength, which makes the material in some way less sensitive to instability effects at elevated temperature.

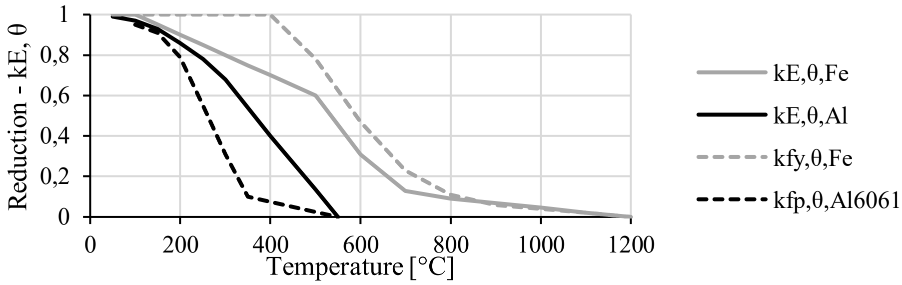

Figure 3. Reduction of mechanical properties according to [15] = (Fe-grey) and [5] = (Al-black)

2.3 Reference fire-test

Several reasons can be found why a standard fire curve is not the best way to assess the fire resistance of bridges or parts of it [16], [17]: i) it is a cellulosic fire developed for buildings and is not representative of bridge fires, ii) the fire is developing in an open air that is completely different from the one in a furnace, iii) there is no post flash-over situation occurring as in a compartment, iv) the elements are not uniformly heated over the length and cross section, v) local fires can generate thermal conditions that are more severe as obtained by uniform heating and vi) in the case of multiple span applications the location of the joints will play a major role.

The fire load magnitudes applied in the experiment are smaller than the fire load of a car, a van, and certainly than a typical tanker truck carrying gasoline. Based on risk management tools, the most severe fire load can be determined in function of the purpose where the bridge will be used for. Facing local fire models such as the Heskestad equation (1) or the Hasemi formulation equation (2) out of [5], [18], this becomes possible.

$$\theta_{(z)} = 20 + 0.25Q_c^{2/3}(z - z_0)^{-5/3} \tag{1}$$

$$\dot{h} = \begin{cases} 100000 \;\; if \;\; y \leq 0.3 \\ 136300 - 121000y \;\; if \;\; 0.3 \leq y \leq 1.0 \\ \dot{h} = 15000y^{-3.7} \;\; if \;\; y \geq 1.0 \end{cases} \; with\, y = \frac{r + H + z'}{L_h + H + z'} \tag{2}$$

where θ is the gas temperature in the plume (°C),

Q_c is the heat release rate of a convective part,

z is the height along the flame,

z_0 is the virtual position of the heat source,

z' is the virtual position of the heat source,

$\dot{h}$ the heat flux received by the ceiling (W/m²) according to [5], [18],

r is the the horizontal distance out of the centre of the plume,

H is the distance between the fire source and the ceiling,

L_h is the horizontal flame length.

By simply changing the position of the fire source, acting on z or H, the effect of a more severe local fire can be simulated in an easy way. In the same way of thinking, increasing the clearance height under a bridge can be the handiest tool to obtain a basic fire protection. In section 3.3, a comparison is made between the applied fire loads and a car or van fire.

2.4 Description of the experimental test set-up

Inspired by the previous work of [17] a test set-up was built at the fire brigade training centre of the province of Antwerp in Belgium (Campus Vesta, Ranst, Belgium), Figure 4.

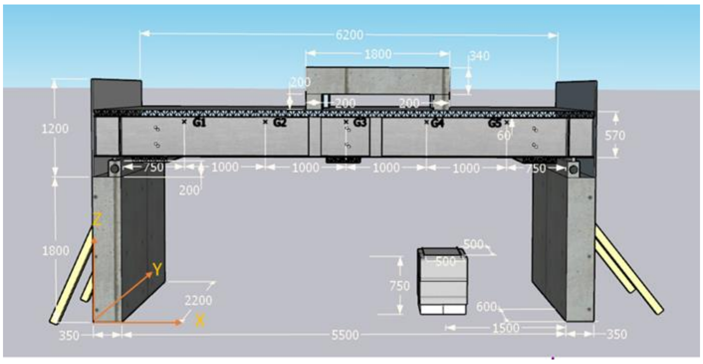

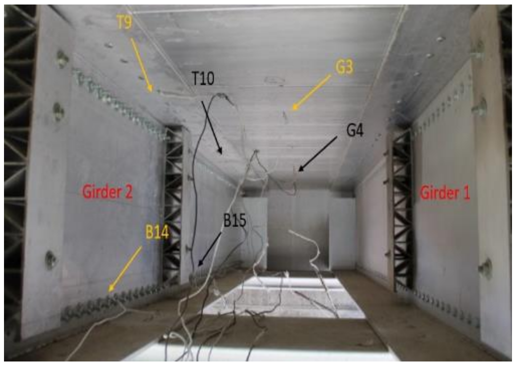

Figure 4. Overview of the test set-up in a schematic way in front view (left), and by a cross section (right)

Abutments have been made out of 1.8 m high concrete blocks, together with a 0.19 m distribution beam and a 0.05 m roll support or square hollow section. With a girder height of 0.50 m, the bridge deck was located 2.55 m above the ground floor. By lifting the pan level to 0.75 m or 1.05 m above ground level, comparable distance between the fire source (pan) and lower level of the bridge deck are reached (i.e., respectively 1.80 and 1.50 m). The free span of the bridge was about 5.69 m (5.50 m between abutments) and as the bridge was constructed with three girders, the fire load was placed between the one in the front and the one in the middle of Figure 4.

2.5 Instrumentation

The reference test [17] used a weight scale, many thermocouples (72), LVDTs (22) and high-temperature optical fibre sensors (17). Alongside these conventional measurement equipment (similar tools but with less quantity compared to the former reference), the authors of the present paper additionally used infrared thermographic cameras to comply with the required amount of data for further processing.

2.5.1 *Weighting scale*

To measure the fuel combustion, a tension and compression load cell of 5 kN with 0.1 % accuracy (combined error) of Sensy was used (model 2712). The operating temperature ranges between -30°C and 70°C. Between the load cell and the pan with fuel, aerated concrete blocks have been placed as a thermal and physical protection, see Figure 4 and Figure 7.

2.5.2 *Thermocouples*

Fibreglass insulated flat twin thermocouple extension cables have been used (Type NX - 7/0.2mm from TC Direct) to measure the gas temperature at 15 different locations: in between the two girders where the fire was positioned (G), near the top (T) and bottom (B) flange of the central girder of the bridge. Facing the origin of the coordinate system in the centre of the bridge and at ground level, coordinates can be found in Table 1. The distance is referring to the x-axis, the width to the y-axis and the level to the z-axis. Similar positions of thermocouples can be found in [17] and will be used as reference for the evaluation of the measurements performed of the actual tests.

Table 1. Location of thermocouples from the ground (level) or centre (distance) in m

TC	Level [m]	TC	TC	TC	Distance [m]
V1	1.20	G1	B1	T1	-2.00
V2	1.54	G2	B2	T2	-1.00
V3	1.79	G3	B3	T3	0.00
V4	2.09	G4	B4	T4	1.00
V5	2.28	G5	B5	T5	2.00
Distance [m]	1.25	2.48	2.06	2.53	Level [m]
Width [m]	-0.37	-0.37	-0.10	-0.10	Width [m]

2.5.3 *Thermographic camera*

Besides the use of thermocouples attached to the material, a thermographic camera (FLIR T650sc 640x480) with infrared (i.e. IR) lenses (45° FOV,13.1 mm) was used during the test. This type of lenses is used to generate an image as wide as possible. A measuring range between 100°C and 650°C was chosen as this corresponds best to the temperatures that are expected. In order to film as accurately as possible and to manage all data, it was decided to record an image set of 5 minutes each time. This was done with a frequency of 30 Hz, corresponding to 30 frames per second for 5 minutes (9000 frames/set).

The emissivity of aluminium is rather low (0.3 according to [5]) which makes it very hard to record temperature profiles. To tackle this issue the front of the web was coated by a thermographic paint for high temperature applications (HERP-HT-MWIR-BK-11), and by doing so, the emissivity is increased up to 0.91 for viewing angles till 30°.

2.5.4 *Laser scan survey*

A Leica P30 terrestrial laser scanner was used to measure at fixed intervals the deflection, misalignments, and expansion of the bridge. To align the scans, 4 artificial targets were placed in a circle around the bridge which were measured with an accuracy of $\sigma_r = 0.001m$. The scanner itself was placed directly in front of the bridge at an elevated position to accurately determine the bridge deck, Figure 5. The bridge's deviations were determined from a) statistical nearest neighbour analysis on all the points on the web and the deck and b) six marking points on the web of the bridge, located near the supports and in the middle of the span, each time at $1/4^{th}$ and $3/4^{th}$ of the height.

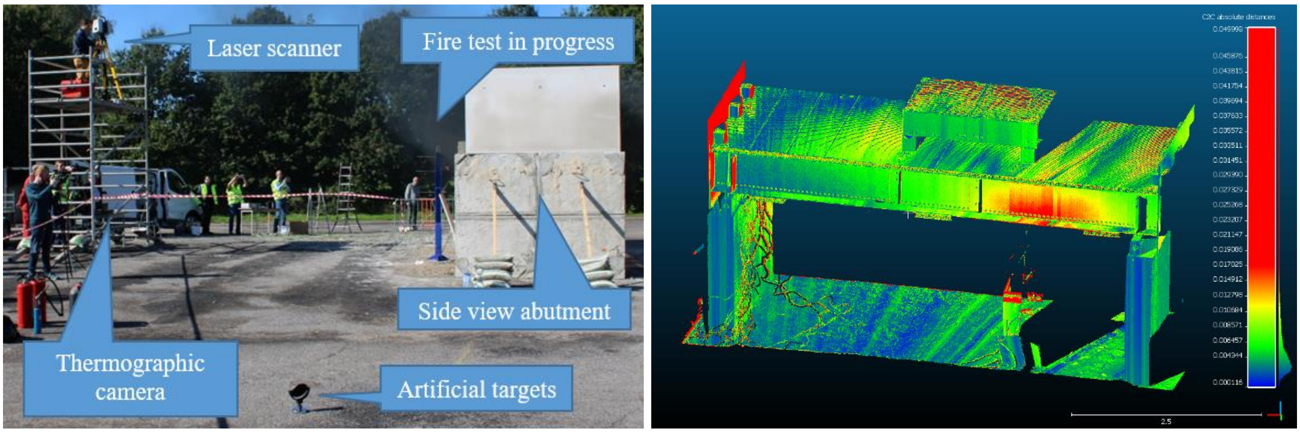

Figure 5: View on the survey tower with on top the terrestrial laser scanner and at ground level the thermographic camera (left) and view of the nearest neighbour analysis between pre-and post-fire scan data (right)

2.6 Execution of the test

The test was executed in two subsequent steps by igniting approximately 20 l of petrol-ether in a 50x50 cm² pan. Between both tests, a time period of about 20 minutes was respected. In that time period, the pan was raised by 30 cm and filled again. Due to the higher position and higher starting temperature, increased temperatures of the aluminium can be reached.

2.7 Post-fire coupon tests.

To cut out coupons, a partial dismantling process of the bridge was needed. Five deck panels of the bridge had to be removed to extract specimens out of the deck panel, the web and the angles. After the grinding process, the parts of the bridge have been cut with a band saw to avoid re-heating. Exact dimensions of the coupons have been machined by wire-EDM (Electrical discharging machine) according to EN ISO 6892-1 (2016) and are dependent of the thickness of the base material, see Figure 6 and Table 2.

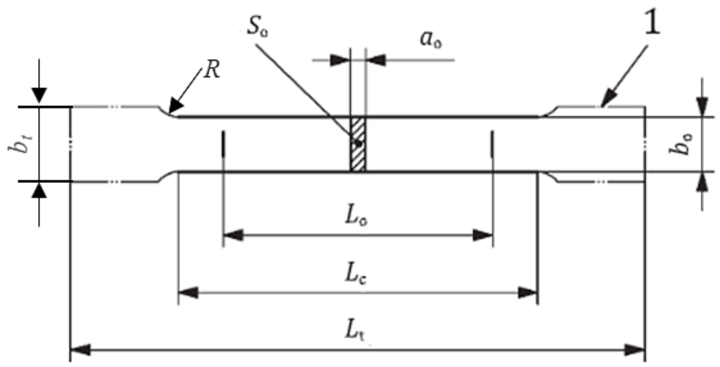

Figure 6. Dimensions of the test coupons taken out of the base material before and after being subjected to fire

Table 2. Overview of test specimen dimensions

Properties	Deck panel [mm]	L-stiffeners [mm]	Web [mm]
Original thickness a_o	4.2	10	2.4
Original width b_o	9	25	15
Original gauge length L_o	35	90	70
Parallel length L_c	50	120	80
Transition radius r	8	12	12
Total length of test piece L_t	146	264	224
Total width of test piece b_t	25	49	39

3 APPLIED LOAD

3.1 Mechanical load

An already published large-scale instrumented test, which can be found in the literature [17], was done in an unloaded condition. No other mechanical loads were present apart from self-weight and other permanent loads. Once moving from nominal fires to local fires (which can be regarded as a natural fire scenario), it may be option to accompany the fire load with actual load condition. This is despite the fact that the code [11] proposes a combination factor $\psi 2 = 0$ to be used for mobile loads on bridges in the combination with fire. However, besides studying the effect of fire on the main girders, the aim was also to investigate the local behaviour of the extruded honeycomb bridge deck plate. For this reason, a concrete block of 14 kN (a medium class car) was placed on the bridge on four cubes with side dimensions of $20\times20\times20$ cm³ (Figure 4), in accordance with the minimum dimensions found in [12].

3.2 Fire load

With a density of about 0,653 kg/l for the petroleum-ether used, and a total of about 21,4 litres, the corresponding mass becomes roughly 14 kg. The mass loss rate was measured during the test (see section 4.1), and by taking into account a net calorific value of 45 MJ/kg out of Table E.3 of [18], a rate of heat release (RHR) of 892 kW for the first test and of 999 kW for the second test can be estimated (see Figure 7). This is in between the tests performed by [17] who figured out a RHR of 415 kW for the 50x50 cm² and 1131 kW for a 75x75 cm² pan. The difference can be explained by the fuel used (they used gasoline) and for that reason the shorter burning time.

Figure 7. Pictures of the test set-up with ignited pans at 75 cm (left), and 105 cm (right) above the ground

3.3 Comparison with real fires

Local fire models allows for a simplified comparison between the applied fire loads impacting the bridge deck during the performed tests (Figure 8) and real fires from a car or a van (Figure 9). The flame length is always higher than the free clearance height for both tests which makes the Hasemi model the most appropriate (see section 2.3 Equation (2)).

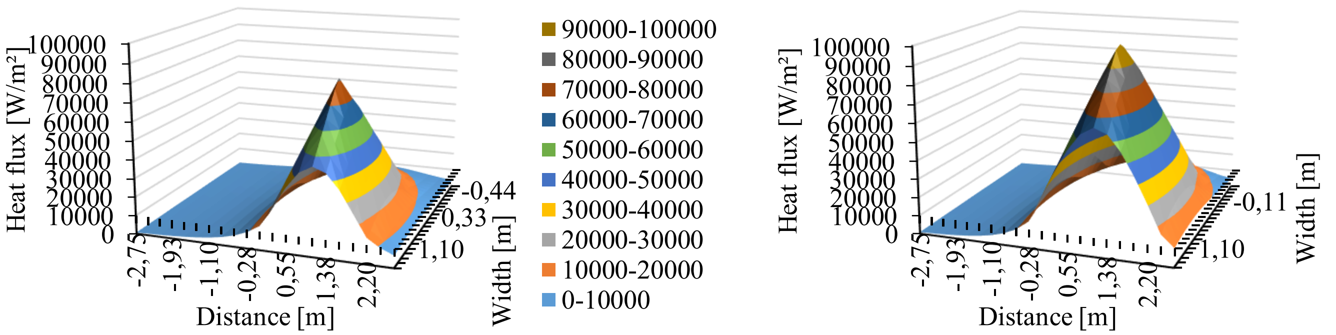

Figure 8. Heat flux for both test set-ups based on the formulation out of [18], for test 1 (left) and 2 (right)

On the other hand, a car and a van fire can be typically described by a 5 and 20 MW fire respectively while a distance of 5 m till the bottom part of the bridge deck is respected (about 4.5 m clearance height under the girders). In combination with an equivalent diameter of 3.2 and 3.57 m, it is shown that the local impact of the executed tests (up to 81 kW/m² for test 1 and 100 kW/m² for test 2) is certainly much higher than a car fire (36 kW/m²) and even a van fire (72 kW/m²). Only a 100 MW truck fire (which is out of the application range) delivers a comparative 97 kW/m². Nevertheless, it should be noted that starting from a van, the infected surface area is increasing.

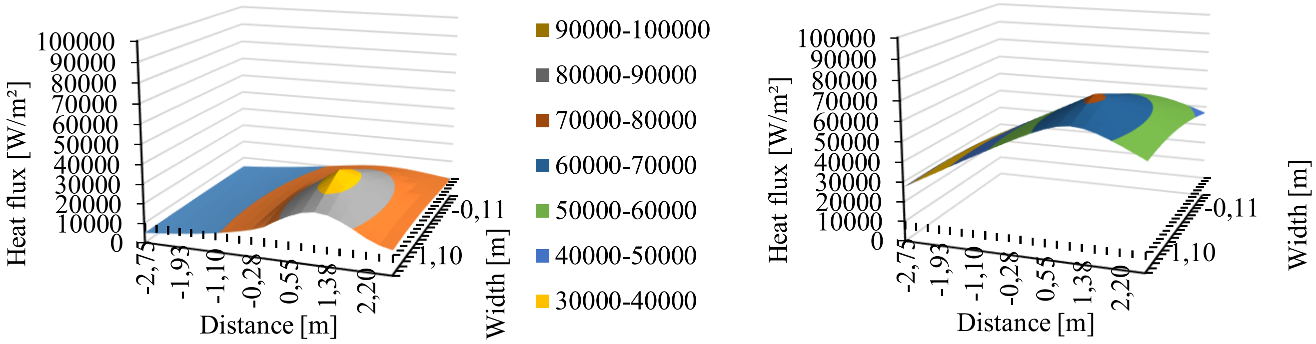

Figure 9. Heat flux based on the formulation out of [18], for a 5MW car (left) and a 20 MW van (right)

4 RESULTS

4.1 Mass loss rate of fuel

The first test ended in about 12 minutes (707 s) after consuming 14.03 kg of fuel, which corresponds to a RHR of 892 kW (= 14.03∗45/707). In Figure 10, it is also seen that even evaporation of the fuel could be measured during the time before ignition. The second test burned 14.63 kg of fuel in about 11 minutes (659 s), resulting in a RHR of 999 kW. While the wind speed was about 1.5 m/s during the first test, it was increasing up till 2 m/s during the second test, which causes this faster burning rate.

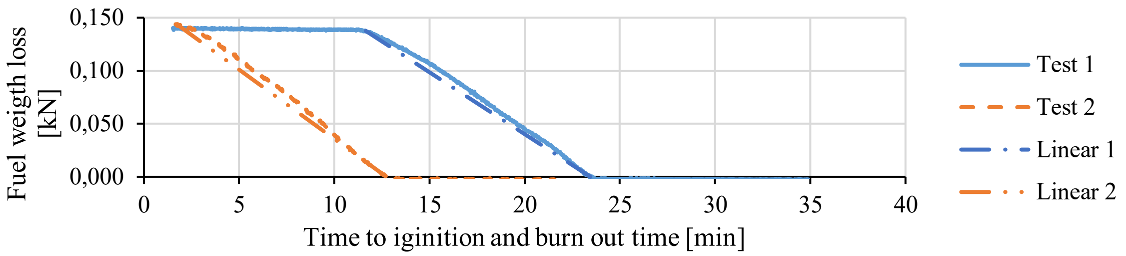

Figure 10. Weight loss rate of fuel (petrol ether) during both tests

To illustrate the severity of the applied fire loads, the expected drop (based on test 2 with the Hasemi and Hesekestad approach), and the real drop (based on measured gas temperatures) of the reduction factors for the proof strength [5]are shown in Figure 11 according to [5].

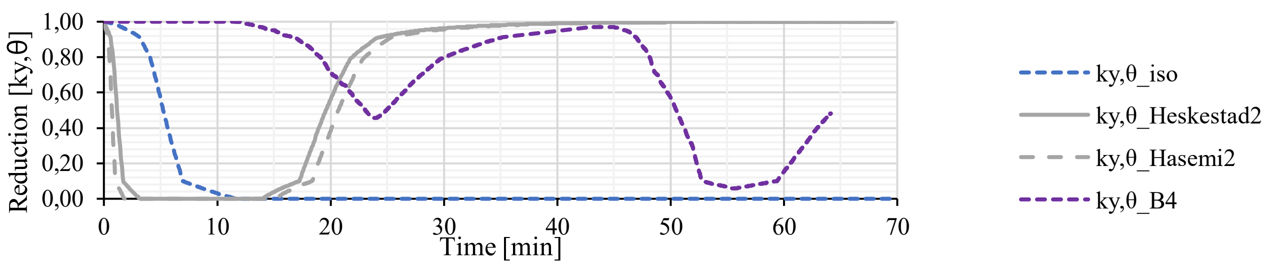

Figure 11. Mechanical response of the aluminium for test 2 with a Hasemi approach, and the real fire

4.2 Dimension analyses during and after the test

The maximum elongation was measured at the side of the roller support, at the left side in Figure 12; up to 14.5 mm. With original distance of 2121.6 mm, 2440.1 mm, 2120.6 mm, 2436.4 mm respectively in between the marking points M1-M3, M4-M6 and a thermal elongation according to equation (3) valid for a temperature range between 0 and 500°C [5], averaged temperatures of 62°C/84°C can be calculated between M1-M2/M4-M5 and 207°C/207°C between M2-M3/M5-M6.

$$ {}^{\Delta L}/_{L} = 0.1 \cdot 10^{-7} \theta_{al}^{2} + 22.5 \cdot 10^{-6} \cdot \theta_{al} - 4.5 \cdot 10^{-4} \quad (3) $$

where ΔL is the thermal bending moment,

L is the initial length,

θ_{al} is the Aluminium temperature.

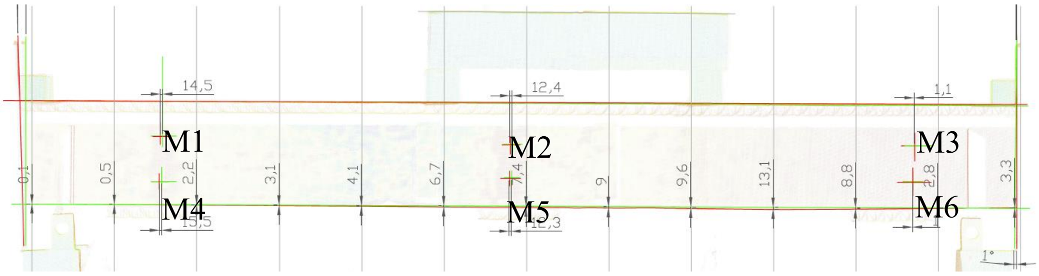

Figure 12. Side view of the target and deck with maximum horizontal and vertical displacements

4.3 Thermal measurements

Comparing the gas temperature along the x-axis of the bridge (direction of the span), Figure 13, it is seen that maximum gas temperatures against the bridge deck are not observed above the centre of the pan (G4 position) but at the centre of the span (G3) and even towards the left support (G2), while G5 seemed to malfunction which possibly points that the effect of the wind caused lower temperatures compared to [17].

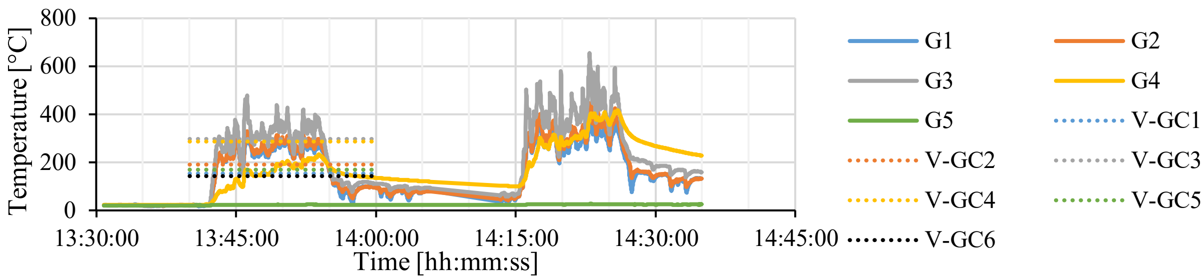

Figure 13. Temperature measurements along the x-axis between girders and comparison with the data from the literature

Also, the gas temperatures measured at 5 cm below the top (T) and 5 cm above the bottom flange (B) confirm the idea of deviations of the flame axis due to the wind. In Figure 14, it can be seen that maximum temperatures are almost equal at the B4 and T5 locations while T4 and B5 are remarkably lower.

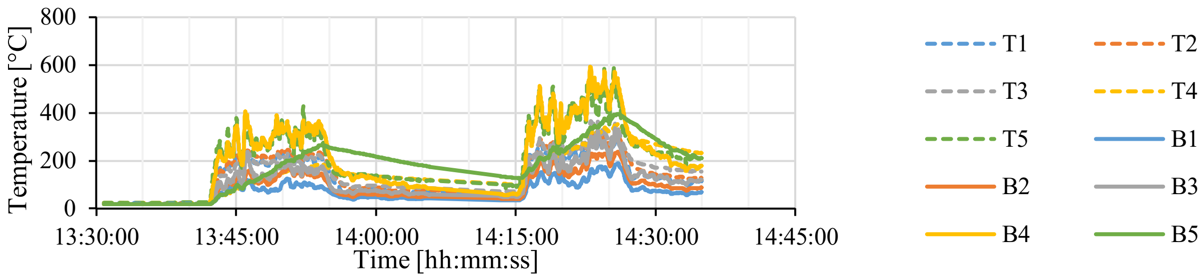

Figure 14. Temperature measurements along the x-axis at the top and bottom flange

Temperature measurements out of [17] showed that the temperatures of the web are almost equal to the one of the bottom flanges. A thermal SAFIR® FEA-model [19], was built up where one side has been subjected to the gas temperatures B4 out of Figure 14 and the opposite side received a 20°C frontier boundary, the convection coefficient α_c at the hot side was set equal to 35 W/m²K in combination with an emissivity coefficient ε of 0.7 since a sooth layer was already present in between both girders during the second test. A maximum aluminium temperature of 256°C after 1380 s was obtained during the first test and 402°C after 3300 s for the second test.

As already indicated in section 2.5.3, use was made of a thermographic camera to measure the material temperatures, the image corresponding to the maximum temperature is given in Figure 15. A first observation is that the temperature profiles are relatively uniform, but the hottest area can be seen above the fire pan (recall B4 in Figure 14). Secondly the maximum observed temperature of 420°C also corresponds very well to the one calculated by SAFIR®, and even to the one obtained by the simplified analytical design equation in [5]. Depending on the emissivity factor ε=0.7, maximum material temperatures of 369°C after 1285 s (238°C/1485s) for test 1, and 430°C after 3300 s (369°C/3360s) for test 2 are obtained, again showing a very good overlap.

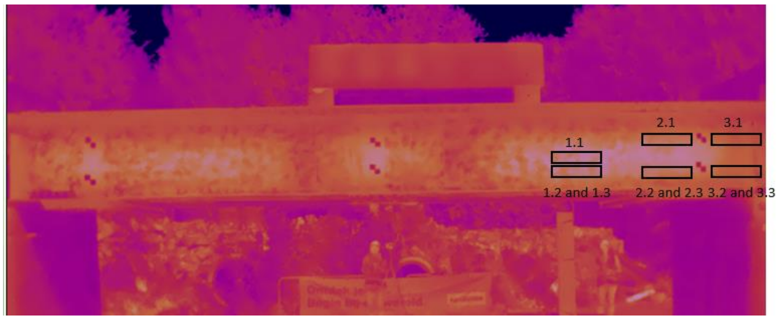

Figure 15. Processed FLIR data with indication coupons 1.X = 380-420°C, 2.X = 270-330°C, and 3.X =200-250°C.

By sampling the pixels out of Figure 15, three temperature zones could be defined which have suffered different temperatures. Out of these zones, coupons have been taken to test the mechanical post-fire properties. The averaged zone temperature is taken as the reference temperature.

4.4 Post-fire mechanical properties

The post-fire mechanical properties have been measured by an Instron 8802 bench. Strain gauges have been used to measure the Young's modulus (following EN-ISO 6892-1, 2016) and initial stress-strain relation. When the measurement range of the strain gauges is exceeded, an extensometer is used (only for the L-profiles), or the stress-strain relation is completed by the Ramberg-Osgood relation till the ultimate strain measured by the testing bench. Including the coupon tests on the virgin material of different components, in total 30 tensile tests have been performed.

4.4.1 L-profiles

Only the coupons taken out of the L-profiles do have a length which allows for the use of extensometers, which allows to determine the applicable n-coefficient from the Ramberg-Osgood relation in the elastic (ne) and plastic range (np). Those coefficients can also be used for the coupons taken out of the web and deck panel once the experimental values are out of the range of the strain gauges used. Note that in Figure 16 beside the experimental values obtained by the extensometers, also the results of an analytical mathematical model (Mat – dotted line) are given besides the Ramberg-Osgood relation (RO – dashed line).

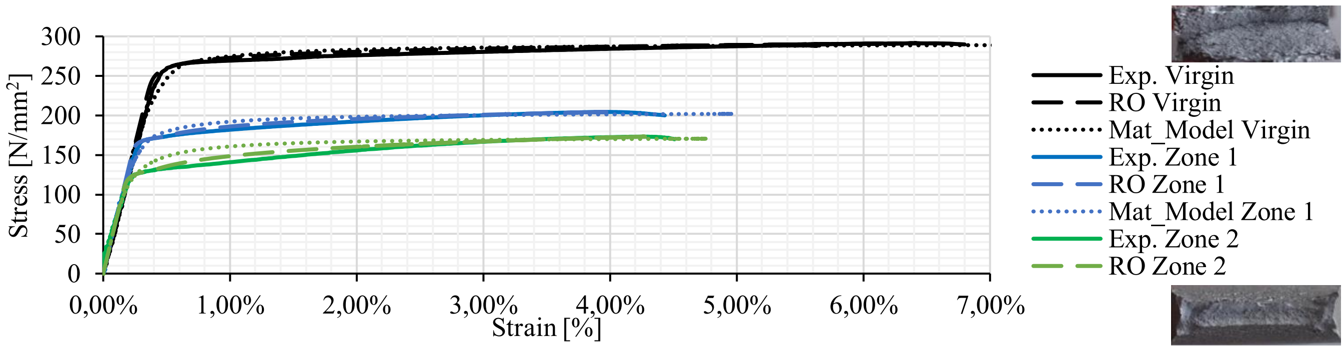

Figure 16. Stress-strain relationship for the L-profiles, virgin, and post-fire coupons + fracture surfaces

It is clear that the RO-model fits the best and the obtained exponent values can also be used in the other tests to complete the graphs beyond the strain gauge limitations. In the plastic region, n_p-exponents of 36, 17 and 11 have been found respectively for the virgin material, zone 1 and zone 2, while [10] suggests values of 20 to 25 for the virgin material. An almost linear decrease of the proof strength can be observed in relation to the maximum temperature measured during the test, which is also the case for the ultimate strength. On the other hand, the fracture surface, is switching from brittle (virgin) to a ductile surface (after fire exposure), Figure 16.

4.4.2 Web panels

As already shown in Figure 15, three sets of coupons have been taken out of three temperature zones for the web panels. The stress strain relation is given in Figure 17. In this case, not a linear decrease can be found which is also remarkably different between the proof and ultimate strength after being submitted to higher temperatures. Likewise, as for the L-profiles, a switch is observed from a brittle to a ductile fracture surface. The dashed lines indicate from which point the Ramberg-Osgood relation (by the n_p-factors of the L-stiffeners) is presented instead of the experimental values.

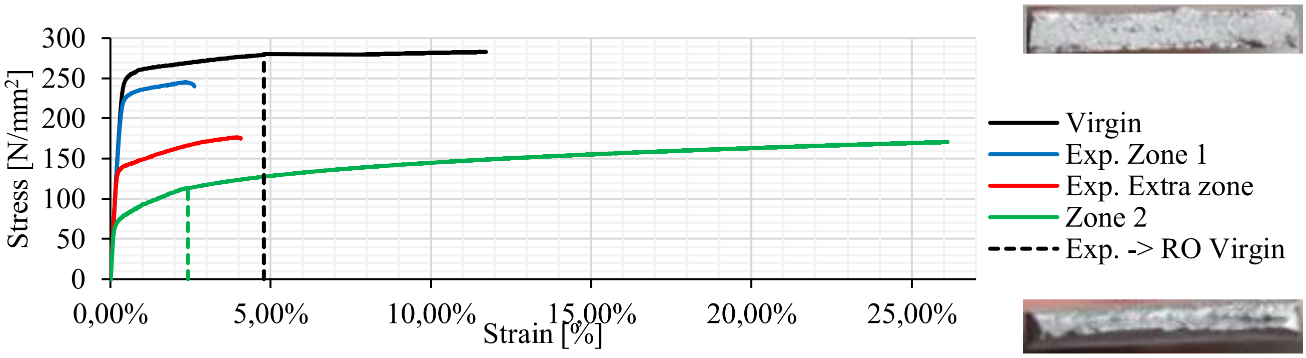

Figure 17. Stress-strain relationship for the web panels, virgin and post-fire coupons + fracture surfaces

4.4.3 Deck panel

While the deck panel has been submitted to the highest temperatures, it did not show considerable difference in the proof strength, which is also the case for the ultimate strength and the fracture surface (always brittle). Nevertheless, the Young-modulus is descending slightly (91%) while there is a noticeable difference for the ultimate strain, see Figure 18. Out of this test, it seems that the EN-AW6005A alloy is less sensitive to fire than the EN-AW6005, see section 3 for more information on the material properties, or an effect of strain hardening was playing a role as the specimens have been taken exactly under the concentrated load.

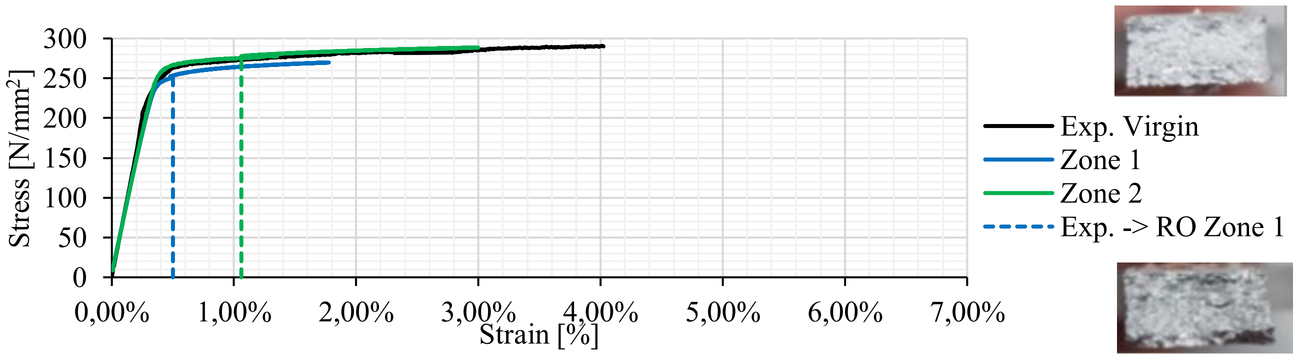

Figure 18. Stress-strain relationship for the deck panels, virgin and post-fire coupons + fracture surfaces

5 CONCLUSIONS

The local fire models are perhaps a straightforward working instrument in a laboratory environment, but in real-world applications, those models are shown to be inadequate. For the experiments performed, it seems that the influence of the wind is the most influencing parameter, even at low wind speed ranges (up to 2 m/s). On the other hand, a very good agreement could be found between the thermal calculations of the web via the FEA-software SAFIR®, but also by the analytical model of EN 1999-1-2, and measurements. 402°C and 430°C have been calculated respectively based on the measured gas temperature at the location of the bottom flange, whilst a maximum temperature of 420 °C was measured.

The aluminium bridge showed, in a first view, an impressive resilience by maintaining the bearing capacity and limited deformations with temperatures that caused reductions on the proof strength till even 0.06 (Figure 11). The extra deformations measured are during the test limited till only around 13 mm for 5.69 m span. However, the residual mechanical properties of the EN-AW6005A (L-profiles + web) grade are strongly reduced after the fire where this was not observed for the EN-AW6005 (deck) material. The system behaviour and local influence of local (non-compartment) fires show that aluminium seems to be an adequate building material with excellent fire resistance if compartment fires can be avoided. Future research on this topic is needed and will be performed at our campus.

ACKNOWLEDGMENT

The execution of this experiment would never be possible without the support of the staff of Campus De Nayer of KU Leuven, especially Luc Willems and the master's students Kobe Uyttersprot and Lander Van Den Bosch from the Rabot campus of KU Leuven. Both students also managed the processing of the Flir camera data, extraction and testing of the coupons in the framework of their master thesis.

REFERENCES

1. European Aluminium, "Recycling: EU net exports of aluminium scrap," 2022.
2. G. Rombach, "Raw material supply by aluminium recycling–Efficiency evaluation and long-term availability," Acta Mater, vol. 61, no. 3, pp. 1012–1020, 2013.
3. J. Fellner and J. Lederer, "Recycling rate–The only practical metric for a circular economy?," *Waste Management*, vol. 113, pp. 319–320, 2020.
4. J. M. Adam, F. Parisi, J. Sagaseta, and X. Lu, "Research and practice on progressive collapse and robustness of building structures in the 21st century," *Eng Struct*, vol. 173, pp. 122–149, 2018.
5. EN 1999-1-2, *European Committee for Standardization, 2007. EN 1999-1-2, Eurocode 9: Design of aluminium structures - Part 1-2: Structural fire design.* CEN, Brussels., 2007.
6. Z. Wang *et al.*, "Structural fire behaviour of aluminium alloy structures: Review and outlook," *Eng Struct*, vol. 268, p. 114746, 2022.
7. C. M. Rippe and B. Y. Lattimer, "Post-fire modeling of aluminum structures using a kinetic driven approach," *Fire Saf J*, vol. 120, p. 103132, 2021.
8. T. Molkens and B. Rossi, "Fire resistance of temporary structures," in *Applications of Structural Fire Engineering 2019*, 2019, pp. 42–48.
9. Y. Akarkach and R. El-Bouchehati, "Ontwerp van een Aluminium Brug," KU Leuven, 2016.
10. EN 1999-1-1, *European Committee for Standardization, 2007. EN 1999-1-1, Eurocode 9: Design of aluminium structures - Part 1-1: General structural rules.* CEN, Brussels., 2007.
11. EN 1990, *European Committee for Standardization, 2002. EN 1990, Eurocode 0 - Basis of structural design.* CEN, Brussels., 2002.
12. EN 1991-2, *European Committee for Standardization, 2003. EN 1991-2, Eurocode 1: Actions on structures - Part 2: Traffic loads on bridges.* CEN, Brussels., 2003.
13. T. Gorinsek and M. Huysmans, "Ontwerp van een Aluminium Brug-Bouwen en Testen van een Schaalmodel," KU Leuven, 2018.
14. P. Saremi, B. Karabulut, and B. Rossi, "Static Structural Response of a Conceptual Aluminium Bridge," in *9th International Conference on Steel and Aluminium Structures (ICSAS19)*, 2019.
15. EN 1993-1-2, *European Committee for Standardization, 2005. EN 1993-1-2, Eurocode 3: Design of steel structures - Part 1-2: General rules - Structural fire design*. CEN, Brussels., 2005.
16. X. Yan and T. Gernay, "Numerical modeling of localized fire exposures on structures using FDS-FEM and simple models," *Eng Struct*, vol. 246, p. 112997, 2021.
17. J. Alos-Moya, I. Paya-Zaforteza, A. Hospitaler, and P. Rinaudo, "Valencia bridge fire tests: Experimental study of a composite bridge under fire," *J Constr Steel Res*, vol. 138, pp. 538–554, 2017.
18. EN 1991-1-2, "European Committee for Standardization, 2002. EN 1991-1-2, Eurocode 1: Actions on structures - Part 1-2: General actions—Actions on structures exposed to fire." European Committee for Standardization Brussels, Belgium, CEN, Brussels., 2002.
19. J.-M. Franssen and T. Gernay, "Modeling structures in fire with SAFIR®: Theoretical background and capabilities," *Journal of Structural Fire Engineering*, 2017.

SiF 2022– The 12th International Conference on Structures in Fire
The Hong Kong Polytechnic University, Nov 30 - Dec 2, 2022

EXPERIMENTAL INVESTIGATION ON MECHANICAL PROPERTIES OF S32001 DUPLEX STAINLESS STEEL AT ELEVATED TEMPERATURES

Ruixin Tan[1], Guobiao Lou[2], Wei Yang[3]

ABSTRACT

This paper presents the mechanical properties data and constitutive model of S32001 stainless steel at elevated temperatures. S32001 stainless steel is a new type of duplex stainless steel, with good corrosion resistance and higher strength. Its yield strength at room temperature is about 1.9 times that of S304 and S316 series stainless steels, while the nickel element content is only 1 %~3 %. When used as structural steel, S32001 has good economy and significant advantages. Therefore, the high-temperature steady-state tensile test study of S32001 duplex stainless steel was conducted, and the main mechanical property indexes such as initial modulus of elasticity, nominal yield strength, tensile strength and elongation after fracture, etc. at elevated temperatures were obtained and compared with other types of stainless steel and Q235B structural steel. The applicability of Rasmussen model and Gardner model was studied using the test data, and the constitutive relation expression at elevated temperatures was established based on Rasmussen model. The study shows that the yield strength and ultimate strength of S32001 stainless steel decreases with increase of temperature, which is lower than 50 % at room temperature at 600°C, but the material strength at elevated temperatures is significantly higher than that of S30408 stainless steel, which has more superior fire resistance properties. The results of this paper can be used in the study of structural fire performance and fire resistance design.

Keywords: Duplex stainless steel; mechanical properties; constitutive relation; high temperature

1 INTRODUCTION

As a building material, stainless steel has beautiful appearance, good corrosion resistance, low whole-life cost, meets the requirements of sustainable development, and has better high-temperature resistance than ordinary carbon steel, so it has broad application prospects in building structures [1-3]. At present, structural stainless steels are mainly S304 series and S316 series, which have a yield strength of about 260MPa at room temperature [4], high content of nickel and chromium, and high price. The newly developed S32001 stainless steel, which is duplex (austenitic-ferritic) stainless steel, not only has the same corrosion resistance as the austenite stainless steel, but also has higher strength and good wear resistance [4,5]. Its yield strength at room temperature is about 490 MPa, which is about 90 % higher than that of S304 series and S316 series; Meanwhile, the content of the nickel element is greatly reduced, so that the S32001stainless steel has better economy and has remarkable advantages when being used as structural steel.

Due to the frequent occurrence of building fires, in order to ensure the safety of structures under fire, it is necessary to study the mechanical properties of stainless steel at elevated temperatures and the structural fire resistance. At present, the research on high-temperature properties of steel mainly focuses on ordinary

[1] College of Civil Engineering, Tongji University, Shanghai 200092, China
e-mail: 2010209@tongji.edu.cn

[2] Associate researcher, College of Civil Engineering, Tongji University, Shanghai 200092, China; State Key Laboratory for Disaster Reduction in Civil Engineering, Tongji University, Shanghai 200092, China
e-mail: gblou@tongji.edu.cn

[3] College of Civil Engineering, Tongji University, Shanghai 200092, China
e-mail: 2032443@tongji.edu.cn
https://doi.org/10.6084/m9.figshare.22178024

steel and high-strength steel [6-8], and a relatively complete mechanical properties and stress-strain relationship of steel at elevated temperatures have been proposed. The constitutive relationship of stainless steel is different from that of ordinary carbon steel [9], with typical nonlinear characteristics, no obvious yield plateau (taking the stress at 0.2 % of the residual strain as the yield strength), significant strain hardening and high ductility, and the high-temperature mechanical properties of the two are quite different. Scholars have conducted relatively mature research on the mechanical properties of stainless steel materials at room temperature [10-19], and put forward a variety of constitutive models with high accuracy [15-17], which are specified in the specifications. For the mechanical properties of stainless steel materials at high temperatures, only the Eurocode EN 1993-1-2 [20] and the Design Manual for Structural Stainless Steel (published by Euro Inox) [21] give the recommended values for ferritic stainless steel EN 1. 4003, austenitic stainless steel EN 1. 4301, EN 1. 4318, EN 1. 4401/4, EN 1. 4571 and duplex stainless steel EN 1. 4462. The researches on mechanical properties of stainless steel materials at high temperature mainly focused on austenitic and ferritic stainless steel [22-32].

Chen and Young [26] proposed a high-temperature stress-strain model for EN 1.4462 grade duplex stainless steel and EN 1.4301 grade austenitic stainless steel on the basis of the room-temperature Rasmussen model [16]. Abdella model [27, 29] and Quach model [17] were both in the form of explicit function, and Abdella model was a two-stage stress-strain relationship of stainless steel at high temperature while Quach model [17] was a three-stage stress-strain relationship. In addition, the parameters calculation of Quach model was complex and inconvenient. Gardner [15, 28] proposed a two-stage constitutive model at elevated temperatures for austenitic stainless steels of EN 1.4301 and EN 1.4401/4 based on his proposed constitutive model for stainless steels at room-temperature. The research on high-temperature mechanical properties of stainless steel materials in China mainly includes: Chen Ju [30], Fan Shenggang [31] and Lou Guobiao[32] carried out tensile tests at elevated temperatures, established the high-temperature stress-strain constitutive relationship and gave the reduction law of mechanical properties indexes at high temperatures. The studies of the three scholars were about EN 1.4462 duplex stainless steel and EN 1.4301 austenitic stainless steel, S30408 austenitic stainless steel, TSZ410 ferritic stainless steel, respectively.

In this paper, the mechanical properties of S32001 duplex stainless steel at high temperature were studied by steady-state tensile tests, and the mechanical properties parameters and their variation rules at elevated temperatures were obtained. Based on Rasmussen model, the calculation formula of hardening exponents of S32001stainless steel is proposed, and the constitutive relationship of stainless steel at elevated temperatures is established. Finally, the test results were compared with those of EN1.4462 duplex stainless steel, Q235B structural steel and other stainless steels.

2 HIGH-TEMPERATURE MECHANICAL PROPERTIES TEST PROGRAMGENERAL

2.1 Test equipment

The tensile tests at elevated temperatures of S32001stainless steel material was carried out in the engineering structure fire resistance laboratory of Tongji University. The MTS E45.305 material testing system was used, with a maximum loading force of 300 kN and a loading rate range of 0.001~250 mm/min. The working temperature range of MTS 653.04 high-temperature furnace was 100 ~ 1400 ℃, and the furnace was divided into upper, middle and lower heating sections, each section had a thermocouple to monitor and control the furnace temperature. The test measuring equipment included displacement sensor, force sensor, 50 mm gauge contact high temperature extensometer (accuracy is 0.001mm) and K-type thermocouple.

2.2 Test specimens

The specimen is taken from 6 mm thick domestic S32001 stainless steel plate, The content of nickel (Ni) in the material is only 1 ~ 3 %, which is economical. The comparison of its main chemical composition with EN 1.4462, TSZ410, S30408 stainless steel and Q235B is shown in Table 1.

Table 1. Comparison of chemical composition between S32001 stainless steel and other steels

Steel type	Substrate	Mass fraction/%							
		C	Si	Mn	P	S	Ni	Cr	N
S32001	Duplex	≤0.030	≤1.00	4.00~6.00	0.04	0.002	1.00~3.00	19.50~21.50	0.050~0.070
EN1.4462	Duplex	0.018	0.54	1.57	0.022	0.001	5.71	22.44	0.175
TSZ410	Ferritic	≤0.060	≤1.00	1.00~2.00	≤0.040	≤0.015	—	11.00~14.00	≤0.300
S30408	Austenitic	0.08	1	2	0.045	0.03	8.00~11.00	18.00~20.00	/
Q235B	/	0.18	0.2	0.45	0.035	0.036	≤0.30	≤0.30	/

The size of the specimens for the tensile tests of materials at room temperature and high temperatures were designed and produced according to GB/T228.1-2010 "Tensile test of metallic materials: Part 1: Room temperature test method" [33] and GB/T 228.2-2015 "Tensile test of metallic materials: Part 2: High temperature test method" [34], respectively. All specimens had rectangular cross sections. 10 groups of test specimens are designed corresponding to 10 temperature points (including one group of normal temperature test pieces), with 3 pieces in each group and 30 pieces in total. The specimen numbers and relevant dimensions of room temperature and high temperature tests are detailed in Table 2.

2.3 Test methods

1. Room-temperature mechanical properties of S32001

According to GB/T228.1-2010, the loading process was divided into two stages. The initial strain rate was kept at 2.5×10-4/s until a strain of 0.05 was reached. Then the displacement was controlled by the test machine crosshead instead of the extensometer. The displacement rate was kept at 1.5mm/min until complete fracture of the specimens. The initial elastic modulus and nominal yield strength of materials was measured during the first stage, the ultimate tensile strength was measured during the second stage, then the elongation after fracture was measured with a vernier caliper.

2. High-temperature mechanical properties of S32001

Steady-state test method was used to determine the high-temperature mechanical properties, that is to say, specimens was loaded under constant temperature. During the tests, the specimen was heated to the specified temperature and kept at the same temperature for 30 min. After the temperature of the gauge section of the specimen was uniform, the two-stage loading process, which is the same as the room-temperature tensile test, was used to tension the specimen until it broke. The target temperatures were 100, 200, 300, 400, 500, 600, 700, 800 and 900 °C, and two samples were tested at each target temperature. Each working condition included 3 test specimens. The heating rate was controlled at 10 ~ 30 ℃/min, and the test specimens were allowed to expand freely during the heating and constant temperature process.

Table 2. Designations and dimensions of specimens

Temperature condition	Specimen number	Specimen width	Specimen thickness	Temperature condition	Specimen number	Specimen width	Specimen thickness
***T*/℃**		***b*/mm**	***t*/mm**	***T*/℃**		***b*/mm**	***t*/mm**
8	P-1	24.95	5.97	500	K5-1	24.98	5.96
	P-2	24.95	5.96		K5-2	24.99	5.95
	P-3	24.96	5.95		K5-3	24.98	5.94
100	K1-1	24.87	6.02	600	K6-1	24.99	5.94
	K1-2	24.88	5.94		K6-2	24.97	5.93
	K1-3	24.91	5.92		K6-3	24.92	5.94
200	K2-1	24.97	5.95	700	K7-1	24.97	5.96
	K2-2	24.92	5.95		K7-2	24.95	5.96
	K2-3	24.93	5.96		K7-3	24.91	5.93
300	K3-1	24.93	5.98	800	K8-1	24.97	5.95
	K3-2	24.94	5.96		K8-2	24.94	5.98
	K3-3	24.92	5.95		K8-3	24.94	5.93

400	K4-1	24.96	5.94	900	K9-1	25	5.95
	K4-2	24.95	5.96		K9-2	24.99	5.97
	K4-3	24.91	5.92		K9-3	24.93	5.94

Note: P-1, P-2 and P-3 in the table are the numbers of test specimens for room-temperature test.

3 ROOM-TEMPERATURE TEST RESULTS AND DISCUSSION

3.1 The mechanical properties at room temperature

The mechanical properties (Table 3) and stress-strain curve test results (Figure. 2) of S32001stainless steel at room temperature were obtained with the test results processing method of stainless steel materials mechanical property proposed by Gardner [15].

Table 3. Mechanical properties of S32001 stainless steel at room temperature

Temperature condition T/°C	**Specimen number**	**E_0/MPa**	**$\sigma_{0.01}$/MPa**	**$\sigma_{0.2}$/MPa**	**$\sigma_{1.0}$/MPa**	**σ_u/MPa**	**ε_u**	**A_0/%**
8	P-1	204327	283.1	488.8	543.1	744.7	0.487	53.3
	P-2	192150	299.3	501.6	563.2	749.2	0.464	48.77
	P-3	191003	287.3	485.6	542.6	747.9	0.493	49.91
Average value		195827	289.9	492	549.6	747.3	0.481	50.66

Note:

1) E_0 is the initial elastic modulus, A_0 is the elongation after fracture;

2) $\sigma_{0.01}$,$\sigma_{0.2}$ and $\sigma_{1.0}$ are the stress corresponding to the residual strain of 0.01%, 0.2% and 1.0 percent, respectively.$\sigma_{0.2}$ is the nominal yield strength;

3) σ_u is the ultimate strength, ε_u is the corresponding strain.

3.2 Stress-strain model at room temperature

The stress-strain model of stainless steel at room temperature recommended by Rasmussen [16] and Gardner [15] was used to fit the test data, and the strain hardening exponents are shown in Table 4. The comparison between the model curve and the test curve is shown in Fig. 2. The formula of stress-strain curve (σ-ε) of stainless steel at room temperature proposed by Rasmussen [16] based on Ramberg-Osgood model [11] is shown in Equation (1).

$$\varepsilon = \begin{cases} \dfrac{\sigma}{E_0} + 0.002\left(\dfrac{\sigma}{\sigma_{0.2}}\right)^n, & \sigma \le \sigma_{0.2} \\ \dfrac{\sigma - \sigma_{0.2}}{E_{0.2}} + \varepsilon_u\left(\dfrac{\sigma - \sigma_{0.2}}{\sigma_u - \sigma_{0.2}}\right)^m + \varepsilon_{0.2}, & \sigma_{0.2} < \sigma < \sigma_u \end{cases} \qquad \begin{aligned} n &= \frac{\ln 20}{\ln\left(\sigma_{0.2}/\sigma_{0.01}\right)} \\ m &= 1 + 3.5\sigma_{0.2}/\sigma_u \\ E_{0.2} &= \frac{E_0}{1 + 0.002nE_0/\sigma_{0.2}} \end{aligned} \tag{1}$$

Where n is the first hardening exponent to consider the strain hardening of stainless steel materials;

m is the second hardening exponent to improve the Ramberg-Osgood model in the second half of the high stress;

$E_{0.2}$ represents the tangential modulus at stress $\sigma_{0.2}$; other symbols are described in the notes to Table 3.

Table 4. Hardening index of mechanical properties of S32001 stainless steel at room temperature

Specimens number	**n**	**m**	**n'**	**m'**	**$n'_{0.2,1.0}$**
P-1	5.48	3.3	7.74	2.89	2.79
P-2	5.8	3.34	7.85	3.24	3.09
P-3	5.71	3.27	7.51	2.96	2.84
Average value	5.67	3.3	7.7	3.03	2.91

Gardner[15] used $\sigma_{1.0}$ instead of σ_u as control parameter, and the proposed room-temperature constitutive model for stainless steel is shown in Equation (2).

$$\varepsilon=\begin{cases}\dfrac{\sigma}{E_0}+0.002\left(\dfrac{\sigma}{\sigma_{0.2}}\right)^n, & \sigma\le\sigma_{0.2}\\[2ex] \dfrac{\sigma-\sigma_{0.2}}{E_{0.2}}+\left(\varepsilon_{t1.0}-\varepsilon_{t0.2}-\dfrac{\sigma_{1.0}-\sigma_{0.2}}{E_{0.2}}\right)\times\left(\dfrac{\sigma-\sigma_{0.2}}{\sigma_{1.0}-\sigma_{0.2}}\right)^{n'_{0.2,1.0}}+\varepsilon_{t0.2}, & \sigma_{0.2}<\sigma<\sigma_u\end{cases}\tag{2}$$

Where $\varepsilon_{t0.2}$ is the total strain at the stress $\sigma_{0.2}$;

$\varepsilon_{t1.0}$ is the total strain at the stress $\sigma_{1.0}$;

$n'_{0.2,1.0}$ is the hardening exponent at the second stage;

other symbols are the same as Equation (1).

Figure 1 includes four curves, where the test curve is a stress-strain curve obtained from the test data; Md1 is a stress-strain curve fitted by the Equation (1); Md3 is an improved curve obtained by modifying the hardening exponents n and m to n' and m' on the basis of the Equation (1); since the Gardner model does not give the reference value of the hardening exponent, Md2 is the stress-strain curve obtained by n', $n'_{0.2, 1.0}$ based on Equation (2), where n', $n'_{0.2, 1.0}$ were fitted results by the use of 1stOpt (First Optimization) nonlinear fitting software. Compared with the test results, the Rasmussen model (Md1 curve) before improvement was significantly higher in the second half of the curve, and the fitting results of the Gardner model (Md2 curve) and the improved Rasmussen model (Md3 curve) are very close to the test results with high accuracy.

4 HIGH-TEMPERATURE TEST RESULTS AND DISCUSSION

4.1 Experimental phenomena

The failure phenomena and characteristics of the high-temperature tensile test specimens are shown in Figure 2 and Table 5. Under different temperature conditions, the necking degree and the surface color changed significantly. The higher the test temperature was, the more obvious the necking occurred at the fracture of the test specimens, and the length of plastic strengthening zone became longer, indicating that S32001 stainless steel material still has good ductility at high temperatures. The specimens at 800 ℃ and 900 ℃ had obvious elongation after fracture, and the specimens at 900 ℃ even have another necking besides the necking at the fracture.

4.2 The high-temperature mechanical properties and mathematical model

Table 6 presents the high-temperature mechanical properties of S32001 stainless steel at high temperature, and variation rules are as follows:

1. The initial modulus of elasticity of S32001 stainless steel, which changes very little at temperatures below 400 °C, decreases at a significantly faster rate above 400 °C, and is only 25 % of room temperature at 900 °C.
2. The yield strength and ultimate strength of S32001 stainless steel decreased with temperature increased, the speed of decline was first fast, then slow, and finally fast; the yield strength and ultimate strength at 600 ℃ are less than 50 % of those at room temperature.
3. Different from the rule that the elongation after fracture (ductility) of most steels increases with the increase of temperature, the tests showed that the elongation after fracture of S32001stainless steel decreased first and then increased with the temperature became higher. When the temperature was below 300 ℃, the elongation after fracture decreased linearly with the increase of temperature, and at 300 ℃ it is 43 % of that at room temperature; when the temperature exceeded 300 ℃, the elongation after fracture began to increase, and at 900 ℃ it almost reached the value at room temperature.

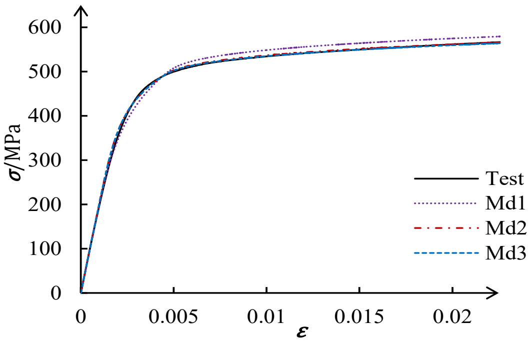

Figure 1. Stress-strain curve of S32001 stainless steel at room temperature

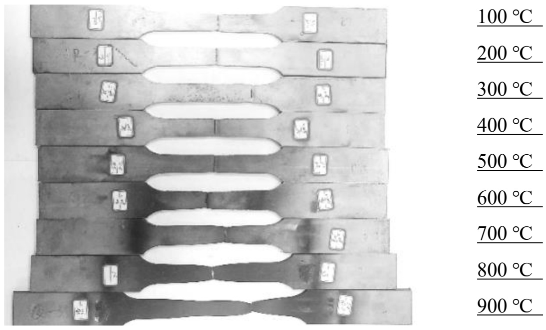

Figure 2. Specimens of S32001 stainless steel after tensile test at elevated temperatures

Table 5. Appearance and damage characteristics of specimens

Temperature(T/°C)	**Surface color of test pieces**	**Necking phenomenon**
100	Silver gray	Exist
200	Close to light yellow	Exist
300	Light yellow	Exist
400	Golden yellow	Exist
500	Brown-yellow	Exist
600	Blue-purple	Exist
700	Brown, metallic luster began to fade	Visibly exist
800	Brown, metallic luster disappeared	Visibly exist
900	Grey black, metallic luster disappeared	Obviously exist

Table 6. Test results of mechanical properties of S32001 stainless steel at elevated temperature

T/°C	$E_{0,T}$/×10^{5}MPa	α_{E_0}	$\sigma_{0.2,T}$ / MPa	$\alpha_{\sigma_{0.2}}$	$\sigma_{u,T}$ /MPa	α_{σ_u}	$\varepsilon_{u,T}$	α_{ε_u}	$A_{0,T}$ /%	α_{A_0}
20	1.958	1	492	1	747.3	1	0.481	1	51	1
100	2.098	1.07	402.2	0.82	594.3	0.8	0.281	0.58	37.2	0.73
200	1.964	1	348.7	0.71	548	0.73	0.264	0.55	30.89	0.61
300	1.956	1	335.2	0.68	556.2	0.74	0.222	0.46	21.89	0.43
400	1.822	0.93	303.6	0.62	553.5	0.74	0.217	0.45	24.65	0.48
500	1.628	0.83	277.8	0.56	488.2	0.65	0.202	0.42	28	0.55
600	1.336	0.68	226.8	0.46	333.2	0.45	0.162	0.34	29.69	0.58
700	1.144	0.58	143.9	0.29	208	0.28	0.18	0.37	36.37	0.71
800	0.871	0.44	82.4	0.17	112.9	0.15	0.134	0.28	48.73	0.96
900	0.489	0.25	45	0.09	57.6	0.08	0.126	0.26	50.59	0.99

Note:

1) At certain temperature(T), $E_{0,T}$,$\sigma_{0.2,T}$,$\sigma_{u,T}$,$\varepsilon_{u,T}$ and $A_{0,T}$ are the initial elastic modulus, nominal yield strength, ultimate strength, ultimate strain and elongation after fracture, respectively.

2) Each data in the table is the average value of three test specimens under the certain temperature condition;

3) α_* is the ratio of the index under this temperature condition to the corresponding index under room temperature, which is expressed by $\alpha_{E_0} = E_{0,T}/E_0$, $\alpha_{\sigma_{0.2}} = \sigma_{0.2,T}/\sigma_{0.2}$, $\alpha_{\sigma_u} = \sigma_{u,T}/\sigma_u$, $\alpha_{\varepsilon_u} = \varepsilon_{u,T}/\varepsilon_u$ and $\alpha_{A_0} = A_{0,T}/A_0$.

The regression analysis of the high temperature test data by the least square method is used to propose a simplified formula for calculating the initial elasticity modulus, nominal yield strength, ultimate strength, ultimate strain and elongation after break of S32001 stainless steel at high temperatures. When the temperature range is 20 ~ 900 °C, the calculation Equation of all mechanical properties a unified form as follow:

$$\alpha_* = a + b(\frac{T}{1000}) \qquad (3)$$

The Equation coefficients are shown in Table 7. Figure 3 indicates the comparison between the Equation calculation values and the test results.

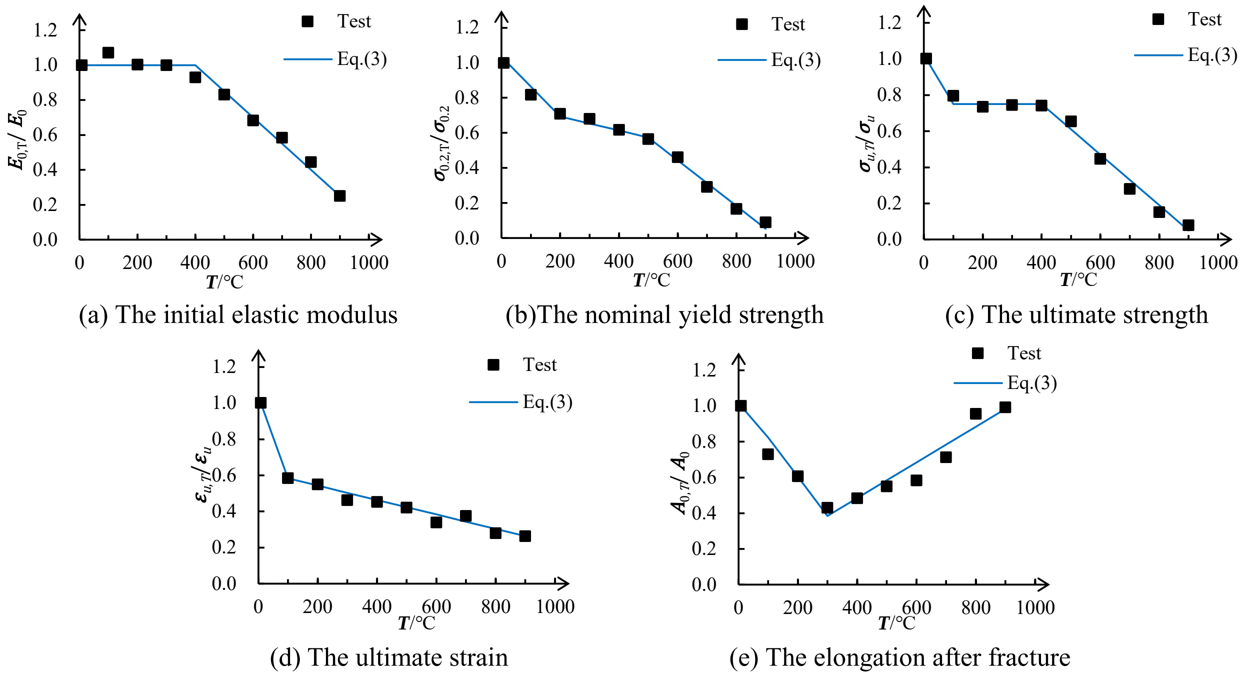

(a) The initial elastic modulus (b)The nominal yield strength (c) The ultimate strength

(d) The ultimate strain (e) The elongation after fracture

Figure 3. Comparison of mathematical model of S32001 stainless steel with test results at elevated temperatures

Table 7. Coefficients of mechanical properties formula

α_*	T/°C	a	b
α_{E_0}	8~400	1	0
	400~900	1.6	-1.5
$\alpha_{\sigma_{0.2}}$	8~200	1.034	-1.7
	200~500	0.774	-0.4
	500~900	1.224	-1.3
α_{σ_u}	8~100	1.02	-2.55
	100~400	0.75	0
	400~900	1.31	-1.4
α_{ε_u}	8~100	1.1	-5.2
	100~900	0.623	-0.4
α_{A_0}	8~300	1.044	-2.2
	300~900	0.084	1

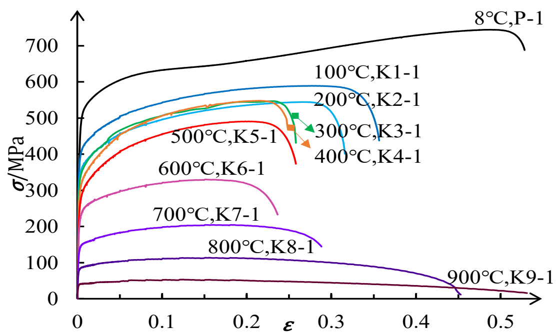

Figure 4. Stress-strain curves of S32001 stainless steel at elevated temperatures

4.3 The stress-strain relationship at high temperatures

For S32001 stainless steel at different temperatures, the test results of stress-strain curves are shown in Figure 4. There is no obvious yield platform at high temperatures. When the test temperature exceeded 800 ℃, the stress fluctuation can be seen. The material ductility decreased first and then increased with the temperature rose, which may be due to the change of microstructure, structure and properties of S32001stainless steel during the heating process [35], and resulting in local strengthening during tension.

The test date was fitted by the constitutive models of stainless steel at elevated temperatures proposed by Chen and Young, which base on Rasmussen model [16, 26] and Gardner model [28] (hereinafter referred to as Rasmussen model and Gardner model). The constitutive model of S32001 stainless steel at elevated temperatures was established, and the two model expressions are Equation (4) Equation (5) respectively.

$$\varepsilon=\begin{cases}\dfrac{\sigma}{E_{0,T}}+0.002\left(\dfrac{\sigma}{\sigma_{0.2,T}}\right)^{n_T}, & \sigma\le\sigma_{0.2,T}\\ \dfrac{\sigma-\sigma_{0.2,T}}{E_{0.2,T}}+\varepsilon_{u,T}\left(\dfrac{\sigma-\sigma_{0.2,T}}{\sigma_{u,T}-\sigma_{0.2,T}}\right)^{m_T}+\varepsilon_{t0.2,T}, & \sigma_{0.2,T}<\sigma<\sigma_{u,T}\end{cases}\qquad \begin{aligned}&n_T=6+0.2\sqrt{T}\\ &m_T=\begin{cases}2.3-0.001T, & EN1.4301\\ 5.6-0.005T, & EN1.4462\end{cases}\end{aligned}\tag{4}$$

Where:At the temperature T, $E_{0.2,T}$ is the tangent modulus;

$\varepsilon_{t0.2,T}$ is the total strain corresponding to $\sigma_{0.2,T}$;

n_T and m_T are the hardening exponent of the first stage and the second stage, respectively;

other symbols are described in the notes of Table 6.

$$\varepsilon=\begin{cases}\dfrac{\sigma}{E_{0,T}}+0.002\left(\dfrac{\sigma}{\sigma_{0.2,T}}\right)^{n_T}, & \sigma\le\sigma_{0.2,T}\\ \dfrac{\sigma-\sigma_{0.2,T}}{E_{0.2,T}}+\left(0.02-\varepsilon_{t0.2,T}-\dfrac{\sigma_{t0.2,T}-\sigma_{0.2,T}}{E_{0.2,T}}\right) & \\ \times\left(\dfrac{\sigma-\sigma_{0.2,T}}{\sigma_{t0.2,T}-\sigma_{0.2,T}}\right)^{n'_T}+\varepsilon_{t0.2,T}, & \sigma_{0.2,T}<\sigma\le\sigma_{u,T}\end{cases}\tag{5}$$

Where: At certain temperature(T), $\sigma_{t0.2,T}$ is the stress corresponding to 2 % total strain;

n'_T is the hardening exponent at the second stage;

the rest is the same as the symbols of Equation (4).

As the recommended values of n_T, m_T and n'_T by Chen, Young and Gardner were suitable for certain stainless steel types, the test results analysis showed that the recommended values of hardening exponent could not simulate the stress-strain relationship of S32001stainless steel accurately. Therefore, in this paper, the strain hardening exponents (Table 8) were obtained by using the McQuart method, the general global optimization method and applying the 1stOpt (First Optimization) nonlinear fitting software. The comparison between the model curves and the test curves are presented in Figure 5, wherein the test curves represent test results, and the Md1 and Md2 curves are stress-strain curves fitted by Equation (4) Equation (5), respectively.

It can be seen from Figure 5 that both the Rasmussen model and the Gardner model (Md1 and Md2) simulate the constitutive relationship of S32001 stainless steel in good agreement with the test results. Because the Rasmussen model has a more concise expression and requires fewer parameters, the Rasmussen model is used in this paper to simulate the constitutive relationship of S32001 stainless steel.

According to the results in Table 8, the hardening exponents n_T and m_T of S32001 stainless steel at elevated temperatures in Equation (4) were numerically simulated to obtain the hardening exponent calculation formulas of S32001 stainless steel, which are shown in the following Equation (6) and Equation (7):

$$n_T=-1.034\times10^{-8}T^3+7.421\times10^{-5}T^2-7.366\times10^{-2}T+26.850,\ \ 100\le T\le 900℃\tag{6}$$

$$m_T=-1.501\times10^{-8}T^3+1.815\times10^{-5}T^2-6.272\times10^{-3}T+3.311,\ \ 100\le T\le 900℃\tag{7}$$

The data in Table 6 and the calculation results of Equation (6) ~ (7) were substituted into the Rasmussen model to establish the stress-strain model of S32001 stainless steel at any temperature. The comparison between the calculation results and the test data is shown in Figure 6. Where the solid line represents the calculation result, and the dotted line indicates the test data. The two fit well, i.e., the above hardening exponents calculation formula is resonable.

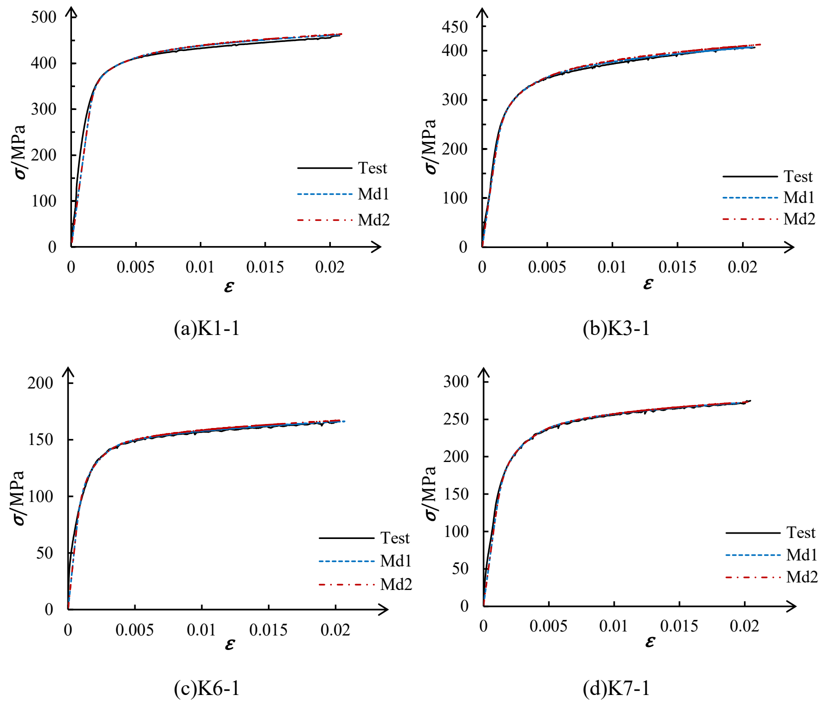

Figure 5. Comparison of stress-strain fitting curve of S32001 stainless steel with test results at elevated temperatures

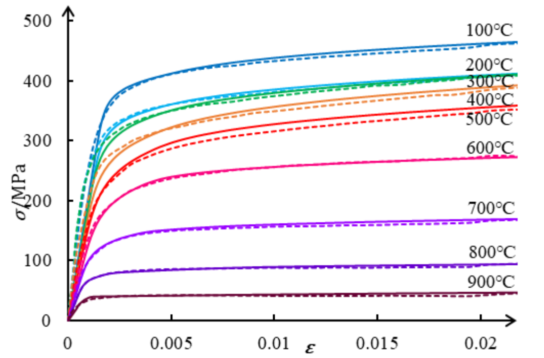

Figure 6. Comparison of stress-strain curves of S32001 stainless steel with test results at different temperatures

Table 8. Hardening index of mechanical properties of S32001 stainless steel at elevated temperatures

T **/°C**	**Specimen number**	**The recommended values of Rasmussen** [26]		**Rasmussen model**		**Gardner model**	
		n_T	m_T	n_T	m_T	n_T	n'_T
100	K1-1	8	5.1	15.62	2.81	15.62	2.83
	K1-2			26.61	3.17	26.61	3.3
	K1-3			19.73	2.67	19.73	2.82
200	K2-1	8.83	4.6	13.63	2.54	13.63	2.6
	K2-2			14.12	2.55	14.12	2.61
	K2-3			15.14	2.63	15.14	2.68
300	K3-1	9.46	4.1	9.53	2.71	9.53	2.79
	K3-2			13.6	2.7	13.6	2.72
	K3-3			10.5	2.59	10.5	2.57
400	K4-1	10	3.6	10.2	2.58	10.2	2.68
	K4-2			8.72	3.24	8.72	3.32
	K4-3			6.01	2.82	6.01	2.91
500	K5-1	10.47	3.1	8.06	2.74	8.06	2.84
	K5-2			6.01	2.48	6.01	2.34
	K5-3			8.45	2.68	8.45	2.79
600	K6-1	10.9	2.6	8.62	3.03	8.62	3.02
	K6-2			7.2	3.15	7.2	3.18
	K6-3			9.04	3.21	9.04	3.06
700	K7-1	11.29	2.1	7.73	2.52	7.73	2.6
	K7-2			6.83	2.21	6.83	2.56
	K7-3			9.3	2.22	9.3	2.26
800	K8-1	11.66	1.6	10.39	2.04	10.39	2.27
	K8-2			9.24	2.29	9.24	2.37
	K8-3			6.25	2.96	6.25	3.5
900	K9-1	12	1.1	9.73	1.73	9.73	1.64
	K9-2			13.81	1.02	13.81	1.46
	K9-3			18.17	1.38	18.17	1.34

5 COMPARISON OF THE HIGH-TEMPERATURE MECHANICAL PROPERTIES OF S32001 STAINLESS STEEL MATERIAL AND OTHER STEELS

The comparison of mechanical properties such as the initial elastic modulus, nominal yield strength and ultimate strength at elevated temperatures of S32001 stainless steel with EN 1.4462 duplex type stainless steel [36], TSZ410 ferritic stainless steel [32], and structural steel Q235B [37,38] is shown in figure (a)~(c).The comparison of S32001 stainless steel with S304 series stainless steels (such as S30408 austenitic stainless steel [31]) for comparison of the yield strength and ultimate strength at high temperatures, see Figure 7(d).

Both S32001 and EN 1.4462 are duplex stainless steel, the variation trend of the mechanical properties at elevated temperatures is almost the same, but the high-temperature mechanical properties of EN 1.4462 is slightly better than S32001.

The initial elastic modulus reduction of S32001 stainless steel at high temperature is similar to that of TSZ410, and the initial elastic modulus is basically unchanged from 20 ℃ to 400 ℃, while the initial elastic modulus of Q235B decreases significantly with the increase of temperature. When the temperature not exceeds 500 ℃, the reduction coefficient of the nominal yield strength of S32001 stainless steel is obviously lower than that of TSZ410 and Q235B, and the maximum difference between the reduction coefficient of S32001 stainless steel and that of Q235B is 0.32; when the temperature is above 500 ℃, the opposite is true.

Compared with S30408 stainless steel, the material strength of S32001 stainless steel at elevated temperatures is much higher than that of S30408 stainless steel, especially in the temperature range of 20 ~ 600 ℃, and the nominal yield strength of S32001 is 2.03 times higher than that of S30408 at 300 ℃.

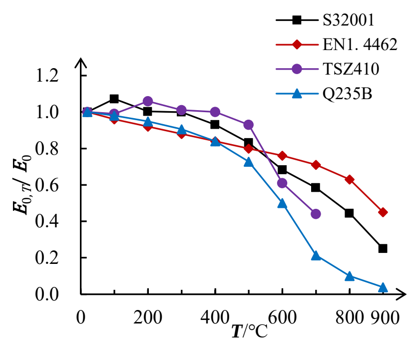

(a) The initial elastic modulus

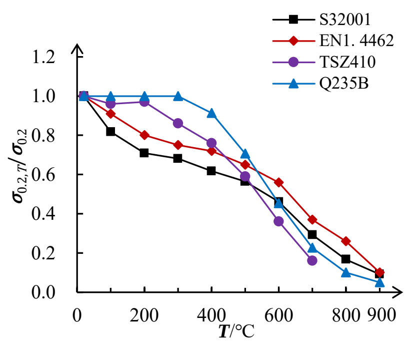

(b) The nominal yield strength

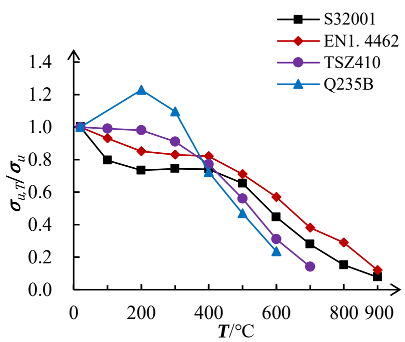

(c) The ultimate strength

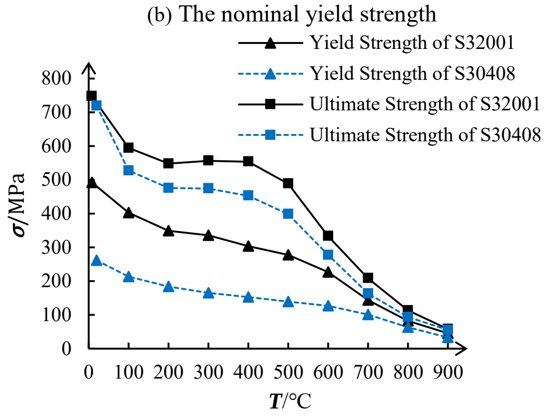

(d) The comparation between S32001 and S30408

Figure 7. Comparison of mechanical properties of different steels at elevated temperatures

6 CONCLUSIONS

1. The nominal yield strength and ultimate strength of S32001 stainless steel show a trend of first fast, then slow and finally fast decline as the temperature increases; 46 % and 45 % of those at room temperature at 600 ℃ , respectively; at 900 °C less than 10 % of those at room temperature.

2. Rasmussen model and Gardner model were used to fit S32001 stainless steel stress-strain relationship at high temperatures, comparison results show that both models have high accuracy. The calculation formula for the hardening exponents of S32001 stainless steel is proposed on the basis of Rasmussen model, which is with simple expression and more convenient for practical engineering applications..
3. When the temperature is below 500 ℃ , S32001 stainless steel strength reduction at elevated temperatures is significantly greater than TSZ410 stainless steel and structural steel Q235B, the opposite when higher than 500 ℃ ; S32001 stainless steel material strength at elevated temperatures is significantly higher than S30408 stainless steel, in the temperature range of 20 ~ 600 ℃ , the nominal yield strength of S32001 is at least 1.8 times that of S30408, with more superior fire resistance.

REFERENCES

1. Burgan BA, Baddoo NR, Gilsenan KA. Structural design of stainless steel members — comparison between Eurocode 3, Part 1.4 and test results. Journal of Constructional Steel Research 54, 51-73(2000). https://doi.org/10.1016/s0143-974x(99)00055-3.
2. Young B. Experimental and numerical investigation of high strength stainless steel structures. Journal of Constructional Steel Research 64, 1225-1230 (2008). https://doi.org/10.1016/j.jcsr.2008.05.004.
3. Wang Yuanqing, Yuan Huanxin, Shi Yongjiu, et al. A review of current applications and research of stainless steel structure. Steel Structure 25, 1-12+18 (2010). https://doi.org/10.3969/j.issn.1007-9963.2010.02.001.
4. Wang Yuanqing, Chang Ting, Shi Yongyong, et al. Experimental study of the stress-strain relation of austenitic stainsteel S31608. Journal of Tsinghua University (Science and Technology) 53, 1231-1234+1240(2013). https://doi.org/10.16511/j.cnki.qhdxxb.2013.09.004.
5. J Charles, P chemelle, HU Jincheng, ZHANG Wei. Development status and future market trend of duplex stainless steel. World Iron & Steel 11, 1-22(2011). https://doi.org/10.3969/j.issn.1672-9587.2012.01.011
6. Tan Wei. Analytical study of steel structure material properties and structural response of steel frames under high temperature (fire) conditions. Industrial Building 11, 1-22(2011). https://doi.org/10.13204/j.gyjz2000.10.016
7. Li Guoqiang, Chen Kai, Jiang Shouchao, et al. Experimental study on material properties of Q345 steel at high temperature . Building structure 31, 53-55, (2001). https://doi.org/10.19701/j.jzjg.2001.01.019
8. Wang Weiyong, Lie Bing, Li Guoqiang. Experimental study on high temperature mechanical properties of high strength Q460 steel. Journal of disaster prevention and mitigation engineering 32, 30-35(2012). https://doi.org/10.13409/j.cnki.jdpme.2012.s1.007
9. Gardner L. The use of stainless steel in structures. Progress in Sturctural Engineering and Materials 7, 45-55(2005).
10. Atchison C S, Miller J A. Tensile and pack compressive tests of some sheets of aluminum alloy, 1025 carbon steel, and chromium-nickel steel. Technical Note, 1-32(1942).
11. Ramberg W, Osgood W R. Description of stress-strain curves by three parameters. Technical Note, 1-28(1943).
12. Hill H N. Determination of stress-strain relations from "offset" yield strength values. Pediatrics 6, 1-7(1944).
13. Macdonald M, Rhodes J, Tayloe G T. Mechanical properties of stainless steel lipped channels. Proceedings of 15th International Specialty Conference on Cold-Formed Steel Structures. St. Louis: University of Missouri—Rolla, 673-686(2000).
14. OLSSON A. Stainless steel plasticity: material modelling and structural applications. Luleå: Luleå Tekniska Universitet, 2001.
15. Gardner L. A new approach to stainless steel structural design. Structural Engineer 82, 21-28(2004).
16. Rasmussen KJR. Full-range stress–strain curves for stainless steel alloys. Journal of Constructional Steel Research 59, 47-61(2003). https://doi.org/10.1016/s0143-974x(02)00018-4.
17. Quach WM, Teng JG, Chung KF. Three-Stage Full-Range Stress-Strain Model for Stainless Steels. Journal of Structural Engineering 134, 1518-1527 (2008). https://doi.org/10.1061/(asce)0733-9445(2008)134:9(1518).
18. Zheng Baofeng, Shu Ganping, Shen Xiaoming, Experimental study on material properties of stainless steel at room temperature. Steel structure 26, 1-6(2011). https://doi.org/10.3969/j.issn.1007-9963.2011.05.001.

19. Zhu Haochuan, Yao Jian. Stress-strain model for stainless steel. Spatial structure 17, 62-69 (2011). https://doi.org/ 10.13849/j.issn.1006-6578.2011.01.011
20. European Committee for Standardization. EN 1993-1-2 Eurocode 3-Design of steel structures-Part 1-2: General rules—structural fire design. Brussels： European Committee for Standardization, 2005.
21. Euro Inox/SCI. Design manual for structural stainless steel. 3rd ed. Building series: Euro Inox and the Steel Construction Institute, 2006.
22. Peckner D, Iirving Melvin Bernstein. Handbook of Stainless Steels. Mcgraw-Hill, 1977.
23. Sakumoto Y, Nakazato T, Matsuzaki A. High-Temperature Properties of Stainless Steel for Building Structures. Journal of Structural Engineering 122, 399-406(1996). https://doi.org/10.1061/(asce)0733-9445(1996)122:4(399).
24. Fujita N, Ohmura K, Kikuchi M, Suzuki T, Funaki S, Hiroshige I. Effect of Nb on high-temperature properties for ferritic stainless steel. Scripta Materialia 35, 705-710(1996). https://doi.org/10.1016/1359-6462(96)00214-x.
25. Brinkman CR. Elevated-Temperature Mechanical Properties of an Advanced-Type 316 Stainless Steel1. Journal of Pressure Vessel Technology 123, 75-80(2000). https://doi.org/10.1115/1.1343911.
26. Chen J, Young B. Stress–strain curves for stainless steel at elevated temperatures. Engineering Structures 28, 229-239(2006). https://doi.org/10.1016/j.engstruct.2005.07.005
27. Abdella K. Explicit full-range stress–strain relations for stainless steel at high temperatures. Journal of Constructional Steel Research 65, 794-800(2009). https://doi.org/10.1016/j.jcsr.2008.09.001.
28. Gardner L, Insausti A, Ng KT, Ashraf M. Elevated temperature material properties of stainless steel alloys. Journal of Constructional Steel Research 66, 634-647(2010). https://doi.org/10.1016/j.jcsr.2009.12.016.
29. KENZU ABDELLA. A Three-Stage Explicit Stress-Strain Relations For Stainless Steel Alloys Applicable In Tension And Compression At Elevated Temperatures. Advanced materials forum VI : Part 2 /.:Trans Tech Publications, 691-696(2011).
30. Chen Ju, Jin Weiliang, Yang Liwei. Behaviour of constructional stainless steel at elevated temperatures. Journal of Zhejiang University (Engineering Science Edition) 42. 1983-1989(2008). https://doi.org/10.3785/j.issn.1008-973X.2008.11.026.
31. Fan Shenggang, Zheng Jiazhen, Sun Wenjun, et al. Experimental investigation on mechanical properties of S30408 austenitic stainless steel at elevated temperatures. Engineering Mechanics 34, 167-176(2017). https://doi.org/10.6052/j.issn.1000-4750.2015.11.0889.
32. Lou Guobiao, Tao Yuchao, Chen Wulong, et al. Experimental Investigation of Mechanical Properties of TSZ410 Ferritic Stainless Steel at Elevated Temperature. Journal of Tongji University (Natural Science) 49. 20-29(2021). https://doi.org/10.11908/j.issn.0253-374x.20205.
33. Standardization Administration of the People's Republic of China. Metallic materials —Tensile testing—Part 1： Method of test at room temperature： GB / T228.1—2010. China Standard Press, Beijing; 2010.
34. Standardization Administration of the People's Republic of China. Metallic materials —Tensile testing—Part 2： Method of test at elevated temperature： GB / T228.2—2015. China Standard Press, Beijing; 2015.
35. Zhu Xueyi. Steel heat treatment manual. China Standard Press, Beijing; 2007.
36. Zhao B. Material behaviour at elevated temperatures: work package 5.1. ECCS project “development of the use of stainless steel in construction” Contract No.7210 SA/ 842. The Steel Construction Institute, UK; 2000.
37. Ministry of Housing and Urban-Rural Development of the People's Republic of China. Code for fire safety of steel structures in buildings: GB 51249—2017. China Planning Press, Beijing; 2017.
38. Ou Manli, Cao Weijun. On the Mechanic Performance of Building-Purpose Q235 Steel Under High-Temperature (Fire). Journal of Hunan University of Technology 20, 99-101(2006). https://doi.org/10.3969/j.issn.1673-9833.2006.04.029.

EXPERIMENTAL INVESTIGATION OF THE FIRE PERFORMANCE OF CIRCULAR CFRP–WRAPPED RC COLUMNS

Salem Khalaf[1], Yazan Alhoubi[2], Farid Abed[3] ,Ahmed El Refai[4], Reem Talo[5]

ABSTRACT

This paper investigates the fire performance of circular Reinforced Concrete (RC) columns wrapped with Carbon Fiber-Reinforced Polymer (CFRP) systems and fire-insulation. Four columns were fabricated and exposed to fire according to ASTM E119 standards for 130 minutes. The columns varied in the number of CFRP layers used and the presence of the fire insulation. All columns had the same length, concrete dimensions, and reinforcement. The columns were exposed to fire inside a full-scale furnace to simulate actual fire scenarios. The temperature readings at different locations within the section were obtained using thermocouples to plot temperature-time curves. The test results showed that the fireproofed columns had 68% lower temperature measurements than those without fireproofing throughout the fire test. The fire insulation layer maintained the CFRP temperature below the glass transition temperature (T_g) of the epoxy resin of the CFRP system for 20 minutes. Furthermore, it was noticed that the CFRP layers did not contribute to any fire isolation since the temperature measurements inside the wrapped and the unwrapped columns were almost identical.

Keywords: Fire; columns; CFRP; fiber-reinforced polymers; fire performance.

1 INTRODUCTION

Over the past decades, the use of externally bonded fiber-reinforced polymer (FRP) systems has increased as a promising method to strengthen existing reinforced concrete (RC) structures. Although FRP systems can improve the performance of the structure, they are vulnerable to elevated temperatures and fire. This temperature vulnerability is mainly associated with the epoxy adhesive that becomes viscous when approaching its glass transition temperature (T_g), which is between 60 and 140 ºC [1]. The FRP systems then lose their strengthening action and the bond between the FRP system and the concrete significantly deteriorates. This phenomenon can happen at relatively low temperatures (65 ºC) as reported in [2]. In addition, the mechanical properties of the FRP system including its stiffness and strength significantly decrease [3]. This poor fire performance of the FRP systems has motivated researchers either to use different fireproofing insulations to maintain the integrity of the FRP systems while in service or to explore alternative strengthening systems that use cementitious matrix as a binder material such as FRCM system

[1] Mr, Graduate Research Assistant at the American University of Sharjah,
e-mail: b00074986@alumni.aus.edu
[2] Mr, Research Associate at the American University of Sharjah,
e-mail: yalhoubi@aus.edu
[3] Dr, Civil Engineering Professor at the American University of Sharjah,
e-mail: fabed@aus.edu
[4] Dr, Civil Engineering Professor at Laval University,
e-mail: Ahmed.ElRefai@gci.ulaval.ca
[5] Ms, Graduate Research Assistant at the American University of Sharjah,
e-mail: g00064227@aus.edu
https://doi.org/10.6084/m9.figshare.22178057

[4-6]. However, the focus of this research paper is going to be on the fire performance of the FRP and fireproofing systems.

Many studies have been devoted to investigate the performance of externally wrapped RC columns exposed to elevated temperatures or fire. For example, Salloum et al. [7] experimentally investigated the performance of circular FRP-wrapped RC columns, with and without fire insulation, when exposed to elevated temperatures up to 800 ºC for 3 hours. The columns were then tested under compression after cooling down to room temperature. The reported results showed a significant decrease in strength (28%) and stiffness (45%) of the non-insulated FRP-wrapped columns when the exposed temperature increased from 100 to 400 ºC. Fire-insulated columns showed 13% reduction in strength when exposed to a temperature of 400 ºC. However, when the fire-insulated columns were exposed to a temperature of 800 ºC, a significant reduction in strength of about 50% was observed, which was attributed to the loss of the fire insulation. Another study conducted by Trapko [8] studied the performance of CFRP-wrapped concrete cylinders exposed to temperatures between 40 and 80 ºC. The results showed a reduction of 20% of the axial capacity of the wrapped cylinders at 80 ºC.

In this paper, full-scale CFRP-wrapped RC circular columns were exposed to fire according to ASTM E119 provisions [9]. The investigated parameters included the number of CFRP layers used, and the existing of the fire insulation. The test setup and the obtained results are detailed below.

2 EXPERIMENTAL PROGRAM

2.1 Test specimens and materials

The experimental program investigated the fire performance of four circular RC columns: one unwrapped and non-fireproofed column (control), one unwrapped and fireproofed column (Control-FP), and two wrapped and fireproofed columns with one and two CFRP layers (C-1-FP and C-2-FP, respectively). Table 1 summarizes the test matrix of this study. No CFRP-wrapped columns were tested without fireproofing as recommended by previous studies [8]. For all columns, a 1-meter steel threaded bar was embedded at the center of the column with half of its length was exposed as shown in Figure 1a. These threaded bars were used to hang the columns from the furnace ceiling (Figure 1b) to prevent the damage that may occur to the furnace slab if the column failed during testing. The column dimensions and reinforcement details are shown in Figure 2.

(a) (b)

Figure 1. (a) Installing threaded bars, (b) columns hung from the furnace ceiling

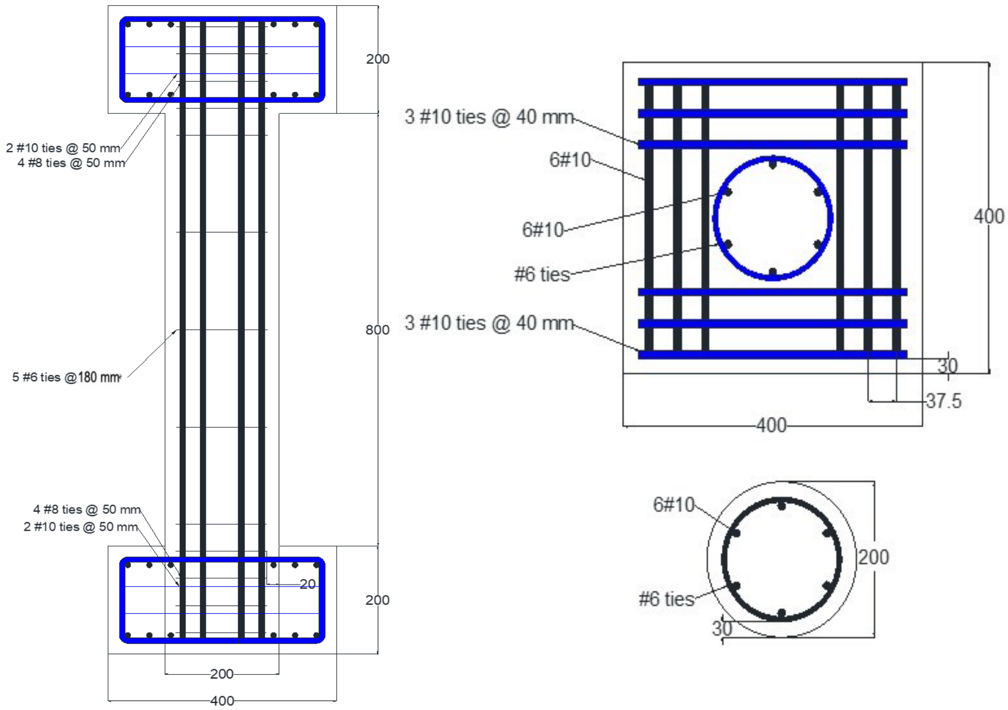

Figure 2. Column dimensions and reinforcement details

Table 1. Test matrix

Specimen label	**Number of CFRP Layers**	**Fireproof Thickness (mm)**
Control	-	-
Control-FP	-	30
C-1-FP	1	30
C-2-FP	2	30

Before casting the columns, three type "*k*" thermocouples are placed within the form at mid height of the columns in the center (location 1), midway between the center and the longitudinal reinforcement (location 2), and close to the longitudinal reinforcement (location 3). The three thermocouples were first fixed on a small steel rod and then placed as shown in Figure 3. The welded end of the thermocouple (inside the concrete) was carefully placed so that it didn't touch the steel reinforcement. The columns were then cast manually and left for curing.

Figure 3. Installing the thermocouples prior to casting

The MapeWrap primer 1 adhesive was used in this study along with a high-strength CFRP sheet (MapeWrap C Uni-Ax 600) from Mapei. According to the manufacturer specifications, the CFRP composite had a design thickness of 1.01 mm, a tensile strength of 1630 MPa, and a tensile modulus of 82 GPa. The fireproof insulation used was the cement-based system Sikacrete-213F with 4-hour fire resistance according to the manufacturer's datasheet. The fireproof had a low density of 1170 kg/m^3 and a thermal conductivity of only 0.23 W/(m*°C).

2.2 CFRP wrapping and fireproof application

After 28 days of casting the columns, the concrete surface was roughened using an electric grinder to ensure good bonding between the CFRP composite and concrete. The concrete surface was first sprayed with water to remove the dust. A thermocouple was then installed on the concrete surface (location 4) and held in place using steel wires. Figure 4 shows the steps used for the CFRP installation. The first layer of epoxy was first applied on the concrete surface, followed by the CFRP sheet and a second layer of epoxy. The sheet was manually rolled to remove any entrapped air bubbles. The sheets were installed with horizontal overlaps of 100 mm.

The Sikacrete 213F fireproof was applied on the CFRP layer after two days of installing it to ensure that the epoxy adhesive was hardened. The fireproof was applied in two layers of 15 mm thickness each at separate times as shown in Figure 4. A thermocouple was placed between the two layers (location 5) to monitor the temperature readings through the fireproof. All five thermocouple locations within the section are shown in Figure 5.

(a) (b) (c) (d)

Figure 4. (a) Applying the first layer of epoxy, (b) wrapping the column with the CFRP sheet, (c) applying the second layer of epoxy and removing the entrapped air, (d) applying the fireproof layers

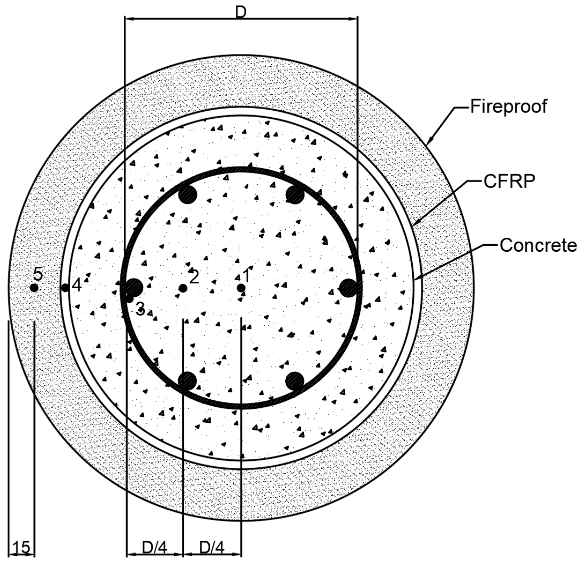

Figure 5. Thermocouple locations within the section

2.3 Fire Test

All columns were fire tested in a 5x5 meter large-scale furnace. The furnace had four fire outlets and the temperature was controlled to follow the ASTM E119 standard fire curve. The thermocouple ends were attached to the laboratory data acquisition system as shown in Figure 6. The test was carried out for 130 minutes for all specimens and the temperature readings were recorded at 0.5 minute intervals.

(a) (b)

Figure 6. (a) Thermocouples connected to wire extensions and (b) the data acquisition system at the fire facility

3 RESULTS AND DISCUSSIONS

The fire performance of the four columns in this study were evaluated based on the temperature response (temperature-time curves) and the final condition of the column after fire exposure. The furnace had 20 thermocouples to calculate the average furnace temperature readings to compare them with the ASTM E119 fire curve. Figure 7 shows the excellent matching between both curves. The temperature response curves for all specimens at all five locations, together with the ASTM E119 fire curve, are shown in Figure 8.

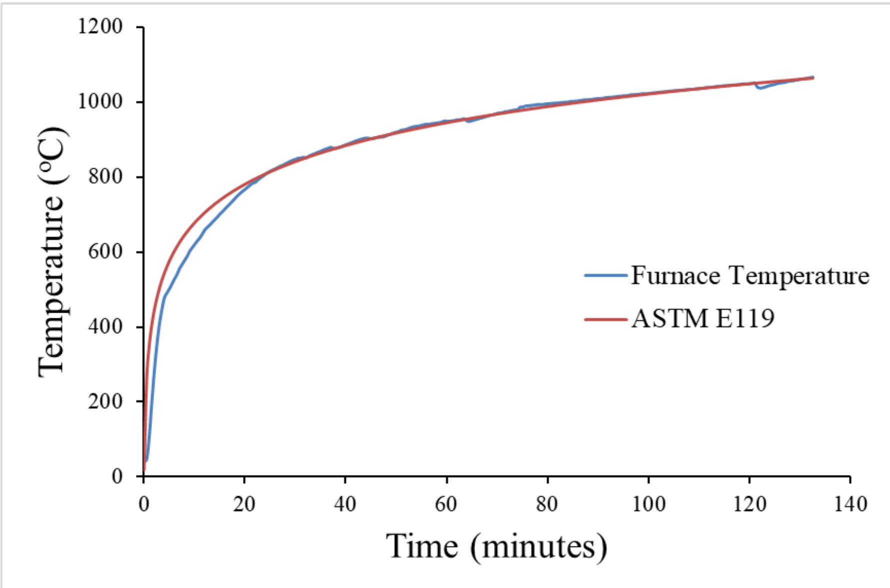

Figure 7. Average furnace temperature and ASTM E119 standard fire curve

At the thermocouples locations 1 to 3 (Figure 8a to c), all three fire insulated columns had approximately the same temperature response, which shows that the CFRP composite didn't provide any added fire insulation. The average final temperature of the three fire insulated columns were 75% lower than that of the Control column in locations 1 to 3. The temperature readings at the concrete surface (Figure 8d) of all columns followed the ASTM fire curve, especially the Control column since the concrete surface was directly exposed to fire

The surface temperature readings (Figure 8d) of the fireproofed columns were significantly lower than the Control column (about 54% in the Control-FP and 36% in the C-2-FP columns). However, a noticeable temperature spike was observed after 120 minutes of fire exposure in the Control-FP column, which was caused by the spalling of the fireproof as shown in Figure 9b.

On the other hand, the fire insulation remained intact to the CFRP layers during the whole exposure duration (about 130 minutes) in the CFRP-wrapped column as shown in Figure 9c and d. However, assuming that the concrete surface temperature was identical to the CFRP temperature, the fire insulation managed to keep the CFRP temperature under 80 °C (T_g) for 20 minutes (Figure 8d) and the final temperature recorded was 720 °C, which was nine times above the critical temperature (T_g).

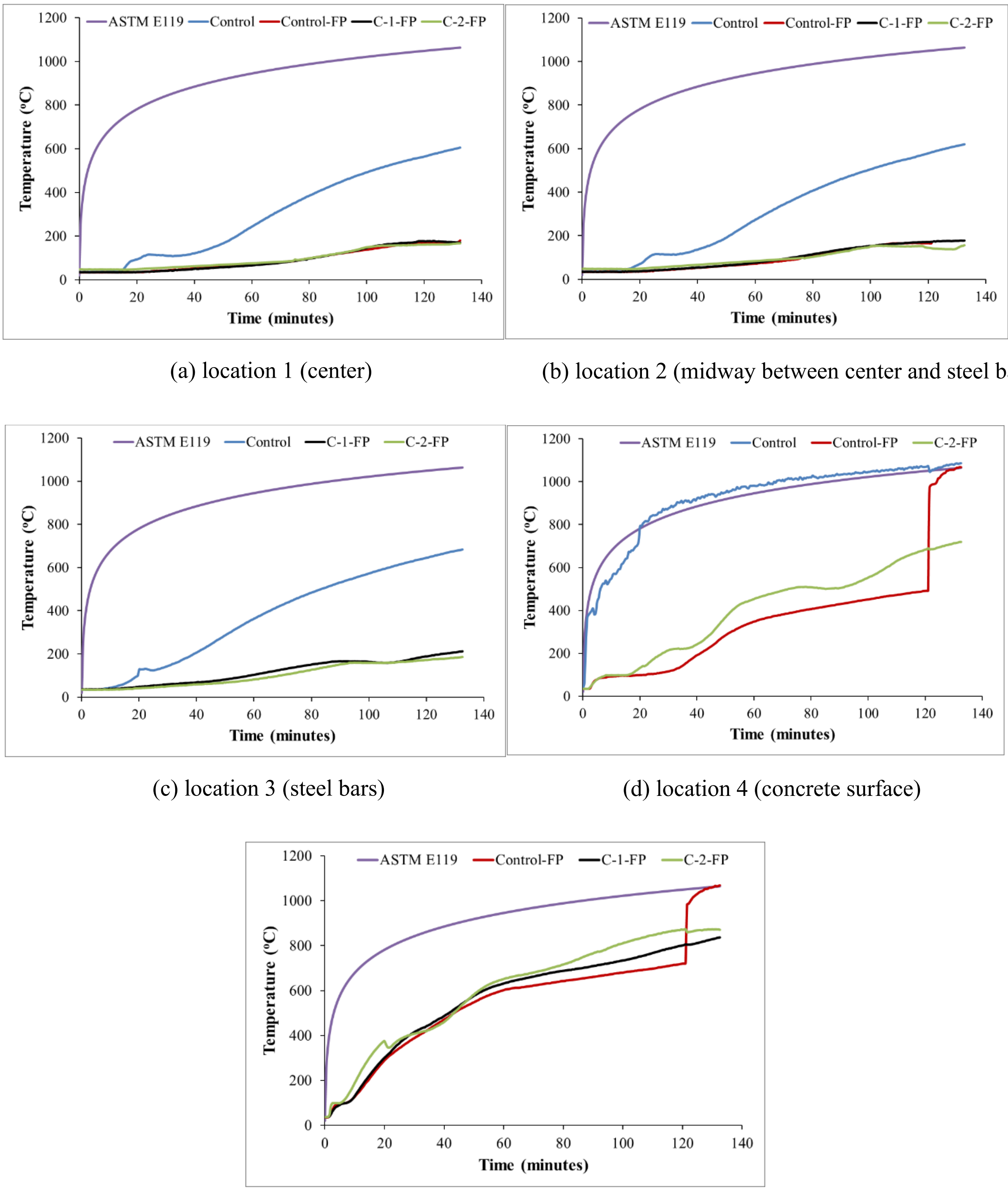

(a) location 1 (center)

(b) location 2 (midway between center and steel bars)

(c) location 3 (steel bars)

(d) location 4 (concrete surface)

(e) location 5 (between the two insulation layers)

Figure 8. Temperature response of all specimens at the five locations

Comparing the condition of the Control and Control-FP columns at the end of the fire exposure (Figure 9a and b), it can be observed that the Control-FP column suffered from more severe spalling. This excessive spalling is expected to occur for columns with relatively high moisture content. It was therefore suggested that the fire insulation trapped the water vapor inside the column, which increased the induced stresses in the concrete pores. When the induced stresses became higher than the tensile strength of the concrete, explosive spalling occurred, which was observed during the test and was confirmed to be a major concern in [10]. The temperature spike in the Control-FP column can also be noticed between the fireproofing layers (Figure 8e), which happened around 2 minutes before the temperature spike at the concrete surface. The CFRP-wrapped columns did not suffer any spalling despite the higher temperature measurements between the insulation layers (16% higher than those of the Control-FP column).

(a) Control

(b) Control-FP

(c) C-1-FP

(d) C-2-FP

Figure 9. Columns' condition before and after the fire test

4 CONCLUSIONS

This paper investigated the fire performance of circular RC columns wrapped with CFRP systems and fire insulation. The following conclusions can be drawn from the test:

- CFRP systems did not contribute to the fire resistance nor the fire insulation of the columns. The temperature measurements at the center, longitudinal reinforcement, and midway between the two were almost identical throughout the exposure period.
- Fireproofing layers significantly contributed to the fire performance of the columns. On average, the temperature measurements at the concrete surface and the center, longitudinal reinforcement, and midway between the two were 45 and 75% less, respectively, for the fireproofed columns compared to the Control column.
- Column Control-FP had significantly lower temperature measurements at the concrete surface compared to the Control specimen for 2 hours. At 120 minutes into the test, explosive spalling

occurred, and the final condition of the column Control-FP was more severe than that of the Control column. No spalling occurred to the fire insulation layers in the fireproofed CFRP columns.

- The fire insulation maintained the temperature of the CFRP layers below the glass transition temperature (T_g) for 20 minutes, and the final temperature at the end of the fire exposure (after 130 minutes) was nine times more than T_g.

REFERENCES

1. R. Correia João, "Mechanical behaviour of pultruded glass fibre reinforced polymer composites at elevated temperature: Experiments and model assessment," Composite Structures, vol. 98, pp. 303-313, 2013.
2. A. Ahmed and V. Kodur, "The experimental behavior of FRP-strengthened RC beams subjected to design fire exposure," Eng. Struct., vol. 33, (7), pp. 2201-2211, 2011. DOI: https://doi.org/10.1016/j.engstruct.2011.03.010.
3. Cao Vui Van, "Experimental behavior of fire-exposed reinforced concrete slabs without and with FRP retrofitting," Journal of Building Engineering, vol. 51, 2022.
4. Abed F, El Refai A, El-Maaddawy T, Tello N, Alhoubi Y. “Strengthening Square and Circular Low-Strength Concrete Columns with Fiber-Reinforced Cementitious Matrix (FRCM): Experimental Investigation.” ASCE Pract Period Struct Des Constr 2022; 27 (2): 04022005. doi: 10.1061/(ASCE)SC.1943-5576.0000676.
5. Alhoubi Y, El Refai A, Abed F, El-Maaddawy T, Tello N, "Strengthening pre-damaged RC square columns with fabric-reinforced cementitious matrix (FRCM): Experimental investigation," Composite Structures, vol. 294, pp. 115784, 2022. DOI: https://doi-org.aus.idm.oclc.org/10.1016/j.compstruct.2022.115784.
6. Tello N, Alhoubi Y, Abed F, El Refai A, El-Maaddawy T. Circular and square columns strengthened with FRCM under concentric load,” Composite Structures, vol. 255, pp. 113000, 2021. DOI: https://doi.org/10.1016/j.compstruct.2020.113000.
7. Y. A. Al-Salloum, T. H. Almusallam, H. M. Elsanadedy, and R. A. Iqbal, “Effect of elevated temperature environments on the residual axial capacity of RC columns strengthened with different techniques,” Constr Build Mater, vol. 115, pp. 345–361, Jul. 2016, doi: 10.1016/j.conbuildmat.2016.04.041.
8. T. Trapko, “The effect of high temperature on the performance of CFRP and FRCM confined concrete elements,” Compos B Eng, vol. 54, no. 1, pp. 138–145, 2013, doi: 10.1016/j.compositesb.2013.05.016.
9. ASTM E119-20 Standard Test Methods for Fire Tests of Building Construction and Materials, (2020), ASTM International, available at: https://doi.org/10.1520/E0119-20, West Conshohocken, PA.
10. L. Bisby, M. Green and V. Kodur, "Response to the fire of concrete structures that incorporate FRP", Progress in Structural Engineering and Materials, vol. 7, no. 3, pp. 136-149, 2005. Available: 10.1002/pse.198.

SiF 2022– The 12th International Conference on Structures in Fire
The Hong Kong Polytechnic University, Nov 30 - Dec 2, 2022

RIGOROUS IMPLEMENTATION OF REAL-TIME HYBRID FIRE SIMULATION APPLYING HIGH HEATING RATES OF THERMAL LOADING

Faranak Faghihi[1], Markus Knobloch[2]

ABSTRACT

Hybrid fire simulation (HFS) has been trending in recent years as a novel method for global performance-based analysis of structures in fire. This method considers the numerical simulation of a global structure while its structural members exposed to fire in fire compartments are tested in experiment. HFS method can capture the beneficial interaction mechanisms developing between fire-exposed structural members and the cooler rest of the structure. Due to rate- and temperature-dependent material behaviour of structures subjected to fire, a real-time performance in hybrid fire simulation counts as a substantial prerequisite. This aspect becomes more challenging in hybrid fire simulations with high applied heating rates in the fire tests. This paper describes a proposed rigorous approach for hybrid fire simulation and presents a thermomechanical benchmark structure for proof-of-concept studies. The results of two representative hybrid fire simulations with high heating rates are investigated. The importance of a proper method for computation of the degrading stiffness of the fire-exposed structural member during HFS procedure is highlighted. The precision of the proposed HFS approach applied in hybrid fire simulations with high heating rates is verified.

Keywords: Hybrid fire simulation; real-time; performance-based design; high heating rate; stiffness-update; structural fire engineering

1 INTRODUCTION

Isolated structural component fire testing cannot represent appropriately the structural fire behaviour of structures subjected to fire since it does not capture the interaction mechanisms between the fire-exposed structural member and the rest of structure. Performance-based design approach is an advancing method that can investigate more accurately the global structural fire behaviour of structures. Hybrid fire simulation as a novel well-suited method of performance-based design approach is a cost-effective addition to full-scale fire tests on entire structures and eliminates the uncertainties existing in purely numerical simulations. This promising method considers the fire-exposed element to be tested in the physical fire test while the surrounding structure is numerically simulated. The numerical model monitors and controls the data of physical element in real-time and updates the mechanical response at the interface of numerical and physical substructures. Various researches have been carried out in recent years to study the HFS methodology. Only few of them have applied physical tests [1-5], while others have presented conceptual virtual frameworks of the method [6, 7]. None of these previous researches have considered an appropriate stiffness-update method in HFS solution procedure for the degrading physical element in fire with respect to real-time thermal-induced phenomena arising during HFS. In addition, several other shortcomings are observed in these studies such as: non-negligible interface errors between the numerical and physical substructures [1, 6], keeping with material elastic range [2] and no consideration of effects of material nonlinearities and

[1] PhD Candidate, Chair of Steel, Lightweight and Composite Structures, Ruhr-Universität Bochum
e-mail: faranak.faghihi@rub.de, ORCID: https://orcid.org/0000-0001-8061-8430
[2] Professor, Chair of Steel, Lightweight and Composite Structures, Ruhr-Universität Bochum
e-mail: markus.knobloch@rub.de, ORCID: https://orcid.org/0000-0002-1289-0691
https://doi.org/10.6084/m9.figshare.22178069

plasticity on HFS response [4], lack of validation of the HFS methodology with full-physical testing [4], and not fulfilling the real-time HFS in nonlinear material behaviour and high heating rates [5].

This paper presents a rigorous methodological approach for hybrid fire simulation. In this study, a benchmark structure consisting of the high strength steel S690QL is introduced and the HFS setup established at Ruhr-Universität Bochum (RUB) is briefly explained. Two representative hybrid fire simulations with high applied heating rates in the fire tests are thoroughly discussed and the computational challenges for real-time performance of hybrid fire simulations with high heating rates are explained. The importance of considering an appropriate stiffness-update method is highlighted. Finally, the precision of the implemented approach is examined for hybrid fire simulations with high heating rates. This study proves the robustness of the proposed real-time HFS method for further applications in structural fire engineering.

2 METHODOLOGY AND FRAMEWORK OF HYBRID FIRE SIMULATION

2.1 Rigorous methodological approach for hybrid fire simulation

In the state-of-the-art studies two conceptually different approaches are available for the methodology of HFS. The first one is centred around the physical fire test and considers the numerical modelling of the surrounding structure as part of the function of physical test's control system during the ongoing fire test. This approach would be confined to laboratory-specific hybrid fire simulations and would not be counted as a generic method for analysis of structures in fire. The second approach considers HFS as an extended numerical simulation that controls and integrates the achieved data of the physical fire test during an ongoing analysis run.

This paper pursues the latter approach that overcomes the shortcomings of the first approach and bears a great potential as a generic tool for more rigorous analysis of structures in fire. An incremental solution procedure is applied in this extended numerical simulation to investigate the thermomechanical response of HFS. Each increment of the ongoing analysis run consists of a thermal stage followed by a mechanical one [5]. In each thermomechanical increment, the mechanical equilibrium at the interface of numerical and physical substructures is controlled in an iterative method with the data obtained from the uninterrupted physical fire test. This incremental solution procedure enables the force and displacement compatibility at the interface of numerical and physical substructures of hybrid fire model.

2.2 Benchmark structure

In this section, a benchmark structure is presented to be analysed further and to validate the HFS approach. This generic thermomechanical benchmark problem is a sufficiently sophisticated yet expediently simple structure representative for structures exposed partially to fire. It is of importance to verify the applied benchmark problem in HFS with full-physical testing's results in order to validate the proposed methodology of hybrid fire simulation in structural fire engineering. In this research, the benchmark structure is adopted from [5], since it fulfils the requirements for the proof-of-concept problem and is validated by full-physical testing in [8].

The benchmark structure consists of a laboratory-scale simply supported beam connected at its mid-span to a truss rod. The fire-exposed element in the fire compartment is the truss element while beam element is kept at ambient temperature. Figure 1 presents the benchmark structure along with the defined loading protocol. The loading protocol includes a mechanical loading followed by a thermal loading. First, an external load $P(t)$, starting from 0 to P_0 in time $t_0 - t_1$, is applied on the mid-span of the beam at ambient temperature θ_0. Thereafter, P_0 is kept constant during the entire analysis while the heating is started from t_1 and the thermal loading $\theta(t)$ is exposed as a determined temperature-time curve to the fire-exposed element in the fire compartment. With respect to initial stiffness-proportionalities between truss and beam element, P_0 is internally distributed to truss F_{truss} and supports of beam element F_{beam}, so that the equilibrium equation $F_{truss} + 2F_{beam} = P_0$ is fulfilled. Start of the fire test and evolution of thermal -induced phenomena such as thermal expansion, stiffness and strength degradation as well as high temperature creep, trigger the load redistribution from truss element to beam supports. By failure of the truss element in fire exposure, beam supports carry completely the external load P_0.

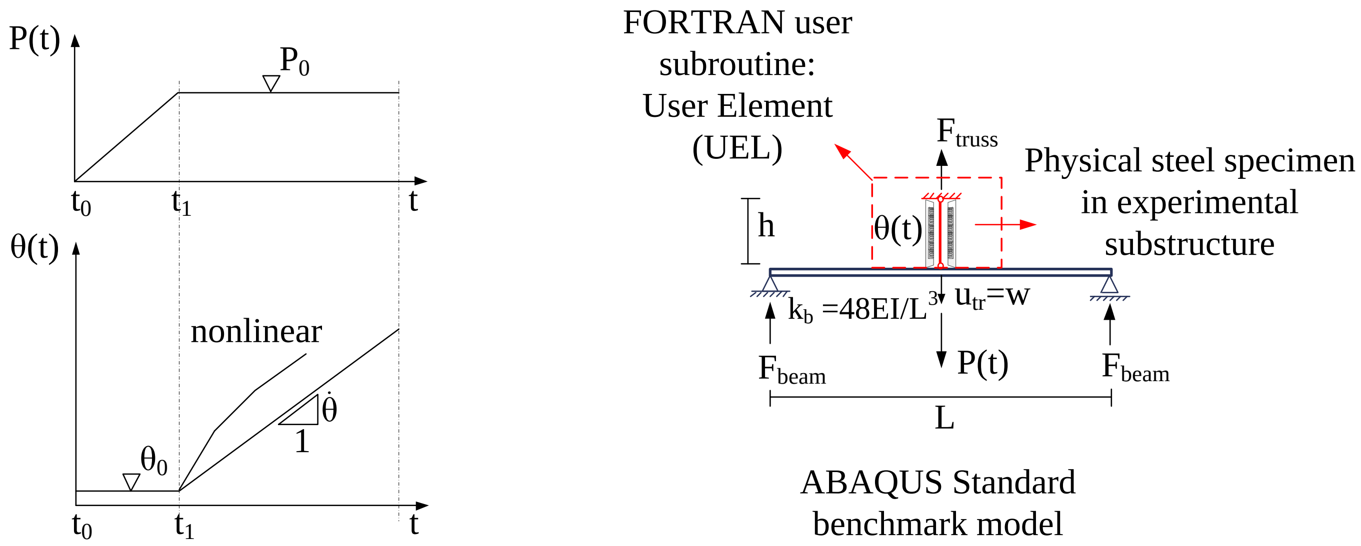

Figure 1. Schematic overview of the thermomechanical benchmark structure (right), Mechanical and thermal loading protocol in current hybrid fire simulation (left)

2.3 Hybrid fire simulation setup

In this research, a computational and experimental setup of hybrid fire simulation is established from ground up at RUB. The numerical simulation is performed in FE-software ABAQUS/Standard with the fire-exposed structural member as a user-defined element written in user subroutine. Beam is modelled with Euler-Bernoulli beam element B23 with length of 600 mm and flexural rigidity of EI = $163.17 \cdot 10^6$ kNmm^2. The interaction and automated communication between numerical simulation and physical element's controlling software is enabled through a middleware software as a server written in python. The physical element in the fire test is a dog-bone shaped specimen with total length of 170 mm, central gauge length L_0 of 45 mm and initial nominal cross section area of A_0 = 54 mm^2 constituted of steel S690QL. Material properties of applied steel is adopted from same batch of S690QL steel plates with thickness of 12 mm [9], derived by means of steady-state tests at different temperatures 20, 400, 550 and 700 °C. The specimen is embedded in a universal testing machine (UTM) and is encompassed in an electric three-zone furnace. A high-temperature resisting extensometer is fixed with its two ceramic rods on the specimen measuring the central deformation at the gauge length of specimen. Therefore, the physical element's displacement refers to measured deformation by extensometer u_{exp}, which equals to truss displacement u_{tr} and mid-span deflection of the beam w at the interface of numerical and physical substructures.

3 EFFECT OF THE HEATING RATE ON THE RESPONSE OF HYBRID FIRE SIMULATION

In this research the effect of high heating rates applied in thermal loading of HFS is studied as a remarkable parameter which investigates the eligibility of proposed HFS method for a real-time hybrid fire simulation. Due to the fact that the physical fire test in HFS would not be halted once initiated and with respect to the existing thermal inertia, it is of great importance to maintain the synchronization of the ongoing numerical simulation with the continuous fire test in order to fulfil a real-time well-synchronized HFS. This challenge becomes more critical when using higher heating rates to keep up with the pace of fire experiment.

In this paper two accomplished hybrid fire simulations are presented as two representative examples of proof-of-concept studies, shown in Table 1, and their results are discussed and analysed. In both of the simulations the initial load-shares between fire-exposed truss and adjacent beam are 90 and 10%, respectively. The hybrid fire procedure is controlled with respect to physical element's temperature which is beneficial to scrutinize more precisely thermal-induced phenomena affecting the thermomechanical response of analyses. The initial load ratio $\mu = F_{t,amb}/F_{y,0.2\%}$ as the ratio of fire-exposed truss element's force to the yielding force of truss at ambient temperature is 40% for both of simulations. As shown in Table 1, the target temperature θ_{targ} is 700 °C for both simulations. The influencing variable in these two HFSs is the applied heating rate. HFS 1 proceeds with the heating rate of 50 °C/min applied to the specimen in the fire test. This heating rate was the highest applicable heating rate with respect to inherent limitations of furnace in fire test. For HFS 2, a nonlinear step-wise target temperature curve is applied to specimen: First, a linear target temperature curve from ambient up to 500 °C with the heating rate of 50 °C/min; second, the linear target temperature curve with the heating rate of 25 °C/min from 500 up to 600 °C; and finally, the linear target temperature curve with the heating rate of 15 °C/min up to the target temperature of 700 °C. It aims to imitate the ISO standard fire test with respect to inherent performance limitations of the furnace in the physical setup.

Table 1. Overview of two presented HFSs

No [-]	P_0 [kN]	μ [%]	θ_{targ} [°C]	Heating rate [°C/min]
HFS 1	18	40	700	50
HFS 2	18	40	700	nonlinear

3.1 Thermal-induced phenomena affecting the thermomechanical response of hybrid fire simulation

By start of the fire test in HFS, the load in the fire-exposed physical element starts degrading and is redistributed to the adjacent substructure. It arises from various thermal-induced phenomena affecting thermomechanical response of HFS. At earlier temperatures, the load in physical element degrades due to restrained thermal expansion. Later, the degradation is additionally caused by reduction of Young's modulus. In case of plastic loading at some temperature points (due to reduction of yielding strength with temperature evolution), the strength degradation occurs as well. High temperature creep also results in additional plastic deformations which yield to degradation of the load in truss element and load redistribution to beam element. With respect to temperature and load ratio, each of these thermal-induced effects contribute individually or simultaneously to thermomechanical response of the structure. Different stages can be assigned during HFS to the response of physical element and consequent load redistribution in the benchmark structure. Figure 2 present the stress as well as tangent stiffness of fire-exposed specimen over specimen temperature for HFS 1 and 2. In addition, the temperature-dependent yielding strength is also shown in Figure 2a. The consisting stages with regard to temperature- and time-dependent material and physical properties are distinguished with circular marks in Figure 2 for HFS 1 and 2.

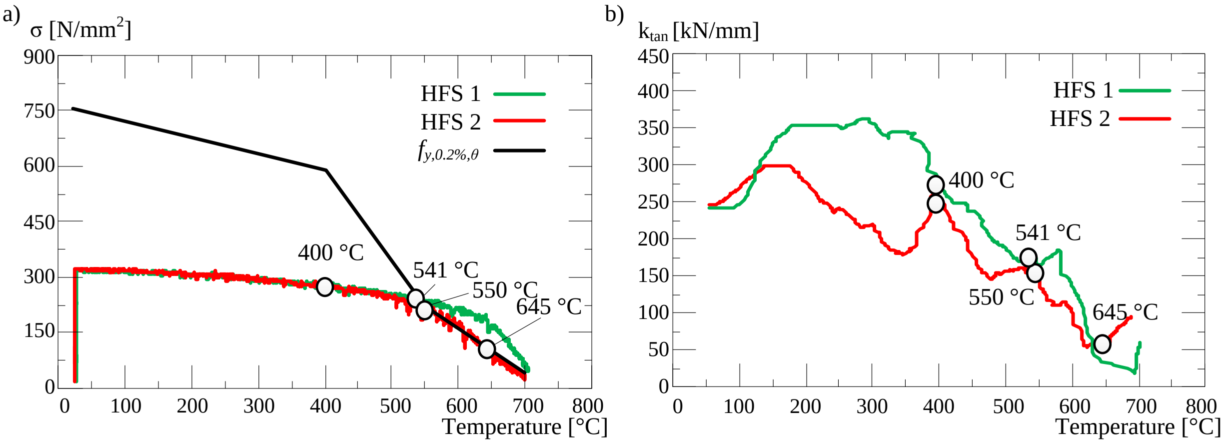

Figure 2. a) Stress-temperature of physical element; b) Tangent stiffness of physical element over temperature

In the first stage up to 400 °C, the stress decrease in physical element is predominantly due to restrained thermal expansion which is verified by the approx. constant tangent stiffness of the specimen at this range (shown in Figure 2b). The tangent stiffness is measured by the method of moving average of a centred data sample consisting of 21 data points. The fluctuations in the stiffness at this stage can be related to the existing oscillations of the force measured in the machine at initial temperatures as well as the method of calculation and modification of the tangent stiffness in the applied approach. The difference of tangent stiffness at initial temperatures (with same heating rate) for HFS 1 and 2 can be explained by dissimilar oscillations of force measured in each HFS (resulting in dissimilar average of measurement points).

Second stage is mainly regarding the temperature-dependent stiffness degradation of the physical element in addition to thermal expansion, marked up to 541 °C and 550 °C for HFS 1 and 2, respectively. These two temperature points refer to transition points where the stress curves hit for the first time the temperature-dependent 0.2% yielding strength curve $f_{y,0.2\%,\theta}$. Gradual reduction of the stiffness at Figure 2b also confirms the degradation of temperature-dependent Young's modulus in this stage.

Third stage starts by onset of plasticity in the physical element and in addition to aforementioned effects, the strength degradation also contributes in the stress decrease of fire-exposed element. The steep decrease of tangent stiffness in this stage for HFS 1 and 2 refer to strength degradation of the element. In HFS 1, stage 3 starts from 541 °C until the end of HFS procedure. Hence, stresses remain in the plastic range for the rest of analysis. Only at the end, the tangent stiffness reduced to approx. zero value starts stabilizing. In HFS 2, stage 3 starts from 550 °C up to 645 °C from which the stresses go below the temperature-dependent 0.2% yielding strength $f_{y,0.2\%,\theta}$. Stage 4 is from 645 °C up to the end of hybrid fire simulation where the stresses are again in elastic range and the stiffness stabilizes gradually.

In addition, the rate-dependent material behaviour and the probable evolution of creep deformations play an important role in the thermomechanical response of the hybrid fire model. In addition to the mentioned temperature-dependent material and physical properties, high temperature creep affects the thermomechanical response of the physical truss element in the HFS procedure as well. Figure 3 shows the first derivative of thermal elongation with respect to specimen's temperature for HFS 1 and 2. In addition, the derivative of free thermal expansions from material tests on S690QL derived from [9] are shown in Figure 3. $du/d\theta$ is approx. constant for free thermal expansions. This is conformed also with HFS 1, which no creep is expected with the fast heating with rate 50 °C/min. In HFS 2, $du/d\theta$ starts to deviate from the constant value at a temperature point before initiation of plasticity (550 °C) in the element. The probable creep evolution is observed in 460 °C, which is the temperature point of the change of heating rate exposed to the physical element (transition temperature point from 50 °C/min to 25 °C/min). The conversion of the heating rate from faster to slower ones in this hybrid fire simulation justifies the rise of creep deformations.

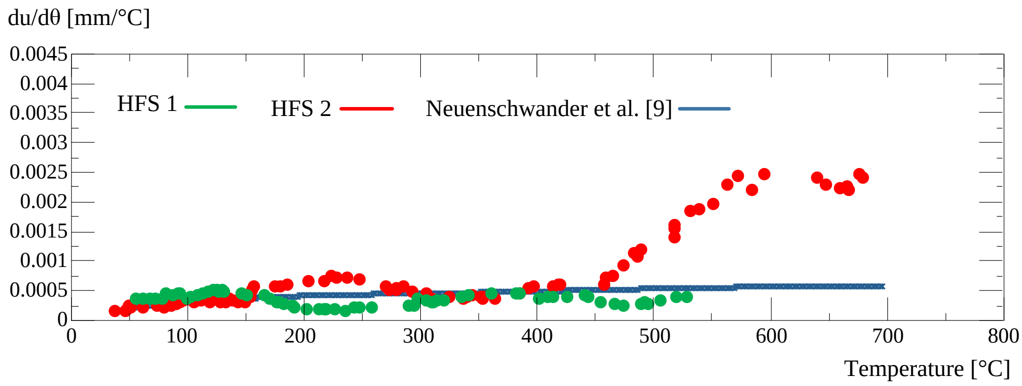

Figure 3. Thermal derivative of thermal elongation with respect to temperature

3.2 Computational challenges of real-time hybrid fire simulation with high heating rates

The main challenge of hybrid fire simulation is the continuous temperature evolution without any hold, like in real fires and fire tests. Therefore, owing to the existing thermal inertia, the temperature may still increase in the mechanical stage of a numerical increment and may exceed the incremental target temperature of that increment. Following this, the iterative numerical solution procedure at the mechanical stage of each increment, explained in [10], has to be fast enough to keep the synchronization between the incremental temperature evolution of numerical simulation and the ongoing fire test. The real-time performance and the well-synchronization of the HFS procedure is more challenging for hybrid fire simulations with higher heating rates, e.g. HFS 1 with 50 °C/min. Figure 4a shows the force-displacement graph of the physical element in HFS 1 in addition to the converged points at the end of each simulation increment. As shown in Figure 4a, one increment is more critical to be converged and the convergence points (red data points) of the preceding and current increment are more distant in comparison to the rest of increments. This increment is scrutinized in Figure 4b.

In case of high plastic loadings or incompatibilities in temperatures of simulation and physical test, higher number of iterations may be required in one increment. Performing more equilibrium iterations in the increment and the continuous temperature increase in the furnace may lag even more the numerical model's assigned temperature from the fire test. In this case, the physical element's temperature in one increment may have already exceeded the incremental target temperature of the next increment. Therefore, the thermal stage of the next increment would be skipped resulting in no or small thermal expansion in that increment. This results in a mismatch between the displacement of the numerical model and the physical element's displacement in the subsequent mechanical stage of that increment. So, an iteration needs to be performed for rectifying this mismatch.

In the proposed approach in this paper, by target displacement corrections (due to mismatch at the interface) that are smaller than the precision limit of the measuring device in the physical setup (1 µm), sending the target displacement to the machine cannot give back a correct restoring force and only causes oscillations in the machine. So, a predictor solver method in numerical model is required. This predictor solves the corresponding force of current iteration purely numerical in the model by using the tangent stiffness of the previous iteration. The mismatch corrections in increments with skipped thermal stages are usually smaller than control precision limit of the physical test. Therefore, they are solved with numerical predictor mechanism. The increments solved purely numerical by hybrid model are generally faster than the increments with normal thermal stage. This mechanism helps the hybrid fire simulation to resynchronize again and to be compatible in time and temperature. Therefore, the latter increments after increments with skipped thermal stage have usually again a normal thermal stage with thermal expansion and are synchronized with the heating state of the fire test. The critical increment (counter i) in Figure 4b has 11 iterations (counter j). The consecutive increments are, however, the faster increments with skipped thermal stage, which compensate the lagged time and temperature and facilitate the simulation to proceed with convergence till the end.

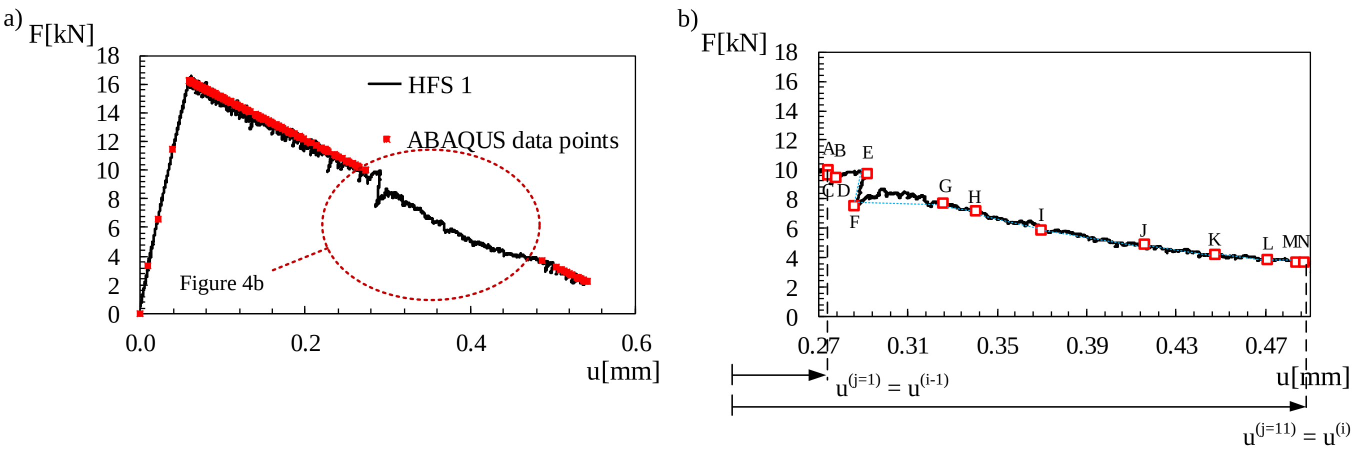

Figure 4. a) Force-displacement of specimen in addition to data points in ABAQUS at each converged increment; b) Analysed increment of HFS 1 including maximum number of iterations

3.3 Update of stiffness in hybrid fire simulations with high heating rates

In addition to the predictor solver, explained in previous section, in the proposed approach of hybrid fire simulation which compensates the desynchronizations over the procedure, computational parameters also have to be improved to solve the real-time challenge of hybrid fire simulations with high heating rates. According to [10], the update of the tangent stiffness is necessitated for the hybrid fire simulations which confront plastic loadings. The actual stiffness k_{act} in each iteration (with counter j) is updated as:

$$k_{act}^{(j)} = \frac{F^{(j)} - F^{(j-1)}}{u^{(j)} - u^{(j-1)}} \quad (1)$$

In calculations of the stiffness-update, an additional condition can be considered in each iteration to avoid the influence of the inevitable oscillations of the machine on deviations occurring in the stiffness-update. Therefore, a 10% threshold is defined to limit higher deviations by update of the tangent stiffness k_{tan}. Hence, if the calculated actual stiffness in current iteration $k_{act}^{(j)}$ deviates more than ±10% from tangent stiffness of the previous iteration $k_{tan}^{(j-1)}$, the updated tangent stiffness of current iteration equals to $k_{tan}^{(j)} = (1 \pm 0.1) \cdot k_{tan}^{(j-1)}$.

For hybrid fire simulations with higher heating rates, e.g. HFS 1, an additional computational condition is also applied in the proposed approach leading the HFS procedure to reach convergence. Due to the contribution of strength degradation in the thermomechanical response of the specimen by initiation of plasticity and the steep decrease of tangent stiffness in this stage (Figure 2b), the stiffness drives in some increments to negative values, which cause divergence and consequent abortion of the simulation. Since the slope of stress-strain curve becomes almost constant reaching to zero by hitting the yielding strength point, negative values of tangent stiffness in the case of plasticity can be substituted with the zero value. This additional condition is applied in the iterative numerical solution procedure of HFS 1. Therefore, for all iterations in the material plastic behaviour which have a negative tangent stiffness as $\partial F/\partial u$, the tangent stiffness is modified to zero. Figure 5 shows the specimen's calculated actual stiffness k_{act} as $\partial F/\partial u$ (black line) as well as the modified tangent stiffness applied in each iteration k_{tan} for HFS 1.

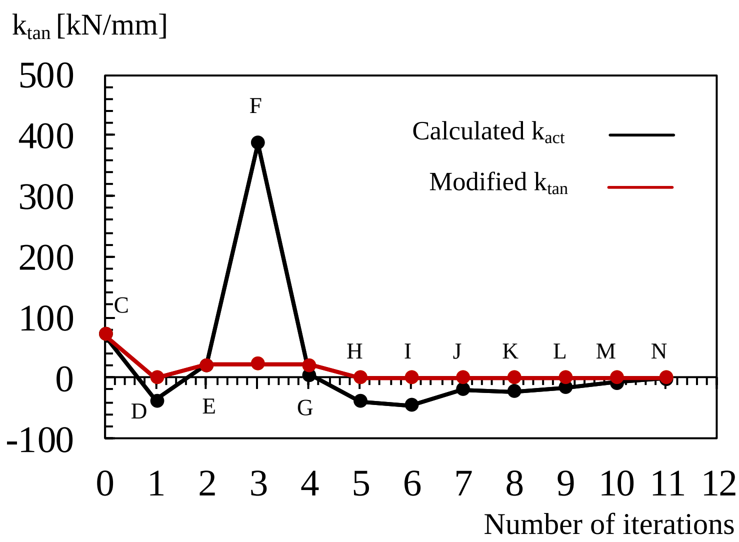

Figure 5. Calculated and implemented tangent stiffness of the specimen in the iterative numerical procedure of HFS 1

4 PRECISION OF PROPOSED APPROACH OF HYBRID FIRE SIMULATION

4.1 Interface error

In this section, the precision of the implemented approach of hybrid fire simulation is investigated. The proposed approach for hybrid fire simulation can be taken as inerrant if at the end of each converged increment of the HFS procedure, the compatibility of displacements and forces at the interface of numerical and physical substructures are completely fulfilled. However, since the last iteration of almost each increment is solely solved with predictor solver of numerical model and due to the fact of limited control precision of the physical setup, an inevitable error exists at the interface. This error is quantified as the mismatch in the displacement $\delta u_{abs} = u - u_{exp}$ and the force $\delta F_{abs} = F - F_{exp}$ at the interface. Figure 6 shows the absolute displacement error, δu_{abs}, the absolute force error, δF_{abs}, and the relative force error δF_{rel} over specimen displacement (measured with extensometer) u_{exp} at the end of each increment of HFS 1 as the representative simulation with highest heating rate.

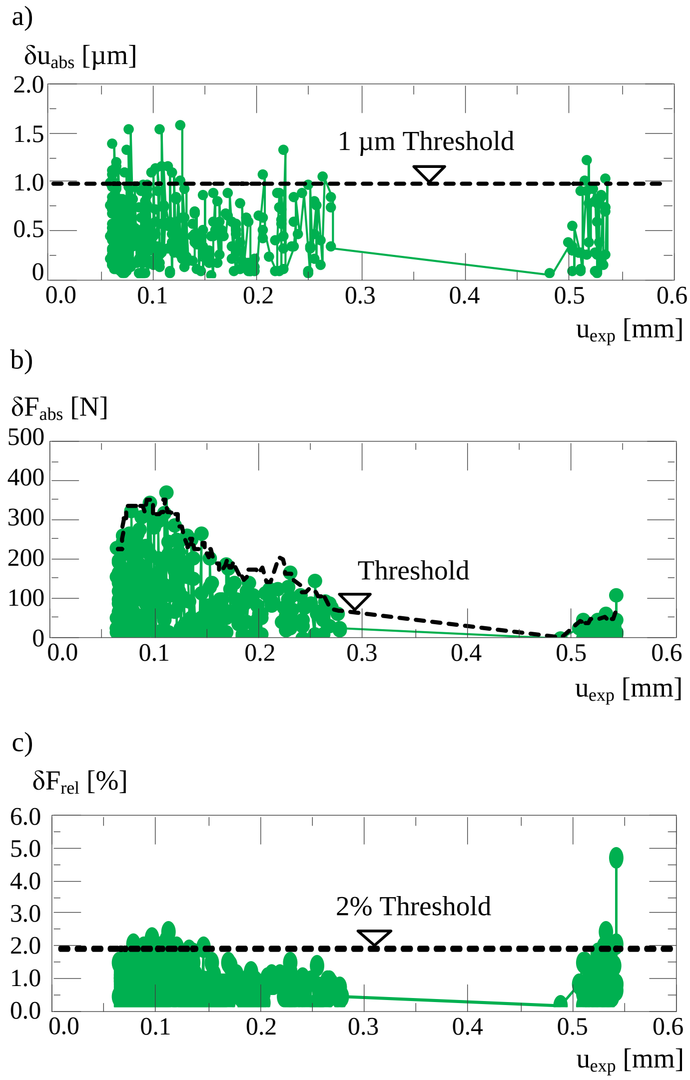

Figure 6. a) Absolute displacement error of HFS 1; b) Absolute force error of HFS 1; c) Relative force error of HFS 1

As mentioned, the predictor solver is applied in the last iteration of almost each increment of the hybrid fire simulation. This originates from the fact that the displacement correction for the last iteration of each increment is usually very small, because the solution of the last iteration and the prior one are very close. If the displacement correction at the two consecutive iterations is smaller than the limit precision of the measuring device in the laboratory (1µm), the machine cannot give back the correct corresponding force to the numerical model. Therefore, a threshold of 1µm is specified to check the displacement correction in each iteration. In last iterations which mostly displacement correction is smaller than this threshold, the numerical simulation applies the predictor solver. The predictor solver computes the resulting nodal force with respect to displacement correction and the tangent stiffness of the previous iteration. It is observed in Figure 6a that the error at the interface in last iteration of each increment lies below this threshold as well.

Exception is also in some increments that mainly have only 1 iteration in which their thermal stage is skipped and the only iteration is performed with the predictor solver. In these cases, the mismatch at the interface has reached to maximum 1.6 µm for HFS 1. It is to note that in the increments in which the last iteration is also interacted with the physical test, the displacement error at the interface is less than 0.1 µm which complies with a very sound accuracy.

In addition, the absolute force error is also in sound precision with respect to the determined threshold, shown in Figure 6b. This force threshold is defined with respect to the displacement threshold of 1 µm multiplied by the tangent stiffness of the corresponding iteration at the end of each increment. The relative force error $\delta F_{rel} = \delta F_{abs} / F_{exp}$ is also chosen to investigate the force compatibility at the interface of the substructures. Figure 6c shows the relative force error. Relative force error in HFS 1 is mainly under 2% fulfilling the sufficient precision. Only at the end of the hybrid fire simulation which F_{exp} is reduced, the relative force error has surpassed the observed threshold. That can be seen in some initial increments as well. It is explained in such increments with regard to the skipped thermal expansion in the increments or not appropriately calculated one due to fluctuations in the measured data of the machine. Hence, with no correct thermal stage, the oscillations in the force values of F_{exp} may also yield to invalid calculated relative force errors.

4.2 Real-time degree

In addition to the interface error as one factor for measurement of the precision of the hybrid fire simulation, several other factors are investigated in this research to study the robustness and accuracy of the implemented approach of hybrid fire simulation. These factors can quantify the synchronization of the HFS procedure and approve the real-time enforcement. The difference between specimen temperature and the determined target temperature in numerical simulation, and the physical time duration over increments as well as its mean value are the parameters which assess the compatibility of time and temperature between numerical and physical substructures. Figure 7 presents the regarding results of HFS 1 and 2. In addition, the results of the most challenging hybrid fire simulation performed with Schulthess et al. [5] including high load ratio and plasticity are also displayed.

Figure 7a confirms the temperature compatibility with showing the difference of specimen temperature and nominal simulation temperature over increments of the hybrid fire simulations. In HFS 1, only in the delayed increment (explained in Figure 4b), the difference of temperatures becomes 74 °C, but it reduces again in next increments. In [5] which have always used initial stiffness of the physical element in their research, this value goes up to approx. 90 °C. It proves that the method of hybrid fire simulation with update of the tangent stiffness as well as the consideration of required modifications for calculation of stiffness is a strong tool and can significantly lead to well-synchronized results. Figure 7b and c present physical time duration, Δt_{real}, in each increment (For HFS 1 and 2, respectively), and their corresponding mean value. It is shown that the mean value of physical time complies with the expected value with respect to the predefined/performed heating rate in HFS 1 and HFS 2. This factor quantifies the real-time degree of the implemented approach for the hybrid fire simulation with a sound accuracy.

5 CONCLUSIONS

Hybrid fire simulation has been an appealing method in recent years. It is a promising tool for global performance-based design in structural fire engineering. Among recent researches in the literature, only few of them have implemented hybrid fire simulations applying physical fire tests. Even these few researches have not succeeded to investigate in real-time all thermal-induced effects arising in the temperature range and heating rates relevant to structural fire engineering. This paper presents a rigorous methodological approach for hybrid fire simulation capable to consider computational and experimental challenges coming from temperature-dependent material behaviour. This research studies, for the first time, the application of high heating rate of 50 °C/min and its challenges in hybrid fire simulations. Two proof-of-concept analyses are investigated in this paper and the effects of various temperature- and time-dependent physical and material properties on thermomechanical response of benchmark problems are discussed. Update of the tangent stiffness with the proposed method and consideration of required modifications for calculation of physical element's stiffness degrading in fire allows to capture thermal-induced effects and enables a precise real-time HFS. Finally, the precision and robustness of the proposed approach for hybrid fire simulation is examined with respect to the errors at the interface of substructures as well as the synchronization and real-time degree of the procedure. The results prove a sound accuracy of the applied approach. As the next step, this powerful method is meant to conduct full-scale hybrid fire simulations on large structural systems.

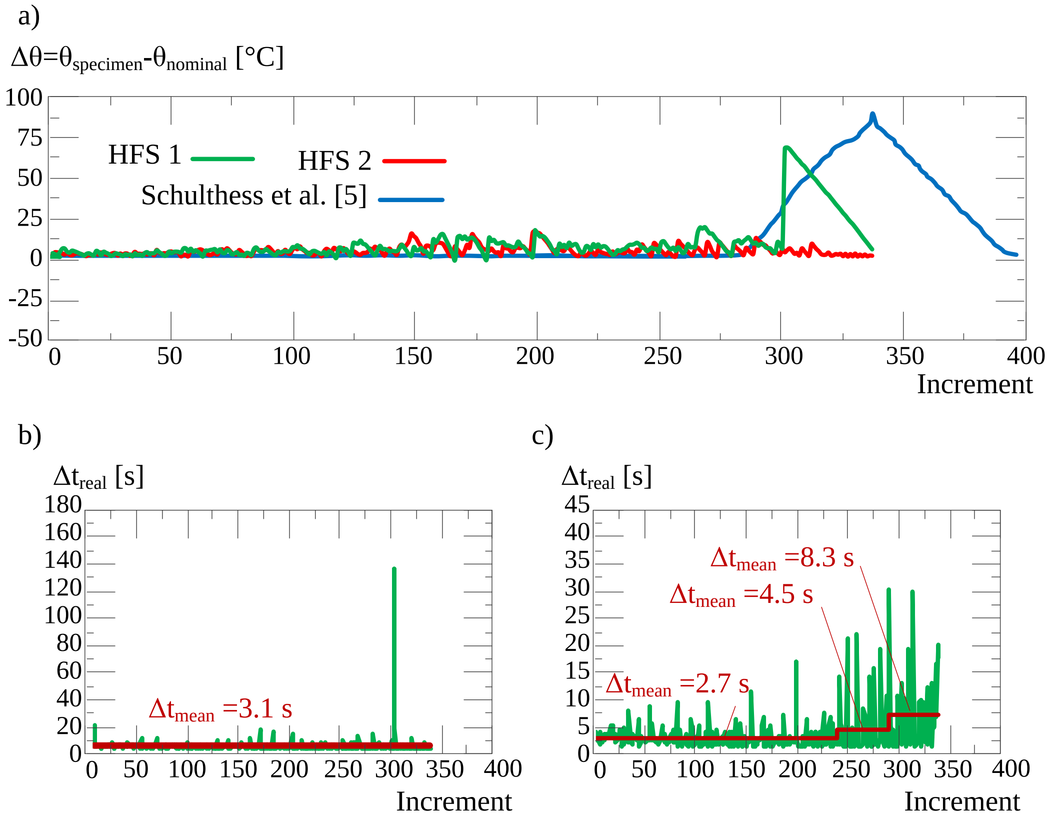

Figure 7. a) Difference of specimen's temperature and nominal target temperature of simulation; b) Physical time in each increment and its mean value for HFS 1; d) Physical time in each increment and its mean value for HFS 2

ACKNOWLEDGMENT

The first author acknowledges the guidance provided by Dr. Martin Neuenschwander, University of California at Berkeley. The authors acknowledge the support provided by the staff in the structural testing laboratory (KIBKON) at Ruhr-Universität Bochum.

REFERENCES

1 Mostafaei, H., Hybrid fire testing for assessing performance of structures in fire—Application. Fire Safety Journal 56, 30–38 (2013). doi: 10.1016/j.firesaf.2012.12.003.

2 Whyte, C. A., Mackie, K. R., Stojadinovic, B., Hybrid Simulation of Thermomechanical Structural Response. Journal of Structural Engineering 142 (2016). doi: 10.1061/(ASCE)ST.1943-541X.0001346.

3 Wang, X., Kim, R. E., Kwon, O.-S., Yeo, I., Hybrid Simulation Method for a Structure Subjected to Fire and Its Application to a Steel Frame. Journal of Structural Engineering 144, 04018118-1 - 04018118-11 (2018). doi: 10.1061/(ASCE)ST.1943-541X.0002113.

4 Mergny, E., Franssen, J.-M., Real-time multi degrees of freedom hybrid fire testing using Pi control. Conference Proceedings of the 11th International Conference on Structures in Fire, 77-88 (2020). The University of Queensland, Australia.

5 Schulthess, P., Neuenschwander, M., Mosalam, K. M., Knobloch, M., A computationally rigorous approach to hybrid fire testing. Computers & Structures 238, 106301–106320 (2020). doi: 10.1016/j.compstruc.2020.106301.
6 Sauca, A., Gernay, T., Robert, F., Tondini, N. and Franssen, J.-M., Hybrid fire testing: Discussion on stability and implementation of a new method in a virtual environment. Journal of Structural Fire Engineering 9, 319–341 (2018), doi: 10.1108/JSFE-01-2017-0017.
7 Qureshi, R., Elhami-Khorasani, N., Gernay, T., Adaption of active boundary conditions in structural fire testing. Journal of Structural Fire Engineering 10, 504–528 (2019). doi: 10.1108/JSFE-12-2018-0042.
8 Neuenschwander, M., Schulthess, P., Mosalam, K. M., Knobloch, M., Validating Hybrid Fire Testing with Full-Physical Twin Experiments. Proceedings of the Royal Society A 478 (2022). doi: 10.1098/rspa.2022.0180.
9 Neuenschwander, M., Scandella, C., Knobloch, M. and Fontana, M., Modeling elevated-temperature mechanical behavior of high and ultra-high strength steels in structural fire design. Materials & Design 136, 81–102 (2017). doi: 10.1016/j.matdes.2017.09.041.
10 Faghihi, F., Knobloch, M., GLOBAL STRUCTURAL FIRE ANALYSIS OF STEEL STRUCTURES IMPLEMENTING HYBRID FIRE SIMULATION. 8th Symposium Structural Fire Engineering, 199-218 (2022). TU Braunschweig, Germany.

FIRE RESILIENCE OF STEEL-CONCRETE COMPOSITE FLOOR SYSTEMS

Selvarajah Ramesh[1], Lisa Choe[2], Matthew Hoehler[3], Matthew Bundy[4]

ABSTRACT

This paper presents the results of compartment fire experiments conducted on 9.1 m × 6.1 m steel-concrete composite floors in a full-scale, two-story, two-bays by three-bays steel gravity frame building to investigate the fire resilience of these widely used floor systems. A total of three composite floor specimens with varying slab reinforcement and fire protection schemes for the secondary beam were tested. The first experiment (Test #1) was designed to achieve a 2-hour fire resistance rating per current U.S. practice and create baseline data for the behaviour of the building. Test #2 and Test #3 were conducted to study the effect of enhanced slab reinforcement with larger area and ductility as well as unprotected secondary beams on the fire resilience of the composite floor systems. The 9.1 m × 6.1 m test floors were exposed to a compartment fire using natural gas fuelled burners while subjected to hydraulically applied gravity loads. The compartment test fire created upper-layer gas temperatures like those in standard fire resistance tests. The Test #1 specimen with steel wire reinforcement of 60 mm^2/m width exhibited mid-panel slab integrity failure at 70 mins of fire exposure. Test #2 and Test #3 showed that the use of deformed steel bars (230 mm^2/m) for the slab reinforcement maintained the structural integrity of the tested slab for more than two hours even with an unprotected secondary beam.

Keywords: Composite floor; compartment fire; steel frame building; large-scale fire experiment

1 INTRODUCTION

Fire safety design of composite floors in the United States (U.S.) is primarily based on prescriptive fire-resistance requirements determined using a standard fire testing method [1]. Standard fire testing of individual building elements does not evaluate the system-level fire resistance of full-scale composite floor assemblies with the realistic restraints from the surrounding structural assemblies. There is a lack of experimental data quantifying the fire performance of full-scale composite steel frames designed in accordance with U.S. building codes and specifications.

Over the last few decades, significant experimental research has been conducted in Europe to evaluate the fire resistance of full-scale composite floor systems [2-5]. In those studies, the fire performance of composite floor systems was found to be superior compared to the standard testing criteria used to determine fire resistance rating of composite beams. These tests showed that the fire performance of composite floors was influenced by the development of tensile membrane action of the reinforced concrete

[1] Guest Researcher, National Institute of Standards and Technology, (corresponding author)
e-mail: selvarajah.ramesh@nist.gov, ORCID: https://orcid.org/0000-0002-9525-6767
[2] Guest Researcher, National Institute of Standards and Technology
e-mail: lisa.choe@nist.gov, ORCID: https://orcid.org/0000-0003-1951-2746
[3] Research Structural Engineer, National Institute of Standards and Technology
e-mail: matthew.hoehler@nist.gov, ORCID: https://orcid.org/0000-0002-6049-7560
[4] Supervisory Mechanical Engineer, National Institute of Standards and Technology
e-mail: matthew.bundy@nist.gov, ORCID: https://orcid.org/0000-0002-1138-0307
https://doi.org/10.6084/m9.figshare.22178072

floor slab at large vertical displacements. The steel reinforcement ratio (equal to the area of steel reinforcement divided by the area of topping concrete) used in the floor specimens was 0.2 % to 0.3 %, which was found to be sufficient to meet the prescriptive fire resistance rating without fireproofing insulation of the secondary beams. In the U.S., a minimum shrinkage steel reinforcement ratio of 0.075 % is permitted for composite floor construction [6] and for the purpose of standard fire testing [7]. This reinforcement ratio is considerably lower than the steel reinforcement used in the European practice [8] as well as in the European experiments detailed above [2-5]. It is noteworthy that the fire resistance design in the U.S. does not consider the slab reinforcement as a factor to determine fire resistance.

Recently, the National Institute of Standards and Technology (NIST) conducted large-scale fire experiments using a two-story steel gravity frame designed and constructed following the U.S. practice. The fire experiments were designed to evaluate the system-level fire resistance, structural performance, and failure modes of the full-scale composite floor assemblies with the most realistic restraints from the surrounding structural assemblies. This test program included three experiments. The first experiment (Test #1) [9, 11] provided baseline data for the fire resistance and behaviour of the full-scale composite floor system designed to achieve a 2-hour fire resistance rating according to U.S. practice. The second experiment (Test #2) [12] was conducted to study fire resilience of the composite floor system with the enhanced slab reinforcement detailed to allow tensile membrane action to develop [10]. The third experiment (Test #3) was conducted to evaluate the effect of the secondary beam without fire protection when combined with the enhanced slab reinforcement. In the tests, all other conditions remained similar, including the specimen geometry, beam-end connections, test fire curves, and imposed gravity loads. Primary focus of this paper is to present comparisons of the test results from Test #1 and Test #3, evaluating the improved fire resilience of the composite floor with the enhanced slab reinforcement without fire protection on the secondary beam.

2 TEST PROGRAM

2.1 Test structure

Figure 1a shows the two-story steel gravity frame, two by three bays in plan, used for the fire tests. Composite floors were constructed on the first floor, whereas the second floor steel framing was erected to mimic continuous steel columns. The same wide-flange steel shapes were used for both first and second story steel framing as shown in Figure 1a. The baseplates of the columns were anchored to the laboratory strong floor with post-tensioned high-strength steel bars. Refer to the American Institute of Steel Construction (AISC) Steel Construction Manual [13] for the dimensions of the W-shapes. The test floor (687 cm × 1008 cm in plan) was situated in the south middle bay of the test building, with the footprint slightly greater than the column grid (610 cm × 914 cm). The fire test bay included 9.1 m long beams with W16×31 shapes and 6.1 m long girders with W18×35 shapes as shown in Figure 1a. The selection of these steel beams was governed by floor vibration criteria [14], which required larger sizes of steel beams compared to the beams designed only for flexural strength at ambient temperature.

The test floor assembly consisted of lightweight aggregate concrete cast on trapezoidal profiled steel decking (Figure 1b). The 7.6 cm deep deck flutes were oriented perpendicular to the 9.1 m long beams. The concrete topping placed over the top rib of the steel deck was 8.3 cm thick to comply with the 2-hour fire resistance rating. The floor slab was partially-composite with the steel beams via 19 mm diameter steel headed stud anchors. The resulting composite action was approximately 65 % of the yield strength of the steel beams. The test bay beams were supported by shear tab connections. Shear tabs (220 mm × 150 mm × 9.5 mm) with three 19 mm diameter structural bolts were used at the ends of the W16×31 beams. Extended shear tabs (370 mm × 250 mm × 9.5 mm), welded to the column webs and bolted to the girder webs using five 19 mm diameter bolts were used at the ends of the W18×35 girders.

For floor slabs, polypropylene microfibers (2.37 kg/m^3) were used in the concrete mixture to reduce thermally induced spalling. Concrete cylinders were cast concurrently with the placement of the concrete floor slab and cured under the same conditions as of the slab. The compressive strengths measured from the concrete cylinders shortly after the day of the fire testing were 67 MPa, 78 MPa, and 68 MPa in Test #1, Test #2, and Test #3, respectively. Purpose-built slab splices (along the blue lines in Figure 1a) were designed to reuse the same surrounding floors throughout the test program, and therefore only the fire-exposed floor assembly was reconstructed for each test. Details of the structural design and construction are provided in Choe et al. [9, 12].

The Test #1 concrete slab was reinforced with steel wire reinforcement of 60 mm^2/m width (6×6 W1.4×W1.4 mesh mat with 3.4 mm diameter plain steel wires spaced 152 mm in both orthogonal directions) as the minimum shrinkage reinforcement permitted in the U.S. (Figure 1b). Both Test #2 and Test #3 specimens were reinforced with No.3 deformed steel bars of 230 mm^2/m of slab width (9.5 mm diameter hot rolled bars spaced 305 mm in both orthogonal directions) determined by the Slab Panel Method [15] incorporating tensile membrane action [10]. In Test #2, mechanical couplers were used to splice the No.3 reinforcing bars to simulate continuous bars across the test bay. In Test #3, American Concrete Institute (ACI) [16] specified details were used to splice the No.3 reinforcing bars. The clear cover to the longitudinal and transverse wires from the top surface of the concrete were 41 mm and 38 mm in Test #1, respectively. They were 48 mm and 38 mm in both Test #2 and Test #3, respectively. The measured 0.2 % offset yield strength, the ultimate tensile strength, and percent elongation after fracture (measured as the ratio of the final elongation after testing to the initial gauge length) of the welded wire reinforcement were 760 MPa, 790 MPa, and 15 %, respectively. The values for the No.3 deformed bars were 480 MPa, 770 MPa, and 22 %, respectively. All the fire exposed beams in Test #1 and Test #2 were protected with sprayed fire resistive materials (SFRM) to meet the 2-hour restrained rating requirements in accordance with the Underwriters Laboratories (UL) directories [7]. A cementitious gypsum-based material with a density ranging from 240 kg/m^3 to 350 kg/m^3 was used for the SFRM. The measured thickness of the SFRM on the secondary beam was 13 mm ± 13 % in Test #1 and 14 mm ± 7 % in Test #2. The connections were over-sprayed with an SFRM thickness of at least 25 mm. In Test #3, however, the secondary beam and its end connections were left unprotected.

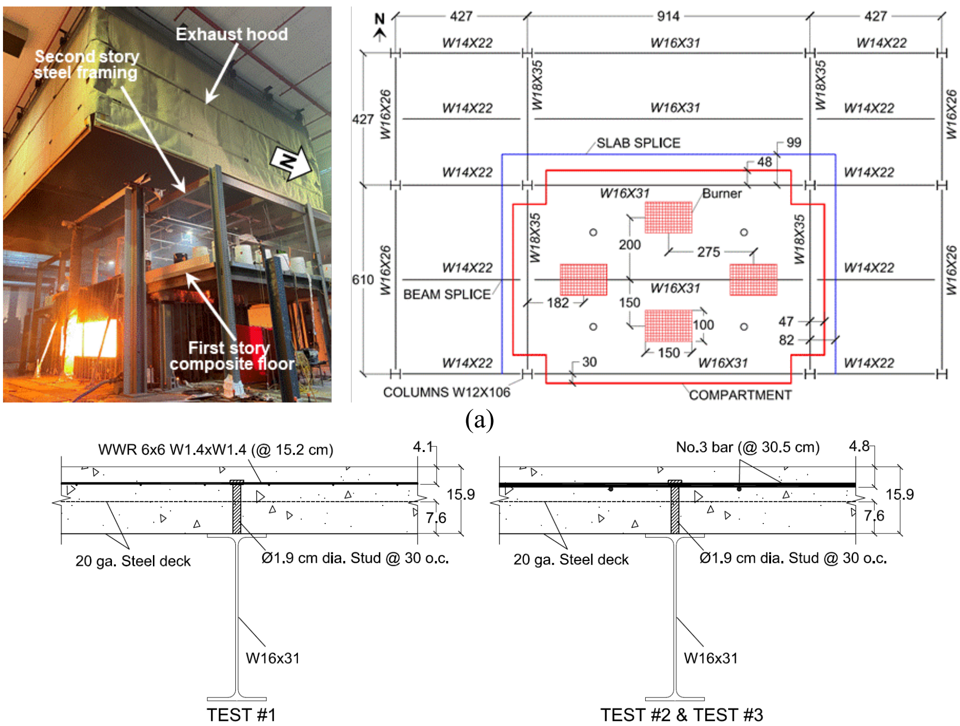

Figure 1. (a) Two-story test structure; (b) secondary beam composite sections (units in cm)

2.2 Test conditions

During the fire experiments, an imposed load of 2.7 kPa was applied to the test floor assembly using four hydraulic actuators and distributed to 24 loading points over the test floor (Figure 2a). The total gravity load including the floor self-weight was 5.2 kPa, which conforms to the gravity load demand determined from the American Society of Civil Engineers (ASCE) 7 [17] load combination for extraordinary events (1.2×dead load + 0.5×live load). The surrounding floors were loaded by water-filled drums (Figure 2a), providing an imposed gravity load of 1.2 kPa, equivalent to 50 % of the office live load considered in the structural design of the test structure. The test floor assembly was exposed to natural gas fire, with peak heat release rates in the range of 10.8 MW to 11.5 MW, using four 1 m × 1.5 m burners and confined under the slab using purpose-built compartmentation (Figure 1a and Figure 2b) to develop upper layer gas temperatures prescribed in American Society of Testing and Materials (ASTM) E119 [1]. The height of the fire compartment, the distance to the composite floor soffit above the top surface of the compartment floor, was 377 cm. Enclosing walls (along the red lines in Figure 1a) were constructed as non-load bearing walls made of sheet steel with gypsum board lining at the exposed surface. Steel columns were not directly exposed to fire except for the upper region where the floor beams and girders were joined in the test bay. The main ventilation opening on the south exterior wall was 150 cm tall × 582 cm wide. The four natural gas burners placed on the ground floor (Figure 2b) created fire exposure to the soffit of the composite floor in the test bay.

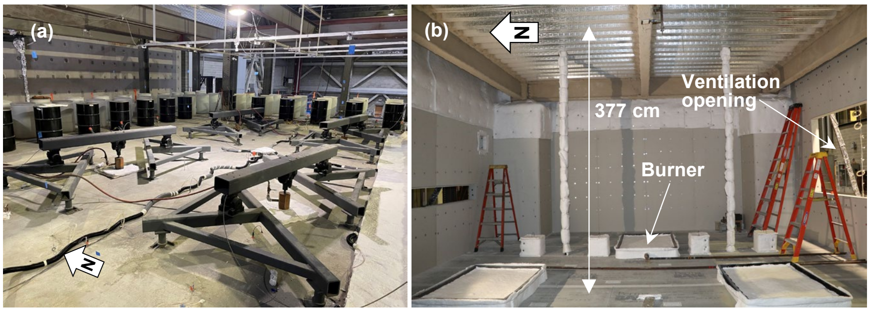

Figure 2. (a) Loading system on the top of the slab; (b) fire compartment

2.3 Instrumentation

The fire test conditions as well as the thermal and structural responses of the specimens were quantified using a variety of measurement systems. The mechanical load applied on the test floor assembly was controlled and measured using servo-hydraulic actuators and the load cells attached to them, respectively. The heat release rate of the test fires was quantified using both the fuel consumption and oxygen consumption calorimetry [18]. The gas temperature within the test compartment and temperatures of the floor specimens at various locations were measured using type-K thermocouples. Figure 3a through Figure 3c show a set of thermocouples mounted at the composite beam sections, secondary beam-to-girder connections, and within the composite floor slab in the test bay, respectively. Displacement transducers, installed outside the fire compartment, were used to measure deflections of the test floor and the surrounding structure. Figure 3d illustrates the selected locations of displacement measurements relevant to this paper, including the vertical displacement (VD) measurements at the centrelines of the test floor assembly and the horizontal displacement (HD) measurements of the test floor. HD4, HD6, HD9, and HD10 were at 15 cm above the top surface of the test floor and HD7 was at the mid-thickness of the topping concrete. The displacement values of HD4 and HD6 indicates thermally induced axial displacements of the connected steel beams. The data plots provided in this manuscript show the standard deviation of the averages of the measured values. The total expanded uncertainties, with a coverage factor of 2 for 95 % confidence level, in the individual measurements of mechanical load, burner heat release rate, temperature, and displacement were estimated to be 1 % at 125 kN, 1.4 % at 11.5 MW, 8 % at 1100 ºC, and 2 % at 655 mm, respectively. Details about the measurement systems and uncertainty in the measurements are presented in Choe et al. [9, 12].

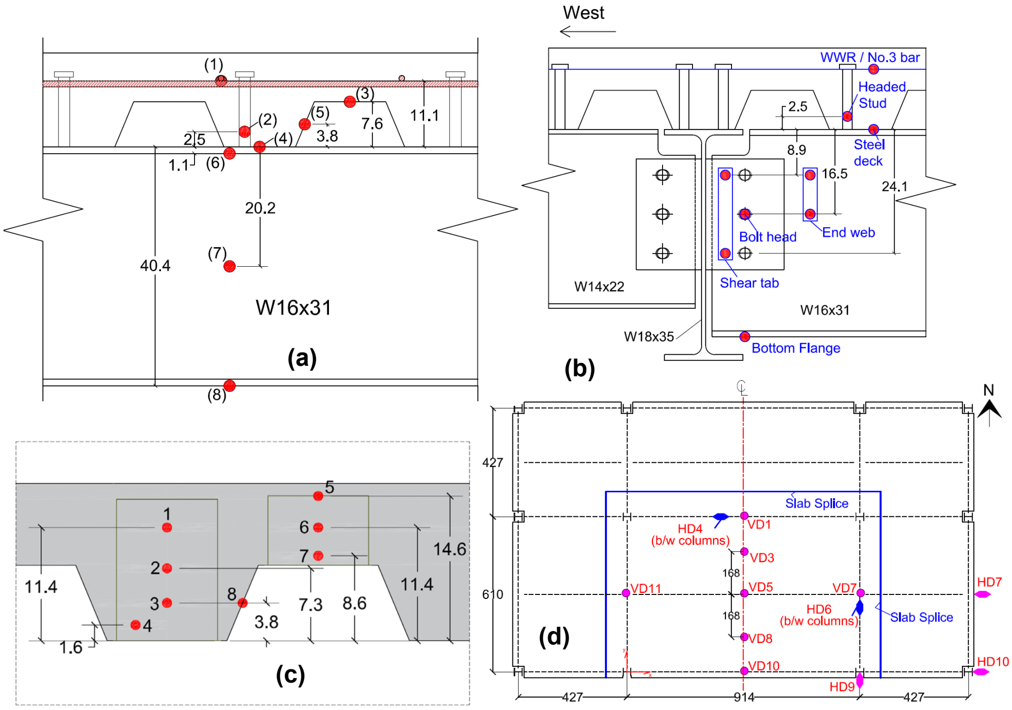

Figure 3. (a) Thermocouple locations at composite beam sections; (b) Thermocouple locations in beam-to-girder connection; (c) Thermocouple locations in concrete; (d) vertical (VD) and horizontal displacement (HD) measurements (units in cm)

3 RESULTS

Figure 4a shows the heat release rate (HRR) of natural gas burners measured based on fuel consumption and the total actuator load (Load) measured after the burner ignition. The test bay floor was imposed by a total actuator load of 125 kN. The HRR values in these tests were comparable. In Test #1, the fire and actuator loads were removed at 107 min due to slab fracture along the longitudinal centreline of the test bay. In Test #3, the actuator loading and the test fire were removed around 140 min due to significant integrity failure of the test floor slab. In Test #2, the fire was extinguished at 131 min due to significant damage of the south compartment wall. However, unlike in Test #1 and Test #3, the actuator loading was continued over a 2-hour cooling period. Details of the test results are presented in the subsequent sections.

Figure 4b shows the average upper layer gas temperatures measured using 12 thermocouple probes located 30.5 cm below the floor specimen soffit, comparable to the temperature-time curves prescribed in the standard fire testing standards (ASTM E119 [1] and International Organization for Standardization (ISO) 834 [19]). As shown in the figure, a small increase in the HRR value (by 0.5 MW) in Test #2 and Test #3 resulted in gas temperatures about 5 % higher than those measured in Test #1. In all three tests, the standard deviation in the upper layer gas temperature measurements at various locations was less than 50 ºC.

The Test #2 composite floor, which was reinforced with the No.3 reinforcing bars and had all the test bay beams protected with SFRM, tested under the same mechanical load and temperature time curve as in Test #1 and Test #3, did not exhibit structural integrity failure after 131 min of standard fire exposure. The mid-span of the SFRM-protected secondary beam reached a mid-panel vertical displacement of 455 mm at 131 min, compared to 530 mm vertical displacement of the unprotected secondary beam at the same fire exposure time in Test #3. The Test #2 floor slab reached a maximum vertical displacement of 465 mm at 145 min, during the cooling phase of the test. Given the superior performance of the Test #2 composite floor, the primary focus of this paper has been to the structural behaviour and failure characteristics of Test #1 and Test #3 composite floor assemblies with the aim to evaluate the improved fire resilience of the composite floor with the enhanced slab reinforcement and unprotected secondary beam. Refer to Choe et al. [12] for more details about Test #2.

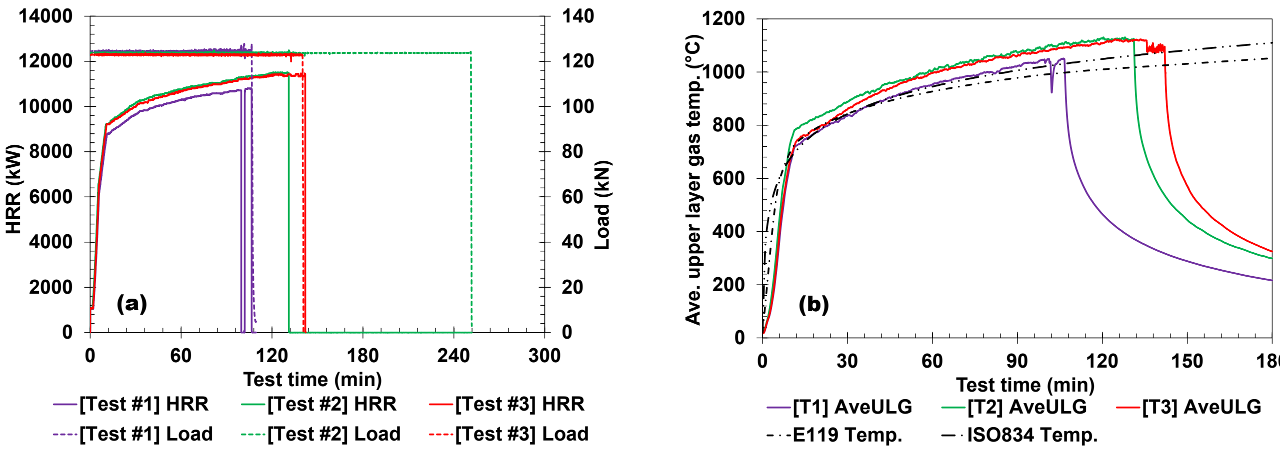

Figure 4. (a) Total actuator load and burner heat release rate (HRR); (b) average upper layer gas temperature (ULT)

3.1 Thermal response

Figure 5a shows the average temperatures of the composite beam sections along the SFRM-protected secondary beam (W16×31) in Test #1 and the unprotected secondary beam in Test #3. Refer to Figure 3a for locations and labels of the corresponding thermocouples. The error bars indicate the maximum standard deviation in temperature measurements at three different sections along the beam span. The web and bottom flange of the secondary beam in Test #1 reached a peak value of 860 °C at 107 min after ignition when the burners were shut off. In Test #3, they reached 1070 °C at 107 min. The temperatures of the unprotected secondary beam in Test #3 were close to the upper layer gas temperature during the test and reached a peak value of 1100 °C at 142 min when the burners were shut off. In Test #3, temperatures of the stud anchors and No.3 reinforcing bars above the secondary beam reached 720 °C and 500 °C, respectively. Figure 5b shows the average temperatures of various parts in the secondary beam-to-girder connection region. Refer to Figure 3b for locations and labels of the thermocouples mounted on these connections. The peak temperatures of end webs, bolt heads, and shear tabs were 640 °C, 500 °C, and 420 °C in Test #1. They were close to the upper layer gas temperature of 1100 °C in Test #3.

Figure 6 shows the averaged values of temperatures at discrete locations within the composite floor slab between steel beams, where the error bars indicate the standard deviation in temperature measurements across the test bay. Refer to Figure 3c for locations and labels of the thermocouples discussed herein. At 107 min in Test #1, the temperatures measured at location 1 (at deep section) and 6 (at shallow section) were 140 °C and 420 °C, respectively. At the same fire exposure time in Test #3, they were 130 °C and 440 °C, respectively, indicating similar temperature-time increment of the concrete slab in both tests.

The temperatures of the steel reinforcement at the deep and shallow sections of the slab placed between the test bay beams in Test #1 and Test #3 are shown in Figure 7. The average temperatures of the steel reinforcement at the deep and shallow sections of the slab in Test #3 were slightly higher than those measured in Test #1 at the same fire exposure time. This is because the bottom concrete cover of the steel reinforcement in Test #3 was smaller than Test #1, as shown in Figure 1b. The slab reinforcement at the deep and shallow sections of the slab in Test #3 reached 320 °C and 600 °C at 142 min, when the burners were shut off. For both tests, the average top surface temperature remained below the ASTM E119 limit.

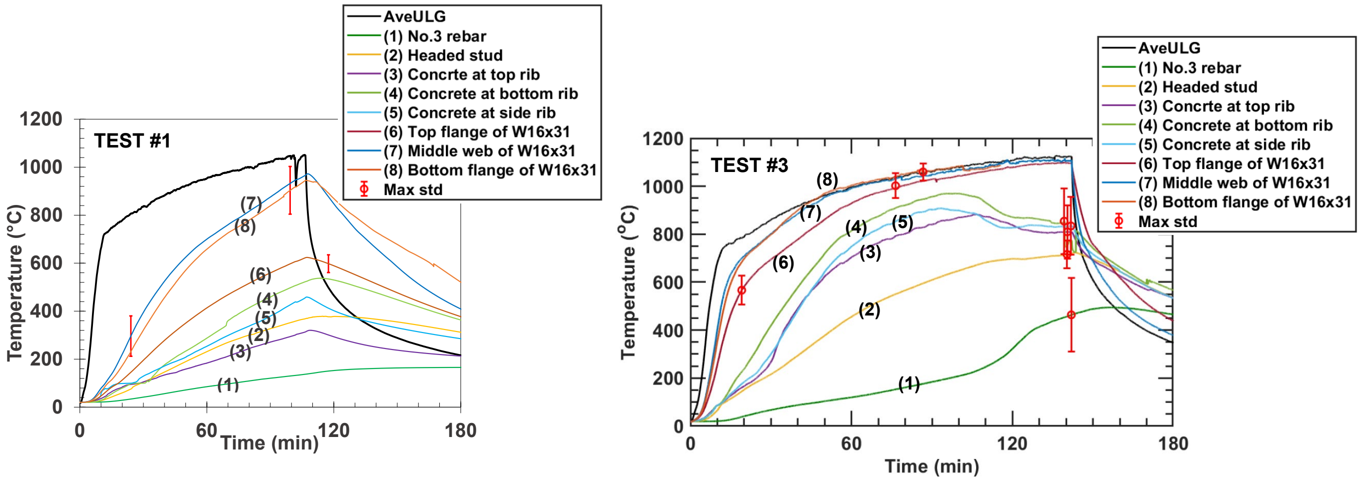

(a)

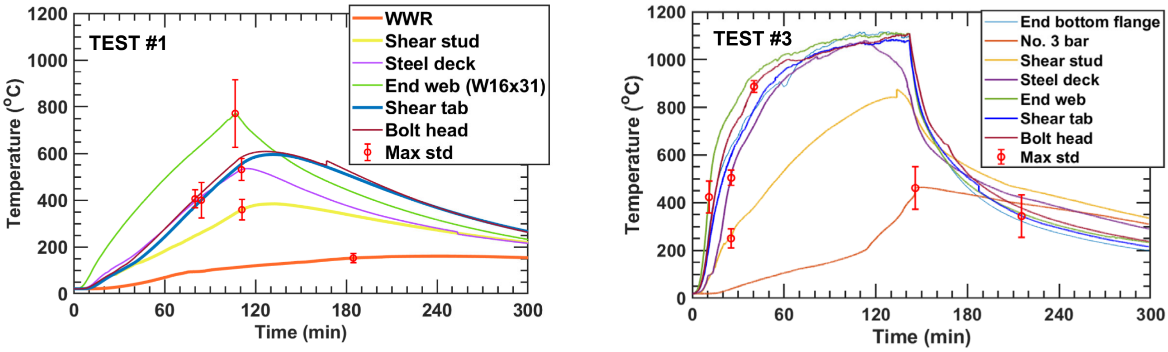

(b)

Figure 5. Measured temperatures (a) across secondary beam sections; (b) at secondary beam-to-girder connections

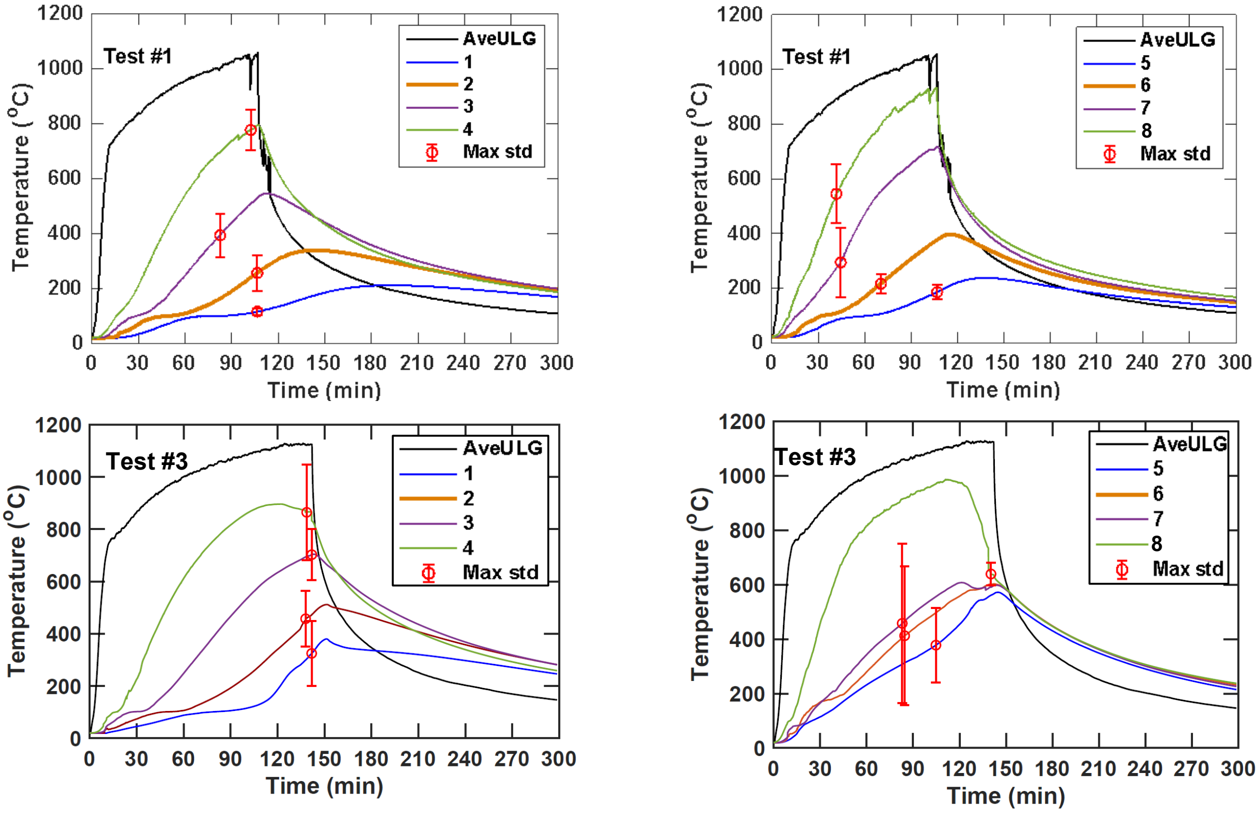

Figure 6. Measured concrete temperature in Test #1 and Test #3

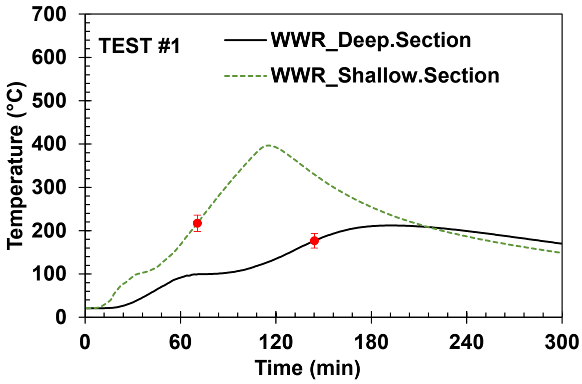

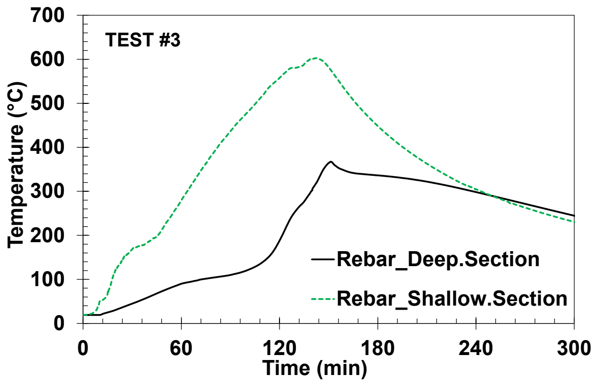

Figure 7. Measured slab reinforcement temperature in Test #1 and Test #3

3.2 Structural response

Figure 8a shows the midspan vertical displacements of the test bay beams varying with the fire exposure time for Test #1 and Test #3. Refer to Figure 3d for the locations and labels of the vertical displacement measurements. In Test #1, the mid-panel vertical displacement (VD5) increased at an approximate rate of 4.2 mm/min until 70 min at which the bottom flange temperature of the secondary beam reached 700 °C. At 70 min after ignition of a test fire, full-depth longitudinal concrete cracking occurred in the middle of the test bay with rupture of reinforcement wires. The crack opening was widen as the wire reinforcement placed in the transverse direction of the test bay ruptured in tension, which was indicated by a noticeable change in the displacements after 70 min (Figure 8a). From 70 min to 107 min in fire, the VD5 value increased at an approximate rate of 7.2 mm/min to its peak value of 565 mm until the fire and mechanical loading were removed at 107 min.

In Test #3, as shown in Figure 8a, the midspan vertical displacement of the secondary beam (VD5) increased at varying rates during the heating phase of the test: (a) 13.4 mm/min between 4 min and 14 min of fire exposure, (b) 3.1 mm/min between 14 min and 132 min, and (c) 13.9 mm/min between 132 min and 140 min. The first displacement rate between 4 min and 14 min indicates the significant loss of flexural strength of the secondary composite beam combined with thermal bowing due to more thermal gradient across the composite beam section as the unprotected secondary beam was heated to approximately 530 °C. The displacement rate change at 132 min corresponds to the occurrence of a transverse crack in the mid-panel region. VD5 reached a peak value of 655 mm (equivalent to the ratio of L/14 where L = 9.1 m, the length of the secondary beam) at 140 min when the actuator loading was removed. Around this time, flame penetration (through concrete cracks) was observed near the southeast corner of the test floor. Burners were shut off at 142 min. As the unprotected secondary beam lost its flexural strength in the early stages of the fire, tensile membrane action was activated in the Test #3 concrete slab which helped maintain the slab integrity longer than two hours.

Compared to Test #1, Test #3 exhibited larger mid-panel deflection at the early stages of the fire, before 73 mins of fire exposure, as the unprotected secondary beam was heated more rapidly. However, Test #3 exhibited smaller mid-panel deflections compared to Test #1 after 73 minutes due to the slab reinforcement of No.3 bars (230 mm^2/m) provided in Test #3 compared to the wire reinforcement (60 mm^2/m) provided in Test #1. At 107 min, the mid-panel displacement (VD5) reached 415 mm in Test #3 compared to 565 mm in Test #1. For both Test #1 and Test #3, the vertical displacement of the south edge beam (VD10) increased more rapidly than north edge beam (VD1) because of the connectivity of the north beam to the surrounding bay. At 107 min, VD10 and VD1 reached 205 mm and 165 mm in Test #1, respectively. They reached 195 mm and 165 mm in Test #1 at the same time, respectively.

Figure 8b shows the horizontal displacements measured in Test #1 and Test #3. In both tests, HD6 and HD9 values increased toward the south due to the restraint provided to the test floor by the north surrounding bay. Overall, the horizontal displacement values of the Test #3 floor specimen reinforced with No.3 bars (230 mm^2/m) were smaller than the Test #1 floor specimen lightly reinforced with wire mesh mats (60 mm^2/m), indicating the effect of slab reinforcement on the horizontal displacements. In Test #1, the values of HD6 and HD9 continuously increased with increasing temperatures, whereas those values in Test #3 seldom increased beyond 80 min.

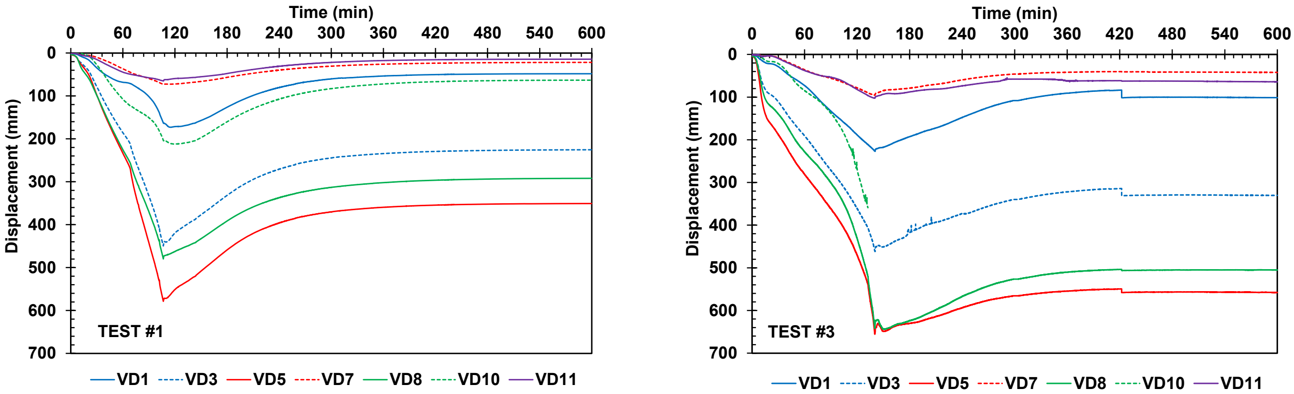

(a)

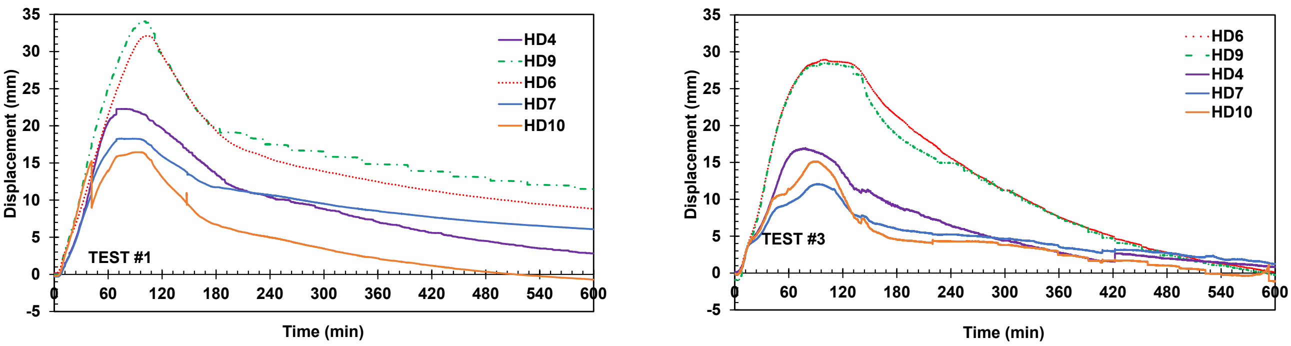

(b)

Figure 8. (a) Measured vertical displacements in Test #1 and Test #3; (b) Measured horizontal displacements in Test #1 and Test #3

Figure 9a and Figure 9b show the concrete crack patterns of the Test #1 and Test #3 floor specimens, respectively. As shown, the differences in the steel reinforcement scheme and in the fire protection of the secondary beam significantly influenced the structural integrity of the composite floor under fire effects. The Test #1 floor reinforced with the wire mesh mats exhibited large crack openings along the east, west, and north edges of the test-bay as well as in the mid-panel zone. Most of the wires within the enlarged cracks (shown in Figure 9a) were fully ruptured. The cracks at the east and west edges of the test bay appeared in the slab next to the top flanges of the girders inside the column grid causing the slab to lose its vertical edge support as well as continuity over the girders. The north edge cracks developed outside the test-bay column grid, close to the tip of the No.4 splice bars extended from the north surrounding floor. With the significant loss of vertical support and slab continuity over girders, the loaded floor slab appeared to be supported by the three longitudinal beams (9.1 m long W16×31) via headed studs with increasing temperatures leading to a tension load path primarily in the transverse direction. After Test #1, it was observed that most of steel deck units in the test bay did not rupture, which contributed to the tension load path during heating.

In Test #3, as shown in Figure 9b, the concrete slab exhibited a large transverse crack opening, approximately 105 cm west of the transverse centreline of the test bay. Most of the No.3 reinforcing bars ruptured in this crack opening. Flame leak above the slab through this transverse crack was observed after 132 min of fire exposure. The test floor exhibited cracks at other three locations (marked 2, 3, and 4 in Figure 9b) at 138 min of fire exposure although these cracks were smaller in size compared to the mid-panel transverse crack (marked 1). Concrete cracks at locations 2 and 3 also exhibited reinforcing bar fractures. The Test #3 specimen also exhibited cracks along the east, west, and north edges of the test-bay column grid (but within the footprint of the fire test compartment); however, only a few bars ruptured. Along the west edge crack, the first five bars from the south end exhibited bar fracture (Figure 9b) and the slab in that region lost continuity over the girders. Although Test #3 had the longer duration of fire exposure than Test #1, the No.3 bars controlled (1) the development of large cracks along the perimeter of the test bay, and (2) significantly delayed the development of mid-panel cracks by 60 min compared to Test #1.

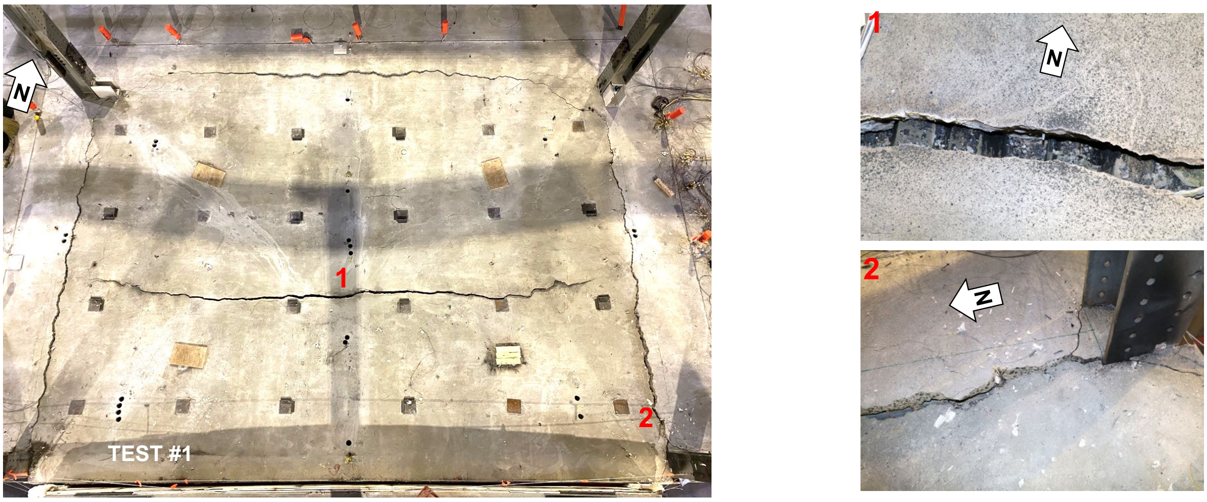

(a)

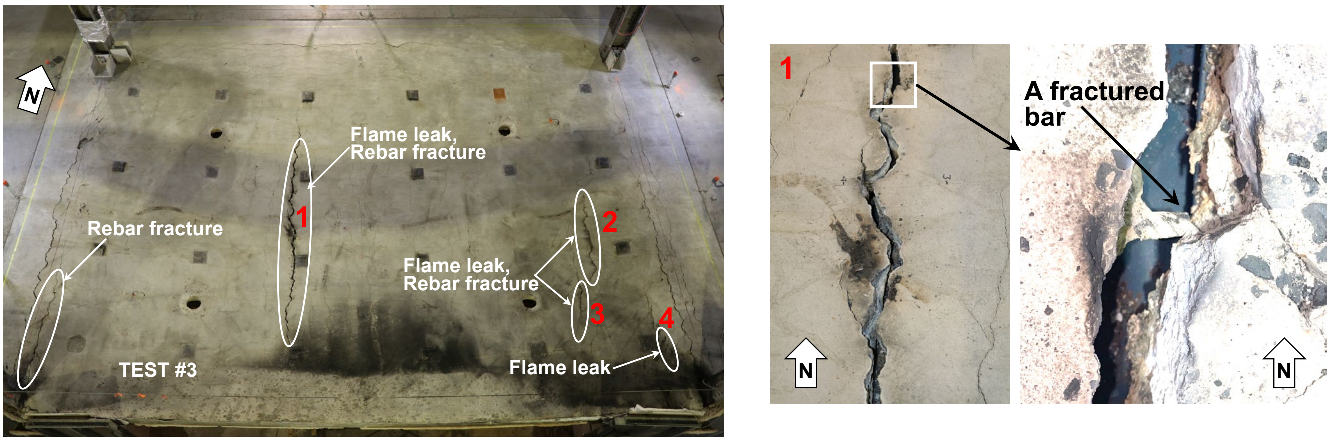

(b)

Figure 9. Concrete crack patterns of the tested floors (a) Test #1; (b) Test #3

All beams in the test bay exhibited permanent global and local deformations after Test #1 and Test #3. The 9.1 m long north and south primary beams exhibited local buckling near the ends as well as twisting and lateral deformations. Along the secondary beam, severe local buckling occurred near the ends of the test bay secondary beam in Test #1 and in the W14×22 secondary beams of the surrounding bays (Figure 1) near their end connections to the test bay girders in Test #3. Relatively minor deformations were exhibited in the east and west girders. Figure 10a through Figure 10c show the failure of the beam-end connections in Test#1 and Test #3. In Test #1, the SFRM-protected shear tab connections at the ends of the longitudinal beams were seldom damaged (Figure 10a). In Test #3 where the secondary beam was unprotected including shear tab connections, all three bolts in the west end shear tab connection fractured during heating (Figure 10b). The west shear tab connection of the north primary beam exhibited bolt fracture during the cooling phase (Figure 10c). This failure is also indicated in Figure 8c where there is a sudden increase in HD4 value in Test #3 around 420 min (about 280 min into cooling). In Test #1 composite floor, no shear stud failure was observed along the test bay beams and girders. However in Test #3, the steel deck together with the concrete in the west half of the secondary beam separated from the steel beam during the test (as shown in Figure 10d) and most of the shear studs in the west half of the secondary beam as well as in the east end of the secondary beam exhibited stud fracture or large bending (Figure 10e), indicating the loss of composite action between the steel beam and concrete. This was because of the higher temperatures of the secondary beam and shear studs as well as due to the failure of the west end connection of the secondary beam in Test #3 compared to Test #1.

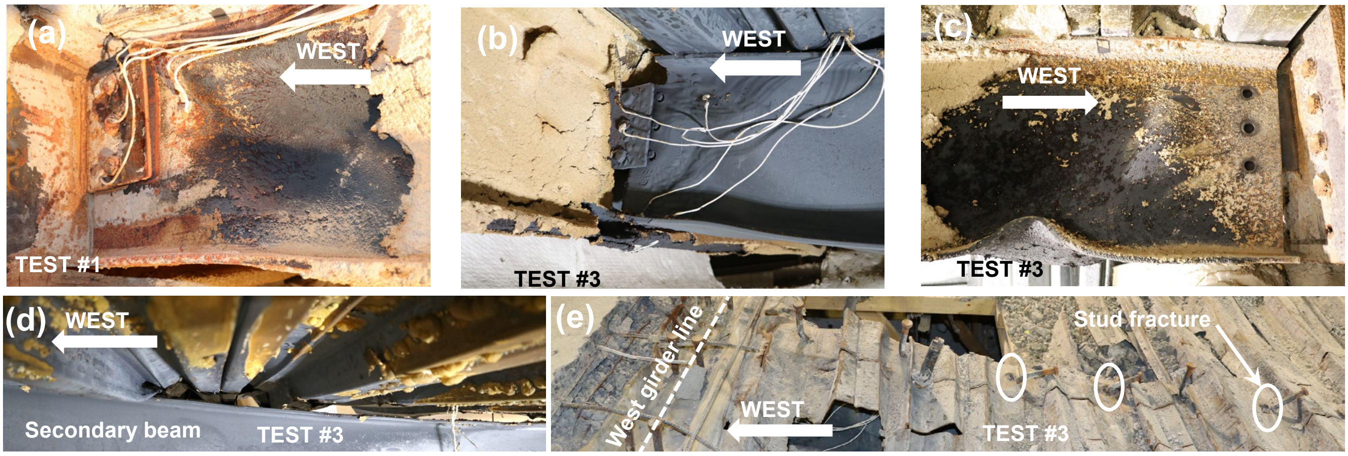

Figure 10. Photographs of test structures after completion of the experiments: (a) shear tab connection at the west end of secondary beam (Test #1); (b) shear tab connection at the west end of secondary beam (Test #3); (c) shear tab connection at the west end of north primary beam (Test #3); (d) Shear stud fracture (Test #3); (e) steel deck separation (Test #3)

4 CONCLUSIONS

The Test #1 specimen which used wire reinforcement of 60 mm^2/m width to meet the minimum shrinkage steel reinforcement permitted in the U.S. standard practice and SFRM to protect all the steel beams and achieve a 2-hour (120 min) fire resistance rating, exhibited slab integrity failure 70 min after fire ignition; i.e., before reaching the specified fire resistance rating period. This result highlights that the minimum required slab reinforcement currently permitted in the U.S. practice may not be sufficient to maintain the structural integrity of a composite floor assembly during a structurally-significant fire. Test #3 showed that the use of No.3 deformed steel bars (230 mm^2/m) for the slab reinforcement determined by incorporating tensile membrane action maintained the structural integrity of the tested slab for more than two hours (120 min) even when no SFRM was provided to the secondary beam or its connections. The additional structural capacity came from force redistribution provided by tensile membrane action of the reinforced concrete slab. The data from these experiments will help to explore engineered solutions to optimize the passive fire protection and slab reinforcement used in the steel-concrete composite floor systems for different structural and fire variables, a necessary step in the performance-based design of steel framed buildings subjected to fire.

ACKNOWLEDGMENT

This work was conducted as part of the *Measurement of Structural Performance in Fire* project under the NIST Engineering Laboratory's *Fire Risk Reduction in Building Program*. The authors thank William Baker (Skidmore, Owings, and Merrill), Craig Beyler (Jensen Hughes), Luke Bisby (University of Edinburgh), Ian Burgess (University of Sheffield), Charles Carter (AISC), Charles Clifton (University of Auckland), Michael Engelhardt (University of Texas), Graeme Flint (Arup), Nestor Iwankiw (Jensen Hughes), Kevin LaMalva (Holmes Fire), Roberto Leon (Virginia Tech.), Kristi Sattler (AISC), and Amit Varma (Purdue University) for their expert consultation. The authors also thank the current and former

NIST colleagues including Brian Story, Laurean DeLauter, Anthony Chakalis, Philip Deardorff, Marco Fernandez, Artur Chernovsky, Michael Selepak, Xu Dai, Rodney Bryant, Giovanni Di Cristina Torres, William Grosshandler, Jonathan Weigand, Joseph Main, Fahim Sadek, Chao Zhang, Ana Sauca, Mina Seif, and John Gross for their significant contributions to design, construction, and execution of this test program.

REFERENCES

1. ASTM International (American Society for Testing and Materials). Standard methods of fire test of building construction and materials, ASTM E119−21. ASTM International, West Conshohocken, PA, 2021.
2. British Steel, The Behaviour of Multi-Story Steel Frame Buildings in Fire, British Steel, Rotherham, United Kingdom, 1999.
3. F. Wald, L.S. Da Silva, D.B. Moore, T. Lennon, M. Chaldna, M. Santiago, M. Benes, L. Borges, 2006, Experimental behaviour of a steel structure under natural fire. Fire Safety Journal. 41 (7) 509–522. https://doi:10.1016/j.firesaf.2006.05.006.
4. B. Zhao, M. Roosefid, O. Vassart, Full scale test of a steel and concrete composite floor exposed to ISO fire and corresponding numerical investigation, Eurosteel, Graz, Austria, 2008.
5. B. Zhao, M. Roosefid, 2011, Experimental and numerical investigations of steel and concrete composite floors subjected to ISO fire condition. Journal of Structural Fire Engineering. 2 (4) 301-310. https://doi.org/10.1260/2040-2317.2.4.301.
6. SDI (Steel Deck Institute), C-2017 Standard for composite steel floor deck–slabs, ANSI/SDI C-17, SDI, 2017.
7. UL (Underwriters Laboratory). Fire Resistance Ratings – ANSI/UL 263. UL, Northbrook, IL, 2011.
8. G.M. Newman, The fire resistance of composite floors with steel decking, SCI Publication P56, second ed., The Steel Construction Institute, 2004.
9. L. Choe, S. Ramesh, X. Dai, M. Hoehler, M. Bundy, R. Bryant, et al. Fire Resilience of a Steel-Concrete Composite Floor System: Full-Scale Experimental Evaluation for U.S. Prescriptive Approach with a 2-Hour Fire-Resistance Rating (Test #1). NIST Technical Note (NIST TN-2165), Gaithersburg, MD, 2021. DOI: 10.6028/NIST.TN.2165.
10. L. Choe, S. Ramesh, C. Zhang, C. Clifton. Behaviour of composite floor assemblies subject to fire: Influence of slab reinforcement. Proceeding of 2021 Eurosteel Conference, September 1-3, 2021, University of Sheffield, United Kingdom.
11. L. Choe, S. Ramesh, X. Dai, M. Hoehler, M. Bundy, 2022, Experimental study on fire resistance of a full-scale composite floor assembly in a two-story steel framed building, Journal of Structural Fire Engineering, Vol. 13 No. 2, pp. 145-161. https://doi.org/10.1108/JSFE-05-2021-0030.
12. L. Choe, S. Ramesh, M. Hoehler, M. Bundy, R. Bryant, X. Dai, et al., Fire Resilience of a Steel-Concrete Composite Floor System: Full-Scale Experimental Evaluation for Influence of Slab Reinforcement (Test #2). NIST Technical Note (NIST TN-2203), Gaithersburg, MD, 2022. DOI: 10.6028/NIST.TN.2203.
13. AISC (American Institute of Steel Construction), Manual of Steel Construction, 15th Edition, AISC, Chicago, IL, 2017.
14. T.M. Murray, D.E. Allen, E.E. Ungar, 2016, AISC Steel Design Guide 11 (Second Edition): Vibrations of Steel Framed Structural Systems due to Human Activity. 2nd Ed. (AISC, Chicago, IL).
15. G. Clifton, A. Gillies, and N. Mago, 2010, The Slab Panel Method: Design of Composite Floor Systems for Dependable Inelastic Response to Severe Fires.
16. American Concrete Institute, Building Code Requriments for Strucutral Concrete (ACI 318-19). Farmington Hills, MI: American Concrete Institute, 2019.
17. ASCE (American Society of Civil Engineers). Minimum design loads for buildings and other structures - ASCE 7-16. ASCE, Reston, VA, 2016.
18. R. Bryant, M. Bundy, The NIST 20 MW calorimetry measurement system for large-fire research, Technical Note (NIST TN) – 2077, 2019. https://doi.org/10.6028/NIST.TN.2077.
19. ISO (International Organization for Standardization). Fire-resistance tests — Elements of building construction — Part 2: Requirements and recommendations for measuring furnace exposure on test samples, ISO 834-2:2019. ISO, Geneva, 2019.

BUSHFIRE RESISTANCE OF LIGHT GAUGE STEEL FRAMED WALL SYSTEMS

Zoe Dart[1], Elise Watkins[2], Anthony Ariyanagam[3], Mahen Mahendran[4]

ABSTRACT

The growing bush-to-urban interface, coupled with the increased severity of climate change impacts, has resulted in more frequent and widespread bushfire events. This increased severity and regularity of bushfire events has resulted in the destruction and costly rebuild of many residential homes across Australia, with over 3000 homes being destroyed in the recent 2019/2020 Black Summer Fires. With the significant and expensive damage caused by such events, incorporating bushfire resilience into residential design has become essential. Increasing the integrity of external wall configurations and thus improving the exterior building envelope is identified as a potential solution to minimise building losses during such events. This paper, therefore, presents the details of a bushfire resistance experiment and associated research conducted for multiple external light gauge steel framed (LSF) wall configurations against various Bushfire Attack Levels (BAL) given in bushfire standards by using relevant radiant heat fire curves. This study aims to improve the knowledge base of the bushfire resistance of external LSF wall configurations, aid in the design of safe bushfire-prone buildings, improve community resilience, limit material wastage, and reduce the economic burden of bushfire attacks.

Keywords: Wall Configurations; Light Gauge Steel; Bushfire; Radiant Heat; Bushfire Curves.

1 INTRODUCTION

As the impacts of climate change become more apparent, causing an increase in temperatures, humidity and fuel moisture content, the severity and regularity of bushfires have become a growing concern [1,2]. Southeast Australia, where most of the population resides, is highly susceptible to large bushfires threatening life and property [3]. The increased intensity and regularity of such bushfire events within Australia highlight the significant importance of research into resilient bushfire design to assist communities in bushfire-prone areas and prevent the destruction of their homes. In particular, the external walls of residential housing have been identified as a key component for bushfire damage prevention as they provide thermal resistance and shielding from bushfires. Furthermore, studying material performance within a wall configuration when exposed to elevated temperatures will deepen the current knowledge, support communities internationally and assist in reducing the damage from bushfire events.

The three main mechanisms of a bushfire are flame front, radiant heat, and ember attack. After analysis of the Australian Capital Territory (ACT) Bushfire in 2003, it was determined that most houses were ignited

[1] Dart Zoe, Queensland University of Technology
e-mail: zoe.dart@connect.qut.edu.au
[2] Watkins Elise, Queensland University of Technology
e-mail: e.watkins@qut.edu.au
[3] Ariyanayagam Anthony, Queensland University of Technology
e-mail: a.ariyanayagam@qut.edu.au, ORCID: https://orcid.org/0000-0001-6732-7735
[4] Mahendran Mahen, Queensland University of Technology
e-mail: m.mahendran@qut.edu.au, ORCID: https://orcid.org/0000-0001-7306-8821
https://doi.org/10.6084/m9.figshare.22178075

from radiant and flame contact from adjacent burning buildings+ or features, with radiant having an impact on the building envelope for a significantly longer period, (approximately an hour) than the fire front [4]. Due to this, radiant heat will be the mechanism of interest in this investigation. To evaluate the bushfire resilience of a property, AS3959 details a Bushfire Attack Level (BAL) and categorises the properties based on the increased risk level of ember attack, burning debris and radiant heat, ranging from 12.5 kW/m^2 to flame zone ($\geq$ 40 kW/m^2) [5]. The BAL rating for a property is attained through the combination of several factors, including the Fire Danger Index, land slope, surrounding vegetation type, and proximity to the property [5]. Further, different construction and materials requirements are detailed based on the BAL rating that a property receives.

Given the complex nature of bushfires and the difficulty of recreating experimental tests to represent actual bushfire events, simple fire curves are often used to aid in the comparative analysis of wall elements in bushfire design [5-7]. Two fire curves are commonly used within this testing program. The first fire curve is based on AS1530.8.1 and comprises a rapid increment phase to a heat flux of 40 kW/m^2, followed by a maintenance phase and, finally, a degree of cooling [8]. The second curve is developed by CSIRO (i.e. in NASH bushfire standards [7]), which is used for steel building construction in bushfire-prone areas and provides a different fire/heat flux versus time curve.

2 EXTERNAL WALLS

As stated in AS1530.8.1, the likelihood of a building being damaged during a bushfire can be attributed to the external building envelope [8]. External walls play an important role in minimising property loss within the building envelope as they can provide the required resistance and shielding to the bushfire's radiant heat, flame, and ember penetration [5-7]. Various wall configurations are currently used to construct a residential home, with the external wall cladding being built with different materials. These materials include timber logs, brick veneers, corrugated steel sheets, other board lining materials and reflective insulations. However, numerous building standards, including AS3959 and NASH, state that non-combustible materials must be used, including steel systems, masonry walls and other non-combustible claddings [5,7]. While certain materials and wall configurations have been recommended, very limited experimental studies are available for external LSF walls at elevated temperatures. As steel is a lightweight, durable and fire-resistant material with considerable cost and structural benefits with increasing use in residential buildings, the overall performance against radiant heat attack must be thoroughly understood [9-11].

Recent experimental studies conducted at the Queensland University of Technology (QUT), Australia, by the authors have shown the severe consequences of radiant heat exposure, particularly for external walls [11]. The wall configurations include light gauge steel framed (LSF) walls externally lined with 7.5 to 9 mm thick boards with and without steel cladding and exposed to bushfire radiant heat and flame zone conditions. The results showed that the rapid increment rate in the heat flux led the wall system to a severe failure, whilst gradual increment resulted in a progressive loss. Furthermore, the investigation revealed the importance of cladding integrity and thermal shock resistance for bushfire building performance. There are many other wall configurations with various materials used in the external wall cladding, including corrugated steel sheets, different board lining materials, and reflective insulations (i.e. sarking). However, only very limited experimental studies are available for external LSF walls compared to internal LSF walls. Even in such studies, the external wall panels were exposed to building fires, where the rate of temperature rise is considered much lower than in the bushfire scenario. In a bushfire scenario, the rate of temperature rise is very rapid and could reach a temperature higher than the standard fire curve in a very short time. Further studies confirmed that the structural adequacy of the wall configuration is determined by the maximum hot flange temperature [12-17]. This highlights the importance of the cladding material to protect the steel stud temperature and act as a thermal barrier to reduce the chances of steel studs buckling. This paper presents the ongoing experimental study on the bushfire resistance of commonly used external LSF wall configurations for various bushfire attack level (BAL) ratings given in bushfire standards using appropriate fire curves.

3 EXPERIMENTAL PROGRAM

The experimental program consisted of three steel framed wall configurations of differing materials, each tested to two separate radiant heat exposures; CSIRO and AS1530.8.1 [7,8]. Overall, six tests were completed. All wall configurations used light-gauge steel frames lined with steel cladding on the fire side and plasterboard on the ambient side. Each configuration was built using 1200mm by 1500mm steel cladding and plasterboard, 1500 mm steel studs and 1200mm steel battens (Figure 1). Tests 1 and 2 used this simple configuration, Tests 3 and 4 included the additional reflective sarking, and Tests 5 and 6 incorporated earth wool glass fibre insulation. To test the wall configurations, the specimen for each test series was bolted to 1400 mm steel tracks to connect the tracks of the wall to the testing frame.

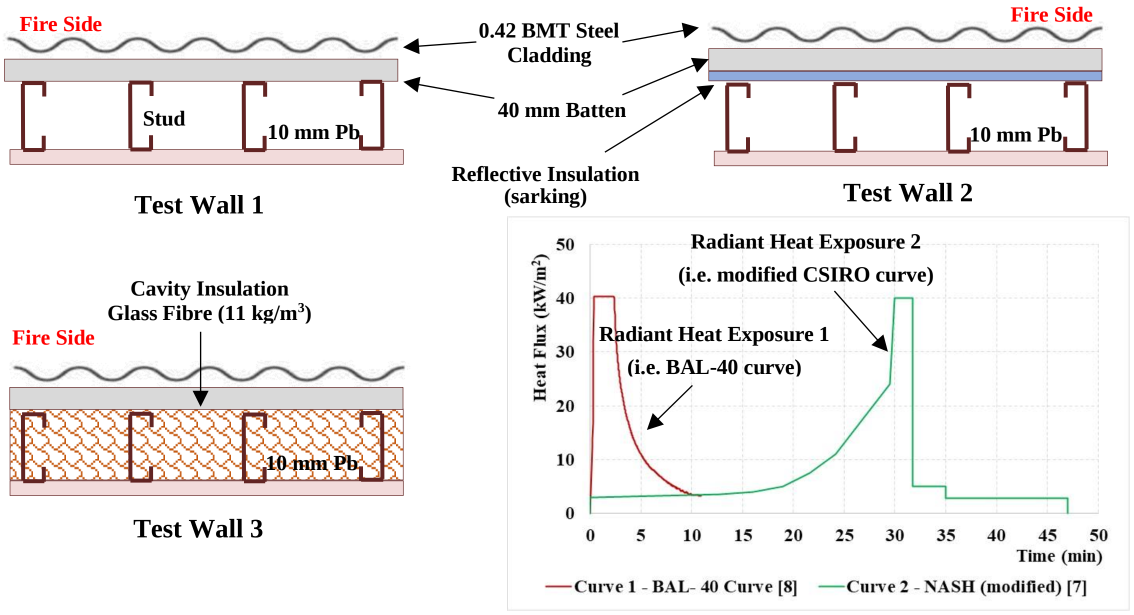

Figure 1. Experimental Program

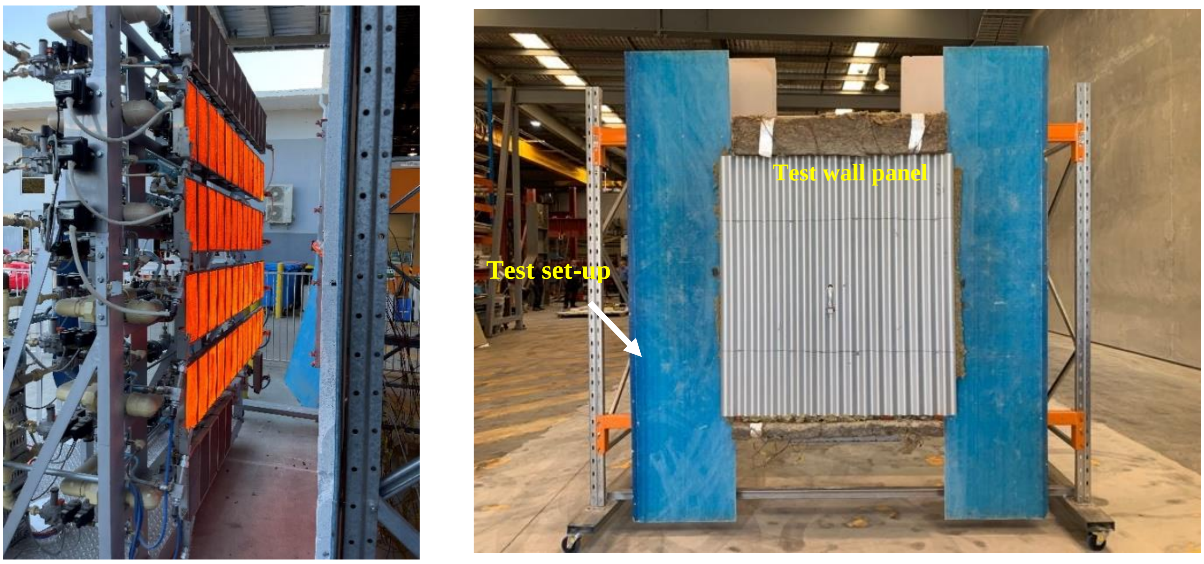

(a) Radiant heat panel (b) Test set-up and wall specimen

Figure 2. Radiant heat panel and test wall specimen

The radiant heat panels used to simulate the radiant heat exposure had 1.7 m by 2 m dimensions. The radiant heat exposure on the wall configurations was controlled manually by adjusting the radiant heat panels towards or away from the wall as needed using rollers on tracks. This was achieved using the information obtained through an SBG01 heat flux meter mounted on the wall configurations. Insulation was placed around the join of the wall configuration and steel frame to prevent excess heat loss. Figure 2 shows the radiant heat panel and test wall specimen.

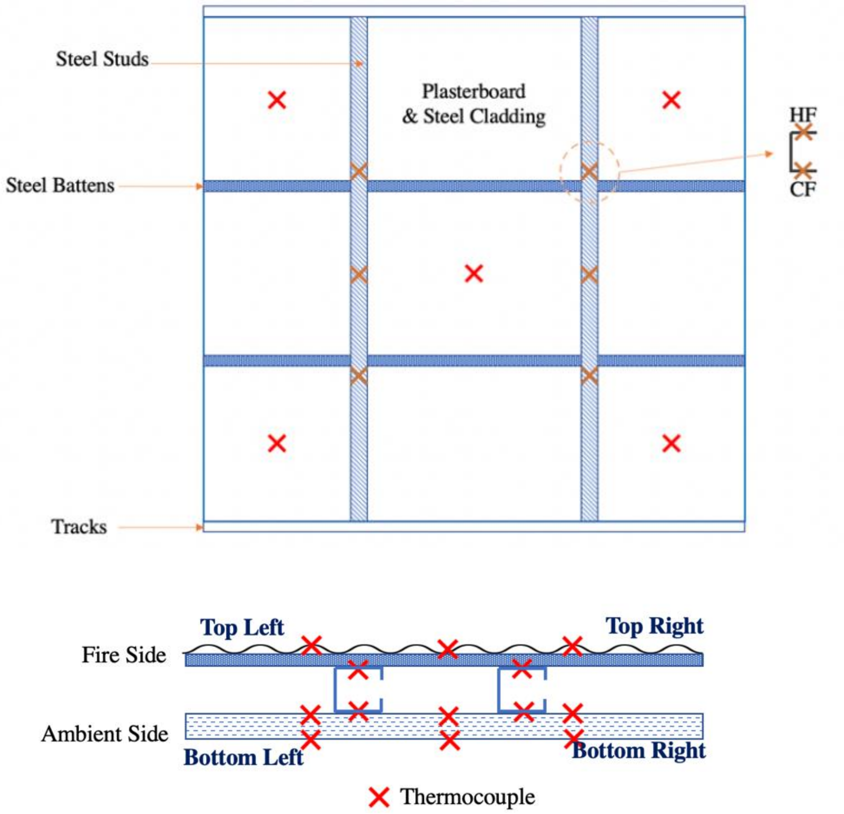

Figure 3. Thermocouple Arrangement on Test Wall Panel

To test and record the temperature rise of the elements of the configurations (i.e. steel studs, cladding, plasterboard), Type K thermocouples were attached using steel brackets and staples. On the external surface of the steel cladding, five thermocouples were placed at quarter heights. Likewise, thermocouples were attached at quarter heights of the plasterboard on both the fire and ambient sides. Additionally, three thermocouples were placed on the hot and cold flanges for each steel stud: top, middle, and bottom. A total number of 27 thermocouples were used per wall configuration. The placement of these thermocouples on the specimen conforms with AS1530.8.1 and can be visualised in Figure 3**.** The Universal DAQ Test System Control Suite software program was used to measure and record the temperatures from the thermocouples.

4 FIRE TEST RESULTS AND DISCUSSIONS

4.1 Test 1(a) – Test Wall 1 exposed to modified CSIRO curve (Radiant Heat Exposure 2)

The following figures reveal the cladding, hot flange, cold flange, and ambient and fire side plasterboard performances during the CSIRO radiant heat flux curve test. The heat flux recorded during the flame immersion phase ranged from approximately 40-49 kW/m^2. The bushfire test results are shown in Figure 4.

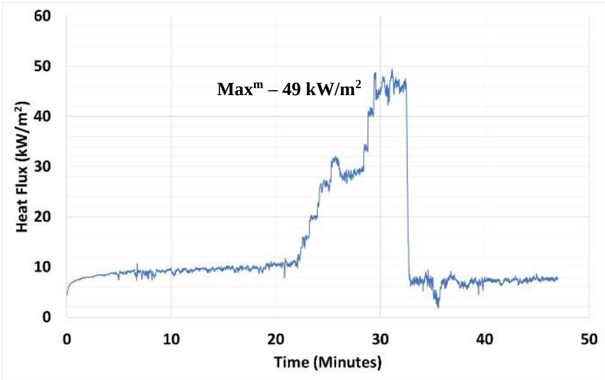

(a) Fire side heat flux

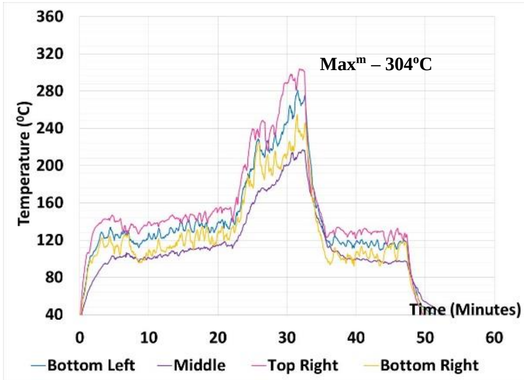

(b) Fire side cladding

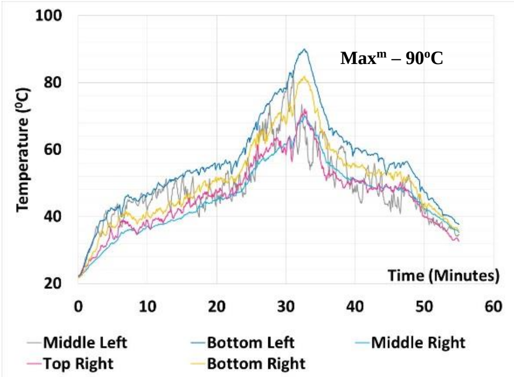

(c) Stud hot flange

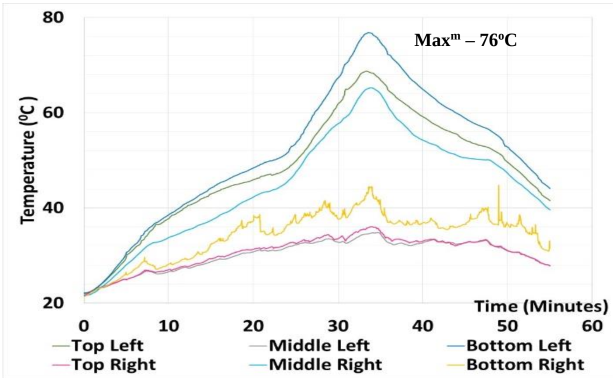

(d) Stud cold flange

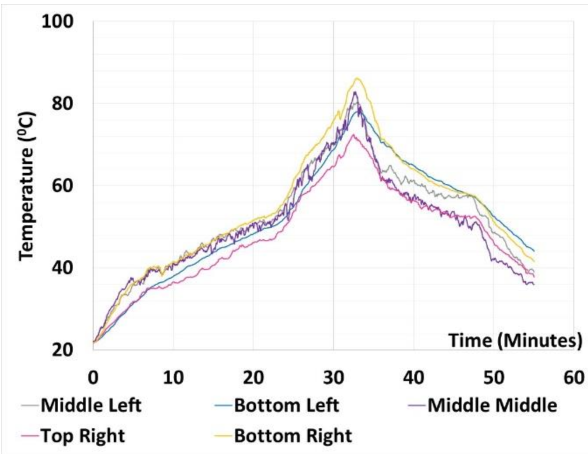

(e) Plasterboard cavity

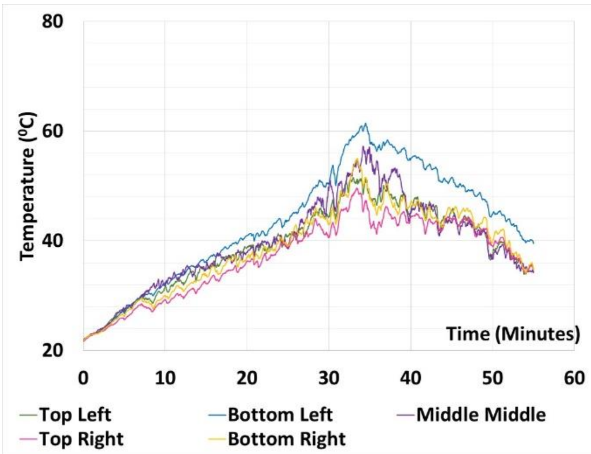

(f) Plasterboard ambient

Figure 4. Fire Test Results of Test 1(a) – Test Wall 1 exposed to modified CSIRO curve (Radiant heat exposure 2)

The cladding achieved the highest temperatures of all the wall elements, peaking at a maximum temperature of 304°C at 32 mins, occurring at the end of the 110 seconds of flame immersion (see Figure 4(b)). This temperature was recorded from the thermocouple positioned at the top right side of the cladding. The hot flange experienced a gradual rise in temperature throughout the pre-flame immersion phase, peaking at a maximum temperature of 90°C during flame immersion taken from the thermocouple positioned on the bottom left (Figure 4(c)). Whilst the hot flange did experience a significant rise in temperature in parallel to the increasing heat flux. It did not reach temperatures that would cause steel buckling or deformation. Similarly, the cold flanges reached a maximum temperature of around 76°C, which did not cause significant damage. The testing results for the cold flange are shown in Figure 4(d). It is also noted that the cavity-facing gypsum plasterboard reached a maximum of 86°C, which is 10°C hotter than the cold flange. The plasterboard's ambient side experienced a steadier temperature increase than the other elements, reaching a maximum temperature of 61°C. The testing results for the gypsum plasterboard, both cavity facing and ambient side, are shown in Figures 4(e) and 4(f), respectively. This reveals that the heat flux has a delayed impact on the ambient side of the wall due to the cladding and hot flanges acting as a thermal barrier, resulting in a slower and reduced increase in temperature. Overall, whilst the wall elements did experience an increase in temperature, they did not reach temperatures significant enough to cause any major damage. Furthermore, it is visually noted that there was no damage or deformation experienced by the wall throughout the testing duration or after testing completion.

4.2 Test 1(b) - Test Wall 1 exposed to BAL-40 curve (Radiant Heat Exposure 1)

This test exposed the wall configuration to the fire curve specified in AS1530.8.1. From the experimental results, it was observed that the maximum heat flux of 59 kW/m^2 was recorded at 1.28 mins (see Figure 5).

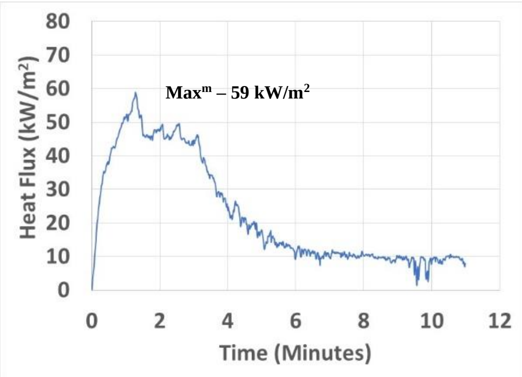

(a) Fire side heat flux

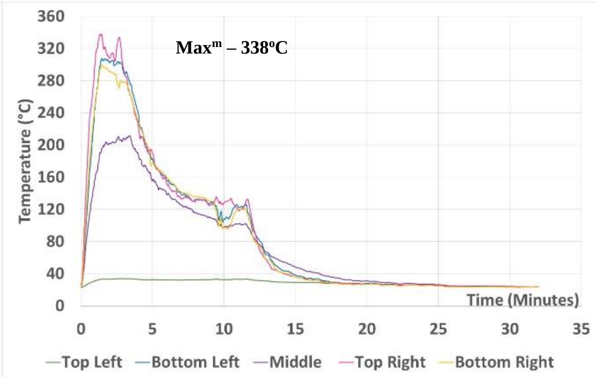

(b) Fire side Cladding

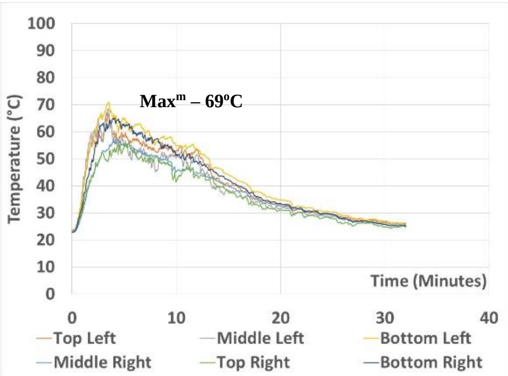

(c) Stud hot flange

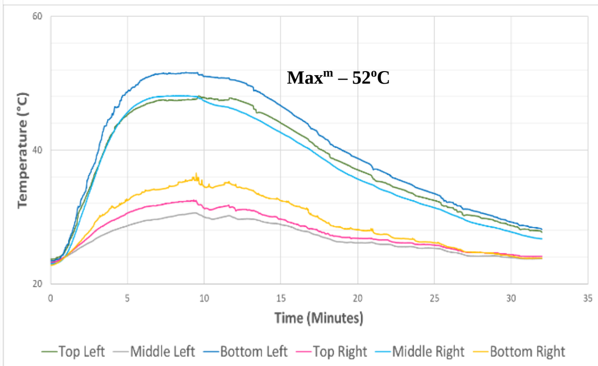

(d) Stud cold flange

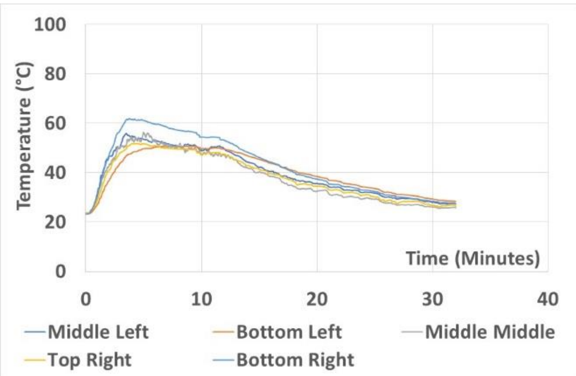

(e) Plasterboard cavity

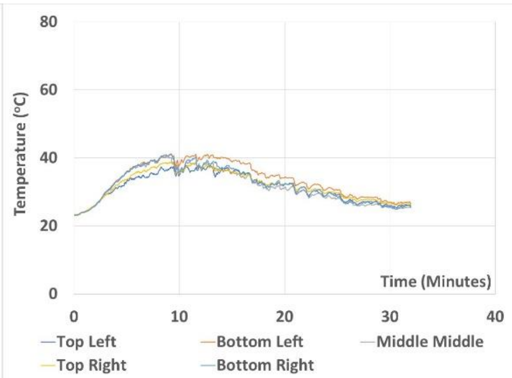

(f) Plasterboard ambient

Figure 5. Fire Test Results of Test 1(b) – Test Wall 1 exposed to BAL-40 curve (Radiant heat exposure 1)

From comparing the various elements of the wall: cladding, hot flange, cold flange, fire side plasterboard, and ambient plasterboard, it was observed that the cladding experienced the greatest average temperature fluctuation of 262°C, and the ambient plasterboard experienced the smallest average temperature fluctuation of 16°C. The top right thermocouple on the cladding recorded a maximum temperature of 338°C at 1.38 mins (see Figure 5(b)). This was closely followed by the bottom left thermocouple with a maximum temperature of 308°C at 1.45 mins. Due to an error with the thermocouple on the top left, an inaccurate temperature reading was recorded throughout the entirety of the test. Thus, the top left results were disregarded for the analysis of the wall configuration performance. From analysing the cladding temperatures, the maximum temperature recorded was 338°C (see Figure 5(b)). Figure 5(c) shows that the maximum hot flange temperature of 71°C was recorded on the bottom left hot flange at about four mins. This temperature is followed closely by the middle-left flange, recording 69°C at 3.43 mins. The cold flange, plasterboard-fire and plasterboard-ambient recorded a maximum temperature of 52°C, 62°C and 41°C, respectively (see Figures 5(d) to 5(f)). Furthermore, from observing the experiment, no physical damage was noted, such as discolouration, cracking or buckling.

4.3 Test 2(a) – Test Wall 2 exposed to modified CSIRO curve (Radiant Heat Exposure 2)

Test Wall 2(a) consisted of a steel stud wall with the addition of sarking tested for CSIRO exposure radiant heat curve. During this test, the heat flux reached its maximum during the 110 seconds simulated flame immersion phase, peaking from 45 – 53 kW/m^2 at approximately 32 mins. The heart flux movement can be seen in Figure 6(a). The cladding reached the maximum temperature of all the wall elements during this test as it was directly exposed to the radiant heat panels without any thermal protection. This temperature of 332 °C occurred at 33 mins within the testing duration, just at the end of the flame immersion phase, as seen in Figure 6(b). This indicates that the cladding took the flame immersion phase to reach the maximum as it did not occur at the start of this phase or simultaneously at the heat flux peak. Furthermore, the hot flange side of the cladding returned the second-highest maximum temperature of 91°C, as revealed in Figure 6(c). This represents a 220 °C difference in maximum temperatures, which can be attributed to the addition of the sarking material. It provides significant thermal protection to the other wall elements from the radiant heat flux emitted by the panels. The cold flange reached a maximum temperature of 70°C, seen in Figure 6(d), which occurred 35 mins into the testing duration, further highlighting the temperature delay experienced through the wall configuration from the fire side to the ambient side. Furthermore, the plasterboard reached maximum temperatures for the fire and ambient side of 68 °C and 44 °C, respectively, as seen in Figures 6(e) and 6(f).

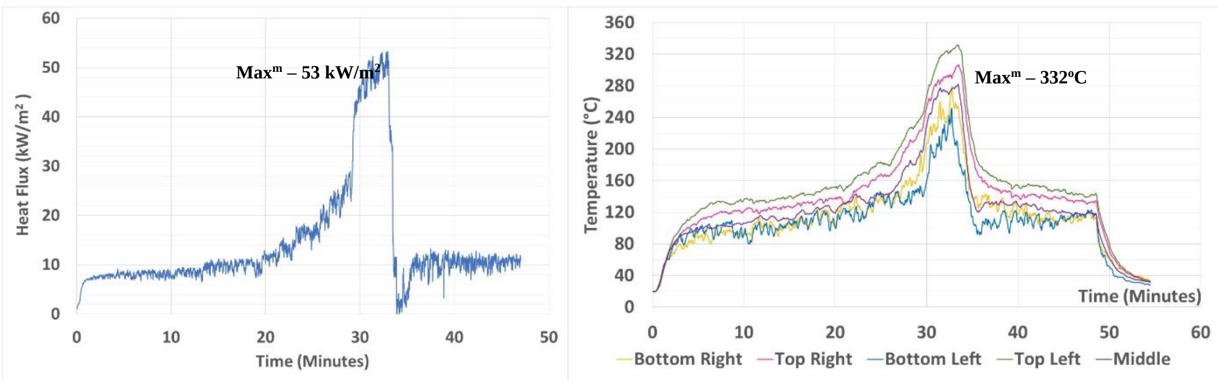

(a) Fire side heat flux

(b) Fire side cladding

Figure 6. Fire Test Results of Test 2(a) – Test Wall 2 exposed to modified CSIRO curve (Radiant heat exposure 2)

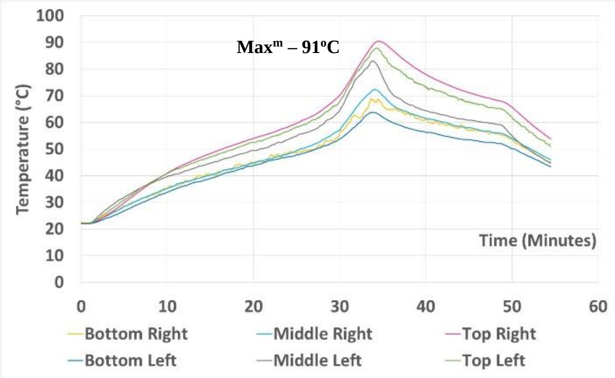

(c) Stud hot flange

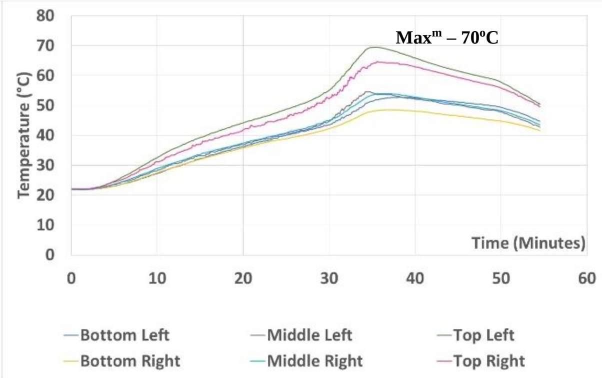

(d) Stud cold flange

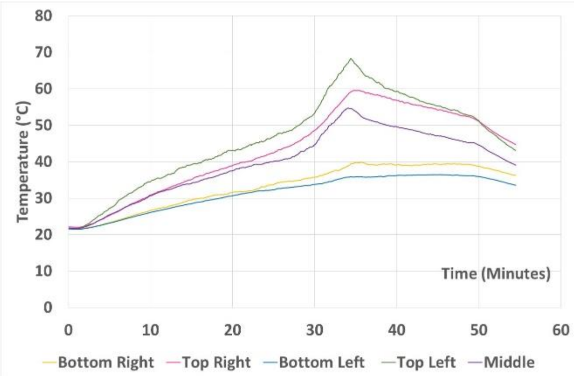

(e) Plasterboard cavity

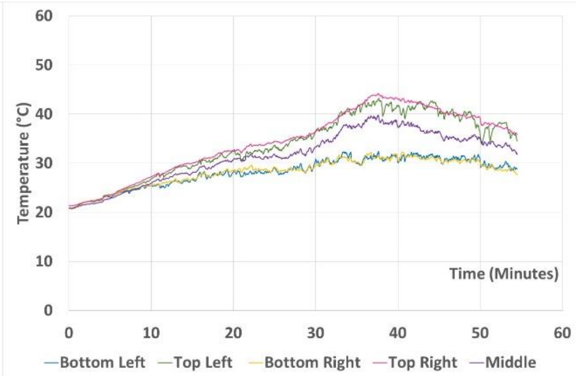

(f) Plasterboard ambient

Figure 6 contd. Fire Test Results of Test 2(a) – Test Wall 2 exposed to modified CSIRO curve (Radiant heat exposure 2)

4.4 Test 2(b) – Test Wall 2 exposed to BAL-40 curve (Radiant Heat Exposure 1)

Figure 7 shows the wall configuration's heat flux and temperature changes with sarking for the AS1530.8.1 radiant heat curve test. During this test, the maximum heat flux of 52 kW/m^2 was recorded at 3 mins, as seen in Figure 7(a). The cladding experienced the largest increase in temperature out of all the wall elements, with the fireside of the cladding reaching a maximum of 328°C at 4 mins. This maximum recording was taken from the top left thermocouple (Figure 7(b)). This reveals an approximate one-minute delay in temperature rise through the cladding element. The hot flange also experienced a significant increase in temperature, peaking at 76°C at 8 mins, as shown in Figure 7(c). In addition, the cold flange reached a maximum temperature of 59°C. This reveals a 17°C degree decrease in temperature along the flange width. The gypsum plasterboard-cavity surface reached a maximum temperature of 55°C approximately 7 mins into the testing duration (Figure 7(e)). The ambient side of the plasterboard experience the smallest fluctuation of temperature rise, with the maximum temperature of 38°C degrees recorded 13 mins after the radiant heat panels were turned off. This delay in temperature can be attributed to the other wall elements acting as a thermal barrier. Lastly, from observing the wall configuration throughout testing time, it was observed that no physical damage, such as discolouration, cracking or buckling, occurred.

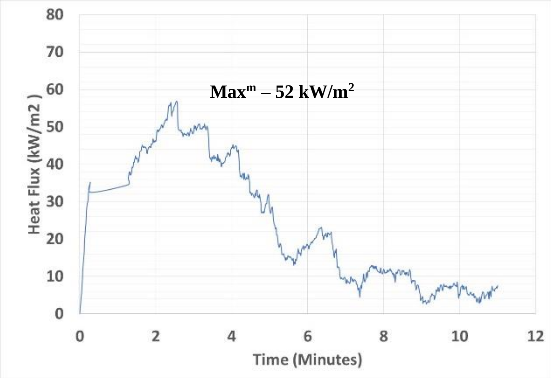

(a) Fire side heat flux

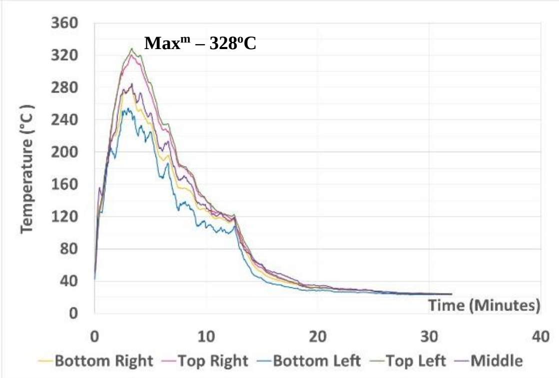

(b) Fire side cladding

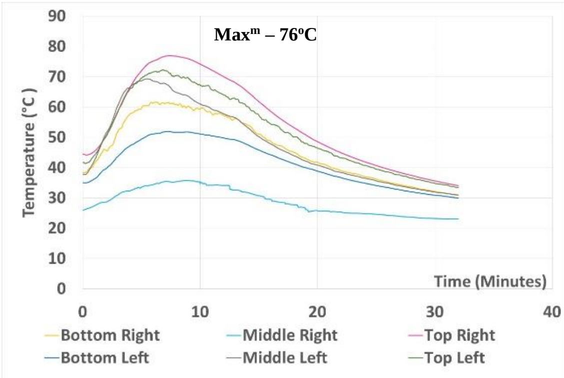

(c) Stud hot flange

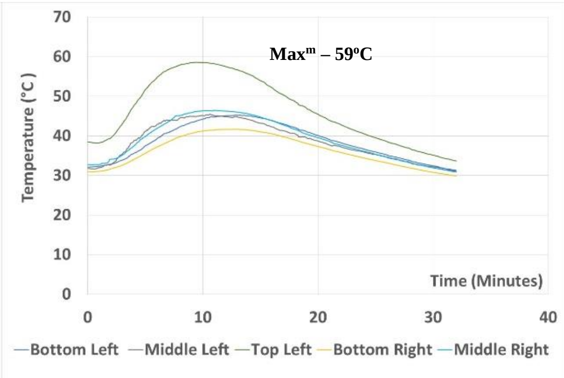

(d) Stud cold flange

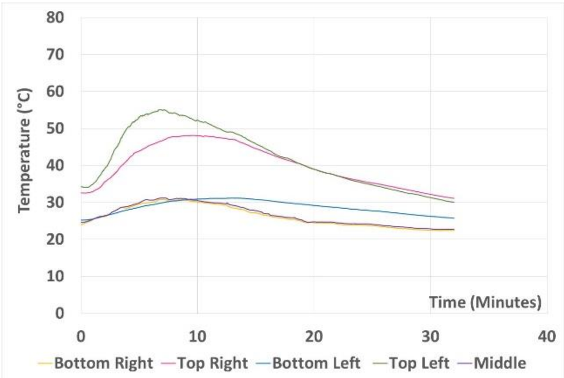

(e) Plasterboard cavity

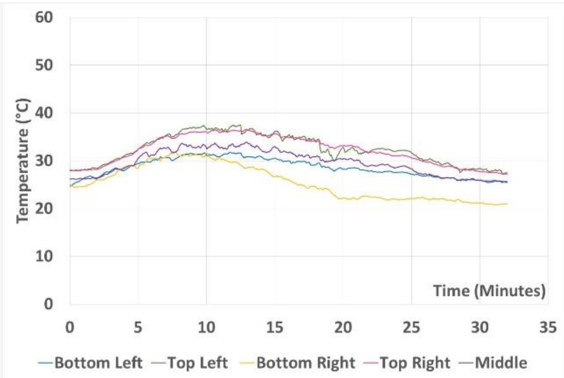

(f) Plasterboard Ambient

Figure 7. Fire Test Results of Test 2(b) – Test Wall 2 exposed to BAL-40 curve (Radiant heat exposure 1)

4.5 Discussions

This experimental investigation was completed to analyse three wall configurations when exposed to two different fire curves. The testing and analysis have been completed for Wall panels 1 and 2. However, Wall panel 3 exposed to both curves (i.e. BAL-40 and modified CSIRO curves) will be completed soon, and the results will be presented at the conference.

Comparing the results from the modified CSIRO and the BAL-40 radiant heat exposure tests show that the temperatures recorded in the materials are different. As previously discussed, the maximum temperature recorded for Tests 1(a) and 1(b) were 304°C and 308°C, respectively (Figures 4(b) and 5(b). Comparing this, the results for Tests 2(a) and 2(b) were 332°C and 328°C, respectively (Figures 6(b) and 7(b). It can be noted that the observations made, with the cladding having the highest temperature, are consistent throughout all exposures. Furthermore, it can be observed that there is no correlation between the maximum recorded temperature and the experimental bushfire curve used. Tests 1(a) and 1(b) revealed that the fire side of the plasterboard returned higher temperatures than the cold flanges, despite being at a greater distance from the radiant heat source. In Test 1(a), the maximum temperature of the fire plasterboard was 86°C, while the cold flange was 76°C. Similarly, Test 1(b) saw the fire side plasterboard reach a maximum temperature of 62°C and a cold flange of 52°C. This discovery can be attributed to increased thermal radiation between the cladding and plasterboard elements due to the lack of insulating materials provided within the wall configuration. This observation is further confirmed through the analysis of Tests 2(a) and 2(b), where the cold flange temperature was greater than the fire side plasterboard. In Test 2(a), the maximum cold flange and fire side plasterboard temperatures were 70°C and 68°C, respectively. In Test 2(b), the maximum cold flange and fire side plasterboard temperatures were 59°C and 55°C, respectively. This proves that the addition of sarking has provided extra thermal protection to the interior plasterboard wall and assisted in reducing the heat transfer between the wall elements.

Moreover, analysis of the tests revealed a delay in heat transfer through the wall elements. This is highlighted by each wall elements maximum temperature peaking at delayed intervals after the maximum heat flux was experienced. This time delay between the maximum temperature and heat flux can be attributed to the protection that is provided by the steel cladding, acting as a thermal shield. Following on from this, the time difference between the maximum heat flux and maximum temperature recorded was shorter for Tests 1(a) and 1(b) compared to Tests 2(a) and 2(b). For Tests 1(a) and 1(b), the hot flange, cold flange, and plasterboard temperatures peaked approximately three to four mins after the maximum heat flux occurred. Comparing this to Tests 2(a) and 2(b), the materials peaked at about six to seven mins after the maximum heat flux exposure. The noticeable time difference in the temperature rise can be attributed to the protection provided by the additional insulating materials. This further reinforces the importance of insulating products in homes to provide comfort and acoustic benefits, assist in the delay of heat transfer between elements, and reduce the temperature fluctuation within the internal materials of an external wall configuration during a bushfire event.

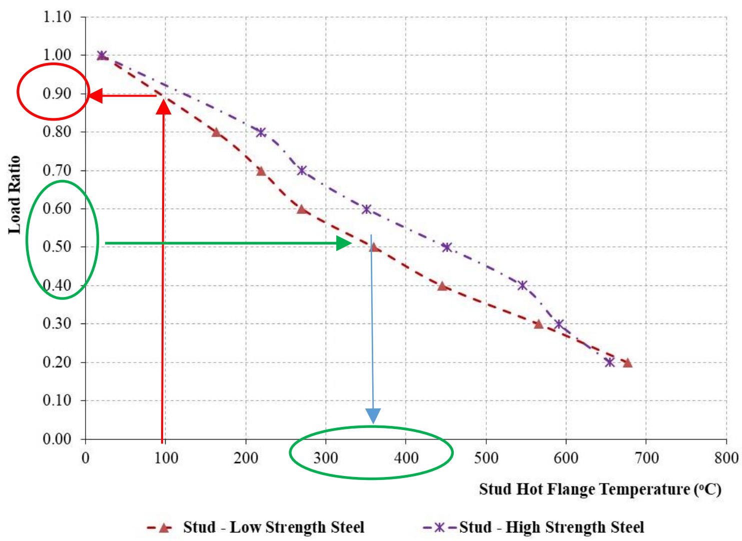

Figure 8. Load ratio vs stud hot flange temperature curves for low and high-strength steel studs.

Past studies have shown that LSF wall stud failures are mostly governed by their hot flange temperatures [12-17]. Figure 8 shows the load ratio vs stud failure times (FRL) of LSF wall stud lined with gypsum plasterboard [12]. The load ratio is the ratio of the axial compression capacity of the stud at elevated temperature to that of ambient temperature capacity (20°C). The difference in stud temperatures is due to the variations in mechanical property reduction factors for low and high-strength steel studs. As seen in Tests 1 and 2, the maximum hot flange temperature is only around 90ºC, which means the stud can carry a load ratio of 0.9 or above. It is to be noted that the maximum heat flux value was limited to 40 kW/m^2 in these tests (the measured maximum heat flux is 59 kW/m^2 in Test 1(b)). However, it can even be more than 40 kW/m^2, and in the flame zone the external wall could be subjected to around 160 kW/m^2. Generally, the design load ratio is between 0.4 to 0.6. Thus, the steel hot flange temperatures can go up to approximately 350ºC. This highlights that the load bearing studs are safe in structural adequacy when exposed to bushfire radiant heat exposures for the wall configurations considered in this study. However, LSF walls exposed to bushfire flame zone conditions need to be investigated for their structural adequacy as it is much more severe exposure than the radiant heat in terms of fire intensity.

5 CONCLUSIONS

This paper has presented an experimental study on the performance of various light gauge steel framed walls lined with plasterboard and steel cladding when exposed to simulated radiant heat exposures. Four experimental studies have been completed and analysed; Tests 1(a) and 1(b) had no insulation, and Tests 2(a) and 2(b) included internal sarking between the cladding and plasterboard. Tests 3(a) and 3(b) are still being completed, and results will be presented at the conference. The radiant heat conditions were simulated using radiant heat burners provided by the QUT Fire and Wind Lab in Banyo. The results of this experimental study have highlighted the suitability of specific materials, including steel cladding, steel studs, steel battens, and plasterboard, against BAL-40 radiant heat exposure. This study has further confirmed the importance of the integrity of cladding in enhancing the bushfire resilience of residential homes. From the elevated thermal radiation conducted within the wall elements, the importance of insulation materials has been highlighted to delay the heat transfer to the interior wall. Therefore, it is suggested to include such materials in future wall configurations to assist in radiant heat protection. To further enhance the experimental study and the usefulness of the results, it is recommended that additional testing of other wall configurations using different materials and simulating load bearing conditions is suggested.

ACKNOWLEDGEMENTS

The authors would like to thank the Australian Research Council (DE180101598) for their financial support, Queensland University of Technology (QUT) for providing the necessary research facilities and support to conduct this research project, and QUT Banyo laboratory staff members for their assistance with fire testing of walls.

REFERENCES

1. Richards, L. and Brew, N. 2019-20 Australian Bushfires – Frequently Asked Questions: A Quick Guide. Parliament of Australia.
2. http://www.bom.gov.au/state-of-the-climate/australias-changingclimate.shtml.
3. Bushfires in Australia, CSIRO Submission 09/355. Prepared for the 2009 Senate Inquiry int Bushfires in Australia
4. https://www.bushfirecrc.com/sites/default/files/downloads/act_bushfire_crc_report.pdf
5. Standards Australia Limited. Construction of buildings in bush fire prone areas. Standard AS 3959:2018, Standards Australia Ltd Sydney, 2018.
6. CSIRO. (2020). Bushfire Resilient Building Guidance for QLD Homes. Queensland: QLD Government. https://www.qra.qld.gov.au/sites/default/files/2020-2/0576_qra_bushfire_guideline_v10_pages_print.pdf
7. National Association of Steel Framed Housing Inc. “Nash Standard Steel Framed Construction in Bushfire Areas, Standard NS300, Australia, 2021

8. Standards Australia Limited. Methods for fire tests on building materials, components and structures, Part 8.1: Tests on elements of construction for buildings exposed to simulated bushfire attack – Radiant heat and small flaming sources. Standard AS1530.8.1:2018, Standards Australia Ltd Sydney, 2018.
9. Pancheti, J., Mahendran, M. and Steau, E. (2021). Fire Resistance of External LSF Walls with Corrugated Steel Cladding. Journal of Constructional Steel Research, 188. https://doi.org/10.1016/j.jcsr.2021.107008
10. Dias. Y. Mahendran, M. and Keerthan, P. (2021). Full-Scale Fire Resistance Tests of Steel and Plasterboard Sheathed Web-Stiffened Stud Walls. Thin-Walled Structures, 137(1), 81-93. https://doi.org/10.1016/j.tws.2018.12.027
11. Hendawitharana, S., Ariyanayagam, A., Mahendran, M. and Steau, E. Experimental Study of LSF Walls Exposed to Simulated Bushfires, Fire Safety Journal, 2022, Under Review.
12. Ariyanayagam, A and Mahendran, M. (2018). Fire performance of Load Bearing LSF Wall Systems Made of Low Strength Steel Studs. Thin-Walled Structures, 130, 487–504. https://doi.org/10.1016/j.tws.2018.05.018
13. Gnanachelvam, S., Ariyanayagam, A. and Mahendran, M. (2020). Fire resistance of LSF wall systems lined with different wallboards including bio-PCM mat. Journal of Building Engineering 32, 101628. https://doi.org/10.1016/j.jobe.2020.101628.
14. Magarabooshanam, H., Ariyanayagam, A. and Mahendran, M. (2020). Fire resistance of non-load bearing LSF walls with varying cavity depth, Thin-Walled Structures 150, 106675. https://doi.org/10.1016/j.tws.2020.106675
15. Ibralebbe, M., Keerthan, P., Ariyanayagam, A. and Mahendran, M. (2015). Numerical studies of gypsum plasterboard and MGO board lined LSF walls exposed to fire, Proceedings of the Second International Conference on Performance-based and Lifecycle Structural Engineering (PLSE 2015), School of Civil Engineering, The University of Queensland.
16. Ariyanayagam, A. and Mahendran, M. (2013). Fire safety of buildings based on realistic fire time-temperature curves. Proceedings of the 19th International CIB World Building Congress, Brisbane 2013: Construction and Society, Queensland University of Technology.
17. Ariyanayagam, A. and Mahendran, M. (2012). Fire tests of load bearing steel stud walls exposed to real building fires. 7th International Conference on Structures in Fire, 105-114.

SiF 2022– The 12th International Conference on Structures in Fire
The Hong Kong Polytechnic University, Nov 30 - Dec 2, 2022

FIRE RESPONSE OF SELF-CENTERING CONCRETE JOINT AND THEIR POST-FIRE SEISMIC PERFORMANCE

Zhenli Wu[1], Lingzhi Li[2], Zhoudao Lu[3]

ABSTRACT

Self-centering joints always show good seismic performance and self-centering capacity. However, there is rare study on fire response of self-centering joint. This paper presents a comprehensive experimental study on the fire response of self-centering beam-column joints as well as their post-fire seismic performance. In total, two joints were designed and fabricated. One was used as reference and the other subjected to constant vertical loads on the beam ends was tested under the ISO-834 fire. The fire test terminated after 171min without reaching failure limit states. The test results indicate that the fire resistance of self-centering joint is satisfactory. Then both joints were tested under quasi-static loading. The fire exposure significantly affected the post-fire seismic performance of self-centering joint. Nevertheless, self-centering joint could sustain severe seismic excitation after fire exposure.

Keywords: self-centering joint; fire response; seismic performance; post-fire

1 INTRODUCTION

With the rapid development of the city, the possibility of fire hazards is in an increasing trend to occur in structures, especially in building. The fire responses of joints have been investigated for years. Effects of fire scenarios [1], pre-damaged structural design [2], and the interaction in the joints [3] were considered. The influences of fire on the material strength loss and degradation in the rotation capacity of the joint [4] were also demonstrated.

In recent years, self-centering joints have been proposed to eliminate the structural damage, residual displacement of the structures [5, 6]. Meanwhile, the preferable seismic performance of self-centering joints was validated [7-9]. Typically, self-centering joints are assembled by using the unbonded prestressing tendons and steel friction-dissipating devices. However, the unbonded prestressing tendons susceptible to stress relaxation and premature rupture during fire [10]. In addition, the influence of the steel friction-dissipating devices is more complex than that at ambient temperature. Thus, self-centering joint has great promise to clarify their fire performance. To data, there has been no detailed study on the post-fire seismic performance of self-centering joint. It remains unknown whether the use of self-centering joint after exposure to fire. Degradation of the material in fire may significantly compromise their post-fire performance.

The aim of this research is to investigate the fire response of self-centering joint and their post-fire seismic performance through experiment. To this end, two self-centering joints were designed and

[1] PHD, Tongji University
e-mail: wzlsdd@tongji.edu.cn
[2] Associate professor, Tongji University
e-mail: lilingzhi@tongji.edu.cn
[3] Professor, Tongji University
e-mail: lzd@tongji.edu.cn
https://doi.org/10.6084/m9.figshare.22178078

fabricated. One joint was exposed to ISO-834 fire; the other joint was taken as the control specimen, not exposed to fire. Then, both joints were tested under constant vertical loading and quasi-static loading.

2 EXPERIMENTAL PROGRAM

The experimental campaign included two full-scale self-centering RC joints was divided into two phases, namely: fire resistance test followed by quasi-static loading test. The control joint SC-S was only tested under quasi-static loading to provide the seismic response of self-centering joint. The other joint SC-F-S was exposed in standard fire testing in a furnace and subsequently tested under quasi-static loading, evaluating the fire resistance and post-fire seismic performance of self-centering joint.

2.1 Design and fabrication of test specimens

Both self-centering joints had identical geometry and reinforcement detailing, as shown in Figure 1. They were designed according to Chinese standard code [11, 12]. A joint was assembled with two beams and one column prefabricated individually to emulate the field conditions. PT tendons and bolted top-seat angles were used as connections. Belleville washers and 2mm thick brass shim were adopted to maintain stable bolt forces.

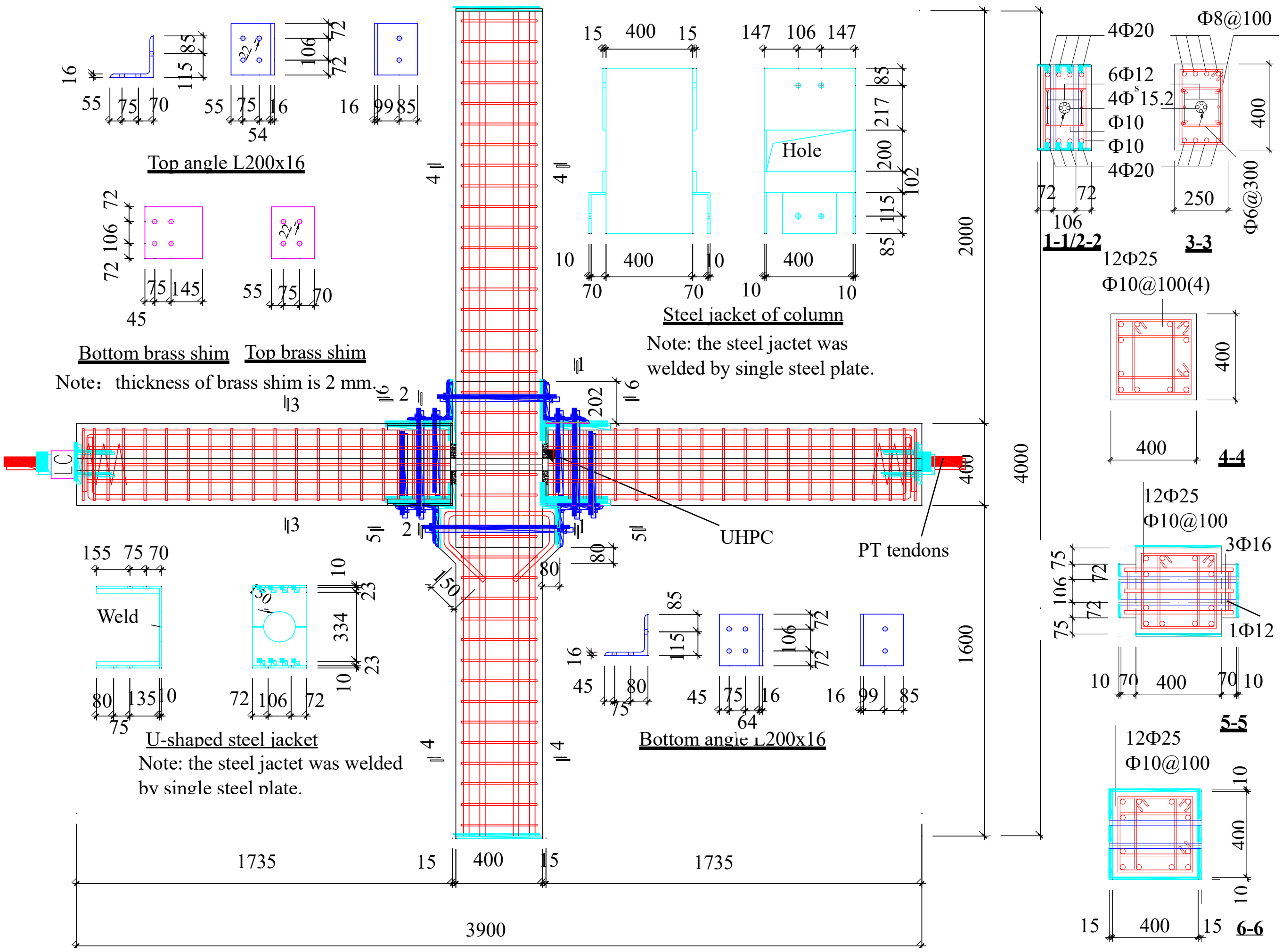

Figure 1 Geometry and reinforcement detailing

The column was 4000 mm height with a square cross section of 400×400 mm dimensions. Steel plates embedded at column core were welded together to protect concrete from local crushing. Four 25-mm-diameter ducts were left inside column to accommodate high strength bolts with diameter of 22 mm. The beams were 1735 mm long with a rectangular cross section of 250×400mm. In order to avoid concrete crushing at beam ends, U-shaped steel jackets were designed. The longitudinal reinforcements and stirrups in U-shaped region were welded to U-shaped jacket for anchoring. Two bolts with diameter of 22 mm were run through the reserved beam-holes to clamp 250 mm long L200×16 angles on the beam face, while the other four bolts were installed in the beam before casting. The bolts were pretensioned to a uniform torsion. Unbonded PT force was provided by four 15.2 mm diameter PT tendons placed in reserved ducts. The initial PT forces in joint SC-S and SC-F-S were 527 kN and 379.9 kN, respectively. In addition, the joint core was thermally insulated with 2 mm thick intumescent fire-retardant coating.

2.2 Material properties

Table 1 summarize the average values of concrete and steel properties, where ultimate strength of concrete is the cube compressive strength. The steel properties were based on tension testing of metallic material in accordance with GB/T 228 [13], where the tension coupons were taken according to GB/T2975 [14]. Each PT tendon was a seven-wire low relaxation Grade 1860 strands with the nominal ultimate strength of 1860 MPa, in a nominal area of 140 mm^2.

Table 2 Average values of concrete and steel mechanical properties

Specimen	Concrete	PT tendon	Angle	Bolt	Reinforcement bars (mm)				
					8	10	12	20	25
Yield strength (MPa)	-	1790.5	339.3	596.5	577.3	541.2	470.1	442.3	447.7
Ultimate strength (MPa)	55.4	1916.0	527.0	691.7	655.9	649.1	578.9	554.1	572.1
Elastic modulus (GPa)	45.0	195.0	201.3	182.3	206.0	207.5	208.2	208.5	204.2

2.3 Test setup and test procedure

2.3.1 Fire test

For fire test, the joint was fixed in the furnace with an internal dimension of 3.2 x 2.2 x 3.2 m as shown in Figure 2a. A hole with a dimension of 490 x 585 mm was set at each firewall to stretch beam end out of furnace. The column axial load was exerted by a jack with a capacity of 1000 kN. A load cell was equipped to monitor the load. Steel column was placed between the load cell and joint to protect load cell. For the beam load, balance weights were used. After a constant load state was reached, the joint was exposed to fire to investigate the influence of fire scenario on the fire response of self-centering joint. The furnace temperature was controlled to obey ISO-834 heating curve [15]. The test was terminated until the joint failed or laboratory rules forbidden in accordance with the failure criterion in ISO-834. After the furnace was turned off, the furnace cover lid was partially opened to allow the joint down to room temperature naturally. The ISO 834 and furnace temperature-time curves were compared in Figure 3a. In heating stage, the measured furnace temperatures were in good agreement with that in ISO 834.

For joint SC-F-S, which would expose to fire, load cell, strain gauges and displacement transducers was also applied to record PT force, joint deformation and the response of reinforcement bars, respectively. Notably, load cells for monitoring bolt forces and strain gauges on steel angles were rescinded in joint SC-F-S, due to their low fire resistance. The temperatures in SC-F-S were monitored by Type-K thermocouples positioned before concrete casting, as shown in Figure 2b.

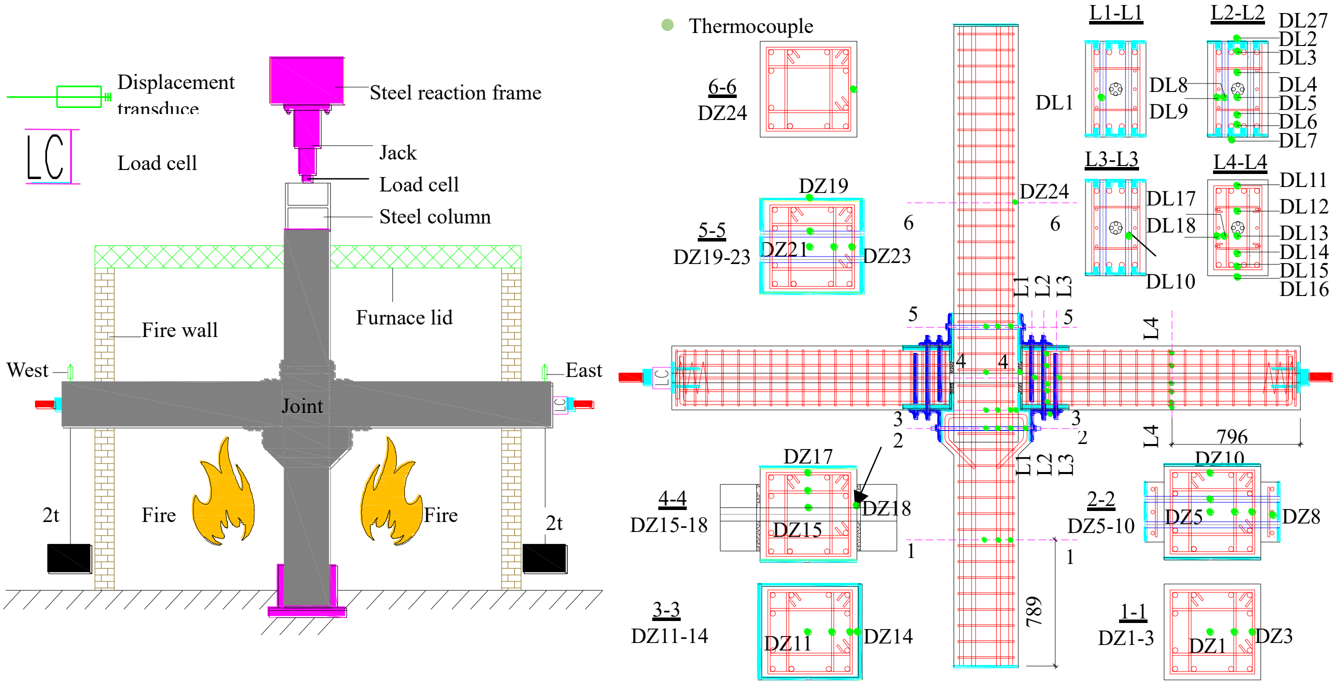

(a) Test setup (b) Layout of thermocouples (dimensions in mm)

Figure 2 Fire test setup and instrumentation

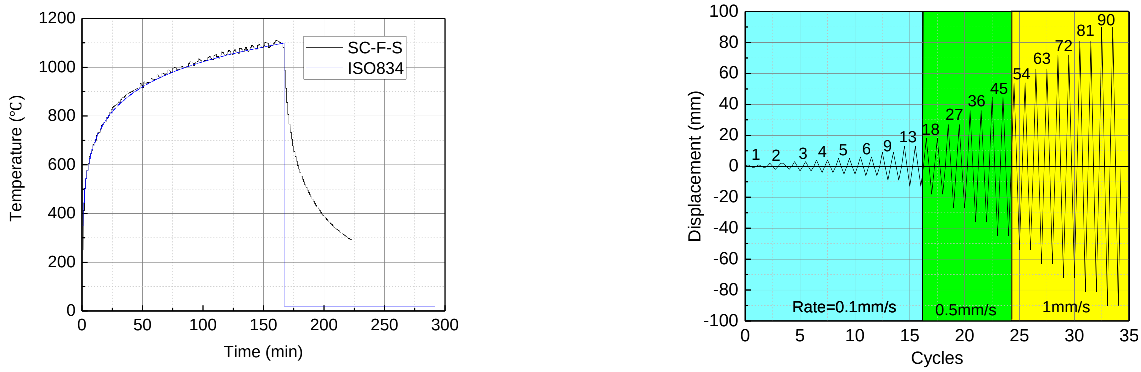

(a) ISO 834 and furnace temperature-time curves (b) Loading protocol for seismic test

Figure 3 Loading protocol

2.3.2 Seismic test

The real and schematic view of test setup are shown in Figure 4. A vertical axial load of column was 650 kN applied by a 1000 kN hydraulic jack. Displacement-controlled antisymmetric cyclic load was exerted by two MTS actuators at the tip of joint beams as shown in Figure 3b. It can be found that the loading cycle amplitudes in protocol were designed in terms of drift ratio of beam end. The distance between column centerline and loading point is 1.8 m. The loading of SC-S was terminated at 5% beam end drift ratio. For SC-F-S, loading was continued until strength degradation occurs.

The instrumentation for the control joint SC-S included: displacement transducers to monitor gap opening and closing at the beam-column interface, the deformations of beam and column, as shown in Figure 4; strain gauges to measure the strain in reinforcement bars, top and seat steel angles; load cells to measure the force in PT tendons and bolts. After cooled to ambient temperature, the joint SC-F-S was moved to the seismic loading system without repair.

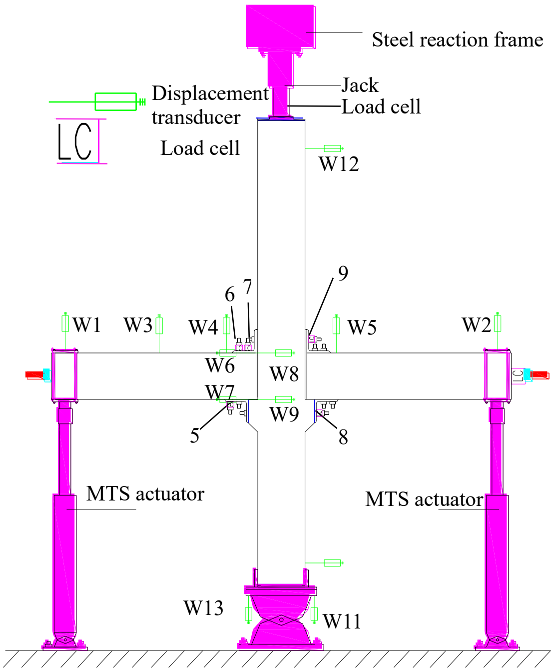

Figure 4 Details of test setup and instrumentation

Note: N is the north direction of the joint, S is the south direction.

3 FIRE TEST RESULTS

3.1 Typical deformation mode

The fire test on joint SC-F-S terminated after approximately 171 min of fire exposure owing to furnace pressure. It means that SC-F-S did not fail, which was still in serviceability limit state. Figure 5a shows the condition of joint SC-F-S after opening the furnace. Following the fire test, the members of SC-F-S appeared in almost the original position. No visible deflection can be observed. Severe discolouration of concrete surface was remarkable, due to the change of concrete composition and texture after reaching a temperature of 800°C. Lots of hairy cracks were observed on the beam and column surface. The conners of beams and column were cracked and fell off. Concrete spalling occurred to column, especially to the out of plane direction of column, where spalling reached the stirrups. Figure 5b presents SC-F-S removed from the furnace to seismic system. In the further inspection of joint fixed in seismic system, a layer of approximately 10-20 mm of concrete cover in post-fire region had flaked and popped off. The pre-tensioned bolt forces were degraded completely. Because the nuts loosed could be screwed by hand.

(a) The condition after opening the furnace (b) Fixed in seismic system

Figure 5 Visual appearance of SC-F-S after fire test

3.2 Thermal response

The temperatures of outer surface of joints in Figure 6-7 were considerably lower than furnace temperature. The temperatures of beam at the same depth were basically in coincidence in beam-height direction as shown in Figure 6. Nevertheless, the temperatures at the side of beam were higher than that of point at the same depth on top and bottom of beam, due to the burners installed on the firewall. The temperatures of connection region protected by fire-retardant coating were lower than that of beam section and column section without fire-retardant coating. In addition, the larger cross-section of joint core was also contributed to its slower growth of temperature.

A plateau phase of the heating curves after reaching 100℃ was observed in the interior concrete, which was longer with the deeper distance in concrete members. This may be due to the vaporization of the remaining free water stored in concrete, which can absorb a large amount of heat input and hence delays the temperature increase at the initial stage. Furthermore, temperature started to rise faster upon the water vaporized completely. It is interesting to found that the maximum temperatures of the interior concrete were achieved in the cooling stage. The temperatures continued to rise after turned off the furnace, primarily resulting from high thermal inertia of concrete. The temperatures of PT tendons were lower than 427℃, the critical temperature of strength failure in the beam according to the codes [16-18].

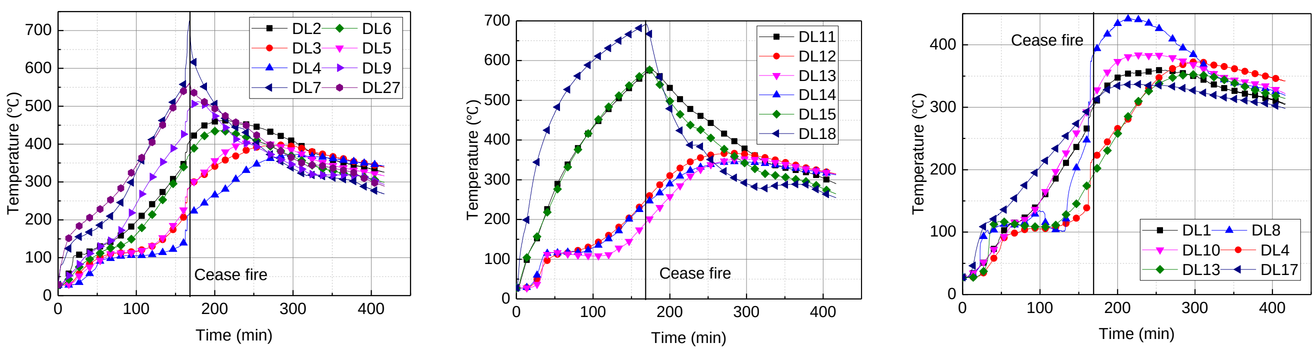

Figure 6 Temperatures for beam

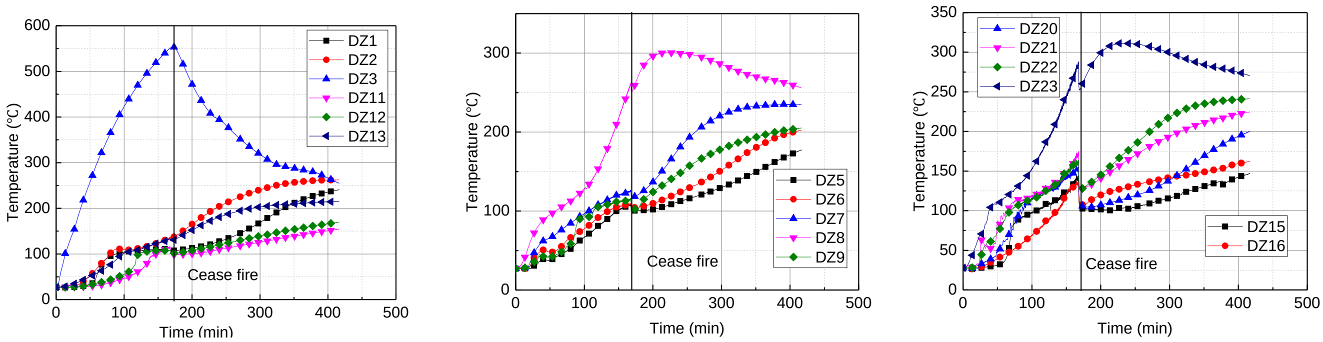

Figure 7 Temperatures for column

3.3 PT force

The evolution of PT force in PT tendons during the fire test was shown in Figure 8. PT force undergone an increase till 118 min of fire exposure and subsequently followed a decease till finished the observation. The increase in PT tendons was mainly attributed to the thermal expansion and increasing deflection of beam. However, once the material degradation caused by increasing temperature overcame the effect of elongation in PT tendons, a consistent reduction in PT tendons occurs. The loss of PT tendons was less than 50% of their strength at the time of turning off the furnace.

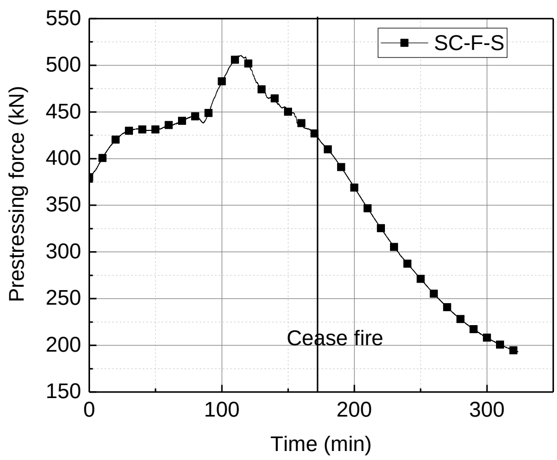

Figure 8 PT force in PT tendons

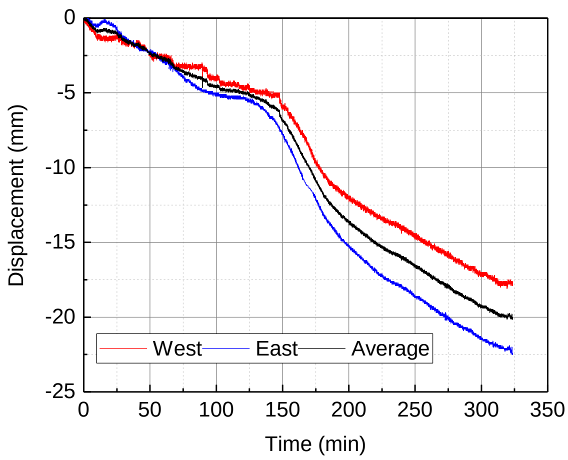

Figure 9 Beam ends deflection of SC-F-S

3.4 Structural response

Structural response of beam in SC-F-S is shown in terms of beam-ends deflection in Figure 9. The displacement of both beam ends increased at a high pace in the first 10 min of fire exposure. A moderate increase in beam-ends displacement occurs till 118 min of fire exposure, resulting from the PT force increase which can overcome the effect caused by material degradation and cracking/crushing of concrete. Once PT force decreased, a significant increase in the pace of displacement occurs till furnace turned off. The deflection of beam ends continued at the cooling stage. This results from the continuous growth of temperature in joint. Remarkably, the displacement at beam ends did not reach the failure criterion of beam in ISO-834. It indicates that the fire resistance of SC-F-S was larger than the testing duration of 171 min, closing to fire resistance of column and joint in ISO-834. Shortly, self-centering joint has an excellent fire resistance.

4 SEISMIC TEST RESULTS

4.1 Test phenomena and failure characteristics

The phenomena of joint SC-S not exposed to fire, which served as control joint for the experimental study, was discussed first. Figure 10 depicts the test phenomenon of joint SC-S at displacement of 90 mm and original position unloaded from 90 mm. Gap-opening and gap-closing at the beam-column interface were observed at the target displacements. Good recentering of joint was achieved after unloading. The damages of joint were mainly concentrated on bolted angle connections. Only fine concrete cracks associated to bending in beam and column. Diagonal cracks developed at column corbel due to its inadequate shear capacity. No concrete crushing was observed. Yielding of reinforcing bars and PT tendons did not appear during the entire test.

(a) At displacement of 90 mm (b) After the test

Figure 10 Deformation phenomena of SC-F-S

Compared to control joint SC-S, post-fire joint SC-F-S was subjected to cyclic loading till failure. SC-F-S failed without visible fracture in bolted angles at displacement of 114 mm, as shown in Figure 11. Unsurprisingly, PT tendons remained elastic during the entire test. Similar to SC-S, no concrete crushing occurred during the gap-opening and gap-closing process. Damages were concentrated on bolted angles. Differently, diagonal cracks appeared initially at loading points. Residual gap was observed at the interface of angle and column after test. The bolt nuts were loose.

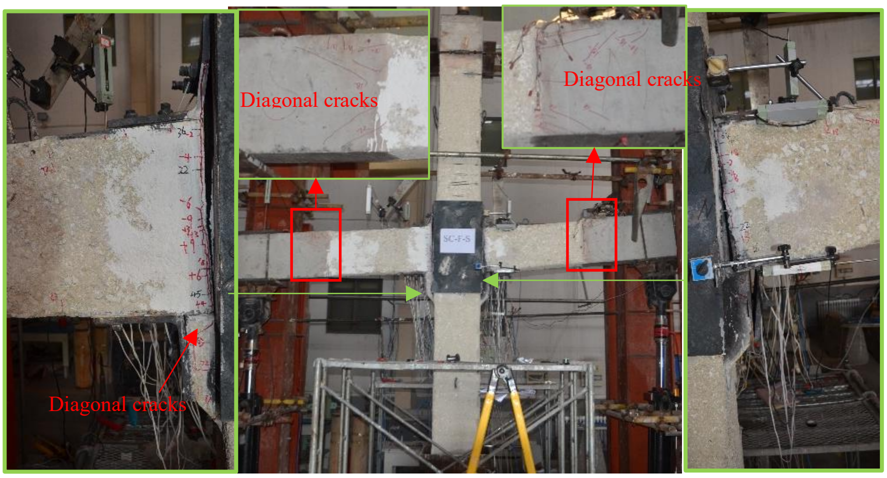

(a) At failed displacement

(c) After the test

Figure 11 Failure mode of joint SC-F-S

4.1.3 PT force

The PT tendons providing a recentering force that varied with displacement, as shown in Figure 12. The initial PT forces of post-fire joint SC-F-S was substantially lower than that of unheated joint SC-S, while the variation of PT tendons for SC-F-S was higher than that for SC-S. The PT forces loses increased with the increased displacement, not exceeding 10% in both joints for the displacement less than 100 mm. According to the records, yielding of PT tendons and concrete crushing did not occur. Therefore, all PT force losses mainly caused by duct friction.

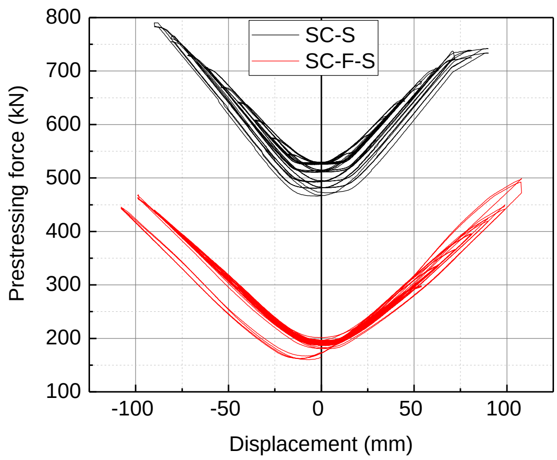

(a) N direction

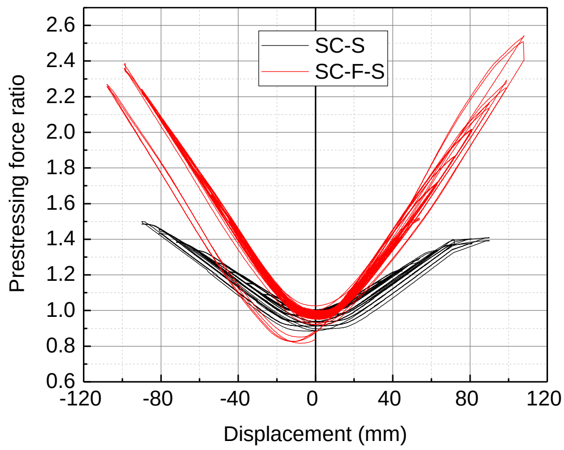

(b) S direction

Figure 12 PT force

4.2 Force vs displacement

The influence of fire-induced damage on the cyclic performance of self-centering joint is evaluated by direct contrast between the results obtained in quasi-static tests of post-fire joint SC-F-S and the control joint SC-S as shown Figure 13. The hysteretic curves of SC-S indicate stable response without strength degradation till 5% drift cycle (displacement of 90 mm). Post-fire joint SC-F-S was failed at displacement of 114 mm. It implies that the deformation capacity of self-centering joint remained adequately high to sustain severe seismic excitation after fire exposure. The hysteresis behavior of joint SC-F-S shows an apparent decrease in initial stiffness and peak force as the control joint. The loss of bearing capacity for post-fire joint SC-F-S is primarily attributed to the loss of PT force and bolt forces. This demonstrates that fire-induced damages have an enormous effect on the hysteresis behavior of self-centering joint.

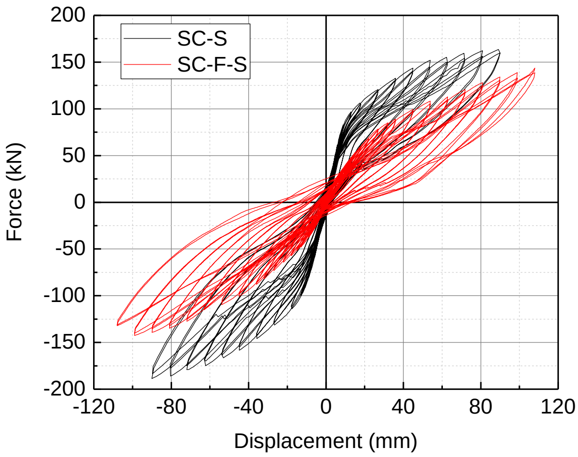

(a) N direction

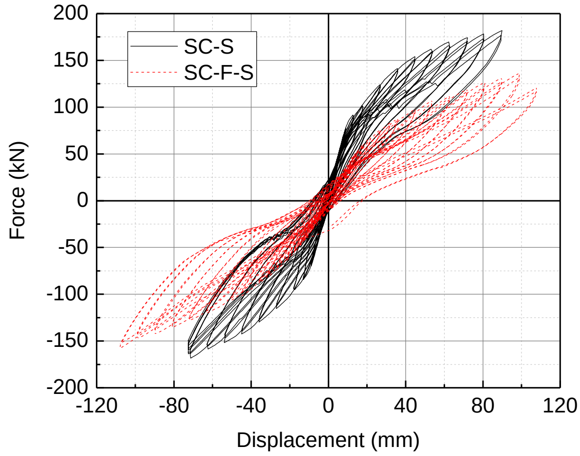

(b) S direction

Figure 13 Load-displacement relationship

5 CONCLUSION

This paper investigated the fire and post-fire response of self-centering joint. Fire test was carried out on a self-centering joint to investigate its fire performance. Cyclic loading tests were conducted on the post-fire joint and unheated joint to investigate the post-fire performance of self-centering. The main conclusions of this paper are as follows:

(1) Self-centering joint exhibited satisfactory fire resistance.

(2) Most damages of self-centering joint occurred at bolted angles. Only some minor cracks appeared at beam and column. PT tendons remained elastic throughout the test, providing a good recentering capacity for the joint.

(3) After fire exposure, the hysteretic behavior of self-centering was significantly reduced. However, self-centering joint could sustain severe seismic excitation after fire exposure.

ACKNOWLEDGMENT

This work was financially supported by the Nation Natural Science Foundation of China (Project No. 51778496 and Project No.51778497).

REFERENCES

1. Li, X. L., Xu, Z. B., Bao, Y., Cong, Z. G., Post-fire seismic behavior of two-bay two-story frames with high-performance fiber-reinforced cementitious composite joints, Engineering Structures, Vol. 183, 2019, pp. 150-159.
2. Cai, Z. W., Yu, J. T., Tian, L. K., Liu, F. C., Yu, K. Q., Fire resistance of post-earthquake steel beams insulated with a novel fire-resistive coating- fr-ecc, Engineering Structures, Vol. 246, 2021, pp. 112887.
3. Wang, Y. C., Dai, X. H., Bailey, C. G., An experimental study of relative structural fire behaviour and robustness of different types of steel joint in restrained steel frames, Journal of Constructional Steel Research,

Vol.67, 2011, pp. 1149-1163.

4. Raouffard, M. M., Nishiyama, M., Fire response of exterior reinforced concrete beam-column subassemblages, Fire Safety Journal, Vol. 91, 2017, pp. 498-505.
5. Nakaki, S. D., Englekirk, R. E., Presss industry seismic workshops: concept development, PCI Journal, Vol. 36, 1991, pp. 54-61.
6. PRIESTLEY, J. M., The presss program: current status and proposed plans for phase III, PCI Journal, Vol. 41, 1996, pp. 22-40.
7. El-Sheikh, M., Seismic analysis, behavior, and design of unbonded post-tensioned precast concrete frames. Pennsylvania: Lehigh University, 1997.
8. Guo, T., Xu, Z., Song, L., Wang, L., Zhang, Z., Seismic resilience upgrade of RC frame building using self-centering concrete walls with distributed friction devices, Journal of Structural Engineering, Vol. 143, 2017, pp. 04017160.1-04017160.11.
9. Morgen, B. G., Kurama, Y. C., Seismic response evaluation of posttensioned precast concrete frames with friction dampers, Journal of Structural Engineering, Vol. 134, 2008, pp. 132-145.
10. Gales, J., Bisby, L., Gillie, M., Unbonded post tensioned concrete slabs in fire–part II–modelling tendon response and the consequences of localized heating, Journal of Structural Fire Engineering, Vol. 2, 2011, pp. 155-171.
11. GB50010-2010. Code for design of concrete structures, Beijing: China Architecture & Building Press, 2015.
12. GB50011-2010. Code for seismic design of buildings, Beijing: China Architecture & Building Press, 2016.
13. GB/T 228. Matallic materials-tensile testing at ambient temperature, Beijing: China Architecture & Building Press, 2010.
14. GB 2975. Rules for sampling in mechanical and technological testing of steel products, Beijing: China Architecture & Building Press, 1998.
15. ISO 834-1. Fire resistance tests-elements of building construction-part 1: general requirements, 1999.
16. ACI 216.1-14. Code requirements for determining fire resistance of concrete and masonry construction assemblies. Farmington Hills: Farmington Hills, MI: American Concrete Institute, 2014.
17. ASTM E119-18. Standard test methods for fire tests of building construction and materials. West Conshohocken, PA: American Society for Testing and Materials, 2018.
18. PCI MNL124-18. Specification for fire resistance of precast/restressed concrete: IL: Precast/Prestressed Concrete Institute, 2018.

LARGE SCALE FIRE TEST: TRAVELLING FIRE WITH FLASHOVER UNDER VENTILATION CONDITIONS AND ITS INFLUENCE ON THE SURROUNDING STEEL STRUCTURE

Ali Nadjai[1], Naveed Alam[2], Marion Charlier[3], Olivier Vassart[4], Jean-Marc Franssen[5], Stephen Welch[6], Johan Sjostrom[7]

ABSTRACT

In the frame of the European RFCS-TRAFIR project, different natural fire tests in large compartment were conducted by Ulster University, involving steel structure and aiming at understanding the conditions in which a travelling fire develops, how it behaves and impacts the surrounding structure. During the experimental programme, the path and geometry of the travelling fire was studied and temperatures, heat fluxes and spread rates were measured. This paper presents the selected experimental data from the third fire test in terms of gas temperatures recorded in the test compartment at different positions and levels. The paper also presents the influence of the traveling fire with flashover on the surrounding structure via temperatures recorded in the selected steel columns and beams. The temperatures in the test compartment were found to be dependent on the positioning of the travelling fire as well as on the height from the floor level. It was found that the non-uniform temperatures in the compartment lead to transient heating of the nearby structural steel elements which is different from a standard furnace test. These non-uniform elevated temperatures result in a reduction of the fire resistance of the structural elements which may influence the global stability of the structure. The results obtained during the test and lessons learnt will help to understand the behaviour of the travelling fires and their influence on the structural members. This knowledge will help to reduce the travelling fire associated risks in future.
Keywords: Travelling fire tests; Natural fire tests; Steel Structure; Large-scale compartment tests, Travelling fire with flashover

1 INTRODUCTION

It is well established that the response of a structure subjected to fire is dependent on the fire exposure conditions. Small compartment fires behave in a well understood manner defined as a post-flashover fire

[1] FireSERT, Ulster University, School Built Environment,
a.nadjai@ulster.ac, ORCID: https://orcid.org/0000-0002-9769-7363
[2] FireSERT, Ulster University, School Built Environment
n.alam@ulster.ac.uk, ORCID: https://sandbox.orcid.org/0000-0003-3637-1113
[3] ArcelorMittal Global R&D (Luxembourg)
marion.charlier@arcelormittal.com, ORCID: https://orcid.org/0000-0001-7690-1946
[4] ArcelorMittal Global R&D (Luxembourg)
olivier.vassart@arcelormittal.com, ORCID: https://orcid.org/0000-0001-5272-173X
[5] Liege University, Civil Engineering Department, Liege, Belgium
jm.franssen@ulg.ac.be, ORCID: https:// orcid.org/0000-0003-2655-5648
[6] School of Engineering, BRE Centre for Fire Safety Engineering, The University of Edinburgh, Edinburgh, United Kingdom
e-mail: firstname.lastname@address, ORCID: https://orcid.org/0000-0002-9060-0223
[7] RISE Research Institutes of Sweden
johan.sjostrom@ri.se, ORCID: https://orcid.org/0000-0001-8670-062X
https://doi.org/10.6084/m9.figshare.22178087

with uniform temperatures. Over time, the building designs have evolved and with modern architecture, there is an increase of open large-floor plan spaces, for which the assumption of post-flashover fire and uniform temperatures does not hold [1,2]. Instead, there is a smaller localised fire that moves across the floor starting in a certain area or a point. The current standard fire as well as the compartment fire exposure conditions have been developed by using data from small compartment tests. The existing test data is available from small compartment tests, the concept of a uniform distribution of gas temperatures fits well when dealing with similar scenarios. In case of large compartments, the assumption of uniform temperature distribution does not hold, and more research is needed to address such cases. During recent fires, the travelling fires have been observed and investigated, which include the destruction of the World Trade Centre Towers in New York City in 2001 [3], the Windsor Tower in Madrid in 2005 [4], and the Faculty of TU Delft Architecture building in Netherlands in 2008 [5]. The detailed investigations on the fire events in large compartments have revealed that such fires have a great deal of non-uniformity unlike the small compartment fires. They generally burn locally and move across floor which generates non-uniform temperatures and transient heating of the surrounding structure and are idealized as the travelling fires [1,2].

Although majority of the fire exposure scenarios provided in the design codes consider uniform temperatures within the compartment, there is also some guidance available related to non-uniform temperatures. In the EC2 (EN1991-1-2) [6], two models are provided which consider a non-uniform temperature distribution, the localised fire model, and the advanced fire models (zone models and computational fluid dynamic models). Although the localised fire is assumed to be static, it is possible to consider several localised fires, one localised fire spreading to other localised fires. Such effect covers a fire spread but does not directly allow to fully capture the science behind the travelling fires. For zone models, the situation starts as a two-zone model which assumes accumulation of combustion products in a layer beneath the ceiling, with a horizontal interface. Uniform characteristics of the gas may be assumed in each layer and the exchanges of mass, energy and chemical substance are calculated between these different zones [6]. Although this model considers a non- uniform temperature distribution within the compartment, it does not translate the travelling nature of a fire. The CFD (computational fluid dynamic) models enable to solve numerically the partial differential equations giving in all points of the compartment, the thermo-dynamic and aero-dynamic variables. These models are consequently complex and imply a high computational cost. Further, these modules need further refining through comparisons with experimental data. The recent years have seen growing interest in investigating travelling fires which underlined the inadequacy of uniform heating in large compartments [6-13]. Further research efforts are needed, especially to extend the experimental data related to such fire scenarios which is scarce, limited, and partial.

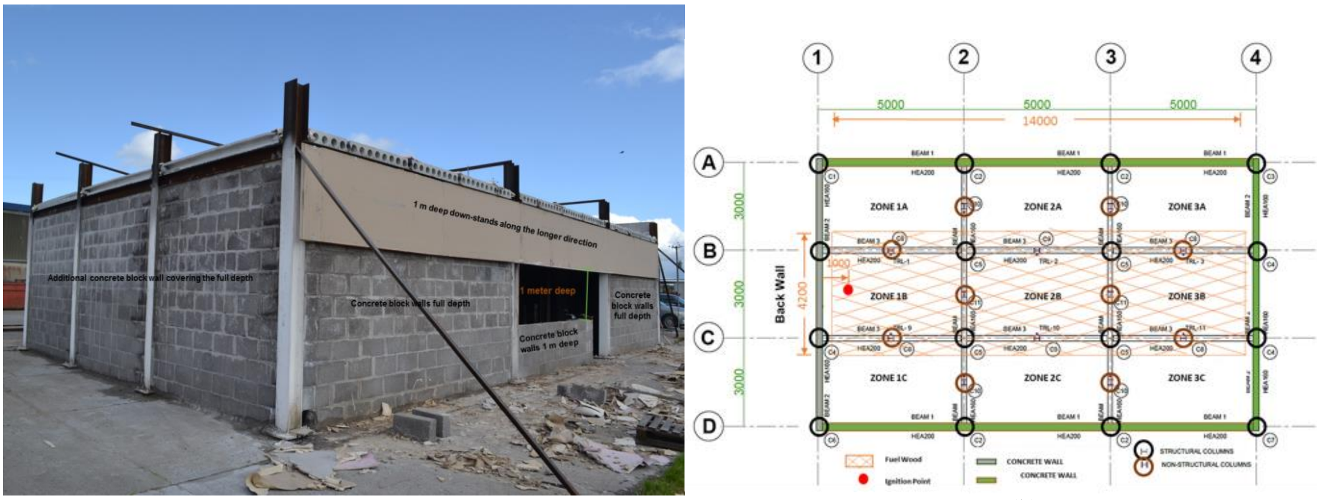

(a) (b)

Figure 1: Test 3 compartment, (a) Perspective view, (b) Plan with boundary conditions

Large scale travelling fire tests were recently conducted by Ulster University which included the fuel controlled and ventilation-controlled fire scenarios. The details of the two fuel-controlled travelling fire tests (Test 1 and Test 2) with different opening sizes were published by Nadjai et al. [14,15] and Alam et al. [16]. Details of the test compartment, instrumentation, fire load and other arrangements are available in the references [14 - 16]. The third tests, Test 3, was conducted to achieve a ventilation-controlled travelling fire scenario. To reduce the opening sizes during Test 3, the height of the soffit was increased along the longer dimension between gridlines 1 & 2 and between gridlines 3 & 4 by adding extra layers of concrete blocks. In these zones, no opening were provided, while the central part of the long walls (between gridlines 2 & 3) was kept identical to Test 2. Hence, the height of the openings between gridlines 2 & 3 remained 1 meter. Such provision of the boundary openings provided a total opening area of $10m^2$ in the test compartment as seen in Figure 1. The selection of opening sizes was conducted based on the outcomes of analysis using OZone software.

2 GENERAL FIRE SPREAD AND OBSERVATIONS DURING TEST 3

The fuel wood arrangement was similar for all three tests and the ignition was triggered using the same approach and position as done during the previous tests [14-16]. Photos taken at different time intervals during Test 3 have been shown in Figure 2. Following observations were made during the Test 3.

- Similar to the previous tests (Test 1 and Test 2), the fire initially spreads in all directions creating a circle around the point of ignition and after 10 mins, the fire flames touch the ceiling of the compartment. It was observed that the fire reaches the back end of the fuel after 9 mins. At this point, the flame thickness is 1 m. After 20 mins, the flame thickness is approximately 1.5 m.
- The fire spreads across the entire width of the fuel bed after 27 mins from ignition. The edges at the back end of the fuel is consumed after 29 mins from ignition. This initiates the travel of the fire towards the fore-end of the fuel bed.
- The travelling fire enters zone 2B of the test compartment after 37 mins. The flame thickness is approximately 2.5 m after 40 mins. The spread of the fire from one stick to another in the central part of the test compartment is steady. Similarly, to the previous tests, the number of sticks burning in the upper layers is higher than the number of sticks burning in the lower layers.
- The fire reaches the centre of the test compartment after 48 mins. At this point, the flame thickness is approximately 3.5 m.
- The flame thickness increases to 4 m after 52 mins from the start of the test. As the travelling fire reaches the centre of the compartment, its length extends to 5 m. The intensity of fire is significantly higher at this point. After 55 mins from ignition, flames escape through the openings of the compartment, which confirms a ventilation-controlled fire.
- After 56 mins, the spread of the travelling fire from stick to stick slows down significantly and the fire remains concentrated in the central part of the test compartment.
- The centre of the travelling fire reaches the middle of the compartment after 57 mins from ignition. After 58 mins, a small part of the fuel bed area near the fore-end of the compartment, (isolated from the actual travelling fire), catches fire. This separate fire at the fore-end of the compartment continues to burn until the 64th min. The intensity of the fire near the fore-end is higher until majority of the fuel wood is consumed. With the consumption of the fuel wood towards the back end of the central zone, the remaining fuel in the last part of the compartment starts to burn, joining the isolated fire. The intensity of the fire reduces after 85 mins.
- The fuel wood in the last compartment continues to burn until the 100th min with moderate intensity. From here onwards, the intensity of the fire reduces further. After 111 mins, no flames were visible as the fuel was totally consumed. The data acquisition continued further to obtain a dataset of more than 120 mins.
- Given the observations detailed above, the evolution of the maximum flame thickness is evaluated and represented in Figure 3. The data in Figure 3 is selected such that only "travelling fire" flame thicknesses are displayed (i.e, no point corresponds to the growing stage of the fire, when the back end hasn't start travelling yet).

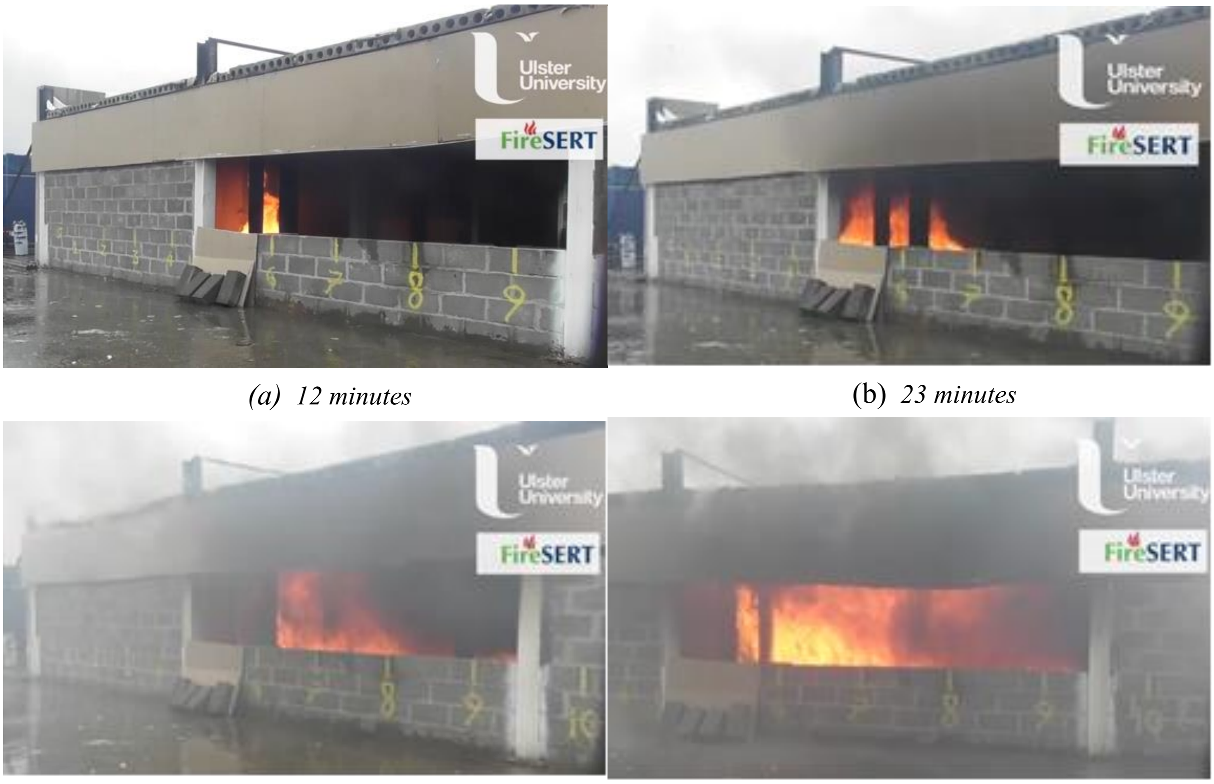

(a) 12 minutes (b) *23 minutes*

(c) *45 minutes* (d) *55 minutes*

Figure 2: Travelling fire along the compartment length after, (a) 12 mins, (b) 23 mins, (c) 45 mins (d) 55 mins

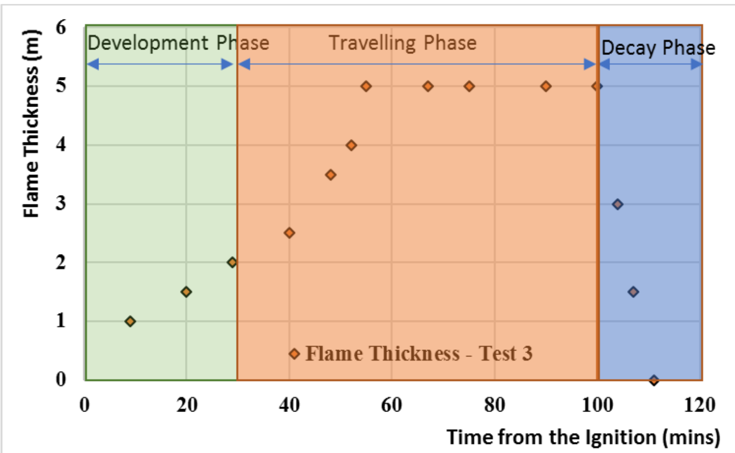

Figure 3: Evolution of the maximum flame thickness during Test 3

3 INSTRUMENTATION

The instrumentation and fuel load during all the fire tests was kept similar as mentioned before. Details of the instrumentation and fuel load for Test 3 shown in Figure 4 are similar to the arrangements made during Test 1 and Test 2 available in the references [14], [15] and [16].

Gas temperatures in the compartment were recorded using thermocouples provided as individual sensors or in groups in terms of thermocouple trees. In this paper, details of the thermocouples provided along the centreline of the test compartment have been provided. The thermocouples along the centreline of the test compartment were provided as thermocouple trees, TRL-4 through TRL-8 as shown in Figure 4 (a). The first thermocouple tree, TRL-4, was positioned at 1.5 m from the back wall while the remaining thermocouple trees were positioned at 2.5 m intervals. The thermocouple trees along the centre were provided with six thermocouples each. The positioning of the first thermocouple from the floor finish level was 0.5 m (L1). The thermocouples at L2, L3, L4 and L5 were at 1.0 m, 1.5 m, 2.0 m, and 2.5 m respectively. The last thermocouple at L6 was provided at 2.7 m from the floor finish level, Figure 4 (c).

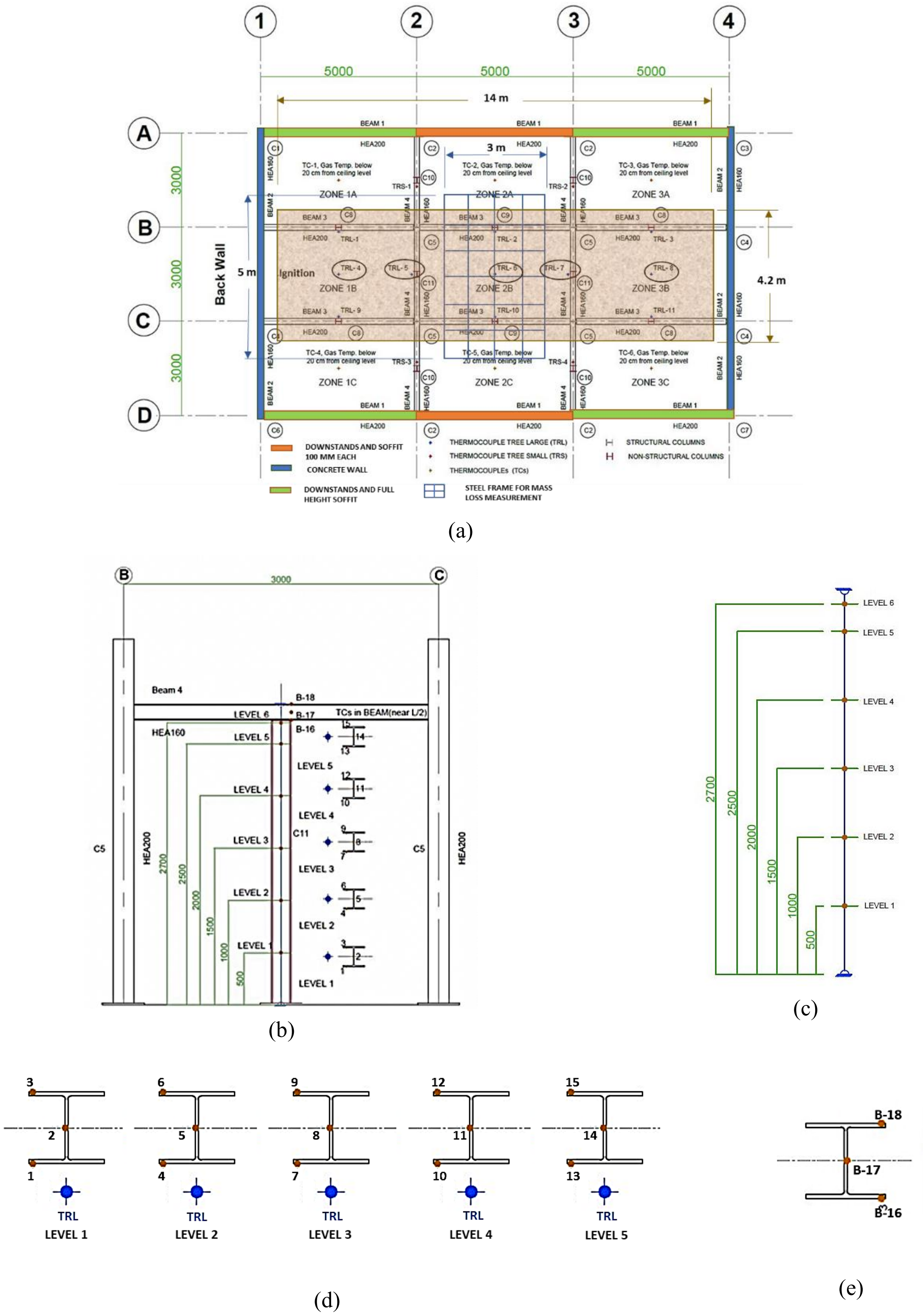

Figure 4: Details of thermocouples, (a) positioning of thermocouple trees (b) thermocouples in beams and columns, (c) thermocouples in large thermocouple trees; (d) thermocouples in columns; (e) thermocouples in beams

To analyse the influence of the travelling fire on the surrounding steel structure, temperatures were monitored in the columns and beams. Details of the instrumentation and recorded temperatures in the dummy column and beam adjacent to TRL-7 have been provided in this article. The column has been identified as C11 while the beam has been identified as BEAM 4 in Figure 4 (a). In total fifteen thermocouples were used in the column and three were used to recorded temperatures in the beam as shown in Figure 4 (b) & (d) and Figure 4 (e) respectively. The column and beam mentioned herein are between the gridlines Ⓑ and Ⓒ provided along the gridline ③ and are adjacent to thermocouple tree TRL-7.

4 GAS TEMPERATURES WITHIN THE FUEL BED ZONE, *TRL-4 THROUGH TRL-8*

The recoded data in the middle of the test compartment within the fuel bed using thermocouple trees TRL-4 through TRL-8 has been presented in Figure 5. The data presented is for thermocouples provided at L1, L3, L4 and L7. The gas temperatures at higher levels starts to rise much earlier as compared to those at lower levels, translating the hot gas layer. It should be noted that thermocouple at L1 (0.5m from the concrete floor level) lies within the fuel load. The following observations can be made from Figure 5:

- Temperatures recorded at L1 are lower as compared to temperatures recorded at higher levels, L3, L4 and L6.
- Temperature recorded in TRL-4 are lower as compared to temperatures recorded using other thermocouple trees. This could be explained by the fact that the fire is still developing at this location. As detailed above, the fire reaches the entire width of the fuel bed only after 27 mins from ignition and the temperature peaks in TRL-4 occur at 28 mins approximately. Similarly, the temperatures recorded at TRL-5 are lower as compared to those recorded using TRL-6 through TRL-8, however, these temperatures are higher as compared to those recorded in TRL-4.
- For Test 1, temperature profiles at L1 and L3 were quite distinct (i.e., shifted in time). For Test 3, such observation can only be made for L1 (at other levels, some coincidence observations can be made). This may result due to the progressively reduced openings from Test 1 to Test 3, enhancing the accumulation of smoke within the compartment and therefore merging the temperature profiles.
- The temperature profiles from TRL-6 and TRL-7 coincides to a certain extent at L4 (while the temperatures from TRL-8 are lower) with those recorded during Test 1. Similarly, the similarities in temperatures are more between Test 3 and Test 2 as compared to Test 3 and test 1. Furthermore, the beginning of the temperature profiles from TRL-6 through TRL8 coincides to a certain extent at L3, L4, and L6 for Test 3 and Test 2. Also, the peak temperatures measured at TRL-6 through TRL8 are in the same order of magnitude at L6 for Test 3 and Test 2.
- Globally for Test 3, the maximum gas temperatures recorded are around 1000°C. The following remarks can be made excluding L1 which is within the fuel bed.
  - TRL-6 through TRL-8 present maximum temperatures between 900-1000°C and are reached at all levels.
  - TRL-5 presents maximum temperatures around 800-900°C and are reached at all levels.
  - The maximum temperatures in TRL-4 are recorded between 750°C and 900°C.
- In case of Test 2, the maximum gas temperatures recorded in TRL-4 through TRL-8 were 1000°C - 1100°C at L1, and between 800°C - 900°C at other levels, i.e., there was a tendency to encounter higher temperature at lower levels.
- For Test 3, the same order of magnitude is reached, whatever the level.
  - The TRL-8 shows a longer period of high temperatures. The period during which temperatures above 600°C are recorded in thermocouple trees is: TRL-4: around 12 mins, TRL-5: around 20 mins, TRL-6: around 25 mins, TRL-7: around 20 mins, TRL-8: around 35 mins (from around 65 to 100 mins).
- The longer duration for TRL-8 can be explained as during the test after 58 mins, a small part of the fuel bed area near the fore-end of the compartment caught fire. This separate fire at the fore-end of the compartment continued to burn until the 64th min, generating a high intensity of the fire near the fore-end, which then reduced after 85 minutes.

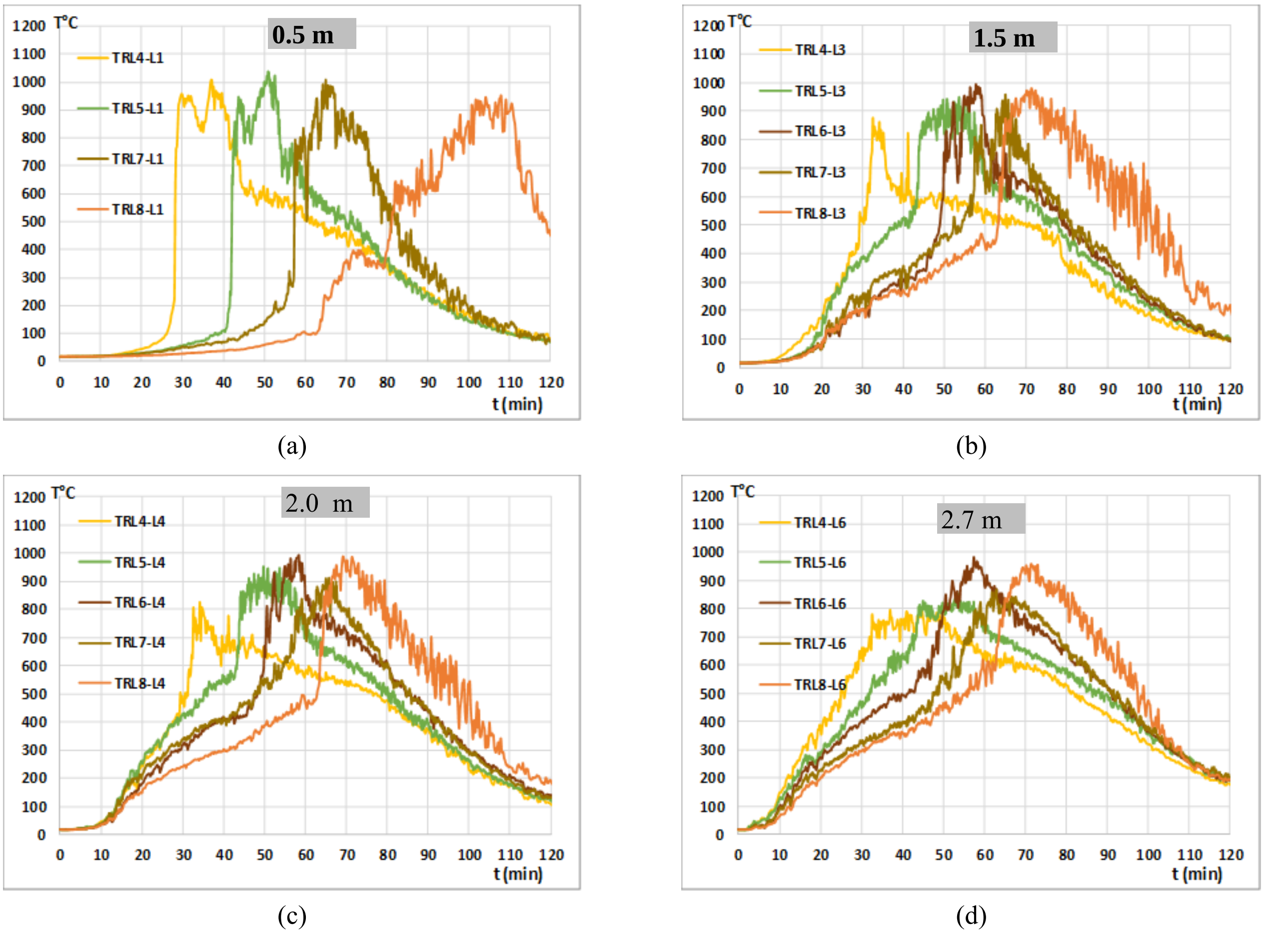

Figure 5: Gas temperature measurements during Test 3 at (a) L1, (b) L3, (c) L4, (d) L6

The thermocouple tree TRL-6 is positioned in the middle of the compartment (both along length and width). Following the observations during the tests, it is known that the centre of the travelling fire reaches TRL-6 after 48 mins during Test 3 (the same was reached after 49.5 and 51 mins during Test 1 and Test 2, respectively). The flame thickness at this point during Test 3 was approximately 3.5 m (the same was 3 m for both Test 1 and Test 2). The comparison of the temperatures recorded in the middle of the test compartment using TRL-6 is made and presented in Figure 6. For comparison purpose, L3 (around mid-height) at 30 mins is considered. At L3 after 30 mins, 40°C are measured for Test 1 while the same is 110°C for Test 2 and 200°C for Test 3. The maximum recorded gas temperature in TRL-6 is approximately 1000ºC during Test 3 (versus 1000°C and 1100°C for Test 1 and Test 2 respectively) after around 58 mins from ignition (nevertheless, measurements at L1 are not considered when finding this maximum). During the peak, contrarily to Test 2 where the higher temperatures are encountered for the lower levels, the temperatures are coinciding (around 1000°C). After the peak, the recorded temperatures reduce as the fire travels towards the end of the compartment. During the whole duration of the test, the higher temperatures are recorded at upper levels, and lesser temperatures for lower levels. It was observed that temperatures measured at upper levels (L6) start to increase at earlier stages of the test due to a hot layer of gases in the upper part of the compartment. It is interesting to note that during Test 1 and Test 2, temperatures at lower levels, especially at L1 and L2, rise suddenly at 45 mins from ignition. In case of the ventilation-controlled Test 3, the rise at lower levels, L1 and L2, is gradual and initiates at earlier stages of the test. During Test 3, due to limited opening sizes, the heat was retained within the compartment as a result, the temperatures of the compartment at all levels, including the lower levels, increased even at earlier stages which is different from the fuel-controlled Test 1 and Test 2. It is also noticed in Figure 6 that sharp decrease in temperatures is recorded for fuel-controlled Test 1 and Test 2. However, due to smaller openings and retaining of the heat, the temperatures recorded during Test 3 show a gradual decrease and remain higher until the recording is discontinued.

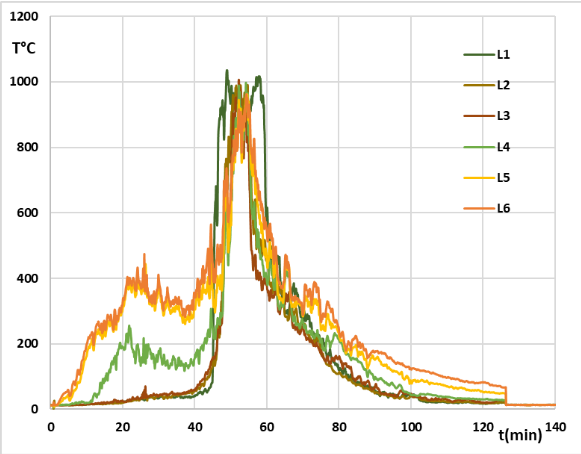

(a)

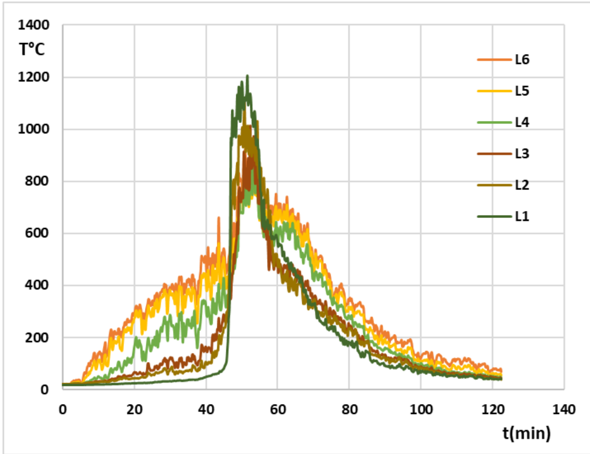

(b)

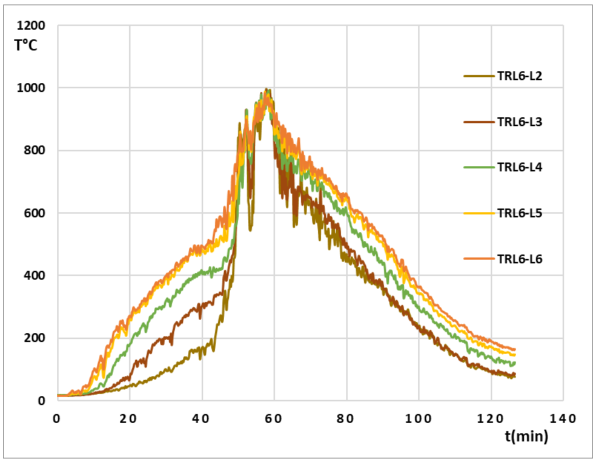

(c)

Figure 6: Gas temperature measurements made in TRL6 during; (a) Test 1, (b) Test c, (c) Test 3

5 TEMPERATURES RECORDED IN THE SURROUNDING STRUCTURE

The temperatures were monitored in beams and unprotected non-structural columns of the steel structure. Within the fuel bed zone, the column and beam (hot rolled, HE 200 A) placed adjacent to TRL-7 have been selected for data presentation purposes. The selected beam and column are along gridline ③ between gridlines Ⓑ and Ⓒ has been selected for data presentation purposes.

5.1 In columns adjacent to TRL-7 with comparison with column adjacent to TRL-5

For the column next to TRL-7, the temperatures recorded during Test 3 are presented in Figure 7. The thermocouple label "LHS-F", "WEB", "RHS-F" correspond to the flange near gridline Ⓒ (thermocouples 1,4,7,10,13), the section web (thermocouples 2,5,8,11,14) and the flanges near gridline Ⓑ (thermocouples 3,6,9,12,15) respectively. The faulty thermocouples 1 and 5 are not considered during the discussion below. The temperatures recorded using TRL-7 are presented in Figure 7 (a). It is clearly seen in Figure 7 that the steel temperature profiles are similar to the recorded gas temperatures, with the following differences:

- The maximum temperature recorded in the column adjacent to TRL-7 during Test 3 is 834°C after 70 mins (it was 833°C after 60 mins for Test 2 and 803°C after 63 mins for Test 1). For this column, the recorded temperatures are slightly higher for Test 2 and m as compared to Test 1. It can nevertheless be noted that the maximum temperatures are reached during Test 3 due to smaller opening sizes. The maximum gas temperature during Test 3 is 1010°C after 65 mins (it was 1021°C at 58 mins for Test 1 and 937°C after 58 mins for Test 2).

- At the exception of L1, the steel temperature descending branch is less steep than the gas temperature one (steel reaches 500°C after around 95 mins while the gas temperature reaches the same after 85 mins).
- During the decay phase of Test 3, the steel temperatures recorded at L1 decrease faster than other levels (this phenomenon was also observed for Test 2 and not for Test 1).
- Temperatures recorded across the section of the column at each level are uniform as seen in Figure 7. Similar observations were also made during Test 1 and Test 2.

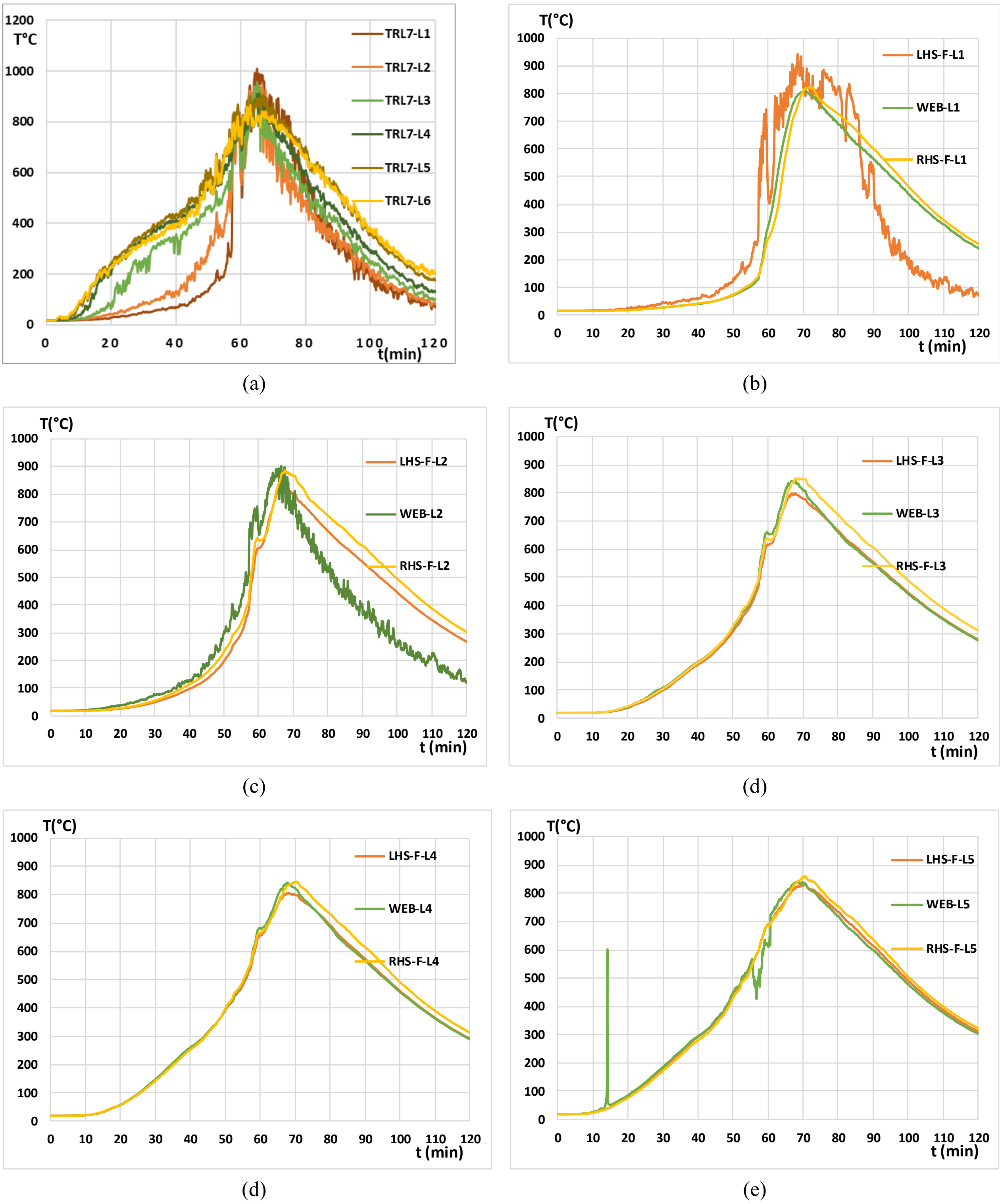

Figure 7: Temperature recordings Test 3: (a) using TRL7, (b) Column L1, (c) Column L2, (d) Column L3, (e) Column L4, (f) Column L5

Temperatures were also recorded at similar points in the column adjacent to TRL-5. Due to space constraints, these have not been presented in this paper, however, a comparison of the maximum temperatures recorded in columns adjacent to TRL-5 and TRL-7 is presented in Table 1. In addition to the maximum recorded temperatures, Table 1 also provides the temperature difference between these values (Δ = TRL7 - TRL5). Also, within each column, the maximum temperature gradient (Δ) is also presented in Table 1. The following observations have been made:

- The maximum steel temperature is 887°C after 68 mins for the column adjacent to TRL-7 (it was 838°C after 63 mins for Test 2 and 799°C after 63 mins for Test 1) while it is 890°C after 56 minutes for the column adjacent to TRL-5 (versus 781°C after 49 mins for Test 2 and 731°C after 46 mins for Test 1). While there was no significant change during comparing Test 1 and Test 2 recorded temperatures, it appears the lower opening factor during Test 3 results in higher steel temperatures (nearly 100°C more).
- For Test 2, the maximum temperature gradient within each column (Δ) was almost identical whereas for Test 1, a lower gradient was observed in column next to TRL-7 as compared to column next to TRL-5. For Test 3, the tendency is same as that for Test 1. This could be explained by the flame thickness which is lesser near TRL-5 as compared to TRL-7. For a similar 'rate of heat released density', a thicker flame (and therefore a bigger diameter if the fire is represented as a localised fire) implies a higher flame length, implying a lower gradient in temperatures for the given heights.
- In previous tests, the gas temperatures from TRL-5 and adjacent column were globally lower than the ones recorded further away in the compartment, which was different in case of Test 3. When looking at the differences between maximum temperatures recorded in the two columns for each level (Δ =TRL-7 – TRL-5), one can see these values are very low, highlighting very similar steel temperatures in TRL-5 and TRL-7. Having less openings compared to previous tests, more heat is contained within the compartment, limiting the differences in the columns.
- When evaluating the period during which higher temperatures (arbitrarily chosen above 600°C) are encountered, it can be observed that this period is quite similar for the column adjacent to TRL-7 (from 60 to 90 mins, i.e. for approximatively 30 minutes) and for the column adjacent to TRL-5 (from 45 to 80 mins, i.e., for approximatively 35 minutes). This period was 20 mins for Test 2, and 15 mins for Test 1, implying that the reduction of opening sizes, elongates the heating time.

Table 1: Maximum steel temperatures measured during Test 3 in columns adjacent to TRL7 and TRL5 (flanges)

	Level 1	Level 2	Level 3	Level 4	Level 5	Δ
TRL5	806°C	890°C	882°C	852°C	850°C	84°C°
TRL7	824°C	887°C	853°C	846°C	859°C	63°C°
Δ (TRL7-TRL5)	18°C	3°C	29°C	6°C	9°C	

5.2 In beam adjacent to TRL-7 during Test 3 and comparison with the previous tests

Each beam was instrumented with three thermocouples, two on the flanges and one on the steel wed as presented earlier in Figure 4 (e). The beam used for data presentation is along gridline ③ between gridlines Ⓑ and Ⓒ in Figure 4 (a). For the beam temperatures presented in Figure 8 (a), "BF", "TF" and "Web" correspond to the bottom flange, the top flange and the web of the beam. The temperatures recorded in the beam follow the same trend as the ones recorded at L5 and L6 of TRL-7. The temperatures in the beam are non-uniform. Similar to the previous tests, temperatures recorded in the top flange are significantly lower than those recorded in the bottom flange. The maximum steel temperatures reached at the bottom flange, the web and the top flange are 783°C, 782°C and 760°C respectively as seen in Figure 8 (a).

The average temperatures recorded in the beam along gridline ③ between gridlines Ⓑ and Ⓒ during all three tests is presented in Figure 8 (b). It can be observed that the temperature recordings are similar for Test 1 and Test 2. However, for Test 3, higher steel temperatures are recorded, and these elevated temperatures are maintained for a longer period. It can be clearly seen that steel temperatures are not affected by the change in ventilation conditions from Test 1 (opening factor 0.316 [$m^{1/2}$]) to Test 2 (opening factor 0.073 [$m^{1/2}$]), while these are significantly affected for Test 3 with smaller openings (opening factor 0.024 [$m^{1/2}$]).

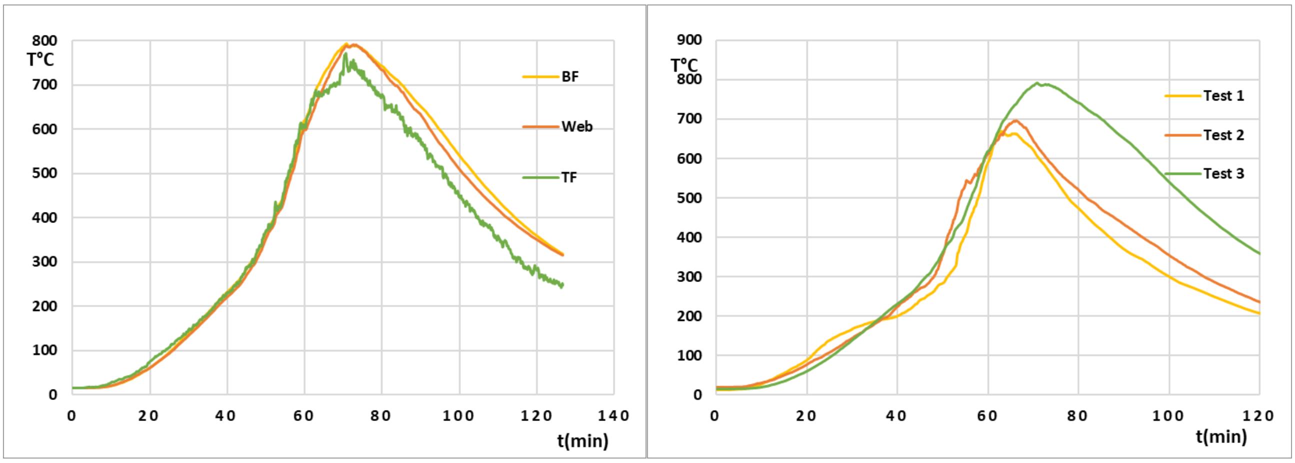

Figure 8: (a) Temperatures recorded in beam adjacent to TRL7, (b) average temperatures recorded in the selected beam during all three tests

6 CONCLUSIONS

Three large scale natural fire tests were conducted in a building with large dimensions. A fire load representative of an office building, defined according to a well-established methodology was used for the three tests, only the ventilation was varied to assess its influence on the fire behaviour. The main objectives of this experimental campaign were to understand in which conditions a travelling fire develops, as well as how it behaves and impacts the surrounding structure. Instrumentation was installed to measure compartment temperatures, heat fluxes and temperature in the steel columns, and beams. This article presented details of Test 3 in terms of gas temperatures recorded in the central part of the compartment, along its length. The details related to the maximum flame thickness, steel temperatures in selected central beams and columns were also provided. Following are major conclusions from the travelling fire Test 3.

- For the fire initiating at a single point, its developing phase consists of increase in the volume of fire in all directions making a circle around the point of ignition. Once the fire is well developed, it continues to travel along the fuel bed. In the case of the test conducted during this research, the fire travelled in the forward direction towards the fore end of the compartment. However, the fire could travel in any direction depending upon the availability of the fuel.
- The rise in temperatures at higher levels starts at the initial stages of test while the rise at lower levels starts once the fuel wood starts to burn locally. The temperatures in the compartment were found to be dependent on the positioning of the travelling fire. The parts of the compartment around the fire are hotter while the parts away from the fire were at lower temperatures.
- The results obtained demonstrated the non-uniform temperature distribution, leading to the heating of the nearby structural steel elements, resulting in a reduction of individual members' resistance, which could influence the global structural stability. Such transient heating of the columns should be considered when analysing the stability of a structure subjected to travelling fires.
- All the connections and steel members performed well and showed no signs of failure during the fire test.

ACKNOWLEDGMENT

This work was carried out in the frame of the TRAFIR project with funding from the Research Fund for Coal and Steel (grant N°754198). Partners are ArcelorMittal, Li ge University, the University of

Edinburgh, RISE Research Institutes of Sweden and the University of Ulster. The authors also wish to acknowledge the supporting of companies Sean Timoney & Sons Ltd, FP McCann Ltd, Saverfield Ltd and Crossfire Ltd.

REFERENCES

1. J. Stern-Gottfried, G. Rein (2012). *Travelling fires for structural design – Part I: Literature review.* Fire Safety Journal 54. pp 74- 85.
2. Dai X, Welch S and Usmani A (2017) A critical review of 'travelling fire' scenarios for performance-based structural engineering. Fire Safety Journal 91: 568–578.
3. R. G. Gann, A. Hamins, K. McGrattan, H. E. Nelson, T. J. Ohlemiller, K. R. Prasad, and W. M. Pitts, (2013) Reconstruction of the fires and thermal environment in World Trade Center buildings 1, 2, and 7, Fire Technol., vol. 49, pp. 679–707.
4. I. Fletcher, A. Borg, N. Hitchen, and S. Welch, (2005) Performance of concrete in fire: A review of the state of the art, with a case study of the Windsor Tower fire," in 4th International Work- shop in Structures in Fire, pp. 779–790.
5. D. M. Zannoni, J. G. H. Bos, D. K. E. Engel, and P. dr. U. (2008) Rosenthal, Brand bij Bouwkunde.
6. EN1991-1-2 (2002). Eurocode 1: Actions on structures – Part 1- 2: General Actions on structures exposed to fire. CEN, Brussels.
7. G. Rein, X. Zhang, P. Williams, B. Hume, A. Heise, A. Jowsey, B. Lane, and J. L. Torero, (2007) Multi-storey fire analysis for high- rise buildings, in Proceedings of the 11th International Inter- flam Conference, London, UK, pp. 605–616.
8. K. Horov , T. J na, F. Wald (2013). Temperature heterogeneity during travelling fire on experimental building. Advances in En- gineering Software 62-63. pp 119-130.
9. J.P. Hidalgo, A. Cowlard, C. Abecassis-Empis, C. Maluk, A.H. Maj- dalani, S. Kahrmann, R. Hilditch, M. Krajcovic, J.L. Torero (2017). An experimental study of full-scale open floor plan en- closure fires. Fire Safety Journal 89. pp 22-40.
10. J. P. Hidalgo, T Goode, V. Gupta, A. Cowlard, C Abecassis-Empis, J. Maclean, A. Barlett, C. Maluk, J.M. Montalva, A. F. Osorio, J. L. Torero (2019). The Malveira fire test: Full-scale demonstration of fire modes in open-plan compartments. Fire Safety Jour- nal vol.108 No 102827.
11. A. Gamba, M. Charlier, J.M. Franssen (2020). Propagation tests with uniformly distributed cellulosic fire load. Fire Safety Journal 117, 103213.
12. J. Degler, A. Eliasson, A. Anderson, D. Lange, D. Rush (2015). A- priori modelling of the Tisova fire test as input to the experimental work. Proc. 1rst Int. Conf. on Struct. Safety under Fire & Blast, Glasgow, UK.
13. M. Charlier, A. Gamba, X. Dai, S. Welch, O. Vassart, J.M. Franssen (2020). Modelling the influence of steel structure compartment geometry on travelling fires. Proceedings of the Institution of Civil Engineers - Structures and Buildings. https://doi.org/10.1680/jstbu.20.00073.
14. A. Nadjai, N. Alam, M. Charlier, O. Vassart, S. Welch, A. Glorieux, J. Sjöström, Large scale fire test: The development of a travelling fire in open ventilation conditions and its influence on the surrounding steel structure, Fire Safety Journal, http://dx.doi.org/10.1016/j.firesaf.2022.103575, April 2022.
15. A. Nadjai, N. Alam, M. Charlier, O. Vassart, S. Xu Dai, JM. Franssen, J. Sjöström, Travelling fire in full scale experimental building subjected to open ventilation conditions, Journal of Structural Fire Engineering, http://dx.doi.org/10.1108/JSFE-06-2021-0037, May 2022
16. A. Naveed, A. Nadjai, M. Charlier, O. Vassart, S. Welch, J. Sjöström, X. Dai. Large-Scale travelling fire tests with open ventilation conditions and their effect on the surrounding steel structure – The second fire test. Journal of Constructional Steel Research, http://dx.doi.org/10.1016/j.jcsr.2021.107032, 2022.

AN APPARATUS FOR APPLYING FIRE-LIKE HEAT FLUX TO BENCH-SCALE SAMPLES

Aleksandra Seweryn[1], Andrea Lucherini[2] and Jean-Marc Franssen[3]

ABSTRACT

The research study presented in this paper concerns an experimental electricity-powered apparatus for applying fire-like heat flux to bench-scale samples. It consists of various elements, of which the most important are ceramic heating pads used to impose a defined heat flux on the exposed side of the sample mounted in a steel holder. The test method allows to control the heating pads' temperature as well as to adjust the distance between the heating pads and the specimen to obtain heat fluxes up to 150 kW/m^2. The thickness of the convective boundary layer at the heating pads' surface is estimated to be around 3 cm, significantly lower than in case of gas-fired radiant panels. The performance of the apparatus was analysed in a case study on soda-lime-silica glass specimen. Experimental results were compared to numerical modelling. This analysis showed that a thermal exposure compared to the ISO 834 fire curve can be imposed on the exposed side of the specimen. There are many research possibilities for future applications of the presented experimental methodology: among others, tests with bigger specimens with heating pads surface up to 1.34 m^2, and tests in controlled atmosphere.

Keywords: H-TRIS; radiant panels; fire testing; heat transfer; glass; heat flux

1 INTRODUCTION

Spread of fire in a building is highly driven by materials which can be found inside and by their reaction to fire. Many researchers have been working to understand the performance in high temperatures of various, sometimes very complex, materials. This is usually analysed through material testing. In this case, a preference is shown for bench-scale tests compared to large-scale furnace tests because of their multiple advantages, for instance lower temporal and economic costs and better-defined thermal boundary conditions.

There are various methods to impose a heat flux on bench-scale samples to study the behaviour of insulating or structural materials at elevated temperatures. Some of them aim at locally imposing a high heat flux, for example with a blowtorch [1]. However, the majority of them aims at imposing a uniform radiative heat flux on the whole specimen surface. The most common methods include the cone calorimeter allowing to test samples of 10x10 cm² [2] as well as the Heat-Transfer Rate Inducing System (H-TRIS) apparatus [3-7] used for bench-scale samples. The first one, cone calorimeter, is limited to imposing constant incident heat flux during a test and its response time is low due to the high thermal inertia of the electrical resistance. On the other hand, H-TRIS is a gas-fired radiant panel that allows to impose constant or varying time-

[1] MSc, Liège University,
e-mail: aleksandra.seweryn@doct.uliege.be, ORCID: https://orcid.org/0000-0002-2990-122X
[2] PhD, Ghent University and Slovenian National Building and Civil Engineering Institute (ZAG)
e-mail:, andrea.lucherini@ugent.be, ORCID: https://orcid.org/0000-0001-8738-1018
[3] Professor, Liège University,
e-mail: jm.franssens@uliege.be, ORCID: https://orcid.org/0000-0003-2655-5648
https://doi.org/10.6084/m9.figshare.22178090

histories of incident heat flux by changing the distance between the radiant panel and the specimen surface. Thanks to its important advantage of well-defined thermal boundary conditions, it has been widely used in research and development studies which included, among others, behaviour analysis of concrete spalling, intumescent coatings, timber structures and glass structures [6-12].

Nevertheless, its relatively high costs and safety concerns due to the presence of gas burners make it an unsuitable solution for some laboratories and researchers. For these reasons, a similar apparatus to H-TRIS but powered by electricity has been designed, easy to maintain and budget-friendly, at the same time providing repeatable and relatively accurate results.

2 APPARATUS AND TEST METHOD

2.1 Apparatus

The first prototype of the apparatus is shown in Figure 1. It has been built with basic and economically available resources to validate the concept before relying on more sophisticated components for a permanent and long-term utilisation.

a) b)

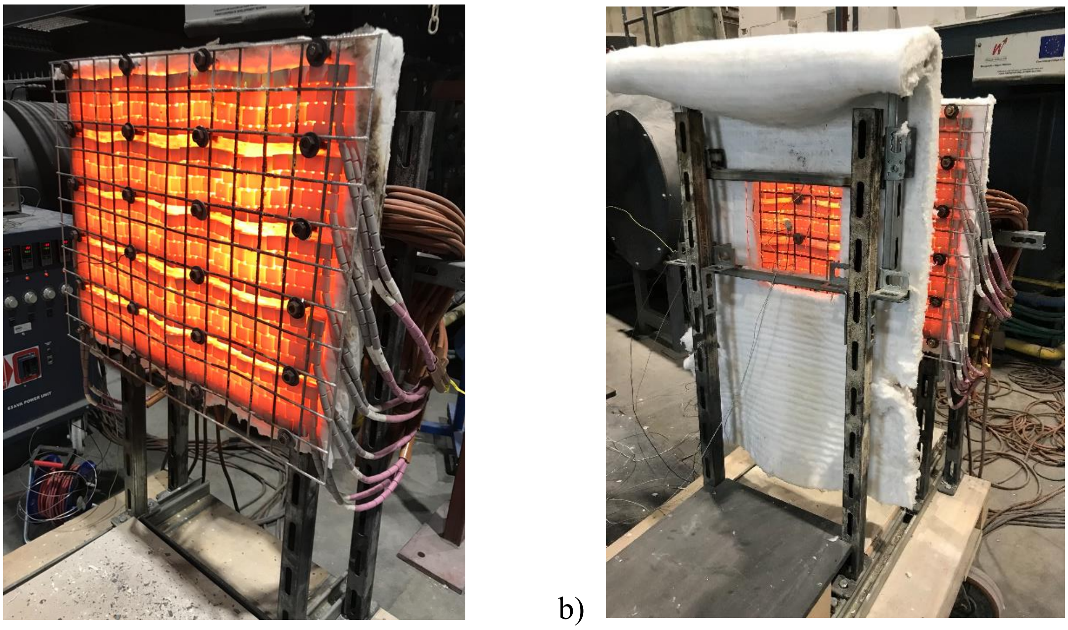

Figure 1. The apparatus a) without the specimen holder, b) with the specimen holder

The apparatus consists of:

1) A 70 x 55 cm² vertical steel plate on which two layers of 5 ceramic heating pads each (Mannings, CP24, 61 x 8.5 cm² each) are fixed. Ceramic fibres insulation is placed between the pads and the steel plate. A steel grid is mounted with screws to support the heating pad strips. The heating surface is 61 x 46 cm². A thermocouple is placed in a special hole very close to the surface of the heating pads and connected to a measuring device.
2) A steel frame serving as a specimen holder.
3) A Mannings 65kVA transformer unit that has the capability to control the temperature of the heating pads in six different zones independently, although in this application only three of them are used (two to four heating pads are connected to each zone) and all of them have the same settings.
4) A wooden base with wheels.

In the present arrangement as shown in Figure 2, the distance between the heating pads and the specimen holder can only be modified from test to test. Limited modifications of the support of the specimen holder could make it possible to vary this distance also during a test.

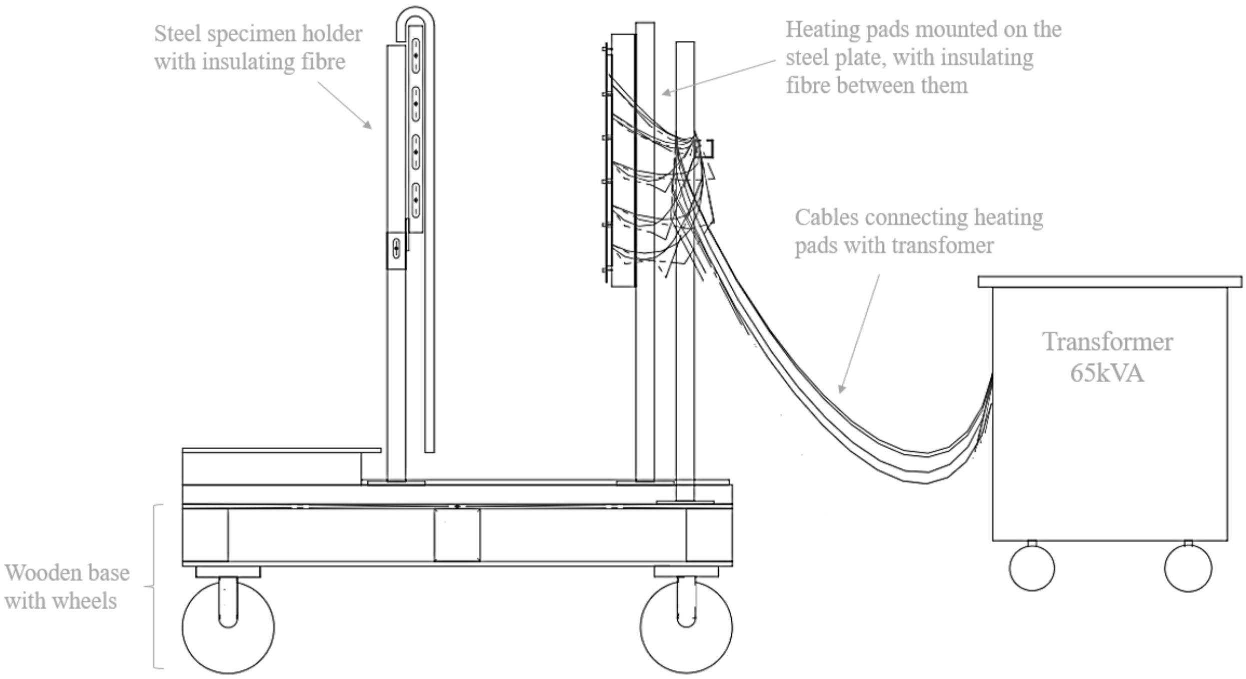

Figure 2. Schematic drawing of the apparatus

2.2 Test method

Two different parameters which can be adjusted to reproduce specific heating regimes.

1. Temperature of the heating pads

The controller allows to impose a predefined temporal evolution of the temperature of the heating pads, for example following a linear or curvilinear evolution; the maximum heating rate that can be achieved on the heating pads is 50°C/min. The temperature can also be maintained at a given constant level up to around 800°C. This temperature is controlled with a thermocouple placed in a special hole in the heating pads, very close to the heating surface, in the central area.

The settings can be assigned separately for six different zones, but it has been observed that, with the dimensions of the radiant panel and of the specimen described here, a sufficiently uniform heating on the specimen's surface is obtained when all zones are set to follow the same evolution. Figure 3 shows the temperature is uniform over the whole surface of the heating pads excluding the area around 3 cm from the edges.

For the tests reported in this paper, the transformer was set to work at full power from the beginning of the test, which leads to temperatures of the heating pads up to 1300°C when a steady state situation has been established.

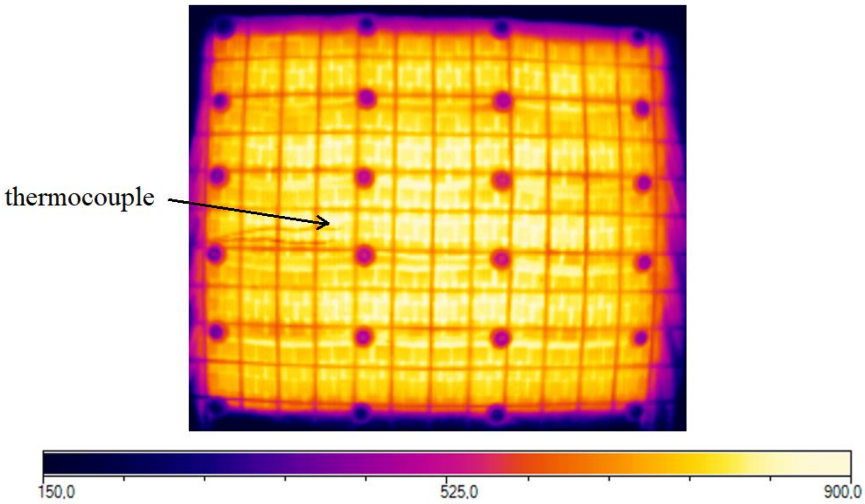

Figure 3. Temperature distribution on the heating pads, captured by infrared camera for temperature 800°C measured by the thermocouple in the centre of the heating pads

Two sets of different heating pads (Mannings CP24) were used until now. The first ones are made of nickel-chrome alloy, allowing a maximum temperature of 1050°C according to the producer. This limitation in temperature, plus the fact that they tend to break after a few utilizations close to the maximum allowed temperature, was the reason to change to the *high temperature* heating pads with the heating wire made of canthal alloy. These heating pads have the maximum temperature of 1300°C, can provide a faster heating rate and they are more robust with no failure observed so far. Their higher price (60 € versus 25 € per heating pad at the time of writing) is easily compensated by the higher durability.

Heating pads can be mounted as one layer or two layers, as shown in Figure 4, or even more. To impose heat fluxes in the range of those corresponding to the ISO 834 curve, it was found that two layers of heating pads were necessary. In this case, the inner layer reaches higher temperatures than the outer layer due to differences in heat losses at the pads surface, for example when the temperature of the outer layer is 1180°C, the inner layer reaches around 1250°C.

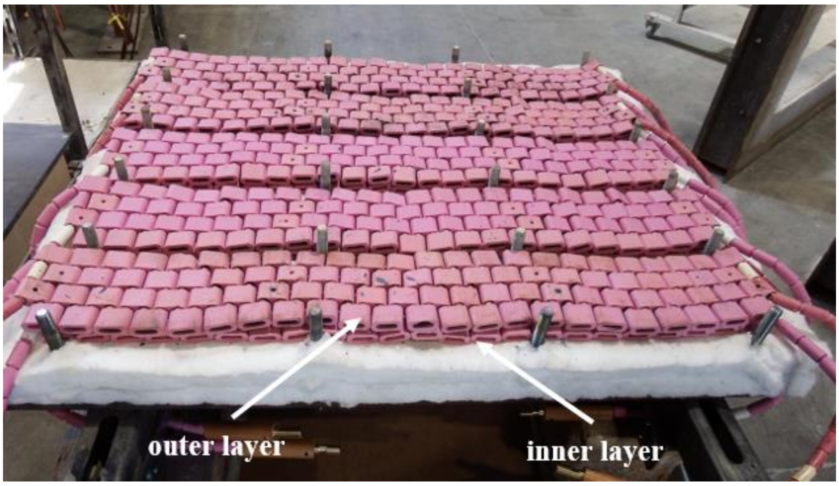

Figure 4. Positioning of two heating pads layers: outer layer and inner layer

2. Distance between heating pads and specimen

Similarly to H-TRIS, the distance between the heating pads and the specimen is crucial to determine the level of heat flux reaching the exposed side of the specimen. Figure 5 shows the evolution of the incident heat flux measured by the Gardon heat flux gauge placed in the specimen holder, positioned in front of the centre of the heating pads, at two different distanced when the full power is applied. The heat flux gauge was surrounded by insulating fibre to recreate conditions used in tests. Due to the limits specified by the producer of the heat flux gauge, the measurements were held until 150 kW/m^2.

It is important to mention that when the transformer is set on full power, the temperature on the heating pads surface (and therefore the heat flux) depends on various factors and might change if one of these factors is changed, for example the presence or not and the type of insulating fibre mats located around the specimen as seen in Figure 1 (providing feedback to the heating pads which increases temperature of the heating pads) and their distance from the heating pads. This means the temperature on the heating pads in this case is not automatically regulated.

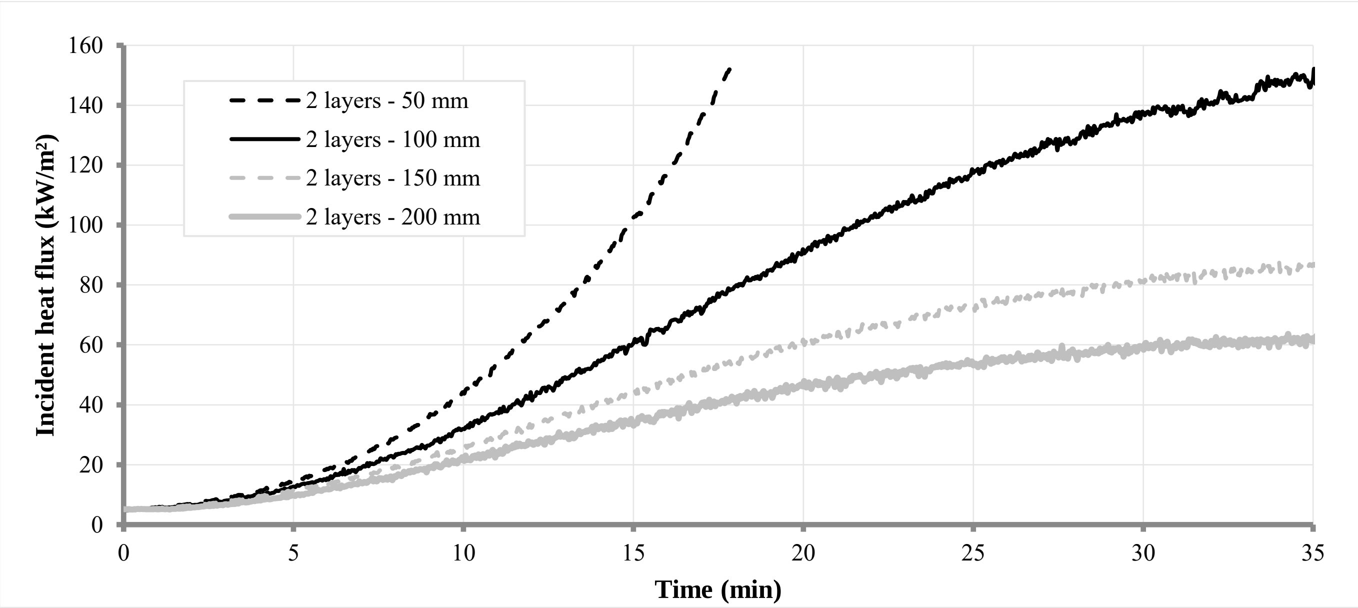

Figure 5. Incident heat flux obtained with two layers of heating pads, and for the distance of 50mm, 100mm, 150mm and 200mm between the heating pads and the specimen, with full power of the transformer

The plot in Figure 6 correlates the temperature at the surface of the heating pads and the incident heat flux measured at different distances from the heating pads. The incident heat flux decreases when the distance increases.

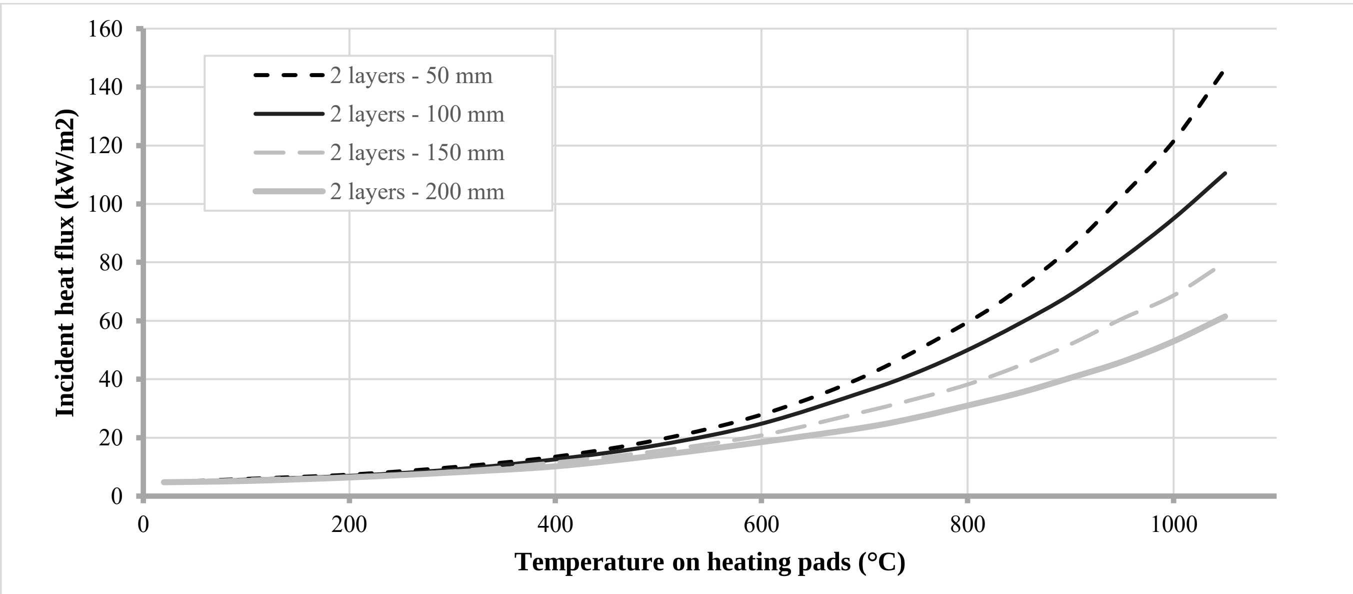

Figure 6. Incident heat flux dependence on temperature obtained on the heating pads for two layers of heating pads, and for the distance of 50mm, 100mm, 150mm and 200mm between the heating pads and the specimen, with full power of the transformer

In order to show the incident heat flux measured at different positions of the heat flux gauge as a function of the distance between the pads and the heat flux gauge, the heating pads were set to automatically regulated temperature of 750°C. It can be noticed that the incident heat flux with stable temperature of 750°C on the heating pads increases smoothly with the decrease of distance between the heat flux gauge and the heating pads (Figure 7). This is the highest temperature of the heating pads which can be obtained when no insulating fibre mat is located around the specimen.

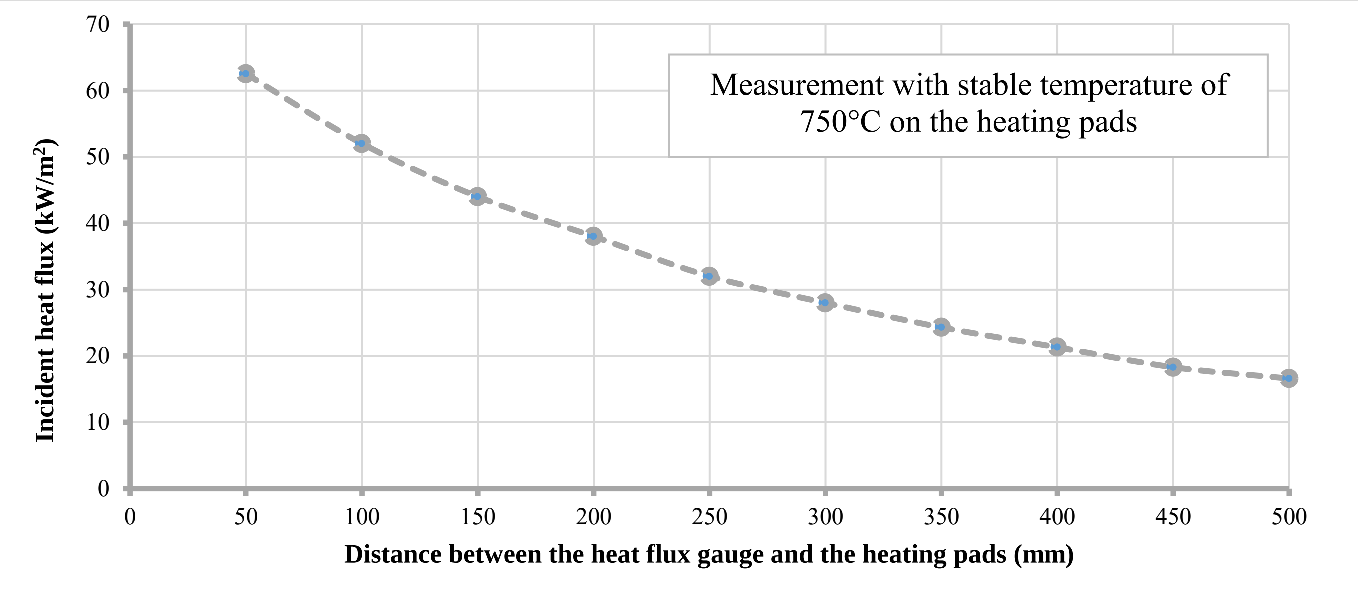

Figure 7. Incident heat flux obtained for different distance between the heating pads and the specimen, with two layers of heating pads, for stabilized temperature on the heating pads of 750°C

The first utilisation of the current apparatus has been for testing the performance of construction products subjected to heat flux comparable to the one pertaining to the ISO 834 curve. Because of the too slow heating rate observed at the start of the heating, an insulating plate is placed between the heating pads and the specimen, and the transformer is set to work at full power. The plate is removed when the temperature of the heating pads reaches 500°C (around 6 minutes from the start of the heating) which creates the thermal shock characteristic of the ISO 834 curve. The same effect could be obtained by a rapid variation of the distance between the specimen and the heating pads, provided a rather simple displacement system is given on the specimen holder.

It may be possible to recreate in a similar way other heating regimes, such as external fire curve or hydrocarbon curve (only for specific materials), however this still has to be investigated.

2.3 Boundary conditions

The heat transfer on test samples is considered unidimensional, following the main direction of the heat flow: from the heated pads to the exposed sample surface and through the sample thickness. The incident heat flux $\dot{q}''_{inc}$ imposed by experimental apparatus at the exposed surface of the test specimen is considered as radiant incident heat flux, therefore the sample receives a surface heat flux due to electromagnetic waves. The surrounding environment is considered at ambient conditions; hence the sample surface has convective and radiative heat loses with this environment. According to this assumption, the thermal boundary conditions in equation (1) are obtained.

In case of stable and homogenous temperature on the heating pads (up to 750°C) and open environment around the test specimen (free convection), the thermal boundary conditions imposed on the exposed surface of test samples can be described as in the following [5, 13]:

$$\dot{q}''_{net} = \alpha \cdot \dot{q}''_{inc} - h_c\left(T_{surf} - T_\infty\right) - F\varepsilon\sigma\left(T^4_{surf} - T^4_\infty\right) \quad (1)$$

Where $\dot{q}''_{inc}$ is the incident heat flux imposed by experimental apparatus at the exposed surface of the test same and $\dot{q}''_{net}$ is net heat flux absorbed by the sample at the exposed surface, which has a surface temperature equal to T_{surf} and it is surrounded by a gas temperature equal to T_{∞}. The absorptivity and the emissivity of the exposed surface are α and ε, respectively. The convective heat losses are described by the convective heat transfer coefficient h_c, while the radiative heat losses are considered by the Stefan-Boltzmann constant σ and the view factor F.

By modifying the relative distance between the heating pads and the sample surface and/or the electric power fed to the experimental apparatus (therefore the heating pads temperature), the incident radiant heat flux $\dot{q}''_{inc}$ can be controlled and quantified through the calibration process (see Figure 7).

However, if the transformer is set at full power, the temperature on the heating pads is not automatically regulated and it might change depending on various factors, for instance the distance between the specimen holder and the heating pads or insulation material used around the specimen. This is the consequence of feedback from the specimen and convection flow caused by the surrounding insulation material and, as a result, the definition of the thermal boundary condition becomes more complex.

2.4 Convective boundary layer

To verify that the main mode of heat transfer is radiation, it is important to understand the convective heat transfer in proximity to the experimental apparatus. In particular, to avoid convective heat transfer between the test sample and the convective boundary layer of the heated pads, a sufficient spatial separation between the heating pads and the exposed surface of the test sample must be ensured [13]. This distance should be at least higher than the thickness of the boundary layer of the radiant panel and the test sample. The test sample one's depends on the sample characteristics, while the boundary layer thickness of the radiant panel composed of heating pads can be estimated following conventional calculations considering it as a vertical hot plate subjected to natural free convection [14]. Assuming the panel surface temperature equal to 900-1000°C, an ambient temperature of 20°C and the panel vertical characteristic dimension equal to 46 cm, the thickness of convective boundary layer of the heating pads panel can be estimated equal to 3.2-3.3 cm. This result was also confirmed by a qualitative measurement using a flag made of several aluminium thin foils, as shown in Figure 8. This outcome highlights that the convective boundary layer of this experimental apparatus is much smaller than the ones for gas-fired radiant panels, typically in the range of 150-200 cm [13, 15].

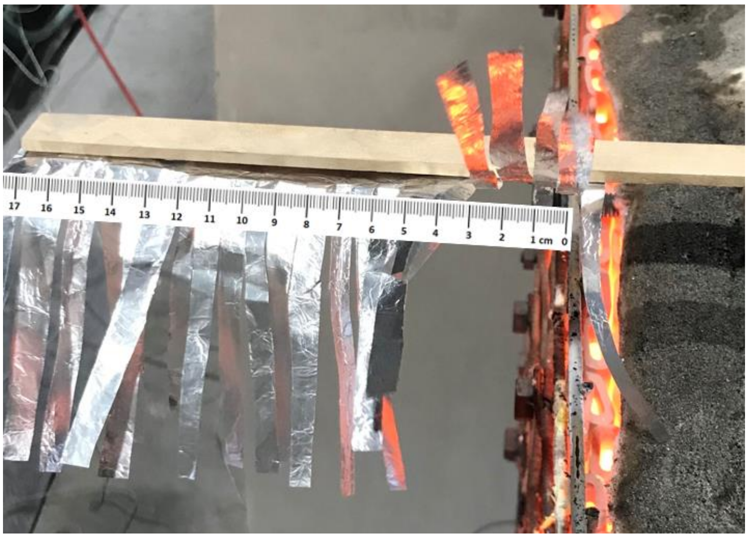

Figure 8. The zone of convective influence coming from the heating pads - qualitative measurement using a flag made of aluminium thin foil

2.5 Advantages and limitations

In addition to easily achieved safety conditions and relatively low cost, the apparatus showed several advantages compared to a gas-fired radiant panel. First, the power and the heating pads temperature can be controlled in a precise way, for most regimes, owing to the automatic regulation of the transformer. Secondly, no combustion and hazardous gases are produced, whereas these can disturb the heat transfer and influence chemical reactions at the surface of reactive materials when the specimen is located too close to a gas-fired panel. The thickness of the convective boundary layer on the panel surface is significantly lower than with gas-fired radiant panel.

The described apparatus is mobile and can be used in most circumstances, provided that there is enough electrical power available. If the tested specimen is non-combustible, it does not require a gas exhaust to collect combustion gases, a requirement which normally imposes a permanent positioning in the laboratory with gas-fired panels.

It is of course necessary to have a certain electrical power in the lab, although the power required to feed the surface of 0,28 m² is well below the 65 kVA capacity of the transformer. Due to thermal inertia of the heating pads, the cooling process is not instantaneous, and the apparatus must be left for 30 to 45 minutes to decrease the temperature back to 500°C. While the maintenance of the apparatus is quite limited, the heating pads may need replacement from time to time.

One of the main limitations of this apparatus is the fact that, when using full power of the transformer, the temperature on the heating pads, and therefore the incident heat flux, depends on the distance between the specimen together with the insulating fibre and the heating pads, as shown in Figure 9. The uniform character of the temperature distribution on the heating pads might also be lost if a specimen made of a material with thermal properties very different from those of the insulating fibre. Therefore, it is difficult to establish the thermal boundary conditions for this complex situation.

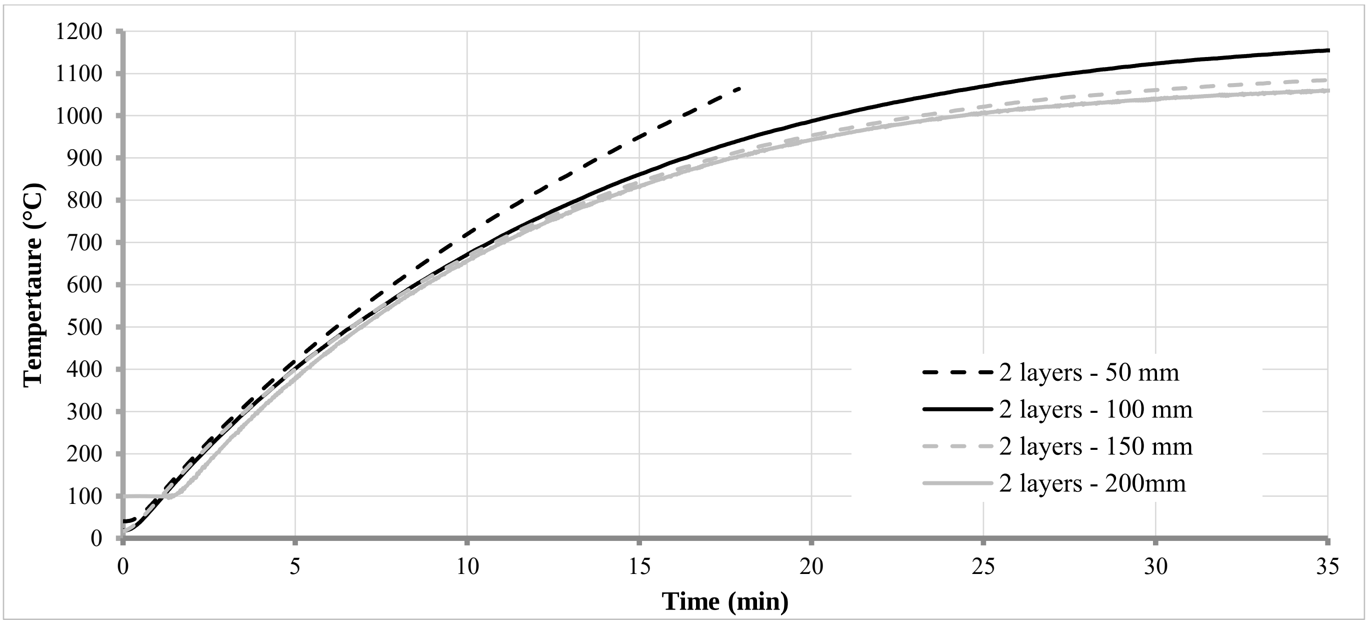

Figure 9. Temperature increase measured on the heating pads' surface for two layers of heating pads, and for the distance of 50mm, 100mm, 150mm and 200mm between the heating pads and the specimen, with full power of the transformer

2.6 Future possibilities

There are many future possibilities of research with use of the apparatus, among others:

- Tests with bigger specimens. It is easy to increase the panel size by increasing the number of heating pads from 10 up to 24 and, therefore, increasing the heating surface to 0.67 m^2 (two layers) or even up to 1.34 m^2 (one layer of heating pads);
- Tests with two different heating zones; the transformer allows to create up to six different temperature zones on the heating pads, for example to recreate specific glass breakage patterns which are caused by temperature gradient;

- Tests in different environments, for example in a controlled oxygen or nitrogen atmosphere, low pressure chamber etc. A special version of cone calorimeter has been already designed for this purpose [16], which could show a direction for future development of the apparatus.

3 APPLICATION TO STUDIES ON A GLASS SPECIMEN

Until now, the apparatus has been used to analyse the behaviour of different materials and objects such as carbon steel tubular section, glass or insulating products subjected to an incident heat flux history similar to the one pertaining to the ISO 834 fire curve. One of these tests is described hereafter.

3.1 Bench-scale tests

The test was performed using two layers of heating pads and following the methodology described in Section 2.2.

Material analysed in the study was commercially available soda-lime-silica glass - a specimen of 20 x 20 cm^2 and thickness of 6 mm. A thermocouple (type K) was glued in the middle of the exposed side to measure the increase of temperature during the test. The glue itself contained a combination of silicate and kaolin and it was left to dry overnight.

The distance between the heating pads and the specimen was 8 cm. There was an insulating fibre placed around the specimen, as shown in Figure 1, and the transformer was set at full power. The specimen is exposed to heat flux when the heating pads reach the temperature of 500°C which compensates for the lack of rapid increase of the temperature present in a standard fire test. These conditions were previously identified for glass specimens through repetition of temperature measurements at different distances between the specimen and the heating pads. Due to lack of clearly defined boundary conditions for the full power set-up, it is not possible at the moment to quantify the net heat flux absorbed by a specimen.

The temperatures measured by the thermocouple on exposed side, as well as the temperature on the centre of the heating pads, are shown in Figure 10. The maximal temperature reached on the heating pads is lower than during the heat flux measurements presented in Figure 9 due to lower feedback provided by the glass specimen towards the heating pads compared to the insulating fibre mat that was used for heat flux measurements.

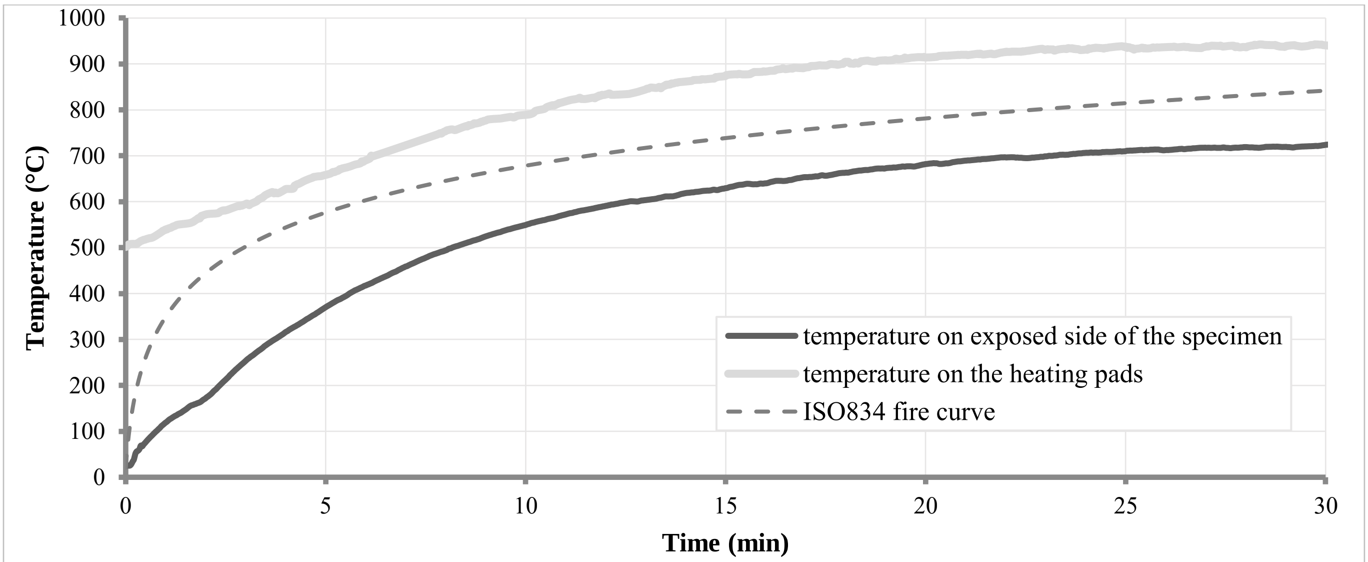

Figure 10. Temperature evolution on exposed side of the glass specimen, compared to temperature on the heating pads and the ISO834 fire curve

During this test, the temperature distribution on unexposed side of the specimen was checked using an infrared camera to control the influence of glass breakage on the temperature measurement. Except for the areas very close to the cracks in the glass and an area 1 cm wide from the edges, the temperature was uniform on the surface of the specimen, as shown in Figure 11. The cracks are not present in the vicinity of the thermocouple, so there was no influence of glass breakage on the temperature measured on the specimen.

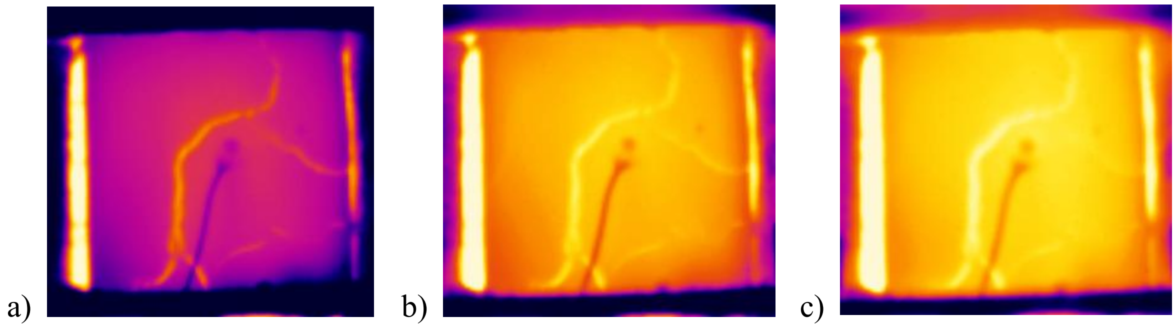

Figure 11. Temperature distribution on the unexposed side of the glass sample, captured by infrared camera for different temperatures on unexposed side: a) 350°C, b) 475°C, c) 550°C

3.2 Numerical modelling

A one-dimensional thermal analysis was performed for the glass specimen using ABAQUS 2019. The boundary conditions included:

- On exposed side heat transfer through radiation and convection with gas and radiation temperatures imposed following the ISO834 standard fire curve; the coefficient of convection was h = 25 W/m^{2}K [17]. and the glass emissivity ε=0.89 [18],
- On unexposed side heat transfer through radiation and convection with the far field at a constant temperature of 20°C; the coefficient of convection was h = 4 W/m^{2}K [17] and the glass emissivity ε=0.89 [18].

Thermal properties of soda-lime-silica glass were included as functions of temperature [19].

The temperature evolution on exposed side of the glass specimen obtained through numerical modelling is shown in Figure 12 and compared with the experimental results. The good fitting is visible with differences only up to approx. 35°C which proves that the apparatus and the methodology applied is suitable for applying ISO 834 fire-like heat flux to bench-scale specimens.

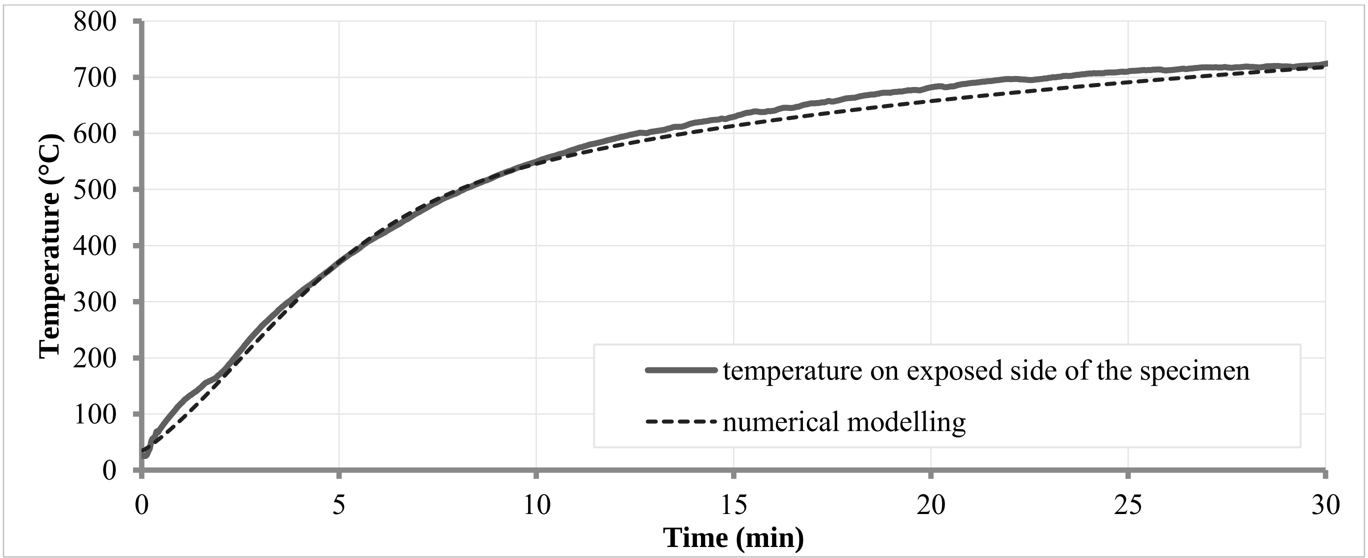

Figure 12. Temperature evolution on exposed side of the glass specimen obtained through numerical modelling and compared to experimental results

4 CONCLUSIONS

The paper presents an apparatus which allows to impose fire-like heat fluxes to bench-scale samples. It is a budget friendly, electricity-powered alternative to the well-known H-TRIS apparatus. However, there are some differences in the two methods for testing. For example, the incident heat flux is controlled by the temperature on the surface of the heating pads, while H-TRIS uses the variability of distance between the gas-fired panels and the specimen. The conditions which have been applied until now include heat flux present in full scale fire resistance test and it is possible to obtain relatively accurate results. It still needs to be verified which other regimes could be imposed.

There are many important advantages of the described apparatus, among others its relatively low cost, its possibility to extend the heating surface up to 1.34m^2 and the thin convective layer of hot gas close to the heating pads which is estimated as around 3.2 cm. On the other hand, the apparatus needs a certain power supply and the thermal inertia of the heating pads is a reason for slow cooling and heating rates. Additionally, more research should be done on the thermal boundary conditions, since they have been well-defined only until 750°C and they are more complex for the full power set-up. Therefore, it is crucial to consider all features of the apparatus when choosing as the testing equipment and method for a specific research program.

ACKNOWLEDGMENT

The authors would like to show their gratitude to Fabien Dumont for work on the mounting and maintenance of the apparatus and AGC Glass Europe for providing the glass specimens for the research. The research was funded by AGC Glass Europe and a grant from Walloon Region – *doctorat en entreprise* project 0000015366.

REFERENCES

1. Huang S., Angelakopoulos H., Pilakoutas K., Burgess I., “Reused tyre polymer fibre for fire-spalling mitigation”, Applications of Structural Fire Engineering, Dubrovnik, Croatia, 2015, doi:10.14311/asfe.2015.056.
2. “BSI Standards Publication ISO 5660-2:3025. Reaction-to-fire tests — Heat release, smoke production and mass loss rate”, vol. 3, no. January, p. 64, 2019.
3. Sakji, S., ”Modélisation probabiliste et validation expérimentale du transfert thermique et du comportement thermomécanique d'une plaque multicouche carton-plâtre-carton soumise au feu”, Ph. D. thesis, Univ. of Marne-La-Vallée, France, 2006.
4. Sakji S., Soize C., Heck J.V., “Probabilistic Uncertainty Modeling for Thermomechanical Analysis of Plasterboard Submitted to Fire Load”, Journal of Structural Engineering, 134 (10), 1611-1618, 2008.
5. Maluk, C., Bisby, L., Krajcovic, M., Torero, J.L., “A Heat-Transfer Rate Inducing System (H-TRIS) Test Method” Fire Saf. J., vol. 105, p. 307-319, 2019, doi:10.1016/j.firesaf.2016.05.001.
6. Elliott A., Temple A., Maluk C., and Bisby L., “Novel Testing to Study the Performance of Intumescent Coatings under Non-Standard Heating Regimes”, Proceedings of the 11th International Symposium on Fire Safety Science (IAFSS), Canterbury, New Zealand, 14 pp., 2014.
7. Lucherini A., Lam H.Y., Jimenez M., Samyn F., Bourbigot S. and Maluk C. “Fire Testing of Intumescent Coatings: Comparison Between Bench-Scale Furnace and Radiant Panels Experimental Methodologies”. Fire Technology, 58, 1737–1766, 2022
8. Lucherini A., Hidalgo J.P., Torero J.L. and Maluk C. “Influence of heating conditions and initial thickness on the effectiveness of thin intumescent coatings”. Fire Safety Journal, 120, 103078, 2021
9. Lucherini A. and Maluk C. “Assessing the onset of swelling for thin intumescent coatings under a range of heating conditions”. Fire Safety Journal, 106, 1-12, 2019
10. Lucherini A. and Maluk C. “Novel test methods for studying the fire performance of thin intumescent coatings”. Proceedings of 2nd International Fire Safety Symposium (IFireSS), pp. 565-572, Naples, Italy, 2017.
11. Maluk C. “Development and Application of a Novel Test Method for Studying the Fire Behaviour of CFRP Prestressed Concrete Structural Elements”, PhD Thesis, The University of Edinburgh, UK, 473 pp., 2014.
12. Lucherini A., Torero J.L., Maluk C., “Effects of substrate thermal conditions on the swelling of thin intumescent coatings”, Fire Mater, p. 1–14, 2020, https:// doi.org/10.1002/fam.284.

13. Lucherini A. “Fundamentals of thin intumescent coatings for the design of fire-safe structures”. PhD thesis, School of Civil Engineering, The University of Queensland, 2020. https://doi.org/10.14264/uql.2020.1021
14. Incropera F.P., DeWitt D.P., Bergman T.L., Lavine A.S. "Fundamental of heat and mass transfer". John Wiley & Sons, 6th Edition, 2006.
15. Mohammed H., Morisset D., Law A., Bisby L., “Quantification of the thermal environment surrounding radiant panel arrays used in fire experiments”, Proceedings of the 12th Asia-Oceania Symposium on Fire Science and Technology (AOSFST), Brisbane, Australia, 2021.
16. Babrauskas V., Twilley W., Janssens M., Yusa S., “A Cone Calorimeter for Controlled-atmosphere Studies” Fire Mater, vol. 16, p. 37-43, 1992, doi:10.1002/fam.810160106
17. EN 1991-1-2: Eurocode 1: Actions on structures - Part 1-2: General actions - Actions on structures exposed to fire
18. AGC technical data sheet – Planibel glass, 2011.
19. Bedon C., Louter C., “Thermo-Mechanical Numerical Modelling of Structural Glass under Fire - Preliminary Considerations and Comparisons.”, Challenging Glass Conference Proceedings 6, 2018, 513–24. https://doi.org/10.7480/cgc.6.2173.

REAL-SCALE FIRE TEST ON PILOTI OF URBAN LIVING HOUSES WITH FRP REINFORCEMENTS

In-Rak Choi[1], Ji-Hye Park[2], Sung-Mo Choi[3], Jeong-Ki Min[4], Jin-Won Shin[5]

ABSTRACT

In this study, real-scale car fire test using mid-size sedan was conducted to verify the fire behavior of the piloti parking space and the fire-resistance performance of the surrounding column members due to the car fire. For the car fire test in the parking area, four columns were installed outside the parking line and roof structure was installed to describe the piloti parking space. During the fire test, heat release rate and temperatures of the inside and outside of the car and the inside of the column were measured. Thermal effect on the columns reinforced with FRP for seismic resistance were observed.

Keywords: Car Fire; Piloti Structures; Reinforced Concrete Column; Fiber Reinforced Plastics; Temperature Distribution.

1 INTRODUCTION

In Korea, most urban living houses constructed as a piloti structure, which generally consists of only a structure that supports a load such as a column on the part facing the ground floor. Because of the piloti space is excluded from the building area and the number of floors according to the building law, the space can be utilized, so it can be used as a community space and parking lot for residents. However, unlike other normal structural members, the members used in the piloti structure are in contact with the outside air and they are exposed to various fire hazards due to different types and arrangements of possible fires and combustibles.

When the piloti space is used as a parking lot, there is a risk of car fire. When a fire occurs in one car, the distance between the cars is close, so the fire spreads quickly to several parked cars, and there is a risk of explosion due to the high heat release rate and increased temperature of the car. Due to the characteristic of the piloti structure, which is vulnerable to fire, the parking space is engulfed in flames for a short period of time, and the fire can spread and cause a fire hazard to the surrounding buildings.

Kang (2013) conducted a study to obtain the fire characteristics and fire-resistant behavior of structural members from car fire for performance-based fire-resistance design of parking space structures. Based on the previous research and existing studies related to the car fire and fire-resistant design of parking space structures, average distance to the column members according to the type of cars were derived. In addition,

[1] Associate Professor, Hoseo University,
e-mail: irchoi@hoseo.edu, ORCID: https://orcid.org/0000-0002-9449-419X
[2] Graduate Student, University of Seoul,
e-mail: jyejye1207@uos.ac.kr, ORCID: https://orcid.org/0000-0001-7180-2076
[3] Professor, University of Seoul,
e-mail: smc@uos.ac.kr, ORCID: https://orcid.org/0000-0002-9391-528X
[4] Senior Researcher, Korea Conformity Laboratories,
e-mail: jkm927@kcl.re.kr, ORCID: https://orcid.org/0000-0001-6371-0702
[5] Assistant Professor, Catholic Kwandong University,
e-mail: jshin@cku.ac.kr, ORCID: https://orcid.org/0000-0001-8152-1761
https://doi.org/10.6084/m9.figshare.22178240

using the mid-size car fire test results, fire curves for car fire were proposed based on the heat release rate of car fire.

In this study, real-scale car fire test was conducted to verify the thermal characteristics in the piloti parking space and the fire-resistance performance of the surrounding column members due to the car fire. For the car fire test in the parking area, four columns were installed outside the parking line of a car and roof structure was installed on it to describe the piloti parking space. Here, assuming that the columns were reinforced with FRP for seismic resistance, the thermal effect on the earthquake-resistant reinforced column member in the event of a car fire were observed.

2 FIRE TEST ON PILOI PARKING SPACE

2.1 Test Program

Real-scale car fire test was conducted to examine the effect on the structural members in the piloti parking space. In the real fire test, as shown in Figure 1, the mid-size sedan was placed in the center and four RC columns and roof structure placed surrounding the car to check the effect of a car fire in the parking space of the piloti structure. During the fire test, temperatures of the inside and outside of the car and the columns were measured. Also, using a large-scale cone calorimeter (LSC), heat release rate during the fire test was measured.

Figure 1. Piloti parking space fire test set-up

Table 1. Specifications of car for fire test

Model	Size (mm)			Engine displacement (cc)	Weight (kg)	Fuel Type
	Length	Width	Height			
SM 520 (1998)	4,825	1,775	1,415	1,998	1,350	Gasoline

Table 2. Test parameters for RC column

Name	Section size (mm)	Height (mm)	Longitudinal rebar	Hoop rebar	Concrete cover (mm)	Material strength (MPa)		Seismic reinforcement	
						Concrete	Rebar	Type	Thickness (mm)
C1	400×400	3,000	8-D22	D10 @150	40	24	400	-	-
C2								CN[1)]	5
C3								CFRP[2)]	0.11
C4								CFRP[2)]	0.4

1) CN: Semi-Incombustible Composite Fiber Panel, 2) CFRP: Carbon Fiber Reinforced Plastic

2.2 Temperature Measurement

During the fire test, temperature distribution of the piloti parking space and inside and outside of the car was measured using thermocouples. To check the flame propagation of the piloti parking space, total 43 thermocouples were installed near the corner of each column (C1′, C2′, C3′, C4 ') and the outside of the car (E, W, S, N, H) (See Figures 2 and 3). Here, sheathed K-Type thermocouples with a diameter of 1.6mm were used. In each location, thermocouples were installed at 0.5m intervals from 1m to 3m. In the location H, due to the presence of car ceiling, thermocouple was installed between 2m and 3m. Thermocouples installed outside the car were installed 200mm away from the car. Inside the car, total four 3.2mm diameter sheathed K-type thermocouples were installed in the center of front and rear seats (I1, I2, I3, I4) (See Figure 3).

In addition, another 112 K-type thermocouples with a diameter of 0.65mm were installed inside the columns. Thus, 28 thermocouples, 14 thermocouples at 1m height and another 14 thermocouples at 2m height, were installed in each column (C1, C2, C3, C4). Location of thermocouples installed inside of the column were presented in Figure 4. 11 thermocouples were installed in the surface of the column and 3 thermocouples were installed in the hoop rebar. Installed thermocouples can measure up to 1,200°C.

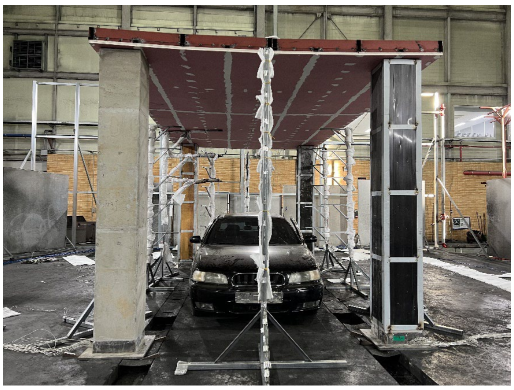

(a) Front side

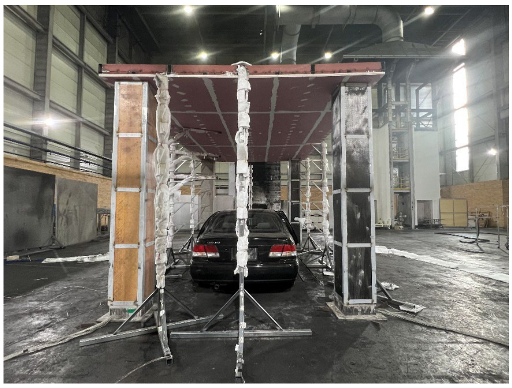

(b) Back side

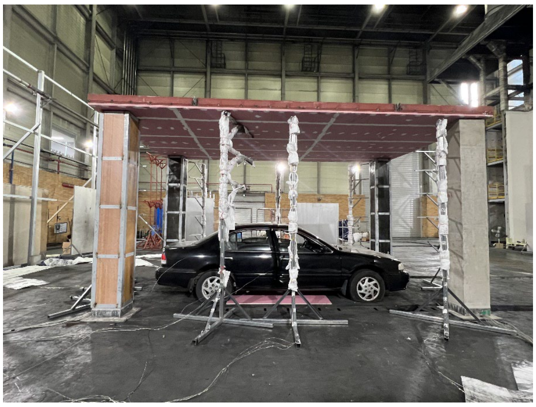

(c) Left side

(d) Right side

Figure 2. Test set-up for real-scale fire test

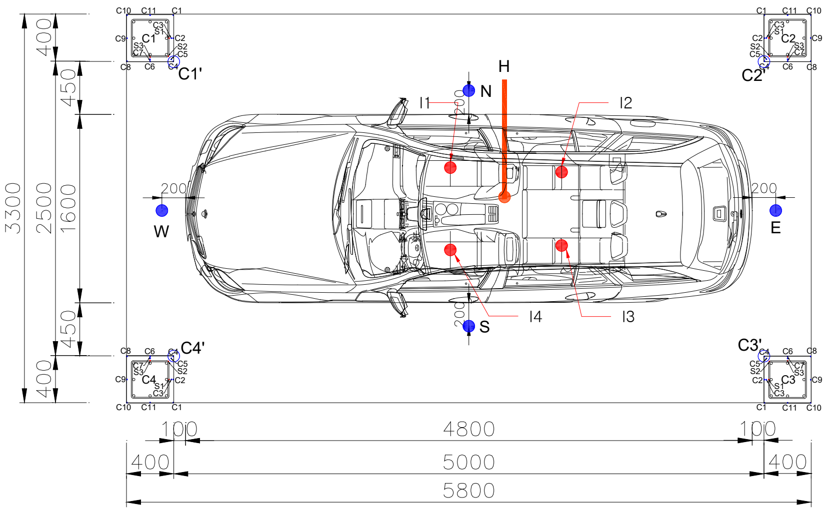

Figure 3. Location of thermocouples (unit: mm)

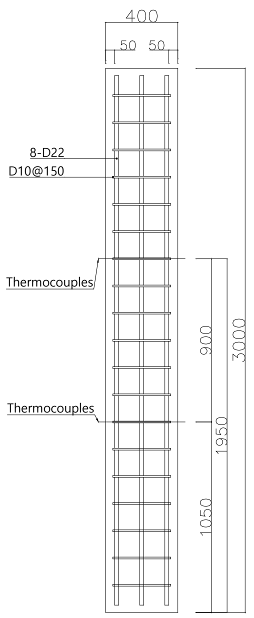

(a) Position by height of thermocouple

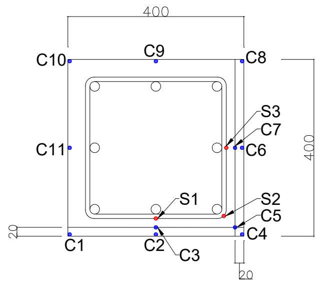

(b) Location of thermocouple inside the column

Figure 4. Location of thermocouples inside the column (unit: mm)

3 TEST RESULTS

3.1 Temperature Distribution of Piloti Parking Space and Column Members

The car after the fire test was shown in Figure 5 and it was found that all the indoor combustible materials were consumed. Figure 6 shows the measured temperatures from the thermocouples over time at different locations. As shown in Figures 6(a~d), the maximum temperature around the column was 332°C at the location of C1′-3.0, and it was due to the explosion of air bag in the front seat. At that time, flames were emitted from the inside to the car and result in a rapid rise in the temperature. Another peak occurred at about 24 minutes in the location of C2' and C3' due to the explosion at the rear part of the car. After that, at about 33 minutes, explosion of the engine room made another peak in the location of C1' and C4'.

As shown in Figures 6(e~i), the maximum temperature of the outside of the car was 640°C in N-3.0 due to the explosion of the airbag in the front seat as the same as the temperature peak of the location of C1′-3.0. The maximum temperature at the top of the car was 728.5°C in H-3.0. The maximum temperature of the inside of the car was 996°C in I4 [See Figure 6(j)]. The temperature measured inside the car was relatively higher than that of the temperature of outside because the flame could not be ejected due to the ceiling of the car. Also, the temperature of the rear seat, location of I2, was higher than that of the front seat, locations of I1 and I4. Except for the location E, the highest temperature was observed at the 3m height, and the height of the flame rose to a maximum of 3m due to the ceiling. Therefore, the temperature and height of the flames have a direct effect on the structures.

In columns, the maximum temperature of column C1 was 173°C in C1-2-C4, 2m height corner location [See Figures 7(a~b)]. In addition, in S1 ~ S3, where the thermocouples installed on the hoop rebar, the maximum temperature was 57.6°C in C1-2-S2 installed at the corner directly exposed to fire. As the flame grew due to the explosion in the engine room, the temperature showed a tendency to rise rapidly, and the hoop rebar located inside the concrete cover showed lower temperature.

In the column C2, the maximum temperature was 92.5°C in C2-2-C6 [See Figures 7(c~d)]. It occurred as the rear bumper fell down and the flames hit the concrete surface. Also, the maximum temperature of rebar was 25.5°C in C2-1-S2, installed at the edge of the column and directly exposed to fire. Thus, the temperature of rebar did not increase significantly. Also, unlike other columns, the temperature at a height of 1m was higher than that at a height of 2m. At a height of 2m, the maximum temperature at the edge of the column surface was 54.9°C at C2-2-C4.

In the column C3, the maximum temperature was 215°C in C3-2-C6 [See Figures 7(e~f)]. It occurred as the flame reached the concrete surface due to the explosion of the car. The maximum temperature of rebar was 33.9°C in C3-2-S2, installed at the edge of the column and directly exposed to fire. The maximum temperature at the edge of the column surface was 123°C at C3-2-C4.

Finally, in the column C4, the maximum temperature was 195°C in C4-2-C6 [See Figures 7(g~h)]. It occurred due to the explosion of tire. The maximum temperature of rebar was 38.3°C in C4-2-S2, installed at the edge of the column and directly exposed to fire. The maximum temperature at the edge of the column surface was 86.6°C at C4-2-C4. On the other hand, at C4′-2.0 around the column, it was 80.5°C, indicating that the temperature at the column surface was about 1.08 times higher than the temperature around the column.
Comparing the temperature by height of the column showed a higher temperature at 1m height than that of 2m height. Also, in the rebars, the temperature of 2m height was higher than the other except for C2 column.

(a) Front side (b) Back side (c) Left side (d) Right side

Figure 5. End shape of real fire test

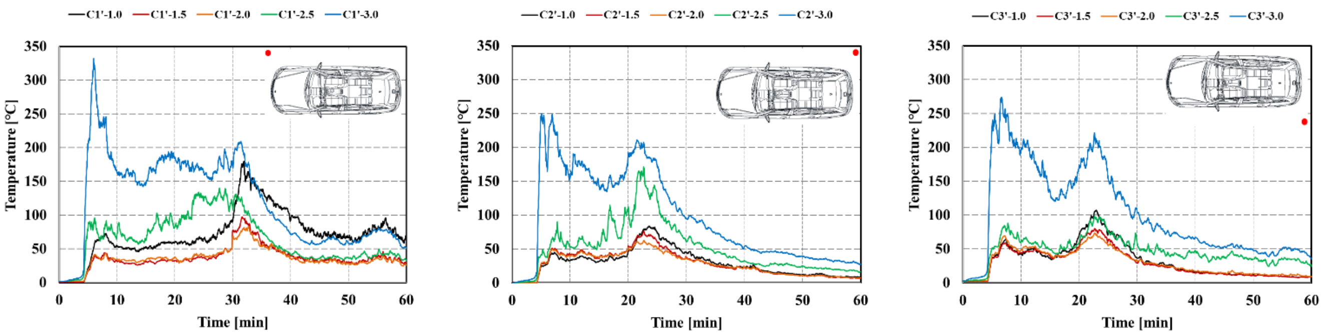

(a) Location of C1´ (b) Location of C2´ (c) Location of C3´

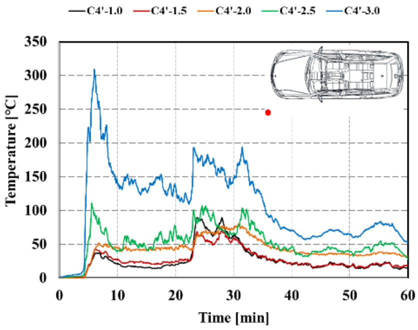

(d) Location of C4´

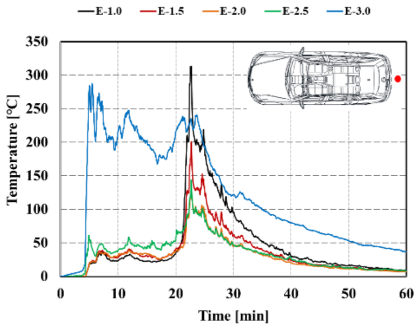

(e) Location of E

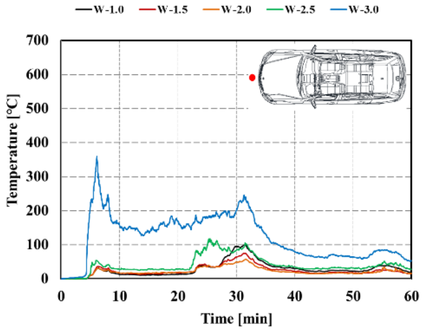

(f) Location of W

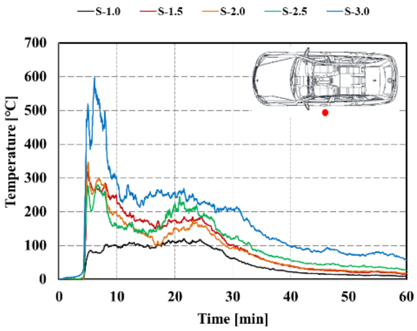

(g) Location of S

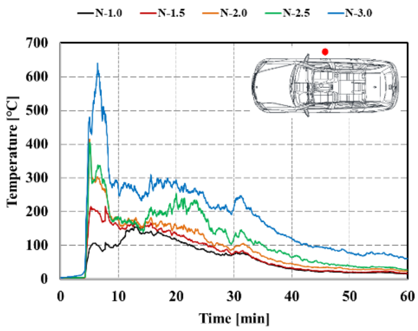

(h) Location of N

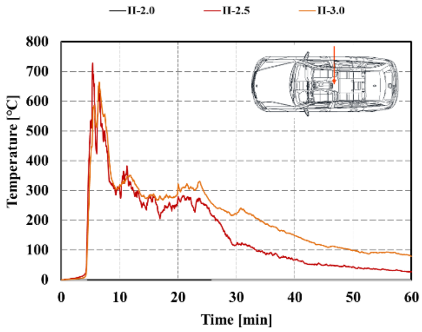

(i) Location of H

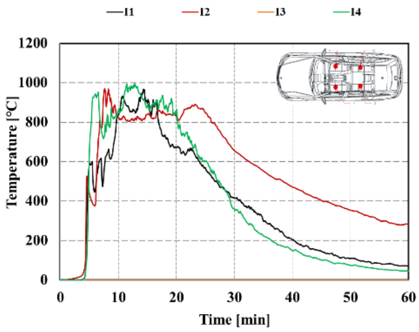

(j) Inside of the car

Figure 6. Measured time-temperature relationships – Inside and outside of car

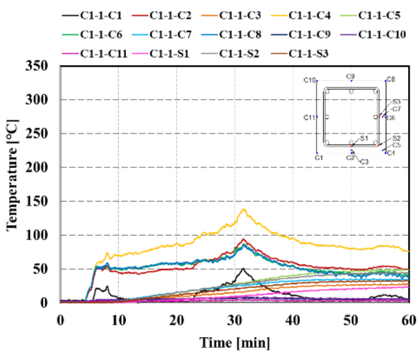

(a) Column C1 – 1m

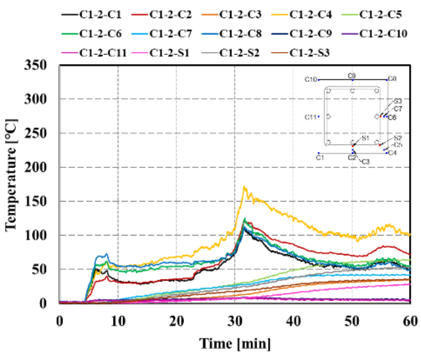

(b) Column C1 – 2m

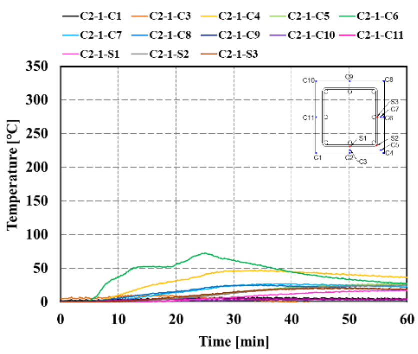

(c) Column C2 – 1m

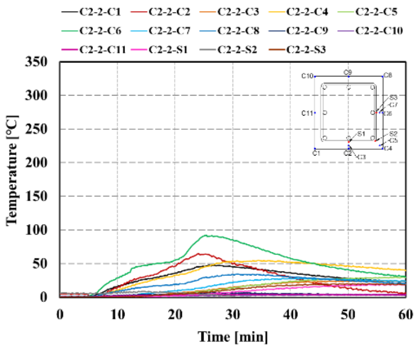

(d) Column C2 – 2m

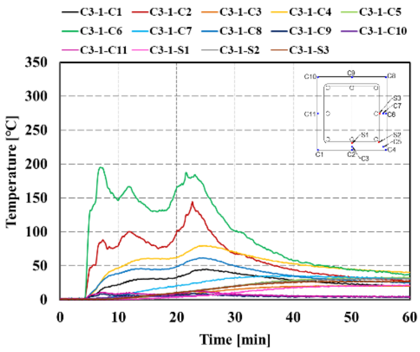

(e) Column C3 – 1m

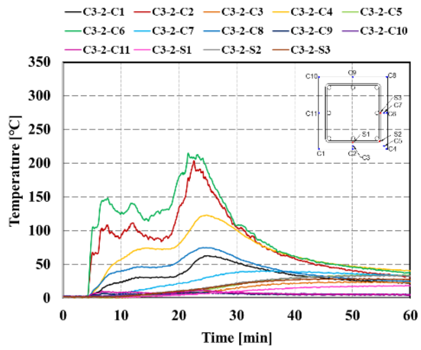

(f) Column C3 – 2m

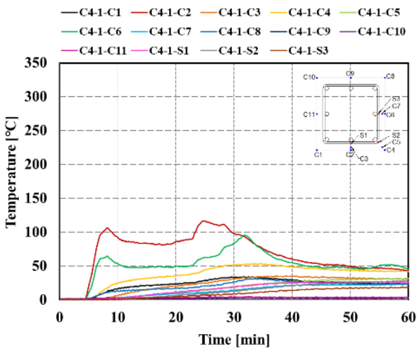

(g) Column C4 – 1m

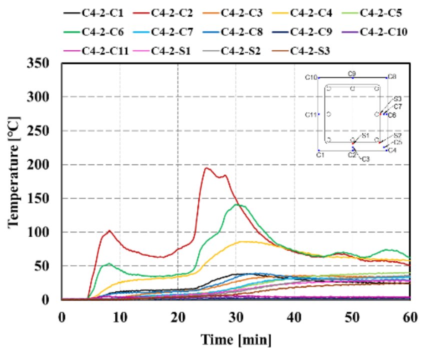

(h) Column C4 – 2m

Figure 7. Measured time-temperature relationships – Inside the column

3.2 Heat Release Rate for Car Fire

Figure 8 shows total heat release and heat release rate for car fire. The maximum heat release rate was 3,752kW at 24 minutes. After ignition, the flame spread to the tires, windows, airbags, and engine room, with the strong flame and explosion sound. In addition, the rate of heat release increased sharply when the explosion occurred. The total heat release after test was 5,575MJ.

3.3 Column Concrete Surface after Test

After the fire test in the car parking space, cracks and burning surface of concrete column was checked. Figure 9 shows a photograph of the surface of the column C1. The maximum temperature of the surface of the concrete column was 92.5°C ~ 215°C for the C1 ~ C4 columns, and only the surface of the column just under the ceiling showed a blackened shape. On the surface of the column that was not directly exposed to the flame, special features were could not be found. Overall, it was found that there was no structural damage on the column members during the car fire because the distance between the flame and the column was sufficient.

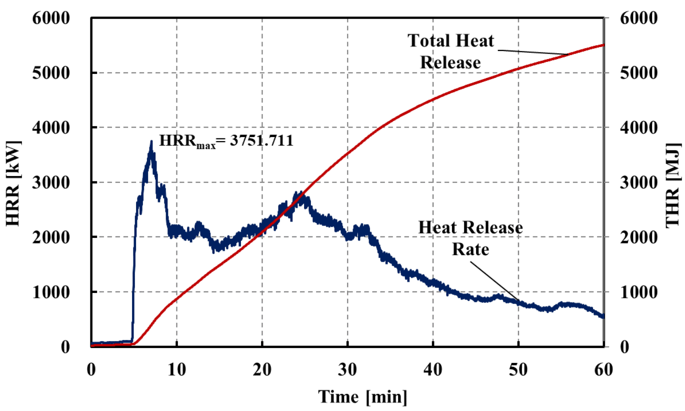

Figure 8. Heat release rate of car fire

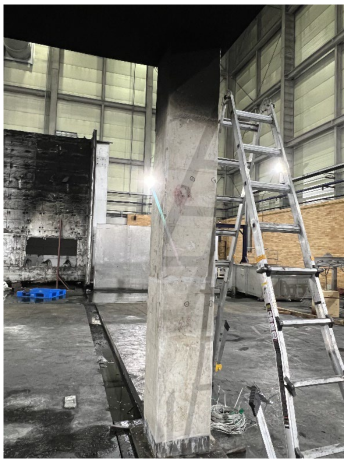

Figure 9. Column surface after test (C1)

4 CONCLUSIONS

In this study, to verify the fire behavior of the piloti parking space and the fire-resistance performance of the surrounding column members due to the car fire, real-scale car fire test was conducted. For the car fire test in the parking area, four columns were installed outside the parking line of a car and roof structure was installed to describe the piloti parking space. During the fire test, heat release rate and temperatures of the inside and outside of the car and the inside of the column were measured. Real-scale car fire test results can be summarized as follows.

- Test results shows that the maximum temperature around the column was varied from 250°C to 332°C according to the measured location. Also, the maximum temperature of the outside of the car was 640°C and that of the inside of the car was 996°C. The temperature measured inside the car was relatively higher than that of the temperature of outside because the flame could not be ejected due to the ceiling of the car.
- The maximum temperature in the column was varied from 92.5°C to 215°C and it was affected by the thickness of seismic reinforcing material. The maximum temperature of the hoop rebar located under the concrete cover was varied from 25.5°C to 57.6°C according to the column.
- The rate of heat release increased sharply when the explosion occurred. The maximum heat release of the mid-size car fire was 3,752kW at 24 minutes. The total heat release after test was 5,575MJ.
- The maximum temperature of the surface of the concrete column was 92.5°C ~ 215°C for the C1 ~ C4 columns, and only the surface of the column just under the ceiling showed a blackened shape. Also, there was no structural damage on the column members during the car fire because the distance between the flame and the column was sufficient.

ACKNOWLEDGEMENTS

This work was supported by the National Research Foundation of Korea (NRF) grant funded by the Korea government (MSIT) (No. 2021R1A4A1031201).

REFERENCES

1. Kang, S.G., A study on the car fire behavior and fire resistance properties for performance: based fire safety design of parking space structures, Master's Thesis, Hoseo University, Asan. (2013).

FIRE BEHAVIOUR OF ALUMINIUM-WOOD JOINTS WITH TOLERANCE GAPS

Hugrún María Friðriksdóttir[1], Finn Larsen[2], Ian Pope[3], Ana Sauca[4], Alexandru Radulescu[5], Frank Markert[6]

ABSTRACT

Tolerance gaps or slips in wood connections are unavoidable, for reasons of constructability and the effects of natural shrinkage in timber elements with changing moisture content. During a fire, these gaps may lead to increased heat transfer through the connection. Aluminium connectors are becoming more popular due to their high malleability and availability, but they are particularly vulnerable to elevated temperatures. Thus, the objective of this study is to investigate the effect of tolerance gaps on the fire performance of aluminium connectors in beam-to-column/wall shear connections. An experimental campaign was designed to study the temperature evolution of the aluminium connectors during standard fire exposure for 1 mm and 6 mm tolerance gaps, as well the mitigation effects of additional intumescent fire protection in a 6 mm tolerance gap connection. The results showed a clear and consistent impact of the connection gap size on the temperature evolution of the aluminium connectors. For the larger 6 mm gap, the temperature of the connector increased much faster, reaching 286 ± 36 °C after 80 minutes, at which time the connector with a 1 mm gap had only reached 97 ± 1 °C. The addition of intumescent protection in a 6 mm gap case led to lower temperatures in the connection after 40 minutes of fire exposure, in comparison to an equivalent tolerance gap without fire protection. This study shows that tolerance gaps can lead to a significant reduction in the capacity of aluminium connectors, but this may be mitigated with additional fire protection.

Keywords: engineered timber; connections; aluminium connectors; wood; tolerance gaps; intumescent; fire resistance; fire protection

1 INTRODUCTION

Engineered timber construction materials are increasingly appealing due to their mechanical properties, aesthetic qualities, and low embodied CO_2 emissions in comparison with more conventional materials. These materials, such as cross-laminated timber (CLT), laminated veneer lumber (LVL), and glulam, consist of modified timber products that are manufactured to increase the strength and stiffness of the elements in comparison to sawn timber. However, the fire performance of engineered timber structures remains a concern. A key issue is the performance of metallic connections between exposed timber elements, which can be particularly vulnerable to fire if not adequately protected [1, 2]. A common practice

[1] MSc Civil Engineering graduate, Denmark's Technical Univeristy
e-mail: hugrunmaria@gmail.com
[2] Wood Specialist, DTI – Danish Technological Institute
e-mail: fla@teknologisk.dk, ORCID: https://orcid.org/0000-0001-6498-9012
[3] Research Consultant, DBI – The Danish Institute of Fire and Security Technology
e-mail: ipo@dbigroup.dk, ORCID: https://orcid.org/0000-0002-3130-6868
[4] Scientific Researcher, DBI – The Danish Institute of Fire and Security Technology
e-mail: as@dbigroup.dk, ORCID: https://orcid.org/0000-0001-5992-998X
[5] Research Consultant, DBI – The Danish Institute of Fire and Security Technology
e-mail: ara@dbigroup.dk
[6] Associate Professor, Denmark's Technical University
e-mail: fram@dtu.dk, ORCID: https://orcid.org/0000-0002-1396-2810
https://doi.org/10.6084/m9.figshare.22178246

for protecting metal connectors is to embed them between the adjoining engineered timber members, so that they are insulated by the surrounding wood and – in case of a fire – by the development of a char layer. The adjoining members shield the connector from direct exposure to radiative and convective heat transfer from the fire, and the relatively lower thermal conductivity of the wood and char can insulate the connector from the high external temperatures. This solution requires a sufficient cover thickness of the wooden elements around the connector, and minimal gap width between the elements, such that convection and radiation through the gap is negligible.

However, ensuring that the joint is completely tight is not feasible, since wood is a natural material that may shrink or swell, and tolerance gaps are unavoidable for constructability. Gaps between members vary in size depending on the type of connection and the extent of any shrinkage or swelling of the wood [3, 4]. The best feasible gap width for connectors that are recessed in holes carved into the wood is 1 mm, but even with this design value, the in-use gap width could foreseeably increase to 6 mm – thus potentially exposing the metal connectors to high temperature gases. In the production phase, often an initial gap of at least 1 mm is made, so that the connection is not too tight and difficult to mount. Subsequently, shrinkage of the wood materials due to changes in moisture content (MC), typically falling from 12-15 % MC down to 6-8 % MC (approximately 8 % change) [5], may result in a longitudinal shrinkage of 4-6 mm for a beam element with a length of 5-9 m, or approximately 2-3 mm at each end. This shrinkage is typically incorporated as a slip possibility in the connections. Furthermore, when the connectors are recessed into a wood-based column or wall, there may also be shrinkage in the depth of the recess around the connector due to aforementioned moisture changes, leading to shrinkage perpendicular to the wood fibres of 1-2 mm. Altogether, this could lead to a gap of 6 mm, even for a designed 1 mm gap.

While the fire performance of these joints has been studied for steel connectors [6, 7, 8], there is a lack of information on the behaviour of aluminium connectors, despite them being widely available and attractive due to their high malleability. For steel connectors, the predominant failure mode is a loss of embedding strength in the timber surrounding the steel [6]. However, aluminium loses 77 % of its yield strength at 300 °C [9], whereas the yield strength of carbon steel is relatively unaffected at this temperature. Thus, exposure to hot gases via tolerance gaps may lead to earlier failure of the aluminium connector itself.

Palma *et al*. [7, 8] showed that increasing the tolerance gap between the beam and the column has a negative influence on the fire resistance of beam-to-column shear connections. This study presented the results of an extensive experimental program on the fire resistance of timber shear connections, where a total of nine different connection typologies were tested. Only two of the considered connections were commercially available, while the others were custom-made. All were steel dowel connections except one, which was an aluminium dovetail connection (AW-6082, EN 755-2 [10]), composed of two interlocking parts that were separately screwed into each member. This aluminium connector was not recessed, so it was exposed around its perimeter by an 18 mm gap between the column and the beam. The member was subjected to 30 % of its ambient shear capacity during the test and failed after 34 minutes of standard fire exposure. The failure occurred in the connector itself, but no temperatures of the metal connectors were reported during the experiment, which is an important parameter to monitor to understand how the fire performance of aluminium-wood connections may be improved.

For timber elements of a given size, it is important to know the extent to which the size of the tolerance gap, charring of the timber, and any additional protection, can affect the temperature evolution of the aluminium connection. For joints with large tolerance gaps or exposed connections, the use of fire protective insulation or intumescent materials is relatively straightforward and generally anticipated in design. However, for small gaps of 1-6 mm, the need for fire protection of aluminium connectors is not established, and solutions are limited by the constructability of the joint. The aim of this study is to investigate the effect of tolerance gaps on the fire behaviour of aluminium connectors in a wood joint. Small-scale experiments were performed in order to investigate the temperature evolution in such connections, char depths, and the estimation of the shear capacity of the aluminium connectors when exposed to elevated temperatures. Two intumescent fire protection measures are proposed, and fire tested, and the results are discussed in this paper.

2 EXPERIMENTAL METHODS

The experimental campaign, presented in Table 1, consisted of four small-scale fire resistance tests. The use of standard fire exposure for testing wooden elements may not be representative of the most severe fire conditions in reality, particularly since the limited availability of oxygen in a standard furnace will inhibit flaming combustion or oxidation of the char layer around the joint [11], and because there is no consideration of cooling-phase heat transfer. Nevertheless, standard fire exposure can allow comparison of the fire performance of different designs, and the convective heat transfer induced is particularly relevant to the vulnerabilities created by tolerance gaps.

In all four tests, samples consisted of a 180 × 366 mm glulam beam with a length of 488-493 mm, connected by an embedded aluminium connector to 500 × 450 mm LVL walls of 160 mm thickness. The connectors used in this experiment were commercially available LOCK75215 aluminium connectors from Rothoblaas, made from alloy AW6005A-T6 (EN 755-2 [10]). Three specimens (used for the Tests 1-3) had 1 mm and 6 mm tolerance gaps at each end, with no additional fire protection, as presented in Figure 1. In Test 4, a specimen with additional fire insulation around the connector was used to investigate the effectiveness of this protection. The specimen in Test 4 had 6 mm tolerance gaps on both ends, with a 1 mm thick intumescent flexible gasket 'fire stripe' [12] surrounding the perimeter of the connector, as presented in Figure 2. The fire stripe's 'reaction to fire' is classified as B-s3, d0 in accordance with EN 13501-1 [13]. At both ends of the specimen, the width of the stripe was 20 mm, with a cover distance of 30 mm from all edges of the beam. The only difference between the cases at each end of the specimen in Test 4 was that at one end the fire stripe was inlaid into a channel carved 1 mm into the surface of the beam (Case I), whereas at the other end, the fire stripe was applied directly to the unaltered surface of the beam (Case II).

No external load was applied to the specimen when exposed to ISO 834 [14] standard fire, but the temperatures of the aluminium connectors were monitored and their reduced load carrying capacity was estimated. As shown in equation (1), the reduced capacity of the aluminium connectors ($R_{v.alu.k.fire}$) was estimated as the product of the shear capacity of the aluminium connector at ambient temperature ($R_{v.alu.k.ambient}$) and the reduction factor of the 0.2 % proof strength at elevated temperatures for aluminium alloy AW6005A ($k_{0.\theta}$) as defined in EN 1999-1-2 [9] .

$$R_{v.alu.k.fire} = k_{0.\theta} \times R_{v.alu.k.ambient} \qquad (1)$$

Additionally, in Test 4, the in-depth temperature of the glulam beam was measured in ten locations at either end of the beam, at a depth of 140 mm from the top of the beam (see Figure 5).

Table 1. Small-scale experimental campaign.

Tests 1-3:		**Test 4:**	
Gap size	**Fire protection**	**Gap size**	**Fire protection**
1 mm	None	6 mm	Case I: fire stripe carved 1 mm into the surface of the beam
6 mm	None	6 mm	Case II: fire stripe glued to the surface of the beam

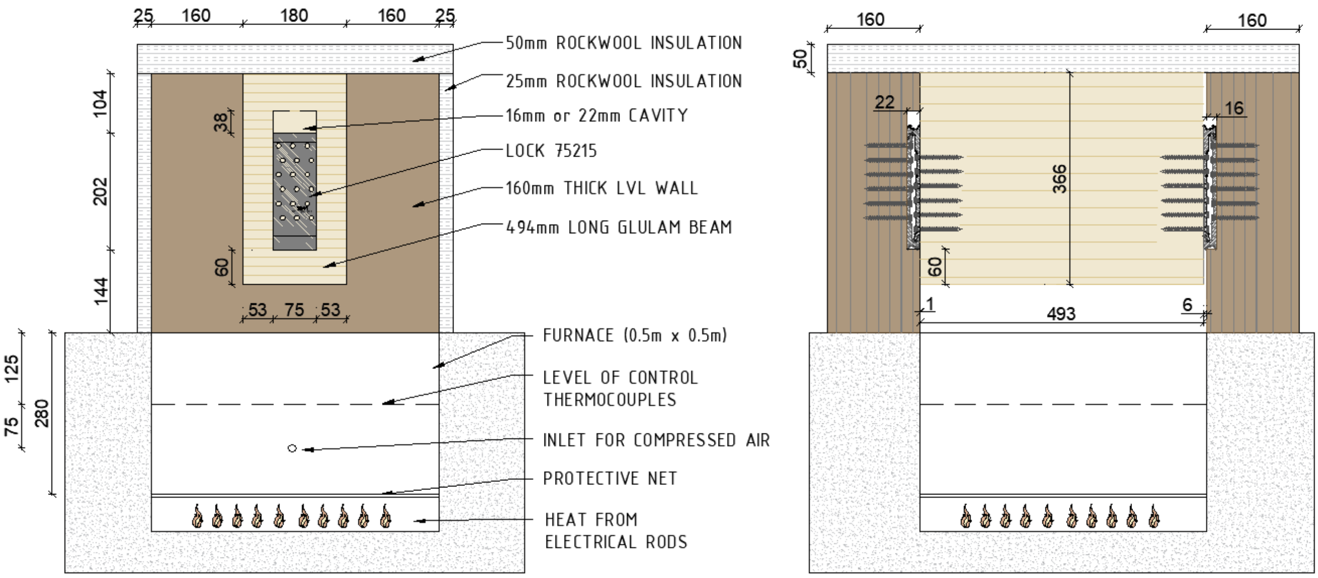

Figure 1. Cross-sections at the joint between the LVL wall and glulam beam (left), and down the length of the specimen (right), for Tests 1, 2, and 3.

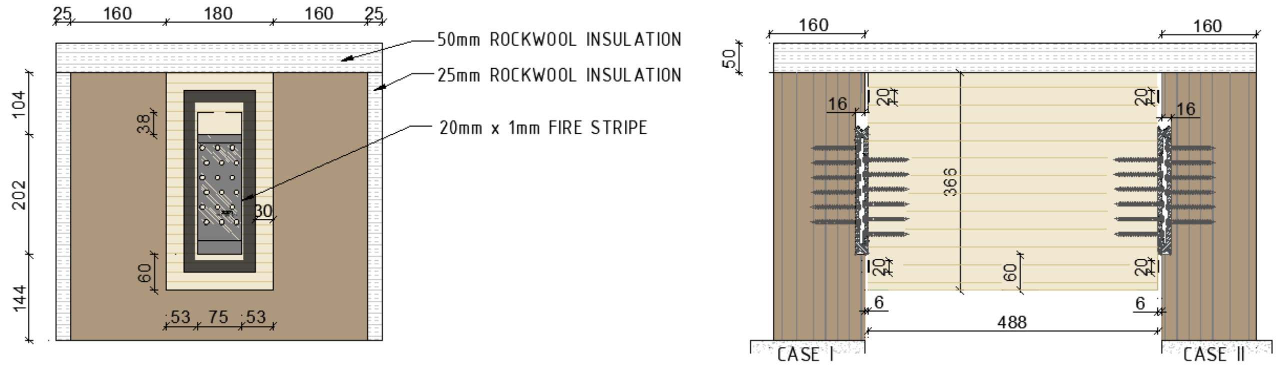

Figure 2. Cross-sections at the joint between the LVL wall and glulam beam (left), and down the length of the specimen (right), for Test 4.

2.1 Testing equipment

The DBI small-scale electrical furnace with opening dimensions of 500 mm × 500 mm, made from a steel frame with ceramic fibre insulation and concrete interface around the opening was used to provide the ISO 834 temperature-time exposure to the specimens. Nine electrical heating rods drive the furnace, with a power of 3×400V/32A at 50 Hz, controlled by three metal-sheathed gas phase thermocouples in the middle of the furnace. Compressed air was supplied to the furnace as needed throughout the experiment to keep the pressure at 20 Pa, controlled with a venturi valve.

The oxygen concentration within the furnace was measured in Test 2, using a 4900 CEMS Analyzer from Servomex [15]. The emission analyser was calibrated based on the ambient oxygen concentration in the laboratory. A steel rod pipe connected to a rubber tube extracted the gases from inside the furnace to the emission analyser.

Agilent data acquisition apparatus was connected to the thermocouples and the data acquisition took place within the Agilent Benchlink software [16]. The temperature time histories were recorded with a sampling interval of 5 seconds.

2.2 Instrumentation of the specimens

The temperatures in the connection area were measured with thermocouples (TCs) at the locations shown in Figure 3 for Tests 1-3, and in Figure 4 for Test 4. These thermocouples were fixed in the gap between the beam and the wall on the left (L), right (R), bottom (B) and top (T) sides of the connector, and also between the aluminium connector and the wall, along the mid-line of the connector (M). During Test 4, additional in-depth TCs were added to the beam, as shown in Figure 5, inserted 140 mm in from the top of the beam at different positions around the screws and the fire stripes. These thermocouples were of type K, with an exposed junction formed by twisted wires of 0.5 mm diameter each, while the rest of the cable was insulated with fibreglass. Three Inconel sheathed type K thermocouples of 2 mm diameter were placed 10 mm below the beam, to measure the gas temperatures near the surface of the beam at each end, and at the centre of the beam.

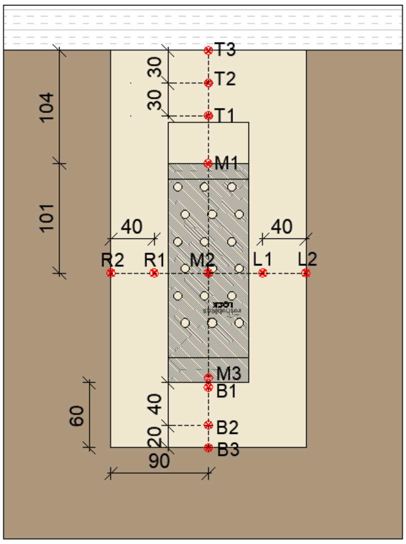

Figure 3. Location of TCs in the connection area - Tests 1, 2 and 3.

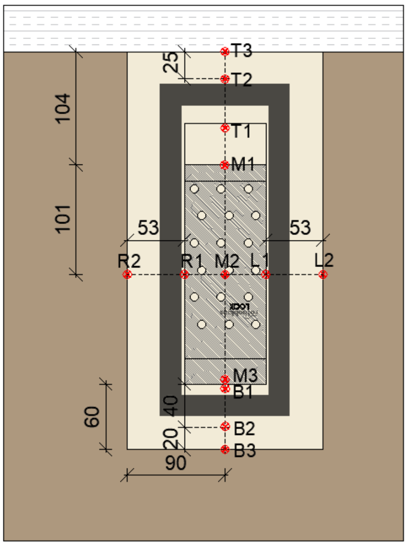

Figure 4. Locations of TCs in the connection area - Test 4.

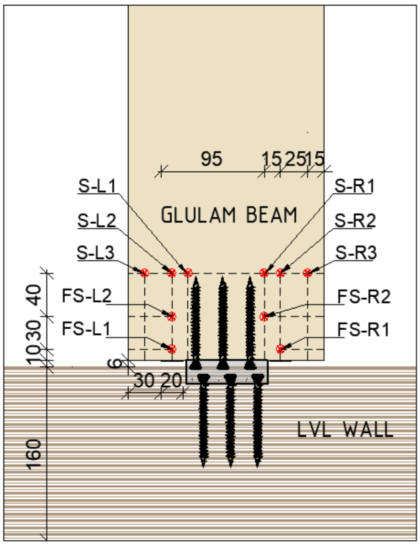

Figure 5. Locations of TCs in the beam - Test 4 (top view).

2.3 Specimen preparation

A cavity of 75 mm × 240 mm, with a depth of either 22 mm or 16 mm, was carved into each LVL wall, at the centre, 144 mm above the bottom edge. The depth of the cavity was 22 mm for the walls where the aluminium connector was to be flush with the surface of the LVL wall specimen. Considering that the connectors had a slip tolerance of 1 mm, this allowed a gap between the wooden elements of 1 mm. For the cases that the connector was to protrude 6 mm out of the LVL wall specimen, the cavity had a depth of 16 mm. In Test 4, the fire stripe was attached to the beam around the connector (see Figure 6 a)).

Pre-drilled holes with a diameter of 5 mm were made in the LVL wall element to allow the insertion of thermocouples from the exterior of the sample. Each thermocouple was then bent 50 mm along the wall surface so that the measuring junction was at the desired location, as shown in Figure 6 b). The pre-drilled holes were sealed at the exterior of the wall specimen with a high-temperature resistant silicate-sealant, to prevent the smoke inside the furnace from passing through the thermocouple holes. For Test 4, an additional ten holes of 2 mm diameter were drilled in the beam, and TCs were inserted as shown in Figure 6 c).

A 50 mm thick mineral wool insulation was fastened on top of the specimen and 25 mm thick mineral wool insulation was placed on both sides of the specimen, to create an enclosed space. A 51 mm diameter hole was made in the top insulation to allow the exhaust of smoke produced during the test.

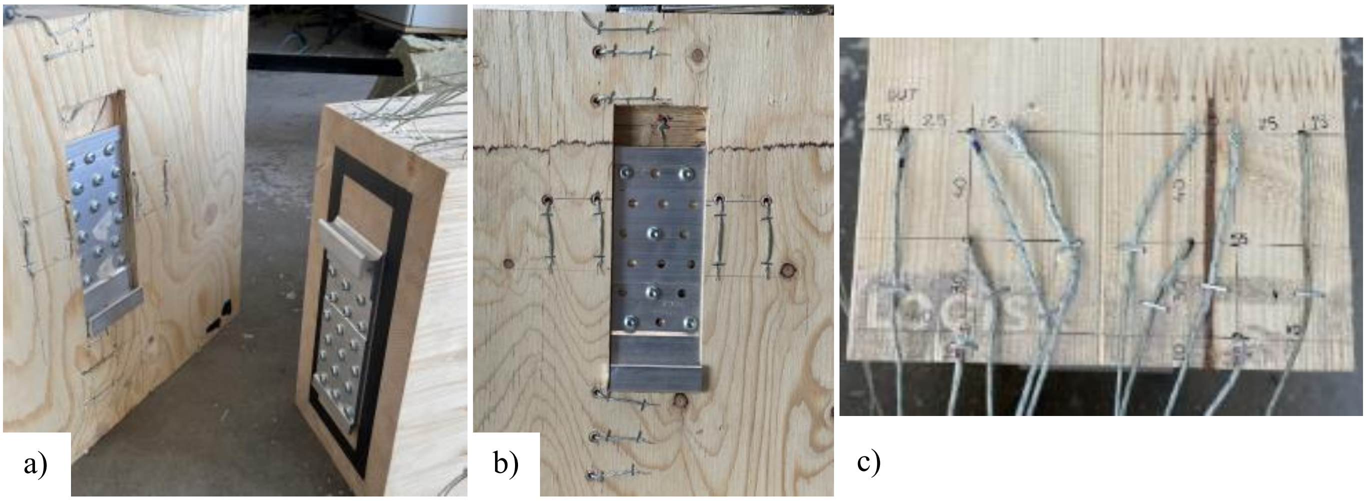

Figure 6. a) fire stripe installed around connector on beam in Test 4, b) aluminium connector installed in LVL wall, along with TCs, c) in-depth TCs installed in the top of the beam in Test 4.

3 RESULTS

3.1 Tests 1-3 with unprotected tolerance gaps

Figure 7 a) shows the averaged temperature measurements of selected thermocouples during Tests 1-3. Maximum and minimum temperatures are also shown, bounding the average values for the thermocouples. Gas temperatures from near the centre and each end of the beam were averaged across the three tests. There was no clear difference between the gas temperatures in each location, and the average was close to the standard value for ISO 834 exposure for most of the test. An initial spike in gas temperatures after two minutes corresponded to ignition of the timber sample, after which the oxygen concentration in the furnace rapidly decreased to zero as an excess of pyrolysis gases was produced by the specimen. In Test 2, the oxygen concentration measured within the furnace had fallen below 3 % within five minutes, and continued to fall after this time. The lack of available oxygen within the fuel-rich atmosphere in the furnace prevents oxidisation of the char layer and flaming combustion, which might otherwise make the influence of the gap on the connection performance even more severe.

The temperatures at the outer edges of the gaps (averages of thermocouples L2, R2, and B3) were similar at either end, which further supports the assumption of equivalent external heating conditions surrounding each connection. Therefore, the difference in temperatures at the connectors can only be explained by the enhanced heat transfer path provided by the larger air gap, increasing the flow of hot gases around the joint.

Figure 7 b) shows the averaged temperatures of the aluminium connectors (M1, M2, and M3) measured in all three tests, along with the reduced capacity of the connector $R_{v.alu.k.fire}$ during the ISO 834 exposure. For the larger 6 mm gap, the temperature of the connector increased much faster, exceeding 150 °C after 60 minutes, and reaching up to 300 °C by around 80 minutes of exposure in all tests – at which time the connector with a 1 mm gap had only reached 100 °C. At 60 minutes, these temperatures corresponded to reductions in the shear capacity of the connectors of 6 % and 22 % for the connections with 1 mm and 6 mm gaps, respectively. At 75 minutes, the temperatures corresponded to reductions of 7 % and 57 % for the connections with 1 mm and 6 mm gaps, respectively. As temperatures behind the connector rise above 150 °C after 60 minutes for the connections with a 6 mm gap, this indicates that the surface of the wood behind the connector has begun to pyrolyse.

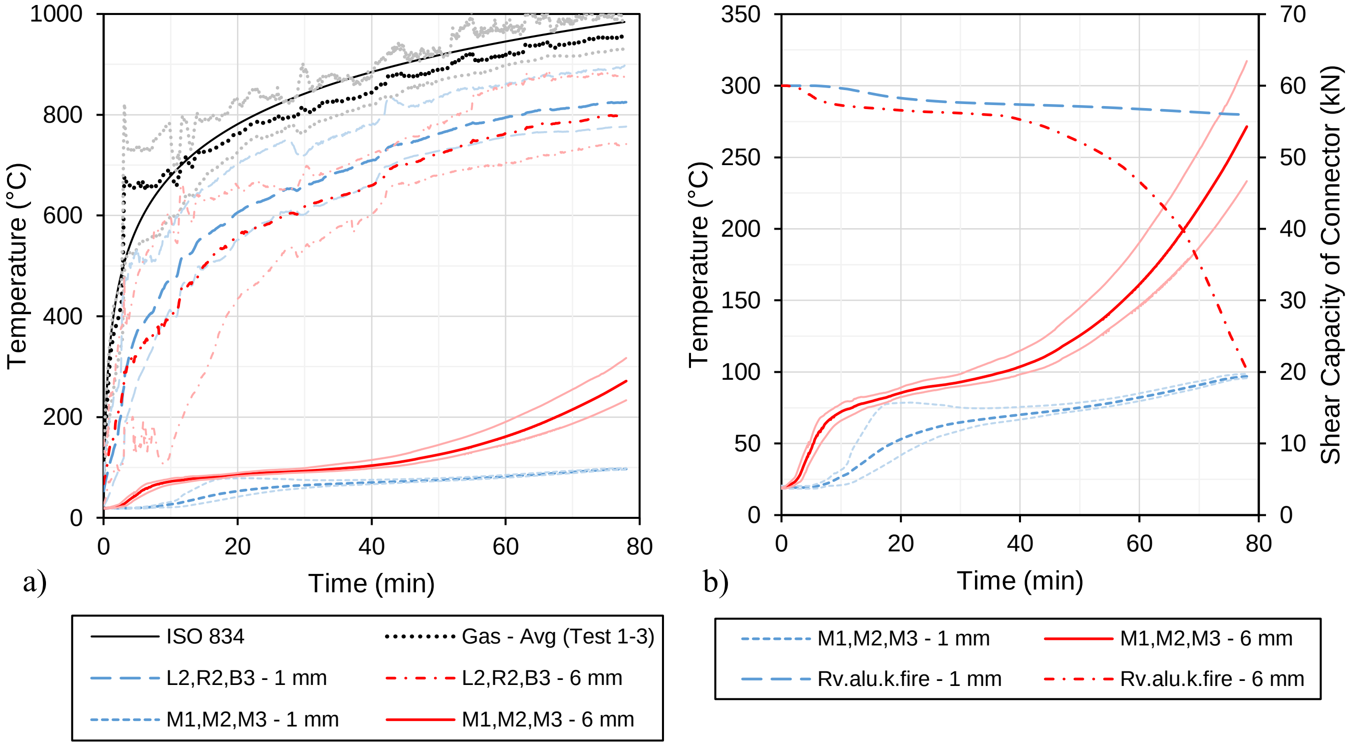

Figure 7. a) averaged temperatures from Tests 1-3 for thermocouples L2, R2, and B3, around the perimeter of the gap at the connection; thermocouples M1, M2, and M3, behind the aluminium connector; and the gas phase thermocouples beneath the beam. b) averaged temperatures behind the connector, and corresponding reduction in shear capacity for each gap width. Darker lines indicate average temperatures, while faded lines bound the maximum and minimum values.

Figure 8 shows the specimen, the connections, and the screws at the end of Test 2, immediately after the specimen has been removed from the furnace. When the test is finished, the specimen continues burning during its removal from the mobile furnace until it is extinguished with water. Therefore, the pictures show the state of the specimen after the water is applied, and some smouldering can still be observed in cracks.

No charring occurred directly behind the aluminium connector for the connections with a tolerance gap of 1 mm, while charring was observed for the 6 mm gap connections. Furthermore, the tolerance gap had increased from 6 mm to approximately 12 mm at the top of the connection, near the connector, due to shrinkage of the char on either side. Discolouration of the connector and screws at the connections with a 6 mm gap indicates exposure to high temperature pyrolysis gases, or contact with the char and tar from the timber. This discoloration was not observed for the 1 mm gap. The discoloured part of the screws for the 6 mm gap was measured, with the greatest length of discoloration being 38 mm and the smallest 24 mm. The discoloured distance is also an indication of the char depth behind the connector.

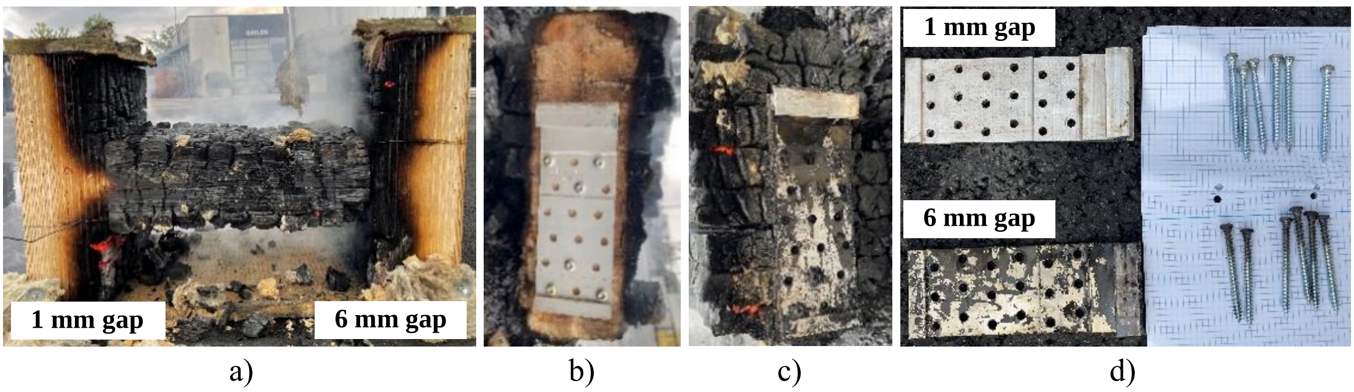

Figure 8. Test 2 specimen after the test: a) top view of the specimen; b) 1 mm gap connection; c) 6 mm gap connection; d) 1 mm and 6 mm gap connections and the adjacent screws.

3.2 Test 4 with additional fire protection of the gaps

Figure 9 a) shows the average temperatures of selected thermocouples from Tests 1-3, compared to those from Test 4. The average gas temperatures measured in Test 4 were slightly higher than those measured for the 6 mm gap in Test 1-3, which could partly explain the higher average temperatures of thermocouples L2, R2, and B3, around the perimeter of the gaps at the connections in Test 4, compared to Test 1-3. This could also be due to activation of the intumescent fire stripe, creating an insulated boundary that reduces heat losses from the perimeter of the gap into the connector. Nonetheless, the eventual temperature rise of the connectors with an unprotected 6 mm gap (Tests 1-3) is less than that for the protected gaps in Test 4.

Figure 9 b) shows the average temperatures of the aluminium connectors measured in all four tests, along with the reduced capacity of the connector during the ISO 834 exposure. In the time interval 0-40 minutes, it can be observed that the average temperatures of the aluminium connectors for the 6 mm tolerance gaps with fire stripes in Test 4 followed the same trajectory as the corresponding temperatures in Tests 1-3 for a 6 mm tolerance gap without a fire stripe. These temperatures begin to diverge significantly after 40 minutes, with the unprotected connector being hotter by approximately 75 °C after 60 minutes, and more than 100 °C by 80 minutes of exposure.

In Test 4, there was no clear difference between the average connector temperatures in the cases with the fire stripe applied directly to the surface of the beam or inset into a channel around the connector. This indicates that both methods of application are similarly effective in reducing the heat transfer to the connector, although additional tests are needed to verify this. In comparison with the unprotected 6 mm gap, the fire stripes did mitigate the temperature rise in the connector, but these temperatures were still significantly higher than for the unprotected 1 mm gap. Even so, the added protection limited the reduction in shear capacity of the connector to approximately 12 % after 60 minutes and 22 % after 75 minutes.

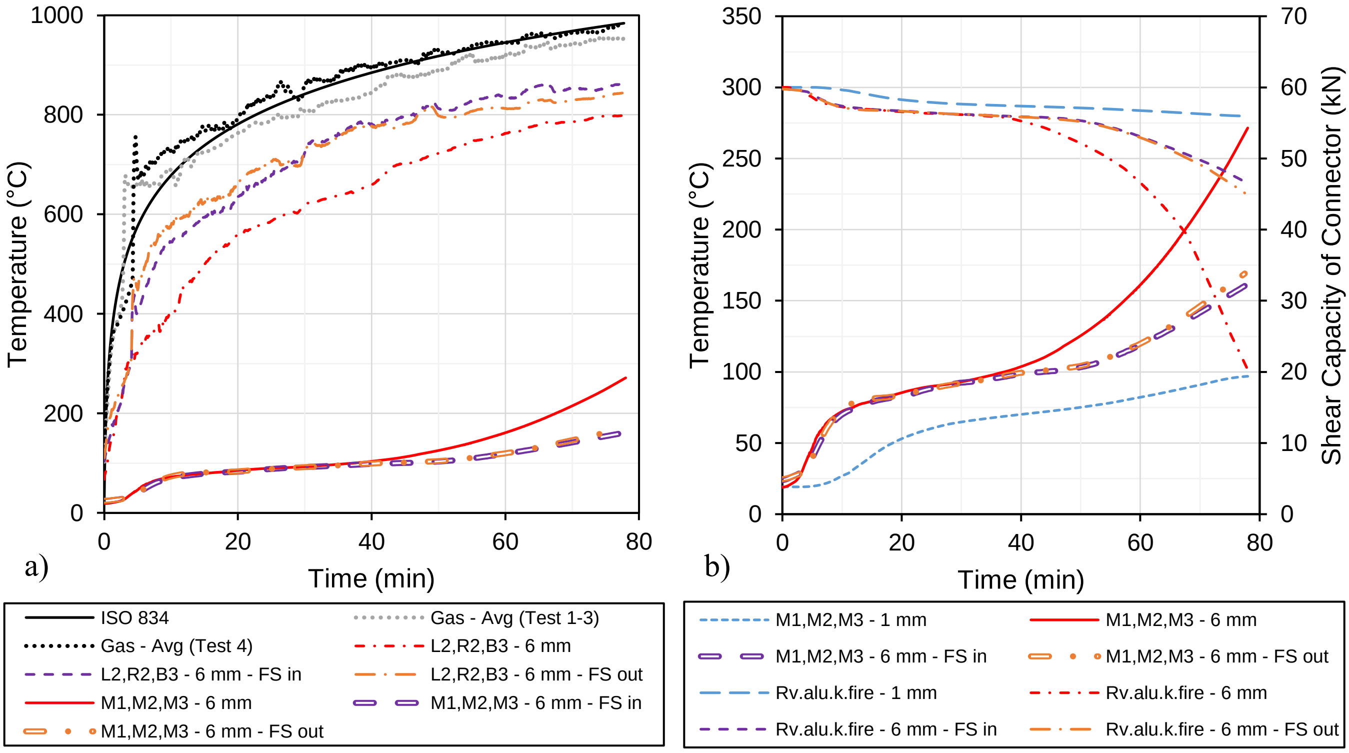

Figure 9. a) averaged temperatures from Tests 1-3 compared with Test 4, for thermocouples L2, R2, and B3, around the perimeter of the gap at the connection; thermocouples M1, M2, and M3, behind the aluminium connector; and the gas phase thermocouples beneath the beam. b) averaged temperatures behind the connector, and corresponding reduction in shear capacity for each unprotected gap width (Tests 1-3) or protection with a fire stripe inset into a carved groove (FS in) or applied directly onto the surface of the beam (FS out).

Figure 10 shows the temperatures on the inner and outer sides of the fire stripe for Test 4, and at the corresponding locations for the unprotected joints in Tests 1-3. The results for each location have been averaged for Tests 1-3, and presented individually for Test 4. No consistent differences were observed between temperatures measured on the left or right side of the connector. Temperatures on the inner side of the fire stripe, at the left and right edges of the connector (L1/R1), were slightly higher for the case with a fire stripe inset into a carved channel than for the case where the fire stripe was directly applied to the beam. Temperatures on the outer side of the fire stripe (L2/R2) were very similar in either of these cases, and slightly higher than the corresponding temperatures for tolerance gaps without protection. As mentioned previously, this may be due to the insulating effect of the intumescent fire stripe reducing heat losses into the connector. However, additional tests with fire stripes are required to verify that these are consistent results, rather than artifacts of experimental variability.

After 10-15 minutes, the temperatures measured by L1 and R1 on the inner sides of the fire stripes started to decrease from an initial peak of 200-250 °C. The temperature decrease could be explained by swelling of the fire stripe closing the gaps around the connector, limiting further convective heat transfer. In contrast, the corresponding temperatures for the unprotected 6 mm gap (Figure 10 a)) continue to increase steadily after this time, and end up more than 100 °C hotter after 60 minutes. Even with the protective effects of the fire stripes, the temperatures at the edge of the connector for the unprotected 1 mm gap (Figure 10 b)) are significantly lower.

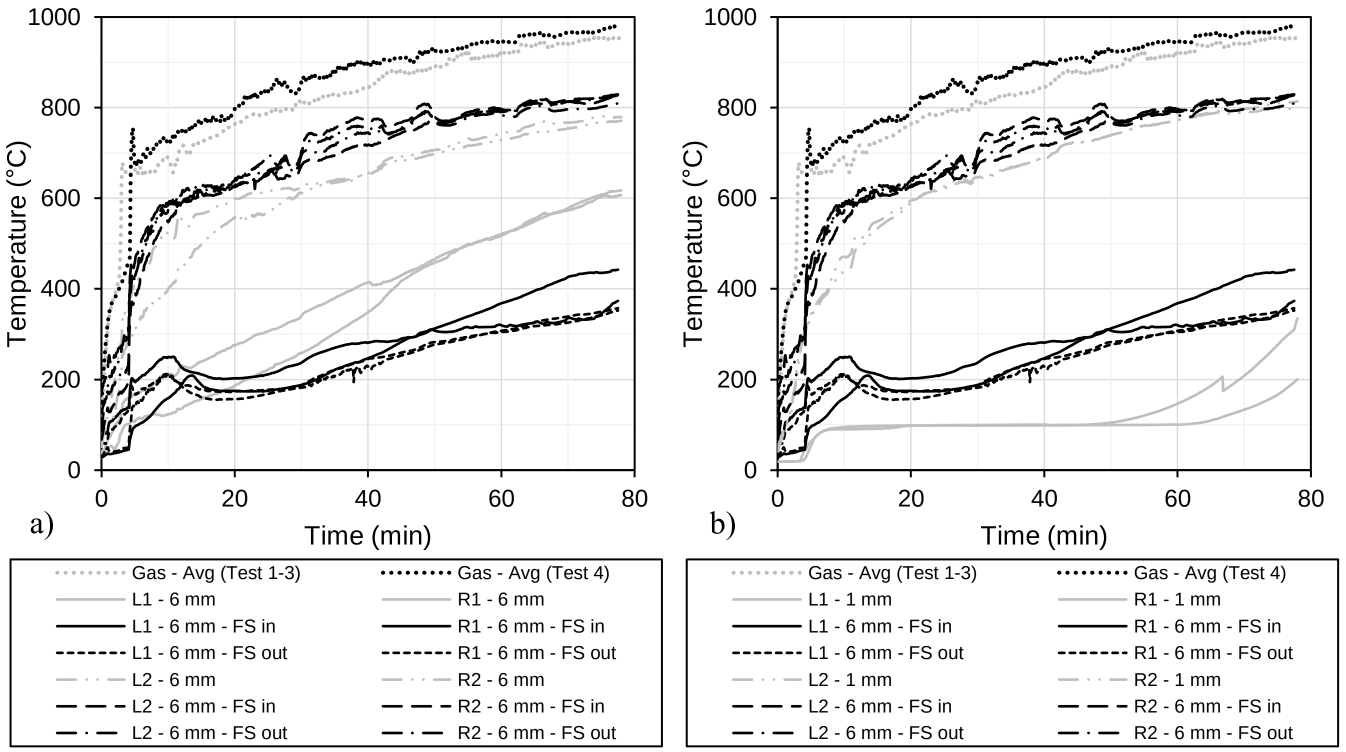

Figure 10: Temperatures on the inner sides of the fire stripe – at the left and right edges of the connector (L1/R1) – and on the outer sides of the fire stripe (L2/R2), for a fire stripe inset into a carved channel (FS in) or applied directly onto the surface of the beam (FS out), compared with corresponding temperatures for a) an unprotected 6 mm gap, and b) an unprotected 1 mm gap.

The in-depth temperatures measured in the beam in Test 4 are presented in Figure 11. Due to potential errors in the drilling angle over the 140 mm depth of the holes, there is some uncertainty in the actual location of the thermocouple tip within the beam. While care was taken to reduce these errors, these in-depth temperatures should be considered as indicative, rather than exact. The temperatures measured closest to the screws, by thermocouples S-L1, S-R1, and FS-R2, remained below 100 °C up until 50 minutes of exposure for both Case I and Case II, and did not exceed 300 °C up to 80 minutes. This suggests that there was no charring of the timber during this period at a depth of approximately 55 mm from the surface of the beam. The temperatures in the beam at a distance of 10 mm behind the fire stripe and 40 mm from the outer surface, i.e., FS-R1 and FS-L1, increase more rapidly, reaching 100-200 °C by 20 minutes and 300 °C by the end of the test for both cases. Considering that the fire stripe has a nominal activation temperature of 150 °C, this supports the conclusion that the fire stripes would have activated within the first 20 minutes, but that the wood behind the fire stripe was charring by the end of the test.

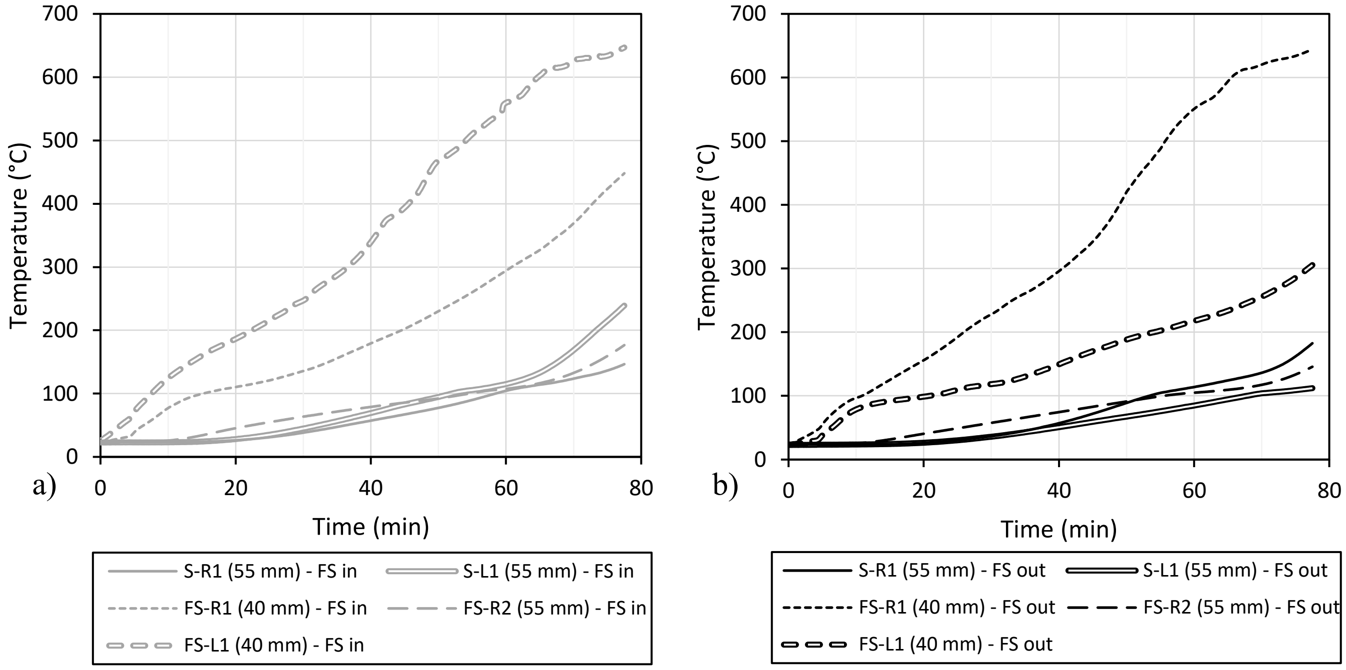

Figure 11. Temperatures measured within the beam in Test 4, at distances of 40 or 55 mm from the side of the beam for a) Case I, with the fire stripe inset into a carved groove (FS in) or b) Case II, with the fire stripe applied directly to the unaltered surface of the beam (FS out).

Figure 12 shows the connections and screws after the fire exposure of Test 4. These images confirm that the wood directly behind the connector and surrounding the screws was uncharred, but that the char layer had just reached the boundary of these areas by the end of the test.

a) b) c)

Figure 12. Test 4 specimen after the test: a) Fire stripe carved into the surface of the beam, b) Fire stripe on the surface of the beam; c) section through the beam, 105 mm from the bottom edge of the original specimen (Case 2).

4 DISCUSSION

In all four tests, aluminium connectors with timber cover distances of 60 mm from the bottom and 53 mm from the sides were exposed to ISO 834 standard fire temperatures for more than 60 minutes. The corresponding reduced capacity of the aluminium connectors during fire was calculated using the measured temperatures of the aluminium and the reduction factor of the 0.2 % proof strength at elevated temperatures for aluminium alloy AW6005A ($k_{0.\theta}$) as defined in EN 1999-1-2 [9]. Temperatures measured in the gas phase beneath the beam and around the perimeter of the connections indicate that the thermal exposure conditions were comparable in each case.

The results of these tests showed a clear and consistent impact of the connection gap size on the temperature evolution of the aluminium connectors. For the larger 6 mm gap, the temperature of the connector increased much faster, and reached 286 ± 36 °C after 80 minutes of exposure in all tests, at which time the connector with a 1 mm gap had only reached 97 ± 1 °C as shown in Figure 7 b). Furthermore, the temperatures of the aluminium connectors for the larger 6 mm gap were on average 35-40 °C higher than for the 1 mm gap until 45 minutes of fire exposure. Further evidence of the impact of the gap size was provided by the observation of significant charring behind the connector with the unprotected 6 mm gap, which was not seen for the 1 mm gap.

When additional intumescent fire protection stripes were used in the 6 mm gap, the temperature evolution of the aluminium connectors followed the same trajectory as the for the unprotected 6 mm gap during the first 40 minutes of exposure, as shown in Figure 9 b). The insulating effect of the fire stripes became apparent after 40 minutes, as the rate of temperature increase for the unprotected 6 mm gap became much higher. By 77 minutes, the temperatures of the protected connectors by the fire stripes were more than 100 °C lower than for the unprotected connectors. In terms of the shear capacity of the connectors, the elevated temperatures at 60 minutes induced an average reduction in capacity of 22 % for the unprotected 6 mm gap, 12 % for the 6 mm gap with a fire stripe, and only 6 % for the 1 mm gap. By 75 minutes, these reductions had increased to 57 %, 22 %, and 7 %, respectively. This shows the significance of the gap width for the fire performance of the connection, and the value of the additional fire protection in cases where a gap of more than 1 mm is unavoidable, particularly for exposure durations beyond 60 minutes. This might be even more critical for exposures with higher oxygen availability, in which additional insulation may provide further protection against flaming or oxidation of the char around the connection.

The fire stripe also prevented the wood around the aluminium connectors from charring, by reducing the heat transfer to the connector and the surrounding wood. This can be observed in Figure 12, in comparison to a connection with no additional fire protection in the 6 mm gap, as shown in Figure 8 c). The in-depth measurements in the beam during Test 4, as presented in Figure 11, show that temperatures in the wood closest to the screws did not reach 300 °C during the test, but they did exceed 100 °C after 50 minutes had passed. Therefore, the base of the char layer had not reached the wood around the fasteners within these exposure periods, but the embedding strength of this wood is likely to have decreased significantly at such elevated temperatures.

No significant difference was observed in the effectiveness of the two fire stripe application methods in Test 4, but further tests are planned to confirm this with greater certainty. Nevertheless, other considerations such as ease of construction, or durability, may be more important in determining whether the fire stripe should be applied directly to the unaltered surface of the beam or inset into a carved channel. Further tests are also planned to investigate the critical failure mode of the connections (e.g., embedment failure or aluminium connector failure) in fire, due to the effects of tolerance gaps. These tests will include external loading under exposure to elevated temperatures, and will be performed at a larger scale.

5 CONCLUSIONS

The objective of this study was to investigate the effects of tolerance gaps on aluminium connectors in a wood joint during fire exposure. Tolerance gaps are unavoidable in connections between timber elements, due to constructability and natural shrinkage or swelling of the wood over time, and this can allow hot gases to travel around the connector during a fire. This convective heat transfer can be critical for aluminium connectors, since the reduction in strength of the connector at elevated temperatures occurs much earlier for aluminium than for steel, which may result in premature failure of the connector during a fire. Tolerance gaps of 1 mm and 6 mm were chosen as they are representative of the minimum gap size range that is currently feasible. The results of this study showed a clear and consistent impact of the connection gap size on the temperature evolution of the aluminium connectors. In all cases, the larger gap size resulted in faster temperature rise of the connector, corresponding to a more severe reduction in capacity.

The addition of an intumescent fire stripe around the connector with a 6 mm tolerance gap improved the performance of the connector after 40 minutes of fire exposure, in comparison with an unprotected gap of equivalent size. There was no clear difference between the effectiveness of fire stripes applied directly to the unaltered surface of the wood or inset into a carved channel around the connector.

To further investigate the critical failure mode of the connections in fire, loaded tests are necessary to conclude whether an embedment failure will occur prior to failure of the aluminium connector. For this purpose, a large-scale test is planned, in which the same connection configuration is subjected to a constant load during fire exposure until failure.

ACKNOWLEDGMENTS

The authors would like to thank Rothoblaas for supplying the connectors and fire-stripes, and Stora Enso, for supplying the wood materials. The authors are also grateful to Lennart Schou Jensen from DBI for his assistance with the tests.

REFERENCES

1. Barber D (2017) Determination of fire resistance ratings for glulam connectors within US high rise timber buildings. Fire Saf J 91:. https://doi.org/10.1016/j.firesaf.2017.04.028
2. Barber D, Gerard R (2015) Summary of the fire protection foundation report - fire safety challenges of tall wood buildings. Fire Sci Rev 4:5. https://doi.org/10.1186/s40038-015-0009-3
3. McKenzie WMC, Zhang B (2007) Design of Structural Timber: To Eurocode 5. Palgrave Macmillan
4. Buchanan A, Östman B (2022) Fire Safe Use of Wood in Buildings: Global Design Guide, 1st ed. CRC Press, Boca Raton
5. Rijsdijk JF, Laming PB (1994) Physical and related properties of 145 timbers: information for practice. Kluwer Academic Publishers, Dordrecht ; Boston
6. Maraveas C, Miamis K, Matthaiou ChE (2015) Performance of Timber Connections Exposed to Fire: A Review. Fire Technol 51:1401–1432. https://doi.org/10.1007/s10694-013-0369-y
7. Palma P, Frangi A, Hugi E, et al (2016) Fire resistance tests on timber beam-to-column shear connections. J Struct Fire Eng 7:41–57. https://doi.org/10.1108/JSFE-03-2016-004
8. Palma P, Frangi A, Hugi E, et al (2014) Fire resistance tests on beam-to-column shear connections
9. EN 1999-1-2: 2007 Design of aluminium structures - Part1-2: Structural fire design (The European Union Per Regulation 305/2011, Directive98/34/EC, Directive 2004/18/EC. EN. Brussels: CEN, 2008.
10. EN 755-2:2016: Aluminium and aluminium alloys - Extruded rod/bar, tube and profiles - Part 2: Mechanical properties EN 755-2:2016: Aluminium and aluminium alloys - Extruded rod/bar, tube and profiles - Part 2: Mechanical properties.
11. Lange D, Sjöström J, Schmid J, et al (2020) A Comparison of the Conditions in a Fire Resistance Furnace When Testing Combustible and Non-combustible Construction. Fire Technol 56:1621–1654. https://doi.org/10.1007/s10694-020-00946-6
12. Rothoblaas Product brochure. Intumescent Thermo-Inflatable Flexible Gasket: Fire stripe. Rothoblaas. Retrieved October 18, 2022, from https://www.rothoblaas.com/products/airtightness-and-waterproofing/tapes-and-sealants/tapes-and-profiles/fire-stripe#documents
13. EN 13501-1: 2018 Fire classification of construction products and building elements - Part 1: Classification using test data from reaction to fire tests.
14. ISO 834. “Fire-resistance tests - elements of building construction”. International Standard ISO, 834 (1975).
15. SERVOPRO 4900 Multigas Product brochure. Servomex. (n.d.). Retrieved October 18, 2022, from https://www.servomex.com/resources/product/4900-multigas/
16. Agilent 34970A/34972A Data Acquisition / Switch Unit. User’s guide. Agilent Technologies, Inc. 2009-2012

Proceedings of the 12th International Conference on Structures in Fire

Numerical Modelling of Structures in Fire

NUMERICAL ANALYSIS OF THE MASONRY BRICK WALL'S DEFORMATION WITH EMBEDDED STEEL DOOR DURING A FIRE RESISTANCE TEST

Rene Prieler[1], Benjamin Ortner[2], Peter Kitzmüller[3], Stefan Thumser[4], Günther Schwabegger[5], Christoph Hochenauer[6]

ABSTRACT

Fire resistance tests (FRTs) are commonly used to determine how long a certain construction (wall, fire safety equipment etc.) or a combination of different construction elements can resist a fire. Although the thermal exposure of the construction, characterized by a pre-defined time-dependent temperature curve, is not representing a real fire scenario, FRTs are used to certify construction elements for a certain fire resistance level. In the present study the deformation of a masonry brick wall was experimentally and numerically investigated during a standardized fire resistance test. Measured data of the temperature and wall deformation are used to validate the numerical model to predict the wall's deformation when a door was embedded in the wall construction, affecting the overall deformation process. The focus of the numerical part of the study was the numerical treatment of the contact faces between the wall and the door as well as the interactions between the bricks and the mortar. It was found that the sliding faces between the wall and the door can be treated by the augmented Lagrange formulation although intumescent material was neglected. The contact behaviour between the single bricks was investigated in a pre-simulation, which showed that the contact can be seen as fixed. A slight displacement between the bricks did not affect the overall deformation of the wall. A comparison with the simulation results showed that the numerical method was capable to predict the wall deformation in close accordance to the measured data.

Keywords: Fire resistance test; Masonry brick wall; Finite element modelling; Deformation; Gap formation

1 INTRODUCTION

In standardized fire resistance tests (FRTs) (see [1]) of different fire safety products (test specimen) the thermal and structural response will be determined. Based on the measured temperature (thermal response) and deformation/structural integrity (structural response) of the test specimen, a certain fire safety certification can be issued. However, during FRTs not only the test specimen is exposed to a fire source, but also the surrounding wall construction (e.g. stud walls, brick walls etc.), where the test specimen is

---

[1] Assistent Professor, Institute of Thermal Engineering, Graz University of Technology, Inffeldgasse 25/B, A-8010 Graz, Austria
e-mail: rene.prieler@tugraz.at, ORCID: https://orcid.org/0000-0003-0102-471X
[2] Junior Researcher, Institute of Thermal Engineering, Graz University of Technology, Inffeldgasse 25/B, A-8010 Graz, Austria
e-mail: benjamin.ortner@tugraz.at
[3] Researcher, IBS-Institut für Brandschutztechnik und Sicherheitsforschung GmbH, Petzoldstraße 45, 4020 Linz, Austria
e-mail: p.kitzmueller@ibs-austria.at
[4] Researcher, IBS-Institut für Brandschutztechnik und Sicherheitsforschung GmbH, Petzoldstraße 45, 4020 Linz, Austria
e-mail: s.thumser@ibs-austria.at
[5] Head, IBS-Institut für Brandschutztechnik und Sicherheitsforschung GmbH, Petzoldstraße 45, 4020 Linz, Austria
e-mail: g.schwabegger@bvs-ooe.at
[6] Professor, Institute of Thermal Engineering, Graz University of Technology, Inffeldgasse 25/B, A-8010 Graz, Austria
e-mail: christoph.hochenauer@tugraz.at
https://doi.org/10.6084/m9.figshare.22178252

embedded. During the heating process caused by the fire source both, wall and test specimen, are heated-up, and, subsequently deform due to their thermal expansion. Since the wall and test specimen are different with regard to their construction and materials used, their heating process as well as their deformation is unique. In the case of a FRT the test specimen is in direct contact with the adjacent wall construction by fixed connections (e.g. locks etc.) and adjoining surfaces. During the heating and deformation, the fixed connections can transfer forces, which affect the deformation process of the wall and test specimen. Furthermore, adjoining surfaces are capable to transfer normal forces when they are getting in direct contact. In the course of the deformation process it is also possible that adjoining surfaces between the wall and test specimen can separate from each other. As a consequence, gaps can occur and flue gas from the fire side can leak through this gap to the ambient side. It can be seen that the mechanical interaction between the wall and test specimen can significantly affect the deformation process of each part as well as the gap formation promoting a possible flue gas leakage.

1.1 Brick walls under fire exposure

Although the interaction between a test specimen (e.g. fire safety door) and the wall is essential for the time from which fire spread can occur, experimental and numerical studies on this topic are sparse. This fact might be based on the issue that there are too many different combinations of test specimen and wall constructions which have to be tested by FRTs. Furthermore, numerical approaches were not applied to have a detailed look on the structural interactions between a test specimen and walls in the past. With special focus on masonry brick walls only a few studies are available considering the deformation process caused by fire exposure. For example, Nguyen and Meftah [2] carried out an experimental campaign where masonry brick walls were exposed to fire. In non-load-bearing cases the maximum deformation was determined at the wall's centre. Applying a load on the wall, which is similar to the mechanical load of an expanding test specimen on the wall, the position of the maximum deformation is different, subsequently affecting the deformation. This is a clear indication that the presence of a test specimen will affecting the overall deformation. In another study Byrne [3] found that the time until a brick wall collapses under fire exposure is also dependent on properties, such as wall size, slenderness etc. Besides experimental studies, also numerical analysis were carried out to predict the wall's deformation (e.g. Nguyen and Meftah, Nguyen et al. [4,5], Prakash et al. [6]). The aforementioned studies considered the thermal response of brick walls without test specimen. However, the study of Nguyen and Meftah [2] showed that additional/external loads can affect the structural response of the wall. Not only the wall's deformation is sensitive to additional forces, but also the test specimen embedded in the wall, which was determined by Prieler et al. [7] in a FRT using an aerated brick wall in combination with a steel door.

Since additional forces and fixtures within the wall (e.g. doors) are leading to a different structural response to a fire source, Prieler et al. [8,9] carried out an experimental campaign where different steel doors are place within a brick wall. It was highlighted, that the size of the doors compared to the size of the entire wall and also the type of the door is crucial for the location as well as the level of the wall's deformation. A numerical approach, which was successfully tested for brick walls by Nadjai et al. [10,11] is the so-called MasSET (masonry subject to elevated temperatures) model. This model was extended by Nadjai et al. [12] to take interface elements between the brick wall and steel slabs into account, which is the only numerical approach considering an interaction between brick walls and surrounding structural elements so far.

1.2 Objectives of the study

The literature in section 1.1 showed that there is lack of research for the interaction between brick walls and other structural elements when they are exposed to fire, although studies highlighted the effect of external/additional forces (e.g. thermally expanding fixtures) on the structural behaviour. Besides one numerical study from Nadjai et al. [12], numerical models where not applied for such interactions in FRTs so far. Therefore, the focus of the present study is the numerical investigation of the structural response of masonry brick walls and the test specimen as well as their mechanical interaction when they are exposed to a standard fire according to [1]. The study presents the numerical treatment of the interfaces between wall and test specimen and between the single brick, which allows to predict the deformation of the components and gap formation between the wall and test specimen. The gap formation is a crucial indication for the fire resistance and fire spread from one compartment to the next one.

2 EXPERIMENTAL SETUP

2.1 Fire resistance testing furnace

In the present study a FRT of a wall made of hollow-bricks with an embedded fire safety steel door (test specimen) was carried out. Measured temperatures and deformation of the wall and the test specimen will be used for the validation of the numerical model. For this purpose, a natural gas fired testing furnace was used (see [8,9]), where the brick wall with the test specimen was placed at the front side. The fuel input to the burners was adapted by the furnace control system to ensure that the temperature in the furnace is in close accordance to the standardized time-temperature curve (see [1]).

2.2 Wall construction and steel door

The masonry brick wall, which consists of hollow bricks, is shown in Figure 1 (left), with the dimension of 4 x 4.5 x 0.17 *m*. Between the rows of bricks mortar was used. At the centre of the wall, a fire safety steel door as test specimen was placed, with a thickness of 64 *mm*. The building dimension width of the door was 1.375 *m* and its corresponding height was 2.5 *m*, whereas the leaf dimension width was 1.337 *m* and the height was 2.475 *m*. In general, the door was made of a steel shell (1 *mm* thickness) and filled with mineral wool. In the centre of the cross-section a gypsum board was arranged with a thickness of 6 *mm* to increase the thermal resistance. The door's frame was fixed with the wall at 11 positions (e.g. in Figure 1 (centre)). Additionally, there are several connections between the door and its frame. At the side of the door lock only one fixed connection (the lock) was available. In contrast, two hinges as well as 3 additional security bolts were used to ensure a fixed connection between the door and the frame when the door is closed (see Figure 1 (right)).

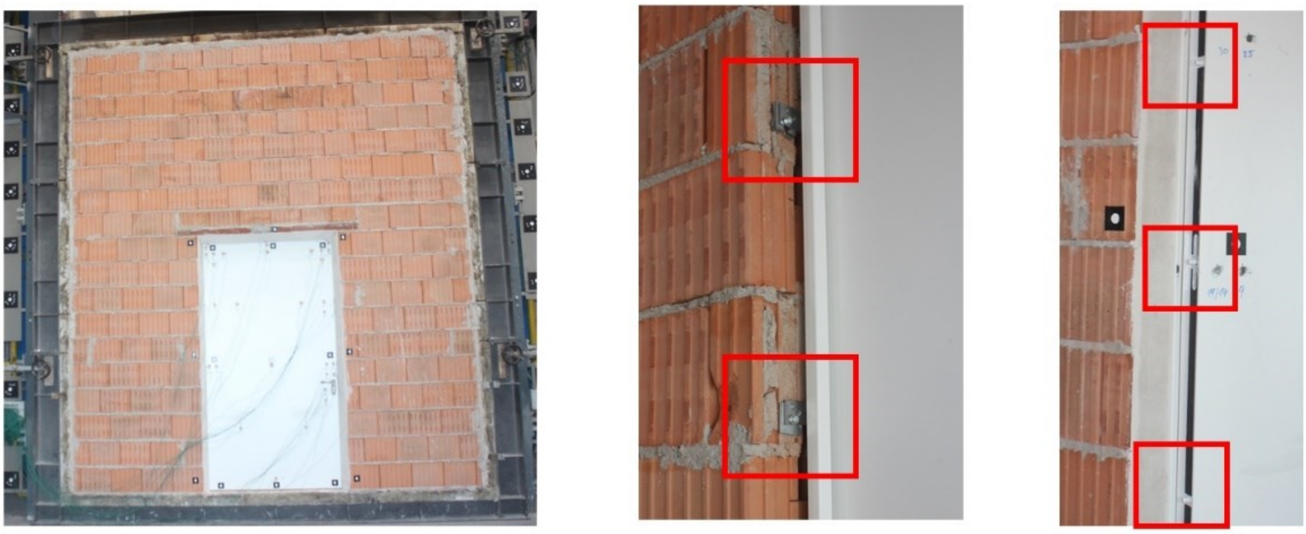

Figure 1. Masonry brick wall with steel door (left), fixing positions between wall and the door's frame (centre) and position of the security bolts (right)

2.3 Material properties

For the thermal and structural analysis temperature-dependent material properties were determined based on literature. The wall consisted of masonry bricks, as shown in Figure 1, and mortar between the rows of bricks. In Nguyen and Meftah [4] the thermal and mechanical properties are presented for the bricks and the mortar. The values at room temperature are presented in Table 1 and the normalized temperature-dependent values (based on the room temperature) are shown in Figure 2.

Table 1. Material properties of masonry bricks and mortar at room temperature [4]

Property	**Brick**	**Mortar**
Density [*kg/m³*]	2100	1500
Therm. conductivity [*W/mK*]	0.7	1.5
Spec. heat capacity [*J/kgK*]	870	1000
Young modulus [*GPa*]	11	3
Poisson ratio [-]	0.22	0.25
Therm. expansion coefficient [*1/K*]	$5.25*10^{-6}$	$10*10^{-6}$

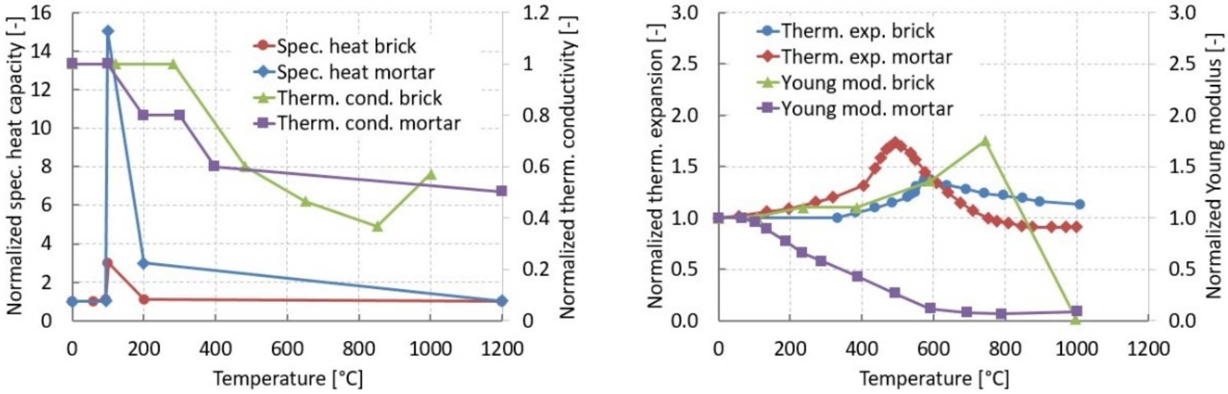

Figure 2. Temperature-dependent specific heat capacity, thermal conductivity, thermal expansion and Young modulus for brick and mortar [4] (normalized values based on Table 1)

The door (test specimen) was made of a steel shell with low-alloy steel, which was filled with mineral wool and a gypsum board in the centre of the cross-section. Prieler et al. [7,13] presented the thermal and mechanical properties for low-alloy steel used in the present study. Besides the temperature-dependency of the thermal conductivity, specific heat capacity, thermal expansion and Poisson ratio, a multi-linear hardening model was applied. The multi-linear hardening was modelled in accordance to [7] for different temperature levels. Figure 3 (left) shows the plastic stress-strain curves at elevated temperature and room temperature.

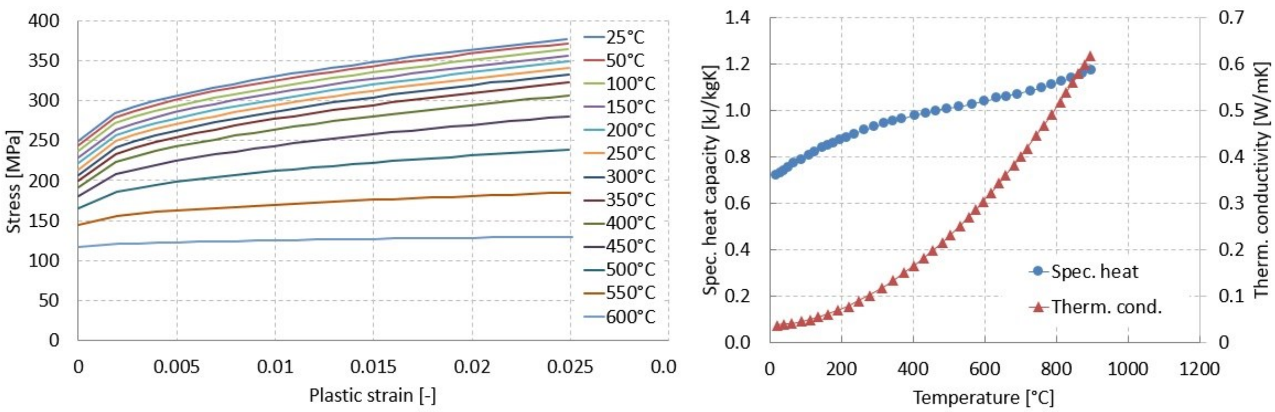

Figure 3. Temperature-dependent plastic stress-strain curves of steel (left) and thermal properties of mineral wool (right)

For the mineral wool and the gypsum board it was assumed that the effect on the structural analysis is negligible. Therefore, only the thermal properties for the thermal analysis were determined. The mineral wool had a density of 50 kg/m³ and the temperature-dependent specific heat capacity as well as the thermal conductivity are shown in Figure 3 (right). Prieler et al. [14] measured the temperature-dependent thermal properties of gypsum, which also represented the chemical reactions (release of water vapour from gypsum) by characteristic peaks in the specific heat capacity curve.

3 NUMERICAL METHODOLOGY

The used numerical model was first introduced by Prieler et al. [7,13] to predict the heating and deformation of fire safety steel doors during FRTs. It was found that it is also essential to consider the adjacent wall construction in the numerical model in order to achieve a higher accuracy when the results are compared to the experimental data. Thus, a wall model for masonry brick walls and interface treatment between the wall and the door will be presented in this section/study. The model of Prieler et al. is also able to simulate the gas phase combustion including the spatial and temporal heat transfer to the wall/door, as well as the mass transfer from the solid test specimen to the gas phase (e.g. water vapour release from gypsum). Thus, also performance-based analyses would be possible instead of FRTs. However, the gas phase combustion (fire) is neglected in this study. For further details, how to couple the fire with the following thermal and structural analysis see [7,13,15]. Therefore, the numerical methodology is limited to the solids (wall/door), which can be seen in Figure 4. All simulations were carried out using the finite element method (FEM).

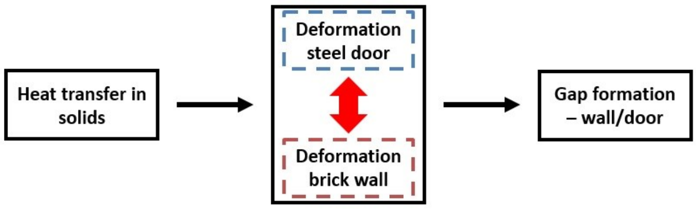

Figure 4. Numerical methodology of the present study

3.1 Numerical grid and boundary conditions for heat transfer modelling

At the fire exposed side of the wall/door construction a convective and radiative boundary condition was defined. The temperature at the fire side was chosen in accordance to the time-dependent temperature curve from [1]. To consider the convective and radiative part of the heat transfer to the test specimen a heat transfer coefficient of 25 W/m^2K and a surface emissivity of 0.9 were used. At the fire unexposed side, the heat transfer coefficient and emissivity were fixed with values of 4 W/m^2K and 0.9, respectively. The heat transfer was calculated in each component (face) of the wall and the door (frame and door leaf). As it can be seen in Figure 5, each brick was modelled in accordance to the real geometry. Thus, not only the heat conduction in the solid was calculated, but also the radiative heat transfer (Surface-to-Surface model) within the holes of the bricks. For the heat transfer through the door only heat conduction with consideration of the chemical reactions in the gypsum board was considered. As a consequence, no transport of water vapour released from gypsum as well as the condensation/evaporation effects within the steel shell of the door were simulated. In contrast, Prieler et al. [16] showed that this effect should to be considered when gypsum is used gypsum. The overall numerical grid consists of about 180,000 cells with mainly hexahedrons in the wall, except in the row of bricks at the height of the lintel and the steel door. For the door approx. 92,000 tetrahedrons were used. For the transient thermal analysis an adaptive time-stepping method was used with a minimum time step size of 0.025 s and a maximum value of 2.5 s. The overall calculation time was 1800 s.

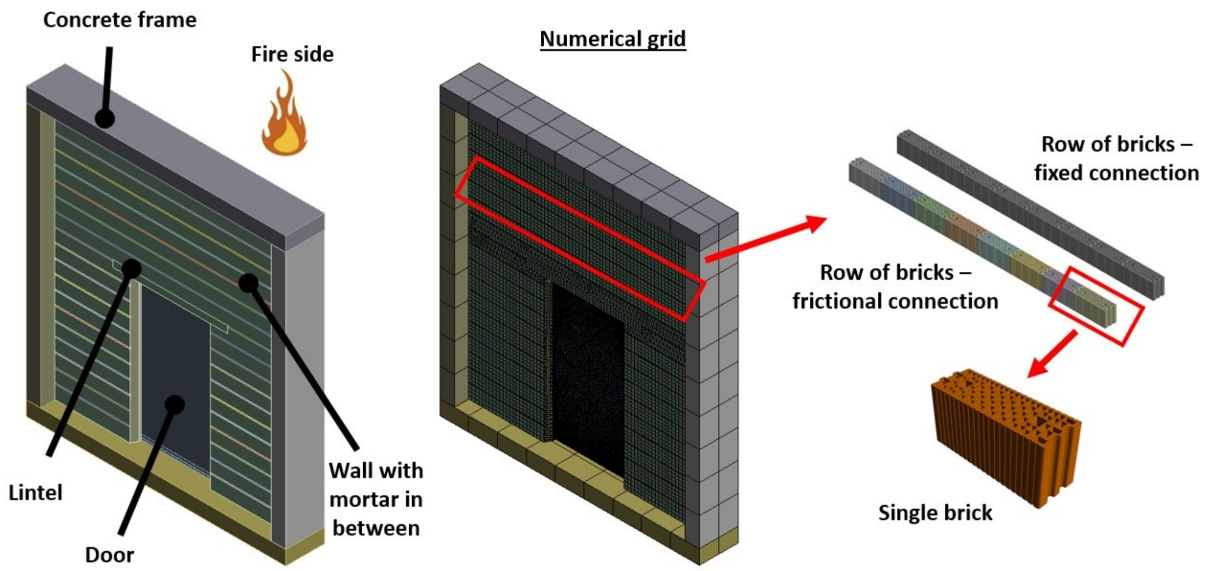

Figure 5. Geometry and numerical grid for the thermal and structural analysis

3.2 Structural analysis

The calculated temperatures of the thermal analysis will be further used for the structural analysis of the wall. The contact treatment between the single bricks as frictional contact would increase the calculation time and memory usage dramatically. Therefore, a structural pre-study was carried out, considering a row of single bricks only. In this pre-study the deformation of a row of bricks will be simulated when (i) the single bricks have frictional contacts to the next ones and (ii) when the bricks have a fixed contact to the next ones. In section 4.2 these results will be presented.

- Boundary conditions for the structural analysis

In accordance to the experimental setup, where the wall construction is surrounded by a concrete frame, this frame was also considered in the simulation. All concrete blocks were defined as rigid bodies. The boundary condition of the concrete block at the bottom is a fixed support. The concrete blocks at the sides and the top are defined with an elastic support (10^{10} N/m³) at the outer surfaces, which allows small movements of these blocks. As mentioned above, the time-dependent and local temperatures in the wall and the door from the thermal analysis will be used as thermal load in the structural analysis.

- Contact treatment between the elements

Crucial for the accuracy of the structural analysis is the treatment of the contact faces between the components used. The contact between the brick wall and the outer concrete blocks was defined as frictional, which allows a displacement of the contact faces to each other. At the beginning of the simulation, the faces between the wall and the concrete blocks are in direct contact to each other. Another frictional contact treatment was chosen between the door leaf and the door's frame. Prieler et al. [7] presented numerical settings for frictional contact treatment for steel doors under fire exposure, which worked successfully for the contact surfaces between two door leafs. Therefore, these settings were also used in the present study for the interaction between the door leaf/door frame as well as the wall and the concrete blocks. The frictional coefficient was chosen to be 0.2. Although the contact faces between the door and the frame is frictional, they are not in direct contact at the beginning of the simulation/FRT. Depending on the construction, there is a gap of about 1 *mm*. Due to the thermal expansion and deformation of all components, the contact surfaces can separate from each other (or increase the initial gap) or get in direct contact. When two faces locally "collide" a contact detection method has to be applied to avoid incomprehensible results due to penetration of the solid bodies. For this purpose, the augmented Lagrange method, which is a penalty-based approach, was used for the contact formulation. Detailed settings can be found in [7].

Besides the frictional contact between the door leaf and the frame, there are also positions where a frictional contact is not appropriate. These positions are the security bolts, the door lock as well as the hinges of the door (see Figure 1). In the simulation the bolts, lock and hinges were considered as fixed connections. Since there is a gap of 1 *mm* between the door leaf and the frame, a solid connection was inserted to bridge the gap and to ensure a direct contact from the beginning of the simulation, where the lock, bolts and hinges are located. The contact faces of this bridge with the door leaf and frame are defined as fixed connections. Additionally, the connections between the door frame and the wall (see Figure 1) were treated as fixed connections. For this treatment a multi-point constraint (MPC) formulation was applied for these contact faces, which does not allow a sliding or separation of the contact faces (bolts, lock and hinges).

Further fixed connections are related to the mortar used in the experimental setup, which can be seen in Figure 6. Firstly, mortar was placed around the door to cover the connections from the frame to the wall as well as partially the door's frame itself. Secondly, mortar was placed between the rows of masonry bricks. It was tried to avoid mortar entering the holes within the bricks. However, a partial filling of the holes with mortar cannot be excluded, but was not considered in the numerical model. All connections of the mortar to the bricks as well as the door's frame was defined as fixed connections also using the MPC formulation.

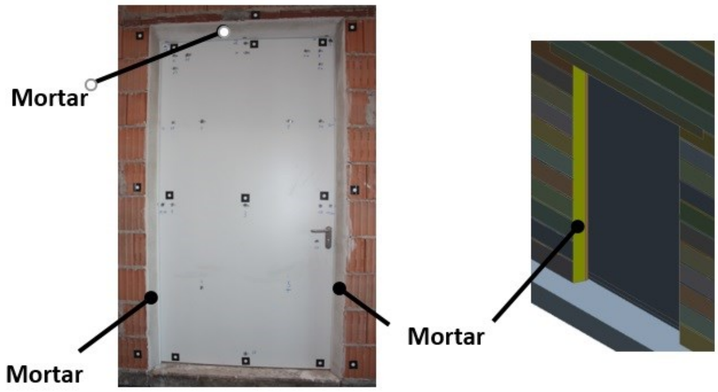

Figure 6. Mortar around the door to cover the connections to the wall

Since frictional contacts are computationally more demanding than a fixed contact formulation, it was tried to avoid too many contact faces with sliding or separating/colliding faces. Despite the contact faces between the door and the wall there is a huge number of contact faces between the bricks within each row, especially when the detailed geometry of each brick (see Figure 5) is taken into account. To decrease the memory usage and computational time, two different contact formulations between the bricks in each row were tested in a pre-study (fixed connection and frictional connections), which is highlighted in section 4.2.

- Other numerical settings

For the transient structural analysis adaptive time-stepping was applied with a minimum time step size of 0.066 s and a maximum of 12 s. The overall calculation time was 1800 s.

4 RESULTS AND DISCUSSION

4.1 Temperature distribution in the wall and steel door

During the FRT no temperature measurements were done within the masonry brick walls, thus, subsequently, the used thermal model (including radiative heat transfer within the holes) cannot be validated by experimental data. As a consequence, the thermal model was tested and validated with data from literature. Nguyen [17] also simulated and validated thermal models to predict the heat transfer in masonry bricks with 20 *cm* thickness. This can be seen in Figure 7 (left). For the bricks, used in the thesis of Nguyen, the thermal model in the present study calculated temperatures, which are in close accordance to the data from Nguyen. This is demonstrated for a short-term fire exposure up to 30 *min* (same as in the FRT in the present study) as well as long-term fire exposure of 180 *min*. Since the thermal model seems appropriate for the masonry brick walls, it was used for the wall tested in the FRT. The predicted temperatures in the brick wall are shown in Figure 7 (right). At the end of the FRT (30 *min*), a higher temperature compared to ambient conditions can be detected up to a thickness of 125 *mm*. From 125 *mm* to the ambient side (175 *mm*) no temperature increase was determined, which means that the heat penetration stops at 125 *mm*.

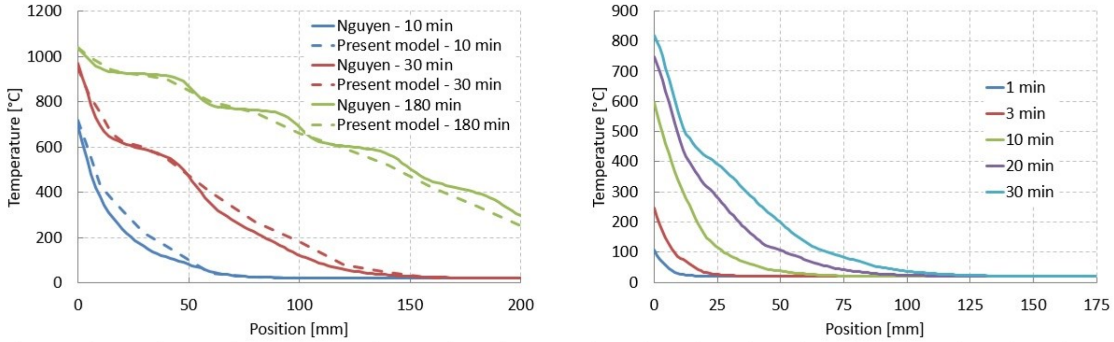

Figure 7. Validation of the thermal model with data from Nguyen [17] for a brick wall with 200 mm thickness (left) and temperature profile in the bricks for the tested masonry brick wall in the present study (right); Position 0 *mm* means fire side and position 200/175 *mm* means ambient side

In Figure 8 the measured temperatures at the fire unexposed side of the door are shown. At the edges and corners of the door more measurement positions were fixed due to the improved heat transfer via the steel shell. Thus, higher temperature gradients are expected there. The red dots mark the measurement 25 *mm* from the edges, the blue dots were placed 100 *mm* from the edges and the black dot is placed in the centre of the door. It can be seen that in a distance of the edges the simulation slightly over-predicts the temperatures after 30 minutes, indicating an improved heat transfer via the steel shell in the simulation. In contrast, the simulated temperature at the door's centre is much lower than the experimental data. The reason for that is the neglected mass transfer of water vapour within the gypsum as well as condensation and evaporation effects in the simulation (see section 3.2). To increase the accuracy of the simulation in the door's centre, these effects have to be considered as presented in Prieler et al. [8]. Nevertheless, the overall temperature is in good agreement to the experimental data and can be used for the structural analysis.

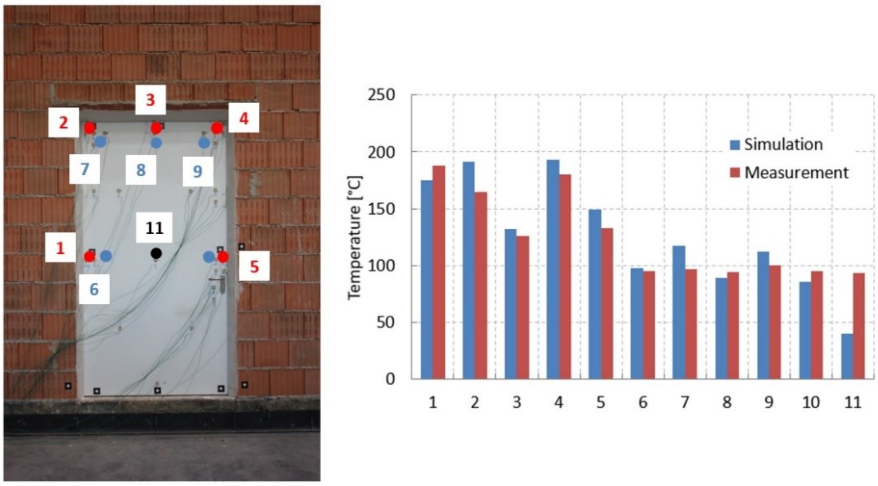

Figure 8. Temperature measurement positions at the steel door (25 mm from edge – red dots; 100 mm from edge – blue dots; door's centre – black dot) (left) and measured temperatures after 30 minutes (right)

4.2 Single row of bricks – Deformation

As mentioned in section 3.2, a pre-study was carried out for a single row of bricks to investigate the effect of different contact formulations between the bricks on the results. The most accurate formulation between the contact faces would be a frictional contact, since a movement between the bricks due to the deformation process is possible. However, the frictional contact is related to a higher computational demand and should be avoid, or in the present study, replaced by a fixed connection between the bricks. Both formulations were tested. In Figure 9 the calculated deformation of the row of bricks is presented. For this purpose, the temperatures from the thermal analysis (see section 4.1) were used. Additionally, the side faces of the row of bricks were defined as fixed support in both cases. It can be seen that the overall deformation is the same in both cases. The detailed view on the contact faces between two bricks also showed that the shifting is very low. Based on these results, a fixed connection between the single bricks in the structural analysis of the entire wall construction can be used. The settings for the fixed contact between the bricks were described in section 3.2.

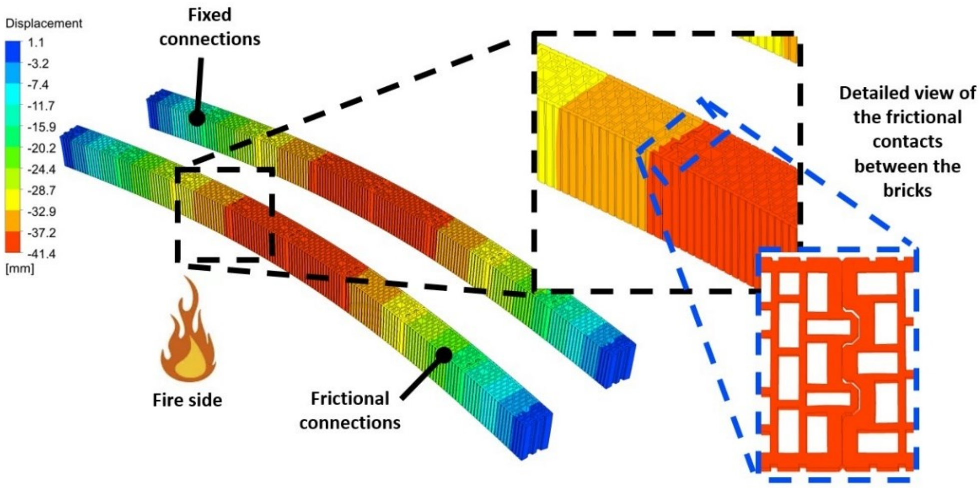

Figure 9. Displacement of a row of bricks with two different contact formulations between the bricks (fixed and frictional) after 30 minutes

4.3 Deformation of the steel door

In Figure 10 the measured and calculated deformation of the steel door after 30 minutes is presented. It can be seen that in the central vertical axis ("D2", "D5" and "D8") the predicted deformation deviates from the experimental values. The FEM simulation predicted a distinct deformation to the fire exposed side at "D5" (negative values), whereas the measured deformation is to the fire unexposed side (positive value). At the left and right hand side of the central axis the predicted deformation is in much better accordance to the FRT results. Due to the water released from gypsum inside the steel shell, the pressure inside the door is increasing during the FRT. It was already described by Prieler et al. [18] that it is inevitable to consider the higher pressure inside the steel shell when doors with gypsum boards inside are tested. Prieler et al. determined that an over-pressure of 0.15 *bar* (compared to ambient) in the simulation is leading to a deformation of the door to the fire unexposed side as well as a better accordance to the measured data. Since the main task of the present study was to find appropriate contact definitions between the parts, the over-pressure in the steel shell of the door was not considered, which would be necessary for a better prediction of the door's deformation.

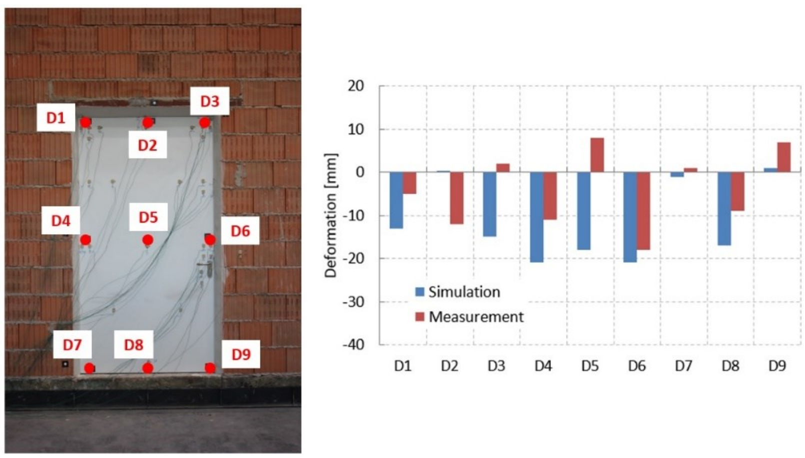

Figure 10. Deformation measurement positions at the steel door (left) and deformation data after 30 minutes (right); (-) means deformation to the fire exposed side, (+) means deformation to the fire unexposed side

4.4 Deformation of the wall

In this section the deformation of the masonry brick wall will be discussed. The deformation (simulation and measurement) of the wall after 30 minutes is shown in Figure 11. A much better agreement between measurement and simulation can be determined compared to the door's deformation. At the upper edge of the door ("W1" to"W3"), the wall was deforming to the fire exposed side between -7 and -4 *mm* in the experiment. The FEM simulation predict a slightly higher deformation of -14 to -9 *mm*. This might be an effect of the much higher deformation of the door in this area (see Figure 10), also affecting the wall due to the fixed connection via the hinges and bolts. At the door's half height ("W4" and "W5") the simulation and measurement determined a deformation of about -19 *mm*. Furthermore, the deformation at the bottom of the wall showed no significant values.

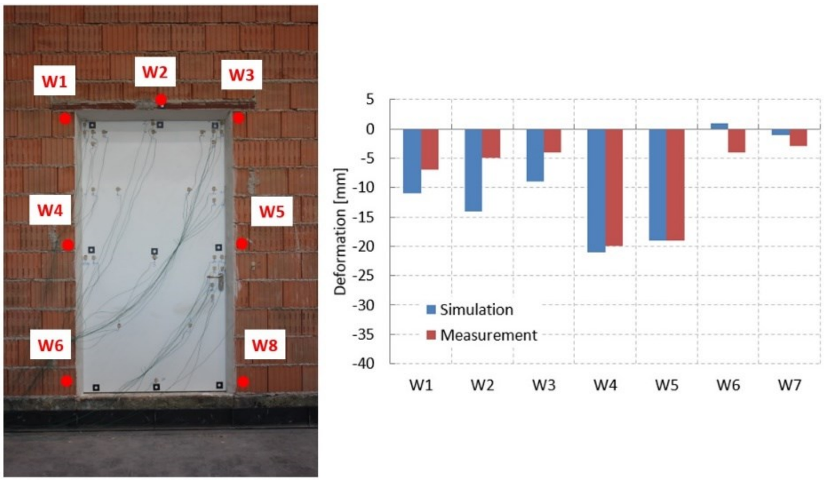

Figure 11. Deformation measurement positions at the brick wall (left) and deformation data after 30 minutes (right); (-) means deformation to the fire exposed side, (+) means deformation to the fire unexposed side

Overall the deformation of the wall can be simulated with high accuracy. At the door's half height, the deformation is well predicted. There is only a slightly higher deformation at the upper edge of the door in the FEM simulation compared to the measurement. In Figure 10 it can be clearly seen that the door is deforming to the fire side (negative values) at the upper edge and the centre. However, due to the over-pressure within the steel casing of the door, a deformation to the fire unexposed side (positive value) was observed in the FRT.

4.5 Gap formation and assessment of the flue gas leakage

Besides the structural integrity, also the assessment of the flue gas leakage from the furnace (fire spread) to ambient via open gaps between the door and the wall is an essential part of FRTs. Thus, the predicted gaps based on the numerical simulations will be compared to the observations during the FRT. At the upper edge of the door a flue gas leakage was observed during the FRT, which is indicated by the condensing water at the mortar (see green mark in Figure 12). The exact size of the gap was not measured during the FRT, thus, a direct comparison with the simulated value was not possible. Furthermore, the intumescent material between the door and the frame was partially sealing the gap, which would have falsified a gap measurement. In Figure 12 (bottom) the predicted gap at the upper edge of the door is presented, where the red mark shows the maximum gap with a value higher than 13 *mm*. Nevertheless, due to the over-predicted deformation of the door at the upper edge, the simulation seems to calculate a gap formation, which is higher than the experimental gap.

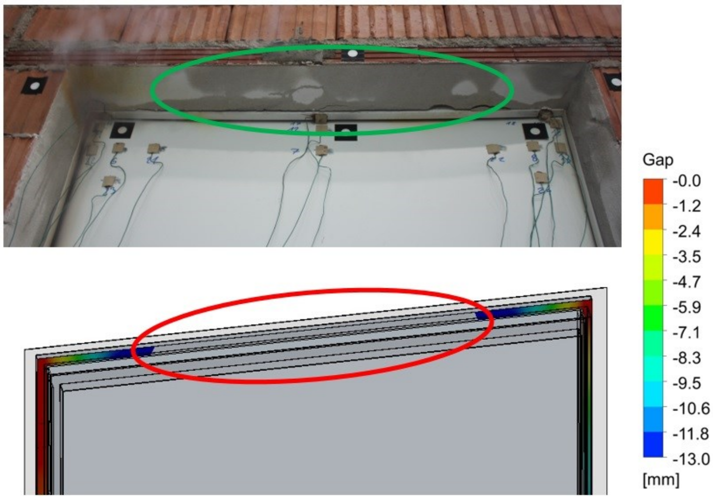

Figure 12. Flue gas exit and gap formation at the door's upper edge after 30 minutes in the experiment (top) and the simulation (bottom)

Further gap formation during the FRT was observed at the right hand side of the door, located above the door lock (see green mark in Figure 13). This was also determined by the FEM simulation (see red mark in Figure 13) with a maximum gap of about 7 *mm*. Although security bolts were arranged on the left hand side of the door, a small gap formation in the simulation can be observed, which was limited to approx. 1.5 *mm*. During the FRT at this position hardly any flue gas leakage was observed.

Figure 13. Flue gas exit and gap formation at the door's left and right edge after 30 minutes in the experiment (left) and the simulation (right)

5 CONCLUSIONS AND OUTLOOK

The presented numerical approach to predict the deformation of a masonry brick wall and fire safety steel door was able to calculate the thermal and structural response to a standard fire. The predicted temperatures at the steel door were in close accordance to the measured data. Furthermore, the thermal model for the bricks considered the heat conduction and radiative heat transfer and showed good agreement to data from literature. The model approach and treatment of the contact faces between all components seemed applicable for the structural analysis of wall constructions with embedded fixtures, since the predicted wall deformation matches the observations from the FRT. Subsequently, the assessment of the gap formation and flue gas leakage (fire spread to the next compartment) is possible with this approach. Future work should be focussed to enhance the model complexity and accuracy (e.g. water vapour transport inside the door in the thermal analysis, over-pressure inside the steel casing in the structural analysis).

ACKNOWLEDGMENT

This work was financially supported by the Austrian Research Promotion Agency (FFG), "FIRE SOLVER" (project 891059, eCall 41897936).

REFERENCES

1. European Committe for Standardization CEN, European standard EN 1363-1, Fire resistance test - Part 1: General requirements. Brussels, Belgium, 2012.
2. Nguyen, T.-D. and Meftah, F., Behavior of clay hollow-brick masonry walls during fire. Part 1: Experimental analysis, Fire Saf J, Vol. 52, 2012, pp. 55-64.
3. Byrne S.M., Fire resistance of load-bearing masonry walls, Fire Technol, Vol. 15, 1979, pp. 180-188.
4. Nguyen T.-D. and Meftah F., Behavior of hollow clay brick masonry walls during fire. Part 2: 3D finite element modeling and spalling assessment, Fire Saf J, Vol. 66, 2014, pp. 35-45.
5. Nguyen T.-D., Meftah F., Chammas R. and Mebarki A., The behaviour of masonry walls subjected to fire: modelling and parametrical studies in the case of hollow burnt-clay bricks, Fire Saf J, Vol. 44, 2009, pp. 629-641.
6. Prakash P.R., Azenha M., Pereira J.M. and Lourenço P.B., Finite element based micro modelling of masonry walls subjected to fire exposure: framework validation and structural implications, Eng Struct, Vol. 213, 2020, pp. 110545.
7. Prieler R., Gerhardter H., Landfahrer M., Gaber C., Schluckner C., Eichhorn-Gruber M., Schwabegger G. and Hochenauer C., Development of a numerically efficient approach based on coupled CFD/FEM analysis for virtual fire resistance tests—Part B: Deformation process of a steel structure. Fire Mater, Vol. 44, 2020, pp. 704-723.
8. Prieler R., Kitzmüller P., Thumser S., Schwabegger G. and Hochenauer C., Experimental analysis of the wall deformation of masonry brick and gypsum-sheathed stud walls during standardized fire resistance tests of steel doors, Fire Mater, pp. 1-17.
9. Prieler R., Ortner B., Thumser S., Schwabegger G. and Hochenauer C., Wall deformation during fire resistance tests – A comparative study between hollow-brick walls and gypsum-sheathed stud walls, in: Proceedings of the International Conference of Structural Fire Engineering, 2021, pp. 137-142.
10. Nadjai A., O'Garra M., Ali F. and Laverty D., A numerical model for the behaviour of masonry under elevated temperatures, Fire Mater, Vol. 27, 2003, pp. 163-182.
11. Nadjai A., O'Garra M. and Ali F., Finite element modelling of compartment masonry walls in fire, Comput Struct, Vol. 81, 2003, pp. 1923-1930.
12. Nadjai A., O'Gara M., Ali F. and Jurgen R., Compartment masonry walls in fire situations, Fire Technol, Vol. 42, 2006, pp. 211-231.
13. Prieler R., Mayrhofer M., Eichhorn-Gruber M., Schwabegger G. and Hochenauer C., Development of a numerical approach based on coupled CFD/FEM analysis for virtual fire resistance tests—Part A: Thermal analysis of the gas phase combustion and different test specimens, Fire Mater, Vol. 43, 2019, pp. 34-50.
14. Prieler R., Kitzmüller P., Thumser S., Schwabegger G., Kaschnitz E. and Hochenauer C., Experimental analysis of moisture transfer and phase change in porous insulation exposed to fire and its effect on heat transfer, Int J Heat Mass Transf, Vol. 160, 2020, pp. 120207.
15. Prieler R., Pletzer S., Thumser S., Schwabegger G. and Hochenauer C., Numerical simulation of a fire resistance test and prediction of the flue gas leakage using CFD/FEM coupling, in: Proceedings of the International Conference of Structural Fire Engineering, 2021, pp. 382-387.
16. Prieler R., Langbauer R., Gerhardter H., Kitzmüller P., Thumser S. Schwabegger G. and Hochenauer C., Modelling approach to predict the fire-related heat transfer in porous gypsum based on multi-phase simulations including water vapour transport, phase change and radiative heat transfer, Appl Therm Eng, Vol. 206, 2022, pp. 118013.
17. Nguyen T.-D., Étude du comportement au feu des maçonneries de briques en terre-cuite: approche expérimentale et modélisation du risque d'écaillage, PhD thesis, University of Paris-Est, 2009.
18. Prieler R., Klemm B., Pletzer S., Thumser S., Schwabegger G. and Hochenauer C., Pressure increase in enclosures of steel doors and its effect on the deformation process during fire resistance tests, in: Proceedings of the International Conference of Structural Fire Engineering, 2021, pp. 174-179.

NUMERICAL SIMULATIONS OF BONDED POST-TENSIONED CONCRETE BRIDGE GIRDERS UNDER HYDROCARBON FIRE

Xiqiang Wu[1], Ting Huang[2], Francis Tat Kwong Au[3]

ABSTRACT

A sequentially coupled 3-step modelling approach is adopted to study the failure mechanism of bonded post-tensioned concrete bridges under hydrocarbon fire. Firstly, a furnace fire model was built and solved. The adiabatic surface temperature (AST) obtained from fire modelling was then applied on the surfaces of the finite element model of the structure to determine the inner temperature field. Finally, the structural response under full range of fire was analysed based on this temperature field. It is noting that the bonding layer between strand and surround grout was modelled at both grouting and fire stages. Special attention was paid to the establishment of the furnace fire model. The calibrated models can be used for estimating the results of new fire tests. The numerical models were validated by fire tests on six scaled bridge beams. Results shows that the fire resistance of prestressed concrete structures depends largely on the strand temperature. In comparison, the box-section bridge beams have better fire resistance than the tee-section bridge beams.

Keywords: Fire simulation; prestressed concrete bridge; thermomechanical analysis; bond failure

1 INTRODUCTION

Post-tensioned concrete bridges have been widely adopted in practical engineering. Although the fire happened on bridges could have significant consequences, it is conventionally deemed as a rare event [1]. Nevertheless, investigation has shown that the quantity of bridge collapse due to fire is around 3 times of that caused by earthquake [1]. However, unlike earthquake, the damaging effect of fire on bridges has not attracted much attention and the risks of bridge fire are seldomly considered in bridge design. The structural-fire behaviour of bridges, especially bonded post-tensioned concrete bridges, has thus been little studied and understood.

It is usually difficult as well as costly to carry out fire tests on bridge structures. Numerical modelling is more cost-effective to determine the structural-fire behaviour of bridges, and the results are not restricted to limited points in the structure as in the fire tests. Recently, a 3-step modelling approach comprising fire simulation, thermal analysis and mechanical analysis has gained wide popularity in the analysis of structural-fire performance of bridges. Choi et al. [2] used this procedure to analyse a composite bridge (I-80/880 interchange, steel girder-concrete slab composite deck bridge) exposed to tanker truck fire. Design recommendations were given based on sensitivity studies on different surface protection materials. The behaviour of another composite bridge (I-65 overpass) exposed to tanker truck fire was extensively analysed with great effort devoted to the verification of their fire models [3–5]. The response of a long-

[1] Associate Professor, Department of Bridge Engineering, Southeast University, Nanjing, China
e-mail: wuxiqiang1988@gmail.com, ORCID: https://orcid.org/0000-0003-2614-0530
[2] Associate Professor, Department of Structural Engineering, Guilin University of Technology, Guilin, China
e-mail: tingingh@glut.edu.cn, ORCID: https://orcid.org/0000-0002-9922-0876
[3] Professor and Head, Department of Civil Engineering, The University of Hong Kong, Hong Kong, China.
e-mail: francis.au@hku.hk, ORCID: https://orcid.org/0000-0002-2163-3531
https://doi.org/10.6084/m9.figshare.22178258

span steel truss bridge during and after fire was analysed with this procedure [6]. In our previous work, the damage of tanker truck fire on post-tensioned concrete bridge decks was analysed [7].

In this study, the 3-step approach was adopted to investigate the structure-fire behaviour of bonded post-tensioned concrete bridge beams. Many efforts were made to the establishment and calibration of the furnace fire model and the modelling of the bonding layer between strand and surround grout. These numerical models were validated by fire tests on six scaled bridge beams.

2 NUMERICAL SIMULATION

The thermomechanical behaviour of scaled bridge beams exposed to the full range of furnace fire is modelled with the 3-step modelling approach. First, the gas temperature profile varying with time and location inside the furnace is simulated with a fire model. Then, the obtained surface temperature is applied to the finite element (FE) model for heat transfer analysis of the structure. Finally, a temperature-dependent mechanical analysis of the FE model of the structure is conducted based on the internal temperature field.

2.1 Furnace fire tests

Furnace fire tests were conducted on six scale specimens labelled as S1 and F1 to F5 [8]. Specimens S1 and F1 - F3 were in box section, as shown in Figure 1, and Specimens F4 and F5 were in bulb-tee section. Specimen S1 was the control specimen tested for its load-carrying capacity at ambient temperature. All specimens have a span of 4300 mm and a total length of 4600 mm to suit the furnace used. The depth of specimens is 400 mm with a span-depth ratio of about 10:1. Tests were conducted using the furnace having a chamber of 1.5 m in height, 3.0 m in width and 4.0 m in length. The gas temperature inside the furnace was designed to following the hydrocarbon fire curve. The surface temperatures of the specimen and the strand temperatures were measured by thermocouples, as illustrated in Figure 1. The downward deflection at mid-span and quarter-span were measured using linear variable differential transformers (LVDTs) during the full range of fire, including heating, cooling and post-fire phases.

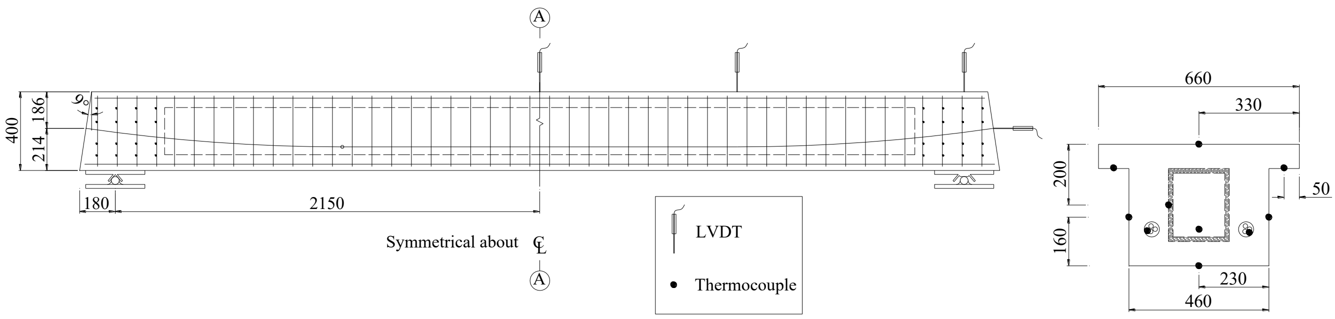

Figure 1. General dimensions of the box specimens and the layout of thermocouples and LVDTs.

2.2 Fire dynamics simulation

The furnace fire model is built up using FDS [9]. Figure 2 show the fire models with the bridge beam specimens located as in the tests for the box and tee specimens respectively. Only a quarter of the furnace was modelled by symmetry. The whole computational domain was defined slightly bigger than the interior volume of furnace. The “mirror” boundary conditions were applied to the planes of symmetry and open boundary conditions were applied to the rest of the domain boundaries.

The accuracy of the computed temperature profiles depends largely on the quality of mesh resolution that can be measured by a dimensionless parameter $D^*/\delta x$ [9], where D^* is the characteristic fire diameter and δx is the nominal size of the mesh cell. A value of $D^*/\delta x = 20$ was adopted in the current models, which satisfies the requirement of no smaller than 13 near the fire source to resolve fire characteristics [10]. The thermal properties of the obstructions, including the concrete specimen and insulated furnace walls were determined according to Eurocode 1 [11] and Eurocode 2 [12].

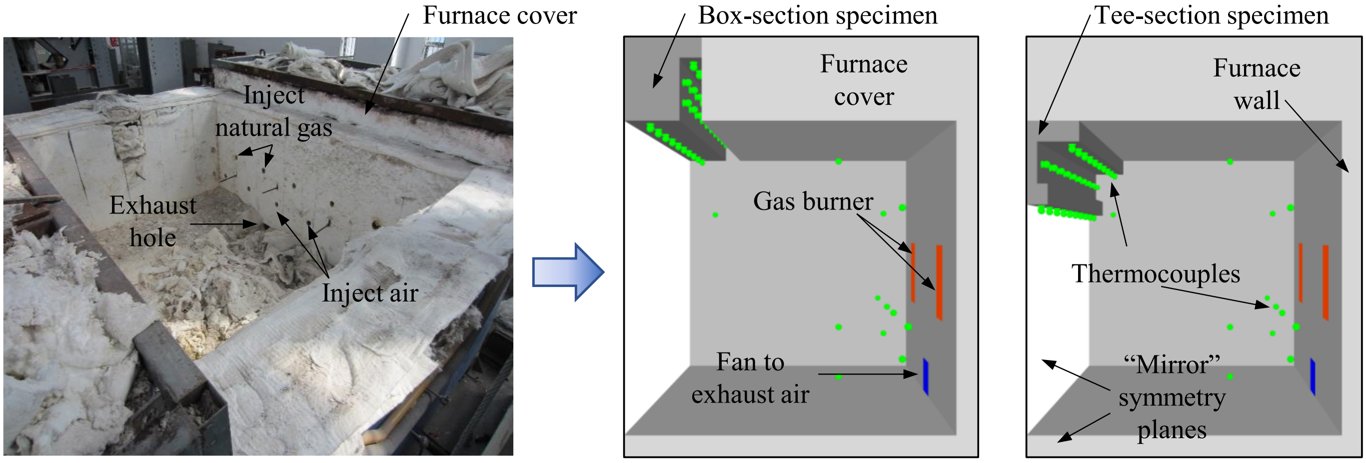

Figure 2. Establishment of the furnace fire models built up using FDS.

The definition of the fire source is the most challenging part in the FDS models. In view of the complexity, the detailed combustion process of the fuel was not modelled. Instead, the combustion products were lumped into hot air injected from vents on the furnace wall. With the observations during the fire tests, i.e., dimensions and materials of the furnace and specimens, the inflow rate of the natural gas was 100 m^3/hour, and the gas pressure inside the furnace was almost constant at 3 Pa, the flow rate of the injected hot air can be determined by the following procedure.

(1) Temperature of the injected hot air. The temperature of the injected hot air was set to increase linearly from 20 °C to 1200 °C in the first minute for the preheating stage in practice. Then, the temperature of the injected hot air kept constant at 1200 °C, i.e., the approximate temperature of the fire flame [1].

(2) The volume rate of injected hot air. This volume rate was roughly determined based on the actual fuel consumption rate during the fire tests. In view of the drastic increase of temperature within a very short duration, the furnace was operated at full capacity at the beginning of each test. The fuel used in the fire tests was natural gas consisting mainly of methane and the inflow rate was 100 m^3/hour, which is the allowed maximum flow rate of the furnace. In the combustion process, one molecule of methane is known to react with two molecules of oxygen to produce one molecule of carbon dioxide and two molecules of water vapor, and every mole of methane releases 810 kJ of energy upon burning. Given that the oxidizer used in the fire tests was air comprising 20.76% of oxygen, 78.25% of nitrogen, 0.95% of water and 0.04% of carbon dioxide, the complete burning of 100 m^3 of methane would require 963.6 m^3 of air under stoichiometric conditions and produce 1063.6 m^3 of combustion products at ambient temperature (20 °C). However, heat would be released, and cause burnt gases to expand. In the fire tests, the gas pressure within the furnace was kept almost constant at 3 Pa above the atmospheric pressure. The amount of burnt gases in the flame (1200 °C) was determined as 5344.8 m^3/h by applying the ideal gas law, giving a volume rate of hot air injection of 1.485 m^3/s.

(3) The flow velocity of the injected hot air. In practice, twelve natural gas burners were alternately mounted on the chamber walls for heating. For simplification, the burners were modelled with two rectangular air inlets of 0.2 m by 0.4 m each for a quarter of the furnace model, as shown in Figure. 2. The flow velocity speed of the hot air at the vent was set to be 2.32 m/s as a result of the flow rate and the vent area. A constant inflow rate of hot air was used throughout heating. The duration of hot air supply was set as the fire exposure time. The analysis also ended upon cessation of hot air supply.

The burnt gases were then discharged outside of the furnace, otherwise the gas pressure inside the surface would continue to increase. A fan at the bottom of the chamber as is located in the real furnace was defined to exhaust the gases, as shown in Figure 2. The definition of the fan uses the “quadratic” fan model, which allows to adjust its flow rate based on the imposed pressure of 3 Pa.

2.3 Heat transfer analysis

Three-dimensional (3D) FE models of the box and tee beams were then built up using ABAQUS [13] .By symmetry, only a quarter of each beam was modelled as shown in Figures 3(a) and (b). The concrete, grout, strand and bond zone between grout and strand were separately modelled with 8-node brick elements DC3D8 to obtain the transient temperature field within the specimen. The reinforcement rebars were modelled with 2-node link elements DC1D2 embedded in the concrete elements. The heat transfer between reinforcement node and the nearest concrete node was realized by defining constraint "Equation" on the temperature degree of freedom (11th degree).

The temperature boundary conditions were applied, as appropriate, to the specimen surfaces. At the exterior surfaces, the adiabatic surface temperature (AST) profiles as obtained from the FDS fire model were applied. Cavity radiation was defined to the interior surfaces of the box specimen to consider the potential heat transfer in this space. For Specimens F2 and F5 exposed to 90-minute heating followed by cooling, the temperature boundary conditions at the exterior surfaces were set to be ambient temperature immediately upon the start of cooling.

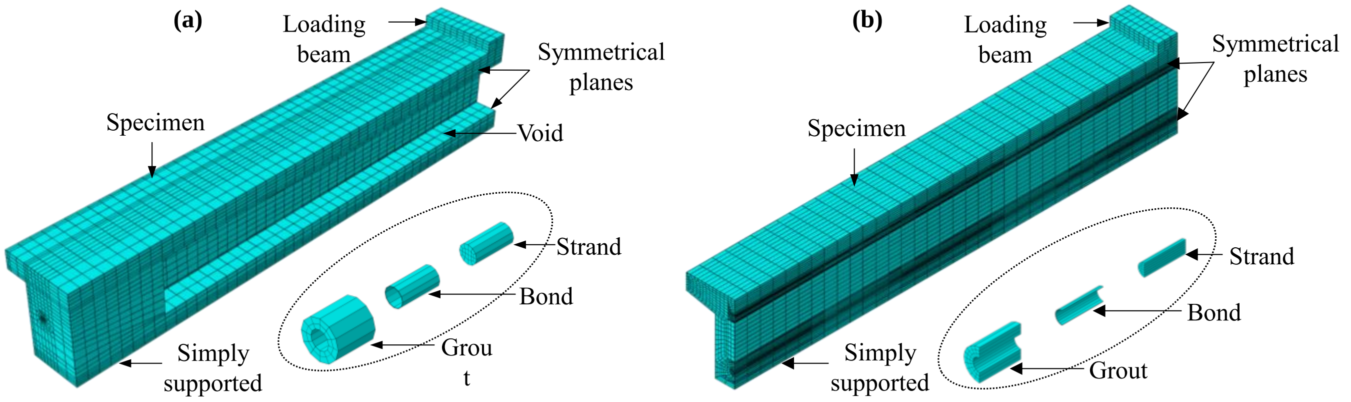

Figure 3. Finite element models for: (a) box-section specimen; (b) tee-section specimen.

Convection and radiation were considered at all the surfaces. The emissivity coefficient for the concrete surface is taken as 0.8. The convective heat transfer coefficient depends on the temperature. A value of 25 W/(m^2·K) was specified for the fire-exposed concrete surfaces at the heating period, while a value of 9 W/(m^2·K) was specified at the cooling period and for the unexposed surfaces [11]. The temperature varied thermal properties of concrete, prestressing steel and reinforcing steel as suggested by Eurocode 2 [12] were used.

2.4 Mechanical analysis

The models used to study the deflection behaviour of the beams were similar to those in Figures 3, except that the models were built by different types of elements. The concrete, grout and strand were modelled using solid element C3D8R. In this study, each 7-wire strand is modelled as an equivalent single solid wire with the same cross-sectional area. The bonding zone between the strand and grout was modelled with 3D cohesive element COH3D8. The longitudinal reinforcing bars and the stirrups were modelled with 3D truss element T3D2 embedded in the concrete element.

The pre-fire, heating, cooling and post-fire phases were modelled sequentially using ABAQUS [13]. The external load was applied with prescribed magnitude in the pre-fire phase and kept constant till the post-fire phase with the exception of Specimen F5 that had load reduction in the cooling phase. The temperature field results from the prior heat transfer analysis were imported so as to consider the effects of fire exposure. For specimens sustaining external load after fire exposure, an imposed increasing displacement was applied at the mid-span of specimen in the post-fire phase in addition to the load to determine the residual load-carrying capacity.

2.5 Material models

Elevated temperature can significantly impair the mechanical properties of concrete, grout, prestressing strand and steel reinforcement, and thus causes damage to structures. The material models adopted for these materials at heating and cooling phases are summarized below. The compressive strength of concrete at ambient temperature for the specimens was 50 MPa. The compressive strength and the corresponding strain, elastic modulus and the ultimate compressive strain of concrete at elevated temperatures were obtained based on Eurocode 2 [12]. Concrete does not recover its mechanical properties during the cooling phase after fire exposure, according to Eurocode 4 [14]. Instead, concrete continuously deteriorates during the cooling down to ambient temperature and will retain no less than 90% of the compressive strength at the maximum temperature experienced. For simplicity, the concrete properties retained at the maximum temperature experienced may be still used when considering the concrete in the cooling phase.

The uniaxial tensile behaviour of concrete was defined according to CEB-FIP [15]. Concrete in tension is assumed to behave linear-elastically until cracking, after which the tensile stress decreases as crack opens. A bilinear relationship between the tensile stress and crack opening displacement as proposed by CEB-FIP [15], being defined by the tensile strength and fracture energy of concrete, was used to describe the behaviour of concrete after cracking. The tensile strength of concrete at elevated temperatures were derived from Eurocode 2 [12]. The fracture energy of concrete was assumed to be 147.6 N/m irrespective of the temperature.

Concrete damaged plasticity constitutive model as specified in ABAQUS was adopted for the analysis of damage of concrete. A viscosity of 0.0005 was found to lead to balanced modelling accuracy and speed. Other parameters such as the flow potential and yield surface were defined by default values provided in ABAQUS. Considering the lack of studies on the grout, the mechanical properties of concrete at elevated temperatures were also applied to the grout.

Similar irreversible adverse effects were also found on mechanical properties of prestressing steel at elevated temperatures [16]. Thus, the material behaviour of the prestressing strand was assumed to be related to the maximum temperature experienced. For steel reinforcement, on the other hand, the mechanical properties corresponding to the current temperature may always be used as an adequate approximation according to Eurocode 4 [14]. The stress-strain relationships for prestressing strand and steel reinforcement at elevated temperatures as proposed by Eurocode 2 [12] were used. The ultimate tensile strength for prestressing strand and steel reinforcement were 1860 MPa and 335 MPa respectively.

It is noting that heat would continue to penetrate into the inner part of the structure even after the ceasing of fire due to the good fire resistance properties of concrete. Therefore, it is unreasonable to assign the mechanical properties at cooling stage to the whole structure at the cease of fire. In this study, a user subroutine was written to allow the material points in each element to follow the appropriate material model based on their current and experienced temperatures. For instance, if the current temperature is no lower than the previous one at the location of a certain element, the material model at heating phase would be used to follow since the temperature is detected to increase, otherwise the material model at cooling phase would be chosen.

2.6 Bonding between prestressing strand and grout

Particular attention was paid to the modelling of the bonding area between strand and grout. In the actual construction, grouting was conducted after post-tensioning. There is no bonding stress before or during prestressing, and the bonding area would start to transfer forces after then. Therefore, the bonding zone was firstly omitted by deactivating the elements in this zone during the self-weight of the beam and prestressing analysis steps. It is noting that though these elements were deactivated, they would still deform since they were sharing the associated nodes with the neighbouring nodes of the strand and grout. The elements in the bonding zone were then re-introduced to the deformed model by reactivating these elements. Since there should be no stress immediately after prestressing, these elements were reactivated without strain. For the prestressing, the stress was introduced to the strands through imposed strain by means of equivalent descending temperature from an elevated temperature to the ambient temperature. To avoid the damage to the strands due to this imposed elevated temperature, the mechanical property of the strand was set as linearly elastic without failure irrespective of the temperature.

The bonding zone between the strand and grout was modelled with a layer of 3D cohesive element COH3D8, as shown in Figure 4(a). This type of elements is specially used for the modelling of bonded interfaces or adhesives having a thin layer. The cohesive elements connect like solid elements, but they can be regarded as being composed of two faces separated by a certain thickness. As shown in Figure 4(a), the relative motion of the bottom and top faces along the thickness direction represents the compressive and tensile behaviours. The relative change in position of the bottom and top faces measured in the plane orthogonal to the thickness direction quantifies the transverse shear behaviour.

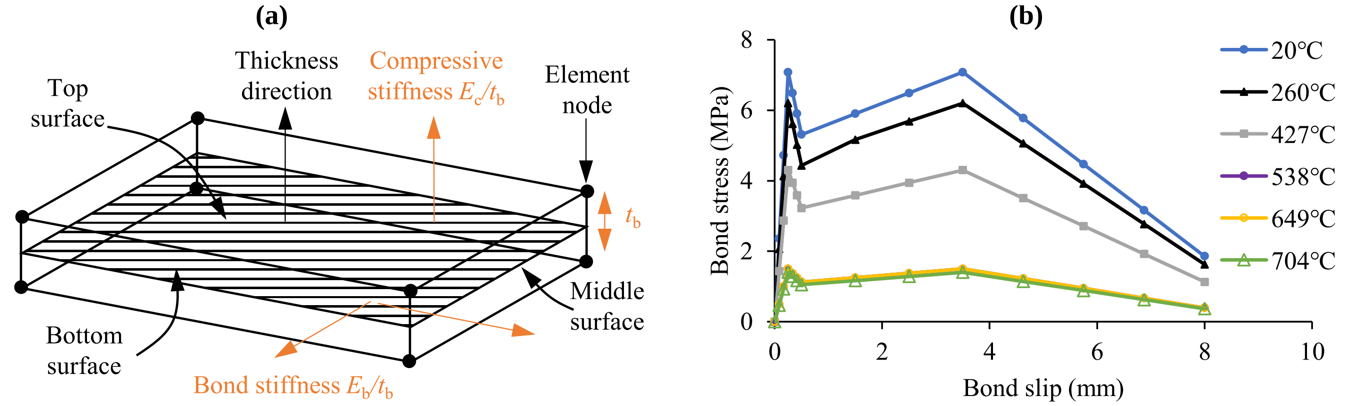

Figure 4. Modelling of the bond zone: (a) spatial representation of the 3D cohesive element; (b) bond-slip relationship at elevated temperatures.

The mechanical properties of the cohesive elements at the thickness and plane directions were defined separately considering their distinct behaviours. In the plane direction, the bond-slip relationship needs to be specified. However, little work has been done on the bonding behaviour between prestressing strand and grout or concrete at elevated temperatures. In this study, the bond-slip relationship between prestressing strand and concrete proposed by Khalaf and Huang [17], as illustrated Figure 4(b), was adopted. The cohesive element was assigned an initial stiffness of E_b/t_b, where E_b is the initial stiffness of the bond and t_b is the thickness of the bond layer taken as 0.5 mm. In the thickness direction, the cohesive element was assumed to behave linear-elastically with a stiffness of E_c/t_b, where E_c is the elastic modulus of concrete.

3 VALIDATION OF NUMERICAL MODELING

3.1 Gas temperature

Numerical results of thermal and structural responses of the bridge beam specimens were compared to the test results to validate the numerical models. The tempo-spatially varied gas temperature field inside the furnace chamber can be visualized in the fire model, as shown in Figure 5(a). However, the temperature distribution is impractical to be compared with the test results since there was no observation window on the furnace wall.

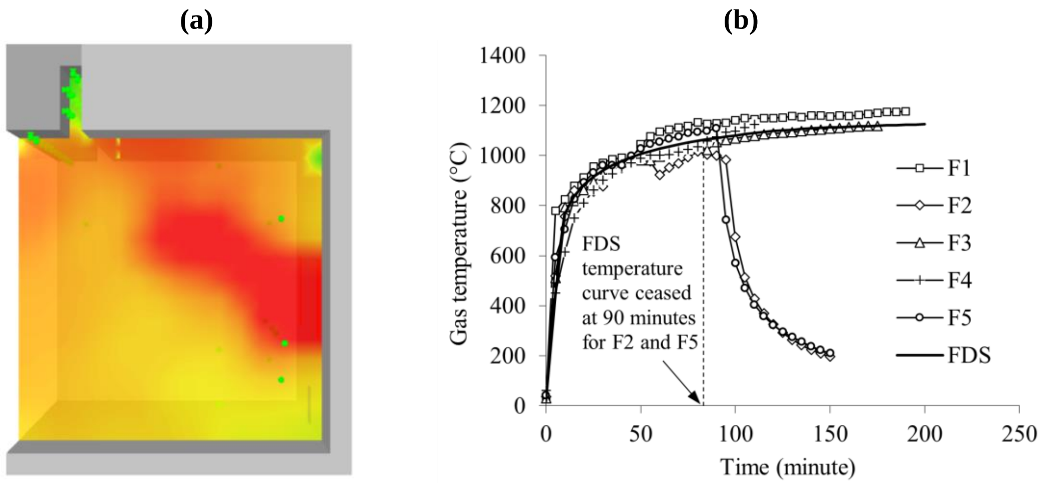

Figure 5. Gas temperatures predicted by FDS model: (a) temperature field 490 s after ignition; (b) temperature measured by thermocouple near the air inlet evolving with time.

Temperature sensors were defined at certain locations in the fire model to obtain the gas temperatures inside the furnace, as shown in Figure 2. The gas temperature near the hot air inlet obtained from the FDS model agree well with those measured at the same location in the fire tests, as illustrated in Figure 5. This validates the capability of the FDS model in predicting the gas temperature of a fire test. The calibrated models can be used for estimating the results of new fire tests using this furnace, which would potentially reduce the unnecessary time and cost spent on the fire tests design.

3.2 Thermal response

The specimen surface temperature curves and strand temperature curves obtained from the heat transfer analysis are presented in Figure 6 along with the fire test results. The predicted maximum strand temperatures are also summarized in Table 1 with the test results. The general agreement between the predicted and measured temperatures indicates that the thermal boundaries exported from the FDS model are competent for the heat transfer analysis.

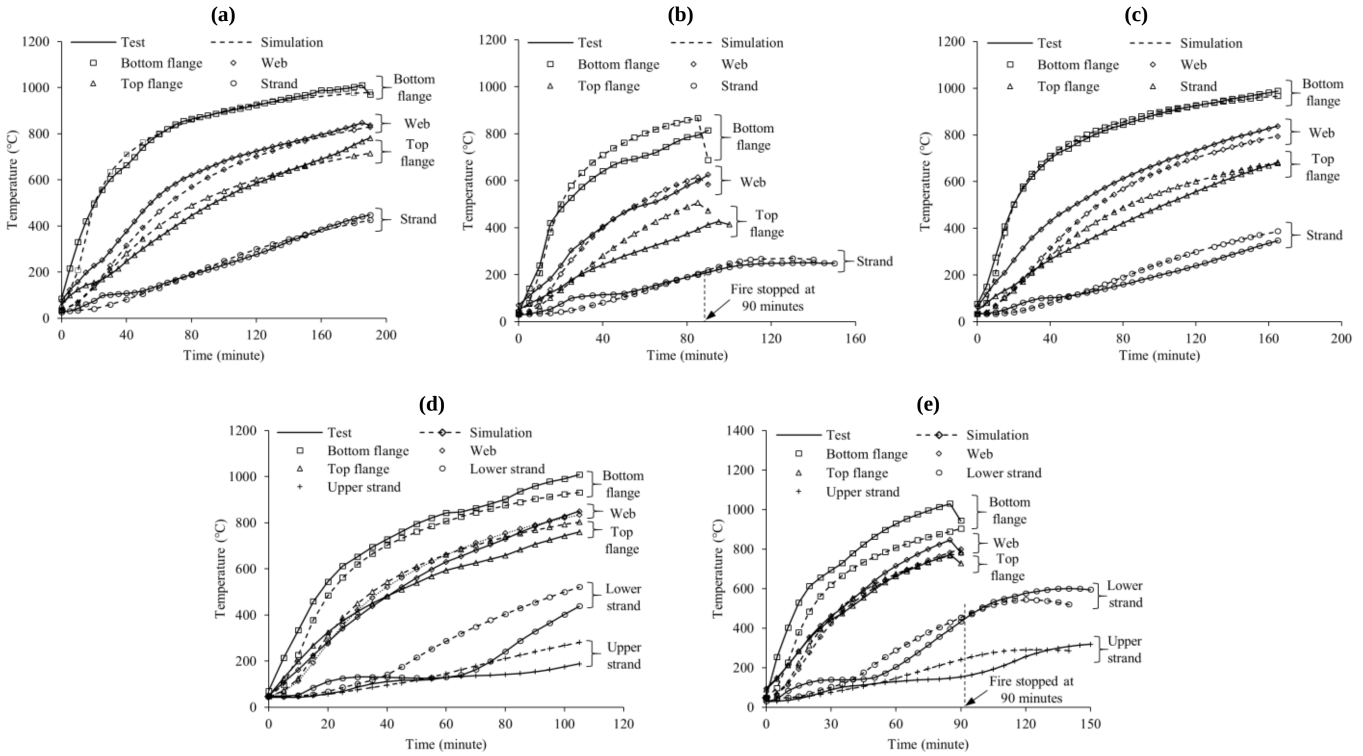

Figure 6. Experimental and numerical results of specimen surface and strand temperatures: (a) F1; (b) F2; (c) F3; (d) F4; (e) F5.

Table 1. Summary of experimental and numerical results

Test	Maximum strand temperature (°C)			Fire resistance duration (min)			Residual load-carrying capacity (%)		
	Test	Simulation	Error (%)	Test	Simulation	Error (%)	Test	Simulation	Error (%)
F1	448	425	-5.1	184	200	+8.7	-	-	-
F2	251	267	+6.4	-	-	-	89	91	+2
F3	347	388	+11.8	165	156	-5.5	-	-	-
F4	438	520	+18.7	105	90	-14.3	-	-	-
F5	600	543	-9.5	-	-	-	62	72	+10

The surface temperatures of the bottom flange, web and top flange of the box specimens vary from high to low, which are well predicted as shown in Figures 6(a) to (c). The gas temperature profiles near the box specimen in Figure 7(a) as obtained from the FDS fire simulation indicate that heat could not effectively reach the web and soffit of top flange due to the presence of furnace cover. For tee specimens, the surface temperature of the top flange was slightly higher than that on the web at the beginning as observed in the fire test. The phenomenon was also successfully predicted as shown in Figures 6(d) and (e). Some vortexes had formed close to the surface of web due to the protruding top flange as shown in Figure 7(b). This may have hindered the convective heat transfer from the gas to the web before the gas inside the furnace got homogenized.

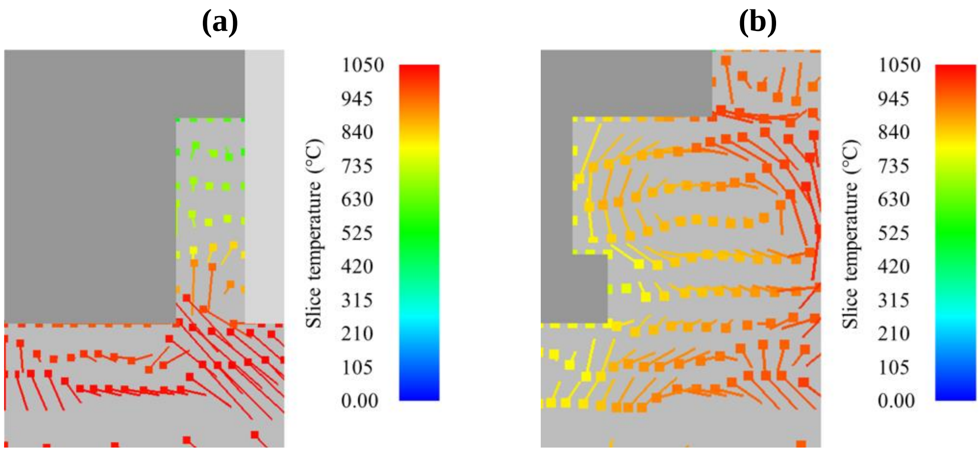

Figure 7. Gas temperature profiles near: (a) box specimen; (b) tee specimen

The strand temperature tended to be underestimated at the beginning and then overestimated afterwards by the simulation as shown in Figure 6. The plateau observed in the experimental strand temperature curves were not well captured by the numerical curves. The occurrence of the plateau has been attributed to the moisture in the concrete and grout. The specific heat of cementitious material is known to increase sharply at temperatures 100 – 115 °C due to evaporation of moisture consuming a large amount of heat, which had delayed further increase of the strand temperature. Based on measurements from concrete cores, the moisture contents of concrete and grout were both taken as 4.0% in the simulation. However, the actual moisture content of grout inside the duct could be higher than 4.0% that was measured for the concrete samples. A higher value of moisture content in grout would theoretically yield a more visible plateau phase in the strand temperature curves.

The strand temperature during the cooling phase was also found to drop faster in the simulation than in the fire tests, especially for Specimen F5 of tee-section as shown in Figure 6(e). This is because the thermal boundaries of specimens were simply set to the ambient temperature immediately after fire exposure in the heat transfer analysis, while the actual surface temperature gradually dropped in the fire tests. Nevertheless, the simulation was able to predict the peak strand temperature that would appear after the fire as for Specimen F2 and F5 with reasonable accuracy.

3.3 In-fire and post-fire structural responses

The simulated evolutions of mid-span deflection and load-deflection curves throughout the fire test agree reasonably well with the corresponding experimental results as shown in Figure 8 and Figure 9 respectively. The predicted fire resistances for Specimens F1, F3 and F4 and residual load-carrying capacities for Specimens F2 and F5 are summarized in Table 1. They are reasonably close to the experimental results with errors within ±15%, indicating that the FDS model in conjunction with the thermo-mechanical model are suitable for structural-fire analysis of post-tensioned concrete bridge beams exposed to furnace fire following the hydrocarbon curve.

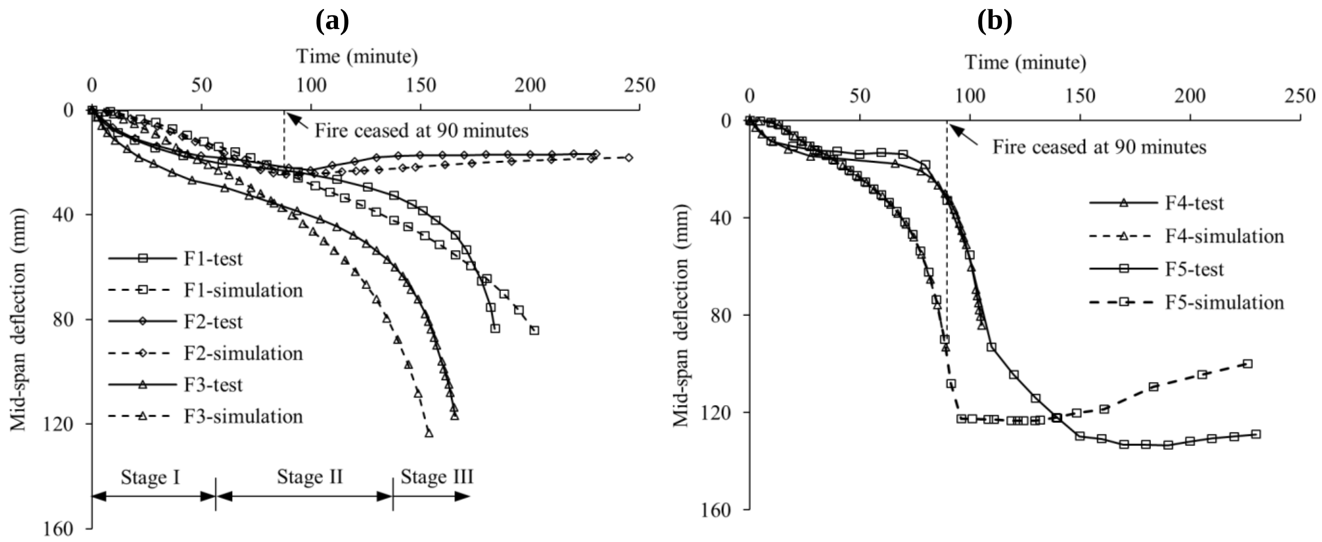

Figure 8. Experimental and numerical results of mid-span deflection: (a) F1 - F3; (b) F4 - F5.

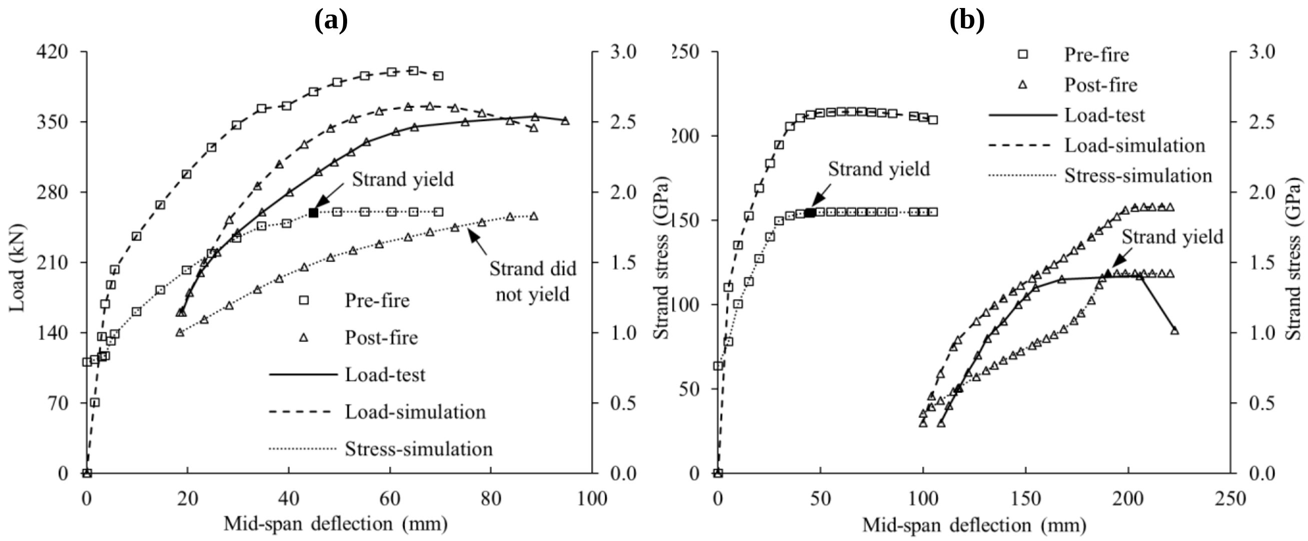

Figure 9. Experimental and numerical results of load-deflection curve: (a) F2; (b) F5.

Examining the numerical and experimental deflection curves, one can attribute the discrepancy to the missing plateau phase in the strand temperature curve from numerical simulation. The deflection was generally underestimated at the beginning and overestimated afterwards by the simulation, exactly the same as the strand temperature was predicted. Take Specimen F1 for example, the predicted strand temperature was lower than the measured value before reaching 100 °C and at the same time the predicted deflection was also smaller. The predicted temperature was higher afterwards while the predicted deflection also became larger as compared to the test results. This indicates that the structural-fire behaviour of prestressed concrete structures depends largely on the strand temperature. In particular, the fire resistance is related to the strand temperature. Both test and simulation results of Specimens F1 and F3 show that a longer fire resistance duration is accompanied by a lower strand temperature as shown in Table 1.

In addition to the residual load-carry capacity, the potential failure modes of Specimens F2 and F5 at ambient temperature after fire exposure are also of interest as both concrete and prestressing strand cannot recover their initial mechanical properties after fire. Figure 9 shows the simulated load-deflection curves of Specimens F2 and F5 before and after fire exposure, together with the simulated stress of strand at mid-span. For the simulated response of Specimen F2 at ambient temperature, the prestressing strand yields at a load of 380 kN followed by concrete crushing and specimen failure at a load of 401 kN as shown in Figure 9(a). After exposure to hydrocarbon fire for 90 minutes, the prestressing strand of Specimen F2 does not show any yielding until the specimen fails upon concrete crushing at a load of 365 kN as shown in Figure

9(a). In other words, fire exposure can change the failure mode of Specimen F2 from the ductile mode to the brittle mode. Actually, the noise of strand fracture was heard in all tests except for the one on Specimen F2. For the simulated response of Specimens F5 at ambient temperature, the prestressing strand yields at 195 kN before the specimen fails at 214 kN as shown in Figure 9(b). After exposure to hydrocarbon fire for 90 minutes, however, the specimen fails at 154 kN following the yielding of prestressing strand at 129 kN as shown in Figure 9(b). Therefore, Specimen F5 is likely to retain ductile performance. However, the external load imposed on Specimen F5 was reduced from 60 kN to 30 kN at the cooling phase; otherwise, the specimen would have collapsed.

4 CONCLUSIONS

In this study, the behaviour of post-tensioned concrete bridge beams exposed to hydrocarbon fire was simulated through a 3-step modelling approach consisting of fire simulation, heat transfer analysis and thermo-mechanical analysis. The numerical method was validated against an experimental study. Based on this study, the following conclusions can be drawn:

- The gas temperature inside the furnace can be predicted by a proper fire model, which was built up mainly based on the general information of the dimensions and materials of the furnace and specimens, the inflow rate of the natural gas and the gas pressure. The fire models would be a cost-effective tool for future fire test designs.
- The simulated thermal and structural response agree well with the experimental results. The simulation results provide insights into the performance of post-tensioned concrete bridges exposed to hydrocarbon fire and hopefully lead to improvements in the design philosophy of such bridges.
- The structural-fire behaviour of a prestressed concrete member tends to depend largely on the strand temperature. Higher strand temperature leads to shorter fire resistance duration and more loss of load-carrying capacity. As a result, the bridge beam of box-section tends to have better fire resistance than the bridge beam of tee-section, since the box-section has fewer fire exposure surfaces due to the presence of enclosed void and thus slows down the rise of strand temperature.
- Fire exposure can cause collapse of a bridge. Limited fire exposure not only reduces the load-carrying capacity of the structure but may also alter the potential failure mode of the structure. Under certain circumstances related to the variation of temperature of prestressing tendons with fire exposure, a bridge that behaves in a ductile manner at ambient temperature may fail in a brittle manner under severe fire exposure.

ACKNOWLEDGMENT

This work is funded by National Natural Science Foundation of China (NSFC grant no. 52108480).

REFERENCES

1. Garlock M, Paya-Zaforteza I, Kodur V, Gu L (2012) Fire hazard in bridges: Review, assessment and repair strategies. Eng Struct 35:89–98. https://doi.org/10.1016/j.engstruct.2011.11.002
2. Choi J, Choi JY (2016) An integrated framework for 24-hours fire detection. In: Lecture Notes in Computer Science(including subseries Lecture Notes in Artificial Intelligence and Lecture Notes in Bioinformatics)
3. Peris-Sayol G, Paya-Zaforteza I, Alos-Moya J, et al (2015) Analysis of the influence of geometric, modeling and environmental parameters on the fire response of steel bridges subjected to realistic fire scenarios. Comput Struct 158:333–345. https://doi.org/10.1016/j.compstruc.2015.06.003
4. Peris-Sayol G, Paya-Zaforteza I, Balasch-Parisi S, Alós-Moya J (2017) Detailed Analysis of the Causes of Bridge Fires and Their Associated Damage Levels. J Perform Constr Facil 31:04016108. https://doi.org/10.1061/(asce)cf.1943-5509.0000977
5. Alos-Moya J, Paya-Zaforteza I, Garlock MEM, et al (2014) Analysis of a bridge failure due to fire using computational fluid dynamics and finite element models. Eng Struct 68:96–110.

https://doi.org/10.1016/j.engstruct.2014.02.022
6. Gong X, Agrawal AK (2015) Numerical Simulation of Fire Damage to a Long-Span Truss Bridge. J Bridg Eng 20:4014109. https://doi.org/10.1061/(asce)be.1943-5592.0000707
7. Wu X qiang, Huang T, Au FTK, Li J (2020) A Localized Fire Model for Predicting the Surface Temperature of Box Girder Bridges Subjected to Tanker Truck Fire. Fire Technol 56:2059–2087. https://doi.org/10.1007/s10694-020-00966-2
8. Wu X, Huang T, Au FTK, Li J (2020) Posttensioned Concrete Bridge Beams Exposed to Hydrocarbon Fire. J Struct Eng 146:04020210. https://doi.org/10.1061/(asce)st.1943-541x.0002791
9. Mcgrattan K, Mcdermott R (2015) Fire Dynamics Simulator User ' s Guide (FDS Version 6.3.0)
10. Lin C-H, Ferng Y-M, Hsu W-S (2009) Investigating the effect of computational grid sizes on the predicted characteristics of thermal radiation for a fire. Appl Therm Eng 29:2243–2250
11. CEN (2002) Eurocode 1: Actions on Structures exposed to fire. Br Stand Institution, BS EN
12. CEN (2004) Eurocode 2: Design of concrete structures-Part 1-2: General rules-structural fire design. Br Stand Institution, BS EN
13. Simulia DS (2013) ABAQUS 6.13 User's manual. Dassault Syst Provid RI 305:306
14. CEN (2005) Eurocode 4 - Design of composite steel and concrete structures - Part 1-2: General rules - Structural fire design. Br Stand Institution, BS EN
15. RILEM/CEB/FIP. (1983) Recommendations on reinforcement steel for reinforced concrete (RC 6, CEB News 73). CEB News
16. Zhang L, Au FTK, Wei Y, Li J (2017) Mechanical properties of prestressing steel in and after fire. Mag Concr Res 69:379–388. https://doi.org/10.1680/jmacr.15.00267
17. Khalaf J, Huang Z (2016) Analysis of the bond behaviour between prestressed strands and concrete in fire. Constr Build Mater 128:12–23. https://doi.org/10.1016/j.conbuildmat.2016.10.016

INCREASED FIRE RESISTANCE OF A STEEL BEAM USING ORIENTED STANDARD BOARD CLADDING – A THERMAL ANALYSIS

Jakub Šejna[1], Kamila Cábová[2], Marie Křišťanová[3], František Wald[4]

ABSTRACT

This article presents the possibility of increasing the fire resistance of a steel member with the use of an OSB (Oriented Standard Board) cladding. Correct design and dimensioning of the OSB cladding to fulfil the targeted fire resistance of the steel member is the main challenge with this type of cladding. The problem lies in the addition of combustible material on the surface of the steel member. When the wood-based material burns, additional heat is generated, and this raises the temperature of the surrounding gas. However, wood material benefits from its extraordinary behaviors when exposed to fire. The burned part forms a char layer that insulates the solid materials below it. It is necessary to ensure the integrity of the cladding and to prevent its premature failure. The aim of the work presented in this article was to determine the functionality of an OSB cladding as a fire protection layer for a steel beam. For this purpose, an FE (Finite Element) model of the heat transfer is developed and is validated against measured data from a fire test in a horizontal furnace. The progression of the charred layer is determined from the validated FE model, and is compared with the standard linear charring rate.

Keywords: fire responsibility; FE model; fire experiment; cladding; char layer, OSB

1 INTRODUCTION

There are many passive protection measures for steel structures, e.g., fire coatings and sprays. Fire cladding appears to be the simplest way to increase the fire resistance of a steel member. Calcium silicate-based boards, gypsum boards and boards with a cement binder are the most widely used claddings. However, these approaches are slow and expensive. With the use of wood or wood-based materials (OSB cladding), excellent structural sustainability can be achieved. In the last ten years, there has been great emphasis on sustainable and ecological design. From a primary energy perspective, ratios of 1: 3 can be determined when comparing wood with cement, ratios of 1:27 when comparing wood with steel, and ratios of 1:70 when comparing wood with aluminum [1].

Wood has excellent fire-resistance properties. Specifically, a char layer develops that exhibits excellent insulating properties and prevents further heat transfer to the structure. If the char layer does not fail, and continues to cover the solid wood members, the wood can be to be made to stop burning due to lack of

---

[1] Ing. Jakub Šejna, Department of Steel and Timber Structures, Faculty of Civil Engineering, Czech Technical University in Prague,
e-mail: jakub.sejna@fsv.cvut.cz, ORCID: https://orcid.org/0000-0002-9968-2026

[2] Ing. Kamila Cábová, Ph.D, Department of Steel and Timber Structures, Faculty of Civil Engineering, Czech Technical University in Prague, Czech Republic
e-mail: kamila.cabova@fsv.cvut.cz, ORCID: https://orcid.org/0000-0002-4446-2472

[3] Bc. Marie Křišťanová, Department of Steel and Timber Structures, Faculty of Civil Engineering, Czech Technical University in Prague, Czech Republic
e-mail: marie.kristanova@fsv.cvut.cz, ORCID: https://orcid.org/my-orcid?orcid=0000-0003-0335-5096

[4] prof. Ing. František Wald, CSc., Department of Steel and Timber Structures, Faculty of Civil Engineering, Czech Technical University in Prague, Czech Republic
e-mail: wald@cvut.cz, ORCID: https://orcid.org/0000-0003-2416-8951

https://doi.org/10.6084/m9.figshare.22178264

oxygen. This assumption cannot be used in the case of cladding, where failure must be assumed to occur within a period that can be predicted according to the charring rate of the wood. The disadvantage of the use of cladding is that combustible material is added to the fire compartment. It is therefore necessary to take into consideration the additional material, which influences the ambient temperatures. There are two ways to predict these temperatures: conservatively by inputting another combustible material in the room, or by taking into consideration the pyrolysis of the wood and the release of combustible gas into the fire compartment. The second option is currently based only on the behavior of the wood in the experimental furnace. Research has been carried out to determine the kinetic coefficients of pyrolysis to calculate the rate of reaction of r_j. Coefficients are obtained in small samples after complete combustion.

Subsequently, based on the selected reaction pattern, the kinetic coefficients of pyrolysis A_j, Ej, *and* n_j are determined, determining the initial mass fraction of the individual reaction elements Y_j of the component. The calculation can then be performed by the reaction rate, as determined by Eq. 1 [2, 3, 4, 5].

$$r_j = A_j \exp\frac{-E_j}{RT} {Y_{s,j}}^{n_j} \qquad (1)$$

where A_j is the preexponential factor, Ej is the activation energy, n_j is the reaction order, T is temperature, $Y_{s,j}$ is the initial mass fraction of the component, and R is the universal gas constant [4].

Research into OSB behaviour in terms of pyrolysis development is reported in the paper by Ira et al. [4], which determines the reaction schematics as three fictitious reactions R1, R2 and R3 with respect to the reaction pattern by Eq. 2. The observed kinetic coefficients of OSB pyrolysis are given in Tab. 1.

$$v_{X,j}X = v_{R,j}R + volatiles \qquad (2)$$

where R denotes a solid residue, and ν denotes a stoichiometric coefficient. The amount of solid residue is derived from the overall thermogravimetric curve, and is considered to be the same for each material component. The number of components X is equal to n [4].

Table 1. Final pyrolysis kinetic coefficients for OSB [4]

	$Y_{s,j}(0)$ (−)	log A_j (log (1/s))	E_j (kJ/mol)	n_j (−)	ν_{char} (−)
R1	39.8	7.6	112	1.2	0.236
R2	34.8	25.4	326	1.5	0.236
R3	25.4	2.7	56	3.1	0.236

The possibility of using wood as a fire protection layer, taking advantage of the insulating properties of the char layer, was introduced in 1974 by Twilt and Witteveen [6]. It was found that even the protective layer provided by a softwood panel 35 mm in thickness can increase the fire resistance of a steel structure by up to 60 min. Very recently, innovations such as the protected steel I and the T profile, using a full or partial wood cladding, have been published [7, 8]. The use of OSB as a fire protective panel has been investigated by Šejna [9], who tested the functionality of OSB claddings in small-scale samples exposed to the standard temperature curve. The OSB reference thickness and a spruce cladding 22 mm in thickness was examined. This prevents heat from entering the steel structure for at least 15 min. Experiments showed that there was a 20-min increase in the fire resistance of the steel element with the cladding [9].

2 FIRE TEST

In a full-scale fire test aimed at verifying the knowledge obtained in small-scale experiments [9], samples were placed to investigate the behaviour of OSB cladding of steel structures. In the furnace, the samples were mechanically loaded [10, 11], and were then unloaded to investigate the behaviour of the OSB cladding. Two short steel beams made of SHS 100×6 mm were protected by one layer or by two layers of OSB cladding (further referred to as 1x OSB and 2x OSB. Each layer of OSB cladding was 22 mm in thickness. The ends of the beam were covered with mineral insulation. Both samples were placed below the ceiling of the furnace (Figs. 1, 2, 3). The temperature load followed the standard temperature curve. The experimental horizontal furnace, measuring 4.0 m in length and 3.0 m in width, was raised by 0.9 m from its original height of 2.35 m to a height of 3.25 m. Horizontal furnace burners were mounted on two walls. The maximum power of one burner was 2,560 kW. The experimental furnace was ventilated through a suction hole on the floor of the furnace. The ventilation of the furnace was controlled by the pressure in the furnace. The horizontal furnace is described in [12].

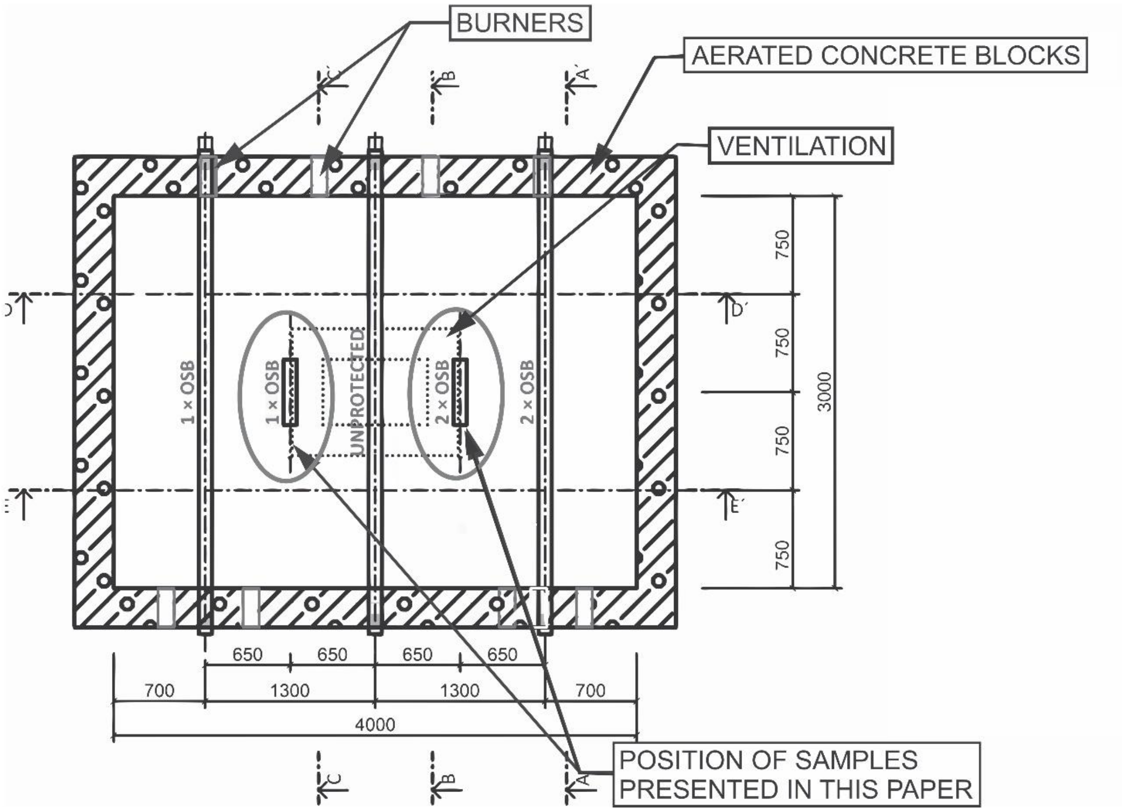

Figure 1. Floor plan of the horizontal furnace

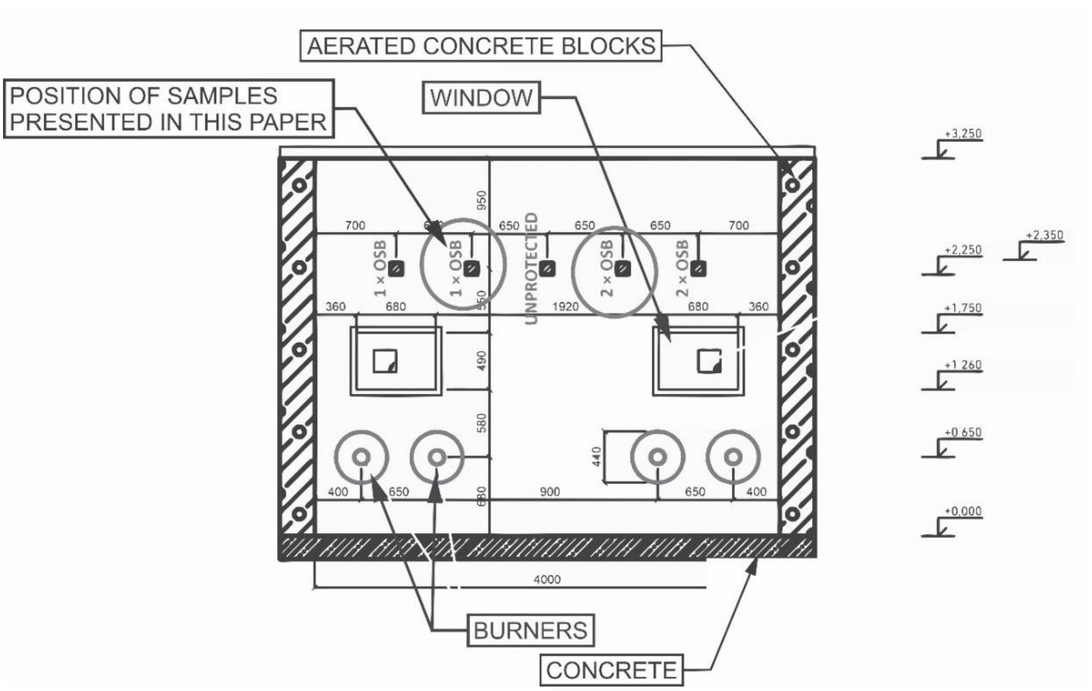

Figure 2. Cross-section of the horizontal furnace

The steel elements were made of SHS 100/6 profile S235JR, length 500 mm. The hollow of the steel profile was filled with mineral wool. The OSB cladding was made using a pneumatic clip, and the clip was 40mm in length. A sample of 2x OSB was made with a second layer of cladding to cover the gap in the cladding (Fig. 4). Thermocouples of type MTC10 /1xK T2 /P1,5 /N3000 /K-MM with a maximum measurement temperature of 1150 ° C and thermocouples of type MTC12 /1xK T2 /N4m /GHGH 2x0,5 / K-MM with declared temperature deviation up to 600 ° C were used to measure the temperature. The thermocouples were placed on the surface of the steel profile. For the two-layer OSB cladding, MTC12 thermocouples were placed between the cladding layers to measure the temperature at which the first layer of OSB cladding failed. The location of the thermocouples was in accordance with the conclusions published by Fahrni [10].

The test was terminated after 60 min. The results of the test show clearly that OSB cladding helps to reduce the temperature in the steel element. The duration of the experiment and the heating method made it possible to monitor the development of the charred layer. The breakage times of each timber cladding were defined in advance, based on the equation for the constant charring rate according to EN 1995-1-2 [14].

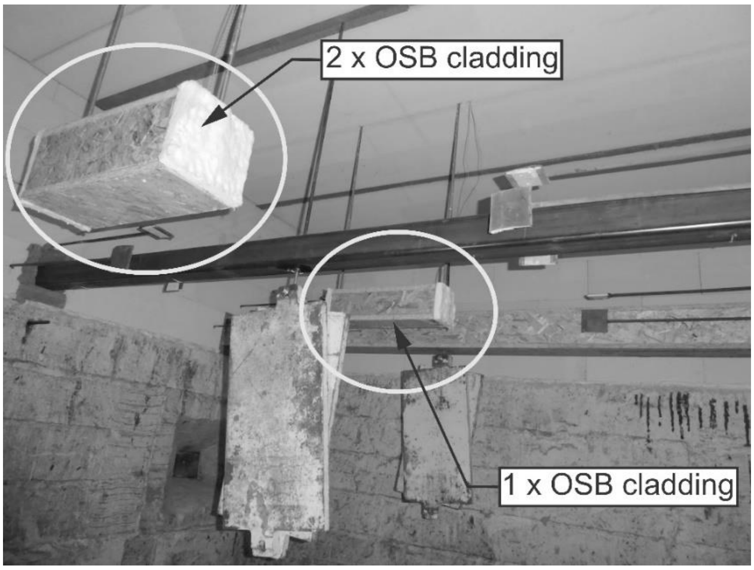

Figure 3. Samples before the fire test

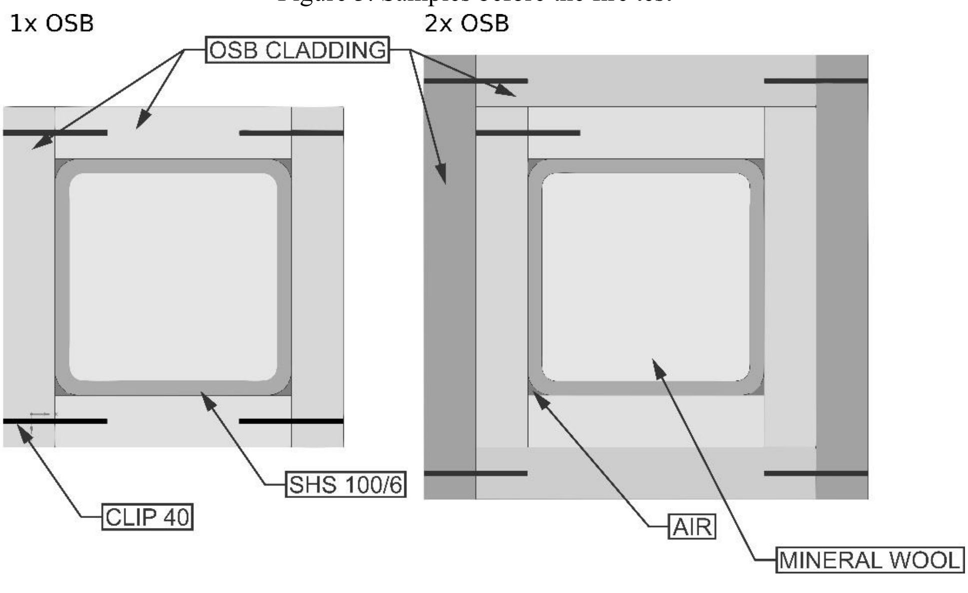

Figure 4. A description of the sample layers

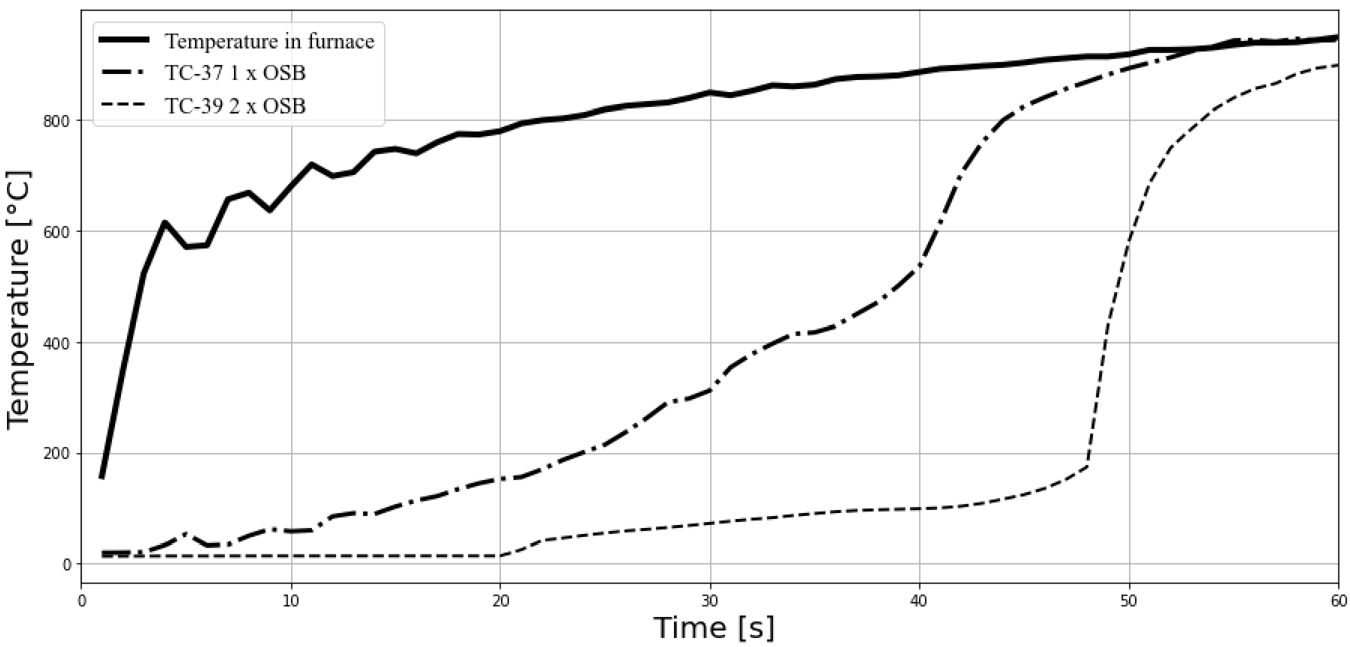

Figure 5. The temperature development in the fire test (members 1 x OSB and 2 x OSB)

The temperatures measured in the experiment are shown in Fig. 5. The failure of the OSB cladding occurred more slowly after 40 min than the failure of the samples loaded mechanically [11, 12], where the completely charred OSB cladding remained on the surface of the steel sample. For the 2x OSB sample, the heating was slower. The 2x OSB cladding failed after a 47-min experiment. The failure of the OSB cladding was about 5 min later than for the mechanically loaded samples mentioned in [10, 11]. Following the failure of the OSB cladding, the steel samples were heated as unprotected steel, and their temperature was considerably higher than the temperature of the gas. Photos of the preparation of the experiment and the fire test are shown in Fig. 6.

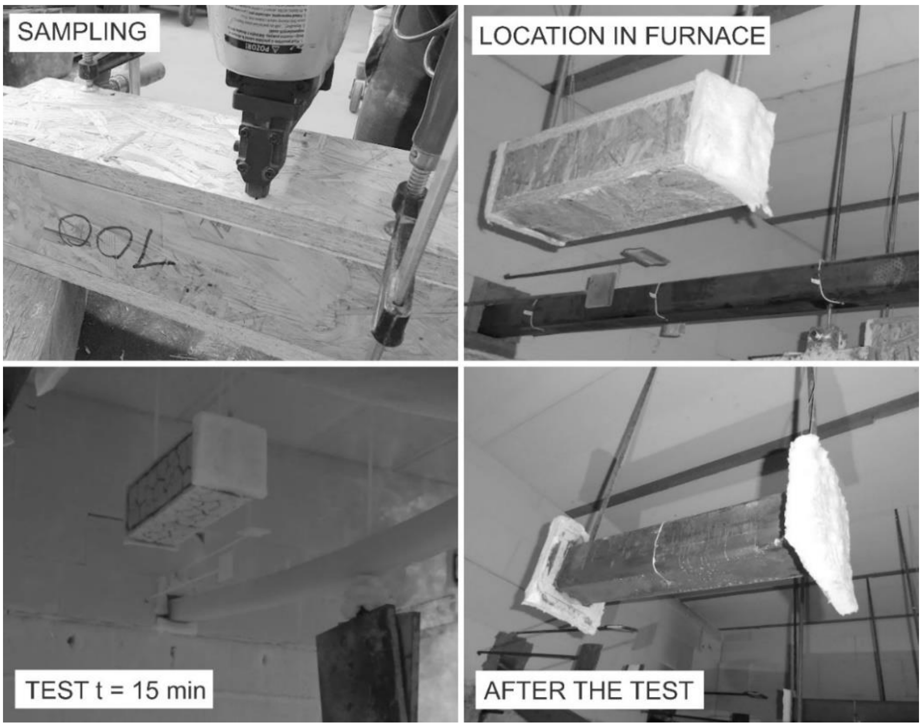

Figure 6. Photos of the fire test

3 NUMERICAL MODEL

The ANSYS mechanical numerical code [15] was used to solve the heat transfer to the protected steel element. The numerical model also determined the development of the charred layer using the isotherm at 300 °C. The dimensions of the steel beam and the OSB layers in the model correspond to the real test dimensions. The material characteristics of the steel were taken from [16], and the material properties of the OSB were taken from [14]. The development of the OSB thermal conductivity has been adjusted in comparison with [14]. The development of the material characteristics of the steel and OSB depending on temperature is shown in Fig. 7. The numerical model created in ANSYS mechanical corresponds with findings that have already been published [9, 17, 18, 19].

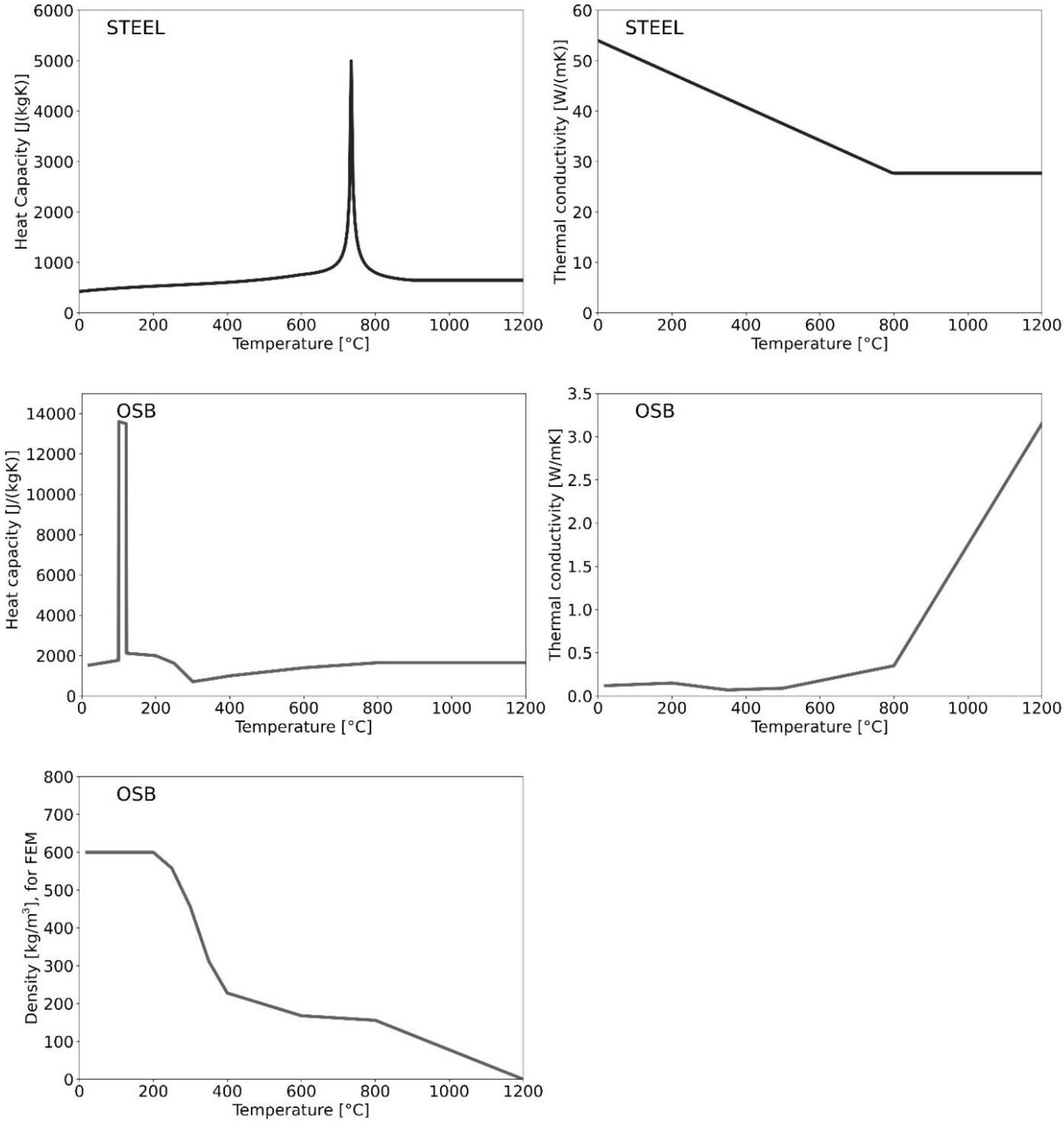

Figure 6. Specific heat, thermal conductivity, and density of steel and OSB

In this model, the previous experience of the authors in numerical modelling of OSB cladding and in small-scale experiments [9] was applied. A hybrid computational mesh was chosen; for each layer, a minimum of 4 elements were chosen for steel across the width with set refinement during the transition between the layers, and the tetrahedral element was used. Different ways of creating MESH (meshing) were compared. The comparison tracked the accuracy of the calculation depending on the computation time and the relevance to the experimental data. The final MESH was selected by MESH No. 4. A comparison of the four MESH models is shown in Tab. 1.

Table 1. Development of the MESH numerical model

	No.1	No.2	No.3	No.4
Nodes	42861	2269313	50772	41946889
Elements	7410	489949	25130	30111563
Type of MESH	hexagonal	hexagonal	tetrahedrons	hybrid-tetrahedrons
Calculation time	1 day	17 days	3 days	23 days

The temperature load was chosen in a combination of convection and radiation. The convection factor was 25 kW/m^2, and the surface emissivity of the OSB cladding was 0.93. The emissivity was chosen according to [21]. The temperature load was used according to the temperatures in the furnace during the experiment. Figs. 7 and 8 show the calculated temperatures of the FE model in comparison with the experiments. The FE model showed the correct temperature development in accordance with the experiments. The difference in the results is due to the input data, the development of the OSB density according to temperature. This development is not yet adequately described. Further FE models could be made by introducing a pyrolysis model. The second difference in temperature development occurs when the OSB cladding fails. The FE model assumes a permanent OSB function, where at the end of the simulations the influence of the insulation properties of the char layer and the low density of the char layer is shown.

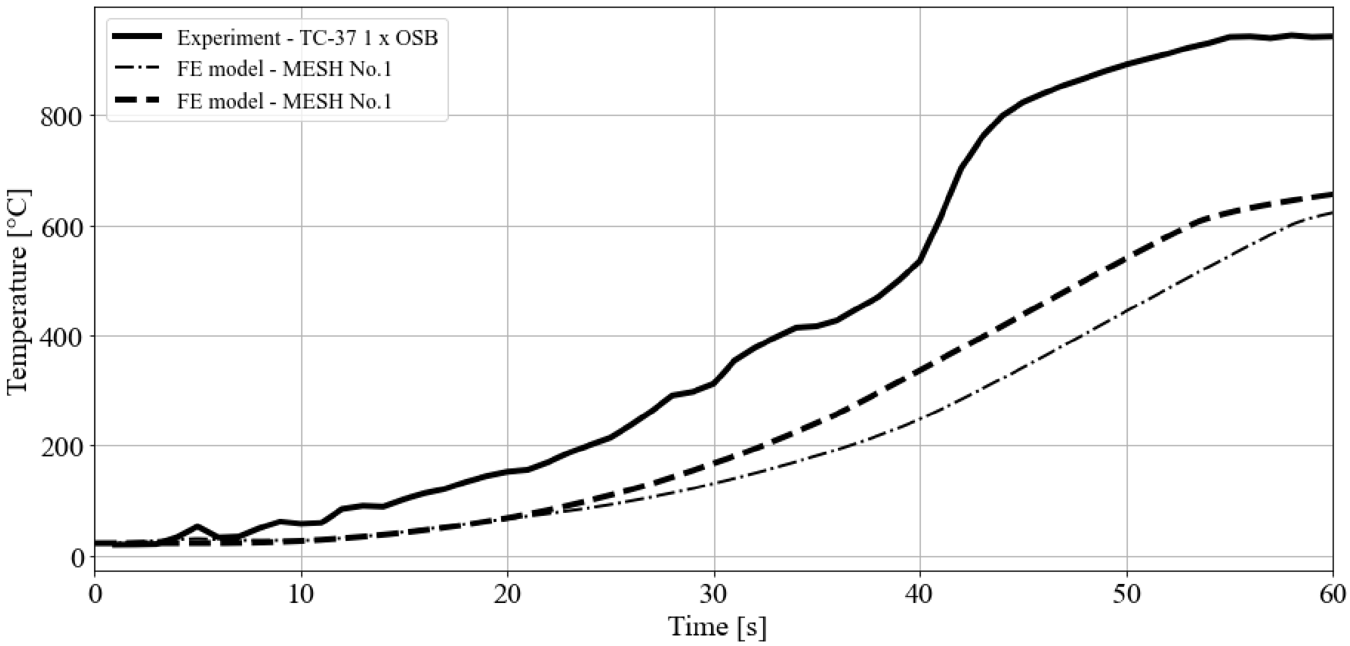

Figure 7. A comparison between the temperatures calculated by the FE model in sample 1 x OSB and the temperatures measured during the experiment

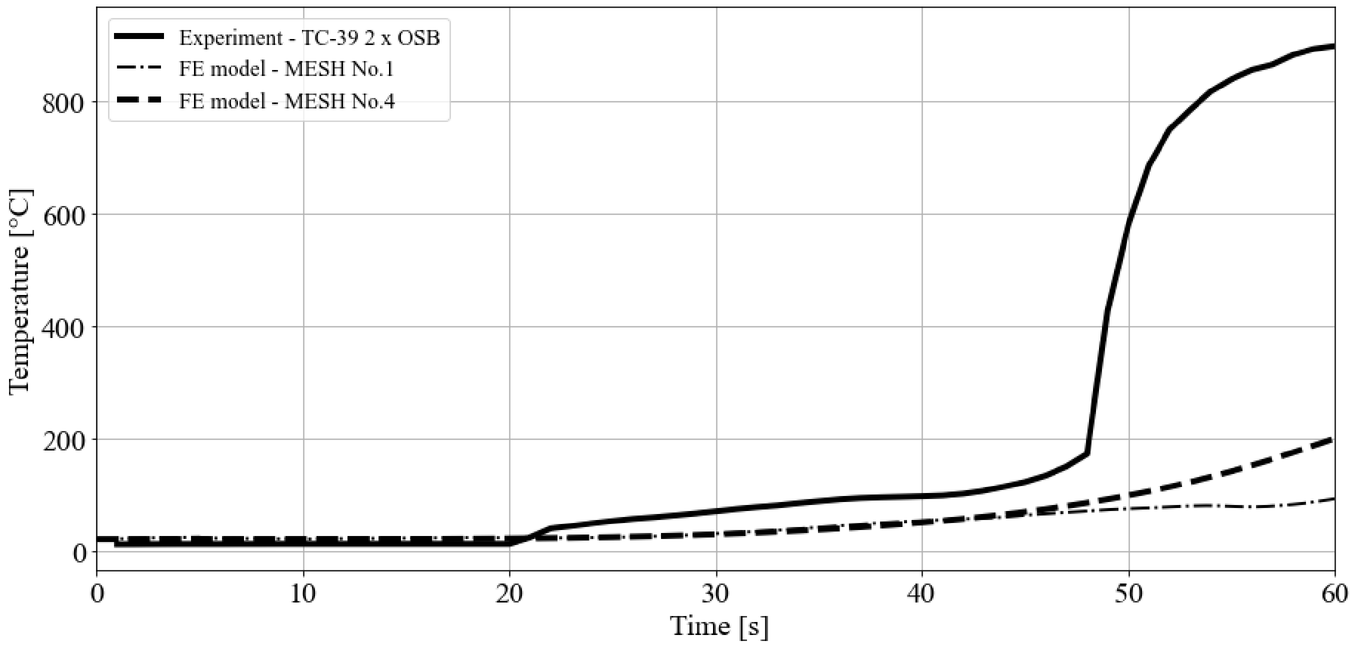

Figure 8. A comparison between the temperatures calculated by the FE model in sample 2 x OSB and the temperatures measured during the experiment

4 CONCLUSIONS

This article has presented the temperature analysis of a steel element protected by an OSB cladding. The samples were not mechanically loaded, so the OSB cladding performed its function for a longer time. Samples 1x OSB and 2x OSB were placed in a horizontal furnace with the same conditions as the mechanically loaded samples. It was therefore possible to compare the behaviour of both types of beams during the fire test. Based on the experiment, FE models were created for a temperature analysis of the heat transfer to the steel beam. The temperatures determined using the FE model were compared with the temperatures measured in the experiment. The findings presented here will lead to a description of the increase in fire resistance of steel structures with an OSB cladding.

The conclusions of the thesis can be summarized as follows:

- Mechanically unloaded samples showed slower heat transfer to the samples. The OSB cladding did not fail due to the mechanical load and remained on the steel until completely burned.
- After the OSB cladding failed, the steel sample was rapidly heated to a temperature close to the gas temperature in the horizontal furnace.
- In the numerical model, a calculated data deviation occurred due to inaccurate input data, where the development of the density of the OSB cladding takes place differently from the standard procedure.
- For the refined FE model, the OSB cladding failures include explicit analyses.
- Connecting the OSB cladding with pneumatic clips confirmed that they were the correct choice; the clips did not significantly contribute heat transfer to the samples.
- Despite the need to refine the development of the density of the OSB cladding for modelling, the FE model can be considered validated.

ACKNOWLEDGMENT

This research was funded by Czech Science Foundation grant 301-3012107A134 “Charring of timber under fully developed natural fire – stochastic modelling”, and the sensitive analysis of the FE models was funded by Student Grant Competition of CTU grant SGS22/144/OHK1/3T/11 “Safety and sustainability of timber and steel structures exposed to fire”.

REFERENCES

1. Hájek, P., Fiala, C.; Kynčlová, M., Life cycle assessments of concrete structures–a step towards environmental savings. Structural Concrete, 2011, 12.1: 13-22. doi: 10.1002/suco.201000026
2. Rinta-Paavola, A., Hostika, S., A model for the pyrolysis of two Nordic structural timbers Fire and materials, 46.1: 55-68., 2021, doi: 10.1002/fam.2947.
3. Wang, X., Fleischmann, Ch. M., Spearpoint, M. J., Parameterising study of tunnel experiment materials for application to the Fire Dynamics Simulator pyrolysis model. Journal of Fire Sciences. 2016, 34(6), 490-514. ISSN 0734-9041. doi:10.1177/0734904116667738.
4. Ira, J., Hasalová, L., Šálek, V., Jahoda, M., Vystrčil, V. Thermal Analysis and Cone Calorimeter Study of Engineered Wood, with an Emphasis on Fire Modelling. Fire Technology, 56(3), 1099-1132, 2020. https://doi.org/10.1007/s10694-019-00922-9
5. Nakrani, D., Wani, T., Srivastava, A. G. Simulation of pyrolysis and combustion of pine wood using two-step reaction scheme. 2020. https://doi.org/10.14264/b582970
6. Twilt L., Witteveen J. (1974) The fire resistance of wood-clad steel columns. Fire Prevention Science and Technology, No. 11, 14-20.
7. Béreyziat, A., Audebert, M., Durif, S., Bouchaïr, A., Si Larbi, A., Dhima, D. (2020). Fire Protection of Steel Beams by Timber: Thermomechanical Analysis, 397-403. https:\/\/doi.org\/10.1007\/978-3-030-41235-7_58
8. Bihina, G., Durif, S., Bouchaïr, A., Saulnier, V., Zhao, B. (2021). Timber encasement of steel structures as an alternative fire insulation. Ce\/papers, 4(2-4), 1289-1296. https://doi.org/10.1002/cepa.1423
9. Šejna, J., Wald, F. Small Furnace Experiments for Wood Burning Pyrolysis Models. Civil Engineering Research Journal, 12, 3, id. 555838. DOI: 10.19080/CERJ.2021.12.555838.
10. Šulc, S., et al. Steel elements with timber fire protection - experiment and numerical analysis, Acta Polytechnica CTU Proceedings, 2022, DOI: 10.14311/APP.2022.34.0116
11. Šejna, J., Šulc, S., Cábová, K., Wald, F. Mechanical analysis of steel beam protected by OSB, In: ENGINEERING MECHANICS 2022. Prague: Institute of Theoretical and Applied Mechanics, AS CR, 2022. p. 365-368, 2022. ISSN 1805-8256. ISBN 978-80-86246-51-2. https://doi.org/ 10.21495/51-2-36
12. Cábová, K., Lišková, N., Novotná, P., Benýšek, M., Zeman, F., Wald, F. (2017). Modelling of standard fire test. Engineering Mechanics, Proceedings Vol. 23 ENGINEERING MECHANICS 2017, 226-229. ISSN 1805-8256.
13. Fahrni, R., et al. Correct temperature measurements in fire exposed wood. In: Proceedings of the 2018 World Conference on Timber Engineering. World Conference on Timber Engineering (WCTE), 2018. https://doi.org/10.3929/ethz-b-000289850
14. EN 1995-1-2 (Eurocode 5): Design of timber structures, Part 1-2: General – Structural fire design, CEN, Brussel, 2010.
15. T. Stolarski, Y. Nakasone and S. Yoshmito “Engineering analysis with ANSYS software.” Butterworth-Heinemann, 2018.
16. G. Li, and P. Wang, “Properties of steel at elevated temperatures” In Advanced Analysis and Design for Fire Safety of Steel Structures. Springer, Berlin, Heidelberg, pp. 37-65. DOI: 10.1007/978-3-642-34393-3_3.
17. Špilák, D.; Majlingová, A.; Kačíková, D.; Tischler, P. Determining the Charred Layer of Wooden Beams with Finite Element Analysis Based on Enthalpy Approach. *Buildings* 2022, *12*, 875. https://doi.org/10.3390/buildings12070875

18. Pierin, I.; Silva, V.P.; La Rovere, H.L. Thermal analysis of two-dimensional structures in fire. Rev. Ibracon De Estrut. Mater. 2015, 8, 25–36. https://doi.org/10.1590/S1983-41952015000100005
19. Martínez-Martínez, J.E.; Alonso-Martínez, M.; Rabanal, F.P.; Díaz, J.J.D.C. Study of the influence of heat transfer of a CLT beam through FEM. In Journal of Physics: Conference Series; IOP Publishing: Bristol, UK, 2018; Volume 1107, p. 032003. doi :10.1088/1742-6596/1107/3/032003
20. Blesak, L., Caldová, E., Wald, F, Unprotected timber-fibre reinforced concrete slab in fire. Wood Research, 2015, 60.4: 605-615.

FIRES FOLLOWING EARTHQUAKE FRAGILITY FUNCTIONS OF STEEL BRACED FRAMES

Patrick Covi[1], Nicola Tondini[2], Amir Sarreshtehdari[3], Negar Elhami-Khorasani[4]

ABSTRACT

The paper describes the outcomes of the analysis of a steel braced frame subjected to fires following earthquake (FFE). Nonlinear time-history analyses were performed in order to evaluate the seismic response. Then, based on the damage suffered by the structure, which was estimated according to the inter-storey drift ratio (IDR) and floor acceleration, the post-earthquake fire ignitions within selected compartments were considered. Natural fire curves were determined by means of zone models. Thus, compartmentation and opening characteristics were included in the analysis. Finally, thermomechanical analyses were run and failure criteria based on the column and beam displacement and rate of displacement were applied. The results of the probabilistic analyses were used to produce fragility functions to evaluate the probability of exceeding a limit state conditioned on an intensity measure in the context of FFE.

Keywords: Fire following earthquake; fragility functions; concentrically braced steel frames; probabilistic framework.

1 INTRODUCTION

The engineering design practice typically analyzes seismic and fire events independently. However, several historical events show that the consequences associated with fire following an earthquake (FFE) event can be significantly higher compared to the damages and losses caused by only the seismic event [1-2]. The 1906 San Francisco earthquake was one of the most significant FFE scenarios, in which fires destroyed around 80% of the city. Other major FFE events that occurred in the past include the Tokyo earthquake (1923), the Kobe earthquake (1995) and the Tohoku earthquake (2011).

Post-earthquake ignition sources identified from past earthquakes are reviewed by Botting (1998) [3]. Also, Scawthorn (1992) [4] discusses ignition sources and predicts post-earthquake ignition rates for typical buildings for different earthquake intensities. In brief, the principal ignition sources are overturning of electrical appliances, short-circuiting of electrical equipment, gas leakage from damaged equipment and pipework, and leakage of flammable fluids. Damaged gas equipment and pipes may cause spark and hold fuel to propagate the fire while electrical household appliances may initiate spark with interior furnishings and other flammable materials. Another major concern is the high potential for ignition as electricity and gas supplies are restored some time after the earthquake. Leaking gas and damaged electrical appliances were identified as initiating fires in the days following the Kobe and Northridge earthquakes. An earthquake can lead to single or multiple ignitions in a building. In this context, the structural fire performance could be deteriorated because the fire acts on a previously damaged structure. The earthquake

[1] Postdoctoral Researcher, Department of Civil, Environmental and Mechanical Engineering, University of Trento (Italy)
e-mail: patrick.covi@unitn.it, ORCID: https://orcid.org/0000-0002-0570-4061
[2] Associate Professor, Department of Civil, Environmental and Mechanical Engineering, University of Trento (Italy)
e-mail: nicola.tondini@unitn.it, ORCID: https://orcid.org/0000-0003-2602-6121
[3] PhD Candidate, Department of Civil, Structural and Environmental Engineering, University at Buffalo (USA)
e-mail: amirsarr@buffalo.edu, ORCID: https://orcid.org/0000-0001-5630-2751
[4] Associate Professor, Department of Civil, Structural and Environmental Engineering, University at Buffalo (USA)
e-mail: negarkho@buffalo.edu, ORCID: https://orcid.org/0000-0003-3228-0097
https://doi.org/10.6084/m9.figshare.22178273

may damage fire protection elements and the compartment measures with the consequence that the fire can spread more rapidly. Moreover, it is harder to control post-earthquake fires as there can be multiple ignitions across a community at once as well as possible disruptions within the infrastructure networks, such as water supply system, that hinder timely intervention [1].

2 FFE FRAMEWORK

The major steps for implementing the FFE probabilistic framework [5] are illustrated in Figure 1. The process is followed to perform probabilistic FFE analyses and to obtain sufficient data to build fragility curves and surfaces. The framework is developed and implemented using a combination of different software, i.e. OpenSees [6,7], Ozone [8], and MATLAB [10]. The seismic analyses and the FFE structural analyses were performed in OpenSees. The zone model software Ozone [8] was used for the fire development analyses, whereas a specific code developed in MATLAB was exploited for the heat transfer analyses.

The geometry of the structural system, cross section sizes, material properties, and applied loads are first defined in a Tcl script. Probabilistic parameters required for the analysis, such as compartment properties, are next generated. Once all the inputs and random variables are defined, the gravity and seismic analyses are performed. Then, OpenSees enters a "standby mode" and a background MATLAB process executes the FFE decision algorithm to automatically generate fire scenarios based on the seismic analysis results, in which the temperature of the hot gases in the compartments is computed using Ozone. Heat transfer is then conducted in MATLAB, followed by the structural analysis at elevated temperatures in OpenSees. Finally, the generated results are used to construct the fragility functions.

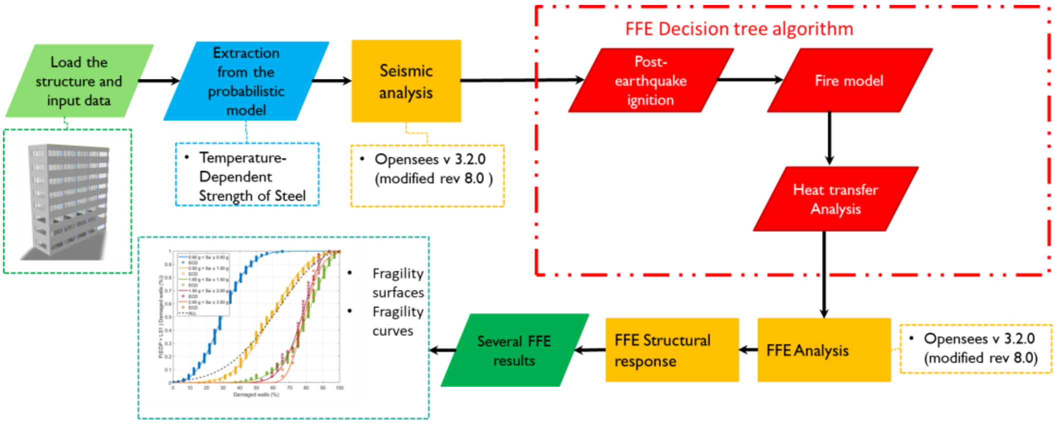

Figure 1. Major steps in the implemented FFE framework

The status of a compartment after an earthquake is based on the combined conditions of the glazing, partition walls, and doors and it is quantified using the fragility functions provided in FEMA P58 [9] background documentation.

The framework determines the possible damage of each compartment (glazing and wall damages) and generates the fire scenario based on the earthquake using the following three thresholds:

- The peak floor acceleration (PFA) of at least one floor must be greater than or equal to 0.7 g, this value corresponds to the 100% probability of exceeding breakage in gas pipe joints according to the fragility curves reported in Ueno et al., (2004) [11].
- The inter-story drift ratio (IDR) of the same floor must be greater than or equal to 1.0 %. This ignition criterion considers the possibility of having some damage to the electric cables that can be characterized as a function of the IDR. According to the FEMA P-356 (2000) [12], the requirements for life safety and collapse prevention performance levels for a steel braced frame structure are 0.5% and 2%, respectively. Therefore, the ignition criterion for a steel braced frame was assumed as 1% IDR, a value in between the two thresholds.

- The maximum IDR must remain below 6%. An IDR equal to 6% was chosen as the threshold for collapse, which is three times the recommended collapse limit state value for a braced steel frame (i.e., 2% IDR) in FEMA P-356 [12]. Extensive yielding, buckling of braces, and connection failure, are expected during the earthquake without the subsequent FFE event.

The yield strength of steel f_y at ambient (seismic analysis) and high temperatures (fire analysis) was modelled as a random variable using a continuous logistic function [13,14] (see Equation 1).

$$k_{y,2\%,T}=\frac{1.7\times\exp\left[\mathrm{logit}\left(\hat{k}^{*}_{y,2\%,T}\right)+0.412\text{-}0.81\times10^{-3}\times T+0.58\times10^{-6}\times T^{1.9}+0.43\times\varepsilon\right]}{\exp\left[\mathrm{logit}\left(\hat{k}^{*}_{y,2\%,T}\right)+0.412\text{-}0.81\times10^{-3}\times T+0.58\times10^{-6}\times T^{1.9}+0.43\times\varepsilon\right]+1} \tag{1}$$

where $\mathrm{logit}\left(\hat{k}^{*}_{y,2\%,T}\right)=\ln\left(\frac{\hat{k}^{*}_{y,2\%,T}}{1\text{-}\hat{k}^{*}_{y,2\%,T}}\right)$, $\hat{k}^{*}_{y,2\%,T}=\frac{\hat{k}_{y,2\%,T}+10^{-6}}{1.7}$, and $\hat{k}_{y,2\%,T}$ is the temperature-specific retention factor as prescribed by EN1993-1-2 [20].

A custom material class, i.e., SteelFFEThermal, was developed for nonlinear FFE analyses in OpenSees. The SteelFFEThermal material has the same definition as the Giuffrè-Menegotto-Pinto uniaxial steel stress-strain model at ambient temperature. However, when the temperature is applied, the material class switches the constitutive law to the stress-strain constitutive law for steel at elevated temperature as for EN 1993-1-2 [22]. For a detailed description of how the FFE probabilistic framework was developed, the reader is referred to the thesis of Covi [5].

3 CASE STUDY

An eight-story three-bay steel frame with concentric bracings in two central bays was selected as a case study, as illustrated in Figure 2. The structure is an office building designed and presented in NIST Technical Note 1863-2 [15]. It is designed according to the ASCE 7-10 [16] recommendations for an area with high seismicity of the West coast of the United States; in particular, the city of Los Angeles was chosen for the case study location.

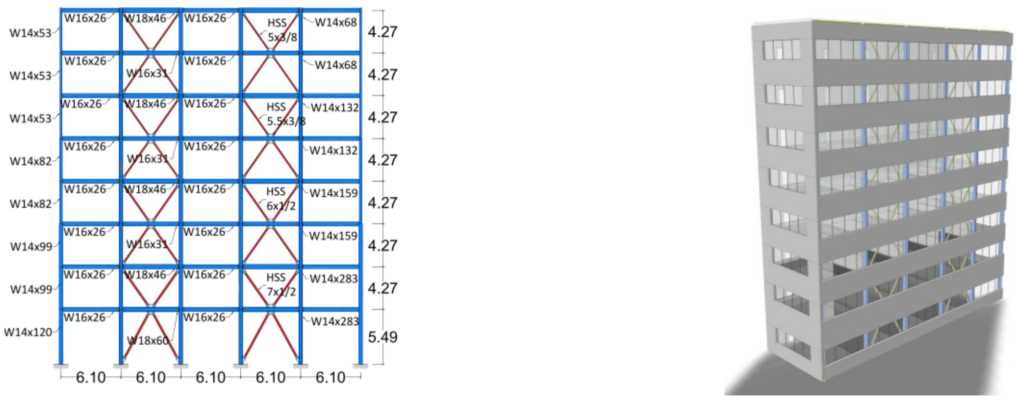

(a) (b)

Figure 2. (a) Configuration of the frame (length in meters); (b) rendering of the building.

The building has a rectangular plan of 46.33 m in the E-W direction, including five 9.14 m bays, and 31.01 m in the N-S direction, including five 6.10 m bays. The story height is 4.28 m with the exception of the first floor, which is 5.49 m high. The width of the windows for the structure was varied from 1.5 to 6 m (5 to 20 ft) with 1.5 m (5 ft) intervals.

3.1 Ground motions

In order to perform non-linear time-history analyses, it was fundamental to model the seismic hazard through adequate selection and scaling of ground motion records. In this respect, a set of 14 accelerograms for the collapse limit state was selected from the FEMA P-695 dataset [17,18] considering the type of spectrum, magnitude range, distance range, style-of-faulting, local site conditions, period range, and ground motion components using the PEER Ground Motion Database [19]. Table 1 summarizes the 14 strong motion records used for the N-S direction in the FFE analyses, including the magnitude and peak ground acceleration and the same ID numbering given in FEMA P-695 [17].

Accelerograms were modified to match the target spectrum in the period range of 0.3 to 2.25s that includes the fundamental period of the structure equal to 1.5 s. Figure 8 illustrates the set of acceleration response spectra, original and scaled, and the scaled average response spectrum. The accelerograms were used to perform the FFE probabilistic analysis and 6 scale factors were applied to the accelerograms: 0.50; 0.75; 1.00; 1.25; 1.50; 1.75.

Table 1. Accelerogram set.

ID	Event name	Station	Year	Mw	PGA (g)
1	Northridge, USA	Beverly Hills - Mulhol	1994	6.7	0.52
2	Northridge, USA	Canyon Country-WLC	1994	6.7	0.48
3	Duzce, Turkey	Bolu	1999	7.1	0.82
5	Imperial Valley, USA	Delta	1979	6.5	0.35
6	Imperial Valley, USA	El Centro Array #11	1979	6.5	0.38
8	Kobe, Japan	Shin-Osaka	1995	6.9	0.24
9	Kocaeli, Turkey	Duzce	1999	7.5	0.36
10	Kocaeli, Turkey	Arcelik	1999	7.5	0.22
11	Landers, USA	Yermo Fire Station	1992	7.3	0.24
14	Loma Prieta, USA	Gilroy Array #3	1989	6.9	0.56
16	Superstition Hills, USA	El Centro Imp. Co.	1987	6.5	0.36
17	Superstition Hills, USA	Poe Road (temp)	1987	6.5	0.45
18	Cape Mendocino, USA	Rio Dell Overpass	1992	7	0.55
19	Chi-Chi, Taiwan	CHY101	1999	7.6	0.44

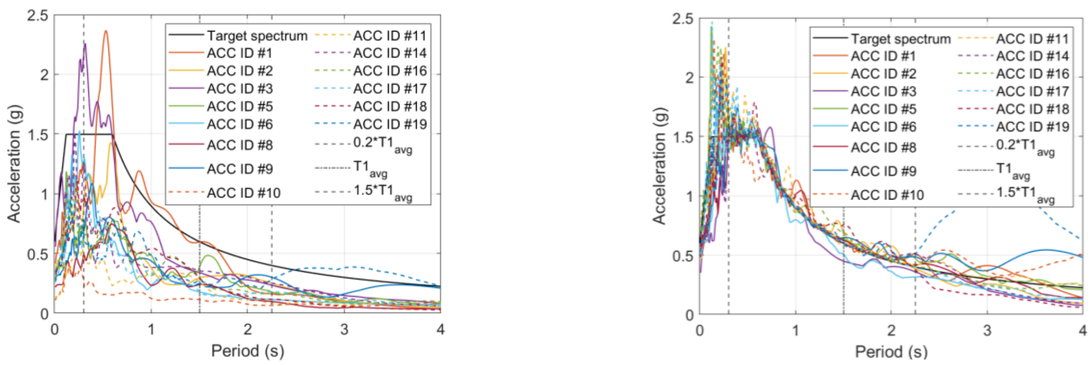

(a) (b)

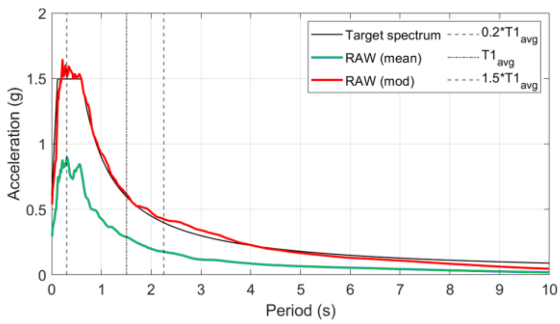

(c)

Figure 3. Acceleration Response Spectra: (a) original, (b) scaled, (c) scaled average spectrum.

3.2 Fire loads

Based on a discrete sampling uniform distribution, five values of fire load density were selected: i.e., 300 MJ/m^2; 600 MJ/m^2; 900 MJ/m^2; 1200 MJ/m^2; 1500 MJ/m^2. In the EN 1991-1-2 [20], an 80% fractile value of fire load density for office occupancies corresponds to 511 MJ/m^2 according to the Gumbel distribution. According to a recent survey conducted in the US, the measured total fire load density, including moveable and fixed content, had a mean value of 1486 MJ/m^2 [21]. For this reason, fire load density values up to 1500 MJ/m^2 were used and fire load density less than 300 MJ/m^2 was considered too low.

3.3 Finite element model

The frame was modelled with non-linear beam elements based on corotational formulation and the uniaxial SteelFFEThermal material was used for the braces, beams and columns. Geometric imperfections were included to allow for flexural buckling according to EN 1993-1-1 [23]. Masses were considered lumped at the floors, following the assumption of rigid diaphragms. Each column was discretized with four elements, while beam and brace elements were discretized using eight elements to get adequate precision in the calculation of displacements, stresses, and strains in sections of each member. Fiber sections were selected to define the cross section of the elements.

4 PROBABILISTIC ANALYSIS RESULTS

4.1 Earthquake simulation

For brevity, one sample simulation is selected as an example to demonstrate the methodology used for the FFE analyses. The selected seismic action is shown in Figure 12. The earthquake, known as the Landers earthquake, occurred at 4:57 am, June 28, 1992 with a magnitude of 7.3.

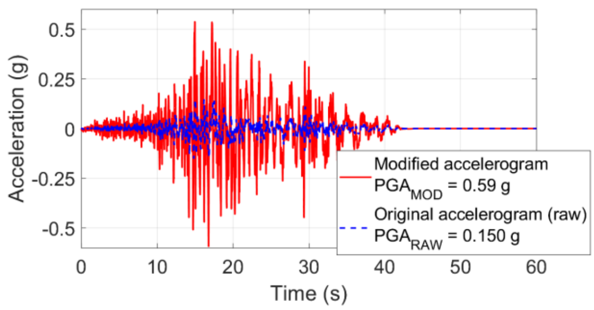

Figure 4. Comparison between the original and modified accelerogram for the FFE simulation.

Figure 5 illustrates the results of the numerical simulation of the non-linear dynamic analysis for the selected acceleration time-history. The energy dissipation was concentrated in the braces. All the columns and beams remained elastic during the seismic event.

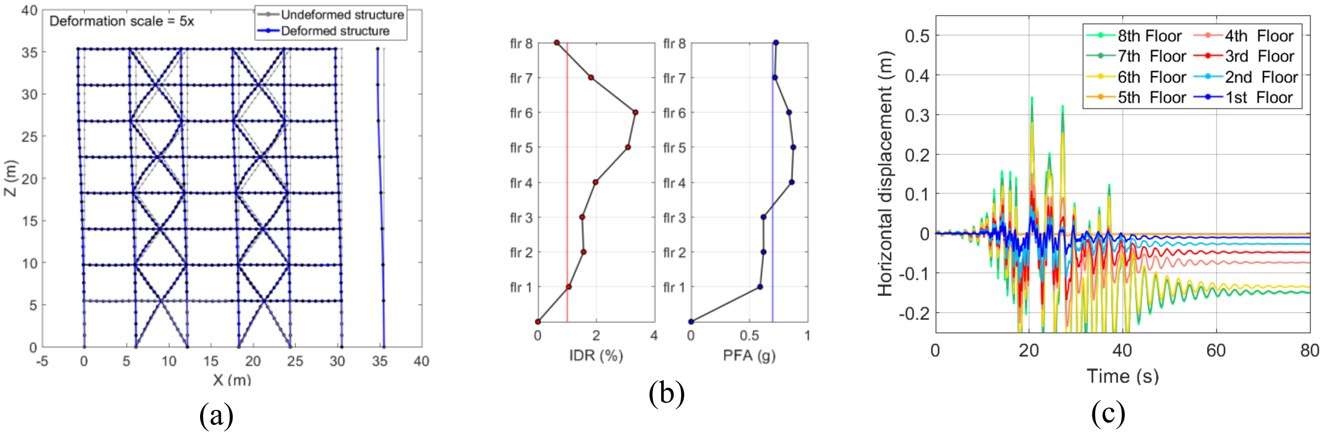

Figure 5. (a) Deformed shape at the end of the seismic event (amplified by a factor of 5); (b) maximum inter-story drift (IDR) and maximum peak floor acceleration (PFA); (c) horizontal displacement of the floors.

4.2 Post-earthquake fire simulation

The probabilistic FFE framework was used to automatically determine the possible damage to each compartment (glazing and wall damages) and generate the fire scenario based on the IDR and PFA thresholds. The framework includes the possibility to have the ignition in more than one compartment, due to multiple damage to the gas or electrical services or appliances in more than one location. For this reason, the framework could select more than one ignition after the earthquake. The flashover time is set as the threshold for the vertical spread between two exterior compartments. In the direction of the horizontal compartment, a delay time for the horizontal fire spreads of 30 minutes or 15 minutes was taken, depending on whether or not the partition remains intact after the earthquake event.

Figure 6a shows the evolution of the fire for the selected FFE scenario, Figure 6b illustrates the time-temperature curves for each compartment at 4th floor, while Figure 6c shows a qualitative representation of the compartment locations and dimensions for the selected case study.

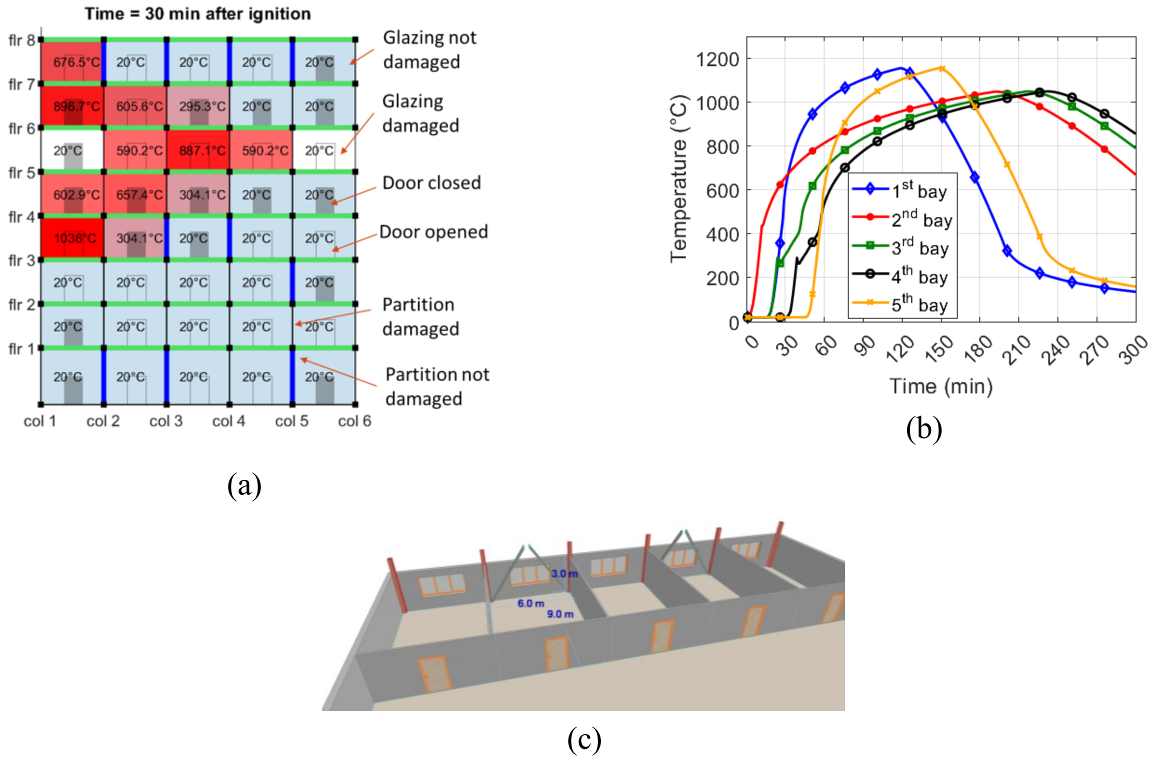

Figure 6. (a) Fire spread within the building after 30 minutes; (b) Time-temperature curve of fire for floor 4; (c) inside view of a compartment.

The time-temperature curve and characteristics of the fire behaviour in the compartments were quantified using Ozone. The heat transfer analysis was automatically performed to obtain steel temperatures for each element in the compartment subjected to fire using the probabilistic FFE framework.

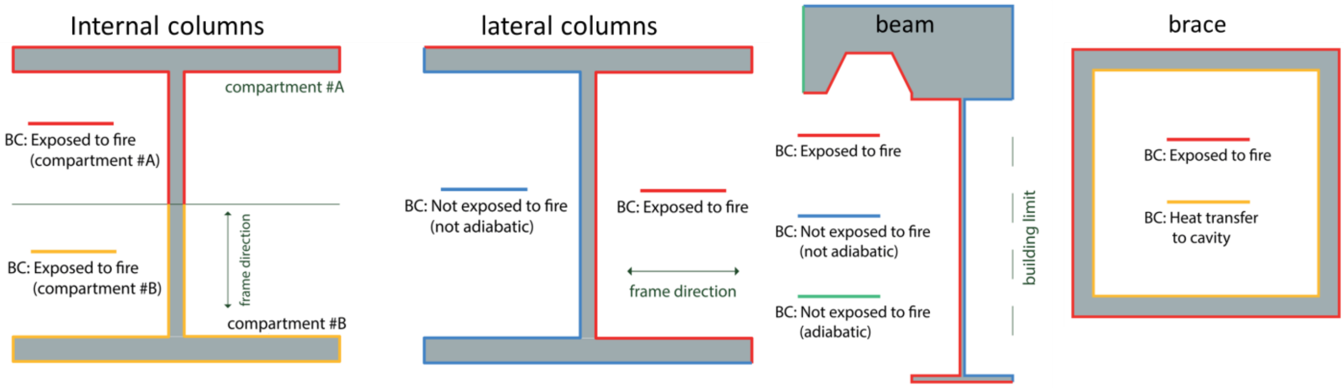

Figure 7: Boundary conditions for thermal analysis.

The FFE structural analysis followed the heat transfer analysis for the selected scenario. Structural partial collapse occurred 30 minutes after the start of the fire due to the excessive rate of vertical deflection in the beams located on the 4th and 7th floors and in the 1st bay, as illustrated in Figure 8a.

Figure 8b shows the final deformed configuration of the steel frame at the end of the simulation. In particular, despite the low utilization factor of the columns, the loss of transverse restraint owing to the beam failure caused an increase in the column effective length that eventually led to column buckling and the collapse of a portion of the building.

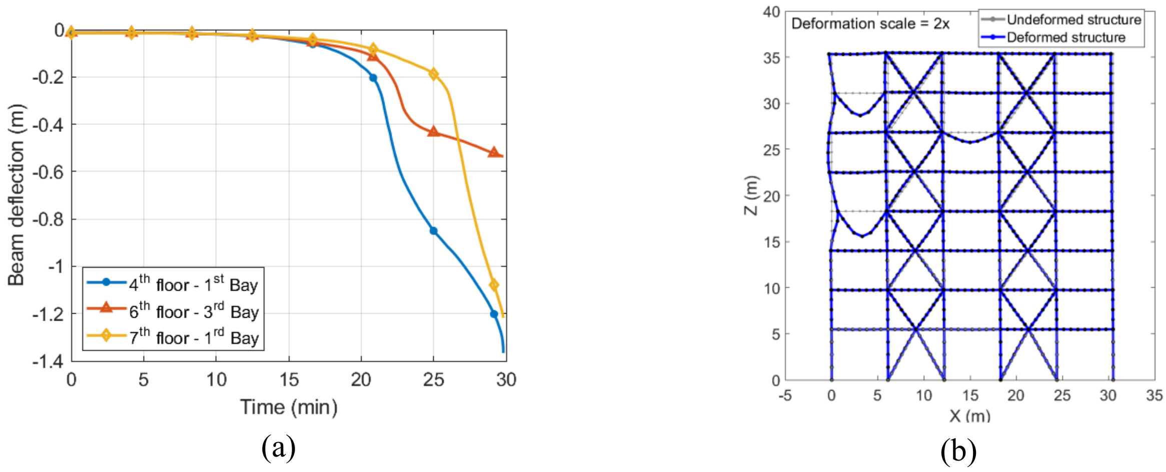

Figure 8. (a) Beams deflection (b) Deformed shape after 30 minutes (collapse).

4.3 Results

A total of 1680 simulations were performed for 14 accelerograms scaled at 6 different intensity values, 4 different values of window width, and 5 different fire load densities, as listed in Table 2. The Latin Hypercube Sampling (LHS) [30] was used to randomly generate the variable ε for steel retention factor $k_{y,2\%,T}$, which was needed to calculate the yield strength at ambient and high-temperatures for each simulation using Equation 1.

Table 2. Analysis parameters.

Parameter	**Values**
Accelerograms	14 accelerograms

Acceleration scale factor	0.50 0.75 1.00 1.25 1.50 1.75
Window width (m)	1.5 3.0 4.5 6.0
Fire load density (MJ/m^2)	300 600 900 1200 1500

Among the 1680 simulations, 1123 analyses did lead to an FFE event because either the PFA and IDR satisfied the three thresholds for an ignition to occur, as explained in the previous section. It is also worth noting that about 500 simulations did not lead to an FFE event because either the ground motion was not strong enough to ignite a fire in a compartment or the ground motion was too strong that caused the collapse of the structure owing to the seismic action. Finally, 43 of 1680 analyses were discarded because they were interrupted due to numerical problems in an early stage of the FFE simulation.

Figure 9a shows the number of ignitions as a function of the maximum Sa at the first period of the structure. It can be observed that for larger values of Sa the number of ignitions is higher. Figure 9b shows the number of ignitions as a function of the percentage of damaged walls and windows after the earthquake event.

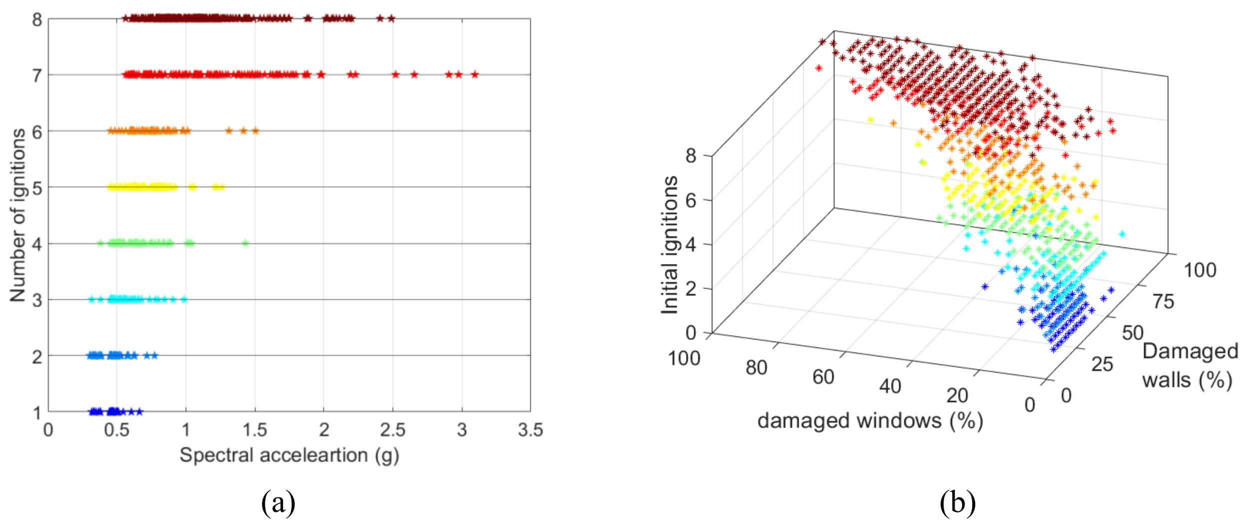

Figure 9. (a) Number of ignitions vs Sa; (b) Number of ignitions vs damaged windows and walls.

4.4 Fragility functions

Based on the results of the FFE simulations, FFE fragility functions were developed in this section. A fragility function expresses the probability *P* of a given engineering demand parameter (EDP), such as IDR exceeding a certain limit state (LS) conditioned on an intensity measure (IM), such as peak ground acceleration or fire load density. Fragility functions are often expressed in terms of a lognormal cumulative distribution and have the form of Equation. 2.

$$P(EDP > LS|IM = x) = \emptyset\left(\frac{\ln\left(\frac{x}{\hat{\theta}}\right)}{\beta}\right) \qquad (2)$$

where ∅ is the standard normal cumulative distribution function (CDF), θ is the median of the IM and β is the standard deviation of the intensity measure. A typical EDP representing the damage induced by a seismic event is IDR, whereas in the case of an FFE, meaningful EDPs as related to structural fire engineering, such as vertical or horizontal displacements and displacement rates of structural members. A representative IM for an FFE scenario is the time to failure of a structural member that reflects the level of damage induced by the earthquake. Many researchers studied statistical procedures for estimating parameters of fragility functions and characterizing the results of probabilistic models, especially in the seismic domain [24-26] but also in the fire domain [27-29].Although the EDP is commonly assumed to follow a lognormal distribution when conditioned on the IM, several other distributions were considered and compared using the Akaike information criterion (AIC) method [31,32], as illustrated in Figure 10. Equation 3 illustrates the AIC mathematical method, which evaluates and compares different possible statistical models and determines which one fits the data best.

$$AIC = -2 \ln L + 2k \qquad (3)$$

where L and $\ln L$ are respectively the likelihood and the log-likelihood at its maximum point of the estimated model and k is the number of parameters. The use of a second-order corrected AIC (AICc) is recommended when the sample size is small compared to the number of parameters (n/k <40) [33], as shown in Equation 4:

$$AIC_c = AIC + \frac{2k^2 + 2k}{n - k - 1} \qquad (4)$$

where n denotes the sample size. Note that for $n \rightarrow \infty$, $AIC_c = AIC$.

AIC uses a model maximum likelihood estimation (log-likelihood) as a measure of fit and adds a penalty term for models with higher parameter complexity to avoid overfitting. Given a set of candidate models for the data, the preferred model is the one with the minimum AIC value.

The outcome of the comparative analysis probability density function (PDF) and function distributions is illustrated in Figure 10. The results in Figure 10 indicate that compared to other statistical models, the lognormal distribution can serve as a candidate distribution to define the FFE fragility functions. However, the Generalized Extreme Value (GEV) distribution showed the best fit to the data.

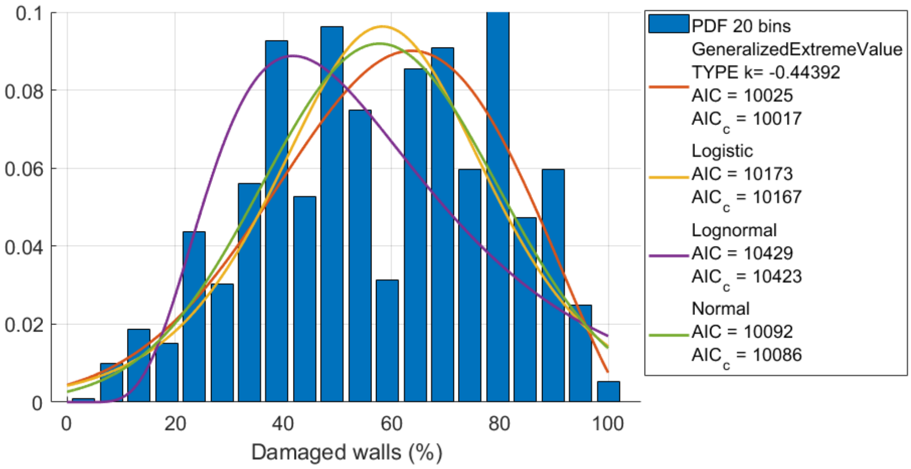

Figure 10. Probability density function (PDF) of the damaged walls and function distributions.

Based on the results of the comparative analysis, the GEV distribution was selected to derive the fragility functions. Not only the distribution provides the best fit, but also can be represented in a simple and closed form function with three parameters. The cumulative probability distribution function for the GEV distribution has the form of Eq 5.

$$P(EDP > LS|IM = x) = \begin{cases} \exp\left\{-\left[1 + k\left(\frac{x-\mu}{\sigma}\right)\right]^{-1/k}\right\} & if\ k \neq 0 \\ \exp\left\{-exp\left[-\left(\frac{x-\mu}{\sigma}\right)\right]\right\} & if\ k = 0 \end{cases} \qquad (5)$$

where σ denotes the scale parameter (statistical dispersion of the probability distribution), μ is the location parameter (shift of the distribution) and k is the shape parameter. The shape parameter k is used to represent three different distribution families (Gumbel distribution, Fréchet distribution, reversed Weibull distribution). The shape value k is always below 0 for the case study analysed in this work (see Table 3). Thus, the GEV Type III was used for the fragility functions. This distribution is equivalent to the reversed Weibull distribution, whose tails are finite, such as the beta distribution.

Table 3. Parameters of the GEV and lognormal distribution for the damaged walls fragility functions and grouped based on S_a

	GEV distribution			Lognormal distribution	
	k	***σ***	***μ***	***σ***	***μ***
0.0 g < Sa ≤ 0.5 g	-0.209	11.89	25.26	0.492	3.306
0.5 g < Sa ≤ 1.0 g	-0.300	16.78	52.93	0.313	4.028
1.0 g < Sa ≤ 1.5 g	-0.535	13.78	75.37	0.183	4.345
1.5 g < Sa ≤ 2.0 g	-0.456	9.903	73.85	0.129	4.327
2.0 g < Sa ≤ 3.5 g	-0.166	7.400	76.03	0.102	4.367

Figure 11a and Figure 11b show the fragility curves for the damaged walls and grouped as a function of the Sa at the first period of the structure, respectively, using the GEV and Lognormal distribution. As expected, the Generalized Extreme Value (GEV) distribution showed a better fit to the data compared to the lognormal distribution.

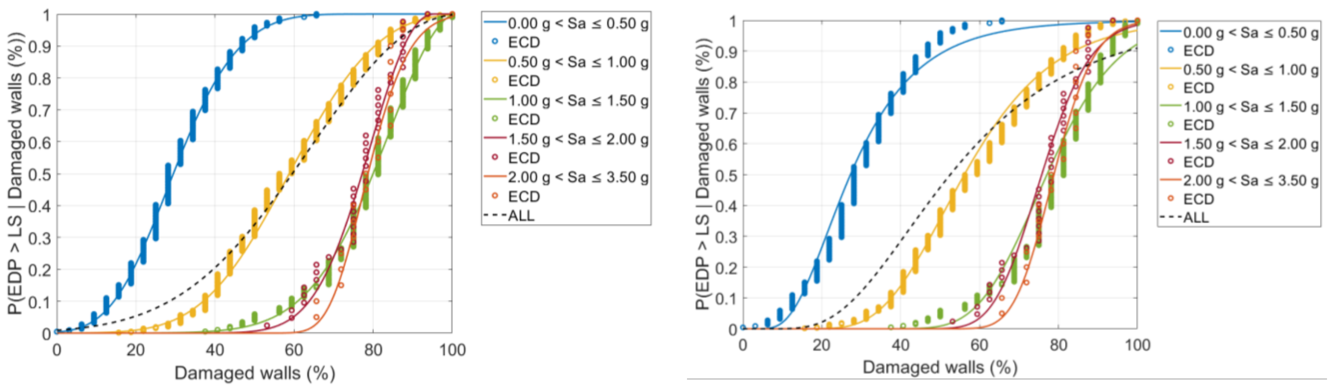

(a) (b)

Figure 11. Empirical cumulative distribution (ECD) and fragility curves for the damaged walls as a function of Sa; (a): GEV distribution (b) Lognormal distribution.

Figure 12 shows the fragility curves for the partial collapse due to fire grouped as a function of the Sa at the first period of the structure.

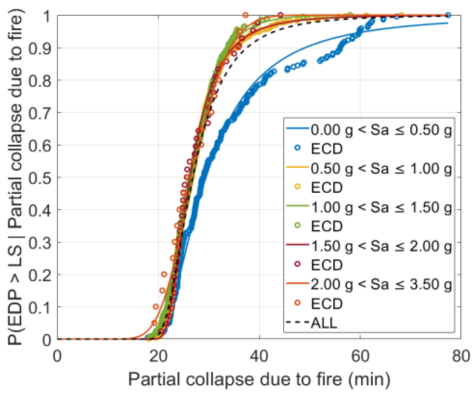

Figure 12. Empirical cumulative distribution (ECD) and fragility curves for the collapse state as a function of Sa

Figure 12 highlights a higher probability of exceedance of reaching partial collapse limit state with shorter times to collapse when the structure is subjected to higher values of spectral acceleration. In fact, at lower Sa values, there is a 90% probability of exceeding the partial collapse limit state in 49 minutes, whereas at higher Sa values, the partial collapse limit state is reached in 33 minutes.

5 CONCLUSIONS

The paper presented a methodology to perform fire following earthquake (FEE) analyses and described the development of a novel probabilistic FFE framework aimed at developing FFE fragility functions of a prototype steel braced frame. A decision tree algorithm was developed to establish the probability of ignition in the compartments within the building after the seismic event. Compartmentation and opening characteristics as well as the potential for fire spread were considered based on seismic damage in windows, doors, and partition walls following seismic fragility functions found in the literature.

The results showed that about 1123 analyses, out of 1680 randomly generated cases, experienced FFE events. The results of the probabilistic analyses were used to produce fragility functions to evaluate the probability of exceeding a damaged state conditioned on an intensity measure in the context of FFE. It was observed a higher probability of exceedance of reaching collapse limit state with shorter times to collapse when the structure is subjected to higher values of spectral acceleration. Moreover, higher values of the spectral acceleration tended to determine higher the number of ignitions. Although this study provided some insights on the performance of unprotected concentrically steel framed buildings subjected to the hazards of earthquake and fire, future research directions can include the study of other type of unprotected and protected steel structure, e.g., other braced frames and moment-resisting frames.

ACKNOWLEDGMENT

The support received from the Italian Ministry of Education, University and Research (MIUR) in the framework of the “Departments of Excellence” (grant L 232/2016) is gratefully acknowledged.

Computational support was provided by the Center for Computational Research at the University at Buffalo [34].

REFERENCES

1. Scawthorn C, Eidinger JM, Schiff AJ. (2005) “Fire following earthquake”. Technical Council on Lifeline Earthquake Engineering Monograph, No. 26. American Society of Civil Engineers
2. Elhami-Khorasani N and Garlock MEM. (2017) “Overview of fire following earthquake: historical events and community responses”, International Journal of Disaster Resilience in the Built Environment.
3. Botting, R. (1998). “The Impact of Post-Earthquake Fire on the Built Urban Environment”. Fire Engineering Research Report 98/1, University of Canterbury, New Zealand.
4. Scawthorn C.R., Khater M. (1992). “Fire follow-ing Earthquake: Conflagration Potential in the in greater Los Angeles, San Francisco, Seattle and Memphis Areas”, EQE International, pre-pared for the National Disaster Coalition, San Francisco, CA (available from the National Committee on Property Insurance, 75 Trem-ont, Suite 510, Boston, MA 02108-3910, (617. 722-0200]).
5. Covi, P. (2021). “Multi-hazard analysis of steel structures subjected to fire following earthquake”, Doctoral dissertation, University of Trento. doi: 10.15168/11572_313383
6. McKenna, F. (2011). “Opensees: a framework for earthquake engineering simulation,”Computing in Science & Engineering, vol. 13, no. 4,pp. 58–66.
7. Elhami-Khorasani, N., Garlock, M. E., and Quiel, S. E. (2015). “Modeling steelstructures in opensees: Enhancements for fire and multi-hazard probabilistic analyses,”Computers & Structures, vol. 157, pp. 218–231.
8. Cadorin, J.F. and Franssen, J.M., (2003). A tool to design steel elements submitted to compartment fires—OZone V2. Part 1: pre-and post-flashover compartment fire model. Fire Safety Journal, 38(5), pp.395-427.
9. Federal Emergency Management Agency (FEMA). (2012). “Next-Generation Methodology for Seismic Performance Assessment of Buildings”. Prepared by the Applied Technology Council for the Federal Emergency Management Agency, Report No. FEMA P-58, Washington, D.C.
10. MATLAB Release 2021b (2021), Natick, Massachusetts: The MathWorks Inc.
11. J. Ueno, S. Takada, Y. Ogawa, M. Matsumoto, S. Fujita, N. Has-sani, and F. S. Ardakani, (2004) “Research and development on fragility of components for the gas distribution system in greater Tehran, Iran,”Conferene Proceed-ings, in Proc. 13th WCEE, Vancouver, BCCanada, Paper, no. 193.

12. FEMA, (2000), “Prestandard and commentary for the seismic rehabilitation of buildings,”
13. Elhami -Khorasani, N., Gardoni, P., and Garlock M., (2015) “Probabilisticfire analysis: material models and evaluation of steel structuralmembers,”Journal of Structural Engineering, vol. 141, no. 12.
14. Qureshi, R., Ni, S., Elhami-Khorasani, N., Van Coile, R., Hopkin, D., and Gernay, T., (2020). “Probabilistic models for temperature-dependentstrength of steel and concrete,”Journal of Structural Engineering,vol. 146, no. 6, p. 04020102.
15. J. L. Harris and M. S. Speicher, (2015), “As-sessment of first generation performance-based seismic design methods for new steel buildings”. volume 2: Special concentrically braced frames .(national institute of standards and technology), NIST TechnicalNote, vol. 2, pp. 1863–2.
16. ASCE 7-10 (2010). “Minimum design loads for buildings and other structures”. American Society of Civil Engineers.[34] ASCE 7-10 (2010). “Minimum design loads for buildings and other structures”. American Society of Civil Engineers.
17. Federal Emergency Management Agency (FEMA) (2008): “FEMA P-695, Quantification of Building Seismic Performance Factors”.
18. Kircher, C., Deierlein, G., Hooper, J., Krawinkler, H., Mahin, S., Shing, B., and Wallace, J., (2010). “Evaluation of the fema p-695 method-ology for quantification of building seismic performance factors,”.
19. PEER 2013/03 “PEER NGA-West2 Database, by: Timothy D. Ancheta, Robert B. Darragh, Jonathan P. Stewart, Emel Seyhan, Walter J. Silva, Brian S.J. Chiou, Katie E. Wooddell, Rob-ert W. Graves, Albert R. Kottke, David M. Boore, Tadahiro Kishida, and Jennifer L. Do-nahue.”
20. CEN (2002): EN 1991-1-2 “Eurocode 1: Actions on structures - Part 1-2: General actions - Actions on structures exposed to fire”.
21. Elhami-Khorasani, N., Salado Castillo, J. G., Saula, E., Josephs, T., Nurlybekova, G., & Gernay, T. (2021). “Application of a digitized fuel load surveying methodology to office buildings”. Fire technology.
22. CEN (2005): EN 1993-1-2 “Eurocode 3: Design of steel structures - Part 1-2: General rules - Structural fire design”.
23. CEN (2005): EN 1993-1-1 “Eurocode 3: Design of steel structures - Part 1-1: General rules and rules for buildings”.
24. Baker, J. W. (2015). “Efficient analytical fragility function fitting using dynamic structural analysis”. Earthquake Spectra, 31(1), 579-599.
25. Calvi, G. M., Pinho, R., Magenes, G., Bommer, J. J., Restrepo-Vélez, L. F., and Crowley, H., (2006). “Development of seismic vulnerability assessment methodologies over the past 30 years”, ISET Journal of Earthquake Technology 43, 75–104.
26. Tondini, N., Zanon, G., Pucinotti, R., Di Filippo, R., & Bursi, O. S. (2018). “Seismic performance and fragility functions of a 3D steel-concrete composite structure made of high-strength steel”. Engineering Structures, 174, 373-383.
27. Lange, D., Devaney, S., & Usmani, A. (2014). “An application of the PEER performance based earthquake engineering framework to structures in fire”. Engineering Structures, 66, 100-115.
28. Gernay, T., Elhami-Khorasani, N., and Garlock, M., (2019). “Fire Fragility Functions for Steel Frame Buildings: Sensitivity Analysis and Reliability Framework,” Fire Technol., vol. 55, no. 4, pp. 1175–1210.
29. Randaxhe J., Popa N., Tondini N., (2021) “Probabilistic fire demand model for steel pipe-racks exposed to localised fires”, Engineering Structures, 226, 111310,
30. Olsson, A., Sandberg, G., and Dahlblom, O. (2003). “On Latin hypercube sampling for structural reliability analysis.” Structural Safety, 25(1), 47–68.
31. Akaike, H. (1998). Information theory and an extension of the maximum likelihood principle. In Selected papers of hirotugu akaike (pp. 199-213). Springer, New York, NY.
32. Akaike, H. (1974). “A new look at the statistical model identification”. IEEE transactions on automatic control, 19(6), 716-723.
33. Burnham, K. P., & Anderson, D. R. (1998). “Practical use of the information-theoretic approach”. In Model selection and inference (pp. 75-117). Springer, New York, NY.
34. Center for Computational Research, University at Buffalo, 2022. http://hdl.handle.net/10477/79221

SiF 2022– The 12th International Conference on Structures in Fire
The Hong Kong Polytechnic University, Nov 30 - Dec 2, 2022

A PARAMETRIC STUDY OF TUBULAR STEEL COLUMNS PROTECTED WITH GYPSUM-BASED MORTARS UNDER FIRE LOAD USING FINITE ELEMENT MODELLING

Pegah Aghabozorgi[1], Aldina Santiago[2], Luís Laím[3], Nuno Cândido[4]

ABSTRACT

This paper presents a study on the thermal performance of gypsum-based mortars as a coating layer on the surface of tubular steel columns. Thermal properties of the fire protection mortars as a function of temperature were determined from the previous studies carried out by the authors and collected from the literature. Based on the measured thermal properties, numerical models were developed for heat transfer and thermo-mechanical analysis. The proposed analysis models were verified based on a set of experimental tests on square hollow section (SHS) steel columns protected with gypsum-based mortars. Finally, a parametric sensitivity study was carried out and the effect of different parameters, including fire protection type and thickness, cross-section width-to-depth ratio, and load level on the fire performance, critical temperature, and failure modes of the protected steel tubular columns under the ISO 834 standard fire curve was investigated.

Keywords: Steel columns; Fire protection mortars; Fire resistance; Numerical analysis; Fire design.

1 INTRODUCTION

For buildings, structural fire safety is generally ensured as far as the supporting members (i.e., columns) maintain their stability during fire [1]. Considering this fact and the vulnerability of steel under fire, it would be necessary to protect the steel members against fire. This protection can be provided by applying fire protection materials (FPM) that can improve the fire resistance rating of steel members and prevent structural collapse by delaying the temperature rise in steel components [2], [3]. Gypsum-based fire protection mortars, one type of passive fire protection materials, have recently attracted interest due to their low cost and excellent thermal properties, such as thermal conductivity, specific heat, and bulk density [4]. Despite their high thermal insulation capacity, they have rarely been discussed in the literature as passive fire protection materials for the improvement of the fire-resistance rating of steel members. However, there is some research investigating the thermal protection of gypsum-based mortars by comparing the fire resistance of protected short steel columns subjected to high temperatures [5].

[1] Ph.D. Researcher, University of Coimbra, ISISE, Department of Civil Engineering, Portugal
e-mail: pegah.aghabozorgi@gmail.com, ORCID: https://orcid.org/0000-0002-9041-5693
[2] Assistant Professor, University of Coimbra, ISISE, Department of Civil Engineering, Portugal
e-mail: aldina@dec.uc.pt, ORCID: https://orcid.org/0000-0003-3646-4926
[3] Research Assistant, University of Coimbra, ISISE, Department of Civil Engineering, Portugal
e-mail: luislaim@uc.pt, ORCID: https://orcid.org/0000-0002-8342-3695
[4] Software developer, Onesource, Coimbra
e-mail: ncandido@onesource.pt,
https://doi.org/10.6084/m9.figshare.22178282

Some tests have also shown that the thermal properties of gypsum-based mortars are changing with increasing temperature [6]. In addition, the performance of gypsum-based mortars is strongly dependent on the composition, and the thermal conductivity may change with changing the thicknesses [7].

In this paper, a numerical model is developed and calibrated based on fire resistance test results previously reported by Santiago and Laim [2] aimed at evaluating the thermal performance of gypsum-based mortars being used as fire protection in steel tubular columns. Steel tubular members were initially used in structural and architectural applications due to their high torsional stiffness, aesthetic appearance, and higher load-bearing capacity being achieved through the concrete filling. Since the thermal properties of fire protection mortars at elevated temperatures are significant in the fire safety design of steel structures, three different ranges of mortar compositions are considered in this study to find the most effective one in terms of cost and thermal performance.

A parametric study is then followed to analyse the influence of different parameters such as fire protection type and thickness, column slenderness, and load level on the structural fire performance of protected steel hollow tubular columns when exposed to ISO 834 standard fire curve [8]. Finally, the numerical results were compared to each other to investigate the effect of each parameter change on the fire resistance of such protected tubular steel columns.

2 FINITE ELEMENT MODELLING

2.1 Geometry

The configuration of the test specimen made of commercial fire protection (CFPM) mortar and square steel tubular column is shown in Figure 1. The steel column had been subjected to fire conditions on all faces with a non-uniform heating rate established by the ISO 834 standard fire curve. The steel tube was composed of S355 structural steel and had a square cross section 150 mm ×150 mm × 8 mm and length 1.25 m. The steel column was also protected with 20 mm thick FPM with a curing duration of around six months.

The test was conducted using the protected steel column placed in the middle of a three-dimensional supporting frame through endplates (see Figure 1). The semi-rigid-ended and pin-ended support conditions were created for the column. Before the fire test, the column was loaded with a constant 748 KN compressive axial load by a hydraulic jacket and then exposed to fire in a square electric furnace controlled according to ISO 834 standard temperature-time curve until the specimen failed [5]. Note that the load level was 50% of the design value of the buckling load at ambient temperature (calculated according to EN 1993-1-1 [9]).

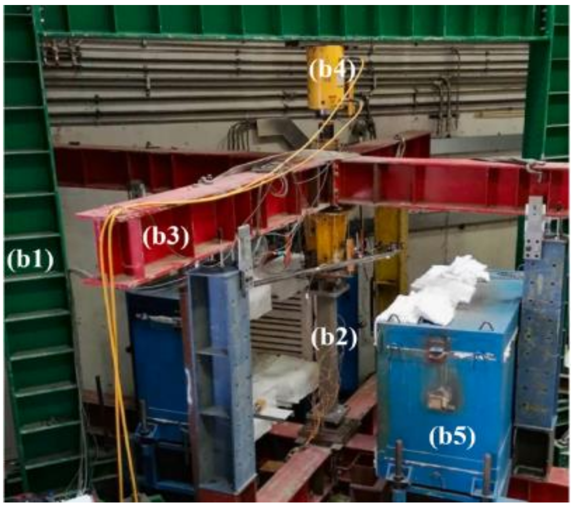

Figure 1: Fire resistance test set-up for SHS steel column [2]

2.2 Material properties

Since the thermal and mechanical properties of both structural steel and mortars vary with temperature, in order to correctly estimate their thermo-mechanical behaviour, the material properties should be accurately defined in advance. Considering the water content, porosity, temperature, heating rate, compositions, etc., different thermal properties are obtained for fire protection mortars. For gypsum-based mortars, thermal and physical properties were derived from the results of tests previously carried out by the authors [2]. Figure 2 illustrates the effective thermal properties of the fire protection mortars being adopted in FEM.

Regarding the variation of mechanical and thermal properties of steel with temperature, there are some design codes providing the steel properties in different temperatures. In this case study, Eurocode 1993-1-2:2005 [10] was adopted.

Furthermore, a nonlinear isotropic material model was adopted with the Von Mises yield criterion for describing the mechanical properties of steel. The stress-strain relationships taken from EN 1993-1-2:2005 were adopted in the FEM with Young's modulus of 210 GPa and steel yield strength of 355 MPa at ambient temperatures. These two parameters were calculated for elevated temperatures considering the reduction factors as recommended in EN 1993-1-1:2005. Furthermore, stress-strain curves needed to be converted into true stress-strain curves to include the large deformation effect of steel in FEM according to equations (1) and (2).

$$\varepsilon = \ln(\varepsilon_{nom} + 1) \tag{1}$$

$$\sigma = \sigma_{nom} \times (1 + nom) \tag{2}$$

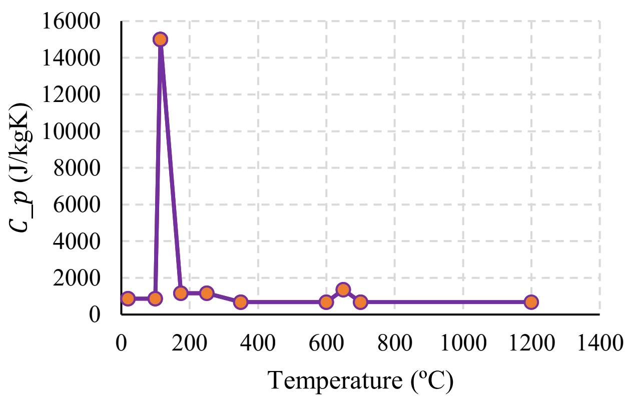

a) Specific heat

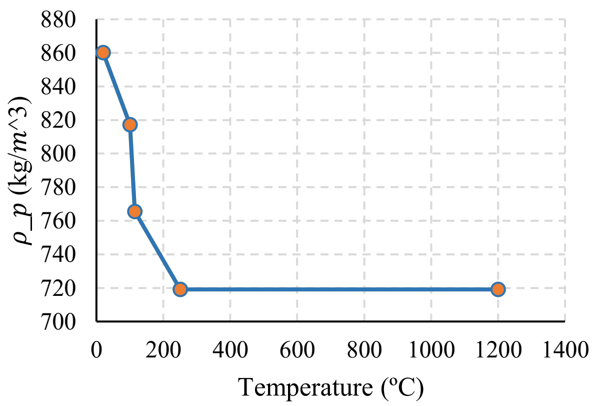

b) Bulk density

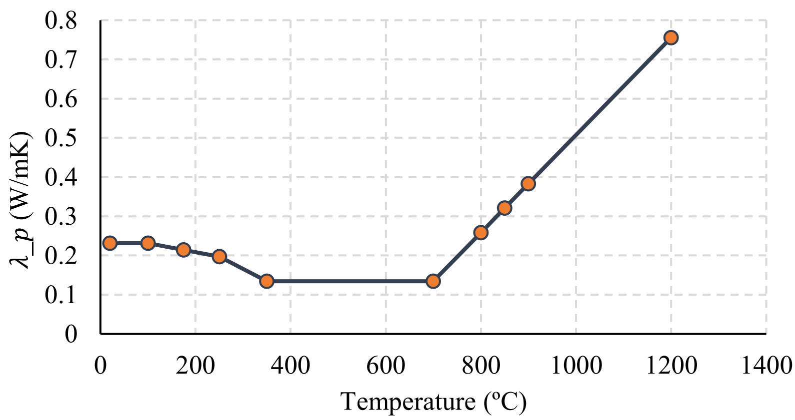

c)Thermal conductivity

Figure 2: Thermal properties of the enhanced fire protection mortar with Perlite [2]

2.3 Numerical modelling

Three types of finite-element analyses using the advanced finite-element program Abaqus [11] were employed to investigate the influence of different parameters on the fire resistance of steel columns protected with gypsum-based mortars. With this purpose, three-dimensional finite-element models (FEM) of test specimens have been developed as depicted in Figure 3. Then, heat transfer, linear buckling, and dynamic implicit quasi-static analysis were sequentially conducted in order to be confront the numerical results against the experimental ones on gypsum-based protected SHS steel columns at elevated temperatures [2]. Moreover, a mesh size of 10 mm on the cross-section of the column was adopted for all three analyses based on a sensitivity analysis.

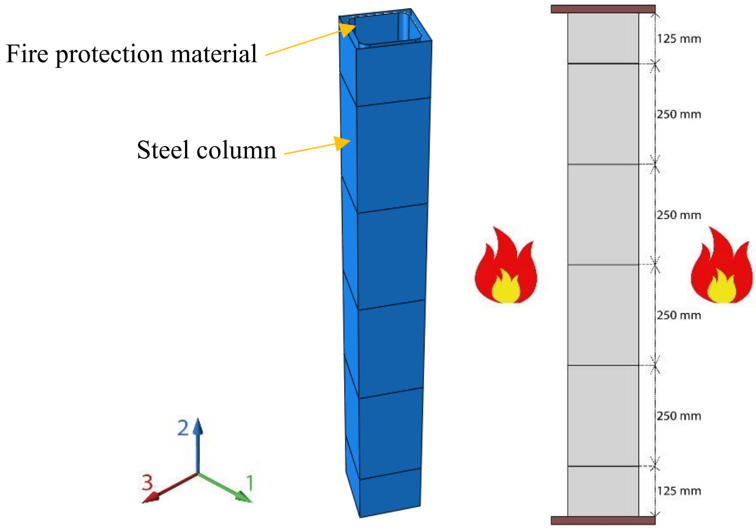

Figure 3: Analysis model of fire protected SHS steel column

2.3.1 Heat transfer analysis

A heat transfer analysis has been undertaken to predict the temperature distribution along a 1 m length of protected steel column when all surfaces are exposed to high temperature by furnace and according to the ISO 834 temperature curve (错误!未找到引用源。). The four-node shell heat transfer element DS4 was employed to measure the thermal responses (temperature-time histories) of the steel tube column. The thermal boundary conditions were defined according to the recommendations in EN 1991-1-2 [12], EN 1992-1-2 [13] , and EN 1996-1-2 [14] using two types of surfaces to obtain the temperature rise in the member. Radiation and convection were modelled as radiation to ambient and film conditions with the emissivity coefficient taken as 0.63 and convective heat transfer coefficient equal to 25 W/(m^2K), respectively. In addition, a thermal contact conductance of 150 W/(m^2K) up to 100ºC and of 80 W/(m^2K) beyond that temperature was considered in order to simulate the thermal resistance to heat conduction at the mortar-steel interface.

2.3.2 Linear buckling analysis

The buckling modes of the specimen, including local and flexural buckling modes, can be obtained using eigenvalue analysis of the finite element model through linear buckling analysis. The combination of buckling modes provides an initial imperfection in the geometry of the specimen with the maximum magnitude of L/1000 and b/200 for global and local imperfection, respectively, as recommended by Eurocode 1993-1-5. This imperfection is used as input into thermo-mechanical analysis in order to predict the over-buckling behaviour of the protected column. Note that both the local and global buckling modes were determined to impose an equivalent final imperfection pattern.

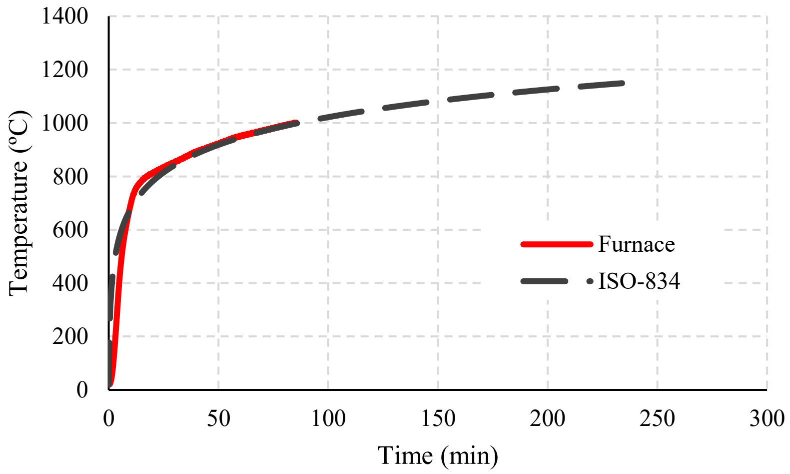

Figure 4: Thermal actions applied on gypsum-based mortar protecting the steel column

2.3.3 Thermo-mechanical analysis

Considering the calculated temperature distribution along the length of the steel column as an input for nonlinear stress analysis, thermo-mechanical actions were applied on the imperfect column during both static general and dynamic implicit analysis. A three-dimensional finite element model of steel tube and mortar has been developed using four-noded S4R shell elements with reduced integration. Furthermore, a general contact model was used to represent the interaction between the steel tube and mortar protection. Two contact behaviours were defined in the general contact models, including tangential and normal behaviour. A friction coefficient equal to 0.3 was assumed for the tangential behaviour, and the normal behaviour was also set to the hard contact mode. In order to apply the constraints and loads, semi-rigid-ended and pin-ended support were established using kinematic coupling constraints. The nodes within the end sections of the members were constrained to a reference point (RP) contained in the plane of the cross-sections where the boundary conditions were defined. All the degrees of freedom were constrained at the lower reference point (U1=U2=U3=UR1=UR2=UR3=0). However, three degrees of freedom were restrained at the top of the column, where the concentrated load was also applied (U1=U= UR3=0). While the reference points were located at the centroid of the cross-sections in the buckling model, in the thermo-mechanical model, both reference points were shifted by L/1000 horizontally to simulate the eccentricity during the test.

2.4 Accuracy of analysis model

Results from fire resistance tests of protected SHS steel tubular columns previously performed in the Coimbra University (UC) [9], [10] has been used as a reference to verify the accuracy of the developed numerical model.

Figure 5 compares the experimental and numerical maximum surface temperature measured in the SHS steel tubular column protected with 20 mm thick commercial fire protection mortar, as an example. The results showed that the numerical model predicted the temperature of the specimen with high accuracy. As seen in Figure 5, the heating time required to increase the steel temperature to 150 °C was longer than that for the temperatures above 150°C. The reduction in heating rate for temperatures above 150 °C (up to 700 °C) was due to the lower thermal conductivity after the evaporation of the moisture in the mortar. In addition, the difference observed in the behaviour of the curves at 100°C can be attributed to the vapour pressure that appeared inside the pores of the mortar as a result of the high heating rate.

Figure 6 (a) represents the final deformed configuration obtained by ABAQUS analysis and a comparison of the axial displacement-temperature curve for both the finite element calculation and the test results. Analysis results showed that as the column is heated, the axial displacement increases (see Figure 6 (b)) due to the thermal elongation of the column. Increasing the temperature leads to gradual degradation in the mechanical properties of steel until the point where the yield strength of the steel is reached. The column temperature at that point corresponds to the critical temperature. At this moment, the axial displacement is sharply reduced to zero, and the column no longer supports the applied load; either it buckles or fails in compression.

The comparisons showed that the developed finite element model could predict the high-temperature behaviour of the column specimen with reasonable precision, and the minor differences in failure time (less than 5%) are negligible. Therefore, the developed FEA model has been proven to be reliable for conducting a series of parametric studies to evaluate the role of each parameter in the structural fire performance of columns when exposed to the standard fire curve ISO 834.

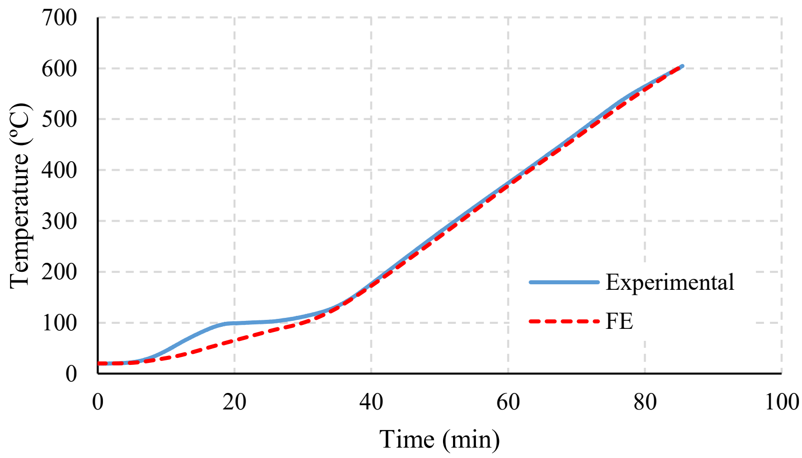

Figure 5: Temperature evolution on steel at the mortar-column interface

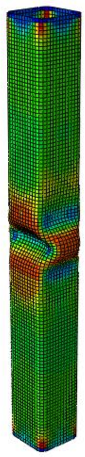

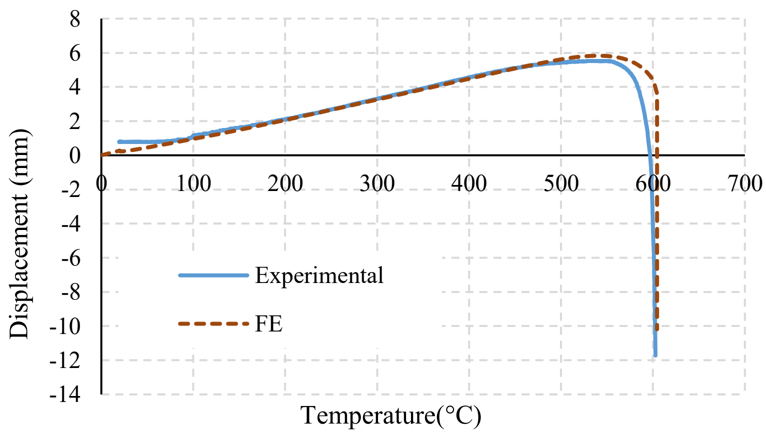

a) Deformed configuration of SHS steel column after the fire test

b) Axial displacement-temperature curve of the column protected with the CFPM

Figure 6: Comparison between experimental and numerical results

3 PARAMETRIC STUDIES

After the development of the accurate numerical model, a parametric study was carried out in order to determine the effect of some parameters such as mortar composition, protection thickness, axial compression load ratio, and cross-section width-to-depth ratio on the fire resistance and critical temperature of protected hollow section steel tubular column. Table 1 provides a summary of the main values of the design parameters selected for the parametric study.

Table 1:Main design parameters for parametric studies of the FE model

Column (C_R/S_tp_LL)	fire protection mortar	Cross-section $\frac{Rectangular}{Square}$ W * D * t_s (mm)	Load level (LL)	Protection thickness (t_p)	
				20 mm	30 mm
C1-S-20-50	DFPM with Perlite	S 150 * 150 * 8	50%	×	
C2-S-20-50	CFPM	S 150 * 150 * 8	50%	×	
C3-S-20-50	DFPM with SMNP	S 150 * 150 * 8	50%	×	
C4-S-30-50	DFPM with Perlite	S 150 * 150 * 8	50%		×
C5-S-20-25	DFPM with Perlite	S 150 * 150 * 8	25%	×	
C6-S-20-15	DFPM with Perlite	S 150 * 150 * 8	15%	×	
C7-R-20-50	DFPM with Perlite	R 350 * 150 * 8	50%	×	

3.1 Influence of the mortar composition

Figure 7 compares the evolution of steel temperature and axial column displacement from different compositions of fire protection mortar, including commercial fire protection mortar (CFPM), the developed fire protection mortar with Perlite (DFPM-Perlite), and the developed one with Silica Micro and Nanoparticles (DFPM-SMNP) [5].

It is observed the same temperature evolution for the SHS steel column protected with DFPMs. On average, the critical time of steel column with 20 mm thickness of FPM increased by 10 min following the application of DFPMs as fire protection material in steel columns as depicted in Fig. From these results, similar fire resistance was achieved for both the DFPM with SMNP and the one with Perlite which the value is higher when compared to CFPM. Therefore, it has been concluded that DFPM with SMNP and Perlite have the benefit over commercial ones regarding the fire resistance rating.

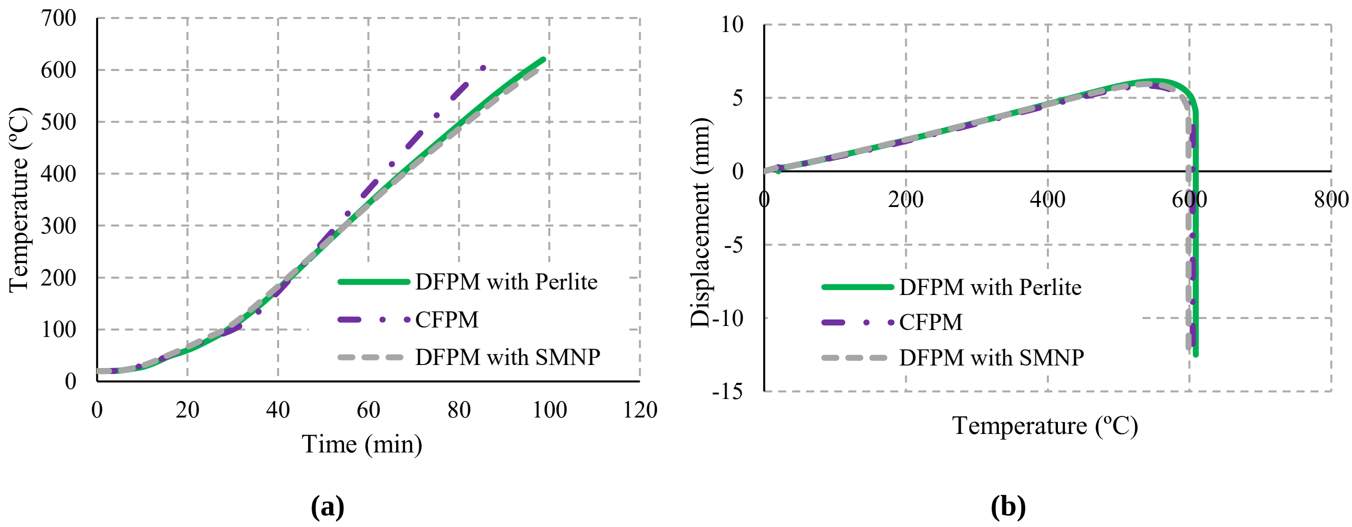

Figure 7: Temperature evolution (a) and axial displacement-temperature curve (b) for steel columns protected with different compositions of fire protection mortar

3.2 Influence of protection thickness

Figure 8 illustrates the influence of the fire protection thickness parameter on the fire resistance rating and critical temperature of steel columns when protected with the developed fire protection materials with Perlite for the load level 50%. The thickness of fire protection plays an important role in the fire resistance rating of these steel members: the fire resistance rating for 20 mm of DFPM with Perlite was R90, while for 30 mm thick, this fire protection was R120. It can be seen that a 10 mm increase in the thickness leads to a significant increase (50 min) in the fire resistance rating of this type of column.

Whereas in the case of the critical temperature of steel columns, the fire protection thickness is independent on that parameter when the fire protection is homogeneous and uniformly distributed along the column, as it is in this case.

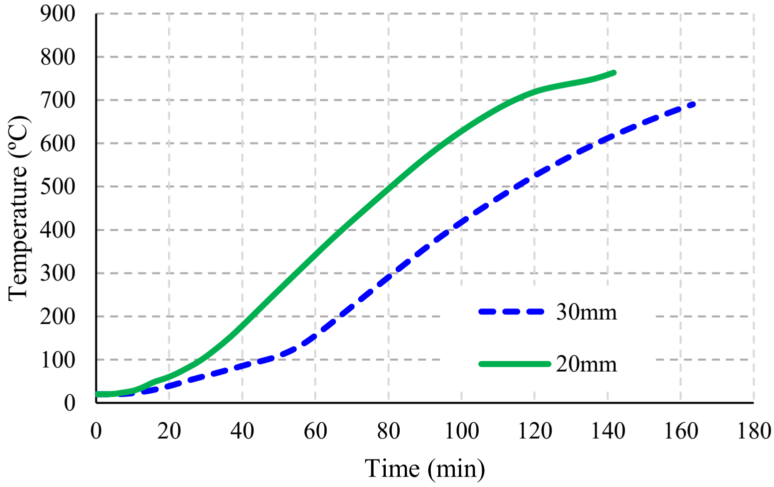

Figure 8: Temperature evolution of steel columns with different thicknesses of FPM

3.3 Influence of axial compression load ratio

The load level is another critical parameter that should be considered in the fire design of steel columns. The thermo-mechanical analysis results for steel columns with three different load levels of 50%, 25%, and 15% of the buckling load at ambient temperature are presented in Figure 9. A comparison of the axial displacement-temperature curve of the steel column directly exposed to standard fire conditions indicated that by changing the load level from 50% to 15%, the critical temperature of 647ºC increased to 760℃ , resulting in a greater fire rating in fire design. Additionally, the lower the load level is, the higher thermal elongation is observed before the failure happens.

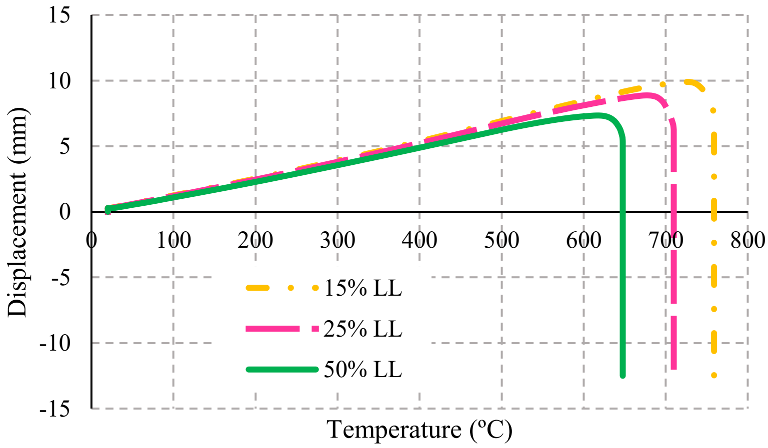

Figure 9: Axial displacement-temperature curve of the protected columns subjected to different load levels

3.4 Influence of column dimensions

To analyse the effect of the width and depth of the steel column on the critical time and fire resistance, two different cross-sections (i.e., square and rectangular) with 8 mm thickness protected with 20 mm DFPM with Perlite: 150×150×8 and 150×300×8 with load ratio of 50% were considered.

As seen in Figure 10, the aspect ratio between the depth and width of the cross-section plays a favourable role in the fire resistance of the columns. The increase of the depth-to-width ratio (β) from 1 to 2, leads to an increase of 112 ºC in the critical temperature of the steel column. Since almost the same temperature evolution is obtained for these two columns from heat transfer analysis, it can result that the rectangular cross-section has a higher critical time and higher fire resistance.

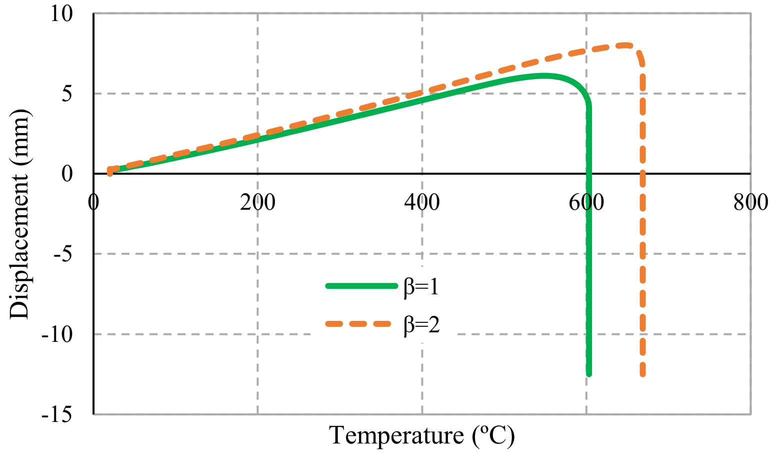

Figure 10: Axial displacement-temperature curve for the steel column with different cross-sections

4 CONCLUSION

This paper describes a numerical and parametric study on the thermo-mechanical behaviour of fire-exposed steel tubular columns when protected with gypsum-based mortars with Perlite.

Based on a set of experimental fire tests on the SHS steel tubular column, a three-dimensional finite element model was developed using ABAQUS. Heat transfer, buckling, and nonlinear implicit dynamic analysis was verified against SHS steel tubular column fire test results. The thermal properties required to calculate for the thermal analysis: thermal conductivity, specific heat, and mass density, were defined based on the previous experimental data.

A comparison between the analysis and test results showed that the analysis model predicts the temperature of the steel tube with reasonable accuracy. Also, the analysis model could reasonably simulate the actual structural response for the steel column specimens protected with commercial fire protection mortar under standard fire conditions.

The findings indicated that the developed gypsum-based fire protection mortars might play a key role in protecting steel structures from fire. As mentioned earlier, compared to the plain commercial fire protection mortars, a 10 min increase in fire resistance was achieved when the column was insulated with 20 mm thick developed gypsum-based mortars.

The analysis results highlight the impact of thickness on the improvement of the fire resistance rating of the column; a 10 mm increase in the thickness of fire protection mortar results in a gain of 50 min in the fire resistance rating of the column, although the optimization of self-weight of protected steel structures should also be taken into account.

In addition, the load level and length-to-depth ratio of the column have proved to have a significant influence on critical times and temperatures.

As approximately similar fire resistance was obtained for the two mentioned compositions of gypsum-based mortars (i.e., gypsum-based mortars with perlite and with silica micro nanoparticles) in this study, it is recommended to develop more compositions of these fire protection mortars and make a comprehensive comparison among them for different thicknesses in the future studies. The findings can also be used to upgrade the existing codes of Eurocodes or create a new version of them.

ACKNOWLEDGMENT

The authors gratefully acknowledge the European Regional Development Fund (FEDER), through the Portugal Operational Program (Portugal 2020) for its funding for the research project CENTRO-01-0247-FEDER-047136 (Switch2Steel - A Calculation Framework for Cost and Material Optimization of Industrial

Buildings in Steel Structures). This work was also financed by FEDER funds through the Competitivity Factors Operational Programme - COMPETE and by national funds through Foundation for Science and Technology (FCT) within the scope of the project POCI-01-0145-FEDER-007633 and the Regional Operational Programme CENTRO2020 within the scope of the project CENTRO-01-0145-FEDER-000006. The authors also acknowledge the

REFERENCES

[1] Y. C. Wang, "Effects of structural continuity on fire resistant design of steel columns in non-sway multi-storey frames," *Fire Saf. J.*, vol. 28, no. 2, pp. 101–116, 1997, doi: 10.1016/S0379-7112(96)00083-5.

[2] L. Laím, A. Santiago, H. Caetano, D. Craveiro, and A. Shahbazian, "Numerical analysis and structural fire design of protected SHS steel columns with thermally enhanced gypsum-based mortars," vol. 54, 2022, doi: 10.1016/j.jobe.2022.104629.

[3] J. Zehfuß and L. Sander, "Gypsum plasterboards under natural fire—Experimental investigations of thermal properties," *Civ. Eng. Des.*, vol. 3, no. 3, pp. 62–72, 2021, doi: 10.1002/cend.202100002.

[4] L. Laím, H. Caetano, and A. Santiago, "Review: Effects of nanoparticles in cementitious construction materials at ambient and high temperatures," *J. Build. Eng.*, vol. 35, no. November 2020, p. 102008, 2021, doi: 10.1016/j.jobe.2020.102008.

[5] H. Caetano, L. Laím, A. Santiago, L. Durães, and A. Shahbazian, "Development of Passive Fire Protection Mortars," *Appl. Sci.*, vol. 12, no. 4, p. 2093, 2022, doi: 10.4324/9781315232140-14.

[6] W. Chen, J. Ye, Y. Bai, and X.-L. Zhao, "Thermal and Mechanical Modeling of Load-Bearing Cold-Formed Steel Wall Systems in Fire," *J. Struct. Eng.*, vol. 140, no. 8, 2014, doi: 10.1061/(asce)st.1943-541x.0000862.

[7] S. Abidi, B. Nait-Ali, Y. Joliff, and C. Favotto, "Impact of perlite, vermiculite and cement on the thermal conductivity of a plaster composite material: Experimental and numerical approaches," *Compos. Part B Eng.*, vol. 68, pp. 392–400, 2015, doi: 10.1016/j.compositesb.2014.07.030.

[8] ISO, "ISO 834-1 Fire resistance tests -Elements of building construction, Part 1: General requirements," *International Organization for Standardization, Geneva, Switzerland*, 1999.

[9] E. 1993-1-1, "Eurocode 3 : Design of steel structures - Part 1-1: General rules and rules for buildings."

[10] E. 1993-1-2, "'Design of steel structures. General Rules. Structural Fire Design' European Committe for Standardization, Brussels, Belgium.," 2005.

[11] "ABAQUS/CAE," *ABAQUS/CAE, Standard User's Manual, Version 2021, Dessault systems, Simulia Crop.,USA*. 2021.

[12] EN 1991-1-2, "Eurocode 1 : Actions on structures - Part 1-2 : General actions - Actions on structures exposed to fire. Brussels, Belgium, European Committee for Standardization," 2002.

[13] EN 1992-1-2, "Eurocode 2 : Design of concrete structures - Part 1-2: General rules - Structural fire design," 2004.

[14] EN 1996-1-2, "Eurocode 6 : Design of masonary structures - Part 1-2: General rules - Structural fire design," 2005.

THERMOMECHANICAL MODELLING OF SANDWICH PANELS WITH CONNECTIONS IN FIRE RESISTANCE TESTS

Qingfeng Xu[1], Hèrm Hofmeyer[2], Johan Maljaars[3], Ruud A.P. van Herpen[4]

ABSTRACT

This paper presents two full-scale fire resistance tests of sandwich panels with connections, to verify one-way coupled fire-structure simulations. The heat transfer simulations agree well with the tests, however, the structural response simulations show some differences compared to the start of the first test, which is a sandwich panel façade. A parameter study is conducted to resolve these differences. It is shown that of little influence are the modelling of the fire, the description of the steel's thermal expansion, the modelling of the tongue and groove connections, and variations of the connection stiffness. Differently, glue decomposition, resulting in delamination, and related sandwich face instabilities are likely to be the cause of the differences. In the second test, a so-called stud bolts test, connection failures by vertical bearing were reported, but further mechanical measurements were not carried out. To simulate the connection failures, in the simulations additionally a two-scale model is incorporated for the connections. This model shows that horizontal bearing occurs in a direction perpendicular to the load due to lateral expansion of the system. As a conclusion, state-of-the-art fire-structure simulations can simulate full-scale fire tests of sandwich panels, however, panel delamination and stability should be modelled in detail. Furthermore, tests should always include detailed measurements with respect to the mechanical behaviour, e.g. with respect to panel buckling, delamination, and connection failures.

Keywords: Sandwich panel; thermomechanical modelling; finite element model; connection; fire test

1 INTRODUCTION

Sandwich panels are widely used for building façades, for they are lightweight, durable, and economical to construct. Their fire resistance must be understood to ensure a fire cannot easily spread to other compartments or buildings. Also, panel failures influence the fire itself, a phenomenon that increasingly receives attention. Design codes exist to verify panel fire resistance. For example, ISO 13784-1 specifies the tests that are needed to evaluate the fire performance of sandwich panels [1]. EN 13501-1 and EN 13823 are used to determine the fire performance of building elements in Europe [2,3]. However, these design codes do not cover all relevant aspects: Axelsson et al. conducted an intermediate scale test for sandwich panels based on EN 13823, and their data showed an unacceptable low level of repeatability [4]. Crewe et al. conducted two types of fire tests for sandwich panels, an ISO 13784-1 standard test and a modified test [5]. Results showed that slight modifications to the standard test could lead to significantly different outcomes. As such, it can be questioned whether standardised tests are good enough to assess all fire scenarios in a safe manner. This is partly solved by the application of non-standard tests, however, these are expensive, especially when full-scale. Besides, a different test is needed for each variation of

[1] PhD student, Eindhoven University of Technology, The Netherlands
e-mail: q.xu1@tue.nl, ORCID: https://orcid.org/0000-0003-3655-1421
[2] Associate Professor, Eindhoven University of Technology, The Netherlands
e-mail: h.hofmeyer@tue.nl, ORCID: https://orcid.org/0000-0001-8353-7054
[3] Principal Scientist at TNO, Full Professor at Eindhoven University of Technology, The Netherlands
e-mail: j.maljaars@tue.nl, ORCID: https://orcid.org/0000-0001-5831-2478
[4] Senior Consultant at Peutz Engineers, Fellow Eindhoven University of Technology, The Netherlands
e-mail: r.a.p.v.herpen@tue.nl
https://doi.org/10.6084/m9.figshare.22178306

parameters. Therefore, simulations are increasingly used, since they are economical and allow for a wide variety of parameters to be studied. They may also provide insights not accessible by tests (e.g. related to internal stresses and strains).

Besides the general setup of a sandwich panel facade, with its panels and frame, details in a sandwich panel system may influence the structural behaviour under fire. This is particulary true for connections, their behaviour even leading to progressive collapse [6]. Cábová et al. tested the shear resistance of sandwich panel screw connections at elevated temperatures [7]. Self-tapping screws were tested, failing by bearing of the sandwich panel faces. When temperatures raised, the bearing area increased significantly due to decreased steel strength. Chen et al. investigated single-shear experiments of screw connections at ambient and elevated temperatures [8]. The failure modes differed as a function of temperature and screw type.

As mentioned earlier, simulations may help to understand sandwich panel behaviour better. Often, these simulations involve thermodynamic and thermomechanical aspects. First, a Heat Transfer (HT) analysis predicts the temperature distribution of the structure, in which thermal boundary conditions come from a standard fire curve or e.g. a fire dynamics simulation, thereby utilising the concept of the Adiabatic Surface Temperature (AST) [9] for transferring the boundary conditions. Subsequently, the thermal data of the HT model is transferred to a Structural Response (SR) analysis to predict the mechanical behaviour. Following these procedures, including a fire dynamics simulation, a so-called One-Way Coupled (OWC) fire-structure simulation is carried out. Additionally, if structural behaviour (e.g., a failure) influences the fire development, this behaviour can be coupled back to the fire dynamics simulation. This is then defined as a Two-Way Coupled (TWC) simulation, as demonstrated by Feenstra et al. [10] and De Boer et al. [11]. So far, in both OWC and TWC simulations, connections are simplified as spring elements or rigid connections, since it is computationally expensive to model a large-scale structural system including the small-scale connections. Only recently, simulations have been developed that include a two-scale method for including the connections [12,13], but besides verification (e.g., by a mesh convergence study), these also need validation (by experiments).

This paper first introduces two sandwich panel fire resistance tests, including data on the temperature distribution (for both tests) and the panel deflection (for the first test). Subsequently, the finite element models as used for the fire-structure simulations are presented. Then the test results are used to verify the principle of OWC fire-structure simulations, including a parameter study. Finally, the second test is used for validating OWC simulations including a two-scale model for the connections. Note that for efficiency most simulations in this paper use a fire curve instead of a fire dynamics simulation, and so strictly are not OWC simulations. However, it is shown in the parameter study that this is a valid approach, and so conclusions also apply to OWC simulations.

2 FIRE RESISTANCE TESTS, FINITE ELEMENT MODELS

2.1 Fire resistance tests

Two sandwich panel fire tests are presented here, both using the same sandwich panel type. The sandwich panel consists of a 0.6 mm thick steel face around and a 100 mm core of mineral wool.

Test 1 was a full-scale sandwich panel façade test, shown in the top row of Figure 1. Four sandwich panels were used, each having dimensions of 5000×4000×100 mm. These panels were fixed to a Rectangular Hollow Section (RHS) frame by 16 screws to each horizontal section and 11 screws to each vertical section, see Figure 1. Self-drilling screws "JT3-D-6H-5.5/6.3×147" were used, with a major diameter of 6.3 mm and 147 mm length. The thickness of the RHS webs and flanges was 5 mm. The complete frame with four panels was positioned in the furnace opening. The internal side of the sandwich panels was exposed to the furnace heat following a standard ISO-834 fire curve, and temperatures and displacements on the external (fire unexposed) side were measured by thermocouples and displacement sensors, shown as red and blue crosses in Figure 1. No failure was observed during the 90 minutes of the test.

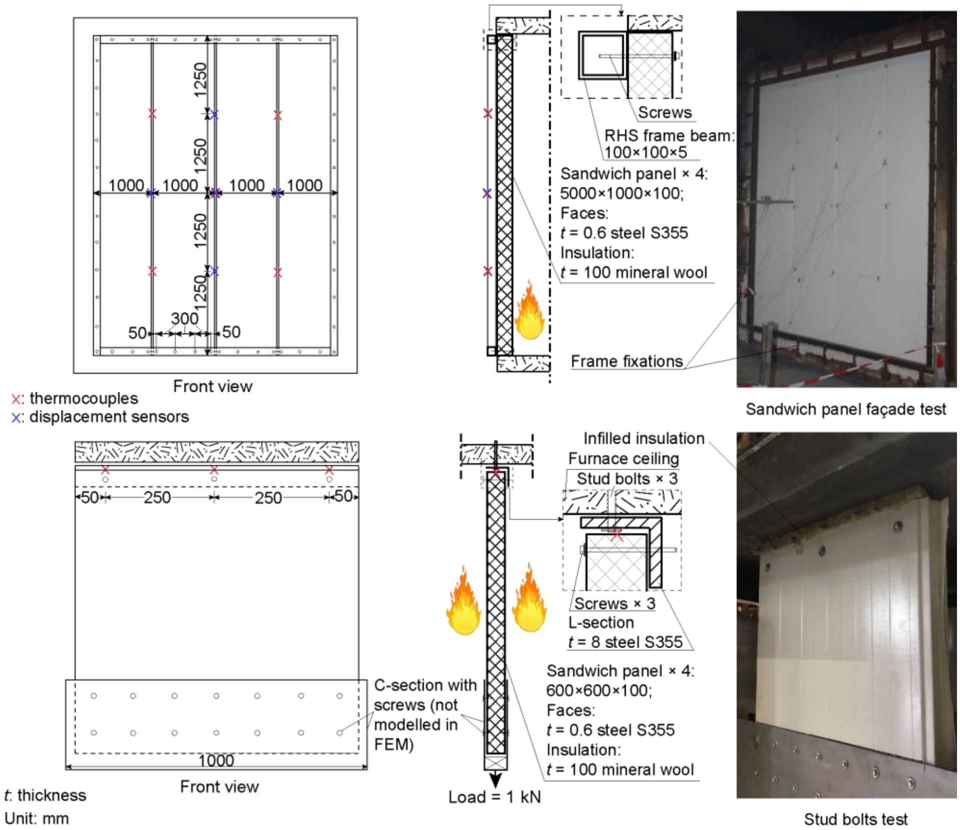

Figure 1. Top row: Sandwich panel facade test, Bottom row: Stud bolts test

Test 2 was carried out to determine the behaviour of a vertically loaded sandwich panel connected to the furnace ceiling, Figure 1, bottom row. A single 600×600×100 mm sandwich panel was used in this test. For its positioning, a steel L-section was clamped to the furnace ceiling via three M10 stud bolts, and the sandwich panel was fixed to the L-section by three self-tapping screws "JZ3-6.3×115-E16", having a major diameter equal to 6.3 mm. The thickness of the L-section web and flange was 8 mm. A steel C-section was fixed at the bottom of the sandwich panel with screws, carrying steel weights for an external load of 1 kN. The sandwich panel was heated in the furnace following an ISO-834 fire. Three thermocouples were embedded inside the insulation layer along the top (the red crosses in Figure 1), and no displacement sensors were used. Test 2 was designed to verify the resistance of the stub bolts, however, the report mentions that the sandwich panel fell down due to plate bearing at the screws, after 50 minutes. No further (quantitative) data are available.

2.2 Finite element models

The fire-structure simulations in this paper utilise finite element models developed in the commercial program Abaqus [14], combined with several in-house developed Python scripts and C++ programs, see for more details [10,11]. For the HT analysis, a standard ISO-834 fire curve is applied on the fire-exposed surface(s) of the sandwich panels. To verify this standard fire curve approach, once a Computational Fluid Dynamics (CFD) simulations is used for the fire in the parametric study, making use of Fire Dynamics Simulator (FDS) [15]. The mentioned two-scale model will be introduced in Section 4.6.

The setup of the finite element models follows the tests in Section 2.1, where irrelevant components (the furnace, frame fixations around the RHS frame in test 1; steel weights, C-section, and the infilled insulation between L-section and sandwich panel in test 2) are not modelled. Sandwich panel faces and frame elements are modelled by shell elements, and the sandwich panel insulation core is made by volume elements, as detailed in Table 1. Figure 2 (on the left and in the middle) shows the finite element models, where orange lines are locations where boundary conditions act in the HT model to impose the ISO 834 fire curve, and the green lines indicate the positions where boundary conditions act in the SR model (restraints or loads). Conductivity and mechanical contact between parts are handled by Abaqus proprietary "interaction properties", indicated by the bold red lines. Material properties are given on the right of the figure. Steel

Table 1. Finite element models: parts, elements, materials, and procedure

	HT analysis		SR analysis	
	Test 1	Test 2	Test 1	Test 2
Parts	Sandwich panel×4 Frame beams×4	Sandwich panel×1 L-section×1	Sandwich panel×4 Frame beams×4 Spring elements×54	Sandwich panel×1 L-section ×1 Spring elements×3
Elements [mm]	Sandwich panel faces DS4(100×100) Sandwich panel insulation DC3D8(100×100×25) Frame beams DS4(50×50)	Sandwich panel faces DS4(12.5×12.5) Sandwich panel insulation DC3D8(12.5×12.5×12.5) L-section frame DS4(12.5×12.5×12.5)	Sandwich panel faces S4(100×100) Sandwich panel insulation C3D8(100×100×25) Frame beams S4(50×50) Spring element CONN3D2	Sandwich panel faces S4(12.5×12.5) Sandwich panel insulation C3D8(12.5×12.5×12.5) L-section S4(12.5×12.5×12.5) Spring element CONN3D2
Mater-ials	Sandwich panel faces: steel Sandwich panel insulation: mineral wool Frame beams: steel	Sandwich panel faces: steel Sandwich panel insulation: mineral wool L-section: steel	Sandwich panel faces: steel Sandwich panel insulation: mineral wool Frame beams: steel	Sandwich panel faces: steel Sandwich panel insulation: mineral wool L-section frame: steel
Procedure	Transient heat transfer	Transient heat transfer	Static	Static

properties are taken from EN 1993-1-2, Section 3 [18] as this section provides detailed temperature dependent thermal and mechanical properties. For the mineral wool insulation, Bai et al. [19] proposed a temperature-dependent conductivity curve for a insulation density between 120 to 140 kg/m^3, and Fredlund [20] found that the conductivity of mineral wool (there having a density of 30 kg/m^3) changes rapidly when the temperature exceeds 600 °C. The density of the mineral wool in the tests was 120 kg/m^3 and, based on the previous information, an assumed curve (dotted) is used. The material behaviour of the mineral wool is assumed to be linear elastic with a Young's modulus equal to 30 N/mm^2.

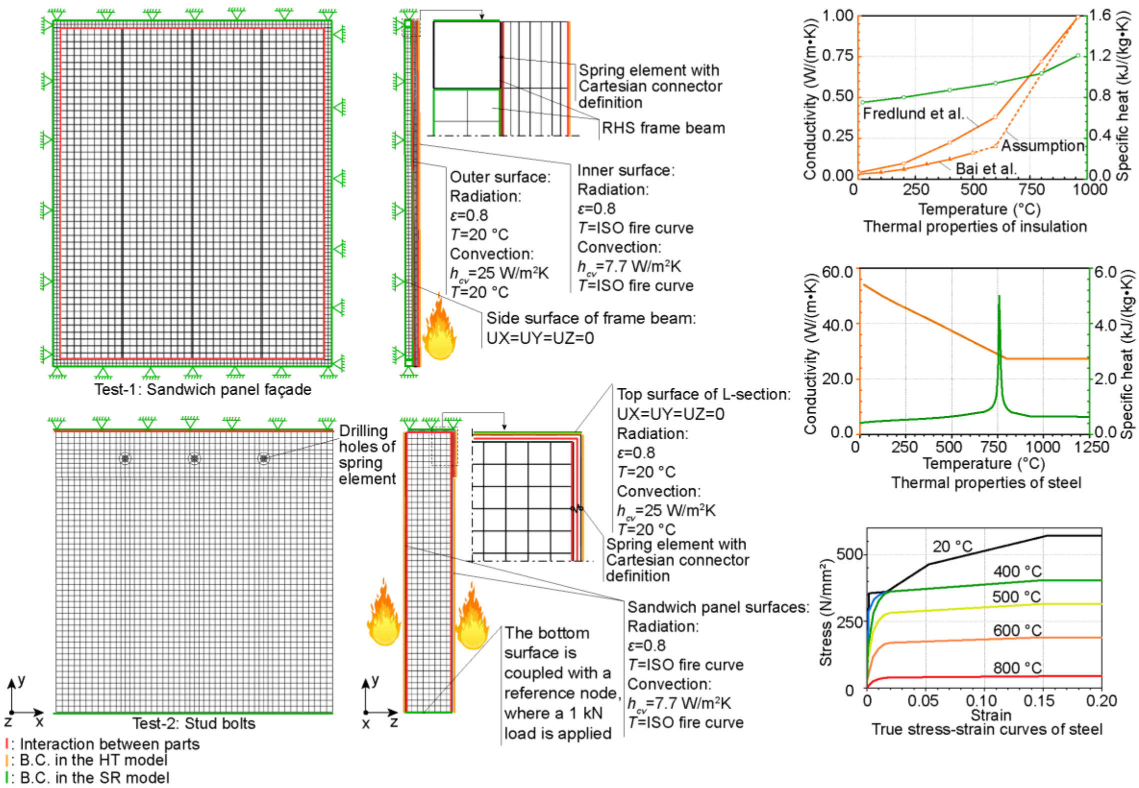

Figure 2. Finite element models (left, middle) and material properties (right)

For the screw connections, spring finite elements were used, their (bi-linear) spring stiffness based on the "component method" in EN 1993-1-8, section 5.2 [16], see for further details Section 4.4.

3 SIMULATION RESULTS

3.1 Heat transfer analyses

Figure 3 shows a comparison of the results of the HT analyses and the test. Temperatures on the fire unexposed side (for Test 1) and the insulation core (for Test 2) are predicted most of the time within the temperature envelope: for the tests an envelope is used, since temperatures were measured at several locations, see Figure 1, whereas the simulations did not show significant temperature differences, because a uniform distributed ISO 834 fire curve was applied. Regarding Test 1, the simulation shows delayed heating up to about 1500 seconds, then a steep increase about 500 seconds earlier than a similar steep increase in the test. This may be due to the approximated material properties for the insulation.

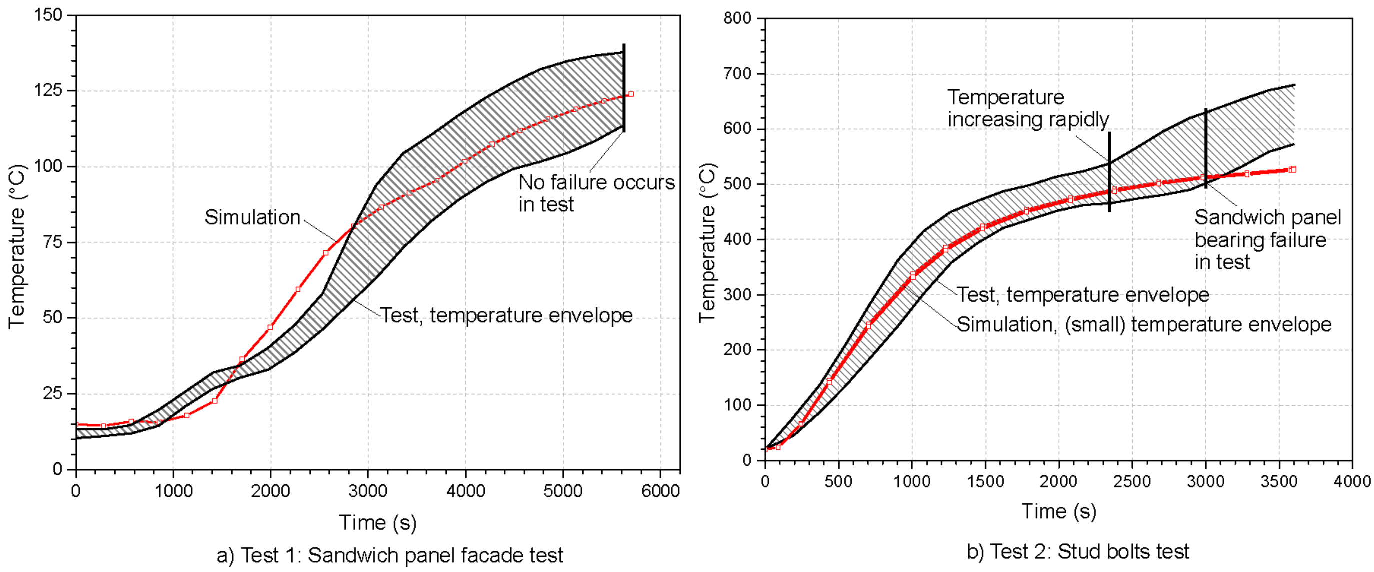

Figure 3. HT analyses vs. tests

For Test 2, temperature measurements were made at the top, see Figure 1. The temperature envelope shows a slightly higher increase around 2300 to 3000 seconds, due to the gap between the panel and L-section opening up. Note that this gap and the thermocouples in test 2 were filled and surrounded by some additional insulation. This is not modelled in the simulation, as it seems not relevant for the results sought here.

In conclusion, the HT analyses show a good agreement with both tests. However, as an ISO 834 temperature curve is used instead of a furnace fire simulation, temperatures in the simulations are relatively equal over the area of the panels, whereas in the test these temperatures fluctuate due to the fire dynamics.

3.2 Structural response analyses

The setup of the SR analyses is given in Section 2. Figure 4(a) on the left shows the panel deflections of Test 1 and its simulation after 5500 seconds, both showing the panel bent toward the fire due to thermal expansion. The centre out-of-plane displacement of the sandwich panel versus time is plotted in black in the graph, whereas the simulation is plotted in red. The simulation agrees well with the test for the first 100 seconds, but hereafter the test first shows irregular behaviour (possibly transient), then shows only limited out-of-plane deflections as compared to the simulation. Only in the final stage, after about 3000 seconds, the simulation predicts the test well again. The differences between the simulation and the test will be studied further in Section 4.

Test 2 did not have measurements with respect to the mechanical behaviour (in the report only a general statement on the bearing failure was made). Therefore, Figure 4(b) can only present the simulation, for which the vertical displacement at the load application point is shown versus time. As equilibrium between

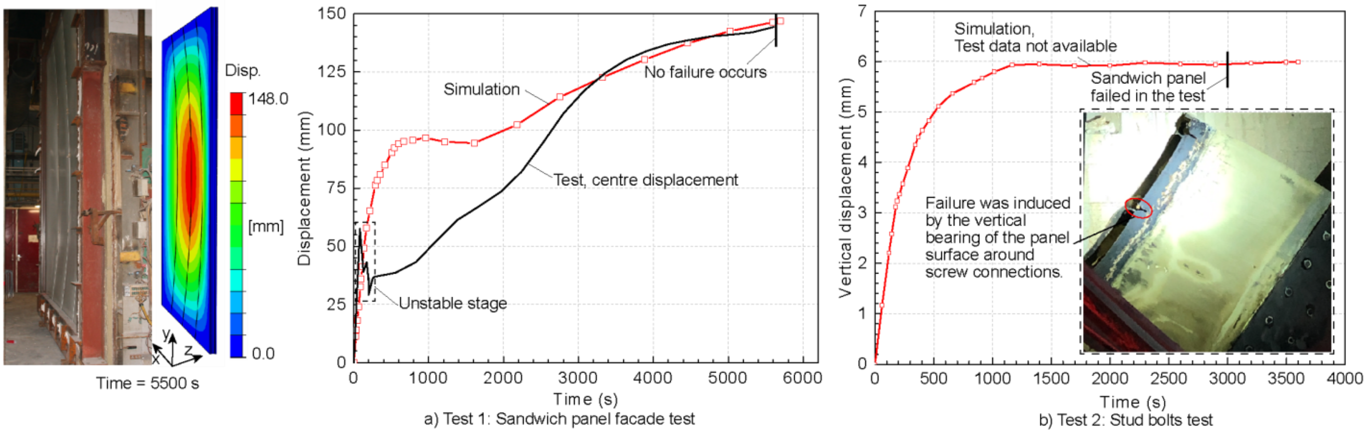

Figure 4. SR analyses deformations; (a) out-of-plane panel displacement of Test 1; (b) vertical displacement of the loaded node of Test 2

the external load and the panel has already been reached at the beginning of the simulation, and additional vertical displacements come from thermal expansion and changing material properties due to the increasing temperatures. The panel failed in the test at around 3000 seconds, reportedly due to bearing failure of the panel to L-section connections. The simulation does not show similar or related failure, due to the limited modelling, and is stopped at 3600 seconds, a while after failure in the test. A more elaborate simulation, including two-scale models, will be studied in Section 4.6.

4 PARAMETER STUDY

The simulations above showed that the HT analyses perform well, however, the SR analyses need improvements. Here, a parameter study for Test 1 is carried out in Section 4.1 to 4.5, to investigate the differences in out-of-plane deflections between the simulation and the test. For Test 2, a two-scale model is applied in Section 4.6 to investigate the connection behaviour in more detail.

4.1 Test 1: FDS instead of fire curve

Simulations in this paper, including the HT analysis in Section 3, use the ISO-834 fire curve as a thermal boundary condition, and so temperatures are evenly distributed over the panel's fire exposed side, different from the test. Here, an OWC fire-structure simulation is conducted. This implies that, instead of using a fire curve, FDS is used, using the Adiabatic Surface Temperature (AST) concept proposed by Wickström [9] to transfer the temperatures from the FDS to the HT analysis, Figure 5(a) and [10,11].

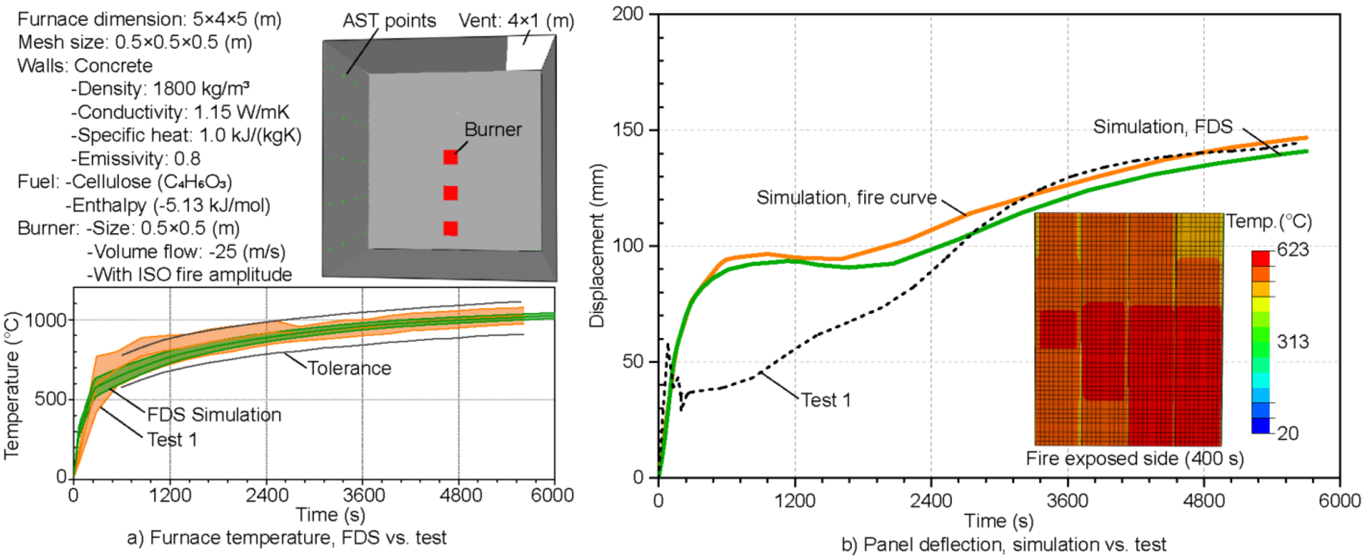

Figure 5. Comparison of simulations with FDS or fire curve

The measured furnace temperatures in the test are shown by the orange envelope in the graph on the left, and these temperatures met the required tolerances of the ISO 834 standard (black curves). The FDS simulation of the furnace yields the temperatures indicated by the green envelope, which are within the experimental envelope. Figure 5(b) shows the panel out-of-plane displacement versus time for the test (dotted line), the HT analysis using the fire curve (orange), and the HT analysis after FDS (green curve). Firstly, it is concluded that the furnace can be modelled well with FDS. Secondly, it is unlikely that the differences between the simulation and the test are caused by differences in the (thermal) load application.

4.2 Test 1: Thermal expansion coefficient

The thermal expansion of the panel steel faces, which may be partly or fully restricted, influences the panel's out-of-plane behaviour. It should therefore be noted that several standards (EN 1993-1-2 [18], BS 5950-8 [21], and ASCE [22]) advise different values for steel's thermal expansion coefficient as a function of temperature, as shown in Figure 6(a).

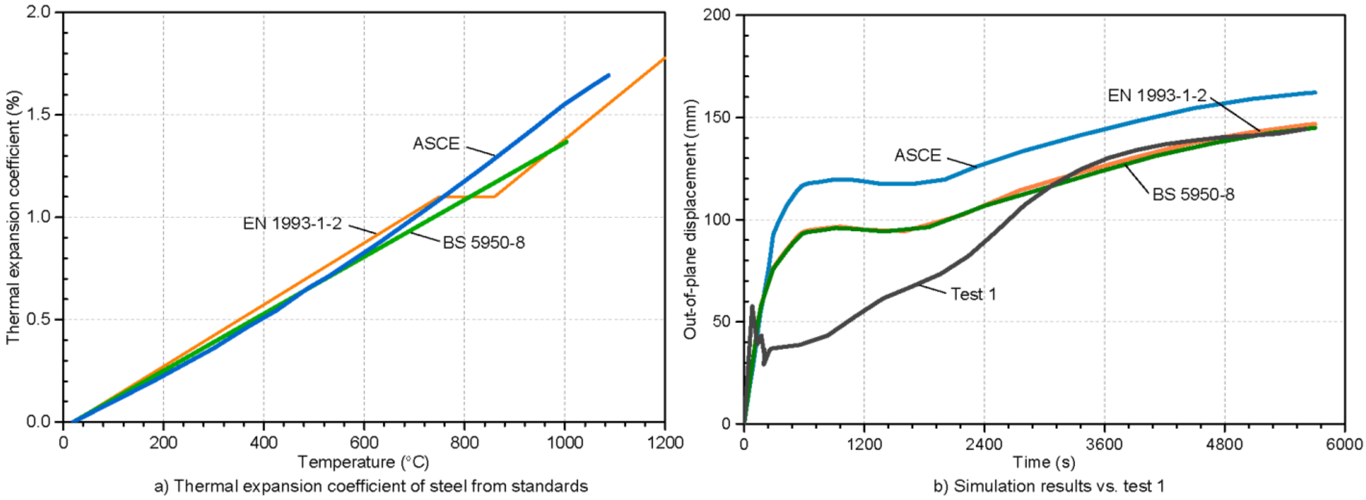

Figure 6. (a) Steel's thermal expansion from several standards, (b) Simulations using the different advised thermal expansion coefficients

In Test 1, the out-of-plane displacements of the fire unexposed face were measured at different locations, here the upper bound (centre point) is shown as the black curve in Figure 6(b). The simulation of Section 3 (using EN 1993-1-2 steel properties) was repeated with the thermal expansion coefficient as advised by the other standards. Figure 6(b) shows that the ASCE advised values overestimate the deformations, whereas the use of BS 5950-8 shows similar behaviour to the already used EN 1993-1-2, both correctly predicting the maximum out-of-plane deflection (in the centre of the plate, at 5500 seconds). Similar to the previous section, it can be seen that assumptions on the steel's thermal expansion cannot be responsible for the differences between the simulations and the test.

4.3 Test 1: Tongue and groove

The sandwich panels in Test 1 are longitudinally connected by tongue and groove connections, see an open connection in Figure 7 on the left. During the test, the (thermally induced) deformations of the panels may lead to these connections being stressed, coming loose, or even a vertical gap may occur, which in turn changes the mechanical boundary conditions, and thus the structural behaviour. In the simulations of Section 3, the longitudinal connections are modelled with a “C” shape for the groove, see Figure 7, for mesh simplicity and conformity. In this section a more realistic groove “E” shape of the grooves is studied. Note that a complete realistic modelled would require an extreme fine mesh, and is therefore not tried yet.

The temperatures from the HT analyses, at the centre of the panel, are similar for the two models, see the red plots in Figure 7 in the middle (note that these temperatures are not available for the test). Some local differences exist near the tongue and groove, as shown in Figure 7 on the right. This is due to the different contact areas for the two types of connections. With respect to the SR analyses (black curves), the “C” shape follows the original simulation of Section 3, whereas the "E" connection, similar to the test, shows

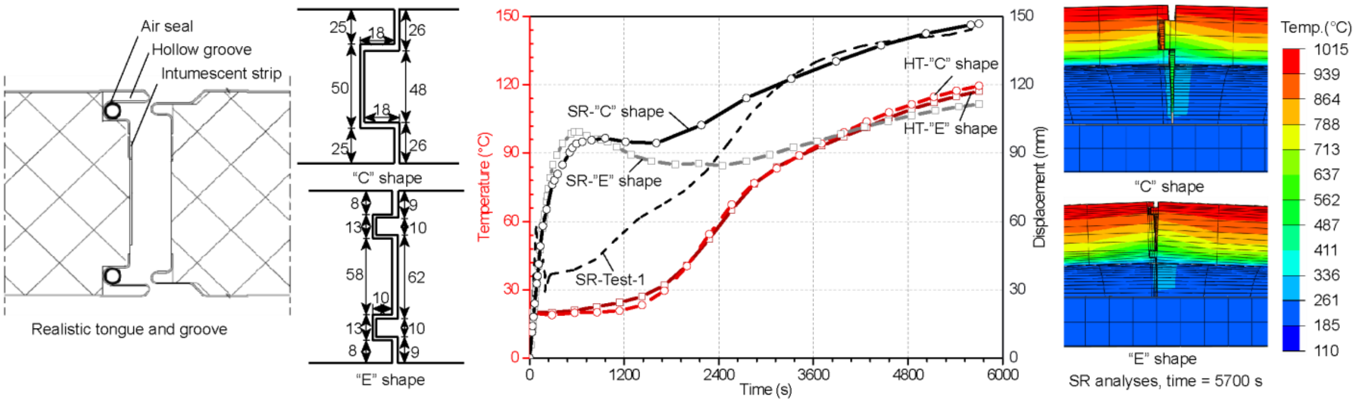

Figure 7. Comparison of simulations with different shapes of tongue and groove

smaller displacements from 1200 seconds on, which suggests the "E" connection is stiffer than the original modelling. Although displacements are confirmed by the final state of the SR models in the figure on the right, these contour plots do not give a further hint on a possible cause for the difference in stiffness between the connection modelling types. Though the "E" shape of the groove is more realistic than "C", it shows less resemblance with the test. This should likely be attributed to the fact that certain details in the connection are not modelled, like the exact lip geometry, the air seal, the intumescent strip, etc. This lack of modelling may offset the "C" model to seemingly correct predictions, and the "E" to too low predictions. In any case, this section makes clear that a precise modelling of the tongue and groove connection is of importance, however, once again it is not likely to explain the large differences between the simulation and the test in the first 2400 seconds.

4.4 Test 1: Connection stiffness

As mentioned earlier, spring finite elements were used for the screw connections, their bi-linear stiffness based on the "component method" in EN 1993-1-8, section 5.2 [16]. However, realistic spring stiffness may differ, and therefore here a parameter study is carried out, see Figure 8. Different types and values of stiffness for a connection are tried to make the panel in the simulation more stiff. Besides the original bi-linear setup, this comprises two values for linear stiffness, and a rigid constraint, i.e. fixation.

Stiffness of spring element	Elasticity (N/m)		Plasticity (N/m) (displacement, force)	
	Tension	Shear	Tension	Shear
Bi-linear	5.56×10⁷	9.964×10⁶	(0, 6200) (0.0055, 7750)	(0, 4200) (0.0055, 5250)
Linear stiffness-1	5.56×10⁷	9.964×10⁶	\	\
Linear stiffness-2	5.56×10⁸	9.964×10⁷	\	\
Rigid constraint	∞	∞	\	\

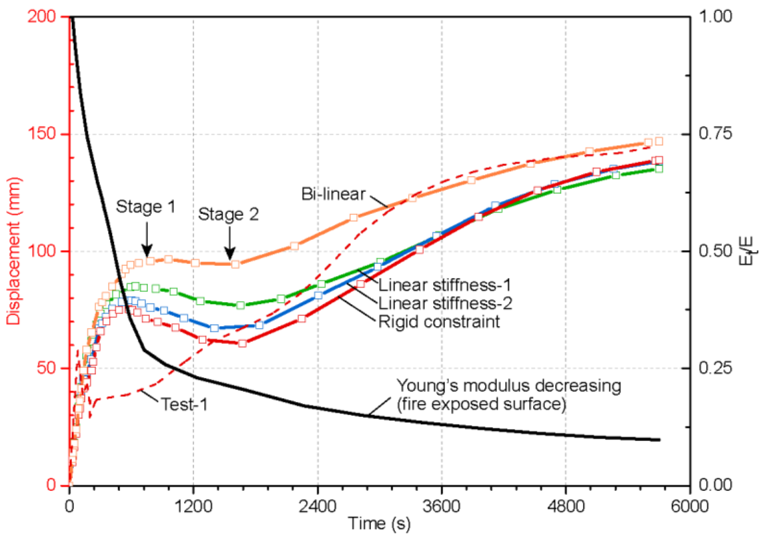

Figure 8. SR analyses for different types of stiffness for the screw connections by spring finite elements

At the very beginning of the test, temperatures increase quickly, and the resulting thermal expansion of the fire exposed face causes rapid out-of-plane deformations. Differences between the several types of stiffness descriptions exist, but are obscured in the graph due to the almost vertical plots. Then starting from "Stage 1", temperatures no longer rise significantly, but the Young's modulus of the steel fire exposed face has reduced strongly as indicated by the black line. This probably overrules thermal expansion between "Stage 1" and "Stage 2" and so the panels bend back a little. Finally, after "Stage 2", Young's modulus only decreases marginally, thermal expansion takes prevalence, and again increases the out-of-plane displacement. Although the modelling of the connection stiffness influences the overall structural behaviour, clearly it is not the cause of the large differences between the simulation and the test during the first 2400 seconds.

4.5 Test 1: Adhesive layer modelling

The final aspect investigated is the behaviour of the adhesive layer between the panel faces and insulation core. Namely, the out-of-plane deflection of the panel comes to a large extent from the expansion of the fire-exposed face, but only if this expansion can be transferred to the panel via the glue layer. Therefore, in this section an adhesive layer (5mm thickness) is modelled to the simulation of Section 3.2, as shown in Figure 9 on the left, with material properties of polyurethane as found in [23]. The adhesive layer is assumed to behave linear elastic with a Young's modulus as given in Figure 9.

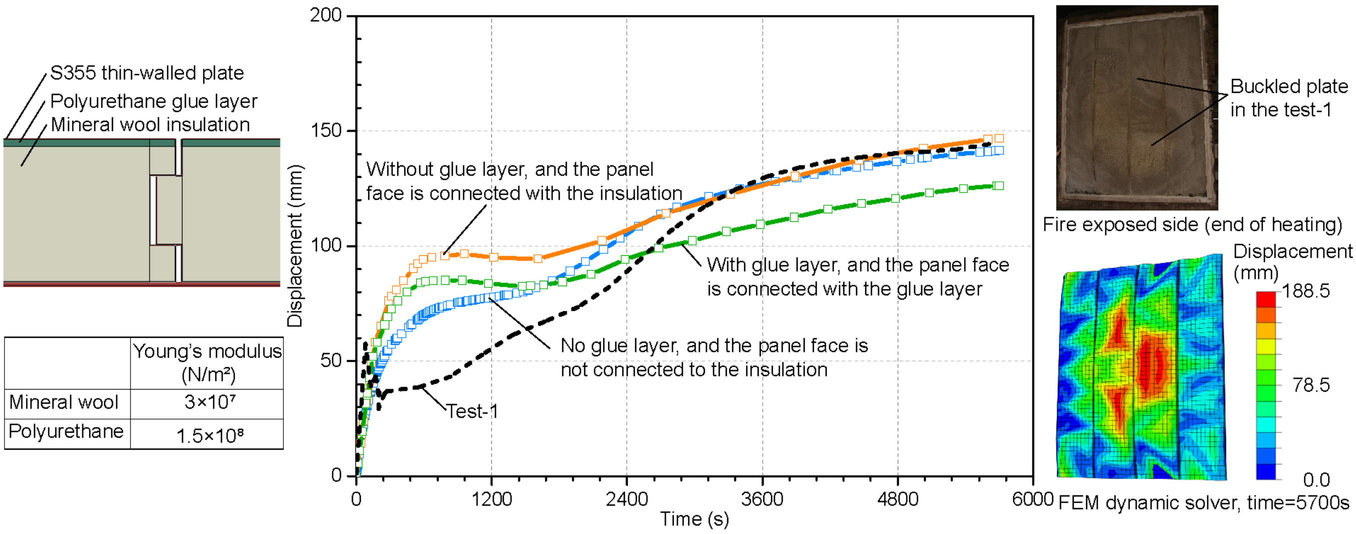

	Young's modulus (N/m²)
Mineral wool	3×10^{7}
Polyurethane	1.5×10^{8}

Figure 9. Modelling of a glue layer, and dynamic simulations with other model.

As the Young's modulus of the glue layer is larger than the insulation of mineral wool, the simulation with the glue layer shows stiffer behaviour along the complete test. However, the melting point of the glue layer is relatively low at approximately 60 °C (not modelled), and so its properties diminish soon after the start of the test. As a consequence, the fire-exposed side of the thin-walled plate may (partly) detach from the insulation layer, which could explain the subsequent transient stage of the test, as indicated in Figure 4(a). As a static solver could have issues with the (partly) loose plate (i.e. due to singularties) or the thin face structural instability modes (transient phenomena due to the lack of elastic support by the glue and insulation), a dynamic solver has been tried without the "tie" constraint between the thin-walled face and the insulation at the fire-exposed side. So the fire exposed face is only connected along its vertical edges. Figure 9 shows that this later simulation directs the equilibrium path in the direction of the test results at the beginning, and leaves the final and correct out-of-plane displacements unchanged. Therefore, it is believed that the glue behaviour and the subsequent fire exposed face behaviour, with structural instabilities and related interactions with the glue, are important factors that may explain the difference between the simulation and the test.

4.6 Test 2: Two-scale model for the stud-bolt test

For Test 2, the HT analysis gave good predictions up to failure at 3000 seconds, however, the SR analysis did not give any indication of failure, which in the test involved vertical bearing at the screw connections. Therefore, in this section a more advanced modelling of the screw connections is presented, using a two-scale model. Here only a brief overview on the two-scale model can be given, and for more details reference is made to [12]. Figure 11(a) shows a large-scale panel (not Test 1 or 2) that is connected to a supporting horizontal L-section by screws, i.e. small-scale components, Figure 11(b).

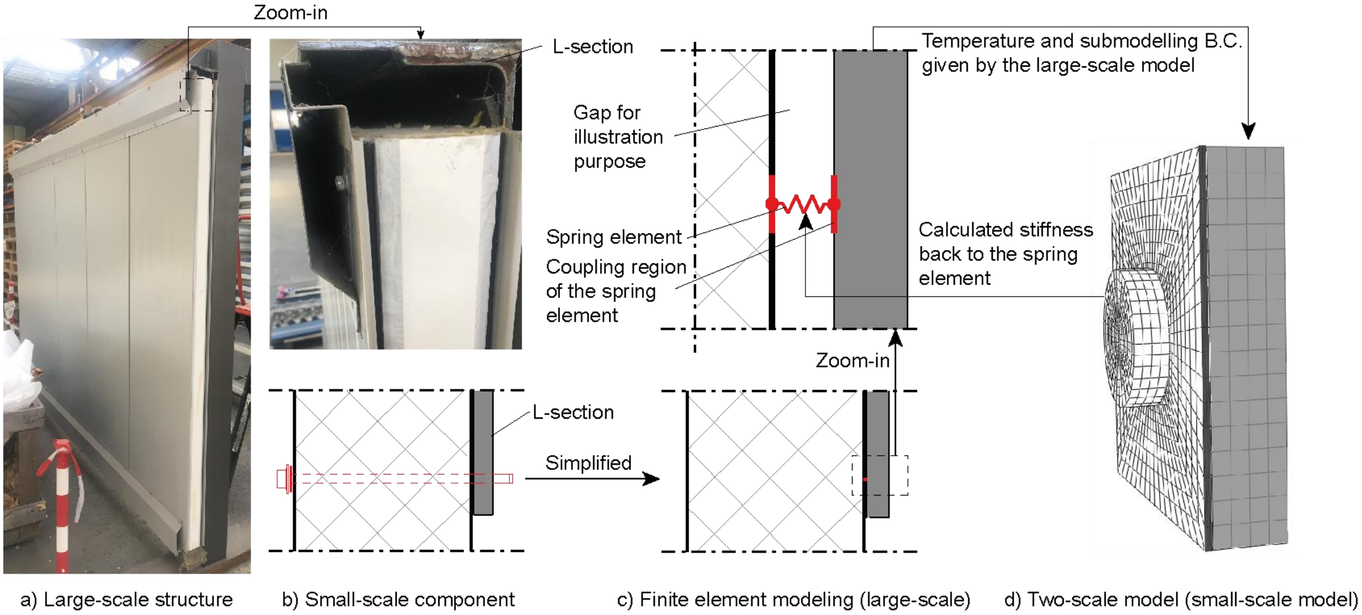

Figure 11. Overview and explanation of the two-scale method (structure for illustration purposes only: is not Test-1 or Test-2)

Commonly, such screw connections are simplified as spring elements in the Finite Element Method (FEM) to avoid computational costs, Figure 11(c), and as also suggested by EN 1993-1-8. However, non-linearities, temperature dependencies, path dependency in case of plasticity, and more phenomena are then not considered. Therefore, Xu et al. propose a so-called two-scale method, which yields accurate stiffness and failure predictions for screw connections in a large-scale structural system under fire [17]. The proposed two-scale method consists of (i) a large-scale model, with a spring element for each connection, Figure 11(c), which accounts for the overall behaviour of the structure. Secondly, it has (ii) for each connection a small-scale model, which accounts for the local and detailed behaviour of the screw connection (Figure 11(d). The large-scale model makes use of so-called "submodelling" to provide boundary conditions (including the temperatures) to the small-scale model, which subsequently predicts the connection tangent stiffness in each direction to be used for the spring element, Figure 11(d). Following the above setup of the two-scale model, Figure 12 on the left shows the specific setup for Test 2.

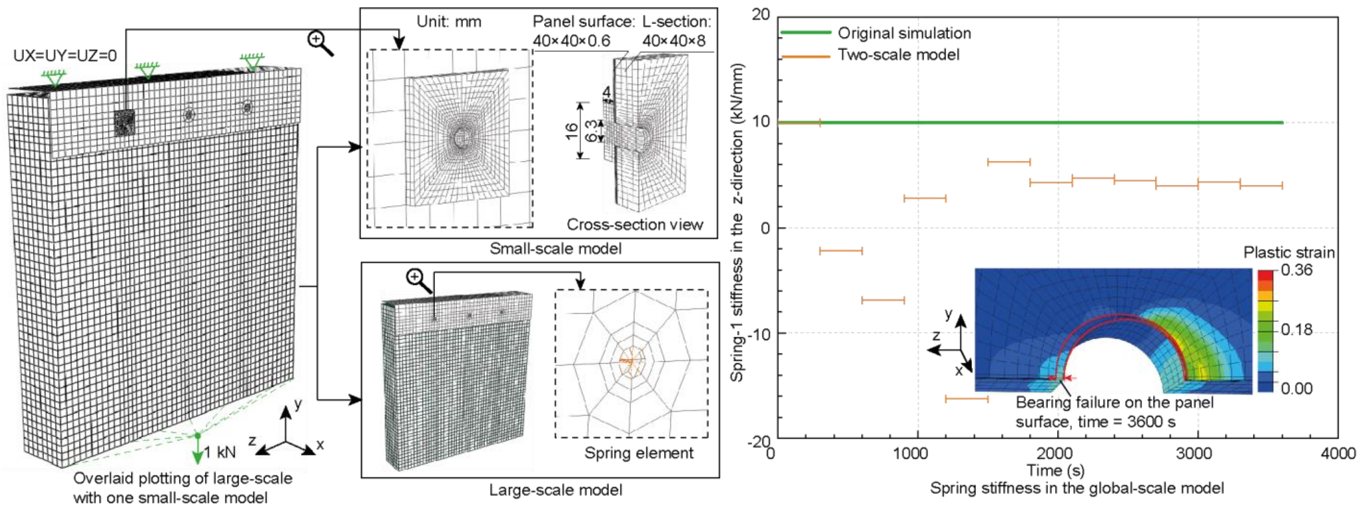

Figure 12. Simulation for Test 2 with a two-scale model: a single large-scale model and a small-scale model for each screw connection.

The large scale model has circular holes (as in practice made by the screw) for the L-section and panel faces at the screw location, with the holes' circumferences tied to the spring finite element. For each spring (screw), the spring stiffness is updated each 300 seconds by a small-scale model, which models the screw connection in detail, including the threads via the Abaqus proprietary thread interaction model [12].

Results are shown in figure 12 on the right, plotting one spring's stiffness in the z-direction versus time. Different from the standard simulation in Section 3.2, the two-scale model shows a different spring stiffness for each load step of 300 seconds, for it takes into account temporarily boundary conditions and temperature dependent (nonlinear) properties. As shown, the tangent stiffness can also be negative, due to softening, and fluctuations are also caused due to mutual interaction and adjustment between the three screw connections. Furthermore, the temperature rate is quite smal after 1800 seconds, whereas the steel stress-strain curve remains the same for the temperatures then above 800 °C (see also Figure 2 on the right). This explains the almost constant screw stiffness after 1800 seconds. On the complete right of the figure, bearing of the screw holes is shown, in z-direction, which starts almost immediately in the simulation, due to thermal expansion.

In the test, reportedly the screw connections failed because of bearing in the load negative y-direction, which could not be modelled by the standard simulation in Section 3.2, using elastic springs. The two-scale model here applies detailed small-scale models that enable the modelling of bearing, as shown in the figure, and this is a positive observation, which potentially leads to a better understanding of the test. However, the vertical bearing failure of the test cannot be seen in the simulation. It is believed that the vertical load may be set too low, for the weight of the C-section and panel have not been taken into account. Future simulations are planned for larger vertical loads, and if needed slightly higher temperatures, to hopefully enforce vertical bearing.

5 CONCLUSIONS

Two full-scale fire resistance tests of sandwich panels with connections were presented, to verify One-Way Coupled (OWC) fire-structure simulations. The simulation's Heat Transfer (HT) parts agree well with the tests, however, the Structural Response (SR) parts show higher out-of-plane deformations compared to the start of the first test.

A parameter study was conducted to resolve these differences. It shows that although (a) the thermal expansion coefficient of steel, (b) the modelling of the tongue and groove connections, and (c) the connection stiffness all do somewhat influence the behaviour of the structure, the most influencing factors are likely to be (d) glue decomposition, resulting in face delamination, and related face instabilities.

The furnace can be successfully modelled by either a standard fire curve or a more elaborate FDS fire simulation, the latter allowing for local temperature variation, if relevant for the problem at hand. This means all conclusions here, made for the (fire curve) simulations, also apply to OWC fire-structure simulations (using FDS).

The second test (a so-called stud bolts test), reportely failed by vertical bearing in load direction. The standard simulations were not able to capture bearing, but if amended by a two-scale model, almost immediate horizontal bearing was predicted, due to thermal expansion. As such, the simulations provide some additional insight in the structure's behaviour. However, vertical bearing was not predicted, and so it is suggested to carry out future simulations with slightly higher loads or temperatures, to enforce vertical besides horizontal bearing.

State-of-the-art OWC fire-structure simulations can simulate full-scale fire tests of sandwich panels, including connections, however, face delamination and instabilities should be modelled in detail. Furthermore, future tests should include detailed measurements with respect to the mechanical behaviour, e.g. panel buckling, delamination, and connections.

REFERENCES

1. ISO 13784-1, Reaction to fire test for sandwich panel building systems — Part 1: Small room test, International Organization for Standardization, Geneva, Switzerland (2019).

2. EN 13501-1, Fire classification of construction products and building elements - Part 1: Classification using data from reaction to fire tests, European Committee: Brussels, Belgium (2019).
3. EN 13823, Reaction to fire tests for building products - Building products excluding floorings to the thermal attack by a single burning item, European Committee: Brussels, Belgium (2020).
4. Axelsson, J., Van Hees, P., New data for sandwich panels on the correlation between the SBI test method and the room corner reference scenario. Fire Mater., 29: 53-59 (2005). https://doi.org/10.1002/fam.879
5. Crewe, R.J., Hidalgo, J.P., Sørensen, M.X. et al., Fire Performance of Sandwich Panels in a Modified ISO 13784-1 Small Room Test: The Influence of Increased Fire Load for Different Insulation Materials. Fire Technol. 54, 819–852 (2018). https://doi.org/10.1007/s10694-018-0703-5
6. Zhang, H. Connections in cold-formed steel modular building structure systems. University of Birmingham. Ph.D. thesis. (2018).
7. Cábová, K., Garifullin, M., Mofrad, A.S., et al., Shear resistance of sandwich panel connection at elevated temperature, J. Struct. Fire Eng., 13: 162-170 (2022). https://doi.org/10.1108/JSFE-03-2021-0013
8. Chen, W., Ye, J. Zhao, M., Steady- and transient-state response of cold-formed steel-to-steel screwed connections at elevated temperatures, J. Constr. Steel Res., 144: 13-20 (2018). https://doi.org/10.1016/j.jcsr.2018.01.016
9. Wickström, U., Duthinh, D., McGrattan, K., Adiabatic surface temperature for calculating heat transfer to fire exposed structures, In: Proceedings 11th International Interflam conference, London, England, Vol. 2, 943-953. (2007).
10. Feenstra, J.A., Hofmeyer, H., Van Herpen, R.A.P., et al., Automated two-way coupling of CFD fire simulations to thermomechanical FE analyses at the overall structural level. Fire Saf. J., 96: 165-175 (2018). https://doi.org/10.1016/j.firesaf.2017.11.007
11. De Boer, J.G.G.M., Hofmeyer, H., Maljaars, J., et al., Two-way coupled CFD fire and thermomechanical FE analyses of a self-supporting sandwich panel façade system. Fire Saf. J., 105: 154-168 (2019). https://doi.org/10.1016/j.firesaf.2019.02.011
12. Xu, Q., Hofmeyer, H., Maljaars, J., A two-scale model for basic screw connection behaviour in two-way coupled fire-structure simulations. To be submitted. (2022).
13. Xu, Q., Hofmeyer, H., Maljaars, J., et al., A two-scale FE model to address connections in coupled fire-structure simulations. ASFE’21, June 10-11, 2021, Ljubljana, Slovenia. (2021).
14. Dassault Systèmes, ABAQUS manuals, Version 6.14, United States, (2014).
15. McGrattan, K., Hostikka, S., McDermott, R., et al., Fire dynamics simulator user’s guide. NIST special publication, 1019: 1-339 (2013).
16. EN 1993-1-8, Eurocode 3: Design of Steel Structures - Part 1-8: Design of Joints, European Committee for Standardisation, Brussels, Belgium, (2005).
17. Xu, Q., Hofmeyer, H., Maljaars, J., A two-scale FE model to address connections in coupled fire-structure simulations. Proceedings ASFE'21, Applications of Structural Fire Engineering, June 10-11, 2021, Ljubljana, Slovenia, 388-393 (2021).
18. EN 1993-1-2, Eurocode 3: Design of Steel Structures - Part 1-2: General rules - Structural fire design, European Committee for Standardisation, Brussels, Belgium, (2005).
19. Bai, Q., Bai, Y., Subsea pipeline design, analysis, and installation. Gulf Professional Publishing, Oxford, 405-433 (2014). https://doi.org/10.1016/B978-0-12-386888-6.00017-1.
20. Fredlund, B., Calculation of the Fire Resistance of Wood Based Boards and Wall Constructions. Lund University, Department of Fire Safety Engineering, Sweden, PhD thesis. (1990).
21. BS 5950–8, British Standards Institution (BSI). Structural use of steelwork in building—Part 8: Code of practice for fire resistant design, London, (1998).
22. ASCE, Structural fire protection. ASCE manual and reports on engineering practice No. 78, New York, (1992).
23. Arvidson, J.M., Sparks, L.L., Low temperature mechanical properties of a polyurethane foam. National Bureau of Standards, U.S. Department of Commerce, Colorado, (1981).

SiF 2022– The 12th International Conference on Structures in Fire
The Hong Kong Polytechnic University, Nov 30 - Dec 2, 2022

PREDICTING THE STRUCTURAL CAPACITY OF FIRE-EXPOSED CLT COMPRESSION MEMBERS

Ahmed Ahmed Ali Awadallah[1,2]*, Luke Bisby[1]

ABSTRACT

Efforts to reduce the carbon footprint of the construction industry have fuelled interests in so-called sustainable construction materials. Engineered wood products such as cross laminated timber (CLT) and glued laminated timber have facilitated this transition owing to numerous advantages over steel or concrete in some structural applications. However, cross laminated timber, like other timber products, degrades and combusts under fire exposure, experiencing reductions in structural capacity in the process. The study presented in this paper aims to numerically evaluate the structural capacity of CLT walls, with reference to properties and procedures suggested in EN 1995-1-2, under both heating and decay phases of potential design fire curves, and then to perform a parametric study to investigate which CLT wall build-ups are better performing in fire, and why. A one-dimensional transient heat transfer model was employed to predict the in-depth temperature distributions in a CLT cross-section whilst accounting for temperature dependent thermal properties (modelled according to the advanced method outlined in Annex B of EN 1995-1-2). A decoupled structural model accounting for the reduction in strength and stiffness based on the thermomechanical properties, also outlined in Annex B of EN 1995-1-2, was then used to predict the crushing and buckling load capacity of the CLT. The widely applied reduced cross-section method (RCSM)of strength during cooling was also studied for illustrative purposes only. The intensity and duration of a fire influence the extent of reduction in capacity, and further strength reductions were observed during the decay phase, as expected. The RCSM, as currently implemented in EN 1995-1-2 was confirmed as being difficult to defend for elements in compression, compared to the advanced model, particularly to estimate the crushing capacity during heating and cooling. It is also shown that the governing mode of failure at ambient temperature may change during a fire (i.e., from crushing to buckling), a fact which should be borne in mind by designers of CLT buildings.

Keywords: CLT; structural fire performance; numerical modelling; timber

1 INTRODUCTION

Cross laminated timber is an engineered timber product that is now widely used for constructing load bearing structural panels such as walls and slabs in multi-storey buildings. The existing code-based methods and assumptions for design of timber members in fire were originally developed for solid and glued laminated timber members when subjected to standardised heating scenarios, and their applicability to the structural fire design of CLT members exposed to so-called natural fires still requires further consideration. Some European designers currently use such methods for CLT design, since alternative design codes specific to CLT have not yet been formally published [1]. Additionally, designers and manufacturers continue to experiment with different parameters to study their influence on the performance of CLT members in fire. Factors such as the number of CLT layers, their thicknesses, adhesive type(s), and configurations all play roles in CLT's structural fire performance.

Cross laminated timber (CLT) refers to an engineered timber product typically made up of an odd number of timber laminations (three, five, seven, and – less commonly – nine) arranged in a crosswise manner and bonded together using adhesives under pressure. The development of CLT began decades ago, particularly in Central Europe (Germany, Switzerland, and Austria) but is currently experiencing rapidly growing interest internationally. In Europe, CLT is often manufactured from softwood species of spruce [2],[3] and

[1] The University of Edinburgh, [2] The Danish Institute of Fire and Security Technology (DBI)
*Correspondence to: aaa@dbigroup.dk
https://doi.org/10.6084/m9.figshare.22178309

in some cases Douglas fir [3]. Unlike solid and glued laminated timber, CLT is capable of withstanding in-plane and out-of-plane loading, making it suitable for use as loadbearing walls and floors [2]. Typical dimensions of CLT are lengths from 18-30 m, breadths ranging from 3-4.8 m, and thicknesses of up to 400 mm [2]. Ply thicknesses commonly range between 12 mm and 45 mm, with thicknesses of 20 mm, 30 mm, and 40 mm generally being adopted in Central Europe [2].

Eurocode 5 Part 1-2 [4] provides three potential methods for the structural fire design of timber members. The most widely used method, the reduced cross-section method (RCSM) and the less known reduced properties method (RPM), as well as an 'advanced method' given in its Annex B. Whilst, as already noted, these methods were developed for other types of solid and glued laminated timber elements, designers and engineers currently use them for CLT design regardless, given that no formally adopted normative codes for CLT currently exist in Europe [1], [5].

The RPM is based on a pre-multiplying modification factor defined as a function of the exposed area and perimeter of the residual cross-section. This method is limited to cross-sections with three or four side exposure, and hence cannot be used for one-sided heating as would occur in a load-bearing wall. Other limitations include inability to capture shear strength reductions [6].

In the RCSM, the design begins by subtracting from the original cross-section of the timber member by the effective char depth (determined as per EC 5 [4]) along with an additional assumed 'zero-strength' layer. The rationale behind using a zero-strength layer stems from the assumption that beyond the charred layer, there exists a heat affected zone with no strength or stiffness. The use of a constant zero-strength layer has been the subject of some debate in the structural fire timber community [7]–[11], however this is outside the scope of this paper and in any case is now widely accepted as being inappropriate for cases involving heated timber in compression. In this paper we use the RCSM purely for illustrative purposes, without any direct or implied criticism, and in full recognition of the fact that necessary updates to the method to address these concerns are currently being proposed.

Annex B of EN 1995-1-2 [4] outlines advanced calculation methods that can be used to assess the fire performance of timber members. These methods can be applied to approximate the evolution and distribution of in-depth temperatures within a timber member using standard heat transfer equations (and effective thermal properties), and for the structural analysis of the structure or part thereof accounting for the temperature-dependent mechanical properties of wood [12].

The study presented in this paper aims to develop a 'thought experiment', to computationally investigate the load-bearing capacity of compressive CLT structural elements, particularly CLT load bearing walls heated from one side in a fire. Analysis of how specific CLT ply configurations may affect the capacity of CLT load bearing walls in fire is included, aiming at guiding engineers and designers with best practice in designing CLT walls for structural fire performance.

2 THE MODELLING APPROACH

2.1 Thermal Analysis

Accurate modelling of heat transfer in timber cross-sections is critical to accurately determine the in-depth temperature profiles and assess mechanical properties. While more complex modelling approaches exist [13] and may be adopted where necessary, an explicit, one-dimensional, transient heat transfer model (without heat generation) using the finite difference method was used in the current study. This scheme was selected as it enabled the time derivative to be measured using forward differences. Small steps in the space and time domains will lead to convergence to the exact solution. Any random errors resulting in the solution for example, round-off error, are thus limited.

Several models for thermal properties of timber exist in literature to approximate its thermal conductivity, specific heat, and density [4] [14]–[20]. While some models are empirical and based on physically measured values, others are instead calibrated against test data to account for processes such as mass transport and the formation of fissures. A choice was made in the current study – for illustrative purposes – to simply employ the temperature dependent thermal properties of timber according to the advanced method outlined in Annex B of EN 1995-1-2 [4]. It was assumed that the temperature inside the timber is initially ambient (20 °C). The surface temperature was obtained by solving the typical heat transfer equations at the timber surface assuming an emissivity of wood of 0.8 and a convective heat transfer coefficient of 25 $W \cdot m^{-2} \cdot K^{-1}$ for standard fire exposure as per EN 1995-1-2 [4].

2.2 Structural Analysis.

The structural analysis uses the resulting temperature data from the thermal analysis as an input to predict the load bearing capacity of the timber member. Similar to the thermal properties, several sets of suggested thermo-mechanical property reduction curves exist in literature [14], [17], [21]–[23]. The compressive strength and elastic modulus reduction factors given in the advanced method of Annex B of EN 1995-1-2 [4] were used in the current work to predict the elastic buckling and compressive load bearing capacity.

For compressive elements, the concentric crushing capacity is the most basic way to determine load bearing capacity for structural design. Cross laminated timber elements present a particular behaviour due their arrangement of timber plies in a crosswise manner (i.e., different loading directions). As such, almost all the load carrying capacity is due to the longitudinal plies, while strength contributions from the crosswise layers are typically neglected [24]. In this study, crosswise layers are assumed to contribute 1/30th of that of the longitudinal layers [1].

Structural design of compression members must also consider for the elastic buckling load so as to prevent instability failures. For slender structural members, buckling may govern the structural design at ambient temperature, and the critical elastic buckling load is given by the classical Euler buckling load. The arrangement of CLT plies necessitates the transformation of crosswise plies into an equivalent depth of longitudinal plies before the second moment of inertia can be calculated, assuming a ratio of the elastic modulus of a longitudinal layer to a crosswise layer of 30 [1].

Additionally, heat induced reductions in the elastic modulus must be considered. Each affected layer of the cross-section can be regarded as a different material (with different E) and must be transformed into an equivalent width of virgin timber, thus resulting in a shift of the neutral axis of the whole cross-section. A stepwise procedure was developed that calculated the reductions in elastic modulus of the heat affected layers, transformed these into to an equivalent width of timber at ambient conditions, and computed the second moment of area of the transformed cross-section using the parallel axis theorem. This is illustrated in Figure 1. Using the coordinates of the transformed cross-section, the transformed second moment of area of the entire cross-section is computed using an procedure outlined in [25]. The input variables are shown in Table 1. For both crushing and buckling calculations, zero strength is assumed once the temperature of any layer exceeds 300 °C [4].

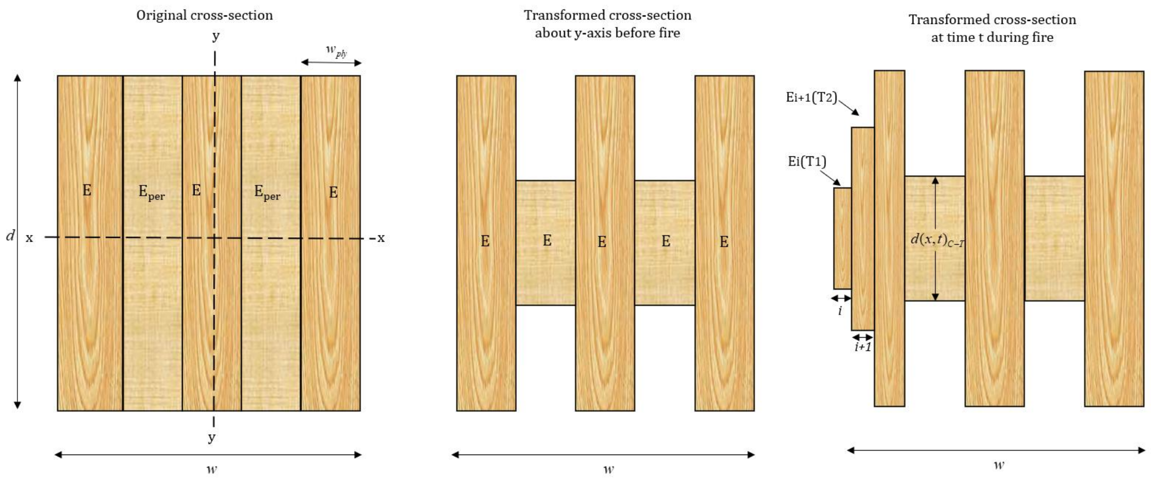

Figure 1 Original 5-ply CLT cross-section (left) and its transformed CLT cross-section (middle) at ambient temperature and transformed section during fire at time t (right). E – ambient elastic modulus, E_{per} – perpendicular elastic modulus, $E(T_i)$ – elastic modulus at temperature T_i. $d(x,t)_{C\text{-}T}$ is the the transformed depth of the cross-section in *mm* at a distance x and time t. $E_i(T1)$ – elastic modulus of slice i at temperature T1

2.1 Fire Scenarios

Fire scenarios implemented in this study consisted of 60-minute and 120-minute standard fires, typically used as an indication of fire resistance (and in essence the *fire performance* of a member). Immediately after the heating phase, the temperature was set to drop immediately to ambient, mimicking what happens when a tested sample is immediately taken out of a fire testing furnace. The authors acknowledge this fire scenario is unrealistic as regards real building fires, but is however implemented for illustrative purposes only (i.e., it is a best case scenario in terms of thermal insult to the timber). Nonetheless, the thermal wave caused by the initial heating phase is accounted for in the model. These fire scenarios are shown in Figure 2.

Table 1 Model input variables

Input Variable	**Value**
Compressive Strength	24 MPa
Elastic Modulus	11000 MPa
Density	470 kg/m3
Moisture Content	12%
Member Length	3 m

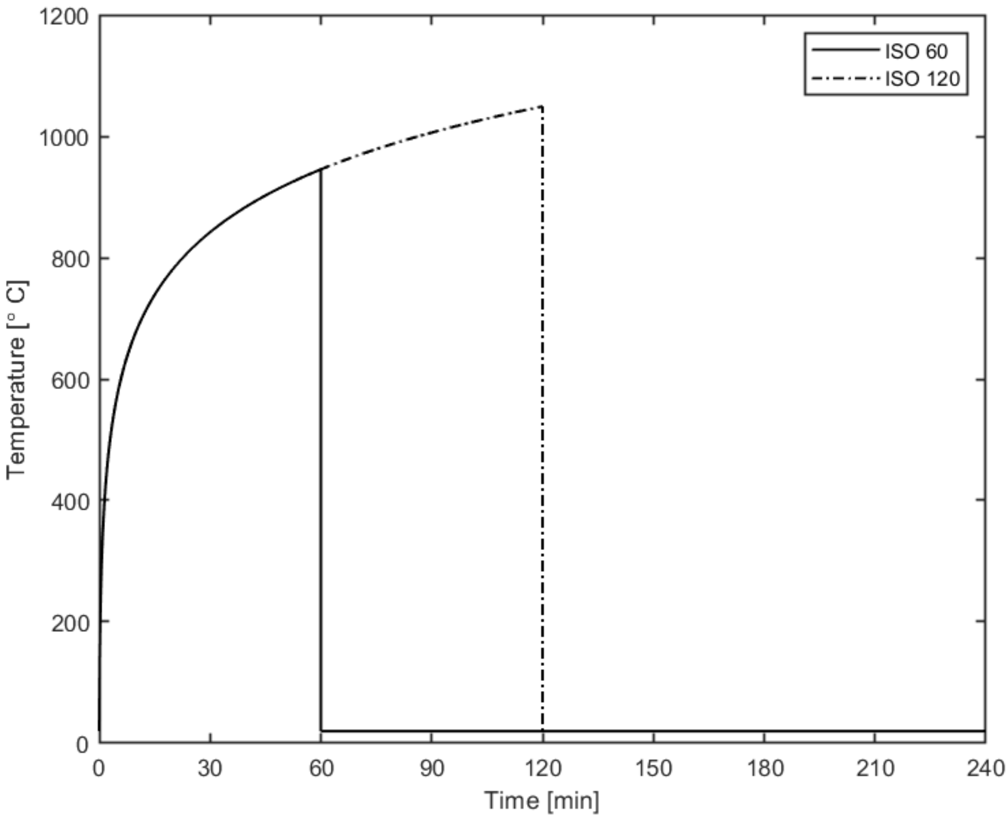

Figure 2 Fire curves used for illustrative purposes in this study.

The simulation campaign first investigated the performance of the different models under the heating scenarios outlined, and then a parametric study on CLT member thickness, number of timber plies, and individual ply thicknesses and arrangements was carried out using the advanced model.

2.2 CLT Configurations

Three CLT configurations were modelled as part of the parametric study, to determine the optimum CLT build-ups for structural fire performance, as distinct from ambient temperature performance. The different CLT configurations all had the same overall thickness of 210 mm, but varied in construction based on the thicknesses of the individual plies. The CLTs considered consisted of either:

1. Plies with uniform thickness (U),
2. Thicker first and last plies (FL),
3. Thicker odd plies (O).

3 RESULTS AND DISCUSSIONS

3.1 Comparison of Strength Prediction Models

The two strength predictions models (i.e. RCSM and EC5-1-2 Advanced) are compared in Figure 3, which shows the normalised load carrying capacity for 3, 5 and 7-ply CLTs with uniform ply thicknesses under 60- and 120-minute ISO fires (heating phase only). All models predict more severe reductions in the buckling load as compared to a gentler reduction in the crushing load. This is logical, since the buckling load is a function of the stiffness and second moment of area of the member's' cross sections, which in turn are functions of the cross-sectional dimensions to the fourth power; and hence the temperature induced reduction in the stiffness will result in a reduced transformed cross-section, thus resulting in more rapid loss of buckling strength. The initial sudden drop in capacities predicted by the RCSM is attributed to the instantaneous 'disappearance' of the so-called zero-strength layer at the smallest time step when calculating the effective char depth, and hence the effective cross-sectional dimensions.

Noteworthy behaviour can be observed in Figure 3; after a certain fire duration, nearly no change in the predicted capacity is recorded. This is readily observed in the predicted load capacity by the RCSM (represented by an almost constant line), and by the advanced method by a sudden change in slope. This is indicative of the progression of the temperature front into a crosswise timber layer, whose contribution to the load capacity is negligible. In other words, the crosswise layers act as 'thermal buffer zones' where minimal strength reduction occurs whilst the layer is thermally penetrated.

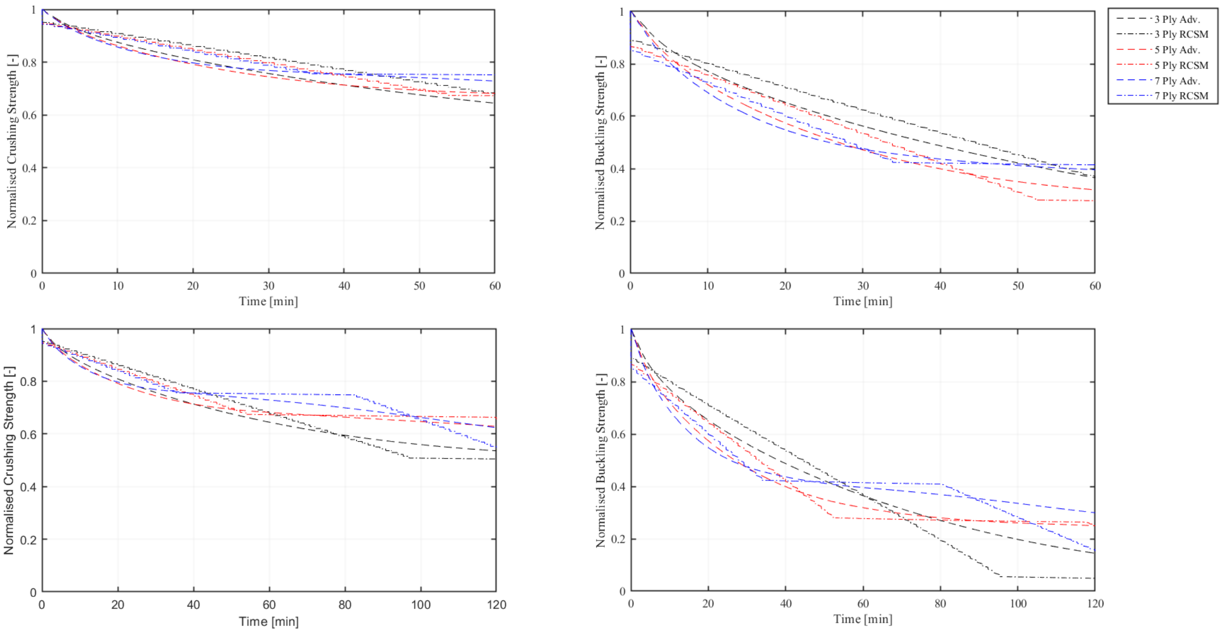

Figure 3 Comparison of strength prediction by advanced and RCSM under ISO-60 (top), ISO-120 (down)

This comparison illustrates that, under short standard heating conditions, the advanced model predicted conservative crushing capacity as compared to the RCSM predictions. However, for the same fire scenario, comparable buckling capacities were obtained using both methods. Under the longer ISO fire however, the RCSM predicted lower crushing capacities for 3- and 7-ply CLTs. For all buckling cases, the RCSM was more conservative to the advanced method.

3.2 Implications of the Decay Phase

The simulation was allowed to run until 240 minutes under both fire exposures to study the effects of the decay phase and internal thermal wave on the structural capacity of the members. It is widely acknowledged that timber starts to degrade mechanically at comparatively low temperatures [1] relative to concrete or steel, hence the effects of the cooling phase ought to be explicitly considered. This is due to the thermal wave that continues to penetrate into the cross-section following the end of the heating duration, owing to heat dissipation through the cross-section. Other authors have commented on similar issues, considered under the banner of 'burnout resistance', both numerically and experimentally for glued-laminated timber columns [26], [27] and for CLT elements [28].

Figure 4 and Figure 5 show the crushing and buckling capacities of 3-, 5- and 7-ply CLTs under the 60- and 120-minute standardised fires with the extended cooling periods. A general trend can be seen, beyond the heating phase, further reduction (albeit mild) in all capacities can be observed. The cooling period results in further losses in strength owing to the continued propagation of the thermal wave through the cross section following the end of heating. Furthermore, it can be observed that the percentage reduction in crushing strength for the 5- and 7-ply CLTs due to the decay phase is comparatively higher than that of their buckling strength, and the opposite is true for 3-ply CLTs. This can be attributed to the arrangement of plies in a CLT, where for a 3-ply CLT – whose strength is provided entirely by the first and last plies – any additional heat induced mechanical degradation of the first ply results in a far more slender cross-section with reduced buckling capacity

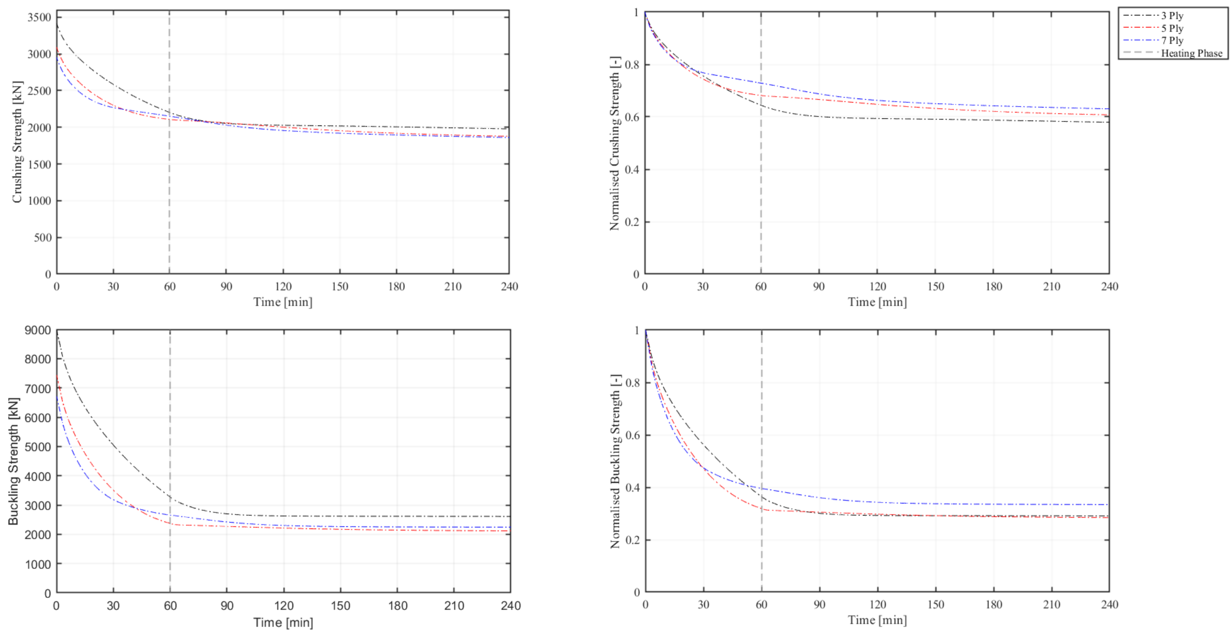

Figure 4 True and normalised load capacities under ISO 60 with immediate cooling

Of the CLTs studied, it is apparent that 3 ply CLTs resulted in the most severe reductions in buckling capacity in fire (taking buckling to be critical) although it results in the highest load bearing capacity at ambient. At first glance, and for the shorter 60 minute standard fire, a 3 ply CLT is predicted to outperform the other CLT layups at 60 minutes (Figure 4). However, during the decay phase, further mechanical degradation results in 7- and 5 ply CLTs performing better. Under a longer fire, 5- and 7- ply CLTs outperform the 3-ply CLT.

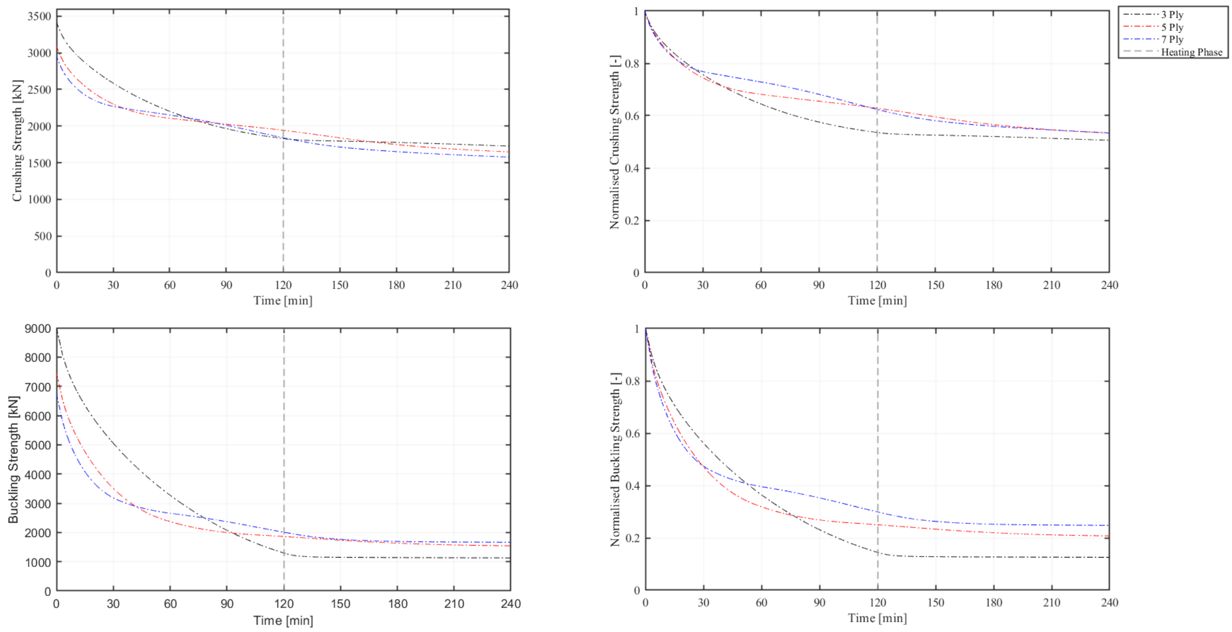

Figure 5 True and normalised load capacities under ISO 120 with immediate cooling

3.3 Critical Load for CLT Walls

Engineering design usually considers the worst credible failure load and designs to resist it. For compression members, this could either be the crushing load or the buckling load depending on the slenderness of the member. However, the distinctive ply arrangement in a CLT member, coupled with the effects of thermo-mechanical degradation, introduce complications specific to the fire limit state that warrant consideration by designers. Results from this study suggest that the governing failure mode under ambient conditions might not necessarily govern under fire; and that a shift from crushing failure to buckling (i.e. instability) failure may occur. This may be particularly important for non-slender CLT walls, which for the wall height considered in this study corresponds to CLTs with a thickness greater than or equal to 150 mm.

Taking for example a 210 mm thick, 3-ply CLT with equal ply thickness subjected to the two-hour standard fire curve (with cooling) shown in Figure 6 below, it is apparent that at ambient conditions (time = 0), the crushing load is automatically the governing load for failure. That is, this wall would fail by crushing under normal conditions and designers will often design against that mode of failure. This can be seen clearly where at ambient conditions, the computed buckling capacity is 8976 kN as opposed to 3415 kN for the crushing capacity, making the buckling capacity about 2.6 times higher than the crushing capacity at ambient.

However, the mechanical degradation induced by the increased temperatures and subsequent charring results in the cross-section suddenly losing a huge proportion of its (already reduced) buckling capacity, eventually becoming the governing mode of failure. This transition in the governing load can be observed at about the 90th minute for the 3-ply CLT. Such transition can also be seen for 5 and 7-ply CLTs with the buckling capacity of the 7-ply CLT going below the crushing capacity during the cooling period. The danger in this therefore becomes apparent postfire, in situations where a structure seemingly stable suddenly collapses, reiterating the importance of accounting for the thermal wave during the decay phase.

3.4 Optimum CLT Wall Design

As outlined in earlier sections, CLT products come in varying numbers of plies, thicknesses, and ply arrangements, which evidently will influence the structural performance in fire. Simulation results revealed the observation, with regards to the makeup of a CLT member, that for the same overall member thickness, the number and arrangement of lamellae, as well as the severity of the fire, are likely to significantly affect structural fire outcomes.

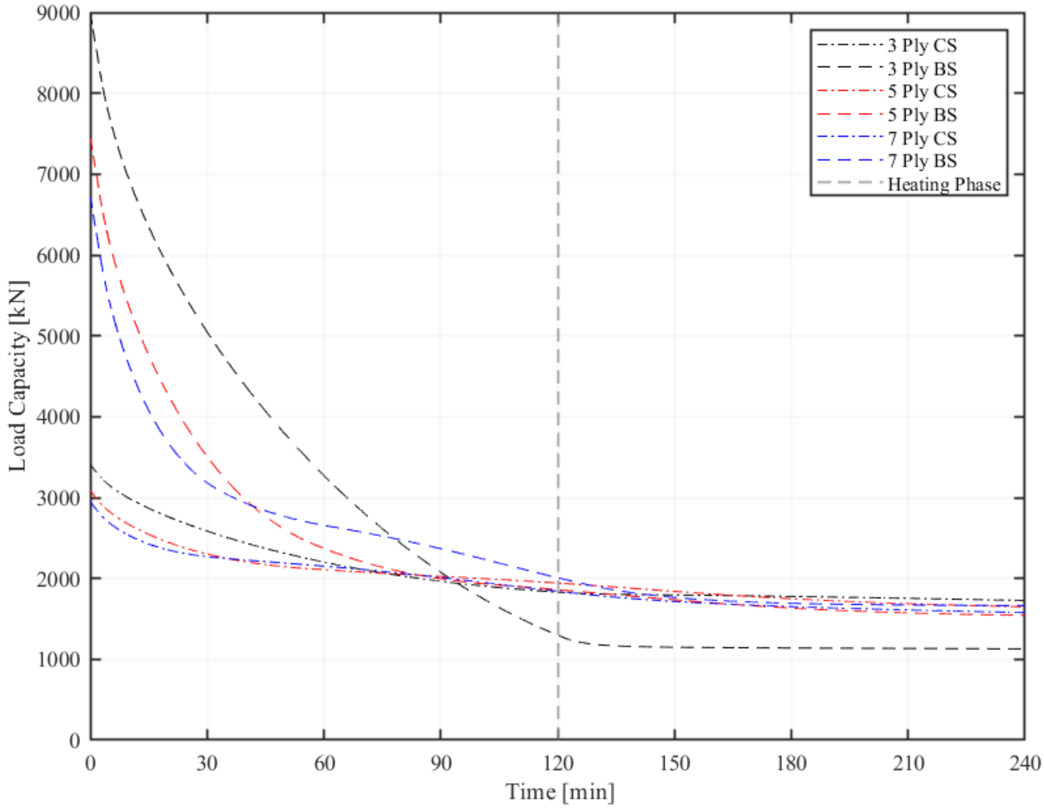

Figure 6 Load capacity for equal ply 210 mm 3, 5 and 7-ply CLTs under ISO 120 with immediate cooling

Structural engineering calculations at ambient temperature will always be based on the weaker calculated strength capacity, which at ambient for non-slender CLT wall members is the crushing capacity. Hence, to illustrate the influence a fire may have, Figure 7 and Figure 8 show the crushing and buckling load capacities normalized against the crushing capacity for a 210 mm thick CLT with the different ply arrangements (U, FL, and O) under the 60- and 120-minute heating curves (with cooling), respectively.

In terms of buckling and under the short fire, the 3-ply CLT outperformed both the 5- and 7-ply CLTs for all arrangements, retaining the highest residual buckling capacity. The opposite was however true for crushing, where the 7- and 5-ply CLTs were able to maintain a higher percentage of their initial capacity. When the same CLTs are subjected to a longer more intense fire, the performance varies. 3-ply CLTs lost most of their first ply and hence become the worst performing with regards to buckling followed by the 5-ply and 7-ply CLTs. Similar residual crushing capacities were obtained for each configuration for each ply number. Of all the CLT arrangements, configuration O, resulted in the highest residual capacity in this study.

A CLT wall's strength comes from its odd-numbered plies (herein called its effective structural thickness, $d_{str,eff}$), while its even-numbered plies act primarily as thermal buffers in fire. For the same wall thickness (and similar ply configuration), a 3-ply CLT would have more $d_{str,eff}$ than a 5-ply, which is slightly higher than a 7-ply CLT's. Under a fire scenario, the heat affected depth will be similar regardless of ply number and evidently the residual structural capacity will be determined by the remaining $d_{str,eff}$. This is especially important for a 3-ply CLT, since its strength is contained in its outer plies. Under the short fire and where the heat affected zone did not penetrate beyond the first ply, 3-ply CLTs outperformed both 5- and 7-ply CLTs since the residual $d_{str,eff}$ was greater. Under the longer fire, however, the heated zone penetrated beyond the first ply of the 3-ply CLT hence $d_{str,eff}$ was halved making it critical under buckling. For the 5- and 7-ply CLTs, although the first ply was 'consumed', the adjacent even ply acted as a buffer where further thermal penetration did not lead to additional loss in strength and the residual $d_{str,eff}$ was greater. Opting for a CLT with thicker odd plies (configuration O) promotes the maximum $d_{str,eff}$ in compressive elements, and consequently the maximum ambient structural capacity as opposed to other configurations, whilst also promoting retention of capacity during a fire for cases involving 3 or 5 plies.

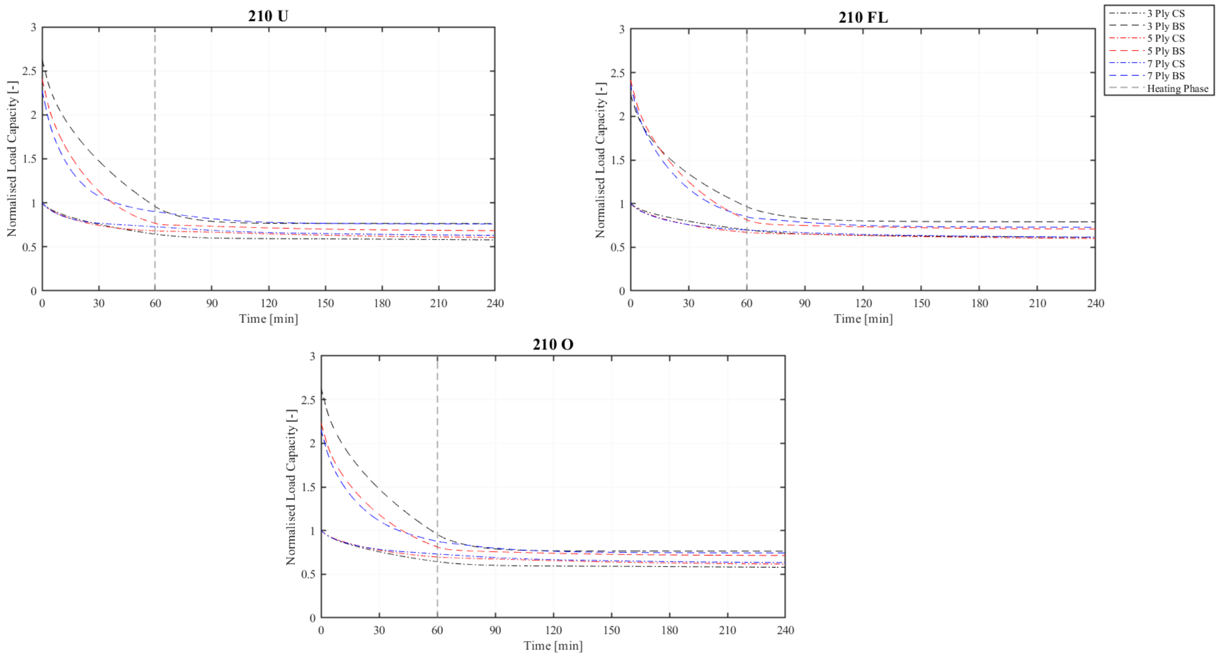

Figure 7 Crushing-normalised load capacities of different CLT arrangements under ISO 60 with immediate cooling

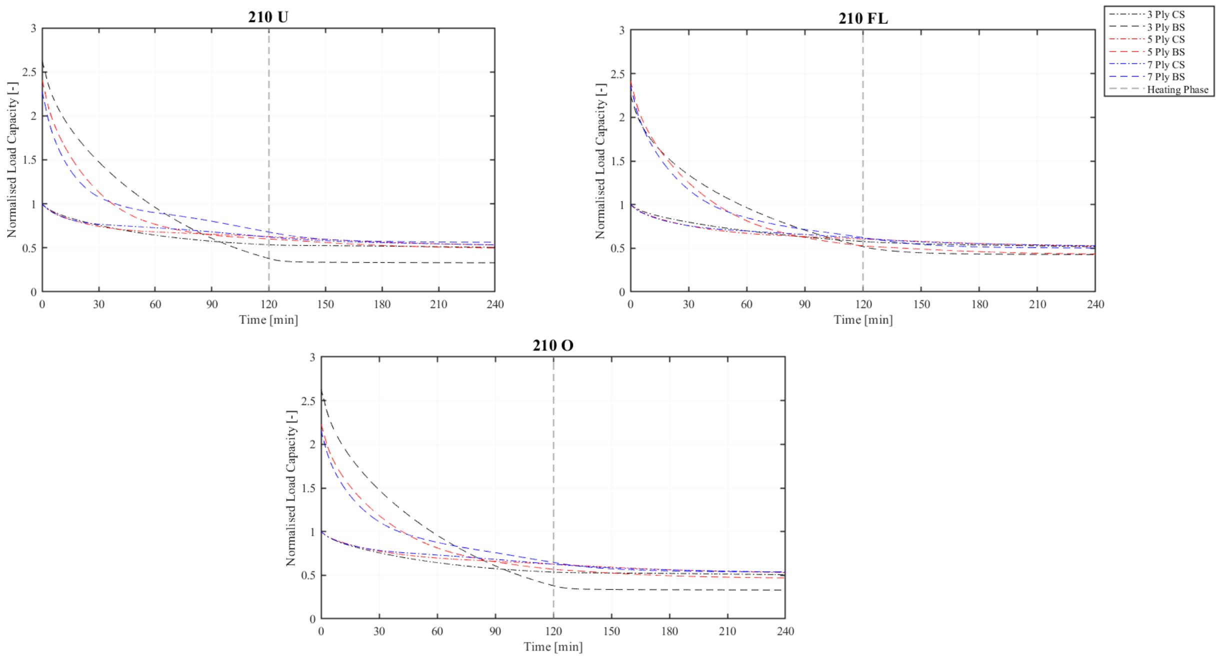

Figure 8 Crushing-normalised load capacities of different CLT arrangements under ISO 120 with immediate cooling

4 CONCLUSIONS

Results from this study confirmed that in fire, the loss in buckling strength is likely to be more pronounced as compared with concentric crushing strength for CLT wall elements. While crushing may appear to be the governing failure mode at ambient temperature, a shift in governing mode of failure from crushing to buckling was predicted for thicker (non-slender) CLT walls during and after a fire. With regards to current design methods, the well-known deficiency of using the RCSM for CLT wall design was reconfirmed, especially for predicting crushing capacity during fire. Accounting for a cooling period (i.e., beyond the period of heating or the normative fire resistance period) confirmed further reductions in capacity due the progressing thermal wave through the cross-section, even after the heating period has ended, albeit these were predicted to be mild for the elements considered in the current paper.

A limited parametric study suggested that the number, arrangement, and thickness of the individual timber plies making up the CLT wall may significantly influence its residual capacity. For the same ply number, CLTs with thicker longitudinal layers performed better in fire. For shorter fires, 3-ply CLTs performed relatively better as compared to 5- and 7-ply CLTs. Under longer fires however, 5- and 7-ply CLTs are recommended. Therefore, designers ought to base their selection of a CLT member (and configuration) with the aim of maximizing the effective structural thickness $d_{str,eff}$ while still keeping in mind the influence of the fire duration. The use of CLT with a higher number of plies (5 and 7) is recommended for structural fire applications of compression elements despite being less structurally efficient at ambient.

5 ACKNOWLEDGEMENT

The work presented in this thesis was performed as part of an International Master of Fire Safety Engineering (IMFSE) MSc thesis project at the University of Edinburgh. The authors gratefully acknowledge the support of the European Commission and the University of Edinburgh in making this programme possible.

REFERENCES

[1] F. Wiesner, “Structural behaviour of cross-laminated timber elements in fires,” The University of Edinburgh, 2019.

[2] R. Brandner, G. Flatscher, A. Ringhofer, G. Schickhofer, and A. Thiel, “Cross laminated timber (CLT): overview and development,” *European Journal of Wood and Wood Products*, vol. 74, no. 3, pp. 331–351, 2016, doi: 10.1007/s00107-015-0999-5.

[3] M. He, X. Sun, and Z. Li, “Bending and compressive properties of cross-laminated timber (CLT) panels made from Canadian hemlock,” *Construction and Building Materials*, vol. 185, pp. 175–183, 2018, doi: 10.1016/j.conbuildmat.2018.07.072.

[4] EN1995-1-2., “Eurocode5: Design of Timber Structures Part 1–2: General Structural Fire Design,” *CEN, European , Committee for standardization: Brussels*, 2004.

[5] F. Wiesner and L. Bisby, “The structural capacity of laminated timber compression elements in fire: A meta-analysis,” *Fire Safety Journal*, vol. 107, no. May 2018, pp. 114–125, 2019, doi: 10.1016/j.firesaf.2018.04.009.

[6] J. König and B. Källsner, “Cross-section properties of fire exposed rectangular timber members,” in *In Proc., Meeting 34 of the Working Commission W18-Timber Structures*.

[7] S. A. Lineham, D. Thomson, A. I. Bartlett, L. A. Bisby, and R. M. Hadden, “Structural response of fire-exposed cross-laminated timber beams under sustained loads,” *Fire Safety Journal*, vol. 85, pp. 23–34, 2016, doi: 10.1016/j.firesaf.2016.08.002.

[8] D. J. Hopkin, J. El-Rimawi, T. Lennon, and V. V. Silberschmidt, “Effect of fire-induced damage on the uniaxial strength characteristics of solid timber: A numerical study,” *Journal of Physics: Conference Series*, vol. 305, no. 1, 2011, doi: 10.1088/1742-6596/305/1/012039.

[9] J. Schmid, A. Menis, M. Fragiacomo, I. Clemente, and G. Bochicchio, “Behaviour of Loaded Cross-Laminated Timber Wall Elements in Fire Conditions,” *Fire Technology*, vol. 51, no. 6, pp. 1341–1370, 2015, doi: 10.1007/s10694-015-0516-8.

[10] J. Schmid, A. Just, M. Klippel, and M. Fragiacomo, “The Reduced Cross-Section Method for Evaluation of the Fire Resistance of Timber Members: Discussion and Determination of the Zero-

Strength Layer," *Fire Technology*, vol. 51, no. 6, pp. 1285–1309, 2015, doi: 10.1007/s10694-014-0421-6.
[11] F. Wiesner, F. Randmael, W. Wan, L. Bisby, and R. M. Hadden, "Structural response of cross-laminated timber compression elements exposed to fire," *Fire Safety Journal*, vol. 91, pp. 56–67, 2017, doi: 10.1016/j.firesaf.2017.05.010.
[12] J. König, "Structural fire design according to Eurocode 5 - Design rules and their background," *Fire and Materials*, vol. 29, no. 3, pp. 147–163, 2005, doi: 10.1002/fam.873.
[13] B. Moghtaderi, "The state-of-the-art in pyrolysis modelling of lignocellulosic solid fuels," *Fire and Materials*, vol. 30, no. 1, pp. 1–34, 2006, doi: 10.1002/fam.891.
[14] J. König and L. Walleij, "Timber frame assemblies exposed to standard and parametric fires Part 2: A design model for standard fire exposure," *Institutet f¨or Tr¨ateknisk Forskning*, no. issn: 1102-1071, pp. 1–76, 2000.
[15] G. Thomas, "Fire resistance of light timber framed walls and floors.," University of Canterbury, 1996.
[16] B. Fredlund, "A model for heat and mass transfer in timber structures during fire: a theoretical, numerical and experimental study.," 1988.
[17] A. P. Knudson, R.M Schniewind, "Performance of structural wood members exposed to fire," 1975.
[18] M. Janssens, "Thermo-physical properties for wood pyrolysis models," in *In Pacific timber engineering conference*.
[19] A. Frangi, *Brandverhalten von Holz-Beton-Verbunddecken*, vol. 269. 2001.
[20] S. Hadvig, "Charring of Wood in Building Fires," Technical University of Denmark: Lyngby., 1981.
[21] I. M. Van Zeeland, J. J. Salinas, and J. R. Mehaffey, "Compressive strength of lumber at high temperatures," *Fire and Materials*, vol. 29, no. 2, pp. 71–90, 2005, doi: 10.1002/fam.871.
[22] M. J. Manríquez Figueroa and P. Dias De Moraes, "Temperature reduction factor for compressive strength parallel to the grain," *Fire Safety Journal*, vol. 83, pp. 99–104, 2016, doi: 10.1016/j.firesaf.2016.05.005.
[23] S. A. Young and P. Clancy, "Compression mechanical properties of wood at temperatures simulating fire conditions," *Fire and Materials*, vol. 25, no. 3, pp. 83–93, 2001, doi: 10.1002/fam.759.
[24] J. Schmid, M. Klippel, A. Just, A. Frangi, and M. Tiso, "Simulation of the Fire Resistance of Cross-laminated Timber (CLT)," *Fire Technology*, vol. 54, no. 5, pp. 1113–1148, 2018, doi: 10.1007/s10694-018-0728-9.
[25] M. Kawakami and A. Ghali, "Time-dependent stresses in prestressed concrete sections of general shape," *PCI Journal*, vol. 41, no. 3, pp. 96–102, 1996, doi: 10.15554/pcij.05011996.96.105.
[26] T. Gernay, "Fire resistance and burnout resistance of timber columns," *Fire Safety Journal*, vol. 122, p. 103350, 2021, doi: 10.1016/j.firesaf.2021.103350.
[27] T. Gernay *et al.*, "Experimental investigation of structural failure during the cooling phase of a fire: Timber columns," *Fire and Materials*, p. fam.3110, Oct. 2022, doi: 10.1002/fam.3110.
[28] F. Wiesner *et al.*, "Structural capacity in fire of laminated timber elements in compartments with exposed timber surfaces," *Engineering Structures*, vol. 179, no. October 2018, pp. 284–295, 2019, doi: 10.1016/j.engstruct.2018.10.084.

BEHAVIOUR CLASSIFICATION OF COMPOSITE BEAMS IN NATURAL FIRES

Mhd Anwar Orabi[1], Asif Usmani[2]

ABSTRACT

When designing composite beams, it is critical to consider the effect of thermal deformation on the adjacent structure and its stability. It is often difficult to judge the type of destabilising forces a composite beam may induce because of the complexity of heat transfer through a composite section consisting of a steel beam and a concrete slab. This paper generates thousands of data points covering the potential behaviour classes of composite beams. This is done by performing heat transfer analyses on a large selection of composite beam sections under different fire exposures and then using an ab-initio analytical approach to estimate the type of behaviour a given beam would have under a specific type of fire exposure. The findings show that long-spanning composite beams with thin slabs under short-hot fires are likely to generate large tensile forces that pull in adjacent supporting structures. Conversely, short-spanning composite beams with thick slabs, and subject to long-cool fires, are expected to generate compressive forces that push against the adjacent structure. The magnitude of these destabilising forces is massive and ought to be considered from the early conceptual design stage.

Keywords: structures; heat transfer; design; thermal deformation

1 INTRODUCTION

The behaviour of composite beams in fire is dependent on multiple factors such as material properties, fire exposure, and boundary conditions. However, A significant portion of the literature over-emphasises material properties as the penultimate factor in fire, which is now evident in prescriptive design approaches which prescribe fire protection to keep steel temperature below a predetermined critical value. One of the issues with such approaches is that they overestimate the importance of material properties, and under-appreciate the severe effects thermal deformations may have on the affected member and adjacent structure. Approaches considering the axial load and moment interaction of members, such as the one presented by Garlock and Spencer [1], offer a more robust method but focus on the response of the member and how it may yield rather than account for its broader impact on the structure. Fundamental studies [2,3] on the behaviour of steel and composite beams in fire have shown that restrained members exert forces into the adjacent structure that vary in both magnitude and direction based on section size, fire exposure, and restraint conditions. It was even shown that restrained thermal deformation forces may have resulted in the collapse of the World Trade Center towers [4].

The 'type' of fire can also have a major impact on the way the structure responds. As presented by Lamont et al. [5], buildings fires can fall into two extreme categories: burns rapidly at a high temperature but for a short time (short-hot), or burns relatively slowly at overall lower temperatures but for a longer duration (long-cool). The type of fire changes the thermal distribution inside the structural members and thus their structural behaviour. It was found that in long-cool fires, temperatures are more uniform within the composite sections because the slab, which has higher thermal inertia than the steel beam, is heated for

[1] Dr, The Hong Kong Polytechnic University, Department of Building Energy and Environment Engineering
e-mail: maorabi@polyu.edu.hk, ORCID: https://orcid.org/0000-0001-5083-3623
[2] Professor, The Hong Kong Polytechnic University, Department of Building Energy and Environment Engineering
e-mail: asif.usmani@polyu.edu.hk, ORCID: https://orcid.org/0000-0003-2454-5737
https://doi.org/10.6084/m9.figshare.22193125

longer. The opposite is true for short-hot fires in which the effect of thermal gradient is more pronounced. This is caused by the temperature differential between the steel beam and slab of the composite section. Quantifying this differential is often non-trivial because the difference in thermal properties of concrete and steel and the difference in thermal mass of the slab and steel beam parts of the composite beam result in a nonlinear temperature distribution within the composite section. Therefore, establishing the temperature profile of composite sections often requires heat transfer analysis using a computational approach such as the finite element method.

Despite the nonlinearity of the thermal profile within the cross section, the mechanical effect of elevated temperatures can be separated into equivalent uniform temperature increase responsible for axial extension, and equivalent thermal gradient resulting in bowing [3]. The corresponding thermomechanical response then falls into one of two classes: uniform temperature dominated, or thermal gradient dominated.

This paper aims to classify a wide range of composite beam sections based on their elastic thermomechanical response class in different types of fire. This can allow engineers working at the conceptual design stage to: (1) establish the type of thermomechanical forces the composite section must resist in fire based on section and material properties, and (2) produce quick estimates of the type and magnitude of secondary action induced into the adjacent structure. This is done by first generating many composite sections dimensions that encompass most of the universal beam sections available for design and a practical range of composite slab thicknesses. These sections are then modelled in OpenSees for heat transfer considering three fire scenarios: a base case using the standard temperature-time curve, and one short-hot and one long-cool fires generated using the parametric temperature-time curve. Ab-initio consideration of the sectional thermomechanical stresses is then used to predict the equivalent uniform and gradient temperatures. Finally, the results of the analyses are studied to classify the composite sections and establish the most important factors governing their classification.

The first section of the paper explains the fire scenarios used for the analysis, the basis for the behaviour classification, and the calculation of equivalent temperatures. After that, the heat transfer analysis and the study parameters are presented, followed by the limitations of the presented work. The results and discussion section then introduces the results of equivalent temperatures and thermal gradients and considers the parameters affecting the effective forces developed in composite sections.

2 METHODOLOGY

2.1 Fire scenarios and types

The standard temperature-time curve is the de facto fire exposure used in structural fire design. While it has many weaknesses, it remains a good benchmark for comparison. This is especially true knowing that many engineers will need to use it for code compliance purposes particularly in the conceptual design stage. The parametric temperature-time exposure as presented in EN1991-1-2 also serves as a good model for use early in design [6]. In this paper, the parametric temperature-time curve was used to model a short-hot fire and a long-cool fire by changing the ventilation factor. The compartment dimensions are assumed to be similar to the Veselí Travelling Fire Test [7] with length × width × height of 12 m × 9 m × 3.5 m. The design value of the fire load density was assumed to be the same as the test at 173.5 MJ/m^2 with fuel-controlled limit t_{lim} of 15 minutes. Opening factors of 0.02 m$^{1/2}$ and 0.039 m$^{1/2}$ were used for the long-cool and short-hot fires respectively. The three fires used for the analyses are shown in Figure 1. Both parametric fires presented are ventilation controlled with the opening factor of 0.039 m$^{1/2}$ being near the transition limit between the ventilation and fuel-controlled regimes as governed by the equation:

$$t_{max} = \max\left[\frac{0.2q_{t,d}}{O\times 1000}, t_{lim}\right] \quad (1)$$

Where the fire is fuel controlled if t_{max} is limited by t_{lim}, and ventilation controlled if otherwise. In equation (1), $q_{t,d}$ is the design fuel load relative to the floor area of the compartment, and O is the opening factor. The long-cool fire, as defined here, burns at a lower temperature but for a longer duration than the short-hot fire. The standard temperature time curve achieves higher temperatures and does not have a time limit for the heating phase. Area under the curve of the long-cool and short-hot fires are 0.69 and 0.58 the area under the curve of the standard temperature time curve, respectively. The total exposure duration for all scenarios is 1 hour.

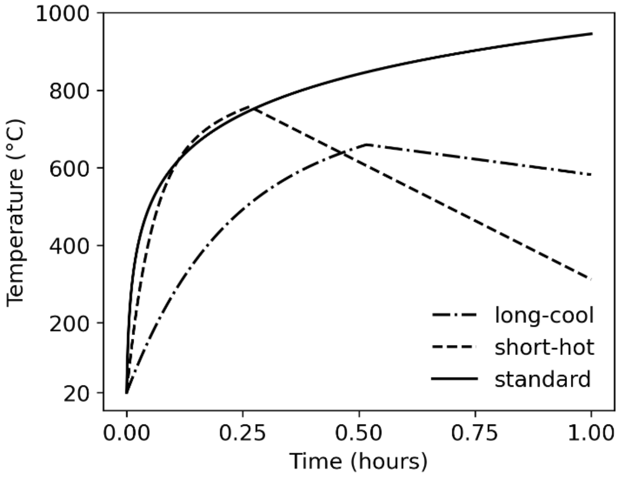

Figure 1. Temperature-time curves used in the analysis

2.2 Behaviour classes

Under ambient conditions, beams primarily act in bending. The heavier the applied load, the larger the resultant deflections. Because of this, large deflections are often associated with a beam that is approaching its capacity and possibly at risk of collapsing. In fire, however, large deformations manifest to accommodate the thermal expansion of the beam and may be completely benign. This has been shown before by Usmani et al. [3], and will be briefly revisited in this section to establish the behaviour classes of composite beams in fire. First, the effect of temperatures on a beam is divided into two distinct types: a uniform temperature growth, and a thermal gradient across the depth. The former represents the overall temperatures of the section and can thought of as the average temperature growth across the depth. The latter is related only to the difference in temperatures across the depth even if the average temperature in the section remains at zero.

If end conditions of a beam allow for extension, then a uniform temperature growth would result in the beam elongating but experiencing no additional stresses. That means that the thermal strains $\varepsilon_{th}$are fully responsible for the total strains of the structural member as shown in equation (2).

$$\varepsilon_{tot} = \varepsilon_{th} \qquad (2)$$

With infinitely rigid end restrains preventing total strains, all thermal strains are translated into mechanical strains:

$$\varepsilon_{tot} = \varepsilon_{th} + \varepsilon_{\sigma} = 0;\ \varepsilon_{\sigma} = -\varepsilon_{th} \qquad (3)$$

By definition, these thermal strains are only related to the uniform temperature ΔT and are not affected by the thermal gradient. This is shown in equation (4) where α is the thermal expansion coefficient.

$$\varepsilon_{th} = \alpha\Delta T \qquad (4)$$

Thus, when fully restrained in translation, the effect of thermal expansion due to a uniform temperature growth is purely compressive and can be calculated as shown in equation (5).

$$N_{th} = -EA\alpha\Delta T \qquad (5)$$

In equation (5), N_{th} is the axial force in the beam due to restrained thermal expansion, E is the Young's modulus of the section, and A is its area.

A beam that is free to rotate at its ends responds in pure stress-free curvature when it is subject to a pure thermal gradient without mean growth in temperature. As there is no uniform growth in temperature, the beam will not have any net increase in length as the top and bottom fibres extend and contract balancing each other out. The resulting thermal curvature in the section is calculated as:

$$\phi_{th} = \alpha \Delta T_{,y} \qquad (6)$$

Where ϕ_{th} is the thermal curvature, and $\Delta T_{,y}$ the thermal gradient across the depth of the section. Assuming simply supported end conditions, the thermal curvature of the beam would result in reducing the distance between the supports as the beam adopts its curved profile. If supports are pinned and not allowed to move laterally, this restrained 'contraction' results in development of tensile forces as calculated by equation (7). As shown in the equation, the curvature-induced axial force depends on length of the beam l.

$$N_{th} = EA\left(1 - \frac{\sin(l\phi_{th}/2)}{l\phi_{th}/2}\right) \qquad (7)$$

Under realistic thermal exposure, composite beams would always be subjected to a combination of both uniform temperature growth and a thermal gradient. As shown in equations (5) and (7), the thermomechanical effects of uniform temperature and thermal gradient on a pin-ended beam result in opposing axial forces. The behaviour class of composite beam corresponds to the value of the effective forces that develop within it due to the combination of uniform temperature growth and thermal gradient:

$$N_{eff} = EA\left(1 - \frac{\sin(l\alpha\Delta T_{,y}/2)}{l\alpha\Delta T_{,y}/2}\right) - EA\alpha\Delta T \qquad (8)$$

If the effective force N_{eff} is negative, then the behaviour is dominated by uniform temperature, and the beam would *push* against the adjacent structure. If the effective force were positive, then the behaviour is dominated by thermal gradient and the beam would *pull* the adjacent structure. If the thermal gradient and uniform temperature growth are of a similar impact, then the beam would induce very little force in the adjacent structure and would diffuse all its restrained thermal deformation in the form of large but innocuous deflections.

2.3 Estimation of equivalent temperatures

It is evident from equation (8) that the elastic behaviour classification of a composite beam is governed by the temperature distribution within the section. As discussed in the last section, the two most important components of the temperature distribution are the uniform temperature and the thermal gradient. It is very difficult to find any composite sections that would be purely subject to one of these two temperature distribution categories. The temperature distribution within the section is governed by many parameters such as the fire exposure conditions, dimensions of the steel beam and depth of the slab, and material properties of the concrete and steel. Because of this, most composite sections have a nonlinear temperature profile $\Delta T(y)$ under most fire conditions, where y is the distance from the neutral axis of the composite section.

One of the primary challenges in classifying the behaviour of a composite beam is estimating the uniform and gradient components of the real temperature distribution. In this section, this is performed by relying on the two definitions made in the previous section but considering fully fixed conditions. That is: (1) the uniform temperature component is solely responsible for thermally induced axial force, and (2) thermal gradient is solely responsible for thermally induced bending moment. Changing the end conditions from pin-ended to fully fixed is to simplify the upcoming equations by causing equation (7) to become zero as all curvatures are converted to moment. This assumption is valid because the temperature profile does not depend on end-conditions, and nor do its uniform and gradient components.

The axial force in the composite section is the sum of the axial force in the steel beam and the concrete flange as shown in equation (9).

$$N_{th} = \int_A \sigma_{th} dA = -\int_{A_s} E_s \alpha_s \Delta T(y) dA - \int_{A_c} E_c \alpha_c \Delta T(y) dA \qquad (9)$$

Where the subscripts s and c refer to the steel beam and concrete flange of the composite section, respectively. The material properties for both steel and concrete are temperature-dependent. As $\Delta T(y)$ is related to the distance to composite section neutral axis y, the integration in equation (9) is performed by dividing the section into fibres along the depth and using the relationship $dA = t(y)dy$ where $t(y)$ is the width of each fibre. The uniform temperature in the section is then found by combining equations (5) and (9) and solving for ΔT in equation (10).

$$\Delta T = \frac{\int_{d_s} E_s \alpha_s t(y) \Delta T(y) dy + \int_{d_c} E_c \alpha_c t(y) \Delta T(y) dy}{EA\alpha} \qquad (10)$$

Where section properties $EA\alpha$ of the composite section the must consider the material type and degradation state of each fibre across the depth of the concrete flange d_c and steel beam d_s.

$$EA\alpha = \int_{d_s} E_s \alpha_s t(y) dy + \int_{d_c} E_c \alpha_c t(y) dy \qquad (11)$$

A similar calculation can be performed for finding the thermal gradient as per equation (12).

$$\Delta T_{,y} = \frac{\int_A \alpha E \Delta T(y) y dA * \int_A E/E_{0,ref} dA}{\int_A y^2 E dA * \int_A E\alpha/E_{0,ref} dA} \qquad (12)$$

Where each integral is evaluated over the entire composite section replacing α and E with the appropriate temperature-dependent values for steel and concrete at the current temperature of the fibre. $E_{0,ref}$ is the exception as it is a reference modulus value set to the modulus of elasticity of steel at ambient conditions regardless of which part of the composite section the integration is being performed over.

2.4 Heat transfer

It was established in section 2.2 that the behaviour classes are dependent on the uniform temperature and the thermal gradient. Subsequently, section 2.3 explained how uniform temperature and thermal gradient are reliant on the temperature distribution within the section. Estimating the nonlinear temperature profile of the section is thus the next challenge in classification of section behaviour. Due to the highly variable nature of fire and the complexity of temperature dependent thermal material properties, this is best performed computationally.

In this work, the heat transfer module of OpenSees [8] was used to analyse the response of several sections to the three fires discussed in section 2.1. The predefined heat transfer sections created as part of the Integrated Simulation Environment allowed for efficiently defining hundreds of composite beam configurations and analysing them in OpenSees [9]. Each analysis was performed assuming the duration of the fire was 1 hour analysed at 5 second intervals. The heat transfer model was two-dimensional as shown in Figure 2. Heat flux boundary conditions were applied to the steel beam and the fire-facing side of the slab. An ambient boundary condition was applied to the cool side of the slab to simulate its interaction with ambient air. It was assumed that the concrete flange is in direct contact with the top of the steel beam as shown in the figure, with equal-temperature boundary conditions applied at the interface. The choice of boundary conditions and how the fire temperatures are converted to heat flux is discussed in more detail in chapter 5 of [10]. A convective heat transfer coefficient of 25 W/(m^2 °K) was assumed for the fire facing side, and 10 W/(m^2 °K) for the cool side.

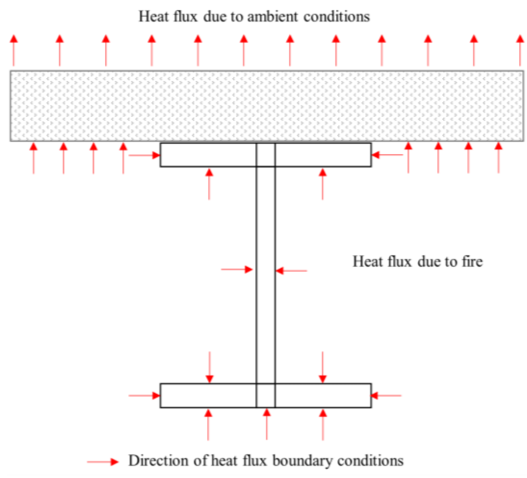

Figure 2. Model used for heat transfer for composite sections

2.5 Study parameters

This work generated a dataset of 55,800 datapoints that represent the effective force induced by 310 different composite beam sections with five lengths at 5-minute intervals through a standard, long-cool, and short-hot fire. This is illustrated more clearly in Figure 3 and the values are presented in Table 1. Section and slab dimensions are major determinants of temperature distribution within a composite beam. A subset of 62 universal beam (UB) sections was chosen from BS EN 10365:2017 with additional sections by the Steel Construction Institute [11,12]. The subset included every section designation from UB127×76 to UB1016×305, and every other section weight. For example, the two section UB610×229×113 and ×140 were chosen from the four available options: UB610×229×140, ×125, ×113, and ×101. If only one mass per length designation was available for a given section, then it was included in the subset. Each of the UB sections were then paired with slab thicknesses of 0.1 m, 0.15 m, 0.2 m, 0.25 m, and 0.3 m for a total of 310 composite sections. Each composite section was then analysed subject to exposure of each of the three fires in section 2.1. Heat transfer analysis was then performed on each composite section with the thermal profile sampled every 5 minutes. Finally, as equation (8) depends on beam length, five lengths (5 m, 10 m, 15 m, 20 m, and 25 m) were assumed for each section for the classification.

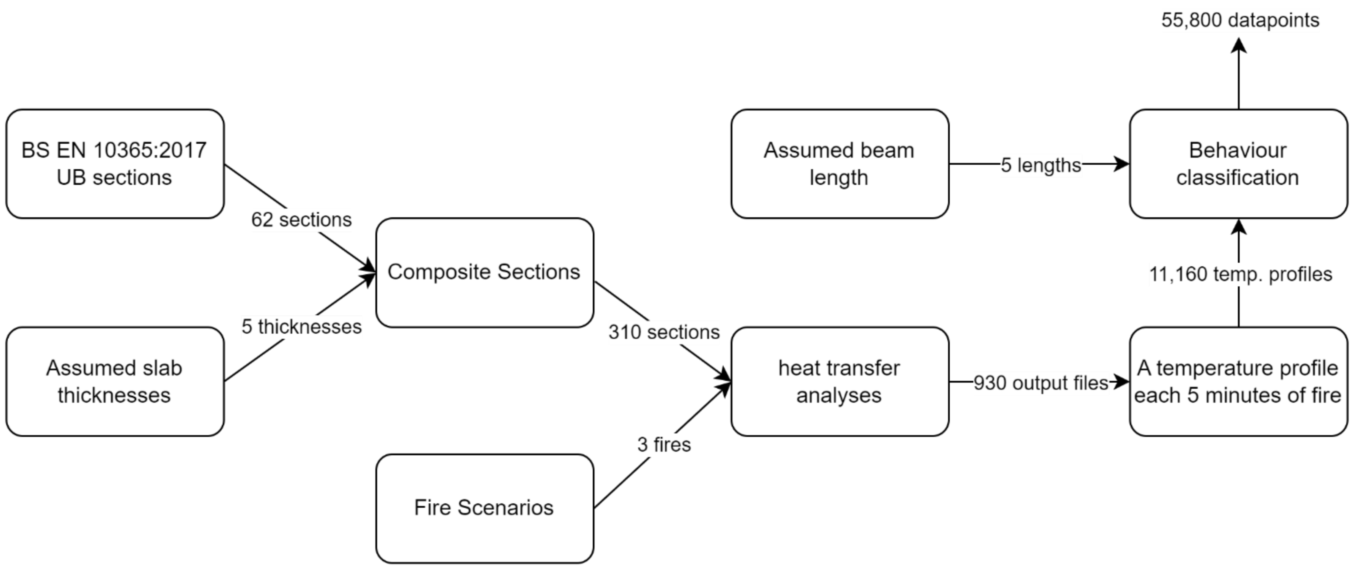

Figure 3. Parametric study flowchart

Table 1. Values for the different parameters of the study

Parameter	Values
Assumed slab thicknesses (m)	0.1, 0.15, 0.2, 0.25, 0.3
Fire scenarios	Standard temperature-time, long-cool, and fast-hot from section 2.1
Assumed beam lengths (m)	5, 10, 15, 20, 25

2.6 Simplifications and Scope

The results presented in this paper are intended to address the early conceptual design stage and allow engineers to consider structural fire performance from the get-go. Some reasonable simplifications were made to streamline the analyses performed. The classes presented in this paper are only valid when the composite beams have not buckled. It is well known that buckling of steel beams can occur at low temperatures of about 60 – 100 °C [3]. However, this work assumes that the beams are fully composite with their concrete flanges, and that the composite section is part of a larger system that restrains and stiffens the beam against buckling. An additional limitation is that the sections are assumed to remain elastic throughout the fire. This is acceptable because the scope of the paper is to provide insight into the potential effects of thermal deformations at the conceptual design stage before performing detailed computational studies. It is not intended to provide a full picture of the thermomechanical behaviour of composite beams throughout a fire. The authors intend to consider plasticity in later iterations of this work where the scope is wider.

Another important simplification made was the utilisation of pinned-pinned end conditions for the analyses. From experimental observation, this simplification is likely acceptable for internal composite beams during heating [2,13]. This is because for a continuous composite floor like that in Figure 4, the opposite cool composite beam and continuous floor would provide significant lateral restraint. Experimental observations have also shown that local buckling/plastic hinging of the steel beam and cracking of the concrete slab happen in the early stages of the fire which relieves the rotational restraint on the heated composite beam [2,14]. The issue is with representing composite beams on the outer bays of the structure. In that case, thermal deformations would be resisted mainly by the edge column or perimeter girder. The thermal deformations may then have the ability to compromise the structural integrity of the building and potentially cause its collapse [4,15]. This would also mean that the thermal deformation stresses would be relieved in the form of large deflections. The assumption of infinite restraint does not represent this case very well and this is a limitation of the current work.

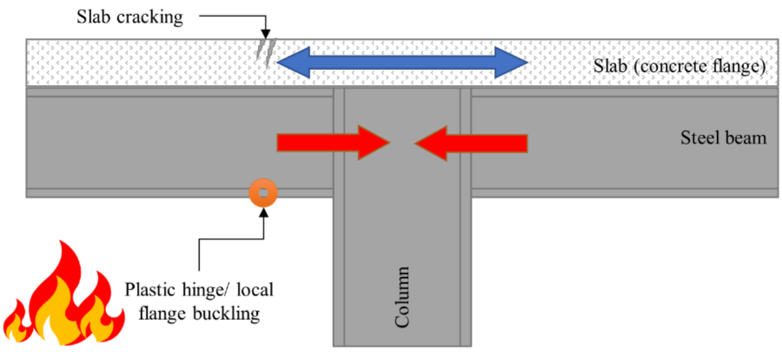

Figure 4. Boundary conditions for composite beams in continuous composite floors

3 RESULTS AND DISCUSSION

3.1 Equivalent temperature and thermal gradient

The mean, median, minimum, and maximum equivalent uniform temperature and thermal gradient of all tested sections are shown against time in Figure 5. Despite the heating phase of the short-hot fire ending after only 15 minutes (Figure 1), the equivalent uniform temperature for sections subjected to it remained high throughout the fire. The maximum uniform temperatures reached in the short-hot, long-cool, and standard fire exposures were 465 °C, 428 °C, and 444 °C, respectively. The maximum gradients reached were 8.22 °C/mm, 6.59 °C/mm, and 9.17 °C/mm for the short-hot, long-cool, and standard exposures respectively. Interestingly, while the uniform temperature kept growing or remained high during the cooling phase, the thermal gradient decreased. The former is due to the thermal inertia of the slab: the slab temperature kept increasing even during the cooling phase, while the steel beam temperature decreased quickly. As the steel beam temperature went down, it resulted in an opposite thermal gradient where the lower fibres of the composite beams were cooling while the upper fibres were heating. The short-hot fire clearly resulted in a higher thermal gradient (and at an earlier point) than the long-cool fire. The decrease in the mean thermal gradient after about 20 minutes for the composite sections subject to standard fire is because the sections had more time for the temperature profile to become more uniform and thus the difference between bottom and top fibres, for most sections, reduced. Despite the intensity of the fire exposure of the natural fires being lower than for the standard fire, they result in a similar equivalent thermal load. This reiterates the findings in [2] which found that standard fire exposure is a deceptive measure; a shorter and 'less intense' fire could have a similar thermal effect, especially the short-hot fire which results in very high gradients and the highest equivalent temperatures. For both the short-hot and long-cool fires, the highest thermal gradient occurred after about 30 minutes of exposure.

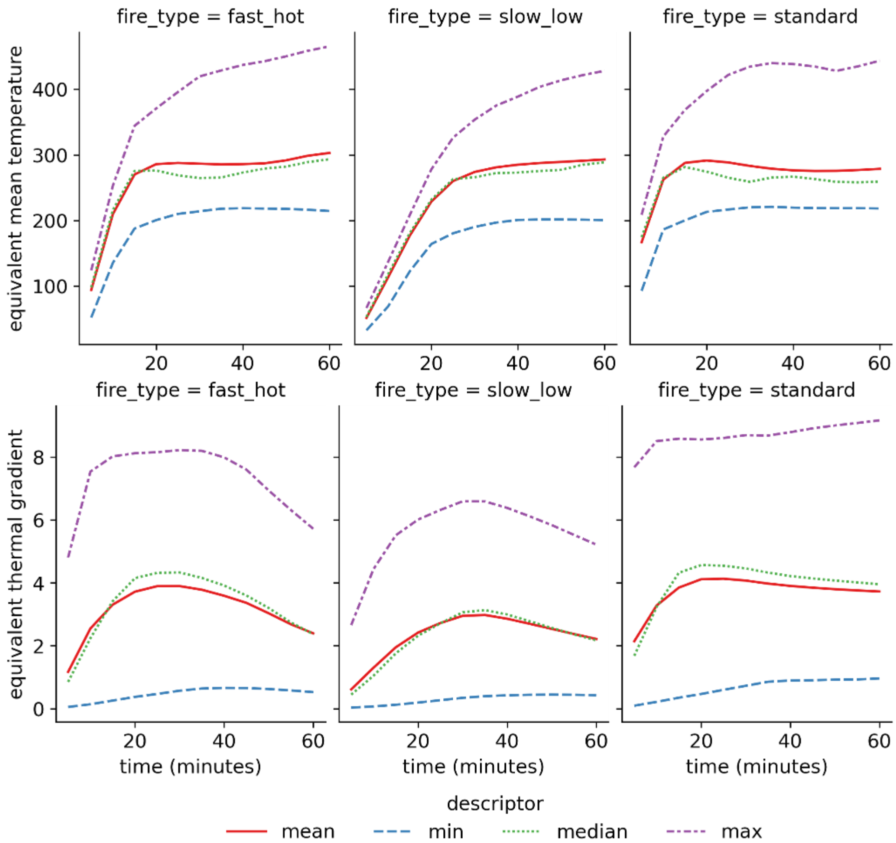

Figure 5. Descriptors of equivalent uniform temperature and thermal gradient for all composite sections. Fast-hot is equivalent to short-hot, and slow-cool is equivalent to long-cool fire

3.2 Slab thickness and equivalent temperatures

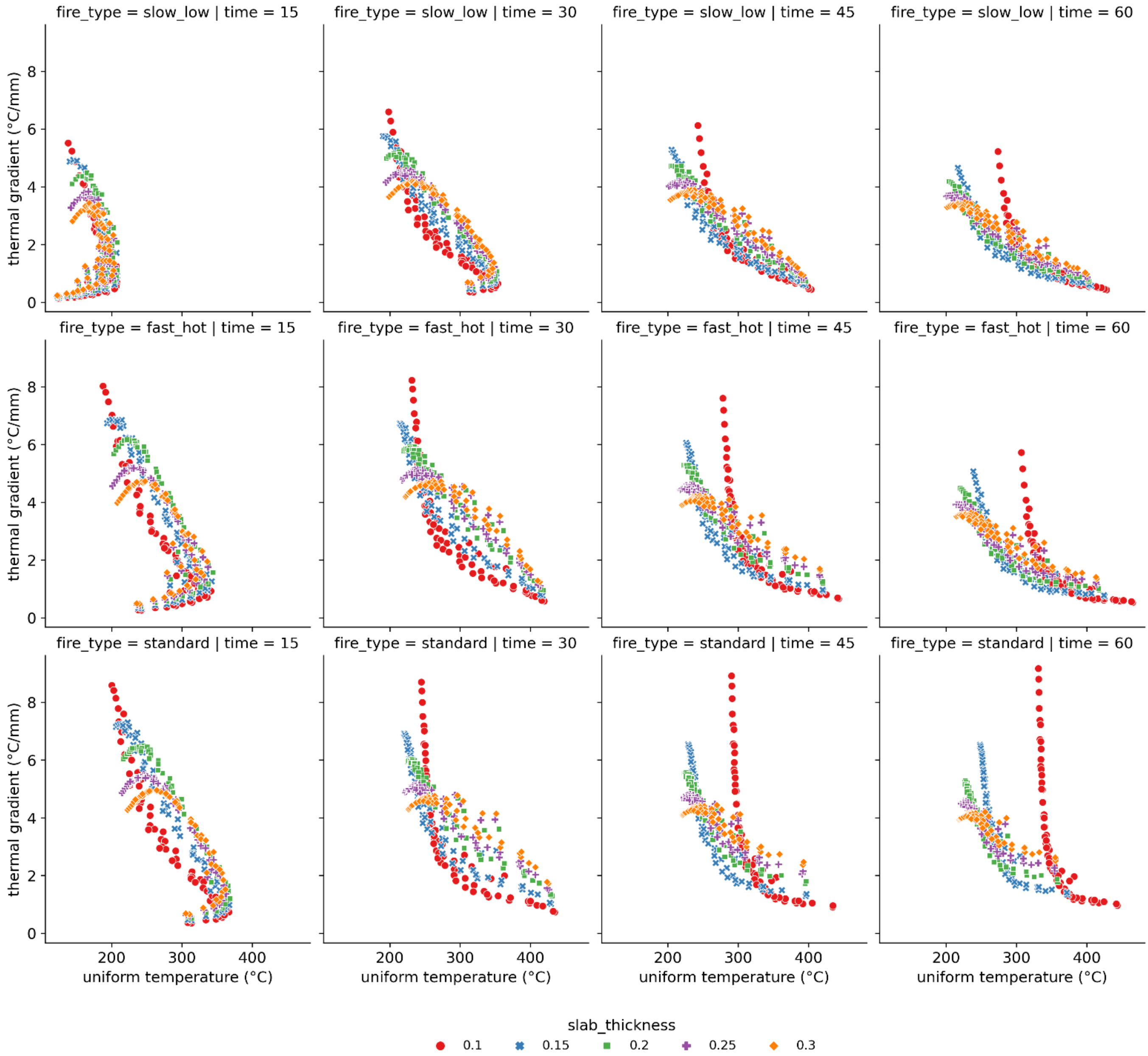

Figure 6. Equivalent temperatures of composite sections in the three fires after 15, 30, 45, and 60 minutes of exposure

Figure 6 shows the uniform temperature and the thermal gradient for all sections based on their thermal profiles after 15, 30, 45, and 60 minutes in the long-cool (slow-low), short-hot (fast-hot), and standard fires. The figure shows that the slab thickness is an important factor in deciding the equivalent temperatures the section is subjected to. Composite sections with thinner slabs generally tend to develop slightly lower thermal gradients than their counterparts with thicker slabs. However, sections with thinner slabs also have a wider range of thermal gradients reaching values that exceed composite sections with thicker slabs. As the time in the fire increases, the sections with the thinner slabs start increasing in thermal gradient and exceeding the other sections in terms of both uniform temperature and thermal gradient. This is particularly interesting when looking at the graphs for the natural fires after 45 and 60 minutes. At this stage, both fires are in their cooling phase. Despite this, the thermal inertia of the slab allows the section to continue to be heated and thus results in higher uniform temperatures.

3.3 Effective thermal load and behaviour classes

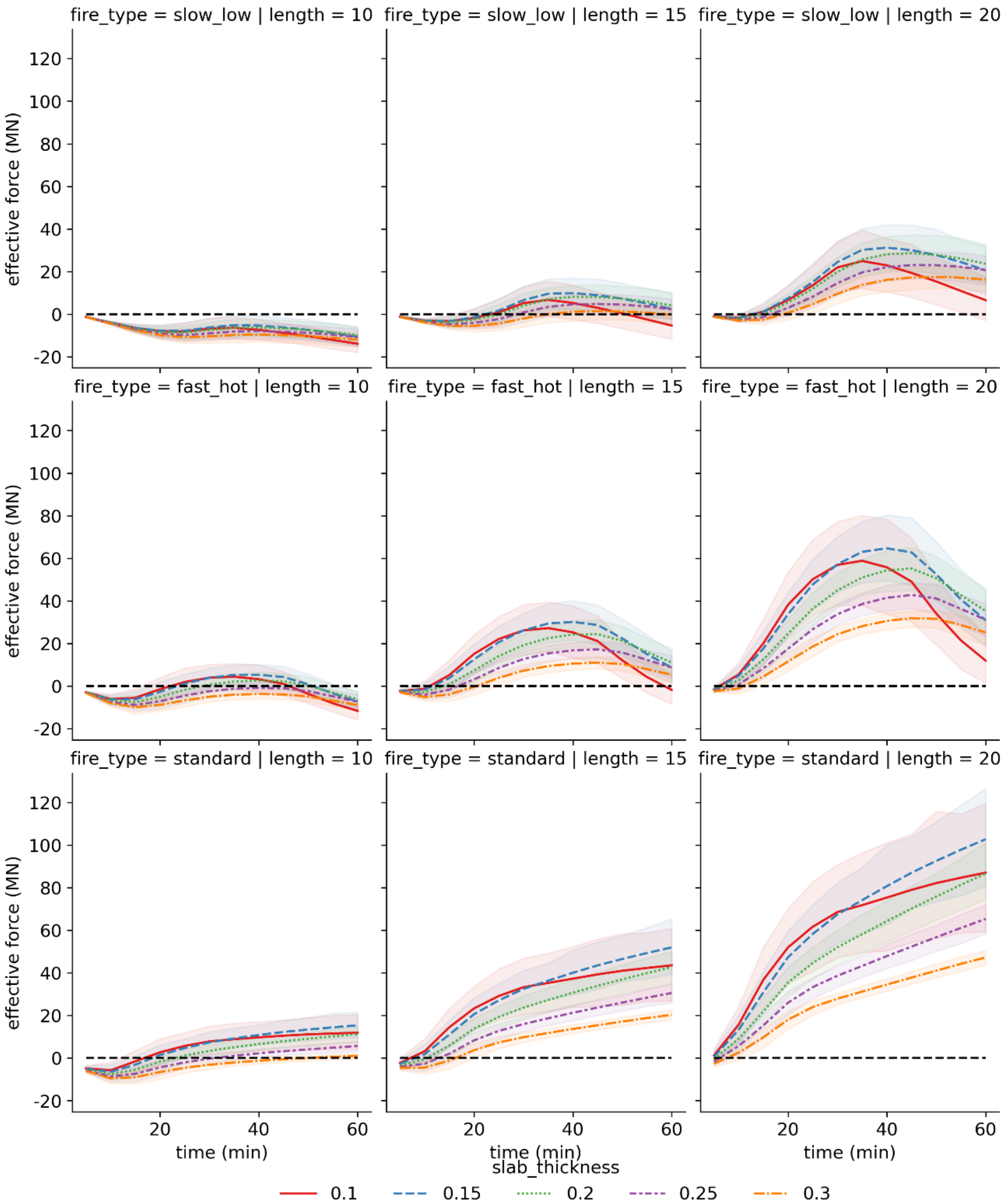

Figure 7. Trendline and in change in effective force over fire time and dependency on beam length

The effective force against time for a subset of the assumed beam lengths is shown in Figure 7 for each fire type. From this figure, it is evident that fire type and beam length are major factors in determining whether a beam would be dominated by uniform temperature and develop compressive forces, or thermal gradient and develop tensile forces. For the longest beam length shown, the behaviour is primarily dominated by thermal gradient. The achieved tensile forces are massive and in the order of mega Newtons. If plasticity were considered or buckling were allowed, then it is expected that this magnitude would have been capped at a lower value earlier in the fire. The magnitude of the force would also be reduced if finite end conditions were considered. Regardless, the data shows that long-spanning composite beams, especially those subject to large thermal gradients, can induce huge tensile forces in the columns or perimeter girders that support them. The tensile forces reduce in the latter stages of the natural fires due to the decrease in thermal gradient during cooling as was shown in Figure 5 and discussed in section 3.1. There is a marked difference between the different fire types for the same beam length. Because of the more gradual heating induced by the long-cool fire, it has the highest number of composite sections that are dominated by uniform temperature. Short-hot and standard fires, on the other hand, are more likely to result in sections that are dominated by thermal gradients. This data is tabulated in Table 2, which shows the classification of all sections after 45 minutes of fire exposure. The length is the biggest determinant of behaviour class with longer beams much more likely to be dominated by thermal gradients, and shorter beams more likely to be dominated by uniform temperature.

Table 2. Classes after 45 minutes of exposure

Fire and class	Long-cool		Short-hot		Standard	
Assumed length (m)	Uniform-dominated	Gradient-dominated	Uniform-dominated	Gradient-dominated	Uniform-dominated	Gradient-dominated
5	306	4	297	13	282	28
10	216	94	145	165	110	200
15	120	190	78	232	56	254
20	83	227	46	264	23	287
25	62	248	24	286	10	300

4 CONCLUSIONS

This paper looked at the behaviour classification of 310 composite sections covering most of the commercially available UB sections and slab thicknesses between 0.1 m and 0.3 m. Each section was subjected to three fire exposures: a long-cool fire, a short-hot fire, and standard temperature-time exposure. Heat transfer analysis was performed for each scenario, and the equivalent thermal gradient and uniform temperature were calculated for each section at 5-minute intervals. The results of the paper can be summarised in the following points:

1. The behaviour of composite beams can be dominated by either equivalent thermal gradients or equivalent uniform temperatures. The former is a result of the difference in temperature between the fibres of the composite beam including the difference in temperature between the steel beam and the slab. The latter represents the mean temperature throughout the entire section.
2. The range of equivalent uniform temperatures for all tested fire scenarios is between about 200 °C and 450 °C. The range for thermal gradients is between about 0.4 °C/mm and 9.2 °C/mm.
3. Long-cool fires are more likely to induce lower thermal gradients due to the gradual nature of the heating. Likewise, short-hot fires result in higher thermal gradients because of the rapid heating coupled with the high thermal inertia of the concrete slab. This reiterates previous findings and extends them to a much larger selection of constructable composite beams.
4. Thicker slabs place an upper limit on the achievable thermal gradient but result in higher gradients earlier in the fire. Composite sections with thinner slabs are more likely to achieve very high thermal gradients and higher uniform temperature later in the fire.
5. Span is one of the most important determinants of the behaviour classification of a composite beam. Longer beams are much more likely to be dominated by thermal gradients, while shorter beams are more likely to be dominated by uniform temperatures.
6. The same beam can be classified as dominated by thermal gradients in a short-hot fire but dominated by uniform temperatures in a long-cool fire.

ACKNOWLEDGMENT

This work is funded by the Hong Kong Research Grants Council Theme-based Research Scheme (T22-505/19-N).

REFERENCES

1. Garlock, M.E., Quiel, S.E. Plastic Axial Load and Moment Interaction Curves for Fire-Exposed Steel Sections with Thermal Gradients. Journal of Structural Engineering 134, 874–80 (2008). https://doi.org/10.1061/(ASCE)0733-9445(2008)134:6(874).
2. Usmani, A.S., Lamont, S. Key events in the structural response of a composite steel frame structure in fire. Fire Mater 28, 281–97 (2004). https://doi.org/10.1002/fam.856.
3. Usmani, A.S., Rotter, J.M., Lamont, S., Sanad, A.M., Gillie, M. Fundamental principles of structural behaviour under thermal effects. Fire Saf J 36, 721–44 (2001). https://doi.org/10.1016/S0379-7112(01)00037-6.
4. Kotsovinos, P., Usmani, A. The World Trade Center 9/11 Disaster and Progressive Collapse of Tall Buildings. Fire Technol 49, 741–65 (2013). https://doi.org/10.1007/s10694-012-0283-8.
5. Lamont, S., Usmani, A.S., Gillie, M. Behaviour of a small composite steel frame structure in a “long-cool” and a “short-hot” fire. Fire Saf J 39, 327–57 (2004). https://doi.org/10.1016/j.firesaf.2004.01.002.
6. BSi. EN 1991-1-2:2002: Eurocode 1: Actions on Structures — General actions-actions on structures exposed to fire.
7. Horová, K., Jána, T., Wald, F. Temperature heterogeneity during travelling fire on experimental building. Advances in Engineering Software 62–63, 119–30 (2013). https://doi.org/10.1016/j.advengsoft.2013.05.001.
8. Jiang, Y. Development and application of a thermal analysis framework in OpenSees for structures in fire. The University of Edinburgh.
9. Orabi, M.A., Khan, A.A., Jiang, L., Yarlagadda, T., Torero, J., Usmani, A. Integrated nonlinear structural simulation of composite buildings in fire. Eng Struct 252 (2022). https://doi.org/10.1016/j.engstruct.2021.113593.
10. Orabi, M.A. State of the Art Large Scale Simulation of Buildings in Fire: The Case of WTC7. The Hong Kong Polytechnic Univeresity.
11. BS EN 10365:2017. BSI Standards Limited; .
12. The Steel Construction Institute. Universal beams (UB) Section properties. Interactive “Blue Book” (2017). https://www.steelforlifebluebook.co.uk/ub/ec3-ukna/section-properties-dimensions-properties/.
13. Lange, D., Röben, C., Usmani, A. Tall building collapse mechanisms initiated by fire: Mechanisms and design methodology. Eng Struct 36, 90–103 (2012). https://doi.org/10.1016/j.engstruct.2011.10.003.
14. Cameron, N.J.K., Usmani, A.S. A new design method to determine the membrane capacity of laterally restrained composite floor slabs in fire Part 2: Validation. Structural Engineer 83, 34–9 (2005).
15. Usmani, A., Röben, C., Al-Remal, A. A Very Simple Method for Assessing Tall Building Safety in Major Fires. Steel Structures 9, 17–28 (2009). https://doi.org/10.1007/BF03249476.

SiF 2022– The 12th International Conference on Structures in Fire
The Hong Kong Polytechnic University, Nov 30 - Dec 2, 2022

RAPID FORECASTING OF THE STRUCTURAL FAILURE OF A FULL-SCALE ALUMINIUM ALLOY RETICULATED SHELL STRUCTURE IN FIRE

Zhuojun Nan[1], Mhd Anwar Orabi[2,*], Xiaoning Zhang[3], Aatif Ali Khan[4], Xinyan Huang[5,*], Liming Jiang[6,*], Yaqiang Jiang[7], Asif Usmani[8]

ABSTRACT

First respondents to fires in structures face severe risks as both the fire and structural behaviour are unpredictable. While structural collapse may manifest some warning signs, these signs are not always easily identified which has led to the death of many fire fighters over the years. Both fire and structural fire simulation have come a long way and are now capable of assessing the thermomechanical behaviour of structures to a good degree of accuracy. However, such simulations take hundreds or thousands of engineering and computation hours. This paper explores performing these analyses a priori and using the generated database to train a recurrent neural network for real time prediction of potential failure. The analysis is performed on an aluminium reticulated roof structure that is constructed in Sichuan Fire Research Institute (Sichuan, China) and is expected to be tested to failure in fire in 2023. One hundred localised fire scenarios were used to cover the potential fire that will be used to induce the failure of the test roof. Heat transfer analyses for each section were then performed in OpenSEES followed by thermomechanical analysis in the same software. The generated results database was then cleaned and the data at several key locations were extracted and used to train a long short term memory recurrent neural network. The results of the predictions show that the artificial intelligence model can infer results with increasing accuracy the closer the structure is to failure. The real test of the accuracy of the model, however, will be during the fire experiment on the real structure. This would be the first time an artificial intelligence model for rapid forecasting of structural response in fire is built a priori and tested against a real fire.

Keywords: structures; real time; artificial intelligence; recurrent neural networks; LSTM

1 INTRODUCTION

The risk from fire continues to increase as taller buildings are erected to accommodate increasingly denser urban populations. There have been many catastrophic fire accidents over the last two decades, some causing the partial or progressive collapse of structures such as the World Trade Center Towers 1, 2 & 7

[1] Ms, The Hong Kong Polytechnic University, Department of Building Energy and Environment Engineering
e-mail: zhuojun.nan@connect.polyu.edu.hk, ORCID: https://orcid.org/0000-0001-8189-5448
[2] Dr, The Hong Kong Polytechnic University, Department of Building Energy and Environment Engineering
e-mail: maorabi@polyu.edu.hk, ORCID: https://orcid.org/0000-0001-5083-3623
[3] Mr, The Hong Kong Polytechnic University, Department of Building Energy and Environment Engineering
e-mail: xiaon.zhang@connect.polyu.edu.hk, ORCID: https://orcid.org/0000-0002-7845-2950
[4] Dr, The Hong Kong Polytechnic University, Department of Building Energy and Environment Engineering
e-mail: alikhan.aatif@connect.polyu.hk, ORCID: https://orcid.org/0000-0001-9181-4795
[5] Dr, The Hong Kong Polytechnic University, Department of Building Energy and Environment Engineering
e-mail: xy.huang@polyu.edu.hk, ORCID: https://orcid.org/0000-0002-0584-8452
[6] Dr, The Hong Kong Polytechnic University, Department of Building Energy and Environment Engineering
e-mail: liming.jiang@polyu.edu.hk, ORCID: https://orcid.org/0000-0001-8112-2330
[7] Dr, Sichuan Fire Research Institute
e-mail: jiang.yaqiang@scfri.cn, ORCID: https://orcid.org/0000-0002-0217-7569
[8] Professor, The Hong Kong Polytechnic University, Department of Building Energy and Environment Engineering
e-mail: asif.usmani@polyu.edu.hk, ORCID: https://orcid.org/0000-0003-2454-5737
https://doi.org/10.6084/m9.figshare.22192006

(2001) [1], the Windsor Tower (2005) [2], the Faculty of Architecture Building at the Delft University of Technology (2008) [3], and the Plasco Building (2018) [4,5]. Structural collapses in fire pose a severe threat to human life in addition to causing massive economic and social impact. Collapse is also a major concern during firefighting and rescue operations. Successful development of rapid forecasting technology for structural failure prediction in fire could help considerably reduce the risk to life and property. This is done by providing emergency responders with key information about the stability of the structure thus allowing them to make informed decisions during their operations.

Modern implementations of machine learning algorithms packaged in accessible and flexible frameworks such as PyTorch and TensorFlow [6,7] have enabled for the proliferation of artificial intelligence (AI) applications in many fields. AI based fire forecasting methods have been used to identify fire sources and temperature distributions in tunnels based on temperature data through limited sensors [8,9]. For structural fire engineering, finite element (FE) based machine learning (ML) models have been applied to real-time prediction of structural fire response in recent years. Ye et al. [10] proposed an FE-based ML model framework to predict the deflection of beams under fire based on real-time thermal data. According to the Critical Temperature Method, Fu developed a ML framework to predict the failure patterns of steel frame structures under two fire scenarios [11]. Ye et al. [12] further developed a Computational Fluid Dynamics (CFD)/ Finite Element Methods (FEM) based framework for real-time structural fire response prediction. Recently, Ji et al. [13] proposed a real-time prediction method for fire-induced building collapse using the long short-term memory network, which is relied on key monitoring physical parameters. This study numerically examined 39 fire scenarios for a portal steel frame building. This paper builds upon the previous research and tackles the problem of real-time forecasting to predict the behaviour of an aluminium roof structure that will be tested until collapse in fire. The paper starts by presenting the roof structure, presenting the parameters used for data generation, and then discussing the development of an LSTM model for forecasting.

2 THE EXPERIMENTAL STRUCTURE

2.1 Geometry, material, and section details

An aluminium reticulated roof structure was constructed in Sichuan Fire Research Institute (SCFRI) to investigate the collapse of structures in fire. The geometric configuration of the roof structure is shown in Figure 1. The roof is 10 m in length and 7.2 m in width, with a height of 8 m. As shown in Figure 1(a), the roof is pinned to a concrete supporting frame. The roof was constructed from rigidly-connected I cross-beams 175×80×5×8 ($H \times B \times t_w \times t_f$ in mm). All beams were made from EN AW-6061-T6 aluminium with density, Young's modulus and yield strength of 2700 kg/m^3, 70 GPa and 270 MPa, respetively. The thermal properties are defined according to Eurocode 9 [14]. Load was applied over the connections as shown Figure 1(b), and ranged between 0.92 kN and 2.21 kN.

2.2 Expected fire conditions

The experimental structure is designed to represent a "slice" of aluminium reticulated roof for an exhibition centre. Piles of wood cribs were used as fire load to create a 24 MW fire lasting approximately 30 minutes. This relatively high fire intensity was chosen in hope to trigger the progressive collapse of the structure. The equivalent fire load density on the whole floor area (i.e., 72 m^2) is 600 MJ/m^2, follows the prescriptive requirement of fire load density for a shopping centre as per Eurocode 1 [15]. The design fire scenario has a character of fuel-controlled fire with sufficient ventilation, as is typical of fire in large open spaces.

2.3 Numerical model

A finite element model of the roof was built in the Integrated Simulation Environment (ISE) and was analysed using OpenSEES. Displacement-based beam-column elements with fibre-based sections were used to represent the beams of the roof. Each member was discretized with 8 elements, for a total of 552 elements modelling 69 structural members. The boundary conditions of the roof structure were pinned at the supports and all the beam-to-beam connections were assumed rigid as in the experimental setup. Both the fire modelling and subsequent heat transfer analysis were also carried out using OpenSEES within the ISE [16,17]. In addition to mesh size, sensitivity analysis was also performed on the scaling of analysis time. The static interval used load-controlled integration with the Band General system of equations, the reverse Cuthill-McKee (RCM) numberer, transformation constraints handler, and the Full Newton-Raphson algorithm. The transient interval used load-controlled integration with the UmfPack system of equations, the RCM numberer, transformation constraints handler, the Krylov Newton algorithm, and performed the integration with the Newmark method with the average acceleration method ($\gamma = 0.5$, $\beta = 0.25$) as recommended by Orabi et al. [18]. Rayleigh damping was also applied with the mass and stiffness damping factors set to 0.05 and 0.005 respectively. It was shown that the duration of fire can be scaled by a time factor of 1/1000 for the implicit dynamic analysis in OpenSEES. The step size was 0.001s, and the total analysis time was set to 1.8 s.

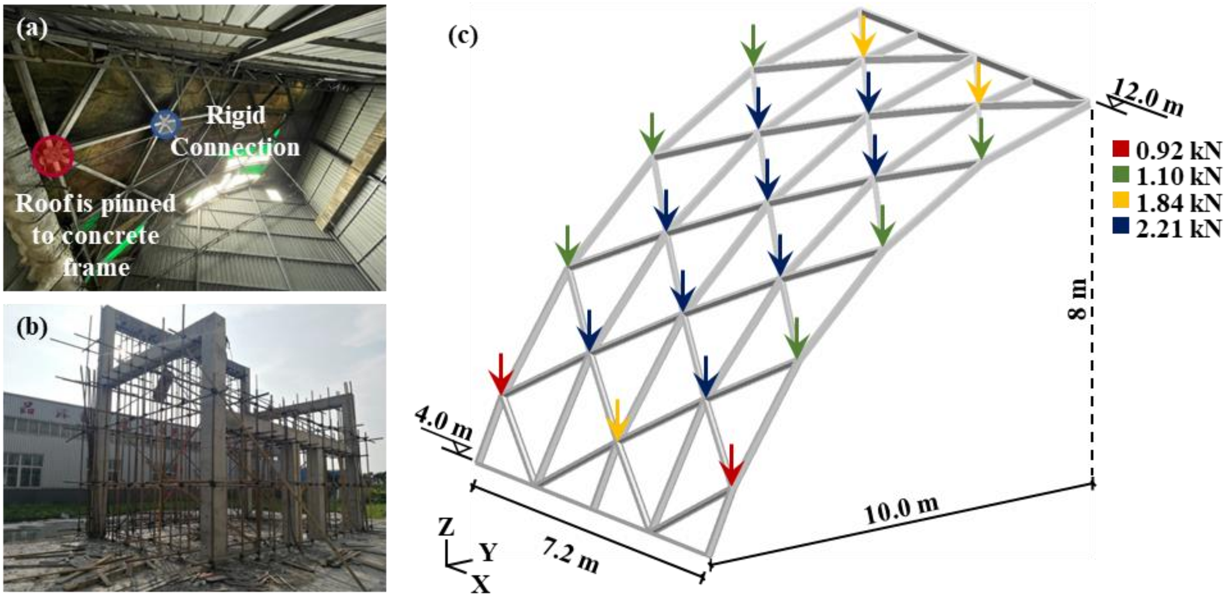

Figure 1. Details of the test structure (a) connection classifications, (b) supporting concrete frame, and (c) dimensions and imposed load

3 GENERATING TRAINING DATA

3.1 Parameters for simulation database

Training a deep learning model requires a significant amount of data. A simulation database of both fire temperatures and corresponding structural deflections was generated using the OpenSEES model above. Figure 2 illustrates the process used to generate the database. First, a library of localised fire scenarios was generated using the fire module of OpenSEES which implements Hasemi's localised fire model [19]. Each fire scenario had a different "location" and "size" to account for the possible spatiotemporal distribution of temperatures that are possible in the fire test. Fire location refers to the point at which the localised fire is concentrated while fire size refers to the intensity of the heat release rate. These two variables are one of the main factors contributing to the spatiotemporal variation in temperatures under localised fires. A series of heat transfer analyses for a subset of fire configurations was performed. It was found that the thermal thinness of the aluminium structural members meant that the gas temperatures and solid temperatures were in steady state heat transfer almost from the beginning of the fire. Therefore, it was concluded that the gas temperatures can be used directly as a uniform thermal load in the FE structural model. The displacement at several key locations of the roof structure were then extracted and included in the database.

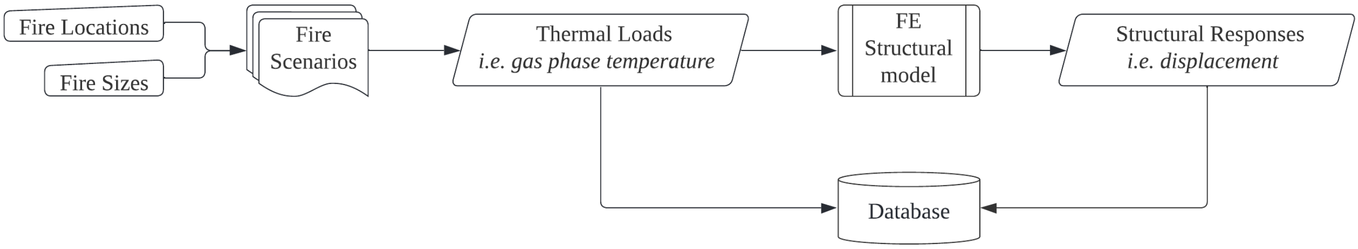

Figure 2. Simulation database flowchart

3.2 Localised fire scenarios

A total of one hundred localised fire scenarios were created considering the ten fire locations highlighted in Figure 3. These locations were combined with ten fire sizes within the range of 0.5 and 40 MW as detailed in Table 1. The relevant parameters of fire scenarios were specified to follow common design practice [15,20,21]: fuel load density on the floor area ≤ 1000 MJ/m^2, heat release rate per unit area (HRRPUA) 1000kW/m^2, fire growth rate "fast" with α value of 0.0469 kW/s^2.

Table 1. Values for the different parameters of the fire scenarios.

Parameters of fire scenarios	Values
Fire location (see Fig. 4)	Loc.1 (bottom centre), Loc.2 (lower centre), Loc.3 (middle centre), Loc.4 (upper centre), Loc.5 (top centre), Loc.6 (lower right), Loc.7 (upper right), Loc.8 (bottom right conner), Loc.9 (middle right edge), Loc.10 (top right conner)
Fire size (MW)	0.5, 2.5, 5.0, 7.5, 10, 15, 20, 25, 30, 40

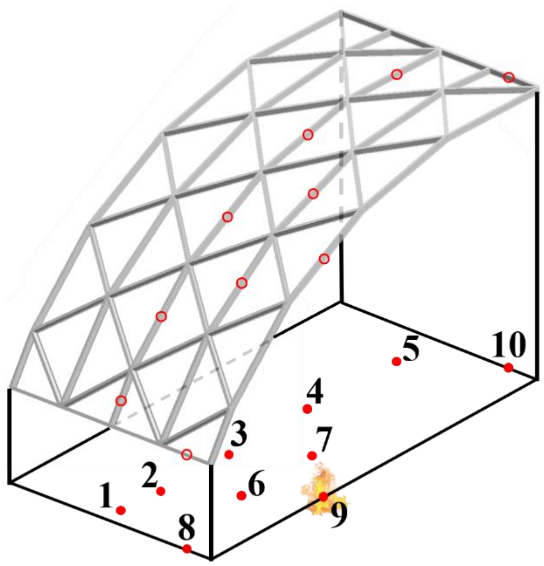

Figure 3. Selected fire locations

Figure 4 and Figure 5 show the effect of fire location and fire size, respectively, on the temperature distribution at the level of the roof. Because of the curvature of the structure, the ceiling height of the structure varies at different locations. As shown in Figure 4, even with the same fire intensity (e.g., 30 MW), due to different fire locations (e.g., bottom centre, middle right edge, and top right corner in this study), the temperature fields are significantly different. Figure 5 shows that, as expected, the larger the fire size, the higher the temperature. This is particularly the case directly above the fire source. The increase in fire sizes also results in a larger area of the structure being significantly affected by the fire.

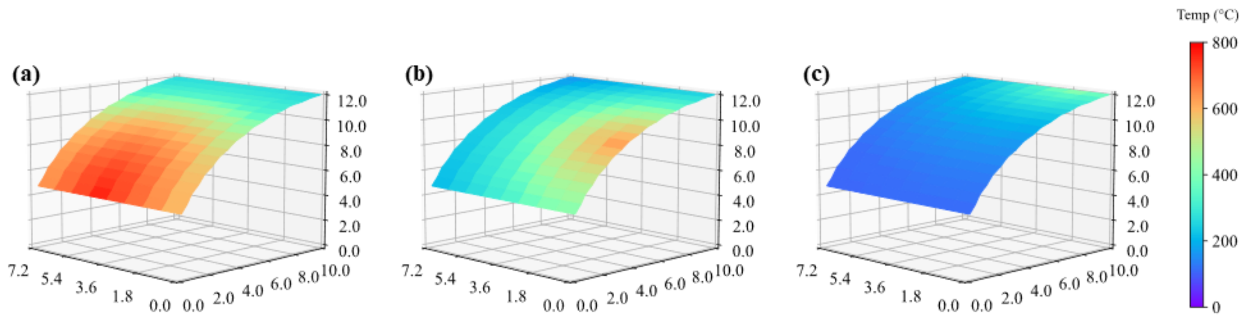

Figure 4. A sample of three cases considering different localised fire locations with the same fire intensity of 30 MW (a) loc. 1 - bottom centre, (b) loc. 9 - middle right edge, and (c) loc. 10 - top right corner

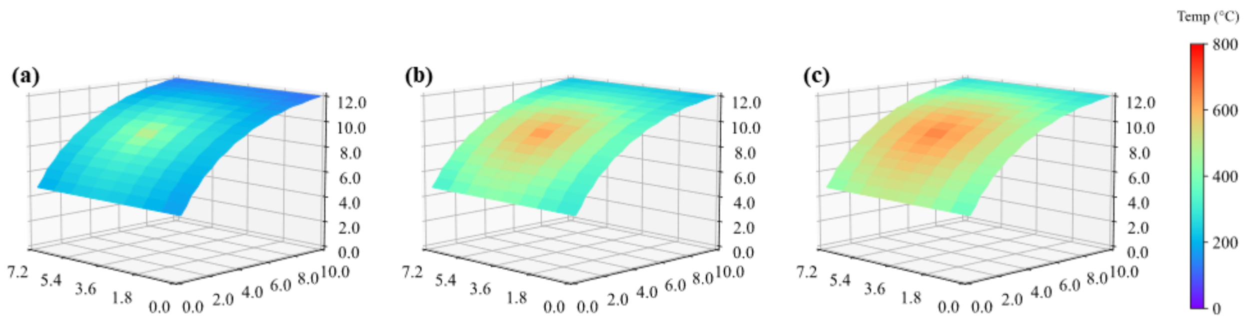

Figure 5. A sample of three cases considering different localised fire intensities at the same fire location (loc.3 - middle centre) (a) case 25 - 15 MW, (b) case 28 – 30 MW, and (c) case 29 – 40 MW

As shown in Figure 6, the data was extracted for 21 monitoring points across the roof. The gas temperature data was collected from 13 monitoring points at the ceiling height as numbered in Figure 6 (a). Displacements were collected at 8 monitoring points corresponding to critical connection locations (Figure 6 (b)). The dataset combined with the gas temperature and the displacement at the selected monitoring points were chosen as the starting point for database generation. Further iterations of this work may consider other information such as axial forces within individual members.

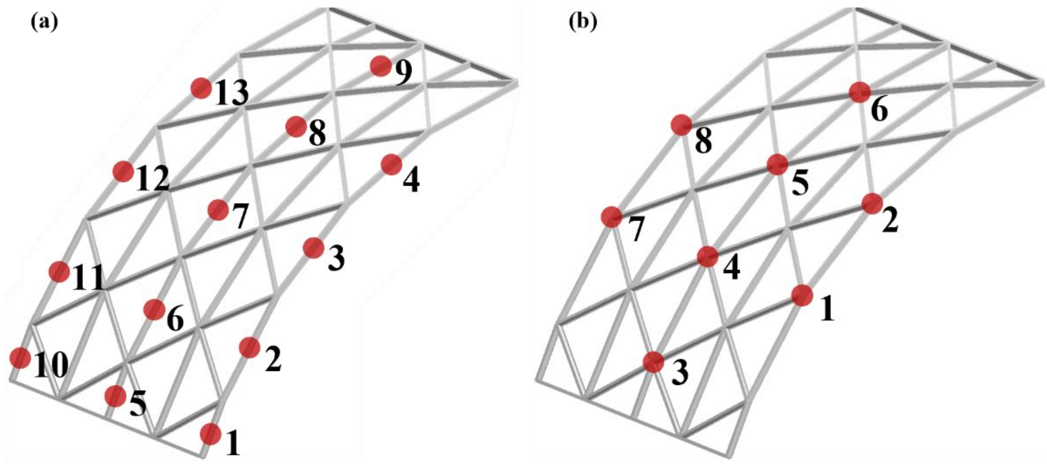

Figure 6. Monitoring points (a) temperature, and (b) vertical displacement.

3.3 Behaviour in fire and failure modes

When subjected to fire, the roof structure first responded by expanding and deflecting upwards as shown in Figure 7 (a). If the fire were intense and long enough, then some members may buckle as shown in Figure 7 (b). Under some circumstances, the structural response really stops there, and the fire extinguishes naturally before any severe structural damage. Some fire cases, however, can lead to partial collapse as shown in Figure 7 (c). Partial collapse here means the severe but limited deflection of only some members of the structure. The rest of the structure remains intact despite some members having failed. Global failure may occur instead of partial failure and is characterized by the rapid and consecutive failure of all members, as shown in Figure 7 (d).

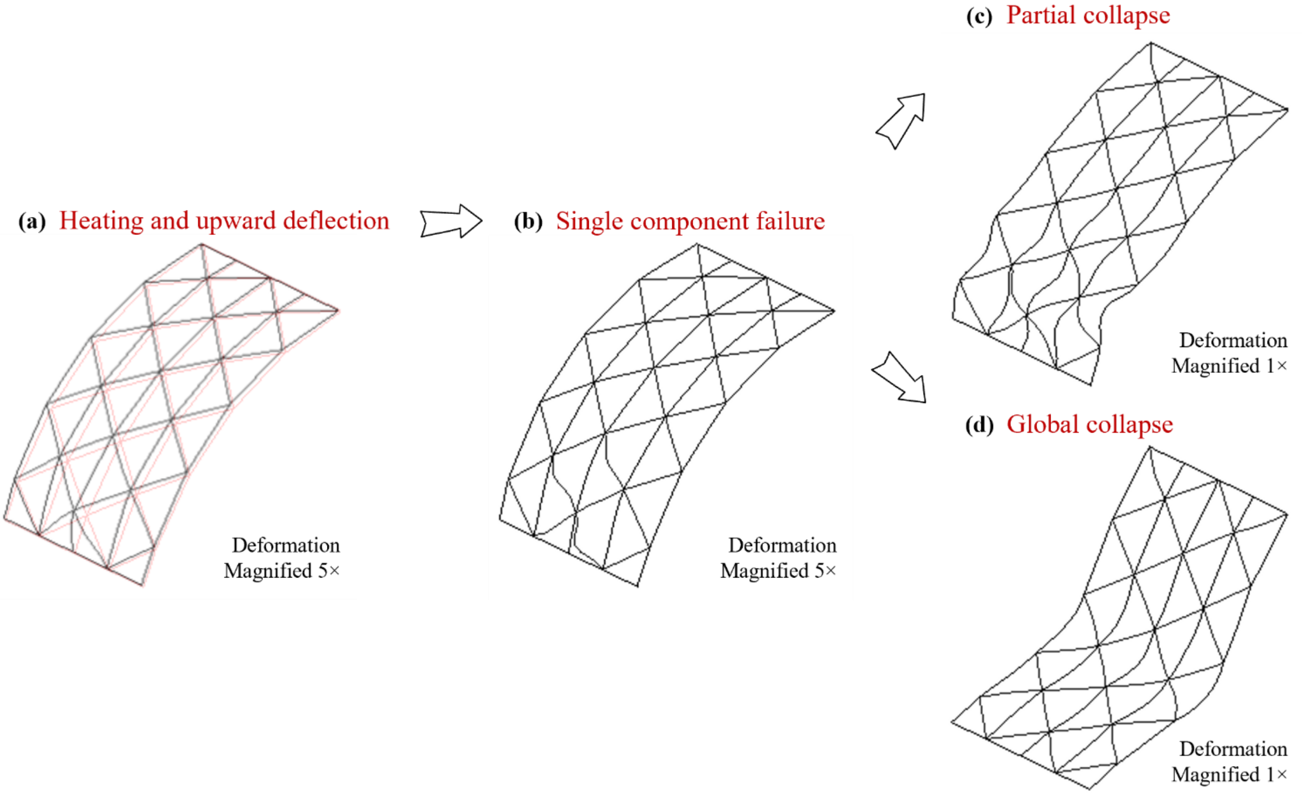

Figure 7. Structural responses under localised fire (a) heating and upward deflection, (b) single component failure, (c) partial collapse, and (d) global collapse

Figure 8 shows the thermal and structural responses of the roof under the fire scenario case 8 (i.e., 30 MW localised fire at the bottom centre of the structure as shown in Figure 4 (a)). For case 8, the gas temperature at the monitoring points are plotted in Figure 8(a). Above the fire source, the gas temperature was as high as 760 ℃ . Even far from the fire ignition location, where the ceiling height is approximately 12 m, the gas temperature still reached 291 ℃ . According to the Eurocode [14], the proof strength of aluminium reaches approximately 45% of its ambient value at 250 ℃ , and loses all its capacity at 550 °C. Thus, under case 8, many of the structural members of the roof reached their material failure point. This resulted in global collapse of the structure. Global collapse can be easily identified from the time-displacement history of the displacement monitoring points. As shown in Figure 8 (b), the displacement at all monitoring points exceeded a critical value of -0.5 m after around 13 minutes of fire exposure. The critical value of 0.5 m roughly corresponds to L/20, where L is the 10 m span of the roof.

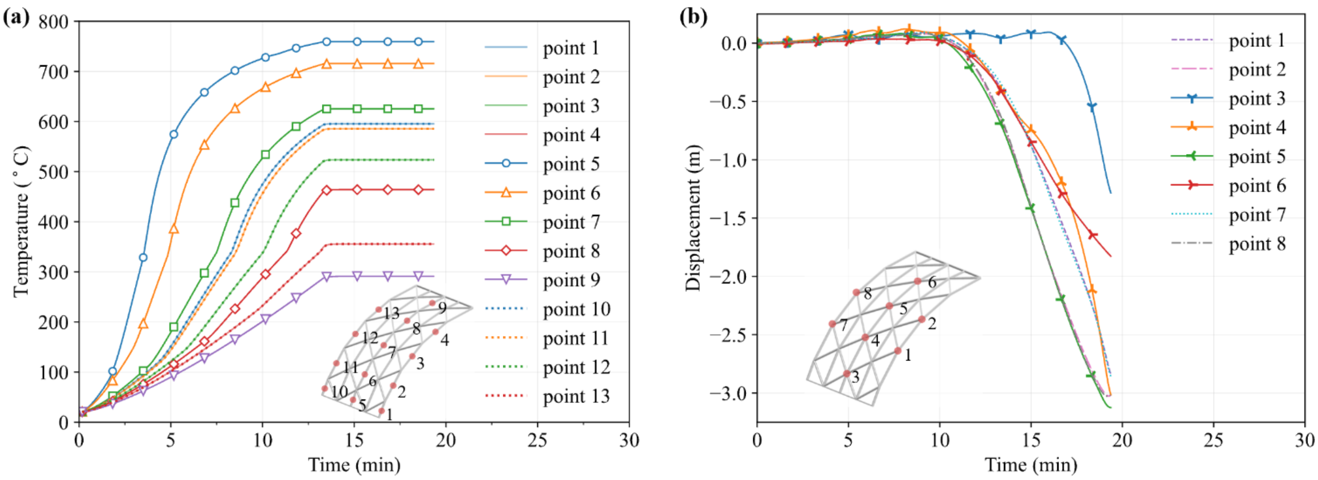

Figure 8. Expected behaviour for case 8 (a) temperatures at the different monitoring points, and (b) displacements of the displacement monitoring points

4 ARTIFICIAL INTELLIGENCE MODEL

4.1 Methodology

The AI model used is an LSTM recurrent neural network. There are two main approaches for fitting the AI model to the data for real-time forecasting: (a) the AI model is trained on all data for temperature and displacement and predicts the next state of displacement for all displacement monitoring points, or (b) an individual LSTM is trained for each displacement monitoring point taking into consideration the surrounding temperature points. The first approach has the benefit of considering the whole state of the structure at any timepoint. This should, hypothetically, make the AI model better at predicting global failure. There are many downsides to this approach, however. First, training on the data of all 21 monitoring points would require a large and complex network that is difficult to train both from a technical and computational standpoint. Another issue is that the network and training framework (data retrieval and cleaning) would not really be transferrable and directly usable for training on and real-time forecasting of another structure.

The second approach, where an LSTM network is trained for each monitoring point, allows for considering each monitoring point irrespective of its neighbours. This means that each AI model would not be trained on the global state of the structure but only on the local monitoring point data and maybe some adjacent thermocouples. It might be more difficult to train such a model to predict global failure, but each individual model would be easier to train and deploy. Additionally, since each model is only trained on a subset of the structure, it would be easy to increase the number of models to increase the prediction coverage for better global state forecasting, or for the prediction of the behaviour of a completely different structure.

4.2 Architecture and training

The architecture of the network used consists of a dropout layer with 50% dropout probability, followed by two hidden layers of size 64, then a fully connected layer with softsign activation and finally an output layer of size 1. This architecture was constructed using PyTorch [6], and was trained in minibatches of size 64. For demonstration, the AI model was trained on the data for displacement monitoring point 4 and temperature monitoring point 6. This AI model would thus predict the displacement at point 4 given the current recorded state of this monitoring point and the corresponding temperatures at temperature monitoring point 6. The data for the 100 cases were divided into a 60-20-20 training-test-validation split. The data in the training set were normalised by dividing by their mean displacement and temperature. Each timeseries in the training set were then further broken down into windows each containing approximately 100 datapoints for both displacement and temperature. These windows were then shuffled and organised into minibatches each containing 64 training windows and their corresponding labels. The network was trained for 10000 epochs, and used the adaptive gradient optimiser and the mean square error loss function. The learning rate was set to an initial value of 0.2 with a decay rate of 0.004. For forecasting, the AI model is fed a short "stump" of data and produces a single prediction. That prediction is then added to the stump and fed back into the model to predict, iteratively, the next point. This is repeated until the entire time-series is predicted.

4.3 Initial predictions and deployment plan

It is hoped to deploy this AI model during the real fire test at the Sichuan Fire Research Institute. A similar network would be trained for each displacement monitoring point, and then the trained models would be fed live temperature data as shown in Figure 9. The models would then keep producing predictions based on the current state of the structure and would issue a warning if the deflections are predicted to go below -0.5 m.

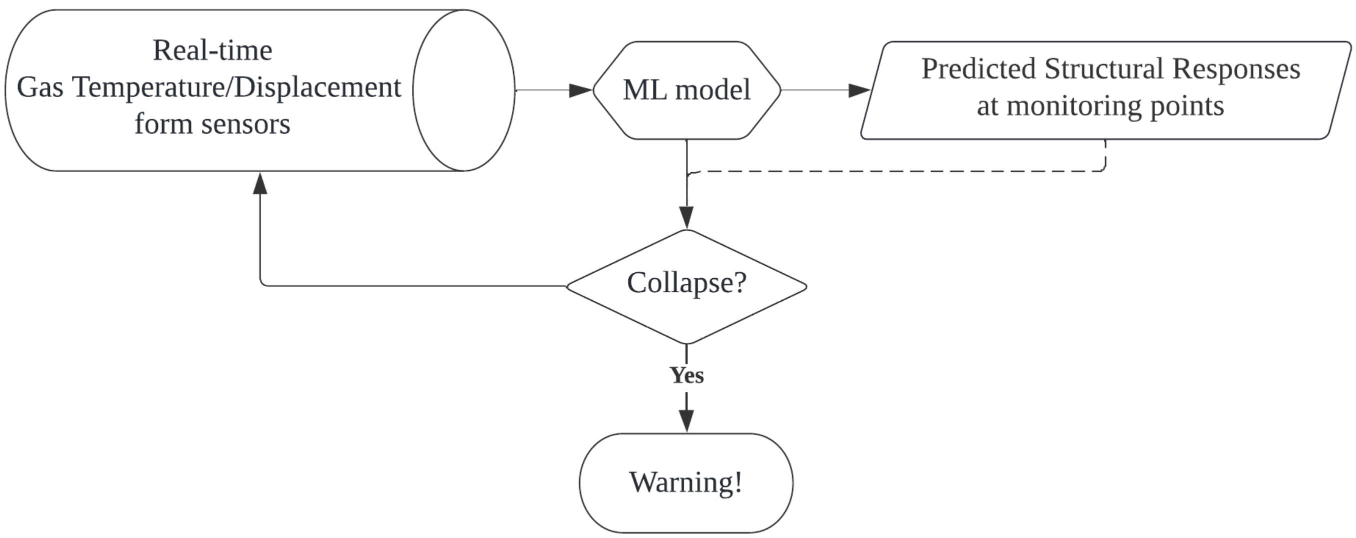

Figure 9. Plan for deploying the AI model during the fire test

Initial attempts at training the AI model have yielded modest results. Take Figure 10, for example. This figure shows the predictions of the displacement at monitoring point 8 given different stumps of data. From this figure, it is clear that the AI model is unable to predict failure until it becomes eminent. There are many reasons for this, most important of which is that most training cases do not experience global collapse, and in fact would experience similar deflections to what the model is predicting given a shorter stump. It was hoped that the inclusion of temperature data would allow the model to overcome this issue. However, with only 18 collapse cases in total, it is expected that a significantly larger database would be needed. Future work will focus on enriching the training database, improving the AI model architecture, and enhancing the training procedure and parameters.

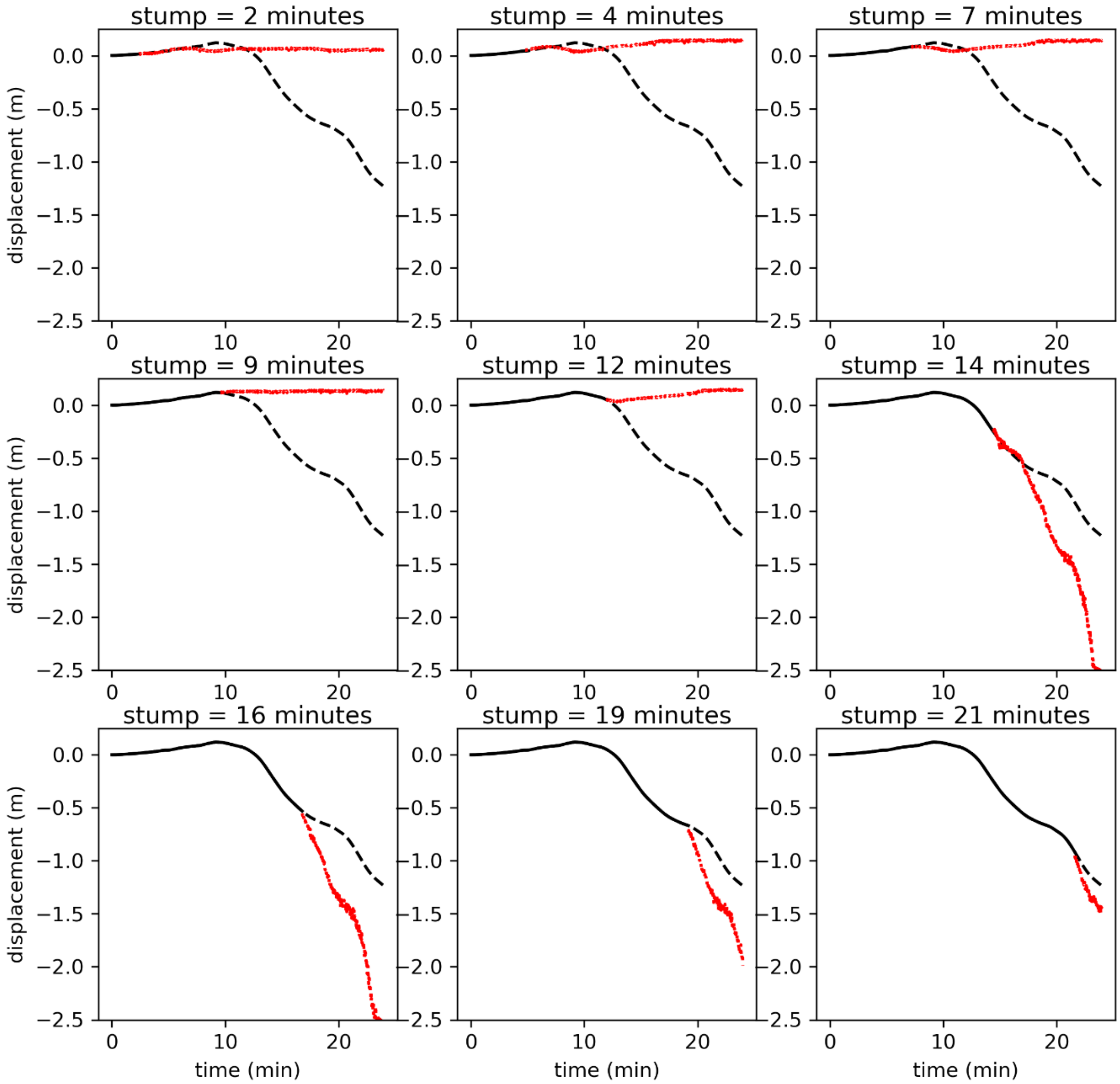

Figure 10. predictions for one of the validation cases which incur structural failure

5 CONCLUSIONS

This paper studied rapid forecasting to predict the behaviour of a roof structure that will be tested until collapse in fire. The proposed AI model will be improved and then deployed in the full-scale test to test its ability to forecast structural collapse in fire. The fire and FEM models were both built in OpenSEES and used to populate a numerical database with 100 localised fire scenarios considering different fire locations and fire sizes. A LSTM RNN was used as the AI model, and the data of temperature and displacement at one displacement and one temperature monitoring points were used as model input. An individual LSTM is to be trained for each displacement monitoring point taking into consideration the surrounding temperature points. For example, the predictions of the displacement at monitoring point 8 given different stumps of data has been presented in this paper. The results of the paper can be summarised in the following points:

1. Under localised fire, the aluminium roof structure reacted by first deflecting upwards. Under some scenarios, this was followed by single component failure. Partial and global collapse also occurred as evidenced by large but controlled deflections, and runaway deflections, respectively.

2. Despite generating over a hundred different fire scenarios, only 18 resulted in global collapse. While this is a large ratio, it makes it difficult to train a neural network to predict global failure; there simply is not enough examples of failure in such a small dataset to train an AI model.
3. Deployment of the AI model will depend on the efficacy of the individual networks trained for each displacement monitoring point. As such, future work will focus first on increasing the quantity of the training data, and then the quality of network architecture and training process.

ACKNOWLEDGMENT

This work is funded by the Hong Kong Research Grants Council Theme-based Research Scheme (T22-505/19-N).

REFERENCES

1. Gann, R.G., Hamins, A., Mcgrattan, K., Nelson, H.E., Ohlemiller, T.J., Prasad, K.R., et al. Reconstruction of the fires and thermal environment in World Trade Center buildings 1, 2, and 7, 679–707 (2013). https://doi.org/10.1007/s10694-012-0288-3.
2. Fletcher, I., Borg, A., Hitchen, N., Welch, S. Performance of concrete in fire: A review of the state of the art, with a case study of the Windsor Tower fire. 4th Int Work Struct Fire, 779–90 (2006).
3. Meacham, B., Park, H., Straalen, I.J. Fire and Collapse , Faculty of Architecture Building , Delft University of Technology : Data Collection and Preliminary Analyses. Architecture, 14 (2008).
4. Yarlagadda, T., Hajiloo, H., Jiang, L., Green, M., Usmani, A. Preliminary modelling of Plasco Tower collapse. Int J High-Rise Build 7, 397–408 (2018). https://doi.org/10.21022/IJHRB.2018.7.4.397.
5. Khan, M.A., Khan, A.A., Usmani, A.S., Huang, X. Can fire cause the collapse of Plasco Building: A numerical investigation. Fire Mater, 1–16 (2021). https://doi.org/10.1002/fam.3003.
6. Paszke, A., Lerer, A., Killeen, T., Antiga, L., Yang, E., Gross, S., et al. PyTorch: An Imperative Style, High-Performance Deep Learning Library, NeurIPS (2019).
7. Abadi, M., Agarwal, A., Barham, P., Brevdo, E., Chen, Z., Citro, C., et al. TensorFlow: Large-Scale Machine Learning on Heterogeneous Distributed Systems (2015).
8. Wu, X., Park, Y., Li, A., Huang, X., Xiao, F., Usmani, A. Smart Detection of Fire Source in Tunnel Based on the Numerical Database and Artificial Intelligence. Fire Technol (2020). https://doi.org/10.1007/s10694-020-00985-z.
9. Wu, X., Zhang, X., Huang, X., Xiao, F., Usmani, A. A real-time forecast of tunnel fire based on numerical database and artificial intelligence. Build Simul 15, 511–24 (2022). https://doi.org/10.1007/s12273-021-0775-x.
10. Ye, Z., Hsu, S.C., Wei, H.H. Real-time prediction of structural fire responses: A finite element-based machine-learning approach. Autom Constr 136, 104165 (2022). https://doi.org/10.1016/j.autcon.2022.104165.
11. Fu, F. Fire induced progressive collapse potential assessment of steel framed buildings using machine learning. J Constr Steel Res 166, 105918 (2020). https://doi.org/10.1016/j.jcsr.2019.105918.
12. Ye, Z., Hsu, S. Automation in Construction Predicting real-time deformation of structure in fire using machine learning with CFD and FEM. Autom Constr 143, 104574 (2022). https://doi.org/10.1016/j.autcon.2022.104574.
13. Ji, W., Li, G., Zhu, S. Real-time prediction of key monitoring physical parameters for early warning of fire-induced building collapse. Comput Struct 272, 106875 (2022). https://doi.org/10.1016/j.compstruc.2022.106875.
14. Mazzolani, F.M. EN1999 Eurocode 9: Design of aluminium structures. Proc. Inst. Civ. Eng. Eng., vol. 144, Thomas Telford Ltd; , p. 61–4.

15. CEN. EN 1991-1-2:2002 - Eurocode 1. Actions on structures. General actions. Actions on structures exposed to fire. Brussels: European Committee for Standardization (CEN).
16. Yaqiang Jiang. Development and application of a thermal analysis framework in OpenSees for Structures in fire. The University of Edinburgh.
17. Jiang, L. Development of an integrated computational tool for modelling structural frames in fire considering local effects. Univ Edinburgh (2015).
18. Orabi, M.A., Jiang, L., Usmani, A., Torero, J. The Collapse of World Trade Center 7: Revisited. Fire Technol (2022). https://doi.org/10.1007/s10694-022-01225-2.
19. Hasemi, Y., Yokobayashi, Y., Wakamatsu, T., Ptchelintsev, A. V. Modelling of heating mechanism and thermal response of structural components exposed to localised fires.Thirteenth Meeting of the UJNR Planel on Fire Research and Safety.
20. Law, M. The origins of the 5 MW design fire. Fire Saf Eng 2, 343–6 (1995).
21. NFPA® 92B. Standard for Smoke Management Systems in Malls , Atria , and Large Spaces.

SiF 2022– The 12th International Conference on Structures in Fire
The Hong Kong Polytechnic University, Nov 30 - Dec 2, 2022

THE SIGNIFICANCE OF SLAB FOR STRUCTURAL RESPONSE UNDER TRAVELLING FIRES

Zhuojun Nan[1], Xu Dai[2,*], Stephen Welch[3], Asif Usmani[4]

ABSTRACT

The role of "travelling fires" is to ensure the robustness of structural design with large compartments under realistic fires, having a fire plume at the near-field, and a hot smoke layer preheating the ceiling at the far-field. Once the fire travels, the near-field has a leading edge representing the fire spread, and a trailing edge representing the burnout of the fuel. Though well understood by its definition, the mainstream of efforts on travelling fires for structural response is limited to 2D finite element modelling (FEM). This paper aims to identify the importance of slab inclusion with a 3D FEM structural model for steel-composite structures under travelling fires, with a special emphasis on the significance of ignoring the slab structural capacity contribution from a 2D simplified structural model. The role of fire protection scheme for 2D model against the 3D model on numerical predictions was also explored. It was found that the structural load path, and the potential structural failure mechanisms could be fundamentally different between the 3D model and the 2D model, i.e., with or without slabs. Although the 2D model tends to predict larger deflections (i.e. more conservative) than the 3D model, it could also significantly underestimate the large internal forces from the beams, which might overlook the connections failure under travelling fires. Further, due to the simplification of the 2D model omitting the significant stiffness contribution from the slab, the effect of the fire protection is likely to be amplified. It may be misleading for the performance-based structural fire design under different travelling fire scenarios. Hence, the 3D model is likely to be considered as necessary and feasible for structural fire analysis for travelling fires as a complement to the 2D model approach.

Keywords: Travelling fires; 3D FEM; steel composite structure; performance-based design

1 INTRODUCTION

In structural fire engineering, the "travelling fire" methodology has been gradually accepted as an appropriate fire boundary condition for fire severity calculations [1]. However, a poor structural model cannot compensate for a rigorous fire model, as is the prevailing situation for travelling fires for performance-based structural engineering. For instance, Rezvani & Ronagh [2] and Rackauskaite et al. [3–5] performed extensive numerical studies on structural response of steel-framed buildings, using 2D generic frame structures under the Travelling Fires Methodology (TFM) [6,7] and its subsequent refined version improved Travelling Fires Methodology (iTFM) [8]. These studies are practically of limited value, as a travelling or spreading fire is by its nature a 3D phenomenon and 2D structural models simply cannot represent the complexity of behaviours presented in a realistic structure, such as the membrane behaviour of floor systems. The Cardington fire tests clearly showed that the slabs carried most of the load at very high temperatures [9]. Jiang and Li [10,11] compared the progressive collapse analysis of steel frames with concrete slabs exposed to localised fire between 2D and 3D models. The results demonstrated that the collapse modes and load redistribution path of the 2D model and 3D model were fundamentally different.

[1] PhD Student, Hong Kong Polytechnic University
e-mail: zhuojun.nan@connect.polyu.hk, ORCID: https://orcid.org/0000-0001-8189-5448
[2] Senior Lecturer, Birmingham City University
e-mail: xu.dai@bcu.ac.uk, xudai1987@gmail.com, *corresponding author, ORCID: https://orcid.org/0000-0002-9617-7681
[3] Seniro Lecturer, University of Edinburgh
e-mail: s.welch@ed.ac.uk , ORCID: https://orcid.org/0000-0002-9060-0223
[4] Chair Professor, Hong Kong Polytechnic University
e-mail: asif.usmani@polyu.edu.hk, ORCID: https://orcid.org/0000-0003-2454-5737
https://doi.org/10.6084/m9.figshare.22249336

Jiang et al. [12] further investigated the disproportionate collapse of a 3D steel-framed gravity building under three travelling fire scenarios (using Clifton's travelling fire model [13]). It was found that a higher level of fire protection may prevent the collapse of structures but may also lead to structural failure in the cooling phase due to the delayed increment of temperatures in the heated members. A lack of understanding persists about the effect of fire protection on failure mechanisms between 2D and 3D FEM models under various travelling fire scenarios.

This paper aims to identify the importance of concrete slab inclusion with a 3D FEM structural model for steel-composite structures under travelling fires, with a special emphasis on the significance of ignoring the slab structural capacity contribution from a 2D simplified structural model. This study further addresses the role of the fire protection scheme on numerical predictions for performance-based structural fire design.

2 THE STRUCTURAL MODEL

Inspired by the BST/FRS 1993 travelling fire test structural layout [14], a prototype structure representing a "slice" of steel framed building with composite floors was developed, see Figure 1(a). It has structural dimensions of 23 m length × 6 m width × 2.75 m height with three bays. This structure was designed by following the Eurocode to resist ambient design load on the floor (1.35 × 4.13 (dead load) + 1.5 × 2.5(live load) = 9.3 kN/m^2). The cross-section of all floor beams and columns were chosen as UB 406 × 178 × 54 with steel grade S355. The Cofraplus 60 [15] composite slab with thickness of 140 mm was used.

In the validated LS-DYNA 3D model [16], the composite slab was simplified as the equivalent self-weight of flat concrete slab with a continuous depth of 110 mm concrete C30/37, reinforced by two structural mesh fabric B502 (i.e., 503 mm^2/1000 mm) placed 25 mm from the edges of the cross-section. The beam elements shared the same nodes with the shell elements to account for composite action effects. The formulation of steel structural members and slabs were Hughes-Liu and Belytschko-Lin-Tsay, respectively. The properties of materials were defined according to Eurocodes [17,18]. All the connections are modelled as pinned.

The corresponding 2D model with three spans (7.5 m, 8.0 m and 7.5 m) was extracted from the longitudinal direction of the 3D prototype structure, i.e., XBeams with the longest beam span in the 3D model and columns, as shown in Fig. 1(b). The concrete slab and the composite action between the beams and the slab were not considered in the 2D model. Nevertheless, the load from the concrete slab was still taken into account, which could have resulted in the equivalent mechanical load compared to the 3D model. Besides, similarly as [5], the heat sink effect due to the concrete slab was considered in the heat transfer analysis of our 2D model. The duration of travelling fire was scaled by a time factor of 1/1000 for the explicit dynamic analysis in LS-DYNA [19].

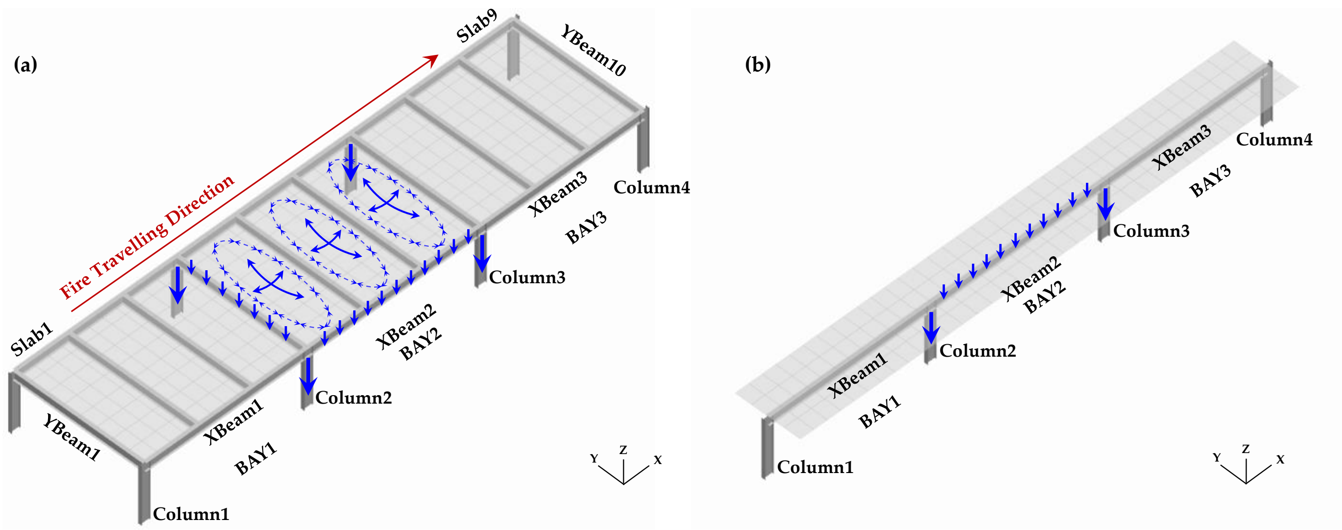

Figure 1. Schematic of the prototype structure load path in the second bay: (a) 3D model; (b) 2D model.

3 THE TRAVELLING FIRE SCENARIOS

A more advanced travelling fire model, the Extended Travelling Fire Methodology (ETFM) framework [20,21] was applied in this study. The EFTM framework is postulated on a "mobilised" version of Hasemi's localised fire model (near-filed), combined with a simple smoke layer calculation using the FIRM zone model (far-filed), which considers both energy and mass conservation for the fire design of the large compartment. Both the travelling fire modelling and subsequent heat transfer analysis were carried out using OpenSEES [21]. The fire was assumed to start at left short end of the compartment, travelling along the longitudinal direction (i.e., left to right as shown in Figure 1).

To investigate the structural response under travelling fires, representative scenarios were defined first. It is critical that the selected fire scenarios are likely to challenge the prototype structure to its failure. The relevant parameters of travelling fire scenarios were selected for typical office buildings [22–24]: fuel load density 511 MJ/m^2, heat release rate per unit area (HRRPUA) 250 kW/m^2, inverse opening factor (IOF) 9.6, total heat loss fraction 0.85 and radiative heat loss fraction 0.35. Travelling fire spread rates are among the most important parameters for the structural fire design, due to their high influence on the thermal and the structural response [16,21]. Hence, this paper would investigate different fire spread rates and the corresponding structural performance for the 2D and 3D models. Within the typical range of fire spread rates, i.e., between 0.1 and 19.3 mm/s based on the previous experimental results [8], two representative travelling fire scenarios were selected for the ETFM framework:

1. Scenario 1: fire spread rate 2.5 mm/s (with resultant HRR 7.7 MW)
2. Scenario 2: fire spread rate 0.5 mm/s (with resultant HRR 1.5 MW)

4 THE SIGNIFICANCE OF SLAB: 3D MODEL VS 2D MODEL

In this section, to maximise the structural response under different travelling fire scenarios for the 3D model against 2D model, all the structural steel members were left unprotected. The effect of fire protection is further investigated in Section 5.

4.1 Travelling fire scenario 1 (2.5 mm/s)

Travelling fire scenario 1 represents a design fire scenario with a resultant HRR of 7.7 MW, which is higher than the typical design value of 5.0 MW for commercial buildings [25]. Meanwhile, the fire duration for each bay was around 60 min with a fire spread rate of 2.5 mm/s. It could provide sufficient heating and cooling time for the structural members, and satisfy the general requirements of structural fire design for fire resistance rating (FRR) (i.e., R60) [26].

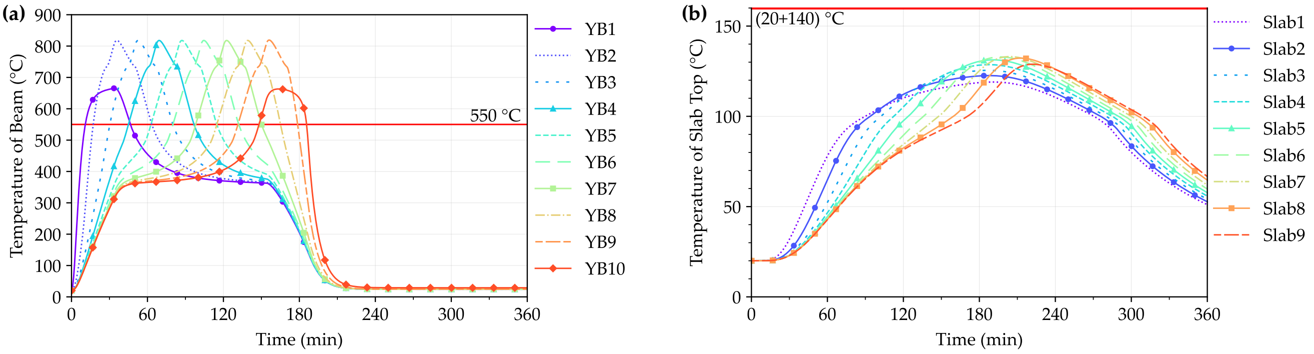

Figure 2. Thermal response of the structural elements in 3D model under the travelling fire scenario 1 (fire spread rate: 2.5 mm/s): (a) YBeam1 to YBeam10; (b) Slab1 to Slab9.

Figure 2 summarises the time-temperature histories of the beams and slabs along the travelling fire path in the 3D model. Full heating and cooling cycles were induced by the travelling fire on the structure. In Figure 2(a), the beams in the latitudinal direction of the compartment (i.e., Y direction refers to Fig. 1) had a peak temperature of 820℃ , exceeding the critical temperature of 550℃ , which was assumed for composite beams supporting concrete floor slabs when the building occupancy is not specified [27]. YBeam1 and

YBeam10 had relatively lower peak temperatures, i.e., approx. 665℃ , as these beams were at the edge of the compartment during the travelling fire initial developing and decaying stages. In Fig. 2(b), note that none of the slab top surfaces reached its critical temperature, i.e., 160℃ , which is defined based on the ASTM E119 [28]. It is worth mentioning that a temperature reduction ratio of 0.7 (from the connected steel beam members) was applied on the columns, the same simplifications as our earlier work [16].

Figure 3 presents the displacement contour development of the 3D and 2D models under the travelling fire scenario 1. Critical structural response events at specific time were selected and demonstrated: 35 min, 95 min, 155 min, and 245 min for the 3D model; 35 min and 75 min for the 2D model respectively. Note that the travelling fire scenario 1 had entered the cooling phase at 245 min. In general, the deflection sequence of the steel beams followed the travelling fire trajectory, i.e., as the fire travelled to each beam it would have the largest deflection; as the fire travelled away from each beam, the deflection would decrease due to cooling. It is worth noting that in Figure 3(a), the second bay which had a slightly longer span (i.e., 8 m) had the largest deflection compared to the other two neighbouring bays with 7.5 m span. This is because the longer primary beams of the second bay had larger deflections in the heating phase due to the thermal expansion. The thermal expansion of the longer primary beams was restrained by the neighbouring cooler bays; hence, relatively larger residual deflection was also induced at the second bay at the cooling phase.

The global structural response, or the potential structural failure mechanism, is very different between the 3D and 2D models. The structural collapse of the 2D model occurred at around 77 min under the travelling fire scenario 1, see Figure 3(b). The maximum deflection of XBeams reached 1.31 m before its failure. This value is significantly larger than the critical deflection 0.4 m, i.e., L/20, where L is the longest XBeam with length of 8 m. In contrast, the largest deflection of the slabs of the 3D model reached 0.33 m at the second bay during the cooling phase, with no indication of structural collapse. This is because the 3D model has higher overall stiffness due to the presence of the composite slab compared with the simplified 2D model.

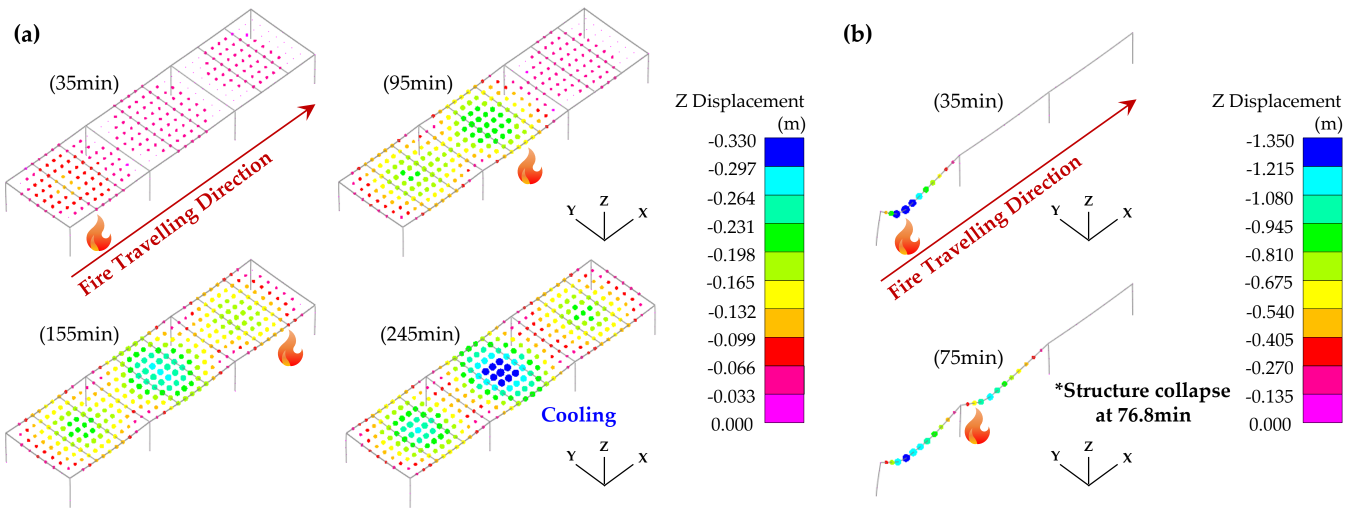

Figure 3. Displacement contour under the travelling fire scenario 1 (fire spread rate: 2.5 mm/s, fuel load density: 511 MJ/m^2, HRRPUA: 250 kW/m^2, and IOF: 9.6): (a) 3D model; (b) 2D model.

The membrane tractions in slab of the 3D model at selected times under travelling fire scenario 1 are presented in Figure 4. The red shaded area represents the fire size, i.e., approx. 30 m^2. In Figure 4(a)-(c), the 3D model was subjected to travelling fire direct flame for the near-field, and pre-heated by the smoke layer for the far-field. The heated composite slabs by the near field led to large displacements and thermal expansion. The expansion of the composite slabs was subsequently restrained by the surrounding bays. As the fire was travelling away, the temperature continued penetrating the slab in-depth, hence yielding even higher compression during the "local" cooling phase, see Figure 4(d). If the deflection was (artificially) increased by enhancing the mechanical loading to a higher magnitude, the composite slab is likely to present an apparent tensile membrane action with features having a compressive ring supporting a central tensile region [29].

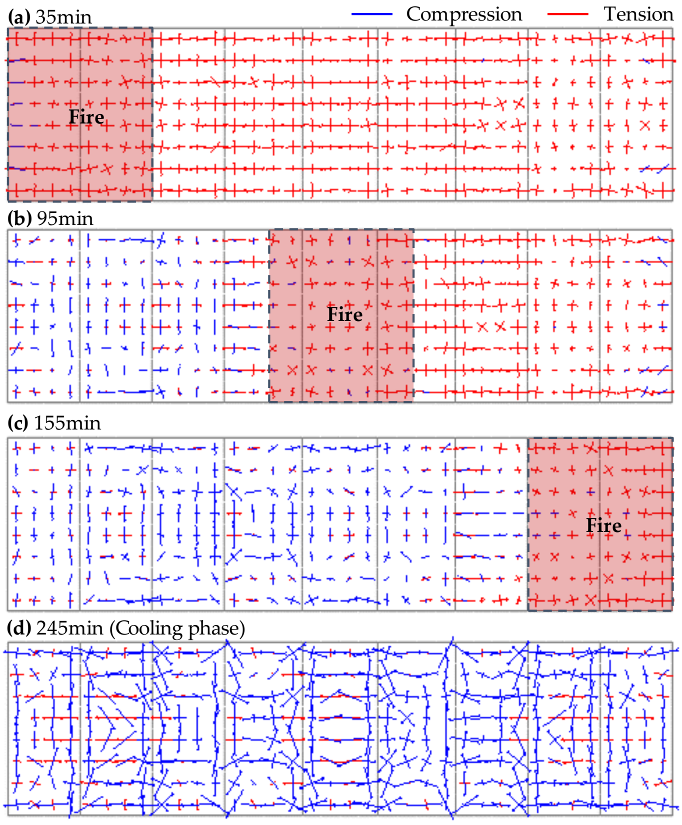

Figure 4. Membrane tractions in the slab under the travelling fire scenario 1 (fire spread rate: 2.5 mm/s): (a) 35 min; (b) 95 min; (c) 155 min; (d) 245 min.

Figure 5 shows the comparison of structural response between the 3D model and the 2D model under the travelling fire scenario 1. In Figure 5(a), the largest deflection of XBeam1 and XBeam2 in the 2D model reached 1.31 m and 0.96 m respectively (both far beyond the critical deflection of 0.4 m), prior to the global structural collapse. In contrast, XBeam2 in the 3D model had the largest deflection of 0.22 m which was below the critical deflection. Figure 5(b)&(c) present the deflection rate at mid-span of XBeams for the 3D model and 2D model respectively. Again, the comparisons of the two figures indicate a fundamental difference in the global structural responses between the 3D and 2D models. In the 3D model, the largest deflection rate of XBeam1 reached 6.4 mm/min, significantly lower than the critical defection rate, i.e., $L^2/9000d$, where L was the longest XBeam length of 8 m and d was the cross-sectional depth of 0.403 m. Whereas the largest deflection rates of XBeam1 and XBeam2 in the 2D model were over an order of magnitude higher. Note that the temperatures of most steel structural members exceeded 600℃ up to 800℃ under the travelling fire scenario 1. It means the loss of steel strength can be as high as 80% to 95% according to the Eurocode [18].

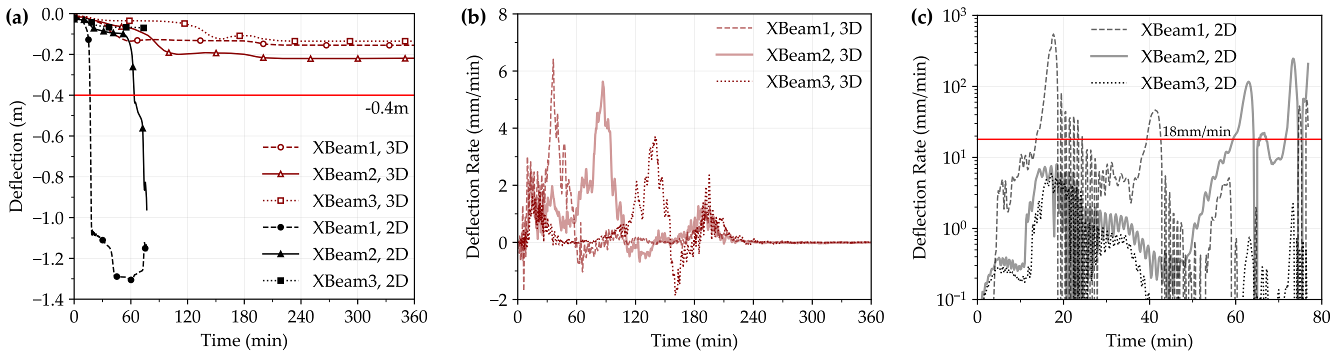

Figure 5. Structural response of XBeam1 to XBeam3 (X direction) at mid-span under the travelling fire scenario 1 (fire spread rate: 2.5 mm/s), 3D model vs 2D model: (a) Deflection; (b) Deflection rate of 3D model; (c) Deflection rate of 2D model.

Figure 6 summarises the axial force and stress utilisation of XBeams under travelling fire scenario 1 for 2D model against 3D model. The stress utilisation at the mid-span of the beam is defined as one of the failure criteria of a single element [16], i.e., the ratio of the axial stress envelope in the whole beam cross-section over the steel yield strength, as shown in Figure 6(b). The failure is defined as the beam reaches its yield capacity at ambient temperature (i.e., 355 MPa at 20℃) and can no longer support the structure above [30], i.e. the stress utilisation reaches 1.0. In Figure 6(b), the stress utilisation of XBeams in the 3D model all approached to 1.0. It is worth noting that the axial forces of XBeam1 to XBeam3 in the 3D model were 2180 kN, 2350 kN, and 2105 kN respectively, close to the axial force capacity of N_{Rd} = 2448 kN (see Figure 6(a)). In contrast, due to lack of neighbouring restraints and stiffness (from the slab and adjacent structural members), the 2D model collapsed in a very early stage of the whole travelling fire duration, and the beam axial forces were also significantly lower compared with the values in the 3D model.

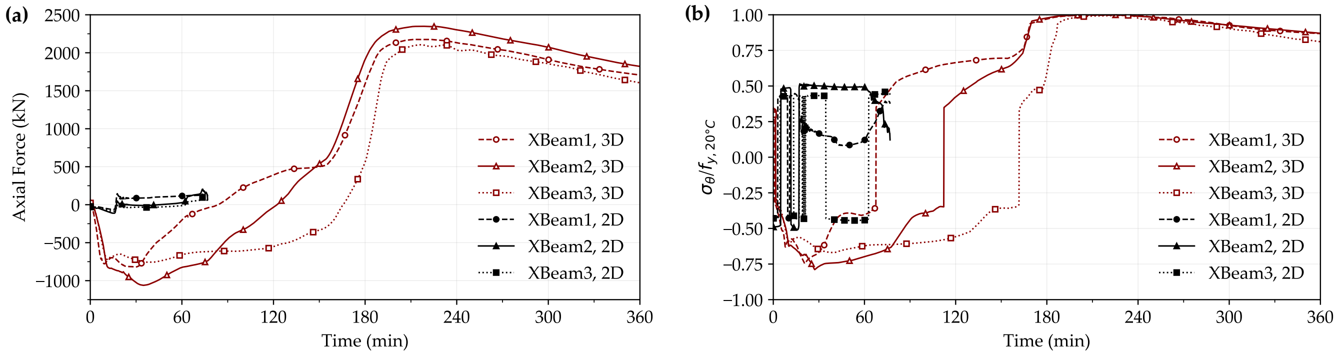

Figure 6. XBeam1 to XBeam3 (X direction) at mid-span under the travelling fire scenario 1 (spread rate: 2.5 mm/s), 3D model vs 2D model: (a) Axial force; (b) Stress utilisation: ratio of the axial stress envelope over the yield strength 355 MPa at 20℃ .

4.2 Travelling fire scenario 2 (0.5 mm/s)

Travelling fire scenario 2 represents a design travelling fire scenario with a “slow” spread rate of 0.5 mm/s, yielding a modest total HRR of 1.5 MW.

As shown in Figure 7, under the travelling fire scenario 2, the peak temperature of YBeams reached 670℃ , exceeding the critical temperature of 550℃ . Further, the “distinguishable” full heating and cooling cycles were observed for all the structural elements. When the slow travelling fire approached a structural member even with a modest total HRR, 1.5 MW, the longer near-field exposure (due to slow fire spread rare) would enable the fire more time to “heat up” the structural member, which may still result in more energy being absorbed by the structural member.

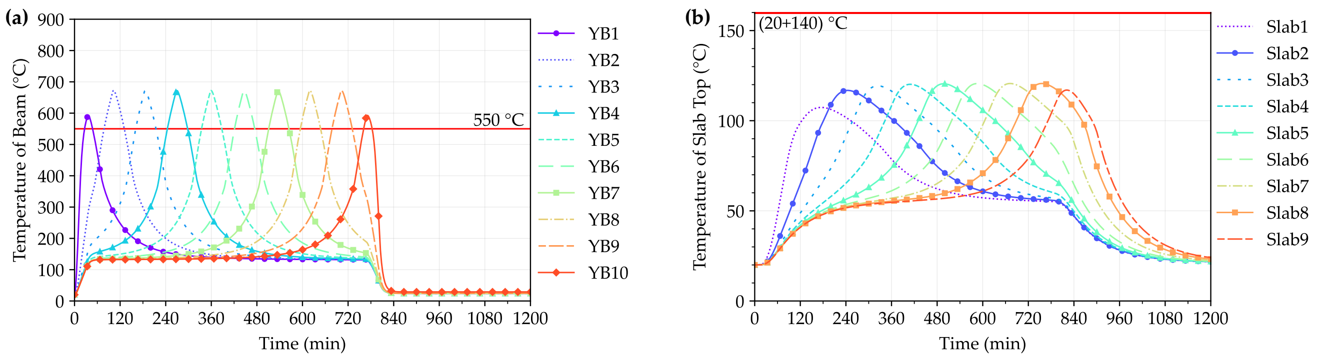

Figure 7. Thermal response of the structural elements in 3D model under the travelling fire scenario 2 (fire spread rate: 0.5 mm/s): (a) YBeam1 to YBeam10 (Y direction); (b) Slab1 to Slab9.

The membrane tractions in slab of the 3D model at the selected time, i.e., 140 min, 400 min, 660 min and 840 min (cooling phase), under travelling fire scenario 2 are presented in Figure 8. In contrast to the membrane tractions presented for the travelling fire scenario 1 in Figure 4, more slab area was demonstrated in tension and lower magnitude of compression during the cooling phase. This is because the fire size of travelling fire scenario 2 was significantly smaller, i.e., approximately 6.0 m^2 with a modest total HRR of 1.5 MW, compared with 30 m^2 with a total HRR of 7.5 MW.

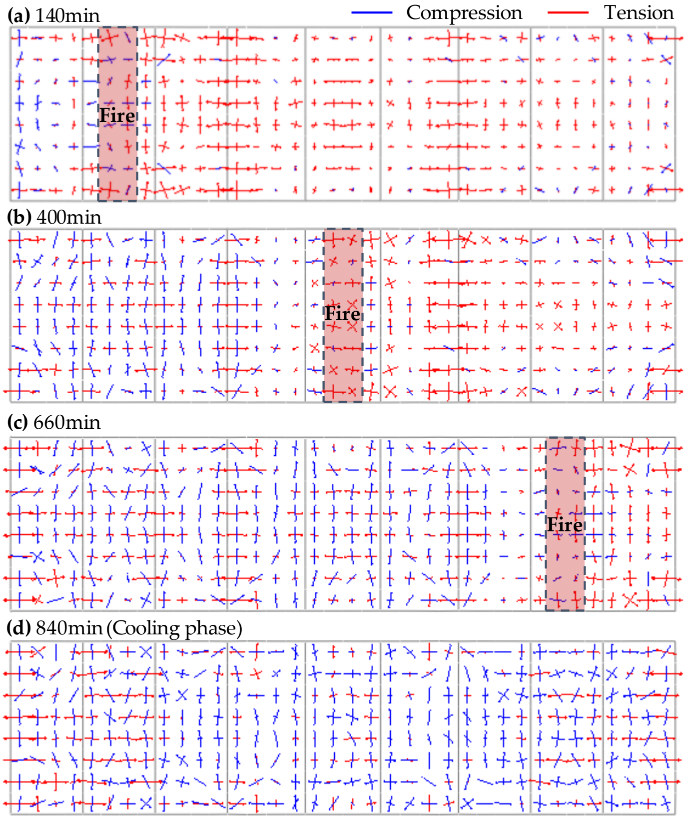

Figure 8. Membrane tractions in the slab under the travelling fire scenario 2 (fire spread rate: 0.5 mm/s): (a) 140 min; (b) 400 min; (c) 660 min; (d) 840 min.

Deflections of 0.07 m and 0.53 m were captured for XBeams in the 3D and 2D model, see Figure 9(a). Compared with the structural response from traveling fire scenario 1, lower deflections from travelling fire scenario 2 are due to its slow travelling fire spread rate, 0.5 mm/s, and the smaller fire size of 1.5 MW which could only "heat up" a limited number of structural elements. Note that the fire area is approximately 6 m^2 for travelling fire scenario 1. This fire could manage to impact a limited area of the structure while the remainder of the structural bays remains at a relatively lower temperature (pre-heated by the smoke temperature for the far field). Hence, the surrounding bays could still provide high stiffness and load redistribution paths to prevent the heated part of the structure from deflection significantly.

As shown in Figure 9(a), the largest deflections of XBeams in the 3D model were between 0.06 m and 0.07 m, whereas the largest deflections of XBeams in the 2D model were between 0.47 m and 0.53 m. The 2D model was observed to predict higher deflections compared with the 3D model, confirming the fundamental load-carrying role of the slab at elevated temperatures [31–33]. Further, lower deflection rates of XBeams were found in the 3D model, below 0.8 mm/min as shown in Figure 9(b). In Figure 9(c), the failure of XBeams could be determined according to the critical deflection rate exceed in the 2D model. For instance, the peak deflection rates of XBeams were 66 mm/min at 58 min, 29 mm/min at 309 min, and 21 mm/min at 576 min for XBeam1, XBeam2 and XBeam3, respectively.

In addition, it is worth noting that there were "small plateaus" at around 0.3 m deflection for the XBeam1 and XBeam2 in the 2D model, see Figure 9(a). Such plateaus were attributed to the over-simplification of the 2D model, that the thermal expansion of the steel members (i.e., beams and columns) had an "interplay" effect on the overall deflection at the mid-span of the beams: the heated beams tended to deflect whereas the heated columns tended to lift-up the structural steel beams on top. Figure 10 demonstrates such "interplay" effect via decoupling the deflections for the beams and the heads of columns vertical displacements respectively. This effect is likely to be avoided by the 3D model due to the presence of the slab.

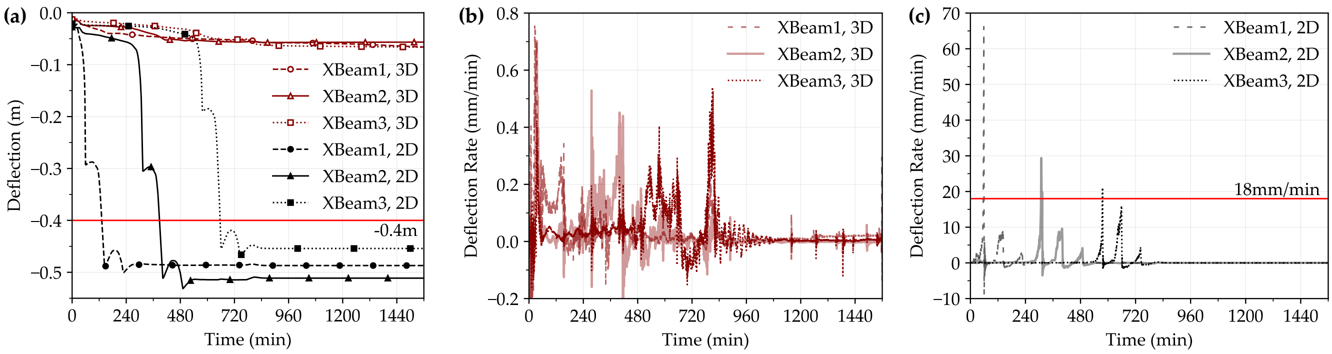

Figure 9. Structural response of XBeam1 to XBeam3 (X direction) at mid-span under the travelling fire scenario 2 (fire spread rate: 0.5 mm/s), 3D model vs 2D model: (a) Deflection; (b) Deflection rate of 3D model; (c) Deflection rate of 2D model.

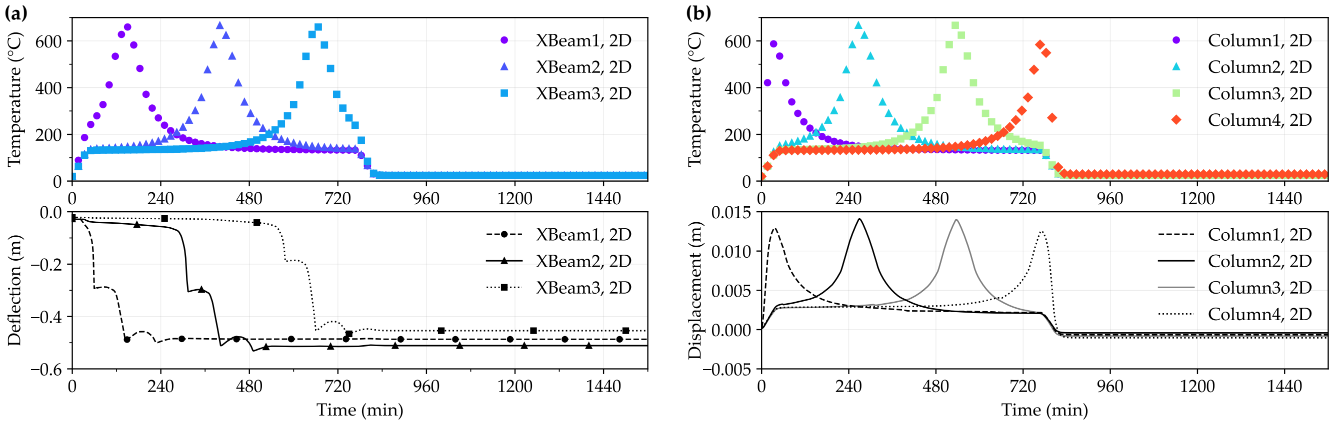

Figure 10. Thermal and structural response of the steel beams in 2D model under the travelling fire scenario 2: (a) XBeam1 to XBeam3 (X direction); (b) The vertical displacements of the heads of Column1 to Column 4.

Figure 11 presents the axial force and stress utilisation of XBeams under the travelling fire scenario 2. The 2D model had maximum axial forces of -105 kN and 251 kN for compression and tension respectively, decreased by over than 85% compared with the 3D model. More conservative axial forces were captured by the 3D model. This large force might induce the connections in a more unfavourable situation, i.e., the structural collapse triggered by the failure of the connections under such shear force, which is unlikely to be addressed in an over-simplified 2D model. Furthermore, Figure 11(b) shows that the stress utilisation of XBeams in the 3D model were above 75% and 90% in the heating phase and cooling phase respectively. In contrast, only the stress utilisation of XBeam3 reached 97% during the cooling phase in the 2D model. The results indicate that the simplification for modelling the composite structure as a 2D frame is not always the most conservative under travelling fires, in terms of internal forces. Further, compared with the travelling fire scenario 1 with a higher fire spread rate of 2.5 mm/s, the peak stress utilisation of XBeams in both 3D and 2D models were both close to 1.0 under the travelling fire scenario 2. This implies that "slow" travelling fires are not advised to be ignored in performance-based structural fire design.

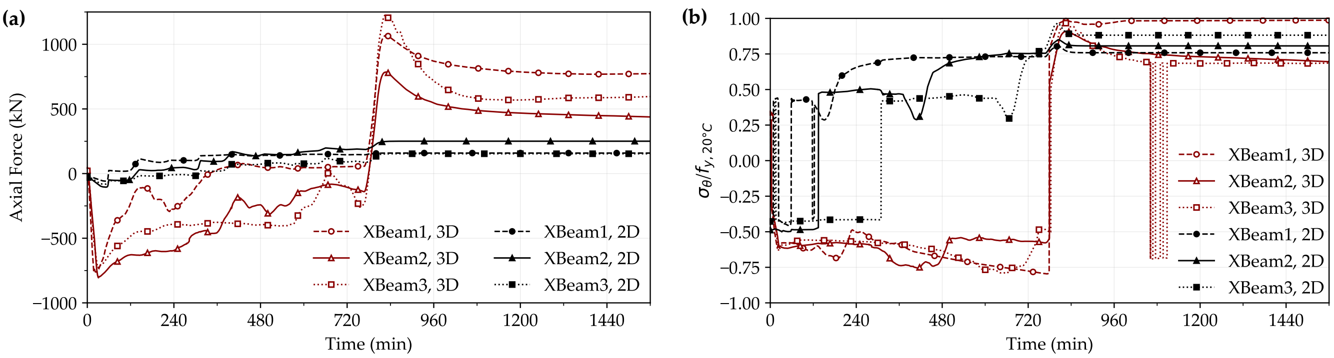

Figure 11. Internal force and stress utilisation of Beam1 - Beam3 (X direction) at mid-span under the travelling fire scenario 2 (fire spread rate: 0.5 mm/s), 3D model vs 2D model: (a) Axial force; (b) Ratio of the axial stress envelope over the yield strength 355 MPa at 20℃ .

5 THE ROLE OF FIRE PROTECTION ON 3D MODEL VS 2D MODEL

Fire protection is a design parameter having a significant effect on the structural behaviour under travelling fires. For conventional fire resistance design, the general approach is to protect all structural steel members to achieve a prespecified fire resistance rating (FRR). However, instead of protecting all steel members, this study protected the columns and primary beams with leaving the secondary beams unprotected. This fire protection scheme is to encourage the development of the tensile membrane action [31–34], which has been gradually applied in practical projects for performance-based structural fire design for steel-composite floor systems. This section investigates the effect of such a fire protection scheme on the structural response for both the 3D and 2D models under travelling fires.

In this study, the thickness of fire protection was required to deliver an equivalent FRR for structural components. The fire protection thickness was based on the simplified calculation in Eurocode 3 [18]. The mineral fibre spray of 15 mm thickness was adopted, with thermal conductivity 0.12 W/(m·K), density 300 kg/m^3 and specific heat 1200 J/(kg·K) following the recommendations from Franssen et al. in 2009 [35]. Note that all primary beams and columns were protected to achieve at least one-hour FRR (i.e., R60) under the travelling fire scenario 1 and travelling fire scenario 2.

The mid-span thermal response of YBeams are presented in Figure 12, for travelling fire scenario 1 (fire spread rate 2.5 mm/s) and travelling fire scenario 2 (fire spread rate 0.5 mm/s) respectively. Note that the secondary beams were left unprotected. The peak temperatures of steel beams can be reduced effectively by fire protection. For instance, under the travelling fire scenario 1, the peak temperature of YBeam7 decreased from 820℃ (without fire protection) to 540℃ (with fire protection); under the travelling fire scenario 2, the peak temperature of YBeam7 with fire protection dropped 170℃ and the occurrence of the peak temperature was delayed approximately for 35 min.

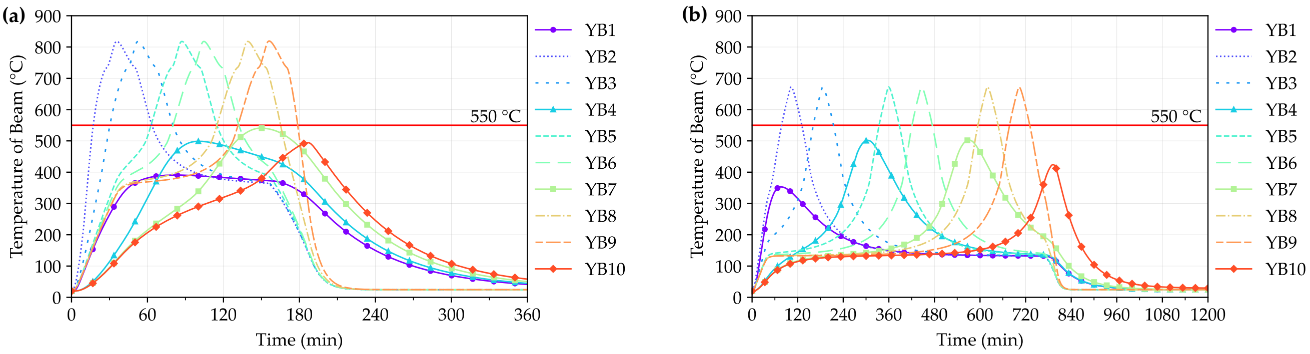

Figure 12. Temperatures of YBeam1 to YBeam10 (Y direction) in the 3D model under travelling fires, with fire protection of primary beams and columns: (a) scenario 1 (fire spread rate: 2.5 mm/s); (b) scenario 2 (fire spread rate: 0.5 mm/s).

Figure 13 presents the defection of the 3D and 2D models under the travelling fire scenario 1, for one case without any fire protection (WOP) against the other case with fire protection (WP) for the primary beams and columns. It was found the effect of fire protection on the deflection of the structure was significant, especially for the 2D model. As shown in Figure 13(a), the maximum deflection at the mid-span of slabs in the 3D model decreased by around 50% on average. For instance, the maximum mid-span deflection decreased from 0.27 m (WOP) to 0.13 m (WP), 0.33 m (WOP) to 0.15 m (WP), and 0.21 m (WOP) to 0.13 m (WP) for BAY1, BAY2, and BAY3, respectively. In the 2D model, Figure 13(b) demonstrates that the fire protection prevented the collapse of the steel frame very effectively, such that the maximum deflection of XBeam2 at mid-span was only 0.15 m, which was far below the critical deflection of 0.4 m. It further proved that the fire protection of steel members plays a critical role to prevent the disproportionate collapse of the steel-framed structures when the slab was absent.

Figure 14 presents the defection of the 3D and 2D models under the travelling fire scenario 2, for one case without any fire protection (WOP) against the other case with fire protection (WP) for the primary beams and columns. In the 3D model, when the fire spread rate decreased to 0.5 mm/s in the travelling fire scenario 2, the effect of fire protection on the deflections become less significant, see Figure 14(a). The maximum deflection of slabs in the 3D model decreased by only approx. 11% on average. For instance, the maximum deflection of the BAY2 decreased from 0.086 m (WOP) to 0.074 m (WP). In contrast, the maximum deflection of XBeams decreased significantly once the fire protection was applied in the 2D model, i.e., from 0.501 m (WOP) to 0.086 m (WP), 0.531 m (WOP) to 0.119 m (WP), and 0.468 m (WOP) to 0.087 m (WP), respectively.

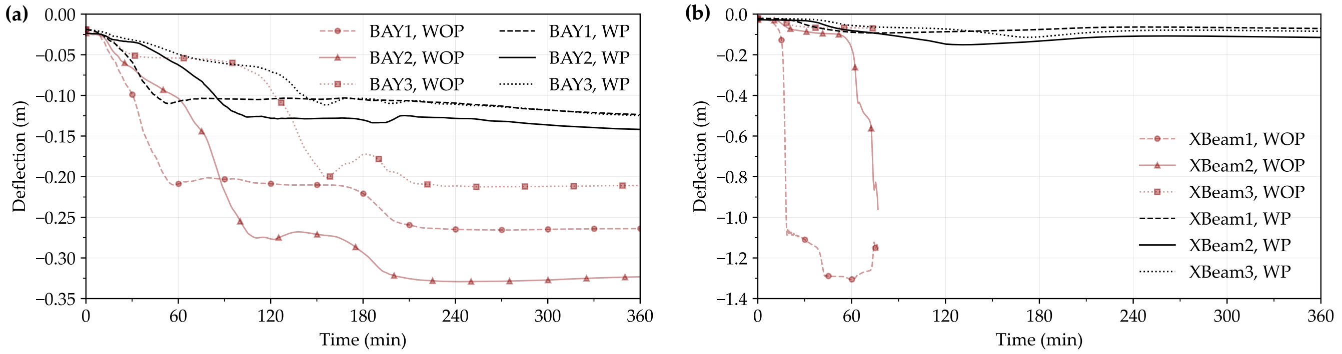

Figure 13. Deflection under the travelling fire scenario 1 (fire spread rate: 2.5 mm/s), without any fire protection (WOP) vs. with fire protection (WP): (a) BAY1 to BAY2 of the 3D model; (b) XBeam1 to XBeam3 of the 2D model.

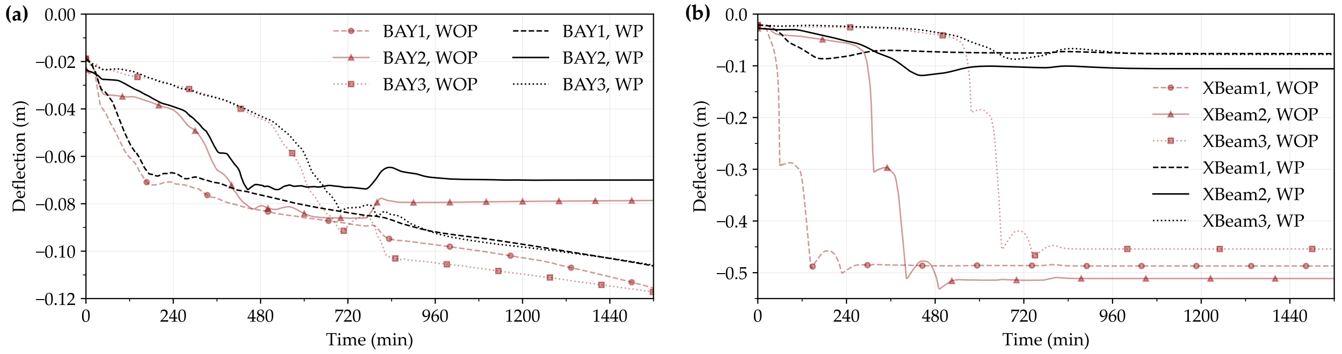

Figure 14. Deflection under the travelling fire scenario 2 (fire spread rate: 0.5 mm/s), without any fire protection (WOP) vs. with fire protection (WP): (a) BAY1 to BAY3 of the 3D model; (b) XBeam1 to XBeam3 of the 2D model.

By comparing Figure 13(a) and Figure 14(a), it can be seen that under the travelling fire scenario 1 with a higher spread rate of 2.5 mm/s, the largest deflection occurred in BAY2 with a longer span (i.e., 8 m). However, under the travelling fire scenario 2 with a "slow" spread rate of 0.5 mm/s, the maximum deflections are likely to occur in the "side" bays of the 3D model (i.e., BAY1 and BAY3 as described in Figure 1(a)) instead of the longer bay (i.e., BAY2). This implies the global structural response, or the potential structural failure mechanism, might be affected by the structure (including with or without concrete slabs and the layout of the structure), in combination with the fire protection and the fire spread rate simultaneously.

6 CONCLUSIONS

The finite element structural models for a story prototype steel-framed building with composite floors were adapted based on the structural layout of the BST/FRS 1993 travelling fire test. The established models investigated the thermal and structural responses as a "slice" of the large open-plan office compartment. The significance of the slabs on the predicted structural responses under travelling fires was studied, via investigating the difference between a 3D model with a 2D model. The analysis includes two representative travelling fire scenarios with different fire spread rates, i.e., 2.5 mm/s and 0.5 mm/s. In addition, the effect of fire protection on the improvement of fire performance between the 3D and 2D models was also investigated. The following conclusions can be drawn:

(1) The global structural response, or the potential structural failure mechanism between the 3D and 2D models, could be fundamentally different. This is likely to be affected by the layout of the structure in combination with the fire protection and the fire spread rate simultaneously.
(2) The 3D model is critical for the performance-based structural fire design for travelling fires, via considering the importance of the slab, since the simplification for modelling the structure as a 2D frame may not always provide the most conservative solution.
(3) Although the 2D model usually predicts larger deflections than the 3D model, the 2D model could significantly underestimate the significant internal force, which might induce the connections failure at a more realistic situation under travelling fires.
(4) The "internal axial force reversal" caused by the heating-cooling cycles of travelling fires is more evident in the 3D model.
(5) Due to the simplification of the 2D model omitting the significant stiffness contribution from the composite slab, the effect of the fire protection is likely to be amplified. Such simplification may be misleading for performance-based structural fire design under different travelling fire scenarios.

ACKNOWLEDGMENT

This work is funded by the Hong Kong Research Grants Council Theme-based Research Scheme (T22-505/19-N).

REFERENCES

1. Dai, X., Welch, S., Usmani, A. A critical review of "travelling fire" scenarios for performance-based structural engineering. Fire Saf J 91, 568–78 (2017). https://doi.org/10.1016/j.firesaf.2017.04.001.
2. Rezvani, F.H., Ronagh, H.R. Structural response of a MRF exposed to travelling fire. Proc Inst Civ Eng Struct Build 168, 619–35 (2015). https://doi.org/10.1680/jstbu.14.00046.
3. Rackauskaite, E., Kotsovinos, P., Jeffers, A., Guillermo, R. Structural analysis of multi-storey steel frames exposed to travelling fires and traditional design fires. Eng Struct 150, 271–87 (2017). https://doi.org/10.1016/j.engstruct.2017.06.055.
4. Rackauskaite, E., Kotsovinos, P., Rein, G. Structural response of a steel-frame building to horizontal and vertical travelling fires in multiple floors. Fire Saf J 91, 542–52 (2017). https://doi.org/10.1016/j.firesaf.2017.04.018.
5. Rackauskaite, E., Kotsovinos, P., Jeffers, A., Rein, G. Computational analysis of thermal and structural failure criteria of a multi-storey steel frame exposed to fire. Eng Struct 180, 524–43 (2019). https://doi.org/10.1016/j.engstruct.2018.11.026.
6. Stern-gottfried, J., Rein, G. Travelling fires for structural design – Part I : Literature review. Fire Saf J 54, 74–85 (2012). https://doi.org/10.1016/j.firesaf.2012.06.003.
7. Stern-Gottfried, J., Rein, G. Travelling fires for structural design-Part II: Design methodology. Fire Saf J 54, 96–112 (2012). https://doi.org/10.1016/j.firesaf.2012.06.011.
8. Rackauskaite, E., Hamel, C., Law, A., Rein, G. Improved Formulation of Travelling Fires and Application to Concrete and Steel Structures. Structures 3, 250–60 (2015). https://doi.org/10.1016/j.istruc.2015.06.001.
9. Gillie, M., Usmani, A.S., Rotter, J.M. A structural analysis of the Cardington British steel corner test. J Constr Steel Res 58, 427–42 (2002). https://doi.org/10.1016/S0143-974X(01)00066-9.
10. Jiang, J., Li, G.-Q. Disproportionate collapse of 3D steel-framed structures exposed to various compartment fires. J Constr Steel Res 138, 594–607 (2017). https://doi.org/10.1016/j.jcsr.2017.08.007.
11. Jiang, J., Li, G.Q. Progressive collapse analysis of 3D steel frames with concrete slabs exposed to localized fire. Eng Struct 149, 21–34 (2017). https://doi.org/10.1016/j.engstruct.2016.07.041.
12. Jiang, J., Lu, Y., Dai, X., Li, G.Q., Chen, W., Ye, J. Disproportionate collapse of steel-framed gravity buildings under travelling fires. Eng Struct 245, 112799 (2021). https://doi.org/10.1016/j.engstruct.2021.112799.
13. Clifton, C. Fire models for large firecells, HERA Report.
14. Kirby, B.R., Wainman, D., Tomlinson, L.N., Kay, T., Peacock, B.N. NATURAL FIRES IN LARGE SCALE COMPARTMENTS. Int. J. Eng. Performance-Based Fire Codes, vol. 1, p. 43–58.

15. ArcelorMittal. Composite floor decking - Cofradal.
16. Nan, Z., Dai, X., Chen, H., Welch, S., Usmani, A. A numerical investigation of 3D structural behavior for steel-composite structures under various travelling fire scenarios. Eng Struct 267, 114587 (2022). https://doi.org/10.14264/a1068ab.
17. CEN. EN 1992-1-2:2004 - Eurocode 2. Design of concrete structures. General rules. Structural fire design. Brussels: European Committee for Standardization (CEN); .
18. CEN. EN 1993-1-2:2005 - Eurocode 3. Design of steel structures. General rules. Structural fire design. Brussels: European Committee for Standardization (CEN); .
19. Rackauskaite, E., Kotsovinos, P., Guillermo, R. Model parameter sensitivity and benchmarking of the explicit dynamic solver of LS-DYNA for structural analysis in case of fire. Fire Saf J 90, 123–38 (2017). https://doi.org/10.1016/j.firesaf.2017.03.002.
20. Dai, X. An extended travelling fire method framework with an OpenSees-based integrated tool SIFBuilder. PhD Thesis, The University of Edinburgh.
21. Dai, X., Welch, S., Vassart, O., Cábová, K., Jiang, L., Maclean, J., et al. An extended travelling fire method framework for performance-based structural design. Fire Mater 44, 437–57 (2020). https://doi.org/10.1002/fam.2810.
22. CEN. EN 1991-1-2:2002 - Eurocode 1. Actions on structures. General actions. Actions on structures exposed to fire. Brussels: European Committee for Standardization (CEN); .
23. Thomas, P.H., Heselden, A.J.M. Fully Developed Fires in Single Compartments. Fire Res Note No 923, Fire Res Station Borehamwood, UK (1972).
24. Janssens, M.L., Birk, D.M. An introduction to mathematical fire modeling. 2nd ed. Lancaster: Pa.: Technomic Pub. Co.; .
25. Morgan, H. Smoke control methods in enclosed shopping complexes of one or more storeys: a design summary. Building Research Establishment, Borehamwood: .
26. CEN. EN 1994-1-2:2008 - Eurocode 4. Design of composite steel and concrete structures. General rules. Structural fire design. Brussels: European Committee for Standardization (CEN); .
27. ASFP. The Yellow Book - Fire protection for structural steel in buildings. vol. 1. 5th ed.
28. ASTM. Standard Specification for Carbon Structural Steel. ASTM A36/A36M - 19. ASTM International, West Conshohocken, PA.: .
29. Orabi, M.A., Qiu, J., Jiang, L., Usmani, A. Modelling concrete slabs subjected to localised fire action with OpenSees. J Struct Fire Eng (2022). https://doi.org/10.1108/JSFE-05-2021-0033.
30. Garlock, M.E., Quiel, S.E. Plastic Axial Load and Moment Interaction Curves for Fire-Exposed Steel Sections with Thermal Gradients. J Struct Eng 134, 874–80 (2008). https://doi.org/10.1061/(asce)0733-9445(2008)134:6(874).
31. Bailey, C.G. Membrane action of unrestrained lightly reinforced concrete slabs at large displacements. Eng Struct 23, 470–83 (2001). https://doi.org/10.1016/S0141-0296(00)00064-X.
32. Usmani, A.S., Cameron, N.J.K. Limit capacity of laterally restrained reinforced concrete floor slabs in fire. Cem Concr Compos 26, 127–40 (2004). https://doi.org/10.1016/S0958-9465(03)00090-8.
33. Burgess, I., Chan, B. An integrated yield-line approach to tensile and compressive membrane actions in thin lightly-reinforced concrete slabs. Eng Struct 208, 110321 (2020). https://doi.org/10.1016/j.engstruct.2020.110321.
34. Barrett BA. Steel Construction: Fire Protection. TATA Steel, British Constructional Steelwork Association (BCSA); .
35. Jean Marc Franssen, Venkatesh Kodur, Zaharia, R. Designing Steel Structures for Fire Safety. Taylor & Francis; .

SiF 2022– The 12th International Conference on Structures in Fire
The Hong Kong Polytechnic University, Nov 30 - Dec 2, 2022

TOWARDS APPLICATION OF AI-FE HYBRID ANALYSES FOR SIMULATING STRUCTURES IN FIRE

Jin Qiu[1], Liming Jiang[2]

ABSTRACT

A novel hybrid simulation scheme combining the finite element (FE) method with artificial intelligence (AI) technique is proposed in this paper. This newly established AI-FE hybrid simulation is based on the existing hybrid simulation concept but introducing a well-trained AI model to replace the previous high-resolution substructure model of high computational demand. The AI-FE hybrid simulation framework is implemented taking advantage of the open-source platform OpenSees for fire with Python interpreter and the advanced machine learning algorithms derived from AI development. The first attempt of AI-FE hybrid simulation is applied for modelling a 2D steel plane frame with central heated column, which has been a reference test of many hybrid simulation research. To realize the real-time communication between the FE structural model and the AI sub-model, a new generic element dispBeamColumnThermalAI is developed. It is ported to an AI model trained using the SVM regression model from the samples generated from a detailed FE model subjected to various loading histories. A comparison between the computed results by the AI-FE model, the traditional FE model and the measured test results in terms of axial displacement and internal axial force demonstrates the robust capability of AI-FE hybrid simulation in capturing the structural response to fires, especially the global buckling of heated column.

Keywords: Fire behaviour; structural system; OpenSees for fire; AI model; hybrid simulation

1 INTRODUCTION

The collapses of WTC buildings in 2001 and Plasco building in 2017 directed the attention to the fire induced collapse in modern structures. In the recent decades, many research efforts have been devoted to the progressive collapse of steel framed structures in fire initiated from local member failure to system-level collapse. Compared with the full-scale fire test, numerical simulation benefiting from its low-cost, easy access to various data collection and flexibility of designing fire scenarios, has been a key research and design tool to analyse and evaluate the structural fire safety performance. Various studies focusing on the structural performance in fire have been conducted using different modelling programs, such as Abaqus, LS-DYNA, SAFIR, Vulcan and OpenSees [1–5].

As illustrated in Figure **1**, when a structure is subjected to fire, it has been recognized that local failure of structural members exists alongside the global load redistribution inside the structural system. It has been found that the progressive collapse of whole structure can be caused by the spread of local failure from element to element [6]. Nevertheless, a system-level structure model usually adopting beam-column elements cannot capture the localised failure at structural members, whereas it is not feasible to use full

[1] Ms., Department of Building Environment and Energy Engineering, The Hong Kong Polytechnic University
e-mail: jinjin.qiu@connect.polyu.hk, ORCID: https://orcid.org/0000-0002-0603-854X
[2] Dr., Department of Building Environment and Energy Engineering, The Hong Kong Polytechnic University
e-mail: liming.jiang@polyu.edu.hk, ORCID: https://orcid.org/0000-0001-8112-2330
https://doi.org/10.6084/m9.figshare.22193272

three-dimensional (3D) model to analyse a structural system subjected to fire. The hybrid simulation approaches [7,8] were developed and implemented to fulfil this need, which use a 2D/3D structural system model with frame elements and slab elements to represent the system-level structural response (master model) and 3D detailed models for single members of potential local failure (slave model). However, the computational cost of the full-3D slave models is too high and the location of the local failure is of uncertainty.

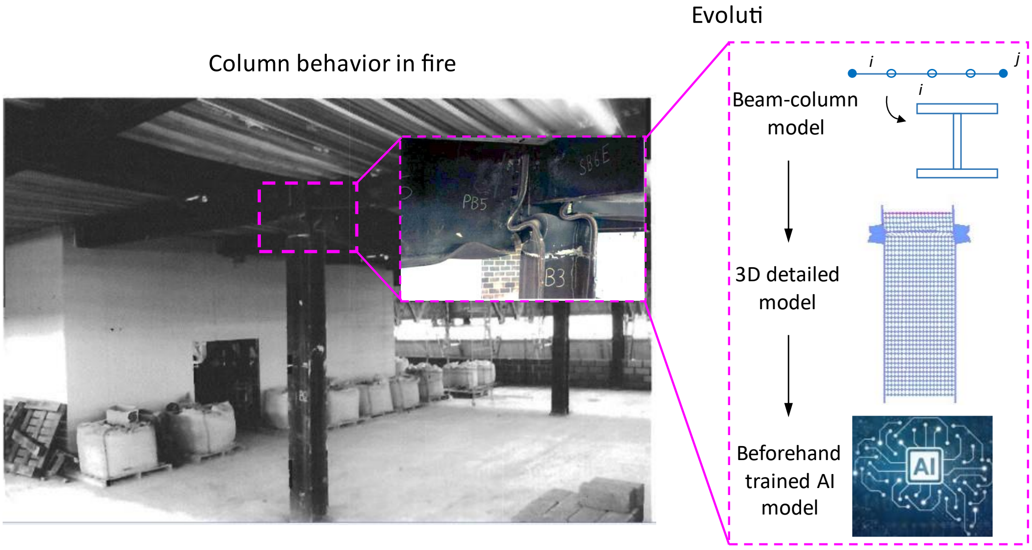

Figure 1. Evolution of numerical models to capture structural behaviour in fire.

In view of these high-resolution models that are typically of regular section types and subjected to locally uniform fire conditions, it is possible to extensively test these components beforehand and to embed it into a trained AI prediction model (see Figure **1**). Ideally, all the structural members can be represented by AI components, which can then be assembled into a complete structure via existing connection modes in current FE models. Machine learning method, as a problem-solving strategy derived from AI technique, is not foreign to structural engineering. The application of machine learning method in the structural engineering field can be traced back to 1980s, when Adeli and Yeh (1989) [9] tried to solve a beam design problem using this method. A comprehensive review of machine learning application for predicting and assessing structural performance can be found in Ref. [10]. In the past few decades, attributable to the development of computer science as well as the renaissance of AI techniques, more and more sophisticated algorithms and tools have been developed within the framework of machine learning, which enables it capable of addressing complex problems with higher computational efficiency. Recently, some researchers have attempted to introduce machine learning method into the area of structures in fires. Hodges [11] predicted spatially resolved temperatures and velocities within a compartment. Wu and his team [12–14] have been dedicated to the real-time forecast of tunnel fire scenarios. Various parameters related to the fire in tunnel space, such as temperatures, fire size, fire location and smoke layer, have been trained and predicted. Ye et al. [15] tried to realize the timely prediction on the deflections of a 3D steel frame subjected to fires based on training a numerical dataset. However, these applications of AI technique associated with structures in fire focus on the single scenario. In other words, the portability of these trained AI models is poor and it is not applicable to other scenarios. The key issue to fully take advantage of the fast response of AI technique in structural engineering is to transform the AI model into the 'component' rather than the specific 'whole structure'. Hence, a hybrid simulation scheme combining the FE method and the AI technique is proposed and established, where some of the components are represented by trained AI models. This AI-FE hybrid simulation allows highly-efficient structural system model and fast response of AI based component behaviour models. Moreover, various hybrid interface to AI component models can be developed to incorporate with the fast-developing research on AI prediction of structural components in fires, which would continuously enrich the model library within the hybrid AI-FE simulation scheme for uncompromised modelling accuracy and efficiency.

This paper is intended to present the conceptual application of this AI-FE hybrid simulation scheme. The first attempt is targeted on the global buckling of the central column as found in the steel moment plane frame fire test [16]. A high-resolution column model built using thermo-mechanical shell elements for the column of interest is extensively tested to generate the training samples. Support vector machine (SVM), which is a powerful machine learning approach for linear and non-linear regression, is employed to formulate the preliminary AI component behaviour model. To realize the real-time communication between AI component model and system-level FE model at each calculation step, the dispBeamColumnThermalAI element, acting as the application interface (API), is added into the source file of OpenSees for fire, which will then be interpreted as Python extension module. The performance of this AI-FE hybrid simulation is examined with reference to the test observed behaviour.

2 CONCEPTUAL AI-FE HYBRID SIMULATION SCHEME FOR MODELLING STRUCTURAL RESPONSES TO FIRES

2.1 Framework of AI-FE hybrid simulation

The AI-FE hybrid simulation scheme proposed in this paper is developed from the virtual hybrid simulation approach for modelling structural response to fires. A hybrid simulation scheme employs a relatively low-resolution model for fast estimation of global behaviour using beam-column elements and shell elements for slabs, which is synchronized with one or multiple high-resolution models to address complex local behaviour. The latter is currently referred to as local buckling and squashing of beams and columns (Fig.2), which cannot be described by beam-column elements and essentially change the structural system response. As mentioned above, it is computationally expensive to employ multiple high-resolution models in one synchronized analysis and the locations of these sub-structures are manually chosen before the analysis.

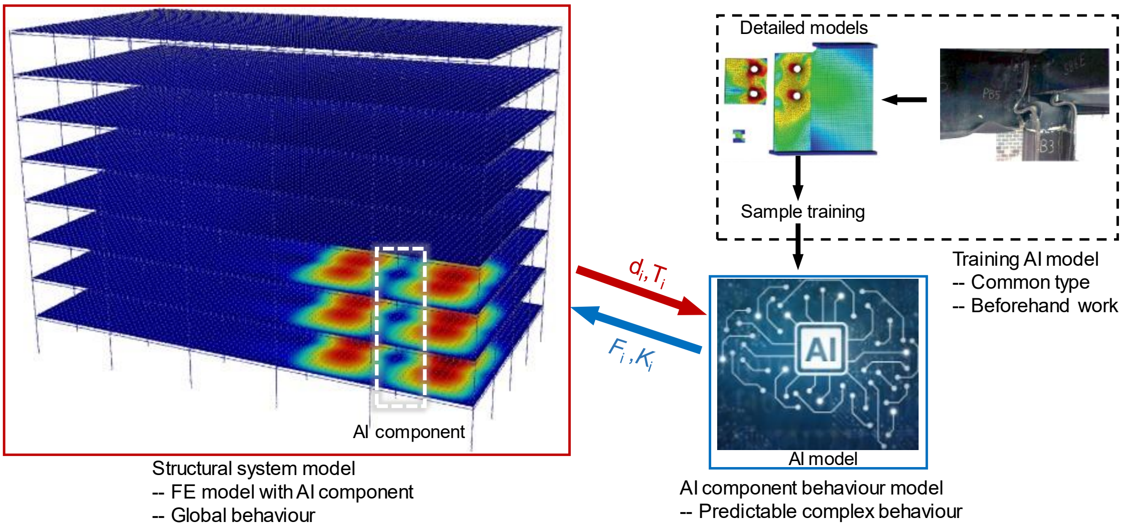

Figure 2. Schematic of the AI-FE hybrid simulation framework.

The AI-FE hybrid analysis scheme adopts a similar concept for hybrid simulation between a system-level FE model and trained AI component model as illustrated in Figure 2. A novel and important approach in this scheme is to bring forward the analyses using detailed models, which are conducted to build up a decent number of case samples for the training of AI component behaviour models. The AI model for different types of structural members can be trained and prepared beforehand based upon the samples generated from validated 3D detailed FE models. Following the calculation flow of FE analysis, the trial displacement (d_i) and temperature (T_i) at each temperature step are transferred from the FE model to the AI model, and the resisting force (F_i) along with tangent stiffness (K_i) enabled by AI prediction will then be fed back to the FE model. This also put requirement on the basic set of data samples for training AI models that is applicable to the AI-FE hybrid simulation, where the d_i and T_i are independent variables and F_i coupled with K_i are dependent variables. To enlarge the applicable scope of the trained AI model, more parameters, like the geometric configuration, material properties, fire scenarios and so on, should be taken as the independent variables.

2.2 Implementation of AI-FE hybrid simulation based on OpenSees for fire

The interaction between the FE model and the AI model can be implemented by adding the corresponding thermo-mechanical AI element into the source code of OpenSees for fire, and then compiling this program into the Python extension module which is named opensees.pyd by default. The opensees.pyd can be imported in the script for FE model written by Python language. In this paper, the first attempt of AI-FE hybrid simulation is to model a 2D steel plane frame subjected to localised fire. Hence, this section will focus on the implementation of AI-FE hybrid simulation on a 2D plane frame structure where the heated column is represented by the AI component model.

Figure 3 shows the communication between the FE plane frame model and the trained AI column model. Herein, the AI models for predicting F_i and K_i were trained separately by using the same samples of independent variables and then were saved independently. A new element class dispBeamColumnThermalAI was added into OpenSees for fire. Two functions, *getPredictedForce* and *getPredictedStiffness*, acting as the application interface between the FE model and the AI model, are embedded into this new element. These two functions are responsible for passing the independent variables obtained from the FE analysis at each temperature step, d_i and T_i, to the external file, LoadModel.py, which is used to load the AI models and obtain predicted F_i and K_i. The predicted values by the AI models will then be returned as the outputs of the two functions. It is worth noting that the independent variables are commonly normalized before training the AI model in order to improve the accuracy of AI models. The scaler for each AI model needs to be saved and the independent variables should be normalized firstly by the same weight to that produced by training samples before they are adopted to make predictions. To perform a AI-FE hybrid simulation analysis, the script for FE model, the opensees.pyd, the file for loading AI models, the saved trained AI models and the saved scalers for normalizing the independent variables should to be contained within one folder.

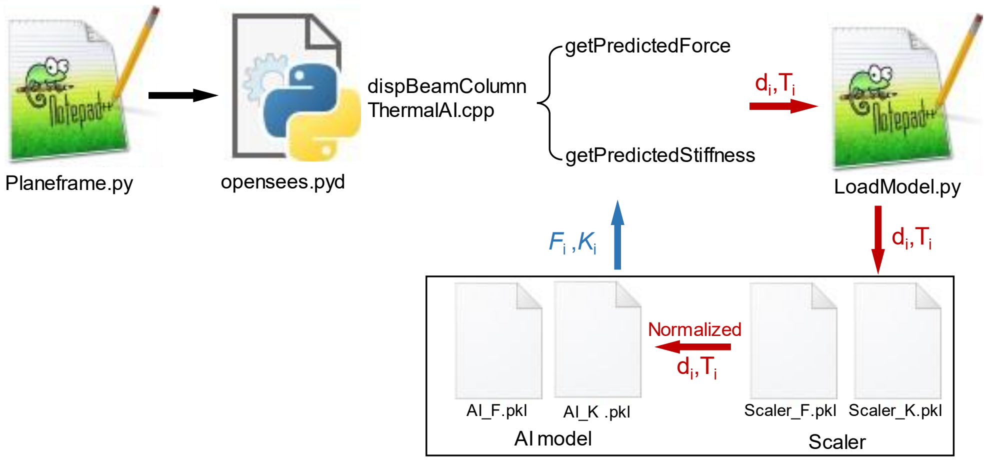

Figure 3. Real-time communication between the FE model and the AI model

The definition of AI column component in the FE model is similar to the definition style of FE column model in Python language:

<*element('dispBeamColumnThermalAI', $eleTag, $iNode, $jNode, $transfTag, $IntgrTag, $secTag)*>

The structural response of the column fed back to the whole structure is predicted by the trained AI model, which is obtained by training the samples generated from a complete column. Therefore, only two nodes, one is at the bottom and one is at the top, need to be defined. In other words, the element size of the AI component is dependent on the length of the column. Additionally, defining one integration point is enough for this AI component element. Because the structural response has already been captured during the process of training AI column model by using 3D detailed FE models.

3 APPLICATION OF AI-FE HYBRID ANALYSES FOR MODELLING STRUCTURES IN FIRES

3.1 Plane frame test configuration

To demonstrate the application of AI-FE hybrid simulation in analysing the structures in fire, the localised fire test performed by Ye et al [16] on the steel plane frame denoted as Frame 2 was numerically modelled and analysed using the AI-FE hybrid simulation framework. Figure **4** shows the detailed test setup. This is a four-bay steel moment plane frame. The span of two middle bays was 2.2 m each and the span of two edge bays was 2 m each, resulting a total length of 8.4 m. The heights of the first storey and the second storey were 1.3 m and 1.2 m respectively. The column top was 0.2 m above the second storey. Hence, the total height of each column was 2.7 m. Steel beams were fully fixed to the columns by welding which were in turn fixed at the bottom and flexible at the top. The columns and beams were taken as universal square steel tubes of the cross-sections of 50×30×3 and 60×40×3.5, respectively. Materials properties for the columns and beams measured at ambient temperature were summarized in Table **1**. Steel boxes were hung on the beams at specified locations illustrated in Figure 4 to simulate the service loading. A customised electrical furnace was installed around the middle column on the first storey to heat up the column. The furnace was turned off when the funace temperature reached 829 °C. At the end of fire test, the global buckling of heated column shown in Figure 5 was observed.

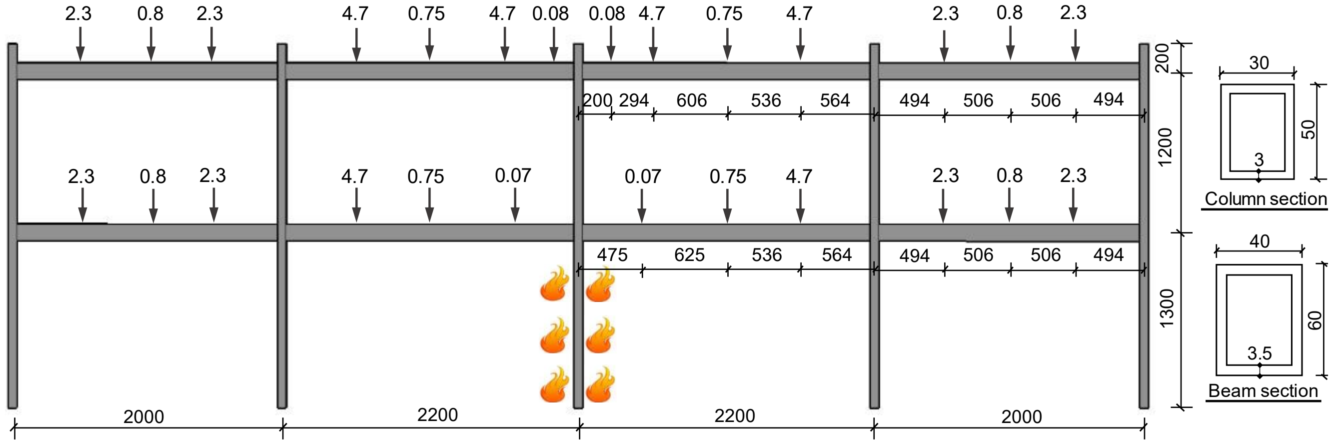

Figure 4. Schematic of test setup and geometric details. (Unit: mm, kN)

Table 1 Material properties at ambient temperature.

Components	Properties			
	f_y (MPa)	f_u (MPa)	E_s (GPa)	ε_u
Column	360.78	534.78	208.23	0.16
Beam	290.03	519.25	208.27	0.18

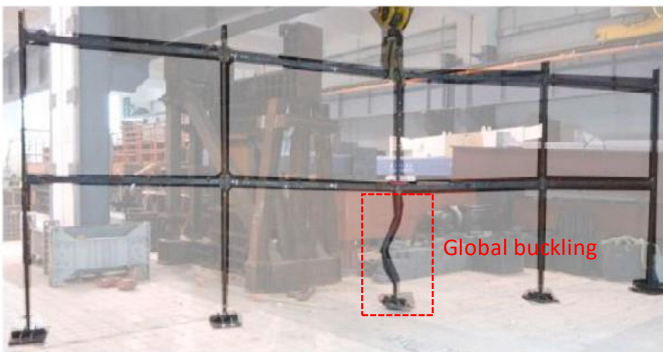

Figure 5. Deformed shape of plane frame after test (Adapted from [16]).

3.2 Model description

The steel beams and unheated columns in the numerical model were represented by dispBeamColumn2DThermal element with uniaxial Steel01Thermal material. A constant mesh of element size of 100 mm was used for both steel beams and steel columns. 5 integration points along the length were specified for each element. Material properties of each structural element summarized in Table **1** were adopted in this model. In this structural model, the base of all columns was fixed and the steel beams were connected to the columns via beam type rigid link.

The central heated column on the first storey is the interested structural member. This column was built using dispBeamColumn2DThermalAI element. To compare the structural performance computed by the AI-FE hybrid simulation model and the traditional beam-column model, a model containing only thermos-mechanical beam-column elements was also built and analysed. The only difference between the two structural models was the element type of the heated column: one adopted dispBeamColumn2DThermalAI element and the other one used dispBeamColumn2DThermal element. The time histories of temperatures for heated column recorded throughout the fire duration were regarded as the thermal load and were applied to the heated column in the numerical models.

3.3 FE-based application-oriented AI column model

3.3.1 Development of AI component model

Figure 6 shows the overall development process of the AI column model. The development of a FE-based AI model mainly contains four stages: 1) establishing reliable numerical model; 2) generating dataset by extracting the required parameters; 3) data processing; and 4) training the model. The following paragraphs discuss each stage in detail in order to clearly present the process of achieving a well-trained AI model that is applicable to AI-FE framework.

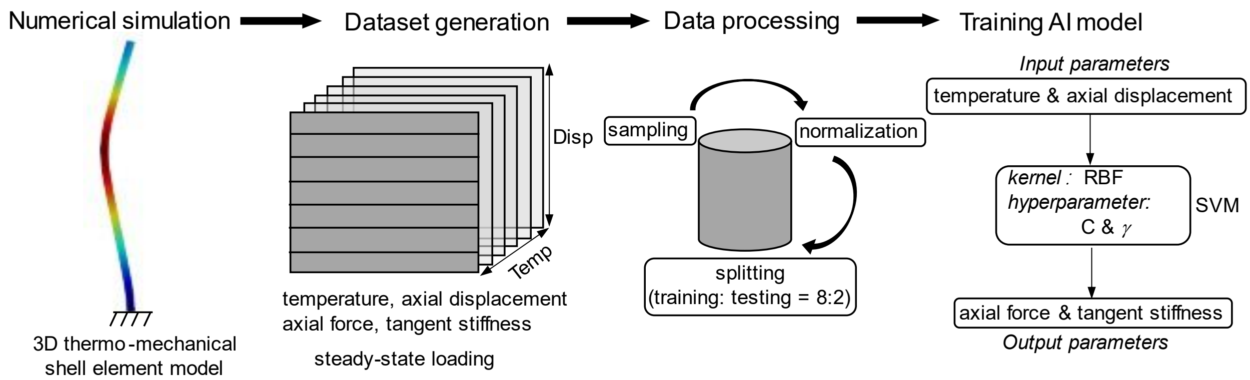

Figure 6. Overall development of AI column model.

To capture the failure of a column in fire, a high-resolution thermo-mechanical shell element (ShellNLDKGQThermal element) based column with the same geometric details and material properties to that in the experimental test described previously was modelled in OpenSees for fire. The J2PlaneStressThermal material model adopting Von-Mises yielding principle was used in the shell section. It is worth noting that the specified geometric configuration and material in this numerical model indicates that the trained AI model is limited to this case. More parameters can be released and be taken as the independent variables in the future to enable larger application of the AI model. The bottom end of the column model was fully fixed and the top end was free. Displacement-controlled steady-state loading (i.e., applying displacement at a constant temperature) was adopted to generate the dataset. In comparison with load control mode, displacement control loading mode can capture the runaway failure characterized with rapidly developed displacement more stably. The applied temperature range was 20 ℃ to 800 ℃ . It is recognized that the column in a whole structure usually fails under the combined action of material degradation and restrained upward thermal expansion at higher temperatures. To improve the training efficiency by simplifying the dataset, a larger temperature interval of 20 ℃ was deployed when the temperature was lower than 700 ℃ and then the temperature interval was decreased to 10 ℃ after the temperature reached 700 ℃ . As a result, 45 temperature scenarios in total were analysed. The applied displacement under each constant temperature was determined based on the principle that the global buckling of column occurred.

At present, only the structural response of the heated column along the length is predicted from the AI model. Hence, the basic set of data samples containing the temperature, the axial displacement, the axial internal force of the column, and the tangent stiffness which was calculated as the ratio of axial force increment to the axial displacement increment were extracted and calculated by taking advantage of the Python packages. After generating the dataset, the data need to be pre-processed and the training and testing samples need to be determined. The two independent parameters (i.e., temperature and axial displacement) were normalized thorough the command of MaxAbsScaler, which can map the data in each column into the range of -1 to 1. The ratio of the number of training samples to the number of testing samples was designated as 8:2. The open-source machine learning library of scikit-learn in Python packages was deployed to develop the SVM regression model, where the Gaussian RBF kernel was selected to transform the low dimensional input space into a higher dimensional space. To improve the model accuracy, the optimal combination of the two hyperparameters, i.e., C, the penalty parameter and γ, the kernel parameter, needs to be tunned. Herein, the grid search approach was adopted to perform the hyperparameter tuning. The search spaces for C and γ are [10, 100000] and [0.0001, 10000], respectively.

3.3.2 Prediction performance of FE-based AI column model

Figure 7 shows the comparison between the computed dependent variables from numerical models and the corresponding predicted dependent variables by AI models. Note that the blue line in each sub-figure was plotted by assuming that the predicted values were exactly equal to the computed values. The closer the predicted values to this blue line, the higher the prediction accuracy of the trained AI model. From this figure we can see that the predicted axial forces are uniformly distributed along the blue line and only very few markers are not on the blue line visibly, which indicates that the majority of axial forces can be accurately predicted by the AI model. However, the tangent stiffness presents significantly wider stripe width and most of the tangent stiffness fall into the range of -75 to 25 kN/mm. The larger discrepancies in Figure 7 (b) means the AI model for predicting tangent stiffness has lower prediction accuracy.

The two numerical performance metrics of coefficient of determination (R^2) and mean absolute error (MAE) were adopted to quantitively evaluate the performance of trained AI models for predicting the axial force (F) and corresponding tangent stiffness (K). The R^2 index with a range of 0 to 1 means the percentage of the variation in the dependent variables that can be predicted by the independent variables. The closer the R^2 to 1, the higher the accuracy of the AI model. The MAE represents the average absolute difference between the dependent variables and the corresponding predicted values. Smaller MAE means higher accuracy. The two performance metrics for both training and testing samples are listed in Table 2. It is clear from this table that the AI model for predicting axial force is more accurate than the AI model for predicting tangent stiffness. The R^2 of AI model for predicting axial force is up to 0.99 for both training samples and testing samples, which are 0.04 and 0.05 higher than the AI model for tangent stiffness respectively. Larger difference between the two AI models can be seen regarding the MAE. The MAE of the model for axial force is lower than 1 while for the model for tangent stiffness, the value reaches 1.92 for training samples and 2.97 for testing samples.

The global buckling of column leads to a sudden change of tangent stiffness. Compared with axial force, the data in the tangent stiffness dataset are more discrete, making it more difficult to obtain an AI model with higher accuracy. However, in the process of finite element calculation, the tangent stiffness primarily influences the convergence rate while has slight influence on the convergence accuracy. This enables it possible to achieve a reliable structural performance even though the AI model for predicting tangent stiffness is not accurate enough.

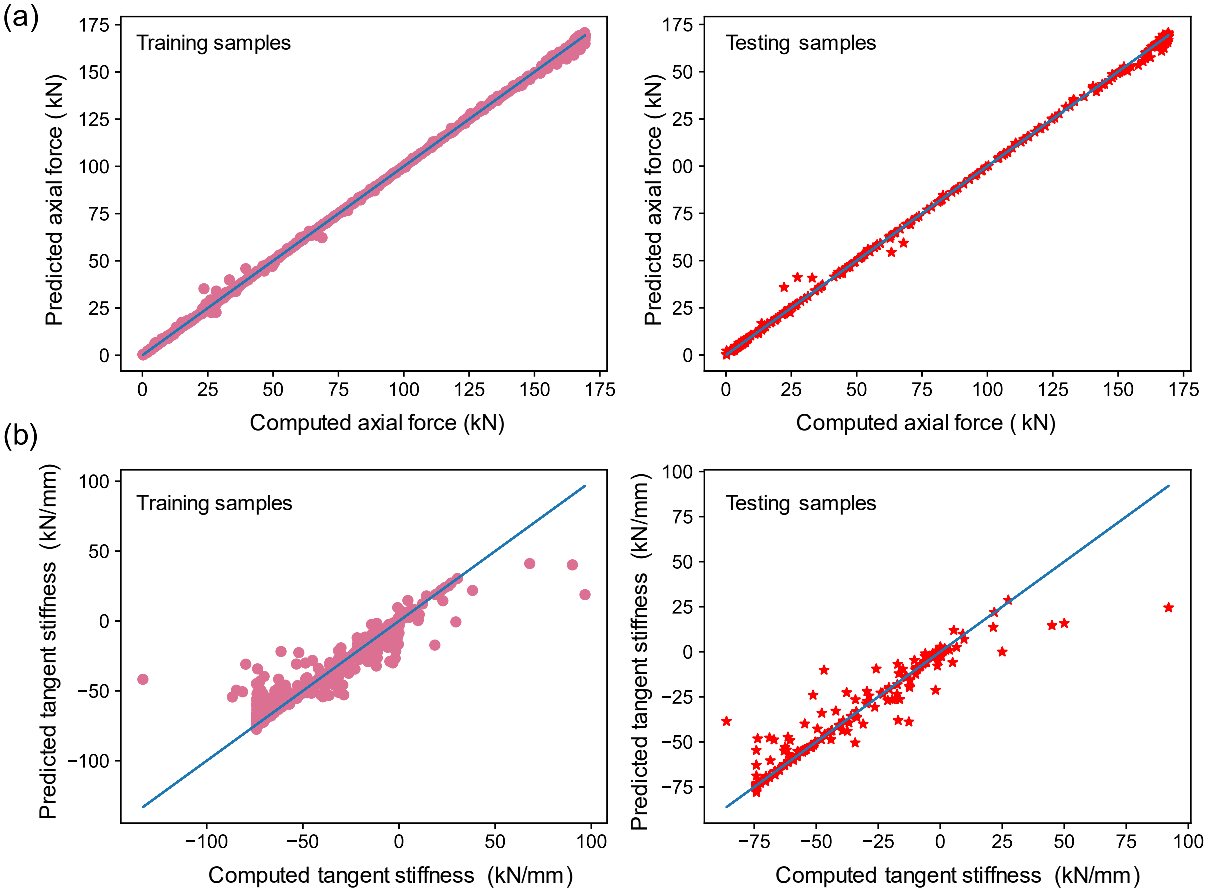

Figure 7. Comparison between computed dependent variables and the predicted dependent variables: (a) axial force; (b) tangent stiffness.

Table 2. Model performance for predicting axial force and tangent stiffness.

Performance metrics	Training		Testing	
	F	*K*	*F*	*K*
R^2	0.99	0.95	0.99	0.94
MAE	0.38	1.92	0.67	2.97

3.4 Result analysis

The axial displacements of the centre column at 2.7 m height and the internal axial force of the heated column computed by the beam element model and AI-FE element model were extracted and plotted in Figure 8 (a) and Figure 8 (b) respectively. The measured time histories of axial displacements in the test were also included in Figure 8 (a) for comparison. The dramatic drop of the axial displacement induced by the global buckling of the heated column on the first storey can be well captured by the two OpenSees for fire models. However, it should be pointed out that a 2 mm initial imperfection was applied horizontally at the centre of heated column in the beam element model. Because the traditional beam element cannot simulate the buckling of the structural members. This is exactly the main motivation for proposing the hybrid simulation scheme of AI-FE. Before the heated column started to buckle, the time-axial displacement curves computed by the OpenSees models are nearly identical to that measured in the experimental test, which validate the capability of AI-FE hybrid simulation model in capturing the structural response to fire. Moreover, as presented in Figure 8 (b), the overlapping internal axial force development computed by the AI-FE hybrid model and the model with only beam elements in the first 50 min further validate the accuracy of AI-FE model.

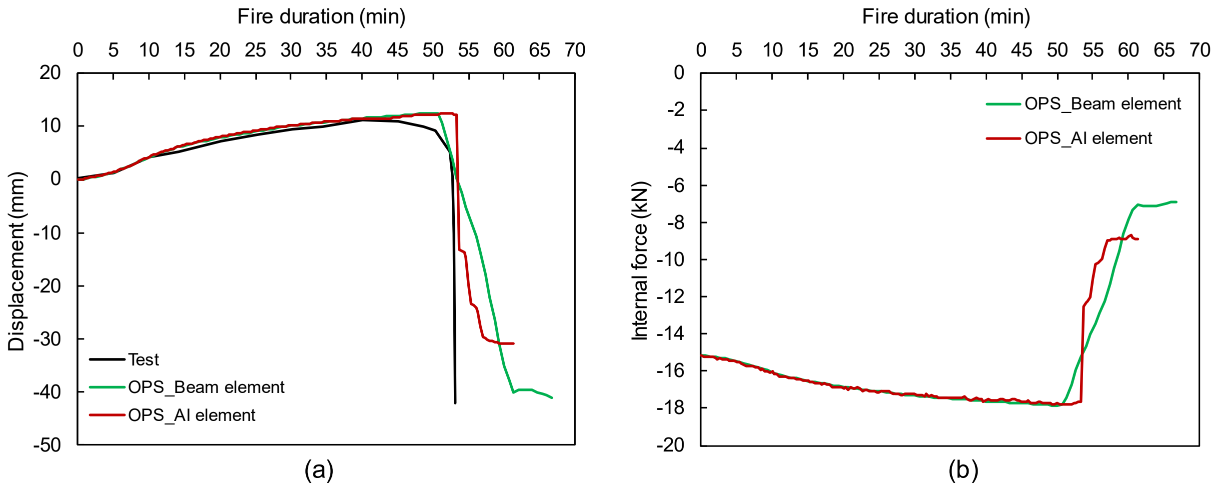

Figure 8. Comparison between AI-FE computed results and test results: (a) axial displacement at the top end; (b) internal axial force.

4 CONCLUSIONS

In this paper, a novel AI-FE hybrid simulation scheme is proposed within OpenSees for fire framwork and demonstrated on a steel plane frame structure subjected to localised fire. The AI-FE hybrid simulation refers to the concept of existing hybrid simulation which aims to capture the failure of some interested structural members in fires. Compared with the existing hybrid simulation where the interested structural members are modelled using 3D high-resolution detailed model, AI-FE simulation has higher computation efficiency as the AI models can be trained beforehand based upon detailed FE models, which is mainly attributable to the regular section types of different structural members in common buildings. Additionally, the idea that transforming the AI model into universal structural members rather than generating an AI model of a specific significantly improves the portability of the trained AI models.

The real-time communication between the FE model and AI model can be achieved by adding corresponding thermo-mechanical AI element class into the source code of OpenSees for fire. The training samples can be generated from 3D detailed structural member models adopting static-state loading. Comparison between the computed results by AI-FE hybrid simulation and test results validates the effectiveness of the AI-FE hybrid simulation in capturing the global buckling of heated columns as well as the structural response to fires.

To further improve and perfect the AI-FE hybrid simulation framework in analysing structures in fire, more research efforts associated with the development of AI models for structural members and the addition of element classes for those structural members in both 2D and 3D structures into the source code of OpenSees for fire are certainly needed in the near future.

ACKNOWLEDGMENT

This research work was supported by the Start-up Fund of the Hong Kong Polytechnic University (P0031564) and the Open Fund from the State Key Laboratory of Disaster Reduction in Civil Engineering (SLDRCE20-02). The financial supports are greatly appreciated.

REFERENCES

[1] Lange D, Röben C, Usmani A. Tall building collapse mechanisms initiated by fire: Mechanisms and design methodology. Eng Struct 2012;36:90–103. https://doi.org/10.1016/j.engstruct.2011.10.003.

[2] Jiang J, Li GQ. Progressive collapse analysis of 3D steel frames with concrete slabs exposed to localized fire. Eng Struct 2017;149:21–34. https://doi.org/10.1016/j.engstruct.2016.07.041.

[3] Gernay T, Gamba A. Progressive collapse triggered by fire induced column loss: Detrimental effect of thermal forces. Eng Struct 2018;172:483–96. https://doi.org/10.1016/j.engstruct.2018.06.060.

[4] Gernay T, Khorasani NE. Recommendations for performance-based fire design of composite steel buildings using computational analysis. J Constr Steel Res 2020;166:105906. https://doi.org/10.1016/j.jcsr.2019.105906.

[5] Jiang J, Li GQ, Usmani A. Progressive collapse mechanisms of steel frames exposed to fire. Adv Struct Eng 2014;17:381–98. https://doi.org/10.1260/1369-4332.17.3.381.

[6] ASCE 7. American Society of Civil Engineers Standard 7 Minimum Design Loads for Buildings and Other Structures, American Society of Civil Engineers; 2005.

[7] Cai X, Jiang L, Qiu J, Orabi MA, Yang C. Dual-3D hybrid fire simulation for modelling steel structures in fire with column failure. J Constr Steel Res 2022;197:107511. https://doi.org/10.1016/j.jcsr.2022.107511.

[8] Khan MA, Jiang L, Cashell KA, Usmani A. Analysis of restrained composite beams exposed to fire using a hybrid simulation approach. Eng Struct 2018;172:956–66. https://doi.org/10.1016/j.engstruct.2018.06.048.

[9] Adeli H, Yeh C. Perceptron learning in engineering design. Microcomput Civ Eng 1989;4:247–56.

[10] Sun H, Burton H V., Huang H. Machine learning applications for building structural design and performance assessment: State-of-the-art review. J Build Eng 2021;33:101816. https://doi.org/10.1016/j.jobe.2020.101816.

[11] Hodges JL, Lattimer BY, Luxbacher KD. Compartment fire predictions using transpose convolutional neural networks. Fire Saf J 2019;108:102854. https://doi.org/10.1016/j.firesaf.2019.102854.

[12] Zhang X, Wu X, Huang X. Smart real-time forecast of transient tunnel fires by a dual-agent deep learning model. Tunn Undergr Sp Technol 2022:104631. https://doi.org/10.1016/j.tust.2022.104631.

[13] Wu X, Zhang X, Huang X, Xiao F, Usmani A. A real-time forecast of tunnel fire based on numerical database and artificial intelligence. Build Simul 2022;15:511–24. https://doi.org/10.1007/s12273-021-0775-x.

[14] Wu X, Zhang X, Jiang Y, Huang X, Huang GGQ, Usmani A. An intelligent tunnel firefighting system and small-scale demonstration. Tunn Undergr Sp Technol 2022;120:104301. https://doi.org/10.1016/j.tust.2021.104301.

[15] Ye Z, Hsu SC, Wei HH. Real-time prediction of structural fire responses: A finite element-based machine-learning approach. Autom Constr 2022;136:104165. https://doi.org/10.1016/j.autcon.2022.104165.

[16] Jiang B, Li G-Q, Li L, Izzuddin BA. Experimental Studies on Progressive Collapse Resistance of Steel Moment Frames under Localized Furnace Loading. J Struct Eng 2018;144:1–10. https://doi.org/10.1061/(asce)st.1943-541x.0001947.

A NUMERICAL SIMULATION METHOD FOR TEMPERATURE FIELDS OF TRAVELLING FIRE BASED ON ANSYS OR ABAQUS

Xinna Wei[1], Suwen Chen[2]

ABSTRACT

In concern of Travelling Fire in a large compartment, normally two temperature fields are classified, which are a near field in the flame region with high temperature and a far field in the rest region with smoke temperature [1]. In 2011, Travelling Fire Methodology (TFM) [1] was proposed, which combines Alpert's ceiling jet correlation, to account for the far field smoke temperature and a uniform temperature zone for the near field. Improved Travelling Fires Methodology (iTFM) [2] was then developed with the gas temperature analytical solution for far-field and flame flapping for near field. Travelling Fire Methodology with flame extension (fTFM) [3] was further developed using heat flux boundary conditions. An Extended Travelling Fire Methodology (ETFM) framework was conceptually proposed by Dai et al. [4] also using heat flux boundary conditions. All these Travelling Fire Methodologies use gas temperature or heat flux as boundary conditions to calculate the thermal response of the component; nevertheless, these methods are mainly applied in calculation software (i.e. MATLAB) or OpenSEES for the fire which is short of visualization of the thermal response of components. And some analysis types, element types, material models are not developed in OpenSEES. The use of Travelling Fire Methodology in finite element software is limited.

In this paper, a numerical simulation method based on ANSYS or Abaqus is proposed for the thermal response of components under travelling fire, which can use either gas temperature or heat flux boundary conditions. The component is divided into different partitions, and then the gas temperature or heat flux history is calculated by user-defined functions and loaded to the corresponding partition, which simulates a component in a temporally and spatially non-uniform temperature distribution. The restart technique is adopted for heat flux boundary conditions. Parametric modelling methods are recommended for this method, and the method can be used for other travelling fire methodologies. The numerical simulation method based on ANSYS or Abaqus could make the best use of the existing finite element software (material model, element type, analysis types, and pre-and post-processing modules) to provide more accurate analysis results.

Keywords: Temperature field; Travelling fire; gas temperature; heat flux

1 INTRODUCTION

Modern buildings prefer to be designed as large spaces. Fire behaviour differs in large spaces and small spaces. In a large space fire, a localized area burns, and the burned area spreads along the floor (unburned fuel) and is extinguished because the fuel is exhausted, so the burned localized area moves. This results in a non-uniform temperature distribution for large space fires, which can be described by a travelling fire methodology [5,6]. The travelling fire phenomenon was found in the collapse of WTC towers [7].

To describe the travelling fire behaviours, the TFMs were proposed. Rackauskaite, Heidari and Rein [2,3] proposed iTFM and fTFM to divide large spaces into near-field and far-field regions based on whether the

[1] PhD student, Tongji University
e-mail: weixinna@tongji.edu.cn
[2] Professor, Tongji University
e-mail: Swchen@tongji.edu.cn, ORCID: https://orcid.org/0000-0001-9308-1564
https://doi.org/10.6084/m9.figshare.22193281

flames hit the ceiling or not. The near-field region uses a specific high temperature or Hasemi, Wakamatsu, and Lattimer models. The far-field temperature, where the hot gas temperature is estimated, is calculated by Alpert correlations. The ETFM proposed by Dai [4] is based on a moving localised fire using Hasemi's model for the near field to quantify the localised fire effect on ceiling structural members, which co-worked with the FIRM zone model for the far field smoke layer. Charlier [8] proposed an analytical model to determine the heat fluxes to a structural element due to a travelling fire. To evaluate the heat fluxes, different zones are defined depending on the location of the target and whether the flame impacts or not the ceiling.

Based on various assumptions, the various TFMs were proposed. Finally, the travelling fire behaviour was described with temperatures or heat flux. Temperature and heat flux could be input parameters to heat transfer in ANSYS and Abaqus.

Rackauskaite[9] used the lumped mass heat transfer method to calculate the temperature of steel and concrete components under the travelling fire by MATLAB. Temperature gradients in cross-sections cannot be captured. The structural performance of steel buildings under travelling fires and blasts was researched based on OpenSEES [10]. Blast analysis is carried out in OpenSEES by applying equivalent dynamic loads to the affected structural members in the numerical model because strain rate effects due to blast loading are not embedded in the definition of the constitutive materials in OpenSees. However, the strain rate effects of constitutive materials (Johnson-Cook model, Cowper-Symonds model) are included in the ANSYS and Abaqus. Therefore, this paper aims to propose a numerical simulation method based on ANSYS or Abaqus to use the existing finite element software (material model, element type, pre-and post-processing modules) to provide more accurate analysis results.

2 TRAVELLING FIRES METHODOLOGY

2.1 Description of the travelling fire model

According to the different boundary conditions, these TFMs can be divided into boundary conditions of heat gas and heat flux. The iTFM with heat gas boundary condition and fTFM with heat flux boundary condition was chosen to represent these TFMs.

In iTFM, a uniform temperature is assumed for the near field. The concept of flapping angle was introduced to account for the near field temperature range from 800 °C to 1200 °C. This may lower the ceiling temperatures for some fire sizes but remains a crude approximation [6]. Therefore, the iTFM was used directly to represent the gas boundary condition, while the comparison with experimental results was ignored. The fTFM was used with a little improvement as below. And the fTFM would be investigated for further study.

2.2 fTFM with a little improvement

2.2.1 improvement

- When the flame is not impacting the ceiling of a compartment.

In the original fTFM, the Hasemi model is adopted for the near field. The model is used to calculate the heat flux received by the fire exposed unit surface area at the level of the ceiling. And this model is used when the flame is impacting the ceiling in EN 1991-1-2:2002 [11]. However, this condition is not considered in the original fTFM.

In the improved fTFM, the Alpert Ceiling Jet fire model and Heskestad model are adopted when the flame is not impacting the ceiling.

Firstly, the flame lengths h_{fire} should be determined by the equation (1). Then, the gas temperature T_g at the ceiling level could be calculated by equation (2).

$$h_{fire} = -1.02D + 0.0148\dot{Q}^{\frac{2}{5}} + z_f \qquad (1)$$

$$\begin{cases} T_g(r) = T_\infty + 16.9\dfrac{(\dot{Q}/1000)^{2/3}}{H^{5/3}}, \ r \leqslant 0.18H \\ T_g(r) = T_\infty + 5.38\dfrac{[(\dot{Q}/1000)/r]^{2/3}}{H}, \ r > 0.18H \end{cases} \quad (2)$$

Where D is the diameter of the localised fire,

$\dot{Q}$ is the heat release rate,

z_f is the height of the fire load base,

T_∞ is the ambient temperature,

H is the height between the ceiling and the fuel surface.

The gas temperature in the plume along the symmetrical vertical flame axis should be the maximum value and calculated by equation (3) (Heskestad model). The gas temperature ($z = H$) at the ceiling level calculated from the equation(2) should be less than the value calculated by the equation (3).

$$T_g(z) = 20 + 0.25\dot{Q}_c^{\frac{2}{3}}(z - z_0)^{-\frac{5}{3}} \leqslant 900°\mathrm{C} \quad (3)$$

Where $\dot{Q}_c$ is the convective part of the rate of heat release, with $\dot{Q}_c = 0.8\dot{Q}$,

z_0 is the virtual origin.

- The limit value of the total power

In the original fTFM, travelling fires are considered fuel controlled. In the improved model, the ventilation controlled are considered, and the simplified equation (4) is adopted.

$$\dot{Q}_{\max} = 0.10 \cdot m \cdot H_u \cdot A_V \cdot \sqrt{h_{eq}} \quad (4)$$

Where $\dot{Q}^*_{\max}$ is the limited value of the heat release rate,

m is the combustion factor,

H_u is the net calorific value of wood,

A_V is the opening area,

h_{eq} is the mean height of the openings.

- The diameter of the localised fire

In the original fTFM, the diameter of the localised fire is the fire length, which is defined as the distance between the travelling fire leading edge and trailing edge along the trajectory. Furthermore, the rectangular flame area is converted into the equivalent diameter (D) according to the principle of equal firepower to carry out the Heskestad and Hasemi model calculation in the improved model.

$$D = \sqrt{\frac{4 \cdot \dot{Q}}{\pi \cdot \dot{Q}^*}} \quad (5)$$

Where $\dot{Q}^*$ is the heat release rate per unit area.

The localised flashover fire will be considered in further study.

2.2.2 *Improved model verification*

The natural fire tests in a large compartment were conducted at Ulster University. This investigation aimed to understand the conditions in which the travelling fires develop and to study the behaviour of such fires on the surrounding steel structure [12]. In this section, the second test results are compared with the improved fTFM results. These experimental data are compared with results obtained while applying the method described in this paper. The comparison is performed for the unprotected steel beam TRL-5 and TRL-7 (highlighted in Figure 1 (a) and (b)).

The key parameters are listed below, and more detailed parameters were summarized in the paper [8].

- The fire load density is 511 MJ/m^2; the rate of heat release rate is 400 kW/m^2; the fire spread rate is 3.2 mm/s.
- The coefficient of convection heat transfer on the steel surface is 35 $W/(m^2 \cdot K)$; the emissivity for the structural member surface is 0.7.
- The beams are hot-rolled profile HEA160 with three surfaces exposed to fire.

In Figure 1 (c) and (d), the steel temperature for each beam (with the label TC for experimental data and the label Model for the fTFM results) is plotted. The steel temperature is calculated by the lumped mass heat transfer method. This method allows for the representation of the spatially transient heating of the steel structure. Nevertheless, it assumes a uniform steel temperature for a given cross-section, i.e., there is no cross-sectional temperature gradient.

In Figure 1 (c) and (d), in the pre-heating and heating phase, the TRL-5 temperature increased faster and over-predicted. This is because, in the early fire development, the surface area of burning fuel in the experiment was semicircle while the surface area is assumed to be a rectangle in fTFM, leading to a higher heat release rate in fTFM. However, the TRL-7 temperature matches well with the experimental data. During the cooling phase, the beam (TRL-5 and TRL-7) temperature decreased faster. This is because the model cannot account for the burnout fuel still providing heat flux. Nevertheless, the error is acceptable.

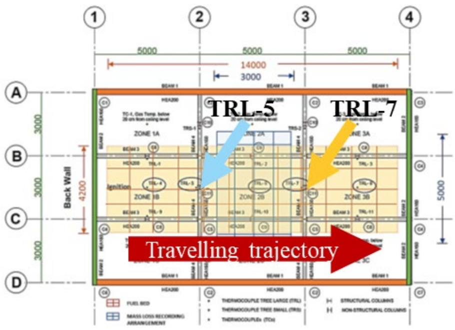

(a) The floor plan [12]

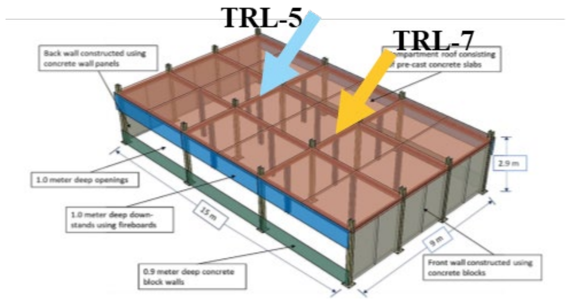

(b) The schematic view [12]

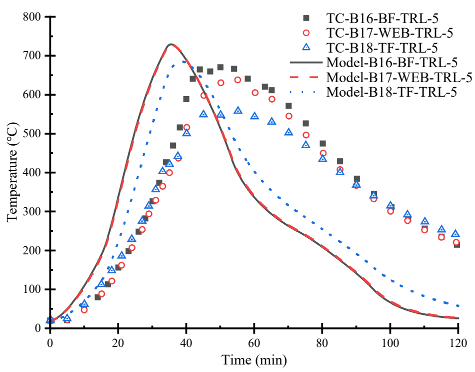

(c) Steel temperature comparison (TRL-5)

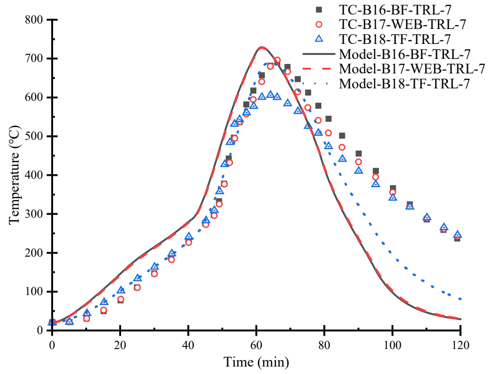

(d) Steel temperature comparison (TRL-7)

Figure 1. Comparison between test and model results

In the numerical simulation with heat flux boundary conditions, this improved fTFM will be used.

3 NUMERICAL SIMULATION METHOD

Based on ANSYS and Abaqus, the simulation of components under travelling fire can take advantage of existing elements types, materials models, analysis types, and pre-and post-processing modules. And cross-sectional temperature gradient is simulated. And heat conduction between adjacent sections can be simulated.

3.1 Gas temperature boundary condition simulation

In FE (Finite Element) analysis, the gas temperature can be input parameters as the boundary condition for heat transfer or couple thermo-mechanical analysis. Firstly, user-defined functions are developed to calculate the gas temperature histories by adopting Travelling Fire Methodologies, such as iTFM. Then, the concerned component is partitioned according to the required accuracy. And then, the gas temperature histories for each partition are calculated and loaded to the corresponding partition, as shown in Figure 2 (a). Figure 2 (b) depicts the results of the heat transfer simulation. Furthermore, the results can be input files as the boundary condition for mechanical analysis. In a couple of thermo-mechanical analyses, the temperature and mechanical results could be obtained simultaneously as shown in Figure 2 (c).

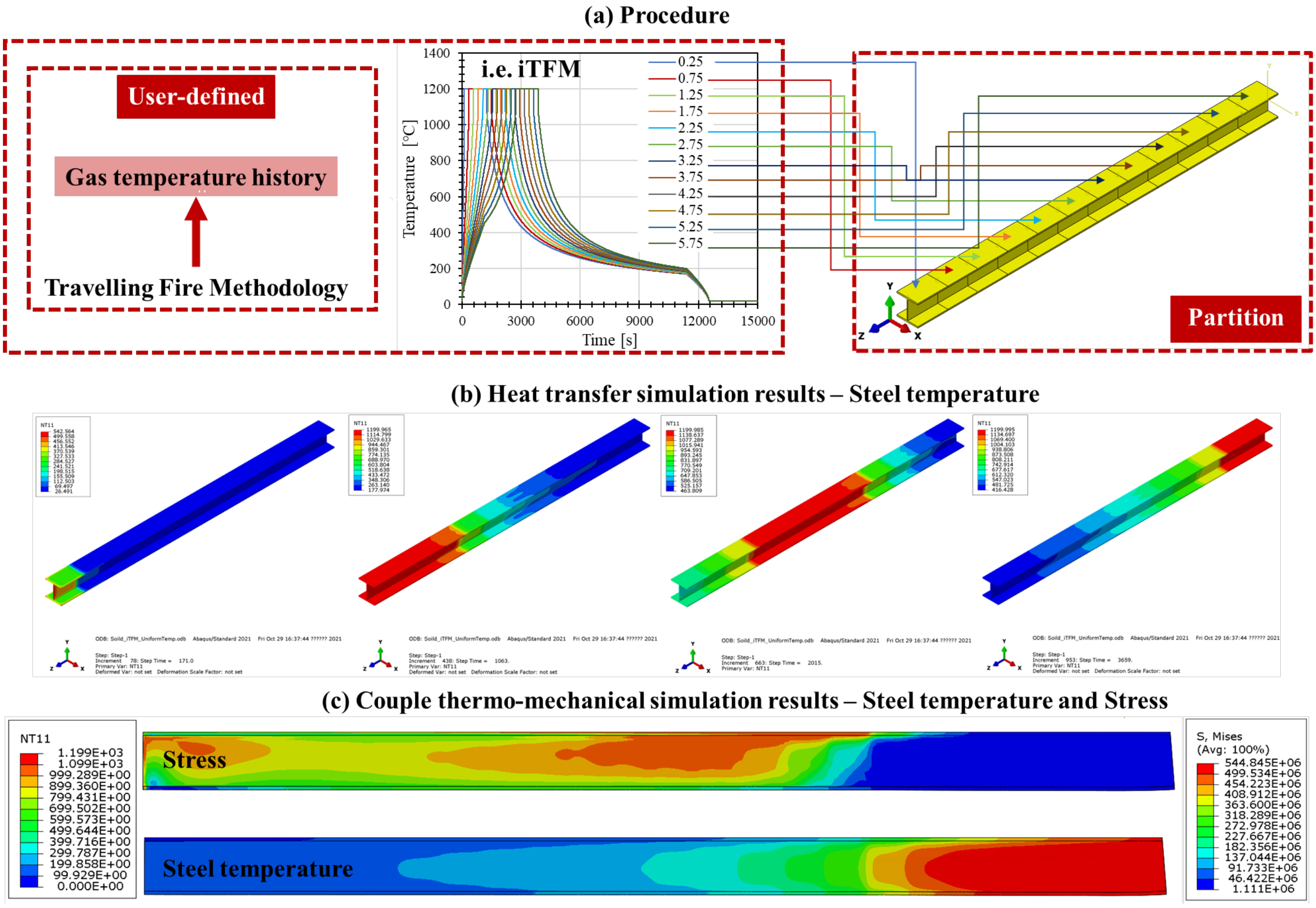

Figure 2. Numerical simulation procedure based on the gas temperature boundary condition

3.2 Heat flux boundary condition simulation

In FE analysis, the heat flux can be input as the boundary condition for heat transfer or couple thermo-mechanical analysis. However, the heat flux should be the net heat flux for calculating the temperature of the component in FE analysis. Therefore, this section describes how to use FE software to perform net heat flux calculations and load them to the component.

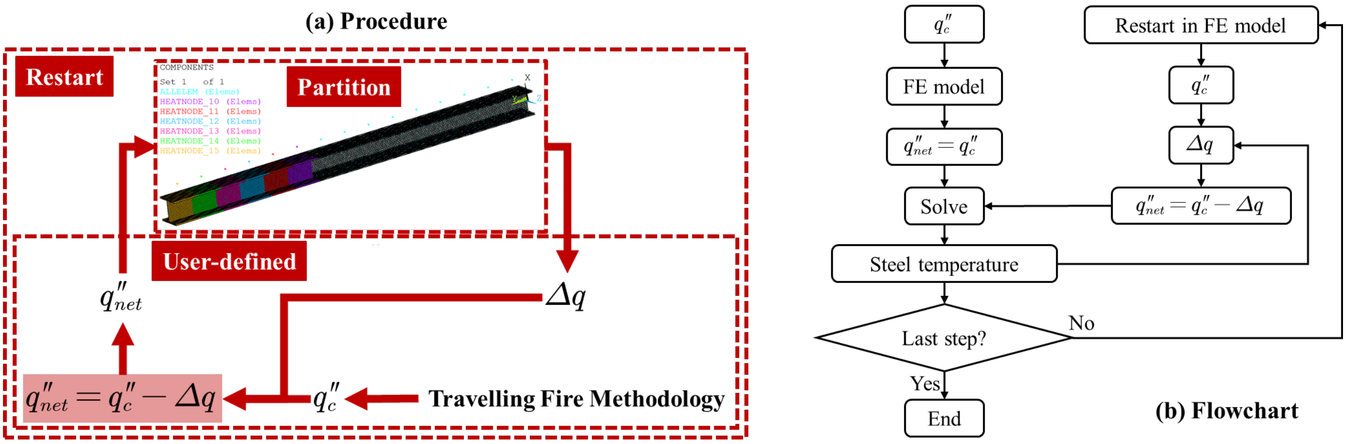

Figure 3. Numerical simulation procedure based on the heat flux boundary condition

The numerical simulation procedure based on the heat flux boundary condition is shown in Figure 3. Firstly, the FE model is established with a suitable partition for the required accuracy. And the incident heat flux

q_c'' is input load parameters, which can be obtained from the TFM model, such as fTFM, and ETFM. In the first step, the net heat flux is equal to the incident heat flux due to the steel temperature being equal to the ambient. Then, the steel temperature after the last analysis step is obtained. Secondly, the last step steel temperature is used to calculate the heat flux exchange Δq by equation (6), and the net heat flux q_{net}'' for this step can be calculated by equation (7). In each subsequent analysis step, the restart technique is required to be used and the net heat flux calculation is repeated until the end of the analysis.

$$\Delta q = \varepsilon\sigma[(T_s+273)^4-(T_\infty+273)^4]-h_c(T_s-T_\infty) \tag{6}$$

Where q_{net}'' is the net heat flux,

q_c'' is the incident heat flux,

ε is the emissivity for structural member surface,

σ is the Stephan Boltzmann constant,

T_s is the steel temperature,

h_c is the convective heat transfer coefficient.

$$q_{net}'' = q_c'' - \Delta q \tag{7}$$

In the following example, a steel beam exposed to ISO834 high-temperature conditions is used to verify the accuracy of the net heat flux and component temperature calculations using the above method.

The ISO834 gas temperature is a high-temperature boundary condition for heat transfer analysis. First of all, the gas temperature is converted to the incident heat flux by equation (8).

$$q_c'' = \varepsilon\cdot\sigma[(T_g+273)^4-(T_\infty+273)^4]+h_c(T_g-T_\infty) \tag{8}$$

In Figure 4, the theoretical steel temperature is obtained by the lumped mass heat transfer method and the net heat flux is calculated by equation (6) and (7). The ANSYS results obtained by the above method match well with the theoretical results, which shows that the above numerical simulation method is feasible.

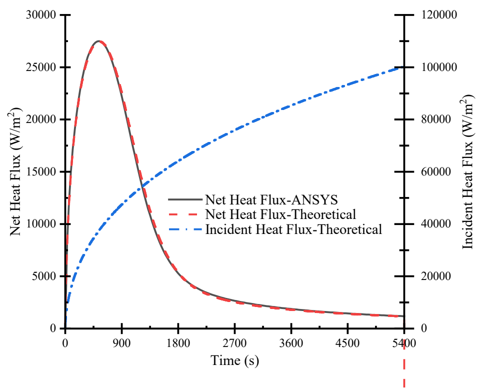

(a) The comparison of heat flux

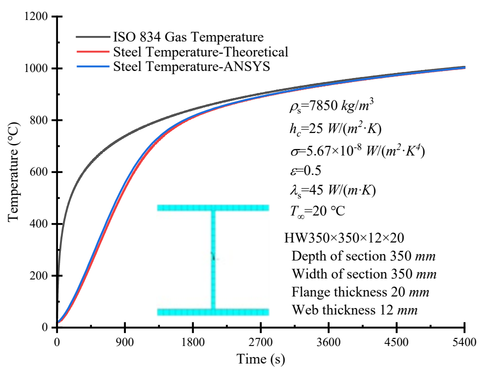

(b) The comparison of temperature

Figure 4. Verification for net heat flux calculation and restart analysis

4 NUMERICAL SIMULATION RESULT

The steel beam temperature field under travelling fire is obtained based on the Abaqus and ANSYS using the above numerical simulation method. Gas temperature and heat flux boundary conditions are calculated from the iTFM and improved fTFM respectively.

4.1 Gas temperature boundary condition simulation result

The height, length and width of the compartment are 24, 18 and 3.5 m respectively. The fire load density is 570 MJ/m^2; the rate of heat release rate is 500 kW/m^2; the dimensionless design fire size is 10%; the fire spread rate is 2.1 mm/s; the near-field temperature is 1200 ℃. These values are within the recommended range [2]. The cross-sectional shape of the steel beam is the same as in Figure 4 (b), and the length is 6 m. The other parameters are the same as in Figure 4 (b). The element types are DC3D8 (an 8-node linear heat transfer brick.) in the heat transfer analysis. The element types are SOLID178 and SURF152 in the ANSYS, and the numerical simulation method is described in section 3.1.

The temperature distribution changes of the components with 12 partitions are shown in Figure 2 (b). In Figure 5, the steel temperature histories at various locations are obtained by theoretical calculation and numerical simulation. The theoretical results are obtained by the lumped mass heat transfer method. And the simulation results are collected by Abaqus with 12 and 24 partitions, and the temperature is the average of the temperature of the whole section.

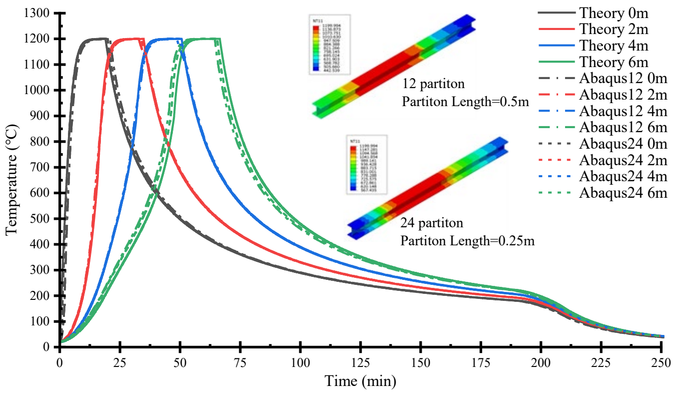

Figure 5. Comparison with a different partition (Heat transfer analyses in Abaqus)

In Figure 5, at both ends of the beam, there is a gap between the theoretical value and the numerical calculation result. The difference at the beginning of the beam was slightly smaller, while the difference at the end of the beam was slightly larger. In the middle part of the beam, the theoretical value is in good agreement with the numerical calculation result. The reason for the analysis is the boundary conditions are different. This shows that lumped mass heat transfer method is feasible in calculating the steel component temperature under the travelling fire, but the cross-section temperature gradient cannot be considered. And the method does not consider the heat conduction of adjacent sections of the beam.

In the numerical calculation, the temperature load is calculated based on different partitions, and the temperature loads are not continuous. The high-temperature load is applied to the different partitions of the steel beam, and the heat transfer between the different partitions is calculated, resulting in the difference. When the partition is smaller, the calculated temperature load is more continuous, and the heat conduction between different partitions due to discontinuous load is smaller. More partitions will result in smoother temperature changes for steel beams under nonuniform high-temperature loads of travelling fire.

A graphical user interface was used in Abaqus. Although the partition length was 0.5 and 0.25 m, the operations were complex, and no distractions were allowed. Therefore, the parametric modelling method is recommended.

In the iTFM simulation by ANSYS, the partition length is 0.02m equal to the one-element mesh size using a parametric model, and the simulation results are shown in Figure 6. In the iTFM, the gas temperature is the input load and is not affected by the simulation results. Therefore, the steel temperature calculated from the ANSYS could be an accurate result.

The numerical results agree well with the theoretical results because of the good thermal conductivity and large shape factor of the steel beams. However, the temperature of the web section varies significantly because both ends of the web are affected by the temperature of the top and bottom flanges due to heat conduction. Since the numerical calculation can consider heat conduction, the temperature change in the cross-section can be more accurately captured.

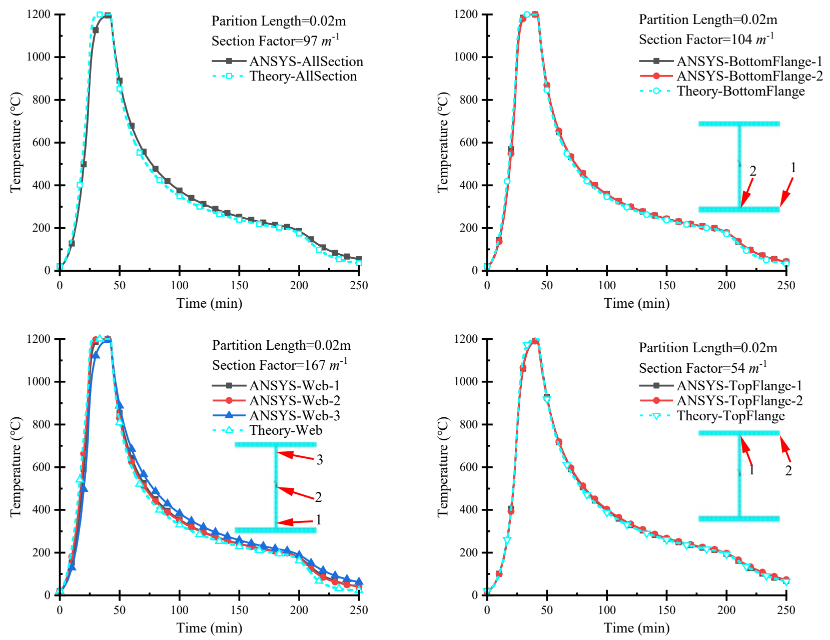

Figure 6. Comparison for section temperature (iTFM-Heat transfer analyses in ANSYS)

4.2 Heat flux boundary condition simulation result

The measured data from natural fire tests in a large compartment conducted at Ulster University is used for comparison. In the test, the improved fTFM could predict the temperature well with the beam (HEA160, TRL-7) measured temperature. Therefore, assuming a beam is hot-rolled profile HEA200 along the room length direction in the test compartment, and the interesting location of steel temperature is at 10 m.

The interested steel temperature is calculated at 10 m by improved fTFM with the lumped mass heat transfer method. To reduce the cost of numerical simulation, only a beam of 3 m is established, representing the beam at 8.5-11.5 m, and the incident heat flux calculated from the improved fTFM at 8.5-11.5 m is inputted to the ANSYS model. Element types are SOLID178 and SURF152 in the ANSYS, and the numerical simulation method is described in section 3.2. The calculation results are shown in Figure 7. Based on the above analysis, the steel temperatures under travelling fire calculated from the theory and numerical simulation are matched well in Figure 7 (a). This illustrates that the numerical simulation method based on ANSYS is credible.

In Figure 7 (b), the temperature distribution in the component is between 8.5 and 11.5 m. This means that if the computational cost is considered, only the part of interest can be calculated. And the temperature distribution of the component section can be accurately captured.

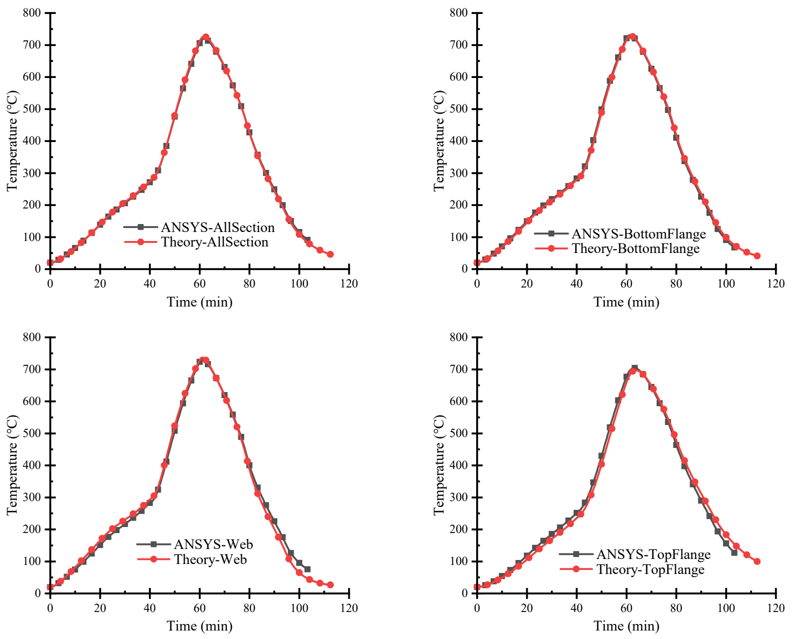

(a) Section temperature history

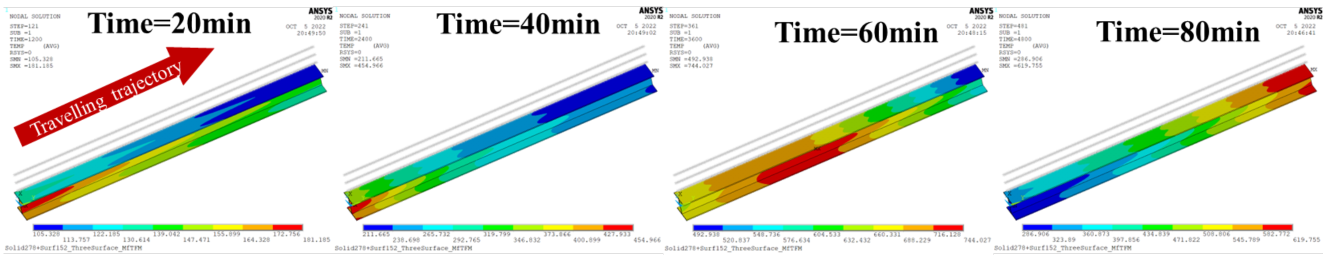

(b) Steel component temperature distribution (8.5-11.5 m)

Figure 7. Comparison for section temperature (improved fTFM-Heat transfer analyses in ANSYS)

Although the steel temperature calculated by the numerical simulation is unnecessary, this numerical simulation could be used for more complex analysis to use the material and element in the software, and the temperature gradient is simulated.

5 CONCLUSIONS

In this paper, a numerical simulation method for temperature fields of travelling fire based on ANSYS and Abaqus is proposed.

Through the simple comparison of the steel beam temperature calculated from the theoretical method and the numerical simulation method, the following conclusions can be drawn:

- The numerical simulation method based on ANSYS and Abaqus can provide accurate temperature field simulation results.
- Based on the proposed numerical simulation method, the elements types, material models and pre-and post-processing modules already available in the software can be used.
- Based on the proposed numerical simulation method, the temperature gradient of the section can be obtained.

- **ACKNOWLEDGMENT**

The authors would like to acknowledge the support from the Ministry of Science and Technology of China (2019YFB2102701).

REFERENCES

[1] Law A, Stern-Gottfried J, Gillie M, Rein G. The influence of travelling fires on a concrete frame. Engineering Structures 2011;33:1635–42. https://doi.org/10.1016/j.engstruct.2011.01.034.

[2] Rackauskaite E, Hamel C, Law A, Rein G. Improved Formulation of Travelling Fires and Application to Concrete and Steel Structures. Structures 2015;3:250–60. https://doi.org/10.1016/j.istruc.2015.06.001.

[3] Heidari M, Kotsovinos P, Rein G. Flame extension and the near field under the ceiling for travelling fires inside large compartments. Fire and Materials 2020;44:423–36. https://doi.org/10.1002/fam.2773.

[4] Dai X, Welch S, Vassart O, Cábová K, Jiang L, Maclean J, et al. An extended travelling fire method framework for performance-based structural design. Fire and Materials 2020;44:437–57. https://doi.org/10.1002/fam.2810.

[5] Stern-Gottfried J, Rein G. Travelling fires for structural design–Part I: Literature review. Fire Safety Journal 2012;54:74–85. https://doi.org/10.1016/j.firesaf.2012.06.003.

[6] Dai X, Welch S, Usmani A. A critical review of “travelling fire” scenarios for performance-based structural engineering. Fire Safety Journal 2017;91:568–78. https://doi.org/10.1016/j.firesaf.2017.04.001.

[7] Gann RG, Hamins A, McGrattan K, Nelson HE, Ohlemiller TJ, Prasad KR, et al. Reconstruction of the Fires and Thermal Environment in World Trade Center Buildings 1, 2, and 7. Fire Technol 2013;49:679–707. https://doi.org/10.1007/s10694-012-0288-3.

[8] Charlier M, Franssen J-M, Dumont F, Nadjai A, Vassart O. Development of an Analytical Model to Determine the Heat Fluxes to a Structural Element Due to a Travelling Fire. Applied Sciences 2021. https://doi.org/10.3390/app11199263.

[9] Rackauskaite E. iTFM: Improved Travelling Fires Methodology for Structural Design and the Effects on Steel Framed Buildings. Imperial College, 2017.

[10] Teslim-Balogun AA. Structural performance of steel buildings under travelling fires and blast. Imperial College, 2020.

[11] EN 1993-1-2, Eurocode 1-Actions on structures -part 1-2: general rules - Actions on structures exposed to fire. 2002.

[12] Alam N, Nadjai A, Charlier M, Vassart O, Welch S, Sjöström J, et al. Large scale travelling fire tests with open ventilation conditions and their effect on the surrounding steel structure– The second fire test. Journal of Constructional Steel Research 2022;188:107032. https://doi.org/10.1016/j.jcsr.2021.107032.

Proceedings of the 12th International Conference on Structures in Fire

Steel Structures in Fire

SiF 2022– The 12th International Conference on Structures in Fire
The Hong Kong Polytechnic University, Nov 30 - Dec 2, 2022

BEHAVIOUR AND DSM DESIGN OF COLD-FORMED STEEL BEAMS AFFECTED BY DISTORTIONAL-GLOBAL INTERACTION AT ELEVATED TEMPERATURES

Natan Sian das Neves[1], Alexandre Landesmann[2], Dinar Camotim[3]

ABSTRACT

This work reports the results of an ongoing numerical investigation dealing with the post-buckling behaviour, strength and Direct Strength Method (DSM) design of cold-formed steel (CFS), simply supported lipped channel beams experiencing distortional-global (D-G) interaction under uniform bending at elevated temperatures. It extends the scope of previous studies, carried out at room temperature, by considering beams (i) exposed to fire conditions (*i.e.*, temperatures up to 800 ºC), (ii) displaying various cross-section dimensions, lengths and yield stresses, and (iii) exhibiting two different support conditions, differing in the end cross-section warping/local displacement/rotation restraints (they are either fully free or fully prevented). The results presented and discussed consist of post-buckling equilibrium paths, failure moments and collapse modes, which are obtained through ABAQUS shell finite element geometrically and materially non-linear analyses. The constitutive model adopted to simulate the temperature dependence of the steel material properties is based on that prescribed by EC3-1.2 for CFS. The D-G interactive failure moment data gathered in this work are used to assess the merits of the available DSM-based design approaches – developed for room temperature and only modified to account for the elevated temperature effects. The findings reported, including a few design considerations, provide encouragement to extend the current research effort with the purpose of searching for an efficient (safe and reliable) DSM-based design approach to estimate the D-G interactive failure moments of CFS beams at elevated temperatures.

Keywords: Cold-formed steel beams; Elevated temperatures; Lipped channels; Distortional-global interaction; Distortional-global interactive failures; Shell finite element analysis; Direct Strength Method design.

1 INTRODUCTION

Cold-formed steel (CFS) is currently widely used in residential, office and commercial/industrial buildings. CFS structural systems exhibit numerous advantages, such as their outstanding strength-to-weight ratio, remarkable ease of fabrication and installation, high usage versatility – moreover, they are not combustible, which is a major advantage under elevated temperatures. However, the combined use of high-strength steel grades and slender cross-sections is responsible for rendering CFS structural members and systems highly susceptible to several instabilities, namely local (L), distortional (D) and global (G) buckling, as well as to coupling phenomena combining two or more of them (L-D, L-G, D-G or L-D-G interaction). The Direct Strength Method (DSM – *e.g.*, [1,2]), included in several specifications for CFS structures, namely the North American [3], Australian/New Zealand [4] and Brazilian [5] ones, is nowadays widely accepted as the most rational approach for the design of such members. The currently codified beam design curves deal only with (i) L, D and G pure, and (ii) L-D interactive failures, at room temperature (20 °C) – the first two design curves are those relevant for this work. However, it should be noted that the currently codified D design curve is replaced, in this study, by the DSM-based strength curves proposed in [6], which were shown to provide superior failure moment predictions (especially in the high slenderness range) – they read

[1] P.hD student, Programa de Engenharia Civil, PEC/COPPE/UFRJ, Universidade Federal do Rio de Janeiro, Brasil.
e-mail: natan.neves@coc.ufrj.br, ORCID: https://orcid.org/ 0000-0002-4679-0461

[2] Full-Professor, Programa de Engenharia Civil, PEC/COPPE/UFRJ, Universidade Federal do Rio de Janeiro, Brasil.
e-mail: alandes@coc.ufrj.br, ORCID: https://orcid.org/0000-0002-3974-5953

[3] Full-Professor (retired), CERIS, DECivil, Instituto Superior Técnico, Universidade de Lisboa, Portugal
e-mail: dcamotim@civil.ist.utl.pt, ORCID: https://orcid.org/ 0000-0002-7994-2687

https://doi.org/10.6084/m9.figshare.22202383

$$M_{nD}=\begin{cases}M_y+(1-C_{yd}^{-2})(M_p-M_y) & \lambda_D\le 0.673\\ (1-a\lambda_D^{-b})\lambda_D^{-c}M_y & \lambda_D>0.673\end{cases},\qquad M_{nG}=\begin{cases}M_p-(M_p-M_y)[(\lambda_G-0.23)/0.37] & \lambda_G\le 0.6\\ 1.11(1-0.278\lambda_G^2)M_y & 0.6<\lambda_G<1.336\\ M_y\lambda_G^{-2} & \lambda_G\ge 1.336\end{cases}\quad (1)$$

where: (i) M_y and M_p are the yield and plastic moments, (ii) $\lambda_D=(M_y/M_{crD})^{0.5}$, $\lambda_G=(M_y/M_{crG})^{0.5}$, M_{crD} and M_{crG} are the distortional and global slenderness values and elastic buckling moments, respectively, (iii) $C_{yd}=(0.673/\lambda_D)^{0.5}\le 3$ is the inelastic strength reserve [3,4], and (iv) the values of parameters a, b and c can be found in [6].

Although, a fair amount of research has been devoted to the development/improvement of DSM-based design methodologies for CFS beams (*e.g.*, [6-12]), only a small fraction of the available studies addresses D-G interactive failures, which may be quite relevant for "intermediate-to-long" beams – to the authors' best knowledge, the available works on D-G interaction in beams consist of (i) experimental and numerical (shell finite element – SFE) investigations concerning lipped channel (LC) stainless beams, conducted at The University of Sydney [11,12], and (ii) numerical studies concerning CFS LC and zed-section (Z) beams, carried out at The University of Lisbon and using SFE and GBT-based (GBT stands for "Generalised Beam Theory") models [13, 14].

Martins *et al.* [14] reported a numerical investigation on the post-buckling behaviour, strength and DSM-based design of CFS simply supported uniformly bent LC and Z beams undergoing D-G interaction. Regarding the LC beams, these authors gathered a total of 902 D-G interactive failure moments concerning (i) 41 beam geometries, (ii) two different support conditions (end cross-sections with the warping displacements and local displacements and rotations fully free or fully prevented), (iii) 11 room-temperature yield stresses, covering wide slenderness ranges, and (iv) beams experiencing "true D-G interaction" ($R_{GD}=M_{crG}/M_{crD}\approx 1.0$) or "secondary (global or distortional)-bifurcation D-G interaction" ($R_{GD}>1.10$ or $R_{GD}<0.90$, respectively, and M_y much larger than the non-critical competing buckling moment). These authors showed that the M_{nD} values provided by Eq. (1_1) (the best available distortional failure moments predictions) overestimate virtually all the numerical D-G interactive failure moments obtained – this overestimation is particularly severe for $\lambda_D>2.0$ and grows rapidly with the slenderness. In addition, it was also shown that the current DSM global design curve (M_{nG} – see Eq. (1_2)) only provides reasonably accurate failure moment predictions for LC beams experiencing "secondary distortional-bifurcation D-G interaction" ($R_{GD}\le 0.85$), which exhibit "practically global" failures (with negligible failure moment erosion). As R_{GD} increases up to and past 1.0, the failure nature switches from "practically global" to "D-G interactive" (*i.e.*, the failure modes combine D and G deformations), and the beam failure moment is gradually eroded (with respect to M_{nG}), due to "true D-G interaction" and "secondary distortional-bifurcation D-G interaction" effects. In order to capture this failure moment erosion, Martins *et al.* [14] followed an approach first put forward by Schafer [15] and prosed two alternative DSM-based design approaches, termed (i) "NDG" (M_{nDG} – involves replacing M_y with M_{nG} in Eq. (1_1)) and (ii) "NGD" (M_{nGD} – replacement of M_y with M_{nD} in Eq. (1_2))– they are given by

$$M_{nDG}=\begin{cases}M_{nG} & \lambda_{DG}\le 0.673\\ (1-a\lambda_{DG}^{-b})\lambda_{DG}^{-c}M_{nG} & \lambda_{DG}>0.673\end{cases},\qquad M_{nGD}=\begin{cases}M_{nD} & \lambda_{GD}<0.6\\ 1.11(1-0.278\lambda_{GD})M_{nD} & 0.6\le\lambda_{GD}\le 1.336\\ M_{nD}\lambda_{GD}^{-2} & \lambda_{GD}>1.336\end{cases}\quad (2)$$

where $\lambda_{DG}=(M_{nG}/M_{crD})^{0.5}$ and $\lambda_{GD}=(M_{nD}/M_{crG})^{0.5}$ are the interactive slenderness values. Furthermore, these authors also concluded that the above two DSM-based design approaches can predict satisfactorily the LC beam D-G interactive failure moments associated with"true" or "secondary global-bifurcation" D-G interaction.

The above findings provided promising indications concerning the possibility of developing an efficient (accurate, safe and reliable) DSM-based design approach for beams undergoing D-G interaction at room temperature, even if experimental validation is still lacking. However, it remains to be assessed whether the available DSM-based strength curves can also be adopted to handle D, G and D-G interactive failures in CFS beams at elevated temperatures caused by fire conditions – naturally, after being modified to account for the temperature-dependence of the steel constitutive law, felt through its Young's modulus, yield strength and amount of non-linearity. Even if some research activity has been devoted to the behaviour and DSM design of CFS beams failing in D and G modes at elevated temperatures (*e.g.*, [16-18]), the authors are not aware of any investigation dealing with CFS beam D-G interaction under fire conditions. Therefore, the purpose of this work is to provide a first contribution towards filling this gap, by presenting and discussing the available results of an ongoing numerical investigation on the behaviour and DSM-based design of uniformly bent (about the major-axis) CFS simply supported LC beams undergoing different D-G interaction levels at (uniform) elevated temperatures, which can be as high as 800 ºC.

2 BEAM GEOMETRY SELECTION – BUCKLING BEHAVIOUR

As done in previous studies (*e.g.*, [6, 14, 18]), the first task of this work consists of selecting the cross-section dimensions and lengths of the CFS single-span LC beams to be analysed. They exhibit two end support conditions, termed here SCA and SCB (as in [6]), both simply supported with respect to major and minor-axis bending and having the end cross-section torsional rotations prevented – the difference resides in the fact that the end cross-section warping and local displacements and rotations are either free (SCA beams − unrestrained end cross-sections) or prevented (SCB beams − rigid plates are attached to their end cross-sections) – see Figs. 1(a)-(b).

This selection procedure involves buckling analysis sequences, performed in the code GBTUL [19] and aimed at identifying beams prone to "true D-G interaction", *i.e.*, such that their D and G buckling moments are (i) fairly close

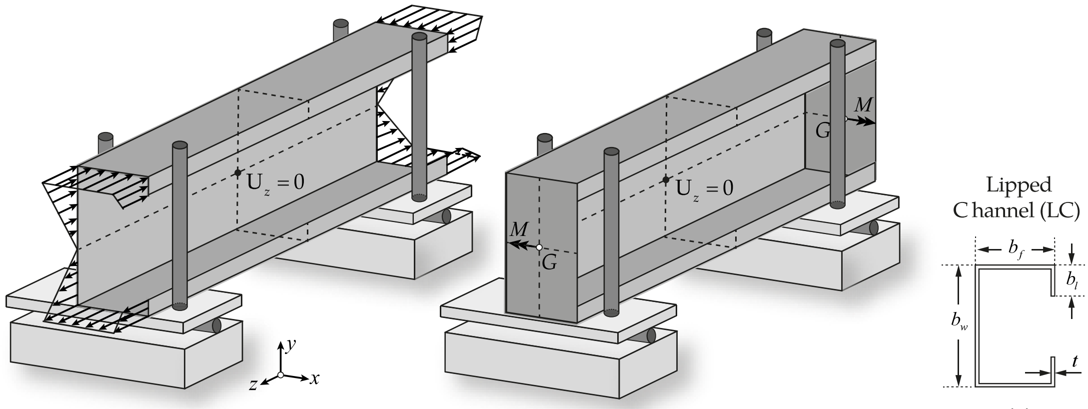

(a) (b) (c)

Figure 1. End support and loading conditions of the (a) SCA and (b) SCB beams, and (c) LC geometry and dimensions.

Table 1. Selected SCA + SCB LC beams prone to "true D-G interaction" [14]: geometries (cm), buckling moments (kNcm) and R_{GD} values.

Beam	SCA								SCB							
	b_w	b_f	b_l	t	L	M_{crG}	M_{crD}	R_{GD}	b_w	b_f	b_l	t	L	M_{crG}	M_{crD}	R_{GD}
LC1	10	5	1.1	0.265	110	1656	1849	0.90	10	5	1.1	0.298	150	2251	2505	0.90
LC2	15	9	1	0.25	350	1089	1195	0.91	16	10	1	0.25	625	1053	1140	0.92
LC3	20	10	1	0.25	440	1279	1397	0.92	18	10	1	0.25	625	1215	1274	0.95
LC4	16	8	1.3	0.35	210	3590	3887	0.92	20	9	1	0.25	525	1506	1579	0.95
LC5	18	10	1	0.25	430	1178	1264	0.93	10	5	1.1	0.33	135	3038	3187	0.95
LC6	15	10	1.2	0.3	350	1772	1890	0.94	15	9	1	0.25	500	1155	1204	0.96
LC7	10	6	1	0.25	155	1182	1258	0.94	10	6	1	0.25	225	1239	1284	0.96
LC8	11	7.5	1	0.3	210	1557	1655	0.94	22	11	1.4	0.35	550	3868	4000	0.97
LC9	16	10	1	0.25	420	1071	1132	0.95	15	10	1.2	0.3	500	1875	1911	0.98
LC10	14	5	1.1	0.35	95	4534	4768	0.95	13.5	8	1	0.3	350	1844	1891	0.98
LC11	13.5	8	1	0.3	240	1799	1867	0.96	16	8	1.3	0.35	300	3870	3941	0.98
LC12	22	11	1.4	0.35	375	3775	3952	0.96	11	7.5	1	0.3	300	1643	1675	0.98
LC13	17.5	10	1.3	0.35	310	3216	3321	0.97	20	10	1	0.25	625	1384	1408	0.98
LC14	20	9	1	0.25	350	1531	1565	0.98	17.5	10	1.3	0.35	450	3338	3368	0.99
LC15	17.5	12	1.5	0.45	350	5366	5489	0.98	14	5	1.1	0.35	135	4923	4981	0.99
LC16	10	5	1.1	0.33	90	3015	3072	0.98	17.5	12	1.5	0.45	500	5560	5565	1.00
LC17	22	10	1	0.25	425	1527	1527	1.00	11	7.5	1.2	0.35	250	2841	2791	1.02
LC18	12.5	7.5	1	0.3	205	1877	1867	1.01	12.5	7.5	1	0.3	300	1921	1886	1.02
LC19	12.5	7	1	0.3	175	2133	2007	1.06	13	8	1	0.35	300	2765	2622	1.05
LC20	11	7.5	1.2	0.35	165	2884	2724	1.06	12.5	7	1	0.3	260	2163	2034	1.06
LC21	13	7	1	0.3	175	2238	2085	1.07	13	7	1	0.3	260	2264	2112	1.07
LC22	13	8	1	0.35	200	2817	2597	1.08	22	10	1	0.25	600	1683	1541	1.09
LC23	18	10	1	0.242	400	1287	1170	1.10	18	10	1	0.24	600	1276	1160	1.10

(0.9≤R_{GD}≤1.10) and (ii) well below their local counterparts (to preclude the occurrence of L-D-G interaction). Table 1 provides the output of this effort, consisting of 23 LC beam cross-section dimensions (b_w, b_f, b_l and t – see Fig. 1(c)), lengths (L), critical distortional (M_{crD}) and global (M_{crG}) buckling moments, and R_{GD} values – note that all the beams considered in this work were previously analysed by Martins *et al.* [14] (at room temperature only).

The illustrative signature curves depicted in Figs. 2(a)-(c) concern the LC18 SCA and SCB beams (same cross-section dimensions) and provide the variation of $M_{cr.T}$ (elastic critical buckling moment at temperature T – min {$M_{crG.T}$; $M_{crD.T}$}) with L (length in logarithmic scale) for four temperatures: 20/100 °C (room/moderate), 400 °C, 600 °C and 800 °C. The temperature-dependent steel constitutive model prescribed in Part 1-2 of Eurocode 3 (EC3-1-2 – [20]), presented in Section 3.1, is adopted and all buckling moments are calculated for E_{20}=210 GPa (Young's modulus at room temperature) and ν=0.3 (Poisson's ratio, deemed temperature-independent). Note that the 2 beam lengths selected (L_{GD}=205 and 300 cm – see Table 1), indicated on the signature curves (Fig. 2(a)), are associated with the D and G buckling mode shapes depicted in Fig. 2(c) – the two L_{GD} lengths are very close to the transition between D and G critical buckling. As for the modal participation diagrams displayed in Fig. 2(b), they show that the so-called "global" (lateral-torsional) buckling modes (corresponding to L_{GD}) combine, in fact, contributions from the minor-axis flexure (**3**), torsion (**4**) and symmetric distortion (**5**) deformation modes (more details are provided in [14]). In other words, they are lateral-torsional-distortional (LTD) buckling modes – for the sake of simplicity, they are denoted "global" in this work. Finally, it is worth noting that a signature curve associated with an elevated temperature (400-600-800 ºC) is obtained through a "vertical translation" of its room-temperature counterpart, whose magnitude depends only on the Young's modulus erosion due to the temperature rise – thus, the buckling moments $M_{crG.T}$ *or* $M_{crD.T}$ correspond to the same length (L_{GD}) regardless of the temperature value.

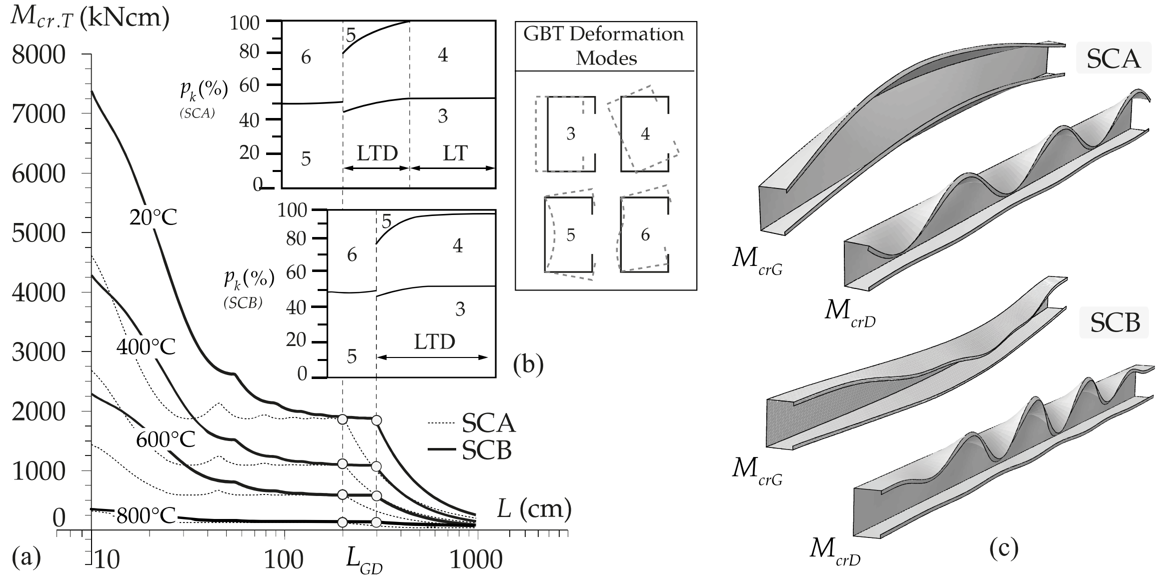

Figure 2. LC18 SCA and SCB beam (a) $M_{cr.T}$ vs. L (signature) curves for T=20/100-400-600-800 ºC associated with the EC3-1-2 constitutive model, (b) GBT modal participation diagrams and, (c) M_{crG} and M_{crD} buckling modes shapes.

3 NUMERICAL MODEL

The beam post-buckling equilibrium paths and failure moments were determined through ABAQUS [21] SFE geometrically and materially non-linear analyses with imperfections (GMNIA), employing models similar to those used in recent studies involving CFS beams at room and elevated temperatures (*e.g.*, [6, 14, 18]). The beams were discretised into fine S4 element meshes (ABAQUS nomenclature – 4-node general-purpose SFE with six degrees of freedom per node and full integration). The analyses (i) were performed by means of an incremental-iterative technique combining Newton-Raphson's method with an arc-length control strategy, and (ii) simulate the response of beams subjected to constant uniform temperature distributions (*i.e.*, the beams are deemed engulfed in flames, thus sharing the surrounding air temperature) and subsequently acted by an increasing uniform major-axis bending moment up to failure – *i.e.*, steady state structural analyses providing failure moments. Previous studies (*e.g.*, [18]) showed that finite element meshes with a length-to-width ratio close to *1* provide accurate results, while involving a reasonable computational effort.

As mentioned earlier (*e.g.*, Fig. 1), the simply supported beams analysed exhibit two end support conditions, termed SCA and SCB – the SCB beams are modelled by attaching rigid plates to the beam end cross-sections. In order to preclude the occurrence of rigid-body motions, the beam longitudinal displacements of all beams analysed were prevented at the mid-span cross-section mid-web point (see Fig. 1). The uniform bending moment diagram is applied by means of either (i) sets of concentrated forces acting on the nodes of both end cross-sections sections (SCA) or (ii) two concentrated moments acting on the rigid end-plates (SCB). The force/moment application is always imposed in small increments, by means of the ABAQUS automatic loading stepping procedure.

All beams analysed contain critical-mode LT initial geometrical imperfections (the most detrimental shape [14]) with amplitude *L*/1000. The critical buckling mode shapes were obtained through preliminary ABAQUS buckling analyses, performed with the same SFE mesh subsequently employed to carry out the GMNIA – this procedure makes it easy to "transform" the buckling analysis output into a GMNIA input. It is still worth noting that strain-hardening, residual stress and rounded corner strength effects were disregarded in this work, since several authors (see the references of [14]) have shown that their combined influence on the failure moments is negligible.

3.1 Steel Material Behaviour

The multi-linear stress-strain curve available in ABAQUS [21] is used to model the steel material behaviour for several yield stresses. The steel constitutive law at elevated temperatures adopted to carry out this research work is defined by the analytical expression provided in EC3-1-2 [20], previously employed to perform the numerical simulations reported in [18, 22]. Figure 3(a) makes it possible to compare the temperature-dependence of the CFS reduction factors concerning the steel Young's modulus ($k_e=E_T/E_{20}$), nominal yield stress ($k_y=f_{y.T}/f_{y.20}$) and proportionality limit stress ($k_p=f_{p.T}/f_{y.20}$), which are tabulated in EC3-1-2. As for Fig. 3(b), it shows the qualitative differences between the steel stress-strain curves $f_T/f_{y.20}$ *vs.* ε prescribed by the EC3-based model for all the temperatures considered in this work – the applied stress at a given temperature f_T is normalised with respect to the room-temperature yield stress $f_{y.20}$.

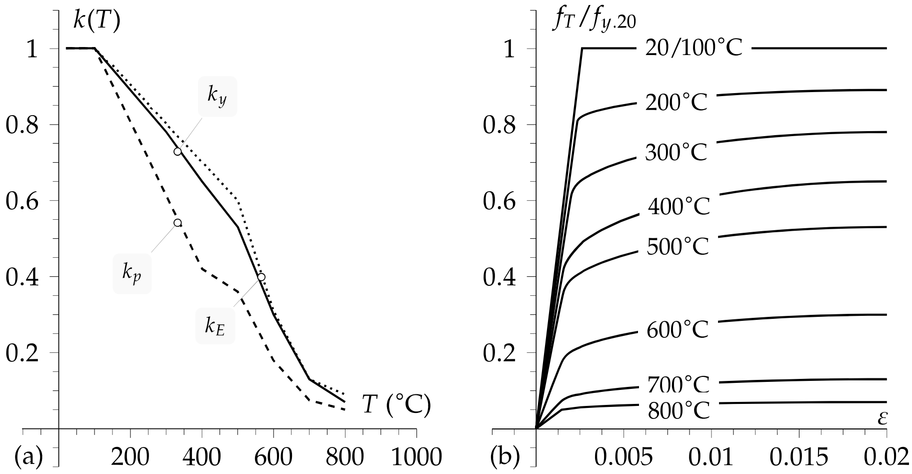

Figure 3. Variation of the CFS material behaviour with *T*: (a) reduction factors and (b) stress-strain curves associated with the various temperatures considered in this work.

4 DISTORTIONAL-GLOBAL INTERACTIVE RESPONSE AT ELEVATED TEMPERATURES

4.1 Elastic-Plastic Post-Buckling Behaviour

The influence of the (elevated) temperature on the elastic-plastic post-buckling behaviour and strength of CFS simply supported LC beams undergoing D-G interaction is examined in this section, for both SCA and SCB beams (see Table 1) and adopting the EC3-based temperature-dependent steel constitutive law presented in Section 3.1 and also considered in [18,22]. Since it was found that such influence is qualitatively identical for all the beams analysed, only the post-buckling results of two beams are presented and discussed here – they constitute a representative sample of the whole set of members dealt with. Figures 4(a)-(b) concern LC18 SCA and SCB beams with $f_{y.20}$=750 MPa

(λ=$[M_y/M_{cr}]^{0.5}$=1.23 and 1.25, respectively) and show their (i) non-linear equilibrium paths $M/M_{cr.20}$ *vs.* $|w|/t$ (w is the mid-span top web-flange corner horizontal displacement) for T=20/100-200-300-400-500-600-700-800 ºC, where the blue (SCA) and grey (SCB) dots identify the failure moments $M_{u.T}$ and the room temperature curve is displayed for comparative purposes, and (ii) the deformed configurations and plastic strains contours at collapse (M=$M_{u.T}$) for the beams at T=20/100-500-800 ºC). The observation of these post-buckling results prompts the following remarks:

(i) Obviously, the various beam equilibrium paths "move downwards" as the temperature T rises, thus leading to lower failure moments, regardless of the end support conditions. Moreover, all beam failure modes (deformed configurations at collapse) exhibit a combination of D and G deformation patterns, thus confirming the occurrence of D-G interaction.

(ii) Concerning the failure modes, note that, since the thermal action effects are negligible (uniform temperature and free-to-deform beams), the failure modes shown in Figs. 4(b$_1$)-(b$_2$) are similar and do not depend on the temperature – the same also applies to the corresponding plastic strain contours (including the yielded region locations). In the SCA beams, plasticity occurs exclusively in the close vicinity of the mid-span cross-section – it starts at the top lip-flange region and progresses towards the top web-flange region, until a kind of "distortional hinge" precipitates the collapse (see Fig. 4(b$_1$)). In the SCB beams, the plastic mechanism is essentially the same, but plasticity can also be observed throughout the beam length prior to failure.

(iii) The equilibrium paths concerning $T\geq600$ ºC are clearly below their $T\leq500$ ºC counterparts for both the SCA and SCB beams, reflecting the heavy degradation of the steel material behaviour taking place between 500 ºC and 600 ºC, namely via the proportionality limit strain and smoothness of the (elliptic) transition between the elastic and plastic ranges (see Fig. 3(b)) – indeed, for $T\geq600$ ºC the stress-strain curve non-linearity diminishes considerably and it almost exhibits again a yield plateau.

(iv) No clear trend was detected concerning the influence of the temperature, geometry and/or steel grade on the amount of elastic-plastic strength reserve and ductility prior to failure. Moreover, all beams exhibit quite similar post-collapse behaviours (equilibrium path descending branches), regardless of the temperature.

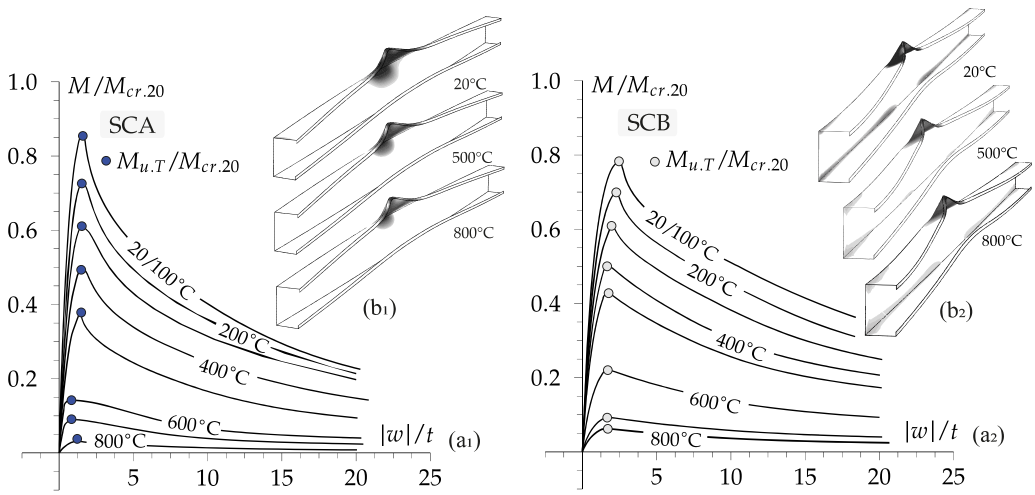

Figure 4. LC18 beams undergoing D-G interaction at elevated temperatures: (a) $M/M_{cr.20}$ vs. $|w|/t$ equilibrium paths and (b) deformed configurations with plastic strain contours for the ($_1$) SCA and ($_2$) SCB beams.

4.2 Failure Moment Data

This section presents and discusses the failure moment data, gathered from the parametric study carried out, that will be used to assess (i) the relevance of the failure moment erosion stemming from D-G interaction at elevated temperatures and (ii) whether the available DSM-based design approaches for LC beams undergoing D-G interaction at room temperature can also be applied to beams at elevated temperatures (after incorporating the modification due to the temperature-dependent CFS constitutive law, of course). This parametric study involves a total of *2944* beams, corresponding to all possible combinations of (i) the 23 geometries given in Table 1, (ii) 2 end support conditions (SCA and SCB), (iii) 8 uniform temperatures (T=20/100-200-300-400-500-600-700-800 ºC) and (iv) 8 room-temperature yield stresses ($f_{y.20}$=150-250-300-350-450-500-550-750 MPa), selected to enable covering wide

D-G slenderness ranges (values comprised between 0.30 and 1.98). Figure 5 shows $M_{u.T}/M_{y.T}$ *vs.* $\lambda_{G.T}$ plots for the various temperatures considered in this work – each of them, concerning both SCA and SCB beams, includes, for comparative purposes, the elastic buckling curve (λ^{-2}). The joint observation of these plots makes it possible to draw the following conclusions:

(i) Regardless of the temperature, the $M_{u.T}/M_{y.T}$ *vs.* $\lambda_{G.T}$ "clouds" follow the trend of "Winter-type" strength curves, even if some "vertical dispersion" exists along the whole slenderness ranges considered – this feature was also observed and discussed in [14], in the context of beams affected by D-G interaction at room temperature.

(ii) In the low-to-moderate slenderness range ($\lambda_{G.T}$<1.20), all the $M_{u.T}/M_{y.T}$ values concerning beams at temperatures T>200 ºC are well below 1.0, in clear contrast with what happens for $T\leq$200 ºC – the differences tend to increase with the temperature and the elastic buckling curves provides a useful reference to quantify these differences. In the moderate and high slenderness ranges ($\lambda_{G.T}$>1.20), this very striking distinction between the $M_{u.T}/M_{y.T}$ values concerning the beams at T>200 ºC and $T\leq$200 ºC ceases to occur.

(iii) Concerning the stocky beams at T>200ºC, note that their $M_{u.T}/M_{y.T}$ values are aligned along clearly descending curves (no "almost plateau" exists, like for $T\leq$200 ºC) that transition fairly smoothly to the curves associated with the beams exhibiting moderate and high slenderness values (invariably located slightly below the elastic buckling curve). Moreover, note that these "stocky beam $M_{u.T}/M_{y.T}$ curves" originate at points ($M_{p.T}$) not ordered according to the temperature value – this stems from the fact that the k_p/k_y values prescribed for CFS in EC3-1.2 are not "logically ordered", since they are equal to 1-0.907-0.786-0.646-<u>0.679</u>-0.6-0.577-<u>0.714</u> for T=20/100-200-300-400-500-600-700-800 ºC (the "out of order" values are underlined).

(iv) Although the results displayed in Fig. 5 provide promising indications concerning the possibility of developing an efficient (safe and accurate) DSM-based design approach to predict D-G interactive failure moments of simply supported CFS LC beams under elevated temperatures, they also clearly show that the failure moment predictions for beams at T>200 ºC and $T\leq$200 ºC must be handled separately in the low-to-moderate slenderness range (at least when the EC3-based CFS constitutive model is adopted). The quantification of these qualitative assertions is addressed in the next section.

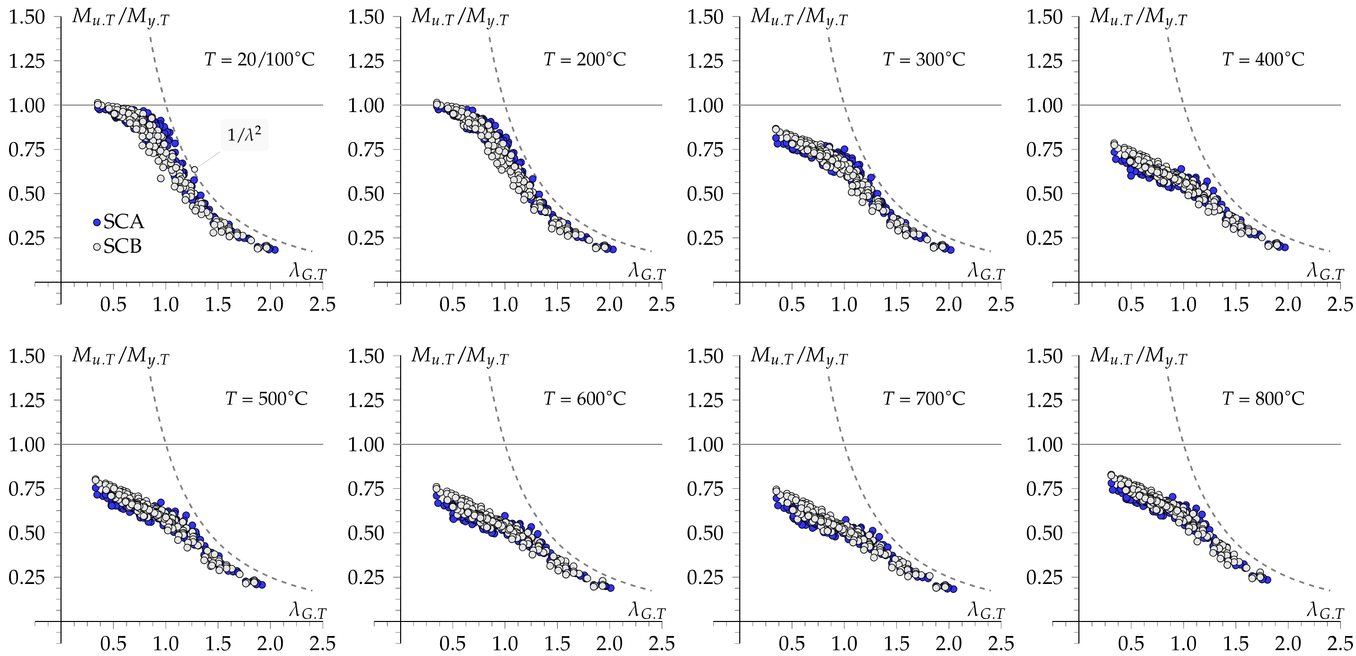

Figure 5. $M_{uT}/M_{y.T}$ *vs.* $\lambda_{G.T}$ values concerning all the SCA and SCB LC beams under elevated temperatures analysed in this work and elastic buckling curves (T=20/100-800 ºC).

5 DSM-BASED DESIGN AT ELEVATED TEMPERATURES

This section addresses the adequacy of the available DSM-based strength curves (appropriately modified to reflect the temperature effects) to predict the numerical D-G interactive failure moments obtained in this work, concerning CFS simply supported LC beams with the two support conditions considered (SCA and SCB). In particular, it is intended to assess (i) the relevance of the failure moments erosion caused by the D-G interaction and (ii) whether the failure moment prediction qualities provided by the available DSM-design approaches specifically developed to handle D-G interaction (M_{nDG} and M_{nGD} [14]) are affected by the temperature effects. The approach followed in this work has already been (partially) explored by the authors [18,23] (among others), in the context of CFS beams and columns failing in pure D modes – it consists of modifying the expressions providing the DSM-based strength curves developed for room temperature, in order to account for the influence of the temperature on the values of the critical buckling, yield and plastic moments. This influence is felt through the Young's modulus and yield stress values, which are progressively eroded as the temperature increases – by changing E and f_y, M_{crD}, M_{crG}, M_y, M_p become $M_{crD.T}$, $M_{crG.T}$, $M_{y.T}$, $M_{p.T}$ (and λ_D, λ_G, λ_{DG}, λ_{GD} become $\lambda_{D.T}$, $\lambda_{G.T}$, $\lambda_{DG.T}$, $\lambda_{GD.T}$).

In order to assess the relevance of D-G interaction in eroding the SCA and SCB beam failure moments, at elevated temperatures, Figs. 6 and 7 show the $M_{u.T}/M_{n.D.T}$ *vs.* $\lambda_{D.T}$ and $M_{u.T}/M_{n.G.T}$ *vs.* $\lambda_{G.T}$ plots for all the beams analysed – they include also the corresponding statistical indicators (averages, standard deviations and minimum/maximum values),

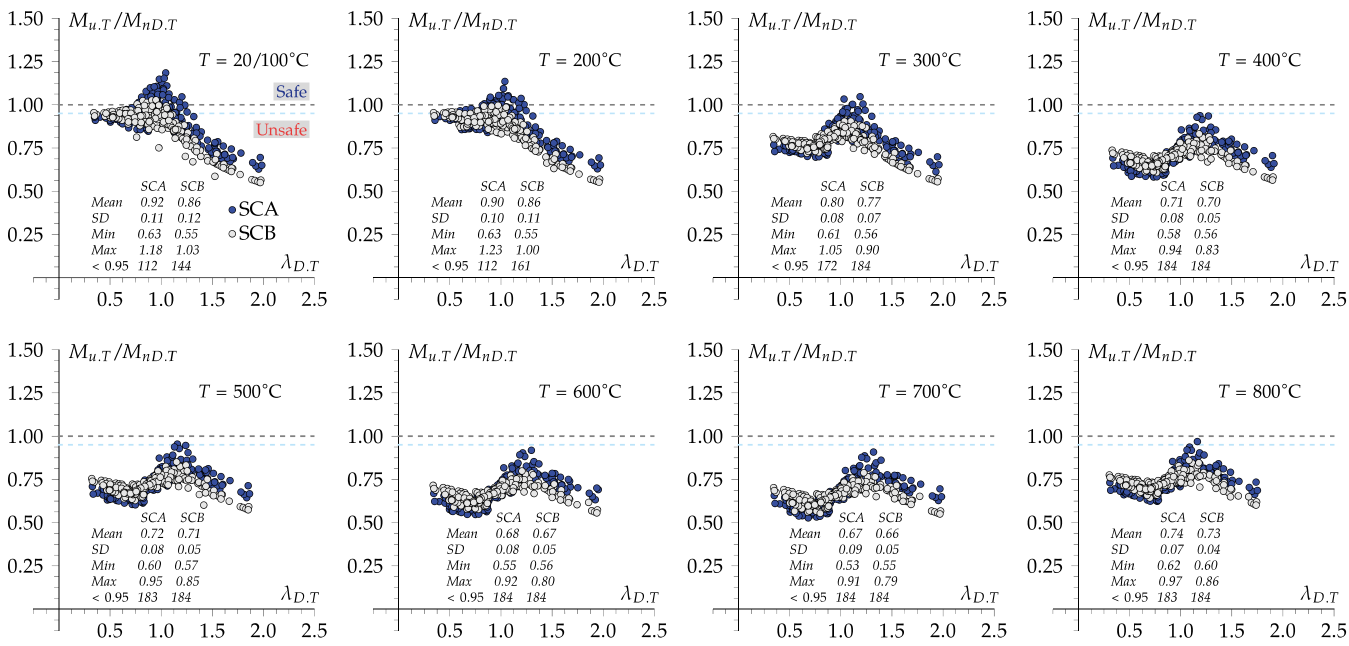

Figure 6. $M_{u.T}/M_{n.D.T}$ *vs.* $\lambda_{D.T}$ plots for all the LC SCA and SCB beams analysed in this work (T=20/100-800 ºC).

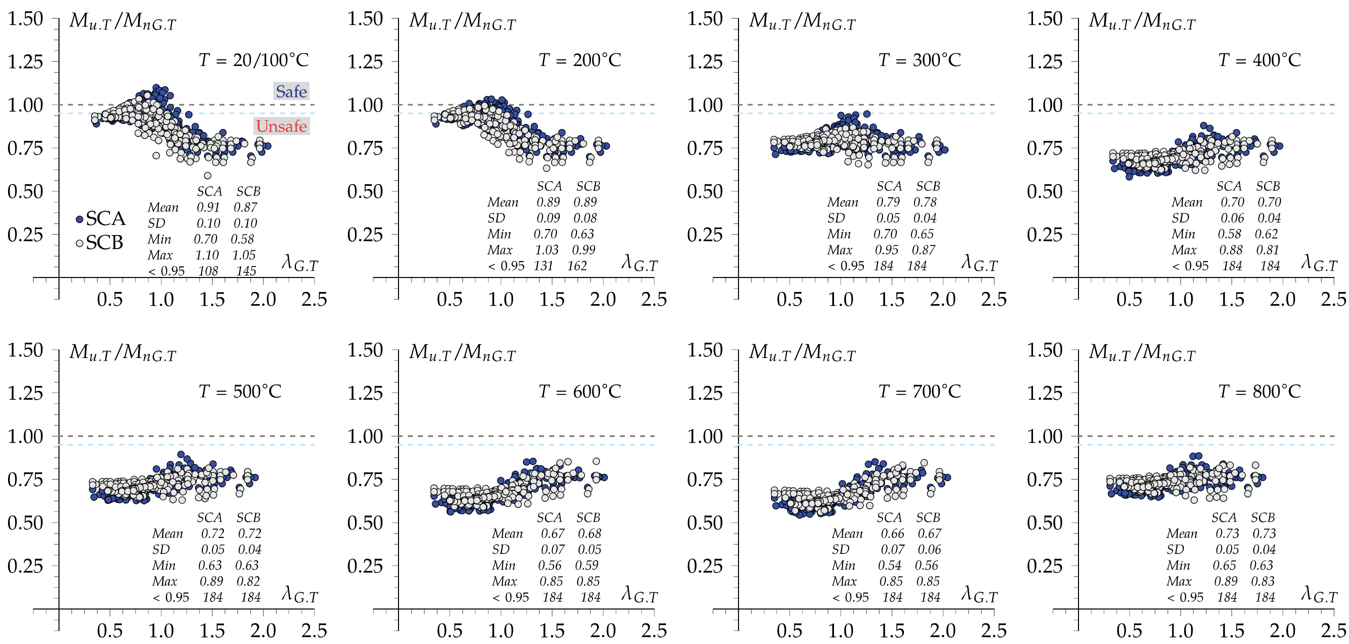

Figure 7. $M_{u.T}/M_{nG.T}$ *vs.* $\lambda_{G.T}$ plots for all the SCA and SCB LC beams analysed in this work (T=20/100-800 ºC).

as well as the numbers of "clearly unsafe" failure moment estimates (in the sense that $M_{u.T}/M_{n.D.T}$ <0.95 or $M_{u.T}/M_{n.G.T}$ <0.95). The observation of the results presented in these two figures prompts the following remarks:

(i) First of all, it should be mentioned that the $M_{nD.T}$ and $M_{nG.T}$ strength curves provide qualitatively very similar failure moment prediction qualities for the SCA and SCB LC beams (naturally, there exist some quantitative differences). Therefore, the contents of the items below, concerning the $M_{nD.T}$ values, apply equally to the $M_{nG.T}$ ones – in addition, they are valid for the beams with both support conditions, even if the number of safe failure moment estimates is slightly larger for the SCA beams.

(ii) For T≤200ºC, the $M_{nD.T}$ values provide only failure moment underestimations for a few beams with moderate slenderness ($0.8 \leq \lambda_{D.T} \leq 1.20$). As for the remaining beams, while the failure moments of the stockier ones ($\lambda_{D.T} \leq 0.80$) are visible overestimated (even if rarely by large amounts), those of the beams such that $\lambda_{D.T}$>1.20 are all considerably overestimated (this overestimation increases with the slenderness).

(iii) For T>200ºC, virtually all the beam failure moments are overestimated by the $M_{nD.T}$ values – except for a few beam with intermediate slenderness range, the amount of overestimation is invariably quite large.

(iv) The fact that the $M_{nD.T}$ and $M_{nG.T}$ strength curves (modified to account for the temperature effects) overestimate the overwhelming majority of the failure moments obtained in this work provides clear evidence concerning the ultimate strength erosion caused by the presence of D-G interaction also at elevated temperatures. Indeed, the failure moments of the beams experiencing D-G interaction fall well below those exhibited by beams failing in pure D or G modes, regardless of the temperature value.

(v) Despite what was mentioned in the previous item, it should be noted that the failure moment prediction qualities of the above $M_{nD.T}$ and $M_{nG.T}$ strength curves were never validated (numerically) for stocky beams at elevated temperatures – indeed, the investigations reported in [18] (distortional failures) and [16] (global failures) dealt almost exclusively with beams with moderate and high slenderness. Since similar investigations on columns [23,24] revealed sizeable failure load overestimations in the low slenderness range, it is possible that the same occurs for the beams. If this is the case, the failure moment overestimation observed in Figs. 6 and 7, for the stocky beams ($\lambda_{D.T} \leq 0.80$ and $\lambda_{G.T} \leq 0.80$) may be due to a combination of (v_1) erosion due to D-G interaction (at elevated temperatures) and (v_2) inadequacy of the $M_{nD.T}$ and $M_{nG.T}$ strength curves in predicting the stocky beam failure moments at elevated temperatures. Naturally, this issue, currently under investigation by the authors, is also bound to influence the failure moment prediction quality assessment of the $M_{nDG.T}$ and $M_{nGD.T}$ strength curves, which is addressed next.

Following the methodology adopted by Martins *et al.* [14], in the context of beams at room temperature, the failure moment prediction qualities provided by the $M_{nDG.T}$ and $M_{nGD.T}$ strength curves (see Eqs. (2_1) and (2_2)), for the SCA and SCB LC beams considered in this work (all undergoing true D-G interaction at elevated temperatures), are assessed now. Figures 8 and 9 show the $M_{u.T}/M_{n.DG.T}$ *vs.* $\lambda_{G.T}$ and $M_{u.T}/M_{n.GD.T}$ *vs.* $\lambda_{G.T}$ plots for all the beams analysed – note that, for the sake of clarity, the slenderness $\lambda_{G.T}$ replaces its interactive counterparts $\lambda_{DG.T}$ and $\lambda_{GD.T}$ in these plots (the $M_{u.T}/M_{n.DG.T}$ *vs.* $\lambda_{DG.T}$ and $M_{u.T}/M_{n.GD.T}$ *vs.* $\lambda_{GD.T}$ plots are more difficult to interpret). As before, the $M_{u.T}/M_{n.DG.T}$ and $M_{u.T}/M_{n.GD.T}$ statistical indicators and numbers of "clearly unsafe" failure moment estimates are included in the figures. The observation of the results presented in these two figures prompts the following remarks:

(i) Although the failure moment prediction qualities of the $M_{nDG.T}$ and $M_{nGD.T}$ values are qualitatively not too different, the close scrutiny of the corresponding "exact"-to-predicted failure moment ratios clearly shows that the former outperforms the latter. Therefore, the contents of the items below concerning exclusively the $M_{nDG.T}$ values – they are again valid for the SCA and SCB beams, even if, as it would be logical to expect, the number of safe failure moment estimates is, once more, slightly larger for the SCA beams.

(ii) For T≤200ºC, the $M_{nDG.T}$ values provide quite reasonable failure moment predictions, as reflected by the corresponding $M_{u.T}/M_{n.DG.T}$ statistical indicators: (ii_1) 1.03-0.09-0.89-1.31 (SCA beams at T=20/100ºC), (ii_2) 0.99-0.06-0.80-1.15 (SCB beams at T=20/100ºC), (ii_3) 1.02-0.08-0.88-1.25 (SCA beams at T=200ºC) and (ii_4) 0.98-0.06-0.87-1.14 (SCB beams at T=200ºC) – naturally, this conclusion is not surprising for the beams at T=20/100ºC, since it just confirms the findings reported in [14]. Most of the unsafe failure moment estimates concern the stockier beams and the larger failure moment underestimations occur for the beams in the moderate slenderness range ($\lambda_{G.T}$ in the vicinity of 1.0).

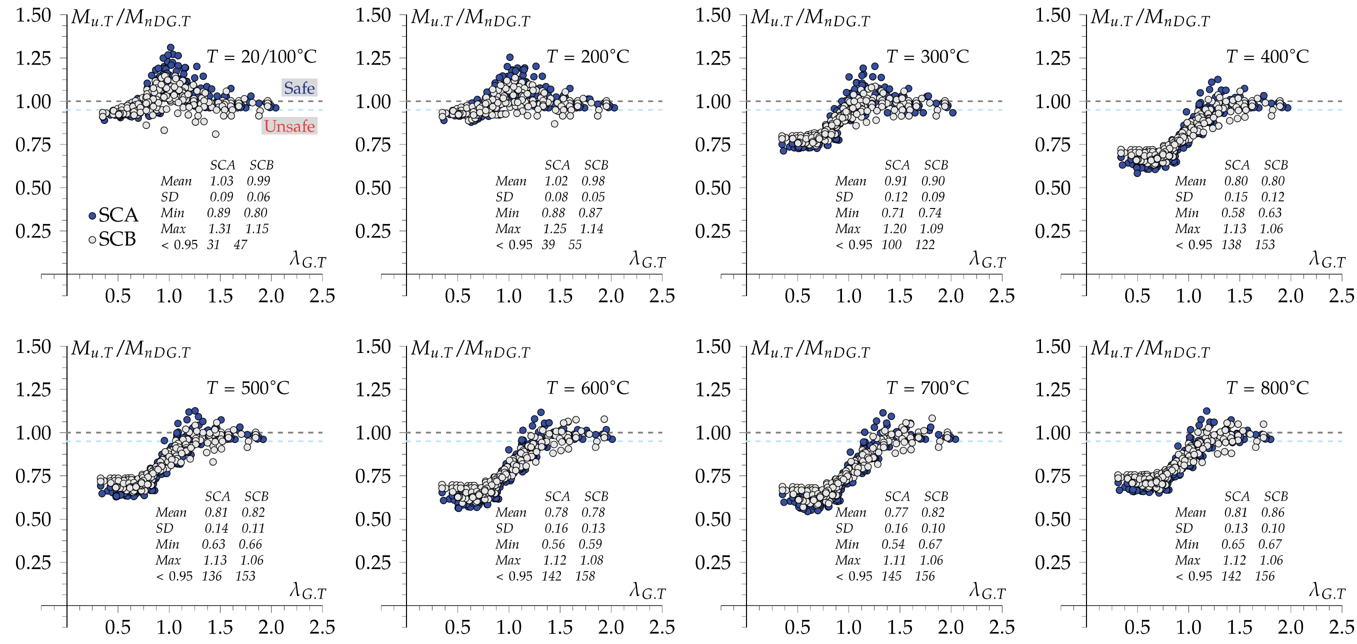

Figure 8. $M_{u.T}/M_{nDG.T}$ *vs.* $\lambda_{G.T}$ plots for all the SCA and SCB LC beams analysed in this work (T=20/100-800 ºC).

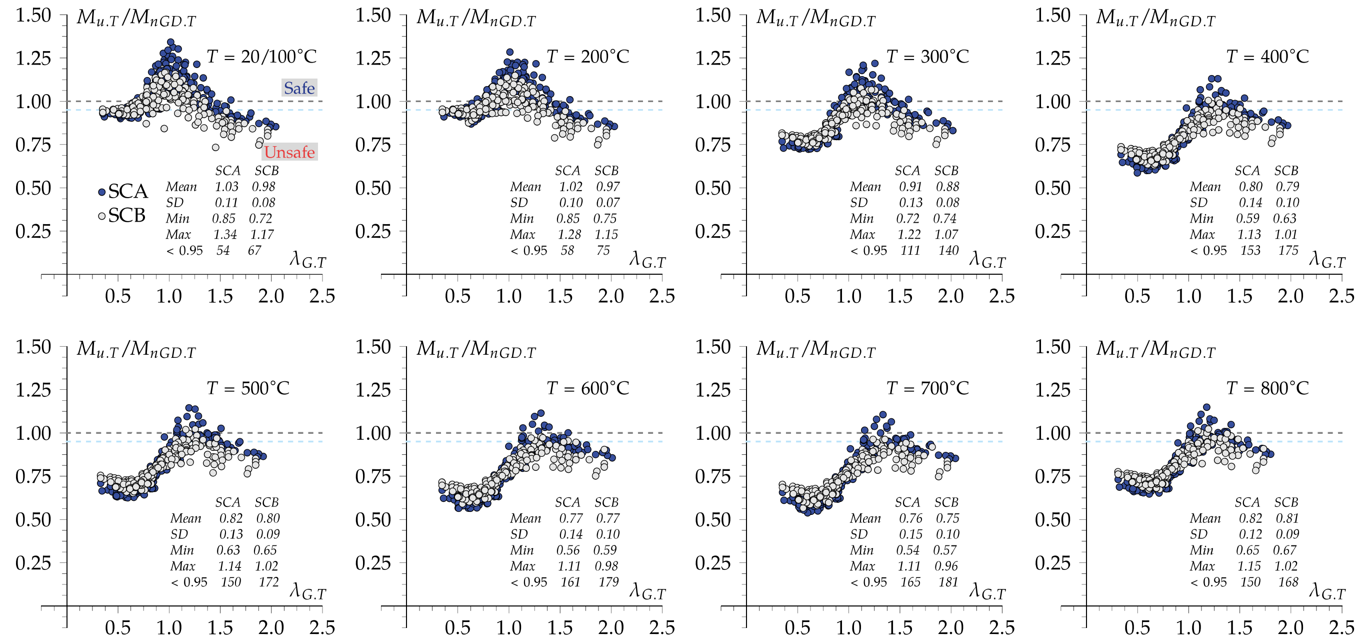

Figure 9. $M_{u.T}/M_{nGD.T}$ *vs.* $\lambda_{G.T}$ plots for all the SCA and SCB LC beams analysed in this work (T=20/100-800 ºC).

(iii) For T>200ºC, the above picture changes drastically and the $M_{nDG.T}$ values cease to provide acceptable failure moment predictions for the beams in the low and moderate slenderness range ($\lambda_{G.T}$≤1.20). The failure moments of the beams with $\lambda_{G.T}$>1.20 continue to be reasonably well predicted by the $M_{nDG.T}$ values, as attested by the corresponding $M_{u.T}/M_{n.DG.T}$ statistical indicators: (iii$_1$) 1.01-0.45-0.93-1.20 (SCA beams at T=300 ºC), (iii$_2$) 0.99-0.43-0.89-1.09 (SCB beams at T=300ºC), (iii$_3$) 0.99-0.43-0.87-1.13 (SCA beams at T=400ºC), (iii$_4$) 0.97-0.41-0.84-1.06 (SCB beams at T=400ºC), (iii$_5$) 0.99-0.42-0.87-1.13 (SCA beams at T=500ºC), (iii$_6$) 0.96-0.40-0.83-1.06 (SCB beams at T=500ºC), (iii$_7$) 0.97-0.44-0.86-1.12 (SCA beams at T=600ºC), (iii$_8$) 0.96-0.42-0.83-1.08 (SCB beams at T=600ºC), (iii$_9$) 0.97-0.44-0.85-1.11 (SCA beams at T=700ºC), (iii$_{10}$) 0.95-0.42-0.82-1.08 (SCB beams at T=700ºC), (iii$_{11}$) 0.99-0.39-0.91-1.07 (SCA beams at T=800ºC) and (iii$_{12}$) 0.97-0.36-0.88-1.06 (SCB beams at T=800ºC). It is worth pointing out how superior these statistical indicators are to those appearing in Fig. 8, concerning the whole sets of beams analysed, thus reflecting the very poor estimation of the failure moments of the beams with $\lambda_{G.T}$≤1.20.

(iv) As anticipated, in the context of the discussion of the results presented in Figs. 6 and 7, there is a fair likelihood that the considerable failure moment overestimation provided by the $M_{nDG.T}$ values for the beams with $\lambda_{G.T}\leq 1.20$ at $T>200\,°C$ stems from the fact that the $M_{nD.T}$ and $M_{nG.T}$ strength curves employed (which consist of Eqs. (1_1) and (1_2), developed for room temperature and only modified to account for the temperature effects) are unable to predict adequately the D and G failures of beams in that low-to-moderate slenderness range and under those (very) elevated temperatures. Only after an adequate prediction of such failures is achieved will it be possible to carry out a truly correct assessment of the $M_{nDG.T}$ failure moment prediction quality.

In the view of the findings reported in the above items, it can just be stated that there are promising indications that the $M_{nDG.T}$ strength curves will provide a good starting point to search for an efficient (safe and reliable) DSM-based design approach to estimate the D-G interactive failure moments of the CFS LC beams at elevated temperatures analysed in this work. In order to confirm (or not) these promising indications, it is indispensable to find DSM-based design curves that predict adequately the D and G failures of CFS beams at elevated temperatures, a task the authors are currently undertaking.

6 CONCLUSION

This paper presented and discussed the available results of an ongoing numerical investigation on the distortional-global (D-G) interactive post-buckling behaviour, ultimate strength and DSM design of CFS simply supported lipped channel beams. After addressing the beam geometry selection (ensuring beams susceptible to "true D-G interaction") and characterising the main features of the beam D-G interactive post-buckling behaviour and strength (adopting the EC3-based temperature-dependent CFS constitutive model), ABAQUS GMNIAs were used to carry out a parametric study, intended to gather a fairly extensive set of D-G interactive failure moments – 2944 beams were analysed, corresponding to all possible combinations of (i) 23 geometries, (ii) two end support conditions (differing mostly in the end cross-section warping restraint), (iii) 8 room-temperature yield stresses, chosen to enable covering wide slenderness ranges, and (iv) 8 uniform temperatures (up to 800 ºC), supposedly caused by fire conditions. The above failure moment data were subsequently used to provide (i) numerical evidence of the occurrence of a visible failure moment erosion stemming from D-G interaction at elevated temperatures and (ii) a first contribution towards the development of an efficient DSM-based design approach to predict beam D-G interactive failure moments at elevated temperatures. Amongst the various findings reported in this work, the following deserve a special mention:

(i) It was clearly shown that the ultimate strength of CFS LC beams is visibly eroded by the presence of D-G interaction also at elevated temperatures, as attested by the fact that both the currently codified $M_{nD.T}$ and $M_{nG.T}$ strength curves (modified to account for the temperature effects) overestimate almost all the failure moments obtained in this work – indeed, they fall well below those concerning beams failing in pure D or G modes.

(ii) After being modified to account for the temperature effects, the NDG DSM-based design approach, developed in the context of beams at room temperature [14], was found to provide quite reasonable failure moment predictions for beams experiencing D-G interaction at $T\leq 200\,°C$, thus extending was already known for beams at room temperature [14] to beams at $T=200\,°C$. Conversely, it was also found that, for $T>200\,°C$, the $M_{nDG.T}$ values cease to provide acceptable failure moment predictions for the beams in the low-to-moderate slenderness range (substantial failure moment overestimations were observed), even if the failure moments of the remaining beams continue to be reasonably well predicted.

(iii) There is a fair likelihood that the substantial failure moment overestimation mentioned in the previous item stems from the fact that the $M_{nD.T}$ and $M_{nG.T}$ strength curves employed are unable to predict adequately the D and G failures of beams in the low-to-moderate slenderness range at significantly elevated temperatures. Only after an adequate prediction of such failures is achieved will it be possible to carry out a truly correct assessment of the $M_{nDG.T}$ failure moment prediction quality – this issue is currently under investigation by the authors.

ACKOWLEDGMENTS

The first two authors gratefully acknowledge the financial support of the Brazilian institutions (i) CAPES (Coordenação de Aperfeiçoamento de Pessoal de Nível Superior) – Finance Code 001, (ii) CNPq (Conselho Nacional de Desenvolvimento Científico e Tecnológico) – Finance Codes 141021/2020-9 and 13197/2020-2, and (iii) FAPERJ (Fundação Carlos Chagas Filho de Amparo à Pesquisa do Estado do Rio de Janeiro) – Finance Code E-26/200.959/2021 (second author). The third author gratefully acknowledges the financial support of FCT (Fundação para a Ciência e a Tecnologia – Portugal), through project UIDB/04625/2020 (funding the research unit CERIS).

REFERENCES

1. Camotim D, Dinis PB, Martins AD. Direct Strength Method (DSM) – a general approach for the design of cold-formed steel structures, *Recent Trends in Cold-Formed Steel Construction*, C. Yu (ed.), Woodhead Publishing (Series in Civil and Structural Engineering), Amsterdam, 69-105, 2016. https://doi.org/10.1016/B978-0-08-100160-8.00004-9
2. Schafer BW. Advances in the Direct Strength Method of cold-formed steel design, *Thin-Walled Struct*, **140**(July), 533-541, 2019. https://doi.org/10.1016/j.tws.2019.03.001
3. AISI (American Iron and Steel Institute). *North American Specification (NAS) for the Design of Cold-Formed Steel Structural Members* (2016 edition reaffirmed in 2020), AISI-S100-16 w/S3-22, Washington DC, 2022.
4. AS/NZS (Standards of Australia and Standards of New Zealand). Cold-Formed Steel Structures (AS/NZS 4600:2018 – 3rd ed.), Sydney-Wellington, 2018.
5. ABNT (Brazilian Standards Association). Brazilian Standard on Design of Cold-Formed Steel Structures (ABNT NBR 14762:2010), Rio de Janeiro, 2010. (Portuguese).
6. Martins AD, Landesmann A, Camotim D, Dinis P B. Distortional failure of cold-formed steel beams under uniform bending: Behaviour, strength and DSM design. *Thin-Walled Structures*, **118**(September), 196-213, 2017. https://doi.org/10.1016/j.tws.2017.04.009.
7. Put BM, Pi Y-L Trahair NS. Lateral buckling tests on cold-formed channel beams, *Journal of Structural Engineering* (ASCE), **125**(5), 532-539, 1999. https://doi.org/10.1061/(ASCE)0733-9445(1999)125:5(532)
8. Pi Y-L, Put BM, Trahair NS. Lateral buckling strengths of cold-formed Z-section beams, *Thin-Walled Structures*, **34**(1), 65-93, 1999. https://doi.org/10.1016/S0263-8231(99)00004-X
9. Yu C, Schafer BW. Distortional buckling tests on cold-formed steel beams, *Journal of Structural Engineering* (ASCE), **132**(4), 515-528, 2006. https://doi.org/10.1061/(ASCE)0733-9445(2006)132:4(515)
10. Yu C, Schafer BW. Simulation of cold-formed steel beams in local and distortional buckling with applications to the direct strength method, *Journal of Constructional Steel Research*, **63**(5), 581-590, 2007.https://doi.org/10.1016/j.jcsr.2006.07.008
11. Niu S, Rasmussen K, Fan F. Distortional-global interaction buckling of stainless steel C-beams: Part I – Experimental investigation, *Journal of Constructional Steel Research*, **96**(May), 127-139, 2014. https://doi.org/10.1016/j.jcsr.2014.01.007
12. Niu S, Rasmussen K, Fan F. Distortional–global interaction buckling of stainless steel C-beams: Part II—Numerical study and design, *Journal of Constructional Steel Research*, **96**(May), 40-53, 2014. https://doi.org/10.1016/j.jcsr.2014.01.008
13. Martins AD, Camotim D, Gonçalves R, Dinis PB. GBT-based assessment of the mechanics of distortional-global interaction in thin-walled lipped channel beams, *Thin-Walled Structures*, **124**(March), 32-47, 2018. https://doi.org/10.1016/j.tws.2017.11.036
14. Martins AD, Camotim D, Dinis PB. Distortional-global interaction in lipped channel and zed-section beams: Strength, relevance and DSM design, *Thin-Walled Structures*, **129**(August), 289-308, 2018. https://doi.org/10.1016/j.tws.2018.02.015
15. Schafer BW. Local, distortional and Euler buckling in thin-walled columns, *Journal of Structural Engineering* (ASCE), **128**(3), 288-299, 2002. https://doi.org/10.1061/(ASCE)0733-9445(2002)128:3(289)
16. Kankanamge ND, Mahendran M. Behaviour and design of cold-formed steel beams subject to lateral–torsional buckling at elevated temperatures, *Thin-Walled Structures*, **61**(December), 213-228, 2012. https://doi.org/10.1016/j.tws.2012.05.009
17. Laím L, Rodrigues JPC, Craveiro HD. Flexural behaviour of axially and rotationally restrained cold-formed steel beams subjected to fire, *Thin-Walled Structures*, **98A**(January), 39-47, 2016. https://doi.org/10.1016/j.tws.2015.03.010
18. Landesmann A, Camotim D. Distortional failure and DSM design of cold-formed steel lipped channel beams under elevated temperatures, *Thin-Walled Structures*, **98A**(January), 75-93, 2016. http://dx.doi.org/10.1016/j.tws.2015.06.004
19. Bebiano R, Camotim D, Gonçalves R. GBTUL 2.0– A second-generation code for the GBT-based buckling and vibration analysis of thin-walled members. *Thin-Walled Structures*, **124**(March), 235-257, 2018. https://doi.org/10.1016/j.tws.2017.12.002
20. CEN (Comité Européen de Normalisation). *Eurocode 3: Design of Steel Structures – Part 1.2: General Rules – Structural Fire Design*, Brussels, 2005.
21. Simulia Inc. ABAQUS Standard (version 6.14-1), 2014.
22. Arrais F, Lopes N, Real PV. Fire design of slender cold-formed lipped channel and sigma section members with uniform temperature under compression, *Fire Safety Journal*, **122**(June), paper 103340 (17 pages), 2021. https://doi.org/10.1016/j.firesaf.2021.103340
23. Landesmann A, Camotim D, Silva FCM. DSM design of cold-formed steel columns failing in distortional modes at elevated temperatures, *International Journal of Steel Structures*, **19**(3), 1023-1041, 2019. https://doi.org/10.1007/s13296-018-0184-x
24. Bicelli AA, Landesmann A, Camotim D, Dinis PB. Flexural-torsional failure and DSM design of fixed-ended cold-formed steel columns at elevated temperatures, *Thin-Walled Structures*, **169**(December), paper 108362 (16 pages), 2021. https://doi.org/10.1016/j.tws.2021.108362

NUMERICAL STUDIES ON POST-FIRE RESIDUAL CAPACITY OF AXIALLY RESTRAINED HIGH STRENGTH STEEL COLUMNS UNDER ECCENTRIC COMPRESSION

Lin-Xin Song[1], Guo-Qiang Li[2]

ABSTRACT

For steel structures, steel columns are the critical load-bearing components and they are usually restrained by other components connected to them. At and after fire, the restraints will induce the deflection and stress in columns, and the mechanical properties of high strength steels may reduce significantly. These two aspects have further effects on the post-fire residual capacity of the restrained columns. This paper presents the details of numerical studies on post-fire residual capacity of axially restrained high strength steel columns under eccentric compression, based on a verified finite element model built in ABAQUS. It can be concluded that the maximum temperature experienced during the fire, axially restraint stiffness ratio, eccentricity, load ratio and slenderness ratio have significant effects on the post-fire residual capacity of axially restrained high strength steel columns.

Keywords: axially restrained; high strength steel columns; post-fire residual capacity; eccentric compression; numerical analysis

1 INTRODUCTION

High strength structural steels have been increasingly applied in construction industry, due to great advantages in terms of safety, reliability, economy and environmental benefits. For steel structures, steel columns are the critical load-bearing components and they are usually restrained by other components connected to them. At and after fire, the restraints will induce the deflection and stress in columns, and the mechanical properties of the steel may reduce significantly, especially for high strength steels. These two aspects have further effects on the ultimate bearing capacity of restrained steel columns after fire, which is named post-fire residual capacity. Therefore, identifying the post-fire residual capacity of restrained high strength steel columns is important for evaluating the safety of continuing use of the high strength steel structures after fire.

Up to now, studies mainly focused on the behaviour of restrained steel columns at fire. It can be found that after buckling at elevated temperature, the post-buckling performance of restrained steel columns can still be used [1-4]. For the post-fire behaviour of steel columns, Liu [5] conducted experimental and numerical studies on non-restrained Q460 high strength steel columns and proposed a simplified method to calculate the stability coefficient of axial compression columns after fire, considering cross-sectional shape, cooling method, maximum temperature experienced during the fire and slenderness ratio. Wang et al. [6] conducted experimental studies on non-restrained, symmetrically restrained and asymmetrically restrained Q345 steel columns to investigate the post-fire axial compression behaviour and found that different restraints resulted in columns with different post-fire strain and different overall stiffness before failure. Li et al. [7] conducted experimental studies on axially restrained Q550 high strength steel

[1] Ph.D. Candidate. College of Civil Engineering, Tongji University, Shanghai, China
e-mail: linlinslx@126.com
[2] Professor. State Key Laboratory of Disaster Reduction in Civil Engineering, Tongji University, Shanghai, China
e-mail: gqli@tongji.edu.cn
https://doi.org/10.6084/m9.figshare.22202422

columns under axial compression to investigate the post-fire residual capacity, and a simplified method was proposed based on parametric study to calculate the post-fire residual capacity of axially restrained high strength steel columns under axial compression, considering maximum temperature, load ratio, axial restrained stiffness ratio, slenderness ratio and steel grade.

Since few studies have been conducted on the post-fire residual capacity of restrained high strength steel columns, it is necessary to fill the research gap. In general, columns in high strength steel structures are eccentrically compressed and axially and rotationally restrained by adjacent components. It has been found that rotational restraints can increase the post-fire residual capacity of high strength steel columns because they can decrease the slenderness of columns [8]. This means that the effect of rotational restraints on post-fire residual capacity can be studied by identifying the effect of slenderness ratios of columns with only axial restraints. Therefore, this paper presents the details of numerical studies on post-fire residual capacity of axially restrained high strength steel columns under eccentric compression.

2 NUMERICAL MODEL

2.1 Basic information of the numerical model

A numerical model is built in ABAQUS.

The cross section of high strength steel column is H200×180×14×10(mm), the width thickness ratio and height thickness ratio of which can avoid local buckling. The longitudinal length of the column is changed according to slenderness ratios. The shape of the initial geometric imperfection is taken as the first-order buckling mode of the column, and the value is taken as 1/1000 of the column length. The eccentric direction is determined on the basis that the bending direction caused by eccentricity is consistent with the initial geometric imperfection. The welding residual stress is introduced based on the model proposed by Ban et al. [9]. The mechanical properties are based on QT Q690 high strength steel. At ambient temperature, the yield strength is 803MPa and the elastic modulus is 206000MPa by measurement. The mechanical properties at and after fire are calculated according to the predictive formulas proposed by Huang et al. [10] and Li et al. [11] respectively.

Shell elements S4R are assigned to the column. The column is divided into 50 units in the length direction, 20 units in the cross section of the web and 10 units in the cross section of each side of the flange. The boundary conditions of the column are set as hinge. Spring elements SPRING1 are set to simulate axial restraints. Four main analysis steps are set up to simulate the process of applying dead load, heating, cooling and static load until failure.

2.2 Validation of the numerical model

A numerical model is established in accordance with the experimental specimens [7] using the above method. In the experiment, the column specimens are axially restrained and axially compressed. The column HC-1 was loaded until failure at ambient temperature without being heated, while the columns HC-2 and HC-3 were loaded until failure after being heated to pre-selected temperatures and then cooling down to ambient temperature. The experimental and numerical results on axial displacement-temperature curve and mid-height lateral displacement-temperature curve are presented in Figure 1 and Figure 2 respectively. The experimental and numerical results on buckling temperature and ultimate bearing capacity are listed in Table 1.

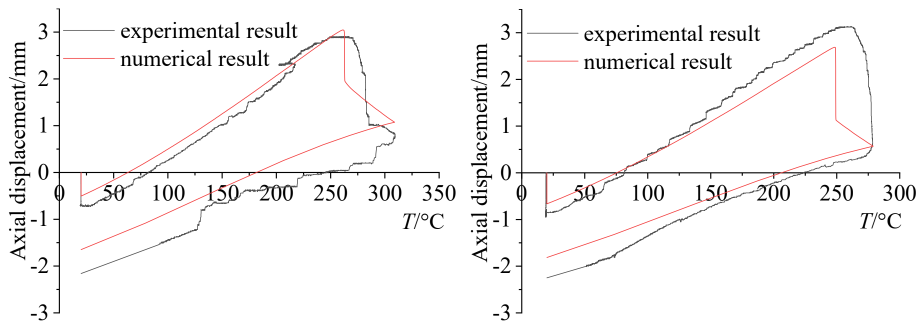

(a) HC-2 (b) HC-3

Figure 1. The experimental and numerical results on axial displacement-temperature curve

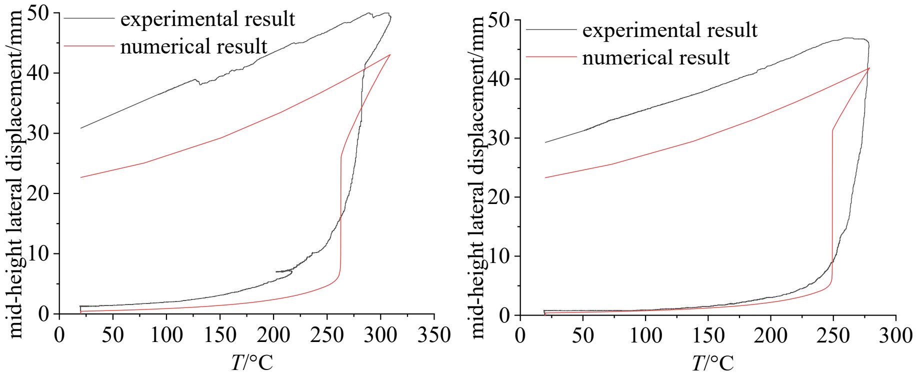

(a) HC-2 (b) HC-3

Figure 2. The experimental and numerical results on mid-height lateral displacement-temperature curve

Table 1 The experimental and numerical results on buckling temperature and ultimate bearing capacity

Specimen no.	buckling temperature /°C			ultimate bearing capacity/kN		
	Experimental	Numerical	Error	Experimental	Numerical	Error
HC-1	-	-	-	723	719	-0.56%
HC-2	268	261	-2.61%	385	381	-1.12%
HC-3	252	248	-1.59%	398	412	3.51%

As it can be seen, the curves obtained from the numerical model accurately reflects the displacement changes of the columns during the experimental heating and cooling process. Compared with the experimental results, the absolute value of errors of the buckling temperature and ultimate bearing capacity of the columns obtained from the numerical model are within 4%. Therefore, the numerical model is validated.

3 PARAMETRIC ANALYSIS

The validated model is used to conduct parametric studies on post-fire residual capacity of axially restrained QT Q690 high strength steel columns under eccentric compression. The residual capacity factor, α, calculated as the ratio of the post-fire residual capacity to the ultimate bearing capacity at ambient temperature without being heated, is used to indicate the degeneration degree of the ultimate bearing capacity after fire. Five influencing factors are considered:

1. Maximum temperature experienced during the fire, T, is considered by relative temperature factor, η. $\eta=(T-T_{bu})/(T_{cr}-T_{bu})$. The buckling temperature, T_{bu}, is the temperature at which restrained columns reach the maximum axial force in the heating phase, as shown in Figure 3. The critical temperature, T_{cr}, is the temperature at which the axial force in the heating phase restored to the initial value at ambient temperature, as shown in Figure 3. The value of η is considered in the range from -0.05 to 1, i.e., the maximum temperature is considered in the range from close to T_{bu} to T_{cr}.
2. Axial restrained stiffness ratio, β_l, in the range from 0.1 to 10, is calculated as the ratio of the axial stiffness of the restraint to the axial stiffness of the column at ambient temperature without being heated.
3. Eccentricity, ε, in the range from 0 to 20, is considered around the weak axis. When columns are axially compressed, ε=0. When columns are eccentrically compressed, ε>0.
4. Load ratio, ρ, in the range from 0.1 to 0.9.
5. Slenderness ratio, λ, in the range from 30 to 150.

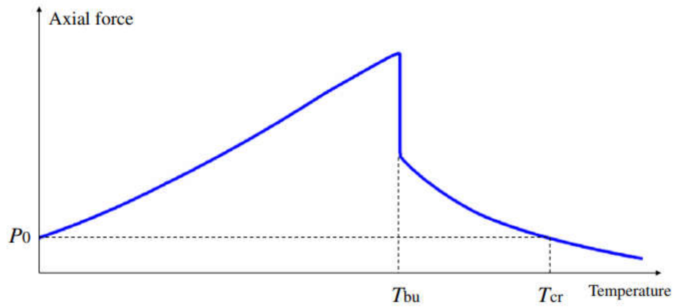

Figure 3. Typical axial force-temperature curve of restrained steel columns at elevated temperature [7]

3.1 Effect of maximum temperature

Take the cases of λ=70, ρ=0.5 as examples, the α-η curves with different eccentricity for the case of β_l=0.3 and β_l=1 are shown in Figure 4.

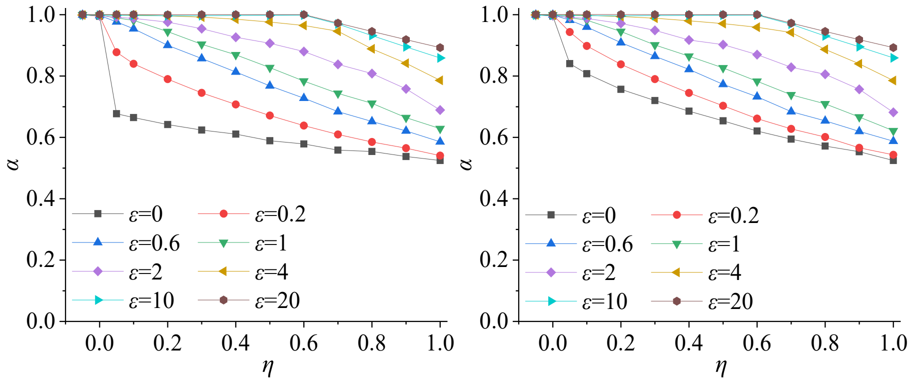

(a) λ=70, ρ=0.5, β_l=0.3 (b) λ=70, ρ=0.5, β_l=1

Figure 4. α-η curves with different eccentricity

It can be found that when $\eta < 0$ ($T < T_{bu}$), the residual capacity factor is close to 1. Therefore, fire process has little effect on the residual capacity when the maximum temperature experienced during the fire is below the buckling temperature. The reason is that columns experience elastic deflection before buckling during the heating and cooling process, which will recover after cooling down to ambient temperature. In addition, when the maximum temperature is lower than the buckling temperature, which is generally less than 600°C for restrained columns, the mechanical properties of high strength steel after fire can almost recover to the original values without being heated. When η=0 (T=T_{bu}), columns reach the critical buckling state and the residual capacity factor may begin to decrease. When 0<η<1 (T_{bu}<T<T_{cr}), the residual capacity factor decreases as the maximum temperature rises. This is because when the maximum temperature rises, the plastic deflection develops and mechanical properties of high strength steel reduce, thereby the residual capacity reduces. The reduction law of the residual capacity factor with the increase of maximum temperature is different among columns for different cases. When η=1 (T=T_{cr}), columns reach the critical failure state. If the temperature is higher, columns will be failure. Therefore, the critical temperature is the maximum temperature considered in this study.

Since η=0 (T=T_{bu}) and η=1 (T=T_{cr}) correspond to critical buckling state and critical failure state respectively, and they correspond to the maximum and minimum residual capacity factor respectively, the following analysis will focus on the influence of axial restrained stiffness ratio, eccentricity, load ratio and slenderness ratio for cases of η=0 (T=T_{bu}) and η=1 (T=T_{cr}).

3.2 Effect of axial restrained stiffness ratio

Take the cases of λ=70, ρ=0.5 as examples, the α-β_l curves with different eccentricity for the case of η=0 and η=1 are shown in Figure 5.

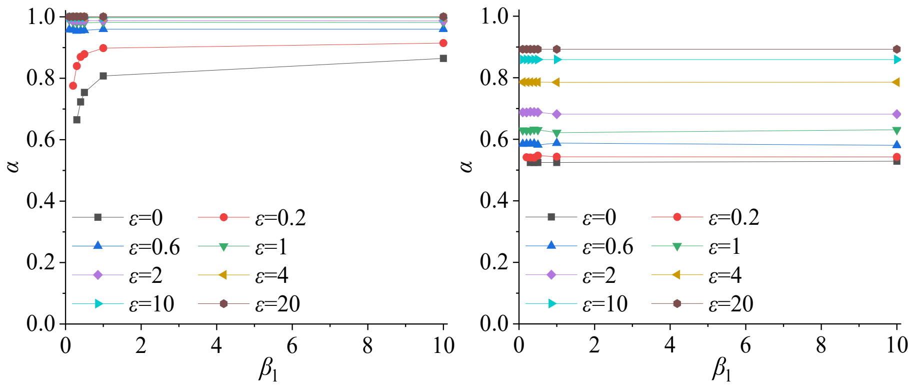

(a) λ=70, ρ=0.5, η=0 (b) λ=70, ρ=0.5, η=1

Figure 5. α-β_l curves with different eccentricity

When η=0 (T=T_{bu}), the residual capacity factor increases as the axial restrained stiffness ratio increases. The reason is that when the axial restrained stiffness increases, the thermal stress induced by unfree thermal expansion in the column will also increase, thereby the buckling state occurs earlier in the heating process, i.e., buckling temperature will be smaller. Therefore, the plastic deflection and reduction of mechanical properties of the high strength steel become less, leading to less reduction on residual capacity. But when the eccentricity exceeds 0.6, the effect of the axial restrained stiffness ratio can be ignored. It can be found that when $\varepsilon \geq 0.6$ and β_l=0.1, the residual capacity factor is close to 1, which has little room to increase even if the axial restrained stiffness ratio increases. When η=1 (T=T_{cr}), the axial restrained stiffness ratio has little effect on the residual capacity factor.

3.3 Effect of eccentricity

Take the cases of λ=70, ρ=0.5 as examples, the α-ε curves with different axial restrained stiffness ratio for the case of η=0 and η=1 are shown in Figure 6.

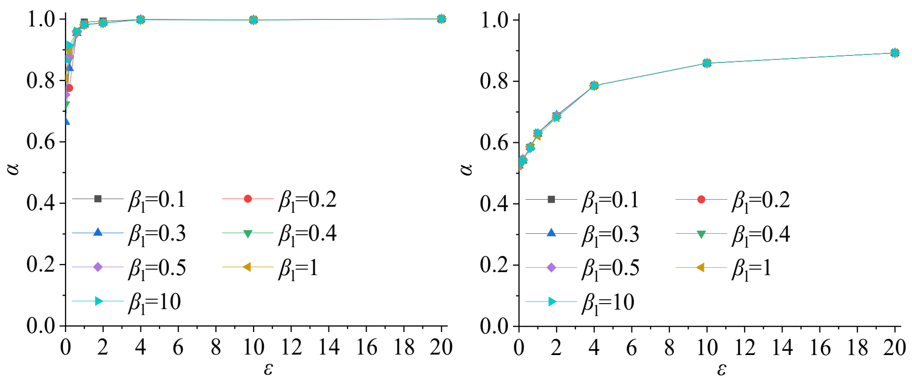

(a) λ=70, ρ=0.5, η=0 (b) λ=70, ρ=0.5, η=1

Figure 6. α-ε curves with different axial restrained stiffness ratio

When η=0 (T=T_{bu}) and η=1 (T=T_{cr}), the residual capacity factor increases as the eccentricity increases. And for the same cases, the reduction degree of residual capacity of columns under axial compression is more severe than that under eccentric compression. This means that the effect of fire process on residual capacity is less than that of eccentricity. When η=0 (T=T_{bu}) and ε>1, the effect of eccentricity can be ignored. In addition, the discussion about the axial restrained stiffness ratio in section 3.3 can also be obtained from Figure 6.

3.4 Effect of load ratio

Take the cases of λ=70 as examples, the α-ρ curves with different axial restrained stiffness ratio for the case of ε=0, ε=20, η=0 and η=1 are shown in Figure 7.

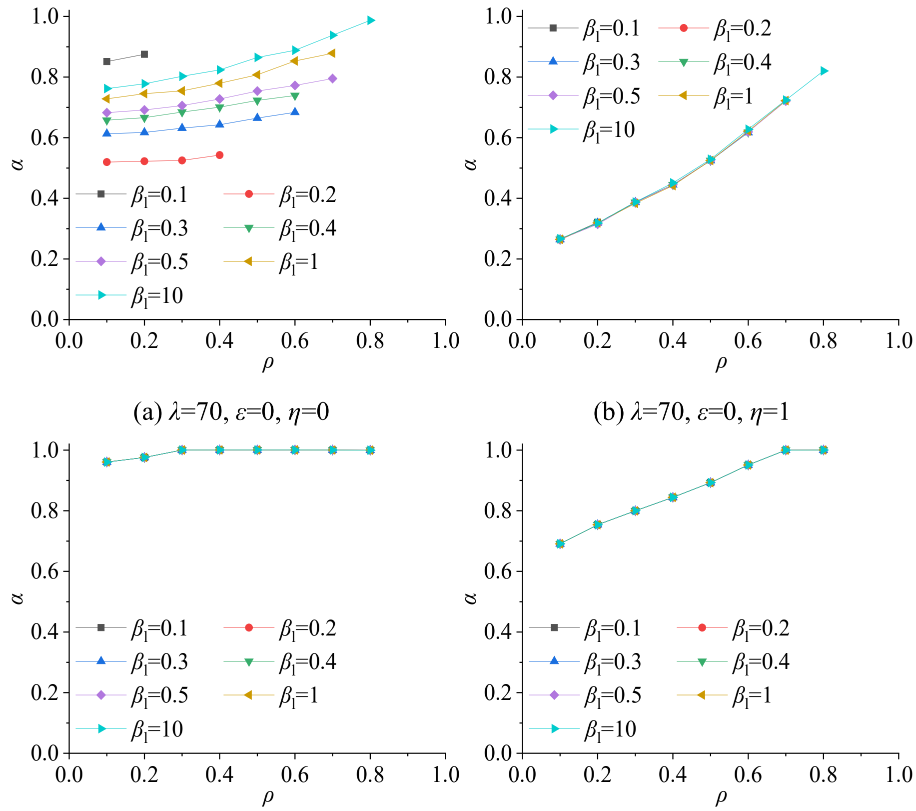

(a) λ=70, ε=0, η=0 (b) λ=70, ε=0, η=1

(c) λ=70, ε=20, η=0 (d) λ=70, ε=20, η=1

Figure 7. α-ρ curves with different axial restrained stiffness ratio

The increase of load ratio leads to the increase of residual capacity factor. When η=0 (T=T_{bu}), the effect is limited and can be ignored when $\varepsilon \geq 4$, while the effect is significant when η=1 (T=T_{cr}). This is because when the load ratio increases, the critical failure state that the axial force of the restrained column restores to the initial value will occur earlier during the heating process, i.e., critical temperature will be smaller. Therefore, the plastic deflection and reduction of mechanical properties of high strength steel become less, leading to less reduction on residual capacity. In addition, the discussion about the axial restrained stiffness ratio in section 3.3 can also be obtained from Figure 7.

3.5 Effect of slenderness ratio

Take the cases of β_l=0.3 as examples, the α-λ curves with different load ratio for the case of ε=0, ε=20, η=0 and η=1 are shown in Figure 8.

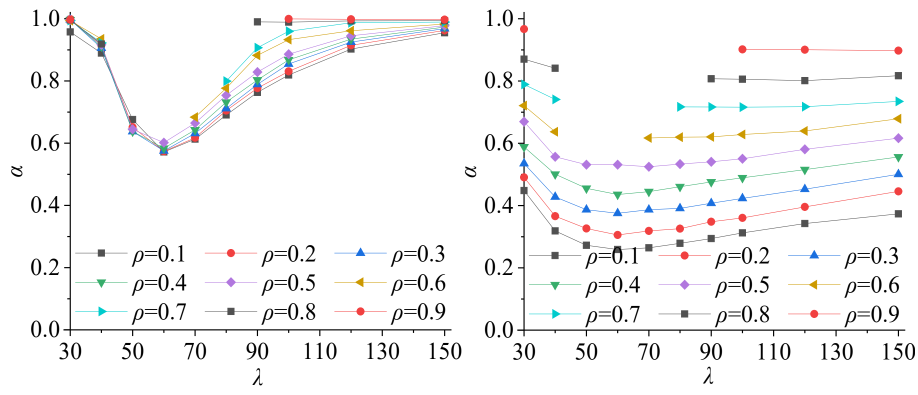

(a) β_l=0.3, ε=0, η=0 (b) β_l=0.3, ε=0, η=1

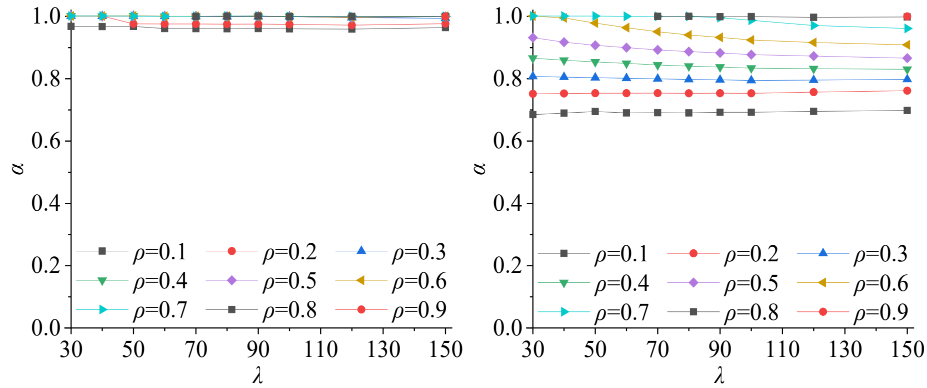

(c) β_l=0.3, ε=20, η=0 (d) β_l=0.3, ε=20, η=1

Figure 8. α-λ curves with different load ratio

For columns under axial compression (ε=0), the residual capacity factor decreases before increases as the slenderness ratio increases when η=0 (T=T_{bu}) and η=1 (T=T_{cr}). It reaches minimum when λ=60. For columns under eccentric compression (ε>0), the slenderness ratio has little effect on the residual capacity when η=0 (T=T_{bu}), while as the slenderness ratio increases, the residual capacity factor decreases before tends to remain unchanged when η=1 (T=T_{cr}). In addition, the discussion about the load ratio in section 3.4 can also be obtained from Figure 8.

4 CONCLUSIONS

The numerical analysis on post-fire residual capacity of axially restrained high strength steel columns under eccentric compression is presented in this paper. The conclusions from this study may be summarized as follows:

1. The maximum temperature experienced during the fire is the key influencing factor for the post-fire residual capacity of axially restrained high strength steel columns. When T<T_{bu}, the fire has little effect on the residual capacity. When T_{bu}≤T≤T_{cr}, the residual capacity decreases as the maximum temperature rises. The reduction law of residual capacity with the increase of maximum temperature is different among columns with different axial restrained stiffness ratio, eccentricity, load ratio and slenderness ratio.
2. The increase of axial restrained stiffness ratio leads to the increase of residual capacity factor when T=T_{bu} and ε<0.6, while it has little effect when T=T_{cr}.
3. For the same cases, the reduction degree of residual capacity of columns under axial compression is more severe than that under eccentric compression. The increase of eccentricity leads to the increase of residual capacity factor. The effect cannot be ignored except when T=T_{bu} and ε>1.
4. The increase of load ratio leads to the increase of residual capacity factor. When T=T_{bu}, the effect is limited and can be ignored when ε≥4, while the effect is significant when T=T_{cr}.
5. For columns under axial compression, as the slenderness ratio increases, the residual capacity factor decreases before increases, and reaches the minimum when λ=60. For columns under eccentric compression, the slenderness ratio has little effect on the residual capacity when T=T_{bu}, while as the slenderness ratio increases, the residual capacity factor decreases before tends to remain unchanged when T=T_{cr}.

ACKNOWLEDGMENT

The research work presented in this paper is supported by the National Natural Science Foundation of China through the contract 51878506. The support is gratefully acknowledged.

REFERENCES

1. Wang Y.C., Moore D. B. Effect of Thermal Restraint on Column Behaviour in a Frame. Fire Safety Science, 4, 1055-1066 (1994).
2. Lennon T., Moore D. The Natural Fire Safety Concept — Full-Scale Tests at Cardington. Fire Safety Journal, 38(7), 623-643 (2003). https://doi.org/10.1016/S0379-7112(03)00028-6.
3. Huang Z.F., Tan K.H. Rankine Approach for Fire Resistance of Axially-and-Flexurally Restrained Steel Columns. Journal of Constructional Steel Research, 59(12), 1553-1571 (2003). https://doi.org/10.1016/S0143-974X(03)00103-2.
4. Li G.Q., Wang P.J., Wang Y.C. Behaviour and Design of Restrained Steel Column in Fire, Part 1: Fire Test. Journal of Constructional Steel Research, 66(8-9), 1138-1147 (2010). https://doi.org/10.1016/j.jcsr.2010.03.017.
5. Liu T.Z. Study on Post-Fire Mechanical Behaviour of High Strength Q460 Steel Columns. Master Thesis, Chongqing University (in China) (2015).
6. Wang X.T., Zhou M., Wang W.Z. Experimental Study of Fire Response and Post-Fire Mechanical Behaviour of Restrained H-Steel Columns After Exposure to Fire. Journal of Building Structures, 33(2), 18-25 (2012). https://doi.org/10.14006/j.jzjgxb.2012.02.004.
7. Li G.Q., Miao J.R., Song L.X., Cai W.Y. & Jiang J. Investigation on Postfire Residual Capacity of High-Strength Steel Columns with Axial Restraint. Journal of Structural Engineering. 146(9), 04020182 (2020). https://doi.org/10.1061/(ASCE)ST.1943-541X.0002759.
8. Song L.X. and Li G.Q. Numerical Analysis on Post-Fire Residual Capacity of the Restrained High Strength Structural Steel Columns Under Axial Compression. 7th International Conference Applications of Structural Fire Engineering. Ljubljana, Slovenia (2021).
9. Ban H.Y., Shi G., Shi Y.J. Experimental and Unified Model Investigations on Residual Stress Within High Strength Steel Welded I-Sections. Engineering Mechanics, 31(8), 83-91 (2014). https://doi.org/10.6052/j.issn.1000-4750.2012.12.0915.
10. Huang L., Li G.Q., Wang X.X., Zhang C., Choe L. & Engelhardt, M. High Temperature Mechanical Properties of High Strength Structural Steels Q550, Q690 and Q890. Fire Technology, 54, 1609-1628 (2018). http://doi.org/10.1007/s10694-018-0765-4.
11. Li G.Q., Lyu H.B., Zhang C. Post-Fire Mechanical Properties of High Strength Q690 Structural Steel. Journal of Constructional Steel Research, 132, 108-116 (2017). http://doi.org/10.14006/j.jzjgxb.2017.05.014.

FRACTURE BEHAVIOR OF HIGH-STRENGTH BOLTS AND CONNECTIONS IN THE WHOLE PROCESS OF FIRE

Qiao Chen[1], Jian Jiang[2], Wei Chen[3], Jihong Ye[4]

ABSTRACT

High-strength bolts have been widely used in steel bolted connections, and fire-induced high temperatures will affect its basic mechanical properties and fracture behavior, leading to failure of the connection and even collapse of the overall structure. Tensile experiments are conducted on Grade 10.9 high-strength bolts to investigate the effect of stress triaxiality and heating history on their mechanical and fracture properties in the whole process of fire. The true stress-strain curves are obtained to determine the material properties. The SMCS fracture model is calibrated based on test results, and parametric studies are conducted on fracture performance of T-stub connections in fire. The experimental results show that the SMCS model can effectively predict the fracture behavior of Grade 10.9 high-strength bolts for a stress triaxiality range of 0.3 to 1.2. There are three failure modes of T-stub connections under different temperature histories: yield fracture of flange plate, simultaneous yield fracture of flange plate and bolt, and yield fracture of bolt.

Keywords: whole process of fire; high-strength bolts; T-stub connection; SMCS fracture model

1 INTRODUCTION

In the fire cooling stage, beam shrinkage may cause tensile failure of steel connections. It is more important to study the failure behavior of steel connections in the whole process of fire. Grade 10.9 high-strength bolts are most widely used in steel connections. The fracture of connections may occur in either the heating phase (thermal expansion) or the cooling phase (shrinkage deformation).Therefore, it is necessary to investigate the fracture behavior of steel bolted connections in the whole process of fire, and fracture behavior of high-strength bolts in fire is an important breakthrough point.

The existing studies mainly focus on the fracture mechanism of structural steels at ambient temperature, and determine the parameters of fracture models and fracture mode of connections [1-3]. Research on fracture properties of structural steels and high-strength bolts in fire is limited. [4-6]. There is still a lack of true stress-strain data used as input in numerical models.

The fracture rate of ductile metals under a given critical plastic strain can be determined by establishing a micro fracture model. The fracture models have been used for simulating the fracture behavior of steel materials at ambient temperature [1, 6, 7, 8]. Among them, the SMCS model assumes that the stress

[1] M.D., China University of Mining and Technology
e-mail: kriya9802@foxmail.com
[2] Prof., China University of Mining and Technology
e-mail: jian.jiang@cumt.edu.cn
[3] Prof., China University of Mining and Technology
e-mail: chenweiseu@163.com
[4] Prof., China University of Mining and Technology
e-mail: jhye@ cumt.edu.cn
https://doi.org/10.6084/m9.figshare.22202428

triaxiality is constant, and the influence of plastic strain and stress triaxiality on cavity expansion are considered.

In summary, there are three main issues on fracture behavior of high-strength bolts and steel connections under fire conditions: (1) There is still a lack of true stress-strain data used as input in numerical models; (2) The fracture models applicability in simulating the fracture behavior of high-strength bolts under fire conditions is in question. (3) Research on behavior of steel connections is concentrated on the heating stage, while less attention is paid to the cooling and post-fire stage. There is a lack of experimental and theoretical basis for the design of steel connections in the whole process of fire.

In this paper, experiments were conducted on Grade 10.9 high-strength bolts which are commonly used for bolted connections. The engineering and true stress-strain curves of high-strength bolts in the whole process of fire were obtained. The SMCS fracture model was used to characterize the fracture behavior of grade 10.9 high-strength bolts in the whole process of fire. The model was calibrated and validated based on test results and finite element simulation. Parametric studies were carried out to investigate the influence of damage criterion and heating conditions on the fracture behavior of T-stub connections exposed to fire.

2 FRACTURE TEST IN THE WHOLE PROCESS OF FIRE

2.1 Specimens and working conditions

The tensile fracture test of grade 10.9 high-strength bolts under the whole process of fire (heating, heating-cooling and post fire stage) was carried out, and 11 temperature conditions were set. Considering the influence of stress triaxiality, three kinds of tensile specimens (smooth and notched) are designed. The temperature conditions and specimen properties are shown in Table 1 and Fig. 1, respectively. The true stress-plastic strain curves are measured by DIC method.

Table 1 Dimensions and properties of bolt specimens

Type of tests	Type of specimens	No. of specimens	Radius of notch R (mm)	Radius at notch root a (mm)	Stress triaxiality $1/3+\ln(1+a/2)$[9]
Heating test	Smooth	SR/SH2/SH4/SH6	$+\infty$	4.5	0.333
	Notched R=6	N6R/N6H2/N6H4/N6H6	6.0	3.0	0.556
	Notched R=3	N3R/N6H2/N6H4/N6H6	3.0	3.0	0.739
Heating-Cooling test	Smooth	SC6-4/SC4-2/SC6-2	$+\infty$	4.5	0.333
	Notched R=6	N6C6-4/N6C4-2/N6C6-2	6.0	3.0	0.556
	Notched R=3	N3C6-4/ N3C4-2/ N3C6-2	3.0	3.0	0.739
Post-fire test	Smooth	SP2/SP4/SP6/SP8	$+\infty$	4.5	0.333
	Notched R=6	N6P2/N6P4/N6P6/N6P8	6.0	3.0	0.556
	Notched R=3	N3P2/N3P4/N3P6/N3P8	3.0	3.0	0.739

Note: S represents smooth bolt specimens; N6 and N3 represent notched bolt specimens with a radius of 6mm and 3mm, respectively; R denotes a test at room temperature; H, C, P denote a heating, heating-cooling, post-fire test, respectively. The heating test includes four target temperatures of 20°C (R), 200°C (H2), 400°C (H4) and 600°C (H6). For the heating-cooling test, three conditions of cooling to 200°C after heating to 400°C (C4-2), cooling to 200°C after heating to 600°C (C6-2), and cooling to 400°C after heating to 600°C (C6-4) were set. There were four maximum temperatures of 200°C (P2), 400°C (P4), 600°C (P6), 800°C (P8) set for the post-fire test. There are 11 temperature working conditions.

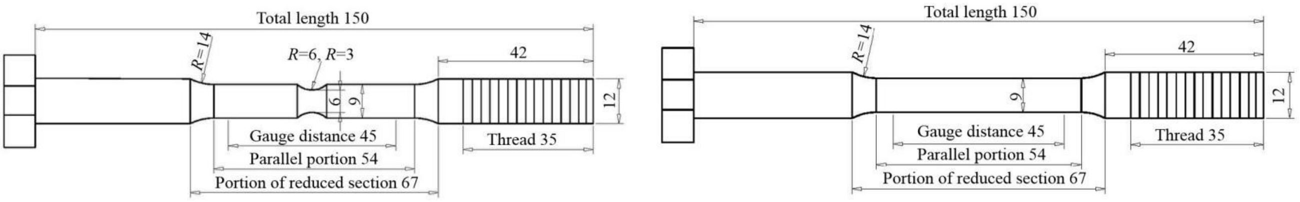

(a) dimension of smooth bolts (b) dimension of notched bolts

Fig.1 Design of smooth and notched bolt specimens

In this study, the DIC system was used to directly obtain the true stress-strain curves in the whole process of fire. The instantaneous cross-sectional area of the specimen was calculated based on variation in transverse width of the necking section monitored by virtual extensometer in DIC, and the longitudinal average strain of the necking area was obtained by DIC as the true strain [10]. Note that the DIC method is to directly measure the cross-sectional area without other assumptions and extrapolation, and the true constitutive relationship of the specimens during the whole loading process can be obtained directly.

Through Eq. (1), the measured data was modified to obtain the true stress-plastic strain curves, as shown in Fig. 3, which can be used as input in numerical models. The strain and stress at fracture were labeled in bracket at the end of curves. The curves in Fig. 2 had common characteristics: (1) at low temperatures, with the increase of strain, the stress increased linearly, showing strain hardening behavior; (2) when the target temperature or maximum temperature reached above 400°C, the material exhibited obvious indigenous softening, and the curve decreased after reaching its peak. This descending path showed the trend of metal flow at high temperatures, which was related to the dynamic recrystallization behavior inside the metal.

$$\varepsilon_{\text{pl}} = \left|\varepsilon_{\text{true}}\right| - \frac{\left|\sigma_{\text{true}}\right|}{E} \tag{1}$$

where ε_{pl} and $\varepsilon_{\text{true}}$ are true plastic strain and true strain respectively; σ_{true} is true stress.

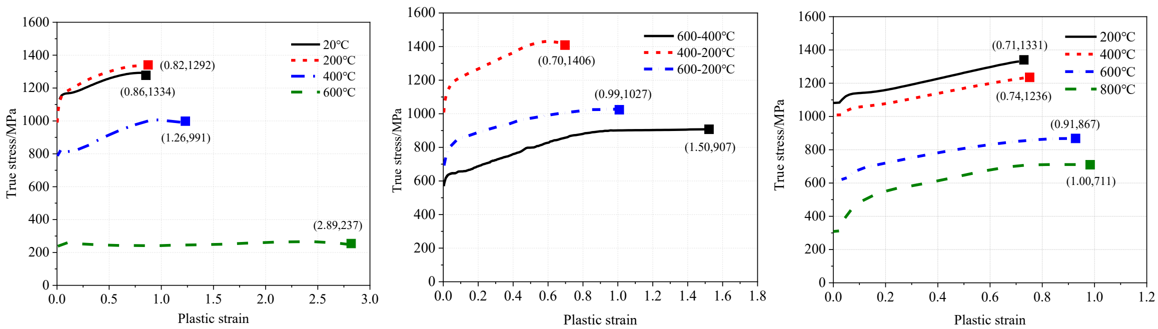

(a) heating test (b) heating-cooling test (c) post-fire test

Fig.2 True stress-plastic strain curves of high-strength bolts in the whole process of fire

3 CALIBRATION AND VALIDATION OF SMCS MODEL

3.1 Parameter calibration of SMCS model

In order to calibrate the parameters in SMCS model, the model of bolt specimens in Fig. 1 was established in ABAQUS. The true stress-plastic strain curves in Fig. 3 were input in the model, and explicit dynamic analyses were conducted to simulate the deformation behavior of the specimen. For simulating the fracture behavior of a material such as fracture point, fracture time, deformation at fracture, it is still necessary to input the corresponding fracture model (i.e. the stress triaxiality-plastic strain relationship), which is difficult to be obtained in an experiment. Therefore, a combination of experiments and numerical analyses is usually used to determine the stress triaxiality-plastic strain relation. From an experiment, we can accurately measure the information of fracture time, and fracture displacement, fracture point, reduction radius of fracture section at this fracture time. From the numerical model with only input of a true stress-strain curve, we can output the information of stress triaxiality and plastic strain at the measured fracture location (obtained from the experiment) at the measured fracture time (obtained from the experiment). The obtained stress triaxiality-plastic strain relationship can be re-input into the finite element model, which include all the fracture information such as when and where the model fractures.

The SMCS model shown in Eq. (3) was used to characterize the fracture behavior of high strength bolts under fire conditions. In order to determine the numerical relationship between the equivalent stress triaxialityand the equivalent plastic strain , $\varepsilon_{\text{p,critical}}$, it is necessary to determine two parameters α and β, which are related to the material. The parameter α represents toughness index, which is the quantification of fracture initiation resistance [11]. For steel materials, the value of β is usually in the range of 1.5 to 2.4 [12]. Table 2 lists the displacement at the fracture time of each specimen Δ_{f}, the equivalent stress triaxiality

$\tilde{\eta}$, the equivalent plastic strain $\varepsilon_{p,critical}$ and the two model parameters (α and β) determined by curve fitting. The comparison of calibrated SMCS model and test results is also plotted in Fig. 3. Under a high stress triaxiality in a tensile state, the critical plastic strain decreased exponentially with the increase of stress triaxiality. The discrete coefficient (CV) was controlled within 10%, indicating that the SMCS model is suitable for predicting the fracture behavior of high-strength bolts in the whole process of fire. Note that the range of stress triaxialities for the specimens in this test was between 0.33 to 0.74, while the range from numerical simulation varied between 0.3 and 1.2. The latter range (0.3 to 1.2) was thus used as the applicability range of the SMCS model for accurately simulate the fracture behavior of high-strength bolts in the whole process of fire.

$$\varepsilon_{\text{p,critical}} = \alpha \mathrm{e}^{-\beta\eta} \tag{3}$$

Table 2 Parameter calibration of the SMCS model

Working condition	Specimen	Δ_f (mm)	$\tilde{\eta}$	$\varepsilon_{p,critical}$	α			β
						CV	AVG	
Heating test	SR	8.33	0.55	0.86	2.57	3.7%	2.61	2
	N6R	2.51	0.79	0.53	2.54			
	N3R	2.10	0.94	0.38	2.72			
	SH2	8.33	0.57	0.82	2.58	1.4%	2.61	2
	N6H2	2.07	0.89	0.45	2.65			
	N3H2	1.72	1.08	0.30	2.60			
	SH4	10.68	0.57	1.26	4.62	2.5%	4.50	2.3
	N6H4	3.37	0.85	0.63	4.48			
	N3H4	2.68	0.97	0.48	4.40			
	SH6	41.07	0.44	2.65	5.44	1.7%	5.50	2
	N6H6	5.40	0.88	0.97	5.61			
	N3H6	5.00	0.97	0.78	5.45			
Heating-cooling test	SC6-4	11.72	0.49	1.50	4.86	1.2%	4.80	2.4
	N6C6-4	5.14	0.87	0.59	4.75			
	N3C6-4	3.10	0.99	0.45	4.79			
	SC4-2	9.73	0.60	0.70	2.56	1.9%	2.61	2.15
	N6C4-2	2.27	0.87	0.41	2.66			
	N3C4-2	1.77	0.95	0.34	2.61			
	SC6-2	10.09	0.45	0.99	2.43	2.6%	2.35	2
	N6C6-2	2.41	0.82	0.45	2.32			
	N3C6-2	1.75	0.87	0.41	2.33			
Post-fire test	SP2	7.56	0.56	0.71	2.17	4.9%	2.07	2
	N6P2	2.03	0.67	0.54	2.02			
	N3P2	1.70	0.84	0.37	1.98			
	SP4	8.27	0.45	0.74	2.38	4.1%	2.50	2.6
	N6P4	1.59	0.82	0.30	2.52			
	N3P4	1.21	0.93	0.23	2.58			
	SP6	11.48	0.46	0.91	2.43	2.9%	2.35	2
	N6P6	2.30	0.69	0.58	2.31			
	N3P6	2.01	0.89	0.39	2.31			
	SP8	19.51	0.43	1.00	2.36	6.8%	2.35	2
	N6P8	2.57	0.61	0.74	2.51			
	N3P8	2.22	0.71	0.53	2.19			

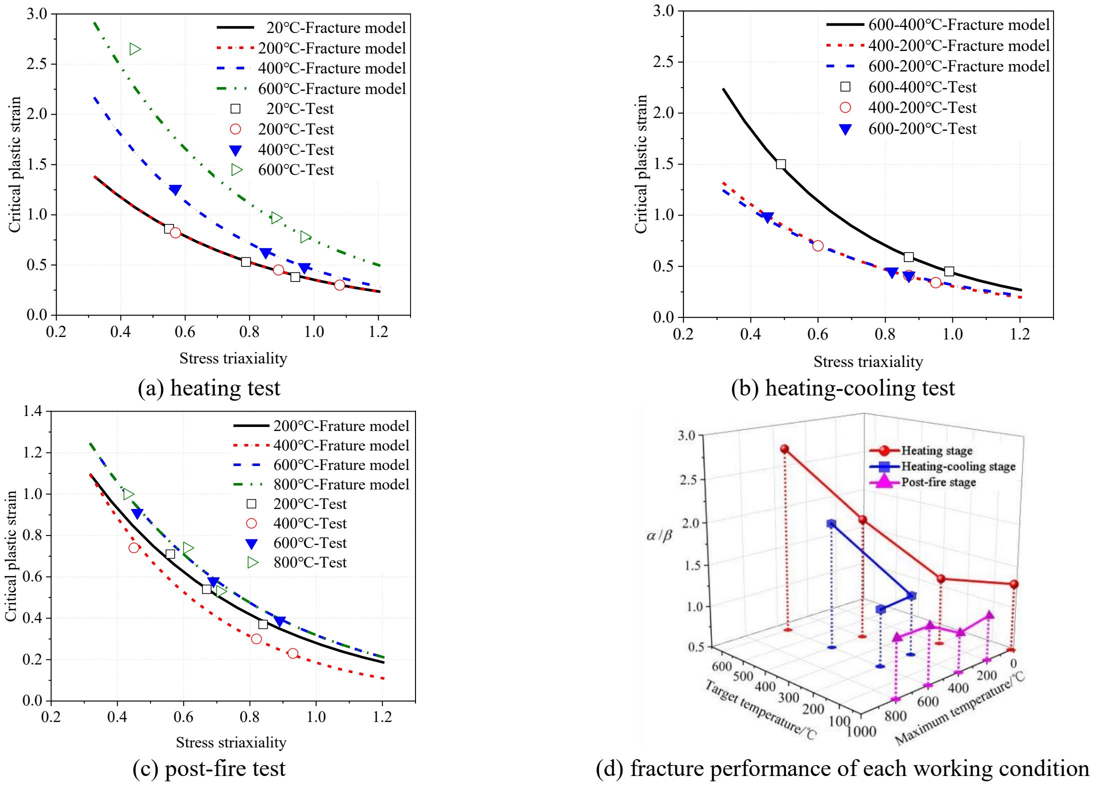

(a) heating test (b) heating-cooling test

(c) post-fire test (d) fracture performance of each working condition

Fig.3 Calibration of SMCS fracture model and fracture performance of bolts

3.2 Validation for stress-strain curves

The true stress-plastic strain curve obtained from the test (Fig. 2) was input into the material model, and the fitted SMCS fracture model (Fig. 3d) was introduced into the ductile damage criterion. The strain rate was set to be 0.001s^{-1} which meets the requirement for a quasi-static tensile test in the design code [13]. The numerical simulation of the fractured specimens was carried out, and a comparison of engineering stress-strain curves were presented as shown in Figs. 4. The results showed that the fracture model had no effect on the stress state of bolts before necking. The prediction error had no obvious correlation with the test type and working condition. The errors for stress and strain at the fracture time were less than 12%, and the simulation results were in a good agreement with the test.

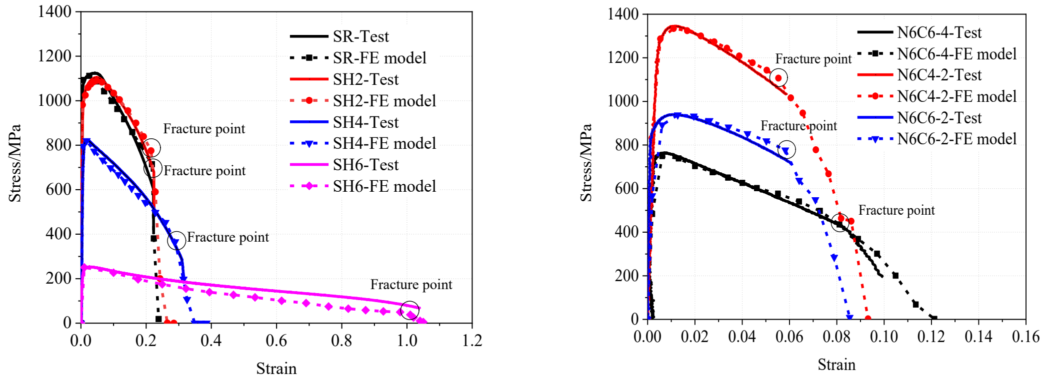

Fig.4 Comparison of predicted and measured stress-strain curves of some bolt specimens

4 FRACTURE PERFORMANCE OF T-STUB CONNECTIONS IN FIRE

4.1 Fracture test of T-stub connections at high temperatures

The calibrated SMCS fracture model was introduced into the ductile damage criterion, and the accuracy of the model was validated by comparing the engineering stress-strain curves of the bolt test and simulation. The high temperature (at 600°C) tensile fracture test of T-stub connections carried out by Barata et al[14] is taken for a further validation.,The T-stub connection specimen consists of T-flange plate, rigid plate and high-strength bolts.

4.2 Validation of T-stub connection models

The finite element model of the T-stub connection was established in ABAQUS. Considering that it is a steady state test, it was assumed that the whole connection was uniformly heated to 600°C without simulating the heating process in the numerical model. The mechanical properties and fracture model of each component of the connection at 600°C were directly input into the model. For the mechanical properties, the elastic modulus and strength of flange and web plate at 600°C were taken from EC3 [15], and test results in Table 4 were used for high-strength bolts at 600°C. For the fracture properties, the limit plastic strain of 0.25 in reference [14] was used as the ductile damage criterion for S355 steel plate at 600°C.

To compare and verify the accuracy of the SMCS fracture model, four different damage criteria were selected for high-strength bolts: (1) No damage criterion. It was assumed that the bolt can infinitely deform without fracture; (2) Ultimate plastic strain criterion. The ultimate strain in a range of 0.2 to 0.25 was taken according to EC3 [15], independent of different temperatures and steel strength; (3) Ultimate plastic strain criterion. The ultimate strain of 0.55 was taken according to Seif [16] on A490 bolts; (4) SMCS model. The SMCS fracture model calibrated in Section 4.1 was used. The damage criterion in the model only predicted the initiation of damage, without considering the process of damage evolution.

4.3 Validation of T-stub connection models

The comparison of predicted and measured load-displacement curves under different damage criteria is shown in Fig. 5. When the displacement reached 34.3mm at Point B in the test, the loading force dropped sharply to Point C where the load became basically zero and the specimen failed completely. For the non-damage criterion model, however, the curve continued to develop to Point D after yielding, and the load remained at about 125kN when the displacement reached 45mm. When the ultimate plastic strain recommended by EC3 was used as the failure criterion, the specimen failed in advance when the displacement at Point A was 16.2mm, and the error of fracture displacement was up to 52.7 %. For the curve with the ultimate plastic strain by Seif [16] as the failure criterion, the specimen fractured when the displacement developed to 27.6mm at Point E, and the error was reduced to 24.3%. The curve from SMCS fracture model calibrated in this paper had the best agreement with experimental results. The sudden change in load occurred at point F (corresponding displacement of 32.7mm and load of 148kN), and the prediction error was only 4.7%. It is concluded that the calibrated SMCS fracture model, considering the effect of stress triaxiality, has a higher accuracy and better applicability for predicting the high-temperature fracture behavior of T-stub connections.

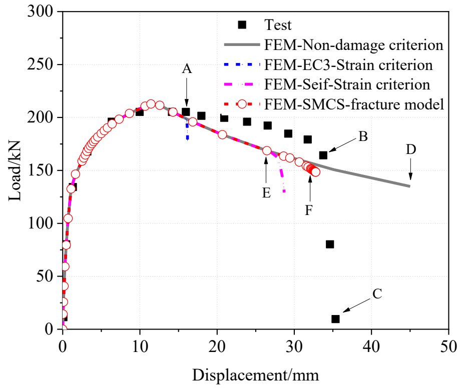

Fig. 5 Load-displacement curves predicted based on different damage criteria (600°C)

4.4 Parametric Analysis on Fracture behavior of T-stub connections

In this section, the validated finite element model was used for parametric analysis to further study the failure mode, bearing capacity and ductility of T-stub connections in the whole process of fire. A wider range of temperatures was considered: three heating-stage conditions of 20°C, 200°C, 400°C; three heating-cooling stage conditions of 600-400°C, 400-200°C, 600-200°C; and four post-fire stage conditions of 200°C, 400°C, 600°C, 800°C.

The T-stub connections exhibited three main failure modes under different temperature conditions, as shown in Fig. 6: (1) In the heating stage of fire, when the temperature was lower than 200°C, the flange near the bolt hole and the weld toe of the web first yielded (before yielding of the bolt), formed plastic hinge, and finally fractured, resulting in failure of T-stub connections. This belongs to Mode 1 (yielding and fracture of flange). In this situation, the bolt deformation was much smaller than the flange plate, and the bolt strength was not fully utilized; (2) When the temperature in the heating stage reached 400°C, the bolt and flange were almost deformed at the same time. The flange at the weld toe of the web yielded and plastic hinges formed. At the same time, the bolt was subjected to yielding fracture in tension, and the bolt strength was fully utilized. This corresponds to Mode 2 (simultaneous yielding and fracture of flange and bolt); (3) When the temperature rose to 600°C, the ductility of high-strength bolts was greatly improved (about 3.5 times) compared with that at ambient temperature, and the bolt had obvious deformation relative to the flange plate. Since degradation of the mechanical properties of high-strength bolts above 600°C (Table 4) is greater and faster than that of the normal-strength steel, the strength and stiffness of the flange plate are stronger than those of the bolt. The connection failed due to fracture of bolts, which is classified to Mode 3 (yielding and fracture of bolt). In this situation, the high-strength bolt becomes the governing factor affecting the deformation of T-stub connections. The failure modes of the connections under other temperature conditions are listed in Table 3. For the heating-cooling and the post-fire stage, the conditions showed failure modes of Mode 1 and Mode 2. With the increase of temperature, the failure mode changed from Mode 1 to Mode 2.

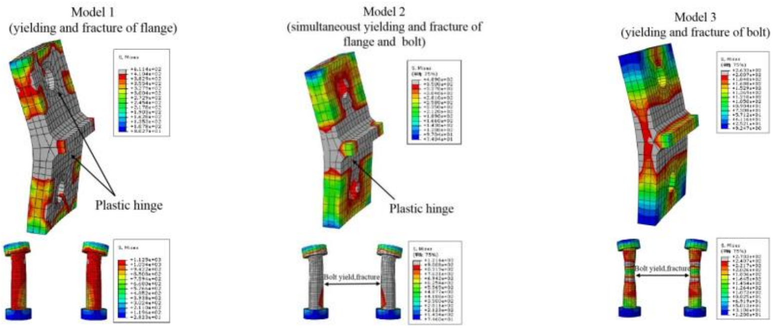

Model1 (20°C) Mode 2 (400°C) Mode 3 (600°C)

Fig.6 Failure modes of T-stub connections

Table 4 Summary on Fracture behavior of T-stub connections in the whole process of fire

Working condition	Temperature (°C)	Ultimate bearing capacity (kN)	Ultimate displacement (mm)	Ductility factor	Failure mode
Heating stage	20	540	19.7	1.00	1
	200	499	19.9	1.01	1
	400	461	14.6	0.74	2
	600	213	32.8	1.67	3
Heating-colling stage	600-400	362	12.4	0.63	2
	400-200	518	19.7	1.00	1
	600-200	426	13.0	0.66	2
Post-fire stage	200	507	21.4	1.08	1
	400	510	19.0	0.97	1
	600	397	13.8	0.70	2
	800	288	14.2	0.72	2

5 CONCLUSIONS

The mechanical and fracture properties of Grade 10.9 high-strength bolts in the whole process of fire (heating, heating-cooling and post-fire stage) were experimentally and numerically studied. The SMCS fracture model was calibrated, and parametric studies were conducted on fracture performance of T-stub connections in fire. The following conclusions can be drawn:

(1) The SMCS model can effectively predict the fracture behavior of Grade 10.9 high-strength bolts in the whole process of fire (errors within 12%) for an applicability range in high stress triaxiality of 0.3 to 1.2. Compared with the limit plastic strain criterion using a constant strain, the SMCS model has a better accuracy for predicting fracture performance of T-stub connections in fire.

(2) There are three failure modes of T-stub connections under different temperature histories: yield fracture of flange plate (Mode 1), simultaneous yield fracture of flange plate and bolt(Mode 2), and yield fracture of bolt (Mode 3). Failure mode 1 occurred when the peak temperature or tensile temperature is lower than 400°C. Failure mode 3 occurred at 600°C in the heating stage. As the temperature rises, the failure mode of the connection changed from mode 1 to mode 3.

ACKNOWLEDGMENT

The work presented in this paper was mainly supported by the National Natural Science Foundation of China with grant 52078478 and 52127814.

REFERENCES

1. F.F. Liao, W. Wang, Y.Y. Chen, Ductile fracture prediction for welded steel connections under monotonic loading based on micromechanical fracture criteria, Engineering Structures 94 (2015) 16-28.
2. M.M. Ran, Y.C. Zhong, Y.Z. Wang, G.Q. Li, F. Xiong, Q. Ge, Fracture prediction in transverse fillet welded joints of high strength structural steel, Journal of Constructional Steel Research 189 (2022) 107101.
3. L.D. A. Padilla, B.W. Schafer, J.F. Hajjar, Cyclic fracture simulation through element deletion in structural steel systems, Journal of Constructional Steel Research 189 (2022) 107082.
4. Y. Du, H.H. Qi, J. Jiang J, Mechanical properties of 1670 MPa parallel wire strands at elevated temperatures, Construction and Building Materials 263(8) (2020) 120582.
5. W.Y. Cai, J. Jiang, G.Q. Li, Analysis and simulation on fracture of structural steel at elevated temperatures based on extended finite element method, Fire Safety Journal 120 (2021) 103022.
6. W.Y. Cai, J. Jiang, Y.B. Wang Y B, Analysis of fracture behavior of high-strength steels in tension after fire exposure, Engineering Structures 231 (2021) 0141-0296.
7. A.T. Myers, A.M. Kanvinde, G.G Deierlein, Calibration of the SMCS criterion for ductile fracture in steels: specimen size dependence and parameter assessment, Journal of Engineering Mechanics 136(11) (2010) 1401-1410.
8. Y. Cao, Y. Zhen, M. Song, Determination of Johnson-Cook parameters and evaluation of Charpy impact test performance for X80 pipeline steel, International Journal of Mechanical Sciences 179(4-5) (2020) 105627.
9. P.M. Bridgman, Studies in large plastic flow and fracture: with special emphasis on the effects of hydrostatic pressure, McGraw-Hill, 1952.
10. V.M. Bac, H.P. Cao, J.H. Gregory, D.N. Giang, Block shear strength and behaviour of cold-reduced G450 steel bolted connections using DIC, Journal of Constructional Steel Research 157 (2019) 151-160.
11. A.M. Kanvinde, A.M. Asce, G.G. Deierlein, The void growth model and the stress modified critical strain model to predict ductile fracture in structural steels, Journal of Structural Engineering 132(12) (2006) 1907-1918.
12. G.R. Johnson, W.H. Cook, Fracture characteristics of three metals subjected to various strains, strain rates, temperatures and pressures, Engineering fracture mechanics 21(1) (1985) 31-48.
13. GB/T 4338.1-2006. Metallic materials-Tensile testing at elevated temperature. Beijing: China Standards Press, 2006.
14. P. Barata, J. Ribeiro, C. Rigueiro, Assessment of the T-stub joint component at ambient and elevated temperatures, Fire Safety Journal 70 (2014) 1-13.
15. CEN. (2005). Eurocode 3, design of steel structures. Part 1-2: general rules-Structural fire design. European Committee for Standardization (CEN), Brussels.
16. M. Seif, J. Main, J. Weigand, Finite element modeling of structural steel component failure at elevated temperatures, Structures 6 (2016) 134-145.

CREEP BEHAVIOR OF 10.9 HIGH STRENGTH BOLTS IN FIRE

Yaoliang Lu[1], Jian Jiang*[2], Wenyu Cai[3] Wei Chen[4] and Jihong Ye[5]

ABSTRACT

As an important component in steel connections, high-strength bolts have a high stress level and may experience creep deformation at high temperatures. This will lead to great deformation and even failure of steel connections, thus affecting progressive collapse resistance of steel structures. This paper experimentally and numerically investigates the creep behavior of 10.9 high-strength bolts under and after fire. The creep strain-time curves at different temperatures and stress levels were obtained using DIC measurement systems. The micromorphology and failure mechanism of high-strength bolts is examined by SEM. The Field & Field creep model is calibrated against test results, and parametric studies are conducted on T-stub connections. The experimental results show that the creep deformation of high-strength bolts is significant at high temperatures, and the creep strain is positively correlated with temperatures and stress ratios. The numerical results show that the Field & Field model is suitable for characterizing the creep behavior of high-strength bolts under fire situation. The fire resistance of T-stub connections is significantly affected by creep-related parameters. It is necessary to consider the effect of creep for predicting the behavior of high-strength bolts and steel connections, ensuring a safe design.

Keywords: high-strength bolt; creep behavior; under fire; after fire; creep model; micro mechanism

1 INTRODUCTION

Connections are an important component of steel structures where high-strength bolt connections are most commonly used [1]. Compared with normal-strength bolt connections, preloads are usually applied in high-strength bolts which are in a higher stress state. On the other hand, fires in high-rise buildings often last for several hours, and the temperature in steel components rises constantly and steadily. The creep deformation of high-strength bolts will be significant as they are in a state of high stresses and high temperatures. Previous studies have shown that structural steels, including normal-strength steels, high-strength steels and high-strength steel wire bundles, have a great difference in material properties under fire due to different heating (transient or steady) and cooling (in air or by water) methods as well as different heat treatment processes (cold drawing or full cooling) [2,3]. The influence of creep deformation should be considered in evaluating the mechanical performance of steel connections under fire, otherwise unsafe results may be obtained [4]. Therefore, it is necessary to study the creep properties of high-strength bolts in case of fire.

[1] PhD student, China University of Mining and Technology
e-mail: ts19030170p31@cumt.edu.cn
[2] Prof., China University of Mining and Technology
e-mail: jian.jiang@cumt.edu.cn
[3] Prof., Hainan University
e-mail: wenyucai@163.com
[4] Prof., China University of Mining and Technology
e-mail: chenweiseu@163.com
[5] Prof., China University of Mining and Technology
e-mail: jhye@ cumt.edu.cn
https://doi.org/10.6084/m9.figshare.22202461

Previous research focuses on the creep performance of normal and high-strength steels in the heating stage [5-7], and there are few on that of steels after fire which leads to the lack of experimental and theoretical basis for the performance evaluation of steel connections after fire. The applicability and pertinence of different creep models are quite different [8,9], which are sensitive to temperatures, loads and steel types. No unified creep model is available. The Field & Field model has the strongest applicability and is widely used to simulate the creep properties of various high-strength steels. In addition, the processing technology of high-strength bolts is different from that of high-strength steels for structural components. This may result in different microstructure, greater stress (smaller section size), and more obvious creep phenomenon in high-strength bolts. Therefore, it is still necessary to study the creep properties of high-strength bolts in the whole process of fire.

In this study, creep tests were conducted on 10.9 high-strength bolts in fire. The DIC strain measuring instrument was used to measure the creep curves of bolts at different temperatures and stress levels. The fracture morphology and failure mechanism of the specimens were studied by scanning electron microscopy. Based on the experimental results, the Field & Field model was calibrated and validated to simulate the creep behavior of high-strength bolts. The finite element model of T-stub connections was established to further validate the model. Parametric studies were carried out to investigate the effect of temperatures, load ratios and loading durations on the fire resistance of T-stub connections.

2 CREEP TEST

2.1 Test preparation

1. Design of specimens

According to the test condition, 10.9 high-strength bolts with a diameter of 12mm (M12) were selected, and the heat treatment process was quenching and tempering. According to the requirements in the relevant specifications, the total length of the specimen was designed to be 150mm, and the length of the middle parallel section is 60mm with a reduced diameter of 9mm. The standard distance of strain measurement is 45mm.

2. Test instruments

The MTS Landmark Servo-hydraulic Test System (Fig. 1a) was used as the loading device under high temperatures and after fire. The high-temperature environmental condition is realized by a medium-sized heating furnace. The specimens in the after fire test were first heated to the target temperature in a muffle furnace, and then cooled with the furnace to complete the preparation.

Digital Image Correlation (DIC) system (Fig. 1a) was used to measure the deformation of the specimens. By observing the speckles sprayed on the specimen surface, the pixel-level displacement information was obtained, and the strain information of the specimen was obtained by using the optimized digital image correlation algorithm.

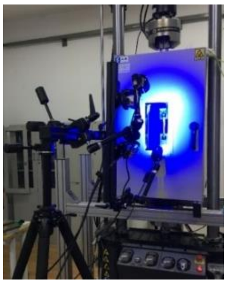

(a) MTS testing machine with DIC strain measurement system

(b) Physical appearance of specimens in under fire creep tests

(c) Physical appearance of specimens in after fire creep tests

Figure 1. Specimens and test equipments

3. Test conditions

Table 1 lists the target temperatures and stress levels of the specimens under two working conditions (under fire and after fire). A total of 23 working conditions were designed.

Table 1 Testing conditions of creep tests on Grade 10.9 high-strength bolts

Conditions	Specimen No.	Temperature T/℃	Yield Strength $f_{0.2,T}$/MPa	Stress σ/MPa	Stress Ratio α
Under fire	UF-400-α	400	860	344/430/516/602/688	0.4/0.5/0.6/0.7/0.8
	UF-500-α	500	400	160/200/240/280/320	0.4/0.5/0.6/0.7/0.8
	UF-600-α	600	220	88/110/132/154/176	0.4/0.5/0.6/0.7/0.8
After fire	AF-200-α	200	1125	900/1125	0.8/0.95
	AF-400-α	400	1050	840/1050	0.8/0.95
	AF-600-α	600	570	456/570	0.8/0.95
	AF-800-α	800	300	240/300	0.8/0.95

2.2 Test phenomena

1. Phenomena of specimens in under fire creep tests

For the creep test at high temperatures, the specimens had obvious creep deformation under high temperatures and high stress ratios, especially when the temperature exceeded 500 ℃ and the stress ratio was greater than 0.6. Some specimens fractured due to creep deformation, showing obvious necking phenomenon, as shown in Fig. 1b. This means that it is necessary to consider the creep deformation of high-strength bolts at high temperatures.

2. Phenomena of specimens in after fire creep tests

For post-fire creep tests, as shown in Fig. 1c, the color of the specimen was almost unchanged after a high temperature of 200 ℃. After 400 ℃, the specimen surface became yellow but still had obvious metal luster. The specimen experiencing a higher temperature of 600 ℃ was white and the surface became rough, almost losing the metallic luster. After 800 ℃, the specimen was gray and white, with pits on the surface.

2.3 Test results

1. Creep curves of under-fire creep tests

At different temperatures, two types of creep curve A and B appeared. When the temperature was 400 ℃ (as shown in Fig. 2a), the creep was dominated by B-type curve, showing only the creep characteristics of the first and second stages. The creep rate became slow, and then tended to be stable. The creep strain was within 0.02. Under a high stress α =0.8, the curve had a complete three-stage creep characteristics (namely A-type curve), where the creep strain reached 0.08. From the morphology of the specimen after test, the creep phenomenon is not obvious.

At the temperature of 500 ℃ (Fig. 2b), the creep deformation of the specimen was obvious, which was still dominated by B-type curve. The creep strain increased exponentially at a high stress ratio. The specimen was destroyed at a stress ratio of α=0.8, and the creep strain was more than 0.4 which is five times that for the specimen UF-400-0.8.

At 600 ℃ (Fig. 2c), the curve was dominated by A-type curve, and with the increase of stress ratios, the proportion of the first and second stages became smaller. The faster it entered the third stage, the shorter the failure time, and therefore the smaller the final creep strain. The maximum creep strain occurred in the specimen UF-600-0.6, where the creep strain was more than 0.8 and the length of the specimen gauge section was nearly doubled, showing particularly obvious creep deformation.

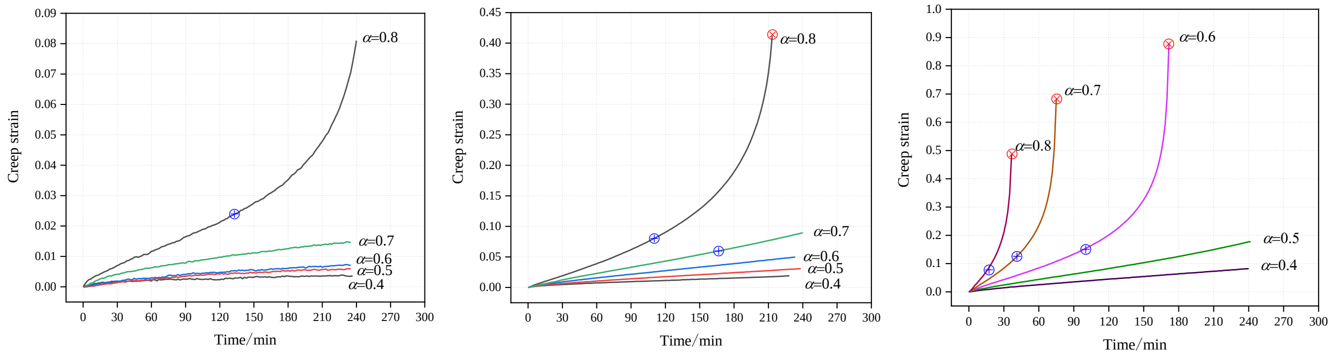

(a) T=400℃ (b) T=500℃ (c) T=600℃

Figure 2. Creep strain-time curves under different stresses from under-fire creep tests

2. Creep curves of after-fire creep tests

In the creep tests after fire, no creep strain was found in the specimens under a high stress ratio of 0.8, and creep phenomenon occurred under an extremely high stress ratio of 0.95, as shown in Fig. 3. When the stress ratio exceeded 0.95, the specimen will fail due to yield during the loading stage rather than creep.

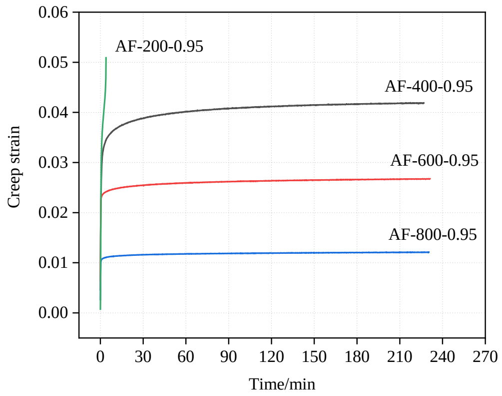

Figure 3 Creep strain-time curve under α = 0.95 from after-fire creep tests

2.4 Micro-analysis of fracture surface of failed specimen

In order to reveal the influence of temperature and stress levels on the creep properties of high-strength bolts from the microscopic point of view, the fracture surface of damaged specimens in creep tests was analyzed by scanning electron microscope (SEM). Fig. 4 shows the microscopic appearance of the fracture center fiber area after 1000 times magnification. It was found that in the fracture fiber area of the specimen after fire (Fig.4a), the dimples were shallow and dense, and there were a large number of small dimples on the cracking grain boundary. This is brittle intergranular fracture appearance. For the specimens at high temperatures, the dimple size at the fracture region of the specimen UF-500-0.8 became larger and deeper (Fig.4b). The fracture area further decreased for the specimen UF-600-0.8 (Fig.4c). With the increase of temperatures, the dimples at the fracture region were deepened, and the fracture crystal plane was in a pattern of smooth rock sugar, showing plastic transgranular fracture appearance and better ductility. This is consistent with the conclusion that the creep deformation observed macroscopically increased with the increase of temperatures.

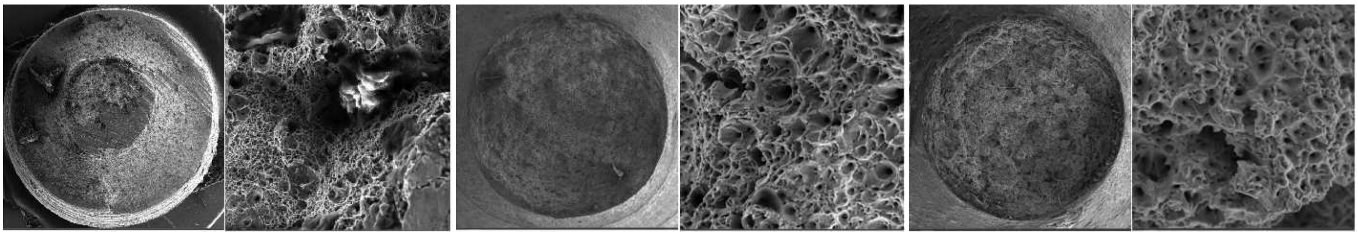

(a) AF-200-0.95 (b) UF-500-0.8 (c) UF-600-0.8

Figure 4 Effect of temperatures on toughness of creep fracture

3 CREEP MODEL

3.1 Field & Field creep model

In this study, the Field & Field creep model was adopted, where the relationship between creep strain, time and stress is provided in the form of power law. This model is simple in expression and has fewer parameters. Moreover, the model can be directly applied to the finite element software ABAQUS after the first derivative on it. The creep in the first and second stages can be considered. The third creep stage indicates that the failure is about to happen, which is usually not simulated. Since the creep deformation after fire is not significant and the time effect is not strong, the Field & Field creep model was thus used to characterize the creep characteristics of high-strength bolts at high temperatures as:

$$\varepsilon_{cr} = at^b\sigma^c \tag{1}$$

where t is time, σ is stress, a, b, c are the parameters related to the temperature T.

Considering the validity of the data, the first and second creep stages of the test data under high temperatures were selected for calibrating the parameters of the model. The model parameters at different temperatures are shown in Table 2. R^2 is the coefficient of determination, which is used to determine the fitting effect. The coefficients of determination in Table 3 were all above 0.95, showing a good fitting effect. The mathematical variation of the model parameters with temperatures is presented as follows:

$$\log(a) = -3.28\times10^{-7}T^3 + 2.72\times10^{-4}T^2 - 3.22\times10^{-3}T - 36.21 \tag{2}$$

$$b = -8.49\times10^{-9}T^3 + 4.34\times10^{-6}T^2 + 3.51\times10^{-3}T - 0.96 \tag{3}$$

$$c = 2.53\times10^{-7}T^3 - 2.81\times10^{-4}T^2 + 8.59\times10^{-2}T - 1.74 \tag{4}$$

Table 2 Parameters of Field & Field creep model for high-strength bolts at high temperatures

Temperature/℃	a	Log(a)	b	c	R^2
400	9.54428E-16	-1.502e+1	0.59510523	3.8681998	0.96547
500	1.28181E-11	-1.089e+1	0.81882105	2.6017868	0.99567
600	6.78879E-12	-1.116e+1	0.87462812	3.2989471	0.99269

3.2 Validation of creep models

The creep behavior of bolts was defined in the material properties, and the aging hardening criterion was used. In ABAQUS, the creep rate is assumed to remain constant in each incremental step, and the creep strain at each step is calculated by using the initial creep rate of each step. Therefore, the expression of creep rate in Eq. (5) can be obtained from the first order derivation on the Field & Field model in Eq. (1). The parameter transformation relationship that needs to be input into the model is obtained as expressed in Eq. (6).

$$\varepsilon'_{cr} = \frac{d\varepsilon_{cr}}{dt} = abt^{b-1}\sigma^c \tag{5}$$

$$A = a*b, n = c, m = b-1 \tag{6}$$

where ε_{cr} is strain of creep, a, b, c are the parameters parameters of Field & Field creep model, A, m, n are input parameters in finite element model.

The comparison between the numerical and the experimental results is shown in Fig. 5. In general, the experimental results were basically consistent with the numerical predictions, where the latter was generally greater than the former, putting the results on the safe side. A great deviation was seen at 400 ℃ with a greatest relative error of 45.7% at the stress ratio of 0.4. This may be related to the less applicability of Field & Field model itself at 400 ℃. Under the temperature of 600 ℃ and stress ratio of 0.6, the maximum absolute error was 0.028. Therefore, the Field & Field model calibrated in this paper is suitable for the numerical prediction of creep effects.

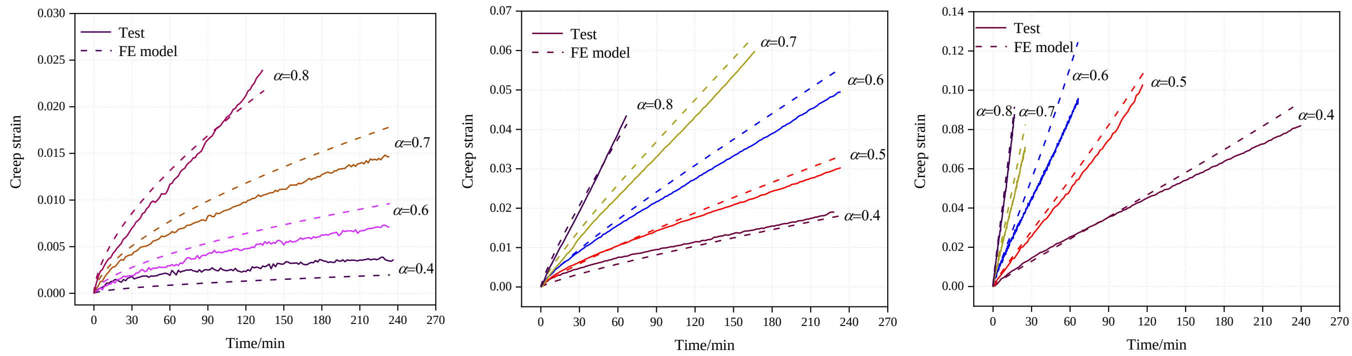

(a) T=400℃ (b) T=500℃ (c) T=600℃

Figure 5. Comparison of creep strain-time curves between numerical and experimental results

4 CREEP PERFORMANCE ANALYSIS OF T-STUB CONNECTIONS

4.1 Camparision between numerical result and experiment

In this section, based on the experimental data of T-stub connections, the accuracy of the Field & Field creep model for high-strength bolts were further validated, and parametric analyses were carried out to investigate the fire resistance of bolted connections considering the effect of creep. The T-stub connection test in the reference [10] was selected, where Grade 10.9 high-strength bolts was used in the test. The test and numerical model of the connection is shown in Fig.6a. The bolt diameter was 24mm, and the flange thickness was 20mm. The test temperature was 600 ℃, and the specimen was loaded until failure under this temperature. Considering the calculation accuracy and efficiency, mesh around the contact part of the component was refined, and that of other parts was coarse. The mesh size of the flange plate was 7mm, and that of the bolt rod (i.e. the gauge section) was the same as the uniaxial tensile specimen in Section 3.2. The same numerical modeling parameters were used. The comparison of the deformation of the numerical model with the test specimen is shown in Fig. 6b, and the failure modes of the two were consistent.

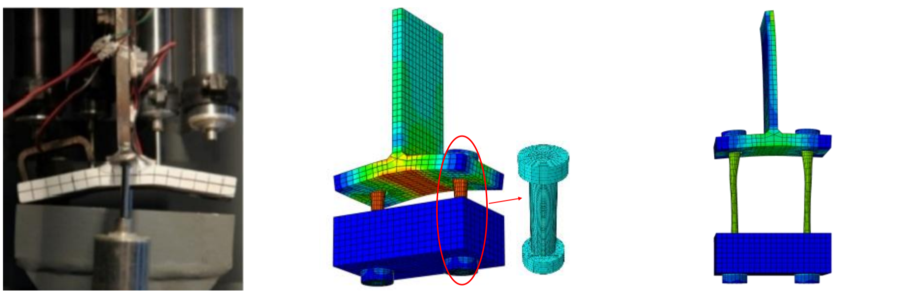

(a) T-stub specimen (b) Finite element model (c) Fracture due to creep

Figure 6. Numerical Simulation of T-stub connection

4.2 Parametric analyses

Parametric analyses were conducted on the T-stub connection model to investigate the effect of creep parameters such as temperature, load ratio and loading duration on the mechanical properties of connections at elevated temperatures. It can be concluded that the sharp growth of creep as temperatures will greatly affect the fire resistance of T-stub connections. While the influence of load ratios on the displacement was less sensitive than that of temperatures. And the time effect of creep was also greater for higher load ratios at high temperatures.

In particular, when the temperature increased to 600 ℃ (equal to the temperature condition in the test), the peak load measured by the test was greater than 200kN. While the numerical simulation showed that the bolt fractured after a loading duration of 70min given a load ratio of 0.3 (absolute load is 150kN), as shown in Fig. 6c. This damage can be considered as the failure due to creep. Therefore, the determination of fire resistance of steel connections needs to consider the effect of creep of high-strength bolts in addition to strength reduction at high temperatures, since creep may lead to excessive deformation and failure of connections

5 CONCLUSIONS

The creep behavior of Grade 10.9 high-strength bolts under and after fire were studied experimentally and numerically. The creep curves under different temperature conditions and stress levels were obtained, and the microscopic fracture mechanism was analyzed by scanning electron microscopy. The Field & Field creep model was established and calibrated, and parametric studies were conducted on creep performance of T-stub connections. The following conclusions can be drawn:

1. At high temperatures, the creep behavior of high-strength bolts were positively correlated with temperatures and stresses. The higher the temperature, the greater the stress, the more significant the creep strain. When the temperature and stress were at a high level (such as 600 ℃ and 0.6), creep quickly entered the third stage, and the bolt fractured with creep strain up to 0.87.
2. After fire, the creep phenomenon of high-strength bolts was not obvious, and was less affected by time. The creep effect of high-strength bolts after fire can be ignored.
3. The Field & Field creep model is suitable for characterizing the high-temperature creep performance of high-strength bolts with an applicable temperature range of 20 ℃-600 ℃ and stress ratio range of 0.4-0.8.
4. The fire resistance of T-stub connections was significantly affected by temperatures, load ratios and loading durations. It is necessary to consider the creep effect on mechanical behavior of steel connections in fire as creep may lead to excessive deformation and failure of steel connections at elevated temperatures.
5. The microscopic fracture morphology of high-strength bolts due to creep varied with temperatures. With the increase of temperatures, the dimple size became larger and deeper, showing a better ductility. High-strength bolts exhibited plastic transgranular fracture and brittle intergranular fracture, respectively, under fire and after fire.

ACKNOWLEDGMENT

The work presented in this paper was mainly supported by the National Natural Science Foundation of China with grant 52078478 and 52127814.

REFERENCES

1. X.D. Wang, M.H. Shen, K.F. Chung, X.H. Zhou, Y. Liao. Experimental investigation into high strength bolted shear connections for simple on-site assembly of composite beams. Engineering Structures, 257 (2022) 113980.

2. F.X. Ding, L.F Lan, Y.J Yu, M.K. Man. Experimental study of the effect of a slow-cooling heat treatment on the mechanical properties of high strength steels. Construction and Building Materials, 241 (2020) 118020.
3. C.T. Zhang, B. Jia, J.J. Wang. Influence of artificial cooling methods on post-fire mechanical properties of Q355 structural steel. Construction and Building Materials, 252 (2020) 119092.
4. M. Morovat, M. Engelhardt, T. Helwig. High-Temperature Creep Buckling Phenomenon of Steel Columns Subjected to Fire. Journal of Structural Fire Engineering, 5(3) (2014) 189-202.
5. T.Z. Harmathy, W.W. Stanzak. Elevated-temperature tensile and creep properties of some structural and pre-stressing steels. Astm Apecial Technical Publication, 1970.
6. X.H. Zhou, J.J. Yang, W.Y. Wang, L. Xu, Y. Shi. Mechanical properties and creep strain of Q355 cold-formed steel at elevated temperature. Journal of Constructional Steel Research, 180 (2021) 106577.
7. G.Q. Li, X.X. Wang, C. Zhang, W.Y. Cai. Creep effect on critical strength of high-strength steel columns exposed to fire. Engineering Structures, 220 (2020) 110971.
8. F.H. Norton. The creep of steel at high temperatures [M]. McGraw-Hill Inc. New York, 1929.
9. F. Fields. The prediction of elevated temperature deformation of structural steel under anisothermal conditions[R]. U.S. Department of Commerce National Institute of Standards and Technology, 1991.
10. P. Barata, J. Ribeiro, C. Rigueiro. Assessment of the T-stub joint component at ambient and elevated temperatures. Fire Safety Journal, 70 (2014) 1-13.

INFLUENCE OF THERMAL GRADIENTS ON THE RESISTANCE OF AXIALLY LOADED STEEL COLUMNS SUBJECTED TO LOCALISED FIRES

Luca Possidente[1], Carlos Couto[2], Nicola Tondini[3], Paulo Vila Real[4]

ABSTRACT

The definition of the resistance and the associated failure time of unprotected steel members in fire is crucial to the safety of steel structures. For this purpose, design standards allow for prescriptive approaches that rely on nominal fire curves that do not represent the physics of a real fire, for instance, a localised fire. Indeed, the thermal actions can be significantly different from the ones based on prescriptive approaches and non-negligible thermal gradients, both in the section and along the length, can develop in the structural members affecting the resistance of steel members. In this paper, three design procedures enabling increasing complexity of the temperature field were compared by investigating axially loaded steel columns characterised by a range of slenderness and load utilisation factors subjected to localised fires. The procedures consisted: i) in exploiting the recently proposed analytical LOCAFI model to compute single steel temperatures at different column heights and calculating the failure time with EN1993-1-2 considering the highest temperature; ii) in determining the failure time with beam finite element analyses in SAFIR by employing the temperatures at the different column heights, iii) in using a more refined version of the LOCAFI model included in SAFIR, which directly allows for the thermal gradients in the cross sections at the different heights of the column. The analysis showed that simplified procedures may predict both higher or lower failure times and therefore the employment of an advanced modelling is recommended.

Keywords: Thermal gradients; localised fires; advanced analysis; analytical methods; steel columns

1 INTRODUCTION

The design of steel structures that meets specific fire requirements is essential to ensure adequate safety in fire situation. Structures should be designed to guarantee sufficient time for evacuation before a structural collapse in case of relevant fire scenarios, or even to prevent collapse. Therefore, it becomes paramount to be able to determine the resistance in fire conditions of the structural elements, and in particular of the columns, whose failure may frequently trigger global structural collapses. The relevance of the definition of the resistance of compressed steel members is demonstrated by the numerous research paper published on the topic [1-3] Concentrically compressed steel sections prone to flexural-torsional and torsional buckling in fire were investigated [1]. The buckling length of columns in braced and unbraced frames was investigated at elevated temperatures in [2]. The influence of the imperfections in I-shape steel members, namely on beams and columns, was studied in [3]. All the mentioned works consider a uniform temperature distribution inside the steel members, as a result of post-flashover compartment fires for which a uniform

[1] PhD, University of Trento, Department of Civil, Environmental and Mechanical Engineering, Via Mesiano 77, 38123, Trento, Italy
e-mail: luca.possidente@unitn.it, ORCID: https://orcid.org/0000-0002-4179-1860
[2] PhD, Assistant Researcher, RISCO, Civil Engineering Department, University of Aveiro, Portugal
[3] PhD, Associate Professor, Department of Civil, Environmental and Mechanical Engineering, University of Trento, Italy
e-mail: nicola.tondini@unitn.it, ORCID: https://orcid.org/0000-0003-2602-6121
[4] Full Professor, RISCO, Civil Engineering Department, University of Aveiro, Portugal
https://doi.org/10.6084/m9.figshare.22202518

gas temperature in space is assumed. However, this is not the case when localised fires are considered, as it was shown that significant temperature gradients may develop inside the cross-sections and along the height of steel columns [4].

The behaviour of compressed steel members with non-uniform temperature distribution was investigated in several publications, among others [5-7], but only few considered a realistic temperature distribution induced by exposure to a localised fire. In this respect, Ren et al. [8] developed an analytical model to perform buckling and post-buckling analysis of non-uniformly heated columns in fire and validated such model against numerical analysis of a tapered H-section steel columns subjected to a localised fire. Bare steel columns exposed to localised fires were analysed in [9,10] by means of numerical simulation based on shell finite elements. The same approach was also used by Chang et al. [11,12] to study the lateral-torsional buckling behaviour of beams exposed to localised fires. These works provide an insight on the behaviour of the steel elements, but lack a quantifiable indication of the consequences of employing simplified procedures rather than an accurate analysis of the effects of non-uniform heating owing to localised fire exposure. Indeed, when comparison between the results of the extensive numerical analyses and simplified procedures is provided, it is presented only in terms of maximum steel temperature reached at failure, and only considering the nominal fire curve in the simplified procedures.

Following the discussion, the aim of this paper is to investigate the influence of thermal gradients on the resistance of axially loaded steel columns subjected to localised fires, by comparing three design procedures suited for localised fires that allow for an increasing complexity of the thermal field inside the steel columns. Localised fires are simulated with the LOCAFI model developed by Tondini et al. [4], which was extensively studied and validated [13,14] and was already employed in different meaningful studies [15,16]. The analysis is conducted on steel elements with different cross-sections, lengths and load levels and varying the severity, the position and the dimensions of the localised fires. In addition to maximum temperatures reached at failure, the failure times obtained with the three design procedures are compared to quantify the consequences of neglecting thermal gradients along the column and in the cross-sections.

2 EVALUATION OF THE TEMPERATURE OF STEEL COLUMNS SUBJECTED TO LOCALISED FIRES

Two applications of the LOCAFI model [4] are employed in this work to determine the temperature of steel columns. Though more complex analyses, e.g. CFD analyses, could be used to reproduce the fire development, the LOCAFI model allows for the definition of complex temperature distributions in the section of the steel members and therefore is sufficient for the purpose of analysing the effects of neglecting thermal gradients when the behaviour of columns subjected to localised fires is investigated. First, the LOCAFI model is described and then the characteristics of the two different applications, i.e. the analytical formulation and the SAFIR [17] implementations, relevant to the definition of temperature gradients are described.

2.1 The LOCAFI model

The LOCAFI model allows for the determination of the radiative heat flux received by the columns when not engulfed into the fire, considering analytical formulae for the definition of configuration factors by discretising the fire in a succession of cylinders to reproduce a conical or a cylindrical fire shape [4], as shown in Figure 1. In this work, conical fires are considered. Depending on the position of the column with respect to the fire, different formulations are exploited to determine the heat flux (Figure 1). For elements or portion of elements located inside a smoke layer zone below a ceiling, i.e. Zones 3 and 4 in Figure 1, the Hasemi model is used, while the heat flux for elements inside the fire, i.e. Zones 1 and 2 in Figure 1, is based on the Heskestad method. Different approaches are used in the calculations for these zones in the two procedures described in the followings and details can be found in [4]. Instead, only columns located outside the fire source that does not impact the ceiling were investigated in this work, as shown in Figure 1.

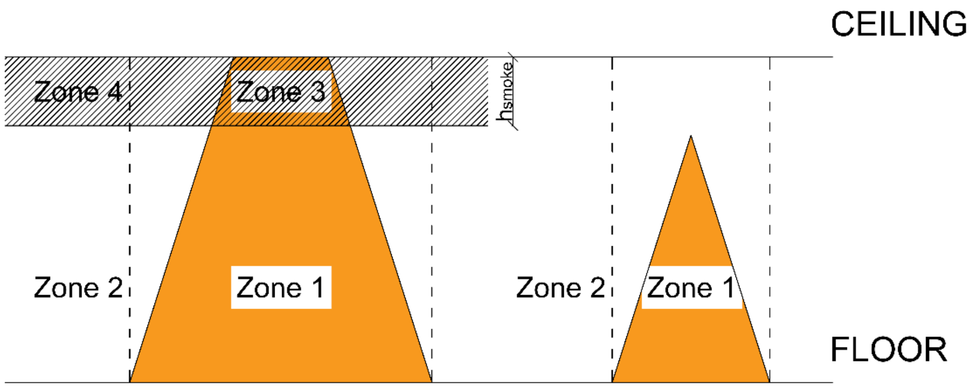

Figure 1 Relevant zones for localised fire impacting the ceiling (left) and not impacting the ceiling (right)

2.2 Analytical formulation of LOCAFI

The simplified analytical formulation of the LOCAFI model is described in Tondini et al. [4] and it based on the discretization of the flame shape into cylinders and rings for which there exist the closed-form solutions of the configuration factors to vertical receiving surfaces, as shown in Figure 2a. In particular, the flux computation $\dot{h}$ received by the columns at given heights is simplified assuming that the normal of Face 1 points to the centre of the fire (Figure 2b). Such heat flux is calculated considering the Heskestad correlations of flame height and flame temperature and computing the configuration factors for each cylinder or ring in which the flame is discretised. The analytical model was implemented in the LF (Localised Fires) software [21] developed inside the LOCAFIplus project [18]. The software makes a further simplification by evaluating a single heat flux that is computed by weighting the heat fluxes received by the 4 faces [17]. In this way, one single steel temperature at each of the selected heights of the steel elements through the simplified equation of heat conduction from EN 1993-1-2 can be obtained

$$\Delta\theta_v = \mathrm{k_{sh}} \frac{A_m V}{\rho_a c_a} \dot{h}_{\mathrm{net}} \Delta \mathrm{t}$$
$$\text{with } \dot{h}_{\mathrm{net}} = \dot{h} - \alpha_c(\theta_m(z_i) - 20) - \phi\sigma\varepsilon_m\varepsilon_f((\theta_m(z_i) + 273)^4 - 293^4) \quad (1)$$

Where ϕ is the configuration factor taken as 1.0, σ is the Stephan-Boltzmann constant, ε_f and ε_m are the fire and steel emissivity respectively (1.0 and 0.7 according to EN 1993-1-2 [19]), $\theta_m(z_i)$ is the surface temperature at height z_i and α_c is the coefficient of heat transfer by convection. The procedure allows for a non-uniform temperature distribution along the column, but no temperature gradient inside the section is defined as only a single steel temperature is determined at each height. Additional details on the procedure can be found in the software user manual [21].

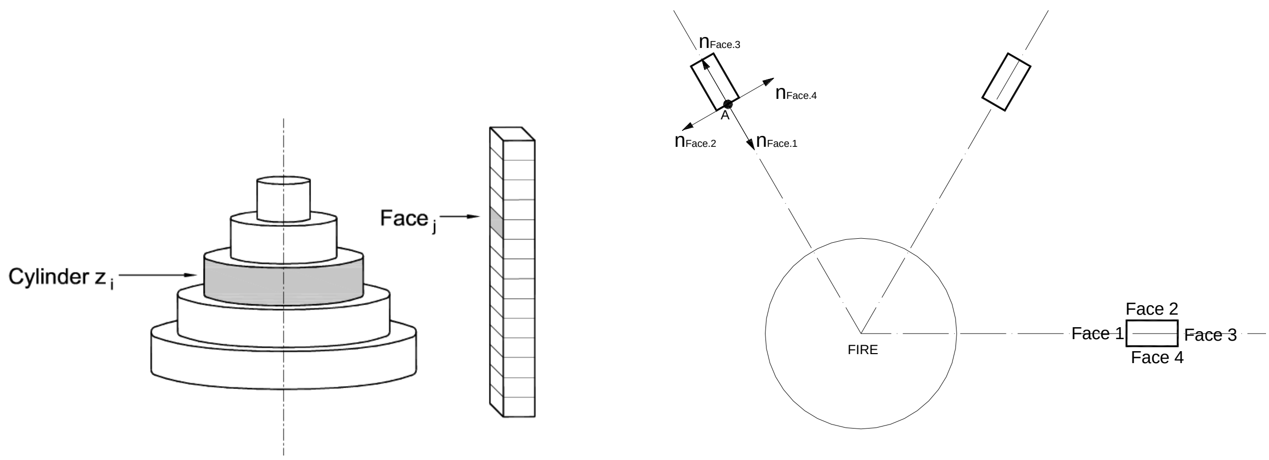

a) b)

Figure 2 Schematic view of the contribution to the heat flux received by *face$_j$* from cylinder *z_i*; b) target orientation towards the centre of the fire

2.3 LOCAFI model integrated in SAFIR

The LOCAFI model was integrated in the software SAFIR [17], enabling a more accurate definition of the thermal field inside the steel section at the selected heights. In detail, the heat fluxes received by the column are calculated with the LOCAFI model by numerically integrating the configuration factors between the discretized flame shape and the discretized column, as shown in Figure 3. However, in this case heat fluxes received by each of the faces of the section are obtained and are considered as boundary condition in a thermal analysis in SAFIR and possible shadow effects are taken into account. By applying the evolution in time of the heat fluxes received by each of the faces of the steel sections, thermal gradients can develop inside the section causing thermal bowing, that may influence the outcomes of the mechanical analysis.

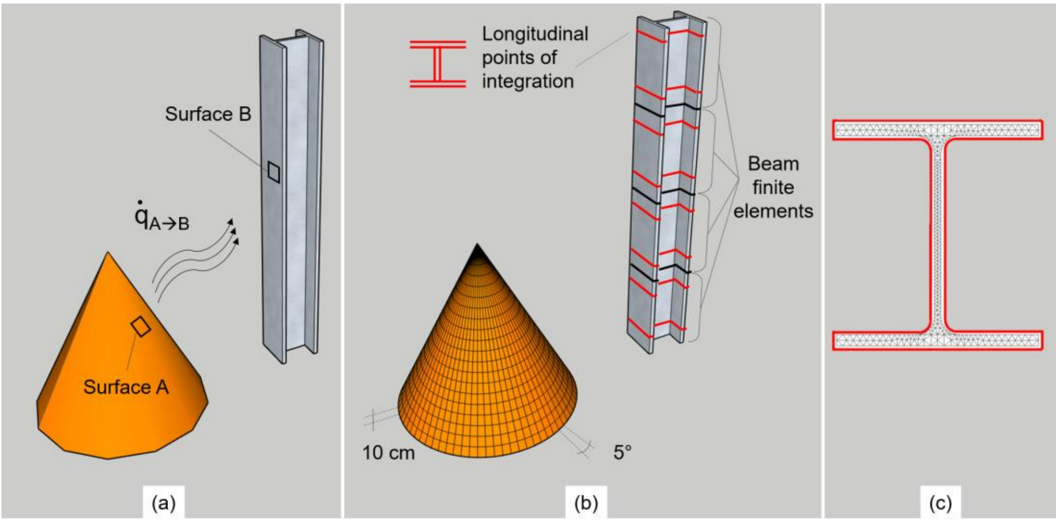

Figure 3 a) Steel column exposed to localised fire; b) LOCAFI numerical model in SAFIR; (c) Cross-section discretization

3 NUMERICAL SIMULATION

3.1 Parametric analysis

The assessment of the capabilities of the different approaches to correctly identify the behaviour of steel compressed elements subjected to localised fire was based on the results of a parametric analysis. As aforementioned, the parametric analysis presented in this paper focused on outdoor fires, i.e. fires outside the structure, implying that the column is located outside the fire and the flame of the fire can develop with no limitations in height given by a ceiling. The main parameters varied in the numerical simulation for both the fire scenario and the steel column definition are summarised in Table 1.

Table 1. Parametric analysis characteristics

Parameters varied			
Fire scenario		Steel column	
3 Positions (°)	α = [0, 45, 90]	**16 Sections**	HE [120, 200, 260, 320] from AA, A, B and M series
2 Fire distances (m)	d = [0.01, 2.00]	**4 Lengths (m)**	L = [2.50, 3.50, 4.50, 5.50]
2 Fire diameters (m)	D = [2.00, 5.00]	**3 Load levels (%)**	L.L. = [60, 75, 90] of $N_{crit,Rd} = N_{\mathrm{b,Rd}}$ [20]
2 Rate of Heat Release density (RHR) (MW/m^2)	q = [0.98, 2.71]		with material partial safety factors γ_M assumed equal to 1 as for the fire situation

The fire scenarios were defined varying the position and the intensity of the localised fires. As depicted in Figure 4, the position of the fire was univocally determined by the distance of the fire *d* from the rectangular envelope of the columns and the orientation α of the line connecting the centroid of the column and the fire. Fires almost impinging the column, i.e. *d* = 0.01 m, and at a distance of 2.00 m were considered and, in order to obtain thermal gradients inside the steel sections with the main components in different directions, three angles α were defined, namely 0°, 45° and 90°.

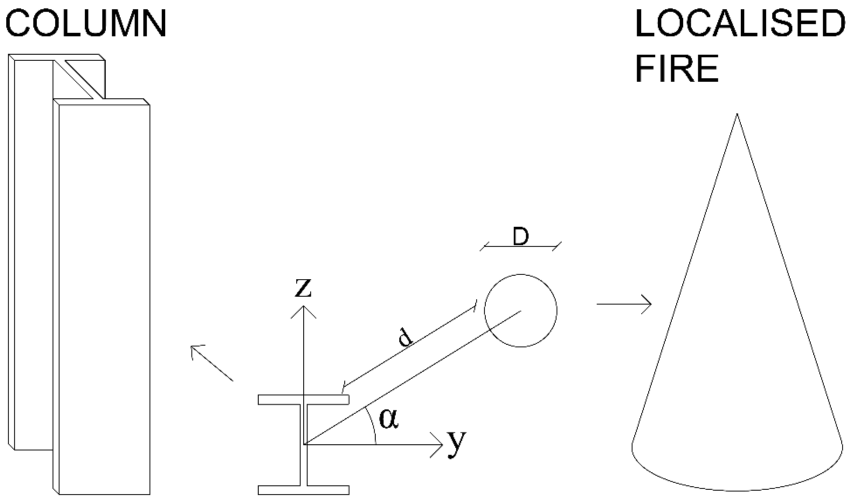

Figure 4 Fire scenario – steel column configuration

The three angles were selected to induce temperature fields inside the cross-sections that could trigger thermal bowing in more than one direction, as depicted in Figure 5 for the integration point immediately below mid-height in the analysis of a 2.5 m long HE120AA column for fire diameter D = 2m and *d* = 0.01m and RHR density equal to 0.98 MW/m^2.

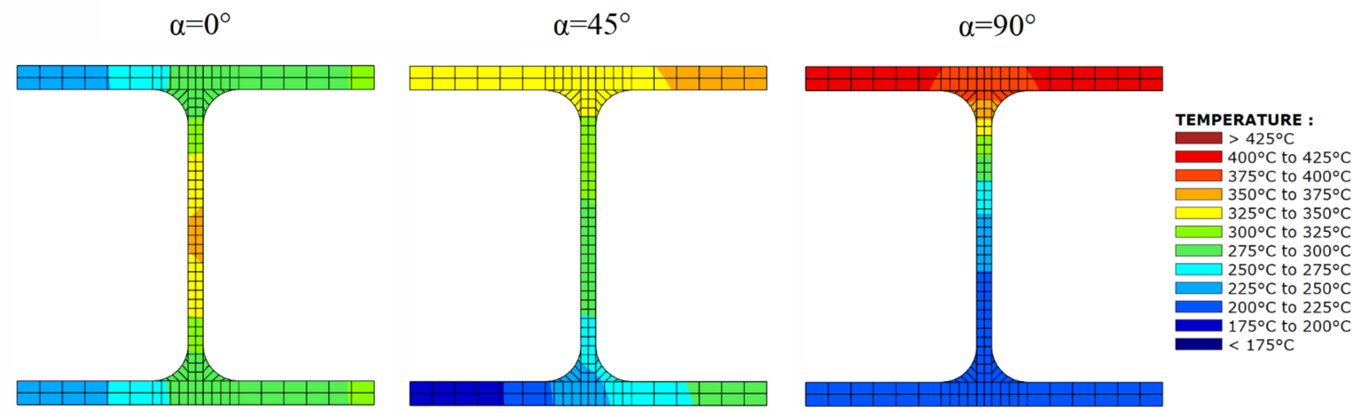

Figure 5. Typical temperature distribution for α equal to 0°, 45° and 90°

Instead, the fire intensity described by the rate of heat release Q (see Eq.(2)) for localised fires with conical shape, was varied employing in the analyses diameters D equal to 2 and 5 meters and RHR density q associated to Acetone and Kerosene, 0.98 MW/m^2 and 2.71 MW/m^2 respectively, as indicated in [16].

$$Q = \min\left(q\left(\frac{\pi D^2}{4}\right); 50MW\right) \tag{2}$$

Columns with sixteen different sections, i.e. HE120, HE200, HE260, HE320 from AA, A, B and M series, and four lengths, namely 2.50, 3.50, 4.50 and 5.50 meters, were selected. This allowed for obtaining steel columns with different non-dimensional slenderness $\bar{\lambda}$, as defined in EN1993-1-1 [20], inside relevant ranges for both the strong (y) and the weak (z) axis. Figure 6 shows the non-dimensional slenderness obtained for each section-length configuration investigated. The load magnitude was defined according to three load levels L.L., i.e. 60%, 75% and 90% of the design compressive force at ambient temperature, determined as the buckling load $N_{b,Rd}$ calculated according to EN1993-1-1 [20], that for values of non-dimensional slenderness less than 0.2 corresponds to the axial plastic resistance for Class 1, 2 and 3 cross sections. The load level equal to 90% was only used for comparison purposes to explore the capacity reserves between the Set 2 and 3 that employ a thermomechanical finite element modelling of the column. Indeed, the probability to have a column loaded to 90% of $N_{b,Rd}$ is very low in reality and it is neglected in design. In total, the parametric analysis consisted of 4608 single case studies (considering column loaded to 90% of of $N_{\mathrm{b,Rd}}$). The steel temperatures and temperature fields obtained with the analytical LOCAFI method implemented in the LF software and the LOCAFI-SAFIR model respectively, were considered in three different sets of analyses to determine the failure time t_{fail} of the columns.

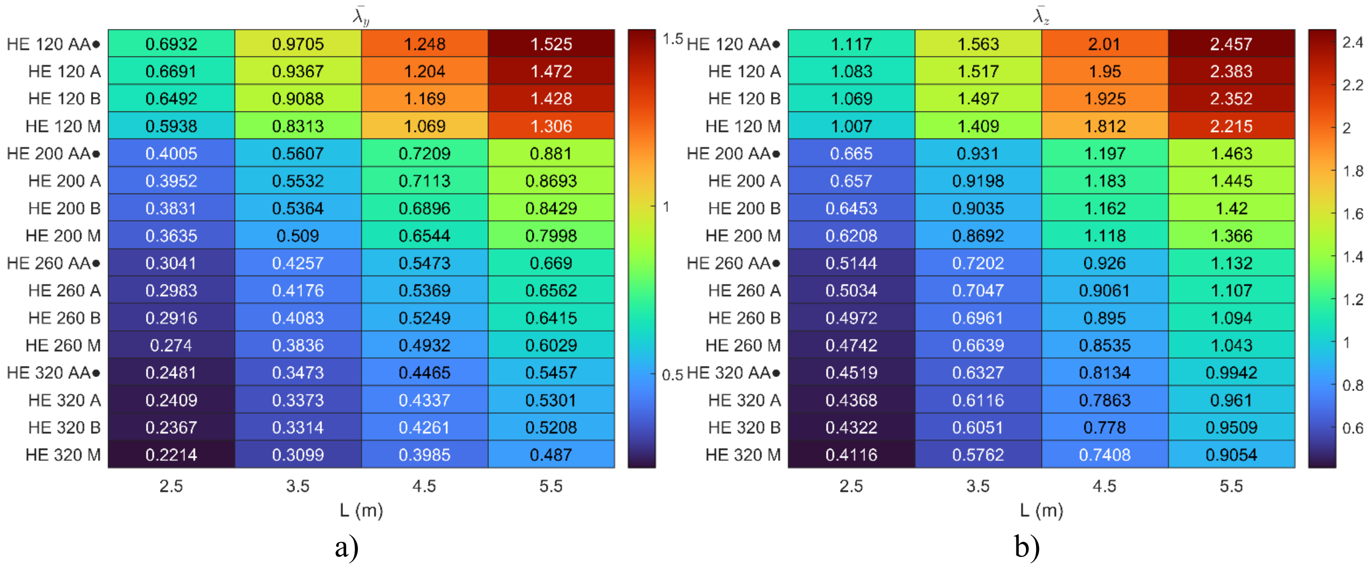

Figure 6. Non-dimensional slenderness vs length of the investigated columns: a) strong axis $\bar{\boldsymbol{\lambda}}_{\boldsymbol{y}}$b) weak axis $\bar{\boldsymbol{\lambda}}_{\boldsymbol{z}}$.

As mentioned, three types of analysis were performed and compared: i) application of the proposed analytical LOCAFI model to compute uniform steel temperatures at different column heights (Section 2.2) and calculation of the failure time with EN1993-1-2 considering the highest temperature; ii) application of i) but computation of the failure time by means of finite element analyses in SAFIR by employing uniform temperatures at the different column heights, iii) use of a more refined version of the LOCAFI model integrated in SAFIR, which directly allows for the thermal gradients in the cross sections at the different heights of the column.

In the first set, assuming that a column fails when the applied load N_{Ed} equals the resistance of the column, the failure time t_{fail} was conservatively obtained at the time when the maximum steel temperature T(t) in the cross section obtained from the LF analysis was such that the buckling resistance of the column $N_{\mathrm{b,fi,t,Rd}}$ as given in EN1993-1-2 [19] equalled the axial force

$$N_{Ed} = N_{\mathrm{b,fi,t,Rd}}(\mathrm{T}(\mathrm{t_{fail}})) \tag{3}$$

Therefore, no mechanical model was necessary to determine the failure time for this set, which represents a simplified procedure that could be employed in the design phase. Instead, a more accurate determination of the failure temperature was involved in the second and the third analysis type, in which mechanical analyses were performed by means of the software SAFIR [17].The numerical model of the column for the mechanical analysis consisted of 10 beam finite elements with two integration points, to which different sectional temperatures could be assigned (Figure 3b). Hence, the uniform steel temperature and temperature fields at the 20 heights associated to the integration points were determined with the LF and the LOCAFI-SAFIR and were introduced in the mechanical models, respectively. The main characteristics of the three sets are summarised in Table 2.

Table 2. Sets of analyses

	Localised fire model	Temperature gradient		Failure time evaluation
		In the section	Along the column	
Set 1	**LF (max temperatures)**	**X**	**X**	**EN 1993-1-2** [19] $N_{\mathrm{b,fi,t,Rd}}$
Set 2	**LF-SAFIR**	**X**	✓	**SAFIR** beam analyses
Set 3	**LOCAFI-SAFIR**	✓	✓	**SAFIR** beam analyses

Simply supported axially compressed columns made of S355 steel subjected to a fire exposure of one hour were studied, a period of time long enough to achieve thermal equilibrium for each fire scenario and column combination. In the numerical model were considered a hinge at the bottom and a roller at the top of the column to permit the application of the axial load. The axial load was linearly applied in the first 100 seconds of the analysis and was then kept constant during the remaining 3600 seconds of fire exposure, as depicted in Figure 7. This solution was adopted to avoid convergence problems in the application of the load, especially for high L.L.s. As a simplification, the localised fires were modelled with a constant diameter, though more complex fire growth models could be employed. In order to consider the effects of both strong and weak axis buckling, initial geometric imperfections were introduced as sinusoidal initial deflections with magnitude of L/1000 and 80% of L/1000 in y and in z direction respectively, see also [3].

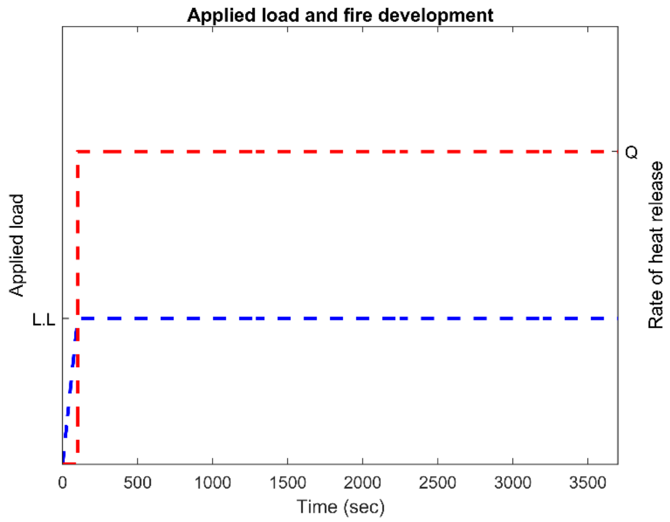

Figure 7. Applied load and fire development

4 DISCUSSION OF THE RESULTS

The failure times and temperatures, hereafter indicated with t and T for simplicity, omitting the subscript “fail”, are compared for the different sets of analyses. The third set is used as reference for comparison, as the LOCAFI-SAFIR procedure offers the most complex and accurate analysis. Moreover, for this comparison, only the columns for which the analyses led to failure in both sets were considered.

4.1 Failure time and temperature for the different approaches

In Figure 8 the results of the simplified procedure employed in the first set of analyses are compared with those of the accurate LOCAFI-SAFIR analysis (set 3) in terms of both temperature and failure time. In Figure 8 and in Figure 9, the results are shown as a function of the non-dimensional slenderness $\bar{\lambda}_y$ with respect to the strong axis. Analogous figures as a function of the non-dimensional slenderness $\bar{\lambda}_z$ with respect to the weak axis could be made, however the distribution of the temperatures and times at failure would be entirely similar to the ones obtained for the strong axis. In addition, due to the presence of thermal gradients leading to thermal bowing, the identification of a failure direction (either about strong or weak axis) is not trivial, and therefore $\bar{\lambda}_y$ is used for the sake of comparison. Figure 8a compares relevant temperatures reached by the columns at failure, i.e. the failure temperature $T_{LF,max\&N_{b,fi,t,Rd}}$ obtained from Eq.(3) and the temperature $T_{max,LOCAFI\text{-}SAFIR,avg}$ obtained with the LOCAFI-SAFIR model as the maximum temperature among the average temperatures in the cross-sections along the column height.

Failure was attained at relatively low temperatures, i.e. between 190° and 470°C, because of quite high L.L., as shown in Figure 8a. As expected, the failure temperature depends on the slenderness of the column, in particular when $N_{b,fi,t,Rd}$ is assumed for checking the column resistance. When applying the Eurocode formula to check buckling at elevated temperature, the failure temperatures decrease with slenderness and range from 255°C to 460°C. The average steel temperatures at failure of the LOCAFI-SAFIR model are located inside a similar range (190°C-470°C), but their variation seems uncorrelated with the slenderness at ambient temperature. One may observe that for stockier columns Set 1 predicts higher temperatures at failures and it is also reflected when considering the failure times depicted in Figure 8b. This is due to the fact that the prediction of the spatial behaviour of a column when subjected to thermal gradients in the cross section and along its length is not trivial. For instance, column buckling occurs with a prevailing strong or weak axis direction depending on the fire scenario, which therefore triggers a much more complex spatial buckling behaviour than the one accounted in a simplified way with the equation of $N_{b,fi,t,Rd}$ in Set 1, for which buckling with respect to the weak axis is always the one providing the lowest $N_{b,fi,t,Rd}$. In Figure 8b the failure times associated with the failure temperatures of Figure 8a are compared in a synthetic manner, by showing the ratio between the failure times of Set 1 and Set 3 with respect to the column slenderness. This representation allows for identifying situations in which the employment of the procedure of Set 1 predicts higher/lower failure temperatures (ratios lower/higher than 1) with respect to the ones of the reference set (Set 3). Following the discussion of the previous figure, Figure 8b show that it is not possible to identify slenderness values for which the Set 1 provides always lower or higher failure time estimates.

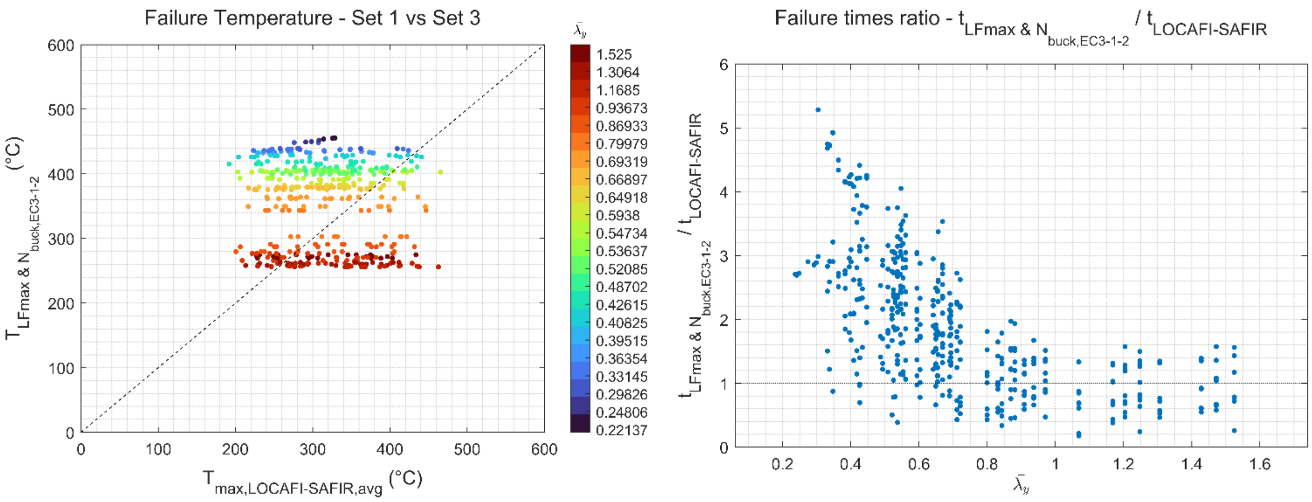

a) b)

Figure 8. Set 1 vs Set 3: a) failure temperatures b) failure temperatures ratio vs slenderness

In Figure 9a, the maximum steel temperature along the column at failure in the LF analyses of set 2 is compared with the maximum average sectional steel temperature in the LOCAFI-SAFIR analyses of set 3. In this case, both failure temperatures are uncorrelated with the slenderness, but some correlation can be seen between them given the slenderness, by observing that points with similar colours are disposed in clouds of data with an orientation of approximately 45°. This reflects the fact that both the LF and the LOCAFI-SAFIR procedures rely on the thermomechanical finite element modelling. With both the procedures columns with a L.L.=90% were considered. Figure 9b illustrates that Set 2 mainly produced higher temperatures at failure than Set 3 and this was also observed by looking at the failure times. With respect to the previous analysis, this fact becomes more evident when the slenderness increases and this can be explained by the presence of significant thermal gradients in the cross section that cause thermal bowing and higher second order effects. Thus, from these preliminary analyses it is recommended to perform an advanced modelling, e.g. using the finite element method, in order to more accurately capture the complex behaviour of axially compressed columns exposed to localised fires.

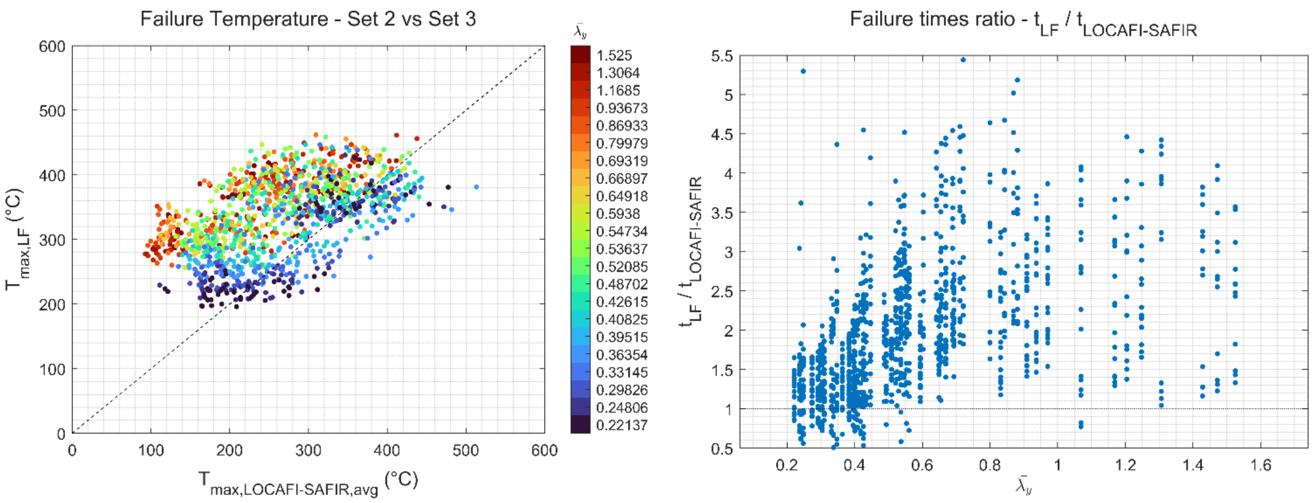

a) b)

Figure 9. Set 2 vs Set 3: a) failure temperatures b) failure temperatures ratio vs slenderness

5 CONCLUSIONS

The work presented in this paper investigates the effects of neglecting thermal gradients, both in the section and along the length, when the resistance of compressed steel members has to be determined. Three possible design procedures that consider temperature fields with an increasing level of complexity were explored, starting with a procedure that provides a single temperature for the whole column (Set 1) and introducing a non-uniform temperature distribution along the column first (Set 2) and then in the cross-section as well (Set 3). The three procedures were applied to a parametric analysis of compressed steel members subjected to localised fires with different severity and location with respect to the steel member. Heat fluxes received by the compressed elements were obtained through the LOCAFI model by means of the analytical LOCAFI model implemented in the LF software in the first two procedures, while a refined version of LOCAFI integrated in SAFIR was employed to determine thermal gradients in the cross-sections in the third procedure. This preliminary analysis showed that the spatial behaviour of an axially compressed columns subjected to thermal gradients in the cross section and along their height is not straightforward to predict. Indeed, simplified procedures, i.e. the ones employed in Set 1 and Set 2, provided different times of failure compared with the more refined procedure of Set 3. In particular both higher and lower failure time predictions were obtained with both the simplified procedures of Set 1 and Set 2 and therefore, the use of advanced thermomechanical simulation allowing for considering thermal gradients both in the cross section and along the column length are recommended when the behaviour of compressed steel elements subjected to localised fires has to be determined. In future applications, axially compressed elements with more fire scenarios, load levels and different supports, representing more realistic boundary conditions and simple steel frames will be investigated to gain more knowledge and provide more detailed indications for practitioners.

ACKNOWLEDGMENT

The support received from the Italian Ministry of Education, University and Research (MIUR) in the frame of the ‘Departments of Excellence’ (grant L 232/2016) is gratefully acknowledged

REFERENCES

1. Possidente L., Tondini N., Battini J.M. (2022). Torsional and flexural-torsional buckling of compressed steel members in fire. J. Construct. Steel Res., 171
2. Couto C, Vila Real P, Lopes N, Rodrigues JP. Buckling analysis of braced and unbraced steel frames exposed to fire. Eng Struct 2013;49:541–59. doi:10.1016/j.engstruct.2012.11.020.

3. Couto C, Vila Real P. The influence of imperfections in the critical temperature of I-section steel members. J Constr Steel Res 2021;179. doi:10.1016/j.jcsr.2021.106540.
4. Tondini N., Thauvoye C., Hanus F., Vassart O. (2019) Development of an analytical model to predict the radiative heat flux to a vertical element due to a localised fire. Fire Saf J;105(March):227–43.
5. Ojeda O. D., Maljaars J., Abspoel R. (2016) Fire exposed steel columns with a thermal gradient over the cross-section. Thin-Walled Structures 98 https://doi.org/10.1016/j.tws.2015.02.009.
6. Tan K.H., Yuan W.F. (2008) Buckling of elastically restrained steel columns under longitudinal non-uniform temperature distribution. Journal of Constructional Steel Research 64(1) https://doi.org/10.1016/j.jcsr.2007.02.003.
7. Usmani A.S., Rotter J.M., Lamont S., Sanad A.M., Gillie M. (2001) Fundamental principles of structural behaviour under thermal effects. Fire Safety Journal 36(8)2001 https://doi.org/10.1016/S0379-7112(01)00037-6.
8. Ren Y., Huo R., Zhou D. (2022) Buckling and post-buckling analysis of restrained non-uniform columns in fire. Engineering Structures 272, https://doi.org/10.1016/j.engstruct.2022.114947.
9. Zhang C., Choe L., Seif M., Zhang Z. (2015) Behavior of axially loaded steel short columns subjected to a localized fire. Journal of Constructional Steel Research 111, https://doi.org/10.1016/j.jcsr.2014.11.012.
10. Zhang C., Gross J. L., McAllister T. P. (2015) Behavior of Unrestrained and Restrained Bare Steel Columns Subjected to Localized Fire. Journal of Structural Engineering 141(10) https://ascelibrary.org/doi/abs/10.1061/%28ASCE%29ST.1943-541X.0001225
11. Zhang C., Gross J. L., McAllister T. P. (2013) Lateral torsional buckling of steel W-beams subjected to localized fires. Journal of Constructional Steel Research 88 http://dx.doi.org/10.1016/j.jcsr.2013.06.004
12. Zhang C., Li G.-Q., Usmani A. (2013) Simulating the behavior of restrained steel beams to flame impingement from localized-fires. Journal of Constructional Steel Research 83 https://doi.org/10.1016/j.jcsr.2013.02.001.
13. Hanus F., Vassart O., Tondini N., Nadjai A., Franssen J. (2016) Temperature assessment of a vertical steel member subjected to localised fire: experimental tests. In: Proceedings of the 9th conference on structures in fire.
14. Tondini N., Franssen J.-M. (2017) Analysis of experimental hydrocarbon localised fires with and without engulfed steel members. Fire Saf J;92(May):9–22.
15. Francis P., Baddo N., Hanus F., Thauvoye C. (2018) Design of columns subject to localised fires. The Steel Construction Institute (SCI).
16. Randaxhe J., Popa N., Tondini N. (2021) Probabilistic fire demand model for steel pipe-racks exposed to localised fires. Engineering Structures 226
17. Franssen J.M., Gernay T. (2017). Modeling structures in fire with SAFIR®: theoretical background and capabilities. J Struct Fire Eng;8(3):300–23.
18. LOCAFIplus - Temperature assessment of a vertical steel member subjected to localised fire – Valorisation, Grant Agreement number: 754072, RFCS-2016, 1/7/2017 - 31/12/2018.
19. European Committee for Standardisation (2005). Eurocode 3 Design of steel structures - Part 1-2: General rules - Structural fire design.
20. European Committee for Standardisation (2005). Eurocode 3 Design of steel structures - Part 1-1: General rules and rules for buildings.
21. Ferreira M., Vila Real, P., LF - Localised Fires, RISCO, Civil Engineering Department, University of Aveiro, Portugal

LATERAL-TORSIONAL BUCKLING FIRE DESIGN OF STAINLESS STEEL I BEAMS UNDER COMBINED END MOMENTS AND TRANSVERSE LOADS

Nuno Lopes[1], Carlos Couto[2], Paulo Vila Real[3], Dinar Camotim[4], Rodrigo Gonçalves[5]

ABSTRACT

New design expressions for stainless steel laterally unrestrained beams under fire conditions have recently been proposed to be incorporated in the second-generation version of Eurocode 3 (EC3) – however, their merit assessment, in the context of beams acted by different bending moment diagrams, is still a relevant issue requiring investigation. Hence, this work presents a numerical study on the lateral-torsional buckling resistance of stainless steel I-beams with slender or non-slender cross-sections, when acted by different combinations of end moments and transverse concentrated or distributed loads at elevated temperatures. The safety and accuracy of the failure moment predictions provided by the EC3 design approaches (current and second-generation version) are assessed through the comparison with extensive numerical failure moment data, obtained with the ANSYS software. It is shown that these methodologies can be improved, as they may lead to overly conservative or unsafe failure moment estimates.

Keywords: Stainless steel beams; fire design; lateral-torsional buckling; combined loading; numerical study

1 INTRODUCTION

Although the main advantage of stainless steels is their corrosion resistance, the aesthetic appearance, ease of maintenance and durability are also valuable features. These advantages can lead to structures enduring a longer life with lower maintenance and repair requirements that compensate for the higher initial cost of stainless steel [1-4]. In addition, the resistance of stainless steel to elevated temperatures is generally higher than that of carbon steel, especially in the common range of steel structural element critical temperatures (500 °C to 700 °C). This fact, which contributes towards reducing the structure initial costs related to fire protection, is thus relevant when performing a complete cost analysis.

Concerning structural design, the relevant European structural design standards (Eurocodes) are Part 1-4 of EC3 [5] (rules for stainless steel structures at normal temperature) and Part 1-2 of EC3 (EN 1993-1-2:2005, fire design guidelines) [6]. These design standards are currently under revision being their second-generation versions already at their final stages of preparation (prEN 1993-1-4:2021 [7] and prEN 1993-1-2:2021 [8]).

Stainless steels exhibit non-linear stress-strain relationships with a low proportional limit stress and an extensive hardening phase [9]. There is no well-defined yield strength, which is usually taken as the 0.2% proof strength $(f_{p0.2})$ at normal temperature design [5,7]. Higher deformations are acceptable in structures

[1] Associate professor, RISCO, Civil Engineering Department, University of Aveiro, Portugal
e-mail: nuno.lopes@ua.pt
[2] Assistant Researcher, RISCO, Civil Engineering Department, University of Aveiro, Portugal
e-mail: ccouto@ua.pt
[3] Full professor, RISCO, Civil Engineering Department, University of Aveiro, Portugal
e-mail: pvreal@ua.pt
[4] Full professor, CERIS, Civil Engineering Department, Technical University of Lisbon, Portugal
e-mail: dcamotim@civil.ist.utl.pt
[5] Associate professor with habilitation, CERIS, Civil Engineering Department, Nova School of Science & Technology, Lisbon, Portugal
e-mail: rodrigo.goncalves@fct.unl.pt
https://doi.org/10.6084/m9.figshare.22202563

under fire situation, which justifies the adoption by Part 1-2 of EC3 [6,8] of the stress corresponding to the 2% total strain as the yield strength at elevated temperatures.

It is well known that the loading type significantly influences the lateral-torsional buckling (LTB) resistance of steel I-beams, which led to the development of EC3 design rules accounting for the beneficial effect of non-uniform bending in laterally unrestrained beams. Researches on carbon steel I-beams with stocky sections susceptible to LTB [10] led to the proposal of new design formulae (to be incorporated in prEN 1993-1-2:2021 [8]), which account for the beneficial effect of non-uniform bending, as was already foreseen in Part 1-1 of EC3 [11]. Subsequent studies [12] have also shown the need for the adoption of a similar approach to design Class 4 carbon steel beams under fire, and proposed small adjustments to the previous proposal for beams with stocky sections. No recommendations for the consideration of non-uniform bending on Class 3 carbon steel beams have yet been proposed for incorporation in EC3. Studies by Vila Real et al. [13], performed on Class 1 and 2 I-section stainless steel beams at elevated temperatures, suggested the implementation of approaches similar to those developed for carbon steel I-beams, which have been validated for different loading cases [14]. But, finally, the second-generation of Part 1-2 of EC3 [8] will prescribe new design approaches for stainless steel members with only two cross-section classes (non-slender and slender) and includes new design formulae accounting for non-uniform bending in LTB fire design. However, information and knowledge concerning the influence of the loading (bending moment diagram shape) on the beam failure moment are still lacking and need to be acquired [15]. In this context, a recent investigation has addressed the fire resistance of stainless steel I-beams acted by equal and unequal end moments [16] – however, the presence of transverse loads on the beams analysed was not considered.

Hence, the purpose of this work is to provide a further contribution towards assessing the safety and accuracy of the existing design rules to estimate the LTB fire resistance of stainless steel beams (namely those included in EN 1993-1-2:2005 and prEN 1993-1-2:2021), when applied to beams under non-uniform bending – note that the above design rules were developed almost exclusively in the context of beams under uniform bending. In particular, this work deals with simply supported beams subjected to bending moment diagrams caused by combinations of end moments and transverse (mid span concentrated and uniformly distributed) loads, all proportional to a single load parameter – these loadings were chosen because they concern situations commonly encountered in practice and, therefore, must be covered by the LTB design formulae.

Geometric and material non-linear analyses with imperfections (GMNIA), using the ANSYS software [17], are performed to obtain the fire resistances of laterally unrestrained I-beams exhibiting different combinations of stainless steel grade, bending moment diagrams, cross-section dimensions and elevated temperature. By comparing the numerical failure moments with their predictions provided by the LTB curves prescribed in EN 1993-1-2:2005, it is possible to conclude that this design approach provides overly conservative estimate. On the other hand, it is also shown that the design approach proposed in prEN 1993-1-2:2021 needs to be modified/adjusted, in order to ensure a better failure moment prediction quality, as it currently provides both too conservative and unsafe estimates of the numerical failure moments obtained in this work.

2 STAINLESS STEEL MECHANICAL PROPERTIES AT ELEVATED TEMPERATURES

This study deals with austenitic (1.4301 and 1.4401), ferritic (1.4003) and duplex (1.4462) stainless steels at elevated temperatures, and their adopted constitutive laws and reduction factors (which vary with the steel grade [9]) are those prescribed in the second-generation Part 1-2 of EC3 [8] – it is worth recalling that they differ from those appearing in the current version of this document [6].

The second-generation of Part 1-2 of EC3 [8] proposes a constitutive model based on a two-phase Ramberg-Osgood formulation [9] to simulate the stainless steel mechanical behaviour at elevated temperatures. Figure 1 illustrates the corresponding constitutive laws of stainless steel grades 1.4301, 1.4401, 1.4462 and 1.4003 at 550 °C [8], which exhibit quite different hardening behaviours, as attested by their ultimate strengths and strains − it is worth noting the very low ductility of the ferritic grade 1.4003.

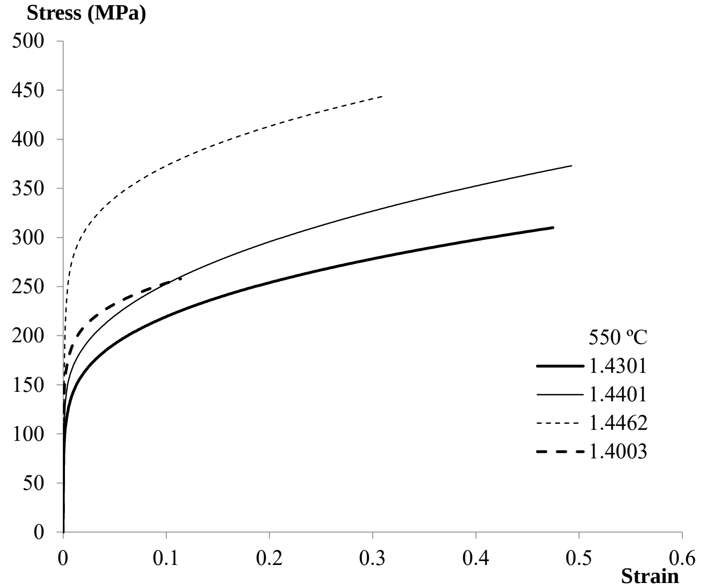

Figure 1. Constitutive laws of the stainless steel grades considered in this work at 550 °C

3 NUMERICAL MODEL FOR UNRESTRAINED I-SECTION BEAMS

This section (i) provides the description and illustrates the numerical model employed in this investigation, and (ii) characterises the loading types considered for the I-section beams involved in the parametric study performed, which exhibit several cross-section slenderness values and lengths.

3.1 Model description

Geometrical and material non-linear analyses with imperfections (GMNIA) were carried out to obtain the failure moments of the selected I-beams, which were discretised using the shell finite element SHELL181 available in the ANSYS [17] library. In addition, linear buckling analyses (LBA) were also performed to define the shape of the initial geometric imperfections considered in the numerical analyses. Regarding the mesh definition, a sensitivity analysis showed that a finite element size of 20 mm and an aspect ratio of 1.0 are adequate to achieve accurate results with a reasonable computational cost. Owing to the high width-to-thickness ratio of the sections considered and the high thermal conductivity of steel, the temperature was deemed uniform within the whole beam. This numerical model was previously validated against experimental tests involving stainless steel beams prone to LTB [16].

The beam failure loadings were obtained using a force-controlled procedure with an increasing load parameter. Bending moments about the y-axis were applied at the beam end cross-sections and a transversal load, either concentrated at mid-span or uniformly distributed, was applied at the lower flange mid-point (by means of nodal forces). A maximum number of iterations was set and an automatic time stepping was allowed by the software – the quality of the solution was assessed later, by inspecting the load-displacement curves obtained.

Simple supports were considered at both ends of the beams, preventing the displacements in the transverse z- and y-directions and torsion. To preclude rigid-body motions, the longitudinal x-direction displacements were restrained at mid-span. Moreover, stiff diaphragms were added at the beam end cross-sections, where 50 mm-thick end plates were included to ensure a correct load distribution and prevent undesirable localised stress concentrations [16] – the presence of these end plates precludes the occurrence of warping at the beam end cross-sections (this also applies to the numerical determination of the beam critical moments – M_{cr} [16]).

Residual stresses and initial geometrical imperfections were included in the numerical models – the former were defined as initial state conditions and consisted of the welded residual stress pattern proposed in [18].

Both local (or plate) and global (or member) geometrical imperfections were included in the numerical models – the corresponding shapes defined by eigenmodes obtained from preliminary LBA. Following the recommendations of Annex C of Part 1-5 of Eurocode 3 [19], the two initial imperfections were combined by (i) taking the critical buckling mode as the leading imperfection and (ii) scaling to 70% the amplitude of the non-critical buckling mode. Concerning the initial imperfection amplitudes, L/1000 was considered for the global imperfection and 80% of the fabrication tolerance values prescribed in EN 1090-2 [20] was taken for the local imperfection (web and flanges) – depending on the most displaced node location, the amplitude was scaled to either the web or flange imperfection value, thus ensuring affinity between the local imperfection shape and critical buckling mode.

3.2 Parametric study

This parametric study deals with doubly symmetric I-section beams whose end cross-sections are simply supported and prevented from warping (due to the presence of end plates). As mentioned before, the stainless steel grades considered are 1.4301, 1.4401, 1.4462 and 1.4003, with yield and ultimate strengths at normal temperature of 230, 240, 500, 280 MPa and 540, 530, 700, 450 MPa, respectively [21].

The I cross-sections considered, identified by the web height x thickness + flange width x thickness (values in mm), are 416x8+150x8, 416x5+135x8, 336x5+150x8, 416x5+200x8, 516x5+225x8, 416x10+150x12, 416x10+135x16, 336x12+135x16 and 336x10+150x16. These dimensions were chosen with the purpose of covering a wide range of cross-section slenderness values, varying from non-slender to slender (according to the classification in prEN 1993-1-2:2021 [9]). The beams are subjected to uniform elevated temperatures equal to 350 °C, 450 °C, 550 °C and 650 °C, chosen to cover the most common critical temperatures in steel structural elements, namely those with slender sections.

The loadings considered in this study consist of combinations of end moments (equal end moments and moment on only one end) and transverse (mid span concentrated or uniformly distributed) loads, all proportional to a single load parameter (*P* or *p*). Two approaches were used to select the end moments: values corresponding to (i) the elastic analysis of beams with fixed-fixed or fixed end supports, and (ii) beams with identical maximum positive and negative moments (occurring in plastic analyses involving the formation of more than one plastic hinge). While the first approach, named "Elastic analyses", can be viewed as a common practical case of beams prone to LTB, the second one, named "Plastic analyses", was often employed in the development of LTB design formulae (it constitutes the most severe situation). Table 1 presents the various loadings and corresponded bending moment diagrams – note that the combination of equal end moments with a mid-span concentrated load leads to the same moment diagram shape for the elastic and plastic analyses.

Finally, 15 lengths are considered for each cross-section, which means that the parametric study carried out in this work involves more than 12000 FEM analyses.

Table 1. Beam loadings considered in this work

	Loading		Bending moment diagram	
	Elastic analyses	Plastic analyses	Elastic analyses	Plastic analyses
Two end moments plus concentrated load	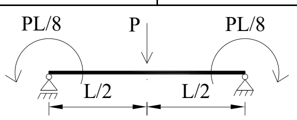			
One end moment plus concentrated load	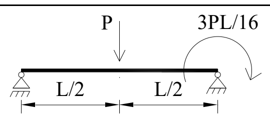	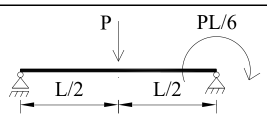		
Two end moments plus distributed load	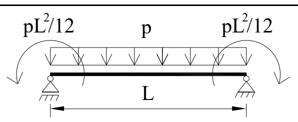	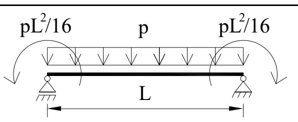		
One end moment plus distributed load	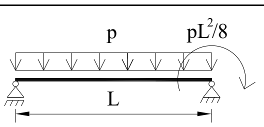	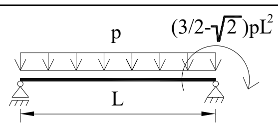		

4 FIRE DESIGN APPROACHES FOR STAINLESS STEEL BEAMS SUSCEPTIBLE TO LTB

The application of the design approaches prescribed in EN 1993-1-2:2005 [6] and prEN 1993-1-2:2021 [8], to beams prone to LTB at elevated temperatures when subjected to the loadings indicated in Table 1, is assessed in this section.

4.1 Design formulae in EN 1993-1-2:2005 [6]

EN 1993-1-2:2005 [6] states that the fire design rules developed for carbon steel members subjected to elevated temperatures must also be used for stainless steel members. As done in other parts of EC3 [5,11], it also considers four cross-section classes, dependent on their compressed internal and outstand wall slenderness values and ranging from stocky (Class 1 and 2) to the slender (Class 4 sections – highly susceptible to the occurrence of local buckling). This classification is based on the slenderness limits given in the current Part 1-4 of EC3 [5], adapted to fire design by means of the reduction factor 0.85, intended to account for the steel strength and stiffness erosion due to the increasing temperature.

The LTB resistant moments are obtained from the expression

$$M_{b,fi,t,Rd} = \chi_{LT,fi} W_y k_{y,\theta} f_y \frac{1}{\gamma_{M,fi}} \tag{1}$$

where W_y is either the plastic section modulus $W_{pl,y}$ (Class 1 and Class 2 sections), elastic section modulus $W_{el,y}$ (Class 3 sections) or effective section modulus $W_{eff,y}$, calculated at normal temperature with the EN 1993-1-4:2006 [5] effective width reduction formulae (Class 4 sections). Moreover, for Class 1, 2 and 3 sections, the yield strength reduction factor $k_{y,\theta}$ must be considered, since the yield strength at elevated temperatures corresponds to the 2% total strain, while for Class 4 sections under fire conditions this yield strength must be taken as the 0.2% proof strength (according to Annex E of EN 1993-1-2:2005 [6]). The LTB reduction factor $\chi_{LT,fi}$ is given by

$$\chi_{LT,fi} = \frac{1}{\Phi_{LT,\theta} + \sqrt{\Phi_{LT,\theta}^{2} - \bar{\lambda}_{LT,\theta}^{2}}} \tag{2}$$

where

$$\Phi_{LT,\theta} = \frac{1}{2}\left[1 + \alpha\bar{\lambda}_{LT,\theta} + \bar{\lambda}_{LT,\theta}^{2}\right] \tag{3}$$

and the imperfection factor α, dependent on the steel grade, is determined from

$$\alpha = 065\sqrt{235/f_y} \tag{4}$$

The relative slenderness for LTB at high temperatures is given by

$$\bar{\lambda}_{LT,\theta} = \bar{\lambda}_{LT}\sqrt{\frac{k_{y,\theta}}{k_{E,\theta}}} \tag{5}$$

where $k_{E,\theta}$ is the reduction factor for Young's modulus at elevated temperatures and the relative slenderness at normal temperature reads

$$\bar{\lambda}_{LT} = \sqrt{\frac{W_y f_y}{M_{cr}}} \tag{6}$$

where M_{cr} is the elastic critical moment concerning the loading and support conditions under consideration, based on gross cross-sectional properties (taken from the literature or obtained numerically). In this study, the M_{cr} values were obtained from numerical LBAs accounting for the presence of the beam end plates, which prevent the end cross-section warping.

The current Part 1-2 of EC3 [6] does not consider the loading influence on the design formulae for laterally unrestrained beams – indeed, the LTB curve is independent of the loading. Figure 2 shows the comparison between the $\chi_{LT,fi}$ values obtained from the numerical failure moments and their EN 1993-1-2:2005 estimates, for the 1.4301 steel beams acted by an uniformly distributed load (elastic and plastic analyses) at elevated temperatures. Results concerning beams under uniform bending at elevated temperatures, analysed previously [16], are also plotted to enable a better understanding of the buckling curve accuracy in the most severe situation (essential to develop LTB design rules). This comparison clearly shows how the moment diagram shape influences considerably the failure moment prediction quality provided by the current LTB design curve. Note that, in order to ensure a more meaningful comparison between the numerical failure moments and their predictions, the stainless steel mechanical property reductions factors at elevated temperatures prescribed in prEN 1993-1-2:2021 [8] were adopted in all the analyses.

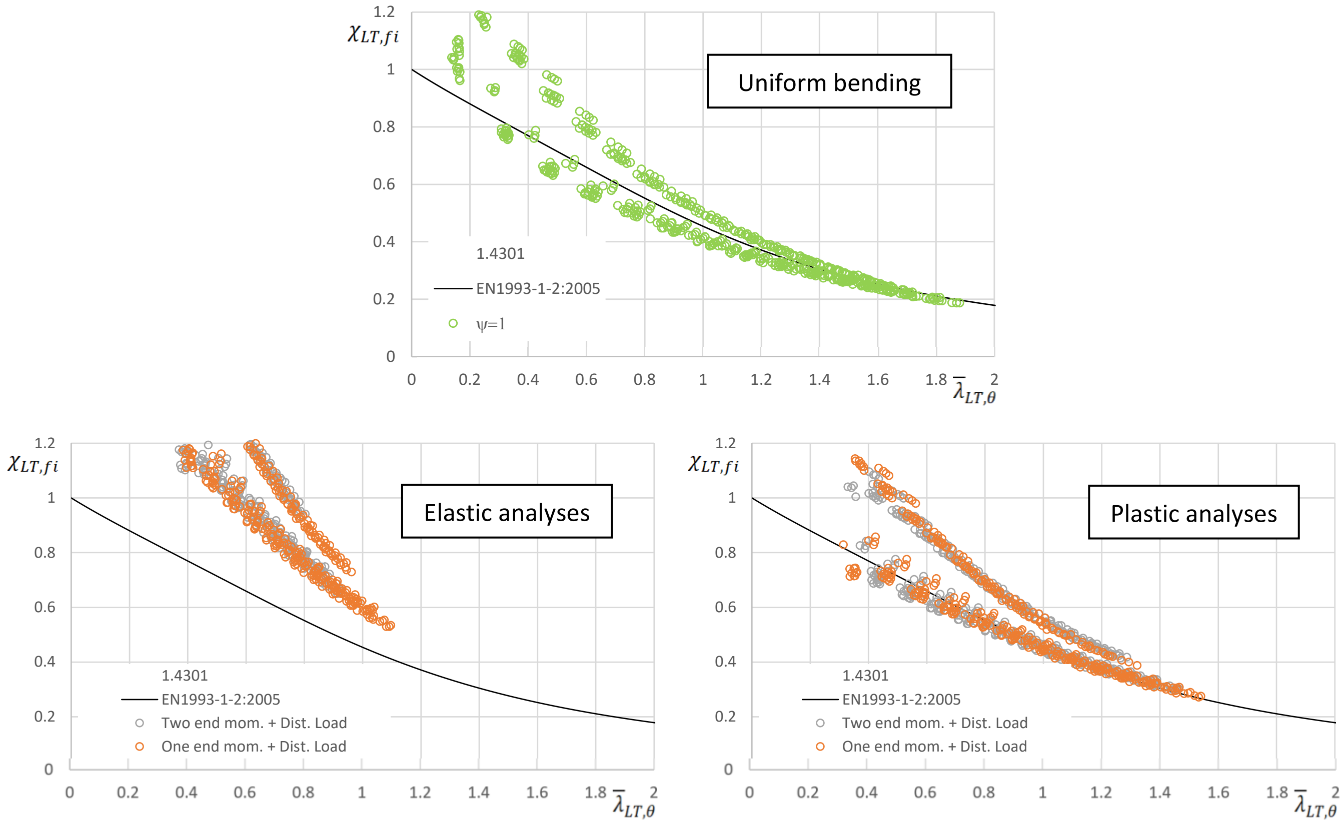

Figure 2. Comparison between the numerical $\chi_{LT,fi}$ values and their EN 1993-1-2:2005 estimates for the 1.4301 steel beams under (i) uniform bending [16] and (ii) end moments plus uniformly distributed load (elastic and plastic analyses) at elevated temperatures

4.2 Design formulae prescribed in prEN 1993-1-2:2021 [8]

The second-generation Part 1-2 of EC3 [8] introduces a number of changes in the design of stainless steel members, namely concerning the beam LTB resistance formulae. The cross-section classification in [8] is based on a new approach, involving only two classes (slender and non-slender) and considering the slenderness of the cross-section internal and outstand compressed walls as a function of the elevated temperature [22]. The fire design resistance of beams susceptible to LTB must be determined according to the expressions

$$\begin{cases} \text{Non}-\text{slender sections: } M_{b,fi,t,Rd} = \chi_{LT,fi} W_{pl,y} k_{2\%,\theta} f_y \frac{1}{\gamma_{M,fi}} \leq M_{c,Rd} \\ \text{Slender sections: } M_{b,fi,t,Rd} = \chi_{LT,fi} W_{eff,y} k_{2\%,\theta} f_y \frac{1}{\gamma_{M,fi}} \leq M_{c,Rd} \end{cases} \tag{7}$$

which involve the stress corresponding to the total strain of 2% for all cross-section classes. The LTB formulae, Equations (2) and (3), are still adopted, but with a different imperfection factor,

$$\alpha = \alpha_{LT} = \alpha_{LT,0} / \xi_{\theta,com} \tag{8}$$

where

$$\xi_\theta = \sqrt{k_{2\%,\theta}/k_{E,\theta}} \tag{9}$$

and $\alpha_{LT,0}$ is a function of the stainless steel group – it is equal to 0.64, 0.45 and 0.4, respectively for welded or hot-rolled beams made of austenitic, duplex and ferritic steel.

The relative LTB slenderness at elevated temperatures is given by

$$\bar{\lambda}_{LT,\theta} = \bar{\lambda}_{LT}\xi_{\theta,com} \tag{10}$$

where $\bar{\lambda}_{LT,\theta}$ is the relative lateral-torsional slenderness at normal temperature, obtained from

$$\begin{cases} \text{Non} - \text{slender sections: } \bar{\lambda}_{LT} = \sqrt{\frac{W_{pl,y}f_y}{M_{cr}}} \\ \text{Slender sections: } \bar{\lambda}_{LT} = \sqrt{\frac{W_{eff,y}f_y}{M_{cr}}} \end{cases} \tag{11}$$

The current Part 1-1 of EC3 [11] accounts for the influence of the loading on the beam failure moments by means of a modified LTB reduction factor $(\chi_{LT,\text{mod}})$, dependent on the bending moment diagram shape. A similar approach is being considered for inclusion in the second-generation Part 1-2 of EC3 [8] – it prescribes that the effect of the bending moment diagram shape, between laterally restrained cross-sections of a stainless steel member, must be taken into account by modifying the LTB reduction factor to

$$\chi_{LT,\text{fi,mod}} = \frac{\chi_{LT,\text{fi}}}{f} \text{ but } \begin{cases} \chi_{LT,\text{fi,mod}} \leq 1.0 \\ \chi_{LT,\text{fi,mod}} \leq \frac{1}{\bar{\lambda}^2_{LT,\theta,com}} \end{cases} \tag{12}$$

where f is determined from

$$\begin{cases} Austenitic: f = 1 - 0.83(1 - k_c) \geq 0.67 \\ Duplex: f = 1 - 0.67(1 - k_c) \geq 0.73 \\ Ferritic: f = 1 - 0.60(1 - k_c) \geq 0.76 \end{cases} \tag{13}$$

with k_c depending on the bending moment diagram shape, as proposed in prEN 1993-1-1:2021 [23] – see Table 2 – note that the values do not vary with the analyses types considered in this work.

Figure 3 concerns the 1.4301 steel beams and shows how the above factor f, accounting for the bending moment diagram shape, influences the LTB fire design curves prescribed in prEN 1993-1-2:2021 [8]. Moreover, it also compares these design curves with the numerically obtained LTB reduction factors, for the beams (i) acted by end moment plus an uniformly distributed load (elastic and plastic analyses) and (ii) under uniform bending (reported in [16]). It can be observed that factor f leads to (i) overly conservative failure moment predictions for all the elastic analysis bending diagrams, and (ii) several unsafe predictions for the plastic analysis bending diagrams (most of them involving one end moment).

Table 2. Correction factor k_c for different bending moment diagram shapes (obtained from prEN 1993-1-1:2021 [23])

Elastic analyses	Plastic analyses	k_c
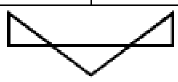		0.77
		0.82
		0.90
		0.91

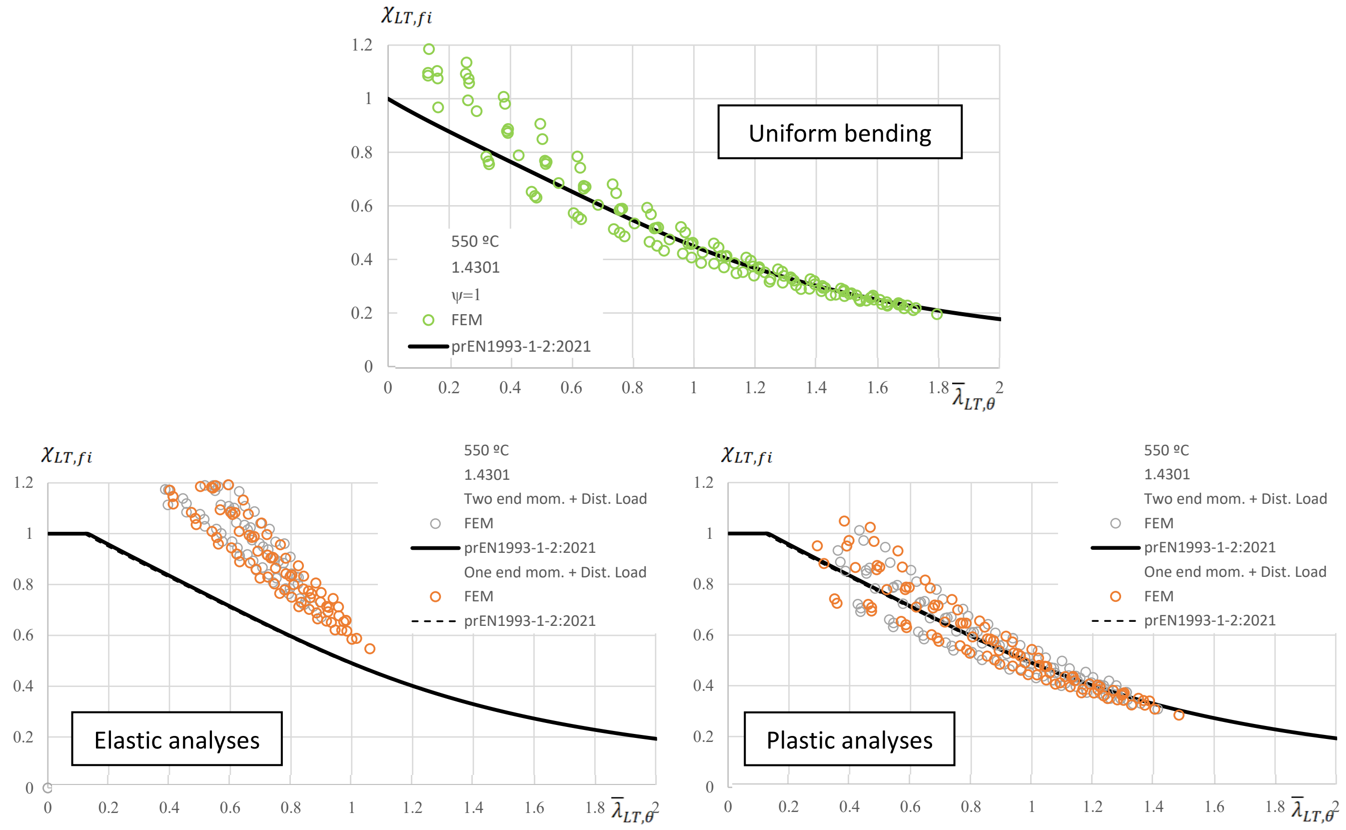

Figure 3. Comparison between the numerical $\chi_{LT,fi}$ values and their prEN 1993-1-2:2021 estimates for the 1.4301 steel beams under (i) uniform bending [16] and (ii) end moments plus uniformly distributed load (elastic and plastic analyses) at 550 °C

5 PRESENTATION AND DISCUSSION OF THE PARAMETRIC STUDY OUTPUT

This section assesses the failure moment prediction quality provided by the different design approaches, using the criteria proposed by Kruppa [24] for the predicted-to-numerical failure moment ratios. According to these criteria, a design approach is considered safe if (i) the ratio average is lower than 1.0, (ii) the number of unsafe predictions (ratios higher than 1.0) is less than 20% of the whole set and (iii) the maximum (unsafe) ratio does not exceed 1.15 – the statistical indicators not satisfying the above criteria are written in red in Table 3 and Table 4, which include also the ratio standard deviations. It should be noted that the short beam numerical failure moments exceeding the cross-section resistance predictions by more than 10% (due to strain-hardening) were disregarded in the statistical evaluation.

5.1 Beams acted by elastic analysis bending moment diagrams

Figure 4 makes it possible to assess the accuracy and safety of the design approaches considered in this work for the beams acted by bending moment diagrams obtained from elastic analyses. A statistical evaluation of the failure moment predictions is presented in Table 3. It can be concluded that, for these loadings, both design approaches are excessively conservative, with the exception of the prEN 1993-1-2:2021 predictions of the failure moments of the beams acted by equal end moments plus a mid-span concentrated load, whose bending moment diagram is the same for elastic and plastic analyses – in the next section, it will be shown that on all the prEN 1993-1-2:2021 failure moment predictions concerning beams acted by with analysed cases with plastic analysis bending moment diagrams need to be improved.

Table 3. Statistical evaluation of the de sign approaches considered (elastic analyses)

		n	average	% unsafe	max. unsafe	st. dev.
EN 1993-1-2:2005	Two end mom. + Conc. Load	1403	0.83	1.6	1.01	0.10
	One end mom. + Conc. Load	1320	0.76	0.0	-	0.08
	Two end mom. + Dist. Load	617	0.65	0.0	-	0.05
	One end mom. + Dist. Load	932	0.67	0.0	-	0.06
prEN 1993-1-2:2021	Two end mom. + Conc. Load	1469	1.01	52.2	1.24	0.11
	One end mom. + Conc. Load	1339	0.89	6.3	1.05	0.08
	Two end mom. + Dist. Load	624	0.71	0.0	0.84	0.05
	One end mom. + Dist. Load	950	0.73	0.0	0.88	0.06

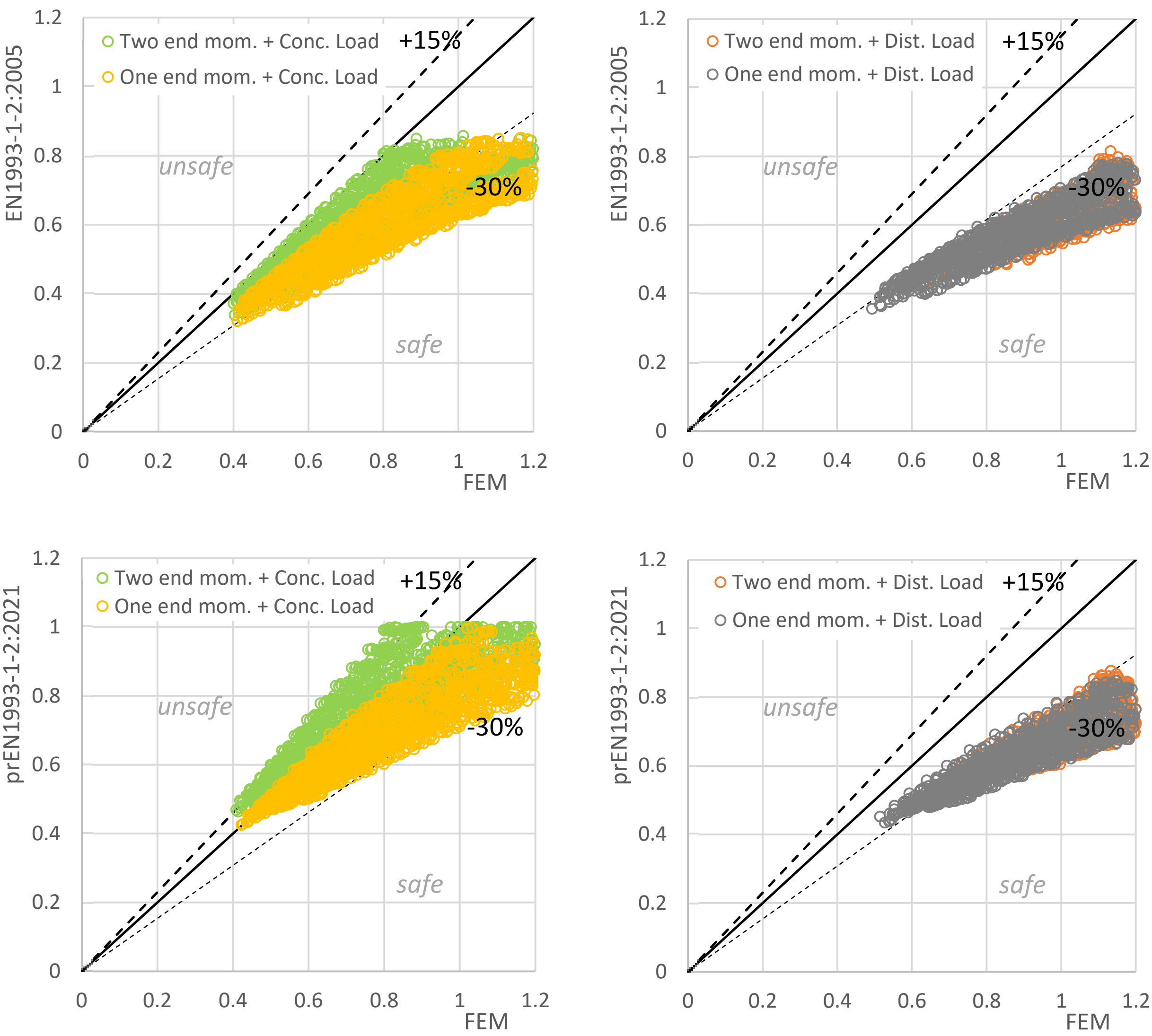

Figure 4. Failure moment prediction quality provided by the design approaches considered (elastic analyses)

5.2 Beams acted by plastic analysis bending moment diagrams

Figure 5 and Table 4. are similar to those presented in Section 5.1, but concern now bending moment diagrams obtained from plastic analyses. It can be observed that the prEN 1993-1-2:2021 failure moment predictions are unsafe for all the beams analysed. On the other hand, the EN 1993-1-2:2005 LTB design curves always underestimate the numerical failure moments.

Table 4. Statistical evaluation of the design approaches considered (plastic analyses)

		n	average	%unsafe	maxunsafe	stdev
EN 1993-1-2:2005	Two end mom. + Conc. Load*	1403	0.83	1.6	1.01	0.10
	One end mom. + Conc. Load	1523	0.83	0.0	-	0.09
	Two end mom. + Dist. Load	1585	0.87	11.7	1.11	0.10
	One end mom. + Dist. Load	1477	0.88	9.5	1.13	0.10
prEN 1993-1-2:2021	Two end mom. + Conc. Load*	1469	1.01	52.2	1.24	0.11
	One end mom. + Conc. Load	1568	0.96	36.7	1.16	0.10
	Two end mom. + Dist. Load	1596	0.96	32.6	1.19	0.09
	One end mom. + Dist. Load	1507	0.95	32.8	1.18	0.09

*These same results were presented in Table 3.

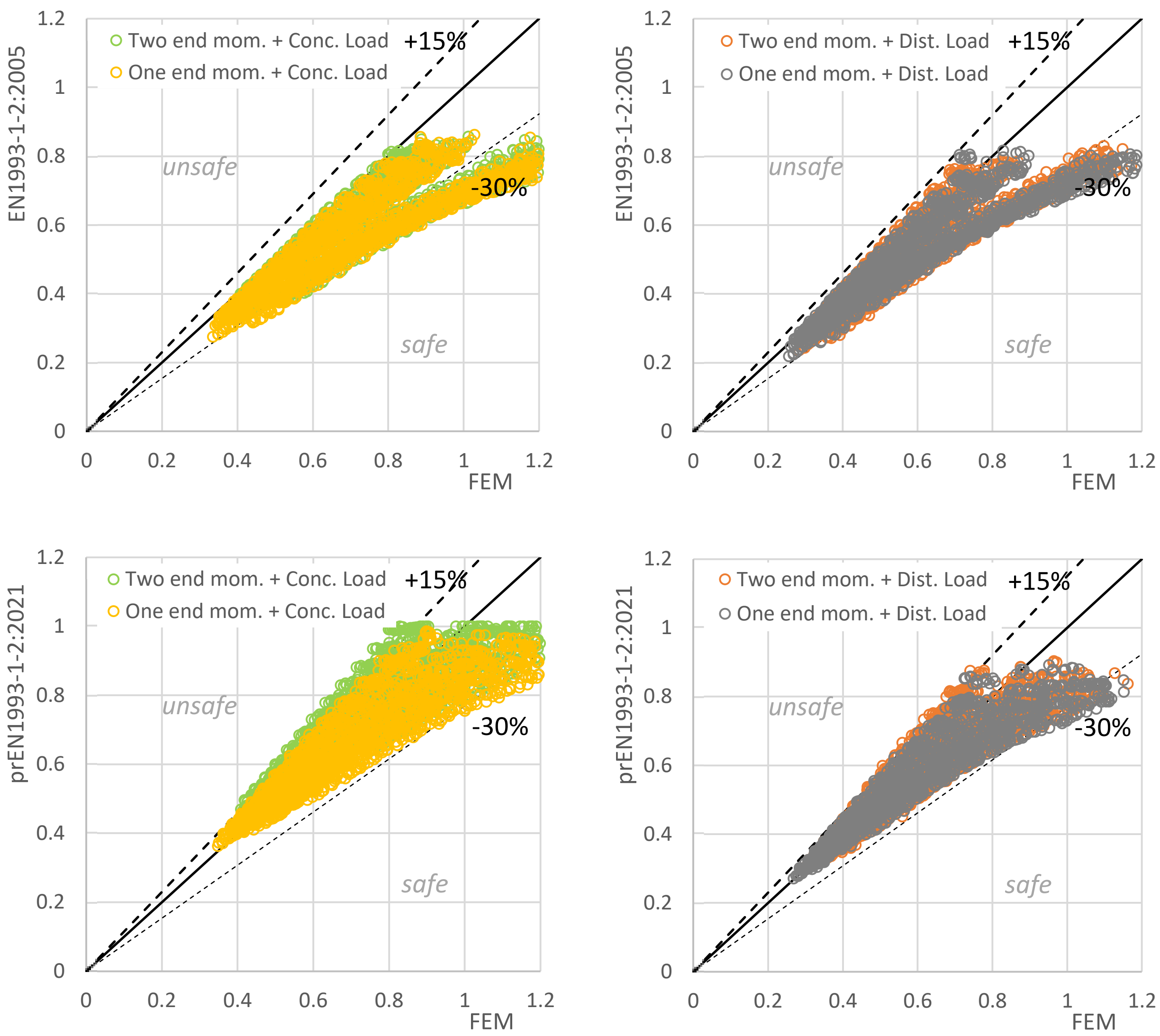

Figure 5. Failure moment prediction quality provided by the design approaches considered (plastic analyses)

6 CONCLUSIONS

A numerical investigation concerning the fire resistance of stainless steel I-beams susceptible to LTB when acted by combinations of end moments and transverse (mid-span concentrated and uniformly distributed) loads was presented in this paper. Its main purpose was to assess how the bending moment diagram shape influences the failure moment prediction quality provided by the EC3 design approaches (current and upcoming second-generation version). This assessment was made through the comparison of numerical beam failure moments, obtained from an extensive parametric study (carried out by means of ANSYS geometric and material non-linear analyses with imperfections), with their predictions provided by the above EC3 design approaches – both beams with non-slender and slender cross-sections were considered. Over 12000 I-section beams were analysed, acted by seven different bending moment diagrams shapes caused by combinations of end moments (equal end moments or moment acting only at one end) and transverse (mid-span concentrated and uniformly distributed) loads. The end moment values were chosen to match the bending moment diagrams obtained from elastic and plastic analyses.

It was observed that the design approach included in the current version of Part 1-2 of EC3 (EN 1993-1-2:2005) provides overly conservative predictions of all the failure moments obtained in this work – the overestimations are smaller for the beams acted by plastic analysis bending moments diagrams. Concerning the design approach to be included in the second-generation version of Part 1-2 of EC3 (prEN 1993-1-2:2021), it also provides overly conservative failure moment estimates for the beams acted by elastic analysis bending moments diagrams – note that beams acted by these bending moments, quite common in practical applications, were not considered in the development of these EC3 LTB design rules. Conversely, the prEN 1993-1-2:2021 provides unsafe failure moment estimates for the stainless steel beams acted by plastic analysis bending moments diagrams – recall that same happened for the beams under uniform bending moments, as previously concluded in [16].

In view of what was mentioned above, it can be readily concluded that the EC3 LTB design rules still need to be modified/improved, in order to achieve an acceptable failure moment prediction quality for beams acted by arbitrary bending moment diagrams.

ACKNOWLEDGMENTS

The financial support of FCT ("Fundação para a Ciência e a Tecnologia" – Portugal) is gratefully acknowledged by the (i) first three authors, through project UIDB/04450/2020 (funding of the research unit RISCO) (ii) second author, through the Scientific Employment Stimulus (Institutional Call) CEECINST/00026/2018, and (iii) fourth and fifth authors, through project UIDB/04625/2020 (funding of the research unit CERIS).

REFERENCES

1. Baddoo, N., "Stainless steel in construction: A review of research, applications, challenges and opportunities", Journal of Constructional Steel Research, 64(11), 1199-1206, 2008.
2. Gardner, L., "Stability and design of stainless steel structures – Review and outlook", Thin-Walled Structures, 141(August), 208-216, 2019.
3. SCI (Steel Construction Institute), "Design Manual for Structural Stainless Steel", SCI publication P413 (4th edition), 2017.
4. Mirambell, E., Real, E., "On the calculation of deflections in structural stainless steel beams: an experimental and numerical investigation", Journal of Constructional Steel Research, 54(1), 109-133, 2000.
5. CEN (European Committee for Standardisation), EN1993-1-4, Eurocode 3, Design of Steel Structures – Part 1-4. General rules – Supplementary Rules for Stainless Steels, Brussels, Belgium, 2006.
6. CEN (European Committee for Standardisation), EN1993-1-2, Eurocode 3, Design of Steel Structures – Part 1-2. General rules – Structural fire design, Brussels, Belgium, 2005.
7. CEN (European Committee for Standardisation), prEN1993-1-4, Eurocode 3, Design of Steel Structures – Part 1-4. General rules – Supplementary Rules for Stainless Steels, Brussels, Belgium, 2021.

8. CEN (European Committee for Standardisation), prEN1993-1-2, Eurocode 3, Design of Steel Structures – Part 1-2. General rules – Structural fire design, Brussels, Belgium, 2021.
9. Liang, Y., Manninen, T., Zhao, O., Walport, F., Gardner, L., "Elevated temperature material properties of a new high-chromium austenitic stainless steel" Journal of Constructional Steel Research, 152(January), 261-273, 2019.
10. Vila Real, P., Lopes, N., Simões da Silva, L., Franssen, J.-M., "Parametric analysis of the lateral-torsional buckling resistance of steel beams in case of fire", Fire Safety Journal, 42(6-7), 416-424, 2007.
11. CEN (European Committee for Standardisation), EN1993-1-1, Eurocode 3, Design of Steel Structures – Part 1-1. General rules and rules for buildings. Brussels, Belgium, 2005.
12. Couto, C., Vila Real, P., Lopes, N., Zhao, B., "Numerical investigation of the lateral-torsional buckling of beams with slender cross sections for the case of fire", Engineering Structures, 106(1 January), 410-421, 2016.
13. Vila Real, P., Lopes, N., Simões da Silva, L., Franssen, J.-M., "Lateral-torsional buckling of stainless steel I-beams in case of fire", Journal of Constructional Steel Research, 64(11), 1302-1309, 2008.
14. Lopes, N., Vila Real, P., Simões da Silva, L., Franssen, J.-M., "Lateral-torsional buckling on carbon steel and stainless steel beams with lateral loads plus end moments in case of fire", Proceedings of 6th International Conference on Structures in Fire (SiF'10 − East Lansing, USA), 67-74, 2010.
15. Martins, A., Camotim, D., Gonçalves, R., Lopes, N., Vila Real, P., "Transversally loaded stainless steel beams under fire: local/global behaviour, strength and design", Journal of Constructional Steel Research, 189(February), paper 107080, 2022.
16. Lopes, N., Couto, C., Vila Real, P., Camotim, D., Gonçalves, R., "Fire design of stainless steel I beams prone to lateral torsional buckling under end moments", Fire Safety Journal, 131(July), paper 103609, 2022.
17. Ansys®, Academic Research Mechanical, Release 18.2.
18. ECCS (European Convention for Constructional Steelwork), New Lateral Torsional Buckling Curves kLT − Numerical Simulations and Design Formulae, ECCS Technical Committee Publication No. 8; 2000.
19. CEN (European Committee for Standardisation), EN1993-1-5, Eurocode 3 - Design of steel structures - Part 1-5: Plated structural elements, 2006.
20. CEN (European Committee for Standardisation), EN1090-2, Execution of Steel Structures and Aluminium Structures − Part 2: Technical Requirements for Steel Structures, Brussels, Belgium, 2018.
21. CEN (European Committee for Standardisation), EN10088-4, Stainless steels. Part 4: Technical delivery conditions for sheet/plate and strip of corrosion resisting steels for construction purposes, Brussels, Belgium, 2009.
22. Xing, Z., Kucukler, M., Gardner, L., "Local buckling of stainless steel I-sections in fire: finite element modelling and design". Thin-Walled Structures, 161(April), paper 107486, 2021.
23. CEN (European Committee for Standardisation), prEN 1993-1-1, Eurocode 3, Design of Steel Structures – Part 1-1. General rules and rules for buildings. Brussels, Belgium, 2021.
24. Kruppa, J., "Eurocodes – Fire Parts, Proposal for a Methodology to Check the Accuracy of Assessment Methods", CEN TC 250, Horizontal Group Fire, Document n° 99/130, 1999.

COMPARING ANALYTICAL AND MACHINE-LEARNING-BASED DESIGN METHODS FOR SLENDER SECTION STEEL MEMBERS IN FIRE

Carlos Couto[1], Qi Tong[2], Thomas Gernay[3]

ABSTRACT

In thin-walled steel members, the complexity of the interaction between the buckling of the plates and the buckling of the member, combined with the reduction of steel properties with increasing temperature, hinders the development of simple accurate analytical models. As a result, analytical design methods tend to be overly conservative for simple situations, and inexistent for more complex situations such as temperature gradients and systems-level response, leading to unreliable fire design methods and affecting the attractiveness of these structures that are designed with optimization in mind. Meanwhile, data-based approaches using Machine Learning (ML) techniques have allowed overcoming complex nonlinear problems in various engineering disciplines. ML may provide fast models surpassing existing analytical methods and achieving accuracy similar to Finite Element-based solutions at much lower computational cost. While the development of ML models requires sophisticated modelling and large datasets, which may not always be available, once a ML model is developed its application to practical design situations within the limits of its validity is straightforward. This paper investigates opportunities from application of ML methods to the problem of thin-walled steel members in fire, including critical comparison of benefits and capabilities between ML methods and existing analytical approaches. With a dataset of 2304 data points for columns and 24516 for beams, the paper shows that ML models can outperform current state-of-the-art analytical models in terms of agreement with high-fidelity shell FE results.

Keywords: Machine learning; Thin-walled members; Fire; Temperature; Shell finite elements; Instability

1 INTRODUCTION

Structures made of thin-walled steel members are widely used, from highly optimized portal frames to structural systems such as light-steel framing. Their exceptional weight-to-strength ratio provides an appealing solution from the cost and material savings point of view. However, these structural members are susceptible to local buckling, a failure mode that can greatly reduce the load bearing capacity of the members. The added complexity resulting from the interaction between local buckling of the plates at the cross-section level and buckling of the member (i.e., flexural buckling and lateral torsional buckling) has hindered the development of more economic yet safe analytical design methods, which goes counter to the advantage of thin-walled members as a means to optimize design and material use. While analytical methods derived from mechanics-based principles and experimental observations are very useful for design, they are necessarily based on simplifying assumptions that lead to conservatism. Further improving their accuracy requires increasing their level of complexity, for example in the form of additional buckling curves for local and/or global buckling, which affects the practicality and makes user mistakes more likely for use as design methods.

[1] Assistant Researcher, RISCO, Civil Engineering Department, University of Aveiro, Portugal
e-mail: ccouto@ua.pt, ORCID: https://orcid.org/0000-0003-0865-2225
[2] PhD Student, Department of Civil and Systems Engineering, Johns Hopkins University, Baltimore, USA
e-mail: qtong5@jhu.edu
[3] Assistant Professor, Department of Civil and Systems Engineering, Johns Hopkins University, Baltimore, USA
e-mail: tgernay@jhu.edu, ORCID: https://orcid.org/0000-0002-3511-9226
https://doi.org/10.6084/m9.figshare.22202605

Stemming from possible failure due to local buckling, Finite Element (FE)-based solutions require more complex models at higher cost. Traditional beam FE models are unable to capture the effects of local buckling thus shell finite models must be used. These complex models are cumbersome to use in a daily basis, since not only the calculation cost is much higher but also the modelling part is harder and time-consuming. Although efforts to enhance the beam FE-based models to include the reduction in capacity due to local buckling were developed [1,2] these techniques are still in their infancy.

Meanwhile, data-based approaches using Machine Learning (ML) techniques have allowed overcoming complex nonlinear problems in many engineering disciplines. ML may provide fast models surpassing analytical methods and achieving accuracy close to that of FE models at much lower computational cost. This has recently led to interest towards their application for the case of structures in fire [3].

This paper investigates the development and application of ML techniques for predicting the capacity of thin-walled columns and beams at elevated temperatures. To construct the ML models, datasets are generated for elevated temperature failure of thin-walled columns and beams using a numerical model with shell finite elements in the software SAFIR [4]. Training of artificial neural networks, support vector machines and polynomial regression is carried out using established numerical methods. The outputs of the ML model are then compared against those from SAFIR and from Eurocode 3 analytical methods.

2 ANALYTICAL MODELS

2.1 Effective cross-section

For slender steel columns under compression, the evaluation of load carry capacity at elevated temperature must consider the effect of local buckling. Part 1.5 of Eurocode 3 provides expressions of reduction factors for plate buckling resistance under compression, based on the concept of effective width method accounting for geometric imperfection and residual stresses [5]. Couto et al. [6] proposed an updated formula to account for the local buckling of slender steel members (Class 3 and Class 4) at elevated temperature and replaced the use of design yield strength corresponding to the 0.2% proof strength with the yield strength at 2% total strain for Class 4.

The effective width of plates at elevated temperature can be calculated as:

$$b_{eff} = \rho_\theta \times b \tag{1}$$

The new expression [6] for a plate reduction factor of internal compression elements is:

$$\rho_\theta = \frac{(\bar{\lambda}_p+\alpha_\theta)^{\beta_\theta} - 0.055(3+\psi)}{(\bar{\lambda}_p+\alpha_\theta)^{2\beta_\theta}} \leq 1.0 \tag{2}$$

For outstand compression element it is:

$$\rho_\theta = \frac{(\bar{\lambda}_p+\alpha_\theta)^{\beta_\theta} - 0.188}{(\bar{\lambda}_p+\alpha_\theta)^{2\beta_\theta}} \leq 1.0 \tag{3}$$

$\bar{\lambda}_p$ is the non-dimensional slenderness of a plate given by:

$$\bar{\lambda}_p = \frac{b/t}{28.4\varepsilon\sqrt{k_\sigma}} \tag{4}$$

where k_σ is the buckling coefficient of plates, b and t are the width and thickness of the plates, ψ is the stress ratio between two ends. Coefficients α_θ and β_θ are given in Table 2 of the paper by Couto et al. [6] for internal compression elements (web) and outstand compression elements (flanges). ε is calculated as:

$$\varepsilon = \sqrt{\frac{235}{f_y}}\sqrt{\frac{E}{210000}} \text{ in which } f_y \text{ and } E \text{ in Mpa} \tag{5}$$

According to the current Eurocode 3 Part 1-2, the effective section is determined for $\alpha_\theta = 0$ and $\beta_\theta = 1$.

2.2 Buckling of columns and beams

Once the effective width of the plates is calculated and the effective properties of the section determined, the load-carrying capacity of the members can be evaluated by making allowance for the flexural buckling or lateral-torsional buckling in the columns and beams using equations (6a) or (6b), respectively.

$$N_{\mathrm{b,fi,t,Rd}} = \chi_{\mathrm{fi}} \cdot A_{\mathrm{eff}} \cdot k_{\mathrm{y},\theta} \cdot f_{\mathrm{y}} \;/\; \gamma_{\mathrm{M,fi}} \tag{6a}$$

$$M_{\mathrm{b,fi,t,Rd}} = \chi_{\mathrm{LT,fi}} \cdot W_{\mathrm{eff}} \cdot k_{\mathrm{y},\theta} \cdot f_{\mathrm{y}} \;/\; \gamma_{\mathrm{M,fi}} \tag{6b}$$

where A_{eff} and W_{eff} are the effective section area and effective sections modulus, k_{θ} is the reduction factor for the yield strength at elevated temperatures, f_{y} is the yield strength, $\gamma_{\mathrm{M,fi}}$ is the safety factor taken as 1.0. According to the present version of the Eurocode 3 Part 1-2, for Class 4 sections, $k_{\mathrm{y},\theta}$ is taken as the reduction factor for the 0.2% proof strength of steel at elevated temperatures ($k_{\mathrm{p},0.2,\theta}$).

For the columns, the buckling reduction factor for flexural buckling χ_{fi} is calculated as:

$$\chi_{fi} = \frac{1}{\phi_\theta + \sqrt{\phi_\theta^2 - \bar{\lambda}_\theta^2}} \quad \text{and} \quad \chi_{fi} \leq 1.0 \tag{7}$$

$\bar{\lambda}_\theta$ is the non-dimensional slenderness at elevated temperature and $\phi_\theta$is calculated as:

$$\phi_\theta = 0.5\left[1 + \alpha\left(\bar{\lambda}_\theta - \lambda_0\right) + \bar{\lambda}_\theta^2\right] \tag{8}$$

$\lambda_0 = 0$ and with α is the imperfection factor calculated as:

$$\alpha = 0.65\varepsilon = 0.65\sqrt{235/f_y} \tag{9}$$

The non-dimensional slenderness at elevated temperature $\bar{\lambda}_\theta$ is calculated as:

$$\bar{\lambda}_\theta = \sqrt{\frac{A_{eff} f_y k_{y,\theta}}{k_{E,\theta} N_{cr,20}}} \tag{10}$$

where $k_{E,\theta}$ is the reduction factor for Young's modulus at elevated temperatures, and $N_{cr,20}$ is the elastic critical capacity at ambient temperature.

For beams, the same procedure given by equations (7)-(10) is used to calculate the lateral-torsional buckling reduction factor $\chi_{\mathrm{LT,fi}}$ with the subscript "LT" added to the parameters. However, α_{LT} and λ_0 take different values for beams with Class 4 cross-sections in the new generation of the Eurocode 3 Part 1-2, with the values proposed given by Couto et al. [7]. A modification factor "f" is also included to take into account the non-uniform bending diagrams as detailed in [8], and the non-dimensional slenderness is calculated as a function of the section resistance to major-axis bending and the elastic critical moment.

3 NUMERICAL MODEL AND DATASET

3.1 Finite element model

Numerical modelling was used to analyse members made of I-shaped slender cross-sections subjected to axial compression and major-axis bending at elevated temperatures. The numerical models were built using shell elements in the nonlinear finite element software SAFIR [4]. Columns and beams with different plate slenderness, lengths and, for the case of beams, end-moment ratios were modelled. The structural members were uniformly heated on four sides. Pinned or fixed support conditions, on the columns, and fork-supports on the beams were considered. A sensitivity analysis on the mesh size was conducted to have a sufficiently refined mesh while preserving an appropriate computational cost.

The constitutive model included in the simulations followed the non-linear stress-strain relationship and reduction factors defined in Eurocode 3 Part 1-2 [9]. Steels with grades S235, S355, and S460 at ambient temperature were used in the numerical models. Young's modulus of elasticity at ambient temperature was taken as 210 GPa and Poisson's ratio as 0.30.

Both geometric imperfections and material imperfections, in the form of residual stresses, were included in the models. For global imperfection, the amplitude followed the design recommendation, i.e. $L/1000$, where L is the length of the member. For local imperfection, the amplitude was calculated as 80% of the geometric fabrication tolerances [10]. The global imperfection and local imperfection were combined following the recommendation of Annex C in Part 1-5 of Eurocode 3 [5]. In accordance with the recommendations of this Annex, the full amplitude was considered for the leading imperfection while that of the accompanying imperfections was reduced to 70%. For the residual stresses, the pattern included in the models followed the one for hot-rolled columns and welded beams [10].

For columns, two rigid 100 mm thick endplates were added at both ends of the column. The load was axially applied on the edge of the vertical plate on the top with no eccentricity such that the load can be distributed evenly on the web and flange. The displacements of two rigid extensions were constrained except for the vertical direction on the top (Uy) which was left free to allow free thermal expansion. The rotations of two rigid extensions were either fixed or pinned in Rx, Ry, and Rz directions (see Figure 1).

For beams, fork-supports were used at both ends of the structural member to prevent the displacements in x-direction and y-direction. To prevent rigid body movement, the displacements in z-direction were constrained at mid-span. The loading was applied by nodal forces to produce end-moments at both ends. Additionally, end-plates were included with a thickness equal to 10 times the web thickness to ensure correct load distribution.

The ultimate load-bearing capacity of the columns was calculated with SAFIR considering steady-state conditions i.e., by first uniformly increasing the temperature in the section up to the target value and then progressively loading the members until failure was reached.

An example of the collapse shape of a IPE500 column and the corresponding boundary conditions are provided in Figure 1. More details about the numerical model can be found in [11,12].

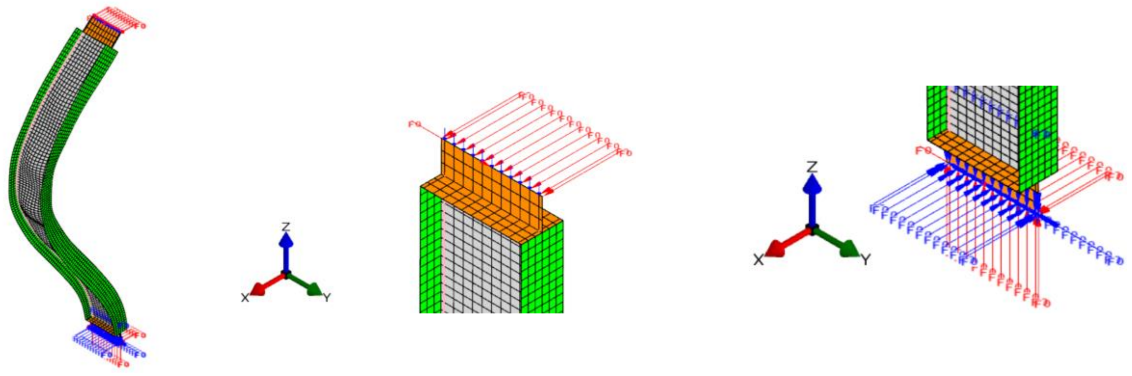

(a) (b)

Figure 1. Numerical model in SAFIR: (a) shell model for IPE500 column at 300 °C and (b) boundary conditions with end plates and pinned-fixed supports.

3.2 Datasets

Two datasets were defined comprising respectively the column and beam cases. For each dataset, the data points were calculated using the numerical model described in the previous section. FE simulations were run to failure. The dataset includes 2304 FE simulations for the columns and 24516 for the beams. For the latter, the same data were used to develop the design rules for the lateral-torsional buckling of beams with slender section [7,8] present in new generation of the Eurocode 3 Part 1-2 and given in Section 2.

The selection of features was carried out using a procedure that combined prior knowledge about the parameters potentially influencing the mechanical response (mechanistic-informed) and a quantitative trial-and-error approach to find the most suitable combination of features. The process of feature selection dealt with both inclusion and exclusion of parameters and their combination, and the best model was selected as the one with fewest parameters for a given accuracy. The ranges of values for the input parameters are listed in Table 1 and Table 2 for columns and beams, respectively, each defining 9 and 8 features for the ML models. Similar features are defined for both cases but with a different order because the ML models originate from two different studies by the authors [11,12]. The order of the features has no influence in the performance of the models.

Table 1. Input parameters for the ML models and for the unseen experimental dataset – columns.

Notation	Feature	Input values	Numerical dataset		Unseen experiment dataset	
			Min.	Max.	Min.	Max.
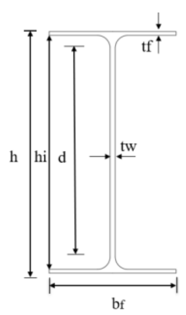	x_1	h_w/t_w	31	52	11.2	50
	x_2	$b_f/2\,t_f$	4.6	8.2	6.25	15.3
	x_3	d/b_f	0.56	2.34	0.56	2
	x_4	t_w/t_f	0.56	1	0.625	1
	x_5	$f_{y_{web}}/E$	$(235/E)$	$(460/E)$	$(321.9/E)$	$(538.1/E)$
	x_6	$f_{y_{flange}}/E$	$(235/E)$	$(460/E)$	$(306.3/E)$	$(538.1/E)$
	x_7	L/b_f	6.7	30	6.8	18.4
	x_8	$(N_{pl,20}/N_{cr,20})^{0.5}$	0.17	2.01	0.17	1.05
	x_9	$temperature$	$300°C$	$800°C$	400°C	700°C

Table 2. Input parameters/features of dataset used for the ML models training – beams.

Notation	Feature	Input values	Min.	Max.
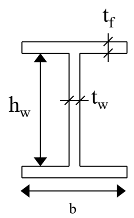	x_1	h_w/t_w	75	200
	x_2	b/t_f	6	50
	x_3	h_w/b	1.8	3.33
	x_4	t_w/t_f	0.16	0.8
	x_5	f_y/E	$(235/E)$	$(460/E)$
	x_6	$temperature$	$300°C$	$700°C$
	x_7	$(M_{pl,20}/M_{cr,20})^{0.5}$	0.097	2.738
	x_8	ψ	-1	1

In these tables, the h_w/t_w and $b_f/2t_f$ are the adimensional web and flange dimensions – note that for beam cases b_f/t_f was considered instead, $F_{y_{web}}/E$, $F_{y_{flange}}/E$ are the adimensional web and flange yield strengths considered for columns and f_y/E is the adimensional yield strength for beams. The L is member length, $N_{pl,20}$ and $M_{pl,20}$ are the section plastic capacity for the column and beam, $N_{cr,20}$ and $M_{cr,20}$ are their elastic critical load at ambient temperature and ψ is the ratio between end-moments applied to beams. The range of feature values considered in the dataset was chosen to cover a common range of design parameters for slender section steel columns and beams in building structures.

The output was defined as $y = N_{u,T}/N_{pl,20}$ with $N_{u,T}$ being the ultimate capacity of a column or $y = M_{u,T}/M_{pl,20}$ with $M_{u,T}$ being the ultimate capacity of a beam.

For columns, in addition to the 2304 numerical data points, 16 experiments on steel columns at elevated temperature were identified from the literature, on axially compressed stud columns with Class 4 cross-sections [13] and on pin-supported steel columns with HEA 100 cross-sections [14]. These experiments were used to test a posteriori the ability of the trained ML models to predict the outcome of the experiments, where the experimental data had not been used in the construction of the ML models. In particular, Table 1 shows that the values of the features for these 16 experimental data points (column "unseen experiment dataset") did not always fit within the boundaries of the feature values used for training and testing the ML models. Consideration of these experiments therefore enables exploring the limits of the data-based approach when extrapolating outside the range of parameters "seen" by the model.

For the column cases, the 2304 data points were randomly divided into two groups with a ratio of 9:1, thus 2073 data points were used for training the ML models and 231 data points were used for testing the ML models. For the beam cases, the 24516 samples were divided on a proportion of 7:3, thus 17161 cases were considered for training and 7355 cases for testing.

4 MACHINE LEARNING MODELS

4.1 Artificial Neural Networks

The artificial neural network (ANN) is a mathematical model that can be described as a group of neurons arranged in layers and their connections forming a network. The ANN can map a certain range of input values (features) to a specific target value (result). The most used type of ANN is the Multilayer Perceptron (MLP), with an input layer, one or more hidden layers, and an output layer. Each neuron of a certain layer is only connected to the neurons in the next layer, and may include an extra, independent, value called the bias. The output of each neuron j can be calculated as:

$$output_j = f\left(\sum_{i=1}^{n} w_{ij} x_i + b_j\right) \tag{11}$$

where $output_j$ is the output of the layer, w_{ij} are the weight coefficients, x_i are the input values, or features, and b_j is the bias values. The $f(x)$ is the so-called transfer or activation function.

Then, the training of ANN is achieved by exposing the network to a set of examples (input patterns) with known outputs (target output). The weights of the internal connections, and the bias values of the neurons, are adjusted to minimize errors between the network output and target output.

Two implementations of the ANN were considered in this study, the one available in the scikit-learn [15] was used for both column and beam cases and *pyrenn* [16] was also considered for the beam case. Regarding the loss function, the *scikit-learn toolkit* implements the square error loss function in the MLP for regression, while the *pyrenn toolkit* used the mean square error loss function.

The hyperparameters were determined by the functionality of a randomized search with the cross-validation of 25 and 5 folds using the *scikit-learn toolkit* for column and beam cases, respectively. The results show that the optimal hidden layer size was 8 with the applied weight optimizer 'lbfgs'. For the beam model, using the 'adam' optimizer the hidden layer size was 64. Using the Levenberg-Marquardt (LM) the hidden layer was reduced to 16 neurons and since no cross-validation was available in *pyrenn* the network architecture was manually fine-tuned.

4.2 Support Vector Machines Regression

SVR is developed as an extension of the support vector machine (SVM), which aims to find a hyperplane in an n-dimensional space (n is the number of features, i.e. input parameters) that classifies the training datasets in different classes. While the objective of SVM is to find a hyperplane that has the maximum margins ($\pm\varepsilon$), the extension SVR aims to find a flat hyperplane with margins ($\pm\varepsilon$) that accept the data points within or on the margins while rejecting the data points outside the margins.

The hyperplane can be written in Equation (12) for linear SVR:

$$y_i = w^T x_i + b \tag{12}$$

in which x_i and y_i are the ith input and output in the training dataset, w is the weight matrix, b is the bias. For nonlinear SVR, the hyperplane can be written as:

$$y_i = w^T \varphi(x_i) + b \tag{13}$$

in which $\varphi(x_i)$ is the nonlinear kernel function that maps the input vectors to a higher dimension space. The deviation of points within the margins ($\pm\varepsilon$) is zero. The deviation of points outside the margins ($\pm\varepsilon$) is the distance of these points to the margins (ξ_i and ξ_i). The loss function of SVR is written as:

$$minimize\colon \frac{1}{2}\|w\|^2 + C\sum_{i=1}^{n}\left(\xi_i + \xi_i\ \right) \tag{14}$$

The constraints are:

$$\begin{aligned} y_i - wx_i - b &\le \varepsilon + \xi_i \\ wx_i + b - y_i &\le \varepsilon + \xi_i \\ \xi_i, \xi_i\ &\ge 0 \end{aligned} \tag{15}$$

in which $\frac{1}{2}\|w\|^2$ is the regularization term added to seek the flattest hyperplane with a small weight. C is a trade-off between the accepted tolerance of deviation ε and the flatness of the solution.

The samples for training and testing are the same as for the ANN. Grid search is applied to tune the hyperparameters. The following values are used for the hyperparameters for the beam: 'rbf' kernel, C=1000, gamma=0.049, and $\varepsilon = 0.05$. The following values are used for the columns: 'rbf' kernel, C=82, gamma=0.263, and $\varepsilon = 0.01$.

4.3 Polynomial regression

The general form for polynomial regression is written as:

$$Y = X\omega + \varepsilon \tag{16}$$

in which Y is the vector of responses, X is the feature matrix, ω is the coefficient and ε is the bias. The polynomial regression extends the inputs of the linear model, which is obtained by raising the initial inputs to a power. The new inputs are created with degrees less than or equal to the specific order. The new feature matrix includes 1) bias; 2) converting the initial inputs to their higher-order terms for each degree; 3) combination of all pairs of initial inputs. For instance, if there are two inputs, $[x_1, x_2]$, a degree-2 polynomial expansion would produce a new feature matrix $[1, x_1, x_2, x_1^2, x_1x_2, x_2^2]$.

Models with higher degrees may closely fit most of the data in the training dataset, but possibly at the cost of over-fitting resulting in a larger error on the testing dataset. To prevent over-fitting in polynomial regression, ridge regression is applied to fit the polynomial feature matrix. The ridge regression adds a regularization term to the sum of squares of residuals. The loss function of ridge regression is written as:

$$minimize: \sum_{i=1}^{n} \|y_i - \sum_{j=0}^{m} x_{ij}w_j\|^2 + \lambda \sum_{j=0}^{m} \|w_j\|^2 \ (\lambda > 0) \tag{17}$$

in which the y_i is the known observation, $\sum_{j=0}^{m} x_{ij}w_j$ is the predicted value, and λ is the tuning parameter which controls the complexity of the model. As λ grows larger, the ridge regression effectively shrinks coefficient w_j to be 0 and selects a small subset of features to build the model, which prevents training a more complex model and thus avoid over-fitting.

For the column, a degree 2 polynomial was found to predict the resistance of columns within the range of features provided in Table 1 of the numerical dataset. The coefficients of the degree 2 polynomial model are given in [11]. This model implemented in a datasheet can provide an almost-immediate prediction of the elevated temperature capacity for slender steel columns, within the range of features considered. For the beam, the model of degree 6 shows the best performance for both training and testing [12].

5 RESULTS AND DISCUSSION

To quantify the performance of the different models, the coefficient of determination R^2 value was evaluated for the models against the training and testing dataset and the unseen experimental data. The R^2 measures how well the observations are replicated by a model and a R^2 close to 1 is preferred. Table 3 gives the results for the SVR, ANN, and PR models for columns and beams respectively. Predictions by the analytical model described in Section 2 are also included.

Table 3. Performance of the ML models and the analytical model.

Regressor (R^2)	Columns			Beams	
	Train	Test	Unseen Experiment	Train	Test
SVR	0.998	0.996	-0.212	0.987	0.987
ANN	0.990	0.990	0.891	0.999	0.999
PR	0.980	0.977	0.914	0.981	0.981
EN1993-1-2:2005		0.928		0.829	
EN 1993-1-2 New Gen.		0.956		0.963	

Figure 2 (a)-(d) plots the predicted capacity $N_{u,T}/N_{pl,20}$ using SVR, ANN, PR, and the analytical models against the numerical estimations from the shell finite element model in SAFIR for the columns. For the training and testing dataset, the results from SVR, ANN, and PR agree better with the capacity evaluated by SAFIR than the analytical model. The ANN and PR models are also able to predict the capacity in the unseen experimental datasets with good agreement.

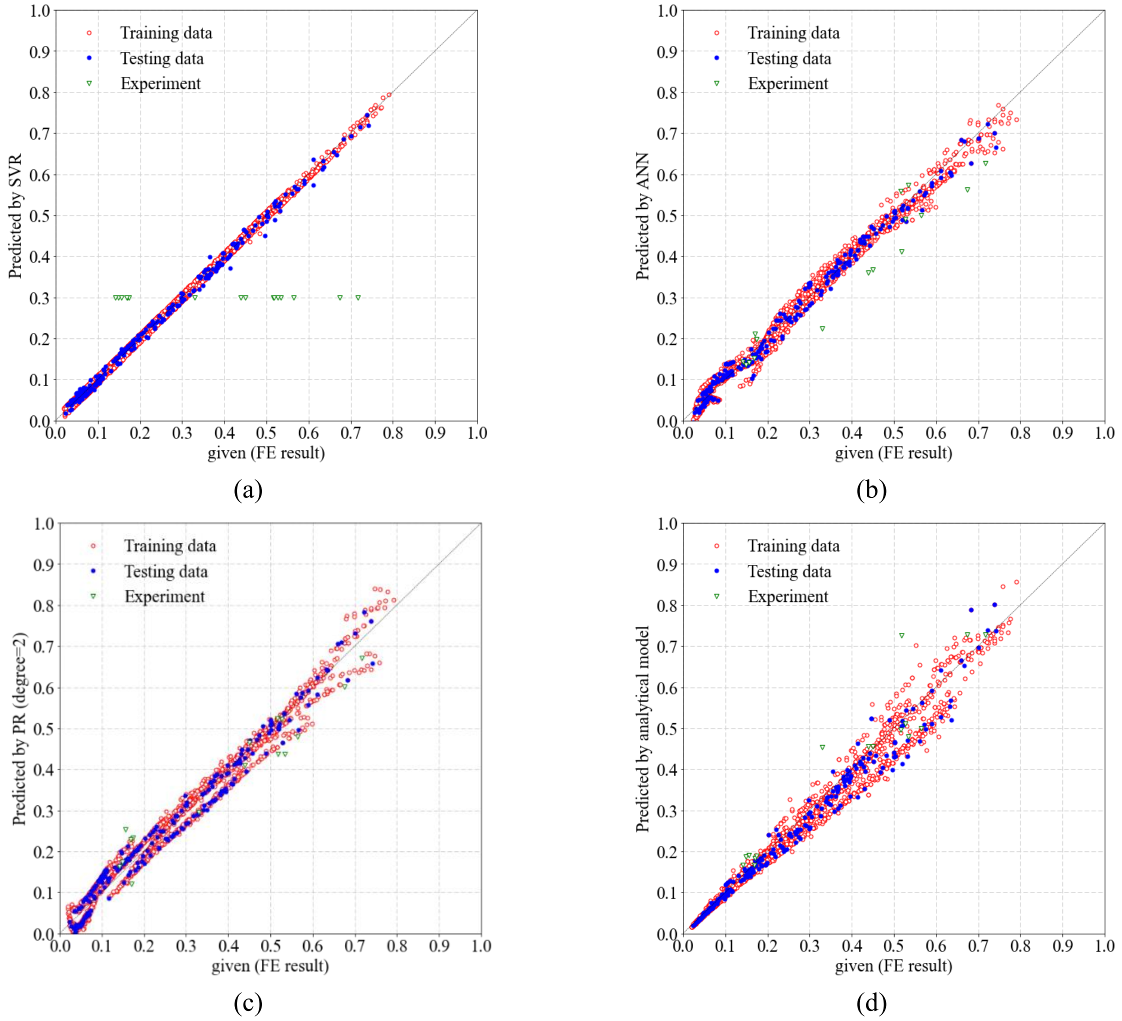

Figure 2. Predicted capacity $N_{u,T}/N_{pl,20}$ for slender steel columns at elevated temperature: Comparison between SAFIR finite element model and (a) SVR; (b) ANN; (c) PR; (d) Analytical model. Training/testing performed based on 2304 data points. "Experiment" refers to 16 experimental data points not used in the construction of the ML models.

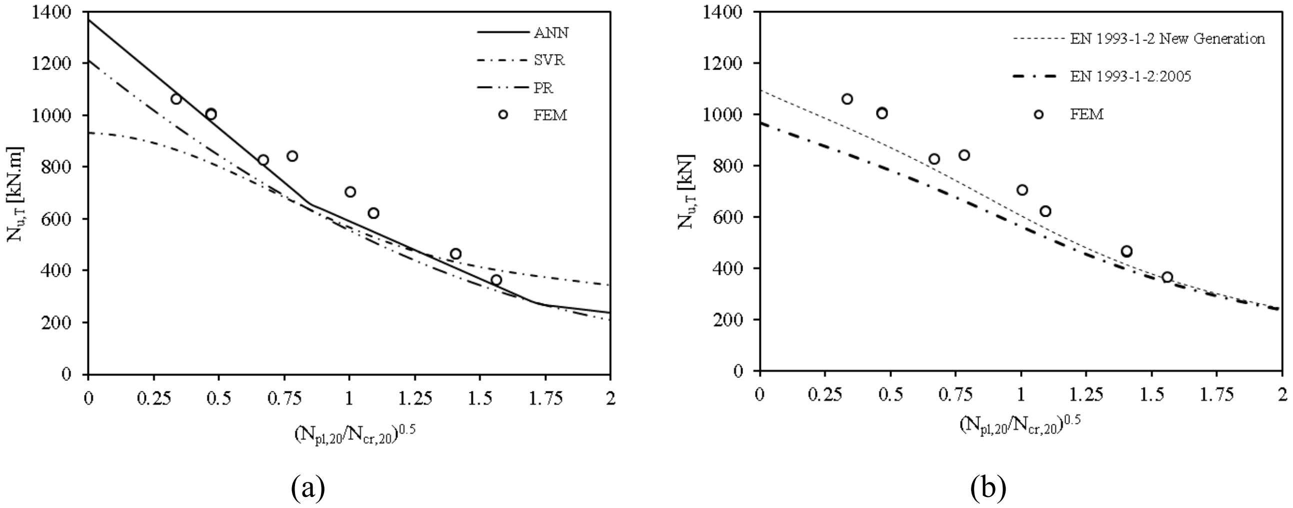

Figure 3. Comparison between numerical results (FEM) and (a) machine learning models or (b) analytical models for columns with cross section IPE A 300 (S460) at 500 $°C$.

In fact, when used to predict the outcome of the experiments from [13,14], which were not used to construct the models, the PR is the most accurate with R^2 of 0.914, followed by ANN, and the analytical model. The SVR model fails to capture the experimental data. The reason is the SVR is sensitive to the range of web slenderness and flange slenderness. Looking at the web and flange slenderness of the training, testing, and experimental data points (Table 1), reveals that the values of these features for the experimental data points fall outside of the range considered in the training and testing data points. When the web slenderness and flange slenderness are beyond the range of the trained model, the SVR fails to accurately extrapolate the outputs and the predictions of $N_{u,T}/N_{pl,20}$ are approximately constant at 0.3. This results from the high degree of nonlinearity of the SVR model. Attempts to improve the predictions with the SVR outside of the range of the parameters (to fit with the experimental data) were made, including by using a linear SVR or addressing the overfitting. However, any improvement of the performance against the experimental dataset was at the cost of a sensible reduction in performance against the training and testing datasets. Therefore, it was concluded that the nonlinear SVR model can provide high performance in the range of the training parameters, but should not be extrapolated outside this range.

For a different visualization of the results, Figure 3 shows the comparison of the different models for columns with IPE A 300 in S460 steel at 500 $°C$, as well as the numerical results obtained with the finite element model described in Section 2, considering different lengths of the column and different support conditions. In this figure, it is possible to observe the good correlation between the ML models and those obtained numerically. The shape of the curve obtained with the ANN might be explained by the number of lengths considered in the training set for the columns, by increasing this number a smoother curve would likely be obtained, as it is the case for the beams that are presented next.

For the beam cases, Figure 4 (a)-(d) plot the predicted capacity $M_{u,T}/M_{pl,20}$ using SVR, ANN, PR, and the analytical models against the numerical estimations from the shell finite element model in SAFIR. As for the columns, the different ML models for beams with slender section outperform the accuracy of the analytical methods defined in the future version of the EN 1993-1-2 which, in turn, provides already a better accuracy over its present version. The artificial neural network developed with *pyrenn* has reached R^2 scores of 0.999 on both the training and testing datasets thus provide an excellent choice to predict the capacity of thin-walled beams.

Figures 5 and 6 shows the comparison of different models for beams with cross-sections I450×4+150×12 and I450×4+200×10, made of S235 and S355 steels and subjected to a constant bending diagram ($\psi = 1$) and a triangular bending diagram ($\psi = 0$), respectively . The beams were calculated for 450 $°C$ using the finite element model described in Section 2. For both sections, it is possible to observe the good correlation between the results predicted by the ML models and the results calculated numerically using the FEM. Regarding the analytical methods while it is noticeable the improvements of the new generation of EN1993-1-2 over the present version of the design code, as expected, both these methods present lower accuracy when compared against the ML models.

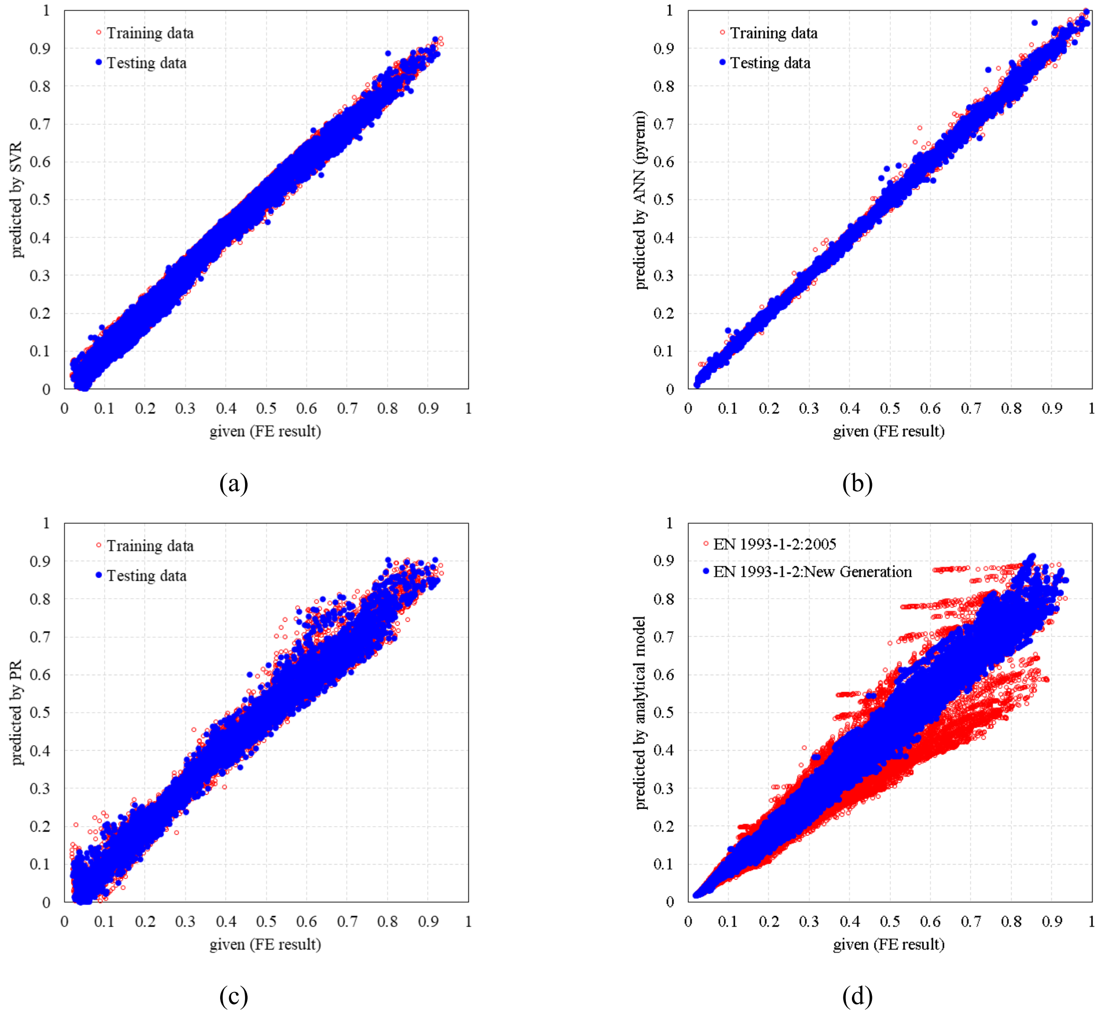

Figure 4. Predicted capacity $M_{u,T}/M_{pl,20}$ for slender steel beams at elevated temperature: Comparison between SAFIR finite element model and (a) SVR; (b) ANN; (c) PR; (d) Analytical models.

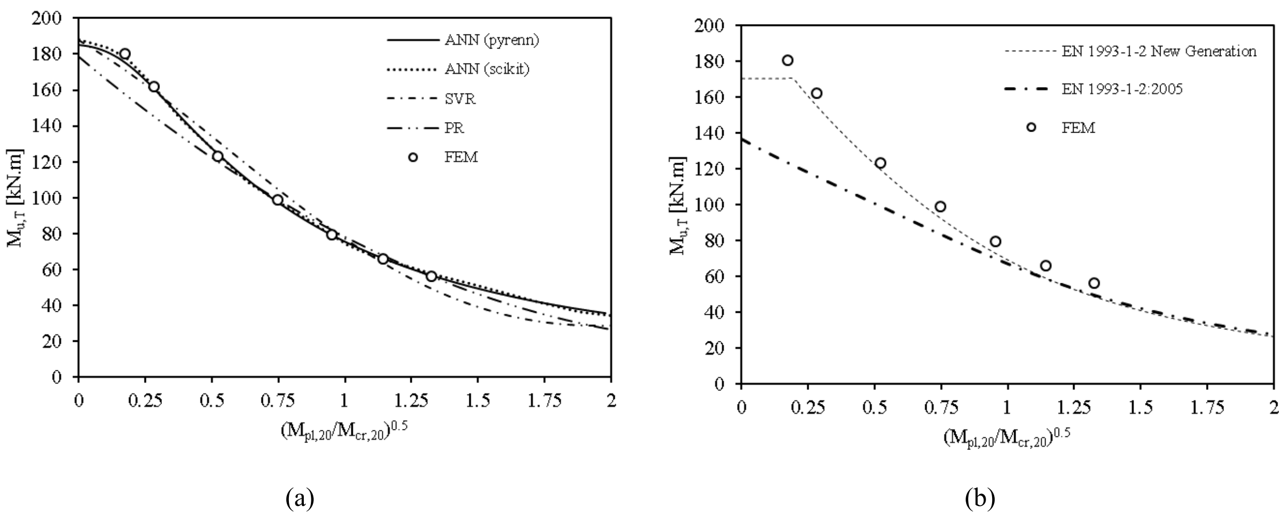

Figure 5. Comparison between numerical results (FEM) and (a) machine learning models or (b) analytical models for beams with cross section I450×4+150×12 (S235) at 450 °C and constant bending moment distribution ($\psi = 1$).

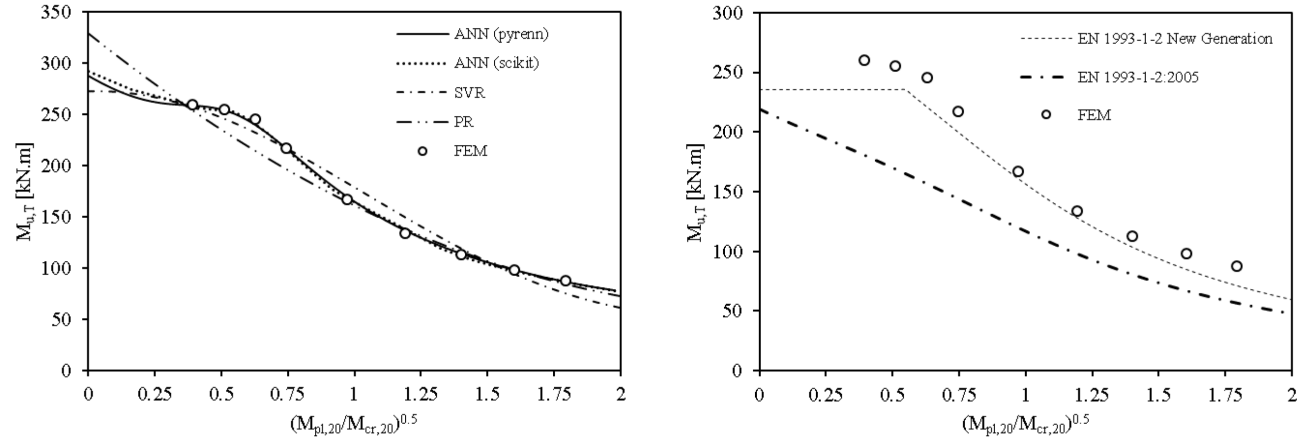

(a) (b)

Figure 6. Comparison between numerical results (FEM) and (a) machine learning models or (b) analytical models for beams with cross section I450×4+200×10 (S355) at 450 $°C$ and triangular bending moment distribution ($\psi = 0$).

6 CONCLUSION

This study investigated the potential of Machine Learning (ML) models to capture the capacity at elevated temperatures of steel members with slender sections which exhibit failure by local buckling and/or global buckling. A numerical study based on validated nonlinear FEM using shell elements was conducted to build a dataset of 2304 data points for columns and 24516 for beams with a range of cross-sections, member length, temperature, yield strength, and boundary conditions. The dataset was used to train and test ML models to predict the elevated temperature capacity of beams and columns. Three types of ML models were applied to the beam and column datasets separately, namely based on artificial neural network (ANN), support vector regression (SVR) and polynomial regression (PR).

For both the beams and columns, the ML models can fit the results of the shell FE models more closely than the state-of-the-art analytical methods to be included in the next generation of the Eurocodes. For columns, the ML models can predict the resistance at elevated temperature, for both the training and testing dataset, with a R^2 greater than 0.990 for SVR and ANN, and greater than 0.977 for PR. For beams, a R^2 greater than 0.981 is obtained for the PR, 0.987 for SVR and 0.999 for the ANN.

For the columns, the PR and ANN models were also able to capture experimental data not used to train the model and with inputs outside the range of the numerical training dataset with a R^2 of 0.914 and 0.891, respectively. The SVR model, while providing the best accuracy against the training and testing datasets, did not provide an acceptable agreement against the experimental data and should thus not be used for inputs outside of the range considered to build the model. It is expected that the accuracy against test data could be further improved by extending the training dataset for the ML models.

In addition, the representation of results in the form of buckling curves illustrates the ability of the ML models to capture the behaviour of the steel members across a large range of slenderness. Generally the ML models agreed better with the FE data than the state-of-the-art analytical models.

This work shows that ML models can accurately predict the resistance of both columns and beams under uniform heating while also being computationally efficient. Large numerical database that were developed as background to the development of analytical methods can be revisited to train ML models, following the procedure described in this paper. In future works, more complex configurations such as structural assemblies or non-uniform fire exposures will be explored.

ACKNOWLEDGMENTS

Carlos Couto acknowledges the funding from FCT – Fundação para a Ciência e a Tecnologia, I.P., under the Scientific Employment Stimulus – Institutional Call – CEECINST/00026/2018, and Rede Nacional de Computação Avançada (RNCA) da FCT, within the scope of the exploratory research project CPCA/A1/6717/2020.

Under a license agreement between Gesval S.A. and the Johns Hopkins University, Dr. Gernay and the University are entitled to royalty distributions related to the technology SAFIR described in the study discussed in this publication. This arrangement has been reviewed and approved by the Johns Hopkins University in accordance with its conflict of interest policies.

REFERENCES

1. Franssen JM, Cowez B, Gernay T. (2014). Effective stress method to be used in beam finite elements to take local instabilities into account. Proceedings of the 11th IAFSS Symposium (pp. 544-557). Christchurch, New Zealand, Feb 10-14. DOI: 10.3801/IAFSS.FSS.11-544.
2. Pallares-Muñoz MR, Payá-Zaforteza I, Hospitaler-Pérez A. New modeling strategies for analyzing lateral-torsional buckling in class-4 steel structural members at elevated temperatures using beam-type elements. Structures 2021;34:3508–32. https://doi.org/10.1016/j.istruc.2021.09.087.
3. Naser MZ. Mechanistically Informed Machine Learning and Artificial Intelligence in Fire Engineering and Sciences. Fire Technol 2021;57:2741–84. https://doi.org/10.1007/s10694-020-01069-8.
4. Franssen J, Gernay T. Modeling structures in fire with SAFIR ® : Theoretical background and capabilities. Journal of Structural Fire Engineering 2017:1–28. https://doi.org/10.1108/JSFE-07-2016-0010.
5. CEN. EN 1993-1-5, Eurocode 3 - Design of steel structures - Part 1-5: Plated structural elements 2006:1–53.
6. Couto C, Vila Real P, Lopes N, Zhao B. Resistance of steel cross-sections with local buckling at elevated temperatures. Journal of Constructional Steel Research 2015;109:101–14. https://doi.org/10.1016/j.jcsr.2015.03.005.
7. Couto C, Vila Real P, Lopes N, Zhao B. Numerical investigation of the lateral–torsional buckling of beams with slender cross sections for the case of fire. Engineering Structures 2016;106:410–21. https://doi.org/10.1016/j.engstruct.2015.10.045.
8. Couto C, Maia É, Vila Real P, Lopes N. The effect of non-uniform bending on the lateral stability of steel beams with slender cross-section at elevated temperatures. Engineering Structures 2018;163:153–66. https://doi.org/10.1016/j.engstruct.2018.02.033.
9. CEN. EN 1993-1-2, Eurocode 3: Design of steel structures - Part 1-2: General rules - Structural fire design 2005.
10. Couto C, Vila Real P. The influence of imperfections in the critical temperature of I-section steel members. Journal of Constructional Steel Research 2021;179:106540. https://doi.org/10.1016/j.jcsr.2021.106540.
11. Tong Q, Couto C, Gernay T. Machine learning models for predicting the resistance of axially loaded slender steel columns at elevated temperatures. Engineering Structures 2022;266:114620. https://doi.org/10.1016/j.engstruct.2022.114620.
12. Couto C, Tong Q, Gernay T. Predicting the capacity of thin-walled beams at elevated temperature with machine learning. Fire Safety Journal 2022;130:103596. https://doi.org/10.1016/j.firesaf.2022.103596.
13. Wang W, Kodur V, Yang X, Li G. Experimental study on local buckling of axially compressed steel stub columns at elevated temperatures. Thin-Walled Structures 2014;82:33–45. https://doi.org/10.1016/j.tws.2014.03.015.
14. Pauli J, Somaini D, Knobloch M, Fontana M. Experiments on steel columns under fire conditions - Test Report No. 340, 2012. , ETH Zurich, Institute of Structural Engineering IBK; 2012.
15. Pedregosa F, Varoquaux G, Gramfort A, Michel V, Thirion B, Grisel O, et al. Scikit-learn: Machine learning in Python. The Journal of Machine Learning Research 2011;12:2825–30.
16. Atabay D. pyrenn: A recurrent neural network toolbox for Python and Matlab. Institute for Energy Economy and Application Technology, Technische Universität, München.

SiF 2022– The 12th International Conference on Structures in Fire
The Hong Kong Polytechnic University, Nov 30 - Dec 2, 2022

EFFECT OF LOCAL INSTABILITIES ON THE ONSET OF FIRE-INDUCED PROGRESSIVE COLLAPSE IN STEEL-FRAMED BUILDINGS

Svetha Venkatachari[1], Venkatesh Kodur[2]

ABSTRACT

This paper examines the influence of temperature-induced local buckling on the onset of fire-induced collapse in steel-framed buildings. A comprehensive finite element model is developed in ABAQUS to trace the overall response of steel-framed buildings under fire conditions, including fire-induced collapse. The model accounts for several critical factors that influence the onset of temperature-induced instabilities in steel-framed buildings, and temperature-induced local buckling is one of the parameters evaluated in this paper. The developed model is applied to predict the overall fire response and failure pattern of a ten-story steel-framed building. Results from the numerical analysis indicate that the occurrence of local buckling in columns has a significant influence on the onset of global instability and this effect is more pronounced in steel columns located on the higher stories of the building. The results indicate that the nonslender steel column, with a sufficiently high slenderness ratio, can transform into a slender section under fire exposure. This can cause the onset of local buckling in the column, which in turn can lead to an early onset of instability at member and global levels.

Keywords: Local instability; fire resistance; fire-induced collapse; steel-framed buildings; slenderness.

1 INTRODUCTION

Steel-framed buildings when exposed to severe fires can experience instability at a local or global level which can lead to the partial or progressive collapse of the structure. With an increasing focus on sustainability, the geometric configuration of steel sections used in buildings is being optimized to achieve cost-effectiveness in construction. For example, columns with high slenderness are being used more prevalently in buildings than before. It has been shown that due to the faster degradation of the modulus of steel than that of yield strength with temperature rise, these sections are susceptible to local buckling at elevated temperatures [1], which can lead to an early onset of instability at local or global levels.

While the stability criterion is given due consideration for the design of steel structures under ambient conditions, it is not specifically considered in fire design. Very limited research has been carried out in the past, primarily at a member level, to study the effect of temperature-induced local instabilities [2, 3]. Seif and McAllister [4] investigated the local and global buckling modes in wide flange steel column sections under varying load and temperature conditions. Local buckling was observed in members with slender flange and/or web elements with a width (b) to thickness (t_f) ratio greater than 10 and depth (h) to thickness (t_w) ratio greater than 35.

Kodur and Naser [2, 5] carried out numerical studies using ANSYS finite element software to study the fire behavior of steel beams taking into consideration the temperature-induced sectional instabilities. Results showed that a compact section under ambient conditions can change to non-compact/slender at elevated

[1] Faculty (on contract), Department of Civil Engineering, National Institute of Technology Puducherry, Karaikal, India
e-mail: svethachari@gmail.com, ORCID: https://orcid.org/0000-0001-6385-5813
[2] University Distinguished Professor, Department of Civil and Environmental Engineering, Michigan State University, East Lansing, MI, USA
e-mail: kodur@egr.msu.edu
https://doi.org/10.6084/m9.figshare.22215685

temperatures and this change can result in the early onset of failure before flexural yielding and/or shear limiting states. Agarwal et al. [6] evaluated the effect of thermal gradients in steel columns subjected to fire loading experimentally and numerically. The study indicated that the main failure modes for columns with non-uniform thermal gradients were flexural buckling about weak and strong axes and flexural torsional buckling. While the prior studies investigated the effect of local buckling at a member level, the effect of temperature-induced local instability is usually ignored at a structural level in most finite element models.

To overcome the above knowledge gaps, a numerical model is developed in ABAQUS to evaluate the influence of temperature-induced local buckling on the onset of fire-induced collapse in steel-framed buildings. In addition to other critical factors such as the variation of material properties with temperature, geometric nonlinearity, and progressive collapse, the effect of local instabilities is explicitly accounted for in the fire resistance analysis. The developed model is applied to predict the behaviour of a ten-story steel-framed building exposed to fire conditions. The influence of temperature-induced local buckling of the progressive collapse timelines is evaluated by comparing the predictions of the model against model predictions that neglect local buckling effects.

2 LOCAL INSTABILITES IN STEEL-FRAMED STRUCTURES

The stability limit state is a key consideration in the ambient temperature design philosophy of steel-framed structures. However, the current fire design provisions neglect the effect of sectional instabilities in evaluating the failure of steel structural members. The susceptibility of a steel section to undergo local buckling depends on the width-to-thickness ratio (slenderness) of each of the cross-sectional elements. This effect is accounted for in evaluating the capacity of the member under room temperature conditions. For instance, the AISC manual [7] classifies the steel sections based on the slenderness ratio of flanges and web into a compact, non-compact, and slender section and recommends a reduced capacity based on the section classification. Limiting values of the width-to-thickness ratio of steel sections are a function of stiffness and strength properties $\left(\sqrt{\mathrm{E}/\mathrm{f_y}}\right)$ of steel, where E and f_y are the Young's modulus and yield strength of steel, respectively.

When steel structures are exposed to fire conditions, the strength and stiffness properties of steel begin to degrade at about 400ºC and 150ºC respectively, and these properties degrade at different rates as shown in Figure 1. Since no specific recommendations are specified in the current standards for the limiting slenderness ratios at elevated temperatures, the room temperature criteria for section classification are often applied to fire conditions in advanced analysis and this can be unrealistic [2]. Moreover, since the stiffness (modulus) starts to degrade at 150ºC itself and at a faster pace, the susceptibility to local buckling at lower temperatures (in the 150ºC to 400ºC range) increases and may lead to a reduction in capacity [2]. This loss in capacity in addition to the temperature-induced strength degradation of steel needs to be properly accounted for in the fire resistance analysis of steel structures.

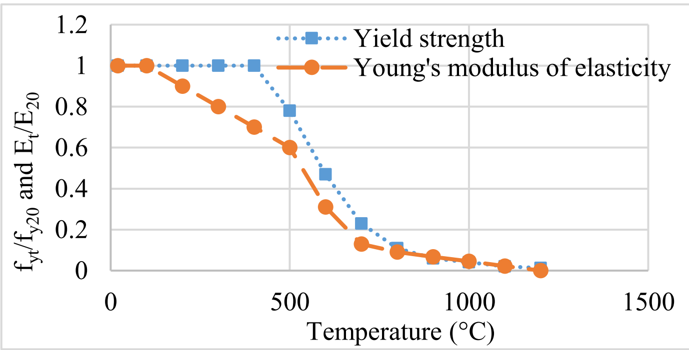

Figure 1. Degradation of strength and stiffness properties of steel at elevated temperatures.

Local instabilities can become dominant particularly when a fire-exposed member is sufficiently slender, when the member is subjected to eccentric loading, or when concentrated loads are placed near the end supports [1]. For tracing the fire-induced progressive collapse in steel framed buildings, the structure is subjected to continuously changing fire spread scenarios and load paths that can expose steel members to nonuniform fire exposure and eccentric loading. Such scenarios increase the susceptibility of steel sections to undergo local buckling, which in turn can lead to an early onset of instability at member and system levels.

3 NUMERICAL MODEL

To study the effect of local instabilities on the onset of fire-induced progressive collapse in steel-framed buildings, a finite element-based model is built in ABAQUS. This model, in addition to several critical factors that influence the onset of temperature-induced instabilities in steel-framed buildings, can explicitly account for the effect of temperature-induced local buckling in steel sections. The general procedure, discretization, material properties, and incorporation of geometric imperfections and local buckling effects are discussed in this section.

3.1 General procedure

The advanced analysis is carried out in two stages, namely, the thermal analysis followed by the structural analysis. Figure 2 shows the steps for tracing the fire-induced progressive collapse in the steel-framed building. For the thermal analysis, the cross-section of each fire-exposed steel member (along with any fire insulation) is discretized using a 4-noded DC2D4 element. The heat transfer calculations are performed by specifying convection and radiation conditions at the boundaries to model the fire temperatures and heat transfer through conduction within the cross-section of the member. Temperature-dependent thermal property relations in Eurocode 3 [8] are provided as input to the model. The variation of sectional temperatures in the fire-exposed steel members are obtained as a function of fire exposure time.

The structural response under ambient and fire conditions is traced using a nonlinear dynamic explicit analysis. In this approach, the force-deformation response of the structural system at room and elevated temperatures is obtained by carrying out the analysis in multiple steps. In the first step, the gravity and lateral loads (as per ASCE 7-16 [9]) are gradually applied until the structure stabilizes. In the next step, the temperatures obtained from the thermal analysis are applied as predefined fields on the fire-exposed members. The explicit dynamic solver has the capability of numerically overcoming the local instability that occurs due to member level failure and the analysis continues until multiple members fail in the structure leading to the onset of global instability. The analysis stops when the structure is no longer able to maintain static equilibrium (or collapse initiation) or till the end of fire exposure duration. The temperature-dependent stress-stain relations in Eurocode 3 [8] are used to model the constitutive behaviour of steel at elevated temperatures. The effect of high-temperature creep in steel is accounted for implicitly through the stress-strain relations in Eurocode 3 [8].

3.2 Discretization of the model for structural analysis

To capture the effect of temperature-induced local instabilities, the steel members in the fire compartment(s) are discretized using 4-noded shell elements (S4R) while the unexposed members in the building are discretized using 2-noded beam elements (B31). The use of shell elements for fire-exposed members is to capture the effects of local buckling, inelastic lateral-torsional buckling, residual stresses, or any other distortions in shape (such as warping) that may occur under elevated temperatures. The beam elements, although computationally efficient, cannot capture the above-mentioned locally induced instability effects in framing members. The connections between the beam and shell elements are modeled using kinematic coupling constraints to achieve either pinned or rigid connections, as per the building description. All remaining connections in the structural system are modeled using connector assignments in ABAQUS as either pinned or completely rigid connections.

3.3 Incorporating geometric imperfections and local buckling effects

The initial member imperfections are applied by superposing a scaled Eigen mode shape obtained from carrying out an eigenvalue buckling analysis on a column subjected to a concentric axial load in ABAQUS. The Eigen modes corresponding to the global buckling modes, i.e., flexural buckling about the weak and strong axes, are scaled to achieve an imperfection amplitude of h/1000, where h is the height of the column, as per AISC-360 specifications [7]. Initial system imperfections that arise typically due to out-of-plumbness of columns are included in the analysis by the application of notional lateral loads at each floor level corresponding to 0.2% of gravity loads on that floor [7].

Further, the initial local imperfections in the fire-exposed members are included in the analysis by superposing additional scaled Eigen mode shapes corresponding to local buckling of flange and web plates. These Eigen mode shapes are obtained from the buckling analysis carried out on steel members in ABAQUS. The scaling factor is chosen such that the maximum imperfection amplitude in the web is $d_w/150$, or the maximum rotation in the flange from its normal orientation is $b_f/150$ at the flange tip, where d_w is the depth of the web and b_f is the width of the flange in a W-section.

The numerical model has been validated both at member and system levels with fire test data reported in the literature. The full details of the validation studies are presented in [10] and are not included here due to space constraints.

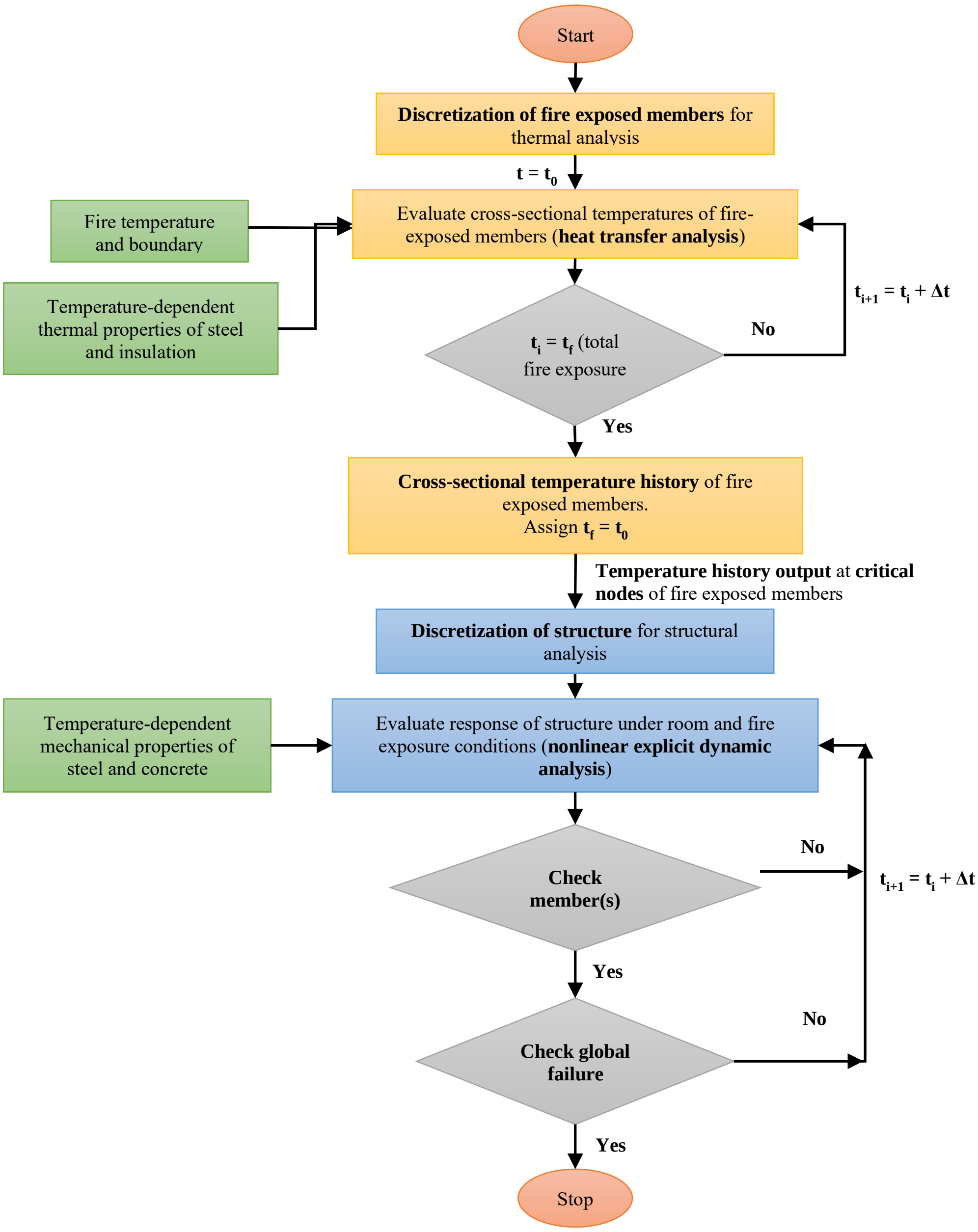

Figure 2. Flowchart illustrating the steps in tracing the fire-induced progressive collapse analysis of the steel-framed building.

4 CASE STUDY

The developed numerical model is applied to predict the effect of temperature-induced local buckling on the onset of instabilities leading to the progressive collapse in a steel-framed building. A ten-story braced steel framed building [11] (shown in Figure 3) is utilized for this study. Complete details of the test building are presented in [10, 12]. The framing members (beams, columns, and braces) in the building are made of grade 50 steel. All columns present in the building are nonslender as per AISC [7] classifications, however, columns used in the higher stories are relatively more slender than columns in the lower stories of a building. Thus, the columns in the higher stories are more susceptible to experiencing local buckling under fire conditions. To evaluate the effect of local instability, the analysis is carried out by assuming standard ASTM E119 [13] fire exposure in two interior compartments in the ninth story of the building. Two scenarios are considered: first, the original building with W14x53 (lateral) columns in the fire compartments, and second, the lateral columns (C3, C4, and C5) in the ninth story are replaced with W14x74 columns. In each scenario, two different structural models are compared; one with only beam elements used for all framing members and the other with shell elements used for fire-exposed steel members and beam elements used for unexposed steel members.

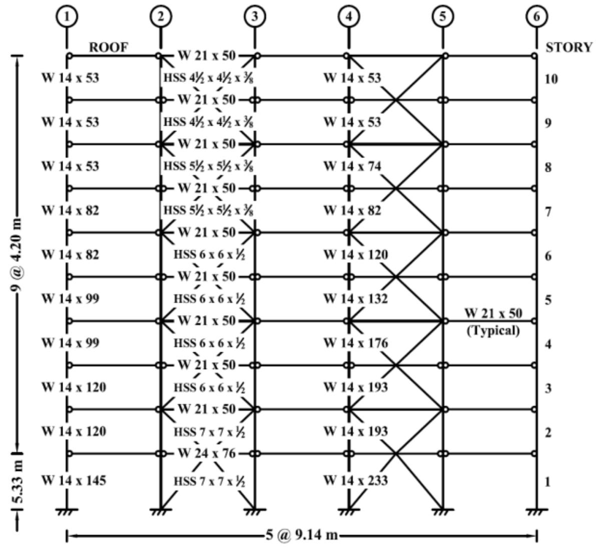

Figure 3. Details of the ten-story braced framed building used.

The temperature-dependent variation of web and flange slenderness limits, under the compression limit state, along with the flange and web slenderness ratios of W14x53 and W14x74 sections are shown in Figure 4. As can be seen from Figure 4, both the columns maintain nonslender flange status for the entire fire duration. However, the web slenderness of the W14x53 section (nonslender at room temperature) becomes slender in the temperature range of 400-800ºC and then transforms back to nonslender beyond 800ºC. The web slenderness of W14x74, on the other hand, remains nonslender throughout the fire exposure duration.

To evaluate the likelihood of progressive collapse in each scenario, the lateral displacement at the top story of the building frame is plotted in Figure 5. In addition, the axial deformation response of column C4 in each scenario is also plotted in the same figure. In the scenario with W14x53 columns, the difference in the predictions of the models with shell elements and only beam elements gradually increases with increasing fire exposure time. At 179 min, the lateral displacement predicted by the model using shell elements increases rapidly indicating the onset of progressive collapse of the structure. This failure time is 20 min earlier than that predicted using beam elements for the same building. The occurrence of local buckling in the middle column (C4) (see Figure 3 for numbering) in the fire compartment leads to a reduction in the axial capacity of the column and an early onset of instability at local and global levels. This is evident from the deformed shape of the building plotted in Figure 6. Further, the beams and columns in the fire compartment undergo significant warping (distortion) due to the nonuniform thermal gradients that develop under fire exposure. These effects are only captured using the model with shell elements.

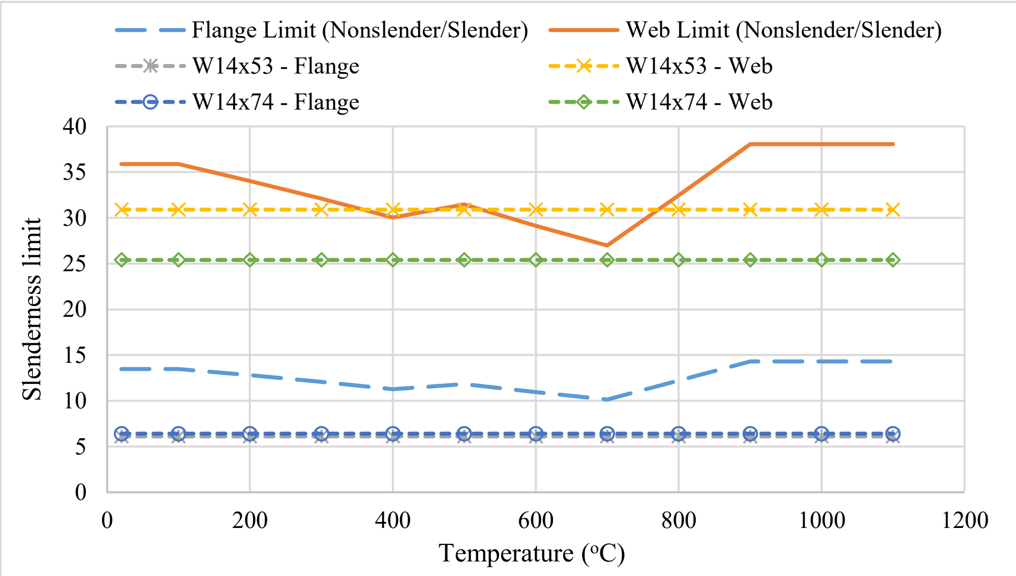

Figure 4. Flange and web slenderness limits for columns.

In the scenario with W14x74 columns, the predictions of the models with shell elements and only beam elements are similar throughout the fire exposure time. This is because the W14x74 columns being relatively less slender and having higher capacity do not experience local buckling and progressive collapse is not triggered in this scenario. The axial deformation response of column C4 in Figure 5 (b) indicate that column W14x74 experiences much less deformation than column W14x53 for the same fire exposure scenario. From this case study, it is evident that for capturing local instability and tracing the fire-induced progressive collapse of steel-framed buildings, shell elements are to be used for discretizing the fire-exposed sections. Further, by limiting the slenderness of the column sections to a certain degree, the instability of the columns under fire conditions can be minimized and thus, minimizing the susceptibility of progressive collapse.

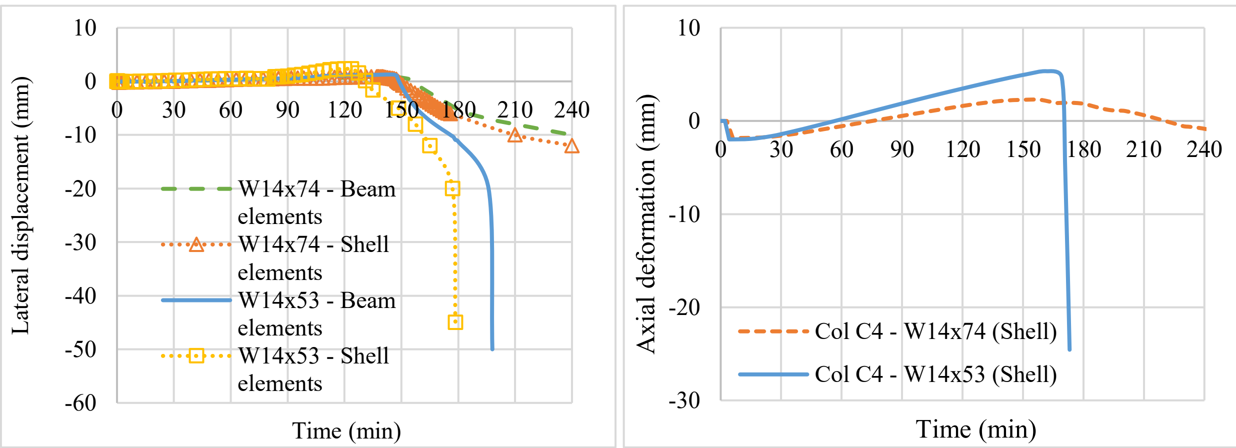

(a) (b)

Figure 5. (a) Lateral displacement at the top floor level of the frame and (b) axial deformation of column A4 with fire exposure time.

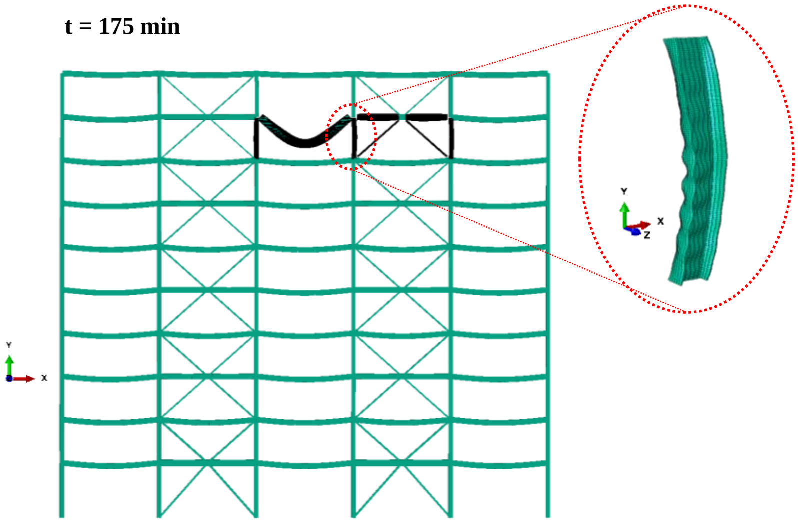

Figure 6. Deformed shape of the steel frame with W14x53 lateral columns in the ninth story.

5 DESIGN RECOMMENDATIONS

The onset of temperature-induced instabilities in steel columns is one of the most critical factors that triggers fire-induced collapse in steel framed buildings [10, 12, 14]. Even if the columns provided in the building are nonslender as per AISC classifications at room temperatures, they can transform to slender sections at elevated temperatures if the provided slenderness is high, making them susceptible to local buckling. The occurrence of local buckling in steel columns can significantly compromise the load-carrying capacity of the column and thus, precipitate the onset of the fire-induced collapse. For this reason, the following recommendations are proposed to minimize the occurrence of local buckling in steel columns (and fire-induced collapse).

In critical buildings, it is recommended to limit the slenderness of column sections to a certain level. The limit can be established as the lowest slenderness limit that can occur at elevated temperatures. For web and flange of steel columns, the slenderness (for compression limit state) can be limited to 25.4 and 10.1 respectively, which are the least slenderness values that occur at 700°C for Grade 50 steel (refer to Figure 4). Additionally, when columns with slenderness values higher than the proposed limits are utilized in critical buildings, it is recommended to explicitly account for the local buckling effects in the fire-induced progressive collapse analysis.

6 CONCLUSIONS

Based on the case study presented, the following conclusions can be drawn on the effect of temperature-induced local buckling on the onset of fire-induced collapse in a steel-framed building.

- Neglecting the effect of local buckling in the finite element model can result in failure times that are 10% higher than models that consider local buckling effects using shell elements for fire-exposed framing members.
- The effect of including the local buckling effects in the fire resistance analysis is sensitive to the slenderness of the steel members present in the fire compartments, where buildings with slenderer columns have larger sensitivities to local buckling effects.
- Limiting the slenderness of the steel columns to a certain level can minimize the susceptibility of instability under fire conditions at member and global levels. The slenderness of web and flange of steel columns (for compression limit state) can be limited to 25.4 and 10.1 respectively, which are the least slenderness values that occur at 700°C for Grade 50 steel.

REFERENCES

1. Kodur, V., Naser, M. Structural Fire Engineering. McGraw Hill Professional, New York, NY, USA; 2020.

2. Kodur, V., Naser, M. Effect of Local Instability on Capacity of Steel Beams Exposed to Fire. Journal of Constructional Steel Research 111, 31–42 (2015). https://doi.org/10.1016/j.jcsr.2015.03.015.

3. Chen, H., Liew, J. Explosion and Fire Analysis of Steel Frames Using Mixed element approach. Journal of Engineering Mechanics 131, 606–616 (2005). https://doi.org/10.1061/(ASCE)0733-9399(2005)131:6(606)

4. Seif, M., McAllister, T. Stability of Wide Flange Structural Steel Columns at Elevated Temperatures. Journal of Constructional Steel Research 84, 17–26 (2013). https://doi.org/10.1016/j.jcsr.2013.02.002.

5. Naser, M., Kodur, V. Factors Governing Onset of Local Instabilities in Fire Exposed Steel Beams. Thin-Walled Structures 98, 48–57 (2016). https://doi.org/10.1016/j.tws.2015.04.005.

6. Agarwal, A., Choe, L., Varma, A.H. Fire Design of Steel Columns: Effects of Thermal Gradients. Journal of Constructional Steel Research 93, 107–118 (2014). https://doi.org/10.1016/j.jcsr.2013.10.023.

7. AISC (American Institute of Steel Construction). Specifications for Structural Steel Buildings. ANSI/AISC 360-16, Chicago, IL, USA; 2016.

8. CEN (European Standards Committee). Eurocode 3-Design of Steel Structures, Part 1-2: General Rules for Structural Fire Design. EN 1993-1-2, Brussels, Belgium; 2005.

9. ASCE (American Society of Civil Engineers). Minimum Design Loads and Associated Criteria for Buildings and Other Structures. ASCE/SEI 7-16, New York, NY, USA; 2016.

10. Venkatachari, S., Kodur, V.K.R. System Level Response of Braced Frame Structures Under Fire Exposure Scenarios. Journal of Constructional Steel Research 170, 106073, (2020). https://doi.org/10.1016/j.jcsr.2020.106073.

11. Liang, X., Shen, Q., Ghosh, S.K. Assessing Ability of Seismic Structural Systems to Withstand Progressive Collapse. S.K. Ghosh Associates, Inc., Palatine, IL, USA; 2006.

12. Venkatachari, S., Kodur, V. Effect of Transient Creep on Fire Induced Instability in Steel Framed Structures. Journal of Constructional Steel Research 181:106618 (2021). https://doi.org/10.1016/j.jcsr.2021.106618.

13. ASTM (American Society for Testing and Materials). Standard Test Methods for Fire Tests of Building Construction and Materials. ASTM E119-18c, West Conshohocken, PA, USA; 2007.

14. Agarwal, A., Varma, A.H. Fire Induced Progressive Collapse of Steel Building Structures: The Role of Interior Gravity Columns. Engineering Structures 58, 129–140 (2014). https://doi.org/10.1016/j.engstruct.2013.09.020.

SiF 2022– The 12th International Conference on Structures in Fire
The Hong Kong Polytechnic University, Nov 30 - Dec 2, 2022

PRELIMINARY STUDY ON MECHANICAL PROPERTIES OF Q460 HIGH STRENGTH STEEL DURING THE COOLING STAGE OF FIRE

Binhui Jiang[1], Mengjie Wang[2,*], Guobiao Lou[3], Guoqiang Li[4]

ABSTRACT

Most previous studies on the fire-related mechanical properties of high-strength steel (HSS) focused on the fire-heating and post-fire stages, with the cooling stage of fire being ignored. In this paper, the mechanical properties of Q460 steel during the cooling stage were experimentally studied. Results show that the mechanical properties of Q460 steel in the cooling stage are not only related to the test temperature (T_t), but also related to the peak heating temperature (T_p). The yield strength and ultimate strength of Q460 steel show an overall download trend with the increase of T_p when T_t is the same. The differences in mechanical properties of Q460 steel between the cooling and heating stages were enlarged after T_p exceeds a certain value. This certain value was different for different mechanical properties. After T_p exceeds 800 °C, the yield strength and ultimate strength in the cooling stage were significantly smaller than those in the heating stage, while the ultimate strain in the cooling stage was greater than that in the heating stage.

Keywords: High-strength steel; Mechanical property; Fire; Cooling stage, Experimental study

1 INTRODUCTION

High-temperature material properties are essential parameters for studying the fire resistance of steel structures. Previous studies on the fire-related mechanical properties of high-strength steel (HSS) focused on the fire-heating and post-fire stages [1-5]. However, steel buildings that survived the heating stage of the fire may suffer further damage or even collapse during the cooling stage [6-9], which emphasises the critical importance of studying the mechanical properties of steel during the cooling stage of fire. Currently, only a few experiments have been conducted to study the mechanical properties of structural steel in the cooling stage of fire.

Mushahary et al. [10] studied the mechanical properties of India-made mild steel E350 in the cooling stage. The results show that the Young's modulus and yield strength lost during the heating stage cannot be completely recovered during the cooling stage. Chen et al. [11, 12] investigated the mechanical properties of cold-formed steel Q345 and G550 during full-range compartment fires, and the results show that the difference in mechanical properties between the heating and cooling stages cannot be ignored. Wang et al. [4] investigated the mechanical properties of Q690 steel in the fire-cooling stage. Azhari et al. [13] studied the effect of creep strain on the mechanical properties of Grade 1200 °C steel (ultra-high strength steel)

[1] Associate professor, National Engineering research center for High Speed Railway construction, Central South University, Changsha 410075, China; School of Civil Engineering, Central South University, Changsha 410075, China
e-mail: binhuijiang@csu.edu.cn, ORCID: https://orcid.org/0000-0003-3774-9587
[2] PhD Candidate, School of Civil Engineering, Tongji University, Shanghai 200092, China; School of Civil Engineering, Central South University, Changsha 410075, China, Corresponding author
e-mail: mengjiewang@tongji.edu.cn
[3] Associate professor, School of Civil Engineering, Tongji University, Shanghai 200092, China
e-mail: gblou@tongji.edu.cn
[4] Professor, School of Civil Engineering, Tongji University, Shanghai 200092, China
e-mail: gqli@tongji.edu.cn
https://doi.org/10.6084/m9.figshare.22215688

during the cooling stage of a fire. Hanus et al. [14, 15] studied the strength of Welds and Grade 8.8 bolts under heating and subsequent cooling stages. Mushahary et al. [16] investigated the tensile and shear strength of 10.9 grade bolts in the fire-heating and cooling stages. However, currently there are no studies on the mechanical properties of hot-rolled HSS Q460 in the cooling stage of fire.

In this paper, the mechanical properties of hot-rolled HSS Q460 in the cooling stage were experimentally studied, by adopting the steady-state method. Reduction factors of Young's modulus, yield strength, ultimate strength and ultimate strain of Q460 steel in the cooling stage were obtained and compared with those in the heating stage.

2 EXPERIMENTAL INVESTIGATION

2.1 Test material and test device

The coupons were extracted from a hot-rolled Q460 steel plate with a nominal thickness of 20 mm. The chemical compositions of the steel are shown in Table 1. The shape and dimensions of the test coupons are presented in Figure 1, which satisfy the requirements of the mainstream material test standards such as GB/T228.2-2015 [17], ISO 6892-2 [18] and EN 10002-5 [19].

The tensile tests were performed with a portal computer-controlled testing machine with a loading capacity of 300 kN, in which the heating equipment was an electric furnace, as shown in Figure 2. Three thermocouples on each of the upper, middle and lower parts of the test coupon were placed to monitor the temperature of the coupons, as shown in Figure 2. In addition, the strains of the coupons were measured by a high-temperature extensometer until the ultimate strain is reached. The strains greater than the ultimate strain were calculated based on the displacement of the crosshead of the test machine.

Table 1 Chemical composition of Q460 steel.

Composition	C	Si	Mn	P	S	Cr	Al	Mo	Ti	Cu	Nb	Ni	V
wt.‰	1.8	2.6	13.5	0.13	0.02	0.5	0.4	0.08	0.02	0.8	0.25	0.15	0.02

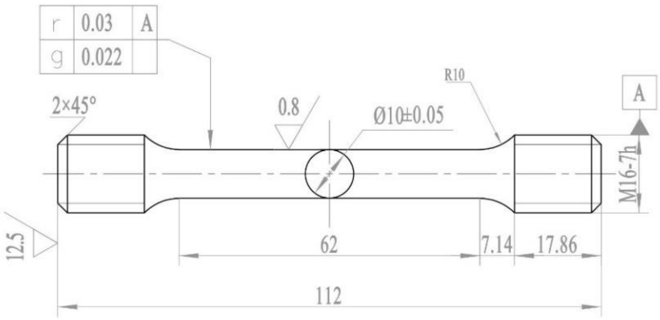

Figure 1 The dimensions of steel coupons (mm)

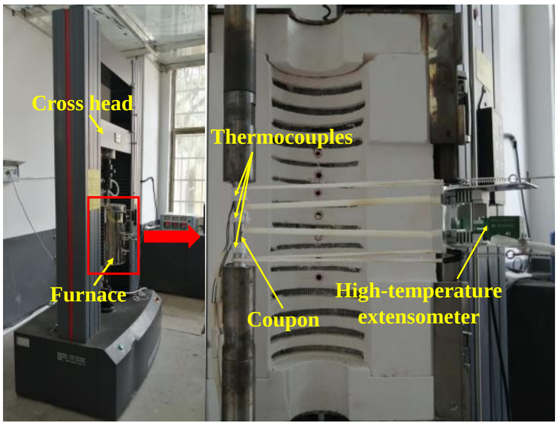

Figure 2 The test device.

2.2 Test method and procedure

The material properties of Q460 during the cooling stage of fire were measured through high-temperature steady-state test. Firstly, the coupons were first heated to a pre-set peak heating temperature (T_p) using a rate of 20 ℃/min and then held at T_p for 15 min. Then, the coupons were cooled to the tensile temperature (T_t) at a rate of 8 ℃/min and held at T_t for a further15 min. Finally, the tensile load was applied to the coupon until fracture, and the temperature was maintained at T_t during loading. The considered peak temperatures were 400 °C, 600 °C and 800 °C, and the tensile temperatures were 20 °C, 200 °C, 300 °C, 400 °C, 500 °C, 600 °C, 700 °C and 800 °C. At least two coupons were tested for each case, and the results were averaged.

3 TEST RESULTS

The mechanical properties studied in this paper involve stress-strain curves, Young's modulus (E), yield strength (f_y), ultimate strength (f_u), and ultimate strain (ε_u). Due to the absence of a clear yield plateau in the stress-strain curve of steel at elevated temperatures, the nominal yield strengths of $f_{0.2}$ and $f_{2.0}$ were adopted in this paper. The change in mechanical properties of the steel during the cooling stage is expressed using a reduction factor, which is the ratio of the mechanical property value at elevated temperature to that at room temperature.

3.1 Stress-strain curves

The stress-strain curves of Q460 steel at the same T_p but different T_t values during the cooling stage are presented in Figure 3. Figure 3(a), (b) and (c) present the stress-strain curves for T_p of 400 °C, 600 °C and 800 °C, respectively. The stress-strain curves have a yield plateau when T_t is 20 °C (room temperature) and 200 °C, while the stress-strain curves at other T_t do not show a yield plateau. When T_p is the same, the stress-strain curve at T_t of 300 °C was generally higher than those at other T_t values, which may be due to the blue-brittle effect at T_t of 300 °C. After T_t exceeds 500 °C, the elastic section of the stress-strain curve shortens and the ultimate strength decreases with the increase of T_t.

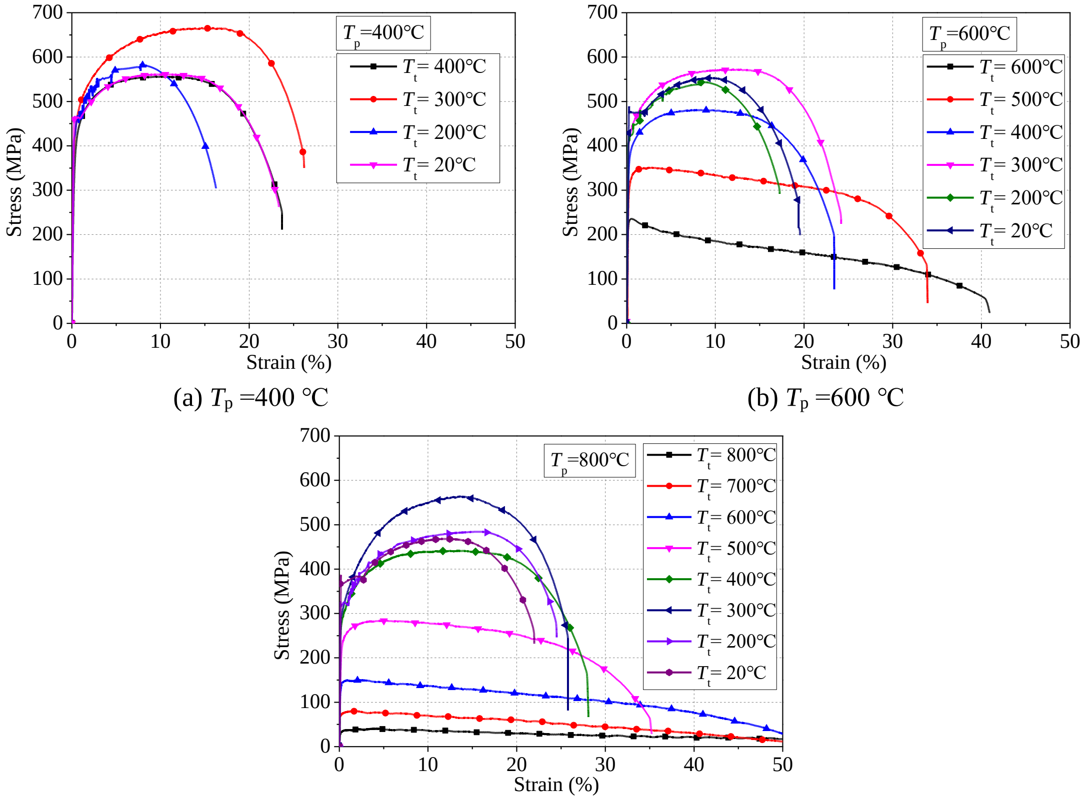

(a) T_p =400 °C
(b) T_p =600 °C
(c) T_p =800 °C

Figure 3 The stress-strain curves of Q460 steel in the cooling stage.

3.2 Young's modulus

The Young's modulus reduction factors of Q460 steel in the cooling stage of fire are presented in Figure 4. It can be seen that the Young's modulus reduction factors of Q460 steel in the cooling stage at the same T_p generally recover with the decrease of T_t. When T_t is the same, the reduction factors of Young's modulus in the cooling stage were generally similar to those in the heating stage. However, there are some exceptions. For example, when T_p is 600 °C and T_t is 400 °C, the Young's modulus reduction factor is 0.971 in the cooling stage, which is significantly greater than that in the heating stage with a reduction factor of 0.827. Besides, when T_p is 800 °C and T_t is 600 °C, the Young's modulus reduction factor is 0.405 in the cooling stage, which is significantly less than the reduction factor of 0.762 in the heating stage.

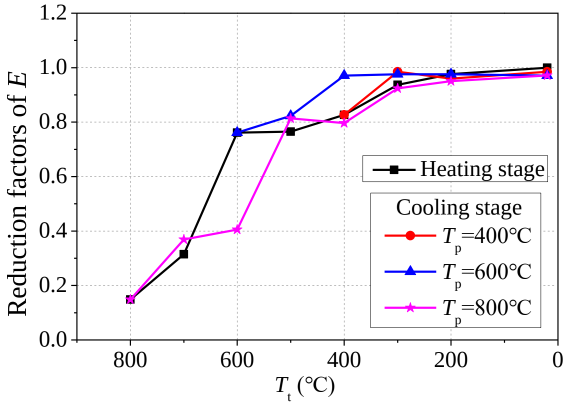

Figure 4 The reduction factors of Q460 steel in the cooling stage

3.3 Yield strength

The yield strength $f_{0.2}$ reduction factors of Q460 steel in the cooling stage are presented in Figure 5(a). The yield strength $f_{0.2}$ reduction factors of each T_p recover with the decrease of T_t. When T_p is within 600 °C, the reduction factors of yield strength $f_{0.2}$ in the cooling stage were similar to those in the heating stage at the same T_t. This phenomenon indicates that the effect of T_p on the $f_{0.2}$ reduction factors of Q460 steel is negligible when T_p is within 600 °C. However, when T_p reaches 800 °C, the $f_{0.2}$ reduction factors in the cooling stage were significantly smaller than those in the heating stage. The yield strength $f_{2.0}$ reduction factors of Q460 steel in the cooling stage are presented in Figure 5(b). When T_t is greater than 300 °C, the $f_{2.0}$ reduction factors of each T_p recover with the decrease of T_t, while they gradually decrease after T_t decreases within 300 °C. The $f_{2.0}$ reduction factors at the same T_t were decreased with the increase of T_p. When T_p is 400 °C, the $f_{2.0}$ reduction factors in the cooling stage were similar to those in the heating stage. After T_p reach 600 °C and 800 °C, the $f_{2.0}$ reduction factors in the cooling stage were evidently smaller than those in the heating stage. It can be seen that after T_p exceeds a certain value, the $f_{0.2}$ reduction factors in the cooling stage are not only related to the test temperature (T_t), but also related to the ultimate peak heating temperature (T_p).

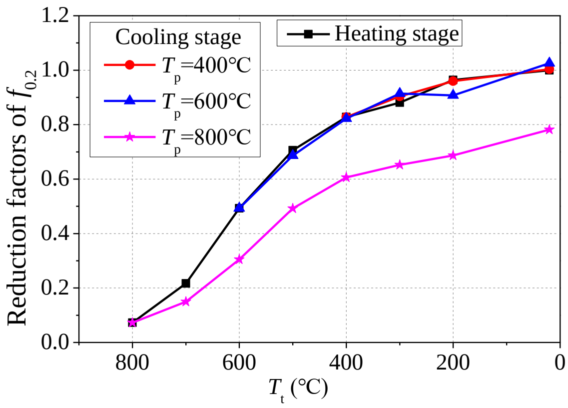

(a) yield strength $f_{0.2}$

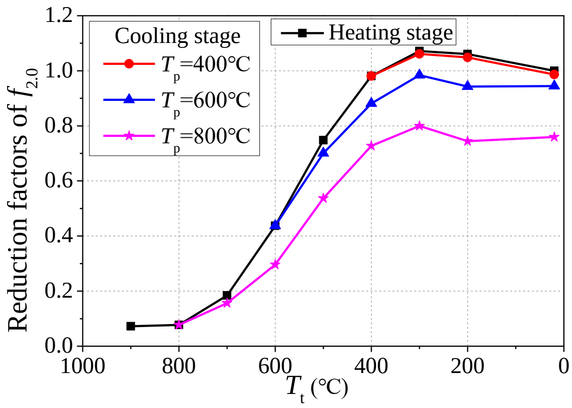

(b) yield strength $f_{2.0}$

Figure 5 The reduction factors of yield strength of Q460 steel in the cooling stage.

3.4 Ultimate strength

Figure 6 illustrates the reduction factors of ultimate strength in the cooling stage. The change trend of ultimate strength of Q460 steel in the cooling stage were generally similar to that of yield strength $f_{2.0}$. When T_t is greater than 300 °C, the ultimate strength reduction factors of each T_p recover with the decrease of T_t, while they gradually decrease after T_t decrease within 300 °C. The ultimate strength reduction factors at the same T_t were decreased within the increase of T_p. When T_p is 400 °C, the ultimate strength reduction factors in the cooling stage were similar to those in the heating stage. After T_p reach 600 °C and 800 °C, the ultimate strength reduction factors in the cooling stage were evidently smaller than those in the heating stage.

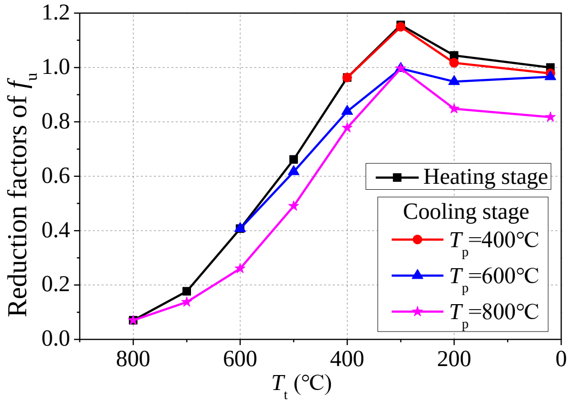

Figure 6 The reduction factors of ultimate strength of Q460 steel in the cooling stage.

3.5 Ultimate strain

Figure 7 illustrates the reduction factors of ultimate strain in the cooling stage of fire. As can be seen from this figure, when T_p is 400 °C and 600 °C, the reduction factors of ultimate strength in the cooling stage were similar to those in the heating stage. When T_p is 800 °C, the reduction factors of ultimate strain in the cooling stage were generally larger than those in the heating stage, especially at T_t of 200 °C.

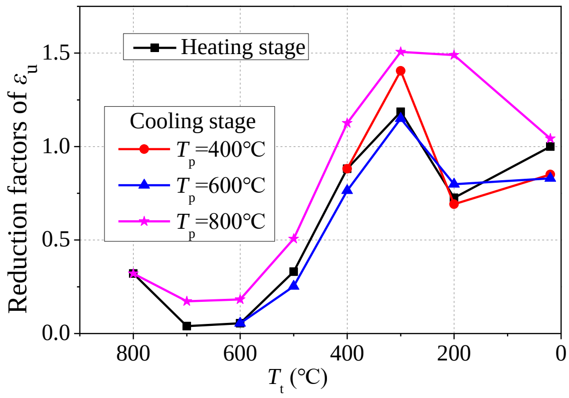

Figure 7 The reduction factors of ultimate strain of Q460 steel in the cooling stage.

4 CONCLUSIONS

In this paper, the mechanical properties of hot-rolled HSS Q460 in the cooling stage of fire were investigated using steady-state test. The test results show that the mechanical properties of Q460 steel in the cooling stage are not only related to the test temperature (T_t), but also related to the peak heating temperature (T_p). After T_t exceeds 500 °C, the elastic section of the stress-strain curve shortens and the ultimate strength decreases with the increase of T_t. The Young's modulus of Q460 steel in the cooling stage was in most cases similar to that in the heating stage when T_p is within 800 °C. The yield strength and ultimate strength of Q460 steel at the same T_t show an overall download trend with the increase of T_p. When T_p is within a certain value, the strength of Q460 steel in the cooling stage was similar to that in the heating stage. However, after T_p exceeds the certain value, the strength of Q460 steel in the cooling stage was significantly smaller than that in the heating stage. The certain value is around 800 °C for yield strength $f_{0.2}$

and around 600 °C for yield strength $f_{2.0}$ and ultimate strength. The ultimate strain of Q460 steel in the cooling stage was generally similar to that in the heating stage when is within 600 °C, while it was larger than that in the heating stage when is 800 °C. In general, the differences in mechanical properties of Q460 steel between the cooling and heating stages were significantly enlarged after T_p exceeds a certain value, and the certain value was different for different mechanical properties. Hence, the mechanical properties of steel in the cooling stage cannot be directly replaced by those of the heating stage.

ACKNOWLEDGMENT

This work is supported by the National Natural Science Foundation of China with Grant No. 51908560.

REFERENCES

[1] X. Qiang, F.S.K. Bijlaard, H. Kolstein. Deterioration of mechanical properties of high strength structural steel S460N under steady state fire condition. MATER DESIGN. 36 (2012), 438-442.

[2] W. Wang, T. Liu, J. Liu. Experimental study on post-fire mechanical properties of high strength Q460 steel. J CONSTR STEEL RES. 114 (2015), 100-109.

[3] M. Wang, Y. Li, G. Li, W. Wang, B. Jiang. Comparative experimental studies of high-temperature mechanical properties of HSSs Q460D and Q690D. J CONSTR STEEL RES. 189 (2022).

[4] M. Wang, G. Lou, G. Li, B. Jiang. Experimental study on mechanical properties of Q690D high strength steel during the cooling stage of fire. FIRE SAFETY J. 132 (2022), 103639.

[5] Y. Li, M. Wang, G. Li, B. Jiang. Mechanical properties of hot-rolled structural steels at elevated Temperatures： A review. FIRE SAFETY J. 119 (2021), 103237.

[6] B.H. Jiang, G.Q. Li, L.L. Li, B.A. Izzuddin. Experimental Studies on Progressive Collapse Resistance of Steel Moment Frames under Localized Furnace Loading. J STRUCT ENG. 2 (2018), 4017190-4017191.

[7] B. Jiang, G. Li, L. Li, B.A. Izzuddin. Simulations on progressive collapse resistance of steel moment frames under localized fire. J CONSTR STEEL RES. 138 (2017), 380-388.

[8] T. Gernay, A. Gamba. Progressive collapse triggered by fire induced column loss: Detrimental effect of thermal forces. ENG STRUCT. 172 (2018), 483-496.

[9] S. Guo. Experimental and numerical study on restrained composite slab during heating and cooling. J CONSTR STEEL RES. 69 (2012), 95-105.

[10] S.K. Mushahary, K.D. Singh, S.A. Jayachandran. Mechanical properties of E350 steel during heating and cooling. THIN WALL STRUCT. 160 (2021), 107351.

[11] W. Chen, K. Liu, J. Ye, J. Jiang, C. Xu, L. Jin, M. Zhang. High-temperature steady-state experiments on G550 cold-formed steel during heating and cooling stages. THIN WALL STRUCT. 151 (2020), 106760.

[12] W. Chen, J. Ye, L. Jin, J. Jiang, K. Liu, M. Zhang, W. Chen, H. Zhang. High-temperature material degradation of Q345 cold-formed steel during full-range compartment fires. J CONSTR STEEL RES. 175 (2020), 106366.

[13] F. Azhari, A. Heidarpour, X. Zhao, C.R. Hutchinson. Mechanical properties of ultra-high strength (Grade 1200) steel tubes under cooling phase of a fire: An experimental investigation. CONSTR BUILD MATER. 93 (2015), 841-850.

[14] F. Hanus, G. Zilli, J.M. Franssen. Behaviour of Grade 8.8 bolts under natural fire conditions—Tests and model. J CONSTR STEEL RES. 67 (2011), 1292-1298.

[15] F. Hanus, G. Zilli, J.M. Franssen. Experimental Tests and Analytical Models for Welds and Grade 8.8 Bolts under Heating and Subsequent Cooling. Journal of structural fire engineering. 2 (2011).

[16] S.K. Mushahary, K.D. Singh, S.A. Jayachandran. Tensile and shear strength of 10.9 grade bolts in heating and cooling fire. J CONSTR STEEL RES. 197 (2022), 107503.

[17] GB/T 228.2 Metallic Materials-Tensile Testing Part 2: Method of test at elevated temperature, Standards Press of China, Beijing, 2015. (in Chinese).

[18] EN ISO 6892-2 Metallic materials. Tensile testing. Part 2: Method of test at elevated temperature, International Organisation for Standardisation, 2011.

[19] European Committee for Standardization. Tensile testing of metallic materials part 5: Method of test at elevated temperatures. EN 10002-5; 1992.

CONVECTIVE HEAT TRANSFER COEFFICIENT OF STEEL MEMBER IN LOCALIZED FIRE CONDITION

Jinggang Zhou[1], Xuanyi Zhou[2,*], Beihua Cong[3], Wei Wang[4]

ABSTRACT

At present, values adopted from specifications are mostly used to define the convective heat transfer coefficient h_c in localized fire researches. In this paper, the specific scenario of the steel column surrounded by fire plume is selected as a typical case to explore the surface h_c change rules of the steel column. This paper conducts a two-way coupling simulation analysis of the fire and the thermal models by means of CFD codes. First, the validity of this simulation methodology is verified. Following this, the distribution laws of the spatial velocity are analyzed, and the h_c coefficient of the steel column surface is explored in detail using two different calculation formulas. The h_c results obtained based on Newton's Law of Cooling is more likely to consider the temperature boundary layer situations above the column surface, which is lower at the bottom of the column and increases with height, with relative maximum value in the lower and middle parts of the column, reaching around 35 W/m^2 K. In contrast, the h_c distributions along the height obtained by the empirically based practical formula are similar to the distribution of fire plume velocity along the height. In other words, it considers mostly the effect of the velocity boundary layer, while the effect of significant changes in fluid temperature on convective heat transfer behavior is less considered.

Keywords: Localized fire; CFD numerical simulation; steel column; convective heat transfer coefficient

1 INTRODUCTION

In structural fire resistance studies, heat convection, as a typical pathway of heat transfer, can cause structural members to be damaged by thermal heating in the fire field, so the selections of h_c coefficient characterizing this behavior are equally critical in structural fire resistance studies. Most of the current structural fire resistance analyses are based on the assumption that the flashover condition is satisfied. In a post-flashover building fire condition, the gas properties are approximately uniform and the interior ambient temperature can be approximated by a time-temperature curve (e.g., ISO-834 curve, EC3 Eurocode [1]). This analytical methodology does not require the introduction of complex computational fluid dynamics (CFD) and can obtain structural response results by direct sequential thermodynamic coupling analysis. In this type of analysis, the value of h_c generally ranges from 5 to 50 W/m^2 K. According to the Eurocode [1], most numerical simulation studies set h_c to 25 W/m^2 K for analysis. For example, Albrifkani and YongChang Wang [2] studied the performance of reinforced concrete beams subjected to axial and

[1] PhD, Tongji University
e-mail: 1910320@tongji.edu.cn
[2] Professor, Tongji University
e-mail: zhouxytj@tongji.edu.cn
[3] Associate Researcher, Tongji University
e-mail: bhcong@tongji.edu.cn
[4] Professor, Tongji University
e-mail: weiwang@tongji.edu.cn
https://doi.org/10.6084/m9.figshare.22215712

rotational restraints in fire, Liu et al. [3] reported a full-scale fire testing of concrete filled thin-walled steel tubular (CFST) column-wall structure. In all these studies, h_c was taken as 25 W/m^2 K.

In actual situations, the threshold of flashover occurrence cannot be reached in large spaces, such as airport terminals, stadiums and parks. In this case, only localized fires will develop. The numerical simulation of localized fires involves the coupling of three analytical processes, in order: fire analysis, thermal analysis and structural analysis. The current mainstream coupled CFD-FEM numerical simulation method for localized fires is based on a new variable proposed by Wickström et al [4], called Adiabatic Surface Temperature (AST), which can accurately describe the complex fire analysis boundary conditions and thus transfer the information from the fire analysis to the subsequent finite element analysis, as shown in Figure 1 below. By using this methodology, Chao Zhang [5] pointed out that the calculated adiabatic temperature AST is influenced by the convective heat transfer coefficient h_c, so the value of h_c coefficient should be carefully chosen, and the results of numerical and experimental agree well when h_c is taken as 9 W/m^2 K for each side of the steel column surfaces when analyzing the buckling time of the steel column surrounding by fire. Silva et al [6] argued that when h_c is set as a constant according to the specification, the relative importance of convective heat flux in a given fire scenario (relative to radiant heat flux) may be reduced or amplified. In their performance-based analysis [7] for cylindrical steel containment vessels exposed to fire, the coefficient was assumed to be 25 W/m^2 K and 4 W/m^2 K, for fire exposed and unexposed surfaces, respectively. Polish scholar Glema [8] applied this performance-based method to evaluate the mechanical properties of CFRP columns in open parking lot fires, assuming that the surface h_c of all parts of the component was 10 W/m^2 K during the analysis. The localized fire with ellipsoidal solid flame (LF-ESF) model proposed by Rivera et al. [9] could be used as an alternative to the highly complex CFD method for application in the structural design under localized fire conditions, where h_c was taken as 25 W/m^2 K.

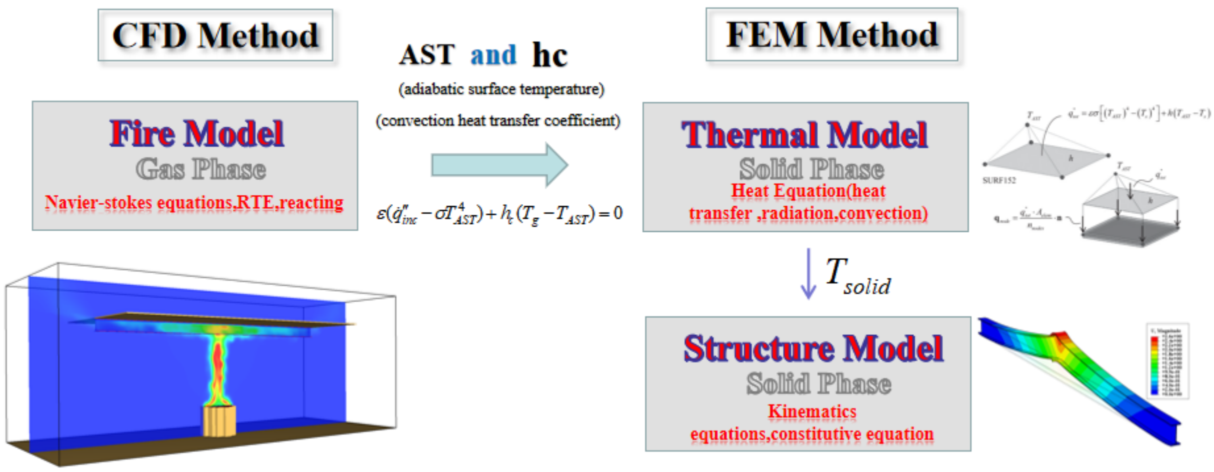

Figure 1. mainstream coupled CFD-FEM simulation approach for structural-fire analysis

As mentioned above, the previous numerical simulation studies of structural fire resistance lack a specific discussion of the h_c parameters, and the values are mostly based on the experience provided by the specifications. Therefore, it is very necessary to analyze and discuss the distribution law of the convection heat transfer coefficient h_c on the surface of the fire-resistant members under the localized fire conditions.

2 METHODOLOGY

2.1 Non-premixed Combustion

The control equations that need to be satisfied in fluid dynamics include the mass, momentum, and energy conservation equations, which are not thoroughly described here. A brief introduction to the non-premix combustion in localized fire scenarios is displayed here. The basis of the non-premixed combustion modeling approach is that under a certain set of simplified assumptions, the instantaneous thermochemical state of the fluid is related to a conserved scalar quantity known as the mixture fraction f [10]:

$$f = \frac{Y_i - Y_{i,ox}}{Y_{i,fuel} - Y_{i,ox}} \tag{1}$$

where Y_i is mass fraction of species i, $Y_{i,fuel}$ means the elemental mass fraction of the species i in the fuel while $Y_{i,ox}$ means that in the oxidant.

The major significance of the application of mixed fraction lies in the elimination of the source term in the species transport equation [11], which is in the following form:

$$\frac{\partial}{\partial t}(\rho f) + \nabla \cdot (\rho V f) = \nabla \cdot (\rho D_{eff} \nabla f) \tag{2}$$

where D_{eff} is effective diffusion coefficient, satisfying the formula $D_{eff} = D_m + \mu_t / \rho Sc_t$. Sc_t is the turbulent Schmidt number, which is generally taken as 0.7.

The relationship between the mean and instantaneous values depends on the interaction between turbulence and chemical reactions which is considered as a probability density function (PDF). Based on the PDF, the time average predicted values $\overline{\phi}$ (such as temperature, specie concentrations, density) can be calculated as (in non-adiabatic systems):

$$\overline{\varphi_i} = \int_0^1 p(f)\varphi_i(f, H)df \tag{3}$$

where H is the total absolute enthalpy of the mixture. The shape of the PDF can be assumed to the β function [12] which is defined by the mean mixture fraction $\overline{f}$ and its variance $\overline{f'^2}$, as given in Prieler et al. [13].

2.2 Formula for Calculating hc coefficient

(a) using the Newton's cooling formula

The convective heat flux depends on the difference between the surrounding gas temperature and the solid surface temperature. It is usually calculated by Newton's Law of Cooling [14], from which h_c can be deduced and solved [15]:

$$h_c = -\frac{\dot{q}''_{\mathrm{conv}}}{T_{amb} - T_s} \tag{4}$$

where $\dot{q}''_{conv}$ is convection heat flux, T_s is solid surface temperature and T_{amb} is ambient temperature.

(b) traditional empirical formula

From the Eq. (4), h_c can be deduced and solved: $h_c = \dot{q}''_{conv} / \Delta T = -k / \Delta T \cdot (\partial T / \partial y)|_{y=0} \approx k / \delta_T$, where δ_T is the thickness of the temperature boundary layer. It can be seen that the h_c coefficient is proportional to the air thermal conductivity k while being inversely proportional to δ_T . As the Reynolds number is connected with the velocity boundary layer thickness δ_v , and the Prandtl number can establish the correlation between δ_T and δ_v, the general relationship equation can be derived: $h_c = K R_e{}^a P_r^b$, where K , a and b are different parameters [16]. In the field of fire safety, fire Dynamic Simulator (FDS) developed by NIST calculate the h_c coefficient of the plate surface with the following formula [17]:

$$h_c = \frac{k}{L} \times 0.0037 \times R_e^{0.8}\, \mathrm{Pr}^{0.33} \quad (5)$$

3 STUDY CASE FOR VALIDATION

The research object is a square steel tube column (section 150mm × 150mm × 4.5mm) surrounded by fire plume under localized fire conditions, and the experimental results [18] from the literature are used to verify the numerical model. The experimental setup is shown in Fig. 2. A 4.5mm thick, 2.50m tall and 0.15m square steel column was located at the center of the diffusion fire source. A 0.50m square diffusion burner with propane as the fuel was used as the fire source (Fig. 2), providing a controlled heat release rate (HRR) of 81 kW. According to the literature [18], the incident radiation heat flow and surface temperature were measured on the surface of the steel column. Temperature was monitored on all the external surfaces of the specimen after the surface temperature had reached a nearly steady state. Incident heat flux was measured for 2 seconds at the interval of 2 minutes, and the average value was recorded.

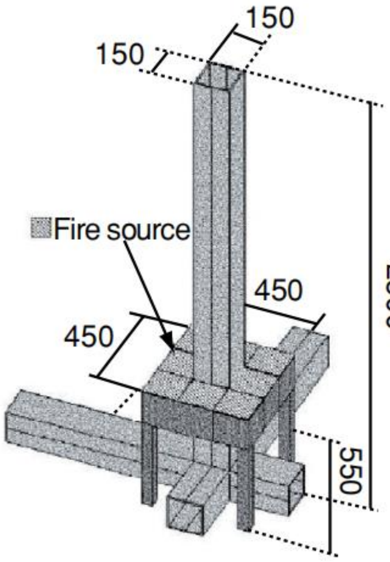

Figure 2. Experimental model of steel column surrounding by fire (unit: mm)

4 NUMERICAL SIMULATION

4.1 Computing domain and grid

The computational domain size of the CFD model was 18m × 6m × 8m, as shown in Fig. 3 below. The model grid adopted unstructured polyhedral mesh. After repairing, smoothing and simplifying, computing domain contained a total of 258,328 polyhedral meshes. To calculate the boundary layer around the steel column, 15 prism layers were located at the surface of the structural component to make the entire surface of the steel column satisfy $y^+<3$.

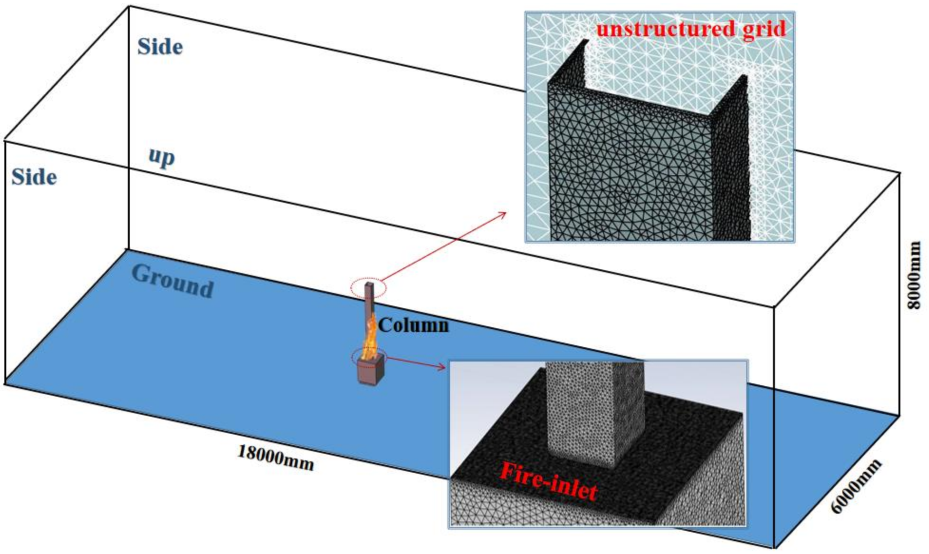

Figure 3. Numerical model of steel column surrounding by fire (unstructured grid)

4.2 Numerical settings

ANSYS FLUENT software is used to implement a coupled solution between the fire analysis model and the thermal analysis model, which includes equations describing physicochemical phenomena such as fluid flow, non-premixed combustion, heat transfer, species transport and steel element conduction.

The transient, pressure-based solver is used for calculation, which takes the effect of gravity into account. In fire analysis, the use of LES method can better simulate the interaction between turbulence and buoyancy with relatively ideal results obtained. The fire development process is considered the turbulent diffusion non-premixed combustion of propane and air. The simple probability density function (PDF) method is used to describe the interaction between turbulence and combustion statistically, and the non-premixed equilibrium chemical model is employed for calculation. The discrete ordinates radiation model [19] is adopted to simulate the radiation heat transfer and the one-step Khan and Greeves model [20] is selected to predict the rate of soot formation, which is based on a simple empirical rate. As for calculating the mixture material density, propane-air is regarded as a non-compressible ideal gas. WSGGM method [21] is used to calculate the absorption coefficient of flame gas products. The thermal properties for steel such as thermal conductivity and specific heat capacity, which affect the elevated temperature of steel, are used as specified in Eurocode 3 [1].

For the boundary conditions, the steel column surface is taken as a two-sided wall (thermally coupled interface), which means the solver can calculate heat transfer directly from the solution in fluid zone adjacent to the solid. The emissivity of steel column surface is set to 0.85. The ground and the brazier surface are considered adiabatic, which do not exchange heat with the outside. Fuel inlet surface is defined as the mass flow inlet, from which the mass flow rate is calculated based on the heat release rate (HRR) in the experiment [18].

The solutions are considered as converged when the residual dropped to 1×10^{-6} for the energy equation and 1×10^{-4} for the other equations. Considering the reasonable value of the Courant number, 0.05 s is set as the time step size, hence a total of 24000 time-steps are performed to complete a 1200-s fire exposure. At this time, the column temperature tend to be stable.

5 RESULTS AND DISCUSSION

5.1 Model validation

Fig. 4 shows the steel column surface temperature distribution at 1200 s. It can be seen that the bottom area is close to the fire source and the temperature there is the highest, exceeding 600°C. gradually decreases as height increases, with the middle area of the column at about 300°C and the top at about 100°C.

From the curve shown in Fig. 4, the four sides of the steel column are heated relatively uniformly, and the simulation results are in good agreement with the experiment results [18], thus verifying the correctness of the numerical simulation coupling method.

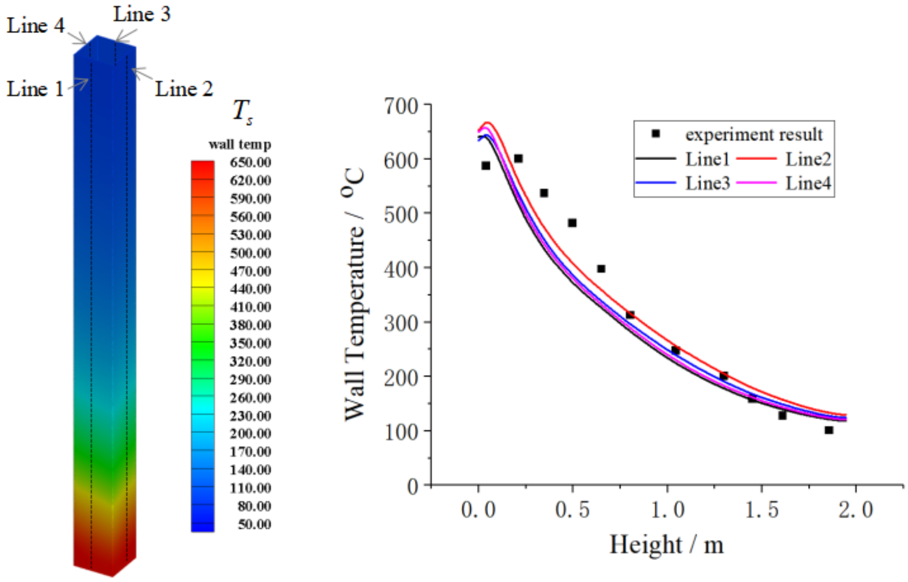

Figure 4. Experimental model of steel column surrounding by fire (unit: mm)

5.2 Fire Environment Analysis

Fig. 5 shows the distribution of velocity slices in the fluid domain at three typical moments obtained from the numerical simulation. As can be seen from the figure, the high temperature gas generated by combustion flows upwards along the wall of the column with a maximum velocity of approximately 5 m/s. Due to the randomness brought by turbulence during the combustion process, the highest velocity region at different moments is not determined in height, but it is always close to the column surfaces.

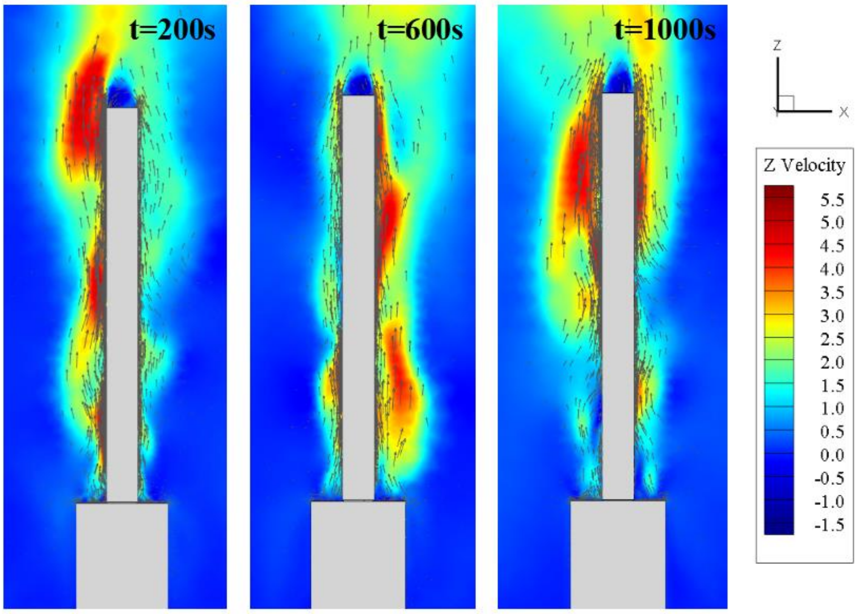

Figure 5. velocity distribution (unit: m/s)

5.3 Convective Heat Transfer Coefficient Analysis

(a) Influencing factors of h_c

Different h_c calculation formulas are proposed in section 2.2 above, but few literature discuss the h_c distribution characteristics of structural members under localized fire conditions. Therefore, this section intends to use a steel column surrounding by flame (with HRR=81.0kW) as the object for exploring the distribution characteristics and influencing factors of the h_c coefficient.

Taking the 800-s situation as an example, as shown in the temperature slice distribution of Fig. 6, the maximum flame temperature is approximately 1250°C, which is mainly distributed at the bottom of the column. The fire plume rises around the column, and the flue gas temperature rising around the column surface is about 300-500°C. From the convection heat flux $\dot{q}''_{conv}$ distribution, the instantaneous convection heat flux value is highly random. For example, $\dot{q}''_{conv}$ at area A1 exceeds 20 kW/m^2, and those at areas A2 and A3 reach 10 kW/m^2. For the area where relatively low temperature near the surface at this time, when T_s is greater than T_g, $\dot{q}''_{conv}$ becomes negative, and the extreme value reaches -15 kW/m^2. The h_c cloud distribution can be obtained in Fig. 6 by applying Eq. 4. It can be seen that the h_c distribution is also highly stochastic with time, with the highest value reaching 65 W/m^2 K. The maximum distribution region of the h_c cloud is very similar to the $\dot{q}''_{conv}$ cloud, namely A1, A2 and A3 regions respectively. It is clear that the surface h_c coefficient obtained by applying Eq. 4 is mainly affected by the the temperature boundary layer and heat flux situations.

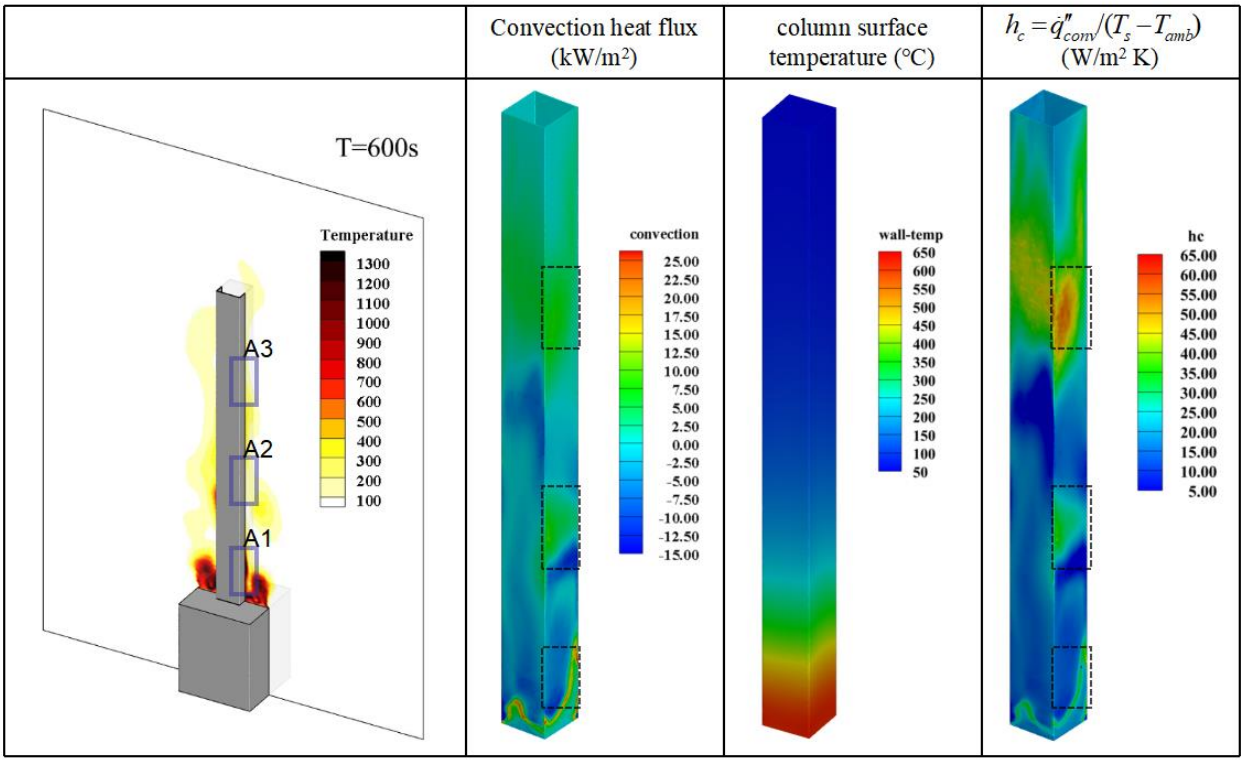

Figure 6. Column surface coefficient display (T=800s)

Again, taking the condition at 800 s moment as an example, as shown in the velocity slice distribution of Fig. 7, the fire plume rises by buoyancy and the highest flow velocity reaches about 4.5 m/s, which is mainly distributed along the column surface. In this figure, two areas B1 and B2 are regions near the surface with higher gas flow velocity, and area B3 is the region where the adjacent gas flow velocity is lower. The Reynolds number has the calculate formula of $R_e = \rho u L / \mu = u L / \nu$, where ν is called the dynamical viscosity coefficient, u is the velocity value obtained from the fluid domain grid close to the surface and L is the characteristic length of the fluid domain, taking 0.15m as its value in this case. The distribution of the R_e number on the surface of the steel column can be obtained as Fig. 7. The value of R_e indicates that the flow field in the fire plume around the column is a typical turbulent flow, with the extreme value of R_e reaching 5.5×10^4 and the region of extreme R_e distribution is where maximum gas velocity near the surface occurs. Regarding the Prandtl number P_r, the general P_r value for gas is in the range of 0.6-0.8. In this analysis, the variation of the effective P_r obtained by the numerical simulation is relatively small, about 0.7 in value as shown in Fig. 7. Taking the Eq. (5) listed in Section 2.2 for calculating the h_c coefficient, it can be observed that the h_c distribution obtained from this equation also show a high degree of randomness, with the highest values close to 60 W/m^2 K. The extreme h_c value distribution area of the cloud map is very similar to the Reynolds number cloud map, with values at B1 and B2 regions being maximum, and values at B3 regions being minimum. It is clear that such formula-applied h_c coefficients are mainly affected by the boundary velocity field situation.

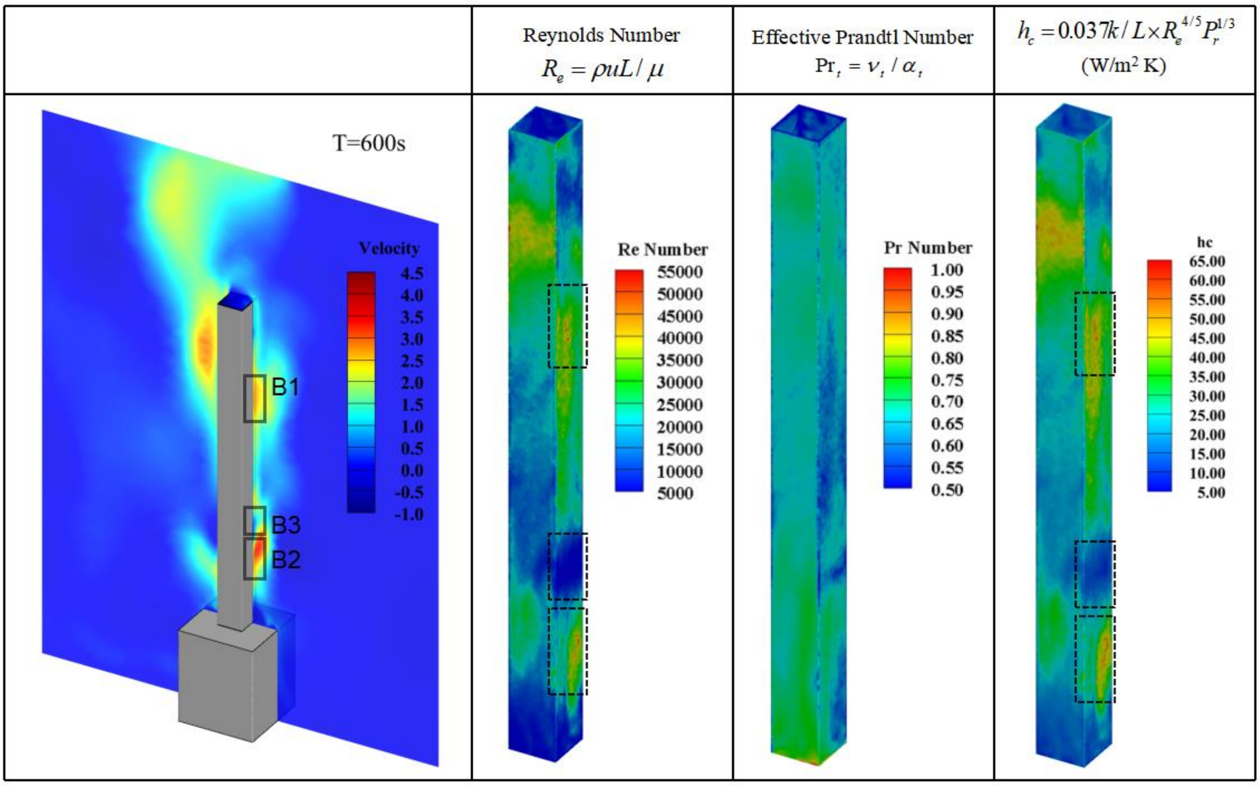

Figure 7. Column surface coefficient display (T=800s)

(b) Different HRR conditions

In order to explore the distribution law of the structure surface h_c coefficient under the localized fire in the field of structural fire resistance, the study was extended to three cases by changing the heat release rate of the fire source (HRR=40.5kW or 81kW or 121.5kW).

Fig. 8 shows the change curve between time-averaged $\overline{h_c}$ and height z. The red curve shows the results of the $h_c(1)$ coefficient applying Eq. 4. It can be found that the $\overline{h_c}$ result at the bottom of the column is small, ranging in the 10-20 W/m^2 K region. The value of $\overline{h_c}$ increases with the rise of height, with largest values at $z = 0.5 \sim 1m$ region, reaching about 35 W/m^2 K, and significantly decreases with the rise of height after reaching the maximum. Moreover, as the HRR gradually increases, the resulting maximum region gradually moves up along the height. The blue curve in Fig. 8 is the $h_c(2)$ coefficient result obtained by the application of Eq. 5. At the bottom of the column, the $\overline{h_c}$ result increases with the height and reaches the maximum. It can be observed that the $\overline{h_c}$ result tends to stabilize after increasing to the maximum and the maximum values after the stabilization are basically not affected by the HRR change of the fire source, which is approximately 25 W/m^2 K. Compared with the results obtained by applying the Newtonian cooling formula, the $\overline{h_c}$ result calculated by the empirical formula from the FDS software in each case is significantly smaller in most of the lower area of the column, and slightly higher in the top area of the column.

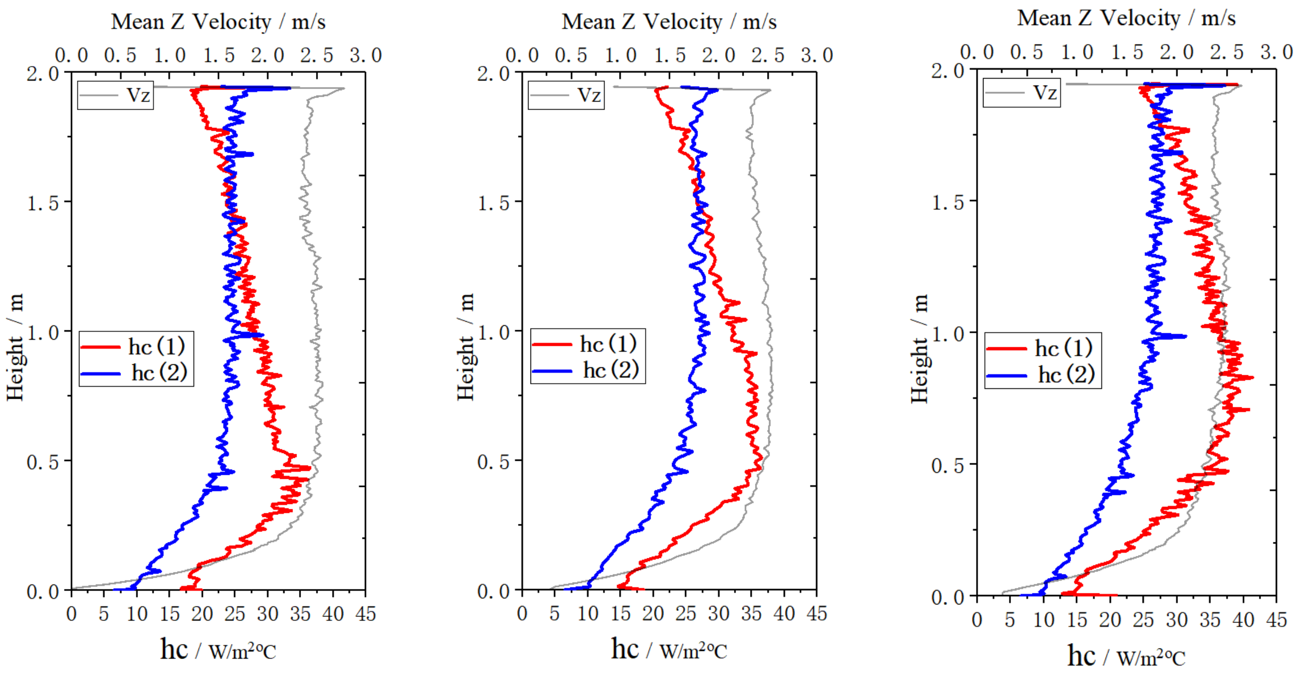

(a) HRR=40.5 kW (b) HRR=81 kW (c) HRR=121.5 kW

Figure 8.Mean convective heat transfer coefficient curves (1200s time averaged results)

As mentioned above, the surface h_c coefficient derived from the application of traditional empirical formula is mainly influenced by the velocity boundary layer situation. It can be tentatively concluded that the results obtained by applying empirical formula in the lower and middle parts of the column are smaller as it ignores the extremely high gas temperature in these regions at the moment; on the other hand, the results are higher in the top region of the column, without considering the fact that the gas temperature at the top has dropped by then.

6 CONCLUSIONS

This paper carries out a detailed discussion on the surface h_c coefficient of square steel column surrounded by flames in localized fire conditions. The detailed tasks are as follows.

The coupling of fire analysis and thermal analysis is combined based on the concept of fluid-solid coupling. Unlike the current international mainstream application of the AST concept, this paper unifies the fire analysis and thermal analysis to establish different equations to solve, thus realizing the two-way coupling of heat transfer between the fluid and the solid domain. The accuracy of this coupling method is verified by comparing the surface temperature of steel members with the experimental results.

The velocity field of the fire plume as well as the surface temperature of the steel members in this scenario are discussed. The distribution rules of the surface h_c results obtained from the two formulas are discussed in detail. The results obtained from the first formula can comprehensively take into account the velocity boundary layer and temperature boundary layer between the fire field and the column surface, and the maximum values obtained are about 35 W/m^2 K. The surface h_c obtained from the second formula focuses more on the influence of the velocity boundary layer situation, and the results are significantly smaller in the lower and middle parts of the column while slightly higher at the top of the column.

ACKNOWLEDGMENT

The financial supports from the National Science Foundation of China with Grant Nos. 52078380, 51820105013 and the Top Discipline Plan of Shanghai Universities-Class I with Grant No. 2022-3-YB-18 are gratefully acknowledged.

REFERENCES

1. EC3-1-2. Eurocode 3: Design of steel structures-Part 1-2: General rules - structural fire design, British Standard, 2005.
2. Albrifkani S, Wang Y C, Behaviour of axially and rotationally restrained reinforced concrete beams in fire. Engineering Structures, Vol. 213, 2020, 110572.
3. Liu J, Han L, Zhao X, Performance of concrete-filled steel tubular column-wall structure subjected to ISO-834 standard fire: Experimental study and FEA modelling. Thin-Walled Structures, Vol. 120, 2017, pp. 479-494.
4. Wickstrom U , Duthinh D D , Mcgrattan K, Adiabatic surface temperature for calculating heat transfer to fire exposed structures. International Interflam Conference 11th Proceedings September 3-5 2007. Interscience, 2007.
5. Zhang C , Silva J G , Weinschenk C , et al., Simulation Methodology for Coupled Fire-Structure Analysis: Modeling Localized Fire Tests on a Steel Column. Fire Technology, Vol. 52, 2015, pp. 239-262.
6. Silva J , Landesmann A , Ribeiro F, Interface model to fire-thermomechanical performance based analysis of structures under fire conditions. Fire and Evacuation Modeling Technical Conference. 2014.
7. Silva J C G , Landesmann A , Ribeiro F L B, Fire-thermomechanical interface model for performance-based analysis of structures exposed to fire. Fire Safety Journal, Vol. 83, 2016, pp. 66-78.
8. Szymku W , Glema A , Malendowski M , et al., Numerical investigation of fire and post-fire performance of CFT columns in an open car park fire. The 10th International Conference on Structures in Fire. 2018.
9. Rivera M R M , Vaz M A , Cyrino J , et al., Evaluation of localized pool fire models to predict the thermal field in offshore topside structures. Journal of the Brazilian Society of Mechanical Sciences and Engineering, Vol. 42, 2020.
10. Sivathanu Y R , Faeth G M . Generalized State Relationships for Scalar Properties in Non-Premixed Hydrocarbon/AirFlames. Combustion and Flame, Vol. 82, 1990, pp. 211-230.
11. Shih T M. Numerical heat transfer. CRC Press, 1984.
12. Prieler, R, Demuth, et al. Evaluation of a steady flamelet approach for use in oxy-fuel combustion. Fuel, Vol. 118, 2014, pp. 55-68.
13. Kays, W.M., and Crawford, M.E., Convective Heal and Mass Transfer,2nd ed., McGraw-Hill, New York, 1980, pp. 76, 172, 176, 211-217.
14. ANSYS Fluent, I. (2002). Fluent 14.5 Theory Guide. Fluent Inc., Lebanon. NH-03766.
15. Bergman T L, Bergman T L, Incropera F P, et al. Fundamentals of heat and mass transfer. John Wiley & Sons, 2011, pp. 378, 396, 397.
16. McGrattan K, Hostikka S, McDermott R, Floyd J, Weinschenk C, Overholt K. Fire dynamics simulator, user’s guide. National Institute of Standards and Technology, Gaithersburg, MD, USA, and VTT Technical Research Centre of Finland, Espoo, Finland, sixth edn, 2013.
17. Kamikawa D , Hasemi Y , Wakarnatsu T , et al., Experimental Flame Heat Transfer and Surface Temperature Correlations for a Steel Column Adjacent to and Surrounded by a Pool Fire. Fire Safety Science--Proceedings of the Seventh International Symposium, 2007, pp. 989-1000.
18. Raithby G D , Chui E H . A Finite-Volume Method for Predicting a Radiant Heat Transfer in Enclosures With Participating Media. Asme Transactions Journal of Heat Transfer, Vol. 112, 1990.
19. Khan I M , Greeves G . A Method for Calculating the Formation and Combustion of Soot in Diesel Engines. Heat Transfer in Flames. Chapter 25Scripta, Washington DC. 1974.
20. T F Smith, Z F Shen , J N Friedman, Evaluation of coefficients for the weighted sum of gray gases model. J Heat Transfer, Vol. 104, 1982, pp. 602.

SiF 2022– The 12th International Conference on Structures in Fire
The Hong Kong Polytechnic University, Nov 30 - Dec 2, 2022

COMPARISONS ON FLUID-SOLID HEAT TRANSFER SIMULATION FOR LOCALIZED FIRE RESISTANCE

Xuanyi Zhou[1,*], Jinggang Zhou[2], Beihua Cong[3], Wei Wang[4]

ABSTRACT

A research idea of multi-physics field coupling can be used to solve the structural fire resistance problem. Most of the previous CFD-FEM numerical simulations in structural fire resistance studies apply adiabatic surface temperature (AST) to accurately describe the complex fire analysis boundary conditions, and this methodology belongs to the use of iterative coupling methods to achieve fluid-solid heat transfer coupling. However, there is less application for another direct two-way coupling method. In this paper, a 2.5-meter-high square steel tube column is selected to investigate the thermodynamic phenomena when surrounding by fire plume. Based on CFD code, the thermal-mechanical coupling in fluid domain is firstly realized, and then the fluid-solid thermal coupling is realized by using iterative coupling method (AST method) and direct coupling method (Conjugate heat transfer method, CHT method) respectively, and the accuracy of this two coupling methodology is verified by comparing with experimental data. The heat flux received at the column surface is analyzed in the CHT method while the characteristics of the AST parameters are analyzed in the AST method. Finally, the mechanical analysis is completed with the solid temperature as the boundary condition and the thermal-mechanical coupling in solid domain is realized.

Keywords: CFD-FEM simulation; Conjugate heat transfer; Adiabatic surface temperature; coupling

1 INTRODUCTION

With the continuous upgrading of analytical tools and the gradual enrichment of computational resources, research in many subjects has started to consider multi-physics field coupling models. In the field of fire safety, the historical development of research on structural fire resistance also reflects the development trend from "single physical field analysis" to "multi-physical field coupling analysis". In the past, traditional fire resistance research in civil engineering relied on standard time-temperature curves, and the fire resistance rating of a building component is determined by a standard fire resistance test conducted on an isolated member subjected to the specified time temperature curve [1]. With the development of the last decade, significant progress has been made in structural fire research, and the basis for conducting research based on performance-based analysis in this field has been initially established. On the experimental side, some scholars have started to try to conduct structural fire resistance tests under realistic fire scenarios [2-5], but for the time being such experimental studies are still very limited [6], especially

[1] Professor, Tongji University
e-mail: zhouxytj@tongji.edu.cn
[2] PhD, Tongji University
e-mail: 1910320@tongji.edu.cn
[3] Associate Researcher, Tongji University
e-mail: bhcong@tongji.edu.cn
[4] Professor, Tongji University
e-mail: weiwang@tongji.edu.cn
https://doi.org/10.6084/m9.figshare.22215715

with respect to structural response under non-uniform heating conditions due to flames. In terms of numerical simulation, the analyses of structural fire resistance can be explained by the research perspective of multi-physical field coupling, where the integrated analysis involves two fields (thermal and mechanical field), and two computational domains (fluid and solid domain), and thus it can be divided into four analysis models, in order: fluid-mechanical analysis, fluid-thermal analysis, solid-thermal analysis and solid-mechanical analysis. In the first two analysis models, the simulation of gas-phase combustion is usually performed by means of computational fluid dynamics (CFD) methods, and therefore these two models are also collectively referred to as fire analysis in many studies [7-9]; Simulation of the heat penetration into the structure is finished in the third analysis model which can be addressed either with CFD or finite element method (FEM) code [10]; for the last fourth analysis, the mechanical response of the structure is often simulated using the FEM method.

The numerical simulation process involves several coupling interfaces. In terms of coupling methods, it can be divided into direct coupling and iterative coupling while in terms of coupling degree, it can be divided into one-way coupling and two-way coupling. Among them, the fluid-solid thermal coupling between the second and third model is the most critical difficulty under this research. Based on this, Wickström et al. [11] proposed a new variable, called adiabatic surface temperature (AST), which can solve the technical difficulty of transmitting a large number of parameters between fire analysis and solid-thermal analysis. The heat flow information is transferred to the finite element analysis by a single scalar AST to accurately describe the complex fire analysis boundary conditions. Essentially, this AST method belongs to iterative coupling. Several scholars have used this simulation method to perform performance-based analysis of structures under fire conditions [7-9, 12-14]. However, this AST method achieves only one-way coupling and suffers from the inherent drawbacks of iterative coupling means, such as difficult operation and poor robustness. In addition, this set of methods had to discard the solid temperature information obtained by CFD methods, which needs to be improved in terms of calculation efficiency.

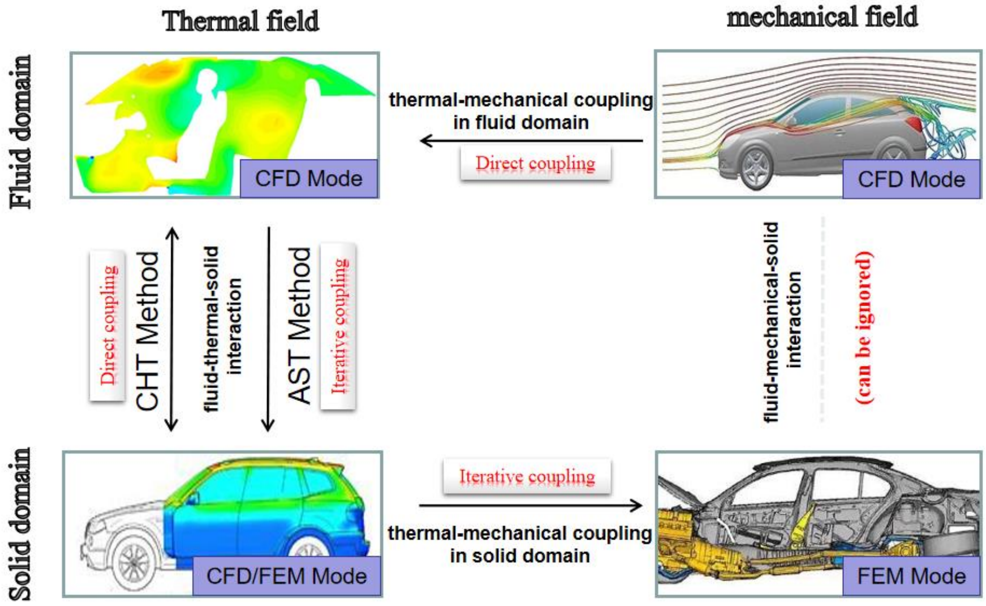

Figure 1. Coupled CFD-FEM simulation approach for structural fire analysis

As mentioned above, most of the previous CFD-FEM numerical simulation studies of structural fire resistance have used iterative coupling methods to solve the fluid-solid heat transfer coupling, with less application for another direct two-way coupling method. Based on this, the CFD-FEM numerical simulation study was carried out for the specific scenario of the steel column surrounded by fire plume. By means of CFD simulation, the fire model in this scenario is firstly analyzed, and the spatial velocity field and temperature field distributions of the fire plume around the column condition are discussed. Then, the fluid-solid heat transfer coupling is completed by AST method and the newly proposed CHT method respectively, and the correctness of the different coupling methods is verified by comparing with the test results. Then the mechanical response characteristics of the steel column are investigated.

2 THEORY

2.1 Combustion in fluid domain

The fire condition involved in this paper belongs to the category of non-premixed combustion. The non-premixed combustion simulation method is based on a series of simplifying assumptions that the instantaneous thermochemical state of fluid can be represented by a conserved quantity, namely the mixing fraction f. The mixing fraction f can be written as follows according to the species mass fraction Y_i [15]:

$$f = \frac{Y_i - Y_{i,ox}}{Y_{i,fuel} - Y_{i,ox}} \tag{1}$$

where $Y_{i,fuel}$ means the elemental mass fraction of the species i in the fuel while $Y_{i,ox}$ means that in the oxidant.

This paper only briefly introduces the species transport equation and the energy conservation equation, as shown in the following:

$$\frac{\partial}{\partial t}(\rho f) + \nabla \cdot (\rho V f) = \nabla \cdot (\rho D \nabla f) \tag{2}$$

$$\frac{\partial}{\partial t}(\rho H) + \nabla \cdot (\rho V H) = \nabla \cdot (\frac{k}{c_p} \nabla H) + S_h \tag{3}$$

In the formula above, D is diffusion coefficient, the magnitude of which is m2/s. S_h is the energy source term. H is the total absolute enthalpy of the mixture, expressed as follows:

$$H = \sum Y_i (h_{f,i}^0 + \int_{T_{ref}}^{T} c_{p,i} dT) \tag{4}$$

where $h_{f,i}^0$ refers to the formation enthalpy in the standard reference state, and $c_{p,i}$ refers to the specific heat capacity of species i at constant pressure.

2.2 Fluid-Solid heat transfer

In this paper, the direct coupling and iterative coupling forms are both used to complete the fluid-solid heat transfer coupling, as shown in Fig. 2 below. In the direct coupling method, the fire analysis and the solid-thermal analysis are solved together in CFD code, where the computational cell has the degrees of freedom of multiple fields, and the mathematical description equations of multiple fields can be solved in a single unit matrix. This method realizes the conjugate heat transfer, so it can be called Conjugate Heat Transfer (CHT) method. In the iterative coupling method, the fire analysis is solved in CFD code and the solid-thermal analysis is solved in FEM format, so it is necessary to use the fire field information obtained from the fire analysis as the boundary conditions of the solid-thermal analysis, and since it is very reasonable to use the AST parameters as the transfer information in this method, it can be called the AST method. In terms of the coupling degree, the CHT method is two-way coupling and the AST method belongs to one-way coupling, which is described in detail below.

(a) Conjugate heat transfer method

Thermal effect at the interface includes radiative heat transfer and convective heat transfer. Most building materials are opaque and can be treated as gray bodies. Therefore, net radiative heat flux is calculated by:

$$\dot{q}''_{rad} = \varepsilon(\dot{q}''_{inc} - \sigma T_s^4) \tag{5}$$

where $\dot{q}''_{rad}$ is radiation heat flux, T_s is solid surface temperature and $\dot{q}''_{inc}$ is surface incident radiation heat flux.

The convective heat flux depends on the difference between the surrounding gas temperature and the solid surface temperature. It is usually calculated by Newton's cooling formula [16]:

$$\dot{q}''_{conv} = h_c(T_g - T_s) \qquad (6)$$

where $\dot{q}''_{conv}$ is convection heat flux, T_g is gas temperature and h_c is surface convective heat transfer coefficient.

(b) Adiabatic surface temperature method

Consider the surface of a perfect insulator exposed to the same heating conditions as the real surface. Its temperature shall be referred to as the adiabatic surface temperature (AST) [11]. The total net heat flux to this ideal surface is by definition zero, thus:

$$\varepsilon(\dot{q}''_{inc} - \sigma T^4_{AST}) + h(T_g - T_{AST}) = 0 \qquad (7)$$

If the emissivity of the adiabatic surface is taken as the emissivity of the real surface, and the convection heat transfer coefficient between the adiabatic surface and the surrounding gas is equal to that between the real surface and the surrounding gas, thus:

$$\dot{q}''_{net} = \varepsilon_s \sigma({T_{AST}}^4 - {T_s}^4) + h_c(T_{AST} - T_s) \qquad (8)$$

The above equation shows that the net heat flux $\dot{q}''_{net}$ can be calculated by the single parameter T_{AST}. By inputting the T_{AST} obtained from the fire analysis as boundary conditions to the solid-thermal analysis and using the iterative solution form, the solid temperature field information can be solved, which is shown as follow:

$$\begin{cases} \dot{q}''^{i}_{net} = \varepsilon\sigma({T^i_{AST}}^4 - T^{i4}_s) + h^i_c(T^i_{AST} - T^i_s) \\ T^{i+1}_s = T^i_s + \dfrac{\dot{q}''^{i}_{net} \cdot A/V\Delta t}{\rho c} \end{cases} \qquad (9)$$

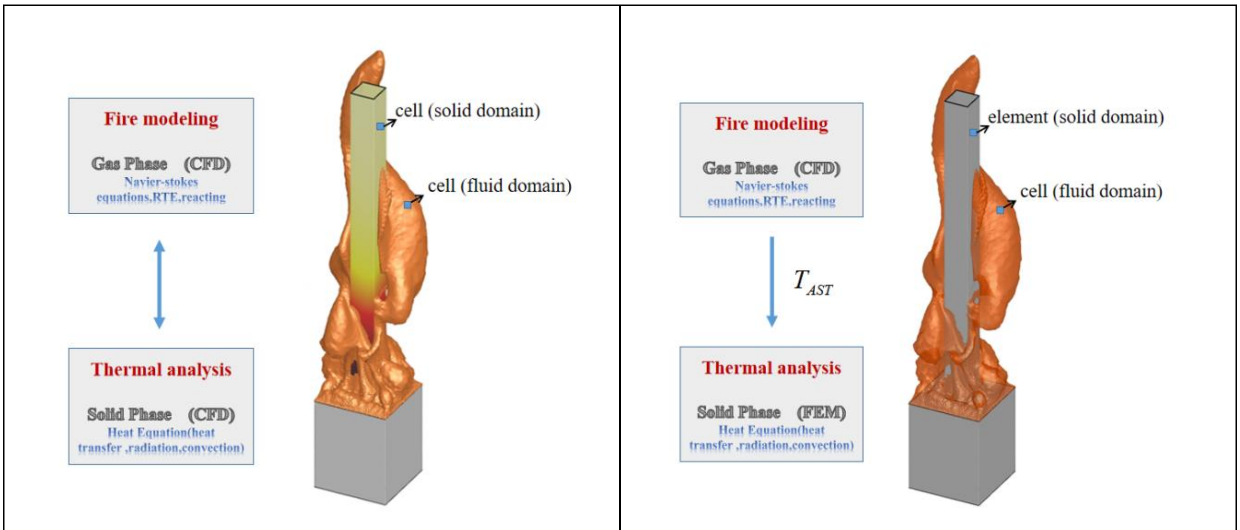

direct coupling form (conjugate heat transfer method)	iterative coupling form (adiabatic surface temperature method)

Figure 2. Comparison between CHT Method and AST Method

3 STUDY CASE FOR VALIDATION

The research object is a square steel column (section 150mm × 150mm × 4.5mm), and the localized fire condition is simulated considering the surround flame generated by the bottom brazier. Experimental

Settings are shown in Fig. 2. A case with HRR of 81kW in literature [2] was selected for analysis. Regarding the size and performance of square steel column and fire source, please refer to the reference [2] for detailed description.

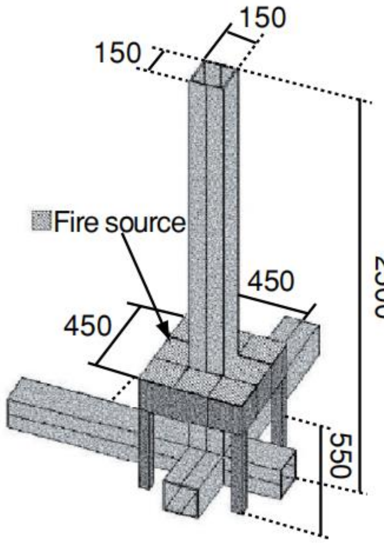

Figure 3. Experimental model of steel column surrounding by fire (unit: mm)

4 NUMERICAL SIMULATION

4.1 Fire model analysis by CFD code

The computational domain size of the CFD model was 18m × 6m × 8m, as shown in Fig. 4 below. The model grid adopted unstructured polyhedral mesh. After repairing, smoothing and simplifying, computing domain contained a total of 258,328 polyhedral meshes. To calculate the boundary layer around the steel column, 15 prism layers were located at the surface of the structural component to make the entire surface of the steel column satisfy $y^+<3$.

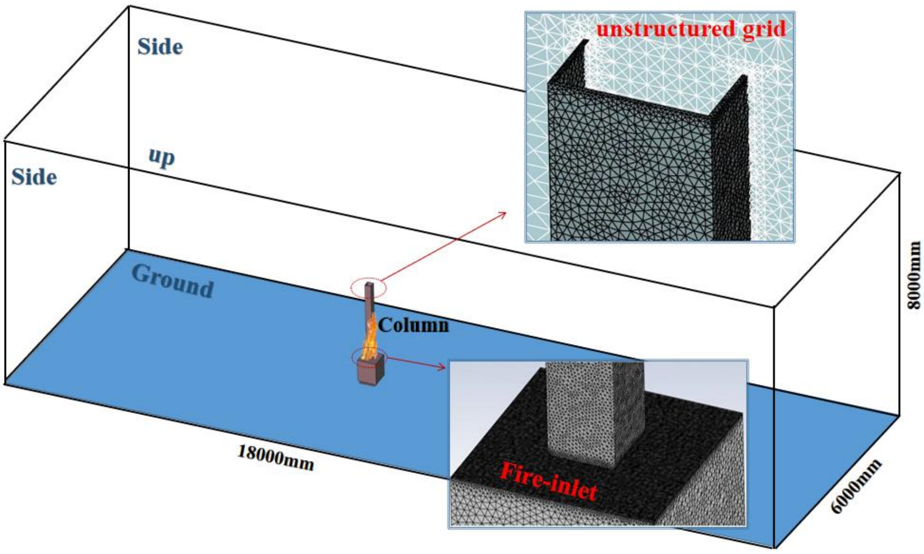

Figure 4. Numerical model of steel column surrounding by fire (unstructured grid)

ANSYS FLUENT software is used to implement the sophisticated fire analysis model, which includes equations describing phenomena such as fluid flow, non-premixed combustion, heat transfer and species transport. Table 1 presents details of the simulation method. Because the fire is time-dependent, the transient, pressure-based solver is used for calculation. The simulation took the effects of gravity into account. As for calculating the mixture material density, propane-air is regarded as a non-compressible ideal gas and WSGGM method [17] is used to calculate the absorption coefficient of flame gas products. The convection term was integrated using the QUICK difference scheme. The SIMPLE algorithm was used for pressure-velocity coupling. The least squares cell-based algorithm was used for gradient discretization. Considering the reasonable value of the Courant number, 0.05 s was set as the time step size, hence a total of 24000 time-steps were performed to complete an 1200-s fire exposure.

Table 1. Numerical scheme (Model settings)

item	Model or status
Solver	Pressure-based, Implicit, Transient
Turbulence model	LES model
Radiation heat transfer	DO model
Combustion	Chemical equilibrium non-premixed combustion
Soot formation	The one-step Khan and Greeves model

The ground and the brazier surface are considered adiabatic, which do not exchange heat with the outside. Fuel inlet surface is defined as the mass flow inlet, from which the mass flow rate is calculated based on the heat release rate (HRR) in the experiment [2].

4.2 Thermal analysis by CFD/FEM code

(a) Conduction Analysis by CFD code

ANSYS FLUENT software is used to implement a coupled solution between the fire analysis and the solid-thermal conduction analysis, so the solver could calculate heat transfer directly from the solution in fluid zone adjacent to solid. The emissivity of steel column surface was set to 0.85. The density of steel is 7850 kg /m^3 and the thermal properties such as thermal conductivity and specific heat capacity, which affect the elevated temperature of steel, are used as specified in Eurocode 3 [18].

(b) Conduction Analysis by FEM code

The Conduction analysis in FEM code is completed by Workbench. The output adiabatic surface temperature T_{AST} (with the convective heat transfer coefficient h_c) obtained by fire analysis model can be converted to inputs to the FEM conduction analysis. The surface effect element SURF152 (ANSYS nomenclature) is employed. This element is attached to the thermal element SHELL181 to prescribe a boundary condition. The data points are interpreted as the effective black body temperature and bulk (gas) temperature to calculate the radiative and convective heat fluxes to the structural elements, respectively. Point measurements are used in this paper because it can be intractable to have measurement devices located in every computational cell where the solid has an exposed surface. Therefore, linear interpolation is used to determine the adiabatic surface temperature between two recorded data.

4.3 Mechanical Analysis by FEM code

The Mechanical analysis in in FEM code is also completed by Workbench. The FE model, with a mesh size of 2.5mm, was adopted for this study. The fix boundary conditions are satisfied by restraining the displacement (UX, UY and UZ) and rotation degrees (RX, RY and RZ) of freedom at the column bottom end. The mechanical material properties for steel need to be defined, for which at elevated temperature are the key parameters in FEM analysis model. The elastic-isotropic option was used to model the Q235 steel materials. The yield strength and the plastic strain values were modeled using the plastic-isotropic option. Poisson's ratio is taken as 0.3 in accordance with EC3 [18]. The T.T. Lie high temperature stress-strain material model for steel [19] was used:

$$\begin{cases} \sigma = E_T \varepsilon & (\varepsilon \le \varepsilon_{pT}) \\ \sigma = (12.5\varepsilon + 0.975) f_{yT} - \dfrac{12.5 f_{yT}^2}{E_T} & (\varepsilon > \varepsilon_{pT}) \end{cases} \qquad (10)$$

The equation for thermal expansion coefficient recommended by NIST TN1681 [20] was used:

$$\alpha_s = 1.17\times10^{-5} + 1.34\times10^{-8} T_s - 9.7\times10^{-12} T_s^2 + 1.67\times10^{-16} T_s^3 \qquad (11)$$

5 RESULTS AND DISCUSSION

5.1 Thermal-mechanical coupling discussion in fluid domain

Fig. 4 shows the velocity and temperature distributions of the fluid domain at a characteristic moment obtained from the numerical simulation. As can be seen from the velocity cloud, the high-temperature gas generated by combustion flows upward along the column surface, and the highest flow velocity can reach about 5 m/s. The randomness brought by turbulence in the combustion process can be clearly observed in the diagram. As shown in the temperature cloud, the maximum temperature of the flame reaches about 1300 °C, which is mainly distributed at the bottom of the column. The fire plume rises around the column, and the temperature of the flue gas rising across the column surface is about 300-500 °C. The coupling between the mechanical and thermal field in fluid domain is not introduced in detail in this paper. Briefly, when a pressure-based solver with SIMPLE algorithm is used for this simulation for the non-premixed combustion process, this coupling belongs to a one-way direct coupling.

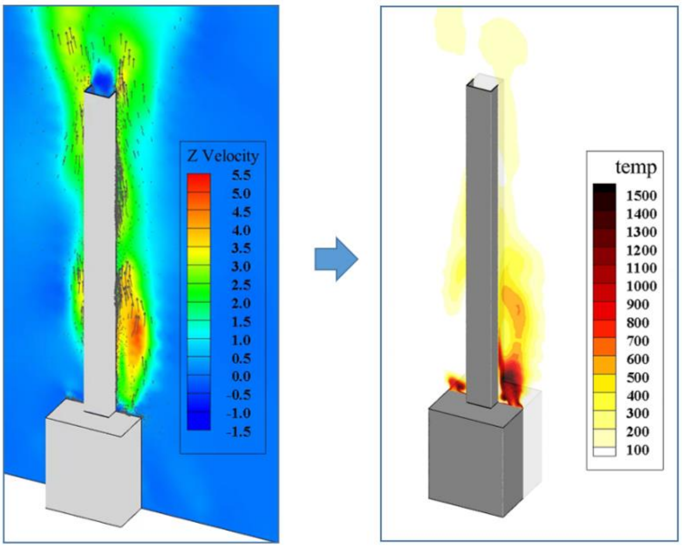

Figure 4. Velocity distribution and Temperature distribution (unit: m/s , °C)

5.2 Fluid-thermal-solid interaction discussion

(a) Conjugate heat transfer method results

In the CHT method, the fire analysis and the solid-thermal analysis use the same calculation cell, and every calculation unit has multi-field degrees of freedom, so the fire analysis model in fluid domain is performed simultaneously with the solid heat conduction analysis, and the heat flux received by the column surface can be obtained directly, as shown in Fig. 5 below. The net heat flux $\dot{q}''_{net}$ received by the steel column from the fire environment contains the radiation heat flux $\dot{q}''_{rad}$ and the convection heat flux $\dot{q}''_{conv}$. The $\dot{q}''_{rad}$ distribution of the column surface is relatively complex. As $\dot{q}''_{inc}$ is very large at the bottom of the column, higher than the radiation flux released by the column itself, leading to the positive $\dot{q}''_{rad}$ in this range with a maximum value close to 16 kW/m^2. As the height rises to $z \approx 0.3m$, $\dot{q}''_{rad}$ drops to zero as $\dot{q}''_{inc}$ decreases, implying that the radiation flux emitted by the column is equal to that received. As the height continues to increase, the radiation emitted to the outside by the steel column is greater than $\dot{q}''_{inc}$, and $\dot{q}''_{rad}$

becomes negative, with a minimum value of approximately -3 kW/m^2. Then along the axial direction upwards, $\overline{\dot{q}''_{rad}}$ at the top gradually drops to near 0, indicating that the thermal radiation phenomenon gradually disappears. For convective heat transfer, as the hot gas temperature around the steel column is higher than the solid surface temperature in most of the time, leading to a positive $\overline{\dot{q}''_{conv}}$ with the maximum value reaching approximately 6 kW/m^2 at $z = 0.3 \sim 0.8m$ region. Statistically, the contribution of thermal radiation is mainly found at the bottom of the column, while the contribution of thermal convection is concentrated in the middle and lower parts of the column.

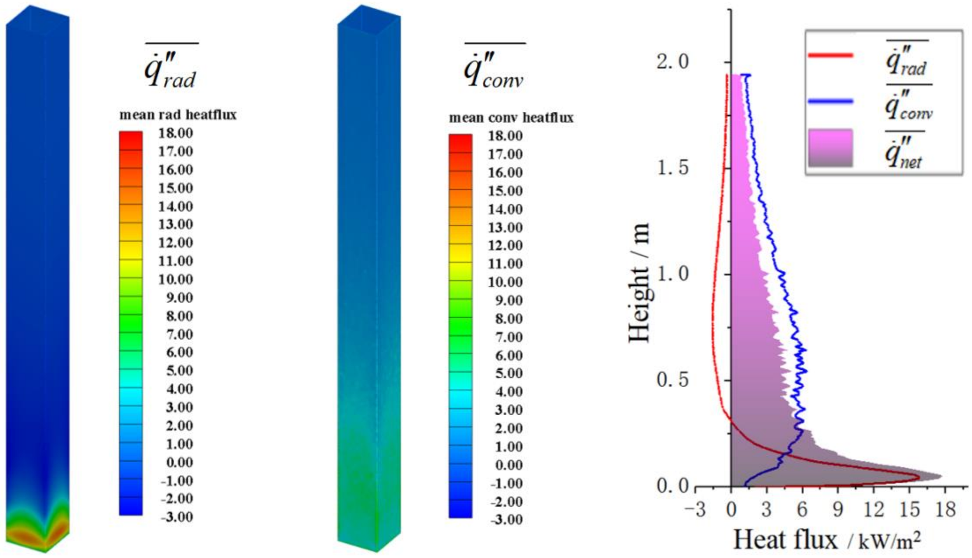

Figure 5. Column heat flux distribution (unit: kW/m2)

(b) Adiabatic surface temperature method results

When the iterative coupling method - i.e., the AST method - is applied, the set of equations should be solved for the fluid domain first (including the conservation equations, the RTE equation, and the soot generation equation, but not including the Fourier heat conduction equation). Fig. 6 below shows the variation curves of three fluid domain parameters ($\dot{q}''_{inc}$, h_c and T_g) obtained by applying the AST method at point A, B and C on the steel column surface during the combustion process, respectively. From this, it can be observed that T_g in the lower region of the column vibrates near 700 °C, $\dot{q}''_{inc}$ varies in the range of 20-50 kW/m^2, and the surface h_c coefficient of this region is slightly more than 25 W/m^2 K. T_{AST} calculated by applying Eq. 7 from these three data oscillates near 600 °C after rising to steady. T_g near the middle region of the column is around 350 °C, $\dot{q}''_{inc}$ decreases to about 2-5 kW/m^2, the surface h_c coefficient is similar to the lower region, and the T_{AST} obtained oscillates near 300 °C. T_g in the top region of the column varies around 175 °C, $\dot{q}''_{inc}$ drops to near zero and h_c is close to 20 W/m^2 K, and the T_{AST} results oscillates at 100 °C. In the AST method applied in the paper, the fluid-solid heat transfer coupling is achieved by using more than 100 characteristic point's T_{AST} results obtained from the fire analysis calculation as the boundary conditions for the solid-thermal analysis. In addition, it can be found that the oscillation interval of the T_{AST} parameter is greatly reduced in comparison with T_g, and it can comprehensively characterize the thermal information of the fire field near the region of the point.

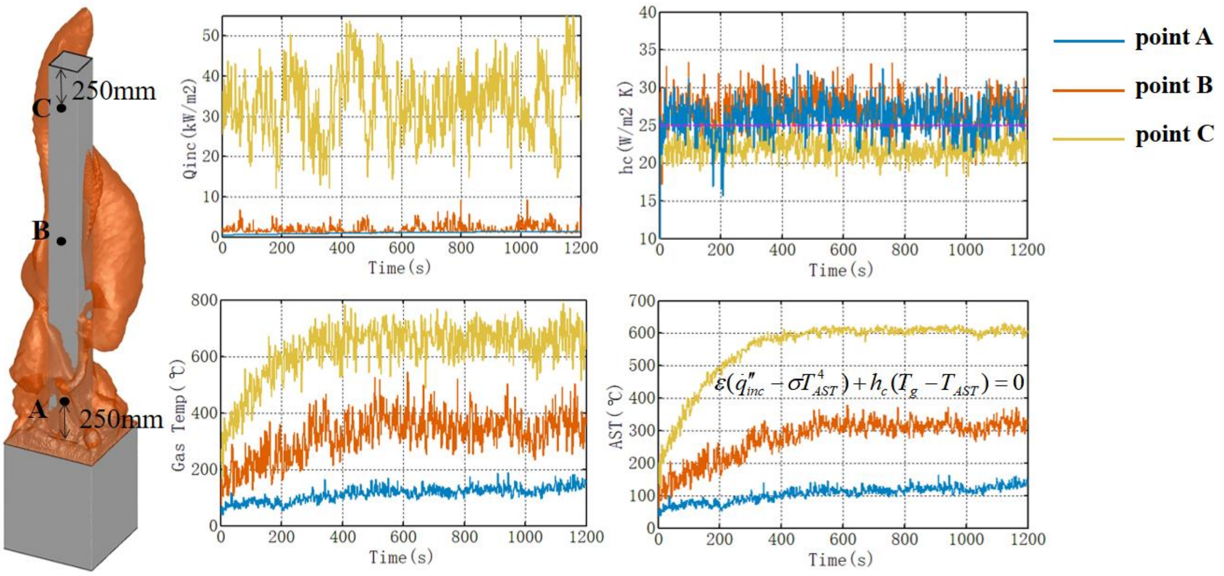

Figure 6. Fluid domain parameters display in AST Method

(c) Comparison between two methods

The surface temperature distributions of the steel column obtained by the CHT method and the AST method, respectively, are shown in Fig. 7 below. It can be noted that the results of the two methods have the same trend. The bottom area is close to the fire source and the temperature there is the highest, exceeding 600 ℃. T_s gradually decreases as height increases, with the middle area of the column at about 300 ℃ and the top at about 100 ℃. The maximum surface temperature of CHT method for steel column is 671.4℃ while that of AST method is 664.2℃, with an error of less than 5%. The temperature curve of the left graph shows that the heat conduction simulation results of the two methods almost overlap and are both in good agreement with the test results [2]. The numerical simulation results at the bottom of the column are slightly larger than the test results, while the wall temperature in the middle of the column is slightly lower than the experimental results. The agreement of the curves verifies the respective rationality of the CHT and AST coupling methods, which shows that both direct and iterative coupling can be achieved by means of CFD-FEM numerical simulation in localized fire researches.

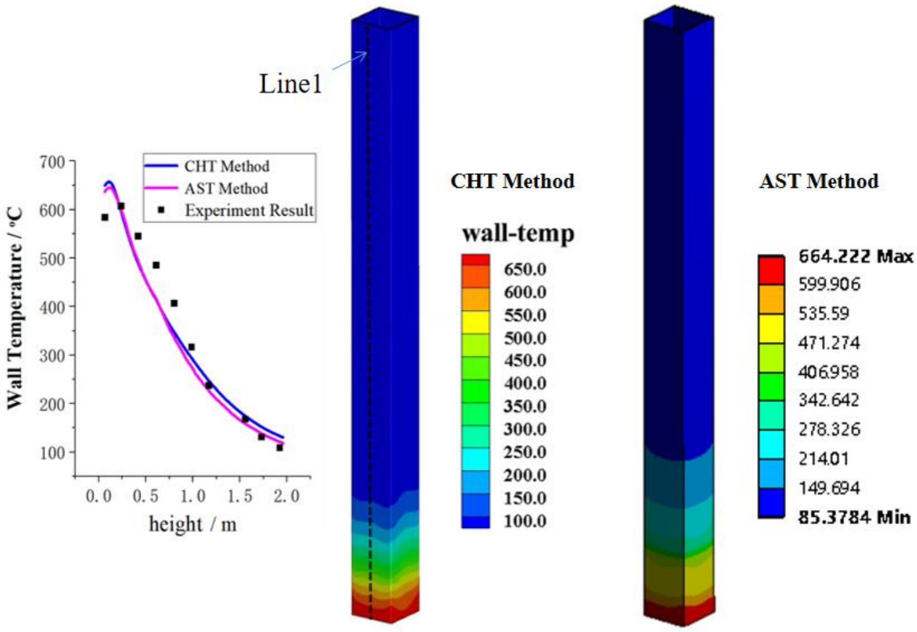

Figure 7. Temperature distributions by different coupling method

5.3 Thermal-mechanical coupling discussion in solid domain

After the solid-thermal analysis, the mechanical analysis can be performed by simply importing the temperature distribution results inside the member into the finite element module. The mechanical response (the Mises stress) of the steel column at different moments during the combustion process is given in Fig. 8. Vertical load of 80 MPa is considered at the top of the steel column to approximate the load from the beam section or the upper ceiling in the real structures. Since the bottom is considered to be fully restrained, this region has the maximum stress, being about 270 MPa at 100s and about 175 MPa at 1200s. It is observed that the maximum stress value of the steel column decreases instead with the increase of the heating time subjected to fire. This is because according to the constitutive relation at high temperature (Eq. 10 above), the maximum temperature of the beam exceeds 550°C and the phenomenon of yield strength degradation at high temperature is already evident. Even if the strain in the highest temperature region reaches the maximum and clearly reaches plastic deformation, the stress value decreases with the decrease of yield strength.

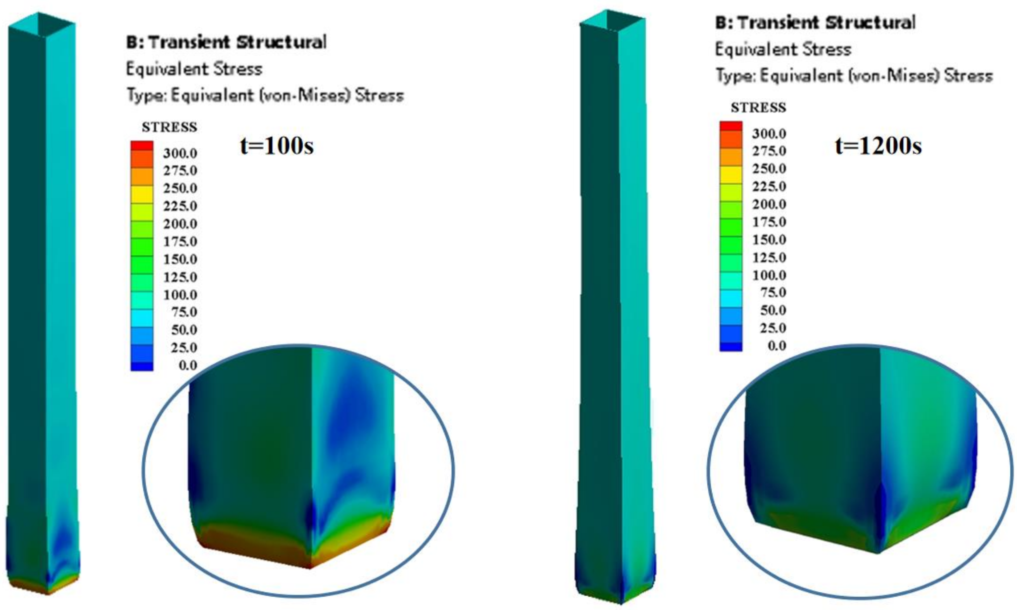

Figure 8. Column Mises stress response distribution at 100s and 1200s moments

6 CONCLUSIONS

Firstly, based on the CFD code, the combustion process in fluid domain for the specific scenario of the steel column surrounded by fire is simulated and the thermal-mechanical coupling of the fluid domain is realized. The spatial velocity field and temperature field distribution are explored. Then, the fluid-solid heat transfer coupling is realized by using the CHT direct coupling method and the AST iterative coupling method respectively. In the CHT method, the radiation and convective heat flux received by the steel column surface are directly obtained and analyzed. In the AST method, the distribution characteristics of AST parameter are expounded. The agreement between the test results and results obtained by these two methods verifies the respective rationality of the CHT and AST coupling methods. Finally, the mechanical analysis i completed with the solid interior temperature as the boundary condition, and the thermal-mechanical coupling of the solid domain is realized. The yield strength degradation of the steel column after heating was discussed.

ACKNOWLEDGMENT

The financial supports from the National Science Foundation of China with Grant Nos. 52078380, 51820105013 and the Top Discipline Plan of Shanghai Universities-Class I with Grant No. 2022-3-YB-18 are gratefully acknowledged.

REFERENCES

1. Zhang C , Li G , and Wang Y , Sensitivity Study on Using Different Formulae for Calculating the Temperature of Insulated Steel Members in Natural Fires, Fire Technology, Vol. 48, 2011, pp. 343-366.
2. Hasemi J , Kamikawa D , Experimental Flame Heat Transfer and Surface Temperature Correlations for a Steel Column Adjacent to and Surrounded by a Pool Fire, Fire Safety Science--Proceedings of the Seventh International Symposium. 2007, pp. 989-1000.
3. Zhang C , et al., Engineering Approach for Designing a Thermal Test of Real-Scale Steel Beam Exposed to Localized Fire, Fire Technology, Vol. 53, 2017, pp. 1535-1554.
4. Yokobayashi Y , Hasemi Y J , and Wakamatsu T , Experimental study on the heating mechanism and thermal response of a steel beam under ceiling exposed to localized fires, J Struct Eng AIJ, Vol.498, 1997, pp. 169−175.
5. Lineham S A , et al., Structural response of fire-exposed cross-laminated timber beams under sustained loads, Fire Safety Journal, Vol. 85, 2016, pp. 23-34.
6. Zhang C , Silva J G , Weinschenk C , et al., Simulation Methodology for Coupled Fire-Structure Analysis: Modeling Localized Fire Tests on a Steel Column, Fire Technology, Vol. 52, 2015, pp: 239-262.
7. Szymku W , Glema A , Malendowski M , et al., Numerical investigation of fire and post-fire performance of CFT columns in an open car park fire. The 10th International Conference on Structures in Fire. 2018.
8. Silva J C G , Landesmann A , and Ribeiro F L B, Fire-thermomechanical interface model for performance-based analysis of structures exposed to fire, Fire Safety Journal, Vol. 83, 2016, pp: 66-78.
9. Yu X , Jeffers A E , A comparison of subcycling algorithms for bridging disparities in temporal scale between the fire and solid domains, Fire Safety Journal, Vol. 59, 2013, pp: 55-61.
10. Welch S , Miles S , Kumar S , et al., FIRESTRUC-Integrating advanced three-dimensional modelling methodologies for predicting thermo-mechanical behavior of steel and composite structures subjected to natural fires, Fire Safety Science, Vol. 9, 2008, pp: 1315-1326.
11. Wickstrom U , Duthinh D D , Mcgrattan K, Adiabatic surface temperature for calculating heat transfer to fire exposed structures. International Interflam Conference 11th Proceedings September 3-5 2007. Interscience, 2007.
12. Silva J , Landesmann A , Ribeiro F, Interface model to fire-thermomechanical performance based analysis of structures under fire conditions. Fire and Evacuation Modeling Technical Conference. 2014.
13. Zhang C , et al., Simulating the fire-thermal-structural behavior in a localized fire test on a bare steel beam, Engineering Structures, Vol. 163, 2018, pp: 61-70.
14. Liu Z, et al., Coupled CFD–FEM Simulation Methodology for Fire-Exposed Bridges, Journal of Bridge Engineering, Vol. 26, 2021, pp: 1-16.
15. Sivathanu Y R , Faeth G M . Generalized State Relationships for Scalar Properties in Non-Premixed Hydrocarbon/AirFlames. Combustion and Flame, Vol. 82, 1990, pp. 211-230.
16. Kays, W.M., and Crawford, M.E., Convective Heal and Mass Transfer,2nd ed., McGraw-Hill, New York, 1980, pp: 211-217.
17. T F Smith, Z F Shen , J N Friedman, Evaluation of coefficients for the weighted sum of gray gases model. J Heat Transfer, Vol. 104, 1982, pp. 602.
18. EC3-1-2. Eurocode 3: Design of steel structures-Part 1-2: General rules - structural fire design, British Standard, 2005.
19. T T Lie and B A Macaulay, Evaluation of the fire resistance of protected steel columns. Internal Report No. 583. National Research Concil Canada, 1989.
20. L T Phan, et al., Best practice guidelines for structural fire resistance design of concrete and steel buildings. NIST technical note 1681, National Institute of Standards and Technology (NIST), Gaithersburg, MD

SiF 2022– The 12th International Conference on Structures in Fire
The Hong Kong Polytechnic University, Nov 30 - Dec 2, 2022

STUDY ON BUCKLING AND CRITICAL TEMPERATURES OF H-SECTION STEEL COLUMNS UNDER FIRE CONSIDERING DYNAMIC EFFECT

Zhengrong Chen[1], Zhongyuan Yin[2], Liping Wang[3], Binhui Jiang[4,*]

ABSTRACT

In this paper, the buckling and critical temperatures of H-section steel columns under fire were studied by parametric analysis. The finite element model of the steel column was verified by test data in literatures. The considered parameters include rotational restraint stiffness ratio (β_R), axial restraint stiffness ratio (β_l), and load ratio (ρ_N). Besides, the buckling and critical temperatures of steel columns under static analysis and explicit dynamic analysis were compared. It was found that the buckling temperatures obtained by these two analysis methods were almost the same, while the critical temperatures obtained by static analysis were slightly less than that obtained by explicit dynamic analysis, and the difference was within 30 ℃. The results of parametric analysis show that the buckling and critical temperatures increased with the increase of β_R, and β_R had greater influence on the critical temperature. In addition, with the increase of β_l and ρ_N, the buckling and critical temperatures of the steel columns both decreased significantly. Finally, the buckling and critical temperatures obtained from the parametric analysis were compared with the existing calculation formulas. Results show that predictions of the existing formulas generally agree well with the analysis results.

Keywords: Restrained steel column; Fire; Dynamic effect; Parametric analysis; Buckling temperature; Critical temperature;

1 INTRODUCTION

Fire is a great threat to steel structures, since the mechanical properties of steel deteriorate significantly at elevated temperatures [1-3]. Steel columns will produce axial expansion due to the increase of temperature under fire. With the existence of axial restraint, the axial thermal expansion will result in additional axial force to the steel columns [4]. Hence, the axial force of the steel columns increases with the increase of temperature. When the axial force reaches the bearing capacity of the steel columns at elevated temperature, the steel column will buckle. After buckling, the axial force of the steel columns starts to decrease due to the release of the thermal expansion. The temperature at which the axial force of the steel columns reaches the peak value is defined as the buckling temperature, and the temperature at which the axial force returns to its initial axial force at room temperature is defined as the critical temperature [5]. Buckling and critical temperatures are important parameters to reflect the fire resistance of restrained steel columns. Therefore, it is essential to understand the influences of various factors on buckling and critical temperatures of steel columns under fire.

There are many research studies on buckling and critical temperatures. Li et al. [4] carried out a group of fire resistance tests on restrained steel columns. The test results showed that the buckling temperature of steel columns with large axial restraint stiffness ratio was lower. Ali et al. [6] studied the influence of axial restraint on the fire resistance of steel columns. The results showed that the critical temperature of steel columns would decrease due to the increase of axial restraint stiffness. Tan et al. [7] conducted a series of

[1] Postgraduate, School of Civil Engineering, Central South University
e-mail: czr19990626@csu.edu.cn
[2] Postgraduate, School of Civil Engineering, Central South University
e-mail: zhongyuanyin@126.com
[3] Associate professor, School of Civil Engineering, Central South University
e-mail: wlp2016@csu.edu.cn
[4] Associate professor, School of Civil Engineering, Central South University
e-mail: binhuijiang@csu.edu.cn, ORCID: https://orcid.org/0000-0003-3774-9587
https://doi.org/10.6084/m9.figshare.22215718

fire resistance tests on restrained steel columns. The results showed that increasing the axial restraint stiffness would increase the additional axial force generated by the steel columns under fire, leading to a significant reduction in the failure time of the steel columns. Zhang et al. [8] studied the fire resistance of axially and rotationally restrained steel columns by numerical simulation. The results showed that increasing the axial restraint stiffness ratio and load ratio will reduce the buckling temperature of steel columns. The numerical analysis results of Valente and Neves et al. [9] showed that increasing the rotational restraint stiffness ratio could increase the critical temperature of steel columns. However, when the rotational restraint stiffness ratio increased sufficiently, its influence on the restraint force and critical temperature at elevated temperature became less obvious. The finite element analysis results of Wang et al. [10] and Wang et al. [11] showed that the buckling temperature of steel columns increases with the increase of the rotational restraint stiffness ratio. In addition, Wang et al. [12] proposed simplified calculation formulas for buckling and critical temperatures through finite element simulation, and the calculation results were in good agreement with the finite element simulation results. For restrained steel columns within the practical application scope, the critical temperatures calculated by the formulas tend to be conservative. Huang et al. [13] proposed a new Rankine method to predict the critical temperature of steel columns by considering column boundary restraints and creep strain. The test and numerical comparison showed that the proposed method provided an accurate and slightly conservative prediction. It is noted that the previous research studies on response of steel columns under fire mostly adopt quasi-static experiment or analysis method. However, research studies [14-15] showed that the failure of steel columns under fire may be accompanied by severe dynamic effects. For steel columns with dynamic failure, it is questionable whether static analysis method can still reasonably predict the buckling and critical temperatures.

In this paper, a validated finite element model using explicit dynamic analysis was adopted to study the influence of dynamic effect on buckling and critical temperatures. The influences of rotational restraint stiffness ratio (β_R), axial restraint stiffness ratio (β_l) and load ratio (ρ_N) on the buckling and critical temperatures of H-section steel columns under fire were studied. Then, the differences on the buckling and critical temperatures of steel columns between static analysis and explicit dynamic analysis were compared. Finally, selected existing formulas of buckling and critical temperatures were verified by the analysis results.

2 FINITE ELEMENT MODEL AND VERIFICATION

The general finite element program ABAQUS [16] was used to conduct a nonlinear explicit dynamic analysis on the response of H-section steel columns under fire. The column model was simulated by four-node shell elements (S4R). The equivalent restraint springs were respectively applied to the top and bottom of the column. The yield strength of steel column at room temperature is 355Mpa and the Young's modulus is 210Gpa. The stress-strain curve of steel columns at elevated temperature was taken according to Eurocode 3 Part 1.2 [17]. In addition, the Cowper-Symonds model [18] was used to consider the effect of strain rate on the yield strength of steel. Figure 1 shows the simplified column model.

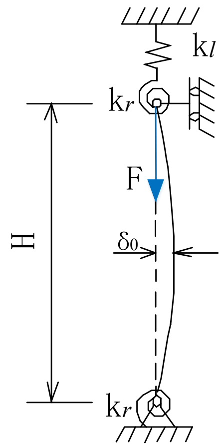

Figure 1. Simplified column model [15]

The tests reported by Li et al. [4] and Jiang et al. [19] are selected to verify the established finite element model. The process of verification has been introduced in Jiang et al. [15, 20] in detail, and here only presents the comparison of results.

Figure 2 compares the test results, simulation results of the current model and simulation results of Li et al. [4] of the fire test of restrained steel column. From the buckling temperature, critical temperature and the final vertical displacement of the column top, the simulation results in this paper generally agree well with the test results and are on the safe side. The effectiveness of the model is further verified by the test data of steel frames subjected to local fire conducted by Jiang et al. [19]. The GLAM method proposed in reference [21] is used to obtain the equivalent axial restraint stiffness for the simplified model, and the temperature distribution of the heated column refers to literature [22]. Figures 3 show the comparison between the test results [19] and the simulation results. It can be seen that the good agreement is also achieved. It is noted that the top of heated column in Frame 2 would further increase after the sudden drop. This is because after the sudden drop, the restrained steel beams connected to column was heated by hot air escaped from the furnace, resulting in the rapid temperature rise of the beams. Hence, the restraint stiffness provided by the beams to the heated column was reduced, which induced the further increase of axial displacement at column top. However, a constant axial restraint stiffness was adopted in current model. Hence, the top of heated column in Frame 2 in simulation tends to be stable after a sudden drop.

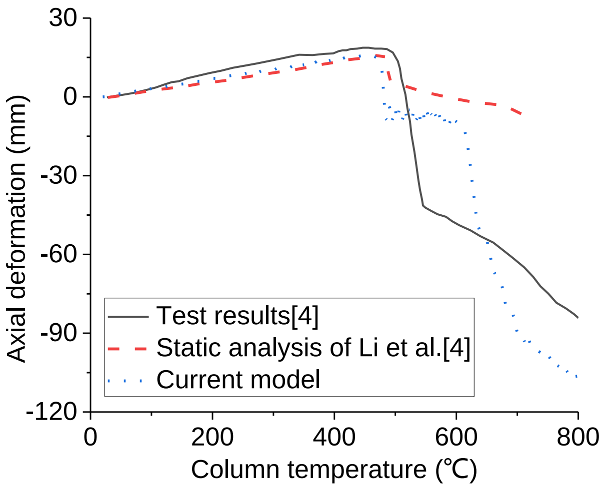

Figure 2. Comparison between simulation results and test results [4]

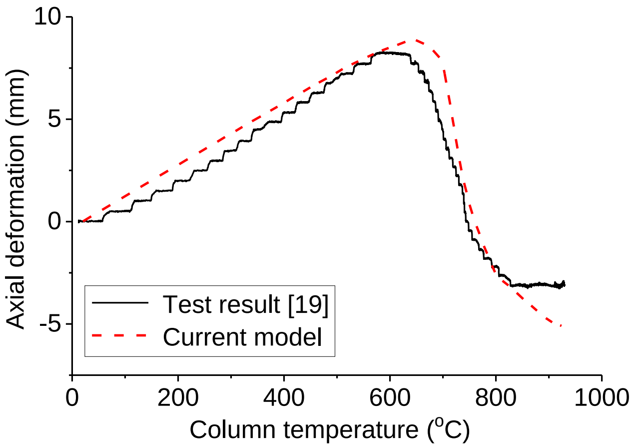

(a). Heated column of frame1

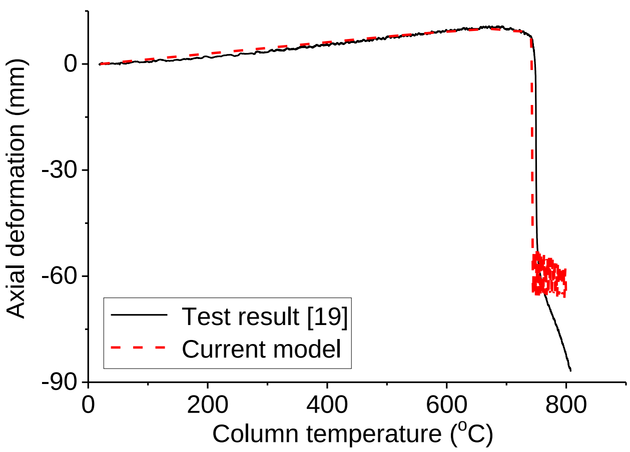

(b). Heated column of frame 2

Figure 3. Comparison between simulation results and test results [19]

3 COMPARISON ON STEEL COLUMN RESPONSES BETWEEN STATIC ANALYSIS AND EXPLICIT DYNAMIC ANALYSIS

The static analysis model also uses the four-node shell elements (S4R) for modelling. The modelling process is basically consistent with the dynamic analysis model, except that the material model does not consider damping and strain rate effect. The maximum and minimum time steps are 1.0×10^{-2} and 1.0×10^{-20}, respectively. To reduce the possibility of numerical non convergence caused by unstable behaviour of steel column under load at elevated temperatures, the adaptive automatic stabilization scheme with 0.0002 default constant damping is adopted.

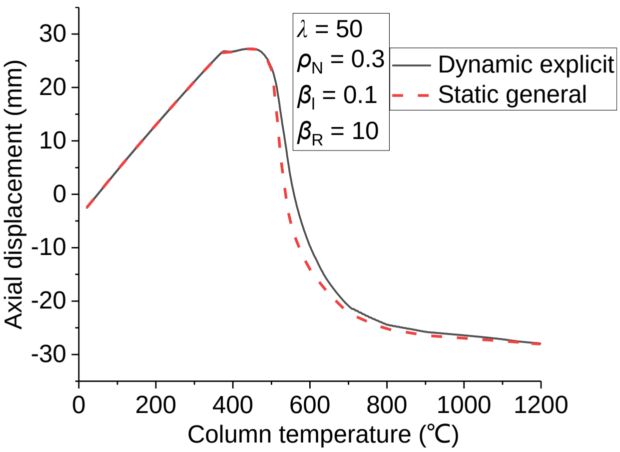

(a). Comparison 1

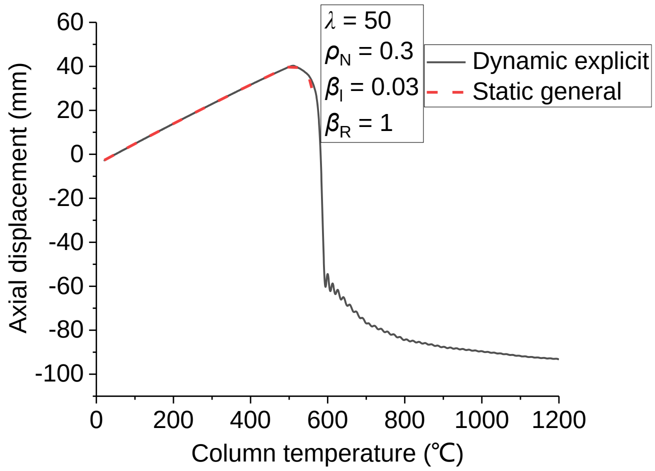

(b). Comparison 2

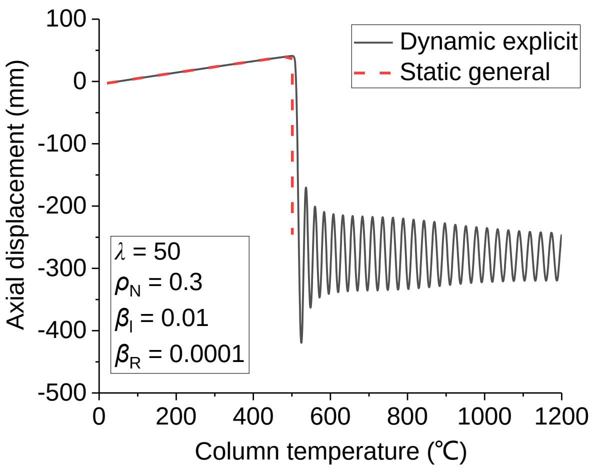

(c). Comparison 3

Figure 4. Comparison on responses of steel columns between static analysis and explicit dynamic analysis

Figure 4 shows the response comparison between static analysis and explicit dynamic analysis for steel columns with weak to severe dynamic effects under fire. It can be seen from Figure 4 that the buckling temperatures of the steel columns and the axial displacements of the column top before buckling obtained by static analysis and explicit dynamic analysis are almost identical. This is because the response of steel columns in the process of temperature rise before buckling is quasi-static. As shown in Figure 4 (a), for steel columns with weak dynamic effects, the difference between the critical temperatures of steel columns obtained by static analysis and explicit dynamic analysis is nearly 30 ℃. This is because the column model of explicit dynamic analysis considers the influence of strain rate on the steel yield strength during the drop of the column top. Besides, the critical temperature of the steel column obtained by static analysis is lower than that obtained by explicit dynamic analysis. As shown in Figure 4 (b) and (c), for steel columns with significant dynamic effects, the calculation is interrupted because the static analysis cannot obtain convergence results. The corresponding steel column temperature at the time of calculation interruption is taken as the critical temperature. It can be seen that the critical temperatures of steel columns obtained by static analysis and explicit dynamic analysis are almost the same, with the differences of 20 ℃ and 9 ℃, respectively.

4 PARAMETRIC ANALYSIS

After verifying the established finite element model, parametric analysis of the response of steel columns under elevated temperatures was carried out, and then the buckling and critical temperatures concerned were obtained. The influences of relevant analysis parameters on the buckling and critical temperatures are specifically discussed. The section size of the restrained steel column is HW300×300×10×15(mm), where 10mm and 15mm are the thickness of the web and flange, respectively. The considered parameters include: rotational restraint stiffness ratio (β_R), axial restraint stiffness ratio (β_l), and load ratio (ρ_N). The values of selected relevant parameters are shown in Table 1.

Table 1. Analysis parameters

λ	ρ_N	β_l	β_R
30	0.1, 0.3, 0.5, 0.7, 0.76	0.001, 0.01, 0.03, 0.05, 0.1	0.0001, 0.1, 0.3, 0.5, 1.0, 5.0, 10.0
50	0.1, 0.3, 0.5, 0.54		
70	0.1, 0.2, 0.3, 0.4		

4.1 Effect of rotational restraint stiffness ratio

Figure 5 shows the variation of buckling and critical temperatures of a group of dynamic failure steel columns with different rotational restraint stiffness ratios β_R. It can be seen from the figure that the buckling and critical temperatures of the steel columns both increase with the increase of β_R. When β_R exceeds 1.0, the effects of further increasing β_R on the buckling and critical temperatures of the steel column both become small. Hence, 1.0 could be considered as the critical rotational restraint stiffness ratio $\beta_{R,cr}$ [15]. In addition, it can be seen from the figure that when β_R increases from 0.0001 to 10, the buckling and critical temperatures increase by 177.73 ℃ and 223.76 ℃ respectively. Therefore, increasing β_R has a greater effect on the critical temperature than on the buckling temperature.

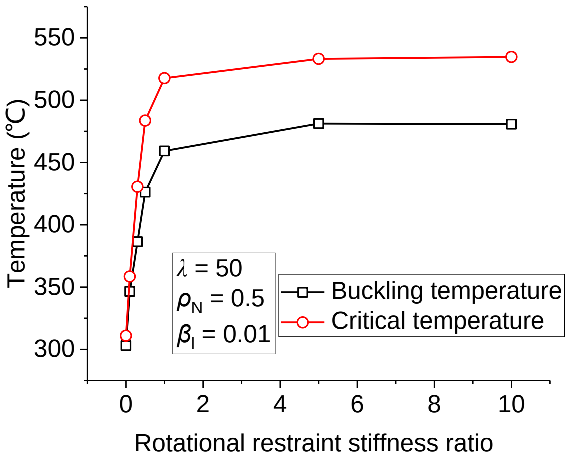

Figure 5. The effect of β_R on buckling and critical temperatures

4.2 Effect of axial restraint stiffness ratio

Figure 6 shows the variations of buckling and critical temperatures of restrained steel columns with λ of 50 and ρ_N of 0.3. It can be seen from Figure 6 that increasing β_l would significantly reduce both the buckling and critical temperatures of steel columns. In addition, it can be seen from the figure that for steel columns with β_R of 0.0001, 0.1 and 10, when β_l increases from 0.001 to 0.1, the buckling temperature decreases by 225.96 °C, 218.1 °C and 119.54 °C respectively, and the critical temperature decreases by 228.14 °C, 139.2 °C and 64.42 °C respectively. This indicates that the impact of increasing β_l on the decrease of the buckling and critical temperatures is weakened with the increase of β_R. And the effect of increasing β_l on the buckling temperature reduction is greater than that on the critical temperature.

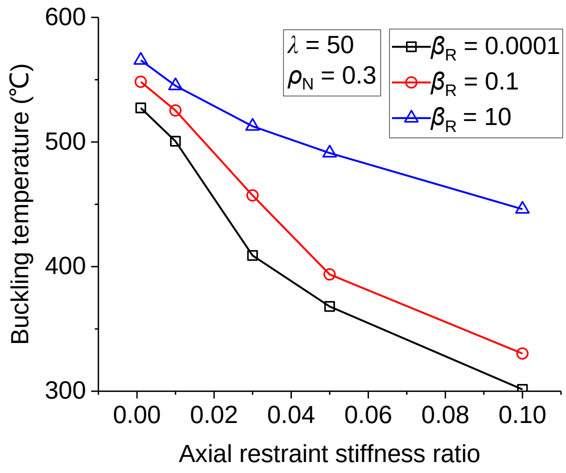

(a). Effect on buckling temperature

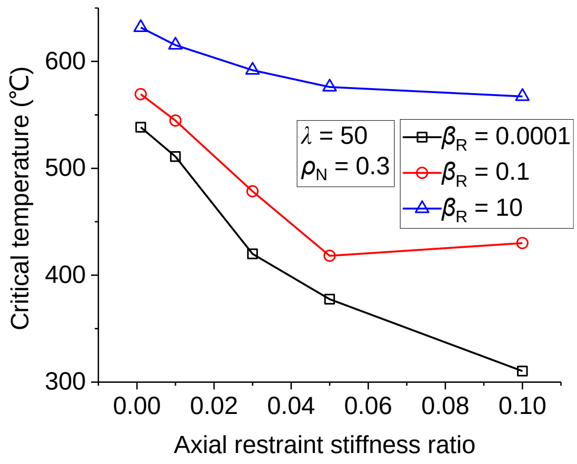

(b). Effect on critical temperature

Figure 6. The effect of β_l on buckling and critical temperatures

4.3 Effect of load ratio

Figure 7 shows the effects of ρ_N on buckling and critical temperatures for steel columns with λ of 70, β_l of 0.1, and β_R of 0.0001. With the increase of ρ_N, the buckling and critical temperatures decreased by 157.81 ℃ and 398.29 ℃, respectively. Besides, it can be found that when β_l is large and β_R is small, the effect of increasing ρ_N on the decrease of critical temperature of steel columns is greater than that of buckling temperature. In other cases, the effect of increasing ρ_N on buckling and critical temperatures reduction is basically the same.

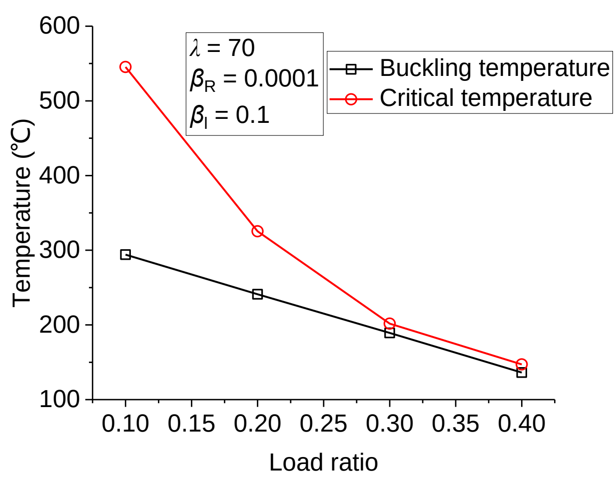

Figure 7. The effect of ρ_N on buckling and critical temperatures

5 COMPARISON ON BUCKLING AND CRITICAL TEMPERATURES BETWEEN EXISTING FORMULAS AND SIMULATION RESULTS

The calculation formula of buckling temperature proposed by Wang et al. [12] is used to compare with the buckling temperature obtained in this paper. The calculation formula is shown in Eqs. (1) - (6). Figure 8 shows the comparison between the calculated buckling temperatures and simulated buckling temperatures of steel columns with slenderness ratios of 50 and 70, respectively, when β_l is 0.1. It can be seen from Figure 8 that the buckling temperatures obtained by the calculation formula proposed by Wang et al. [12] generally agree well with those obtained by simulation, and the error is mostly within 20%.

$$T_b = T_0 - \Delta T_b \tag{1}$$

$$T_0 = -355.7\rho_N + 745.4 \tag{2}$$

$$\Delta T_b = B_{\rho_N} B_\lambda B_{\beta_l} \tag{3}$$

$$B_{\rho_N} = 3.224 - 2.654\rho_N + 2.761\rho_N^2 \tag{4}$$

$$B_\lambda = 25.483 - 0.137\lambda + 0.001\lambda^2 \tag{5}$$

$$B_{\beta_l} = 7.329 - 7.220e^{-\beta_l/0.145} \tag{6}$$

where T_b is the buckling temperature of a restrained column,

T_0 is the buckling temperature of an unrestrained column,

ΔT_b is the reduction in column buckling temperature due to restrained thermal expansion,

B_{ρ_N} is the influence of load ratio on buckling temperature reduction,

B_λ is the influence of column slenderness on buckling temperature reduction,

B_{β_l} is the influence of axial restraint on buckling temperature reduction.

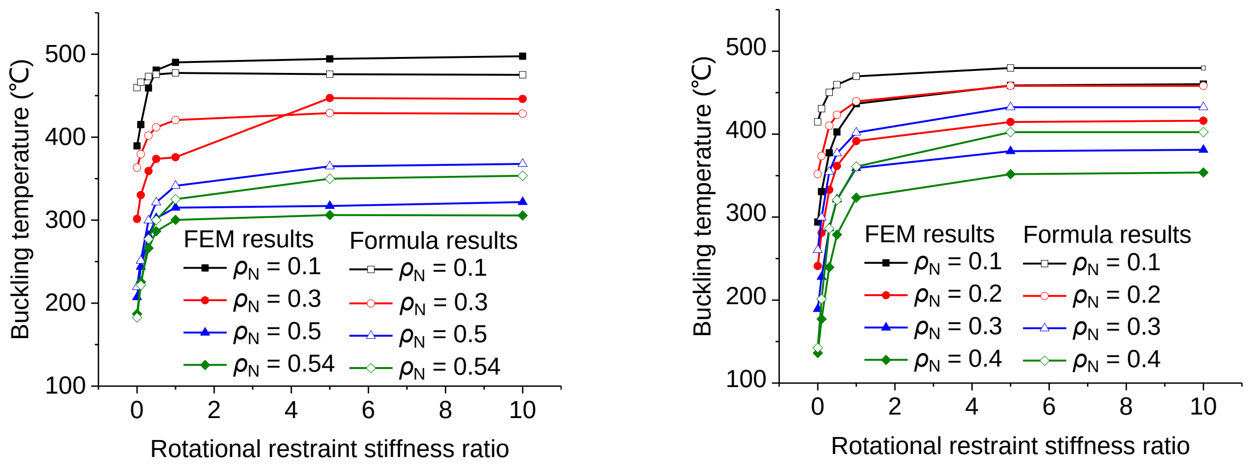

(a). Column slenderness ratio λ=50 (b). Column slenderness ratio λ=70

Figure 8. Comparison of buckling temperatures between simulation and formula

The critical temperature is calculated using the formula in Eurocode 3 Part 1.2 [17]. The calculation formula is shown in Eqs. (7) - (13). Figure 9 shows the comparison between the calculated critical temperature according to formula in Eurocode 3 and the current simulated results of steel columns with slenderness ratios of 50 and 70, respectively. It can be seen from Figure 9 that the critical temperature calculated by the formula in Eurocode 3 Part 1.2 [17] is in good agreement with the results obtained by simulation, and the error is mostly within 5%.

$$T_c = 39.19\, ln\left(\frac{1}{0.9674{\mu_0}^{3.833}} - 1\right) + 482 \tag{7}$$

$$\mu_0 = \frac{P_T}{N_{b,0}} \tag{8}$$

$$N_{b,T} = \chi_T A f_{yT} \tag{9}$$

$$\chi_T = \frac{1}{\varphi_T + \sqrt{\varphi_T^2 - \bar{\lambda}_T^2}} \tag{10}$$

$$\varphi_T = \frac{1}{2}[1 + \alpha\bar{\lambda}_T + \bar{\lambda}_T^2] \tag{11}$$

$$\alpha = 0.65\sqrt{\frac{235}{f_{y20}}} \tag{12}$$

$$\bar{\lambda}_T = \bar{\lambda}_{20}\sqrt{\frac{k_{yT}}{k_{ET}}} = \sqrt{\frac{Af_{yT}}{P_{ET}}} \tag{13}$$

where T_c is the critical temperature of a restrained column,
μ_0 is the utilization factor,
P_T is the column service load at fire condition,
$N_{b,0}$ is the buckling resistance of steel columns at room temperature,
$N_{b,T}$ is the buckling resistance of steel columns at temperature *T*,
α is the imperfection factor,
$\bar{\lambda}_T$ is the non-dimensional slenderness ratio at elevated temperature,
$\bar{\lambda}_{20}$ is the non-dimensional slenderness ratio at room temperature,
f_{yT} is high temperature yield strength,
k_{yT} is the reduction factor for the yield strength of steel at temperature *T*,
k_{ET} is the reduction factor for elastic modulus of steel at temperature *T*.

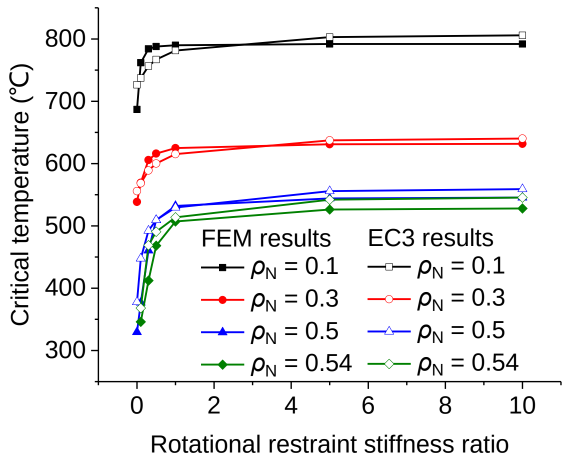

(a). Column slenderness ratio λ=50

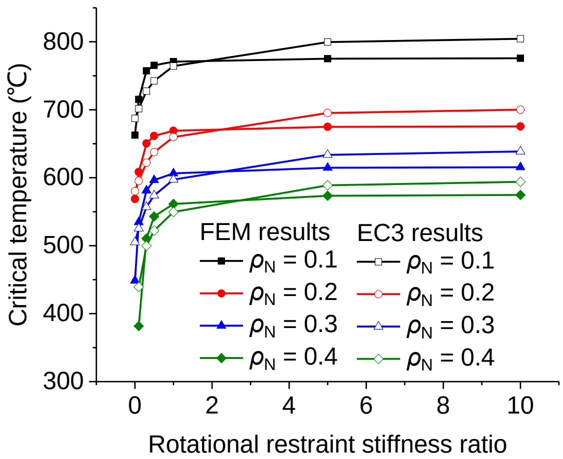

(b). Column slenderness ratio λ=70

Figure 9. Comparison of critical temperatures between simulation and formula

6 CONCLUSIONS

In this paper, a verified finite element model using explicit dynamic analysis method was adopted for parametric analysis on the buckling and critical temperatures of H-section steel columns under fire. The considered parameters include rotational restraint stiffness ratio (β_R), axial restraint stiffness ratio (β_l) and load ratio (ρ_N). Besides, results of static analysis and explicit dynamic analysis were compared. Moreover, selected formulas were verified by the analysis results. The following main conclusions were noted:

1. The buckling temperature of steel columns obtained by static analysis and explicit dynamic analysis are almost the same. The critical temperature obtained by static analysis is slightly less than that obtained by explicit dynamic analysis. Within the parameters considered, the difference is within 30°C.
2. When β_R is small, the buckling and critical temperatures increase with the increase of β_R. When β_R exceeds the critical rotational restraint stiffness ratio $\beta_{R,cr}$, the effects of further increasing β_R on the buckling and critical temperatures of steel columns become negligible. In the simulation of this paper, $\beta_{R,cr}$ does not exceed 2.0 for most cases. In addition, the influence of β_R on the critical temperature of steel columns is greater than that on the buckling temperature.
3. With the increase of β_l, the buckling and critical temperatures of the restrained steel column decrease obviously. However, with the increase of β_R, the effect of increasing β_l on the reduction of buckling and critical temperatures of steel columns decreases. Besides, β_l has greater influence on the buckling temperature than that on the critical temperature.
4. When β_l is large and β_R is small, the effect of ρ_N on critical temperature is greater than that on buckling temperature. In other cases, the effects of ρ_N on buckling and critical temperatures are basically the same.
5. The calculation formula proposed by Wang et al. can generally predict the buckling temperature well, with the errors mostly being within 20%. Besides, Eurocode 3 Part 1.2 formula can predict the critical temperature very well, with the error mostly being within 5%.

ACKNOWLEDGMENT

This work was supported by the National Natural Science Foundation of China with Grant No. 51908560.

REFERENCES

1. Y. Li, M. Wang, G. Li, B Jiang. Mechanical properties of hot-rolled structural steels at elevated Temperatures: A review. Fire Safety J. 119 (2021), 103237.
2. M. Wang, Y. Li, G. Li, W. Wang, B. Jiang. Comparative experimental studies of high-temperature mechanical properties of HSSs Q460D and Q690D. J Constr Steel Res. 189 (2022), 107065.
3. M. Wang, G. Lou, G. Li, B. Jiang. Experimental study on mechanical properties of Q690D high strength steel during the cooling stage of fire. Fire Safety J. 132 (2022), 103639.
4. G. Li, P. Wang, Y. Wang. Behaviour and design of restrained steel column in fire, Part 1: Fire test. J Constr Steel Res. 66 (2010), 1138-1147.
5. Y.C. Wang. Postbuckling Behavior of Axially Restrained and Axially Loaded Steel Columns under Fire Conditions. J Struct Eng. 130 (2004), 371-380.
6. F.A. Ali, P. Shepherd, M. Randall, I.W. Simms, D.J. O'Connor, I. Burgess. The effect of axial restraint on the fire resistance of steel columns. J Constr Steel Res. 46 (1998), 305-306.
7. K. Tan, W. Toh, Z. Huang, G. Phng. Structural responses of restrained steel columns at elevated temperatures. Part 1: Experiments. Eng Struct. 29 (2007), 1641-1652.
8. Zhang C, Gross JL, McAllister TP, Li GQ. Behavior of unrestrained and restrained bare steel columns subjected to localized fire. J Struct Eng 2015;141.
9. J.C. Valente, I.C. Neves. Fire resistance of steel columns with elastically restrained axial elongation and bending. J Constr Steel Res. 52 (1999), 319-331.
10. W. Wang, L. Zhang, Y. Ge, L. Xu. Behaviour of restrained high strength steel columns at elevated temperature. J Constr Steel Res. 148 (2018), 251-264.

11. P. Wang, Y. Wang, G. Li. Behaviour and design of restrained steel column in fire: Part 2. Parameter study. J Constr Steel Res. 66 (2010), 1148-1154.
12. P. Wang, Y. Wang, G. Li. A new design method for calculating critical temperatures of restrained steel column in fire. Fire Safety J. 45 (2010), 349-360.
13. Z. Huang, K. Tan. Rankine approach for fire resistance of axially-and-flexurally restrained steel columns. J Constr Steel Res. 59 (2003), 1553-1571.
14. B. Jiang, G. Li, B.A. Izzuddin. Dynamic performance of axially and rotationally restrained steel columns under fire. J Constr Steel Res. 122 (2016), 308-315.
15. B. Jiang, Z. Yin, J. Zhang, C. Fan, Y. Li. Effect of rotational restraint conditions on performance of steel columns in fire. Eng Struct. 238 (2021), 112237.
16. Dassault Systemes Simulia Corp, Getting Started with ABAQUS Interactive Edition, Version 6.14–1, 2014.
17. EN 1993-1-2, Design of Steel Structures, Part 1.2: General Rules - Structural Fire Design, European Committee for Standardization (CEN), Brussels, 2005.
18. G. Cowper, P. Symonds, Strain Hardening and Strain Rate Effect in the Impact Loading of Cantilever Beams, Division of Applied Mathematics, Brown University, 1957.
19. B. Jiang, G. Li, L. Li, B.A. Izzuddin, Experimental studies on progressive collapse resistance of steel moment frames under localized furnace loading, J. Struct. Eng.144 (2018) 04017190.
20. B. Jiang, Z. Yin, M.C.H. Yam, J. Zhang, L. Wang. Influence of rotational restraints on response of H-section steel columns under fire. J Constr Steel Res. 190 (2022), 107104.
21. B. Jiang, G. Li, M.C.H. Yam, Simplified robustness assessment of steel framed structures under fire-induced column failure, Steel Compos. Struct. 35 (2020) 199–213.
22. B. Jiang, G. Li, L. Li, B.A. Izzuddin, Simulations on progressive collapse resistance of steel moment frames under localized fire, J. Constr. Steel Res. 138 (2017) 380–388.

EXPERIMENTAL STUDY ON FAILURE MECHANISM OF TOP AND SEAT WITH WEB ANGLE CONNECTIONS UNDER FIRE

Jun Jiang[1], Jian Jiang*[2]

ABSTRACT

As an important component in steel structures, beam-to-column connections may experience fracture at high temperatures, affecting progressive collapse resistance of steel structures. This paper experimentally investigates the failure mechanism of top and seat with web angle (TSWA) connections in the whole process of fire. The experimental results show that TSWA connections may fail is due to either fracture of lower angle bolt or fracture of angle plate around bolt hole. Loading during the heating-cooling stage has a great influence on the residual ultimate bearing capacity of connections after fire, and it is unsafe to ignore the influence of loading.

Keywords: Fire; experiment; top and seat with web angle connection; failure mechanism

1. INTRODUCTION

A beam-column connection is the key component in a steel structure, which plays an important role in the stability and reliability of the structure. The collapse analysis of WTC5 and WTC7 after the 9.11 event showed that the collapse scope of WTC5 was influenced by the fracture of the internal beam-column connections, while the collapse of WTC7 was caused by the destruction of the inner lower floors which also contributed to the failure of beam-column connections. It can be concluded that the tensile fracture of connections were the main factors of structural collapse [1-3]. Therefore, the performance of steel beam-column connections in the whole process of fire is the premise and foundation for evaluating fire resistance of steel structures.

In this study, experiments were conducted on top and seat with web angle (TSWA) connections in the heating, cooling and post-fire stage of a fire. The failure mechanism of this connection was investigated.

2. MATERIAL PROPERTY TEST

The bolts used in the test are 10.9 high-strength bolt, with the nominal diameter of M12 and the screw length of 80mm. The Q245 steel cut from the angle steel and Q355 steel from the test beam were used to process the sheet specimen for tension, of which the gauge length section was polished. The nominal dimensions of the two shapes of tensile test pieces are shown in Fig. 1, while physical drawings are shown in Fig. 2.

[1] Master student, China University of Mining and Technology
e-mail: 418328187@qq.com
[2] Prof., China University of Mining and Technology
e-mail: jian.jiang@cumt.edu.cn
https://doi.org/10.6084/m9.figshare.22215721

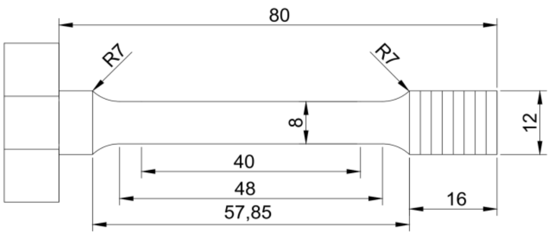

（a）Size of smooth round bar specimen

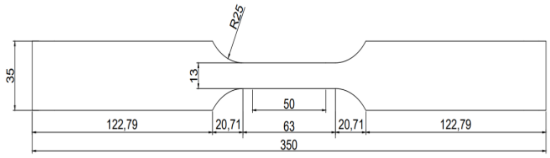

（b）Size of sheet specimen

Figure 1 Size of tensile specimens (mm)

（a）Smooth round bar specimen in the test

（b）Sheet specimen in the test

Figure 2 Tensile specimens in the test

This test was completed in the Jiangsu Key Laboratory of Environmental Impact and Structural Safety in Engineering, China University of Mining and Technology. The test loading system is MTS universal testing machine (Fig.3), with a load limit of 120kN. The digital image correlation measurement system (DIC) was used to measure the strain of the test specimen (Fig. 4). The real stress-strain curve of the material can be obtained through DIC. The yield strength of Q245 steel, Q355 steel and 10.9 bolt was measured as 290MPa, 400MPa and 1200MPa, respectively.

Figure 3 MTS Land Mark system

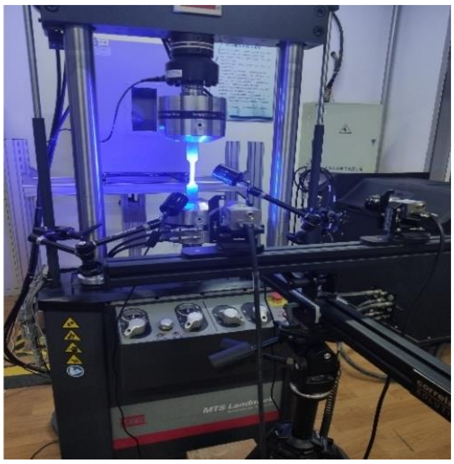

Figure 4 DIC measurement

3. CONNECTION FAILURE TEST

3.1 Test preparation

The test was conducted in the multipurpose horizontal furnace as shown in Fig. 5. The internal dimension of the furnace is 4.5m×3 m×1 .5m, of which the space can be separated as required. It is equipped with 10 sets of integrated burners, 12 sets of S-type thermocouples and 2 sets of high-definition cameras in the furnace. There is a self-balanced reaction frame on the upper part, with a vertical design load of 150 tons.

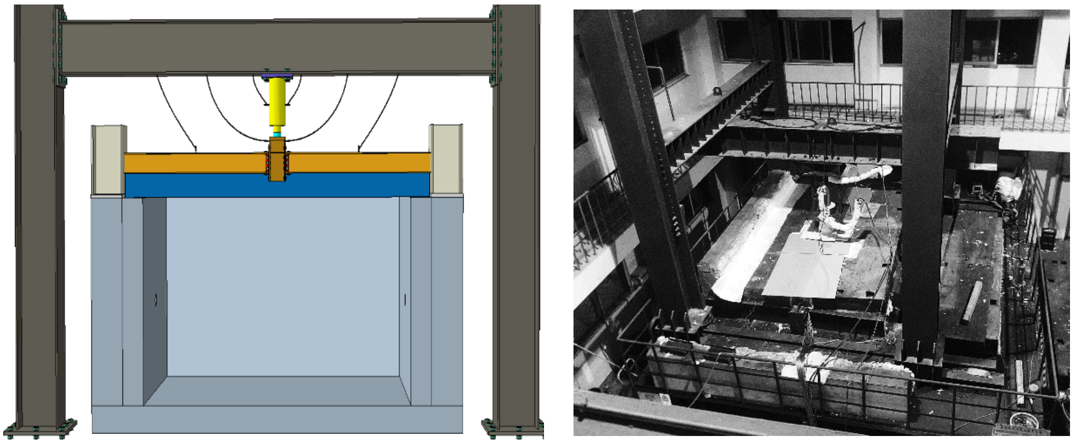

（a）Room temperature test device diagram （b）High temperature test device diagram

Figure 5 The experimental device

Four specimens were tested, including ambient-temperature test, heating test, heating-cooling test and post-fire test. The working conditions for these four specimens is shown in the Fig.6. For the latter three fire-related tests, after loading to the target load ratio, the specimen was heated following standard ISO834 fire curve, and cooled down to ambient temperature. A load with a load ratio of 0.2 was imposed on the specimen for the heating-cooling test, compared to zero load in the post-fire test. For the heating test, a higher load ratio of 0.5 was applied.

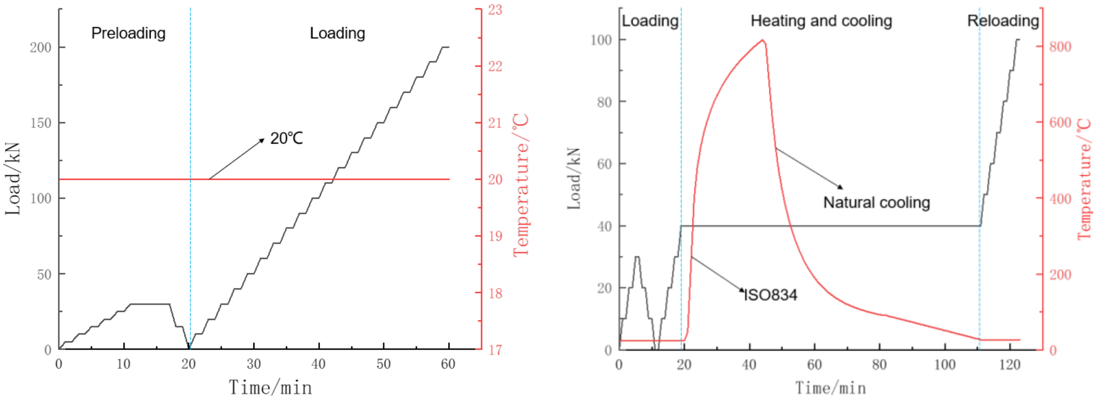

（a）Ambient temperature （b）Fire test

Figure 6 Working conditions

The cable displacement meter was used to monitor the vertical displacement of the middle column, and the load of the jack was output through the load sensor. K-type thermocouples were used to monitor specimen temperature in the fire-related tests, the specific layout is shown in Fig. 7.

In addition to the loading device, in order to prevent the central column from falling during the test after the connection failure, the steel wire rope was used to connect the jack and the vertical reaction frame. The sealing of the furnace body is required for the test conditions involving high temperature. In order to ensure the temperature rise effect of the structure and the safety of the surrounding personnel and facilities, fire protection covers were applied on both sides of the structure, aluminum silicate cotton was wrapped at the ends of key instruments: pipelines, beams and the gap between the two fire covers. Finally, a layer of fireproof gypsum board was covered to complete the sealing of the furnace body which are shown in Fig.8.

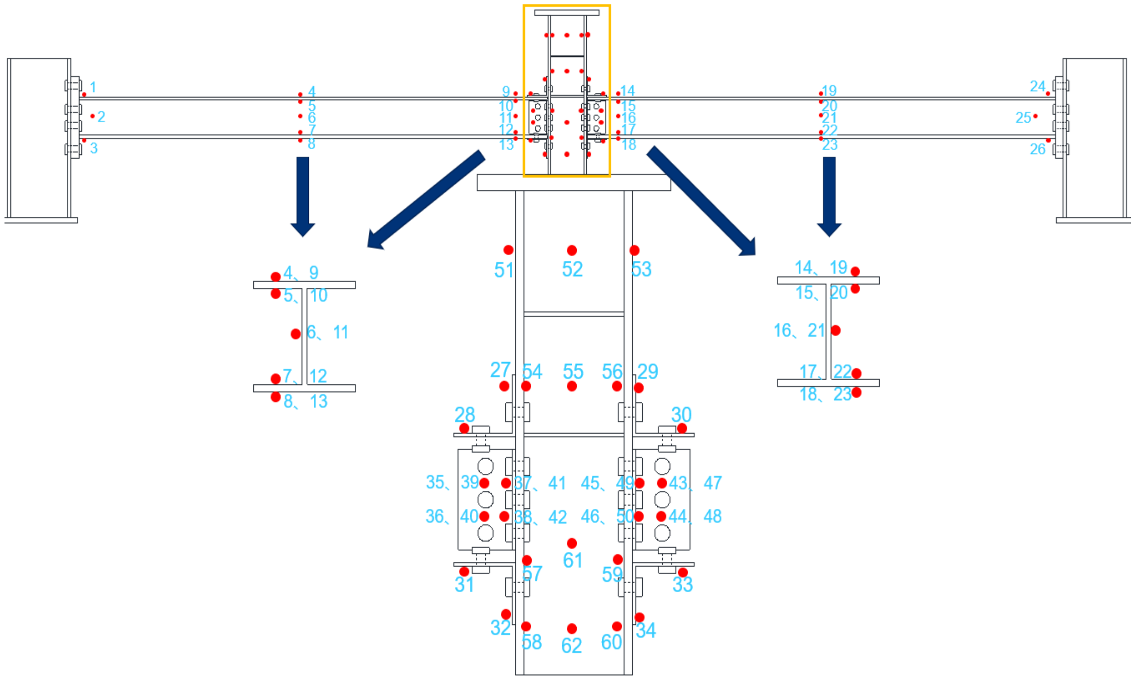

Figure 7 Distribution of temperature measuring points

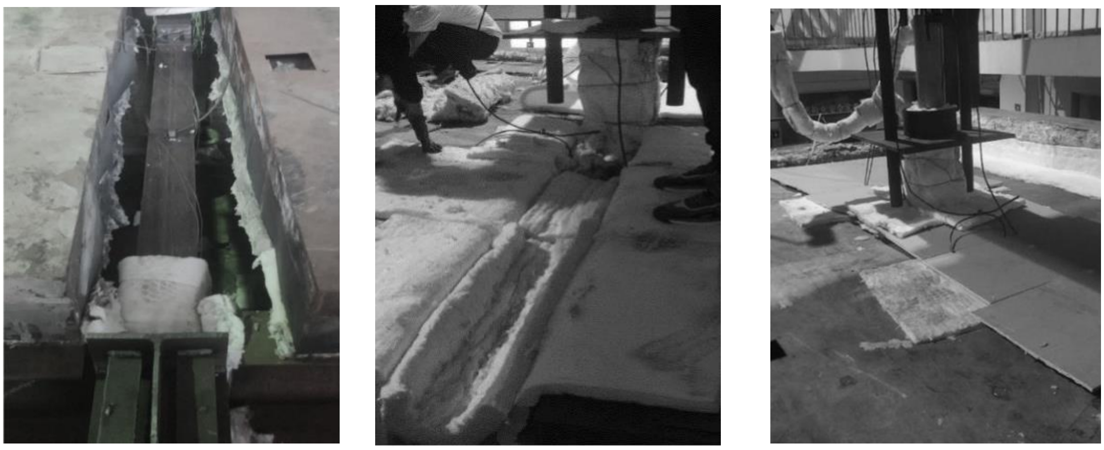

（a）Key parts are coated with aluminum silicate cotton

（b）Laying and filling rock wool at the gap

（c）Covered with fireproof gypsum board

Figure 8 Fire protection process

3.2 Test results

1. Test phenomena

The failure of connections is shown in the Fig.9. The failure mode of ambient-temperature test and heating test was tensile failure of lower angle steel bolt hole. While in the heating-cooling test and post-fire test, the bolts on the side of the lower angle plate were damaged by shearing.

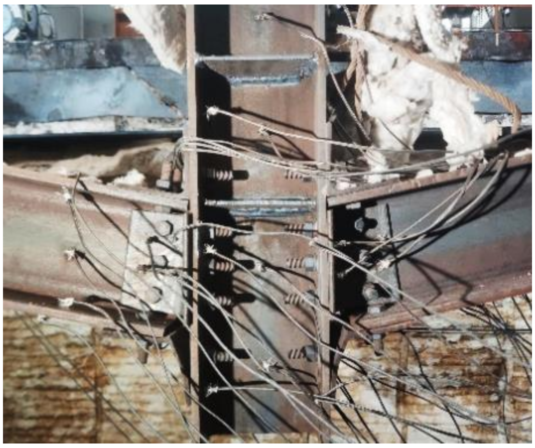

（a）Ambient-temperature test （b）Heating test

（c）Heating-cooling test （d）post-fire test

Figure 9 Connection failure

The overall deformation under four working conditions is shown in the Fig. 10. Among them, the residual deformation of the heating-cooling test was the largest.

（a）Ambient-temperature test

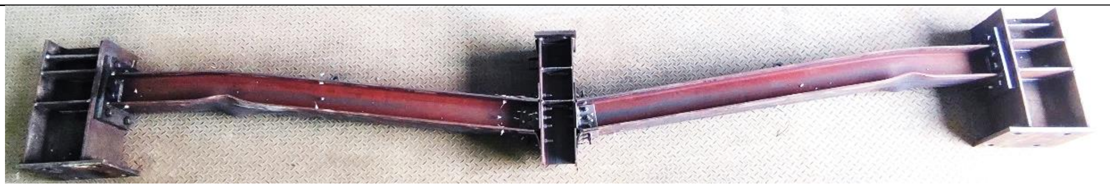

（b）Heating test

Figure 10 Overall deformation of structure

By comparing the load-displacement curves for the four tests, it was found that the residual bearing capacity of natural cooling to room temperature after rising to 980℃ through ISO834 curve was about 80% of the ambient-temperature value. The bearing capacity of the connection decreased significantly with the increase of temperatures. When the temperature rised to 650 ℃, the bearing capacity was less than 50% of that at ambient temperature. The load ratio had a great influence on the critical temperature of the connection in the heating section. The higher the load ratio, the lower the critical temperature of the structure and the shorter the fire resistance time. The results showed that the residual ultimate bearing capacity of the connection in the heating-cooling test was 100kN for the load ratio of 0.2, while the residual ultimate bearing capacity was 160kN for the post-fire test where no load was applied.

This means that applying load in the fire test had a great influence on the residual ultimate bearing capacity of the connections after fire, and it is unsafe to ignore the influence of loads.

4. CONCLUSIONS

Experiments were conducted on failure mechanism of top and seat with web angle connections in the whole process of fire. It was found that the failure mode of this connection is mainly the failure of lower angle plate and bolt hole. Loading under fire had a great influence on the residual ultimate bearing capacity of the connections after fire, and it is unsafe to ignore the effect of loads.

REFERENCES

1. Jian Jiang, Wenyu Cai, Guo-Qiang Li, Wei Chen, Jihong Ye. (2021) Progressive collapse of steel-framed gravity buildings under parametric fires. Steel & Composite Structures: An International Journal. 36(4):383-398.
2. Jian Jiang, Wenyu Cai, Wei Chen, Jihong Ye, Guo-Qiang Li. (2020) An Insight into Eurocode 4 Design Rules for Thermal Behaviour of Composite Slabs. Fire Safety Journal, 103084.
3. Guo-Qiang Li, Jiarong Miao, Linxin Song, Wenyu Cai, Jian Jiang. (2020) Investigation on Post-fire Residual Capacity of High Strength Steel Columns with Axial Restraint. Journal of Structural Engineering, 146(9): 04020182.

AN IMPROVED ANALYTICAL FORMULA FOR PREDICTING THE TEMPERATURE OF HEAVILY PROTECTED STEEL SECTIONS

Luca Possidente[1], Nicola Tondini[2], Ulf Wickström[3]

ABSTRACT

Fire verification might be particularly demanding for steel structures and insulation is a common option to slow down the temperature increase in the steel elements without modifying the original structural design. Simple analytical formulae, as provided for instance in EN1993-1-2 design standard, allow a quick estimate of the temperature of insulated steelwork, without determining the thermal field inside a steel cross-section by performing in-depth experimental or numerical analyses. However, the EN1993-1-2 formulation considers heat transfer with temperature boundary conditions, rather than more realistic conditions on the heat flux, and is inaccurate for heavily insulated steel sections, in which protective solutions with high heat capacity are adopted. In this paper a new analytical formula aimed at estimating the temperature of protected steel members is proposed. Its accuracy is assessed by comparing the predictions of the proposed and the EN1993-1-2 formulations with the results of a parametric analysis consisting of 1-D models. Several steel thicknesses, insulation materials and thicknesses and an exposure to the ISO 834 heating curve are considered in the analyses. It is shown that the EN1993-1-2 can be both conservative and unconservative depending on the ratio between the insulation and the steel heat capacities μ and is not suited for heavily insulated steel sections with high values of μ. On the contrary, the proposed formulation results in being always safe and particularly suited for heavily insulated steel sections.

Keywords: Fire protection; steel temperature; heat transfer; steel structures; Fire safety engineering

1 INTRODUCTION

Fire safety requirements may be particularly demanding for steel structures, due to the inherent vulnerability of steel to thermal attack and the small thickness of the cross-sections, and thus the fire design of unprotected steel members can govern the size of the profiles. Passive fire protection allows the temperature in the steel elements to be slowed down to meet the fire requirements and is one of the most popular solutions as it does not require modifications of the structural design. For this reason, fire protective measures were extensively studied aiming at accurately characterising existing measures and at developing new and optimised solutions [1-7]. For instance, several literature reviews describing the main features and strengths of protective measures were published. Among others, The National Institute of Standards and Technology (NIST) [1], Leborgne and Thomas [2] reviewed different types of fire protections as intumescent paints, sprayed-based protections and board systems, while Mariappan [3] focused on intumescent fire coating. Extensive experimental investigations are available in the literature for steel-concrete solutions as well, in which steel columns are encased in concrete, which provides fire protection

[1] PhD, University of Trento, Department of Civil, Environmental and Mechanical Engineering, Via Mesiano 77, 38123, Trento, Italy
e-mail: possidentel@gmail.com , ORCID: https://orcid.org/0000-0002-4179-1860
[2] PhD, Associate Professor, University of Trento, Department of Civil, Environmental and Mechanical Engineering, Via Mesiano 77, 38123, Trento, Italy
e-mail: nicola.tondini@unitn.it
[3] Professor Emeritus at Luleå University of Technology
https://doi.org/10.6084/m9.figshare.22215730

to the inner steel core [4-7]. Moreover, in the last decades there have been continuous efforts to find new solutions, as fire-retardant products [8], spray-applied fire-resistive composites [9] or plug-and-play protections systems [10].

Despite the extensive research carried out so far and the improvement of computer capabilities that may allow to accurately characterise the behaviour of protected steel elements, easy-to-use hand-calculations are used for a quick assessment of the fire protection suitability to comply with the fire resistance requirements and are still preferred by designers owing to the flexibility required in the design process. Indeed, simple predictive equations support engineers and researchers in rapidly estimating the temperature of insulated steelwork, without performing extensive analyses, as experimental tests or numerical simulation. The predictive formula currently prescribed in the European standard for the fire design of steel structures EN1993-1-2 [11] was developed and calibrated in [12]. It was shown that this formula presents some limitations. In particular, starting from the formulation proposed in [12] and to ECCS recommendations [13], Melinek and Tomas [14] defined a more effective time delay term t_d, which accounts for the retardant effect of insulation on the steel temperature increase, to be substituted in the EN1993-1-2 formulation. Wang et al. [15] suggested the same time delay t_d for insulation materials with high heat capacity C, which typically consist in materials with high density as bricks or concrete. Moreover, it should be highlighted that a Dirichlet boundary condition was assumed in the derivation of the EN 1993-1-2 formulation by assigning the temperature of adjacent gas to the exposed surface $T_s(t, x = x_0) = T_g(t)$. Wong and Ghojel [16] highlighted that the total heat transfer coefficient h_{tot}, that accounts for convection and radiation, should be considered and thus, a more realistic condition on the total heat flux received by the surface $-k \cdot \left.\frac{\partial T_s}{\partial x}\right|_{x=x_0} = \dot{q}''_{tot}$ should be preferred.

This paper presents a simple predictive formula to estimate the temperature of insulated steel elements suited for insulation materials with relatively high insulation capacities and derived considering heat flux boundary conditions. The formula is based on a lumped approach and considers both radiative and convective components, while terms accounting for the time delay are neglected to keep the formulation simple. The proposed formulation was assessed against results of numerical simulation and compared with the EN1993-1-2 formula. For this purpose, a parametric study was conducted, performing 1-D finite element analyses covering different insulation materials and thicknesses as well as different steel thicknesses. Considerations are provided about the range of applicability of the two predictive formulae and the implications of their employment in the classification of protected steel elements in respect to the fire resistance.

2 LUMPED MASS APPROACHES FOR THE ESTIMATE OF THE EQUIVALENT TEMPERATURE OF INSULATED STEEL MEMBERS

In the described formulations, since steel has a very high thermal diffusivity, it is assumed that the temperature is uniform in sufficiently thin sections and all the heat of the section can be lumped into a zero-dimension point. Therefore, no temperature distributions in the solids are considered and temperatures are only time-dependent.

2.1 EN 1993-1-2 formulation

EN-1993-1-2 [11] provides a recursive equation for the estimate of a uniform temperature distribution in an insulated steel cross-section T_{st}. This formulation is derived assuming a Dirichlet boundary condition in the heat transfer equations, assigning to the exposed surface the temperature of adjacent gas. In detail, the temperature increase ΔT_{st}^{i+1} during the time interval $\Delta t = t_{i+1} - t_i$ is obtained as follows

$$\Delta T_{st}^{i+1} = \frac{\lambda_{in} A_{st}/V_{st}}{d_{in} c_{st} \rho_{st}} \frac{\left(T_g^i - T_{st}^i\right)}{\left(1 + \frac{\mu}{3}\right)} \Delta t - \left(e^{\frac{\mu}{10}} - 1\right) \Delta T_g^{i+1}$$
$$T_{st}^{i+1} = T_{st}^i + \Delta T_{st}^{i+1} \qquad (1)$$

$$\text{with } \Delta T_{st}^{i+1} \geq 0 \text{ if } \Delta T_g^{i+1} = T_g^{i+1} - T_g^i > 0$$

where T_g is the gas temperature and the parameter μ is calculated as

$$\mu = \frac{c_{in}\rho_{in}}{c_{st}\rho_{st}} d_{in} \frac{A_{st}}{V_{st}} \tag{2}$$

the exponential term of Eq.(1) account for a time delay t_d in the temperature increase of the steel member. As prescribed in EN1993-1-2, the value of Δt should not be greater than 30 seconds.

2.2 Proposed formulation

The derivation of the proposed recursive equations is based on thermal equilibrium. The total received heat flux $\dot{q}''_{tot}$ by the exposed area A in a time dt should be equal to heat stored in the volume V, which is proportional to the temperature rise of the solid dT. Hence, can be defined as

$$\begin{gathered} \dot{q}''_{tot} \cdot A \cdot dt = V \cdot \rho \cdot c \cdot dT \\ \frac{dT}{dt} = \frac{A}{V \cdot \rho \cdot c} \dot{q}''_{tot} = \frac{\dot{q}''_{tot}}{C} \end{gathered} \tag{3}$$

where dT/dt is the temperature rise rate, and ρ, c and C are the density, the specific heat capacity and the heat capacity of the heated solid. Consistently with the assumption of lumping the system into a single temperature point, $\dot{q}''_{tot}$ can be taken proportional to the difference between the gas and the steel temperature, as depicted in the electric circuit analogy in Figure 1a, and the rate of steel temperature increase can be expressed as follows

$$\dot{q}''_{tot} = \frac{(T_g - T_{st})}{R_{h+in}} = \frac{(T_g - T_{st})}{\frac{1}{h_{tot}} + \frac{d_{in}}{\lambda_{in}}} \tag{4}$$

where d_{in} is the insulation thickness, λ_{in} is the insulation conductivity and h_{tot} is the total heat transfer coefficient. For heavily insulated steel sections, the contribution of the insulation material to the total heat capacity is relevant and should be accounted as follows

$$\begin{gathered} C = C_{st} + \chi C_{in} \\ \text{with } C_{st} = \frac{V_{st}}{A_{st}} \cdot \rho_{st} \cdot c_{st} = d_{st} \cdot \rho_{st} \cdot c_{st} \text{ and } C_{in} = d_{in} \cdot \rho_{in} \cdot c_{in} \end{gathered} \tag{5}$$

d_{st}, ρ_{st}, c_{st} and d_{in}, ρ_{in}, c_{in} are the thickness, the density and the specific heat capacity of steel and insulation respectively. V_{st}/A_{st} is the ratio between the volume per unit length and the enveloping area of the steel section, equivalent to the effective steel thickness d_{st} in the one-dimensional case. The parameter χ quantifies the contribution of the insulation to the heat capacity of the system and is assumed constant for simplicity. In detail, based on preliminary analyses, it was found that considering half of the insulation heat capacity in the total heat capacity, i.e., χ=0.5, allows for good and conservative predictions. Hence, assuming the time derivative of temperature with a differential $\frac{dT}{dt} \approx \frac{\Delta T}{\Delta t}$, and a constant time increment $\Delta t = t_{i+1} - t_i$ between two consecutive steps i and i+1, the following formulation is obtained from Eq. (3), Eq. (4) and Eq. (5)

$$\begin{gathered} T_{st}^{i+1} = T_{st}^i + \frac{1}{(C_{st} + \frac{d_{in}\rho_{in}c_{in}}{2})} \frac{1}{\left(\frac{1}{h_{tot}^i} + \frac{d_{in}}{\lambda_{in}}\right)} (T_g^i - T_{st}^i)\Delta t \\ \text{with } h_{tot}^i = h_r^i + h_c = \varepsilon_s \cdot \sigma(T_g^2 + T_s^2) \cdot (T_g + T_s) \approx 4\varepsilon_{in}\sigma(T_g^i)^3 + h_c \end{gathered} \tag{6}$$

Where h_r^i is the radiation heat transfer coefficient at step i, h_c is the convection heat transfer coefficient and T_s is the temperature of the exposed insulation surface. It should be observed that the simplification $T_s = T_g$ was employed only in the h_r^i term, differently from the EN 1993-1-2 in which $T_s = T_g$ was assumed as boundary condition. This simplification was introduced since the equation becomes easier to use and, as confirmed by preliminary numerical analyses, no significant variation in the steel temperatures predictions

T_{st} is obtained. Similarly, in order to keep the formulation simple, an explicit term to account for a time delay t_d was not considered. As for the EN 1993-1-2 formulation, if temperature-dependant material properties are used, e.g., $c_{st} = c_{st}(T_{st})$, they should be updated at each step as $c_{st}^i = c_{st}(T_{st}^i)$.

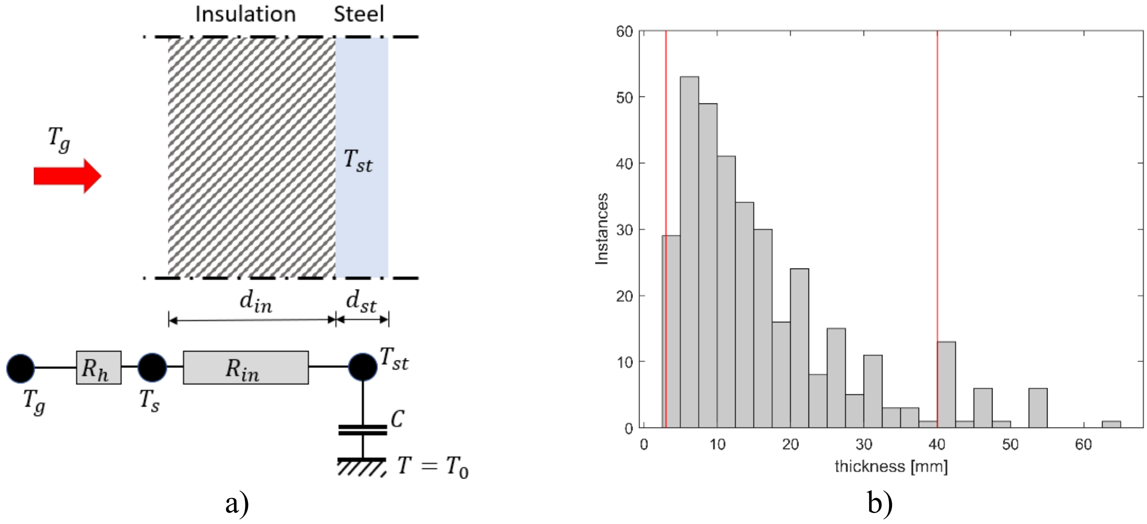

Figure 1. a) Protected steel sections: electric analogy of the thermal model; b) Thickness of plates composing H and I steel profiles

3 NUMERICAL SIMULATION

3.1 Parametric analysis

Predictions obtained with the EN1993-1-2 and the proposed formulations were compared against the results of a parametric study, consisting of 1-D thermal analyses. 1-D analyses are employed since the heat transfer through the thickness of the steel components composing typical steel sections, e.g. H and I profiles, is relevant and corner effects are usually neglected in the applications to which the investigated formulations apply. In order to investigate different steel-insulation configurations, 10 insulation materials, 9 insulation thicknesses d_{in} and 15 steel thicknesses d_{st} were considered, as reported in Table 1. The insulation thickness was varied in a range relevant to each of the insulation materials, i.e., 10 mm, 15 mm, 20 mm, 25 mm, 30 mm, 35 mm, 40 mm, 45 mm, 50 mm for all the materials except bricks, for which thicknesses of 100 mm, 125 mm, 150 mm, 175 mm, 200 mm, 225 mm, 250 mm, 275 mm, 300 mm were studied. The values of steel thickness d_{st} were selected inside a range relevant for plates composing steel sections, as confirmed by Figure 1b in which the distribution of the thickness of plates composing H and I steel sections and the limits of the thicknesses considered in the parametric analysis are shown. In detail, the values of d_{st} employed were 3 mm, 5 mm, 8 mm, 10 mm, 13 mm, 16 mm, 18 mm, 21 mm, 24 mm, 26 mm, 29 mm, 32 mm, 34 mm, 37 mm, 40 mm.

Table 1. Investigated insulation materials

	ρ_{in} (kg/m^3)	λ_{in} (W/mK)	c_{in} (J/kgK)	d_{in} (mm) range
Calcareous concrete	2200	1.30	1200	10-50
Concrete with voids	600	0.30	1200	10-50
Lightweight concrete	1600	0.80	1200	10-50
Siliceous concrete	2400	1.70	1200	10-50
Mineral fibres	250	0.10	1100	10-50
Gypsum boards	800	0.20	1700	10-50
Rockwool	120	0.25	1100	10-50
Silicate boards	450	0.15	1100	10-50
Bricks	2000	1.00	1200	100-300
Vermiculite	300	0.15	1100	10-50

3.2 Numerical model

For each of the steel-insulation configurations of the parametric analysis, a numerical simulation was performed by means of the finite element software SAFIR [17]. In the numerical model, shown in Figure 2a, an insulation layer exposed on the upper surface, and a steel layer with an adiabatic condition at the bottom surface were defined. On the lateral surfaces adiabatic conditions were imposed. On the exposed surface a ISO834 flux boundary condition was applied. As 360 minutes is typically the highest requirement of fire resistance of civil structures, a fire exposure of 360 minutes was considered. The analyses were performed setting the timestep Δt=10 seconds. 4 quadrangular elements for the material with the smallest thickness and a variable number of elements for the material with the larger thickness, as shown in Figure 2a, were employed in the numerical models to have finite elements with comparable dimensions The selected mesh discretization was sufficiently accurate since by increasing the number of elements in exploratory analyses the difference in the obtained steel temperatures was negligible.

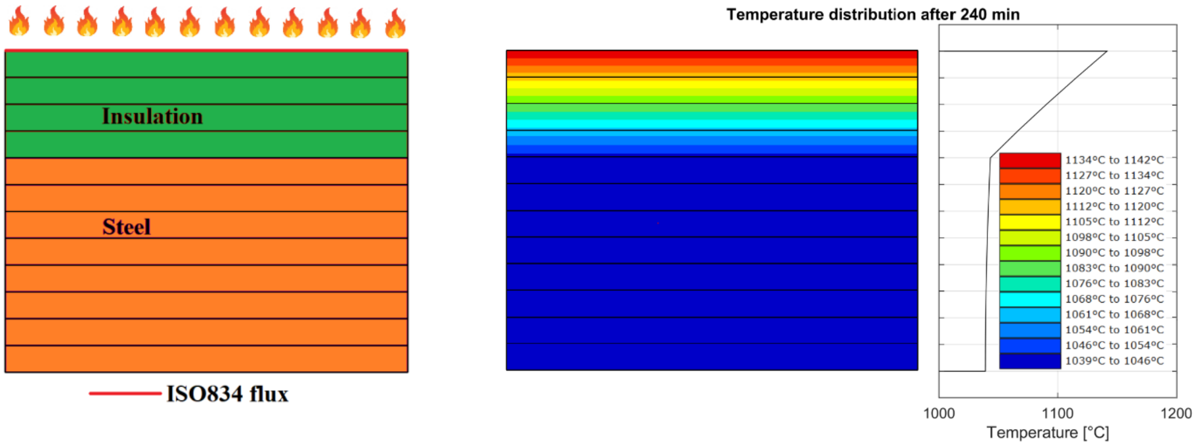

a) b)

According to EN 1993-12 [11], the specific heat c_{st} and the thermal conductivity λ_{st} of steel were considered to vary with the steel temperature T_{st}. These and further relevant model properties are reported in Table 2.

Figure 2. a) Numerical model; b) Typical temperature distribution at t=240 min

Table 2. Model properties

Additional properties			
Heat transfer coefficient h_c (W/m^{2}K)	25	**Specific heat of steel** c_{st} (J/kgK)	$c_{st} = c_{st}(T_{st})$ [11]
Emissivity of steel ε_{st}	0.7	**Thermal conductivity of steel** λ_{st} (W/mK)	$\lambda_{st} = \lambda_{st}(T_{st})$ [11]
Emissivity of insulation ε_{in}	0.9	**Unit mass of steel** (kg/m^3)	7850

Though the temperature distribution was essentially uniform in the steel in most of the analyses, as shown in Figure 2b in which the typical temperature distribution inside a section is depicted, different temperatures were available at each finite element node. Hence, only the maximum steel temperature, found at the steel-insulation interface one temperature was conservatively chosen as the temperature $T_{st,FEM}$ to be compared with the predictions from the two investigated formulations.

4 COMPARISON BETWEEN NUMERICAL RESULTS AND PREDICTIVE EQUATIONS

The maximum steel temperatures $T_{st,FEM}$ obtained in the parametric analyses were stored at each time of analysis t, or step of analysis i, where the uniform time increment between two consecutive steps was Δt=10 seconds. These temperatures compared with the predictions of the steel temperature T_{st} obtained with the EN1993-1-2 and the proposed formulations at the same step of the analysis and employing the same time increment, i.e., Δt=10 seconds. In this respect, Figure 3 provides a synthetic representation of the comparisons with the EN1993-1-2 and the proposed formulation. To identify over- and underestimated predictions in both relative and absolute terms, ranges from -10% to +10% and from -100°C and +100°C in respect to a perfect match between predicted and numerical temperatures (bisector line) are clearly indicated in the figure. As shown in Figure 3a, EN1993-1-2 predictions (may be both safe (data above the bisector line) and unsafe (data below the bisector line), and significantly higher than +10% or lower than -10% of the FEM temperature. In particular, temperatures higher or lower than $T_{st,FEM}$ for more than 100°C were found until 900°C were not exceeded. Predictions obtained with the proposed formulation (Figure 3b) are much well distributed in the -10% to +10% range, especially for steel temperatures $T_{st,FEM}$ higher than 600°C, when the temperature overestimation becomes much lower than 100°C. Only at very low temperatures predictions are unsafe for more than 10%, but this is not particularly relevant as such predictions are never unsafe for more than 20°C. Indeed, in general an initial overestimation is found at low temperatures, but predictions gradually improve when the steel temperature increases. In addition, considering that failures of steel elements in fire, typically occur for steel temperatures 400°C≤T_{st}≤800°C [18-20], a reference critical temperature T_{crit}=550°C within this range was indicated in Figure 3 with a dashed line. Though different temperatures could be assumed as critical for the stability of the steel elements, this temperature was selected as it entails a significant reduction of the yield strength at elevated temperature of 62.5% [11]. It can be observed that when $T_{st,FEM}$ attains T_{crit}, for the EN1993-1-2 (Figure 3a) a maximum and a minimum temperature of 706 °C and 20 °C are obtained (-96% to +28% of T_{crit}), whereas the proposal (Figure 3b) provides conservative predictions between 549°C and 626 °C (0% to +14% of T_{crit}).

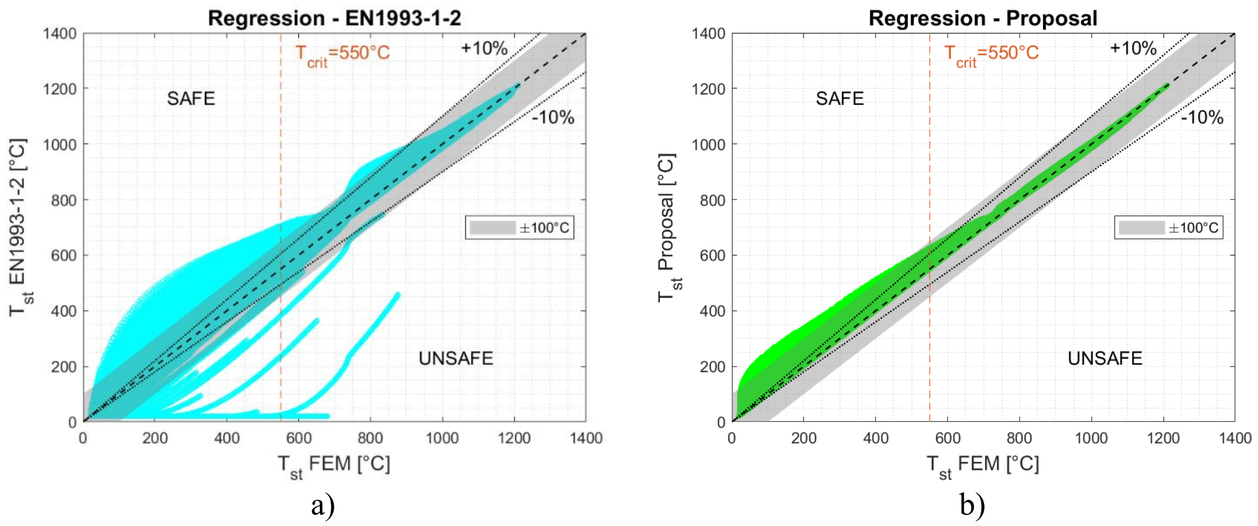

Figure 3. Predicted vs numerical steel temperatures: a) EN1993-1-2 b) Proposed formulation.

Figure 4 compares the results in terms of absolute error, evaluated as the difference between the numerical and the predicted steel temperatures, where each bin spans for an error range of 10°C. The dashed line indicates the zero-error line and unsafe and safe predictions can be found respectively on the left and right of this line. The higher the bins close to dashed line, the better the temperatures predictions. In this respect, the EN1993-1-2 formulation (Figure 4a) ensures fewer predictions in the -10 to 0°C error range compared with the proposed formulation, but in general more predictions are found in more unsafe ranges, i.e., errors <-10°C. Furthermore, higher percentage values are found for safe predictions in the 10 to 80°C range, while a lower percentage is attained for the 0 to 10°C range. Instead, the proposed formulation ensures higher percentages compared for the -10°C to 0°C and the 0°C to +10°C ranges, and no predictions are unsafe for more than 20°C (Figure 4b). Nevertheless, this formulation provides very conservative values for low steel temperatures and therefore, percentages higher than 1% are found until an error value of 150°C is attained. It is interesting to note that limiting the analysis to data for which $T_{st,FEM}$ is inside a relevant range, i.e., $0.9T_{crit} < T_{st} < 1.1T_{crit}$, the error distribution does not significantly differ from the one of the full dataset for the EN1993-1-2 (Figure 4a), while the error percentages become already negligible for an error less than +70°C and a higher percentage is reached in the 0 to +10°C error range for the proposed formulation(Figure 4b).

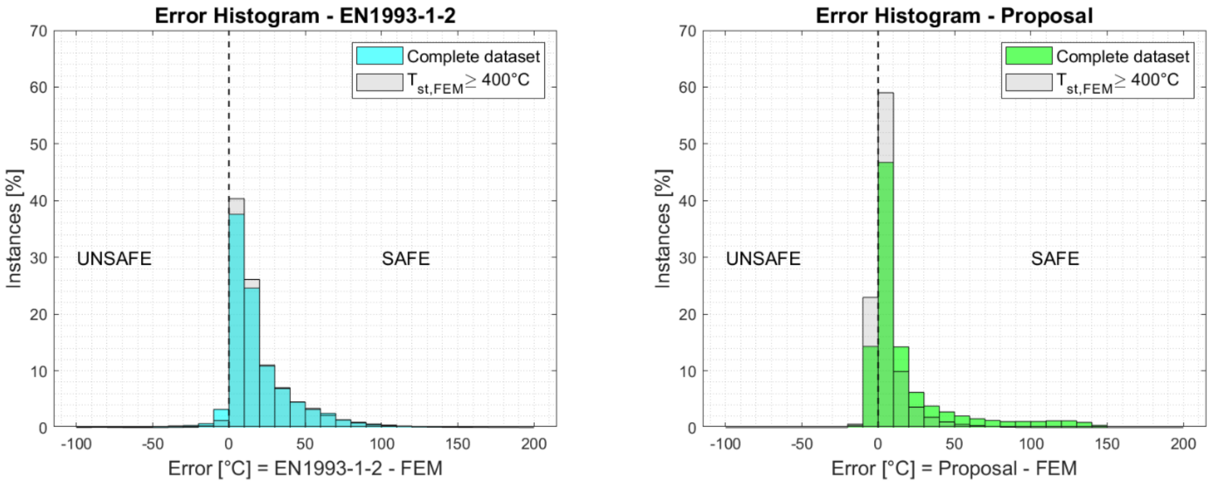

a) b)

Figure 4. Error distribution: a) EN1993-1-2; b) Proposed formulation

In order to distinguish when the EN1993-1-2 provisions can still provide good predictions and when the proposed formulation should be preferred, results are compared in respect to the parameter μ in Figure 5. The parameter μ, defined as in Eq. (2) represents the ratio between the heat capacities of the insulation and the steel, and assumes higher values for heavy insulations, which typically ensure low temperature rise inside the steel sections. The parameter μ was selected since the EN1993-1-2 is particularly sensitive to this parameter, therefore allowing for the identification of a marked change in the ability to provide safe predictions. In Figure 5 the ratio between predictions and numerical results is reported for predictions associated with $T_{st,FEM}$ values that surpassed a relevant temperature threshold, i.e. T_{crit}=550°C. This reference value was conventionally chosen since failure of steel structural elements is typically observed inside the 400°C to 800°C temperatures range owing to the degradation of mechanical properties of steel and in particular of the yield strength [18-20]. In order to provide a clearer representation, the constant value c_{st}=460 J/kgK was used to calculate μ in Figure 5.

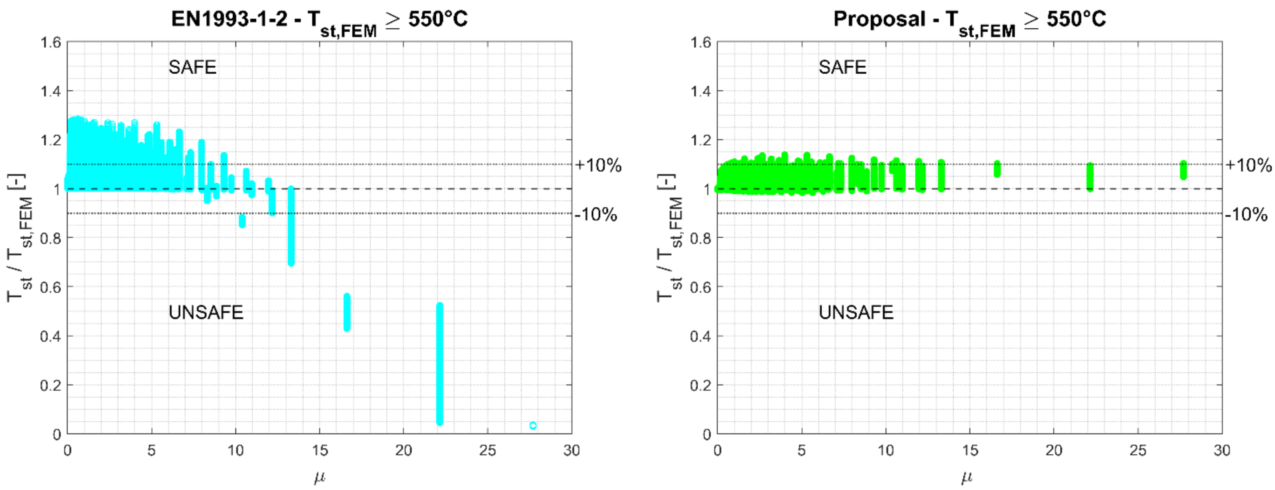

a) b)

Figure 5. Predicted-numerical temperatures ratio depending on μ for $T_{st,FEM}$>550°C: a) EN1993-1-2; b) Proposed formulation.

Figure 5a shows that the EN1993-1-2 formulation provides predictions of temperatures equal to or higher than T_{crit} that are always safe only for μ<7 and always unsafe for μ>14. Instead, the proposed formulation always provides safe or slightly unsafe predictions regardless of the value of μ (Figure 5b). However, differently form the EN1993-1-2 predictions, the predictions obtained with the proposed formulation are well disposed in the 0% to +10% range. It can be concluded that the proposed formulation should be preferred to the one of EN1993-1-2 for predicting relevant steel temperatures of heavily insulated steel member, and in particular for μ>14. For μ<7 the EN1993-1-2 formulation can be employed as it provides safe and not excessively overestimated prediction, though more accurate predictions of relevant temperatures may be obtained with the proposal. For 7<μ<14 the EN1993-1-2 prediction may be better or worse than the proposal depending on the case, but the proposal seems more reliable for relevant temperatures. It should be observed that the proposed formulation gives higher overestimation of the steel temperature for low temperatures and therefore, a term accounting for a time delay t_d could be introduced in Eq.(6) to reduce the error. However, a more complex formulation would be obtained, and such a refinement is beyond the scope of this work, though the formulation could be improved in future developments.

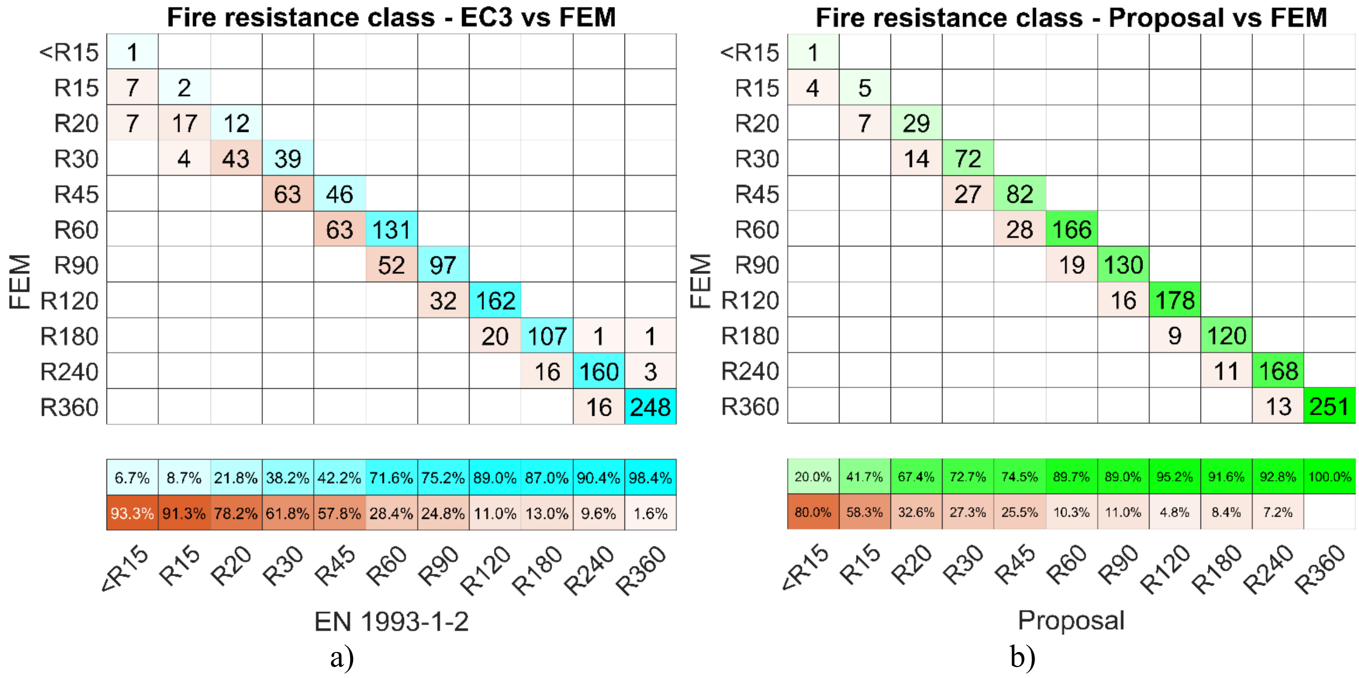

Figure 6. Fire resistance class misclassification for T_{crit}=550°C: a) EN1993-1-2; b) Proposed formulation.

Finally, the consequences of the use of the two proposals for the classification of fire resistance was investigated, assuming that the results of the numerical analysis provide the actual resistance class. For simplicity, it was considered that the resistance requirement is met until the temperature does not exceed T_{crit}=550°C. Therefore, for each of the studied steel-insulation configurations the times t_{crit} for which the critical temperature T_{crit} was exceeded in the numerical analyses were identified and the associated resistance classes were determined for both formulations. Since the number in the class label, e.g. 15 in R15, represents the minutes for which the resistance of the steel element is guaranteed, the fire resistance class was determined as the highest class time exceeded by t_{crit}, e.g. an analysis with t_{crit}=32 minutes is classified as R30. The results of the classification are reported in two confusion matrices in Figure 6 comparing the classification of numerical analyses with the ones of the EN1993-1-2 and the proposal, respectively. The diagonal values correspond to the number of correct identifications for each resistance class, i.e. same classification as for the numerical analyses, while out-of-diagonal values represent the misclassified resistances, where over- and underestimated classes are found above and below the diagonal respectively. It can be observed that the proposal allows for a better classification as a higher number of analyses are found on the diagonal in respect to EN1993-1-2. The analyses misclassified with the proposal, see Figure 6b, are always below the diagonal and therefore on the safe side, and never for more than one class. As expected, more relevant misclassifications are found for lower classes, when the time between two classes is smaller than for higher classes. Instead, the misclassified analyses obtained with the EN1993-1-2 formulation (Figure 6a) sometimes differ from the classification of finite element analyses for more than one class and are not always on the safe side. In fact, a too conservative classification is obtained for the lowest classes, where some analyses cannot even be classified in the lowest resistance class (<R15), while some analyses are unsafe for the highest classes, where a variation of one class implies a difference in t_{crit} of 60 minutes or 120 minutes. The accuracy of the classifications can be evaluated with a synthetic indicator that spans from 0 (no class correctly identified) to 1 (all classes correctly identified), defined as

the ratio between the sum of the diagonal values and the sum of the diagonal and off-diagonal values. This indicator assumes the value of 0.74 and 0.89 for the EN1993-1-2 and the proposal respectively.

5 CONCLUSIONS

In this paper a new analytical formulation based on a mass lumped approach is proposed to predict the temperature of insulated steel elements. The proposed formulation is suited for heavily insulated steel, widening the applicability range of the current equation provided in EN1993-1-2, which was demonstrated to be inaccurate for insulation materials with relatively high heat capacity C. In particular, in contrast with the equation provided in EN1993-1-2, in which it is conservatively assumed that the temperature of the exposed surface equals the temperature of the surrounding gas, the new predictive equation is based on more realistic heat flux boundary conditions. In order to emphasise the improvement introduced, results of a parametric analysis consisting of 1-D heat-transfer finite element analyses were compared with the predictions of the proposed and the EN1993-1-2 formulations. Different steel-insulation configurations, obtained by varying the insulation properties and the steel and insulations thicknesses, were investigated for an exposure to an ISO834 fire for 360 minutes. The proposed formulation always ensured safe or just slightly unsafe predictions (unsafe for no more than 20°C), while the EN1993-1-2 formulation gave both safe and unsafe predictions and was significantly unsafe for high values of the ratio between the insulation and the steel heat capacities μ. In specific, considering only steel temperatures above a reference critical temperature above which it is assumed that a protected steel member has lost its bearing capacity, i.e. 550°C, the EN1993-1-2 gives predictions that are always safe for μ<7 , always unsafe for μ>14, and can be both safe and unsafe otherwise. The proposed formulation instead, provides safe predictions that fit very well the safe 0 to +10% range. In addition, the consequences of the employment of the two different formulations were quantified in terms of fire resistance class, assuming 550°C as the reference critical temperature. It was observed that a more accurate classification is obtained with the new proposal, whereas a more relevant misclassification was found considering the EN1993-1-2 equation, for which too conservative and unconservative classifications were obtained for low and high fire resistance classes, respectively. In light of the presented analysis, the proposed formulation is suggested for heavily insulated steel sections, especially for μ>14, but it can also be employed regardless from the value of μ. More thorough numerical analyses, e.g. 2-D, and experimental results will be considered in future developments for further validations, as well as a more detailed evaluation of the consequences of the used of different predictive equations.

ACKNOWLEDGMENT

The support received from the Italian Ministry of Education, University and Research (MIUR) in the frame of the ‘Departments of Excellence’ (grant L 232/2016) is gratefully acknowledged

REFERENCES

1. National Institute of Standards and Technology – NIST (2004), Fire Protection of Structural Steel in High-Rise Buildings.
2. Leborgne H., Thomas L. (1999), Techniques de protections rapportées des structures en acier, Constr. Met. (CTICM) 3 pp. 123–135
3. Mariappan T. (2016), Recent developments of intumescent fire protection coatings for structural steel : a review, J. Fire Sci. 34 (2) pp. 120–163.
4. L.-H. Han, K. Zhou, Q.-H. Tan, T.-Y. Song (2016). Performance of Steel-Reinforced Concrete Column after Exposure to Fire: FEA Model and Experiments. Journal of Structural Engineering, 142, 9
5. J. P. C. Rodrigues, A. J. M. Correia, T. A. C. Pires (2015). Behaviour of composite columns made of totally encased steel sections in fire, J. Construct. Steel Res., 105 .pp. 97–106
6. Z.-F. Huang, K.-H. Tana, W.-S. Tohb, G.-H. Phnga (2008). Fire resistance of composite columns with embedded I-section steel - Effects of section size and load level, J. Construct. Steel Res., 64 pp. 312–325

7. Z.-F. Huang, K.-H. Tana, G.-H. Phnga (2008). Axial restraint effects on the fire resistance of composite columns encasing I-section steel, J. Construct. Steel Res., 63 pp. 437–447
8. Fulmer G.E., Method of Making a Fire-Retardant Product Having a Foamed Lore and a Fire-Retardant Protective Layer, 1982. US 4349494.
9. Zhang Q., Li V.C. (2015), Development of durable spray-applied fire-resistive engineered cementitious composites (SFR-ECC), Cement Concr. Compos. 60 pp. 10–16.
10. Jerome Randaxhe, Nicoleta Popa, Olivier Vassart, Nicola Tondini (2021). Development of a plug-and-play fire protection system for steel column, Fire Safety Journal, 121
11. European Comitee for Standardisation (2005). Eurocode 3 Design of steel structures - Part 1-2: General rules - Structural fire design.
12. Wickström U. (1985). Temperature analysis of heavily-insulated steel structures exposed to fire. Fire Saf J 9, pp. 281-285.
13. ECCS Technical Committee 3 (1983). European Recommendations for the Fire Safety of Steel Structures. Amsterdam: Elsevier Scientific Publishing Company.
14. Melinek S.J., Thomas P.H. (1987). Heat flow to insulated steel. Fire Saf J 12, pp. 1–8.
15. Wang Z.-H., Kang H.T. (2006). Sensitivity study of time delay coefficient of heat transfer formulations for insulated steel members exposed to fire. Fire Saf J 41, pp. 31-38.
16. Wong M.B., Ghojel J.I. (2003). Sensitivity analysis of heat transfer formulations for insulated structural steel components. Fire Saf J 38, pp. 187-201
17. Franssen J.M., Gernay T. (2017). Modeling structures in fire with SAFIR®: theoretical background and capabilities. J Struct Fire Eng;8(3):300–23.
18. Franssen J.M., Schleich J.B., Cajot L.G. (1995). A simple Model for the Fire Resistance of Axially-loaded Members According to Eurocode 3. Journal of Constructional Steel Research, 35, pp. 49-69.
19. C. Couto, P. Vila Real, N. Lopes, B. Zhao (2015). Resistance of steel cross-sections with local buckling at elevated temperatures. J. Construct. Steel Res., 109, pp. 101-114.
20. Possidente L., Tondini N., Battini J.M. (2022). Torsional and flexural-torsional buckling of compressed steel members in fire. J. Construct. Steel Res., 171

ASSESSMENT OF STRUCTURAL STEEL MEMBERS TEMPERATURES IN OPEN CAR PARK FIRES: DIFFERENT MODELLING APPROACHES

Xia Yan[1], Marion Charlier[2], Thomas Gernay[3]

ABSTRACT

Open car parks, as defined based on ventilation conditions, are one of the most common types of car park buildings. For such structures, adopting a performance-based structural fire design based on localised fires is often justified and allowed because the fire does not reach flashover. As this approach requires assessing the temperatures in the structure, this paper focuses on the numerical analysis of the temperatures reached in open car park steel beams under localised fires through different approaches. Simple analytical localised fire models and advanced CFD-FEM coupling methods are used to evaluate the beam temperatures. Several parameters are considered and varied: the dimensions of the steel elements, layout of burning vehicles, galvanization of the steel, and the modelling approaches. Results show that the temperatures reached in the investigated steel profiles are influenced by the location and number of burning vehicles; open car park fires generate thermal exposure conditions vastly different from the nominal fires. Galvanization of the steel profiles has the effect of delayed heating and reduced peak temperature under open car park fires. In terms of the modelling approach, Hasemi model is overconservative and gives erroneous results with galvanization, while adopting an advanced CFD-FEM modelling approach shows advantages and benefits for the performance-based design of open car parks in fire conditions.

Keywords: Open car park, localised fire, steel frame, numerical modelling, CFD-FEM.

1 INTRODUCTION

In open car parks, a spatially uniform temperature field does not capture the thermal exposure conditions for the structure. Instead, localised fire models are preferred to simulate burning cars and assess the heating of adjacent structural members. The definition of open car park depends on the country or jurisdiction under consideration [1], and it usually relies on a ratio of openings to surface of the boundaries of enclosure (openings present on opposite façades also have an influence). Modelling of localised fires can either be based on simple models, e.g., the models by Heskestad [2], Hasemi [3], and LOCAFI [4], which have each their field of application; or on advanced numerical modelling such as computational fluid dynamics [5]. In previous studies, the Hasemi model was used to analyse the thermal effect from burning vehicles on a steel beam [6] and to analyse multi-story car parks [7]. In another study, the Hasemi and the LOCAFI models were applied to study the fire performance of a steel open car park subjected to the fire scenario relevant for the columns [8]. While these studies provided insights into the thermal response of structural members in car park fires, no comparison of the temperatures predicted by different modelling approaches were performed, with the exception of a study that suggested that application of the Hasemi model led to

[1] Department of Civil and Systems Engineering, Johns Hopkins University, Baltimore, U.S.A. (now work at Simpson Gumpertz & Heger)
e-mail: xyan18@jhu.edu, ORCID: https://orcid.org/0000-0002-1263-3417
[2] ArcelorMittal Steligence, Esch-sur-Alzette, Luxembourg
e-mail: marion.charlier@arcelormittal.com, ORCID: https://orcid.org/0000-0001-7690-1946
[3] Department of Civil and Systems Engineering, Johns Hopkins University, Baltimore, U.S.A.
e-mail: tgernay@jhu.edu, ORCID: https://orcid.org/0000-0002-3511-9226
https://doi.org/10.6084/m9.figshare.22215736

more conservative thermal actions than the FDS-FEM coupling [9]. Further, the effect of steel galvanization on the temperature rise in steel framing members has not been studied in the context of open car park fires, yet galvanization is expected to affect the heat transfer through a reduction of the steel emissivity. This research therefore aims to assess the influence of galvanization when assessing the steel beam temperatures in an open car park, and to perform a systematic comparison of simple and advanced modelling approaches. This study focuses on the analysis of the temperatures reached in open car park steel beams subjected to car fires. Various modelling approaches are adopted to simulate the localised fires. Both simple analytical localised fire models and advanced CFD-FEM (Computational Fluid Dynamics – Finite Elements Method) coupling methods are used. The simple models in this study include the Heskestad [2], Hasemi [3], and LOCAFI [4] models. As each of these models have their own scope of application, the choice made between these models depends on the structural member under consideration (beam or column) and on its relative position from the burning vehicles. For the advanced numerical modelling, the FDS software is adopted with two methods to interface the FDS simulation of the localised fires with the subsequent FEM thermal analysis. The first one uses the concept of Adiabatic Surface Temperature (AST), while the second method, referred to as the FDS-FEM interface, uses a transfer file containing the gas temperatures and radiant intensities from FDS in a format readable by the FEM software. In addition, analyses are carried out to investigate the effects on steel temperatures of parameters including the dimensions of the steel members, the layout of burning vehicles, and galvanization of the steel. The case study considers a medium-sized multi-story open car park with a typical steel-concrete composite structure with steel framing and concrete flat slabs.

2 DEFINITION OF THE CAR PARK LAYOUT

2.1 Steel beams

The study focuses on a medium-sized multi-story open car park [9]. The distance between the floor and the bottom part of the ceiling is 2.5 m. The floor plan of the car park is 60 × 48 m, with 5 × 2.5 m standard parking bays. The structure is a steel-concrete composite structure with steel framing and concrete flat slabs. Two members are considered for the beams: a steel hot rolled profile IPE450 (common design in composite steel-concrete car parks for 16 m primary beams spaced 2.5 meters apart), and a steel hot rolled profile HEA600 (common design for 16 m primary beams spaced 5 meters apart) [9]. The dimensions of the profiles are shown in Figure 1. No fire protection is applied to the structure. To study the influence of galvanization on steel temperatures, the analysis is conducted for both ungalvanized profiles and galvanized profiles. Following EN 1993-1-2 [10], the emissivity of ungalvanized steel is taken as 0.7 (value independent of the temperature). The thermal behaviour of the galvanized steel is the same as that of ungalvanized steel except that the emissivity is 0.35 up to first heating to 500 °C, and 0.7 beyond. This is because the zinc coating applied on the surface of the steel irreversibly melts at a temperature of 500 °C.

2.2 Localised fires: burning cars layout

The heat release rate (HRR) for burning vehicles (class 3 cars) is adopted from the CTICM Guidebook for the verification of open car parks subjected to fire [11]. This HRR curve car was obtained from experimental campaigns (more details can be found in [12]). In “Development of design rules for steel structures subjected to natural fires in closed car parks” [12] , an experimental campaign which took place in a semi-closed carpark with large dimensions (85x55x3m) is described. The time shift of fire propagation between nearby cars was observed and served as reference for open car park fire design. Thus, the ignition of cars next to the first car igniting the fire is delayed by 12 minutes.

For the heating of the steel beams, three scenarios were considered that involve between one and three burning cars, as shown in Figure 2. In the first scenario, a single car is burning, and it is positioned right below the beam. In the second scenario, a single car is burning, but with an offset from the axis of the beam. This layout is representative of situations where the beam is located above the boundary between two adjacent car park bays. In the third scenario, three cars are burning underneath the beam, which axis is aligned with the middle car.

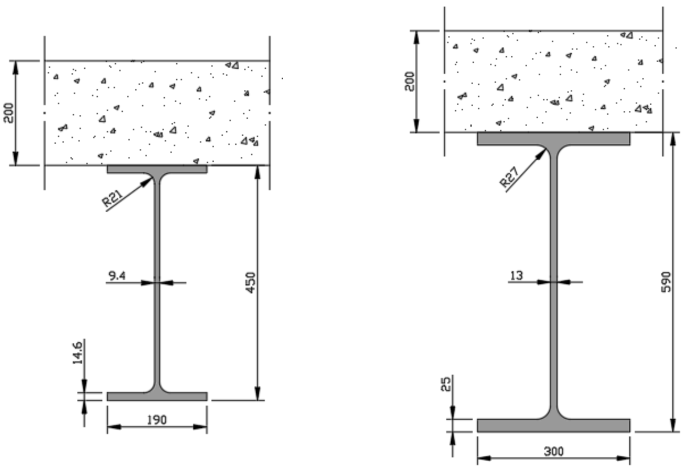

(a) IPE450 (b) HE600A

Figure 1. Dimensions of the steel beam profiles (units: mm).

Fire scenario	Layout	Heat release rate
1	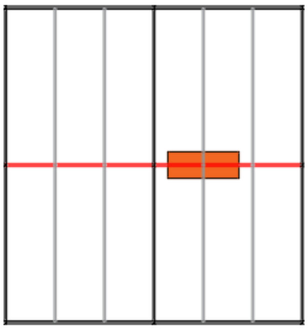	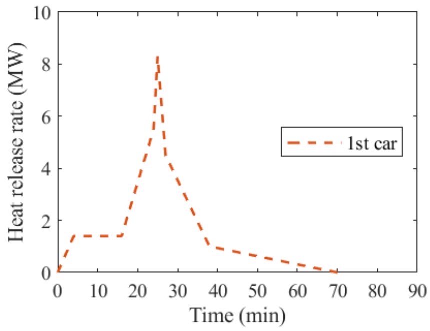
2	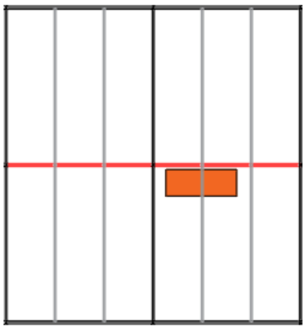	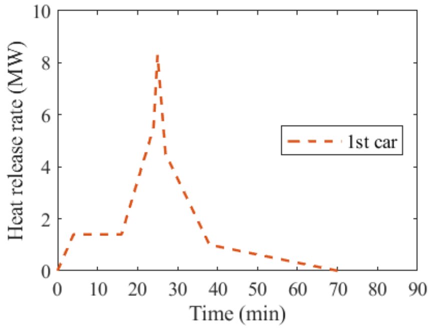
3	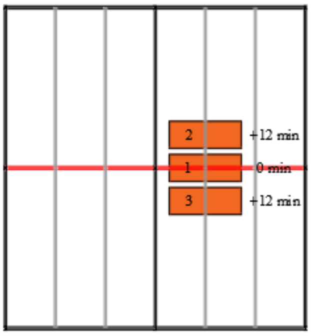	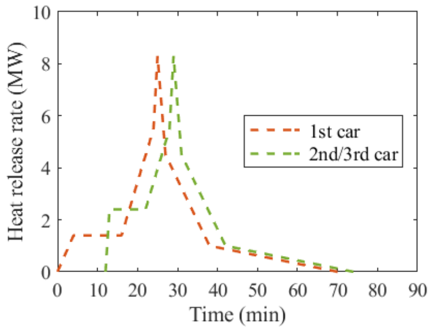

Figure 2. Fire scenarios considered for the modelling of the thermal exposure on steel beams (burning cars are shown in orange, structure of interest is shown in red).

The Guidebook from CTICM [11] recommends a scenario with seven cars placed transversally when studying the fire response of open car park beams. Given that the present study focuses on the heating modelling at a given section, the scenario with seven cars was not further considered. This assumption was validated by localised fire analyses conducted in OZone [13] (in accordance with the Annex C in EN1991-1-2 [14]). Indeed, these analyses allowed to verify that the considered beam temperatures under five burning cars and three burning cars (located transversally in the mid-span cross-section of both the IPE450 and HE600A sections) are similar, as shown on Figure 3. As a result, it can be assumed that peak steel temperatures in the beams would not be higher with seven cars transversally than with three cars.

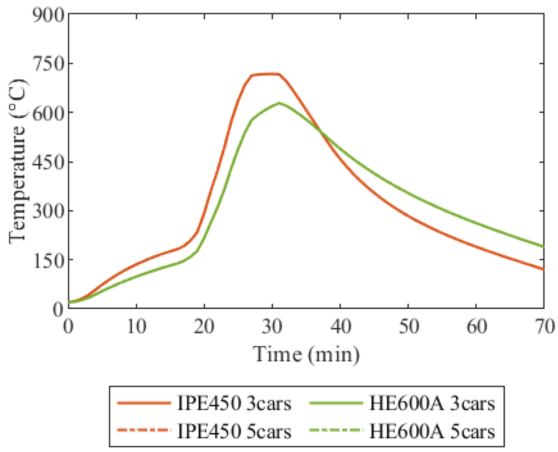

Figure 3. Temperature in IPE450 and HE600A beams when subjected to 3 and 5 burning cars positioned transversally to the beam axis, as calculated with OZone (localised fires). The temperature curves for 3 and 5 cars for a given profile are superposed.

3 THE FIRE MODELLING APPROACHES

3.1 Application domain

Both simple models and advanced modelling approaches are available for simulating member temperatures under localised fires. Benchmarking against test data is provided in a recent study by the authors [15]. The main features of the models are summarized hereafter.

The simple modelling approaches for localised fires include the Heskestad, Hasemi, and LOCAFI models. The Heskestad model is used to evaluate the flame temperature along the vertical centreline of the fire when the flame is not impacting the ceiling (e.g., for columns coinciding with the centreline of the fire or for part of the beam located just above the fire). The Hasemi model evaluates the heat flux received by the unit surface area at the ceiling level when the flame touches the ceiling (e.g., for beams or for column tops). The LOCAFI model calculates the radiative heat flux received by a vertical member not engulfed in the fire area (e.g., a column). As these models have different scopes of application, the selection of the applicable simple model results from the situation which is under consideration.

Advanced numerical modelling approaches rely on CFD to simulate the localised fire. A commonly used tool is FDS [5]. There are two main approaches to interface a FDS simulation with a subsequent FEM thermal analysis. The first uses the concept of Adiabatic Surface Temperature (AST) to transfer the thermal boundary information [16]. It assumes the surface to be a perfect insulator and the net heat flux is thus zero. The fictitious temperature T_{AST} is calculated based on the incident radiative heat flux and the gas temperature near the surface [17]. Then the T_{AST} is applied to the FEM thermal analysis as thermal boundary condition. This method is referred to as the FDS-FEM AST method. The second method is referred to as the FDS-FEM interface method. It uses a transfer file containing the gas temperature and radiant intensities in the field of interest in FDS in a format readable by the FEM software [9]. Then the transfer file is processed by the FEM software that interprets the quantities in terms of thermal boundary conditions [18].

Figure 4 shows the applicable fire models based on the configuration between the localised fire and the steel member. The study focuses on beams. When using simple models for analysing beam sections outside the fire area (section ‘B1’ and ‘B2’), the heat flux should be taken from the Hasemi model. However, if beam sections are inside the fire area (section ‘B3’), the heat flux should be taken as the maximum between the Hasemi flux and the flux computed based on the flame temperature from the Hesketad model. When selecting CFD-based modelling approaches, the FDS-FEM AST method is applicable to all configurations. The structural frame members should be included in the FDS model when adopting the AST method. The FDS-FEM interface method is applicable for structural members that are far from the fire source (section ‘B1’); the relevant distance being such that the presence of the structural members does not noticeably affect the continuity of the temperature and radiative fields. These frame members should be omitted in the FDS model when using the interface method [15]. The ability to omit the frame members from the FDS simulation and to rely on an automatic transfer file between FDS and a FEM software is advantageous in terms of modelling effort. For sections closer to the heat source, which significantly influence the mass flow or radiative flow in the compartment (section ‘B2’), the frame members should be included in the FDS model and the AST method is preferred for the transfer of thermal information; except if the section is right above the heat source (section ‘B3’), in which case owing to symmetry both FDS-FEM AST and FDS-FEM interface methods are applicable.

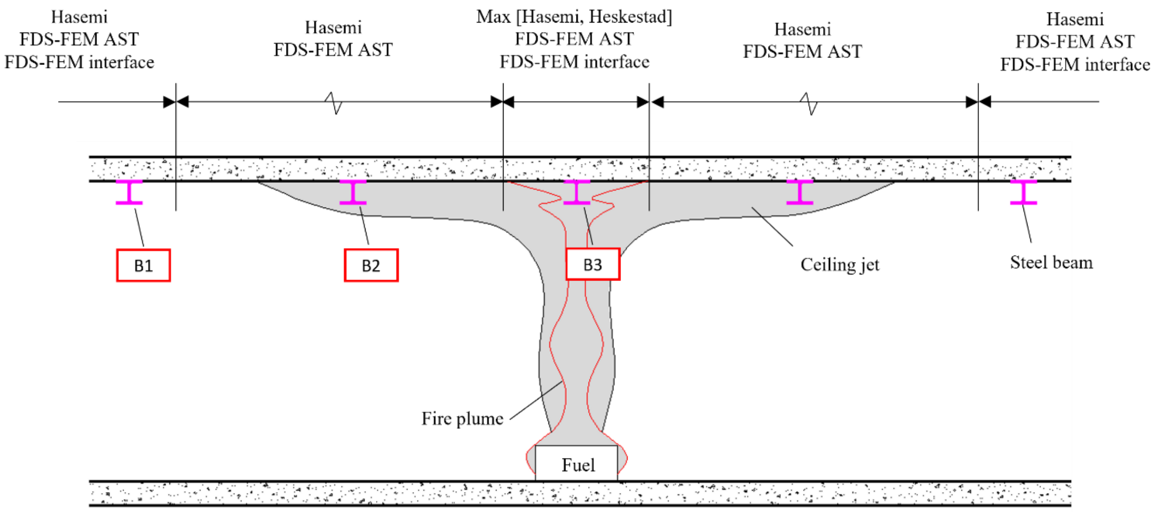

Figure 4. Application domain of localised fire modelling approaches for localised fires (not to scale).

3.2 CFD simulations and analytical models: fire development

The Fire Dynamics Simulator (FDS, version 6.7.1) is adopted to run the CFD simulations. The computational domain in FDS is 30 × 22.5 × 3 m (length × width × height) for the simulations of fire scenarios. A sensitivity analysis was conducted on the computation domain to minimize the border effects with respect to the smoke flow. Burning cars are modelled as rectangular blocks with dimension of 4.8 × 1.8 × 0.3 m each. The heat release rate of the burning car is taken as the heat flux curves in Figure 2. Based on research for car fires, the soot yield is set to 0.22 [19], and heat of combustion is set to 44.4 MJ/kg, typical of gasoline [9]. A mesh size of 0.1 × 0.2 × 0.1 m is selected. The special resolution $R^* = dx/ D^*$, where dx is the characteristic length of a cell for a given grid and D^* is the characteristic diameter of a plume, calculated with the selected mesh size falls into a reasonable range of 1/10 ~ 1/20 [5].

The fire development is also investigated with the simple models described above. The burning car is modelled as a 3.2 m-diameter circular plan area with equivalent fire area for a typical car park spot. The axis of the localised fire is at the center of car. The heat release rate of the burning car is consistent with the heat flux curves in Figure 2.

3.3 FEM simulations: heat transfer to the steel beams

The heat transfer analysis to the steel member is conducted with the FEM software SAFIR [21]. SAFIR allows applying thermal boundary conditions to the surfaces of the steel members which are imported from

FDS simulations or from the simple localised fire models provided in the Eurocodes, i.e., Hasemi, Heskestad, and LOCAFI (i.e., solid flame) [20]. A series of 2D thermal analyses are conducted at each longitudinal integration point of the structural member. Thermal analysis of the cross section is carried out using solid conductive elements and capturing the convection and radiation at the boundaries. The equations to capture radiative and convective heat flux to the steel member are in accordance with the Eurocode EN1991-1-2 [14] and are detailed in [21]. Longitudinal variations in temperature distributions are captured by analysing several cross-sections along the beam length; heat transfer in the longitudinal direction of the steel beam and column is neglected as the longitudinal dimension of the member is order of magnitudes larger than the thickness of the plates.

The steel member is included in the FDS analysis when using the AST method. 14 sensors are attached onto the structural surface of cross sections at an interval of 0.2 m in the longitudinal direction to measure the AST. Then, the AST outputs from FDS are applied onto the SAFIR 2D thermal model as boundary condition (temperature-time Frontier constraint). For the interface method, the structural member is not included in the FDS model. The gas temperature and radiant intensities are output from FDS at the grids surrounding the structural member with a time step of 10 seconds and written into a transfer file. The transfer file is applied onto the SAFIR 2D thermal model as thermal boundary condition (Flux constraint).

When the fire development is computed through analytical models, different flux constraints are available in SAFIR. The flux constraint 'Hasemi' computes the flux applied to each point of integration of the steel beams based on the simple Hasemi model, for situations where the localised fire flame is touching the ceiling. For columns not engulfed into the fire, the LOCAFI model can be applied. SAFIR then evaluates the flux using the solid flame model, assuming that the burning car is represented by a cone shape fire. For members in the axis of the flame (columns and beams, if the localised fire flame is not touching the ceiling), the Heskestad model is applied, as depicted on Figure 4. The equations from Eurocode EN1991-1-2 are used to evaluate the flame temperature along the vertical axis of the fire. The heat flux to the member is then evaluated considering both the convective and radiative heat flux. It is worth noting that the Hesketad model is embedded in the flux constraint named 'LOCAFI' in SAFIR. With the flux constraint 'LOCAFI' applied, the heat transfer computation in SAFIR automatically shifts between the virtual solid flame model and the Heskestad model considering the relative position of the point of integration and the fire flame. When the point of integration (POI) is in the flame, a convective flux with the flame temperature and radiative heat flux with this temperature and a view factor of 1 are considered. The flame temperature is calculated by the Heskestad model in the centreline of the flame at the height of the POI. When the POI is located outside the flame, only the radiative heat flux is considered with the LOCAFI model.

The thermal properties of the steel are in accordance with Eurocode EN1993-1-2 [10]. The conductivity and specific heat vary with the temperature. The convection coefficient is taken as 35 W/m^{2}K, in accordance with Eurocode EN1991-1-2 for natural fire exposures [14]. The emissivity of the ungalvanized profiles is taken as ε = 0.7, while for the galvanized profiles, a newly developed material named GALVASTEEL is implemented in SAFIR: it is such that ε = 0.35 up to 500 °C and then ε = 0.7 beyond that. A mesh size of 0.01 m is adopted for all the thermal analyses (see Figure 5 (a) and (b)).

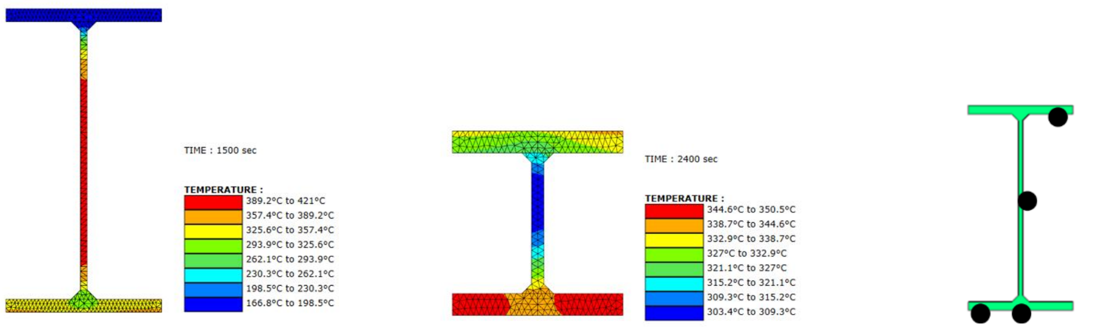

(a) Steel beam HE600A (b) Steel column HE240M (c) Node location

Figure 5. Finite element mesh for the thermal analysis of (a) HE600A, (b) HE240M, and (c) location of the nodes used to compute average steel temperatures.

4 TEMPERATURE DEVELOPMENT IN THE BEAMS

4.1 Fire Scenario 1

Localised fire scenario 1 includes a single burning car directly underneath the beam (Figure 2). The steel beam temperatures at the lower flange of the mid-span cross section are plotted in Figure 6 (a) and (b). Solid and dashed lines are used for the ungalvanized and galvanized profiles, respectively. The two FDS-FEM methods yield similar results for the IPE450 profile, while the interface method is slightly more conservative than the AST method for the HE600A profile. This verifies that for the structures located at the ceiling level and right above the heat source, the interface method is applicable, as shown in Figure 4 B3. In the FDS interface simulation, the beam is not modelled in FDS, but the flat slab ceiling is. When comparing the member temperatures reached in different profiles, the IPE450 experiences temperatures higher by almost 120 °C than HE600A due to the higher section factor.

Galvanization reduces the emissivity and hence the amount of heat transferred into the section. Both the AST method and interface method indeed predict reduced temperatures when the profile is galvanized. The peak temperature is reduced by 53 °C in the web and 69 °C in the flange of IPE450 at the center section. As for the HE600A profile, the peak temperature is reduced by 68 °C in the web and 73 °C in the flange at the center section. The time to reach the peak temperature is also delayed by about 1 minute for IPE450 and 2 minutes for HE600A due to galvanization.

Results are also given for simple models of localised fires. For the configuration of scenario 1, two analyses are completed. The first is with the Hasemi model. Strictly speaking, the Hasemi model only applies when the flame touches the ceiling, while in the early stage of the fire this is not the case. Evaluating the heat flux throughout the localised fire event with the Hasemi model ("Hasemi" flux boundary condition in SAFIR) is thus expected to yield conservative results. Another approach is to evaluate the flux based on the flame temperature from the Hesketad model. This second approach ("LOCAFI" flux boundary condition in SAFIR) evaluates the flame temperature along the vertical axis of the fire, then applies either the virtual solid flame model to compute radiative flux to the beam at the early stage of the fire when it is outside the flame or computes the convective and radiative flux to the beam once it is inside the flame. In this second approach, the FE software automatically transitions from the former flux computation to the latter based on the flame height. To indicate that both LOCAFI and Heskestad models are combined in this second approach, the curves in Figure 6 are labelled as LOCAFI/Heskestad.

The Hasemi model significantly overestimates the steel temperatures, compared to the FDS-FEM AST/interface method. The overestimation is greatest during the initial heating phase. At 15 min, the temperature difference between the Hasemi model and AST method reaches 420 °C in the lower flange of the ungalvanized HE600A profile, as shown in Figure 6 (1). Differences in peak temperatures are also notable; the peak temperature difference between Hasemi model and AST method is 260 °C in the lower flange of ungalvanized HE600A profile. Another issue with the Hasemi model is that it erroneously represents the influence of galvanization on the member temperature. Contrary to the observation with FDS-FEM, Hasemi yields slightly higher steel temperature in the galvanized profile compared with the ungalvanized one. The causes for these shortcomings of the Hasemi model are discussed in Section 4.3.

Regarding the LOCAFI/Heskestad model ("LOCAFI" flux boundary condition in SAFIR), during the initial stage when the HRR from the burning car is small and the analysed section is outside the flame, lower temperatures are obtained compared with the FDS-FEM AST method. In this initial stage, the flux is computed based on the virtual solid flame, hence convection is neglected. After the flame touches the ceiling and the section is inside the flame, both the convective and radiative heat flux are taken into account, evaluated based on the flame temperature from the Heskestad model. The model yields similar estimations of the peak temperatures reached in the profiles as the FDS-FEM AST method. The ability of this implementation of the simple model to transition from virtual solid flame when the member is outside the flame to convection and radiation once the member becomes engulfed is clearly visible in the results, with a sudden increase in temperatures that matches that obtained with FDS. It also captures the influence of galvanization with lower emissivity leading to lower temperature.

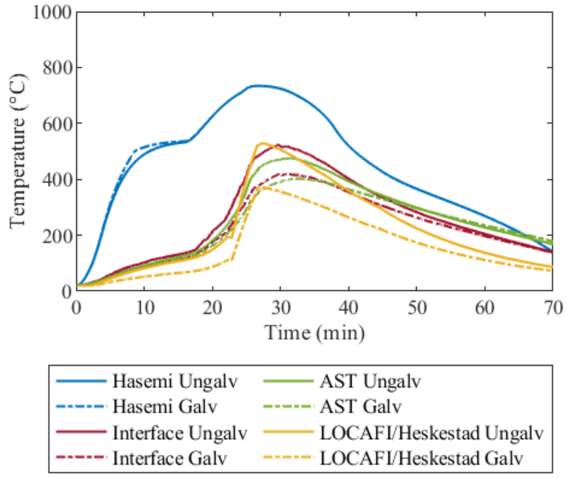

(a) Lower flange of HE600A – Scenario 1

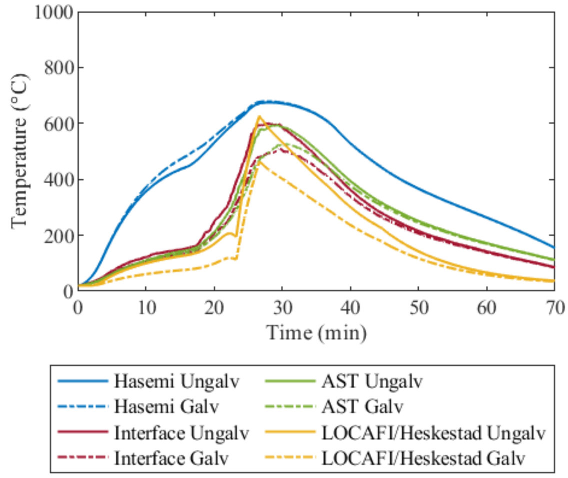

(b) Lower flange of IPE450 – Scenario 1

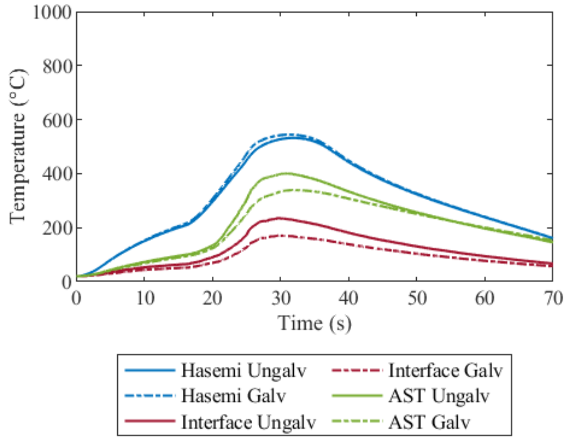

(c) Lower flange of HE600A – Scenario 2

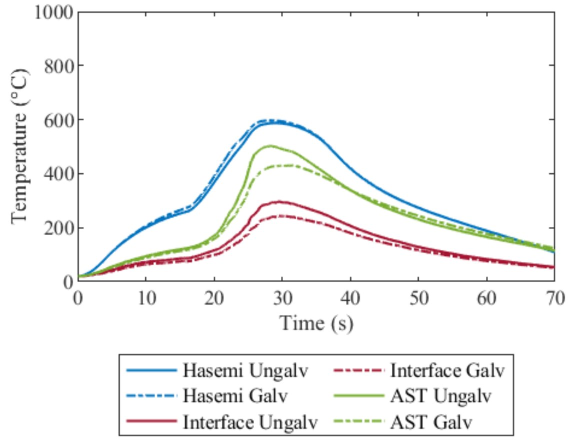

(d) Lower flange of IPE450 – Scenario 2

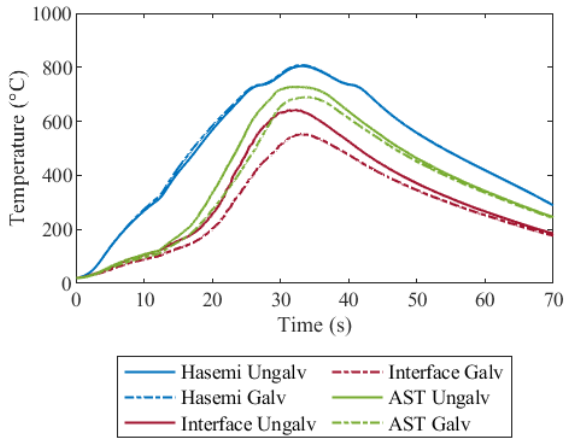

(e) Lower flange of HE600A – Scenario 3

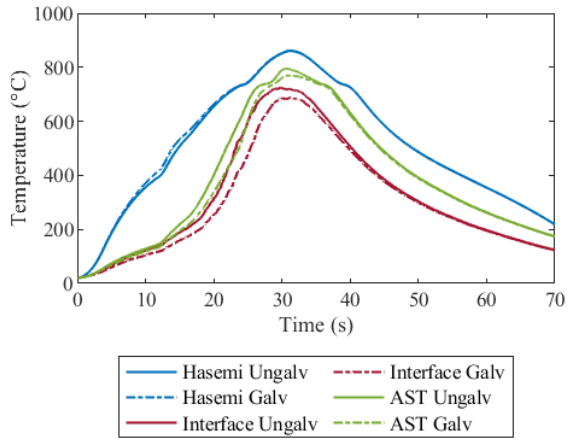

(f) Lower flange of IPE450 – Scenario 3

Figure 6. Temperature evolution in the lower flange of HE600A and IPE450 profiles under the three scenarios.

4.2 Fire Scenarios 2 and 3

The steel beam temperatures at the mid-span cross section obtained from various methods under localised fire scenarios 2 and 3 are shown in Figure 6 (c) to (f). The FDS-FEM interface method yields lower member temperatures than the FDS-FEM AST method, especially at the lower flange. It is worth nothing that the steel beam is not modelled in FDS with the interface method. Omitting the beam is necessary to avoid unwanted averaging effects in the spatial integration of the temperature and flux fields by the FEM as shown in [15]. However, this means the impact of the presence of structural member on the fire development is neglected. The discrepancy in terms of the member temperature obtained with the FDS-FEM AST and interface method indicates that when the section is not right above the heat source, the influence of the presence of the structural member should not be neglected. Thus, the interface method is not recommended for this situation. Due to galvanization, the peak temperature is reduced by more than 60 °C for HE600A and IPE450 profiles in fire scenario 2.

In fire scenario 3, the galvanization has less dominant effect on the peak temperature due to the more intense heating. The peak temperatures reached in fire scenario 2 are lower than those reached in fire scenario 1 due to the offset of the beam, while the peak temperatures reached in fire scenario 3 are higher than those reached in fire scenario 1 due to the higher heat release rate when three cars are burning instead of one. When comparing the member temperatures in different profiles, IPE450 experiences temperatures about 60 °C to 100 °C higher than the HE600A due to the different section factor.

The Hasemi model again overestimates the member temperatures compared with the FDS-FEM AST method. It is on the conservative side, with discrepancies not as large as for scenario 1, but still possibly making it overconservative for design. As observed previously, the Hasemi model also yields erroneous results on the effect of galvanization, because it cannot correctly capture the effect of a change in emissivity on the absorbed heat flux (See Section 4.3).

The peak temperatures obtained from the FDS-FEM AST method are summarized in Table 1. The listed values are obtained at the time of peak temperature in the profile and are the average of the temperatures at the bottom of lower flange, center of lower flange, mid web, and bottom of upper flange, as shown in Figure 5 (c). When subject to open car park fires, galvanization has the effect of delayed heating and reduced peak temperature. As listed in Table 1, the peak temperatures in HE600A are reduced by more than 60 °C and those in IPE450 are reduced by more than 50 °C under localised fire scenarios 1 and 2 when galvanization is applied to the steel members. The influence of galvanization on reduced peak temperature is less dominant in localised fire scenarios 3, see Figure 6. This is because the zinc coating applied on the surface of the steel melts at a temperature of 500 °C, so the member temperatures gradually catch up with the fire temperature for severe fire exposures.

4.3 Limitations linked to the use of Hasemi model

It was shown that the Hasemi model leads to higher predicted steel temperatures than the FDS-FEM coupling methods. The main reasons of this noticeable difference are the following:

(i) The Hasemi model assumes that the flame touches the ceiling. It is an empirical model which flux is calibrated on an experiment during which the flame was touching the ceiling. Figure 7 shows the HRR cloud map captured at different time steps in the FDS simulation of localised fire scenario 1. It can be observed that the flame is not impacting the ceiling (grey block in Figure 7) before 1000 s (growing phase in the HRR curve of class 3 car shown in Figure 2) and after 1900 s (cooling phase) in the FDS simulation. In other words, as can be observed in FDS modelling, the flame touches the ceiling during only one sixth of the whole fire duration.

(ii) The Hasemi model was derived from experimental tests in which the ceiling was made of perlite boards. The concrete slab in a car park behaves as a heat sink that absorbs a large amount of energy (larger than with perlite boards), which causes a decrease in gas temperature at the ceiling level.

(iii) The Hasemi model does not capture the shadow effect, i.e., all boundaries of the section receive the same heat flux with the value calculated at the point of integration in FEM software. For open sections with concave parts, the received heat flux evaluated by the Hasemi model is therefore overestimated.

Table 1. Peak temperatures of galvanized and ungalvanized profiles under localised fire scenarios (obtained from FDS-FEM AST method, averaged over the profile section).

Profile		Average temperatures under scenario 1 (°C)	Average temperatures under scenario 2 (°C)	Average temperatures under scenario 3 (°C)
HE600A	Ungalva	428	355	671
	Galva	369	309	628
	Difference	59	46	43
IPE450	Ungalva	551	453	749
	Galva	494	397	718
	Difference	57	56	31

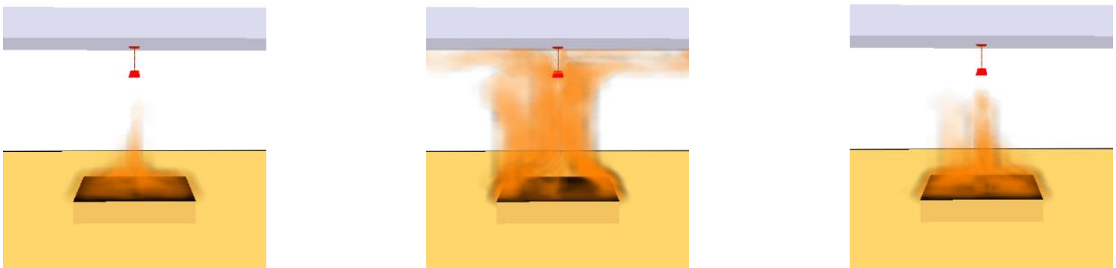

(1) t = 1000 s (Flame is not impacting ceiling)

(2) t = 1500 s (Flame is impacting ceiling)

(3) t = 1900 s (Flame is not impacting ceiling)

Figure 7. HRR cloud map obtained from FDS simulation of the localised fire scenario 1 shows that the flame does not touch the ceiling (grey block) for most of the fire duration.

Besides, the Hasemi model gives erroneous results when applied to a material with different thermal properties than the ones for which the model was calibrated. More specifically, Hasemi model gives higher member temperatures with lower emissivity. This is because the heat flux given by the Hasemi model is in fact inherently an absorbed heat flux, meaning that it does not depend on the thermal properties of the receiving member (because it is already implicitly multiplied by the thermal properties of the material for which it was calibrated). When using the Hasemi model, the net heat flux on the boundary of a solid is evaluated with Eq. (1).

$$\dot{q}_{net} = \dot{q}_{hasemi} - h_{hot}(T_s - T_{amb}) - \sigma\,\varepsilon\,(T_s^4 - T_{amb}^4) \tag{1}$$

where $\dot{q}_{hasemi}$ is the flux computed according to Eq. (C.4) of EN 1991-1-2 [14] (incoming “absorbed” flux from the plume) [10]; h_{hot} is the coefficient of convection on exposed surfaces; T_s is the temperature at the surface of the solid at the boundary; T_{amb} is the ambient temperature; σ is the constant of Stefan Boltzmann; ε is the emissivity of the material of the solid. As can be seen in Eq. 1, the incoming (absorbed) part is independent of the thermal properties of the solid, whereas the outgoing (re-emitted) part depends on h_{hot} and ε. In this study, the steel member is analysed in two configurations: ungalvanized (ε = 0.7) and galvanized (ε = 0.35). The incoming flux $\dot{q}_{hasemi}$ is the same for the two configurations, which does not capture the fact that reducing emissivity physically leads to less radiant heat absorbed in a solid. The outgoing flux, in contrast, accounts for the term ε and therefore will be larger for the material with larger emissivity (as the latter is able to re-radiate more heat to the far field as its temperature increases). The result is that the net heat flux on the boundary of the ungalvanized steel would be smaller than that of the galvanized steel. This contradicts the physics and erroneously leads to higher temperatures in galvanized steel members than in (otherwise identical) ungalvanized members.

This contradicts the physics and erroneously leads to higher temperatures in galvanized steel members than in (otherwise identical) ungalvanized members. A possible solution to circumvent this limitation is the following [22]. First, an equivalent hot gas temperature can be estimated using Eq. (2)., which equates the total incident heat flux from Hasemi's model to the incident heat flux from the equivalent hot gas temperature T_g. Next, these equivalent hot gas temperatures are applied as boundary conditions to the steel members, and heat transfer at the boundary is evaluated from convection and radiation taking into account the appropriate emissivity for galvanization. As the Hasemi incident flux varies with time, so do the equivalent hot gas temperatures. It is noted though that this method is not mentioned in the Eurocode and requires specific implementation.

$$\dot{q}_{hasemi} = 35\left(T_g - T_{amb}\right) + 0.7\left(T_g^4 - T_{amb}^4\right) \tag{2}$$

5 CONCLUSIONS

This study focuses on the temperatures reached in steel framing members subjected to open car park fire scenarios. A parametric study was carried out considering the influence of the steel profiles, layout and number of burning vehicles, galvanization of the steel, and the modelling approaches adopted. The following conclusions are drawn:

- When subject to localised open car park fire, galvanization has the effect of delayed heating and reduced peak temperature. The peak temperatures in the investigated steel beam profiles are reduced by more than 50 °C under a scenario with a single burning car. However, this effect is reduced when subjected to localised fires with multiple burning vehicles because the steel temperature largely exceeds the melting temperature of the galvanization. As temperature rise in the steel members is also delayed owing to the galvanization, the member critical temperature may be reached a few minutes later when the member is galvanized.
- In terms of modelling approach, the Hasemi model is overconservative in predicting the temperatures in the steel beams at the ceiling level under open car park fires. This is mostly due to the assumption in the Hasemi model that flames are touching the ceiling during the whole fire duration, which contradicts observations from FDS modelling. While this study shows that applying Hasemi in open car park fire studies would be conservative, it could in fact be recommended to adopt more advanced modelling techniques (e.g., CFD-FEM) to complete the design based on a fire prediction that is not overly severe.
- Another limitation of the Hasemi model is that, since it provides an absorbed heat flux, it incorrectly predicts that reduced steel emissivity leads to higher steel temperatures. Indeed, the predicted absorbed heat flux in Hasemi is independent of the emissivity but the reemitted heat flux decreases with a reduction in emissivity. In general, the Hasemi model cannot capture the effect of different thermal properties on the absorbed heat flux. If engineers want to model the temperature elevation in galvanized steel structures, they need to adopt a model that can account for the modified emissivity, such as a CFD-FEM approach with a suitable steel thermal model.

Future works could focus on further improvements of simple fire models for open car parks. Specifically, a unified simple model predicting the heat flux received by the different members of the structure would facilitate analyses. The estimation of the heat flux should capture the effect of the thermal properties of the receiving surface, unlike the current version of the Hasemi model. An important challenge is for simple models to capture the transition between different phases of the fire-structure interaction, including when the structural member becomes engulfed in the flame.

ACKNOWLEDGMENT

The authors declare the following financial interests/personal relationships which may be considered as potential competing interests: Under a license agreement between Gesval S.A. and the Johns Hopkins University, Dr. Gernay and the University are entitled to royalty distributions related to the technology SAFIR described in the study discussed in this publication. This arrangement has been reviewed and approved by the Johns Hopkins University in accordance with its conflict of interest policies.

REFERENCES

[1] F.S. of S.S. European Convention for Constructional Steelwork. Technical Committee 3, Fire Safety in Open Car Parks: Modern Fire Engineering, in: European Convention for Constructional Steelwork, 1993.

[2] G. Heskestad, Engineering relations for fire plumes, Fire Saf. J. 7 (1984) 25–32.

[3] A. Pchelintsev, Y. Hasemi, T. Wakamatsu, Y. Yokobayashi, Experimental and numerical study on the behaviour of a steel beam under ceiling exposed to a localized fire, Fire Saf. Sci. 5 (1997) 1153–1164.

[4] N. Tondini, C. Thauvoye, F. Hanus, O. Vassart, Development of an analytical model to predict the radiative heat flux to a vertical element due to a localised fire, Fire Saf. J. 105 (2019) 227–243.

[5] K. McGrattan, S. Hostikka, R. McDermott, J. Floyd, C. Weinschenk, K. Overholt, Fire dynamics simulator user's guide, NIST Spec. Publ. 1019 (2013).

[6] B. Fettah, Fire Analysis of Car Park Building Structures, (2016).

[7] C. Fang, B.A. Izzuddin, R. Obiala, A.Y. Elghazouli, D.A. Nethercot, Robustness of multi-storey car parks under vehicle fire, J. Constr. Steel Res. 75 (2012) 72–84.

[8] M. Sommavilla, N. Tondini, Fire performance of a steel open car park in the light of the recent development of the localised fire model" LOCAFI", (2020).

[9] O. Vassart, A. Morbioli, N. Tondini, J.-M. Franssen, S. Lechêne, An integrated modelling strategy between a CFD and an FE software, J. Struct. Fire Eng. 7 (2017) 217–233.

[10] E. 1993-1-2, Eurocode 3: Design of Steel Structures - Part 1-2: General Rules – Structural Fire Design, European Committee for Standardization (CEN), Brussels, 2005.

[11] B. Zhao, M. Roosefid, Guide pour la vérification du comportement au feu de parcs de stationnement largement ventilés en superstructure métallique, CTICM document (SRI – 11/110h– MR-BZ/NB), 2014.

[12] J.B. Schleich, L.G. Cajot, J.M. Franssen, J. Kruppa, D. Joyeux, L. Twilt, J. Van Oerle, G. Aurtenetxe, Development of design rules for steel structures subjected to natural fires in closed car parks (1997), EUR 18867EN, Rep. (1997).

[13] J.-F. Cadorin, J.-M. Franssen, A tool to design steel elements submitted to compartment fires—OZone V2. Part 1: pre-and post-flashover compartment fire model, Fire Saf. J. 38 (2003) 395–427.

[14] E. 1991-1-2, Eurocode 1: Actions on structures–Part 1-2: General actions–Actions on structures exposed to fire, Eur. Stand. (2002).

[15] X. Yan, T. Gernay, Numerical modeling of localized fire exposures on structures using FDS-FEM and simple models, Eng. Struct. 246 (2021) 112997.

[16] U. Wickström, D. Duthinh, K. McGrattan, Adiabatic surface temperature for calculating heat transfer to fire exposed structures, in: Proc. Elev. Int. Interflam Conf. Intersci. Commun. London, 2007.

[17] U. Wickström, S. Hunt, B. Lattimer, J. Barnett, C. Beyler, Technical comment—Ten fundamental principles on defining and expressing thermal exposure as boundary conditions in fire safety engineering, Fire Mater. 42 (2018) 985–988.

[18] M. Charlier, A. Glorieux, X. Dai, N. Alam, S. Welch, J. Anderson, O. Vassart, A. Nadjai, Travelling fire experiments in steel-framed structure: numerical investigations with CFD and FEM, J. Struct. Fire Eng. (2021).

[19] X. Deckers, S. Haga, N. Tilley, B. Merci, Smoke control in case of fire in a large car park: CFD simulations of full-scale configurations, Fire Saf. J. 57 (2013) 22–34.

[20] T. Gernay, P. Kotsovinos, Advanced Analysis, in: Int. Handb. Struct. Fire Eng., Springer, 2021: pp. 413–467.

[21] J.-M. Franssen, T. Gernay, Modeling structures in fire with SAFIR®: Theoretical background and capabilities, J. Struct. Fire Eng. (2017).

[22] Zhao B., CTICM, email communication, Oct 6, 2022.

SiF 2022– The 12th International Conference on Structures in Fire
The Hong Kong Polytechnic University, Nov 30 - Dec 2, 2022

EFFECTS OF CLADDING MATERIALS ON THE FIRE RESISTANCE OF EXTERNAL LIGHT GAUGE STEEL FRAMED WALLS EXPOSED TO INTERNAL FIRE

Jashnav Pancheti[1], Mahen Mahendran[2]

ABSTRACT

This paper presents finite element heat transfer modelling of external light gauge steel framed (LSF) walls with autoclaved aerated concrete and brick veneer cladding exposed to fire from the inside. There has been research on the fire resistance of internal LSF walls (gypsum plasterboard layers on both sides of the cold-formed steel (CFS) studs) [1,2] and fire resistance of external LSF walls (gypsum plasterboard on the internal side and any cladding on the external side) exposed to fire from the external side [3–5]. But no research is available on the fire resistance of external LSF walls exposed to fire from the internal side and whether the cladding has any influence on the fire resistance of these LSF walls. Finite element heat transfer models were first validated against the fire test results presented in Refs. [3,5]. They were then used to evaluate the fire resistance of these LSF walls exposed to fire from the internal side. Two configurations with and without cavity insulation, when exposed to fire from the internal side, were investigated. When compared to internal LSF walls, while minor differences were noticed in the case of cavity insulated walls, a significant difference was observed when there was no cavity insulation in the wall.

Keywords: Cladding; light gauge steel; external wall; fire resistance

1 INTRODUCTION

Several cladding fire accidents have occurred recently endangering the lives of the occupants in those buildings. Unlike in high rise buildings where external cladding does not influence the structural performance of the building, external cladding is an integral part of the walls in light gauge steel framed construction. Hence fire resistance of cladding influences the structural fire performance of the cold-formed steel (CFS) studs as well as the stability of the wall and the entire building, especially in the case of load bearing walls. In Refs. [3–5] the fire resistance of three external LSF walls clad with autoclaved aerated concrete (AAC) panels, corrugated steel cladding and brick veneer cladding exposed to fire from the external side was investigated by conducting several fire resistance tests. But it is equally important to understand if the cladding has any influence on the fire resistance of LSF walls when exposed to fire from the internal side and how the stud temperatures compare with the results of an internal LSF wall exposed to fire. Figure 1 shows the cross-sections of typical external and internal LSF walls. This paper presents the results from a fire resistance test and finite element heat transfer models to understand the influence of cladding materials on the fire resistance of external LSF walls exposed to internal fires.

[1] PhD student, Queensland University of Technology,
e-mail: jashnav.pancheti@hdr.qut.edu.au, ORCID: https://orcid.org/0000-0002-4437-0690
[2] Professor, Queensland University of Technology
e-mail: m.mahendran@qut.edu.au, ORCID: https://orcid.org/0000-0001-7306-8821
https://doi.org/10.6084/m9.figshare.22215739

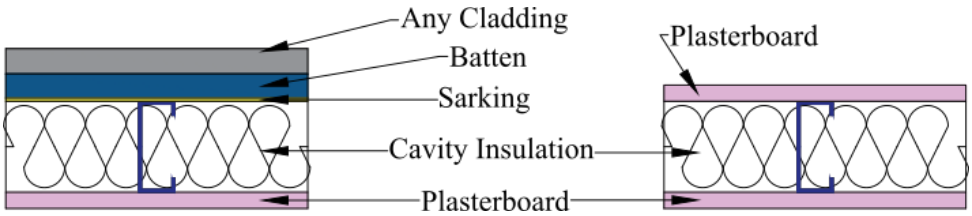

Figure 1. Cross-sections of typical external (left) and internal LSF walls (right).

2 METHODOLOGY

In the case of external LSF walls with corrugated steel cladding [4], two layers of 16 mm gypsum plasterboards were used on both sides of the stud. Hence when exposed to fire from the internal side, the temperature development in the studs would be very similar to internal LSF walls as the configuration is the same. The steel cladding has no direct influence on the temperature development in the wall and the studs. In the case of external LSF walls with AAC panels and brick veneer, the configuration is very similar to the cross-section shown in Figure 1. They can influence the temperatures in the wall and studs when exposed to fire from the internal side. Hence, only external LSF walls with AAC panels and brick veneer are considered in this study.

Two-dimensional finite element heat transfer analysis models were developed in ABAQUS as shown in Figure 2 (a). The details of the model are presented in Table 1. A solid part was first created along with any cavities and then partitioned accordingly to assign the material properties. This way, the tie constraints required are eliminated reducing the running time. The models were first validated using the fire test results presented in Refs. [2,3]. Apparent thermal properties of AAC, brick and insulation were used to account for physical changes in the material such as cracks, melting, loss of moisture etc. Using the validated models, a parametric study was conducted. Two wall configurations were considered for each cladding material – with and without cavity insulation. Hence a total of four heat transfer models were developed for the external LSF walls with two cladding materials – AAC panels and brick veneer. The heat transfer model developed for cavity insulated external LSF with AAC panels and the temperature development is shown in Figure 2. The wall consists of 75 mm thick AAC panels, 24 mm cavity (for batten), 90 mm deep CFS studs and glass fibre cavity insulation and a 16 mm thick fire rated gypsum plasterboard. In the case of LSF wall with brick veneer cladding, the bricks were 110 mm thick and 50 mm cavity (for ties) were the only differences. Cored brick units of void ratio 0.38 were used.

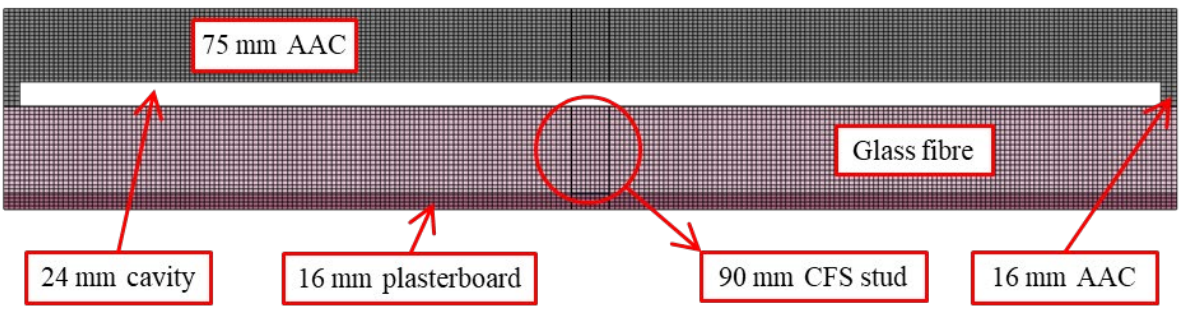

(a) Two-dimensional heat transfer ABAQUS model

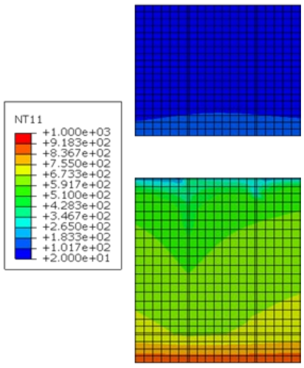

(b) Temperatures in the wall at 60 min (a small section of the model with CFS stud is shown)

Figure 2. Heat transfer model and results of external LSF wall with AAC panels.

Table 1. Finite element heat transfer model details

Parameter	Details
Model dimensions	AAC panels: 1.2 m (width) x 0.195 m (depth) Brick veneer: 1.2 m (width) x 0.266 m (depth)
Mesh size	Global: 5 mm Plasterboard: 4mm
Element type	DC2D4
Fire side boundary conditions	Radiation: Emissivity – 0.9 Convection: Convective heat transfer coefficient – 25 W/m2°C Sink temperature: Standard fire curve (Parametric study) Fire side temperatures from fire test (Validation model)
Ambient side boundary conditions	Radiation – Emissivity: 0.9 Convection - Convective heat transfer coefficient: 10 W/m2°C Sink temperature: 20 °C
Cavity	Radiation – Emissivity: 0.9
Thermal properties	Based on the results presented in Refs. [3,5]

3 VALIDATION RESULTS

Ref. [3] presented the fire test result of an external LSF wall clad with AAC panels exposed to fire from the external side, that is, AAC panels exposed to fire. This test was used for validation, the model developed is shown in Figure 2 (a) and the boundary conditions are mentioned in Table 1. The validation of the finite element heat transfer model in terms of surface and stud temperatures comparison is shown in Figure 3. A reasonable agreement between the test and finite element model results could be observed. The model was similarly validated against the fire test results of external LSF walls with brick veneer cladding presented in Ref. [5].

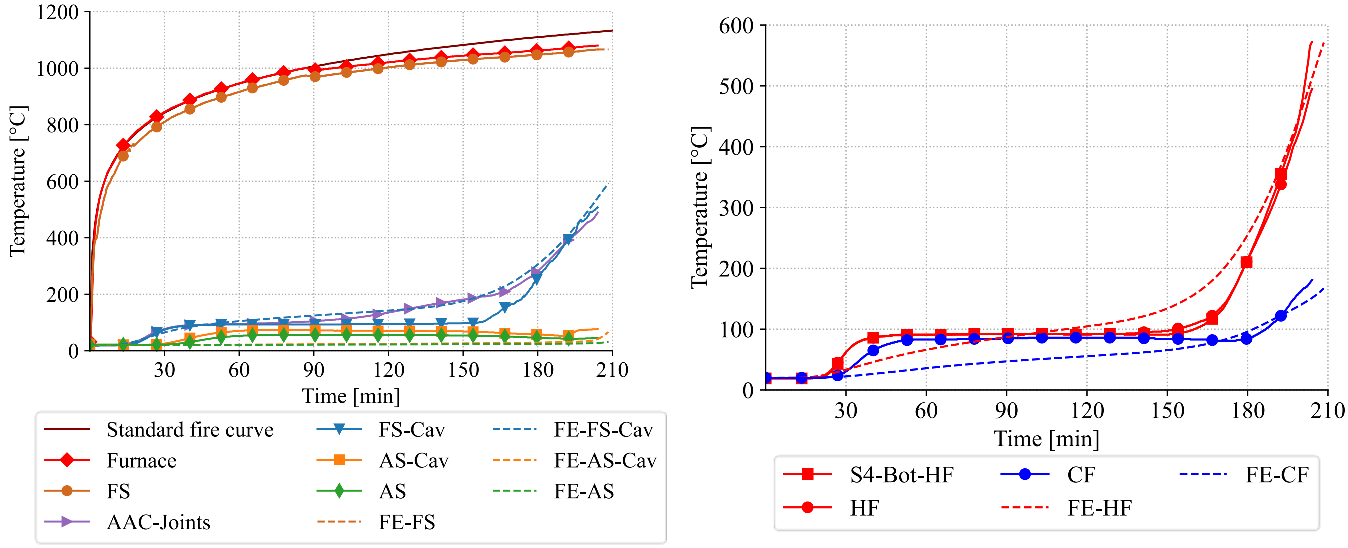

(a) Comparison of AAC and plasterboard surface temperatures

(b) Comparison of stud temperatures

Figure 3. Validation of heat transfer FE model

4 PARAMETRIC STUDY

Finite element heat transfer models were developed for four different wall configurations. Wall configuration details and the FE model cross-sections are shown in Table 2.

Table 2. Parametric study LSF wall configurations

Case	Wall configuration	FE model cross-section
Case 1	75 mm AAC panels (1) 24 mm cavity (Battens) (2) 90 mm studs (3) with cavity insulation (4) 16 mm gypsum plasterboard (5) - exposed to fire	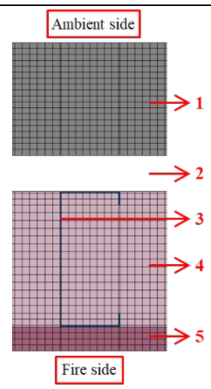
Case 2	75 mm AAC panels (1) 24 mm cavity (Battens) (2) 90 mm studs (3) 16 mm gypsum plasterboard (4) - exposed to fire	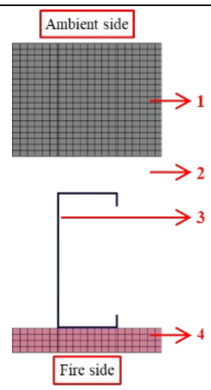

Case 3	110 mm cored (38 % void ratio) bricks (1) 50 mm cavity (2) 90 mm studs (3) with cavity insulation (4) 16 mm gypsum plasterboard (5) - exposed to fire	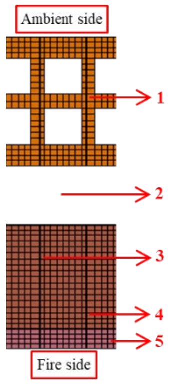
Case 4	110 mm cored (38 % void ratio) bricks (1) 50 mm cavity (2) 90 mm studs (3) 16 mm gypsum plasterboard (4) - exposed to fire	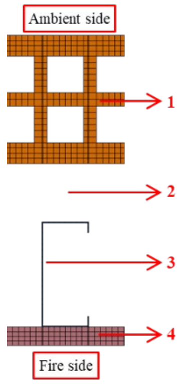

5 RESULTS AND DISCUSSION

5.1 External LSF walls clad with AAC panels

Figure 4 shows the temperature-time plots for Case 1 (referred to as C1) compared with those for an internal LSF wall with single layer plasterboard on both sides and glass fibre cavity insulation (referred to as Int1) from Ref. [6]. Fire side cavity temperatures are similar till 25 min after which differences are noticed, i.e., temperatures in the external LSF wall are higher compared to the internal LSF wall. Initially, the ambient side cavity temperatures of Case 1 are lower than those of the internal wall but then increase after about 60 min (Figure 4 (a)). Stud hot flange temperatures are very similar to internal LSF wall temperatures till about 90 min, after which they are higher in Case 1 (Figure 4 (b).

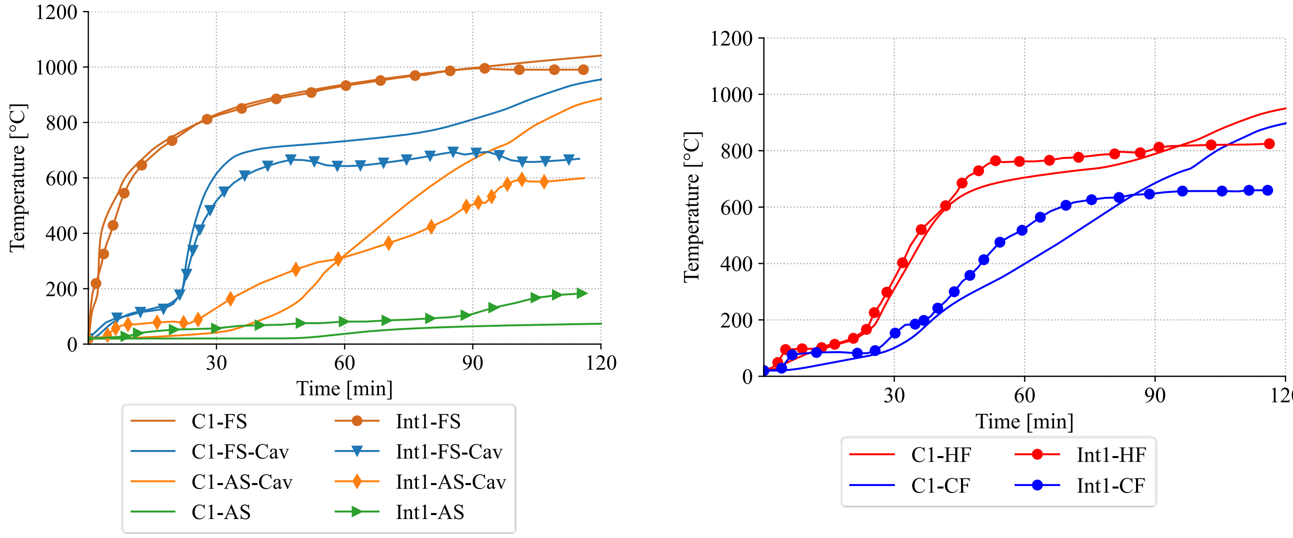

(a) AAC and plasterboard surface temperatures

(b) Stud temperatures

Figure 4. Comparison of temperature-time plots of Case 1 external wall (C1) with internal LSF wall (Int1).

The temperature-time plots for Case 2 (referred to as C2) are compared with those from another internal LSF wall fire test with single layer plasterboard on both sides of the stud and no cavity insulation (referred to as Int2) presented by Ref. [6] in Figure 5. Fire side cavity temperatures are similar till 30 min after which significant differences are noticed. Temperatures in the wall for Case 2 are much higher compared to those in the internal LSF wall (Figure 5 (a)). Stud hot flange temperatures in Case 2 are very similar to internal LSF wall temperatures initially, but they are much higher after about 40 min (Figure 5 (b)), which can lead to lower FRLs at low load ratios for Case 2.

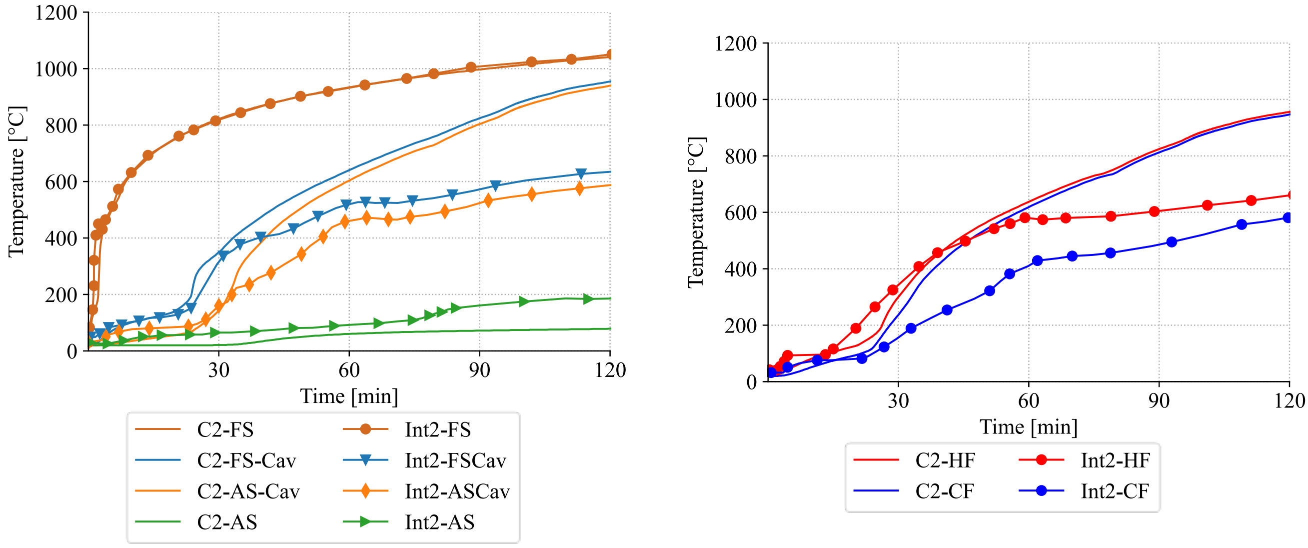

(a) AAC and plasterboard surface temperatures

(b) Stud temperatures

Figure 5. Comparison of temperature-time plots of Case 2 external wall (C2) with internal LSF wall (Int2).

5.2 External LSF walls with brick veneer cladding exposed to fire from the internal side

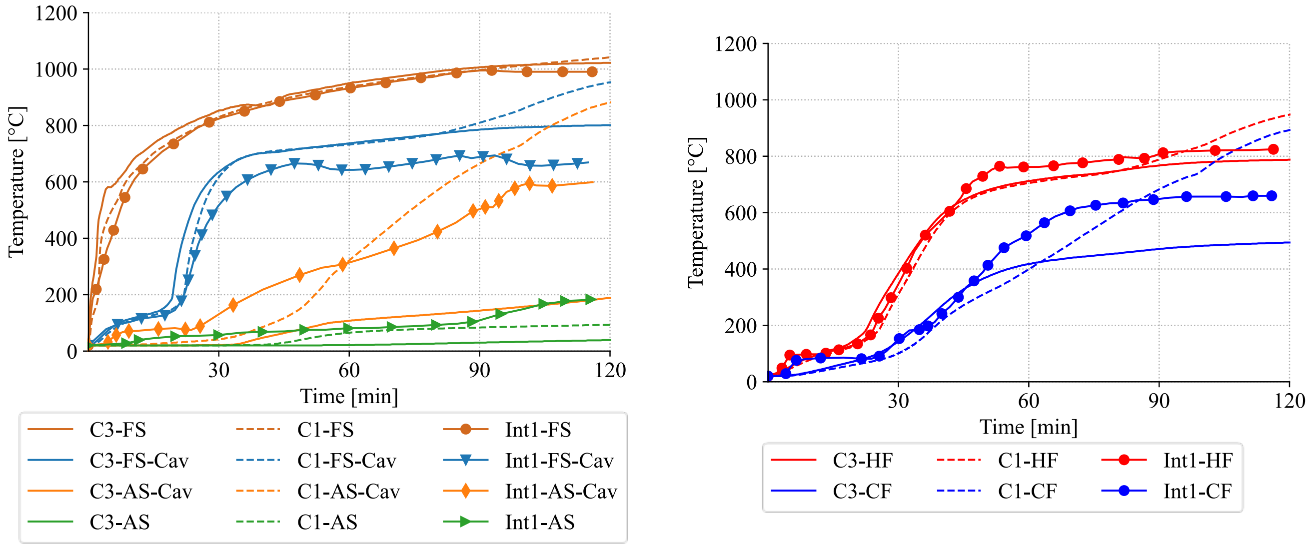

(a) Surface temperatures

(b) Stud temperatures

Figure 6. Comparison of temperature-time plots of Case 3 wall (C3), Case 1 wall (C1) and internal LSF wall (Int1).

Case 3 wall with cavity insulation and Case 4 wall without cavity insulation were exposed to fire on the internal plasterboard side with brick veneer cladding on the ambient side. To understand the influence of different ambient side sheathing materials (AAC panels, brick veneer cladding and gypsum plasterboards) on the temperatures, Case 3 results (brick veneer wall, referred to as C3) are compared with Case 1 results (AAC panel wall) and internal LSF wall with single layer plasterboard and cavity insulation (Int1) results from Ref. [6] in Figure 6. Similarly, Case 4 results (brick veneer wall, referred to as C4) are compared with Case 2 results (AAC panel wall) and internal LSF wall with single layer plasterboard and no cavity insulation (Int2) results from Ref. [6] in Figure 7.

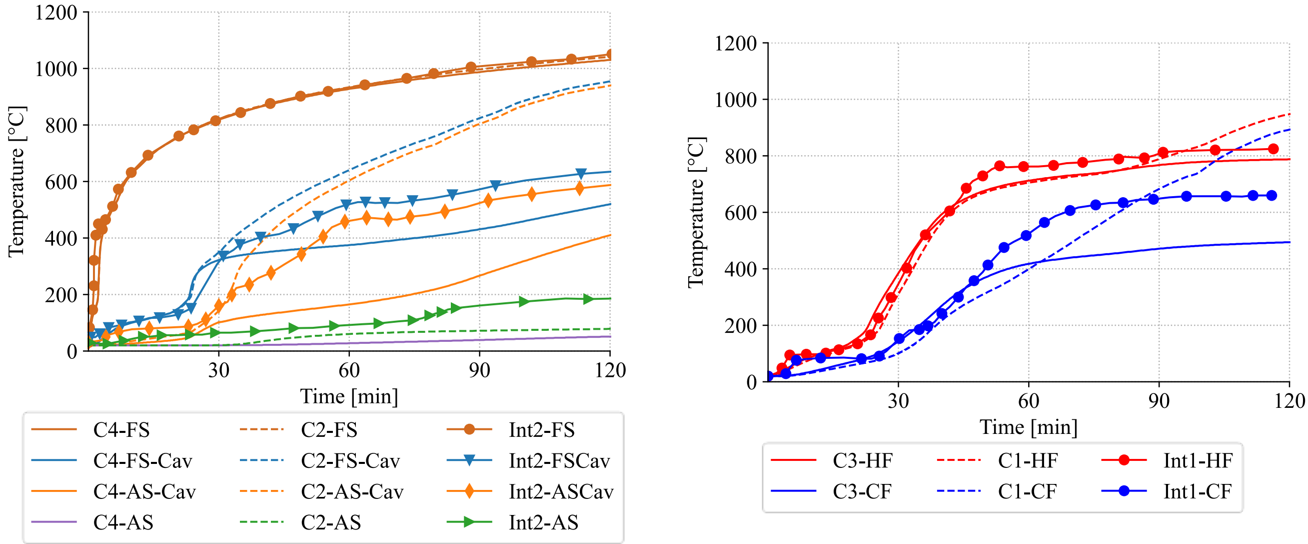

(a) Surface temperatures (b) Stud temperatures

Figure 7. Comparison of temperature-time plots in Case 4 wall (C4), Case 2 wall (C2) and internal LSF wall (Int2).

Although the wall configurations are very similar except for the cladding/sheathing on the ambient side, clear differences were observed. For the cavity insulated walls with AAC panels (C1), the temperature-time plots were very similar to those of the internal LSF wall (Int1) when exposed to fire from the internal plasterboard side. But in the case of the brick veneer wall (C3), the ambient side cavity temperatures were much lower compared to the other two walls (C1 and Int1) (Figure 6 (a)). In the case of stud temperatures, hot flange temperatures were very similar in all three cases. But cold flange temperatures were similar in the initial 45 min after which they were lower in C3 wall (Figure 6 (b)) compared to the other two walls (C1 and Int1).

In the case of non-cavity insulated walls (Figure 7) also, the ambient side temperatures are lower in C4. It was observed that AAC panels (C1) on the ambient side resulted in higher temperatures in the stud compared to internal LSF wall (Int2) as AAC panels block the heat. But in the case of brick veneer wall (C4), the stud temperatures including the hot flange are much lower after 30 min compared to the other two walls (C2 and Int2).

Thermal conductivities of plasterboard (0.26 W/m°C) and AAC (0.104 W/m°C) are very low compared to bricks (1.45 W/m°C). Hence plasterboard and AAC panels block the heat resulting in higher ambient side cavity and stud cold flange temperatures in both non-cavity insulated, and cavity insulated walls. A higher cavity depth (50 mm) in brick walls compared to AAC walls (24 mm) and comparatively very high thermal conductivity of bricks (more than 10 times AAC) resulted in much lower stud temperatures. The cross-sections and thermal conductivities of AAC, plasterboard and brick are presented in Table 3.

Table 3. Thermal conductivity of AAC, plasterboard and brick

Thermal Conductivity (W/m°C)	AAC	Plasterboard	Brick
	0.104	0.26	1.45

<table>
<tr><td>Cross-section</td><td>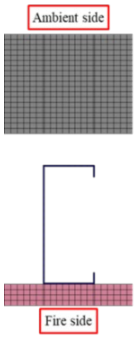
</td><td>
</td><td>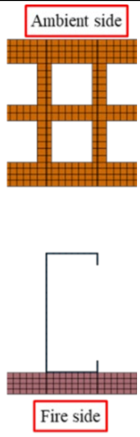
</td></tr>
</table>

6 CONCLUSIONS

The main conclusions from the finite element heat transfer modelling results of the four external LSF wall configurations and comparison with internal LSF walls are,

- The temperatures were very similar to the internal LSF wall temperatures in the case of cavity insulated walls and hence the FRLs of internal LSF walls can be used.
- In the walls with no cavity insulation exposed to internal fires, AAC panels with very low thermal conductivity block the heat resulting in higher stud temperatures (thus reduced FRLs) compared to brick veneer walls and internal LSF walls.
- The reason for the differences in the stud temperatures is simple, i.e., the thermal conductivity of the unexposed side (ambient side) cladding/sheathing.
- AAC with the lowest thermal conductivity acts as insulation blocking the heat in the cavity, resulting in higher temperatures.
- Brick on the other hand with high thermal conductivity and moisture takes away heat resulting in lower temperatures in the cavity and studs.
- The difference in the cavity (24 mm in the case of AAC walls and 50 mm in the case of brick veneer walls) could also have an impact on the difference in the temperatures.

REFERENCES

[1] V.K.R. Kodur, M.A. Sultan, Factors Influencing Fire Resistance of Load-bearing Steel Stud Walls. Fire Technology. 42 (2006) 5–26. DOI:10.1007/s10694-005-3730-y.

[2] A.D. Ariyanayagam, M. Mahendran, Influence of cavity insulation on the fire resistance of light gauge steel framed walls. Construction and Building Materials. 203 (2019) 687–710. DOI:10.1016/J.CONBUILDMAT.2019.01.076.

[3] J. Pancheti, M. Mahendran, Fire resistance of external light gauge steel framed walls clad with autoclaved aerated concrete panels. Thin-Walled Structures. 167 (2021) 108201. DOI:https://doi.org/10.1016/j.tws.2021.108201.

[4] J. Pancheti, M. Mahendran, E. Steau, Fire resistance of external LSF walls with corrugated steel cladding. Journal of Constructional Steel Research. 188 (2022) 107008. DOI:https://doi.org/10.1016/j.jcsr.2021.107008.

[5] J. Pancheti, M. Mahendran, Fire resistance of external light gauge steel framed walls with brick veneer cladding. Thin-Walled Structures. 182 (2023) 110162. DOI:https://doi.org/10.1016/j.tws.2022.110162.

[6] A.D. Ariyanayagam, M. Mahendran, Experimental study of non-load bearing light gauge steel framed walls in fire. Journal of Constructional Steel Research. 145 (2018) 529–551. DOI:10.1016/j.jcsr.2018.02.023.

MATERIAL CHARACTERIZATION TESTS AND ADVANCED MODELING OF HIGH- AND ULTRA-HIGH-STRENGTH STEELS UNDER NATURAL FIRE CONDITIONS

Sara Uszball[1], Markus Knobloch[2]

ABSTRACT

For mild steels it has been proven by experimental evidence that the mechanical material behaviour is reversible in the cooling phase of natural fire scenarios. Regarding the material behaviour of high-strength steels during cooling there are no results available in literature so far. Therefore, the application range of existing code models, such as the Eurocode material model, remain restricted for fire scenarios with steadily increasing temperatures and to steel grades up to S500 in the cooling phase of natural fires. The paper provides the first test program regarding the constitutive material behaviour of high- and ultra-high-strength steels of grades S690QL and S960QL as well as mild steel S355 J2+N in the case of natural fires. It is elaborated that the mechanical material behaviour of high-strength steels in the cooling phase differs from the behaviour in the heating phase and is not reversible due to phase changes of the microstructure. A constitutive material model for future extensions of the 2nd generation of the Eurocode to high-strength steels under natural fire conditions is developed on the basis of experimental data of natural fire and residual strength tests; and the numerical implementation of the temperature-dependent material behaviour in the finite-elemente software Abaqus/Standard is described.

Keywords: High-strength steels, Natural fire tests, Constitutive modeling, Case study

1 INTRODUCTION

Comprehensive knowledge of the material behaviour in case of fire is the basis for a thorough understanding as well as a realistic modeling of the structural fire behaviour of steel structures. For state-of-the-art buildings with architecturally sophisticated design and increasing requirements, the use of structural components made of high-strength structural steels is appealing, as their good strength-to-weight ratio can contribute to reduced static cross sections and therefore to resource and energy efficiency. Based on the results of material characterization tests, in particular [1-6], regarding the temperature-dependent behaviour of high-strength steels under steady state and transient temperature conditions it has been decided to expand the application range of the stress-strain response model in prEN 1993-1-2:2022 [7] to steels up to and including S700 for fire scenarios with steadily increasing temperatures. An application of the constitutive model to the cooling phase of natural fire scenarios implicitly assumes that the mechanical material behaviour is reversible, which has been proven by experimental evidence for mild steels [8]. For high-strength steel bolts, however, Hanus [9] has shown that the mechanical material behaviour in the cooling phase differs from the behaviour in the heating phase due to phase changes of the microstructure. Further, the results of rare post fire tests on high-strength steels [10-14] indicate that the behaviour is not fully reversible. Accordingly, the Eurocode material model remains restricted for the cooling phase of natural fires to steel grades up to S500, as there have been no results available in literature regarding the material behaviour of high-strength steels during cooling.

[1] M. Sc., Ruhr-Universität Bochum,
e-mail: sara.uszball@rub.de
[2] Prof. Dr., Ruhr-Universität Bochum
e-mail: markus.knobloch@rub.de, ORCID: https://orcid.org/000-0002-1289-0691
https://doi.org/10.6084/m9.figshare.22215748

Therefore, the present study provides the first comprehensive test program regarding the constitutive material behaviour of high- and ultra-high-strength quenched and tempered steels of grades S690QL and S960QL as well as mild steel S355 J2+N in the case of natural fire scenarios. The influence of different maximum temperatures in the heating phase on the material behaviour during and after the cooling process is pointed out. Then, a constitutive material model for high- and ultra-high-strength steels under natural fire conditions is developed based on the experimental data of natural fire tests and residual strength tests. Finally, the numerical implementation of the temperature-dependent material behaviour in the finite-elemente software Abaqus/Standard for the use in case studies is described.

2 MATERIALS AND METHODS

The experimental study consisted of an extensive tensile test program of natural fire tests and post fire tests on small scale specimens made of high-strength (HSS) and ultra-high-strength (UHSS) quenched and tempered structural steels of grades S690QL and S960QL and of mild steel of grade S355 J2+N. The tensile tests were performed under steady state temperature conditions after heating the specimens to predefined maximum temperatures T_u and subsequently cooling them down to specified test temperatures T_t. The maximum temperatures of the tests were T_u= 400°C, 550°C, 700°C, 900°C in order to cover the temperature ranges relevant for structural steel in terms of material technology. Analogous to the maximum temperatures, the test temperatures were set as T_t= 700°C, 550°C, 400°C, 20°C. Each test combination of maximum temperature and test temperature was performed twice.

2.1 Test Specimens

For the tensile tests, dog-bone shaped specimens were manufactured from plate material with an initial thickness of 12 mm made of HSS of grade S690QL and UHSS of grade S960QL as well as from the flanges of a HEA 100 section with a nominal thickness of 8 mm made of mild steel of grade S355 J2+N. The following abbrevations are used to indicate the test series: M1: HSS S690QL, 12 mm; M2: mild steel S355 J2+N, HEA 100; M3: UHSS S960, 12 mm.

The geometry of the specimens was chosen according to the requirements of the test setup and is presented in Fig. 1(a). The specimens had a total length of L= 170 mm and the thickness of the specimens was chosen to t= 6 mm. Further, a geometry with two fillet radii was selected. The first fillet radius of R_1= 15 mm served the form-fitted installation in the specimen holder while the second radius of R_2= 10 mm was chosen to ensure that the fracture of the specimens occured within the gauge length.

2.2 Test Setup

For the tensile tests, a combined test setup of a universal testing machine with a maximum load capacity of 250 kN (manufacturer Schenck) and an electric furnace (manufacturer KÖNN) is used. The test setup is shown in Fig. 1(b) and (c). The furnace has three independent controllable heating zones in vertical direction with a maximum temperature of 1200°C for each zone.

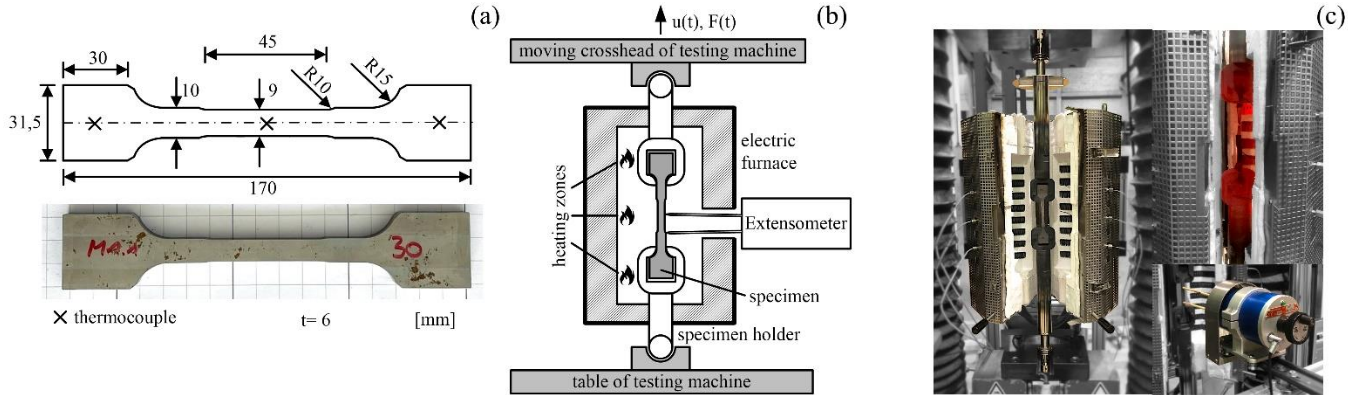

Figure 1. (a) Test specimens, (b) schematic illustration of the test setup and (c) test setup.

The air temperature inside the furnace was measured by three mantle thermocouples, type N (D= 3,0 mm). The heating of the furnace was controlled by three further mantle thermocouples, type N (D= 1,5 mm), which were positioned on the surface of the test specimens. In Fig. 1(a), the positions of the thermocouples on the specimens are marked. A vertical opening is provided at the front of the furnace so that a strain measurement can be made using a temperature-resistant strain sensor. In the present study, the strain was measured using a high-temperature extensometer from manufacturer MAYTEC with two ceramic rods, which were placed directly on the specimens surface. The gauge length of the extensometer was set as L_0= 45 mm. The measured strain also served as feedback variable for the closed-loop-feedback control during the strain-rate controlled tensile tests. The specimens were placed in the furnace respectively in the universal testing machine using a high-temperature resistant specimen holder with a maximum load capacity of 50 kN at a test temperature of 1100°C.

2.3 Test Procedure

For the natural fire tests as well as the post fire tests, a test procedure, which consisted of five successive phases was defined. The test procedure is shown schematically in Fig. 2(a) by the time-force and in Fig. 2(b) by the time-temperature relationship.

In the first phase of the test, the temperature was kept ambient. The specimen was subjected to five strain-rate controlled loading and unloading cycles with a maximum applied load corresponding to 80 % of the nominal yield strength to ensure the centric alignment of the specimen in the testing machine and to determine the Young's modulus at ambient temperature. The second phase comprised the heating of the specimen. A constant tensile force of F_{hold}= 0,5 kN was applied force-controlled to allow and measure the (free) thermal expansion while the specimen was heated with a constant heating rate of $\dot{T}$= 15°C/min until the specimen temperature reached the specified maximum temperature T_u. The temperature was then kept constant for 30 min, so that it could be assumed that the entire cross-section of the specimen reached the target temperature. In phase 3 of the procedure the specimen was cooled down to the test temperature T_t under natural ventilation conditions, i.e. the heating device of the furnace was switched off, but no additional cooling medium (water or similar) was used to cool the specimen. To avoid damage to the test setup, the furnace remained closed throughout the entire cooling process. The holding load F_{hold}= 0,5 kN continued to be applied during the cooling.

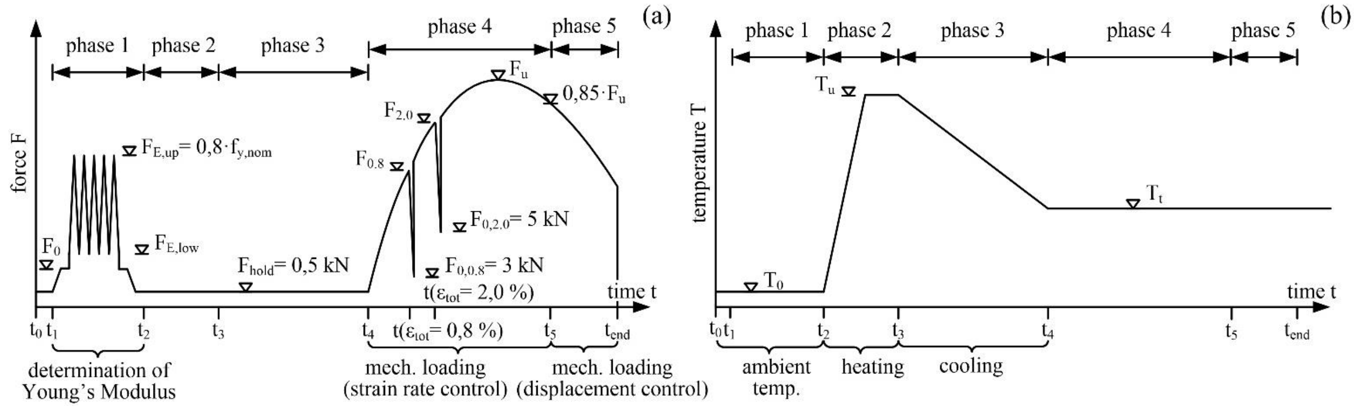

Figure 2. (a) Time-force and (b) time-temperature relationship of the test procedure.

Once the target test temperature T_t was reached, the mechanical loading of the tensile tests was carried out in the subsequent phases 4 and 5. The test temperature T_t was kept constant. In phase 4 the loading was realized strain-rate controlled with a constant strain rate of $\dot{\varepsilon}$= 1 %/min, using a closed-loop-feedback control via the high-temperature extensometer. Two elastic unloading-reloading cycles at predefined total strain levels of ε_{tot}= 0.8 % and ε_{tot}= 2.0 % were performed. After the second unloading step, the specimen was loaded beyond the tensile strength. In order to avoid damage of the extensometer by the sudden rupture of the specimen or too large deflection of the ceramic rods, the extensometer was removed at a force reduction of 15 % based on the maximum achieved load. At this point, for the fifth and final phase, the test was switched to a displacement-controlled loading with a constant velocity of v= 0,8 mm/min via the crosshead displacement of the testing machine until the rupture of the specimen.

3 RESULTS AND DISCUSSION

This section presents the results of the natural fire and post fire tests are presented in the form of experimentally determined stress-strain curves from material characterization tests as well as reduction factor-temperature relationships for material properties, which were derived from the stress-strain curves.

3.1 Stress-Strain Response

Fig. 3 shows the stress-strain relationships for the investigated materials, which were obtained from the natural fire tests during the cooling phase and the post fire tests at ambient temperature. Each graph shows the stress-strain curves at a predefined test temperature T_t after a previous heating to higher maximum temperatures T_u for the strain range up to 2 % total strain (left) as well as up to 15 % (right). The stress-strain curves with solid lines are assigned to series M1, the dashed lines represent the results of series M2 and the dotted lines belong to series M3. The test temperatures T_t decrease from Fig. 3(a) to (d). The coloring of the curves indicates the maximum temperatures T_u. Additionally, Fig. 3(d) contains the reference curves of the materials at ambient temperature. The curves with equal test temperature T_t and maximum temperature T_u represent the results of steady state tests, in which no cooling takes place before the mechanical loading of the specimens. In the case of the mild steel of series M2 the results of steady state tests correspond to the study presented in [15] and for the HSS of series M1 and the UHSS of series M3, the results of the steady state tests were taken from [1]. In both reference studies the exact same plate material was used to prepare the test specimens and also the test procedure was the same as in the current study.

The reference curves of all investigated materials at ambient temperature show linear-elastic material behaviour for small strains. Additionally, a distinct change from the linear-elastic range to the beginning of plastic flow is obvious. At elevated test temperatures in the heating as well as in the cooling phase, no distinctive yield plateau can be observed for any of the investigated materials. The mechanical material behaviour is non-linear. In particular at test temperatures above 400°C, it also becomes clear, that the material strengths are significantly reduced compared to the initial values at ambient temperature, since the stress-strain curves here are considerably below the reference curves.

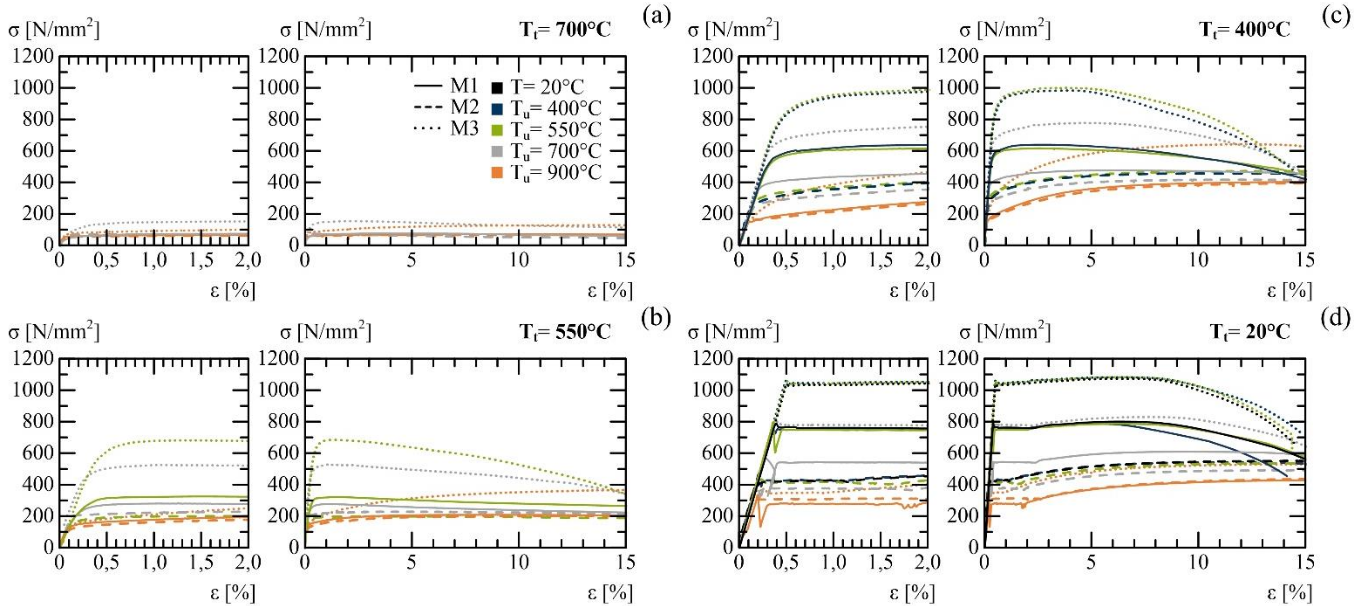

Figure 3. Stress-strain curves of natural fire tests on series M1, M2 and M3 at test temperatures of (a) T_t= 700°C, (b) T_t= 550°C, (c) T_t= 400°C and (d) T_t= 20°C.

For normal-strength structural steel, it is generally assumed that the material behaviour is completely reversible in the cooling phase of a fire. The stress-strain curves in Fig. 3(d) partly verify this assumption. Up to a maximum temperature of T_u= 550°C in the heating phase, it appears that the strength of series M2, which is reduced by high temperatures during the heating process, increases again during the cooling phase up to the initial value. Accordingly, there is complete reversibility. Very high maximum temperatures of T_u= 900°C lead to a slight reduction of the post fire strength compared to the initial value.

In case of the investigated materials M1 and M3 it can be observed that the maximum temperature has a higher impact on the material behaviour during cooling than in case of mild steel. In cases with maximum temperatures up to T_u= 550°C a full regression of the material behaviour can be seen in Fig. 3(d). However, for maximum temperatures above T_u= 700°C the post-fire strengths of the materials M1 and M3 are remarkably reduced compared to the initial values. After an exposure to T_u= 900°C, the initial higher strengths of the series M1 and M3 do not recover and materials with characteristic strength values of mild steel are present in both cases. It can be assumed that this is due to the phase transformation when exceeding the A_1-phase change-temperature and the subsequent slow cooling under natural ventilation conditions. As a result of the carbon precipitation, the fine-grained predominantly austenitic microstructure of the initial HSS and UHSS, which was obtained through the quenching and tempering process during production, is transformed into a coarser-grained structure consisting of mostly ferrite and pearlite phases, which results in materials with lower strengths.

3.2 Young's Modulus

Table 1 summarizes the mean values of the temperature dependent material properties of series M2, which were derived from the stress strain curves of two natural fire tests (Fig. 3) each with the same material and temperature conditions. Table 2 and Table 3 contain the determined material properties of series M1 and series M3 respectively. Some values of the fracture strain $\varepsilon_{u,\theta}$ are not given in the tables, as those could not be clearly determined from the test data at high test temperatures. Fig. 4 shows the reduction factor-temperature relationships for the Young's modulus E_θ (a), the effective yield strength $f_{y,2.0,\theta}$ (b) and the tensile strength $f_{t,\theta}$ (c) which were derived from the material parameters by relating the temperature-dependent values to the initial value at ambient temperature and displaying them with respect to the test temperature T_t. In accordance to the decreasing test temperature T_t during cooling, the graphs in Fig. 4 each are to be read from right to left. The colors of the datapoints in Fig. 4 indicate the maximum temperatures T_u of the natural fire tests.

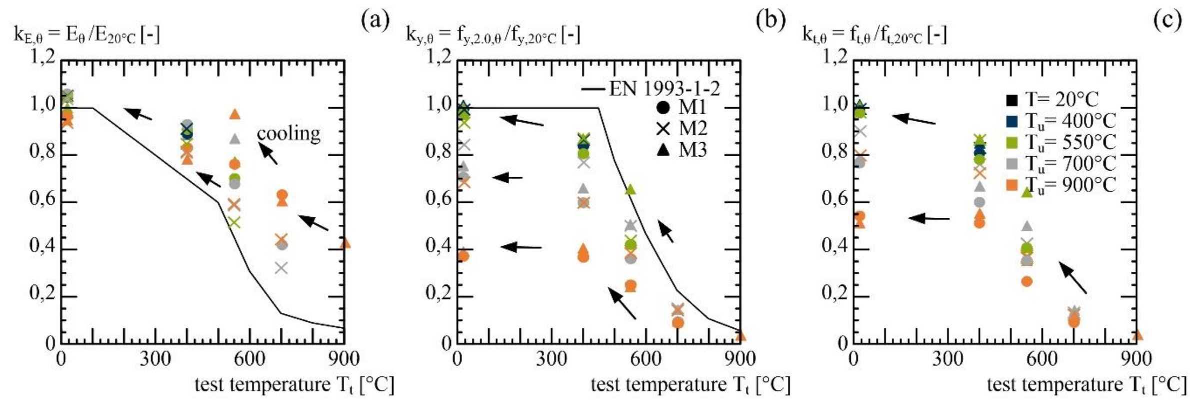

Figure 4. Reduction factor-temperature relationship of natural fire tests for (a) the Young's modulus E_θ, (b) the effective yield strength $f_{y,2.0,\theta}$ and (c) the tensile strength $f_{t,\theta}$ during cooling.

The development of the Young's modulus during cooling is illustrated in Fig. 4(a). It can be noted that the mild steel of series M2 regains its initial stiffness completely and the regeneration is independent from the maximum temperature T_u, which has been reached during the heating phase, as the reduction factor-temperature relationships with different maximum temperatures almost coincide and reach a value of about $k_{E,\theta}$= 1,0 at post fire conditions.

For the HSS and UHSS of series M1 and M3, the maximum temperature also has only a small impact on the development of E_θ during cooling as the scatter of the values of natural fire tests are small and in post fire test the initial values of the Young's modulus were reached. An effect of the heating process on the development of the Young's modulus in the cooling phase therefore can be seen as negligible for mild steel as well as for HSS and UHSS.

In Fig. 4(a), further, the reduction factors $k_{E,\theta}$ of prEN 1993-1-2:2022 [7] are depicted. The reduction factors $k_{E,\theta}$ represent a conservative approximation of the experimentally determined Young's moduli in the heating and the cooling phase for all investigated materials.

3.3 Effective Yield Strength

In Fig. 4(b), the reduction factor-temperature relationships for the effective yield strength at ε_{tot}= 2,0 % are presented. It appears that there are differences in the strength development during the cooling of mild steel and HSS, respectively UHSS. In case of the HSS of series M1 and the UHSS of series M3, the relative development of the material strength during the cooling process depends significantly on the maximum temperature T_u, which has been reached in the heating phase of the tests. The reduction factor-temperature relationships in Fig. 4(b) show that higher maximum temperatures T_u lead to lower material strengths for identical test temperatures T_t in the cooling phase and in the residual strength range at ambient temperature. Up to a maximum temperature of T_u= 550°C, the initial strengths of all investigated materials can be fully recovered in post fire tests. Exceeding higher maximum temperatures during heating, significant strength losses can be observed in the cooling phase. After a maximum temperature of T_u= 900°C, it can be seen that only about 40 % of the initial strength values of the high-strength materials were reached. This dependence is less prominent in case of the investigated mild steel of series M2. Here, about 70 % of the initial strength was reached in post fire tests with T_u= 900°C.

The comparison of the test results with the reduction factors $k_{y,\theta}$ of the Eurocode 3 shows that the normative values lead to an overestimation of the strength values of all investigated materials in the heating and the cooling phase. However, for all materials in the heating phase and for M2 in the cooling phase the deviations between normative values and test results are minor. For M1 and M3 there are major deviations in the cooling phase in cases with T_u= 700°C and T_u= 900°C so that it can be assumed that the code model is not suitable to describe the strength development of HSS and UHSS during the cooling phase of natural fires.

Table 1. Material properties of series M2 from natural fire tests

T_t [°C]	T_u [°C]	E_θ [N/mm^2]	$f_{p,\theta}$ [N/mm^2]	$f_{y,0.2,\theta}$ [N/mm^2]	$f_{y,0.5,\theta}$ [N/mm^2]	$f_{y,1.5,\theta}$ [N/mm^2]	$f_{y,2.0,\theta}$ [N/mm^2]	$f_{t,\theta}$ [N/mm^2]	$\varepsilon_{u,\theta}$ [%]
20	20	212316	423.0	390.2	425.2	442.1	457.4	553.6	27.6
	400	222352	467.0	429.2	431.7	443.0	453.2	547.9	24.0
	550	221985	446.6	421.6	419.0	414.3	428.2	539.5	26.7
	700	219464	357.3	383.4	380.1	378.7	385.4	496.8	29.2
	900	198384	255.6	313.6	312.5	313.1	312.5	439.8	33.9
400	400	193000	198.0	301.0	321.0	378.0	395.0	459.0	-
	550	179511	249.1	323.6	333.8	382.8	397.9	476.0	30.4
	700	165574	211.2	281.3	290.5	337.0	351.1	384.3	27.8
	900	177382	189.2	198.4	211.1	264.8	282.4	395.2	30.7
550	550	109000	137.0	185.0	191.0	199.6	200.0	202.6	-
	700	124313	185.6	210.6	214.8	227.1	228.5	234.9	40.2
	900	112785	109.4	138.6	147.1	171.4	179.1	205.5	73.2
700	700	68100	58.5	72.7	73.0	70.2	69.0	73.6	-
	900	93795	46.6	58.5	60.6	64.1	65.2	68.6	133.0

3.4 Tensile Strength

In Fig. 4(c), the reduction factor-temperature relationship for the tensile strength $f_{t,\theta}$ are presented. It can be observed that the dependency of the strength development on the maximum temperature T_u, which was found for the effective yield strength $f_{y,2.0,\theta}$ of HSS and UHSS, also appears for the tensile strength $f_{t,\theta}$ of series M1 and M3. The initial values of the tensile strengths were reached in cases with $T_u \leq 550$°C. Higher maximum temperatures cause lower tensile strengths during cooling and after a temperature exposure of T_u= 700°C only about 80 % of the initial tensile strengths were reached. After T_u= 900°C the reduction of the tensile strength was even higher.

In case of the mild steel of series M2, it can be seen that the tensile strength recovered completely for $T_u \leq 550$°C. At higher maximum temperatures slight decreases in the strength recovery are obvious.

However, the strength reduction of the tensile strength of mild steel is minor compared to HSS and UHSS even in cases with very high maximum temperatures of T_u= 900°C.

Table 2. Material properties of series M1 from natural fire tests

T_t [°C]	T_u [°C]	E_θ [N/mm^2]	$f_{p,\theta}$ [N/mm^2]	$f_{y,0.2,\theta}$ [N/mm^2]	$f_{y,0.5,\theta}$ [N/mm^2]	$f_{y,1.5,\theta}$ [N/mm^2]	$f_{y,2.0,\theta}$ [N/mm^2]	$f_{t,\theta}$ [N/mm^2]	$\varepsilon_{u,\theta}$ [%]
20	20	204764	786.0	763.4	759.5	760.3	760.0	794.4	16.7
	400	213736	717.0	742.5	744.2	752.7	755.5	783.4	14.2
	550	214417	744.7	737.9	739.6	736.1	737.2	775.7	16.1
	700	216825	575.6	537.3	536.3	538.5	537.5	607.7	21.7
	900	197603	314.5	272.4	274.7	273.4	283.4	430.4	32.4
400	400	182304	432.4	592.9	588.4	633.3	638.2	641.3	18.1
	550	186031	441.9	575.1	573.9	610.5	612.9	619.7	18.2
	700	190447	290.7	405.0	412.1	445.7	455.1	477.0	25.0
	900	170199	147.9	180.6	197.0	256.3	279.8	406.7	34.7
550	550	143836	119.8	302.1	313.9	322.9	320.4	324.2	46.7
	700	138885	150.4	262.2	269.8	277.8	275.4	280.9	-
	900	155987	107.6	155.2	166.2	184.8	191.0	211.4	-
700	700	86200	19.0	57.0	63.1	70.9	72.5	74.3	83.5
	900	129556	42.8	58.9	61.5	66.2	67.9	72.8	-

Table 3. Material properties of series M3 from natural fire tests

T_t [°C]	T_u [°C]	E_θ [N/mm^2]	$f_{p,\theta}$ [N/mm^2]	$f_{y,0.2,\theta}$ [N/mm^2]	$f_{y,0.5,\theta}$ [N/mm^2]	$f_{y,1.5,\theta}$ [N/mm^2]	$f_{y,2.0,\theta}$ [N/mm^2]	$f_{t,\theta}$ [N/mm^2]	$\varepsilon_{u,\theta}$ [%]
20	20	206788	1036.8	1026.9	1031.6	1034.8	1038.8	1069.1	14.5
	400	218929	1045.6	1039.5	1055.2	1046.4	1049.7	1078.5	14.6
	550	206523	1040.6	1027.5	1033.4	1034.9	1039.0	1069.6	14.1
	700	217613	702.5	785.6	786.4	783.3	783.0	834.5	16.5
	900	196032	349.3	354.1	355.9	398.2	407.2	545.5	23.7
400	400	183520	605.1	812.0	760.6	881.5	893.0	904.5	14.4
	550	186329	594.9	820.9	768.8	892.8	903.7	922.1	13.8
	700	183791	519.3	619.3	613.0	672.9	686.1	710.6	15.4
	900	161858	110.2	246.5	281.7	390.8	422.6	589.6	21.8
550	550	159578	385.0	644.8	616.4	683.8	681.4	685.5	17.3
	700	179664	380.4	505.4	505.6	529.2	526.9	533.4	18.9
	900	201423	131.8	170.5	187.1	236.9	253.8	375.8	36.1
700	700	90037	60.9	130.1	140.4	152.4	152.6	153.2	56.3
	900	125301	61.3	82.7	85.8	97.4	101.5	128.9	61.7
900	900	88919	19.8	34.6	36.3	39.5	40.7	43.8	93.9

4 PREDICTIVE EQUATIONS

The constitutive material model given in the European standard [7] to describe the material behaviour of structural steel during a fire is based on the general assumption that the mechanical material behaviour of mild steels is reversible after a fire exposion. Therefore, according to the model, for the same temperatures in the heating and cooling phase of natural fire scenarios, the same reduction factors for the material properties are used in structural fire design. For HSS and UHSS in the cooling phase, the present tests have shown that the assumption of a complete reversibility of the mechnical material behaviour is not applicable, as it has been observed a dependence of the strength development during the cooling process on the reached maximum temperature of the heating phase. The present study therefore indended to adapt the given constitutive material model of Eurocode 3 for the application to HSS and UHSS in the cooling phase of natural fires. The focus was particularly on a user-friendly and easy-applicable model. Accordingly, the existing model was used as a basis and modified respectively extended by simple approaches.

The present tests have shown that the stiffness of the investigated materials is fully reversible and the influence of the maximum temperature on the development of the Young's modulus during cooling is negligible. Further, it has been found that the reduction factors $k_{E,\theta}$ are conservative for the investigated materials. The developed model therefore includes the reduction factors $k_{E,\theta}$ according to EC 3 for HSS and UHSS in the heating and cooling phase without any adjustments of the reduction factors (Eq. (1)).

The strength development during cooling depends significantly on the maximum temperature of the heating phase. Therefore, a novel reduction factor for the effective yield strength $f_{y,2.0,\theta}$ and the proportional limit $f_{p,\theta}$, which depends on the maximum temperature T_u is provided. The novel reduction factor considers an influence of maximum temperatures above 500°C on the development of material properties during cooling. Therefore, a stress strain model without hardening is used according to EC 3 so that the tensile strength is not affected by the novel reduction factor. According to the developed model, the effective yield strength and the proportional limit of HSS and UHSS during the cooling phase of natural fires can be determined according to Eqs. (2)-(4). Fig. 5 shows the reduction factor-temperature relationships according to Eqs. (2)-(4). The reduction factors are sorted by the maximum temperatures T_u and displayed over the test temperatures T_t.

Young's modulus: $E_{\theta,c} = E_\theta \cdot k_{E,\theta}$ (1)

Effective yield strength: $f_{y,\theta,c} = f_{y,\theta} \cdot g(T_u) = f_{y,20°C} \cdot k_{y,\theta} \cdot g(T_u)$ (2)

Proportional limit: $f_{p,\theta,c} = f_{p,\theta} \cdot g(T_u) = f_{y,20°C} \cdot k_{p,\theta} \cdot g(T_u)$ (3)

with:

$T_u \leq 500°C$: $g(T_u) = 1,0$

$T_u > 500°C$: $g(T_u) = 1,75 - 1,5 \cdot T_u \cdot 10^{-3}$ (4)

where

$k_{i,\theta}$ the reduction factors for material properties at elevated temperatures according to EC 3;

$E_{\theta,c}$ the Young's modulus in the cooling phase of natural fire scenarios;

$f_{y,\theta,c}$ the effective yield strength in the cooling phase of natural fire scenarios;

$f_{p,\theta,c}$ the proportional limit in the cooling phase of natural fire scenarios;

$g(T_u)$ the reduction factor for $f_{y,\theta,c}$ and $f_{p,\theta,c}$ in the cooling phase of natural fires depending on T_u [°C].

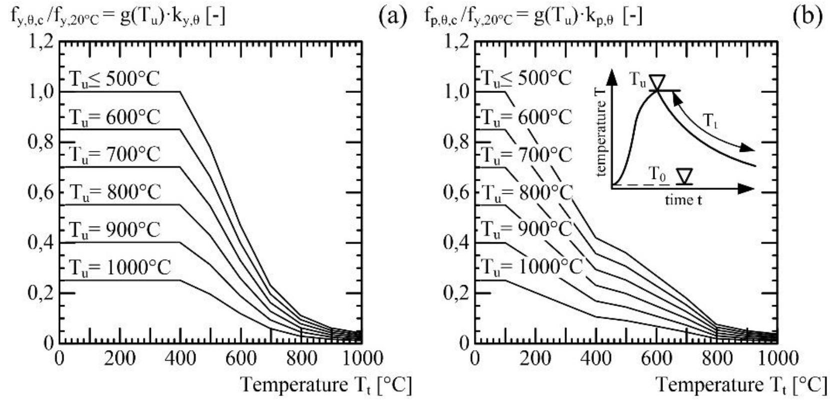

Figure 5. Proposed reduction factors for (a) the effective yield strength $f_{y,\theta,c}$ and (b) the proportional limit $f_{p,\theta,c}$ for HSS and UHSS in the cooling phase of natural fire scenarios.

In Fig. 6, the comparison between stress-strain curves from post fire tests and analytical determined stress-strain curves based on the developed material model is presented for series M1 of the present study as well as for S690QL from [10] and for tests on 8.8 bolts from [9]. It can be seen that the analytical curves lead to an applicable approximation of the post fire material behaviour in each case and the consideration of the maximum temperature for the calculation of the post fire strength is necessary for the characterization of the measured material behaviour of various high-strength materials.

In Table 4, the relative deviations between the reduction factors for the effective yield strength $k_{y,\theta}$ and test results from natural fire tests and post fire tests are summarized. The test results include the present study as well as results from literature [9-14]. On the one hand the original model from EC 3 and on the other hand the developed material model of the present study is considered. It can be seen that for both, the cooling phase of natural fire scenarios and the post fire range, the consideration of the maximum temperature in the determination of the strength values according to the developed model for HSS and UHSS of the present study leads to a more accurate description of the measured material behaviour, since the average values of the relative deviation between model values and test results are remarably smaller compared to the original model of EC 3.

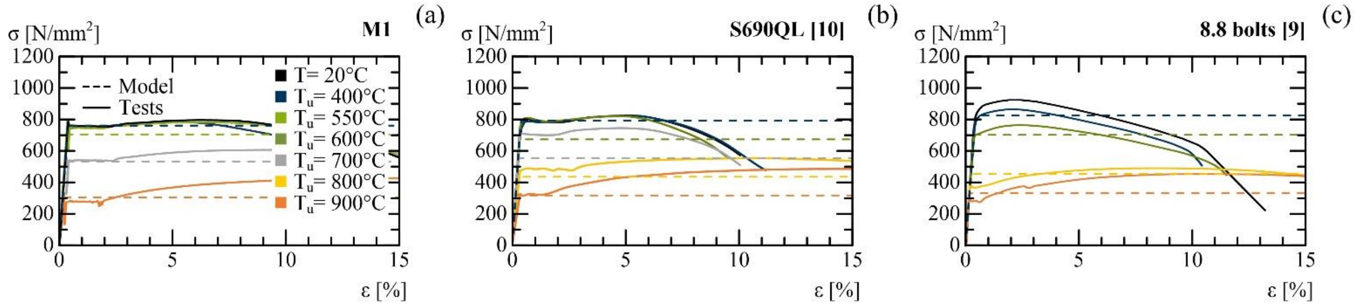

Figure 6. Comparison between stress-strain curves from post fire tests with T_t= 20°C and analytical stress-strain curves based on the developed material model for (a) series M1, (b) series M3, (c) S690QL from [10] and (d) 8.8 bolts of [9].

Table 4. Deviations between reduction factors for the effective yield strength from material models and test results

		$\bar{x}_{EC3}^{1)}$	$s_{EC3}^{2)}$	$\bar{x}_{Model}^{1)}$	$s_{Model}^{2)}$
natural fire tests	$f_{y,nom} \leq 460$ N/mm²	-0,314	0,226	-	-
	460 N/mm² < $f_{y,nom} \leq 700$ N/mm²	-0,556	0,536	-0,058	0,239
	700 N/mm² < $f_{y,nom}$	-0,526	0,647	0,009	0,249
post fire tests	$f_{y,nom} \leq 500$ N/mm²	-0,054	0,071	-	-
	500 N/mm² < $f_{y,nom} \leq 700$ N/mm²	-0,206	0,295	0,058	0,077
	700 N/mm² < $f_{y,nom}$	-0,203	0,385	0,026	0,135

1) $\bar{x}=\frac{1}{n}\sum_{i=1}^{n} x_i$, 2) $s=\sqrt{\frac{1}{n-1}\sum_{i=1}^{n}(x_i-\bar{x})^2}$ mit $x_i=(k_{y,\theta,test}-k_{y,\theta,model})/k_{y,\theta,test}$

5 CASE STUDIES

For the extended structural analysis of steel structures in the case of fire, taking into account natural fire scenarios, the temperature-dependent material behaviour of high-strength structural steels was made accessible for the finite element software Abaqus/Standard by means of a user subroutine UMAT and used for case studies on a structural component. As an example, a girder as part of a structure of an open car park in composite construction was chosen for the case study. The girder consists of an IPE 450 section and a composite ceiling with a thickness of h_c= 100 mm. The composite ceiling of the girder is neglected and not modelled in the present study. For the steel component of the girder it is assumed that it is made of HSS of grade S690 and has a total length of L= 8,00 m. As part of the German national IGF research project No. 20453 N [16], extensive studies were carried out on the development of the temperature of the composite girder in various fire scenarios and selected examples of the determined temperature-time curves are used in the present study for the analysis of the load-bearing capacity of the steel component of the composite girder.

The temperature-dependent mechanical material behaviour of the high-strength steel is defined in a subroutine UMAT. The structure of the used subroutine is presented in Fig. 7. The UMAT subroutine of the present study is developed for calculations with volume elements, i.e. a three-dimensional stress state is defined. The required input parameters for the use of the subroutine are the material parameters Young's modulus E_{ini}, proportional limit $f_{p,ini}$, yield strength $f_{y,ini}$ as well as the Poisson's ratio ν at ambient temperature. It is assumed that the Poisson's ratio is independent of temperature. Accordingly, a constant value of ν= 0,3 is used in the elastic range. In addition, it needs to be defined the value of the ambient temperature T_{ini}. In the present study, a value of T_{ini}= 20°C is assumed. Further, as input parameters for the material behaviour at ambient temperature, nominal values were specified. Therefore it is E_{ini}= 210000 N/mm^2, $f_{y,ini}$= 690 N/mm^2, $f_{p,ini}$= 690 N/mm^2. Further, a constant load of q= 15 kN/m is assumed.

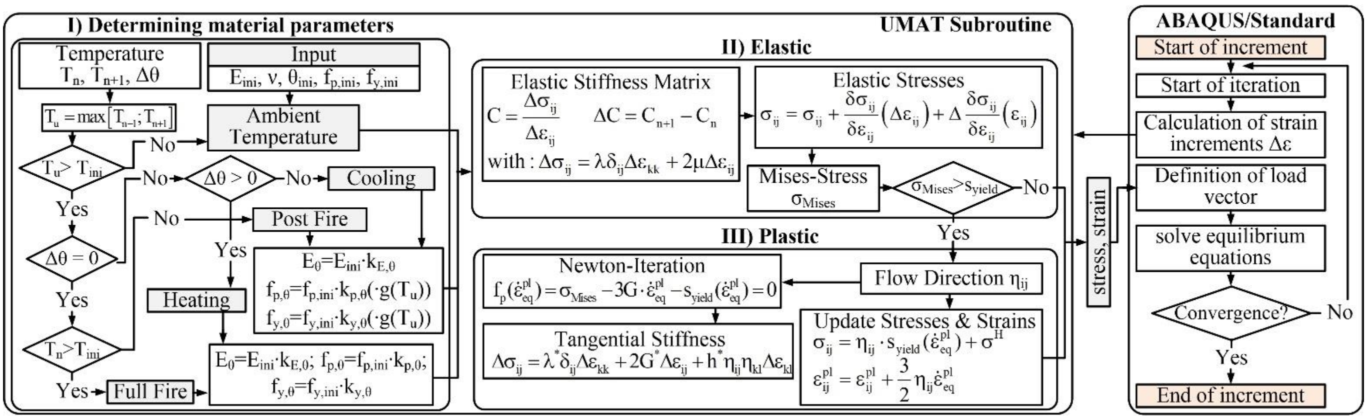

Figure 7. Structure of the developed subroutine UMAT for the temperature-dependent material behaviour of HSS.

The UMAT subroutine is used to define the temperature-dependent mechanical material behaviour in the different phases of a natural fire. An automatised recognition of the fire phases heating, full-fire phase, cooling and post fire phase is generated using Eqs. (5) and (6).

$$T_n = T;\ T_{n+1} = T+\Delta\theta;\ T_u = max[T_n; T_{n+1}] \tag{5}$$

$$T_u \leq T_{ini} \rightarrow (initial)\ ambient\ temp.;\ T_u > T_{ini} \rightarrow \Delta\theta \begin{cases} > 0 \rightarrow heating\ phase \\ < 0 \rightarrow cooling\ phase \\ = 0 \begin{cases} T > T_{ini} \rightarrow full\text{-}fire \\ T = T_{ini} \rightarrow post\ fire \end{cases} \end{cases} \tag{6}$$

Depending on the phase, the material properties are modified using the reduction factors of EC 3 for the heating and full-fire phase and the extended model with the novel reduction factor g(T_u) (Eq. (4)) for the cooling phase as well as the post fire range. Subsequently, isotropic elastic-plastic material behaviour according to the stress-strain-curve given in EC 3 is defined.

Fig. 8 summarizes the results of the simulation of the girder for one of the selected fire scenarios as an example. The scenario corresponds to the simulation of two burning vehicles underneath the girder (scenario ICEV-KK-SUV, [16]). For the individual parts of the steel girder (upper flange (OF), web (ST), lower flange (UF)) result different temperature-time curves, which are shown in Fig. 8(a). The lowest maximum temperatures occur in the upper flange, since the upper side is protected by the concrete ceiling. The highest maximum temperature is reached in the web, as this part of the girder heated faster compared to the flanges due to the lower plate thickness. The total fire duration is 40 min.

In Fig. 8(c), the development of the vertical deformations w in the middle of the beam is presented by relating the temperature-dependent values during the fire scenario to the initial value at ambient temperature. It can be seen that the relative development of the vertical deformation w for all beam components is identical and qualitatively affine to the temperature development, i.e. the maximum deformation occurs at the time of the maximum temperature. It is noticeable that the deformation increases slowly at first, but accelerates significantly after exceeding a component temperature of 400°C. This can be attributed to the decreasing stiffness due to the reduction of the Young's modulus when the temperature exceeds 400°C.

Fig. 8(b) shows the stress σ_x at section points on top of the upper and on the bottom of the lower flange and in the quarter-points of the web of the beam during the fire scenario. As a result of the temperature-induced deformation of the beam, the stress state changes. It can be seen that the transition between pressure and tension shifts towards the colder upper part of the section during heating. Further, it is noticeble that the stress state of the upper flange is fully reversible whereas the stresses in the lower flange and the web are changed after the fire exposure compared to the initial state. This is caused by plasticifications in those components, which occur due to the high temperatures and the respective low yield strengths during the fire scenario. This is also underlined by the stress-strain responses at the examined section points, which are pictured in Fig. 8(d). In case of the upper flange it can be seen that the stress-strain curves return to the linear-elastic initial straight line. In case of the lower flange and the web, however, the stress-strain responses do not recover.

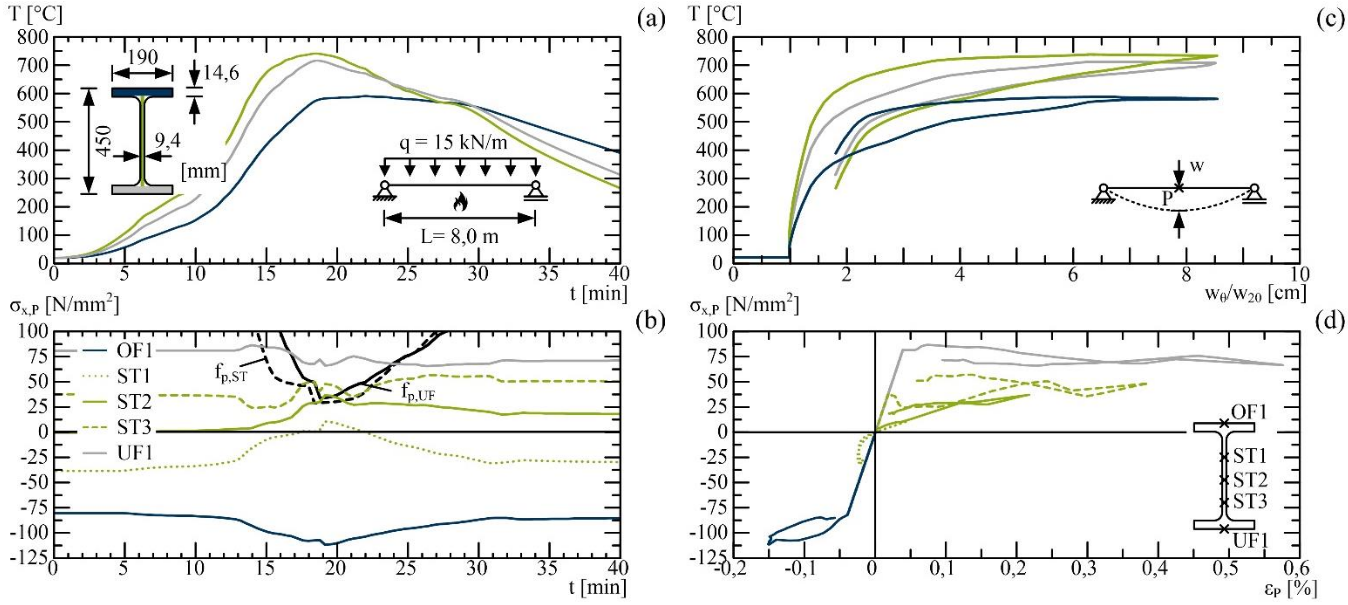

Figure 8. Numerical determined (a) time-temperature relationship, (b) relative development of the vertical deformation, (c) stress-temperature relationship and (d) stress-strain curves of the case study.

6 CONCLUSIONS

An extensive test program of natural fire tests has been carried out to investigate the constitutive behaviour in the cooling phase of natural fire scenarios as well as the residual behaviour of quenched and tempered steels of grades S690QL and S960QL. Further, tests on mild steel S355 J2+N have been performed to compare the temperature dependent mechanical material behaviour of HSS and UHSS to mild steel.

The general assumption of a complete reversibility of the material behaviour of mild steels during cooling has been proofen by the test results. However, the mechnical material behaviour of quenched and tempered HSS and UHSS is not completely reversible, as the recovery of the strength during cooling depends on the maximum temperature, which has been reached in the heating phase. Up to a maximum temperature of T_u= 550°C it can be observed full reversibility, but higher maximum temperatures lead to significant degradations of the residual strengths. In case of the stiffness, the temperature dependent relative change in material behaviour of all investigated materials is qualitatively almost similar during the cooling process. Further, it is almost independent of the maximum temperature and fully reversible in the post fire range.

The comparison of the test results to the material model of prEN 1993-1-2:2022 has shown that modifications of the model are required for HSS and UHSS in the cooling phase of natural fires to predict the measured material behaviour accurately. Therefore, a constitutive material model has been developed, which is based on the existing Eurocode model and a supplementary reduction factor for the effective yield strength and the proportional limit in the cooling phase. For the novel reduction factor, an approach depending on the maximum temperature of the heating phase has been proven adequately.

The developed model has been used for case studies with the FE-software Abaqus. A user subroutine UMAT has been developed, which enables the automatic recognition of the different phases of a natural fire and the respective modification of the material behaviour. It has been shown that the consideration of the altered material behaviour of HSS and UHSS is necessary for an accurate estimation of the structural fire behaviour of steels structures in natural fires including the cooling phase and the post fire behaviour.

ACKNOWLEDGMENT

The research project IFG 20915 N “Material properties for the cooling phase of natural fire conditions (CoolFire)” from the German Committee for Steel Construction (DASt), Düsseldorf, was supported by the Federal Ministry of Economic Affairs and Climate Action through the German Federation of Industrial Research Associations (AiF) as part of the programme for promoting industrial cooperative research (IGF) on the basis of a decision by the German Bundestag. The project was carried out at Ruhr-Universität Bochum.

REFERENCES

1. Neuenschwander, M.; Scandella, C.; Knobloch, M.; Fontana, M.: Modeling elevated-temperature mechanical behavior of high and ultra-high strength steels in structural fire design, Materials & Design 136, 2017, pp. 81–102, doi: 10.1016/j.matdes.2017.09.041.
2. Lange, J.; Wohlfeil, N.: Untersuchungen zum Werkstoffverhalten des Feinkornbaustahls S 460 unter erhöhten Temperaturen, Bautechnik 84, 2007, pp. 711–720, doi: 10.1002/bate.200710061.
3. Qiang, X.; Bijlaard, F.; Kolstein, H.: Deterioration of mechanical properties of high strength structural steel S460N under steady state fire condition, Materials & Design 36, 2012, pp. 438–442, doi: 10.1016/j.matdes.2011.11.069.
4. Qiang, X.; Bijlaard, F.; Kolstein, H.: Deterioration of mechanical properties of high strength structural steel S460N under transient state fire condition, Materials & Design 40, 2012, pp. 521–527.
5. Qiang, X.; Bijlaard, F.; Kolstein, H.: Dependence of mechanical properties of high strength steel S690 on elevated temperatures, Construction and Building Materials 30, 2012, pp. 73-79, doi: 10.1016/j.conbuildmat.2011.12.018.
6. Qiang, X.; Jiang, X.; Bijlaard, F.; Kolstein, H.: Mechanical properties and design recommendations of very high strength steel S960 in fire, Engineering Structures 112, 2016, pp. 60–70, doi: 10.1016/j.engstruct.2016.01.008.
7. CEN/TC250/SC3/WG2, N119: prEN 1993-1-2:2021-Eurocode 3: Design of steel structures- Part 1-2: General rules – Structural fire design, 2021.
8. Lapwood, D.G.: The Effect of Fire Damage on the Mechanical Properties of Structural Steels Assessed using Laboratory Heat Treatment simulations, BSI, 1980.
9. Hanus, F.; Zilli, G.; Franssen, J.-M.: Behaviour of Grade 8.8 bolts under natural fire conditions-Tests and model, Journal of Constructional Steel Research 67, 2011, pp. 1292–1298, doi: 10.1016/j.jcsr.2011.03.012.
10. Qiang, X.; Bijlaard, F.; Kolstein, H.: Post-fire mechanical properties of high strength structural steels S460 and S690, Engineering Structures 35, 2012, pp. 1–10, doi: 10.1016/j.engstruct.2011.11.005.
11. Qiang, X.; Bijlaard, F.; Kolstein, H.: Post-fire performance of very high strength steel S960, Journal of Constructional Steel Research 80, 2013, pp. 235–242, doi: 10.1016/j.jcsr.2012.09.002.
12. Li, G.-Q. et al.: Experimental Studies on the Properties of Constructional Steel at Elevated Temperatures, Journal of Structural Engineering, 2003, pp. 1717–1721. doi: 10.1061/(ASCE)0733-9445(2003)129:12(1717)
13. Chiew, S. P.; Zhao, M. S.; Lee, C. K.: Mechanical properties of heat-treated high strength steel under fire/post-fire conditions, Journal of Constructional Steel Research 98, 2014, pp. 12–19, doi: 10.1016/j.jcsr.2014.02.003.
14. Wang, W.; Liu, T.; Liu, J.: Experimental study on post-fire mechanical properties of high strength Q460 steel, Journal of Constructional Steel Research 114, 2015, pp. 100–109, doi: 10.1016/j.jcsr.2015.07.019.
15. Knobloch, M.; Pauli, J.; Fontana, M.: Influence of the strain-rate on the mechanical properties of mild carbon steel at elevated temperatures, Materials & Design 49, 2013, pp. 553-565, doi: 10.1016/j.matdes.2013.01.021.
16. Schaumann, P.; Zehfuß, J.: Untersuchung zur Tragsicherheit offener Parkgaragen in Stahl- und Verbundbauweise unter Brandeinwirkungen von E-Fahrzeugen und kraftstoffbetriebenen Fahrzeugen. German national IGF-AiF/DASt Research Project 20453N, Research report, 2021.

SiF 2022– The 12th International Conference on Structures in Fire
The Hong Kong Polytechnic University, Nov 30 - Dec 2, 2022

FIRE PERFORMANCE OF BUILT-UP COLD-FORMED STEEL COLUMNS

Hélder D. Craveiro[1], Rohola Rahnavard[2], Luís Laím[3], Aldina Satntiago[4]

ABSTRACT

Cold-formed steel (CFS) products are nowadays widely used in multiple structural applications, exploring their versatility. More recently CFS products and structural solutions have been used successfully in multi-storey buildings, enabling prefabrication, and easy and fast assembly procedures. To further extend the applicability of such products in new structures, their versatility must be intelligently explored, for instance by combining multiple individual sections effectively to attain higher load-bearing capacity and torsional stiffness. The behaviour of built-up elements has been investigated worldwide in order the address the demands arising from the construction sector about the urgent need for specific guidelines for the design of built-up elements. However, under accidental fire conditions, research on the behaviour of CFS built-up elements is still scarce, and no specific provisions exist for these types of structural elements.

In this investigation, the fire performance of short built-up cold-formed steel columns is assessed using experimental tests and numerical modelling. Closed built-up cross-sections were investigated in fire using 3 basic cross-section shapes, namely C, U and Σ. The composite action between the individual shapes and local buckling phenomena was investigated, considering the influence of fastener spacing in the overall behaviour of the short built-up columns in fire

Keywords: Cold-formed steel; built-up, fire; local buckling; critical temperature

1 INTRODUCTION

Cold-formed steel (CFS) products are nowadays widely used in the building construction industry, exploring efficiently their versatility. Increasing the competitiveness of CFS requires expanding the field of applicability of CFS structural solutions, for instance, for multi-storey buildings. This trend is pushing the increasing demand from the industry to the development of comprehensive design guidelines for their structural design. Built-up cold-formed steel elements are commonly used in light steel framing structural systems, providing higher load-bearing capacity (reducing as well the global slenderness) and torsional stiffness. The versatility of single sections allows that those can be combined using self-drilling screws to fabricate open and closed built-up sections [1]. As stated by Rasmussen et al. [2] the behaviour of built-up CFS elements is governed by the partial composite action, ensured by the use of fasteners positioned at the cross-section level and along the length of the elements. The partial composite action will greatly depend on the spacing between the fasteners, shear displacements, and forces in the fasteners [2]. Also, the overlapping steel plates may play a relevant role in the way the individual shapes interact.

[1] Researcher, ISISE – Institute for Sustainability and Innovation in Structural Engineering, University of Coimbra,
e-mail: heldercraveiro.eng@uc.pt, ORCID: https://orcid.org/ 0000-0001-8590-5885
[2] PhD Candidate, ISISE – Institute for Sustainability and Innovation in Structural Engineering, University of Coimbra
e-mail: rahnavard@uc.pt, ORCID: https://orcid.org/ 0000-0001-9399-104X
[3] Researcher, ISISE – Institute for Sustainability and Innovation in Structural Engineering, University of Coimbra
e-mail: luislaim@uc.pt, ORCID: https://orcid.org/ 0000-0002-8342-3695
[4] Professor, ISISE – Institute for Sustainability and Innovation in Structural Engineering, University of Coimbra
e-mail: aldina@dec.uc.pt, ORCID: https://orcid.org/ 0000-0003-3646-4926
https://doi.org/10.6084/m9.figshare.22215751

At ambient temperature, the design of CFS members can be performed considering the Effective Width Method (EWM) and the Direct Strength Method (DSM), used in the EN 1993-1-3 [3] and AISI S100 [4]. However, the design standards almost exclusively deal with elements comprising a single section. The same is observed when discussing design methodologies for accidental fire action [5].

Traditionally, CFS elements require passive fire protection due to the high section factor of the individual shapes, high thermal conductivity, and fast degradation of mechanical properties with increasing temperature [6]. However, research on built-up elements in fire is still relatively scarce, and no specific provisions are provided in the current version of the Eurocode for these types of elements [5]. For single sections and wall systems extensive research has been conducted in the past few decades [7 - 13], however, research on the structural fire performance of built-up cold-formed steel columns is still very scarce [6, 11 - 13].

Arrais et al. [13] investigated and proposed improvements to the design methodologies for CFS lipped channels and Sigma channels under compression, by introducing a new parameter β (as a function of cross-section shape) to the calculation of the imperfection factor α in fire situation. The authors recommended a β value of 0.65 for lipped channels and 0.4 for sigma channels. No indications were given for built-up sections, but the proposed methodology can be considered for built-up elements by adjusting the β parameter.

Yang et al. [14, 15] investigated built-up box CFS columns in fire conditions with and without the influence of restraint to thermal elongation. In both studies, the authors used plain and lipped channels to fabricate the built-up box section. The authors reported the impact of restraint to thermal elongation and initial serviceability load level in the overall fire resistance of CFS built-up box columns, however, no comparisons were made against design predictions using relevant standards. Also, no detailed discussion was presented concerning the composite action between the individual shapes. Similar observations were reported by Craveiro et al. [1, 6] concerning the influence of restraint to thermal elongation, for both built-up open and built-up closed sections.

In the numerical models, Yang et al. [15] discussed the relevance of the input data, mainly related to mechanical and thermal properties. Generally, researchers consider that the information presented in current design standards such as the EN 1993-1-2 [5] is not accurate, since the reduction factors in the EN 1993-1-2 [5] are higher than the ones obtained in experimental tests [16 - 18].

The behaviour of CFS columns in fire is complex, especially if several profiles are considered simultaneously and if the partial composite action between the individual shapes is a critical influencing parameter. The partial composite action influences significantly the load-bearing capacity of built-up columns at ambient temperature, hence the lack of accurate and reliable design guidelines will provide inaccurate fire resistance estimations for built-up CFS columns.

In this investigation, the fire performance of short built-up cold-formed steel columns is assessed using experimental tests and numerical modelling. Closed built-up cross-sections were investigated in fire using 3 basic cross-section shapes, namely C, U, and Σ. In all experimental tests, temperature evolution, loading, and deformations of the tested specimens were monitored. The fire resistance of the built-up columns was determined. It is worth mentioning that the serviceability compressive load considered in the fire resistance tests was determined based on experimental results obtained at ambient temperature. The composite action between the individual shapes and local buckling phenomena was investigated, considering the influence of fastener spacing in the overall behaviour of the short built-up columns in fire. The complex buckling phenomena were also investigated and predominant buckling modes characterized. All data collected was used for the development and validation of accurate and reliable finite element models.

2 EXPERIMENTAL TESTING

2.1 Geometry of the built-up sections

Exploring the versatility of the individual CFS cross-section shapes, four built-up cross-sections were fabricated using 3 individual shapes, namely, C, U and Σ. Each closed built-up box CFS section comprised

4 profiles. In Figure 1 the geometric configuration of the individual shapes is presented. The individual sections were fabricated with S280GD+Z structural steel, hot-dip galvanized with zinc (zinc coating of 0.04 mm – 275 g/m^2) with a nominal yield strength of 280 MPa and ultimate strength of 360 MPa.

The built-up cross-sections were a) rectangular built-up cross-section comprising two C-shaped profiles fastened back-to-back and two U-shaped profiles (R-2C+2U); b) square built-up cross-section comprising two C-shaped profiles and two U-shaped profiles (S-2C+2U); c) rectangular built-up cross-section with two Σ-shaped profiles fastened back-to-back and two U-shaped profiles (R-2Σ+2U); and, d) a square built-up cross-section with two Σ-shaped and two U-shaped profiles (S-2Σ+2U). The cross-sections are depicted in Figure 2. The length of the steel profiles was 1050 mm.

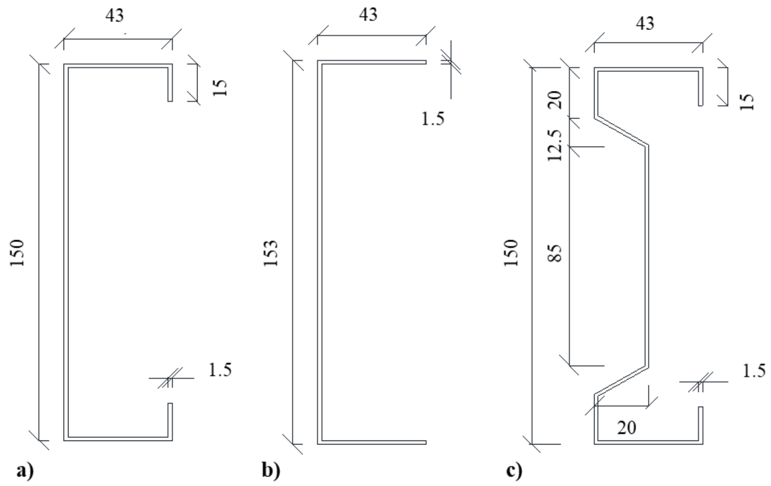

Figure 1. Dimensions of the individual cross-section shapes used. A) C-shape. B) U-shape. C) Σ-shape.

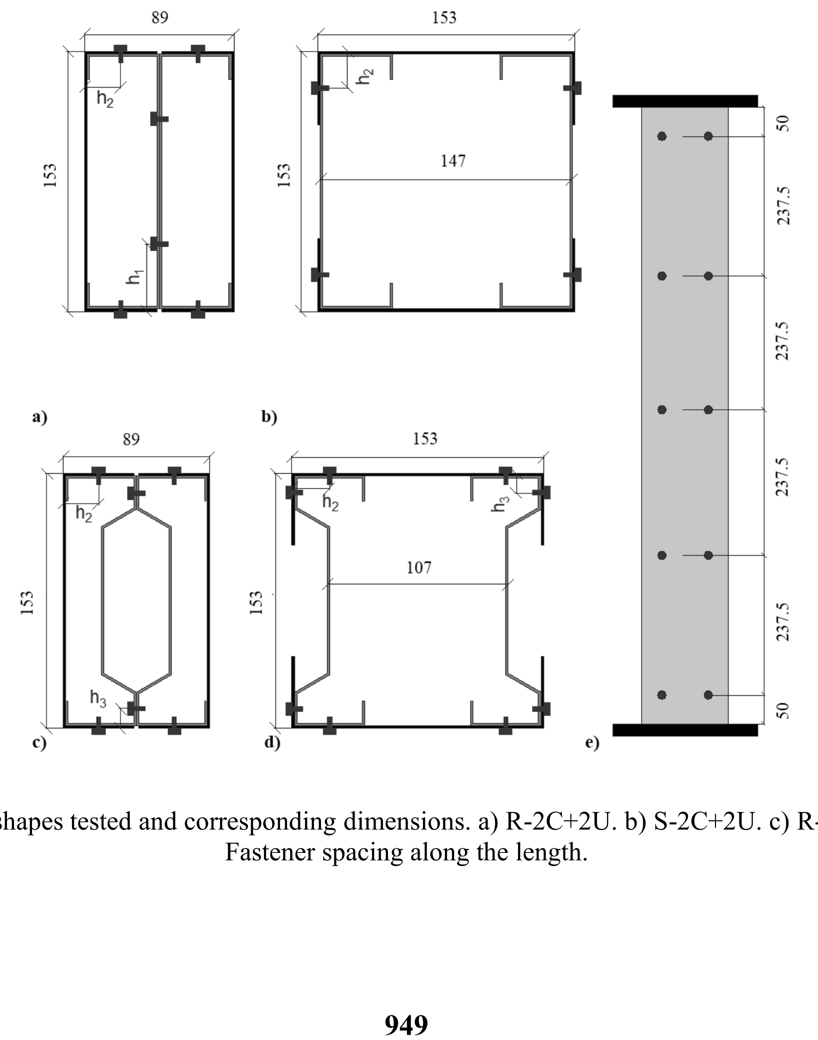

Figure 2. Cross-section shapes tested and corresponding dimensions. a) R-2C+2U. b) S-2C+2U. c) R-2Σ+2U. d) S-2Σ+2U. e) Fastener spacing along the length.

The selected spacing for the fasteners was 237.5 mm ($^{L-(2\times 50)}/_{4}$), considering that additional fasteners were positioned at 50 mm from the ends of the built-up columns. The selected spacing along the length of the built-up member was selected based on preliminary numerical modelling, current practice, and data from the literature, namely in research studies conducted by Meza et al. [19] and Nie Shaofeng et al. [20, 21]. The fasteners' distances at the cross-section level are also detailed in Figure 2. The fasteners were positioned at the mid-span of the overlapping steel plates, except in the web of the R-2C+2U section, as depicted in Figure 2. To connect the individual shapes, self-drilling screws 6.3 mm in diameter were used.

The short square columns were designed to fail predominantly by sectional buckling of the individual profiles between the connectors. The total length was larger than 3 times the length of the web and smaller than 20 times the least radius of gyration [22], especially for the square columns (i.e., 1150 mm). Some interaction between sectional and global buckling for the rectangular columns could occur. Hence, the obtained results were used to validate and perform additional numerical studies. Additionally, the selected length was the most suitable to match the existing limitations of the electric furnaces used in this investigation.

2.2 Load-bearing capacity tests

At ambient temperature, the load-bearing capacity of the innovative built-up CFS columns was assessed. 12 compressive tests were performed on identical built-up columns considering fixed boundary conditions, as depicted in Figure 3. The obtained experimental results are presented in Table 1.

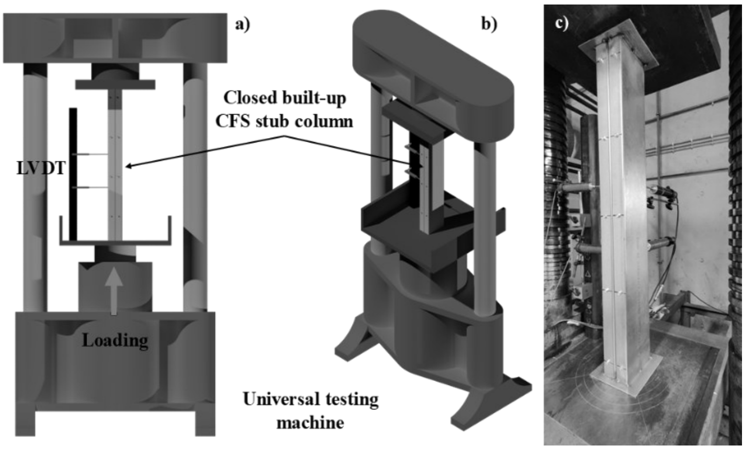

Figure 3. a) and b) Schematic representation of the test set-up. c) Test set-up [23].

Table 1. Buckling loads recorded in the experimental tests at ambient temperature.

Test	$P_{u,test}$ (kN)	$P_{u,test}/A_g$ (N/mm²)	$P_{u,test}/A_{eff}$ (N/mm²)	Test	$P_{u,test}$ (kN)	$P_{u,test}/A_g$ (N/mm²)	$P_{u,test}/A_{eff}$ (N/mm²)
R-2C+2U-1	259.60	178.66	312.41	**S-2C+2U-1**	232.78	160.21	280.13
R-2C+2U-2	267.00	183.76	321.32	**S-2C+2U-2**	248.00	170.68	298.45
R-2C+2U-3	242.50	166.90	291.83	**S-2C+2U-3**	241.89	166.48	291.10
μ	256.37	176.44	308.52	μ	240.89	165.79	289.89
σ	10.26	7.06	12.35	σ	6.25	4.30	7.53
CV (%)	4.00	4.00	4.00	**CV (%)**	2.60	2.60	2.60
Test	**$P_{u,test}$ (kN)**	**$P_{u,test}/A_g$ (N/mm²)**	**$P_{u,test}/A_{eff}$ (N/mm²)**	**Test**	**$P_{u,test}$ (kN)**	**$P_{u,test}/A_g$ (N/mm²)**	**$P_{u,test}/A_{eff}$ (N/mm²)**
R-2Σ+2U-1	320.70	209.47	284.10	**S-2Σ+2U-1**	320.30	209.21	283.74
R-2Σ+2U-2	310.20	202.61	274.80	**S-2Σ+2U-2**	295.40	192.95	261.68
R-2Σ+2U-2	302.30	197.45	267.80	**S-2Σ+2U-3**	311.90	203.72	276.30
μ	311.07	203.18	275.56	μ	309.20	201.96	273.91
σ	7.54	4.92	6.68	σ	10.34	6.76	9.16
CV (%)	2.42	2.42	2.42	**CV (%)**	3.35	3.35	3.35

The obtained results were then used to determine the service load to be considered in the experimental fire resistance tests. In Table 2 the used serviceability loads are presented.

Table 2. Determination of the serviceability load.

Test	$P_{u,Test}$ (kN)	$\overline{P}_{u,Test}$ (kN)	$0.4 \times \overline{P}_{u,Test}$ (kN)	Test	$P_{u,test}$ (kN)	$\overline{P}_{u,Test}$ (kN)	$0.4 \times \overline{P}_{u,Test}$ (kN)
R-2C+2U-1	259.60			**S-2C+2U-1**	232.78		
R-2C+2U-2	267.00	256.4	102.5	**S-2C+2U-2**	248.00	240.89	96.4
R-2C+2U-3	242.50			**S-2C+2U-3**	241.89		
R-2Σ+2U-1	320.70			**S-2Σ+2U-1**	320.30		
R-2Σ+2U-2	310.20	311.1	124.4	**S-2Σ+2U-2**	295.40	309.2	123.6
R-2Σ+2U-2	302.30			**S-2Σ+2U-3**	311.90		

2.3 Mechanical properties

The determination of the mechanical properties of cold-formed steels at elevated temperatures is a key topic in the research of the behaviour of CFS structural elements in fire. In this investigation, tensile coupon tests were only performed at ambient temperature, but data previously obtained for the S280GD+Z steel by Craveiro et al. [17] was used. The data obtained in this investigation was critical for the developed finite element models. The mechanical properties determined at ambient temperature are presented in Table 3, including the data for flat (*Fi*) and corner (*Ci*) coupon specimens. In Figure 4 the stress-strain curves at elevated temperatures for the S280GD+Z steel are depicted.

Table 3. Mechanical properties of the S280GD+Z steel [23].

Test	E_s (GPa)	$\overline{E}_s$ (GPa)	f_y (MPa)	$\overline{f}_y$ (MPa)	f_u (MPa)	$\overline{f}_u$ (MPa)	f_p (MPa)	$\overline{f}_p$ (MPa)	ε (%)	$\overline{\varepsilon}$ (%)	n	$\overline{n}$
F1	205.23		302.54		422.47		208.28		22.71		12.49	
F2	203.9	204.7	308.92	305.9	426.61	426.1	210.97	214.5	23.05	22.9	14.16	12.8
F3	203.42		308.98		423.04		218.24		22.75		12.91	
F4	206.4		303.12		432.11		220.43		23.48		11.77	
C1	205.21		378.31		449.94		240.14		12.78		20.87	
C2	209.56	205.1	381.43	378.6	454.38	451.0	238.15	241.9	12.79	13.2	17.90	18.9
C3	202.04		376.88		452.15		240.17		13.67		18.74	
C4	203.43		377.67		447.63		249.22		13.66		18.22	

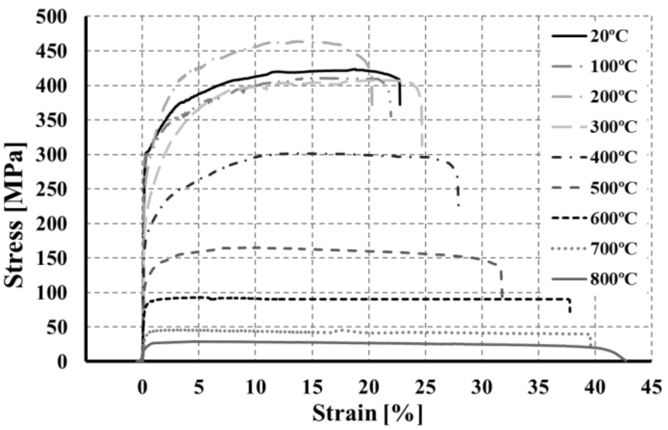

Figure 4. Stress vs strain curves for the S280GD+Z steel at elevated temperatures [17].

2.4 Experimental tests, test set-up and instrumentation

The experimental fire resistance tests were performed at the laboratory of Civil Engineering at the University of Coimbra. The test set-up comprises a large reaction steel frame a 3D auxiliary steel frame that can be used to apply different levels of restraint to thermal elongation. In this experimental investigation, no restraint to thermal elongation was imposed to the CFS built-up column in fire, hence during the fire resistance test the built-up column could freely expand. The built-up CFS columns were fixed to the 3D surrounding steel frame using special devices. In Figure 5 a global view of the test set-up is presented and in Figure 6 the positioning of the Type-K thermocouples.

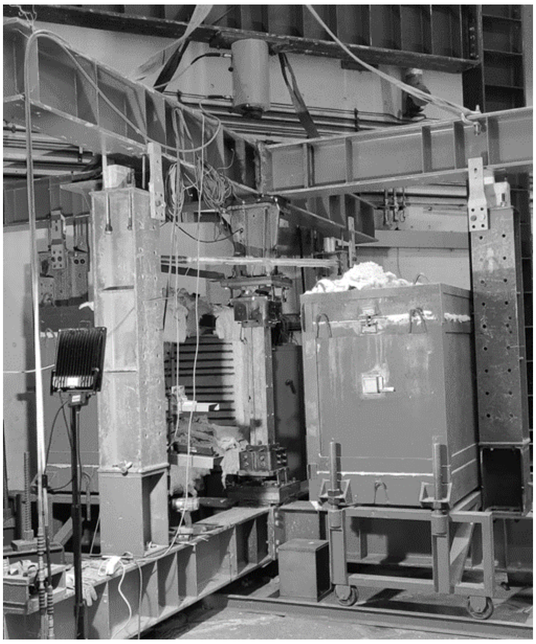

Figure 5. Global view of the experimental test set-up.

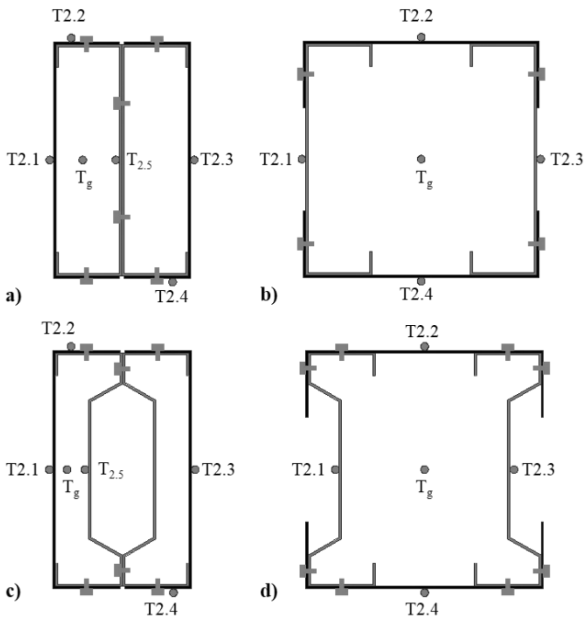

Figure 6. Positioning of the Type-K thermocouples.

The test procedure consisted of applying the previously defined serviceability load to each one of the built-up configurations. The load was applied under force control, and after the established load was applied the electrical furnaces, programmed to reproduce the ISO 834 fire curve, were turned on. During the fire resistance test, the service load was kept constant and the test specimen could freely expand. With increasing temperature, the mechanical properties of the S280GD+Z steel would degrade, up to an instant when the column was no longer able to withstand the service load.

In all tests loads, displacements and temperatures were monitored and recorded.

3 NUMERICAL MODELLING

3.1 Modelling strategies and assumptions

Exploiting the experimental results and all data gathered, finite element models were developed to accurately reproduce the observed experimental behaviour. In this investigation, both heat transfer and mechanical behaviour were reproduced using the finite element software Abaqus [24]. A sequential temperature-displacement analysis with imperfections was adopted, hence the heat transfer analysis was performed on the 3D model and then the nodal temperatures were imported to the structural model including imperfections and degradation of the mechanical properties of the steel as a function of temperature.

The adopted procedure included the heat transfer analysis, the linear buckling analysis and the mechanical analysis including imperfections and nodal temperatures determined in the heat transfer analysis. The procedure is detailed in Figure 7.

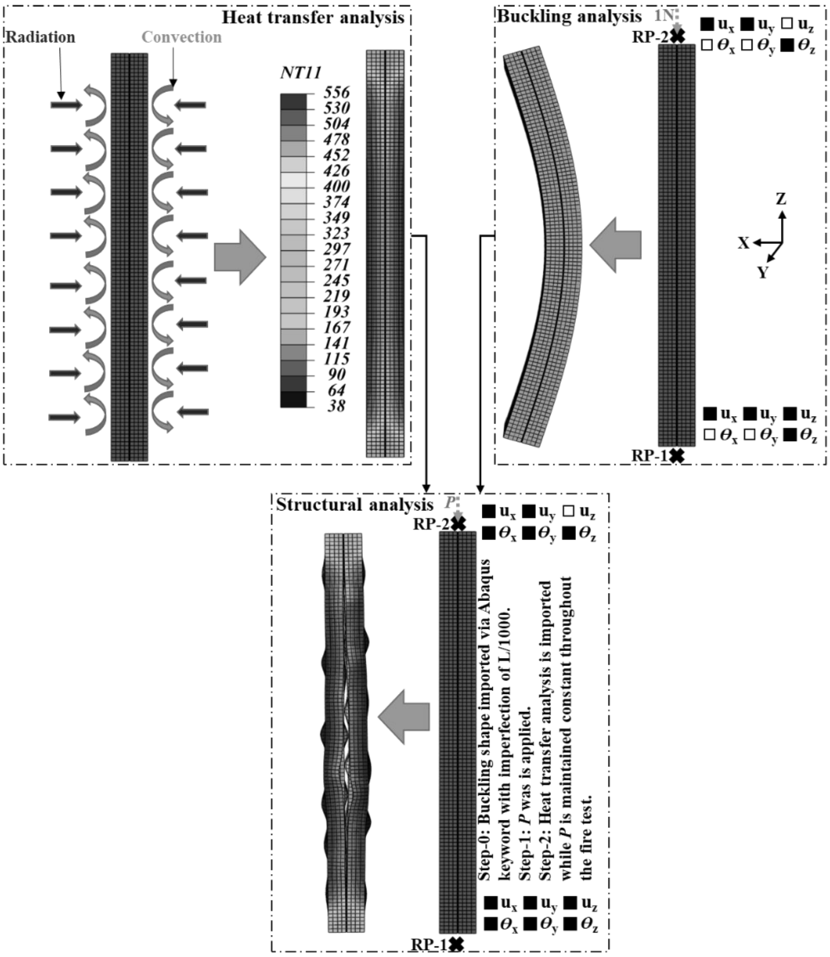

Figure 7. Strategy adopted to reproduce the experimental tests using the finite element model.

The heat transfer analysis was performed to obtain the temperature distribution at the cross-section level and along the length of the column. The gas temperature monitored in the experimental tests at different locations was used as input, considering a resultant emissivity of 0.16 (emissivity of electrical resistances of 0.7; emissivity of galvanized steel of 0.23) and a coefficient of heat transfer by convection of 15 $Wm^{-2}K^{-1}$. The Stefan-Boltzmann constant was 5.67×10^{-8} $Wm^{-2}K^{-4}$ and the thermal conductance between the steel plates was 7×10^{3} $Wm^{-2}K^{-1}$.

In the structural analysis, the magnitude of the global and local imperfections was L/1000 and h/200, respectively, taking into consideration the indications provided by several other authors [25 - 28].

The material properties of CFS were defined as an elastoplastic material considering temperature-dependent data. The plastic behaviour with isotropic hardening was from the experimental results presented by Craveiro et al. [17] and depicted in Figure 4. All thermal properties used were also extracted from the results reported by Craveiro et al. [17].

The contact interaction for all surfaces was defined using *surface-to-surface* contacts including normal hard contact and penalty tangential contact with a friction coefficient of 0.2. The fasteners were reproduced using the combined *Beam connector and fastener* approach in Abaqus. In this scenario, the beam connector defined the connection between the nodes of the adjacent surfaces. Using the fastener tool, the actual radius of the fasteners is introduced.

All cross-section shapes were modelled considering S4R shell elements with a size of 10 mm.

4 DISCUSSION OF RESULTS

4.1 Failure modes

The observed buckling modes for the innovative built-up short columns are depicted in Figure 8. As expected, the governing buckling mode was local buckling. Since the specimens were inside the furnace it was not easy to identify where local buckling started but it was clear that the phenomenon started between the fasteners. Significant deformations are identified for the external plain channels (U profiles). In all tested specimens no damage was observed in the fasteners, hence it can be stated that during the fire resistance test the fasteners contributed effectively to mitigate distortional buckling phenomena at their location.

It was also observed that deformation by compatibility occurred in the connected overlapping steel plates. No global buckling was identified.

The final deformed shapes show the relevant role of fasteners in preventing local buckling phenomena.

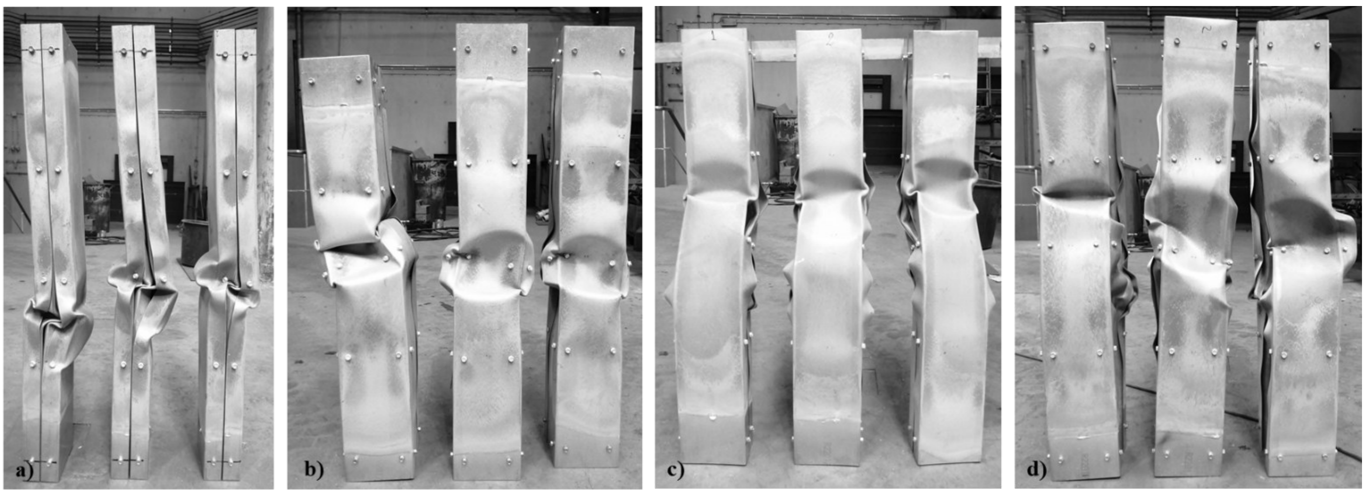

Figure 8. a) R-2C+2U. b) S-2C+2U. c) R-2Σ+2U. d) S-2Σ+2U.

It is interesting to note that overlapping plates tend to deform as a group which may indicate that if the fasteners' spacing is close to or smaller than the local buckle half-wavelength the composite action will be greatly enhanced.

4.2 Temperature evolution

The monitored temperature evolution of the steel was compared with the numerical results using the finite element method and considering all the assumptions and strategies presented in Chapter 3 for the heat transfer analysis. The experimental and numerical results are depicted in Figure 9. Overall, a very good agreement was obtained between experimental and numerical results in the heat transfer analysis. Hence, the adopted strategies and assumptions enable larger parametric studies that are still required.

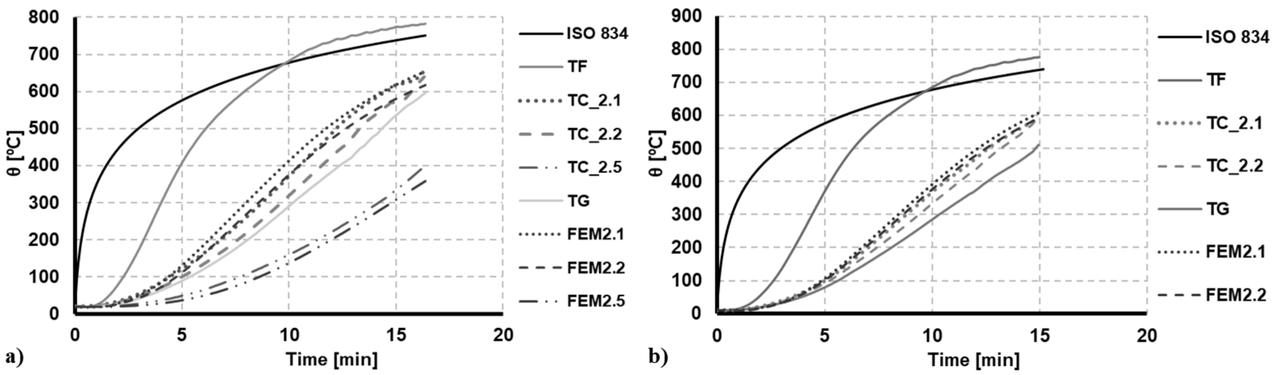

Figure 9. Temperature evolution in the steel profiles

4.3 Fire resistance

The fire resistance of the tested specimens was assessed both in terms of time (t_{cr}) and critical temperature (θ_{cr}). Specifically for the data presented in Table 4, the critical temperatures were the ones extracted from the cross-section where the highest temperatures were recorded. Overall, in terms of time, the results are relatively similar, however, it is worth mentioning that for an initial load level of $0.4N_{b,Rd}$ the observed critical temperatures were always significantly higher than 350 ºC. Consequently, the 350 ºC critical temperature limit established in the EN 1993-1-2 for class 4 members is too simplistic and conservative. On average, the critical temperatures ranged from 538 ºC up to 606 ºC, respectively for the S-2C+2U and R-2Σ+2U cross-sections.

Table 4. Summary of the experimental results.

Section	**P_0 [kN]**	**t_{cr} [min]**	**θ_{cr} [ºC]**	**Section**	**P_0 [kN]**	**t_{cr} [min]**	**θ_{cr} [ºC]**
R-2C+2U_1		14.78	542	**R-2Σ+2U_1**		15.90	584
R-2C+2U_2	102	14.71	558	**R-2Σ+2U_2**	124	16.40	596
R-2C+2U_3		14.31	555	**R-2Σ+2U_3**		16.40	640
	$\overline{X}$	14.6	551.7		$\overline{X}$	16.2	606.7
	σ	0.2	6.9		**σ**	0.2	24.1
	COV	1.4	1.3		**COV**	1.5	4.0
Section	**P_0 [kN]**	**t_{cr} [min]**	**θ_{cr} [ºC]**	**Section**	**P_0 [kN]**	**t_{cr} [min]**	**θ_{cr} [ºC]**
S-2C+2U_1		13.78	517	**S-2Σ+2U_1**		14.20	575
S-2C+2U_2	96.4	14.50	538	**S-2Σ+2U_2**	123.6	14.00	563
S-2C+2U_3		15.30	561	**S-2Σ+2U_3**		14.90	562
	$\overline{X}$	14.5	538.7		$\overline{X}$	14.4	566.6
	σ	0.6	18.0		**σ**	0.4	5.6
	COV	4.3	3.3		**COV**	2.7	1.0

The experimental results were reproduced using the finite element method and the software Abaqus using all assumptions and techniques described in Chapter 3. As depicted in Figure 10, the numerical results are in good agreement with the experimental ones. This enables the use of finite element models to perform larger parametric studies assessing the influence of several parameters outside the bounds of the experimental investigation already performed.

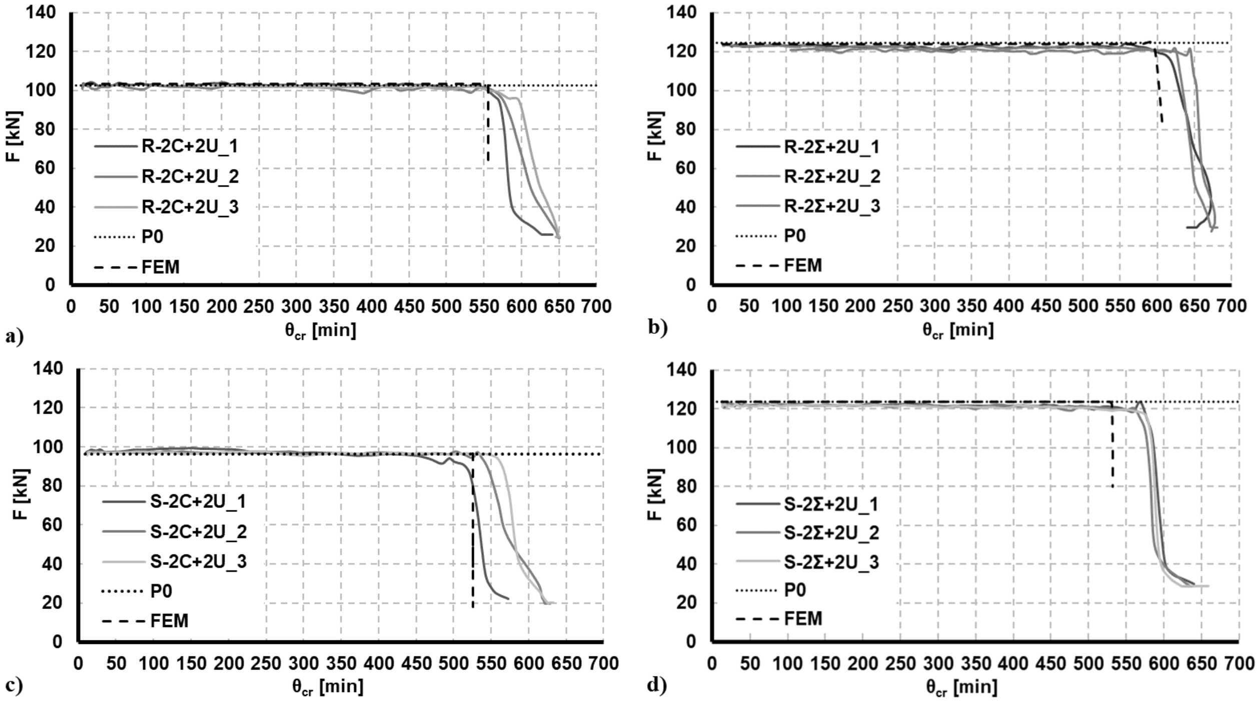

Figure 10. Force vs temperature graphs for all tested cross-sections and comparison against numerical results. a) R-2C+2U. b) R-2Σ+2U. c) S-2C+2U. d) S-2Σ+2U.

5 CONCLUSIONS

This paper reports an experimental investigation on the complex behaviour of built-up CFS short columns under compression in fire. Fire resistance of the short built-up CFS columns in terms of temperature and time. Also, the complex buckling phenomena were identified and discussed. Local buckling phenomena governed the overall behaviour of the built-up columns, and it was observed that the distance between fasteners influenced the deformation of the overlapping plates. The shorter the spacing between fasteners the stronger will be the composite action. Consequently, the overlapping steel plates will deform as a group.

The numerical models were able to reproduce accurately the observed experimental behaviour, enabling extensive parametric studies. The future work includes assessing the suitability of design guidelines according to the EN 1993-1-2 [5] and AISI S100 [4], and assessing the influence of the spacing between fasteners in promoting the composite action between the individual shapes. Also, the stiffness of the fasteners and considering explicitly the degradation of the mechanical fasteners with increasing temperature shall be considered.

ACKNOWLEDGMENT

This work is financed by national funds through FCT - Foundation for Science and Technology, under grant agreement 2021.06528.BD attributed to the 1st author and under the grant agreement 2020.03588.CEECIND attributed to the 2nd author.

The authors gratefully acknowledge the Portuguese Foundation for Science and Technology (FCT) for its support under the framework of the research project PCIF/AGT/0062/2018 – INTERFACESEGURA –

Segurança e Resiliência ao Fogo das Zonas e Interface Urbana-Florestal, financed by FCT through National funds.

This work was partly financed by FCT/MCTES through national funds (PIDDAC) under the R&D Unit Institute for Sustainability and Innovation in Structural Engineering (ISISE), under reference UIDB/04029/2020.

REFERENCES

1. Hélder D. Craveiro, João Paulo C. Rodrigues, Luís Laím. (2016). Buckling resistance of axially loaded cold-formed steel columns. Thin-Walled Structures 106 358-375.
2. Rasmussen Kim J.R., Khezri Mani, Schafer Benjamin W., Zhang Hao (2020), The mechanics of built-up cold-formed steel members, Thin-Walled Struct., 154 (2020), Article 106756, 10.1016/j.tws.2020.106756
3. EN1993-1-3:2004, Eurocode 3: Design of steel structures, Part 1–3: General Rules, Supplementary Rules for Cold-formed Members and Sheeting, European Committee For Standardization, Brussels, Belgium, p.125.
4. AISI-S100, North American Specification for the Design of Cold-Formed Steel Structural Members, American Iron and Steel Institute, Washington, D.C., 2016.
5. EN 1993-1-2:2005, Eurocode 3: Design of Steel Structures, Part 1-2: General Rules, Structural Fire Design, European Committee for Standardization, Brussels, Belgium, 2005.
6. Hélder D. Craveiro, João Paulo C. Rodrigues, Luís Laím, (2016). Experimental analysis of built-up closed cold-formed steel columns with restrained thermal elongation under fire conditions, Thin-Walled Structures, Volume 107, pages 564-579.
7. Ashkan Shahbazian, Yong Chang Wang (2011). Application of the Direct Strength Method to local buckling resistance of thin-walled steel members with non-uniform elevated temperatures under axial compression, Thin-Walled Structures, Volume 49, issue 12, Pages 1573-1583. https://doi.org/10.1016/j.tws.2011.08.005
8. Ahkan Shahbazian, Yong Chang Wang (2012). Direct Strength Method for calculating distortional buckling capacity of cold-formed thin-walled steel columns with uniform and non-uniform elevated temperatures, Thin-Walled Structures, Volume 53, pages 188-199. https://doi.org/10.1016/j.tws.2011.08.005
9. Y. Dias, M. Mahendran, K. Poologanathan (2019), Full-scale fire resistance tests of steel and plasterboard sheathed web-stiffened stud walls, Thin-Walled Struct., 137 (2019), pp. 81-93
10. A.D. Ariyanayagam, M. Mahendran, (2018), Fire performance of load bearing LSF wall systems made of low strength steel studs, Thin-Walled Struct., 130 (2018), pp. 487-504. https://doi.org/10.1016/j.tws.2018.05.018
11. M. Feng, Y.C. Wang, J. M. Davies, (2003), Structural behaviour of cold-formed thin-walled short steel channel columns at elevated temperatures. Part 1: Experiments, Thin-Walled Structures, Volume 41, Issue 6, Pages 543-570. https://doi.org/10.1016/j.jcsr.2015.01.011
12. Luís Laím, Hélder D. Craveiro, Rui Simões, André Escudeiro, Alexandre Mota (2020). Experimental analysis of cold-formed steel columns with intermediate and edge stiffeners in fire, Thin-Walled Structures, Volume 146, 106481. https://doi.org/10.1016/j.tws.2019.106481
13. Flávio Arrais, Nuno Lopes, Paulo Vila Real, (2021), Fire design of slender cold-formed lipped channel and sigma section members with uniform temperature under compression, Fire Safety Journal, Volume 122, 103340. https://doi.org/10.1016/j.jcsr.2019.105851
14. Jingjie Yang, Weiyong Wang, Yu Shi, Lei Xu (2020). Experimental study on fire resistance of cold-formed steel built-up box columns, Thin-Walled Structures, Volume 147, 106564. https://doi.org/10.1016/j.tws.2019.106564
15. Jingjie Yang, Weiyong Wang, Lei Xu, Hisham Al-azzani, (2020). Experimental and numerical studies on axially restrained cold-formed steel built-up box columns at elevated temperatures, Journal of Constructional Steel Research, Volume 171, 106143. https://doi.org/10.1016/j.jcsr.2020.106495
16. Ju Chen, Ben Young, (2007). Experimental investigation of cold-formed steel material at elevated temperatures, Thin-Walled Structures, Volume 45, Issue 1, Pages 96-110. https://doi.org/10.1016/j.tws.2006.11.003
17. Hélder D. Craveiro, João Paulo C. Rodrigues, Aldina Santiago, Luís Laím, (2016). Review of the high temperature mechanical and thermal properties of the steels used in cold-formed steel structures – The case of the S280GD+Z steel, Thin-Walled Structures, Volume 98, Part A, Pages 154-168. https://doi.org/10.1016/j.tws.2015.06.002

18. N.D. Kankanamge, M. Mahendran (2011), Mechanical properties of cold-formed steels at elevated temperatures, Thin-Walled Structures, Volume 49, pages 26-44. https://doi.org/10.1016/j.tws.2010.08.004
19. Meza, Francisco J., Becque, Jurgen, Hajirasouliha, Iman. (2020). Experimental study of cold-formed steel built-up columns, Thin-Walled Structures, 149, 1076291. https://doi.org/10.1016/j.tws.2019.106291
20. Nie, Shao-Feng, Zhou, Tian-Hua, Zhang, Yang, Liu, Bo. (2020). Compressive behaviour of built-up closed box section columns consisting of two cold-formed steel channels, Thin-Walled Structures, 151, 106762. https://doi.org/10.1016/j.tws.2020.106762
21. Nie, Shafeng, Zhou, Tianhua, Eatherton, Matthew R., Li, Jiang, Zhang, Yang. (2020). Compressive behaviour of built-up double-box columns consisting of four cold-formed steel channels, Engineering Structures, 222, 111133. https://doi.org/10.1016/j.engstruct.2020.111133
22. R.D. Ziemian, Appendix B - Technical Memoranda of Structural Stability Research Council, 2010.
23. Craveiro, Hélder D., Rahnavard, R., Laím, L., Simões, R., Santiago, A., (2022), Buckling behaviour of closed built-up cold-formed steel columns under compression, Thin-Walled Structures, Volume 179, 109493. https://doi.org/10.1016/j.tws.2022.109493
24. Abaqus Analysis User's Guide, Version 6.17 Dassault Systèmes Simulia USA (2017).
25. Dongdong Yang, Faqi Liu, Shan-Shan Huang, Hua Yang (2021), Structural fire safety design of square and rectangular tubed-reinforced-concrete columns, Structure, 29 (2021), pp. 1286-1321, 10.1016/j.istruc.2020.12.014
26. N.D. Kankanamge, M. Mahendran, Behaviour and design of cold-formed steel beams subject to lateral–torsional buckling at elevated temperatures, Thin-Wall Struct, 61 (2012), pp. 213-228
27. J. Ye, I. Hajirasouliha, J. Becque, K. Pilakoutas, Development of more efficient cold-formed steel channel sections in bending, Thin-Wall Struct, 101 (2016), pp. 1-13.
28. C. Yu, B.W. Schafer, Simulation of cold-formed steel beams in local and distortional buckling with applications to the direct strength method, J Constr Steel Res, 63 (2007), pp. 581-590

FIRE RESISTANCE OF SHORT STEEL COLUMNS PROTECTED WITH DEVELOPED GYPSUM-BASED MORTARS

Hugo Caetano[1], Aldina Santiago[2], Luís Laím[3], Ashkan Shahbazian[4]

ABSTRACT

During a fire event, the stability of steel members may be compromised, and the structural collapse may occur, due to the loss of its mechanical resistance as the temperature increase. One of the solutions to reduce this problem is the protection with a coating using enhanced fire-resistant mortars. In this sense, the main objective of this experimental work was to develop a gypsum mortar as a passive fire protection for steel members and to compare the mechanical behaviour of steel columns subject to axial compression and high temperatures when protected with: i) the developed gypsum mortar, ii) a commercial mortar and iii) without any kind of thermal protection. In addition, the thermal effect provided by the respective mortars with a coating of 2 and 3 cm on the steel columns was also studied. The results showed that when compared with the non-protected steel column, 2 cm of commercial mortar and laboratory developed mortar increased the fire resistance of the column by about 4.5 and 5.8 times more, respectively. When a 3 cm thick coating was applied, the commercial mortar and the laboratory developed mortar increased their fire resistance by about 7.4 and 8.0 times more, respectively. These results demonstrated the actual impact of the application of such mortars as passive fire protection of steels structures.

Keywords: Gypsum mortar; perlite; passive protection materials; steel structural elements; high temperatures.

1 INTRODUCTION

There is a growing interest in the development of alternative and sustainable materials with enhanced properties. As far as steel structures are concerned, this demand includes the development of high strength steels, but also the development of materials that can efficiently protect these structures in case of fire [1]. During a fire, the stability of steel members may be compromised, and the structural collapse may occur, due to the loss of its mechanical resistance as the temperature increase [2,3].

The thermal protection of these members is of significant importance. One of the solutions to this protection is the coating with mortars with enhanced fire resistance due to the introduction of thermally stable and porous aggregates [4]. Vermiculite and/or perlite have been incorporated in cement mortars (as a substitution for sand), with the objective of improving their thermal performance when subjected to high temperatures [5].

[1] PhD Researcher, University of Coimbra, ISISE, Department of Civil Engineering, Portugal
e-mail: hugo.caetano@uc.pt, ORCID: https://orcid.org/0000-0002-5447-2236
[2] Assistant Professor, University of Coimbra, ISISE, Department of Civil Engineering, Portugal
e-mail: aldina@dec.uc.pt, ORCID: https://orcid.org/0000-0003-3646-4926
[3] PhD Researcher, University of Coimbra, ISISE, Department of Civil Engineering, Portugal
e-mail: luislaim@uc.pt, ORCID: https://orcid.org/0000-0002-8342-3695
[4] PhD Researcher, University of Coimbra, ISISE, Department of Civil Engineering, Portugal
e-mail: ashkanshahbazian@yahoo.co.uk, ORCID: https://orcid.org/0000-0002-0716-1582
https://doi.org/10.6084/m9.figshare.22215754

Due to their highly porous structure, these materials absorb moisture in varying degrees (depending on their type), extending their durability during the fire, until the moment when this moisture evaporates from the material. As they are materials with good thermal properties, there is the potential to be used in the development of plaster or cement mortars as a passive fire protection solution in steel structures [6].

Vermiculite consists of a micalike mineral containing a shiny flake (the phyllosilicate group). It is produced at ambient conditions from the weathering/hydrothermal alteration of phlogopite or biotite [7]. Similar to perlite, when vermiculite particles are subjected to high temperatures (from 650 to 950 °C), they expand, presenting a density of 80 to 120 kg/m^3, a melting point between 1240 to 1430 °C and a thermal conductivity between 0.04 to 0.12 W/mK [8]. Moreover, due to their highly porous structure, these materials absorb moisture in varying degrees (depending on their type), which when combined with the low thermal conductivity, extends their durability during the fire.

Perlite may be a better supplement than vermiculite, not only due to its thermal conductivity but also to the high retraction effect of vermiculite [9]. As they are materials with good thermal properties, they can be used in the development of plaster or cement mortars as a passive fire protection solution in steel structures.

In addition to cement, plaster can also be used as a binder and combined with perlite and/or vermiculite to develop mortars for passive fire protection. Compared to cement, gypsum is much cheaper, easier to produce, and provides a more effective thermal barrier because it has a lower thermal conductivity than cement. It also contributes to the energy loss from fire due to its endothermic dehydration process [10,11].

Studies have shown that perlite–Portland cement and perlite–gypsum coatings are the most effective plasters as fire barriers and in retarding the conduction of high temperatures across their thickness among different kinds of coatings, such as traditional-cement plaster, vermiculite cement/gypsum-based mortar, intumescent coating, calcium silicate board, and LECA-cement plaster [12-14].

The main objective of this experimental work was to develop a gypsum mortar as a passive fire protection for steel elements and to compare the mechanical behaviour of steel columns subjected to axial compression and high temperatures when protected with: i) the developed gypsum mortar, ii) a commercial mortar and iii) without any type of thermal protection. In addition, the thermal effect provided by the application of these mortars with different coating thicknesses: 2 and 3 cm was evaluated.

2 MATERIALS AND METHODS

2.1 Compositions and Materials

In a preliminary phase, several laboratorial mortars based on cement or gypsum were developed, with different dosages of raw materials [1]. Of these various mortars, the one that presented the best thermal performance was selected (LDM). Furthermore, two commercial passive protection solutions were tested, to identify the commercial solution (CS) that provided one of the best thermal insulation results, which came to be considered as the reference mortar. The LDM was prepared with gypsum powder (40%), perlite (60%) with dimensions between 1 and 5 mm and water (water binder ratio of 1.25). The quantity of materials used in preparation of LDM composition was in volume (%).

2.2 Experimental Program

To evaluate the thermal efficiency provided by the CS and LDM as passive fire protection, experimental tests were carried out on five short tubular steel columns (SSC) at high temperatures: one without any type of coating, the second one with a mortar commercial and the third one with a mortar developed in the laboratory. The thermal effect provided by the respective mortars with a covering of 2 and 3 cm on the SSC was also studied. Table 1 presents the experimental program defined in this experimental work.

Table 1. Experimental program on short steel columns.

Different types of tested columns		Specimens designation	Number of Specimens
Steel columns without passive fire protection		SSC1	5
Short Steel column coated with 2 cm of protection	Commercial solution (CS)	SSC2	
	Laboratory developed mortar (LDM)	SSC3	
Short Steel column coated with 3 cm of protection	Commercial solution (CS)	SSC4	
	Laboratory developed mortar (LDM)	SSC5	

2.3 Specimens

Specimens were defined by a hollow square section 150 × 150 × 8 mm, with a height of 1250 mm, and the steel grade was S355. At the column ends, it was centered and welded a steel plate (section 300 × 300 × 20 mm), as shown in Figure 2. To evaluate the temperature evolution on the external surfaces of the steel columns during the test, 12 type K thermocouples were welded, equidistant from each other on all the specimen’s surfaces, applied in 3 groups of 4 thermocouples at different heights.

These thermocouples were welded in the middle of the surfaces of the steel tubular columns. To guarantee a constant and uniform mortar thickness of 20 and 30 mm along the steel columns, two modular formworks were developed with the ability to assign the desired geometric shape with easy assembly and disassembly while concreting the specimen. Figure 1 depicts the location of the three groups of thermocouples and the different concreting steps of the steel columns. The specimens were tested after curing for 6 months.

(a) **(b)** **(c)** **(d)**

Figure 1. Distribution of thermocouples (a) and fabrication of specimens, preconcreting (b), concreting on the short steel columns (c), and concrete specimen without formwork (d).

2.4 Experimental Testing System and Procedure

The experimental layout for the short steel columns under fire conditions (Figure 2) consisted essentially of a reaction steel frame (A) to apply the serviceability load on the specimen, a support steel frame (B), a hydraulic jack (C), and an electric furnace (H).

This steel frame was defined by HEB 500 columns and a HEB 600 beam (A), with a high stiffness to minimize possible displacements of this steel structure during the tests. Additionally, a support 3D steel frame consisting of two frames (B) with HEB 300 columns and HEB 400 beams accommodate the testing specimen to similar actual boundary conditions. Regarding the test equipment, a 3 MN hydraulic jack (C) and its controller (J), a 3 MN load cell (D), and a 1 MN load cell (E) were used for measuring the compression forces. Ten linear variable displacement transducers were used for displacements measurements (F), a Datalogger (G) for data acquisition, and an electric furnace (H) to heat up the steel columns (I).

A hydraulic jack controlled by a servo-controlled central was used, and a preload of 50% of the design value of the loadbearing capacity of the columns at ambient temperature (ULS) was applied (727.8 kN) to simulate a service load on the specimen. After stabilising this loading in the specimen, the furnace was switched on and the specimen heated according to the temperature evolution established by the ISO 834 standard fire curve [7].

Due to the increase in temperature during the test, significant thermal elongation was generated in the specimen. The test was stopped based on the axial contraction criterion defined by ISO 834-1: 1999 [8], which define a limit shortening of the specimen according to its initial length, i.e., when the heated specimen could no longer support the initial applied load. Thus, the final value of vertical deformation measured was 12.5 mm. Finally, the degree of detachment of the protective mortar and the failure mode in each specimen were observed.

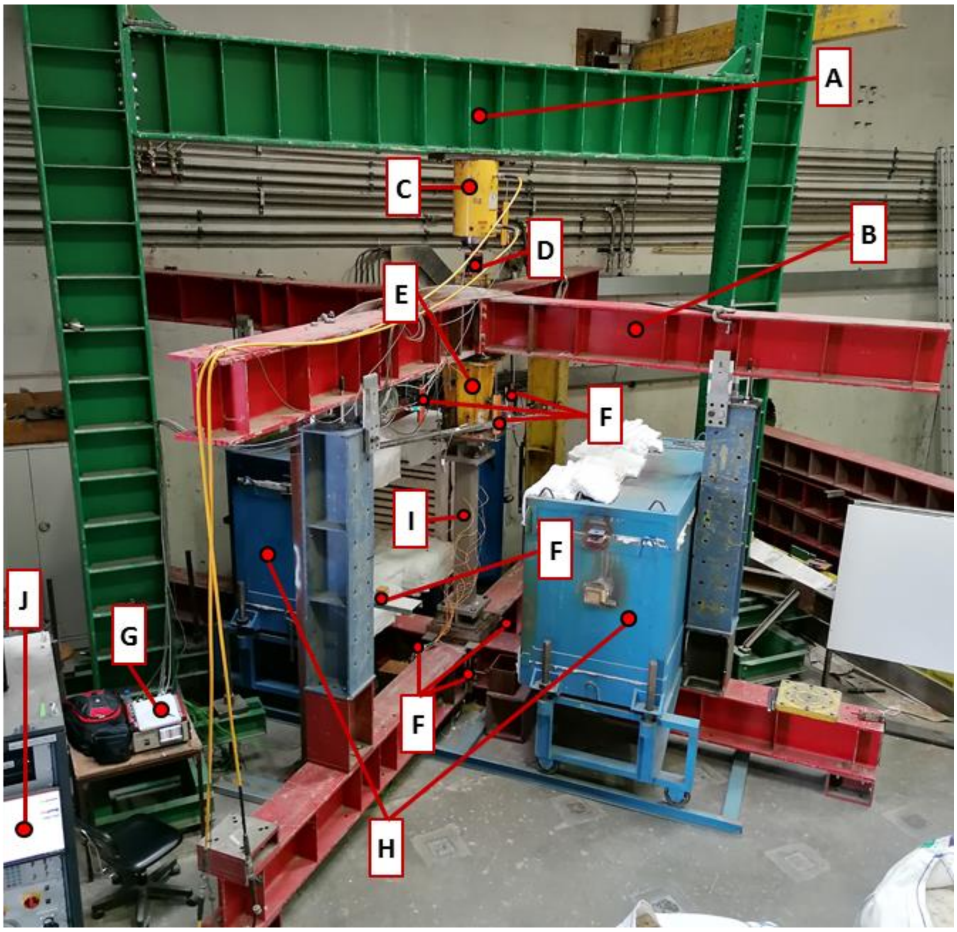

Figure 2. Experimental system used in the laboratory to test SSCS [1]. The letters in this figure are defined in the text.

3 RESULTS AND DISCUSSION

Regarding the protected square-section short steel columns, the assessment of the column temperature was based on the arithmetic average of the temperatures obtained from the 12 thermocouples (TH) welded to the steel column, which were distributed into three sections with four thermocouples each one (Figures 1 and 3). As an example, Figure 4 shows the temperature evolution in steel at the lower section of the column where temperatures were recorded (Figure 1).

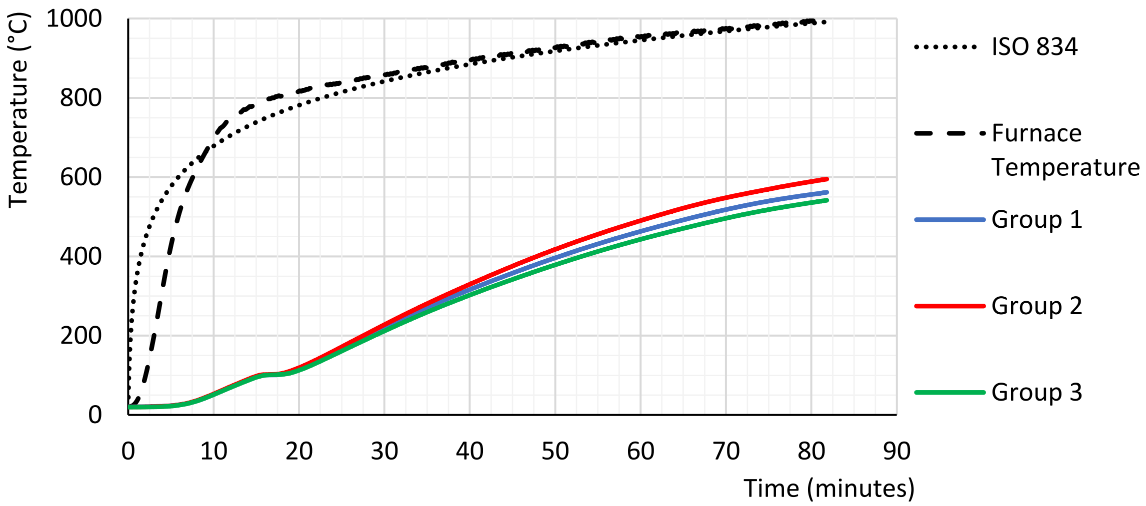

Figure 3. Evolution of the average temperature in the three groups of thermocouples [1].

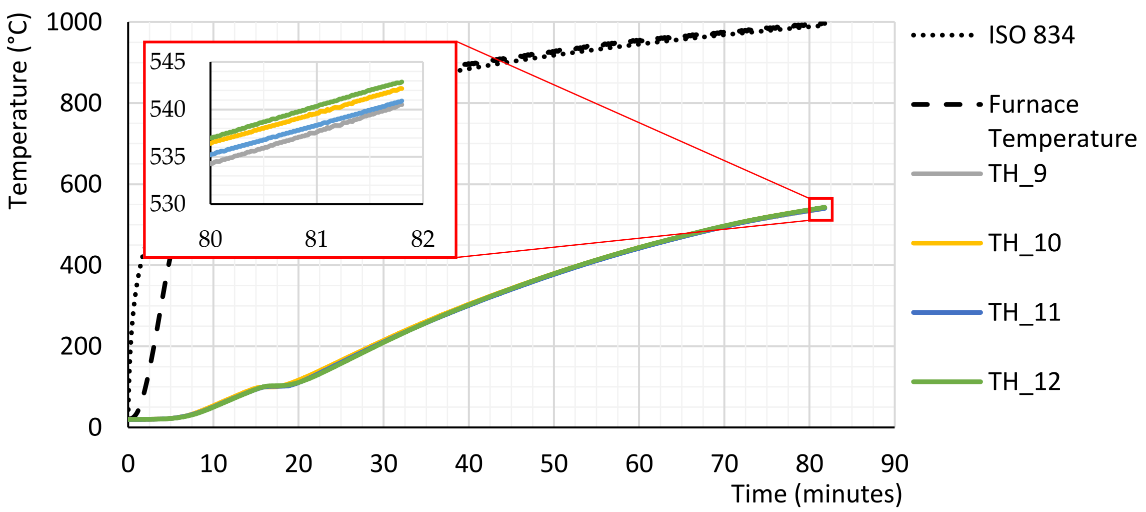

Figure 4. Evolution of the average specimen´s temperature in the four thermocouples (TH) of group 3 [1].

In Figure 3, shows the furnace temperatures have a slight delay during the initial minutes when compared to the ISO 834 standard fire curve. This part of the curve is difficult to reproduce in an electric furnace, and this becomes worse for larger furnaces (high initial thermal inertia).

However, near 9 minutes after the beginning of the heating, the furnace temperatures followed close to the ISO 834 standard fire curve. Nevertheless, the evolution of temperatures inside the furnace over time was uniform in all fire tests, meaning that the tests were comparable. Based on Figure 4, it is possible to observe that the temperature development recorded in the four thermocouples of group 3 was similar. There is only a difference of 3.3 °C between the thermocouple with the highest (TH_12) and the lowest temperature (TH_9) at column failure. Until the specimens became unstable, graphs were generated with the temperature evolution and the evolution of the vertical deformation of the specimen as a function of time (Figures 5 and 6), in order to identify the critical experimental temperature.

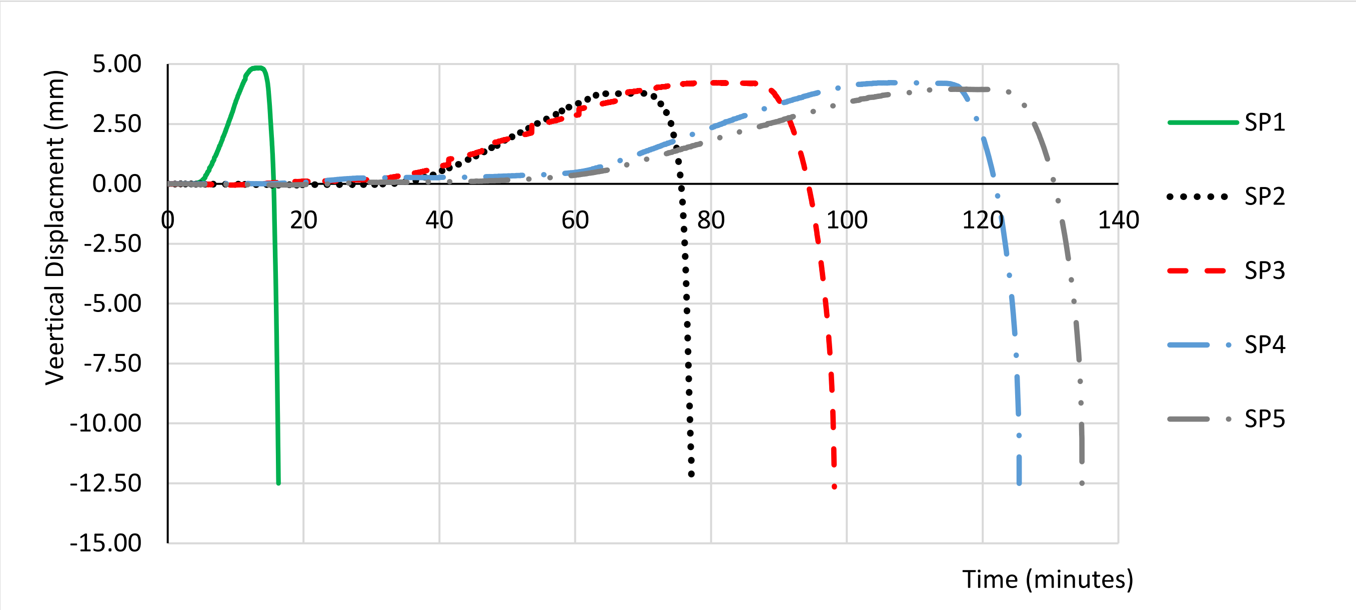

Figure 5. Evolution of vertical deformation in the specimens as a function of time.

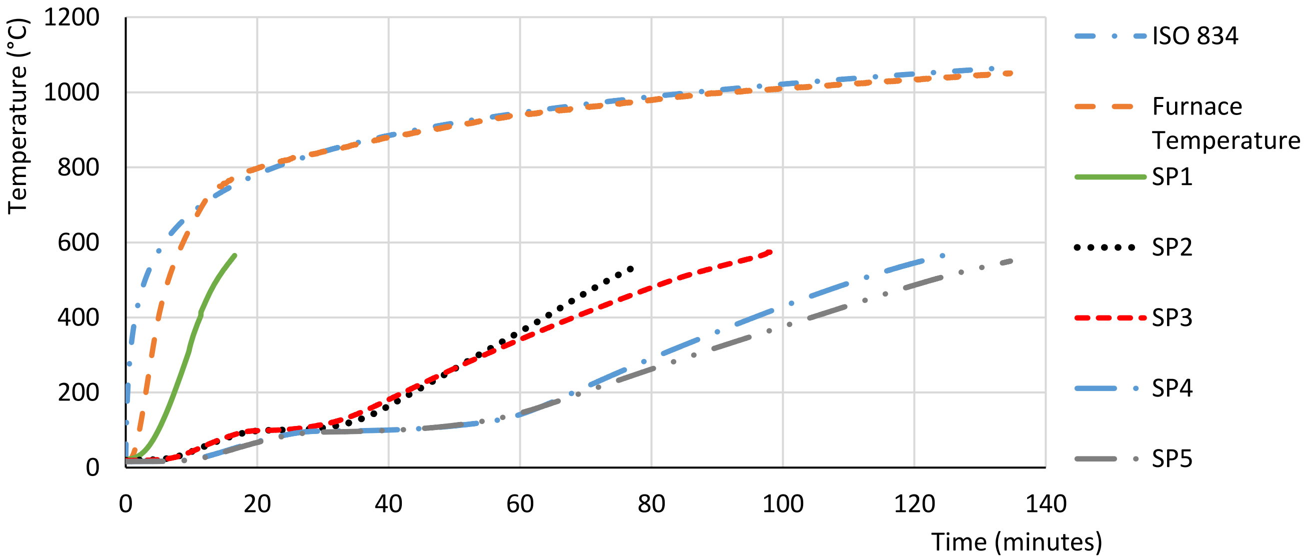

Figure 6. Evolution of temperature in the specimens of SSC as a function of time.

In Figure 5, the tested SSC1 failed at 17 minutes, SSC2 at 77 minutes, SSC3 at 98 minutes, SSC4 at 125 minutes and SSC5 at 135 minutes, corresponding to the temperature of 560, 530, 576, 570 and 550°C, respectively. In Figure 6 the specimens coating with commercial mortar has a more effective thermal protection for lower temperatures (the highest delay in the temperature rises at the beginning of the test). However, for temperatures higher than 400°C, its thermal capacity tends to decrease due to the degradation of the mortar (the highest temperature rise rate at the ending of the test). It was observed that the material degradation was high for high fire protection thicknesses, since the thermal performance reduced by approximate 27% when de thickness of fire protection materials increased from 20 to 30 mm for high temperatures (higher than 200°C).

Table 2 shows the temperature values acquired in the specimens after 15, 30, 60, 90 and 120 minutes, as well as the temperature values for the instability instants of each specimen. The design critical temperature calculated according EN 1993-1-2: 2005 was 586.7ºC.

Table 2. Average temperature measured on the specimens.

Steel column without protection	Time (min.)	**15**	**17**	-	-	-	-
	Temperature (°C)	525	560	-	-	-	-
Comercial Solution (2 cm thick coating)	Time (min.)	**15**	**30**	**60**	**77**	-	-
	Temperature (°C)	77	108	360	530	-	-
Laboratory developed mortar (2 cm thick coating)	Time (min.)	**15**	**30**	**60**	**90**	**98**	-
	Temperature (°C)	75	119	342	572	576	-
Comercial Solution (3 cm thick coating)	Time (min.)	**15**	**30**	**0**	**90**	**120**	**125**
	Temperature (°C)	44	97	141	366	545	570
Laboratory developed mortar (3 cm thick coating)	Time (min.)	**15**	**30**	**60**	**90**	**120**	**135**
	Temperature (°C)	42	95	145	320	486	550

The results showed that when compared with the steel column without any passive fire protection with the 2 cm thick coated steel columns, commercial mortar and laboratory developed mortar increased their fire resistance by about 4.5 and 5.8 times more, respectively. When a 3 cm thick coating was applied, the commercial mortar and the laboratory developed mortar increased their fire resistance by about 7.4 and 8.0 times more, respectively. In both cases: 2 and 3 cm coating, the mortar developed in the laboratory provided approximately 10% and 8% more effective thermal protection than the commercial solution, respectively.

The developed mortar and commercial mortar applied to the steel columns as passive fire protection proved to be an effective solution, since the standard fire rating of a column increased from R15 (without thermal protection) to R60. Standard fire rating of R90 or even R120 can be reached when a 3 cm cover was applied. These results demonstrated the actual impact that the application of such mortars can have as passive fire protection of steels structures.

The catalog of the commercial mortar, indicate that for a section factor of 130 and for a covering thickness of only 21 mm (slightly higher than the 20 mm tested) the standard rating of fire resistance should be R90 minutes. However, the results obtained in the test of specimen SSC2 (R90) clearly showed that they do not have the announced performance. The same conclusions might be observed for fire resistance rating of R120, since the commercial table requires only a minimum thickness of 26 mm, and it was experimentally observed that this fire resistance rating is hardly achieved when 30 mm of fire protection is employed. Figure 7 depicts the specimen before and after being tested. Regarding the instability modes of the steel columns, local instability was observed despite the column being a class 1 cross-section under fire conditions.

Figure 7. Photos of the specimens before and after tested, as an example.

4 CONCLUSIONS

The main objective of this experimental work was to develop a gypsum mortar as a passive fire protection for steel elements and to compare the mechanical behaviour of steel columns subjected to axial compression and high temperatures when protected with: i) the developed gypsum mortar, ii) a commercial mortar and iii) without any type of thermal protection. In addition, the thermal effect provided by the application of these mortars with different coating thicknesses: 2 and 3 cm was evaluated. The following conclusions can be taken from the results of this work:

- The results showed that when compared with the non-protected steel column, 2 cm of commercial mortar and laboratory developed mortar increased the fire resistance of the column by about 4.5 and 5.8 times more, respectively.
- When a 3 cm thick coating was applied, the commercial mortar and the laboratory developed mortar increased their fire resistance by about 7.4 and 8.0 times more, respectively.
- In both cases (2 and 3 cm coating), the mortar developed in the laboratory provided approximately 10% and 8% more effective thermal protection than the commercial solution, respectively.
- The developed mortar and commercial mortar applied to the steel columns as passive fire protection proved to be an effective solution, since the standard fire rating of a column increased from R15 (without thermal protection) to R60. Standard fire rating of R90 or even R120 can be reached when a 3 cm cover was applied.
- Regarding the instability modes of the steel columns, local instability was observed despite the fact that the column was class 1 cross-section.
- The higher of fire protection material, the higher the degradation level of the material is.

These results demonstrated the actual impact that the application of such mortars can have as passive fire protection of steels structures.

ACKNOWLEDGMENT

The authors gratefully acknowledge the Portuguese Foundation for Science and Technology (FCT) for its support under the framework of research project PTDC/ECI-EGC/31850/2017 (NANOFIRE - Thermal and Mechanical behaviour of Nano Cements and their application in steel construction as fire protection) and also to the University of Coimbra (UC) for their support under the Scientific Employment Stimulus Programme given to the first author, as well as to the European Regional Development Fund, the European Social Fund, and European Structural and Investment Funds. This work was also financed by FEDER funds through the Competitivity Factors Operational Programme - COMPETE and by national funds through FCT within the scope of the project POCI-01-0145-FEDER-007633 and the Regional Operational Programme CENTRO2020 within the scope of the project CENTRO-01-0145-FEDER-000006. The authors also acknowledge the European Regional Development Fund (FEDER), through the Portugal Operational Program (Portugal 2020) for its funding for the research project CENTRO-01-0247-FEDER-047136 (Switch2Steel - A Calculation Framework for Cost and Material Optimization of Industrial Buildings in Steel Structures).

REFERENCES

1. Caetano, H., Laím, L., Santiago, A., Durães, D. and Shahbazian, A., 2022, "Development of Passive Fire Protection Mortars", Applied Science, 12, 2093, https://doi.org/10.3390/app12042093.
2. Santiago, A., Simões da Silva, L., Vaz, G., Vila Real, P. e Gameiro Lopes, A., 2008, Experimental investigation of the behaviour of a steel sub-frame under a natural fire, International Journal of Steel and Composite Structures 8, p. 243-264.
3. Franssen, J.M., Cooke, G.M.E. and Latham, D.J., 1993. "Numerical simulation of a Full Scale Fire Test on a Loaded Steel Framework, Journal of Constructional Steel Research, Vol. 35, Issue 3, p. 377-408.

4. Caetano, H., Vaz-Ramos, J., Santiago, A., Dur es, L., Portugal, A., 2019, Desenvolvimento de argamassas cimentícias com nanosílica como proteção passiva para elementos metálicos, XII Congresso de Construção Metálica e Mista.
5. Laím, L.; Caetano, H.; Santiago, A., 2021, Review: Effects of nanoparticles in cementitious construction materials at ambient and high temperatures. J. Build. Eng., 35, 102008.
6. Laím, L., Santiago, A., Caetano, H., Craveiro, H., Shahbazian, A., 2022, Numerical analysis and structural fire design of protected SHS steel columns with thermally enhanced gypsum-based mortars, Journal of Building Engineering, Volume 54, 104629, ISSN 2352-7102.
7. Singh, M. and Garg, M. Perlite-based building materials - a review of current applications. Constr. Build. Mater. 1991, vol. 5, 75–81.
8. Rashad, A. M. Vermiculite as a construction material – A short guide for Civil Engineer. Constr. Build. Mater. 2016, 125, 53–62.
9. Abidi, S., Nait-Ali, B., Joliff, Y. and Favotto, C. Impact of perlite, vermiculite and cement on the thermal conductivity of a plaster composite material: Experimental and numerical approaches. Compos. Part B Eng. 2015, 68, 392–400.
10. Abdel-Hafez, L. M., Abouelezz, A. E. Y. and Hassan, A. M. Behavior of RC columns retrofitted with CFRP exposed to fire under axial load. HBRC J. 2015, 11, 68–81.
11. Manzello, S. L., Gann, R. G., Kukuck, S. R. and Lenhert, D. B. Influence of gypsum board type (X or C) on real fire performance of partition assemblies. Fire Mater. 2007, 31, 425–442.
12. Hodhod, O. A., Rashad, A. M., Abdel-Razek, M. M., and Ragab, A. M. Coating protection of loaded RC columns to resist elevated temperature. Fire Saf. J. 2009, 44, 241–249.
13. Correia, J. R., Branco, F. A. and Ferreira, J. G. The effect of different passive fire protection systems on the fire reaction properties of GFRP pultruded profiles for civil construction. Compos. Part A. 2010, 41, 441–452.
14. Kamal, O. A., Hamdy, G. A. and Abou-Atteya, M. A. Efficiency of coating layers used for thermal protection of FRP strengthened beams. HBRC J. 2014, 10, 183–190.
15. EN 1993-1-2, 2005. Eurocódigo 3 – Projecto de estruturas de aço – Parte 1-2: Regras gerais, Verificação da resistência ao fogo, Comité Europeu de Normalização, Bruxelas, 2005.
16. ISO 834-1, 1999. Ensaios de resistência ao fogo - Elementos de construção de edifícios - Parte 1: Requisitos gerais, International Organization for Standardization: Geneva, Switzerland, 1999; pp. 1-33.

SiF 2022– The 12th International Conference on Structures in Fire
The Hong Kong Polytechnic University, Nov 30 - Dec 2, 2022

PERFORMANCE OF VERTICAL LOAD CARRYING BEAM TO COLUMN SUBASSEMBLAGES IN SEISMIC RESISTING STEEL FRAMED BUILDINGS UNDER FULLY DEVELOPED FIRE

Fanqin Meng[1], Anthony Abu[2], G Charles Clifton[3]

ABSTRACT

Steel-framed buildings, comprising a structural steel frame supporting composite concrete floors, are commonly used in highly seismically active areas. However, predominant design guidelines are obtained from studies on isolated structural components and disregard the interaction of structural components during a fire. Thus, this paper uses a validated numerical modelling method in ABAQUS to analyze the performance of beam-to-steel column assemblage with composite slabs in fires. The simulation results reveal that the interior columns in the structural assemblage may fail to research the designed fire resistance because the continuous bending beams squeeze the column from two orientations. Although the recommended continuity stiffeners enhance column performance in the structural assemblage, the structural assemblage presents limited reserve fire resistance. Thus, new reduction factors, SQRT, are proposed herein to provide a reasonable robustness margin for steel columns to resist a fire severer than the designed FRR. The simulation results show that using SQRT reduction factors generates a reserve fire resistance ratio of 1.30 for steel columns, which is more appropriate compared with the 1.14 using the ones from EN 1993-1-2.

Keywords: Structural fire performance; compartment fires; steel structures; robustness

1 INTRODUCTION

Steel-framed structures comprising a structural steel frame supporting composite concrete floors are commonly used as commercial buildings worldwide. In highly seismically active countries the structural system is typically separated into a gravity system, designed to support vertical loading, and a seismic resisting system, which resists lateral loading. The gravity system columns are designed to be continuous throughout the building height and support beams with connections designed and detailed to transfer vertical shear forces but not high moments under beam end rotation. Typical continuous steel columns are shown in Figure 1. Because steel loses appreciable strength at temperatures above 400℃, such gravity system columns are vulnerable to fire and have been the subject of ongoing research [1-5].

The fire resistance rating (FRR) is a measure of structural fire severity as given by a specified length of time exposure to the ISO Standard Fire condition [6]. It applies to structural components in isolation according to each element's performance in the standard fire test [7-9]. However, some research has concluded that the interactive relationship between different could lead to the premature failure of structural elements. For example, Han et al. [10] tested six reinforced concrete beams to CFST column assemblages in the ISO-834 Standard Fire. The tested columns reached failure 36mins earlier than the design limit because of the impact of the unbalanced bending moment from the composite beam. This conclusion agrees

[1] Structural fire research engineer, HERA,
e-mail: fmeng@hera.org.nz,
[2] Associate professor, University of Canterbury,
e-mail: anthony.abu@canterbury.ac.nz,
[3] Associate professor, The University of Auckland,
e-mail: c.clifton@auckland.ac.nz, ORCID: https://orcid.org/0000-0003-0723-1699
https://doi.org/10.6084/m9.figshare.22215763

with other research findings [11-13]; Yang et al. conducted experimental research on composite beam and concrete-filled steel tubular (CFST) columns. It was found that the structural assemblage failure changed from beam failure to column failure with the decreasing load ratio of beams; Fire tests from the United Kingdom [14] used different connection types between beam and column to evaluate their performance. It was found that the beam deflection was highly related to the stiffness of connected columns. Moreover, the structural performance of structural components is different under parametric fire and standard fire. As detailed in the research on the assemblage under full-phase fire [15, 16], the thermal expansion of the beam in fire produced significant compression demand on the column first and then switched to tension demand, which is not considered in the structural fire design. Based on these studies, it can be concluded that the fire performance of structural components is highly affected by the connected elements and fire scenarios. However, most structural fire design guides neglect the interactive relationship between different components. Very little research has been conducted on evaluating the fire performance of continuous steel columns in structural steel buildings.

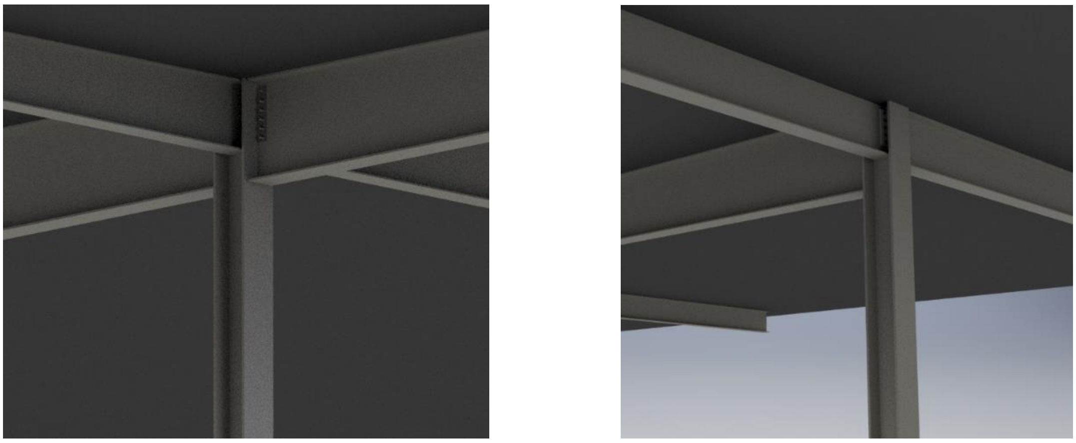

(a) Interior column (b) Exterior column

Figure 1 Typical interior columns and exterior columns in the building

Although there is some research on the fire performance of steel columns in the structural assemblage, none have thoroughly investigated the steel columns' fire performance in steel-framed structures designed by up-to-date design methods. To fully investigate the structural fire performance of structural assemblage in the building, a four-storey steel-framed building with a span of 12 m and a storey height of 4 m is designed, whose structural components are simulated and analysed in ABAQUS [17] using the validated simulation method.

2 GENERAL

2.1 Numerical validation

Because the thermal performance of steel-framed buildings is not heavily reliant on their structural performance, the conventional sequential thermal-stress analysis is adopted herein. Consequently, thermal analysis is performed first to obtain node temperatures for the following stress analysis. In the first phase of stress analysis, structural loads are applied to the structure and then held constant. Then, in the second stage, the thermal load is applied to the structure in the form of node temperature to model the temperature evolution of structural parts. As this research does not contain any experimental testing, and does not find any similar experimental tests, the validation procedure shown here is comprised of three phases using data from published experimental tests. The validation process began with the column specimen and ended up with the whole structural assembly. Subsequently, the applicability of model established model is evaluated by comparing it to experimental data. More information about the numerical validation is detailed in the thesis [18]. It should be pointed out that the effects of mesh size, starting defect, and constraint stiffness was studied during the validation.

2.2 Structural fire model design

A four-story, strongly loaded, steel-framed office structure was designed to investigate the effect of beam and slab interaction on the steel column. The building's design adheres to the New Zealand building standards, primarily AS/NZS 2327 [6], Design of composite steel floor systems for severe fires [19] AS/NZS Structural design actions 2002, and NZS 3404 Steel structures standard [20]. The isometric view of the structure is shown in Figure 2.

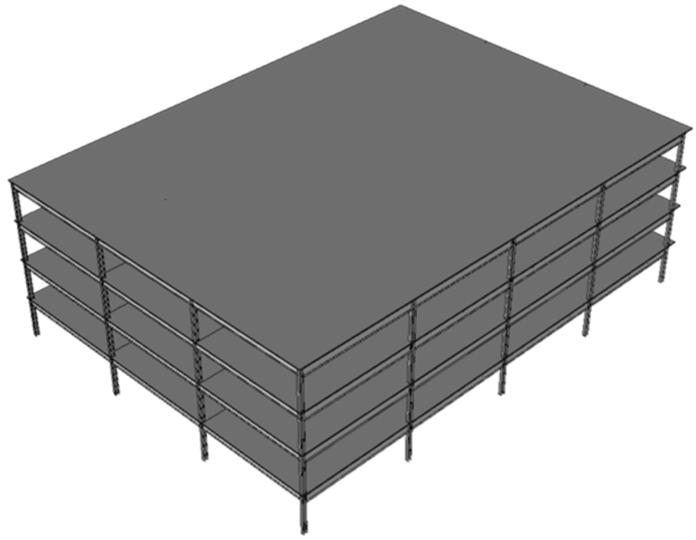

Figure 2. Isometric view of the designed four-storey steel-framed building.

The designed building has an identical layout at each storey, with a storey height of 4 m and continuous columns 12 m apart in both directions. Web plate connections are used to connect the structural components. The adopted permanent load and live loads are 4.0 kN/m2 and 3.5 kN/m2. The 130mm thick composite floor system, Comflor60, with the 30 MPa concrete compressive strength, a 0.89 mm thick steel deck, is used herein. DH10 reinforcing bars with a 10 mm diameter were embedded at a distance of 200 mm (393 mm^2/m) apart in concrete. The mesh and steel deck has a 500 MPa yield strength. The secondary beams on all levels were 530UB82, whereas the major beams were 800WB122. The structural arrangement in one flooris as given in Figure 3.

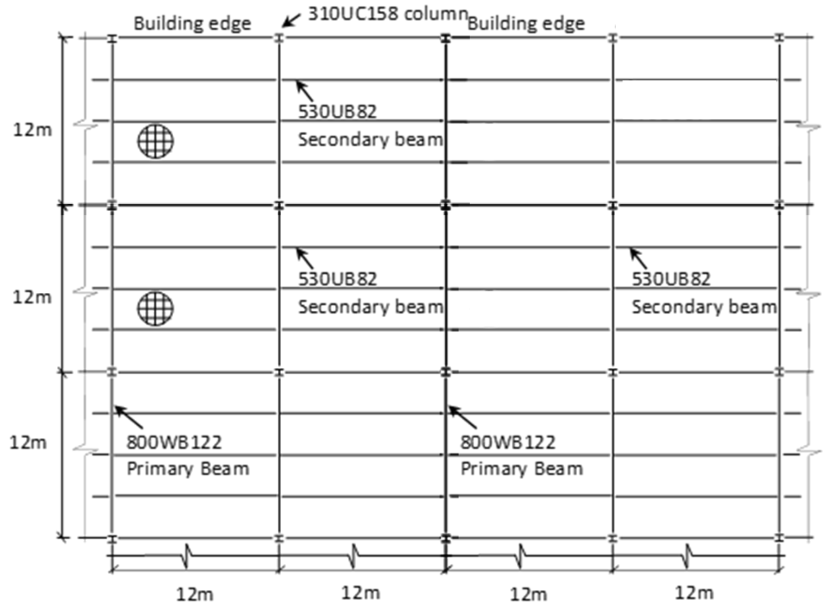

Figure 3. Detailed structural arrangement of a typical floor

2.3 Discussion of simulation results

Figure 4 depicts time-axial displacement curves of exterior and interior columns. The dashed line represents column failure limits. In general, the top end of columns expands upward due to the thermal expansion of steel columns induced by heating. Later, the deterioration of steel materials and deformation of connected composite beam in fire leads to the axial compression of columns. The vertical deformation continuously develops with the increasing time and temperature until the column could no longer support the axial stress and collapsed in the end. According to the modelling findings, the fire resistance of external columns achieved their deflection limits at 95 minutes and 125 minutes for FRR= 60 and 90 minutes, respectively. It demonstrates that the reserve fire resistance ratio (the ratio of achieved fire resistance in the simulation to specified FRR) for external columns with FRR=60 min and FRR=90 min is 1.58 and 1.39, respectively. Regarding internal columns, the column demonstrated a reserve fire resistance ratio of 1.07 in the FRR=60min instance. In the FRR=90min scenario, however, the internal column fails to achieve its intended fire resistance. This finding agrees with the design, in which the exterior column has the same cross-section with interior column assemblage, but carries less compression load than the interior column.

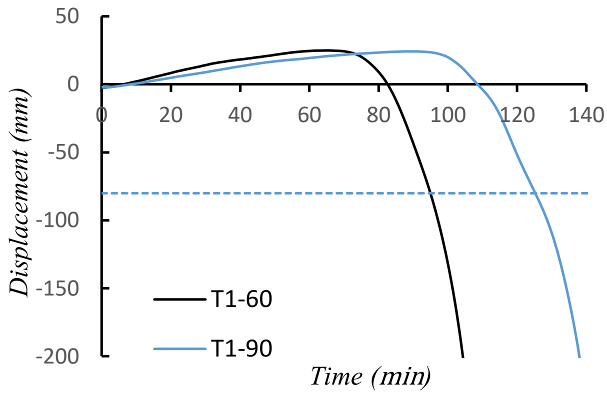

(a) Exterior column assemblage

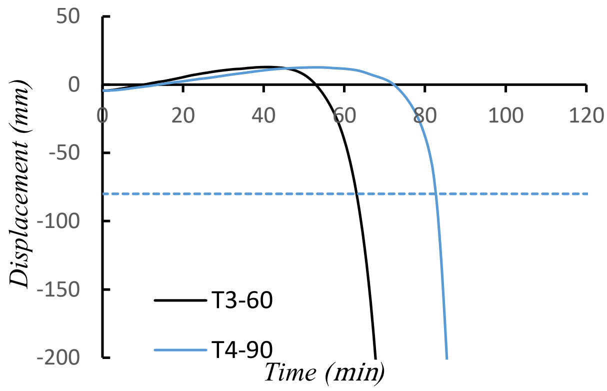

(b) Interior column assemblage

Figure 4. Vertical displacement-time curve of steel columns.

2.4 Discussion of column failure models

For exterior columns, the steel beam ends rotate in fire and make contact with the column surface. The joint area of the column is naturally pulled inwards by the beam's continual bending. The external column ultimately failed, as shown in Figure 5 (a). For interior columns, the beam end contact from two opposite orientations forms the "squeeze load" on the column. The steel column capacity cannot withstand the "squeeze stress," and the column web buckles along its minor axis. Then the column then reaches the loading capacity, as seen in Figure 5 (b). Meanwhile, the beam bottom flange buckled laterally, which was not observed in the exterior column assemblage.

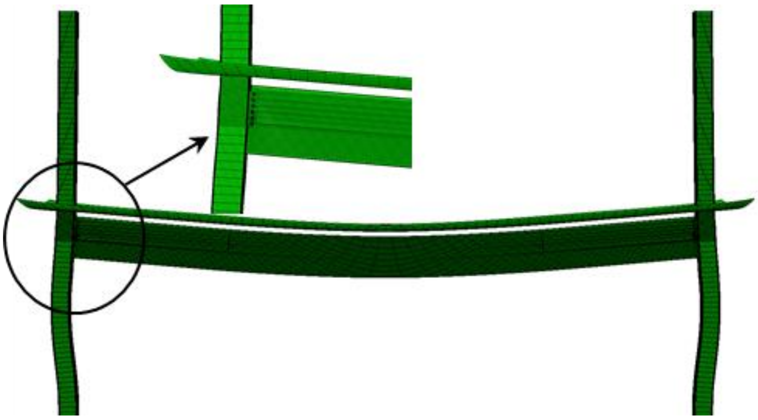

(a) Exterior column assemblage

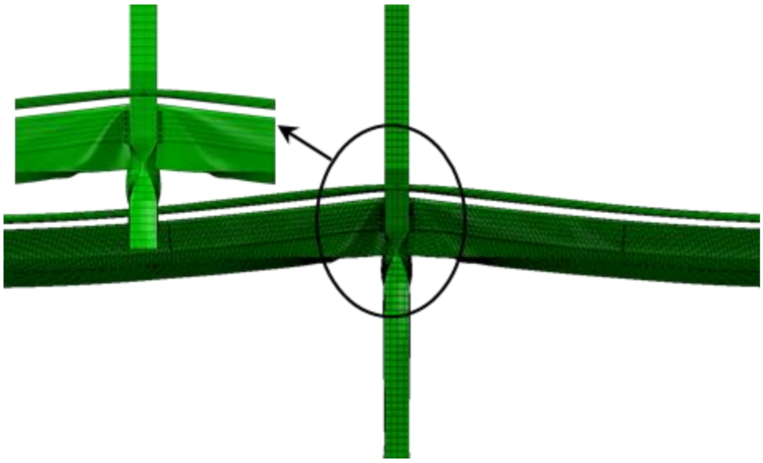

(b) Interior column assemblage

Figure 5. The failure modes of simulated columns in the assemblage

3 SENSITIVE STUDY OF CRITICAL PARAMETERS

3.1 Continuity stiffener

The steel column in the interior assembly reaches the designed FRR=60min, but not FRR=90min. The unexpected collapse for the FRR=90 min case was caused by the local buckling of the column flange and web induced by the compressive "squeeze load" from the continuous bending beam. A pair of continuity stiffeners is recommended to be installed at the same level as the beam's bottom flange with the same beam flange thickness, as shown in Figure 6. In the meantime, the continual bending of the beam leads to a stress concentration at the beam end, with considerable compressive stress in the beam's bottom flange in contact with the column. When the bottom flange of the beam is unable to bear the contact force, local buckling occurs, resulting in a localised shortening. Web diagonal buckling developed simultaneously with beam bottom flange buckling because of the necessity to preserve deformation compatibility. Regardless of the existence of the pair of rib stiffeners, this local buckling pattern is observed in the beam's bottom flange and web.

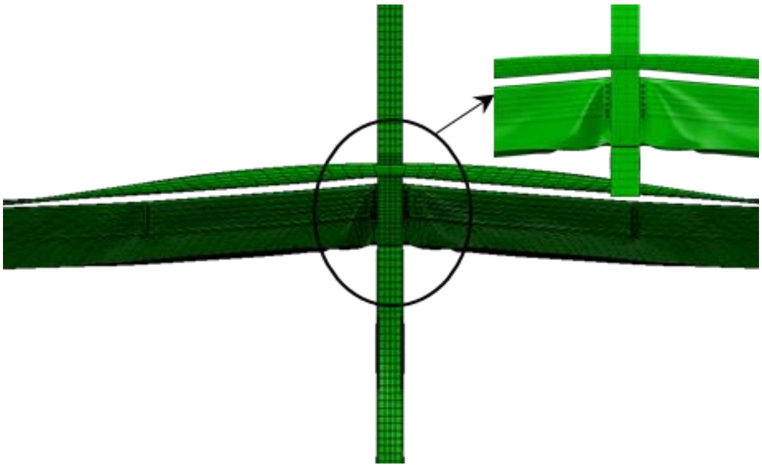

Figure 6. Deformation-time curves of the interior columns with rib stiffeners in the fire

It can be observed that the failure mechanism of columns with or without rib stiffeners is notably different. For the unreinforced T3-60 and T4-90 columns, the significant localised compression stress results in localised column web buckling, as seen in Figure 5, which leads to the ultimate collapse. For the strengthened T3-60-Rib and T4-90-Rib columns, there is no local buckling, but column members buckle about the minor axis, causing the column failure. The overall deformation-time curves of the interior columns with rib stiffeners in the fire is given in Figure 7. It can be seen that the usage of continuity stiffeners increases the fire resistance of steel columns in fire compared with these columns without continuity stiffeners. For FRR= 60 min, the fire resistance of interior column assemblage increases from 64 min to 69 min. For FRR= 90 min, the fire resistance of interior column assemblage increases from 83 min to 91 min. Thus, it can be concluded that the usage of continuity stiffeners is essential to columns to reach the designed FRR in the structural assemblage, at least for FRRs of 60 mins or greater.

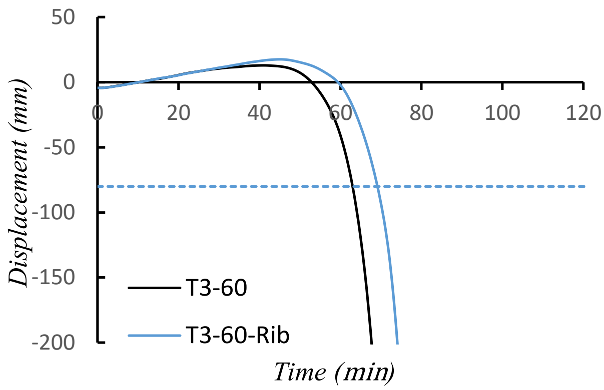

(a) FRR=60min

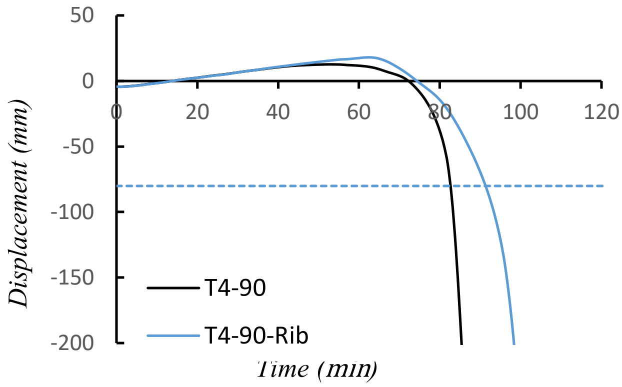

(b) FRR=90min

Figure 7. Deformation-time curves of the interior columns with rib stiffeners in the fire

3.2 Restraint effect

The thermal expansion of columns could generate a significant internal force in steel columns because of the existence of connected structural components. The increasing internal force could lead to the premature buckling of steel columns in fire. This section is to explore the overall performance of steel columns in the assemblage considering the restraint effect coming from connected element. The adopted restraint level have 0 kN/mm, 1 kN/mm and 10 kN/mm. Figure 8 shows the deformation-time curves of interior column assemblies under various axial restraint levels. It can be seen that the 1 kN/mm stiffness does not result in any difference compared to the case with no axial constraint. With a restraint stiffness of 10 kN/mm, the column reaches its deflection limit more slowly. Meanwhile, the maximum deformation of steel columns is less for columns with a restraint stiffness of 10 kN/mm. The less thermal expansion indicates that the column could have generated some permanent deformation, but the generated some permanent deformation has a limited effect on the overall performance of steel columns in fire.

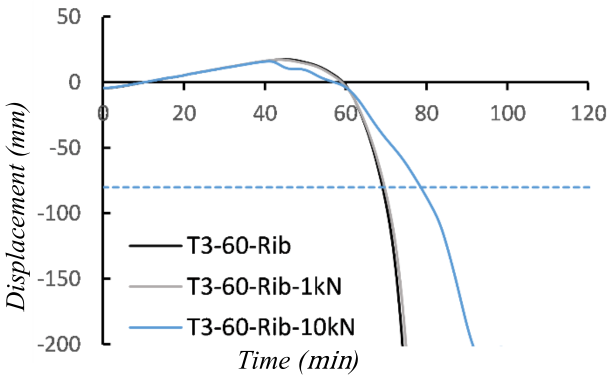

(a) FRR=60min.

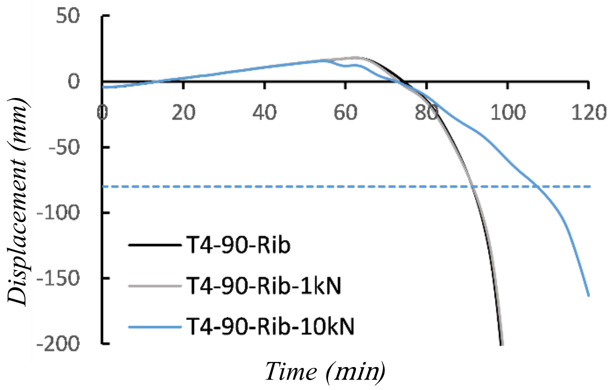

(b) FRR=90min.

Figure 8. Deformation-time curves of interior column assemblies under three restraint levels.
Note: 1kN and 10kN are short for axial restraint stiffness 1kN/mm and 10kN/mm.

3.3 Mechanical strength reduction factors at elevated temperature

Despite the fact that rib stiffeners improve the overall structural fire performance of the columns in simulation, the T4-fire 90-Rib's resistance is only 91 minutes, leaving a one-minute safety margin. One purpose of this research is to develop a design method with a Capacity/Demand ratio of at least 1.25. One of the possible reasons for current design methods failing to reach this purpose is the adoption of yield strength with 2% strain. In practice, part of the section starts to yield and deform first, but the other parts are still in the elastic stage. The member buckling capacity is controlled by a mixture of elastic and inelastic material properties and buckling begins when the material starts to behave in the non-linear elastic range. This section is to investigate a range of column elevated temperature reduction factors on the time to failure of columns under the Standard Fire Test exposure. These included using the proportionality limit reduction factor (k_{yp}), the 2% strain reduction factor ($k_{y,2\%strain}$) and a new factor, called k_{SQRT} , representing the square root of the $k_{y,2\%strain} * k_{yp}$. These three factors are presented in Table 1.

Table 1. Proposed SQRT reduction factors of structural steel at different temperatures

Steel Temperature (℃)	$k_{y,2\%strain}$	k_{yp}	k_{SQRT} ($k_{y,2\%strain} * k_{yp}$)
20	1.000	1.000	1.00
100	1.000	1.000	1.00
200	1.000	0.807	0.90
300	1.000	0.613	0.78
400	1.000	0.420	0.65
500	0.780	0.360	0.53
600	0.470	0.180	0.29
700	0.230	0.075	0.13
800	0.110	0.050	0.07
900	0.060	0.038	0.05
1000	0.040	0.025	0.03
1100	0.020	0.013	0.02
1200	0.000	0.000	0.00

Four reduction factors are adopted in the design and simulation, including the proportionate and yield strength reduction factors from EN 1993-1-2 [21], the SQRT reduction factors, and the yield strength reduction factors from NZS 3404:1997 [20]. The simulation results are given in Table 2. It can be seen that using the proportionate limit of EN 1993-1-2 [21] with an average reserve fire resistance ratio of 1.58 is too conservative in engineering practice design. The reduction factors of yield strength from EN 1993-1-2 [21] do not provide sufficient reserve fire resistance for steel columns, especially for the column of T4-60-Rib-EN and T4-90-Rib-EN-1, for which the reserve fire resistance ratio is 1.01. The reserve fire resistance ratio of 1.14 specified by NZS 3404:1997 [20] for steel columns with 0 kN/mm and 1 kN/mm axial stiffness is insufficient for column reserve fire resistance. Using the SQRT reduction factor in column design resulted in an average reserve fire resistance ratio of 1.30, which is the most acceptable value and comparable to the minimum reserve strength expected for columns of seismic resisting systems during an earthquake, where there is an expaction that a seismic resisting system designed for ultimate limit state earthquake conditions will behave in a fundamentally similar manner under an earthquake intensity of up to 1.5 times the ULS design level. This is desirable to give a reserve of toughness against a more severe earthquake than has been designed for and this exceedence of the ULS design level is commonly observed in severe earthquakes. .

Table 2. Simulated fire resistance using different properties of structural steel

Assemblage name	Design Code	Designed FRR (min)	Stiffness (0 kN/mm)		Stiffness (1 kN/mm)		Stiffness (10 kN/mm)		Average
			FEA FRR (min)	$\frac{Resistance}{Design}$	FEA FRR (min)	$\frac{Resistance}{Design}$	FEA FRR (min)	$\frac{Resistance}{Design}$	$\frac{Resistance}{Design}$
T3-60-Rib-EN	EN 1993-1-2	60	69	*1.15*	69	*1.15*	78	*1.30*	1.14
T4-90-Rib-EN		90	91	*1.01*	91	*1.01*	107	*1.19*	
T3-60-Rib-NZS	NZS 3404	60	69	*1.15*	69	*1.15*	78	*1.30*	1.19
T4-90-Rib-NZS		90	101	*1.12*	103	*1.14*	115	*1.28*	
T3-60-Rib-SQRT	SQRT	60	77	*1.28*	77	*1.28*	86	*1.43*	1.30
T4-90-Rib-SQRT		90	109	*1.21*	111	*1.23*	123	*1.37*	
T3-60-Rib-Prop	Proportional limit	60	94	*1.57*	96	*1.60*	105	*1.75*	1.58
T4-90-Rib-Prop		90	132	*1.47*	134	*1.49*	145	*1.61*	

3.4 Parametric fire

The use of standard fire models has significantly promoted structural fire research in the past several decades [14, 22-26]. However, it is generally recognised that standard fire models cannot accurately capture the time-temperature characteristics of a fire within a compartment. For instance, the heating and cooling phases of compartment fires are dependent on thermal boundary conditions, ventilation conditions and fuel load density, which are absent from traditional fire models. Consequently, a more realistic fire mode shall be used to assess the structural performance of buildings, for example the parametric fire curve from the Annex A of EN 1991-1-2 [27], which is more appropriate for compartment fire design. The structural performance of the designed assemblage is investigated here.

Using Equation 1, the corresponding fire load density of $920MJ/m^2$ in parametric fire curves for FRR=60 min, $1370MJ/m^2$ for FRR= 90 min.

$$t_e = e_f k_b k_m w_f \tag{1}$$

where e_f is the fire load energy density; k_b is the conversion factor of the thermal property of the structure; and k_m is the modification factor for the structural material. For normal-weight concrete, k_b takes the value of 0.065 and k_m takes the value of 1.0.

The sensitiveity study conducted in Section 3.1 indicates that adopting continuity stiffeners increases the fire resistance of interior steel columns in the assemblage. Thus, the structural performance of an internal column assembly under parametric fire is investigated for the interior columns utilizing continuity stiffeners. The results of the simulation are shown in Table 3. The reduction factors used for the structural fire design of columns here are the SQRT reduction factors. The slash "/" in Table 3 indicates that the column does not fail in the assemblage. For the columns with FRR=60min, S1-Rib-SQRT-800, S1-Rib-SQRT-900, and S1-Rib-SQRT-920 do not fail in the simulation. S1-Rib-SQRT-1000 and S1-Rib-SQRT-Standard reached failure with sufficient reserve fire resistance. For the columns with FRR=90 min, all columns presented sufficient reserve strength as well. Moreover, the failure temperature of columns with FRR=60min or FRR=90min was higher than the designed limiting temperature.

Table 3. Results of steel columns with rib stiffeners designed by SQRT strength reduction factors

Specimen No.	FRR	Fire load MJ/m^2	Design temperature limit (°C)	Failure temperature (°C)	Failure time (min)	Outcome
S1-Rib-SQRT-800	60	800	500	/	/	P
S1-Rib-SQRT-900	60	900	500	/	/	P
S1-Rib-SQRT-920	60	920	500	/	/	P
S1-Rib-SQRT-1000	60	1000	500	503	68	F
S1-Rib-SQRT-Standard	60	Standard	500	556	77	P(1.28)
S2-Rib-SQRT-1200	90	1200	500	/	/	P
S2-Rib-SQRT-1300	90	1300	500	/	/	P
S2-Rib-SQRT-1370	90	1370	500	/	/	p
S2-Rib-SQRT-1400	90	1400	500	504	109	F
S2-Rib-SQRT-1500	90	1500	500	518	106	F
S2-Rib-SQRT-Standard	90	Standard	500	547	109	P(1.21)

Note: The "outcome" in the table depicts whether the column was exposed to the parametric fire condition or to the standard fire condition. For the parametric fire cases, F is short for the failure, meaning the column failed during either the heating phase or the cooling phase of the fire. If the column didn't fail in either phase, no failure temperature is given and the outcome is a pass. For the standard fire case, if the simulated time to failure is greater than the design fire resistance time, it is designated P; if less, it is designated F. The number in brackets represents the ratio of (simulated fire resistance time to failure)/(designed fire resistance).

4 CONCLUSIONS

This paper presents numerical research simulating the realistic structural fire performance of interior gravity system steel columns, including primary steel beams and composite slabs under ISO-834 Standard Fire. In addition, the effect of continuity stiffeners in the column was simulated in order to assess their impact on the fire resistance of steel columns. The stiffened constructions were then subjected to three degrees of axial constraint stiffness: 0 kN/mm, 1 kN/mm and 10 kN/mm. Then, the structural performance of designed structures is assessed under parametric fire based on the proposed SQRT reduction factors. The main results of this research can be summarized as follows:

- The structural assemblage involving the interior gravity column has lower robustness in the fire than the structural assemblage involving the exterior gravity column;
- Using the continuity stiffener in the column at the bottom flange level significantly improves the robustness of the interior gravity column by resisting the contact force resulting from the continuous bending beam. This is especially the case for structural fire severity equal to or exceeding 60 minutes but has less benefit for the exterior gravity column;
- The restraint effect from connected structural components would suppress the thermal expansion of steel columns in fire, inducing the increase of internal force in the columns. However, the influence of restraint against thermal expansion is not detrimental to the overall fire resistance of a compact column;
- The elevated temperature material strength reduction factors for columns should be based on square root of the $\sqrt{k_{y,2\%strain} * k_{yp}}$, where$k_{y,2\%strain}$is the factor associated with developing 2% strain and k_{yp} is the proportionality limit, which gives the steel columns a reasonable robustness margin.

REFERENCES

1. Bailey, C. and D. Moore, The structural behaviour of steel frames with composite floorslabs subject to fire. Pt. 2: design. Structural Engineer, 2000.
2. Clifton, C. and C. Beck, Design of multi-storey steel framed buildings with unprotected secondary beams or joists for dependable inelastic response in severe fires. Steel Design and Construction Bulletin, 2001. **60**: p. 1-58.
3. Huang, Z., I.W. Burgess, and R.J. Plank, Modeling membrane action of concrete slabs in composite buildings in fire. I: Theoretical development. Journal of Structural Engineering, 2003. **129**(8): p. 1093-1102.
4. Wald, F., et al., Experimental behaviour of a steel structure under natural fire. Fire Safety Journal, 2006. **41**(7): p. 509-522.
5. Sun, R. and I.W. Burgess, An analytical and numerical prediction for ductility demand on steel beam-to-column connections in fire. Engineering Structures, 2016. **115**: p. 55-66.
6. AS/NZS 2327, Composite structures—Composite steel-concrete construction in buildings. 2017: New South Wales/Wellington, Australia/New Zealand.
7. Ali, F. and D. O'Connor, Structural performance of rotationally restrained steel columns in fire. Fire Safety Journal, 2001. **36**(7): p. 679-691.
8. Espinos, A., M.L. Romero, and A. Hospitaler, Advanced model for predicting the fire response of concrete filled tubular columns. Journal of constructional steel research, 2010. **66**(8-9): p. 1030-1046.
9. Li, G.-Q., P. Wang, and Y. Wang, Behaviour and design of restrained steel column in fire, Part 1: Fire test. Journal of Constructional Steel Research, 2010. **66**(8-9): p. 1138-1147.
10. Han, L.-H., W.-H. Wang, and H.-X. Yu, Experimental behaviour of reinforced concrete (RC) beam to concrete-filled steel tubular (CFST) column frames subjected to ISO-834 standard fire. Engineering Structures, 2010. **32**(10): p. 3130-3144.
11. Han, L.-H., W.-H. Wang, and H.-X. Yu, Analytical behaviour of RC beam to CFST column frames subjected to fire. Engineering structures, 2012. **36**: p. 394-410.
12. Li, G.-Q., et al., Modeling of end-plate bolted composite connection in fire considering axial force effects. Journal of Constructional Steel Research, 2012. **76**: p. 133-143.
13. Li, J.-T., et al., Experimental investigation on flush end-plate bolted composite connection in fire. Journal of Constructional Steel Research, 2012. **76**: p. 121-132.
14. Wang, Y., X. Dai, and C. Bailey, An experimental study of relative structural fire behaviour and robustness of different types of steel joint in restrained steel frames. Journal of Constructional Steel Research, 2011. **67**(7): p. 1149-1163.
15. Liu, Y., S.-S. Huang, and I. Burgess, Performance of a novel ductile connection in steel-framed structures under fire conditions. Journal of Constructional Steel Research, 2020. **169**: p. 106034.
16. Liu, Y., S.-S. Huang, and I. Burgess, Component-based modelling of a novel ductile steel connection. Engineering Structures, 2020. **208**: p. 110320.
17. Abaqus, F., Abaqus Inc. Providence, Rhode Island, United States, 2017.
18. Meng, F.-Q., The performance of steel beam to column gravity frame subassemblages with composite slabs in severe fires in multi-storey buildings, in The University of Auckland. 2022.
19. Clifton, G. and A. Abu, Fire Engineering Design of Multi-storey Steel and Composite Steel; Concrete Structures; Draft DemandCapacity Document: Recommendations and Questions. 2019.
20. NZS 3404: 1997 Part 1: Steel structures standard. 1997, SNZ Wellington, New Zealand.
21. Burgess, I. and S.-S. Huang. Tensile Membrane Action and the Performance of Composite Slabs in Fire. in Protect 2015. 2015. Lansing, Michigan, USA.
22. Rodrigues, J.P.C. and L. Laím, Fire resistance of restrained composite columns made of concrete filled hollow sections. Journal of Constructional Steel Research, 2017. **133**: p. 65-76.
23. Espinos, A., et al., Experimental investigation on the fire behaviour of rectangular and elliptical slender concrete-filled tubular columns. Thin-Walled Structures, 2015. **93**: p. 137-148.
24. Li, G.-Q., N. Zhang, and J. Jiang, Experimental investigation on thermal and mechanical behaviour of composite floors exposed to standard fire. Fire Safety Journal, 2017. **89**: p. 63-76.

25. Lim, L., et al., Numerical modelling of two-way reinforced concrete slabs in fire. Engineering structures, 2004. **26**(8): p. 1081-1091.
26. Ding, J. and Y. Wang, Experimental study of structural fire behaviour of steel beam to concrete filled tubular column assemblies with different types of joints. Engineering Structures, 2007. **29**(12): p. 3485-3502.
27. EN 1991-1-2, Eurocode 1: Actions on structures. Part 1-2. General actions – Actions on structures exposed to fire. 2002, European Committee for Standardization (CEN): Belgium.

SiF 2022– The 12th International Conference on Structures in Fire
The Hong Kong Polytechnic University, Nov 30 - Dec 2, 2022

BEHAVIORS OF HIGH STRENGTH STEEL CONNECTIONS IN FIRE

Weiyong Wang [1], Haojie Fang[2], Hisham Al-azzani [3]

ABSTRACT

Experimental and numerical studies were presented in this paper to investigate the fire behavior of high strength steel (Q690 and Q960) shear and T-stub connections. The load–displacement curves, failure modes, and load capacities at elevated temperatures were obtained from the experiment. Finite element models were established by ABAQUS software and validated by the test results. The test capacities of shear connections were compared with those predicted by EC3, AISC 360-16, and GB50017, while the test capacities of T-stubs were compared with that predicted by EC3. Results show that the failure temperature from brittle failure to ductile failure is approximately 500 ℃ for shear connections. The load capacity predicted by AISC 360-16 is accurate, while EC3 and GB50017-2017 are conservative for shear connections. The failure mode of T-stubs changed from the flange rupture to the bolt failure with yielding of the flange when the temperature was higher than 600 ℃. EC3 provides conservative results, while the modified equations accurately predict the first yield resistance for the T-stubs.

Keywords: Shear connection; T-stub; High strength steel; Fire test; Finite element method

1 INTRODUCTION

Connections play an important role in high strength steel structures. The connection failure not only causes the redistribution of internal force but also leads to the structure collapse. The strength and elastic modulus of steel severely decrease at elevated temperatures, and additional thermal force is generated in the structure because of the constrained thermal expansion of steel members, resulting in connection failure. Therefore, studying the behavior of the connection at elevated temperatures is of considerable importance.

Design methods of bolt shear connection for mild steel structures at elevated temperatures are provided in international specifications for steel structures, such as European Code (EC3) [1, 2], American Specification (AISC 360-16) [3], British Specification (BS 5950: 2000) [4], and Australian Standard (AS 4100) [5]. EC3 [1] also recommends three failure modes and provides methods to predict the corresponding tension capacity for the T-stub connection. All the codes used the strength reduction method to predict the load capacity at elevated temperatures. However, some researchers found that the strength reduction factors provided in these specifications might be unsafe for high strength steel structures. For example, Qiang et al. [6-8] investigated the material properties of S460N, S690, and S960 steel at elevated temperatures. They found that the reduction factors of the yield strength recommended in EC3 [2], BS 5950 [3], and AISC [2] were generally unsafe. Wang et al. [9-11] also performed experimental investigations on the material properties of high strength steel Q460, Q690, and Q960 at elevated temperatures. They also found that the

[1] Professor, Chongqing University,
e-mail: wywang@cqu.edu.cn, ORCID: https://orcid.org/ 0000-0002-8607-3379

[2] Master student, Chongqing University,
e-mail: 20174898@cqu.edu.cn

[3] Ph D candidate, Chongqing University,
e-mail: hisham.alazzani@gmail.com, ORCID: https://orcid.org/ 0000-0003-1980-8002
https://doi.org/10.6084/m9.figshare.22215766

reduction factors of the yield strength recommended in EC3 [2], AISC [2], and BS5950 [3] were conservative for Q460 steel, while those in EC3 [2] and AISC [2] were unsafe for Q690 and Q960 steel.

Some researchers studied the shear behaviors of the steel connection at elevated temperatures using experimental and numerical methods. For example, Yan et al. [12] conducted high-temperature steady-state tests on G450, G500, and G550 thin sheet steel bolted bearing connections. Cho et al. [13] conducted tensile tests and analytical studies on the ultra-high strength sheet steel bolted connection at elevated temperatures. Cai et al. [14] performed tensile tests on the cold-formed stainless steel double shear connections at elevated temperatures.

Moreover, Barata et al. [15] conducted steady-state tests and numerical studies on T-stub joint components at ambient and elevated temperatures. Based on the experiment, the numerical results were compared with those calculated by previous analytical models. P. Wang et al. [16] and Y. You et al. [17] conducted steady- and transient-state tests on thread-fixed one-side bolted T-stubs. They found that the large bolt could increase the ductility of the connection and the thick flange would raise the stiffness and ultimate strength while maintaining good deformation capacity.

Most previous studies are involved in investigating the fire performance of mild strength steel connections. However, data to describe the behavior of high strength steel connections at elevated temperatures, such as Q690 and Q960, are insufficient. This paper presents static-state tensile tests on high strength Q690 and Q960 steel shear and T-stub connections at elevated temperatures to address these knowledge gaps, and finite elements models were also established.

2 EXPERIMENTAL PROGRAM

2.1 Test setup

The testing machine used in the experiments was an electromechanical universal testing machine (SANS-CMT5305) with 300 kN tension capacity, as shown in Figure 1(a). A high-temperature furnace with a temperature controller (GX-1200A), which can achieve a temperature of 1000 °C, was used to heat specimens. Figure 1(b) shows the details of the furnace. Three thermocouples were installed in the furnace.

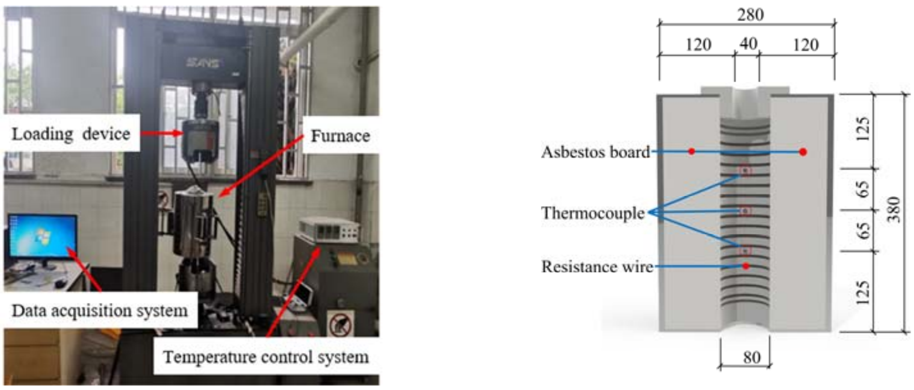

(a) Test device (b) Furnace

Figure 1. Test device and dimensions of furnace.

2.2 Test specimens

Figure 2 shows the dimension of the shear connection specimens. Each specimen included three plates, one Grade 12.9 bolt (M8), and one 1.6 mm shim used to fix the cover plate end. A total of 20 specimens were tested (10 for Q690 steel connection and 10 for Q960 steel connection). Nine target temperatures were considered: 200 °C, 300 °C, 400 °C, 500 °C, 550 °C, 600 °C, 650 °C, 700 °C, and 800 °C. The ambient temperature was also considered for comparison.

Figure 3 shows the nominal dimensions of the T-stub specimens. Each specimen includes two webs, two flanges, and two Grade 12.9 bolt (M6), and the web and the flange were welded by the T-butt weld with a weld leg size of 5 mm and a welding technology of gas-shielded arc welding. The E70 electrode was used for the specimens.

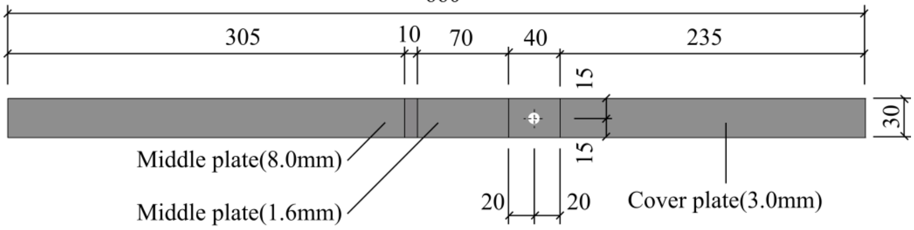

(a) Top view

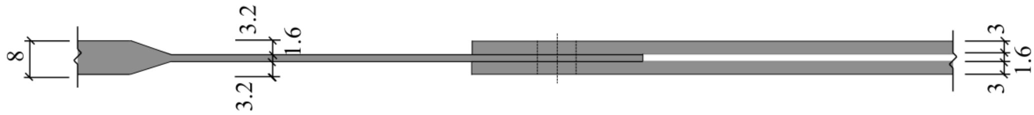

(b) Front view

Figure 2. Dimensions of the shear connection.

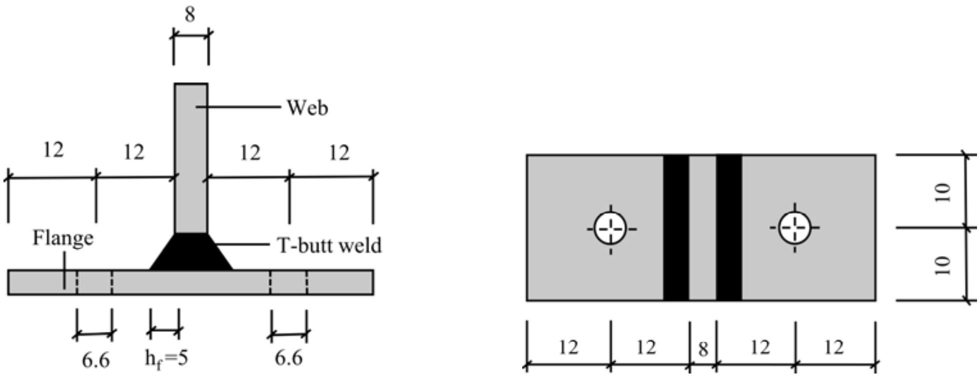

(a) Front view (b) Top view

Figure 3. Dimensions of the T-stub connection.

2.3 Test method

Eight bolts were randomly selected in the torque coefficient test for M8 and M6 bolts. The torque was applied by a torque wrench. Meanwhile, the pretension was read by an axial force sensor. Figure 4 shows the relationship between the preload and the torque of M8 and M6 bolts. The torque coefficient was calculated as follows:

$$K = T/(Pd) \quad . \tag{1}$$

The average torque coefficient, the standard deviation, and the variation coefficient are 0.218, 0.00975, and 4.47% for M8 bolts, respectively, while those for M6 bolts are 0.238, 0.00916, and 3.86%, respectively, indicating that the pretension applied to bolts is relatively accurate.

Steady-state tests were conducted after the torque coefficient tests. The heating process started immediately to avoid considerable preload loss once the preload (25 and 15 kN for shear and T-stub connections) was applied. Each specimen was heated up to a target temperature. After maintaining that temperature for the scheduled time, the specimen was loaded until it failed. The critical part of specimens was installed in the middle part of the furnace to heat the specimens sufficiently. The heating rate was set as 20 °C/min. The temperatures were maintained for 25 min after the reading of the middle thermocouple achieved the target value to ensure that the specimen temperature could reach the target value and was uniformly distributed. To avoid axial force caused by thermal expansion, the lower end of the specimen was gripped, whereas the upper end was free during the heating and heat preservation stages. After the heat preservation stage, the upper end was gripped and a tensile load was applied to the specimen by displacement control with a loading rate of 5 mm/min until the specimen failed.

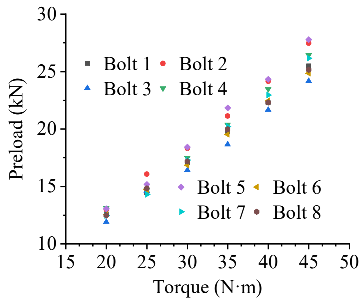

(a) M8 bolt

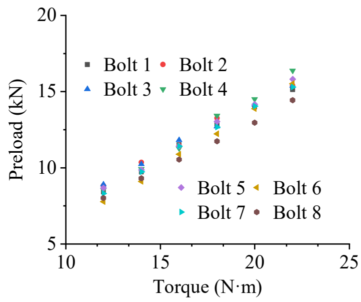

(b) M6 bolt

Figure 4. Relationship between preload and torque.

3 TEST RESULT AND DISCUSSION

3.1 Failure modes of shear connections

Figure 5 shows the failure modes of specimens. Considerable deformation of the hole was observed in most specimens, which indicated that those specimens underwent steel plate strength bearing failure. However, the final failure mode varied with temperature and steel grade.

When the tested temperature was lower than 500 °C, two failure modes were observed in Q690 and Q960 specimens: net section failure and block shear (the combination of net section fracture and tearing out). For specimens with net section failure such as Q690S-25, Q690S-200, Q690S-300, and Q960S-200, after the bolt shank contacted the hole wall, the tensile stress concentration formed at the interior of the hole results in a local tearing, which gradually developed as the load increased and finally led to a sudden fracture of the net section. For specimens with block shear such as Q690S-400, Q960S-300, and Q960S-400, besides the fracture of a portion of the net area, there was also a tearing caused by shear stress.

When the tested temperature was higher than 500 °C, most specimens failed due to tearing out of the plate, except for the specimens Q690S-700, Q960S-600, and Q960S-650, which failed due to the bolt shear failure. As the temperature increased from 550 °C to 800 °C, the failure mode of Q960 specimens changed from tearing out to net section fracture, which indicated that the net section capacity might decrease more rapidly than the tearing out capacity for Q960 specimens when the temperature is from 550 °C to 800 °C.

3.2 Failure modes of T-stubs

Figure 6 shows the failure mode of specimens in tests. Most specimens underwent the yield of the flange due to its large deformation.

The failures mainly occurred at the flange when the tested temperature was lower than 600 °C. All Q690 specimens failed due to the rupture of the flange at the weld toe. Meanwhile, considerable deformation at the flange near the bolts was also observed.

When the tested temperature was higher than 600 °C, all specimens demonstrated bolt failure with yielding of the flange. The deformation of all specimens was quite considerable, but no rupture behavior was observed. The failure modes of the T-stub change from the flange rupture to the bolt failure with the yielding of the flange after 600 °C.

Figure 5. Failure modes of shear connections.

Figure 6. Failure modes of T-stub

3.3 Load–displacement curves and capacities of shear connections

Figure 7 shows the load–displacement curve of Q690 specimens, and Table 1 also presents their load capacity. The ultimate and slip loads decreased with the increasing temperature overall. The ultimate capacity of Q690T-25 was reduced to 76.5%, 45.8%, and 13.0% at 500 °C, 600 °C, and 800 °C, respectively. The slip load decreased more rapidly than the ultimate load and reduced to 82.8%, 49.2%, 24.6%, and 10.9% at 400 °C, 500 °C, 600 °C, and 800 °C, respectively. The ductility of the specimens improved with the increase in temperature. A steep drop was observed in load–displacement curves at a low temperature (≤ 500 °C), indicating that the specimens fractured suddenly. However, the steep drop disappeared at a temperature larger than 500 °C, and the progress of failure was slow. Therefore, the failure temperature from brittle to ductile failure was approximately 500 °C.

Figure 8 shows the load–displacement curve of Q960 specimens, and Table 2 also presents the load capacity. The results suggest that the ultimate and slip loads decreased with the increasing temperature overall. The ultimate capacity of Q960-25 was reduced to 78.4%, 42.7%, and 11.7% at 500 °C, 600 °C, and 800 °C, respectively. The slip load decreased more rapidly than the ultimate load and reduced to 76.4%, 42.0%, 33.7%, and 10.2% at 400 °C, 500 °C, 600 °C, and 800 °C, respectively. The steep drop of the curve disappeared at temperatures larger than 550 °C, but the failure displacement of Q960-550 is 15 mm, which is even larger than that of Q960-600. Therefore, the failure temperature from brittle failure to plastic failure was 500 °C.

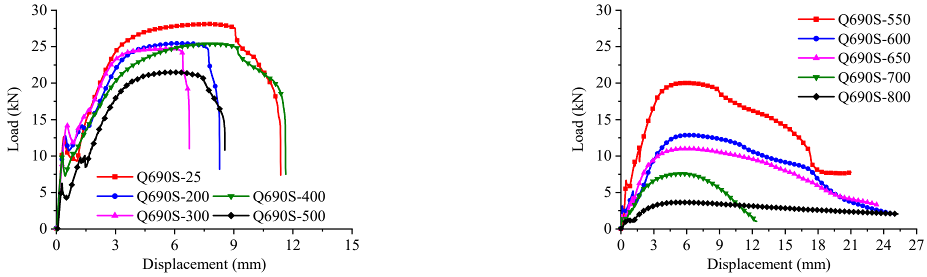

(a) At ambient, 200 °C, 300 °C, 400 °C, 500 °C (b) At 550 °C, 600 °C, 650 °C, 700 °C, 800 °C

Figure 7. Load–displacement curves of Q690 shear connections.

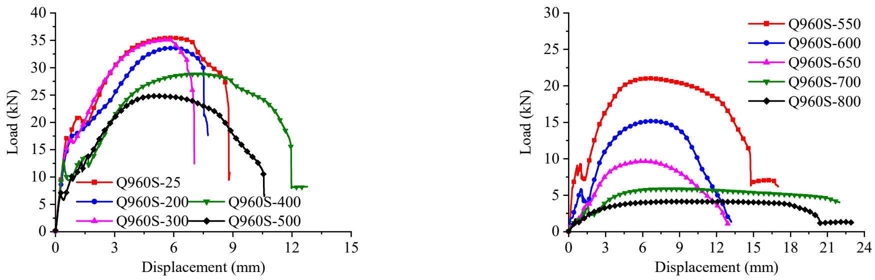

(a) At ambient, 200 °C, 300 °C, 400 °C, 500 °C (b) At 550 °C, 600 °C, 650 °C, 700 °C, 800 °C

Figure 8. Load–displacement curves of Q960 shear connections.

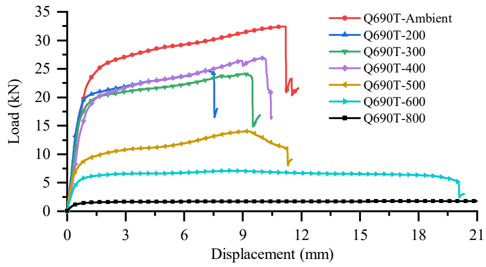

Figure 9. Load–displacement curves of T-stubs.

3.4 Load–displacement curves and capacities of T-stubs

Figure 9 shows the load–displacement curves of T-stub connections, and Table 3 also presents their load capacity. When the temperature was lower than 600 °C, the load–displacement curves contained a sudden drop, representing the brittle rupture of the flange at the weld toe. However, the sudden drop disappeared when the temperature was higher than 600 °C, indicating that the plastic hinge can comprehensively develop, and the specimens demonstrated ductile failure. Moreover, the strengthening behavior at the plastic hinge developing stage disappeared. Even the negative post-limit stiffness was observed in some specimens, such as Q690-800. However, the yield ratio of steel usually decreases with increasing temperature[10, 11]. Therefore, the disappearance of the strengthening behavior was mainly due to the severe decrease in bolt strength at elevated temperatures [18]. The first yield resistance was reduced to 36.8% at 500 °C and 6.9% at 800 °C. Meanwhile, the ultimate load was reduced to 43.2% at 500 °C and 5.5% at 800 °C.

Table 1. Load capacities of Q690 shear connections.

Specimens	First slip load (kN)	Second slip load (kN)	Ultimate load (kN)	Failure Mode
Q690S-25	12.67	-	28.10	N
Q690S-200	12.79	14.25	25.45	N
Q690S-300	14.22	-	24.74	N
Q690S-400	10.49	-	25.39	NT
Q690S-500	6.23	9.98	21.49	N
Q690S-550	6.65	-	20.02	T
Q690S-600	3.12	5.18	12.86	T
Q690S-650	1.68	-	11.00	T
Q690S-700	1.56	-	7.59	S
Q690S-800	1.38	-	3.65	T

Note: "N" means the net section failure, "T" means the tearing out failure, "NT" means the block shear, and "S" means bolt shear failure.

Table 2. Load capacities of Q960 shear connections.

Specimen	Slip load 1 (kN)	Slip load 2 (kN)	Ultimate load (kN)	Failure Mode
Q960S-25	17.18	21.04	35.45	T
Q960S-200	17.69	-	33.60	N
Q960S-300	17.00	-	35.07	T
Q960S-400	13.12	-	28.80	NT
Q960S-500	7.22	-	24.81	NT
Q960S-550	9.10	-	21.02	T
Q960S-600	5.79	-	15.15	S
Q960S-650	3.96	-	10.70	S
Q960S-700	3.29	-	5.85	NT
Q960S-800	1.75	-	4.13	NT

Table 3. Load capacities of Q690 T-stubs.

Specimens	P_{yield} (kN)	$P_{ultimate}$ (kN)	Initial stiffness (kN/mm)	Post limit stiffness (kN/mm)	Failure mode
Q690T-25	25.87	32.42	29.17	0.74	1
Q690T-200	20.20	24.72	32.78	0.78	1
Q690T-300	19.86	24.09	27.78	0.52	1
Q690T-400	19.37	26.88	24.95	1.04	1
Q690T-500	9.53	14.02	13.81	0.52	1
Q690T-600	6.53	7.09	10.82	0.03	2
Q690T-800	1.78	1.78	1.70	-	2

Note: P_{yield} and $P_{ultimate}$ means the first yield resistance and the ultimate resistance, respectively. Failure mode 1 is the complete yielding of the flange. Failure mode 2 is the bolt failure with yielding of the flange.

4 NUMERICAL MODEL

4.1 Overview

The high strength steel shear and T-stub connections conducted by steady-state tests were simulated using the finite element program ABAQUS 6.14 with standard solver. A quarter model was developed due to the symmetry of the structure to improve the computing efficiency, as shown in Figure 10. The bolt in FEM was simplified as the form without washers and threads. Temperature variation was defined by the predefined field as a uniform distribution of all parts. Geometric nonlinear was defined in each step.

The steel plates and bolts were meshed with C3D8R solid elements. The C3D8R element is an eight-node three-dimensional element with only one integral point, which could reduce the computation. Three layers of the mesh of the middle plate were used for shear connections, and five layers of mesh were used for T-stub connections to avoid the hourglass phenomenon.

The material properties of Q690, Q960, and bolt were determined by previous studies [10, 11, 18, 19]. The engineering stresses and strains were converted into the true stresses and strains, respectively.

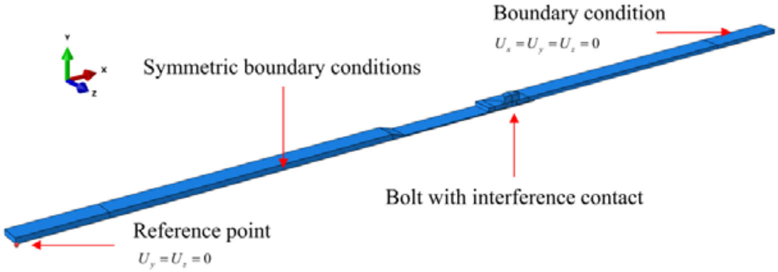

(a) Shear connection

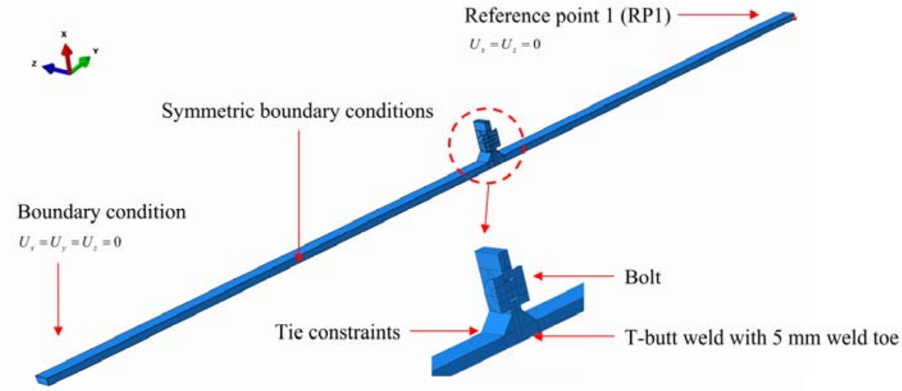

(b) T-stub

Figure 10. Finite element model for double shear connection.

4.2 Model validation

Table 4 shows the comparison of simulation and test results of shear connections considering the first stage of slip and ultimate loads. Table 5 presents the comparison between the simulation and test results of T-stubs considering the first yield resistance. Overall, the simulation results are reasonable. The simulation ultimate load of Q690S-800 (2.16 kN) was 59% of that in the test (3.65 kN), which might be due to the accidental difference of materials between the connection and material property tests.

Figure 11 shows the comparison of load–displacement curves from tests and FEM for some typical specimens. The load–displacement curves obtained by FEM are in good agreement with that in the tests. Figure 12 shows the failure modes in FEM for some specimens. The figure reveals that the load–displacement curves and the failure modes obtained by FEM are in good agreement with that in tests.

5 COMPARISON WITH DESIGN SPECIFICATIONS

5.1 Modified equations of T-stub connections

EC3 [1] specifies three failure modes considering the prying force: (1) complete yielding of the flange, (2) bolt failure with yielding of the flange, and (3) bolt failure. Considering the effect of the bolt nut, EC3 [1] also provides two methods to predict the tension resistance for failure mode 1.

Method 1:

$$F_{T,1} = \frac{4M_{pl,1}}{m}. \tag{2}$$

Method 2:

$$F_{T,1} = \frac{(8n-2e_w)M_{pl,1}}{2mn-e_w(m+n)}, \tag{3}$$

where $F_{T,i}$ is the tension resistance for failure mode i, $M_{pl,i}$ is the flange plastic moment resistance of T-stub for failure mode i, and e_w is quarter of the diameter of the washer. m and n are the distance, which are 8 and 10 mm in this paper, respectively.

The tension resistance of T-stub for failure mode 2 can be predicted by Equation (4).

$$F_{T,2} = \frac{2M_{pl,2}+n\sum F_{tb}}{m+n}, \tag{4}$$

where $\sum F_{tb}$ is the total tension resistance of all bolts.

However, the weld toe could increase the plastic moment resistance of the flange, especially when the flange is quite thin. The equations in EC3 [1] are modified as follows based on force equilibrium theory of beams to consider the aforementioned phenomenon.

Method 1:

$$F_{T,1} = \frac{2M_{pl,b}+2M_{pl,w}}{m}. \tag{5}$$

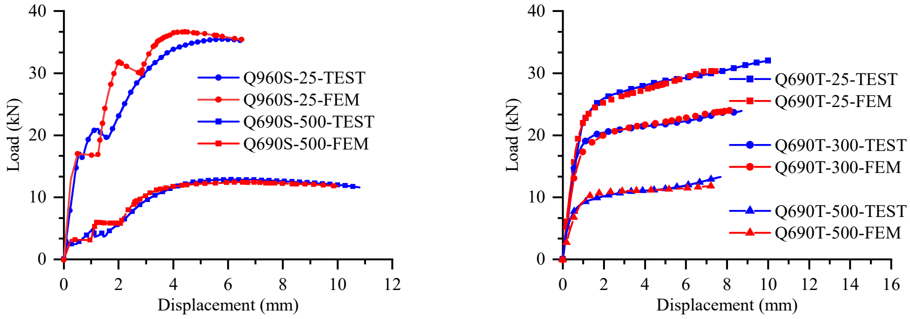

(a) Shear connections (b) T-stubs

Figure 11. Comparison of load–displacement curve between test and FEM.

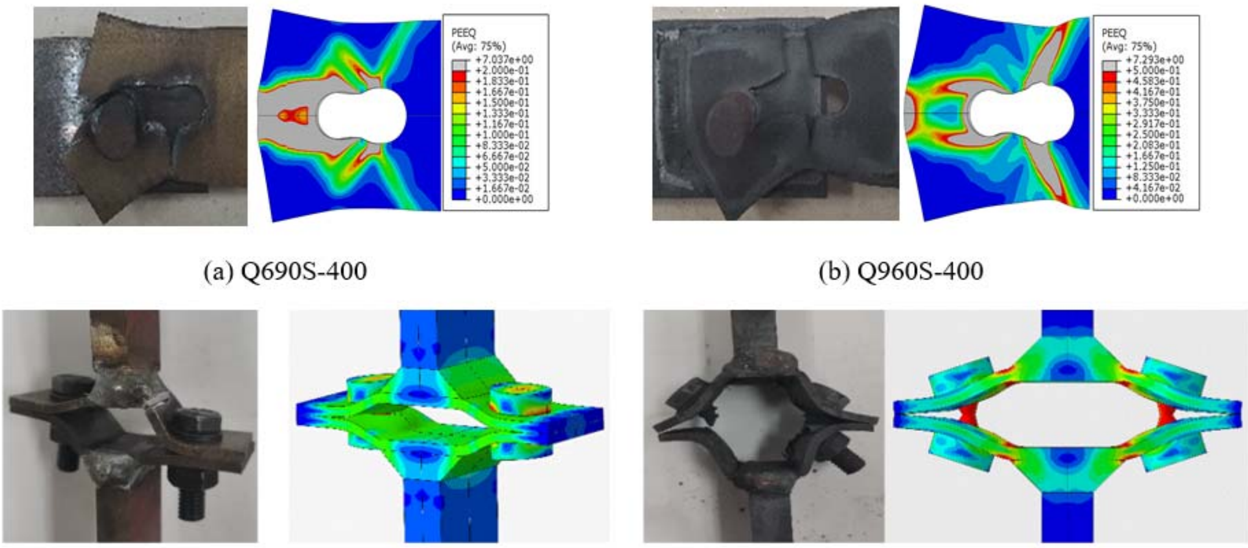

(a) Q690S-400 (b) Q960S-400

(c) Q690T-25 (d) Q690T-800

Figure 12. Failure modes simulated by FEM.

Table 4. Simulation verification of the shear connection at elevated temperatures.

Specimen series	$P_{s,FEM}$ (kN)	$P_{u,FEM}$ (kN)	$P_{s,test}$ (kN)	$P_{u,test}$ (kN)	$P_{s,FEM}/P_{s,test}$	$P_{u,FEM}/P_{u,test}$
Q690S-Ambient	12.19	28.58	12.67	28.10	0.96	1.02
Q690S-T300	14.52	25.74	14.22	24.74	1.02	1.04
Q690S-T400	10.48	26.64	10.49	25.39	1.00	1.05
Q690S-T500	6.33	20.68	6.23	21.49	1.02	0.96
Q690S-T600	3.16	12.42	3.12	12.86	1.01	0.97
Q690S-T800	1.37	2.16	1.38	3.65	0.99	0.59
			Average		1.01	0.94
			Coefficient of variation		0.03	0.18
Q960S-Ambient	17.00	36.64	17.18	35.45	0.99	1.03
Q960S-T300	17.34	35.22	17.00	35.07	1.01	1.00
Q960S-T400	13.26	32.16	13.12	28.80	1.01	1.12
Q960S-T500	7.33	27.54	7.22	24.81	1.02	1.11
Q960S-T700	3.39	7.44	3.29	5.85	1.03	1.27
Q960S-T800	1.79	3.02	1.75	4.13	1.02	0.73
			Average		1.01	1.04
			Coefficient of variation		0.01	0.17

Table 5. Simulation verification of the T-stub at elevated temperatures.

Specimens	P_{FEM} (kN)	P_{test} (kN)	Failure mode (FEM)	Failure mode (TEST)	P_{FEM}/P_{test}
Q690T-25	24.43	25.14	1	1	0.97
Q690T-200	19.55	20.20	1	1	0.97
Q690T-300	19.70	19.86	1	1	0.99
Q690T-400	19.64	19.37	1	1	1.01
Q690T-500	10.68	9.53	1	1	1.12
Q690T-600	5.94	6.53	2	2	0.91
Q690T-800	1.50	1.78	2	2	0.84
				Average	0.97
				Coefficient of variation	0.08

Method 2:

$$F_{T,1} = \frac{4nM_{pl,b} + (4n - 2e_w)M_{pl,w}}{2mn - e_w(m+n)}, \tag{6}$$

$$F_{T,2} = \frac{2M_{pl,w} + n\sum F_{tb}}{m+n}, \tag{7}$$

$$M_{pl,b} = 0.25 l_{eff} t_f^2 f_y, \tag{8}$$

$$M_{pl,w} = 0.25 l_{eff} (t_f + 0.2h_f)^2 f_y, \tag{9}$$

where $M_{pl,b}$ and $M_{pl,w}$ are the flange plastic moment resistance at the bolt and the weld toe, respectively; h_f is the size of the welding foot and f_y is the yield strength of the flange.

5.2 Comparison of specifications with test results

Table 6 shows the ultimate loads calculated by GB50017-2017 [20] , EN 1993-1-8 [1] and AISC 360-16 [3] for shear connections. The reduction factors of the ultimate strength of steel at elevated temperatures were taken from the specification of the corresponding nation, that is, GB51249-2017 [21], EN 1993-1-2 [2], and AISC 360-16 [3]. Table 7 shows that AISC 360-16 [3] provides the most accurate estimate of the ultimate load of Q690 and Q960 specimens. Meanwhile, GB50017-2017 [20] and EN 1993-1-8 [1] are all conservative, and GB50017-2017 [20] is more conservative than EC3 [1].

Table 7 shows the comparison of the first yield resistance between tests and EC3 for T-stubs. Overall, EC3 [1] provides conservative results. The results calculated by Equation (3) are slightly higher and more accurate than those predicted by Equation (2) because Equation (3) considered the effect of the bolt nut.

The predicted values are 39% less than the test results on average possibly because Equation (3) ignores the effect of the weld toe. Considering the weld toe, the results calculated by the modified equations are close to the test results.

Table 6. Comparison of the load capacity (in kN) results obtained by test and specifications (shear connections).

Specimens	P_{EC3}	$P_{AISC\ 360}$	$P_{GB50017\text{-}2017}$	P_{test}	P_{EC3}/P_{test}	P_{AISC}/P_{test}	$P_{GB50017}/P_{test}$
Q690S-25	23.48	29.28	14.10	28.10	0.84	1.04	0.50
Q690S-200	21.70	27.01	13.03	25.45	0.85	1.06	0.51
Q690S-300	20.86	26.01	12.52	24.74	0.84	1.05	0.51
Q690S-400	19.29	30.00	13.24	25.39	0.76	1.18	0.52
Q690S-500	14.61	21.51	9.94	21.49	0.68	1.00	0.46
Q690S-550	11.77	18.41	8.21	20.02	0.59	0.92	0.41
Q690S-600	8.02	12.93	5.80	12.86	0.62	1.01	0.45
Q690S-650	6.55	10.21	4.65	11.00	0.60	0.93	0.42
Q690S-800	2.10	3.81	1.43	3.65	0.58	1.04	0.39
Q960S-25	30.34	35.84	17.20	35.45	0.86	1.01	0.49
Q960S-200	28.77	33.91	16.31	33.60	0.86	1.01	0.49
Q960S-300	31.21	36.80	17.70	35.07	0.89	1.05	0.50
Q960S-400	23.47	34.55	15.21	28.80	0.81	1.20	0.53
Q960S-500	18.47	26.28	11.87	24.81	0.74	1.05	0.48
Q960S-550	14.99	22.13	9.88	21.02	0.71	1.05	0.47
Q960S-700	5.37	9.03	3.73	5.85	0.92	1.54	0.64
Q960S-800	2.64	4.51	1.70	4.13	0.64	1.09	0.41

Table 7. Comparison of the load capacity (in kN) results obtained by test, EC3, and modified equations (T-stubs).

Specimens	$F_{T,1}$ (EC3)		$F_{T,2}$ (EC3)	$F_{T,1}$ (Modified)		$F_{T,2}$ (Modified)	Test	P_{EC3}/P_{test}	P_{mod}/P_{test}
	Equation (2)	Equation (3)		Equation (5)	Equation (6)				
Q690T-25	7.98	11.13	28.13	12.96	17.53	30.35	25.87	0.43	0.68
Q690T-200	7.98	11.13	26.42	12.96	17.53	28.64	20.20	0.55	0.87
Q690T-300	7.98	11.13	25.58	12.96	17.53	27.79	19.86	0.56	0.88
Q690T-400	7.98	11.13	22.20	12.96	17.53	24.42	19.37	0.57	0.91
Q690T-500	6.22	8.69	15.88	10.11	13.67	17.61	9.53	0.91	1.43
Q690T-600	3.75	5.23	6.63	6.09	8.24	7.67	6.53	0.80	1.18
Q690T-800	0.88	1.22	1.96	1.43	1.93	2.20	1.78	0.69	1.08

6 CONCLUSIONS

Experimental and numerical investigations of high strength steel connections at elevated temperatures are reported in this paper. The finite element model was established and validated by the test results. The load capacities predicted by the specifications were compared with the test results. Moreover, modified equations were developed to predict the first yield resistance for the T-stubs. The following conclusions are drawn from this study.

1) The slip load of the shear connection decreases more rapidly than the ultimate load at elevated temperatures. They all reduce to approximately 10% at 800 °C for Q690 and Q960 specimens. The failure temperature from brittle failure to ductile failure is approximately 500 °C for Q690 and Q960 specimens.

2) AISC 360-16 predicts the ultimate load relatively accurately, while EC3 [1] and GB50017-2017 [20] respectively underestimate the ultimate load by 29% and 54% for Q690 specimens and 20% and 50% for Q960 specimens.

3) The T-stubs demonstrated the flange rupture when the temperature was lower than 600 °C, while the failure mode changed to the bolt failure with yielding of the flange when the temperature was higher than 600 °C.

4) The results predicted by EC3 were 39% less than the test results on average. Considering the effect of the weld toe, the modified equations provide relatively accurate results.

REFERENCES

1. European Committee for Standardization, Eurocode 3: Design of steel structures-Part 1-8: Design of joints, EN 1993-1-8, Brussels, 2005.
2. European Committee for Standardization, Eurocode 3: Design of steel structures-Part 1-2: General rules-Structural fire design, EN 1993-1-2, Brussels, 2005.
3. American Institute of Steel Construction, Specification for Structure Steel Buildings, ANSI/AISC 360-16, Chicago IL, 2016.
4. British Standards Institution (BSI), Structural use of steel work in building-Part 1: Code of practice for design-Rolled and welded sections, BS 5950-1: 2000, London, 2001.
5. Australian Standard, Steel Structures, AS 4100, Sydney, Australia, 1998.
6. Qiang, X., Bijlaard, F.S.K., Kolstein, H., Elevated-temperature mechanical properties of high strength structural steel S460N: Experimental study and recommendations for fire-resistance design, Fire Safety Journal, 55 (2013), pp. 15-21.
7. Qiang, X., Bijlaard, F., Kolstein, H., Dependence of mechanical properties of high strength steel S690 on elevated temperatures, Construction and Building Materials, 30 (2012), pp. 73-79.
8. Qiang, X., Jiang, X., Bijlaard, F.S.K., Kolstein, H., Mechanical properties and design recommendations of very high strength steel S960 in fire, Engineering Structures, 112 (2016), pp. 60-70.
9. Wang, W.Y., Liu, B., Kodur, V., Effect of temperature on strength and elastic modulus of high-strength steel, Journal of Materials in Civil Engineering, 25(2), 2013, pp. 174-182.
10. Wang, W.Y., Wang, K., Kodur, V., Wang, B., Mechanical properties of high-strength Q690 steel at elevated temperature, Journal of Materials in Civil Engineering, 30(5), 2018.
11. Wang, W.Y., Zhang, Y., Xu, L., Li, X., Mechanical properties of high-strength Q960 steel at elevated temperature, Fire Safety Journal, 114 (2020).
12. Yan, S., Young, B., Tests of single shear bolted connections of thin sheet steels at elevated temperatures—Part I: Steady state tests, Thin-Walled Structures, 49(10), 2011, pp. 1320-1333.
13. Cho, Y., Teh, L.H., Young, B., Ahmed, A., Net section tension strength of bolted connections in ultra-high strength sheet steel during and after fire, Journal of Constructional Steel Research, 172 (2020).
14. Cai, Y., Young, B., High temperature tests of cold-formed stainless steel double shear bolted connections, Journal of Constructional Steel Research, 104 (2015), pp. 49-63.
15. Barata, P., Ribeiro, J., Rigueiro, C., Santiago, A., Rodrigues, J.P., Assessment of the T-stub joint component at ambient and elevated temperatures, Fire Safety Journal, 70 (2014), pp. 1-13.
16. Wang, P., You, Y., Liu, M., Zhang, B., Zhou, S., Chen, J., Behavior of thread-fixed one-side bolted T-stubs with backing plates at ambient and elevated temperatures, Journal of Constructional Steel Research, 170 (2020).
17. You, Y., Liu, M., Liu, Y., Wang, P., Zhou, S., Chen, J., Experimental studies on thread-fixed one-side bolted T-stubs in tension at elevated temperatures, Journal of Constructional Steel Research, 171 (2020).
18. Pang, X.P., Hu, Y., Tang, S.-L., Xiang, Z., Wu, G., Xu, T., Wang, X.Q., Physical properties of high-strength bolt materials at elevated temperatures, Results in Physics, 13 (2019).
19. Huang, D., Zhang, L., Wang, W., Mu, H., Test on post-fire residual mechanical properties of high strength Q690 steel considering tensile stress in fire, Journal of Constructional Steel Research, 194 (2022).
20. Ministry of Housing and Urban-Rural Development of the People's Republic of China (MOHURD), GB50017-2017 Standard for design of steel structures, Architecture & Building Press, Beijing, 2018.
21. Ministry of Housing and Urban-Rural Development of the People's Republic of China (MOHURD), Code for fire safety of steel structures in buildings, GB51249-2017, China Plan Press, Beijing, 2017.

NUMERICAL INVESTIGATION OF A DUCTILE CONNECTION TO IMPROVE STRUCTURAL ROBUSYNESS IN FIRE

Yu Liu[1], Shan-Shan Huang[2], Ian Burgess[3]

ABSTRACT

A novel steel connection with high axial and rotational ductility has been proposed with the objective to improve the performance of steel-framed buildings in fire. A series of sub-frame models with this ductile connection have been built using Abaqus to study the influence of the characteristics of the part of the connection between the fin-plate which connects to the beam web and face-plate which connects to the column face on the overall connection behaviour. Measures to improve the bolt pull-out failure mode of the connection have also been tested using the Abaqus models, including adding a strengthening plate to the face-plate and increasing the connection thickness.

Keywords: Fire; connections; ductility; finite element modelling

1 INTRODUCTION

Connections are potentially the most vulnerable structural elements of a steel building frame in fire. The collapse of buildings at the World Trade Centre [1] and the Cardington full-scale fire tests [2] showed that connection fractures may occur, which can potentially trigger the collapse of floors, buckling of columns, and eventually the disproportionate collapse of an entire building. Connections are usually designed to carry forces under ambient-temperature loadings which are easily defined and calculated. However, in fire conditions, the deformation of the weakened connected beams causes a complex variation of forces in the structure. During the initial stage of a fire event, heating of a steel downstand beam causes a free thermal expansion which, if stiffly restrained by surrounding structure, generates very high axial compression. The net compression, hogging bending and shear tend to cause localised shear buckling of the beam web and lower-flange buckling. If the free thermal expansion of the beam can be accommodated by soft, ductile surrounding structure, then the initial build-up of compressive force can be greatly reduced. At very high temperatures, a beam hangs, essentially in catenary tension, between its end connections. When the beam is cooled from any peak temperature, its contraction will generate high tensile forces between its ends. If the connections are ductile during this phase, then this tension force will be reduced.

To improve the resistance of modern buildings with steel framing and composite steel-concrete floor systems, to progressive collapse in fire, a novel ductile connection has been proposed [3-12] by the authors. Component-based models of the ductile connection have been proposed by the authors, and converted into connection elements, following the principles of the finite element method, and incorporated into the software Vulcan [5, 6, 8]. Comparisons have been made, using sub-frame models, between the fire performance of the new connection and that of other connection types, including conventional end-plate

[1] Dr. Yu Liu, University of Shanghai for Science and Technology,
e-mail: liuyu651020@163.com, ORCID: https://orcid.org/0000-0001-7468-1089
[2] Dr. Shan-Shan Huang, The University of Sheffield
e-mail: s.huang@sheffield.ac.uk, ORCID: https://orcid.org/0000-0003-2816-7104
[3] Prof. Ian Burgess, The University of Sheffield
e-mail: ian.burgess@sheffield.ac.uk, ORCID: https://orcid.org/0000-0001-9348-2915
https://doi.org/10.6084/m9.figshare.22215769

and web-cleat connections, and ideally rigid and pinned connections [6, 12]. The results show that the ductile connection can provide much higher axial and rotational ductility to accommodate the deformations generated by the connected beams as their temperatures rise, significantly reducing axial force and preventing abrupt fracture. In previous studies, the failure temperatures of the ductile connection have been higher than those of commonly-used connection types, but the differences are not large. The current critical failure mode for the ductile connection is the bolt pull-out from the face-plate zone. At very high temperatures, the top bolt row of the face-plate part is pulled out of the bolt holes first, and then the remaining bolt rows are pulled out successively.

In this paper, the proposed connection is introduced. A series of Abaqus sub-frame models with ductile connections are built to investigate the influence of the characteristics of the part between the face-plate and fin-plate parts of the connection on the overall connection performance. In addition, Abaqus sub-frame models are also used to test measures to improve the bolt pull-out failure of the connection, including adding an additional strengthening plate to the face-plate part, or increasing the connection thickness directly.

2 THE PROPOSED DUCTILE CONNECTION

Figure 1 shows the detailed design of the ductile connection proposed by the authors. It consists of two identical parts, each of which includes a fin-plate which is bolted to the beam web, a face-plate bolted to either the column flange or web, and a semi-cylindrical section between these zones. The latter provides additional ductility by allowing the fin-plate to move away from or towards the face-plate and to use this horizontal movement to provide high rotation capacity. Therefore, the diameter of the semi-cylindrical section should be determined according to the ductility demand of the connected beam under fire conditions, which can be approximated by equations (1) – (3) which have been proposed in the previous papers [3, 8]. The basic element of this connection can be manufactured simply by bending a steel plate.

$$\Delta_{low-temp} = \frac{1}{2}(\alpha l T + h\theta) - \frac{4}{3}\delta^2 / l \qquad (1)$$

$$\Delta_{high-temp} = \frac{4}{3}\delta_{\max}{}^2 / l - \frac{1}{2}(\alpha l T + h\theta) \qquad (2)$$

$$\Delta_{high-temp,\max} = \frac{4}{3}\delta_{\max}{}^2 / l - \frac{1}{2}(\alpha l T - h\theta) \qquad (3)$$

where $\Delta_{low-temp}$ is the displacement at the bottom of the beam end at low temperatures, caused by the beam thermal expansion, the beam end rotation, and the effective shortening due to beam deflection. The movements $\Delta_{high-temp,max}$ and $\Delta_{high-temp,max}$ are those at the top and bottom of the beam end in the high temperature range.

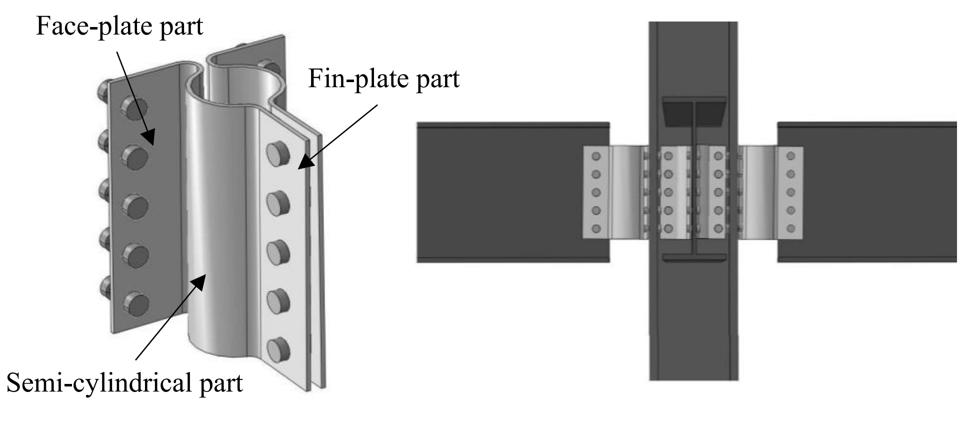

Figure 1. The design of the ductile connection

3 THE GEOMETRY OF THE SECTION BETWEEN THE FIN-PLATE AND FACE-PLATE

As mentioned previously, the connection part between the fin-plate and the face-plate can provide additional deformability for the ductile connection, and is designed as a semi-cylindrical section preliminarily. The diameter of the semi-cylindrical section should be determined according to the ductility demands of the beam in fire, calculated using equations (1) – (3). From these equations, it can be found that the ductility demands of the beam in tensile and compressive directions are different, implying that the part between the fin-plate and the face-plate should not necessarily be semi-cylindrical, but rather semi-elliptical. In this section, the influence of the geometry of the part between the fin-plate and the face-plate on the high-temperature connection behaviour will be studied

3.1 Development of Abaqus sub-frame models

A series of two-storey three-bay steel frame models with different beam spans and beam sections, as shown in Figure 2, were established using Abaqus. Due to the symmetry of the frame, only half of each model needed to be built. It was assumed that fire occurs only on the ground floor of the central bay, and the ISO standard fire curve was adopted. Three beam spans, 6m, 9m and 12m, are selected and the corresponding beam sections are listed in Table 1. A uniformly distributed line load of 42.64 kN/m is applied to the beams of each frame model, generating a load ratio of 0.4 with respect to simply supported conditions. For each beam span the ductility demands of the beam are calculated first, and then the ductile connections with semi-cylindrical and semi-elliptical configurations are designed according to the range of ductility demand conditions, as listed in Table 1. The dimensions of the fin-plate and face-plate parts of the connection are designed based on Eurocode 3 [13]. The complex contacts involved in the connection zone of the frame model may lead to numerical singularities if the Abaqus static solver is used, and so the dynamic explicit solver is used to analyse the frame models in this paper, as long as the response of the whole system remains static.

Table 1. Parameters of the steel frame models

Span (mm)	Beam section	Load ratio	Connection size	
			Semi-cylindrical (radius: mm)	Semi-elliptical (semi-major axis × semi-minor axis: mm×mm)
6000	UKB 457×152×82	0.40	55	60 × 45
9000	UKB 533×312×151	0.39	75	80 × 65
12000	UKB 610×305×238	0.39	125	130 × 115

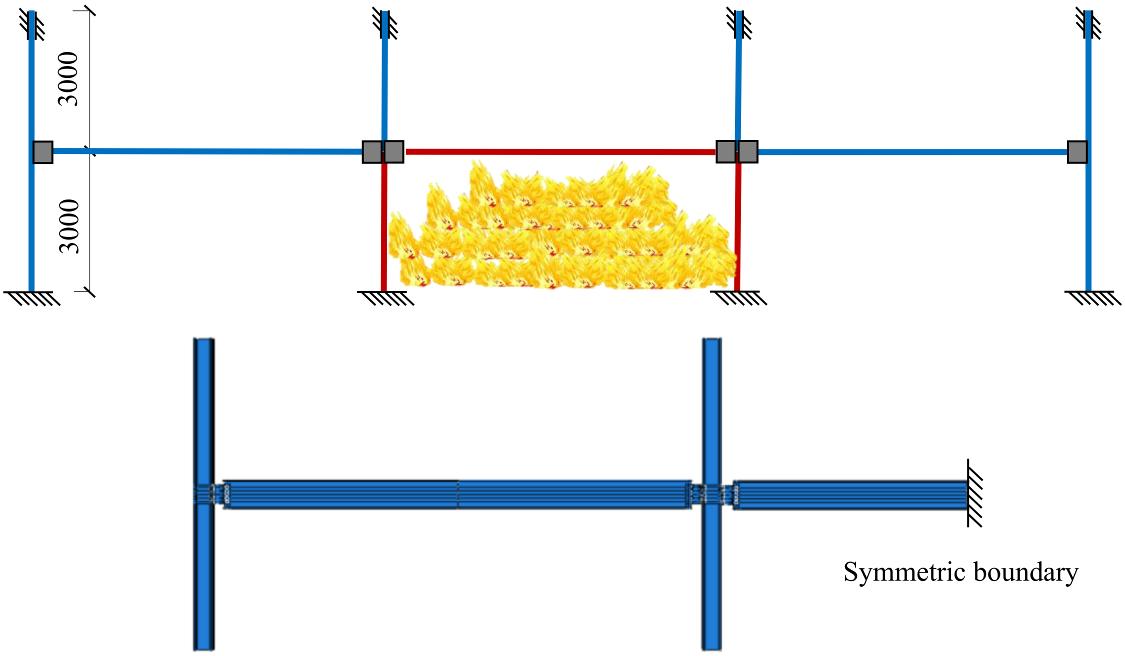

Figure 2. Abaqus steel frame model

3.2 Influence of the geometry of the section between the fin-plate and the face-plate

Figures 3 – 5 show comparative results from the Abaqus frame models with connections of different shapes. It can be seen from these figures that the beam mid-span deflections and connection axial forces of the frame models with connections of semi-cylindrical section are almost the same as those of the models with connections of semi-elliptical section. This illustrates that the geometry of the section between the fin-plate and the face-plate has negligible influence on the overall connection performance, as long as the deformability of the connection can meet the ductility demands of the beam.

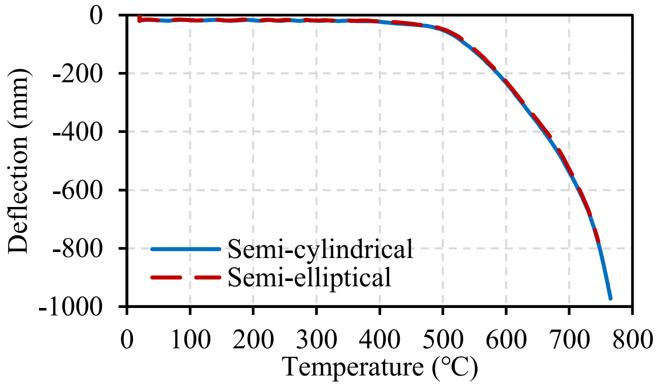

(a) Mid-span deflection of the beam of the central bay

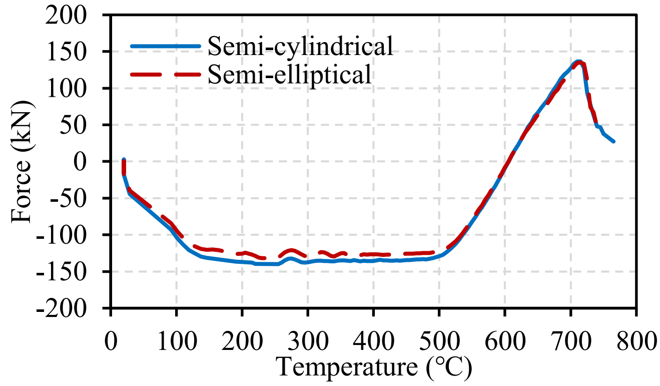

(b) Axial force of the connection of the central bay

Figure 3. Results of the frame models with 6m beam span

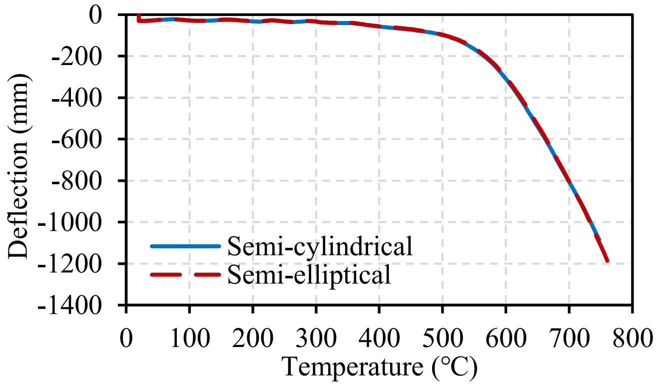

(a) Mid-span deflection of the beam of the central bay

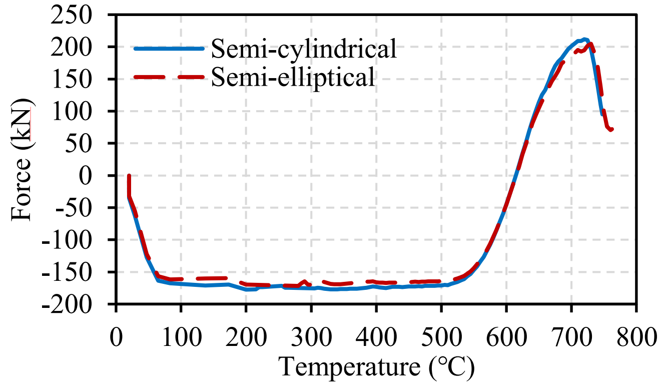

(b) Axial force of the connection of the central bay

Figure 4. Results of the frame models with 9m beam span

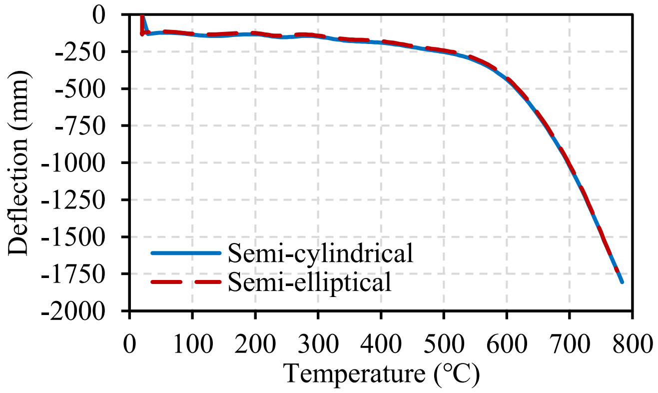

(a) Mid-span deflection of the beam of the central bay

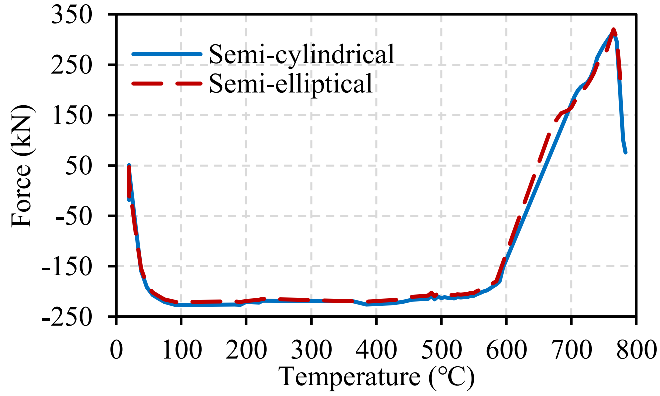

(b) Axial force of the connection of the central bay

Figure 5. Results of the frame models with 12m beam span

4 MEASURES TO IMPROVE BOLT PULL-OUT FAILURE

Currently the critical failure mode of the ductile connection is bolt pull-out failure from the face-plate zone. At very high temperatures, coinciding with very high rotations, the top bolt row is first pulled out from its bolt holes, and a sequence of pull-out of the remaining bolt rows then follows very closely, resulting in a progressive failure of the whole connection. However, when the whole connection fails, the semi-cylindrical section is not completely stretched flat, so the tensile deformation capacity of the connection is not fully utilized. To improve the bolt pull-out failure of the connection, the Abaqus steel frame models introduced in the previous section are used here to test some measures, including adding an additional strengthening plate to the face-plate of the connection (as shown in Figure 6 (a)), and increasing the connection's plate thickness.

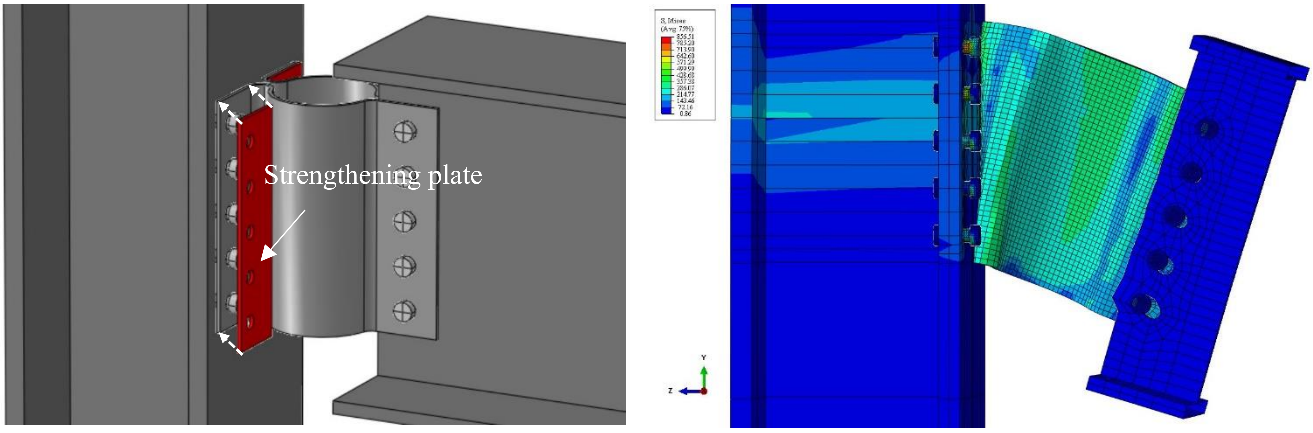

(a) Additional strengthening plate (b) Bearing failure of the fin-plate part

Figure 6. Additional strengthening plate and bearing failure of the fin-plate part

A series of frame models with strengthening plates of different thicknesses installed on the face-plate part of the ductile connection were built, and the simulation results are compared in Figure 7. The black solid curves in Figure 7 represent the results of the model without strengthening plates on the ductile connection. It can be seen from Figure 7 (b) that the compressive connection axial forces of different models are very close to each other, whereas the tensile connection forces are slightly different. In addition, the tensile connection force increases with the increase of the strengthening plate thickness. This is reasonable since the face-plate part and the semi-cylindrical part both contribute to the tensile deformation of the ductile connection, while the compressive deformation of the connection is only related to the semi-cylindrical part. The overall tensile deformation capacity of the connection decreases with the increase of the strengthening plate thickness, resulting in an increase of the tensile connection force (Figure 7 (b)), and a decrease of the beam mid-span deflection (Figure 7 (a)). The critical failure mode of the connection changes from bolt pull-out failure to beam web bearing failure, as shown in Figure 6 (b), with the increase of the strengthening plate thickness. It should be noted that the use of the thicker strengthening plate does not necessarily mean that the failure temperature of the connection is increased. The failure temperature of the connection with a 2mm strengthening plate reaches the highest value of the five models, which is 753°C. Further research will be needed to provide design recommendations concerning the most appropriate thickness for the strengthening plate.

The effect of increasing the connection plate thickness on elimination of bolt pull-out failure has also been examined, and the results are shown in Figure 8. As can be seen from this figure, the deformability of the connection decreases with increase of the connection plate thickness; this is reflected in a decrease of the beam mid-span deflection, and a significant increase of the connection axial force. With the increase of connection plate thickness, the failure mode of the connection also changes from bolt pull-out to beam web bearing failure.

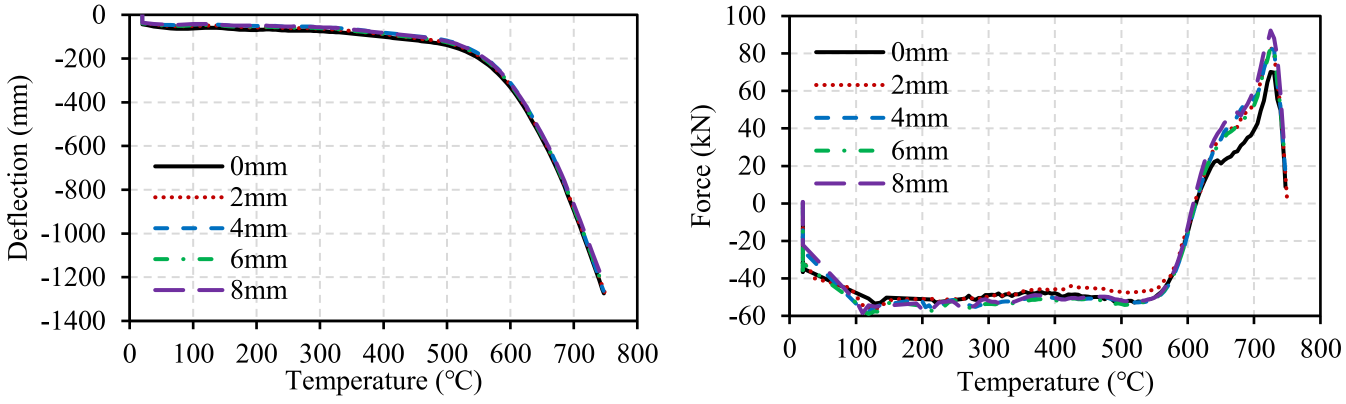

(a) Mid-span deflection of the beam of the central bay (b) Axial force of the connection of the central bay

Figure 7. Ductile connections with additional face-plate strengthening plates of different thickness

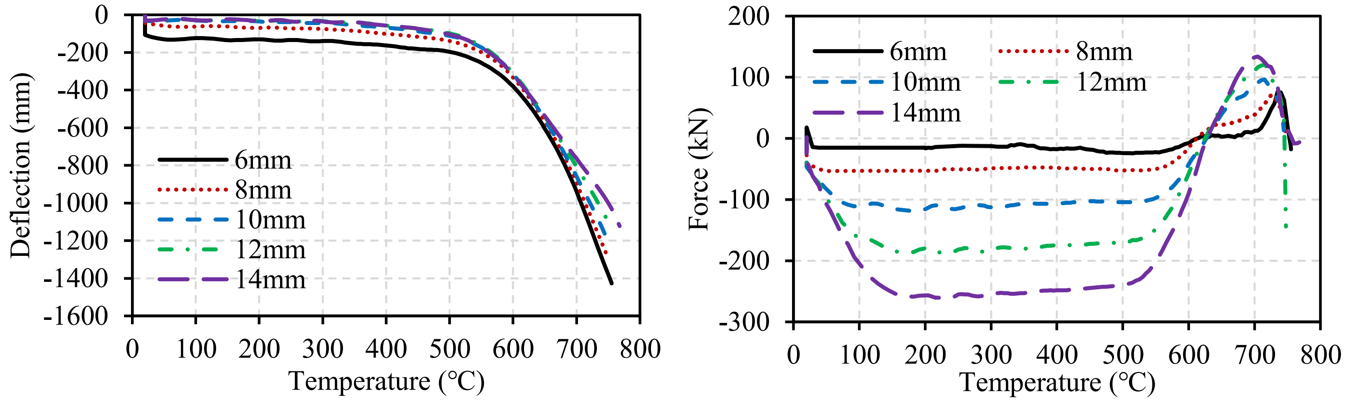

(a) Mid-span deflection of the beam of the central bay (b) Axial force of the connection of the central bay

Figure 8. Ductile connections of different plate thickness

5 CONCLUSIONS

Connection ductility is vital to the survival of steel-framed structures under fire conditions. A novel ductile connection has been proposed by the authors to improve this aspect of connection performance. The present study is attempting to make these connections more effective, particularly in the highest-temperature range of a heating curve. A series of two-storey three-bay steel frame models with different beam spans and beam sections have been built using Abaqus, to test the influence of the geometry of the ductile connection zone between the fin-plate and face-plate parts of the connection on the overall connection performance. It is found that the shape of the middle part of the connection has negligible influence on the high-temperature connection behaviour, as long as its deformability can meet the ductility demands of the beam which it supports.

Abaqus steel frame models have also been used to test some measures to eliminate bolt pull-out failure of the connection, including the addition of a strengthening plate to the face-plate part, and increase of the connection plate thickness. The results show that the failure mode of the connection changes from bolt pull-out failure to beam web bearing failure with the increase of either strengthening plate thickness, or the connection plate thickness. Further study will be required to specify general design guidelines for the strengthening plate thickness and the overall connector thickness.

ACKNOWLEDGMENT

The authors gratefully acknowledge the financial support of the National Natural Science Foundation of China (52208489), and the Shanghai Pujiang Program (22PJ1411500).

REFERENCES

1. McAllister T, Corley G. World Trade Center Building performance study: Data collection, preliminary observations, and recommendations: Federal Emergency Management Agency; 2002.
2. Lennon T, Moore D. The natural fire safety concept—full-scale tests at Cardington. Fire Safety Journal. 2003;38:623-43.
3. Liu Y, Huang S-S, Burgess I. Investigation of a steel connection to accommodate ductility demand of beams in fire. Journal of Constructional Steel Research. 2019;157:182-97.
4. Liu Y, Huang S-S, Burgess I. Ductile connections to improve structural robustness in fire. Proceedings of the 6th Applications of Structural Fire Engineering Conference (ASFE'19). Singapore: Nanyang University of Technology 2019.
5. Liu Y, Huang S-S, Burgess I. Component-based modelling of a novel ductile steel connection. Engineering Structures. 2020;208:110320.
6. Liu Y, Huang S-S, Burgess I. Performance of a novel ductile connection in steel-framed structures under fire conditions. Journal of Constructional Steel Research. 2020;169:106034.
7. Liu Y, Huang S-S, Burgess I. Investigation of the performance of a novel ductile connection within bare-steel and composite frames in fire. Proceedings of the 11th International Conference on Structures in Fire (SiF2020). Asutralia, Queensland: The University of Queensland; 2020. p. 662-72.
8. Liu Y, Huang S-S, Burgess I. Fire performance of axially ductile connections in composite construction. Fire Safety Journal. 2021:103311.
9. Liu Y, Huang S-S, Burgess I. Ductile connection to improve the fire performance of bare-steel and composite frames. Journal of Structural Fire Engineering. 2021.
10. Liu Y, Huang SS, Burgess I. A numerical study on the structural performance of a ductile connection under fire conditions. ce/papers. 2021;4:1196-202.
11. Liu Y, Huang S-S, Burgess I. Performance of ductile connections in 3-D composite frames under fire conditions. Proceedings of the 7th Applications of Structural Fire Engineering (ASFE'21). Ljubljana: University of Ljubljana; 2021. p. 43-8.
12. Liu Y, Huang S-S, Burgess I. Three-dimensional modelling of composite frames with ductile connections in fire. Structures. 2022;36:665-77.
13. BSI E. 3: design of steel structures: part 1-8 design of joints, BS EN 1993-1-8. London: British Standard Institution. 2005;18.

EXPERIMENTAL INVESTIGATION ON MECHANICAL PROPERTIES OF DOUBLE-SIDED STAINLESS-CLAD BIMETALLIC STEEL AT ELEVATED TEMPERATURES

Chen-Yu XU [1], Miao WANG [2], Hai-Ting LI [3*], Jia-Hui ZHANG [4], Bo YAN [5]

ABSTRACT

An experimental investigation on material properties of double-sided stainless-clad bimetallic steel at elevated temperatures is reported in this paper. Totally, twenty-one tensile coupon specimens were extracted from a 3 mm thick bimetallic steel plate. The elevated temperature coupon tests were carried out applying the steady-state test method and the test temperatures were up to 900 °C. In addition, the impact of varying heat soak time on elevated temperature material properties was examined. Key material properties such as the elastic modulus, yield stress, ultimate strength and elongation after fracture were fully reported. The obtained elevated temperature reduction factors were compared with the predictions by various existing design rules, including AISC 360 and EN 1993-1-2 for carbon steel as well as AISC 370 and EN 1993-1-4 for stainless steel, to assess their applicability to this novel material. Overall, it is revealed that the existing design rules cannot accurately predict the stiffness and yield stress deteriorations of this new type of material at elevated temperatures.

Keywords: Stainless-clad bimetallic steel; material properties; elevated temperatures; fire resistance

1 INTRODUCTION

Stainless-clad (SC) bimetallic steel is a type of high-performance steel produced by bonding stainless steel (cladding metal) to structural steel (substrate metal) via roll bonding, explosive cladding or compound casting process [1]. In SC bimetallic steel, the proportion of rare metals such as nickel and chromium can be reduced significantly while retaining almost the same corrosion resistance as stainless steel [2]. Therefore, SC bimetallic steel is regarded as a cost-effective solution [3] and may result in substantial price and market advantages for structural applications.

SC bimetallic steel can be divided into two categories: single-sided SC bimetallic steel and double-sided SC bimetallic steel [4,5]. Single-sided SC bimetallic steel is deemed suitable for fabricating tubular sections or similar closed profiles where only one side of the section is exposed to corrosive environment, whereas double-sided SC bimetallic steel may be preferable for applications where both sides of the section are exposed. Channels, angles and I-sections, for instance, are widely employed cross-section types in construction, and the double-sided SC bimetallic steel has great potential in such structural applications, particularly in corrosive environments owing to the superior corrosion resistance of the cladding layers.

Fire safety is a key issue for steel structures to be tackled and the material properties at elevated temperatures have a crucial role in the fire resistance design of steel structures [6]. Ban et al. [5] conducted a series of steady-state tests and investigated the material properties of single-sided SC bimetallic steel at various temperatures. It was revealed that both the elastic modulus and strengths of the material reduced markedly as temperature increased; a set of specific equations were proposed for predicting the stiffness

[1] Undergraduate Student, Department of Civil Engineering, Shanghai Jiao Tong University, E-mail: xcy010109@sjtu.edu.cn
[2] PhD Candidate, Department of Civil Engineering, Shanghai Jiao Tong University, E-mail: wang_miao@sjtu.edu.cn
[3] Associate Professor, Department of Civil Engineering, Shanghai Jiao Tong University (corresponding author), E-mail: haiting.li@sjtu.edu.cn
[4] Lecturer, Department of Civil Engineering, University of Shanghai for Science and Technology, E-mail: zhangjh316@163.com
[5] Professorate Senior Engineer, Cnetral Research Institute, Baoshan Iron & Steel Co., Ltd., E-mail: yanbo@baosteel.com
https://doi.org/10.6084/m9.figshare.22215772

and the strengths of the single-sided SC bimetallic steel at elevated temperatures [5], which laid down a sound understanding of the material behaviour of SC bimetallic steel in fire. To date, however, the material properties of double-sided SC bimetallic steel at elevated temperatures have not yet been investigated. This may hinder the vast potential applications of such a promising material to be used in construction. This paper intends to address this deficiency by presenting test results of an experimental investigation into the material properties of a typical double-sided SC bimetallic steel at elevated temperatures up to 900 °C.

2 EXPERIMENTAL INVESTIGATION

2.1 Test specimens

The double-sided SC bimetallic steel material investigated in this study is a 3mm thick plate manufactured through hot-rolling bonding process. The substrate metal of the plate is grade Q235 carbon steel (with nominal yield stress of 235 MPa) and the cladding metal is grade 304L stainless steel (equivalent to UNS S30403 and EN 1.4307). The clad ratio, or the ratio of thickness of cladding metal to substrate metal to cladding metal, is 1:4:1. Tensile coupon specimens were cut from the plate and the dimensions of the coupon specimens were prepared in accordance with the ASTM E 21 [7] for tensile testing of metallic materials at elevated temperatures by utilising 6 mm wide coupon of 25 mm gauge length. Detailed geometric parameters of the coupon specimens are shown in Figure 1.

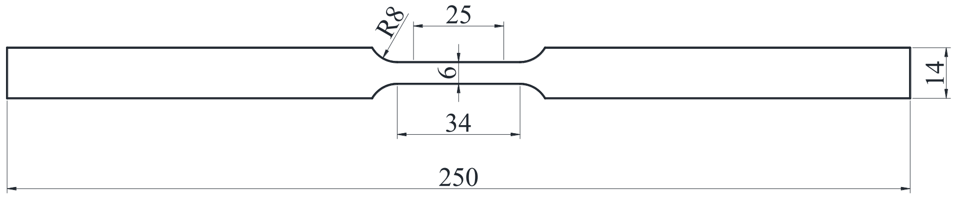

Figure 1. Dimensions of coupons

The specimens were labelled such that the applied nominal temperature, soak time and repeatability of the test could be identified, as shown in Tables 1-3. For example, the labels “T200-R_1” and “T500-1min” define the following specimens: “T200” and “T500” indicate the specimens were tested under nominal target temperatures of 200 °C and 500 ℃ , respectively; “1min” indicates that the soak time of the test was 1 min instead of the default soak time of 15 min (as applied for specimen T200-R_1). The letter "R" denotes that the test was repeated. When there are two repeated tests, the subscripts 1 and 2 denote the tests individually, as in "T200-R_1."

2.2 Test devices

The set-up of the test devices is shown in Figure 2. An MTS universal material testing machine was used in the tensile coupon tests. An MTS 653 high-temperature furnace was used as the heating device for the tensile tests at elevated temperatures. A calibrated MTS high-temperature extensometer of 25 mm gauge length was used to measure the longitudinal strain of the coupon specimens. To obtain the actual temperature of the specimens, two external thermal couples were employed to measure the surface temperature of the specimens, one near each end of the reduced sections as required by ASTM E 21 [7].

2.3 Test procedures

A total of 21 experiments were conducted using the steady-state test method, from which continuous stress-strain curves could be obtained. It should be noted that two additional steady-state tests at nominal temperature of 500 ℃ with soak time of 1 min and 60 mins were carried out to investigate the impact of different heat soak time on material properties. For the 19 steady-state tests using default soak time of 15 mins, the targeted temperatures selected were set to be ambient temperature (20 ℃), 100 °C, 200 °C, 300 °C, 400 °C, 450 °C, 500 °C, 550 °C, 600 °C, 650 °C, 700 °C, 800 °C and 900 °C. The heating rate was set as 50 °C/min for all the tests. After reaching the targeted temperature, a 15-min heat soak time (except for the two tests with soak time of 1 min and 60 mins) was provided to make sure that the temperature distribution of the specimen was uniform. During the heating process, the upper end of the specimen was gripped whilst the lower end was allowed to expand freely so as to let the thermal expansion take place while ensuring zero load. Two external thermal couples were mounted on the surface of both ends of the parallel length to measure the temperature throughout testing. When the readings of the two thermal couples stabilized, with a difference of less than 1%, the lower end of the specimen was gripped. The MTS universal material testing machine was used to apply the load to the specimen. The tensile load was applied to the specimen by strain control at a rate of 0.005 mm/mm/min until strain reached 15%, which is the limit of the employed high-temperature extensometer. Afterwards, the high-temperature extensometer was dismounted and the machine was switched to displacement control at a cross-head speed of 1.36 mm/min (resulted in a strain rate of approximately 0.04 mm/mm/min) until the specimen failed; the 0.04 mm/mm/min is the lower bound speed for strain measurements after yield strength determination, as codified in Clause 9.6.1.2 of the ASTM E 21 [7]. The strain of the specimen was measured by the high-temperature extensometer up to 15%, after which the strain was obtained by converting the displacement data recorded by the tensile testing machine. The complete stress-strain curves of the material were obtained by using the data processing method as suggested by Huang and Young [8].

Figure 2. Test devices

3 TEST RESULTS

3.1 General

Figure 3 shows the failed double-sided SC bimetallic steel coupons. The data obtained from the tests were converted into stress-strain curves, as plotted in Figure 4. The elastic modulus at ambient temperature (E_{20}) and the elastic modulus at elevated temperatures (E_T) were determined from the initial linear parts of the stress-strain curves. As shown in Figure 4, no obvious yield plateau could be seen from the stress-strain curves at both ambient and elevated temperatures. Therefore, the 0.2% proof stress at ambient temperature ($\sigma_{0.2,20}$) and the 0.2% proof stress at elevated temperatures ($\sigma_{0.2,T}$) were taken as the yield stress of this material in this paper. In addition, the stress at 2.0% strain ($\sigma_{2.0,20}$), ultimate strength ($\sigma_{u,20}$) and elongation after fracture ($\varepsilon_{f,20}$) at ambient temperature and the stress at 2.0% strain ($\sigma_{2.0,T}$), ultimate strength ($\sigma_{u,T}$) and elongation after fracture ($\varepsilon_{f,T}$) at elevated temperatures are also obtained from the stress-strain curves. Table 1 shows the material properties of double-sided SC bimetallic steel at ambient temperature. The reduction factors of elastic modulus (k_E=E_T/E_{20}), reduction factors of yield stress (k_y=$\sigma_{0.2,T}$/$\sigma_{0.2,20}$), reduction factors of stress at 2.0% strain ($k_{2.0}=\sigma_{2.0,T}/\sigma_{2.0,20}$), reduction factors of ultimate strength ($k_u=\sigma_{u,T}/\sigma_{u,20}$) and reduction factors of elongation after fracture ($k_\varepsilon=\varepsilon_{f,T}/\varepsilon_{f,20}$) are fully reported in Tables 2 and 3. Six repeated tests were conducted at 20 °C, 200 ℃ (twice), 300 °C, 550 ℃ and 700 ℃. The repeated test results echoed well with the first test results, and the differences between the repeated tests are within 1% for most of the results, which demonstrated the reliability of the obtained test results.

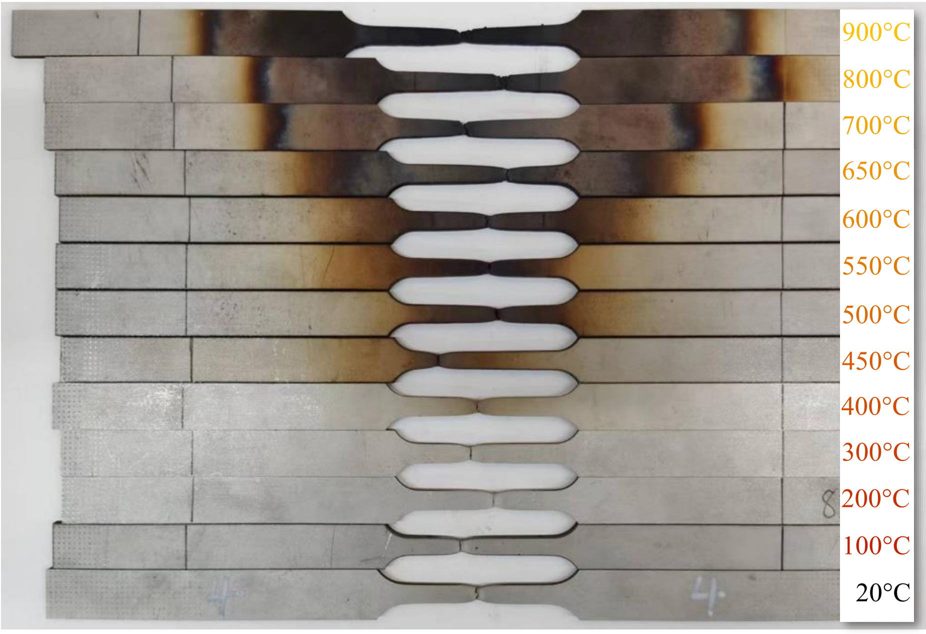

Figure 3. Failed double-sided SC bimetallic steel coupons

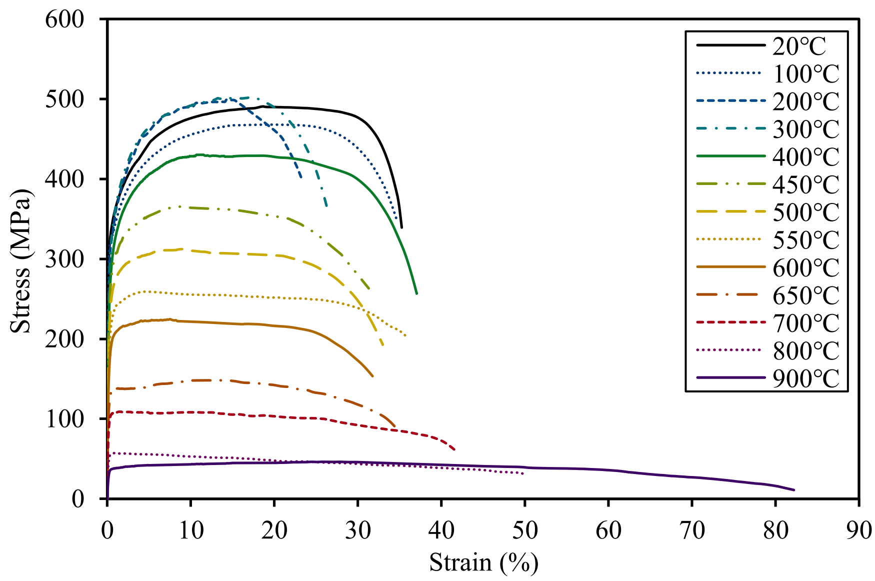

Figure 4. Stress-strain curves of double-sided SC bimetallic steel at elevated temperatures

3.2 Material properties at ambient temperature

Table 1 lists the material properties of the investigated double-sided SC bimetallic steel at ambient temperature, including the elastic modulus (E_{20}), 0.2% proof stress ($\sigma_{0.2,20}$), stress at 2.0% strain ($\sigma_{2.0,20}$), ultimate strength ($\sigma_{u,20}$) and elongation after fracture ($\varepsilon_{f,20}$). One repeated test was conducted and the difference between the first (Specimen: T20) and second (Specimen: T20-R) test results in terms of elastic modulus, 0.2% proof stress, stress at 2.0% strain, ultimate strength and elongation after fracture is 0.55%, 0.15%, 0.63%, 0.33% and 3.50%, respectively. The obtained $\varepsilon_{f,20}$ values of the specimens are over 30%, indicating good ductility of the studied SC bimetallic steel.

Table 1. Material properties of double-sided SC bimetallic steel at ambient temperature

Specimen	Temperature (°C)	E_{20} (GPa)	$\sigma_{0.2,20}$ (MPa)	$\sigma_{2.0,20}$ (MPa)	$\sigma_{u,20}$ (MPa)	$\varepsilon_{f,20}$ (%)
T20	19.3	199.1	325.5	393.8	490.8	34.3
T20-R	19.3	198.0	325.0	391.3	489.2	33.1

3.3 Material properties at elevated temperatures

The full stress-strain curves of the test specimens at ambient and elevated temperatures are illustrated in Figure 4. Table 2 lists the obtained reduction factors of the material properties at elevated temperatures, including reduction factors of elastic modulus $k_E=E_T/E_{20}$, yield strength $k_y=\sigma_{0.2,T}/\sigma_{0.2,20}$, stress at 2.0% strain $k_{2.0}=\sigma_{2.0,T}/\sigma_{2.0,20}$, ultimate strength $k_u=\sigma_{u,T}/\sigma_{u,20}$ and elongation after fracture $k_\varepsilon=\varepsilon_{f,T}/\varepsilon_{f,20}$. Generally, as the temperature rises over 400 °C, the elastic modulus and the strengths of the material decrease rapidly. Figure 3 depicts the failed double-sided SC bimetallic steel tensile coupon specimens at various elevated temperatures; all of the specimens clearly went through the necking stage. Table 2 lists all of the reduction factors of elongation after fracture. It should be noted that the ductility of the material decreases before 400 °C and then increases, exceeding that at ambient temperature.

Table 2. Reduction factors of material properties of double-sided SC bimetallic steel at elevated temperatures

Specimen	Temperature (°C)	$\frac{E_T}{E_{20}}$	$\frac{\sigma_{0.2,T}}{\sigma_{0.2,20}}$	$\frac{\sigma_{2.0,T}}{\sigma_{2.0,20}}$	$\frac{\sigma_{u,T}}{\sigma_{u,20}}$	$\frac{\varepsilon_{f,T}}{\varepsilon_{f,20}}$
T100	101.9	1.02	0.99	0.96	0.96	1.06
T200	199.3	0.97	0.95	1.01	1.01	0.71
T200-R_1	199.1	0.97	0.94	1.00	0.98	0.72
T200-R_2	199.8	0.98	0.94	1.01	1.02	0.71
T300	297.1	0.94	0.95	1.04	1.02	0.81
T300-R	299.0	0.94	0.94	1.02	0.98	0.83
T400	400.6	0.89	0.83	0.92	0.88	1.13
T450	450.9	0.87	0.80	0.84	0.75	1.08
T500	501.3	0.83	0.71	0.74	0.64	1.01
T550	552.4	0.77	0.61	0.62	0.51	1.08
T550-R	552.6	0.79	0.59	0.60	0.50	1.04
T600	598.0	0.66	0.55	0.55	0.46	0.97
T650	648.9	0.58	0.39	0.35	0.31	1.05
T700	700.3	0.56	0.30	0.28	0.22	1.26
T700-R	701.8	0.55	0.30	0.27	0.22	1.22
T800	797.2	0.32	0.17	0.14	0.12	1.48
T900	901.2	0.13	0.11	0.10	0.10	2.46

3.4 Comparison of material properties at elevated temperatures with different soak time

The influence of soak time on the material properties of double-sided SC bimetallic steel at elevated temperatures was also investigated. Three steady-state tests at 500 °C with soak time of 1 min, 15 mins and

60 mins were conducted. The stress-strain curves and corresponding material properties are depicted in Figure 5 and Table 3, respectively. The reduction factors of elastic modulus, ultimate strength and elongation after fracture of the material with a 1 min soak time were 8.2%, 5.4% and 5.8% higher than that from their counterparts with 15 mins soak time, and the difference for 0.2% proof stress and stress at 2.0% strain results were found to be neglectable (within 1.5%). With regards to the comparison between results from specimens of 15 mins and 60 mins soak time, there is marginal difference (less than 1.5%) between the material properties. Therefore, it may be concluded from the test results that the changing of soak time has minor impact on the steady state test results of the investigated material, and the applied 15 mins soak time is sufficient enough for the tested specimens to reach their demanded steady-state condition.

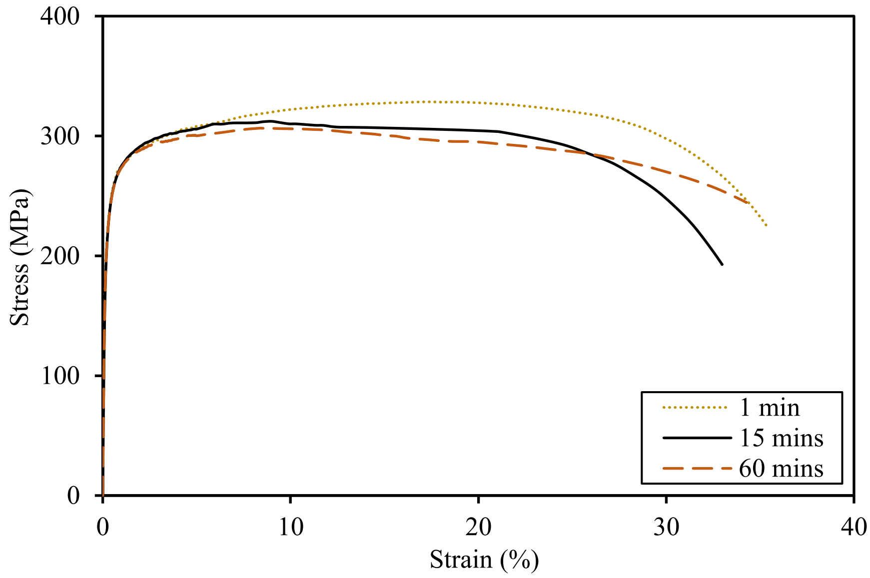

Figure 5. Stress-strain curves at 500°C with different soak time

Table 3. Reduction factors of material properties of double-sided SC bimetallic steel at 500°C with different soak time

Specimen	Temperature (°C)	Soak time (min)	$\frac{E_T}{E_{20}}$	$\frac{\sigma_{0.2,T}}{\sigma_{0.2,20}}$	$\frac{\sigma_{2.0,T}}{\sigma_{2.0,20}}$	$\frac{\sigma_{u,T}}{\sigma_{u,20}}$	$\frac{\varepsilon_{f,T}}{\varepsilon_{f,20}}$
T500	502.1	15	0.83	0.71	0.74	0.64	1.01
T500-1min	497.4	1	0.90	0.72	0.74	0.67	1.07
T500-60min	502.1	60	0.82	0.72	0.74	0.63	1.05

4 COMPARISON OF TEST RESULTS WITH EXISTING DESIGN RULES AND DATA

4.1 Elastic modulus

The elastic modulus of the double-sided SC bimetallic steel at various temperatures were obtained from the initial linear parts of the stress-strain curves. The reduction factors of elastic modulus (k_E=E_T/E_{20}) can be calculated by dividing the elastic modulus at elevated temperatures (E_T) by the elastic modulus at ambient temperature (E_{20}). Figure 6 shows the comparison of k_E with existing design rules provided in AISC 360 [9] and EN 1993-1-2 [10] for carbon steel as well as codified in AISC 370 [11] for S30403 and EN 1993-1-4 [12] for EN 1.4307 stainless steel. In addition, the results reported by Ban et al. [5] for single-sided SC bimetallic steel, Zhang [13] for Q235 (the substrate metal), and Fan et al. [14] for 304L (the cladding metal), are included for comparison in Figure 6.

It is demonstrated that the obtained k_E values undergo a steadily decrease up to 550℃ , beyond which a sharper decline in k_E occurs which is earlier than that of the knee value (around 800°C) as per the AISC 370 [11] and EN 1993-1-4 [12] for stainless steel. The k_E predictions from these two stainless steel specifications are generally conservative within 550 °C, while would yield unconservative prediction if being used for the investigated material after 550 °C. On the other hand, the predicted reduction factors of k_E by AISC 360 [9] and EN 1993-1-2 [10] are rather conservative, particularly for temperatures between 400 ℃ and 800 ℃ . The results of single-sided SC bimetallic steel [5] generally align with the test results obtained from this paper up to 500 ℃ , following the same downward trend with temperatures rise over this temperature range. In addition, it is found that the test results generally lie between that of Q235 [13] and 304L [14] reported in the literatures. In general, neither the design curves for mild steel nor stainless steel can accurately predict the deterioration of the elastic modulus of the double-sided SC bimetallic steel at elevated temperatures.

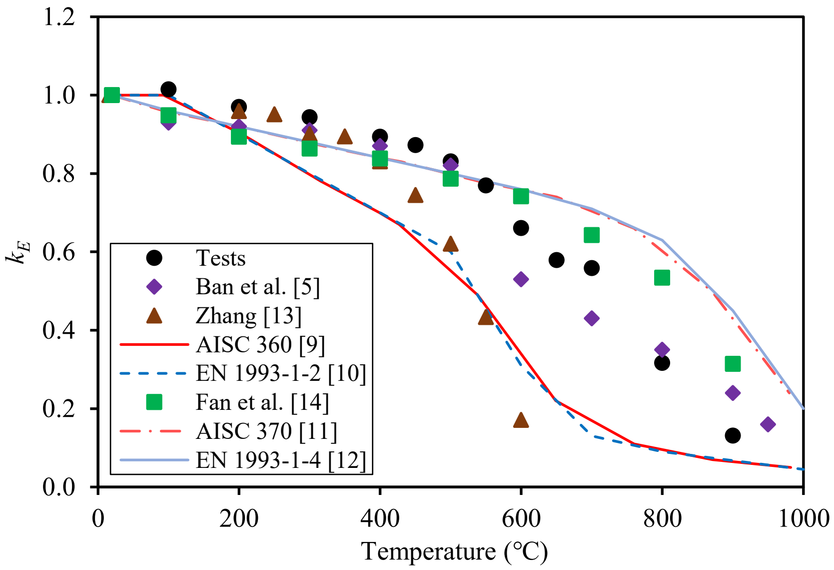

Figure 6. Comparison of reduction factors of elastic modulus

4.2 Yield stress

The stress-strain curves in Figure 4 show that, unlike typical mild steel and carbon steel, no obvious yield plateau exists for the studied material at both ambient and elevated temperatures; this can be attributed to the presence of stainless steel cladding metal which has no distinct yield plateau. To this end, the 0.2% proof stresses at ambient temperature ($\sigma_{0.2,20}$) and at elevated temperatures ($\sigma_{0.2,T}$) were taken as the yield stresses of the double-sided SC bimetallic steel. The reduction factors of the yield stress, namely, $k_y=\sigma_{0.2,T}/\sigma_{0.2,20}$, which are defined as the ratio of the yield stress at elevated temperatures to that of at ambient temperature, are fully reported in Table 2.

The obtained k_y values were plotted in Figure 7 and compared with the current AISC 360 [9] and EN 1993-1-2 [10] predictions for carbon steel, AISC 370 [11] predictions for stainless steel of grade S30403, and EN 1993-1-4 [12] predictions for stainless steel of grade EN 1.4307. Overall, it is shown that the obtained k_y values are between the codified predictions for carbon steel and stainless steel. For temperatures up to 550 °C, the predictions by AISC 370 [11] and EN 1993-1-4 [12] are rather conservative to be used for the investigated material; on the other hand, for temperatures beyond this temperature, the converse is true. The AISC 360 [9] and EN 1993-1-2 [10] predictions are unconservative for temperatures before 550 ℃ , while yield generally conservative predictions for temperatures above 550 ℃ . The k_y reported from the single-sided SC bimetallic steel by Ban et al. [5], Q235 by Zhang [13] and 304L by Fan et al. [14] are also plotted in Figure 7.

It is noteworthy that in the fire safety design of steel structures, greater deformation could be tolerated to enable higher member strengths to be developed. Consequently, stress at 2.0% strain is also used in the fire design of steel members. The reduction factors $k_{2.0}=\sigma_{2.0,T}/\sigma_{2.0,20}$, as reported in Table 2, were plotted in Figure 8. In Figure 8, the obtained $k_{2.0}$ values are compared with the reduction factors predicted by existing design rules [9-12] as well as the results of single-sided SC bimetallic steel reported by Ban et al. [5]. In general, the $k_{2.0}$ values obtained from this test program are well aligned with the predictions (for yield stress) by AISC 360 [9] and EN 1993-1-2 [10] for carbon steel. The AISC 370 [11] and EN 1993-1-4 [12] codify a reduction factor k_2, defined as the ratio of $\sigma_{2.0,T}$ to σ_y (0.2% proof strength at ambient temperature). The codified k_2 values for stainless steel were converted into the $k_{2,0}$ values and plotted in Figure 8 for comparison. It is shown that for temperatures lie between 100 ℃ and 600 °C, the AISC 370 [11] and EN 1993-1-4 [12] predictions for stainless steel would be overly conservative to be used for the studied material, while for the temperatures exceed 600 °C, the predictions become unconservative.

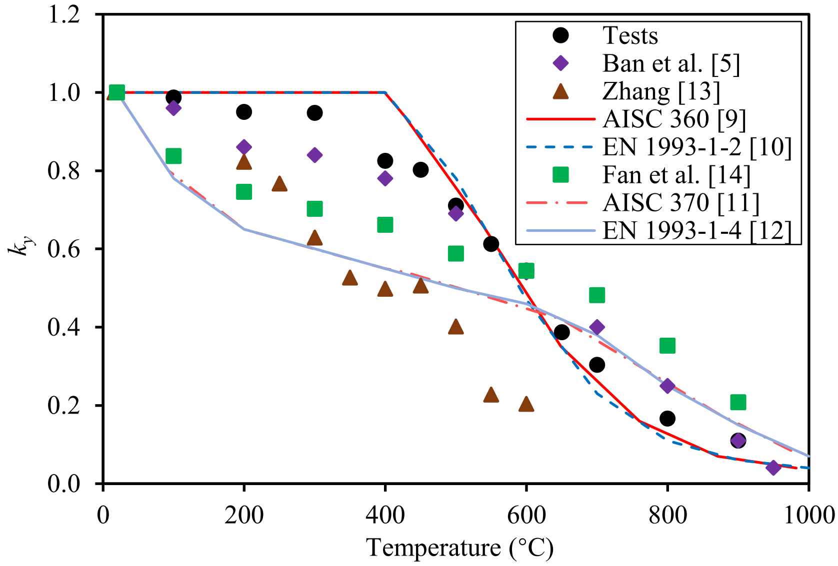

Figure 7. Comparison of reduction factors of yield stress

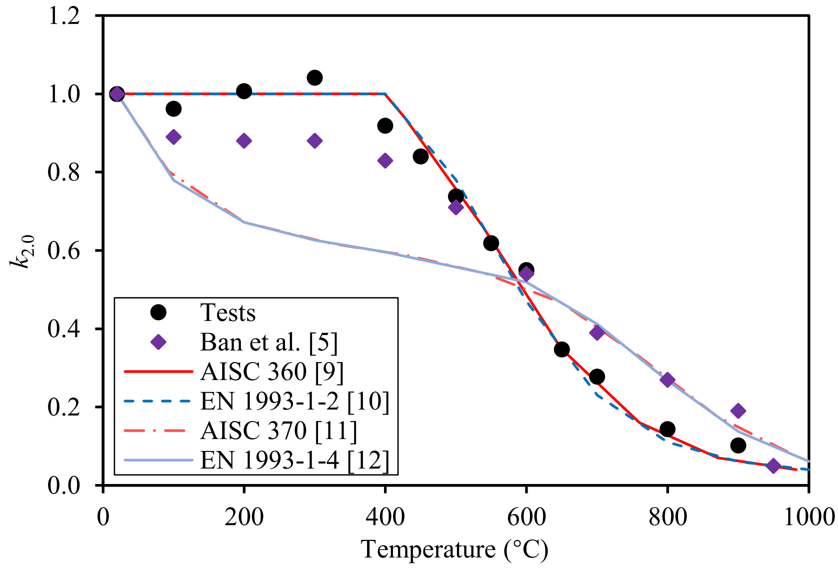

Figure 8. Comparison of reduction factors of stress at 2.0% strain

4.3 Ultimate strength

The reduction factors for the ultimate strength $k_u=\sigma_{u,T}/\sigma_{u,20}$ were calculated as the ratio of the ultimate strength at elevated temperatures to that at ambient temperature. The k_u values at various elevated temperatures are listed in Table 2 and plotted in Figure 9 to compare with the predictions by AISC 360 [9] and EN 1993-1-2 [10] for carbon steel, AISC 370 [11] for S30403, EN 1993-1-4 [12] for EN 1.4307, as well as test results of the related materials reported in [5,13,14].

As shown in Figure 9, the k_u values keep at unity for temperatures up to 300 °C, beyond which the k_u decreases rapidly and linearly for temperatures up to 800 °C. The predictions by EN 1993-1-2 [10] are in good agreement with the test results and are generally safe-sided as well. Regarding the AISC 370 [11] and EN 1993-1-4 [12], which are in line with the test results of 304L [14], the predictions are found to be overly pessimistic for temperatures less than 500 ℃ ; by contrast, for temperatures above 550 °C, the predictions are unconservative for the double-sided SC bimetallic steel. In general, the obtained k_u values of the studied material fall between that of Q235 and 304L, showing obvious relevance of the bimetallic steel to its substrate and cladding metals. The k_u obtained in this paper generally share a same trend with that from the single-sided SC bimetallic steel [5].

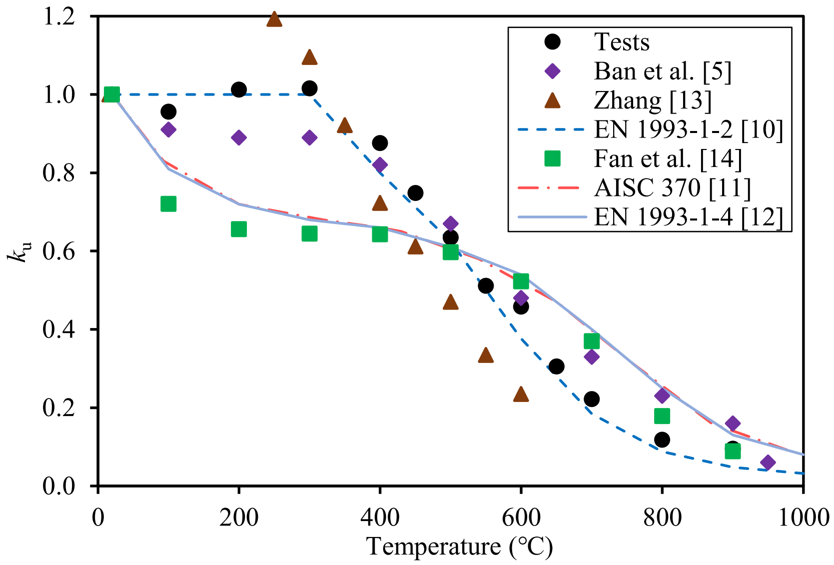

Figure 9. Comparison of reduction factors of ultimate strength

5 CONCLUSIONS

This paper presents an experimental investigation on the material properties of a double-sided stainless-clad (SC) bimetallic steel at elevated temperatures. A total of 21 tensile coupon specimens were extracted and tested by using the steady-state test method for temperatures up to 900°C. Stress-strain curves as well as key properties including the elastic modulus, yield stress, ultimate strength and elongation after fracture were obtained from the tests. The effect of soak time on the material properties of the bimetallic steel at elevated temperature was also investigated. The test results indicate the soak time may have a neglectable effect on the material properties of the steady-state test results. In general, it is revealed that the current design rules cannot properly predict the reduction of elastic modulus and 0.2% proof stress of the investigated double-sided SC bimetallic steel at elevated temperatures. The reduction factors for yield stress codified in the AISC 360 [9] and EN 1993-1-2 [10] can be used in predicting the deterioration of the stress at 2.0% strain; the reduction factors for the ultimate strength provided in EN 1993-1-4 [12] can be used to for the studied material. New design curves to determine the deterioration of elastic modulus and yield strength of double-sided SC bimetallic steel at elevated temperatures are currently ongoing.

ACKNOWLEDGMENTS

This research work was supported by a seed fund at Shanghai Jiao Tong University (Project No. IPP23013). The authors are grateful to Baoshan Iron & Steel Co., Ltd. for providing the material and are also grateful to Mr. Xiao-Jing Cai and Mr. Di-Yang Zhu for their assistance in the experimental program.

REFERENCES

1. Su, H., Luo, X., Chai, F., Shen, J., Sun, X. and Lu, F., Manufacturing technology and application trends of titanium clad steel plates, Journal of Iron and Steel Research, Vol. 22, no. 11, 2015, pp. 977-982.
2. Ban, H. and Shi, Y., An innovative high performance steel product for structural engineering: Bimetallic steel, Proceedings of the International Conference on Engineering Research and Practice for Steel Construction, Vol. 09, 2018, pp. 424-430.
3. Smith, L., Engineering with clad steel, Nickel Institute Technical Series No 10064, 2nd Edition, Vol. 10064, 2012, pp. 1-24.
4. Shi, Y., Ban, H. and Tao, X., Use of clad steel in engineering structures, The Fifteenth East Asia-Pacific Conference on Structural Engineering & Construction, 2017, pp. 343-343.
5. Ban, H., Bai, R., Yang, L. and Bai, Y., Mechanical properties of stainless-clad bimetallic steel at elevated temperatures, Journal of Constructional Steel Research, Vol. 162, 2019, 105704.
6. Li, H. T. and Young, B., Material properties of cold-formed high strength steel at elevated temperatures, Thin-Walled Structures, Vol. 115, 2017, pp. 289-299.
7. ASTM E 21, Standard test methods for elevated temperature tension tests of metallic materials, American Society for Testing and Materials (ASTM), 2020.
8. Huang, Y. and Young, B., The art of coupon tests, Journal of Constructional Steel Research, Vol. 96, 2014, pp. 159-175.
9. AISC 360, Specification for structural steel buildings, American Institute of Steel Construction (AISC), 2016.
10. EN 1993-1-2, Eurocode 3: Design of steel structures, Part 1-2: General rules-Structural fire design, Brussels, Belgium: CEN, 2005.
11. AISC 370, Specification for structural stainless steel buildings, American Institute of Steel Construction (AISC), 2021.
12. EN 1993-1-4, Eurocode 3: Design of steel structures, Part 1-4: General rules-Supplementary rules for stainless steels, Brussels, Belgium: CEN, 2020
13. Zhang, H., Material properties of Q235 in fire, Fire Safety Science, Vol. 13, 2004, pp.74-77. (in Chinese)
14. Fan, S., Ding, R., Zheng, J., Xie, F. and Wu, Q., Refined model for the stress-strain curve of austenitic stainless-steel materials at elevated temperatures, Journal of Materials in Civil Engineering, Vol.32, 2020, 04020032.

NUMERICAL STUDY OF THE RESPONSE OF COLD-FORMED STEEL SECTIONS USED IN WALL PANELS WHEN SUBJECTED TO FIRE

Mohammed Hassoune[1], Abdelhak Kada[2], Belkacem Menadi[3], Belkacem Lamri[4]

ABSTRACT

In recent years, building construction industry in Algeria has started to include light gauge steel framed (LSF) wall systems as an alternative building solution especially in seismic regions. This is due to the advantages brought by the use of Cold Formed Section (CFS) that offers high durability, flexibility and strength to weight ratio. As these steel elements are slender, they are characterized with high shape factor, and the effect of the exposure to fire conducts to the possibility of the material properties degradation under high temperature. Thus causing different failure modes of stud members when subjected to a compression loading which could be leads to the collapse of the LSF panel. In this research work, different element models of single and double Lipped Channel (LC) stud that isolated from LSF panel, protected by plasterboard are produced using ANSYS APDL software. A parametric study is done, with the variation of type of cross-section for double stud including open and closed built-up sections. The main objective of this work is to study the influence of these sections on the behaviour of CFS stud LC members and the determination of the load capacity leading to understand the different buckling failure modes that could be occur under an axial compression loading at ambient and when exposed to fire ISO834. The results predict temperature profiles, progression of temperature, critical and ultimate load, critical temperatures and the failure mode.

Keywords: Cold formed section; Light gauge steel framed; Thermomechanical response; Fire ISO834; ANSYS.

1 INTRODUCTION

It has become a current trend in construction industry to employ steel as one of the most versatile material to achieve flexible, durable, lightweight structures with long spans [1]. Recently, developers in Algeria has adopted a new alternative building solution, in the form of a light structure made from lateral and horizontal panels with Cold Formed Steel (CFS) framing. Another reason is that it offers a new and a feasible solution in seismic region when a decrease in the structure weight is most needed. One of the common feature of CFSs cross-section is its simple geometry, C-sections, U-sections and Z-sections, based on a thin thickness and variety of sizes, used for stud element in load-bearing Light Gauge steel Frame (LSF) panel [2]. However at ambient, the behavior of CFS structures is complex because the

[1] PhD student, Laboratory of Geo-Materials and Civil Engineering, Department of Civil Engineering, University of Blida1, Blida, Algeria.
e-mail: hassoune.mohammed@etu.univ-blida.dz, ORCID: https://orcid.org/0000-0002-7527-1353

[2] Senior lecturer, Laboratory Fire Safety Engineering of Constructions and Protection of their Environment LISICPE, Department of Civil Engineering, University of Hassiba Benbouali, Chlef, Algeria.
e-mail: a.kada@univ-chlef.dz

[3] Professor, Laboratory of Geo-Materials and Civil Engineering, Department of Civil Engineering, University of Blida1, Blida, Algeria.
e-mail: bmenadi@yahoo.com

[4] Professor, Laboratory Fire Safety Engineering of Constructions and Protection of their Environment LISICPE, Department of Civil Engineering, University of Hassiba Benbouali, Chlef, Algeria.
e-mail: b.lamri@univ-chlef.dz

https://doi.org/10.6084/m9.figshare.22215775

members made of thin open cross sections develop several mode of stability, global as well as local or in some cases coupled modes [3, 4]. Extensive research studies on steel structures when subjected to fire have focused on the behavior of Hot Rolled Section (HRS) elements under fire condition both unprotected [5-9] or protected members such as IPE and HE [10-12]. Few research studies have tackled the behaviour of CFS elements and their protection when subjected to fire, and there is a need for more investigations to encounter the complexity of the problem peculiar to slender sections of class 4. In the case of fire, these sections suffer from a rapid increase of temperature due to the high thermal conductivity and shape factor therefore the fire resistance must be based on protective materials [13]. Mesquita, et al. [14] presented an experimental and numerical study of the behavior of cold-formed thin steel sheeting screwed connections at ambient and elevated temperatures. The results show that the use of self-drilling screwed connections of thin steel sheets leads to an increase of the temperature. Gunalan, et al. [15], did experimental, numerical and analytical studies to investigate the local buckling behavior of stud LSF compression members at ambient and under uniform temperature. They concluded that the design rules provided could be used to predict the local buckling capacities using the effective areas, both at ambient and elevated temperature. Several researches have introduced the fire response of CFS protected by different insulations, when being used as cavity and external insulations [16-19]. The results showed that the presence of insulations within the panel leads to the rapid increase of temperature within the hot flange of the stud, unlike when they are between two layers of protection providing a high fire performance. Piloto, et al. [20] did experimental and numerical investigations on the thermal and structural response of load-bearing walls, considering the insulation criterion and load-bearing capacity under fire exposure. The results demonstrated the worst fire performance of using cork with plasterboard as composite solution for the protection compared to OSB, and the fire resistance decreases with the increase of the load level. Other studies have investigated the influence of some parameters of single CFS stud element, such as grade of steel [21], stud web width [22] and width-thickness ratio [23]. These researches showed that increasing these parameters lead to an increase in ultimate compression capacity of stud and fire resistance rating (FRR). In this study, element models of single and double stud Lipped Channel (LC) that isolated from LSF panel protected by plasterboard are produced, with the variation of cross-section for double stud including open and closed built-up sections. This work aims to study the influence of these sections on the behaviour of CFS stud LC members subjected to an axial compression, and the determination of the load capacity at ambient and under non uniform thermal temperature. This is leading to understand the different buckling failure modes that could be occur under an axial compression loading, at ambient and when exposed to fire ISO834 with the using of ANSYS APDL software[24]. The results predict temperature profiles, progression of temperature, critical and ultimate load, critical temperatures and the failure mode.

2 PROPERTIES OF STEEL AND PROTECTION MATERIALS AT ELEVATED TEMPERATURE

2.1 Material properties of CFS

The progression of temperature within the CFS sections depends on the thermal conductivity, specific heat and density, Figure 1, as given by EN 1993-1-2 [25]. CFS mechanical properties at elevated temperatures, that is the elastic modulus and yield stress reduction factors as proposed by Dolamune Kankanamge [26] are considered in this study, Figure 2a. It is noticed that as, the elasticity modulus and the yield strength reduction factors decrease rapidly from 100°C and 300°C, respectively. For all simulations using ANSYS software, the true stress-strain curve is adopted as defined by equation (1), based on the engineering stress–strain curve (strain hardening), Figure 2b, issued from equation developed by Ranawaka and Mahendran [27], equation (2).

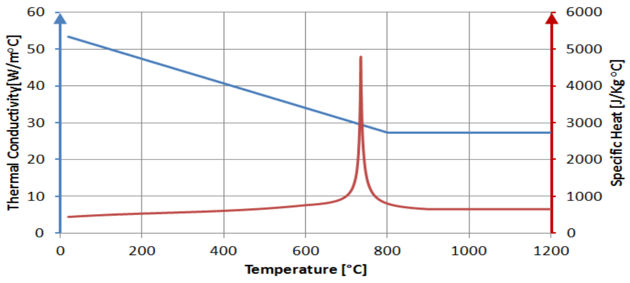

Figure 1. CFS thermal conductivity & specific heat versus temperature

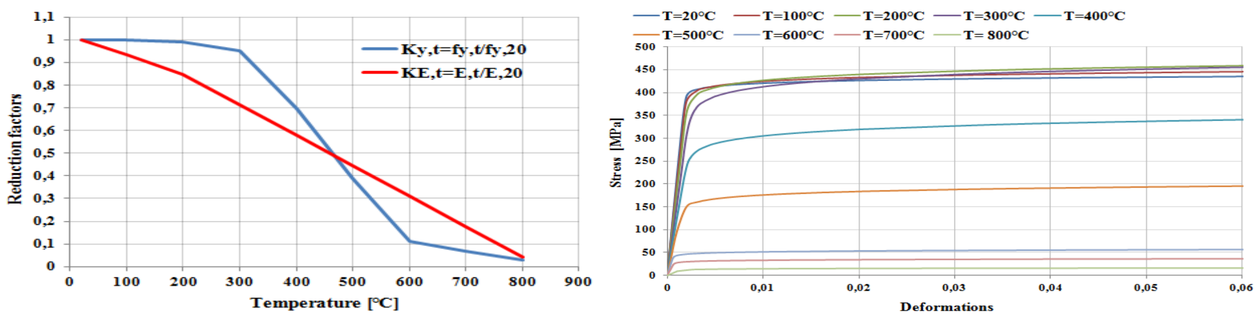

(a) Reduction factors of elastic modulus and yield stress

(b) Stress-strain curve

Figure 2. CFS mechanical properties

$$\sigma_{true} = \sigma_{eng}\left(1+\varepsilon_{eng}\right)$$

$$\varepsilon^{pl}{}_{true} = \ln\left(1+\varepsilon_{eng}\right) - \frac{\sigma_{true}}{E} \quad (1)$$

$$\text{With, } \varepsilon_{eng} = \frac{\sigma_{eng}}{E_T} + \beta\left(\frac{f_{y,T}}{E_T}\right)\left(\frac{\sigma_{eng}}{f_{y,T}}\right)^{\eta_T} \quad (2)$$

Where ε_{eng} is the strain corresponding to a given stress σ_{eng}, E_T is the elastic modulus at temperature T, $f_{y,T}$ is the yield strength at temperature T, β is a parameter taken as 0.86 and η is given by the equation 3 [27].

$$\eta_T = -3.05\times10^{-7}T^3 + 0.0005T^2 - 0.2615T + 62.653 \text{ for } 20°C \le T \le 800°C \quad (3)$$

All types of CFSs used in parametric study have a steel grade of G345, a yield stress of 410 MPa, a modulus of elasticity of 211040 MPa, a density of 7850 kg/m^3 and a poisson's ratio of 0.3 and remains unchanged with temperature increase. Non-uniform temperature distribution on stud surfaces induces displacements due to thermal expansion when exposed to fire [28]. The coefficient of the thermal expansion considered for the thermomechanical analysis is given by EN1993-1-2 [25], equation (4).

$$\alpha = 1.2\times10^{-5} + 0.4\times10^{-8}T - 2.416\times10^{-4}/T \text{ for } 20°C \le T \le 750°C \quad (4)$$

2.2 Material properties of plasterboard

The fire resistance of wall panels with LSF system must be ensured for time duration and when necessary protection by different boards is included to improve their fire safety [13]. In this study, all CFS models are protected by 16 mm of plasterboard. Thermal properties of the later, Figure 3, is taken from studies developed by Sultan [29].

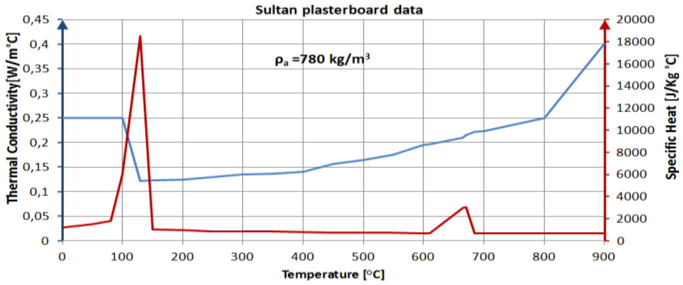

Figure 3. Plasterboard thermal properties

3 FINITE ELEMENT MODELLING AND VALIDATION

In this study, numerical simulations are conducted using ANSYS APDL for both thermal and mechanical analyses while taking into account material and geometric imperfections. For the later, elastic buckling analysis is done to determine the appropriate buckling mode at ambient temperature to be included in the forthcoming mechanical analysis. The thermal transient analysis is performed under fire ISO834 to obtain the temperature distribution within CFS in respect to time. The mechanical analysis is done with the aim to determine the load bearing capacity of CFS, critical time and temperature at elevated temperature and failure mode.

3.1 Study cases

Different CFS element models from LSF panel, single and doubles Lipped Channel stud, Figure 4, are considered to study their thermal and mechanical response at ambient and when exposed to fire. Four cases of CFS open and closed cross-sections with configurations, single, Figure 4a, back-to-back (B-B), Figure 4b, face-to-face (F-F), Figure 4c, and box (B), Figure 4d. All CFS models have the same dimensions with 3.72m of length protected by 16 mm thick of plasterboard and the section geometry details are presented in Figure 5.

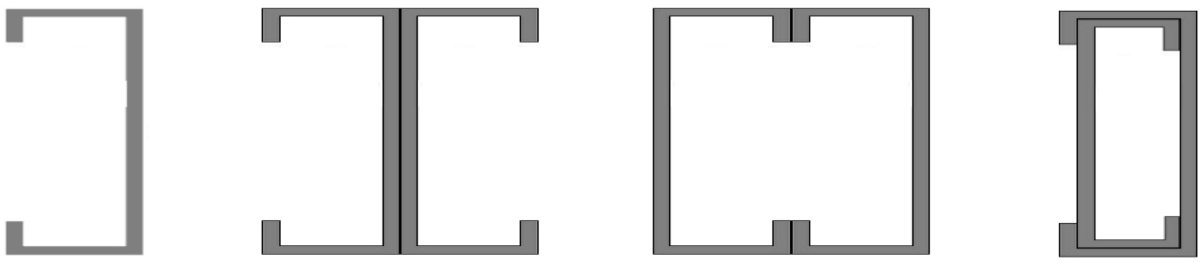

(a) Single stud (b) B-B Double stud (c) F-F Double stud (d) Box Double stud

Figure 4. Types of stud cross-section used in parametric study

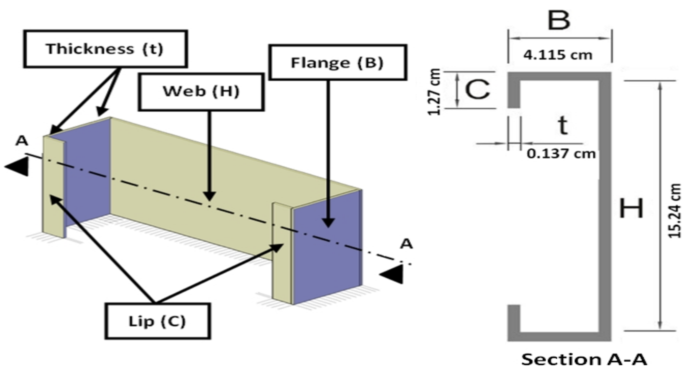

Figure 5. Geometry details of CFS members (LC H×B×C×t)

3.2 Element type

Structural finite element models both at ambient and elevated temperature are modelled using SHELL181 for CFS elements, with six degree of freedom at each node, and SOLID65 for ended rigid plate that used for the distribution of the load. Thermal finite element analyses are conducted based on SHELL131, for CFS members, having four nodes with up to 32 temperature degrees of freedom at each node, and SOLID70 for plasterboard, having eight nodes and a single degree of freedom, temperature, at each node. The contact between solids and shells is considered perfect.

3.3 Mesh size and boundary conditions

All structural and thermal models including CFS members, plasterboard and rigid plate are meshed with size of 4 mm × 10 mm, Figure 6a. The boundary conditions for structural models are defined such that the restrained displacements at one end, where the load is applied at the centroid of the section, are UX,UY, RZ rotation and at the other end, are UX,UY,UZ and RZ. Boundary condition for horizontal displacement UX is applied at distance intervals of 300 mm of the member length to account for the constrained on CFS member exerted by the plasterboard, Figure 6a. Figure 6b shows the boundary conditions used for thermal analyses under the ISO834 fire action with heat transfer by convection coefficient of 25 W/m2 for the exposed face and 9 W/m^2 which include the radiation effect as recommended by EN-1991-1-2 [30]. The radiation is applied with an emissivity coefficient of 1 both on exposed side and on empty cavity.

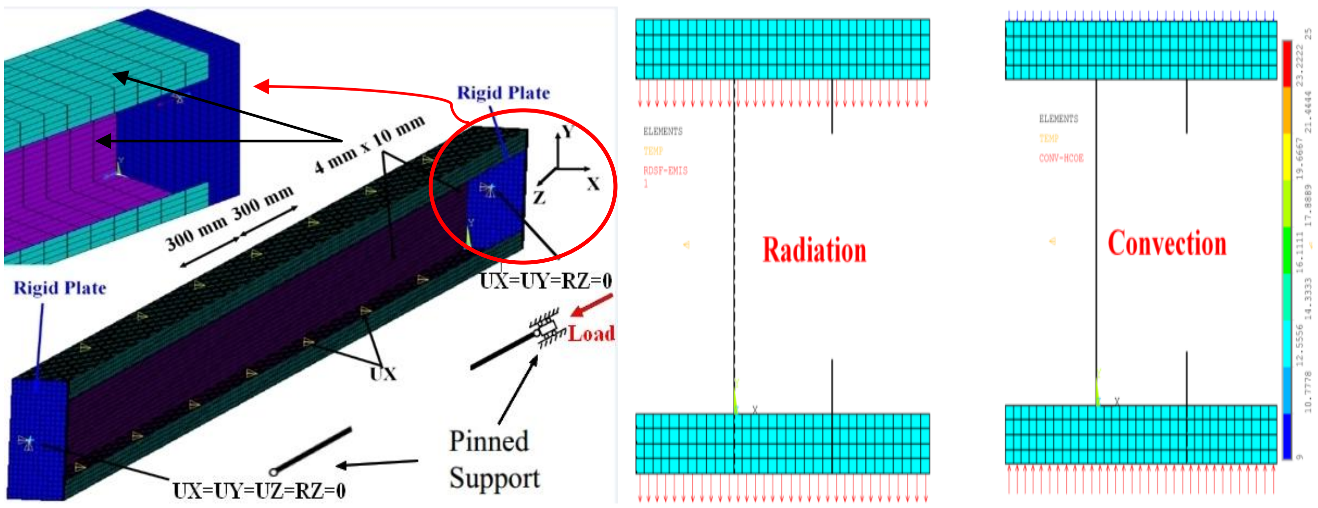

(a) Mesh size structural boundary condition (b) Thermal boundary condition

Figure 6. Mesh size and boundary condition applied to the numerical models

3.4 Geometric imperfection

The initial geometric imperfection for CFS to account cross-sectional instabilities are included in the numerical models of this study by adopting an amplitude of 0.006H as recommended by Schafer and Peköz [31]. As with regard to residual stresses effect, many studies [19, 31, 32] have proved that they can be neglected due to their small effect.

3.5 Validation of numerical models

Thermal and structural finite element models for stud LC (90×40×15×1.15) mm are validated using the fire test conducted by Kolarkar [33] and the numerical study done by Gunalan [28]. The test wall model was built with G500 four studs LC of 2.4 m height equally spaced by 600 mm, fixed between two tracks of 2.4 m width at the top and the bottom, and protected by 16 mm thick of plasterboard. The yield strength and elasticity modulus at room temperature were 569 MPa and 213,520 GPa, respectively. The most exposed element among LC studs of the panel is modelled with geometric imperfection and boundary conditions discussed above.

Results for the thermal FE model is presented and compared with the fire test result obtained by Kolarkar [33]. Figure 7 shows a comparison between the numerical thermal results obtained by ANSYS to those of experimental study, including the temperature progression at mid-height Hot Flange (HF) and Cold Flange (CF). The thermal FE model has produced a good prediction for temperature evolutions as by the thermocouples from the test.

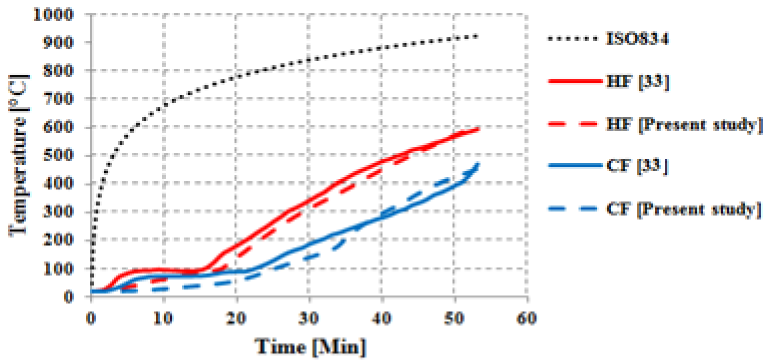

Figure 7. Temperature progression within CFS surfaces from fire test and thermal FE analysis

Results for the structural model at ambient temperature are presented and compared with the experimental and numerical results [28, 33] in table 1 and Figure 8.The predicted results are close with those from experimental and numerical ones. The difference in the failure ultimate load is 1.5% with the experiment and 0.6% with the numerical, Table1.

Table 1. Comparison of ultimate failure load

Studies	Experimental [33]	Numerical [28]	Present study
Failure ultimate load [kN]	79	77.3	77.8

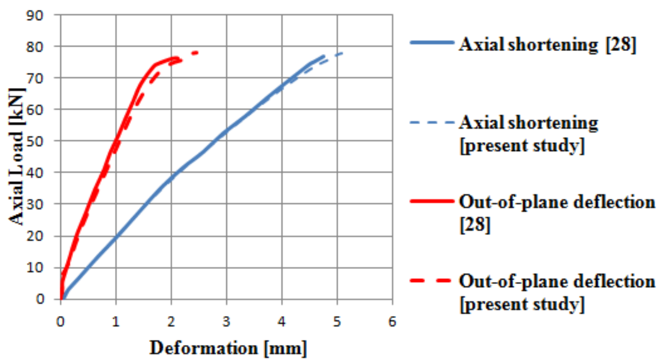

Figure 8. Comparison of the deformation of LC stud at ambient temperature

At elevated temperature, results for the structural model are presented and compared to results obtained from fire test [33]. Table 2 and Figure 9a, show a good agreement between the numerical results and the fire test results obtained by Kolarkar [33]. The load ratio (LR)-time curves obtained both by Gunalan [28] and present study are presented in Figure 9b. The comparison between the curves indicates a good agreement between the two numerical studies and the failure time obtained confirms the validation of structural FE model under steady state.

Table 2. Comparison between failure time and critical temperature under transient state condition

Studies	Experimental [33]	Numerical [28]	Present study
Failure time [minutes]	53	52	53
Critical temperature [°C]	607	598	612

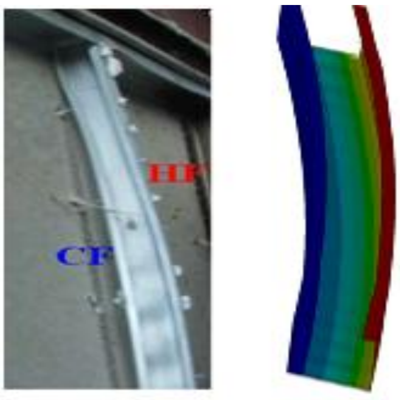

(a) Failure mode under transient state condition

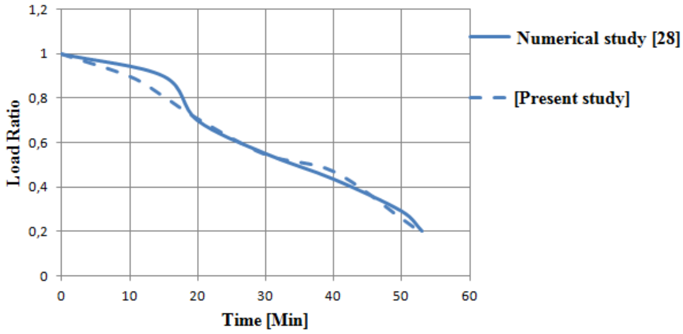

(b) LR-time under steady state condition

Figure 9. Validation of structural FE models at elevated temperature

4 ANALYSES AND RESULTS

This study aims to investigate the fire response of the presented cases in section 3.1, for single and doubles LC stud CFS, subjected to an axial compression loading, at ambient temperature and under non-uniform elevated temperature distributions. The mechanical analysis include results for failure ultimate load, axial shortening and the buckling mode of each section type at ambient. The thermal analysis results present the determination of the progression and distribution of temperatures across the stud cross-sections. The thermomechanical analysis considers results for the load ratio (LR), varying from 1 to 0.2, calculated with respect to the failure load at room temperature for each model. This is to define the fire resistance rating (FRR) and the corresponding failure mode at high temperature under transient state condition.

4.1 Thermal analysis results

The temperature evolution at the mid-height of the Hot Flange (HF) and Cold Flange (CF) of different sections of studs is presented in Figure 10. It can be observed that the single stud, B-B double stud and F-F double stud have the same temperatures progressions and the same maximum of temperature for both HF and CF at 60 minutes, which are approximately 630 °C and 500 °C, respectively. However, for the box double stud, a large difference of temperature evolution of both HF and CF is observed compared to the other three section type. It can be seen that the HF and CF temperature of box double stud are lower than the other temperatures, with a slow rise in temperature progression. The maximums temperature for box double stud does not exceed 400 °C and 250 °C at 60 minutes for HF and CF respectively. It can be concluded that an increase of the thickness of CFS flanges results in a decrease of the temperature. An increase in the thickness of the web and lips did not affect the temperature progression. This is due to the radiation effect which allows for the transfer of the temperature from the cavity exposed side to the cavity ambient side as described in boundary condition section.

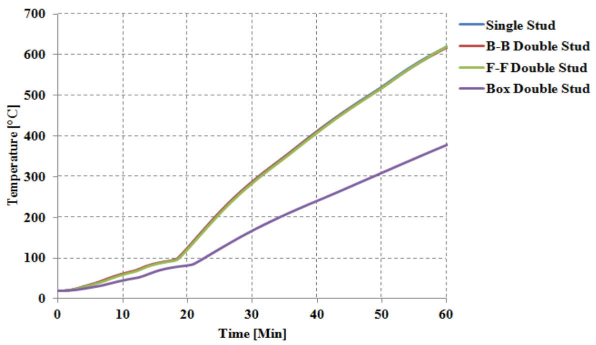

(a) HF Temperature

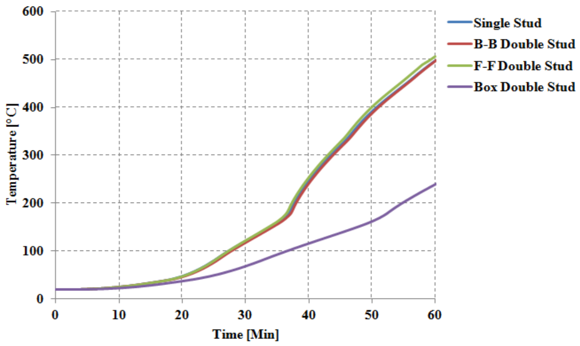

(b) CF Temperature

Figure 10. Temperature evolution at mid-height stud

4.2 Mechanical analysis results at room temperature

The elastic buckling loads and the failure loads at ambient temperature of different studs sections are presented in table 3. It can be observed that the use of double stud regardless of their configurations, leads to the increase in the failure load. The highest and the lowest failure load for double stud configurations reach 207.8 kN and 186.8 kN for the B-B and F-F sections, respectively. Figure 11a and Figure 11b show the axial shortening created by the failure compression loads presented in table 3 for each stud and the corresponding failure buckling modes, respectively. In Figure 11a, B-B double stud provided a better structural response with less deformation at high loads. F-F double stud that has showed a weaker structural response compared to other double stud section. Figure 11b shows that the predominant failure mode for all stud elements, exception made for B-B section, is the local buckling of the web, which has occurred due to the high stud web depth, with high slenderness of the stud section

Table 3. Elastic buckling load and failure ultimate load at room temperature

Section types	Single Stud	B-B double stud	F-F double stud	Box double stud
Elastic buckling load [kN]	30.66	199.40	61.77	82.06
Failure load [kN]	75.3	207.8	186.8	203.7

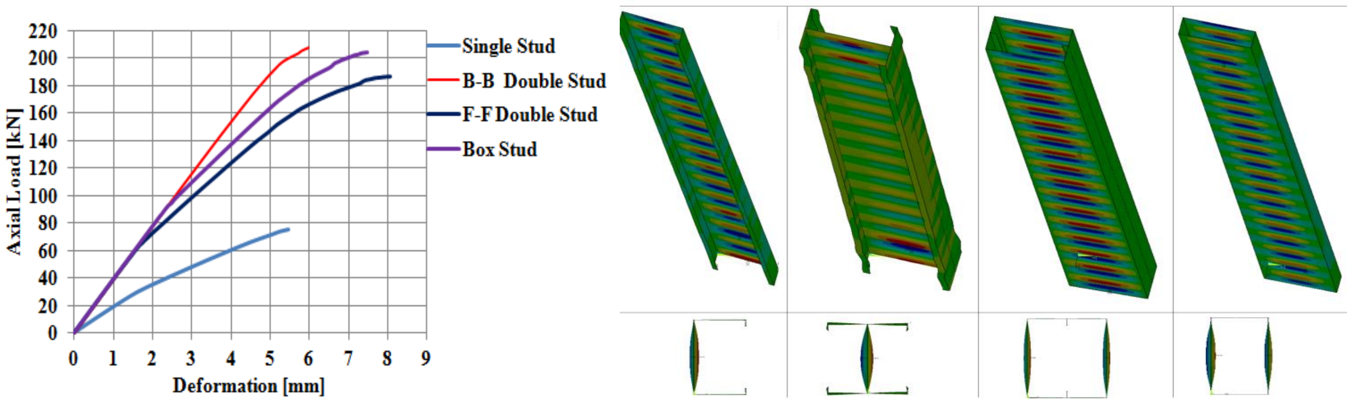

(a) Axial shortening versus axial compression load

(b) Failure buckling mode at room temperature

Figure 11. Structural behaviour of different stud cross section at ambient temperature

4.3 Thermomechanical analysis results

The FRR is presented in the form of LR versus time curve as is illustrated in Figure 12a. The later shows a comparison of FRR of different types of double stud cross section to study their influence on the fire response of CFS. It can be observed, Figure 12a, that the single stud, B-B and F-F double stud reached nearly the same failure time of 57, 59.5 and 60 minutes, respectively. A FRR of 60 minutes is observed at a minimum of LR of 0.55 for box double stud and did not reached failure expected at 0.2. A difference in FRR of more than 20 minutes is observed between box double stud and others at LR of 0.55. The temperature distribution obtained from thermal analyses shows similarities of temperature profiles for single stud, B-B and F-F double stud and provided the same FRR. Although, B-B double stud element with higher ultimate compression capacity at ambient temperature giving a better resistance for the wall, it has less load compression capacity at elevated temperature. Figure 12b shows the temperature contours and the buckling mode of single stud, B-B and F-F double stud that occurred at the failure (LR of 0.2) when exposed to fire. It can be observed that the B-B section failed by local buckling that occurred in HF which is slender than at the web. Flexural and local buckling of the web and HF near supports occurred in the single and F-F double stud. Critical temperatures for all models have reached 622, 606 and 630°C for single stud, F-F and B-B double stud, respectively.

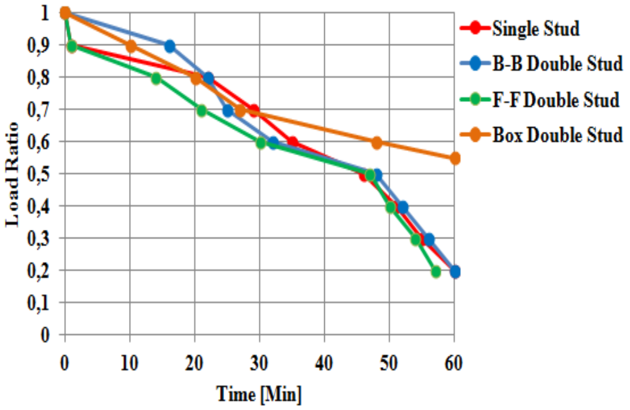

(a) Load ratio versus time

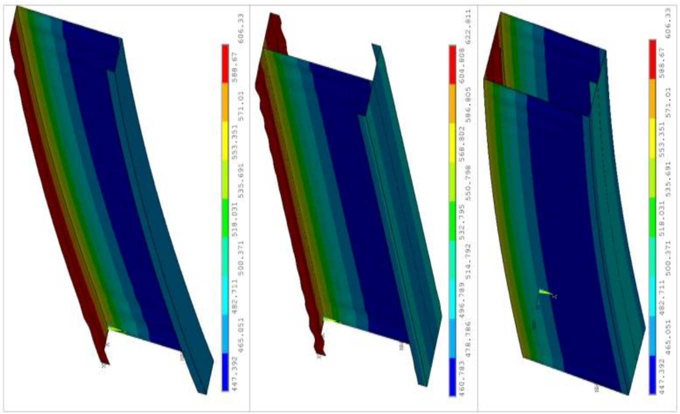

(b) Failure buckling load at elevated temperature

Figure 12. Structural behaviour of different stud cross section under fire condition

5 CONCLUSIONS

In this paper, cases of study for different types of cold formed sections including single and double stud are investigated at ambient and elevated temperatures based on the validated finite element model.

Thermal and structural responses are evaluated for each case and the following conclusions are drawn:

- Although, the increase of the thickness of CFS flanges conducts to the decrease of the temperature, the increase of the thickness of the web and lips did not affect the progression of the temperature.
- The predominant failure mode at room temperature for all stud elements is the local buckling of the web, exception made for B-B section case which occurred in web and at both flanges near supports.
- The box double stud provided a better fire response with higher FRR than other sections during 60 minutes.
- All models failed by flexural and local buckling of the web and HF near supports at elevated temperature, exception made for B-B section, which failed by local buckling that occurred in HF.
- The box section did not fail during one hour of the fire exposure.

REFERENCES

1. Cashell, K. A., Malaska, M., Khan, M., Alanen, M., and Mela, K., Experimental and numerical analysis of stainless steel cellular beams in fire. Fire safety journal 121, 103277 (2021). https://doi.org/10.1016/j.firesaf.2021.103277
2. Dar, M. A., Subramanian, N., Dar, A. R., Anbarasu, M., Lim, J. B., and Atif, M., Behaviour of partly stiffened cold-formed steel built-up beams: Experimental investigation and numerical validation. Advances in Structural Engineering 22, 172-186 (2019). https://doi.org/10.1177/1369433218782767
3. Dundu, M., Buckling of short cold-formed lipped channels in compression. Journal of the South African Institution of Civil Engineering= Joernaal van die Suid-Afrikaanse Instituut van Siviele Ingenieurswese 56, 46-53 (2014). https://hdl.handle.net/10520/EJC158377
4. Maraveas, C., Local buckling of steel members under fire conditions: A review. Fire Technology 55, 51-80 (2019). https://doi.org/10.1007/s10694-018-0768-1
5. Benyettou Oribi, S., Kada, A., Lamri, B., and Mesquita, L. M., Investigation of residual stresses on the fire resistance of unrestrained cellular beams. ce/papers 4, 1386-1394 (2021). https://doi.org/10.1002/cepa.1436
6. Kada, A. and Lamri, B., Numerical analysis of non-restrained long-span steel beams at high temperatures due to fire. Asian Journal of Civil Engineering 20, 261-267 (2019). https://doi.org/10.1007/s42107-018-0103-7

7. Merouani, M. R., Lamri, B., Kada, A., and Piloto, P., Mechanical analysis of a portal steel frame when subjected to a post-earthquake fire. Fire Research 3, (2019). https://doi.org/10.4081/fire.2019.76
8. Mesquita, L., Piloto, P., Vaz, M., and Vila Real, P., Experimental and numerical research on the critical temperature of laterally unrestrained steel I beams. Journal of Constructional Steel Research 61, 1435-1446 (2005). https://doi.org/10.1016/j.jcsr.2005.04.003
9. Nadjai, A., Petrou, K., Han, S., and Ali, F., Performance of unprotected and protected cellular beams in fire conditions. Construction and Building Materials 105, 579-588 (2016). https://doi.org/10.1016/j.conbuildmat.2015.12.150
10. Bailey, C., Indicative fire tests to investigate the behaviour of cellular beams protected with intumescent coatings. Fire safety journal 39, 689-709 (2004). https://doi.org/10.1016/j.firesaf.2004.06.007
11. Lamri, B., Mesquita, L., Abdelhak, K., and Piloto, P., Behavior of cellular beams protected with intumescent coatings. Fire Research 1, (2016). https://doi.org/10.4081/fire.2017.27
12. Mesquita, L., Gonçalves, J., Gonçalves, G., Piloto, P., and Kada, A., Intumescente fire protection of cellular beams. X Congresso de Construção Metálica e Mista, pp. 623-630 Coimbra, Portugal, 2015.
13. Buchanan, A. H. and Abu, A. K., Structural design for fire safety, John Wiley & Sons, 2017.
14. Mesquita, L., Dias, R. P. S., Parente, A., and Piloto, P., Computational modelling of cold-formed steel screwed connections at ambient and elevated temperatures. VII European Congress on Computational Methods in Applied Sciences and Engineering (ECCOMAS Congress 2016), 2016.
15. Gunalan, S., Heva, Y. B., and Mahendran, M., Local buckling studies of cold-formed steel compression members at elevated temperatures. Journal of Constructional Steel Research 108, 31-45 (2015). https://doi.org/10.1016/j.jcsr.2015.01.011
16. Ariyanayagam, A. D. and Mahendran, M., Influence of cavity insulation on the fire resistance of light gauge steel framed walls. Construction and Building Materials 203, 687-710 (2019). https://doi.org/10.1016/j.conbuildmat.2019.01.076
17. Baleshan, B. and Mahendran, M., Numerical study of high strength LSF floor systems in fire. Thin-Walled Structures 101, 85-99 (2016). https://doi.org/10.1016/j.tws.2015.12.018
18. Hassoune, M., Kada, A., Menadi, B., and Lamri, B., Finite element models for the prediction of thermal response of light steel guage steel panels when subjected to fire. First International Conference on Geotechnical, Structural And Materials Engineering ICGSAME2021, Biskra-Algeria-, 2021
19. Rokilan, M. and Mahendran, M., Design of cold-formed steel wall studs subject to non-uniform elevated temperature distributions. Thin-Walled Structures 171, 108625 (2022). https://doi.org/10.1016/j.tws.2021.108625
20. Piloto, A. G. P., Khetata, S. M., and Gavilán, B. R. A., LOADBEARING CAPACITY OF LSF WALLS UNDER FIRE EXPOSURE. MATTER: International Journal of Science and Technology 4, (2018). https://doi.org/10.20319/mijst.2018.43.104124
21. Samiee, P., Niari, S. E., and Ghandi, E., Fire performance of cold-formed steel shear wall with different steel grade and thicknesses. Structures, pp. 751-770, (2021). https://doi.org/10.1016/j.istruc.2020.11.073
22. Samiee, P., Niari, S. E., and Ghandi, E., Thermal and structural behavior of cold-formed steel frame wall under fire condition. Engineering Structures 252, 113563 (2022). https://doi.org/10.1016/j.engstruct.2021.113563
23. Senthilkumar, R., Kumar, C. P. A. S., Saravanakumar, R., and Kumar, D. P., Numerical study on restrained thermal elongation of cold-formed steel Column subjected to non-uniform thermal loading under transient state. Fire safety journal 103608 (2022). https://doi.org/10.1016/j.firesaf.2022.103608
24. ANSYS®, "Academic Research, Release 16.2," ed: ANSYS, Canonsburg, PA, USA, 2015.
25. EN1993-1-2, Eurocode 3: Design of steel structures - Part 1-2: General rules - Structural fire design [Authority: The European Union Per Regulation 305/2011, Directive 98/34/EC, Directive 2004/18/EC]. 78 (2005).
26. Dolamune Kankanamge, N., Structural behaviour and design of cold-formed steel beams at elevated temperatures. PhD thesis, Queensland University of Technology, 2010.

27. Ranawaka, T. and Mahendran, M., Experimental study of the mechanical properties of light gauge cold-formed steels at elevated temperatures. Fire safety journal 44, 219-229 (2009). https://doi.org/10.1016/j.firesaf.2008.06.006
28. Gunalan, S., Structural behaviour and design of cold-formed steel wall systems under fire conditions. PhD thesis, Faculty of built environment and engineering, Queensland University of Technology, 2011.
29. Sultan, M. A., A model for predicting heat transfer through noninsulated unloaded steel-stud gypsum board wall assemblies exposed to fire. Fire Technology 32, 239-259 (1996). https://doi.org/10.1007/BF01040217
30. EN-1991-1-2, Eurocode 1: Actions on structures—Part 1-2: General actions—Actions on structures exposed to fire [Authority: The European Union Per Regulation 305/2011, Directive 98/34/EC, Directive 2004/18/EC]. British Standards 58 (2002).
31. Schafer, B. W. and Peköz, T., Computational modeling of cold-formed steel: characterizing geometric imperfections and residual stresses. Journal of Constructional Steel Research 47, 193-210 (1998). https://doi.org/10.1016/S0143-974X(98)00007-8
32. Kanthasamy, E., Chandramohan, D. L., Shanmuganathan, G., Poologanathan, K., Gatheeshgar, P., Corradi, M., and Mcintosh, A., Web crippling behaviour of cold-formed high-strength steel unlipped channel beams under End-One-Flange load case. Case Studies in Construction Materials 16, e01022 (2022). https://doi.org/10.1016/j.cscm.2022.e01022
33. Kolarkar, P. N., Structural and thermal performance of cold-formed steel stud wall systems under fire conditions. PhD Thesis, School of urban development, Queensland University of Technology, India, 2010.

FIRE RESISTANCE ASSESSMENT OF AUTOMATED RACK SUPPORTED WAREHOUSES

Margherita Autiero[1], Donatella de Silva[2], Antonio Bilotta[3], Emidio Nigro[4]

ABSTRACT

Automated Rack Supported Warehouses (ARSW) combine the structural efficiency of metal construction with automated machines for handling the stored products. A fundamental distinction exists between traditional Steel Racks (SR) and ARSW, indeed ARSW are self-bearing rack structures committed to support, besides self-weight and weight of products, also environmental loads (i.e., wind, snow and seismic action) and all the other non-structural elements such as clads, equipment, etc. The peculiarity of these structures makes them a topic of great interest both for the scientific community and for the manufacturers of industrial racks. In the last years, a lot of research has been carried out to better understand the behaviour of these structures from the seismic point of view, while their behaviour in case of fire is still poorly known. Since the lack of regulations and technical references, this paper aims to provide a state of the art on ARSW structures in case of fire, with a discussion of the most critical aspects. For this reason, this paper provides first results about an advanced thermos-mechanical analysis of a case study, by considering a fire model that allows us to consider the vertical and horizontal propagation starting from a localized fire and providing a comparison between the capacity models that the regulations in case of fire propose for cold-formed steel members (CFS), which mainly made these structures.
Keywords: Structures; finite element modelling; compartment fires; fire tests

1 INTRODUCTION

The warehouse is a building where many goods can be stored after their production and before their distribution to the consumers. The demand for storage space is growing, due to the increasing mass production of goods and increasing consumption levels, therefore highly optimized and reliable warehouses are needed. Automated Rack Supported Warehouses (ARSW) are used in industrial facilities to optimize storage spaces; these structures combine the structural efficiency of metal construction with automated machines for handling the stored products.
A fundamental distinction exists between traditional Steel Racks (SR) and Automated Rack Supported Warehouses (ARSW). SR are designed to carry on the structural self-weight and the weight of the stored goods. ARSW are self-bearing rack structures committed to support, besides self-weight and weight of products, also environmental loads (i.e., wind, snow and seismic action) and all the other non-structural elements such as clads, equipment, etc. The traditional structural scheme of steel racking consists of a regular sequence of upright frames connected by coupled pallet beams devoted to bring the goods, as widely presented by Bernuzzi [1]. SR have two principal directions, as indicated in Figure 1 the cross-aisle

[1] Margherita Autiero, Department of Structures for Engineering and Architecture, University of Naples Federico II (Italy),
e-mail: margherita.autiero2@unina.it ,
[2] Donatella de Silva, Department of Structures for Engineering and Architecture, University of Naples Federico II (Italy)
e-mail: donatella.desilva@unina.it , https://orcid.org/0000-0002-4058-902X
[3] Antonio Bilotta, Department of Structures for Engineering and Architecture, University of Naples Federico II (Italy)
e-mail: antonio.bilotta@unina.it , https://orcid.org/0000-0002-2414-5488
[4] Emidio Nigro, Department of Structures for Engineering and Architecture, University of Naples Federico II (Italy)
e-mail: eminigro@unina.it , https://orcid.org/0000-0002-3848-7454
https://doi.org/10.6084/m9.figshare.22215778

(CA) direction where two (often perforated) upright sections are linked together by a system of bracing members to provide lateral stability of the structure in this direction; and the down-aisle (DA) where the main lateral force resisting system is provided by vertical bracing [2].
To design ARSW, designers usually refer to the EN 15512 [3] which provides principles for the structural design of pallet racking systems, and EN 16681 [4] which indicates principles for the seismic design for pallet racking systems, applying them in combination with thecnical experience. Well-established principles and rules supported by experimental evidence and theoretical research could be found in Bernuzzi 2015 [1]. Because the ARSWs are systems larger, taller, and more complex than usual pallet racks producers and design offices are question the suitability of these regulations, for high-tech massive, automated warehouses.

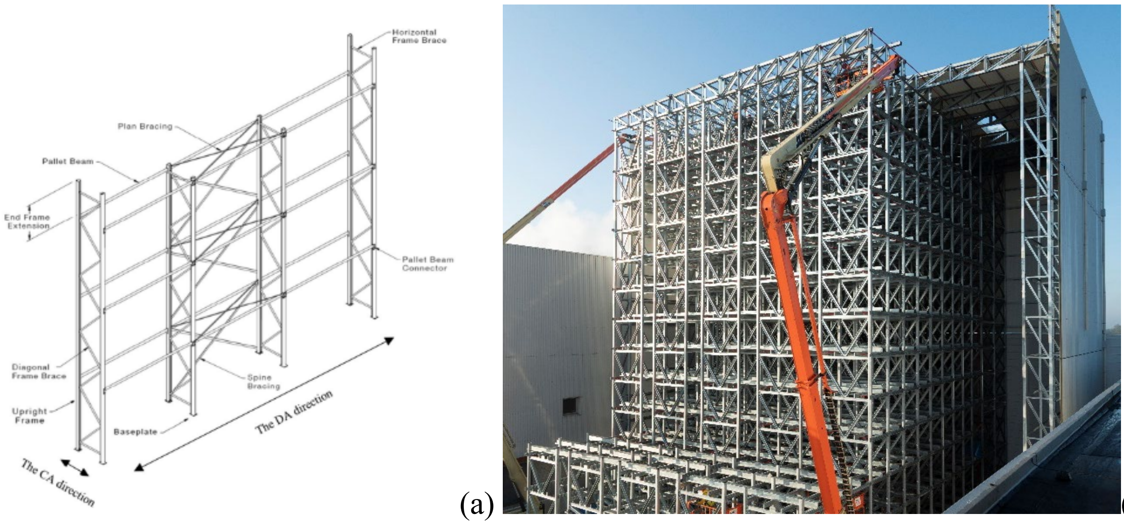

(a) (b)

Figure 1 Cross-aisle and down-aisle directions (a), ARSW during its construction (https://www.rosss.it/) (b)

These structures mainly consist of cold-formed steel members (CFS); that optimize the structural performance by reducing the steel weight, the costs, and the assembly time, however, under fire conditions, the thin thickness of these profiles, combined to the steel high thermal conductivity, induce fast increase on the steel temperature with a significant loss in material stiffness and strength. As this type of sections is usually classified as class 4 cross-section, according to EN 1993-1-1 [5] and it has much lower strength and stiffness than hot-rolled steel members, CFS members can fail by a variety of buckling modes including global, local and distortional buckling and their interactions [6] (see Figure 2).
At ambient temperatures, the EN 1993-1-5 [7] gives two methods to account for the effects of local buckling in the design, i.e., the effective width method and the reduced stress method. On the other hand, Eurocode considers the distortional buckling strength by using a reduced thickness in the edge stiffener and/or distorted part of the compression flange.
At present, fire design methods for cold-formed steel members are not so developed as for hot-rolled ones. Indeed, at elevated temperatures, EN 1993-1-2 [8] suggests for Class 4 cross-sections a default critical temperature of 350 °C if no fire design is conducted, which means that even for a requirement of 15 min of fire resistance, passive fire protection should normally be used for current profiles. Alternatively, the informative Annex E of this Eurocode suggests the use of a reduced cross-section calculated with the effective width method using the steel properties at ambient temperature and for the design yield strength of steel the 0.2% proof strength ($f_{0.2p,\theta}$). According to Kankanamge and Mahendran [9], EN 1993-1-2:2005 [8] predictions were found to be over-conservative for high temperatures except for beams with very high slenderness. EN 1993-1-3:2004 [9] design method with buckling curve 'b' was found to be over-conservative or unsafe for some temperatures and slenderness ratios. Actually, Kankanamge and Mahendran [10] have already proposed a new fire design methodology for CFS lipped channel beams subjected to lateral-torsional buckling, based on modified AS/NZS4600 [11] design rules. The proposed formulae is an adaptation of the ambient temperature design method by replacing the mechanical properties at ambient temperature with the respective reduction factors depending on the temperature ($E = k_{E,\theta} \cdot E_{20}$, $f_y = k_{y,\theta} \cdot f_{y,20}$) and using the $f_{p,\theta}/f_{y,\theta}$ factor for considering the non-linearity in the stress-strain curve of steel.

However, this design method did not provide accurate load- bearing capacity predictions for the full range of temperatures and slenderness ratios [10]. Other new simplified fire design rules were proposed [12] but they were specifically developed for CFS floor systems.
Laíma and Rodrigues [6] developed a simplified fire design methodology for single and built-up cold-formed steel beams based on the European guidelines. The proposed formula is an adaptation of the ambient temperature design method [8] by modifying the dimensional slenderness at elevated temperatures ($\lambda_{LT\,\theta}$) taking into account the smooth relationship between the parameters $k_{y,\theta}$ and $k_{E,\theta}$. As well as that the coefficient values of 0.5 and α were modified to β and α' in order to consider higher geometric imperfections in members under higher initial load levels.

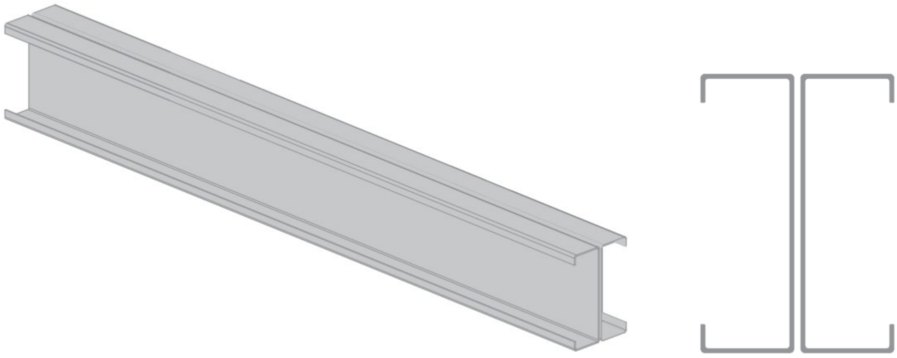

Figure 2 an example of cold-formed steel member

Couto et al. 2014 [13] developed new expressions to determine the effective width of steel sections at high temperatures. This design curve has been calibrated as close as possible to the existing design curve of the Eurocode 3 by introducing the factors α_θ and β_θ on the expressions of Part 1.5 of Eurocode 3, hence the influence of the imperfections is taken into account as in the original formulas developed by Winter and additionally the non-linear steel constitutive law at elevated temperatures is also accounted for, furthermore by using the factor ε_θ steel grade is also taken into account in this new proposal. It is worth saying that by using these expressions the strength at a total strain of 2% can be used to calculate the resulting effective cross-sectional resistance, instead of using the 0.2% proof strength as recommended in the Annex E.
The new expressions are temperature dependant leading to a variation on the effective cross-section properties under fire situation. For this reason, a simplified proposal, not temperature dependant, is investigated from Couto et al. 2015 [14] based on the assumption that the influence of the temperature on the range of the critical temperatures usually expectable for steel members (from 350 °C to 750 °C) are negligible leading to a simpler yet accurate design.
Therefore, also in light of the previous considerations, it is certainly necessary to consider design and verification against both seism and fire, for these structures. Nevertheless, in the last years, a lot of research has been carried out to better understand the behaviour of these structures from the seismic point of view [15], while their behaviour in case of fire is still poorly known. Since the lack of regulations and technical references, this paper aims at providing a state of the art on Automated Rack Supported Warehouses structures in case of fire, with a discussion of the most critical aspects, research addresses to develop design and verification guidelines in fire conditions are also provided.

2 CRITICAL ASPECTS

In the context of the modern technical codes, as the new Italian technical fire prevention regulation [16], the fire resistance is defined as a passive fire protection measure to guarantee load-bearing and compartmentation capabilities of structures according to performance levels, selected by the designer in order to achieve the defined fire safety objectives. The Italian code, in accordance with European ones, defines five performance levels (PL) depending on the importance of the building; for example, in the case of industrial ones, PLI and PLII can be chosen. In particular, in PLI the absence of external consequences due to structural collapse has to be demonstrated, whereas according to the PLII the structure has also to

maintain its fire resistance capacity for a period of time sufficient for the evacuation of occupants to a safe area outside of the building.
In order to comply with the performance level, different design solutions can be chosen, based on prescriptive or performance-based approaches.
In this particular type of structure is essential to consider the performance-based approach, instead of the prescriptive one, because this one generally requires a minimum fire resistance performance for structural elements that lead to the use of traditional passive fire protection systems, that in the case of these metal profiles are difficult to apply, because of their high section factors and very small critical collapse temperatures. Indeed, considering the intumescent paints, in order to ensure the bearing capacity against fire, a very high thickness of more than 1,000μ should be applied to the element [17]. Moreover, this paint should be applied when the rack is already built, therefore the practical application would be very difficult due to the particularity of these profiles. All these aspects would lead to high costs.
Since their fire vulnerability, these structures are typically protected by active fire protection measures in order to limit any structural damage. The fire protection of a warehouse is a big challenge, because they have generally a high fire load, in addition to the goods, they contain other elements that facilitate the propagation of flames, among them: plastic, cardboard or wood. To minimise risks, warehouses must be equipped with fire prevention, detection and extinguishing systems.
Moreover, in these Automated Rack Supported Warehouses can be stored a lot of different types of goods, such as paper rolls, flammable liquids, plastics, etc therefore also the choice of active fire protection could be different, such as sprinkler system with water, with lather or even oxygen reduction systems (especially in freezing cells where no people operate). This system injects nitrogen into the warehouse, decreasing the concentration of oxygen and thus preventing the development of a fire.
It is worth saying that the use of active fire protection can lead to lose the stocked goods and therefore the study of the fire scenario without these systems should be deeply analysed. However, recent studies [18] have shown that in many cases these systems may not work and therefore to consider the fire scenario without active system is necessary as one of the most critical for mechanical analyses, is necessary.
For these reasons, moving in the context of alternative solutions, or rather in the performance-based approach, the absence of external consequences due to structural collapse has to be demonstrated, which means that the designer has to demonstrate analytically that the collapse mechanism is implosive using, for example, one or more technical measures to guide the collapse, such as:

- adoption of criteria of the hierarchy of the fire resistance (e.g., assignment of an over fire resistance to the perimeter structures elements compared to the internal ones;
- spatial distribution of the fire loads towards inner areas;
- adoption of convenient structural forms (e.g. with inclination towards the interior, ...);
- use of fire control systems with higher availability;
- pyramidal stacking of the fuel materials;
- adoption of constraints that facilitate implosive collapse;

Starting from these considerations, it has been studied one structural typological of a self-supporting automated warehouse, starting from the fire modelling and coming to the collapse study.

3 ASSESMENT AT ELEVATED TEMPERATURE

3.1 Description of the typological structure

The structure object of this study is a self-supporting automated warehouse consisting of a steel supporting structure and equipped with infill panels and roofing consisting of sandwich panels. This automated warehouse, having a rectangular plan, will consist of a central block, used for the storage of the reels, and two side lanes served by stacker cranes for handling the reels. It is characterized by 13 load levels placed at an inter-axis distance of 2 m, a total length of 52 m, a width of 35m and a height of 29.8 m. In the down-aisle direction (Figure 3a)., the central block consists of a succession of frames, each of which composed of five shoulders with V-shaped braces (see Figure 3b). In this direction, the frames are connected with beams made up of open section steel profiles. At either end of the warehouse in down-aisle direction, the first two spans of the structure host the bracing towers. The warehouse structural scheme consists of hot-rolled tubular columns and cold formed horizontal and diagonal elements. For each span, a unit load (a paper reel) is stored; the UDCs are supported by specially designed channels resting on the principal beams. The system is braced in both directions. The type of Supports have been assumed to be pin supports in Y-direction and fixed supports in X-direction. The handling of units load is realized by a system of shuttles and satellites that move goods along rails in the warehouse X and Y-directions.

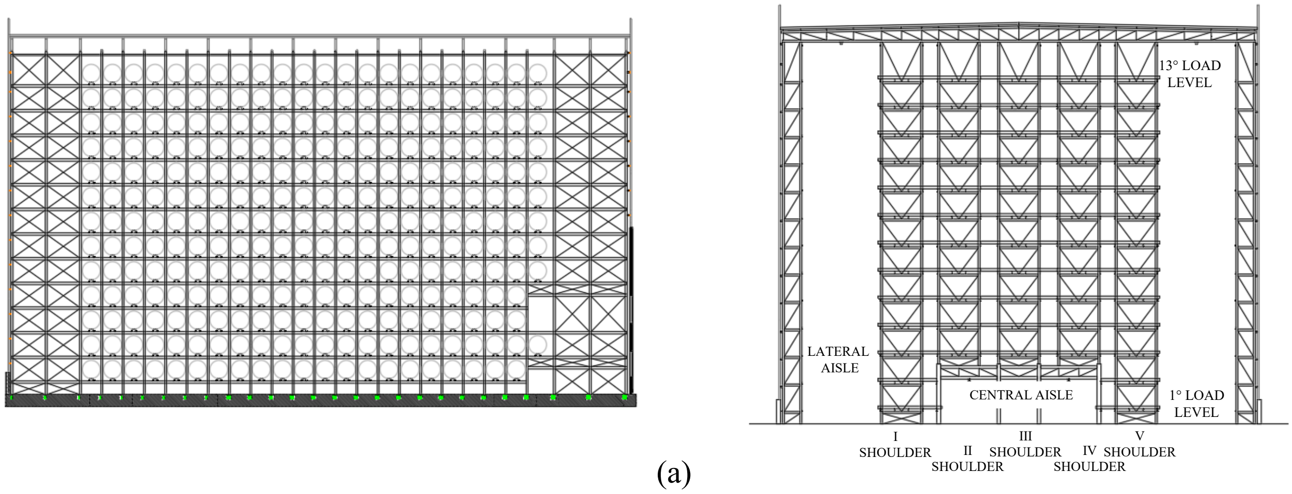

(a) (b)

Figure 3 down-aisle direction (a) and Cross-aisle one (b)

3.2 Application of performance-based approach

3.2.1 Fire modelling

For the application of the performance-based approach, the first step is the selection of the design fire scenarios, that for this type of structure, can be very significant, especially for their locations. After the choice of these fire scenarios, for each of them, the designer has to define the natural fire curve, determined on the basis of fire models. Also, the choice of the fire model can be crucial, because in these Automated Rack Supported Warehouses can be stored a lot of different types of goods, such as paper rolls, flammable liquids, plastics, etc. and for this reason, to consider different types of models such as localized fire (e.g., LOCAFI), and a vertically traveling fire in the upright frames, with different types of heat release rate (HRR), may be necessary. Starting from these considerations to better study the behaviour of these structures in case of fire, it was deemed necessary to study the scientific literature about fire spread in warehouses, in order to obtain a fire model which considers the vertical propagation of localized fires, validated against some experimental results. The work used as principal references to build this fire model is the one carried out by Lönnermark and Ingason [19], which carried out model scale tests (1:5), in order to investigate the fire spread in rack storages. In particular, the focus was on the fire spread from an initial fire in rack storage to adjacent racks without the interaction of a suppression system. The test program presented in the report [18], consisted of six different test series, to study the effects on the fire spread with regard to the enclosure, the ceiling height above the top of the rack storage (clearance height), beams in the ceiling and ventilation. The height of the rack storage as well as the distances between boxes and the thickness of the box material varied. The effect of beams and clearance height on response of virtual sprinklers in the ceiling was explored as well as the risk of fire spread between low stacks of goods. In particular the results of the following test series were used in this work:

- Test series 1: Cone calorimeter tests of the materials in the cardboard boxes used in the rack storage tests;
- Test series 2: Fire spread tests with one small rack;
- Test series 5: Fire spread tests with four racks (2x12x5) under a ceiling with varied height and slope, and cases with or without beams.

These tests were simulated by using the software CFAST software (Jones et al. 2006) [20] developed by NIST which is a two-zone fire model that predicts the thermal environment caused by a fire within a compartmented structure, in particular CFAST allows to model different compartments which can communicate among them. Therefore, in order to model the vertical propagation of a localized fire, making the best use of the information contained in the publication, it was decided to refer to Test 5.3 i.e. fire spread tests with four racks (2x12x5) with boxes in each rack. This test was selected also because it is the only one that provided the vertical fire spread between levels of the racks, but in order to have all the data and according to a bottom-up approach, it was necessary starts from Test 1 and 2, which provide the necessary input data. Indeed, to study the fire resistance of structures according to the performance-based approach, the first step is the modelling of possible fire scenarios that lead to the design natural fire curves. First of all, the Heat Release Rate (HRR) curves that characterize the fire scenarios have to be defined. For this reason, the test 2.2 was modelled first. In particular, since test 2.2 refers to double-thickness boxes, the HRR curve was set from test results 1.2, which provides the Maximum Heat Release Rate (kW/m^2) equal to 247 kW/m^2, the Total developed energy q_f=23,9 MJ/m^2 , which was amplificated to consider the presence of 4 boxes per level, obtaining q_f =95,6 MJ/m^2. While the value of $t\alpha$ was considered equal to 250 s, which is the value between the ones defined by Eurocode for bookshops (150 s) and offices (300 s), similar uses for paper and paperboard content. The combination of these parameters allowed us to obtain the input HRR, which was compared with the experimental one and therefore HRR calculated can be considered representative of test 2.2 and can be used in Cfast. In Cfast it has been modelled a single compartment with the rack dimensions, all the surfaces have the thermal properties of the steel. Along the walls were defined 4 openings per side (always considered totally open) so that, net of openings, the compartment represents the metal structure of the rack. It was then placed a steel flat thermocouple in the middle point of the rack, such as the thermocouple 2 in the test 2.2. The comparison between the experimental temperatures and the numerical ones obtained from CFAST allowed us to say that the numerical model in Cfast can be considered reliable.

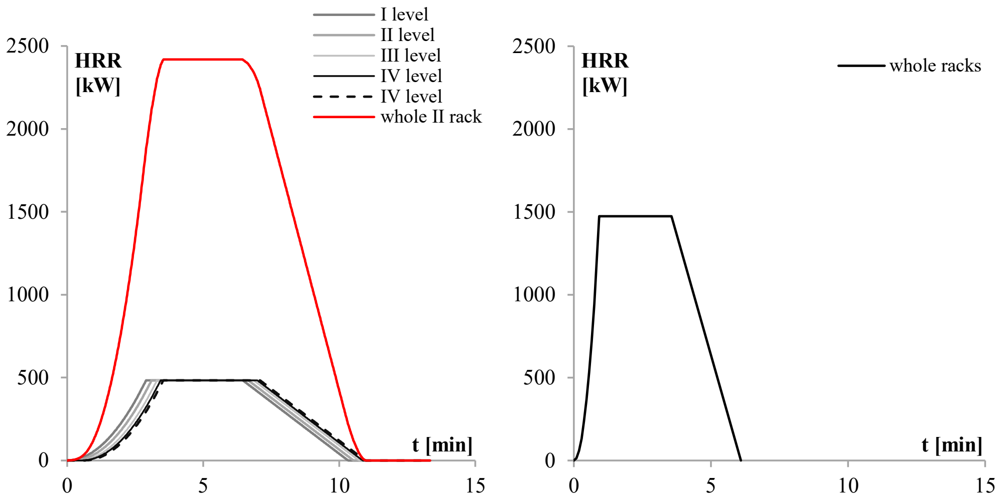

Figure 4 HRR curves of the second rack of test5.3 (a) and of the lateral ones (b)

Starting from these results, it was possible to simulate Test 5.3, which consists of the study of the vertical and horizontal propagation of the fire in a group of four racks containing 120 boxes under a flat ceiling at a distance of 60 cm from the top of the higher box. In particular, in the test configuration the ignition took place at the bottom of rack 2, containing double-thickness boxes (i.e., with the same characteristics of test 2.2 and 1.2 and described previously), but in order to model the ignition delay of the different levels and then reconstruct the vertical propagation, it was necessary to obtain first the HRR curves of the single rack level of test 2.2 (four boxes), in order to define the HRR curve of the single level of the second rack of test5.3 (twenty-four double thickness boxes) which were then summed up moment by moment, referring to the time delays provided by Lönnermark and Ingason’s work [19], obtaining finally the HRR curve of the whole rack, see Figure 4a.

For the remaining three racks (placed one to the left and two to the right of the rack mentioned before), although having the same geometrical characteristics, they are filled with single-thickness boxes, therefore the HRR curves must be reconstructed from tests 1.1 and 2.1. with the same procedure described before for tests 1.2 and 2.2. But since the test results didn't provide the vertical time delays, in this case, it was defined the HRR curve of the whole rack directly, see Figure 4b. These HRR curves provided the input of the CFAST program, in particular to model test 5.3 a large compartment of 16x15m in plan and 1.85 m in high was modelled. Within this one, 4 compartments representing the 4 racks were modelled and divided into 5 levels. The surfaces of the large compartment were plasterboard to simulate the walls of the environment in which the test was carried out, while the compartments representing the racks are characterized by the thermal properties of the steel. See Figure 6. Along the walls were defined 5 openings per side (always considered totally open) so that, net of openings, the compartment represents the metal structure of the rack. A steel flat thermocouple was placed in the aisle between the second and the third racks, a few centimetres from the ceiling, such as the thermocouple 10 in test 5.3. For each rack, the corresponding fire was placed in the middle of the compartment at the base. In particular, the fire of the second shelf was modelled by the red HRR curve (Figure 5a) which starts at 0:00 (already considers vertical propagation). As regards the lateral racks, the fire of the third, first and fourth racks were modelled using the HRR curve (Figure 4b) applied at 129, 130 and 150 seconds respectively, as defined in report [18].

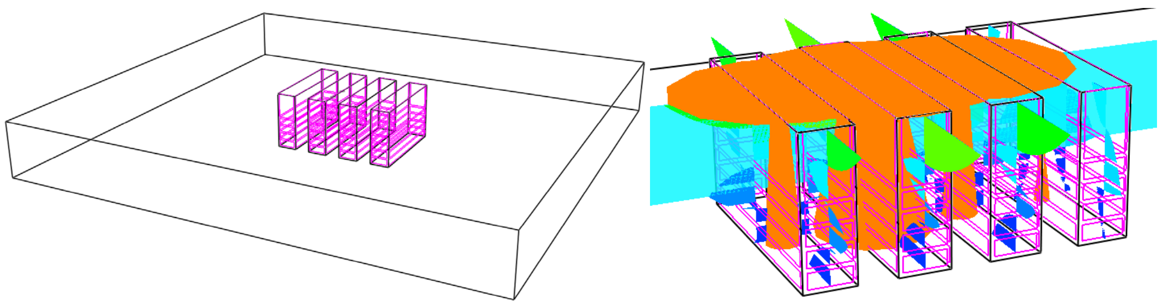

Figure 5 Cfast model of the 5.3 test

In following Figure 6 it is possible to see the comparison between the experimental results and the numerical ones, in terms of temperature distribution recorded by the thermocouple, in particular the temperature calculated with CFAST is, in terms of maximum temperature, coherent with the one recorded experimentally. The pre-peak phase is not too different while the next cooling phase is very different: Fast cooling occurs in the CFAST reconstruction, while the experimental test does not show a sharp drop in temperature, but on the contrary slow cooling extends over at least eight minutes. This different behavior of the cooling phase led us to assume that not all the thermal power expressed by the input RHR curve has actually been used,

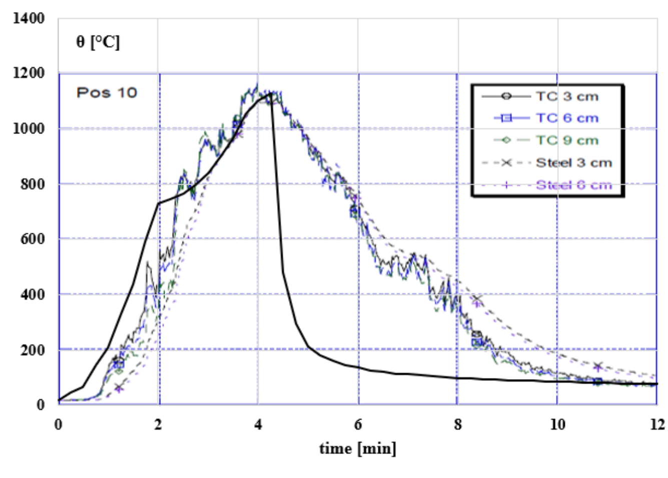

Figure 6 comparison between numerical and experimental results

From the previous figure it can be seen that the temperature calculated in CFAST is, regards the maximum temperature, coherent with the one recorded experimentally in the test. Moreover, the heating phase is not too different, unlike the cooling phase, which is faster in the numerical model. This different behaviour of the cooling phase could be caused by the fact that not all the thermal power expressed by the input RHR curve has actually been used.

After the validation of the fire model, it was possible to analyse the structure showed in Figure 3. In order to obtain a HRR curve in real scale, it was necessary to modify the HRR curves of the model scale test. The new HRR curves were obtained by using the *Froude scale factors* presented in [21] by Y. Z. Li and H. Ingason modelled ad hoc on cellulosic material fires that develop in steel racks structures. These coefficients can be used for scaling the parameters that define a fire in terms of HRH value, volumetric flow, propagation speed, time, energy released, mass and temperature, in relation to the geometric ratio between the full-scale dimensions L_f (in real scale) and the model scale dimensions L_m (in reduced scale). In particular considering our case it was obtained a geometrical ratio equal to 11.76, which leads to different scale factor used for the time and the HRR values. While for the value of $t\alpha$ which is the time needed to reach a HRR of 1 MW it was used the Italian value for paper material equal to 150s. The HRR curve obtained is shown in the following figure.

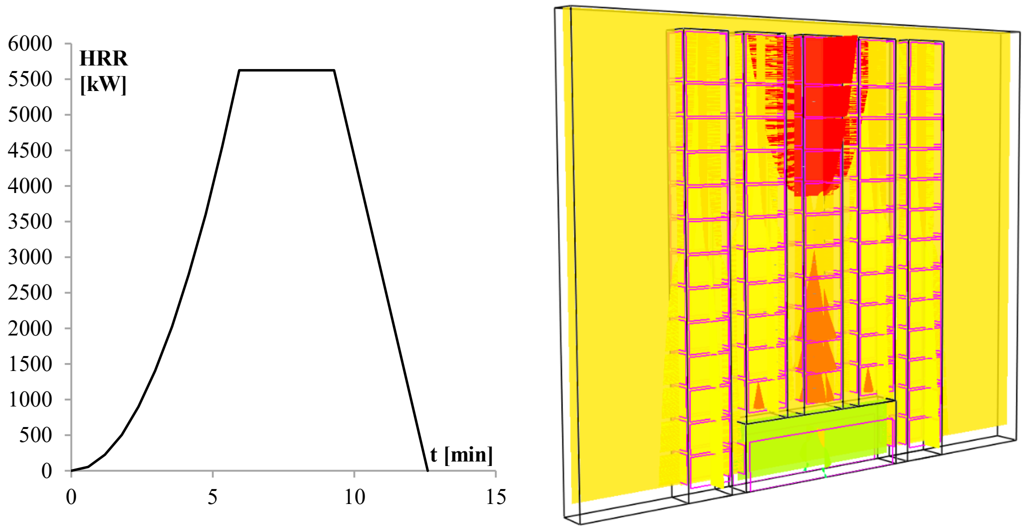

Figure 7 HRR curve and CFAST model

In order to model the vertical propagation, it was necessary first to validate the propagation times of test 5.3 in order to define a generalized model capable of being representative of the fires that develop along a vertical. It was found that these times are equal to the times the flame reaches the upper level of the racks (see Table 1), calculated by using the flame lengths L_f of a localised fire formula indicated in the EN1991-1-2 [5].

Table 1

Level	Experimental time	Calculated time
I	0	0
II	12	13
III	24	25
IV	32	38
V	38	50

Therefore, starting from this consideration, it was possible to calculate the vertical propagation times in our case, considering that the inter-axis distance of the load cell is 2, m, the ignition time is considered to be the time at which the flame height reaches this heigh and its multiples. For this reason, from the instant t=0s of ignition of the first load level, the vertical propagation times are: 107s for the II level, 244s for the II level, 368s for the IV level, 515s for the V level and finally 691s for the VI level.

Regarding the study of the horizontal fire propagation, a time delay between the ignition of the first shoulder and the ignition of the adjacent ones was evaluated, this is equal to 506 seconds, and it is the time required for the fuel stored in the adjacent load cells to reach a temperature of 230 ºC, that is the paper auto-ignition temperature.

After defining the HRR curve of the generic load cell and validating the vertical and horizontal propagation times of the fire through the different load levels, it was possible to carry out the thermo-fluid analysis. In CFAST, therefore, was modelled a first large compartment that represents the entire cross section considered. Inside it, other compartments were defined, representing the five central shoulders and a compartment related to the portal that is at the base, all the surfaces so defined were characterized by the thermal properties of the steel. The lateral shoulders were not modelled as a compartment because they were considered cold. Along the walls were defined the openings so that, net of openings, the compartment represents the metal structure of the rack, consisting of uprights and traverse beams, in this model. For the analysed fire scenario. In the following Figure 8 it is possible to see the temperatures distributions recorded by the thermocouples, for each element at the first four levels.

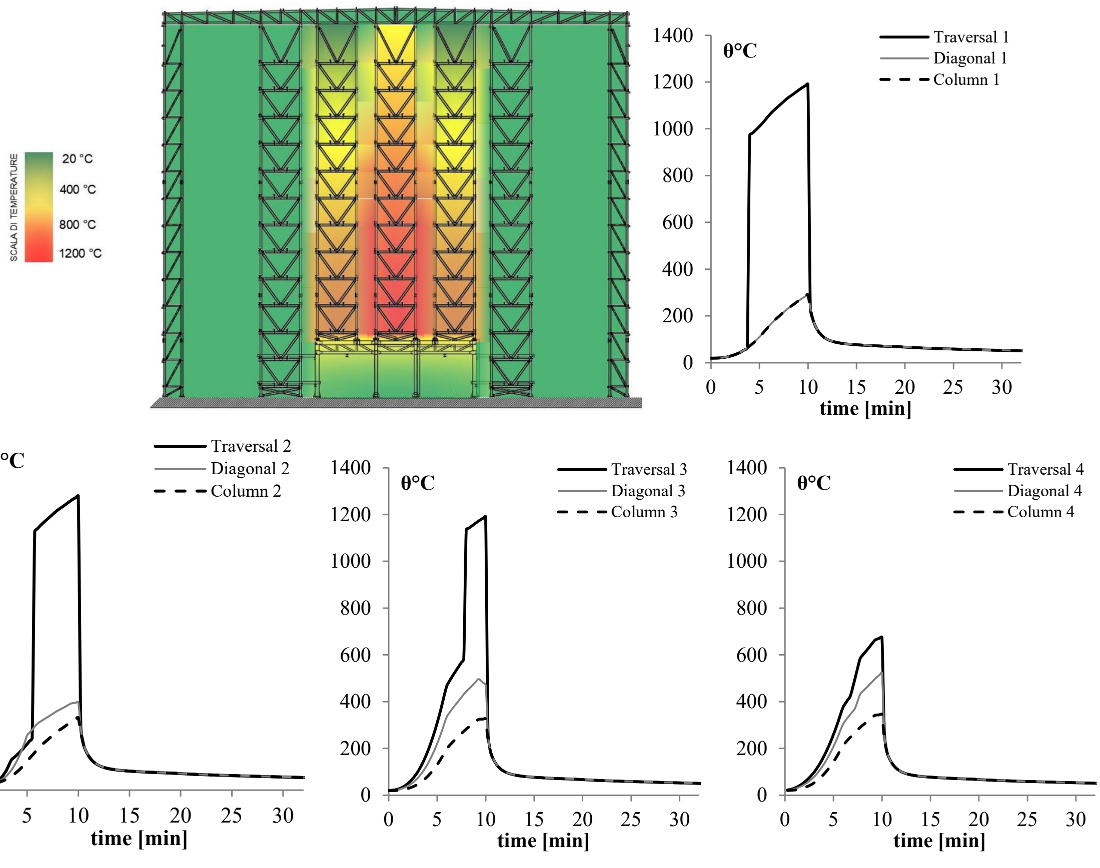

Figure 8 temperature distribution in the structure

3.2.2 *Thermo-mechanical analysis*

Therefore, by using the previous natural fire curves as input, it was possible to perform the thermo-mechanical analysis, which was carried out by using the SAFIR software [22]. The selected frame has been analysed in 3D space by allowing the out-of-plane displacements, the base restrains of the uprights were considered fixed with additional fixations provided by beams in the third direction. For correct modelling of Class 4 steel elements, by using *beam* elements, it has been needed assign a modified effective low that considers, the local instabilities that can occur in slender sections, proposed by Franssen J.M. et al [23]. The stress-strain relationship in compression is modified by a reduction of the proportionality limit, of the effective yield strength and of the strain corresponding to the beginning of the horizontal plateau. The elastic stiffness during unloading after first plasticisation in compression is also reduced according to a damage model in order to take into account the plastic deformation of the plate. The level of reduction depends on the slenderness of each plate that makes the section and the conditions at the edge of the plate.

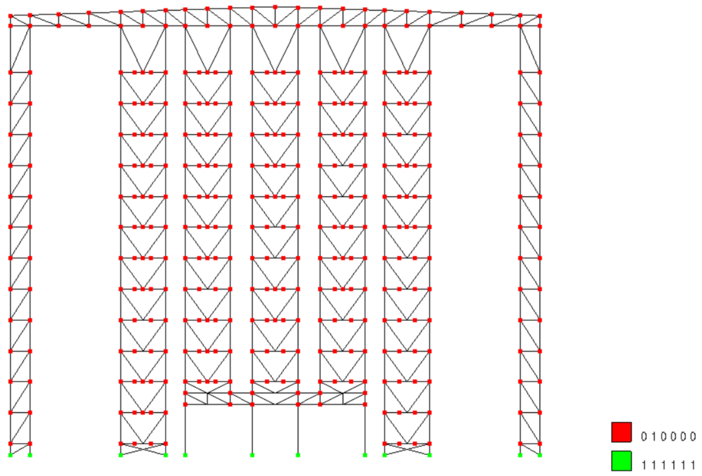

Figure 9 structural model

In this fire scenario, the critical element that leads to the collapse of the structure at a time t = 366 s is the traverse beam belonging to the first load level of the third shoulder, as well as the element most affected by the fire. Which is a coupled C section 150x150x15mm and 2mm thickness. In Figure 10a is possible to see the temperature distribution in the cross section, and it is possible to observe that in this case the flange and lip have a little temperature difference compared to the web one. Therefore, in order to assess the beam collapse in terms of resistance axial force in compression, it was necessary to consider this non-uniform temperature distribution, combined with the assessment of the effective width to consider the local instability, the reduced thickness to consider the distortional one and the assessment of χ coefficient to consider the global instability in compression. Figure 10b shows the comparison between the normal stress in compression and the resistance one calculated with both methods, explained before.

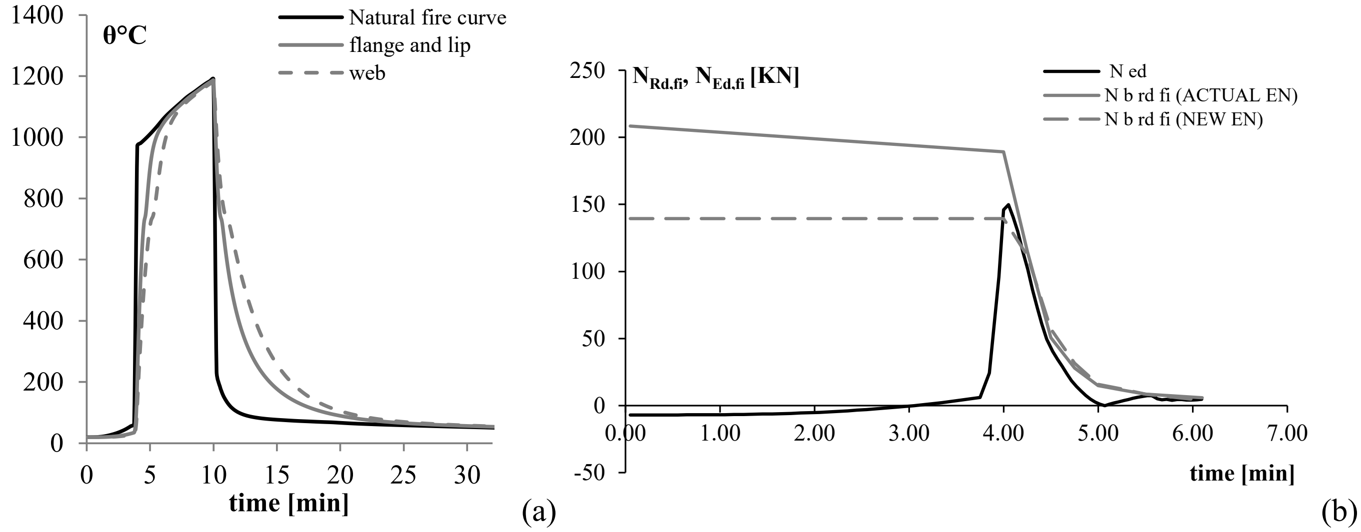

Figure 10 temperature distribution (a) comparison between stress and resistance (b)

This comparison confirms that the critical element is this traverse beam, in particular, we see how it is necessary to consider the non-uniform temperature distribution, but that the capacity method that best provides the capacity of the section seems to be the current Eurocode one and not the new one that would underestimate the resistance.

On the basis of the common mechanical model, presented before, the mechanical analysis of the substructure was carried out by considering the nominal fire curve ISO834. In this fire scenario, the critical element that leads to the collapse of the structure at a time t = 748 seconds is the upright of the central fifth shoulder of the sixth load level, which is an hot-rolled tubular section 150x150x3, which have an uniform temperature distribution, and for this reason to calculate the resistance axial force in compression in this case it was necessary only considering the effective width to consider the local instability, the reduced thickness to consider the distortional one and the assessment of χ coefficient to consider the global instability in compression. Figure 11b shows the comparison between the normal stress in compression and the resistance one calculated with both methods, explained before.

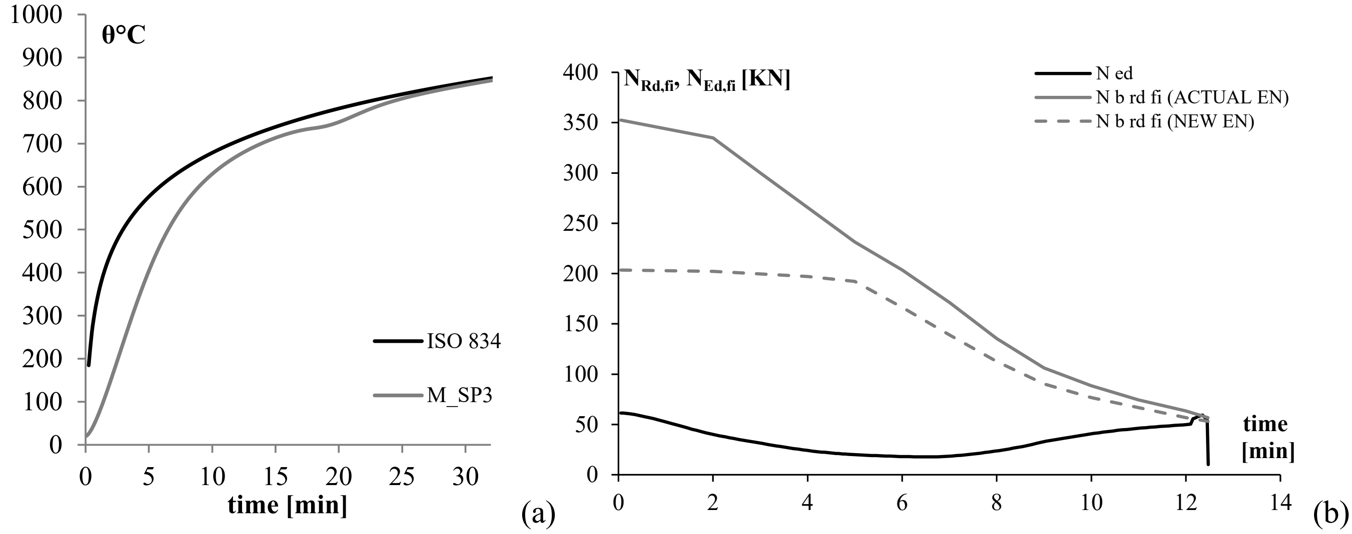

Figure 11 temperature distribution (a) comparison between stress and resistance (b)

This comparison confirms that the critical element is this traverse beam, in particular, we see how it is necessary to consider the non-uniform temperature distribution, but also in this case, the capacity method that best provides the capacity of the section seems to be the current Eurocode one and not the new one that would underestimate the resistance by anticipate the collapse around the second 730.

4 CONCLUSIONS

The peculiarity of these structures make them a topic of great interest both for the scientific community and for the manufacturers of industrial racks; After a deep study of the state of art and the study of the structural typology, a fire model that allows us to consider the vertical and horizontal propagation starting from a localized fire was modelled. This fire is confirmed to be very heavy for these structures being made with thin profiles bent cold, making them subject to all types of instability e.g. local, distortive and global. Regarding the methods of fire verification of these structures, it was pointed out how important and necessary it is for this type of structure, not only to carry out analyses according to advanced methods, but also to refine them as much as possible, for example, in the field of non-uniform temperature distribution for the study of instability phenomena. A mechanical finite element model has been created using the Safir 2019 software that allows modelling of these elements even if of class 4 with beam elements, with a constitutive low validated on shell elements. The comparison between the standard ISO834 fire curve and the natural fire curve showed that, for the structures in question, the natural one is heavier reducing the collapse time. It was finally made a comparison between the capacity models that the regulations propose for these structural elements. In particular, it was observed that the method that best provides the capacity of the section seems to be that of the current Eurocode and not that of the new Eurocode that would understate the resistance.

REFERENCES

1. Bernuzzi C, Draskovic N, Simoncelli M. "European and United States approaches for steel storage pallet rack design". Part 2: practical applications. Thin walled Structures 97:321–341. (2015)
2. Kondratenko A., Kanyilmaz A., Castiglioni C.A., Morelli F., Kohrangi M., "Structural performance of automated multi-depth shuttle warehouses (AMSWs) under low-to-moderate seismic actions". Bulletin of Earthquake Engineering (2022) 20:1247–1295
3. EN 15512 (2009) Steel static storage systems—Adjustable pallet racking systems—Principles for structural design.
4. EN 16681 (2016) Steel static storage systems—Adjustable pallet racking systems—Principles for seismic design.
5. EN 1993-1-1: Eurocode 3: Design of steel structures. General rules and rules for buildings. Brussels (Belgium): European Committee for Standardization; (2004).
6. Laíma L., Rodrigues J.P.C. "Fire design methodologies for cold-formed steel beams made with open and closed cross-sections". Engineering Structures 171 (2018) 759–778 Contents
7. EN 1993-1-5: Eurocode 3: Design of steel structures - Part 1-5: General rules - Plated structural elements, (2006).
8. EN 1993-1-2, Eurocode 3: Design of steel structures - Part 1-2: General rules -Structural fire design, (2005).
9. EN 1993-1-3: Eurocode 3: Design of steel structures - Part 1-3: General rules - Supplementary rules for cold-formed members and sheeting, (2006).
10. Kankanamge ND, Mahendran M. Behaviour and design of cold-formed steel beams subject to lateral–torsional buckling. Thin-Wall Struct 2012;61:213–28
11. AS/NZS 4600. Cold-formed steel structures. Sydney Australian/New Zealand Standard Australia; (2005).
12. Baleshan B, Mahendran M. Fire design rules to predict the moment capacities of thin-walled floor joists subject to non-uniform temperature distributions. Thin-Wall Struct 2016;105:29–43. (2016)
13. Couto, C. et al. 'Effective width method to account for the local buckling of steel thin plates at elevated temperatures', Thin-Walled Structures, 84. (2014)
14. Couto, C. et al. 'Resistance of steel cross-sections with local buckling at elevated temperatures', Journal of Constructional Steel Research, 109, pp. 101–114. (2015)
15. Caprili S., Morelli F., Salvatore W. and Natali A., "Design and Analysis of Automated Rack Supported Warehouses", The Open Civil Engineering Journal, (2018), 12, 150-166
16. D.M. 3 agosto 2015 "Approvazione di norme tecniche di prevenzione incendi, ai sensi dell'articolo 15 del decreto legislativo 8 marzo 2006, n. 139", GU n. 192 del 20/8/2015 – S.O. n. 51.
17. de Silva, D., Bilotta, A., Nigro, E. Approach for modelling thermal properties of intumescent coating applied on steel members. Fire Safety Journal, (2020), 116, 103200
18. P. Cancelliere, D. de Silva, A. Marino, E. Nigro, L. Possidente, P. Princi, S. Pustorino, N. Tondini. (2021) "Impiego di un impianto a disponibilità superiore nel progetto delle prestazioni di resistenza al fuoco di strutture di acciaio". Fondazione Promozione Acciaio, Redazione: giugno 2021.
19. Lönnermark A., Ingason H. Fire Spread in Large Industrial Premises and Warehouses. BRANDFORSK project 630-021. (2005)
20. Jones W., Forney G., Peacock, R. and Reneke, P. 2003. A Technical Reference for CFAST: An Engineering Tool for Estimating Fire and Smoke Transport, Technical Note (NIST TN), National Institute of Standards and Technolo-gy,Gaithersburg,MD, May 2, (2022).
21. Ying Zhen Li, Haukur Ingason .Scaling of wood pallet fires - SP Technical Research Institute of Sweden SP Report 2014:57, (2014).
22. Franssen, J.M., Gernay, T. (2017), Modeling structures in fire with SAFIR®: Theoretical background and capabilities, Journal of Structural Fire Engineering, 8(3):300-323.
23. Franssen J.M., Cowez B, Gernay T. (2014). Effective stress method to be used in beam finite elements to take local instabilities into account. Fire safety science-proceedings of the eleventh international symposium pp. 544-557

POST-FIRE TENSILE BEHAVIOR OF HOLE-ANCHORED BOLTS BOLTED T-STUB CONNECTION

Peijun Wang[1], Yang You[2], Mei liu[3], Fangzhou Liu[4], Wenchao Zhang[5]

ABSTRACT

A test was designed and conducted to investigate the post-fire tensile behavior of the novel Hole-anchored Bolt (HB) bolted T-stub connection. The HB was anchored by the bolt hole with internal threads, for which the HB could be installed from one-side and is very suitable for the installation of the closed-section steel component. The full-period test method was used to consider the influence of load level and the fire temperature on the residual mechanical behavior of the HB bolted connection, including the failure mode, the failure stage, and the resistance. The diameter of the HB and the thickness of the bolt hole decided the failure mode of the connection. Fire temperature and the load level had little influence on the failure mode but had obvious impact on the failure stage of the connection. The T-stubs that not fail in fire still have good load carrying capacity after cooling down. The un-failed T-stubs could recover at least 87.1% of their yielding load and 80.9% of their ultimate load under post-fire circumstances.

Keywords: Hole-anchored Bolt; Tensile behavior; Bolted T-stub; Post-fire

1 INTRODUCTION

The blind bolt is the bolt that could be anchored by itself and need no nut to provide anchorage to the bolt. The self-anchored property made the blind bolt very suitable for the connection of steel components with closed sections. Many researchers focused on the behavior of different kinds of novel blind bolted connections recently.

Wan et al. [1] researched the performance of Obround-head blind bolt. This kind of blind bolt patches an obround bolt hole. Before going into the blind end the obround head and the obround bolt hole kept in same direction. And after the bolt head going into the blind end rotate bolt shank to let the bolt head overlap the bolt hole to anchor the bole in the blind end. Result showed that the best length-width ratio of the obround bolt head is 1.7 to control the slippage of the bolt and the stress concentration near the bolt hole. Wang et al. [2] studied the behavior of the Hollo Bolt that is a kind of blind anchored by deformable sleeve by both experimental and numerical methods. Methods for predicting the resistance and initial stiffness of Hollo Bolt bolted connections were given.

Fire is a serve threat to the safety of building structures for the high temperature could decrease the property of building material and the bearing resistance of structural components. Full understanding of the deteriorating law of different structural components is an essential precondition for reasonable design of building structures. Many researchers focused on the fire behavior of blind bolted connections already. Tao [3] et al. conducted tests to acquire the strength of Hollo Bolt at different temperatures. Tensile strength

[1] Professor, School of Civil Engineering, Shandong university.
e-mail: pjwang@sdu.edu.cn
[2] Lecturer, School of Transportation and Civil Engineering, Shandong Jiaotong University
e-mail: 574948117@qq.com, ORCID: https://orcid.org/0000-0002-8111-7766
[3] Associate Professor, Scho ol of Civil Engineering, Shandong university.
e-mail: liumei@sdu.edu.cn
[4] Postdoctoral, School of Civil Engineering, Shandong university.
e-mail: lfzseven@126.com
[5] Associate Professor, School of Civil Engineering, Shandong university.
e-mail: 770946569@qq.com
https://doi.org/10.6084/m9.figshare.22215781

and shear strength all decreased quickly when the temperature exceed 400°C. Song [4][5] et al. conducted full-scale tests on Hollo Bolt bolted composite beam to concrete-filled column connections. Test result showed that the load ratio of the beam and the fire protection measure had a great influence on the fire performance of the connection.

Despite the high frequency of fires, most of the happened fires can be extinguished timely and do not cause mortal damage to the building due to complete firefighting efforts. The buildings that are less affected by the fire can be quickly re-used after necessary repair. Therefore, it is necessary to study the residual mechanical properties of different structures after cooling from fire, to provide a basis for the reuse of buildings after the fire.

Other than the blind bolts mentioned above, there is another way to achieve one-side installation of the bolt. The bolt could be anchored by the threads on the bolt hole, as shown in F1, which is called the Hole-anchored Bolt (HB). The HB need not special installation tools and could use the standard bolt directly, for which the HB has the advantages of low-cost and quick installation compared to other kinds of blind bolt.

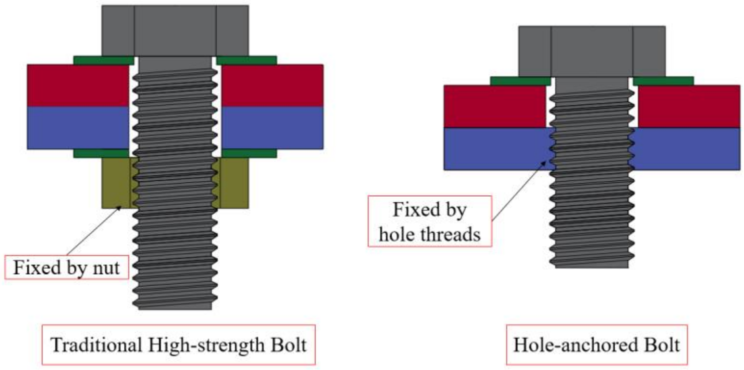

Figure 1. Schematic diagram of the anchorage mechanism of HB

You [6] and Wang et al. [7] tested the tensile behavior of HB bolted connections by using the T-stub model. Typical failure mode of HB bolted T-stub were presented. Thickness of the threaded bolt had a great influence on the behavior of the HB bolted T-stub. The welded backing plate could improve the tensile performance of HB significantly. The HB bolted T-stub strengthened by the backing plate could comparable to the standard bolt connected T-stub at both ambient and high temperatures. Wang et al. [8] also studied the shear behavior of the HB bolt lap connections at different temperatures. The shear resistance of HB bolted lap connection was similar to the lap connection bolted by standard bolt with the same configuration at the same temperature.

To date, there are few published papers that focus on the post-fire behavior of HB bolted connection. Test was carried out to investigate the tensile behavior of HB bolted connection after cooling from fire to provide the reference for engineering application of this kind of novel HB. The full-period test method was used in test to simulate the whole progress of a real fire. Key parameters including the HB diameter, threaded bolt hole thickness, load ratio and the suffered temperature to the residual tensile behavior of the HB, including the failure mode, failure stage, the yielding load and the ductility, were studied.

2 TEST DESIGN

2.1 Paper title, authors and affiliation Test specimen

For the limitation of the test condition, the simplified T-stub model was used to carry out the test. The T-stub model was simplified from the tension zone in an end-plate beam to column connection by the component method and was widely used in the research on different kinds of bolted connections. The specimens in the test consisted of two different T-stubs and two HBs, as shown in F2. The upper T-stub was a rigid base T-stub with normal bolt holes without internal threads. The diameter of the bolt hole of the base T-stub was 1-2mm larger than the diameter of HBs. The bolt of the lower T-stub was threaded bolt hole which provided the anchorage to the HBs. The diameter of the threaded bolt holes on the lower T-stub was the same with the diameter of the HBs. The HBs used the standard high strength bolt with a hexagonal head [9]. The thickness of the flange of lower T-stub t_b and the HB diameter D ranged in different groups, as listed in T1.

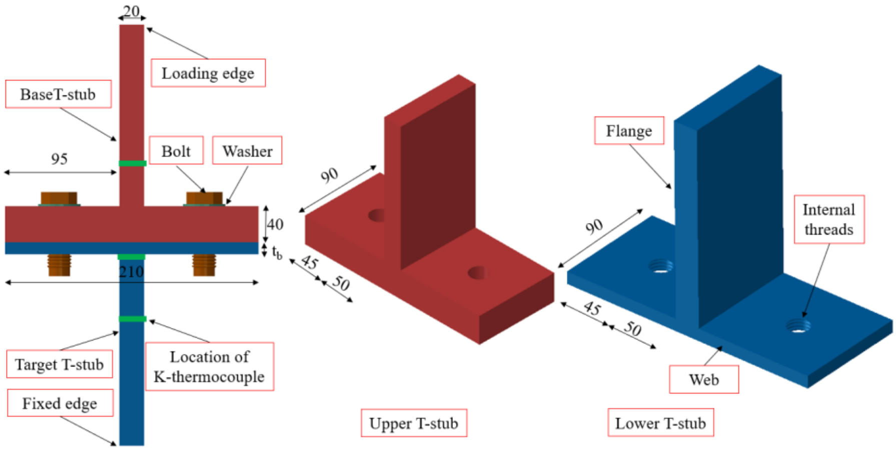

Figure 2. The test specimens in test.

Table 1. The specimens in test.

Group	Specimen	HB diameter D/mm	Bolt holt thickness t_b/mm	Applied load F_μ/kN	Load ratio μ	Suffered temperature /°C
G1	B10-P18-0-20	10	18			20
	B10-P18-0.5-500	10	18	40.5	0.5	500
	B10-P18-0.5-700	10	18	40.5	0.5	700
	B10-P18-0.25-500	10	18	20.3	0.25	500
	B10-P18-0.25-700	10	18	20.3	0.25	700
G2	B20-P06-0-20	20	6			20
	B20-P06-0.5-500	20	6	15.5	0.5	500
	B20-P06-0.5-700	20	6	15.5	0.5	700
	B20-P06-0.25-500	20	6	7.8	0.25	500
	B20-P06-0.25-700	20	6	7.8	0.25	700
G3	B20-P10-0-20	20	10			20
	B20-P10-0.5-500	20	10	40.0	0.5	500
	B20-P10-0.5-700	20	10	40.0	0.5	700
	B20-P10-0.25-500	20	10	20.0	0.25	500
	B20-P10-0.25-700	20	10	20.0	0.25	700
G4	B20-P18-0-20	20	18			20
	B20-P18-0.5-500	20	18	109.0	0.5	500
	B20-P18-0.5-700	20	18	109.0	0.5	700
	B20-P18-0.25-500	20	18	54.5	0.25	500
	B20-P18-0.25-700	20	18	54.5	0.25	700

2.2 Paper size, margins and numbering Test set-up and loading procedure

The test in this paper was conducted in the Structural Laboratory of Shandong University. The whole test setup consisted of two parts, which were the loading system and the heating system, as shown in F3 The loading system was the computer-controlled universal testing machine WAW-1000C with a maximum 1000kN load capacity. The applied load and the displacement of the specimen could be controlled and recorded by the controlling computer. Another extensometer was used in the loading progress at ambient temperature to ensure the accuracy of the recorded deformation of the specimen. The heating progress was a customised electronic furnace which matched the testing machine. The furnace was supported by a movable brace and the furnace could move along the brace. There were reserved holes on the top face and bottom face on the electronic furnace, which could help the end of the specimen across the furnace, as shown in F2 (b). The controlling box and the furnace were connected by three thermocouples. Measure points of the thermocouples were shown in F2. The heating progress inside the furnace could be controlled and recorded by the controlling box and the average temperature of the three thermocouples was taken as the instant temperature inside the furnace. The real heating progress in test was shown in F4 (a).

The specimens were tested at ambient temperature firstly to acquire their basic result including the failure mode, the yielding load F_Y and the ultimate load F_U. The ambient test result was then used as a reference to carried out the post-fire test.

The post-fire test used the full-period method to simulate the whole progress of a real fire from happening to extinguishing. The test progress included three stages and could be illustrated by F4 (b). In stage 1, the specimen was loaded to specified load F_μ at ambient temperature by the speed of 2mm/min and kept the F_μ unchanged. In stage 2, the F_μ still kept unchanged, and at the same time the specimen was heated to specified high temperature and then naturally cooled to ambient temperature as the progress shown in F4 (a). Stage 2 represented the connection in a real structure that suffered a fire while still sustained the load. The value of the applied constant load F_μ was determined by the load ratio μ, which was the ratio of the applied constant load F_μ and the yielding load F_Y of the specimen acquired from ambient test. In stage 3 the specimen was reloaded to failure directly from the constant load F_μ at speed of 2mm/min if the specimen not failed in stage 2. Stage 2 could present the residual performance of the HB bolted connection after cooling from fire.

F5 (a) shows the load-displacement curve in the ambient temperature test. The curve shows no obvious yielding point, for which the tangent line method is used to define the yielding point of the curve. F5 (b) shows the load-displacement curve in the post-fire test. Corresponding to the test progress, the curve could be divided into three stages. In stage 1, the specimen is in elastic state and the force increases linearly with the displacement. In stage 2, the displacement increases obviously and then decreases slightly for the combination influence of the change of temperature and the constant load F_μ. In stage 3 the curve shows nonlinearity and the tangent line method is used to define the yielding load F_Y, as shown in F5 (b).

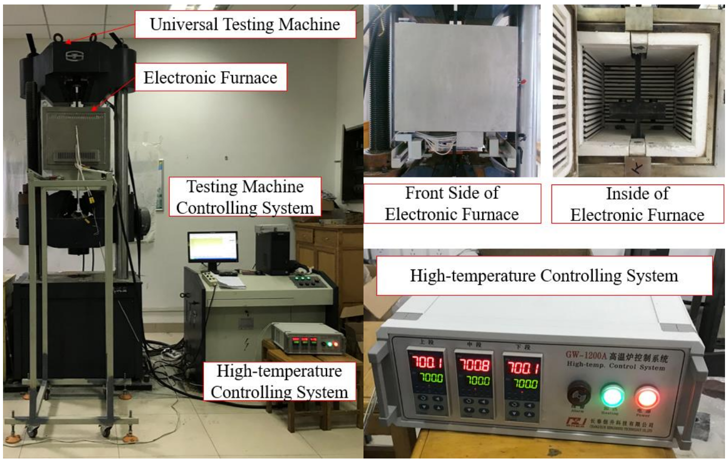

(a) The test set-ups (b) The electronic furnace and the controlling box
Figure 3. Test set-ups.

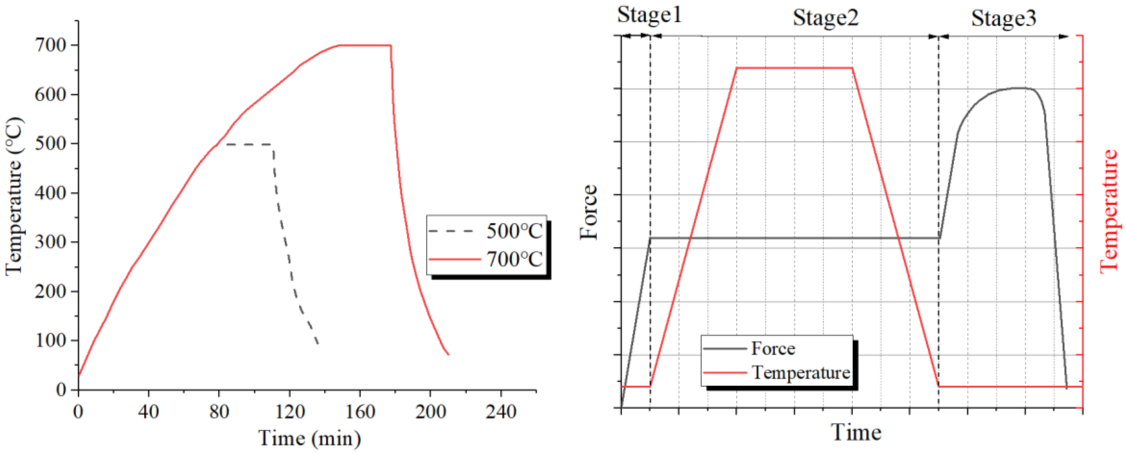

(a) The temperature change progress recorded in test (b) The loading progress in test
Figure 4. Test progress and the recorded temperature changing progress.

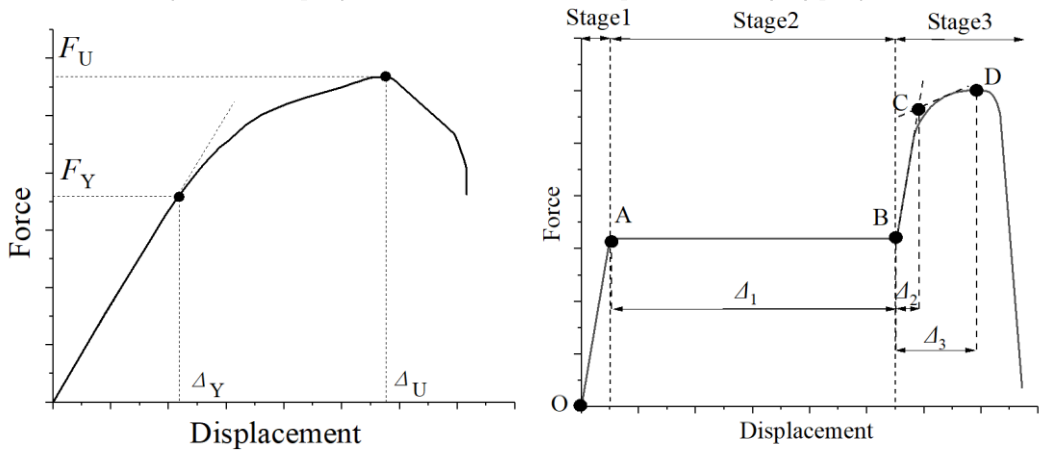

(a) Ambient temperature test (b) Post-fire test
Figure 5. The load-displacement curve in test.

3 TEST RESULT

3.1 Failure mode

The test results of the ambient temperature test and the post-fire test were summarised in T2, including the failure mode, the yielding load, and the ultimate load of different specimens.

The failure mode of the HB bolted T-stub connections could be divided into three types: yielding of the T-stub flange (mode 1), yielding of the T-stub flange accompanied with bolt failure (mode 2), the bolt failure (mode 3).

The flange thickness of the T-stub of the specimens in the S1 group, which was equal to the bolt hole thickness, was only 6mm. In the ambient temperature test, the specimen in the S1 group failed by mode 1, the yielding of the T-stub flange, as shown in F6 (a). The flange of the T-stub deformed severely with the increase of the applied load. The hole threads separated with the bolt for the deformation of the T-stub flange, which finally caused the failure of the specimen. In the post-fire test, the failure mode of the T-stub was still failure mode 1, which was the same as the ambient temperature test. F6 (b) shows the failure mode of the T-stub in the S1 group in the post-fire test (θ=500°C, μ=0.25). In stage 1, the specimen was in elastic stage and there was no obvious deformation. In stage 2, uncoverable plastic deformation occurred in the flange of the T-stub under the combination of high temperature and constant load F_μ. But the specimens still not failed and the constant load F_μ could still be sustained. In stage 3, the deformation of the T-stub flange continued to increase with the reloading progress. The HBs separated from the threaded bolt hole finally when the deformation was large enough, which caused the failure of the T-stub. Failure mode of other specimens in S1 group was also mode 1, as summarized in T2. Although the failure mode of the specimen not change in post-fire test, the failure stage might change with the change of test condition. In the test whose fire temperature was 700℃ and load ratio was 0.5, the specimen failed in stage 2 directly, which indicated that the test condition had a certain influence on the failure stage of the HB bolted T-stub.

Flange thickness of the specimens in S2 group was 10mm, which was larger than that of S1 group. Failure mode of specimen in S2 group at ambient temperature test was failure mode 1, which was same with S1 group, as shown in F7 (a). In the post-fire test, failure mode of specimens in S2 group at different test condition did not change, as shown in F7 (a). But the specimen in S2 group had better fire resistance capacity for larger flange thickness. None of the specimen in S2 group failed in stage 2 previously at any test condition, as shown in T2.

Flange thickness of the specimens in S3 group was 10mm. In ambient temperature test, the specimen failed by mode 2, yielding of the T-stub flange accompanied with bolt failure, as shown in F8 (a). Deformation occurred on the T-stub flange firstly, but the deformation would not lead to the pull-out of the HBs. With the further increase of the load, the bolt reached their ultimate strength and fractured, which caused the failure of the whole specimen. In post-fire test, failure mode of the specimen in S3 group not change, as shown in F8 (b). All the specimens failed by mode 2 in post-fire test. Change in fire temperature θ and load ratio μ will not change the failure mode but might change the failure stage. In the θ=700℃, μ=0.5 post-fire test, the specimen failed in stage 2 previously, as listed in T2.

Bolt diameter and flange thickness of specimens in S3 group was 10mm and 18mm, respectively. In ambient temperature test, the specimens failed by mode 3, the bolt failure. The bolt fractured abruptly without obvious T-stub flange deformation in test, which was typical fragile failure, as shown in F9 (a). Failure mode of the specimen did not change in post-fire test, as shown in F9 (b). But the fire temperature θ and load ratio μ had more obvious influence on the failure stage on the specimen in S3 group. In the θ=700℃, μ=0.25 post-fire test, only the specimen in S3 group failed in stage 2, as shown in T2.

The test result showed the HB bolted T-stub connection had a stable tensile performance in both before and post-fire circumstances. The failure mode of the T-stub was decided by dimension parameters including the flange thickness and the bolt diameter. Increase in the fire temperature θ and load ratio μ might make the specimen fail previously in fire. The failure stage of the T-stub whose failure mode was bolt failure was more sensitive to the change of fire temperature θ and load ratio μ.

(a) Ambient temperature test (b) Post-fire test (θ=500℃, μ=0.25)
Figure 6. Phenomenon of the specimens in S1 group.

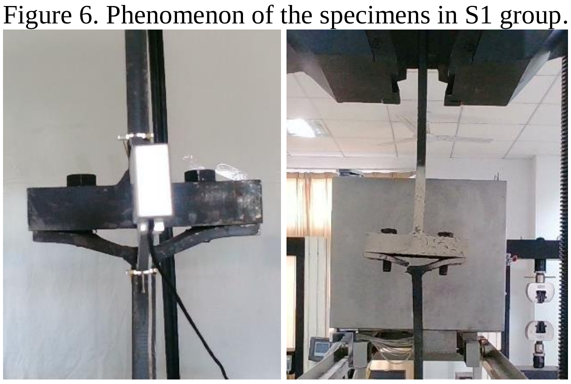

(a) Ambient temperature test (b) Post-fire test (θ=500℃, μ=0.25)
Figure 7. Phenomenon of the specimens in S2 group.

(a) Ambient temperature test (b) Post-fire test (θ=500℃, μ=0.25)
Figure 8. Phenomenon of the specimens in S3 group.

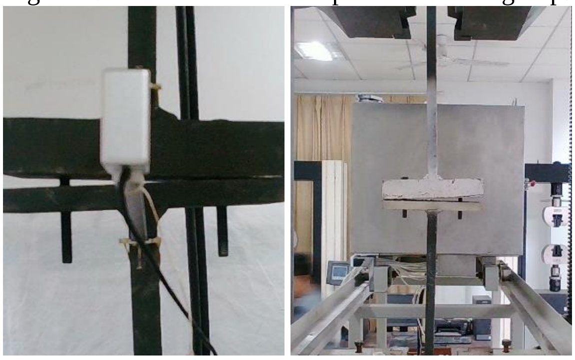

(a) Ambient temperature test (b) Post-fire test (θ=500℃, μ=0.25)
Figure 9. Phenomenon of the specimens in S4 group.

Table 2. Summary of the test result.

Group	Failure mode	Ambienr yielding load F_Y/kN	Ambient utimate load F_U/kN	Temperature θ/℃	Load ratio μ	Applied load F_μ/kN	Failre stage	Failure mode	Residual yielding load $F_{Y,R}$/kN	$F_{Y,R}/F_Y$	Residual ultimate load $F_{U,R}$/kN	$F_{U,R}/F_U$
S1	mode1	31.0	64.0	500	0.25		stage3	mode1	29.3	94.5%	58.2	91%
				700	0.25		stage3	mode1	28.8	92.9%	54.2	84.7%
				500	0.5		stage3	mode1	29.8	96.1%	51.9	81%
				700	0.5		stage2	mode1	-	-	15.9	-
S2	mode1	80.1	98.0	500	0.25		stage3	mode1	72.7	90.9%	89.9	91.7%
				700	0.25		stage3	mode1	73.7	92.1%	94.4	96.3%
				500	0.5		stage3	mode1	74.6	93.3%	96.3	98.3%
				700	0.5		stage3	mode1	78.1	97.6%	98.9	100.9%
S3	mode2	218.2	262.3	500	0.25		stage3	mode2	196.5	90.1%	256.2	97.8%
				700	0.25		stage3	mode2	194.1	89.0%	259.2	98.9%
				500	0.5		stage3	mode2	189.9	87.1%	258.1	98.5%
				700	0.5		stage2	mode2	-	-	109.7	-
S4	mode3	81.5	101.3	500	0.25		stage3	mode3	74.2	88.1%	84.2	83.4%
				700	0.25		stage2	mode3	-	-	20.6	-
				500	0.5		stage3	mode3	71.4	88.1%	81.7	80.9%
				700	0.5		stage2	mode3	-	-	41.0	-

3.2 Load-displacement curve

The load-displacement curves of the specimens in the S1 to S4 group are shown in F10 to F13, respectively. And the resistance of different groups is summarized in T2.

F10 (a) and (b) compares the load-displacement curves of specimens in S1 group. Comparison shows that the stiffness and the resistance of the specimens decreased after cooling from fire. The decrease also influenced by the fire temperature θ and load ratio μ. In the θ=500℃, μ=0.25 post-fire test, the residual yielding load $F_{Y,R}$, and the residual ultimate load $F_{U,R}$ was 94.5% and 91% of that at ambient temperature, respectively. And in the θ=700°C, μ=0.25 post-fire test, the residual yielding load $F_{Y,R}$, and the residual ultimate load $F_{U,R}$ further decreased to 94.5% and 91% of that at ambient temperature, respectively. And in the θ=700°C, μ=0.5 post-fire test, the specimen failed in stage 2 directly, and the load-displacement curve was platform shape, as shown in F10 (b). The HB bolted T-stubs showed good tensile resistance in post-fire circumstances if not failed in the fire stage.

The comparison of the load-displacement curves in F11 to F13 also shows the stiffness and resistance of the specimens in the S2, S3, and S4 groups decreased after cooling from fire compared to ambient temperature. An increase in the fire temperature θ and load ratio μ will further decrease the stiffness and the resistance of the specimen. Failure mode of the specimen also influenced the post-fire behavior of HB bolted T-stub. Specimens in S2 group all failed by mode 1, yielding of the T-stub flange. Ratio of the ultimate load F_U and the yielding load F_Y (F_Y/F_U) of specimen in S2 group at ambient temperature was larger than that of the specimen in other groups, for which the specimen in S2 group had better fire-resistance capacity than other specimen in other groups. In the θ=700°C, μ=0.5 post-fire test, only the specimen in S2 group not failed in stage 2 previously, as shown in T2. Similarly, the specimens in S4 group all failed by mode 3, the bolt failure. The ratio of F_Y/F_U of the specimens in S4 group at ambient temperature was smaller than that of the specimen in other groups, for which the fire resistance of the specimens in S4 group was worse than that of the specimen in other groups. In the θ=700°C, μ=0.25 post-fire test, only the specimens in the S4 group failed in stage 2 previously, as shown in T2. In general, the HB bolted T-stub still showed good tensile behavior after cooling from high temperature. The T-stubs that have not failed previously in stage 2 could recover at least 87.1% of their yielding load F_Y and 80.9% of their ultimate load F_U at ambient temperature, as listed in T2.

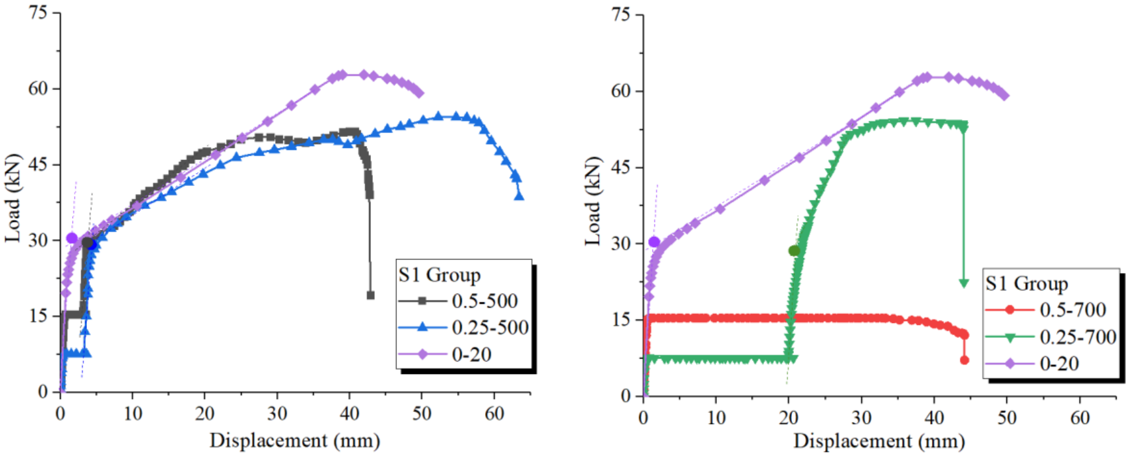

(a) θ=500°C (b) θ=700°C

Figure 10. Load-displacement curves of the specimens in S1 group.

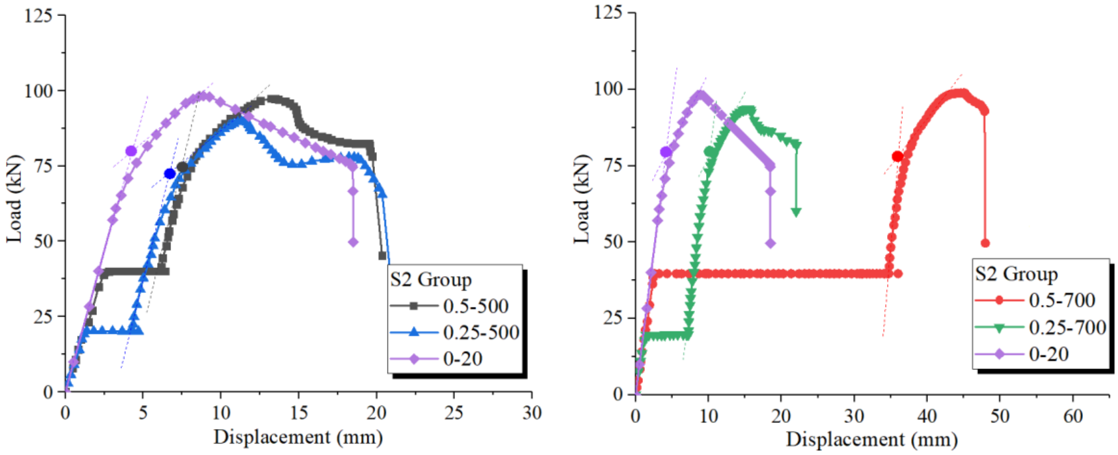

(a) θ=500°C (b) θ=700°C

Figure 11. Load-displacement curves of the specimens in S2 group.

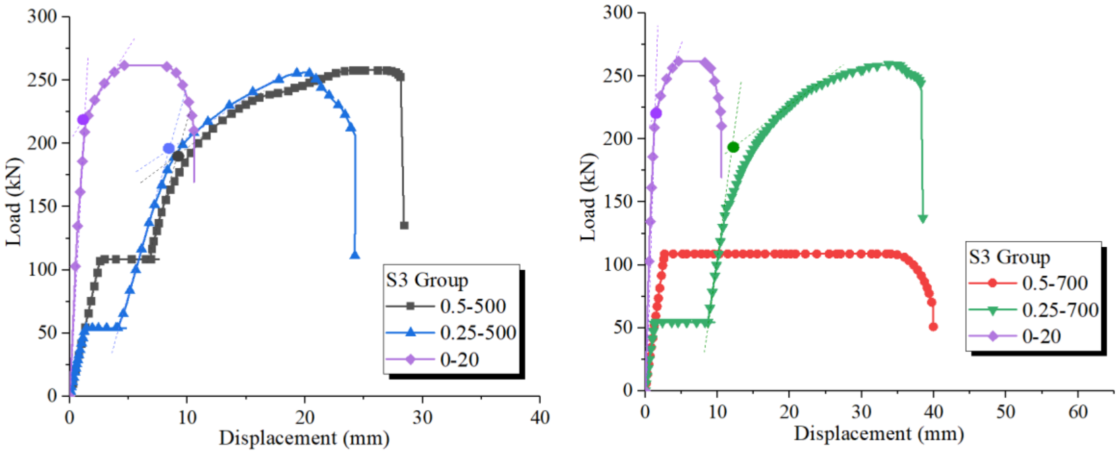

(a) θ=500℃ (b) θ=700℃

Figure 12. Load-displacement curves of the specimens in S3 group.

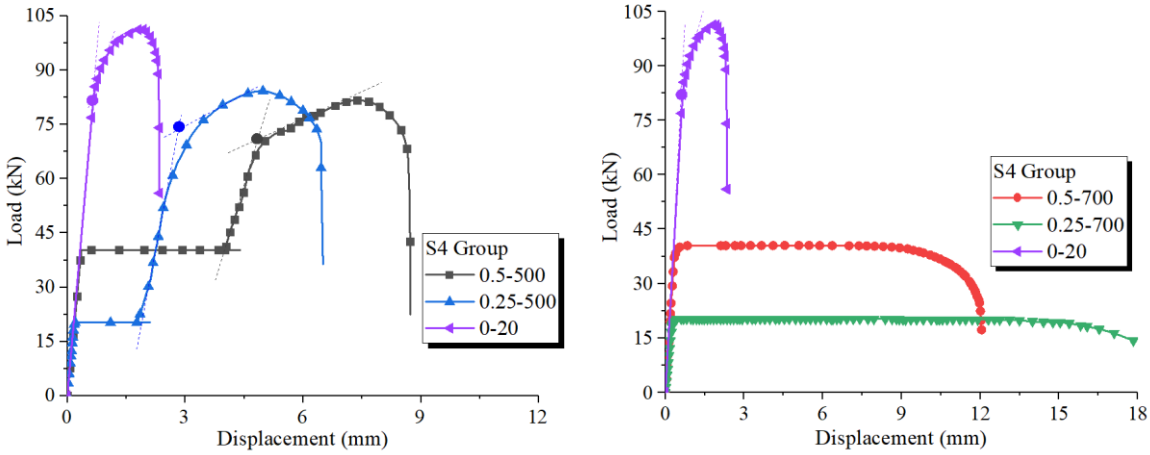

(a) θ=500℃ (b) θ=700℃

Figure 13. Load-displacement curves of the specimens in S4 group.

4 DISSCUSSION ON PARAMETERS

4.1 Dimension of the T-stub connection

HB bolted T-stub connections with different bolt diameter and flange thickness were tested in different conditions and the influence of these parameters on the behavior of the T-stub could be analysed.

Thickness of T-stub flange decides the depth of the threaded bolt hole and the out-of-plane stiffness. Bolt diameter decides the tensile resistance of bolt. The relative relationship between the flange thickness and the bolt diameter decides the failure mode of the HB bolted T-stub. When the bolt diameter is large and the thickness of the T-stub flange is small, the bending resistance of the T-stub flange is small and the T-stub flange would deform severely, which will lead the HB pulled out from the threaded bolt hole, such as the specimens in S1 group. When the bolt diameter is small and the flange thickness is large, there is no obvious deformation on the flange, and the bolt fractures abruptly, such as the specimens in S4 group. When the flange thickness matches the bolt diameter, the flange could deform fully and the tensile resistance of the bolt could be fully used, such as the specimens in S2 and S3 groups. Decrease in tensile resistance after cooling from high temperature of S2 group was smaller than that of other specimens, and the specimens in S2 group was much less likely to fail in stage 2 at same conditions, as shown in T2. Decrease in tensile resistance after cooling from the high temperature of the S2 group was smaller than that of other specimens, and the specimens in the S2 group were much less likely to fail in stage 2 under the same conditions, as shown in T2. Reasonable selection in flange thickness and bolt diameter could control the failure mode of the HB bolted T-stub connection and increase the fire-resistance capacity, which is very beneficial to decrease the possibility of the connection failing in fire directly and to re-use the connection after a fire.

4.2 Fire condition

The full-period test method, which means the specimen sustained constant load when exposed to high temperature, was used in test to simulate the real connection at fire. Different fire conditions were designed by the combination of different temperature θ and load ratio μ in test.

The test result showed the change in high temperature θ and load ratio μ will not change the failure mode of the specimen, but an increase in the high temperature θ and load ratio μ might make the specimen fail previously in the fire stage. At the same time, increase in the high temperature θ and load ratio μ will slightly decrease the residual resistance in the post-fire circumstance. But all the T-stubs could recover most of their resistance after cooling if not failed in the fire. The un-failed connection could at least recover 87.1% of its yielding load F_Y at ambient temperature and 80.9% of its ultimate load F_U at ambient temperature.

The influence of high temperature θ was more obvious than the load ratio μ. In the θ=500°C, μ=0.25 post-fire test, none of the T-stubs failed previously in stage 2. In the θ=500°C, μ=0.5 post-fire test, there was also no specimen failed in stage 2. When the test condition changed to θ=700°C, μ=0.25, the specimen in the S4 group failed previously in stage 2, as shown in T2. And in the θ=500°C, μ=0.5 post-fire test, specimens in the S1, S3, and S4 groups all failed in stage 2. These facts showed that controlling the fire scale or increasing the safety reserve could all improve the fire-resistance capacity.

The influence of high temperature θ and load ratio μ on different T-stubs with different failure mode was different. In the θ=700°C, μ=0.25 post-fire test, only specimen in S4 group failed in stage 2. And the decrease in load of specimen in S4 group was more obvious than other specimens after exposing to same fire conditions, as shown in T2. The reason was that the failure mode of S4 group specimen was bolt fracture. The bolt fractured abruptly without obvious deformation, which was typical brittle failure. The ratio of yielding load F_Y and ultimate load F_U was larger than the specimens in other specimens, for which the specimen in S4 group was closer to the ultimate load under same load ratio μ than the specimen in other groups. Controlling the failure mode of the HB bolted T-stub in design progress was important to avoid the pre-failure of the connection in fire stage and re-use of the connection after cooling.

5 CONCLUSIONS

A test on the post-fire tensile behavior of the novel HB bolted T-stub connections was carried out in this paper by the full-period methods and the main conclusions acquired from the test were summarized below:

(1) Three failure modes of the HB bolted T-stub connection were found in the test, which was the yielding of the flange, the yielding of the flange accompanied with the bolt fracture, and the bolt fracture. The failure mode of the HB bolted T-stub was decided by the thickness of the bolt hole and the diameter of the HB.

(2) The load ratio and the fire temperature had little influence on the failure mode of the HB bolted T-stub but had obvious influence on the failure stage of the T-stub. Increase of the load ratio or the fire temperature might make the T-stub fail in fire stage directly. The T-stub failed by the flange yielding accompanied with bolt failure showed better fire resistance capacity than the other T-stubs failed by other failure modes. And the T-stubs failed by the flange yielding accompanied with bolt failure, is least likely to fail in fire stage.

(3) Deformation of the T-stub in the fire stage increased with the elevation of the load ratio and the fire temperature. Deformation of the T-stub connection in the reloading stage after cooling down from fire fluctuated with the change of fire temperature and the load ratio.

(4) The residual load of the HB bolted T-stub was decided by the dimension of the connection, including the thickness of the bolt hole and the diameter of the HB diameter. The T-stubs could recover at least 87.1% of their yielding load and 80.9% of their ultimate load after cooling down, which showed the T-stub still had good carrying capacity in post-fire circumstances.

ACKNOWLEDGMENT

The authors wish to acknowledge supported by the National Natural Science Foundation of China (52078280).

REFERENCES

1. Wan Chuqi, Bai Yu, Ding Chenting, et al. Mechanical performance of novel steel one-sided bolted joints in shear [J]. Journal of Constructional Steel Research,2020,165:105815.
2. Z.Y. Wang, W. Tizani,Q.Y. Wang. Strength and initial stiffness of a blind-bolt connection based on the T-stub model [J]. Engineering Structures,2010,32(9): 2505-2517.
3. Tao Z, Song T Y, Razzazzadeh A. Tensile and shear behaviour of Hollo-Bolts at elevated temperatures[C]//Mechanics of Structures and Materials: Advancements and Challenges: Proceedings of the 24th Australasian Conference on the Mechanics of Structures and Materials (ACMSM24), Perth, Australia, 6-9 December 2016. 2017: 921-926.
4. TY Song, Z Tao, Ali Razzazzadeh, LH Han, K Zhou. Fire performance of blind bolted composite beam to column joints[J]. Journal of Constructional Steel Research, 2017, 132(1) 29-42.
5. Song, Tian-Yi, Hassan, et al. Experimental study on blind bolted connections to concrete-filled stainless steel columns[J]. Journal of Constructional Steel Research, 2017, 128(1) 825-838.
6. Yang You, Mei Liu, Yuanjian Liu, Peijun Wang, Shengzhan Zhou, Junxia Chen, Experimental studies on Hole-anchored Bolted T-stubs in tension at elevated temperatures, J. Constr. Steel Res. 171(1) (2020) 106139.
7. Peijun Wang, Yang You, Mei Liu, Boxun Zhang, Shengzhan Zhou, Junxia Chen, Behavior of Hole-anchored Bolted T-stubs with backing plates at ambient and elevated temperatures, J. Constr. Steel Res. 170(1) (2020) 106093.
8. Peijun Wang, Yang You, Qingfeng Xu, Qishuai Wang, Fangzhou Liu, Shear Behavior of Lapped Connections Bolted by thread-fixed one-side bolts at elevated temperatures, Fire Safety Journal, 125(2015) 103415.
9. High strength bolts with large hexagon head for steel structures: GB/T 1228-2006 [S]. Beijing: China Architecture Publishing & Media Co., Ltd. 2006. (in Chinese)

SiF 2022– The 12th International Conference on Structures in Fire
The Hong Kong Polytechnic University, Nov 30 - Dec 2, 2022

BEHAVIOUR OF COLD-FORMED HIGH-STRENGTH STEEL TUBULAR COLUMNS AT ELEVATED TEMPERATURES

Syed Muhammad Shamaim ALI [1], Ke-Jiang ZHAN [2], Jie-Yong YUAN [3], Hai-Ting LI [4*], Jia-Lin MA [5]

ABSTRACT

In this study, the behaviour and resistances of cold-formed high-strength steel (CFHSS) square and rectangular hollow section (SHS and RHS) columns at elevated temperatures up to 1000°C were numerically investigated. A finite element model was developed and developed finite element model was validated with available test results of CFHSS SHS and RHS columns in terms of ultimate capacities, failure modes and load-deflection curves. After validation, a parametric study was performed by utilising stress-strain relationships of CFHSS at elevated temperatures developed based on prior research. A total of 280 CFHSS tubular columns of steel grade S700 were studied, covering a wide range of cross-sectional classes and member slenderness ratios. The applicability of current column design provisions in Eurocode 3 and AISI S100 Specification to the studied tubular columns at elevated temperatures was evaluated. Overall, it is shown that the codified design provisions may be used for the resistance predictions of the CFHSS tubular columns at elevated temperatures, while further improvement in terms of accuracy and consistency remains possible.

Keywords: Cold-formed steel; high-strength steel; columns; elevated temperatures; tubular sections

1 INTRODUCTION

Cold-formed high-strength steel (CFHSS) tubular sections are being increasingly applied in civil engineering applications due to their superior resistance against torsional buckling, aesthetic appearance as well as high strength-to-weight ratio, which leads to material savings and easier handling during construction [1,2]. With the advances in steel production technologies, CFHSS tubular sections with yield strength up to 1300 MPa are available for structural use. The past decade has witnessed extensive research efforts performed globally to understand the fundamental behaviour of CFHSS tubular section materials (e.g. [1]), beams (e.g. [3]), columns (e.g. [4,5]) as well as hollow and composite joints [6,7], shedding light on design methods of the square, rectangular, and circular hollow section (SHS, RHS, and CHS) structural members and joints. On the other hand, fire safety is a critical issue in designing steel structures, as the strength and stiffness of steel materials will deteriorate remarkably at high temperatures [8,9]. However, research work on high-strength steel tubular structural members at elevated temperatures is rather limited.

The behaviour of high-strength steel fabricated box section (also I-section) stub and slender columns at elevated temperatures were numerically investigated by Chen and Young [10]. The studied high-strength steel sections had a nominal yield strength of 690 MPa. The column strengths at various elevated temperatures obtained from finite element analyses were compared with the results predicted by AISC 360,

[1] Postgraduate Student, Department of Civil Engineering, Shanghai Jiao Tong University, E-mail: smsa_179@sjtu.edu.cn
[2] Postgraduate Student, Department of Civil Engineering, Shanghai Jiao Tong University, E-mail: zhankejiang@sjtu.edu.cn
[3] Postgraduate Student, Department of Civil Engineering, Shanghai Jiao Tong University, E-mail: desperadooo@sjtu.edu.cn
[4] Associate Professor, Department of Civil Engineering, Shanghai Jiao Tong University (corresponding author), E-mail: haiting.li@sjtu.edu.cn
[5] Researcher, Building Research Center, Vanke Co. Ltd., Email: kmconi@hotmail.com
https://doi.org/10.6084/m9.figshare.22215787

EN 1993-1-2, AS 4100 provisions, and direct strength method (DSM) for members in compression by substituting the material properties at elevated temperatures. Winful et al. [11] conducted a numerical study on behaviour of high-strength steel tubular section columns at elevated temperatures; two steel grades, i.e., S690QL and S700MC, were considered in their study. It was concluded that the predictions of EN 1993-1-2 were generally safe, while a lower buckling curve may be needed for S690QL compression members at elevated temperatures. Regarding CFHSS tubular section material and member behaviour at elevated temperatures, Li and Young [8] carried out a test program and studied the mechanical properties of CFHSS tubular sections at elevated temperatures. More recently, a numerical investigation was conducted by Li and Young [9] to explore the structural responses of CFHSS tubular section beams at elevated temperatures. The finite element (FE) results were adopted to evaluate the applicability of existing cross-section slenderness limits to CFHSS tubular sections at elevated temperatures. The suitability of current flexural design provisions in EN 1993-1-2, AISC 360, and AISI S100 specifications to the studied CFHSS tubular beams at elevated temperatures were also evaluated. It was shown that the predictions of the existing provisions were quite conservative; meanwhile, an improved design rule was proposed by modifying the direct strength method (DSM) in the AISI specification [9].

In this paper, the behaviour of CFHSS tubular columns at elevated temperatures is numerically studied by using the same methodology as previously used by Li and Young [9] for beams. The finite element software ABAQUS was used for the numerical investigation. An accurate finite element model was established and verified against the column tests at ambient temperature conducted by Ma et al. [5]. A parametric study was performed to investigate structural performance of CFHSS SHS and RHS of grade S700 columns at various temperatures up to 1000℃. The applicability of current column design provisions in Eurocode 3 [12,13] and the DSM as per AISI S100 [14] to the studied CFHSS tubular columns at elevated temperatures was evaluated.

2 BRIEF SUMMARY OF EXPERIMENTAL STUDIES

The behaviour of CFHSS SHS and RHS columns at ambient temperature were carefully studied in the past and test results on the tubular columns under concentric and eccentric compression were reported by Ma et al. [5]. The cross-section dimensions of the studied SHS and RHS of grade S700 were 80×80×4 and 100×50×4 (depth×width×thickness in millimetres), respectively. A hydraulic testing machine with 1000kN capacity was used to apply compressive forces to the test specimens [5]. The specimens were loaded between two parallel knife edges, which allowed the specimen to rotate in the bending plane. Displacement control was used to apply the axial compression load to the specimens at a constant speed of 0.5 mm/min for all test specimens. Three displacement transducers were used to measure both the axial shortening and end-rotation of the specimens. In addition, two extra transducers were set up at the mid-height of the specimens on the two sides in the bending plane to capture the horizontal deflections. Four strain gauges were attached to the two faces in the bending plane to determine the loading eccentricities. The column tests are detailed in Ma et al. [5].

On the other hand, Li and Young [8] conducted a test program to explore the material characteristics of the CFHSS tubular sections at elevated temperatures up to 1000°C. Two SHS/RHS of grade S700 (i.e., H140×140×6 and H50×100×4) were studied. Based on the test results, a stress-strain model was developed for CFHSS SHS and RHS at elevated temperatures, and it is recommended that the proposed stress-strain model be used for the numerical investigation of CFHSS members at elevated temperatures [9]. It should be noted that the materials tested by Li and Young [8] are of the same batch of SHS and RHS tubes used by Ma et al. [5] for column tests. The abovementioned previous studies conducted by the authors [5,8,9] laid down a solid foundation for carrying out a numerical investigation into the structural performance of CFHSS SHS and RHS columns at elevated temperatures, which is the focus of this presented paper.

3 NUMERICAL INVESTIGATION

3.1 General

A numerical investigation was performed to study the structural behaviour of CFHSS tubular columns at elevated temperatures. A finite element (FE) model was developed using ABAQUS software [15]. The developed FE model was validated against the test results of CFHSS tubular columns conducted by Ma et al. [5]. Upon verification, a numerical parametric study was carried out based on the verified FE model to explore the structural performance of the CFHSS tubular columns at elevated temperatures.

3.2 FE Modelling and Validation

The CFHSS tubular columns were modelled using the four-noded S4R shell element with reduced integration. This type of element has been successfully used in prior FE modelling of steel tubular columns [5,16-18]. The FE model was built based on centreline dimensions of the CFHSS tubular cross-sections. A mesh size of $(B + H)/20$ was adopted for modelling the SHS and RHS columns. Both local and global geometric imperfections were used in the developed FE model. The initial local imperfection pattern was assumed as the form of the lowest elastic local buckling mode shape under compression and the initial global geometric imperfection distribution was taken as a quarter-sine wave along the member length due to symmetry used in the modelling. The longitudinal residual stresses, which composed of bending and membrane residual stresses, have been measured for tubular columns [1]. It has been found that the bending residual stresses were significantly greater than the membrane residual stresses, and the values of which were found to be below 20% of the 0.2% proof stresses [1,19]. Note that the effect of bending residual stresses can be inherently included in FE model by incorporating measured material properties [9,20-22]. On the other hand, the effect of membrane residual stresses on the strength of CFHSS columns can be deemed quite minimal [1] and therefore were not included in this FE modelling.

The CFHSS columns displayed symmetry in geometries, boundary conditions and experimental failure modes. Hence, only half of the cross-section over half of the column length was included in the FE modelling; symmetry constraints were applied to the X and Z planes for the applied quarter model, as illustrated in Figure 1. The nodes of each end surface of any column were coupled with a reference point offset by 87.5 mm longitudinally; this is in accordance with the test setup used by Ma et al. [5]. The two reference locations were constrained in all degrees of freedom except for the rotation along the minor axis of the cross-section (if any) and the longitudinal displacement along the loading point, as shown in Figure 1. Compression forces were applied to the specimens through the top reference point by specifying longitudinal displacement in the Static, Riks analysis step in ABAQUS. The geometric non-linearity was enabled throughout the analysis and the maximum step increase was limited to obtain a smooth load-deformation curve.

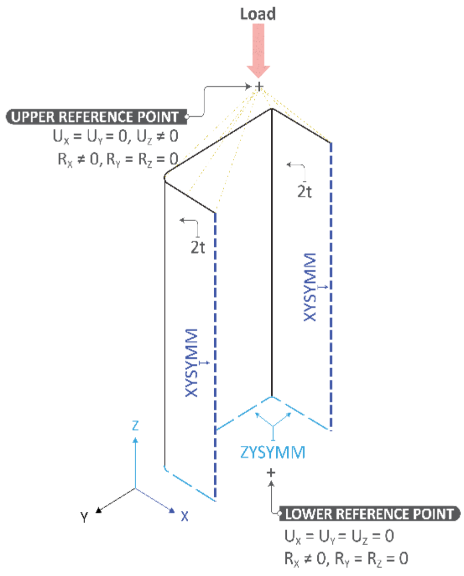

Figure 1. Boundary conditions for FE modelling.

The FE model introduced above was validated against the column test results reported by Ma et al. [5]. During the validation, the incorporated stress-strain relationships in the FE analyses were obtained based on the measurements by Ma et al. [1]. The local imperfection magnitudes reported in Ma et al. [1] and the global imperfection magnitudes tabulated in Ma et al. [5] were used during the validation. The experimental results of 21 SHS/RHS columns were compared with those obtained numerically in terms of ultimate capacities, failure modes and load-deflection curves to validate the accuracy of the developed FE model. The test-to-FE ultimate capacity ratios ($P_{\mathrm{Test}}/P_{\mathrm{FEA}}$) ranged from 0.93 to 1.02 with the mean value and coefficient of variation (COV) of 0.98 and 0.024, respectively. The experimentally obtained failure modes and load-mid height deformation responses were all compared with their numerical counterparts with typical comparisons presented in Figures 2 and 3 which show good agreements. The comparisons indicate that the developed FE model can accurately predict the structural performance of the CFHSS SHS and RHS columns.

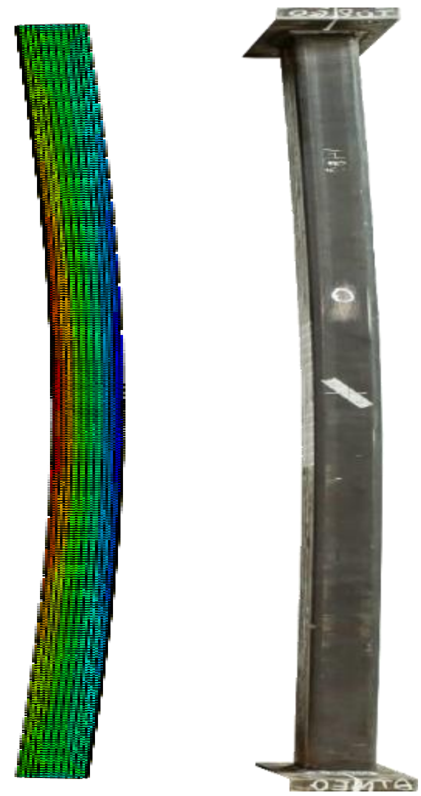

Figure 2. Comparison of numerical and experimental [20] failure modes of specimen H100×50×4-e0.

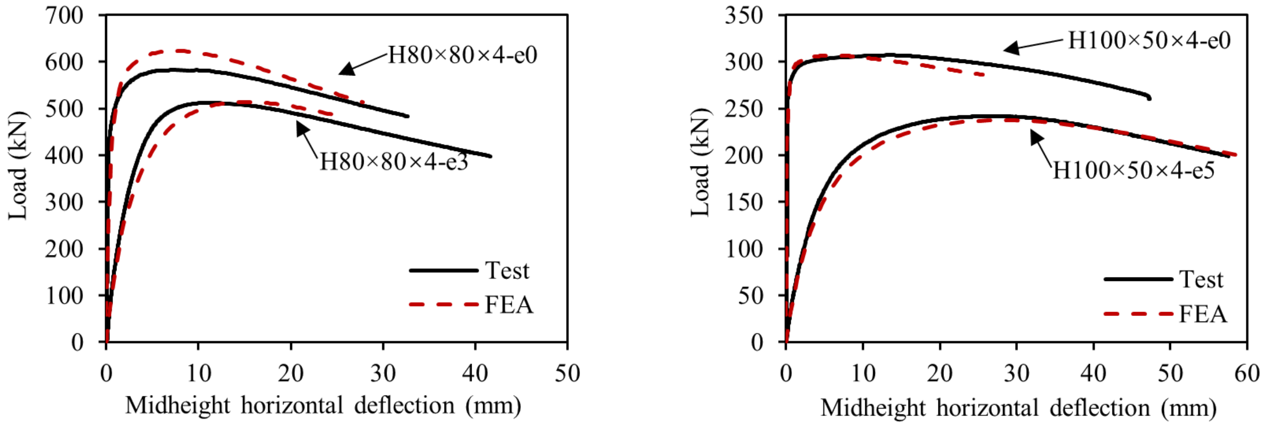

(a) Specimens form H80×80×3 series

(b) Specimens form H100×50×4 series

Figure 3. Comparison of experimental [5] and numerical load-midheight deformation curves.

3.3 Parametric Study

Upon verification, a parametric study was carried out to investigate the behaviour of concentrically loaded CFHSS SHS and RHS columns at elevated temperatures up to 1000°C by incorporating stress-strain relationships at elevated temperatures proposed by Li and Young [9]. Seven temperatures, i.e., ambient, 400°C, 500°C, 600°C, 700°C, 800°C and 1000°C, were studied, as tabulated in Table 1; these temperatures were selected based on the deterioration of the CFHSS material that previously revealed in [8]. Initial local and global geometric imperfections were applied in this parametric study, during which the average measured global and local imperfection magnitudes (equal to $L/3749$) and ($0.0119\times(B\text{-}2R)\times t$) of the grade S700 SHS and RHS reported in [20] were applied.

Table 1. Parametric study results at various temperatures

CFHSS Specimen	$P_{FEA,\theta}$ (kN)						
($D\times B\times t$)	ambient	400 °C	500 °C	600 °C	700 °C	800 °C	1000 °C
80×80×3L660	592.7	525.8	422.4	302.3	146.9	71.6	19.7
80×80×5L630	1050.3	926.2	732.8	511.1	240.9	115.5	31.9
120×120×4L1140	1104.2	981.8	795.5	579.5	287.9	142.9	39.0
120×120×5L1070	1604.8	1417.7	1125.1	788.4	372.8	179.7	49.5
100×50×3L410	503.4	446.9	360.0	260.6	129.9	65.1	17.7
100×50×5L350	987.3	870.6	688.2	479.1	225.8	108.2	29.9
150×100×4L1000	1044.3	927.3	749.1	548.3	276.9	142.8	38.5
150×100×6L900	1994.5	1760.9	1395.5	975.8	460.3	222.0	61.2
80×80×3L1490	418.1	371.5	300.3	218.0	107.9	55.9	14.9
80×80×5L1440	670.6	595.7	481.2	218.0	107.9	55.9	14.9
120×120×4L2460	799.9	711.4	576.7	420.9	210.2	109.3	29.1
120×120×5L2310	1044.1	927.4	749.2	543.3	268.5	139.0	37.0
100×50×3L990	380.1	338.0	274.0	199.9	99.6	51.7	13.8
100×50×5L880	625.7	555.8	448.9	325.2	160.3	82.9	22.1
150×100×4L2180	783.1	697.8	568.4	419.6	212.8	111.3	29.6
150×100×6L1960	1290.0	1145.9	925.6	671.0	331.2	171.3	45.7
80×80×3L2320	253.5	227.0	188.3	144.5	78.9	42.9	11.3
80×80×5L2250	401.9	360.0	298.7	229.4	125.4	68.3	18.0
120×120×4L3770	473.1	424.0	352.9	272.0	151.7	83.4	21.9
120×120×5L3550	629.5	563.9	467.7	358.9	196.0	106.6	28.0
100×50×3L1580	232.6	208.4	173.1	133.1	73.0	39.8	10.5
100×50×5L1410	374.7	335.6	278.5	214.0	116.8	63.5	16.7
150×100×4L3360	467.1	418.9	349.6	270.7	153.2	84.6	22.2
150×100×6L3030	776.8	695.8	577.2	443.2	242.0	131.5	34.6
80×80×3L3150	154.5	138.8	117.0	93.0	56.6	33.3	8.6
80×80×5L3060	243.6	219.0	184.7	146.7	89.6	52.7	13.6
120×120×4L5090	283.7	255.1	215.4	171.8	106.5	63.2	16.3
120×120×5L4800	381.7	343.1	289.2	229.8	140.1	82.3	21.3
100×50×3L2160	142.5	128.1	108.0	85.9	52.5	30.9	8.0
100×50×5L1940	227.0	204.0	172.0	136.8	83.5	49.1	12.7
150×100×4L4530	280.6	252.4	213.3	170.6	106.9	63.9	16.5
150×100×6L4100	472.1	424.3	357.8	284.3	173.3	101.9	26.4

Table 1. Parametric study results at various temperatures (Continued)

CFHSS Specimen	$P_{\mathrm{FEA},\theta}$ (kN)						
(D×B×t)	ambient	400 °C	500 °C	600 °C	700 °C	800 °C	1000 °C
80×80×3L3990	100.5	90.5	76.6	61.7	40.3	25.3	6.4
80×80×5L3870	159.0	143.0	121.2	97.6	63.7	40.1	10.2
120×120×4L6400	185.2	166.7	141.2	113.9	75.0	47.9	12.1
120×120×5L6040	249.6	224.7	190.2	153.2	100.0	62.9	16.0
100×50×3L2740	93.5	84.1	71.3	57.4	37.5	23.6	6.0
100×50×5L2470	148.0	133.2	112.8	90.9	59.4	37.4	9.5
150×100×4L5710	182.7	164.4	139.4	112.5	74.5	48.0	12.1
150×100×6L5170	308.3	277.4	235.0	189.3	123.6	77.7	19.8

A total of 280 CFHSS numerical specimens were studied, covering 8 SHS/RHS over a wide range of cross-section classes (Classes 1 to 4 as per the EN 1993-1-1 [12]), 5 member slenderness ratios (non-dimensional slenderness of 0.5, 1.0, 1.5, 2.0 and 2.5 at ambient temperature) at 7 different temperatures. These non-dimensional member slenderness ratios are calculated based on the Eqs. (6.50) and (6.51) in EN 1993-1-1 [12] for Class 1-3 and Class 4 sections, respectively. The SHS and RHS sections were selected from the range of practical sizes for structural applications. The cross-section dimensions (D×B×t in millimetres) for the SHS were 80×80×3, 80×80×5, 120×120×4 and 120×20×5; the D×B×t for RHS were 100×50×3, 100×50×5, 150×100×4 and 150×100×6, as tabulated in Table 1.

In Table 1, the specimens are labelled such that the cross-sectional dimensions and specimen lengths could be identified. For example, the label "120×120×4L1140" defines the following specimen. The 120×120×4 are the nominal cross-sectional dimensions, arrange as D×B×t, of the specimen in millimetres (120×120×4 means D = 120mm, B = 120mm, and t=4mm); the following notation L1140 shows that the specimen length was 1140mm. The generated ultimate capacities $P_{\mathrm{FEA},\theta}$ of the CFHSS SHS and RHS columns under concentric loading at various temperatures are fully reported in Table 1.

4 APPLICABILITY ASSESSMENT OF EXISTING DESIGN PROVISIONS

4.1 Eurocode 3

The Eurocode 3 has specific design guidance for steel members in fire with detailed design provisions codified in EN 1993-1-2 [13]. In this study, the $P_{\mathrm{FEA},\theta}$ of the CFHSS SHS and RHS columns at elevated temperatures were compared with the nominal column resistances $P_{\mathrm{EC3},\theta}$ calculated based on provisions as per the EN 1993-1-2 [13]. During the assessment, the reduced material properties at elevated temperatures were used to compute the elevated temperature column resistances $P_{\mathrm{EC3},\theta}$.

According to the EN 1993-1-2 [13], the cross-sections shall be classified at ambient temperature based on EN 1993-1-1 [12] and shall employ the ε value, as provided in Eq. (4.2) of the EN 1993-1-2 [13], in obtaining the classification of cross-sections. The design provisions for columns with Classes 1-3 sections are codified in Clause 4.2.3.2 of the EN 1993-1-2 [13], while for columns with Class 4 sections, the Annex E.2 can be referred. The comparisons of the $P_{\mathrm{FEA},\theta}$ with the computed $P_{\mathrm{EC3},\theta}$ calculated from the EN 1993-1-2 [13] provisions are shown in Table 2, where the mean value of $P_{\mathrm{FEA},\theta}/P_{\mathrm{EC3},\theta}$ ratios for a total of 240 (out of 280) specimens at elevated temperatures is 1.13 with a corresponding COV of 0.057. This indicate that the current EN 1993-1-2 [13] provisions can provide quite conservative and consistent strength predictions for the CFHSS SHS/RHS columns at elevated temperatures. The numerically obtained column buckling strengths $P_{\mathrm{FEA},\theta}$ are graphically compared with the obtained $P_{\mathrm{EC3},\theta}$ in Figure 4, where conservative predictions are illustrated with the maximum and minimum $P_{\mathrm{FEA},\theta}/P_{\mathrm{EC3},\theta}$ values of 1.36 and 0.98, respectively. The comparison of EN 1993-1-2 buckling curve with numerical results at various temperatures are shown in Figure 5, where the vertical axis is the $P_{FEA,\theta}$ values normalized by their corresponding $Af_yk_{y,\theta}$. It is found that the column buckling curve can be applied for the CFHSS SHS/RHS columns at elevated temperatures.

Table 2. Comparison of numerical results with predicted column capacities at elevated temperatures

FEA: 240	$\frac{P_{FEA,\theta}}{P_{EC3,\theta}}$	$\frac{P_{FEA,\theta}}{P_{EC3\#,\theta}}$	$\frac{P_{FEA,\theta}}{P_{DSM,\theta}}$
Mean	1.13	1.12	0.98
COV	0.057	0.062	0.091

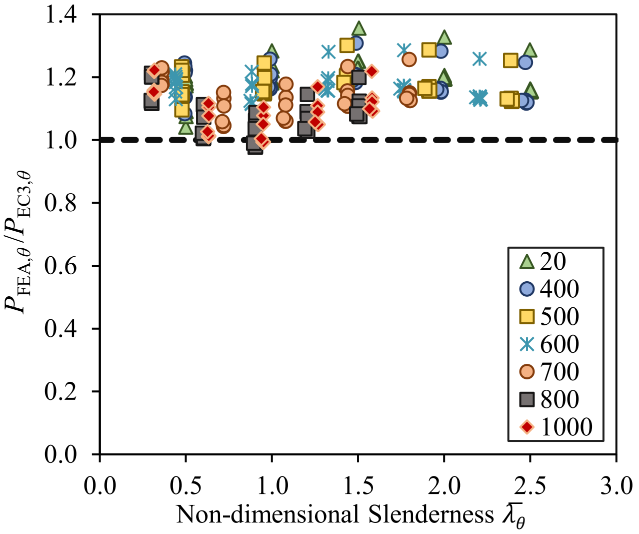

Figure 4. Comparison of column buckling strengths $P_{FEA,\theta}$ with $P_{EC3,\theta}$ obtained at various temperatures

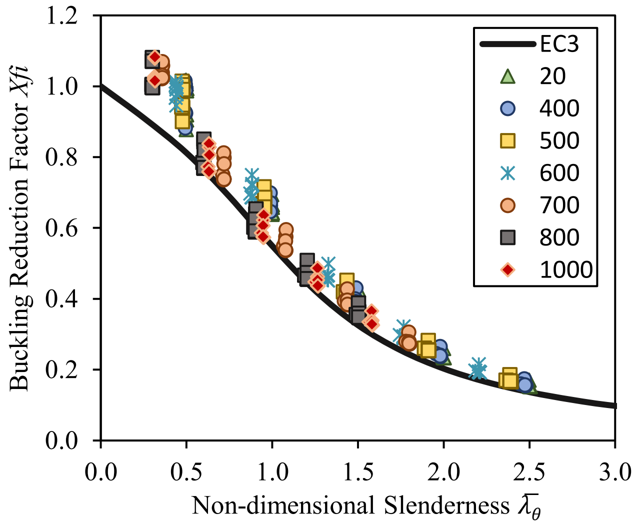

Figure 5. Comparison of EN 1993-1-2 buckling curve with numerical results at various temperatures

The constant value of 0.85 in Eq. (4.2) of the EN 1993-1-2 [13] is reduction factor to consider influences due to increasing temperature, yet it is noteworthy that this value is an approximation of the $(k_{E,\theta}/k_{y,\theta})^{0.5}$ function ($k_{E,\theta}$ and $k_{y,\theta}$ are reduction factors for elastic modulus and yield strength, respectively) and has been codified in EN 1993-1-2 [13] for simplicity [23]. In this study, the Eq. (1) of this paper was also used to replace the Eq. (4.2) of the EN 1993-1-2 [13] in an extra assessment; a new series of nominal column resistances $P_{EC3\#,\theta}$ for the CFHSS SHS/RHS at elevated temperatures were obtained accordingly. Namely, the $P_{EC3\#,\theta}$ were computed based upon the EN 1993-1-2 [13] but by incorporating the actual material strength and stiffness reduction factors rather than using the approximation value of 0.85.

$$\varepsilon = \sqrt{\frac{k_{E,\theta}}{k_{y,\theta}}}\sqrt{\frac{235}{f_y}} \tag{1}$$

The mean value of $P_{FEA,\theta}/P_{EC3\#,\theta}$ ratios of the 240 elevated temperature specimens is 1.12 and the corresponding COV is 0.062, as reported in Table 2. It is found that the $P_{EC3\#,\theta}$ results are slightly more accurate than the $P_{EC3,\theta}$ results by 1% in average, while the adoption of the 0.85 approximation for $(k_{E,\theta}/k_{y,\theta})^{0.5}$ results still yielded rather consistent predictions for the studied columns.

4.2 AISI S100

The AISI S100 [14] is a specific specification for the design of cold-formed steel structural members in North America. The Direct strength method known as the DSM, which requires no cross-section classification nor any effective length calculation, is provided in the main clauses of the AISI S100 since its 2016 version. In this study, the applicability of the DSM for members in compression, as detailed in Chapter E of the specification, to the CFHSS SHS and RHS columns at elevated temperatures is assessed.

The DSM in this study was based on Equation E3.2.1-1 and E3.2.1-2 codified in the AISI S100 [14]. The nominal member capacity $P_{DSM,\theta}$ of a compression member shall be the minimum value of the nominal capacity in compression for global buckling (P_{ne}) and member in compression for local buckling (P_{nl}). Note that distortional buckling was not occur for the studied SHS and RHS, and therefore, the determination of distortion buckling is not considered. In this assessment of the AISI S100 DSM provision, the global flexural buckling strength P_{ne} were calculated by using A_g multiplied by F_n according to Clause E2 of the AISI S100 [14], where A_g is gross area and F_n is compressive stress which can be calculated by Eqs. (E2-2) and (E2-3). Regarding to the P_{nl} calculations, the required P_{crl} of the SHS and RHS were obtained from numerical software CUFSM in this study.

The assessment of applicability of the DSM as per the AISI S100 to CFHSS SHS and RHS columns at elevated temperatures is similar to the assessment at ambient temperature condition, whereas the material properties of CFHSS at elevated temperatures were used in calculations. The $P_{FEA,\theta}$ of the CFHSS SHS/RHS columns at elevated temperatures were compared with the $P_{DSM,\theta}$ calculated by the abovementioned AISI S100 [14] DSM provisions. Overall, the mean value of $P_{FEA,\theta}/P_{DSM,\theta}$ ratios for a total of 240 specimens at elevated temperatures is 0.98 with a corresponding COV of 0.091, as tabulated in Table 2. The $P_{FEA,\theta}$ are graphically compared with the obtained $P_{DSM,\theta}$ in Figure 6, where the maximum and minimum $P_{FEA,\theta}/P_{DSM,\theta}$ values are 1.21 and 0.82, respectively. It is found that the DSM would lead to some overestimated predictions for specimens with $\bar{\lambda}_\theta$ 0.5 to 1.6 especially for temperatures above 700℃ .

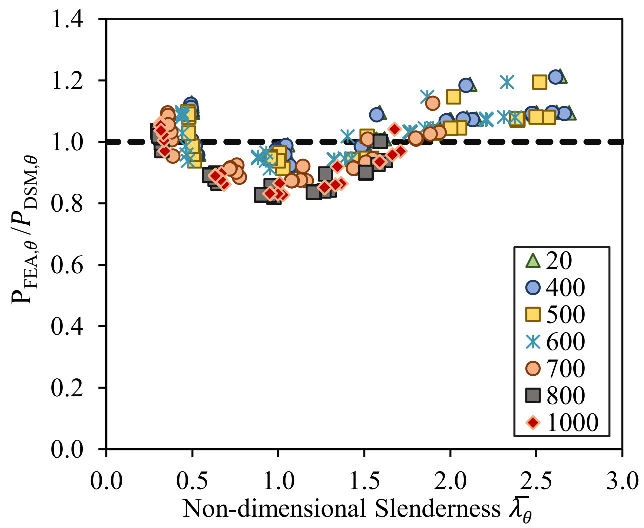

Figure 6. Comparison of column buckling strengths $P_{FEA,\theta}$ with $P_{DSM,\theta}$ obtained at various temperatures

5 CONCLUSIONS

The structural performance and design of cold-formed high-strength steel (CFHSS) SHS and RHS columns subjected to concentric loading at elevated temperatures was numerically investigated in this paper. A FE model was developed. The developed model was carefully validated against the experimental results of available cold-formed SHS, and RHS column test results made of grade S700 high-strength steel conducted by Ma et al. [5] at ambient temperature. A parametric study was conducted on the CFHSS SHS/RHS columns with a wide range of cross-sectional dimensions, member slenderness subject to various temperatures from ambient temperature up to 1000℃. A total of 280 numerical column capacities were obtained. The newly obtained column strengths were compared with the predictions based on codified provisions in Eurocode 3 and AIS1 S100 in order to check their applicability to the studied tubular columns at elevated temperatures. It is shown that the Eurocode 3 provide quite conservative predictions for the CFHSS SHS and RHS at elevated temperatures. Overall, the DSM provided in the AISI S100 are generally conservative for column strengths at ambient temperature, but less conservative in predicting column strengths at elevated temperatures. Further improvement of the DSM for CFHSS SHS and RHS columns at elevated temperatures is currently underway.

REFERENCES

1. Ma, J.-L., Chan, T.-M. and Young, B., Material properties and residual stresses of cold-formed high strength steel hollow sections, Journal of Constructional Steel Research 2015; 109: 152–165.
2. Li, H.-T. and Young, B., Cold-formed high-strength steel tubular structural members under combined bending and bearing, Journal of Structural Engineering 2019; 145(8): 04019081.
3. Ma, J.-L., Chan, T.-M. and Young, B., Design of cold-formed high strength steel tubular beams, Engineering Structures 2017; 151: 432–443.
4. Ma, J.-L., Chan, T.-M. and Young, B., Experimental investigation on stub-column behavior of cold-formed high-strength steel tubular sections, Journal of Structural Engineering 2016; 142(5): 04015174.
5. Ma, J.-L., Chan, T.-M. and Young, B., Cold-formed high strength steel tubular beam-columns, Engineering Structures 2021; 230: 111618.
6. Li, H.-T. and Young, B., Design of concrete-filled high strength steel tubular joints subjected to compression, Journal of Constructional Steel Research 2018; 150: 209–220.
7. Pandey, M., Chung K.-F. and Young, B., Numerical investigation and design of fully chord supported tubular T-joints, Engineering Structures 2021; 239: 112063.
8. Li, H.-T. and Young, B., Material properties of cold-formed high strength steel at elevated temperatures, Thin-Walled Structures 2017; 115: 289–299.
9. Li, H.-T. and Young, B., Cold-formed high strength steel SHS and RHS beams at elevated temperatures, Journal of Constructional Steel Research 2019; 158: 475–485.
10. Chen, J. and Young, B., Design of high strength steel columns at elevated temperatures, Journal of Constructional Steel Research 2008; 64(6): 689–703.
11. Winful, D.A., Cashell, K.A., Afshan, S., Barnes, A.M. and Pargeter, R.J., Behaviour of high strength steel columns under fire conditions, Journal of Constructional Steel Research 2018; 150: 392–404.
12. CEN (European Committee for Standardization), Eurocode 3: Design of steel structures, Part 1-1: General rules and rules for buildings, EN 1993-1-1:2005+A1: 2014, Brussels, Belgium, 2014.
13. CEN (European Committee for Standardization), Eurocode 3: Design of steel structures, Part 1-2: General rules-Structural fire design, EN 1993-1-2, Brussels, Belgium: CEN, 2005.
14. AISI (American Iron and Steel Institute), North American Specification for the Design of Cold-Formed Steel Structural Members, AISI S100-16, Washington D.C., USA, 2016.
15. ABAQUS, Version 6.14-4 (2015). Dassault Systèmes, Providence, RI.
16. Chan, T.M. and Gardner, L., Flexural buckling of elliptical hollow section columns, Journal of Structural Engineering 2009; 135: 546–557.

17. Fang, H. and Chan, T.M., Axial compressive strength of welded S460 steel columns at elevated temperatures, Thin-Walled Structures 2018; 129: 213–24.
18. Chan, T.M. and Gardner, L., Compressive resistance of hot-rolled elliptical hollow sections, Engineering Structures 2009; 30: 522–532.
19. Somodi, B. and Kövesdi, B., Residual stress measurements on cold-formed HSS hollow section columns, Journal of Constructional Steel Research 2017; 128: 706–720.
20. Ma, J.-L., Behaviour and design of cold-formed high strength steel tubular members. Ph.D. thesis. Department of Civil Engineering, The University of Hong Kong; 2016.
21. Rasmussen, K.J.R. and Hancock, G.J, Design of cold-formed stainless steel tubular members. I: columns, Journal of Structural Engineering 1993; 119: 2349–2367.
22. Theofanous, M. and Gardner, L., Testing and numerical modelling of lean duplex stainless steel hollow section columns, Engineering Structures 2009; 31: 3047–3058.
23. Franssen, J.-M., Kodur, V. and Zaharia, R., Designing Steel Structures for Fire Safety, Taylor and Francis, The Netherlands, 2009.

Proceedings of the 12th International Conference on Structures in Fire

Timber Structures in Fire

EVALUATION OF FIRE PERFORMANCE OF PRE-CHARRED WOODS

Shaorun Lin[1], Yunzhu Qin[2], Xinyan Huang[3]

ABSTRACT

Wood, as one of the most sustainable construction materials, has regained global attention under the initiative of the carbon-neutral world, but its flammable nature is still a primary public concern. Pre-charring is an ancient approach to protect wooden construction materials against biochemical impacts, but its effectiveness in fire retardancy is still poorly understood. This work proposes a novel method to generate engineered wood with a uniform and robust surface char layer under low thermal irradiation. We found the pre-charred wood can achieve an extraordinary fire-retardant performance under intense irradiation by increasing the ignition time by up to seven-fold and doubling the ignition temperature to about 670 °C. For the first time, we quantify the minimum char-layer thickness of 6 ± 1 mm for achieving effective fire retardancy. The fire hazards of the pre-charred wood are also mitigated significantly, where its flame becomes weaker, thinner, and bluer than that of the original wood. The peak heat release rate of burning pre-charred wood is reduced by over 50%, helping maintain the fire resilience of timber structures. This work reveals the fire performances of pre-charred wood, highlighting a promising direction toward fire-retardant timber construction materials.

Keywords: Thermal resistance; ignition time; peak heat release rate; timber structure; fire retardancy

1 INTRODUCTION

Woods have significantly contributed to the development of human civilisation and have been adopted as one of the longest-standing construction materials for more than 10,000 years [1, 2]. For example, the world's oldest surviving wooden building, the Horyuji Temple near Nara, Japan, was reconstructed at least 1,300 years ago [3]. Despite the long-lasting history of wooden construction and timber buildings, steel and concrete have dominated the construction since the industrial revolution. Nevertheless, in the past few decades, wood has gained a renaissance as a green and renewable construction material for high-rise buildings, aiming to pave the way for a future carbon-neutral world [4–8]. Compared with modern construction materials such as steels, concretes and glasses, the production processes of the woods and engineered wood products require lower energy consumption and emit less carbon [9]. In recent years, the mushrooming high-rise timber buildings have marked a firm commitment to innovation, sustainability and modernity by combining the vision of ecological and innovative architectures [7, 10]. For example, the new 84-meter, 24-story high 'HoHo Tower' in Vienna, Austria, is the world's new milestone of the tallest timber skyscraper.

Woods are inhomogeneous and anisotropic natural composites of celluloses that are strong in tension and embedded in a matrix of lignin that resists compressive strength [11–13]. However, due to the flammable

[1] Postdoctoral Researcher, The Hong Kong Polytechnic University
e-mail: shaorun@outlook.com, ORCID: https://orcid.org/0000-0003-4090-1148
[2] PhD Student, The Hong Kong Polytechnic University
e-mail: yunzhu.qin@connect.polyu.hk, ORCID: https://orcid.org/0000-0001-9704-8630
[3] Assistant Professor, The Hong Kong Polytechnic University
e-mail: xy.huang@polyu.edu.hk, ORCID: https://orcid.org/0000-0002-0584-8452
https://doi.org/10.6084/m9.figshare.22193293

nature of the wooden material, except the cost, supply and issues of moisture control during its lifetime, the fear of fire is probably the single largest contributor to the abandonment of wood as a construction material [14–16]. For example, the 16-story Lingguan Tower in China, which was the tallest wooden pagoda in the world, was completely burnt to the ground after being engulfed in flames for around 4 h. Currently, despite new fire retardant and prevention techniques [17], the never-ending fire accidents have continuously raised the fire safety issue to be a public concern and led to strict fire safety and structural requirements that increase its cost and limit its popularity [18, 19]. Therefore, it is urgent to deepen our understanding of the fire dynamics of wood materials and improve their fire resilience for future timber structures.

As a typical charring material, wood can sustain both forms of flaming and smouldering combustion [20]. Currently, the fire dynamics of wood materials have been thoroughly studied and revealed many insights into ignition [21, 22], fire spread [23, 24], deformation [13, 25, 26], and extinction [27, 28]. On the other hand, methods that may improve the reaction to fire of the wood materials have also been well explored, especially the application of fire-retardant systems [29–37]. The mechanisms of fire-retardant systems include endothermic degradation (e.g., magnesium and aluminium hydroxides) [34], thermal shielding (e.g., intumescent additives) [38], dilution of gas fuels (e.g., inert gas produced by thermal degradation) [39], and gas-phase radical quenching (e.g., chlorinated and brominated materials) [33]. For example, the intumescent coating is an effective method for fire retardancy by massive volume expansion of porous charred layer [33, 40]. Additionally, chemical modifications of woods have offered an alternative to provide protection against water, corrosion, ultraviolet and thermal degradation (fire), showing excellent application prospects [41].

Charring is a historical approach to generating a protective surface layer for wood against biochemical impacts [42–44]. During the first century BC, Vitruvius, a Roman architect and engineer, also recommended using carbonisation to increase the service life of bridges and fortification fences [33]. In the 1600s, the technique of 'charring wood' was further developed in Japan to improve the biological resistance and fire-harden the fast-growing wooden structures, known as 'shou sugi ban', 'sugi ban' or 'yakisugi' [42, 45]. Recently, several studies have been performed to investigate the surface characteristic of the charred woods. For example, Kymalainen et al. [46, 47] introduced charring on the wood surface using a hot plate and found that spruce sapwood exhibits promising characteristics in terms of reduced sorption. Machova et al. [43] also concluded that charring at a particular temperature and duration improved the properties of the beech wood such as discolouration and surface roughness. Moreover, the charring process is also believed to improve the fire retardancy of wood materials due to the lower thermal conductivity of char compared to virgin wood [48].

However, few studies have evaluated the fire performances of woods with charred surfaces. Hasburgh et al. [42] tested several commercial 'shou sugi ban' but found that the thin char layer did not systematically improve the fire performance of the wood materials. Machova et al. [43] suggested that charring should be conducted at a suitable combination of temperature and time for an effective char layer against fires. Gan et al. [49] generated an insulating char layer on the densified wood in a tube furnace at 500 ºC that doubled the ignition time and decreased the maximum heat release rate, but the thickness of the char layer was not mentioned. Therefore, our understandings of the fire-retardant performance of charred woods and the required char-layer thickness for an effective protective layer against fires are still limited, requiring more fundamental research and quantitative analyses.

Herein, we develop a novel and low-cost strategy to generate a controllable and uniform char layer on the wood surface under low irradiation. The thickness of the char layer is accurately controlled by the irradiation durations (0-20 min). The fire-retardant performances (reaction-to-fire behaviours) of the pre-charred woods are evaluated in terms of the piloted ignition delay time, ignition temperature, and fire heat release rate under intense irradiation up to 50 kW/m^2 that simulates real fire scenarios.

2 EXPERIMENTAL DETAILS

2.1 Virgin wood sample

The virgin wood sample used in this work is Merbau wood from Southeast Asia, and its dry bulk density was measured to be around 900 kg/m^3. Initially, the wood samples were uniformly cut into the dimension of 10 cm × 10 cm × 3 cm. To prevent cracking due to high-temperature heating, the wood samples were oven-dried at a low temperature of 50 °C for at least 48 h, and then placed into an electronic dry cabinet to avoid the re-absorption of moisture from the ambient [27].

2.2 Controlling surface charring process

The charring process was conducted using the cone calorimeter (FTT I-Cone Plus) [50, 51], which mainly consists of a conical heater, a sample holder and a precision scale. The conical heater could provide relatively constant and even irradiation to the sample area of 10 cm × 10 cm, thus ensuring that the whole exposed surface of the wood sample would receive uniform irradiation [27, 50]. The periphery of the wood sample was wrapped by a 1-cm insulation cotton layer, which reduced the heat loss and ensured a steady 1-D charring process perpendicular to the top surface (see Fig. 1).

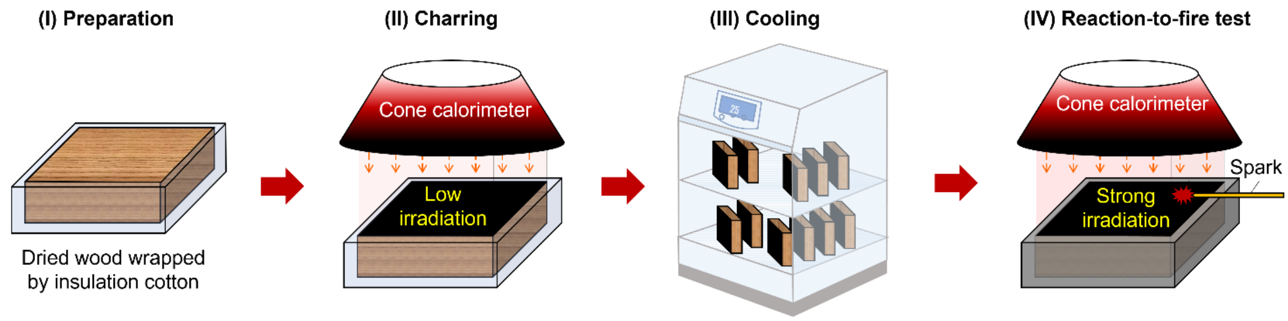

Figure 1. Schematic diagrams of test procedures

The charring irradiation was adjusted to a relatively low level of 20 kW/m^2 that was measured by a radiometer and was further calibrated by the temperature of the conical heater. After that, irradiation was shielded by two steel panels, and the sample was installed on the precision scale where the unwrapped surface was exposed to the conical heater. Once the steel shield was removed, the prescribed irradiation was applied to the exposed wood surface. The charring duration lasted for 5 min, 10 min, 15 min and 20 min, respectively. After charring, some shallow and random fissures were observed on the charred surfaces, and a uniform char layer was observed on the cross-section of the charred wood samples.

Fig. 2 summarises the thicknesses of the pre-charred layer (δ_c) with different charring durations (t_c). As expected, the thickness of the char layer increases almost linearly with the charring duration, with a near-constant charring rate of 0.7 mm/min, consistent with the data in the literature [52]. For example, as the charring duration increases from 5 min to 20 min, the thickness of the charred layer increases from 4.2 mm to 13.8 mm. An empirical correlation between the thickness of the charred layer [mm] and the charring duration [s] was found to be $\delta_c = 0.7t_c$ with R^2=0.99. Note that the charring rate of the wood may vary with the wood species and densities, and the charring rate may decrease if the char layer further expands [52].

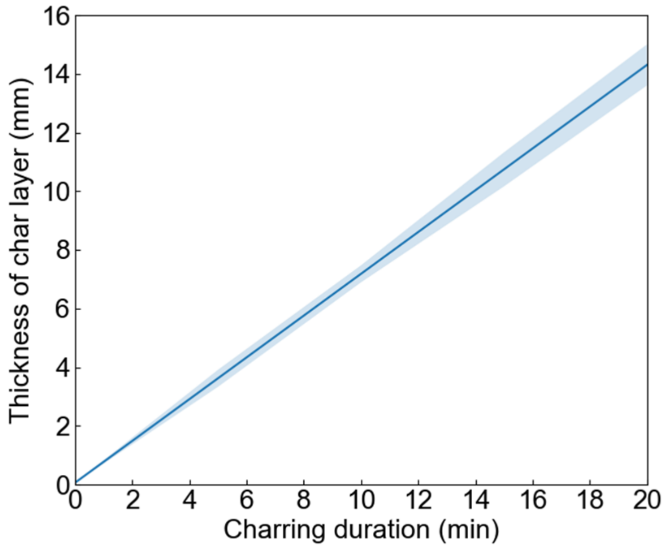

Figure 2. Relationship between the thickness of charred layer and charring duration, where the linear fitting is $\delta_c = 0.7t_c$ with R^2=0.99

2.3 Reaction-to-fire test

The standard reaction-to-fire test was conducted using the cone calorimeter under strong irradiations of 40 kW/m^2 and 50 kW/m^2 following ASTM E1354 and ISO 5660 [50]. The pilot ignition is the initiation of flaming combustion in the vicinity of a small pilot source located in the boundary layer, such as a flame, spark, electrical arc, or glowing wire [53]. The pre-charred wood samples were installed into a stainless-steel box to prevent the edge or curvature effect, as recommended in [50]. The pilot source (a spark) was placed 15 mm above the top surface of the sample during the heating. Once a flame was piloted, the spark was removed while the heating was continued to measure the burning rate and fire heat release rate until flame extinction. The surface temperatures of the samples were carefully monitored using two K-type thermocouples (0.5-mm bead diameter) that were closely attached to the top surface [27]. The test process was fully recorded by a side-view camera. During the test, the ambient temperature was maintained at 25 ± 2°C, while the relative humidity was kept at 50 ± 5%. For each test, at least three repeating experiments were performed for uncertainty analysis.

3 RESULT AND DISCUSSION

3.1 Fire phenomena

Fig. 3 shows some typical examples of the piloted flaming ignition processes of the wood samples with different thicknesses of pre-charred layers under irradiation of 40 kW/m^2, where the original videos can be found in the Supplemental materials. For the virgin wood (Fig. 3a), once exposed to irradiation, dense smoke was always observed, which could be a mixture of pyrolysis gases and condensed water vapours [54]. After being heated for about 48 s, a typical buoyancy-controlled strong yellow flame was successfully piloted and maintained above the wood surface. For the wood with a 4.2-mm char layer (Fig. 3b), although less smoke was observed during heating, a strong yellow flame was also piloted at about 46 s, similar to that of virgin wood. Thus, a char layer with a thickness of 4.2 mm is not effective to improve the fire retardancy of wood materials.

By increasing the thickness of the char layer to 7.5 mm (Fig. 3c), although a glowing process was first achieved on the char surface, no visible smoke was observed during the heating process. After being heated for about 118 s, a flame was also piloted, but the ignition was delayed by 70 s compared to that of virgin wood in Fig. 3a. Meanwhile, the flame height was decreased due to a smaller fuel burning mass flux and the flame intensity was also weakened. Therefore, the fire performance of wood has been well improved by the pre-charred surface. Further increasing the char thickness to 11.5 mm and 13.8 mm, compared with the virgin wood, the flaming ignition could be further delayed by about 150 s and 250 s, respectively. Moreover, after ignition, only a weak, thin, flat, blue and discrete flame was observed floating above the hot charred surface, analogous to the near-limit blue flame observed in our previous work [27]. As the flame height was very small due to a smaller fuel mass flux, the flame was only slightly affected by the buoyancy. Note that the temperature of the observed blue flame was not necessarily lower than the yellow flame, whereas it only indicated a lower soot concentration in the flame or soot standing away from hotter regions [27].

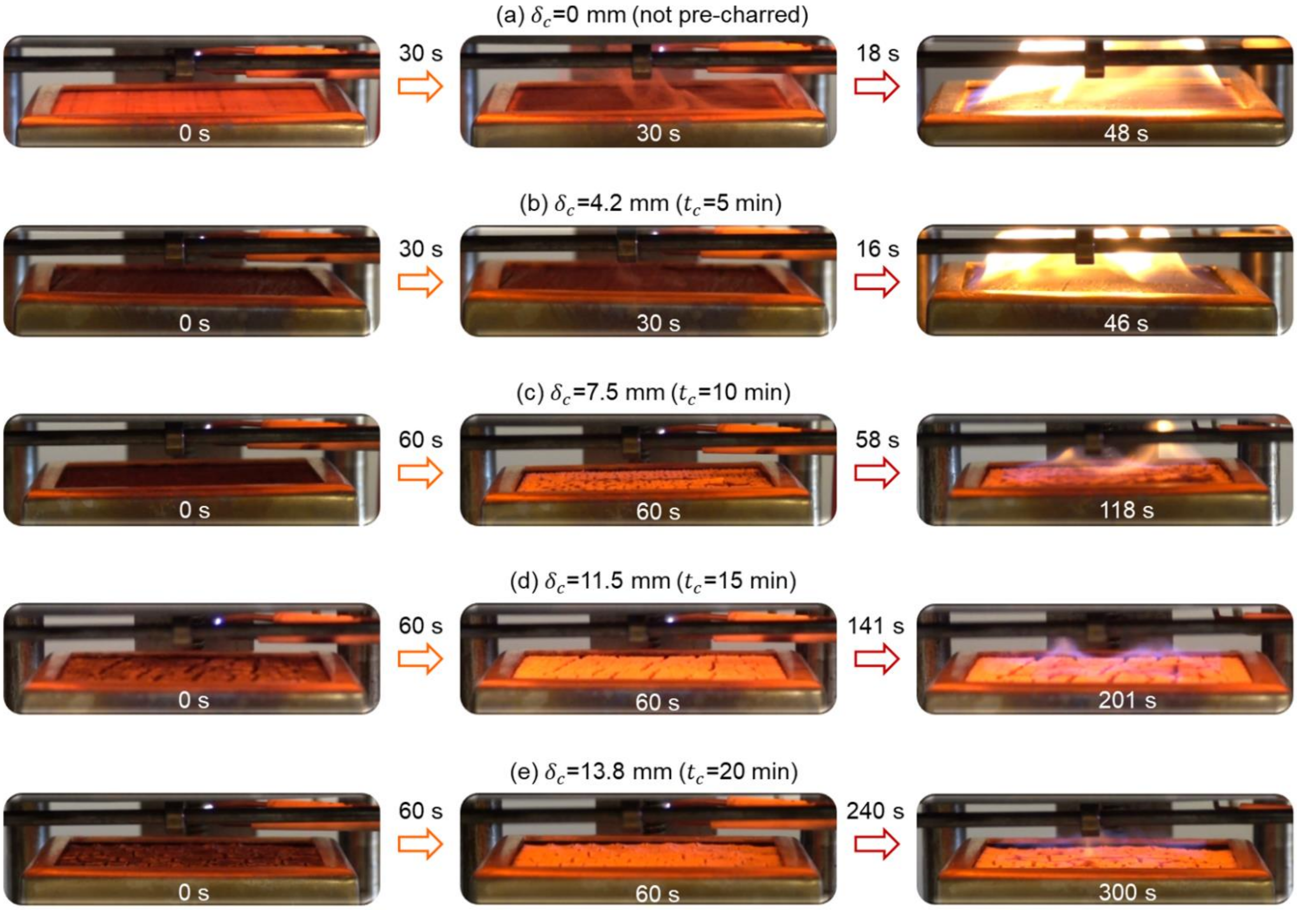

Figure 3. Snapshots of piloted flaming ignition of woods under irradiation of 40 kW/m^2, where thicknesses of char layers are (a) 0 mm without charring, (b) 4.2 mm with 5-min charring, (c) 7.5 mm with 10-min charring, (d) 11.5 mm with 15-min charring, and (e) 13.8 mm with 20-min charring

3.2 Ignition time and thermal inertia

Fig. 4(a) summarises the piloted flaming ignition time (t_{ig}) of virgin woods and pre-charred woods with different thicknesses of char layers under irradiations of 40 kW/m^2 and 50 kW/m^2. As expected, given the thickness of the char layers, the required ignition time decreases with the increasing radiant heat flux, well agreeing with the trend in the literature [22]. On the other hand, when the thickness of the char layer is smaller than 6 ± 1 mm, given an irradiation level, the ignition difficulty is insensitive to the thickness of the char layer, as the ignition time is almost the same as that of virgin wood. Therefore, a thin layer of char surface (<6 mm) is not sufficient to protect the underlying virgin woods against fires.

In terms of conductive heat transfer, a char layer thinner than such value does not exceed the thermal penetration depth ($\delta_T \sim \sqrt{8\alpha t_{ig}} \approx \sqrt{8 \times 0.1 \times 40} = 5.7$ mm) of the virgin wood at the ignition moment, where $\alpha \approx 0.1\ \mathrm{mm}^2/\mathrm{s}$ is the thermal diffusivity of wood [53, 55]. Comparatively, as the thickness of the char layer exceeds 6±1 mm, the required ignition time starts to increase greatly with the thickness of the char layer. For example, given irradiation of 40 kW/m^2, compared with that of virgin wood (39 s), the ignition time increases by around 5 times to 197 s and 7 times to 272 s, as the thickness of the char layer increases to 11.5 mm and 13.8 mm, respectively. Therefore, an effective char layer could remarkably improve the fire performance or retardancy of wood materials.

For a thermally thick fuel where the fuel thickness is generally larger than 2 mm [53], the ignition time (t_{ig}) can be estimated as

$$t_{ig} \approx k\rho c \left(\frac{T_{ig} - T_{\infty}}{\dot{q}''_{ir}}\right)^2 \tag{1}$$

where k, ρ, c are the thermal conductivity, bulk density and specific heat, respectively; T_{ig} and T_{∞} are the ignition temperature and ambient temperature (25 °C); and $\dot{q}''_{ir}$ is the irradiation. As the irradiation increases, the ignition time decreases, agreeing with the experimental observations (Fig. 4a). By rearranging Eq. (1), we can estimate the fuel **thermal inertia** (I) as

$$I = \sqrt{k\rho c} = \sqrt{t_{ig}}\left(\frac{\dot{q}''_{ir}}{T_{ig} - T_{\infty}}\right) \tag{2}$$

which is a measure of its resilience to the external thermal impact [53].

Fig. 4(b) plots the calculated thermal inertia of engineered woods with different thicknesses of char layers. Firstly, the thermal inertia of virgin wood is around 1062 $J{\cdot}m^{-2}{\cdot}K^{-1}{\cdot}s^{-1/2}$, similar to the literature values [53]. However, as the thickness of the char layer increases to 11.5 mm and 13.8 mm, the thermal inertia increases to 2022 $J{\cdot}m^{-2}{\cdot}K^{-1}{\cdot}s^{-1/2}$ and 2071 $J{\cdot}m^{-2}{\cdot}K^{-1}{\cdot}s^{-1/2}$, further demonstrating the improved fire performances of woods with effective pre-charred surfaces.

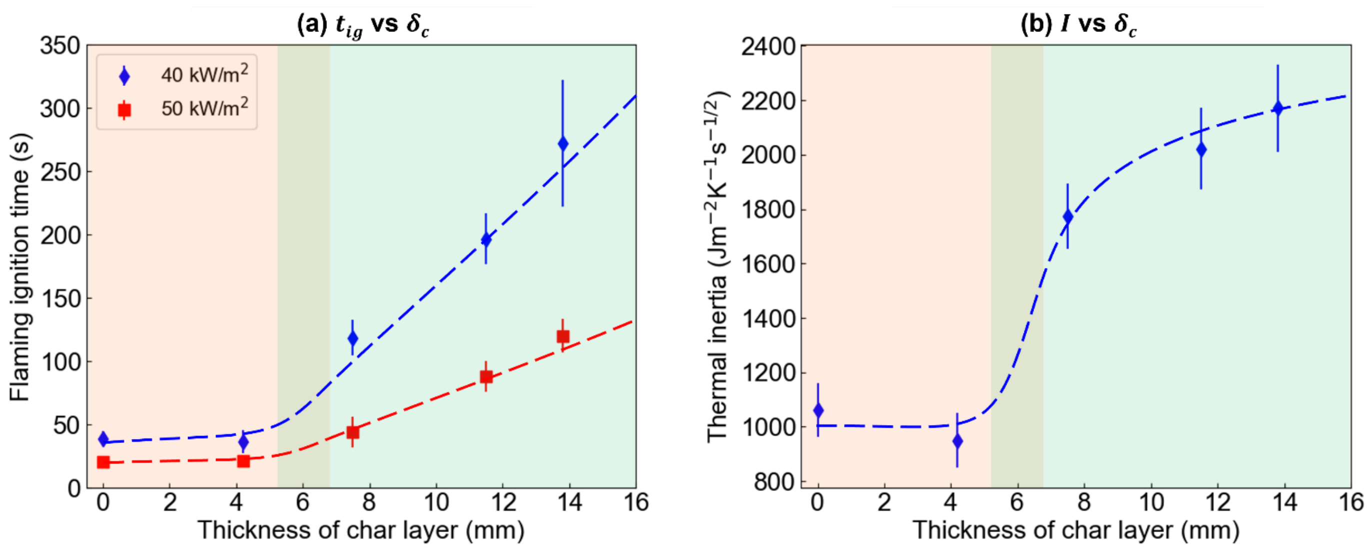

Figure 4. (a) Piloted flaming ignition delay time under irradiations of 40 kW/m^2 and 50 kW/m^2, and (b) calculated thermal inertia for pre-charred wood, where markers represent the average values, error bars represent the standard deviations, and dashed lines represent the fitting

3.3 Ignition temperature and minimum irradiation

For the ignition criteria, it is a common practice to assume an ignition temperature [53]. That is, flaming ignition will occur when the fuel surface temperature reaches a critical value, and such critical temperature is also most useful to predict the fire spread rate [53, 54]. Fig. 5(a) further summarises the ignition temperatures of virgin woods and pre-charred woods with different thicknesses of char layers. Analogous to the pattern of the ignition time, for the virgin wood or pre-charred wood with a 4.2-mm char layer, the ignition temperatures remain constant at around 350 °C, well agreeing with the literature data [53]. However, as the thickness of the char layer exceeds 6 mm, the ignition temperature witnesses a sudden increase. For example, as the thicknesses of the char layer increase to 11.5 mm and 13.8 mm, the ignition temperatures dramatically increase to 655 ºC and 683 ºC, which is almost twice the ignition temperature of virgin wood. For the virgin wood, the minimum irradiation for the piloted ignition is measured as $\dot{q}''_{min} = 13\ \mathrm{kW/m^2}$. Theoretically, this value should approximately balance the overall environmental heat loss ($\dot{q}''_{loss}$) [53] as

$$\dot{q}''_{min} = \dot{q}''_{loss} = \varepsilon\sigma\left(T_{ig}^4 - T_\infty^4\right) + h\left(T_{ig} - T_\infty\right) \tag{3}$$

where ε is the emissivity, $\sigma = 5.67 \times 10^{-8}\ \mathrm{Jm^{-2}s^{-1}K^{-4}}$ is the Stefan-Boltzmann constant, $h = 1.52\left(T_{ig} - T_\infty\right)^{1/3}$ is the free convection heat transfer coefficient for a horizontal hot plate [53, 56]. Fig. 5(b) summarises the calculated minimum irradiation, where the pre-charred wood can resist the irradiation above 30 kW/m^2, if the char layer is thicker than 10 mm.

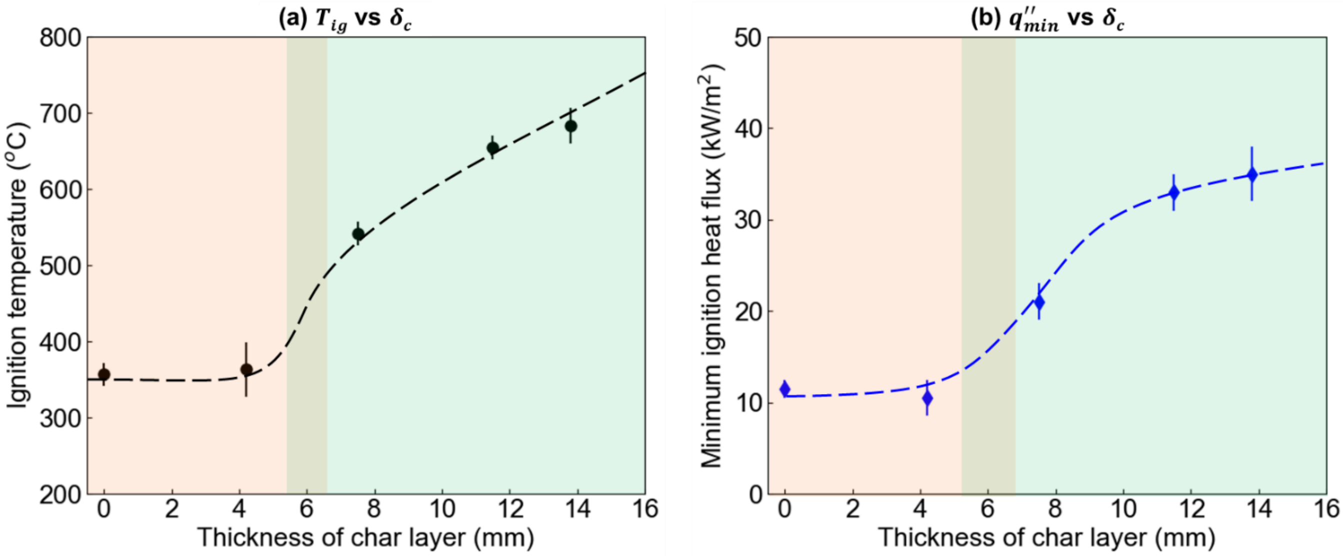

Figure 5. (a) The measured ignition temperatures and (b) the calculated minimum ignition irradiation for engineered wood with different char-layer thicknesses.

4 CONCLUSIONS

This work applies a novel and low-cost method to generate a uniform insulating pre-charred layer on the inner virgin wood using low irradiation of 20 kW/m^2. The thickness of the char layer is found to increase linearly with a constant charring rate of ~0.7 mm/min. For this kind of wood, we found the minimum thickness of an effective pre-charred layer to be 6 ± 1 mm, which should be larger than the thermal penetration depth of the virgin wood. Compared with the virgin woods, an effective char layer could remarkably increase the thermal inertia of the pre-charred woods. The difficulty of ignition increases greatly in terms of the ignition delay time, ignition temperature, and minimum irradiation. For example, with a 13.8-mm char layer, under irradiation of 40 kW/m^2, the required ignition time increases by seven-fold to 272 s, and the ignition temperature increases above 670 ºC. This work provides a promising approach to improving the fire-retardant performance of the wood materials, which may pave a way for the popularisation of wooden buildings for future carbon-neutral construction. Future work will examine other properties essential for future application, including durability, surface roughness, decay resistance and mechanical properties.

ACKNOWLEDGMENT

This work is funded by the National Natural Science Foundation of China (NSFC) No. 51876183 and the Joint Postdoc Scheme of the Hong Kong Polytechnic University and University of California at Berkeley (No. P0038960).

REFERENCES

1. Karlen C (2021) Multiple Scales Insight into Using Timber for a Sustainable and Future Approach to Buildings. In: Sayigh A (ed) The Importance of Wood and Timber in Sustainable Buildings. Springer Nature, Switzerland, pp 195–211
2. Kim DH, Na IY, Jang HK, et al (2019) Anisotropic electrical and thermal characteristics of carbon nanotube-embedded wood. Cellulose 26:5719–5730. https://doi.org/10.1007/s10570-019-02485-y
3. Beasley W (1999) The Japanese Experience: A Short History of Japan. University of California Press, California
4. Wang J, Wang L, Gardner DJ, et al (2021) Towards a cellulose-based society: opportunities and challenges. Springer Netherlands
5. Tollefson J (2017) Wood Grows Up. Nature 545:280–282. https://doi.org/10.1038/545280a
6. Barber D (2015) Tall Timber Buildings: What's Next in Fire Safety ? Fire Technol 51:1279–1284. https://doi.org/10.1007/s10694-015-0497-7
7. Bowyer J, Bratkovich S, Howe J, et al (2016) Modern Tall Wood Buildings: Opportunities for Innovation. Minneapolis
8. Chen C, Kuang Y, Zhu S, et al (2020) Structure–property–function relationships of natural and engineered wood. Nat. Rev. Mater. 19–21
9. Ahn N, Dodoo A, Riggio M, et al (2022) Circular economy in mass timber construction: State-of-the-art, gaps and pressing research needs. J Build Eng 53:104562. https://doi.org/10.1016/j.jobe.2022.104562
10. Wimmers G (2017) Wood: A construction material for tall buildings. Nat Rev Mater 2:1–3. https://doi.org/10.1038/natrevmats.2017.51
11. Stoeckel F, Konnerth J, Gindl-Altmutter W (2013) Mechanical properties of adhesives for bonding wood-A review. Int J Adhes Adhes 45:32–41. https://doi.org/10.1016/j.ijadhadh.2013.03.013
12. Ayanleye S, Udele K, Nasir V, et al (2022) Durability and protection of mass timber structures: A review. J Build Eng 46:103731. https://doi.org/10.1016/j.jobe.2021.103731
13. Wang D, Lin L, Fu F (2020) Deformation mechanisms of wood cell walls under tensile loading: a comparative study of compression wood (CW) and normal wood (NW). Cellulose 27:4161–4172. https://doi.org/10.1007/s10570-020-03095-9
14. Lu Y, Feng M, Zhan H (2014) Preparation of SiO2–wood composites by an ultrasonic-assisted sol–gel technique. Cellulose 21:4393–4403. https://doi.org/10.1007/s10570-014-0437-6
15. Vaks A, Mason AJ, Breitenbach SFM, et al (2020) Palaeoclimate evidence of vulnerable permafrost during times of low sea ice. Nature 577:221–225. https://doi.org/10.1038/s41586-019-1880-1
16. Wang K, Wang S, Meng D, et al (2021) A facile preparation of environmentally-benign and flame-retardant coating on wood by comprising polysilicate and boric acid. Cellulose 28:11551–11566. https://doi.org/10.1007/s10570-021-04238-2
17. Yang WJ, Wei CX, Yuen ACY, et al (2022) Fire-retarded nanocomposite aerogels for multifunctional applications: A review. Compos Part B Eng 237:109866. https://doi.org/10.1016/j.compositesb.2022.109866
18. Cobian-Iñiguez J, Richter F, Camignani L, et al (2022) Wind Effects on Smoldering Behavior of Simulated Wildland Fuels. Combust Sci Technol 00:1–18. https://doi.org/10.1080/00102202.2021.2019239
19. Richter F, Jervis FX, Huang X, Rein G (2021) Effect of oxygen on the burning rate of wood. Combust Flame 234:111591. https://doi.org/10.1016/j.combustflame.2021.111591
20. Xing Z, Wang Y, Zhang J, Ma H (2021) Comparative study on fire resistance and zero strength layer thickness of CLT floor under natural fire and standard fire. Constr Build Mater 302:124368. https://doi.org/10.1016/j.conbuildmat.2021.124368
21. Jiang L, Zhao Z, Tang W, et al (2019) Flame spread and burning rates through vertical arrays of wooden dowels. Proc Combust Inst 37:3767–3774. https://doi.org/10.1016/j.proci.2018.09.008
22. Wang S, Ding P, Lin S, et al (2021) Smoldering and Flaming of Disc Wood Particles Under External Radiation: Autoignition and Size Effect. Front Mech Eng 7:1–11. https://doi.org/10.3389/fmech.2021.686638
23. Engel T, Werther N (2021) Structural Means for Fire-Safe Wooden. Fire Technol. https://doi.org/10.1007/s10694-021-01174-2

24. Kallada Janardhan R, Hostikka S (2019) Predictive Computational Fluid Dynamics Simulation of Fire Spread on Wood Cribs. Fire Technol 55:2245–2268. https://doi.org/10.1007/s10694-019-00855-3
25. Lineham SA, Thomson D, Bartlett AI, et al (2016) Structural response of fire-exposed cross-laminated timber beams under sustained loads. Fire Saf J 85:23–34. https://doi.org/10.1016/j.firesaf.2016.08.002
26. Wang S, Ding P, Lin S, et al (2021) Deformation of wood slice in fire: Interactions between heterogeneous chemistry and thermomechanical stress. Proc Combust Inst 38:5081–5090. https://doi.org/10.1016/j.proci.2020.08.060
27. Lin S, Huang X, Gao J, Ji J (2022) Extinction of wood fire: A near-limit blue flame above smoldering surface. Fire Technol 58:415–434. https://doi.org/10.1007/s10694-021-01146-6
28. Arnórsson SM, Hadden RM, Law A (2020) The Variability of Critical Mass Loss Rate at Auto-Extinction. Fire Technol. https://doi.org/10.1007/s10694-020-01002-z
29. Ilhan F, Kıyan E, Yüzer N (2022) Use of sheep slaughterhouse-derived struvite in the production of environmentally sustainable cement and fire-resistant wooden structures. 366:. https://doi.org/10.1016/j.jclepro.2022.132948
30. Zhou X, Fu Q, Zhang Z, et al (2021) Efficient flame-retardant hybrid coatings on wood plastic composites by layer-by-layer assembly. J Clean Prod 321:128949. https://doi.org/10.1016/j.jclepro.2021.128949
31. Jiang T, Feng X, Wang Q, et al (2014) Fire performance of oak wood modified with N-methylol resin and methylolated guanylurea phosphate/boric acid-based fire retardant. Constr Build Mater 72:1–6. https://doi.org/10.1016/j.conbuildmat.2014.09.004
32. Jiang J, Li J, Hu J, Fan D (2010) Effect of nitrogen phosphorus flame retardants on thermal degradation of wood. Constr Build Mater 24:2633–2637. https://doi.org/10.1016/j.conbuildmat.2010.04.064
33. Popescu CM, Pfriem A (2020) Treatments and modification to improve the reaction to fire of wood and wood based products—An overview. Fire Mater 44:100–111. https://doi.org/10.1002/fam.2779
34. Uddin M, Kiviranta K, Suvanto S, et al (2020) Casein-magnesium composite as an intumescent fire retardant coating for wood. Fire Saf J 112:102943. https://doi.org/10.1016/j.firesaf.2019.102943
35. Gaff M, Kačík F, Gašparík M, et al (2019) The effect of synthetic and natural fire-retardants on burning and chemical characteristics of thermally modified teak (Tectona grandis L. f.) wood. Constr Build Mater 200:551–558. https://doi.org/10.1016/j.conbuildmat.2018.12.106
36. Sun L, Xie Y, Ou R, et al (2020) The influence of double-layered distribution of fire retardants on the fire retardancy and mechanical properties of wood fiber polypropylene composites. Constr Build Mater 242:118047. https://doi.org/10.1016/j.conbuildmat.2020.118047
37. Zhang L, Liang S, Chen Z (2018) Influence of particle size and addition of recycling phenolic foam on mechanical and flame retardant properties of wood-phenolic composites. Constr Build Mater 168:1–10. https://doi.org/10.1016/j.conbuildmat.2018.01.173
38. Nasirzadeh M, Yahyaei H, Mohseni M (2022) Effects of inorganic fillers on the performance of the water-based intumescent fire-retardant coating. Fire Mater 1–11. https://doi.org/10.1002/fam.3067
39. Sevda BT, Ayfer DC, Turgay O (2020) The synergistic effect of intumescent coating containing titanium dioxide and antimony trioxide onto spruce and alder wood species. J Build Eng 31:101407. https://doi.org/10.1016/j.jobe.2020.101407
40. Yasemin A, Doğan M, Bayramlı E (2009) The effect of red phosphorus on the fire properties of intumescent pine wood flour – LDPE composites Yasemin. Finnish-Swedish Flame Days 2009 4B. https://doi.org/10.1002/fam
41. Rowell RM (2006) Chemical modification of wood: A short review. Wood Mater Sci Eng 1:29–33. https://doi.org/10.1080/17480270600670923
42. Hasburgh LE, Zelinka SL, Bishell AB, Kirker GT (2021) Durability and fire performance of charred wood siding (Shou sugi ban). Forests 12:. https://doi.org/10.3390/f12091262
43. Machová D, Oberle A, Zárybnická L, et al (2021) Surface characteristics of one-sided charred beech wood. Polymers (Basel) 13:1–15. https://doi.org/10.3390/polym13101551
44. Gaff M, Babiak M, Kačík F, et al (2019) Plasticity properties of thermally modified timber in bending – The effect of chemical changes during modification of European oak and Norway spruce. Compos Part B Eng 165:613–625. https://doi.org/10.1016/j.compositesb.2019.02.019

45. Hein C (2010) Shaping Tokyo: Land development and planning practice in the early modern Japanese metropolis. J Urban Hist 36:447–484. https://doi.org/10.1177/0096144209347737
46. Kymäläinen M, Hautamäki S, Lillqvist K, et al (2017) Surface modification of solid wood by charring. J Mater Sci 52:6111–6119. https://doi.org/10.1007/s10853-017-0850-y
47. Kymäläinen M, Turunen H, Čermák P, et al (2018) Sorption-related characteristics of surface charred spruce wood. Materials (Basel) 11:. https://doi.org/10.3390/ma11112083
48. Gupta M, Yang J, Roy C (2003) Gupta, Yang, Roy - 2003 - Specific heat and thermal conductivity of softwood bark and softwood char particles. Fuel 82:919–927. https://doi.org/10.1016/S0016-2361(02)00398-8
49. Gan W, Chen C, Wang Z, et al (2019) Dense, Self-Formed Char Layer Enables a Fire-Retardant Wood Structural Material. Adv Funct Mater 29:1–9. https://doi.org/10.1002/adfm.201807444
50. Babrauskas V (2016) The Cone Calorimeter. In: Hurley M (ed) SFPE Handbook of Fire Protection Engineering, 5th Editio. Springer, London, pp 952–980
51. Dutta S, Kim NK, Das R, Bhattacharyya D (2019) Effects of sample orientation on the fire reaction properties of natural fibre composites. Compos Part B Eng 157:195–206. https://doi.org/10.1016/j.compositesb.2018.08.118
52. Qin R, Zhou A, Chow CL, Lau D (2021) Structural performance and charring of loaded wood under fire. Eng Struct 228:111491. https://doi.org/10.1016/j.engstruct.2020.111491
53. Quintiere JG (2006) Fundamentals of Fire Phenomena. John Wiley, New York
54. Lin S, Huang X, Urban J, et al (2019) Piloted ignition of cylindrical wildland fuels under irradiation. Front Mech Eng 5:54. https://doi.org/10.3389/fmech.2019.00054
55. Huang X, Gao J (2020) A review of near-limit opposed fire spread. Fire Saf J 103141. https://doi.org/10.1016/j.firesaf.2020.103141
56. Incropera FP (2007) Principles of heat and mass transfer. John Wiley

SiF 2022– The 12th International Conference on Structures in Fire
The Hong Kong Polytechnic University, Nov 30 - Dec 2, 2022

NUMERICAL MODEL FOR NON-LINEAR M - θ RELATIONSHIPS OF DOWEL-TYPE TIMBER CONNECTIONS EXPOSED TO FIRE

Yukito Nakayama[1], Takayuki Kikuchi[2], Marina Totsuka[3], Takeo Hirashima[4]

ABSTRACT

The most common connection type in mass timber construction is wood–steel–wood dowel-type connections, which are semi-rigid. A model for moment–rotation ($M-\theta$) relationships of dowel-type connections is required to account for their semi-rigidity in analyses using beam elements. This study develops a numerical model for non-linear $M-\theta$ relationships under fire conditions (non-linear $M-\theta$ model) that considers the temperature and plasticisation of dowels and timber. This paper also introduces a theoretical model for linear elastic $M-\theta$ relationships (linear $M-\theta$ model), which provides the basis of the non-linear $M-\theta$ model. The numerical model divides dowels into a series of elements on an elastoplastic foundation and performs a direct stiffness method in a time incremental procedure, using an element stiffness matrix derived from beam-on-elastic-foundation theory. The theoretical model agreed well with the ambient test result in the elastic range, and the numerical model corresponded to the fire test results. The three numerical analyses where the dowels are considered to be rigid, linear elastic and elastoplastic bodies are also performed. These three results converged to the same value after 65 min of heating, which suggests that the ultimate states of beams with dowel-type connections exposed to fire can be modelled by assuming that dowels are rigid bodies.

Keywords: Numerical modelling; dowel-type timber connections; moment-rotation relationships; fire

1 INTRODUCTION

The use of mass timber as a primary building material has been increasing for the past few decades. The most common connection type in mass timber construction is a wood–steel–wood (WSW) dowel-type connection, which consists of multiple cylindrical dowels penetrating holes pre-drilled in the timber and a slotted-in steel plate. Because dowel-type connections exhibit semi-rigidity [1,2], their resistance to angle changes falls between those of the fully rigid and pinned types. Thus, a model for moment–rotation ($M-\theta$) relationships of dowel-type connections are essential to account for their semi-rigid behaviour in analyses using beam elements, such as [3]. Studies have been performed on $M-\theta$ relationships under ambient conditions; however, limited research is available to evaluate $M-\theta$ relationships under fire conditions.

Under ambient conditions, the modelling of dowel-type connections is commonly based on beam-on-elastic-foundation (BOEF) theory. Kuenzi adopted the BOEF theory to theoretically describe the elastic deformation of nails and bolts in timber [4]. The BOEF theory was then applied to a 2D numerical analysis

[1] Master's Student, Graduate School of Science and Engineering, Chiba University, Chiba, Japan
e-mail: yukiton@chiba-u.jp, ORCID: https://orcid.org/0000-0002-3814-4902
[2] PhD Candidate, Graduate School of Science and Engineering, Chiba University, Chiba, Japan
e-mail: kikuchi.takayuki@chiba-u.jp, ORCID: https://orcid.org/0000-0001-9972-6386
[3] Assistant Professor, Graduate School of Science and Engineering, Chiba University, Chiba, Japan
e-mail: mtotsuka@chiba-u.jp, ORCID: https://orcid.org/0000-0001-8548-4996
[4] Professor, Graduate School of Science and Engineering, Chiba University, Chiba, Japan
e-mail: hirashima@faculty.chiba-u.jp, ORCID: https://orcid.org/0000-0003-1462-5370
https://doi.org/10.6084/m9.figshare.22193785

to address the elastoplastic deformation problem of nails [5] and bolts [6 – 8]. In recent years, these single-fastener models have been used in models for linear elastic $M-\theta$ relationships [9] and elastoplastic $M-\theta$ relationships [10,11].

Under fire conditions, the modelling of timber connections is very complex as the mechanical properties of steel and timber depend on temperature and plasticisation. The 3D finite element method is the most common solution for this complexity [12,13]. However, it cannot be combined with analyses using beam elements. Some studies have been conducted using numerical models of a single fastener under fire loading [14 – 16]. However, these single-fastener models cannot simulate the fire behaviour of the entire connection. To the best of our knowledge, no model has been developed for the $M-\theta$ relationships under fire conditions.

This study aims to develop a numerical model for non-linear $M-\theta$ relationships (non-linear $M-\theta$ model) that considers the temperature and plasticisation of dowels and timber. This paper first introduces the theoretical model for the linear elastic $M-\theta$ relationships [9] (a linear $M-\theta$ model), which is the basis of the non-linear $M-\theta$ model, and then presents the numerical framework developed to investigate the non-linear $M-\theta$ relationships under fire conditions. This paper also describes load-carrying tests on timber frames with dowel-type connections, under ambient and fire conditions, and compares the experimental results with the theoretical and numerical results to verify the proposed non-linear $M-\theta$ model.

The subscripts and superscripts used in this paper are defined as follows:

t denotes the time step number,
c denotes the convergence step number for the determination of the neutral axis,
i denotes the element number (When written in Romans, i denotes the imaginary unit),
j denotes the node number,
and *m* denotes the dowel number.

2 LINEAR M - θ MODEL AT AMBIENT TEMPERATURE

2.1 Linear M - θ relationships

When a bending moment acts on a dowel-type connection, the dowels contact the slotted-in steel plate and bear the reaction forces from the contact points, as shown in Figure 1. The relationship between the force applied to the dowel and the displacement at the loading point is generally called the load–slip relationship, which is almost linear in the elastic range at ambient temperature. Thus, dowel-type connections can be modelled simply in two dimensions by representing the load-slip relationships of dowels as linear springs, as shown in Figure 2. The linear $M-\theta$ relationships of the dowel-type connections at ambient temperature [9] are expressed as follows:

$$M=\left(\sum_{m=1}^{n_d} K_m r_m^2\right)\theta, \tag{1}$$

where n_d is the total number of dowels, K_m is the slip modulus of dowel *m*, and r_m is the distance from the rotation centre to dowel *m*.

The present paper has described the procedure used to simulate the $M-\theta$ behaviour of a double-shear connection with dowels arranged in one vertical line, which is the connection type used in the test specimens. The rotation centre of this connection type is always on the neutral axis, and the dowels deform in the grain direction when the connection rotates. Thus, this paper considered the rotation centre and the neutral axis to be synonymous and defined the embedding stiffness of timber, k, and the embedding strength of timber, σ_h, as the values parallel to the grain unless otherwise noted. However, the linear and non-linear $M-\theta$ models can be applied to connections with dowels arranged in multiple vertical lines.

2.2 Slip modulus

The objective here is to derive the slip modulus using the BOEF theory. According to the BOEF theory, the deflection curve of a dowel in timber, $y(x)$, satisfies the differential equation:

$$EI\frac{d^4y(x)}{dx^4}+kdy(x)=0, \tag{2}$$

where EI denotes bending stiffness and d denotes dowel diameter. Assuming that the general solution is $y(x)=\mathrm{e}^{\alpha x}$, the constant α is expressed as

$$EI\alpha^4+kd=0,$$

$$\therefore \alpha=\pm\sqrt[4]{kd/4EI}\,(1\pm \mathrm{i}). \tag{3}$$

Substituting Equation (3) into $y(x)=\mathrm{e}^{\alpha x}$ gives the general solution of Equation (2):

$$y(x)=\mathrm{e}^{\lambda x}\left[A\cos(\lambda x)+B\sin(\lambda x)\right]+\mathrm{e}^{-\lambda x}\left[C\cos(\lambda x)+D\sin(\lambda x)\right], \tag{4}$$

where A, B, C, and D are constants of integration and λ stands for $\sqrt[4]{kd/4EI}$. As shown in Figure 2, the boundary conditions of a dowel in the WSW connections are:

$$\ddot{y}(0)=0,\ \dddot{y}(0)=0,\ \dot{y}(l/2)=0, \text{ and } \dddot{y}(l/2)=-p/2EI, \tag{5}$$

where l is the dowel length and p is the reaction force. For simplicity, the axial force is ignored, and the half of the dowel is modelled. The integration constants that satisfy the boundary conditions above are:

$$A=\frac{\left(3+\mathrm{e}^{\lambda l}\right)\cos(\lambda l/2)+\left(1+\mathrm{e}^{\lambda l}\right)\sin(\lambda l/2)}{4kd\cdot \mathrm{e}^{\lambda l/2}\left[\sinh(\lambda l)+\sin(\lambda l)\right]}p\lambda,\ B=D=\frac{\left(1-\mathrm{e}^{\lambda l}\right)\cos(\lambda l/2)+\left(1+\mathrm{e}^{\lambda l}\right)\sin(\lambda l/2)}{4kd\cdot \mathrm{e}^{\lambda l/2}\left[\sinh(\lambda l)+\sin(\lambda l)\right]}p\lambda, \text{ and}$$

$$C=\frac{\left(1+3\mathrm{e}^{\lambda l}\right)\cos(\lambda l/2)-\left(1+\mathrm{e}^{\lambda l}\right)\sin(\lambda l/2)}{4kd\cdot \mathrm{e}^{\lambda l/2}\left[\sinh(\lambda l)+\sin(\lambda l)\right]}p\lambda. \tag{6}$$

Using the constants of integration defined above, the deflection of any point of the dowel can be calculated using Equation (4). The deflection at the contact point $x=l/2$ is:

$$y(l/2)=\frac{\lambda}{2kd}\cdot\frac{\cosh(\lambda l)+\cos(\lambda l)+2}{\sinh(\lambda l)+\sin(\lambda l)}\cdot p. \tag{7}$$

Because $y(l/2)$ coincides with the slip caused by the reaction force, the slip modulus can be obtained by:

$$K=\frac{p}{y(l/2)}=\frac{2kd}{\lambda}\cdot\frac{\sinh(\lambda l)+\sin(\lambda l)}{\cosh(\lambda l)+\cos(\lambda l)+2}. \tag{8}$$

3 NON-LINEAR M - θ MODEL AT HIGH TEMPERATURE

3.1 General approach

Under fire exposure, the load–slip relationships exhibit nonlinearity because the mechanical properties of timber and steel vary with heating time; thus, they are represented as non-linear springs in the non-linear $M-\theta$ model, as shown in Figure 3. Within a given time step, t, the relationship between the current bending moment, M^t, and rotation, θ^t, is given by:

$$M^t=\sum_{m=1}^{n_d}p_m^t\left(\theta^t r_m^t\right)\cdot r_m^t, \tag{9}$$

where r_m^t is the current distance from the neutral axis to dowel m and $\theta^t r_m^t$ is the current slip of dowel m. Because the neutral axis position varies with the heating time, r_m^t must be updated at each time step using:

$$r_m^t=y_m-e^t, \tag{10}$$

where y_m is the distance from the centroid axis to dowel m and e^t is the current distance from the centroid axis to the neutral axis. It should be noted that e denotes the natural logarithm when written in Romans. The procedure used to determine e^t is outlined in Section 3.6. In Equation (9), the non-linear load–slip relationships for each dowel, $p_m^t(\theta^t r_m^t)$, are unknown functions. To obtain $p_m^t(\theta^t r_m^t)$, the non-linear $M-\theta$ model divides dowels into a series of elements on an elastoplastic foundation and uses a direct stiffness method in a time incremental procedure. By updating the element properties at each time step, the load–slip relationships can be simulated considering the time history of temperature distribution and plasticisation. For simplicity, the non-linear $M-\theta$ model ignores the axial forces within the elements and model only the half of the dowel due to symmetry.

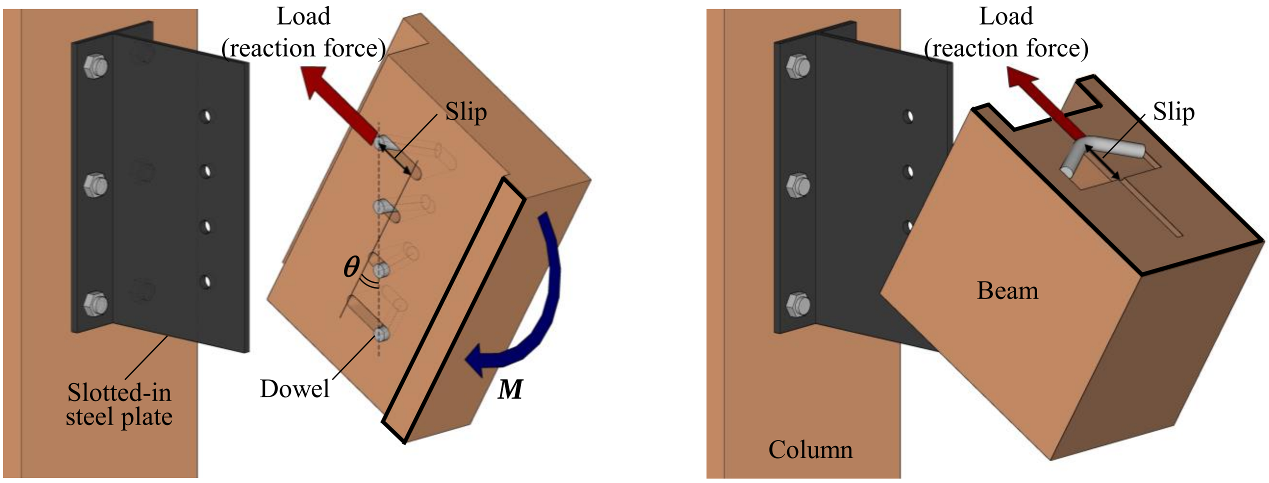

Figure 1. Resistance mechanism of dowel-type connections subjected to a bending moment

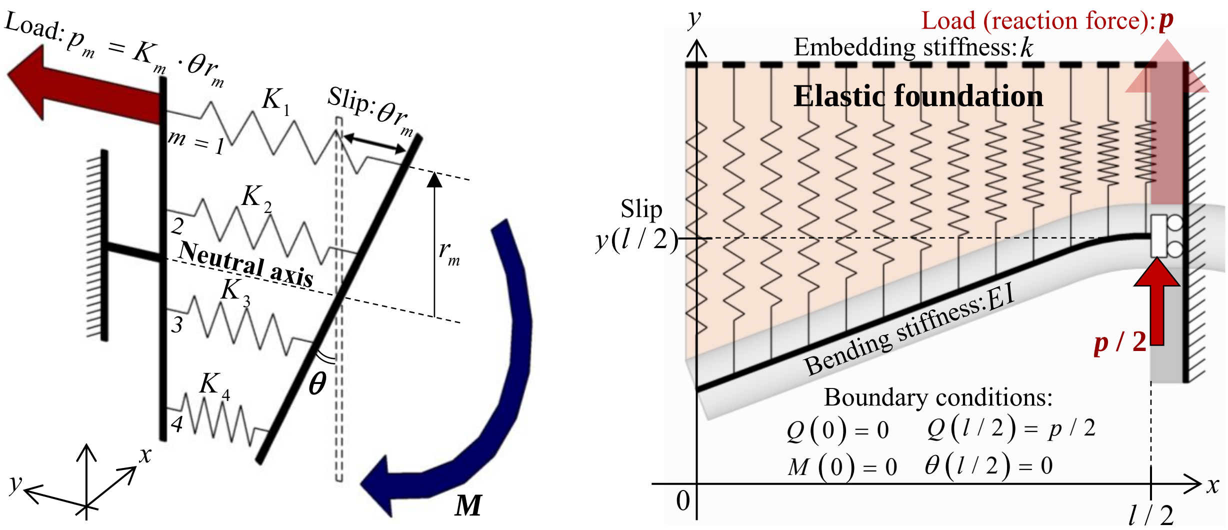

Figure 2. Linear $M-\theta$ model at ambient temperature

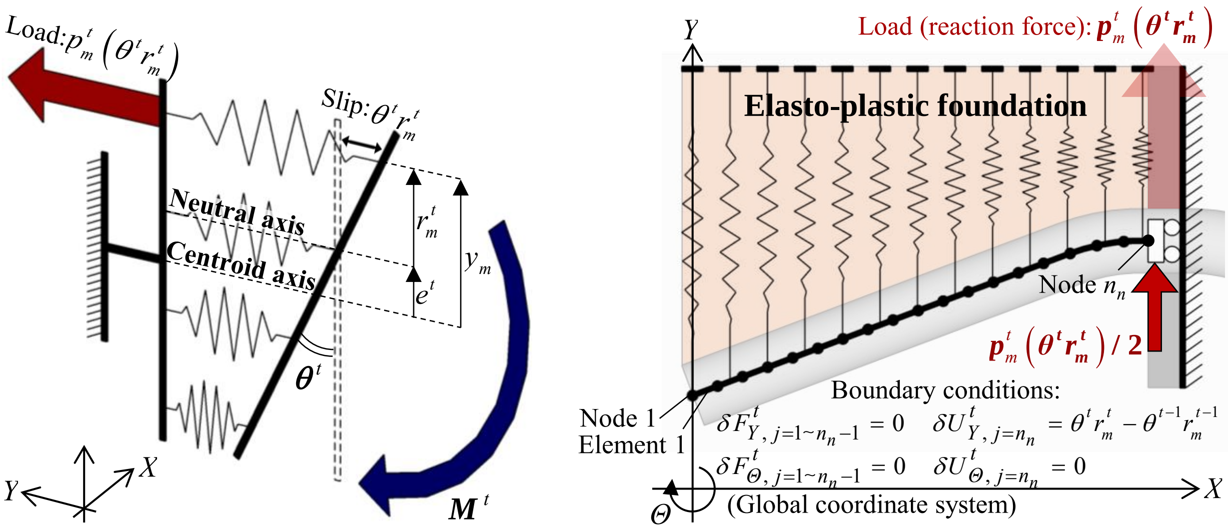

Figure 3. Non-linear $M-\theta$ model at high temperature

3.2 Stress–displacement relationship of elastoplastic foundation

Using Foschi's approach [5], the stress–displacement relationship of the elastoplastic foundation parallel to the grain was assumed to take the form:

$$\sigma_i^t(v) = R_\sigma\left(T_i^t\right)\sigma_h\left(1-\exp\left(\frac{-R_k\left(T_i^t\right)\cdot k}{R_\sigma\left(T_i^t\right)\cdot\sigma_h}v\right)\right), \tag{11}$$

where R_σ and R_k are the reduction factors for the embedding strength and stiffness, respectively, T is the element temperature, and v is the element displacement, which was calculated using the average of the element end displacements of the two adjacent nodes. As shown in Figure 7, the embedding stiffness for each element can be updated using the element displacements from the previous time step, $t-1$, that is:

$$k_i^t = \frac{\partial\sigma_i^{t-1}}{\partial v_i^{t-1}} = R_k(T_i^t)\cdot k\cdot\exp\left(\frac{-R_k(T_i^t)\cdot k}{R_f(T_i^t)\cdot f}\cdot v_i^{t-1}\right). \tag{12}$$

3.3 Stress–strain relationship of steel

The stress–strain relationship of the steel was assumed to have a bilinear form, as shown in Figure 4. The bending stiffness for each element can be updated from the following condition branch, assuming that the plane sections remain planar, namely:

$$EI_i^t = \begin{cases} R_E\left(T_i^t\right)EI & \text{Case I: } (M_{\max,i}^t \le M_i^{t-1} < M_y) \\ R_E\left(T_i^t\right)E\left[\mu I + \frac{I}{\pi}(1-\mu)\left(2\alpha - \frac{\sin 4\alpha}{2}\right)\right] & \text{Case II: } (M_y \le M_{\max,i}^t \le M_i^{t-1}), \\ R_E\left(T_i^t\right)EI & \text{Case III: } (M_i^{t-1} < M_{\max,i}^t) \end{cases} \tag{13}$$

where R_E is the reduction factor for the modulus of elasticity of steel, μ is the ratio of the modulus of elasticity to the modulus of plasticity, and $M_{\max,i}^t$ is the maximum bending moment that element i has experienced before the time step t. Figure 5 shows the schematic diagram of the condition branch. The parameter α in Case II denotes arcsin(l_e/d), which is a function of the bending moment of the previous time step, $t-1$, given below:

$$\left|M_i^{t-1}\right| = \int\sigma y\cdot dA = 2R_f\left(T_i^t\right)\cdot f_y\left[\frac{\mu I + \frac{I}{\pi}(1-\mu)\left(2\alpha-\frac{\sin 4\alpha}{2}\right)}{d\sin\alpha} + \frac{d^3}{16}(1-\mu)\left(\cos\alpha + \frac{\cos 3\alpha}{3}\right)\right], \tag{14}$$

where l_e denotes the length of the elastic area, R_f is the reduction factor for yield stress of steel, and f_y is the yield stress of steel. Because α cannot be transformed into an explicit function of M_i^{t-1}, α is determined numerically using the bisection method within the interval $[0,\ \pi/2]$.

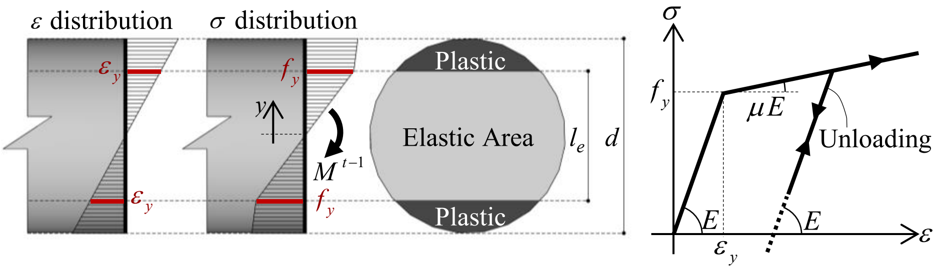

Figure 4. Assumed stress-strain relationship of steel

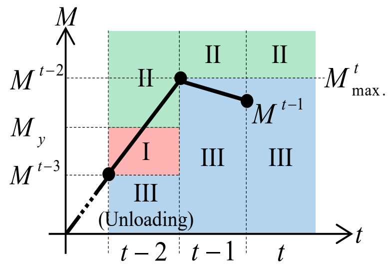

Figure 5. Condition branch for updating bending stiffness

3.4 Element stiffness matrix based on BOEF theory

The objective here is to derive the element stiffness matrix using the general solution, Equation (4), of BOEF theory. As shown in Figure 6, the boundary conditions of element i are as follows:

$$y(0) = \delta v_j^t,\ \dot{y}(0) = -\delta\theta_j^t,\ \ddot{y}(0) = \delta M_j^t / EI_{i=j}^t, \text{ and } \dddot{y}(0) = \delta Q_j^t / EI_{i=j}^t, \tag{15}$$

where δv_j^t, $\delta\theta_j^t$, δM_j^t, and δQ_j^t denote the incremental displacement, rotation, bending moment, and shearing force of the element end at node j, respectively. The element number i coincide with the node number of the left element end. By substituting Equation (15) into Equation (4), the deflection curve for each element can be expressed using the following integration constants:

$$A = \frac{\delta v_j^t}{2} - \frac{\delta\theta_j^t}{4\lambda_{i=j}^t} - \frac{\delta Q_j^t}{8EI_{i=j}^t\,{\lambda_{i=j}^t}^3},\ B = -\frac{\delta\theta_j^t}{4\lambda_{i=j}^t} + \frac{\delta M_j^t}{4EI_{i=j}^t\,{\lambda_{i=j}^t}^2} + \frac{\delta Q_j^t}{8EI_{i=j}^t\,{\lambda_{i=j}^t}^3},$$

$$C = \frac{\delta v_j^t}{2} + \frac{\delta\theta_j^t}{4\lambda_{i=j}^t} + \frac{\delta Q_j^t}{8EI_{i=j}^t\,{\lambda_{i=j}^t}^3},\ \text{and}\ D = -\frac{\delta\theta_j^t}{4\lambda_{i=j}^t} - \frac{\delta M_j^t}{4EI_{i=j}^t\,{\lambda_{i=j}^t}^2} + \frac{\delta Q_j^t}{8EI_{i=j}^t\,{\lambda_{i=j}^t}^3}. \tag{16}$$

With the values of all constants of integration, the incremental deformations and forces at the opposite element end, that is $x = L_i$, can be expressed using δv_j^t, $\delta\theta_j^t$, δQ_j^t, and δM_j^t by recalling:

$$y(L_i) = \delta v_{j+1}^t,\ \dot{y}(L_i) = -\delta\theta_{j+1}^t,\ \ddot{y}(L_i) = -\delta M_{j+1}^t \big/ EI_{i=j}^t,\ \text{and}\ \dddot{y}(L_i) = -\delta Q_{j+1}^t \big/ EI_{i=j}^t. \tag{17}$$

The incremental element end forces can then be expressed using the incremental element end deformations. The element stiffness matrix is now expressed as:

$$\begin{bmatrix} \delta Q_j^t \\ \delta M_j^t \\ \delta Q_{j+1}^t \\ \delta M_{j+1}^t \end{bmatrix} = \frac{2EI_{i=j}^t}{sh^2 - s^2} \begin{bmatrix} 2{\lambda_{i=j}^t}^3(sh\cdot ch + s\cdot c) & -{\lambda_{i=j}^t}^2(sh^2+s^2) & -2{\lambda_{i=j}^t}^3(sh\cdot c + ch\cdot s) & -2{\lambda_{i=j}^t}^2 sh\cdot s \\ & \lambda_{i=j}^t(sh\cdot ch - s\cdot c) & 2{\lambda_{i=j}^t}^2 sh\cdot s & -\lambda_{i=j}^t(sh\cdot c - ch\cdot s) \\ & & 2{\lambda_{i=j}^t}^3(sh\cdot ch + s\cdot c) & {\lambda_{i=j}^t}^2(sh^2+s^2) \\ & \text{Sym.} & & \lambda_{i=j}^t(sh\cdot ch - s\cdot c) \end{bmatrix} \begin{bmatrix} \delta v_j^t \\ \delta\theta_j^t \\ \delta v_{j+1}^t \\ \delta\theta_{j+1}^t \end{bmatrix}, \tag{18}$$

where $\lambda_{i=j}^t = \sqrt[4]{k_{i=j}^t d \big/ 4EI_{i=j}^t}$, $sh = \sinh(\lambda_{i=j}^t L_{i=j})$, $s = \sin(\lambda_{i=j}^t L_{i=j})$, $ch = \cosh(\lambda_{i=j}^t L_{i=j})$, and $c = \cos(\lambda_{i=j}^t L_{i=j})$. Once the current embedding stiffness and bending stiffness of all elements are obtained from Equations (12) and (13), the current element stiffness matrices are assembled into the current global stiffness matrix of the dowel such that the system can be expressed as:

$$\delta\mathbf{F}^t = \mathbf{K}^t \cdot \delta\mathbf{P}^t, \tag{19}$$

where $\mathbf{K}^t$ denotes the current global stiffness matrix, $\delta\mathbf{F}^t$ denotes the current incremental nodal force vector, and $\delta\mathbf{U}^t$ denotes the current incremental nodal displacement vector. Inserting the known values shown in Figure 3 into Equation (19) leads to:

$$\begin{bmatrix} \delta F_{Y,j=1}^t = 0 \\ \vdots \\ \delta F_{\Theta,j=n_n-1}^t = 0 \\ \delta F_{Y,j=n_n}^t \\ \delta F_{\Theta,j=n_n}^t \end{bmatrix} = \mathbf{K}^t \cdot \begin{bmatrix} \delta U_{Y,j=1}^t \\ \vdots \\ \delta U_{\Theta,j=n_n-1}^t \\ \delta U_{Y,j=n_n}^t = \theta^t r_m^t - \theta^{t-1} r_m^{t-1}\,(= \text{current slip increment}) \\ \delta U_{\Theta,j=n_n}^t = 0 \end{bmatrix}, \tag{20}$$

where the subscripts Y and Θ denotes directions in the global coordinate system and n_n is the total number of nodes. Now, Equation (19) is solvable, and the unknown nodal deformations and forces can be calculated. The current element end deformations can then be determined by the following summations:

$$v_j^t = v_j^{t-1} + \delta v_j^t = v_j^{t-1} + \delta U_{Y,j}^t, \tag{21}$$

$$\theta_j^t = \theta_j^{t-1} + \delta\theta_j^t = \theta_j^{t-1} + \delta U_{\Theta,j}^t. \tag{22}$$

3.5 Element end force and reaction force

Once all the current element end displacements are obtained, in Equation (21), the current element end forces can be calculated by equilibrium with the σ calculated from Equation (11). As shown in Figure 8, the current shearing forces and bending moments can be calculated by the following integrations:

$$Q_j^t = \sum_{i=1}^{j-1} \sigma_i^t \left(v_i^t \right) \cdot L_i \cdot d \ , \tag{23}$$

$$M_j^t = \sum_{i=1}^{j-1} \left[\sigma_i^t \left(v_i^t \right) \cdot L_i \cdot d \cdot \left(\frac{L_i}{2} + L_{i+1} + L_{i+2} + \cdots + L_{j-1} \right) \right] . \tag{24}$$

The node $j = n_n$ is the contact point with the steel plate. Thus, the current reaction force for each dowel p_m^t is obtained using:

$$p_m^t \left(\theta^t r_m^t \right) = 2Q_{j=n_n,m}^t = 2\sum_{i=1}^{n_n-1} \sigma_{i,m}^t \left(v_{i,m}^t \right) \cdot L_{i,m} \cdot d \ . \tag{25}$$

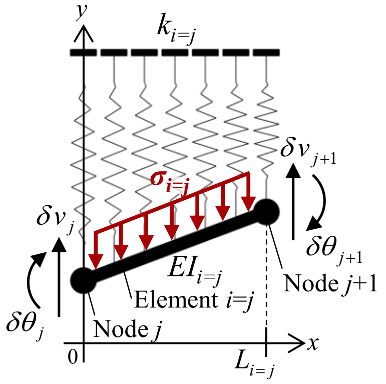

Figure 6. Element on an elastoplastic foundation

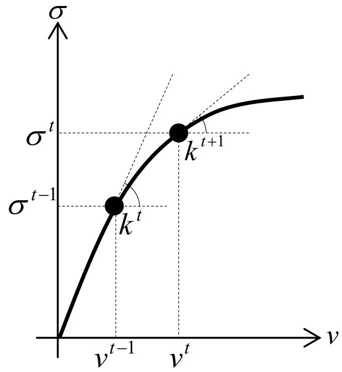

Figure 7. Assumed stress-displacement relationship of timber

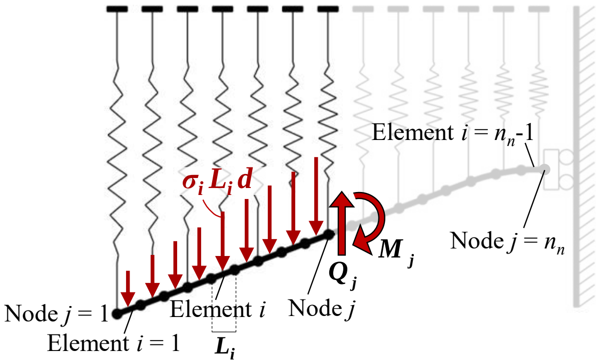

Figure 8. Equilibrium between element end forces and σ

3.6 Distance from centroid axis to the neutral axis

The axial force caused by the rotation around the neutral axis must be 0. Thus, the amount of $p_m^t \left(\theta^t r_m^t \right)$ was checked against the permissible error:

$$\left| \sum_{m=1}^{n_d} p_m^t \left(\theta^t r_m^t \right) \right| \le \text{permissible error} \ . \tag{26}$$

If convergence was not obtained, the interval for the bisection method and the current distance from the centroid axis to the neutral axis, $e^{t,c}$, were updated from the following condition branch:

$$\left[e_{\text{high}}^{t,c+1}, e_{\text{low}}^{t,c+1} \right] = \begin{cases} \left[e_{\text{high}}^{t,c}, e^{t,c} \right] & \left(\sum_{m=1}^{n_d} p_m^t \left(\theta^t r_m^t \right) > \text{permissible error} \right) \\ \left[e^{t,c}, e_{\text{low}}^{t,c} \right] & \left(\sum_{m=1}^{n_d} p_m^t \left(\theta^t r_m^t \right) < \text{permissible error} \right) \end{cases}, \quad e^{t,c+1} = \frac{e_{\text{high}}^{t,c+1} + e_{\text{low}}^{t,c+1}}{2} . \tag{27}$$

The initial values, $e_{\text{high}}^{t,c=1}$ and $e_{\text{low}}^{t,c=1}$, represent the distances from the centroid axis to the uppermost and downmost dowels, respectively. After redetermining r_m^t from Equation (10) using $e^{t,c+1}$, the calculation is reduced from Equation (18), with the current slip increment $\theta^t r_m^t - \theta^{t-1} r_m^{t-1}$ being recalculated. Figure 11 shows the flow chart of the calculation procedure of the non-linear $M - \theta$ model.

3.7 Reduction factor

The modulus of elasticity and yield strength of steel at elevated temperatures were reduced according to the reduction factors recommended in Eurocode 3 [17]. Meanwhile, the reduction factors for the embedding stiffness and strength of timber were determined from available experimental data [18] because there are no recommendations in Eurocode 5. The reduction factors are shown in Figure 9. The experimental procedure [18] were as follows: first, the single-dowelled specimens were heated for 1–2 h in an electric furnace with an air temperature of 100, 150 or 200 °C; subsequently, the specimens were removed from the furnace and covered with a heat-resistant glass cloth; and finally, the specimens were compressed. The temperature of the specimen was measured using two thermocouples attached to the centre of the dowel.

The reduction factors were calculated based on the time history data of the element temperatures. They were then multiplied by the corresponding mechanical properties at each time step, as shown in Equations (11)–(14). The time history data of the element temperatures was obtained using 3D heat transfer analysis. The non-linear $M-\theta$ model can be applied to the standard and also non-standard fire exposure by appropriately setting the heat transfer analysis conditions.

3.8 Load–slip relationships of non-linear springs at high temperature

Figure 10 shows the load–slip relationships of the non-linear springs at high temperature obtained using Equations (11)–(25), which agreed well with the available experimental results at 20, 60, and 100 °C [18].

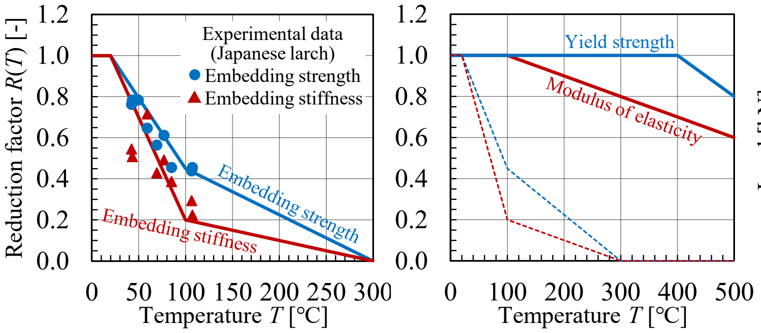

(a) Timber (b) Steel

Figure 9. Reduction factor

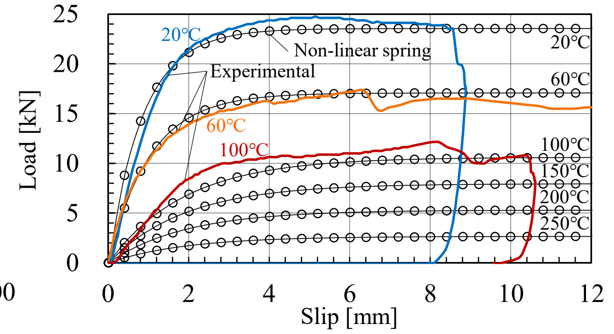

Figure 10. Load–slip relationship of non-linear springs

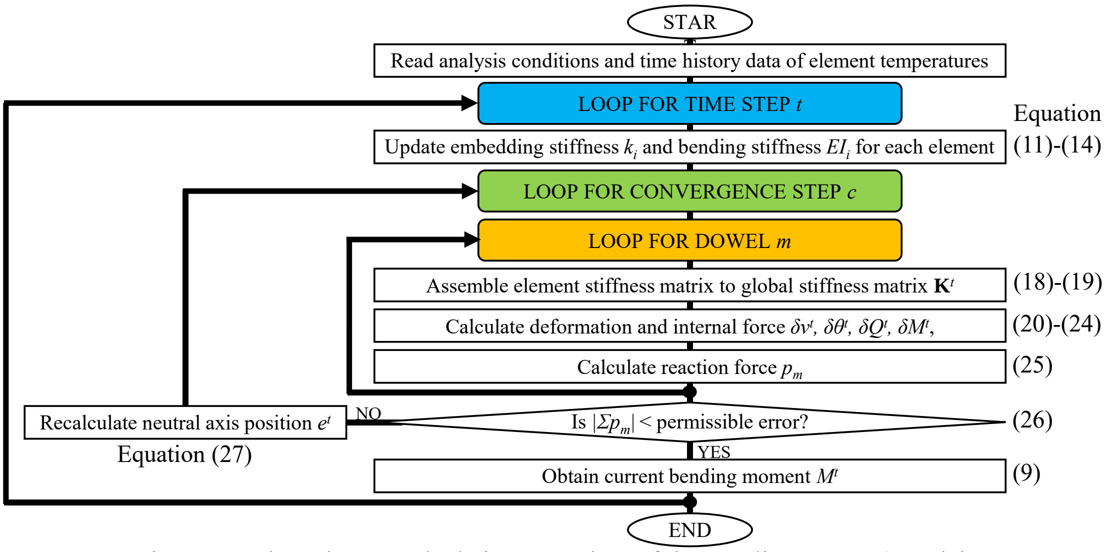

Figure 11. Flow chart – Calculation procedure of the non-linear $M-\theta$ model

4 EXPERIMENTAL PROGRAM

4.1 Test setup

Two load-bearing tests were conducted on large-scale glulam frames under ambient and fire conditions. The detailed configurations of the specimens are shown in Figures 12 and 13. The specimens were cut from Japanese larch with an average density of 0.473 g/cm^3. The loads on point D7s were controlled to fix their vertical displacements of point D7s during both tests. In the ambient test, the loads on point D2s were increased until failure was confirmed. In the fire test, the specimen was first pre-loaded to 100 % of the allowable load for 60 min of fire resistance, calculated according to the reduced cross-section method recommended in the Japanese *Standard for Structural Design of Timber Structures* [19]. The preload was 45 % of the design load of the dowel-type connections at ambient temperature [19]. The specimen was then exposed to fire following the ISO834 standard fire curve with the loads on point D2s being controlled to be constant. The loading spans were different in the ambient and the fire tests.

4.2 Measurement of M - θ relationships during experiments

As shown in Figure 12, the specimens can be modelled as a simply supported beam that is subject to bending moments from the beam-to-column joints, M_{joint}, and vertical loads on point D2s, L_{D2}. The experimental results of the $M-\theta$ relationships are the relationship between the bending moment at the dowel location, M_{con}, and the relative rotation angle between the beam end and column head, θ_{con}:

$$M_{con} = 150L_{D2} - M_{joint} = 150L_{D2} - \left(1050L_{D7} + M_{col}\right), \tag{28}$$

$$\theta_{con} = \theta_{beam} - \theta_{col} = \arcsin\left(\frac{D_4 - D_5}{420}\right) - \arcsin\left(\frac{D_{h1} - D_{h2}}{500}\right), \tag{29}$$

where L_{D7} is the measured load on point D7, M_{col} is the bending moment within the column, θ_{beam} is the rotation angle of the beam end, θ_{col} is the rotation angle of the column head, and D_4, D_5, D_{h1}, and D_{h2} are the displacements (mm) at the corresponding measurement points. The bending moment in an optimised roller-supported column must be zero; however, in the experiments, the grounding surface of the column could resist rotation owing to axial compression, which resulted in the pure bending of the column. In the ambient test, M_{col} was measured using:

$$M_{col} = Z \cdot E \frac{\varepsilon_{S1} - \varepsilon_{S2}}{2}, \tag{30}$$

where Z is the section modulus of the columns (4.5×10^6 mm^3), E is the modulus of elasticity of the columns (9500 N/mm^2, [19]), and ε_{S1} and ε_{S2} are the strains at the corresponding measurement points. Because the strain gauges were only attached to the left column, the experimental result illustrated as a red line in Figure 14 is measured with M_{col} and θ_{col} on the left-side connection.

To calculate fire test's M_{col}, the relationship between M_{col} and θ_{col} in the ambient test was applied to both columns. It should be noted that this overestimates the fire test's M_{col} because the bending stiffness of the columns in reality decreases as the temperature increases.

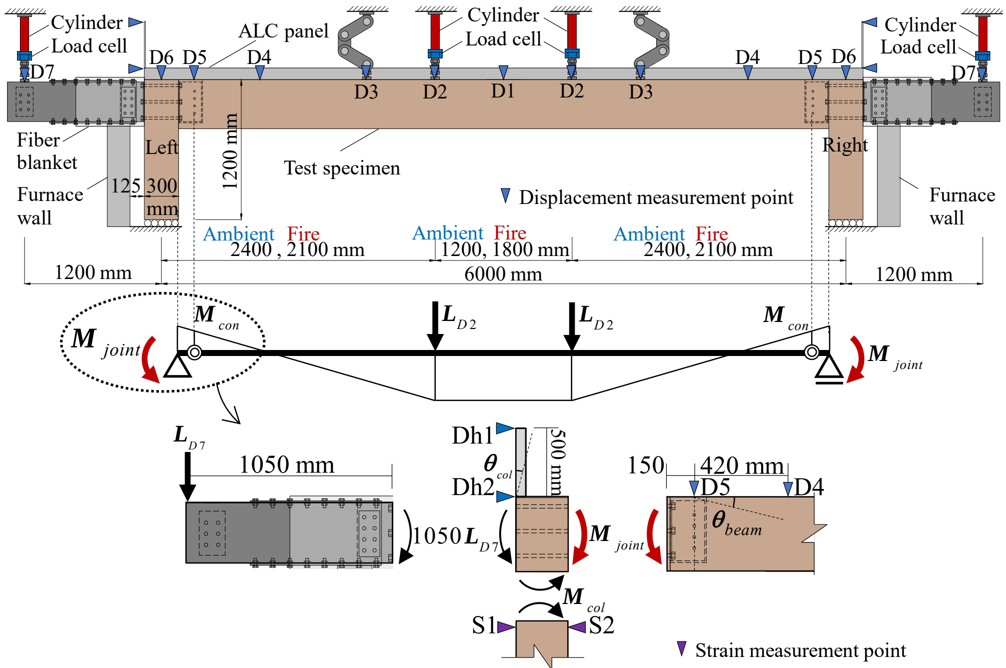

Figure 12. Test setup

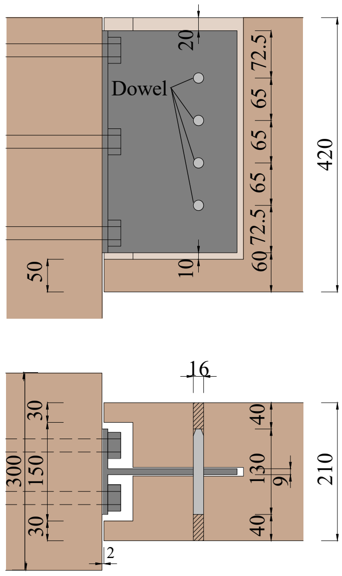

Figure 13. Connection configuration (unit: mm)

5 RESULTS AND DISCUSSIONS

5.1 Model validation at ambient temperature

In the ambient test, the beam failed to bend at the centre and the D2 loads reached their maximum value (91 kN). No shearing or splitting failures of the connections ware observed. Figure 14 compares the experimental result with the theoretical result calculated using the linear $M-\theta$ model (Equation 1). The dotted line in Figure 14 shows the $M-\theta$ relationship calculated using:

$$M=\sum_{m=1}^{n_d}\left(k_m\cdot d\cdot l\cdot r_m^2\right)\theta\ . \tag{31}$$

Equation (31) assumes that dowels are rigid bodies, which in turn overestimated the experimental result. However, the theoretical and experimental results agreed well up until the rotation surpassed 0.003. At higher rotations, the rotational stiffness of the specimen connection increased owing to the contact between the lower beam end and the column. When the rotation surpassed 0.006 rad, the rotational stiffness of the specimen connection began to decrease owing to yielding. However, the theoretical model simulated the elastic $M-\theta$ relationship at ambient temperatures with good accuracy.

5.2 Model validation at high temperature

In the fire test, the centre of the beam failed to bend at 92 min, and the specimen lost its load-bearing capacity. No shearing or splitting failures of the connections ware observed. Figures 15 and 16 compare the experimental fire test results of the left and right connection, respectively, with the numerical results calculated by the non-linear $M-\theta$ model. The time history of the rotations, θ^t, required in the numerical analysis (Equation 9) was obtained from the test results measured by Equation (29). The two test results exhibited different behaviours.

As shown in Figure 15, the experimental result of the left-side connection increased during the pre-loading phase and until 50 min, decreased after 50 min, and remained almost constant after 75 min. The non-linear $M-\theta$ model simulated this increasing, decreasing, and stagnating behaviour. As shown in Figure 16, the non-linear $M-\theta$ model agreed well with the test result of the right-side connection during the pre-loading phase and until 50 min. The numerical result began to decrease after 50 min, and both the numerical and experimental results remained almost constant after approximately 65 min. The time history data of the element temperatures used in the numerical analysis is shown in Figure 17. The temperature of all elements increased as the heating progressed and exceeded 100 °C between 60 and 70 min. Because the decline in the reduction factors of timber above 100 °C was slower than that below 100 °C (Figure 9), the numerical results of both the left and right-side connections decreased after 50 min, whereas they became almost constant after approximately 65 min.

Figure 18 compares the three numerical results where the stress-strain relationship of the dowels is set to be rigid, linear elastic, and elastoplastic. The rigid and linear elastic body assumption of the dowels overestimated the elastoplastic result until 65 min; however, the three results converged to the same value after 65 min. This result indicates that the failure mode of the dowels was determined only by the embedding failure of timber, and not by the formation of plastic hinges. This phenomenon can be described in Figure 19, which shows the bending moment distribution along the downmost dowel obtained through the elastoplastic analysis in Figure 16. As shown in Figure 19, the bending moment distribution reached its maximum value at 50 min and monotonically declined after 50 min as the stress on each element calculated from Equation (11) decreased. The decline in the bending moment distribution means that the stress–strain states of the plasticised beam elements entered their linear unloading phase (Case III in Equation 13) after 50 min, and their bending stiffness recovered to elasticity, while the contacting timber was charred and plasticised. Accordingly, the three numerical results showed little difference after 65 min. The convergence of the three numerical results suggests that the ultimate states of beams with dowel-type connections exposed to fire can be approximated by assuming that dowels are rigid bodies.

6 CONCLUSIONS

A theoretical model for the linear elastic $M-\theta$ relationships of dowel-type connections under ambient conditions was introduced. The theoretical model was then applied to develop a numerical model for non-linear $M-\theta$ relationships of dowel-type connections exposed to fire. To verify the numerical model, two load-bearing tests were performed on large-scale glulam frames, each under ambient and fire conditions, and the experimental results were compared with theoretical and numerical results.

The theoretical model provided good approximations of the measured $M-\theta$ relationships in the elastic range. The non-linear numerical model coincided with the $M-\theta$ behaviour of the left-side connection in the fire test. The numerical result agreed well with the fire test results for the right-side connection until 50 min, and both the numerical and experimental results were almost constant after approximately 65 min.

Three numerical analyses were performed, in which the stress-strain relationship of the dowel was set to be rigid, linear elastic, and elastoplastic. The three numerical results showed little difference after 65 min as the stress-strain states of the plasticised elements entered their linear unloading phase, and their bending stiffness recovered to elasticity after 50 min. This result suggests that the ultimate states of beams with dowel-type connections exposed to fire can be approximated by assuming that dowels are rigid bodies.

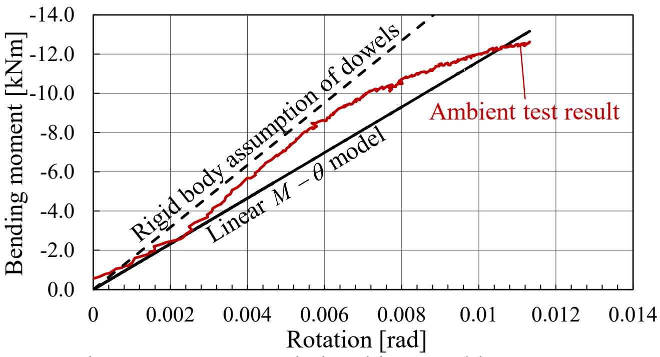

Figure 14. $M-\theta$ relationship at ambient temperature

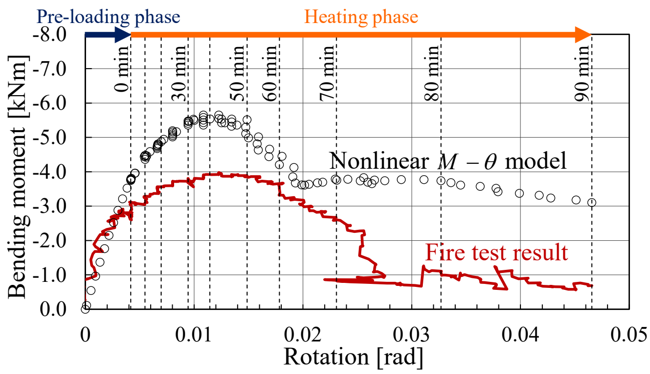

Figure 15. $M-\theta$ relationship at high temperature (left-side connection)

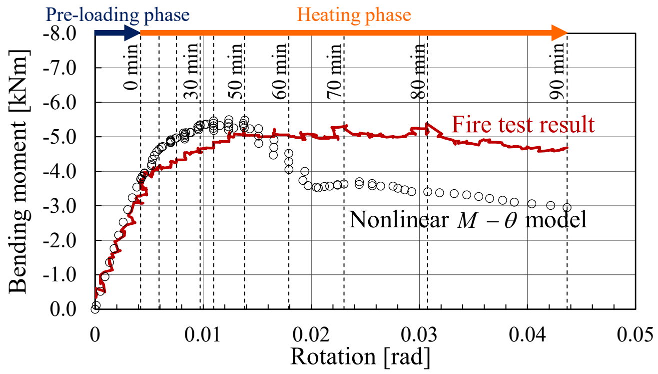

Figure 16. $M-\theta$ relationship at high temperature (right-side connection)

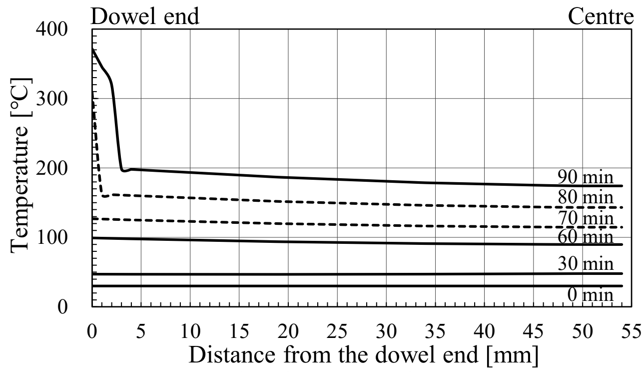

Figure 17. Time history of element temperatures

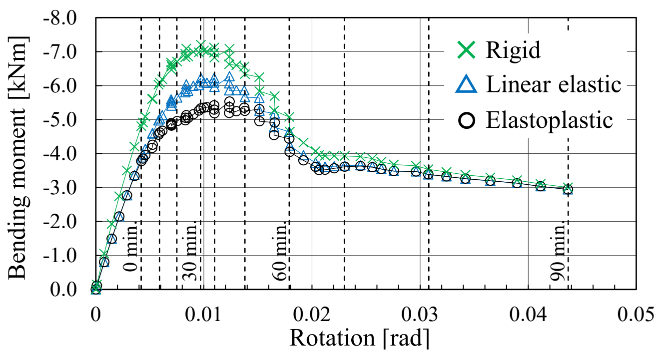

Figure 18. Comparison of three numerical analyses where dowels are considered rigid, linear elastic, and elastoplastic bodies

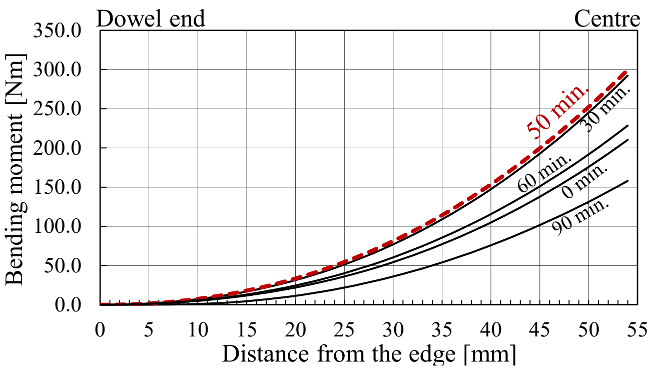

Figure 19. Bending moment distribution along the downmost dowel

7 FUTURE WORK

The non-linear $M-\theta$ model developed in this study will be adopted into the fire response analysis model for timber beams based on [3] to make it possible to simulate the fire behaviour of timber frames considering the semi-rigidity of dowel-type connections. The analytical results will be compared with the time–displacement relationship and fire-resistance time obtained by the fire test introduced in this study.

REFERENCES

1. Chen, Z., Zhao, J., Zhao, S., Wang, X., Liu, H., Zhang, L. and Xu, Q., Experimental Study and Theoretical Analysis on the Rotational Performance of Large-Size Bolted Joints with Slotted-in Steel Plates, Construction and Building Materials, 341 (2022) 127785.
2. Okunrounmu, O., Salem, O. and Hadjisophocleous, G., Fire Performance of Hybrid Mass Timber Beam-End Connections with Perpendicular-to-Wood Grain Reinforcement, Journal of Structural Fire Engineering, Emerald Publishing Limited, DOI:10.1108/JSFE-06-2021-0036.
3. Becker, J. and Bresler, B., A Computer Program for the Fire Response of Structures-Reinforced Concrete Frames, Fire research group, University of California, Berkley, 1974.
4. Kuenzi, E. W., Theoretical Design of a Nailed or Bolted Joint Under Lateral Load, Forest Products Laboratory, Forest Service, United States Department of Agriculture, Madison, USA, 1955.
5. Foschi, R. O., Load-Slip Characteristics of Nails, WOOD SCIENCE, Vol. 7, 1974, pp. 69-76.
6. Tsujino, T. and Hirai, T., Nonlinear Load-Slip Relationship of Bolted Wood-Joints with Steel Side-Members I. Numerical Analysis Based Upon a Finite Element Method, Mokuzai Gakkaishi, Vol. 29, No. 12, 1983, pp. 833-838 (in Japanese).
7. Hirai, T., Nonlinear Load-Slip Relationship of Bolted Wood-Joints with Steel Side-Members II. Application of the Generalized Theory of a Beam on an Elastic Foundation, Mokuzai Gakkaishi, Vol. 29, No. 29, 1983, pp. 839-844.
8. Hirai, T., Nonlinear Load-Slip Relationship of Bolted Wood-Joints with Steel Side-Members III. Advanced Numerical Analysis Based on the Generalized Theory of a Beam on an Elastic Foundation, Vol. 31, No. 3, 1985, pp. 165-170.
9. Architectural Institute of Japan, Design Manual for Engineered Timber Joints, 2015 (in Japanese).
10. Awaludin, A., Smittakorn, W., Hayashikawa, T. and Hirai, T., M-θ Curve of timber Connection with Various Bolt Arrangements Under Monotonic Loading, Journal of Structural Engineering, Vol. 53A, 2007, pp. 853-862.
11. Yasuda, Y., Aoki, K. and Inayama, M., Comparison of the Test and Analysis of Moment-Resisting Joint – Verification of Approximate Analysis by Beam-Model for the Load-Slip Characteristics of Drift-Pinned Joints with the Steel Plate Inserted Part2 –, J. Stust. Constr. Eng., Architectural Institute of Japan, Vol. 83, No. 744, 2018, pp. 275-283 (in Japanese).
12. Khelifa, M., Khennane, A., Ganaoui, M. E. and Rogaume, Y., Analysis of the Behavior of Multiple Dowel Timber Connections in Fire, Fire Safety Journal, 68 (2014) 119–128.
13. Racher, P., Laplanche, K., Dhima, D. and Bouchair, A., Thermo-Mechanical Analysis of the Fire Performance of Dowelled Timber Connection, Engineering Structures, 32 (2010) 1148–1157
14. Cachim, P. B. and Franssen, Jean-Marc, Numerical Modelling of Timber Connections under Fire Loading Using a Component Model, Fire Safety Journal, 44 (2009) 840–853.
15. Palma, P. and Frangi, A., Modelling the Fire resistance of Steel-toTimber Dowelled Connections Loaded Perpendicularly to the Grain, Fire Safety Journal, 107 (2019) 54–74.
16. Erchinger, C., Frangi, A. and Fontana, M., Fire Design of Steel-to-Timber Dowelled Connections, Engineering Structures, 32 (2010) 580–589.
17. EN 1993-1-1: Eurocode 3: Design of Steel Structures– Part 1-2: General Rules–Structural fire Design, 2005.
18. Kawarabayashi, F., Kikuchi, T., Totsuka, M. and Hirashima, T., Embedding Behaviors of a Dowelled Connection in Structural Glulam Timbers at High Temperature, J. Stust. Constr. Eng., Architectural Institute of Japan, Vol. 87, No. 795, 2022, pp. 498-509 (in Japanese).
19. Architectural Institute of Japan, Standard for Structural Design of Timber Structures, 2006 (in Jananese).

SiF 2022– The 12th International Conference on Structures in Fire
The Hong Kong Polytechnic University, Nov 30 - Dec 2, 2022

CHARRING OF STEEL-TIMBER HYBRID BEAM SECTION

Mikko Malaska[1], Mikko Salminen[2], Timo Jokinen[3], Risto Ranua[4]

ABSTRACT

Tampere University is currently investigating a steel-timber hybrid floor system which uses steel beams contained within the depth of the cross-laminated timber (CLT) floor slab. The steel-beam section consists of a rectangular steel hollow section welded to a steel bottom plate, and the CLT panels are installed on the top of the bottom plate. Two furnace tests and numerical simulations have been conducted to investigate the thermal profiles of the steel member and CLT slabs and to obtain more realistic and reliable information on the temperature development and charring of the hybrid-beam section when it is exposed to standard fire conditions. Also, the effects of intumescent fire protection on temperatures and charring performance were investigated. The results show that the charring of CLT panels at the slab support is extensive if the steel beam is unprotected. Intumescent protection applied to the steel section exposed to fire reduced the temperatures of the steel and CLT components as well as charring depth significantly. Numerical 2D thermal simulations for unprotected and protected cases were conducted using SAFIR software, and the agreement between experiments and numerical-analysis predictions were in general very good. Based on the temperature profiles found, the fire-protected hybrid beam has still load-bearing capacity left at 60 minutes of fire exposure, but further research is needed to determine whether the effective cross-section is sufficient to meet all the structural fire resistance requirements of composite-beam sections.

Keywords: steel-timber composite; slim floor beam; CLT; fire resistance; charring; charring depth

1 INTRODUCTION

Steel-timber hybrid beam systems have recently been studied and developed in many configurations, with the most typical solution being a structural steel section located beneath the timber floor slab. Tampere University is currently investigating a slim-floor-type system with the steel beams contained within the depth of the CLT floor slab [1]. The floor consists of CLT panels installed on the top of a steel plate welded to a steel hollow section, as Figure 1 shows. The composite solution enables light and shallow floor construction with longer spans compared to traditional timber construction. Other benefits include high speed in installation, totally dry construction and recyclable components. Timber's good fire-resisting qualities can also be utilized to enhance the beam's fire performance.

In addition to load-bearing capacity at ambient temperature, hybrid floor systems' fire resistance needs to be considered, including structural stability and separating function. The structural fire design of CLT panels is normally based on standardised fire tests as well as approved calculation methods and charring

[1] Professor, D.Sc., Tampere University, Finland,
e-mail: mikko.malaska@tuni.fi, ORCID: https://orcid.org/0000-0002-8215-9765
[2] Senior Fire Safety Specialist, D.Sc., Markku Kauriala Ltd Fire Engineering and Fire Safety Design Consultants, Finland
e-mail: mikko.salminen@kauriala.fi
[3] Senior Fire Safety Specialist, M.Sc., Markku Kauriala Ltd Fire Engineering and Fire Safety Design Consultants, Finland
e-mail: timo.jokinen@kauriala.fi
[4] Senior Fire Safety Consultant, M.Sc., Markku Kauriala Ltd Fire Engineering and Fire Safety Design Consultants, Finland
e-mail: risto.ranua@kauriala.fi
https://doi.org/10.6084/m9.figshare.22193791

rates presented, for example, in EN 1995-1-2 [2]. At present, there is very limited information about the fire performance of CLT panels at a slim-floor construction's steel-beam support, where the steel beam protects the panel ends from direct fire exposure but also transfers heat deeper into the floor, thereby increasing the temperature of the wood adjacent to the steel section. Charring of the CLT floor slab affects the floor slab's shear and bearing resistance and can also reduce the efficiency of possible shear connectors used to attain composite action between the slab and beam. It is therefore important for the slab and beam design that there is reliable information available on the thermal profile and charring of the hybrid beam section.

Figure 1. Slim-floor type of a steel-timber hybrid beam consisting of a CLT slab and a steel beam consisting of an RHS section and steel bottom plate

No design guidance is available to help determine the amount of heat transferred through the steel hollow section into CLT slabs or to assess the char depths at the slab support area. The American Wood Council's [3] recommended practise requires that all of a connection's components be protected so that no part of the connection is exposed to an individual temperature rise of 181 °C. The method limits the temperatures well below the level of charring of wood and meets the required significant fire protection for the steel bottom flange plate. Moreover, this method suggests that intumescent paint may not effectively protect the steel elements at the hybrid connection, as it typically activates at higher temperatures than the criterion.

Tampere University has investigated the thermal profiles of the steel member and CLT slabs experimentally and numerically to obtain more realistic and reliable information on the temperature development and charring of the hybrid-beam section when it is exposed to standard fire conditions. The aim of the study is to determine how the charring of the CLT slab should be considered in the structural fire design of the slabs and hybrid beams. Heat transfer mechanisms throughout the cavity of the steel hollow section and effects of fire paint protection on temperatures and charring performance were also investigated.

2 EXPERIMENTAL RESEARCH

Two fire tests were carried out to investigate temperatures in CLT and steel components as well as the charring of CLT adjacent to the steel-beam section. The beam sections, unprotected in the first test and fire protected in the second test, were exposed to standard fire test conditions in accordance with EN 1363-1:2020 [4]. The test specimens were installed on the top of a full-scale fire test furnace chamber with internal dimensions of 3000 mm x 3000 mm x 1200 mm (height x width x depth), and they formed part of the furnace roof structure. The char development in CLT members was estimated based on visual observations made after tests and on temperatures measured inside the specimens during the test. The position of the char line in the test specimen was assumed as the position of the 300 °C isotherm.

2.1 Test specimen and setup

In a fire test, the steel beam was installed across the furnace chamber's 1.2-m-wide opening. The beam section was made of a 150 x 100 x 6 mm (RHS) rectangular steel hollow section welded to a 300-mm-wide and 6-mm-thick steel bottom plate, as Figure 2 shows. In the first test, the steel beam was unprotected. In the second test, the underside and sides of the steel bottom plate were fire protected with intumescent paint (Tikkurila Fontefire ST60-1). The coating thickness was chosen in such a way that it would limit steel members' temperature to less than 600 °C at 60 minutes. The paint was applied using a brush in the testing laboratory.

On both sides, the steel beam's 600 x 1200 mm CLT panels were installed and supported on the bottom flange plate of the beam. 10-mm air gaps were left between the steel beam web and the CLT panels' vertical faces. The gaps were closed with cement-bonded fibreboard strips mounted on the top of the gap, as Figure 2 shows. Aerated concrete slabs supported the other ends of the panels. The panels were unsupported along the furnace walls. The panel thickness was 140 mm, consisting of five layers (20, 40, 20, 40, and 20 mm). The 20-mm-thick lamellae ran perpendicular to the beam span. The CLT panels were made of spruce timber with a density of 425 kg/m^3 and strength class of C24. The specimens had polyurethane (PUR) adhesive. Before testing, test specimens were conditioned in climate conditions with temperature of 22 °C and relative humidity of 50 %. The CLT specimens' moisture content on the day of testing was 10.7 – 11.0 %.

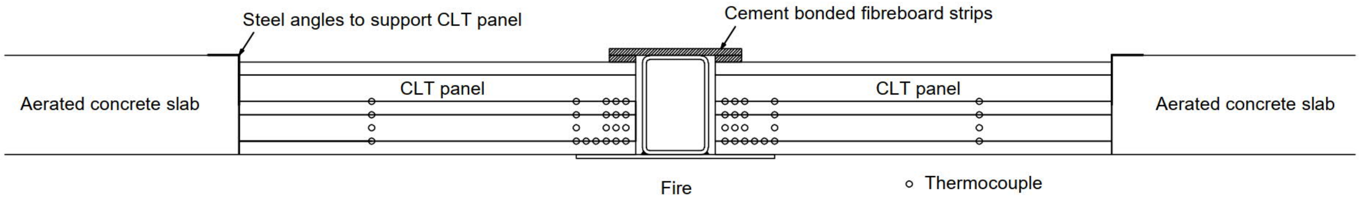

Figure 2. Vertical cross-section through the test specimen

Figure 3. Test set-up seen from above

The tests were conducted unloaded and according to EN 1363-1 [4]. During the tests, furnace temperature, specimen temperatures, oxygen content within the furnace and the pressure differences between the furnace and test hall were monitored. Four plate thermometers were used to monitor the furnace temperature. The furnace pressure at the furnace ceiling level was set to 20 Pa. The oxygen content was monitored in the middle of the furnace chamber using a Dräger EM200-E multi gas detector. After the termination of the test, the CLT elements were extinguished by immersing them in a pool of water. A crane located above the furnace chamber was used to lift and move the CLT panels. The first of the two CLT panels in a test was moved to the pool in less than 30 seconds. The visual observations presented below were made from this first panel.

2.2 Instrumentation

Steel temperatures were recorded using fibreglass-wrapped Type K24-2-305 thermocouples (Ø 0.5 mm). Five thermocouples with a welded junction were installed into pre-drilled holes in an RHS section, and eight thermocouples were weld-fixed to the steel bottom plate and the bottom flange of the RHS section.

A total of 44 thermocouples were used to measure temperatures inside the CLT panels, as Figure 2 shows. The distance between the vertical edge of CLT panels and the first set of measurement points and the horizontal distance between measurement points was 15 mm. In the unprotected-beam test, sheathed K-type thermocouples installed in holes drilled horizontally and parallel to the exposed surface were used. The thermocouples were run through the air gap between steel web and CLT panels. The test results showed that this installation was not satisfactory because the heat transferred from the air gap and along the metal sheath affected the measurements, so they were considered unreliable. Therefore, for the fire-protected case, the charring of the CLT panels is estimated based on visual inspection only. In the second test, with the fire-protected steel beam, temperatures inside the CLT panels were measured with fibreglass-wrapped Type K24-2-305 thermocouples (Ø 0.5 mm) installed in vertical holes drilled in the panels' unexposed face. To ensure the correct installation depth, the thermocouple wire installation was assisted with thin wooden sticks. After installation, the holes were sealed with fire-resistant mastic sealant.

2.3 Test results

Figure 4 shows the cross-section of the charred CLT panel supported by the unprotected steel bottom plate. This first test was terminated at 70 minutes, and the specimen was immediately extinguished. Based on visual inspection, the vertical charring had progressed through the first two lamella layers (20 mm + 40 mm). The charring depth is almost constant across the panel's width, and the steel bottom plate did not reduce charring behind the plate. Visual observations through the furnace camera showed that the first lamellae layer had fallen off at 36 minutes, but the part on top of the steel bottom plate remained in place until the end of the test. Horizontal charring depth measured from the vertical face of CLT panels adjacent to the steel web at 71 minutes was 11 mm.

Figure 4. Residual cross-section of a CLT panel supported by an unprotected steel beam at 71 minutes of fire exposure. The CAD drawing corresponds to original dimensions

Figure 5 presents steel temperatures measured during the test. At 70 minutes, the temperatures of the steel bottom plate and the web were around 850 °C and 700 °C, respectively. At this stage, radiation from the steel web and the entry of hot gases through cracks formed in the charred layer above the steel bottom plate increased temperatures in the air gap and on the vertical surface of the CLT panel. The oxygen content within the furnace varied between 4 % and 8 %.

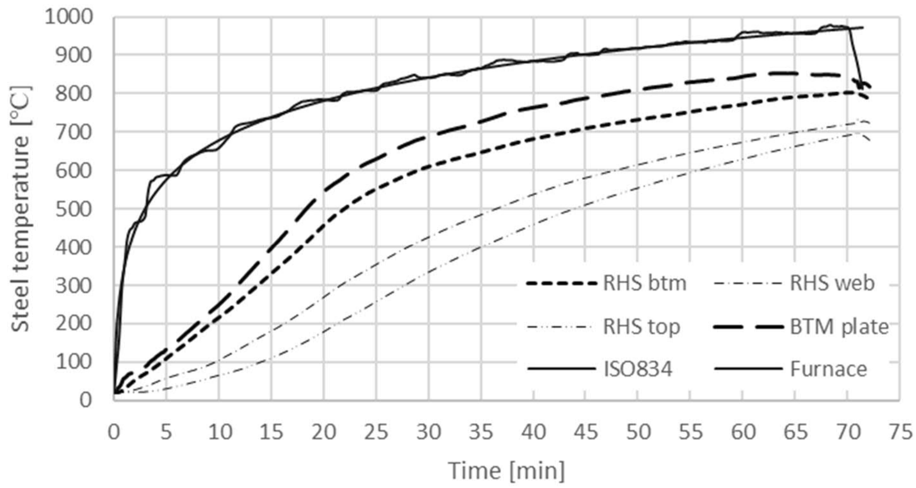

Figure 5. Temperatures of unprotected steel profile

Figure 6 shows the cross-section of the charred CLT panel supported by a fire-protected steel bottom plate. The test was terminated at 60 minutes, and the specimen was immediately extinguished. Based on visual inspection, the vertical charring of CLT panels far from the beam support was progressing in the second lamella layer. The position of the char line passed the first lamella layer and the mid-depth of the second layer at 30 minutes and 52 minutes after the commencement of the test, respectively. The temperature measured at the interface between the second and third layers at 60 minutes was 100 °C. The charring depth was significantly reduced at the beam support, where the fire paint limits the heating of the steel. The charring affected the first lamella layer, and horizontal charring adjacent to the steel web was insignificant.

Figure 6. Charring of a CLT panel supported by a fire-protected steel beam at 61 minutes of fire exposure

Figure 7 presents temperatures of the fire-protected steel-beam members. The results show that the temperature of the beam bottom plate and the web were around 580 °C and 400 °C at 60 minutes, respectively. The oxygen content varied between 5 % and 7 %.

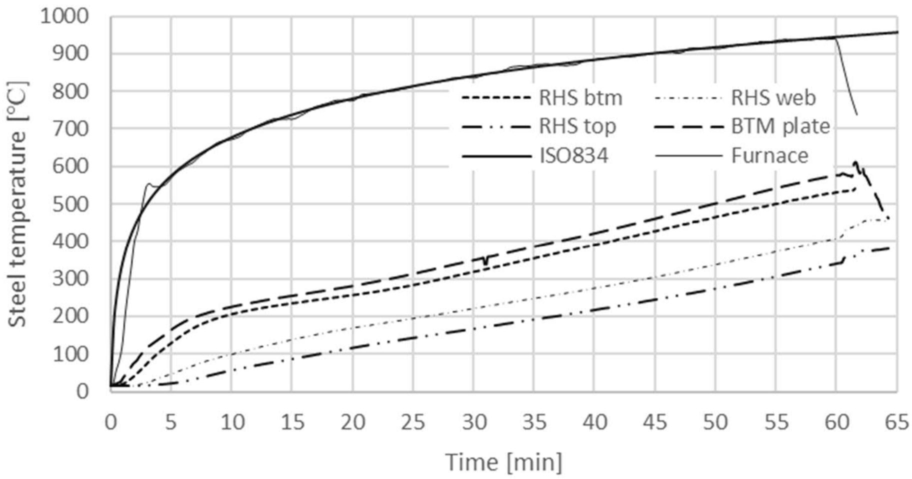

Figure 7. Temperatures of fire-protected steel profile

3 NUMERICAL SIMULATIONS

3.1 Numerical model

Numerical 2D thermal simulations for unprotected and protected cases were conducted using SAFIR [5]. The results from the numerical model are compared to those from the tests. The main objective is to investigate how well the thermal behaviours (including charring of CLT, radiation in cavities, behaviours of intumescent paint) of the considered section can be predicted using relatively simple numerical models that could be applicable to everyday structural fire design applications.

Figure 8 presents the numerical model for the fire-protected case. The model for the unprotected case is similar but naturally does not include the fire protection material. ISO 834 fire was applied to the model's lower edge, and 20 °C ambient temperature was applied to the model's upper edge. Symmetry-boundary conditions were applied on the model's left and right edges.

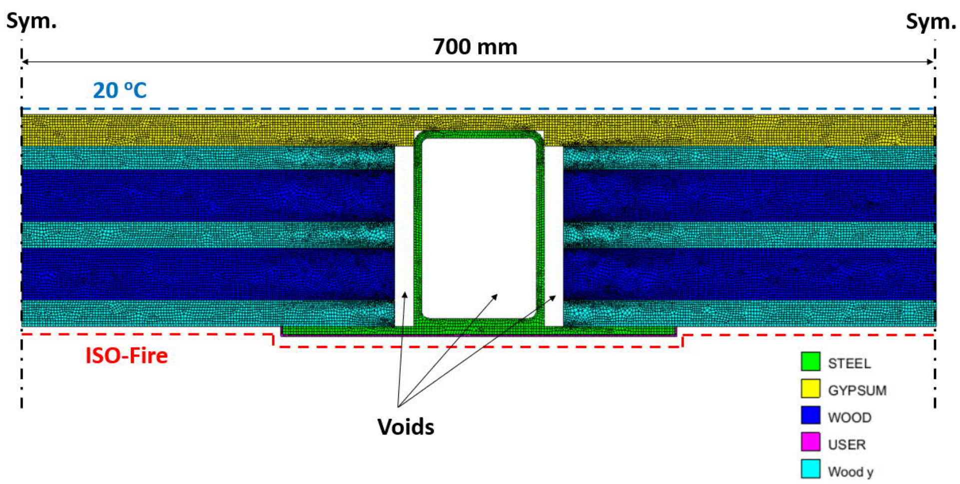

Figure 8. Numerical model of the fire-protected case

The following coefficients of heat transfer by convection were applied in the model: 25 W/m^{2}K for fire-exposed side and 4 W/m^{2}K for the non-exposed side [6]. Surface emissivities were as follows: 0.7 for steel [7], 0.9 for intumescent paint [11] and 0.8 for other materials [2]. Rectangular elements approximately 2 mm x 2 mm were applied in the model (total of approx. 32 000 elements). The three cavities shown in Figure 8 were modelled by using the VOID command in SAFIR, which required the use of a relatively small time step in the calculations (1 s in this case). The VOID command in SAFIR takes the convection and radiation in the cavity into account. Table 1 summarizes the material properties and models applied.

Table 1. Assumptions related to material properties and models

Material	Material model
Steel	Density: 7850 kg/m^3 [7]. Temperature-dependent values for specific heat and thermal conductivity per EN 1993-1-2 [7].
Timber	Density: 425 kg/m^3, based on the average value of the tested specimens. Moisture content: 11 %, based on the average value of the tested specimens. Temperature-dependent values for specific heat and density per EN 1995-1-2 [2]. Temperature-dependent values for thermal conductivity per EN 1995-1-2. Note that for the layers where the heat transfer occurs mainly in the direction of the grains (indicated as material Wood y in Figure 8), thermal conductivity increased by a factor of 1.2, which is the custom value in SAFIR. Delamination of CLT was outside the scope of this paper, and it was not taken into account in any way. It is assumed that delamination does not have much effect on the temperature development and charring close to the support and steel bottom plate.
Gypsum board	The custom values of SAFIR type X gypsum board were applied. These values are based on studies by Cooper [8]. It is assumed that these values do not significantly affect the objective of this study because the gypsum boards are located on the non-exposed side of the structures, where the temperatures are relatively low.
Intumescent paint	Density: 100 kg/m^3 [9] Specific heat: 1200 J/kg K [10] Thermal conductivity: Varies from 0.3 W/mK (0 °C – 150 °C) to 0.05 W/mK (starting at 400 °C after full swelling has occurred), as Lucherini [11] proposed based on multiple effective thermal conductivity curves. See also Figure 9. This model was chosen to take the swelling of intumescent paint into account in some (relatively simple) way. The thickness of the protection was determined iteratively so that the temperature of the protected plate at 60 minutes was the same as designed. The thickness was determined to be 1,7 mm.

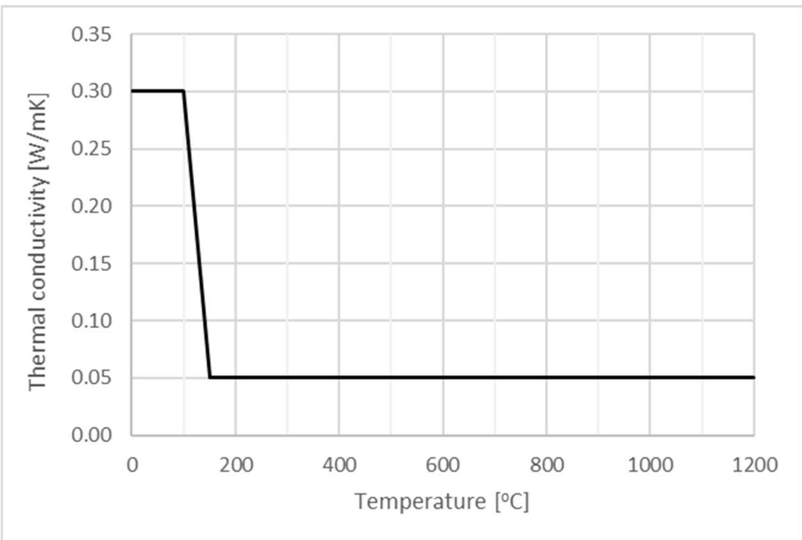

Figure 9. The applied model of the intumescent paint's thermal conductivity, based on [11]

3.2 Results from numerical analysis

Figures 10 and 11 present the temperatures of the steel profiles from numerical analysis and a comparison to test results. Based on the figures, it can be concluded that on average, the steel temperatures from numerical analysis are slightly higher (conservative) than those from the tests. Figure 11 shows that the numerical model underestimates the protected plate's temperatures in the early phases of the fire (approx. 2 – 13 min), then overestimates the temperatures until approximately 55 minutes, and finally leads to approximately the same temperature with the tests at 60 minutes. This behaviour was expected because in the test, the bottom plate heats up quickly during the first minutes of the fire because the intumescent paint has not swelled up yet. Even though the swelling is taken into account indirectly (using temperature-dependent thermal conductivity), the model cannot capture the temperature development of the intumescent-painted steel part perfectly. However, it is assumed that this model can capture the temperature development relatively well so that it can be utilized in typical design cases.

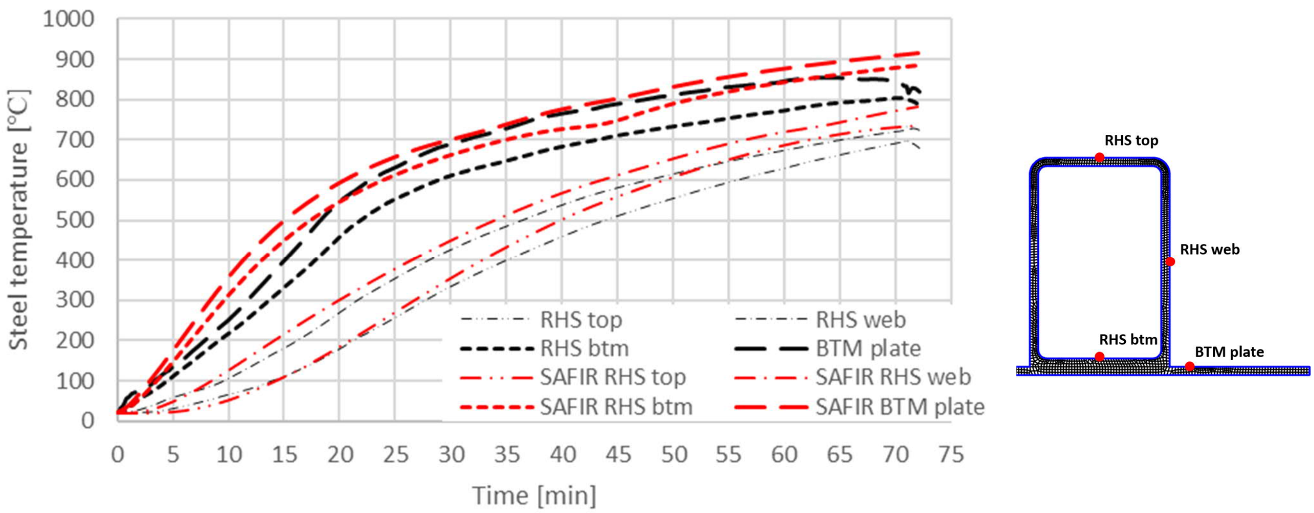

Figure 10. Temperatures of the unprotected steel profile from the numerical analysis as well as a comparison to test results

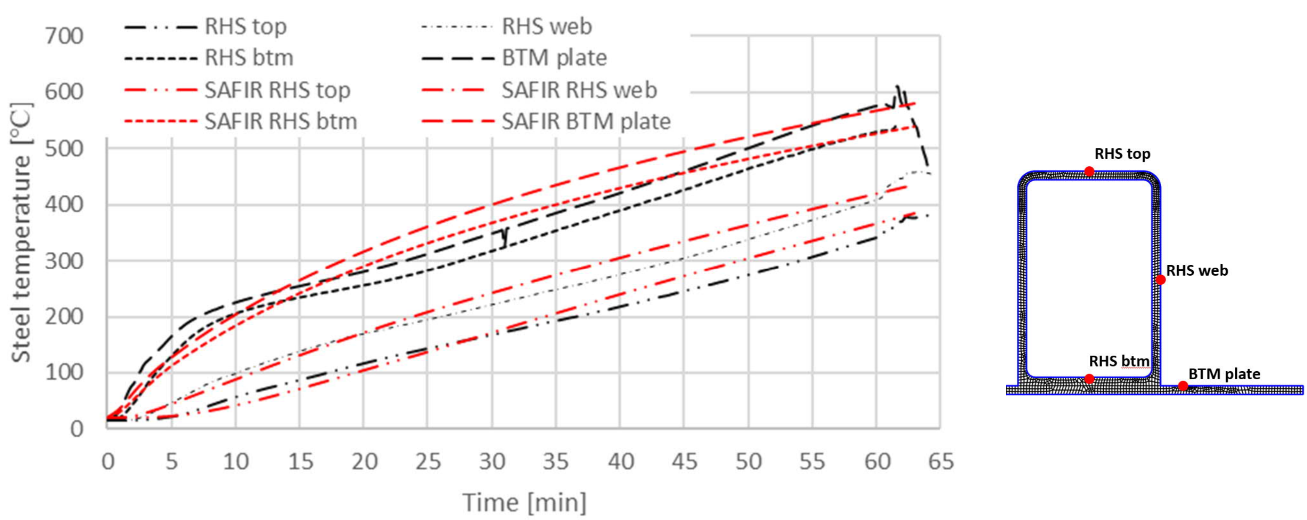

Figure 11. Temperatures of the fire-protected steel profile from the numerical analysis as well as a comparison to test results

Figures 12 and 13 present the (a) charred part of the CLT panel (300 °C isotherm [2]) from the numerical analysis and (b) a comparison to the test results. In Figure (a), the red portion indicates members and areas where temperatures are above 300 °C, and the brown line in Figure (b) indicates the 300 °C isotherm from the numerical analysis and can be considered the charring line of the CLT panel. The figures show that numerical analysis predicts the charring depths relatively well at the support. For the unprotected steel beam, the horizontal charring depth is slightly underestimated and on the unsafe side. For the protected beam, the horizontal charring depth is overestimated, leading to conservative results. In both cases, the vertical charring depth above the bottom plate is slightly higher than from the test, leading to a conservative estimate. However, when moving further from the support or the bottom plate, the numerical model underestimates the charring depth of CLT due to the delamination, for which the model does not account. This suggests that delamination should be included in the model if it is a relevant factor in the connection design. In this case, it is assumed that delamination does not affect the connection's behaviour but naturally needs to be accounted for in the fire design of the CLT panel.

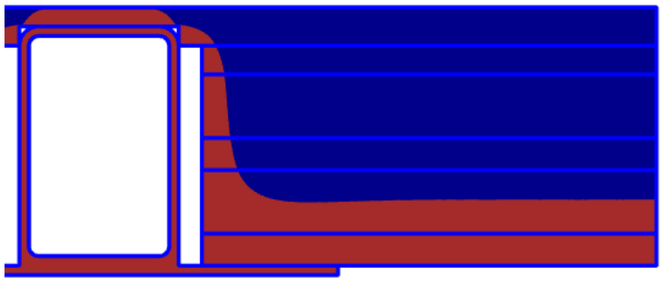

(a)

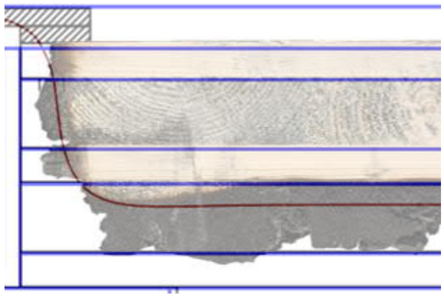

(b)

Figure 12. Charring depth of the CLT panel above the unprotected steel beam bottom plate: (a) red area representing areas where temperatures exceed 300 °C at 60 minutes and (b) comparison to test results at 71 minutes of fire exposure

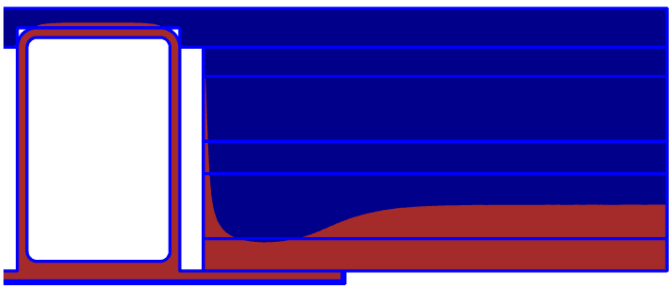

(a)

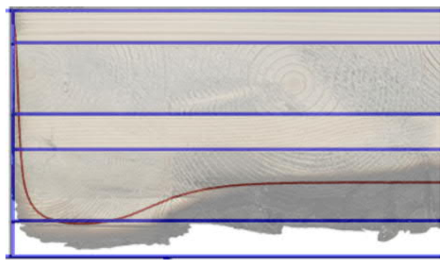

(b)

Figure 13. Charring depth of the CLT panel above the fire protected steel beam bottom plate: (a) red area representing areas where temperatures exceed 300 °C at 60 minutes and (b) comparison to test results at 61 minutes of fire exposure

Figure 14 presents charring depths calculated by numerical simulations in different locations and directions. C1 and C2 refer to vertical charring depth over time far from the beam support (symmetry edge of the model) and at mid-width of the steel bottom plate, respectively. C3 refer to the horizontal charring depth at mid-depth of the CLT panel.

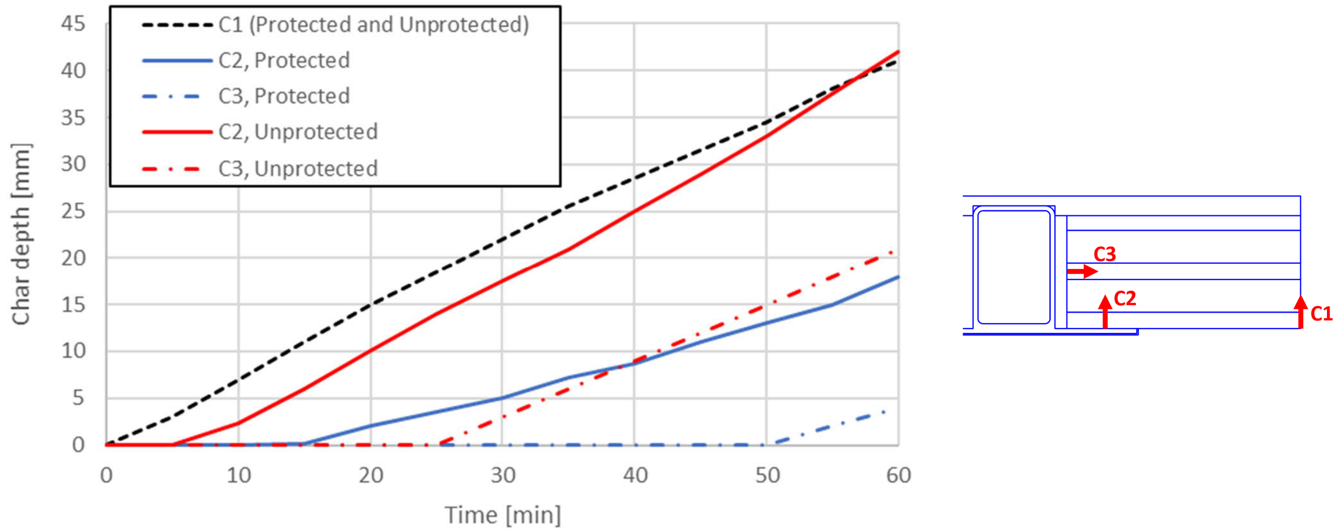

Figure 14. Numerically simulated charring depths of the CLT panel as a function of time in different locations

The comparison between curves C1 and C2 (Unprotected) shows that the unprotected bottom plate causes a slight delay (approximately 5 min) in the vertical charring. However, after this initial delay, the charring rate is basically the same as in the CLT far from the beam support. Actually, in this case the rate increases to even higher values after approximately at 40 minutes because of the heat transfer and charring in horizontal direction (C3). In the protected case, the vertical charring rate at the support (C2, Protected) is clearly smaller than in the unprotected case. However, even this lower rate can be significant for the mechanical behaviour of the hybrid beam. If the design criteria do not allow charring of CLT panels at beam support, it may be challenging to meet the criteria by using intumescent coating as fire protection material.

4 CONCLUSIONS

Two fire tests on steel-timber hybrid floor beams were conducted to investigate the thermal profiles of the steel member and CLT slabs and to obtain more realistic and reliable information on the temperature development and charring of the beam section when it is exposed to standard fire conditions. Also, a relatively simple numerical model applicable to everyday structural fire design applications was developed to analyse the temperatures in the hybrid-beam section. Numerical 2D thermal simulations for the unprotected and protected cases were conducted using SAFIR-software, and the agreement between experiments and numerical analysis predictions were in general very good.

The experimental and numerical results reported above show that charring of CLT panels supported on the bottom flange plate of a slim floor beam is significant unless the heat transfer to a CLT structure through the steel beam is restricted. Intumescent protection applied to the steel section exposed to fire was an effective way to reduce the temperatures of the steel and CLT components as well as the charring depth. Based on the temperature profiles found, the fire-protected hybrid beam has still load-bearing capacity left at 60 minutes of fire exposure. In the case tested, the vertical charring depth was limited to the first lamella layer and the horizontal charring of the panel end was negligible. Further research is needed to determine whether the effective cross-section is sufficient to meet all the structural fire resistance requirements of composite beams and CLT floor slabs.

REFERENCES

1. Heinisuo, M., Mela, K., Pajunen, S. and Malaska, M., New steel-timber composite beam, Nordic system, XII Conference on Steel and Composite Construction, 21-22 November 2019, Coimbra, Portugal, ce/papers, Ernst&Sohn, pp. 193-202, 2020, https://doi.org/10.1002/cepa.1194
2. EN 1995-1-2, Eurocode 5: Design of timber structures – Part 1-2: General – Structural fire design, Brussel, European committee for standardization, 69 p., 2004
3. American Wood Council (AWC), Calculating the Fire Resistance of Wood Members and Assemblies, Technical Report No. 10, Leesburg, VA, USA, 137 p, 2021.
4. EN 1363-1:2020, Fire resistance tests. Part 1: General requirements, Brussel, European committee for standardization, 47 p., 2020
5. Franssen, J.-M. and Gernay, T., Modeling structures in fire with SAFIR®: Theoretical background and capabilities, Journal of Structural Fire Engineering, pp. 300-323, 2017, doi 10.1108/JSFE-07-2016-0010
6. EN 1991-1-2, Eurocode 1: Actions on structures. Part 1-2: General actions. Actions on structures exposed to fire, Brussels, European committee for standardization, 61 p., 2003.
7. EN 1993-1-2, Eurocode 3: Design of steel structures. Part 1-2: General rules. Structural fire design, Brussels, European committee for standardization, 83 p. 2005.
8. Cooper, L.Y. (1997), The thermal response of gypsum-panel/steel-stud wall systems exposed to fire environments - a simulation for use in zone-type fire models, NISTIR 6027, National Institute of Standards and Technology, Gaithersburg MD.
9. Kolsek J. and Cesarek P. "Performance-based fire modelling of intumescent painted steel structures and comparison to EC3". Journal of Constructional Steel Research, vol. 104, pp. 91-103, 2015.
10. de Silva, Bilotta A. and Nigro E. "Experimental investigation on steel elements protected with intumescent coating". Construction and Building Materials, vol. 205, pp. 232-244, 2019.
11. Lucherini, A. Fundamentals of thin intumescent coatings for the design of fire-safe structures. A thesis submitted for the degree of Doctor of Philosophy at the University of Queensland in 2020.

SiF 2022– The 12th International Conference on Structures in Fire
The Hong Kong Polytechnic University, Nov 30 - Dec 2, 2022

THE STRUCTURAL BEHAVIOUR OF CROSS-LAMINATED TIMBER RIB PANELS IN FIRE

Miriam Kleinhenz[1], Alar Just[2], Andrea Frangi[3]

ABSTRACT

In the frame of a research project, the structural behaviour in fire and the fire resistance of cross-laminated timber rib panels were studied based on experimental and numerical investigations. The floor system consists of cross-laminated timber plates rigidly bonded to glued-laminated timber ribs. The full composite action between the composite components is provided by means of screw-press gluing. The results of the reference tests showed good agreement with results based on the method of rigidly bonded components and the effective width according to the final European draft of cross-laminated timber design [1]. The fire resistance tests resulted in fire resistances up to 120 min and confirmed the assumption that the effect of the composite action was maintained in fire. In this paper, the numerical investigations cover thermal, and uncoupled thermo-mechanical simulations using a 2D FE model of a linear beam system for discussion of the mechanical behaviour under fire exposure. The numerical results of the tested cross-sections are compared with the experimental results of the fire resistance tests. Depending on the modelled cross-section, the influence of the effective width on the numerical results is investigated.

Keywords: Massive timber rib panel; fire resistance; fire tests; finite element; effective width

1 INTRODUCTION

Long-span floor systems are required for building types such as commercial office buildings, residential buildings, schools, and industrial buildings. As a long-span floor system with spans up to 16 m, cross-laminated timber rib panels consist of cross-laminated timber (CLT) plates connected to glued-laminated timber (glulam) ribs (Figure 1). Full composite action is provided by a rigid connection between the composite components by means of screw-press gluing [2]. For ribbed cross-sections, the assumption that the cross-section remains plane is incorrect. The simple beam theory according to Euler-Bernoulli is not applicable because the strains in the flange vary with the distance from the rib due to the in-plane shear flexibility of the flange. This leads to a non-uniform distribution of the longitudinal strains along the flange width. For simplified structural analysis, the effective width defines an equivalent cross-section that provides the same maximum bending stress and effective bending stiffness as the actual cross-section [3]. The final European draft of CLT design [1] for a revised version of EN 1995-1-1 [4] proposes simplified formulae to estimate the effective width for ribbed plates build up from cross-laminated timber plates. In the case of uniformly distributed loads, equation (1) determines the effective width at normal temperature b_{ef} according to prEN 1995-1-1:20xx [1], as explained in Figure 1

[1] Dipl.-Ing., Institute of Structural Engineering, ETH Zurich, Switzerland
e-mail: kleinhenz@ibk.baug.ethz.ch, ORCID: https://orcid.org/0000-0001-9948-6378
[2] Prof. Dr., Institute of Civil Engineering and Architecture, Tallinn University of Technology, Estonia
e-mail: alar.just@taltech.ee, ORCID: https://orcid.org/0000-0002-8001-401X
[3] Prof. Dr., Institute of Structural Engineering, ETH Zurich, Switzerland
e-mail: frangi@ibk.baug.ethz.ch, ORCID: https://orcid.org/0000-0002-2735-1260
https://doi.org/10.6084/m9.figshare.22193779

$$b_{ef} = b_{rib} + \sum b_{ef,i} = b_{rib} + b_{f,i} \cdot \left(0.5 - 0.35 \cdot \left(\frac{b_{f,i}}{l}\right)^{0.9} \cdot \left(\frac{(EA)_x}{(GA)_{xy}}\right)^{0.45}\right) \tag{1}$$

where $b_{ef,i}$ is the effective width at each side of the rib width b_{rib}, $b_{f,i} = (b - b_{rib})$ is the clear rib distance, l is the span, and $(EA)_x/(GA)_{xy}$ is the ratio per meter width between the in-plane stiffness of the longitudinal CLT layers and the shear stiffness in plane of the gross CLT cross-section.

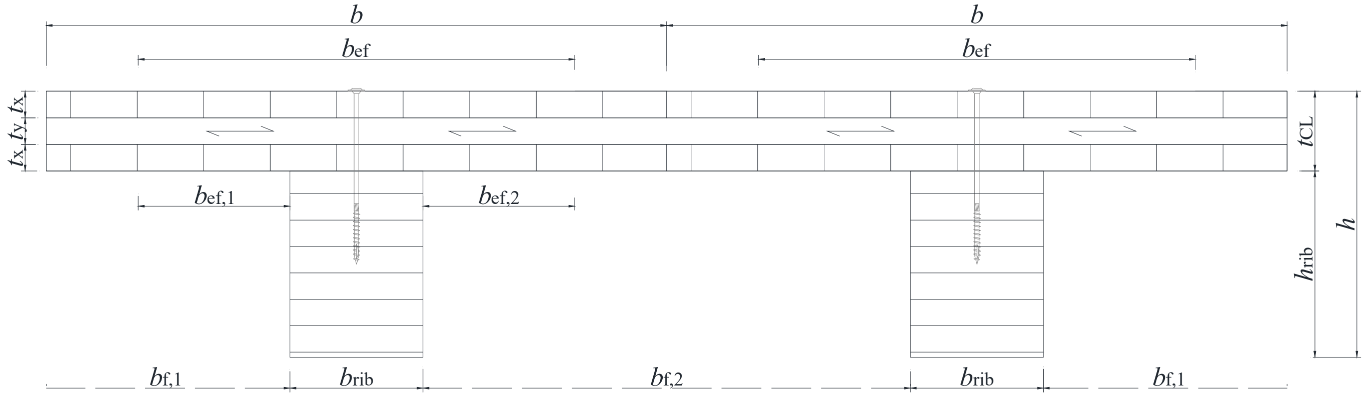

Figure 1. Geometry of the cross-section of cross-laminated timber rib panels.

In a research project, the structural behaviour in fire and the fire resistance of CLT rib panels were studied based on experimental and numerical investigations. The results of the reference tests showed good agreement with results based on the method of rigidly bonded components and the effective width according to prEN 1995-1-1:20xx [1]. The experimental results of the full-scale fire tests showed more than 90 and 120 min of fire resistance and confirmed the assumption that the effect of the composite action was maintained under standard fire. This paper focuses on the numerical simulations of the structural behaviour of CLT rib panels under standard fire. First, the results of the thermal simulations of the tested cross-sections are validated against the experimental results of the fire resistance tests. Then, a 2D FE model of a linear beam system is presented modelling the floor system as Bernoulli-type beams. The deflections of the thermo-mechanical simulations are compared with the experimental deflections. Depending on the modelled cross-section, the influence of the effective width on the numerical results is investigated.

2 EXPERIMENTAL INVESTIGATIONS

2.1 Overview

The experimental program cover ultimate-load tests at normal temperature as reference tests, and fire resistance tests exposed to standard fire. Test setup and experimental results are presented and discussed in detail in Kleinhenz et al. [5]. For the design, a simply supported system was defined with a length of 9 m and a CLT width b of 0.933 m. The target bending moment was calculated using a uniformly distributed load ($g_k = g_{k,self\text{-}weight} + 1.50$ kN/m^2; $q_k = 4.50$ kN/m^2) and the combination of loads for accidental design situations based on office areas according to EN 1990 [6]. Four different cross-sections were evaluated, including two T-sections (one CLT plate as top flange) and two box-sections (CLT plates as top and bottom flanges), as presented in Figure 2 (A, B, C, and D). The cross-sections were designed initially unprotected for a fire resistance time of 60 min (A, C), and initially protected for a fire resistance time of 90 min (B, D). No insulation material was used in the cavity. The rigid composite action is achieved through screw-press gluing method (SPG) using the one-component polyurethane adhesive Purbond HB S709. Gypsum plasterboards type F according to EN 520 [7] were installed at the bottom of cross-sections B and D.

2.2 Reference tests

The ultimate-load tests were performed as 4-point bending tests in accordance with EN 408 [8]. Based on the size of the furnace, the cross-sections were tested at a span l of 5.2 m. The experimental results confirmed the rigid composite action between CLT plate and glulam rib. They also confirmed the importance to consider the shear flexibility out of shear lag for the design of the composite cross-section. While the experimental effective width $b_{ef,test}$ was on average 80% of the CLT width, it would be estimated at 60% for the given system based on the effective width b_{ef} according to prEN 1995-1-1:20xx [1] (see equation 1). For test specimens tested as T-sections, the experimental loadbearing capacity showed very good agreement with the estimated loadbearing capacity. The experimental and estimated deflections showed perfect correlation. For test specimens tested as box-section, the design rules of prEN 1995-1-1:20xx [1] were conservative and the effective bending stiffness was substantially underestimated.

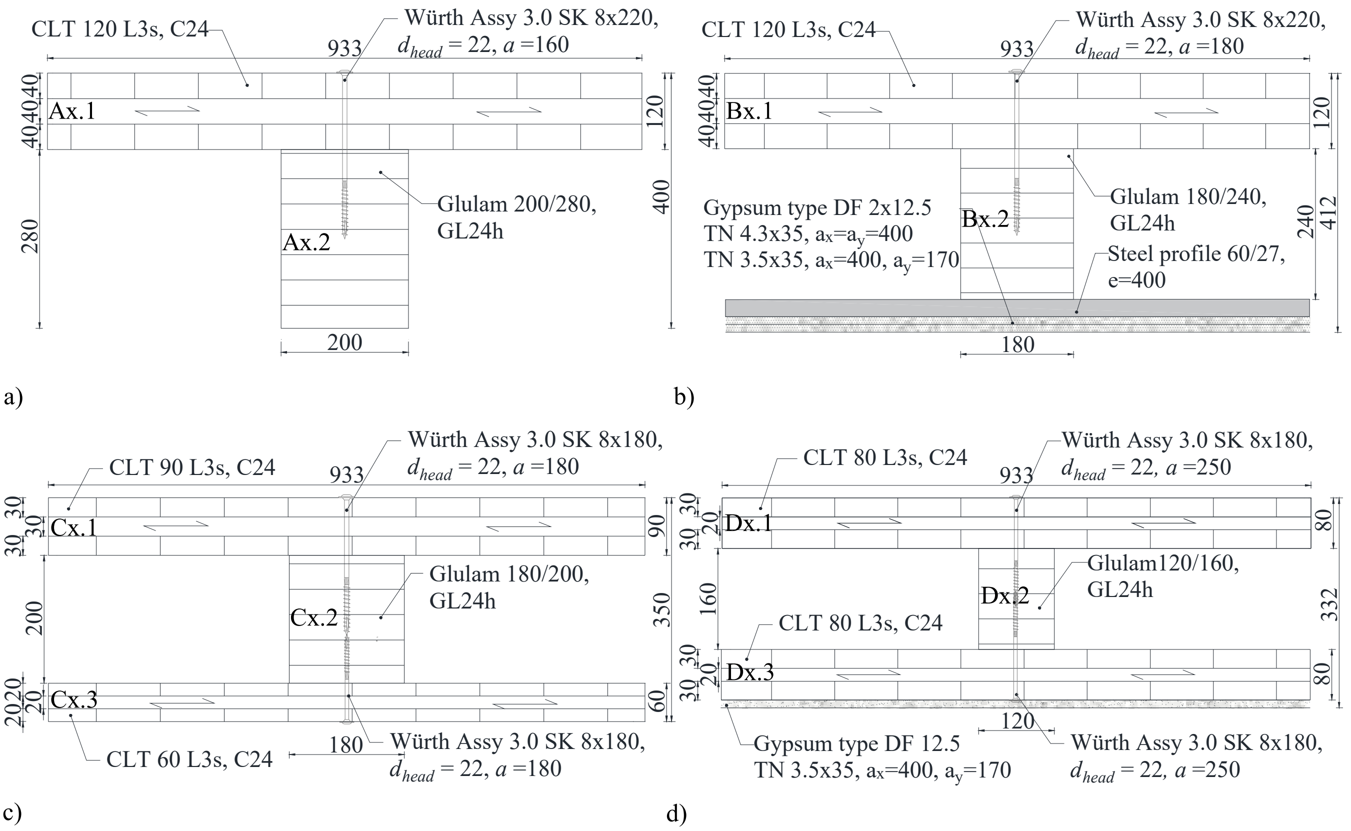

Figure 2. Cross-sections of the experimental program, in [mm]: a) T-section (A); b) T-section initially protected (B); c) Box-section (C); d) Box-section initially protected (D).

2.3 Fire resistance tests

The full-scale fire resistance tests were performed according to European test standards [9,10]. Four tests were performed (A, B, C, and D), one test specimen per cross-section of Figure 2. The horizontal furnace had a length l of 5.20 m and a width of 3.00 m. The test specimens were tested as three-ribbed system with a CLT width per rib b of 0.933 m. In the test setup, a constant mechanical load was applied uniformly via evenly distributed loading points, whereby the moment in the middle of the span corresponded to the target bending moment of the design. The deflection at midspan was measured at each rib. The furnace was controlled with plate thermometers to follow the ISO standard time-temperature curve [11]. Thermocouples of type K-w-e-0.5/2.2/in-pa were inlaid between and on top of gypsum plasterboards and CLT layers according to the recommendations by Fahrni et al. [12].

Failure times of the fire protection systems $t_{f,test}$ were defined as the first local fall-offs of gypsum plasterboards parts. In the case of initially protected test specimens B and D, the start time of charring $t_{ch,test}$ was defined when the average temperature on the fire-exposed side of the CLT plate reached 300°C. Sudden increases of the temperature measurements to the furnace temperature confirmed the fall-off of charred

CLT layers and that the bond line integrity was not maintained in fire. The fall-off times of charred CLT layers $t_{300°C,test}$ were defined as the average temperature of 300°C between the CLT layers. The fire resistance tests confirmed the assumptions that the bond line remained intact and the effect of the composite action was maintained in fire. The screws remaining after screw-press gluing had negligible influence on the fire behaviour of the floor system. After termination of the test, the test specimens were lifted from the furnace and extinguished. However, duration of the process lasted around 25 min.

3 FINITE ELEMENT MODELLING

3.1 Modelling assumptions

The numerical investigations comprised thermal and uncoupled thermo-mechanical simulations using SAFIR® version 2019.b.0, a nonlinear finite element software for modelling structures in fire [13]. The modelling framework was developed using the Python programming language [14]. The following assumptions were derived from the experimental investigations:

- The composite action is maintained under standard fire exposure.
- The influence of the screws and thus the screws themselves are neglected in the thermal simulation. Their loadbearing behaviour is neglected in the thermo-mechanical simulation.
- The thermal simulation takes into account the fall-off of charred CLT layers but not the fall-off of charred glulam layers.
- For comparison with the experimental results, the charred depth is tracked along the 300°C-isotherm according to EN 1995-1-2 [15].

3.2 Thermal simulations

Thermal simulations were conducted as 2D FE heat transfer analyses modelling the cross-section of a T-section or box-section. The nodeline was defined as the position of the neutral axis of the original cross-section. The vertical symmetry in the middle of the cross section was exploited by modelling it as an adiabatic surface. Convective and radiative thermal interactions were defined for the outer timber surfaces with the coefficient of convection taken as 25 W/(m^{2}K) on exposed surfaces and 4 W/(m^{2}K) on unexposed surfaces, and emissivity as 0.8 for timber and gypsum plasterboards [16]. The standard fire exposure was applied at the bottom edge. The top edge was exposed to a constant temperature of 20°C. The heat transfer is influenced by the void cavities. For radiation inside the void cavity, the emissivity of the materials enclosing the void was considered. For convection inside the void cavity, the coefficient of convection on unexposed surfaces was used, regardless of the temperature of the air in the void. Air movement within the cavity was not considered. The simulated sections were discretised into rectangular elements. The sizes of the elements varied between 4x4 mm^2 and 5x5 mm^2. The intervals between the time steps were kept at 5 seconds.

As criterion for the fall-off of gypsum plasterboards, the fall-off times observed in the fire tests $t_{f,test}$ were used to remove the elements defined as gypsum plasterboards in the FE model. Fall-offs of charred CLT layers $t_{300°C,sim}$ were defined as time steps of the thermal simulation when the average temperature between CLT layers exceeded 300°C. In a further simulation step, the FE model was re-created without the fallen-off CLT layer and the calculation was continued until the next CLT layer has fallen off.

The heat transfer analyses were based on the temperature-dependent thermal properties for wood according to EN 1995-1-2 [15] and a new set presented by Kleinhenz et al. [17]. The new set has been validated for after the fall-off of charred CLT layers to take into account the post-fall-off behaviour of wood. For this paper, the new set of thermal properties was also used for the glulam ribs after either the fall-off of the gypsum plasterboards (cross-sections B) or the fall-off of the bottom CLT plates (cross-sections C and D). Thus, the numerical results were calculated applying the new set after a fall-off on the entire composite cross-section and not only on the CLT plates. Thermal properties were used for gypsum plasterboards according to FSITB [18]. The moisture content of CLT plates and glulam ribs was measured as 10%. The mean density of the CLT plates was assumed as 465 kg/m^3 according to Stora Enso. The mean density of the ribs certificated as quality of GL 24h was assumed as 420 kg/m^3 according to EN 14080 [19]. For the gypsum plasterboards, the mean density was chosen as 800 kg/m^3 according to EN 520 [7].

3.3 Thermo-mechanical simulations

Uncoupled thermo-mechanical simulations were performed using a 2D FE model of a linear beam system. The system of the fire resistance tests was modelled as simply supported with a span l of 5.20 m in accordance with the length of the furnace. The structure was discretized by 16 beam elements of 0.352 m length, thus smaller than the height of the cross-sections (compare with Figure 2). The loads were applied per rib. As in the test setup, eight loading points represented the uniformly distributed load over the length (see Figure 3). The self-weight was taken as constant value. Mass-loss of the cross-section due to pyrolysis was neglected, as its share in the total load is negligible. The cross-section and its temperature history was imported from the thermal simulations' TEM-files.

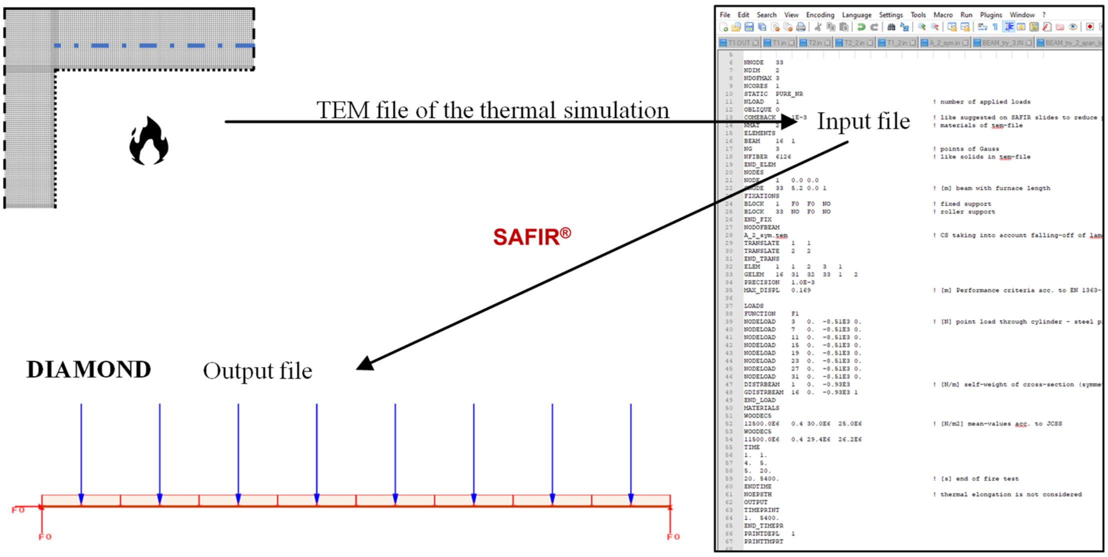

Figure 3. Linear FE beam model of the thermo-mechanical simulations.

Material properties were modelled as linear-elastic, brittle in tension and in compression. The mechanical properties at normal temperature (20°C) were defined by the modulus of elasticity in longitudinal direction, the Poisson's ratio, and the compressive and tensile mean strength values, as presented in Table 1. For the determination of the mean strength values, probabilistic models were used according to the JCSS guidelines for structural timber [20]. The stiffness and strength values for the transversal CLT layers and the gypsum plasterboards were set close to zero as non-loadbearing material. The temperature-dependent reduction in stiffness and strength properties was modelled by the bi-linear simplification according to EN 1995-1-2 [15]. The intervals between the time steps were kept at maximum 20 seconds.

Table 1. Mechanical properties for the longitudinal cross-laminated timber layers [1] and glued-laminated timber [19].

Material	E_x	v	f_c	f_t
	[N/mm^2]	[-]	[N/mm^2]	[N/mm^2]
CLT24	12500[1)]	0.40	33.9	27.1
GL24h	11500	0.40	29.4	26.2

[1)] Value based on Stora Enso.

SAFIR® uses Bernoulli-type beam finite elements. Thus, the influence of shear deformations is neglected and the stress distribution along the CLT width is uniform. The shear lag effect of the ribbed cross-sections needed to be taken into account by applying an effective width to the cross-section. For each cross-section, three cross-sections were submitted to SAFIR® for thermal simulations. A certain percentage of the CLT width b of 0.933 m was assumed as effective width based on the following cases:

- Case 1: 60% of the CLT width, representing the average result for the effective width at normal temperature according to prEN 1995-1-1:20xx [1] (see sub-section 2.2)
- Case 2: 80% of the CLT width, representing the average result for the effective width of the reference tests (see sub-section 2.2)
- Case 3: 100% of the CLT width, representing the extreme case

For each cross-section and effective width, thermo-mechanical simulations were conducted importing the thermal fields of the thermal simulations. At the end, the numerical results were sequenced together.

4 RESULTS

4.1 Thermal simulations

Figure 4 presents on the left side the experimental and numerical residual cross-sections after extinguishment. After the fire resistance tests, the experimental residual cross-sections at the centre rib's midspan were brushed, measured, and photographed. Figure 4 presents on the left side the experimental residual cross-sections' extracted coordinates per test specimen. All test specimens show the residual cross-section of a T-section. The numerical residual cross-section was created by extracting the 300°C iso-surface at a specified time step, which agrees with the time duration in the fire resistance tests until extinguishment. The 300°C iso-surfaces in the glulam ribs fit perfectly the experimental shapes, except for cross-section D. Figure 4 complements these results on the right side with the analysis of the corresponding charring behaviour of the CLT plates from the start time of charring until extinguishment. The charring developments of the charred depth in the CLT layers are shown as a function of the time for each test specimen. The experimental charring developments are based on the fall-off times of charred CLT layers $t_{300°C,test}$ and the mean charred depths measured at the experimental residual cross-sections $d_{char,test}$. The numerical charring developments are based on the fall-off times of charred CLT layers of the thermal simulations $t_{300°C,sim}$. Until test termination, the numerical charred depths fit well with the experimental charred depths. After test termination, they show a faster progression of the charred depths.

The results are compared to the estimated results according to prEN 1995-1-2:20xx [21]: the estimated rectangular residual cross-sections of the glulam ribs and the estimated charred depths in the CLT plates. The notional charring rate of 0.70 mm/min was used for the glulam ribs. The charred depths of the CLT plates were estimated according to the simplified design method including fall-off of charred CLT layers. After fall-off of gypsum plasterboard or of a charred CLT layer, the charring rate β_0 for solid wood of 0.65 mm/min is doubled to 1.30 mm/min until the charred layer reaches a thickness of 25 mm. Then, the charring rate decreases again to the basic value of the charring rate β_0. In the case of initial protection, encapsulated phases (no charring) and protected charring phases (decreased charring rate) were defined by the estimated start times of charring $t_{ch,EC5}$ and the estimated fall-off times of gypsum plasterboards $t_{f,EC5}$. The estimated results including fall-off of charred CLT layers lead to safe results for the charred depth in the CLT layers. An exception is the charred depth at the end of the second layer of cross-section C, where the charring progressed in a relatively short time. The charred depths in the CLT layers propagate less severe for the numerical calculation than the estimated calculation.

4.2 Thermo-mechanical simulations

Figure 5 presents per cross-section the experimental deflections as single (grey colour) and mean values (black colour). Furthermore, it presents the numerical deflections for the three cases of the effective width (60%, 80%, and 100% of the CLT width) until simulation stop. The simulation stop occurred, when SAFIR® has not obtained convergence. The convergence aims an equilibrium of stresses over the height of the cross-section based on the defined restrictions for the mechanical properties. The distribution of stresses depend on the reduced stiffness per fibre (= element of the thermal simulation) based on the temperature-dependent reduction factors for stiffness. The maximum stress per fibre depends on the reduced strength value based on the temperature-dependent reduction factors for strength.

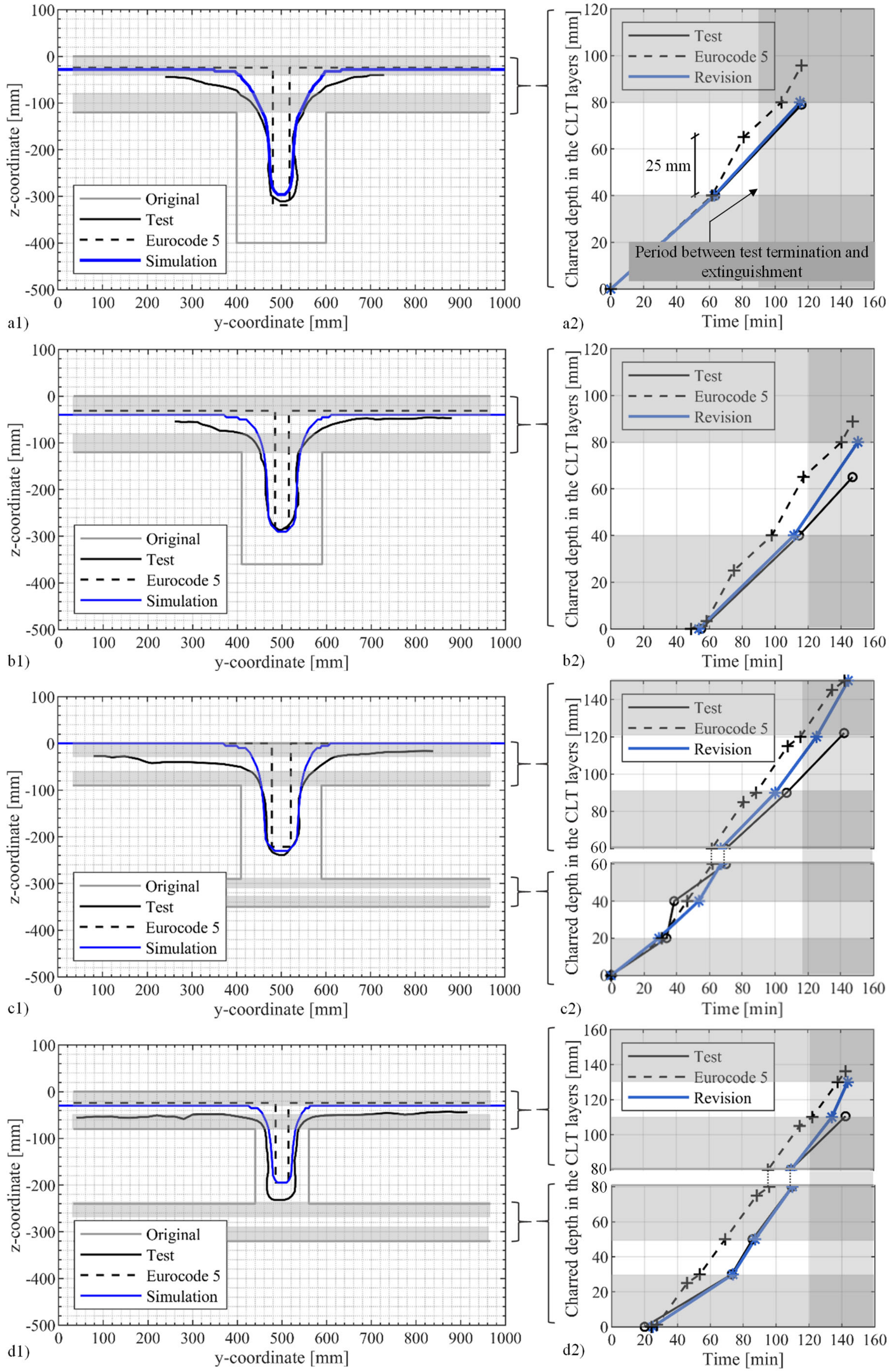

Figure 4. Experimental, estimated, and numerical residual cross-sections (after extinguishment) and the corresponding charred depths in the cross-laminated timber plates based on the revision: a) A; b) B; c) C; d) D.

The instantaneous deflections due to self-weight were removed from the experimental and numerical deflections. Figure 5a and b present the deflections of the T-sections (A, B). The numerical deflections show higher values for a cross-section with a smaller effective width. The original numerical results (light blue colour) show a clear underestimation of the experimental measurements. The linear FE beam model does not account for deflections caused by shear deformations. To compensate for the neglected shear deflections, a certain proportion is added to the numerical bending deflections (blue colour). From the reference tests, the proportion due to shear deflections w_V/w was determined on average as 28% of the deflections for cross-section A, and as 18% of the deflections for cross-section B. Multiplying the original numerical results by the ratio $100/(100-w_V/w)$, the revised numerical results show very good agreement with the experimental measurements. The difference between the results based on the cross-sections with 60% and 100% CLT widths is up to 7 mm. For cross-section B, the influence of the initial fire protection becomes visible through the comparison with the equivalent initially unprotected cross-section. The temperature increase in the initially protected cross-section is delayed by the failure time t_f of the fire protection system.

In the fire resistance tests, the test specimens were screwed on top of a wood frame for lifting on the furnace. In the case of T-sections (A, B), the wood frame was attached to non-loadbearing elements of the test specimens. In the case of box-sections (C, D), the wood frame was attached to the bottom CLT plates. In Figure 5c and d, the numerical results disagree with the experimental measurements using a roller support. In Figure 6, both supports of the FE beam model were defined as fixed support for cross-sections C and D. Figure 6c and d present the results of the box-sections (C, D). Again, a certain proportion is added to the numerical bending deflections (light blue colour) to account for the neglected shear deflections (blue colour). From the reference tests, the proportion due to shear deflections w_V/w was determined on average as 26% of the deflections. The numerical results show a higher increase in the rate of change after the fall-off of the second charred CLT layer than the experimental measurements. The difference between the results based on the cross-sections with 60% and 100% CLT widths is up to 18 mm.

5 DISCUSSION

5.1 Thermal simulations

The thermal simulations give good approximations of the residual cross-sections. However, the numerical residual cross-sections show lower degrees of corner rounding in the corners of the composite section than the experimental residual cross-sections. A reason for this could be a less severe fall-off of charred CLT layers but a dropping of charred CLT layer parts. The thermal simulations assume a sudden fall-off of the entire charred CLT layer, resulting in less visible corner rounding. After test termination, the numerical results show a faster progression of the charred depths in the CLT layers. In the fire resistance tests, the fire exposure cannot be defined as standard fire exposure in the period between test termination and extinguishment (up to 25 minutes). The furnace was turned off and the gas temperature did not follow the standard time-temperature curve, anymore.

The fall-offs of gypsum plasterboards are well predicted according to prEN 1995-1-2:20xx [21]. The estimated results give a good approximation of the residual cross-section of the glulam rib and confirms that fall-off of charred glulam layers did not occur. The simplified bi-linear model including fall-off of charred CLT layers according to prEN 1995-1-2:20xx [21] leads to safe results for the charred depth in the CLT plates. The fall-off of charred CLT layers was less pronounced as expected. As for the thermal simulations, the analytical calculations assume a sudden fall-off of the entire charred CLT layer.

5.2 Thermo-mechanical simulations

The numerical results show good agreement with the experimental measurements. In the case of cross-sections C and D, changing the roller support of the simply supported beam system to another fixed support (no resistance to rotation) improved the compatibility with the experimental measurements. The numerical results of cross-section C show the greatest discrepancy with the experimental measurements as in the thermal simulations.

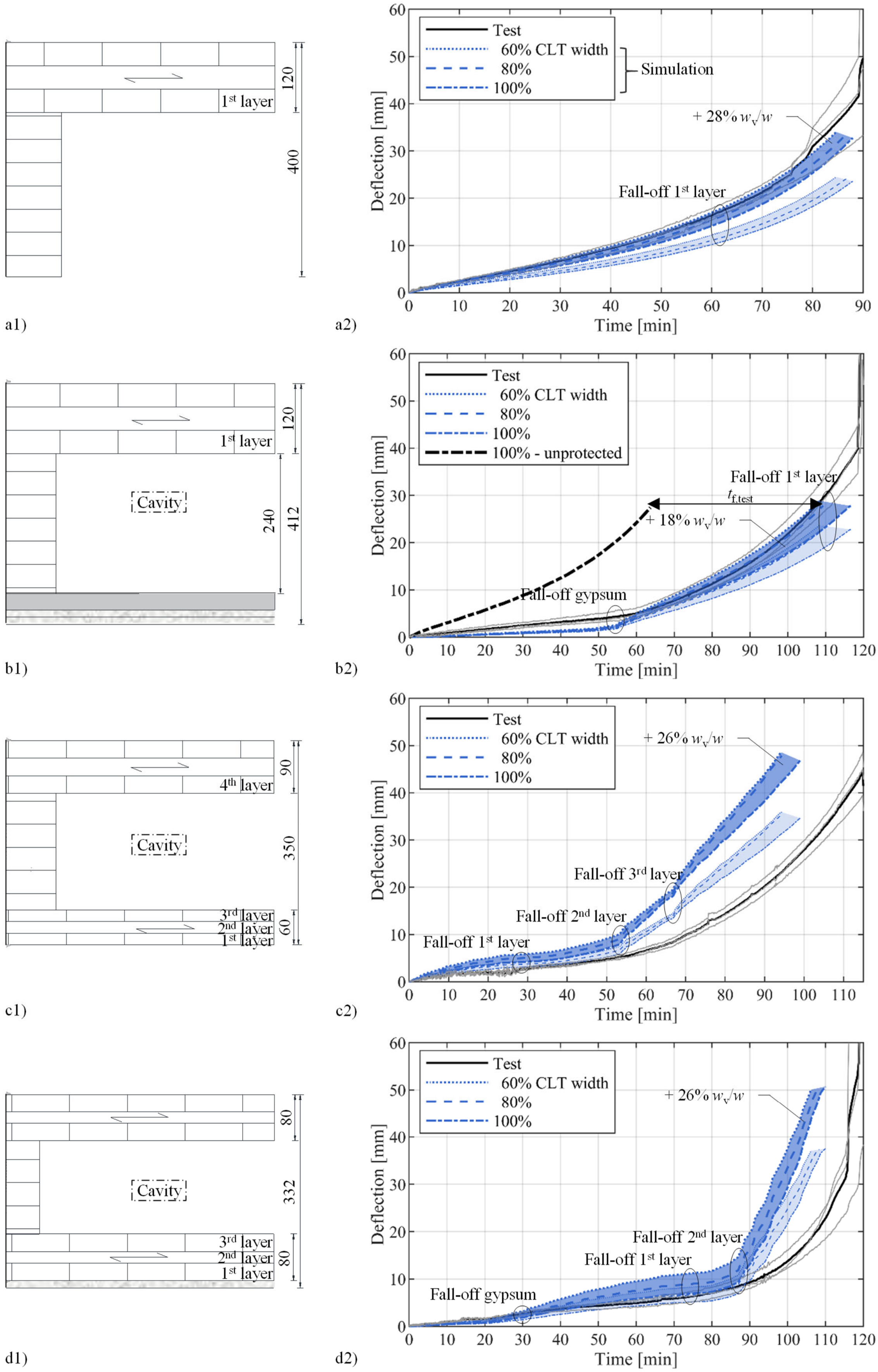

Figure 5. Numerical deflections of the cross-sections for the three cases of the effective width (until simulation stop) excl./incl. the proportion due to shear deflections in comparison to the experimental results (until test termination): a) A; b) B; c) C; d) D.

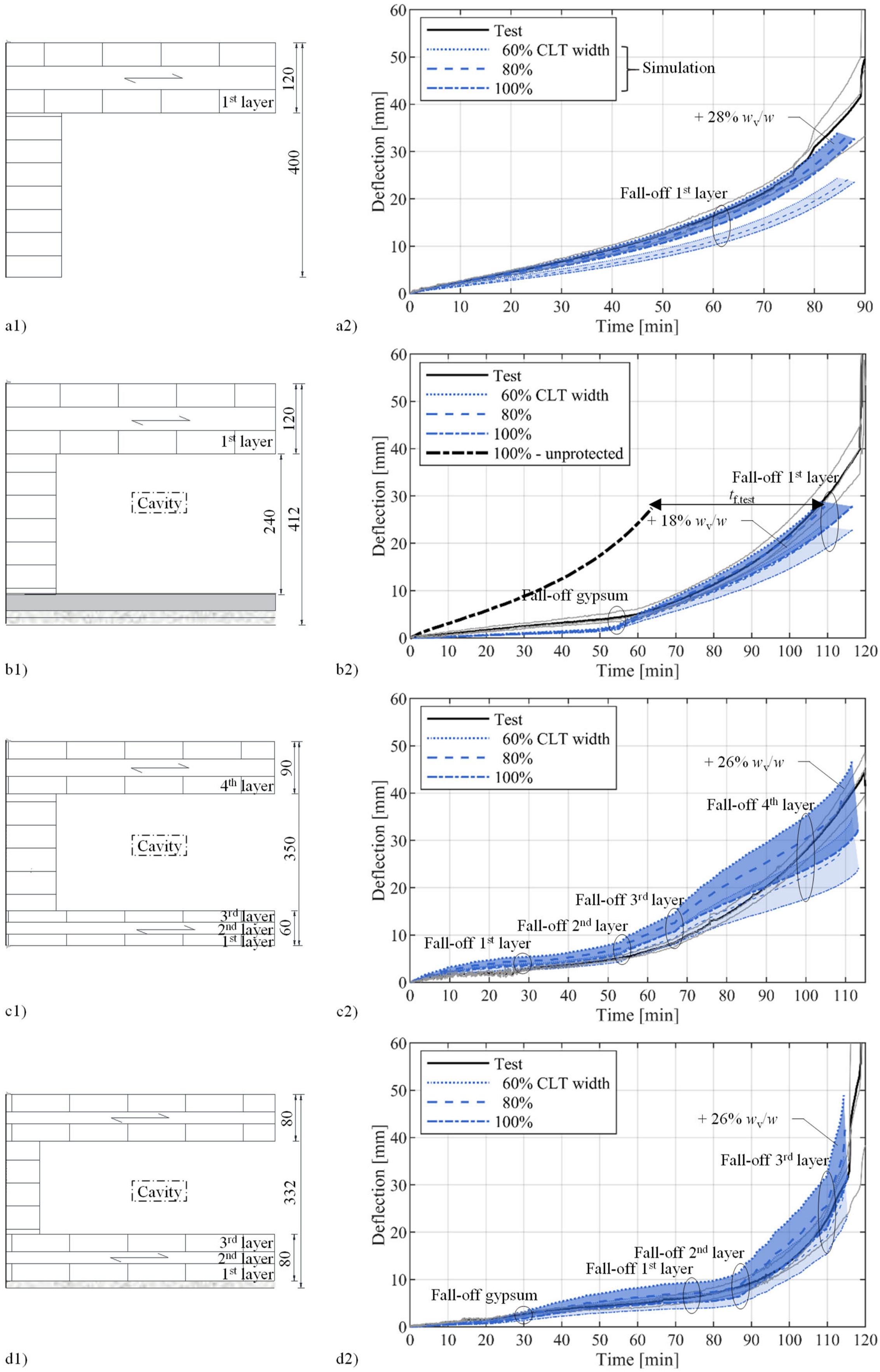

Figure 6. Numerical deflections of the cross-sections for the three cases of the effective width (until simulation stop) excl./incl. the proportion due to shear deflections in comparison to the experimental results (until test termination): a) A; b) B; c) C (fixed supports); d) D (fixed supports).

The numerical deflections outline the importance to take into account the shear deflections. The shear flexibility is increased by the effect of shear lag of the composite cross-section, and to a certain extent by the shear-soft transversal layers of the CLT plates. Especially in the case of box-sections, the proportion due to shear deflections w_v/w cannot be considered as constant value over time. Based on the increased charring process, the residual cross-section of the CLT plates is reduced and the proportion due to shear deflection w_v/w will decrease.

Higher deflections are obtained for a cross-section with a smaller effective width. The results based on the cross-sections with 60% and 100% CLT widths show a larger difference for the box-sections than for the T-sections. The reason therefor are the smaller ribs of the box-sections in combination with a higher number of longitudinal CLT layers (Figure 2). This increases the influence of the CLT layers on the bending stiffness of the composite system, and the influence of the effective width on the deflections. As for the shear deflections, the effective width during fire exposure cannot be considered as a constant value or equal to the initial value at normal temperature. Based on the increased charring process, the effective width during fire exposure will decrease over time. However, the differences between different CLT widths are small in all cases. The results indicate that the cross-sections with 60% CLT width give an approximation on the safe side.

6 CONCLUSIONS

The FE heat transfer models provide good estimates of the experimental temperatures. The experimental residual cross-sections show good agreement with the numerical residual cross-sections (= 300°C iso-surface) when the new set of thermal properties [17] is applied after fall-off to all timber materials; i.e. also for the glulam ribs. The degrees of corner rounding are more pronounced in the corners of the composite section of the experimental cross-sections. The 2D FE model of a linear beam system gives very good approximations of the mechanical behaviour in fire. A good fit is obtained based on the temperature-dependent reduction factors according to EN 1995-1-2 [15], and linear-elastic brittle material behaviour.

The FE linear beam system is modelled by SAFIR® as Bernoulli-beam. Thus, the influence of shear deformations is neglected and the stress distribution along the CLT width is uniform. The numerical results outline the importance to take into account the deflections caused by shear deformations w_v. Different effective widths were chosen for modelling the tested cross-sections (60%, 80%, and 100% of the CLT width). Higher deflections are obtained for a cross-section with a smaller effective width. The influence on the resulting deflections based on different effective widths are larger for the box-sections than for the T-sections, as already concluded from the reference tests (see subsection 2.2). However, the differences are small in all cases. Therefore, it can be concluded that an underestimation of the effective width in fire will still result in good approximations. The results indicate that the cross-sections with 60% CLT width, representing the effective width at normal temperature b_{ef} according to prEN 1995-1-1:20xx [1], can give an approximation on the safe side of the effective width in fire $b_{ef,fi}$.

The numerical investigations of the FE linear beam formed the basis for further investigations using a 3D FE model resulting in a non-uniform, temperature-dependent strain distribution along the CLT width [22]. A parametric study analysed the effective width in fire $b_{ef,fi}$ for a parameter range expected in practice. Simplified design rules were proposed for prEN 1995-1-2:20xx [21].

ACKNOWLEDGMENT

The authors gratefully acknowledge the financial support from Stora Enso Wood Products GmbH in Ybbs, Austria, with special thanks to Niko Kumer, Thomas Demschner, and Julien Lapere. The process of Python scripting has been brought forward thanks to the work of two former students: Jonas Fischer and Janine Kipfer. The authors gratefully acknowledge the contributions of Pedro Palma (Empa, Dübendorf). The authors would like to thank Thomas Gernay for his dedicated support with SAFIR®.

REFERENCES

[1] CEN/TC 250/SC 5 N 892: M515 SC5.T1 Phase 1 Final deliverables - SC5.T1 Final Document of prEN 1995-1-1 on CLT, CEN - CENELEC, Brussels, 2018.

[2] K. Bratulic, M. Augustin, G. Schickhofer, Investigations concerning screw-press gluing of assemblies with CLT, in: International Network on Timber Engineering Research (INTER) – Proceedings of the 6th Meeting, Tacoma, USA, 2019. http://holz.vaka.kit.edu/392.php (accessed November 2, 2020).

[3] E. Chwalla, Die Formeln zur Berechnung der voll mittragenden Breite dünner Gurt- und Rippenplatten, Bautechnik. 10 (1936) 73–78.

[4] EN 1995-1-1, Eurocode 5: Design of timber structures - Part 1-1: General - Common rules and rules for buildings, European Committee for Standardization (CEN), Brussels, 2004.

[5] M. Kleinhenz, A. Just, A. Frangi, Experimental analysis of cross-laminated timber rib panels at normal temperature and in fire, Engineering Structures. 246 (2021) 113091. https://doi.org/10.1016/j.engstruct.2021.113091.

[6] EN 1990:2002/A1:2005/AC:2010, Eurocode - Basis of structural design, European Committee for Standardization (CEN), Brussels, 2002.

[7] EN 520:2009, Gypsum plasterboards – Definitions, requirements and test methods, European Committee for Standardization (CEN), Brussels, 2009.

[8] EN 408:2012, Timber structures - Structural timber and glued laminated timber - Determination of some physical and mechanical properties, European Committee for Standardization (CEN), Brussels, 2012.

[9] EN 1363-1:2012, Fire resistance tests - Part 1: General requirements, European Committee for Standardization (CEN), Brussels, 2012.

[10] EN 1365-2:2014, Fire resistance tests for loadbearing elements - Part 2: Floors and roofs, European Committee for Standardization (CEN), Brussels, 2014.

[11] ISO 834-1:1999, Fire-resistance tests - Elements of building construction - Part 1: General requirements, International Organization for Standardization (ISO), 1999.

[12] R. Fahrni, J. Schmid, M. Klippel, A. Frangi, Correct temperature measurements in fire exposed wood, in: World Conference on Timber Engineering (WCTE) - 10th World Conference on Timber Engineering, Seoul, South Korea, 2018.

[13] J.-M. Franssen, T. Gernay, Modeling structures in fire with SAFIR: theoretical background and capabilities, Fire Engineering. 8 (2017) 300–323. https://doi.org/10.1108/JSFE-07-2016-0010.

[14] Python Software Foundation, Python (version 3.7), (2018). https://www.python.org/.

[15] EN 1995-1-2, Eurocode 5: Design of timber structures - Part 1-2: General - Structural fire design, European Committee for Standardization (CEN), Brussels, 2004.

[16] EN 1991-1-2:2002, Eurocode 1: Actions on structures – Part 1-2: General actions – Actions on structures exposed to fire, European Committee for Standardization (CEN), Brussels, 2002.

[17] M. Kleinhenz, A. Just, A. Frangi, Temperature-dependent thermal properties for cross-laminated timber exposed to standard fire, in: International Network on Timber Engineering Research (INTER) – Proceedings of the 6th Meeting, Online, 2021. http://holz.vaka.kit.edu/392.php (accessed November 2, 2020).

[18] Fire Safety in Timber Buildings – Technical Guideline for Europe, SP Report 19, Science Technical Research Institute of Sweden, 2010.

[19] EN 14080:2013, Timber structures - Glued laminated timber and glued solid timber - Requirements, European Committee for Standardization (CEN), Brussels, 2013.

[20] JCSS, JCSS Probabilistic Model Code Part 3: Resistance Models, 3.5 Properties of timber, 2006. https://www.jcss-lc.org/jcss-probabilistic-model-code/ (accessed November 1, 2020).

[21] CEN/TC 250/SC 5/WG 4 N 193: Consolidated draft prEN 1995-1-2 for informal enquiry, CEN - CENELEC, Brussels, 2021.

[22] M. Kleinhenz, A. Frangi, A. Just, The effective width of cross-laminated timber rib panels in fire, in: International Network on Timber Engineering Research (INTER) – Proceedings of the 7th Meeting, Bad Aibling, Germany, 2022. http://holz.vaka.kit.edu/392.php (accessed November 2, 2020).

SiF 2022– The 12th International Conference on Structures in Fire
The Hong Kong Polytechnic University, Nov 30 - Dec 2, 2022

VALIDATION OF A VIRTUAL ROOM CORNER FIRE TEST WITH SPRUCE MEMBERS AND THE DEVELOPMENT OF THE CHAR LAYER

Jakub Šejna[1], Kamila Cábová[2], Robert Pečenko[3], Tomaž Hozjan[4], Marie Křišťanová[5], František Wald[6]

ABSTRACT

This article presents the validation of the Computational Fluid Dynamics (CFD) model of the Room Corner Test (RCT). In the RCT experiment, a natural fire with two columns and one beam is studied. The specimens were made of spruce wood. The CFD model integrates the calculation of complex pyrolysis. The Fire Dynamics Simulator (FDS) was used, and the input data was created. In the experience of previous models, emphasis was placed on the selection of input data for the pyrolysis model. Various pyrolysis models with a single reaction pattern or with parallel reactions were studied in a numerical simulation.

This work provides insight for advanced modelling of wood samples in a natural fire, taking into consideration the pyrolysis model. The CFD model with pyrolysis, considering massive specimens, has not previously been adequately validated and presented. To show the applicability of the model, the development of the char layer of the timber column most exposed to fire is presented.

Keywords: Virtual test; CFD; fire test; timber column; timber beam; pyrolysis; char layer

1 INTRODUCTION

A full-scale fire test provides the best demonstration of the behavior and the fire resistance of each member of a structure, including its joints. While the benefits of full-scale fire tests are clear, however, they are very complex to design and very expensive to carry out. The timber members expand only slightly due to the high temperatures in fire, so the behavior of the members and connections can be considered separately. However, it has been shown that uneven spatial radiation on the timber structure has significant effects on the behavior and the load-bearing capacity of timber members. The validated CFD model of the room corner test (RCT) [1] provides an option for virtual radiation to the structure. The validated model can be used to test timber specimens. In this case, the tested specimens are made of a flammable material and at the same time serve as a supplementary source of the fire.

[1] Ing. Jakub Šejna, Department of Steel and Timber Structures, Faculty of Civil Engineering, Czech Technical University in Prague,
e-mail: jakub.sejna@fsv.cvut.cz, ORCID: https://orcid.org/0000-0002-9968-2026
[2] Ing. Kamila Cábová, Ph.D., Department of Steel and Timber Structures, Faculty of Civil Engineering, Czech Technical University in Prague, Czech Republic
e-mail: kamila.cabova@fsv.cvut.cz, ORCID: https://orcid.org/0000-0002-4446-2472
[3] doc. dr. Robert Pečenko, univ. dipl. inž. grad., Chair of Mechanics, Faculty of Civil and Geodetic Engineering, Univerza v Ljubljani, Slovenia
e-mail: robert.pecenko@fgg.uni-lj.si, ORCID: https://orcid.org/0000-0003-4521-905X
[4] prof. dr. Tomaž Hozjan, univ. dipl. inž. grad., Chair of Mechanics, Faculty of Civil and Geodetic Engineering, Univerza v Ljubljani, Slovenia
e-mail: tomaz.hozjan@fgg.uni-lj.si, ORCID: https://orcid.org/0000-0002-9300-4267
[5] Bc. Marie Křišťanová, Department of Steel and Timber Structures, Faculty of Civil Engineering, Czech Technical University in Prague, Czech Republic
e-mail: marie.kristanova@fsv.cvut.cz, ORCID: https://orcid.org/0000-0003-2416-8951
[6] prof. Ing. František Wald, CSc., Department of Steel and Timber Structures, Faculty of Civil Engineering, Czech Technical University in Prague, Czech Republic
e-mail: wald@cvut.cz, ORCID: https://orcid.org/0000-0003-2416-8951
https://doi.org/10.6084/m9.figshare.22193773

In this paper, the validated RCT model with spruce structural elements is used to investigate the development of the char layer in structural elements exposed to local fire, and the influence of pyrolysis on the fire conditions inside the RCT. The RCT model has already been used for virtual testing of timber cladding that protects wall structures [2]. In the application of the RCT model, the fundamental question concerns the kinetic coefficients of pyrolysis, which are obtained from small-scale cone calorimeter tests. The application of the coefficients to a virtual large-scale simulation [2, 5] may limit the predictive value of this model.

2 FIRE TEST

2.1 Room corner test

The room corner test measuring 3.6 × 2.4 × 2.4 m with an opening for ventilation in the form of a door was used for the fire test. The burner is located in the corner of the furnace [1]. The RCT walls are made of aerated concrete blocks, and the floor and ceiling are made of concrete. Three structural elements, namely two columns and a beam made of spruce wood, were located at different distances from the burner. The distribution of the elements was determined by CFD pre-simulation investigating the effect of their location on the flow of the gases in the furnace. The location of the wood elements, the burner, and the ventilation opening are shown in Fig. 1 and Fig. 2.

2.2 Description of the experiment

The beginning of the combustion of all the timber elements was monitored during the test. The gas temperatures in the furnace were measured using thermocouples (TC) type MTC12 /1xK T2 /N4m /GHGH 2x0,5 / K-MM located according to [1]. The timber element temperatures were recorded by thermocouples type MTC12 /1xK T2 /N4m /GHGH 2x0,5 / K-MM and MTC10 /1xK T2 /P1,5 /N3000 /K-MM mounted into the specimens at depths of 5, 15, 25, and 50 mm at a height of 0.8 m and 2.02 m from the floor, directed to the burner and to the short wall of the RCT, and the adiabatic surface temperature (AST) was measured on each element using plate thermometers at the height of the thermocouples located in the specimens. [3] The thermocouples named in this article are illustrated in Fig. 2.

The burner power was set to 100 kW for 10 min, followed by 300 kW, to be terminated at 30 min. The standard ventilator [1] was set constantly to 30 % power for the full experiment. During the experiments, temperatures of up to 800° C were measured on the surface of the wood. After the experiments, the individual elements were cut, and the char layer and the pyrolysis layer were measured to validate the predictive ability of the CFD virtual model.

Within 10 mins of the start of the experiment, the water had been evaporated from the specimens. After the burner power had increased to 300 kW in 600 s of the experiment, Column 1 started burning on the sides exposed to fire at the height of the smoke layer. During the experiment, the flame on the surface of Column 1 gradually spread. The samples in column 2 burned only on the side exposed to fire at the height of the smoke layer. The beam caught fire repeatedly only on the side exposed to fire. After the end of the experiment, the surface of column 1 continued to burn for 30 s. Subsequently, the specimens were extinguished and were cooled with a water jet.

3 THE CFD MODEL OF AN RCT FURNACE

3.1 Pyrolysis model

Fire Dynamics Simulator (FDS) 6.7.9 was used as a CFD tool to simulate the fire test of timber elements in an RCT furnace. The geometry of the model corresponds to the actual test dimensions (Fig. 1 and 2). The properties of the wood material were taken from [5]. The authors' experience in modelling small test furnaces [6] and the virtual RCT model [2] was applied to the large RCT test model.

Various sources [4, 7, 8] were considered when selecting the correct pyrolysis kinetic coefficients for the CFD model. As these coefficients are obtained on small specimens in a conical calorimeter, it is necessary to validate their applicability to the simulation of massive specimens.

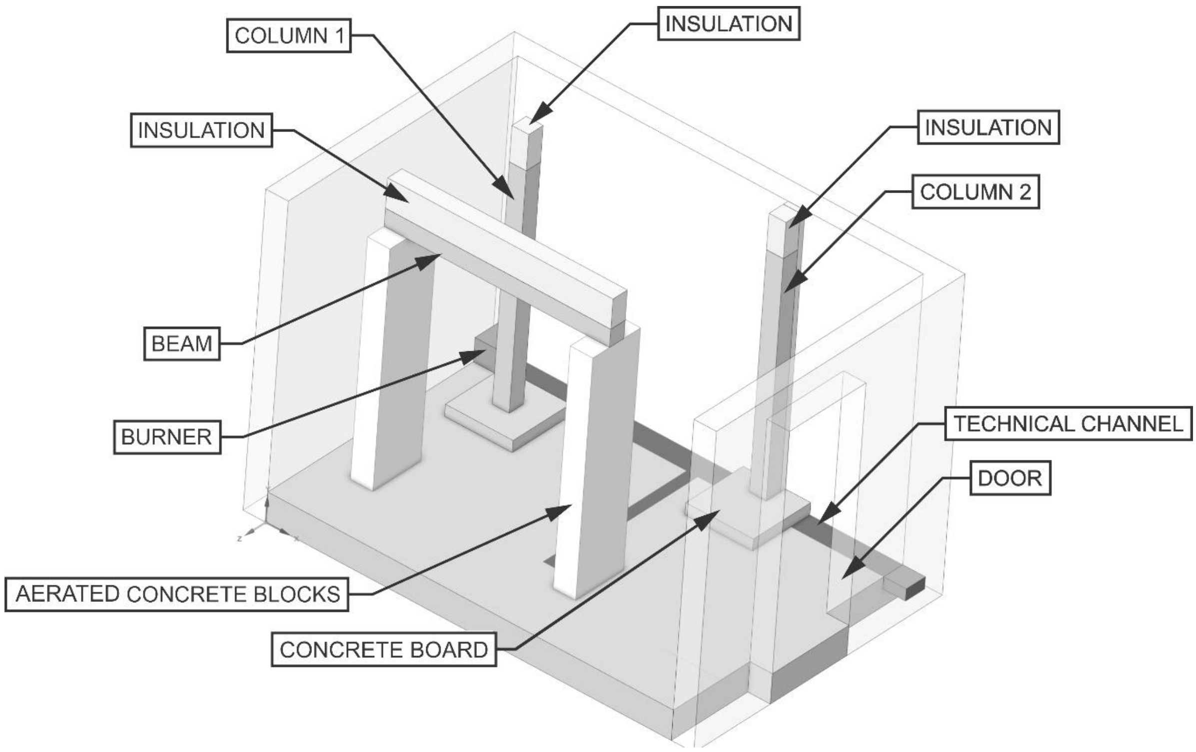

Figure 1. 3D model of RCT

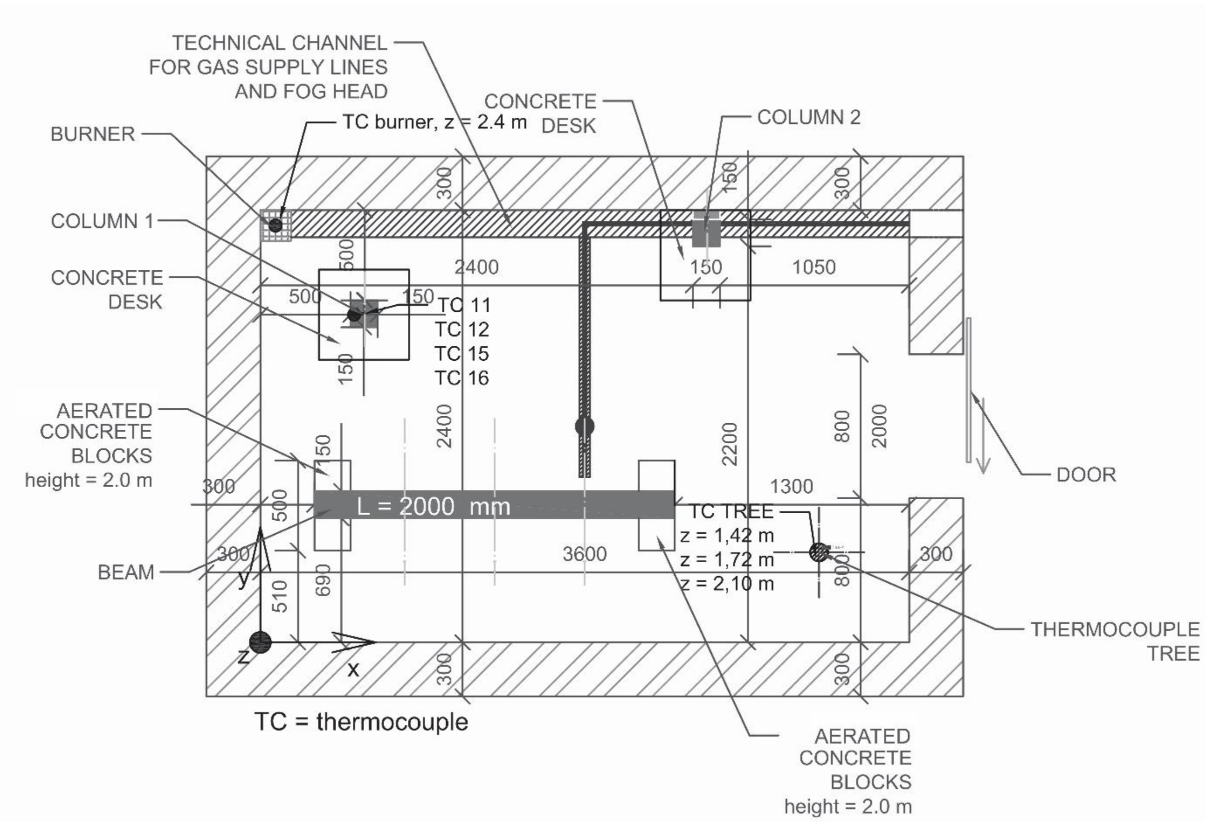

Figure 2. Floor plan of the RCT

For comparison, the temperatures were measured in the RCT CFD model at the farthest point from the burner (TC tree, z = 1720 mm, and 2100 mm). They were calculated to accommodate the rate of reaction r_j defined in Eq. 1 [4].

$$r_j = A_\alpha \exp\frac{-E_j}{RT} Y_{s,\alpha}{}^{n_\alpha} \quad (1)$$

where A_α is the pre-exponential factor, E_α is the activation energy, n_α is the reaction order, T is temperature, $Y_{s,\alpha}$ is the initial mass fraction of the component, and R is the universal gas constant [4, 9, 10].

Pyrolysis can be modelled using kinetic coefficients using fictitious reactions that can be compared to lignin, cellulose, and hemicellulose, but cannot be considered identical to [6, 10]. It is very important to monitor the individual representations of the kinetic coefficients of pyrolysis and the series of reactions that can negatively affect the resulting model. For a correct model of pyrolysis, it is necessary to consider the correct reaction pattern and the number of reactions, for example, Eq. 2 [4].

$$parallel\ reaction \begin{cases} extractives \rightarrow char_e + volatiles \\ reaction\ 1\ (fictional\ hemicellulose \rightarrow char_{hc} + volatiles \\ reaction\ 2\ (fictional\ cellulose \rightarrow char_c + volatiles \\ reaction\ 3\ (fictional\ lignin \rightarrow char_l + volatiles \end{cases} \quad (2)$$

Failure to follow the reaction pattern or the number of reactions may result in the introduction of an error into the calculation. The error causes a decrease in the development of the temperatures. When comparing the calculated values, the most appropriate data from Rinta-Paavola [4] were chosen. The kinetic coefficients of pyrolysis are given in Table 1.

Table 1. Final pyrolysis kinetic coefficients for the RCT CFD model [3]

	$Y_{s,\alpha}(0)$ (−)	A_α (1/s)	E_α (kJ/mol)	n_α (−)	ν_{char} (−)
Extractives	0.0167	4.411×10^{8}	107.1	1.0	0.0
Hemicellulose	0.2785	5.426×10^{13}	168.1	2.5	0.0
Cellulose	0.4103	4.239×10^{13}	195.1	0.62	0.043
Lignin	0.2696	2.46×10^{12}	157.5	6.11	0.517

The calculated temperatures from the comparison are shown in Fig. 3 and Fig. 4. The graphs shown for the RCT CFD model using one reaction burning scheme, i.e., the burner model with the power specified as HRRPUA (defining the burner power without the burner fuel burning reaction), appeared to be inaccurate. In the RCT CFD model, temperatures greater than 1100 ℃ were reached, which was refuted by the experiment. In the advanced CFD models, two reactions were considered in the simulation. The first was the reaction of burning propane as a fuel. The second reaction was the pyrolysis of the wood.

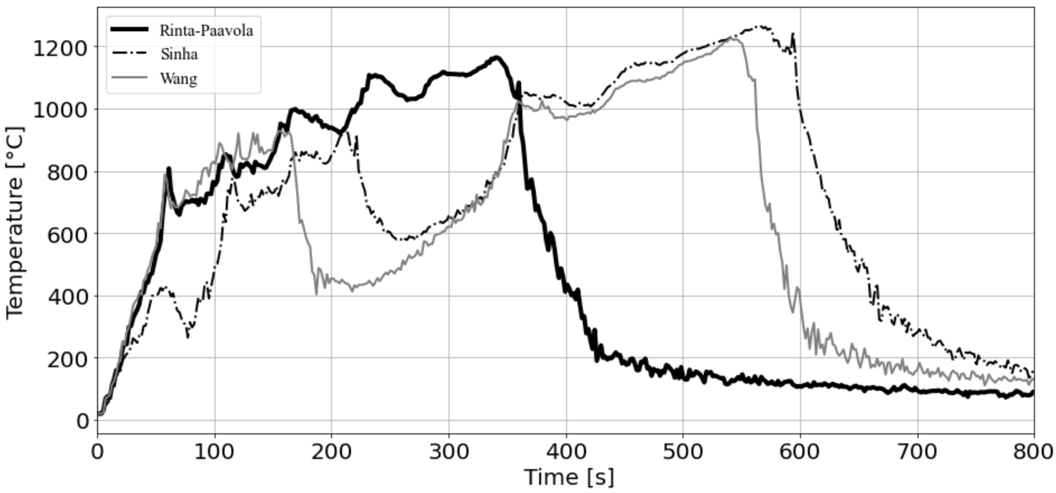

Figure 3. Temperature development at a height of 1720 mm in the area of the thermocouple tree

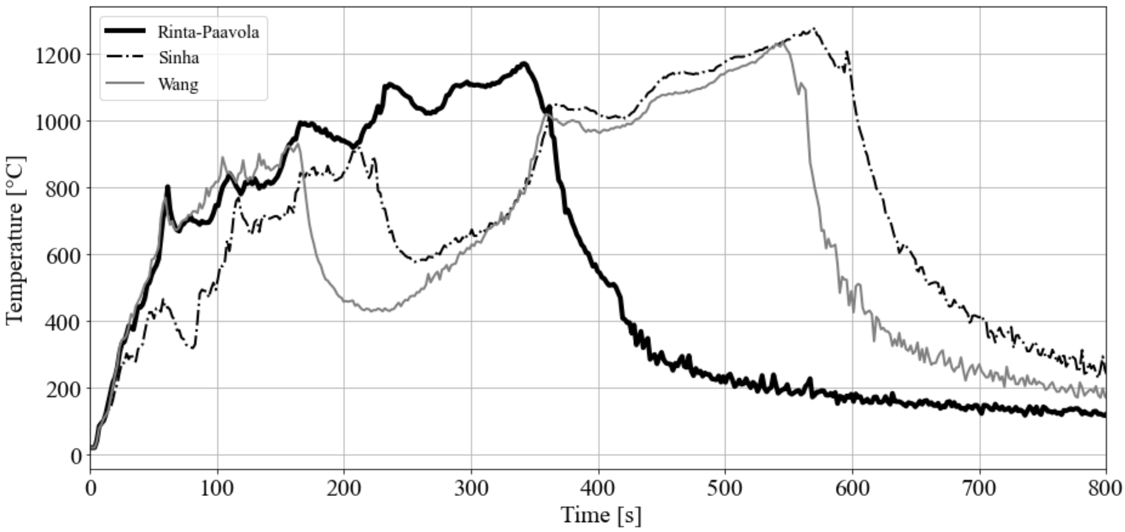

Figure 4. Temperature development at a height of 2100 mm in the area of the thermocouple tree

3.2 Validation of the CFD model

For the validation of the CFD model, the results from the models were compared with the temperatures measured in the experiment. For the possibility of a correct comparison, a CFD model without the influence of pyrolysis was also calculated. The model without the inclusion of pyrolysis can be taken as a reference value for a comparison of the influence of the pyrolysis assignment as a second reaction for the calculation of the CFD model. The difference in the simulations is due to the energy consumed in the endothermic phase of pyrolysis. Due to the time-consuming nature of the calculation, the algal section was selected up to 1400 s for validation, at which point the experiment was considered stable. The size of the individual calculation cells was selected with an edge of 50 mm, based on previous experience [2, 6], resulting in the number of calculation cells being 206 652. The burner power and the fan power were set the same as in the experiment. The geometry of the FDS model is shown in Fig. 5. The temperature courses obtained in the experiment and the calculated CDF models are shown in Figs. 6-8.

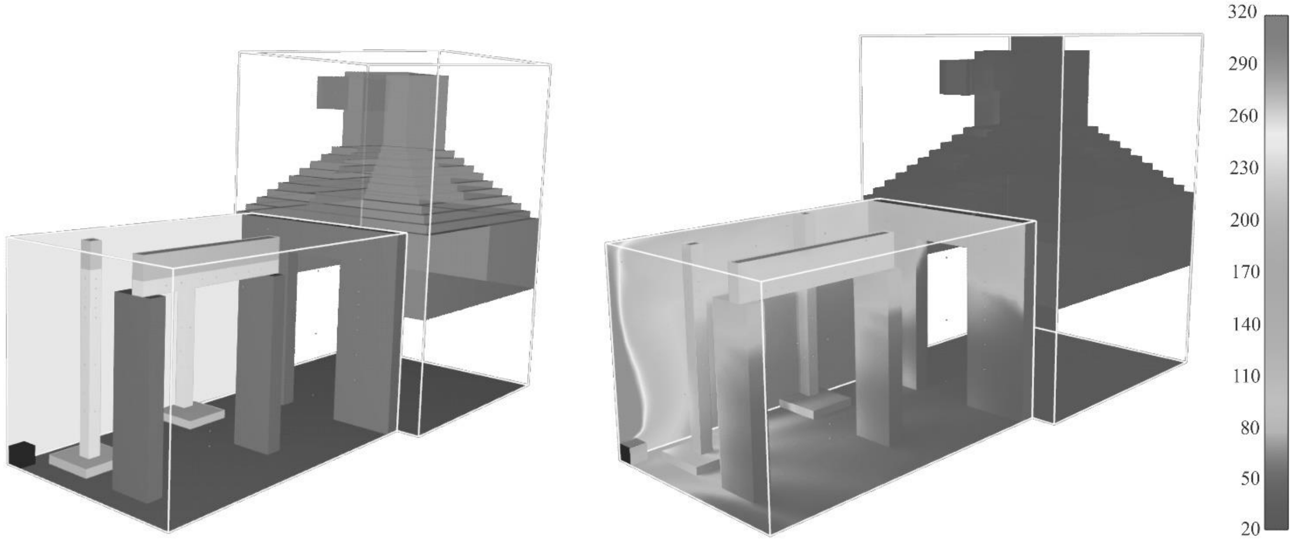

Figure 5. Geometry of the CFD model (left) and the surface adiabatic temperature after 600 s of the experiment (right).

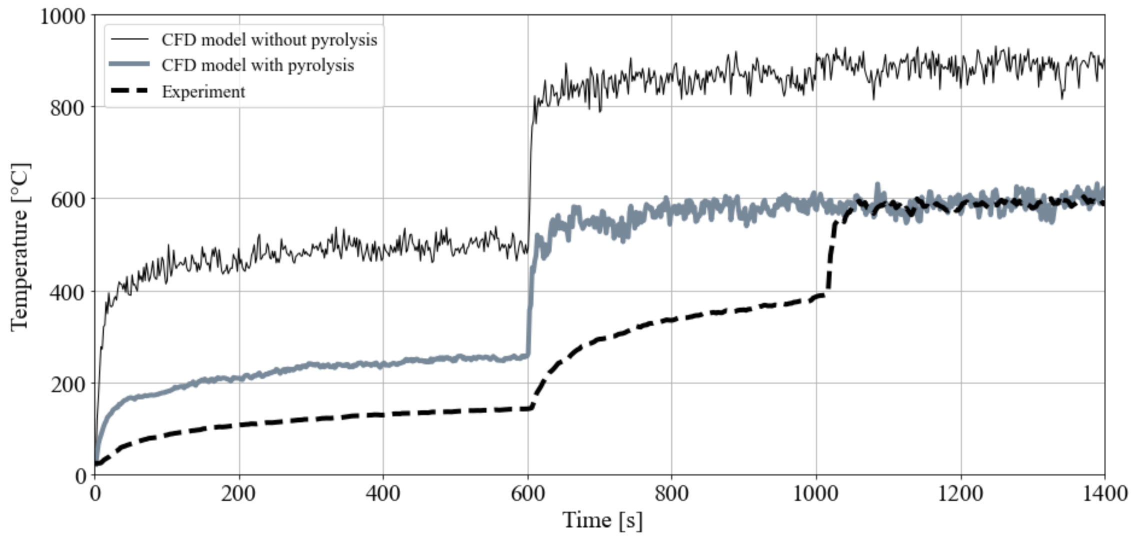

Figure 6. Temperature development at a height of 2400 mm in the burner area

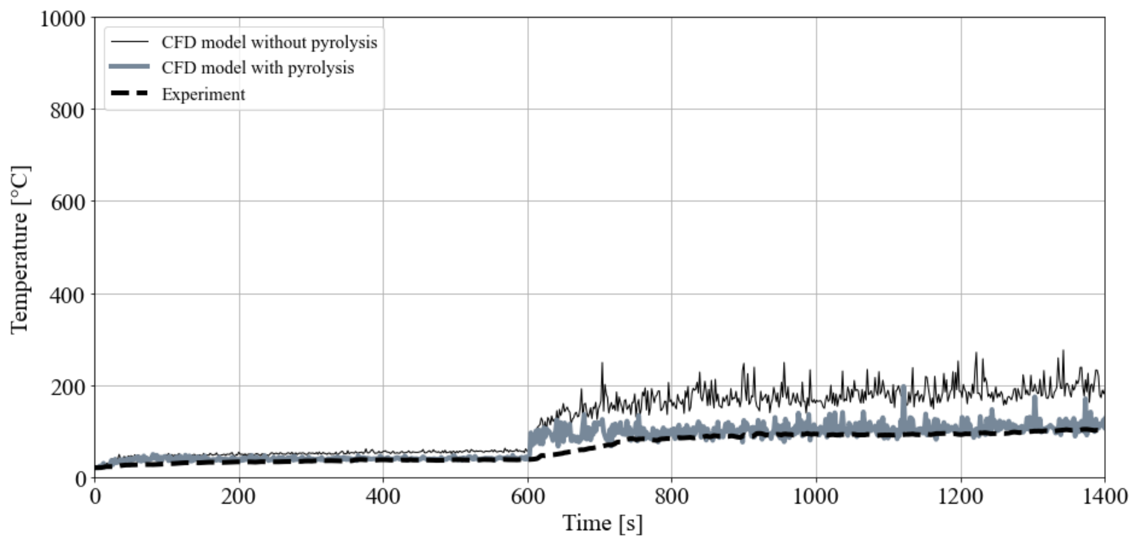

Figure 7. Temperature development at a height of 1420 mm in the area of the thermocouple tree

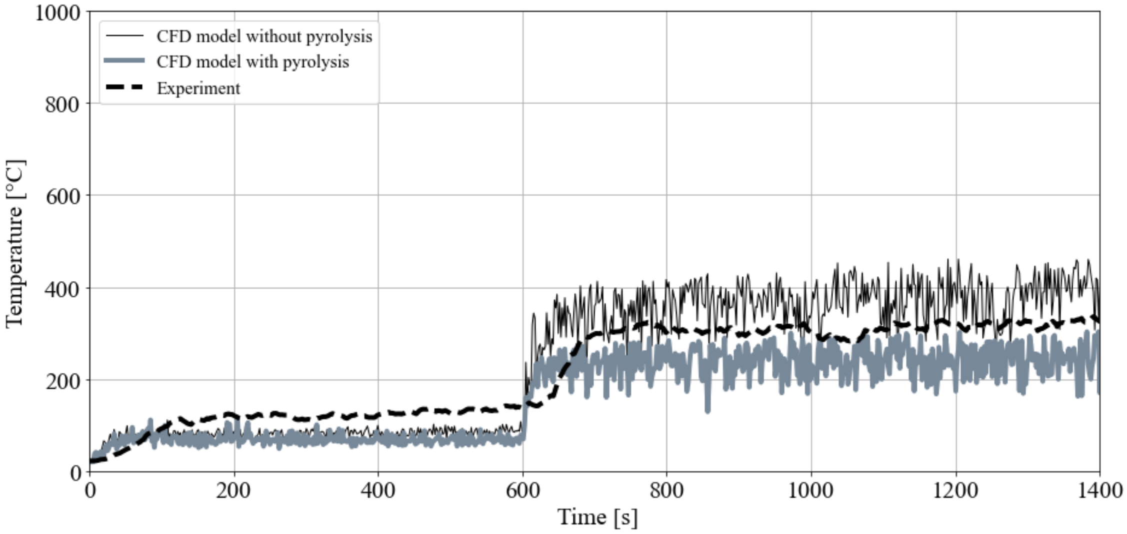

Figure 8. Temperature development at a height of 1720 mm in the area of the thermocouple tree

In the CFD model, the temperatures inside the timber specimens were measured at the positions of the thermocouples. The chosen number of calculation cells allowed us to compare the temperatures of the thermocouples 5 mm and 15 mm below the surface of the wood. The correct results were obtained considering the pyrolysis of the wood and the development of the properties of the wood. The calculated temperatures at a depth of 5 mm and 15 mm below the surface of the wood in the CFD model were the same as in the experiment. Figures 9-12 show the patterns in column 1. Column 2 and the beam did not show large heat transfer to the samples. A small difference occurs only in TC-13 and TC-15 (Figs. 10 and 11), when there was significant exposure to fire, and only in the later part of the experiment.

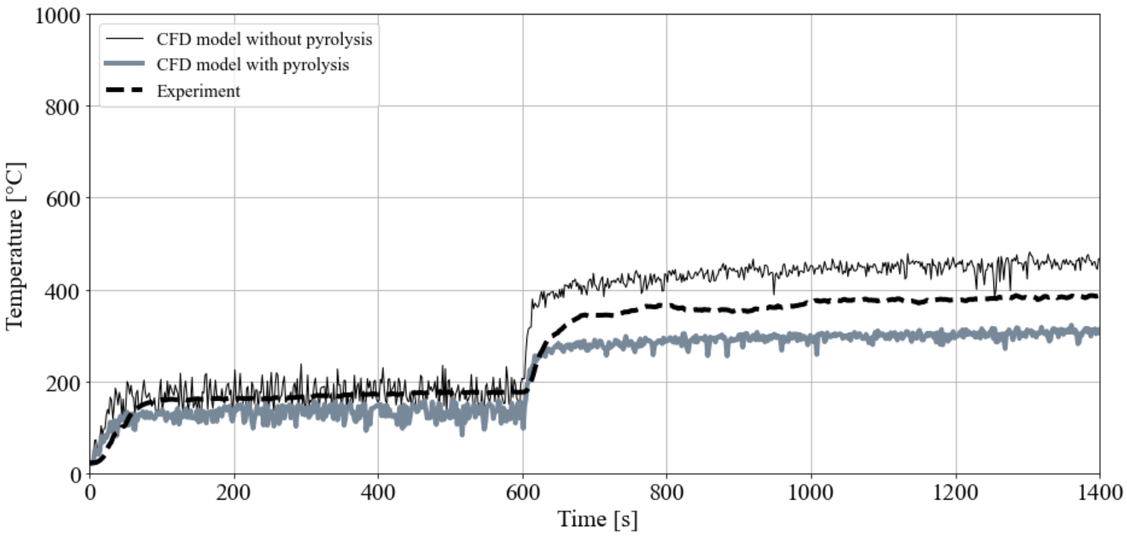

Figure 9. Temperature development in column 1, at a depth of 15 mm below the surface, height 2020 mm - TC-12

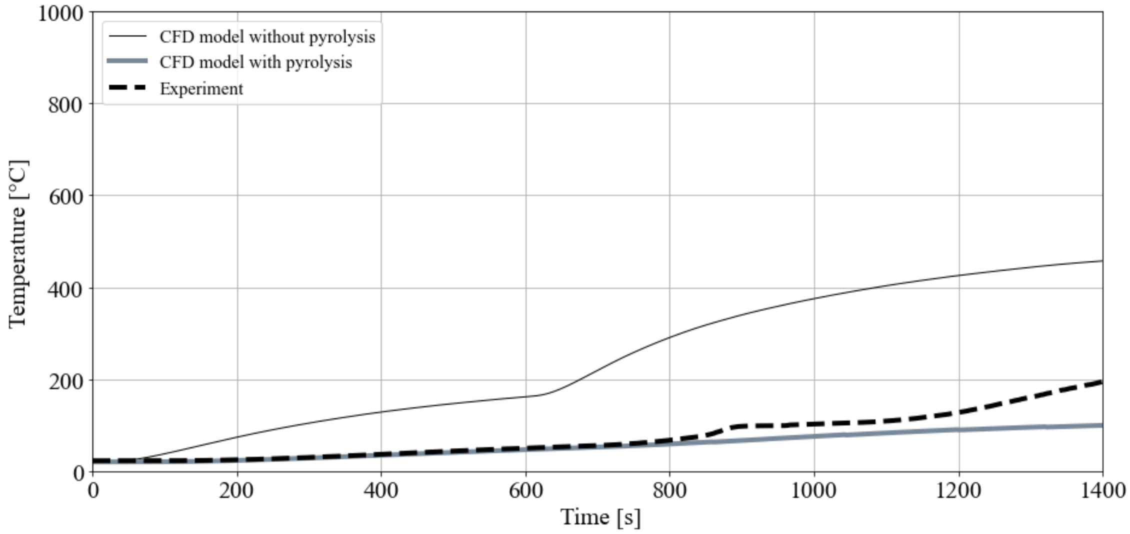

Figure 10. Temperature development in column 1, at a depth of 25 mm below the surface, height 2020 mm - TC-13

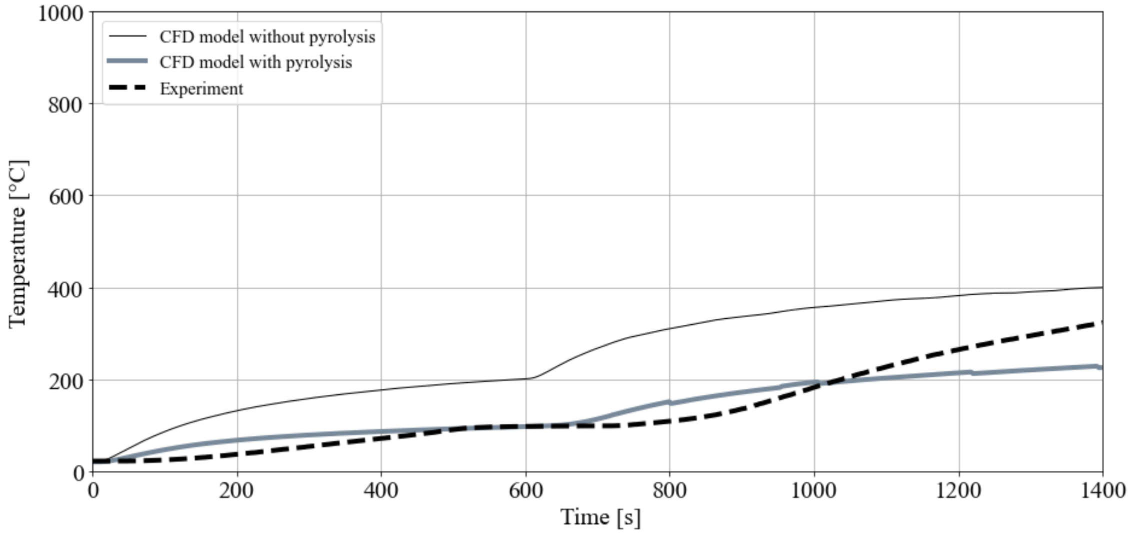

Figure 11. Temperature development in column 1, at a depth of 5 mm below the surface, height 800 mm - TC-15

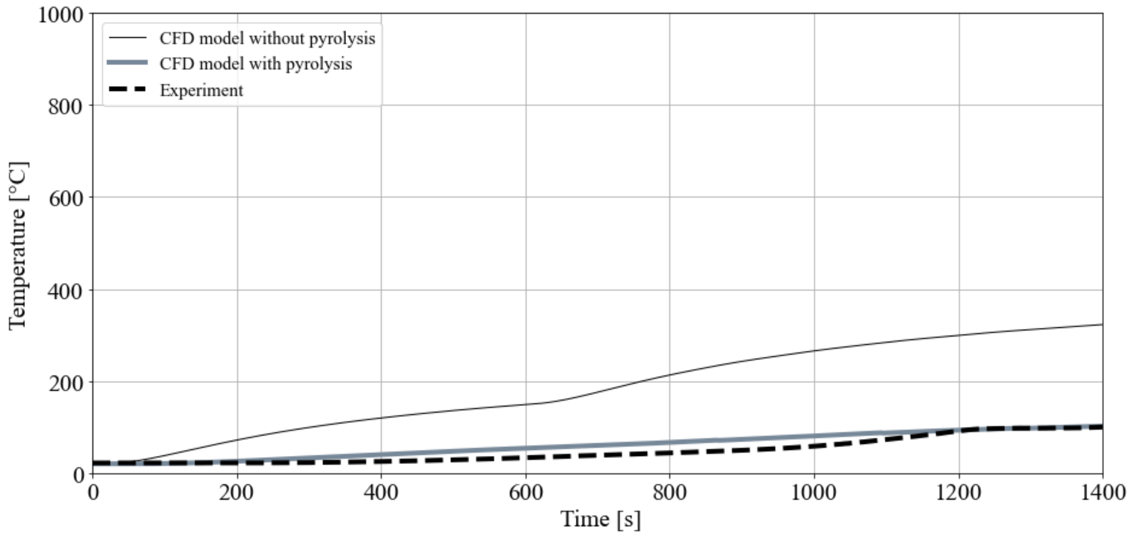

Figure 12. Temperature development in column 1, at a depth of 15 mm below the surface, height 800 mm - TC-16

4 DEVELOPMENT OF THE CHAR LAYER

After the experiment was completed, the wood samples were cooled. To observe the development of the charred layer in a natural fire, the specimens were cut in 50 mm increments and were then photographed for an evaluation. The development of the char layer and the pyrolysis layer was monitored. The boundary between the char layer and the pyrolysis layer was determined by using the zero-strength line of the char layer, which was detected mechanically. Fig. 13 (left) shows the measurement method. Measurements were always carried out in five lines in both directions.

In the places in the wood elements where intense burning occurred, the thickness of the char layer was very close to the linear rate of char, according to [11]. However, on the sides facing away from the burner, the char rate was only one third.

Fig. 13 (right) shows the development of the char layer and the pyrolysis layer at the top of the columns.

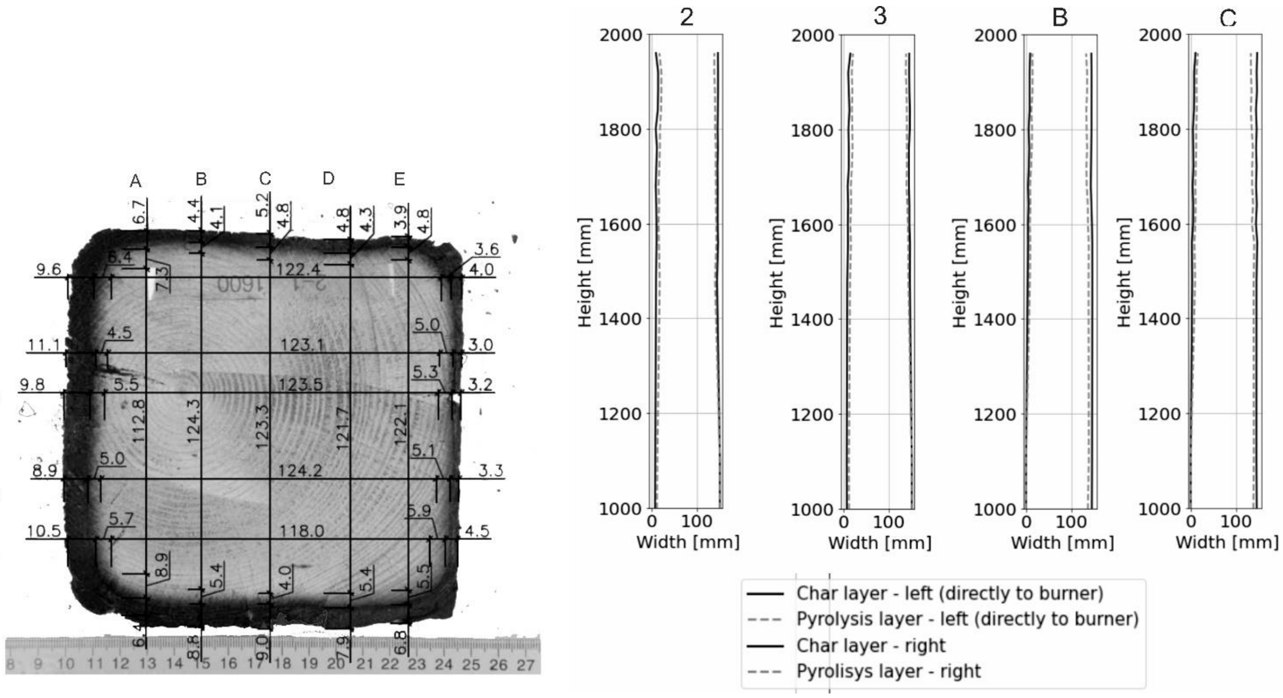

Figure 13. Cross section of column 1 at a height of 1600 mm with measured values (left), development of the char layer and the pyrolysis layer on column 1 (right).

5 CONCLUSIONS

This article has provided an overview of a real-scale validation of the CFD fire experiment model. Three members were exposed to fire during the experiment, i.e., two columns and one beam. Two simulation reactions were used in the CFD model. The first was the reaction of burning propane in the burner. The second reaction was a pyrolysis model with a parallel scheme. The challenge was to correctly apply the kinetic coefficients of pyrolysis. The comparison simulations that were performed helped to determine values suitable for transfer to massive elements. The development of the char layer and the pyrolysis layer was measured for further advanced research.

The conclusions of the thesis can be summarized as follows:

- When the kinetic coefficients of pyrolysis are selected, it is necessary to consider the pyrolysis scheme, the number of reactions, and the possibility of performing a comparison simulation with different values before modelling the final simulation.
- The thermocouple cable cover placed in the sample must be at least 70 mm in length; however, this may increase the measurement inaccuracy. For thermocouples with assumed exposure to fire in the case of wood burnout, choose a less conductive surface.

- In the first 600 s of the experiment, the samples evaporated the water and began to burn after the power of the burner increased to 300 kW, at which point the ignition temperature was reached.
- The measured temperatures in elements at a depth of 25 and 50 mm can be compared when the calculation cells are increased, so that the course of the temperatures can be calculated in greater detail.
- The measured thicknesses of the char layer and the pyrolysis layer in column 1 on the sides exposed directly to fire are the same as the depths calculated according to the linear rate of char. The thicknesses of these layers on the upside are about one-third of the thickness of the layers on the underside.
- The measured thicknesses of the char layer and the pyrolysis layer will be used for advanced modelling of the development of the char layer under the effects of a natural fire.
- Based on the calculated temperatures in the CFD model and the temperatures in the wood elements, the CFD model can be considered validated.

ACKNOWLEDGMENTS

This research was funded by Czech Science Foundation grant 301-3012107A134 "Charring of timber under fully developed natural fire – stochastic modelling", and determining the char layer was funded by Student Grant Competition of CTU grant SGS22/144/OHK1/3T/11 "Safety and sustainability of timber and steel structures exposed to fire".

REFERENCES

1. ISO 9705-1:2016, Reaction to fire tests — Room corner test for wall and ceiling lining products — Part 1: Test method for a small room configuration
2. Šálek, V., Cábová, K., Wald, F., Jahoda, M., Numerical modelling of fire test with timber fire protection, Journal of Structural Fire Engineering. 13(1), 99-117, 2021 ISSN 2040-2317, doi: 10.1108/JSFE-04-2021-0017.
3. Fahrni, R., et al. Correct temperature measurements in fire exposed wood. In: Proceedings of the 2018 World Conference on Timber Engineering. World Conference on Timber Engineering (WCTE), 2018. https://doi.org/10.3929/ethz-b-000289850
4. Rinta-Paavola, A., Hostika, S., A model for the pyrolysis of two Nordic structural timbers Fire and materials, 46.1: 55-68., 2021, doi: 10.1002/fam.2947.
5. Wade, C., et al., Enclosure fire model for mass timber construction—Benchmarking with a kinetic wood pyrolysis sub model. In: Interflam: 15th International Conference on Fire Safety Engineering. 2019.
6. Šejna, J., Wald, F., Small Furnace Experiments for Wood Burning Pyrolysis Models. Civil Engineering Research Journal, 12, 3, id. 555838. doi: 10.19080/CERJ.2021.12.555838.
7. Sinha, S., et al. Modelling of pyrolysis in wood: a review. SESI Journal, 2000, 10.1: 41-62., Corpus ID: 32941193.
8. Wang, X., Fleischmann, Ch. M., Spearpoint, M. J., Parameterising study of tunnel experiment materials for application to the Fire Dynamics Simulator pyrolysis model. Journal of Fire Sciences. 2016, 34(6), 490-514. ISSN 0734-9041. doi:10.1177/0734904116667738.
9. Ira, J., Hasalová, L., Šálek, V., Jahoda, M., Vystrčil, V. Thermal Analysis and Cone Calorimeter Study of Engineered Wood, with an Emphasis on Fire Modelling. Fire Technology, 56(3), 1099-1132, 2020. https://doi.org/10.1007/s10694-019-00922-9
10. Nakrani, D., Wani, T., Srivastava, A. G., Simulation of pyrolysis and combustion of pine wood using two-step reaction scheme. 2020. https://doi.org/10.14264/b582970
11. EN 1995-1-2:2006, Eurocode 5: Design of timber structures - Part 1-2: General - Structural fire design.

SiF 2022– The 12th International Conference on Structures in Fire
The Hong Kong Polytechnic University, Nov 30 - Dec 2, 2022

PERFORMANCE OF POST-TENSIONED TIMBER BEAM-COLUMN CONNECTIONS IN FIRE

Paul Horne[1], Anthony Abu[2], Alessandro Palermo[3]

ABSTRACT

Post-Tensioned Timber (PTT) frames combine high-strength tendons with heavy timber elements to create low-damage or longer span timber structures. The seismic, long-term and fire response of these structures is governed by the detailing of the connections. A specific detail which improves connection performance under one action may degrade the response under other actions. To investigate the response of PTT beam-column connections detailed to current practice, a full-scale PTT beam-column sub-assembly was loaded and exposed to the Standard Fire. This experiment showed that internal steel tubes and screw reinforcement, which were installed for ambient-temperature performance improved the behaviour of the connection in fire. The moment resistance of the connection was maintained for approximately 40 minutes. The presence of the tendon is found to improve the performance of the connection in comparison to scenarios where the tendon is neglected.

Keywords: Post-Tensioned; Timber; connection, experiment

1 INTRODUCTION

Post-Tensioned Timber (PTT) is a structural system that uses unbonded high-strength steel tendons inside timber elements with energy dissipation devices, to create rocking ductile moment resisting frame or wall structures. This structural system meets increasing demands from developers and architects for a timber structure and for a low-damage structure in high seismic areas, which can be easily reinstated faster and cheaper than conventionally designed structures. When applied to framed structures, as shown in Figure 1a, many moment-resisting connections can be formed in a single stressing operation, facilitating faster construction of the primary structure. Under a lateral load the timber elements behave elastically, and a gap opens at each beam-column connection, engaging the energy dissipaters, as illustrated in Figure 1b. Moment resistance is provided by the force-couple from the dissipaters in tension and compression and from the tendon and compression of the beam against the column. The stressed tendon re-centres the structure after the conclusion of the lateral action. This system can also be applied in low seismic regions to achieve longer spans than possible with a conventional timber element of the same size by using deviated tendons (see Figure 1), and in this case energy dissipation is not required. The performance of PTT structures at ambient temperature, under gravity and seismic loads, has been well investigated [1–7] and design guidance published [8]. Buildings using a PTT structural system have been constructed in New Zealand, for example the Trimble [9], Merrit and Von Haast [10] buildings, and overseas such as the House of Natural Resources Engineering at ETH Zurich, Switzerland [11].

[1] PhD Student, University of Canterbury, New Zealand
e-mail: paul.horne@pg.canterbury.ac.nz, ORCID: https://orcid.org/0000-0003-2254-6250
[2] Associate Professor, University of Canterbury, New Zealand
e-mail: anthony.abu@canterbury.ac.nz, ORCID: https://orcid.org/0000-0001-6237-3361
[3] Professor, University of Canterbury, New Zealand
e-mail: alessandro.palermo@canterbury.ac.nz, ORCID: https://orcid.org/0000-0001-8259-9050
https://doi.org/10.6084/m9.figshare.22193767

Although the behaviour of Post-Tensioned Timber box beams in fire has been investigated [12–14], the performance of PTT connections and frames in fire has received little attention. The design guidance [8], therefore, proposes two approaches to the design of PTT structures in fire: the protected and unprotected approach. In the protected approach (see Figure 2a) the tendon is protected from the effects of fire so that the tendon force is maintained. Although the cross-section of the timber elements is reduced by charring, the moment resisting connections and moment-frame are maintained. In the unprotected approach (see Figure 2b), the tendon is not explicitly protected from the fire, so the contribution of the tendon force is neglected, and so the beams are designed as simply supported with reduced cross-sections. All the PTT buildings built in New Zealand so far have used the unprotected approach, because no protection is required to the tendon, making the design check simple [12].

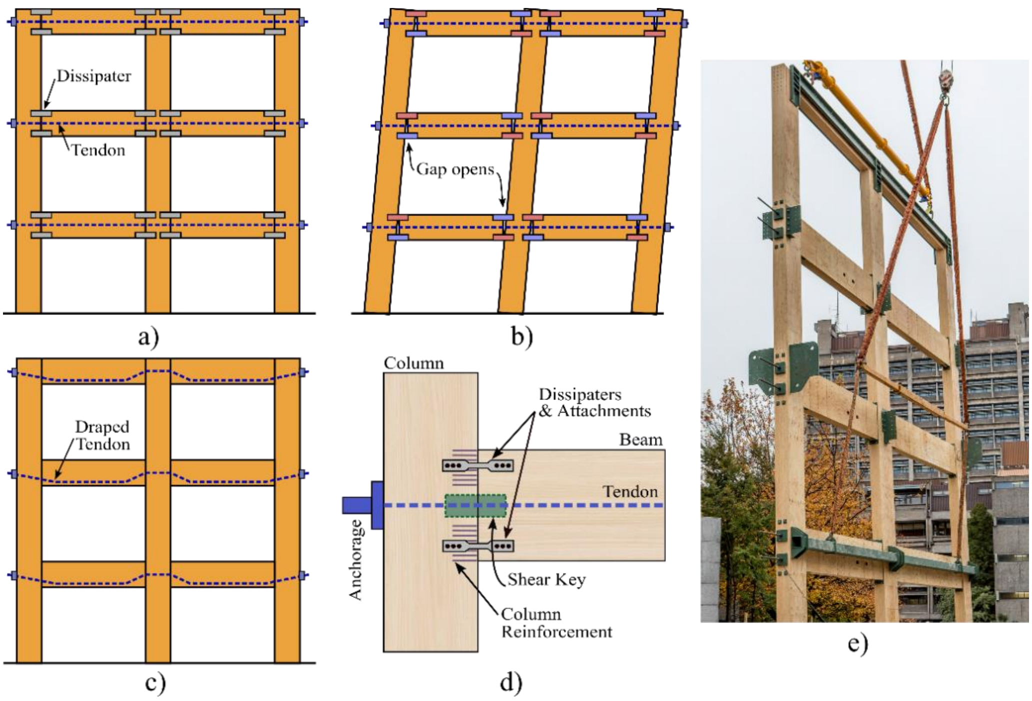

Figure 1. Illustration of PTT frames a) in a high seismic area at rest and b) under a lateral load and c) in a low seismic area, d) a schematic of a PTT beam-column connection and e) a PTT frame during construction

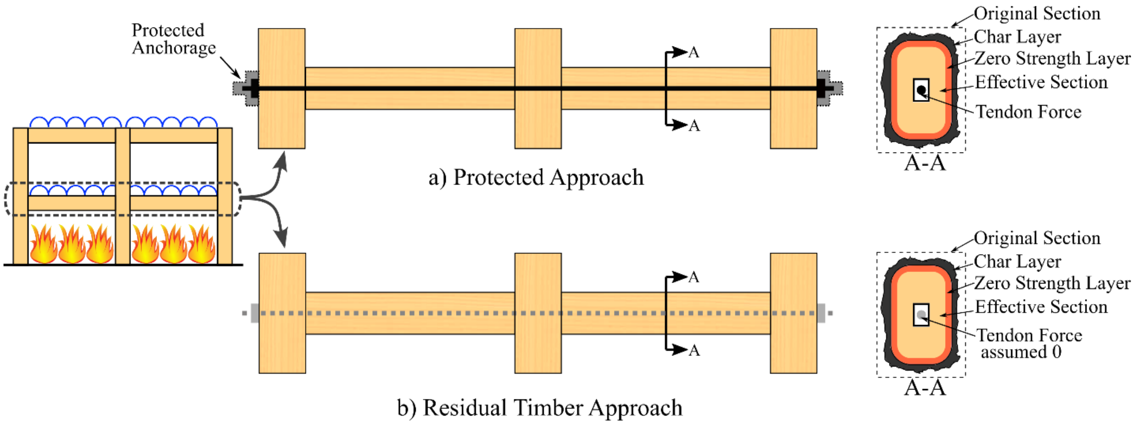

Figure 2. Illustration of the a) Protected and b) Unprotected approaches to the design of PTT frames

While these approaches are easy for designers to implement, they do not evaluate the actual response of the structure in a fire. Even in the unprotected case, the tendon takes some time to be heated through the anchorage and for the force in the tendon to decrease. Features for advantageous fire performance may already be present in a building designed for seismic loads, e.g. larger column sizes for increased lateral stiffness can withstand greater charring in a fire. Therefore, there is an opportunity for economy and optimization if these features can be harnessed for advantageous fire performance. This increased performance in fire is not guaranteed by seismic design and detailing; it has been shown that PTT beam-column connections detailed for good seismic performance may impair performance in fire [15].

2 PTT BEAM-COLUMN CONNECTIONS

Since timber elements are designed to stay within their elastic limits, beam-column connections are responsible for ductile rocking behaviour of the system. At its simplest, a PTT beam-column connection must contain (see Figure 1d):

1. A tendon passing through ducts in the beam and column,
2. Dissipaters and attachments to the timber elements, which can take several forms from buckling restrained necked bars to reduced cross-section angles,
3. Corbel or shear key to transfer shear from the beam to the column, which can be external or internal, and
4. A tendon anchorage at beam-column connections at each end of the frame.

However, further detailing of the connection must be considered to ensure the desired performance is achieved (see Figure 1d):

1. The rocking interface must be sufficiently stiff so that drift limits under Serviceability Limit State (SLS) lateral actions are achieved. The interface stiffness depends on the material properties and size of the timber elements, and whether there is a steel interface plate.
2. Perpendicular-to-grain crushing of the timber column must be avoided under large gap angles when the bearing area is small.
3. Creep deformations from the compression of timber column perpendicular-to-grain must be limited so the required tendon force is maintained over the life of the building.

Connection detailing to address these considerations includes screw reinforcement in the column, a steel jacket around the column or steel compression elements inside the column or the column can be fabricated with rotated blocks at the beam-column zone do the grain is parallel to the compressive forces.

A previous study [15] examined the response of individual components of PTT beam-column connections to fire and demonstrated that while the existing analytical design method for PTT connections at ambient conditions (Modified Monolithic Beam Analogy) could be combined with a reduced cross-section method to determine the moment-rotation response in fire, localised damage at the connections would result in poorer performance than predicted. Since the response of these connections in fire is governed by their detailing, the detailing choices made for ambient performance could result in improved or degraded performance in fire. Since the performance of PTT beam-column connections is dependent on the complex interaction between many components, experiments are required to observe the behaviour in fire and validate a design method that evaluates the true performance of these connections in fire.

The mechanical behaviour of PTT beam-column connections in fire strongly depends on the specific connection detailing and the thermal field established in the joint. As explained previously, PTT beam-column connections in multi-storey buildings contain other features which influence the connection in fire, e.g. creep prevention and external corbels. Before the analytical method is used in design, it should be validated to against an experiment of a 100%-scale connection to include “size effect” of larger elements and components. To address these points, an experiment on a full-scale PTT beam-column connection that was detailed to current design practice in New Zealand was undertaken. This paper presents the result of this experiment, which investigated the moment resistance of the PTT beam-column connection exposed to fire, the adaptions to the analytical model to account for the effects of the connection detailing and makes the necessary recommendations for designers.

3 EXPERIMENT SETUP

A 1:1 scale realistically sized PTT beam-column connection sub-assembly was setup based on a case-study design of a four-storey office building in Christchurch, New Zealand. The connection was based on the connection detailing of recently constructed PTT framed structures [10] and published design guidance [8]. The tested sub-assembly (see Figure 3) was constructed from LVL13 (E=13.2 GPa [16]) 700x310 mm beam and 800x310 mm column. Two 75 mm square ducts were formed in the beam and column for the tendons. The tendons were 26.5 mm diameter high-strength Macalloy 1030 bars [17] tensioned to 160 kN (28% of UTS) with 200 mm square, 40 mm thick anchorage plates. Reinforcing screws (7 rows of 9 screws) were installed in the column at the top and bottom of the beam-column contact area to prevent crushing of the column perpendicular to the grain under large gap angles in seismic events. Two 75 mm square hollow steel sections (5 mm wall thickness) were installed inside the ducts to prevent long-term creep perpendicular to the grain of the column. The corbel was a stiffened steel bracket (16 mm thick) which was fixed to the column with 10x M20 coach screws.

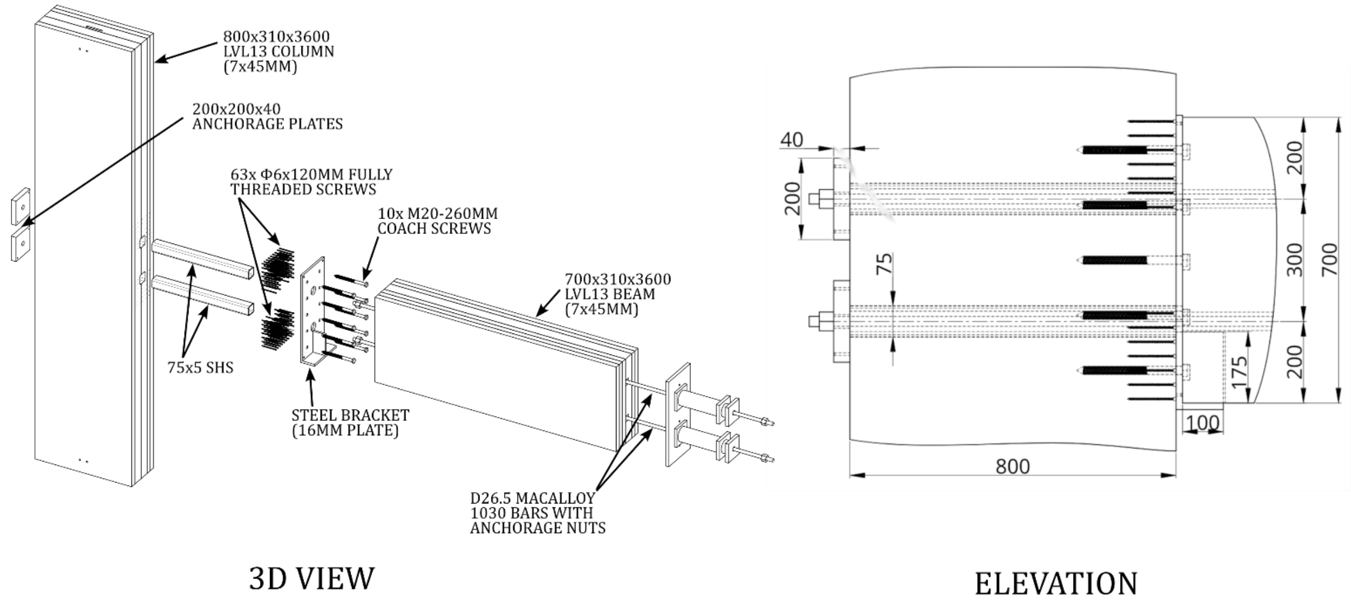

Figure 3. a) 3D view of the tested beam-column sub-assembly and b) elevation view

The timber beam and column were fabricated from seven 45 mm thick LVL laminations glued to form the 310 mm thick elements. Gluing of the laminations was performed by a commercial structural timber fabricator with a phenol-resorcinol adhesive in accordance with the adhesive manufacturer's instructions. Bare wire K-Type thermocouples were laid in small grooves (approximately 1x1 mm formed with a router) on the surface of the seven 45 mm laminations. Thermocouples were installed in this way because it resulted in a more precise placement than drilling, allowed 50 mm of the wire to be placed parallel to the isotherm were possible [18] and the wires exited the specimen outside the furnace enclosure. Thermocouple "trees" were placed in the column and beam, away from the connection, adjacent to the bottom of the bracket and at shallow depths up the height of bracket and in the column under the anchorage. Thermocouples were also installed at the interface between the steel bracket and column.

The beam-column sub-assembly was placed in a purpose-built enclosure, so that the beam was exposed on three sides and the column was exposed on four sides below a floor level. The enclosure was made from 13 mm calcium silicate board lined internally with an alkaline earth silicate fibre blanket. The effect of a floor was simulated with a 100 mm thick slab of concrete on the beam. Two viewing windows were installed in the enclosure for visual observations. This enclosure was placed on a 3 x 4 m standard fire resistance testing furnace in its vertical orientation (see Figure 4).

A point load of 16 kN was applied to the end of the beam to achieve a total connection moment of 29.6 kNm (90% decompression moment). An axial force of 50 kN was applied to the top of the column (limited by hydraulic jack capacity). Rotation of the connection was calculated from vertical displacement measured by a potentiometer outside the enclosure. The furnace was controlled following AS 1530.4 [18] which adopts the ISO 834 Standard Fire [19] until failure.

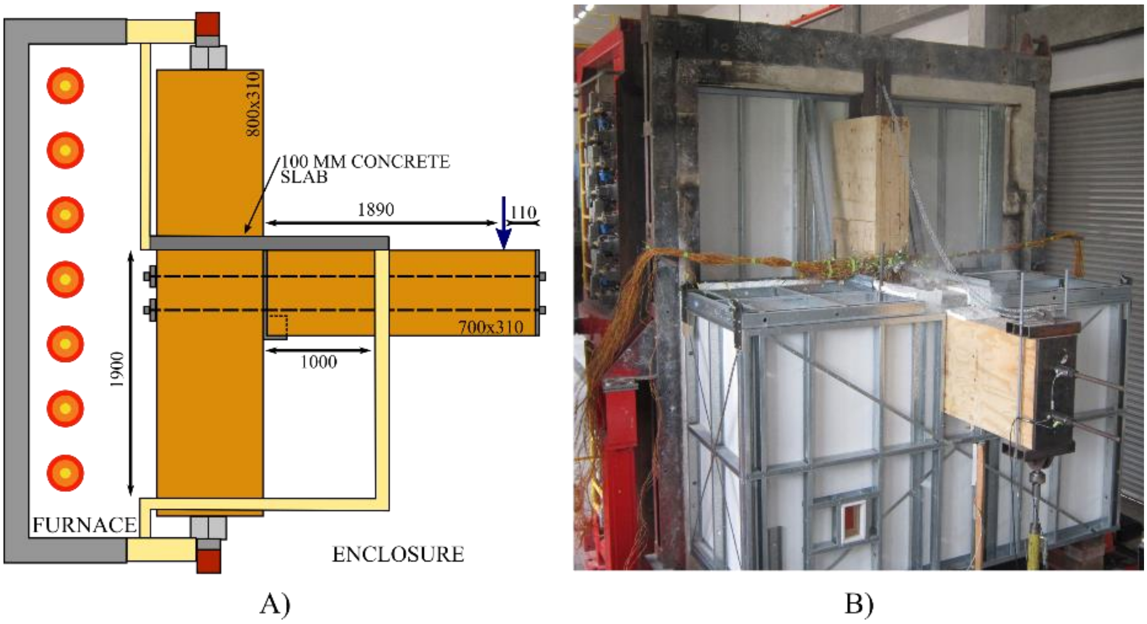

Figure 4. a) Schematic of beam-column subassembly in enclosure on furnace and b) photo of experimental setup

4 RESULTS

4.1 Observations

Flaming of the timber beam and column began after 5 minutes. At a similar time, a gap began to open at the top of the beam-column interface, i.e. the connection decompressed. The connection rotation increased slowly at a constant rate until it started increasing exponentially at 37 minutes. The test was terminated at 44 minutes when the rotation was too large to sustain the applied load. The connection and residual cross-section of the timber elements are shown in Figure 5. The temperature of the furnace control thermocouple probes and plate thermocouples adjacent to the beam and column are shown in Figure 6.

4.2 Thermal Field

Char rates, determined from thermocouples in the beam and column away from the connection (using a 300 °C isotherm), ranged from 0.62 to 0.78 mm/min with a mean of 0.70 mm/min. A previous study of the charring of LVL elements in the Standard Fire reported a mean charring rate of 0.72 mm/min [20].

Figure 5. Photographs of the (a) connection and (b) residual cross-section after the experiment

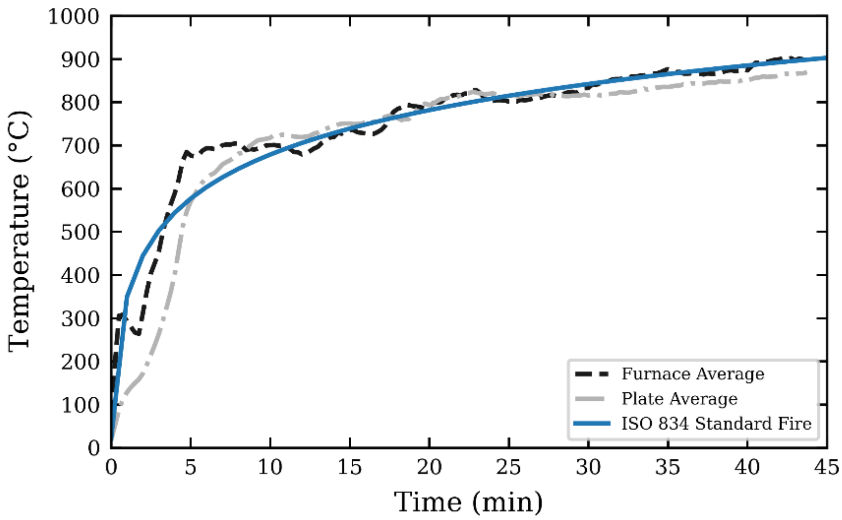

Figure 6. Furnace Temperature

The bearing plate of the steel bracket, which supported the beam, was exposed to the fire on three sides but only the edges of the interface plate (the vertical plate of the bracket) were exposed. The bearing plate heated quickly due to its direct exposure to the fire. Charring at the interface between this plate and the beam began at 21 minutes. Heat was conducted from the exposed surfaces throughout the bracket. The temperatures measured at the interface between the steel bracket and the column are shown in Figure 7. The temperature developments at locations A-D show that a 2D thermal field was established in the lower third of the interface. Heat was conducted up the interface from the exposed bearing plate and from the exposed sides of the interface plate. In the top two-thirds of the interface plate the thermal field was one-dimensional, decreasing in temperature from the exposed edges to the centre of the bracket. The maximum temperature near the middle of the bracket was 200 °C.

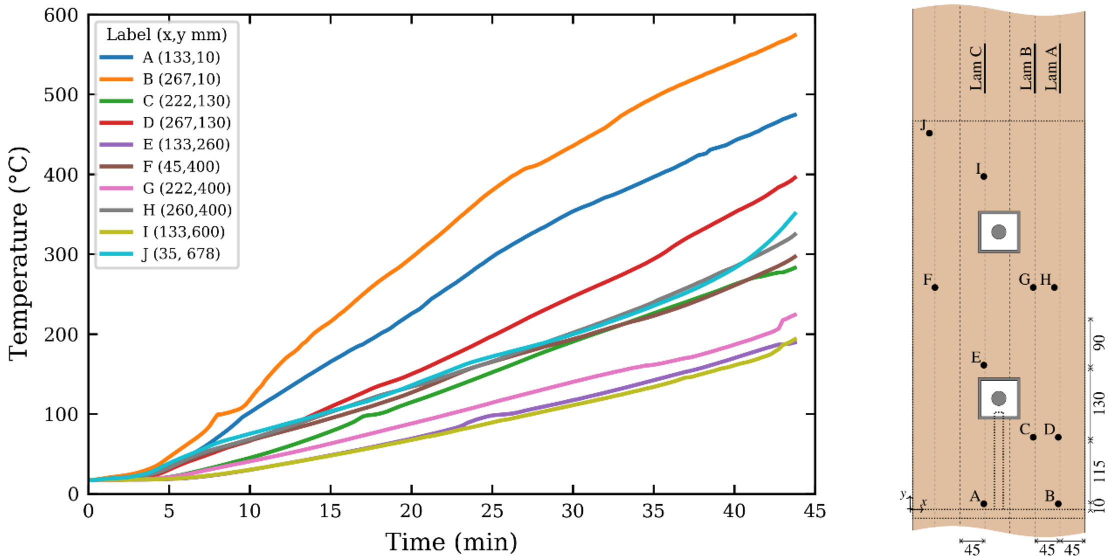

Figure 7. Temperatures at the interface between the timber column and steel bracket

At the corner of the beam, where it was supported by the bracket, the beam was heated from the underside and from the interface plate, as well as the sides of the beam. The temperatures in this location are shown in Figure 8 for Laminations A and B which were 45 and 90 mm from the sides of the beam. The steel bracket offered some shielding to the corner of the timber beam, as the thermocouples at a depth of 10 mm from the underside of the beam exceeded 300 °C at 30 minutes compared to 15 minutes away from the connection in the beam. At a depth of 10 mm, the dominant heat flow was from the underside of beam because the temperature at these locations exceeded 300 °C at the same time in Lamination A. The temperature at the same location on Lamination B exceeded 300 °C a few minutes later since Lamination A was closer to the end of the beam than Lamination B. Ten minutes later, as the test was terminated, the temperature at a depth of 30 mm from the underside of the beam and 10 mm from the interface on Lamination B was about to exceed 300 °C. At the same depth from the underside of the beam, the temperature at 30 mm from the interface increased ahead of the temperature at 50 mm, indicating that while there was a small amount of conduction along the grain of the beam the dominant heating was from the underside of the beam. The temperature at a depth of 50 mm from the interface and underside of the beam reached approximately 100 °C at the end of the test which was the same temperature measured in the beam away from the connection.

The temperatures in the column underneath the anchorage plates are shown in Figure 9. The anchorage plate shielded the timber for some time; the temperature at a depth of 10 mm exceeded 300 °C 14 minutes after that in the column away from the column. Except for the shielding delay the temperature development underneath the anchorage followed the typical thermal field in timber exposed to the Standard Fire perpendicular-to-grain. The temperatures at depths of 5 and 10 mm were 600 °C at the end of the test, indicating that all surfaces of anchorage plate exceeded this temperature.

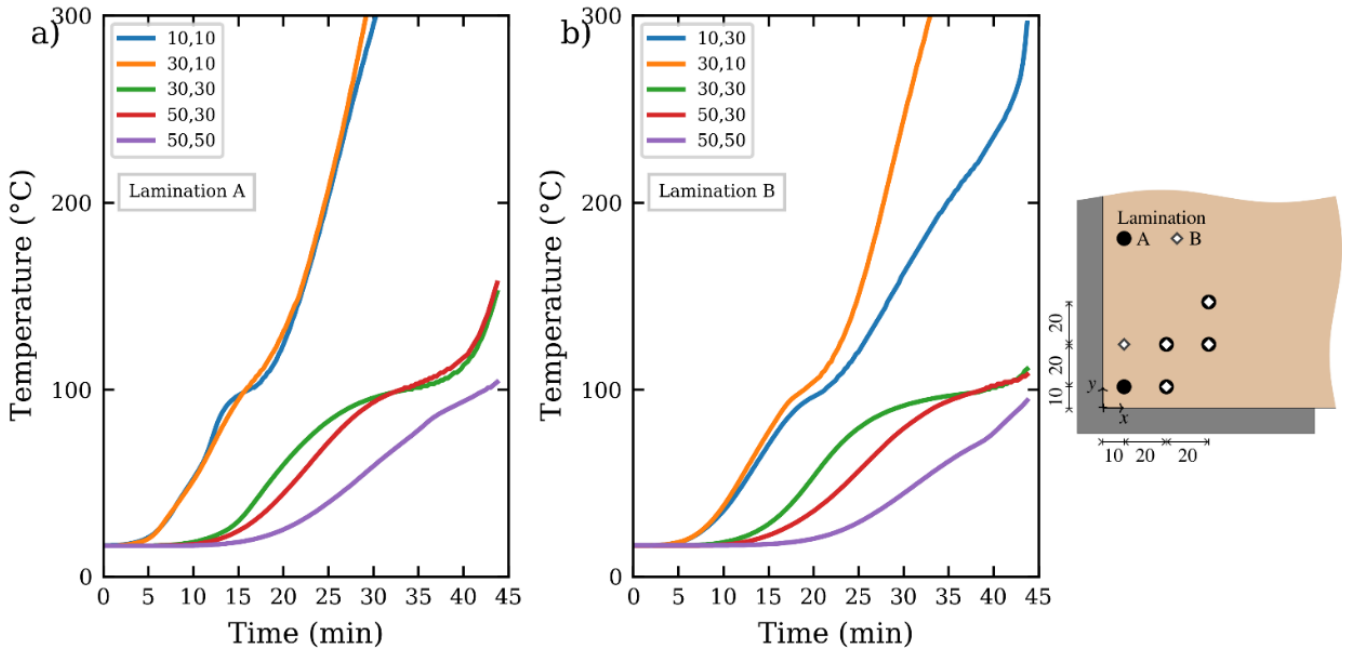

Figure 8. Temperatures in the corner of the beam supported by the steel bracket

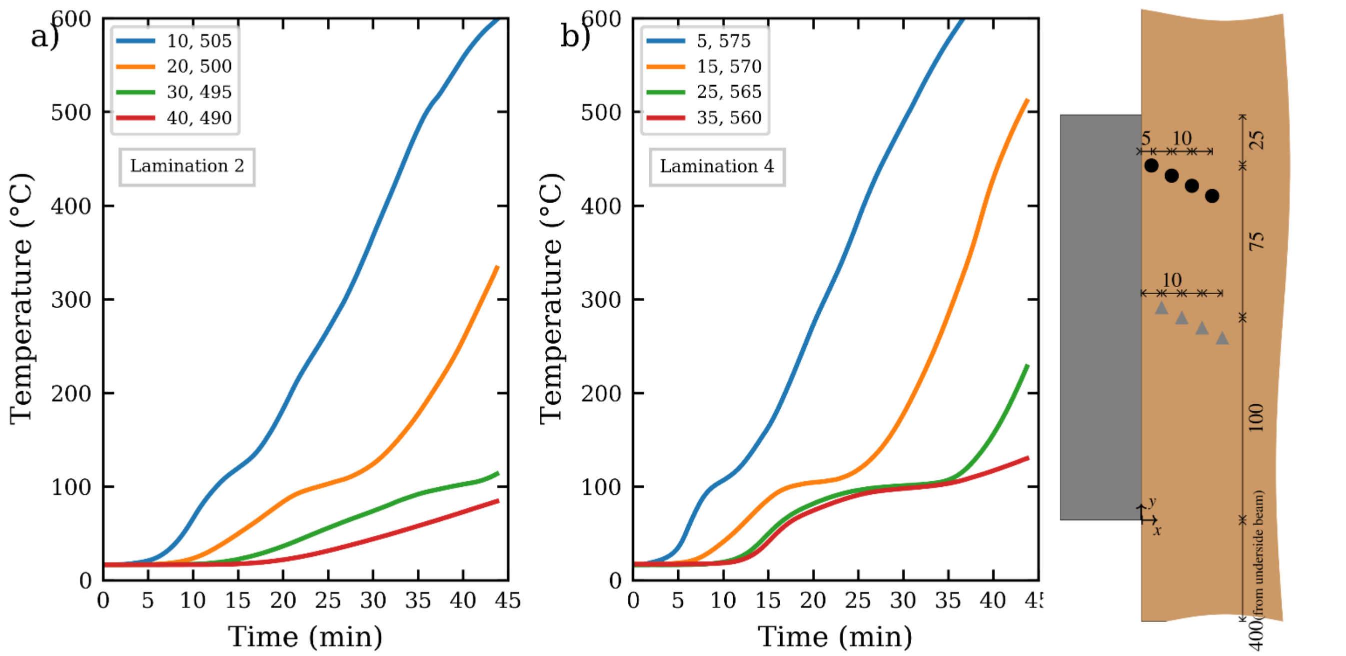

Figure 9. Temperatures in the timber column underneath the top anchorage

A strong thermal gradient was recorded along the tendon; this was between the exposed free length of the bar tendon at effectively the furnace temperature to less than 100 °C 300 mm along the tendon from the anchorage plate (Figure 10). The temperature of the tendon underneath the anchorage nut increased quickly and reached a maximum temperature of over 700 °C at the end of the experiment. However, the temperature 100 mm along the tendon was 270 °C at the same time. The temperature of the tendon was also monitored at the beam-column interface to determine if the tendon was heated by the opening at the interface. The temperature of the bottom tendon was the same as that at 300 mm from the anchorage as the tendon was heated from the steel bracket. The temperature of the top tendon was the same as the bottom tendon except for the final five minutes, when the temperature increased rapidly to 200 °C as hot gases penetrated the gap at the beam-column interface.

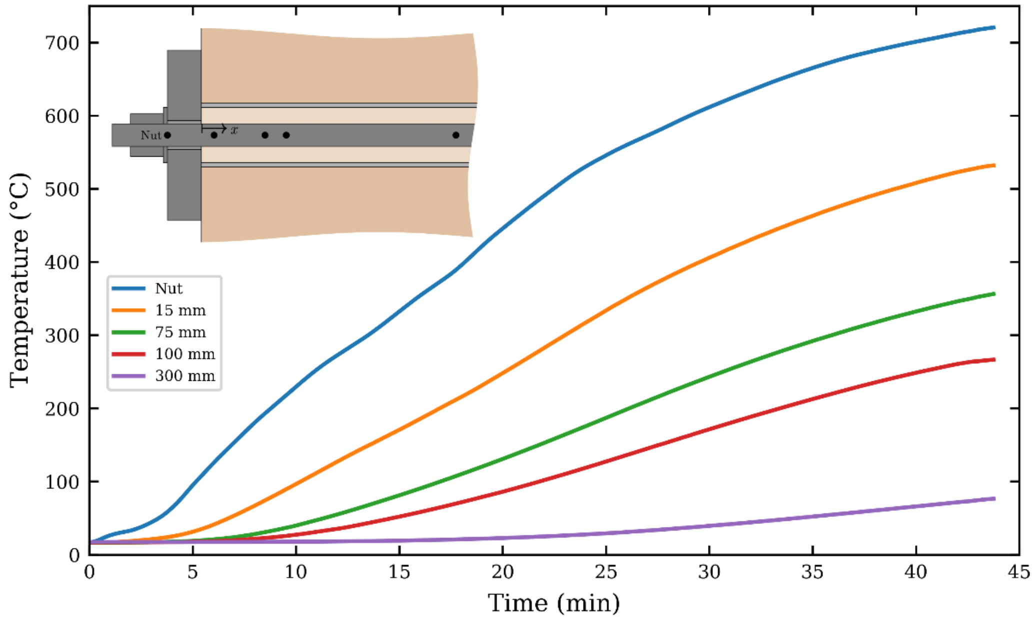

Figure 10. Temperatures measured along the tendons

4.3 Mechanical Response

The connection decompressed after 5 minutes of fire exposure and increased linearly (approximately 0.0014 rad/min) until 37 minutes (rotation of 0.05 rad). The connection rotation then increased rapidly and the test was terminated at 44 minutes at a peak rotation of more than 0.05 rad. The tendons were initially stressed to 160 kN each. The force in the top tendon increased by around 5kN and the force in the bottom tendon decreased by a similar amount in response to the applied moment on the connection. Between 5 and 10 minutes the tendon force decreased by 13% and 7% in the top and bottom tendon respectively. The force in the bottom tendon remained slightly greater than the top tendon until 27 minutes, at which the force had decreased to 75% of the initial force. After this, the rate of reduction in tendon force increased. The force in the bottom tendon decreased to 25% of the initial force. The force in the top tendon decreased to 52% at 37 minutes and remained constant for five minutes. At the end of the test, the gap was sufficiently deep that the bottom tendon was engaged and its tendon force increased as the top tendon was unable to sustain its force.

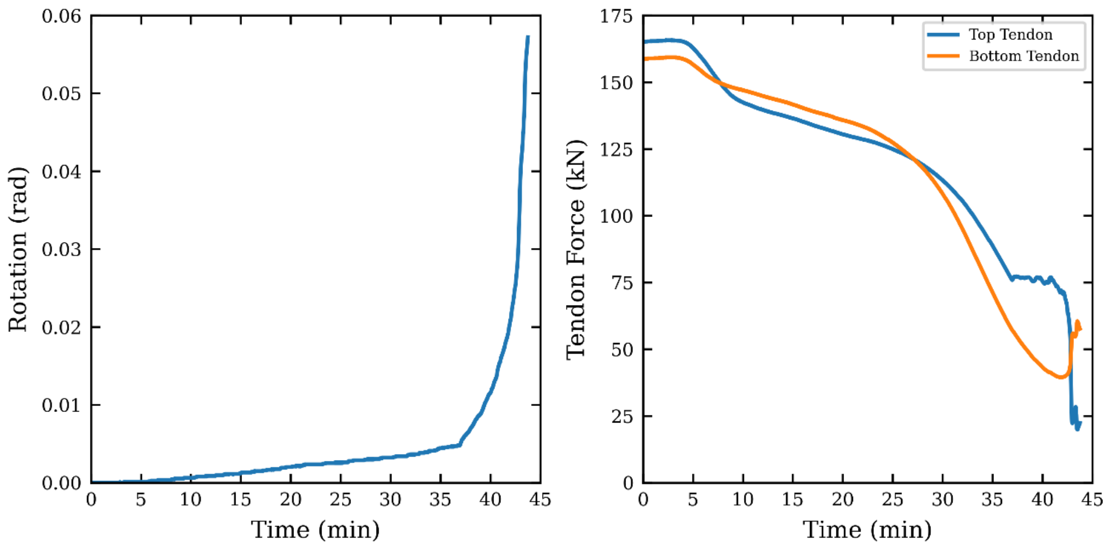

Figure 11. a) Rotation of the connection and b) forces in the tendons

5 DISCUSSION

The thermal field in the timber beam and column (away from the connection) was typical of heavy timber elements exposed to the Standard Fire. At the connection, however, the partially exposed steel plate disturbed this thermal field locally (not more than 100 mm from the connection). The heating of the steel bracket from the exposed edge and bottom bearing plate resulted in a 2D thermal field in the bottom third of the timber-steel interface and a 1D thermal field in the remainder of the interface. The temperature of the wood at the beam-column interface is important because the elastic modulus of wood decreases at relatively low temperatures [21], and a decrease in elastic modulus reduces the rotational stiffness of the connection.

In a PTT frame under gravity loads, a compressive block occurs at bottom of the beam-column interface when a gap opens at the top of the interface. However, when the underside of the beam chars, the depth of the compression block is reduced. The timber in the heated layer beneath the char layer has reduced strength and elastic modulus, decreasing the effective depth of the compressive block further. This experiment showed that while the exposed steel bracket does provide some shielding to the timber behind (delaying charring by 15 minutes), this effect decreases as the char surface recedes and combustion occurs behind the bracket. Charring of the beam from heat conduction up the interface plate and along the grain, results in greater connection rotations since crushing is needed to maintain the compression block against the column.

Similar to any unprotected steel components exposed to a fire, the anchorage nut and free length of the tendon heated quickly and conducted heat along the tendon. Thermal elongation and the reduced elastic modulus in the heated portion of the tendon resulted in a decreased tendon force. The portion of the tendon that was heated more than 100 °C extended less than 300 mm from the anchorage. For most of this experiment, at small angles of gap openings, the protection of the tendon from direct exposure was large enough that the tendon was not heated at the beam-column interface. It was when the gap angle became large that the temperature of the tendon increased, and only in the localised area of the gap. The reduction in tendon force from exposed anchorages in a PTT frame will be less than observed in this experiment on a beam-column joint because of the different tendon lengths. In the initial stressing operation, a tendon is stretched in proportion to its length to achieve the desired tendon force i.e., the axial stiffness of the tendon. However, the reduction in tendon force from thermal elongation and reduced elastic modulus is proportional to thermal distribution along the heated length of the tendon at each exposed anchorage (two per tendon). Consequently, in a realistic PTT frame (> 15 m length), the change in tendon length resulting from the effects of heating two exposed anchorages is typically an order of magnitude less than the reduction in tendon length to stress the tendon in the first place. Based on this experiment, it is observed that where the width of the gap at the beam-column interface is small and the depth to the tendon is large, heating of the tendon is limited to exposure from the surrounding surfaces. For design purposes, localised heating of the tendon though a gap at the interface can be included by determining the effect of a portion of heated tendon at each connection.

The rapid increase in connection rotation, that began at 37 minutes, coincided with the plateau in the force in the top tendon. At the conclusion of the experiment, the top tendon had pulled through the anchorage nut (see Figure 12). A bar pulling through a nut involves plastic deformation of the threads, which would explain the constant tendon force but also the rapid increase in rotation. If the bar where to pull right through the nut, the tendon would not provide any force and the moment resistance at all connections which utilised this tendon would be lost.

Also evident in Figure 12 is the effect of anchorage reinforcement; in this case, the anchorage plates are held off the char surface. Although the 40 mm thick anchorage plates provided some shielding to the timber underneath (approximately 15-minute delay in charring), the large bearing stress from the anchorage resulted in crushing of the timber column perpendicular-to-grain at low temperatures. In this connection, the detailing to prevent long-term creep (the SHS tubes inside the column) formed an alternative load carrying mechanism and supported the anchorage plates as the timber underneath charred. Without an alternate load carrying mechanism to resist the high bearing stress from the anchorage, hot wood/char underneath and anchorage plates would be crushed, and the tendon force would decrease from shortening of the tendon. Therefore, if the moment resistance of connections and the frame is to be maintained, the exterior frame connections should be detailed to avoid this failure mechanism.

Conduction through the steel bracket and the exposed timber column below caused charring of the column underneath the bottom of the bracket. Since this is where the compressive block formed, this char would have been crushed resulting in greater connection rotation to maintain the compressive block. However, in this connection the column was screw reinforced to prevent crushing of the column perpendicular-to-grain at large gap openings under seismic loads. So, for the connection in this experiment, as the timber charred the screw reinforcement transferred the compressive forces from the compressive block to the sound timber underneath the char layer (see Figure 13), avoiding the additional connection rotation from char crushing.

Figure 12. Tendon Anchorages after experiment

Figure 13. Screw reinforcing resisting bearing from the compression block in the beam

6 CONCLUSIONS

The performance of Post-Tensioned Timber frames is governed by the behaviour of the beam-column connections. The response of these connections is dependent on their detailing. An experiment of a loaded full-scale PTT beam-column sub-assembly, with current seismic detailing, showed that:

- internal SHS tubes, installed to avoid long-term creep of the column, formed an alternate load carrying mechanism when the timber under the anchorage plates charred, and
- screw reinforcing of the column, installed to avoid crushing the column under large seismic demands, resisted the compressive block at the bottom of the beam-column interface despite the timber column charring locally.

Despite the tendon anchorages being exposed directly to the fire, the tendon force was maintained for approximately 40 minutes in opposition to the Unprotected design approach which neglects the tendon contribution from the start of the fire exposure. Moment resistance of the connection was lost when the top tendon pulled through the anchorage nut resulting in a rapid increase in connection rotation. Tendon anchorages could be protected to limit anchorage and tendon temperatures to avoid this failure mode.

This experiment has demonstrated that when carefully chosen, detailing which improves ambient performance can also result in better connection behaviour in fire. If the fire exposure is maintained, the connection will eventually fail by another mode, which requires further experimental investigation.

ACKNOWLEDGMENT

George Hare and Logan Cooper for their assistance in setting up this experiment.

REFERENCES

[1] A. Palermo, S. Pampanin, A. Buchanan, M. Newcombe, Seismic design of multi-storey buildings using Laminated Veneer Lumber (LVL), in: Proceedings of the NZSEE Conference 2005, NZSEE, Taupo, New Zealand, 2005.

[2] A. Buchanan, B. Deam, M. Fragiacomo, S. Pampanin, A. Palermo, Multi-Storey Prestressed Timber Buildings in New Zealand, Structural Engineering International. 18 (2008) 166–173. https://doi.org/10.2749/101686608784218635.

[3] G. Granello, A. Palermo, S. Pampanin, S. Pei, J. van de Lindt, Pres-Lam Buildings: State-of-the-Art, J. Struct. Eng. 146 (2020) 04020085. https://doi.org/10.1061/(ASCE)ST.1943-541X.0002603.

[4] T. Smith, Post-tensioned Timber Frames with Supplemental Damping Devices, PhD, University of Canterbury, 2014.

[5] F. Sarti, Seismic Design of Low-Damage Post-Tensioned Timber Wall Systems, PhD, University of Canterbury, 2015.

[6] D. Moroder, Floor Diaphragms in Multi-Storey Timber Buildings, PhD, University of Canterbury, 2016.

[7] W. van Beerschoten, Structural Performance of Post-tensioned Timber Frames under Gravity Loading, PhD Thesis, University of Canterbury, 2013.

[8] S. Pampanin, A. Palermo, A. Buchanan, Design Guide Australia and New Zealand: Post-tensioned Timber Buildings, Structural Timber Innovations Company, 2013.

[9] A. Brown, J. Lester, S. Pampanin, Re-building Trimble Navigation’s offices using a damage-limiting seismic system, in: Proceedings of the World Conference on Timber Engineering 2014, World Conference on Timber Engineering 2014, Quebec City, Canada, 2014.

[10] A. Kirstein, J. Siracusa, T. Smith, The new timber von Haast replacement building in Christchurch, in: Proceedings of the NZSEE Conference 2018, NZSEE, Auckland, New Zealand, 2018.

[11] C. Leyder, F. Wanninger, A. Frangi, E. Chatzi, Dynamic response of an innovative hybrid structure in hardwood, Proceedings of the Institution of Civil Engineers - Construction Materials. 168 (2015) 132–143. https://doi.org/10.1680/coma.14.00043.

[12] P.M. Spellman, The Fire Performance of Post-Tensioned Timber Beams, Master’s Thesis, University of Canterbury, New Zealand, 2012.

[13] R.S. Costello, The Fire Performance of Post-Tensioned Timber Buildings, Master’s Thesis, University of Canterbury, 2013.

[14] H. Quiquero, J. Gales, A. Abu, R. Al Hamd, Finite Element Modelling of Post-tensioned Timber Beams at Ambient and Fire Conditions, Fire Technol. 56 (2020) 737–767. https://doi.org/10.1007/s10694-019-00901-0.

[15] P. Horne, A. Palermo, A. Abu, P. Moss, Implications of seismic design detailing on the fire performance of Post-Tensioned Timber frames, in: Proceedings of the Pacific Conference on Earthquake Engineering 2019, Auckland, New Zealand, 2019: p. 12.

[16] Nelson Pine, Nelson Pine LVL - Specific Engineering Design Guide, (2016).

[17] Macalloy, Macalloy Post Tensioning System, (2017).

[18] Standards Australia, AS 1530 Methods for fire tests on building materials, components and structures Part 4: Fire-resistance tests for elements of construction, (2014).

[19] ISO, ISO 834-1:1999 Fire Resistance Tests - Elements of Building Construction - Part 1: General Requirements, (1999).

[20] W. Lane, Ignition, Charring and Structural Performance of Laminated Veneer Lumber, Master’s Thesis, University of Canterbury, 2005.

[21] CEN, Eurocode 5—Design of timber structures Part 1-2: General—Structural fire design, (2004).

SiF 2022– The 12th International Conference on Structures in Fire
The Hong Kong Polytechnic University, Nov 30 - Dec 2, 2022

APPLICATION OF THE LAW AND O'BRIEN CORRELATION FOR EXTERNAL FLAMES TO MASS TIMBER COMPARTMENTS

Adam Glew*[1], Eoin O'Loughlin[2], Panagiotis Kotsovinos[3], David Barber[4] and Judith Schulz[5]

ABSTRACT

Buildings generate nearly 40% of global carbon dioxide (CO_2) emissions. Embodied carbon accounts for roughly a quarter of that. Innovations in engineered timber products present opportunities for designers to use timber for larger structures now. Such buildings need to be both safe and sustainable.

Small- and medium-scale compartment experiments conducted to date have shown that exposed mass timber results in larger external flaming. Empirical correlations, first developed by Law and O'Brien in the 1970s, exist for predicting the characteristics of such flames. The correlation is reproduced in Eurocodes 1 and 3 (to allow designers to calculate heat transfer to external unprotected structure) and BR 187 (to allow external fire spread radiation assessments from external flames to relevant boundaries). However, the correlation does not consider structural fuel load.

This paper presents external temperature data from three large-scale (352 m^2 floor area) compartment fire experiments; the *CodeRed* experimental series. External temperature data from *CodeRed* and two other experimental programmes (RISE and Épernon) is compared with predictions made using the Law and O'Brien correlation. The correlation underpredicts temperature along the flame axis. This paper therefore highlights the need for a modified approach, taking account of the structural fuel load, to enable designers to estimate external flame characteristics from exposed mass timber compartments.

Keywords: timber; large-scale compartment fire experiment; external flaming; external structural steel; Law and O'Brien correlation

1 INTRODUCTION

1.1 Setting the scene

In recent decades, there has been rapid global urbanisation and population growth. More than half of the world's population now live in urban areas. That portion is predicted to increase to two-thirds by 2050 [1], [2]. Consequentially, pressure on our planet's resources will increase.

* Corresponding author.
[1] Engineer, Arup, 8 Fitzroy St, London, W1T 4BJ, UK
e-mail: Adam.Glew@arup.com, ORCID: https://orcid.org/0000-0002-3238-6708
[2] Associate, Arup, 8 Fitzroy St, London, W1T 4BJ, UK
e-mail: Eoin.OLoughlin@arup.com
[3] Senior Engineer, Arup, 6th Floor, Three Piccadilly Place, Manchester, M1 3BN, UK
e-mail: Panos.Kotsovinos@arup.com, ORCID: https://orcid.org/0000-0003-2234-0420
[4] Principal, Arup, Sky Park, One Melbourne Quarter, 699 Collins Street, Docklands, VIC 3008, Australia
e-mail: David.Barber@arup.com
[5] Director, Arup, 8 Fitzroy St, London, W1T 4BJ, UK
e-mail: Judith.Schulz@arup.com
https://doi.org/10.6084/m9.figshare.22193761

The Sixth Assessment Report (AR6), published by the Intergovernmental Panel on Climate Change (IPCC) ahead of COP26, warned that the world is heading towards 1.5 °C of temperature rise (above pre-industrial levels) within the next two decades. Global surface temperature in 2011-2020 was already 1.1 °C above 1850-1900. Drastic cuts in carbon emissions are needed if the Paris Agreement [3] is to be met.

Buildings are responsible for nearly 40% of global carbon dioxide (CO_2) emissions. Embodied carbon (associated with the sourcing of materials and the construction process) accounts for approximately a quarter of that (i.e. 10% of global CO_2 emissions) [4].

The IPCC also reported on climate change mitigation options and highlighted the importance of buildings [5]. "Enhanced use of wood products" is one of six mitigation options presented. Timber is renewable and sequesters carbon during its growth. Engineered timber, such as cross-laminated timber (CLT) and glued laminated timber (glulam), presents an opportunity for building designers to use sustainable construction materials on a large scale. When the timber is sustainably-sourced, used efficiently and the building is designed with its end-of-life scenario considered, an asset with lower whole-life carbon can result [6], [7].

Whilst timber holds many benefits, it is not devoid of drawbacks. Timber burns if it gets hot, and swells, moulds and/or rots if it gets wet. Furthermore, timber can present acoustic and vibration design challenges. A holistic, integrated design approach is needed to ensure timber buildings are safe and sustainable.

1.2 Exposed mass timber and external flaming

There has been considerable research effort into the presence and properties of external flames from compartment fires, with the early experiments dating back to the 1950s [8]. To date, the vast majority of research has used non-combustible construction. Comparatively little research (summarised below) has investigated external flaming from compartment fires with exposed timber surfaces.

Gorska et al. showed that exposed mass timber can result in larger external flames by conducting a series of 24 small (0.25 m^2 floor area) and one medium-scale (12.25 m^2 floor area) compartment experiments with varying exposed CLT area [9], [10].

Bartlett et al. published results from the Épernon programme, which consisted of a series of six medium-scale (24 m^2 floor area) compartment experiments; three with concrete ceilings and three with exposed CLT ceilings. The CLT compartment with the smallest opening factor (more openings) resulted in double the heat flux received at a distance of 3 m from the opening than from the equivalent concrete compartment. This increase was attributed to increased flame size, and higher external and internal temperatures [11].

Bartlett et al. also carried out eight small-scale (0.49 m^2 floor area) experiments and found that the heat flux to the façade increased when the CLT surface area increased [12].

Brandon et al. carried out five large-scale (47.95 m^2 floor area) experiments and varied exposed timber area. Four experiments represented residential compartments, and one represented a well-ventilated office [13]. An increase in exposed timber area led to increased flame height externally [14].

Most recently, the *TIMpuls* programme of three medium- (20.25 m^2 floor area) and two large-scale (40.50 m^2 floor area) experiments has been completed. The opening factor was kept constant and the area of exposed CLT was varied. No noticeable difference in external flame profiles/temperatures was reported [15]. However, the movable fuel load was very high (1085 MJ/m^2) in these experiments, therefore the influence of the structural fuel load is expected to be less significant.

The compartments used in research to date vary considerably in size, generally capturing common apartment-type arrangements, however are not representative of large, open-plan offices [16] which can have floor areas well in excess of multiple hundred or thousand square metres.

1.3 Potential implications for building designers

The observations from previous research highlight three practical questions for building designers;

1. **Large-scale façade fire tests** – are industry 'standard' testing methods still fit-for-purpose for buildings with large areas of exposed mass timber?

2. **Radiation assessments to neighbouring buildings** – are existing design approaches for external fire spread still appropriate to predict radiation from exposed mass timber building fires to inform analyses of fire spread risk to nearby buildings?
3. **Heat transfer analyses to external structural steelwork** – do existing correlations for external flames accurately predict flame size/temperatures from building fires including mass timber?

This paper focuses on the latter. Mass timber is often used in combination with either steel, concrete, or both. Hybrid typologies make up more than half of all mass timber buildings eight storeys and taller [17]. Some hybrid proposals feature external structural steel exoskeletons. In some non-combustible buildings, the external steelwork is left unprotected (which brings carbon, cost and aesthetic benefits), based on heat transfer analyses from external flame correlations. However, it is not yet known whether those correlations hold for compartments with large areas of exposed mass timber.

1.4 The Law and O'Brien correlation

Law and O'Brien developed a method for assessing fire exposure to external steel members in their seminal work [18]. The method is widely used today and is found in Eurocode 1 [19] and Eurocode 3 [20], and is also presented in abridged form in BR 187 [21] in the context of external fire spread radiation assessments. The current version of Eurocode 5 – a key guidance document for the design of timber buildings – does not have guidance on external flaming from timber structures [22]. It is currently being reviewed and updated.

1.4.1 Assumptions

The assumptions underlying the original Law and O'Brien method are summarised below:

- Only the highest fire temperature is considered. Any fluctuations in temperature are ignored.
- Fire loads are expressed in mass of wood, which was deemed representative of the types of furnishings and contents normally found in buildings at the time.
- The fuel burns uniformly across the compartment and the temperature distribution is uniform.
- Temperature across the width and through the thickness of the flame is constant.
- The flame has distinct boundaries, beyond which there is no convective heat transfer. (This is unconservative, but is offset by the previous conservative assumption).
- All flames take an idealised shape; flame width is taken as the window width. Flame depth is taken as 2/3 of the window height. Maximum lateral deflection by wind is 45°. Gusts are ignored.
- The flame tip exists at the point at which the temperature is 540 °C.
- All steel members are approximated to rectangular sections enclosing the volume of the actual section.
- Steel temperature calculated is an average across the section. Temperature gradients are ignored.
- The steel reaches equilibrium temperature (steady-state conditions) and is generally considered satisfactory if the calculated maximum steel temperature does not exceed 550 °C.
- Emissivity of the fire is assumed as unity (1). Steel emissivity is assumed as unity (1).
- Convective heat transfer coefficient is the same for steel and flame.
- The rate of heat loss by conduction away from the heated area is neglected.

As stated in the original paper, the assumptions generally err on the side of safety.

1.4.2 Method

The relevant input parameters for the correlation are the fire load, the mass burning rate, and the compartment and opening geometry. Law [23] states that the mass loss rate is approximately steady over the fully developed period, when the mass falls from 80% to 30% of its initial value. In other words, half of the fuel load combusts during the peak burning period at a constant rate. The duration of this peak burning period under free-burning conditions (i.e. not ventilation-controlled) is described as the free-burning fire duration, τ_F. Law and O'Brien [18] state that, for most types of furniture found in buildings, τ_F is about 1200 seconds (20 minutes). They then proceed to define the fuel-controlled rate of burning, R_{fuel}, as:

$$R_{fuel} = \frac{A_F \times q}{1200} = \frac{L}{1200} \qquad [\text{kg/s}] \qquad (1)$$

where L is the fire load which is the product of the floor area, A_F, (m^2) and the fire load density, q, (kg/m^2). It is unclear why equation 1 does not define the average rate of burning as:

$$R_{fuel} = \frac{0.5L}{1200} \qquad [\text{kg/s}] \qquad (2)$$

which would align with the theory presented prior.

The ventilation-controlled rate of burning is then given by:

$$R_{vent} = 0.18(1 - e^{-0.036\eta})\left(\frac{D}{W}\right)^{-1/2} A_w h^{1/2} \qquad [\text{kg/s}] \qquad (3)$$

where η is the opening factor, D/W is the ratio of compartment depth over width (however it is not always simply calculated as such), A_w is the window area or sum of window areas on all walls and h is the window height or weighted average of window height on all walls.

The actual burning rate, R, given by:

$$R = \min\,(R_{fuel}, R_{vent}) \qquad [\text{kg/s}] \qquad (4)$$

is then used to determine flame height and the flame temperature along its axis (and at the opening).

Average flame height, z, is given by:

$$z = 12.8\left(\frac{R}{w}\right)^{\frac{2}{3}} - h_{eq} \qquad [\text{m}] \qquad (5)$$

where w is the total opening width and h_{eq} is the area-weighted average opening height.

This is then used to calculate the length of the flame axis (from the opening plane to the flame tip), X, when there is a wall above the opening and $h_{op} < 1.25w_{op}$:

$$X = z + \frac{h_{op}\sqrt{2}}{3} \qquad [\text{m}] \qquad (6)$$

Flame temperature at the opening is given by:

$$T_o = \frac{813.15 - T_a}{\left[1 - 0.027\left(\frac{Xw}{R}\right)\right]} + T_a - 273.15 \qquad [°\text{C}] \qquad (7)$$

Flame temperature at any point, l, along the flame axis (centreline) (shown in Figure 1) is then given by:

$$T_z = \frac{T_o - T_a}{\left[1 - 0.027\left(\frac{lw}{R}\right)\right]} + T_a - 273.15 \qquad [°\text{C}] \qquad (8)$$

Compartment fire temperature is calculated based on fire load, ventilation and compartment dimensions. Flame temperature can exceed compartment fire temperature if substantial amounts of unburnt gas are emitted from the compartment and combust outside.

Law & O'Brien present correlations for the emissivity of the flame, the convective heat transfer coefficient, and flame geometry. Heat transfer calculations (based on energy balances) are then presented for;

- Column not engulfed in flame
- Column engulfed in flame
- Spandrel beam engulfed in flame.

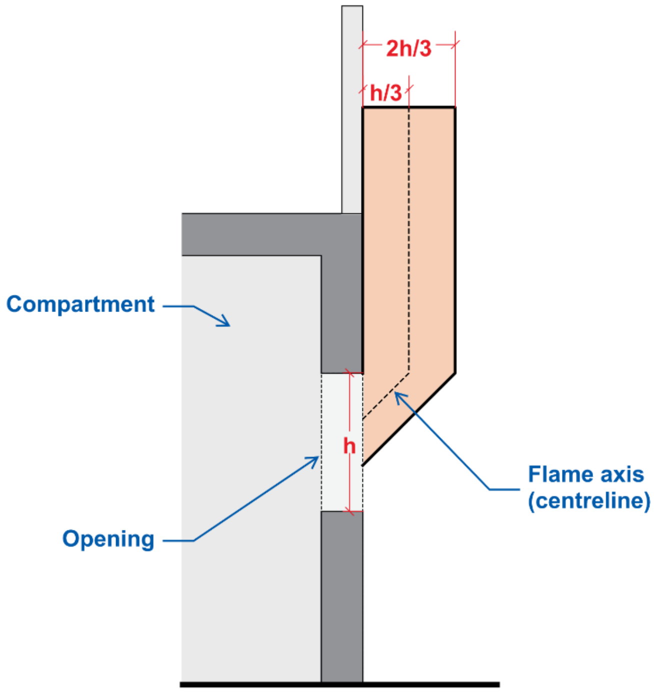

Figure 1: Section showing idealised flame geometry when the flame adheres to the facade.

Generally, the steelwork nearest the top of the windows is analysed. If the column is engulfed in flame, it will almost always exceed the critical temperature unless shielding is used.

Based on equation (7), a higher burning rate results in lower temperatures at the opening. However, from equation (5), a higher burning rate results in a taller flame. This presents challenges for designers wishing to analyse heat transfer from external flames venting from compartments to unprotected external structural steel. The designer may wish to estimate flame temperatures based on correlations, and then carry out sensitivity studies to gain insight on the margin of safety.

1.4.3 Limitations

The main limitation with the original Law and O'Brien method is in the determination of the burning rate. Only the movable fuel load is considered. No guidance currently exists on accounting for any structural fuel load, such as in exposed mass timber compartments.

1.5 Hypothesis and objectives

Based on the method and limitations presented, this paper raises the hypothesis:

The existing empirical Law and O'Brien correlation, which is presented in Eurocode 1 and Eurocode 3, does not consider structural fuel load and therefore may require adjustments before it is applied to the design of buildings with large areas of exposed mass timber

and aims to fulfil the following objectives:

1. Present external temperature data from the *CodeRed* experimental series.
2. Investigate whether the Law & O'Brien correlation adequately predicts external flaming from mass timber compartments.
3. Carry out the same analysis using data from other timber compartment fire experiments.

2 THE *CODERED* EXPERIMENTS

In 2021, a series of four full-scale (352 m^2 floor area) experiments were conducted in a purpose-built compartment with a mass timber ceiling at CERIB's Centre d'Essais au Feu. The experiments aimed to study the fire dynamics in large, open-plan compartments with exposed timber. Chosen parameters (those in **bold** in Table 1) were varied.

Table 1: Summary of key parameters of the *CodeRed* experiments without suppression.

Experiment		*CodeRed #01*	*CodeRed #02*	*CodeRed #04*
Date		09 Mar 2021	01 Jun 2021	14 Dec 2021
Ignition time (CET)		23:11:55	23:22:33	23:06:43
Internal floor area, A_F	[m^2]	352	352	352
Total area of openings, A_w	[m^2]	56.6	**28.3**	56.6
Exposed CLT area, A_{CLT}	[m^2]	352	352	**176.7**
Total internal surface area of compartment (floor, ceiling and walls), **inc. opening area**, A_t	[m^2]	980	980	980
Total internal surface area **minus opening area**, A_T	[m^2]	923	952	923
Area-weighted average window height, h_{eq}	[m]	1.488	1.818	1.488
Opening factor as per Eurocode [19] $A_t/(A_w h_{eq}^{1/2})$	[m$^{-1/2}$]	14.2	25.6	14.2
Opening factor as per L&O'B [18] $A_T/(A_w h_{eq}^{1/2})$	[m$^{-1/2}$]	13.4	24.9	13.4
Modified opening factor as per [10] $(A_T\text{-}A_{CLT})/(A_w h_{eq}^{1/2})$	[m$^{-1/2}$]	8.3	15.7	10.8

The compartment (shown in Figure 2) had walls which were constructed from aerated concrete blocks and a CLT ceiling. This paper will focus on the results from *CodeRed #01*, *CodeRed #02* and *CodeRed #04*; *CodeRed #03* investigated the efficacy of a water mist suppression system and is not relevant to the scope of this paper.

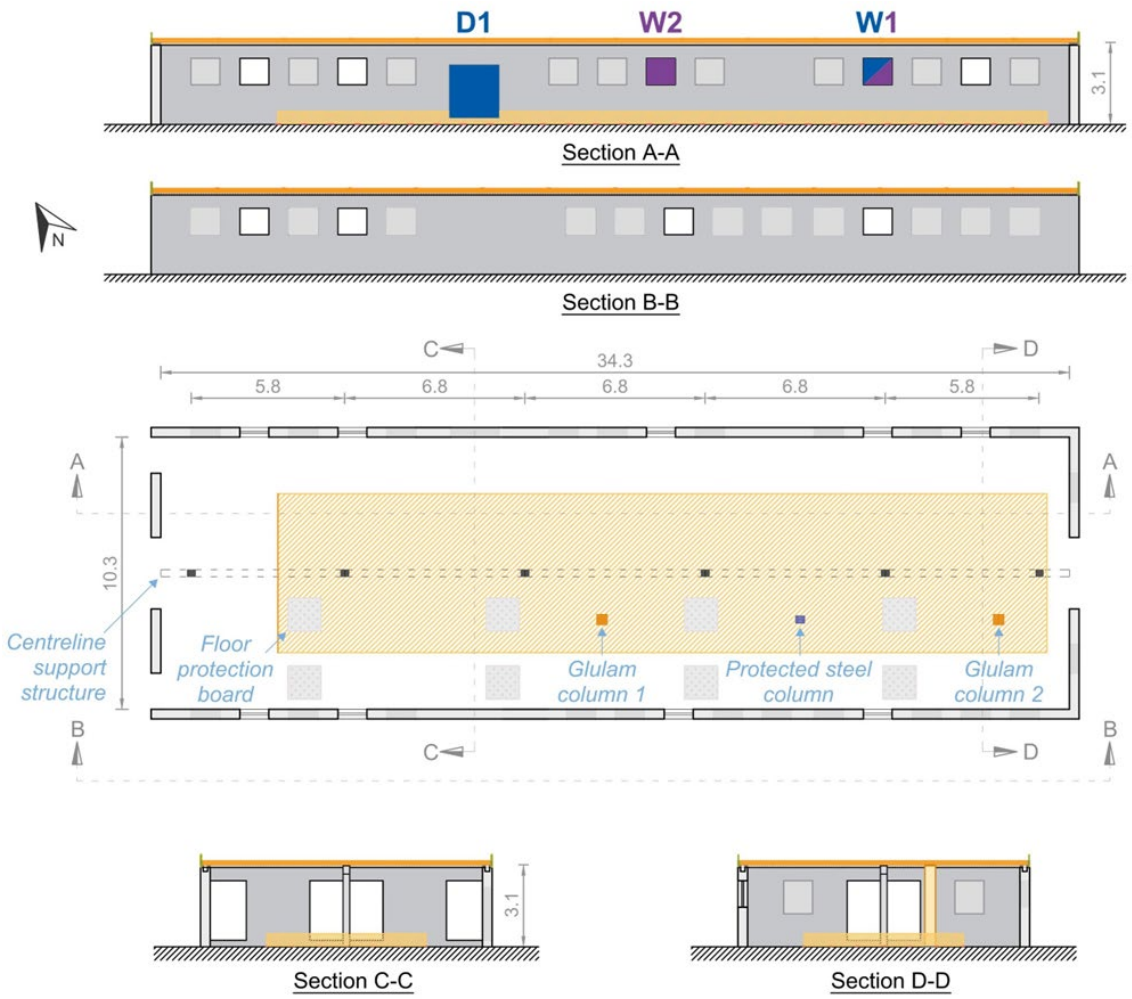

Figure 2: Floor plan and sections of the compartment used for the *CodeRed* experiments. Units in metres. The greyed-out openings represent those filled in *CodeRed #02*. These were open for *CodeRed #01* and *CodeRed #04*.

The fuel bed constructed was identical in all experiments and consisted of continuous wood cribs with a fuel load density of ~380 MJ/m^2 over a floor area of 174 m^2. The fuel load was chosen to be within the range of typical fuel load densities in office buildings [24].

The fuel load density and the ventilation used for the *CodeRed* experiments mirrored those of previous travelling fire experiments within non-combustible compartments [25], [26] to allow for a direct comparison of the influence of the CLT ceiling.

3 EXPERIMENTAL DATA ANALYSIS

3.1 Temperature of the external flame and plume

The external flame/plume temperatures recorded outside the instrumented openings of the three unsuppressed *CodeRed* experiments are shown in Figure 2. Data is presented for the first 45 minutes of the experiments. The temperatures have not undergone any correction for radiation (as radiation errors are expected to be low outside the compartment). The data has been smoothed using the Savitzky–Golay [27] filter available within SciPy , using a time frame of 60 s and a 2nd-order polynomial, to reduce noise.

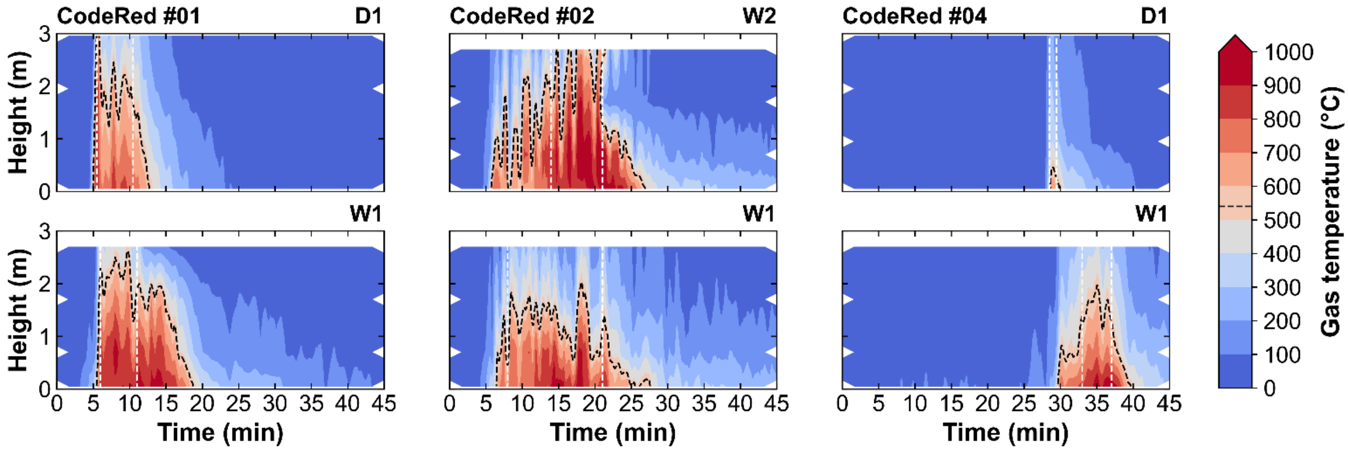

Figure 3: *CodeRed* external gas temperature development. Temperatures recorded at 300 mm offset from the façade screens. White triangles indicate the position of the thermocouples. Temperatures are linearly interpolated. The black dashed lines show an approximation of flame height (at the 540 °C isotherm), based on external flame theory [18]. The white dashed lines indicate the peak external flaming period for each opening, to the nearest 30 seconds.

In *CodeRed #01*, the external flaming from the door opening D1 lasted for approximately half the duration than from the window opening W1. Figure 2 shows the locations of both openings. The fire spread past the door opening, and the crib at the ignition-end of the compartment was burnt out, which caused the cessation of external burning outside opening D1 whilst flaming continued outside opening W1. The maximum external flame height during *CodeRed #01* was approximately 3 m [28].

When the ventilation area was halved in *CodeRed #02*, the fire lasted for longer. External flaming commenced at approximately the same time as *CodeRed #01*, at just after five minutes, but lasted until after 25 minutes. Maximum flame heights were slightly taller in *CodeRed #02*, at approximately 3.5 m [29].

Encapsulation of 50% of the CLT in *CodeRed #04* (with the same ventilation as in *CodeRed #01*) reduced the maximum flame height to similar levels as seen from a similar non-combustible compartment [26].

3.2 Comparison to the existing Law & O'Brien correlation which considers movable fuel load only

So that the data can be compared with Law and O'Brien's correlation for temperature along the flame axis (equation (8)), a peak period is defined (shown in Figure 3) over which temperatures are averaged. All peak burning periods defined are shorter than the 20 minutes assumed by Law and O'Brien (L&O'B) [18].

The flame/plume centreline is typically assumed as being located a distance of $h/3$ from the façade [18]. The window openings have a height, h, of 1 m, therefore the centreline should be at an offset of 333 mm from the façade. Images recorded during the experiments indicate that this is an accurate prediction.

The door openings have a height of 2 m. Therefore, the centreline should be at an offset of 666 mm from the façade. However, no significant difference in flame thickness was observed between the window and door openings on the long sides of the compartments.

Therefore, it is assumed that the thermocouples at a 300 mm offset from the façade are located on the flame centreline for both the window and door openings. The external temperatures recorded by each thermocouple have been averaged over the peak periods and plotted with lines of best fit in Figure 4.

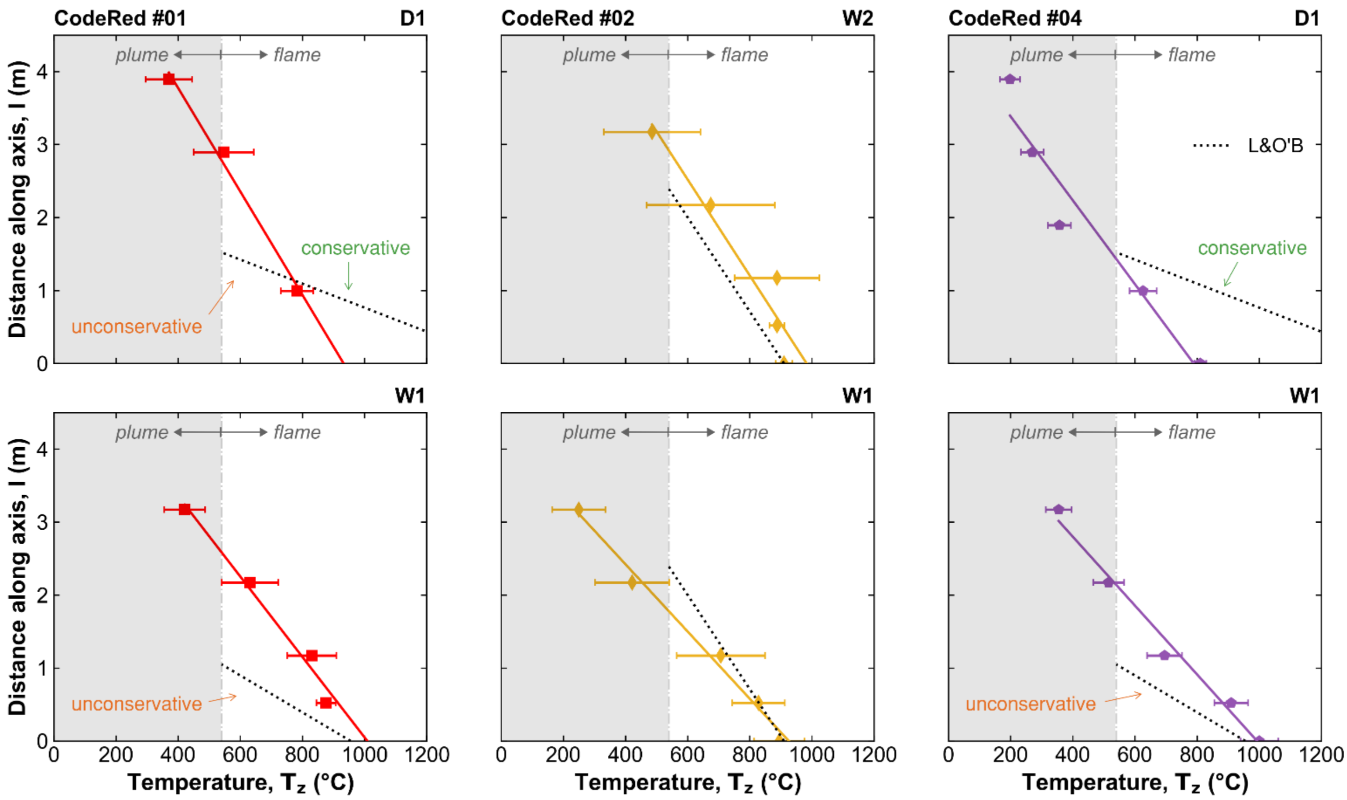

Figure 4: Comparison between temperatures recorded in the external flame/plume (averaged over the peak period), and predictions made following the Law & O'Brien (L&O'B) correlation. Flame tip is assumed at 540 °C [18]. Error bars indicate min. and max. temperatures.

The L&O'B correlation generally makes inaccurate predictions for *CodeRed #01* and *#04*. These experiments had ample ventilation (i.e. the burning rate was fuel-controlled and given by equation (1)).

For the larger door (D1) openings, the correlation overpredicts the temperature in the opening and underpredicts the flame height. For the smaller window (W1) openings, the correlation slightly underpredicts the temperature in the openings and underpredicts the flame height.

The prediction is more accurate for *CodeRed #02*, which had the ventilation area reduced by 50%.

4 SUPPLEMENTARY ANALYSIS OF AVAILABLE DATA FROM OTHER EXPERIMENTS

To further broaden the analysis rather than focusing on one experimental series, the Law & O'Brien correlation has been applied to other medium-scale timber compartment fire experiments.

4.1 RISE

4.1.1 The experiments

RISE conducted experiments on compartments with a floor area of 48 m^2 with instrumentation outside two identical openings [13]. Data is presented from Tests 1 – 4.

Tests 1 – 4 had exposed areas of CLT of 53.8, 91.2, 96.2, and 77.9 m^2 respectively. In all experiments, the openings were 'open' from the beginning, i.e., it was assumed that all glass had broken before the fire grew and flashed over.

Tests 1 – 3 had fewer openings (an opening factor of 15.3 m$^{-1/2}$ calculated following Law & O'Brien [18] and Drysdale [30]), with the intention of replicating a residential compartment. Test 4 had much greater opening area (an opening factor of 3.1 m$^{-1/2}$), which replicated an office compartment.

4.1.2 Instrumentation

In all experiments, the thermocouple offset distance from the façade varied from 25 to 100 mm. For this study, it is assumed that the temperatures recorded by the thermocouples (regardless of offset) represent the flame centreline temperature. This is likely to introduce error (through underestimating the centreline temperature). The error would be smallest if the flame adhered to the façade. From observing available image data, the flame did not always adhere to the mock-up façade panel, therefore errors will exist.

In all tests, mass was recorded. The movable fuel load on the floor and the structural fuel load (CLT slabs) were weighted independently.

4.1.3 Comparison of data to Law & O'Brien prediction

In Figure 5, the L&O'B correlation generally makes slightly better (however, still unconservative) predictions for compartments with little ventilation (Test 1 – 3) than for those with ample ventilation (Test 4). The L&O'B correlation only slightly underpredicted flame temperatures for Tests 1 – 3. However, as noted prior, the recorded temperatures are likely to be cooler than the actual flame centreline temperatures, as the thermocouples are located close to the façade.

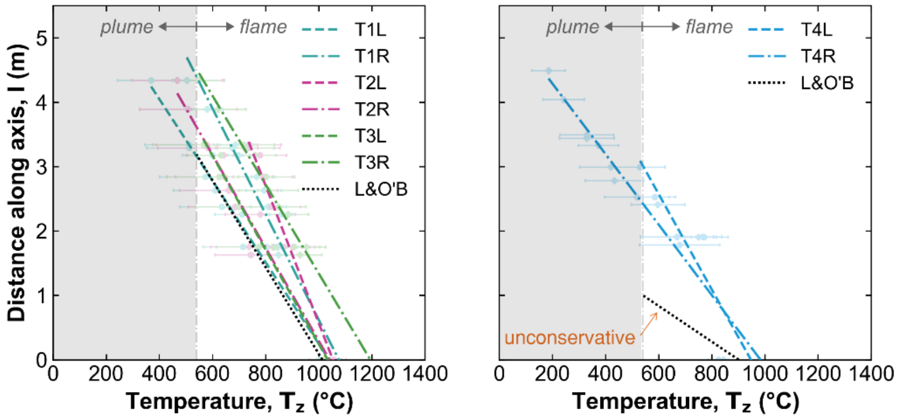

Figure 5: Comparison between recorded temperatures (which may not have been on the flame centreline) and predictions made by the Law and O'Brien (L&O'B) correlation for RISE Tests 1 – 4 from both left (L) and right (R) openings. Flame tip is assumed at 540 °C [18]. Error bars indicate min. and max. temperatures.

For Tests 1 – 3, L&O'B predicts that the rate of burning is ventilation-controlled (R_{vent} = 0.8 kg/s).

For Test 4, which had significantly increased ventilation, L&O'B predicts that the rate of burning is fuel-controlled (R_{fuel} = 1.0 kg/s).

The final project report presents independent mass loss rates for Test 2 only [31]. The mass loss rate for the movable fuel varied between approximately 0.4 – 0.9 kg/s, and the mass loss rate of the timber structure varied between approximately 0.4 – 1.4 kg/s (i.e., a total mass burning rate, R, of between approximately 0.8 – 2.3 kg/s) during the peak burning period. The L&O'B prediction of ventilation-controlled rate of burning for Tests 1 – 3 (of R_{vent} = 0.8 kg/s) is towards the lower end of this range. This explains the slight underprediction for Tests 1 – 3 in Figure 5.

For Test 4, which was fuel-controlled, L&O'B underestimated temperature along the flame axis.

These observations are similar to those from *CodeRed*, whereby the L&O'B correlation appears to perform better for under-ventilated compartments and worse for well-ventilated timber compartments.

4.2 Épernon

The Épernon experiments had a floor area of 24 m^2. The programme involved three 'scenarios'. Scenario 1 (S1), which had an opening factor of 6.2 m$^{-1/2}$, did not have any instrumentation in the external flaming region. External instrumentation was introduced for Scenarios 2 (S2) and 3 (S3).

Each scenario had two compartment experiments; one with a non-combustible concrete ceiling (S21 and S31) and another with a CLT ceiling (S22 and S32) [16].

Scenarios 2 and 3 both had very little ventilation (opening factors of 19.0 and 30.8 m$^{-1/2}$ respectively). Both scenarios featured a mock-up façade with thermocouples. The thermocouples were placed close to the façade, therefore (like in the RISE experiments), may underestimate centreline temperature.

Figure 6 presents the façade temperature data and the predictions of flame centreline temperature made using the Law and O'Brien correlation.

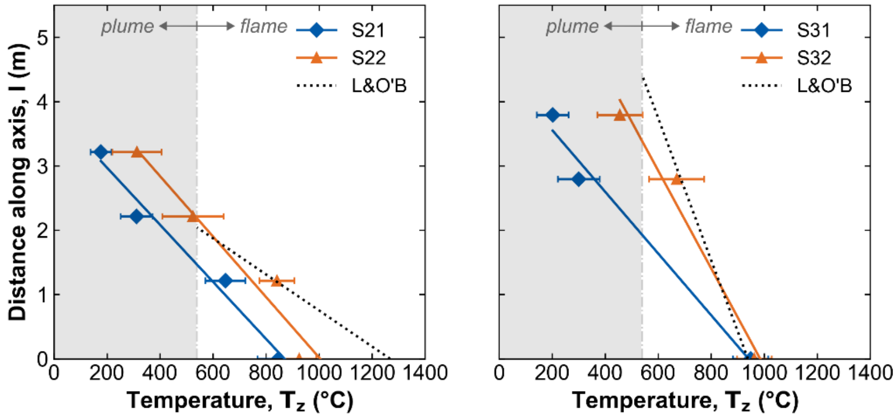

Figure 6: Comparison between recorded temperatures and predictions made by the Law and O'Brien (L&O'B) correlation for Épernon Scenarios 2 and 3. Data is presented from both non-combustible (S21 and S31) and combustible (S22 and S32) experiments.

The L&O'B correlation overpredicts opening temperature for S21 and S22, and slightly underpredicts flame height for S22 (which had a timber ceiling). For both S31 and S32, opening temperature is slightly underpredicted, and flame height is overpredicted. All four scenarios are ventilation-controlled.

5 DISCUSSION

The analysis has shown that the Law & O'Brien correlation, which was derived in the 1970s based on experiments in non-combustible compartments, can lead to significant underestimations of both flame height and temperature from compartments with large areas of exposed mass timber.

Similar observations were made on both the large-scale *CodeRed* experiments and medium-scale RISE and Épernon experiments; the greatest errors were seen for timber compartments with ample ventilation.

For timber compartments with less ventilation, the burning rate is more likely to be ventilation-controlled. In this case, omission of structural fuel load when using the Law and O'Brien correlation should not have an impact (as equation (3) for R_{vent} governs).

For a well-ventilated compartment, the burning rate is more likely to be fuel-controlled (and equation (1) for R_{fuel} governs). Equation (1) currently ignores structural fuel load (i.e. no fuel load contribution from the exposed timber is taken into account). When the contribution to the fuel load by the combustible structure is not taken into consideration, the mass burning rate is likely to be underestimated and the temperature along the flame centreline is subsequently also likely to be underestimated. This was seen in the analysis of both the *CodeRed* and RISE experiments.

Flame heights were generally underpredicted by the correlation. Underpredictions ranged from 20% to 75% for the *CodeRed* and RISE experiments.

Significant errors for temperature at the opening were seen, particularly for large openings. For the door (D1) openings in *CodeRed #01* and *CodeRed #04*, opening temperatures were conservatively overpredicted by around 60% and 90% respectively. In other experiments, they were often slightly underpredicted.

Many contemporary timber office buildings feature large areas of glazed façade. Such buildings are more likely to exhibit fuel-controlled burning (if the façade fails in a fire). If the existing Law and O'Brien correlation is applied to such buildings without accounting for the structural fuel load, large underestimations of external flaming are to be expected.

There is a need for a modified Law and O'Brien correlation which can be applied to the design of buildings with large areas of exposed mass timber. In the interim, designers could make conservative assumptions for external flame height and temperature. Whilst outside the scope of this paper, designers also need to consider the potential impacts (if any) on the validity of large-scale façade fire tests and radiation assessments to neighbouring buildings in their jurisdiction. Further work is needed in these areas.

6 CONCLUSIONS

The analysis presented in this paper has confirmed the hypothesis that *the existing empirical Law and O'Brien correlation, which is presented in Eurocode 1, Eurocode 3 and BR 187, does not consider structural fuel load and requires adjustments before it is applied to the design of buildings with large areas of exposed mass timber*.

There is a need for a new, modified approach for predicting external flame characteristics (height and temperature along axis) from compartments with large areas of exposed mass timber. Such an approach needs to consider the structural fuel load as well as the movable fuel load.

Further work is required in this area to develop guidance which will allow designers to develop safe and sustainable buildings which can help tackle the climate crisis.

REFERENCES

[1] H. Ritchie and M. Roser, "Urbanization," *Published online at OurWorldInData.org*, 2018. https://ourworldindata.org/urbanization (accessed Sep. 21, 2022).

[2] M. Roser, H. Ritchie, and E. Ortiz-Ospina, "World Population Growth," *Published online at OurWorldInData.org*, 2013. https://ourworldindata.org/world-population-growth (accessed Sep. 22, 2022).

[3] United Nations / Framework Convention on Climate Change, *Paris Agreement*. Paris: United Nations, 2015.

[4] Architecture 2030, "Why The Building Sector?," 2022. https://architecture2030.org/why-the-building-sector/ (accessed Mar. 26, 2022).

[5] IPCC, "Summary for Policymakers," in *Climate Change 2022: Mitigation of Climate Change. Contribution of Working Group III to the Sixth Assessment Report of the Intergovernmental Panel on Climate Change*, P. R. Shukla, J. Skea, R. Slade, A. Al Khourdajie, R. van Diemen, D. McCollum, M. Pathak, S. Some, P. Vyas, R. Fradera, M. Belkacemi, A. Hasija, G. Lisboa, S. Luz, and J. Malley, Eds. Cambridge: Cambridge University Press, 2022. doi: 10.1017/9781009157926.001.

[6] W. Hawkins, "Timber and carbon sequestration," *Struct. Eng.*, vol. 99, no. 1, pp. 18–20, 2021.

[7] Arup, "Net Zero Carbon Buildings: Three Steps to Take Now," 2020.

[8] S. Yokoi, "Study on the Prevention of Fire-Spread Caused by Hot Upward Current," 1960.

[9] C. Gorska, "Fire Dynamics in Multi-Scale Timber Compartments," University of Queensland, 2019. [Online]. Available: https://espace.library.uq.edu.au/view/UQ:ec263ab/s4408332_final_thesis.pdf

[10] C. Gorska, J. Hidalgo, and J. Torero, "Fire dynamics in mass timber compartments," *Fire Saf. J.*, 2020, doi: 10.1016/j.firesaf.2020.103098.

[11] A. Bartlett *et al.*, "Heat fluxes to a facade resulting from compartment fires with combustible and non-combustible ceilings," in *FSF 2019 – 3nd International Symposium on Fire Safety of Facades*,

2019, pp. 62–69.

[12] A. Bartlett, G. Kanellopoulos, and A. Law, "Heat flux distribution on a facade from timber-lined compartments," in *15th International Conference and Exhibition on Fire Science and Engineering (Interflam)*, 2019, pp. 2–9.

[13] D. Brandon, J. Sjöström, A. Temple, E. Hallberg, and F. Kahl, "Fire Safe implementation of visible mass timber in tall buildings – compartment fire testing," 2021. [Online]. Available: http://urn.kb.se/resolve?urn=urn:nbn:se:ri:diva-58153

[14] J. Sjöström, A. Temple, D. Brandon, E. Hallberg, and F. Kahl, "Exposure from mass timber compartment fires to facades," Brandforsk, 2021.

[15] T. Engel *et al.*, "Schlussbericht zum Verbundvorhaben TIMpuls - Brandschutztechnische Grundlagenuntersuchung zur Fortschreibung bauaufsichtlicher Regelungen im Hinblick auf eine erweiterte Anwendung des Holzbaus," Gülzow-Prüzen, 2022.

[16] The University of Edinburgh and CERIB, "Épernon Fire Tests Programme," 2020.

[17] D. Safarik, J. Elbrecht, and W. Miranda, "State of Tall Timber 2022," *CTBUH J.*, vol. 2022, no. I, pp. 22–31, 2022.

[18] M. Law and T. O'Brien, "Fire Safety of Bare External Structural Steel," *Constrado*, 1981.

[19] The British Standards Institution, *Eurocode 1: Actions on structures Part 1-2: General actions – Actions on structures exposed to fire*. 2013.

[20] The British Standards Institution, *Eurocode 3: Design of steel structures Part 1-2: General rules – Structural fire design*. 2009.

[21] R. Chitty, *BR 187 External fire spread: building separation and boundary distances*, Second., vol. 1, no. 2. Watford: IHS BRE Press, 2014.

[22] The British Standards Institution, *Eurocode 5: Design of timber structures Part 1-2: General — Structural fire design*. 2004. doi: 10.1680/cien.144.6.39.40613.

[23] M. Law, "Fire Safety of External Building Elements - The Design Approach," *Eng. J.*, vol. 15, no. 2, pp. 59–74, 1978.

[24] The British Standards Institution, *PD 7974-1:2019 Application of fire safety engineering principles to the design of buildings - Part 1: Initiation and development of fire within the enclosure of origin (Sub-system 1)*. 2019.

[25] E. Rackauskaite *et al.*, "Fire Experiment Inside a Very Large and Open-Plan Compartment: x-ONE," *Fire Technol.*, 2021, doi: 10.1007/s10694-021-01162-6.

[26] M. Heidari *et al.*, "Fire experiments inside a very large and open-plan compartment: x-TWO," in *SiF 2020 – The 11th International Conference on Structures in Fire*, 2020, no. November, pp. 479–491. doi: 10.14264/b666dc1.

[27] A. Savitzky and M. J. E. Golay, "Smoothing and Differentiation of Data by Simplified Least Squares Procedures," *Anal. Chem.*, vol. 36, no. 8, pp. 1627–1639, Jul. 1964, doi: 10.1021/ac60214a047.

[28] P. Kotsovinos *et al.*, "Fire dynamics inside a large and open-plan compartment with exposed timber ceiling and columns: CodeRed #01," *Fire Mater.*, pp. 1–27, 2022, doi: 10.1002/fam.3049.

[29] P. Kotsovinos *et al.*, "Impact of ventilation on the fire dynamics of an open-plan compartment with exposed timber ceiling and columns: CodeRed #02," *Fire Mater.*, pp. 1–28, 2022, doi: 10.1002/fam.3049.

[30] D. Drysdale, *An Introduction to Fire Dynamics*, 3rd ed. Chichester: John Wiley & Sons, Ltd, 2011. doi: 10.1016/0379-7112(86)90046-9.

[31] D. Brandon, J. Sjöström, E. Hallberg, A. Temple, and F. Kahl, "Fire Safe implementation of visible mass timber in tall buildings – compartment fire testing," 2020.

SiF 2022– The 12th International Conference on Structures in Fire
The Hong Kong Polytechnic University, Nov 30 - Dec 2, 2022

BURNING BEHAVIOUR OF GLT WALLS DURING COOLING PERIOD AFTER ISO 834 EXPOSURE IN A SMALL FURNACE

Kazunori Harada[1], Anyang Sun[2], Shoma Makino[3], Daisaku Nii[4]

ABSTRACT

Fire resistance of timber structures is mainly investigated by ISO 834 standard fire resistance tests. In the tests, specimens are heated in accordance with prescribed standard time-temperature curve and the time to failure is measured, but no information is available with regard to the behaviours during post-heating period. In case of timber constructions, post-heating behaviour is important because the self-burning continues during cooing period. To investigate the behaviour during cooling period, fire resistance tests of larch GLT (Glue Laminated Timber) walls were carried out. The wall thickness was 100mm. The walls were heated in accordance with ISO 834 for 60 minutes. After heating, the furnace was supplied with fresh air at various rates. By changing the air supply rate, 8 experiments were carried out. Behaviours, such as self-burning, were observed and recorded by video. Heat release rates by self-burning was measured by the oxygen consumption technique. Time-dependent temperature and water content values were measured at internal points of the specimen. As a result, the post-heating self-burning behaviour depended on the rate of air supply. In case of large air supply rate, self-burning was intense right after the end of heating. However, the self-burning ceased fairly quickly because the furnace was cooled down rapidly due to the large amount of supplied air. In case of small air supply rate, self-burning was relatively mild because the oxygen is not enough. However, the decrease of furnace temperatures was slow because the air supply rate was small. As a result, charring of specimen was deeper as the air supply rate was smaller.

Keywords: Fire resistance test; cooling period; GLT wall; air supply rate; cooling temperature; charring depth

1 INTRODUCTION

The use of timber structure is wide spreading due to its environmental friendliness. However, the use is limited to relatively small buildings because of its concerns on fire resistance. In case of large-scale buildings, collapse of building should be avoided to prevent damage to people, property and surrounding area. In this sense, large-scale buildings should not collapse at least during evacuation, rescue, and firefighting. In practical sense, large buildings should not collapse by fire during whole process of fire including cooling period. For example, the Building Standards Law of Japan requires large buildings with more than four stories not to collapse during the complete process of fire. [1]

[1] Professor, dept. Architecture and Architectural Eng., Kyoto University, Japan
e-mail: harada@archi.kyoto-u.ac.jp, ORCID: https://orcid.org/0000-0001-8270-1692
[2] Ph.D student, *ibid*.
e-mail: sun.anyang.78r@st.kyoto-u.ac.jp, ORCID: https://orcid.org/0000-0003-0456-8835
[3] Graduate student, *ibid*.
e-mail: makino.shoma.55z@st.kyoto-u.ac.jp
[4] Assistant Professor, *ibid*.
e-mail: nii@archi.kyoto-u.ac.jp, ORCID: https://orcid.org/0000-0002-5821-7494
https://doi.org/10.6084/m9.figshare.22193746

In case of timber buildings, structural elements are required to support mechanical load during and after fire. The fire resistance of timber structures is usually investigated by ISO 834 standard fire test [2]. The specimen is heated until failure, but the post-heating behaviour is not usually investigated. However, the post-heating behaviour is important because the self-burning takes place during the cooling period. For example, König proposed a model for charring of wood under natural fires including decay phase[3]. He used an effective heating temperature during decay phase to consider the effect of self-burning flame. Schmid *et al.*[4] discussed the possibility of using fire resistance furnace to evaluate the fire resistance of timber structures against natural fires including decay phase. In addition, they investigated the charring rate of wood during decay phase using bench scale equipment [5]. The structural performance of beams during cooling period is investigated by Hirashima *et al.*[6].

However general information is still missing on the burning behaviour of timber structures during cooling period. In case of fire resistance tests as shown in Figure 1, the timber specimen does not burn with flame but is simply charred from the heated surface because there is almost no oxygen in the furnace during the heating period. During the cooling period, fuel supply to the furnace is stopped and fresh air is introduced. As a result, the timber specimen starts to burn with flame. Depending on the rate of air supply, the burning behaviour varies. If the air supply is large, the furnace temperature is decreased rapidly and the thermal damage to timber element may be reduced. At the same time, fresh air may increase the self-burning of timber element and the damage to timber element may be increased. The correlation between damage and air supply rate is not quantified yet.

In this paper, eight experiments were conducted on GLT (Glue Laminated Timber) walls. The specimens were heated by ISO 834 fire, then subjected to cooling at various air supply rates [7]. The burning behaviour, furnace and specimen temperatures, moisture content, damage to the specimens were investigated.

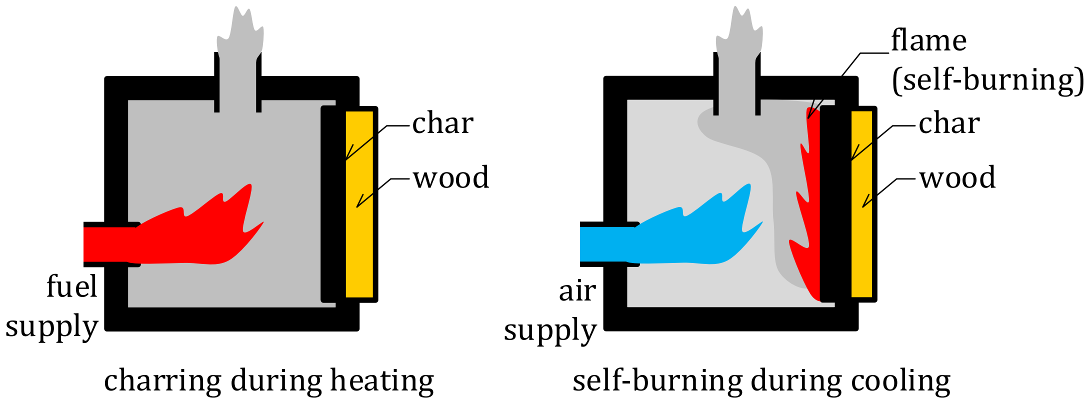

Figure 1. schematics of burning behaviour of a timber wall specimen during and after heating in a fire resistance furnace

2 EXPERIMENTAL METHODS

2.1 Schematics of experiments

The specimens were 100mm thick GLT walls made of larch. The specimens were heated by ISO 834 fire for 60 minutes using a cube furnace of 800 x 800 x 800mm as shown in Figure 2. After heating, the furnace was cooled down by air supply. By changing the air supply rates, eight experiments were carried out.

2.2 Specimens

The specimens were GLT wall of larch. The wall thickness was 100mm. Oven dry density was 463kg/m^3. Water content was 11.0% by weight. Laminas of thickness of 30.5mm were laminated to manufacture a wall specimen of W1,200×H1,000×D100mm. The initial water content of each specimen was in the range of 10.7 to 13.0 % by weight (see Table1 shown later) as measured by a moisture meter. The specimens were fairly air-dried.

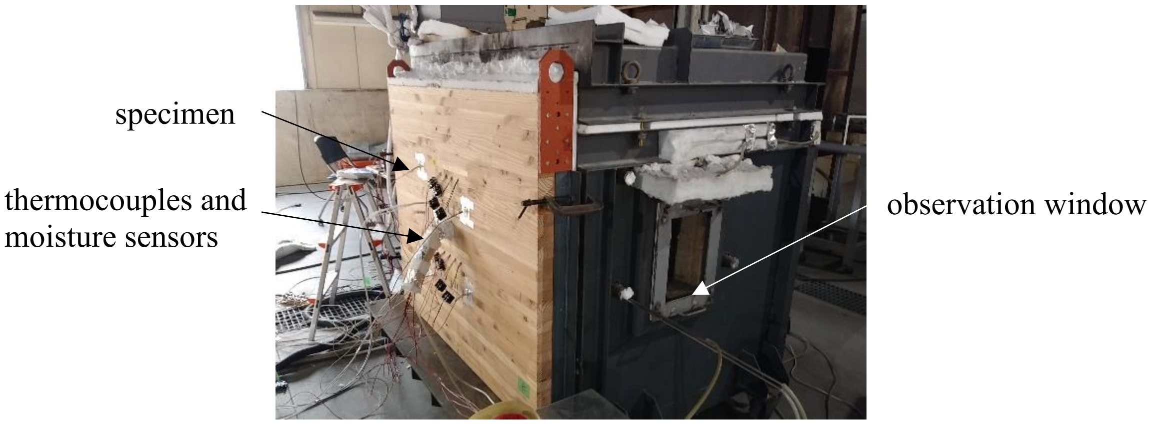

Figure 2. view of testing situation

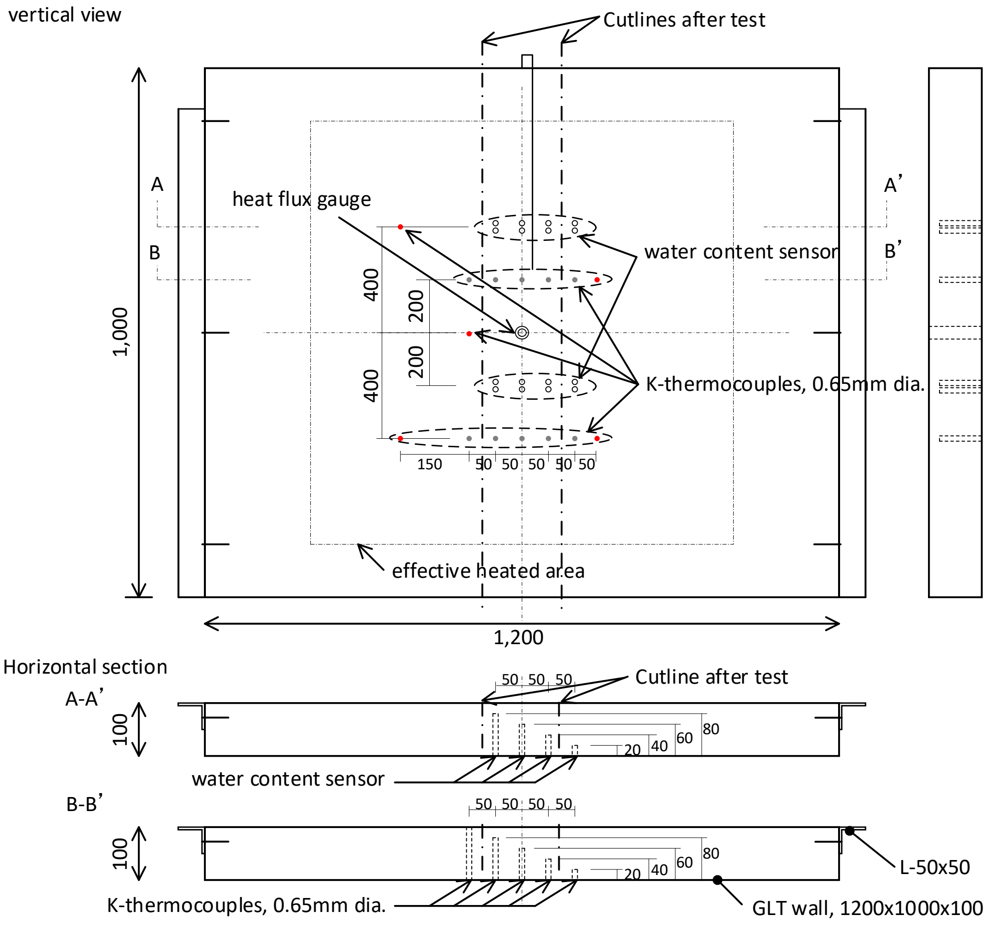

Figure 3. schematics of specimen

2.3 Measurements

Specimen temperatures, water contents and incident heat flux were measured at the locations shown in Figure 3. Temperatures were measured at exposed surface, at internal points (20, 40, 60 and 80mm from exposed surface) and at unexposed surface. Type K thermocouples of 0.65 diameter were used. As to the water contend, pairs of stainless wires were embedded in the specimen. The electric resistance between the wires was measured by insulation continuity tester and converted to water content.

2.4 Testing apparatus

A small box furnace was utilized in the experiments as shown in Figure 4. Inner dimension of the furnace was 800mm cube. On one side of the cube, a wall specimen was equipped. Single gas burner is equipped on the wall opposite to the specimen. The burner was fired by natural gas. Furnace gas was exhausted naturally through a duct hole equipped at a side wall.

The furnace wall is constructed by fire clays made of silica-alumina compounds (density ρ=2,000 kg/m^3, thermal conductivity k=0.16 W/m·K). An observation window was equipped on a side wall. During heating and cooling, the condition of exposed surface was recorded by a video camera through the observation window.

To measure the air supply rate during cooling period, supply air pressure was measured by a gauge pressure manometer. By correlating the degree of opening of air supply valve and air supply pressure, air supply rate was monitored continuously.

During cooling period, furnace gas was sampled, and the concentration of oxygen was measured by a gas tester. Using the oxygen consumption technique, heat release rate from specimen due to self-burning was estimated.

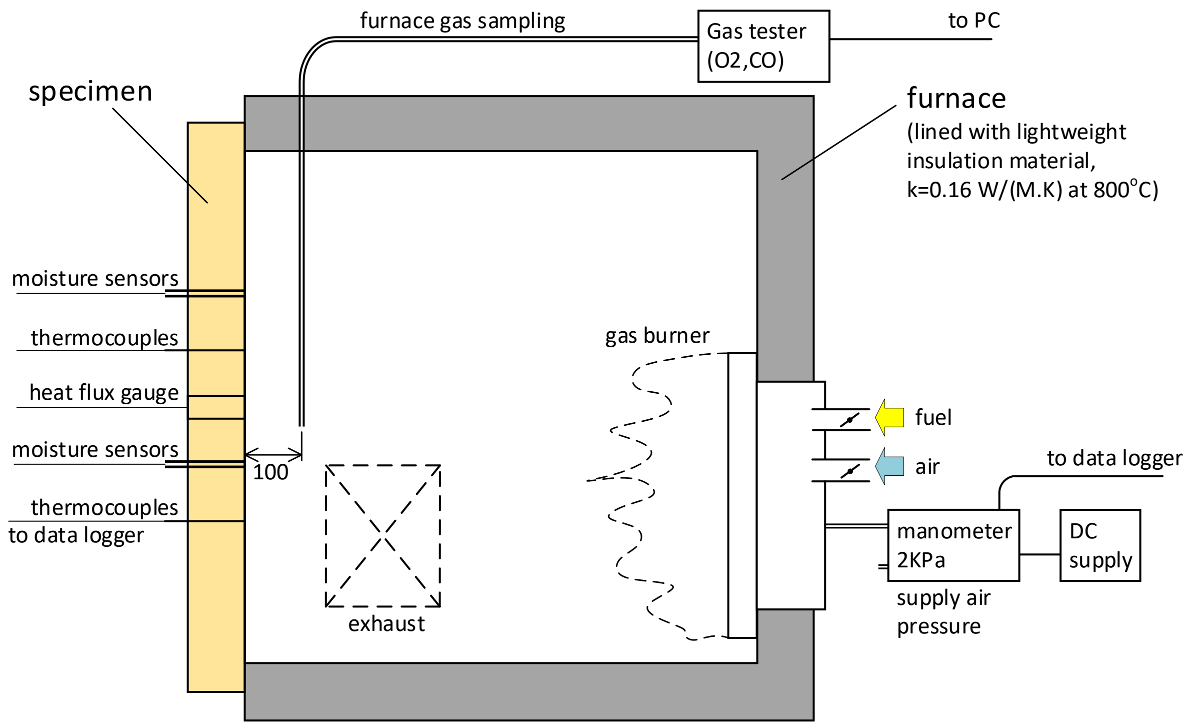

Figure 4. testing furnace

2.5 Testing conditions

The furnace was controlled following the ISO 834 standard time- temperature curve [2] as

$$T_f = 345 \log_{10}(8t+1) + 20 \qquad (1)$$

where T_f is the furnace temperature [°C]

t is the time [min.].

Heating was continued for 60 minutes. After 60 minutes, fuel supply was stopped. To cool down the furnace, air was supplied at constant rate. The supply rate m_a[kg/s] per wall area of specimen A_{fuel}(=0.64m^2) was selected between m_a/A_{fuel} = 0.0067 and 0.0786 kg/(m^2·s). By changing the air supply rate, eight experiments were conducted. Table 1 shows the air supply rate of each experiment. For wooden materials, it is said that

$m_a/A_{fuel} = 0.04$ kg/(m^2·s) is the border of ventilation control (fuel rich) and fuel control (fuel lean) fires [8]. In this series, experiments 8,1 and 5 belong to ventilation control condition, while other five experiments belong to fuel control condition.

Table 1. air supply rates and initial water content of specimen

Experiment No.*)	Burning type	Air supply per surface area of wall, m_a/A_{fuel} [kg/(m^2·s)]	Initial water content [%-wt.]
8	Ventilation control	0.0067	10.7
1		0.0144	12.5
5		0.0266	12.0
7	Fuel control	0.0410	12.2
6		0.0469	11.4
3		0.0552	13.0
4		0.0668	11.8
2		0.0786	12.3

*) Experiments were numbered in the order of execution but tabulated in the ascending order of air supply rate.

3 EXPERIMENTAL RESULTS

3.1 Burning behaviour

The burning behaviours during cooling period are shown in Figure 5. Up to 60 minutes, furnace gas was fuel rich due to the supplied fuel and generated pyrolysis gas. As the furnace gas was sooty, no observation was possible. After 60 minutes, fuel supply was stopped and only air was supplied to furnace.

In case of small air supply rates (exp. 1), furnace gas was sooty even after stop of heating for a long period. Due to the soot adhered on the observation window, specimen's surface could not be observed but it seemed that smouldering combustion continued. In case of medium air supply rates (exp. 5 and 7), the self-burning was intensified as the air and fuel ratio was close to stoichiometric. Flaming combustion was observed up to 90 (exp. 5) to 80 minutes (exp. 7). After that, glowing combustion continued partially. In case of large air supply rate (Exp. 2), flaming combustion was intense right after the start of cooling. Fallout of char layers was observed. The flaming combustion ceased fairly quick. At 80 minutes, no flaming was observed but glowing combustion continued. In summary, it can be said that flaming combustion is intense in case of large air supply rate, but the duration is short. In contrast, mild combustion continues for a long period in case of small air supply rates.

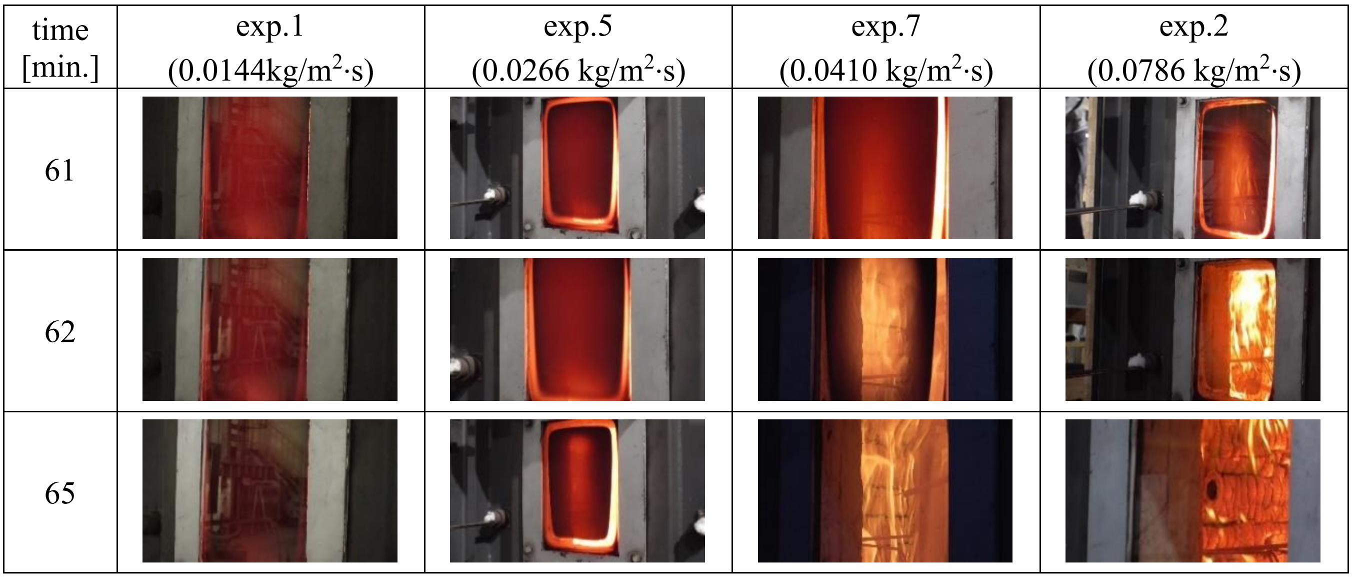

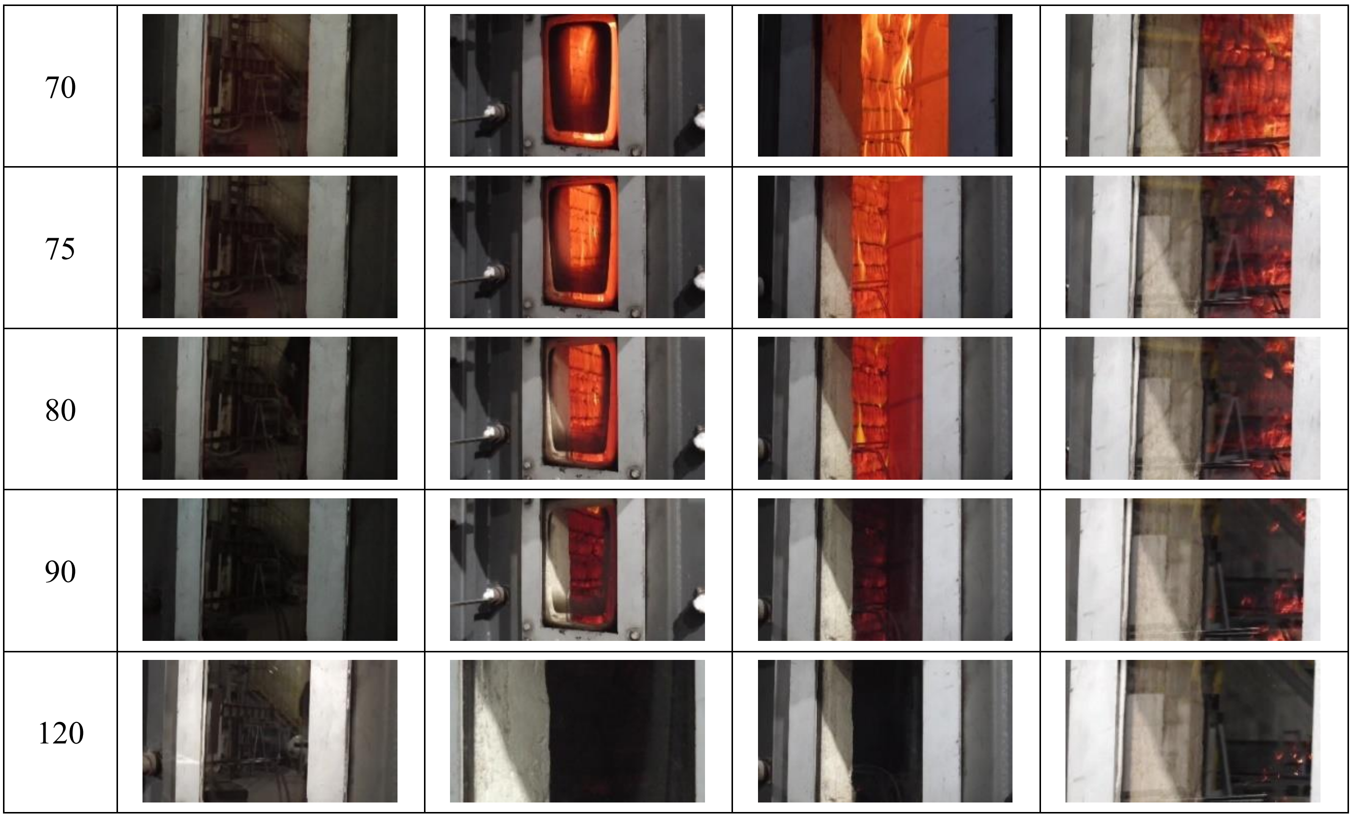

Figure 5. self-burning behaviour during post-heating periods as observed through window

3.2 Furnace temperatures

The furnace temperatures during eight experiments are summarized in Figure 6. As shown in Figure 6a), decrease of furnace temperature was slow in cases of small air supply rates. It seems that large difference exists between ventilation control experiments (exp. 8, 1 and 5) and fuel control experiments. As summarised in Figure 6b), the correlation between air supply rate is somewhat complex. Among all the experiments, the furnace temperature was highest in exp. 1, when air supply rate m_a/A_{fuel} was 0.0144 kg/m^2·s. In case of smallest air supply rate (m_a/A_{fuel} = 0.0067, exp.8), furnace temperature was lower than that in exp.1 because the heat release rate in exp. 8 was small due to lack of oxygen as will be shown in 3.3. In case of fuel control fires, furnace temperature monotonically decreased as the air supply rate was increased.

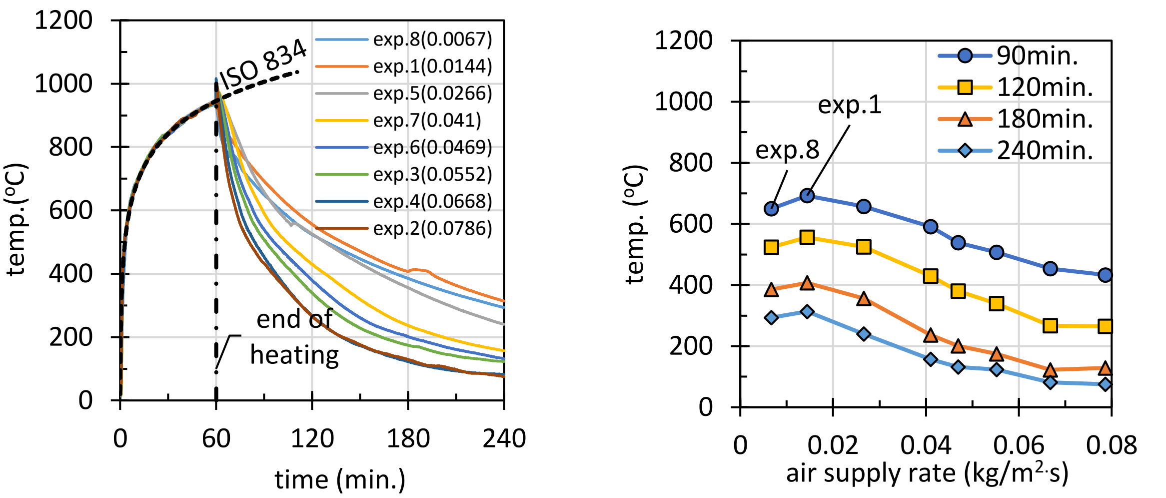

a) Time- temperature plot

b) Air supply rate vs temperatures at specific times

Figure 6. furnace temperatures during heating and cooling period

3.3 Heat release rates during cooling period

Measured oxygen concentrations in the furnace are shown in Figure 7. During the heating, oxygen concentration was almost zero. After heating had stopped, oxygen concentration recovered gradually. However, the recovery is slow in case of small air supply rates. Even at 240 minutes, the oxygen concentration is about 18% in case of exp.1. It implies that some sort of combustion continued.

Using the oxygen consumption method [9], the heat release rate due to self-burning was calculated by

$$Q/A_{\text{fuel}} = 13{,}100\,(X_{O2,f}\text{-}X_{O2,amb})\,m_a/A_{\text{fuel}} \qquad (2)$$

where Q/A_{fuel} is the heat release rate per surface area of wall [kW/m^2]

$X_{O2,f}$ is the mass fraction of oxygen in the furnace [kg/kg]

$X_{O2,amb}$ is the mass fraction of oxygen in the ambient air [kg/kg].

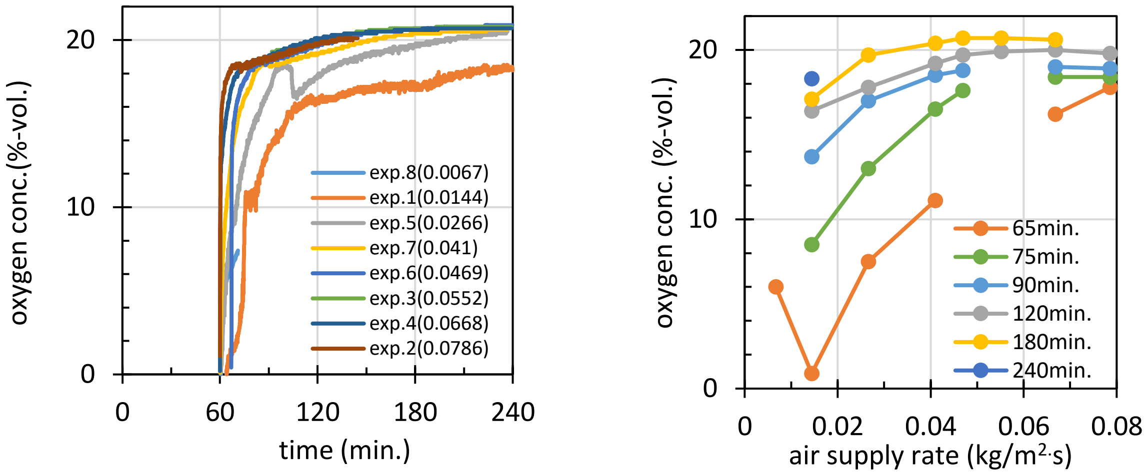

a) Time-oxygen concentration plot

b) Air supply rate vs oxygen concentration at specific times

Figure 7. oxygen concentration of furnace gas during post heating period

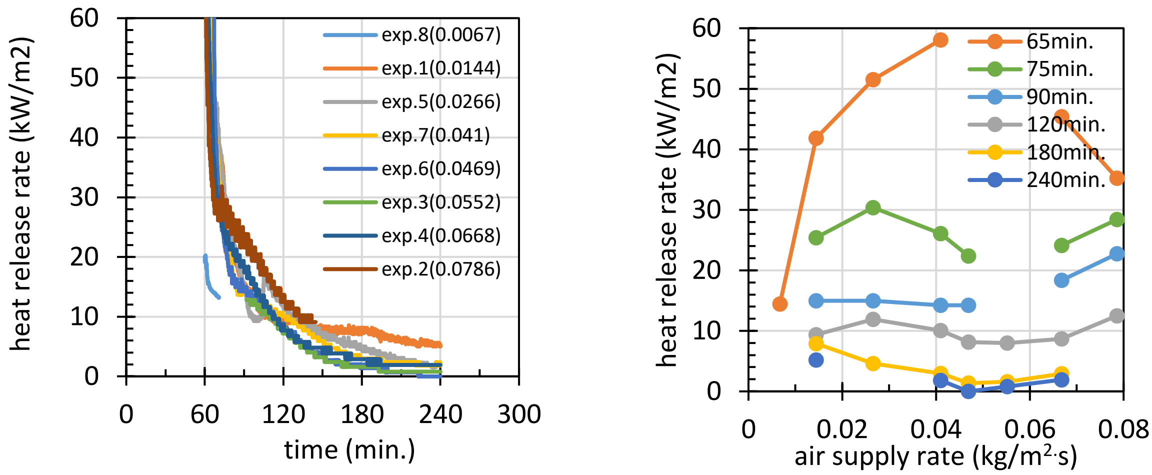

a) Time-heat release rate plot

b) Air supply rate vs heat release rate at specific times

Figure 8. heat release rate from specimen due to self-burning

The results are shown in Figure 8. Large heat release rate values were obtained soon after the stop of heating in all the cases. Maximum value was obtained in case of exp.7, which corresponds with the border of ventilation-control and fuel-control fires. The heat release rate is gradually decreased with time, but the decrease is slow in case of small air supply rate. Due to the slow decrease in furnace temperatures, heat release from self-burning continues for long duration.

3.4 Specimen temperature

The specimen temperatures are shown in Figure 9. At 0mm (exposed surface) the temperature is almost close to furnace temperature. Temperatures are high in cases of the three ventilation-controlled experiments (exp. 8,1 and 5). It should be noted that temperature was increased during 190 to 240 minutes unexpectedly in case of exp. 2. Due to the fallout of surface char layers, virgin wood surface might be exposed, and re-burning took place. Similar tendency appeared in the temperatures at 20mm from exposed surface. The effect of re-burning in case of exp.2 can be identified. At 40mm, the effect of another self-burning is seen in case of exp.2. Unexpected temperature rise at 180 minutes might correspond with self-burning at around 40mm. At 60 and 80mm, the differences between experiments were small. The effect of self-burning did not arrive to those positions.

Consulting the relationships to air supply rates, it can be seen that the specimen temperatures are high in case of small air supply rates. Temperatures are relatively low in case of large air supply rate. However, the temperature is unexpectedly increased at the maximum air supply rate, which is caused by re-burning following the dropping of char layers.

<table>
<tr><th>position</th><th>Time-temperature plot</th><th>Air supply rate vs temp. at specific time</th></tr>
<tr><td>0
(exposed surface)</td><td>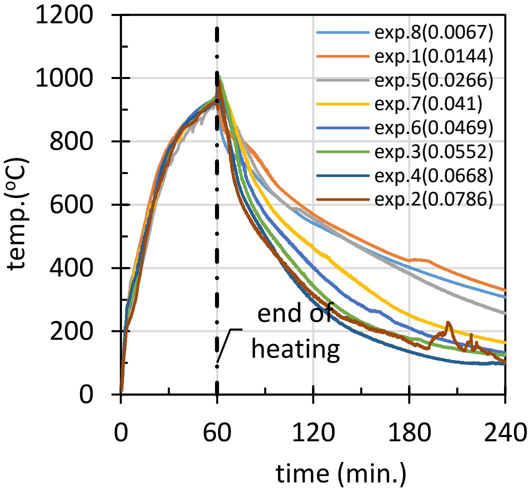
</td><td>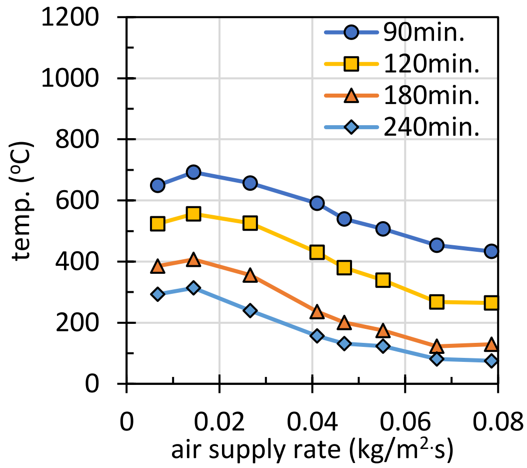
</td></tr>
<tr><td>20mm</td><td>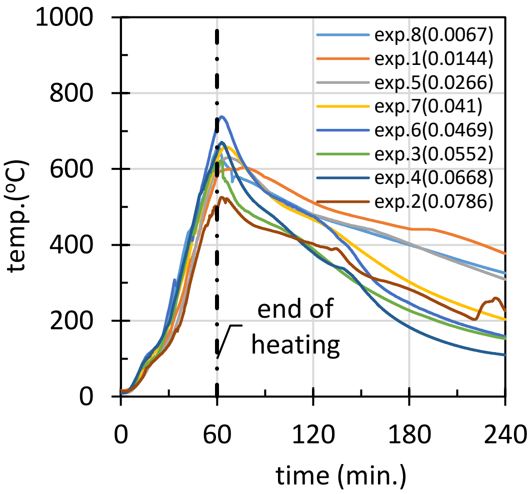
</td><td>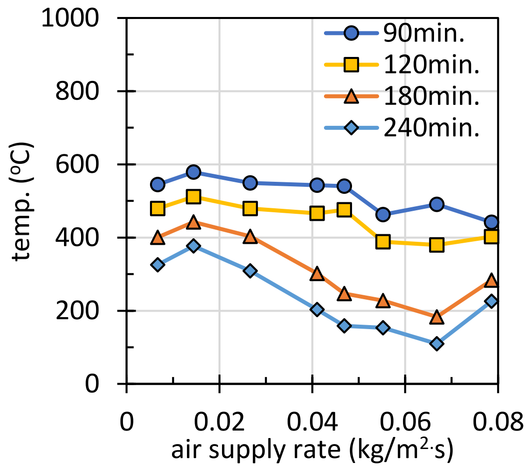
</td></tr>
</table>

Figure 9. temperature histories at internal points (continue to next page)

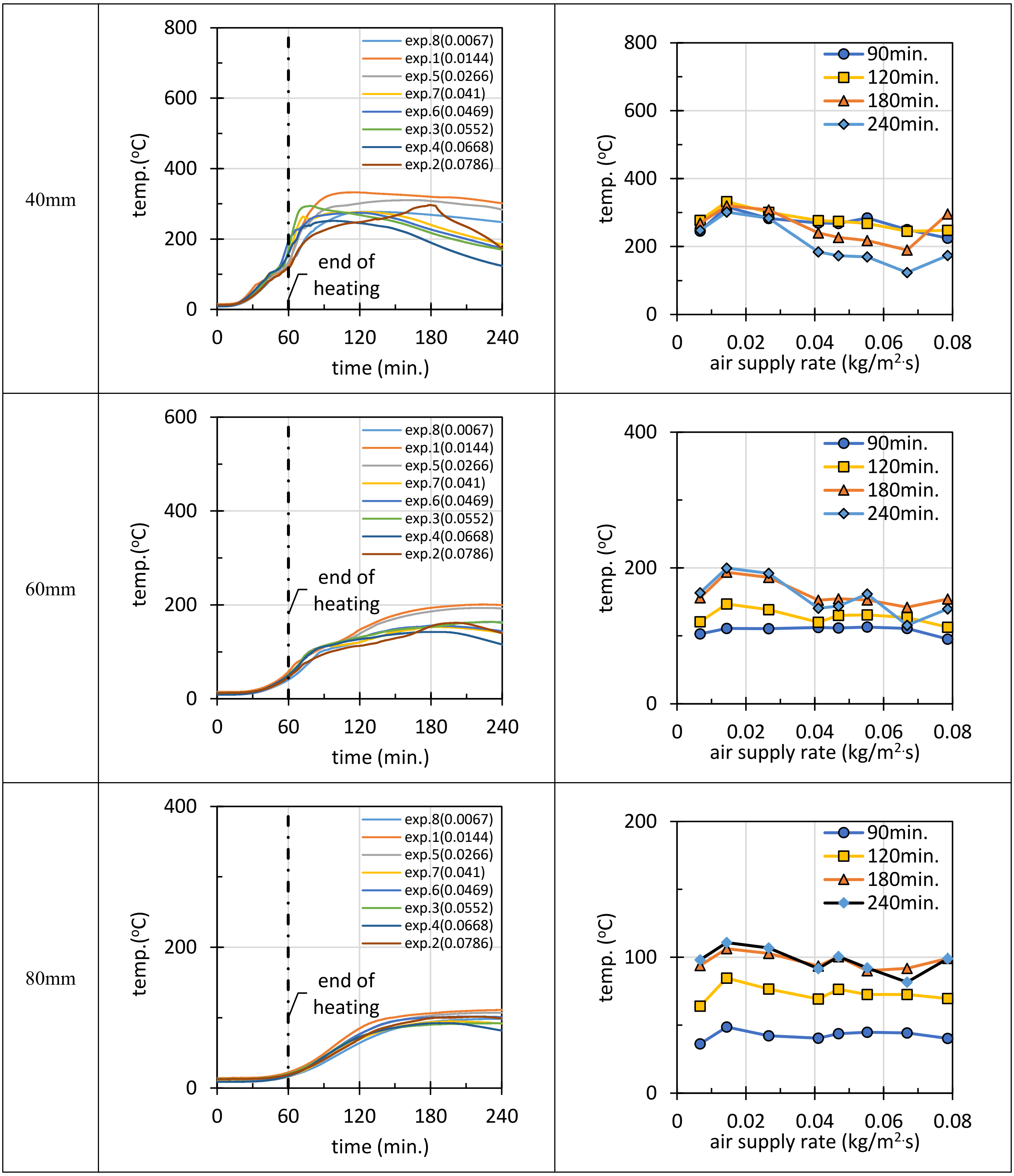

Figure 9. temperature histories at internal points (continued)

3.5 Water content

The measured water content values are shown in Figure 10. At 40mm, water content values rose due to the condensation of water vapor generated and transferred from the zone of exposed surface. There is no meaningful difference, but scatter of measurement errors dominates as the major changes are within the heating period. At 60 and 80mm, water content values tend to increase in cases of small air supply rates. As the specimen temperatures in the zone of exposed surface is high, large amount of water vapor has generated and transferred to the direction of unexposed surface.

<table>
<tr><th>position</th><th>Time-water content plot</th><th>Air supply rate vs water content at specific time</th></tr>
<tr><td>40mm</td><td>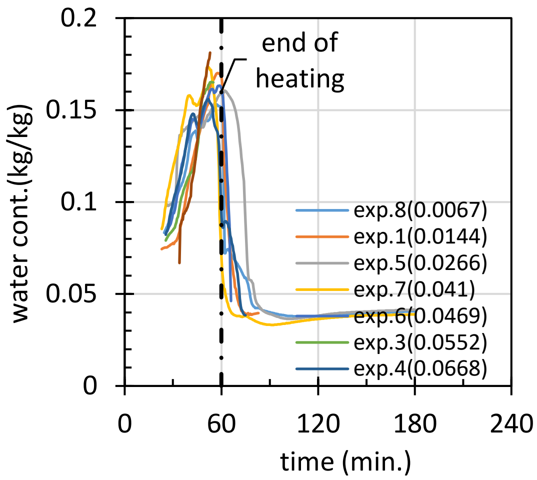
</td><td>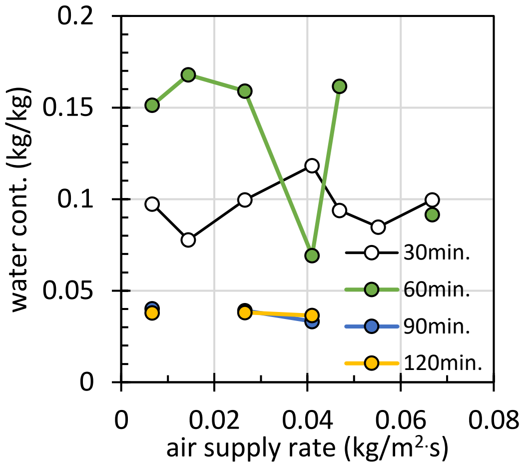
</td></tr>
<tr><td>60mm</td><td>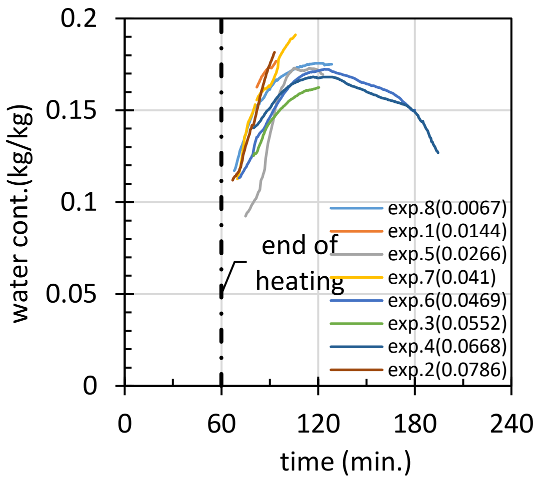
</td><td>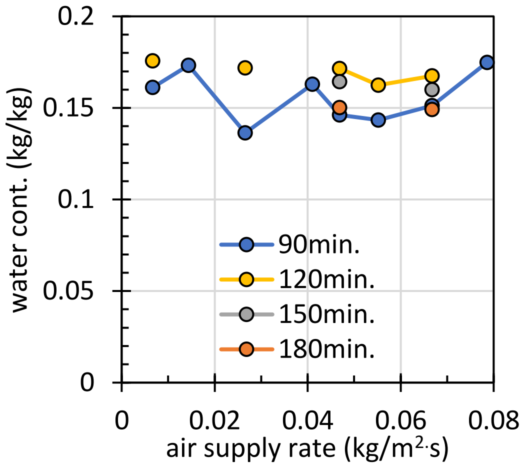
</td></tr>
<tr><td>80mm</td><td>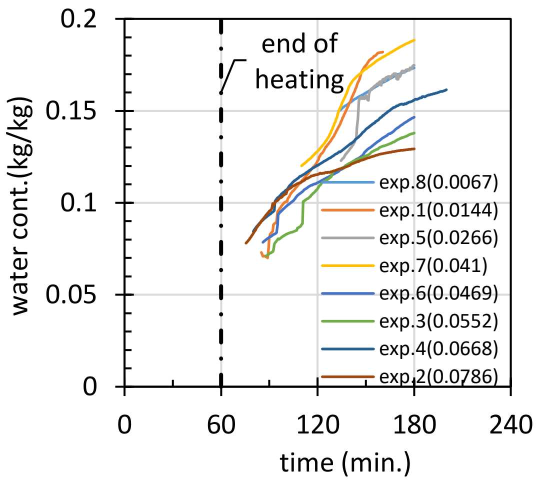
</td><td>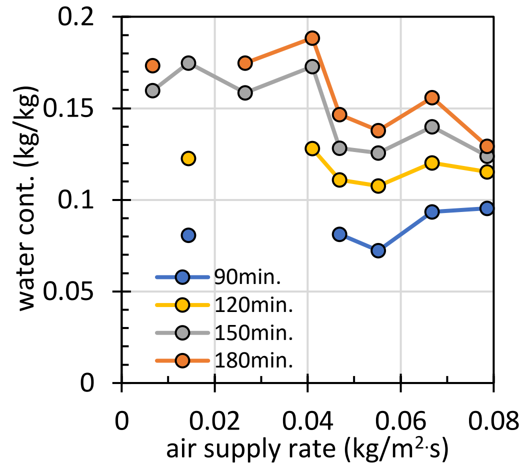
</td></tr>
</table>

Figure 10. water content histories at internal points

3.6 Post cooling state

The photographs of exposed surface after 240 minutes (three hours of cooling) and cut sections are shown in Figure 11. In cases of small air supply rates (exp. 8,1 and 5), surface damage seemed to be minor, because the self-burning was mild, and fallout of char layer was not significant. However, the charred layer was deep in these experiments. As indicated by circles, small glowing combustion still remained even at 240 minutes.

In case of large air supply rates, the damage of surface char layer is obvious. Especially in exp.2, large portion of surface char layer had dropped. However, the charred depth was relatively shallow in comparison with those in small air supply rates. No glowing combustion was observed in exp.4 and 2.

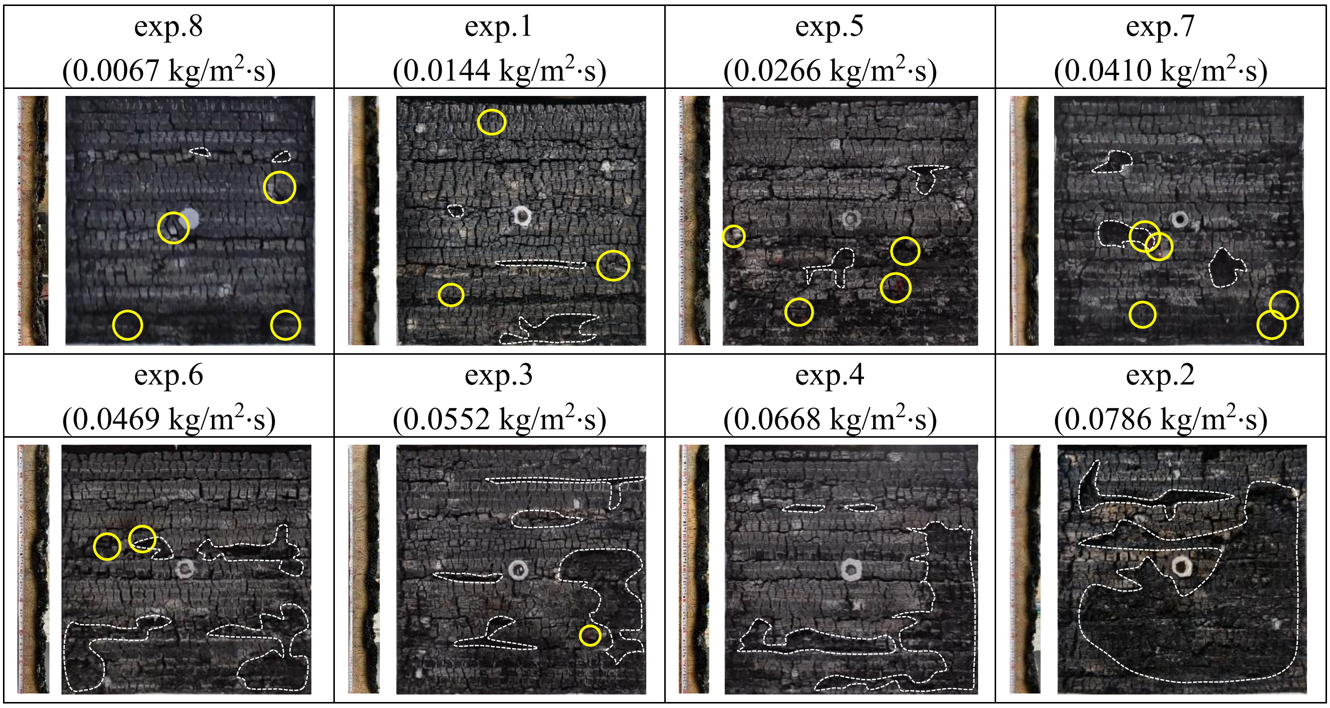

Figure 11. Post cooling surface conditions and residual sections (dashed line: region of dropped char, solid circle: glowing)

3.7 Burnt-out, charred and coloured depth

The burnt-out, charred and coloured depth of the specimens at the cut sections are summarised in Figure 12. As the air supply rate was decreased, the charred and coloured depths were increased. This is because of the slow decrease of furnace temperature as shown in Figure 6a). On the contrary, the burnt-out depth is largest in case of large air supply rate. This is because of intense self-burning during cooling period.

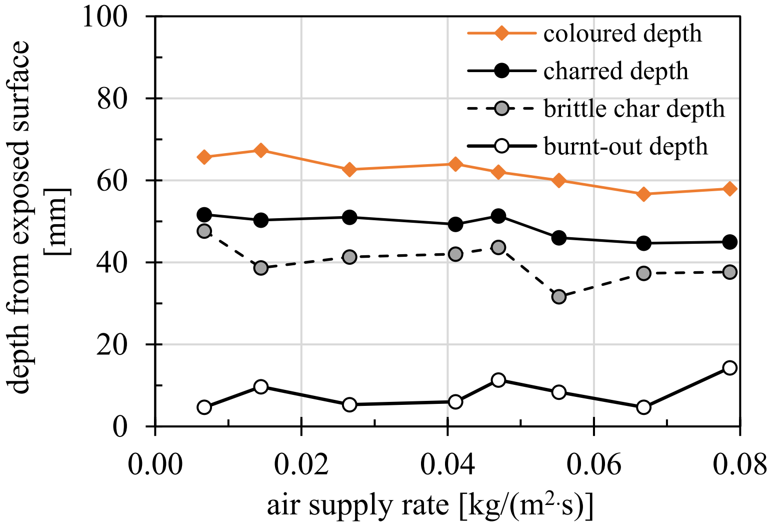

Figure 12. summary of burnt-out, charred and coloured depth

4 CONCLUSIONS

Fire resistance tests were conducted on GLT larch wood wall to investigate the effect of air supply rate on the self-burning behaviour and damage to wood specimens. Main findings are as follows:

1) In case of large air supply rate during cooling, surface damage of specimen is intensified due to the intense self-burning and fallout of char layers. As the furnace temperature decreases rapidly, charred depth and coloured depth are relatively small.
2) In case of small air supply rate during cooling, self-burning continues mildly for a long period. As the decrease of furnace temperature is slow, charred depth and coloured depth are increased.
3) In case of very small air supply rate, self-burning is reduced due to the lack of oxygen. As a result, furnace temperature is slightly decreased.

ACKNOWLEDGMENT

This work was financially supported by JSPS KAKENHI (Grant-in-Aid for Scientific Research (B), Grant Number 21H01490). The fire resistance tests were carried out at General Building Research Corporation of Japan (GBRC). The technical supports by Mr. Komiya, Mr Azuma and all the staff in correspondence are highly appreciated.

REFERENCES

1. Article 27, The building standards law of Japan
2. International Organization for Standardization, ISO 834, Fire-resistance tests — Elements of building construction
3. König J., Effective thermal actions and thermal properties of timber members in natural fires, Fire and Materials, 30, pp. 51–63, 2006
4. Schmid J., Lange D., Sjöström J., Brandon D., Klippel M., Frangi A., the Use of Furnace Tests to Describe Real Fires of Timber Structures, proc. SiF 2018, pp.241-248
5. Schmid J., Totaro A., Frangi A., the Behaviour of Timber in Fire Including the Decay Phase - Charring Rates, Char Recession and Smouldering, proc. SiF 2020, pp.842-851
6. Hirashima T., Katakura Y., Ichikawa M., Ishii S., Influence of Gas Temperature during Cooling Phase on Load-Bearing Period of Structural Glued Laminated Timber Beams Exposed to Fire, proc. SiF 2018, pp.291-298
7. Harada K., Makino S., Sun A. and Nii D., A study on the relationships between burning behavior of wood and air supply rate, Architectural Inst. of Japan, Kinki branch, Research reports, vol. 62, pp. 89-100, 2022
8. Ohmiya, Y., Sato, M., Tanaka, T., Wakamatsu, T., Incident heat flux to fuel and burning rate in ventilation controlled fires, Transactions of AIJ, No. 472, pp.169-176, 1995 (in Japanese)
9. Hugget C., Estimation of rate of heat release by means of oxygen consumption measurements, Fire and Materials, vol. 4, pp. 61-65, 1980

EXPERIMENTAL RESEARCH ABOUT MOISTURE TRANSFER, BURNING BEHAVIOUR AND CHARRING BEHAVIOUR OF GLUE LAMINATED LARCH UNDER FIRE HEATING USING CONE CALORIMETER

Anyang Sun[1], Kazunori Harada[2], Daisaku nii[3]

ABSTRACT

Cone calorimeter tests were conducted to investigate the moisture transfer, burning behaviour and charring behaviour of timber material under fire heating. 100 x 100 x 50mm glue laminated larch specimens were made in cross grain and straight grain directions. The initial surface moisture contents were 15.1 wt. % (cross grain specimens) and 13.5 wt.% (straight grain specimens). Twenty specimens were heated at 50kW/m^2 of irradiance. The heating duration was varied between 10 to 50 minutes. Internal temperature, surface temperature, heat release rate, and water content were measured during heating. Charred depth, coloured depth and burnt-out depth was measured after cooling. Heat release rate was measured by oxygen consumption method. Temperature was measured by an IR camera and type K thermocouples. Moisture content was measured by electrical resistance method. Charring temperature and colouring temperature were estimated by using the measured charred or coloured depth data and temperature histories. Burnt-out depth, charred depth and coloured depth was slightly larger in case of straight grain specimens than that in cross grain specimens. Heat release rates were almost constant after reaching the first peak values. Steady state values were slightly larger in straight grain specimens. Temperature creep was observed in each location at about 100°C, according to phase change of water. Maximum internal temperature of each specimen at each location increased while heating duration increased. Peak value of moisture content varied by each specimen, but the temperatures corresponding with peak moisture content were almost the same, i.e., around 100 to 120ºC. Moving speed of moisture peak is about 1.30mm/min. Temperatures of charring front and colouring front were about 380 and 260°C, respectively.

Keywords: Cone calorimeter; Radiant heating; Moisture content; Heat release rate; Charring temperature, Glue Laminated Larch

1 INTRODUCTION

As the wood is a sustainable and environmentally friendly material, it has been widely used in construction in many countries. However, wood will be decomposed into char and combustible gas by pyrolysis when exposed to high temperatures. The progress of pyrolysis of timber material will result in failure of structure. In addition, once the pyrolysis gas will be ignited, heat generated by the combustion of pyrolysis gas will cause further pyrolysis, making the reaction self-sustaining. Special attentions must be paid to flammability when using timber elements to buildings.

[1] Ph.D. Student, Department of Architecture and Architectural Engineering, Graduate school of Engineering, Kyoto University.
e-mail: sun.anyang.78r@st.kyoto-u.ac.jp, ORCID: https://orcid.org/0000-0003-0456-8835
[2] Professor, Department of Architecture and Architectural Engineering, Graduate school of Engineering, Kyoto University.
e-mail: harada@archi.kyoto-u.ac.jp, ORCID: https://orcid.org/0000-0001-8270-1692
[3] Assisiant Professor, Department of Architecture and Architectural Engineering, Graduate school of Engineering, Kyoto University.
e-mail: nii@archi.kyoto-u.ac.jp, ORCID: https://orcid.org/0000-0002-5821-7494
https://doi.org/10.6084/m9.figshare.22193740

Many researches about fire safety of timber materials were reported in the past. Terrei *et al*. [1] conducted a heating experiment using cone calorimeter to investigate the critical heat flux of ignition of spruce wood. They have found that ignition only occurs when heating intensity is above 45kW/m^2. For lower heat flux, ignition is not observed but smouldering combustion takes place. Li *et al.*[2] used medium density fibreboard as specimen and found that the mass loss rate of the sample is linear to heating intensity. Chatani *et al.*[3] studied the rate of char oxidation during glowing combustion. They found that the critical heating intensity for continuation of char oxidation is above 8.4kW/m^2. The corresponding surface temperature was 286°C. As to large scale tests, for example, Niwa *et al.*[4] conducted large scale furnace tests of laminated veneer lumber (LVL) columns and beams under ISO834 heating. Lennon *et al.* [5] conducted large scale fire tests to investigate the burning behaviour of various timber floor system, using a compartment with internal dimension of 4m x 3m. Suzuki *et al.*[6] conducted loaded and unloaded large-scale fire resistant test for timber panels and walls to investigate the burning behaviour of timber panel, and to develop a simple method for estimating the fire resistance of timber panels. Xu *et al.*[7] investigated the fire resistance of timber floor assemblies exposed to ISO 834 standard fire heating protected by different fire protection. However, although so many researches were conducted to investigate the fire safety about timber materials, there are still some topics needed to be investigated.

First topic is about moisture transfer inside timber material under fire heating. Most of the experimental research have focused on the heat transfer process (temperature, HRR, etc.). However, the moisture transfer process, should also be considered. Although there are also some research conducted, (like [8] by Kimura *et.al*) experimental research on measuring moisture contents change over time is rare. One of the reasons for investigating moisture transfer inside timber material is that moisture content influences many kinds of physical properties, like mechanical properties. A literature review by Gerhards[9] shows that the shear modulus decreases by 20% while bending strength decreases 25% when moisture context increases from 12% to 20%. Similar results were also found by other researchers [10] [11]. For moisture contents inside timber element, internal liquid moisture transfer occurs by temperature gradient, moisture content gradient and pressure gradient[12][13]. Moisture content will change with time and position due to phase change of water. Non-uniform moisture distribution will be developed inside timber material under fire heating. This leads to difference of physical properties in different location, which complicates the behaviour of timber elements in fire.

The second topic is about charring temperature. Since wood and char have different thermal properties, it is important to identify the temperature that wood pyrolyzed into char while conducting numerical simulation of timber material under fire heating. Also, calculation results of charring depth can be derived by using calculated temperature history and charring depth, which broaden the applicable range of calculation results. However, the charring temperature of wood is unclear. According to a review by Frangi *et.al*[14], temperature of charring front measured by different researchers varies in a range of 253℃~360℃, which is too wide to use in simulation. A precise charring temperature is needed.

The target of this research is to analyse the moisture transfer, burning factor and charring behaviour of glue laminated larch under fire heating. For that purpose, cone calorimeter was used to heat timber specimen with high intensity for 10 to 50 minutes. Heat release rate from surface, internal temperature, moisture content, charred depth, burnt-out depth and coloured depth were measured.

The authors would like to mention that earlier version of this work have been presented on the annual symposium of Japan Association for Fire Science and Engineering(JAFSE)[15] and the annual symposium of Architectural Institute of Japan(AIJ)[16]. This paper includes more details about the experiment, comprehensive results and discussion.

2 MATERIALS AND METHODS

2.1 Experimental setup

The experiments were conducted using a cone calorimeter. **Figure 1** shows the experimental setup. Each specimen was exposed to radiation with intensity of 50kW/m^2 for 10 to 50 minutes. A spark igniter was placed between the specimen and the cone heater to ignite the combustible mixed gas generated by pyrolysis of the specimen. The spark igniter was removed after the combustible gas was ignited. Heat release rate was measured by oxygen consumption method. After the heating period, specimen was placed on ceramic fibre wool for cooling down in room temperature.

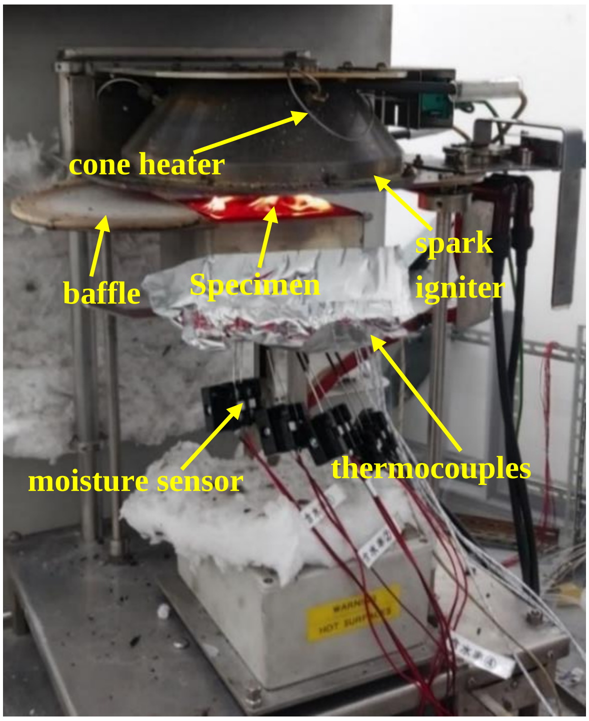

Figure 1: Experimental setup

2.2 Specimens

Specimens used in this work were laminated larch wood with 100 x 100mm in size and 50mm thickness. 20 specimens were used in experiments, 10 of cross grains specimens and 10 of straight grain specimens. Laminar thickness was about 25mm. Experiments was named in the format of "Specimen type-heating time-experiment number". For example, C-10-1 means the cross-grain specimen (C) for 10 minutes heating, first run. **Figure 2** illustrates examples of straight grain and cross grain specimens used in this experiment. The cross grains specimens were created so that the cross-grain surface is heated from top. Straight grain specimens were created so that the cutting edge is heated from top. Red arrow in **Figure 2** represents the direction of heating. In creating straight grain specimens, it was difficult to unify the direction of annual ring, thus the cross and straight grain laminas were partially mixed.

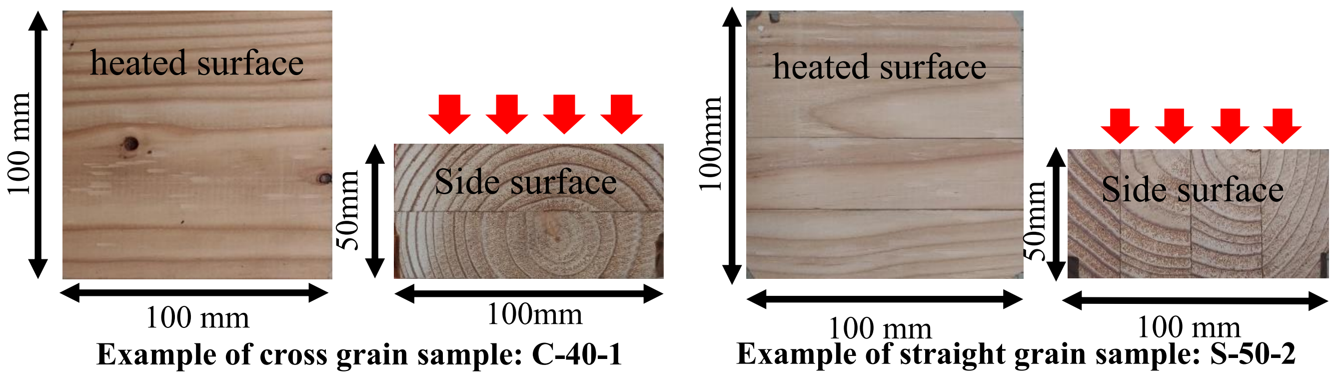

Figure 2: photographs of specimens

Side surfaces of the specimen were wrapped by aluminium foil tape to reduce the inflow of oxygen. Note that aluminium foil tape was broken in experiments C-40-2 and C-50-1. These experiments were thought to be in failure and an additional experiment C-40-3 was conducted. Summary of experimental conditions is shown in Table 1.

Table 1 Summary of experimental conditions

Type/Time	10min	20min	30min	40min	50min
Cross grain(C)	C-10-1 C-10-2	C-20-1 C-20-2	C-30-1 C-30-2	C-40-1 C-40-2 C-40-3	C-50-1
Straight grain(S)	S-10-1 S-10-2	S-20-1 S-20-2	S-30-1 S-30-2	S-40-1 S-40-2	S-50-1 S-50-2

Specimens were cured in a room with constant temperature (23°C) and relative humidity (50%) for one month. Density of specimens was measured via specimens created with same condition. Air dry density of cross grain specimens (C) are 565±16.8 (average value ± unbiased standard deviation) kg/m^3, while density of straight grain specimens(S) is 531±18.3 kg/m^3. Initial moisture contents of each specimen were measured by non-destructive high frequency wood moisture meter. Initial moisture contents (air dry) of cross grain specimens(C) are 15.1±1.6wt.%. For straight grain specimens (S), the initial moisture contents are 13.5±2.7wt.%.

2.3 Measurement of temperature and moisture contents

It is desirable to measure the moisture content inside timber material continuously and non-destructively during heating. Many non-destructive moisture contents measurement technique was developed in the past, including the NMR technique, γ-ray attenuation technique, electrical resistance method, etc[17][18]. Special equipment is needed to use contactless measurement method by NMR technique or by γ-ray technique [18], which is difficult to apply to high temperature conditions. Therefore, moisture content was measured based on electrical resistance method in this work.

The arrangement of sensors on specimen is shown in **Figure 3**. Type K thermocouples were placed at 10 to 50mm at every 10mm from heated surface. The temperature was measured at every 10 seconds. Surface temperature of specimen was measured by an infrared camera at every second.

Moisture content inside wood was measured by electrical resistance method. Pairs of stainless-steel electrodes were inserted inside specimen with 5mm interval and 10mm length. The electrical resistance between electrodes was measured by insulation resistance testers (Kyoritsu KEW 3551, 0.01 MΩ – 4,199 MΩ) and/or by a data logger (Eto Denki, CADAC-3, 0 - 99MΩ). The electrodes were set at 10 - 40mm from heating surface at every 10mm. Electrical resistance was measured at every 30 seconds. In each measurement, resistance data was recorded after 5 seconds since the start of measurement to ensure the stability of data.

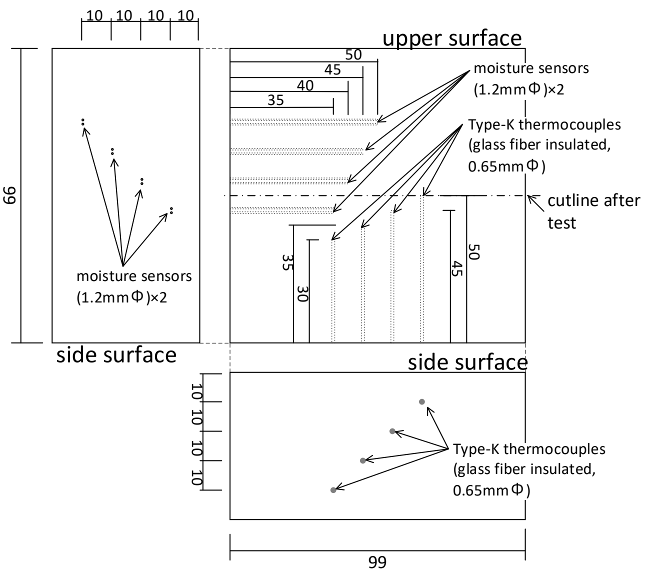

Figure 3: arrangement of sensors

According to Vermaas[19], the logarithm of moisture contents W and electrical resistance r is in a linear relation. Measurement data by James[20] were used to obtain a formula between moisture contents and electrical resistance, by using the relation of W and r mentioned above. The formula was then calibrated since interval and length of electrodes in James'[20] experiment were different from electrodes in this experiment, by considering current flows only perpendicular to electrodes. Temperature dependency of electrical resistance was also considered, following the fact that specific volume conductivity (reciprocal of resistance) changes with temperature following Arrhenius type exponential function[21], by using activation energy data at 24% moisture contents summarised by Vermaas[22]. Calibrated formula between electrical resistance r[MΩ] and moisture contents W[kg/kg] can be written in the following form:

$$W = \left(\frac{2.0\,r}{3.0 \times 10^{-6}\,exp(E/RT)}\right)^{-0.115} \tag{1}$$

Where E is activation energy [$4.33*10^4$J/mol], R is ideal gas constant [8.314J/(K*mol)], T is absolute temperature[K]. E/R is equal to about 5207.

3 RESULTS AND DISCUSSION

3.1 Specimen after heating

After heating, specimens were cut vertically in the direction of fibre. **Figure 4** shows the vertically cut sections. Charring depth increased with heating time increase gradually. At sample C-40-2 and C-50-1, oxygen inflow from side and burning combustion occurred at side face, so charring also happens at side. 3~4 deep cracks were observed in all samples, with the crack interval at different samples are similar. Crack depth is almost equal to charring depth.

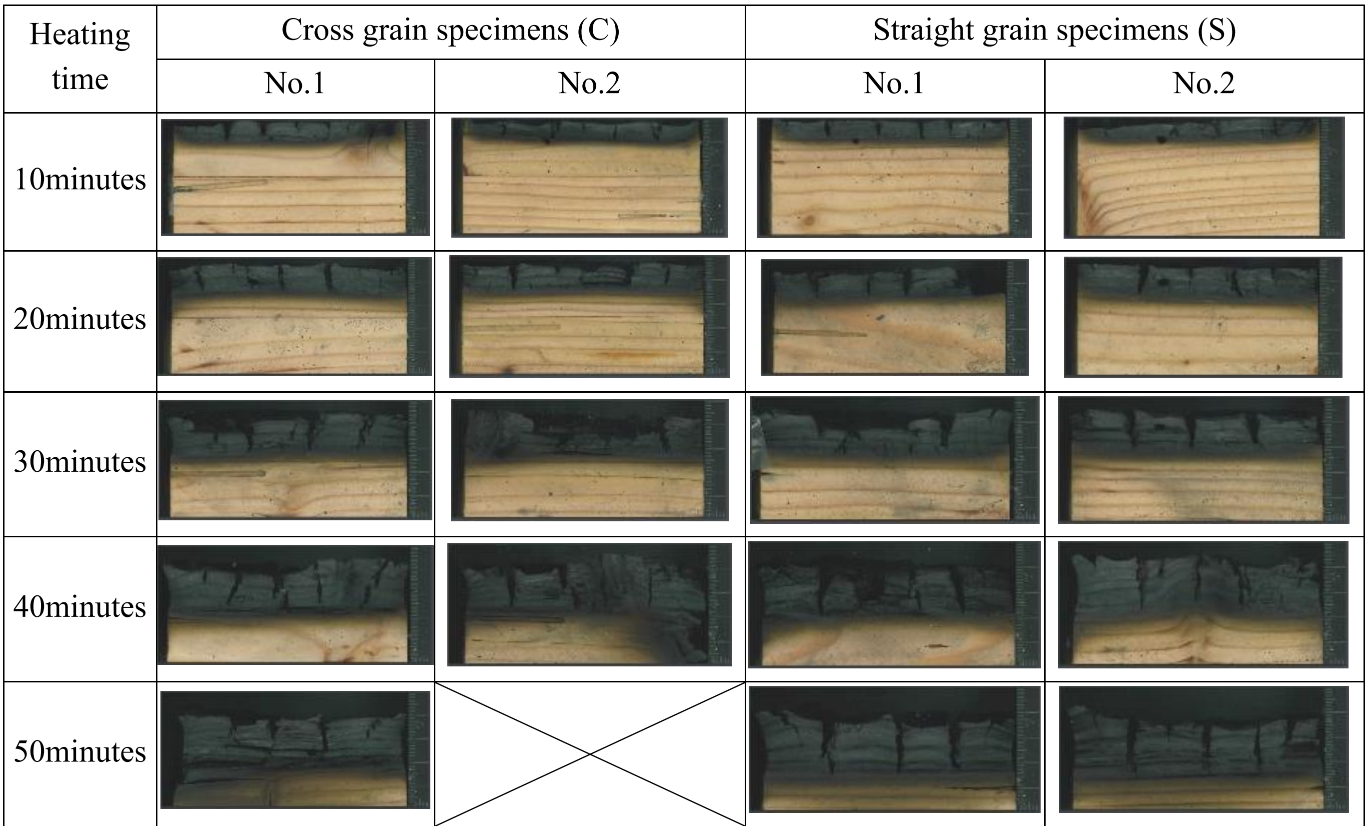

Figure 4: Image of specimen after heating

Coloured depth, charred depth, brittle charred depth and burnt-out depth was measured by tape measurements (1 mm accuracy). Measurement was conducted twice at different location for each specimen. Measured data were presented in **Figure 5**. The charred depth at 50min of heating was about 33mm for cross grain and 36mm for straight grain. The charring rate was about 0.72~0.76mm/min, which is similar to the results obtained in previous large-scale tests[6]. Coloured depth was about 12 mm when heating

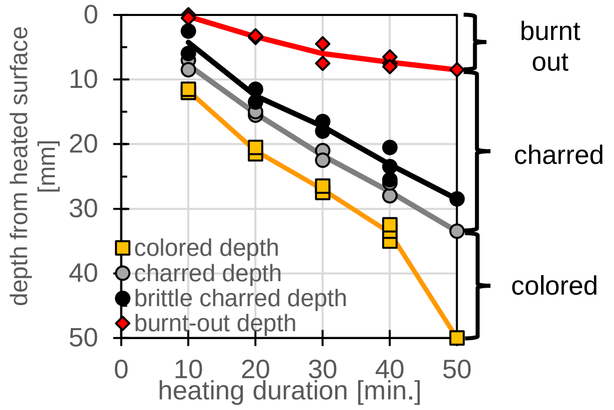

(a) Cross grain specimen

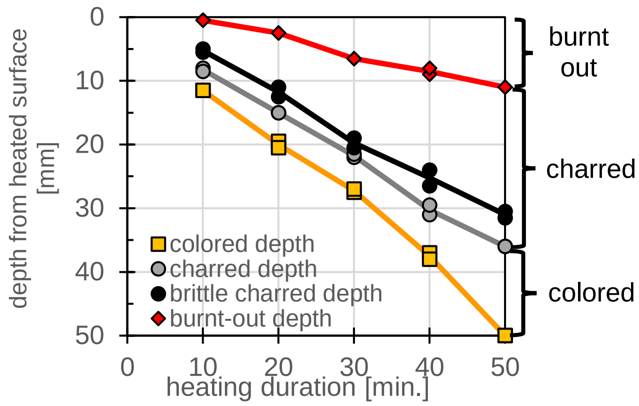

(b) Straight grain specimen

Figure 5: Coloured depth, charring depth and burned depth from heating surface

duration was 10 minutes, while the colour was completely changed in case of 50 minutes heating. Colouring rate was about 0.98~1.00 mm/min. Burnt-out depth was about 1/3~1/4 of charred depth. Charred depth, brittle charred depth and burnt-out depth changed almost linearly with heating duration in both specimens. In comparison, the coloured depth, charred depth and burnt-out depth is slightly larger in straight grain samples.

3.2 Ignition time, ignition temperature and heat release rate

Surface temperature measured by infrared camera at 0~60 seconds were presented in **Figure 6**. Ignition time and ignition temperature were identified based on the occurrence of sharp temperature rise. The average ignition time of cross grain specimens(C) is 23.9±6.0s (average value ± unbiased standard deviation) and 360±13.9°C, respectively. For straight grain specimens, the result is 15.7±3.8s and 340±31.3°C, respectively. The average value of ignition time and ignition temperature for cross grain specimens are higher than straight grain specimens. This is because of the difference of thermal inertia of wood in different direction.

Measured heat release rate is shown in **Figure 7**. The heat release rate of all the experiments increased rapidly after ignition. After reached a peak value of about 150kW/m^2, heat release rate decreased to about 50kW/m^2 within 5 minutes and kept constant afterwards. Heat release rate at steady states in all the experiments are similar but heat release rates in cross grain specimens are slightly larger than straight grain specimens. In the experiments C-40-2 and C-50-1, heat release rate increased after reaching the steady period. This was caused by the failure of aluminium foil insulation on the side surfaces. Fresh air might have entered the specimen from the side surface and initiated the burning from the rear side.

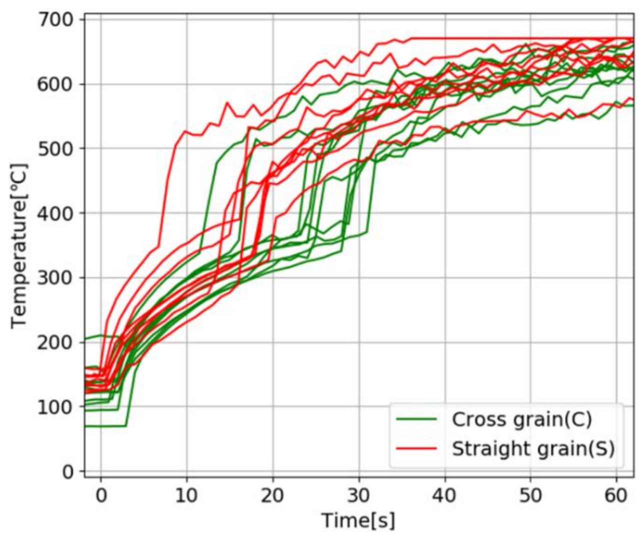

Figure 6: Surface temperature

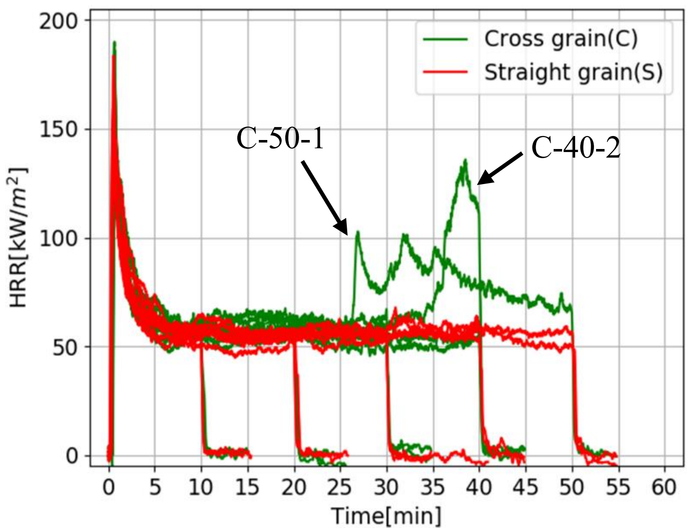

Figure 7: Heat release rate Graphs

3.3 Internal temperature

Figure 8 shows the internal temperature measured by the thermocouples. Solid lines mean data measured in the first run and dashed lines mean data measured in the second run. In case of experiments C-40, the second run was in failure. Thus, the dashed line represents the result in the third experiment C-40-3.

Heating Time **cross grain specimens (C)** **Straight grain specimens (S)**

10min

20min

30min

40min

50min

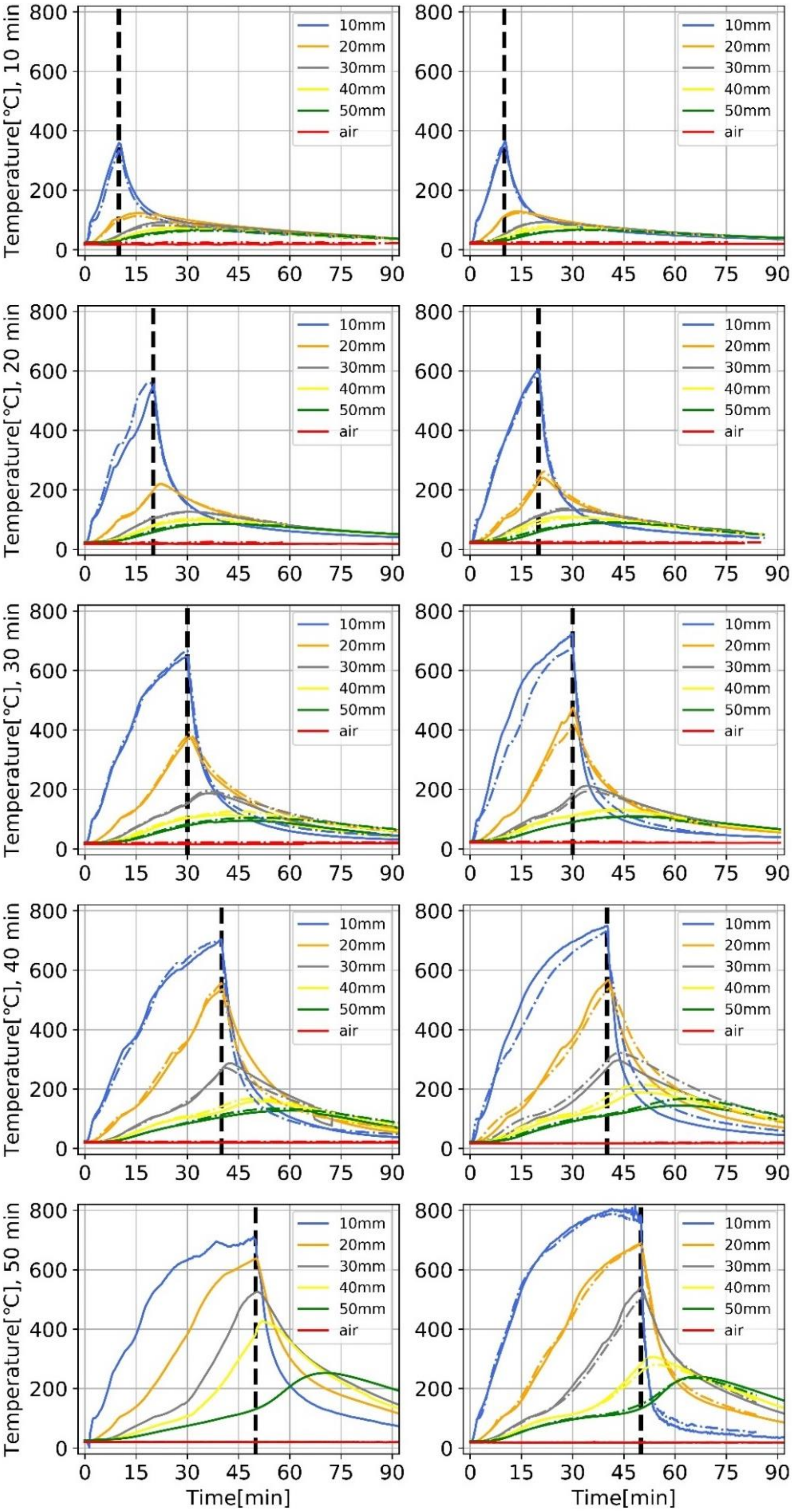

Figure 8 internal temperature measured by thermocouple on each condition

Temperature creep was observed at each location at about 100°C at almost all of the locations in all experiments. This is caused by the heat generation by adsorption of water vapor first, then followed by desorption of water. The period of temperature creep also increased while distance from heating surface increased. Since the creep period approximately represent the time of water evaporation, increase of creep period was thought according to following reasons. One reason is because of the difference on inflow heat flux. Locations near the heated surface receive larger heat flow than locations inside. Secondary, according to moisture transfer inside wood conduit driven by pressure gradient, moisture gradient and temperature gradient, moisture content inside was higher than that at heated surface. Lower heat flux and high moisture content finally leads to increase on time of evaporation of water inside.

Wood pyrolysis is also an endothermic process. However, the temperature creep did not exist near the pyrolysis temperature (about 250°C). The reason why this phenomenon occurs is that pyrolysis gas combustion happens after the gas was released from surface. The combustion of pyrolysis gas is an exothermic process with large heat of reaction, and the sum of reaction heat of wood pyrolysis and gas combustion is positive.

Temperature at locations near heating surface started to decrease quickly after heating period ends. For location near rear surface, temperatures were still rising after heating stopped since the temperature lower than temperature of heating surface, which means total heat inflow is still positive. Temperature at each location converge to a close value at about 50~60 minutes after heating stopped, besides temperature at 10mm location (or 20mm location in experiment with 40min or 50min heating time). This is because of the shrinkage and crack formation on charring layer. Thermocouples installed on these locations contacted with air due to shrinkage and crack formation in char layer, which leads to convective heat exchange during cooling period.

Internal temperature of straight grain specimens is slightly higher than cross grain specimens. Although difference of thermal conductivity at tangential direction and radial direction of wood is very small and had been neglected in past researches[23][24], combustion is easier to occur in the directions tangential to annual rings according to the difference of local density, which will corresponds with low thermal inertia.

3.4 Moisture contents

Measured moisture contents are shown in **Figure 9** as functions of temperatures. Only results measured by insulation resistance testers were properly measured and shown here. Moisture contents start to increase at about 60 - 80°C. After reaching the peak value at about 100-120°C, moisture content starts to decrease. Although moisture contents differed by specimens, local temperature at the peak value of moisture content is almost the same, e.g., 100 - 120°C. This temperature is thought to be the boiling point of liquid water in wood. Almost all the experiments followed this tendency, except at 20mm location in S-40-1. Moisture content at this location showed unrealistic increased at about 40°C. This is thought to be caused by the malfunction of moisture sensor.

Results of moisture contents showed strong temperature dependence. Besides the peak period, moisture content decreased continuously at temperatures below about 60~80°C. This is thought to be resulted from the formula (1) used to express temperature dependency of resistance of wood. However, it is reported that the activation energy could depend on temperature and moisture contents[25]. Temperature and water content dependence of coefficient might be needed to improve the precision of calibration function. Times at peak of moisture content at each location (besides S-40-1, at 20mm) are shown in **Figure 10**. The average times to peak moisture content were about 3 minute (10mm), 9.8 minute (20mm), 18.6minute (30mm) and 25.3 minutes (40mm) at the measuring points, and the average moisture peak moving speed is about 1.30 mm/min, according to the slope of regression line in **Figure 10**. Although the peak values shown in **Figure 9** varies by experiments and locations considerably, time to peak moisture content has a fairly small scatter. Relation between time to peak water content and depth from heated surface is linear.

It is worthy to note that regression line in **Figure 10** did not pass (0,0), which means peak moving speed at 0~10mm is different to other locations. Combustion of wood and pyrolysis gas at the initial stage after heating leads to rapid temperature increase, which also influenced moisture transfer. This leads to the phenomena that peak moving rate of moisture content at first 10mm is higher than those in other locations.

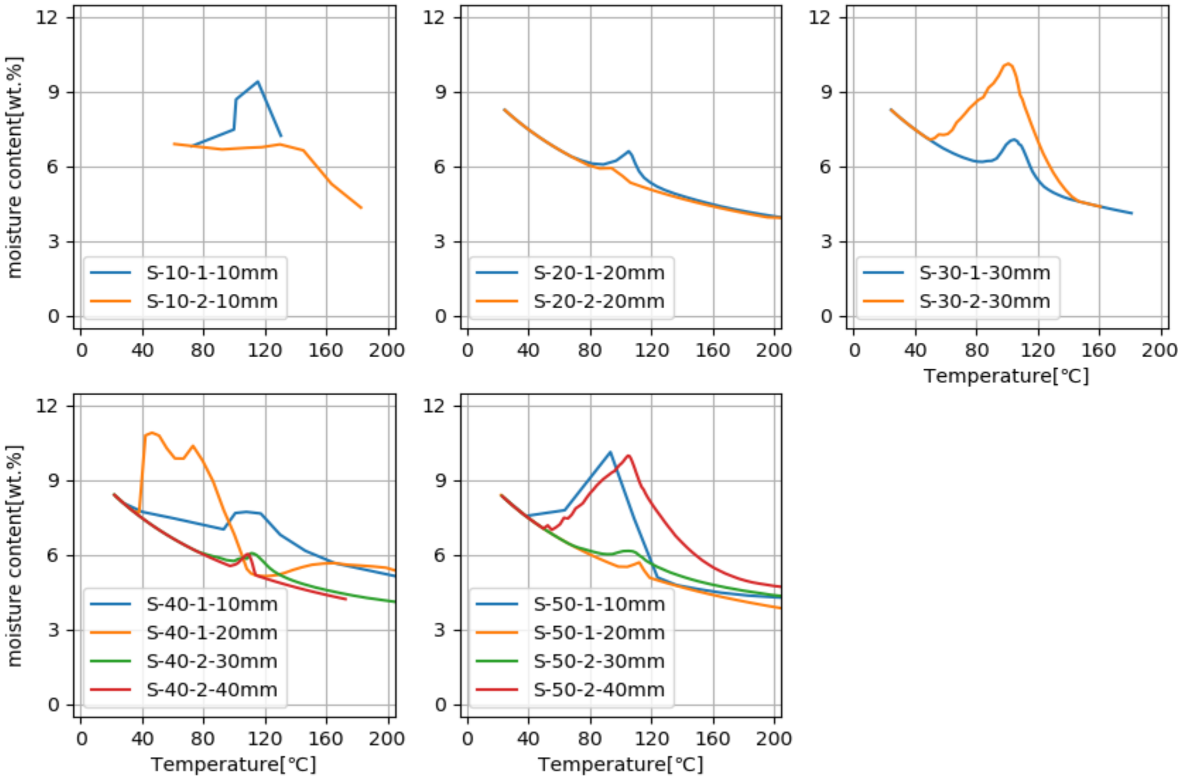

Figure 9 Relation between moisture contents and temperature

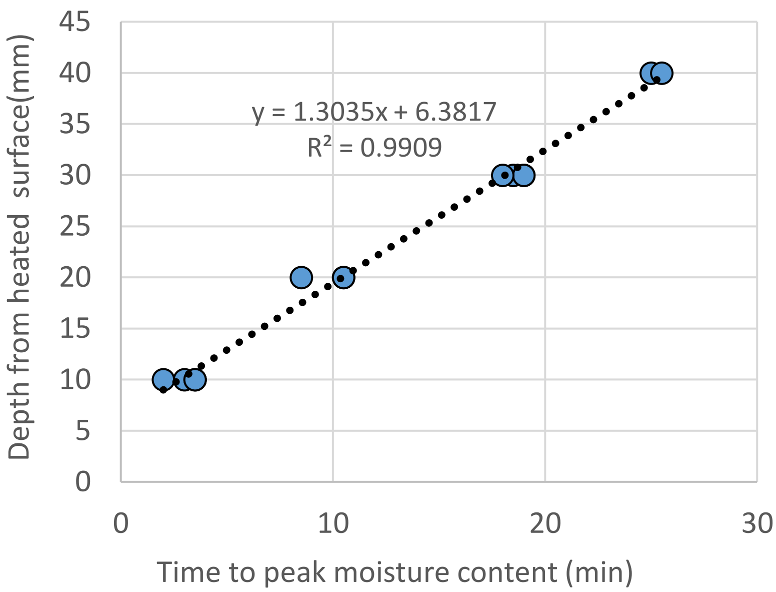

Figure 10 Time that moisture content reached peak value in different location

3.5 Charring Temperature and colouring temperature

Charring and colouring temperatures were estimated based on temperature history and observation of charred and coloured depth. To explain the estimation method, an example of C-30-1 is shown in **Figure 11.** Following the measured internal temperature history, the maximum temperatures at each location are plotted in **Figure 11(b)** against the depth from heated surface. Using the results in **Figure 5**, charred depth and coloured depth are plotted on **Figure11(b)** by vertical lines. By reading the temperatures at the crossing points, temperature at charring and colouring front were obtained. Since temperature gradually decrease with the direction from heated surface to rear surface, temperature of charring front and colouring front were thought to be the charring and colouring temperature. As for the example shown in **Figure 11**, charring and colouring temperatures were 355℃ and 234℃, respectively.

Charring temperature and colouring temperature of all the other experiments were also calculated in the same way. The results are shown in **Figure 12.** For cross grain specimens, the charring temperature was about 336~491°C, colouring temperature is in the range of 206~312°C. Average value for charring and colouring temperature is 381°C and 254°C, respectively. For straight grain specimens, the average charring and colouring temperature is 381°C and 264°C, respectively. Colouring and charring temperature on cross grain and straight grain specimens is similar. This charring temperature estimated in this work(about 380°C) is much higher than charring temperature reported by Schaffer[26](indirect reference from[14]), as 288°C, which is widely used as the charring temperature[27].

According to the results of thermogravimetric analysis (TGA) of larch[28], mass loss start to grow rapidly at 250°C~260°C, which is caused by pyrolysis of wood. The rate of pyrolysis starts to become slowly at about 380~390°C. Since the boundary of colouring and charring represents the location where rapid pyrolysis start and terminate, it can be concluded that the colouring and charring temperatures by the cone calorimeter is properly estimated.

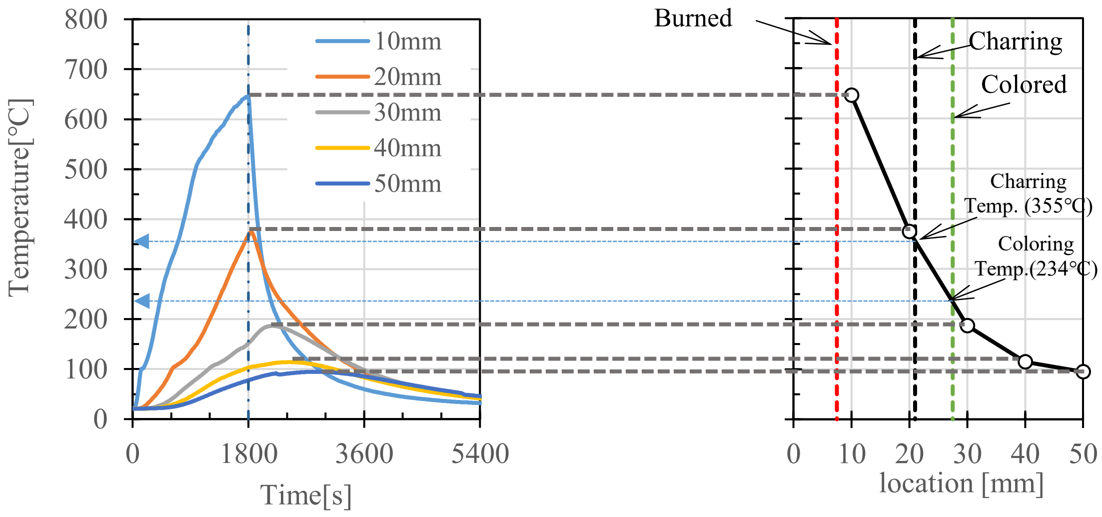

(a)Temperature history (b) Maximum temperature at each location

Figure 11 Temperature history of C-30-1

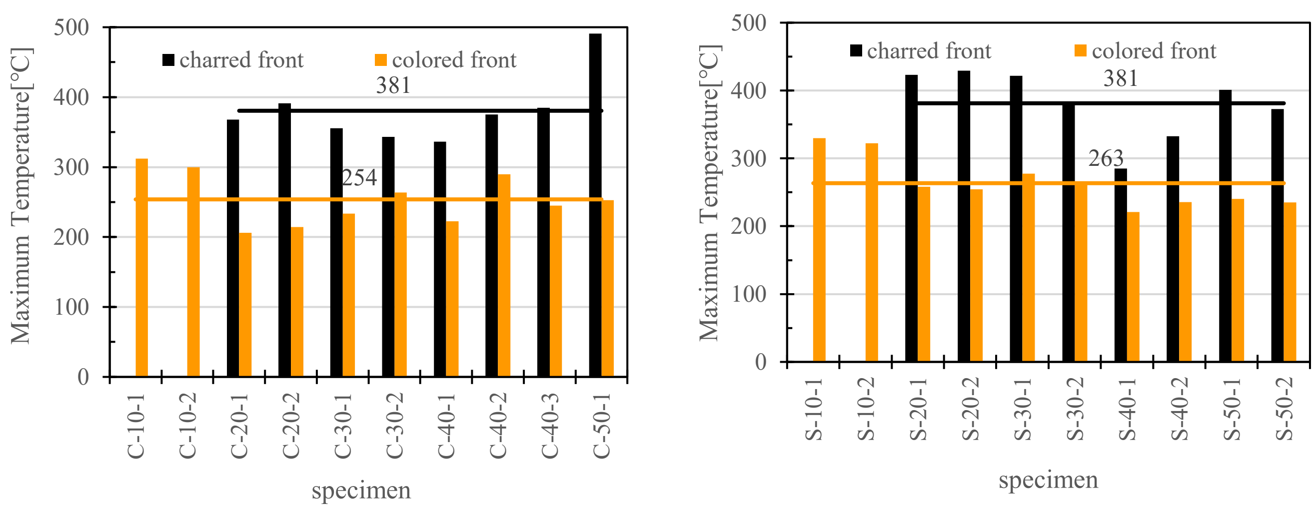

(a) Results of cross grain specimens(C) (b) Results of straight grain specimens(S)

Figure 12 Charring and Colouring temperature measured by highest temperature history

4 CONCLUSIONS

In this paper, cone calorimeter tests were conducted on 20 glue laminated larch specimens to investigate moisture transfer, burning behaviour and charring behaviour under heating. Internal temperature, moisture content and heat release rate were measured during experiment. Charred depth and coloured depth of each specimen were measured after experiment. Charring temperature and colouring temperature was calculated using measured temperature history, charred depth, and coloured depth.

Temperature creep was observed to start at about 100°C, which is thought to be caused by phase change of water. The duration of temperature creep increased with increasing distance from heating surface because the heat flux was relatively small and moisture content was large at locations near rear surface. As a result, time to vaporize liquid water increased. Internal temperatures of straight grain specimens are slightly higher than those cross-grain specimens. This is thought to be caused by the difference of direction of annual rings.

Peak heat release rate of each specimen was observed right after ignition with a value of about 150kW/m^2. The heat release rate decreased to about 50kW/m^2 within 5 minutes and maintained constant value afterwards, regardless of heating duration. Heat release rate of cross grain samples is slightly higher than straight grain samples.

Moisture content was measured by electrical resistance method. Although the measured moisture content varied by experiments, the relation between temperature and moisture distribution is almost identical. Moisture content started to increase at about 60~80°C, and the peak of moisture content was reached at about 100~120°C. After reaching the peak value, moisture content starts to decrease. Peak moisture content was thought to be the point that vapor condensation changes to liquid water vaporization. Time for moisture content to reach to peak values increased with depth linearly. Moving rate of peak water content was about 1.30 mm/min according to the regression result. The peak moving rate at 0~10mm is faster than this value.

Charred depth, coloured depth and burnt-out depth increased according to heating duration. Charring rate was 0.72~0.76mm/min. similar to results reported in previous large-scale tests. Colouring rate was 0.98~1.00 mm/min. Colouring and charring temperature at cross grain specimen and straight grain specimen is very close, at about 260°C and 380°C, respectively. Charring temperature estimated in this work is much higher than previously reported results.

5 FUTURE WORKS

The next step is to develop a numerical model to analyse heat and mass transfer, burning behaviour and charring behaviour of timber material under fire heating, and compare with measurements of temperature, moisture content and heat release rate.

ACKNOWLEDGMENT

This work was supported by JSPS KAKENHI (Grant-in-Aid for Scientific Research (B)), Grant Number 21H01490. Cone calorimeter experiments were conducted at General Building Research Corporation of Japan, supported by Mr. Masato Komiya, Mr. Hidekazu Suzuki, and Ms. Takako Oue. Measurement of charring depth was assisted by Mr. Shoma Makino (Graduate student at Kyoto University). The authors appreciate all the supports received.

REFERENCES

1. L. Terrei, Z. Acem, V. Georges, P. Lardet, P. Boulet, and G. Parent, "Experimental tools applied to ignition study of spruce wood under cone calorimeter," *Fire Saf. J.*, vol. 108, no. July, p. 102845, 2019, doi: 10.1016/j.firesaf.2019.102845.
2. K. Li, D. S. W. Pau, J. Wang, and J. Ji, "Modelling pyrolysis of charring materials: Determining flame heat flux using bench-scale experiments of medium density fibreboard (MDF)," *Chem. Eng. Sci.*, vol. 123, pp. 39–48, 2015, doi: 10.1016/j.ces.2014.10.043.
3. Y. Chatani and K. Harada, "Measurement of char oxidation rate of larch glue laminated timber," *12th Asia-Oceania Symp. Fire Sci. Technol.*, 2021.

4. H. Niwa, H. Enomoto, N. Sakata, M. Sadahiro, and Y. Kurihara, “Fire Resistance Performance of Build-up Laminated Veneer Lumber: Part 3 Fire Resistance Tests of Column and Beam,” in *Fire safety, Summaries of technical papers of annual meeting, AIJ*, 2020, pp. 211–212.
5. T. Lennon, D. Hopkin, J. El-Rimawi, and V. Silberschmidt, “Large scale natural fire tests on protected engineered timber floor systems,” *Fire Saf. J.*, vol. 45, no. 3, pp. 168–182, 2010, doi: 10.1016/j.firesaf.2010.02.006.
6. J. Suzuki, T. Mizukami, T. Naruse, and Y. Araki, “Fire Resistance of Timber Panel Structures Under Standard Fire Exposure,” *Fire Technol.*, vol. 52, no. 4, pp. 1015–1034, 2016, doi: 10.1007/s10694-016-0578-2.
7. Q. Xu, Y. Wang, L. Chen, R. Gao, and X. Li, “Comparative experimental study of fire-resistance ratings of timber assemblies with different fire protection measures,” *Adv. Struct. Eng.*, vol. 19, no. 3, pp. 500–512, 2016, doi: 10.1177/1369433216630044.
8. H. Kimura *et al.*, “Dynamic Measurement of Temperature and Moisture Content changing in Glulam Timber Beam exposed to Fire Heating,” *Fire safety, Summ. Tech. Pap. Annu. Meet. AIJ*, 2022.
9. C. C. Gerhards, “Effect of Moisture Content and Temperature on the Mechanical Properties of Wood: An Analysis of Immediate Effects,” *Wood Fiber*, vol. 14, no. 1, pp. 4–36, 1982.
10. M. Báder and R. Németh, “Moisture-dependent mechanical properties of longitudinally compressed wood,” *Eur. J. Wood Wood Prod.*, vol. 77, no. 6, pp. 1009–1019, 2019, doi: 10.1007/s00107-019-01448-1.
11. M. Aydın and T. Yılmaz Aydın, “Moisture dependent elastic properties of naturally aged black pine wood,” *Constr. Build. Mater.*, vol. 262, 2020, doi: 10.1016/j.conbuildmat.2020.120752.
12. H. L. Frandsen, “Selected Constitutive Models for Simulating the Hygromechanical Response of Wood,” 2007.
13. G. A. Spolek and O. A. Plumb, “Capillary pressure in softwoods,” *Wood Sci. Technol.*, vol. 15, no. 3, pp. 189–199, 1981, doi: 10.1007/BF00353471.
14. A. Frangi and M. Fontana, “Charring rates and temperature profiles of wood sections,” *Fire Mater.*, vol. 27, no. 2, pp. 91–102, 2003, doi: 10.1002/fam.819.
15. A. Sun, D. Nii, and K. Harada, “An experimental study of heat and mass transfer inside timber specimen under radiant heating,” *Proc. JAFSE Annu. Symp.*, 2022.
16. K. Harada, A. Sun, and D. Nii, “A study on charring depth and temperature history on laminated larch wood,” *Fire safety, Summ. Tech. Pap. Annu. Meet. AIJ*, 2022.
17. S. Roels *et al.*, “A Comparison of Different Techniques to Quantify Moisture Content Profiles in Porous Building Materials,” *J. Build. Phys.*, vol. 27, no. 4, pp. 261–276, 2004, doi: 10.1177/1097196304042117.
18. T. Arends, A. J. Barakat, and L. Pel, “Moisture transport in pine wood during one-sided heating studied by NMR,” *Exp. Therm. Fluid Sci.*, vol. 99, no. June, pp. 259–271, 2018, doi: 10.1016/j.expthermflusci.2018.08.004.
19. H. F. Vermaas, “D.C. resistance moisture meters for wood: Part I: Review of some fundamental considerations,” *South African For. J.*, vol. 121, no. 1, pp. 88–92, 1982, doi: 10.1080/00382167.1982.9628815.
20. W. L. James, “Electric Moisture Meters for Wood.,” *Gen. Tech. Rep. FPL-GTR-6, U.S. Dep. Agric.*, 1988.
21. J. D. Clark and J. W. Williams, “The electrical conductivity of commercial dielectrics and its variation with temperature,” *J. Phys. Chem.*, vol. 37, no. 1, pp. 119–131, 1933, doi: 10.1021/j150343a015.
22. H. F. Vermaas, “D.C resistance moisture meters for wood. Part III: Temperature Correction of Moisture meter Readings for a Proposed new Moisture Meter(Calibrated for 20°C) for P.pinaster and P.radiata and Calibration Equations for a Commercial Moisture Meter,” *South African For. J.*, vol. 123, no. 1, pp. 63–71, 1982, doi: 10.1080/00382167.1982.9628855.
23. B. Adl-Zarrabi, L. Boström, and U. Wickström, “Using the TPS method for determining the thermal properties of concrete and wood at elevated temperature,” *Fire Mater.*, vol. 30, no. 5, pp. 359–369, 2006, doi: 10.1002/fam.915.
24. T. Harada, “A Study on the Combustibility and the Fire Resistance of Wood,” *Bull. For. For. Prod. Resourse Institude*, vol. 378, pp. 1–85, 2000.
25. H. F. Vermaas, “D.C. resistance moisture meters for wood: Part II: The Influence of Temperature and Miosture Content on the Resistance of Two South Africal Pines,” *South African For. J.*, vol. 122, no. 1, pp. 70–81, 1982, doi: 10.1080/00382167.1982.9628838.
26. E. L. Schaffer, “Charring Rate Of Selected Woods - Transverse To Grain,” *FPL Res. Pap. 69*, no. April, p. 1967, 1967.
27. R. H. White and E. V. Nordheim, “Charring rate of wood for ASTM E 119 exposure,” *Fire Technol.*, vol. 28, no. 1, pp. 5–30, 1992, doi: 10.1007/BF01858049.
28. A. Sun, K. Harada, D. Nii, and J. Yamaguchi, “Measurements of Thermal Decomposition Rates of Several Types of Wood and Estimation of Reaction Rate Parameters,” *Bull. Japan Assoc. fire Sci. Eng.*, vol. 71, no. 2, pp. 1–12, 2021.

SiF 2022– The 12th International Conference on Structures in Fire
The Hong Kong Polytechnic University, Nov 30 - Dec 2, 2022

THE CODERED EXPERIMENTS AND STRUCTURAL FIRE SEVERITY OF OPEN-PLAN COMPARTMENTS WITH EXPOSED TIMBER CEILINGS

Panagiotis Kotsovinos[1], Eirik G.Christensen[2], Mohammad Heidari[3], David Barber[4], Guillermo Rein[5], Judith Schulz[6]

ABSTRACT

None.

Keywords: Structural fire severity; exposed timber; time equivalence; design fires

1 INTRODUCTION

Architects and engineers around the world want to explore the use of mass-timber as a structural material in buildings due to its perceived advantages as a natural and pre-manufactured material. Mass-timber members are however combustible and therefore can influence fire dynamics in a compartment and alter the resulting structural fire severity when compared to non-combustible compartments. Additionally, knowledge from the fire dynamics of open-plan non-combustible compartments has shown that there are different phenomena from those observed in smaller compartments. Fire dynamics in open-plan compartments with an exposed timber ceiling were recently explored in the CodeRed experiments [1]–[3].

This work aims to extend previous work by presenting the lessons learnt from the CodeRed series of experiments on the structural fire severity of open-plan compartments with an exposed timber ceiling. The time equivalence results for structural members included within the experiments, will be presented for the first time based on the observed charring depth of the exposed CLT ceiling and glulam columns, and the observed temperatures of the protected steel column.

2 CODERED EXPERIMENTS

Three fire experiments with a floor area of 352 m2 (10.27 m width, 34.27 m length), the largest experiments in terms of compartment floor area to date, with an exposed timber surface, were carried out in 2021 in a bespoke facility that was built in Épernon, France. The construction of the facility closely followed the design of a previous non-combustible experiment that was carried near Warsaw, Poland which investigated travelling fire dynamics in open-plan compartments [4]. The fire dynamics observed in these experiments and a detailed description of the experimental method have been presented in [1]–[3]. A high-level summary of the facility and set up is provided here for convenience.

[1] Fire Engineer, Arup, London, UK
e-mail: panos.kotsovinos@arup.com
[2] Fire Engineer, Arup, London, UK
[3] Dr., Fire Testing Centre, CERIB, France
ORCID: https://orcid.org/0000-0002-4411-390X
[4] Principal, Arup, Australia
e-mail: David.Barber@arup.com
[5] Prof., Imperial College London, UK
e-mail: g.rein@imperial.ac.uk, ORCID: https://orcid.org/0000-0001-7207-2685
[6] Fire Engineer, Arup, London, UK
https://doi.org/10.6084/m9.figshare.22193734

CodeRed #01 had a fully exposed timber ceiling. CodeRed #02 had 50% of the ventilation provided in CodeRed #01 (Figure 1 indicates which openings were closed for CodeRed #02). CodeRed #04 had 50% of the ceiling encapsulated when compared with that of CodeRed #01 with all other parameters being the same. The encapsulation was provided in the middle of the compartment, away from the perimeter (Figure 1 illustrates the extent of the encapsulation). CodeRed #03 is not included as its aim is not related to this study. Table 1 summarises the differences in the key parameters of interest between the previous non-combustible travelling fire experiment and the CodeRed experiments.

CodeRed used a similar fuel load design and ignition procedure as per the original non-combustible experiments. The fuel load consisted of a continuous wood crib, with a fuel load density of 394 MJ/m2 and covered a floor area of 174 m2 (6 m × 29 m). The fuel was ignited simultaneously along the northwest edge of the crib and allowed to naturally spread across the compartment, with no firefighting intervention. A consistent CLT and glulam performance was observed in all the CodeRed experiments. The timber was specified such that it would not show glue-line integrity failure. As a result, no char fall-off of the ceiling was observed.

A CLT ceiling, two glulam columns and a protected steel column were included in the experiments (Figure 2). All structural members were unloaded, as such this research focuses on structural fire severity. Temperature measurements were taken throughout the compartment and within the members. Figure 1 presents the location of thermocouples which measure the gas phase temperatures within the compartment and the positioning of thermocouples on the protected steel column. For both the protected steel column and the gas phase measurements thermocouples were located at 100, 700 and 2100 mm below the ceiling. In a limited number of positions thermocouples were also located at 2800 mm below the ceiling, measuring the gas temperature. This suite of experiments and instrumentation allowed the study of both the influence of exposed timber area and ventilation on the expected structural fire severity.

Several cuts were made through the timber columns and CLT ceiling panels several days after the end of the experiment to enable the measurement of the char depth and allowed for an estimation of the time equivalent severity of the fire.

Table 1 Summary of the differences in the key parameters of interest between the previous non-combustible travelling fire experiment and the CodeRed experiments.

Parameter	Previous non-combustible experiment [4], [5]	*CodeRed #01* [1]	*CodeRed #02* [2]	*CodeRed #04* [3]
Ceiling	Non-combustible	*Fully exposed ceiling (CLT)*	*Fully exposed ceiling (CLT)*	*52% exposed and 48% encapsulated CLT*
Ventilation	20%	*21%*	*10%*	*21%*
Area	380m^2	*352m^2*	*352m^2*	*352m^2*

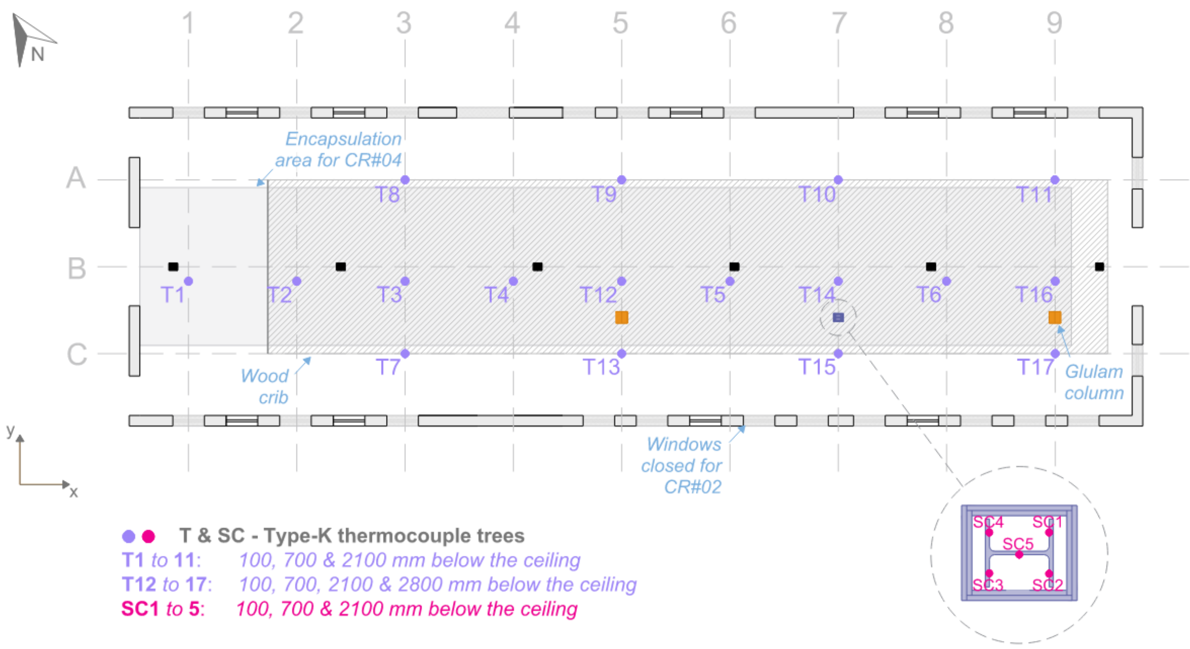

Figure 1. CodeRed compartment overview with gas and steel column thermocouple locations indicated. Openings which were closed for CodeRed #02, and extent of encapsulation in CodeRed #04 are also indicated.

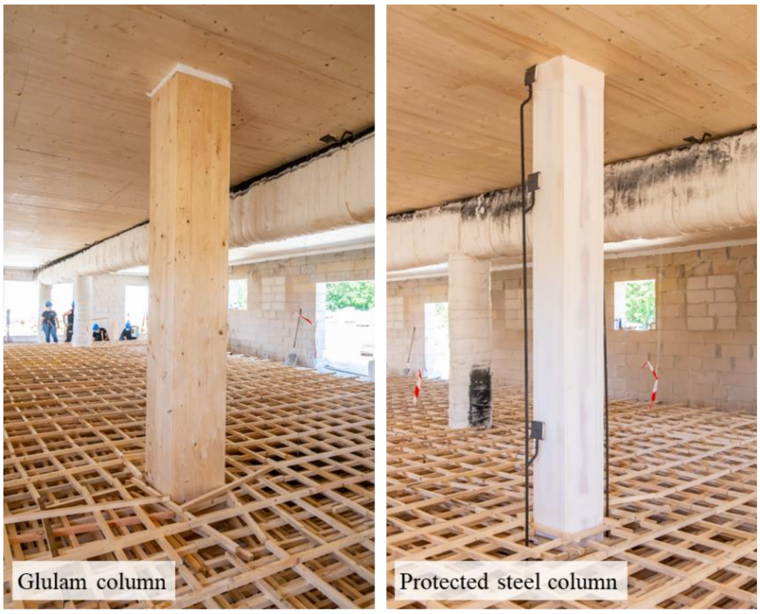

Figure 1. Timber and protected steel columns in the *CodeRed* experiments

3 RESULTS

Approaches involving the concept of "time equivalence" are typically employed in design practice to compare natural fires against the standard fire that is used for the qualification testing of fire resistance products. For protected steel members the equivalent time of fire exposure is most commonly established by comparing metrics such as the peak temperature reached under both the natural fire and a standard fire. For timber, the time equivalence is often made on the basis of an equivalent final char depth. For all considered CodeRed experiments, the time equivalence based on the above principles were estimated for the protected steel column, the CLT ceiling and the glulam columns. These results are presented in Table 1. This enables the comparison of the experimental time equivalence against the calculated time equivalence from prescribed design fire curves. For CodeRed #02 one of the timber columns experienced prolonged smouldering at the base and eventually lost its limited attachment with the ceiling and fell to the ground and continued smouldering; therefore its time equivalence cannot be reported.

The thermal response of the protected steel column is also shown in Figure 3. The peak average steel temperature was 103°C, 155°C, and 98°C for CodeRed #01, #02 and #04 respectively. The maximum temperatures in the steel columns were reached at a similar time despite the variations in flaming duration, gas temperature distribution, and gas temperature development. In addition, adjusting for the difference in the CLT ignition between CodeRed #01 and #04, the temperature development very similar and resulted in 5% difference in the maximum temperatures despite the difference in the percentage of the encapsulation of the ceiling. On the other hand, reducing the ventilation by 50% (CodeRed #02) led to a significant increase in maximum steel temperatures due to the increase in flaming duration and slower rate of decay in the compartment. During peak flaming period the temperature development of the steel column was similar between CodeRed #01 and #02 until approximately 30 min. After this time, the fire had ceased, and the gas temperature was decaying. However, the extended peak flaming period of CodeRed #02 delayed the decay phase, resulting in higher temperatures giving an overall greater heat transfer to the column.

Table 1. Average time equivalence results

Member type	Experiment	Measured values	Average time equivalence	Relative increase
Protected steel column	CodeRed #01	103°C peak average steel temperature	23.0 min	Base case
	CodeRed #02	155°C peak average steel temperature	31.6 min	+8.6 min (+37.4%)
	CodeRed #04	98°C peak average steel temperature	22.2 min	-0.8 min (-3.5%)
Glulam columns	CodeRed #01	Average char depth for Column 1: 30.2 mm Column 2: 30.4 mm	Column 1: 43.1 min Column 2: 43.4 min	Base case
	CodeRed #02	Average char depth of Column 1: n/a Column 2: 32 mm	Column 1: N/A Column 2: 45.7 min	N/A +5.3%
	CodeRed #04	Average char depth for Column 1: 23.0 mm Column 2: 18.2 mm	Column 1: 32.8 min Column 2: 26.0 min	-10.3 min (-23.9%) -17.4 min (-40.1%)

Member type	Experiment	Measured values	Average time equivalence	Relative increase
CLT ceiling	CodeRed #01	Weighted average char depth: 25.4 mm	35.3 min	Base case
	CodeRed #02	Weighted average char depth: 28.0 mm	38.9 min	+3.6min (+12%)
	CodeRed #04	Weighted average char depth: 25.0 mm	34.7 min	-0.6min (-1.7%)

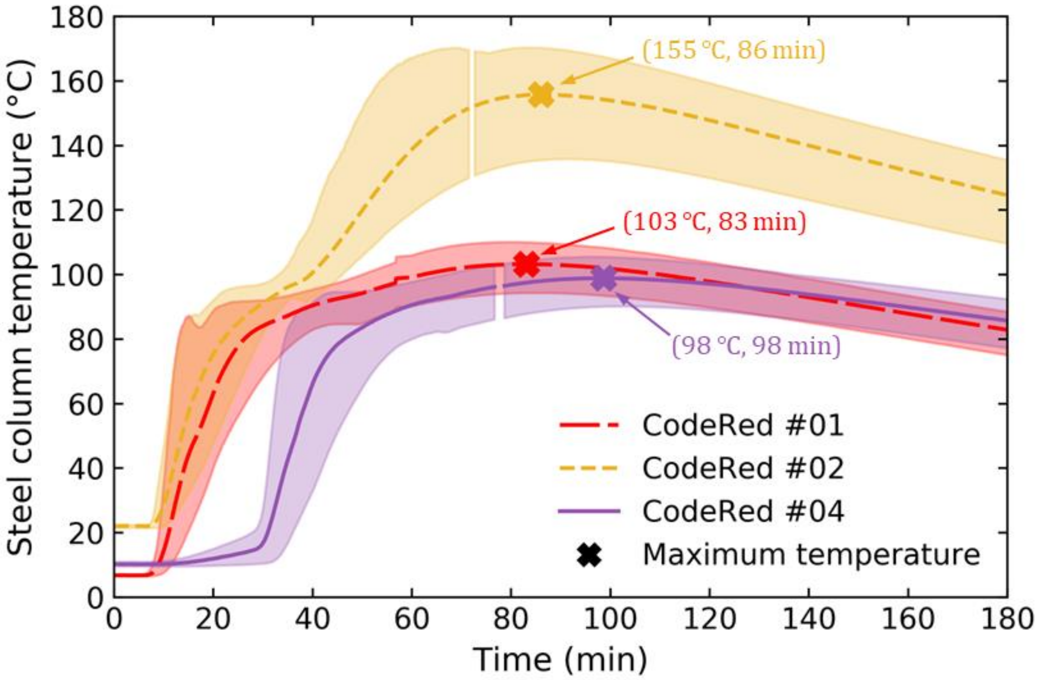

Figure 3. Protected steel column thermal response. The shaded area provides the range of temperatures measured by the thermocouples installed along the height of the column.

4 KEY FINDINGS

This work presented the obtained results on the time equivalence for all CodeRed experiments in order to characterise observations and trends in structural fire severity of open-plan compartments with a timber ceiling.

The concept of time equivalence with a single value for all members in the same compartment as it is used in non-combustible structures cannot be adopted for combustible compartments. The time equivalence found for the protected steel column, CLT ceiling, and glulam columns were shown to vary within each experiment. This points to the complexity in assessing the fire severity of combustible and non-combustible members using a common factor based on differing methodologies (charring rates and peak temperatures). Even for combustible members, the structural fire severity varied spatially depending their orientation and location in the compartment.

Comparing the results in CodeRed #02 to #01, it was observed that a reduction in available ventilation results in an increased structural fire severity due to the increase of the duration of the fire. For the well-ventilated experiments, CodeRed #01 and CodeRed #04, it was observed that the structural fire resistance inside the compartment was not impacted significantly by the amount of exposed timber in the ceiling for the CLT ceiling and the steel columns. For the glulam columns there is a significant variation with the reduction in exposed timber surface area.

In all experiments smouldering was observed to be sustained in joints and junctions, continuing to spread for days following the cessation of flaming. In many locations smouldering spread through the full thickness (160 mm) of the CLT ceiling slab. This presents additional complexity when considering predicted fire severity and time equivalence. In particular it was found that the lower parts of timber columns are particularly vulnerable during the decay period and the on-going smouldering of the fuel leading to additional charring and therefore loss of structural capacity. This is a new phenomenon that has not been observed in previous literature and needs to be addressed in structural fire design.

5 PRESET FORMATS

The experiments have shown that charring and thermal penetration continues after extinction of flaming combustion due to high compartment temperatures at ‘extinction’. This highlights the importance in accurately capturing the full decay phase in predicting the fire severity on structural members. The design fires curves available in the literature needs to be compared against the observed gas temperatures in the experiments to investigate their adequacy in modelling open-plan compartments with an exposed timber ceiling. The results from CodeRed can be used as a benchmark to determine the suitability of a design fire methodology for open-plan timber compartments. More specifically, the curves considered are EN1991-1-2 Parametric Fire curves, an iterative version of these curves as per Barber, Zehfuss & Hosser and its iterative version, and the curve proposed by Brandon et al [6].

The comparison against CodeRed #01 and #04 is included in Figure 4 indicatively. It can be seen that Zehfuss & Hosser approach (iterative) fits best during the growth (adjusting for the experimental growth period), but overpredicts temperatures and does not capture the decay ‘tail’ observed during the experiment. The Brandon method was found to underpredicts results. The Eurocode methods underpredict peak temperatures and overpredicts duration. Therefore, Zehfuss & Hosser appears to have best fit for all metrics and consistently conservative although for some cases too conservative. A fast fire growth has been assumed for the comparison reported which is the greatest available in EN991-1-2 for commercial use based on knowledge from non-combustible compartments. An ultra-fast fire should also be explored, as it may be more relevant to combustible compartments based on the results from CodeRed. In addition, further research is necessary to compare against all CodeRed experiments and other published results.

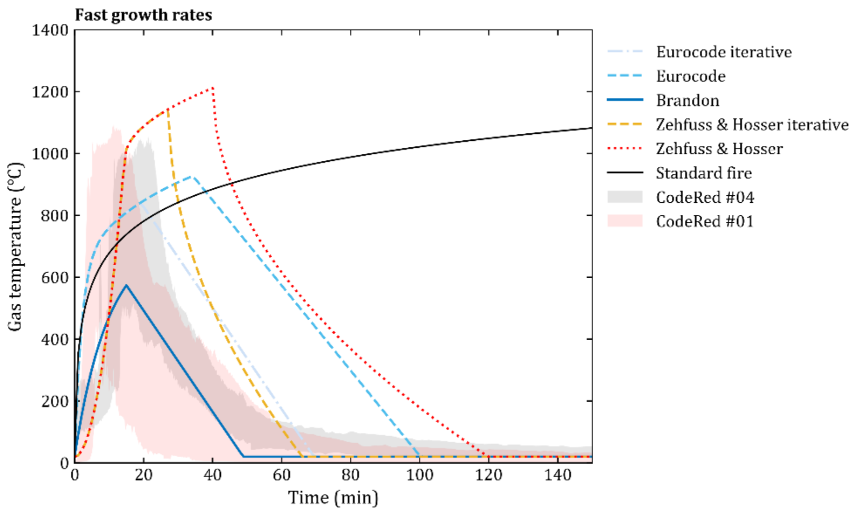

Figure 4. comparing prescribed design fires against the temperatures measured near the ceiling in CodeRed #04

ACKNOWLEDGMENT

Acknowledgments are optional.

The references provided should be in a numbered list as shown below. This numbered list should be in the order in which the references first appear in the manuscript. Corresponding numbers should be provided in the manuscript included in square brackets, e.g. [1]. If two non-consecutive references should be added in one location then these can be separated by a comma in the square brackets, e.g. [1,3]. If consecutive references should be added in the text then the first and last of these should be given in the brackets, separated by a hyphen, e.g. [1–3].

REFERENCES

1. P. Kotsovinos, E. Rackauskaite, E. Christensen, A. Glew, E. O'Loughlin, H. Mitchell, R. Amin, F. Robert, M. Heidari, D. Barber, G. Rein and J. Schulz (2022) Fire dynamics inside an open-plan compartment with an exposed CLT ceiling and glulam columns: CodeRed #01, Fire and Materials.
2. P. Kotsovinos, E. Christensen, E. Rackauskaite, A. Glew, E. O'Loughlin, H. Mitchell, R. Amin, F. Robert, M. Heidari, D. Barber, G. Rein and J. Schulz (2022) Impact of ventilation on the fire dynamics of an open-plan compartment with exposed CLT ceiling and glulam columns: CodeRed #02, Fire and Materials.
3. P. Kotsovinos, E. Christensen, A. Glew, E. O'Loughlin, H. Mitchell, R. Amin, F. Robert, M. Heidari, D. Barber, G. Rein and J. Schulz (2022) Impact of partial encapsulation on the fire dynamics of an open-plan compartment with exposed CLT ceiling and glulam columns: CodeRed #04, Fire and Materials
4. E. Rackauskaite, P. Kotsovinos and D. Barber (2021) Letter to the Editor: Design Fires for Open-Plan Buildings with Exposed Mass-Timber Ceiling, Fire Technology, 57 (2), 487-495.

SiF 2022– The 12th International Conference on Structures in Fire
The Hong Kong Polytechnic University, Nov 30 - Dec 2, 2022

FLEXURAL BEHAVIOR OF HYBRID GLULAM-FRP BEAM DURING AND AFTER A FIRE

Abdulrahman Zaben[1], Joseph Michael Gattas[2], Cristian Maluk[3]

ABSTRACT

This work considers an experimental investigation of rationalized manufacturing techniques for hybrid Glulam beams combined with Fibre Reinforced Polymers (FRP) for the manufacturing of floor timber structures with improved fire and serviceability performance. In essence, introducing FRP with a relatively higher residual capacity at elevated temperatures, compared to timber, compensates for timber's loss of strength and stiffness at elevated temperatures or even when charring during a fire. This is a shift in how FRP materials are currently constrained in load-bearing applications where structural integrity must be maintained during or after a fire. In applications where a certain fire performance is needed for the load-bearing mass timber structure of a building, the end-result of this work aims at setting the basis for a prototype Hybrid Glulam-FRP (HGF) beam that could be used to deliver load-bearing floor timber structures with enhanced fire performance. Experimental tests were conducted in four-point bending arrangement at ambient conditions, and during or after exposing the midspan section of the beams to a fire.

Keywords: Glulam beam, Hybrid Glulam-FRP (HGF); fire performance; bending behaviour

1 INTRODUCTION

1.1 Hybrid Timber-Fibre Reinforced Polymers systems

The reinforcement of timber and Glulam beam elements by using fibre-reinforced polymer (FRP) laminates, sheets, and bars has been extensively researched in recent decades. The primary goal of most existing research has been to improve beam strength and serviceability performances under flexural loads at ambient (non-fire) conditions. Hybrid Glulam-FRP beams have been reported to be significantly stronger and stiffer in bending than unreinforced elements of equal size (Martin and Tingley, 2000; Yang *et al.*, 2016). However, limited work to date has been done to understand the load-bearing structural performance of HGF beams in a fire. There is also a lack of robust experimental findings to provide a comprehensive understanding of this issue (Martin and Tingley, 2000; Romani and Blaß, 2001; Raftery and Rodd, 2015).

1.2 Objective of the present study

Two proposed manufacturing techniques for the prototype HGF beam were investigated within the scope of this work. The techniques rely on using CFRP sheets or strips impeded inside the Glulam elements and aim to provide partial protection for the FRP when a section is heated, thereby retaining the contribution of the FRP to the hybrid system and not unduly influencing the timber’s aesthetic appeal. The techniques also

[1] The University of Queensland, Australia
e-mail: a.zaben@uq.edu.au, ORCID: https://orcid.org/0000-0001-7229-9193
[2] The University of Queensland, Australia
e-mail: j.gattas@uq.edu.au, ORCID: https://orcid.org/0000-0002-0878-583X
[3] The University of Queensland, Australia and Semper, UK
e-mail: c.maluk@sempergrp.com, ORCID: https://orcid.org/0000-0002-1662-6943
https://doi.org/10.6084/m9.figshare.22193728

aim to achieve a feasible manufacturing process for effective implementation at an industrial scale, by minimizing technical intervention to the conventional manufacturing process of laminated timber with enough precautions to eliminate or mitigate the debonding between timber and FRP. Relatedly, an adhesive typically used in laminated timber was also used to bond timber and FRP, ensuring the bonding interface between the two elements in the composite system and avoid long duration incompatibility between timber and FRP. A schematic diagram of the two techniques is shown in Figure 1.

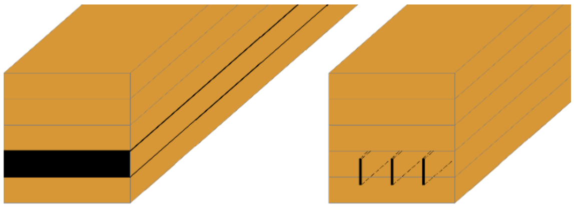

Figure 1: Schematic diagram shows cross section of Hybrid Glulam-FRP (HGF) beams of two different prototypes.

To assess the bending behaviour of HGF beams during and after a fire, a comprehensive investigation conducted herein through an experimental approach based on four-point bending loading conditions. The experimental framework comprised four-point bending experiments for mid-scale HGF beams at normal ambient conditions, residual testing conditions after burning and cooling of the midspan section of the beams. Beams were also tested under transient testing conditions by heating the midspan section of the beams to a well-controlled heating condition defined by a target incident heat flux, applying a sustained four-point bending load. Heating conditioning (for residual and transient conditions) was done using gas-fired radiant panels coupled with a purpose-built four-point bending setup. The heating condition was controlled to achieve a specific target incident radiant heat flux; for residual testing conditions beams were heated up to a target charring depth, and for transient-state testing conditions beams were heated up until the moment of failure

2 MATERIALS AND FABRICATION DETAILS

Beam specimens were fabricated in compliance with industry standards (AS/NZS 1328.1:1998) when possible. Glulam beams and HGF beams fabricated within the scope of this paper were made using Australian southern pine boards of Machine Graded Pine (MGP) rating, with an initial cross-section of 90 mm × 35 mm. Australian standard AS 1720.1 “Design Methods for Timber structures” includes more details about the characteristic values for design of MGP timber. The moisture content of the timber was measured to be at an average of 12% using the oven-drying method based on (AS/NZS 1080.1: 2012) for twenty one timber specimens with a coefficient of variation equal to 7%.

The Glulam beams were fabricated using five timber lamellas, with unreinforced specimens designated as UR. CFRP sheets of type *Sika-Wrap®-300C* and CFRP strips of type *Sika-CarboDur®-S* were used to reinforce the two types of HGF beams. The CFRP fabric sheet thickness is 0.166 mm based on total unidirectional fibre content, with tensile strength and Modulus of Elasticity (MoE) of 3900 MPa and 230 GPa, respectively, as provided by the manufacturer’s technical data sheet. The CFRP strips have a thickness of 1.4 mm, a width of 30 mm, and a fibre volume content over 68%. The CFRP laminates have a mean value for elongation at break of 1.8%, and design values for the tensile strength and MoE of 2900 MPa and 165 GPa, respectively, as provided by the manufacturer’s technical data sheet. To further improve the homogeneity of the beams and to avoid undesired failures triggered by timber defects, all beams were fabricated using timber lamellas free of knots or visual defects in the middle portion.

2.1 First reinforcement technique using CFRP fabric

An extended description of the first fabrication methodology utilised for the first group of beams is given in (Zaben et al., 2021), with the process and materials summarised here as follows.

The process started by cutting the planks into smaller lamellas of dimensions 1200 mm × 90 mm × 35 mm, sorting the timber lamellas and dressing them down to a thickness of 33 mm to activate the timber surface to improve the gluing efficiency during the lamination process. After dressing, timber lamellas were glued together using a commercially available single component prepolymer polyurethane adhesive (*Jowat Jowapur 681.40*). The adhesive was applied at a mass to surface area ratio of 200 g/m^2. Specimens were pressed for 90 minutes at ambient conditions at a sustained surface pressure of 1.0 MPa using a hydraulic system in a Glulam press table. Control test specimens were fabricated from five timber lamellas without CFRP reinforcement fabric.

For the first type of HGF beams, during the timber lamination process, one CFRP sheet was wrapped around a timber lamella to be positioned second to last from the beam's soffit, in a longitudinal direction starting at the bottom face. The adhesive was applied to the timber lamella at a mass to surface area ratio of 300 g/m^2. The CFRP sheet was then secured using a block of solid timber hammered into a pre-cut groove, as shown in Figure 2. The groove was positioned at 50 mm from the edge of the beam to be placed outside the supporting points of the beam during the four-point bending tests and not directly beneath the load. A sufficient amount of adhesive was then poured onto the CFRP sheet to impregnate the fibres completely with adhesive. The reinforced lamella after that was joined with the other timber lamellas and pressed for 90 minutes in a similar process to the fabrication of the control beams. The beams of this group had a total depth and width of 165 mm and 90 mm, respectively. *Table 1* summarizes the different types of specimens tested within this first group of beams.

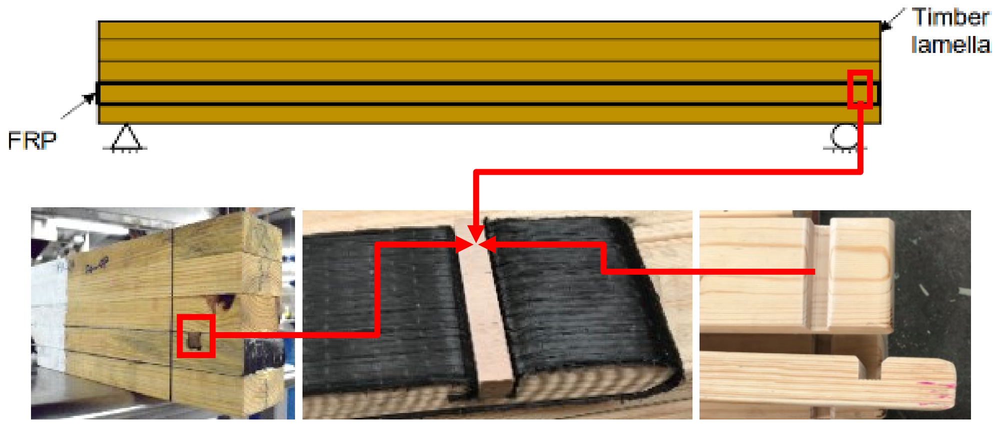

Figure 2: Detailed view for the method of securing the CFRP fabric around the reinforced lamella.

Table 1: Summary of the different types of beams tested within first fabrication technique group (FT1).

Beam type	Timber grade	Span length (mm)	Shear span (mm)	Beam depth (mm)	Beam width (mm)	Beam cross-section area (mm^2)	CFRP sheet thick. (mm)	CFRP strips width (mm)	CFRP cross-section area (mm^2)	FRP/Timber ratio (%)
FT1-UR	MGP 15	1020	410	165	90	14850	---	---	---	0 %
FT1-Rsheet							0.166	90	15 x 2 Layers	0.2 %

2.2 Second reinforcement technique using CFRP strips

Similar to the first fabrication technique, the process started by cutting the planks into smaller lamellas of dimensions 2600 mm × 90 mm × 35 mm, sorting the timber lamellas and dressing them down to a thickness of 31 mm. Since the timber in this group was subjected to a preservative treatment, further dressing was done for the timber lamellas of this group of beams to remove the surface layer which was subjected to preservative treatment. After dressing, timber lamellas were glued together using a commercially available single component prepolymer polyurethane adhesive (*Jowat Jowapur 681.70*). The adhesive was applied at a mass to surface area ratio of 200 g/m^2. Specimens were pressed for 120 minutes at ambient conditions at a sustained surface pressure of 0.7 MPa using a hydraulic system in a Glulam press table. Control test specimens were fabricated from five timber lamellas without CFRP reinforcement fabric.

The CFRP reinforcement strips in the second type of HGF beams were included during the typical Glulam lamination process, without introducing a significant complexity to the typical Glulam manufacturing process. During the timber lamination process, three CFRP strips were pressed vertically inside pre-cut longitudinal notches that were made in the bottom two lamellas, as shown in Figure 3.

Figure 3: Steps of reinforcing the Glulam beams using CFRP strips embedded in between timber lamellas.

The notches in the timber were perfectly aligned in the two adjacent lamellas, with a depth of 15.5 mm in each lamella and a thickness slightly larger than the thickness of each type of strips. The surface of the CFRP strips were sanded by fine sandpapers and wiped with acetone to prepare it for the adhesive application. The same adhesive was applied initially inside the notches and then on the lamellas' surface and the CFRP strips' surface; after that, the strips were pressed inside the notches, and the two lamellas were joined together. The beams of this group had a total depth and width of 155 mm and 86 mm, respectively. *Table 2* summarizes the different types specimens tested within this second group of beams.

Table 2: Summary of the different types of beams tested within second fabrication technique group (FT2).

Beam type	Timber grade	Total Span length (mm)	Shear span (mm)	Beam depth (mm)	Beam width (mm)	Beam cross-section area (mm^2)	CFRP strips height (mm)	CFRP strips width (mm)	CFRP cross-section area (mm^2)	FRP/Timber ratio (%)
FT2-UR	MGP 12	2300	900	155	86	13330	---	---	---	0 %
FT2-R126							30	1.4	126	1 %
FT2-R270							30	3	270	2 %

3 EXPERIMENTAL METHODOLOGY

3.1 Loading procedure

An experimental approach based on four-point bending loading conditions was conducted to investigate the change in the bending strength and stiffness of the Glulam beams through the inclusion of relatively rigid CFRP reinforcement fabric. As an initial proof of concept, the experiments were conducted to test the mechanical response of the beams at normal ambient conditions and their residual bending capacity during and after being exposed to fire.

The four-point bending tests were conducted according to ASTM D198-15. For the first group of HGF beams, the simply supported beams were tested across a span of 1020 mm, with a shear span of 410 mm. For the second group of HGF beams, the were tested across a span of 2300 mm, with a shear span of 900 mm. The span of the second HGF beams was decided to be increased from 1020 mm to 2300 mm after experiencing a significant shear failure in the first group of beams.

Based on that, the Glulam beams of the first and second fabrication techniques groups were tested under bending with a slenderness coefficient for lateral buckling of 3.7 and 5.4, respectively. This means that the stability factor (k_{12}) is equal to 1.0 for both cases, according to AS1720. Therefore, there was no need to use lateral stiffeners during the experiments (Australian Standard AS 1720.1, 2010).

The specimens were loaded at a constant rate until reaching failure. The loading rate was performed at 2 mm/min for the first group of beams, and at 10kN/min for the second group of beams. For experiments conducted under normal ambient conditions, failure of the tested beams was obtained in less than 10 minutes from the start of loading. According to ASTM D198-15, failure should be achieved withing 5 to 20 minutes.

3.2 Testing procedure for heating and residual testing at ambient conditions

The heating condition for specimens undergoing heating and cooling was defined in order to achieve a depth of char that would compromise the internal FRP sheets. Heating was conducted by radiant panels calibrated to apply a constant incident heat flux of 42 kW/m^2, which was chosen to achieve self-ignition and avoid the occurrence of self-extinguishment during heating for a long enough duration, based on a previous study conducted by (Emberley, 2017) on bench scale cross laminated timber specimens. Only the midspans of the beams were heated and exposure size was limited to a distance which was 100 mm shorter than the distance between loading points at midspan. This means only a midspan length of 100 mm were heated.

The heating method was not conducted according to an existing standard. The exposure to a fixed incident heat flux until failure was chosen to provide basic proof of the concept by testing many specimens within reasonable time and cost and with good repeatability.

Unloaded control heating tests were conducted with type K thermocouples embedded inside small-scale timber specimens, short length span beams of 180 - 360 mm length with identical cross-sections to those tested in four-point bending, to predict the through depth temperature distribution. The small-scale Glulam specimens and the Glulam beams were heated using rotated radiant panels from above while they were flipped so that the tensile face in bending was directly exposed to the heat from the radiant panels, as shown in Figure 4. The flipped orientation helped to avoid the flame effect on the remaining timber section to achieve good consistency. An insulation board with an exposure window was placed between the radiant panels and the timber specimens to control the size of the heated section. After 90 minutes of heat exposure, the Glulam beams were cooled down and then tested for residual bending capacity in four-point bending arrangement. The beams were loaded at a constant rate of 2 mm/min until reaching failure.

Figure 4: Testing setup during burning one of the beams (left), and during burning one of the small control specimens using rotated radiant panels (right).

3.3 Transient testing procedure

Transient capacity experiments were conducted by exposing the midspan section of the beams to a fixed incident heat flux while the beams are subjected to a sustained four-point bending load for a specific duration until failure. Only the second group of HGF beams were tested in transient conditions; the beams of that group were loaded until reaching a target level of 50% of the expected failure load of the control unreinforced Glulam beams at ambient conditions, which was fixed to 30 kN. After reaching the target load level, the beams were heated at midspan from the soffit tensile surface under a constant incident heat flux of 42 kW/m^2, for a midspan length equal to 400 mm. The test finished once the beam had reached failure due to the loss in their bending capacity as an effect of the reduced cross-section and the reduced mechanical properties of timber at elevated temperatures. All beams were tested in an inverted position as described previously in the heating procedure section.

4 EXERIMENTAL RESULTS AND ANALYSIS

4.1 Ambient testing conditions

Two and three Glulam beams were tested at ambient conditions for each of the specimen types described in the first and second groups of beams, respectively. The average results and coefficient of variation for all the ambient experiments are shown in *Table 3* and *Table 4*. The experimental load-deflection curves Figure 5. *Table 3 Table 4* also include calculations of the modulus of rupture (MoR), the average slope of the initial linear-elastic portion of the load-deflection curves, which was used to calculate the global modulus of elasticity (MoE). This can be used as an indication of the flexural rigidity of the beams. According to ASTM D198-15, this slope has been determined for the linear portion between two different stress levels below the proportional limit. The range used was between 10% and 40% of the ultimate capacity of the beams with a coefficient of determination (R^2) higher than 0.98.

Table 3: Average ambient results for bending experiments of FT1 beams from first fabrication technique group.

Beam type	Average Failure load (kN)	Avg. Failure moment (kN.m)	Avg. MoR (MPa)	Capacity increase %	CV %	Avg. Load/Def. slope (N/mm)	Avg. MoE (GPa)	Stiffness increase %	CV %
FT1-UR	145	29.7	72.8		3.4%	17400	10.8		2.3%
FT1-Rsheet	85.5	17.5	42.9	**-41%**	8.8%	13300	8.3	**-24%**	8.3%

Table 4: Average ambient results for bending experiments of FT2 beams from second fabrication technique group.

Beam type	Average Failure load (kN)	Avg. Failure moment (kN.m)	Avg. MoR (MPa)	Capacity increase %	CV %	Avg. Load/Def. slope (N/mm)	Avg. MoE (GPa)	Stiffness increase %	CV %
FT2-UR	59.7	26.9	78.0		2.1%	1342	11.9		2.8%
FT2-R126	65.7	29.6	85.8	**10%**	7.6%	1536	13.6	**14%**	5.0%
FT2-R270	63.7	28.7	83.2	**7%**	4.1%	1694	15.0	**26%**	2.6%

The reinforced beams from first fabrication technique group experienced an early-stage delamination of the reinforced lamellas, which limited the relevance of the data for analysing the bending behaviour of the first group of Glulam beams. Lower failure loads and stiffness of the HGF beams compared to the control Glulam beams were observed mainly due to delamination of the reinforced lamella that happened at the early stage of loading. All beams of the second prototype demonstrated a clear flexural failure without any sign of shear failure or delamination; the increased loading span, compared to the previous span used in the first prototype HGF beam, helped to achieve this consistency in flexural failure.

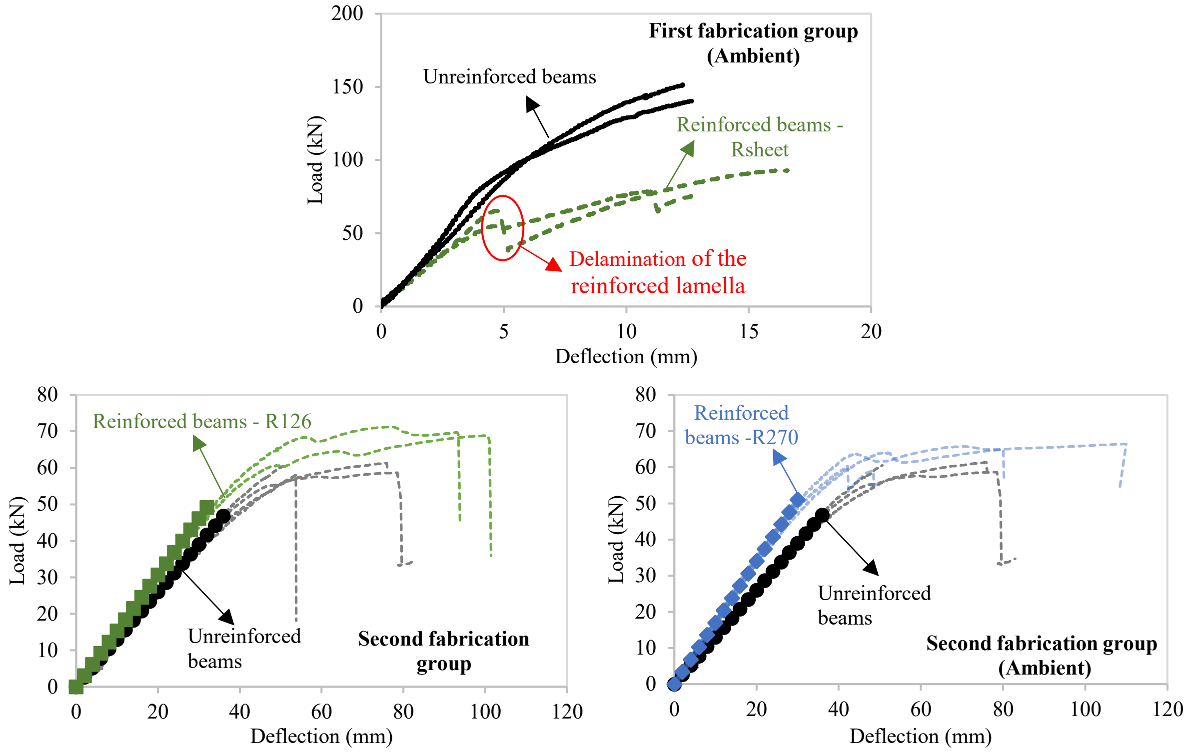

Figure 5: Load-deflection curves for the ambient testing conditions

Reinforcing the Glulam beams with CFRP strips enhanced their bending strength and their deformation behaviour. An increase in the ultimate bending capacity of the second prototype Glulam beams was around 10% and 7% for the HGF beams reinforced with R126 and R270 with a reinforcement ratio of 1% and 2%, respectively. Increasing the reinforcement ratio for the Glulam beams did not result in further enhancement of the ultimate capacity. This is mainly because of the failure of the FT2-R270 beams induced by the ductile yielding in the compression zone; the degree of ductility was dependent on the quality of the bottom timber lamellas. Therefore, over-reinforcing the Glulam beams in the tension zone did not show an additional contribution to the ultimate bending capacity. However, it was still effective to enhance their flexural rigidity and deformation behaviour.

The global MoE of the timber beams, which directly demonstrates the global bending stiffness, was calculated from the elastic stage of the load-deflection curves by using the equation from the standard test methods of static tests of lumber in structures (ASTM D198, 2015):

$$E_{global} = \frac{a.\Delta P}{4bd^3\Delta\delta}(3L^2 - 4a^2) \qquad (1)$$

where E_{global} is the global MoE; ΔP refers to the given range of the applied load in the elastic region; $\Delta\delta$ refers to the range of the deflection corresponding to ΔP; b and d represent the beam width and depth respectively; L is the beam span distance; a is the shear span distance between the support point and the loading point.

It is noteworthy that equation (1) does not include a shear correction factor as the shear modulus of the timber was not measured experimentally as part of this study. This is an important factor which affect the calculated values of global MoE and hinder any direct comparison between the beams with different shear spans.

4.2 Residual testing conditions

Residual bending capacity of the Glulam and the HGF beams were tested after undergoing heating at a constant incident heat flux of 42 kW/m^2 and then cooling down to ambient temperature before being tested in four-point bending. The duration of heating was determined based on the temperature measurements to be 30, 60, and 90 minutes to achieve three distinct charring depths equivalent to 30, 45, and 60 mm, respectively. Residual heating conditions of 30, 60, and 90 minutes are called HC30, HC60, and HC90, respectively.

Two or three Glulam beams were tested at residual testing conditions for each specimen type. The average results for all the ambient experiments are shown in *Table 5*, and the load-deflection curves are shown in Figure 6.

Table 5: Average residual results for bending experiments of FT1 beams from first fabrication technique group.

		Glulam beams				HGF beams				
Heating condition	Reinf. Ratio (%)	Average Failure Load (kN)	Avg. Failure moment (kN.m)	Capacity decrease as an effect of charring %	CV %	Average Failure Load (kN)	Avg. Failure moment (kN.m)	Capacity decrease as an effect of charring %	CV %	Relative capacity % (Rsheet/UR)
Ambient	0.0%	145.0	29.7		3%	85.5	17.5		9%	59%
HC30	0.1%	101.0	20.7	-30%	6%	78.5	16.1	-8%	15%	78%
HC60	0.1%	70.7	14.5	-51%	13%	74.0	15.2	-13%	7%	105%
HC90	0.1%	43.7	9.0	-70%	11%	77.0	15.8	-10%	10%	176%

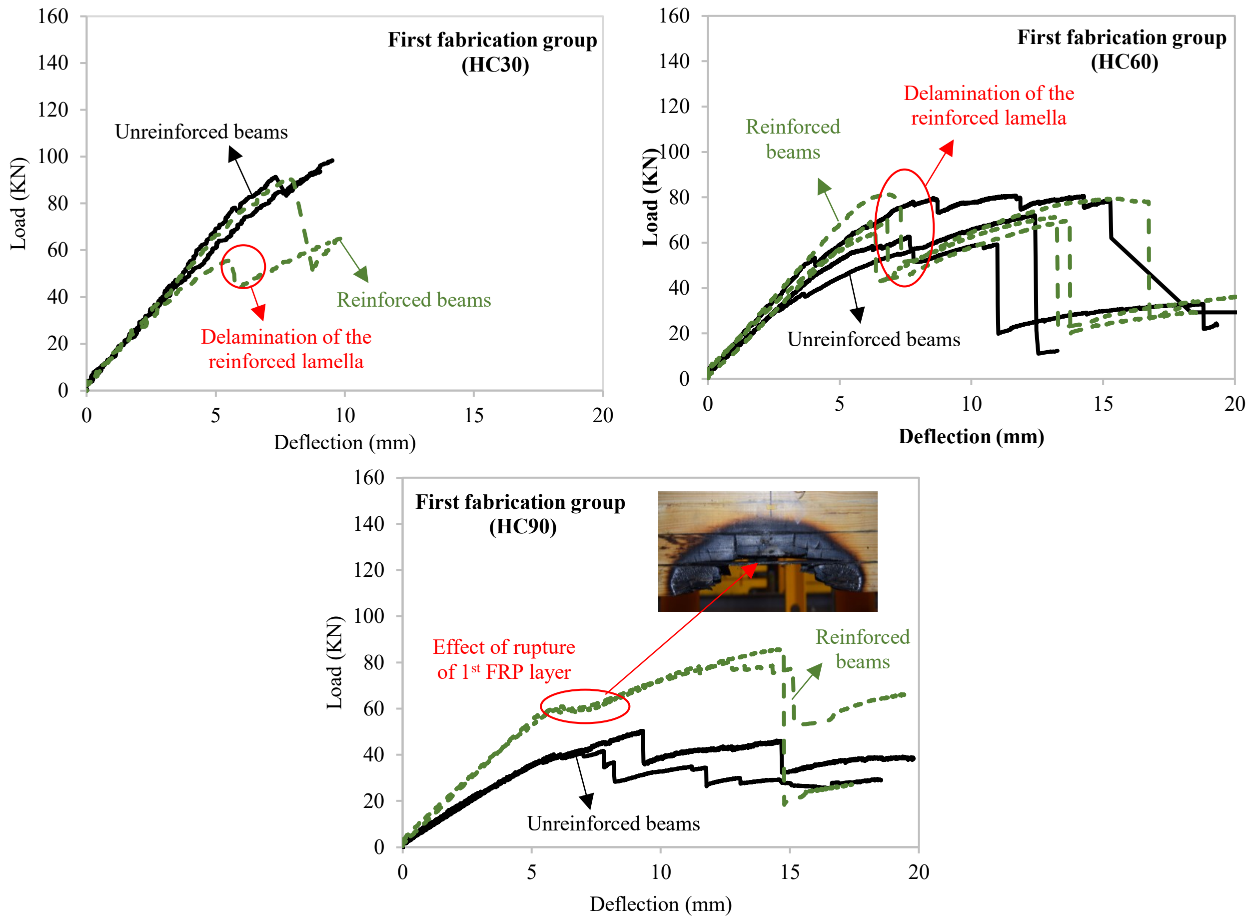

Figure 6: Load-deflection curves for the residual testing conditions

It is clear from the results that the bending capacity and stiffness of the beams were decreased for increasing durations of heating, as expected due to the increased loss of cross-section. The reduction in the capacity of the HGF beams was less severe compared to the control Glulam beams, as shown in Figure 7; this could be a result of the consistent mechanical properties of the CFRP reinforcing layer, as the CFRP layer was not significantly affected by the current degree of heating (Foster, S.K. and Bisby, 2005). In Figure 7, the failure of the hybrid beams tested at ambient conditions and after exposure to HC30 was mainly due to delamination of the reinforced lamella. Therefore, the failure loads for the hybrid beams in these groups were less than the failure loads of the control Glulam beams under the same heating conditions. As the loss of cross-section in the flexural region of the HC90 group was the highest, more significant contribution of the CFRP reinforcement fabric was achieved which resulted in much higher residual bending capacity and stiffness for the HGF beams.

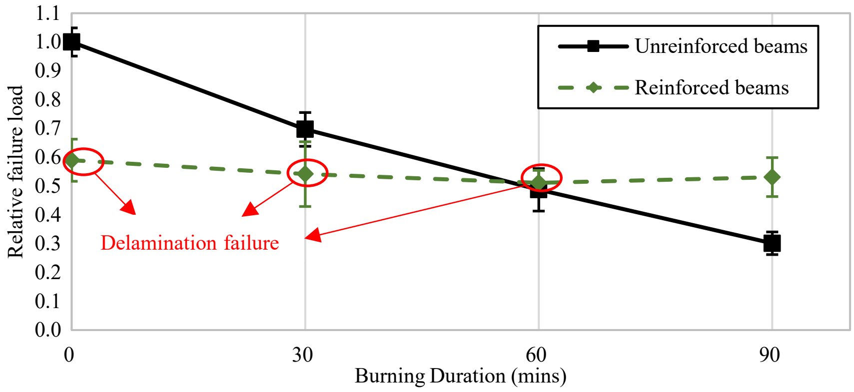

Figure 7: Normalised failure load for control Glulam (unreinforced) beams and HGF (reinforced) beams. At normal ambient testing conditions (HC0) and at residual testing conditions.

The significant reduction in the beam's cross section after being exposed to 90 minutes of heating decreased their bending capacity to the limit where the beams experienced normal bending failure before any shear or delamination effect. Therefore, the CFRP reinforcement fabric contribution to the residual bending capacity of the HGF beams was clear as shown in Figure 7. The failure of the HGF beams started with an initial rupture to the bottom CFRP layer, which was associated with clear drop in the slope of the load deflection curve, followed by overall flexural rupture of the remaining timber section and the upper CFRP sheet together.

4.3 Transient testing conditions

Three Glulam beams were tested for each of the specimen types described in the second fabrication technique group of beams at transient condition under exposure to a fixed incident HF of 42 kW/m2. The average exposure times until failure for the beams with different reinforcement ratios along with the average maximum deflections at midspan of the beams before failure are summarised in Table 6. The table also shows the average charring depths at the mid-span of the beams, which was measured after the beams collapsed and cooled down. Water quenching was applied at the burning area directly after the failure of the beams to avoid a further smouldering effect on charring depth. Figure 8 shows the effect of CFRP reinforcement in extending the fire exposure duration until failure for each group of beams.

Table 6: Average transient bending experiments results of FT2 beams from second fabrication technique group.

Beam type	Reinforc--ement Ratio (%)	Transient Heating Condition	Average Failure Time (min)	Average Equivalent Applied Thermal Energy (MJ/m^2)	Increase in Failure Time (%)	Coefficient of Variation (%)	Average Maximum Deflection (mm)	Average Charring Depth (mm)
FT2-UR	0 %	THC1	26	66		11.0 %	45	24
FT2-R126	1 %	THC1	44	111	**69 %**	3.4 %	63	37
FT2-R270	2 %	THC1	107	270	**312 %**	8.1 %	47	42

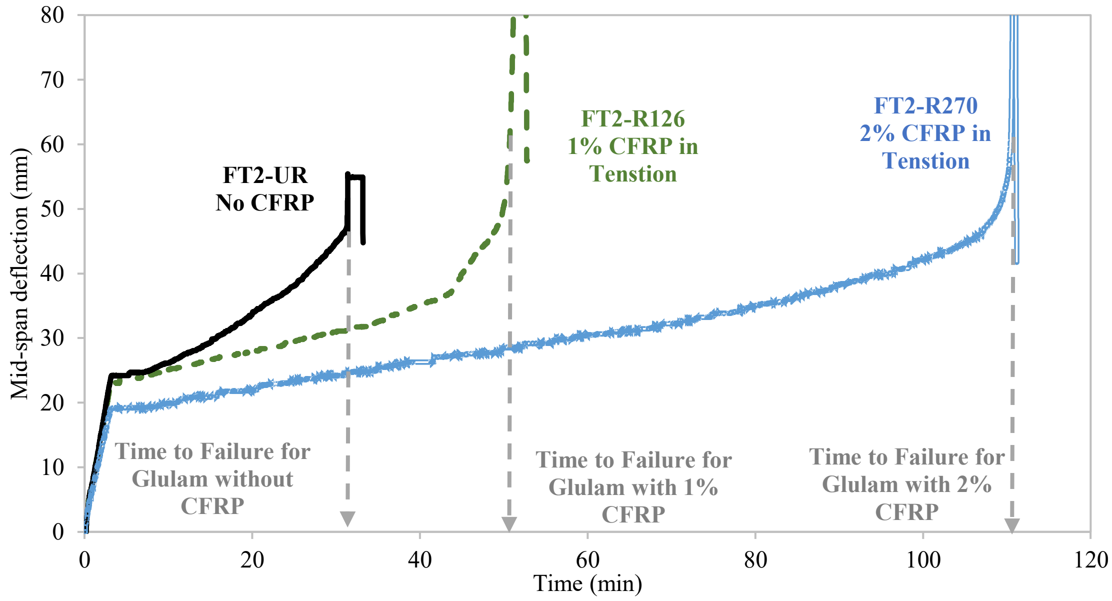

Figure 8: Exemplar time-deflection curves at mid-span for the FT2 beams from the second fabrication technique group during exposure to a fixed incident HF of 42 kW/m^2 while tested under sustained load.

The fire exposure duration until failure was quantified and compared for different types of beams. Based on the failure time, the equivalent applied thermal energy can be quantified using the following equation:

$$Equivelent\ applied\ thermal\ energy\ (kJ/m^2) = Applied\ incident\ HF\ (kW/m^2) \times Exposure\ duration\ (seconds) \quad (2)$$

Results clearly show that beams incorporating FRP reinforcement have an increased bending moment capacity during fire exposure reflected by the extensive increase in the exposure time to reach the failure of the HGF beams compared to the control Glulam beams under the same thermal boundary conditions. This increase in failure time was larger for the beams with a higher reinforcement ratio in the tension zone. The HGF beams experienced extensive yielding in the compression zone before failure; the plasticization in the compression zone of the beams led to extensive deflections before reaching the failure.

During the heating process, the CFRP strips used to reinforce the Glulam beams were heated up to temperatures in the range of 700°C. Even after exposure to this range of elevated temperatures, the CFRP was still able to contribute to the strength and stiffness of the HGF beams, considering that a sufficient cold anchorage zone was provided at each side of the beam. No apparent signs of decomposition were shown on the Carbon fibres themselves after heating.

Moreover, the CFRP reinforcements in the tension zone of the beams were able to increase the fire exposure duration to reach failure by reducing the charring rate and at the same time by compensating the loss in the timber section capacity with the strong CFRP grains. Once the CFRP strips in the tension side of the beams became exposed as an effect of timber burning, they were partially insulating the inner timber section of the beam. As a result, they decelerated the charring rate and decreased the overall charring depth.

5 CONCLUSIONS

Outcomes of the experimental studies show that hybrid Glulam-FRP (HGF) beams have an increased bending moment capacity and stiffness at ambient conditions, and during and after fire. Beams with FRP show an increase of up to 26% for bending stiffness at normal ambient conditions and an increase of 76% for residual bending capacity. When loaded during heating, the HGF beams show an increase in the time-to-failure of more than 100%.

Within the first fabrication technique described in this study, the CFRP reinforcement managed to be incorporated inside the timber by using Polyurethane adhesive as a bonding agent without affecting the timber aesthetic appeal, and they demonstrated an efficient performance after exposure to elevated temperatures. However, the first fabrication technique proposed herein was not completely effective as it initiated an early-stage delamination between lamellas.

The second fabrication technique described in this study yielded a consistent mechanism of failure in bending – away from the inter-lamella delamination observed for the first fabrication technique. This emphasised the contribution of the FRP reinforcement to the structural behaviour of Glulam beams at normal ambient conditions and during fire exposure.

Based on the analysis of the testing results for the four-point bending tests, the following may be concluded:

- The FRP strip was able to moderately increase the flexural capacity and stiffness of the Glulam beams at ambient condition and to significantly increase the residual flexural capacity and stiffness for the beams during and after thermal exposure.
- The capacity and stiffness of the unreinforced beams were decreased after thermal exposure due to the loss of cross-section. The reduction in the capacity of the reinforced beams was less severe compared to the unreinforced beams which could be a result of the consistent mechanical properties of the CFRP reinforcing layer that did not get significantly affected by the current degree of thermal exposure.
- Beams incorporating CFRP reinforcement strips have an increased bending moment capacity during fire exposure, reflected by the extensive increase in the exposure time to reach failure.
- No detrimental effects induced by the presence of the CFRP strips inside the timber beams during the ambient and the transient experiments.
- The experimental quantification of the reinforcement contribution in this study represents an important outcome which can lead to better understanding for the role of the CFRP reinforcement during or after exposure to fire. Further investigation is still required to understand the effect of different reinforcement ratios and their efficiency under different thermal boundary conditions.

ACKNOWLEDGMENT

The authors are grateful for the financial support received from the Australian Research Council under the Industrial Transformation Hub for Advanced Solutions to Transform Tall Timber Buildings (IH150100030). The support provided by the Queensland Government, Department of Agriculture and Fisheries (DAF) through the provision of the unique facilitates located at the Salisbury Research Facility is acknowledged as critical to facilitate studies of this nature. Authors would also like to acknowledge the intellectual and technical contribution of Daniel Field, Eric Littee, Andrew Outhwaite and Adam Faircloth from the Department of Agriculture and Fisheries, Queensland Government.

REFERENCES

1. Australian/New Zealand Standard AS/NZS 1080.1 (2012) ‘Timber-Method of test Moisture content’.
2. Australian/New Zealand Standard AS/NZS 1328.1 (1998) ‘Glued laminated structural timber Performance requirements and minimum production requirements’.
3. Australian Standard AS 1720.1 (2010) ‘Design Methods for Timber Structures’.
4. Emberley, R. L. (2017) ‘Fundamentals for the Fire Design of Cross Laminated Timber Buildings’. (PhD Thesis), University of Queensland, Brisbane, Australia.
5. Foster, S.K. and Bisby, L. A. (2005) ‘High temperature residual properties of externally-bonded FRP systems’, in Proceedings of the 7th international symposium on fiber reinforced polymer reinforcement for reinforced concrete structures (FRPRCS-7), p. SP-230-70.
6. Martin, A. and Tingley, A. (2000) ‘Fire resistance of FRP reinforced glulam beams’, World Conference on Timber Engineering, Whistler Resort, British Columbia, Canada.
7. Raftery, G. M. and Rodd, P. D. (2015) ‘FRP reinforcement of low-grade glulam timber bonded with wood adhesive’, Construction and Building Materials, 91, pp. 116–125. doi: 10.1016/J.CONBUILDMAT.2015.05.026.
8. Romani, M. and Blaß, H. J. (2001) ‘Design model for FRP reinforced glulam beams’, in Proceedings of the International Council for Research and Innovation in Building and Construction (CIB), Working Commission W18 Timber Structures, Meeting, p. Vol. 34.
9. Yang, H. et al. (2016) ‘Prestressed glulam beams reinforced with CFRP bars’, Construction and Building Materials, 109, pp. 73–83. doi: 10.1016/J.CONBUILDMAT.2016.02.008.
10. Zaben, A., Bailleres, H., Vella, R., McGavin, R.L., Fernando, D., Lange, D. and Maluk, C. (2021) ‘Residual performance of a prototype hybrid Timber-FRP glulam beam after fire’, in. World Conference on Timber Engineering 2021, WCTE 2021 9-12 August 2021.

IMPLICATIONS ON MASS TIMBER STRUCTURES FROM THE FINDINGS OF THE VERY LARGE COMPARTMENT FIRE EXPERIMENTS

David Barber[1], Panos Kotsovinos[2], Eirik Christensen[3], Eoin O'Loughlin[4], Judith Schultz[5]

ABSTRACT

Mass timber buildings using cross laminated timber (CLT) and glulam have significantly increased in number globally due to benefits with regards to sustainability as well as other architectural and commercial drivers. This paper presents an introduction and overview of the results from the experimental series CodeRed, highlighting the implications for the engineering design of large open plan mass timber structures. CodeRed is a series of four real scale fire experiments carried out inside a purpose-built, open-plan compartment to capture fire dynamics in large compartments with exposed timber. The aim of the CodeRed series was to study the impact on fire dynamics when introducing CLT floors (CodeRed #01), making it intentionally similar to the traveling fire experiments, x-ONE and x-TWO.1, which had a non-combustible ceiling. Additional parameters were studied also, including reduced ventilation (CodeRed #02) and CLT encapsulation (CodeRed #04), by keeping all other parameters the same as CodeRed #01. CodeRed #03 investigated the efficacy of water mist suppression and falls outside the scope of this paper.

The experiments showed the reduced ventilation impacts fire dynamics inside and outside the compartment by slowing the fire spread and burning rate. The reduced ventilation in CodeRed #02 led to an increased fire duration 20% longer duration compared to CodeRed #01. The overall fire dynamics experienced in CodeRed #04, corelate with CodeRed #01, x-ONE and x-TWO.1, with a delay in the ignition of the CLT ceiling, as the CLT directly above the crib was encapsulated. Once the CLT ceiling ignited, fire spread rapidly throughout the compartment, with the resulting fire duration, maximum temperatures and heat fluxes broadly similar to CodeRed #01. Long term fire behaviour in the compartment without firefighting intervention was also monitored; smouldering hot spots occurred in the CLT at junctions in CodeRed #01, #02 and #04. The experimental data, observations and findings from this research will assist engineers to understand how exposed mass timber structures impact fire dynamics and apply appropriate solutions for the fire safety design of exposed mass timber buildings.

Keywords: Large compartments, fire experiments, structural fire engineering, mass timber, cross-laminated timber

1 INTRODUCTION

Mass timber buildings utilising engineered timber products such as glulam and cross laminated timber (CLT) have become prevalent globally. The design of high-rise mass timber buildings has been predominantly based on protecting the mass timber elements with fire rated board systems, to improve fire resistance ratings (FRR) and to mitigate the issues of a combustible structure. Accompanying the movement for taller mass timber buildings is a significant interest in visually exposing the timber structure. For high-

[1] Principal, Arup, 699 Collin Street, Melbourne, VIC 3002 e-mail: David.Barber@arup.com ORCID: https://orcid.org/0000-0001-8658-8009
[2] Senior Engineer, Arup, 3 Piccadilly Place, Manchester, M1 3BN e-mail: Panos.Kotsovinos@arup.com, ORCID: https://orcid.org/0000-0003-2234-0420
[3] Fire Engineer, Arup, 8 Fitzroy St, London, W1T 4BJ e-mail: Eirik.Christensen@arup.com ORCID: https://orcid.org/0000- 0001-8927-1437
[4] Associate, Arup, 8 Fitzroy St, London, W1T 4BJ e-mail: Eoin.OLoughlin@arup.com
[5] Director, Arup, 8 Fitzroy St, London, W1T 4BJ e-mail: Judith.Schulz@arup.com
https://doi.org/10.6084/m9.figshare.22193689

rise buildings, a key issue to be addressed is the building code requirement for the structure to withstand a fully developed fire, which is a complex problem when the load-bearing timber is exposed. Timber is a combustible material and therefore when left exposed (i.e., not encapsulated), the compartment fire dynamics will be altered due to the additional fuel load coming from the combustion of the timber [1]. Understanding fire dynamics in timber compartments is a significant knowledge gap. To date, research with exposed timber has been limited in scale, but very informative [2 – 6], with the following key findings:

- Heat release rates (HRR) are greater in compartments with exposed timber surfaces due to the additional fuel from the timber contributing.
- In some experiments fire growth was found to be faster in combustible compartments and flashover was more quickly reached.
- Longer fire duration occurs, particularly where ventilation is limited.
- External flaming is greater as more heat flows outside with the increased HRR.
- The fire decay is extended when compared with non-combustible construction and thermal degradation of the timber during fire decay will occur after flaming has ceased. Smouldering may also be factor, though not often assessed in experiments.
- Timber susceptible to glue-line integrity failure (i.e., adhesive dependent falling off of the charred layer exposing fresh timber in the fire) may experience increased charring and lead to the fire reaching a secondary flashover or not reaching a decay phase after the contents have burnt.

Compartment fire experiments with exposed timber have been based on residential type spaces with the largest being only 84 m^2 in floor area. The fire behaviour in smaller compartments (less than ~150m^2) is proportional to the ventilation available and if flashover occurs. As a result, these exposed mass timber experiments are not necessarily representative of larger compartments such as open-plan offices with proposed floor areas in the range 1,000 to 4,000 m^2, used in the design of commercial buildings [7]. For non-combustible compartments, fire dynamics can differ significantly between small compartments and large open-plan compartments. In large open-plan non-combustible compartments, travelling fires have been observed [8, 9] and compartment fires tend to be fuel controlled rather than ventilation controlled, as is often the case for small compartments [10]. The CodeRed experimental series is the first of its kind worldwide to investigate the fire dynamics experienced in large compartments (> 100 m^2) with exposed timber and how these differ from small compartments and non-combustible large compartments. This paper provides a summary of the findings to date, as they relate to timber structures.

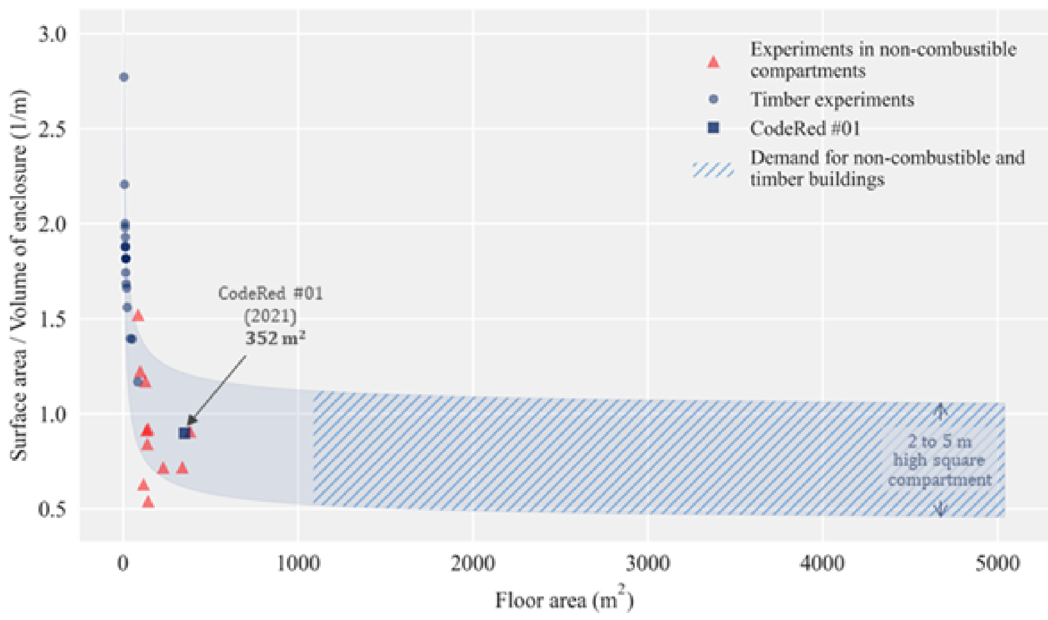

Figure 1. Comparison of the surface area to volume ratio of compartments within which experiments have been carried out to date, and demand for non-combustible and timber buildings worldwide. Shaded area represents a range of typical surface area to volume of enclosure ratios for a rectangular compartment with floor to ceiling heights between 2 and 5 m

2 LARGE COMPARTMENT FIRE EXPERIMENTS WITH EXPOSED MASS TIMBER

Globally, there is no validated design methodology for quantifying the effect of exposed timber on the fire dynamics of large compartments, for the full duration of a fire. Open-plan compartment floor areas up to 5000m^2 are currently being proposed for mass timber buildings which are significantly larger than timber compartments for which experimental data is available. Given this lack of connectivity between the smaller scale experiments and planned buildings, Arup in collaboration with CERIB and Imperial College London have completed four experiments on a very large open plan compartment with exposed CLT, referred to as "CodeRed".

The large-scale fire experiments are carried out in a purpose-built, open-plan compartment with a floor area of 352 m^2. The facility used for the CodeRed series was built at CERIB's site in Epernon, France. The configuration resembles that of an existing non-combustible building used in a series of experiments, known as x-ONE [11] and x-TWO [9], that studied travelling fire dynamics in open-plan compartments, to be able compare the impact of exposed timber on fire dynamics. The large-scale compartment had a fully exposed CLT ceiling and two glued laminated timber columns. At 352 m^2 floor area, this is the largest compartment fire experiment with exposed timber carried out to date as illustrated in figure 1. The primary aim of the CodeRed experiments was to assess the impact of exposed timber on the fire dynamics. Secondary goals related to determining the impact of the exposed timber on (1) structural fire resistance and (2) external flaming and fire spread.

2.1 Experimental Setup

Internally, the compartment is 10.27 m wide, 34.27 m long and 3.1 m tall (see Figure 2). The building was constructed from concrete blocks (365 mm thick) to provide a robust non-combustible enclosure and support the ends of each CLT panel. A load bearing 34.27 m long concrete beam (0.25 m × 0.55 m) runs along the centreline of the compartment, supported by 6 concrete columns (0.25 × 0.30 m) to support the centre of the CLT panels. The CodeRed compartment included two glulam columns and a protected steel column to evaluate their performance during and after a fire. The two glulam columns were installed 1.75 m offset from the centreline, at 16.64 and 31.60 m from the start of the compartment (12.22 and 27.18 m from ignition). The steel column was included to establish a comparative fire severity for a non-combustible structural member. The column section was HEB 200, was 3.05 m high and protected with two layers of 15 mm plasterboard to achieve a load-bearing fire resistance of 90 min. It was positioned between the two glulam columns. None of the CLT ceiling, glulam or steel columns were load bearing as the experiment intent was to investigate compartment fire dynamics while minimising the risk of structural collapse to mitigate potential health and safety risks. The ceiling (roof) was constructed from a commercially available CLT supplier using an adhesive that has proven glue-line integrity in fire (non-delaminating). The CLT ceiling comprises 5 ply (40-20-20-20-40 mm) spruce wood with MUF adhesive. Due to the size of the compartment the CLT ceiling was constructed of 14 panels laid side by side with each panel spanning the width of the compartment and centrally supported by the continuous concrete beam.

Four experiments were completed over a number of months during the year of 2021 (see Table 1). Due to covid restrictions, the experimental schedule was extended. CodeRed #02 was a variant of CodeRed #01 with ventilation reduced by half. CodeRed #04 was a variant of CodeRed #01 with the amount of exposed CLT reduced by approximately half. CodeRed #03 was a variant of CodeRed #01 with the installation of water suppression (CodeRed #03 is not covered in this paper).

Table 1. Summary of four CodeRed experiments completed

Parameter	CodeRed #01	CodeRed #02	CodeRed #03	CodeRed #04
Ceiling	Fully exposed CLT ceiling	Fully exposed CLT ceiling	Fully exposed CLT ceiling with water suppression	52% exposed and 48% encapsulated CLT ceiling
Ventilation	21%	10%	21%	21%
Area	352m^2	352m^2	352m^2	352m^2

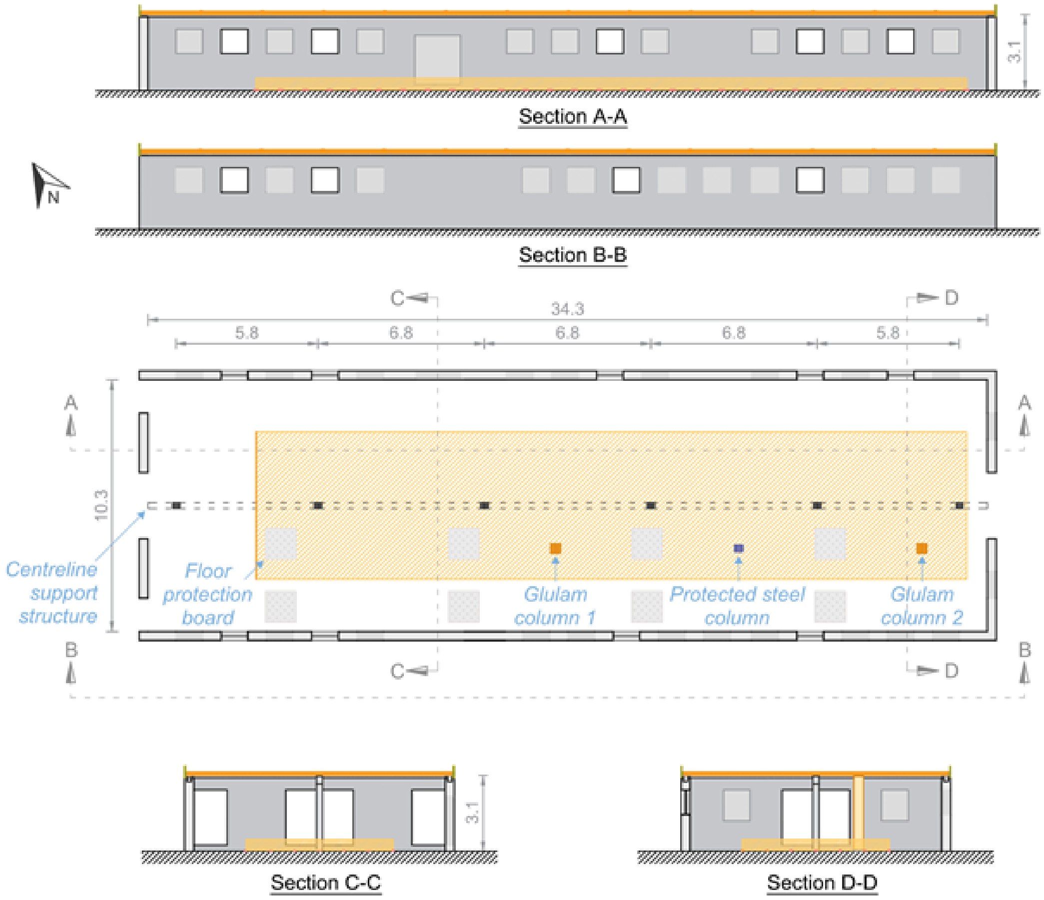

Figure 2. Floor plan and sections of the compartment used for the CodeRed #01 experiment (units in metre)

The fuel load was a wood crib with an approximate fuel density of 374 MJ/m^2 (see Figure 3). The wood crib comprised softwood sticks with the dimensions of 30 mm × 30 mm × 1000 mm, density of ~455 kg/m^3 (average), heat of combustion of 19.05 ± 0.14 MJ/kg, and moisture content of 13.5 ± 0.8 % (on dry basis). The ignition procedure for the fuel was placing a line of 12 pans (150 × 250 mm), each filled with 0.5 l methanol, below one end of the continuous wood crib.

2.1.1 *Ventilation*

The CodeRed building was constructed with five door and 31 window openings. In total, 21% of the compartment wall surface area constituted of openings (i.e., area of window opening, $A_w = 57$ m^2), resulting in an opening factor of 0.071 m$^{1/2}$ ($A_w\sqrt{h}/A_{total}$, where A_{total} is the total surface area) with a weighted average opening height, h, of 1.49 m as defined in Annex A of Eurocode 1 [12]. Opening factors are commonly used to describe the amount of ventilation in a fire compartment. The higher the opening factor, the more likely the fire is to be fuel controlled. For CodeRed #02 the ventilation was reduced to 10% of the compartment wall surface area ($A_w = 28$ m^2), resulting in an opening factor of 0.039 m$^{1/2}$ with a weighted average opening height, h, of 0.91 m

2.1.2 *Instrumentation*

Extensive instrumentation was installed to measure the fire dynamics and the thermal exposure. The temperature development of the gas, CLT ceiling, glulam and steel columns were measured, as well as the incident heat flux received by the ceiling and protected steel column. Additionally, gas temperature and heat flux measurements were recorded of the external flaming from one door and one window. Data was recorded for 60 hours with no fire-fighter intervention to capture the temperature development within the timber elements during the cooling phase and to observe post fire behaviour of the compartment following the burn out of the crib, such as smouldering or transition back to flaming. This behaviour is noted to be important with respect to structural capacity. To date, to the best of the knowledge of the authors, no such data exist which capture the timber behaviour for an extended duration following the experiment.

Figure 3. Image of pre-ignition setup from CodeRed #01 showing the exposed CLT ceiling and columns.

2.1.3 Encapsulation

For CodeRed #04 the encapsulation was installed in the middle of the compartment with the perimeter of the ceiling left exposed (i.e., 2.41 m from each longitudinal wall). The encapsulation was located centrally to test the performance and effectiveness in the most onerous location from a fire severity perspective (i.e., just above the fuel load) and to maximise the potential of external flaming by keeping the timber in the perimeter of the building exposed. It is also representative of preferred architectural arrangements. The area covered by the encapsulation was 161 m^2, 32.17m in length and 5.00 m in width, comprising 48% of the total ceiling area. The encapsulation consisted of three layers of 12.5 mm fire rated boards. The commercial encapsulation product was selected on the basis that it was been classified to BS EN 13501-2 and BS EN 13501-1 to achieve a K_2 60 A2-s1,d0 standard, as reported by the manufacturer.

3 IMPLICATIONS FROM CODERED EXPERIMENTS FOR MASS TIMBER STRUCTURES

The following sections provide an overview of the implications of the CodeRed experiment series results applicable to the engineering design of mass timber structures.

3.1 Fire dynamics characteristics – change in ventilation

The timber compartment fire framework presented by Gorska et al. [5] characterised fires as fuel or ventilation controlled based on the opening factor and maximum average temperature in the compartment. Based on their opening factors, CodeRed #01 [13] and CodeRed #02 [14] would be classified as fuel and ventilation controlled respectively. However, this framework cannot be directly applied for CodeRed #01 and CodeRed #02 as these are large compartments that naturally fall outside of the original scope, as described Gorska et al. The CodeRed experiments present dynamics where conditions are more complex and potentially best described as moving between traditional definitions.

The heat release rate of CodeRed #02 is estimated to be 99MW which is 18% lower than the 121 MW estimated for CodeRed #01. This assumes that combustion efficiency is the same between the two experiments for comparison purposes although it is recognised that in CodeRed #02 combustion was less efficient due to lack of ventilation, evident in the increased smoke production observed. The peak heat release rate in CodeRed #04 [15] was estimated to be approximately 103 MW, a 14% decrease from CodeRed #01, reflecting the lesser fuel available due to encapsulation of the CLT. The fire and resultant heat flux to the timber is influenced by the available fuel, type of CLT and available ventilation. Ventilation was reduced by 50% between experiment #01 and #02 and the area of exposed CLT reduced by 50% between experiment #01 and #04. The reduction in ventilation followed classical fire theory with the resultant fire exposure longer and with a slower decay, negatively influencing char depth. The reduction in exposed CLT slowed fire growth and changed the decay phase with improved results for the resultant char depth. Peak gas temperatures recorded at thermocouple tree locations, at set heights are shown for CodeRed #01, #02 and #04 in fFigure 4 and Figure 5. Figure 6 and Figure 7 show the peak gas temperature results and Figure 7 also includes a comparison with non-combustible compartment x-ONE and x-TWO.1.

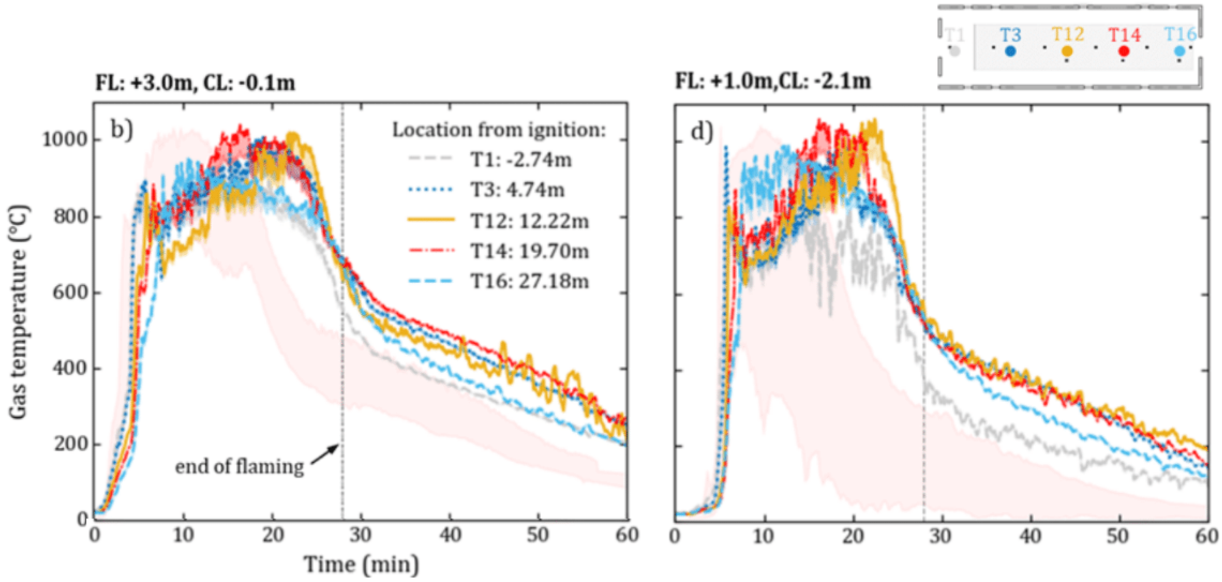

Figure 4. Code Red #02 peak gas temperatures along the centreline measured at +3.0 m above floor level = - 0.1 m below ceiling level (left), +1.0 m above floor level = -2.1 m below ceiling level (right), compared with CodeRed #01. The temperature range measured during CodeRed #01 is presented as a red cloud, using the same thermocouple locations as for CodeRed #02.

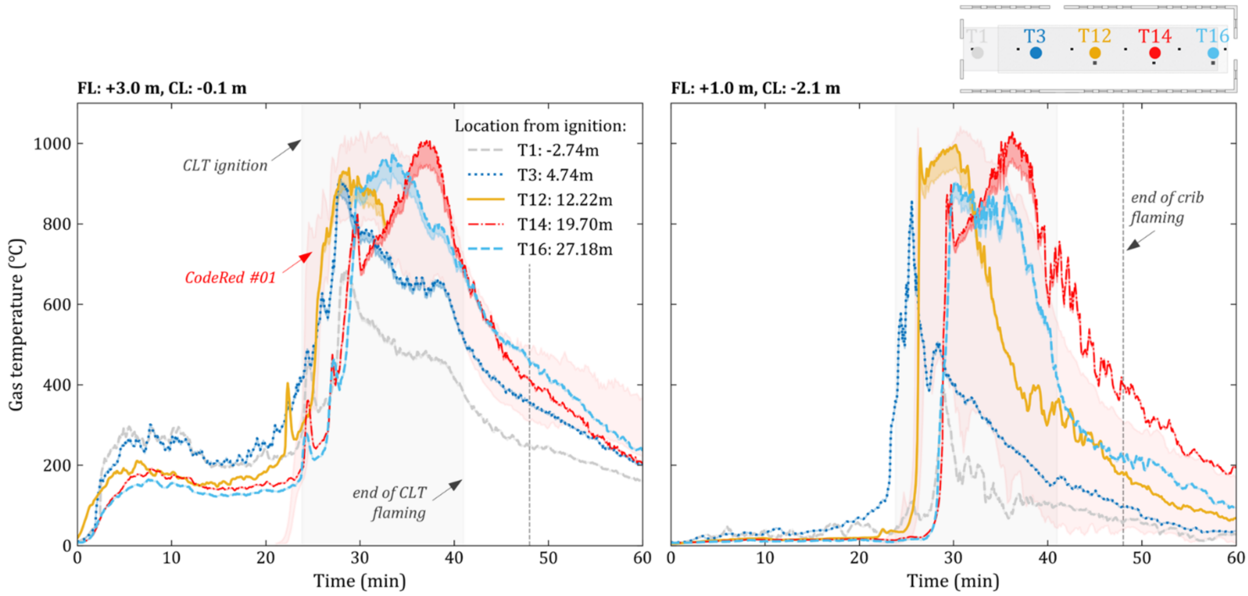

Figure 5. CodeRed #04 peak gas temperatures along the centreline measured at +3.0 m above floor level = - 0.1 m below ceiling level (left), +1.0 m above floor level = -2.1 m below ceiling level (right). Uncertainty in the radiation correction is represented by a cloud around the temperature profile. The temperature range measured during CodeRed #01 is presented as a red cloud, using the same thermocouple locations as for CodeRed #04

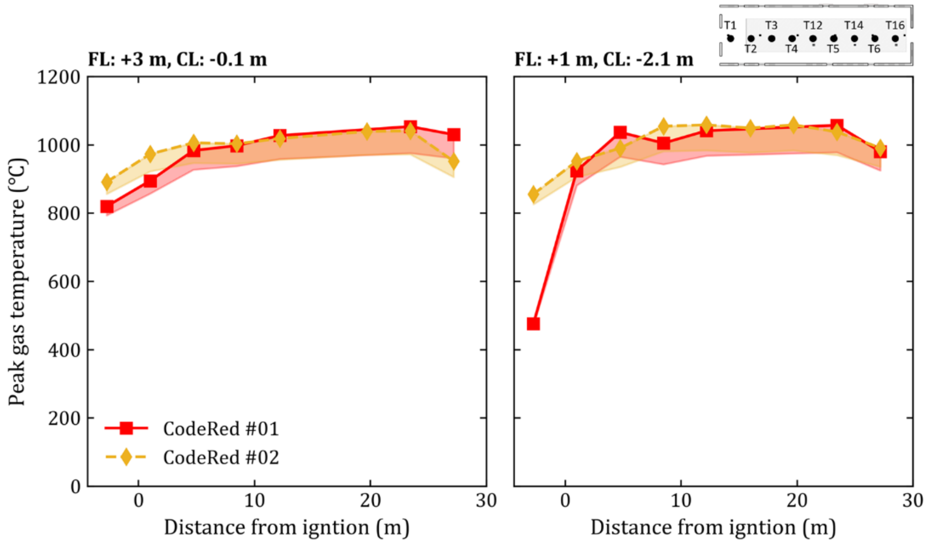

Figure 6. Comparison of peak gas temperatures CodeRed #01 and CodeRed #02 at varying positions from ignition and at two different heights above the floor level.

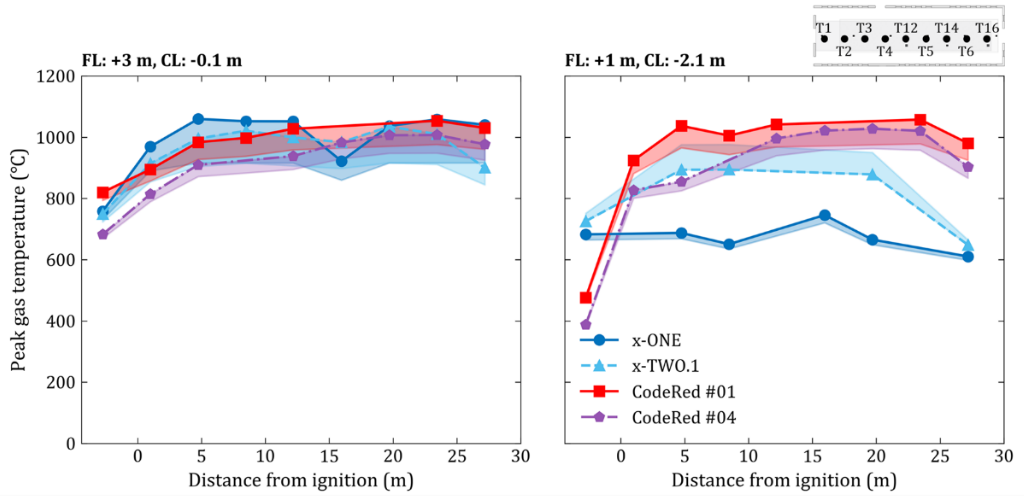

Figure 7. Comparison of peak gas temperatures CodeRed #01, CodeRed #04, x-ONE, and x-TWO.1 at varying positions from ignition and at two different heights above the floor level.

The observations of the flame propagation, external flaming, and temperature development suggest that CodeRed #02 was limited by the ventilation, when compared with CodeRed #01, resulting in a greater quantity of the combustion occurring outside of the compartment. In both CodeRed #01 and CodeRed #02 a leading edge was observed to spread across the compartment. Similarly, a trailing edge was observed with video cameras, particularly in CodeRed #01 and less so in CodeRed #02, characteristic of fuel controlled travelling fires. In both experiments there was a period when the fire was burning across the entire wood crib and there was external flaming from all openings simultaneously. Previous studies have refereed to similar phenomena as “localised flashover” [16]. The presence of the timber ceiling resulted in more rapid fire spread in comparison to the equivalent non-combustible structure. The average fire spread rate across the wood crib in CodeRed #01 and CodeRed #02 was 160 and 150 mm/s, while for x-ONE and x-TWO.1 it was 73 and 35 mm/s, respectively. The average flame spread rate across the CLT was 150 mm/s in CodeRed #02 compared to 200 mm/s for CodeRed #01. The fire dynamics in large open compartments with an exposed timber ceiling presents complex characteristics, beyond traditional definitions.

3.2 Structural resistance

The structural capacity of mass timber elements exposed to fire is based on determining an effective cross-section, based on a depth of char and reduced strength zone, for a specified design fire. For a high-rise building the full growth, development and decay phases of the fire needs to be assessed as these phases impact the final effective char depth and hence, the structural capacity. CodeRed #02 highlighted the impact of reduced ventilation on the structure by extending the overall flaming duration by 20% (15.6% considering the time after CLT ignition). Additionally, while the peak temperatures and heat fluxes reached are similar, they occur later and at different times when compared to CodeRed #01 that was well ventilated. The CLT additionally experienced more charring in CodeRed#02. Also observed is that the highest temperature inside the compartment occurred near the end of the fire duration as the compartment has been heating up and re-radiating since the ignition of the fire, which has an impact on the observed charring. Another impact of the reduced ventilation were the gas temperatures of CodeRed #02 being more spatially uniform for a longer period, for the length of compartment and over the internal height.

The charring in timber structures that occurs in the decay phase of a fire is of particular importance and often ignored in design, potentially leading to non-conservative results. The rate of decay of gas temperatures in CodeRed #02 after the end of flaming was 9.7 °C/min, compared to 11.2 °C/min for CodeRed #01. The 13% reduction in decay rate suggests that the 50% change in ventilation increased the overall time period of decay, resulting in increased charring in all timber members. Weighted average char depths along the compartment between CodeRed#01 and #02 were measured post-fire from residual cross-sections for selected CLT panels. For CodeRed #02 the average char depth across the CLT ceiling was ~28 mm, whereas in CodeRed #01 this was 25 mm, an 11% increase in overall char depth (see figure 8).

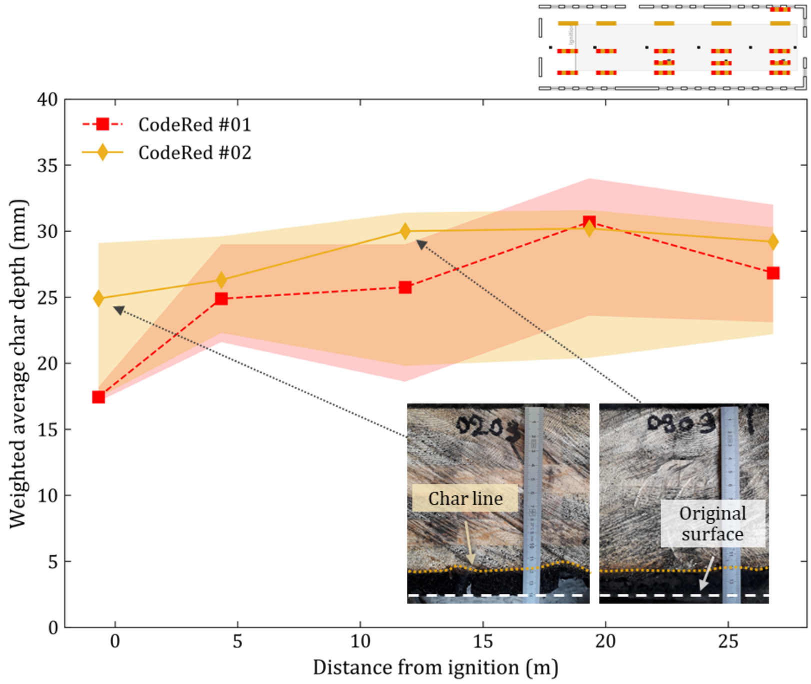

Figure 8. Comparison of weighted average char depths along the compartment between CodeRed#01 and #02. Char depths were measured post-fire from residual cross-sections for selected CLT panels. The char depths are weighted based on lateral distance between cuts. Diagram at the top indicates locations of the panel section cuts. The shaded cloud represents the minimum and maximum average char depth from cuts in a relevant panel.

3.3 Impact of encapsulation

The fire dynamics observed in CodeRed #04 corelates with the characteristics observed in CodeRed #01 and the reference non-combustible experiments, x-ONE and x-TWO.1. The peak HRR of CodeRed #04 was 14% lower than in CodeRed #01, but 47 % and 76% greater than x-ONE and x-TWO.1 respectively. CodeRed #04 showed that despite the encapsulation preventing direct flame impingement onto the exposed CLT during the early growth stage, the CLT ceiling still ignited because of exposure from the convection of hot gas layer and radiation. Once the ceiling was consistently flaming, the fire quickly spread across the full extent of the CLT and wood crib. The presence and positioning of the encapsulation impacted the development of the fire, as it delayed the ignition of the CLT, given the area directly above the wood crib was encapsulated, so wood crib flaming did not directly impinge on the CLT. This delayed CLT ignition however, provided a prolonged preheating period, where the hot smoke layer could heat and dry the exposed CLT. Once the CLT did ignite the average spread across the CLT, taken from after the consistent flaming of the CLT, was greater than that of CodeRed #01, with 222 mm/s compared to 200 mm/s in CodeRed #01. This highlights the relationship between the movable fuel fire development, CLT and encapsulation placement. The greater the delay in CLT ignition, the more rapid the fire spread may be once ignited. As a result, the fire growth is based on several complex parameters and cannot be easily predicted a-priori.

Again, the fire was observed to travel with a distinct leading and trailing edge. Although the leading edge on the crib spread rapidly after the CLT ignition resulting in a large fire size, the fire was broadly observed to be predominantly fuel controlled. This is indicated by the external flaming, which was unevenly distributed through the openings, and the temperature measurements which showed a rapid increase in gas temperatures before reaching steady values around flame temperature (~1000°C). Visual inspection confirmed that the CLT was largely uncharred beneath the encapsulation. The weighted average char depth for the CLT panels (where exposed) was found to be like CodeRed #01 (25 mm), suggesting that the resulting fire severity from the two experiments is approximately equal. This is consistent with the expectations about burning duration from classic fire dynamics theory for well ventilated compartments. Measurements taken at the end of the encapsulation (southeast border), showed CLT charring approximately 40 mm from the edge (beneath) the encapsulation. Smouldering also occurred below the encapsulation within the CLT. Average charring depth for the two columns was 19 mm and 25 mm respectively, significantly less than the 30 mm char depth measured in CodeRed #01, which is likely related to the reduced radiation feedback from the partly encapsulated ceiling to the lower parts of the compartment.

3.4 Decay phase thermal degradation

The relative rate of decay of a fire slows with a greater area of exposed mass timber. CodeRed has provided significant data regarding the impact of continued thermal degradation in the timber that occurs after the peak compartment temperatures and after flaming has ceased (see Figure 9). Peak gas temperatures in CodeRed #01 and #02 occurred between 10 and 27 mins, whereas peak temperatures in the glulam columns occurred from 19 mins through to 73 mins. The time-lag between peak compartment temperatures and peak temperatures in the timber, and the resultant slow cooling of temperatures in the timber is very important for engineering design, as temperatures above 100^{o}C in the timber member will cause a reduction in strength and stiffness [17]. This continued reduction in timber properties needs to be accounted for throughout the fire decay phase, even when the compartment temperatures are below 100^{o}C. The impact is particularly relevant for the engineering design of columns as critical vertical load paths, which could reach their weakest load-bearing state in a severe fire well after flaming combustion has ceased.

3.5 External flaming

External flaming is important when evaluating vertical fire spread between floors and fire spread to adjacent properties. Observations and data from CodeRed #01, #02 and #04 indicate that existing engineering methods for predicting flame extension and temperatures are not accurate where large area of CLT are exposed at the ceiling. New design tools that can capture exposed CLT need to be developed. Data and observations from CodeRed #02 (see Figure 10) indicate external flaming was observed to extend further laterally from the compartment, when compared with Code Red #01, indicating the impact of the reduced ventilation. The external flames in CodeRed #02 reached heights of up 3 to 3.5 m depending on the window location, which is taller than CodeRed #01 and from the end openings protruded much further (laterally) from the compartment. The duration of the external flaming was also longer. The conditions were generally more onerous with regards to external fire spread compared to observations made in the equivalent non-combustible compartments. In CodeRed #04, flames outside the door opening were small (around 0.5 m high). The window opening produced greater flame heights compared to the door opening, of around 2.0 m at their peak, however the encapsulation reduced the burning rate such that external flames were smaller than those seen in CodeRed #01. External flaming in CodeRed #04 appears to be approximately similar to that observed from non-combustible compartments of the same geometry [11] in terms of flame height.

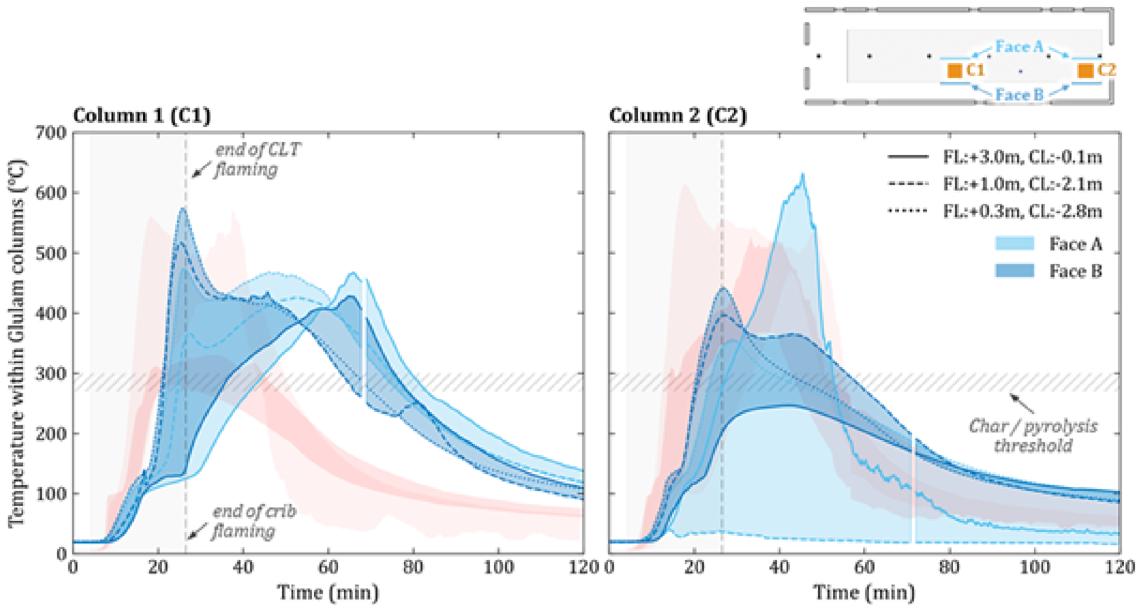

Figure 9. CodeRed #02 recorded thermocouple temperatures at 20mm depth from the exposed surface in glulam column 1 and column 2 at heights of approx. 3 m, 1 m and 0.3 m above the floor in Face A and Face B. Vertical thermocouple positions in Face A are 6 cm lower than in Face B. The red clouds are the results from CodeRed#01, with the lighter and darker cloud corresponding to Face A and B respectively.

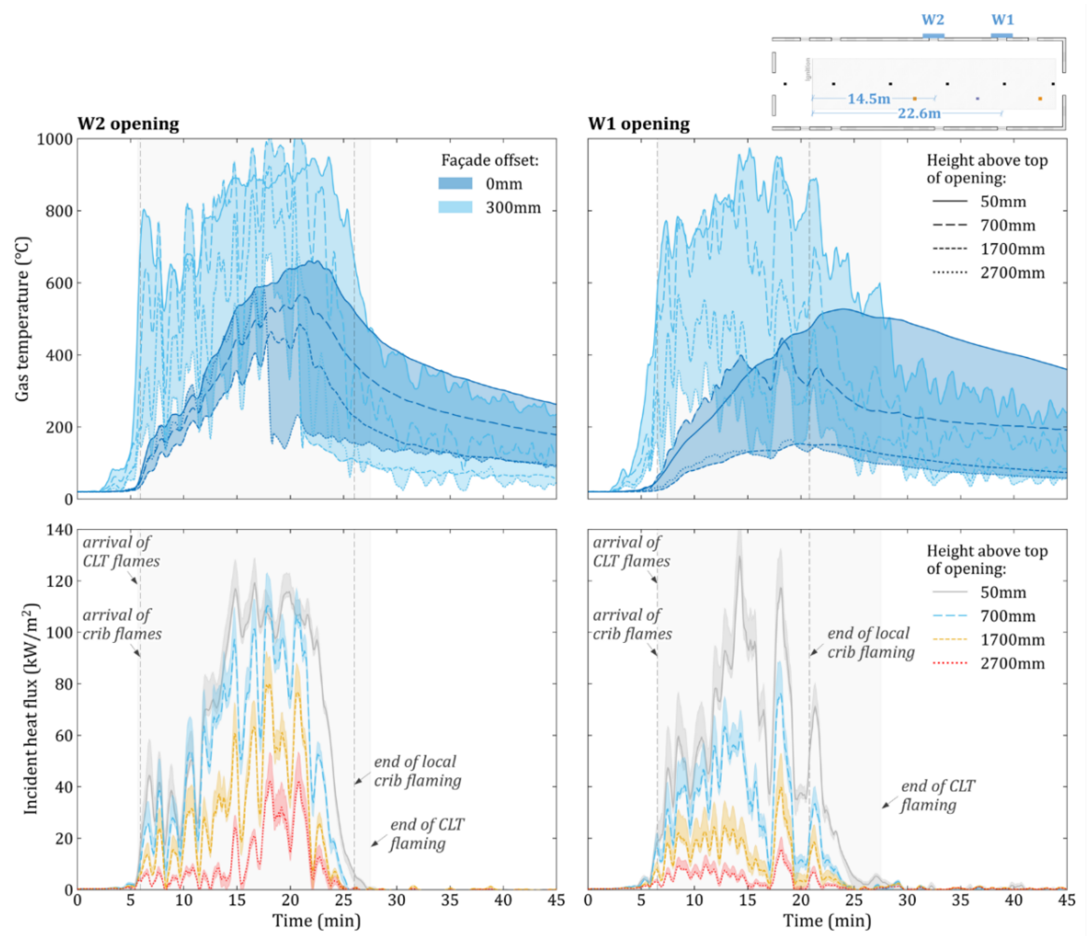

Figure 10: External flame/plume gas temperatures and incident heat fluxes to the façade measured at various heights above the opening soffit during CodeRed #02. The cloud in the incident heat flux plots represents the maximum and minimum heat fluxes of all permutations of uncertainty in emissivity (0.7 to 0.9) and the heat transfer coefficient (5 to 25 W/m²K).

3.6 Smouldering in timber interfaces

Smouldering within timber interfaces has been analysed to understand where the smouldering is likely to occur, the rate of smouldering, how this can be detected and methods for suppression. Smouldering occurred in CodeRed #01, #02 and #04, at timber junctions and interfaces between the CLT panels and the central beam or at the external walls. This was observed to occur for the following 60 hours after ignition, until suppression or natural extinction. In CodeRed #01, #02 and #04, hot spots were identified after the end of flaming that resulted in holes being created in the CLT slab. In CodeRed #02 one of the hotspots transitioned to flaming and was successfully suppressed with a water hose. Further research is necessary to establish potential links between smouldering and the conditions that affect its occurrence in specific locations such as junctions. Understanding where smouldering may occur is important as connections are critical locations for the loadbearing capacity of structural members and the risk of on-going smouldering may remain in difficult to access areas.

4 CONCLUSIONS

This paper presents an overview of the experimental data and observations from the CodeRed series of fire experiments carried out inside a purpose-built, open-plan compartment with exposed mass timber elements. CodeRed #01 studied the impact of fully exposed CLT slab compared to an equivalent non-combustible compartment. CodeRed #02 was set-up to assess the impact of a circa 50% reduced ventilation on fire dynamics while keeping all other relevant parameters the same as CodeRed #01. Code Red #04 was set-up to assess the impact of a circa 50% encapsulation of the CLT ceiling while keeping all other relevant parameters the same as Code Red #01. The presence of CLT ceiling accelerated fire spread across the wood crib and the CLT, increased the extension of external flaming and resulted in more sustained higher compartment temperatures, when compared to the equivalent non-combustible compartment. The observations indicate that CodeRed #02 was limited by the reduced ventilation and impacted the spread rate of flames across the CLT, more than the crib. Similar observations of CodeRed #04 indicate that fire spread was initially slowed by the encapsulation as there was no direct flame impingement on the CLT, but the prolonged period of pre-heating then resulted in faster flame spread across the CLT surface.

Also relevant was the choice of CLT. The resultant fire conditions observed during the decay phase of the fire may not have occurred if the CLT did not have proven glue-line integrity in fire, i.e. if the CLT suffered from delamination under fire exposure. For engineering design of buildings with exposed mass timber structural elements, the fire decay phase needs to be predictable and reliable, and able to be correlated to the moveable (floor) fuel and the area of available ventilation. If the CLT being used does not have proven glue line integrity in fire, then the connectivity between exposed timber surfaces, moveable fuel and ventilation cannot be reliably determined, as the CLT delaminating event(s) then need to be incorporated into the analysis. Methods to predict how a CLT delaminating event occurs, the timing, and most importantly, the impact on the compartment fire dynamics, have not been established and are highly complex.

The implications on mass timber structures have been presented in this paper, highlighting how the exposed mass timber, changed ventilation conditions and encapsulation impacts fire severity, charring of timber, decay phase of the fire, assessment of timber strength in the decay phase, fire spread through external flaming and smouldering at interfaces.

ACKNOWLEDGMENT

This research has been fully funded by Arup and was undertaken in partnership with CERIB, France and Imperial College London. All CERIB staff involved in the experiment are gratefully acknowledged as well as the Imperial College London PhD students (Harry Mitchel, Rikesh Amin and Simona Dossi). The following Arup staff that helped in the analysis included in this work are acknowledged Clara Bermejo Bordons, Alexandra Dakin, Tess Van Der Veen and Daniel Thompson.

REFERENCES

1. Hadden, R. Bartlett, A. Hidalgo, J. Santamaria, S. Wiesner, F. Bisby, L. Deeny, S .and Lane, B., 2017, "Effects of exposed cross laminated timber on compartment fire dynamics," Fire Safety Journal, Vol. 91, No. February, pp. 480–489.
2. Su, J., LaFrance, P., Hoehler, M., Bundy, M., 2018, "Fire Safety Challenges of Tall Wood Buildings – Phase 2: Task 2 & 3 Cross Laminated Timber Compartment Fire Tests" Fire Protection Research Foundation, Report No. FPRF-2018-01
3. Zelinka, S., Hasburgh, L., Bourne, K., Tucholski, D., Ouellette, J., 2018, "Compartment Fire Testing of a Two-Story Mass Timber Building" General Technical Report FPL–GTR–247, May 2018
4. Brandon, D., Sjöström, J., Hallberg, E., Temple, A., and Kahl, F., 2020, "Fire safe implementation of visible mass timber in tall buildings – compartment fire testing," Final Project Report RISE Report 2021:40
5. Gorska, C. Hidalgo, J. and Torero, J., 2021, "Fire dynamics in mass timber compartments," Fire Safety Journal, Vol. 120, No. April 2020, p. 103098.
6. McNamee, R. Zehfuss, J. Bartlett, A. Heidari, M. Robert, F. and Bisby, L., 2021, "Enclosure fire dynamics with a cross-laminated timber ceiling," Fire and Materials, Vol. 45, No. 7, pp. 847–857.
7. Rackauskaite, E., Kotsovinos, P. & Barber, D. 2021, Letter to the Editor: Design Fires for Open-Plan Buildings with Exposed Mass-Timber Ceiling. Fire Technology 57, 487–495
8. Rackauskaite, E. Kotsovinos, P. and Rein, G., 2017, "Structural response of a steel-frame building to horizontal and vertical travelling fires in multiple floors," Fire Safety Journal, Vol. 91, No. February, pp. 542–552.
9. Heidari, M., 2021, "Travelling fires methodology and probabilistic design of structures," Imperial College London.
10. Torero, J. Majdalani, A. Cecilia, A. and Cowlard, A., 2014, "Revisiting the compartment fire," Fire Safety Science, Vol. 11, pp. 28–45.
11. Rackauskaite, E. Bonner, M. Restuccia, F. Fernandez Anez, N. Christensen, E. Roenner, N. Wegrzynski, W. Turkowski, P. Tofilo, P. Heidari, M. Kotsovinos, P. Vermesi, I. Richter, F. Hu, Y. Jeanneret, C. Wadhwani, R. and Rein, G., 2021, "Fire Experiment Inside a Very Large and Open-Plan Compartment: x-ONE," Fire Technology.
12. CEN, 2002, EN 1991-1-2 - Eurocode 1. Actions on structures. General actions. Actions on structures exposed to fire. Brussels.
13. P. Kotsovinos, E. Rackauskaite, E. Christensen, A. Glew, E. O'Loughlin, H. Mitchell, R. Amin, F. Robert, M. Heidari, D. Barber, G. Rein and J. Schulz, 2022 "Fire dynamics inside an open-plan compartment with an exposed CLT ceiling and glulam columns: CodeRed #01", Fire and Materials.
14. P. Kotsovinos, E. Christensen, E. Rackauskaite, A. Glew, E. O'Loughlin, H. Mitchell, R. Amin, F. Robert, M. Heidari, D. Barber, G. Rein and J. Schulz, 2022 "Impact of ventilation on the fire dynamics of an open-plan compartment with exposed CLT ceiling and glulam columns: CodeRed #02", Fire and Materials.
15. P. Kotsovinos, E. Christensen, A. Glew, E. O'Loughlin, H. Mitchell, R. Amin, F. Robert, M. Heidari, D. Barber, G. Rein and J. Schulz, 2022 "Impact of partial encapsulation on the fire dynamics of an open-plan compartment with exposed CLT ceiling and glulam columns: CodeRed #04", Fire and Materials.
16. Hidalgo, J. Goode, T. Gupta, V. Cowlard, A. Abecassis-Empis, C. Maclean, J. Bartlett, A. Maluk, C. Montalvá, J. Osorio, A. and Torero, J., 2019, "The Malveira fire test: Full-scale demonstration of fire modes in open-plan compartments," Fire Safety Journal, Vol. 108, No. May, p. 102827.
17. CEN, 2009, "Eurocode 5: Design of Timber Structures – Part 1-2: General – Structural Fire Design", EN 1995-1-2

Proceedings of the 12th International Conference on Structures in Fire

Other Topics Related to Structures in Fire

SiF 2022– The 12th International Conference on Structures in Fire
The Hong Kong Polytechnic University, Nov 30 - Dec 2, 2022

THE BURNING SEARCH FOR CAUSALITY AND KNOWLEDGE DISCOVERY: BEYOND FIRE TESTS AND EXPLAINABLE ARTIFICIAL INTELLIGENCE

M.Z. Naser[1]

ABSTRACT

Most of our research effort revolves around uncovering data generating processes (i.e., the how and why phenomena come to be). In this pursuit, we hope that by knowing the *how* and *why*, we can discover new knowledge, or perhaps advance our existing knowledge. This short paper presents a look into causal discovery and causal inference from the lens of fire resistance and then contrasts that to traditional artificial intelligence (AI) methods. Thus, two sets of algorithms are used; causal discovery algorithms are adopted to uncover the causal structure between key variables pertaining to the fire resistance of reinforced concrete (RC) columns, and causal inference algorithms are applied to estimate the influence of key predictors on the fire resistance of the same columns.

Keywords: Causality; Fire; Artificial intelligence; Machine learning.

1 INTRODUCTION

Discovering new knowledge implies the realization of the data generating process (DGP) responsible for creating the phenomena we happen to be interested in [1]. Such realization is often identified via fire tests or experiments. A typical experiment is planned to quantify, for example, the influence of some form of intervention (i.e., changing the construction material from A to B) on the outcome of interest (e.g., fire resistance). Hence, the outcome of such an experiment is thought of as a *cause(s)* → *effect* approach [2].

Once a true DGP is identified, then an engineer may opt to utilize the identified DGP to estimate the outcome of a particular testing intervention. This may, in fact, reduce our heavy reliance on expensive fire tests. At a minimum, a DGP will allow us to complete our understanding of a particular problem or phenomenon. The same could also open the door for new hypotheses and, most importantly, intelligently narrow the vast search space of our problems (rather than relying on outdated information that we do not seem to break free from).

Fire resistance is one such problem that is elemental to structural fire engineers. For example, predicting fire resistance of structural members is a complex problem that remains, and rightfully so, to be confined to the standard fire testing method. It is very likely that the DGP for fire resistance already exists in the thousands of fire tests conducted so far. At the end of the day, many such tests were conducted on specimens of, more or less, similar features (i.e., columns tend to have a practical range of size, length, reinforcement, etc.), which further narrows our search space. This may also ease the identification of possible DGPs.

For instance, reinforced concrete (RC) columns made from normal strength concrete (NSC) often display good performance under fire conditions. Recent works argue that NSC columns may outperform other columns made from high strength concrete (HSC) and ultra high-performance concrete (UHPC) [3].

[1] Assistant Professor, School of Civil and Environmental Engineering & Earth Sciences (SCEEES), Clemson University, Clemson, SC 29634, USA.
AI Research Institute for Science and Engineering (AIRISE), Clemson University, Clemson, SC 29634, USA
e-mail: mznaser@clemson.edu, ORCID: https://orcid.org/0000-0003-1350-3654
https://doi.org/10.6084/m9.figshare.22223938

Although HSC and UHPC columns inherently have high strength than NSC, such a strength does not correlate to improved fire resistance. Figure 1 illustrates this very point by plotting the relationship between compressive strength and fire resistance of about 100 RC columns. As one can see, there is a weak correlation. Not surprisingly, columns of relatively low grade strength (NSC) do not seem to guarantee achieving high fire resistance.

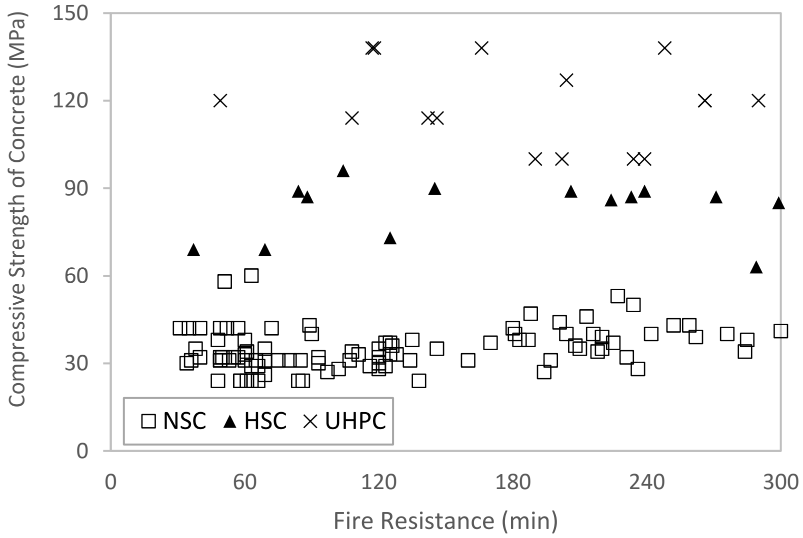

Fig. 1 Examination of compressive strength and fire resistance of fire-tested RC columns

The fire resistance of RC columns can be evaluated through codal charts/tables, or hand calculation methods, or via finite element simulations, and/or artificial intelligence (AI)/machine learning (ML). These methods deliver fire resistance predictions for RC columns *given* a set of variables. Interestingly, these methods do not often agree if applied to a particular and/or a group of columns [4–6]. As such, re-visiting the classical phenomenon of fire resistance of RC columns is of interest to this paper.

This paper presents a casual approach to discovering and inferring the causal mechanism responsible for the DGP of the fire resistance of RC columns. Then, this paper compares the newly discovered knowledge against domain knowledge and traditional machine learning. For completion, a companion discussion on causality can be found in a recent paper from the author's group [7].

2 CAUSAL APPROACH

In a traditional sense, a regression-based approach can be used to *predict* an outcome, *Y*, through a set of predictors. In such an approach, a predictive expression does not imply that the predictors are causes of *Y* but rather notes the outcome can be predicted using the predictors. On the other hand, a causal analysis strives to establish if a set of predictors are likely to cause *Y*. A look into Fig. 2 showcases a visual depiction of how regression differs from causation.

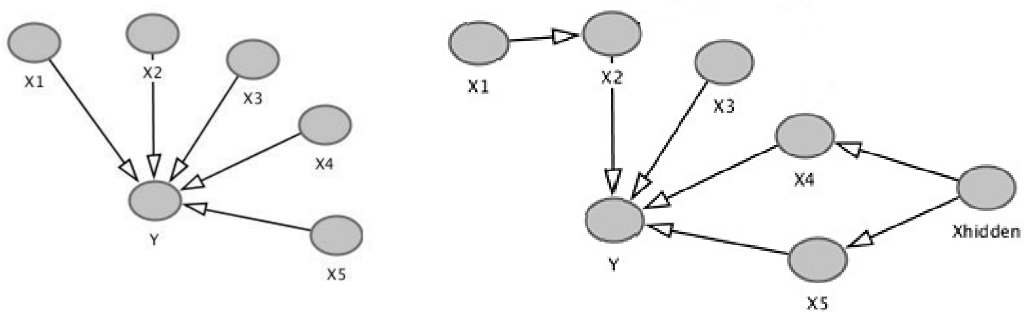

Fig. 2 Regression vs. causation

A causal approach comprises four primary steps (see Fig. 3):

1) Collecting data on the phenomena of interest.
2) Causal discovery to uncover the underlying DGP by satisfying causal principles. These principles include the Markov causal assumption, the causal faithfulness assumption, and the causal sufficiency assumption. Following such assumptions lead to the creation of a direct acyclic graph (DAG). Full details on such assumptions can be found elsewhere [8–10].
3) Causal inference is applied to infer how the output (i.e., fire resistance) would change by intervening on a predictor. An intervention equates to *setting* $X = x$ (what is the fire resistance of a RC column if its width is *increased* to 300 mm?) vs. *observing* $X = x$. (what is the fire resistance of a RC column, *given* it has a width of 300 mm?).
4) Finally, the outcome of the causal analysis can be compared to that of existing methods.

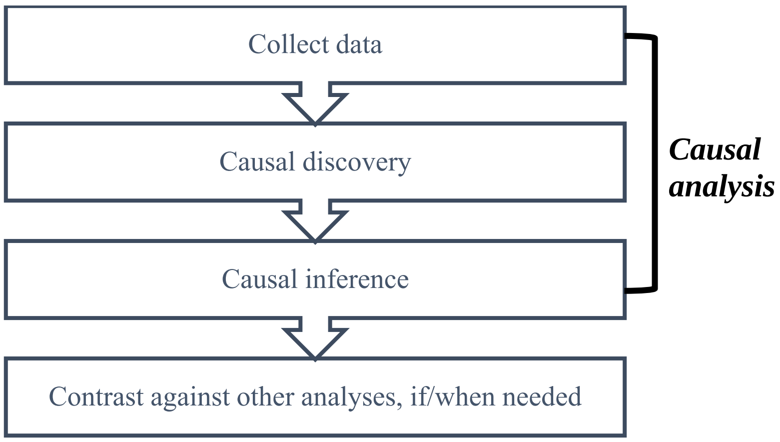

Fig. 3 Flowchart of the proposed approach

3 DATABASE

The database used in this short study compiles information on 144 fire-exposed RC columns that were tested at full scale and under standard fire conditions. The following predictors were collected 1) column width, *W*, 2) steel reinforcement ratio, *r*, 3) column length, *L*, 4) concrete compressive strength, f_c, 5) column effective length factor, *K*, 6) concrete cover to steel reinforcement, *C*, 7) the magnitude of applied loading, *P*, and 8) fire resistance time, *FR*.

Table 1 Statistics on collected database

	W (mm)	***r*** (%)	***L*** (m)	f_c (MPa)	***C*** (mm)	***P*** (kN)	***FR*** (min)
Minimum	203	0.9	2.1	24	25	0	55
Maximum	610	4.4	5.7	138	64	5373	389
Average	350.4	2.1	3.9	55.7	42.4	1501.8	176.6
Standard Deviation	105.3	0.5	0.5	33	7.1	1168.6	82
Skewness	1.1	1	-0.5	0.9	-1	1.3	0.4

4 METHODOLOGY

This paper starts by creating a machine learning (ML) ensemble for the above dataset. Then, this paper applies a common causal discovery algorithm and then compares its result to that of a previously used interpretable machine learning model [11].

The selected ensemble contains three algorithms: random forest (RF), extreme gradient boosted trees (ExGBT), and deep learning (DL). The RF algorithm randomly generates multiple decision trees to analyze the dataset [12]; such that:

$$Y = \frac{1}{J}\sum_{j=1}^{J} C_{j,full} + \sum_{k=1}^{K}\left(\frac{1}{J}\sum_{j=1}^{J} contribution_j(x,k)\right) \quad (1)$$

where, J is the number of trees in the forest, k represents a feature in the observation, K is the total number of features, c_{full} is the average of the entire dataset (initial node).

The ExGBT algorithm re-samples the collected observations into decision trees, where each tree sees a boostrap sample of the database in each iteration. ExGBT shares some aspects with RF, except that it fits successive trees to the residual errors from all the previous trees combined (see Eq. 2).

$$Y = \sum_{k=1}^{M} f_k(x_i)\,, f_k \in F = \{f_x = w_{q(x)}, q: R^p \rightarrow T, w \in R^T\} \quad (2)$$

where, M is additive functions, T is the number of leaves in the tree, w is a leaf weights vector, w_i is a score on i-th leaf, and $q(x)$ represents the structure of each tree that maps an observation to the corresponding leaf index [13]. The RF algorithm incorporates 50 leaf nodes, with a minimum of 5 samples to split an internal node.

Deep learning algorithm contains a number of layers that are connected via nonlinear activation functions e.g., *Logistic*, *PReLu*, etc. [14]. This algorithm aims to achieve a general and primarily implicit representation that best exemplifies a phenomenon; such that:

$$net_j = \sum_{i=1}^{n} In_i w_{ij} + b_j \quad (3)$$

$$Y = f(net_j) \quad (4)$$

where, In_i and b_j are the ith input signal and the bias value of jth neuron, respectively, w_{ij} is the connecting weight between ith input signal and jth neuron, and f is a *PReLu* activation function. The number of used layers are 64, with 3% learning rate, and *Adam* optimizer to enhance the processing of observations.

Finally, the causal analysis carried out in this short paper starts by disregarding the effects of all predictors on each other and assuming that they only have an influence on *FR* as shown in the DAG listed in Fig. 4. As one can see, this DAG also represents how a typical machine learning model assumes the relationships with *FR* and the one used in an earlier study [11].

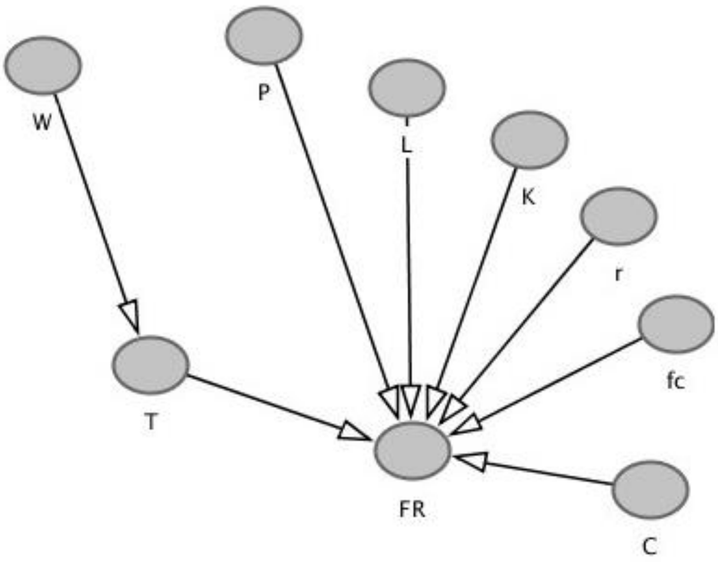

Fig. 4 Hypothetical model [Note: T: intervention/treatment, FR: fire resistance]

5 RESULTS AND DISCUSSION

This section highlights the main findings of this short paper.
In order to further highlight the accuracy of the developed ensemble, fire resistance predictions obtained herein are also compared against Eurocode 2 [15], as plotted in Fig. 5. This figure infers the good predictions from the ensemble and the adequacy of Eurocode 2 predictions for columns within the 60-240 minute range beyond which these predictions seem to be underestimated.

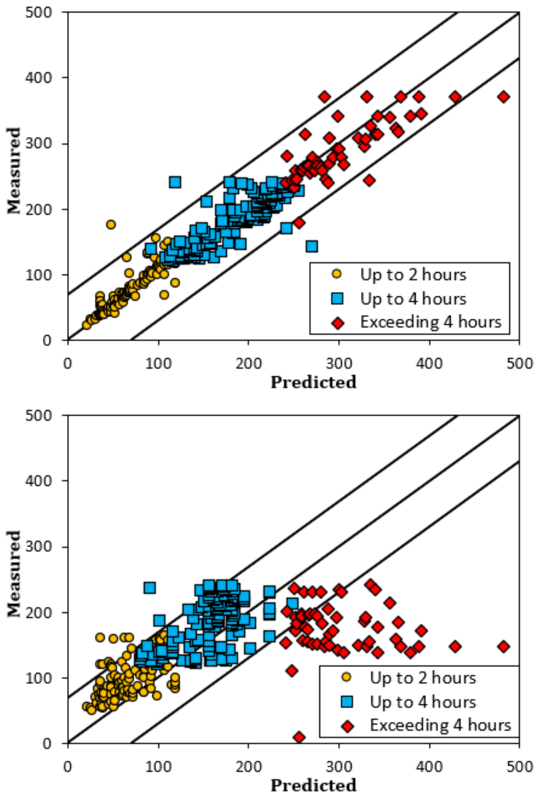

(a) Predictions from ensemble

(b) Eurocode 2 method

$R = 120\left(\frac{R_{fi}+R_a+R_l+R_b+R_n}{120}\right)^{1.8}$, and $R_{fi} = 83\left(1-\mu_{fi}\frac{1+\omega}{\frac{0.85}{\alpha_{cc}}+\omega}\right)$, $\omega = \frac{A_s f_{yd}}{A_c f_{cd}}$

where,
R = fire resistance of column (min),
α_{cc} = coefficient for compressive strength,
$R_a = 1.6(a\text{-}30)$; a is the axis distance to the longitudinal steel bars (mm); 25 mm $\leq a \leq$ 80 mm,
$R_l = 9.6(5\text{-}l_{o,fi})$; $l_{o,fi}$ is the effective length of the column under fire conditions; 2 m $\leq l_{o,fi} \leq$ 6 m; values corresponding to $l_{o,fi}$ = 2 m give safe results for columns with $l_{o,fi}$ < 2 m,
$R_b = 0.09b'$; $b' = A_c/(b+h)$ for rectangular cross-sections or the diameter of circular cross sections,
$R_n = 0$, if 4 rebars are used, and 12 for more than 4 rebars.
Performance metrics: R = 0.7, R^2 = 0.49

Fig. 5 Comparison of fire resistance prediction in RC columns

The ML ensemble can also be used to identify the importance of each predictor. The analysis shows that the following predictors C (100%), P (63%), K (54%), e_x (52%), and b (39%), are the most impactful features. Figure 6 shares additional insights into the impact of each of these features on the increased possibility of improved fire resistance (when all other features remain constant). For example, larger columns are expected to have higher fire resistance.

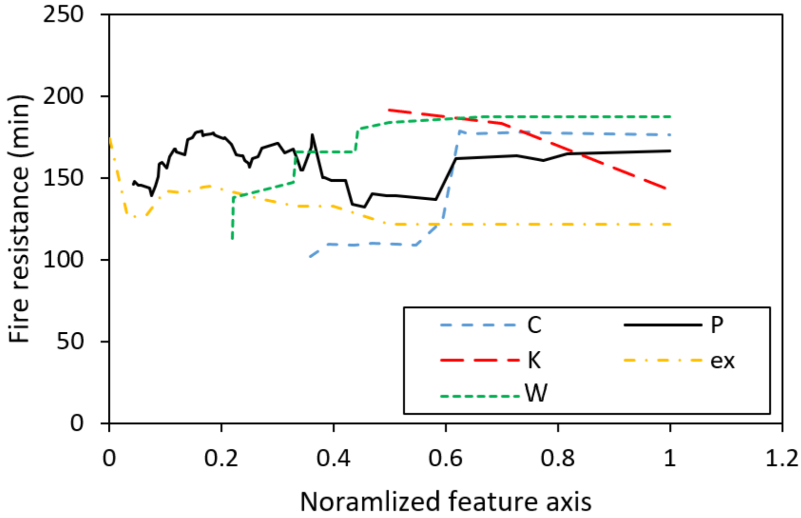

Fig. 6 Insights into key factors influencing fire resistance of RC columns

Since machine learning predictions cannot account for intervention as they are based on observational distribution, then a comparison is drawn between ensemble predictions and the causal algorithm. Figure 7 shows how intervening by substituting the average value of a given predictor into the ensemble does not turn well. In other words, the ensemble is used to estimate *FR* for a given column with predictors having a value equal to the average value noted in Table 1. This action leads to shifting in each of the method's predictions which can be explained by the reliance on the association of both methods to minimize the variance of the outcome instead of displaying the actual causal mechanism tying each variable to the fire resistance of RC columns.

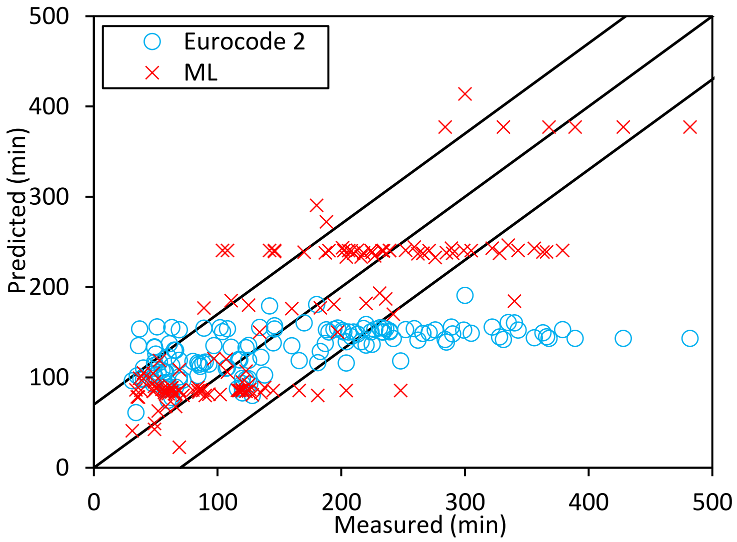

Fig. 7 Comparision applied due to interventions

On the other hand, Table 2 shows that when all variables are assessed for their interventional impact on *FR*. For example, positive interventions/treatments negatively influence *FR* for *W*, *L*, and *K*, whereas they positively influence *FR* for *r*, f_c, *C*, and *P*. In this instance, having a RC column with average steel reinforming ratio (2.1%) will increase FR by about 19 min, while having the same column with an average concrete cover (42.4 mm) will increase FR by 87.8 min.

Table 2 Results of analysis for fire resistance (min)

Treatment variable	Estimate	
	Mean value	*p*-value
W	-245.0	0.11
r	19.0	0.76
L	-82.0	0.97
f_c	40.9	0.85
K	-81.1	0.02
C	87.8	5.8e-9
P	36.3	0.004

6 CONCLUSIONS

This paper presents a look into causal discovery and causal inference to quantify the magnitude of interventions on the fire resistance of RC columns. The following list of inferences can also be drawn from the findings of this study:

- Integrating causality can further accelerate knowledge discovery in our domain.
- Interventions are seen to be highly influential in terms of column width, column length, and concrete cover. Interventions on the level of applied loading and/or reinforcement ratio did not significantly alter fire resistance.
- Unlike traditional ML analysis, the causal analysis provides us with the most realistic predictions as it can accommodate interventions (without needing new tests or experiments).

REFERENCES

[1] N. Huntington-Klein, The Effect : An Introduction to Research Design and Causality, Chapman and Hall/CRC, Boca Raton, 2021. https://doi.org/10.1201/9781003226055.

[2] D.F. Chambliss, R.K. Schutt, Causation and experimental design., in: Mak. Sense Soc. World Methods Investig., 2013. https://us.sagepub.com/sites/default/files/upm-assets/103318_book_item_103318.pdf.

[3] V. Kodur, Properties of concrete at elevated temperatures, ISRN Civ. Eng. (2014). https://doi.org/10.1155/2014/468510.

[4] S.H. Buch, U.K. Sharma, Empirical model for determining fire resistance of Reinforced Concrete columns, Constr. Build. Mater. (2019). https://doi.org/10.1016/j.conbuildmat.2019.07.183.

[5] S.H. Buch, U.K. Sharma, Fire resistance of reinforced concrete columns: A systematic review, in: Appl. Fire Eng. - Proc. Int. Conf. Appl. Struct. Fire Eng. ASFE 2017, 2018. https://doi.org/10.1201/9781315107202-16.

[6] M.Z. Naser, Heuristic machine cognition to predict fire-induced spalling and fire resistance of concrete structures, Autom. Constr. 106 (2019) 102916. https://doi.org/10.1016/J.AUTCON.2019.102916.

[7] M.Z. Naser, A.O. Ciftcioglu, Causal Discovery and Causal Learning for Fire Resistance Evaluation: Incorporating Domain Knowledge, (2022). https://doi.org/10.48550/arxiv.2204.05311.

[8] J. Pearl, Causal inference in statistics: An overview, Stat. Surv. (2009). https://doi.org/10.1214/09-SS057.

[9] C. Heinze-Deml, M.H. Maathuis, N. Meinshausen, Causal Structure Learning, Annu. Rev. Stat. Its Appl. (2018). https://doi.org/10.1146/annurev-statistics-031017-100630.

[10] R. Scheines, An Introduction to Causal Inference *, (n.d.).

[11] M.Z. Naser, V.K. Kodur, Explainable Machine Learning using Real, Synthetic and Augmented Fire

Tests to Predict Fire Resistance and Spalling of RC Columns, Eng. Struct. 253 (2021) 113824. https://doi.org/10.1016/J.ENGSTRUCT.2021.113824.

[12] A. Liaw, M. Wiener, Classification and Regression by RandomForest, 2002. https://www.researchgate.net/publication/228451484 (accessed April 8, 2019).

[13] Gradient boosted tree (GBT), (2019). https://software.intel.com/en-us/daal-programming-guide-details-24 (accessed April 9, 2019).

[14] Y. Bengio, Learning deep architectures for AI, Found. Trends Mach. Learn. (2009). https://doi.org/10.1561/2200000006.

[15] BSI, European Committee for Standardization, Design of concrete structures - Part 1-2: General rules - Structural fire design, 2004. https://doi.org/10.1002/jcp.25002.

SiF 2022– The 12th International Conference on Structures in Fire
The Hong Kong Polytechnic University, Nov 30 - Dec 2, 2022

POST-FIRE EVALUATION OF THE NEW ZEALAND INTERNATIONAL CONVENTION CENTRE

G Charles Clifton[1], Lucas Hogan[2], Linus Lim[3], Peter Nguyen[4], Martin Feeney[5], Guzhao Li[6], Emily R. McCarthy[7], Paul B Summers[8], Alistair Remmington[9], Leonard King[10], Gordon Carle[11], Ryan Clifton[12], Neha Raphael[13]

ABSTRACT

In October 2019, the largest fire in a commercial building in New Zealand since 1947 burned for over four days through the roof and upper floor of the 120m wide x 100m long New Zealand International Convention Centre, which was under construction and nearing completion at the time. The steel composite and reinforced concrete framed building with composite floors features five above grade storeys of structural steel framing with composite floors, comprising heavy, intricate steel work that were impacted by the fire.

The main steel structure performed very well in response to fire exposure, with minimal damage and distortion to the heavy steel roof members in general, considering the severity of the fire. Secondary steel angles, tubular steel, and wide-flange members at the roof elevation were locally more heavily distorted.

A very detailed post-fire evaluation of the structure was carried out, comprising mapping of the fire effects, deflections, metallurgical changes, extensive numerical modelling, and full scale in-situ experimental testing. The outcome resulted in retention of 95% of the total roof steelwork (2500 tonnes).

This paper provides an overview of the fire and the key steps involved in the post-fire structural evaluation.

Keywords: Structures, fire, assessment, restoration

[1] Associate Professor of Civil Engineering, The University of Auckland
e-mail: c.clifton@auckland.ac.nz, ORCID: https://orcid.org/0000-0003-0723-1699
[2] Lecturer; Civil and Envionmental Engineering, The University of Auckland
e-mail lucas.hogan@auckland.ac.nz, ORCID: https://orcid.org/0000-0001-5151-1378
[3] Technical Director; Holmes Australia LP
e-mail Linus.Lim@holmesfire.com
[4] Fire Engineer; Holmes New Zealand LP
e-mail: peter.nguyen@holmesgroup.com
[5] Principal, Holmes New Zealand LP
e-mail: martin.feeney@holmesgroup.com
[6] Technical Director, Simpson Gumpertz & Heger (USA)
e-mail: gli@sgh.com
[7] Senior Consulting Engineer, Simpson Gumpertz & Heger (USA)
e-mail: ermccarthy@sgh.com
[8] Senior Principal, Simpson Gumpertz & Heger (USA)
e-mail: pbsummers@sgh.com
[9] Materials Engineer, Industries and Environment, SGS New Zealand Ltd
e-mail: alistair.remmington@sgs.com
[10] Operations Manager Industrial NDT and Materials, SGS New Zealand Ltd
e-mail: leonard.kong@sgs.com
[11] Project Engineer, Buildings, The Fletcher Construction Company, Ltd.
e-mail: gordonc@fcc.co.nz
[12] Site Manager, Buildings, The Fletcher Construction Company, Ltd
e-mail: ryanc@fcc.co.nz
[13] Site Engineer, Buildings, The Fletcher Construction Company, Ltd
e-mail: nehar@fcc.co.nz
https://doi.org/10.6084/m9.figshare.22223947

1 INTRODUCTION

In October 2019, the largest fire in a commercial building in New Zealand since 1947 burned for over four days through the roof and upper floor of the 120m wide x 100m long New Zealand International Convention Centre (NZICC), which was under construction and nearing completion at the time. The structure primarily comprised of steel composite and reinforced concrete framing with composite floors. The five above grade storeys have structural steel framing with composite floors, comprising heavy and intricate steel work, while the four below grade floors have traditional composite floors supported on reinforced concrete and concrete encased steel columns.

The roof area, which was directly impacted by the fire, consisted of large primary and secondary steel trusses, with spans of up to 36m and 39.9m respectively, giving clear spans of up to 64.5m. Some of the roof trusses were 13m clear height above the top floor.

The main steel structure performed very well in response to the fire exposure, considering the severity of the fire, with minimal damage and distortion to the heavy steel roof members, in general. Secondary steel angles, tubular steel, and wide-flange members at the roof elevation underwent some local buckling and sagging. No collapses of these structural steel components occurred.

A very detailed post-fire evaluation of the structure was carried out. This involved heat mapping of the fire (based on activation of the intumescent coating, material testing of purlins and cleats, and video evidence of the fire migration), measurement of post-fire deflections, metallurgical investigation of many components, advanced numerical modelling, and full scale in-situ experimental testing of selected roof trusses.

This paper starts with a brief overview of the structure and fire, followed by details of the post-fire evaluation. It then covers post-fire restoration and ends with conclusions and acknowledgements.

2 STRUCTURE AND FIRE

When completed, following the post-fire rehabilitation, the NZICC will be New Zealand's largest and most versatile conference and exhibition venue, encompassing 32,500m^2 of floor area. The conference and exhibition spaces are spread over three levels and will be able to accommodate a wide variety of functions, from a 2,850m^2 top floor theatre (Level 5) to multiple break-out spaces and small meeting rooms.

The ground floor (Level 3) has 8,100m^2 of floor space which can accommodate 3,150 delegates across three column-free halls. The ground floor has a 9m clear height and vehicular access from adjacent roads.

The structural steel frame to meet the needs of this facility is complex. Figure **1** shows an isometric view of the two level roof steelwork which spans over the upper floors of the conference and exhibition venue.

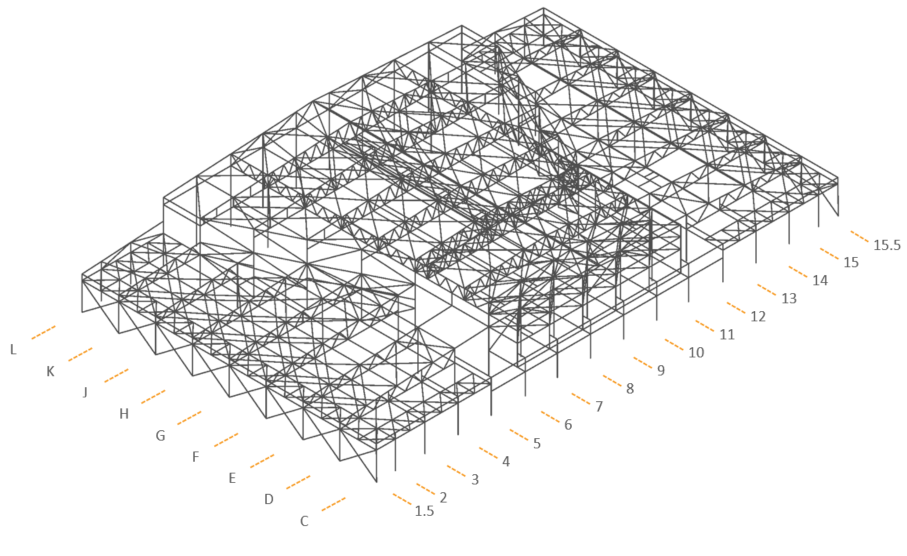

Figure 1. Isometric view of upper level steelwork

The fire commenced in the early afternoon of 22 October 2019, near the north-west corner of the roof, which was nearing completion. The roofing system comprised a sandwich construction with multiple thermal and acoustic layers spanning between structural purlins, all topped with a structural plywood layer over which was placed a torch applied bituminous weathertight membrane. At the time of the fire, over 95% of the roof system was in place and fitout of the lower levels was nearing completion. The fire started in the bituminous roofing membrane system that was being placed near the north-west corner (see Figure **5**) being fanned by strong gusting winds. The wind played a key role in the development of the initial fire and its spread across the roof. Once established, the fire burned through the various layers of the roof and spread through the building. The mechanisms of travel included direct drop down of burning materials into cavities in walls and ceilings, on to construction equipment which included multiple gas cylinders, petrol fuelled lifts and other assorted equipment and via incomplete fire separations due to ongoing construction. Despite intensive fire-fighting efforts, which started within 15 minutes of the alert, putting the fire out was challenging due to the roof construction, uncertain fire affected roof capacity, limited roof access that required fire-fighters to project water from the street, and the strong winds. For many reasons, the fire was allowed to burn out, while efforts focused on protecting adjacent buildings and a tower crane still installed. The fire was declared to have been extinguished after 10 days of firefighting. Fire and Emergency New Zealand (FENZ) investigated the cause of the fire and found it was accidental and likely the inadvertent ignition of the cardboard centre roll of the bituminous weathertight membrane.

Despite concern reported in the local press that the steel framed building might collapse, no collapse occurred and as reported below, the damage to the structural members was in general relatively minor. However, the post-fire remediation was complicated by three on-site factors: first, the contaminated fire-fighting water and burnt debris generated a hazardous work zone and limited timely access to de-water the basement and to remove damaged elements throughout the building; secondly, the resulting growth of toxic black mould required significant health and safety measures for access; and thirdly, the loss of the roof left the almost completed structure below open to the weather for 18 months..

3 PERFORMANCE IN FIRE

3.1 Physical observations – distortions and coating damage

Figure **2** shows a view looking up through the roof trusses from the top floor through to the open sky above. This was taken in July 2020, by which time the upper levels had been made sufficiently safe from physical hazards to allow detailed evaluation of the state of the roof and upper levels. In this image the extent and variation of damage is visible. Note that: the coating system on the bottom chord of the truss is less damaged than the top chord, there is visible surface corrosion on steel members, and hanging and loose debris create falling hazards. These were characteristic observations during the post-fire investigation.

Figure 2. View from underside of fire and smoke damaged roof trusses through to the sky, showing coating and steel damage.

Intumescent coating was used on most of the roof steelwork, to achieve a Fire Resistance Rating (FRR) of between 60 and 120 minutes, with most truss steelwork having a 90 min FRR. The intumescent coating on roof members was generally damaged either by the fire, ie., the coating intumesced to create a barrier between the steel and fire, or by fire-fighting water and long weather exposure.

3.2 Survey data – roof trusses and columns

Surveys of the trusses' post-fire positions were originally attempted with Lidar, however surface damage to the intumescent coating made the readings unreliable. Instead, a total station survey with a combination of stick-on targets and fixed prisms was used and gave an accuracy of 1-2mm. These survey results informed the damage assessment team about the level of fire induced deflections in the roof trusses. Surveys were also carried out on all the Level 5 (the level below the roof) columns to compare as-built and post-fire positions vs design for position and verticality. These initial post-fire profiles provided a benchmark against which the in-situ experimental testing would be compared, to assure the testing did not introduce further residual deformations into the roof system. Some outputs from the survey data are given in section 4.1.

3.3 Component testing

SGS was engaged as the primary mechanical and metallurgical testing laboratory for the purlins, truss splice plates, and bolts removed from the roof of the NZICC. The purpose of component testing was to estimate fire temperatures reached by the components, which could then be used to further corroborate the temperature mapping estimations. Testing was also carried out to determine whether the steel components were still mechanically sound after being affected by the fire. Removal of all tested components was witnessed by SGS to confirm the exact location of each sample.

Maximum temperatures reached in the fire were estimated using two different methods, microstructural analysis and experimentally determined correlations. The purlins used in the roof were made of cold-formed, low alloy steel which allowed for analysis of the microstructures present to be used to estimate the peak, localised temperatures reached during the fire. Temperature estimation was based on the recrystallisation of the cold-worked microstructure, estimation of the austenite grain size formed during the fire, and the presence of complex microstructures caused by rapid cooling from the fire extinguishing efforts.

Several of the high strength bolts (Grade 8.8 and higher) used in the trusses were removed and tested experimentally to find correlations between temperature, time, and bolt hardness. Due to the effects of high temperatures on the quenched and tempered structure of the high strength bolts, their hardness decreases as temperature increases, due to the bolts becoming over-tempered. These correlations were then applied to bolts removed from fire affected areas of several trusses, to estimate the fire temperature reached in those areas.

Mechanical testing of components was also carried out to compare the fire affected components to those that were unaffected, to examine any changes that may have occurred due to the fire. This testing incorporated tensile testing, Charpy impact testing and Vickers hardness testing (used for bolts too small for tensile testing). All tested low-alloy steel components retained their original mechanical properties irrespective of the maximum temperatures reached in the fire.

3.4 Heat mapping

In order to undertake the structural fire modelling of the fire exposed upper roof and lower roofs, the thermal exposure of the structural elements over the four day fire duration needed to be determined. A heat map was developed for the structural steel roof, by mapping the thermal exposure to all the steel members across the entire roof. Numerous site investigations were undertaken to inspect the post-fire damage and the post-fire state of the reactive fire protection coatings.

The primary method of identifying the surface temperatures on the structural steel, which forms the basis of the structural fire analyses, comprised visual inspections to check the surface appearance of the structural steel and the coating on the structural steel. This is because the surface of the steel and intumescent coating has different appearances under different levels of thermal exposure (see for example high temperature exposure in Figure **3**). This led to a relatively large number of groups of temperature ranges on the steel structure.

The suppliers and applicators of the intumescent coating were consulted to provide information on the range of temperatures corresponding to the surface appearances of the structural steel and the intumescent coating. Different temperature ranges were derived, as shown in Table 1, which were then used for mapping the possible temperature exposures on the structural steel members throughout the building. Figure **4** shows an example of the heat map on one of the trusses.

Figure 3. Appearance of expanded intumescent coating

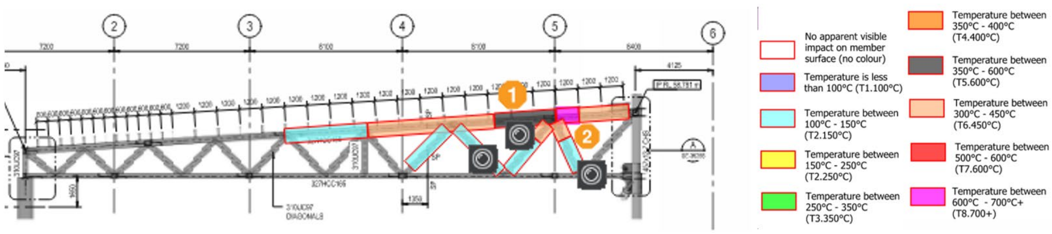

Figure 4. Example of heat map for one of the trusses.

Table 1. Upper Bound and Lower Bound Surface Temperatures Considered in the Analysis

Surface Category Number	Temperature Range (°C)	Temperature exposure for structural fire analysis	
		Lower Bound (°C)	Upper Bound (°C)
T1.100	20 - 100	20	100
T2.150	100 - 150	100	150
T2.250	150 - 250	150	250
T3.350	250 - 350	250	350
T4.400	350 - 400	350	400
T5.600	350 - 600	350	600
T6.450	300 - 450	300	450
T7.600	500 - 600	500	600
T8.700	600 - 700	600	700

Video footage of the entire fire event, from a CCTV mounted near the building site, was also reviewed to determine the time when flames were observed at the different locations of the roof. This was crucial to estimate the time when different parts of the structure were exposed to the fire, and the durations of fire exposure. This enabled a migrating fire behaviour to be modelled at different locations on the upper roof for the structural fire analysis, in order to estimate the likely forces and deflections in the structure. A simpler heating approach such as simultaneous heating of the entire roof for an indefinite period of time was not used as it would have resulted in different behaviours and forces in the structure, compared to those observed.

Seven zones were defined for the migrating fire based on the observations from the video footage (see Figure **5** and Figure **6.**). Within each zone, the heating to the structural elements in that zone followed the temperature time curve corresponding to that zone and based on the maximum heating temperature, as shown in the heat map temperature distribution.

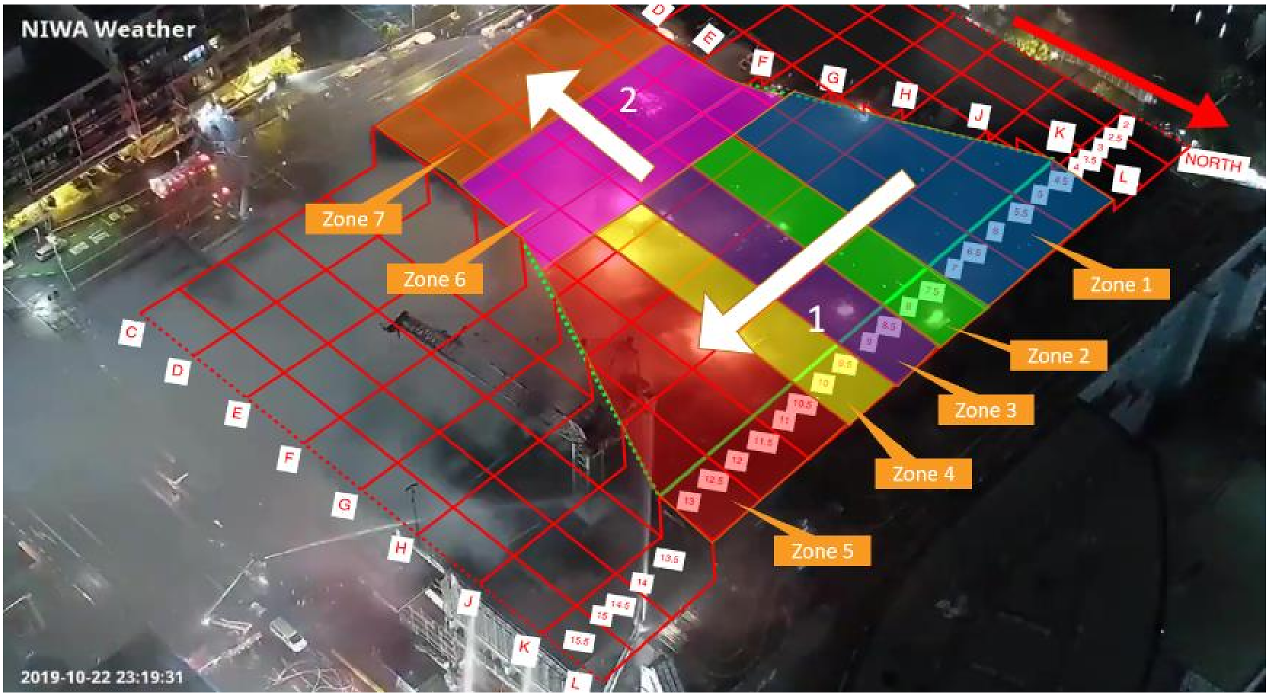

Figure 5. Simplified progression of fire spread on Upper Roof for structural fire analysis

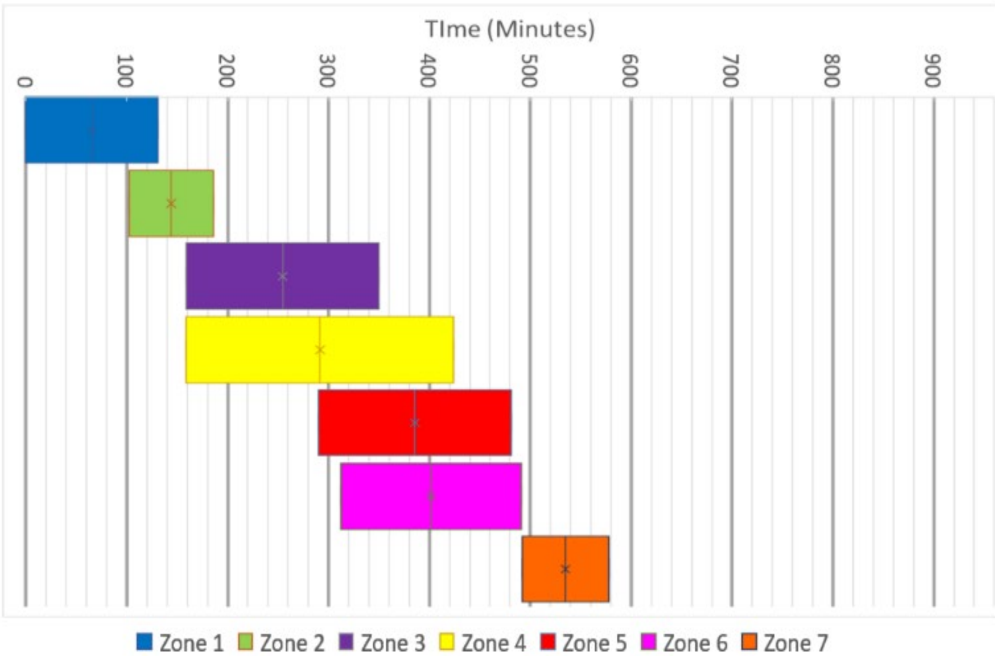

Figure 6. Progression and duration of fire spread on Upper Roof

3.5 Thermal and structural fire analyses

The analysis involved finite element (FE) 2D heat transfer modelling and 3D structural fire response modelling of the roof structure. The primary analysis objective was to determine the residual forces in the steel roof truss members exposed to fire and to evaluate whether structural components needed to be replaced or retrofitted due to fire damage, and potential locations where structural elements could have experienced high fire-induced residual stresses. The structural fire analysis was also undertaken to identify methods of relieving residual stresses where these were shown by the fire and large-scale experimental testing to be significant.

3.5.1 Heat transfer analyses

The temperatures across the heated structural elements were determined using 2D thermal analysis for each structural member exposed to the specified temperature-time curves on the surface of the structural section. The representative cross-sectional geometry of the structural members was analysed using the SAFIR [1] FE program to obtain detailed time-temperature distributions through the section of the member. The thermal properties of the structural steel members, such as specific heat and thermal conductivity, were based on Eurocode EN 1993-1-2 [2] for carbon steel. Where the heat map shows that the members were exposed to elevated temperatures, the protected and unprotected steel members were assumed to be exposed to the thermal exposure on four-sides of the structural section. The respective structural members within the building were subjected to the maximum temperatures obtained from the heat map that was developed from the site surveys and also subjected to the durations of fire exposure derived from the time-lapse video observations (see Figure 5 and Figure 6).

Figure **7** shows an example temperature time history of four selected nodes across the section of a beam segment (with three-sided insulation) on the upper roof with maximum applied temperature of 500°C and with total simulation time of 24000 seconds.

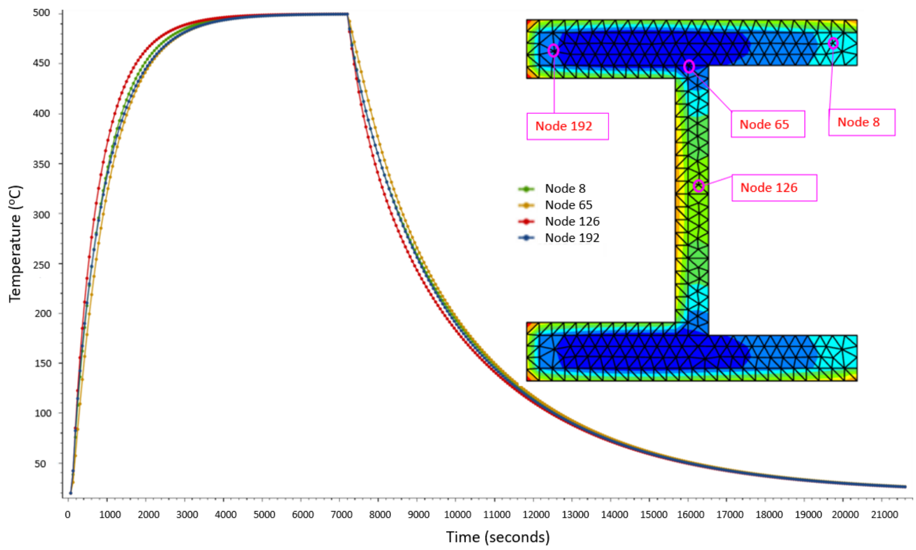

Figure 7. Temperature Time History of Selected Nodes across a Beam Section with Three-Sided Insulation

3.5.2 Structural fire response analysis

The detailed thermal data from the 2D heat transfer analysis for all the heated structural members was used in the structural fire response analysis models to determine the response of the overall structure and individual members. The structural fire response analysis was performed using the SAFIR non-linear FE analysis program and was independently verified using the ABAQUS [3] non-linear FE analysis program.

Non-linear material models were used to model the structural response at elevated temperatures. The yield strengths of the steel at ambient ranged from 300MPa to 355MPa, depending on structural shape. The material models for steel considered strength and stiffness degradation of the ambient materials as a function of temperature as per Eurocode EN 1993-1-2. The material models also considered thermal expansion and contraction associated with heating and cooling, respectively. As an example, Figure **8** shows the stress-strain curves of structural steel with ambient grade of 350 MPa used in both the SAFIR and ABAQUS structural analysis models.

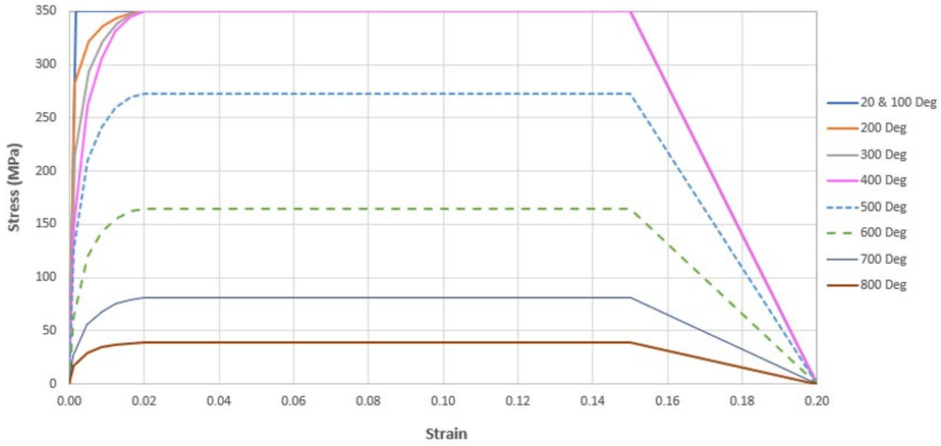

Figure 8. Stress-Strain Curves for Ambient Steel Grade of 350 MPa with Temperature

Boundary conditions were applied at the bottom of the columns to simulate continuity of the columns at Level 5 and at other locations as applicable. Gravity loads were applied prior to the application of thermal loads. The whole structure was modelled to provide a better representation of the lateral stiffness and boundary conditions of the fire exposed structural elements. This was done instead of only modelling a sub-assembly of part of the structure which would require idealised supports at the boundary conditions (e.g.: full lateral fixity), which in turn could result in overprediction of the restraint stiffnesses, and hence the residual forces within the structural members at the conclusion of the fire.

Three separate analyses were undertaken to simulate the fires at the different roof locations (west lower roof, upper roof and east lower roof), using the same structural model. For each of the fire locations, upper bound and lower bound temperatures for each of the surface categories as shown in the heat map were modelled in the structural analysis. The structural models were able to predict the deformations and deflections consistent with those measured in the post-fire surveys. Figure **9** shows the calculated vertical deflections for the scenario of fire exposure on the upper roof. The deflections are shown at the end of the cooling stage of the simulation, modelled as six hours after the last observed fire on the upper roof.

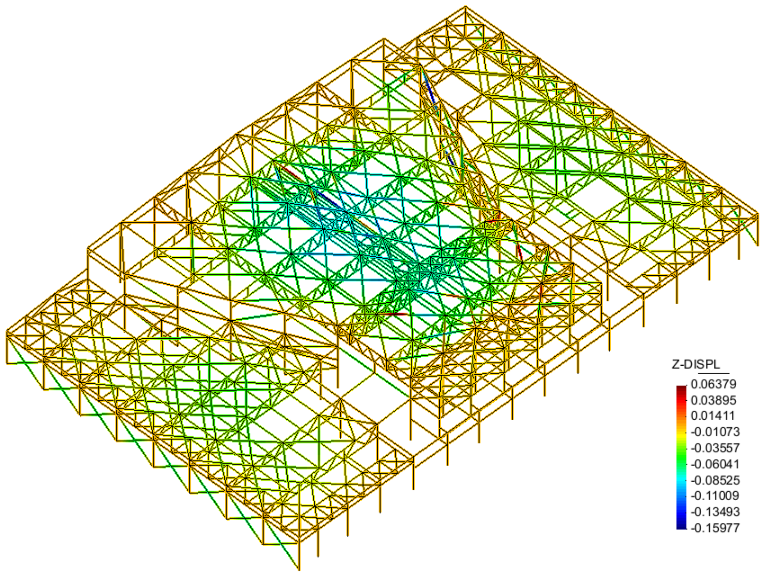

Figure 9. Calculated Deflection of Structure at the Conclusion of the Fire on the Upper Roof

Some of the members that were heated to relatively low temperatures (less than 400°C) could develop substantial locked-in residual forces despite not showing any visible signs of yielding or deformation. This is attributed to the steel exceeding its proportional limit during heating, resulting in a residual strain after cooling and a corresponding potential residual stress. There was debate over whether these high residual stresses resulting from exceeding the proportionality limit would be influential in post-fire strength and one of the principal purposes for conducting the large-scale experimental tests was to answer this question. The analyses also demonstrated that the post-fire residual forces in the structural members could be relieved to some extent through the disconnection of some bracing and strut members. In addition, the sensitivity of the restraining condition of the slotted connections on the west lower roof was also considered.

In addition to the global analysis, local analysis models were also developed to predict the local response of structural members. As an example, Figure **10** shows the local bucking analysis of one top chord segment on the west lower roof. The local deformation predicted from the analysis matches the deformation measured on site reasonably well.

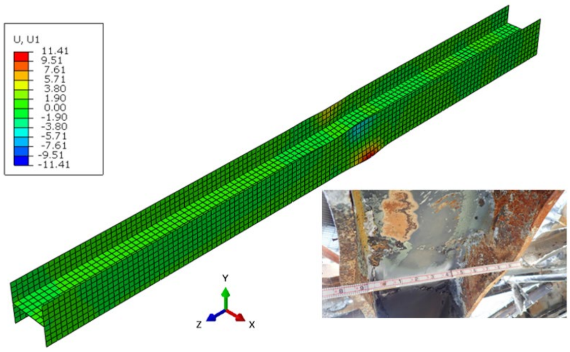

Figure 10. Local Buckling Analysis of One Top Chord Segment on the West Lower Roof

4 LARGE SCALE PROOF TESTING

The principal purpose of the large-scale proof load testing was to provide experimental validation of the post-fire ultimate limit state vertical load carrying capacity of the roof trusses that were to be retained in the post-fire remediation in accordance with Clause 17.4 Proof Testing, NZS 3404 Steel Structures Standard [4]. Successful compliance with these provisions, which was achieved, offered a path for meeting the requirements of the New Zealand Building Control System for demonstrating the post-fire strength of the roof truss system.

To demonstrate compliance via the above clause required careful selection of trusses and careful execution of the in-situ experimental testing on a scale not before undertaken in New Zealand.

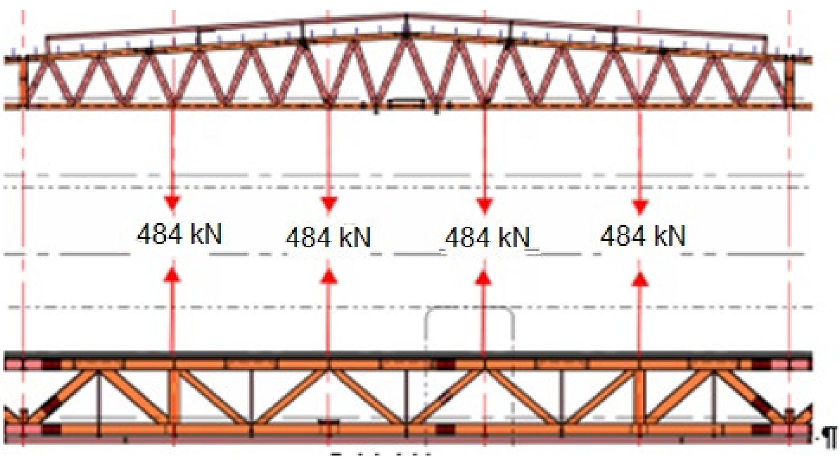

Figure 11. Maximum applied loads for full scale testing of 39m span roof truss

Figure 11 shows the maximum loading applied to the largest truss tested (in the upper roof). This comprised four equally distanced loads applied incrementally up to the design ultimate limit state factored vertical design load. The loading sequence cycled through loading and unloading to capture the threshold of elastic behaviour and stiffness retention.

Evaluation of the load-deflection behaviour of all trusses certified they remained in the elastic range during the full extent of testing.

4.1 Proof testing survey

Three surveys were carried out on the roof trusses during the damage assessment and testing process. The objective of each survey was to document:

- The post-fire position of every truss on Level 5.
- The position of all Level 5 trusses before and after selected struts and braces were removed to attempt to relieve residual stresses in the roof (see monitoring positions in Figure 12).
- The deflection at each load increment for each of the three trusses that were load tested (see Figure 13).

In addition to the target locations used for the total station survey, stick-on and fixed prism targets for the load test monitoring were placed:

- Directly over the load points on the bottom chord.
- Between node points on the top chord to pick up any out-of-plane deflections.
- Above the highest stressed section of top chord so movement could be monitored while the load is applied.

As the Level 5 slab was used as a reaction floor, its deflection was measured using a digital level to normalize the roof truss deflections. At each load rig a barcode staff was secured to the Level 5 slab/truss so the levels could be read at each load increment without anyone approaching the test area.

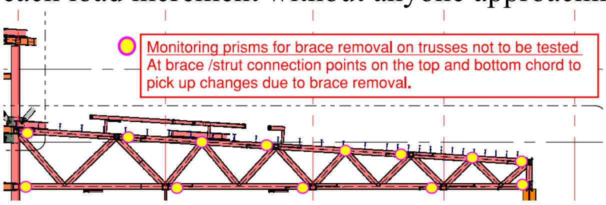

Figure 12. Monitoring positions for brace and strut removal

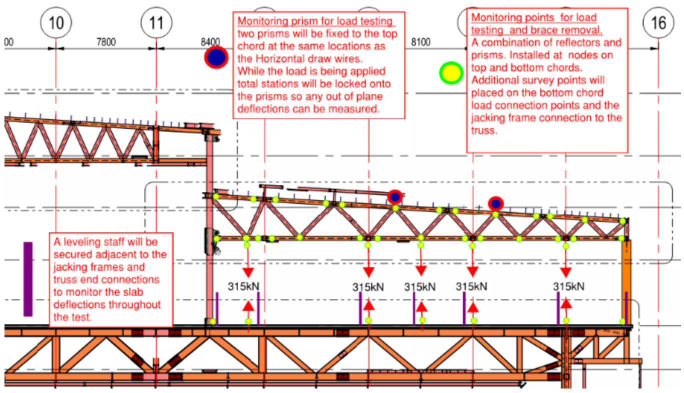

Figure 13. Additional monitoring points for load testing

Measured deflections during the load test were tabulated and later graphed for each load increment, at each load point (i.e. jacking position) at the Level 5 slab level, as seen in Figure 14.

Truss - vertical and lateral at load points

Test Location:-		Load point 1					
Total Load (kN)	Load %	point load (kN)	Deflection (mm) est. vertical	Vertical West	Vertical East	lateral West	lateral East
0	0	0	0	0	0	0	0
315	20	63	10.2	7	8.0	0	1 nth
630	40	126	20.4	14	16.0	1 sth	0
945	60	189	30.6	23	24.0	0	1 sth
1103	70	221	35.7	28	29.0	1 sth	1 sth
1260	80	252	40.8	32	33.0	1 sth	1 sth
1418	90	284	45.9	37	36.0	2 sth	1 sth
1575	100	315	51	42	41.0	2 sth	1 sth

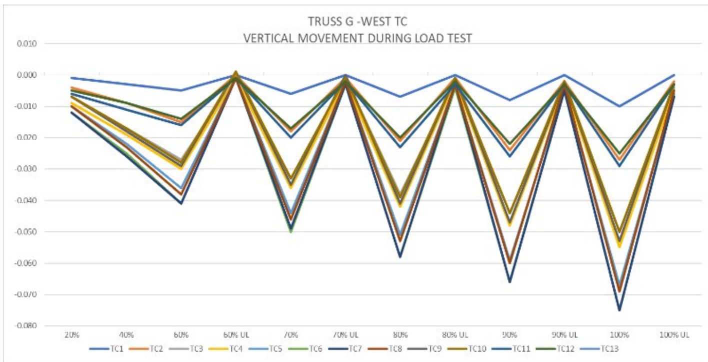

Figure 14. Tabulated deflections for a single load point (left) and deflections in graphical form for multiple load points (right)

5 POST-FIRE RESTORATION

The structural fire damage was confined to the upper and lower roof steel and the parapet and façade steel between the upper and lower roof at several locations, especially at the southern end of the building.

From the damage assessment, it was determined that it was more appropriate to replace, rather than try to remediate, any structural stick steel member that showed signs of damage, especially when weighed against the labour costs and schedule implications required to replace the member's coating. This included all the roof purlins, all the equal angle top chord diagonal roof bracing members, some top chord roof bracing struts, and some secondary beams and columns on the southern facade of the building.

The large heavily fabricated members, such as the roof trusses, were inspected by the steel supplier. The steel supplier provided repair details to the contractor and engineer of record for approval and acceptance, rather than proposing full replacement of any individual roof truss. No roof trusses were replaced.

Figure 15. TTR13011 Top chord sagging 70mm

Figure 16. TTR16007 Local buckling of roof truss top chord

All roof trusses were removed from site for remedial work including blasting and recoating. Typical roof truss remedial work consisted of heat straightening bent truss members and replacing segments of truss members that showed excessive local buckling.

Truss designation TTR13011, seen in Figure 15, is an example where the heat straightening method was applied. Measurements showed that the top chord at one end of the truss had sagged 70mm and the same end also showed an out of plane sweep of approximately 40mm. Initially a segment of the top chord was to be removed and replaced, but the fabricator decided that it could be straightened if the weld between the top chord and the diagonal members was released and rewelded after straightening. This was successfully completed, together with heat straightening of the bottom chord and diagonal members at this end of the truss. Truss designation TTR16007 displayed excessive local buckling to the top chord which left no option but to replace a segment of the top chord. The local buckling can be seen in Figure **16.**

In terms of steel restoration, from the 15,171 total number of roof steel pieces only 542 pieces were replaced. By weight 95% of the total roof steel (2500T) was retained.

Whilst the structural fire damage to the steel was generally small, the intumescent coating on the steel was an internal coating system which was either damaged by fire, fire water, or environmental exposure because the roof fabric was destroyed leaving the building totally exposed to the elements for eighteen months. Removal of the damaged intumescent coating could not be executed without compromising the primer coat, which meant that all steel with intumescent coatings had the intumescent coating scraped off, blasted, then reprimed and the intumescent coating then reapplied. This was a site-wide need. The in-situ blasting, repriming, and reapplication of the intumescent coating proved challenging and has had a significant impact on the post-fire restoration construction programme.

6 CONCLUSIONS

Although the path to restoration has been extensive, the 22 October 2019 fire at the New Zealand International Convention Centre led to globally recognised fire analysis and never before seen in New Zealand large-scale in-situ experimental testing of heavy steel trusses. Key parts of the extensive damage assessment process included:

- Reliably capturing damage through site observations, testing, historical review of any live feed (photo or video), and collaboration with key stakeholders and subject matter experts.
- Performing localized and informed destructive testing to corroborate visual observations.
- Modelling a best estimate of the fire demands on a reasonably accurate representation of the structure.
- Performing a non-liner structural analysis of the post-fire structure to understand demand to capacity margins considering future demands.
- Undertaking full scale testing of select members to assess potential damage e.g. from post-fire residual stresses.
- Conducting a cost-benefit analysis of repair/replacement options to guide reinstatement.

When completed, this iconic convention centre will draw events from around the world. Delegates and attendees can be assured that extensive and thorough damage assessment and reinstatement methodologies were implemented for their health and safety.

ACKNOWLEDGMENTS

We are grateful to SkyCity, the owner of the NZICC, for permission to publish this work. Acknowledgement and gratitude go to contributors from Beca Engineering, Fletcher Construction Company, SkyCity, Holmes Fire, The University of Auckland, SGS, Simpson Gumpertz & Heger and Culham Engineering for the many hours of effort they applied over several years.

REFERENCES

1. Franssen J.M., Gernay, T., “User Manual for SAFIR 2019. A Computer Program for Analysis of Structures at Elevated Temperature Conditions,” University of Liege, 2019.
2. BSI, “Eurocode 3 - Design of Steel Structures General Rules - Structural Fire Design, BS EN 1993-1-2,” British Standards Institution, 2005.
3. ABAQUS, Inc., “ABAQUS/Standard, User’s Manual”, Version 2020, Distributed by Dassault Systemes SIMULIA
4. NZS 3404 1997/2001/2007 Steel Structures Standard Incorporating Amendments 1 and 2, Standards New Zealand, Wellington, New Zealand.

SiF 2022– The 12th International Conference on Structures in Fire
The Hong Kong Polytechnic University, Nov 30 - Dec 2, 2022

ESTIMATION OF THERMAL IMPACT ON VERTICAL COMPONENTS DUE TO LOCALISED BURNING IN LARGE COMPARTMENT FIRES

Tianwei CHU[1], Liming Jiang[2], Asif Usmani[3]

ABSTRACT

This paper proposes an engineering model to provide estimation of thermal impact on vertical components subject to a localised burning, which regarded the radiant energy as discharged along the flame axis. Non-uniform radiant power and flame radius distributions along the flame height are derived after normalisation and approximation. Multiple datasets obtained from experimental tests are used to validate the proposed model, which demonstrated good performance with mostly 20% or lower deviation. In built environment, the convective heat nearby the localised fire or in the smoke layer are found to be the main source of errors in prediction. Further applications are discussed and demonstrated in large unconfined spaces, and semi-confined compartments, showing promising results compared with FDS models.

Keywords: Localised fire; large compartment fires; fire impact; vertical members; smoke layer

1 INTRODUCTION

A fire could remain localised in a modern large compartment due to the efficiently ventilated smoke layer preventing flashover. The current traveling fire models focus on the thermal impact on horizontal structural members at the ceiling level. These members are exposed to the fire plume when the localised burning region travels [1]. Localised fire models describing the horizontal thermal impact have been often studied [2] and have been written in design standards for structural fire safety engineering [3]. However, fire models to estimate the thermal impact on vertical building components are not well established. Serval attempts [4–7] on characterizing the localised fire impact on vertical surfaces have been made in recent decades, which can be categorized as point source models and solid flame models, as shown in Figure 1.

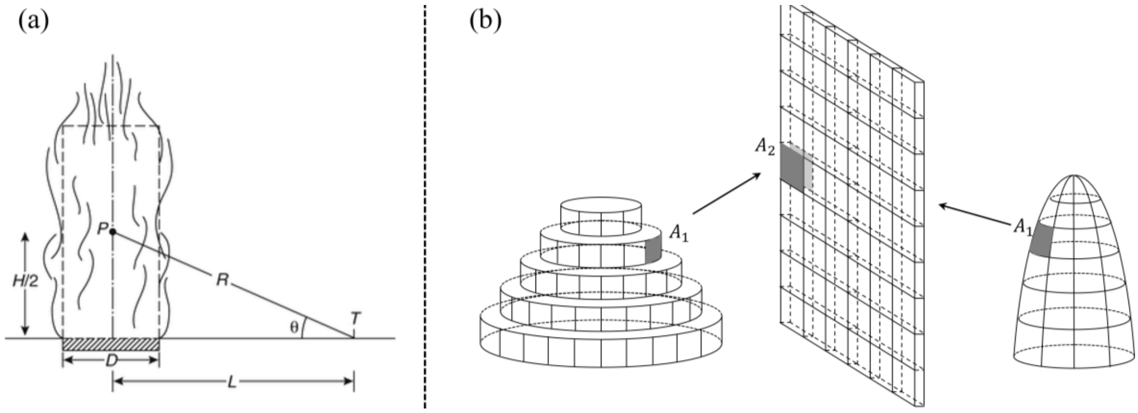

Figure 1 Simple models: (a) point source model[4], and (b) solid flame models.

[1] Mr., Deparment of Building Services Engineering, The Hong Kong Polytechnic University,
e-mail: tianwei.chu@connect.polyu.hk, ORCID: https://orcid.org/0000-0003-3286-6856
[2] Dr., Deparment of Building Services Engineering, The Hong Kong Polytechnic University,
e-mail: liming.jiang@polyu.edu.hk, ORCID: https://orcid.org/0000-0001-8112-2330
[3] Prof., Deparment of Building Services Engineering, The Hong Kong Polytechnic University,
e-mail: asif.usmani@polyu.edu.hk, ORCID: https://orcid.org/0000-0003-2454-5737
https://doi.org/10.6084/m9.figshare.22223953

The single point source model [4] assumed radiation emitting from a single point at the tridimensional centre P of the flame bulk (see Figure 1a), and the radiative heat flux $\dot{q}''_{rad}$ received by the target point T at a distance R (m) from the point source can be calculated as:

$$\dot{q}''_{rad} = \chi_{rad} \frac{\tau \dot{Q}}{4\pi R^2} \cos\theta \tag{1}$$

The point source model preferably of a simple form presented some large deviations in calculating the thermal radiation, especially in the near-field range [8]. The solid flame models, on the other hand, are slightly more complex, which assumed that the radiation from the flames is uniformly emitted from the flame surface. The solid flame surface is discretized into several finite surfaces (see Figure 1b), and the contribution of each surface to the target surface is then calculated separately and summed. The existing models [6, 7, 9] primarily differed in the flame shapes, thereby leading to differences of calculating the view factors. The calculation of view factor adopted a complicated form, which can be expressed as:

$$F_{1\to2} = \frac{1}{A_1} \int_{A_1} \int_{A_2} \frac{\cos\theta_1 \cos\theta_2}{\pi R^2} dA_2\, dA_1 \tag{2}$$

As given in Eq.(2), it requires a double integration and complex calculation of view factors between the finite surfaces and the target receiving surfaces. Computationally, these solid flame models involve a large number of finite surfaces, inhibiting their uses in engineering problems.

In this paper, an engineering fire model is proposed to quantify the thermal impact on vertical surface from localised burning. A comprehensive description of the proposed model, as well as the validation with the experimental dataset is provided. The application of this model in large compartment fire scenarios is examined regarding various smoke layer conditions, and shows promising performance compared with FDS (Fire Dynamics Simulator) models, as well as scaled compartment tests in laboratory.

2 DESCRIPTION OF THE LINE SOURCE MODEL

2.1 Assumptions used in line source model

In the line source model, the localised burning is portrayed as an approximately axisymmetric envelope of flame over the fuel source, as shown in Figure 2. The vertical axis is regarded as the line source of the model, from which all the radiant energy is assumed to be generated. It is assumed that there is no energy loss inside the flame, so the generated radiative power is transmitted intact to the nearest flame contour to the target, and then emitted to the surroundings in a manner similar to the point source.

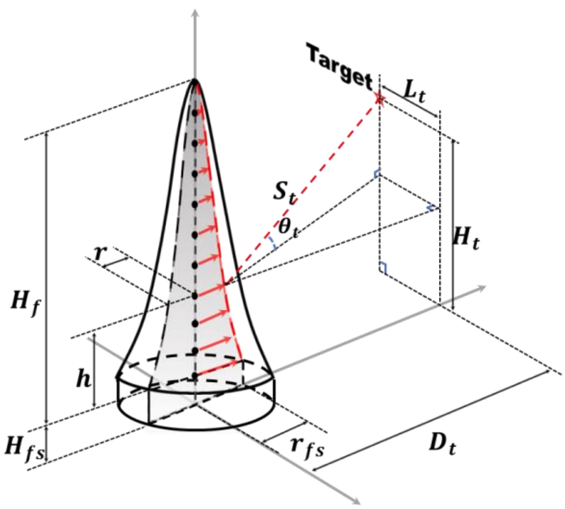

Figure 2 Schematic diagram of the line source model.

The height of the line source, i.e., the flame height over fuel surface, can be estimated using the Heskestad model [10]:

$$H_f = 0.235\dot{Q}^{2/5} + 1.02D_{fs} \tag{3}$$

where $\dot{Q}$ is the heat release rate of the fire source (kW), and D_{fs} is the diameter of the fire source (m). Along this height, the non-uniform energy distribution $\dot{q}(h)$ and flame radius distribution for plume shapes $r(h)$ are developed, and the heating impact towards a target from a line source element of height h can be then estimated using Eq.(4).

$$d\dot{q}''_{t,rad} = \tau \frac{\dot{q}_{rad}(h)}{4\pi S_t(h)^2} \cos\big(\theta_t(h)\big)\, dh \tag{4}$$

where $S_t(h)$ and $\theta_t(h)$ represent the distance from the target (m), and the elevation angle (°) to target of line source element at a height of h. τ is the atmospheric transmissivity (assumed as 1.0) over the distance S_t. Thus, the radiation received by a target $\dot{q}''_{t,rad}$ can be given by:

$$\dot{q}''_{t,rad} = \tau \int_0^{H_f} \frac{\dot{q}_{rad}(h)}{4\pi S_t(h)^2} \cos\big(\theta_t(h)\big)\, dh \tag{5}$$

As indicated in Eq.(5), except for the flame height that governs the integration range, the calculation of the radiation is determined by the radiated power and the relative position between the fire source and the target surface. Hence, these two essential parameters are discussed below to determine their dependency on height.

2.2 Radiative power along the line source

The non-uniform distribution of radiative power along the line source can be derived from the flame temperature distribution, which has been discussed by Zukoski [11] and other researchers [10, 12–14] (shown in Figure 3a). Based on these previous efforts, the following form is recommended to represent the axial flame temperature versus height:

$$T^* \propto (h^*)^{-5/3} \tag{6}$$

where h^* is the normalised height of fire h/H_f, and h is the height of interest (m). Similarly, T^* is the normalised temperature $T(h)/T_{max}$, where $T(h)$ is the gas phase flame temperature (K) at the height of h and T_{max} is the maximum temperature (K) along the flame axis. The radiant power released by the line source is related to its local temperature, which conforms to the principal law of thermal radiation:

$$\dot{q}_{rad} = \varepsilon\sigma T^4 \tag{7}$$

where ε denotes the emissivity of line source, and σ is the Stefan–Boltzmann constant (σ =5.67×10^{-8} W/m^{2}K^4). Combined with Eq.(6), the radiation distribution along the flame axis can be described as:

$$\dot{q}^*_{rad} = \varepsilon\sigma(T^*)^4 \propto (h^*)^{-20/3} \tag{8}$$

where $\dot{q}^*_{rad}$ is the normalised radiative power and can be estimated as $\dot{q}^*_{rad} = \dot{q}_{rad}(h)/\dot{q}_{rad,max}$. Hereby, $\dot{q}_{rad}(h)$ is the radiative power (kW) at the height of h, and $\dot{q}_{rad,max}$ is the maximum radiative power (kW) along the flame axis. Following the above form, an equation based on the fitting of experimental data is proposed to describe the distribution of normalised radiative power (shown in Figure 3b), which is given as:

$$\dot{q}^*_{rad} = \frac{1}{1 + (h^*/0.625)^{20/3}} \tag{9}$$

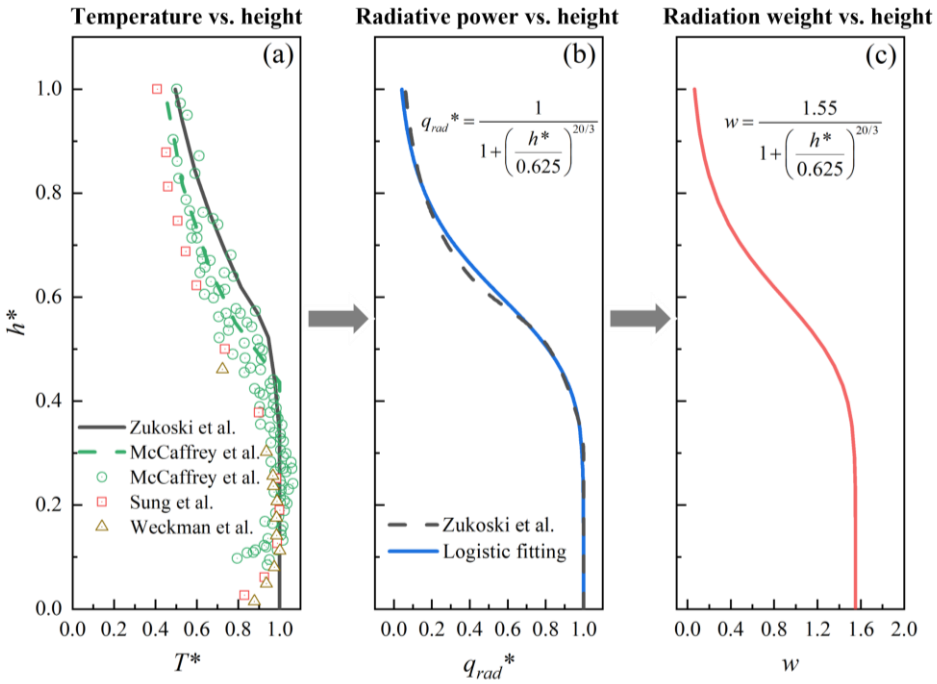

Figure 3 Distribution along the flame axis for: (a) normalized temperature; (b) normalized radiative power; and (c) radiation weight

Eq.(9) represents the normalised radiation distribution with respect to the maximum radiative power $\dot{q}_{rad,max}$, which means that the acquisition of the maximum radiated power is of great importance. However, it may be a challenging task to determine the maximum radiative power $\dot{q}_{rad,max}$ as the calculation of emissivity is complex and sensitive. The present model introduces a radiation weight (shown in Figure 3c) to convert the radiation distribution to be relative to the average radiation energy, which adopts a parameter related to the HRR of the fire source to enable convenient estimation. It is expressed as:

$$\dot{q}_{rad} = \dot{q}^*_{rad}\dot{q}_{rad,max} = w(h^*)\dot{q}_{rad,ave} = w(h^*)\frac{\chi_{rad}\dot{Q}}{H_f} \tag{10}$$

where $w(h^*)$ is the weight of radiation distribution at the normalised height of h^*, and χ_{rad} is the radiative fraction (assumed as 0.35) of the total heat release rate $\dot{Q}$ of fire. It follows the same form of calculating $\dot{q}^*_{rad}$, and its integral should equal to 1. Hence, the expression of weight is as follows:

$$w = \frac{1.55}{1+(h^*/0.625)^{20/3}} = \frac{1.55}{1+\left[(h/H_f)/0.625\right]^{20/3}} \tag{11}$$

The total radiation emitted by the line source can be thereafter calculated by:

$$\dot{Q}_{rad} = \int_0^{H_f} \dot{q}_{rad}(h)\,dh = \int_0^{H_f} w(h/H_f)\frac{\chi_{rad}\dot{Q}}{H_f}\,dh \tag{12}$$

2.3 Flame radius along the line source

The radius of flame envelope can be non-uniform at different height, and this paper uses an empirical correlation to characterize the relationship between the normalised flame radius and the normalised height, as shown in Figure 4. The mathematic description of flame envelope is derived through the fitting of datapoints of typical pool fires, which is expressed as:

$$r^* = -3(h^*)^3 + 5.5(h^*)^2 - 3.5\,h^* + 1 \tag{13}$$

where $r^* = r(h)/r_{max}$ is the normalised radius of flame envelope. $r(h)$ is the radius (m) of flame envelope at the height of h, while r_{max} is the maximum radius (m) of flame envelope, usually being denoted as the radius of fuel surface r_{fs}.

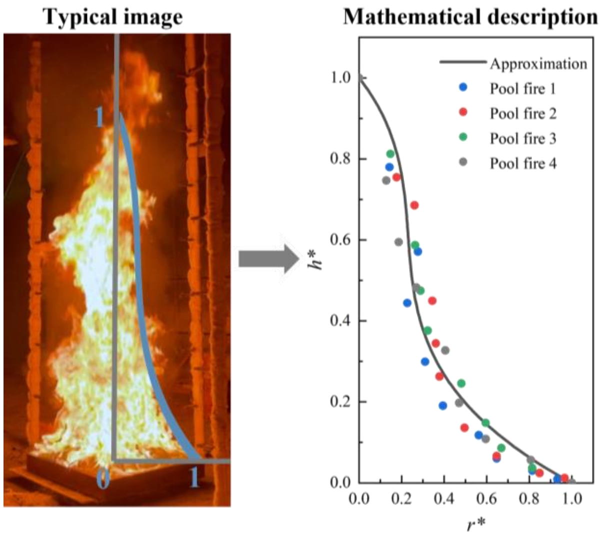

Figure 4 Approximation of the flame radius along line source.

With Eq.(13), it is possible to determine the distance S_t and view angle θ_t from the target to the component at a height of h on the flame envelope, using Eq. (14) and Eq. (15), respectively.

$$S_t = \sqrt{\left(\sqrt{D_t^2 + L_t^2} - r^* r_{fs}\right)^2 + \left(H_t - H_{fs} - h\right)^2} \tag{14}$$

$$\cos\theta_t = \frac{\sqrt{D_t^2 + L_t^2} - r^* r_{fs}}{S_t} \tag{15}$$

where D_t and L_t are the horizontal offset distances (m) from the target to the flame axis. H_t is the height of target (m), and H_{fs} is the height of fuel surface (m). Eventually, the integral form of the line source model can be expressed as:

$$\dot{q}''_{t,rad} = \frac{\chi_{rad}\tau\dot{Q}}{4\pi H_f}\int_0^{H_f} \frac{w\sqrt{D_t^2 + L_t^2} - r_i^* r_{fs}}{\left[\left(\sqrt{D_t^2 + L_t^2} - r_i^* r_{fs}\right)^2 + \left(H_t - H_{fs} - h_i\right)^2\right]^{3/2}} dh \tag{16}$$

2.4 Engineering form of line source model

As indicated in Eq.(16), the model requires the HRR of fire source ($\dot{Q}$), the radius and height of fuel surface (r_{fs}, H_{fs}), and the location of target (D_t, L_t, H_t) as the input parameters to obtain the radiative heat flux $\dot{q}''_{t,rad}$ received by the target. However, this integral form may be inconvenient to implement for engineering applications. Therefore, an engineering form is established by evenly dividing the flame envelope into slices using N points that evenly distributed along the line source, as shown in Figure 5a. For each slice, its thermal impact on the target can be approximately derived by multiplying the average of the heat fluxes at the height of its upper and lower points by their height difference, as expressed by Eq.(17).

$$\dot{q}''_{t,rad} = \sum_{i=1}^{N-1}\left(\dot{q}_{rad,i} + \dot{q}_{rad,i+1}\right)\frac{H_f}{N-1} \tag{17}$$

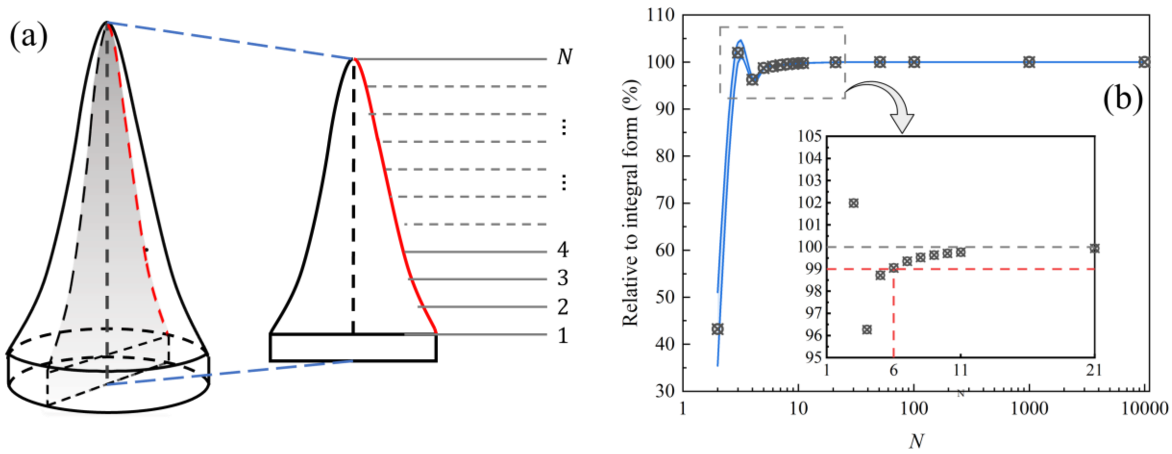

Figure 5 (a) Line source model sliced by N points, and (b) determination of the optimum number of points.

Based on this procedure, an approximated estimation can be obtained, which slightly differs from the full integral form of the proposed line source model. As indicated in Figure 5b, more points could lead to better accuracy comparing to the integral form. The relative deviation ratio is about 1% when using 6 points to slice the line source, and this discrepancy is almost negligible when raising the number of points to 21. By doing so, it inevitably increased the complexity of the engineering form. In this paper, the 6-point form is adopted to balance the accuracy and efficiency of the engineering approximation, given as:

$$\dot{q}''_{t,rad} = 0.0028\dot{Q}\sum_{i=1}^{5}(R_i + R_{i+1}) \tag{18}$$

$$R_i = \frac{w_i\sqrt{D_t^2 + L_t^2} - r_i^* r_{fs}}{\left[\left(\sqrt{D_t^2 + L_t^2} - r_i^* r_{fs}\right)^2 + \left(H_t - H_{fs} - h_i\right)^2\right]^{\frac{3}{2}}} \tag{19}$$

where D_t, L_t and H_t are parameters determined by the location of the target. Similarly, H_{fs} and r_{fs} are the given parameters for fuel surface as shown previously in Figure 2. The subscript i represent the ith slice of localised fire plume, the parameters required for calculation are listed in the Table 1.

Table 1 Parameters for the engineering form of vertical localised fire model

i	h_i	w_i	r_i^*
1	0	1.550	1
2	$0.2H_f$	1.549	0.496
3	$0.4H_f$	1.475	0.288
4	$0.6H_f$	0.880	0.232
5	$0.8H_f$	0.251	0.184
6	H_f	0.065	0

3 VALIDATION OF THE PROPOSED MODEL

3.1 Experimental dataset for validation

The previous four series of localised fire tests have been selected as validation dataset to the proposed line source model. The details of these test series are briefly summarized in Table 2.

Table 2 Summary of experimental dataset of localised fires.

Data source	Compartment type	Fuel type	HRR range (kW)
LOCAFI[5]	Unconfined	Heptane/Diesel	[145, 1901]
LOCAFI+[15]	Unconfined/Confined	Kerosene/Diesel	[442, 2506]
ECSC[16]	Confined	Heptane	[486, 3905]
ICFMP[17]	Confined	Heptane	[400, 2300]

The setup of localised fires in the above projects are all pool fires, involving a wide range of HRRs from 145kW to 3905kW. There are several heat flux gauges installed beside the fire source to detect the heating impact, and the performance of the proposed model is examined by comparisons against the experimental data measured in the tests.

3.2 Performance of line source model

The validation results have been shown in Figure 6a. The horizontal axis in Figure 6a represents the experimentally recorded data of heat fluxes at various locations, which are extracted from the aforementioned reports. Meanwhile, the vertical axis represents the estimation using the proposed engineering solution. Therefore, the diagonal dash lines indicate the performance of present model in comparison to the test data.

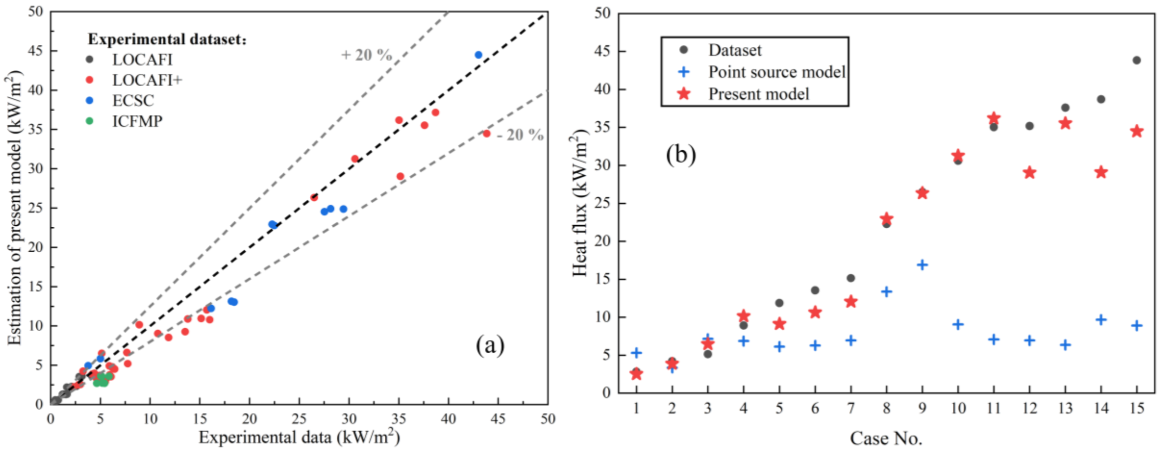

Figure 6 Comparison of calculated results of line source model with experimental data, point source model: (a) estimation VS test data; (b) comparison regarding test cases.

It can be seen that the proposed model is able to estimate the fire impact with deviations mostly below 20%. The majority of the predicted heat fluxes are found to be lower than those measured in experimental tests, and this underestimation is considered to originate from the contribution of convective heat from hot (smoke) layer, which is out of the scope of present model. As shown in Figure 6b, the line source model generally presents better performance compared to the point source model. A total number of 15 cases covering a variety of fire sizes (HRRs) are chosen to show the prediction of the line source model and the point source model comparing to the same data sets. While the case numbers are sorted in terms of HRRs of localised fires, the point source model predicts much lower heat fluxes in higher HRR range. These higher heat fluxes were due to the relatively shorter distance to the localised fire plume or due to a larger fire. In general, the discrepancies observed between the line source model and test data exist due to the uncertainties of fire behaviour but the discrepancies are at an acceptable level.

4 APPLICATIONS OF LINE SOURCE MODEL

The application of the present model focuses on the fire scenarios where the thermal impact on vertical members is dominated by heat radiation, which can be modified for an upper layer of smoke. Two scenarios can be therefore considered for application, large unconfined spaces, and semi-confined compartments [18]. The former represents fire scenarios of nearly unconfined boundaries, such as sports stadiums, where the thermal impact on vertical elements is dominated by the radiation energy from a localized burning. For this case, an FDS model comprising a heptane pool fire of a diameter of 1 m and a vertical wall 2 m away from the flame axis, is used to demonstrate the application of present model, as shown in Figure 7. While the HRR of fire source is 3 MW at static state, the proposed model predicts the non-uniform heat flux distribution on a targeted surface in the large unconfined space, which is very similar to the FDS model.

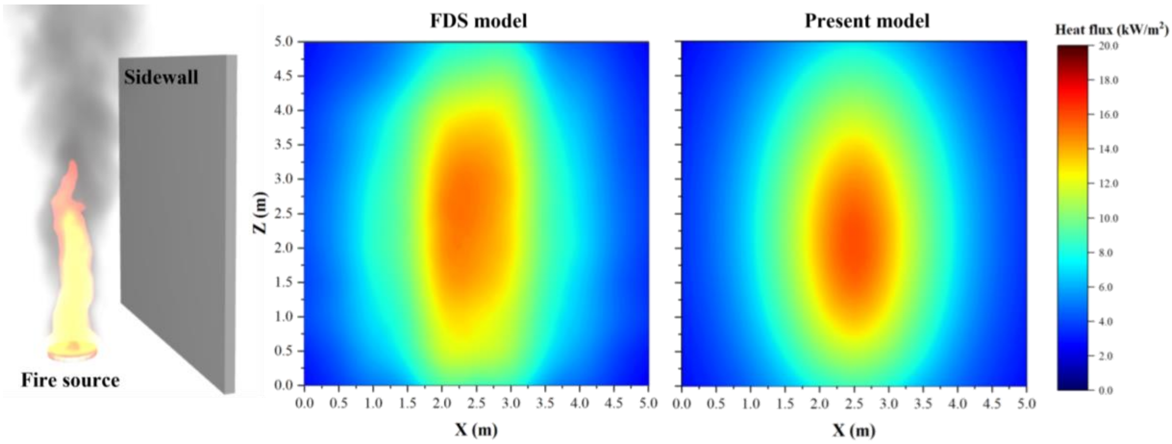

Figure 7 Application in large unconfined space.

The concept of the semi-confined compartment fire [18] denotes the open-plan compartment with various ventilation conditions leading to different smoke layer statuses. The smoke generated from a moving localized fire exists accumulates underneath the ceiling and can lead to various fire impact and fire development. In these fire scenarios, the vertical building component in the compartment receives the heat from the localised burning fire and the smoke layer, as shown in Figure 8. For these fire scenarios, the present model should be adapted with convective components to estimate the heat fluxes on vertical components due to the smoke layer. A validation setup is realised in a laboratory scale compartment (1.8 m × 1.2 m × 0.9 m) with a soffit (0.3 m high) on each side to accumulate a certain thickness of smoke.

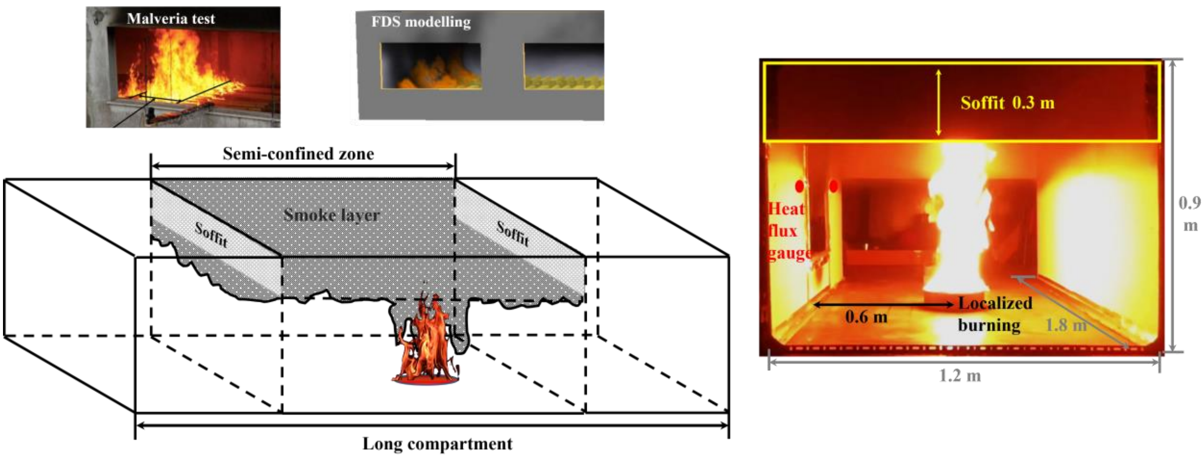

Figure 8 Semi-confined compartment and its demonstration in laboratory scale.

A propanol pool fire of a 0.28 m diameter was placed in the centre of the compartment as a localised burning source. Its mass loss rate was captured serving as the time-variant input parameter to the FDS model. The data from two heat flux gauges and five thermocouples were used for the validation of the FDS model, and then the validated FDS model could provide additional information on the thermal impact received by the sidewall, which can be compared with the present model for demonstration. As shown in Figure 9, the application of present model to this fire scenario can yield relatively promising results, with the exception of the minor underestimation in the area above the soffit.

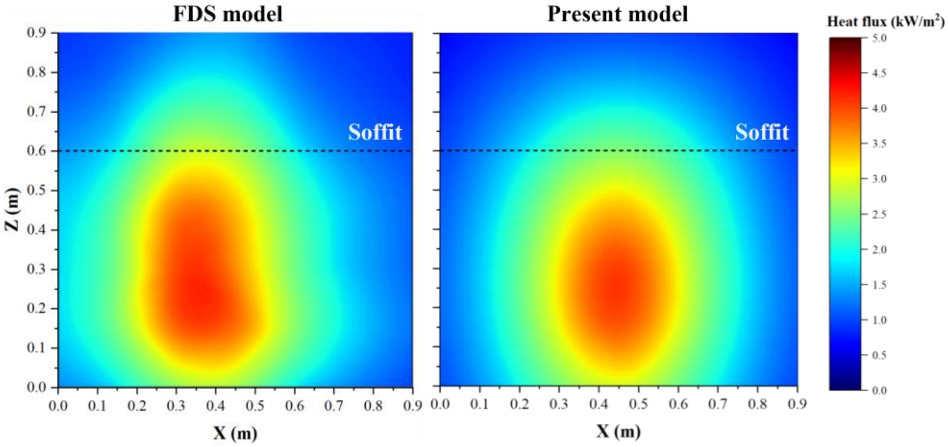

Figure 9 Application in semi-confined compartment.

The use of the FDS model typically require sound understanding and expertise on the modelling process and detailed simulation requires high computational cost. Using the above cases, the good performance of line source model in estimating thermal action of a localised fire on vertical components has been demonstrated. The model can be potentially used as vertical heating boundary models for localised fire scenarios, which could facilitate the heat transfer analyses of building components and structural members of vertical surfaces similar to the use of Hasemi localised fire models for ceiling heat fluxes.

5 CONCLUSIONS

Most of localised fire models currently focus on the heating impact on horizontal members in built environment. In this paper, a line source model and an engineering solution has been derived to estimate the received heat fluxes on vertical surface from a localised fire. The model is validated by experimental datasets of different localised fire cases, which has shown generally good performance and the discrepancy are mostly within 20 %. Limitations can be found for the cases where the heat convection becomes major contribution to thermal impact, which occur at the target surfaces close to the fire flames or in the smoke layer. For large unconfined spaces and semi-confined fire scenarios representing large compartment fires, the line source model has exhibited good prediction capability when comparing the model to the FDS models in terms of surface heat fluxes. This model can facilitate the heat transfer analyses involving vertical surfaces, which can be thereafter implemented in the heat transfer modules in the simulation package for structures in fire such as Opensees for Fire [19].

REFERENCES

1. Khan, A.A., Usmani, A., Torero, J.L.: Evolution of fire models for estimating structural fire-resistance. Fire Safety Journal. 124, 103367 (2021). https://doi.org/10.1016/j.firesaf.2021.103367
2. Wakarnatsu, T., Hasemi, Y., Kagiya, K., Kamikawa, D.: Heating mechanism of unprotected steel beam installed beneath ceiling and exposed to a localized fire: verification using the real-scale experiment and effects of the smoke layer. Fire Safety Science. 7, 1099–1110 (2003). https://doi.org/10.3801/IAFSS.FSS.7-1099
3. British Standards Institution: Eurocode 1: Actions on structures: Part 1.2 General actions: actions on structures exposed to fire. BSI, London (2002)
4. Beyler, C.L.: Fire hazard calculations for large, open hydrocarbon fires. In: Hurley, M.J., Gottuk, D., Hall, J.R., Harada, K., Kuligowski, E., Puchovsky, M., Torero, J., Watts, J.M., and Wieczorek, C. (eds.) SFPE Handbook of Fire Protection Engineering. pp. 2591–2663. Springer New York, New York, NY (2016)
5. Tondini, N., Franssen, J.-M.: Analysis of experimental hydrocarbon localised fires with and without engulfed steel members. Fire Safety Journal. 92, 9–22 (2017). https://doi.org/10.1016/j.firesaf.2017.05.011

6. Manco, M.R., Vaz, M.A., Cyrino, J.C.R., Landesmann, A.: Ellipsoidal solid flame model for structures under localized fire. Fire Technology. 54, 1505–1532 (2018). https://doi.org/10.1007/s10694-018-0750-y
7. Tondini, N., Thauvoye, C., Hanus, F., Vassart, O.: Development of an analytical model to predict the radiative heat flux to a vertical element due to a localised fire. Fire Safety Journal. 105, 227–243 (2019). https://doi.org/10.1016/j.firesaf.2019.03.001
8. Iqbal, N., Salley, H.M.: Fire Dynamics Tools (FDTs): quantitative fire hazard analysis methods for the U.S. nuclear regulatory commission fire protection inspection program. U.S. Nuclear Regulatory Commission, Washington, DC (2004)
9. Rew, P.J., Hulbert, W.G., Deaves, D.M.: Modelling of thermal radiation from external hydrocarbon pool fires. Process Safety and Environmental Protection. 75, 81–89 (1997). https://doi.org/10.1205/095758297528841
10. Heskestad, G.: Engineering relations for fire plumes. Fire Safety Journal. 7, 25–32 (1984). https://doi.org/10.1016/0379-7112(84)90005-5
11. Zukoski, E.: Fluid dynamic aspects of room fires. Fire Safety Science. 1, 1–30 (1986). https://doi.org/10.3801/IAFSS.FSS.1-1
12. McCaffrey, B.J.: Purely buoyant diffusion flames: some experimental results. National Bureau of Standards, Gaithersburg, MD (1979)
13. Sung, K., Chen, J., Bundy, M., Hamins, A.: The characteristics of a 1 m methanol pool fire. Fire Safety Journal. 120, 103121 (2021). https://doi.org/10.1016/j.firesaf.2020.103121
14. Weckman, E.J., Strong, A.B.: Experimental investigation of the turbulence structure of medium-scale methanol pool fires. Combustion and Flame. 105, 245–266 (1996). https://doi.org/10.1016/0010-2180(95)00103-4
15. Francis, P., Baddoo, N., Hanus, F., Thauvoye, C.: Design of columns subject to localised fires (LOCAFI+). SCI Assessment, Silwood Park, Ascot, Berkshire (2018)
16. Hostikka, S., Kokkala, M., Vaari, J.: Experimental study of the localized room fires. NFSC2 Test Series. 98 (2001)
17. Hamins, A., Maranghides, A., Johnsson, R., Donnelly, M., Yang, J., Mulholland, G., Anleitner, R.L.: Report of experimental results for the international fire model benchmarking and validation exercise #3. National Institute of Standards and Technology, Gaithersburg, MD (2006)
18. Khan, A.A., Nan, Z., Jiang, L., Gupta, V., Chen, S., Khan, M.A., Hidalgo, J., Usmani, A.: Model characterisation of localised burning impact from localised fire tests to travelling fire scenarios. Journal of Building Engineering. 54, 104601 (2022). https://doi.org/10.1016/j.jobe.2022.104601
19. Jiang, L., Usmani, A.: Towards scenario fires – modelling structural response to fire using an integrated computational tool. Advances in Structural Engineering. 21, 2056–2067 (2018). https://doi.org/10.1177/1369433218765832

A STUDY TO DETERMINE SUITABLE AND ROBUST INTENSITY MEASURES FOR REINFORCED CONCRETE SLAB SUBJECTED TO FIRE

Akshay Baheti[1], David Lange[2], Vasant Matsagar[3]

ABSTRACT

Performance-based structural design is still in a comparatively developmental phase for fire hazard when compared to that of, for example, earthquake excitation. Addressing a significant weakness in performance-based design for fire, the present study aims to propose appropriate intensity measures (IM) for a fire hazard that has a robust correlation with certain engineering demand parameter (EDP) and which may subsequently be linked to the damage / loss estimation a priori, in a structure subjected to a fire event. In this context, 12 plausible variables are identified for consideration as IMs for the EDPs of maximum deflection and maximum rate of deflection in an isolated simply supported reinforced concrete (RC) slab element. A correlation matrix is established based on the outcome from detailed nonlinear analyses of an RC slab subject to various fire profiles from the literature. Based on the important traits that a certain IM should possess as suggested in previous studies, maximum rebar temperature and maximum net heat flux are recommended as suitable IMs for the respective EDPs. The robustness of both the correlations is established by performing sensitivity analysis for changes in material and geometric properties of the RC slab element.

Keywords: RC slab; Fire risk analysis; Intensity measure; Engineering demand parameter; Correlation matrix.

1 INTRODUCTION

Major fires result in significant damage to structural and non-structural members. Whilst most design standards allow the structural engineer to primarily focus on the principal performance driver, i.e., life safety in fire scenarios, comparatively little to no attention is given to the performance of structural members and the subsequent damages caused in fire [1]. Modern buildings are exposed to a high risk of fire-induced damage due to various factors which are otherwise not considered by several national codes. These factors include gas pipelines, modern electric appliances, a large volume of combustibles compartments, open architecture, etc. [2]. The concept of performance-based design in structural engineering offers a solution to these issues as it is based on achieving results that achieve certain end objective(s) rather than through the provision of restrictive deemed to satisfy solutions or technical guidance. The PEER (Pacific Earthquake Engineering Research) Centre's performance-based earthquake engineering framework, later extended for structural fire engineering [3], is a well-accepted tool for performance-based structural design. This framework proposes a solution based on the outcomes at the end of the "loss analysis" step which is preceded by the "structural analysis" and "hazard analysis" steps. Using the PEER framework, the evaluation of damage or loss in any structure, subjected to a fire event, is therefore based on its post-fire condition rather than on limiting criteria commonly adopted to determine fire resistance levels.

[1] PhD Research Scholar, The University of Queensland - IIT Delhi Academy of Research (UQIDAR), India
e-mail: as.baheti11@gmail.com, ORCID: https://orcid.org/0000-0002-8172-1103
[2] Senior Lecturer, The University of Queensland, Australia
e-mail: d.lange@uq.edu.au, ORCID: https://orcid.org/0000-0002-4551-1045
[3] Dogra Chair Professor, Indian Institute of Technology (IIT) Delhi, India
e-mail: matsagar@civil.iitd.ac.in, ORCID: https://orcid.org/0000-0002-7600-0520
https://doi.org/10.6084/m9.figshare.22223968

A recent study [4] has developed a framework to evaluate probabilistic fire loss in an RC structure based on numerical analysis; however, a strong correlation between and demonstration of the suitability of the chosen intensity measures (IM) and engineering demand parameters (EDP) was not established. Previous studies indicate that it is essential to demonstrate a correlation between IMs and EDPs of the structure as post-hazard vulnerability may be underestimated if correlations between the chosen variables are poor. Another recent study [5] established a correlation between several IMs and an EDP for a composite slab; however, this was limited to a fire based on the parametric fire curve defined in EN 1991-1-2 [6].

Several experimental studies inferred that the fully developed fire profiles such as parametric fire or standard fire may not represent a real fire which may occur in the pre-flashover, moving or spreading phase. There remains work to explore the correlation of different IMs based on other fire models, such as those proposed by the travelling fire frameworks, e.g. [7] and the large compartment fire framework [8]. The present study is an analysis for selecting a suitable and robust parameter for the IM which is suitably correlated to EDP so that this could prove a benchmark for future risk assessment studies of RC structures subjected to fire. Objectives of the present study are summarised as follows: (1) to prepare an exhaustive list of potential candidate intensity measures (IM) and engineering demand parameters (EDP) for various structural fire events on a reinforced concrete slab element; (2) to establish possible correlations between different IM and EDP candidates by performing detailed stochastic analysis for each kind of fire event; (3) to perform sensitivity analysis for the established correlation between IM and EDP by varying material and geometric properties of RC slab element.

2 IDENTIFICATION OF VARIABLES IN STRUCTURAL FIRE ENGINEERING

2.1 Introduction

An essential component of the risk estimation procedure is the quantification of the structure's fragility, i.e., the likelihood of the structure experiencing damage of a certain magnitude if a hazardous event, such as fire, occurs. In the PEER framework, a structure's fragility is assessed by explicitly incorporating uncertainty arising from various sources, for example, uncertainty in the fire model, heat transfer model, and structural model [9]. The PEER framework handles the uncertainties by constructing two key interrelationships. The first of these relates to fire intensity (referred to as intensity measure) followed by the structural response (referred to as engineering demand parameter) based on which structural damage state is determined using a damage function.

Reinforced concrete (RC) structures may experience degradation in their physical, chemical, and mechanical characteristics if subjected to significant fire. Some recent studies [1, 4-5, 10-11] evaluated damage in RC structures due to fire by primarily focussing on the basic unit of the structure such as a structural member or a portal frame. Therefore, the present study is targeted at developing an IM-EDP correlation matrix for an isolated RC slab element.

2.2 Plausible candidates for intensity measures

Uncertainty in a fire event depends on the type of time-temperature profile considered while analysing the structure. For example, standard fire formulation is identical in every case whereas equivalent duration standard fire [6] (referred to as EDSF now onwards) limits the duration of standard fire depending on compartment characteristics. Parametric fire profile depends on several inputs such as fuel load density, ventilation factor, material properties, and heat release rate. Travelling fire profiles, such as those proposed by the improved Travelling Fire Methodology (the iTFM) [7] assume that the compartment is fully ventilated and therefore, the temperature profile depends on fuel load density, fire spread rate, and heat release rate. The large compartment fire framework (LCFF) [8] considers the transition of compartment fire from travelling phase to the fully developed phase and hence, its temperature profile depends on the combination of the variables described before.

Plausible candidates for fire intensity measure, suggested in previous studies are peak compartment temperature (T_{max}) [3], fire duration (t_{dur}), peak rebar temperature ($T_{\mathrm{r,max}}$), area under the time-temperature curve (AUC) [1], fuel load density (f_{d}) [4, 10, 11], time to reach maximum temperature (t_{peak}), cumulative incident radiation (CIR) [5]. All these parameters, except fuel load density, may be derived from the time-temperature curve of the fire. LCFF inputs a fire scenario as flux-time history like other fire frameworks such as localised fires [6] or flame extension travelling fire model [12]. Therefore, heat flux-dependent parameters, as with time-temperature profile-dependent parameters, can also be considered plausible candidates for intensity measures. These include maximum, e.g. net heat flux ($\dot{q}''_{\text{net,max}}$), average net heat flux ($\dot{q}''_{\text{net,avg}}$), the area under flux time history or the energy stored in the member considering adiabatic boundary condition at the unexposed surface (E_i), energy stored in the member considering Neumann boundary condition at its unexposed surface (E_s). The computation of the variable E_i and E_s is presented in equations (1) and (2), respectively.

$$E_{\text{i}} = \int_0^{t_{\text{h}}} \dot{q}''_{\text{net, exposed}}(t)\,dt \tag{1}$$

$$E_{\text{s}} = \int_0^{t_{\text{h}}} \left(\dot{q}''_{\text{net, exposed}}(t) - \dot{q}''_{\text{net, unexposed}}(t)\right)dt \tag{2}$$

where, t_h is the time up to which heating is observed in the member, i.e., the gas temperature in the compartment is greater than the slab temperature at its exposed surface. Another parameter that can be considered as an IM is the maximum temperature difference between the exposed and unexposed surface of the RC slab element (ΔT_{max}). This parameter is related directly to the temperature gradient across the section of the slab which is responsible for the induction of curvature and possibly thermally induced bending moment (in the case of rotational restraint) on the slab element.

2.3 Plausible candidates for engineering demand parameter

The critical response of a structure to fire hazard is recorded using the engineering demand parameter (EDP) which may subsequently be related to the damage/ loss estimation. Plausible candidates for EDP for structural members suggested in previous studies are percentage of spalling, residual capacity, peak rebar temperature, residual deflection, maximum deflection, residual drift, and maximum rate of deflection [1, 4, 5, 10]. Numerical estimation of spalling in reinforced concrete elements is still in development. Residual capacity and residual deflection are determined based on field tests or post-fire structural assessment. Therefore, maximum deflection (δ_{max}) and maximum rate of deflection ($\dot{\delta}_{max}$) at centre of the slab are considered as EDPs for the RC slab element in the present study. In the future limits of these two variables may be correlated to decision variables however this is outside of the scope of the current work.

3 NUMERICAL MODELLING

3.1 Structural model

The floor plan of the large compartment under consideration is shown in Figure 1a. Floor height is taken as 3.6 m. Compartment plan, floor height, and member dimensions are adopted from the study on a 9-storey structure [14]. Grade of concrete and steel rebar are M25 (characteristic compressive strength, f_{ck} = 25 MPa) and Fe500 (characteristic yield strength, f_y = 500 MPa), respectively. A 7 m × 7 m slab in each bay is of overall depth, D 200 mm, and is reinforced with 335 mm^2 steel bars per meter width in its lateral and longitudinal directions near its bottom surface with a 20 mm clear cover provided to them. A schematic of the section of reinforced concrete (RC) slab is presented in Figure 1b. The RC slab element is subjected to external heat at its bottom surface and the top surface is exposed to ambient air condition (air temperature, T_a = 20 °C).

The temperature profile across the section is obtained by conducting a heat transfer analysis of the slab element by subjecting it to uniform temperature history at its bottom surface along the entire length as shown in Figure 1b. Heat transfer analysis of slab is conducted in OpenSees for fire framework [15]. RC slab element is modelled as 2D Block element with the initial temperature set to 20 °C across its section. Temperature histories from various fire scenarios, as discussed in the next section, are given as input for gas temperature in the compartment. The RC slab receives heat from the compartment fire through convective and radiative modes of heat transfer, assuming a black body radiation temperature equal to the temperature history calculated. The convective heat transfer coefficient, h_c at the exposed surface of RC slab is taken as 25 W/m^2.K for EDSF and 35 W/m^2.K for other fire profiles and the emissivity, ε is assumed 0.7 [6]. Values of h_c and ε at the unexposed surface are taken as 4 W/m^2.K and 0.7, respectively. Thermal properties of concrete, i.e., conductivity, specific heat, and density are adopted from the temperature-dependent relations in EN 1992-1-2 [16]. The reinforcement bars are not modelled while conducting heat transfer analysis of slab as their area is small compared to the surrounding concrete. The temperature of the reinforcement bars is assumed equal to the temperature of the concrete at the depth they are located.

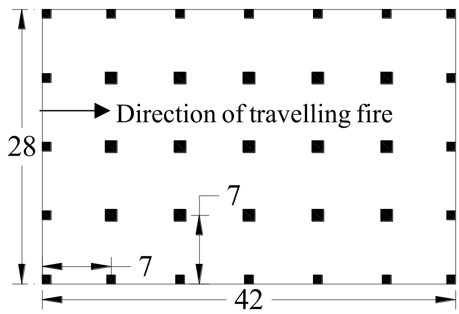

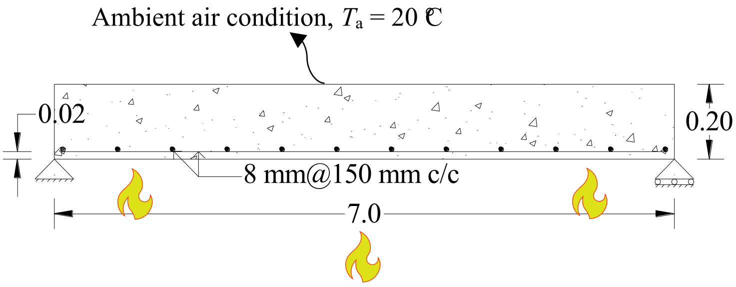

Figure 1: (a) Plan of the large compartment under consideration [14]; (b) schematic of the section of RC slab element subjected to uniform fire loading on the entire length.
(note: all the dimensions are in 'm' unless stated otherwise)

After obtaining the temperature profile across the depth of the slab, its nonlinear thermo-mechanical analysis is performed in OpenSees for fire framework [17]. RC slab element is modelled using nonlinear shell elements. The slab is divided into small layers of shell element having thickness of 10 mm each across its depth. Concrete is modelled using the concrete damage plasticity model using strength and stiffness reduction factors and thermal expansion properties defined in EN 1992-1-2 [16]. Steel reinforcement bars are modelled using the J2 plasticity material (von-Mises stress yielding principle) using strength and stiffness reduction factors and thermal expansion properties defined in EN 1992-1-2. The slab is simply supported on all its four edges. The slab element is subjected to static uniformly distributed load (UDL) equivalent to the combination of self-weight, super-imposed dead load, and live load whose values are obtained from the relevant Indian standards. The structural analysis for static loads is performed before the application of thermal load.

3.2 Fire models

The uncertainty associated with different fire profiles include those related to fuel load density in a compartment, ventilation properties of the compartment, heat release rate, thermal inertia of the compartment lining material, and compartment geometry. Since the scope of the present study is limited to the reinforced concrete (RC) structure, compartment geometry and lining material properties are not expected to vary and therefore, are assumed deterministic. The occupancy of the structure is categorised as dwelling and hence, the heat release rate is assumed constant having a value of 250 kW/m^2.

The remaining two uncertainties, i.e., fuel load density and ventilation factor are the variables to generate random fire profiles with different formulations available in the literature. Fuel load density is following the Gumbel type I distribution having an average value of 780 MJ/m^2 and a standard deviation of 234 MJ/m^2 [6]. There is only one probabilistic model in the literature which considers uncertainty related to the opening factor (ϕ) of the compartment and it is presented in equation (3) [13].

$$\phi = \phi_{max}\left(1-\zeta\right) \tag{3}$$

where, ϕ_{max} is a physical maximum value of the opening factor in a compartment and ζ is a dimensionless random parameter varying as per lognormal distribution with a mean of 0.2 and a standard deviation of 0.2 and is curtailed to a maximum value equal to 1 as an opening factor cannot be a negative number. The basis this expression, whether it is mathematically or physically based, is unclear. In addition, it is mathematically incorrect as the area under its probability density curve is less than 1 due to it being curtailed at 1.

Nonetheless, the expression is still being used in this study to get random fire profiles. The conclusions of this paper are not affected by the use of this function. Parametric fire and EDSF time-temperature profiles are obtained for a single bay (7 m × 7 m) of the compartment shown in Figure 1a. Two windows of uniform dimension 0.9 m × 1.2 m are present on each side of this small compartment which acts as the source of opening. The fire spread rate, s_f depends on the nature of fuel inside the compartment and lies in the range of 0.1 mm/s to 19.3 mm/s [7]. Hence, five different cases of iTFM with spread rate $s_{f,min}$ (= 0.1 mm/s), 1 mm/s, 5 mm/s, 10 mm/s, and $s_{f,max}$ (= 19.3 mm/s) are considered in present study to cover the entire domain of iTFM. The near-field temperature in iTFM framework is taken as 1200 °C. In travelling fire phase of LCFF, the fire spread rate is taken 1 mm/s corresponding to the spread rate for wood crib in open [7]. Fire profiles obtained from both iTFM and LCFF are uniform across the width of the compartment. Time-temperature profile in iTFM and LCFF is evaluated at the centre of the slab in the first bay from the left in Figure 1a. 50 random fire profiles are generated for each framework by varying f_d and ϕ, as discussed earlier. A detailed nonlinear analysis of the RC slab element is conducted to record values of all the variables being considered either as IM or EDP. For example, input time-temperature profiles evaluated for f_d = 780 MJ/m^2 and ζ = 0, from each fire framework are presented in Figure 2. It is observed that all the fire profiles have quite different characteristics which may result in more devastating effects than what are observed for fully developed fire profiles from the code and design standards.

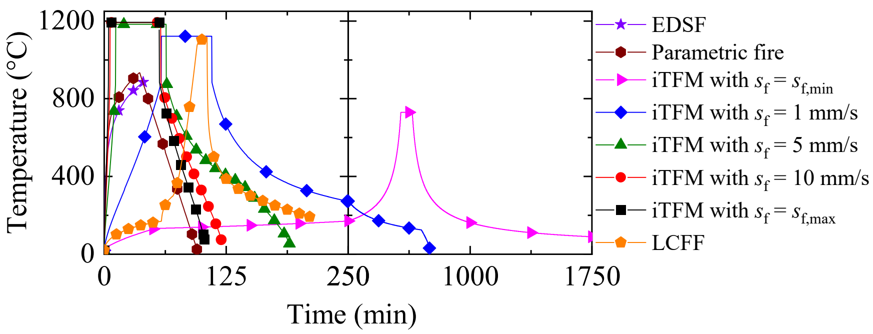

Figure 2: Temperature-time curves obtained with different fire frameworks for f_d = 780 MJ/m^2 and ζ = 0.

3.3 Validation of numerical models

Studies of RC slab element subjected to fire are undertaken to establish the credibility of the numerical models developed in OpenSees for fire framework in the present study. The first study undertaken is to check the correctness of the heat transfer model. An RC slab of depth 100 mm is modelled in the OpenSees for fire framework following the procedure described in Section 3.1 and is subjected to a standard fire profile at its bottom surface for 180 minutes. Temperature profiles thus obtained at various depths across the section of the slab are compared with the observations made by Jiang et al. [15] and are presented in Figure 3a. A good overlap of the temperature profiles across the depth of section is observed for the developed numerical model demonstrating the accuracy of the heat transfer model.

Another validation study is undertaken for a cantilever RC beam of width 0.2 m and depth 0.1 m [17]. It is reinforced with 393 mm^2 steel bars per meter width in lateral and longitudinal directions with a clear cover of 20 mm from both surfaces. Concrete is modelled using the concrete damage plasticity model with its tensile and compressive strength equal to 3 MPa and 30 MPa, respectively. The tensile strength of the reinforcement bar is 345 MPa. The beam is subjected to a 0.5 kN concentrated load at its free end and its top surface is maintained at 0 °C all the time during the analysis. The temperature of its bottom surface is gradually increased from 0 °C to 1000 °C and the corresponding deflection at a free end of the beam is observed. The beam is modelled using layered shell element following the procedure described in Section 3.1 and the observations from the numerical analysis are compared with those obtained by Jiang et al. [17] in Figure 3b. A good overlap is observed indicating the numerical model developed for conducting thermo-mechanical analysis of RC slab is quite accurate. The same numerical models are used throughout the present study.

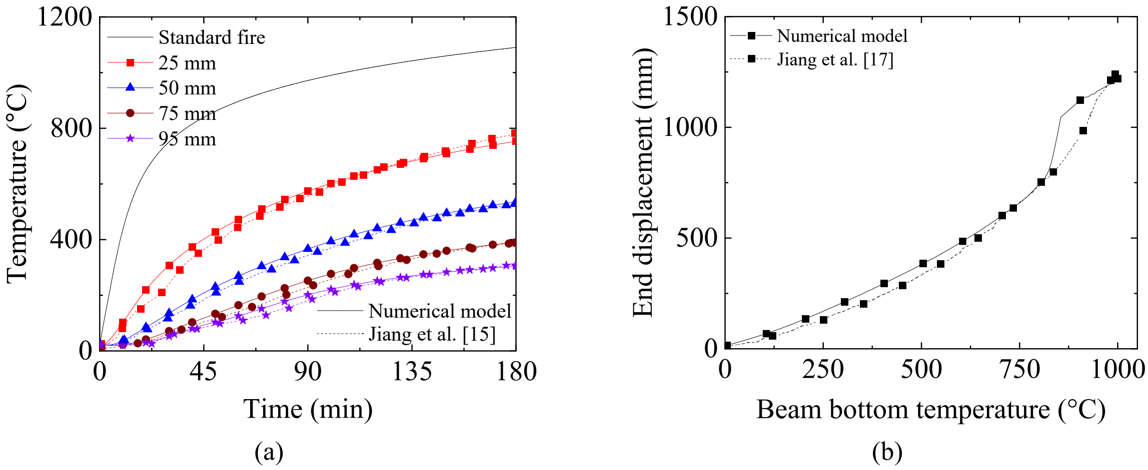

Figure 3: (a) Validation of a numerical model for heat transfer analysis of RC slab with Jiang et al. [15]; (b) validation study of a numerical model for thermo-mechanical analysis of RC cantilever beam with Jiang et al. [17].

4 DEVELOPMENT OF CORRELATION MATRIX FOR RC SLAB

4.1 Analysis of RC slab to various fire events

A reinforced concrete (RC) slab is modelled in OpenSees for fire framework following the procedure described in Section 3.1. The RC slab is analysed for 50 random fire profiles from various frameworks described in Section 3.2. Heat transfer analysis was performed to obtain temperature history across the depth of the slab. This temperature history is applied as an input for performing a nonlinear thermo-mechanical analysis of the RC slab in its deflected position due to the action of static loads. A well-established KrylovNewton algorithm is used to get accelerated convergence in the modified Newton Raphson algorithm. Convergence criterion is defined in terms of the norm of displacement increment in each step of the analysis. The maximum value of displacement and rate of displacement at centre of the slab is recorded for each fire profile along with the corresponding values of the variables to be considered as intensity measures. Since the correlation between IM-EDP variables is seemingly nonlinear, the use of popular Pearson's coefficient to show correlation between the IMs and EDPs is not appropriate. Hence, Kendall's rank correlation coefficient, tau [18] is instead used to illustrate the correlation between IM-EDP variables. The tau values obtained for the set of IM and EDP variables are presented in Table 1.

The positive tau values in Table 1 represents that there is a positive correlation between the two variables under consideration, i.e., if the value of one variable increase, the value of the other variable increases and vice versa. A tau value close to 1 indicates a reasonable degree of monotonicity between the two variables under consideration. Both these attributes are strongly encouraged between the finalised IM and EDP variables. However, some values of the tau coefficient are not obtained due to lack of variation in the observed values of certain variables, for example, for the case of the maximum rate of deflection in slab subject to EDSF profile and the maximum net heat flux recorded in the same case.

From the table, it is inferred that the variables CIR, E_i, $T_{r,max}$, and ΔT_{max} have a good degree of monotonicity with a maximum deflection of slab for all the kinds of fire profiles. Hence, these could all be the potential candidates to be considered as intensity measures (IM) for an EDP maximum central deflection (δ_{max}) of RC slab. Similarly, variables $\dot{q}''_{net,max}$ and ΔT_{max} have a good degree of monotonicity with a maximum rate of deflection in the slab. Hence, these are potential candidates for IM for an EDP maximum rate of deflection at centre of the RC slab. A comparison of the correlation between the shortlisted variables as IM and the corresponding EDPs is presented in Section 4.2 to arrive at the most suitable parameter for IM in each case.

4.2 Determination of the most suitable intensity measure

The intensity measure is a key input for fragility analysis since it quantifies the hazard. It too has a probabilistic distribution due to the varying nature of the hazard. An IM aims to provide a single parameter

Table 1: IM-EDP correlation matrix for RC slab (Figure 1b) subjected to fire, presented in terms of Kendall's coefficient, tau

IM → EDP ↓	Fire framework	f_d	T_{max}	t_{dur}	AUC	t_{peak}	CIR	$\dot{q}''_{net,max}$	$\dot{q}''_{net,avg}$	E_i	E_s	$T_{r,max}$	ΔT_{max}
δ_{max}	EDSF	0.72	0.98	1.00	1.00	1.00	1.00	ND	-1.00	1.00	1.00	1.00	1.00
	Parametric fire	0.59	0.38	0.12	0.69	0.52	0.87	0.18	0.04	0.84	0.84	0.97	0.73
	iTFM with $s_f = s_{f,min}$	-0.41	-0.41	0.44	0.35	-0.41	-0.02	0.45	-0.44	0.08	-0.02	0.00	0.83
	iTFM with s_f = 1 mm/s	0.19	0.19	0.57	0.62	ND	0.77	0.19	0.67	0.84	0.88	0.95	0.19
	iTFM with s_f = 5 mm/s	0.00	0.00	0.67	0.67	ND	0.86	0.00	-0.40	0.96	0.96	0.91	0.41
	iTFM with s_f = 10 mm/s	0.19	0.19	0.66	0.73	0.09	0.91	0.19	-0.71	0.97	0.97	0.94	0.66
	iTFM with $s_f = s_{f,max}$	0.18	0.15	0.74	0.79	0.17	0.87	-0.14	-0.78	0.92	0.92	0.88	0.89
	LCFF	0.12	0.01	0.77	0.81	0.09	0.87	0.39	0.86	0.87	0.87	0.94	0.62
$\dot{\delta}_{max}$	EDSF	ND	ND	ND	ND	ND	ND	ND	ND	ND	ND	ND	ND
	Parametric fire	0.03	0.30	-0.62	-0.17	-0.18	-0.03	0.67	0.68	-0.08	-0.07	0.07	0.29
	iTFM with $s_f = s_{f,min}$	-0.31	-0.31	0.35	-0.34	-0.31	-0.42	0.35	-0.35	-0.41	-0.42	-0.40	0.10
	iTFM with s_f = 1 mm/s	0.14	0.14	0.08	0.09	ND	0.12	0.14	0.04	0.04	-0.07	0.03	0.14
	iTFM with s_f = 5 mm/s	0.74	0.74	-0.21	-0.20	ND	0.02	0.74	0.28	0.11	0.12	0.07	0.55
	iTFM with s_f = 10 mm/s	0.90	0.90	-0.13	-0.05	0.20	0.14	0.90	0.08	0.20	0.20	0.17	0.53
	iTFM with $s_f = s_{f,max}$	-0.37	-0.31	-0.06	-0.08	-0.42	-0.14	0.54	0.19	-0.18	-0.18	-0.15	-0.18
	LCFF	0.10	0.10	0.62	0.64	-0.02	0.69	0.45	0.82	0.69	0.69	0.75	0.66

(Note: ND represents Kendall's tau coefficient is not defined for the variable combination due to lack of variation in data)

encompassing many variations of the hazard such that these can be directly compared and associated with one another. The most important trait that IM should possess is efficiency. Other desirable traits include sufficiency, predictability, hazard computability, and scaling robustness [5]. Efficiency is related to the variance in the IM-EDP relationship. Thus, it helps to reduce the number of analyses and loading scenarios to estimate the damage with adequate precision, i.e., with adequately small uncertainty. Sufficiency of an IM renders the damage measure conditionally independent in the risk function, i.e., it leads to accurate prediction of a damage measure for the given IM. Predictability of an IM is related to the accuracy with which an IM can be determined. It helps to reduce errors in the prediction of subsequent damage function. Hazard computability is related to the efforts required by a risk evaluator to develop hazard curves in terms of the IM. Scaling robustness is related to the unbiased nature of an IM against scaling of various records of a hazard.

The correlation curves are developed separately for EDP – maximum deflection and maximum rate of deflection with the shortlisted variables of IM, described in Section 4.1. The choice of the most appropriate variable for fire intensity measure will be based on all the traits discussed earlier. Therefore, correlation curves for maximum deflection of the slab at its centre are obtained by mapping it against ΔT_{max}, E_i, CIR, and $T_{r,max}$ and the same are presented in Figure 4a. Similarly, correlation curves for maximum rate of deflection of slab at its centre are obtained by mapping it against $\dot{q}''_{net,max}$ and ΔT_{max} and the same are presented in Figure 4b.

4.3 Result and discussion

The tau values obtained for the parameter E_i are highest among those observed for other parameters for their probable correlation with the EDP – maximum deflection of RC slab element which indicate a greater degree of monotonicity. However, it is concluded that the maximum rebar temperature ($T_{r,max}$) has the most efficient correlation, compared to other variables, with an EDP of maximum central deflection (δ_{max}) as the

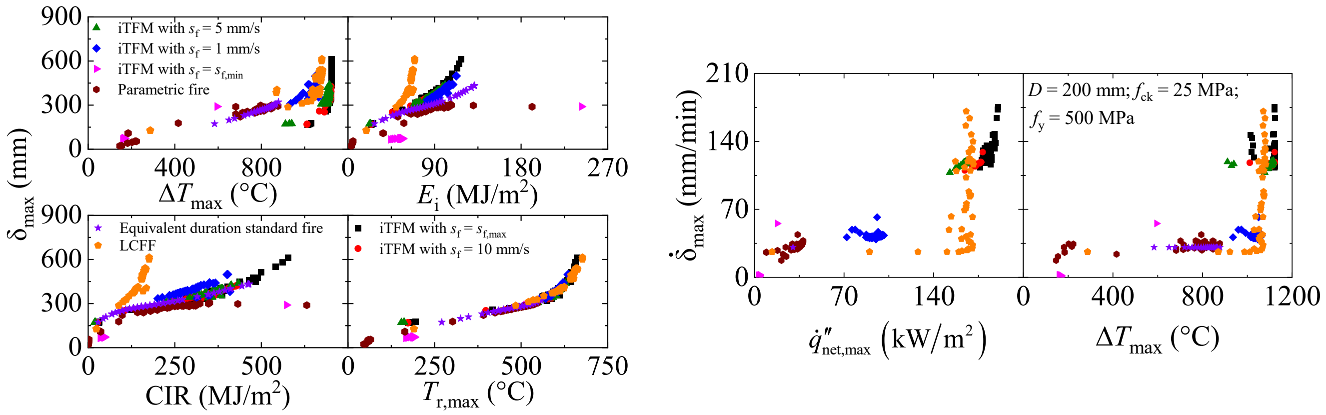

(a) (b)

Figure 4: Correlation curves of plausible candidates for intensity measures for an engineering demand parameter: (a) maximum deflection and (b) maximum rate of deflection, at centre of the RC slab.

scatter in its correlation curves with the EDP, for all the kinds of fire profiles, is least among those observed for other plausible candidates for IM. In addition, the correlation curve between $T_{r,max}$ and δ_{max} is monotonic without any jumps in between. Thus, the value of δ_{max} can be predicted with reasonable accuracy if the value of $T_{r,max}$ is known (satisfaction of the trait – sufficiency). The maximum reinforcement temperature can be predicted with reasonable accuracy from heat transfer analysis of RC slab for a certain fire hazard (satisfaction of the trait – predictability). The single drawback of $T_{r,max}$ is that the fire hazard curve do not exist in its term and therefore, the risk evaluator has to put some efforts in the computation of fire hazard. The rebar temperature is the result of the heat energy stored in the rebar due to the external heat flux on the RC slab element and it is more relatable than the heat energy in the reinforcement bar. The stiffness of reinforcement bar reduces with rise in its temperature [16] which is crucial in the overall response of the member. Therefore, if the desirable trait, hazard computability, is not considered for the time being, the maximum rebar temperature ($T_{r,max}$) is a clear choice for the most suitable IM for the EDP δ_{max}. This observation is in agreement with one of the hypotheses by Ioannou et al. [1].

Whereas, both $\dot{q}''_{net,max}$ and ΔT_{max} have a similar level of efficiency in correlation with the EDP maximum rate of deflection ($\dot{\delta}_{max}$) as is observed from Figure 4b. The data presented in Table 1 indicates that the maximum net heat flux, $\dot{q}''_{net,max}$ has a better monotonicity with $\dot{\delta}_{max}$ as Kendall's tau coefficient values for $\dot{q}''_{net,max}$ are greater than those observed for ΔT_{max} except for those obtained for the LCFF framework. In addition, there is a continuous increase in the maximum rate of deflection with the increase in maximum net heat flux, except for the case of LCFF; whereas, correlation curves of $\dot{\delta}_{max}$ with ΔT_{max} demonstrate a disproportionate relationship between the IM and the EDP which may not go well with the desirable trait for an IM – sufficiency. For the desirable trait predictability, both the variables can be estimated from the heat transfer analysis of RC slab with the same level of accuracy and the fire hazard curve does not exist, to date, in terms of both the variables. Heat flux represent the rate of heat energy input in the system and it is reasonable that if the rate of input energy increases, there is increase in rate of deflection in an element for example, RC slab in the present study. Therefore, $\dot{q}''_{net,max}$ is proposed as the most suitable IM for an EDP $\dot{\delta}_{max}$ based on its advantage in desirable trait for an IM – sufficiency.

5 SENSITIVITY STUDY FOR THE MOST SUITABLE IM

The robustness of the selected fire intensity measures is established by performing sensitivity analysis for the reinforced concrete (RC) slab element. Two different cases for depth of the slab element, i.e., 175 mm and 225 mm are considered while keeping other geometric properties (length and width) constant. Lower values for depth of the slab section are not considered for it will not satisfy the serviceability condition as

per the relevant Indian standards. Four grades of concrete, i.e., M20, M30, M40, and M50, and two grades of steel reinforcement, i.e., Fe415 and Fe550 are also considered to analyse the effect of change in material properties on the IM-EDP correlations. Results from the sensitivity analysis are presented in Figure 5a and 5b for variation of depth, Figure 6a and 6b for the variation in grade of concrete, and Figure 7a and 7b for the variation in grade of a steel reinforcement bar. Two figures in each case represent the results from the sensitivity analysis for an EDP – maximum deflection and maximum rate of deflection, respectively.
From the graphs presented in Figure 5a, 6a, and 7a, it is observed that there exist an efficient correlation between maximum rebar temperature ($T_{r,max}$) and maximum displacement (δ_{max}) of RC slab even with the variation in geometric and material properties of RC slab. Therefore, it is inferred that $T_{r,max}$ is the most suitable and robust intensity measure (IM) for engineering demand parameter (EDP) δ_{max}.

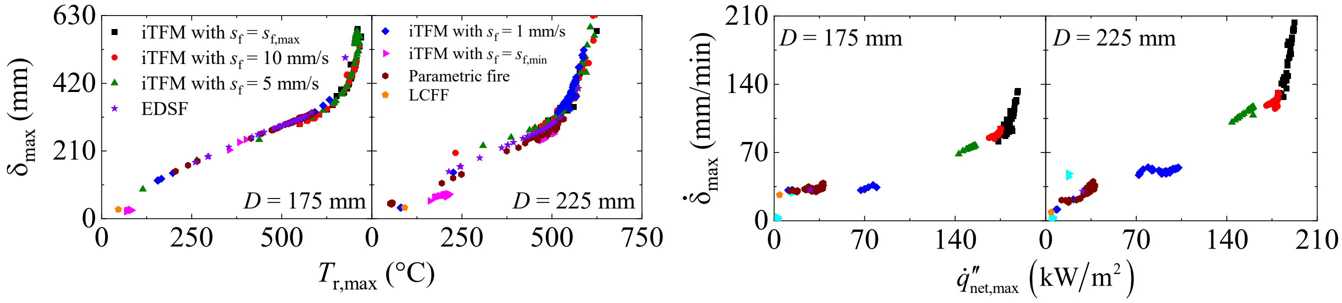

(a) (b)

Figure 5: Results from the sensitivity analysis of RC slab performed by varying its depth for: (a) $T_{r,max}$ - δ_{max} correlation; (b) $\dot{q}''_{net,max}$ - $\dot{\delta}_{max}$ correlation.

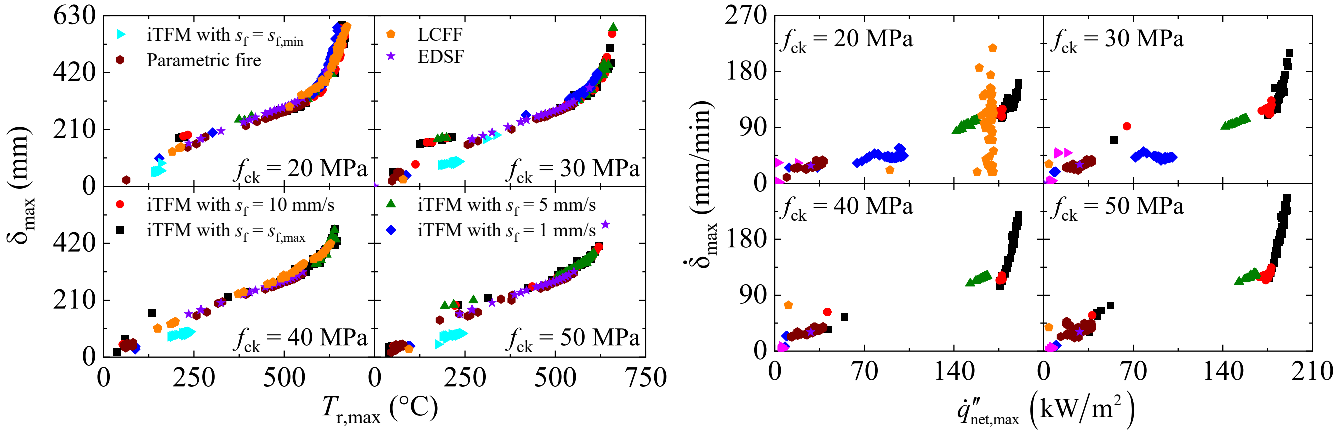

(a) (b)

Figure 6: Results from the sensitivity analysis of RC slab performed by varying grade of concrete for: (a) $T_{r,max}$ - δ_{max} correlation; (b) $\dot{q}''_{net,max}$ - $\dot{\delta}_{max}$ correlation.

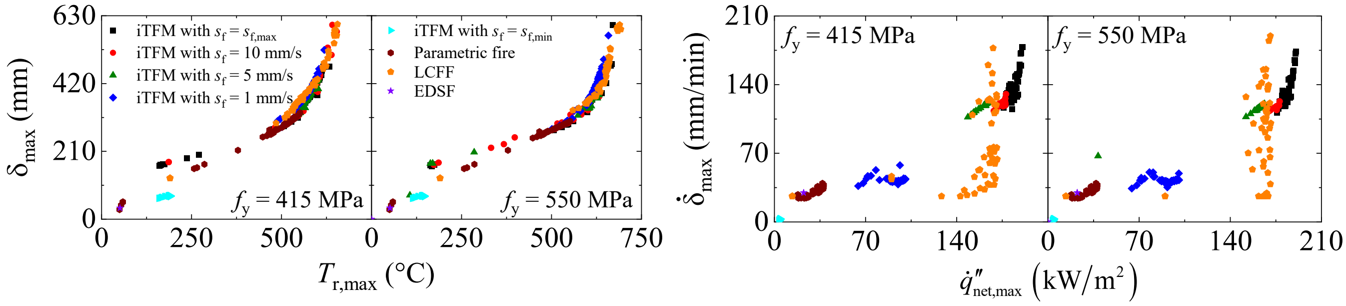

(a) (b)

Figure 7: Results from the sensitivity analysis of RC slab performed by varying grade of reinforcement bars for: (a) $T_{r,max}$ - δ_{max} correlation; (b) $\dot{q}''_{net,max}$ - $\dot{\delta}_{max}$ correlation.

Similarly, From the graphs presented in Figure 5b, 6b, and 7b, it is observed that maximum net heat flux ($\dot{q}''_{\text{net,max}}$) incident on RC slab has an efficient correlation with the maximum rate of deflection ($\dot{\delta}_{\max}$) for all the kinds of fire profiles except the LCFF profile, even with the changes in material and geometric properties of RC slab. Moreover, it is observed that the correlation curve between $\dot{q}''_{\text{net,max}}$ and $\dot{\delta}_{\max}$ for the LCFF profile is in concordance with the correlation curves developed for other fire profiles, for greater values of $\dot{\delta}_{\max}$. Therefore, $\dot{q}''_{\text{net,max}}$ is a suitable and robust IM for and EDP $\dot{\delta}_{\max}$.

6 CONCLUSIONS

The present study summarises the importance of the existence of the correlation between intensity measure (IM) and engineering demand parameter (EDP) for a hazard for its risk evaluation and is an effort to establish suitable pairings for a reinforced concrete (RC) slab subjected to fire hazard. The following conclusions are drawn based on the results observed in the present study:

- 7 time-temperature profile-dependent variables from an extensive literature survey and 5 more variables having flux-time profile-dependent properties are suggested for their consideration of probable IMs. Thus, 12 different variables are identified, in total, which is quite an extensive range for the fire intensity measure.
- An isolated simply supported RC slab element is analysed for random fire profiles generated using well-established fire frameworks from the literature and a correlation matrix is formulated using Kendall's rank correlation coefficient to shortlist the variables for IM which possess a positive and monotonic relationship with the corresponding EDP.
- On comparing the probable correlation for the shortlisted variables based on essential and desirable traits for an IM, it is concluded that the maximum rebar temperature ($T_{\text{r,max}}$) is the most suitable IM for an EDP – maximum deflection ($\delta_{\max}$) in RC slab and maximum net heat flux ($\dot{q}''_{\text{net,max}}$) is the most suitable IM for an EDP – maximum rate of deflection ($\dot{\delta}_{\max}$) in RC slab.
- A sensitivity analysis is performed by varying the overall depth of RC slab, grade of concrete, and grade of steel reinforcement bars to check the robustness of the developed IM-EDP correlations. It is observed that both the IM-EDP correlations, i.e., the $T_{\text{r,max}}$ - $\delta_{\max}$ and $\dot{q}''_{\text{net,max}}$ - $\dot{\delta}_{\max}$ correlations, are quite robust for the variation in geometric and material properties of RC slab, thus demonstrating their suitability for risk evaluation strategies in future studies.

ACKNOWLEDGMENT

The research work presented herein is supported by the Government of India's Ministry of Education under its Scheme for Promotion of Academic and Research Collaboration (SPARC) for the project 'Fire Safety in Underground Tunnels' (Project Code: P920). The PhD study of the first author is supported by a fellowship from Indian Institute of Technology (IIT) Delhi, India and The University of Queensland (UQ), Australia under their joint PhD program, UQIDAR.

REFERENCES

1. Ioannou, I., Aspinall, W., Rush, D., Bisby, L. & Rossetto, T., Expert Judgment-based Fragility Assessment of Reinforced Concrete Buildings Exposed to Fire, Reliab Eng Syst Saf 167, 105-127 (2017). https://doi.org/10.1016/j.ress.2017.05.011.
2. Zhang, H. Y., Li, Q. Y., Kodur, V. & Lv, H. R., Effect of Cracking and Residual Deformation on Behavior of Concrete Beams with Different Scales under Fire Exposure, Eng Struct 245, 112886 (2021). https://doi.org/10.1016/j.engstruct.2021.112886.
3. Lange, D., Devaney, S. & Usmani, A., An Application of the PEER Performance Based Earthquake Engineering Framework to Structures in Fire, Eng Struct 66, 100-115 (2014). https://doi.org/10.1016/j.engstruct.2014.01.052.

4. Ni, S. & Gernay, T., A Framework for Probabilistic Fire Loss Estimation in Concrete Building Structures, Struct Saf 88, 102029 (2021). https://doi.org/10.1007/s10694-012-0291-8.
5. Shrivastava, M., Abu, A. K., Dhakal, R. P., Moss, P. J. & Yeow, T. Z., Probabilistic Structural Fire Engineering using Incremental Fire Analysis and Cloud Analysis, Proc Inst Civ Eng: Eng Comput Mech 173(2), 47-58 (2020). https://doi.org/10.1680/jencm.18.00001.
6. CEN (European Committee for Standardization): EN 1991-1-2: Eurocode 1: Actions on Structures - Part 1-2: General Actions - Actions on Structures Exposed to Fire. Brussels; 2002.
7. Rackauskaite, E., Hamel, C., Law, A. & Rein, G., Improved Formulation of Travelling Fires and Application to Concrete and Steel Structures, Structures 3, 250-260 (2015). https://doi.org/10.1016/j.istruc.2015.06.001.
8. Gupta, V: Open-plan Compartment Fire Dynamics, PhD Thesis. The University of Queensland, Brisbane; 2021.
9. Van Coile, R, Elhami Khorasani, N, Lange, D and Hopkin, D: Uncertainty in Structural Fire Design, In International Handbook of Structural Fire Engineering, 323-411. Springer, Cham; 2021.
10. Chaudhary, R. K., Roy, T. & Matsagar, V., Member and Structural Fragility of Reinforced Concrete Structure under Fire, J Struct Fire Eng 11(4), 409-435 (2020). https://doi.org/10.1108/JSFE-02-2019-0015.
11. Chaudhary, R. K., Roy, T. & Matsagar, V., Framework for Fragility Assessment of Reinforced Concrete Portal Frame subjected to Elevated Temperature, Structures 28, 2785-2800 (2020). https://doi.org/10.1016/j.istruc.2020.10.078.
12. Heidari, M., Kotsovinos, P. & Rein, G., Flame Extension and the Near Field under the Ceiling for Travelling Fires inside Large Compartments, Fire Mater 44(3), 423-436 (2020). https://doi.org/10.1002/fam.2773.
13. Lungu, D, Rackwitz, R: Joint Committee on Structural Safety-Probabilistic Model Code - Part 2: Loads, Joint Committee on Structural Safety (JCSS), Section 2.20. https://www.jcss-lc.org/publications/jcsspmc/fire.pdf; 2001.
14. Law, A., Stern-Gottfried, J., Gillie, M. & Rein, G., The Influence of Travelling Fires on a Concrete Frame, Eng Struct 33(5), 1635-1642 (2011). https://doi.org/10.1016/j.engstruct.2011.01.034.
15. Jiang, L., Jiang, Y., Zhang, Z. & Usmani, A., Thermal Analysis Infrastructure in OpenSees for Fire and its Smart Application Interface towards Natural Fire Modelling, Fire Technol 57(6), 2955-2980 (2021). https://doi.org/10.1007/s10694-020-01071-0.
16. CEN (European Committee for Standardization): EN 1992-1-2: Eurocode 2: Design of Concrete Structures - Part 1-2: General Rules - Structural Fire Design. Brussels; 2004.
17. Jiang, L., Orabi, M. A., Jiang, J. & Usmani, A., Modelling Concrete Slabs subjected to Fires using Nonlinear Layered Shell Elements and Concrete Damage-plasticity Material, Eng Struct 234, 111977 (2021). https://doi.org/10.1016/j.engstruct.2021.111977.
18. Kendall, M. G., A New Measure of Rank Correlation, Biometrika 30(1/2), 81-93 (1938). https://doi.org/10.2307/2332226.

"SCALING-UP" FIRE SPREAD ON WOOD CRIBS TO PREDICT A LARGE-SCALE TRAVELLING FIRE TEST USING CFD

Xu Dai[1,*], Naveed Alam[2], Chang Liu[3], Ali Nadjai[4], David Rush[5], Stephen Welch[6]

ABSTRACT

Simulation-based approaches for characterising the fire behaviour of travelling fires in large compartments are a potentially valuable complement to experimental studies, providing useful insights on evolving boundary conditions for structural response. They are attractive in reduced costs and the possibility of carrying out systematic parametric studies free from some of the experimental uncertainties, but sufficiently general models have not been previously demonstrated. Here, we explore the potential for "scaling-up" a "stick-by-stick" CFD model which had been carefully calibrated against the results of experiments on an isolated crib, of 2.8 m diameter, to a uniformly distributed fuel bed of extent 4.2 × 14.0 m located within an open compartment 9 × 15 m in plan, with an internal height of 2.9 m. The results in terms of the fire spread and burn out predictions are very encouraging, and the heat release rate evolution is also consistent with the experimental value. There are some discrepancies in predicted gas phase temperatures, nevertheless, such discrepancies with this aspect of the model are unlikely to have any great significance in the prediction of fire spread on a horizontally orientated flat fuel bed, which is the prime interest of the current work. Thus, the established "numerical simulator" looks to have good potential as a tool to explore and characterise the behaviour of travelling fires subject to different compartment boundary conditions.

Keywords: Flame spread; CFD modelling; FDS; Large-scale wood crib fire tests; Travelling fires

1 INTRODUCTION

One of the key foundations in fire engineering is the compartment fire, which is used to describe a fire confined within an enclosure. Travelling fires are now regarded as a very relevant fire scenario in large compartments, following research in the past decade towards providing simplified design tools for performance-based structural fire design [1, 2]. Typical features of this fire scenario are the fire plume in the near-field and the hot smoke layer providing pre-heating in the far field. Once the fire is "travelling",

[1] Senior Lecturer, School of Engineering and the Built Environment, Birmingham City University
e-mail: xu.dai@bcu.ac.uk; xudai1987@gmail.com (corresponding author), ORCID: https://orcid.org/0000-0002-9617-7681
[2] Lecturer, FireSERT, Ulster University
e-mail: n.alam@ulster.ac.uk, ORCID: https://orcid.org/0000-0003-3637-1113
[3] PhD student, School of Engineering, University of Edinburgh
e-mail: chang.a.liu@ed.ac.uk, ORCID: https://orcid.org/0000-0002-1812-5480
[4] Professor, FireSERT, Ulster University
e-mail: a.nadjai@ulster.ac.uk, ORCID: https://orcid.org/0000-0002-9769-7363
[5] Senior lecturer, School of Engineering, University of Edinburgh
e-mail: d.rush@ed.ac.uk, ORCID: https://orcid.org/0000-0002-6439-8607
[6] Senior lecturer, School of Engineering, University of Edinburgh
e-mail: s.welch@ed.ac.uk, ORCID: https://orcid.org/0000-0002-9060-0223
https://doi.org/10.6084/m9.figshare.22223980

the near-field has a leading edge representing the fire spread, and a trailing edge representing the burnout of the fuel [3, 4].

In the long development history of experimental and theoretical treatments for compartment fires wood cribs were often adopted as the main fuel. Examples of this include: the pioneer compartment fire theory by Harmathy in the 1970s [5], the full-scale tests for Natural Fire Safety Concept for Eurocodes in 2000s [6], and various travelling fire test series in 2010s [2]. Nevertheless, the experimental costs for travelling fires are particularly high, as they require very large experimental compartments (usually > 100 m^2); time-consuming intensive test instrumentation work; and significant demands on resources and staffing, an example being the recent TRAFIR Ulster Travelling Fire Test series [7-9]. This is due to the essential nature of the travelling fires, with the requirement to adequately characterise the spatial and temporal variation of thermal boundary conditions for the extensive structural elements, inside the very large open-plan compartments which are of interest for structural fire engineering design.

2 RESEARCH OBJECTIVES AND METHOD

This paper aims to push the boundaries of fire modelling using CFD via "scaling-up" a calibrated model, to explore if an adequate level of fire spread prediction can be achieved at a large compartment scale for an idealised fuel bed (i.e., uniformly distributed wood crib). If the predictive capability could be demonstrated in the fire modelling field, it means "numerical experiments" can be potentially performed in the future for assessing underlying physical mechanisms that are currently out of reach through traditional large-scale onsite experiments. This would go some way to addressing the issues with the high expense of the large compartment fire tests for travelling fires.

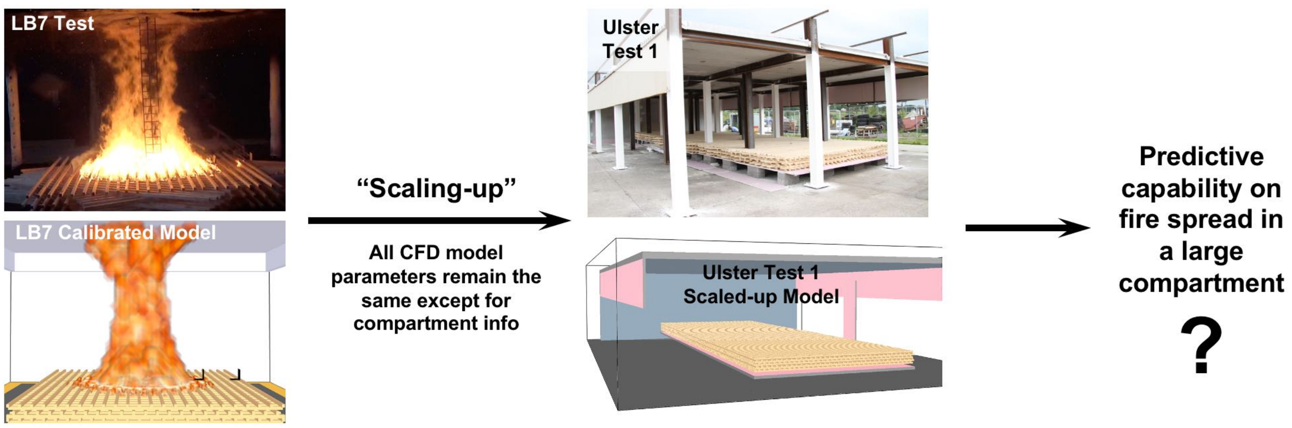

Figure 1. Research method in this paper.

The research method relies on "scaling-up" the model for fire spread calibrated on a single wood crib test (i.e., LB7 Test) [10], to a large-scale compartment travelling fire test with an extended wood crib distribution (i.e., Ulster Travelling Fire Test 1) [7]. Both the calibrated model and the scaled-up model have an identical high resolution for wood crib fuel bed representation (i.e., stick-by-stick). During the "scaling-up" exercise, all the CFD model setup parameters (e.g., wood characteristics) remain strictly the same except for updating the compartment dimensions (9 × 15 × 2.9 m in height). Then the method credibility could be assessed via comparing the scaled-up CFD model prediction against the large-scale compartment fire test measurements, as illustrated in Figure 1. The assessed parameters include fire spread, burn-away, heat release rate, gas phase temperatures, and incident radiant heat flux on the fuel bed.

Note that the CFD model presented in this paper is fundamentally different from that of one earlier publication [11], which used larger "wood block" objects to represent the fuel load as a simplification, with a direct model calibration against the same large-scale compartment travelling fire tests [7-9]. In theory the approach presented in this paper should result in a more general model, provided the wood crib specification is maintained, i.e., the one which does not require further calibration at a large compartment scale. It therefore provides a potential method with predictive capability on fire spread, as a cost-effective alternative to large-scale structural fire testing for travelling fires.

3 THE "SCALED-UP" CFD MODEL

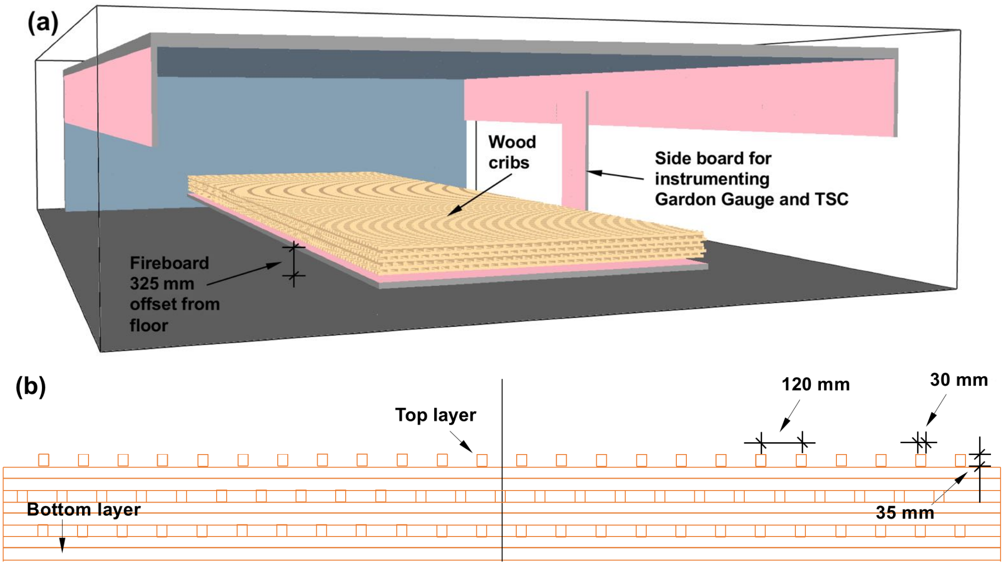

Figure 2. The "scaled-up" CFD model, (a) Skewed view, and (b) Representation of the wood sticks in side-elevation view.

As explained earlier, the "scaled-up" CFD model for the Ulster Travelling Fire Test 1 strictly inherited all the setup parameters from the calibrated model for the LB7 test (e.g., wood characteristics [10]), except for updating the dimensions of the compartment, fuel bed, and test rig, as shown in Figure 2 (a). The 2.8 m × 2.8 m square wood crib with nine layers of sticks in the calibrated LB7 model was extended to a 14.0 m × 4.2 m rectangular wood crib with the same wood sticks arrangement for the Ulster Test 1 [7]. Note that both the calibrated model and the scaled-up model had the same high resolution for wood crib fuel bed representation 30 mm (breadth) × 35 mm (height), referred as "stick-by-stick" models, see Figure 2 (b). Further, the cell size of the "scaled-up" model within the crib volume was 15 mm × 15 mm × 17.5 mm (i.e., half that of the physical dimensions of the sticks, the same as the calibrated LB7 model). Sensitivity studies on grid cell size for representing heat release rate (HRR) and the fire spread on the wood crib top layer were demonstrated in the calibrated LB7 model study [10].

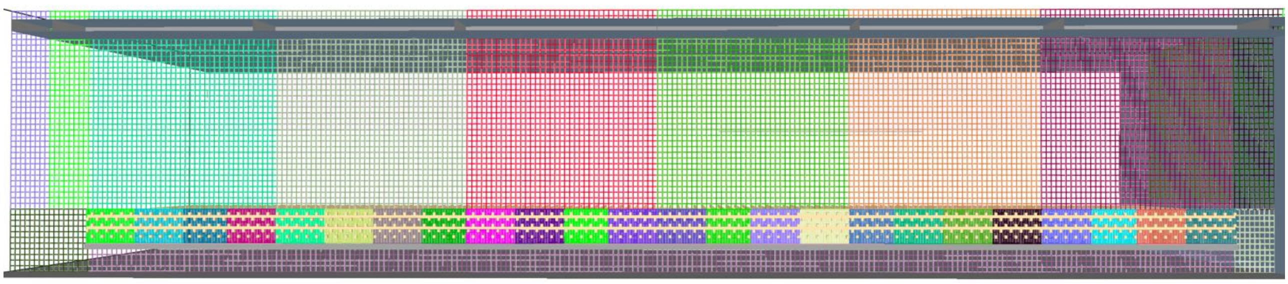

Figure 3. Grid cell resolution of the model: 15 mm × 15 mm × 17.5 mm per cell for the wood sticks at solid phase, 60 mm × 60 mm × 70 mm and 30 mm × 30 mm × 35 mm cell size at the gas phase, total number of cells ~8.3 million with 125 meshes.

The cell size of the gas phase in the horizontal surrounds of the crib, as well as above the top surface of the crib was 60 mm × 60 mm × 70 mm, see Figure 3. In addition, to better represent the heat transfer process at the crib top surface, an additional layer was inserted with two cells of identical size as in the fine mesh, functioning as a "transition layer" between the crib and the gas phase. The total computational domain size was 16.20 m × 10.20 m × 3.22 m, thus the total number of cells was approximately 8.3 million, which were divided into 125 meshes and each mesh was assigned to a single MPI process on the computational cluster. The simulations were performed using the compute cluster ARCHER2 [12], with the run taking around 40 days clock time of computation to complete a 7200 s simulation for the Ulster Test 1.

The compartment ceiling, back wall, downstands, and fireboard platform for supporting the wood sticks were all represented in the model according to the exact dimensions in the test. The material thermal properties for the compartment boundaries are summarized in Table 1. The moisture content of the normal weight concrete (NWC) was assumed to be 10%, which was equivalent to the water saturated status due to the consistent rain on the test day. Moisture migration, *per se*, was neglected in the model, but its energetic influence was considered via a modified specific heat value. In addition, the compartment test floor adopted the same NWC material, also with 10% moisture. The concrete blocks below the fireboard platform were not included in the model due to its limited impact on heat transfer for the wood cribs above. An elevated vertical fireboard screen located externally beside the wood cribs for Thin Skin Calorimeter (TSC) and Gardon Gauge (GG) instrumentation was also represented in the model, as shown in Figure 2 (a).

Table 1. Summary of the compartment thermal properties in the "scaled-up" model (Temperature, T, unit in ºC).

Material	Density (kg/m^3)	Emissivity	Conductivity (W m^{-1}K^{-1})	Specific heat (kJ kg^{-1}K^{-1})	References
Normal weight concrete (10% moisture)	2300	0.8	1.6	T=20, F=0.9 T=100, F=0.9 T=115, F=5.6 T=200, F=1.0 T=400, F=1.1 T=1200, F=1.1	Eurocode 2 [13]
Fireboard	900	0.89	0.24	1.25	SFPE Handbook [14], Kirby et al. [15]
Rockwool Flexi	45	0.9	0.09	0.66	Rockwool [16]

The igniter for the "scaled-up" model herein was simplified as being the same for the calibrated LB7 model, accounting for the fact that prediction of the initial ignition stage was not regarded as a prime research interest in this study, and also to minimise the modelling uncertainties for this "scaling-up" exercise due to the ignition difference between the Ulster Test 1 and the LB7 test. As explained in our earlier publication [10], the ignitor was modelled as a square burner with dimensions of 90 mm × 90 mm, prescribed with a 323 kW/m^2 HRRPUA (heat release rate per unit area) lasting for 240 s to ensure the energy and mass are conserved for the 40 ml of methylated ethanol at 96% used in the LB7 test.

Furthermore, thermocouples and incident radiant heat flux measurement devices (e.g., TSC/GG) in the model were placed at the same locations as the experimental instrumentations. Thermocouples were represented in FDS using a value of 1.5 mm bead diameter and emissivity of 0.85.

4 COMPARISON BETWEEN THE MODEL AND THE TEST

Due to the ignition difference between the Ulster Test 1 and the "scaled-up" model (inherited from the LB7 calibrated model), it should be noted that a 13 mins fire development delay was consistently applied to all the modelling results herein, including fire spread, burn-away, HRR, gas phase temperature, and incident radiant heat flux. This 13 mins offset was determined by matching the initial spread away from the burner, which itself is only represented approximately in the simulation.

4.1 Fire spread & burn-away

Figure 4 demonstrates the fire spread comparison captured from the video recording of the Ulster Travelling Fire Test 1 and the FDS Smokeview (a visualisation tool supplied with FDS) at 20-minute intervals. In the model, the fire spread was represented with the gas temperature “slice” at the centreline of the compartment along the fire trajectory (elevation view), and via the burning rate of the wood cribs fuel bed (plan view). Figure 4 suggests the simulated fire spread on the wood sticks top layer and the flame shape are both qualitatively comparable to the test observation.

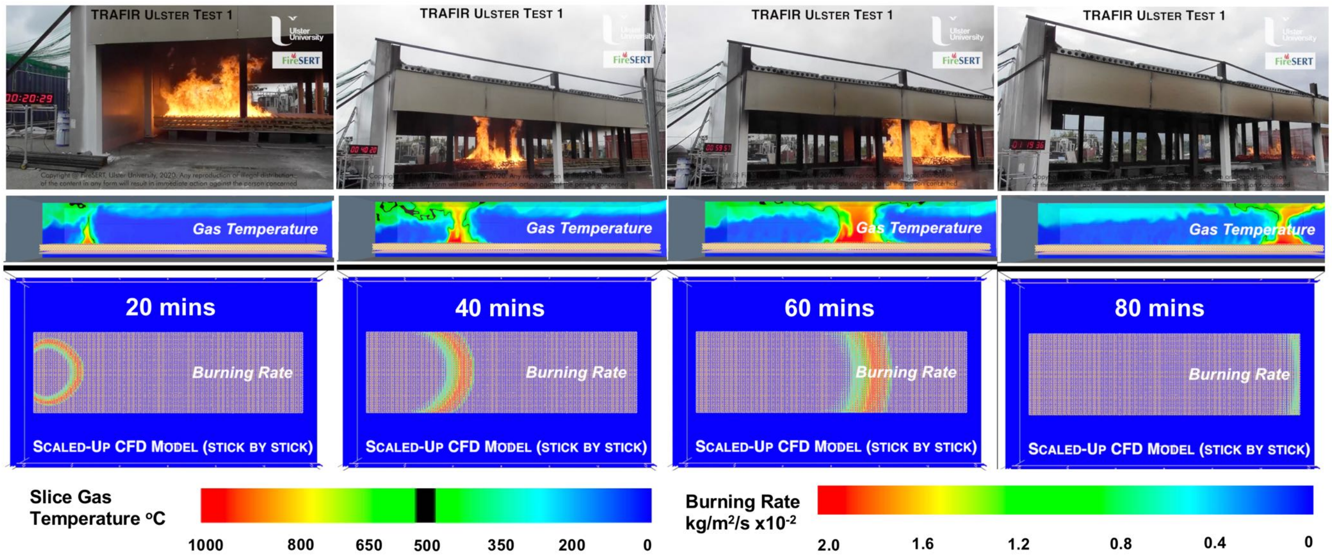

Figure 4. Scaled-up CFD model predicted fire spread comparison with the test, at 20 mins, 40 mins, 60 mins, and 80 mins.

Looking closely at the comparison of the fire spread and burn-away in Figure 5 (a), both the fire leading edge and the trailing edge of the model and the test are in remarkably good agreement, though for the stage after around 50 mins the model showed a slight 2-3 mins delay compared with the test until the fire reached 14.0 m, i.e. the fuel bed far end, at 67 mins. Figure 5 (b) shows the fire spread rate of the model gradually increased with the fire development, from 0 mm/s to 7 mm/s, generally in line with the trend observed in the test.

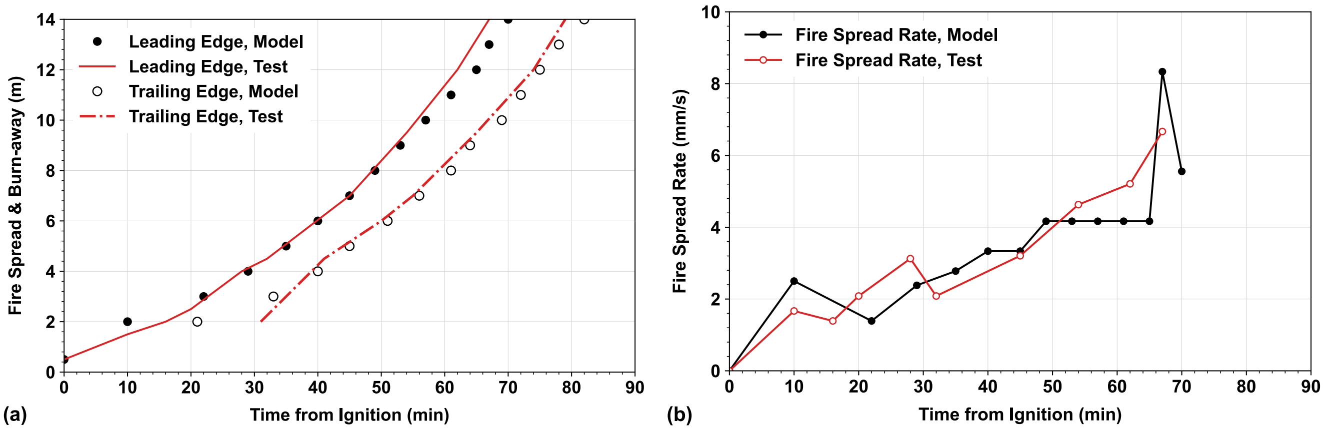

Figure 5. Comparison between the test and the model at compartment centreline along fire trajectory, (a) Fire spread distance & burn-away, and (b) Fire spread rate.

In the literature of the large-scale compartment fires, three fire “modes” were identified at the Malveira Fire Test [17] and similarly at the Tisova Fire Test [18], with both of them having a steady travelling fire, a growing fire, and a fully developed fire. Those three fire modes were quantified through the relationships between the velocity of the fire spread front, V_s, and the velocity of the fire burnout front, V_{BO}. Hence, a travelling fire mode refers to $V_s/V_{BO} \approx 1$, a growing fire mode means $V_s/V_{BO} > 1$, a decaying fire mode means $V_s/V_{BO} < 1$, and a fully developed fire mode is equivalent to $V_s/V_{BO} \to \infty$. Figure 6 demonstrates the fire mode comparison between the model and the test. It shows that the ratios of V_s/V_{BO} were both close but slightly higher than 1 at a later stage, indicating that the travelling fire mode was gradually trending towards a growing fire mode both in the model and the test.

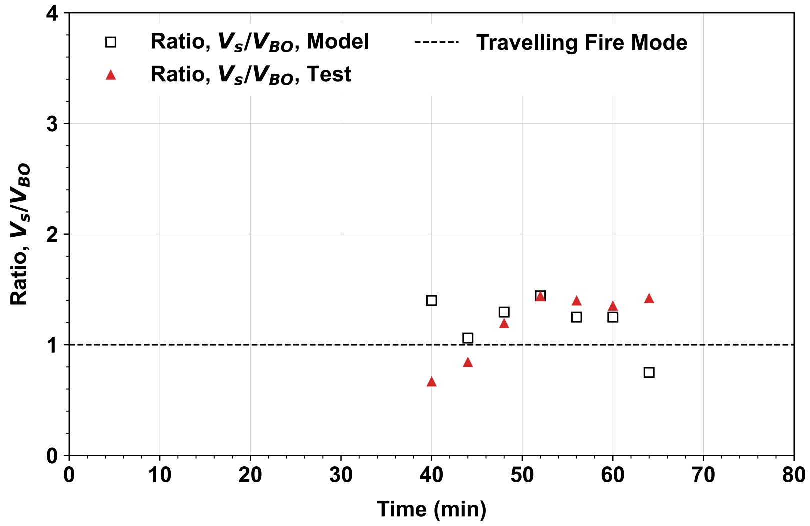

Figure 6. Comparison on fire mode, V_S/V_{BO}: velocity of the flame spread front to velocity of the flame burnout front.

4.2 Heat release rate (HRR)

In the experiment, the mass loss for *part* of the continuous fuel bed was measured to quantify the fire size development (i.e. HRR). A steel platform (3.0 m × 5.0 m) was placed below the centre of the continuous fuel bed with two layers of fireboards (3.6 m × 4.2 m) holding the wood cribs above, see Figure 7. Four load cells were used to support the steel platform to measure the total mass loss rate. Note that the fireboards border for the mass loss measurement area, 3.6 m × 4.2 m in dashed line shown in Figure 7 (a), was deliberately cut in order to separate the mass loss change from the neighbouring fireboard, holding another part of the extended wood crib [7]. Although only part of the continuous fuel bed was measured for mass loss, due to constraints on the experimental resources, a valuable HRR "data point" can be estimated while the fire was fully "sitting" on the platform at a specific time, for model validation purposes, i.e., at around 50 mins shown in Figure 7 (b).

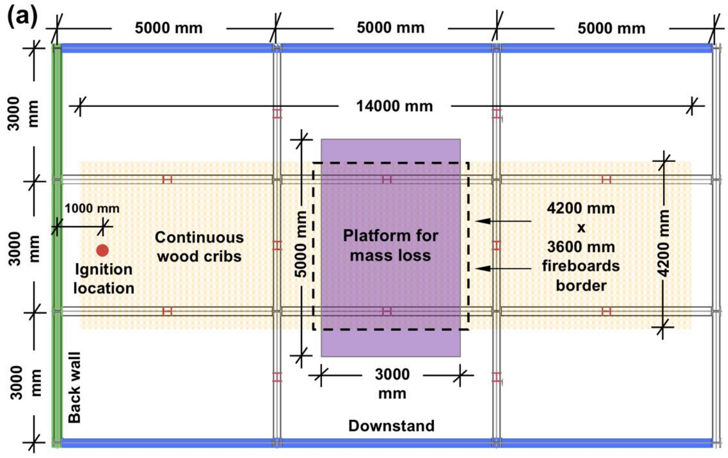

Figure 7. Mass loss measurement, (a) Position of platform for measuring mass loss (purple shaded area), and (b) Platform measuring mass loss at 51 mins.

Figure 8 compares the model HRR with the interpreted test data, based upon the measured mass loss while assuming the same effective heat of combustion of 10.84 MJ/kg as for the virgin fuel in the model. It is worth noting that the test HRR data was smoothed using a Savitzky-Golay filter with a low window length 5 and a medium window length 31, respectively, as advised by Morrisset et al. [19] who suggest that a high-order window length (e.g. 51) is likely to truncate up to 30% of the peak HRR for charring materials. Figure

8 shows that prior to the fire leading edge arriving to the mass loss platform at around 40 mins, the predicted fire size gradually increased to about 6.2 MW. When the fire was fully "sitting" on the platform at around 50 mins, the predicted HRR was about 7.9 MW, falling well in the range between 10.3 MW and 6.9 MW using the window lengths 5 and 31, respectively, for the interpreted test HRR, with an average value of 8.6 MW which is slightly higher than the predicted 7.9 MW. At around 63 mins, the fire left the mass loss platform and was predicted to reach its peak HRR of about 12.2 MW at around 72 minutes. Immediately thereafter the heat release rate declined due to the exhaustion of new fuel.

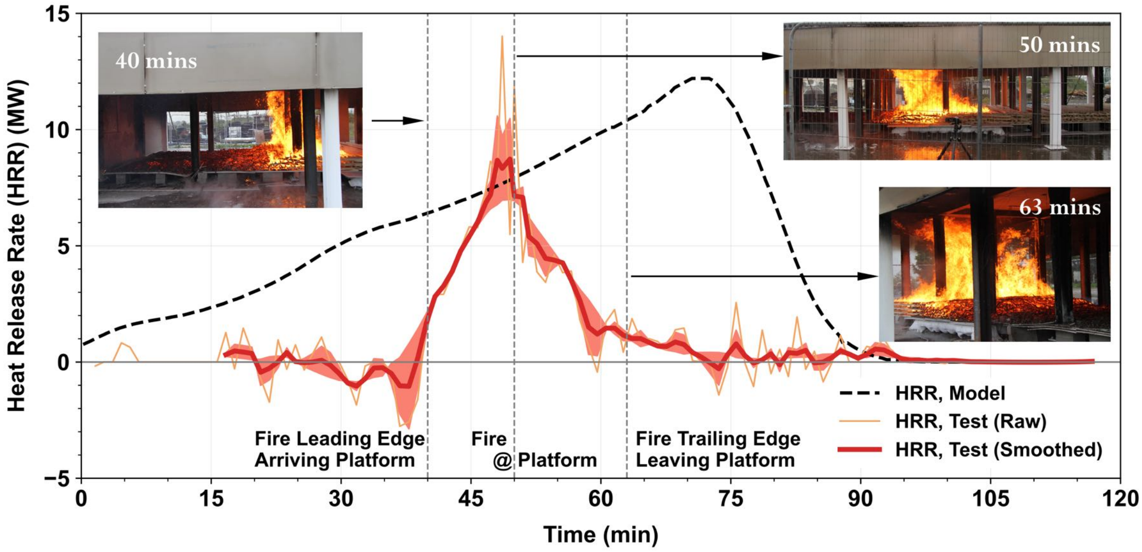

Figure 8. Comparison between the test and the model on HRR
(The translucent pink band represents the range of smoothing sensitivity via using Savitzky-Golay filter with a low window length, 5, and a medium window length, 31).

4.3 Thermocouple temperatures

To further characterise the gas phase temperatures and fire spread, thermocouple trees "TRL-1" to "TRL-11" were placed above the wood cribs, as presented in Figure 9. In addition, six thermocouples "TC-1" to "TC-6" were instrumented 200 mm beneath the ceiling level to quantify the travelling fire "far-field" temperatures. The thermocouples were modelled with the same diameter as the test, i.e., 1.5 mm bead diameter and assuming emissivity of 0.85.

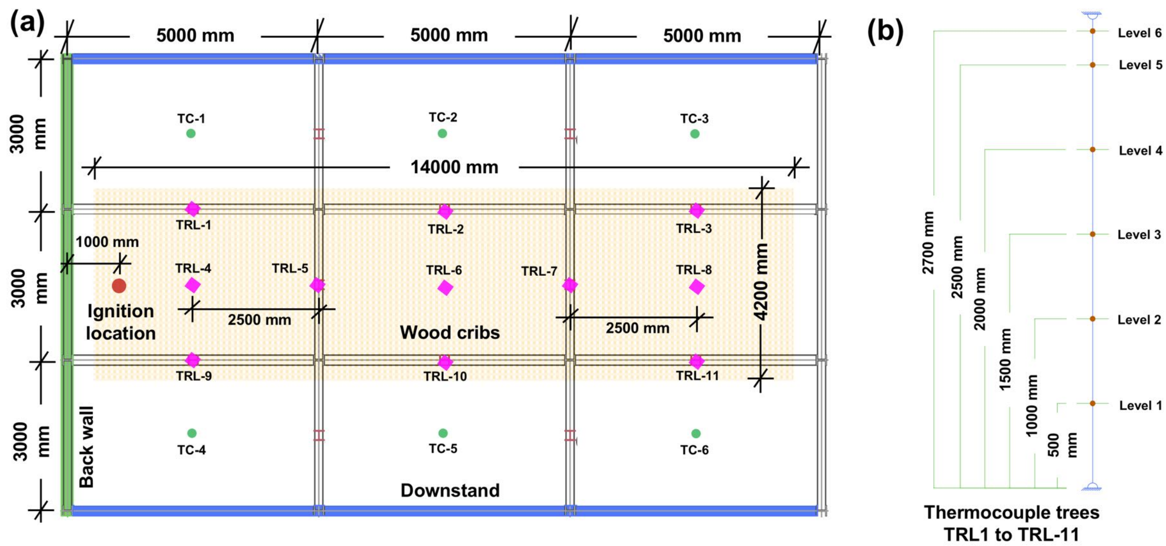

Figure 9. Location of the thermocouples for measuring gas phase temperatures, (a) plan view, TC-1 to TC-6 were thermocouples 200 mm below ceiling, (b) elevation view, TRL-1 to TRL-11 were thermocouple trees above the wood cribs.

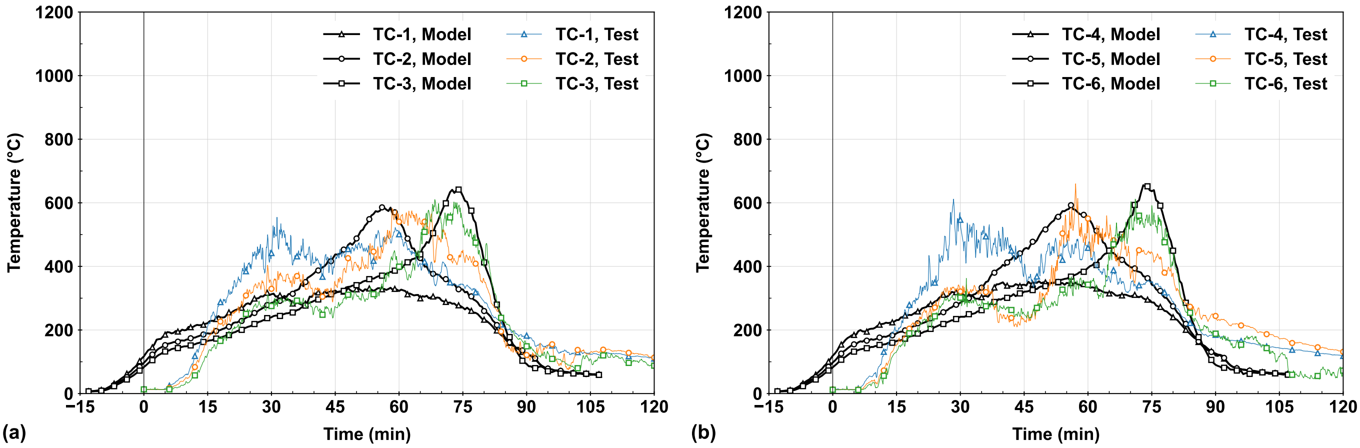

Figure 11. Comparison of the thermocouple temperatures, 200 mm from the ceiling level at side bays, (a) TC-1 to TC-3, and (b) TC-4 to TC-6.

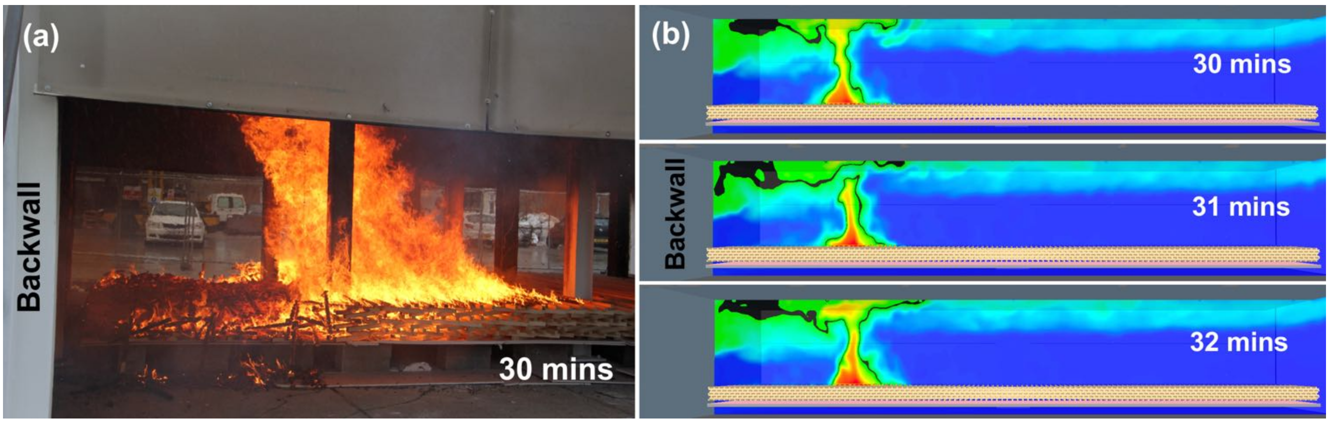

Figure 10. Fire plume shape at around 30 mins, (a) experiment showing the fire plume "leaning" (photo reversed), and (b) scaled-up model.

Figure 11 shows the comparison of the thermocouple temperatures "TC-1" to "TC-6", located 200 mm beneath the ceiling at the side bays of the large compartment. Apart from the temperatures discrepancy due to the aforementioned initial ignition difference from 0 – 15 mins, thermocouple temperatures of the model show good agreement with the test data for the rest of duration except for "TC-1"/"TC-4", which presented an under-prediction of around 250 °C compared with the test data at about 30 mins.

This discrepancy is likely associated with: 1) the absence of glowing char representation for heat transfer in the model; 2) the "leaning" fire plume in the first bay during the test affected by the external wind, in combination with the local effect of air entrainment and recirculation due to the presence of the backwall, see Figure 10 (a). Such external wind effect was not considered and explored in the scaled-up model, as shown in Figure 10 (b). Note that the TRAFIR Ulster Travelling Fire Test series were undertaken outdoors due to the large test scale [7].

Further, once the fire size grew from 5 MW at 30 mins to larger sizes, (i.e., 10 MW and 12 MW at 60 mins and 75 mins, respectively, as illustrated in Figure 8), the maximum discrepancy of the thermocouples at "TC-2"/"TC-5" and "TC-3"/"TC-6" was greatly improved. This is because the flame extension and smoke flows beneath the ceiling level became more dominant at "TC-2"/"TC-5" and "TC-3"/"TC-6".

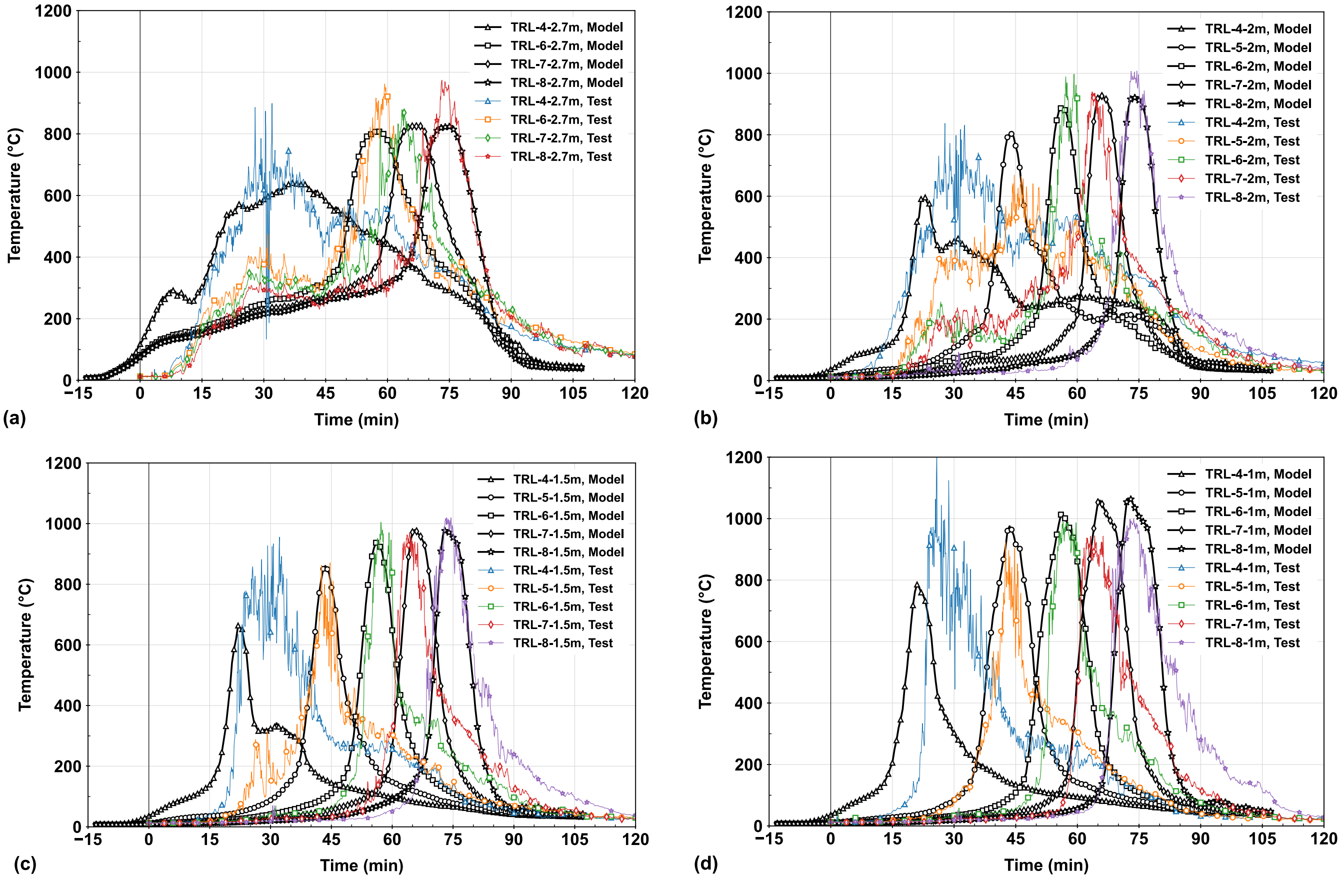

Figure 12. Comparison of the thermocouple temperatures at compartment centreline along fire trajectory, TRL-4 to TRL-8, (a) ceiling level (note: TRL-5-2.7m failed during test data acquisition), (b) 2 m from floor level, (c) 1.5 m from the floor level, and (d) 1 m from the floor level (i.e., 0.265 m from the fuel bed top level).

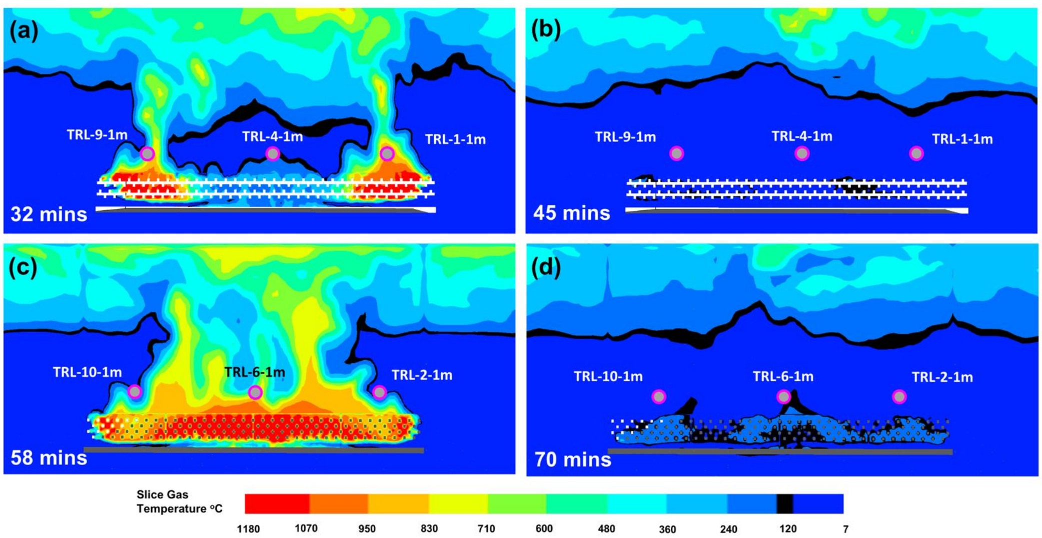

Figure 13. Gas phase temperature contour of the compartment 'slice' at specific time, (a) TRL-1/4/9 'slice' at 32 mins, (b) TRL-1/4/9 'slice' at 45 mins, (c) TRL-2/6/10 'slice' at 58 mins, and (d) TRL-2/6/10 'slice' at 70 mins.

Figure 12 demonstrates an excellent capability of the model in predicting the evolution of fire spread and burn-away, and in reproducing the gas phase temperatures along the fire travelling trajectory. Nevertheless, a discrepancy is still presented in the thermocouple temperatures close to the ignition location at a lower level (e.g., TRL-4-1m), because of: 1) the ignition difference between the model and the test; and 2) deficiencies in the model representation of the heat transfer for the radiation from the glowing embers, with high surface temperatures to the thermocouples close to the fuel bed (see Figure 13 (a) and (b) for TRL-4-1m at 32 mins and 45 mins respectively); a similar issue was also identified in the calibrated LB7 model [10]. Also, the fire at an early developing stage is more susceptible to sources of disturbance, e.g., wind.

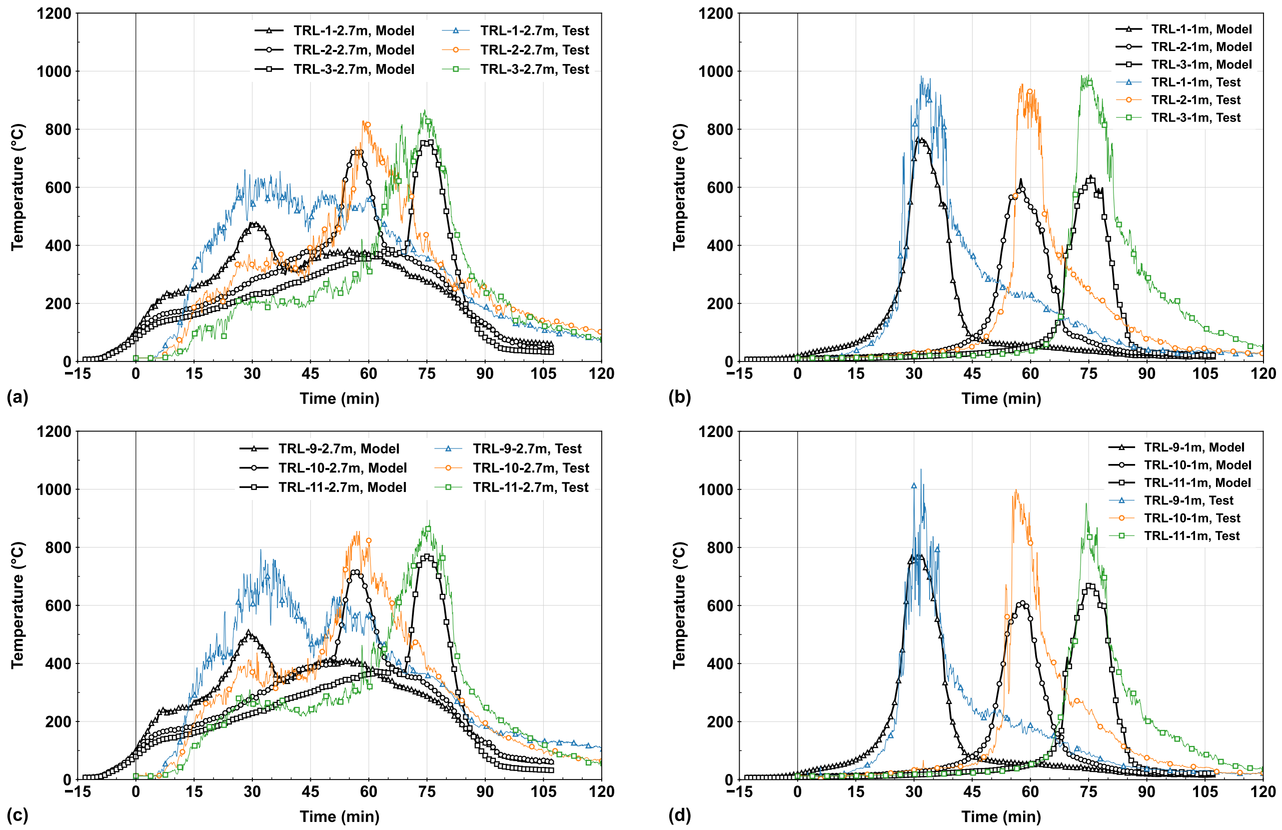

Figure 14. Comparison of the thermocouple temperatures along fire trajectory and the longitudinal fuel bed edges, (a) TRL-1 to TRL-3 at ceiling level, (b) TRL-1 to TRL-3 at 1 m from the floor level (i.e., 0.265 m from the fuel bed top level), (c) TRL-9 to TRL-11 at ceiling level, (d) TRL-9 to TRL-11 at 1 m from the floor level (i.e., 0.265 m from the fuel bed top level).

Figure 14 (a) and (c) demonstrate a good level of fire spread model prediction, but a similar discrepancy (as Figure 11) for the thermocouple temperatures along the longitudinal edges of the continuous fuel bed, but close to the ceiling level, was identified. Again, such a discrepancy might be induced by a slightly different shape of the fire plume, especially while those thermocouples were not engulfed in the extended flame or smoke at ceiling level (i.e., TRL-1-2.7m; TRL-9-2.7m) for the fire size of 5 MW at 30 mins.

For the thermocouples close to the fuel bed longitudinal edges presented in Figure 14 (b) and (d), the model predicted TRL-1-1m maximum temperature around 220 °C, which is lower than the test at 30 mins, while it was engulfed into the flame due to the "ring" like fire development (see Figure 4, and Figure 13 (a)). At 58 mins, the maximum temperature difference between the model and the test at TRL-2-1m reached an even higher level, around 380 °C, while it was "beside" the fire plume due to the entrainment of the cold air, see Figure 13 (c). Further, the missing element of the model representation in heat transfer for the radiation from "hot" glowing embers, was again manifested in the "local" cooling phase on thermocouples close to the fuel bed level. For example, at TRL-1-1m at 45 mins, the model predicted a temperature of 80 °C whereas the experimentally measured value was 350 °C, see Figure 13 (b) and Figure 14 (b).

5 CONCLUSIONS

Porous wood cribs, with shielding of internal surfaces, are recognised as a rather artificial fire source, hence with different fire spread sensitivities than many real-world fuels, but have been a dominant choice in fire experiments over many decades and are an important steppingstone towards more complex scenarios. Gaining a proper understanding of the sensitivities of fire spread over distributed fuel beds in large compartments would be greatly facilitated by the availability of validated models that could be used for parametric studies.

In this work, the potential for "scaling up" a "stick-by-stick" CFD model which had been carefully calibrated against the results of experiments on an isolated crib, of 2.8m diameter, to a distributed fuel bed in a full-scale compartment, has been demonstrated. With no changes of any model parameters between these two scenarios of very different scale, fire spread and burn out predictions were found to be in excellent agreement, and the single experimental data point for heat release rate also fits very well with the evolution of the predicted value.

Some differences in gas phase temperatures were seen, and the reasons for them have been carefully considered. Firstly, there is some uncertainty associated with the representation of the ignitor and the initial fire development – an identical ignitor was used in both cases in the model, while a bigger fuel tray located higher in the fuel bed was adopted in the experimental compartment test. But it is important to stress that the modelling of the early fire development is not a prime concern since it is subject to many uncertainties but is largely irrelevant to the evolution of fire conditions of interest for structural response – nevertheless the differences at the very start do introduce uncertainties in matching up the evolving fire timelines. Other temperature discrepancies seen early in the fire, when the main plume is located only halfway along the first bay, are likely to derive substantially from differences in the shape of the fire plume, with the model significantly underpredicting the peak temperatures at ceiling level at the compartment edge, and outside, the fuel bed. However, the test values reveal some asymmetry, and it is likely that the shape of the plume was affected to some degree by the prevailing wind, with an observed deflection towards the back wall, and this is not represented in the model. But as the fire size increases, more than doubling before the end of the test, it will be more robust to external disturbances.

The final temperature discrepancy is the most noticeable, with an acknowledged inability of the model to properly represent the heat transfer effects of the glowing char, resulting in a very significant underprediction of peak thermocouple temperatures near the fuel bed and the failure to capture the extended "cooling phase" seen in the test. This issue is known to have broadly affected previous model comparisons in the literature, but is particularly clear for this travelling fire where its impact can be seen progressively at each measurement location, i.e., there is effectively a local "cooling phase" for each sector of the extended fuel bed, in addition to a final cooling once all the fuel is burning out. Though potentially important for local structural elements, various avenues might be explored to remedy the discrepancies with this aspect of the model, but it is unlikely to have any great significance in the prediction of fire spread on a horizontally orientated flat fuel bed, which is the prime interest of the current work.

Thus, the established "numerical simulator" looks to have good potential as a tool to explore and characterise the behaviour of travelling fires subject to different compartment boundary conditions, including, but not limited to, the effects of 1) compartment geometry, opening locations and sizes, 2) extent and location of fuel bed, and 3) thermal properties of the boundaries. The equivalent experimental studies of this range of parameters would be infeasible, and would also be subject to significant uncertainties including the effects of varying ambient conditions (temperature and wind) as well as differences in fuel moisture.

ACKNOWLEDGMENT

This work was carried out in the frame of the TRAFIR project with funding from the Research Fund for Coal and Steel (grant N°754198). Partners are ArcelorMittal Belval & Differdange, Liège Univ., the Univ. of Edinburgh, RISE Research Inst. of Sweden and the Univ. of Ulster. This work used the ARCHER2 UK National Supercomputing Service (http://www.archer2.ac.uk), and assistance of relevant administrators is acknowledged. The authors are grateful to EPSRC (grant number: EP/R029369/1) and ARCHER2 for financial and computational support as a part of their funding to the UK Consortium on Turbulent Reacting Flows (www.ukctrf.com). The UKCTRF Consortium benefits from the support of CoSeC, the Computational Science Centre for Research Community. The authors would like to thank many students from the University of Ulster and University of Edinburgh who contributed to the experiment and analysis of the test data.

REFERENCES

1. Stern-Gottfried, J., Rein, G., Travelling Fires for Structural Design–Part I: Literature Review, Fire Safety Journal, Vol. 54, 2012, pp. 74-85.
2. Dai, X., Welch, S., and Usmani, A., A Critical Review of 'Travelling Fire' Scenarios for Performance-based Structural Engineering, Fire Safety Journal, Vol. 91, 2017, pp. 568–578.
3. Rackauskaite, E., Hamel, C., Law, A., Rein, G., Improved Formulation of Travelling Fires and Application to Concrete and Steel Structures, Structures, Vol. 3, 2015, pp. 250-260.
4. Dai, X., Welch, S., Vassart, O., Cábová, K., Jiang, L., Maclean, J., Clifton, C., Usmani, A., An Extended Travelling Fire Method Framework for Performance-based Structural Design, Fire and Materials, Vol. 44, 2020, pp. 437-457.
5. Harmathy, T. Z., A New Look at Compartment Fires, Part I&II, Fire Technology, Vol. 8, 1972, pp. 196-217.
6. European Commission, Natural Fire Safety Concept - Full-scale Tests, Implementation in the Eurocodes and Development of a User-Friendly Design Tool, European Communities, 2003.
7. Nadjai, A., Alam, N., Charlier, M., Vassart, O., Dai, X., Franssen, J., and Sjöström, J., Travelling Fire in Full Scale Experimental Building Subjected to Open Ventilation Conditions, Journal of Structural Fire Engineering, 2022, https://doi: 10.1108/JSFE-06-2021-0037.
8. Nadjai, A., Alam, N., Charlier, M., Vassart, O., Welch, S., Glorieux, A., Sjöström, J., Large scale fire test: The development of a travelling fire in open ventilation conditions and its influence on the surrounding steel structure, Fire Safety Journal, Vol. 130, 2022, http://dx.doi.org/10.1016/j.firesaf.2022.103575
9. Alam, N., Nadjai, A., Charlier, M., Vassart, O., Welch, S., Sjöström, J., and Dai, X., Large Scale Travelling Fire Tests with Open Ventilation Conditions and Their Effect on the Surrounding Steel Structure – The Second Fire Test, Journal of Constructional Steel Research, Vol. 188, 2022, 107032.
10. Dai, X., Gamba, A., Liu, C., Anderson, J., Charlier, M., Rush, D., Welch, S. An Engineering CFD Model for Fire Spread on Wood Cribs for Travelling Fires, Advances in Engineering Software, Vol. 173, 2022, 103213.
11. Charlier, M., Glorieux, A., Dai, X., Alam, N., Welch, S., Anderson, J., Vassart, O., Nadjai, A., Travelling Fire Experiments in Steel-Framed Structure: Numerical Investigations with CFD and FEM, Journal of Structural Fire Engineering, 2021, https://doi.org/10.1108/JSFE-11-2020-0034
12. UK National Supercomputing Service (ARCHER2), [online] [Viewed 27 July 2022]. Available from: http://www.archer2.ac.uk
13. Eurocode 2. Design of Concrete Structures—Part 1-2: General Rules — Structural Fire Design, European Standard EN 1992-1-2, CEN, Brussels. 2004.
14. Lautenberger, C., Tien, C.L., Lee, K.Y., Stretton, A.J., Radiation Heat Transfer, SFPE Handbook of Fire Protection Engineering, 5th Edition, Society of Fire Protection Engineers, 2016.
15. Kirby, B.R., Wainman, D.E., Tomlinson, L.N., Kay, T.R., Peacock, B.N., Natural Fires in Large Scale Compartments. British Steel Technical, Fire Research Station Collaborative Project Report, UK, 1994.
16. ROCKWOOL FLEXI, [online] [Viewed April 2014]. Available from: https://www.rockwool.com
17. Hidalgo, J.P., Goode, T., Gupta, V., Cowlard, A., Abecassis-Empis, C., Maclean, J., Bartlett, A. I., Maluk, C., Montalvá, J. M., Osorio, A. F., Torero, J. L., The Malveira Fire Test: Full-Scale Demonstration of Fire Modes in Open-Plan Compartments, Fire Safety Journal, Vol. 108, 2019, 102827.
18. Rush, D., Dai, X., Lange, D., Tisova Fire Test – Fire Behaviours and Lessons Learnt, Fire Safety Journal, Vol. 173, 2021, 103261.
19. Morrisset, D., Santamaria, S., Hadden, R., Emberley, R., Implications of Data Smoothing on Experimental Mass Loss Rates, Fire Safety Journal, Vol. 131, 2022, 103611.

SiF 2022– The 12th International Conference on Structures in Fire
The Hong Kong Polytechnic University, Nov 30 - Dec 2, 2022

MAXIMUM ALLOWABLE CONSEQUENCE APPROACH TO FIRE SAFETY DESIGN OF BRIDGES

Andrea Franchini[1], Carmine Galasso[2], Jose L. Torero[3]

ABSTRACT

Structural damage and collapse of bridges due to fire have increased in recent years, emphasising the need for appropriate fire-safety-oriented design approaches. Current methods of fire-safe design often consist of a simple extrapolation of rules used originally for buildings and do not provide bridge-specific guidance as for other hazards. Available design methodologies (deterministic and/or probabilistic) for extreme loads start by characterising the hazard at the site. Next, they involve structural response analysis to estimate hazard consequences in terms of damage or loss metrics of interest. These metrics are eventually appraised to verify whether various performance objectives are achieved. While the same approach has been applied to fire (as an extreme load), the results' appropriateness is unclear. Dynamic coupling between structures and fire exists, where the fire affects a structure, but the characteristics of the structure also affect the fire. This makes the workflow mentioned above unsuitable for delivering optimised solutions. Indeed, the structural design choices define the fire scenarios that could potentially affect the structure over its lifespan.

This paper proposes a Maximum Allowable Consequence (MAC) approach to the fire safety design of bridges that considers fire scenarios as additional design variables and delivers them as outputs. A single-span bridge subject to a car fire is considered to illustrate the proposed MAC approach, and the following performance metrics are selected: 1) the time t_u to reach unsatisfactory conditions (i.e., the bridge's collapse); 2) the probability of that time being lower than a MAC threshold of 20 min. The design variables are the clearance and girder height. Numerical optimisation is applied to calculate fire scenario features that minimise t_u. Then, the effect of input uncertainties in steel material properties on the estimated fire consequences is investigated through Monte Carlo sampling. Finally, these metrics inform the selection of an optimal design configuration.

Keywords: Bridge; fire hazard; performance-based design; uncertainty analysis

1 INTRODUCTION

Garlock et al. [1] and Hu et al. [2] reported that fire-accident occurrence on bridges has increased in recent years, leading to substantial direct and indirect losses worldwide. In addition, Lee et al. [3] indicated that fire-induced bridge failures occurred at a similar rate to other hazards that have received significant research attention in past years, such as earthquakes. Nevertheless, fire loads are often neglected in the bridge design process and are scarcely discussed in design codes and standards.

Prescriptive code-based design approaches to fire safety are often inadequate. Hence, alternative deterministic (e.g., Quiel et al. [4]) and probabilistic (e.g., Ma et al. [5]) fire performance assessment procedures for bridges have been proposed in the framework of performance-based fire design and

[1] PhD Student, Department of Civil, Environmental and Geomatic Engineering, University College London, London, UK
e-mail: andrea.franchini.19@ucl.ac.uk, ORCID: https://orcid.org/0000-0001-9732-2484
[2] Professor, Department of Civil, Environmental and Geomatic Engineering, University College London, London, UK
e-mail: c.galasso@ucl.ac.uk, ORCID: https://orcid.org/0000-0001-5445-4911
[3] Professor, Department of Civil, Environmental and Geomatic Engineering, University College London, London, UK
e-mail: j.torero@ucl.ac.uk, ORCID: https://orcid.org/0000-0001-6265-9327
https://doi.org/10.6084/m9.figshare.22223974

assessment. Similar to practices adopted for other extreme events, fire performance assessment often starts by characterising the hazard through structure-independent hazard scenarios. Then, the resulting structural response is analysed, and fire consequences are estimated in terms of damage or loss metrics of interest to stakeholders. Finally, if the considered performance objectives (in terms of such damage or loss metrics) are not achieved, the structural design is updated, and the structural performance is iteratively checked against those pre-set hazard scenarios. This unavoidably results in design solutions for worst-case scenarios. In contrast, an optimised design solution positively affects the potential nature of the fire. Thus, much of the designer's capability to reduce the overall impact of a fire is lost. Furthermore, designing a structure starting from a predefined hazard scenario constrains the design choices and conditions them on a fire scenario that is a consequence rather than a causation.

Indeed, several criticisms of probabilistic risk assessment approaches in fire engineering have been highlighted in the literature [6], such as the acceptance of significant consequences characterised by low likelihoods and the fact that fire scenarios must depend on the structure to design rather than be an input to the design. Concerning this latter aspect, Torero [7, 8] highlighted that structural and fire behaviour are dynamically coupled, resulting in a feedback loop by which a fire affects a structure as much as the structure modifies fire behaviour. This viewpoint was discussed in several other studies (e.g., [9-11]), implying that design choices in terms of structural geometry, layout, materials, and fire safety strategies determine fire growth, spread, and decay. Consequently, a simultaneous design of the structure and the fire hazard is possible, enabling optimised design solutions that entail an acceptable level of consequence.

For bridge structures in which vehicle-borne or pool fires are considered, structural design choices influence fire development and spread in terms of:

- Possible locations where the fire might start (which depend on barriers on the deck), the location of cables (for cable-supported bridges), and under-deck clearance;
- The number of lanes and their arrangement, affecting the spread of fire during traffic jams and the time required by the fire service to intervene;
- The deck shape and water management system, influencing the potential development of pool fires, both above and beneath the deck, determining the potential for fire spread;
- Flammable materials, such as wooden components or the materials implemented for cables' environmental protection (in cable-supported bridges), potentially causing further fire spread.

This study introduces a maximum allowable consequence (MAC) approach to the fire safety design and assessment of bridges. The proposed approach extends the fire risk assessment methodology by Cadena et al. [6]. Numerical structural optimisation is adopted to estimate fire scenarios resulting in the most severe consequences (e.g., time to unsatisfactory conditions, residual bearing capacity, repair cost, downtime) as a design output. Such an output is a function of the bridge design variables. Therefore, the methodology concurrently designs structural features and fire hazard scenarios. Such a strategy aligns well with the proposal of designing structures to obtain a minimum fire damage potential as an alternative to the use of input design fires [7].

The proposed MAC approach is described in Section 2 and applied in Section 3 for the fire safety design of a case-study bridge. Finally, Section 4 draws conclusions and discusses future developments of the study.

2 MAXIMUM ALLOWABLE CONSEQUENCE APPROACH

The proposed methodology is shown in Figure 1 and consists of six steps. In Step #1, performance objectives are set following the requirements suggested by the National Fire Protection Association [12]: a) support firefighter accessibility; b) minimise economic impact; c) mitigate structural damage. A feasible option to address them consists in selecting as the performance metric of interest the time necessary for the bridge to reach conditions, when subject to a fire, that are deemed to challenge all three points above (unsatisfactory time, t_u). Indeed, designing the bridge to achieve an appropriate value of this metric can ensure structural stability until the fire services arrive and contain the fire or until burnout. In both cases, structural damage would be reduced, and traffic flow could continue, limiting direct and indirect losses.

This approach is adopted in the current paper, and unsatisfactory conditions are identified with the bridge's partial or global structural collapse, which would result in disproportionate structural damage and direct/indirect economic impact. The precise definition of collapse is case-specific, and examples are provided for the case study of Section 3. Consequences are as more significant as lower t_u is. An initial design configuration $\boldsymbol{X}_1$ is also selected in this step.

It is worth noting that the methodology can be easily extended to any performance metric of interest other than t_u. For instance, the available bearing capacity after fire extinction might be of interest because structural damage is the primary concern for structural stability and indirect loss control for bridges.

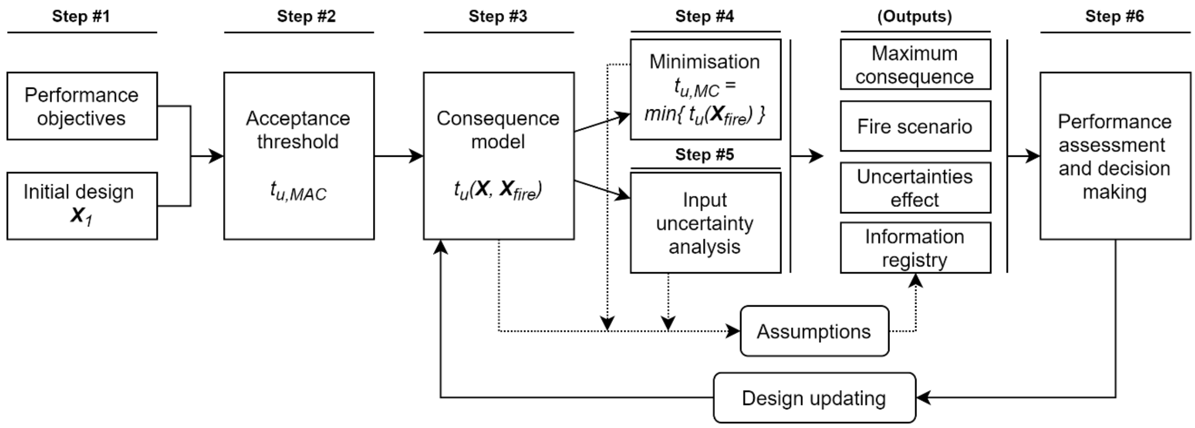

Figure 1. Proposed MAC methodology.

In Step #2, stakeholders choose the acceptance threshold, i.e., the maximum level of consequence they are willing to accept (MAC). This corresponds to a minimum value for the time to reach unsatisfactory conditions, defined $t_{u,MAC}$. Additionally, when considering different sources of uncertainties, a critical value of the probability of t_u being lower than $t_{u,MAC}$ can also be selected.

The following step (Step #3) builds a consequence model $t_u(\boldsymbol{X}, \boldsymbol{X}_{fire})$ to quantify the potential of fire-induced consequences (in terms of t_u) as a function of the structural design variables $\boldsymbol{X}$ and the fire scenario variables $\boldsymbol{X}_{fire}$. Such a model is obtained through numerical simulation of the bridge's thermomechanical response to the fire, which usually consists of four analysis steps [4]: 1) fire modelling; 2) heat transfer; 3) thermal response; 4) structural response.

For a given realisation of the design variables $\boldsymbol{X} = \boldsymbol{X}'$, numerical optimisation is adopted to compute the maximum consequence and the generating fire scenario (Step #4). Because the time to reach unsatisfactory conditions is used as the performance metric, the maximum consequence corresponds to the minimum value of the function $t_u(\boldsymbol{X}', \boldsymbol{X}_{fire})$, named $t_{u,MC}$. The fire scenario characteristics that maximise consequences ($\boldsymbol{X}_{fire,MC}$) are also obtained as a procedure output.

Step #5 investigates the effect of uncertainties in the analysis inputs (e.g., materials properties and geometry) on the estimated $t_{u,MC}$. More in detail, plain Monte Carlo sampling is implemented to calculate the probabilistic distribution of the random variable $\bar{t}_{u,MC}$ (of which $t_{u,MC}$ is a given realisation) and evaluate the probability that $\bar{t}_{u,MC} \leq t_{u,MAC}$. This probability represents an additional information layer for decision-making. Additionally, it might be used to design optimised solutions from a lifecycle cost perspective. An assessment is required to identify which random variables should be considered in the uncertainty analysis and characterise them through ad-hoc probability models (i.e., distributions). Other variables can be set to deterministic values, notwithstanding the possibility of performing sensitivity studies on their impact on the consequence estimates. As Cadena et al. [6] suggested, the fire safety assessment's uncertainties, assumptions, and limitations are tracked into an information registry.

The final phase of the MAC approach (Step #6) consists of decision-making. The process is based on the four obtained analysis outputs: 1) the minimum time to reach unsatisfactory conditions ($t_{u,MC}$); 2) the features $\boldsymbol{X}_{fire,MC}$ of the designed fire scenario; 3) the input uncertainties effect; 4) the information registry of all the assumptions drawn during the assessment. If the assessment is successful, the information registry provides insights into the actions required for the assumptions to remain valid. Otherwise, the registry supports updating the design variables.

A case study is presented in the next section, where the MAC methodology is applied to design a bridge girder subject to vehicle-borne fires.

3 CASE STUDY

3.1 Initial bridge design and fire scenario

The single-span bridge studied by Peris-Sayol et al. [13] and illustrated in Figure 2 is considered a reference to demonstrate the applicability of the proposed MAC approach. The bridge has a vertical clearance $H_1 = 5.00\ m$ and is made of five W36x300 girders with height $H_{1,gir} = 0.91\ m$ and span $L_{gir} = 21.34\ m$. The subscript "1" identifies the initial design configuration. The girders, which support a 0.20 m concrete slab, are made of steel with a yielding stress of $250\ MPa$; an elastic modulus $E = 210\ GPa$ is assumed. Only the central girder is considered in this paper and a 2D analysis in the X-Y is conducted (see Figure 2b).

In the reference, the girders are simply supported. However, Figure 2b shows that a fixed end is assumed on the left-hand side to show the proposed methodology's capability to calculate fire scenarios as outputs (otherwise, the problem would be symmetric, and the most unfavourable condition would result from a fire at the midspan, where both the peak bending moment and the peak deflection are found). The fixed-end might represent specific design details aimed at controlling the girders' deflection or could be a simplified analysis approach for a two-span continuous girder bridge. For a fixed-roller beam subject to a uniformly distributed load, the maximum bending moment and the maximum deflection are located at $x = 0.625L_{gir}$ and $= 0.579L_{gir}$, respectively. The properties of this bridge represent the initial design features $\boldsymbol{X}_1$ in the flowchart of Figure 1. A fire safety assessment and design through the MAC methodology is then performed.

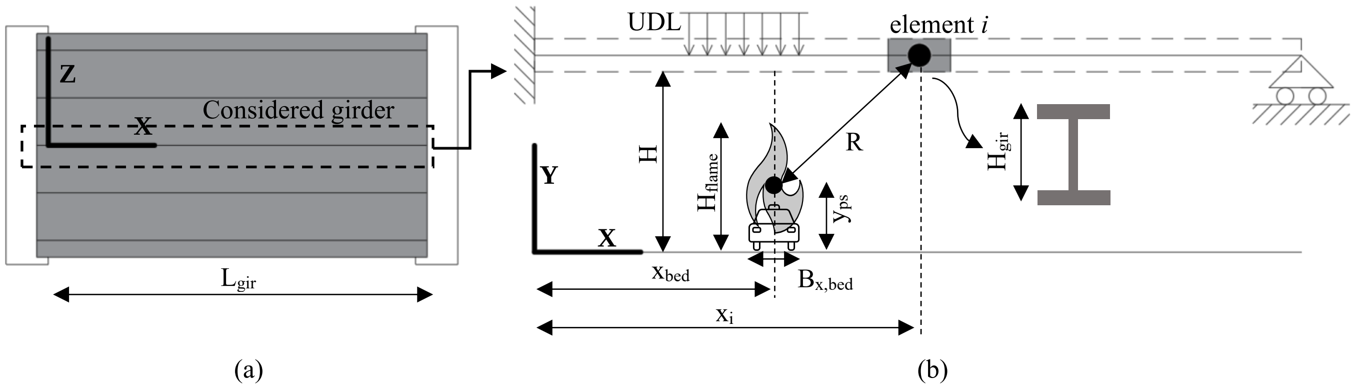

Figure 2. Case study bridge and model geometry: (a) top view; (b) front view.

A car fire located at x_{bed} and with dimensions $B_{x,bed} \times B_{z,bed} = 1.5\ m\ \times 4m$ is considered as the fire scenario. The heat release rate curve (i.e., the time history of the amount of energy released by the fire) is assumed to grow linearly up to a representative peak heat release rate $hrr_{max} = 5\ MW$, which is reached at a time $t_{hrr,max} = 10\ min$ and lasts until burnout ($t_{burning} = 45\ min$). These values are consistent with vehicle fire properties published in the literature [2, 5]. The fuel bed location that maximises consequences ($x_{bed,MC}$) has to be calculated.

3.2 Performance objectives and maximum allowable consequence

The performance objectives are defined in terms of time for the bridge to reach unsatisfactory conditions (t_u) when subject to a car fire. Therefore, consequences are as more severe as lower t_u is.

For illustrative purposes only, it is assumed that stakeholders require the bridge to resist any car fire accident for 20 min without collapsing. This value represents the maximum allowable consequence (MAC) and is defined $t_{u,MAC}$. A design solution is acceptable if $t_{u,MC,design} > t_{u,MAC}$. The effect of uncertainties and the assumptions drawn to build the consequence model are also accounted for in the decision-making process. Finally, an acceptance threshold for the probability that $\bar{t}_{u,MC,design} \leq t_{u,MAC}$ due to uncertainties should be selected. However, this study only discusses such probability estimates, leaving the definition of an acceptable threshold as a subject for future research.

3.3 Consequence model

The consequence model estimates consequences induced by combinations of structural design variables $\boldsymbol{X}$ and fire scenario variables $\boldsymbol{X}_{fire}$. Because the time to reach unsatisfactory conditions is adopted as the performance metric, the model is a function $t_{u,design}(\boldsymbol{X}, \boldsymbol{X}_{fire})$. Such a function can be obtained through the four steps listed in Section 2, for which further details are provided in the following subsections. The first three steps are performed in MATLAB software [14], whereas the structural response is calculated using the OpenSees for fire software [15]. Details about the fire modelling phase were provided in Section 3.1.

3.3.1 Heat transfer

This section describes the calculation of heat flux $\dot{q}''_{fire}$ from the fire to the bridge girder. With reference to Figure 2b, the girder is divided into elements of 0.5 m in length, and it is assumed that the heat flux to a given element is constant for a given time step. Such a heat flux should account for the effect of convection and radiation from both the flames and the smoke.

The proposed calculation procedure is summarised in Table 1 and combines several heat transfer models from localised fires (point source model [16]; Hasemi's model from Eurocode 1-Part 1.2 [17]; and peak heat fluxes measured on objects immersed in flames [16]).

Table 1. Heat flux calculation methodology.

<table>
<tr><td colspan="4">∀ time step: calculate the mean flame height: $H_{flame} = -1.02D_{eq} + 0.235hrr^{2/5}$ (Chapter 13, [16])</td></tr>
<tr><td colspan="2">Case 1: $H_{flame} \leq H + H_{gir}$</td><td colspan="2">Case 2: $H_{flame} > H + H_{gir}$</td></tr>
<tr><td>$|x_i - x_{bed}| \leq D_{eq}/2$</td><td>$|x_i - x_{bed}| > D_{eq}/2$</td><td>$|x_i - x_{bed}| \leq L_{h,flame}$</td><td>$|x_i - x_{bed}| > L_{h,flame}$</td></tr>
<tr><td>Radiative heat transfer from the flames: point source model (Chapter 66, [16]).
Convective and radiative heat transfer from the smoke: Hasemi's localised fire model for flames not impinging the ceiling [17].</td><td>Radiative heat transfer from the flames: point source model (Chapter 66, [16]).</td><td>Constant heat flux to object immersed in flames $\dot{q}''_{flame} = 85\ kW/m^2$ (Chapter 25, [16])</td><td>Radiative heat transfer from the flames: point source model (Chapter 66, [16])</td></tr>
</table>

At each time step, the height of the flames H_{flame} is calculated and compared to the clearance of the bridge. The equivalent diameter of the fire is obtained as $D_{eq} = \sqrt{4B_xB_z/\pi}$ by making the area equal to that of a circular fuel [16]. This comparison distinguishes the two cases of the flame not impinging (Case 1) or impinging (Case 2) on the bridge deck.

In Case 1, the deck elements are classified based on their longitudinal location falling within or outside the fuel bed. For those falling within the bed, a smoke layer is assumed to form above the bed area. Its temperature at the height of the deck is computed through Hasemi's model. This temperature is then used to obtain the radiative and convective heat transfer from the smoke layer to the girder. Additionally, assuming that a small optical thickness characterises the smoke layer, the radiative heat flux from the flame to the deck is added. This contribution is calculated through the point source model, assuming the point source to be located at $y_{ps} = H_{flame}/2$. The radiative heat flux from the point source is assumed as the only heat transfer mechanism to girder elements located outside the fuel bed boundaries.

In Case 2, the flame impinges on the bridge deck. In such a situation, Heskestad and Hamada [18] observed that the mean horizontal flame length is approximately equal to the difference between the free flame height and the height of the obstructing surface ($L_h \approx H_{flame} - H - H_{gir}$). A constant value of heat flux $\dot{q}''_{flame} = 85\ kW/m^2$ is assigned to girder elements whose centre locates within a distance $L_{h,flame}$ from the centre of the fuel bed. This value is representative of measured heat fluxes to objects immersed in flames [16]. Only radiative heat fluxes are instead considered for elements located at a distance larger than $L_{h,flame}$. For this calculation, it is assumed that the point source locates at $y_{ps} = \left(H + H_{gir}\right)/2$.

3.3.2 Thermal response

The thermal response of each girder element is calculated through a lumped thermal mass approach as described by Quiel et al. [4]. This approach assumes a constant temperature distribution across the section (lumped capacitance), which is acceptable for steel girders. At each time step dt, the temperature increase ΔT_i in the *i-th* girder element is calculated through the energy balance equation:

$$\Delta T_i = \frac{dt}{V_i \rho c_p(T)} \times \left(\dot{Q}_{fire,i} - \dot{Q}_{out,i} + \dot{Q}_{i-1,i} + \dot{Q}_{i,i+1}\right) \qquad (1)$$

where V_i is the volume of the *i-th* element; $\rho = 7850\ kg/m^3$ is the density of steel; $c_p(T)$ is the temperature-dependent specific heat of steel [19]; $\dot{Q}_{fire,i}$ is the heat transferred from the fire, obtained multiplying $\dot{q}''_{fire}$ by the exposed surface of the girder; $\dot{Q}_{out,i}$ is heat loss to the ambient through radiation and convection; $\dot{Q}_{i-1,j}$ and $\dot{Q}_{i,j+1}$ are the conductive heat transfer terms from the element *i-1* to *i* and from the element *i* to $i{+}1$, respectively. The latter two terms are calculated considering a temperature-dependent thermal conductivity coefficient [19]. Other studies that used the lumped capacitance approach (e.g., [4]) recommended a maximum time step of 1 min. Here, a time step of 5 s was selected to estimate the time to unsatisfactory conditions more accurately.

3.3.3 Structural response

The bridge's structural response is estimated through thermomechanical analysis in the OpenSees for fire software [15], assigning the temperature time histories obtained from Section 3.3.2 to each element. Displacement-based elements with thermo-mechanical fibre sections are adopted to model the girder, which is discretised in the same way as for the thermal analysis. The uniaxial material model *Steel01Thermal* [15] is assigned to each fibre. This material class was created by modifying the existing OpenSees material class *Steel01* and including the temperature-dependent properties provided in Eurocode 3-Part 1.2 [19].

The displacement history of each girder node is monitored during the thermomechanical analysis, which starts from the deformed configuration induced by dead and traffic loads. These loads are modelled through a uniformly distributed load $UDL = 80\ kN/m$, which is maintained constant over the analysis.

As discussed above, the analysis adopts a time step of 5 s and runs until the burnout time $t_{burning}$ unless earlier collapse arises. As mentioned in Section 0, the selected performance metric is the time required to reach unsatisfactory conditions (t_u), i.e., global structural collapse. Therefore, a failure criterion should be defined to calculate t_u. Here, global failure is defined as the condition in which any point of the girder exceeds a deflection limit of $L_{gir}/20$ [2].

3.4 Maximum consequence calculation

The minimum time to unsatisfactory conditions ($t_{u,MC,design}$) is obtained by numerical optimisation using MATLAB software [14]. For illustrative purposes, the vector of design variables includes only the deck clearance and the girder height ($\boldsymbol{X} = [\beta_H \cdot H_1;\ \beta_{Hgir} \cdot H_{1,gir}]$). β_H and β_{Hgir} are multiplicative factors to facilitate the design updating process. Increasing H_1 distances the girder from the flames, delaying the time to impingement or possibly causing the flame to never impinge on the deck. From a heat transfer perspective, $H_{1,gir}$ has a similar (despite less relevant) effect to H_1. Additionally, it changes the volume and the girder surface exposed to the fire. On the thermo-mechanical side, this design parameter increases the stiffness of the girder, reducing deflections.

The vector of fire scenario properties to consider in the minimisation problem only includes the location of the fuel bed centre, i.e., $\boldsymbol{X}_{fire} = [x_{bed}]$. In principle, any fire property falling within the selected modelling framework can be considered in the optimisation process. For example, the procedure might be adopted to identify the worst-case scenario between the two extreme situations of short-hot or long-cold fires. However, this is outside the scope of the current paper. To ease the comparison between different design solutions, the nondimensional fuel bed location $\alpha = x_{bed}/L_{gir}$ is defined. Hence, the output of the t_u minimisation process is the nondimensional fuel bed location α_{MC}.

Table 2. Minimum time to unsatisfactory conditions for different designs.

Design	β_H [-]	β_{Hgir} [-]	α_{MC} [-]	$t_{u,MC}$ [min]	$Pr[\bar{t}_{u,MC} < t_{u,MAC}]$
#1	1.00	1.00	0.643	16.58	0.98
#2	1.15	1.05	0.681	20.75	2e-4
#3	1.05	1.15	0.690	19.33	0.11
#1	1.00	1.00	0.625 (max bending)	16.67	-
#1	1.00	1.00	0.579 (max deflection)	17.00	-

The initial bridge design configuration is referred to as Design #1. The first row of Table 2 shows that $t_{u,\#1}$ is minimised if $\alpha = \alpha_{MC} = 0.643$, yielding $t_{u,MC,\#1} = 16.58\ min$. This value is lower than the MAC selected by stakeholders ($t_{u,MAC} = 20\ min$), requiring updating the bridge design.

To select feasible design updating solutions, a sensitivity study on the effect of the design variables' multiplicative factors β_H and β_{Hgir} on $t_{u,MC}$ was performed. The results are reported in Figure 3a, where the horizontal axis shows the variation of β_H and each line refers to a different value of β_{Hgir}. Based on this analysis, two design alternatives (Design #2 and #3) were selected. Their properties are listed in Table 2 and provide $t_{u,MC}$ equal to 20.75 min and 19.33 min, respectively. Design #3 provides a $t_{u,MC}$ lower than the set MAC. However, its acceptability will be further discussed with respect to the uncertainties effect reported in Section 3.5.

Figure 3b compares the effect of the fuel bed locations on t_u for the three considered design configurations. If the car ignites closer to the fixed end of the girder ($\alpha \leq 0.4$ approximately), higher times to unsatisfactory conditions are observed, with designs #2 and # 3 resisting the fire until burnout. For these fire scenarios, Design #1 might still be acceptable since it provides a t_u larger than $t_{u,MAC}$. A t_u drop is instead observed if the fuel bed moves towards the hinged end of the girder (right-hand side), and minimum values are found for $\alpha_{MC} \in [0.643, 0.690]$. In cases where a vehicle cannot ignite in the range of α values causing $t_u < t_{u,MAC}$ (e.g., the bridge is crossing a river, or a proper stand-off distance has been put into place), Designs #1 and #3 might still be acceptable. Figure 3b can also inform the optimal use of an eventual fire protection layer, whose thickness can represent an additional design variable.

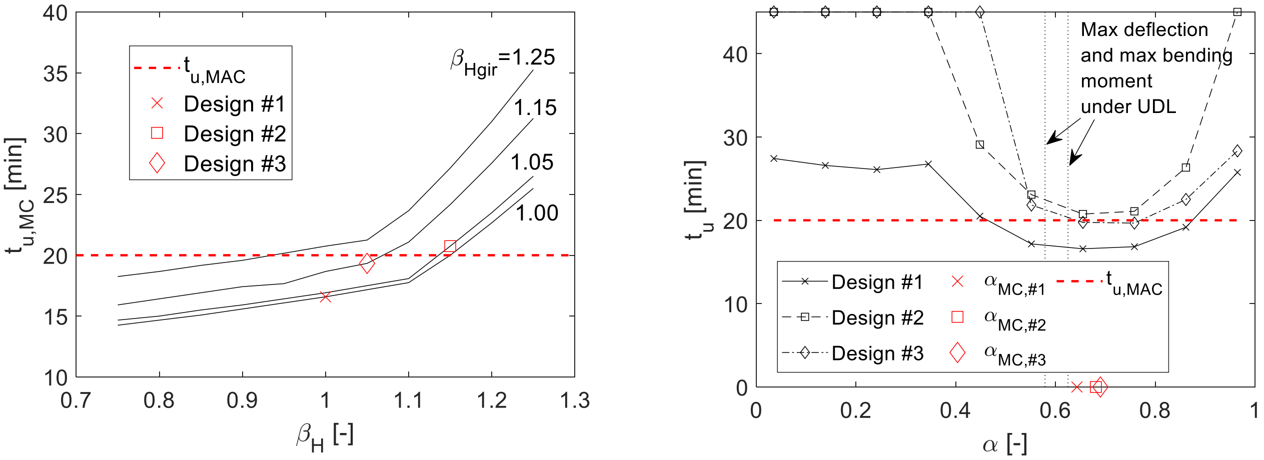

(a) (b)

Figure 3. Comparison of design options: (a) effect of design variables on the minimum time to reach unsatisfactory conditions; (b) effect of fuel bed location on the time to reach unsatisfactory conditions.

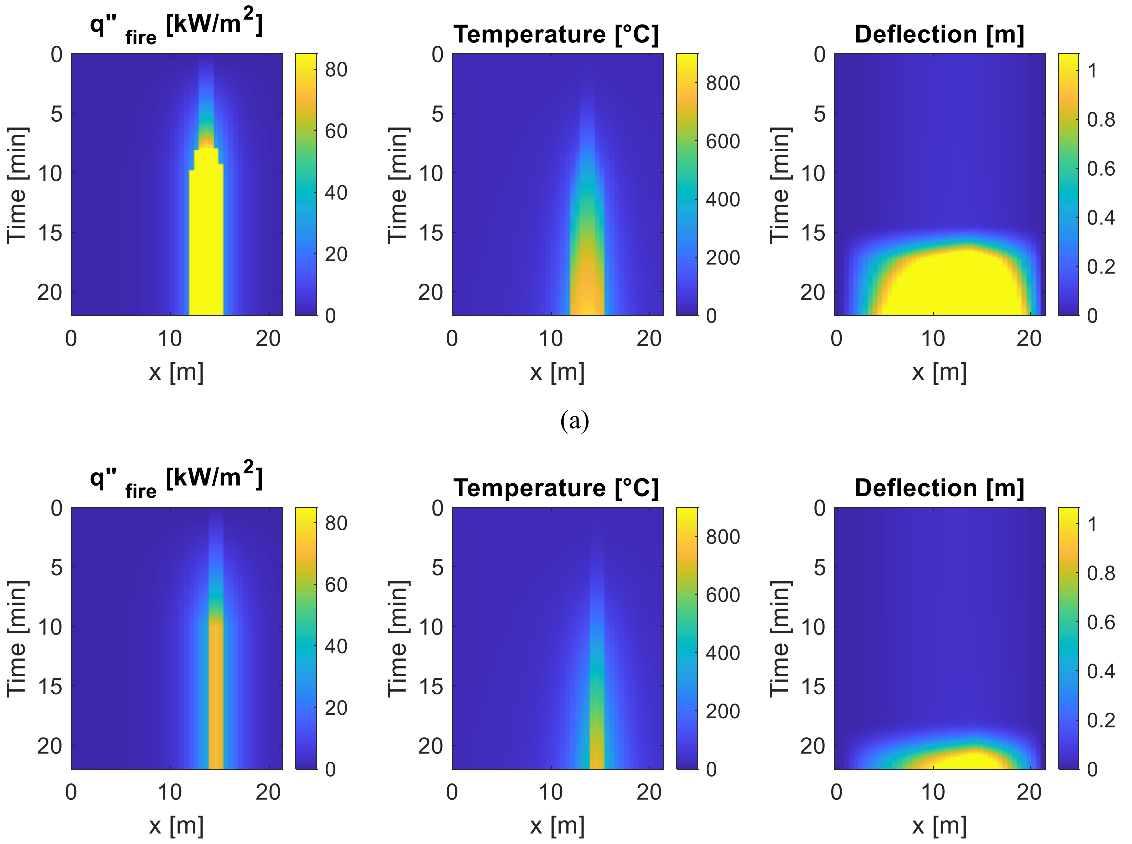

(a)

(b)

Figure 4. Time history of the heat flux from the fire, girder temperature and deflection for: (a) Design #1; (b) Design #2.

The nondimensional fuel bed location yielding $t_{u,MC}$ (i.e., α_{MC} in Table 2 and single markers in Figure 3b) deserves some discussion. Indeed, it can be observed that its value varies for the different design configurations, suggesting that the fire scenario properties generating the maximum consequences cannot be determined independently of the structural properties. Additionally, the fuel bed location that maximises consequences does not correspond to the positions of maximum deflection or maximum bending moment under uniformly distributed load. Indeed, as shown by Figure 3b and the last two rows in Table 2, setting the fuel bed location in one of those two locations (which might be an intuitive preliminary assumption) provides misleading and larger values of t_u. Therefore, the fire scenario cannot be defined independently of the investigated structure.

It is observed that the variation of α_{MC} for the three selected design configurations is small. However, this results from the assumptions drawn on the fire scenario features, from the simple bridge configuration considered as the case-study and from the selected time step. Consequently, a wider range of variation is to be expected if any of the mentioned factors changes.

It is also essential to remark that changing the design variables varies the fire scenario, suggesting the possibility of a simultaneous design of both the fire and the structure. This concept can be better noted in Figure 4, which compares the time histories of the heat flux from the fire, girder temperature and deflection for Design #1 and Design #2. Specifically, the increased clearance and girder height of Design #2 cause the flame not to impinge on the bridge deck. This reduces the heat flux, limits the lateral flame spread, and delays the increase of the girder temperature. Smaller deflections are also attributed to the increased girder stiffness. Consequently, Design #2 requires a longer time to reach unsatisfactory conditions (girder deflection exceeding $L/20$ =1.07 m).

3.5 Uncertainty analysis and effect

A further objective of the MAC methodology is assessing input uncertainties' effect on the estimated maximum consequence. Plain Monte Carlo sampling (MCS) is adopted for such an aim. In this study, the goal is to assess the effect of the steel material properties uncertainty on the $t_{u,MC}$ computed as in Section 3.4. The considered random variables (and their probability models) are shown in Table 3 and are obtained from the work of Devaney [20]. In this table, CoV is the coefficient of variation, i.e., the ratio of the standard deviation to the mean.

Table 3. Assumed random variables (and their probability models) for MCS.

Variable	Distribution	Mean	CoV	Units
Yielding stress	Lognormal	281	0.07	MPa
Elastic modulus	Lognormal	210	0.03	GPa
Density	Normal	7850	0.01	Kg/m^3

MCS provides an estimate of the probabilistic distribution of $\bar{t}_{u,MC}$. This distribution can be used to calculate the probability $p_f = Pr\left[\bar{t}_{u,MC} < t_{u,MAC}\right]$ that, for a given design, the time to unsatisfactory conditions results lower than the minimum acceptable limit. The required sample size N to estimate p_f through MCS can be obtained from the expression of the CoV of a random binomial variable, which provides $N = \left(1 - p_f\right)/\left(CoV^2 \times p_f\right)$. For this study, it was chosen to estimate p_f values as low as 0.001 with a CoV of less than 15%. This requires a sample size of 50000.

The results of MCS are reported in Figure 5. Each histogram shows the variability of $t_{u,MC}$ for the three considered designs. The deterministic estimates obtained in Section 3.4 are also plotted for comparison. The fact that they lay in the lower percentile range of each distribution suggests that they are conservative estimates.

The vertical line in Figure 5 shows the $t_{u,MAC}$ set by stakeholders, whereas the probabilities $Pr\left[\bar{t}_{u,MC} < t_{u,MAC}\right]$ are reported in Table 2 above. Design #1 exhibits a 0.98 probability of yielding a $t_{u,MC}$ lower than the acceptable threshold. Such a probability reduces to 0.11 and 2e-4 for Design #3 and #2, respectively.

In the case of a bridge as in this study, the structure can likely be evacuated quickly enough for the fire not to represent a risk to people's life. Therefore, stakeholders might decide what value of $Pr\left[\bar{t}_{u,MC} < t_{u,MAC}\right]$ they are willing to accept in relation to the cost of making such a probability lower (or considering any other criteria). This assessment lies beyond the scope of this paper, but it is subject for future research by the authors.

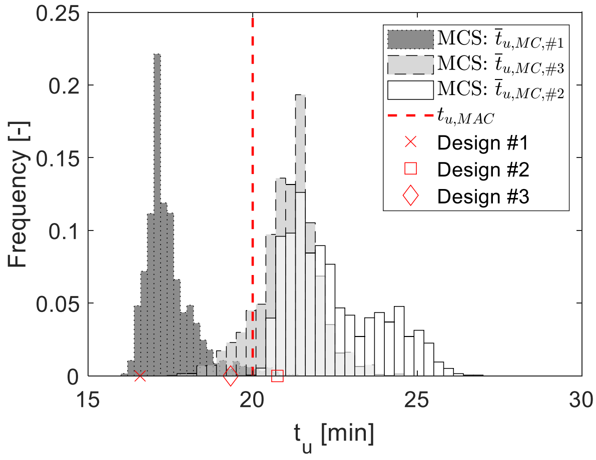

Figure 5. Effect of input uncertainties on the estimated time to unsatisfactory conditions.

3.6 Decision making

The final phase of the MAC approach consists of decision-making. Combining the four analysis outputs listed in Figure 1 suggests opting for Design #2, which provides the highest $t_{u,MC}$ and a low probability of this value is lower than $t_{u,MC}$ (see Table 2). Design #3 might also be selected if a 0.11 failure probability is acceptable following a cost-benefit analysis. Finally, if the site and/or traffic conditions allow barriers to guarantee an appropriate stand-off distance, a different fire scenario would be designed, and Design #1 and #2 might also be acceptable. This would require a re-assessment of the uncertainties' effect.

It is observed that this study deliberately did not consider the use of fire protection materials. This was chosen to investigate the possible improvement of the structure's inherent (i.e., without additional protection layers) fire resistance, as Hu et al. [2] suggested. Future research should focus on the optimal combination of the two design strategies.

4 CONCLUSIONS

This paper introduced a maximum consequence (MAC) approach for the fire safety assessment and design of bridge structures. The approach recognises the existence of dynamic coupling between the structure and the fire. It implements numerical optimisation to calculate fire scenarios maximising consequences as analysis outputs (rather than inputs as in the current practice). Moreover, the effect of input uncertainties is quantified through Monte Carlo sampling. Based on the obtained results, the following conclusions are drawn:

- The proposed MAC methodology allows the simultaneous design of both the bridge structure and an optimised fire hazard, obtaining optimised structures that bind consequences to an acceptable level. Additionally, Monte Carlo sampling provides insights into the effect of input uncertainties.
- A single-span case-study bridge analysis revealed that the fire scenario properties maximising consequences could not be defined independently of the structure.
- It was shown that modifying the bridge design variables (clearance and girder height) or the environment layout (e.g., placing barriers to guarantee a stand-off distance) also influences the fire growth and the heat flux reaching the girders. Thus, three bridge configurations (#1, #2 and #3) were investigated, and it was possible to design the structure and the fire so that the consequence level lays below the acceptance threshold (i.e., to resist any car fire for 20 min).
- Design #2 and #3 yielded a probability of time to unsatisfactory conditions being lower than the acceptance threshold of 2e-4 and 0.11, respectively. Design #3 might still be acceptable following a cost-benefit analysis.

The scenario studied here is purposely oversimplified to illustrate the method, so future research should extend the proposed methodology to more complex structures. Furthermore, approaches to define an acceptance threshold on the probability that the maximum consequence exceeds the allowable threshold due to uncertainties.

ACKNOWLEDGMENT

The first author greatly acknowledges the financial support of: the Maurice Franses Memorial Trust; the UCL's Department of Civil, Environmental and Geomatic Engineering; the Society for Fire Protection Engineering through a Student Research Grant as part of the May 2022 Grant Cycle.

REFERENCES

1. Garlock, M., Paya-Zaforteza, I., Kodur, V. and Gu, L., Fire hazard in bridges: Review, assessment and repair strategies, Engineering structures, 35, pp.89-98 (2012).
2. Hu, J., Carvel, R. and Usmani, A., Bridge fires in the 21st century: A literature review, Fire Safety Journal, 126, p.103487 (2021).
3. Lee, G.C., Mohan, S.B., Huang, C. and Fard, B.N., A study of US bridge failures, Technical Rep. No. MCEER-13-0008, Univ. at Buffalo, Buffalo, NY (2013).
4. Quiel, S.E., Yokoyama, T., Bregman, L.S., Mueller, K.A. and Marjanishvili, S.M., A streamlined framework for calculating the response of steel-supported bridges to open-air tanker truck fires, Fire Safety Journal, 73, pp.63-75 (2015).
5. Ma, R., Cui, C., Ma, M. and Chen, A., Performance-based design of bridge structures under vehicle-induced fire accidents: basic framework and a case study, Engineering Structures, 197, p.109390 (2019).
6. Cadena, J.E., McLaggan, M., Osorio, A.F., Torero, J.L. and Lange, D., Maximum allowable damage approach to fire safety performance quantification, Fire Safety Journal, 128, p.103537 (2022).
7. Torero, J.L., The risk imposed by fire to buildings and how to address it, Protection of civilian infrastructure from acts of terrorism, pp. 41-57, Springer (2006).
8. Torero, J.L., Structures in fire or fires in structures? Assessing the true performance of structures in fire, Proceedings of the 5th International Conference on Structural Engineering, pp. 1919-1923 (2013).
9. Karlsson, B. and Quintiere, J., Enclosure fire dynamics, CRC press (1999).
10. Hadjisophocleous, G.V. and Mehaffey, J.R., Fire scenarios, SFPE handbook of fire protection engineering (pp. 1262-1288). Springer, New York (2016).
11. Park, H., Meacham, B.J., Dembsey, N.A. and Goulthorpe, M., Conceptual model development for holistic building fire safety performance analysis, Fire Technology, 51(1), pp.173-193 (2015).
12. National Fire Protection Association, NFPA 502, Standard for road tunnels, bridges, and other limited access highways. 2020: NFPA.
13. Peris-Sayol, G., Paya-Zaforteza, I., Alos-Moya, J. and Hospitaler, A., Analysis of the influence of structural models in fire responses of steel girder bridges, Structures Congress 2015, pp. 160-171 (2015).
14. Mathworks Inc., MATLAB version 9.5.0.1298439 (R2018b) Update 7. 2018: Natick, Massachusetts.
15. Jiang, J., Jiang, L., Kotsovinos, P., Zhang, J., Usmani, A., McKenna, F. and Li, G.Q., OpenSees software architecture for the analysis of structures in fire, Journal of Computing in Civil Engineering, 29(1), p.04014030 (2015).
16. Hurley, M.J., Gottuk, D.T., Hall Jr, J.R., Harada, K., Kuligowski, E.D., Puchovsky, M., Watts Jr, J.M. and Wieczorek, C.J., SFPE handbook of fire protection engineering. Springer (2015).
17. EN 1991-1-2, Eurocode 1: Actions on structures - Part 1-2: General actions - Actions on structures exposed to fire, European Committee for Standardisation (2002).
18. Heskestad, G. and Hamada, T., Ceiling jets of strong fire plumes, Fire Safety Journal, 21(1), pp.69-82 (1993).
19. EN 1993-1-2, Eurocode 3: Design of steel structures - Part 1-2: General rules - Structural fire design, European Committee for Standardisation (2005).
20. Devaney, S., Development of software for reliability based design of steel framed structures in fire, Doctoral dissertation, University of Edinburgh (2015).

Proceedings of the 12th International Conference on Structures in Fire

Nov.30 – Dec.2 2022

Hong Kong, China

THE HONG KONG POLYTECHNIC UNIVERSITY
香港理工大學

Department of Building Environment and Energy Engineering
建築環境及能源工程學系